Pierre L. Fauchais
Joachim V.R. Heberlein
Maher I. Boulos

Thermal Spray Fundamentals

From Powder to Part

Springer

Thermal Spray Fundamentals

Pierre L. Fauchais • Joachim V.R. Heberlein
Maher I. Boulos

Thermal Spray Fundamentals

From Powder to Part

Springer

Pierre L. Fauchais
Sciences des Procédés
Céramiques et de Traitements
de Surface (SPCTS)
Université de Limoges
Limoges, France

Maher I. Boulos
Department of Chemical Engineering
University of Sherbrooke
Sherbrooke, QC, Canada

Joachim V.R. Heberlein
Department of Mechanical Engineering
University of Minnesota
Minneapolis, MN, USA

ISBN 978-0-387-28319-7 ISBN 978-0-387-68991-3 (eBook)
DOI 10.1007/978-0-387-68991-3
Springer New York Heidelberg Dordrecht London

Library of Congress Control Number: 2013956523

© Springer Science+Business Media New York 2014
This work is subject to copyright. All rights are reserved by the Publisher, whether the whole or part of the material is concerned, specifically the rights of translation, reprinting, reuse of illustrations, recitation, broadcasting, reproduction on microfilms or in any other physical way, and transmission or information storage and retrieval, electronic adaptation, computer software, or by similar or dissimilar methodology now known or hereafter developed. Exempted from this legal reservation are brief excerpts in connection with reviews or scholarly analysis or material supplied specifically for the purpose of being entered and executed on a computer system, for exclusive use by the purchaser of the work. Duplication of this publication or parts thereof is permitted only under the provisions of the Copyright Law of the Publisher's location, in its current version, and permission for use must always be obtained from Springer. Permissions for use may be obtained through RightsLink at the Copyright Clearance Center. Violations are liable to prosecution under the respective Copyright Law.
The use of general descriptive names, registered names, trademarks, service marks, etc. in this publication does not imply, even in the absence of a specific statement, that such names are exempt from the relevant protective laws and regulations and therefore free for general use.
While the advice and information in this book are believed to be true and accurate at the date of publication, neither the authors nor the editors nor the publisher can accept any legal responsibility for any errors or omissions that may be made. The publisher makes no warranty, express or implied, with respect to the material contained herein.

Printed on acid-free paper

Springer is part of Springer Science+Business Media (www.springer.com)

Foreword

Thermal spraying was invented and applied for the first time close to a century ago. In 1909 the Swiss engineer Max Ulrich Schoop got a first patent for the application of lead and zinc as protective coatings. Initially, he used a combustion process as a heat source for melting of metal wires. A high velocity flow of air or inert gas served to atomize the liquefied metal and to propel the formed droplets toward the substrate where it solidified as a layer. Later on he also used an electrical arc for this purpose.

These inventions represent in principle the beginning of the flame and wire arc spray technology. Over the following decades, thermal spraying evolved in terms of both technology and the great variety of the materials that could be sprayed. The driving force has been mostly economical since it offered means of modifying surface properties of parts and components where only the surface has to be made of expensive materials. Due to the relatively low process temperature of flame spraying, the selection of materials which could be processed at that time was limited and hence the variety of producible coatings and intended applications. In the middle of the last century the need for coatings with materials of higher quality and melting temperature increased notably and with the development of first plasma spray torches in mid-1950s by Thermal Dynamics Corporation, by Metco, and by Plasmadyne. These devices allowed for the generation of considerably higher process temperatures, which in turn extended the range of materials and applications that could be coated, and improved the overall quality and economics of the products.

The stringent requirements of the aerospace industry were strong technology drivers at these times. Based on the first plasma torch designs, new spray devices have been developed which continued up to now. For instance, besides the standard torches with plasma generation by a direct current (d.c.) arcs struck between two electrodes, electrodeless devices such as inductively coupling radio frequency (r.f.) plasma torches have been developed and are increasingly used for powder processing and the deposition of near net-shaped parts. Several process modifications also came into application, such as plasma spraying in vacuum or low pressure (VPS) or controlled atmospheric spraying. Also in the lower temperature range

improvements and new processes could be attained, like spraying with high velocity flames (HVOF and HVAF) and eventually the so-called "Cold Spraying." Concerning the precursor materials the spectrum increased considerably. In addition to the conventional wires and powders of metals, ceramics, and polymers, suspensions and liquids can now be used by new spraying methods. In particular, with suspension spraying, the grain size of powders suitable for processing can be extended into the sub-micron range, for nanostructured coatings, giving rise to considerable improvement of coating qualities.

With these new process modifications and the enlarged spectrum of precursor materials, the variety of coatings and their industrial applications increased to an impressive extent. New surface qualities and interesting combinations of substrate and surface properties could be made, which otherwise were not possible, at least not with acceptable price and effort. These include coatings for protection against corrosion or wear, for electrical or thermal insulation, for high mechanical stability and hardness, for specific electrical, optical, electrochemical, or catalytic properties, etc., which could now be produced on an industrial scale.

A main precondition for improving quality, economy, and reproducibility, and for the acceptance in new application fields, was the need to gain a fundamental knowledge about the basic physics of the whole process chain concerning:

- The interaction of the deposition material with the heat source
- The transient melting and accelerating phase of the material
- The interaction with the surrounding atmosphere
- The material deposition, where surface conditions of the substrate has a critical impact on the resulting coating quality

In its early stages, thermal spraying could be considered as an "art," where empiricism and experience together with a "hot hand" of the operator for selecting the right set of the numerous process parameters guaranteed the success. Over the past three decades, thermal spraying evolved into a mature science. This important step was greatly helped by improved fast diagnostics methods, mainly based on lasers and computers and the use of numerical modeling for the prediction of the influence of the different process parameters on the coating quality and its performance.

The three authors, worldwide leading scientists in the field of thermal spray, have presented in this book a large volume of knowledge and experience gathered over many years of successful research and development work. This book is by far one of the most comprehensive reviews of the state of the art in this field. As indicated in its title, it covers the field of thermal spray from the powder all the way to the final part. On the one hand, a systematic survey is given of the different types of power sources and process characteristics in thermal spraying for a large spectrum of applications, together with information about the necessary components like materials, equipment, control units, and applied diagnostic methods. On the other hand, the analysis of process fundamentals is not restricted to a phenomenological description, but is supported by extended theoretical considerations to understand the basic phenomena involved behind the whole processes.

Separate chapters are also devoted to feedstock preparation, whether in the form of powders, wires, cords, or rods, surface preparation, coating formation and characterization, online diagnostics and control, process integration, and industrial applications. An impressive number of figures and extensive list of references facilitate considerably the understanding of the material and allow for going further into details, whenever necessary.

This impressive book is addressed to newcomers in the field of thermal spray as well as experienced researchers and engineers, wanting to know more about the scientific details, either to improve the quality of their own products, and of their process efficiency, or to have guidance in a decision phase, when new applications or processes for increasing the product portfolio are the goal.

Stuttgart, Germany Rudolf Henne

Preface

This book is based on a series of continuing education courses which have been offered by the authors across the world in conjunction with the International Symposium on Plasma Chemistry (ISPC) as part of its summer school over the period 1995–2011. A similar course, though more oriented toward thermal spray technology, was also offered by the authors in conjunction with ASM International Thermal Spray Conferences (ITSC) over the period 1998–2010. Both courses were offered to graduate students, practicing engineers, and researchers actively involved in the field of thermal plasmas. Their emphasis was on the fundamentals behind plasma processing and thermal spray technology, and the aim was to provide a grassroot understanding of the basic phenomena involved, necessary for taking the technology over the crucial step from being an "art" based on operator talent and experience to a mature science with quantitative predictive capabilities.

This step did not come easily and without the intense involvement of many leading researchers in this field across the world. The three determining factors which were of critical importance to the evolution of this field over the past three decades are as follows:

- Major improvement in process diagnostics and online controls
- The fast and significant development of numerical modeling and computing capabilities
- Major development in materials science and materials characterization techniques

In the process of preparation of the manuscript for this book, which spans many years, the authors were confronted with the critical need to strike a good balance between the need to be concise in the overall presentation of the subject and being inclusive in stressing the fundaments without overlooking the important applications which were the economical driver of the technology. New technologies were also developed over this period which, while not being "plasma technologies," were relevant to the overall field of surface treatment and coating. These were accordingly included in the book such as the combustion-based technologies and "cold spray."

We have no pretensions about having covered every aspect of this technology or exhaustively reported on every relevant publication in this field. Exhaustive lists of references are given at the end of each chapter. For those who were not cited, our apologies, it was not intentional. A book of this size and scope could not have been possible without the extensive help of students, research assistants, colleagues, and associates. Our sincere thanks to all who have helped make this book a reality. Particular thanks are due to Dr. Rudolf Henne who so generously gave his time in the process of reviewing the manuscript of the book in its final preparation stage. We also appreciate his willingness to write the foreword for this book which reflects his long and broad experience in the field of thermal spray. The financial assistance of the numerous government and private funding agencies and industrial partners who have also supported the basic and applied research behind this technology in our respective research laboratories is gratefully acknowledged. Our sincere thanks to our respective families and life partners, Paulette Fauchais, Yuko Heberlein, and Alice Boulos who had to cope with the long hours of intense personal efforts that were needed to complete this book.

Limoges, France — Pierre L. Fauchais
Minneapolis, MN, USA — Joachim V.R. Heberlein
Sherbrooke, QC, Canada — Maher I. Boulos

Contents

1 Introduction 1
1.1 Needs for Coatings 1
1.2 Thin Films vs. Thick Films 2
1.3 Thermal Spray Coating Concept 2
1.4 Description of Different Thermal Spray Coating Processes 4
1.5 History of Thermal Spray 7
1.6 Thermal Spray Applications 8
1.7 Overview of Book Content 13
References 14

2 Overview of Thermal Spray 17
2.1 Surface Treatments or Coatings 17
2.1.1 Why Surface Treatment or Coatings 17
2.1.2 Surface Treatments 18
2.1.3 Coatings 19
2.2 Brief Descriptions of Thermal Spray Applications 25
2.3 Overview of Thermal Spray Processes 27
2.3.1 Compressed Gas Expansion 28
2.3.2 Combustion Spraying 28
2.3.3 Electrical Discharge Plasma Spraying 28
2.4 Substrate Preparation 32
2.5 Energetic Gas Flow Generation 33
2.5.1 Cold Spray 33
2.5.2 Flame Spray 35
2.5.3 High-Velocity Oxy-fuel Spraying 36
2.5.4 Detonation Gun Spraying 38
2.5.5 Direct Current Blown Arc Spraying or d.c. Plasma Spraying 39
2.5.6 Vacuum Induction Plasma Spraying 40
2.5.7 Wire Arc Spraying 42
2.5.8 Plasma-Transferred Arc Deposition 43

2.6 Material Injection 44
2.6.1 Powder Injection 44
2.6.2 Wire, Rod, or Cord Injection 47
2.6.3 Liquid Injection 50
2.7 Energetic Gas–Particle Interactions 51
2.7.1 Momentum Transfer 51
2.7.2 Heat Transfer 52
2.7.3 Effect of the Surrounding Atmosphere 54
2.8 Coating Formation 57
2.8.1 Coatings from Fully or Partially Melted Particles in Conventional Spraying 57
2.8.2 Adhesion of Conventional Coatings 60
2.8.3 Coatings Resulting from Solution or Suspension Spraying 63
2.8.4 Residual Stresses 64
2.9 Control of Coating Formation 65
2.9.1 Coating Temperature Control Before, During, and After Spraying 65
2.9.2 Control of Other Spray Parameters 67
2.10 Summary and Conclusions 69
References 70

3 Fundamentals of Combustion and Thermal Plasma 73
3.1 Combustion 73
3.1.1 Definitions 73
3.1.2 Combustion at Equilibrium 74
3.1.3 Combustion Kinetics 76
3.1.4 Combustion or Deflagrations, Detonations 79
3.2 Thermal Plasmas Used for Spraying 84
3.2.1 Definition 84
3.2.2 Plasma Composition 85
3.2.3 Thermodynamic Properties 88
3.2.4 Transport Properties 89
3.3 Basic Concepts in Modeling 95
3.3.1 Introduction 95
3.3.2 Conservation Equations 95
3.3.3 Gas Composition, Thermodynamic, and Transport Properties 104
3.4 Summary and Conclusions 106
References 110

4 Gas Flow–Particle Interaction 113
4.1 Introduction 113
4.2 Single Particle Trajectory 114
4.2.1 Single Particle Motion 114
4.2.2 Particle Injection and Trajectory 116
4.2.3 Drag Coefficient: Micrometer Sized Single Sphere 128

4.2.4 Drag Coefficient: Submicron and Nanometer-Sized Particles . . . 138
4.3 In-Flight Single Particle Heat and Mass Transfer and Chemical Reactions . . . 140
4.3.1 Basic Conduction, Convection, and Radiation Heat Transfers . . . 140
4.3.2 In-Flight Particle Heating and Melting . . . 142
4.3.3 Heat Transfer to a Single Sphere . . . 148
4.4 Ensemble of Particles and High-Energy Jet . . . 176
4.4.1 General Remarks . . . 176
4.4.2 Particle Injection . . . 178
4.4.3 Particles and Plasma Jet with No Loading Effect . . . 187
4.4.4 Loading Effect . . . 191
4.5 Liquid or Suspension Injection into a Plasma Flow . . . 195
4.5.1 Liquid Injection . . . 196
4.5.2 Liquid Penetration into the Plasma Flow . . . 202
4.5.3 Liquid Fragmentation . . . 203
4.5.4 In-Flight Heat Transfer to Droplets . . . 207
4.5.5 Cooling of the Plasma Flow by the Liquid . . . 208
4.5.6 Influence of Arc Root Fluctuations . . . 209
4.5.7 Case of No Fragmentation . . . 211
4.6 Summary and Conclusions . . . 212
References . . . 215

5 Combustion Spraying Systems . . . 227
5.1 Historical Perspective and General Remarks . . . 227
5.2 Flame Spraying . . . 228
5.2.1 Principle . . . 228
5.2.2 Powder Flame Spraying . . . 229
5.2.3 Liquid Flame Spraying . . . 235
5.2.4 Wire, Rod, or Cord Spraying . . . 235
5.2.5 Flame Modeling . . . 238
5.3 High Velocity Flame Spraying (HVOF–HVAF) . . . 239
5.3.1 HVOF or HVAF Powder Spraying . . . 239
5.3.2 HVOF Wire Spraying . . . 260
5.3.3 Applications: General Remarks . . . 262
5.3.4 Coatings Sprayed with Combustible Gases and Oxygen . . . 262
5.3.5 Coatings Sprayed with Liquid Fuel and Oxygen . . . 265
5.3.6 HVOF–HVAF Modeling . . . 266
5.4 Detonation Gun (D-Gun) . . . 269
5.4.1 Process Description . . . 269
5.4.2 In-Flight Particle Properties . . . 275
5.4.3 Graded Coatings . . . 278
5.4.4 Coating Properties . . . 278
5.5 Summary and Conclusions . . . 290
References . . . 292

6 Cold Spray 305
6.1 Introduction to the Different Cold Spray Processes 305
6.1.1 High-Pressure Cold Spray 305
6.1.2 Low Pressure Cold Spray 309
6.1.3 Vacuum Cold Spray 311
6.2 High-Pressure Cold Spray Process 312
6.2.1 Process Gas Dynamics 312
6.2.2 Coating Adhesion and Cohesion 326
6.2.3 Deposition Parameters 342
6.3 Coating Materials and Applications 356
6.3.1 General Remarks 356
6.3.2 Metals 356
6.3.3 Composites 363
6.3.4 Ceramics 366
6.4 Low Pressure Cold Spray (LPCS) 369
6.4.1 Coating Formation 369
6.4.2 Examples of Coatings 370
6.5 Summary and Conclusions 372
References 374

7 D.C. Plasma Spraying 383
7.1 Description of Concept 383
7.2 Equipment and Operating Parameters 386
7.3 Fundamentals of Plasma Torch Design 388
7.3.1 Torch Cathode 389
7.3.2 Arc Column 391
7.3.3 Torch Anode 393
7.3.4 Arc Voltage and Power Dissipation 394
7.3.5 Arc Stability 394
7.3.6 Electrode Erosion 400
7.4 Particle Injection 403
7.5 Plasma Torch and Spray Process Modeling 408
7.6 Plasma Torch and Jet Characterization: Time Averaged 412
7.6.1 Effect of Plasma Gas 413
7.6.2 Effect of Plasma Gas Injector Design 416
7.6.3 Effect of Anode Nozzle Design 418
7.6.4 Effect of Surrounding Atmosphere 421
7.6.5 Effect of Cathode Shape 421
7.6.6 Effect of Standoff Distance 422
7.6.7 Summary of Design and Operating Parameters 424
7.7 Plasma Jet Characterization: Transient Behavior 424
7.7.1 Plasma Jet Instability 424
7.7.2 Effect of Arc Voltage Fluctuations on Plasma Jet and Particle Characteristics 427

7.8 Different Plasma Torch Concepts 433
7.8.1 Shrouds and Other Fluid Dynamic Jet Stabilization 433
7.8.2 Fixed Anode Attachment Position 437
7.8.3 Central Injection Torches 440
7.8.4 Torches for Inside Diameter Coatings 443
7.8.5 High-Power Plasma Spray Torch 444
7.8.6 Water-Stabilized Plasma Torch 444
7.9 Low Pressure and Controlled Atmosphere Plasma Spraying . . . 446
7.10 Plasma-Sprayed Materials and Coatings 454
7.10.1 Oxide Materials 455
7.10.2 Non-oxide Ceramics 460
7.10.3 Cermets 462
7.10.4 Metals or Alloys 463
7.11 Summary and Conclusions 465
References 467

8 R.F. Induction Plasma Spraying 479
8.1 Introduction 479
8.2 The r.f. Induction Plasma Torch 481
8.2.1 Basic Concepts 481
8.2.2 Energy Coupling Mechanism 483
8.2.3 Induction Plasma Torch Design 490
8.2.4 Temperature, Fluid Flow, and Concentration Fields 497
8.3 Modeling of the Inductively Coupled Plasma Discharge 509
8.3.1 Basic Assumption 511
8.3.2 Governing Equations 511
8.3.3 Typical Results of Fluid Dynamic Modeling 521
8.4 Plasma–Particle Interaction Model 532
8.4.1 Governing Equations 534
8.4.2 Typical Result: Effect of Particle Loading 536
8.5 Vacuum Induction Plasma Spraying 549
8.5.1 Basic Equipment Design 549
8.5.2 Parametric Analysis and Operating Conditions 554
8.5.3 Reactive Induction Plasma Spraying 562
8.5.4 Suspension Induction Plasma Spraying 564
8.5.5 Supersonic Induction Plasma Spraying 567
8.6 Summary and Conclusions 569
References 571

9 Wire Arc Spraying 577
9.1 Description of Concept 577
9.2 Equipment and Operating Parameters 579
9.3 Wire Materials and Specific Applications 582
9.3.1 Wires 582
9.3.2 Cored Wires 585
9.4 Metal Droplet Formation 587

9.5 Process Characterization . . . 597
9.5.1 Gas Velocity Measurements . . . 599
9.5.2 Metal Droplet Velocity Distributions . . . 600
9.5.3 Metal Droplet Temperature . . . 607
9.5.4 Coating Characteristics . . . 608
9.5.5 Fume Formation . . . 612
9.6 Process Modeling . . . 613
9.7 Single Wire Arc Spraying . . . 618
9.8 Special Developments: Low-Pressure Wire Arc and 90° Angle Spraying . . . 622
9.9 Summary and Conclusions . . . 623
References . . . 624

10 Plasma-Transferred Arc . . . 631
10.1 Description of Concept . . . 631
10.1.1 Tungsten Inert Gas . . . 633
10.1.2 Metal Inert Gas . . . 633
10.2 Equipment and Operating Parameters . . . 634
10.3 Coating Materials and Applications . . . 639
10.3.1 Corrosion and Wear . . . 639
10.3.2 Self-Lubricating Coatings . . . 641
10.3.3 Rebuilding of Parts . . . 642
10.3.4 Free-Standing Shapes . . . 642
10.4 Process Characterization . . . 642
10.4.1 Temperature Distributions in the Arc and Arc Voltages . . . 643
10.4.2 Heat Flux to the Substrate . . . 646
10.4.3 PTA Process Modeling . . . 650
10.5 Effect of Process Parameter Changes on Coating Properties . . . 652
10.6 Process Modifications and Adaptations . . . 655
10.6.1 Variation of Ratio of Pilot Arc Current to Transfer Arc Current . . . 656
10.6.2 Variation of Powder Feed . . . 656
10.6.3 Nitriding of Coating . . . 656
10.6.4 Modulation of Deposition Parameters . . . 657
10.6.5 High-Energy PTA . . . 658
10.6.6 PTA Combined with Tape Casting . . . 660
10.6.7 PTA Deposition with a Negative Work Piece Polarity . . . 660
10.6.8 Hard Coatings on Magnesium . . . 661
10.7 Examples of Specific Applications . . . 661
10.7.1 Increasing Hardness . . . 661
10.7.2 Increasing Wear Resistance . . . 662

10.7.3 Abrasive Wear in Petrochemical, Mining, and Agricultural Applications . . . 664
10.7.4 Combined Corrosion and wear . . . 665
10.7.5 Refurbishing of Worn Parts . . . 666
10.7.6 Freestanding Shape Fabrication . . . 666
10.8 Summary and Conclusions . . . 667
References . . . 669

11 Powders, Wires, Cords, and Rods . . . 675
11.1 Powders . . . 676
11.1.1 Introduction . . . 676
11.1.2 Powders Manufacturing Techniques . . . 678
11.1.3 Examples of the Influence of Powder Morphologies on Coating Properties . . . 716
11.1.4 Conventional Particle Classification Method . . . 719
11.1.5 Characterization . . . 722
11.1.6 Powder Feeders . . . 728
11.1.7 Hazards Related to Particulate Materials . . . 732
11.2 Wires . . . 734
11.2.1 Wire Materials . . . 734
11.2.2 Cored Wires . . . 735
11.2.3 Wire Feeders . . . 736
11.3 Rods . . . 736
11.4 Cords . . . 736
11.5 Polymer Particles . . . 737
11.5.1 General Remarks . . . 737
11.5.2 Sprayed Polymer Powders . . . 739
11.6 Summary and Conclusions . . . 744
References . . . 746

12 Surface Preparation . . . 755
12.1 Introduction . . . 755
12.2 Machining . . . 755
12.3 Cleaning . . . 757
12.3.1 Vapor Degreasing . . . 757
12.3.2 Baking in an Oven . . . 758
12.3.3 Ultrasonic Cleaning . . . 758
12.3.4 Wet or Dry Blasting . . . 758
12.3.5 Acid Pickling . . . 758
12.3.6 Brushing . . . 758
12.3.7 Dry Ice Blasting . . . 759
12.4 Masking . . . 760
12.5 Roughening by Grit Blasting . . . 761
12.5.1 Roughness Measurement . . . 761
12.5.2 Grit-Blasting Equipment . . . 766

12.5.3 Grit-Blasting Nozzles . . . 767
12.5.4 Grit Material . . . 768
12.5.5 Blasting Parameters . . . 771
12.5.6 Grit Residues . . . 776
12.5.7 Grit Wear . . . 781
12.5.8 Residual Stress Induced by Grit Blasting . . . 783
12.5.9 Conclusion . . . 784
12.6 High-Pressure Water Jet Roughening . . . 786
12.6.1 Equipment and Description of the Process . . . 786
12.6.2 Water Jet-Blasting Parameters . . . 788
12.6.3 Comparison Grit and Water Jet Blasting . . . 792
12.7 Abrasive Water Jetting . . . 793
12.8 Laser Treatment: Protal® Process . . . 793
12.8.1 Laser Ablation . . . 793
12.8.2 Protal® Experimental Setup . . . 795
12.8.3 Example of Results . . . 796
12.9 Summary and Conclusions . . . 799
References . . . 801

13 Conventional Coating Formation . . . 807
13.1 Introduction . . . 807
13.2 Spray Parameters . . . 810
13.3 Physical and Chemical Description of Substrates . . . 812
13.3.1 Physical Aspect of Substrate Surfaces . . . 813
13.3.2 Oxide Layer Development on Metals or Alloys . . . 816
13.4 Single Particle Impact, Flattening, and Solidification (When Melted) . . . 820
13.4.1 Introduction . . . 820
13.4.2 Different Possibilities of Particle or Splat–Substrate Adhesion . . . 822
13.4.3 Splat Formation from Unmelted Particles Impacting on Smooth Substrates . . . 832
13.4.4 Splat Formation from Molten Particles Impacting onto Smooth Substrates . . . 839
13.4.5 Splat Formation from Partially Molten Particles on Smooth Substrates . . . 863
13.4.6 Splat Formation from Unmelted Particles Off Normal on Smooth Substrates . . . 866
13.4.7 Flattening and Solidification of Molten Particle on a Smooth Substrate . . . 866
13.5 Splat Formation on Rough Surfaces . . . 868
13.5.1 Solid Ductile Particles . . . 868
13.5.2 Molten Metal, Alloy, Ceramic, and Cermet Particles . . . 869
13.5.3 Polymer Particles . . . 873

13.6 Coating Formation 874
13.6.1 Molten Particles Deposited by Thermal Spraying 874
13.6.2 Polymer Coatings 887
13.6.3 Ductile Particles 892
13.6.4 PTA Coatings 896
13.6.5 Coatings Obtained by Very Low Pressure Plasma Spray 897
13.6.6 Use of Robot Manipulators 900
13.6.7 Coating Structure Modeling 902
13.7 Temperature Control of Substrate and Coating in Thermal Spraying 903
13.7.1 Introduction 903
13.7.2 Splat Cooling 905
13.7.3 Cooling Methods 908
13.7.4 Coating Mean Temperature Control 913
13.8 Influence of Powder Manufacturing Process on Coating Properties 915
13.8.1 Chemical Reactions 915
13.8.2 Particle Morphology 917
13.8.3 Nanostructured Agglomerated Particles 919
13.9 Influence of Wire, Cored Wires, Rods, and Cords on Coating Properties 920
13.9.1 Flame or HVOF or HVAF-Sprayed Wires 920
13.9.2 Flame-Sprayed Rods 922
13.9.3 Arc Sprayed 922
13.10 Stresses Within Coatings 924
13.10.1 Residual Stress 924
13.10.2 Service Stresses 937
13.10.3 Conclusions Relative to Residual Stresses 941
13.11 Finishing Coatings 941
13.11.1 Machining (Turning, Milling) 941
13.11.2 Grinding 941
13.11.3 Abrasive Belt Grinding and Polishing 942
13.11.4 Other Finishing Methods 943
13.12 Post Treatment of Coatings 943
13.12.1 Fusion of Self-Fluxing Alloys 944
13.12.2 Heat Treating or Annealing 946
13.12.3 Hot Isostatic Pressing 948
13.12.4 Austempering Heat Treatment 949
13.12.5 Laser Glazing 949
13.12.6 Sealing 952
13.12.7 Spark Plasma Sintering 956
13.12.8 Peening or Rolling Densification 957
13.12.9 Diffusion 958
13.13 Summary and Conclusions 958
References 962

14 Nanostructured or Finely Structured Coatings 981
14.1 Introduction 982
14.1.1 Why Nanostructured Coatings 982
14.1.2 How to Spray Nanostructure Coatings? 985
14.2 Spraying of Complex Alloys Containing Multiple Elements to Form Amorphous Coatings 987
14.2.1 Amorphous Alloys Containing Phosphorus 987
14.2.2 NiCrB and FeCrB Alloys 988
14.2.3 Iron-Based Amorphous Alloys 989
14.3 Agglomerated Ceramic Particles Spraying with Hot Gases 993
14.3.1 Spray Conditions 993
14.3.2 Applications 1004
14.4 Attrition or Ball Milled Cermets or Alloy Particles Sprayed with Hot Gases 1013
14.4.1 Alloys 1014
14.4.2 Cermets 1015
14.5 Spraying Hypereutectic Alloys with Hot Gases 1017
14.6 Production of Nanostructured Coatings by Cold Spray 1019
14.6.1 Alloys 1019
14.6.2 Composites 1020
14.6.3 Amorphous Alloys 1022
14.7 Solutions or Suspensions Spraying 1023
14.7.1 Sub-Micrometer and Nanometer-Sized Particles in Plasma or HVOF Jets 1024
14.7.2 Liquid Injection 1030
14.7.3 Spray Torches Used 1037
14.7.4 Solutions or Suspensions Preparation 1040
14.7.5 Liquid Stream: Hot Flow Interactions 1045
14.7.6 Coating Manufacturing Mechanisms 1056
14.7.7 Applications 1083
14.8 Summary and Conclusions 1093
References 1096

15 Coating Characterizations 1113
15.1 Introduction to Coating Characterizations and Testing Methods 1115
15.1.1 Differences Between Coatings and Bulk Materials 1115
15.1.2 Characterization and Testing Methods Used for Coatings 1116
15.1.3 Statistical Methods 1117
15.2 Nondestructive Methods 1121
15.2.1 Visual Inspection 1121

15.2.2 Laser Inspection 1122
15.2.3 Coordinate Measuring Machines 1122
15.2.4 Machine Vision and Robotic Evaluation 1122
15.2.5 Acoustic Emission 1123
15.2.6 Laser-Ultrasonic Techniques 1123
15.2.7 Thermography 1124
15.2.8 Coating Thickness 1125
15.3 Metallography and Image Analysis 1125
15.3.1 Coating Preparation 1126
15.3.2 Microscopy 1131
15.4 Materials Characterization 1137
15.4.1 X-Ray Spectroscopy or X-Ray Fluorescence 1138
15.4.2 Infrared Spectroscopy 1138
15.4.3 Mössbauer Spectroscopy 1139
15.4.4 X-Ray Diffraction 1139
15.4.5 Small- and Ultrasmall-Angle X-Ray Diffraction (USAXF) 1141
15.4.6 Neutron Scattering 1143
15.4.7 X-Ray Absorption Spectroscopy 1145
15.4.8 Electron Probe X-Ray Microanalysis 1146
15.4.9 Auger Electron Spectroscopy 1146
15.4.10 X-Ray Photoelectron Spectroscopy 1146
15.4.11 Other Techniques 1147
15.5 Void Content and Network Architecture 1147
15.5.1 Archimedean Porosimetry 1149
15.5.2 Mercury Intrusion Porosimetry (MIP) 1150
15.5.3 Gas Permeation and Pycnometry 1150
15.5.4 Small-Angle Neutrons Scattering 1152
15.5.5 Ultrasmall-Angle X-Ray Scattering 1153
15.5.6 Stereological Protocols (Coupled to Image Analysis) (ST) 1155
15.5.7 Electrochemical Impedance Spectroscopy 1160
15.6 Adhesion–Cohesion 1161
15.6.1 Introduction 1161
15.6.2 Simple Adhesion Tensile Test 1162
15.6.3 Other Types of Tensile Tests 1164
15.6.4 Shear Stress 1166
15.6.5 Fracture Mechanics Approach 1167
15.6.6 Bending Test: Adhesion and Interface Toughness Measurements 1169
15.6.7 Indentation: Interface Toughness Measurement 1171
15.6.8 Other Methods 1173
15.7 Mechanical Properties 1177
15.7.1 Hardness and Indentation Test 1177
15.7.2 Young's Modulus 1184

15.7.3 Toughness 1186
15.7.4 Residual Stress 1187
15.8 Thermal Properties 1193
15.8.1 Mass Density 1193
15.8.2 Expansion Coefficient 1194
15.8.3 Thermal Conductivity and Thermal Diffusivity 1194
15.8.4 Specific Heat at Constant Pressure 1196
15.8.5 Thermal Shock Resistance 1197
15.8.6 Differential Thermal Analysis, Thermogravimetry, and Differential Scanning Calorimetry 1199
15.9 Wear Resistance 1203
15.9.1 Abrasive Wears 1203
15.9.2 Adhesive Wears 1204
15.9.3 Erosive Wear 1206
15.9.4 Surface Fatigue 1209
15.9.5 Corrosive Wears 1213
15.9.6 Fretting 1217
15.10 Corrosion Resistance 1218
15.10.1 General Remarks 1218
15.10.2 Corrosion Characterization 1222
15.11 Summary and Conclusions 1225
References 1235

16 Process Diagnostics and Online Monitoring and Control 1251
16.1 Introduction 1252
16.1.1 What Is Expected from Thermal-Sprayed Coatings? 1252
16.1.2 Coatings Repeatability, Reliability, and Reproducibility 1252
16.1.3 How Sprayed Coatings Quality Was Improved Through the Spray Process Monitoring 1255
16.1.4 Spray Process Parameters That Should Be Controlled 1257
16.2 High-Energy Jets Characterization 1258
16.2.1 Plasma Jets 1259
16.2.2 Flames and Cold Spray 1266
16.3 Sensors 1269
16.3.1 Hot Gases Flow: Enthalpy Probe 1270
16.3.2 Particles In-Flight Distribution 1274
16.3.3 In-Flight Hot Particle Temperature and Velocity Measurement 1284
16.3.4 In-Flight Velocity Measurements of Cold Particles 1303
16.3.5 Are Such Measurements Sufficient to Monitor Coating Properties? 1306
16.3.6 Coating Under Formation 1308

16.4 Online Control or Monitoring? . . . 1311
16.4.1 Coating Properties Monitoring . . . 1311
16.4.2 Online Control? . . . 1320
16.5 Other Possible Measurements . . . 1320
16.5.1 Particle Vaporization . . . 1320
16.5.2 Splat Formation . . . 1321
16.5.3 Plasma-Liquid Injection . . . 1328
16.6 Summary and Conclusions . . . 1333
References . . . 1337

17 Process Integration . . . 1351
17.1 Introduction . . . 1352
17.2 Potential and Real Risks . . . 1352
17.2.1 Powders: Respiratory Problems and Explosions . . . 1353
17.2.2 Gases . . . 1355
17.2.3 Prevention and Safety Measures . . . 1357
17.2.4 Other Risks . . . 1359
17.3 Ancillary Equipment . . . 1362
17.3.1 The Spray Booth . . . 1362
17.3.2 Exhaust Systems . . . 1365
17.3.3 Power Supply . . . 1365
17.3.4 Gas Supply . . . 1366
17.3.5 Compressed Air Supply . . . 1366
17.3.6 Cooling Water . . . 1366
17.3.7 Micrometer-Sized Powder Feeders and Solutions or Suspensions Feeders . . . 1367
17.3.8 Gun Movements . . . 1368
17.3.9 Control Panel . . . 1368
17.4 Controlled Atmosphere . . . 1368
17.4.1 Soft Vacuum Plasma Spraying . . . 1368
17.4.2 Vapor Phase Deposition . . . 1373
17.4.3 Inert Plasma Spraying . . . 1374
17.4.4 Cold Spray with Helium . . . 1375
17.5 Finishing and Post-Treatment of Coatings . . . 1375
17.5.1 Finishing . . . 1376
17.5.2 Fusion of Self-Fluxing Alloys . . . 1378
17.5.3 Heat Treating or Annealing . . . 1381
17.5.4 Hot Isostatic Pressing . . . 1383
17.5.5 Austempering Heat Treatment . . . 1384
17.5.6 Laser Glazing . . . 1384
17.5.7 Sealing . . . 1387
17.5.8 Spark Plasma Sintering . . . 1392
17.5.9 Peening or Rolling Densification . . . 1392
17.5.10 Diffusion . . . 1393
17.6 Summary and Conclusions . . . 1393
References . . . 1394

18 Industrial Applications of Thermal Spraying Technology 1401
18.1 Introduction 1403
18.2 Advantages and Limitations of the Different Spray Processes 1404
18.2.1 Flame Spraying 1404
18.2.2 D-Gun Spraying 1406
18.2.3 HVOF–HVAF Spraying 1406
18.2.4 Wire Arc Spraying 1407
18.2.5 Plasma Spraying 1407
18.2.6 Plasma-Transferred Arcs (PTA) 1409
18.2.7 Plasma Transferred Arc 1410
18.2.8 Cold Spray 1411
18.3 Thermal-Sprayed Coating Applications 1411
18.3.1 Wear Resistant Coatings 1412
18.3.2 Corrosion and Oxidation Resistant Coating 1433
18.3.3 Thermal Protection Coatings 1446
18.3.4 Clearance Control Coatings 1455
18.3.5 Bonding Coatings 1457
18.3.6 Electrical and Electronic Coatings 1458
18.3.7 Freestanding Spray-Formed Parts 1462
18.3.8 Medical Applications 1466
18.3.9 Replacement of Hard Chromium 1469
18.3.10 Applications Under Developments 1471
18.4 Thermal-Sprayed Coatings by Industry 1474
18.4.1 Aerospace 1475
18.4.2 Land-Based Turbines 1478
18.4.3 Automotive 1478
18.4.4 Electrical and Electronic Industries 1481
18.4.5 Corrosion Applications for Land-Based and Marine Applications 1483
18.4.6 Medical Applications 1486
18.4.7 Ceramic and Glass Manufacturing 1487
18.4.8 Printing Industry 1488
18.4.9 Pulp and Paper 1490
18.4.10 Metal Processing Industries 1492
18.4.11 Petroleum and Chemical Industries 1495
18.4.12 Electrical Utilities 1498
18.4.13 Textile and Plastic Industries 1499
18.4.14 Polymers 1499
18.4.15 Reclamation 1501
18.4.16 Other Applications 1503
18.4.17 Thermal-Sprayed Coatings in the Different Countries 1505

18.5 Economic Analysis of the Different Spray Processes 1513
18.5.1 Different Cost Contribution Factors 1513
18.5.2 Direct Cost Factors 1514
18.5.3 Indirect or Fixed Cost Factors 1521
18.5.4 Few Examples 1522
18.6 Summary and Conclusions 1529
References 1545

About the Authors

Maher I. Boulos, Professor Boulos is a chemical engineer, with a bachelor's degree from Cairo University, Egypt 1963, and Master's and Ph.D. degrees from the University of Waterloo, Ontario, Canada in 1968 and 1972. He has a long experience in the areas of fluid dynamics and heat and mass transfer under plasma conditions. He has been at the University de Sherbrooke since 1973 where he founded the Plasma Technology Research Center in 1985. In 1990, he founded Tekna Plasma Systems Inc., a spin-off the University of Sherbrooke with the mandate of developing and promoting industrial applications of thermal plasma technology. Since January 2007 he retired from his regular faculty position to focus on running the Tekna Group which has grown to be a world leader in induction plasma technology. Over his 35 years career at the University of Sherbrooke, Professor's Boulos supervised/co-supervised 57 M.Sc. and Ph.D. students, published more than 150 papers in refereed scientific Journals, and contributed to 30 patents and patent applications. He coauthored a textbook on thermal plasma fundamentals and applications, published by Plenum in 1994. He is a Fellow of the Canadian Academy of Engineering and has been the recipient of numerous distinctions including TSS Hall of Fame in 2003 and the "Lieonel Boulet" Prix du Québec in November 2007, the highest scientific distention in Québec, for his contribution to scientific and economical development in Québec.

Pierre L. Fauchais, Pierre Fauchais is a professor emeritus at University of Limoges, France. He received at the University of Poitiers, France, his Diplomas both in Engineering: Aeronautics and related Thermal Problems (1961) and in Physics (1961), his Ph.D. in Mechanics and Aeronautics (1963), and his State Thesis in Physics (1968). From 1961 to 1968 he was Researcher at National Research Centre (CNRS) at ENSMA Poitiers, and in 1968 became Assistant Professor at the University of Limoges, then Full Professor in 1973, and Exceptional Professor in 1988. His work was devoted to thermodynamic and transport properties of thermal plasmas, arc technology, plasma diagnostics (temperatures and velocities), sensors for particles in flight and at impact (laser anemometry, fast pyrometers (50 ns), and imaging, plasma spraying, and production of finely or

nanostructured coatings. He has about 400 papers published, 9 book chapters, one book, 280 peer-reviewed international conference papers, 430 international conference papers, and 8 patents. He has given 52 plenary lectures and 82 topical lectures at international meetings. He was inducted to the ASM-TSS Hall of Fame in 1998 and received the Plasma Chemistry Society award in 2001 and 34 best paper awards. He is fellow ASM since 2002. He has directed or codirected 92 Ph.D. thesis and 15 State thesis or equivalent (HDR). Besides regular teaching, he has given and organized numerous continuing education short courses in conjunction with international conferences and specialized courses adapted to industrial needs.

Joachim V.R. Heberlein, Professor J. V. R. Heberlein received the Diploma in Physics from the Technical University Stuttgart, Germany, and the Ph.D. degree in Mechanical Engineering from the University of Minnesota in 1966 and 1975, respectively. From 1975 to 1989 he was at the Westinghouse R&D Center involved in a variety of plasma-related applications, first as senior engineer in Power Interruption Research and then as manager of Lamp Research, Applied Plasma Research, and Nuclear and Radiation Technology. Since 1989 he has been at the Mechanical Engineering Department at the University of Minnesota working in the areas of plasma heat transfer, electrode effects, plasma instabilities, and various plasma process developments. In particular he has described arc plasma effects theoretically and numerically and performed experimental verifications for a variety of applications, including plasma spray torch development and plasma cutting. He has over 330 published papers, 7 book chapters, and 14 patents issued and has received a number of awards and distinctions and inducted to TSS Hall of Fame in 2004.

Chapter 1
Introduction

The motto of the Olympic games "citius, altius, fortius" (faster, higher, stronger) entices athletes to continuously establish new records. Similarly, there is a continuous push in every part of industry to set new performance standards for the improvement of one particular part of human life. These performance improvements can be summarized as better functional performance, longer component life, and lower component cost. Besides the geometrical design, it is the choice of materials that will determine the performance and cost of the component. Materials have been developed for exceptional functional performance in specific applications, such as a number of specialty steels or super alloys; however, the increasing demands for combined functional requirements such as high temperatures and corrosive atmospheres in addition to abrasive wear, and the difficulty in machining some of the specialty alloys to the final form, as well as the costs of having an entire part made of such a material has led to the ever increasing demand for coatings.

1.1 Needs for Coatings

The motivation for coating structural parts can be summarized by the following needs:

(1) improve functional performance by, e.g., allowing higher temperature exposure through the use of thermal barrier coatings,
(2) improve component life by reducing wear due to abrasion, erosion, and corrosion,
(3) extend the component life by rebuilding the worn part to its original dimensions avoiding the need for replacing the entire component, e.g., a shaft or axle.
(4) reduce component cost by improving functionality of a low cost material with an expensive coating.

In each of these uses of coating technologies there should be no or minimal machining required of the coated part.

P.L. Fauchais et al., *Thermal Spray Fundamentals: From Powder to Part*,
DOI 10.1007/978-0-387-68991-3_1, © Springer Science+Business Media New York 2014

1.2 Thin Films vs. Thick Films

Coating technologies can be roughly divided into deposition of thin films and deposition of thick films. Thin films with thicknesses of less than 20 μm offer excellent enhancement of surface properties. Chemical vapor deposition (CVD) or physical vapor deposition (PVD) can provide surfaces with unparalleled hardness or corrosion resistance. However, most thin film technologies require a reduced pressure environment and, therefore, are more expensive and impose a limit on the size and shape of the substrate. The exceptions are the super thin surface modification films of large polymer sheets using atmospheric pressure nonequilibrium discharges. Thick films have a thickness of >30 μm, up to several millimeters. They are required when the functional performance depends on the layer thickness, e.g., in thermal barrier coatings, when strong erosion and corrosion conditions result in wear and the component life depends on the layer thickness, or when the original dimensions of worn parts are being restored. Thick film deposition methods include chemical/electrochemical plating, brazing, weld overlays, and thermal spray. Each of these methods offers certain advantages and has certain limitations. Wet chemical methods suffer from environmental hazards; brazing and weld overlays have limitations with regard to the materials that can be deposited and with regard to the shape of the substrate, and thermal spray may require an after-treatment to reach full density or eliminate all open porosity.

1.3 Thermal Spray Coating Concept

This book is devoted to all aspects related to thermal spray technology. The definition of thermal spray technology is given in the Thermal Spray Terminology compendium [1] as: "Thermal spraying comprises a group of coating processes in which finely divided metallic or nonmetallic materials are deposited in a molten or semi-molten condition to form a coating. The coating material may be in the form of powder, ceramic rod, wire, or molten materials." Weld overlays could be included in this definition; however, from all the weld coating processes only plasma transferred arc (PTA) deposition is usually included as a thermal spray process. The cold spray process is strictly not conforming to this definition because the powders are neither molten nor semi-molten, but this process is anyway included as part of thermal spray technology and, therefore also in this book. The general concept of thermal spray is depicted in Fig. 1.1. The central part of the system is a torch, which converts the supplied energy, chemical energy for combustion or electrical energy for plasma based processes, into a stream of heated gases. The coating material is heated, eventually melted, and accelerated by this high-temperature, high-velocity gas stream toward a substrate, where the particle/droplet deforms to generate a splat, and where multiple layered splats form the coating. The droplets may be generated by the melting of powders or by melting the

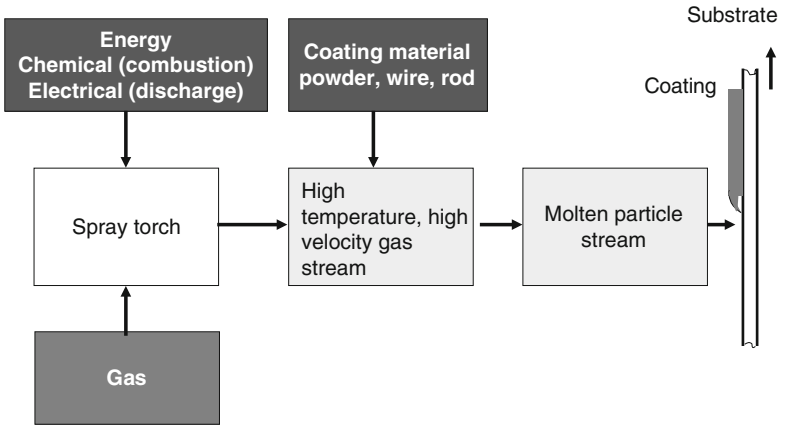


Fig. 1.1 Schematic of the thermal spray concept

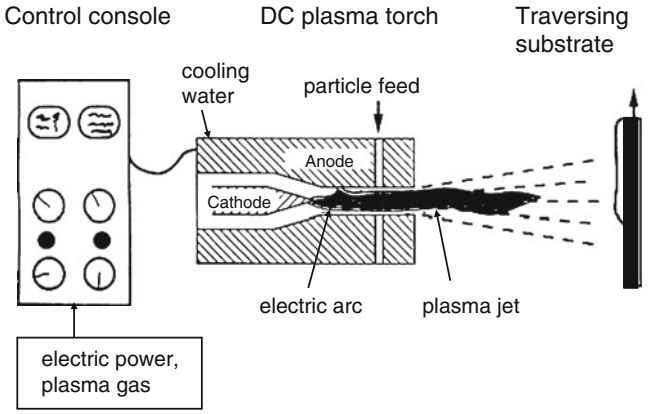


Fig. 1.2 Schematic of a plasma spray torch as an example for a thermal spray system

tips of wires or rods using the high-energy gas stream. Figure 1.2 shows a schematic of a plasma spray torch as an illustration of the process operation, and Fig. 1.3 [courtesy of Sulzer Metco] shows photographs of thermal spray torches using either powders or wires as the starting material. A thermal spray system can be understood as consisting of five subsystems [2]: (1) the high-energy, high-velocity jet generation, including the torch, power supply, gas supply, and of course the associated controls; (2) the coating material preparation, i.e., the powder size distribution and morphology, its injection into the high-energy gas stream, and its transformation into a stream of molten droplets; (3) the surrounding atmosphere, i.e., atmospheric air, controlled atmosphere (including humidity control), low pressure, etc.; (4) the substrate material and the substrate surface preparation; and (5) mechanical equipment for controlling the motion of the torch and the substrate relative to each other. It is the understanding and the control of the interaction between these subsystems which are required for implementation of reliable coating processes.

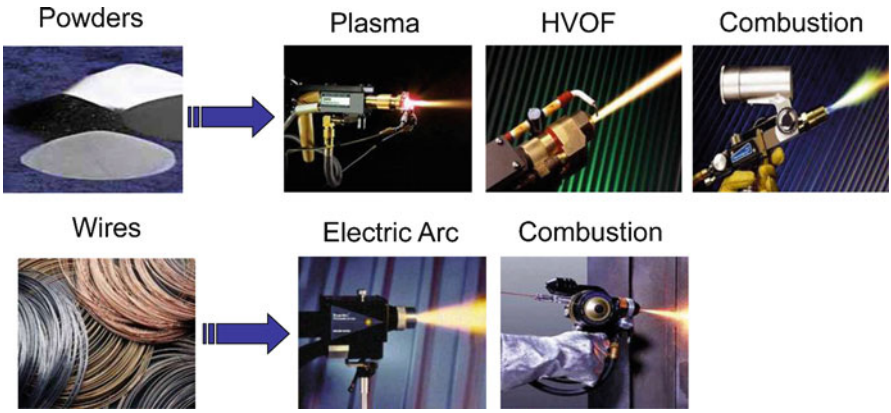


Fig. 1.3 Illustration of thermal spray processes using powders and wires [Reproduced with kind permission of Sulzer Metco AG (Switzerland)]

1.4 Description of Different Thermal Spray Coating Processes

Thermal spray is divided first according to the way the energy or heat is provided to melt the material or give it enough plasticity to allow the formation of the coating, i.e., the "thermal" part of thermal spray. This energy or heat is provided by combustion, by dissipation of electrical energy creating plasma, or in the case of cold spray by high-pressure gases. A second level for dividing the processes is according to the form in which the coating material is introduced, as powder, wires, or rods. A further division can be introduced according to the environment upstream or downstream of an accelerating nozzle, (1) high or very high pressures upstream of the nozzle and atmospheric air downstream of it, or (2) reduced pressure and controlled atmosphere in a chamber downstream of the nozzle. Lastly, the processes can be divided according to power consumption and deposition rate. Figure 1.4 gives an overview of the different thermal spray processes, not including cold spray.

The combustion spray processes are (1) the flame spraying of powders, wires, or rods, (2) the high-velocity oxy-fuel (HVOF) or the high-velocity air fuel (HVAF) processes with significantly higher upstream pressures and a Laval nozzle allowing attainment of supersonic speeds, using mostly powders, and (3) the detonation spray process where an explosive mixture is ignited upstream of a Laval nozzle to create a detonation with high pressure and temperature for heating and accelerating the powders. The drawbacks of any combustion spray process are that the highest gas temperature for melting the spray material is given by the adiabatic flame temperature of the combustion gas mixture, reducing its value for spraying high temperature ceramics. Also, the environment of the products of the combustion process may lead to chemical reactions of the sprayed material with these

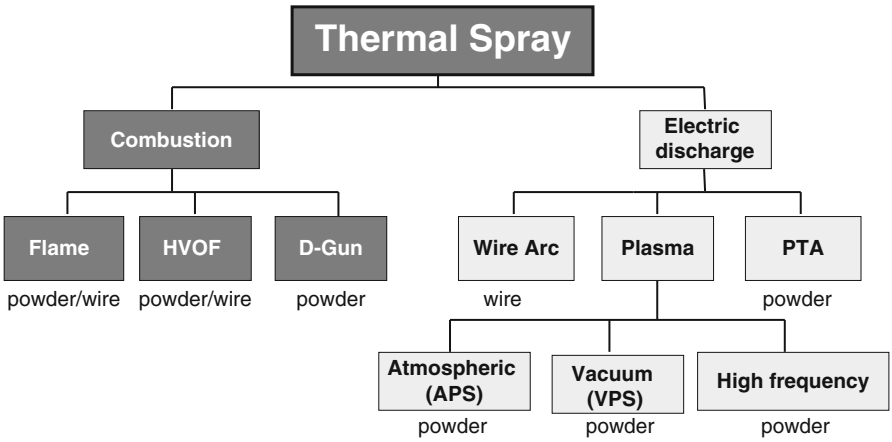


Fig. 1.4 Classification of thermal spray technologies

gases. Still, flame spraying is the most widely used spray coating process because of its economics. In the plasma-based processes the gas is heated by an electrical discharge, i.e., an arc discharge or a radio frequency discharge. The plasma-based processes are plasma spraying, wire arc spraying, and plasma transferred arc (PTA) deposition, the latter process being also part of the weld overlay family of coating processes. The use of wires is listed separately as a different process because the material melting is accomplished directly by an arc rather than in the plasma jet. Plasma spraying is probably the most versatile of all thermal spray processes because there are few limitations on the materials that can be sprayed and few limitations on the material, size, and shape of the substrate. The coating quality is in general higher than that obtained with flame spraying. While the majority of the plasma spray processes exhaust the plasma jet into the open air environment (atmospheric pressure plasma spraying or APS), the coating quality, i.e., density, uniformity, and reproducibility can be enhanced by spraying in a controlled environment, i.e., a controlled atmosphere chamber or in a low pressure environment (low pressure plasma spraying or vacuum plasma spraying, LPPS or VPS), making the process significantly more expensive. In wire arc spraying, an arc between two wires is melting the wire tips and a high-velocity gas stream is propelling the droplets toward the substrate. This process is more economical because of the use of wires instead of powders, but the choice of materials is limited because the wires need to be electrically conducting and ductile. The coatings usually have higher porosity than those of the other plasma-based processes. A variant of the plasma spray process is the high frequency or radio frequency (r.f.) plasma spray process, where the electrical discharge is not a direct current (d.c.) arc but a high frequency ($>$400 kHz) discharge, offering a larger plasma volume and longer residence times of the particles in the plasma suitable for melting larger size particles. The PTA deposition process is different from the other thermal spray processes because the substrate serves as one electrode, usually the anode, of the arc that heats the process

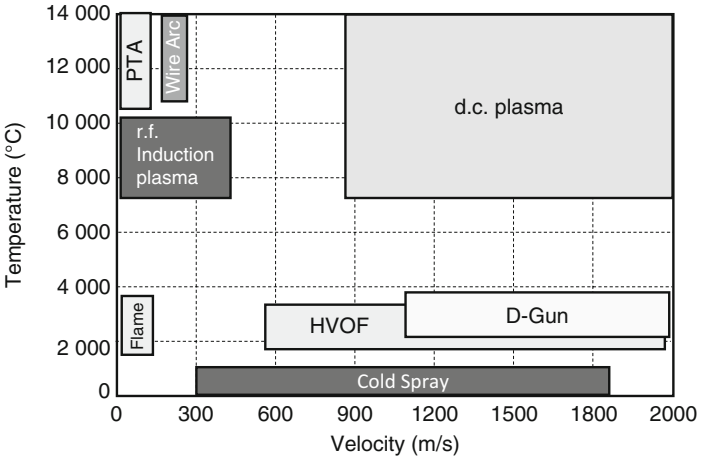


Fig. 1.5 Gas temperatures and velocities obtained with different thermal spray systems

gases and the spray material. This feature allows the attainment of excellent bonding between the substrate and the coating and very high coating densities. The transferred arc deposition can also use wires as the starting material; however, in this case the process is essentially a weld overlay process.

The coating properties are determined by the coating material and the form in which it is provided and by a large number of process parameters. Besides the parameters characterizing the substrate condition, it is the parameters that control the particle/droplet temperature and velocity at impact that have generally the strongest impact on the coating characteristics. These particle characteristics depend primarily on the gas temperatures and velocities. Figure 1.5 shows on a temperature–velocity diagram the range of values that one can expect for the gases heated by the different thermal spray processes. One has to keep in mind that (1) different materials require different deposit conditions, (2) specific coating properties (high density or desired porosity) may require specific particle velocity/temperature characteristics, (3) the heat fluxes to the substrate vary for the different coating methods and for some substrates the heat flux has to be minimized, (4) substrate preheating and temperature control during spraying strongly influence coating properties, in particular residual stresses, and (5) frequently a trade-off exists between coating quality and process economics. Consequently, if plasma spray can offer a high-temperature /high-velocity environment for the injected powders, there will be a strong heating of the substrate under these conditions, and the powder material may change during the deposition due to excessive heating, e.g., WC–Co may decompose. Chapter 2 will provide more details of the comparison of the different processes. It is clear, however, that every process has some unique features that make it particularly suited for a specific coating, i.e., the thermal spray processes are to a large degree complementary rather than competing with each other. But there exists an overlap between the coatings that can be achieved with the different processes.

1.5 History of Thermal Spray

The invention of thermal spray is credited to M.U. Schoop, who received with several collaborators a number of patents on various aspects of thermal spray and was able to commercialize the process. His impact on thermal spray technology is well described by Berndt [3] and by Knight [4], and several of his important patents are discussed. It shall only be mentioned that in his patents and some of his review articles, M.U. Schoop anticipated many future developments. In his early patents he describes the atomization of liquid metals by a high-pressure air or inert gas stream [5], the use of metallic or ceramic powders heated by a flame [6], the use of wires or rods of various materials in a patent by Morf [7], or a description of the twin wire arc spray process [8]. It also should be mentioned that he recognized the importance of the droplet velocity and temperature on the coating, e.g., by commenting in anticipation of HVOF and cold spray: "*At a gas pressure of 20 atmospheres, for example, coatings are produced, the density and hardness of which are above normal values; at a gas pressure of only 5 atmospheres the density and hardness are below normal values*." [5]. While thermal spray technology was widely applied, the need for coatings was limited. Until the 1950s, thermal spray technology consisted essentially of flame spraying. In the mid-1950s, the first plasma spray torch was developed by Thermal Dynamics Corporation, followed by developments by Metco and by Plasmadyne, and these torches form the basis of many of the torches that are being used today. Figure 1.6 [courtesy of Sulzer Metco] illustrates the history of thermal spray and the improvement of the performance through new developments.

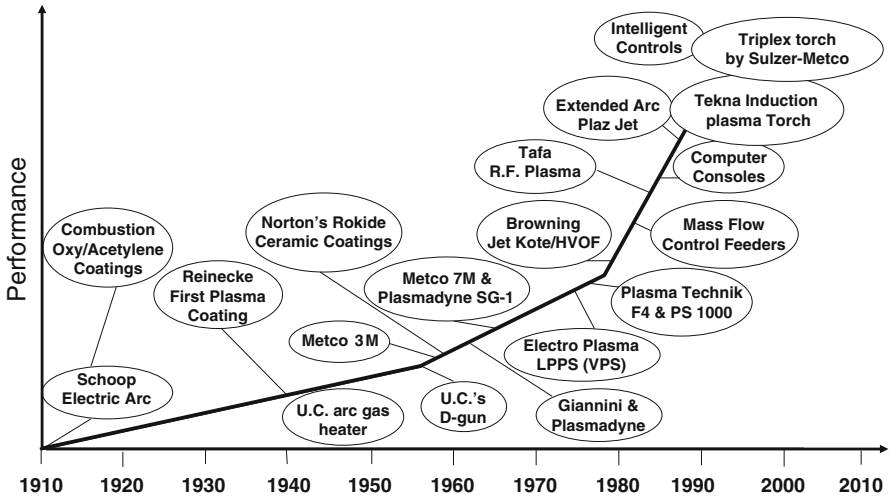


Fig. 1.6 Milestones in the development of the thermal spray industry [Reproduced with kind permission of Sulzer Metco AG (Switzerland)]

The requirements for new materials in the aeronautical and space industries led to a rapid development of thermal spray technology in the 1960s. Since then there has been an accelerating pace of developments for spray coating devices and processes, materials, process diagnostics and controls, and new applications. The 1970s saw the development of low pressure plasma spraying and of induction plasma spraying, of HVOF, and of many process improvements. A trend was pursued to extend the process conditions to higher particle velocities and lower particle temperatures, through the introduction of HVAF and eventually that of cold spray. The use of coatings spread to more and more industries, and the increased requirements for improved process reliability led to an increase in research and development activities. At the same time, robotic systems were developed for the coating of complex shapes. Thermal spray technology became a truly interdisciplinary field, with research in plasma diagnostics, fluid dynamic modeling, new developments in describing plasma heat transfer, awareness of transient phenomena (instabilities), diagnostics for describing the in-flight properties of individual particles, and lastly the description of the coating formation. This research stimulated the development of more robust torches, as well as sensors, which are able to characterize properties of particles and of the substrate. These sensors not only allowed unprecedented gathering of information on the influence of process parameters on the particle states, they also set the stage for developing effective online control systems. Among the new torch developments, the torches with multiple cathodes [9, 10] or multiple anodes should be mentioned [11] as well as the central injection torch [12, 13]. At the same time, cold spray technology became part of the family of industrially accepted coating technologies, and strong developments of this technology are continuing. This low temperature deposition process avoids the formation of oxides and the properties of the deposited films are close to those of the wrought material. The discovery of the special properties of materials consisting of nanometer-sized grains (nanophase materials or nanomaterial) has led to developments of depositing coatings of such materials, either by using powders consisting of nanoparticle agglomerates or by using newly developed techniques of suspension spraying, where droplets of a suspension of nanoparticles are injected into the plasma, or solution spraying, where precursors of nanoparticles are injected as a liquid into the plasma where nanoparticles then nucleate. A separate chapter in this book is devoted to these new developments.

1.6 Thermal Spray Applications

An overview of the applications in Europe in 2002 in Fig. 1.7 [14] shows that the earlier domination of aerospace applications (around 50 % 10 years earlier) has been reduced by an increasing use in the automotive and chemical process industries, an extension from high-value added products to high-volume production items, indicating a maturity of the process. This increase in process maturity and reliability is continuously opening up new markets. While the diversity of

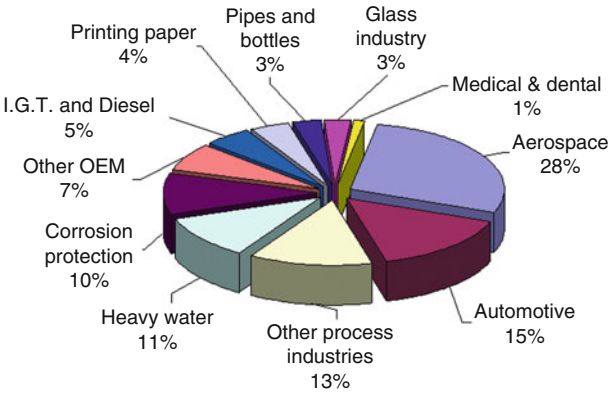


Fig. 1.7 Industrial applications of thermal spray technology in Europe in 2001, after Ducos and Durand [14]. Reprinted with permission of ASM International. All rights reserved

applications is likely to increase, the main pillars of users are still the aerospace, automotive, power, and chemical industries [15], and thermal spray technology will have to continue to adjust to respond to the needs of these industries. One could not imagine modern aircraft engines without thermal spray coatings nor high-efficiency gas turbines—thermal spray is a truly enabling technology. Thermal spray technology makes in many applications substitution of steel with lighter weight materials Al or Mg economically sensible. The use of aluminum engine blocks in automobiles to reduce the weight is an example for how thermal spray technology can respond to an industrial/societal need. Spray torches have been developed to coat the inside walls of the Al alloy cylinder blocks with materials withstanding the high temperatures and corrosive environment of the internal combustion chamber [16, 17]. A strong driver for expanding thermal spray technology is the need for replacement of wear-resistant hard chrome coatings [18]: thermal spray coatings (1) reduce the environmental concerns associated with exposure to hexavalent chromium, (2) allow deposition of thicker coatings, (3) offer improved corrosion resistance and higher fatigue life, and (4) offer cost savings because of higher process speeds, and a wider range of materials that can be deposited, having no limitations on the size of the part to be coated, and providing longer life of the coated part [18]. A comparison of wear resistance of chrome-plated surfaces with surfaces coated by HVOF or plasma spraying demonstrated the advantages of the thermally sprayed coatings in applications in the paper and textile industries [18]. However, it is the large variety of materials that can be chosen for the coatings that are responsible for the continued diversification of the thermal spray market. Ceramic coatings can offer besides good wear resistance, good tribological properties reducing friction, or can have high acceptance of color ink for printing presses [19]. Hip or knee or dental implants rely on biocompatible or bioactive coatings that increase the speed of connecting with the bone tissue.

An estimate of the 2003 thermal spray market size as presented by J. Read [20] is shown in Table 1.1. The overall market is significant, and the service of providing

Table 1.1 Estimated thermal spray market size in 2003 as compiled by J. Read [20], reproduced with kind permission of ITSA Spraytime

OEM/end users	1,400 M$ US
Large coating service companies	800 M$ US
Small coating companies	600 M$ US
Powder/equipment sales	700 M$ US
Estimated total market	3,500 M$ US

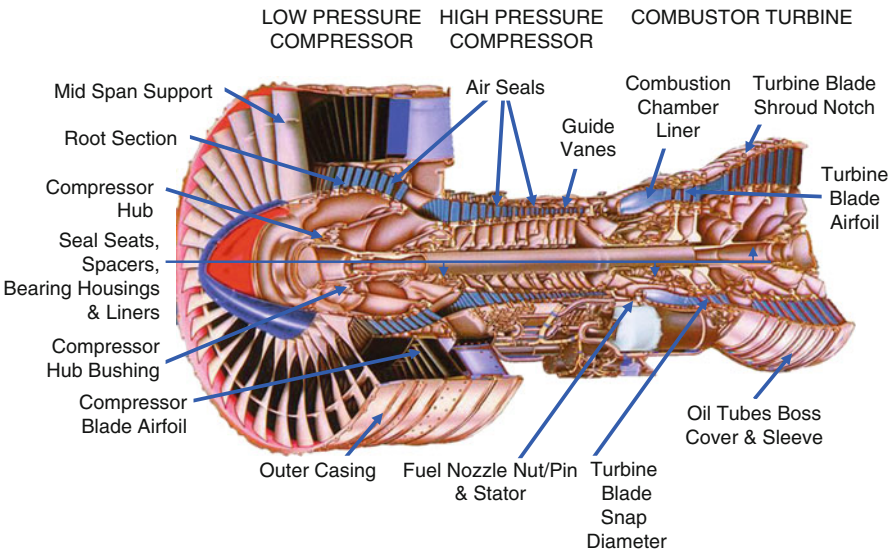


Fig. 1.8 Thermal-sprayed coatings on aircraft turbine engine parts [15] [Reproduced with kind permission of Sulzer Metco AG (Switzerland)]

the coatings constitutes the largest part of it. It must be kept in mind that, as mentioned already, in several applications the coating is the enabling technology for components with a much larger market value.

The diversity of the applications is shown in Figs. 1.8, 1.9, 1.10, 1.11, 1.12, and 1.13. Figures 1.8 and 1.9 [both courtesy of Sulzer Metco] show the multitude of parts that are coated using thermal spray technology in a jet engine and in an automobile [15]. Figure 1.10 (courtesy of Sulzer Metco) shows the spray deposition of a coating on a turbine blade and the assembly of coated blades in a gas turbine. Typically, such a blade is coated with at least two layers of different materials. Figure 1.11 (courtesy of Sulzer Metco) illustrates the coating of a large drum for manufacturing paper, and Fig. 1.12 (courtesy of Sulzer Metco) shows spray-coated spindles used in the textile industry, both coated for reducing wear. Figure 1.13 (courtesy of Sulzer Metco] shows a hip implant—coating of such implants is a rapidly growing market.

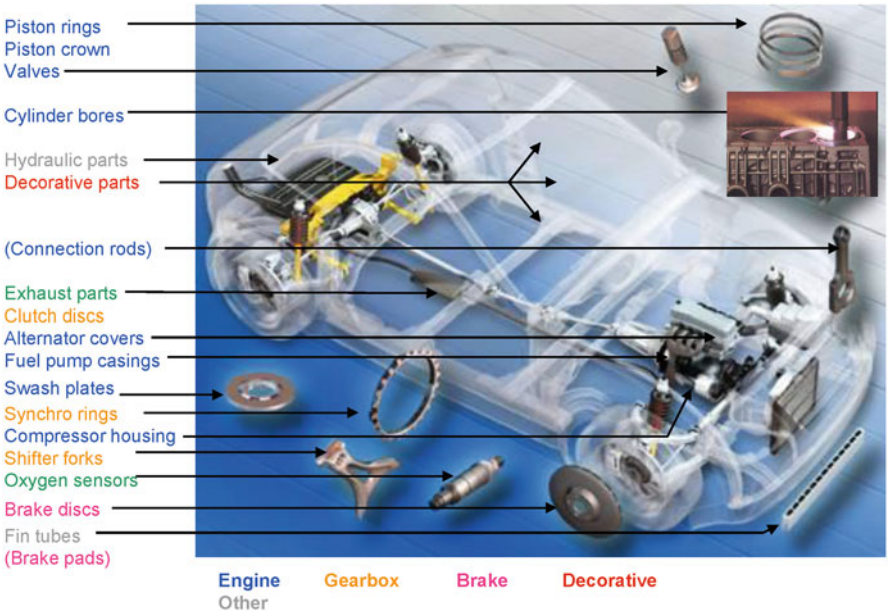


Fig. 1.9 Thermal spray components in the automotive industry [15] [Reproduced with kind permission of Sulzer Metco AG (Switzerland)]

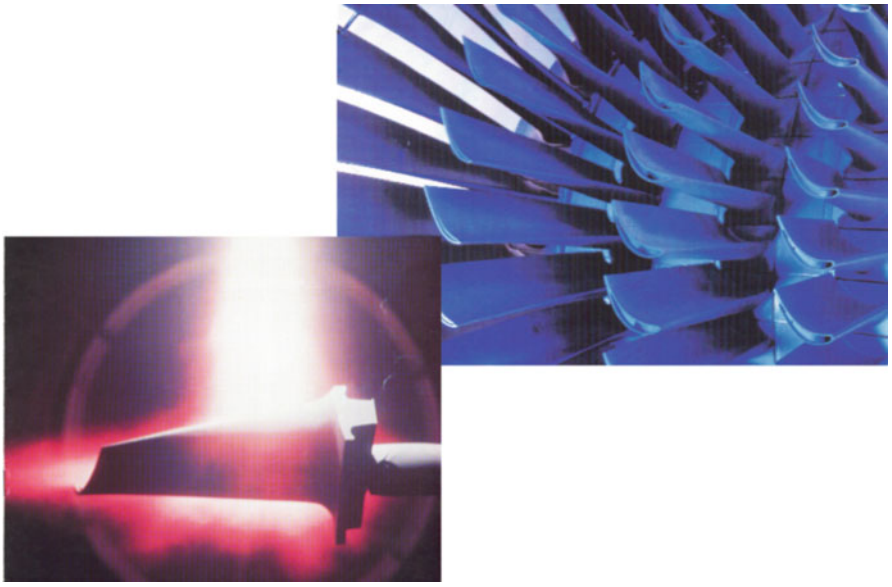


Fig. 1.10 Plasma-sprayed turbine blade coating [Reproduced with kind permission of Sulzer Metco AG (Switzerland)]

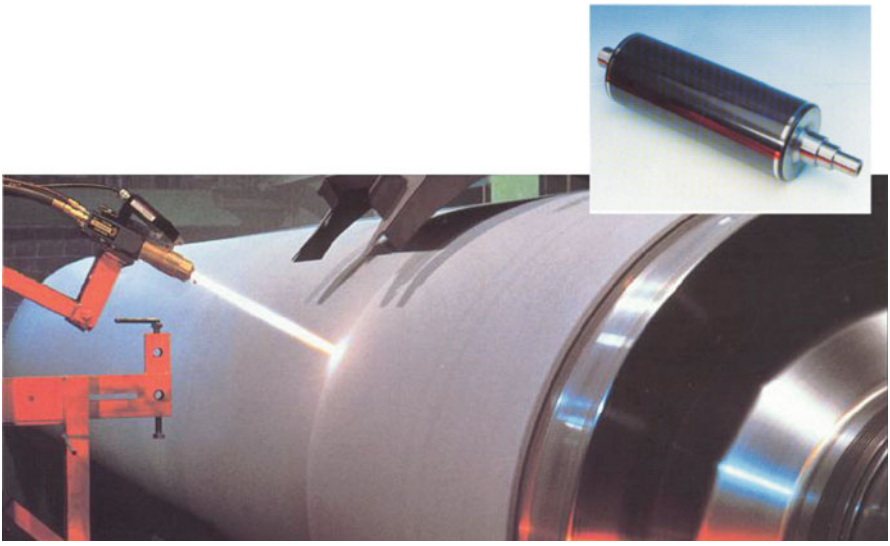


Fig. 1.11 Plasma spray applications in the paper and printing industry [Reproduced with kind permission of Sulzer Metco AG (Switzerland)]

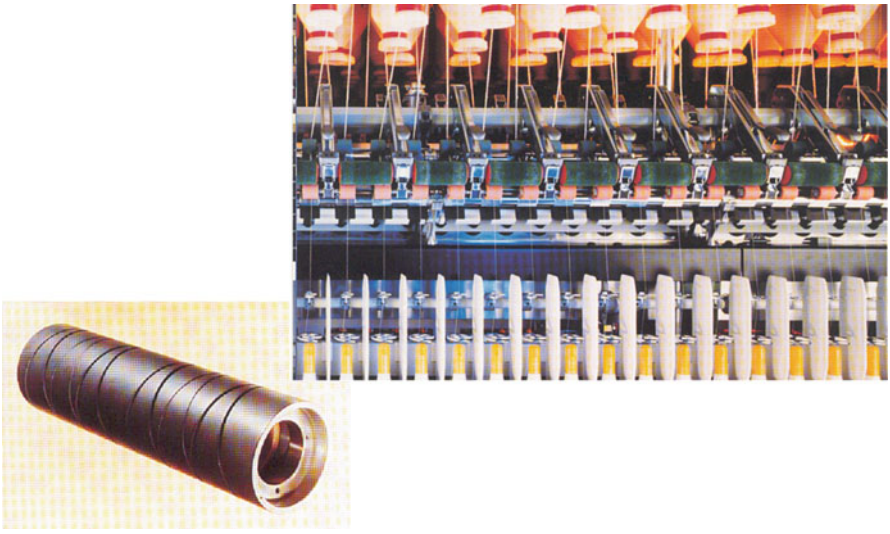


Fig. 1.12 Applications of plasma spray technology for the coating of spools and high wear parts in the textile industry [Reproduced with kind permission of Sulzer Metco AG (Switzerland)]

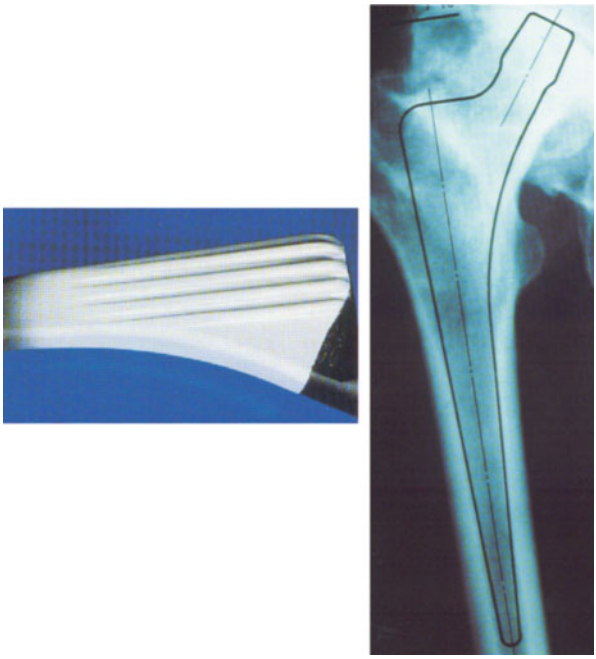


Fig. 1.13 Medical applications of plasma spray technology for the coating of hip and dental implants [Reproduced with kind permission of Sulzer Metco AG (Switzerland)]

1.7 Overview of Book Content

Understanding and controlling the entire coating process require more than just using one of the spray processes to form a layer on a substrate. In this book, all issues related to having a part that has the desired surface properties and performance characteristics are discussed. Chapter 2 is presenting an overview of thermal spray technology and serves as a summary of the major parts of the book. Chapters 3 and 4 provide the theoretical background on the generation of the necessary heat using either combustion or electrical discharges, and the transfer of this heat (or -high-energy flow) to particles of the material for the coating. These descriptions are used to understand and control the trajectories and particle heating histories in a flame or a plasma stream. Chapters 5–10 describe details of the different deposition techniques—the different processes based on combustion in Chap. 5, cold spray in Chap. 6, d.c. and r.f. plasma spraying in Chaps. 7 and 8, and wire arc spraying and PTA deposition in Chaps. 9 and 10. Chapters 11 and 12 deal with the important issues of preparing the deposition materials, i.e., the manufacturing processes for powders, wires, and rods, and with the preparation of the surface which is necessary for obtaining well-adhering coatings. Over the past decade, immense progress has been made in understanding the details of the coating formation process, through modeling and sophisticated experiments, and this understanding is presented in Chap. 13. The relatively new efforts on developing coatings with nanostructures to take advantage of some of the properties that nanoscale materials possess are

described in Chap. 14. Chapter 15 is devoted to the various surface analysis techniques used to characterize the coatings and to describe both their material properties and their functional properties. Chapter 16 deals with a topic that also has seen a large amount of developments in recent years that of process diagnostics and online control, describing the progress that has been made in having truly feedback-based process controls. The remaining issues related to manufacturing the coating, such as spray booths and occupational hazards, are discussed in Chap. 17, devoted to process integration. Finally, Chap. 18 presents an overview of industrial applications. While specific applications are discussed in the description of the deposition processes, Chap. 18, an overview of industrial applications, will form a basis for selecting the appropriate coating process for a specific application.

References

1. Hermanek FJ (2001) Thermal spray terminology and company origins. ASM International, Materials Park, OH
2. Fauchais P, Vardelle A, Dussoubs B (2001) Quo vadis thermal spraying? J Therm Spray Technol 10(1):44–66
3. Berndt CC (2001) The origin of thermal spray literature. In: Berndt CC, Khor KA, Lugscheider EF (eds) Proceedings of the international thermal spray conference, Singapore. ASM International, Materials Park, OH, pp 1351–1360
4. Knight R (2005) Thermal spray: past, present and future. In: Mostaghimi J (ed) Proceedings of the international symposium on plasma chemistry, Toronto, Canada, p unpaginated CD
5. Schoop MU (1910) Improvements in or connected with the coating of surfaces with metal, applicable also for soldering or uniting metals and other materials. UK Patent 5,712
6. Schoop MU (1911) An improved process of applying deposits of metal or metallic compounds to surfaces. UK Patent 21,066
7. Morf E (1912) A method of producing bodies and coatings of glass and other substances. UK Patent 28,001
8. Schoop MU (1915) Apparatus for spraying molten metal and other fusible substances. US Patent 1,133,507
9. Zierhut J, Haslbeck P, Landes KD, Barbezat G, Muller M, Schutz M (1998) TRIPLEX – an innovative three-cathode plasma torch. In: Coddet C (ed) Proceedings of the international thermal spray conference, Nice, France. ASM International, Materials Park, OH, pp 1374–1379
10. Barbezat G, Landes K (2000) Plasma technology TRIPLEX for the deposition of ceramic coatings in the industry. In: Berndt CC (ed) Proceedings of the 1st international thermal spray conference, Montreal, Canada. ASM International, Materials Park, OH, pp 881–885
11. Dzulko H, Forster G, Landes KD, Zierhut J, Nassenstein K (2005) Plasma torch developments. In: Proceedings of the international thermal spray conference, Basel, Switzerland. DVS, Düsseldorf, Germany, p unpagniated CD
12. Moreau C, Gougeon P, Burgess A, Ross D (1995) Characterization of particle flows in an axial injection plasma torch. In: Berndt CC, Sampath S (eds) Proceedings of the 8th national thermal spray conference, Houston, TX. ASM International, Materials Park, OH, pp 141–147
13. Burgess A (2002) Hastelloy C-276 parameter study using the Axial III plasma spray system. In: Lugscheider E (ed) Proceedings of the international thermal spray conference, Essen, Germany. ASM International, Materials Park, OH, pp 516–518

14. Ducos M, Durand JP (2001) Thermal coatings in Europe: a business perspective. In: Berndt CC, Khor KA, Lugscheider EF (eds) Proceedings of international thermal spray conference, Singapore. ASM International, Materials Park, OH, pp 1267–1271
15. Walser B (2003) The importance of thermal spray for current and future applications in key industries. Spraytime 10(4):1–7
16. McCune RC Jr, Reatherford LV, Zaluzec M (1993) Thermally spraying metal/solid lubricant composites using wire feedstock. US Patent No. 5,194,304
17. Barbezat G (2001) The internal plasma spraying on powerful technology for the aerospace and automotive industries. In: Berndt CC, Khor KA, Lugscheider E (eds) Proceedings of the international thermal spray conference, Singapore. ASM International, Materials Park, OH, pp 135–139
18. Wasserman C, Boeckling R, Gustafsson S (2001) Replacement of hard chromeplating in printing machinery. In: Berndt CC, Khor KA, Lugscheider E (eds) Proceedings of the international thermal spray conference, Singapore. ASM International, Materials Park, OH, pp 135–139
19. Wewel M, Langer G, Wassermann C (2002) The world of thermal spraying—some practical applications. In: Lugscheider E (ed) Proceedings of the international thermal spray conference, Essen, Germany. DVS, Düsseldorf, Germany, pp 161–164
20. Read J (2003) Keynote address at the China international thermal spray conference. In: Proceedings, Dalian, China

Chapter 2
Overview of Thermal Spray

Abbreviations

ALR	Mass ratio between gas and suspension
CFD	Computational fluid dynamics
d.c.	direct current
D-gun	Detonation gun
HVOF	High-velocity oxy-fuel flame
PACVD	Plasma-assisted chemical vapor deposition
PECVD	Plasma-enhanced chemical vapor deposition
PSZ	Partially stabilized zirconia
PTA	Plasma-transferred arc
PVD	Physical vapor deposition
r.f.	Radio frequency
RGS	Gas to liquid volume flow rates (generally over 100)
slm	Standard liter per minute
TBC	Thermal barrier coating

2.1 Surface Treatments or Coatings

2.1.1 Why Surface Treatment or Coatings

In order to be competitive in the market, it is important to be able to produce surfaces that wear only a little, are more resistant to tarnishing and corrosion, and retain their electrical, optical, or thermal properties over a long period. It is also interesting to have technologies to simplify product ranges or maintenance requirements. Surface treatments and coatings have a prominent role to play in this respect [1].

P.L. Fauchais et al., *Thermal Spray Fundamentals: From Powder to Part*,
DOI 10.1007/978-0-387-68991-3_2, © Springer Science+Business Media New York 2014

2.1.2 Surface Treatments

For surface treatments many solutions exist [1–3] and only the most important ones will be cited.

2.1.2.1 Strain Hardening

In strain hardening, materials are submitted to plastic deformation processes either prior to the application by rolling and impact loading, peening (shot or water jet), or are strain hardened in service (when using materials with a high rate of strain hardening such as austenitic manganese, stainless steel,. . .). The depth of hardening is below 1 mm for rolling but it can reach a depth as high as 20 mm for impact loading and it is around 0.5 mm with shot peening while with a water jet it is below 0.1 mm.

2.1.2.2 Surface Hardening

In surface hardening by thermal treatment, hardenable grades of steels are heated to the austenitizing temperature and cooled faster than the critical cooling rate of the steel. This can be achieved by heating with flame, induction, high-frequency resistance, plasma, laser, and electron beam. The depth of hardening is between 0.5 and 5 mm.

2.1.2.3 Thermo Chemical Treatments

In thermo chemical treatments: chemical elements are introduced by diffusion into surfaces at elevated temperatures (around 930 °C for carburizing low-carbon steel and 500–540 °C for nitriding). The elements are mainly not only carbon and nitrogen but also niobium and vanadium, which are diffused into steels to form, for example, very hard carbon layers. The different treatments comprise carburizing, carbonitriding, nitriding, nitrocarburizing, and boriding. In the normal carburizing cycle the depth of the carburized area is $x(\text{mm}) = 0.635\sqrt{t}$, where t is the treatment time in hours. Shorter times are obtained with gas (CO, CH_4. . .) carburizing: 4 h for a depth of 1–1.25 mm and this treatment time can be reduced with plasmas.

2.1.3 Coatings

If in surface treatment the process must be adapted to the part material, coatings allow depositing at the part surface various materials, which are quite different from that of the part, and almost independent of it [1–3]. They are generally categorized into thin (roughly below a few micrometers) and thick coatings (about over 50 μm), with of course intermediate thicknesses. It is generally admitted that four different techniques can be used to deposit coatings.

2.1.3.1 Electro/Electroless Plating

Electrochemical treatments [4]: In electroplating a coating is electrodeposited upon an electrode (the part to be coated), which is generally the cathode. Metals and alloys are deposited that way, except aluminum and titanium. In brush plating, handheld plating tool is used instead of a bath. For anodizing aluminum and its alloys, where an oxide layer is developed at their surface, the materials are the anodes in an aqueous electrolytic solution.

Chemical treatments [5]: In electroless plating the deposited material is reduced from its ionic state in solution by means of a chemical reducing agent, instead of the electric current. In phosphating, a metal surface reacts with an aqueous solution of a heavy metal salt, primarily phosphate, plus free phosphoric acid, to produce an adherent layer of insoluble complex phosphates,

Hot dip coatings [6]: the parts to be coated are dipped into a molten bath of coating material. Metals used, generally to protect steels from corrosion, are low-melting temperature ones such as zinc, zinc alloys, aluminum, aluminum alloys, and lead–tin alloys. The zinc is the most used material in an operation called galvanizing.

Metal coatings obtained with these techniques have thicknesses between about 10 μm and 1 mm. Their advantages are that they are omnidirectional (all surfaces exposed to the liquid are coated, including blind holes where the liquid can penetrate) the substrate is kept at a relatively low temperature and their cost (equipment and operating) is low.

2.1.3.2 Chemical Vapor Deposition

Coatings are obtained from the gaseous or vapor state [7, 8]. The coating results from the decomposition of chlorides, fluorides, bromides, iodides, hydrocarbons, phosphorus, and ammonia complexes. The gaseous precursor is thermally decomposed to produce the coating on the component surface, which is at high temperature (800–1,100 °C), thus limiting the choice of the substrate material. When exothermic chemical reactions occur at temperatures lower than the decomposition temperature the substrate surface temperature is correspondingly lowered.

The process, working at pressures between 13 and 100 kPa, is omnidirectional and gaseous mixture can easily penetrate into blind holes and deposit the coating, even on the internal surfaces of porous bodies. When using organometallic precursors the part temperature is lowered (400–600 °C) and the pressure range varies from 0.13 and 10^5 Pa.

With Chemical vapor deposition (CVD), metals, alloys, intermetallic, boron silicon, borides, silicides, carbides, oxides, and sulfides are deposited. The control of the coating microstructure depends on the temperature and the super saturation (ratio of the local effective concentration of the deposited material to its equilibrium concentration). With the high temperature of the substrate, diffusion between coating and substrate occurs easily resulting in a good diffusion bonding.

To coat small components (3 μm to 3 mm) fluidized beds are used. The bulk density of the bed can be varied between 1,800 and 19,000 kg/m^3 and it can be easily adjusted to that of the parts to be treated, and the reactive gases circulate in the bed kept in a furnace at the right temperature for the CVD reaction to occur.

To work at lower temperatures (25–400 °C), the decomposition of the precursor is achieved with plasma (Plasma-enhanced chemical vapor deposition: PECVD or Plasma-assisted chemical vapor deposition: PACVD) [9, 10]. It allows using all types of substrates including polymers and the deposition rates are higher than those of thermal CVD. The energy necessary for the activation of the gas is supplied by means of plasmas produced by either glow discharges (d.c. voltage, pulsed d.c. voltage, radio frequency) or microwaves. For example, it is possible to achieve hard coatings of amorphous carbon (DLC: diamond-like coatings) at temperatures below 200 °C with pulsed or RF discharges where acetylene is introduced. Unfortunately the pressure is in the range 0.13 Pa and 13 kPa, thus reducing drastically the deposition rate and restricting the use to thin films (below 50 μm). Moreover the process becomes monodirectional. This process allows achieving coatings with rather complex architectures.

Even if it is possible to achieve rather thick coatings, usually CVD coating thicknesses are below 50 μm.

2.1.3.3 Physical Vapor Deposition

Physical vapor deposition includes evaporation, sputtering, and ion plating. Virtually any solid material (except certain polymers) can be deposited onto any solid material. It is a line of sight method, the processes being operated at rather low pressures (1.3×10^{-6} to 13 Pa), which implies depositing thin coatings (typically below 1 μm) with a rather low-deposition rate [11, 12].

The process comprises:

– *Evaporation*, where vapors, produced by heating a solid by different means (direct resistance, only for metals, laser, electron beam, for metals and ceramics, arc discharge, for metals,...) are condensing onto the substrate surface after almost collision less line of sight transport. Mainly metals or alloys are

evaporated but reactive gases in surrounding atmosphere allow production of carbides, nitrides, or oxides. The coating formed on a plane surface has an inhomogeneous thickness because the fraction of the total mass deposited depends on radius and angles locating the surface (cosine law). To achieve homogeneous thickness several sources must be used or the substrate subjected to an oscillatory movement. The kinetic energy of particles impacting the substrate and then the coating is low (0.1–0.5 eV) resulting in relatively poor coating adhesion. These coatings are mainly used for their optical properties and for decoration

– *Sputtering* (at pressures between 0.13 and 13 Pa), where the energy of particles ejected from the target and impacting the substrate can reach hundreds of eV (up to 1,000 eV) creating adherent and dense coatings. Sputtering with plasma is achieved with excited molecules or atoms or ions. With the diode process, ions of a heavy inert gas (argon), impact (with energies up to 1,000 eV) onto the negatively biased target from which they eject material atoms. The sputtered material flux deposits onto the substrate, which is connected or not to the positive terminal. Nonconductive materials such as refractory carbides, nitrides, and oxides cannot be deposited by sputtering while using the direct current (d.c.) glow discharge mode. Reactive d.c. sputtering or radio frequency (r.f.) sputtering must be used for these nonconductive coatings. The densities of sputtered deposits are dependent on substrate temperature and deposition rate. The deposition rate is rather low. The introduction of a magnetic field under the target intensifies the sputtering by increasing the electrons density and thus that of ions in the area where the magnetic field is parallel to the target surface: magnetron sputtering. Reactive PVD can also be used where the metal target is sputtered and then the resulting particles react with the corresponding gas to form the ceramic (for example, Al particles sputtered react with oxygen). To improve the reaction, a RF coil is disposed close to the reactive gases injection close to the substrate. However collision frequencies must be increased to promote reactions and for that the chamber pressure must be increased (0.1–1 Pa). To increase the deposition rate, arcs are used. An interruption arc, a laser flash or a high-voltage flashover arc initiates cathodic Arc PVD between the cathode (the material to be evaporated) and an anode (the chamber wall in many cases). A stream of electrons (a few tens to hundreds A) is generated and flows through the cathode, melting locally at numerous cathodic spots on the cathode surface. Cathodic Arc PVD is used for the evaporation of metals (Ti, Al, Cr, . . . and their alloys) but also carbon for hard DLC coatings. The addition of reactive gases permits deposition of nitrides, carbides,. . . This technique is more and more used in industry to coat all types of tools, for car and engine components, for hydraulic components, for medical tools and instruments, for turbine blades, in decorative coatings,. . .
– *Ion plating* equipment consists of an ion source with the extraction and acceleration system for the ions. Ions are extracted from the plasma by extractor grids while suppressor grids prevent electrons escape. The ions extracted from the plasma source drift through a field free space to reach the substrate. The flux of

high-energy particles causes changes in the interfacial region or film properties, compared to the non-bombarded deposition. The working pressure is around 1 Pa, the surrounding atmosphere being generally argon, and a negative potential of 2–5 kV is applied to the work piece that becomes the cathode of a glow discharge formed between it and the grounded parts of the setup. Argon ion bombardment initially cleans the surface and continues, while the coating material is evaporated into the plasma and deposited onto the substrate. Compared to sputtering this continuing bombardment increases nucleation and improves adhesion. PVD coating thickness is usually below 5 μm.

2.1.3.4 Pulsed Laser Deposition

Pulsed Laser Deposition (PLD) [13] uses a high-power laser beam (mostly an excimer laser $200 < \lambda < 400$ nm) focused periodically onto a target material with laser pulses of a few tens of ns and frequencies of a few tens of Hz. Locally the target material is heated by the absorbed laser energy; it evaporates or sublimed, and if the laser flux is sufficient, the gas is transformed into a dense plasma inside the plume of the evaporated material. Resulting atoms, electrons, and ions are driven away from the target at high speeds into the vacuum of controlled conditions and strike the surface of the substrate leading to the nucleation and growth of thin films with the same chemical composition as the evaporated material. Additionally, gases can be introduced inside the reaction chamber to react with the atoms or molecules from the plume and modify the chemical composition of the material deposited on the substrate surface. As already pointed out for PVD the increase of the deposition pressure confines the plume expansion allowing a homogeneous deposition over several cm^2 of substrate surface. Of course it is a line of sight process with the cone angle of about 10° above the laser impact point. Thus the process is not well adapted for large surfaces and it is limited to electronics or optic applications with thicknesses below a few μm.

2.1.3.5 Thermal Spray

Thermal spray is a generic term [1, 2, 14, 15] for a group of coating processes where the coating is deposited on *a prepared substrate* by applying *a stream of particles*, *metallic or nonmetallic*, *which flatten more or less forming platelets, called splats, with several layers of these splats forming the coating*. Upon impact a bond forms with the surface, with subsequent particles causing a build-up of the coating to its final thickness. Figure 2.1 illustrates the principle of the plasma spray process. Alternate spray processes use either axial or radial powder injection in a high-energy flow resulting from combustion or high-velocity gas streams (cold spray). Coating thicknesses are between 50 μm and a few mm.

The process consists of generating an energetic gas flow (hot or cold gases) with an appropriate torch or gun (described in detail later on), generally flowing into the open-air environment, or sometimes into a controlled atmosphere. Thermal spray torches are devices for feeding, accelerating, heating, and directing the flow of a

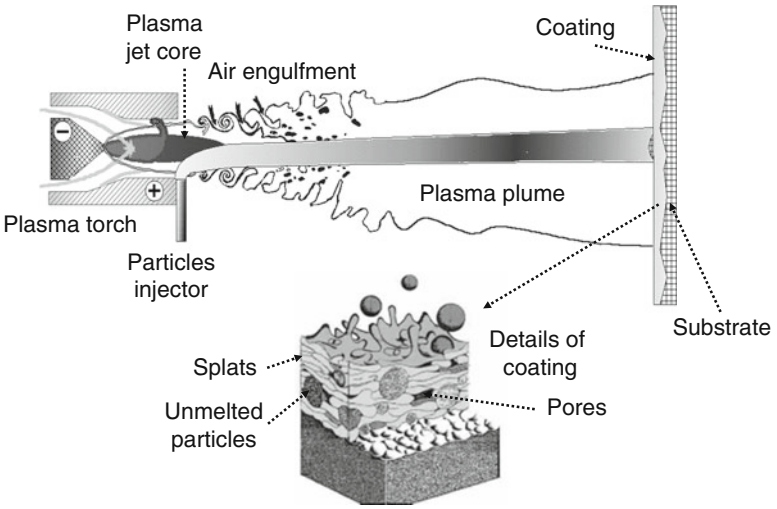


Fig. 2.1 Schematic of the different steps of the plasma spray process with radial injection of the powder in a d.c. plasma jet [16]

thermal spray material toward the substrate. The feedstock is introduced as powder, wire, rod, or cord. Wires, rods, and cords are continuously advanced (in most cases axially) at a velocity allowing the spray gun to melt their tips. The molten material is generally atomized and accelerated by an auxiliary gas fed into the spray gun, and *only molten particles are accelerated towards the substrate*. This is not the case when powders are used as the feed material. The powders are introduced into the jet of hot gases, are *accelerated but not necessarily melted before impacting on the substrate* (depending on their size and trajectories). When sprayed with a cold gas, *ductile* particles stick to the substrate and then to the previously deposited layer if their velocity is above a critical velocity, which cannot necessarily be attained by all particles of a powder with a given size distribution. As particles residence times within the spray gas, which temperature is below 600 °C, are very short (a few tens to a few hundred μs), the oxide content of coatings is almost that of sprayed particles.

Most spray processes operate in air as the surrounding atmosphere, resulting in some coating oxidation, which is drastically increasing with the temperature of the sprayed particles. This oxidation can be suppressed, or at least significantly reduced, if spraying is performed in a controlled atmosphere or a soft vacuum or achieved with the cold spray process. Moreover, for plasma-sprayed coatings of metals or alloys, a soft vacuum allows keeping the substrate at a high temperature promoting good adhesion by diffusion bonding, provided the substrate has been cleaned from its oxide layer for example by a reverse arc. However, the cost of the controlled atmosphere or soft vacuum equipment is significantly higher, almost by an order of magnitude, compared to the equipment designed for spraying in an open

Table 2.1 General characteristics of main coating methods [2]

Characteristics	Electro/electroless plating	CVD	PVD	Thermal spray
Equipment cost	Low	Moderate	Moderate to high	Moderate to high
Operating cost	Low	Low to moderate	Moderate to high	Low to high
Process environment	Aqueous solutions	Atmospheric to medium vacuum	Hard vacuum	Atmospheric to soft vacuum
Coating geometry	Omnidirectional	Omnidirectional	Line of sight	Line of sight
Coating thickness	Moderate to thick 10 μm–mm	Thin to thick 10 μm–mm	Very thin to moderate	Thick 50 μm–cm
Substrate temperature	Low	Moderate to high	Low	Low to moderate
Adherence	Moderate mechanical bond to very good chemical bond	Very good chemical bond to excellent diffusion bond	Moderate mechanical bond to good chemical bond	Good mechanical bond
Surface finish	Moderately coarse to glossy	Smooth to glossy	Smooth to high gloss	Coarse to smooth
Coating materials	Metals	Metals, ceramics, polymers	Metals, ceramics, polymers	Metals, cermets, ceramics, polymers

air environment. Besides the increased cost, the finite volume of the containment vessel limits the size of the parts that can be sprayed.

The enthalpy of the hot gas jet can be adjusted for spraying metals, alloys, cermets, or ceramics. Whatever spray process is used, it is a line-of-sight process. Thus only parts that the spray gun or torch can "see" are coated. It is for example impossible to coat small deep cavities into which the spray gun cannot fit.

Recently new processes based on the injection of a liquid into thermal spray jets have been developed [17]. The liquid is either a solution of different precursors (mixture of nitrates in water/ethanol, mixtures of nitrates, and metal-organics in isopropanol, mixed citrate/nitrate solution, etc.), or a suspension of submicron or nanometric particles. Finely structured or nanostructured coatings are obtained with thicknesses between 5 and 100 μm, bridging the gap between conventional spraying (>50 μm) and PVD (< few μm) processes. Table 2.1 from T. Bernecki [2] summarizes the different properties of the major coating methods, which are complementary and not competitive.

Thermal spray, to which this book is devoted, comprises only a small part of the total coating sales. In the next section the applications of thermal spray processes will be briefly discussed. This section is followed by a description of the different thermal spray processes and the various components of the process, i.e., preparation of the substrate, introduction of the spray material, energy transfer to the gas, interaction of the spray material with the gas, and the formation of the coating.

2.2 Brief Descriptions of Thermal Spray Applications

Choosing a thermal spray material for an application is more complex than selecting a wrought or cast material for the same applications because coating properties are not as predictable as those of conventional materials. However, now many applications are well established and new ones are continuously being developed. The optimal pairing of base material and surface coating properties is now possible and it allows obtaining a combination of characteristics that would not be possible with homogeneous materials. Aircraft and aerospace industries have provided an ideal proving ground for testing and integrating a few coating concepts. The technology has advanced to a point where it has increased the credibility and reliability of coatings. They have led to applications in other markets such as paper machines, printing, steel and metal processing, in the textile, chemical, oil, gas, automotive industries, for coatings on plastic, parts of pumps, pneumatic and hydraulic systems, near net shaped parts in rapid prototyping, and parts in the turbine, nuclear, electronic, and electrical industries. However it must be kept in mind that different spray techniques exist which are complementary and not competitive in the majority of cases, i.e., most of the time an optimal spray technique exists for a specific application. The most common functions of thermal sprayed coatings are [2, 14, 15]:

- *Wear-resistant coatings* against abrasion, erosion, cavitation wear, galling, fretting, friction, etc., and often more than one aspect of wear can be addressed. For example, cermets combine hardness, ductility, and acceptable thermal conductivity. Nonstick materials with low-friction coefficients can be combined with hard coatings. Self-lubricating materials can be deposited (for example, materials containing free carbon, or MoS_2). Very hard materials can be obtained with ceramics, which can also be combined (for example, ZrO_2 and Al_2O_3). Corrosion and wear-resistant materials can be combined.
- *Corrosion-resistant coatings*: many materials are used such as zinc, aluminum (which represents the broadest atmospheric protection), nickel-base alloys, copper–nickel alloys, chemically inert ceramics, plastics, and noble metals. One of the big concerns with thermally sprayed coatings used against corrosion is the interconnected porosity. To make the coatings impervious, high-energy thermal sprays are used, or sealants, of course, depending on service temperature. Coatings can achieve protections against high-temperature ($<$1,500 °C) corrosion or oxidation. Cold spraying seems to offer interesting possibilities against corrosion due to their high density, especially for Al, Zn, Zn–Al coatings.
- *Thermal insulation coatings*: thermal barrier coatings (TBCs) became a great success of thermal spray technology. They are made of stabilized or partially stabilized zirconia (a low-thermal conductivity ceramic material: $K < 1.5$ W/m.K when sprayed) sprayed on a superalloy bond coat protecting the substrate from oxidation or corrosion. It is worth to note that corrosion by hot gases decreases through the temperature drop achieved within the ceramic coating.

The latest TBCs are vertically segmented to have a better compliance to the stress generated when heating and cooling them. Much effort is also devoted to develop deposition processes for nanostructured TBCs, and new materials, for example, with pyrochlore structure, which has no phase transformation at high temperature as zirconia does.

- *Abradable and abrasive coatings*: these coatings are used in gas turbine engines for clearance control. Blade tips are designed or coated to make grooves in the relatively soft abradable coating face. The coating thus creates a gas-path seal that prevents gases from bypassing the blades, increasing the engine performance. Nickel/graphite, nickel/bentonite, nickel/polyester, and aluminum/polyester are used or more generally a metal matrix with a nonmetallic filler (graphite, polyester, polyimide, boron nitride, or a friable mineral). The abrasive coatings made of oxides or carbides which can also be imbedded in a metallic matrix are applied to the blade tip to reduce wear as it rubs against the abradable coating.
- *Electrically conductive coatings*: electrical contacts are made of silver, copper, aluminum, tin alloys, and bronze alloys. Thus electrical conductivity depends on the spray technique used and is generally between 40 and 90 % of that of the bulk material.
- *Electromagnetic shielding* can reduce electromagnetic or radio frequency interference, which can damage electronic components or disturb low-level signals. Such shielding is, for example, achieved by a metallic coating, often wire arc sprayed, on the inside surface of an instrumentation cabinet which is usually made of plastic or a composite material. In another application, conductive material coatings are cold sprayed on aluminum surfaces. Microwave integrated circuits (MIC) are made by plasma-sprayed Mg–Mn ferrite. Al, Ta, and Nb capacitor electrodes are sprayed in air. Unusual conductors such as aluminum titanate, barium titanate, molybdenum di-silicide, and other ceramic compounds are also sprayed.
- *Electrically resistive or insulating coatings*: electrically insulating surfaces (mostly oxides and especially alumina) are used for dielectrics (for example, in ozonizers), high-temperature strain gages, oxygen sensors (ionic conduction of zirconia), and insulation of heating coils. Resistors are made of NiCr or super alloys doped with alumina particles to tailor their electrical conductivity.
- *Electrochemical active coatings* including solid oxide fuel cells (SOFCs) and high-temperature electrolyser (HTE) are very efficient devices that electrochemically convert fuel energy into electricity and heat (SOFC) or electricity into hydrogen (HTE). SOFCs are well suited as cogeneration units for providing electricity and heat to buildings. They could greatly reduce the consumption of fuels, lowering greenhouse gas and pollutant emissions, but their development is hindered by high cost of manufacturing through wet-ceramic techniques (tape casting and screen printing). The HTE, working according to the reverse reaction of SOFC, produce hydrogen from water vapor. Plasma spray processes instead

of wet-ceramic techniques could significantly reduce manufacturing costs and many works, with industrial applications, have been devoted to these techniques.
- *Heat transfer improvement* is achieved with high-thermal conductivity coatings such as Cu or Al, or BeO for ceramics when electrical insulation is mandatory.
- *Medical coatings* can be bioactive or biocompatible or bioinert. Bioactive coatings are made of hydroxyapatite, or tricalcium phosphate, that emulates the characteristics of bone material and induces the growth of new bone attached to the implant. Biocompatible materials are made of titanium alloys, mainly Ti-6Al-4V, and Ti-6Al-7Nb, Ti-13Nb-13Zr,. . . as well as TiO_2. Titanium alloys have big pores at their surface allowing the growth of new tissue to secure the implant. SiO_2–CaO–P_2O_5-based bioactive glasses and glass ceramics are attractive materials for biomedical applications, because of the excellent levels of bioactivity. The main applications are dental, hip, and knee implants.
- *Dimensional restoration coatings* are used for salvage of worn or over-machined parts. All spray processes are used for this salvage work and very often NiCr and NiAl materials are used. With plasma-transferred arc processes coating thicknesses can reach a few mm. Cold spray has been successfully used to impart surface protection and restore dimensional tolerances to magnesium alloy components.
- *Free-standing shapes*: parts are fabricated from hard-to-machine materials by building a coating on a removal form. This process is often less costly than conventional processing methods such as sintering or hot isostatic pressing. Ceramic membranes, ceramic tubes (1 m in diameter, 10 m long, and with wall thickness of a few mm), rocket nozzles, and ceramic or refractory material crucibles are manufactured this way.
- Nuclear applications: in addition to the usual mechanical applications (however with short lifetime elements: no cobalt, for example) thermally sprayed coatings are used in Tokomak reactors and magnetic fusion devices.
- *Polymer coatings* are used as protection against chemical attack, corrosion, or abrasion. Unlike inorganic coatings polymer coatings may have equal or better properties than their cast or molded counterpart.

To conclude, this list is far from being exhaustive but it shows the wide variety of applications of thermal spray coatings. A more detailed discussion of thermal spray applications is given in Chap. 18.

2.3 Overview of Thermal Spray Processes

The thermal spray processes can be categorized in three basic groups according to the method of energy generation.

2.3.1 Compressed Gas Expansion

Commonly known as cold spray or cold gas dynamic spraying (CGDS) makes use of a converging–diverging nozzle for the creation of a high-velocity gas stream which is used for the acceleration of the powder particles in the spraying process. In this case only cold ductile metallic or alloyed particles are sprayed, with of course no oxidation during the process. For details see Chap. 6.

2.3.2 Combustion Spraying

For the definitions see Chaps. 3 and 5 for details about processes. Three types of combustion spray guns are used:

- *Flame Spray* torches that work at atmospheric pressure using mostly oxyacetylene mixtures achieving combustion temperatures up to about 3,000 K. Sprayed materials are introduced axially. Flame velocities below 100 m/s characterize this process, and powders or wires, rods, or cords are used.
- *High-Velocity Oxy-fuel Flame (HVOF).* The combustion of a hydrocarbon molecule (C_xH_y) is achieved with an oxidizer, which is either oxygen or air in a chamber at pressures between 0.24 and 0.82 MPa, or slightly more for high-power guns fed with kerosene. A convergent–divergent Laval nozzle follows the chamber achieving very high gas velocities (up to 2,000 m/s). Mostly powders are used, which are injected either axially or radially or both, depending on the gun design. Recently liquid injection (suspensions or solutions) has been developed, mainly for axial injection. Few guns have been designed to use wires or cored wires.
- *Detonation gun or D-gun*. The detonation is mainly generated using acetylene or hydrogen–oxygen mixtures (with some nitrogen to modify the detonation parameters) contained in a tube closed at one end. The shock wave created by the combustion of the highly compressed explosive medium results in a high-pressure wave (about 2 MPa) pushing the particles, which are heated by the combustion gases. Gas velocities of more than 2,000 m/s are achieved. Contrary to the two previous devices where combustible gases and powders are continuously fed into the gun, combustible gases and the powders are fed in the D-gun in cycles repeated at a frequency of 3–100 Hz.

2.3.3 Electrical Discharge Plasma Spraying

This is achieved using arcs or plasmas with four different types of torches:

Direct Current (d.c.) plasma torches generate a plasma jet from a continuously flowing gas heated by an electric arc inside a nozzle (for details see Chap. 7). They

work with Ar, Ar–H_2, Ar–He, Ar–He–H_2, N_2, and N_2–H_2 mixtures resulting in temperatures above 8,000 K (up to 14,000 K) and subsonic velocities between 500 and 2,800 m/s. When operated under atmospheric pressure, the process is commonly known as Atmospheric Plasma Spraying (APS), while under soft vacuum conditions, it is commonly referred to as Vacuum Plasma Spraying (VPS). In a few cases supersonic plasma jets could be generated using such torches when the design of the anode nozzle is adapted. Most of the applications use powders but more recently has been used solution and suspensions precursors

Radio Frequency (R.F.) inductively coupled plasma torches in which the plasma is generated though the electromagnetic coupling of the energy into the discharge cavity. It is an electroless plasma torch that can be used for the generation of plasmas of a wide range of gases including inert, reducing, or oxidizing gas mixtures such as Ar, Ar/H_2, Ar/H_2/He, Ar/O_2, Air, etc. The plasma generated is generally of a large volume, low-energy density, and low velocity (in the 10 to 100 m/s). The plasma bulk temperatures in typically in the range of 6,000–9,000 K. Induction plasma torches are characterized by their ability to allow for the internal axial injection of powders or suspensions in the discharge cavity. Induction plasma spraying is typically carried out under reduced pressure and commonly referred to as vacuum induction plasma spraying (VIPS) (for more details see Chap. 8).

Wire arc spraying: instead of using dedicated electrodes, the arc is struck between two continuously advancing wires, one being the cathode and the other the anode. The melted tips of the wires are fragmented into tiny droplets (a few tens of μm) by the atomizing gas blown between both wires (for details see Chap. 9). The wires are necessarily made of ductile material or of a ductile envelope filled with a nonductile material such as a ceramic powder. These are commonly known as cored wires.

Direct current (d.c.) transferred arc plasma: The principle is the same as that of the blown arc in a d.c. plasma torch with the exception that the arc is transferred between a floating electrode and the substrate, necessarily metallic, which, in most cases, becomes the anode. The transferred arc induces a local melting of the substrate and the particles, heated in the plasma column, stick to the molten pool where they are melted by the transferred arc. This process is essentially similar to a welding process (for details see Chap. 10).

Figure 1.5 summarizes the gas temperature and velocity ranges in the different spray processes. To illustrate the effect of particle impact velocities and temperatures, as well as of the surrounding atmosphere, the cross sections of a coating obtained by Scrivani et al. [18] with the same CoNiCrAlY commercial powder (Sulzer Metco Amdry 955) sprayed with three different processes are shown in Fig. 2.2a–c.

The quality of the coating obtained by either of these techniques depends to a large extent on the nature of the powder or precursor and the characteristics of the spraying device. For example, coatings made using VPS, Fig. 2.2a, is generally of a superior quality that obtained by means of HVOF, Fig. 2.2b, which in turn is better than APS Fig. 2.2c. The VPS plasma jet yields very dense and oxide-free coatings.

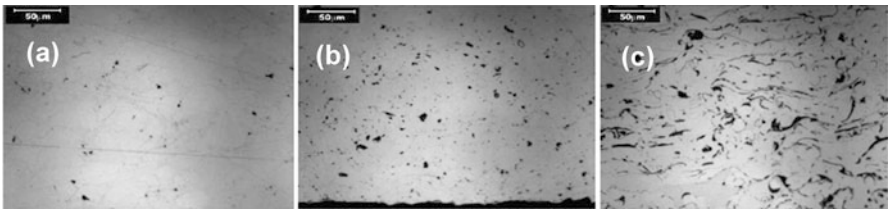


Fig. 2.2 Same CoNiCrAlY powder sprayed respectively with (**a**) the EPI system Sulzer Metco® torch working in a soft vacuum chamber, (**b**) the HVOF TAFA® JP 5000 equipment, and (**c**) the Mettech Axial III Tri-electrode Model 600 [8]

The axial plasma spray Fig. 2.2c has much better deposition efficiency than other methods, but the coating presents higher porosity, larger amounts of unmelted particles, and higher degree of oxidation. The HVOF coating in Fig. 2.2b shows low-porosity levels due to the high velocity of its flame, but the oxide content is still high compared to that of the VPS coating. Such results show that the different processes are not competitive but complementary. The choice between each of these coating techniques depends on the coating properties that are desired, the material to be sprayed, and also (probably one of the most important items) on the price the customer is ready to pay for the coating. For example, to spray a ceramic material, plasma is the most widely adopted process, as long as a high porosity coating is acceptable, flame spraying of ceramic rods is cheaper (see Chap. 18). HVOF is also possible but it requires small particles with narrow size distribution, and the deposition efficiency becomes rather low. Other spray techniques derived from the previously listed ones also exist and will be described in the corresponding chapters.

It should be noted, however, that independent of the energy source used, thermal spray processes can be divided into the following five distinct steps illustrated in Fig. 2.3.

1. *Substrate preparation* (cleaning, roughening) achieved prior to spraying and preheating. As shown in Fig. 2.4 from Yankee et al. [19] the surface preparation will define the substrate roughness characterized by its R_a, R_t, $R_{\Delta q}$,... (see Chap. 12 for definitions). Preheating the substrate above a certain temperature allows desorption of adsorbates and condensates, but this preheating also modifies the oxide layer thickness and composition with metallic substrates.
2. *Generation of the energetic gas flow*
   Expanding gas in cold spray, combustion flame or detonation, plasma or arcs, and their interaction with the surrounding atmosphere.
3. *Particle or wire or rod or cord injection*
   For powder injection, melting of particles depends on their morphology (function of their manufacturing technology, see Chap. 11), specific mass, size distribution, and trajectories that are a function of their injection parameters and the hot gases used. The choice between wires, rods, and cords depends on

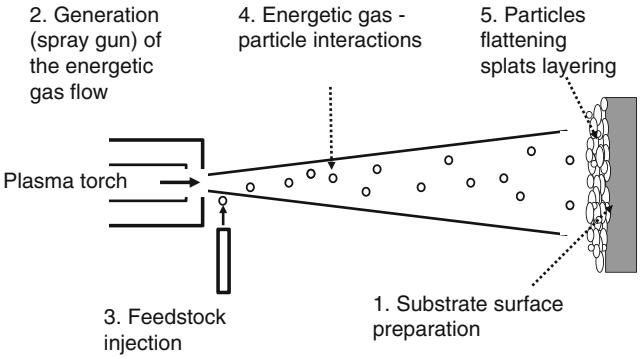


Fig. 2.3 Schematic of the different steps involved in a the thermal spray process

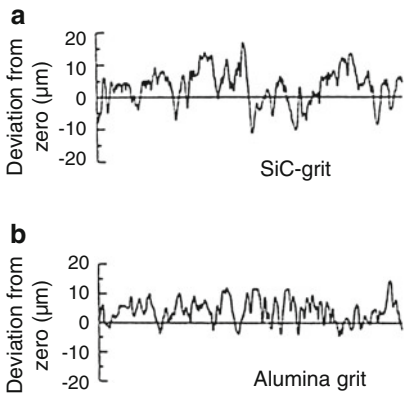


Fig. 2.4 Typical surface roughness obtained from samples roughened with (**a**) SiC and (**b**) alumina grit [19]

the material to be sprayed and the spray process chosen, and the injection velocity is controlled by the time necessary for the energetic gas to melt their tips. With this type of feeding only melted drops are sent toward the substrate.

4. *Energetic gas particle or droplet interaction*
   Involving acceleration, heating, melting, oxidation, or modification of surface chemistry of the particles or droplets (see Chap. 4). This step determines for a particle of diameter d_p, the trajectory, the impact temperature and velocity, as well as the impact angle (relative to the normal to the substrate). Depending on the entrainment of the surrounding atmosphere and the particle temperature, the particle can have its surface chemistry modified for example by oxidation (see Fig. 2.5).
5. *Coating formation*
   This depends on the particle or droplet impact, flattening, splat formation, and cooling, and splat layering first on the prepared substrate and then on already deposited layers. Particle flattening, cooling, and solidification is strongly linked, besides to its impact parameters (temperature, velocity, diameter, surface

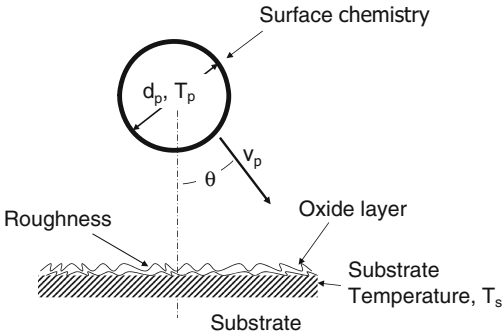


Fig. 2.5 Impacting particle and substrate parameters controlling particle flattening [20]

chemistry, and impact angle), to the substrate roughness, oxide layer thickness and composition, preheating temperature relative to the evaporation of adsorbates and condensates at its surface (for details see Chap. 13). It also depends on the relative movement between the torch and the substrate which controls the formation of beads and passes.

In the following these different steps will be described in detail.

2.4 Substrate Preparation

Substrates can be metals, ceramics, composites, glasses, woods, plastics, etc. All of these materials have very different melting or decomposition temperatures, as well as different oxidation rates generating oxide layers from thin (<50 nm) to thick (>100 nm). This means that with most spray processes, except cold spray and wire arc spraying, the substrate temperature must be controlled during spraying.

Whatever the substrate may be, its preparation prior to spraying is the most critical step for the bonding and adhesion of the coating. This preparation comprises generally three steps:

Cleaning the surface to eliminate contamination, particularly from oil or grease. Solvent rinsing or vapor degreasing are commonly used processes to remove oil, grease, and other organic compounds. For porous materials, baking is sometimes necessary. For more information see Chap. 12.

Roughening the surface (see Chap. 12 for details) to provide asperities or irregularities to enhance coating adhesion and provide a larger effective surface, as shown in Fig. 2.4. The substrate roughening in most cases is achieved by grit blasting. It is also possible to use water jets with pressures between 200 and 400 MPa. Grit blasting or water jet roughening also induces compressive stress, which can reach up to 2,000 MPa, in the first tenths of mm below the substrate-roughened surface. This stress contributes to the final stress distribution within the coating and the substrate. Some substrates (e.g., composites, plastics) require special preparations such as acid pickling.

A second cleaning step after grit blasting is necessary to remove as much as possible of the grit residues by blowing compressed air jets, using ultrasonic baths or both. Any grit particle (generally made of a ceramic material) imbedded in the substrate surface will create a defect, which is drastically magnified by an exposure to a temperature variation in most cases because of the expansion mismatch between substrate and grit materials. Of course the advantage of water roughening is that no grit residue is left. For more details see Chap. 12.

2.5 Energetic Gas Flow Generation

All devices presented below use powders or wires, rods, or cords, and introducing them into the gas flow is summarily described in Sect. 2.6, and in detail in Chaps. 4 and 11.

2.5.1 Cold Spray

2.5.1.1 Conventional High-Pressure Cold Spray

This process is "a kinetic spray process utilizing supersonic jets of a compressed gas to accelerate, at or near-room temperature, powder particles to ultra high velocities (up to 1,500 m/s). The *unmolten* particles traveling at speeds between 500 and 1,500 m/s plastically deform and consolidate on impact with their substrate to create a coating" [21].

The basis of the cold spray process [21–24] is the gas-dynamic acceleration of particles to supersonic velocities and hence high kinetic energies. This is achieved using convergent–divergent Laval nozzles. The upstream pressure is between 2 and 2.5 MPa for typical nozzle throat internal diameters in the range of 2–3 mm. Gases used are N_2, He, or their mixtures at very high flow rates (up to 5 m^3/min). For stable conditions, typically the mass flow rate of the gas must be ten times that of the entrained powder. For a powder flow rate of 6 kg/h, this means a volumetric flow rate of 336 m^3/h for helium and 52.3 m^3/h for nitrogen. Gases introduced (nitrogen or helium) are preheated up to 700–800 °C to avoid their liquefaction under expansion and increase their velocity. With the highest gas flow rate this means that the heating device must be capable of heating 90 m^3/min to temperatures up to 700–800 °C. As particles are injected upstream of the nozzle throat, the powder feeder has to be at a slightly higher pressure compared to the upstream chamber pressure. Especially when spraying with He, the spray is performed within an enclosure in order to recycle the gas.

Particles adhere to the substrate only if their impact velocity is above a critical value, depending on the sprayed material varying between about 500 and 900 m/s. The spray pattern covers an area of roughly 20–60 mm^2, and spray rates are about

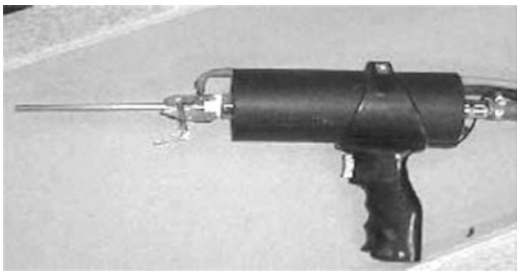


Fig. 2.6 Cold spray handgun of DYMET-402DC in 2001 [27]

3–6 kg/h. Feed stock particle sizes are typically between 1 and 50 μm and deposition efficiencies reach easily 70–90%. Only ductile metals or alloys are sprayed (Zn, Ag, Cu, Al, Ti, Nb, Mo, Ni–Cr, Cu–Al, Ni alloys, MCrAlYs, and polymers), owing to the impact-fusion coating build-up. Blends of ductile materials (>50 vol. %) with brittle metals or ceramics are also used. It is also important to emphasize that the substrate is not really heated by the gas exiting the gun (up to 200 °C at the maximum). Current and expected applications for cold spray coatings are electronic and electrical coatings (Cu, Fe–NdFeB), and coatings for the aircraft (superalloy) and automotive industries for localized corrosion protection (Al, Zn), rapid tooling repair, etc. [2]. For more details about the process see Chap. 6.

2.5.1.2 Low-Pressure Cold Spray

The cost of high-pressure spray processes is rather high, especially because of the quantity of gases consumed (especially if it is helium), and the process is not adapted at all to spraying for onsite repair of parts. Portable equipment using air has been developed [25–27] where the upstream pressure is below 1 MPa, typically 0.5 MPa with a much lower gas consumption of about 0.4 m^3/min. Figure 2.6 shows the Dymet gun developed for such a reduced pressure process.

Of course, less power (3.5 kW for the Dymet gun) is necessary to preheat the air, and the spray gas is much less expensive than N_2 or He [25]. The powder feeder can be simplified because pressurization is not necessary and the powder can be injected downstream of the nozzle throat. With gas velocities in the 300–400 m/s range the critical velocity of particles is not attained. To achieve coatings, small metal particles are mixed with bigger ones, which can be ceramics. Big particles mostly rebound upon impact, their role being to "press" the small metal particles onto the substrate and the previously deposited layers [26] (shot peening effect). Powder recuperation is hardly possible for multicomponent powder mixtures. Of course the deposition efficiency is much lower than with high-pressure guns, but the process is attractive for short production runs [27]. For more details about the process see Chap. 6.

2.5.2 *Flame Spray*

2.5.2.1 Powder Flame Spraying

This process is "a thermal spray process in which the material to be sprayed is in powder form" [28]. It is the simplest and among the oldest spray processes. The powder is fed, with a simple powder hopper or a more sophisticated powder feeder, through the central bore of a nozzle where it is heated by the oxy-fuel flame and carried by the carrier gas and the hot gas to the work piece. The flame temperature and enthalpy are determined by the fuel gas composition (C_xH_y) and flow rate and by the oxidizer (oxygen or air) flow rate [29]. For more details about the combustion process see Chap. 3. The process takes place at atmospheric pressure. One has to be reminded that one mole of air as oxidizer contains only 0.2 moles of O_2 which are used for the combustion, while the 0.8 moles of N_2 do not burn and must be heated by the flame. Thus for the same total quantity of O_2 and hydrocarbon molecules, the flame using air as oxidizer will have a lower bulk temperature.

At atmospheric pressure, the maximum temperature is achieved theoretically with the stoichiometric combustion of acetylene ($2C_2H_2 + 5O_2$) and is 3,410 K. Flame velocities depend on the combustible gas flow rates and are generally below 100 m/s. Typical flow rates are about 30 slm of O_2 and 18 slm C_2H_2 and provide a power level of about 40 kW. The specific mass of hot gas is about one-tenth of that of the cold gas at room temperature. Coatings in the "as-sprayed" condition exhibit high porosity (>10 %) and low adhesion (<30 MPa) but the coating process is easy to perform, cheap, and many materials are available. These flame spray systems are easily portable and used for many applications [30], especially to spray self-fluxing alloys, as illustrated in Fig. 2.7 for a paper machine roll coated by NiCrBSi (self-fluxing alloy). A self-fluxing alloy contains boron and silicon, which serve as fluxing agents limiting oxidation. Metallurgical bonding is achieved by heating the coating to its melting temperature after spraying. For more details about such powders see Chap. 11. The melting temperature of the substrate is necessarily higher than that of the self-fluxing alloy, and for example aluminum alloys cannot be sprayed with self-fluxing alloys and then reheated at the coating melting temperature. The process is also used for depositing wear-resistant coatings under low-load conditions, for spraying thermoplastics, rebuilding worn parts, etc., and deposition of composite coatings is possible. These coatings are used against abrasive wear (friction, erosion) and corrosion (cold or hot). For more detail about the process see Chap. 5.

2.5.2.2 Wire, Rod, or Cord Flame Spraying

This process is "a spray process in which the feed stock is in form of a wire or rod" [28] or a cord. It was the very first spray process, developed by Dr. Schoop in 1912. The setup consists of a nozzle in which acetylene is mixed with oxygen and burned

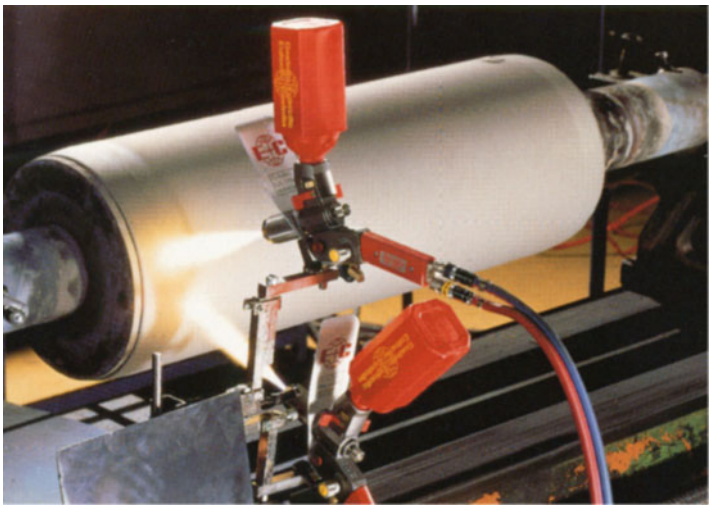


Fig. 2.7 Paper machine roll coated by NiCrBSi (self-fluxing alloy) using two powder flame guns (Courtesy of Castoline)

at the nozzle face, the flame extending into an air cap. The wire, rod, or cord is fed axially and continuously at a velocity such that the tip is melted in the flame. A stream of compressed air, surrounding the flame, atomizes and generates material droplets in a continuous stream. The advantage of the system is that only molten droplets are propelled towards the substrate. If the material is fed at a too high velocity the wire (rod or cord) comes out of the gun cap. Another advantage of the process is that the nozzle's flame is concentric with the wire or rod or cord, which maximizes the uniform heating. For example, the Master Jet of Saint Gobain can spray metal wires, cored wires, flexicords, and ceramic rods, propelled by an electromotor. The gun is lightweight and it is easy to use for spraying onto complicated shapes by hand. Of course the gun can be fixed onto a robot. For more details about the process see Chap. 6.

The remarks made previously about powder flame spraying apply to coating properties. A very wide range of materials (wires, cored wire, rods, cords) can be sprayed. All kinds of substrates can be used and the process can be manual or automated. The main applications are abrasion-resistant coatings for low-load conditions, protection against atmospheric corrosion, and copper layers for cooling. An example of a copper coating is shown in Fig. 2.8.

2.5.3 High-Velocity Oxy-fuel Spraying

This process is a "high-velocity flame-spray process" [31]. The combustion is achieved in a pressurized chamber, water-cooled or not, followed by a Laval-type nozzle (see Fig. 2.9). The combustion at pressures higher than atmospheric pressure

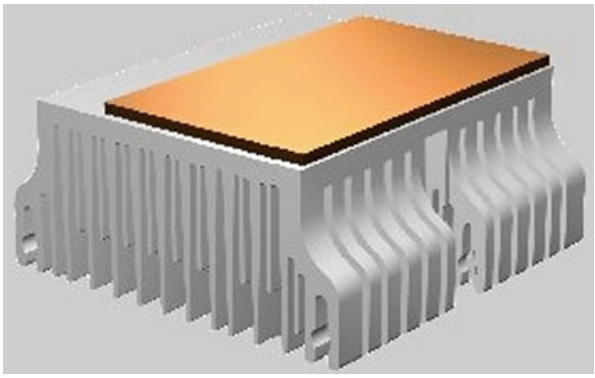


Fig. 2.8 Example of flame wire spraying: copper layer on a computer cooling system [30]

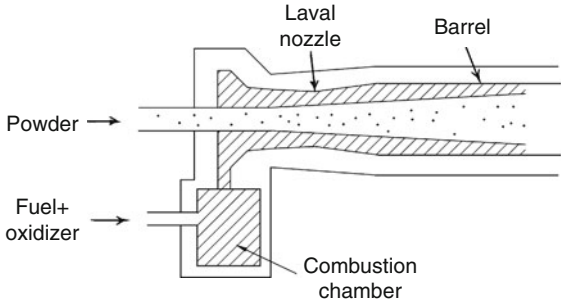


Fig. 2.9 Schematic of the HVOF process based on the Jet Kote gun [31]

(between 0.2 and 1 MPa) increases slightly the combustion temperature (see Chap. 3). For example, stoichiometric combustion of methane with oxygen at atmospheric pressure results in a temperature of 3,030 K, while at 2 MPa it is 3,733 K [29]. But the main advantage is the high gas velocity (up to 2,000 m/s, see Fig. 1.5) achieved due to the hot gas expansion through the Laval nozzle. Such velocities are supersonic as shown by shock diamonds observed downstream of the nozzle. Two types of guns exist characterized by the chamber pressure. The low-pressure HVOF uses a gun at pressures between 0.24 and 0.6 MPa with heat inputs below 600–700 MJ, while the high-pressure guns are operated in the pressure range of 0.62–0.82 MPa, generally fueled with kerosene burning either with oxygen or air with heat inputs over 1 GJ. These guns are often termed "hyper velocity guns." The "low" pressure guns are fed with hydrogen, propylene, methane, propane, heptane, and a few trademark gases together with oxygen, or also kerosene with air. The first HVOF gun was introduced in the early eighties by Browning and Witfield. Particles are injected either axially upstream of the nozzle (a pressurized powder feeder is required), as shown in Fig. 2.9 or radially downstream of the nozzle (with a conventional powder feeder). Compared to flame spraying, HVOF guns are fed with high fuel gas flow rates of 60–120 slm, and oxygen flow rates ranging from 280 to 600 slm, which corresponds to power levels of a few hundreds

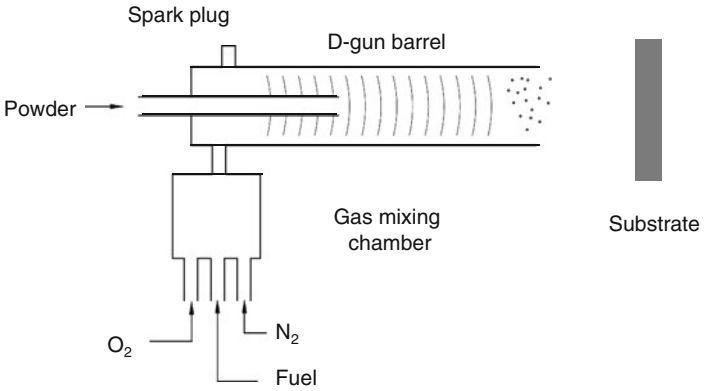


Fig. 2.10 Schematic of the D-gun [33]

of kW. With kerosene the liquid is fed between 20 and 30 slm with oxygen flows in the order of 1 m^3/min, or air up to 5 m^3/min. In flame spraying, the gas-specific mass is about one-tenth of that of the cold gas. The coupling of having highly plasticized particles impacting with high inertia allows achieving very dense coatings. The flame mixing with surrounding air can be delayed and the particles can be kept accelerating by extending the gun nozzle using a barrel (see Fig. 2.9). For the spraying of wires, special HVOF guns have been developed [32]. The principle is the same as that of wire flame spraying. The flame (propane–oxygen) is positioned at the nozzle face and the molten tip of the wire is atomized both by the pressurized flame and the airflow. Under such conditions, the gas temperature reaches values of 3,100 K, and the velocities reach values of up to 1,600 m/s, and particle velocities are much higher than with wire flame spraying.

The initial success of HVOF was in spraying dense and wear-resistant WC–Co coatings, almost as good as those sprayed by the D-gun, which at that time was only available as a service. The HVOF coatings (metals, alloys, and cermets) are dense, adherent with low-oxide content, compared to flame spraying, and they compare favorably with high-energy plasma-sprayed coatings. Typically with WC + Co (WC + NiCr or CrCo are also used) and dependent on the applications hardness values between 1,100 and 1,400 $\pm$ 150 HV_{5N} are obtained. For more details about the process see Chap. 5.

2.5.4 Detonation Gun Spraying

This process is a "thermal spray process variation in which the controlled explosion of a mixture of fuel gas, oxygen, and powdered coating material is utilized to melt and propel the material to the work piece" [28]. First developed in Russia it was introduced in the early 1950s by Gfeller and Baiker working for Union Carbide. As shown in Fig. 2.10 oxygen and acetylene are introduced in a barrel or tube (about

1 m long), closed at one end. The ignition of the mixture by a spark plug close to the closed end generates a detonation [33].

Pressures around 2 MPa are generated and particles injected about in the middle of the tube (see Fig. 2.10) are accelerated and heated, and in most cases melted. Pressures from the detonation close the gas feed valves until the chamber pressure is equalized. When this occurs the tube is flushed with nitrogen, filled with combustion gases, and the cycle is repeated (between 4 and 8 times per second or more with the recent guns). In contrast to most other spray processes the specific mass of the gas that accelerates and propels particles toward the substrate is higher than that of the cold gas (about five times) resulting in very high particle velocities. The detonation speed is the sound velocity in the combustion products (Chapman Jouget condition [29]) plus the velocity of these gases behind the wave front, as defined by Kadyrov [33]. Velocities between 1,000 and 3,000 m/s can be reached. They depend strongly on the combustible gas mixture composition and also on pressure [33]. For more details about the process see Chap. 5.

The D-Gun produces premium coatings, especially metallic and cermet ones, with properties which have been the goal of all other spraying processes to reproduce, i.e., higher density, improved corrosion barrier, higher hardness, better wear resistance, higher bonding and cohesive strength, almost no oxidation, thicker coatings, and smoother as-sprayed surfaces.

2.5.5 Direct Current Blown Arc Spraying or d.c. Plasma Spraying

This process is usually called plasma spraying. It is "a thermal spray process in which a nontransferred arc as a source of heat, ionizes a gas which melts the coating material, in-flight, and propels it to the work piece" [28]. Plasma is an electrically neutral (same amount of ions and electrons) mixture of molecules, atoms, ions (in fundamental and excited states), electrons, and photons. For gases used in plasma spraying, thermal plasma exists as soon as the gas temperature is higher than 7,000–8,000 K at atmospheric pressure (for details see Chap. 3). The plasma-forming gases: Ar, Ar–H_2, Ar–He, Ar–He–H_2, N_2, N_2–H_2 always contain a primary heavy gas (Ar or N_2) for the flow and particle entrainment and a secondary gas to improve the heat transfer (H_2, He). The high temperatures are achieved through a direct current arc struck between the cathode and the anode nozzle of the torch [34]: see Fig. 2.1. Two types of cathodes are used. Rod-type cathodes, as shown in Fig. 2.1, are usually made of thoriated tungsten, not permitting traces of oxygen or water vapor in the plasma-forming gas (tungsten oxidation starts at 1,800 K, while the cathode tip is above 3,600 K). Plasma jet temperatures are in the range of 8,000–14,000 K (at the nozzle exit on the axis). Gas flow rates are between 0.8 and 2 g/s, and it must be emphasized that the mass of the secondary gas, generally helium or hydrogen, is generally negligible compared to that of the primary gas (argon or nitrogen). Gas velocities for conventional anode nozzle internal diameters

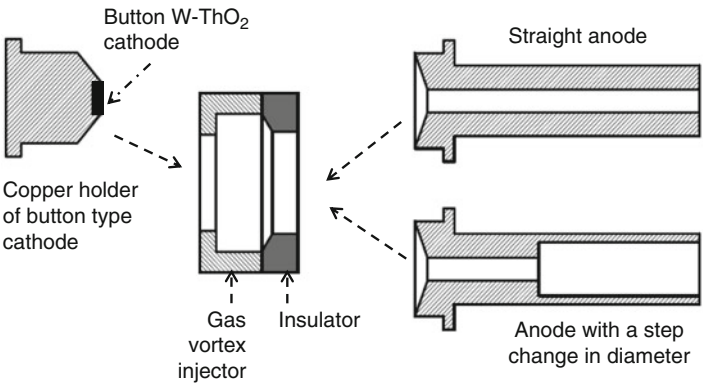


Fig. 2.11 Schematic of a d.c. plasma torch with a button-type hot cathode [35]

between 6 and 8 mm range between 500 and 2,600 m/s (subsonic velocities at these temperatures). Power levels are between 20 and 80 kW. With such temperatures the specific mass of the gas in the hottest zones of the plasma jet is about one-thirtieth to one-fortieth of that of the cold gas. Typical powder flow rates are about 3–6 kg/h. The majority of plasma spray torches make use of this type of cathode arrangement.

Button-type cathodes use a button of thoriated tungsten or other refractory metals imbedded in a copper holder, the arc being centered on it by a strong vortex flow of the plasma-forming gases. This vortex allows elongating the arc in the anode nozzle, see Fig. 2.11 [35]. Plasma-forming gas flow rates are higher (5–7 g/s) than those with a stick-type cathode, and the anode nozzle internal diameter is in 8–10 mm range. The plasma jet bulk temperature is in the 8,000–10,000 K range, with velocities below 2,000 m/s. These velocities can be supersonic at temperatures below 9,000–10,000 K. Power levels are 200–250 kW. Typical powder flow rates are up to 20 kg/h. These types of torches are used mainly for high-power/high-deposition rate applications, where the cathode attachment has high current densities. Of course other types of plasma torches exist, which are described in Chap. 7, with more detail about the plasma spray process.

The high degree of particle melting, including ceramics and the relatively high particle velocities (100–300 m/s) obtained with the plasma torches, results in higher deposit density and bond strengths compared to most flame and electric arc spray coatings [2]. To avoid any oxidation, for example, when spraying super alloys for thermal barrier bond coats, plasma spraying is performed in soft vacuum.

2.5.6 Vacuum Induction Plasma Spraying

The induction plasma spray process uses an inductively coupled r.f. plasma torch for the generation of the hot energetic gas stream in which the powder, or suspension to be sprayed, is axially injected into the center of the discharge cavity [36].

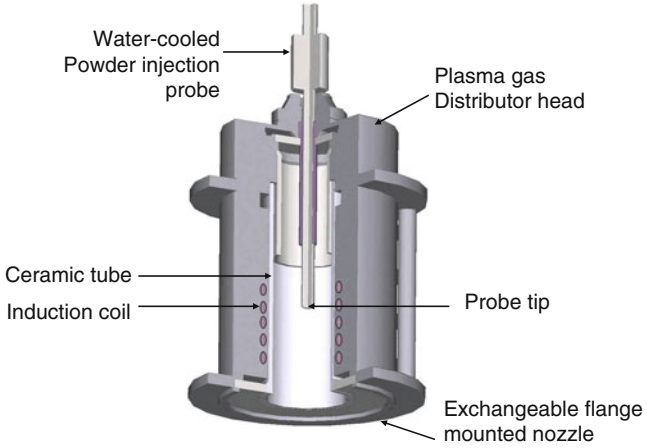


Fig. 2.12 RF induction plasma-spraying torch of Tekna (courtesy of Tekna Plasma Systems Inc., Sherbrooke, Québec Canada)

A typical design of an induction plasma torch developed by Tekna Plasma Systems Inc is shown in Fig. 2.12. The torch consists essentially of a plasma confinement ceramic tube with its outer surface cooled using a high-velocity thin-film water stream. A water-cooled induction copper coil surrounds the ceramic tube creating an alternating magnetic field in the discharge cavity. On ignition a conductive plasma load is produced within the discharge cavity, in which the energy is transferred through electromagnetic coupling. An internal gas flow introduced through the gas distributor head insures the shielding of the internal surface of the ceramic tube from the intense heat to which it is exposed. The hot plasma gases exit the torch cavity through the downstream flange-mounted nozzle. For plasma torches with r.f. power ratings between 30 up to 100 kW (mostly used in plasma spraying) and plasma gas flow rates of 50–100 slm, the bulk plasma temperature is between 8,000 K and 10,000 K, and the mean exit plasma velocity is below 100 m/s. As shown in Fig. 2.12, these torches allow for the internal axial injection of the powder or precursor, into the center of the discharge cavity using a water-cooled powder injection probe. Such torches work at pressures between 30 and 100 kPa, thus requiring a controlled atmosphere spray chamber. For more detail about the process see Chap. 8.

RF plasmas are well suited [36] for materials processing when a long dwell time of particles in the plasma is advantageous. They also offer the possibility to use reactive gases to alter or modify the particles in flight, and there is no contamination by electrode materials (no electrodes). It is a niche technology, with a big commercial success for spray powder preparation such as particle densification and spheroidization (not exclusively for spraying), as illustrated in Fig. 2.13.

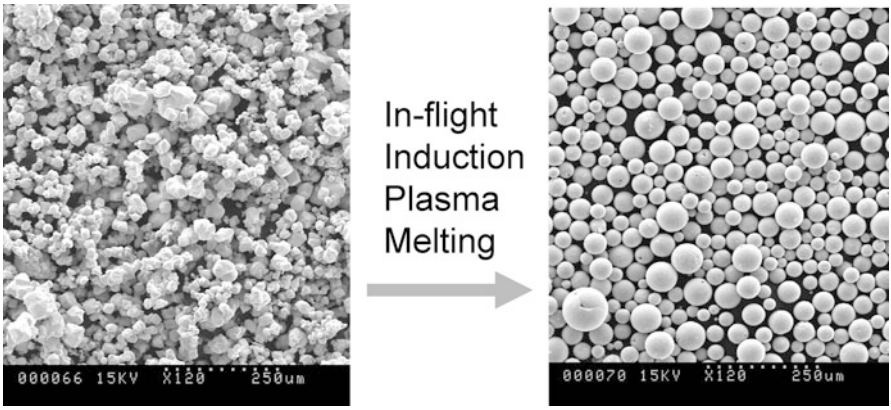


Fig. 2.13 Spheroidization of tungsten particles: initial particles diameter $d_{50} = 78$ μm, $\rho_o = 7{,}400$ kg/m3, after plasma treatment $d_{50} = 69$ μm, $\rho_o = 11{,}600$ kg/m3 (courtesy of Tekna Inc., Sherbrooke, Canada)

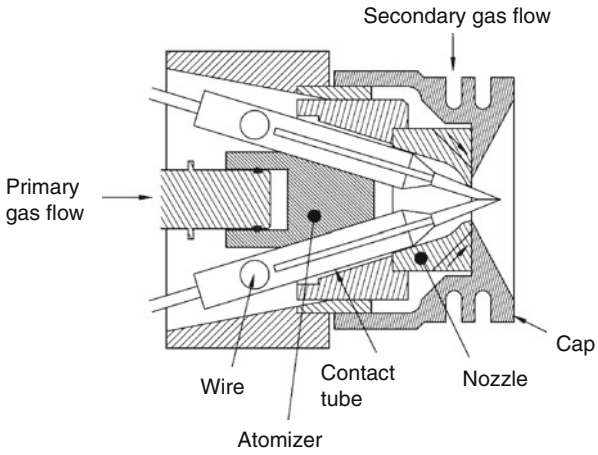


Fig. 2.14 Schematic of the wire arc spray device [37], reprinted with the kind permission of Elsevier

2.5.7 Wire Arc Spraying

This process is "a thermal spray process in which an arc is struck between two consumable electrodes of a coating material, compressed gas is used to atomize and propel the material to the substrate" [28]. In this process, shown schematically in Fig. 2.14, the two wire tips (one is the cathode and the other the anode) are continuously melted and fragmented into droplets by air jets injected with more or less sophisticated nozzles [2]. Gas velocities are a few hundreds of m/s but the gas is practically not heated by the arc, allowing one to keep the substrate temperature below a few tens of °C without cooling. Arc power levels are generally

between 2 and 10 kW, airflow ranges from 0.8 to about 3 m^3/min. The temperature within the arc can be higher than 20,000 K but the corresponding volume is relatively small. Particles are generally heated to temperatures above the melting temperature. For more details about the process see Chap. 9.

One of the main advantages of the process is the lack of substrate heating, very convenient for low-melting point substrates such as polymers. The second advantage is that the process is well suited to high-rate deposition primarily for coatings against corrosion (zinc, aluminum, zinc–aluminum) with arcs operated up to 1,500 A (with 400 A or less in conventional guns). Coatings are rather porous; contain resolidified particles and oxides (up to 25 wt%). Soft coatings can be densified by online shot peening just after deposition. Zinc is particularly efficient as cathodic protection against corrosion, especially when impregnated with epoxy paints, sealing the porosity in the coating. This process is extensively used for the protection of steel bridges.

2.5.8 Plasma-Transferred Arc Deposition

This process is "a welding process utilizing plasma. Instead of using neutral plasma, the arc is transferred to the substrate (the anode). Powder is fed into the plasma, heated, and fused to the substrate. Coatings are similar to weldments" [28]. To achieve welding the substrate (the anode) as well as the coating material must be metallic. Welding implies the formation of a molten pool on the substrate surface, which must not be blown out by the plasma flow. The plasma velocity must be low: large nozzle i.d. with a short length, low-gas flow rate, argon as plasma-forming gas with flow rates below 0.5 g/s. Figure 2.15 [38] shows a typical PTA gun. The transferred arc stability is very often improved by using an auxiliary arc between the cathode and the torch nozzle, the nozzle thus becoming an auxiliary anode at a lower potential than that of the substrate. Particles are introduced into the arc where they are heated but not melted. They stick onto the substrate where the transferred arc melts them. Depending on the gun power rather high-powder flow rates can be deposited (up to 30 kg/h). At higher power levels and higher velocities, the process allows reducing drastically the mixing of the molten materials of the substrate and the coating. It is also possible to inject two different types of powders: a metal powder close to the nozzle exit and heated below their melting temperature, and a ceramic one close to the molten bath to be included unmolten within the coating. An example of such a coating on the tooth of an excavator is presented in Fig. 2.16a, with a cross section of the coating (Fig. 2.16b) showing a good dispersion of WC irregular particles (with no evidence of melting and spheroidizing). For more details about the process see Chap. 10.

PTA deposition is generally performed on horizontal surfaces and is usually mechanized; such coatings on electrically conductive materials are often used for applications requiring repetitive operations. Compared to thermal coatings, a PTA deposit is generally more localized, denser, and metallurgically bonded to the base.

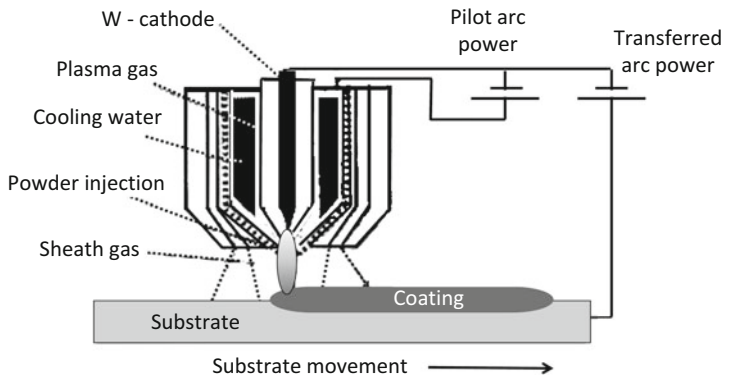


Fig. 2.15 Schematic of plasma-transferred arc (PTA) deposition [38]



Fig. 2.16 (**a**) PTA-coated tooth of excavator with Ni base coating + WC (25 kg/h) and (**b**) cross section of the coating (courtesy of Castolin)

The absence of slag removes a source of impurities. The coating is smoother and more uniform because melting takes place with a slow plasma flow and an inert gas shroud. The selection of coating materials is limited as well as the kind of substrates that can be used (for example, aluminum alloys cannot be treated by conventional PTA).

2.6 Material Injection

2.6.1 Powder Injection

Sprayed powders have sizes typically between about 10 μm and 110 μm, except for PTA where they can reach 200 μm. However, the choice of the size distribution is a key issue for the coating quality. It must be chosen according to the material sprayed, especially the difficulty of melting it, and a size distribution as narrow as possible to

limit the particle trajectory dispersion. It is important to keep in mind that the injection force of a particle is proportional to its mass, itself depending on the cube of its diameter! Particle injection is performed with an injector (in most cases a straight tube, with an internal diameter between 1.5 and 2 mm). Particles, carried by a carrier gas, collide between themselves, and the injector wall resulting in a slightly divergent particle jet at the injector exit (conical jet shape with an angle between 10 and 20°). The divergence angle increases when the particle sizes are below 20 μm and their specific mass is lower than 6,000 kg/m^3. Compared to the gas, particles have much more inertia, thus with curved injectors they will be slowed down by their friction with the curved wall, and a homogeneous distribution will be restored only 4–6 cm downstream of the bend. For more details about injection see Chap. 4.

Powders are generally characterized by their minimum and maximum diameters: for example, 22–45 μm. This means that less than 10 vol.% of the powder is below 22 μm and less than 10 vol.% is over 45 μm. However particles with the same size distribution and same chemistry can be very different. Particles can be produced through different manufacturing processes resulting in different morphologies, characterized by different densities or specific masses, various thermal conductivities, and different flow abilities (see Chap. 11). Depending on its morphology, the same particle, for a given injection velocity will have different trajectories and thus different heat and momentum transfers.

Depending on the spray gun used, powders are introduced into the energetic jet either radially or axially. Radial injection is used with d.c. plasma guns and some of the HVOF guns and sometimes in cold spray. To illustrate the radial injection, plasma spraying has been chosen, as illustrated in Fig. 2.1 from Seyed [16]. As the injected particles have divergent trajectories at the injector exit, their trajectories within the jet are also dispersed and they hit the substrate with different velocities and temperatures and of course different melting stages. For the particle penetration into the jet, it is mandatory that their mean injection force be about the same as that given to them by the energetic gas [39]. The optimum mean trajectory corresponds roughly to an angle of about 3.5–4° with the torch axis. Figure 2.17a illustrates the interaction of particles with the jet. The injection acceleration is imparted to particles by the carrier gas (see Chap. 4 where the equations for particles movement are presented in Sect. 4.2.1). The gas gives to particles of different sizes a mean velocity, which is almost independent of their size [39] and the gas velocity in the injector is also almost constant (with internal diameters of the injector below 2 mm, the Reynolds number is larger than 2,000 corresponding to turbulent flows). Thus the acceleration of particles, with a given diameter, depends only of carrier gas flow rate (see Eq. 4.4). In Fig. 2.18a the trajectory of one particle of mass m_p is optimal [39] for an acceleration γ_{p2}, where it corresponds to a trajectory making an angle of 3.5–4° with the jet axis. In contrast, the particle with the same mass but a lower acceleration γ_{p1} hardly penetrates the jet while that with a higher acceleration γ_{p3} crosses it. The major problem is, however, that particles have a size distribution with, in the best case, a value of 2 for the ratio of the larger diameter to the smaller one, corresponding to a mass ratio of 8! Thus trajectories will be necessarily dispersed as shown in Fig. 2.19 illustrating the envelope of particle trajectories

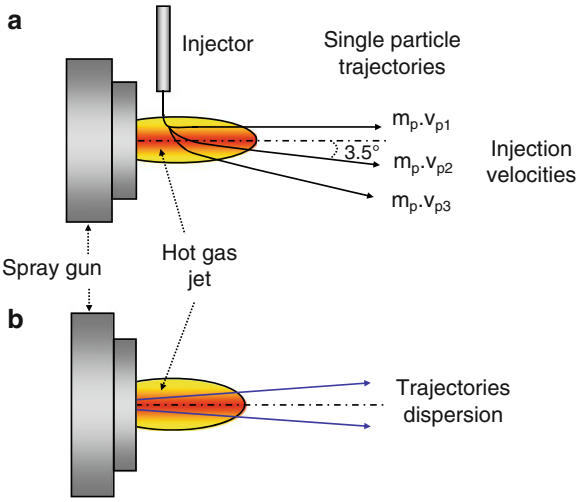


Fig. 2.17 (**a**) Trajectories of single particle injected radially with the same mass but with different injection velocities and (**b**) dispersion of particles injected axially

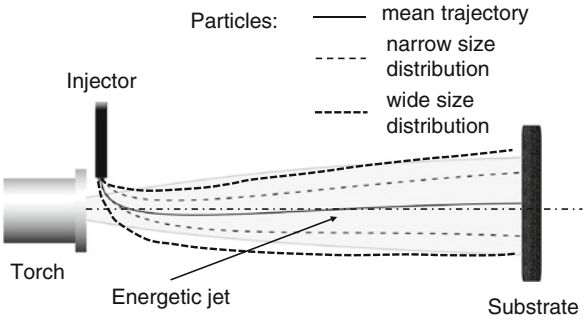


Fig. 2.18 Envelope of trajectories of particles injected radially for two powder size distributions (with one larger than the other) with the same mean size and same optimum trajectory

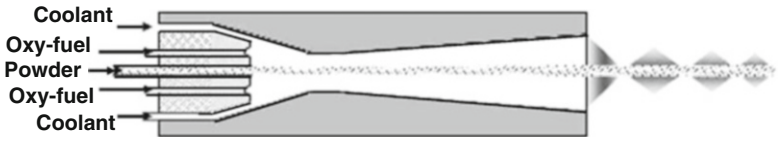


Fig. 2.19 Schematic of the axial powder injection in a HVOF gun. Reprinted with kind permission from Springer Science Business Media [40], copyright © ASM International

for two powder size distributions (with one larger than the other) with the same mean size and the same optimum trajectory. The mean trajectory is determined for the mean particle size. One can easily imagine the problem if the diameter ratio is 10 resulting in a mass ratio of 1,000!

The position of the injector relative to the nozzle exit (external or internal injection) and the torch axis plays also a key role [39]. The particle acceleration must be higher for an injection internal to the nozzle (the jet has not yet expanded).

It can be reduced with external injection, this reduction increasing with the distance from the nozzle exit due to the jet expansion. The injector must not be too close to the jet to avoid its overheating which could induce particle melting inside the injector and clogging. On the other hand, if the injector is too far away from hot gases, the injected particles bypass the plasma or flame jet.

The injection using a carrier gas is impossible for particles below 5–10 μm in diameter because the particle injection acceleration, and thus the carrier gas flow rate, would have to be increased as the square of the particle diameter. The acceleration by the carrier gas depends on the cross section of the particle (see Sect. 4.3.1) and the necessary amount of carrier gas to achieve the same acceleration of a 10 μm particle compared to a 40 μm one (16 times higher) perturbs considerably the plasma jet [39]. Moreover most powder feeders are not adapted to such small particle sizes.

Axial injection, as shown in Fig. 2.17b, is used in cold spray, flame spraying, part of HVOF spraying, certain d.c. torches such as the Mettech Axial III torch, D-gun, and RF plasma spraying. The dispersion of particles is due to on the one hand their collisions between themselves and with the injector wall and on the other to the flow turbulence. Their acceleration is much less critical than with radial injection. However when the gases flow in the spray gun is rather low, as with flame or r.f. spraying, a too high injection acceleration can perturb drastically the hot gas interaction with particles. To illustrate axial injection, the HVOF gun, shown in Fig. 2.19 from Dolatabadi et al. [40], has been chosen. As in the case of radial injection, particles at the injector exit have slightly divergent trajectories, and this divergence must be controlled to avoid that particles hit the nozzle wall, especially where the cross section is the smallest at the nozzle throat. Compared to radial injection, the particle dwell times in the hot zones of the energetic gases are longer with axial injection. The initial velocities, conferred to particles by the carrier gas are less critical than with radial injection because the gas, the flame, or the plasma flow entrains the particles, but the final particle velocities depend on their initial velocities.

Radial injection allows spraying simultaneously particles with very different properties such as ceramic and metals by using two or more injectors located at different positions. This is illustrated in Fig. 2.20 representing the injection of two different powders with two opposite injectors, thus allowing the adaptation of the carrier gas flow rates to each powder. In this figure different configurations of multi-injectors are also shown.

2.6.2 Wire, Rod, or Cord Injection

Wires, as those shown in Fig. 2.21a, are necessarily made of ductile materials. They are supplied wound on plastic spools. Their diameters are typically in the range between 1.2 and 4.76 mm. Larger, stiffer wires ($d > 2$ mm) are more difficult to feed as uncoiling requires more force and larger wire tension. Nonductile materials

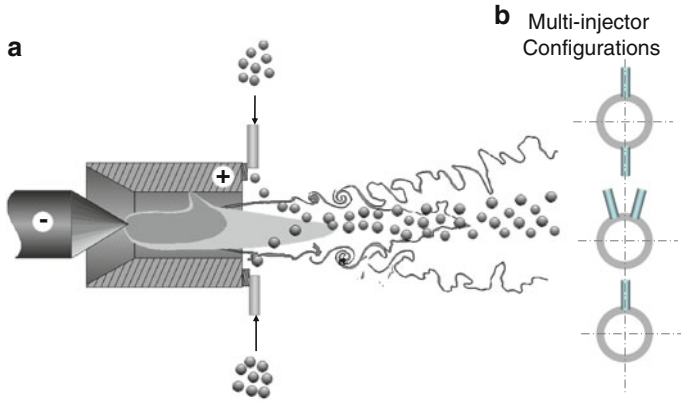


Fig. 2.20 (**a**) Injection of two different powders with opposite radial injectors and (**b**) illustration of possible configurations of radial injectors [16]

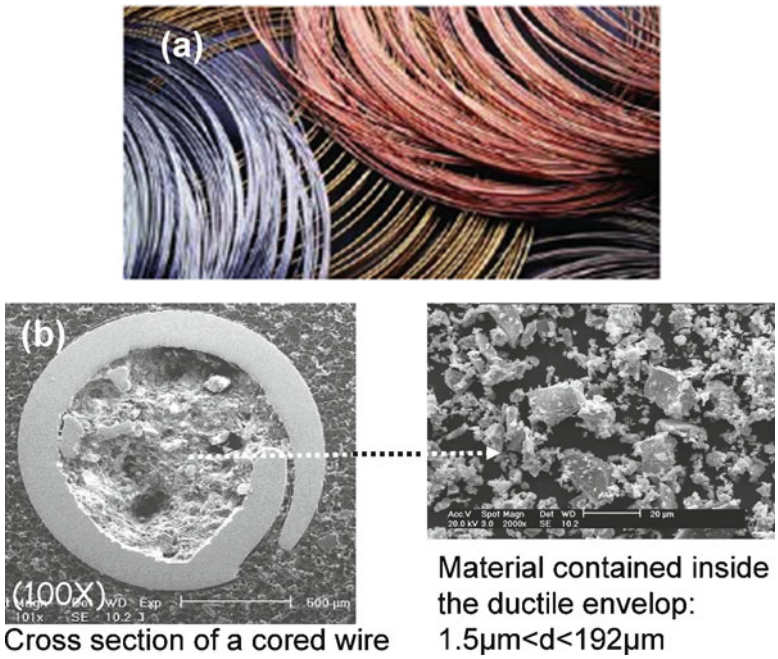


Fig. 2.21 (**a**) Different wires from Sulzer Metco (courtesy of Sulzer Metco) and (**b**) cored wire cross section

can also be used in cored wires. They consist of an outer sheath made of a ductile material surrounding one or more powdered nonductile metals or ceramics, as shown in Fig. 2.21b. Rods and cords are mainly used for ceramic materials. Rods of ceramic materials 3.16, 4.75, 6.35, or 7.94 mm in diameter have a limited length of 608 mm, which corresponds to spray times of a few minutes. Cords are made of a cellulosic or plastic casing filled with ceramic particles. The ceramic particles are within either an organic binder which starts decomposing at 250 °C and has completely disappeared at about 400 °C, or within a mineral binder such as bohemite, $Al(OH)_3$, which keeps them together up to close to their melting temperatures. Compared to rods, cords are supplied on plastic spools and their length is 120 m allowing spraying for hours. Their diameters are between 3.16 and 6.35 mm.

Wire, rod, and cords are introduced into the torch by simple mechanical devices consisting of electrical- or air-driven motors [2, 4], drive rolls, and associated speed controllers. It is of primary importance to maintain a very stable feeding rate of the material into the flame, plasma, or wire arc. The torque of the motors must be high enough to overcome the friction of the system. Drive rolls must grip the wire, rod, or cord sufficiently to prevent slipping, while not deforming the wire or crushing the rod or cord. The feeding of wires is achieved by systems, which pull only, push only, or push and pull, the latter being more complex because of the need to synchronize the two drive motors. Besides the wire guides and drive wheel geometry, critical feed issues include wire tension, wire straightness, wire diameter consistency, and wire surface characteristics.

The steady motion of the wire, rod, or cord must be adapted to the gas composition and flow rate as well as to their diameter and composition. If the wire velocity is too high, the tip cannot melt because its residence time in the flame is too short. When using low-velocity spray guns, such as a flame gun, the molten material is atomized and accelerated by an auxiliary gas fed into the spray gun. The compressed atomizing gas (generally air), fed around the flame (see Chap. 5), creates liquid metal sheets, which are disintegrating, their flapping motion is responsible for creating showers of drops. The size distribution of drops and their divergence angle depend strongly on the atomizing gas nozzle design and its flow rate. When using HVOF, instead of flame, the melted wire tip can be atomized directly by the hot gas flow.

Compared to powder feeding, the advantage of devices working with wires, rods, and cords is that *only fully melted drops are directed toward the substrate*. The way the molten wire tip form droplets has been the subject of extensive study for wire arc spraying [41]. The atomizing gas deforms the molten tips into sheets of molten metal which become self aligned in the flow, the instabilities creating droplets at their extremities (see Fig. 2.22).

For example, in the wire arc spray process, the control of the wire velocity is obtained through the control of the arc voltage, the latter depending strongly on the distance between both wires.

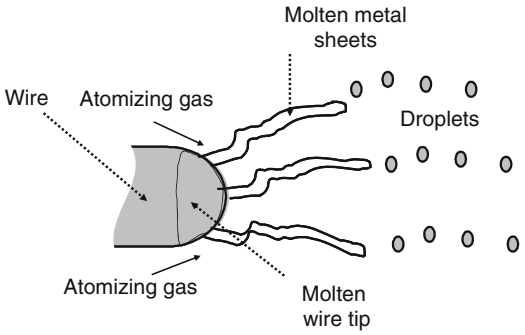


Fig. 2.22 Schematic of droplet detachment from the tip of a molten wire by the atomizing gas

2.6.3 Liquid Injection

For deposition of coatings with nanometer-sized structure, liquids (suspensions or solutions) are injected into the hot gases in the thermal spray processes. To assure sufficient energy to compensate for the cooling of the hot gases by the evaporation of the liquid and the heating of the vapor, processes where the gases have a sufficient enthalpy are used, such as HVOF or plasma spraying [17]. The liquid can be injected either by atomization with a gas or by mechanical injection (for details see Chaps. 5 and 14).

2.6.3.1 Gas Atomization

Very often coaxial atomization is used. This process consists of injecting a low-velocity liquid inside a nozzle where it is fragmented by a gas (usually Ar because of its high-specific mass) expanding within the nozzle bore [42]. The atomization is affected by the following parameters: the relative velocity liquid–gas, the ratio of the gas to liquid volume flow rates, called RGS (generally over 100), or the mass ratio between gas and suspension, called ALR (below 1), the nozzle design, and the properties of the liquid (density, surface tension, dynamic viscosity). The drawbacks of this atomization are the space, droplet diameter range (typically 5–100 μm for an air cap atomizer), divergence of the atomized droplet jet, and droplet velocity distribution (see Chaps. 4 and 14). Moreover, the atomizing gas can also perturb the hot gas flow.

2.6.3.2 Mechanical Injection

Two main techniques are possible: either to have the liquid in a pressurized reservoir from where it is forced through a nozzle of given diameter, d_i, or to add to the previous setup a magnetostrictive rod at the back side of the nozzle which superimposes pressure pulses at variable frequencies (up to a few tens of

kHz). The reservoir is connected to an injector consisting of a stainless steel tube with a laser-machined nozzle with a calibrated injection hole. The drawback of the system is that the reservoir pressure varies as the inverse of the fourth power of d_i. According to this relationship, if for a given liquid flow rate the pressure is a few tenths of MPa with a nozzle of 150 µm internal diameter, the required pressure becomes a few tens MPa if the nozzle i.d. is reduced to 50 µm (the pressure is multiplied by 81). The liquid exits the nozzle with a constant diameter jet, which is between 1.2 and 1.8 times the nozzle i.d. depending on the nozzle shape and reservoir pressure. After a distance of about 120–150 times the injector nozzle internal diameter, instabilities can be observed in the jet and a stream of uniform droplets is observed (see Sect. 4.5.1).

When using a magnetostrictive drive rod at the backside of the nozzle, giving pressure pulses with a frequency of up to 30 kHz, droplets with a constant diameter are produced, having a specific velocity. A constant distance separates these droplets.

In all these injection methods, the key issue is to control the size and the velocity of the droplets. Mechanical injection offers a controlled velocity and a constant size, although it may not be simple to achieve drop diameters below 100 µm. This control is by far more difficult with gas atomization. Besides having a distribution of droplet sizes, droplets have a more or less broad velocities distribution and the trajectories show different dispersion spray angles (see Chap. 4). Thus the injection control is sometimes tricky. For more detail about liquid injection see Chaps. 4 and 13.

2.7 Energetic Gas–Particle Interactions

2.7.1 Momentum Transfer

The particle trajectory within the high-energy jet depends on its acceleration $\frac{\partial v_p}{\partial t}$, which is linked to the force exerted on it. This acceleration is given by

$$\frac{dv_p}{dt} = \frac{18\mu_g}{\rho_p \cdot d_p^2}\left(v_g - v_p\right) \tag{2.1}$$

where μ_g and v_g are the gas viscosity and velocity respectively, ρ_p, d_p, and v_p the specific mass, diameter, and velocity of the particle.

From Eq. (2.1) it is obvious that the particle acceleration increases if the specific mass of the particle material decreases as well as its diameter, and if the gas viscosity and its velocity increases. Typical velocities of particles with their mean size range for different spray guns are summarized in Table 2.2. For more details about momentum transfer see Sect. 4.2.

According to the particle size distribution (generally Gaussian) and injection acceleration vectors, which are not all parallel to the injection axis, particles have a

Table 2.2 Typical particle size range and velocities with different spray guns

		Powder flame	Wire flame	HVOF	D-gun	d.c. plasma	r.f. plasma	Wire arc	PTA
Particle size range (μm)	Metal	10–90	Wire	<45	<45	10–90	<150	Wire	0–200
	Oxides	No	Rods–cords	<15	<15	<45	<90	No	0
Particle velocities (m/s)		<100	<200	200–700	<1,200	<350	<100	<200	20–30

rather wide distribution of trajectories within the jets and a rather broad range of velocities. It is the same with molten droplets resulting from wire, rod, or cord atomization.

2.7.2 Heat Transfer

The heat transfer mechanisms between a hot gas and a single sphere are mainly those resulting from gas convection and radiative loss of the particle to its surroundings (for details see Sect. 4.3). In the following, to simplify the presentation only the basic assumptions will be considered. For example, the heat propagation within the heated particle, depending on the value of its thermal conductivity relatively to that of the hot gases, will not be considered (for details about it, see Sect. 4.3.3). The heat from the hot gas q_{cv} (W) depends on the heat transfer coefficient h (W/m^2 K), the particle surface a (m^2), and the gas temperature T_s (K). The main energy loss of the hot particles, especially for high-temperature particles (>1,800 K), is the radiative loss to the surroundings. It is characterized by the global emission coefficient ε of the particle and the Stefan–Boltzmann radiation constant σ_S(5.671 × 10^{-8}W/m^2 K^4). Finally the most important term is the energy (J) necessary to melt the particle:

$$\int_0^{\tau} Q_{\text{int}} \cdot \mathrm{d}t > m \cdot c_p \cdot (T_m - T_0) + m \cdot L_m = Q_F \tag{2.2}$$

where τ is the residence time of the particle in the hot jet, m the mass of the particle (proportional to the cube of its diameter), c_p the specific heat (J/kg K), and L_m the latent heat of melting (J/kg). The residence time depends on the length of the hot jet and the particle velocity. These equations define the requirement for melting a particle by Q_L (J m$^{3/2}$/kg$^{1/2}$) [43]:

$$Q_L = \left(m \cdot c_p \cdot (T_m - T_0) + mL_m\right) / \sqrt{\rho_p} \tag{2.3}$$

Table 2.3 summarizes some values of Q_L for different materials. It can be seen that it is not necessarily materials with the highest melting temperature which are

Table 2.3 Values of Q_L for different materials

	T_M (°C)	c_p (J/kg K)	L_m (kJ/kg)	Q_F (kJ/kg)	$Q_L = Q_F/\sqrt{\rho_p}$
Al_2O_3	2,313	1,090	1,095	2,564	27.07
Mo	2,890	251	290	1,010	10.25
Ti	1,933	527	376	1,338	27.87
ZrO_2	2,677	566	769	2,272	30.09

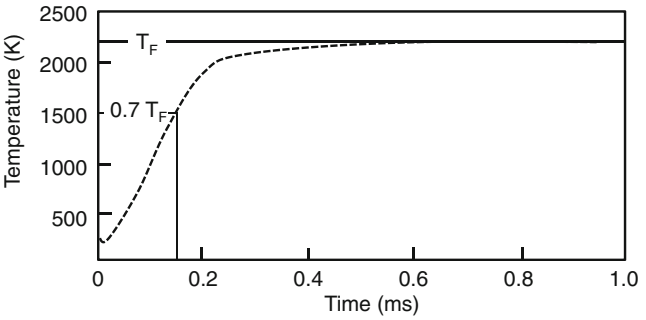


Fig. 2.23 Temperature evolution for a single particle immersed in infinite plasma at temperature T_F

the most difficult to melt, provided the gas temperature is a few hundreds of °C above the particle melting temperature.

Another important point is that when heating a single particle in an infinite medium at a uniform temperature, T_F, the particle temperature reaches that of the medium very slowly once its temperature is above about $0.7 \times T_F$ (see Fig. 2.23).

This means that when injecting a particle into a hot medium, with a limited length, particles will hardly reach 0.7 times the flame temperature. For example, with an acetylene-oxygen flame at about 3,000 K, it will be difficult to melt particles requiring heating above a value of 2,100 K. With a plasma jet at over 8,000 K, any material can be melted. Of course, this consideration does not apply when using wire, rod, or cord, the residence time of the wire tip being much longer than that of a particle (about 1 ms). Thus, it becomes possible to reach temperatures up to 0.9–0.95 times that of the flame. For a stoichiometric acetylene–oxygen flame at about 3,400 K, a zirconia rod or cord can be melted.

When the particle temperature approaches its melting temperature, particle melting and evaporation starts with the evaporation rate increasing rapidly as the boiling temperature of the material is approached. This means that it will be almost impossible to spray materials for which the melting temperature is not separated by at least 300 K from its boiling temperature (the deposition efficiency will become very low). The same considerations apply if instead of vaporizing, the material decomposes, which explains why it is generally difficult to spray most nitrides, carbides, and borides.

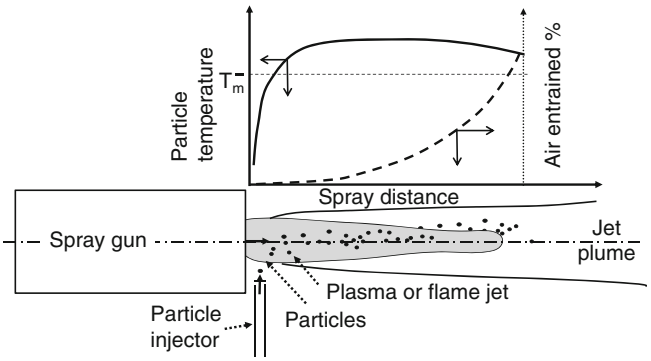


Fig. 2.24 Schematic of the air entrainment within the hot plasma jets as function of the spray distance and particle temperature evolution

Finally, due to the dispersion of their trajectories, hot particles within the jet are not uniformly distributed. The energy radiated by the hot particles can be approximated by a Gaussian distribution over the jet diameter at a specific axial location. Any variation of the spray parameters, for example, arc current or plasma-forming gas with a d.c. plasma torch, modifies the force the hot gases impart on the particles as represented by $S_p \cdot \rho \cdot v^2$; where S_p is the projected surface of the particle, ρ and v the specific mass and velocity of the high-energy plasma jet. Thus changing the carrier gas flow rate to keep an optimum mean trajectory is essential to modify the injected particle accelerations. *The key issue is that the carrier gas flow rate must be adjusted as any of the spray parameter is modified*. For more detail about particle trajectories and heat transfer see Chap. 4.

2.7.3 Effect of the Surrounding Atmosphere

Most spray processes are operated in air (atmospheric spraying). Air, or the surrounding gas if spraying is performed in a controlled atmosphere chamber, is always entrained by the high-energy jet. Thus, when spraying in air, entrained oxygen (diatomic or monoatomic in case of plasma) can react with the sprayed materials. The penetration of the entrained air in the jet increases with the distance from the nozzle exit with the expansion of the jet. For example, for a d.c. Ar–H_2 plasma jet, the entrained air penetration in the jet is limited (less than 30–40 vol.%) during the first 40–50 mm from the torch nozzle exit. Further downstream the jet becomes more and more oxidizing. At 100 mm more than 95 vol.% of the hot gas mixture is air at temperatures in the 2,500–3,500 K range (see Fig. 2.24).

2.7.3.1 Particle In-Flight Oxidation

The Arrhenius law controls the oxidation kinetics: the rate of change of concentration of a given species is proportional to the specific reaction rate constant k. The Arrhenius form of k is

$$k = A \ \exp\left(-E_A/k_B T\right) \tag{2.4}$$

where, A is a term accounting for the collision terms with mild temperature dependence, k_B is the Boltzmann constant, and E_A the activation energy of the reaction. Roughly, k increases by one order of magnitude when T increases by 100–200 K. Thus oxidation reactions will be strongly promoted when sprayed materials are heated to high temperatures. This is especially the case when the temperature is above the melting temperature where, besides the diffusion phenomenon, oxidation can be promoted by the convective movement induced within the fully melted particle by the hot gas flow around it. This situation is encountered under certain conditions in plasma, HVOF, and wire arc spraying. In that case, internal recirculation within the particle is responsible for continuously bringing fresh metal to the particle surface, while molten oxide or oxygen is entrained inside the molten particle. Compared to diffusion-controlled oxidation, the oxide content of the particle is such a case can be larger by a factor of 4 to 6!

This situation is important when the Reynolds number relative to the particle is higher than 20, and the ratio of kinematic viscosities of the gas to the liquid particle ν_g/ν_p is higher than 50 [44]. The phenomenon is particularly important when the melting temperature of the oxide is close to that of the metal, for example, in low carbon and stainless steel. The convective oxidation can result in the formation of up to 15 wt% of oxide with low-carbon steel. For more details see Sect. 4.3.3.7. To limit the oxidation of the particle, its temperature must be kept as low as possible. This is possible when increasing the particle velocity to spray it close to or below its melting temperature, as with the D-gun or high-pressure HVOF. Increasing the particle velocities also reduces their residence time within the hot gas stream where oxidation reactions occur. Of course, when using cold spray, particle temperatures are kept below a few hundred °C, suppressing or limiting the effects of high temperatures: melting, evaporation, decomposition, gas release, and oxidation.

2.7.3.2 Substrate and Successive Passes

Substrate oxidation occurs during the preheating stage before spraying; preheating performed to get rid of adsorbates and condensates. This preheating (at temperatures between 200 and 400 °C depending on the substrate material), which can also result in the partial oxidation of the substrate surface, is generally performed with the spray torch, at least when the part dimensions are not too large (less than 1 m). By controlling the preheating rate, depending on the distance and

relative torch–substrate velocity, the preheating time, and temperature, substrate oxidation can be limited. It is important to control this oxidation, especially with materials that oxidize easily, such as low-carbon steels. A thick oxide layer is generally not mechanically sound, and coatings are detaching from their substrate not because of poor coating quality, but due to the poor adhesion to the oxide layer on which they were sprayed! Once spraying has started, the substrate oxidation by the hot gases is relatively small. However, successive passes of the hot jet can increase oxidation when the coating does not consist of an oxide.

2.7.3.3 Chemical Reactions Other Than Oxidation

Chemical reactions can occur within particles in-flight and also during coating formation. Liquid–solid reactions occur within cermet particles when the ceramic particle, in the solid state, is partially dissolved in the surrounding liquid metal. One typical example is the dissolution of tungsten carbide grains (WC) in the liquid cobalt when spraying WC–Co particles. These reaction times are generally rather long (characteristic times of a few seconds) and are thus limited by the rather short flight time of the particles in the hot jets (a few milliseconds). However, these reactions, as is the case with all chemical reactions, are following Arrhenius law, and the reaction rate increases drastically with the particle superheat, for example when the cobalt matrix is above its melting temperature. This fact explains the better results that are obtained when spraying WC–Co particles with a HVOF gun (temperatures close to the Co melting point) compared to a plasma sprayed coating, where the cobalt is largely overheated.

The second type of reaction is that related to the synthesis of condensed materials by a "self-supported" heating generated by the exothermic reaction between components (SHS: self-propagation high-temperature synthesis). The reaction occurs between both materials within the particle as soon as the particle in-flight has reached the ignition temperature. Such reactions are longer than the residence time of the particle in the hot gas and they can continue after the deposition. A well-known example is the formation of NiAl when spraying particles made of a Ni core surrounded by an aluminum shell, or when spraying silicides, borides, carbides in form of agglomerated particles made for example of Ti–bronze and boron. For more details see Chap. 4.

2.7.3.4 Limiting Gas-Induced Reactions

At the end of the 1960s and at the beginning of the 1970s, inert gases have substituted air as the environment for plasma spraying. This can be achieved by spraying in a controlled atmosphere chamber either filled with a neutral gas (generally argon) or in a soft vacuum (≈10 kPa). As the process is rather costly in terms of gas consumption and equipment cost (up to one order of magnitude more than that working at atmospheric pressure in air) it is generally used only in

connection with conventional plasma spray equipment (gas flow rates below 100 slm). In controlled atmosphere spraying, the chamber walls are not necessarily cooled if the chamber volume is large enough (few m^3). The chamber air is removed with vacuum pumps and then the chamber is back filled with argon. The oxygen content is less than 7 ppm when a liquid argon source is used. Under these conditions the plasma jets are a little longer and wider than in air, because in air the dissociation of the entrained oxygen consumes a lot of energy and cools the plasma. As shown in Chapter 4, spraying in controlled atmosphere is not necessarily accompanied by an improvement of heat transfer between the plasma and the particles. The oxide content in the coatings is limited, however, to that already present in the sprayed powders.

Shroud nozzles have also been used, mostly with plasmas. The shroud nozzle is attached to the front of the plasma gun and a blanket of inert gas (argon or nitrogen) is used to displace air around the jet. Unfortunately high-inert gas flow rates are necessary (300–500 slm for conventional d.c. spray torches). Other types of shrouds supply a concentric sheath of inert gas between the hot plasma and the air. The flow rates are slightly lower. For more details see Chap. 7.

2.8 Coating Formation

2.8.1 Coatings from Fully or Partially Melted Particles in Conventional Spraying

Particles with given temperatures (above or close to their melting temperature) and velocities impact and flatten *on the prepared substrate* forming splats. The particle and substrate parameters playing a role in the particle flattening are summarized in Fig. 2.5. The critical particle parameters comprise the particle velocity and temperature at impact, the impact angle relative to the substrate (best results being obtained when the particle impacts perpendicularly to the substrate), the oxidation of the particle, and the temperature gradient within the particle (especially for low-thermal conductivity materials). Most particle flattening studies, for experimental reasons or modeling simplification, have been performed on smooth surfaces. For the substrate the key parameters are its surface roughness, as resulting from its preparation or from its oxidation (most substrates are made of metals or alloys) or both, and the substrate preheating temperature. The oxide layer thickness and composition also play an important role [20]. Modeling results of particle flattening on a smooth substrate are illustrated in Fig. 2.25 illustrating the flattening of a nickel droplets on a stainless steel substrate preheated to 563 K [45]. In experiments and models, the flattening time is in the range of a few μs, and the solidification time is longer though solidification starts before flattening is completed.

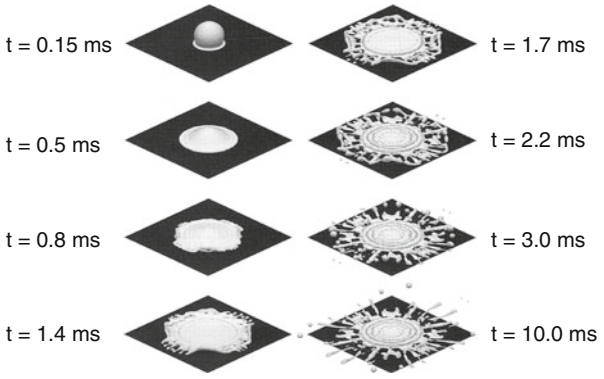


Fig. 2.25 Modeling of a nickel droplet ($d_p = 60$ µm) impacting on a smooth stainless steel substrate preheated at 563 K. Reprinted with kind permission from Springer Science Business Media [45], copyright © ASM International

As can be seen, after a relatively symmetrical flattening stage (up to 1.4 ms) digitations start to appear resulting in an extensively fingered splat. In fact, the phenomenon is very complex, depending on the dynamic wetting angles, drop surface tension and velocity, and on solidification taking place before flattening is completed and modification of the liquid flow [20]. For more details see Chaps. 4 and 13. Most experimental studies show that, for smooth substrates, above a critical preheating temperature, called transition temperature, T_t, [20, 46] splats are disk shaped, while below such a temperature they are extensively fingered. Among the different explanations the most plausible one seems to be the evaporation of adsorbates and condensates present at the substrate surface [20, 47]. Without this preheating and the evaporation of adsorbates and condensates, the local pressure under the flattening melted droplet increases rapidly resulting in the lifting of the liquid that is flowing on the substrate surface. Thus, compared to a surface where adsorbates and condensates have been eliminated, the contact surface between flattening particle and substrate is reduced by a ratio of 2 to 6 inducing the fragmentation of the liquid flow. For more details see Sect. 13.5.1.

For micrometer-sized particles, depending on their degree of superheat (above the melting temperature) and on their impact velocity (key parameter), for a substrate preheated above T_t, the ratio of the splat diameters, D, to the initial droplet diameter, d_p, is in the range $2 < D/d_p < 6$. For most sprayed materials on different substrates, the transition temperature is below $0.3T_m$ (T_m being the particle melting temperature). Thus the cooling rate of the flattening particle is practically not affected by the substrate preheating at the transition temperature. The flattening behavior of the drop above the transition temperature is mainly due to desorption of adsorbates and condensates from the substrate surface when preheated above T_t. The contact between the splat and the substrate represents up to about 60 % of the splat surface on substrates preheated above T_t, compared to possibly less than 20 % on cold substrates. Accordingly, when spraying on rough substrates preheated above T_t the coating adhesion is higher by a factor of 3 to 4 compared to that obtained on a cold substrate.

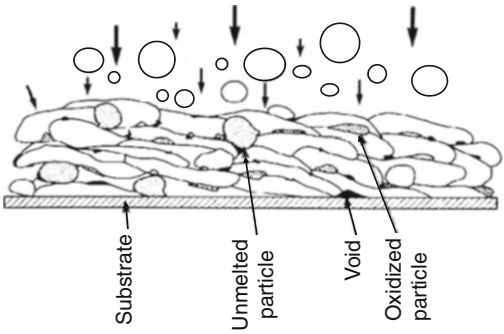


Fig. 2.26 Schematic cross section of a thermally sprayed coating

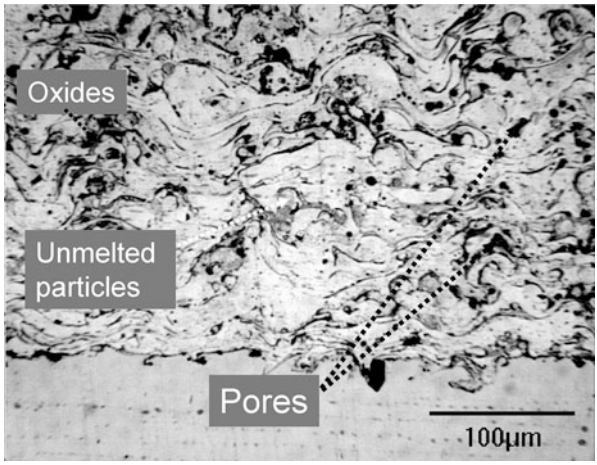


Fig. 2.27 Stainless steel coating (304L) deposited by air plasma spraying on a low-carbon (1040) steel substrate

The time between two successive impacts is typically in the range of ten to a few tens of µs. Thus the next particle impacts on an already solidified splat. The splat layering is controlled by the powder flow rate, the process deposition efficiency, and finally the spray pattern including the relative torch–substrate velocity. Coatings contain layered splats, porosities (often due to the poor ability of the flattening particle to follow the cavities present in the previously deposited layer), unmolten or partially melted particles, and oxides for metals and alloys. This is schematically illustrated in Fig. 2.26.

Coatings obtained by conventional spraying (sprayed particles with sizes of a few tens of micrometers) have thicknesses between about 50 µm and a few millimeters. Figure 2.27 presents the cross sections of a plasma-sprayed ($Ar–H_2$) stainless steel coating and Fig. 2.28 that of a plasma-sprayed yttria partially stabilized zirconia coating. Figure 2.28 shows all the coating characteristics shown in the schematic cross section in Fig. 2.26, but in Fig. 2.28 (YSZ coating) of course no oxidation is present, and the lamellar structure is more pronounced.

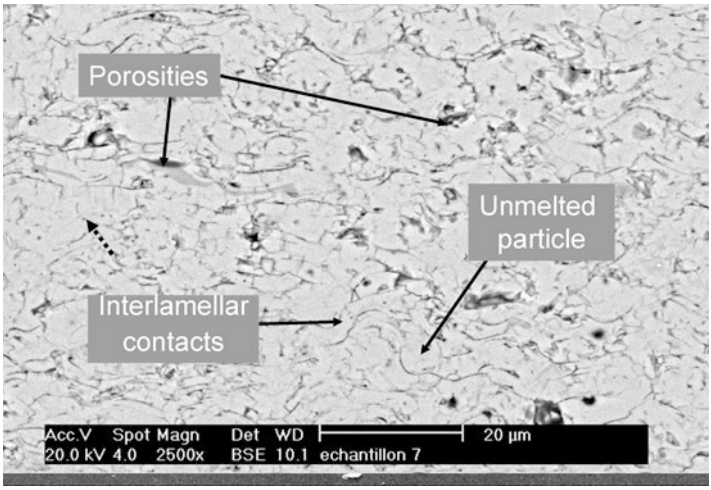


Fig. 2.28 YSZ (8 wt%) coating plasma sprayed on a super alloy

Cold-sprayed ductile particles are not melted at all at impact and they need a velocity above a critical value to form a coating. This critical velocity depends on the particle size, material, manufacturing process, and the substrate material and properties [22]. At the time when the substrate surface is placed in front of the impacting particle jet, none of the particles adhere to it and rebound. They only clean and deform the surface. After a certain "induction time" t_i, the particles begin to adhere in an avalanche-like manner, rapidly forming the coating. This induction time depends on the surface preparation [48]. The deposited particles of the first layer are little deformed and have a diameter D which is close to that of the impacting particle d_p ($D/d_p < 1.5$). For the next layers, upon impact particles are plastically deformed and the previously deposited ones are consolidated by the impact of the incoming ones. This is illustrated in Fig. 2.29.

Figure 2.29 demonstrates that such coatings can be obtained with porosities of far less than 1 %. The etching of sample cross sections reveals the internal grain boundaries of former spray particles and highly deformed grains close to particle–particle interfaces.

2.8.2 Adhesion of Conventional Coatings

2.8.2.1 Hot Particles

The bond between splats and substrate and afterwards between splat and already deposited layers is essentially mechanical. However in this case the splat diameter

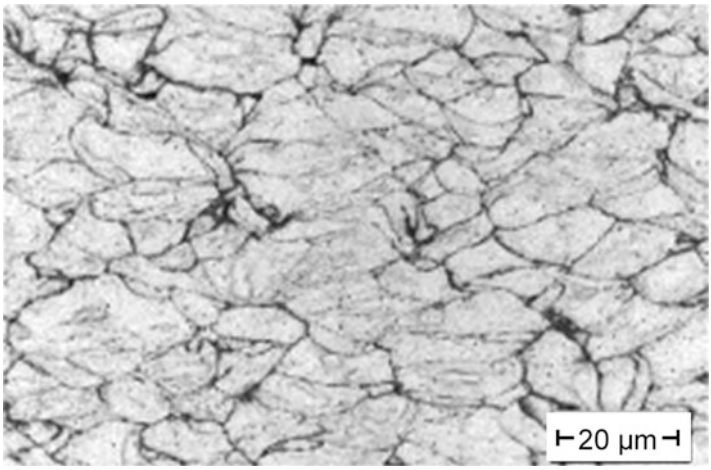


Fig. 2.29 Cu cold sprayed on Cu substrate with a trumpet-shaped standard nozzle (powder −22 + 5 µm; process gas N_2; temperature 320 °C; pressure 3 MPa): close-up view of the cross section revealing grain boundaries and particle–particle interfaces. Reprinted with kind permission from Springer Science Business Media [21], copyright © ASM International

has to be adapted to the peak heights. Roughly the splat diameter, D, must be such that

$$D = 2 - 3 \times R_t \tag{2.5}$$

where, R_t is the distance between the highest peak and deepest valley. If the splat diameter D is much smaller than R_t, the adhesion is poor. The distance between peaks is also of primary importance, because the liquid has to penetrate into the undercuts, and R_a and R_t do not account for this parameter. Thus another quantity must be considered: the root mean square value $R_{\Delta q}$ which is obtained from the local profile slope $dz(x)/dx$ of the roughness profile within the single measurement length (for details see Sect. 12.5.1). For example, for plasma-sprayed coatings on non-preheated substrates, even with the optimal roughness, the maximum coating adhesion is about 20 MPa, while with substrates preheated above the transition temperature, it is between 40 and 70 MPa. Desorption of adsorbates and condensates and sometimes the improved liquid drop–substrate wettability are responsible for the better adhesion. It must be noted that for splats impacting on already deposited layers, the liquid drop–substrate wettability is good (a liquid wets well a solid of the same material), and in most cases the next layers of splats impact on layers hotter than the substrate, especially if the sprayed material has a poor thermal conductivity as most oxides.

With the D-gun or high-power HVOF guns, particles must be at least in a plastic state at impact. This is particularly true for ceramic materials usually characterized by low densities and high melting points. The limitation in this case is not the

particle velocity, generally high, but the degree of melting or the plasticity. For example, for D-gun spraying, the presence of unmolten ceramic particles produces an erosive blasting effect both on the substrate and on the coating [49]. For particles in a plastic or molten state the impact of the new incoming particles results in an impact consolidation and densification of previously deposited layers (similar to shot peening effect).

Another type of adhesion is obtained when diffusion occurs between substrate and sprayed material. However, according to Eq. (2.4), this occurs only at high-substrate temperatures (about 0.6–0.7 T_m where T_m is the melting temperature), and *if the oxide layer at the substrate surface has almost disappeared*. Thus such adhesion is observed when spraying in soft vacuum a super alloy onto a super alloy substrate, and after destroying the oxide layer at the substrate surface with a reversed arc (substrate as cathode see Chap. 7).

Finally, chemical bonding can occur if the impacting droplet melts the surface and if both materials can make a new material. For that to occur, the particle effusivity e_p has to be larger than that of the substrate. The effusivity is defined as

$$e_p = \sqrt{\rho_p \cdot \kappa_p \cdot c_p} \tag{2.6}$$

where ρ_p, κ_p, and c_p are, respectively, the particle specific mass (kg/m^3), thermal conductivity (W/m s), and specific heat (J/kg K). This is the case, for example, if Mo particles are sprayed onto an iron substrate, liquid Mo can react with liquid Fe to form $MoFe_2$. For more details about particle adhesion in conventional spraying, see Sects. 13.5 and 13.6, and for submicrometric or nanometric ones, see Sect. 14.7.6.1.

2.8.2.2 Cold Particles

In the case of cold spray, the resulting splats are quite different because the deformation at impact is much less than that obtained with particles in a semimolten or molten state. Even if the adhesion process is not yet completely understood, authors agree that the high kinetic energy of particles impacting on the substrate results in cleaning and activation of the surface during what is called an induction time, generating favorable conditions for adhesion for the subsequently impacting particles [50]. As already mentioned, adhesion of the first particles to the substrate leads to a rapid increase in the number of particles attached to the substrate and consequently to the formation of a continuous coating. It seems that the plastic deformation at impact results in the rupture of superficial films, such as the oxide layer, and allows achieving an excellent contact between both pure metals at high pressure forming a metallurgical bond. Moreover, the impact of the next particle results in an impact densification of the previously deposited layers. The improvement of the contact quality increases with the impact velocity [51]. The critical velocity depends on the spray particle material and size distribution as well as the substrate material composition, roughness, hardness, and elastic modulus. For more details see Sects. 6.2.2 and 6.2.3.

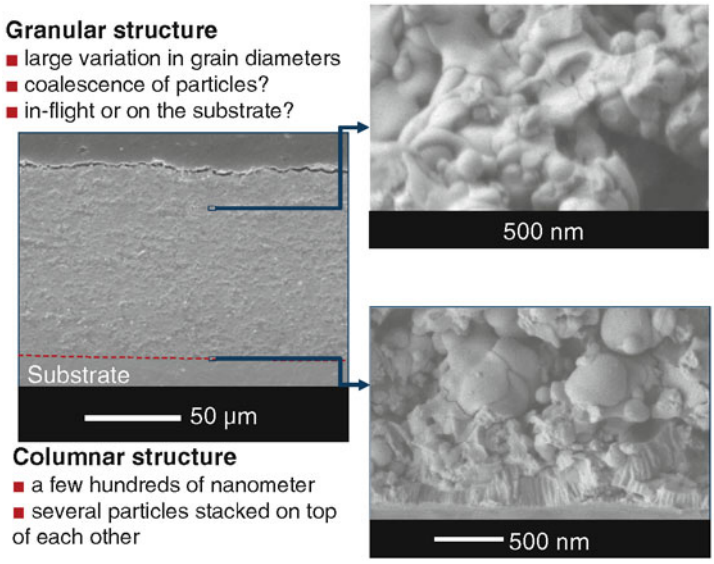


Fig. 2.30 Fractured cross section of YSZ suspension plasma sprayed (Ar–He 40–20 slm, 12 MJ/kg) onto a stainless steel substrate and detached from its substrate. Reprinted with kind permission from Springer Science Business Media [52], copyright © ASM International

2.8.3 Coatings Resulting from Solution or Suspension Spraying

At the present development stage, essentially oxide coatings or WC–Co coatings are deposited with solution or suspension spraying. For suspensions, solid particles contained in droplets, which have traveled in the hot jet core, are melted, will form splats on smooth substrates [17]. The splat diameters are at the maximum two times the initial particle diameters. Surprisingly, the corresponding coatings have a lamellar structure close to the substrate and a granular one above a few µm from the substrate as shown in Fig. 2.30.

This appearance is probably due to the very high heat flux imposed by the plasma jet at the spray distance of 3 cm (up to 40 MW/m^2) together with the Weber number of particles below 500. As the splat solidification is delayed by this strong heating, as soon as a sufficiently thick layer of zirconia has been deposited, the surface tension force takes over and the recoil phenomenon takes place. Therefore, such coatings are dense with pore sizes in the nanometer to the few hundreds of nanometers range and possess a granular structure completely different from the lamellar one obtained with conventional spraying, as illustrated in Fig. 2.32. Coatings deposited with this technology have thicknesses ranging from 5 µm to hundreds of micrometers, thus bridging the gap between coatings obtained through gaseous phase and thermally sprayed coatings.

For solutions, Gell et al. [53] have described the different mechanisms that included precursor solute precipitation, pyrolysis, sintering, melting, and crystallization. The droplet treatment by the plasma jet differs with their sizes: the larger particles correspond to the condensation of the precursor precipitating in the droplet periphery and the production of hollow spheres. Smaller droplets result in a uniform precipitation. Upon impact on the substrate, fully melted particles will produce splats as with suspensions and then, depending on spray conditions a granular structure, as with suspensions. If the standoff distance increases molten particles may resolidify and crystallize before impact. For droplets traveling in the low-temperature regions of the jet, some precursor solution can reach the substrate in liquid form (for more details see Sect. 14.7.6).

When most of the solution drops penetrate into the plasma core, mostly small droplets are obtained resulting in well-melted particles. Coatings are then dense as that shown in Fig. 2.30 suspension plasma sprayed. When drops are fragmented in the jet fringes, unpyrolized droplets are imbedded in the coating during its formation. Upon reheating by the plasma jet during the successive passes, these materials are pyrolized, sintered, and the resulting volume shrinkage promotes the formation of vertical cracks if the quantity of unpyrolized material is sufficiently high.

2.8.4 Residual Stresses

Stresses encountered during the spray process are [54]:

- *The quenching stress* (always tensile) due to cooling of each individual splat is increasing with the quality of the contact between the splat and the substrate or the splat and the previously deposited layer. This contact is improved by substrate preheating above the transition temperature.
- *The compressive stress* is due to particles impacting at high velocity (HVOF, D-gun, cold spray) equivalent to shot peening, and it can be affected by the coating temperature. These are often more important than the quenching stresses.
- *The temperature-gradient stress* develops especially within low-thermal conductivity coatings. This stress must be avoided and suppressing or reducing drastically the temperature gradients within the coating during its formation can achieve that.
- *The phase change stress* occurs when the crystal in a new phase after deposition is smaller or larger than in the preceding phase. This is for example the case when sprayed coatings essentially composed of γ alumina transform into α alumina at about 950 °C. This situation is generally encountered during service conditions, but it can also occur if too high temperature gradients are encountered during spraying of low-thermal conductivity materials. Such transformations must be avoided because ceramic coatings are generally destroyed when this transformation occurs.
- *The expansion mismatch stress* occurs during substrate and coating cooling from the mean temperature they had during spraying (deposition temperature) to room

temperature. This stress increases with the mean deposition temperature and the mismatch between the expansion coefficients of coating and substrate. Here also, for low-thermal conductivity coatings, a too fast cooling can induce damaging temperature gradients.

Of course, the final stress distribution within coating and substrate is the addition of all the previously described stresses, plus that created in the substrate by its preparation such as grit blasting. Service conditions will bring new stress, generally due to temperature gradients developed between coating surface and substrate interface either during heating or cooling phases. This stress will be added to the residual one and can result in coating detachment. The control of these different stresses, depends strongly on coating and substrate temperature during spraying, and is of primary importance for coating service conditions. With a too high residual stress, coatings can peel off, especially thick ones [54]. The level of stress-induced peeling-off depends on the coating toughness, which is drastically improved for nanostructured coatings.

2.9 Control of Coating Formation

2.9.1 Coating Temperature Control Before, During, and After Spraying

The temperature control of the substrate and coating before (preheating), during (spraying) and after spraying (cooling down) is of primary importance. Heating has to be controlled:

- During preheating with a temperature high enough to desorb adsorbates and condensates (substrate surface cleaning just before spraying during the preheating stage), but with the substrate oxidation limited as much as possible.
- At the beginning of spraying and during spraying of successive passes to limit the substrate oxidation.
- During spraying to control residual stresses formed during coating formation and then, when spraying is terminated, those due to the cooling of coating and substrate.

To limit as much as possible on the one hand the oxidation phenomena and on the other to control the stress distribution, it is necessary to control the preheating and deposition temperatures and keep them as constant as possible, especially within coating under construction when the sprayed material has a poor thermal conductivity. These temperatures depend on:

The heat flux from the hot gases during the preheating and spraying stages
The heat flux from the molten, or semimolten, droplets as they impact and stick to the substrate surface, during the spraying stage

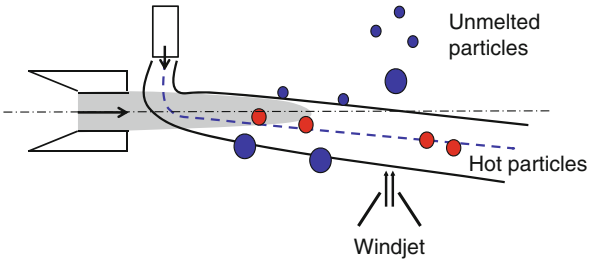


Fig. 2.31 Illustration of cold particles elimination by a windjet

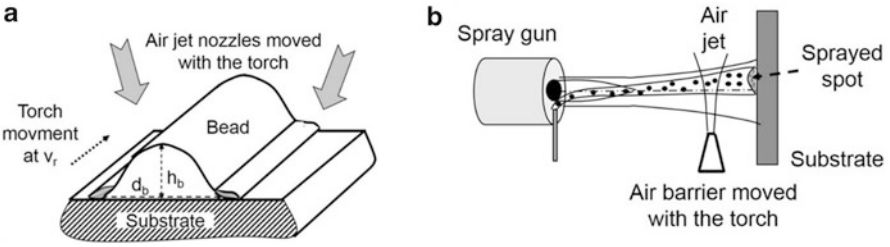


Fig. 2.32 Debris: (**a**) elimination by air jets and (**b**) reduction by an air barrier

The cooling systems used (during spraying and cooling stages). Two types of cooling systems are used with air as cooling medium: air nozzles fixed or moving with the torch and blowing onto the substrate and coating under construction, and/or wind jets moved with the torch and blowing orthogonally to the hot gases jet. Besides the reduction of the heat flux of the hot gases (up to a factor of 5), the wind jet allows eliminating those particles traveling in the fringes of the hot gas jet (see Fig. 2.31). Such particles, which generally are not melted, create defects in the coating when sticking between successive passes. The wind jet can separate them from those traveling in the hot core of the jet because their velocities are lower than those travelling in the jet core. This is achieved of course at the expense of a decrease of the in-flight hot particle temperatures (by less than 200 K) and velocity (by less than 20 m/s). Figure 2.32a shows two air jets blowing on each side of the sprayed spot and moved with the torch. These air jets also allow eliminating debris sticking to the substrate, after one pass (Fig. 2.33). Figure 2.32b shows a single air jet blown orthogonally to the hot gas jet about 2 cm in front of the substrate. It must also be kept in mind that if the coating surface is very hot, fine particles have the tendency to stick to it and form a deposit when the torch is translated to spray the next pass (see Fig. 2.33).

The heat flux of the hot gases depends on the spray process used (for example, heat fluxes increase when using HVOF spraying instead of flame), the combustion or plasma-forming gases, the spray distance (for example, with d.c. plasma jets the heat flux diminishes exponentially with the distance from the nozzle), and the relative movement torch–substrate (spray pattern) that can have a very important effect. The heat content of the sprayed particles increases with their quantity

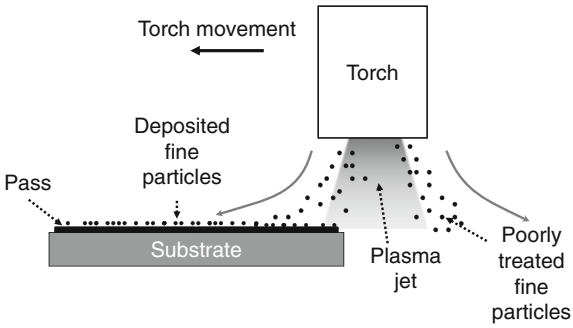


Fig. 2.33 Fine particles sticking on a hot pass

deposited during each pass. However, whatever may be the cooling system used (even cryogenic ones), most of the heat is withdrawn through conduction through the substrate. When depositing high-thermal conductivity materials (copper, for example) thick deposits can be achieved without generating steep temperature gradients. But this is not the case when spraying low-thermal conductivity materials (below 20–30 W/m K) for which thin layers (a few μm) must be deposited. For details about substrate and coating heating during the spray process see Sect. 13.8.

With plasma spraying, the mean deposition temperature is easily maintained around 400 °C during deposition, thanks to the thin passes when spraying low-thermal conductivity materials and the cooling air slot.

For stronger cooling (but also more expensive), cryogenic cooling can be used either with CO_2 snow or atomized liquid argon.

2.9.2 Control of Other Spray Parameters

Besides being influenced by the substrate temperature, any coating depends strongly on the control of the other following variables:

- The surface preparation
- The standoff distance
- The angle of impingement
- The relative velocity between the spray gun and the part to be coated
- The spray pattern

2.9.2.1 Surface Preparation

It is mandatory to clean, roughen, and clean again (to get rid of grit-blasting residues) the substrate prior to spraying. Otherwise coatings will not at all adhere to the substrate. For more details see Chap. 12 devoted to surface preparation (see Sect. 12.3).

2.9.2.2 Standoff Distance

This distance, also called spray distance, i.e., the distance between the nozzle exit and the part to be coated, is a compromise. It should be the distance where the average sized particle has reached the maximum temperature and velocity because farther downstream both these quantities diminish. However, at this distance (except for cold spray), in most cases the heat flux of the hot jet is still very high, especially for plasma spraying. For example, in plasma spraying with an Ar–H_2 jet, the optimum distance for particles is in the 50–60 mm range. However the heat flux values are in the range 4–8 MW/m^2. Thus spray distances are chosen between 90 and 120 mm in order to have heat fluxes below 2 MW/m^2.

2.9.2.3 Impact Angle

Studies have been devoted to this topic [55]. Splats collected on inclined surfaces present the same adhesion as those sprayed with an impact angle of 90° as long as the angle is between 60 and 90°. Depending on substrate and sprayed material, the adhesion is acceptable down to 45° and decreases drastically after that. Thus it is recommended to spray with an impact angle as close as possible to 90°. For more details see Sect. 13.5.2.

2.9.2.4 Beads

A bead is obtained when translating the torch relative to the substrate at a given relative velocity v_r. The bead height h_b and width d_b at mid-height depend on v_r, the powder mass flow rate, deposition efficiency, torch nozzle internal diameter, and injection conditions. In most cases the bead shape is Gaussian in good agreement with the distribution of hot particles. In the wings of the bead (see Fig. 2.32a), frequently particles appear which are not well exposed to the hot jet, but are sufficiently heated to stick. These particles, at least the metallic ones, are easily oxidized and they may form the major source of oxide inclusions in sprayed coatings, and thus create defects. Another important point is the risk, when spraying off-normal angles [55], to have particles intercepted by the bead rebounding and splashing on the other side of it. The adhesion of the splashed material being very poor, it will be the same with the next bead deposited on top of it [56]. For more details see Sect. 13.7.1.3.

2.9.2.5 Passes

A pass results from the overlapping of successive beads depending on the spray pattern (see Sect. 13.7.1.4 for details). The choice of the beads overlapping ratio depends on their thickness and the surface undulation that is acceptable. For a

medium thick bead (7–8 μm) an overlap of one half-bead width results in an undulation of about 3 μm, while with an overlap ratio of 1/6, the undulation is about 1 μm [57]. The resulting pass thickness depends on the bead thickness, and the successive beads overlap. The pass thickness generally ranges between 5 and 40 μm. For materials with thermal conductivities below 20–30 W/m K, it is necessary to have thin passes (below 10 μm) to avoid too high temperature gradients in coatings. The thinner the pass, the easier is the coating and substrate cooling and thus the control of the mean temperature.

2.10 Summary and Conclusions

This section aimed at presenting globally the different thermal spray processes, the sprayed materials (powders, wire, cored wire, cord, rod), the interactions of sprayed materials, and high-energy jets produced by the different spray processes, the way coatings are constructed with the influence of the in-flight parameters and substrate preparation on coating properties and residual stresses… All these phenomena and the fundamental mechanisms involved are described in detail in the following chapters (from 3 to 18).

Nomenclature

Latin Alphabet

a Particle surface (m^2)
c_p The specific heat of the particle (J/kg K)
d_i Nozzle internal diameter (mm)
d_p Particle diameter (μm)
e_p Effusivity $e_p = \sqrt{\rho_p \cdot \kappa_p \cdot c_p}$ $\left(J/m^2\,K\,s^{0.5}\right)$
E_A Activation energy of the reaction (J)
h Gas heat transfer coefficient (W/m^2 K)
k Specific reaction rate constant
k_B Boltzmann constant (1.38×10^{-23} J/K)
L_m Latent heat of melting of the particle (J/kg)
m_p Mass of the particle (kg)
q_{cv} Heat transferred to a particle by the hot gas (W)
Q_F Energy necessary to melt the particle (J)
Q_L Define the requirement for melting a particle ($J\,m^{3/2}/kg^{0.5}$)
v_g Gas velocity (m/s)
v_p Particle velocity (m/s)
T_s Gas temperature (K)

Greek Alphabet

ε Global emission coefficient of the particle
μ_g Gas viscosity (xx)
κ Thermal conductivity (W/m K)
ρ_p Particle specific mass (kg/m^3)
σ_S Stefan–Boltzmann radiation constant (5.671×10^{-8} W/m^2 K^4)
τ Residence time of the particle in the hot jet (s)

References

1. Cartier M (2003) Handbook of surface treatments and coatings. ASME Press, New York, NY
2. Davis JR (ed) (2004) Handbook of thermal spray technology. ASM International, Materials Park, OH
3. Chattopadhyay R (2001) Surface wear. ASM International, Materials Park, OH
4. Kanani N (2004) Electroplating, basic principles, processes and practice. Elsevier, Amsterdam
5. Djokic SS (2010) Electroless deposition: theory and applications, chapter 6. In: Djokic SS, Cavallotti P (eds) Modern aspects of electrochemistry, vol 48. Springer, New York, NY, pp 251–289
6. Maaß P, Peißker P (2011) Handbook of hot-dip galvanization. Wiley, New York, NY, 494 p
7. Dobkin DM, Zuraw MK (2003) Principles of chemical vapor deposition. Kluwer Academic, Dordrecht
8. Pawlowski L (2003) Dépôts physiques. Presses polytechniques et universitaires romandes, Lausanne
9. Glocker DA, Shah SI (1995) Handbook of thin film process technology (2 vol. set). Institute of Physics, Bristol
10. Mahan JE (2000) Physical vapor deposition of thin films. Wiley, New York, NY
11. Erkens G, Vetter J, Müller J, auf dem Brinke T, Fromme M, Mohnfeld A (2011) Plasma-assisted surface coating processes, methods, systems and applications. Sulzer Metco, Süddeutscher Verlag onpact GmbH, Munich
12. Frey H, Khan HR (2013) Handbook of thin film technology. Springer, Berlin, 550 pages
13. Gladush GG, Smurov I (2011) Physics of laser materials processing: theory and experiment, Springer series in materials science. Springer, Berlin
14. American Welding Society (1985) Thermal spraying, practice, theory and application. American Welding Society, Miami, FL
15. Pawlowski L. The science and engineering of thermal spray coatings. Wiley, New York, NY, 1st edition (1995) and 2nd edition (2008)
16. Seyed A. Co-spraying of alumina and stainless steel by d.c. plasma jets. PhD Thesis, University of Limoges France and GIK Institute, Topi, Pakistan, 26 Feb 2004, Limoges France
17. Fauchais P, Etchart-Salas R, Rat V, Coudert J-F, Caron N, Wittmann-Ténèze K (2008) Parameters controlling liquid plasma spraying: solutions, sols or suspensions. J Therm Spray Technol 17(1):31–59
18. Scrivani A, Bardi U, Carrafiello L, Lavacchi A, Niccolai F, Rizzi G (2003) A comparative study of high velocity oxygen fuel, vacuum plasma spray, and axial plasma spray for the deposition of CoNiCrAlY bond coat alloy. J Therm Spray Technol 12(4):504–507
19. Yankee SJ, Salsbury RL, Pletka BJ (1991) Quality control of hydroxylapatite coating: properties, processes and applications. In: Bernecki T (ed) Thermal spray 1991. ASM International, Materials Park, OH, pp 475–483

20. Fauchais P, Fukumoto M, Vardelle A, Vardelle M (2004) Knowledge concerning splat formation: an invited review. J Therm Spray Technol 13(3):337–360
21. Gärtner F, Stoltenhoff T, Schmidt T, Kreye H (2006) The cold spray process and its potential for industrial applications. J Therm Spray Technol 15(2):223–232
22. Champagne VK (ed) (2007) The cold spray materials deposition process. Woodhead Publishing Limited, England
23. Alkhimov AP, Papyrin AN, Kosarev VF, Nesterovich NI, Shushpanov MM. Gas-dynamic spraying method of applying a coating. US Patent 5, 302,414, April 12.
24. Stoltenhoff T, Kreye H, Richter HJ (1994) An analysis of the cold spray process and its coatings. J Therm Spray Technol 11(4):542–550
25. Kashirin AI, Klynev OF, Buzdygar TV (2002) Apparatus dynamic coating. US patent 6, 402, 050, June 11
26. Shkodkin A, Kashirin A, Klynev O, Buzdygar T (2006) Metal particle deposition simulation by surface abrasive treatment in gas dynamic spraying. J Therm Spray Technol 15(3):382–386
27. Kashirin A, Klynev O, Buzdygar T, Shkodin A (2007) DYMET technology evolution and application. In: Marple BR et al (eds) Thermal spray 2007: global coating solutions. ASM International, Materials Park, OH, e-proceedings
28. Hermanek FJ (2001) Thermal spray terminology and company origins. ASM International, Materials Park, OH
29. Glassmann I (1977) Combustion. Academic, New York, NY
30. Ducos M (2006) Evaluation des coûts de projection thermique (Costs evaluation in thermal spraying). Cours, ALIDERTE, Limoges
31. Thorpe ML, Richter HJ (1992) A pragmatic analysis and comparison of HVOF processes. J Therm Spray Technol 1(2):161–170
32. Smith MF, Dykhuisen RC, Neiser RA (1997) Oxidation in HVOF sprayed steels. In: Berndt CC (ed) Thermal spray: a united forum for scientific and technological advances. ASM International, Materials Park, OH, pp 885–892
33. Kadyrov E, Kadyrov V (1995) Gas dynamical parameters of detonation powder spraying. J Therm Spray Technol 4(3):280–286
34. Fauchais P (2004) Understanding plasma spraying, an invited review. J Phys D Appl Phys 37:2232–2246
35. Morishita T (1991) In: Blum–Sandmeier S et al. Plasma Technik 2nd symposium, vol. 1. Plasma Technik, Wohlen, pp 137–145
36. Boulos M (1992) RF induction plasma spraying: state-of-the-art review. J Therm Spray Technol 1:33–40
37. Bolot R, Planche M-P, Liao H, Coddet C (2008) A three-dimensional model of the wire-arc spray process and its experimental validation. J Mater Process Technol 200:94–105
38. Wilden J, Bergmann JP, Frank H (2006) Plasma transferred arc welding-modeling and experimental optimization. J Therm Spray Technol 15(4):779–784
39. Vardelle M, Vardelle A, Fauchais P, Li K-I, Dussoubs B, Themelis NJ (2001) Controlling particle injection in plasma spraying. J Therm Spray Technol 10:267–286
40. Dolatabadi A, Pershin V, Mostaghimi J (2005) New attachment for controlling gas flow in the HVOF process. J Therm Spray Technol 14(1):91–99
41. Hussary NA, Heberlein JVR (2001) Atomization and particle jet interactions in the wire-arc spraying process. J Therm Spray Technol 10(4):604–610
42. Filkova I, Cedik P (1984) Nozzle atomization in spray drying, vol 3. In: Mujumdar AS (ed) Advances drying. Hemisphere Publishing Corporation, pp 181–215
43. Savkar FD, Siemers PA (1989) Some recent developments in rapid solidification plasma deposition technology. In: Boulos M (ed) Workshop applications, pp 80–89
44. Neiser RA, Smith MF, Dykhuisen RC (1998) Oxidation in wire HVOF-sprayed steel. J Therm Spray Technol 7(4):537–545
45. Pasandideh-Fard M, Pershin V, Chandra S, Mostaghimi J (2002) Splat shapes in a thermal spray coating process: simulations and experiments. J Therm Spray Technol 11(2):206–217

46. Fukumoto M, Haang Y (1999) Flattening mechanism in thermal sprayed Ni particles impinging on flat substrate. J Therm Spray Technol 8(2):427–432
47. Chandra S, Fauchais P (2009) Formation of solid splats during thermal spray deposition. J Therm Spray Technol 18(2):148–180
48. Klinkov SV, Kosarev VF (2006) Measurements of cold spray deposition efficiency. J Therm Spray Technol 15(3):364–371
49. Kadyrov V (1992) Detonation coating technology. J Jpn Therm Spray Soc 29(4):14–25
50. Raletz F, Vardelle M, Ezoo G (2006) Critical particle velocity under cold spray conditions. Surf Coat Technol 201(5):1942–1947
51. Papyrin AN, Klinkov SV, Kosarev VF (2005) Effect of the substrate surface activation on the process of cold spray coating formation. In: Lugscheider E (ed) Thermal spray 2005. DVS, Dusseldorf, Germany, e-proceedings
52. Bacciochini A (2010) Quantification of porous architecture of finely structured deposits of yttria stabilized zirconia manufactured by suspension plasma spraying. PhD Thesis, University of Limoges, France, 24 Nov
53. Gell M, Jordan E, Teicholz M, Cetegem BM, Padture NP, Xie L, Chen D, Ma X, Roth J (2008) Thermal barrier coatings made by the solution precursor plasma spray process. J Therm Spray Technol 17(1):124–135
54. Clyne TW, Gill SC (1996) Residual stresses in thermal spray coatings and their effect on interfacial adhesion: a review of recent work. J Therm Spray Technol 5(4):401–418
55. Smith MF, Neiser RA, Dykhuizen RL (1994) An investigation of the effects of droplet impact angle in thermal spray deposition. In: Berndt CC, Sampath S (eds) Thermal spray: industrial applications. ASM International, Materials Park, OH, pp 603–608
56. Kanaouff MP, Neiser RA, Roemer TJ (1998) Surface roughness of thermal spray coatings made with off-normal spray angle. J Therm Spray Technol 7(2):219–231
57. Montillet D, Dombre E, Valentin FD, Goubot JM (1999) Modeling, simulating and optimizing the robotized plasma deposition: an expression approach. In: Lugsheider E, Kammer PA (eds) Thermal spray. DVS, Düsseldorf, Germany, pp 507–512

Chapter 3
Fundamentals of Combustion and Thermal Plasma

Abbreviations

1D	One dimension
2D	Two dimensions
3D	Three dimensions
d.c.	Direct current
LHS	Left hand side
r.f.	Radio frequency
RHS	Right hand side

3.1 Combustion

Except for cold spray, thermal spray processes are based either on combustion or thermal plasmas. This chapter recalls the basic phenomena involved allowing understanding how the high temperature jets are generated and what are their properties. General equations presented in this chapter are then used in the different chapters related to the various spray processes.

In this section are recalled the bases of combustion, according mainly to the work of Glassman [1].

3.1.1 Definitions

In spray technology combustion results from the chemical reaction between fuels which are hydrocarbon molecules: C_xH_y (or sometimes hydrogen H_2) and oxygen (O_2). The combustion can be studied either at equilibrium and is characterized by its temperature, pressure and composition, or out of equilibrium, corresponding to fast reactions, where the chemical kinetics defines the flame propagation within the

P.L. Fauchais et al., *Thermal Spray Fundamentals: From Powder to Part*,
DOI 10.1007/978-0-387-68991-3_3, © Springer Science+Business Media New York 2014

combustible mixture, its possible explosive behavior, and its flammability limits (explosive limits are quite different from flammability limits!).

3.1.2 Combustion at Equilibrium

The combustion reaction involves a significant heat release. The stoichiometry of the reaction corresponds to the case were all carbon and hydrogen atoms are reacted into carbon dioxide and water as in Eq (3.1):

$$C_xH_y + (x + y/4) \cdot O_2 \rightarrow x \cdot CO_2 + (y/2) \cdot H_2O \tag{3.1}$$

In general the combustion is characterized by the molar ratio of fuel to oxidizer F/A

$$F/A = nC_xH_y \cdot \left(mO_2\right)^{-1} \tag{3.2}$$

where n and m are mole numbers of hydrocarbon and oxygen molecules, respectively.

When the mixture is stoichiometric $F/A = 1/(x + y/4)$, x and y being the coefficients defined in Eq. (3.1), but usually the parameter used is R', called either equivalence ratio or richness and defined by

$$R^{'} = (F/A)/\left(F/A\right)_{\text{stoichiometry}} \tag{3.3}$$

For fuel-rich systems, there is more than the stoichiometric amount of fuel and $R' > 1$. For overoxidized or fuel-lean systems: $R' < 1$. Obviously at stoichiometry $R' = 1$. If there is too much oxidizer, part of it will not be burned but will have to be heated to the combustion temperature without participating in it and thus the final temperature will be lower than that obtained with the stoichiometric mixture. Similarly, in a fuel-rich mixture, the excess of fuel will have to be heated by the reaction and the temperature will be lower than with the stoichiometric mixture. This is illustrated in Fig. 3.1 from Glassman [1].

In fact some systems have their temperature peak slightly on the rich side of stoichiometry that is the case when the system is slightly underoxidized [1]. If air is used as oxidizer instead of oxygen, as 1 mole of air contains only 0.2 moles of O_2 the remaining being in first approximation 0.8 moles of N_2, for achieving the stoichiometry five times more air by volume must be used to obtain the required quantity of oxygen. The combustion temperature with air will accordingly be lower than that obtained with pure oxygen, since the nitrogen in the air which will need to be heated (Table 3.1). This is illustrated in Table 3.1 (from Glassman [1]), where it can be seen that using air instead of oxygen reduces the temperature by about 600–800 K. (Note also that the use of air as oxidizer results in the formation of NO_x

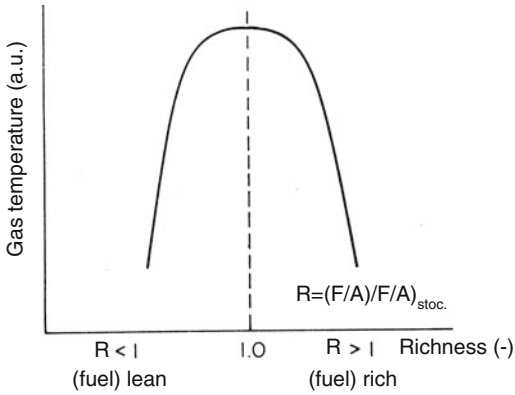


Fig. 3.1 Variation of combustion temperature with richness ratio [1], reprinted with the kind permission of Elsevier

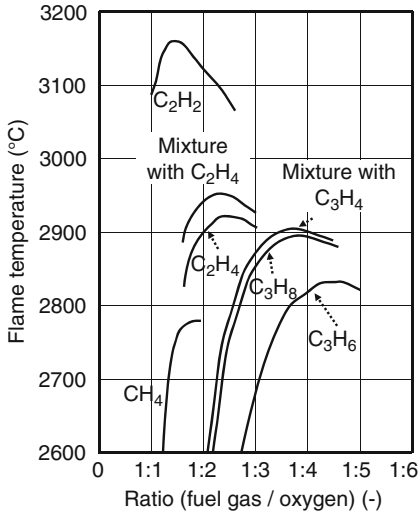


Fig. 3.2 Flame temperatures as function of the fuel/oxygen ratio for different mixtures fuel/oxygen by volumes (m^3/m^3) and for different hydrocarbon fuel gases [2], reprinted with the kind permission of Linde Co

Table 3.1 Approximate flame temperatures of various stoichiometric mixtures (initial temperature 298 K, atmospheric pressure) [1], reprinted with the kind permission of Elsevier

Fuel	Flame temperature (K) Air as oxidizer	Flame temperature (K) Oxygen as oxidizer
Acetylene	2,600[a]	3,410[b]
Carbon monoxide	2,400	3,220
Heptane	2,290	3,100
Hydrogen	2,400	3,080
Methane	2,210	3,030

[a]This maximum exists at $R' = 1.3$
[b]This maximum exists at $R' = 1.7$

in the exhaust gases, which is not necessarily wanted. The % of formed NO_x increases with the increase of the flame temperature).

The most commonly used gases are:

- For flame and D-gun spraying and also in specific HVOF guns such as Top gun: acetylene (C_2H_2 unsaturated compound with triple bonds)
- For HVOF: ethene (C_2H_4 containing two double bonds) available with the same purity as hydrogen, propane (C_3H_8 saturated component with single bonds), methane (CH_4 saturated component with single bonds), propene or propylene (C_3H_6 with double bonds), methyl-acetylene (C_3H_4 unsaturated compound with triple bonds), and also mixtures such as acetylene–ethene or methyl-acetylene
- For flames and HVOF: hydrogen

Increasing the pressure raises slightly the flame temperature, as illustrated for methane: increasing the pressure to 2 MPa results in a flame temperature of 3,460 K compared to 3,030 K at atmospheric pressure. The increase is rather small when using air instead of oxygen: for methane 2,270 K at 20 MPa against 2,230 K at 0.1 MPa [1].

3.1.3 Combustion Kinetics

3.1.3.1 One-Step Reactions

In fact, any one step chemical reaction can be represented by

$$\sum_{j=1}^{n'} \nu'_j M_j \rightarrow \sum_{j=1}^{n'} \nu''_j M_j \tag{3.4}$$

where ν'_j is the stoichiometric coefficient of the reactants, ν''_j the stoichiometric coefficient of the products, M the arbitrary specification of all chemical species and n' the total number of compounds involved. If a species involved does not occur as a reactant or product, its ν_j equals zero [1].

In an actual reacting system, the rate of change of the concentration of a given species is given by

$$\mathrm{d}(M_i)/\mathrm{d}t = \left(\nu''_i - \nu'_i\right) \cdot k_\mathrm{R} \cdot \Pi\left(M_j\right)^{\nu_j} \tag{3.5}$$

where (M_i) is the concentration of species i and k_R the specific reaction rate constant.

This expression corresponds to the law of mass action stating that the disappearance of a chemical species is proportional to the product of the concentrations of the

reacting chemical species, each concentration raised to a power equal to the corresponding stoichiometric coefficient.

For example, the formation of dihydrogen through recombination of hydrogen atoms in the presence of a third body M is written:

$$\mathrm{H} + \mathrm{H} + \mathrm{M} \rightarrow \mathrm{H_2} + \mathrm{M} \tag{3.6}$$

and Eq. (3.5) becomes $\mathrm{d(H_2)} = k_\mathrm{R} \cdot (\mathrm{H})^2 \cdot (\mathrm{M})$

The specific reaction rate constants k_R are expressed by

$$k_\mathrm{R} = c(T) \cdot \exp(-E_\mathrm{A}/k_\mathrm{B} \cdot T) \tag{3.7}$$

where $c(T)$ takes into account the collision terms of reactants and has a mild temperature dependence and E_A is the critical energy for the reaction to occur (Arrhenius law). Values of k_R can be found in papers devoted to specific reactions, such as, for example, in [3] for the mixture $\mathrm{C_2H_2}$–$\mathrm{O_2}$ or in tables such as those of Kee et al. [4].

3.1.3.2 Simultaneous Interdependent and Chain Reactions

In combustion processes a simple one-step reaction is the exception rather than the rule, and one finds generally simultaneous, interdependent reactions, or chain reactions [1]. Generally, two reacting molecules do not react directly, as $\mathrm{O_2}$ and $\mathrm{H_2}$, for example, but react by one or both dissociating to form radicals O* and H*, which then initiate a chain of steps. This is illustrated below for the reaction $\mathrm{H_2} + \mathrm{Br_2} \rightarrow 2\mathrm{HBr}$:

$$\begin{array}{lll}
(1) & \mathrm{Br_2} \rightarrow 2\mathrm{Br}^*(k_1) & \text{initiation} \\
(2) & \mathrm{Br}^* + \mathrm{H_2} \rightarrow \mathrm{HBr} + \mathrm{H}^*(k_2) & \text{chain carrying step} \\
(3) & \mathrm{H}^* + \mathrm{Br_2} \rightarrow \mathrm{HBr} + \mathrm{Br}^*(k_3) & \text{chain carrying step} \\
(4) & \mathrm{H}^* + \mathrm{HBr} \rightarrow \mathrm{H_2} + \mathrm{Br}^*(k_4) & \text{chain carrying step} \\
(5) & 2\mathrm{Br}^* \rightarrow \mathrm{Br_2}(k_5) & \text{chain breaking}
\end{array} \tag{3.8}$$

The reaction is initiated by the dissociation of $\mathrm{Br_2}$ because the energy required at room temperature is about half that of $\mathrm{H_2}$ dissociation. Of course it is not the case when the reaction takes place in gases at very high temperatures because $\mathrm{H_2}$ dissociation starts at about 3,000 K. The HBr formation rate ($\mathrm{d(HBr)}/\mathrm{d}t$) is calculated by considering reactions (2), (3) (HBr formation), and (4) (HBr destruction). Assuming that radicals react very fast it can be postulated that their concentration reaches a steady state and thus the formation rates of both radicals ($\mathrm{d(H^*)}/\mathrm{d}t$ and $\mathrm{d(Br^*)}/\mathrm{d}t$) can be set to zero. It allows calculating [1] the HBr formation rate as a function of the five reaction rate constants of Eq. (3.8).

3.1.3.3 Criterion for Explosion

In order for combustion, whether deflagrations (flames) or detonation, to propagate, the reaction kinetics must be fast enough for the mixture to be explosive. Explosions in fuel–oxidizer mixtures occur under certain conditions depending on temperature and/or pressure. They can occur only if in the chain system the multiplication factor of radicals, often called α', is larger than one (more radicals R created than destroyed). A simple calculation by Glassman [1] illustrates this point: he assumed that in a straight chain reaction there are 10^8 collisions/s, 1 chain particle/cm^3, and 10^{19} molecules/cm^3. Thus the molecules will be consumed in 10^{11} s ~ 30 years! If, in the same conditions, a particular branched chain reaction is assumed with a multiplication factor $\alpha' = 2$ it comes

$$2^N = 10^{19} \rightarrow N = 62 \text{ generations}$$

All molecules will be consumed in 62 generations corresponding to a time 62×10^{-8}~10^{-6} s. For $\alpha' = 1.01$ the time is 10^{-4} s, which is still very fast!

In the following the branched chain reaction system is illustrated [1]:

(1)	$M \rightarrow R^*(k_1)$	initiation (radical production)
(2)	$R^* + M \rightarrow M + \alpha' R^*(k_2)$	chain branching : increased R production
(3)	$R^* + M \rightarrow P(k_3)$	chain branching : increased R production
(4)	$R^* + \text{wall} \rightarrow \text{destruction}\ (k_4)$	chain termination (very efficient)
(5)	$R^* + \text{gas} \rightarrow \text{destruction}\ (k_5)$	chain termination

(3.9)

Writing that d(R*)/dt equals zero (steady state) and calculating d(P)/dt shows that the rate of product formation becomes infinite, or the system is explosive, when the denominator becomes zero, corresponding to a critical value of $\alpha' = \alpha'_{\text{crit}}$:

$$\alpha'_{\text{crit}} = (1 + k_3/k_2) + (k_4 + k_5)/(k_2 \cdot (M)) \tag{3.10}$$

The dependence of the critical value α_{crit} on the concentration (M), as given in Eq. (3.10), as well as the other multiplication factor of radicals, partially explains why α'_{crit} depends on pressure and temperature. In fact the mixture is explosive if $\alpha' > \alpha'_{\text{crit}}$, while for $\alpha' < \alpha'_{\text{crit}}$ the product forming reactions are too slow. Explosion limits for combustion mixtures are well defined and represented as the temperature–pressure boundary separating the regions of slow and fast reactions.

One must have fast reactions for a flame to propagate. *The explosive limits are not flammability limits, corresponding to the lean and rich fuel mixture ratios beyond which no flame will propagate*. These limits are calculated or measured according to the range of a concentration (by volume) of a gas or vapor that will burn (or explode) if an ignition source is introduced. For example, according to Glassman [1] with a mixture of H_2–air the flammability and explosive limits are respectively for the lean part 4 and 18 and for the rich part 74.2 and 59, the stoichiometry being 29.2.

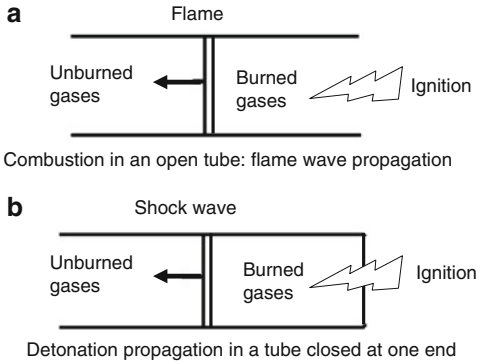


Fig. 3.3 Combustion in a tube initially filled with a premixed mixture of fuel and oxidizer [1]. (**a**) Tube opened at both ends, with ignition at one end resulting in flame wave propagation. (**b**) Tube open at only one end, with ignition at that location resulting in detonation wave propagation [1], reprinted with the kind permission of Elsevier

Generally, detonation limits are narrower than flammability limits. A general rule of thumb is that with oxygen the upper limit is about three times the stoichiometric mixture ratio and the lower limit is about half the stoichiometry [1]. The lower limit is the same for oxygen or air, while the higher limit is much higher in oxygen than in air.

3.1.4 Combustion or Deflagrations, Detonations

It is first important to define the terms used [1]:

- Explosion refers to rapid heat release or pressure increase
- Subsonic combustion wave or flame or deflagration are terms used interchangeably
- Detonation is a shock wave sustained by the energy of the chemical reaction in the highly compressed explosive medium
- A pure explosion does not necessarily require the passage of a combustion wave through the explosive medium, whereas an explosive gas mixture must exist to have either deflagration or detonation. It can also be said that deflagrations (subsonic waves) or detonations (supersonic waves) require a rapid energy release, while explosions do not require the presence of a waveform. Of course, explosion limits depend on the mixture composition (particularly the mixture ratio), its pressure, and its temperature

3.1.4.1 Combustion (Deflagration)

To explain simply the difference between combustion and detonation one can consider a tube filled with a premixed mixture of fuel and oxidizer Fig. 3.3 [1].

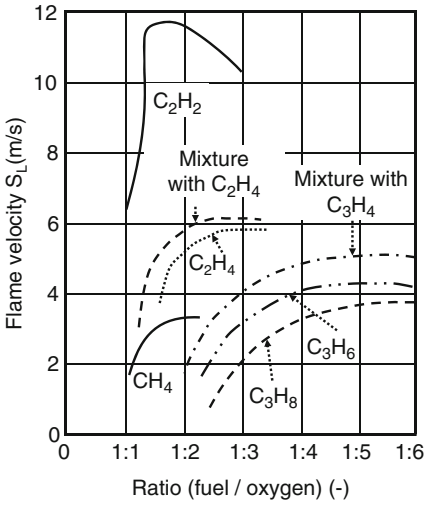


Fig. 3.4 Flame velocity dependence on the fuel/oxygen ratio for different gases fuels [2], reprinted with the kind permission of Linde Co

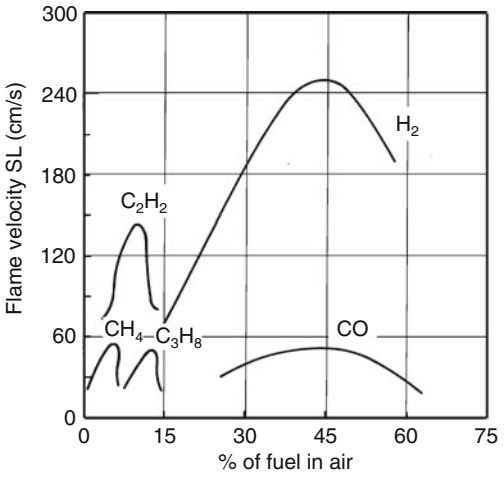


Fig. 3.5 Flame velocity dependence on the percentage of fuel in air for different gases fuels [1], reprinted with the kind permission of Elsevier

First both ends of the tube are closed to keep the mixture enclosed and then both ends are opened simultaneously and an ignition source applied at one end Fig. 3.3a. A flame appears in the tube. It is characterized by a very luminous zone less than 1 mm thick, which is composed of a preheat zone, a reaction zone, and a recombination zone. In front of the flame the unburnt gases are at room temperature and at the end of the luminous zone the temperature is the highest and corresponds to the adiabatic flame temperature as shown in Fig. 3.2. In the reaction zone the reactions are very fast. Within the burnt gases, slow reactions can occur. The flame can be considered as a subsonic wave sustained by combustion which propagates at velocities between 1 and 11.5 m/s with oxygen, and between a few tens of cm/s and a few m/s in air as shown in Figs. 3.4 and 3.5.

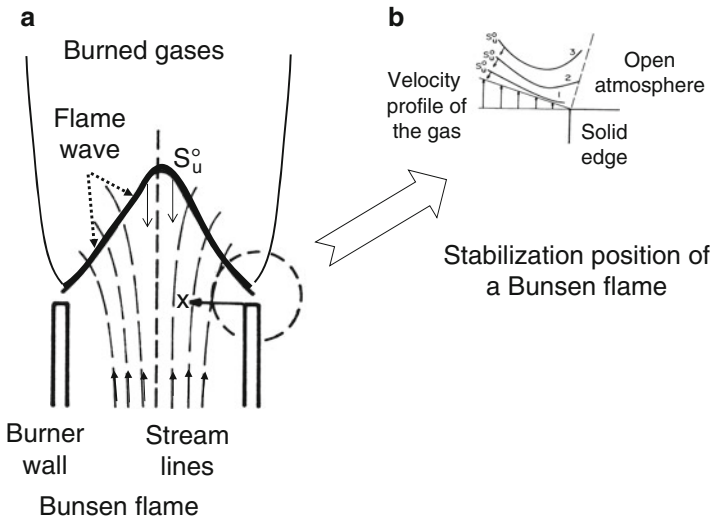


Fig. 3.6 (**a**) Schematic diagram of a Bunsen burner with the combustible gas flow streams, the wave flame and the burned gases [1]. (**b**) Detail closeup to the burner wall: flame stabilization [1]

The flame velocity S_L, in laminar conditions, is given by Eq. (3.11):

$$S_L \sim (a \cdot RR)^{1/2} \tag{3.11}$$

where a is the diffusivity in the combustion wave and RR the reaction rate. The burnt gases (index b) have a pressure slightly lower ($p_b \sim 0.8 - 0.9 \times p_u$) than that of the unburnt ones (*premixed* mixture of gaseous fuel and oxidizer, characterized by index u), and its specific mass is lower ($\rho_b \sim 0.06 - 0.25\rho_u$).

In a burner the combustion wave can be maintained at a fixed position as illustrated in Fig. 3.6a [1]. This is possible because a competition exists between the wave velocity S_u° directing the flame towards the unburnt gases flowing in the cylindrical tube of the Bunsen burner and the velocity of these gases flowing in the tube and directed towards the tube exit.

Assuming the flow is laminar, the gas velocity profile at the tube exit, close to the wall, has been represented as being zero at the wall and varying linearly with the tube radius (see Fig. 3.6b). The wave velocity far away from the rim, attains its maximum S_u°, while when it approaches the burner rim it decreases as heat, and chain carriers are lost to the rim. If the distance of the wave from the rim increases, losses diminish, and the wave velocity increases. This illustrated in Fig. 3.6b for different positions of the wave, numbered 1–3. Finally a position can be found for a cold gas mean velocity where equilibrium exists.

If the unburnt gas velocities diminish too much, the flame will penetrate into the tube, a phenomenon called flash back. Close to the wall, the unburnt gas velocity tends to zero, but quenching of radicals increases, thus chain carriers are lost

resulting in no possible flash back in this area. To avoid this unwanted phenomenon in the central part of the tube, one has to reduce its internal diameter to increase drastically the radical destruction and reduce the flame velocity. If the burner hole is small enough (smaller than the fluid boundary layer thickness) no flash back is possible. It is also possible on the other hand to blow out the flame if the hole is too small, and the velocity of unburned gases is increased too much, a phenomenon called blow-off. Flash arrestors which are commonly introduced in the flow of combustible gases to avoid "flash backs" consists essentially of a fine metal mesh which acts as a heat sink thus cooling the flame and impairing its propagation across the metal wire mesh.

The color of the luminous zone of the flame depends on the fuel/oxidizer ratio [1]: the radiation is deep violet for fuel-lean mixture (due to CH radicals), while it is green in fuel-rich mixtures (due to C_2 molecules). In the burnt high temperature gases, a reddish glow arises from CO_2 and H_2O vapor radiation. When the mixture is adjusted to be fuel rich, free carbon soot particles are formed. These are responsible for the intense yellow emission observed in such flames.

In thermal spray processes, flame spraying uses flames at atmospheric pressure, while HVOF or HVAF spraying uses flames but at pressures generally below 1 MPa.

3.1.4.2 Detonation

As in the case of deflagration or flame, one considers a tube filled with a premixed mixture of fuel and oxidizer (see Fig. 3.3) [1]. First, both ends of the tube are closed to keep the mixture enclosed, and then one end (instead of both) is opened and an ignition source is applied simultaneously at the closed end (see Fig. 3.3b). Again a flame or a wave propagates, except its velocity is not between a few tens of centimeters per second and about 10 m per second, but reaches thousands meters per second. Such velocities are supersonic with respect to the unburned gases. Chapman performed the first studies of this phenomenon at the end of the nineteenth century followed by Jouget at the beginning of the twentieth century. It was demonstrated that the only possible velocity for a detonation wave was the velocity of sound in gases behind the detonation wave (burned gases), plus the velocity of the burned gases relatively to the tube, also called mass velocity [1]. The velocity of sound is depending on the square root of temperature, which results in an adiabatic shock front for the propagating wave.

The theoretical works of Neumann (1942), Döring (1943), and Zeldovich (1950) have clarified the structure of the detonation wave: it consists of a shock moving at the detonation velocity, leaving heated and compressed gases behind it. The chemical reaction then starts and as it progresses, the temperature rises and the specific mass and pressure fall until they reach the Chapman–Jouget (C–J) values and the reaction attains equilibrium. Behind the C–J shock, energy is generated by thermal reactions [1]. Figure 3.7 is a representation of the theory of Zeldovich–von

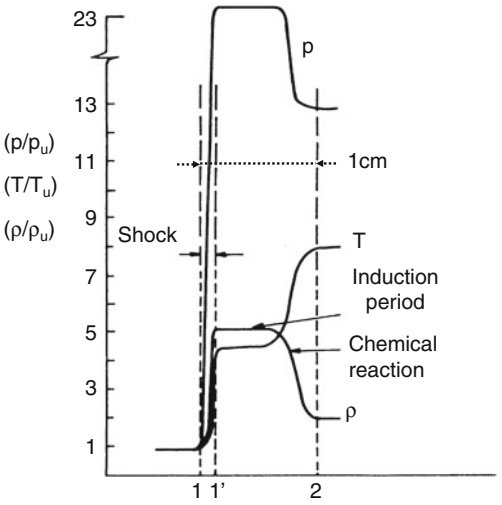


Fig. 3.7 Structure of a detonation wave: variation of physical parameters through it [1], reprinted with the kind permission of Elsevier

Table 3.2 Calculated values of the physical parameters at the positions 1, 1′ and 2 indicated in Fig. 3.7 in a 20 vol.% H_2–air detonation [1], reprinted with the kind permission of Elsevier

	1	1′	2
M(-)	4.5	0.42	1.0
u (m/s)	1,524	305	549
p (MPa)	0.1	2.3	1.3
T (K)	298	1,350	2,425
ρ/ρ_u	1	5	1.8

Neumann showing the variation of the different physical parameters. Plane 1 corresponds to the shock front, plane 1' is that immediately after the shock and plane 2 is the Chapman–Jouget plane. Table 3.2 presents the calculated values of the physical parameters related to a 20 vol.% H2–air detonation.

As it can be seen, when the gas passes from the shock front to the C–J state, its pressure drops by a factor of almost two, while its temperature is almost doubled and its specific mass is reduced by about a factor three. Compared to the flame wave, the ratio ρ_b/ρ_u is higher than ten (against 0.8–0.9), while the ratio ρ_b/ρ_u has values between 1.5 and 2 (against 0.06–0.25 for flames) with, of course, much higher velocities (about two orders of magnitude).

At last it must be emphasized that, as for flames, detonation limits exist depending on the mixture used (lean or rich), and which, as previously explained in Sect. 3.1.3.3, are different from deflagration limits. The difference comes from the fact that the shock provides the detonation mechanism whereby the combustion process is continually sustained. The energy to drive the shock is not the same as that for the combustion wave.

In thermal spray processes Detonation guns consist in a barrel close at one of its ends as shown in Fig. 3.3b.

3.2 Thermal Plasmas Used for Spraying

The bases of thermal plasma properties presented below rely mainly on the work of Boulos et al. [5].

3.2.1 Definition

Plasmas, considered in this book, consist of a mixture of electrons, neutral molecules, and atoms as well as ions, in the fundamental or excited states. The oscillation of molecules, atoms, and ions between their excited state and lower or ground state results in the emission of photons that constitute the luminous signature of the plasma. Such a mixture, however, is qualified as plasma only if the negative and positive charges balance each other, i.e., overall the plasma is electrically neutral. Thermal plasmas exist only if their electrical conductivity exceeds a given threshold, which for the mixtures used in plasma spraying at atmospheric pressure corresponds to temperatures roughly between 7,000 and 8,000 K [5].

Commonly used thermal plasmas are optically thin, i.e., all the radiation escapes and does not participate in establishing an equilibrium. However it is no more the case when plasma contains metallic vapors resulting from sprayed particle evaporation. In plasmas the ions and electrons are accelerated, and thus gain energy, under the influence of the applied electric field. The exchange of energy between elementary particles either of the same species or of different species is a direct result of particle collisions. The energy exchanged in any such collision between two species with masses m_1 and m_2 is proportional to $2\ m_1\ m_2/(m_1 + m_2)^2$. Thus the energy exchange between two heavy species is rather fast (50 % if they have the same mass). It is not the case with electrons that have a very low mass compared to that of other species except photons (m_H, the lightest atom, has a mass 1,836 times larger than that of electrons!). Correspondingly the energy exchange between an electron and a heavy species is rather small (proportional to $2\ m_e/m_h$, i.e., for an argon atom 1/37,120!). Accordingly a very large number of collisions is required for the electrons and heavy particles to reach thermal equilibrium. A unique temperature can characterize thermal plasmas if collisions are numerous enough to thermalize all species including electrons. This condition is fulfilled in thermal plasmas where temperatures are between 8,000 and 15,000 K with electron densities ranging from 10^{21} to 10^{24} m^{-3}. Of course, deviations from equilibrium must be expected in some areas, especially close to electrodes or where a cold gas or a liquid jet is injected with a high-energy momentum density or pressure ($\rho \cdot v^2$) compared to that of the plasma, and in the presence of steep temperature gradients. In the following this situation will not be discussed.

In combustion, the composition of the fuel–oxidizer mixture and its pressure determine the energy dissipated. In contrast, in thermal plasmas, external energy (electrical energy through a direct current arc or inductively coupled radio

Table 3.3 Ionization and dissociation energies of the main spray plasma gases and surrounding atmosphere [5], reprinted with the kind permission of Springer

Species	Ar	He	H	N	O	H_2	N_2	O_2
Ionization energy(eV)	15.755	24.481	13.659	14.534	13.614	15.426	15.58	12.06
Dissociation energy (eV)	–	–	–	–	–	4.588	9.756	5.08

frequency discharge) is supplied to the plasma forming gas. If this energy is sufficiently high, it results first in the dissociation of molecules (presenting the case of molecular gases) and then in ionization of atoms. Table 3.3 summarizes the ionization ($X \rightarrow X^+ + e$) and dissociation energies ($X_2 \rightarrow 2\ X$) of the main plasma forming gases and air (X represents the species considered). The first observation is that the ionization energies of all plasma gases, except He, are rather close together (less than 2.1 eV difference). That means that ionization for all gases, except for helium, will be completed at about the same temperature (about 15,000 K at atmospheric pressure). However it does not mean that the energy required for achieving a number density of electrons within the plasma forming gas (which will result in an electrical conductivity sufficiently high to sustain the plasma with an arc or a r.f. discharge), will be the same whatever the plasma gas may be. Dissociation energies are lower than ionization energies, which means that dissociation will be completed at temperatures lower than that of ionization (at atmospheric pressure about 3,500 K for hydrogen and oxygen, and 7,500 K for nitrogen). The ionization of molecular gases are far more energy demanding than most monatomic gases because of the need to supply both dissociation and ionization energies (4.588 + 13.481 eV) for H^+ ion compared with (15.755 eV) for Ar^+. It is important to note that in all plasma sources used in thermal spray applications, the degree of ionization of the gas is relatively small (less than 1–3 %) which explains why it is possible to have a plasma with an average bulk gas temperature (specific energy level) that is almost one order of magnitude smaller than that needed for full ionization of the plasma gas.

3.2.2 Plasma Composition

Plasma composition is calculated by minimizing the Gibbs free enthalpy, taking into account the van't Hoff's laws for dissociation and ionization, the conservation of different elements, the electrical neutrality, and Dalton's law. For details the interested reader is referred to [5]. Results are traditionally represented as the evolution of the species number densities with temperature at a given pressure. In the following only atmospheric pressure conditions, at which most plasma torches work, will be considered.

Figure 3.8 represents the dependence of the argon number density on temperature at atmospheric pressure. As the temperature increases, n_{Ar}, the density of argon atoms, decreases monotonically first due to the temperature increase ($n_{Ar} = p/k_B \cdot T$), and then due to ionization, with the progressive increase of $n_{Ar}{}^+$ and

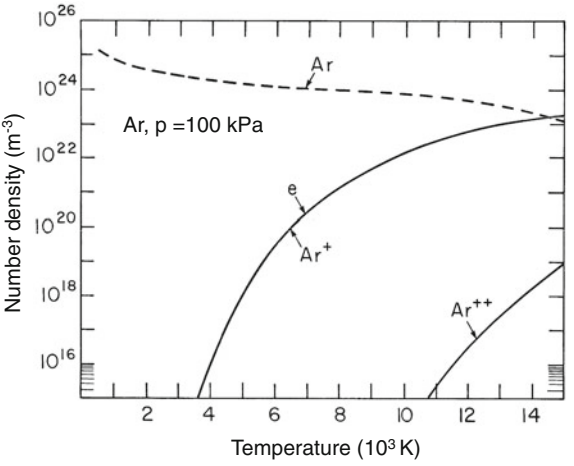


Fig. 3.8 Temperature dependence of number densities of argon plasma species at atmospheric pressure [5], reprinted with the kind permission of Springer

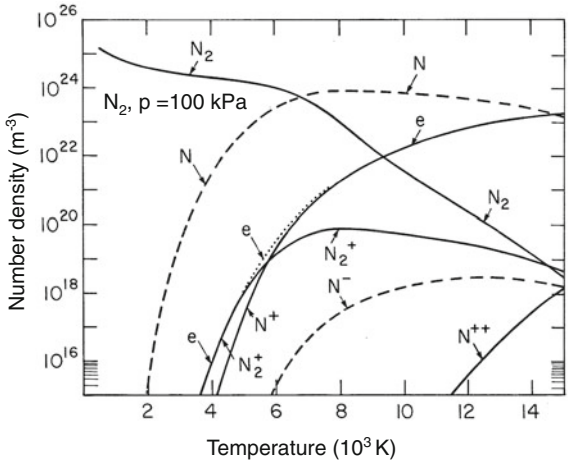


Fig. 3.9 Temperature dependence of number densities of nitrogen plasma species at atmospheric pressure [5], reprinted with the kind permission of Springer

correspondingly of n_e (electrical neutrality). Ionization is completed at about 15,000 K. It must be noted that the second ionization (Ar^{++}) represents a density of 10^{15} m^{-3} at about 10,700 K, i.e., 10^{-9} less than Ar atoms. At 8,000 K, electrons and ions represent about 2 % of the total species.

With helium results are quite similar, except of course that ionization is completed at about 25,000 K (against 15,000 K for argon). The percentage of electrons reaches about 1 % at temperatures higher than 15,000 K. Thus in any Ar–He mixtures (except with less than 5 vol.% Ar) electrons and ions are all due to argon ionization.

With nitrogen, as shown in Fig. 3.9, the evolution is different from that obtained with argon. First nitrogen must be dissociated and, at the beginning, n_{N2} diminishes fast with temperature ($n_{N2} = p/k_B \cdot T$) and then faster with N_2 dissociation. The latter is completed at about 10,000 K. As the ionization energies of N and N_2 are

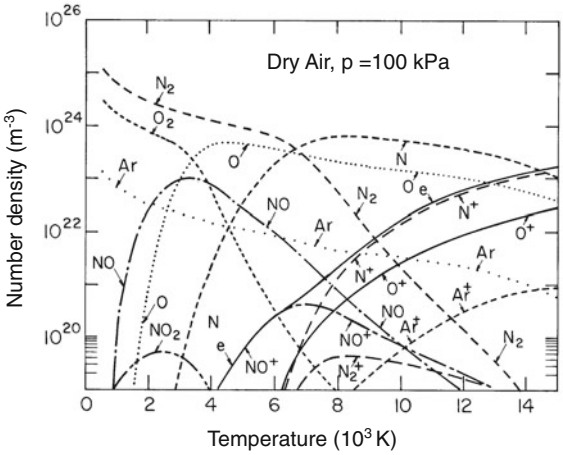


Fig. 3.10 Temperature dependence of number densities of air plasma species at atmospheric pressure [5], reprinted with the kind permission of Springer

rather close (see Table 3.3), the ionization of these species starts at about the same temperature.

However, in spite of the slightly lower ionization energy of N, N_2^+ ions appear before N^+ ions because the number density of N_2 is higher than that of N at this temperature. Of course the density of N_2^+ ions decreases above about 7,000 K because of their dissociation. The presence of negative ions N^- must also be noticed. However, under spraying conditions N_2^+ and N^- ions have no practical influence. At the end of dissociation, nitrogen atoms start to ionize and ionization is completed above 15,000 K.

Other diatomic molecules, used in plasma spraying or existing in the surrounding atmosphere, behave similarly to nitrogen. This is the case of O_2, but according to the dissociation energy being about half that of nitrogen (see Table 3.3), dissociation is completed above about 3,500 K and ionization above 15,000 K. Molecular ions O_2^+ and O^- ions also exist at levels slightly different from those of nitrogen. With hydrogen, dissociation is completed above 3,500 K, and if H_2^+ does not exist, H^- is formed above 4,000 K. As for nitrogen, these molecular positive and atomic negative ions have no practical influence in spraying conditions. Figure 3.10 presents the composition of air plasma (dry air with no water vapor) at atmospheric pressure.

In this calculation air is considered to be a mixture of nitrogen (78.09 vol.%), oxygen (20.95 vol.%), and argon (0.93 vol.%), with no water vapor. The following species are important: e, N, O, Ar, N^+, O^+, Ar^+, N_2, N_2^+, O_2, O_2^+, NO, NO^+, NO_2, and N_2O. The main ions are NO^+ below 6,000 K, while N^+ and O^+ are dominant above 9,000 K. In practice, the surrounding air cools plasma jets faster than flames because the air entrained into the plasma jet reaches rapidly temperatures above 3,000–3,500 K, and the induced molecular oxygen dissociation reaction reduces the energy in the plasma.

The last comment is about the specific mass which decreases when the temperature is raised. Between room temperature and 15,000 K, for heavy gases which

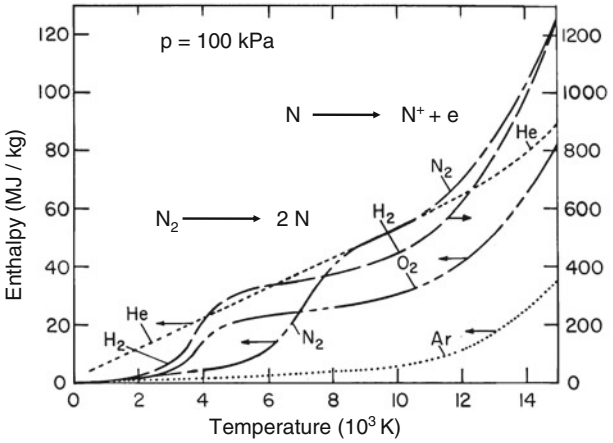


Fig. 3.11 Temperature dependence of the specific enthalpy (MJ/kg) of Ar, He, N_2, O_2 and H_2 at atmospheric pressure [5], reprinted with the kind permission of Springer

entrain particles in plasma spraying, $\rho_{300}/\rho_{15,000} = 46$ for argon and 145 for nitrogen. This means that the spray particle acceleration will be the smallest for the highest plasma temperature at the same flow velocity.

3.2.3 Thermodynamic Properties

The plasma enthalpy depends strongly upon the dissociation and ionization phenomena. Figure 3.11 represents the variation with temperature of the specific enthalpy (MJ kg^{-1}) of the different plasma gases (Ar, He, N_2, O_2, and H_2). The interested reader can refer to [5] for details about the calculations. The steep variations of enthalpy are due to the heats of reaction (dissociation and ionization). The very high enthalpy of pure hydrogen is due to its low mass. At the maximum temperature of this figure, the ionization for helium has not yet started, thus, in spite of its low mass, helium enthalpy is lower than that of hydrogen but higher than that of argon. This figure illustrates the important economics of using plasmas, in which the energy supply is independent of the gas, and the temperature is not determined by the chemical reactions (as in flames). Specifically, if an oxygen-fuel flame at 3,000 K is used to heat a particle up to 2,500 K, only 20 % of its energy is used. If nitrogen plasma at 10,000 K is used for the same purpose, it is possible to recover almost 95 % of the available energy in the gas. Adding secondary gases such as helium or hydrogen to the primary ones, argon or nitrogen, increases the enthalpy of the mixture.

Figure 3.12 represents the dependence on temperature of the specific heat at constant pressure (0.1 MPa) of Ar, He, N_2, and H_2. All curves show peaks at dissociation and ionization. As it could be expected, these peaks are the highest

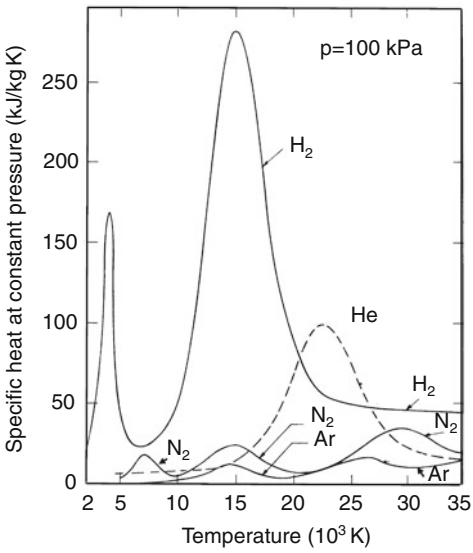


Fig. 3.12 Temperature dependence of the specific heat at constant pressure (MJ/kg K) of Ar, He, N_2 and H_2 at atmospheric pressure [5], reprinted with the kind permission of Springer

for the light gases: helium and hydrogen. These peaks correspond to the large values of the derivatives of the specific enthalpy with respect to temperature.

3.2.4 Transport Properties

3.2.4.1 Electrical Conductivity

The electrical conductivity σ_e is proportional to the electron number density. Thus it is not surprising, according to the rather close ionization energies (see Table 3.3) that values of σ_e are rather close (within a temperature difference of 1,000 K) for Ar, N_2, H_2, and O_2 as represented in Fig. 3.13 for the first three species. In contrast, for helium the difference is more significant (values shifted by about 5,000 K). It is important to note that Fig. 3.13 has a decimal logarithmic scale for σ_e.

Below a few hundreds of Siemens per meter, no arc or r.f. discharge at atmospheric pressure can be sustained. In Fig. 3.14 where the σ_e scale is linear, it can be seen that electrical conductivities of Ar, Ar–H_2 (25 vol.%), and N_2 are very close together.

This observation explains why in plasma spraying the temperature values T_c, where current flow can be established, are in general above 7,000 to 8,000 K. For example, for an electric arc, one can define an isothermal envelope at $T = T_c$, outside of which no electrical conduction is possible, and which appears as a boundary between the arc column and the "cold" sheath. If the electrical conductivity is expressed as function of the gas specific enthalpy, one can see large

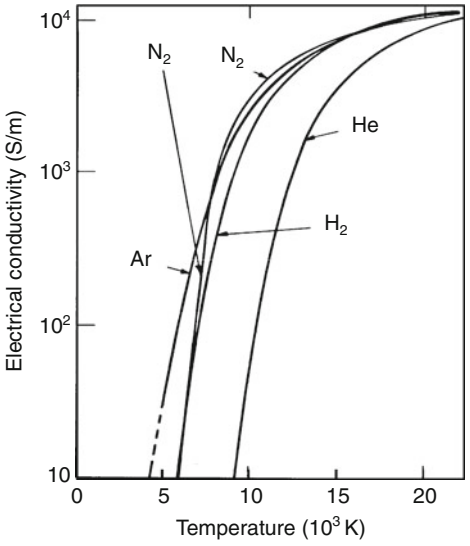


Fig. 3.13 Temperature dependence of the electrical conductivity (decimal logarithmic scale) (S/m) of Ar, He, N_2 and H_2 at atmospheric pressure [5], reprinted with the kind permission of Springer

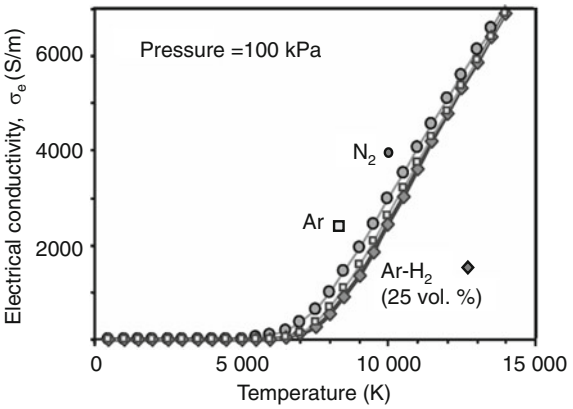


Fig. 3.14 Electrical conductivity (linear scale) (S/m) as function of temperature for Ar, N_2 and Ar–H_2 (25 vol.%) at atmospheric pressure [5], reprinted with the kind permission of Springer

differences between the properties of different gases. The electric conduction requires much more energy for nitrogen (about ten times more) than for argon, as shown in Fig. 3.15, the argon–hydrogen mixture being in between (about five times less energy than for nitrogen).

3.2.4.2 Molecular Viscosity

The molecular viscosity μ establishes the proportionality between the friction force in the direction of the flow and the velocity gradient in the orthogonal direction. Figure 3.16 presents the dependence on temperature of μ for Ar, H_2, and He at atmospheric pressure.

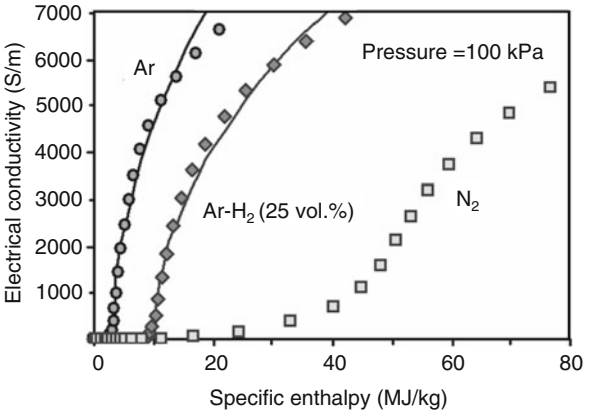


Fig. 3.15 Electrical conductivity (linear scale) (S/m) as function of the specific enthalpy for Ar, N_2 and Ar–H_2 (25 vol.%) at atmospheric pressure [5], reprinted with the kind permission of Springer

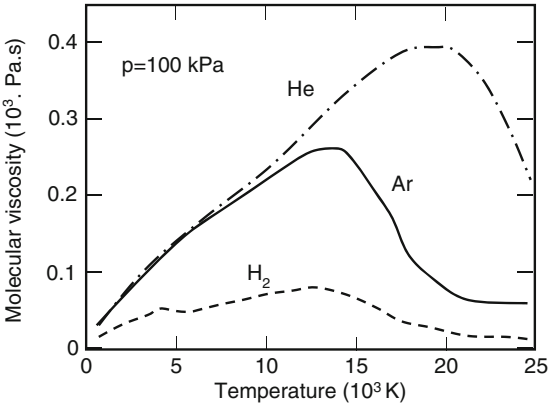


Fig. 3.16 Molecular viscosity (Pa s) as function of temperature for Ar, He and H_2 at atmospheric pressure [5], reprinted with the kind permission of Springer

The molecular viscosity of thermal plasmas reaches its maximum when the volume fraction of electrons in this plasma reaches about 3 %. For higher percentages of charged particles, the long distance interactions between such particles diminish drastically the interactions between the gas particles and the viscosity decreases. At its maximum, the plasma molecular viscosity is about ten times that of the cold gas. This difference partly explains the difficulty of mixing cold gases with plasmas. However, the difference also protects the plasma core from rapid cooling by mixing with the air entrained by the high velocity plasma jet.

When mixing hydrogen with argon (less than 30 vol.% in plasma spraying), the viscosity of argon is only slightly reduced because the mixture mass is mainly controlled by that of argon. The viscosity of nitrogen is about that of argon, and hydrogen addition does not modify it appreciably. When adding helium (up to 60 vol.%) to argon, the decrease of the viscosity above 10,000 K is not so fast, and the viscosity keeps increasing up to about 15,000 K (where it starts to decrease due to the beginning of helium ionization). This effect allows running slightly longer Ar–He jets than those obtained with Ar–H_2 mixtures in air atmosphere.

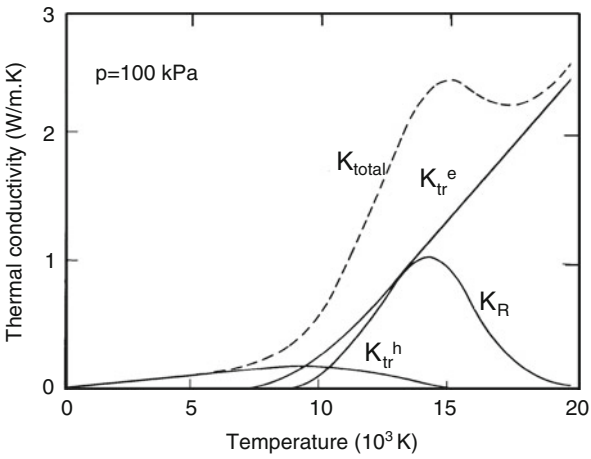


Fig. 3.17 Temperature dependence of the total, κ_{total}, electron translational, κ_{tr}^{e}, heavy species translational, κ_{tr}^{h}, reactional, κ_R, and total thermal conductivities (W/m K) of Ar at atmospheric pressure [5], reprinted with the kind permission of Springer

3.2.4.3 Thermal Conductivity

The thermal conductivity of thermal plasmas is of primary importance because it controls the energy losses in the arc or r.f. discharge fringes, and thus the discharge behavior, as well as the heat transfer to solid materials or sprayed particles. Thermal conductivity κ can be split into three important terms:

- κ_{tr}^{h} corresponding to the translational thermal conductivity of heavy species and thus decreasing when the electron percentage is about 3 % and of course tending to zero for temperatures where ionization is almost completed: about 15,000 K for argon
- κ_{tr}^{e} corresponding to the translational thermal conductivity of electrons, which becomes important above 8,000 K (electron percentage over 1 %)
- κ_R reactional thermal conductivity, which can be very important as soon as dissociation and ionization occur

Finally one has

$$\kappa_{total} = \kappa_{tr}^{h} + \kappa_{tr}^{e} + \kappa_R \tag{3.12}$$

Figure 3.17 illustrates the temperature dependence of these three terms and their sum for argon at atmospheric pressure. The reactional thermal conductivity appears when ionization starts and it goes towards zero when ionization is fully completed.

The dominance of the reactional thermal conductivity when dissociation occurs explains why hydrogen is added to argon: it improves the heat transfer at temperatures above about 3,000 K where dissociation starts. Figure 3.18 shows how the thermal conductivity increases with the volume percentage of hydrogen in an argon–hydrogen mixture, especially when dissociation and ionization occur. With 30 vol.% hydrogen, which is generally the maximum used in plasma spraying, the thermal conductivity of the mixture is increased by a factor of 12.

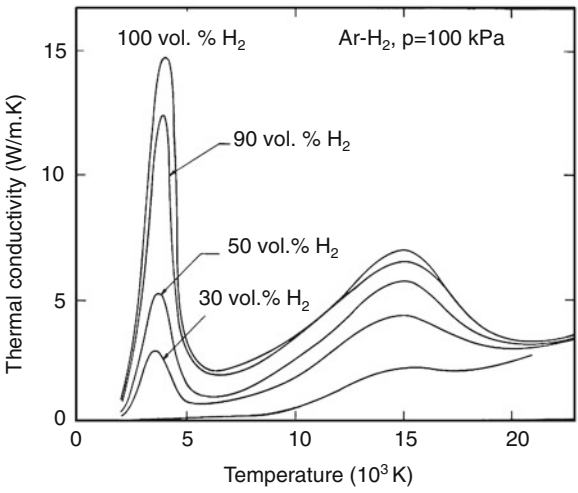


Fig. 3.18 Temperature dependence of the total, κ_{total}, thermal conductivity (W/m K) of the mixture Ar–H_2, with volume percentages varying between 0 and 100 %, at atmospheric pressure [5], reprinted with the kind permission of Springer

The influence of the addition of light gases to argon on the thermal conductivity of the mixture is illustrated in Fig. 3.19 presenting its dependence on temperature for three conventional spray mixtures: Ar, Ar–He (50 vol.%), and Ar–H_2 (25 vol.%). As can be seen, the best result is obtained with the Ar–H_2 mixture with the strong dissociation peak between about 2,500 and 5,000 K. The addition of helium increases the thermal conductivity more regularly, resulting in a value between that of pure argon and the argon–hydrogen mixture. Of course, at temperatures above 15,000 K, the ionization of helium boosts the mixture thermal conductivity.

In the presence of steep temperature gradients, such as those observed in the thermal boundary layer surrounding a particle in flight in a plasma jet, careful attention must be given to the way the heat transfer is calculated. Bourdin et al. [6] have suggested using the mean effective or integrated thermal conductivity κ' to calculate the heat transfer coefficient. κ' is defined as

$$\kappa' = \left[1/\left(T_p - T_s\right)\right]\int_{T_s}^{T_p}\kappa(T)\cdot dT = \frac{I_p - I_s}{\left(T_p - T_s\right)} \tag{3.13}$$

with

$$I_x = \int_{T_O}^{T_X}\kappa(T)\cdot dT \tag{3.14}$$

where T_x corresponds to the temperature limits across which the energy transfer is taking place, T_p the plasma temperature outside the boundary layer and T_s the particle surface temperature. Figure 3.20 presents κ' for three different plasma spray mixtures: Ar–H_2 (26 vol.%), Ar–H_2 (11 vol.%), and Ar–N_2 (11 vol.%). This figure highlights the advantage of using diatomic gases to improve the integrated thermal conductivity of the mixture. When adding hydrogen to argon, κ' increases over

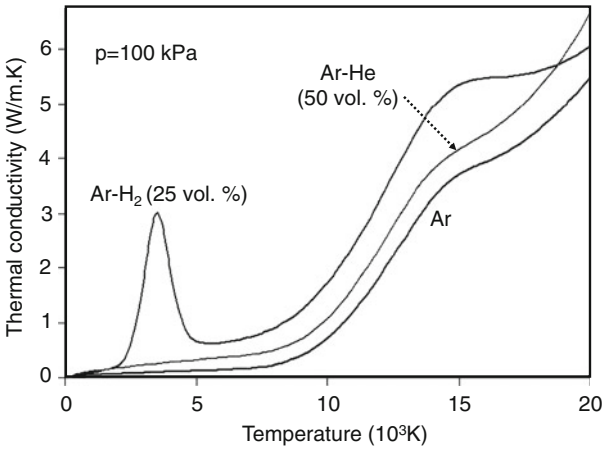


Fig. 3.19 Temperature dependence of the total, κ_{total}, thermal conductivity (W/m K) of mixtures Ar–H_2 (25 vol.%), Ar–He (50 vol.%), and pure Ar at atmospheric pressure [5], reprinted with the kind permission of Springer

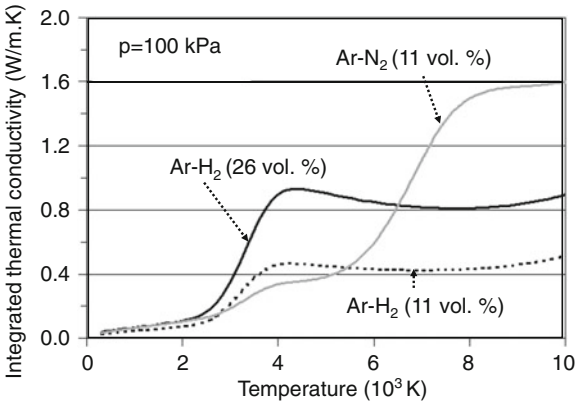


Fig. 3.20 Temperature dependence of the mean effective or integrated thermal conductivity κ' (W/m K) of mixtures Ar–H_2 (26 vol.%), Ar–H_2 (11 vol. %), and N_2–H_2 (11 vol.%) at atmospheric pressure [5], reprinted with the kind permission of Springer

3,000 K and becomes almost constant over 4,000 K, but larger by a factor of about four for the 11 vol.% of H_2 mixture and of about ten for the 26 vol.% mixture. In nitrogen–hydrogen plasmas, where the hydrogen percentage is generally below 12 vol.%, first κ' increases between 3,000 and 4,000 K, but then the nitrogen dissociation, between about 6,000 and 8,500 K, raises it drastically, κ' being multiplied by a factor of about sixteen above temperatures of 8,500 K compared to its value at 2,000 K. This strong increase of the heat transfer at 8,500 K, which is also the temperature at which the plasma can sustain an arc (see Fig. 3.14), explains the particular behavior of nitrogen arc columns [7]. Thus the arc column is self-constricted, which is not the case of the argon–hydrogen plasma, where the heat transfer between the arc column and its cold boundary layer depends strongly on the amount of hydrogen.

3.3 Basic Concepts in Modeling

3.3.1 Introduction

Physical and chemical processes occurring in heat and/or momentum sources of spray processes and the interaction with particulate matter in spray guns are highly complex and still poorly understood phenomena. They involve intricate interactions between fluid dynamics, turbulent transport, thermal radiation, chemical reactions, and changes in phases. Modeling of such processes has been a long-standing challenge.

Such developments have been possible thanks to the improvement of our knowledge base of thermodynamic and transport properties that were a prerequisite for modeling especially of thermal plasmas.

Another complication which modeling of thermal plasma systems has to face are deviations from Local Thermodynamic Equilibrium (LTE). Regions of steep gradients in plasmas and/or high velocities in plasma jets are mainly responsible for such deviations that impose severe problems on modeling work. However such problems are beyond the aim of this book and will not be discussed.

The thermal spray processes are multiphase flow systems in which the gas dynamics and particle dynamics are coupled with each other. However, because the particle loading is generally low, the assumption of one-way coupling is usually made. With this assumption the existence of particles has a minimal influence on the gas dynamics, while the particle velocity and temperature can be determined based on the two-phase momentum and heat transfer equations. It is however important to check this loading effect in spray processes where too many injected particles reduce their temperatures and velocities.

To summarize, in most cases, a realistic model should be three dimensional to enable taking into consideration the transverse injection of a cold gas and three-dimensional character of turbulence structures. It should also take into account the effect of the arc root movement on the d.c. plasma flow (nonstationary model). At last the compressibility effects, which are obvious for plasma jets flowing in a low pressure atmosphere (below 30–20 kPa), HVOF or HVAF, D-gun, and cold spray, must be considered.

3.3.2 Conservation Equations

Serious modeling efforts have to be based on first principles, i.e., on solutions of the conservation equations with appropriate boundary conditions [8–12]. The conservation equations represent a set of coupled, nonlinear differential equations, which have to be solved simultaneously to obtain the desired results that include temperature and velocity fields, species concentrations, heat and enthalpy fluxes and electrical characteristics for plasmas. The general equations used to model the

different spray processes are presented below. In each chapter, related to a given spray process, they will be either redevelop or the modifications to be used in equations presented below summarily described. In all cases the reader will be redirected to the corresponding references.

3.3.2.1 Continuity Equations

The continuity equations comprise a set of equations describing conservation of mass, conservation of species, and conservation of electrical charges (electrical current in plasmas). Conservation of electrical current applies only to "active," current-carrying plasmas (for example, to electric arcs), not to "passive," non-current-carrying plasmas such as plasma jets. Considering a gas comprised of k different species (for example, electrons, ionic species, neutral species for plasmas), the species conservation equation for species of type k may be written as

$$\frac{\partial \rho_k}{\partial t} + \nabla \cdot \left(\rho_k \vec{\nu}_k \right) = \Gamma_k \tag{3.15}$$

where ρ_k represents the mass density, v_k the velocity and Γ_k the mass generation rate of species of type k. By introducing the concentration

$$c_k = \rho_k / \rho \quad \text{with} \rho = \sum_k \rho_k \tag{3.16}$$

and the mass flux

$$\vec{I}_k = \rho_k \left(\vec{\nu}_k - \vec{\nu}_g \right) \tag{3.17}$$

where v_g is the velocity of the center of mass, Eq. (3.16) may be transformed into

$$\rho \frac{Dc_k}{\mathrm{d}t} + \nabla \cdot I_k = \Gamma_k \tag{3.18}$$

by using the substantive derivative

$$\frac{D}{\mathrm{d}t} = \frac{\partial}{\partial t} + \left(\vec{\nu}_g \cdot \nabla \right) \tag{3.19}$$

Equation (3.19) is an alternate equation describing species conservation.

Summation over all species k transforms Eq. (3.16) into an overall mass conservation equation

$$\frac{\partial \rho}{\partial t} + \nabla \cdot \left(\rho \vec{\nu}_g \right) = 0 \tag{3.20}$$

making use of the fact that $\sum_k \Gamma_k = 0$

An alternate form of Eq. (3.19) may be obtained by introducing Eq. (3.18) into Eq. (3.19):

$$\frac{\mathrm{d}\rho}{\mathrm{d}t} + \rho \cdot \nabla \cdot \nu_g = 0 \tag{3.21}$$

For plasmas, the space charge density is given by

$$\rho_{\mathrm{el}} = e(n_{\mathrm{i}} - n_{\mathrm{e}}) \tag{3.22}$$

The charge or current conservation equation may be expressed by (for derivation see Sect. 5.7 of [5])

$$\frac{\partial \rho_{\mathrm{el}}}{\partial t} + \nabla \cdot \vec{j} = 0 \tag{3.23}$$

where e is the elementary charge, n_{i} and n_{e} are ion and electron density, respectively, and $\vec{j}$ is the current density vector.

By specifying a particular coordinate system (one-, two-, or three dimensional), these continuity equations can be expressed in terms of this coordinate system.

As an example, a steady and $\left(\frac{\partial}{\partial t} = 0 \right)$ rotationally symmetric plasma flow will be considered, which implies that cylinder coordinates (r, z, φ) should be used. The velocity vector shall have two components

$$\vec{\nu}_g = \vec{\nu}_g(u, v, o) \tag{3.24}$$

With these assumptions Eq. (3.16) translates into

$$\frac{\partial}{\partial z}(\rho_k u_k) + \frac{1}{r}\frac{\partial}{\partial r}(\rho_k r v_k) = \Gamma_k \tag{3.25}$$

where the index k indicates the different species present in the plasma (electrons, ions, neutrals) and Γ_k accounts for the mass generation rate of species of type k due to chemical reactions.

In a similar way, Eq. (3.21) translates into

$$\frac{\partial}{\partial z}(\rho u) + \frac{1}{r}\frac{\partial}{\partial r}(\rho r v) = 0 \tag{3.26}$$

which is the overall mass conservation equation for this particular situation.

Assuming that the electric current has only a z- and r-component, Eq. (3.24) translates into

$$\frac{dj_z}{dz} + \frac{1}{r}\frac{\partial}{\partial r}(r \cdot j_r) = 0 \tag{3.27}$$

Besides this simple example, the previously discussed continuity equations may be written for other coordinate systems and for steady as well as for nonsteady situations.

3.3.2.2 Momentum Equations

The overall momentum equation, which is identical to the basic equation of hydrodynamics, may be written as

$$\rho \frac{D\vec{v}_g}{\mathrm{d}t} = -\nabla p + \sum_k \rho_k \vec{F}_k \tag{3.28}$$

where p is the total pressure considering contributions from all species present in the plasma and $\vec{F}_k$ represents external forces. Possible external forces are important electric forces due to applied electric fields, magnetic forces due to external or self-magnetic fields for plasmas, pressure forces provided that there are significant pressure gradients, pressure jump when the detonation wave front passes. . .. Forces due to gravity are generally negligible for spray guns.

Internal forces do not appear in Eq. (3.29), because internal forces cannot move the center of gravity. But internal forces, such as friction and thermal diffusion may play an important role. Such forces will appear in the momentum equation of individual species. For species of type k the momentum equation assumes the form

$$\frac{\partial \rho_k \vec{\nu}_k}{\partial t} + \nabla \cdot \left(\rho_k \vec{\nu}_k \vec{\nu}_k\right) = -\nabla p_k - \nabla \cdot \overline{\overline{\tau}}_k + \rho_k \vec{F}_k + \sum_j \vec{F}_{kj} \tag{3.29}$$

where v_k is the velocity vector of species k,

$\overline{\overline{\tau}}_k$ is the stress tensor of species k and

$$p_k = n_k \cdot k_\mathrm{B} \cdot T \tag{3.30}$$

is the partial pressure of species k.

$\vec{F}_k$ represents the rate of momentum transfer between species k and other species j. For example, in d.c. plasmas, assuming that only electric and magnetic forces are present, the term describing external forces can be expressed by

$$\rho_k \vec{F}_k = e_k n_k \vec{E} + e_k n_k \left(\vec{\nu}_k x \vec{B} \right) \tag{3.31}$$

where e_k is the electric charge,

n_k is the number density of species of type k,

$\vec{E}$ is the applied electric field

and $\vec{B}$ represents the magnetic induction.

Assuming charge neutrality

$$\sum_k e_k n_k = 0 \tag{3.32}$$

the mass-averaged momentum equation assumes the form

$$\frac{\partial \rho \vec{\nu}_g}{\partial t} + \nabla \cdot \left(\rho \vec{\nu}_g \vec{\nu}_g \right) = -\nabla p - \nabla \cdot \overline{\overline{\tau}} + \vec{j} \times \vec{\mathrm{B}} \tag{3.33}$$

This equation may be written for any desired coordinate system.

As an example, the same two-dimensional situation will be considered specified in the previous section (cylindrical coordinates r, z, φ). In this case, Eq. (3.34) transforms into two equations for the z- and r-direction:

z-direction:

$$\rho u \frac{\partial u}{\partial z} + \rho v \frac{\partial u}{\partial r} = -\frac{\partial p}{\partial z} + 2\frac{\partial}{\partial z}\left(\mu \frac{\partial u}{\partial z} \right) + \frac{1}{r}\frac{\partial}{\partial r}\left(\mu r \frac{\partial u}{\partial r} \right) + \frac{1}{r}\frac{\partial}{\partial r}\left(\mu r \frac{\partial v}{\partial r} \right) + j_r \mathrm{B}_\varphi \tag{3.34}$$

r-direction:

$$\rho u \frac{\partial v}{\partial z} + \rho v \frac{\partial v}{\partial r} = -\frac{\partial p}{\partial z} + \frac{\partial}{\partial z}\left(\mu \frac{\partial v}{\partial z} \right) + \frac{2}{r}\frac{\partial}{\partial r}\left(\mu r \frac{\partial v}{\partial r} \right) + \frac{\partial}{\partial z}\left(\frac{\partial v}{\partial r} \right) - \frac{2\mu v}{r^2} - j_z \mathrm{B}_\varphi \tag{3.35}$$

3.3.2.3 Energy Equations

The energy equation may be written in the form (for derivation see Chap. 5 in [5]):

$$\rho \frac{d}{dt}\left(\frac{v_g^2}{2} + u_g \right) = -\nabla \cdot \left(p \vec{v}_g + \vec{W} \right) + \sum \vec{F}_k \cdot \rho_k \vec{v}_k \tag{3.36}$$

In this equation, u_g is the internal energy of the system and W is the heat flux vector. This equation represents a typical balance equation, i.e., (rate of change of

the total energy in the system) = (net flux of work and heat into the system) + (energy dissipation in the system).

By introducing the expression for the substantive derivative, Eq. (3.35) transforms into

$$\rho\frac{\partial}{\partial t}\left(\frac{v_g^2}{2}+u_g\right)+\rho\vec{v}_g\nabla\left(\frac{v_g^2}{2}+u_g\right)=-\nabla\cdot\left(p\vec{v}_g+\vec{w}\right)+\sum\vec{F}_k\cdot\rho_k\vec{v}_k \quad (3.37)$$

For example, in the case of steady-state plasma in LTE with negligible viscous dissipation and under optically thin conditions this equation reduces to

$$\rho\vec{v}_g\nabla\left(\frac{v_g^2}{2}+h\right)+\nabla\cdot\vec{W}=\vec{j}\cdot\vec{E}+\frac{5}{2}\vec{j}\cdot\nabla T-S_R(\rho,T) \quad (3.38)$$

where h is the enthalpy. The first two terms on the r.h.s. of Eq. (3.39) represent the Ohmic heating term and an energy dissipation term which becomes important if $\vec{j}$ and ∇T are parallel which is, for example, the case in the electrode boundary layer of electric arcs. In the case of a fully developed arc column, $\vec{j}$ and ∇T are perpendicular to each other, i.e., $\vec{j}\cdot\nabla T=0$.

Again, the energy equations [Eq. (3.37) or (3.38)] may be written for any desired coordinate system. As an example, the same two-dimensional situation as discussed in (a) and (b) of this section will be adopted resulting in the following equation:

$$\begin{aligned}\rho u\frac{\partial h}{\partial z}+\rho v\frac{\partial h}{\partial r}=&\frac{\partial}{\partial z}\left(\frac{\kappa}{c_p}\frac{\partial h}{\partial z}\right)+\frac{1}{r}\frac{\partial}{\partial r}\left(\frac{\kappa}{c_p}\frac{\partial h}{\partial r}\right)+\frac{j_z^2+j_r^2}{\sigma_e}\\&+\frac{5}{2}\frac{k}{e}\left(\frac{j_z}{c_p}\frac{\partial h}{\partial z}+\frac{j_r}{c_p}\frac{\partial h}{\partial r}\right)-S_r(\rho,T)\end{aligned} \quad (3.39)$$

where c_p is the specific heat at constant pressure and $S_R(\rho,T)$ the optically thin radiation term. The LHS of this equation represents two convection terms, followed by two heat conduction terms on the RHS. The next term accounts for Joule heat dissipation, followed by another heat dissipation term which is not negligible for situations in which $\frac{\partial h}{\partial z}\neq 0$ and $j_r\neq 0$. The last term in Eq. (3.38) accounts for optically thin radiation.

3.3.2.4 Electromagnetic Field Equations

Electromagnetic field equations required for modeling of arcs and plasma jets include:

- Charge or current conservation equation
- Poisson equation

- Ohm's law
- Magnetic field equation

For $\frac{\partial \vec{B}}{\partial t} = \frac{\partial \vec{E}}{\partial t} \approx 0$ modeling of arcs, changes of electric or magnetic fields may be assumed to be relatively slow.

Conservation of charge has been already discussed in part (a) and will not be reiterated here. The Poisson equation reads as

$$\nabla . \vec{E} = \frac{\rho_{\mathrm{el}}}{\varepsilon_0} = \frac{e \cdot (n_{\mathrm{i}} - n_{\mathrm{e}})}{\varepsilon_0} \tag{3.40}$$

where ρ_{el} is the space charge density, n_{i} and n_{e} the ion and electron density, respectively, and ε_0 is the dielectric constant. With

$$\vec{E} = -\nabla \Phi \tag{3.41}$$

Equation (3.41) becomes

$$\nabla^2 \Phi = -\frac{\rho_{\mathrm{el}}}{\varepsilon_0} \tag{3.42}$$

Ohm's law in the simplest form may be written as

$$\vec{j} = \sigma_e \vec{E} \tag{3.43}$$

which implies that there are no other significant driving forces for the electric current besides the applied electric field. As shown in Chap. 5 of the book of Boulos et al. [5], there may be additional driving forces such as temperature gradients, pressure gradients, $\vec{v}_e x \vec{B}$ force induced by a magnetic field on electrons, etc., which contribute to the current flow.

The magnetic induction, which appears in the momentum equations may be determined from one of Maxwell's equations, i.e.,

$$\nabla \times \vec{B} = \mu_0 \vec{j} \tag{3.44}$$

where μ_0 is the magnetic permeability constant. The electromagnetic field equations may be written in terms of any desirable coordinate system. As an example, the transformation of Eq. (3.45) into cylindrical coordinates will be considered assuming that $\vec{B}$ has only a φ-component, i.e.,

$$B_\varphi = \frac{\mu_0}{r} \int_0^r j_z \zeta d\zeta \tag{3.45}$$

where ζ is a dummy variable.

3.3.2.5 Laminar or Turbulent Flows

The assumption of laminar flow entails relatively low mass flow rates. For example, arcs with little or no superimposed flow are mainly used in laboratories. In contrast arcs exposed to substantial flows are of great practical interest, as, for example, in the development of arc gas heaters and plasma torches. The flow in this case is usually turbulent, except that in the plasma core it is laminar, which requires models able to treat both laminar and turbulent flows.

Turbulence is one of the most puzzling phenomena in fluid dynamics and even more so in thermal plasma technology, which is, to a large degree, governed by turbulent flow situations. In spite of many successful commercial developments over the years, the underlying physics of turbulence in plasma flows is still poorly understood. Therefore, it is not surprising that the presence of turbulence adds another dimension of complexity to the already complex situation in spray flow systems.

Turbulence is characterized by highly random, nonsteady, and three-dimensional effects in the flow. Turbulent flow, in principle, can be described by the Navier–Stokes (NS) equations. Unfortunately, these equations cannot be solved for most practical problems, because such turbulent flows encompass a wide range of turbulent eddy sizes from the size of the domain of interest, down to sizes below those at which viscous dissipation and chemical reactions occur. This fact translates into corresponding requirements in terms of the number of spatial grid cells and the resultant time steps for all-scale resolution which is far beyond the capacity and speed of available computers today.

Turbulent transport properties require closure assumptions, because information is lost in the averaging process. Due to the nonlinearity of the governing equations, the averaging process introduces unknown correlations, e.g., between fluctuating velocities and between velocities and scalar fluctuations. This implies that the governing equations can only be solved if the turbulence correlations are specified. Determining such correlations is one of the main problems in calculating turbulent flow. The choice of the closure assumptions requires specification of the proper turbulence model. A number of models have been proposed to solve this closure problem, including

- Zero-equation models
- One-equation models
- Two-equation models
- Stress/flux-equation models
- Scalar-fluctuation models

These models have been classified according to the number of turbulence parameters that appear as dependent variables in the differential equations. All these models listed above have been reviewed in detailed surveys [13–25]. The simplest models relate the turbulence correlations directly to the local mean flow quantities, while the most complex models solve differential transport equations for the individual turbulence correlations. The choice of the proper turbulence model

depends on the requirements of the problem and thus on the compromise between two factors: (1) the complexity of the model and the availability of computational resources and (2) the applicability and accuracy of the information needed. A good turbulence model should provide sufficient universality, but should not be too complex to use. A rather simple assumption is that of the mixing length. In the mixing length model, the turbulent viscosity μ_t is given by

$$\mu_t = L_m \frac{du}{dy} \tag{3.46}$$

and the main problem is to find an expression giving the mixing length L_m.

A very popular model is the two-equation k–ε turbulence model. In this model, the three turbulent fluctuation components, u', v', and w' are integrated in the expression of the turbulent kinetic energy through

$$k = \frac{1}{2}\left(\overline{u'^2} + \overline{v'^2} + \overline{w'^2}\right) \tag{3.47}$$

It allows modeling the *isotropic* turbulence by solving one equation related to k and another one to ε the turbulent energy dissipation. It is possible to combine a k–ε turbulence model with a mass-weighted averaging concept in his model. A multiple time scale turbulence model, using one time scale for velocity fields and another for scalar fields, was first proposed for parabolic-type flows. The ability to predict both unweighted and mass-weighted mean temperatures can be achieved by adopting mass-weighted averaging for transport equations and a probability density function. This model offers a linkage for correlating different measurement methods, e.g., spectroscopy and enthalpy probes for plasma temperatures. The aforementioned parabolic model has been extended to more general situations for two-dimensional plasma flows, allowing, for example, the presence of a swirl component, a cross-stream pressure gradient, or even recirculation. However, the coefficients involved in the closure model must be reoptimized to achieve better overall agreement with available experimental data. Caution has to be exercised in applying the various turbulence models. For example, the traditional high-Reynolds-number k–ε modeling method, which has been successfully used in fully developed flow regions, may not be appropriate for modeling of plasma jets. k–ε models are not well adapted to describe flows where the turbulence intensity is low or comprising a laminar core followed by a turbulent plume as in plasma jets. The turbulence intensity in k–ε low Reynolds models is addressing this issue by defining a turbulent Reynolds number Re_t representing the ratio between turbulent and laminar viscosities

$$\mathrm{Re}_t = \frac{\overline{\rho} k^2}{\mu \varepsilon} \tag{3.48}$$

and by modifying the turbulence constants C_μ and C_z of the standard k–ε model by expressions depending on Re_t. Another point where the k–ε models are poor (even

the low Reynolds ones) is when the jet impacts on a surface (for example, the substrate in various spray processes). The model cannot be applied for boundary layers where the flow is laminar and also where laws are used to describe the friction and the thermal exchange with the wall. To solve this problem, Yap [26] has proposed to add a source term in the equation of turbulent energy to modify the characteristic turbulence length towards a local equilibrium value close to the wall. Chen and Kim [27] have also proposed to add a source term in the equation of turbulent energy which represents the transition of the turbulence energy transfer at large scale to that at small scale within the boundary layer.

Other models have also been used for the turbulence:

- The R_{ij}–ε model solving transport equations of Reynolds stress ($R_{ij} = \overline{u'_i u'_j}$) and the heat fluxes of turbulence. This approach allows solving the weakness of the k–ε model linked to the turbulent viscosity and the assumption of isotropic turbulence. This model is however time expensive. In 3D cases it is necessary to solve 8 equations instead of 2 for the standard k–ε model and the use of a finer grid. It also requires more empirical constants than the standard k–ε [17].
- The *Re* Normalization Group (RNG) $|k$–$\varepsilon|$ model is derived from the use of a rigorous statistics applied to Navier–Stokes equations. It represents, better than the k–ε low Reynolds model, flows with low Reynolds numbers, especially close to walls [17].

To illustrate the differences between the turbulence models, E. Legros [28] has calculated a 2D-stationary d.c. plasma jet using the k–ε and two versions of the R_{ij}–ε models and compared results with experimental values. The plasma jet was produced by a d.c. plasma torch PTF4 type with a 7 mm i.d. anode nozzle working with 45 splm argon and 15 splm hydrogen, an arc current of 600 A, corresponding to a voltage of 65 V and a thermal efficiency of 55 %. Figure 3.21a, b represents respectively the velocities and temperatures calculated along the torch axis. As can be seen, the differences between the different turbulence models are not very significant while the computation time between k–ε and R_{ij}–ε is more than one order of magnitude. Compared to experimental results the cooling down of the jet is much faster than that given by the experiment (see Fig. 3.21b). The air entrainment is also under estimated compared to experiments (see Fig. 3.21c).

3.3.3 Gas Composition, Thermodynamic, and Transport Properties

3.3.3.1 Gas Composition

The gas composition depends on reaction rates linked to local temperature and pressure. Different assumptions can be assumed regarding the reaction rates, including:

1. Infinitely fast reaction rate (equilibrium calculation): equilibrium compositions are obtained by minimizing the Gibbs free energy [29]. The data are given in

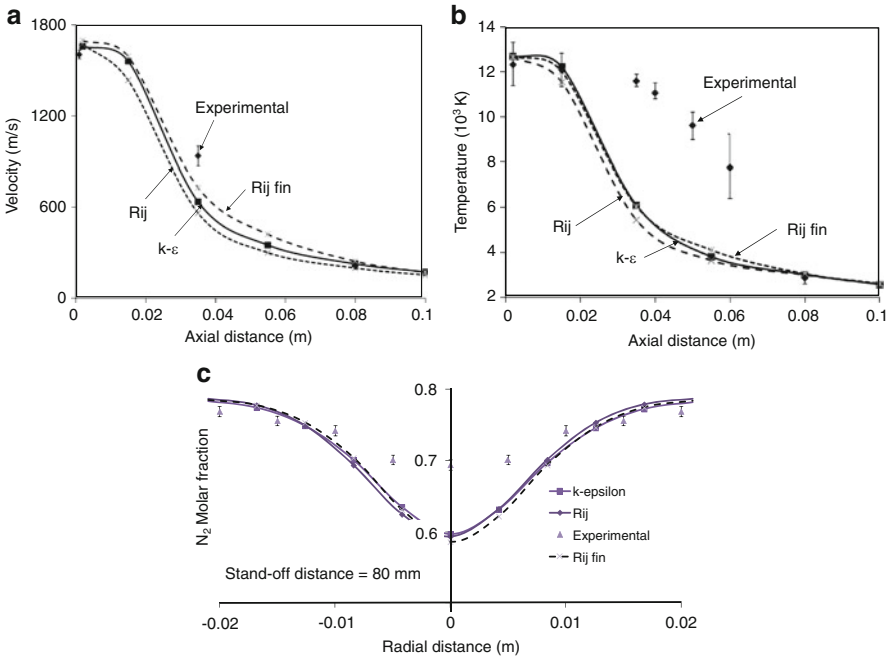


Fig. 3.21 Velocity (**a**) and temperature (**b**) profiles along the axis of a d.c. plasma jet calculated with different turbulence models (the k–ε and two versions of the R_{ij}–ε), evolutions and (**c**) the corresponding radial profile of the volume percentage of nitrogen in the air entrained along the jet at a standoff distance of 80 mm [28]

different tables such as those of Thermodata [30], Janaf [31], and Gurvich et al. [32]. The data in each table are coherent among themselves, but not necessarily between tables, especially for plasmas over 6,000 K. In most cases plasma flows are calculated at equilibrium.

2. Finite reaction rate in Arrhenius (see Eq. 3.7): the multireaction simulations use a number of intermediate chemical species the number of which increases with temperature when dissociation and of course ionization (at higher temperatures) occur. For example, in combustion a few tens of reactions should be considered and a higher number of reversible reactions. Then the time rate of change of the concentration of a given species is given by Eq. (3.5). This results in a set of nonlinear equations, which can be solved numerically, knowing the initial values of n_i, to determine the composition at time t [33]. The data for calculations have to be checked carefully and they must satisfy the following equation:

$$k_f/k_r = K_x \tag{3.49}$$

where k_f is the forward reaction rate, k_r the reverse reaction rate and K_x the molar fraction equilibrium constant related to the considered reaction. Many of the data

are gathered in the database of Chemkin [34]. However these rates can be computed from the Arrhenius rate expressions (see Eq. 3.7) when turbulence is not the dominating mechanism, which is not the case in flames and HVOF. For plasmas, kinetic calculations are used when a cold gas, reacting or not, is injected into the plasma jet and the induced reactions are of interest. In most cases in spray processes the plasma jet perturbation by the cold carrier gas is neglected as soon as the carrier gas mass flow rate does not exceed 10 % of the plasma gas mass flow rate (for more details see Sect. 4.4.2.4). In flame or HVOF spraying such kinetic calculations have been used in most cases to demonstrate that equilibrium calculation is sufficient to characterize the flame.

3. Finite reaction rate limited by turbulent mixing, which assumes that the reaction rate is limited by the turbulent mixing rate of components, or the reaction is instantaneous as the reactants are mixed together. This approach is currently used in combustion processes; see, for example, Bandyopadhyay and Nylén [35], but not in plasmas where the jet characteristics mainly depend on phenomena occurring in the laminar core.

3.3.3.2 Thermodynamic Properties

Once the composition is determined the different thermodynamic properties are relatively easy to calculate, even in plasmas [5].

3.3.3.3 Transport Properties

They are rather complex to calculate in plasmas, because, up to now, they have been calculated only for a few species and mixtures containing only two different species. The calculation of complex mixtures is rather long even if all interactions potentials are known, which is not necessarily the case. Thus simplified mixing rules are used [5]. However the diffusion coefficients, which must be used to account for species diffusion within flows, are very often unknown.

3.4 Summary and Conclusions

Many spray processes are based on combustion flames at atmospheric or higher pressures, or on thermal plasmas produced by blown or transferred arcs, or radio frequency inductively coupled discharges, mainly at atmospheric pressure but also at lower pressures and in some cases above atmospheric pressure. The principal objective of this chapter is to present a comparative overview of the different available technologies for thermal spraying, without going at this stage into details of the properties of flames and plasmas to which books have been devoted.

This chapter is devoted to the description of the thermodynamic and transport properties of these high-energy jets: composition of the gas, enthalpy and specific heats, transport properties such as electrical conductivity, thermal conductivity, and viscosity, which are of critical importance for the understanding of the basic phenomena in the transfer heat between hot jets and particles and particles entrainment. For flames and plasmas the differences between kinetic and equilibrium conditions are also discussed because of their importance close to walls, controlling the flame, or plasma development.

Of course for flames, besides hot gas properties, flammability, and explosive conditions are very important for working and safety conditions. The design principle of the gun to achieve flame or detonation is discussed to introduce D-guns.

At last the conservation equations are represented by a set of coupled, nonlinear differential equations, which have to be solved simultaneously to obtain the desired results that include temperature and velocity fields, species concentrations, heat and enthalpy fluxes, and electrical characteristics for plasmas. The heat, mass, and momentum transfers' hot gas particles are discussed in Chap. 4, while the description of spray guns is presented in Chap. 5 for flames and Chaps. 7–10 for plasmas.

Nomenclature

In the following when no unit is given in parenthesis, it means that the quantity is dimensionless

a	Thermal diffusivity of the combustion wave ($\kappa/\rho\ c_\mathrm{p}$) ($\mathrm{m^2/s}$)
B	Magnetic induction (T)
c_k	Concentration of species of type k
c_p	Specific heat at constant pressure (J/K kg)
D	Detonation velocity (m/s)
e	Elementary charge (C)
E	Electric field strength (V/m) or energy (J)
E_I	Ionization energy (J or eV)
F	External forces per unit mass (N/kg)
F_k	Represents external forces (N)
F_{kj}	Rate of momentum transfer between species k and other species j ($\mathrm{kg/m^2\ s^2}$)
F/A	Molar ratio of fuel to oxidizer
g	Statistical weight
h	Planck's constant (6.6×10^{-34} J s)
h_m	Enthalpy per unit mass (J/kg)
k_B	Boltzmann constant (1.13×10 J/kg particle)
k_R	Specific reaction rate constant
I_k	Mass flux of particles of type k ($\mathrm{kg/m^2\ s}$)
I_p	Heat flux potential: $I_\mathrm{p} = \int_{T_\mathrm{o}}^{T_\mathrm{p}} \kappa(T)\mathrm{d}T(\mathrm{W/m})$

I_s Heat flux potential: $I_s = \int_{T_o}^{T_s} \kappa(T)\mathrm{d}T(\mathrm{W/m})$
j Current density ($\mathrm{A/m^2}$)
k_f Forward reaction rate, $k_f = A \times T^B \times \exp(-E/kT)$ ($\mathrm{m^3}$/part s)
k_r Reverse reaction rate, for a binary reaction ($\mathrm{m^3}$/part s)
K_x Molar equilibrium constant ($K_x = k_f/k_r$)
M Arbitrary specification of all chemical species
M_e Mach number
(M_i) Concentration of species i ($\mathrm{m^{-3}}$)
m Mass (kg)
N_i Number species i
n' Total number of compounds involved in a chemical reaction
n Number density of particles ($\mathrm{m^{-3}}$)
n_i Number density of species i: $n_i = N_i/V$ ($\mathrm{m^{-3}}$)
p_i Pressure of species i (Pa)
p Total pressure (Pa)
q Chemical energy release at constant pressure (J/kg)
Q Partition function
R Perfect gas law constant (J/K kg)
R' Equivalence ratio or richness: $R = (F/A)/(F/A)_{\mathrm{stoichiometry}}$
R* Radical
RR Reaction rate (units depend on the species number involved)
r Radial coordinate (m)
S Entropy (J/K)
S_L Flame velocity (m/s)
S_R Optically thin radiation losses ($\mathrm{W/m^3}$)
S_u° Combustion wave velocity (m/s)
T Temperature (K)
t Time (s)
u Axial velocity component (m/s)
V Volume ($\mathrm{m^3}$)
v Radial velocity component (m/s)
v_g velocity of the center of mass (m/s)
v_k Velocity of particles of type k (m/s)
W Heat flux ($\mathrm{W/m^2}$)
x Coordinate (m)
z Axial coordinate (m); ion charge number

Mathematical Symbols

∇ Spatial derivative ($\mathrm{m^{-1}}$)
$\frac{\partial}{\partial t}$ Time derivative ($\mathrm{s^{-1}}$)

Greek Symbols

α' Multiplication factor of radicals
α Thermal diffusion factor (A/V m)
ΔE_{I} Lowering of the ionization energy (J or eV)
ε_{o} Dielectric constant (A s/V m)
Φ Electric potential (V)
Φ Dummy variable
Φ Time averaged dummy variable
Φ' Time fluctuating dummy variable
Γ_k Mass generation rate of species of type k (kg/m^3 s)
γ Ratio of specific heats
κ Thermal conductivity (W/m K)
κ' Integrated mean thermal conductivity

$$\kappa' = \left[1/\left(T_{\mathrm{p}} - T_{\mathrm{s}}\right)\right] \int_{T_{\mathrm{s}}}^{T_{\mathrm{p}}} \kappa(T) \cdot \mathrm{d}T (\mathrm{W/m\,K})$$

κ_{total} Thermal conductivity also noted κ (W/m K)
$\kappa_{\mathrm{tr}}^{\mathrm{h}}$ Translational thermal conductivity of heavy species (W/m K)
$\kappa_{\mathrm{tr}}^{\mathrm{e}}$ Translational thermal conductivity of electrons (W/m K)
κ_{R} Reactional thermal conductivity (W/m K)
μ Molecular viscosity (Pa s)
ν'_j Stoichiometric coefficient of the reactants
ν''_j Stoichiometric coefficient of the products
ρ_i Specific mass (kg/m^3)
ρ Total mass density (kg/m^3)
ρ_{el} Space charge density (C/m^3)
σ Electrical conductivity (S/m)
$\overline{\overline{\tau}}_k$ Stress tensor of species k (Pa)
ζ Dummy variable (m)

Subscripts

a Atoms
amb Ambipolar
b Burned gas
e Electrons
eff Effective value
i Ions
j Summation index
k Summation index
LES Large Eddy Simulation
max Maximum
NS Navier–Stokes

o	Reference value
r	Radial direction
u	Unburned gas
w	Wall
z	Axial direction
φ	Circumferential direction

References

1. Glassman I (1977) Combustion. Academic, New York, NY
2. Linde catalogue, Acetylene… there is no better fuel gas for Oxyfuel gas processes, Linde AG, Head Office, Klosterhofstr. 1, 80331 Munich, Germany
3. Mackie JC, Smith JC (1990) Inhibition of C_2 oxidation by methane under oxidative coupling conditions. Energy Fuels 4(3):277–85
4. Kee RJ, Rupley FM, Miller JA (1998) A Fortran chemical kinetics package for the analysis of gas-phase chemical kinetics, Sandia National Laboratories Report, SAND89-8009
5. Boulos M, Fauchais P, Pfender E (1994) Thermal plasmas, fundamentals and applications. Plenum Press, New York and London
6. Bourdin E, Boulos M, Fauchais P (1983) Transient conduction to a single sphere under plasma conditions. Int J Heat Mass Transfer 26:567–579
7. Nogues E, Fauchais P, Vardelle M, Granger P (2007) Relation between the arc-root fluctuations, the cold boundary layer thickness and the particle thermal treatment. J Therm Spray Technol 16(5–6):919–926
8. Oran ES, Boris JP (2001) Numerical simulation of reactive flow, 2nd edn. Cambridge University Press, Cambridge
9. Hirsch C (1988) Numerical computation of internal and external flows; vol I: Fundamentals of numerical discretization and numerical computation of internal and external flows and vol II: Computational methods for inviscid and viscous flows. Wiley, New York, NY
10. Hoffman KA, Chiang ST (1993) Computational fluid dynamics for engineers, vol 1. Engineering Educational Systems, Kansas
11. Kundu Pijush K, Ira Cohen M (2008) Fluid mechanics. Academic (4th revised ed.)
12. Falkovich G (2011) Fluid mechanics (a short course for physists). Cambridge University Press, Cambridge
13. Launder BE, Spalding DB (1972) Lectures in mathematical models of turbulence. Academic, London
14. Launder BE, Spalding DB (1974) The numerical computation of turbulent flow. Comput Methods Appl Mech Eng 35:269–289
15. Reynolds WC, Cebeci T (1976) Calculation of turbulent flows. In: Bradshaw P (ed) Turbulence. Springer, Berlin, p 193
16. Rodi W (1980) Turbulence models for environmental problems. In: Kollmann W (ed) Prediction methods for turbulent flows. Hemisphere Publishing Company, Washington, DC, p 260
17. Schiestel R. Modeling and simulation of turbulent flows, new technologies. Dunod University, Paris, France (in French)
18. Favre A, Kovasznay LSG, Dumas R, Gaviglio J, Coantic M (1977) The turbulence in fluid mechanics. Gauthier-Villars Editors, Paris
19. Pozorski J, Minier JP (1994) Lagrangian modeling of turbulent flows. EDF Report HE.106, 44/94

20. Shih TH, Liou WW, Shabbir A, Yang Z, Zhu J (1995) A new eddy viscosity model for high Reynolds number turbulent flows model development and validation. Comput Fluids 24:227–238
21. Sagaut P (1998) Introduction to large eddy scale simulations for the modeling of uncompresible flows, vol 30 (in French). Mathématiques et Applications. Springer
22. Pope SB (2000) Turbulent flows. Cambridge University Press, Cambridge
23. Archambeau F, Méchitoua N, Sakiz M (2004) Code_Saturne: a finite volume code for the computation of turbulent incompressible flows—industrial applications. Int J Finite Vol 1 (1):1–62
24. Pope SB (2004) Ten questions concerning the large-eddy simulation of turbulent flows. New J Phys 6(35):1–24
25. Bazilevs Y, Calo VM, Cottrell JA, Hughes TJR, Reali A, Scovazzi G (2007) Variational multiscale residual-based turbulence modeling for large eddy simulation of compressible flows. Comput Methods Appl Mech Eng 197(1–4):173–201
26. Yap C (1987) Turbulent heat and momentum transfer in recirculating and impinging flows. Ph.D., University of Manchester, G.B
27. Chen YS, Kim SW (1987) Computation of turbulent flows, turbulence closure models using and extended k-ε. NASA, CR-179204
28. Legros E. Contribution to 3D modelling of the plasma spray process and application to a two-torch process. University of Limoges, France, Nov 2003 (in French)
29. Storey SH, van Zeggeren F (1970) The computation of chemical equilibria. Cambridge University Press, Cambridge
30. Thermodata Data Bank, Scientific Group Thermodata Europe (SGTE), 6 rue du Tour de l'Eau, 38402 St Martin d'Hères, France
31. Janaf Thermochemical Tables, Part I and II, Published by the American Chemical Society and The American Institute of Physics for the National Bureau of Standards (1985) Michigan
32. Gurvich LV, Veyts IV, Alcock CB (1990) Thermodynamic properties of individual substances, 4th ed. Hemisphere Publishing Corporation, A member of the Taylor and Francis Group, New York
33. Benson SW (1976) Thermochemical kinetics, 2nd edn. Wiley, New York, NY
34. Kee RJ, Rupley FM, Miller JA, Chemkin II (1989) A Fortran chemical kinetics package for the analysis of gas-phase chemical kinetics, Sandia Nat. Lab. Sept. See also Kee RJ, Dixon-Lewis G, Warnatz J, Coltrin ME, Miller JA (1986) Sandia National Laboratories, Report SAND 86-8246
35. Bandyopadhyay R, Nylén P (2003) A computational fluid dynamic analysis of gas and particle flow in flame spraying. J Therm Spray Technol 12(4):492–503

Chapter 4
Gas Flow–Particle Interaction

Abbreviations

d.c.	direct current
D-gun	Detonation gun
FTIR	Fourier transform infra red
GLR	Gas-to-liquid mass ratio
HVAF	High velocity air fuel
HVOF	High velocity oxygen fuel
i.d.	internal diameter
L.T.E.	Local Thermodynamic Equilibrium
PIV	Particle Image Velocimetry
r.f.	radio frequency
XRD	X-Ray Diffraction

4.1 Introduction

In the thermal processing of powders for spraying of protective coatings or free-standing bodies, the proper control of the trajectories of the particles or droplets (suspension or solution) and their temperature and momentum histories in the gas flow represents one of the critical aspects on which the overall success of the operation strongly depends. In fact, a slight deviation from near-optimal conditions can easily lead to poor results due to either the lack of melting of particles, or insufficient impact velocities, or the modification of their composition due to particle evaporation or unwanted chemical reactions. In most spray processes, except cold spray or some HVAF and HVOF processes or D-gun process, particles are melted after a few millimeters of their trajectory. Thus, for most calculations particles are considered to be spherical (the shape they achieve, due to surface tension, as soon as they melt).

P.L. Fauchais et al., *Thermal Spray Fundamentals: From Powder to Part*,
DOI 10.1007/978-0-387-68991-3_4, © Springer Science+Business Media New York 2014

This chapter is mainly devoted to a review of the different fundamental phenomena encountered in the processing of particles. Comprehensive studies have been published in the 1980s and 1990s by various authors, especially for plasma flows [1–11]. More recently, corresponding studies and developments were published for cold spray, HVOF, and D-gun, as well as for suspension and solution precursor spraying. The basic phenomena governing the momentum, trajectory, heat, and mass transfer between a single particle and a high-energy gas flow will be discussed in the first place. This includes a review of the basic equations used for the calculation of the trajectory of a single particle or a liquid droplet in a gas flow. Then the heating, melting, evaporation, chemical reactions, and heat propagation within the particle with the basic equations involved will be discussed. The treatment of ensembles of particles in gas flows will be described next including the different problems related to particle injection and the important problem of thermal loading effects resulting from high-energy gas–particle or plasma–droplet interactions. At last, the problems of the interaction of hot gases with liquid drops or jets will be addressed to account for the recent developments of suspensions or solutions spraying.

4.2 Single Particle Trajectory

Flow field–particle interactions have been extensively studied since the end of the 1960s [12–18]. However, the high-energy jet–particle interaction studies have mainly started in the 1980s. This section will essentially deal with the calculation of a single particle trajectory and temperature history under spray conditions. As illustrated by the equations, results depend strongly on the particle entrainment mainly through its drag coefficient. Once the calculations of this dimensionless number have been presented, the basic assumptions, the governing equations, and typical results obtained for different spray processes will be presented. The section will end with the treatment of liquid drops by hot jets (suspension and solution plasma spraying).

4.2.1 Single Particle Motion

During its displacement a particle in a hot gas or high energy stream is subjected to a number of forces, which act simultaneously on it and have varying influence on its trajectory and residence time in the plasma. Among the most important forces which invariably are taken into account are the inertia forces, F_i, and the viscous drag forces, F_D, which are defined as [1, 19]

$$F_{\mathrm{i}} = \frac{\pi d_{\mathrm{p}}^3}{6} \cdot \rho_{\mathrm{p}} \cdot \frac{du_{\mathrm{p}}}{dt} \tag{4.1}$$

$$F_{\mathrm{D}} = \frac{\pi d_{\mathrm{p}}^2}{4} \cdot C_{\mathrm{D}} \cdot \frac{1}{2}\rho \cdot u_{\mathrm{R}}^2 \tag{4.2}$$

with d_{p} particle diameter (m), ρ_{p} particle density (kg/m^3), ρ plasma density (kg/m^3), C_{D} drag coefficient (−), u_{p} particle velocity (m/s), u_{R} relative velocity between the plasma and the particle (m/s), t time (s).

The gravity force, F_{g} (N) defined as

$$F_{\mathrm{g}} = \frac{\pi d_{\mathrm{p}}^3}{6} \cdot \rho_{\mathrm{p}} \cdot g \tag{4.3}$$

may also be relatively important for low-velocity flows with large size and heavy particles such as those encountered in r.f. discharges. Other forces, which may have an influence on the trajectory of the particle, depending on the particular situation, are F_{p}(N) the pressure gradient force which can be important in the presence of steep pressure gradients in the flow field, F_{B}(N) the Basset history term which can be important under very high acceleration conditions, F_{T}(N) thermophoresis effects which can be important for very fine particles $d_{\mathrm{p}} < 1$ μm in the presence of steep temperature gradients, F_{C}(N) Coriolis forces, which result from the rotation of the particles about an axis parallel to the direction of relative motion.

Considering that in most cases encountered in melting and processing of powders under plasma conditions, F_{P} (except for D-gun, cold spray, and sometimes HVOF) F_{B}, F_{T}, and F_{C} are negligible compared to F_{i}, F_{D}, and F_{g}. Therefore, a force balance around a single particle in motion in a plasma flow can be written simply as

$$F_{\mathrm{i}} = F_{\mathrm{D}} + F_{\mathrm{g}} \tag{4.4}$$

Substituting Eqs. (4.1), (4.42), and (4.33) in Eq. (4.4), the latter can be written in axis-symmetric cylindrical coordinates as follows:

$$\frac{du_{\mathrm{p}}}{dt} = -\frac{3}{4} C_{\mathrm{D}} \left(u_{\mathrm{p}} - u\right) u_{\mathrm{R}} \left(\frac{\rho}{\rho_{\mathrm{p}}.d_{\mathrm{p}}}\right) \pm g \tag{4.5}$$

$$\frac{dv_{\mathrm{p}}}{dt} = -\frac{3}{4} C_{\mathrm{D}} \left(v_{\mathrm{p}} - v\right) v_{\mathrm{R}} \left(\frac{\rho}{\rho_{\mathrm{p}}.d_{\mathrm{p}}}\right) \pm g \tag{4.6}$$

u_{p} is the particle velocity (m/s) in the z direction that of the plasma jet axis, u is the plasma velocity (m/s) in the z-direction, u_{R} is the relative velocity plasma–particle, v_{p} is the particle velocity (m/s) in the r-direction, v is the plasma velocity (m/s) in the r-direction, and v_{R} the relative velocity plasma–particle in the r direction.

The acceleration due to gravity force ($\pm g$) has to be added or subtracted from either the axial or radial velocity components equations depending on flow orientation.

In the case of RF plasmas generally oriented vertically, the + or − sign in front of the gravitational acceleration, g, corresponds to a flow in axial direction with the positive direction for the velocity of the particles being downwards or upwards, respectively.

For a d.c. plasma, HVOF, or flame torch, where the axis is generally horizontal, + corresponds to a vertical injection downward and—to the upward injection.

If cylindrical symmetry does not exist anymore, and this is the actual case when injecting particles radially, Eqs. (4.5) or (4.6) hold but the velocity vector and its derivative, as well as the gravity acceleration vector, must be described in a specific equation. When turbulent effects are taken into account, which is particularly important for small particles (<20 μm) and those with a low specific mass such as alumina, the turbulent component u' and v' must be added to the velocity components u and v [17, 19, 20].

At last it must be recalled that the drag coefficient C_D must be corrected by the temperature gradient effect, Knudsen effect, etc. (see Sect. 4.2.2.2). Integrating once the Eqs. (4.55) and (4.56), or their vectorial expression, gives the particle velocity evolution, while integrating them twice provides the position vector of the particle as a function of time.

4.2.2 Particle Injection and Trajectory

The problem is different between radial and axial injection. Later the calculation of the drag coefficient will be explained (Sect. 4.2.3); however, whatever the equation used to calculate the drag coefficient, results will present the same trend: for a given powder carrier gas any change of spray conditions will modify the particle trajectories, especially for radial injection.

4.2.2.1 Radial Injection

The particles injected radially (most d.c. plasma guns, some of the HVOF guns, and a few cold spray devices) encounter a flow whose momentum density (ρv^2) varies along the jet radius: the velocities and temperatures are increasing from the jet fringes to its axis, but ρ is decreasing correspondingly. This is especially the case for d.c. plasma jets, where ρ is about more than one order of magnitude higher in the jet fringes than on the plasma jet axis, while the reverse is true for the jet velocity (up to 2,200 m/s on the jet axis against a few hundreds of m/s in the jet fringes). Roughly, to achieve a good penetration, the particle force should be close to the force imparted to it by the plasma along its trajectory ($S_p \rho v^2$ where S_p is the particle cross section) [21, 22].

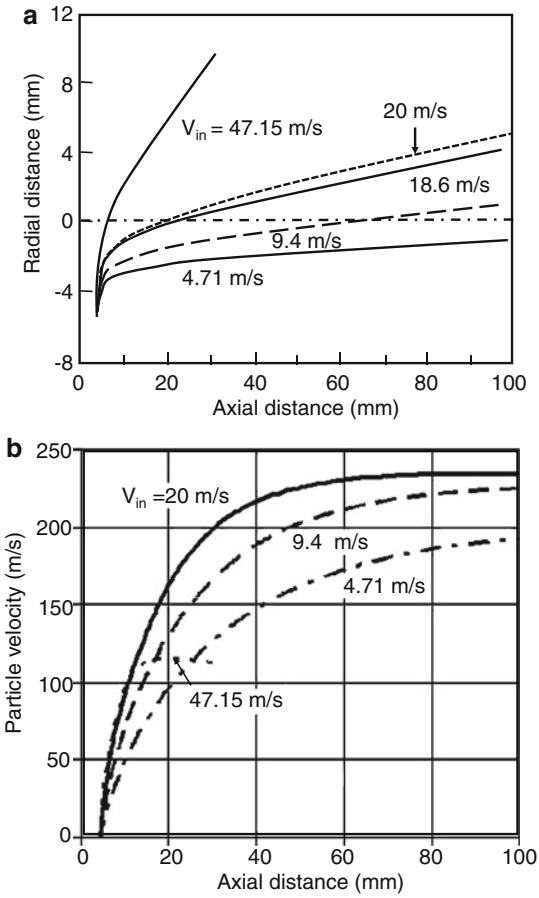


Fig. 4.1 Zirconia particle 30 μm in diameter injected externally into a d.c. plasma jet (45 kW, 45 slm Ar, 15 slm H_2) with different injection velocities, V_{in} (radial distance = 0 corresponds to the torch axis) and their influence on the particle trajectories (**a**) and velocities (**b**) [26]

(a) Influence of the Injection Conditions

The importance of the injection conditions in d.c. plasma jets has been emphasized by many authors [21–30]. This is illustrated below with the results of Delluc et al. [26] for fully dense zirconia particles of different diameters injected into a d.c. plasma produced by a torch working at 43 kW with a thermal efficiency of 60 %. Ar–H_2 plasma-forming gases were used (45 slm Ar and 15 slm H_2) and a 7 mm i.d. torch nozzle. The particles are externally injected 4.5 mm downstream of the nozzle exit and at 8.5 mm from the torch axis. The injection, except when specified differently, is orthogonal to the jet axis. In all cases corrections for temperature gradients, Knudsen effect and particle vaporization have been taken into account (see Sect. 4.2.3). Figure 4.1a shows, for a given plasma jet, the different trajectories followed by a zirconia particle 30 μm in diameter and injected with velocities between 4.71 and 47.15 m/s. The carrier gas imparts a given velocity

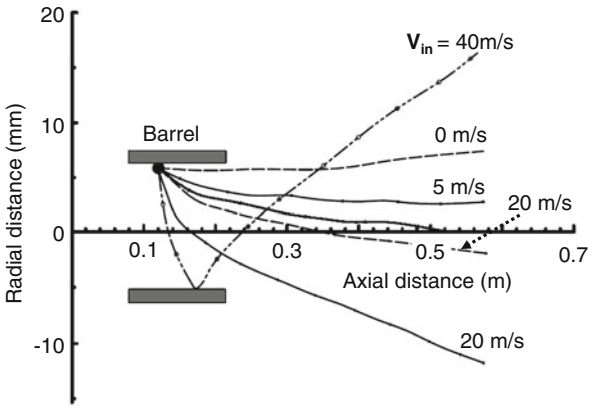


Fig. 4.2 Inconel 718 20 µm particle trajectories at different injection velocities, V_{in}: radial injection downstream the nozzle throat in HVOF gun working with kerosene and oxygen. Reprinted with kind permission from Elsevier [32]

to the particle, velocity easy to calculate or measure. From this velocity and that of the carrier gas, the particle acceleration can be calculated through Eq. (4.1). Obviously the particle acceleration is too small, with a velocity of 4.71 m/s, the particle crosses the torch axis only 15 cm downstream of the nozzle exit (i.e. practically in the plasma plume where the temperature is below 2,000 K).

To achieve a good heat and momentum transfer in spray conditions, an angle of 3.5–4° between the particle trajectory and the torch axis seems to give the best results [21]. In Fig. 4.1a, such a trajectory corresponds to a particle velocity of about 20 m/s, which gives the best momentum transfer, i.e., the highest particle velocity (see Fig. 4.1b).

Similar results are obtained with HVOF, when the injection is performed radially downstream of the nozzle throat [31]. In the calculation presented in Fig. 4.2, 20 µm diameter Inconel 718 particles are injected from the axial distance of 0.12 m. The injection velocities vary in the range 0–40 m/s. The particle trajectories show that the particle is driven by the gas flow and travels along the edge of the barrel with zero injection velocity; the increase of injection velocity enables the particle to travel across the gas flow and move toward the center of the jet. At injection velocities between 8 and 10 m/s the particle travels across the center of the gun and moves outwards. At an injection velocity of 40 m/s the particle hits the internal surface of the barrel and the trajectory is changed to the opposite direction as the result of an elastic collision. Nozzle wear is one of most frequently encountered problem for operating HVOF guns and the nozzle needs to be replaced after about 10 h spraying. Thus the injection velocity of particles has to be carefully chosen [32].

Finally experiments show that in d.c. plasma spraying an optimum mean trajectory (corresponding to the highest particle temperature and velocity) is that which makes an angle between 3.5 and 4° with the torch axis [21].

In some cold spray guns the particle feeder is placed at the beginning of the throat and injects particles, in the flow direction, at an angle of 45° with respect to the nozzle axis [33] or in the divergent part of the nozzle again in the flow direction

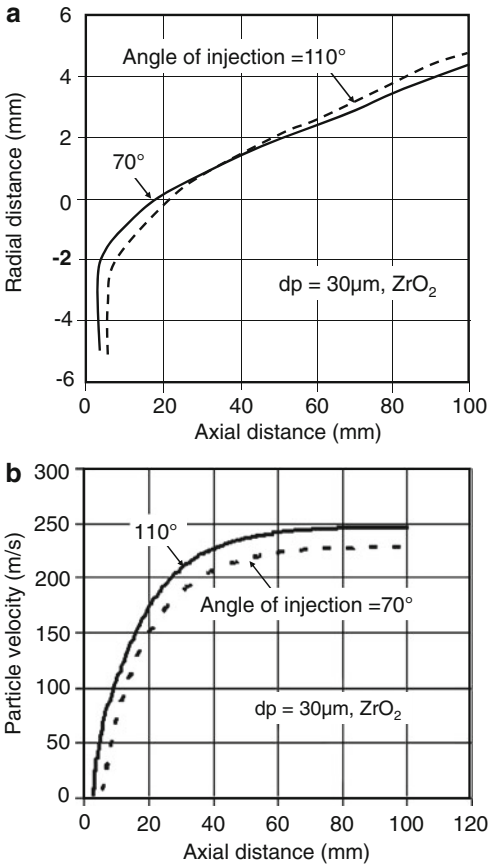


Fig. 4.3 Zirconia particles 30 μm in diameter injected externally into a d.c. plasma jet (45 kW, 45slm Ar, 15slm H_2) with a velocity vector inclined by 70° and 110° (slightly against the flow) relative to the torch axis (radial distance = 0 corresponds to the torch axis). (**a**) Trajectories, (**b**) Velocities [26]

at an angle of 80° with respect to the nozzle axis [34] or orthogonally to it [35]. It is worth to emphasize that the injection in the expanding jet avoids using a powder feeder pressurized to a pressure above the cold spray chamber pressure.

(b) Influence of the Injector Acceleration and Inclination

In fact, inside injectors particles collide among themselves and with the injector wall resulting in trajectories with an angle of up to 20° relative to the injector axis [21]. In Fig. 4.3a, b the injector has been inclined by 70° relative to the torch axis (particles are injected slightly in the flow direction) and 110° (particles are injected slightly against the flow).

In real world where a powder is injected and not a particle, particles have different trajectories, due to their collisions with the injector wall and between themselves, and they exhibit a divergence angle relative to the injector axis which can reach a total value of 40°, especially for small <20 μm and light particles such

as alumina (see Sect. 4.4.2.3 for details). Such trajectory distributions make calculations more difficult, but they show that the injection of a single particle with the proper injection velocity for the optimum trajectory represents rather well the mean trajectory of an ensemble of particles, which mean size (d_{50}) is that of the single particle. As expected, particles injected in against the flow have their trajectories in the hottest and highest velocity zones of the plasma (see Fig. 4.3a), resulting in higher particle velocities (see Fig. 4.3b).

(c) Influence of Other Parameters

When any parameter (power level gas flow rates,. . .) modifying the hot jet temperature and velocity distributions, i.e., the jet momentum density, is changed or modified by wear (of electrodes in d.c. plasma spraying or nozzle internal diameter in HVOF or HVAF), the particle injection velocity must be varied accordingly to keep the trajectory optimum. This is illustrated in Fig. 4.4 showing the influence of the power level for 30 μm zirconia particles injected into a d.c. plasma jet with a velocity of 20 m/s, which is the optimum velocity for a 43 kW power level. As the plasma momentum density increases with increasing power level, the particle penetration will be less. On the other hand if the power level decreases, the particle will cross more easily the plasma jet (see Fig. 4.4a). The particle velocity increases with the increase of the power level (see Fig. 4.4b) provided the injection velocity is adapted to the each power level to achieve the optimum trajectory.

It is also worth noting that when the injection distance increases, due to the jet expansion, the jet momentum density decreases and, accordingly, the injection velocity for a trajectory close to the torch axis decreases. This is illustrated by the work of Hanson et al. [36] who have studied an HVOF thermal spray torch that has a conical supersonic nozzle with several different particle injection locations. Particle injection location was found to determine the residence time of particles within the nozzle, thus providing a means to control particle temperature. Finally, injection location had a negligible effect on particle velocity according to the numerical model.

(d) Optimization of the Injection

Vardelle et al. [37] have calculated in a d.c. plasma jet the rate of change of momentum of particles due to the drag force in their direction of motion, assuming that the drag force corresponds to one in a Stokes regime with a constant plasma viscosity μ_g. Under these conditions the total time of flight of the particle depends on a reference time t_r:

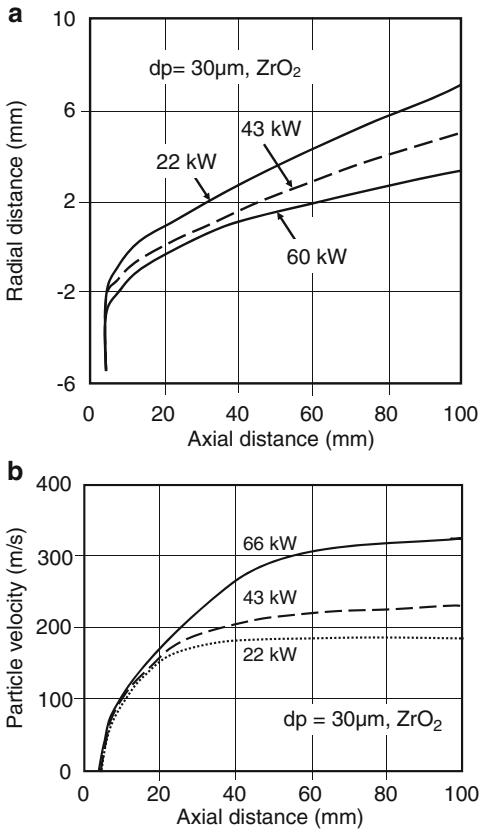


Fig. 4.4 Influence of the plasma power level (Ar 45 slm, H_2 15 slm, $\rho_{th} = 60$ %, nozzle i.d. 7 mm) on (**a**) a 30 μm diameter zirconia particle trajectory and (**b**) the particle velocities (injection velocity optimized for 43 kW) [26]

$$t_r = \frac{\rho_p \cdot d_p^2}{\mu_g} \tag{4.7}$$

Thus they have established the residence time of various particles as a function of their specific mass and diameter (see Fig. 4.5) in an Ar–H_2 (45 slm–15 slm) d.c. plasma jet with an effective power level of 21.5 kW and a nozzle i.d. of 7 mm. They have then calculated the required injection velocity for the different particles to "land" on nearly the same location on the substrate. Results are plotted on the right-hand y-coordinate of Fig. 4.5. For a given plasma jet, the injection velocity varies drastically with the particle size and specific mass.

(e) Influence of Plasma Jet Fluctuations

As described in Chap. 7 on plasma spraying, the restrike mode, observed with plasmas containing diatomic gases, corresponds to voltage fluctuations such that the

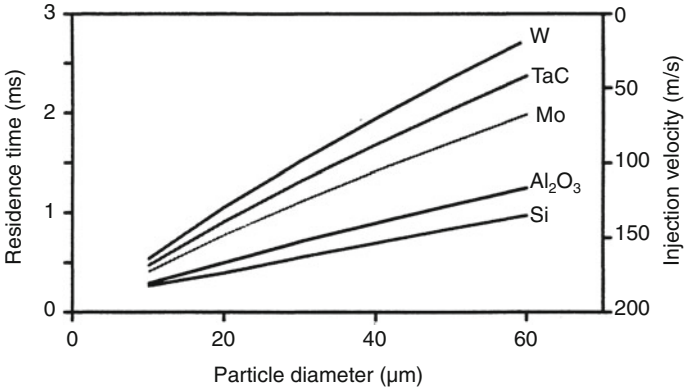


Fig. 4.5 Particle residence time as a function of particle diameter, for different materials with a wide range of specific mass (plasma forming gas: 45 slm Ar + 15 slm H_2, effective power: 21.5 kW, nozzle i.d.: 7 mm) [37], Reprinted with kind permission from Springer Science Business Media

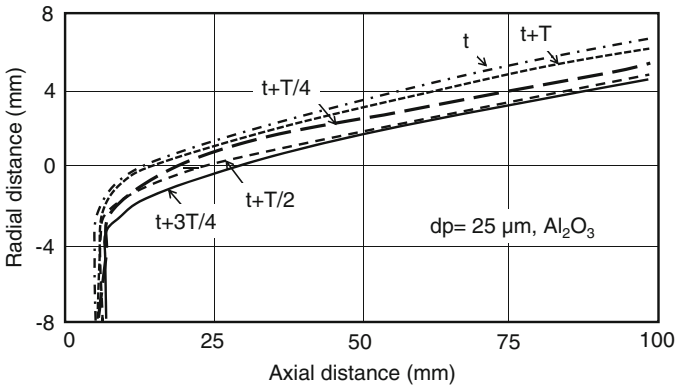


Fig. 4.6 Trajectories of 25 μm alumina particles injected into an Ar–H_2 d.c. plasma jet (45–15 slm, 600A, anode-nozzle i.d. 7 mm) at different instants of the fluctuation period with an injection velocity of 20 m/s (y–z plane) [38], Reprinted with kind permission from Springer Science Business Media, copyright © ASM International

highest voltage can be more than twice the lowest one. As the power supply is generally a current source, it results in power fluctuations proportional to those of the voltage. The frequency of these fluctuations being a few 1,000 Hz, the carrier gas cannot follow them because its response time is in the 10-Hz range. Thus the carrier gas flow rate is constant when the instant power varies, resulting in a constant injection velocity, generally adapted to achieve the optimum trajectory with the time averaged value of the power dissipated in the torch. This is illustrated in Fig. 4.6 [38] showing the trajectories, in the y–z plane, of 25 μm alumina particles injected into the Ar–H_2 plasma jet at different instants of the arc fluctuation period but with the same injection conditions: particles are located on the axis of the injector, and they leave the injector with an axial velocity of 20 m/s. Under the

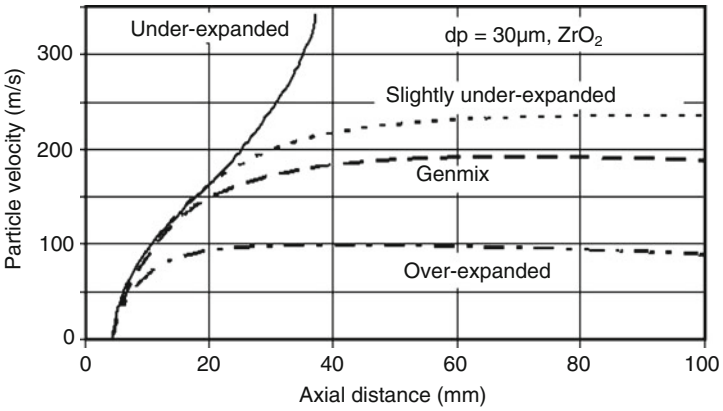


Fig. 4.7 Influence of turbulent mixing length on a 30 μm Zirconia particle velocity. The particle is injected in such a way that it has the same trajectory in the jets calculated with different mixing lengths for a 43 kW plasma, 45 slm Ar, 15 slm H_2, and nozzle i.d. 7 mm [26]

conditions of the study, the way the trajectory is affected by flow fluctuations depends essentially on the particle momentum with respect to the instantaneous momentum of the gas at the point where the particle penetrates the jet flow. The width of the particle spray jet, on impact at the substrate, is 3.5 mm for 25 μm particles, but is as large as 6.6 mm for 10 μm particles. Meillot and Balmigere [39] obtained similar results

(f) Influence of the Plasma Flow Computational Model

The way the flow is calculated of course plays a key role on the particle trajectories and, accordingly, its temperature and velocity. Thus the temperature and velocity distributions of the gaseous flow have to be checked carefully, if possible by comparison with measurements. When using, for example, a simple turbulence model with a mixing length as defined in the Genmix 2-D axisymmetric algorithm [26], different results can be obtained according to the choice of the mixing length L (m). This length can be taken (a) from the Genmix program (calculated for flows below 1,500 K), and (b) with the value corrected by a factor of 0.5 to achieve an under-expanded jet, or (c) by a factor of 1.5 (over-expanded jet), or (d) corrected by a factor related to the radial temperature distribution $(T(r)/300)^{1/9}$) to account for the laminar behavior of the jet at $T > 8{,}000$ K and resulting in a slightly under-expanded jet. The particle momentum has been adapted to the four cases in order to achieve trajectories with an angle of 4° with the torch axis. Figure 4.7 shows that the more the jet is constricted, the higher the particle velocity will be.

The influence of the choice of the turbulence model has also been emphasized by Legros [40] using 3D models: K–ε and different R_{ij}–ε models resulting, for the same spraying conditions, in different temperature and velocity distributions, thus in different particle trajectories.

4.2.2.2 Axial Injection

Axial injection is used for flame spraying, part of HVOF spraying, detonation spraying, in a few d.c. plasma torches, and in of all r.f. induction plasma torches, and finally mostly in cold spray guns. Injectors play a key role first by their position and then by the particle injection velocity, especially when the gas flow velocity is low (flame or RF torches).

(a) Flame Spraying

The main remark is that the principal parameter is the particle injection velocity which can increase slightly the particle velocity (a few m/s compared to its mean velocity, which is in the range of a few tens of m/s in the flame (see Fig. 5.5 in Chap. 5). Calculation and comparison with experimental measurements of particles in-flight in the flame show a rather good agreement [41].

(b) HVOF

Gu et al. [42] have studied the particle dynamic behavior in an HV2000-type HVOF spray gun, using the propylene as fuel premixed with oxygen. The model employed a Lagrangian particle tracking frame coupled with a steady-state gas flow field to examine particle motion and heating during HVOF spraying. Results showed that an increase in particle injection velocity only slightly reduces the particle temperature development and has virtually no effect on the particle velocity profile. This feature is attributed to the relatively uniform heat input and acceleration within the HVOF system with axial injection of particles; thus, the small variation in the particle dwell time that is brought about by changing the injection speed has little effect in this HVOF spraying.

Unfortunately no information was found about the influence of the injector position within the combustion chamber.

(c) D-Gun

The position of the end of the injector, relative to the point of the detonation wave initiation, also called loading distance, is critical [43]. The particle velocity attains a maximum for a given position, as shown, for example, in Fig. 4.8 for a 30 μm tungsten carbide particle in a propane–oxygen mixture [43]. This maximum is due to the peculiar profile of gas velocity and pressure in the detonation pulse and to the non-monotonic nature of particle acceleration.

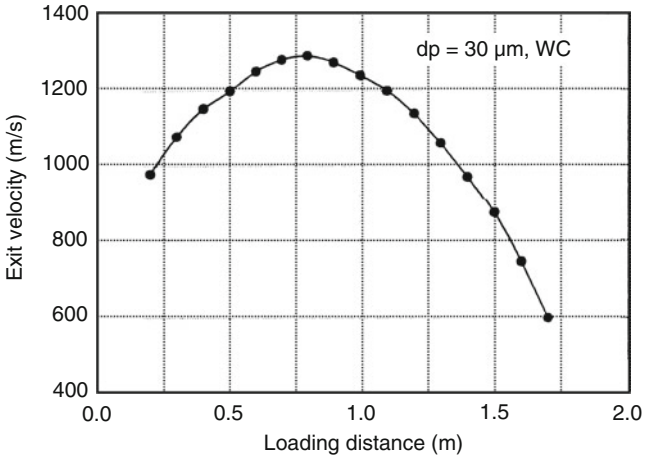


Fig. 4.8 Exit velocity of 30 µm tungsten carbide particles as a function of the loading distance in a D-gun working with a propane–oxygen stoichiometric mixture [43]. Reprinted with kind permission from Springer Science Business Media, copyright © ASM International

Attempts have been made to spray soft particles (copper for example) with the D-gun and inject at the barrel exit hard particles (alumina) to be imbedded within the coating during its formation [44]. The position of the external injector and its orientation are key issues.

(d) Plasma Spraying

The injector position is also very important in r.f. plasma spraying. Computations have been reported by Boulos [45–47] for alumina particles with a particle size distribution in the range from 10 to 200 µm, injected axially into the discharge region of inductively coupled r.f. plasma. Computations were carried out in two separate and independent steps: computation of the flow and temperature fields in the discharge followed by computation of individual particle trajectories and their temperature histories.

Typical results obtained for argon plasma at atmospheric pressure are given in Fig. 4.9 for spatial flow, temperature fields, and particle trajectories, respectively. The plasma confinement tube had an internal diameter of 28 mm. The central powder carrier gas, the intermediate and the sheath gas flow rates were set to 0.4, 2.0, and 16.0 slm, respectively. The oscillator frequency was 3 MHz and the net power dissipated in the discharge was 3.77 kW.

In the representation of the trajectories given in Fig. 4.9, the size of the circles indicates the position of the particles is also an indication, although not to scale, of their diameter. Particles with different sizes (10, 30, and 100 µm) were injected

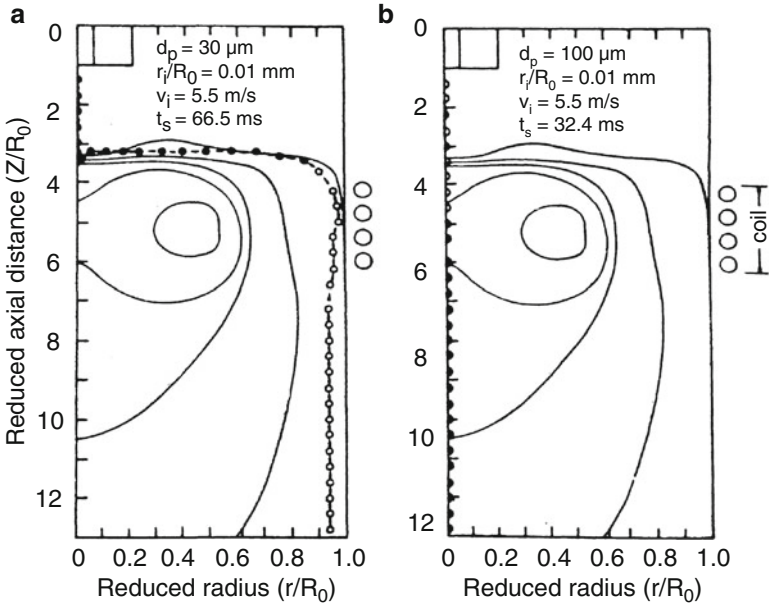


Fig. 4.9 Particle trajectories for alumina powder injected into an r.f. induction plasma: $f = 3$ MHz, $P_t = 3.77$ kW, powder gas $Q_1 = 0.4$, central gas, $Q_2 = 2.0$, Sheath gas $Q_3 = 16.0$ slm, (**a**) 30 μm particle, (**b**) 100 μm particle after Boulos. Reprinted with kind permission from Springer Science Business Media, copyright © ASM International [46, 47]

axially with the same injection velocity of 5.5 m/s. Moreover, an open circle indicates a solid particle while a dark circle represents a liquid droplet.

Recirculation occurring upstream of the injection coil can entrain the particles towards the plasma fringes (see Fig. 4.9a), resulting in a poor treatment especially for 30 μm particles which are not sucked into the hot core as the 10 μm particles. The 100 μm particles retain an axial trajectory (Fig. 4.9b).

In practice, due to the flow pattern in the discharge region, the position of the tip of the powder injection probe is of critical importance [47]. If located above the first turn of the induction coil, it could result in excessive deposition of powder on the walls of the confinement tube, which may lead to its eventual failure. A low position of the powder-injection probe at the downstream end of the induction coil will result in excessive cooling of the central part of the plasma (heated mainly by conduction–convection) and a reduction of the particle residence time in the discharge. This will cause a reduction of the ability of the plasma to completely melt the particles in-flight. Practically, in industrial r.f. plasma torches of TEKNA, the double-walled and water cooled injector tip is disposed about at the level of the upper third of the coil (see Chap. 8). With a Mettech d.c. torch with axial injection the maximum temperature of particles injected was at the same location as that of the maximum number of particles, which is not the case with radial injection [48]. This demonstrates that axial injection is the most efficient way of heating particles.

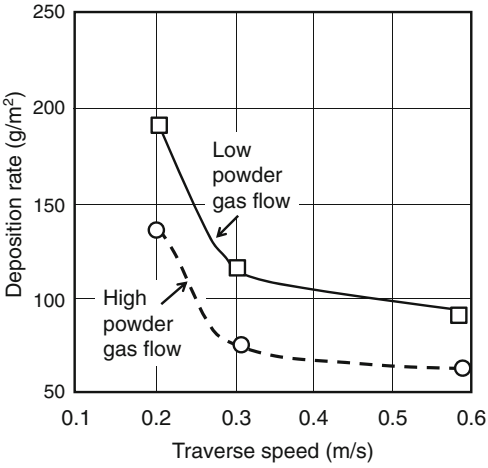


Fig. 4.10 Effect of the powder gas flow rate on the deposition per unit area for Al coatings: cold spray with nitrogen gas: low nitrogen carrier gas flow: 2.8 g/s, high nitrogen carrier gas flow 6.1 g/s. Reprinted with kind permission from Springer Science Business Media, copyright © ASM International [49]

(e) Cold Spray

Because of the strong acceleration of the gas, and thus particles, in the divergent part of the nozzle, the initial velocity of the particles at the injector exit does not have an important effect on particle velocities at the nozzle exit. The particle velocity at the injector exit depends on the carrier gas flow rate, which is controlled primarily by the injector internal diameter and the differential pressure between the powder feeder and the pre-nozzle chamber. An important factor is that the carrier gas is generally cold and because the injector is largely submerged inside the heated gas flow, and a sufficient powder gas flow is needed to prevent the injector from build-up/clogging by particles [34, 35, 49]. However, it has also been observed that too much powder gas flow can degrade coating formation. Figure 4.10 [49] shows the effects of powder gas flow on Al coatings deposited using 63–90 μm particles. Note that under the same nominal spray conditions, spraying with the smaller nitrogen flow rate (2.8 g/s) has consistently resulted in coatings with higher deposition rates than with the larger powder gas flow rate (6.1 g/s).

Downstream of the injector the carrier gas is actually a mixture of the heated main gas (nitrogen) and the room-temperature powder feed gas (nitrogen). Only the main gas is heated to elevated temperatures, and the powder feed gas is at a room temperature. Simulations using FLUENT have been performed for an axially symmetric nozzle with a throat diameter of 2.8 mm with the nozzle expansion ratio of 6.34. Computations have shown that the main gas flow rate varies with the powder gas flow rate to maintain a nearly constant total inlet gas flow. With the lower powder gas flow rate, the particle velocity (particles with a 63 μm diameter) is predicted to be lower than that with the high powder gas flow rate in the converging section of the nozzle before the throat [50]. Most of the particle heating occurs before the diverging section of the nozzle. Due to relatively high surrounding gas temperatures and large residence time associated with the low particle velocities, particles are heated to nearly 400 K at their arrival of the substrate with the lower

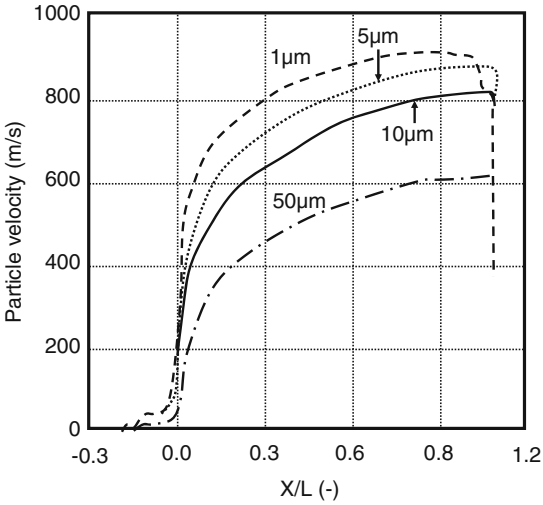


Fig. 4.11 Effects of bow shock on the particle velocities for various aluminum particle sizes. *X* position relative to the nozzle throat, *L* length of the divergent nozzle part. Spray gun working with nitrogen at 2.07 MPa at a temperature of 643 K and a nozzle expansion ratio of 6.37. Reprinted with kind permission from Springer Science Business Media [49], copyright © ASM International

powder gas flow, compared with 360 K with the higher powder gas flow. This higher impact temperature enhances coating formation [50].

As discussed in Chap. 6, the best results in cold spray are obtained with helium as spray gas. It is thus important when spraying with helium to use the same gas as carrier gas [50]. Depending on the spray standoff distance, a bow shock wave occurs near the substrate where the impinging supersonic jet decelerates rapidly in front of the substrate. There are abrupt changes in the flow properties, such as pressure, temperature, density, and velocity across the bow shock. The bow shock wave decelerates the gas flow to a subsonic velocity. Across the bow shock, particles [49] could be slowed down due to increased gas density and decreased gas velocity. In particular, small aluminum particles are easily decelerated by the compression shocks and are severely deflected before they reach the substrate, as shown in Fig. 4.11. However, the large aluminum particles (>50 μm) appear to be able to penetrate the compression shock near the substrate with little deceleration, due to their relatively large inertia.

4.2.3 Drag Coefficient: Micrometer Sized Single Sphere

4.2.3.1 Calculations Without Any Correction

Considerable attention has been given to study the flow and the temperature fields around single spheres [12]. Typical flow patterns as a function of the particle Reynolds number, Re, are, for example, given in Fig. 4.12. The Reynolds number is given by

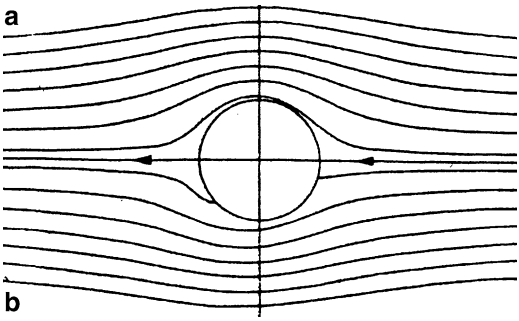


Fig. 4.12 Streamlines over a spherical solid particle at low N_{Re}. (**a**) Stoke's solution (**b**) Oseen approximation, after Clift et al. [12]. Reprinted with kind permission from Elsevier

$$\mathrm{Re} = \frac{\rho \cdot u_R \cdot d_p}{\mu} \tag{4.8}$$

ρ fluid specific mass (kg/m^3)
μ fluid viscosity (Pa s)
d_p particle diameter (m)
u_R relative velocity between the particle and its surroundings (m/s):

$$u_R = \sqrt{\left(u - u_p\right)^2 + \left(v - v_p\right)^2} \tag{4.9}$$

u_p and u are particle and gas velocity components along the torch axis direction, respectively, v_p and v are particle and gas velocity components in the radial direction, respectively.

It may be noted from Fig. 4.12 that the increase of the particle Reynolds number is accompanied by a gradual shift of the flow pattern from the typical symmetric Stokes flow regime shown in Fig. 4.12a for Re < 0.01, to the viscous but slightly nonsymmetric (upstream vs. downstream) flow pattern represented by the Oseen approximation for Reynolds number between 0.01 and 1.0, shown in Fig. 4.12b. At Reynolds numbers above 1.0, the flow pattern, while still being in the laminar region, becomes increasingly nonsymmetric with the eventual development of a separation bubble behind the particle at Reynolds number higher than 50.

Obviously these changes in the flow pattern around the particle will have a direct influence on the drag, C_D, and the heat transfer coefficients, h, between the particle and its surrounding, where

$$C_D = \frac{F_D/A}{\frac{1}{2}\rho \cdot u_R^2} \tag{4.10}$$

with

F_D the total drag force exerted by the fluid on the particle (N)
A the particle projected surface area perpendicular to the flow ($A = \pi d_p^2/4)(m^2$).

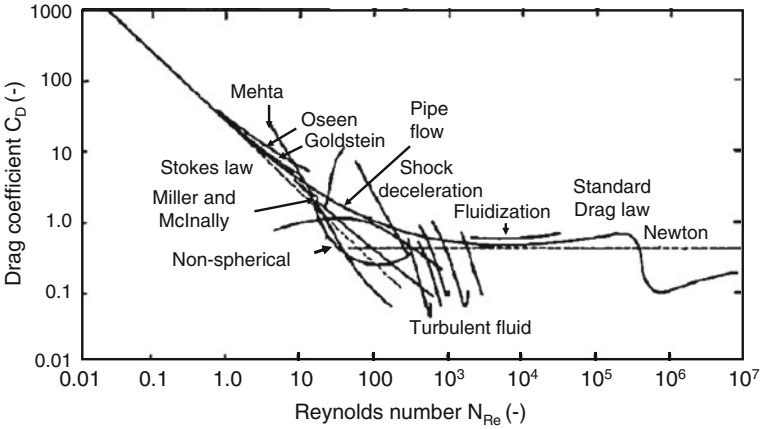


Fig. 4.13 Drag coefficient as function of the Reynolds number for a single sphere. Reprinted with kind permission from Elsevier [12]

Table 4.1 Equations proposed for the Drag coefficient of a single sphere according to the Reynolds number

$C_D = \frac{24}{Re}$	$Re < 0.2$	(4.11)
$C_D = \frac{24}{Re}[1 + 0.187 \times Re]$	$0.2 \leq Re < 2$	(4.12)
$C_D = \frac{24}{Re}\left[1 + 0.110 \times Re^{0.81}\right]$	$2 \leq Re < 20$	(4.13)
$C_D = \frac{24}{Re}\left[1 + 0.189 \times Re^{0.62}\right]$	$20 \leq Re < 200$	(4.14)
$C_D = \frac{24}{Re} + \frac{6}{1+\sqrt{Re}} + 0.4$	$N_{Re} \geq 200$	(4.15)

Typical results for C_D as function of the Reynolds number Re are given in Fig. 4.13. These are mostly based on experimental measurements and flow modeling studies under normal ambient temperatures and pressures. Corresponding correlations proposed by various authors [12–14, 51, 52] for Reynolds numbers less than 200, are given in Table 4.1.

Other expressions have also been proposed, such as that given by White [13]:

$$C_D = \frac{24}{Re} + \frac{6}{1 + Re^{0.5}} + 0.4 \quad Re < 100 \tag{4.16}$$

or those proposed by Oberkampf and Talpallikar [52] which are valid for a wide range of Reynolds numbers:

$$C_D = 24/Re \quad \text{for } Re < 1 \tag{4.17}$$

$$C_D = 24\left(1 + 0.15 \times Re^{0.687}\right)/Re \quad \text{for } 1 < Re < 1,000 \tag{4.18}$$

$$C_D = 0.44 \quad \text{for } Re > 1,000 \tag{4.19}$$

For compressible flows, as those found in cold spray or HVOF, drag coefficient calculations are far more complex due to the need of the particles to cross the shock wave upstream of the substrate on which they are deposited. The reader is referred to extensive literature on the subject [53–58].

4.2.3.2 Corrections Due to Various Effects

Under thermal spray conditions the presence of steep temperature gradients across the boundary layer surrounding the particle, especially for thermal plasmas, has a significant effect on momentum and heat exchange between the gas and the particle. Special attention has to be given to the correction of the drag coefficient predicted using correlations obtained under normal temperatures and pressures. While the need for such corrections is essential under plasma conditions, it is much less important in combustion-based thermal spray processes and negligible in cold spray processes.

Other corrections are also necessary under rarified flow conditions mostly encountered during low-pressure plasma spraying. Under these conditions the mean free path of the gas molecules at high temperature can reach a few μm at 10,000 K and 0.1 MPa, which starts to be comparable with the characteristic dimension of the particles. Under such conditions non-continuum effects (Knudsen effect) can be important and requires special corrections to the drag coefficient predicted using continuum fluid mechanics under normal temperature and pressure conditions.

(a) Influence of the Temperature Gradients

Under plasma conditions [59] the plasma temperature outside the boundary layer surrounding the particle can exceed 10,000 K, while the particle surface temperature does not exceed 3,000 K. Thus, a drastic temperature gradient will exist over a few hundreds of micrometers, causing strong nonlinear variations of transport properties (see [60]) with temperature.

The gradient effect is demonstrated in Fig. 4.14, after Sayegh and Gauvin [14], who computed the flow and temperature fields for a particle Reynolds number of 50, assuming in one case constant fluid property and taking into account in the second case property variations across the boundary layer (lower and upper parts of the figures, respectively). The parameter T_o in Fig. 4.14 was defined as the ratio of the temperature of the sphere surface, T_s, to that of the gas stream T_∞.

Based on their results (obtained for an argon plasma), Sayegh and Gauvin [14] recommended the estimation of the fluid properties (kinematic viscosity, $\nu = \mu/\rho$, and thermal conductivity, κ) at a reference temperature defined as, $T_{0.19}$, where

$$T_{0.19} = T_s + 0.19(T_\infty - T_s) \tag{4.20}$$

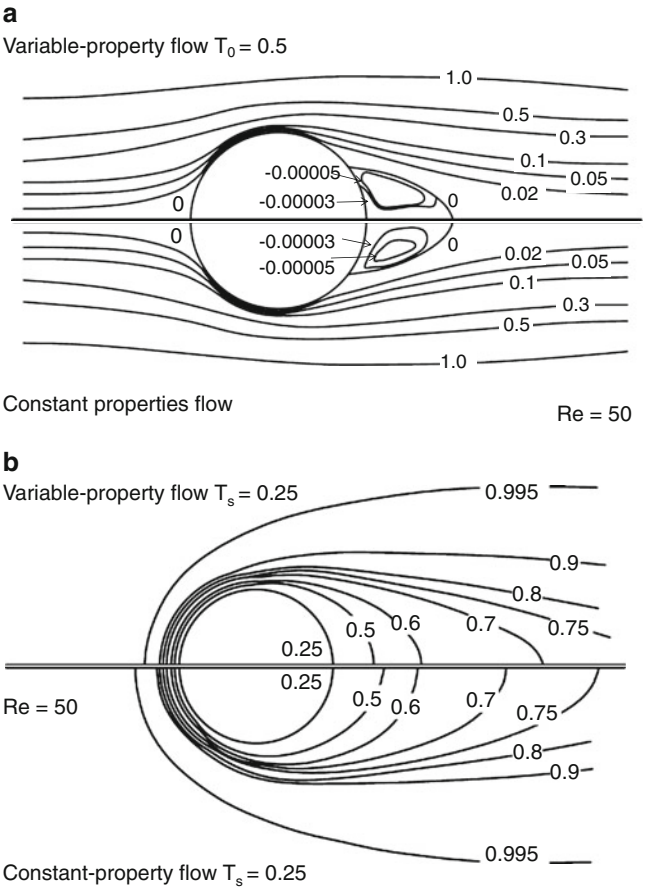


Fig. 4.14 (**a**) Streamlines and (**b**) temperature isocontours for constant and variable fluid property flows, $N_{Re} = 50$, $T_o = 0.25$ (ratio of the temperature of the sphere surface, T_s, to that of the gas stream T_∞) after Sayegh and Gauvin. Reprinted with kind permission from John Wiley and Sons for AIChE Journal [14]

However, considerably simpler corrections for the drag coefficient and the heat transfer coefficient have been widely accepted in the literature [6].

One such correction factor proposed by Lewis and Gauvin [51] involves the estimation of the drag coefficient based on the arithmetic mean film temperature across the boundary layer:

$$T_f = (T_s + T_\infty)/2.0 \tag{4.21}$$

The obtained drag coefficient (C_{DF}) is further corrected using the ratio of kinematic viscosity estimated at the mean film temperature, ν_f, to that estimated at the free stream temperature, ν_∞, taken to the power 0.15, i.e.

Table 4.2 Drag coefficients for an argon plasma calculated using different correction factors [11]

T_w (K)	T_∞ (K)	Simulation	Re = 0.1	Re = 1.0	Re = 10.0	Re = 20.0	Re = 50.0
1,000	4,000	Simulation	100.8	15.4	2.9	1.8	1.0
		Lee et al. [9]	100.6	12.3	2.4	1.6	1.1
		Film temp.	115.6	14.2	2.7	1.9	1.2
		Lee et al. [9]	146.1	17.9	3.4	2.4	1.6
		Lewis and Gauvin [51]					
2,500	10,000	Simulation	151.9	17.6	3.3	2.1	1.2
		Lee et al. [9]	112.9	13.7	2.5	1.7	1.1
		Film temp.	136.9	16.6	3.1	2.1	1.4
		Lee et al. [9]	164.5	19.9	3.7	2.5	1.7
		Lewis and Gauvin [51]					
3,000	12,000	Simulation	199.9	22.4	4.2	2.6	1.4
		Lee et al. [9]	137.6	16.2	2.9	1.9	1.2
		Film temp.	202.3	23.9	4.2	2.8	1.8
		Lee et al. [9]	226.8	26.8	4.7	3.2	2.0
		Lewis and Gauvin [51]					

$$C_D = C_{DF}(\nu_f/\nu_\infty)^{0.15} \tag{4.22}$$

Lee et al. [60] on the other hand, proposed another correction factor based on their computations (performed mostly for argon):

$$C_D = C_{DF}(\rho_\infty \mu_\infty/\rho_s \mu_s)^{0.45} \tag{4.23}$$

The index "*s*" meaning that the plasma properties are calculated at the particle surface temperature.

The difference between these two corrections is well within the experimental error of the available data (±25 %).

Table 4.2, summarizes results obtained with different expressions of the drag coefficient in a d.c. plasma jet. This table shows that, for a given Reynolds number, the drag coefficient calculated by different methods, can vary by up to 50 % between different correlations and simulation methods. They also show a strong dependence on the particle and free stream plasma temperatures.

(b) Influence of the non-Continuum Effect

Other corrections which might be necessary when dealing with the transport and heating of fine particles ($d_p < 10$ μm) under plasma conditions, whether at atmospheric pressure or under soft vacuum conditions, are due to the non-continuum effect. These can be particularly important when the mean free path of the plasma,

Table 4.3 Knudsen effect correction factor to the Drag coefficient of small zirconia particles immersed in an infinite Ar–H_2 (25 vol.%) plasma at 10,000 K [64]

d_p (μm)	5	1	0.1
T_p = 1,000 (K)	0.33	0.17	0.06
T_p = 2,000 (K)	0.28	0.14	0.05
T_p = 3,000 (K)	0.26	0.13	0.046

λ, is of the same order of magnitude as the diameter of the particles, d_p. According to Chen and Pfender [61, 62] and Chen et al. [63], the Knudsen effect should be taken into account in the Knudsen number regime $0.01 < \mathrm{Kn} < 1.0$, where $\mathrm{Kn} = \lambda/d_p$.

The following correction for the drag coefficient was proposed [62]:

$$C_D = (C_D)_{\text{cont.}} \left[\frac{1}{1 + \left(\frac{2-a}{a}\right)\left(\frac{\gamma}{1+\gamma}\right)\frac{4}{\Pr(s)}\mathrm{Kn}} \right]^{0.45} \tag{4.24}$$

where a is the thermal accommodation coefficient (−), γ the isentropic coefficient (c_p/c_v), Pr(s) the Prandtl number of the gas at the surface temperature of the particle. Typical numerical values of the correction factor in square brackets can vary from 1.0 to 0.4, with an increase of the Knudsen number from 0.01 to 1.0. The correction to the drag coefficient can be important when considering particles in the size range 0.1–5 μm as used in suspension plasma spraying. This is illustrated in Table 4.3 from J. Fazilleau [64] related to zirconia particles immersed in an infinite Ar–H_2 (25 vol.%) plasma at 10,000 K.

4.2.3.3 Trajectory Corrections Due to Various Effects

Results are presented for d.c. plasma jets where these corrections are the most important.

(a) Effect of Temperature Gradient

As already emphasized in Section “Flame Spraying”, temperature gradients modify, depending on the calculation method, the drag coefficient, and thus particle trajectories. For example, the calculation according to [19] presented in Fig. 4.15 was obtained with alumina particles injected internally into an Ar–H_2 d.c. plasma jet using the isotherms and velocities measured by Fauchais et al. [66]. The choice of the correction to the drag coefficient plays a great role on the 60 μm alumina particle trajectory (for a given injection velocity) as shown in Fig. 4.15.

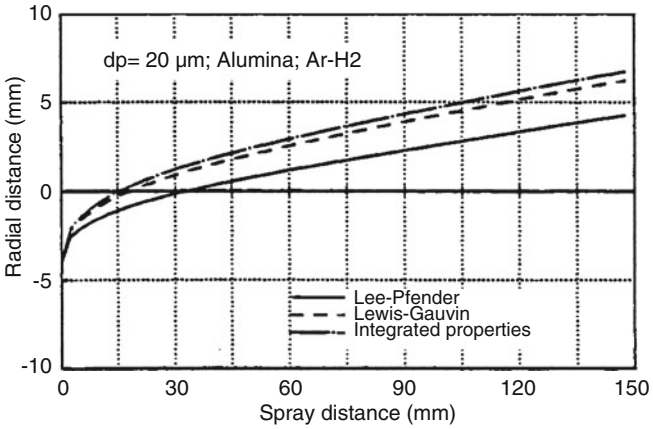


Fig. 4.15 Effect of the drag coefficient on the trajectories of 60 μm diameter alumina particles injected at 8 m/s into the plasma jet ($Ar–H_2$, 75–15 slm, $P = 29$ kW, $\rho_{th} = 63$ %, nozzle i.d. 8 mm) [19]: Lee et al. [60], Lewis and Gauvin [49], integrated properties [65]

(b) Effect of Rarefaction and Vaporization

Once the correction for the steep gradients has been chosen, the corrections for non-continuum effects and vaporization have also to be determined. This is illustrated in Fig. 4.16 for 20 μm diameter alumina particles (this size is chosen because it shows a significant non-continuum effect) injected at 25 m/s (to obtain about the same trajectory as that of the 60 μm particles). Here again the different types of corrections used are shown to have an important effect on the calculated particle trajectory. The corresponding effect on the particle velocity along each of these trajectories is shown in Fig. 4.17.

(c) Effect of Turbulence

The effect of turbulence on the particle motion has also been shown to have an important influence on the small particle trajectory by Pfender [11]. Typical results for 10–50 μm alumina particles injected into an argon d.c. turbulent plasma jet are given in Fig. 4.18.

The ranges of dispersed particle trajectories are obviously larger for the smaller particles (10 μm). This is due to the small mass of such particles which follow easier the motion within eddies. It is also observed that the dispersion becomes larger downstream. This is caused by the accumulated "random walk" influence. Comparing Fig. 4.18 to Figs. 4.15–4.17 it seems that the different corrections by the equations of motion may still exceed the influence of turbulence, for particles larger than 15 μm in diameter.

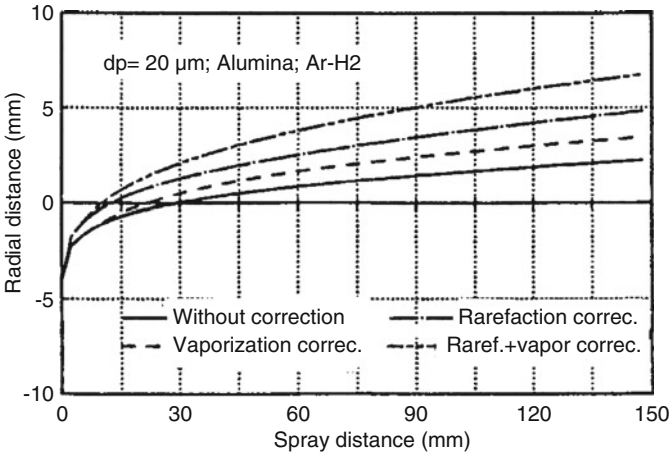


Fig. 4.16 Trajectories of 20 μm in diameter alumina particles injected at 25 m/s into the plasma jet depicted in Fig. 4.15 (radial distance = 0 corresponds to the torch axis). The temperature gradient correction has been calculated using the mean integrated properties [65]

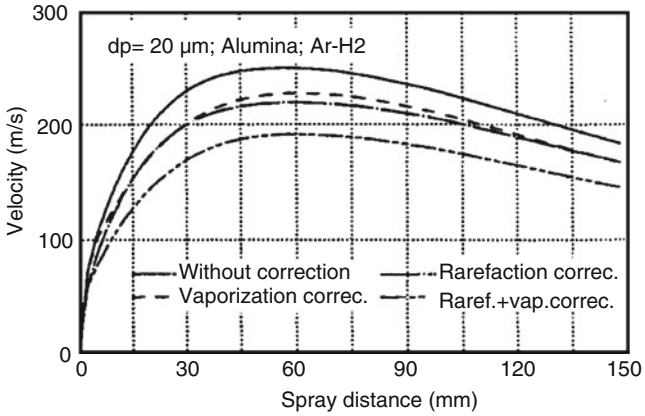


Fig. 4.17 Particle velocity along the trajectories shown in Fig. 4.15 with different drag coefficient corrections for non-continuum effects and particle vaporization [65]

4.2.3.4 Other Effects

(a) Particle Shape

In all preceding calculations, the particles have been assumed to be spherical. If this is the case for agglomerated, spray dried, atomized powders, or those produced by sol–gel techniques, it is not at all true for fused and crushed particles, which can have angular shapes with a low shape factor. The shape of the particle modifies its drag coefficient [67], which, for example, can be correlated to the particle sphericity

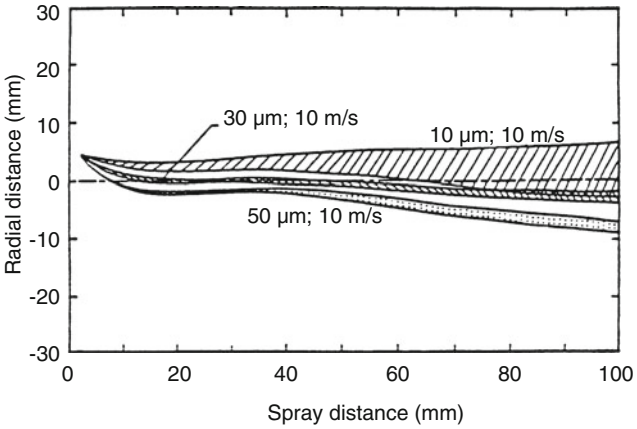


Fig. 4.18 Dispersed alumina particle trajectories in an argon, d.c. turbulent plasma jet. Reprinted with kind permission from Springer Science Business Media [11]

factor in a limited range of shape effects [68]. However it must be emphasized that particles when injected into the plasma or HVOF or flame jets are rapidly (~ a few tens of μs) heated above or close to their melting point, thus attaining a spherical shape. For example, in d.c. plasma spraying, the non-sphericity effect plays a role mainly close to the injector. However, the increase in drag force of oblate spheroids compared to those of equal volume spheres, may appreciably affect the particle trajectory, thus its heating [68, 69]. This non-sphericity modifies much more the behavior of particles within the injector.

Measurements have shown in cold spray that irregular titanium particles were accelerated and decelerated more rapidly than the spherical aluminum and copper powders [70]. It was proposed that this occurred as a result of the greater drag force experienced by the titanium particles. In-flight particle velocity and deposition efficiency measurements, under cold spraying conditions, of two different stainless steel powders were carried out [68]. It was found that the angular particle had a faster velocity than the spherical one and resulted in greater deposition efficiency. The critical velocity of both powders was almost the same and did not depend on their micro-hardness. However, more work is needed to understand and quantify this effect. Equations have been proposed to calculate the acceleration of nonspherical particles. For example, the shape of the particle and its drag coefficient in this case can be correlated with the particle sphericity factor for a limited range of shapes [68]. Similar calculations have been performed for nonspherical particles in d.c. plasmas [69].

(b) Particle Charging

Particle charging can also have a limited effect on its trajectory in plasma jets, since a particle injected into thermal plasma will always assume a negative charge due to

the difference between the thermal velocities and mobilities of electrons and ions. Whether or not this affects particles drag in thermal plasmas has never been explored. Under LTE conditions [11, 19, 63] in the boundary layer, particle charging will be of minor importance, because of the low charge concentration that can exist in the region near the particle surface. This may, however, be different for frozen chemistry, under non-continuum conditions in the case of low pressure plasma spraying.

Deviations from LTE conditions in the plasma can also be important, particularly close to the particle surface. Whether or not such deviations from LTE will substantially affect heat and momentum transfer to particles in the condensed phase, remains still a matter for further study. Studies of momentum and heat transfer between low-pressure plasma and particles are generally based on molecular dynamics and they are beyond the scope of this book. However, the interested reader can find information in refs. [71–76].

4.2.4 Drag Coefficient: Submicron and Nanometer-Sized Particles

4.2.4.1 Problem of Particle Inertia

When spraying fine particles in the micrometer or nanometer size range they tend to follow the flow over the surface where they are to be deposited. The following question must be considered: under which conditions will such small particles reach the surface of the substrate and not continue to follow the gas flow, as expected according to their low inertia? The answer is given by the Stokes number [77]:

$$\mathrm{St} = \frac{\rho_\mathrm{p} \cdot d_\mathrm{p}^2 \cdot \nu_\mathrm{p}}{\mu_\mathrm{g} \cdot l_\mathrm{BL}} \tag{4.25}$$

where the index p relates to the liquid particle, g to the gas, and BL is the fluid boundary layer thickness. St must be larger than 1 for the particle to cross the boundary layer and reach the substrate. Considering a zirconia particle with an impact velocity of 300 m/s, a boundary layer of 1 mm, and an Ar–H_2 plasma containing 30 % air (50 mm spray distance), with a Stokes number of 10, a 1-μm particle impacts onto the substrate, but St = 1 for a 0.3 μm particle and with sizes below none of them will impact the substrate. The limiting size depends strongly on the particle impact velocity at the edge of the boundary layer, and on the flow velocity close to the substrate, controlling the boundary layer thickness. The latter is inversely proportional to the square root of the flow velocity. Particle impact thus depends on the spray gun used, its working conditions, especially its nozzle design, the gas flow rate, the power dissipated, and the spray distance, especially when it is below 50 mm as in suspension plasma spraying. The longer the spray distance, the more the hot jet

expands and mixes with the surrounding atmosphere, thus increasing the flow boundary layer thickness and reducing the Stokes number [Eq. (4.25)].

4.2.4.2 Thermophoresis Effect

As underlined previously (see Sect. 4.2.1) Thermophoresis forces, $F_{\text{th,}}$ occur when small particles are subjected to in the presence of steep temperature gradients [1].

$$F_{\text{th}} = \frac{p \cdot \lambda \cdot d_{\text{p}}^2 \cdot \nabla T}{T_{\text{p}}} \tag{4.26}$$

where p is the gas pressure, λ the gas mean free path, d_{p} the particle diameter, ∇T the temperature gradient between the front and rear faces of the particle, and T_{p} the particle temperature. This effect is important for particle sizes below 1 μm and becomes negligible for particles over 5 μm. Figure 4.19 shows the influence of the thermophoresis effect on a 1 μm particle trajectory injected at a radial distance of 2 mm from the jet axis. The particle trajectory is almost parallel to the torch axis (an angle of 3–4°) and once it arrives in strong gradient region, it is ejected towards the jet periphery and once the temperature gradient is reduced, the particle tends to come back parallel to the jet axis. The phenomenon is enhanced if the particle size decreases. It means that small particles, even correctly entering the plasma, can escape from the core and travel in the fringes. Of course this phenomenon is mainly observed with plasma jets.

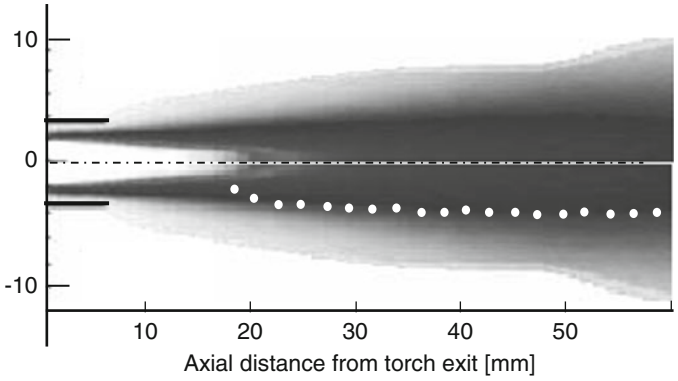


Fig. 4.19 Thermophoresis effect on the trajectory of a 1-μm zirconia particle. The velocities and temperature fields are computed [77] for an Ar–H_2 plasma jet with a 6 mm nozzle diameter and a net power of 32 kW supplied to the gas. The bright part of the jet core is surrounded by the 11,000 K isotherm and the particle trajectory starts at a radial distance of 2 mm from the jet axis and 15 mm from the nozzle exit. Reprinted with kind permission from Springer Science Business Media [78]

4.3 In-Flight Single Particle Heat and Mass Transfer and Chemical Reactions

4.3.1 Basic Conduction, Convection, and Radiation Heat Transfers

The balance between conduction and convection heat transfers from the hot gas to the particle and particle cooling due to radiative heat losses to the surroundings governs the particle temperature (see Fig. 4.20). In most cases the radiative heat transfer from the hot gas, especially the plasma gas, to the particle can be neglected, because it is generally considered as optically thin (see [59]). The net heat exchange between the hot gas and the particle can be expressed as

$$Q = h\left(\pi d_{\mathrm{p}}^2\right)\left(T_\infty - T_{\mathrm{s}}\right) - \left(\pi d_{\mathrm{p}}^2\right)\varepsilon\sigma_{\mathrm{s}}\left(T_{\mathrm{s}}^4 - T_{\mathrm{a}}^4\right) \tag{4.27}$$

where, T_{s} and d_{p} are, respectively, the surface temperature and diameter of the particle, ε is the particle emissivity, σ_{s} the Stefan–Boltzmann constant (5.67×10^{-8} W/m^2·K^4), T_{a} the temperature of the surroundings (K), Q is expressed in (W).

Assuming a uniform particle temperature implies that the thermal conductivity of the particle material κ_{p} is much higher than that of the gas κ, i.e.

$$\mathrm{Bi} = \frac{\kappa}{\kappa_{\mathrm{p}}} < 0.01 \tag{4.28}$$

where Bi is the Biot number.

The heat transfer coefficient between the plasma and the particle may be expressed in terms of the Nusselt number defined as

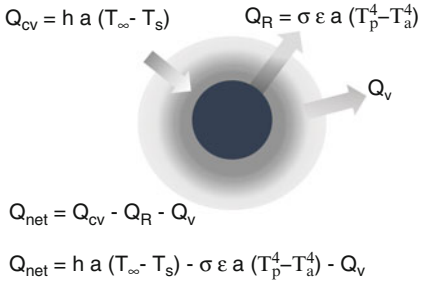


Fig. 4.20 Schematic of the net heat transfer to a particle, q_{net} , where, q_{R} radiative loss from the surface of a solid particle and q_{v}, heat loss from radiating vapor

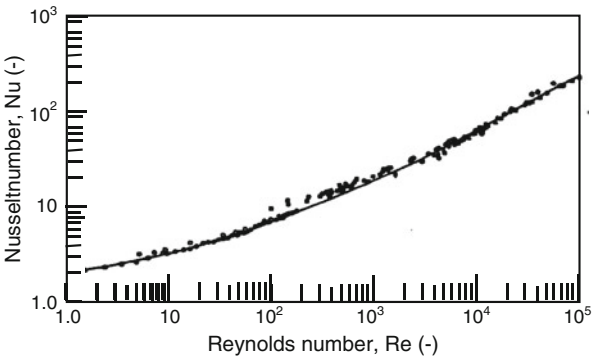


Fig. 4.21 Nusselt number as function of the Reynolds number for a single sphere in air, after Clift et al. Reprinted with kind permission from Elsevier [12]

$$\mathrm{Nu} = \frac{h d_\mathrm{p}}{\kappa} \tag{4.29}$$

where h is the heat transfer coefficient (W/m^2·K) and κ the thermal conductivity of the fluid (W/m·K).

Typical data for the Nusselt as function of the Reynolds number are given in Fig. 4.21. These can be correlated through the following relationship, often called semi-empirical Ranz–Marshall correlation, for Reynolds numbers lower than 200.

$$Nu = 2.0 + 0.6 \times \mathrm{Re}^{0.5} \times \mathrm{Pr}^{0.33} \quad \mathrm{Re} < 200 \text{ and } 0.5 < \mathrm{Pr} < 1.0 \tag{4.30}$$

The radiative losses are not negligible when the temperature and size of the particles are relatively high. They will mainly affect the heat transfer when h is low, i.e., for pure argon plasmas (see [59]) and combustion processes. This is illustrated in Fig. 4.22 (after Boulos [5]) for metallic particles immersed in infinite plasma, respectively, of pure Ar and Ar–H_2 (10 vol.%) plasmas. The emissivity has been set to one. For pure Ar plasma, the plasma temperature has to be slightly over 11,000 K for a tungsten particle with a diameter of 500 μm, immersed in the plasma to reach its melting temperature of 3,680 K (Fig. 4.22a). The effect is due to the intense radiation losses from the surface to the surroundings of the particle.

With the Ar–H_2 plasma, a temperature close to 9,000 K is sufficient to melt the 500 μm tungsten particle (see Fig. 4.22b). For conventional plasma sprayed tungsten particles (50 μm in diameter) argon r.f. plasma over 7,000 K is sufficient (Fig. 4.22a), while an Ar–H_2 plasma must have about 4,000 K (see Fig. 4.22b). Similar results [5] were reported for oxide particles heated by air plasma where heat transfer is higher than that for pure argon.

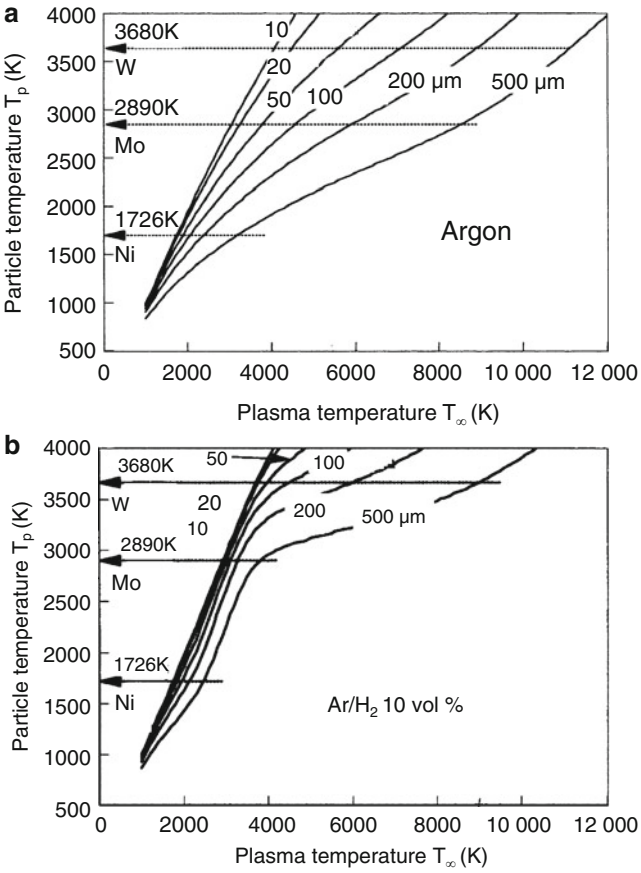


Fig. 4.22 Radiative losses from metal particles immersed in infinite plasma of (**a**)- pure argon (**b**)- Ar–H_2 (10 vol.%) [5]

4.3.2 In-Flight Particle Heating and Melting

4.3.2.1 Basic Assumptions and Governing Equations

For the instantaneous particle temperature (see Sect. 4.3.1) the heat transfer, Q, to the particle can be calculated using Eq. (4.27), where the hot gas temperature T_∞ is that "seen" by the particle along its trajectory, and which has to be calculated first (see Sect. 4.2). Assuming a particle of infinite conductivity (relative to the hot gas) and corresponding to Bi = 0 (see Eq. (4.28)), results in a uniform temperature within the particle ($T_p = T_s = T_c$, where T_s and T_c are the surface and center temperatures, respectively) and under these conditions the variation of the particle temperature during its trajectory can be calculated by any of the following equations, depending whether the particle is undergoing a phase change or not.

For $T < T_m$ or $T_m < T < T_v$:

$$\frac{dT_p}{dt} = \frac{6Q}{\pi d_p^3 \rho_p c_{ps}} \tag{4.31}$$

where T_m and T_v are the melting and boiling temperatures of the particle material, respectively, and c_{ps} is the specific heat of the solid particle.

For $T = T_m$, the particle undergoes a phase change with the mass fraction which is molten, x, given by Eq. (4.32) as follows:

$$\frac{dx}{dt} = \frac{6Q}{\pi d_p^3 \rho_p \Delta H_m} \tag{4.32}$$

where ΔH_m is the latent heat of fusion of the particle material.

For $T = T_v$, the particle evaporates with the rate of change of the particle diameter given by Eq. (4.60) as

$$\frac{dd_p}{dt} = \frac{6Q}{\pi d_p^3 \rho_p \Delta H_v} \tag{4.33}$$

where ΔH_v is the latent heat of vaporization of the particle material.

It should be pointed out that Eq. (4.33) is only an approximation and that evaporation is likely to take place well below the boiling point of the material (see Section "Radiation of the Vapor"). As shown by Chen et al. [79] (see also Sect. 4.3.3.5), the shielding effect of the particle by the evolving vapor cloud could lead to considerable slowing down of the heating rate of the liquid droplet with the possibility of complete evaporation of the particle before it ever reaches its boiling temperature (see Sect. 4.3.3.5). Interestingly, they also show that these phenomena do not seem to affect, to any considerable extent, the estimate of the time required for the complete evaporation of the particle.

4.3.2.2 Example of Results

(a) DC Plasma Jets

Figure 4.23 from [80, 81] represents the axial velocity and temperature evolution of stainless steel particles 95 and 50 μm in diameter injected so that they assume the same trajectory in an Ar–H_2 d.c. plasma jet. As expected the larger particles reach a lower temperature (about 800 K less) than the smaller ones in spite of a higher velocity for the smaller particle (35 m/s more), resulting in a residence time almost twice as long for the larger particle (19 ms against 10.7 ms). The heating is rather fast and the maximum temperature is reached in both cases after less than 20 mm travel. The particle inertia is relatively high as shown upon cooling. The melting

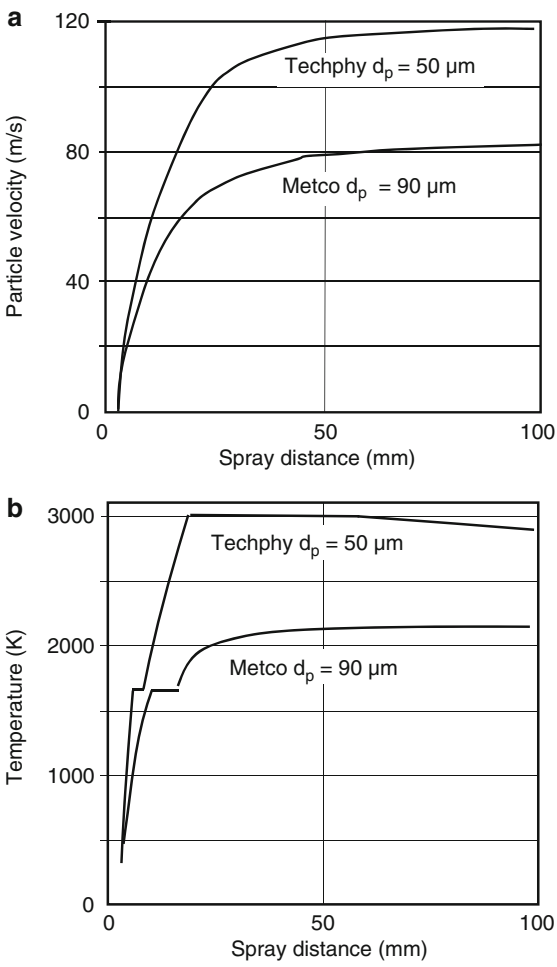


Fig. 4.23 Computed [80] downstream axial profiles of stainless steel particles, velocity, (**a**) and temperature (**b**). Particles with a mean size of 60 and 95 µm, respectively, were injected externally (at 4 mm downstream of the nozzle exit) in an Ar–H_2 plasma ($I = 550$ A, Ar 45 slm, H_2 15 slm, nozzle i.d. 7 mm), Reprinted with kind permission of the author

time of the small particle (constant temperature at about 1,750 K) is shorter than that of the bigger one. However it must be underlined that with $Bi = 0$ propagation phenomena are neglected and during melting the temperature is constant. As for particle trajectories, particles temperatures are linked to the corrections chosen to account for temperature gradients, Knudsen effect, and vaporization effect. The choice of the correction method results in different temperature histories.

(b) RF Inductively Coupled Plasmas

With r.f. plasmas, calculations are quite similar, and the main difference compared to a d.c. plasma is twofold:

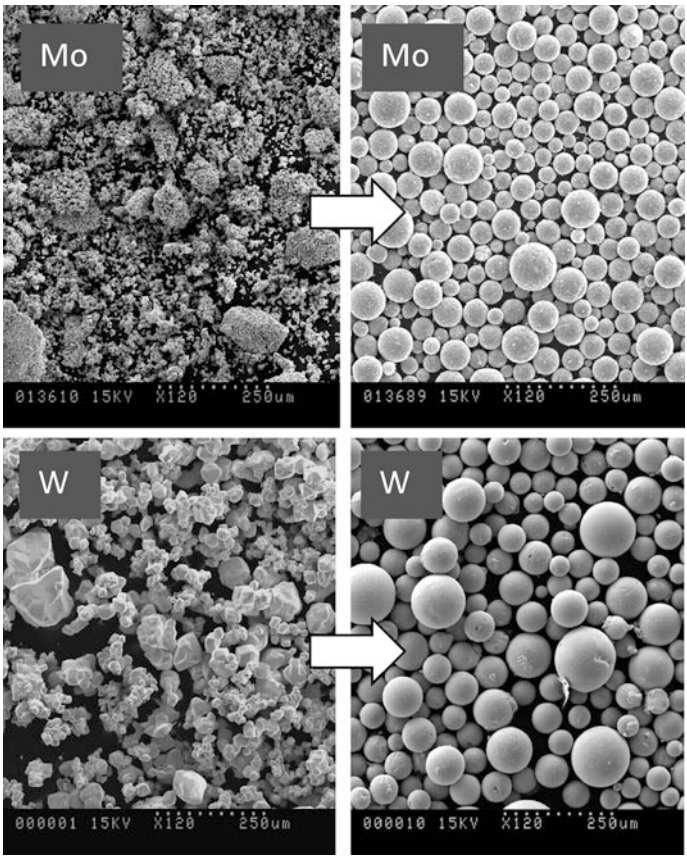


Fig. 4.24 Example of particles spheroidized by r.f. induction plasmas. Reprinted with kind permission of Tekna Plasma Systems Inc. [82]

– According to the plasma velocity, the corresponding residence times will be one to two orders of magnitude shorter in d.c. plasmas and only metal particles smaller than 60–80 μm and ceramic particles smaller than 50 μm can be fully melted in d.c. plasma jets, while for conventional r.f. plasmas melting of particles occurs up to 150–200 μm.
– In the case of d.c. plasma, spraying is generally performed in air, which is rapidly entrained into the jet, the oxygen, and in some cases nitrogen reacting with particles. Of course d.c. plasma spraying can also be performed in a controlled atmosphere, which is always the case in r.f. plasmas. However, they can work with an oxidizing atmosphere with oxygen injected in their sheath and entrained in their plume. r.f. plasmas are thus used for spraying of larger particles for composite materials reinforced with fibers (usually ~150 μm in diameter) or for powder densification and spheroidization as illustrated in Fig. 4.24 after Boulos [82].

(c) HVOF Spraying

i. Radial Injection

In these calculations [31], different-sized Inconel 718 particles ranging from 5 to 40 μm were injected at an axial distance of 0.12 m (downstream of the nozzle throat) with a speed of 8 m/s in an HVOF gun working with kerosene and oxygen. The particle trajectories in Fig. 4.25a show that the small particles are blown away by the gas flow, e.g., 5 μm particle travel along the edge of the barrel and spread outwards at the external domain as the jet expands outside the nozzle. The 10 μm particle remains at the outer region of the jet throughout the domain while the large particles, e.g., 30 and 40 μm move across the center of the gun and spread outwards into the external domain [31]. The particle velocity profiles in Fig. 4.25b clearly demonstrate that the smaller particles are accelerated more throughout the computational domain. When the particle velocity is higher than the gas velocity, as the gas jet decays outside the gun, the drag force on the particle then changes direction and becomes a resistance to the particle motion. The velocity of the particle is then decreased. The smaller the particle size, the more easily it is decelerated. A larger particle, on the other hand, has greater ability to maintain its velocity during the deceleration stage, because of its larger inertia. The surface temperature plots in Fig. 4.25c show the particles smaller than 10 μm undergo melting and solidification during the process.

ii. Axial Injection

To compare radial injection to axial one, results are presented of the experimental work conducted by Yang et al. [83] with a prototype HVOF torch of the chamber-stabilized type, using natural gas with oxygen with a stoichiometric factor of 1.4, corresponding to an adiabatic flame temperature of about 3,220 K. The sprayed powder was Amdry (Sulzer Metco, Troy, MI) 9,954 r (Co–32 %Ni–21 %Cr–8 % Al–0.5 %Y). Velocity profiles calculated for various particle sizes are shown in Fig. 4.26a. For particles smaller than 30 μm, the maximum velocity is obtained at a distance of less than 300 mm from the nozzle exit. Figure 4.26b shows the temperature evolution in the core of the particles versus the distance from the nozzle exit. In this figure, flat parts correspond to the melting point and result from the high latent heat of fusion of the CoNiCrAlY alloy. A flat section is also found in the resolidification process, which, for the smaller particles, starts not very far from nozzle exit. The 11 μm particles appear to be entirely resolidified at the distance of 250 mm and then rapidly cool down to a temperature of 430 °C below the melting point at the distance of 300 mm. The 60 μm particles begin to be molten at the position of −50 mm, inside the torch nozzle, and the melting front moves to half of the radius (15 μm) at the distance of 130 mm from the nozzle exit. From this position on, this partially molten particle resolidifies progressively and becomes

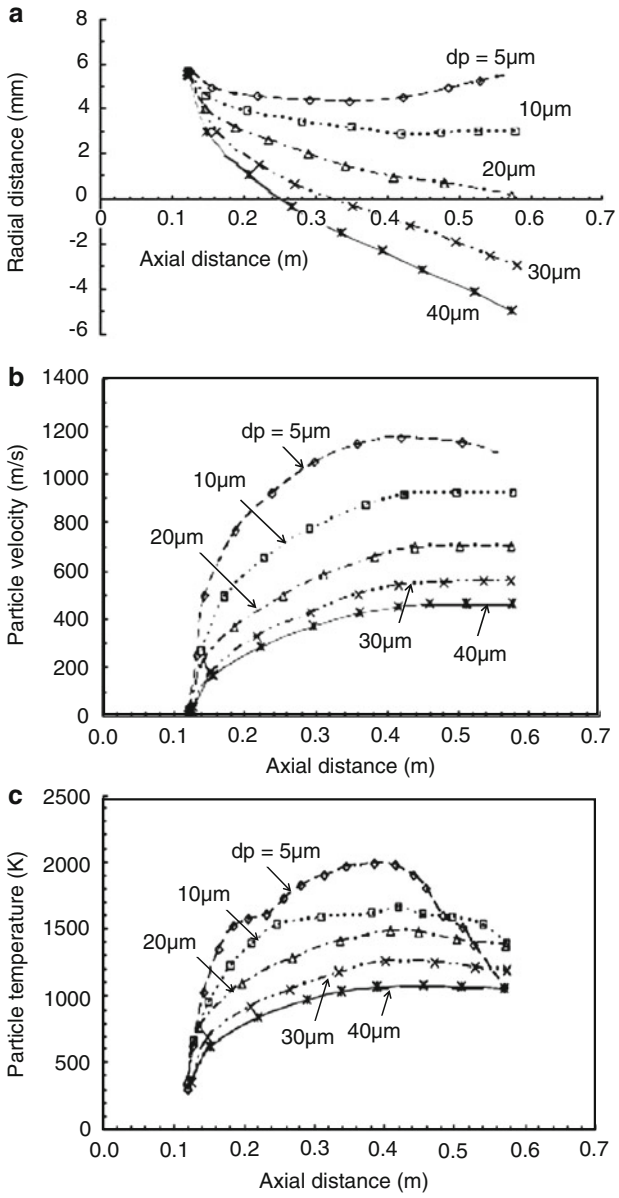


Fig. 4.25 Inconel 718 particles injected downstream of the nozzle throat in a kerosene–oxygen gun, (**a**) trajectory, (**b**) velocity profiles for different size particles, (**c**) temperature profiles for particles at different sizes. Reprinted with kind permission from Elsevier [31]

completely solid at a distance of 170 mm. At a distance of 300 mm, the core temperature of this particle is about 100 °C below its melting point. Globally, for the two superalloys considered (In 718 and CoNiCrAlY) similar velocities are achieved but particle temperatures are higher for axial injection.

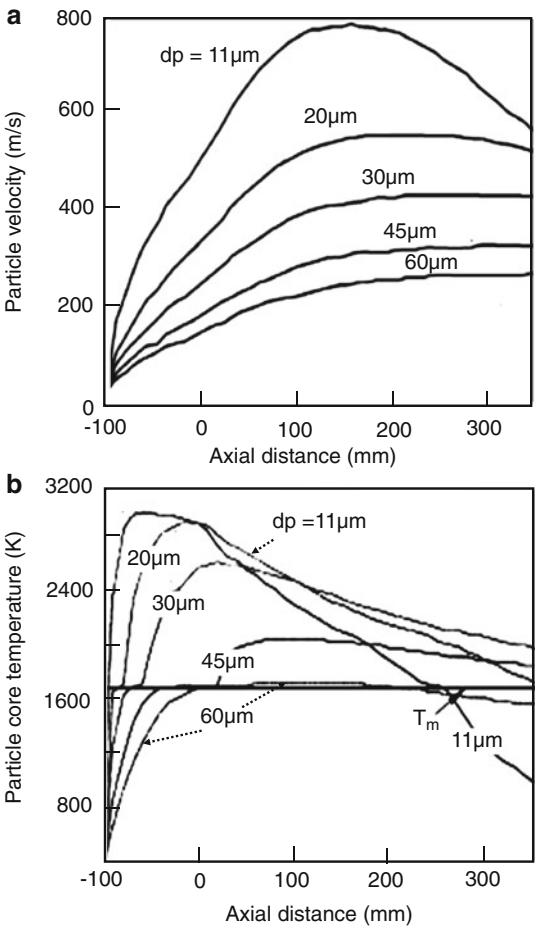


Fig. 4.26 CoNiCrAlY particles (**a**) velocity profiles (**b**) temperature (supposed to be uniform) calculated for the HVOF natural gas–oxygen mixture (stoichiometric factor of 1.4 corresponding to an adiabatic temperature of about 3,220 K), axial injection. Reprinted with kind permission from Springer Science Business Media [83], copyright © ASM International

4.3.3 Heat Transfer to a Single Sphere

4.3.3.1 Influence of Temperature Gradients

Because of high temperature gradients and strong nonlinear variations of the thermal conductivity, κ, with temperature, essentially for plasmas, one of the key problems for heat transfer coefficient calculations using the Nusselt number [Eq. (4.29)] is to determine at which temperature the thermal conductivity has to be evaluated. It can be the film temperature [Eq. (4.21)], $T_{0.19}$ [Eq. (4.20)] or any other temperature. This problem is especially important when considering diatomic gases for which a strong peak of κ is observed at the dissociation temperature of the gas.

A detailed theoretical analysis of the problem of pure conduction by Bourdin et al. [84] showed that the standard heat transfer equation (Eq. 4.20) holds even

under plasma conditions, provided that the properties are evaluated as an integrated mean value defined as:

$$\overline{\kappa} = \frac{I}{(T_\infty - T_s)} \left[\int_{T_s}^{T_\infty} \kappa(T) dT \right] \tag{4.34}$$

It is interesting to note that if the thermal conductivity, κ is a linear function of temperature, Eq. (4.34) reduces to the commonly used practice of evaluating the property values at the arithmetic mean film temperature, i.e. $\overline{\kappa}(T) = \kappa(T_f)$.

The application of Eq. (4.34) can be considerably simplified by splitting the integral with respect to some reference temperature, $T_o = 300$ K, as follows:

$$\overline{\kappa} = \frac{I}{(T_\infty - T_s)} \left[\int_{T_{300}}^{T_\infty} \kappa(T) dT - \int_{T_{300}}^{T_s} \kappa(T) dT \right] \tag{4.35}$$

$$\overline{\kappa} = \frac{I}{(T_\infty - T_s)} [I(T_\infty) - I(T_s)] \tag{4.36}$$

Values of κ, and $I(T)$, known as the heat conduction potential, are given in Fig. 4.27 for different plasma gases at atmospheric pressure as a function of temperature.

It should be noted that the analysis of Bourdin et al. [84] is restricted to pure conduction. In most practical cases for plasma spraying (Re $<$ 20 and Pr $<$ 1 dimensionless numbers related to particles) the convection term contributes less than 25 % to the heat transfer under plasma conditions [84]. However, in HVOF or HVAF slightly higher percentages are obtained.

To account for temperature gradients, Sayegh and Gauvin [14] proposed to calculate the fluid properties at the reference temperature $T_{0.19}$ defined in Eq. (4.20) and to use:

$$\mathrm{Nu} = 2.0 \times f_o + 0.473 \times \mathrm{Pr}^m \times \mathrm{Re}^{0.552} \tag{4.37}$$

where m and f_o are given by Eqs. (4.38) and (4.39).

$$m = 0.78 \times \mathrm{Re}^{0.552} \times \mathrm{Pr}^{0.36} \tag{4.38}$$

and

$$f_o = \left(1 - T_o^{1+x}\right) / \left[(1+x)(1 - T_o) T_o^x\right] \tag{4.39}$$

where x is the value of the exponent of T in the expression relating the viscosity and the thermal conductivity to the absolute temperature ($x = 0.8$ for Ar at $T < 10{,}000$ K and $p = 10^5$ Pa).

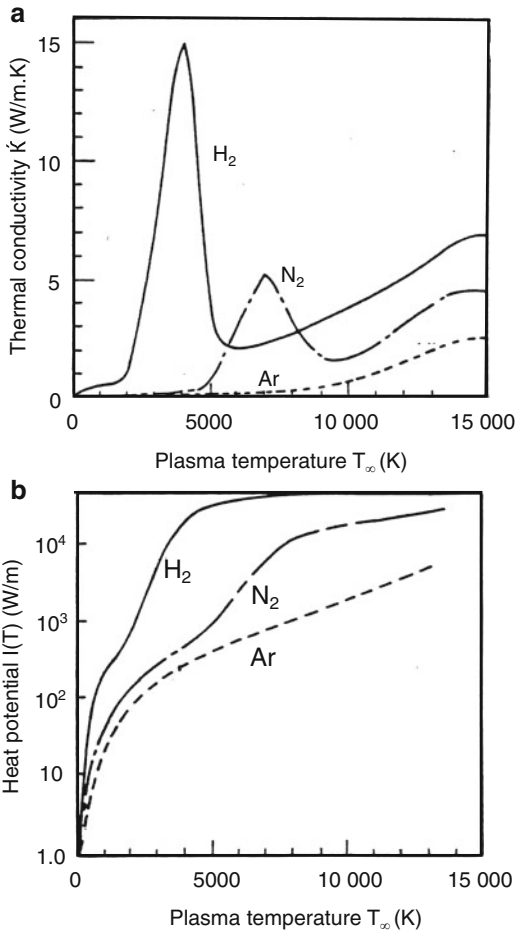


Fig. 4.27 Thermal conductivity (**a**) and heat conduction potential (**b**) for different gases at atmospheric pressure as function of temperature, after Bourdin et al. Reprinted with kind permission from Elsevier for Journal of Heat and Mass Transfer [84]

Lewis and Gauvin [15] suggested for pure argon,

$$\mathrm{Nu} = \left(2 + 0.515 \times \mathrm{Re}^{1/2}\right)\left(\nu_\mathrm{f}/\nu_\infty\right)^{0.15} \tag{4.40}$$

where T_f is the film temperature at which Re is evaluated. Fizsdon [85], on the other hand, suggested using

$$\mathrm{Nu} = \left(2 + 0.6 \times \mathrm{Re}_\mathrm{f}^{0.5} \times Pr^{1/3}\right)\left(\frac{\rho_\infty \mu_\infty}{\rho_\mathrm{s} \mu_\mathrm{s}}\right)^{0.6} \tag{4.41}$$

where Re and Pr are calculated at the film temperature. Lee et al. [60] proposed to use

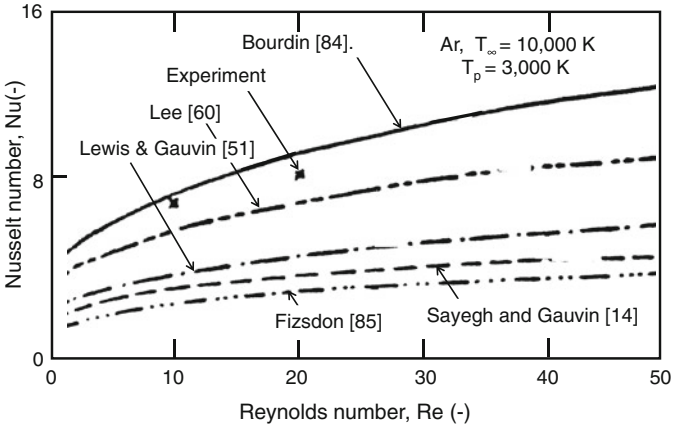


Fig. 4.28 Nusselt number derived by different authors and computer simulation [6]

$$\mathrm{Nu} = \left(2 + 0.6 \times \mathrm{Re}^{1/2} \times \mathrm{Pr}^{1/3}\right)\left(\frac{\rho_\infty \mu_\infty}{\rho_s \mu_s}\right)^{0.6}\left(\frac{c_{p\infty}}{c_{ps}}\right) \tag{4.42}$$

and finally Chen et al. [10, 61, 62, 86] gave an even more complex relationship

$$\mathrm{Nu} = 2\left[1 + 0.63 \times \mathrm{Re}_\infty \times \mathrm{Pr}_\infty^{0.8}\left(\mathrm{Pr}_S/\mathrm{Pr}_\infty\right)^{0.42}\left(\frac{\rho_\infty \mu_\infty}{\rho_s \mu_s}\right)^{0.52} C^2\right] \tag{4.43}$$

in which

$$C = \left[1 - \left(h_s/h_\infty\right)^{1.1}\right] \Big/ \left[1 - \left(h_s/h_\infty\right)^2\right] \tag{4.44}$$

where h_i is the specific enthalpy of the plasma calculated, respectively, at the particle surface temperature (index s) and at the plasma temperature (index ∞). The values of the Nusselt number, Nu, obtained using these different correlations and computation schemes have been shown by Pfender [6] for atmospheric argon plasma at 4,000 K, to be consistent from one expression to the other. The differences at 12,000 K, are significantly more important than at lower temperatures, because of ionization effects, as illustrated in Fig. 4.28.

These differences are particularly important when considering diatomic gases such as Ar–H_2 (17 vol.%) mixture. This is illustrated in Fig. 4.29 representing the heat transfer coefficients calculated by A. Vardelle [87] versus temperature for a 50 μm particle, at T_s = 1,000 K, and traveling at 50 m/s.

Correlations 1, 2, 4 in Fig. 4.29 were evaluated at T_f and they exhibit similar evolution with a peak close to 6,000 K corresponding to T_f = (6,000 + 1,000)/2 = 3,500 K, i.e., the dissociation temperature of hydrogen, where κ, as well as c_p, exhibit high peaks as shown in Fig. 4.27a. It can be seen that the difference between

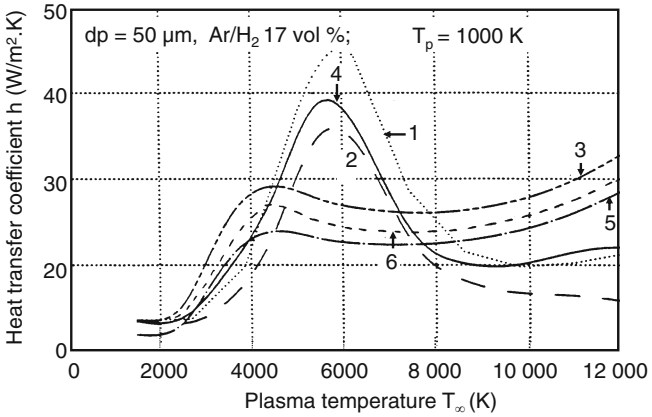


Fig. 4.29 Heat transfer coefficient for a 50 µm diameter particle traveling at 50 m/s with T_s = 1,000 K in a Ar–H_2 (17 vol.%) plasma (1) Lewis and Gauvin [51], (2)—Fizsdon [85], (3) Convection and conduction calculated with integrated properties, (4) Lee et al. [60], (5) Nu = 2 : Bourdin et al. [84], (6) Chen [86]

the values of the heat transfer coefficient, h, for pure conduction (curve 5 in Fig. 4.29) and that including convection effects (curve 3 in Fig. 4.29) is less than 20 %.

Finally, the question is what Nusselt number relationship should be used. Chen [10] has tried to answer this question by comparing the compiled results from eight different relationships, cited in the literature, with experimental results for spheres 6 mm in diameter in an argon plasma jet, and 8 mm diameter in an air plasma jet. The results, limited to a temperature range from 7,000 to 9,200 K due to the experimental conditions, show that the best fit is obtained with Eq. (4.43).

For calculating particle heating in combustion and cold spray processes, practically the Ranz–Marshall correlation [see Eq. (4.30)] is systematically used, where Reynolds and Prandlt numbers are calculated at the mean value of the free stream fluid temperature, T_∞, and the particle surface temperature, T_s, [see Eq. (4.14)].

In D-gun spraying, authors use the Ranz–Marshall correlation [see Eq. (4.30)] [56] or more sophisticated ones [88]:

$$\mathrm{Nu} = 2 \cdot \exp\left(-\mathrm{Ma_p}\right) + 0.459\mathrm{Re}^{0.55}\mathrm{Pr}^{0.33} \tag{4.45}$$

4.3.3.2 Influence of non-Continuum Effect

The effect, essentially in thermal plasmas, is quite similar to that observed for the drag coefficient (see Section "HVOF") and generally Eq. (4.22) is used with an accommodation coefficient of 0.8. A corresponding correction to account for non-continuum effects in plasma–particle heat transfer over the same Knudsen number range ($0.01 < \mathrm{Kn} < 1.0$) has also been proposed by Chen and Pfender [62].

In this case they made use of the temperature jump concept resulting in the following correction:

$$q = (q)_{\text{cont}} \left[\frac{1}{1 + \left(2Z^*/d_{\text{p}}\right)} \right] \tag{4.46}$$

where $(q)_{\text{cont}}$ is the heat flux calculated using an available correlation for continuum flow and Z^* is the jump distance. Typical numerical values of the correction factor in square brackets in this case could be as low as 0.4–0.5 for a Knudsen number of about 0.1. It is important to note that the Knudsen effect is stronger for plasmas with higher enthalpies [62]. For small particles (0.1–5 μm, for example) corrections with a magnitude similar to those already presented for C_{D} (see Section "HVOF") have to be made [64].

In combustion processes, generally the Knudsen effect is negligible. For example, Sobolev et al. [58] have shown that for particles 20 μm in diameter, the Knudsen effect changes values by less than 4 %. Of course when spraying suspensions with sub-micrometer- or nanometer-sized particles, this effect will be more important, but less than that observed in plasma spraying, due to the lower gas temperature.

4.3.3.3 Role of Heat Conduction in Fully Dense Particles

(a) Particle Immersed in an Infinite Hot Gas at Constant Temperature

To achieve no heat propagation within the in-flight particle the condition of Eq. (4.28) must be fulfilled. The two important factors to be considered are the thermal conductivities of both the hot gas and particle. The gas thermal conductivity is the highest for plasmas, especially for those containing diatomic gases at temperatures over that of dissociation (for example, see Fig. 3.20). Flames thermal conductivities are generally below 0.3 W/m K. Thus the value of the Biot number depends strongly on the particle material considered: roughly over 30 W/m K heat propagation must be considered. It is especially the case of zirconia ($\kappa_{\text{p}} \approx 1$ W/m K) and polymer materials ($\kappa_{\text{p}} \approx$ few tenths of W/m K). It must also be kept in mind that the morphology of the particles, depending on the manufacturing process plays an important role in the particle thermal conductivity that can be up to 5–6 times lower than that of the bulk material. For example, it is the case of agglomerated particles that are not or poorly densified. Moreover the thermal conductivity for the same densification conditions drops when the size of the agglomerated particles diminishes. The problem of the heat propagation lies in short the residence time of the particles in the hot gases: if $\text{Bi} > 0.3$ the particle can reach the substrate with its core still solid modifying deeply its flattening.

As will be shown later, one of the important problems facing most researchers dealing with the calculations of trajectories and temperature histories of particles

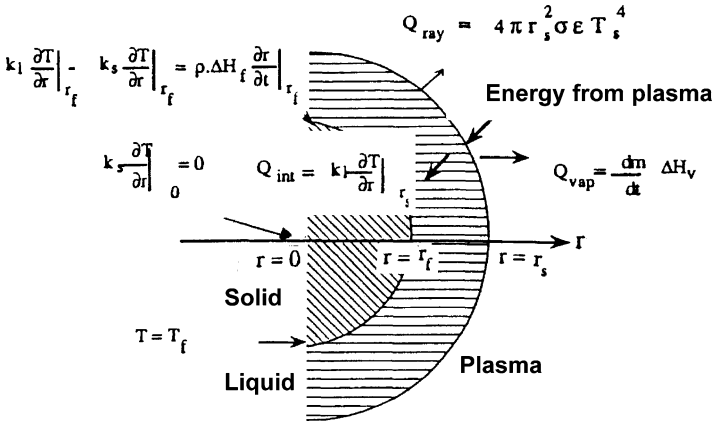


Fig. 4.30 Boundary conditions for the propagation of a melting front within a spherical particle

injected into a plasma is how to decide, a priori, whether internal conduction in the particle should be taken into account or not. Intuitively, it should always be possible to treat small particles of diameters in the range of 5–20 μm as isothermal and neglect the effect of internal heat conduction on the overall heat transfer process. But, whatever maybe the particle size, heat propagation has to be taken into account as soon as Eq. (4.28) is not fulfilled. Then the time evolution of the temperature field within the particle is described by the following conduction equation:

$$\frac{1}{r^2}\frac{\partial}{\partial r}\left(\kappa_p r^2 \frac{\partial T}{\partial r}\right) = \rho_p c_{pp} \frac{\partial T}{\partial t} \tag{4.47}$$

where the index p refers to the particle and r is the radial distance from the center of the particle. The velocity of propagation of a melting front $\left(\frac{\partial r}{\partial t}\right)_{r_m}$ is given by

$$\left(\frac{\partial r}{\partial t}\right)_{r_m} = \frac{1}{\rho_l \Delta H_m}\left[\kappa_{pl}\left(\frac{\partial T}{\partial r}\right)_{r_m} - \kappa_{ps}\left(\frac{\partial T}{\partial r}\right)_{r_m}\right] \tag{4.48}$$

where κ_{pl} and κ_{ps} are the thermal conductivities (W/m K), respectively, of the liquid and solid phases, r_m is the radial position (m) of the melting front, ρ_l the specific mass of the liquid (kg/m^3), and ΔH_m the latent heat of fusion (J/kg). The boundaries conditions for Eqs. (4.47) and (4.48) are summarized in Fig. 4.30.

Bourdin et al. [84] carried out a systematic study of the transient heating of spherical particles of different materials (Ni, Si, Al_2O_3, W, SiO_2) and different particle sizes (d_p = 20–400 μm) as they are suddenly immersed in different plasmas (Ar, N_2, H_2) at atmospheric pressure and different temperatures (T_∞ = 4,000–10,000 K).

Typical results obtained for alumina particles of different diameters in nitrogen plasma at 10,000 K are given in Fig. 4.31. This figure shows temperature

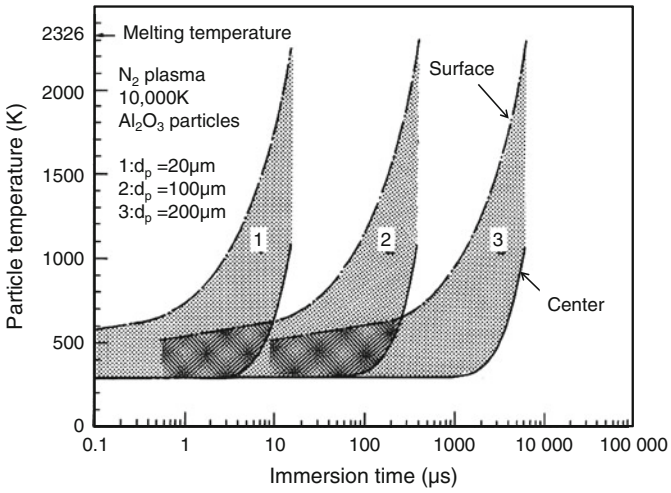


Fig. 4.31 Temperature history of alumina particles of different diameters suddenly immersed in a nitrogen plasma at 10,000 K, after Bourdin et al. [84]. Reprinted with kind permission from Elsevier for Journal of Heat and Mass Transfer

differences between the surface (dotted line) and that of the center of the particle (solid line) as high as 1,000 K even for the 20 μm diameter particles.

As expected, the difference between the temperature of the surface of the particle and that of its center depends on the temperature of the plasma (Fig. 4.32), the nature of the plasma gas (Fig. 4.33), as well as on the thermal conductivity of the material of the particle (Fig. 4.34).

Based on the above results Bourdin et al. [84] concluded that a good estimate of the relative importance of the phenomena of internal heat conduction in the particle can be made based on the value of the Biot number, see Eq. (4.28) $\left(Bi = \overline{\kappa}/\kappa_p\right)$ with, $\overline{\kappa}$, the integrated mean thermal conductivity of the gas (W/m K), Eq. (4.34), and κ_p the thermal conductivity of the material of the particle. As a general rule they observed that important differences can exist between the temperature at the surface of the particle and that at its center, when the Biot number is larger than 0.03.

Chen and Pfender [86] reached a similar conclusion in their study of the unsteady heating of small particles in thermal plasmas. Their results showed, however, that for an approximate estimate of the melting time required for a given particle, the infinite thermal conductivity assumption was still reasonably acceptable. It should be stressed that the phenomenon of internal heat propagation in the particle should be taken into account in the case of high thermal conductivity plasmas (mainly those containing diatomic molecules) in which ceramic particles are injected. A typical result, presented as the time temperature history of alumina particles in nitrogen plasma, is given in Fig. 4.35.

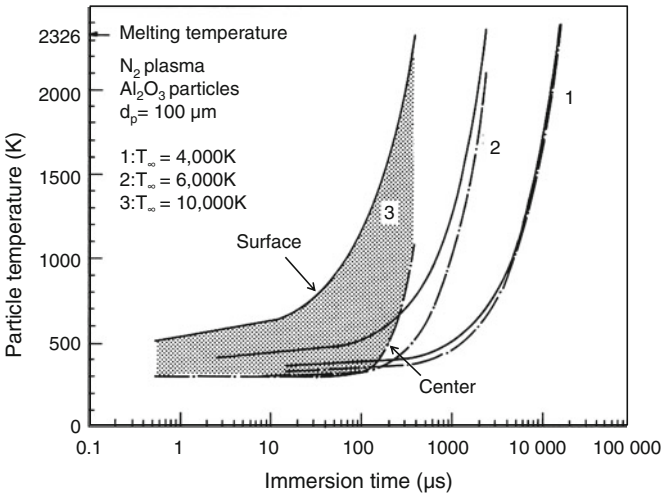


Fig. 4.32 Temperature history of 100 μm diameter alumina particles immersed in nitrogen plasma at different temperatures, after Bourdin et al. [84]. Reprinted with kind permission from Elsevier for Journal of Heat and Mass Transfer

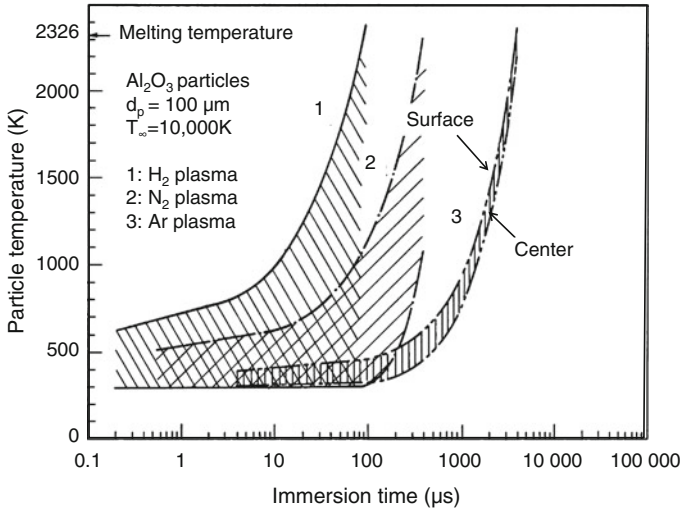


Fig. 4.33 Temperature history of 100 μm diameter alumina particles immersed in different plasmas at 10,000 K, after Bourdin et al. [84]. Reprinted with kind permission from Elsevier for Journal of Heat and Mass Transfer

The phase change problem can also be accounted for by using an explicit enthalpy model which eliminates the need to track the phase bounding interface explicitly as proposed in Eq. (4.35). Associated with finite difference/finite volume methods, the explicit enthalpy method is easy and robust to implement. In this case instead of Eq. (4.35) the following equations are used:

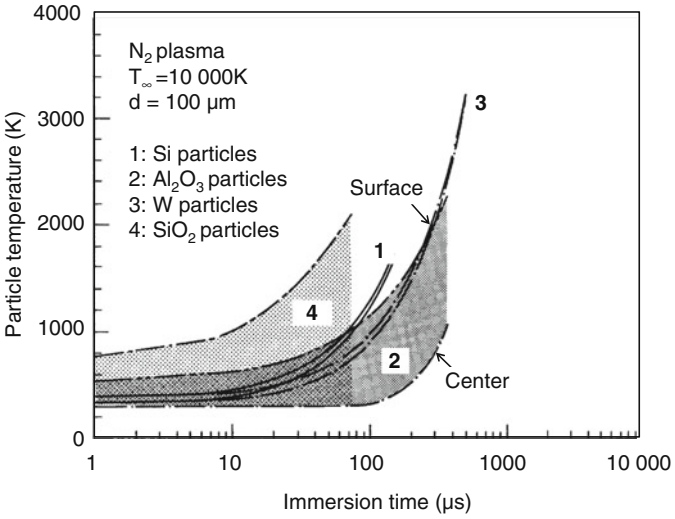


Fig. 4.34 Temperature history of 100 μm diameter particles of different materials immersed in a nitrogen plasma at 10,000 K, after Bourdin et al. [84]. Reprinted with kind permission from Elsevier for Journal of Heat and Mass Transfer

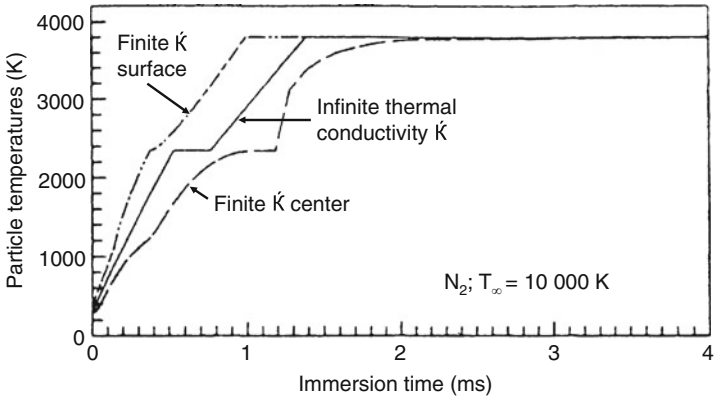


Fig. 4.35 Temperature history of an alumina particle exposed to a nitrogen plasma at 10,000 K, after Chen and Pfender. Reprinted with kind permission from Springer Science Business Media [86]

$$\frac{\partial h_g}{\partial t} = \frac{1}{r^2} \times \frac{\partial}{\partial r}\left(r^2 \kappa_{\mathrm{p}}(T)\frac{dT}{dr}\right)$$

with

$$\begin{aligned} T(r,0) &= T_{\mathrm{ini}} \\ \left(\frac{\partial T}{\partial r}\right)_{r=0} &= 0 \\ \kappa_{\mathrm{p}}(T)\left(\frac{\partial T}{\partial r}\right)_{\mathrm{R}} &= h(T(R,t))(T(R,t)-T_\infty) - \varepsilon\sigma_{\mathrm{s}}\left(T(R,t)^4 - T_{\mathrm{e}}^4\right) \end{aligned} \tag{4.49}$$

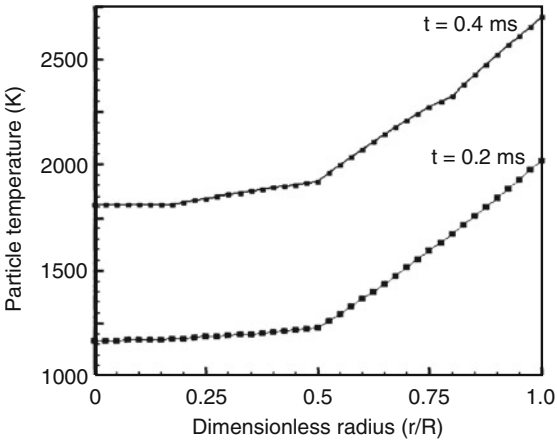


Fig. 4.36 Radial evolution of the temperature at two different times of a mechanofused particle (Fe_2O_3 with Al_2O_3 shell) 25 μm in radius, with the alumina shell 12.5 μm thick, immersed in an infinite plasma at 10,000 K ($R_{th} = 10^{-8}$ m^2 K/W). Reprinted with kind permission from author [89]

In these equations R is the radius of the particle, T_{ini} its initial temperature, ε the emission coefficient, σ_s the Stefan–Boltzmann constant, T_e the environment temperature, h is the heat transfer coefficient, and T_∞ the plasma temperature outside the boundary layer surrounding the particle. For example, Fig. 4.36 represents the temperature distribution within a mechanofused particle (iron core 12.5 μm in radius surrounded by an alumina shell 12.5 μm thick with a very low contact resistance of 10^{-8} m^2 K/W) at two successive times of 0.2 and 0.4 ms after its immersion in infinite Ar–H_2 (25 vol.%) plasma at 10,000 K [89].

At 0.2 ms neither the iron nor the alumina are melted, but the alumina temperature is larger with an important temperature gradient (due to its low thermal conductivity $\kappa = 5$ W/m K). At 0.4 ms alumina and iron have started to melt. This can be observed through the slight slope change of iron at 1,810 K for a dimensionless radius of 0.2. Below a dimensionless radius of 0.8, alumina is still solid and over that radius it becomes liquid with slope change.

In combustion conditions the heat propagation phenomenon is not so important because the heat transfer is less and generally metals, alloys, and cermet are sprayed and not ceramics, however, it is drastic when polymers are sprayed

(b) Particles in-Flight

Figure 4.37 shows the core and surface temperature profiles for a 45 μm CoNiCrAlY particle (again, for the HVOF-spraying parameters given in Fig. 4.26). This particle begins to melt at the position of −80 mm inside the torch nozzle and is completely molten at a distance of 30 mm. The maximum difference reached between the core and the surface temperatures is approximately 400 °C.

Similar results are obtained with d.c. plasma jets, as illustrated in Fig. 4.38 for alumina particles, respectively 20, 40, and 60 μm in diameter injected into an Ar–H_2 d.c. plasma jet.

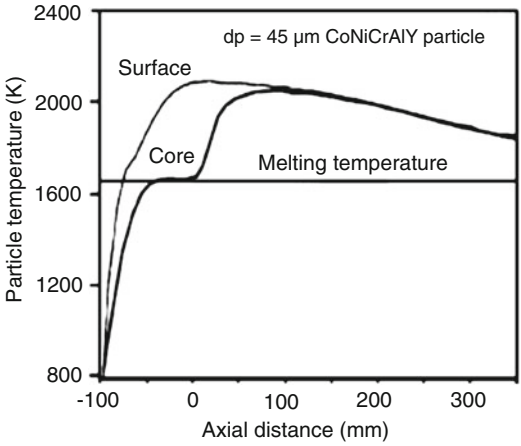


Fig. 4.37 Surface and core temperature profiles of a 45 µm CoNiCrAlY particle (calculated for the HVOF parameters given in Fig. 4.26), coordinate zero = barrel exit. Reprinted with kind permission from Springer Science Business Media [83], copyright © ASM International

Figure 4.38a represents the velocities along their mean trajectories and Fig. 4.38b shows the surface and center temperatures of the particles. The particles were injected in the plasma jet with different velocities in order to follow as closely as possible the same trajectory. As expected, the smallest particles reach the highest velocity, but they decelerate faster than the larger ones (see Fig. 4.38a). In spite of a ratio of almost 2 in the residence times of the 60 µm particles compared to the 20 µm ones, their surface temperature is almost 1,200 K lower (see Fig. 4.38b). The heat propagation phenomenon is also more important with the larger particles. When considering 40 µm particles, the center temperature reaches that of the surface only 80 mm downstream of the nozzle exit (see Fig. 4.38b). It is clear that when the heat propagation phenomenon is neglected, the real conditions are not represented at all. To limit the calculation time, recent work uses the enthalpy model with the finite volume technique of the second order in time and space [89, 90] that allows discretizing equations. Another model is based on the Stefan problem with an explicit determination of the position of the interface solid/liquid. Vaporization is described according to the approach "back pressure" of C.J. Knight [91]. An adaptive grid is used in which the positions of different phase change fronts are fixed. The transformation of co-ordinates thus depends only on the interface velocities [92]. In this frame of reference, an implicit scheme of finished differences is written. With this method, calculation time costs are minimized (approximately 10 s) to calculate the trajectory and heat transfer to a single particle injected into a d.c. plasma jet on a PC operating with Windows XP, against about one hour for a second-order enthalpy method [92].

With polymer particles, which thermal conductivities are few tenths of W/m K, heat propagation is generally the rule rather than the exception, even when they are flame or HVOF sprayed. It must also be kept in mind that with HVOF-forced convection is important resulting in high convective heat transfer coefficient (4,000–18,000 W/m^2/K). For example, Ivosevic et al. [93] have studied the behavior of Nylon 11 (κ_p = 0.25 W/m K) particles 90 µm in diameter sprayed by HVOF

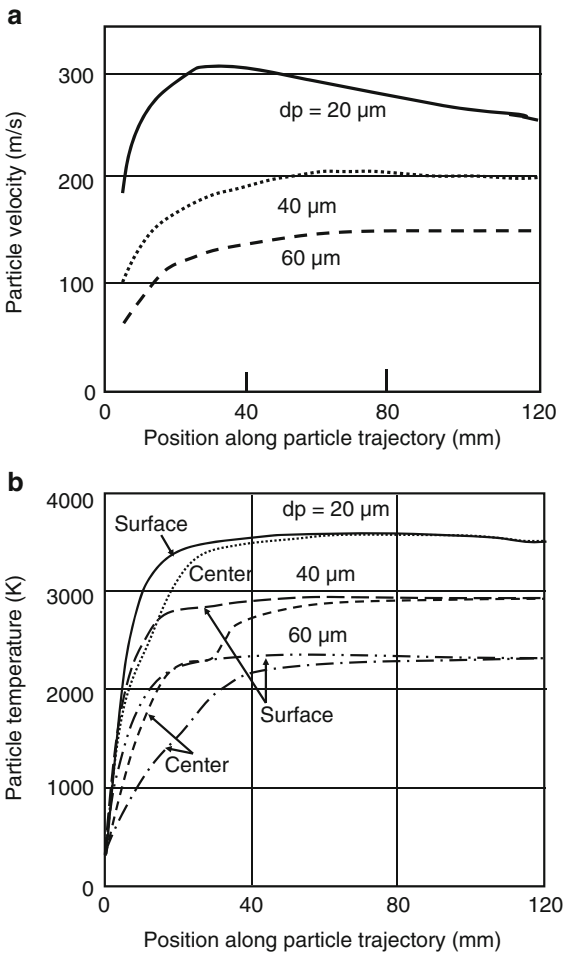


Fig. 4.38 Computed particle velocity (**a**) and temperature history (**b**) for dense Zirconia particles injected into an Ar–H_2 DC plasma jet: nozzle i.d. 6 mm, 35 slm Ar, 12 slm H_2, $I = 600$ A, $P = 35$ kW, $\eta_{th} = 55$ % [87]

Jet-Kote II® working with hydrogen–oxygen with $\Phi = 0.83$ with $\Phi = (H_2/O_2)/(H_2/O_2)_{sto.}$, and $(H_2/O_2)_{sto}$ the stoichiometric ratio of H_2/O_2. Figure 4.39 represents the particle temperature evolution along its trajectory respectively at its surface, mid-distance surface center, and center. If the surface temperature reaches about 900 °C, it does not attains 200 °C at mid-distance surface center (melting temperature 182 °C) when reaching the impact distance.

4.3.3.4 Heat Conduction in Porous Particles

The heat propagation phenomenon is particularly important for particles with a low effective thermal conductivity, such as with agglomerated particles [94–96], which can have a porosity as high as 45 % vol., compared to dense fused and crushed

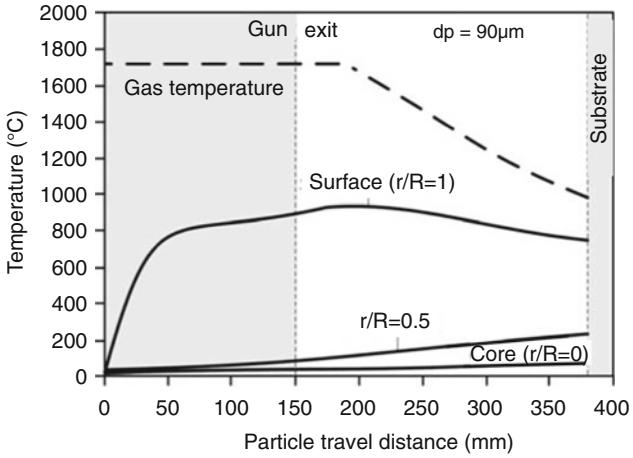


Fig. 4.39 Temperatures of a Nylon 11 particle 90 μm in diameter with respect to travel distance in HVOF Jet-Kote II working with hydrogen–oxygen. Reprinted with kind permission from Elsevier for Journal of Heat and Mass Transfer [93]

(FC) particles. Typical results showing the temperature profile in a 60-μm diameter zirconia (ZrO_2) particle immersed in Ar/H_2 plasma at 10,000 K are given in Fig. 4.40. The profiles given in Fig. 4.40a were calculated for a fully dense particle (FC), while those in Fig. 4.40b correspond to a porous particle (45 % vol.) with a mean pore diameter of 50 nm.

As shown by Hurevich et al. [94], the effect of porosity is taken into account by reducing the thermal conductivity of the bulk material. However, experiments have shown that the phenomenon is more complex, especially when spraying zirconia with $Ar–H_2$ (25 vol.%) plasmas (heat propagation is very important). Experiments have shown that the gas included in the pores, or created by the evaporation of the organic binder in agglomerated particles, must escape from the particle. This is rather easy when spraying small particles ($d \sim 30$ μm) where the molten shell reaches temperatures beyond 3,500–4,500 K, thus allowing the gas to escape through the liquid shell, which has a low viscosity [95]. Thus particles collected after their flight in a d.c. plasma jet are spherical and fully dense. In contrast, bigger particles ($d = 60$ μm) are not sufficiently heated to allow the entrapped gas to escape through the molten shell, which may be partly inflated by the gas pressure. Thus the corresponding collected particles are hollow spheres containing unmolten material. Diez et al. [96] have also confirmed experimentally these results, and similar results were also reported for hydroxyapatite particles [97]. Unfortunately, to our best knowledge, no model of these phenomena has been developed.

Plasma or HVOF spraying of nanometer-sized agglomerated particles aims at building partially nanostructured coatings (see Chap. 14 Sect. 14.4). Particles must be only partially melted to keep their nanostructured core. So the control of the melting of particles is the key point to achieve successful plasma sprayed partially nanostructured *coatings*. For example, Ben-Ettouil et al. [98] have calculated the heat transfer to

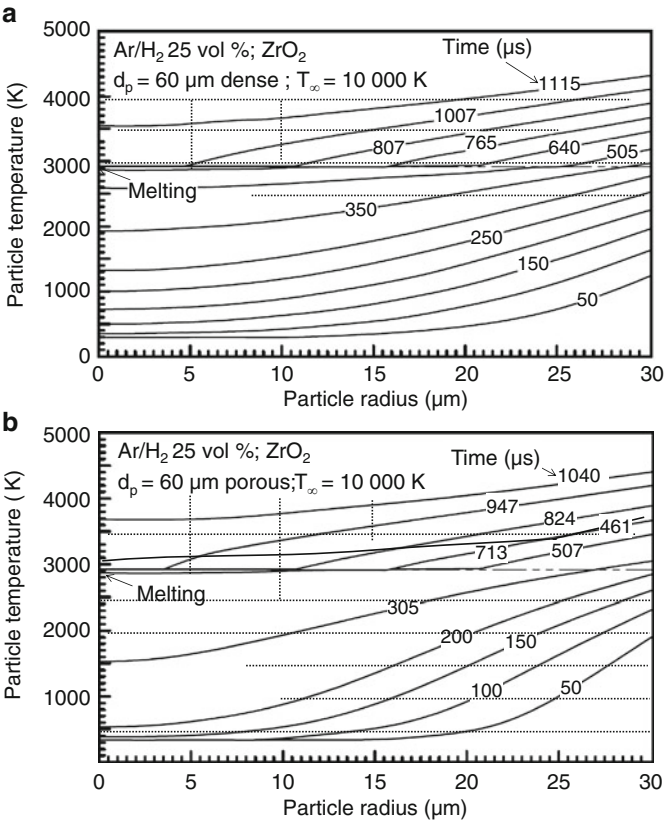


Fig. 4.40 Effect of particle porosity on internal temperature gradients. Example for a 60-µm diameter ZrO_2 particle in an Ar/H_2 (17 vol.%) plasma at 10,000 K: (**a**) dense particle (FC, **b**) agglomerated particle: (45 % porosity), mean pore diameter 0.05 µm. Reprinted with kind permission from Cambridge University Press for MRS [95]

dense and porous yttria partially stabilized zirconia particles in-flight in $Ar–H_2$ (45–15 L/min) d.c. plasma jet (32 kW, 7 mm i.d. anode nozzle), particles being externally injected to achieve the optimum trajectory whatever their porosities. The first remark that must be done for porous particles is that with heating their size diminishes first with their sintering, which is not very important, but also with their melting resulting in a non-negligible radius reduction increasing with porosity, as shown in Fig. 4.41. Thus it has to be taken into account to calculate the trajectory. Figure 4.42 represents the axial evolution of the melting front for different particle diameters all with a porosity of 50 %, except for the 50 µm particle, which has also been calculated for a dense particle. It allows evaluating the size of the nanostructured core, preserved at the end of the heat treatment of zirconia particles. The particle 40 µm in diameter is totally melted after 40 mm trajectory, when within particles of 50 and 60 µm remains nanostructured solid cores, respectively, of 27 and 56 µm corresponding to 54 and

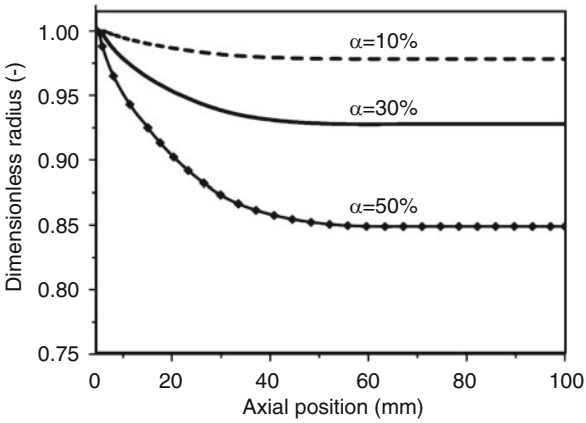


Fig. 4.41 Axial evolution of the agglomerated zirconia particle size (initial size $d_p = 60$ μm) for particles with different porosities. Reprinted with kind permission from Elsevier [98]

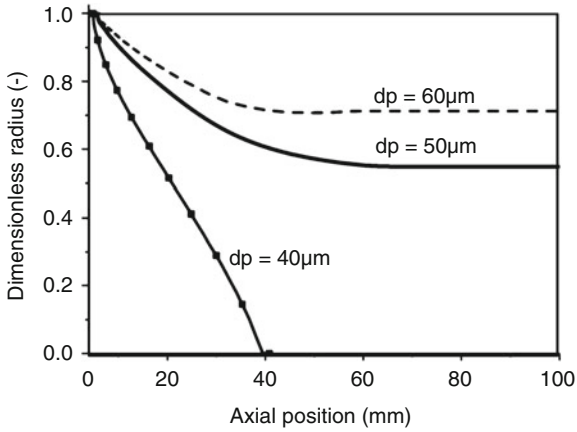


Fig. 4.42 Axial evolution of the melting front in agglomerated zirconia particles of different diameters. For comparison the evolution has been represented for a dense zirconia particle 50 μm in diameter. For the four cases the particle trajectory was the same. Reprinted with kind permission from Elsevier [98]

71 % of their initial diameter. This result shows that, for this spray conditions, there is a lower limit to the particle size below which nanostructured solid core cannot be obtained. Comparatively the dense zirconia particle, 50 μm in diameter, melts much less than the porous particle due to the better heat propagation. However it cools more rapidly, its surface solidification starting before reaching the substrate (positioned at 100 mm standoff distance).

4.3.3.5 Vaporization

Hot gas–particle heat transfer becomes much more complex in the presence of simultaneous mass transfer. The simplest case of mass transfer is particle vaporization, which will modify the heat transfer through the vapor layer created around the particle and acting as a sort of buffer. This phenomenon often occurs in the plasma treatment of medium and low vaporization temperature materials.

Moreover, the radiation from the vapor cloud surrounding the particle/droplet is generally much higher than that of the plasma gas, due to the lower ionization potential of the evaporated atoms, giving rise to a significant increase in volumetric radiation losses. The mass transfer and evaporation rate of the particle or droplet, will depend, on the vapor diffusion within the boundary layer provided that the saturation pressure of the vapor p_s is lower than that of the surrounding atmosphere. Of course, if convection removes the vapor created at the particle surface, and the equilibrium vapor pressure at the surface of the particle is higher than the ambient pressure of the plasma, particle or droplet evaporation will control the heat transfer. The complexities of the calculations increase substantially when chemical reactions take place, either between the vapor and the plasma, or between the plasma and the molten droplet.

Vaporization will start to take place as the particle surface temperature approaches its boiling point. The generated vapor cloud will surround the particle affecting the heat transfer rate between the hot gas and the particle. This phenomenon will be particularly important with low thermal conductivity materials and high thermal conductivity hot gases, such as, for example, ZrO_2 particles in Ar/H_2 plasmas, or when treating low boiling point materials, even in low thermal conductivity gases.

The maximum molar flux of vaporization, N_{max}, from a droplet at surface temperature T_s may be predicted from the Langmuir equation:

$$N_{\max} = \frac{p_s}{\sqrt{2\pi \mathrm{M} \mathrm{R} T_s}} \tag{4.50}$$

where p_s is the vapor pressure of the liquid material (Pa) at the absolute temperature T (K), R the perfect gas constant (J/K mol), and M the molecular weight of the material. For example, the maximum molar flux of vaporization N_{max} of Fe near its melting point (1,878 K) is 2×10^{-4} kg mol/m^2 s or 15×10^{-3} kg/m^2 s and, near its boiling point (3,135 K), 50 kg/m^2 s [65].

Equation (4.50) describes the maximum rate of vaporization that may be expected from a liquid surface under vacuum conditions. In the case of vaporization in a gaseous atmosphere and vapor pressures lower than atmospheric pressure, the rate of vaporization will be controlled by diffusion of the vapor through the boundary layer around the droplet. If forced convection reduces drastically the boundary layer thickness, the rate of evaporation will be increased. At the liquid–vapor interface, a vapor pressure $p_{v,s}$ will prevail such that the chemical potentials are the same within the liquid and the vapor. If the vapor pressure far away from the interface is lower than that of the saturated vapor $p_{v,s}$, mass transfer from the surface of the liquid droplet to the vapor cloud will take place. The evaporation rate for a metallic particle in a pseudo steady state is given [85, 99, 100] by

$$\frac{dm_p}{dt} = S \cdot k_d \left(c_g - c_s\right) \rho_g \tag{4.51}$$

where S is the surface area of the particle (πd_p^2)(m^2), k_d is the mass transfer coefficient of the metal vapor (m/s), c_g is the mass fraction of metal vapor in the bulk gas, and c_s is the mass fraction of metal vapor at the surface of the particle, and ρ_g is the specific mass of the gaseous material.

c_s is defined by

$$c_s = \frac{p_s M}{\rho_g R T} \tag{4.52}$$

where M is the molar weight of metal, R the universal gas constant (J/K/mol), T the fluid temperature (K), and p_s the saturation vapor pressure at T determined by the Clausius–Clapeyron relationship:

$$p_s = p_{ref} \times \exp\left[-\frac{\Delta Hv \cdot M}{R T_{ref}}\left(\frac{T_{ref}}{T} - 1\right)\right] \tag{4.53}$$

where p_{ref} and T_{ref} are a pair of values corresponding to one point on the Clausius–Clapeyron curve. In case of pure diffusion, the concentration driving force is then the logarithmic difference of the prevailing concentrations at the surface of the particle and in the bulk of the gas surrounding the particle [65]

$$N_v = \frac{D_{v,g}}{\delta} \times c \times \ln\left(\frac{p - p_{v,b}}{p - p_{v,s}}\right) = k_d \times c \times \ln\left(\frac{p - p_{v,b}}{p - p_{v,s}}\right) \tag{4.54}$$

where N_v is the molar flux of vapor (mol/m^2 s), $D_{v,g}$ the diffusion coefficient of the vapor through the enveloping gas (m^2/s), δ the thickness of the boundary layer (m), k_d the corresponding mass transfer coefficient (m/s), p the total system pressure (Pa), $p_{v,b}$ the vapor pressure of the evaporated material in the enveloping gas (Pa), and $p_{v,s}$ the vapor pressure of the liquid material at T_p, and c the molar density of the bulk gas at T_p. It is clear from the preceding formula that when the temperature of the surface is close to the boiling point, the particle is subjected to an intense evaporation. The mass transfer coefficient is calculated [100] using the Ranz–Marshall [101, 102] correlation, and if necessary, using a correction factor of the same type as that used for the Nusselt number (see Eqs. (4.37) to (4.45), through the Sherwood number ($Sh = k_d \times d_p/D_{v,g}$)

$$Sh = 2 + 0.6 \times Re^{1/2} \times Sc^{1/3} \tag{4.55}$$

where, $D_{v,g}$ is the diffusion coefficient and N_{Sc}=$\nu/D_{v,g}$ (ν being the dynamic viscosity (m^2/s)).

Typical values of the Sherwood number range from 2 to 6 and correspondingly for particles 30 μm in diameter, k_d varies between 10 and 200 m/s. Under conditions of high mass transfer rates, the particle vaporization process can be heat transfer controlled. The particle vaporization rate in this case is given by the following energy balance equation:

$$\frac{dm_p}{dt} = \frac{Q}{\Delta H_v} \tag{4.56}$$

where m_p is the mass of the particle and Q is the net heat exchange between the plasma and the particle (W) and ΔH_v is the latent heat of vaporization (J/kg).

(a) Heating of the Vapor

At the interface between the liquid and vapor phases, a heat balance is maintained and at the same time a bulk flow of material crosses the interface. For high mass transfer rates, the transfer coefficients become functions of the mass transfer rate, thus causing non-linearity in the transport equations. For example, Chen and Pfender [79, 86, 99] have shown that the heat flux through a liquid–vapor interface is reduced due to absorption of heat by the vapor. The heat received by the particle can be written [99] as

$$Q = 2\pi d_p \Delta H_v \int_{T_s}^{T_\infty} \frac{\kappa_g dT}{h'_{pl} - h'_s + c'} \tag{4.57}$$

with

$$c' = \Delta H_v + \frac{2\pi d_p^2 \varepsilon \sigma_s T_s^4}{\frac{dm}{dt}} \tag{4.58}$$

where h'_{pl} is the plasma specific enthalpy at T, h'_s being that at T_s. This expression has been deduced assuming that the plasma thermodynamic and transport properties (h, κ) are not modified by the vapor diffusion.

Assuming that $\kappa/c_p = \left(\overline{\kappa}/\overline{c}_p\right)$ in the boundary layer, Eq. (4.57) applies because

$$Q = \frac{\Delta H_v}{h_\infty - h_s} \ln\left(1 + \frac{h'_\infty - h'_s}{\Delta H_v}\right) 2\pi d_p \left(\frac{\overline{\kappa}}{\overline{c}_p}\right)\left(h'_\infty - h'_s\right) \tag{4.59}$$

Equation (4.57) is equivalent to the introduction of a correction factor λ_c to the thermal flux due to the plasma [see Eq. (4.34)], i.e.

$$\lambda_c = \frac{\Delta H_v}{h'_\infty - h'_s} \ln\left[1 + \left(\frac{h'_\infty - h'_s}{\Delta H_v}\right)\right] \tag{4.60}$$

is the correction factor proposed by Borgianni et al. [103].

Typical results are presented in Figs. 4.43 and 4.44 as the ratio of the heat flux to the particles in the presence of vaporization, Q_1, to that in the absence of vaporization, Q_o, as a function of the plasma temperature.

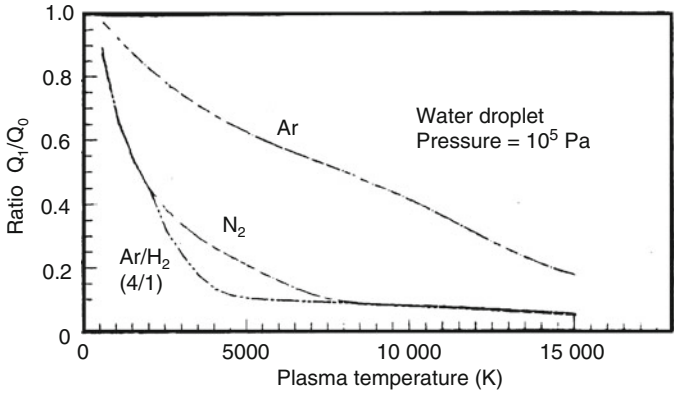


Fig. 4.43 Effect of evaporation on heat transfer to a water droplet under different plasma conditions, after Chen and Pfender. Reprinted with kind permission from Springer Science Business Media [99]

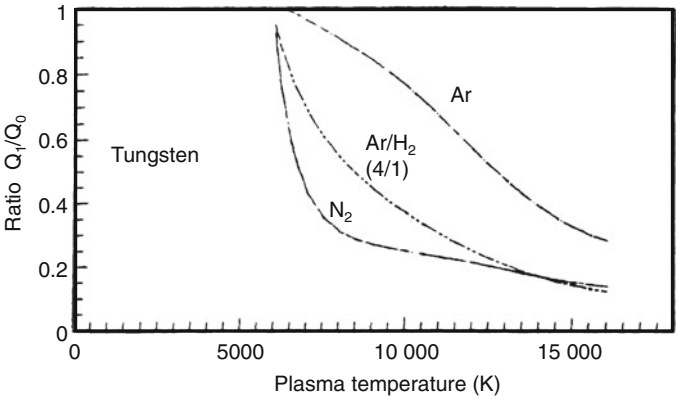


Fig. 4.44 Effect of evaporation on heat transfer to a tungsten particle under different plasma conditions, after Chen and Pfender. Reprinted with kind permission from Springer Science Business Media [99]

These figures show a substantial reduction of the heat flux to the particle with the increase of the vaporization rate. The effect is more pronounced for an Ar/H_2 or N_2 plasma compared to that for a pure Ar plasma.

The approach described above is however relatively simplified. In a more rigorous approach the following phenomena should be taken into account:

- Mass conservation which, according to the prefect gas law can be expressed as function of temperature.
- The conservation of the chemical species taking into account the diffusion transport of each species.
- The momentum conservation.
- The energy conservation including the transport of energy due to diffusion.

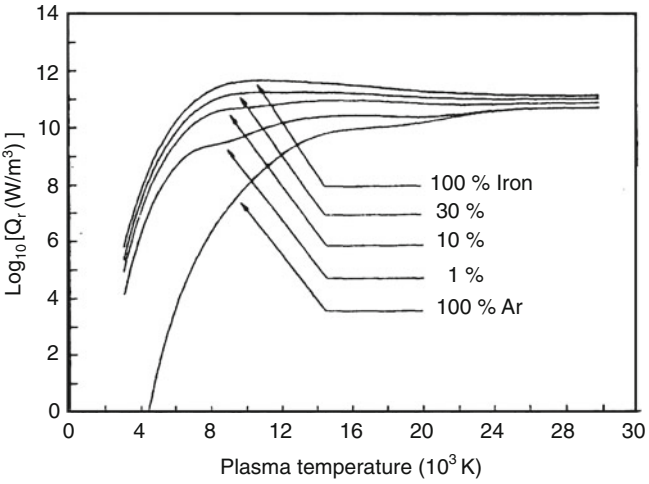


Fig. 4.45 Volumetric radiation losses for an Ar/Fe plasma as function of temperature and the molar fraction of iron vapor, plasma radius $R = 1$ mm, after Essoltani et al. Reprinted with kind permission of J. Analytical Atomic Spectrometry [105]

What makes the problem very complex is the fact that all the transport properties (including the different diffusion coefficients) have to be determined at each step of the calculation. At a given time the composition of the gas/vapor at the interface (supposed to be at the particle surface temperature) has first to be defined in order to calculate the thermodynamic and transport properties of the gas/vapor. The mass conservation equation then allows calculating the molar barycentric velocity, the momentum equation allows determining the radial distribution of the pressure $p(r)$, the conservation of the chemical species equation allows determining the molar fraction of the different species, and finally the energy equation gives the radial temperature distribution $T(r)$. The latter can then be used to recalculate a new value of the composition at the interface up to convergence [104].

(b) Radiation of the Vapor

During the evaporation of metallic particles, radiative energy losses from the metal vapor cloud surrounding the particle cannot be neglected in contrast to that of the plasma and of course that of flames, HVOF,... [105–110]. This is illustrated in Fig. 4.45 after Essoltani et al. [105] showing that in the temperature range from 3,000 to 8,000 K the radiation losses of the vapor can be several orders of magnitude higher than those of a pure argon plasma. In this figure the effective radiation (including absorption) has been calculated for plasma of 1 mm in radius.

This effect has been observed with different metals, though its extent varies with the nature of the vapor as illustrated in Fig. 4.46 from Essoltani et al. [108]. Self-absorption reduces the net radiation losses [105] and the radiation of the vapor cloud reduces drastically the heat transfer to the particle [109].

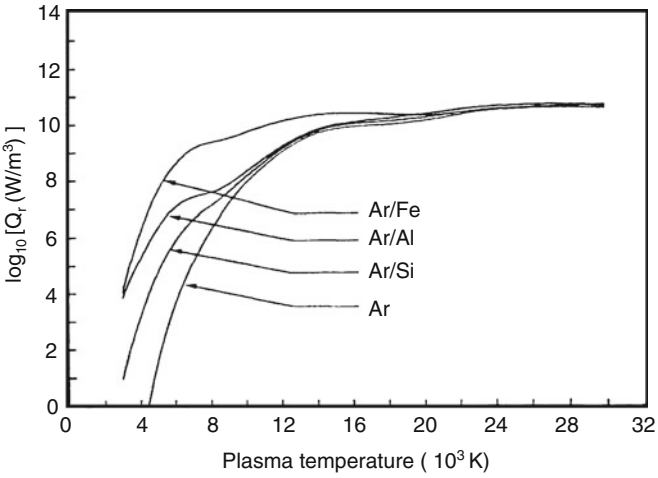


Fig. 4.46 Volumetric emission for an argon plasma in the presence of 1 % molar fraction of different metallic vapors, plasma radius = 1 mm, after Essoltani et al. [108]. Reprinted with kind permission from Springer

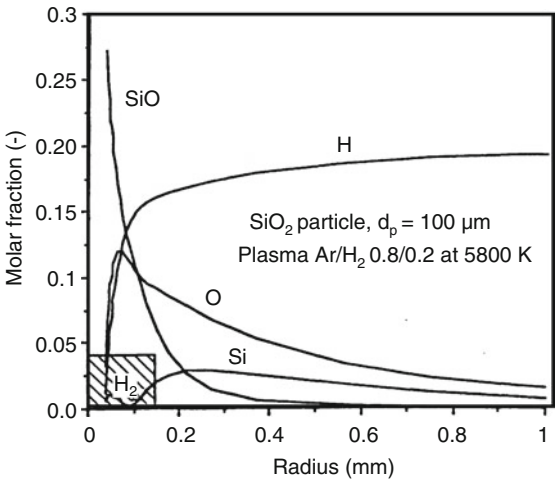


Fig. 4.47 Evolution of the molar fraction of the different chemical species around a 100 µm diameter SiO_2 particle in an infinite Ar/H_2 (20 vol.%) plasma at 5,800 K, after Humbert [104]

4.3.3.6 Chemical Reactions with the Vapor

The approach described above has to be used for calculating reactions with the vapor, but a source term representing the variation of the mole numbers of the different chemical species has to be added to the conservation equations. A typical result is illustrated in Fig. 4.47 from [104] for a SiO_2 particle, 100 µm in diameter, immersed in argon/hydrogen plasma (20 vol.% H_2) at 5,800 K.

This figure shows that very close to the particle surface, particle mass evaporates as SiO which is progressively reduced by H atoms as the vapor moves farther from the particle surface.

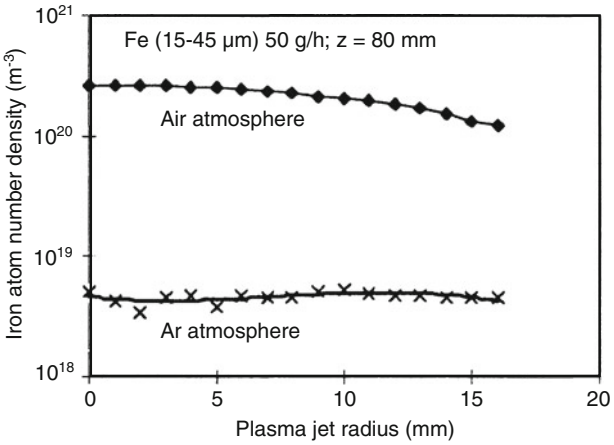


Fig. 4.48 Radial profiles of iron density in an Ar–H_2 plasma jet (600 A, 65 V, Ar 45 slm, H_2 15 slm, nozzle i.d. 7 mm) issuing into air or argon atmosphere, with iron particles with a mean diameter of 40 µm injected. Reprinted with kind permission from IUPAC organization for Pure and Applied Chemistry [110]

The presence of a reactive gas in the atmosphere around liquid particles may affect their vaporization [65]. In the case of metal particles sprayed in air, two types of mechanisms may be responsible for an increased rate of vaporization: a chemical process involving the formation of volatile metal compounds and a transport process involving the counter diffusion of oxygen and metal vapor within the boundary layer around the particles. These interact and the homogeneous oxidation reaction consumes the metal vapor and thereby increases its evaporation rate from the liquid surface. In fact it was observed that the rate of vaporization of a number of metals increased with oxygen pressure in the atmosphere. Above a critical value of oxygen pressure, the flux of oxygen toward the surface is greater than the counter flux of metal vapor; a solid or liquid oxide layer may then form on the particle surface and change drastically the rate of vaporization.

When spraying in an inert atmosphere, the vapor molecules produced by particle vaporization diffuse without reacting, through the boundary layer around particles; therefore the metal vapor pressure around the droplets builds up and the rate of vaporization decreases. An example of this behavior is shown in Fig. 4.48 from [110]. This figure compares the observed radial profiles of the density of iron atoms produced by vaporization of iron particles injected into an argon–hydrogen plasma issuing either into an air or an argon atmosphere [110]. The density of iron atoms is two orders of magnitude higher when the surrounding gas is air, despite a lower plasma temperature because of cooling of the flow by the mixing with ambient air and the dissociation of O_2 molecules.

A simple calculation can also determine if the oxidation is controlled by diffusion or chemistry. It has been shown (Sect. 4.3.2.5) how the mass transfer coefficient could be calculated with the help of the Sherwood number. For example, with a relative velocity of 10 m/s for a 30 µm Fe particle in the gas, the Sherwood

number at 2,000 K is about 2.5 resulting in a k_d of 37.3 m/s. The rate of transfer of oxygen can be calculated by estimating the concentration driving force across the boundary layer. For argon plasma flowing into air, the plasma gas may contain 50 % of entrained air, in which case the mass concentration of oxygen in the bulk of the gas will be one-half of that of air, i.e., $X'_{o_{2,b}} = 0.115$; at the particle surface, the oxygen is consumed by the following irreversible reaction

$$2Fe + O_2 = 2FeO \tag{4.61}$$

and therefore $X'_{o_{2,s}} = 0$.

The corresponding mass flux of oxygen to the iron particle is

$$N_{o_2} = k_d \cdot c \cdot \left(X'_{o_{2,b}} - X'_{o_{2,s}}\right) \tag{4.62}$$

From the equation above, the corresponding flux causing oxidation of iron to FeO is calculated to be 2.0 kg/m^2 s. This value can be compared with the rate of oxidation of iron in pure oxygen gas calculated by Robertson and Jenkins [111], of 3.61 kg/m^2 s; the corresponding rate in a gas containing a mass fraction of only 0.115 of oxygen is 0.415 kg/m^2 s. The rate of oxidation of the iron particles will obviously be controlled in this case by chemical reactions since the indicated reaction rate is almost five times slower than the oxygen diffusion to the surface of the particle as computed using Eq. (4.62). Besides the value of k_d of 37.5 m/s is a minimum because, for example, with the same relative velocity of 10 m/s but an average temperature of 4,000 K, k_d = 140 m/s. If the mass flux due to evaporation is very high, for example, when the particle is close to its boiling temperature, the oxygen will be consumed mainly by the reaction in the vapor phase rather than at the surface of the iron droplet.

Once the gaseous oxide is formed and mixed with the plasma flow [112–114], it condenses in the regions where the temperature decreases and, according to the steep temperature gradients in the plasma jet fringes, submicron, or even nanometer size particles, called fumes, are formed. For example, with the conditions prevailing in Fig. 4.48 fume concentration in the plasma jet envelope can range from 2.5×10^{14} m^{-3} at a distance of 20 mm from the torch exit to 5×10^{15} m^{-3} at 110 mm. Oxides are mostly formed but other compounds can also be obtained such as nitrides, carbides, etc., depending on the surrounding atmosphere. For example, the volatilization of Al particles in a nitrogen plasma jet results in the formation of AlN (s) [115].

4.3.3.7 Chemical Reactions with the Particle

(a) Diffusion Controlled Reactions

When the partial pressure of the reacting gas in the bulk of the hot gas surrounding a particle reaches a specific value, defined as the critical pressure, the flux of reacting

species toward the surface of the droplet exceeds the counter flux of metal vapor, and a liquid or solid oxide, nitride, carbide, etc., layer (depending on the hot gas forming gas composition and surrounding atmosphere) forms on the droplet surface. For example, for an oxidation reaction the critical pressure of oxygen can be calculated from

$$\left(p_{O_2}\right)_{max} = \frac{p_i}{\alpha k_{dO_2}} \sqrt{\frac{RT}{2\pi M_i}} \tag{4.63}$$

where α is the number of gram-atoms of metal vapor required to combine with one mole of oxygen at the surface of the droplet, k_d is the mass transfer coefficient (m/s), M_i is the atomic mass of the metal (kg), and p_i is the vapor pressure as defined by Eq. (4.53).

Under plasma spraying conditions, oxidation of the sprayed metal can take place either in the vapor phase surrounding the droplet or at the surface of the droplet. In the latter case the formed oxide layer can result in a considerable reduction of the evaporation rate from the droplet surface.

This is illustrated in Fig. 4.49 for iron particles injected into an Ar–H_2 d.c; plasma jet (conditions of Fig. 4.48) showing the mole fraction of evaporated and oxidized iron along the torch axial distance for two particles respectively 40 and 80 μm in diameter, injected with the same velocity of 10 m/s.

This implies that if the trajectory of the 40 μm particle is optimum, the 80 μm particle will cross earlier the jet and thus is less heated. This results in a much lower evaporation in the latter case with a strong oxidation, while the opposite is true for the smaller particle.

The compound that will be obtained at the particle surface depends on the reactants present within the plasma, provided that they can reach the particle surface, and it also depends very strongly on the particle temperature. The first step to be performed in order to obtain the chemical composition of the particles prior to their impact on the surface of the substrate is the thermodynamic equilibrium calculation. Though the plasma conditions often differ from equilibrium, the knowledge of which phases are thermodynamically stable under given conditions, and the comparison with the presence of these phases in real systems is very informative. This has been demonstrated for example for the oxides in plasma-sprayed chromium steel [116].

The next step consists of calculating the diffusion phenomena occurring at the interfaces; diffusion of the reactant through the shell formed at the particle surface (in liquid or solid state); diffusion of gaseous reaction products formed (if any) through the shell and then through the boundary layer (see the shrinking core model described [117–119]). The diffusion coefficients can be strongly affected by the expansion mismatch between the nonreacted particle core and the reacted shell formed around the core which can be easily broken if it is in the solid phase.

A few examples of oxidation reactions can be found in Refs. [105, 110, 112, 114, 116, 120–124] and for many other species: TiC + Ti, SiC + Si, W + W_xC_y, Mo + MoC_2, NiCr/Ti + TiC + Cr_xC_y, FeCrAlY + Cr_xFe_y + Fe_xC_y, Mo + $MoSi_2$, Ti + TiB_2, etc. (see Refs. [125–133]).

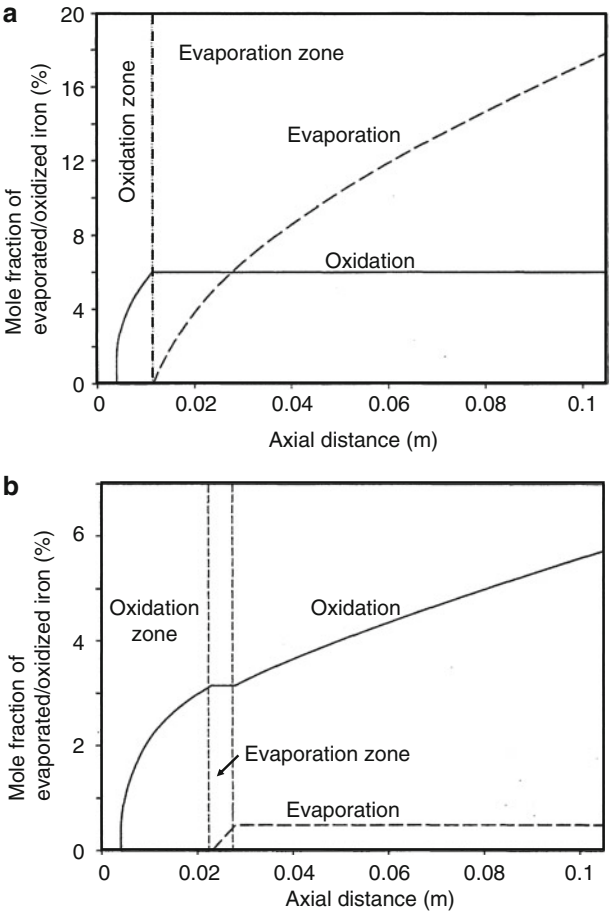


Fig. 4.49 Mole fraction of evaporated and oxidized iron along particle trajectory. (**a**) initial particle size: 40 μm, injection velocity: 10 m/s (**b**) 80 μm, injection velocity : 10 m/s. Reprinted with kind permission from IUPAC organization for Pure and Applied Chemistry [110]

(b) Reactions Taking Place Between Condensed Phases

In this case the basic reactants are in the solid phase either as agglomerated or cladded particles [133–139] (see Fig. 4.50). The most common cladded particle is the Ni–Al where an Al core is surrounded by a Ni shell. Upon melting, Al reacts with the Ni creating intermetallic species such as Ni_3Al, NiAl, etc., through an exothermic reaction. The same holds for agglomerated particles of Ti and C, for example [133]. Hot gases heating of the particle triggers the reaction and initiates the Self-propagation High Temperature Synthesis (SHS). The reaction depends strongly on the size of agglomerated particles and the possibility to heat the agglomerated particles without destroying the agglomerates by the produced gas

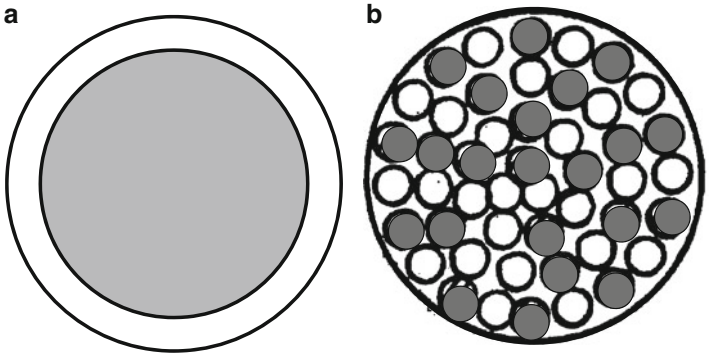


Fig. 4.50 (**a**) Cladded, (**b**) agglomerated composite particles which can be used for SHS plasma spraying. Reprinted with kind permission from ASM International [134]

expansion. As the speed of SHS is typically between 1 and 150 mm/s, the SHS reaction propagation is not necessarily completed during the flight of particles and it may proceed after their impact resulting in very dense and hard coatings [139].

Many coatings have been produced by this method:

- Mixtures of transition metals with refractory compounds such as Cr-SiC or Cr-B_4C and Ti-SiC or Ti-B_4C or Ti-Si_3N_4, which gives rise to excellent resistance to wear [135, 140–144].
- Copper–TiB_2 coatings starting from agglomerated particles of Ti–bronze and boron, the TiB_2 particles in coatings increase considerably the hardness of copper [142].
- TiB_2 or TiC particles in ferrous matrices to increase their hardness and wear resistance [143–145].
- Al and metal oxides to produce intermetallic compounds with aluminum particles [138].

(c) Reactions Controlled by Convection Within the Liquid Phase

Such reactions within droplets occur only in d.c. plasma or HVOF jets, as well as in wire arc spraying where the velocity difference between the molten particle in-flight and the gas flow induces a convective motion within the droplet. Under such conditions, when the ratio of the kinematics viscosities of the plasma and the droplet is higher than 50, and the Reynolds number of the flow relative to droplet higher than 20, a convective phenomenon is induced within the droplet [146]. Therefore, the presence of a flow-induced vortex in the molten particle can be expected [146]. The motion inside the droplet can be represented by a Hill vortex that is an inviscid axisymmetric vortex [147]. For a low carbon 60 μm iron droplet in a d.c. Ar–H_2 plasma jet, the calculation was performed by using a commercial code, FIDAP7-62, dedicated to the materials processing field [148]. Figure 4.51

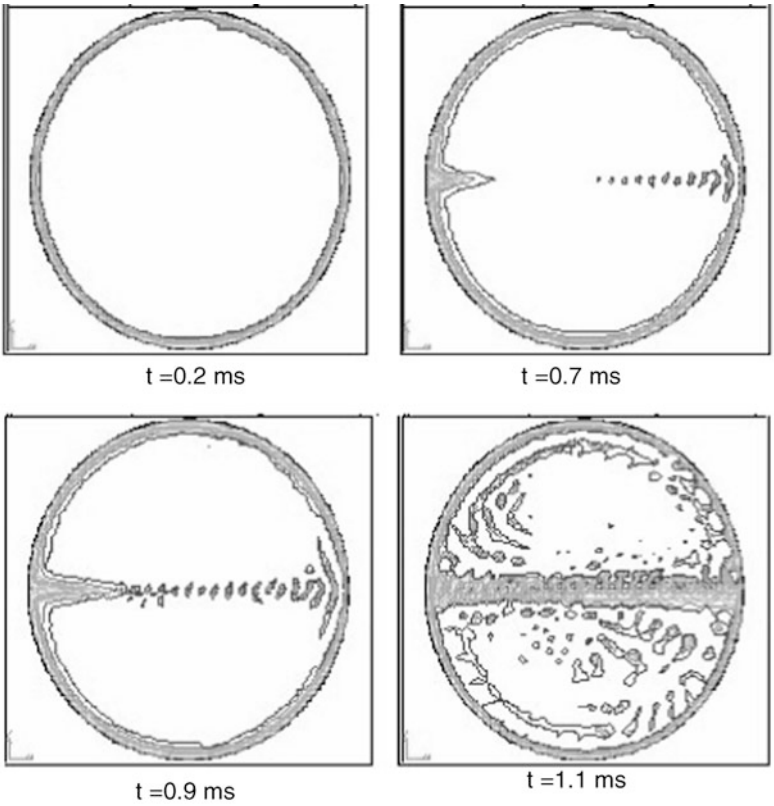


Fig. 4.51 Time-resolved modeling of internal convection and oxide penetration by a spherical vortex of Hill. Reprinted with kind permission from Annals of the New York Academy of Sciences [147]

shows the time resolved presentation of internal convection and oxide penetration by the spherical Hill vortex.

The internal circulation in the liquid metal droplet continuously sweeps fresh liquid to its surface and makes it available for oxidation. This circulation then entrains portions of the outer layer or of the dissolved oxygen at the droplet surface and transports it to the inside of the droplet. With the low carbon iron particles the oxide formed at the surface is liquid Fe_xO. Liquid iron and liquid Fe_xO are not miscible due to their difference in surface tension (1,778 mJ m^2 for pure iron and 585 mJ m^2 for the wüstite [116]). Thus upon cooling both phases, separate and spherical Fe_xO nodules are formed within the solidified particle as shown in Fig. 4.52. The recirculating flow within the droplet results in an increase of the oxygen content compared to that estimated assuming a pure diffusion model [147].

For example, under spraying conditions as shown in Fig. 4.52, the captured FeO mass percentage is 15 wt.%, while diffusion calculations estimate the Fe_2O_3 and

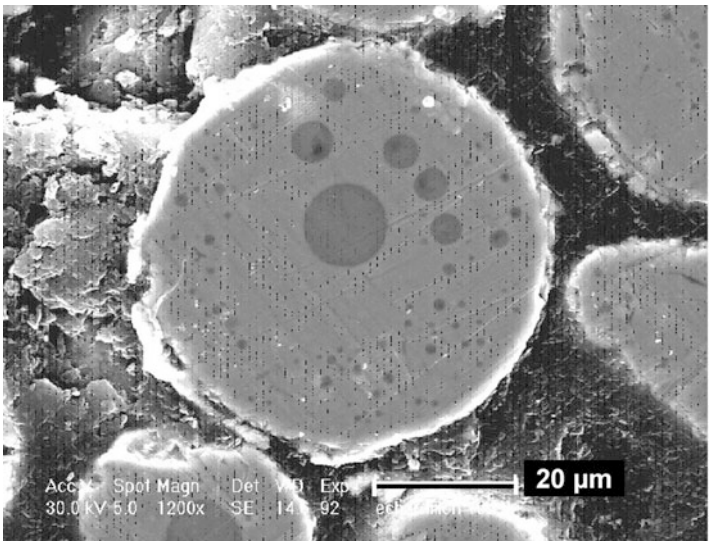


Fig. 4.52 Cross sections of a low carbon steel particle collected at $z = 100$ mm after its flight in a D.C. plasma jet: Ar 50 slm, H_2 10 slm, $I = 500$ A, nozzle i.d. 7 mm. SEM analysis at 30 keV. Scale 20 µm. Reprinted with kind permission from Annals of the New York Academy of Sciences [147]

Fe_3O_4 concentration to be less than 3 wt.%. The oxide shell formed at the surface of particles, with no inside convective movement, is made of Fe_2O_3 and Fe_3O_4. Such oxides are observed in the thin shell surrounding the particle (see Fig. 4.52) formed at the end of the particle trajectory when the particle velocity is about the same as that of the surrounding plasma plume (no more convective effect). The same effect was observed with stainless steel particles plasma sprayed with Ar–H_2 plasma-forming gas [124]

Similar results with convection have been observed when spraying Ti4Al6V particles in a d.c. nitrogen plasma either under controlled atmosphere or in air. Inside the particles TiN and TiO are formed with, of course, much less TiO in controlled atmosphere [149].

4.4 Ensemble of Particles and High-Energy Jet

4.4.1 General Remarks

Development of theoretical/computational models which can predict the percentage of melted particles in a thermal spray process can potentially reduce the cost of the development. This is especially important for spraying if this modeling is extended to particle flattening and layering, i.e., the prediction of the microstructure

of the coating. In principle, the models should provide a better understanding of the processes and help to improve and optimize the design of the existing spray torches. The following steps must be considered:

- Gas flow modeling inside the spray torch, which is now well established for combustion, cold spray, D-gun, and RF torches, but is still in its infancy for d.c. plasma torches. In the latter case the problem is related to the arc root fluctuations, which require 3D time-dependent modeling.
- Particle injection, which is a full 3D problem for devices where injection is orthogonal to the jet and where the inner diameter of the injector (usually below 2 mm), implies a carrier gas momentum close to that of the flow, thus disturbing it drastically. The problem of the collision of the particles between themselves and with the injector wall is also very complex, and it determines the distribution of the injection velocity vectors at the injector exit. So far no reliable model has been developed.
- The particle trajectory distributions within the plasma jet, which is again closely linked to the injection velocity vector distribution. For each particle, equations required are those described in the previous Sect. 4.2 for a single particle; then a stochastic discrete-particle model is applied. Computational particles are stochastically generated by sampling from probability distributions of particle properties (size, velocity vector, etc.) at the injection point.
- The loading effect when increasing the mass flow rate of particles injected into the plasma. This effect has to be taken into account by introducing source terms in mass, momentum and energy equations to include the effect of particles on the gas phase. Indeed in most cases for spray processes the particle mass flow rate has to be limited to avoid the cooling and deceleration of the gas flow. For example, when spraying with conventional d.c. plasma spray torches (power level of about 40 W) the powder flow rate is limited 4–6 kg/h. Under such conditions, if particle vaporization is of minor importance, the cooling and slowing down of particles are not too important and in a first approximation they can be neglected. This is not the case when higher flow rates are used, for example in particle spheroidization, or when a strong evaporation takes place, and this loading phenomenon has to be considered.

Once the flow field (temperature, velocity, composition, enthalpy, etc. distributions) has been calculated or measured, the flow-particle momentum and heat transfers can be calculated. To conclude, in spite of the great strides that have been made over the last decades, results are still very dependent on the various assumptions made for the flow modeling (for example the turbulence model chosen, the thermodynamic and transport properties of gases and mixtures used, etc.), and on the way particle velocity and size distributions are taken into account at the injector exit. Thus comparison of calculated values with measurements, for example velocities and temperatures of particles in-flight, must be used to validate the results of such calculations.

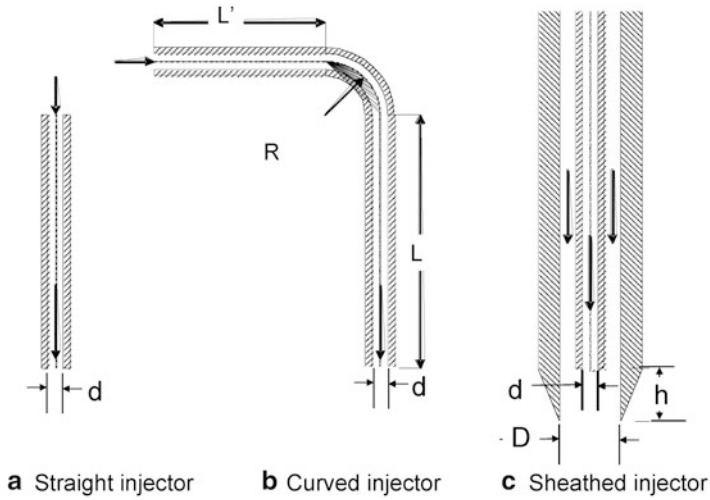


Fig. 4.53 Injector geometries typically used for radial injection (**a**) straight injector, (**b**) curved injector, (**c**) double-flux injector. Reprinted with kind permission from Springer Science Business Media [114], copyright © ASM International

4.4.2 Particle Injection

4.4.2.1 Types of Injector

Particle injectors are generally very simple and for radial injection can be categorized roughly [110] as straight (Fig. 4.53a), or curved (Fig. 4.53b) injector, or double flow injector (Fig. 4.53c).

For axial injection only straight injectors are used which can be water-cooled depending on the heat flux to which they are exposed. The curved injector is in fact mainly used for design reasons for example of d.c. plasma torches: as particles are injected orthogonally to the torch axis at its nozzle exit, the injector is curved to follow the torch body, thus allowing all the pipes, including the powder transport pipe, to be connected at the rear end of the torch. The curved injector disturbs the gas and particle flows, and an important point is the length L necessary to dampen out this perturbation. Double flow injectors are used to focus the particle stream exiting the injector, especially when small ($d < 20$ μm) and light particles are used [150]. Typical injector diameters used in d.c. plasma spraying range between 1 and 2 mm (generally 1.6 or 1.8 mm) and the carrier gas is mostly argon and sometimes helium.

The main problem is the positioning of the injector relative to the hot gas flow as shown schematically in Fig. 4.54. For example, in a d.c. plasma jet, when the injector is too far from the jet, particles at the periphery of the injection cone (generally the smallest ones) by-pass the plasma jet as shown by the measurement of Vardelle et al. [110].

They are then re-entrained farther downstream, creating defects in the coating. However, if the distance D between the jet axis and the injector exit is shortened,

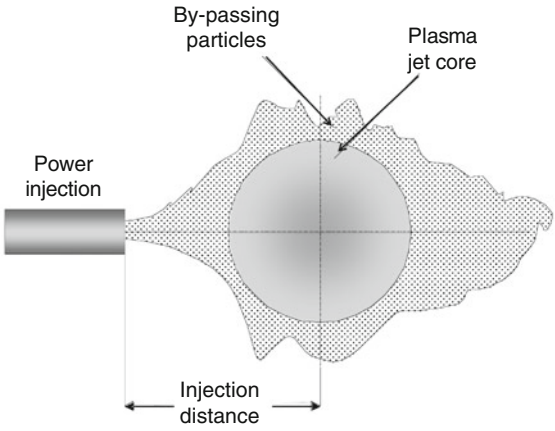


Fig. 4.54 Illustration of spatial distribution of particles by-passing the plasma core. Reprinted with kind permission from Springer Science Business Media [110], copyright © ASM International

the tip of the injector may be too much heated, resulting in clogging. Thus, to avoid clogging, injectors may be water-cooled. This is a prerequisite for RF plasma torches where the injector must be positioned almost at the level of the second turn of the coil.

4.4.2.2 Gas Flow Within the Injector

According to the gas pressure difference between the inlet and outlet of the injector the flow inside may reach high velocities and frequently it may be compressible. Thus, the gas velocity can no longer be derived from the mass conservation equation:

$$m_{\mathrm{cg}}^{\mathrm{o}} = S \cdot \rho_{\mathrm{cg}} \cdot v_{\mathrm{cg}} \tag{4.64}$$

where $m_{\mathrm{cg}}^{\mathrm{o}}$ is the carrier gas mass flow rate (kg/s), S the cross section of the injector tube (m^2) and v_{cg} the carrier gas velocity (m/s). Instead, the compressible fluid equation of St Venant has to be used:

$$v_{\mathrm{cg}} = \left(2 \cdot \left(\frac{\gamma}{\gamma - 1} \right) \left(\frac{p_{\mathrm{in}}}{\rho} \right) \left[1 - \left(\frac{p_{\mathrm{out}}}{p_{\mathrm{in}}} \right)^{\frac{\gamma - 1}{\gamma}} \right] \right)^{1/2} \tag{4.65}$$

where γ is the isentropic constant of the cold gas, p_{in} the pressure at the injector inlet and p_{out} the pressure at the outlet of the injector (Pa).

For an argon gas flow of 3–8 slm, the Reynolds number in a 1.75 mm i.d. injector ranges from 3,000 to 8,000. The transition from laminar to turbulent flow starts at about $\mathrm{Re} > 2{,}100$, and the flow is considered to become fully turbulent at

Re > 4,000. If it is assumed that the flow within the straight injector is fully turbulent, the carrier gas velocity distribution $u(r)$ may be expressed by

$$u(r) = \frac{u_m}{0.875}\left(1 - \frac{r}{R_{inj}}\right)^{1/7} \tag{4.66}$$

where u_m is the average velocity determined from the gas flow rate and R_{inj} the radius of the injector tube.

Computations of the gas flow through various curved injectors showed that the streamlines are distorted toward the outer periphery of the curvature and are re-established in the straight portion of the tube after the curvature. As a result, the computed gas velocity profiles at the exit were similar for both straight and curved injectors. For turbulent flow, the minimum length, L_e, necessary for the complete development of the velocity profile in the tube can be estimated from [151]:

$$L_e = 8.8\,\mathrm{Re}^{1/6} R_{inj} \tag{4.67}$$

For 3,000 < Re < 8,000, this relationship yields an L_e ranging from 29 to 34 mm and is within the range of straight sections following curved injectors, as discussed earlier. This calculation supports the conclusion that the carrier gas exiting from a curved injector with $L_e > 35$ mm is not affected by the presence of curvature, but unfortunately this is not the case for particles (see next section).

4.4.2.3 Particle Flow at the Injector Exit

The results presented in the following were either measured using laser sheets or laser illumination (see Chap. 16), or calculated.

(a) Straight Injector

The internal diameter of the injector affects the particle velocity which increases, for a given carrier gas flow rate, when the injector i.d. decreases, and also on the jet divergence, decreasing with the injector i.d. [90]. It is also interesting to note that for small particles (zirconia with $d_p < 20$ μm), their velocity is higher with He than with Ar as carrier gas for the same gas flow rate [150].

Ben Ettouil [152] has developed a statistical model of powder transportation within a straight injector, 1.6 mm in internal diameter. A turbulent flow, except close to wall is assumed, taking into account the friction on the wall. Particle size distribution is simulated according to a discrete law. Particle collisions with the wall are treated according to the method of Milencovic, and their collisions between themselves are calculated assuming they are spherical and that collisions are elastic. The method allows determining velocity vector distributions at the injector exit.

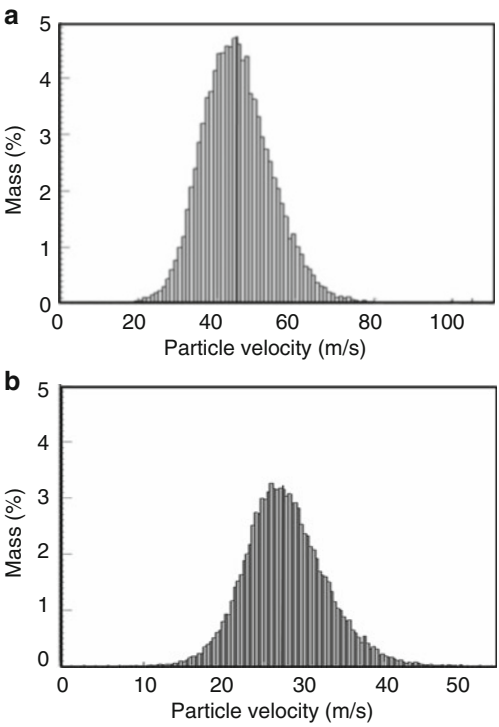


Fig. 4.55 Mass percentage distribution of the particle velocities at the injector exit for (**a**) alumina particles, (**b**) Zirconia particles. Reprinted with kind permission from Dr. Ben Ettouil [152]

However it must be emphasized that the maximum number of particles considered is about 10 000, which is a few orders of magnitude lower than one encounters in real conditions.

For example two powder size distributions have been studied for a straight injector, 1.6 mm in internal diameter: alumina 45–10 μm and Zirconia 110–10 μm. At the injector exit no size segregation is observed and the mean particle size at different radii from the injector axis is that of the size distribution of both powders. The quantity of particles increases as the square of the radius of the surface considered, with a larger concentration close to the wall where the gas velocity is low. The distributions of particle velocities at the injector exit are presented in Fig. 4.55 as a function of the powder mass percentages for the alumina and zirconia particles. Both distributions are centered on a mean velocity equal to that of the carrier gas, 47 m/s for alumina and 37 m/s for zirconia, respectively.

When presenting the velocity distribution as a function of the particle size (see Fig. 4.56) the main velocity is about the same for each size class. However, globally the smaller the particles the larger is their velocity spread.

An interesting parameter is the angle, δ, of the velocity vector relative to the injector axis. It is represented in Fig. 4.57 for both distributions. Ninety-three percent of the alumina particles and 94 % of the zirconia ones are within a cone with a half angle of 20°. As for the velocity, this result is the same for each size class,

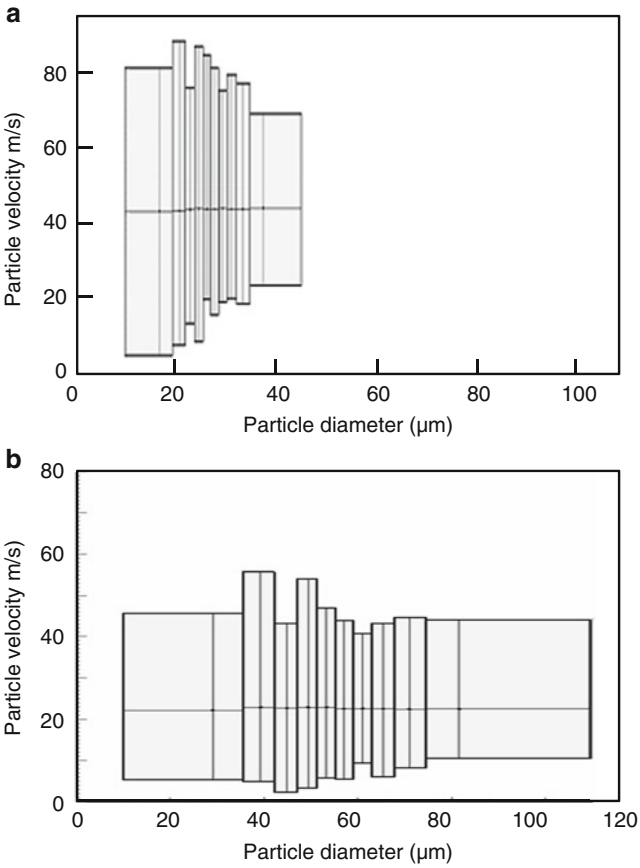


Fig. 4.56 Particle velocity distribution dependence on particle diameters, (**a**) alumina, (**b**) zirconia. Reprinted with kind permission from Dr. Ben Ettouil [152]

resulting in no segregation of particles according to their sizes. It has been checked experimentally by collecting particles in different tubes, 3 mm in internal diameter, with their axes parallel to that of the injector and positioned 150 mm downstream of the injector exit. In each tube the size distribution of particles collected is close to that of the original powder. Of course, as shown in Fig. 4.3, the modification of the injection angle changes the particle trajectory.

(b) Straight Double-Flow Injector

The usefulness of such injectors is again important for small ($d_p < 20$ μm) and light particles, which are difficult to collimate. This is illustrated in Fig. 4.58 [150] for the injector depicted in Fig. 4.53c and zirconia particles (45–5 μm).

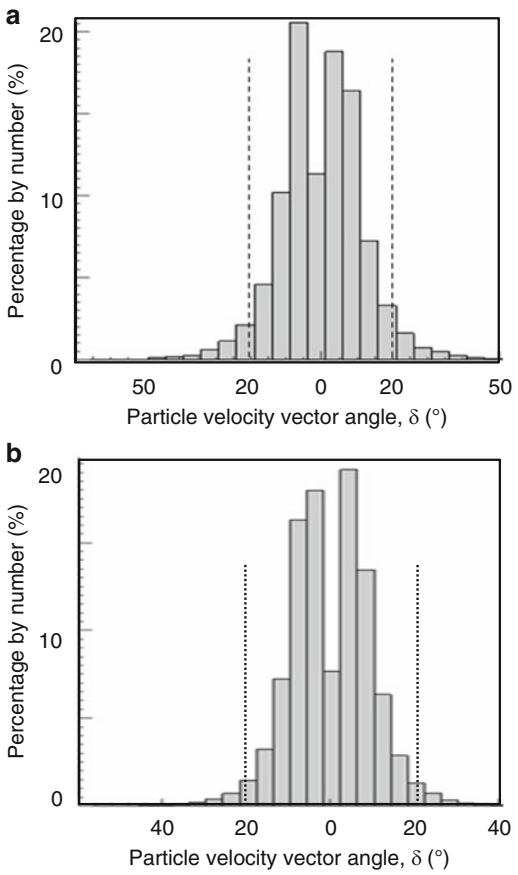


Fig. 4.57 The relative number distribution of particles at an angle, δ, of the particle velocity vectors, relative to the injector axis, at the injector exit, (**a**) alumina, (**b**) zirconia. Reprinted with kind permission from Dr. Ben Ettouil [152]

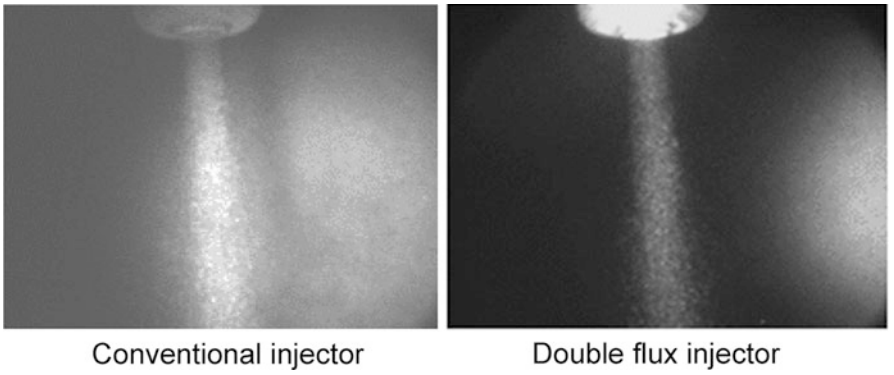


Fig. 4.58 Pictures of zirconia (45–5 μm) particles (obtained with laser flashes) at the exit of conventional and double flux injectors. Reprinted with kind permission from Dr. Renouard Vallet [150]

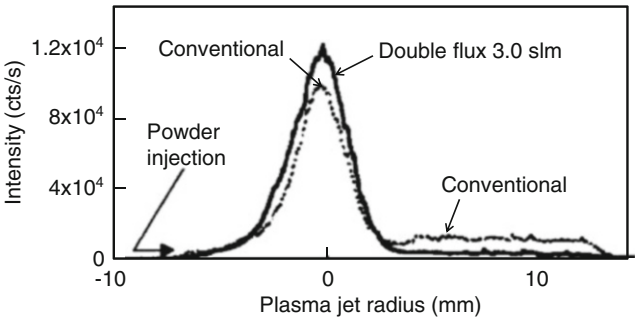


Fig. 4.59 Penetration of particles (zirconia 45–5 μm) into a d.c. plasma jet. Measurements performed at 20 mm downstream of the nozzle exit with conventional and double flux injectors. Reprinted with kind permission from ASM International [112]

The figure shows that the double flux injector constricts efficiently the particle flux. Particle distributions measured by laser scattering within the plasma jet 20 mm downstream of the injector, are presented in Fig. 4.59 [112]. It is obvious from this figure that the particle jet within the plasma jet is well confined by the double flux injector with an argon external gas injection of 3 slm. This gas makes the particle distribution much more symmetrical compared to that with a conventional injector. Moreover, the maximum of the profile with a double flux injector exhibits a higher peak than that with the normal injector. The unsymmetrical appearance of the profile with a conventional injector is due to the particles by-passing the plasma (see Fig. 4.54). These particles are sucked downstream back into the jet, and defects are created in the coating when these unmolten particles stick to the coating being deposited.

(c) Curved Injector

The geometry of the curved injector has a great effect on particle behavior. As the particles approach the bend, they decelerate and are driven to the outer regions of the bend due to the centrifugal forces imparted by the flow. In this zone, the gas has a lower velocity, resulting in a decrease of the drag force exerted on the particles by the enveloping fluid. The particle distribution within the injector is no longer symmetrical, 90 % of the particles are concentrated in the outer part of the curvature [114]. Figure 4.60 from [114] shows the computed change of the velocity profile with particle size for both types of injectors. The slightly lower velocity obtained with the injector having the larger radius is due to the longer friction times of particles with the injector wall. The curved injector reduces drastically the particle velocity but, as with a straight injector, the velocities of particles with diameters over 20 μm are only slightly affected by the curvature of the injector.

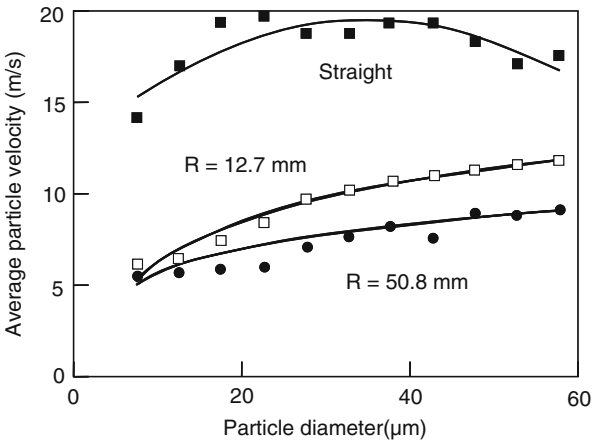


Fig. 4.60 Computed mean particle velocity vs. particle diameter for ZrO_2 powder injected into different tubes; carrier gas flow rate: 4 slm, and $L = 35$ mm. Reprinted with kind permission from Springer Science Business Media [114], copyright © ASM International

4.4.2.4 Interaction Between the Plasma Flow and the Carrier Gas Jet

Calculations have been performed [114] for d.c. plasma jets using the Estet commercial fluid dynamic code. In this code, the mass diffusion of species is assumed to behave similarly to heat diffusion: i.e., the effective diffusivity of each species is equal to its thermal diffusivity. In addition, the Schmidt turbulence number, Sc, (the ratio of momentum diffusivity to molecular mass diffusivity), is fixed at 0.7. The thermodynamic and transport properties of the gas mixture, consisting of the plasma-forming gas, the carrier gas, and the ambient atmosphere, are determined on the basis of the mixture laws using the properties of pure argon, air, and argon–hydrogen mixtures.

A rectangular mesh is used, subdivided into a non-uniform $49 \times 49 \times 43$ grid. The length of the calculation domain is 100 mm and its radius of 21 mm is about 7 times the radius of the torch nozzle. At the two inlets of the domain, i.e., at the plasma torch and injector exits, the values of all variables are defined. The effect of the powder carrier gas is more noticeable for internal injection, as can be seen by comparing the computed data of Fig. 4.61a, b. In these tests, the plasma forming gas is a mixture of 27 slm of argon and 7 slm of hydrogen and the carrier gas flow consists of 8 slm of argon; the effective power dissipated in the gas is 13 kW, the plasma torch i.d. 6 mm, and the injector i.d. 1.6 mm. Under these conditions, the angles of the plasma jet axis with the torch axis were calculated to be 6 and 2° for internal and external injection, respectively. For internal injection, the deflection of the jet is noticeable when the carrier gas mass flow rate exceeds 10 % of the plasma gas mass flow rate.

It should be noted that for internal injection of 22–45 μm alumina particles, the optimum carrier gas injection flow rate is 6 slm. This flow rate induces a relatively high deflection of the plasma jet. On the other hand, the optimum flow rate for external injection is only 4.5 slm. When the injector is moved further downstream, the carrier gas effect on the plasma jet becomes almost negligible. Such results

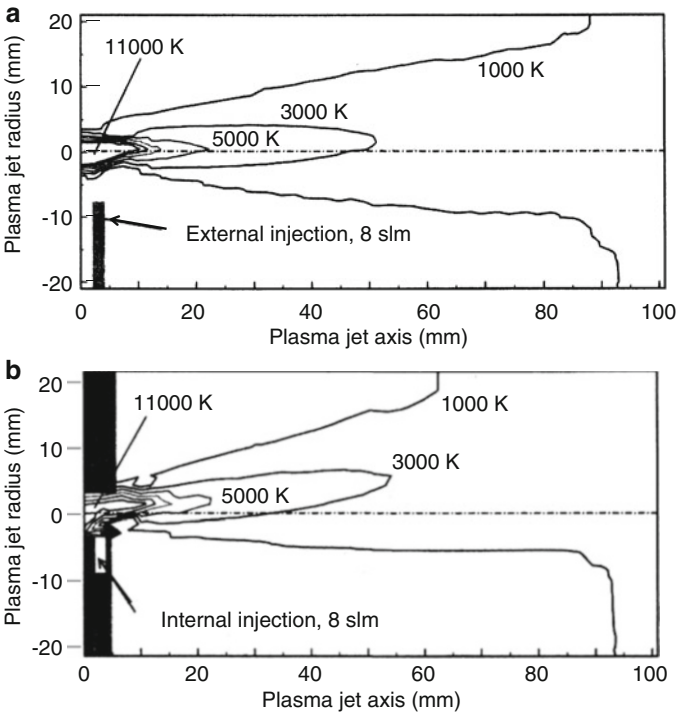


Fig. 4.61 Isotherms at intervals of 2,000 K for (**a**) external powder injection (injector i.d. 1.8 mm, plasma forming gas: 27 slm Ar + 7 slm H_2, carrier gas flow rate 8 slm, $I = 500$ A, $V = 65$ V, thermal efficiency 56 % and plasma anode-nozzle i.d. 6 mm), (**b**) internal injection. Reprinted with kind permission from Springer Science Business Media [114], copyright © ASM International

explain why it is not possible to inject particles below five μm in diameter: the carrier gas flow rate would have to be a few tens of liters per minute inducing a drastic perturbation of the plasma jet.

With axial injection in HVOF (Sulzer-Metco Diamond Jet gun) the carrier gas flow rate (nitrogen), although very low compared to the fuel (propylene)-oxygen-air flow rate (4.45×10^{-5} kg/s against 6.9×10^{-3} kg/s) can perturb the flow close to the axis [153]. When increasing the nitrogen flow rate the flame temperature and velocity, especially the temperature, near the centerline of the nozzle, are decreased. With the flow rate values given above, the maximum gas temperature along the centerline is about 3,000 K. When doubling the nitrogen flow rate, the maximum temperature dramatically decreases to 1,700 K and the velocity at the nozzle exit decreases from 1,950 to 1,800 m/s. Since nitrogen gas does not take part in the chemical reaction, it absorbs the thermal energy generated by the oxy-fuel reaction. As a result, the flame temperature and velocity are decreased, which, in turn, decreases the efficiency of the thermal spray device. Nevertheless, the calculated results show that it is wise to keep a minimum nitrogen flow rate when assuring smooth feeding [153] of particles, in order to get a maximum flame velocity and temperature over the entire particle flow path.

4.4.2.5 Concluding Remarks About Particle Injection

Particle injection is a key issue for particle treatment (acceleration, heating, melting, etc.). Results depend strongly on:

- The positioning of the injector, when it is done internally, the heating and acceleration of particles are optimal, but the perturbation of the hot flow may increase. To diminish this effect, in d.c. plasma spraying the nozzle must be designed to give the carrier gas a possibility to escape before penetrating the plasma jet. With external injection, the flow perturbation by the carrier gas is reduced, but the distance between injector exit and torch axis becomes very critical. If the injector is too close, particles do not by-pass the plasma jet, but clogging or even melting of the injector tip occurs; if it is too far, particle bypassing of the plasma flow will increase.
- The injector inclination can also play a role: when it is in counter-flow direction heating and acceleration are improved, but clogging is enhanced; when it is in the flow direction, heating and acceleration of particles decrease. The positioning is also very important, for example when using high power plasma torches with a strong vortex injection of the plasma forming gases. In this case powder injection must be adjusted to compensate for the deflection caused by the swirl to ensure that the particle spray coincides with the plasma plume [154].
- The injector i.d must be optimized. When it is reduced, the particle jet divergence (important for light particles below 20 μm) diminishes. Using a double-flux injector can also reduce this jet divergence.

When injecting radially it is important that the mean force of injected particles is about the same as that imparted to them by the hot flow, a condition that will lead to optimum trajectories of the particles and thus acceleration and heating [114]. It is clear that the particle jet divergence will drastically increase with the diameter ratio of the smallest and the largest particles of the distribution. This ratio should be kept, if possible, below 2 (already corresponding to a mass ratio of 8!). Thus when co-spraying particles with different characteristics (size distribution and specific mass) for example alumina and iron, the only way to have a uniform melting of all of them (without over-heating for example of iron) is to adapt their size distribution and use two injectors not necessarily disposed at the same distance from the nozzle exit [114].

4.4.3 Particles and Plasma Jet with No Loading Effect

4.4.3.1 Modeling of Interactions with Particles

Tracking particles in a Lagrangian frame requires the second phase to be dilute enough so that the particle–particle interactions and the effect of the particles on the gas phase can be neglected. This assumption requires the second phase to have a low

volume fraction. Many studies, starting with the early works of [155], have been devoted to the problem of distributions of particles. Such calculations require that:

- The projected area of the particle feeder on the nozzle wall is used as the inlet boundary for the particles.
- The particles inside the flow field, are injected in a complete random order, in order to resemble the stochastic behavior.
- Particle diameters are selected randomly in each size range in such a way that they resemble the given distribution.
- Finally, an initial velocity between two values at an angle between two other values with respect to the nozzle axis must be selected randomly for injection.

For plasma spraying, some authors used the LAVA code, for example Chang [20], based on previous studies of liquid sprays [156], some adopted a stochastic approach [157]. Others have introduced injection velocity and direction distributions (often selected based on experimental results) as well as size distributions (see the review of Pfender and Chang [158] and references [156, 159–162]). A few papers related to HVOF processes have been published [162, 163] as well as for Cold Spray [33].

However, at the moment nobody really has determined how representative these models are. Once the starting distributions have been chosen, particles are divided into different classes, for example for diameter classes ranging between both extremes of the size distribution and following a log–normal law. Injection velocity distributions are often approximated by Gaussian distributions. Then each computational particle, p, represents a number N_p of particles of similar physical properties, and the equations of motion and energy transfer are applied to them as defined in Sect. 4.2.

4.4.3.2 Example of Results

(a) d.c. Plasma Jet

The calculation [38] has been performed for Al_2O_3 particles in a size range from 5 to 46 μm divided into two classes and used in an Ar–H_2 d.c. plasma jet (45–15 slm, $I = 600$ A, $U = 65$ V, thermal efficiency = 55 %, anode-nozzle internal diameter 7 mm, flowing into air) neglecting voltage fluctuations and then taking them into account ($\Delta U = 50$ V). Particles were injected vertically (z axis) from below the plasma jet, which had a horizontal orientation, and with the injector disposed externally at 4 mm downstream of the nozzle exit and at 8 mm from the torch axis. The injection velocity distribution was between 5 and 20 m/s and the injection velocity vectors were randomly distributed between two angles: α varying from 0 to 360° and δ (defining the cone angle) between 0 and 10°. Calculations were performed for 2,000 particles. The results obtained are presented in Fig. 4.62 for steady (left) and transient flow (right) showing that the effect of turbulent dispersion

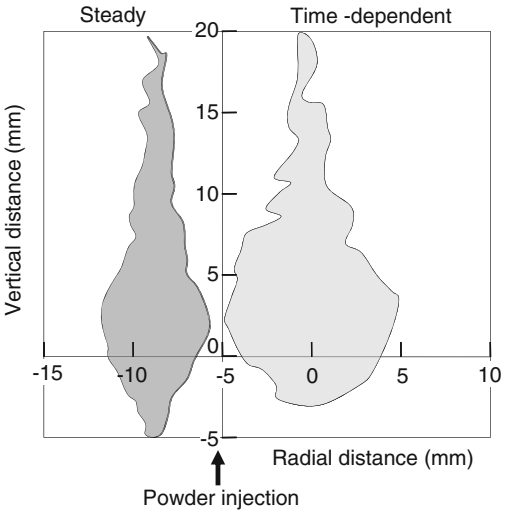


Fig. 4.62 Distribution of two thousand alumina particles in a plane at a stand off distance of 100 mm. Calculations were performed for spray conditions described above, particles being injected vertically in z direction at 4 mm downstream of the nozzle exit and 8 mm from the torch axis. Coordinates on horizontal axis do not indicate the position of the particles cloud but only their dimensions along this axis. *Left*: steady flow, *Right*: transient flow. Reprinted with kind permission from Springer Science Business Media [38], copyright © ASM International

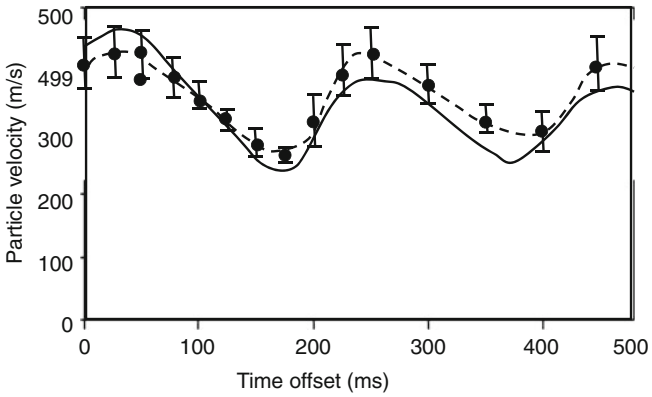


Fig. 4.63 Calculated (*continuous line*) [125] time dependence of the velocity of alumina particles (5– 45 μm) in a fluctuating Ar–H_2 d.c. plasma jet (nozzle i.d. 7 mm, Ar 35 slm, H_2 10 slm, $I = 550$ A, $P_{\text{eff}} = 19.25$ kW). Measurements points taken at 50 mm downstream from the nozzle exit on the jet axis. Reprinted with kind permission from Springer Science Business Media [164], copyright © ASM International

is very high for small particles, their cloud extending up to 2 cm from the torch axis in the vertical direction (Fig. 4.63).

With larger particles with high inertia (top part of the left figure) the cloud of particles is limited to an area of 2–3 mm in width. When considering the voltage

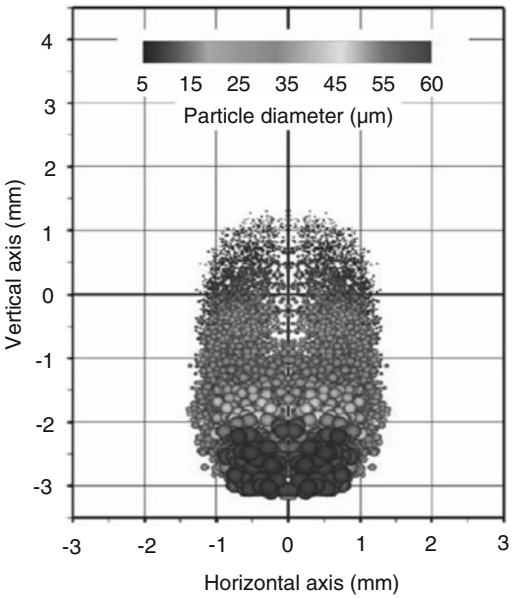


Fig. 4.64 Footprint of a stream of particles ranging between 5 and 60 μm at a distance of 10 mm from the nozzle exit when there is no substrate blocking the free jet. Reprinted with kind permission from Springer Science Business Media [33], copyright © ASM International

fluctuation corresponding to the restrike mode with the Ar–H_2 plasma forming gases, the effective power varies between 12 and 35 kW. This results in plasma jets varying in velocity and temperature with time as well as position and length as shown in Fig. 7.36 of Chap. 7, representing pictures of plasma jets and molybdenum particles injected taken with a Control Vision set-up (see Chap. 16) and a laser flash duration of 5 ns.

As the plasma jet momentum continuously fluctuates (±30 %) while that of particles with a given carrier gas flow rate is constant, the particles will either cross the plasma jet or they will not penetrate into it. Figure 4.50 shows the time evolution of alumina particle velocity at 50 mm from the nozzle exit and on the torch axis.

The calculations are those of Legros [40] while the measurements are those of Bisson and Moreau [164]. Both were performed for an Ar–H_2 (35–10 slm) plasma jet, a 7 mm i.d. nozzle, an arc current of 550 A and an effective power of 19.25 kW. Particles with diameters between 5 and 45 μm were injected externally with a 1.5 mm i.d. injector and a carrier gas flow rate of 3 slm Ar. The good agreement between predicted and measured velocities and velocity fluctuations is remarkable, the fluctuations reaching about 200 m/s over a fluctuation period.

(b) Cold Spray

B. Samareh and A. Dolatabadi [33] have studied the effect of particle distribution on the Cold Spray process with the effect of the flow on particles, especially the smallest. Figure 4.64 shows the footprint of the particles at a distance of 10 mm from the nozzle exit when there is no substrate blocking the high-speed jet. The

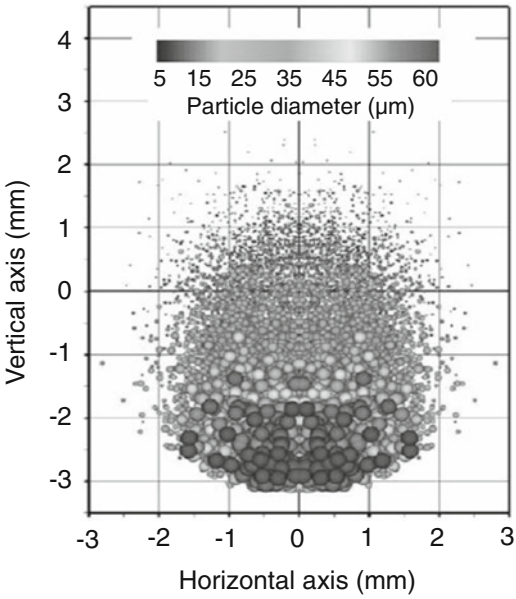


Fig. 4.65 Landing locations for a stream of particles ranging between 5 and 60 μm for a flat substrate, placed at a standoff distance of 10 mm. Reprinted with kind permission from Springer Science Business Media [33], copyright © ASM International

landing location for a range of particle sizes varying between 5 and 60 μm, impinging on a flat square substrate located at a standoff distance of 10 mm is shown in Fig. 4.65. A particle deviation in both vertical and lateral directions due to the three-dimensional nature of the flow is shown in this figure. Smaller particles, having low Stokes numbers, are more affected by the gas flow and are deviating more compared to the heavy ones. Particles are injected from the topside of the nozzle at random angles between 40 and 50°. As the heavier particles are less affected by the flow, they shift below the nozzle centerline while the smaller particles are dispersed above and below the centerline.

4.4.4 Loading Effect

4.4.4.1 Modeling

While the assumption of dilute systems has generally been accepted for the calculation of individual particle trajectories and temperature histories under plasma conditions, the interpretation of the results obtained is greatly hindered by the simple fact that any application of plasma technology for the in-flight processing of powders will have to be carried out under sufficiently high loading conditions, in order to make efficient use of the energy available in the hot or cold flow. With hot flows the main effect is the local modification of the flow energy due to the presence of the particles, and model predictions using the low-loading assumptions are

substantially in error when the currently used powder loadings in spray processes are considered. It is generally admitted that the loading effect has to be considered as soon as the particle mass flow rate is higher than 4 % of the mass flow rate. Such a situation occurs in plasma spraying (d.c. and r.f.), and flame spraying, but is generally negligible in PTA and has almost no possibility to occur in HVOF or HVAF spraying as well as in Cold Spray. However in this case, a different loading effect can occur as described in Chap. 6 Section "Loading Effect".

In an attempt to take into account the plasma–particle interaction effects, Boulos and his collaborators [165–167] developed a mathematical model, which, through the interactive procedure illustrated in Fig. 8.48 of Chap. 8. This procedure up-dates continuously the computed plasma temperature, velocity and concentration fields to take into account the plasma–particle interaction effects. The interaction between the stochastic single particle trajectory calculations and those of the continuum flow, temperature and concentration fields is incorporated through the use of appropriate source–sink terms in the respective continuity, momentum, energy and mass transfer equations. These are estimated using the so-called particle-source-in-cell model (PSI-Cell). For more details about these calculations see Sect. 8.4 in Chap. 8.

4.4.4.2 Examples of Results

(a) Ar R.F. Induction Plasma with Copper Particles

As an example of possible plasma–particle interaction effects in induction plasma spraying under heavy loading conditions, results reported by Proulx et al. [167] will be given in this section. These were obtained for an inductively coupled plasma torch operated with argon at atmospheric pressure, 3 kW power level, working at 3 MHz with an internal diameter of 25 mm. The torch description and its working conditions are presented in Fig. 8.47 in Chap. 8.

Copper powder with a mean particle diameter of 70 μm and a standard deviation of 30 μm was injected through the central tube into the coil region of the discharge. The physical properties of copper, which were used in the calculations, are those of Mostaghimi and Pfender [168]. It was thus possible to take into account the effect of the presence of copper vapor on the transport properties of argon under plasma condition. Particularly the presence of even small amounts of copper vapor can have a pronounced effect on the electrical conductivity of argon. The Gaussian particle size distribution of copper powder was discretized and the injection velocity of the particles was assumed to be equal to that of the carrier gas velocity at the point of injection. Results were reported [167] for different mass feed rates of the copper powder varying between 1.0 and 20.0 g/min (Fig. 4.66, Table 4.4).

Because the trajectories of the particles in this case are very close to the axis of the torch, the plasma gas is significantly cooled down in this region (Fig. 4.66). Figure 4.67, reveals, however that the loading effect caused by the copper powder injection is limited to the central region of the discharge (+/−) 5 mm from the axis where most of the copper powder trajectories are concentrated. On the other hand,

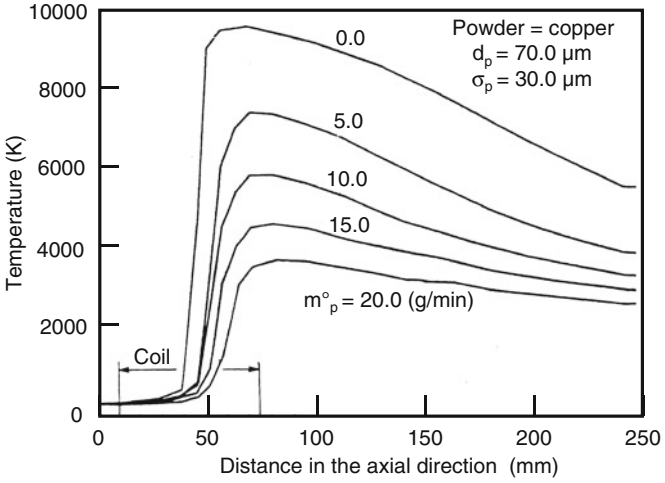


Fig. 4.66 Effect of the powder feed rate on the axial temperature profile at $r = 0.0$ mm for an induction plasma torch, (see Table 4.4 for spray conditions) after Proulx et al. Reprinted with kind permission from Elsevier for Journal of Heat and Mass Transfer [167]

Table 4.4 RF torch dimension and summary of the operating conditions. Reprinted with kind permission from Elsevier for Journal of Heat and Mass Transfer [167]

$r_1 = 1.7$ mm	$L_1 = 10.0$ mm	$Q_1 = 3.0$ slm
$r_2 = 3.7$ mm	$L_2 = 74.0$ mm	$Q_2 = 3.0$ slm
$r_3 = 8.8$ mm	$L_T = 250.0$ mm	$Q_3 = 14.0$ slm
$R_o = 25.0$ mm	$w = 2.0$ mm	$P_o = 3.0$ kW
$R_c = 33.0$ mm		$f = 3.0$ MHz

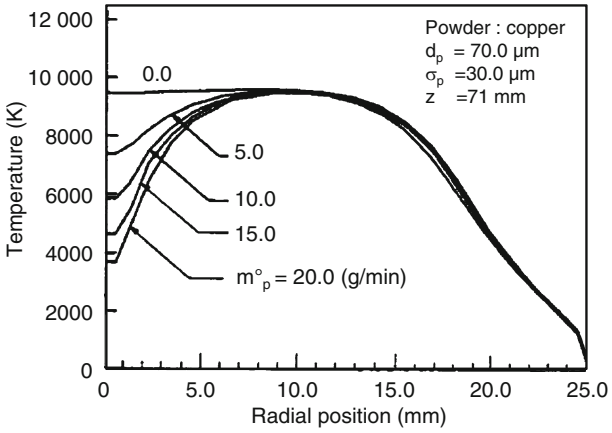


Fig. 4.67 Effect of copper powder feed rate on the radial temperature profile at the middle of the coil region, $z = 71.0$ mm. After Proulx et al. Reprinted with kind permission from Elsevier for Journal of Heat and Mass Transfer [167]

the outer region of the plasma, where most of the power is dissipated, remains largely unaffected by the increase in the copper feed rate. The results clearly demonstrate that although the overall loading ratio of the copper powder to plasma gas might be small (0.19 g copper/3 g argon), the local cooling effects are significant. This is a clear indication that the plasma–particle interaction effects could be locally very important under loading conditions for which it is frequently assumed to neglect the changes in plasma temperature due to the presence of the powder.

The momentum transfer between the gas and the particle is negligibly affected, and the flow field is affected only through changes of the local plasma temperature. As the particles pass through the plasma, a portion of the powder evaporates and the vapor diffuses into the plasma medium and the total energy absorbed by the powder is between 3.1 % and 17.8 % of the input plasma power. Thus the injection conditions will have a very important effect on the loading effect in r.f. plasma torches, as illustrated in Sect. 8.4 in Chap. 8.

Of course, as underlined by Proulx et al. [169] the importance of the loading effect is directly linked to thermal properties of particles: alumina, for example, has the highest latent heat of melting and boiling as well as high specific heats of the solid and liquid phase. The lowest values are those of tungsten, nickel being between alumina and tungsten. Similar results are obtained for the plasma velocity along its axis, which suffers a reduction due to particles, but less than that observed for the temperature. For more details see Chap. 8 Sect. 8.4.

(b) d.c. Plasma with Alumina Particles

Calculations and measurements were performed [170] for alumina particles (fused and crushed –62 + 18 μm) injected into a d.c. plasma jet. The spraying parameters in this case were: nozzle i.d. 7 mm, 32 slm Ar, 12 slm H_2, $I = 600$ A, $V = 58$ V, $\eta = 52$ %, injector i.d. 1.8 mm, external injection $r = 9$ mm, $z = 6$ mm. The distributions of particle velocities and surface temperatures were measured at a point situated on the jet centerline at 120 mm from the nozzle exit for different powder mass flow rates. Results given in Fig. 4.68 show that the velocity of the particles is reduced by 11 % when the powder mass flow rate is increased from 0.03 to 2 kg/h, while their surface temperature is reduced by about 14 %.

When calculating the particle velocities, the mean value is within 10 % of the experimental values for a low mass flow rate of 0.2 kg/h. However, significant differences are observed for a powder flow rate of 2 kg/h. The effect is the same, but more pronounced for the particle temperature. This discrepancy underlines the importance of representing the particle injection more accurately.

(c) HVOF

Since the particle loading in HVOF is very low (less than 4 % of the gas mass flow rate), it can be assumed that the presence of particles will have negligible effect on the gas velocity and temperature field in the barrel and in the free jet [171].

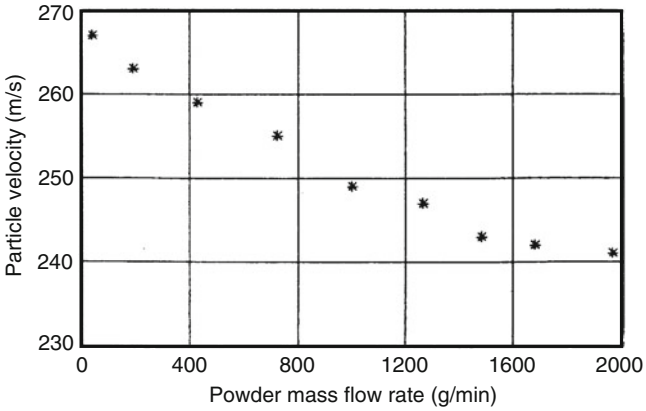


Fig. 4.68 Measured Al_2O_3 particle velocity as function of the powder feed rate at 120 mm from the nozzle exit, after Vardelle et al. Reprinted with kind permission from ASM International [170]

(d) Cold Spray

Varying the mass flow rate at which the copper feedstock particles are fed into the carrier gas stream can change the thickness of the coatings on aluminum substrates [172]. Increasing the powder feed rate increases the thickness of the coating linearly until a maximum powder mass flow rate is reached for which there are too many particles impacting the surface of the substrate, resulting in excessive residual stresses causing the coating to peel. It was shown by Taylor et al. [172] that the peeling was not a result of flow saturation, as in plasmas, but, instead, of excessive particle bombardment per unit area of the substrate. By increasing the travel speed of the substrate or elevating the propellant gas temperature, this can be overcome, and once again well-bonded dense coatings are obtained [172]. Some authors also suggest that a high particle loading could slow the flow but no evidence to this effect has been reported.

4.5 Liquid or Suspension Injection into a Plasma Flow

For almost one decade, work has been devoted to spraying of sub-micrometer or nanometer sized particles, especially through suspensions and solutions [173–200]. The main problem is that the carrier gas has to have a high flow rate to impart a sufficiently high momentum to particles for their penetration into the plasma. For example, with a 1.8 mm i.d. injector the flow rate required for 1 μm alumina particles is about 80 slm thus disturbing drastically the plasma jet (see the plasma jet deviation in Fig. 4.61b for an injection of 8 slm of Ar as carrier gas!).

Therefore, the only way to inject small particles is to use a liquid carrier. Two ways are possible for this injection [180–183]:

- Atomization which will perturb the plasma drastically by the atomizing gas and also result in wide ranges of particle diameters and velocities.
- Mechanical injection where a pressurized liquid is pushed through a tiny nozzle (diameters between 50 and 200 μm) resulting in drops with a unique size and with velocities that can be easily controlled.

Whatever the injection mode may be (see Sect. 4.5.1), the main question that needs to be addressed in this section is what happens when the injected liquid droplets interact with the plasma flow?

To understand what happens to liquid droplets it is possible to develop Computer Fluid Dynamic (CFD) complex calculations as Kolman did for d.c. plasma jets [201] or Shan and Mostaghimi [202] for RF plasmas. More sophisticated numerical models have been developed to account for those mechanisms [203–207]. They consider usually at least (1) 3D transient or stationary description of the turbulent plasma flow and its mixing with the ambient atmosphere, (2) a suitable description of the liquid feedstock injection as jet, drops or droplets into the plasma jet, and (3) an accurate description of the possible mechanisms that will control the treatment of the liquid material in the plasma flow (i.e. mechanical break-up, thermal break-up, coalescence). Afterwards, a number of factors must be considered for suspensions: heating, evaporation, boiling, melting of the solid phase and re-condensation; and for solutions: precipitation, pyrolysis, crystallization, sintering and melting. However, here we will mainly be concerned of using simple 0-D or 1-D equations pointing out the key parameters controlling the processes of fragmentation (see Sect. 4.5.2) and evaporation (Sect. 4.3.3.5) [77].

4.5.1 Liquid Injection

Two main techniques are used: atomization or mechanical injection.

4.5.1.1 Spray Atomization

This method has been used for suspensions and solutions [196, 208–214]. Very often co-axial atomization is used. It consists in injecting a low velocity liquid inside a nozzle where it is fragmented by a gas (mostly Ar because of its high mass) expanding within the body of the nozzle [215]. For liquids of viscosity between a few tenths to a few tens of mPa s, their break-up into drops depends on the Weber number, which is the ratio of the force exerted by the flow on the liquid to the surface tension force:

$$\mathrm{We} = \frac{\rho_g \times u_r^2 \times d_l}{\sigma_l} \tag{4.68}$$

where ρ_g is the gas mass density (kg/m^3), u_r the relative velocity gas–liquid (m/s), d_l the drop or jet diameter (m) and σ_l (N/m) the surface tension of the liquid.

Fragmentation of the liquid occurs when We $>$ 12–14 according to the different authors. This means that, for a liquid with a given surface tension, atomization depends on gas velocity and specific mass. Atomization also depends, but to lesser extent, on the Ohnesorge number, Z, including the effect of liquid viscosity (see, e. g., the studies of Rampon et al. [216] and Marchand et al. [217]):

$$Z = \frac{\mu_l}{\sqrt{\rho_l \times d_l \times \sigma_l}} \tag{4.69}$$

where μ_l is the liquid viscosity (Pa s), ρ_l the liquid mass density (kg/m^3), d_l the drop or jet diameter (m) and σ_l (N/m) the surface tension of the liquid. However, if the viscosity is too high (>0.8 mPa s), difficulties with feeding the liquid may appear [216]. Sizes and velocities of drops exiting the injection nozzle have been characterized by laser scattering. Measurements show that atomization is affected by the gas-to-liquid mass ratio (GLR), the nozzle design, and the properties of the liquid (density, surface tension, dynamic viscosity) [215–217]. For example with alcohol, depending on the Ar atomizing flow rate, the mean droplet diameters vary between 18 and 110 μm [211]. Of course, with the same injection parameters, shifting from ethanol ($\sigma_{eth} = 22 \times 10^{-3}$ N/m at 293 K) to water ($\sigma_w = 72 \times 10^{-3}$ N/m) modifies the mean diameter from 70 to 200 μm. If increasing the atomizing gas constricts the droplet jet, it also perturbs the plasma jet (see Fig. 4.69a).

Similar results have been obtained [212]: the droplet size is diminished with the increase of GLR. Quadrupling the GLR leads to a decrease in the droplet size by a factor of ten and allows obtaining a narrower Gaussian curve. It is also interesting to note that the weight percentage of solid in the suspension broadens the particle size distribution. Marchand et al. [217] studied, an internal- and an external mixing two-fluid atomizing nozzles to transfer the suspension feedstock to the plasma jet. A dedicated Particle Image Velocimetry, PIV, system (see Sect. 16.7.3.1 of Chap. 16) was implemented to record information on the injection of liquid feedstock and characterize the liquid stream penetration and behavior in the plasma jet. Thus the atomization modes, the drop size distributions, and the corresponding mean sizes were investigated according to suspension properties (surface tension, liquid viscosity, and GLR) and nozzle design. Several different injection modes were achieved from a liquid jet to various sprays with different drop size distributions by changing mainly the design of the atomizing nozzle. By adjusting the surface tension and the GLR, for both nozzles, a modification of the spray from a Rayleigh break-up mode [218] to a super pulsating mode can be observed. Figure 4.70a, b presents a few examples of different atomized liquid jets obtained. Except for the first mode (Rayleigh break-up mode) corresponding to a round liquid jet diameter of about 350 μm, all the other sprays showed multimodal drop size

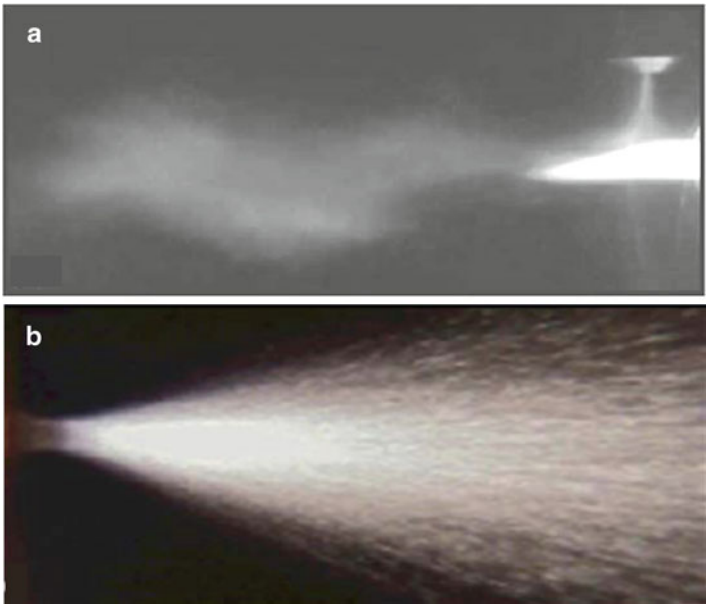


Fig. 4.69 Interaction of an Ar–H_2 (45–15 slm) dc plasma jet ($I = 600$ A, anode-nozzle i.d. 7 mm) with an atomized ethanol flow [182]. (**a**) Atomized ethanol jet, (**b**) interaction plasma-atomized jet

distributions. Membrane like and fiber-like break-up modes led to tri-modal modes (15, 65, and 300 μm). Depending on the atomization conditions, the ratio between large and medium drop size modes was changing, while the ratio of fine drops seemed to be constant (Fig. 4.70b, c). Finally, when a super pulsating mode was reached, a mist was generated, characterized by a bimodal drop size distribution (10 and 30 μm) the drop size distribution being narrow.

For more details about atomization see the book of Lefebvre [218] where one can find, for example, the relationship between the Sauter mean diameter (SMD) and the variables σ_l, ρ, ρ_l. ALR, μ, and the diameter of the discharge orifice of the atomizing probe. However, at least for suspensions that have a non-Newtonian behavior (generally thixotrope) these expressions, established for Newtonian liquids, must be taken with caution. Similar results about the effect of atomizing gas flow were obtained for solutions [196]. Of course, the liquid pressure as well as the atomizing gas mass flow rate and pressure control droplet velocities and sizes [196, 213], unfortunately not independently of each other. Typical sizes obtained are in the range 2–100 μm with velocities varying between 60 and 5 m/s. For example with a YSZ suspension the average droplet size is 38 μm with an average velocity of 13 m/s [203]. At last it must be emphasized that the injector must be water-cooled in order to bring it as close as possible to the plasma jet to avoid too much dispersion of the droplet jet before its penetration into the plasma jet. Jordan et al. [219] have developed a homemade capillary atomizer with a liquid exiting one capillary and an

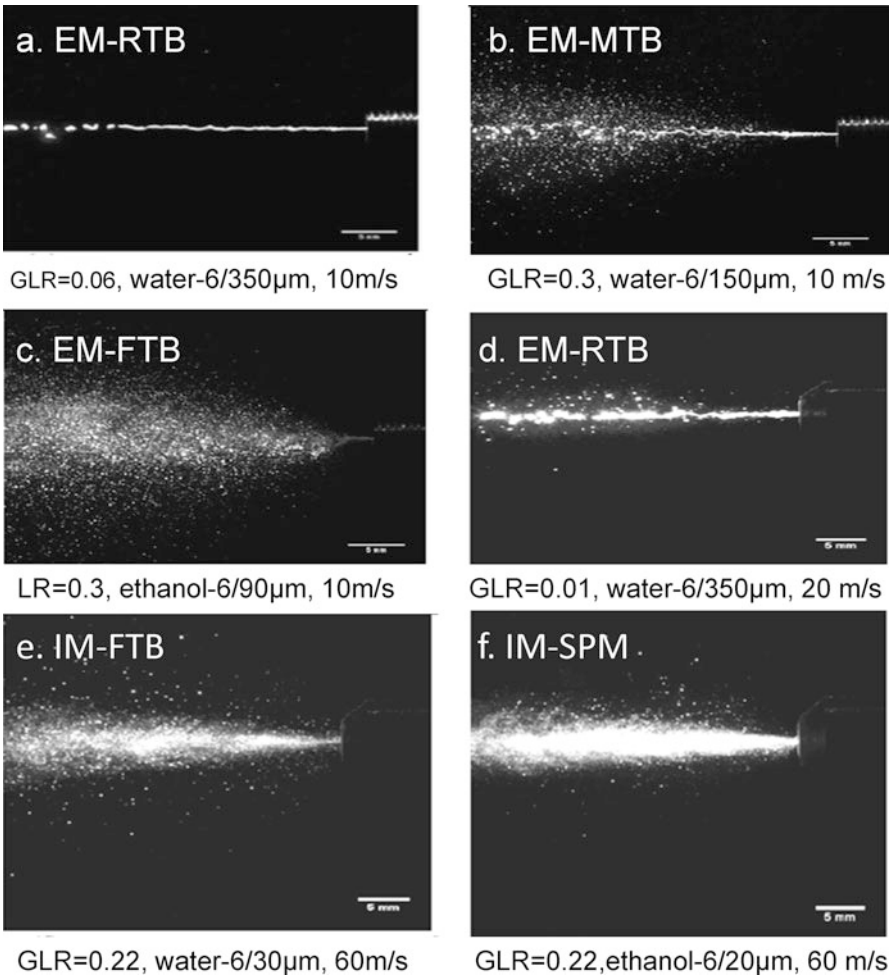


Fig. 4.70 Images of the atomized suspensions as a function of the nozzle design (External mixing nozzle, EM or Internal mixing nozzle, IM) and operating conditions associated with the break-up mode (Rayleigh-type break-up mode, RTB, Membrane-type break-up mode, MTB, Fiber-type break-up mode, FTB) and the mean drop size and velocity. Reprinted with kind permission from Springer Science Business Media [217], copyright © ASM International

air atomizing jet at 90° to the liquid discharge used as a transverse atomizer. This arrangement results in a rather narrow spray jet and droplet size distribution in the 1–20 µm diameter range. Figure 4.71 shows typical droplet size distributions measured by Phase Doppler Particle Anemometry (PDPD) [219]. Three different types of atomizers were used: (a) a home made capillary atomizer with a liquid exiting one capillary, (b) a narrow angle hydraulic atomizing fan nozzle, (c) an air cap transverse air blast atomizing nozzle with a relatively large spray angle, and (d) an air datomizing jet at 90° to the liquid discharge used as a transverse jet

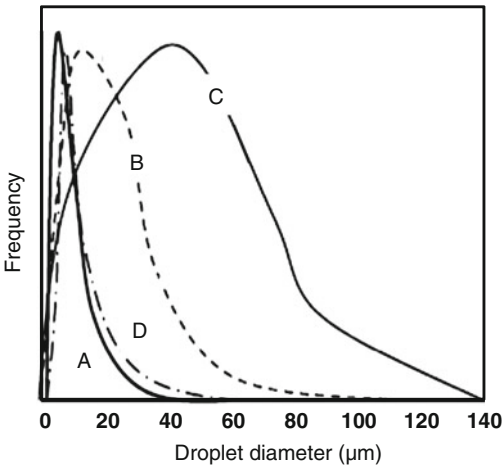


Fig. 4.71 Drop size distributions obtained with different atomizers: (A) capillary atomizer, (B) Fan nozzle, (C) Transverse air blast atomizer, (D) nebulizer. Reprinted with kind permission from ASM International [219]

atomizer. For comparison the size distribution with a nebulizer is also shown. It is apparent that the broadest particle size distribution is for the air cap atomizer and the narrowest is for the capillary atomizer.

Cotler et al. [220] have developed and tested an industrial liquid-based feedstock feeder prototype in continuous operation to produce well-bonded coatings from liquid feedstock suspensions of alumina, titania, and YSZ. As emphasized in Sect. 4.5.5, the authors have applied gun power compensation for the effect of liquid media against established dry feedstock regimes.

4.5.1.2 Mechanical Injection

Two main techniques are possible: either to have the liquid in a pressurized reservoir from where it is forced through a nozzle of given i.d., or to add to the previous set-up a magnetostrictive rod at the back side of the nozzle which superimposes pressure pulses at variable frequencies (up to a few tens of kHz). The first device has been developed at the SPCTS in Limoges, France [182, 185, 188, 190, 191, 221]. It consists of four tanks in which different suspensions and one solvent are stored. Any reservoir or both of them can be connected to an injector consisting of a stainless steel tube with a laser-machined nozzle with a calibrated injection hole. A hole of diameter d_i produces a liquid jet with a velocity v_l (m/s) linked to the incompressible liquid mass flow rate m_l^* (kg/s) by:

$$m_l^* = \rho_l v_l S_i \tag{4.70}$$

where ρ_l is the liquid specific mass (kg/m^3) and S_i the cross sectional area of the nozzle hole (m^2). Assuming that the liquid is non-viscous and ideal, v_l depends on

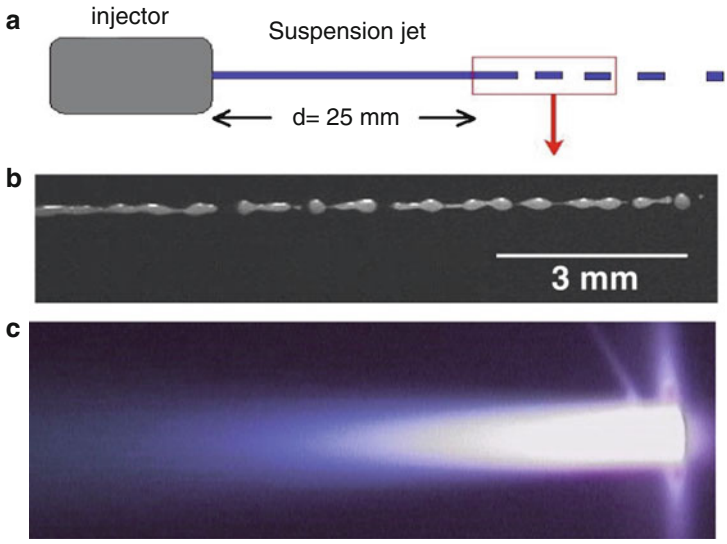


Fig. 4.72 Suspension mechanical injection, (**a**) Schematic of the liquid jet at the injector exit, (**b**) Picture of the transition between the jet and droplets, (**c**) Interaction of the liquid jet and the plasma jet. Reproduced with kind permission of IOP organization [221]

the pressure drop Δp between the tank and surrounding atmosphere through the Bernoulli equation:

$$\Delta p = 0.5\rho_l v_l^2 \tag{4.71}$$

However, the right-hand side of this equation has to be multiplied by a correction factor to take into account the friction along the nozzle wall (depending on its shape, length, and roughness) as well as the viscous dissipation. Correction factors between 0.6 and 0.9 are often used. For example, in the experiments performed at Limoges (SPCTS) [182, 185, 188, 190, 191, 221], d_i was 150 µm and the tank pressure was varied between 0.2 and 0.6 MPa. If, for example, one wants to achieve the same m_l^* as that obtained at 0.5 MPa with $d_i = 150$ µm with a smaller d_i of 50 µm, it can be deduced from Eqs. (4.70 and 4.71) that the pressure should be multiplied by 81 (a pressure of 40.5 MPa requires adapted equipment and special precautions!). The liquid exiting the nozzle, characterized with a CCD camera (diameter and droplet velocity), flows as a liquid jet, with a diameter between 1.2 and $1.5 \cdot d_i$ depending on the tank pressure and nozzle shape. After a length of about 100–150 times d_i, Rayleigh–Taylor instabilities lead to fragmentation of the jet into droplets with a diameter of about 1.3–1.6 times that of the jet. This is illustrated in Fig. 4.72 for a 150 µm internal diameter injector. Compared to the atomization injection, (see Fig. 4.69b obtained with the same Ar–H_2 plasma jet) the jet perturbation is drastically reduced.

Thus, depending on the position of the injector exit relative to the plasma jet (radial injection), it is possible to inject either the liquid jet or droplets. For example, with $d_i = 150$ µm and a pressure of 0.5 MPa, the droplet diameter was 300 µm and the flow rate of liquid was 0.47 cm^3/s. Siegert et al. [222] used a similar device with a nozzle i.d. of 250 µm. To overcome the high-pressure problem, Blazdell and Kuroda [179] used a continuous ink jet printer, which allowed uniformly spaced droplets to be produced by superimposing a periodic disturbance on a high-velocity ink stream. They used a nozzle 50 µm i.d. (d_i) and a frequency f of 74 MHz producing 64,000 droplets/s. The theoretical diameter d_l of drops is given by Eq. (4.72):

$$d_l = \left(\frac{3d_i^2 v_l}{2f}\right)^{1/3} \tag{4.72}$$

where v_l is the liquid velocity. This expression shows that d_l is a function of the liquid flow velocity and therefore these two parameters cannot be controlled separately. It is also possible to replace v_l by m_l^* using Eq. (4.70). In their experiments, Blazdell and Kuroda [179] used a tank pressure of 0.12 MPa corresponding to a 87 µm mean droplet diameter with a theoretical velocity of 11.5 m/s. According to the nozzle i.d. and the number of droplets, the liquid flow rate is about 20 times less than that in the preceding case (see previous section) where a nozzle of 150 µm i.d. was used. Oberste–Berghaus et al. [223] have used a similar set-up with a magnetostrictive drive rod (Etrema AU-010, Ames, Iowa) at the backside of the nozzle, working up to 30 kHz. They produced 400 µm drops with 10 µs delay between each and with a velocity of 20 m/s. Siegert et al. [224] have used a peristaltic pump with single boring injection, where the i.d. is between 0.2 and 0.7 mm. The velocity was varied through changing the i.d. between 0.7 and 18 m/s.

4.5.2 *Liquid Penetration into the Plasma Flow*

In conventional particle spraying the optimum particle trajectory is achieved when the injection force of the particle is about that imparted to it by the plasma jet, i.e. $S_p \rho v^2$, where S_p is the apparent surface of the particle and ρv^2 the momentum density of the jet, corresponding to a pressure, (of course varying along its radius or more precisely along the particle trajectory within the jet). For liquid jet injection the momentum density of the liquid $\rho_l v_l^2$, has to be compared to that of the plasma ρv^2. As shown in the next section, when the liquid jet or liquid droplets penetrate the jet they are progressively fragmented and thus their volumes and apparent surfaces become smaller. Accordingly, the injection force of the droplets is reduced as well as the force imparted to them by the gas jet. Thus, rapidly there penetration ceases, and the condition for good penetration implies that:

$$\rho_l v_l^2 \gg \rho v^2 \tag{4.73}$$

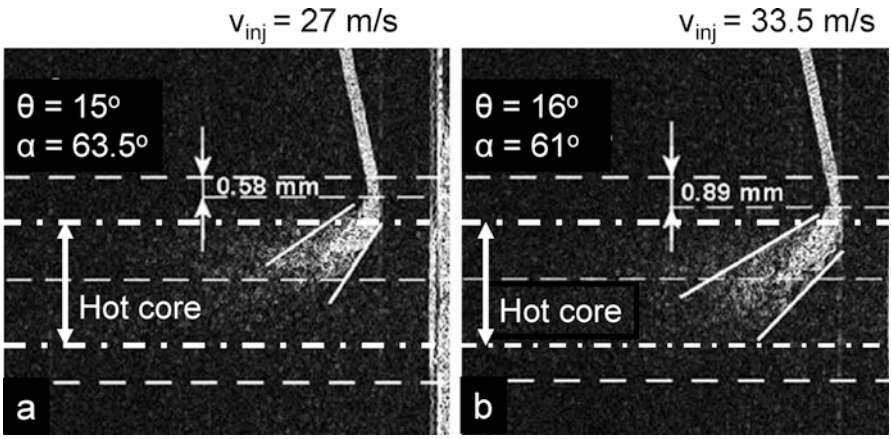


Fig. 4.73 Penetration of a zirconia suspension in ethanol injected with two different injection velocities (27 and 33.5 m/s) into an Ar–He d.c. plasma jet (30–30 slm, 700 A, anode-nozzle i.d. 6.0 mm). Reprinted with kind permission from Springer Science Business Media [77], copyright © ASM International

For example, considering a suspension of zirconia in ethanol injected into Ar–He d.c. plasma jet, Fig. 4.73 shows a better penetration of the liquid jet within the plasma jet core when its velocity is 33.5 m/s instead of 27 m/s. In the first case, the liquid jet momentum density is 0.96 MPa against 0.02 MPa for the mean value of that of the plasma jet.

Upon penetration within the plasma jet the drops are submitted both to a strong shear stress due to the plasma flow, which, under conditions described later, will fragment them into smaller droplets, and to a very high heat flux which will vaporize the liquid. Thus, a very important point is the value of the fragmentation time, t_f, relatively to the vaporization time, t_v, in order to see if both phenomena can be separated.

4.5.3 Liquid Fragmentation

4.5.3.1 Simple Approach

In itself droplet fragmentation is a very complex phenomenon, which has been extensively studied for fuel injection. Different break-up regimes exist depending on the Weber number and break-up should happen according to the catastrophic regime where Rayleigh–Taylor and Kelvin–Helmholtz waves develop at different stages of drop destruction [225]. Moreover, the problem becomes even more complex when the drop encounters steep gradients of velocity and temperature as it penetrates the d.c. plasma jet. For example, a 150 μm diameter drop will have, between its front and trailing edges, a velocity difference of about 50 m/s and a

Table 4.5 Calculation of droplet diameters d_d for different plasma jet droplets

	u (m/s)		
Calculation of d_d (μm)	500	1,000	2,000
Water $\sigma = 72 \times 10^{-3}$ N/m	40.4	10.1	2.5
Ethanol $\sigma = 22 \times 10^{-3}$ N/m	12.4	3.1	0.8

temperature difference of 500–1,000 K. This will result in a strong deformation, and the deformed drop will experience very different drag coefficients. With very high atomizing gas flow momenta as those obtained, for example, in wire arc spraying, molten metal droplets are torn into sheets of metals, as shown by Hussary and Heberlein [226]. The eddy structure in the flow leads to the sheet disintegration in a shower of droplets with varying trajectories. Thus, calculations presented below are only very crude approximations.

To determine order of magnitude estimates for what happens to a suspension drop entering a hot gas flow, only a simple force balance can be considered. The drop will be fragmented as soon as the aerodynamic force acting on it will exceed the surface tension force. This practically never occurs in r.f. plasmas where flow velocities are only a few tens of m/s, but it occurs in d.c. plasma or HVOF jets where velocities are much higher (up to 2,200 m/s). To determine the diameter d_d of the resulting droplet, the equality of the aerodynamic force F_p acting on it and the surface tension force F_s will be considered:

$$\frac{\pi}{8} \cdot C_D \cdot d_d^2 \cdot \rho \cdot u^2 = \pi \cdot d_d \cdot \sigma \tag{4.74}$$

where C_D is the flow drag coefficient, ρ is its specific mass (kg/m^3), the relative velocity, u, between flow and drop or droplet: $u = u_p - u_d$ (m/s) where u_p is the flow velocity and u_d the droplet velocity, and σ is the droplet surface tension (N/m).

If it is assumed that $u \gg u_d$ the droplet diameter is then given by:

$$d_d = \frac{8 \cdot \sigma}{C_D \cdot \rho \cdot u^2} \tag{4.75}$$

Of course, d_d depends on the liquid used and the flow velocity as shown in Table 4.5 for an Ar–H_2 d.c. plasma jet assumed to be at 10,000 K.

This calculation shows that the fragmentation can be very important in d.c. plasmas and depends very strongly on the plasma velocity. The viscosity of a suspension or solution will be higher (the value being linked to the wt.% of solid particles in a suspension) than that of the solvent, but this calculation provides reasonable trends.

It is important to determine how long fragmentation will take. For that it can be assumed that an initial drop of radius r_s is fragmented into n droplets of radius

Table 4.6 Calculation of fragmentation times t_d (μs) for different plasma jet velocities

	u (m/s)		
Calculation of d_d (μs)	500	1,000	2,000
Water	0.52	0.29	0.15
Ethanol	0.57	0.3	0.14

$r_d(n \cdot r_d^3 = r_s^3)$. The variation of the surface energy for a liquid of surface tension σ, during the step of fragmentation results in work:

$$\Delta E_s = \sigma \cdot \Delta S = \sigma 4\pi\left(n r_d^2 - r_s^2\right) = \sigma \cdot \pi r_s^2 \left(\frac{r_s}{r_d} - 1\right) \tag{4.76}$$

The work W_F of the drag force F_D during t_d, the destruction time, can be calculated from:

$$W_F = F_D \cdot u \cdot t_d$$

resulting in:

$$t_d = \frac{\Delta E_s}{F_D \cdot u} = \frac{8\sigma\left(\frac{r_s}{r_d} - 1\right)}{C_D \cdot \rho \cdot u^3} \tag{4.77}$$

The estimation of the destruction time for an ethanol drop, 300 μm in diameter, entering an Ar/H_2 plasma jet at 10,000 K with different velocities is given in Table 4.6. The results show that the fragmentation time of the initial drops takes place in about 1 μs.

4.5.3.2 More Elaborated Description

The study of Hwang et al. [225] describes fragmentation of fuel drops 189 μm in diameter injected at 16 m/s into an air jet with velocities between 70 and 200 m/s at 450 K. The values correspond to typical sizes of droplets used in plasmas with similar gas momentum densities. The different mechanisms depend strongly on the Weber number Eq. (4.68) and the different regimes for break-up are defined in [227]. For practical purposes, We ≈ 14 has been chosen as the critical value over which particles break up [228]. Other authors propose We ≈ 12. The former value is the criterion adopted by Ozturk et al. [229, 230] and Basu et al. [231]; with Ar–H_2 and Ar–He conventional d.c. plasma jets, in the jet core and its fringes ($T > 3{,}000$ K), ρv^2 values are between 15 and 120 kPa. Thus, ethanol droplets down to 15 μm can be broken up in the jet fringes, but if $\rho v^2 = 50$ kPa, 4 μm droplets will be broken up. In good agreement with the simplified calculations presented in the previous section, this particle fragmentation will be more the rule than the exception. Of course, increasing σ_l, for example, by replacing ethanol with water modifies

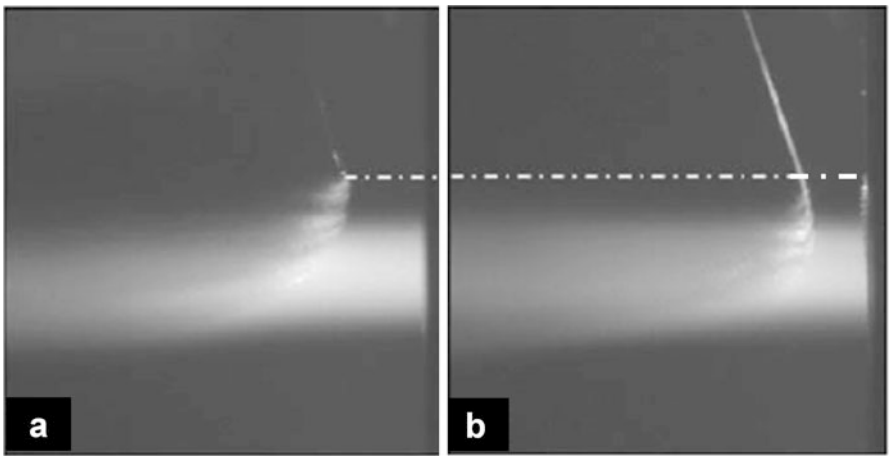


Fig. 4.74 Influence of the liquid jet composition upon its break-up by Ar–H_2 dc plasma jet. (**a**) Pure ethanol and (**b**) zirconia suspension in ethanol. Exposure time 50 μs, five laser flashes of 1 μs duration with 5 μs between each. Reprinted with kind permission from Springer Science Business Media [77], copyright © ASM International

the minimum size of droplet break-up which is multiplied by a factor of 3.27 (ratio of the surface tensions) and thus small droplets (below 40–50 μm) will be mainly fragmented deeper in the plasma jet and not in its fringes.

Another criterion has to be taken into account when considering suspensions: what modification of fragmentation will occur when the weight percentage of solid particles within the suspension will be increased? The answer lies in the Ohnesorge number, Z [Eq. (4.69)]. With the increase of the particle loading within the suspension, its viscosity is raised but not its surface tension, thus the Ohnesorge number increases. Correlatively, the critical value of the Weber number over which fragmentation occurs also increases and fragmentation is thus delayed. This is illustrated in Fig. 4.74 representing the penetration of mechanically injected pure ethanol and the corresponding suspension with 7 wt.% zirconia particles. The addition of solid particles and dispersant enforces the cohesion of the droplet. The fragmentation of the ethanol (left) starts before that of the suspension (right), the white dotted line corresponding to the nozzle diameter.

Droplet trajectories are determined using the momentum equations, in the axial and radial directions, as used when spraying micrometric particles [1]. Along the trajectory, when they penetrate into the plasma jet, their break-up can be calculated by simple expressions such as those from which Eq. (4.75) is derived. More sophisticated models such the Taylor Analogy Break-up model [232] can be used (see Basu et al. [231]). The new trajectories of the new droplets are again calculated through the momentum equations, taking into account their vaporization. In Eqs. (4.75) and (4.68), the surface tension σ of drops and droplets plays a key role. It diminishes with liquid heating:

$$\sigma = \sigma^0 - aT \tag{4.78}$$

and in principle, the drop or droplet heating along its trajectory should be calculated. However, taking into account the considerations presented in the next Sect. 4.5.4, vaporization is a very slow process compared to fragmentation, and droplet heating can be calculated on the basis of a lumped capacity model.

A complete model of the liquid–plasma interaction is still a challenge and would require as far as possible the independent study and validation of the various sub-processes that govern the droplet behavior in the flow and at impact. Sophisticated numerical models have also been developed for fragmentation and vaporization of drops [204–206, 233–236]. However the effect of vaporization on the plasma flow is generally neglected, which is far from the reality. The breakup models that have been used for plasma conditions are essentially those developed for the interaction of a cold flow with a liquid. The Taylor-analogy break-up (TAB) model [204, 206, 233, 234] is based on the analogy between a spring mass system and an oscillating and distorting droplet and the wave model that supposes that the break-up time and the resulting droplet size are related to the fastest growing Kelvin–Helmholtz instability and applies better for larger Weber numbers. However, in both models, the We and Oh numbers as well as the constants and parameters of the models have been established for conditions rather different of that prevailing in liquid plasma spraying and their extension to these conditions should be validated.

4.5.4 *In-Flight Heat Transfer to Droplets*

It is interesting to evaluate the vaporization time of drops and droplets. As already discussed in Sect. 4.3.3, the heat flux balance for heating and vaporizing a drop is given by:

$$4\pi r_s^2 \cdot h \cdot (T - T_s) = \left(\Delta H_v + c_{pl}\left(T_s - T_g\right)\right) \cdot \rho_l \cdot \frac{dV_s}{dt} \tag{4.79}$$

where $\frac{dV_s}{dt}$ is the volume variation of the drop $\left(\frac{dV_s}{dt} = 4\pi r_s^2 \frac{dr_s}{dt}\right)$ and c_{pl} the specific heat at constant pressure of the liquid (J/kg/K). Assuming that the vaporization time, t_s, is that necessary for the drop to shift from radius r_s to radius zero one finds:

$$t_s = \frac{\left(\Delta H_v + c_{ps}\left(T_s - T_g\right)\right) \cdot \rho_s \cdot 2 \cdot r_s^2}{(T - T_s)\kappa \cdot \mathrm{Nu}} \tag{4.80}$$

As shown in Fig. 4.75, the characteristic times to fragment and vaporize droplets of different sizes along the radius of a d.c. plasma jet (Ar–H_2, 45–15 slm, 500 A, anode nozzle i.d. 7 mm) differ by at least 3–4 orders of magnitude for diameters over 1 μm. The vaporization time of a 300 μm ethanol drop is 500 μs in a 10,000 K plasma against 1 μs for its fragmentation. For a fragmented droplet of 1.5 μm

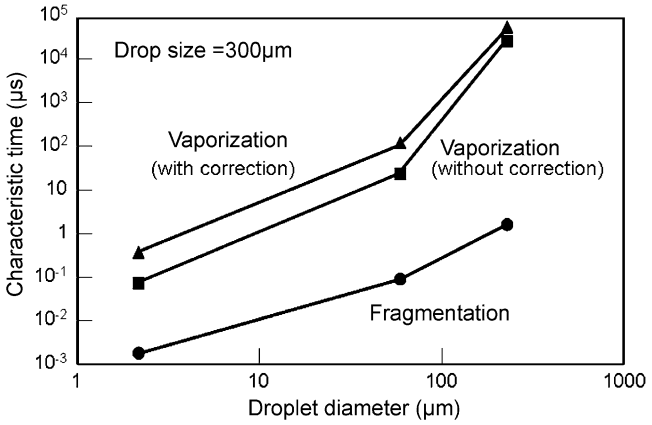


Fig. 4.75 Evolution along the Ar–H_2 plasma jet (45–15slm, 500 A, anode-nozzle i.d. 7 mm) of the vaporization and fragmentation times for different droplet radii. Reprinted with kind permission from Springer Science Business Media [191], copyright © ASM International

diameter the evaporation time is only 0.05 μs. The Knudsen effect, the temperature gradient and the evaporation effects should correct these times. The net result of these corrections is the lengthening of the time, t_s, by a factor of up to 60, depending on particle sizes.

4.5.5 Cooling of the Plasma Flow by the Liquid

When injecting water drops 300 μm diameter into a d.c. plasma jet (Ar 45 slm–H_2 15 slm, $P_{eff} = 25$ kW, nozzle i.d. 7 mm) the plasma jet is cut into two parts almost instantly [180]. This is illustrated in Fig. 4.76 showing two orthogonal pictures of the jet: one taken orthogonally to the injection, while the other is parallel to it.

This local cooling is caused by drop vaporization, dissociation of water and ionization of H and O (only about 3 % of the jet energy is consumed). But 15 mm downstream from the injection point, the plasma jet has recovered its axial symmetry and is a uniform mixture of Ar, H and O in its hottest zone ($T > 8{,}000$ K), as shown in Fig. 4.77 [180].

No more liquid is present after 15 mm, and the solid particles contained initially within a droplet are then accelerated and heated by the plasma.

It is important to note that as the plasma jet is cooled by the liquid injection and with the very low inertia of particles below 1 μm, the spray distances are very short compared to conventional spraying. With stand-off distances as short as 30–50 mm instead of 100–120 mm in conventional spraying the transient heat fluxes of the plasma jet on the substrate will be multiplied by about one order of magnitude: in the 20–40 MW/m^2 instead of 2 MW/m^2!

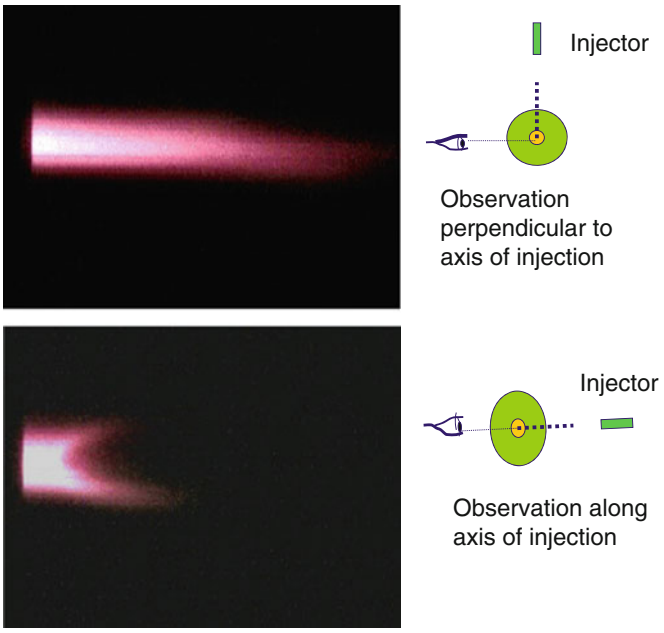


Fig. 4.76 Two orthogonal pictures of the plasma jet (Ar 45 slm–H_2 15 slm, $P_{eff} = 25$ kW, nozzle i.d. 7 mm): one taken orthogonally to the injection, while the other is parallel to it. Reprinted with kind permission from ASM International [180]

4.5.6 Influence of Arc Root Fluctuations

The voltage fluctuations (in the restrike mode with a PTF4 torch and an Ar–H_2 mixture) correspond to a voltage varying between 40 and 80 V for the same arc current of 503 A. The torch velocity follows the corresponding enthalpy variations while the temperature is almost constant (<1,000 K difference when the enthalpy is doubled) due to the "inertia wheel" effect of ionization. Thus, the momentum density of the plasma varies drastically, especially in the jet fringes. Marchand et al. [237] have calculated the transient momentum density values. They have used a three-dimensional (3D) and time-dependent model of the plasma jet issuing into air in conjunction with a Large Eddy Simulation (LES) turbulence model to examine the influence of the arc voltage fluctuation amplitude and frequency on the time evolution of the plasma jet flow fields and droplet injection. Typical results of the values of the momentum density of the plasma, ρv^2, in a plane orthogonal to the jet axis and located at 8 mm from the nozzle exit, are presented in Fig. 4.78. These results were obtained for an Ar–H_2 plasma jet at 600 A. With T as the period of the restrike mode, Fig. 4.78 represents five images of ρv^2 calculated at times differing by $T/5$; in this figure the isotherm 8,000 K is represented as a white line. This figure shows that the momentum density varies drastically with time for the same position as well as the position of the hot zone of the plasma (8,000 K isotherm).

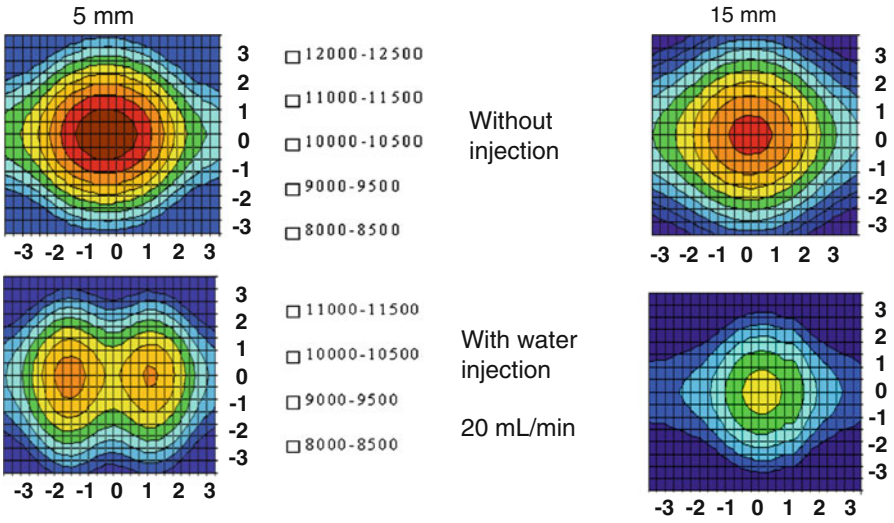


Fig. 4.77 Spectroscopic measurements at 5 and 15 mm downstream of the nozzle exit of the plasma jet presented in Fig. 4.74 without and with liquid injection. Reprinted with kind permission from ASM International [180]

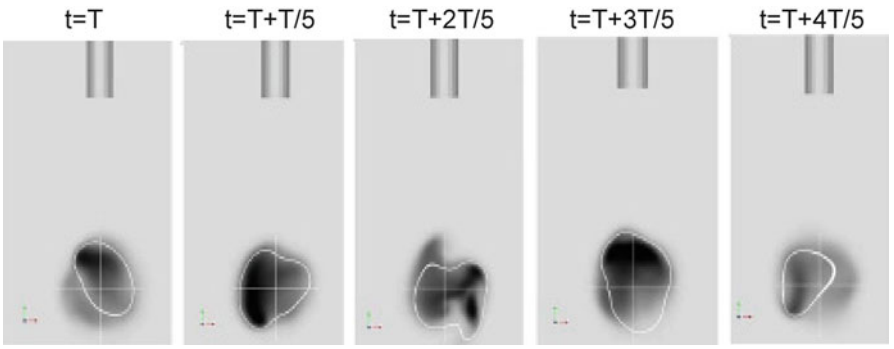


Fig. 4.78 Calculated momentum density (Pa) of a d.c. plasma jet in an orthogonal plane to the jet axis at 8 mm from the nozzle. Ar–H_2 (45–15 slm), $I = 600$ A. Reprinted with kind permission from ASM International [237]

As already emphasized, this variation is due to the variation in length of the electric arc, and the location of the anodic arc root. Such calculations well underline the very inhomogeneous dynamic treatment that droplets could undergo. To get more information from images as those presented in Fig. 4.74, up to 10 images have been superposed and their treatment has allowed determining their envelope and thus measuring the liquid droplet dispersion angle θ and mean deviation α, as shown in Fig. 4.73 for an Ar–He stable plasma jet. Of course, the results obtained depend on the torch voltage level at which images are taken, as illustrated in Fig. 4.79 for zirconia suspension in ethanol. It can be readily seen that the deviation

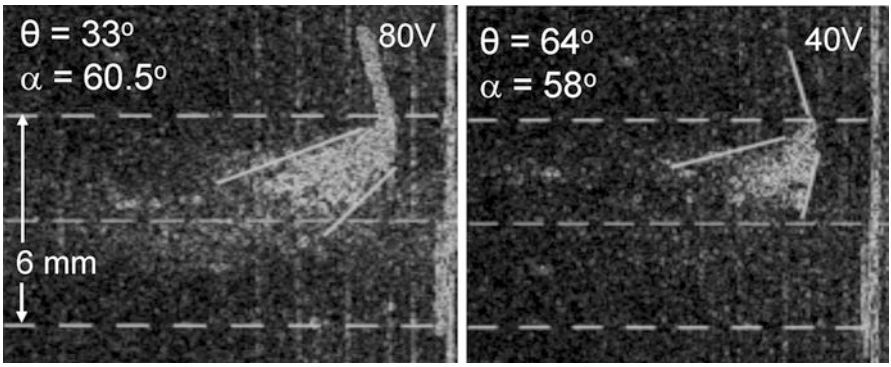


Fig. 4.79 Dependence of the dispersion angle θ and deviation angle α of the liquid droplets cloud ($Ar–H_2$ dc plasma jet) on arc voltage for two transient voltages corresponding to their minimum (40 V) and maximum (80 V) values. Reprinted with kind permission from Springer Science Business Media [238], copyright © ASM International

angle is not very sensitive to the voltage fluctuation (58° at 40 V against 60.5° at 80 V). However, this is not the case of the dispersion angle which varies from 33° at 80 V against 64° at 40 V.

In contrast, with stable plasma, such as that presented in Fig. 4.73 ($\Delta V/V = 0.25$ instead of 1 for the $Ar–H_2$ plasma) the liquid penetration is better, and especially the dispersion angle is much lower (more uniform treatment of droplets) and less fragmentation occurs in the jet fringes.

4.5.7 Case of No Fragmentation

Fragmentation of drops by the plasma jet plays a key role in their further heat treatment. This is due first to the vaporization time of the solvent, which varies as the square of the drop diameter and second to droplet trajectories in the plasma jet core or in its fringes. Based on We $\approx$ 14, fragmentation will never occur in r.f. torches according to the very low plasma velocity ($v < 100$ m/s) for drops injected with sizes between 30 and 280 μm. Thus, all phenomena will be governed by particle heating and solvent vaporization, which are long processes requiring times between a few tens and few hundreds of microseconds depending on droplet size distribution.

For example Bouyer et al. [239, 240] have used suspension plasma spraying to prepare dense hydroxyapatite (HA) particles starting from a water suspension with tiny needles of HA (less than 1 μm). As pointed out, once drops have been formed in the atomizer, the plasma flow is unable to fragment them (We < 12) and thus, progressively the water solvent is evaporated. Then the HA grains, contained within drops, are either consolidated or flash sintered and then melted, resulting either in spheroidized particles when collected far downstream, or in coatings when the substrate is disposed at the conventional stand-off distance.

4.6 Summary and Conclusions

Three-dimensional simulations with full coupling between a single particle and gas flow, employing a Lagrangian particle-tracking frame coupled with a steady-state gas flow, have been developed to examine particle motion and heat transfer. These models, when necessary, are compressible and consider the effect on particles of compression and expansion waves. Since the nineties models have shown the importance of the different corrections adopted to the process for flames, HVOF or HVAF, D-Gun, and plasma spraying processes: high temperature gradients, particle evaporation or vaporization, rarefaction effect (Knudsen effect), shock waves, supersonic flow effect, ... Such models have shown the drastic influence of the particle injection (position, velocity vector) on its velocity and temperature at impact. Different effects such as loading effect, particle morphology and shape have been considered. However the way the particle velocity vector distribution at the injector exit is calculated is still in its infancy in spite of its drastic influence on the particle treatment within the hot or cold gas flow. The first studies of the interaction between hot gas flows and a liquid (solution or suspension spraying) have also been presented, this technique being very promising for the deposition of finely or nano structured coatings with thicknesses between a few micrometers and hundreds of them.

Nomenclature

Units are indicated in parentheses, when no unit is indicated the parameter is dimensionless

Latin Alphabet

a	Accommodation coefficient
a_i	Sound velocity (m/s)
A	Particle projected surface area perpendicular to the flow ($A = \pi d_p^2/4$) (m^2)
Bi	Biot number $\left(\frac{\kappa}{\kappa_p}\right)$
c	The molar density of the bulk gas (mol/m^3)
C_D	Drag coefficient $(F_D/A)/(0.5\rho v^2)$
c_i	Mass fraction of metal vapor at the location i
c_{pi}	Specific heat at constant pressure in the state i (J/kg.K)
c_{vi}	Specific heat at constant volume in the state i (J/kg.K)
d_d	Drop diameter (m)
d_l	Drop or liquid jet diameter (m)
d_p	Particle diameter (m)
D_{vg}	Diffusion coefficient of metal vapor through the surrounding gas (m^2/s)

F_B Basset history term (N)
F_c Coriolis force (N)
F_b Body force per unit particle mass (N)
F_d Force related to the pressure jump in the detonation wave $F_d = \frac{\pi d_p^2}{4}\Delta p$ (N)
F_D Drag force exerted by the fluid on the particle (N)
F_g Gravity force (N)
F_i Inertia force ($m_p.\gamma_p$) (N)
F_p Pressure gradient force (N)
F_S Surface tension force (N)
F_T Thermophoresis force (N)
g Gravity acceleration (9.81 m/s^2)
h Heat transfer coefficient (W/m^2·K)
h_g Enthalpy (J/m^3)
h'_i Specific enthalpy of the plasma calculated at i (J/kg)
I Arc current (A)
$I(T)$ Heat conduction potential $\left(\int_{T_{300}}^{T} \kappa(s)\cdot ds\right)$ (W/m)
Kn Knudsen number (λ/dp)
k_d Mass transfer coefficient (m/s)
L Mixing length in turbulent model (m)
m_{cg}^o Carrier gas mass flow rate (kg/s)
m_p Particle mass (kg)
M Molecular weight (kg/mol)
Ma Mach number (v_g/a_g)
N_{max} Maximum molar flux of vaporization from a droplet (m^2/s)
Nu Nusselt number (hd/κ)
N_v Molar flux of vapor (mol/m^2·s)
p Total pressure (Pa)
p_i Partial pressure of species i (Pa)
p_o Saturation vapor pressure of a liquid (Pa)
P Torch power (kW)
P_l Splat parameter (m)
P_{eff} Torch effective power (kW)
Pr Prandtl number ($\mu\cdot c_p/\kappa$)
q Heat flux (W/m^2)
Q Heat transferred to a particle in 1 s (W)
r Plasma or particle radius (m)
r_d Liquid droplet radius (m)
r_s Initial liquid drop radius (m)
R Plasma torch internal or particle radius (m)
R' Universal ideal gas constant ($R' = 8.32$ J/K · mol)
Re Reynolds' number ($\rho\cdot U_R.d_p/\mu$)
R_{inj} Internal radius of injection tube (m)
S_p Surface area of the particle ($\pi d_p^2/4$) or of the splat ($\pi\cdot D_p^2/4$) (m^2)

S Cross section of injection tube (m^2)
Sc Schmidt number ($\nu/D_{v,g}$)
Sh Sherwood number ($k_d.d_p/D_{v,g}$)
St Stokes number $St = \rho_p d_p^2 v_p/(\mu_g l_{BL})$
Ste Stephan number; $Ste = c_{pi}(T_m - T_s)/\Delta H_m$
t_d Drop fragmentation time (s)
t_r Time of flight of particles (s)
t_s Vaporization time (s)
T_a Ambient temperature (K)
T_f Mean film temperature ($(T_s + T_\infty)/2$) (K)
T_s Particle surface temperature (K)
T_∞ Temperature of the flow out of the boundary layer around the particle (K)
U Mean arc voltage (V)
$U(t)$ Transient arc voltage (V)
u Gas velocity component in the axial direction (m/s)
u_p Particle velocity component in the axial direction (m/s)
u_R Relative velocity between the particle and its surrounding (m/s)
u_r Relative velocity gas–liquid (m/s)
v Gas velocity component in the radial direction (m/s)
v_p Particle velocity component in the radial direction (m/s)
V Volume (m^3)
V_p Particle volume (m^3)
V_s Liquid drop volume (m^3)
w_s Work resulting from the drag force (J)
We Weber number ($We = \frac{\rho_g \times u_r^2 \times d_l}{\sigma_l}$)
Z Ohnesorge number $\left(Z = \frac{\mu_l}{\sqrt{\rho_l \times d_l \times \sigma_l}}\right)$

Greek Alphabet

γ Isentropic coefficient (c_p/c_v)
δ Boundary layer thickness (m)
ΔE_s Variation of surface energy (J)
ΔH_m Latent heat of fusion (J/kg)
ΔH_v Latent heat of vaporization (J/kg)
ε Particle emissivity (integrated over all wave lengths)
$\phi(r)$ Function representing temperature, enthalpy, velocity
γ_p Particle acceleration (m/s^2)
η_{th} Torch thermal efficiency (%)
κ Thermal conductivity of the fluid (W/m K)
κ_p Thermal conductivity of the particle (W/m K)
$\overline{\kappa}$ Mean integrated thermal conductivity $\left(\frac{1}{T\infty - T_s}\int_{T_s}^{T\infty} \kappa(s) \cdot ds\right)$ (W/m K)

λ	Plasma mean free path (m)
μ_i	Fluid viscosity (Pa·s)
ν_{cg}	Carrier gas velocity (m/s)
ν_i	Kinematic viscosity (μ/ρ) (m^2/s)
ρ_g	Gas mass density (kg/m^3)
ρ_i	Fluid density or specific mass (kg/m^3)
σ	Droplet surface tension (N/m)
σ_s	Stephan–Boltzmann constant (5.670×10^{-8} $W/m^2\cdot K^4$)
ξ	Ratio of the cylindrical splat to droplet diameter ($\xi = D_p/d_p$)

Subscripts

i	Index that relates to temperature at which the property is evaluated, or to indicate a specific species
$i = s$	Property evaluated at surface temperature
$i = \infty$ or g	Property evaluated at plasma temperature
$i = g$	Gas
$i = p$	Particle
$i = l$	Liquid

References

1. Boulos MI, Fauchais P, Vardelle A, Pfender E (1993) Fundamentals of plasma particle momentum and heat transfer. In: Suryanarayanan R (ed) Plasma spraying theory and applications. World Scientific, Singapore
2. Pfender E (1999) Thermal plasma technology: where do we stand and where are we going? Plasma Chem Plasma Proc 19(1):1–31
3. Pfender E, Chang CH (1998) Plasma spray jets and plasma-particulate interaction: modeling and experiments. In: Coddet C (ed) Thermal spray: meeting the challenges of the 21st century, vol 1. ASM International, Materials Park, OH, pp 315–321
4. Fauchais P, Léger AC, Vardelle M, Vardelle (1997) Formation of plasma sprayed oxide coatings. In: Sohn HY, Evans JW, Apelian D (eds) Proceedings of the Julian Szekely Memorial Symposium on Materials Processing. T.M.S. pp 571–582
5. Boulos MI Plasma interaction with a dispersed medium. In: Heberlein J (ed) Ch 6.2. Continuing education course in conjunction with ITSC2004. University of Minnesota, MN
6. Pfender E (1985) Heat and momentum transfer to particles in thermal plasma flows. Pure Appl Chem 57:1179–1196
7. Pfender E, Lee YC (1985) Particle dynamics and particle heat and mass transfer in thermal plasmas. Part I. The motion of a single particle without thermal effects. Plasma Chem Plasma Proc 5(3):211–237
8. Lee YC, Chyou YP, Pfender E (1985) Particle dynamics and particle heat and mass transfer in thermal plasmas. Part II. Particle heat and mass transfer in thermal plasmas. Plasma Chem Plasma Proc 5(4):391–414

9. Lee YC, Chyou YP, Pfender E (1997) Particle dynamics and particle heat and mass transfer in thermal plasmas. Part III. Thermal plasma jet reactors and multiparticle injection. Plasma Chem Plasma Proc 7(1):1–27
10. Chen X (1988) Particle heating in a thermal plasma. Pure Appl Chem 60:651–662
11. Pfender E (1989) Particle behavior in thermal plasmas. Plasma Chem Plasma Proc 9 (Sup.1):167S–194S
12. Clift R, Grace JR, Weber JE (1978) Bubbles, drops and particles. Academic, New York, NY
13. White FM (1974) Viscous fluid flow. Mc Graw Hill, New York, NY
14. Sayegh NN, Gauvin WH (1979) Analysis of variable property heat transfer to a single sphere in high temperature surrounding. AIChE J 25:522–534
15. Boothroyd RG (1971) Flowing gas-solid suspension. Chapman and Hall, London
16. Ishii M (1975) Thermofluid dynamic theory of two phase flow. Eyrolles, Paris
17. Rudinger G (1980) Fundamentals of gas-solid particle flow. Elsevier, Amsterdam
18. Chang CH, Ramshaw JD (1994) Numerical simulation of non-equilibrium effects in an argon plasma jet. Phys Plasmas 1:3698–3708
19. Chyou YP, Pfender E (1989) Behavior of particulates in thermal plasma flows. Plasma Chem Plasma Proc 9(1):45–71
20. Chang CH (1992) Numerical simulation of alumina spraying in an argon-helium plasma jet. In: Berndt CC (ed) Thermal spray: international advances in coatings technology. ASM International, Materials Park, OH, pp 793–798
21. Vardelle M, Vardelle A, Fauchais P, Li K-I, Dussoubs B, Themelis NJ (2001) Controlling particle injection in plasma spraying. J Therm Spray Technol 10(2):267–284
22. Janisson S, Meillot E, Vardelle A, Coudert JF, Pateyron B, Fauchais P (1999) Plasma spraying using Ar-He-H_2 gas mixtures. J Therm Spray Technol 8(4):545–552
23. Planche MP, Bolot R, Landemarre O, Coddet C (1998) Comparison between experimental and numerical results obtained on in-flight particles characteristics. In: Coddet C (ed) Thermal spray: meeting the challenges of the 21st century, vol 2. ASM International, Materials Park, OH, pp 355–360
24. Bolot R, Morin V, Coddet C (2001) Correlation between simulations and plasma spray coatings properties. In: Berndt CC, Khor KA, Lugsheider E (eds) Thermal spray 2001: new surface for a new millenium. 883, 888
25. Dussoubs B, Vardelle A, Mariaux G, Themelis NJ, Fauchais P (2001) Modeling of plasma spraying of two powders. J Therm Spray Technol 10(1):105–110
26. Delluc G, Perrin L, Ageorges H, Fauchais P, Pateyron B (2004) Modelling of plasma jet and particle behavior in spraying conditions. In: Rom CD (ed) ITSC2004, in modeling and simulation V. DVS, Düsseldorf, Germany
27. Planche MP, Bolot R, Coddet C (2003) In-flight characteristics of plasma sprayed alumina particles: measurements, modeling, and comparison. J Therm Spray Technol 12(1):101–111
28. Zhang T, Gawne DT, Liu B (2000) Computer modelling of the influence of process parameters on the heating and acceleration of particles during plasma spraying. Surf Coat Technol 132:233–243
29. Devasenapathi A, Ang CB, Yu SCM, Ng HW (2001) Role of particle injection velocity on coating microstructure of plasma sprayed alumina - validation of process chart. Surf Coat Technol 139:44–54
30. Wilden J, Frank H, Bergmann J-P (2006) Process and microstructure simulation in thermal spraying. Surf Coat Technol 201:1962–1968
31. Kamnis S, Gu S, Zeoli N (2008) Mathematical modelling of Inconel 718 particles in HVOF thermal spraying. Surf Coat Technol 202:2715–2724
32. Li M, Christofides PD (2004) Feedback control of HVOF spray process accounting for powder size distribution. J Therm Spray Technol 13(1):108–120
33. Samareh B, Dolatabadi A (2007) A three-dimensional analysis of the cold spray process: the effects of substrate location and shape. J Therm Spray Technol 16(5–6):634–642

34. Katanoda H, Matsuoka T, Matsuo K (2007) Experimental study on shock wave structures in constant-area passage of cold spray nozzle. J Therm Sci 16(1):40–45
35. Nickel R, Bobzin K, Lugscheider E, Parkot D, Varava W, Olivier H, Luo X (2007) Numerical studies of the application of shock tube technology for cold gas dynamic spray process. J Therm Spray Technol 16(5–6):729–735
36. Hanson TC, Hackett CM, Settles GS (2002) Independent control of HVOF particle velocity and temperature. J Therm Spray Technol 11(1):75–85
37. Vardelle A, Fauchais P, Dussoubs B, Themelis NJ (1998) Heat generation and particle injection in a thermal plasma torch. Plasma Chem Plasma Proc 18(4):551–574
38. Moreau E, Chazelas C, Mariaux G, Vardelle A (2006) Modeling the restrike mode operation of a d.c. plasma spray torch. J Therm Spray Technol 15(4):524–530
39. Meillot E, Balmigere G (2008) Plasma spraying modeling: particle injection in a time-fluctuating plasma jet. Surf Coat Technol 202:4465–4469
40. Legros E (2003) 3D modeling of the spray process. Ph.D. Thesis, University of Limoges, France
41. Bandyopadhyay R, Nylén P (2003) A computational fluid dynamic analysisof gas and particle flow in flame spraying. J Therm Spray Technol 12(4):492–503
42. Gu S, McCartney DG, Eastwick CN, Simmons K (2004) Numerical modeling of in-flight characteristics of inconel 625 particles during high-velocity oxy-fuel thermal spraying. J Therm Spray Technol 13(2):200–211
43. Kadyrov E (1996) Gas-particle interaction in detonation spraying process. J Therm Spray Technol 5(2):185–195
44. Tillmann W, Vogli E, Nebel J (2007) Development of detonation flame sprayed cu-base coatings containing large ceramic particles. J Therm Spray Technol 16(5–6):751–758
45. Boulos MI (1978) Heating of powders in the fire ball of an induction plasma. IEEE Trans Plasma Sci 6(2):93–106
46. Boulos MI (1985) The inductively coupled R.F. (radio frequency) plasma. Pure Appl Chem 57(9):1321–1352
47. Boulos MI (1992) RF induction plasma spraying: state-of-the-art review. J Therm Spray Technol 1(1):33–40
48. Abukawa S, Takabate T, Tani K (2006) Effect of powder injection of deposit efficiency in plasma spraying. In: Marple B et al (eds) Proceedings of the 2006 international thermal spray conference. ASM International, Materials Park, OH, e-proc
49. Han T, Zhao Z, Gillispie BA, Smith JR (2005) Effects of spray conditions on coating formation by the kinetic spray process. J Therm Spray Technol 14(3):373–383
50. Balani K, Laha T, Agarwal A, Karthikeyan J, Munroe N (2005) Effect of carrier gases on microstructural and electrochemical behavior of cold-sprayed 1100 aluminum coating. Surf Coat Technol 195:272–279
51. Lewis JW, Gauvin WH (1973) Motion of particles entrained in a plasma jet. AIChE J 19 (6):982–990
52. Oberkampf WL, Talpallikar M (1994) Analysis of a high velocity oxygen-fuel (HVOF) thermal spray torch, part 1: numerical formulation. In: Berndt CC, Sampath S (eds) Thermal spray industrial applications. ASM International, Materials Park, OH, pp 381–386
53. Crowe CT (1967) Drag coefficient on particles in a rocket nozzle. J AIAA 5(5):1021–1022
54. Lopez AR, Hassan B, Oberkampf WL, Neiser RA, Roemer TJ (1998) Computational fluid dynamics, analysis of a wire-feed, high –velocity oxygen fuel (HVOF) thermal spray torch. J Therm Spray Technol 7(3):374–382
55. Kadyrov E, Kadyrov V (1995) Gas dynamical parameters of detonation powder spraying. J Therm Spray Technol 4(3):280–286
56. Henderson CB (1976) Drag coefficients of spheres in continuum and rarefied flows. AIAA J 14(6):707–708
57. Walsh MJ (1975) Drag coefficient equations for small particles in high speed flows. Am Inst Aeronaut Astronaut J 13(11):1526–1528

58. Sobolev VV, Guilemany JM, Nutting J (2004) High-velocity oxy-fuel spraying. Maney for the Institute of Materials, Minerals and Mining, London, p 397
59. Boulos M, Fauchais P, Pfender E (1994) Thermal plasmas fundamental and applications. Plenum Press, London, p 452
60. Lee YC, Hsu C, Pfender E (1981) Modelling of particle injection into a D.C plasma jet 5th international symposium on plasma chemistry. Edinburgh, Scotland, 2, pp 795-801
61. Chen X, Pfender E (1983) Effect of the Knudsen number on heat transfer to a particle immersed into a thermal plasma. Plasma Chem Plasma Proc 3:97–113
62. Chen X, Pfender E (1983) Behavior of small particles in a thermal plasma flow. Plasma Chem Plasma Proc 3:351–366
63. Xi C, Ping H (1986) Heat transfer from a rarefied plasma flow to a metallic or nonmetallic particle. Plasma Chem Plasma Proc 6(4):313–333
64. Fazilleau J (2003) Contribution to the understanding of the phenomena implied in the achievement of finely structured oxide coatings by suspension plasma spraying. PhD. Thesis, In French, University of Limoges France
65. Vardelle A, Themelis NJ, Dussoubs B, Vardelle M, Fauchais P (1997) Transport phenomena in thermal plasmas. J High Temp Mater Proc 1(3):295–317
66. Fauchais P, Coudert JF, Vardelle M (1989) Diagnostics in thermal plasma processing. In: Ociello O, Flamm DL (eds) Plasma diagnostics, vol 1. Academic, New York, p 349
67. Ganser GH (1993) A rational approach to drag prediction of spherical and nonspherical particles. Powder Technol 77:43–52
68. Fukanuma H, Ohno N, Sun B, Huang R (2006) The influence of particle morphology on in-flight particle velocity in cold spray. In: Proceedings of the 2006 International Conference of Thermal Spray. ASM International, Materials Park, OH, e-proc
69. Xu D-Y, X-C W, Chen X (2002) Motion and heating of non-spherical particles in a plasma jet. Surf Coat Technol 171(1–3):149–156
70. Fukanuma H, Ohno N, Sun B, Huang R (2006) In-flight particle velocity measurements with DPV-2000 in cold spray. Surf Coat Technol 201:1935–1941
71. Xi C, Chen X (1989) Drag on a metallic or non-metallic particle exposed to a rarefied plasma flow. Plasma Chem Plasma Proc 9(3):387–408
72. Uglov AA, Gnedovets AG (1991) Effect of particle charging on momentum and heat transfer from rarefied plasma flow. Plasma Chem Plasma Proc 11(2):251–267
73. Gnedovets AG, Uglov AA (1992) Heat transfer to non-spherical particles in a rarefied plasma flow. Plasma Chem Plasma Proc 12(4):383–402
74. Gnedovets AG, Uglov AA (1992) Enhancement of heat transfer from a rarefied plasma flow to thermo-emitting particle. Plasma Chem Plasma Proc 12(4):371–382
75. Xi C, Chen J, Wang Y (1995) Unsteady heating of metallic particles in a rarefied plasma. Plasma Chem Plasma Proc 15(2):199–219
76. Soo SL (1967) Fluid dynamics of multiphase systems. Blaisdell, New York, NY
77. Fauchais P, Etchart-Salas R, Rat V, Coudert JF, Caron N, Wittmann K (2008) Parameters controlling liquid plasma spraying: solutions, sols or suspensions. J Therm Spray Technol 17 (1):31–59
78. Delbos C, Fazilleau J, Rat V, Coudert JF, Fauchais P, Pateyron B (2006) Phenomena involved in suspension plasma spraying, part 2: zirconia particle treatment and coating formation. Plasma Chem Plasma Proc 26(4):393–414
79. Chen XI, Chyou YP, Lee YC, Pfender E (1985) Heat transfer to a particle under plasma conditions with vapor contamination from the particle. Plasma Chem Plasma Proc 5 (2):119–141
80. Seyed AA, Denoirjean A, Denoirjean P, Labbe JC, Fauchais P (2004) Investigation of phenomena influencing properties of plasma sprayed ceramic-metal composite deposits. High Temp Mater Proc 8(2):253–276
81. Seyed A (2004) Co-spraying in air of alumina and stainless steel particles by DC plasma jet. Ph.D. Thesis, University of Limoges, F. and Ghalam Ishaq Khan Institute, Islamabad, Pa, Feb

82. Boulos MI (2003) Spheroïdization and densification of powders" Continuing education course on thermal plasmas, held in conjunction with 16th International Symposium on Plasma Chemistry, Fauchais P (ed) University of Limoges
83. Yang Y-M, Liao H, Coddet C (2002) Simulation and application of a HVOF process for MCrAlY thermal spraying. J Therm Spray Technol 11(1):36–43
84. Bourdin E, Fauchais P, Boulos MI (1983) Transient heat conduction under plasma conditions. Int J Heat Mass Transfer 26:567–582
85. Fizdon JK (1979) Melting of powder grains in a plasma flame. Int J Heat Mass Transfer 22:749–761
86. Chen XI, Pfender E (1982) Unsteady heating and radiation effects of small particles in a thermal plasma. Plasma Chem Plasma Proc 2:293–316
87. Vardelle A (1988) Numerical study of heat, momentum and mass transfers between an arc plasma at atmospheric pressure and solid particles, Thesis of Doctorate, University of Limoges, France
88. Gavrilenko TP, Nikolaev YA (2007) Calculation of detonation gas spraying. Combust Explos Shock Waves 43(6):724–731
89. Bouneder M, El Ganaoui M, Pateyron B, Fauchais P (2003) Thermal modeling of composite iron/alumina particles sprayed under plasma conditions Part I: Pure conduction. High Temp Mater Proc 7(4):547–555
90. Bouneder M (2006) Modelling of heat and mass transfer within composite metal/ceramic particles in DC plasma spraying. PhD thesis University of Limoges France
91. Knight CJ (1979) Theoretical modeling of rapid surface vaporization with back pressure. AIAA J 17(5):519–523
92. Ben-Ettouil F, Mazhorova O, Pateyron B, Ageorges H, El Ganaoui M, Fauchais P (2007) Fast modelling with "back pressure" model of phase changes along the trajectory of a single particle within a DC plasma jet. J Therm Spray Technol 16(5–6):744–750
93. Ivosevic M, Cairncross RA, Knight R (2006) 3D predictions of thermally sprayed polymer splats: modeling particle acceleration, heating and deformation on impact with a flat substrate. Int J Heat Mass Transfer 49:3285–3297
94. Hurevich V, Smurnov I, Pawlowski L (2002) Theoretical study of the powder behavior of porous particles in a flame during plasma spraying. Surf Coat Technol 151–152:370–376
95. Vardelle M, Vardelle A, Denoirjean A, Fauchais P (1990) Heat treatment of zirconia powders with different morphologies under thermal spray conditions. In: Apelian D, Szekely J (eds) MRS Spring Meeting Proceedings, MRS 190:175–183
96. Diez P, Smith RW (1993) The influence of powder agglomeration methods on plasma sprayed yttria coatings. J Therm Spray Technol 2(2):165–172
97. Chang P, Khor KA (1996) Influence of powder characteristics on plasma sprayed hydroxyapatite coatings. J Therm Spray Technol 5(3):310–316
98. Ben-Ettouil F, Mazhorova O, Pateyron B, Ageorges H, El-Ganaoui M, Fauchais P (2008) Predicting dynamic and thermal histories of agglomerated particles injected within a d.c. Plasma Jet Surf Coat Technol 202:4491–4495
99. Xi C, Pfender E (1982) Heat transfer to a single particle exposed to a thermal plasma. Plasma Chem Plasma Proc 2(2):185–212
100. Yoshida T, Akashi K (1977) Particle heating in a radio-frequency plasma torch. J Appl Phys 48(6):2252–2264
101. Ranz WE, Marshall WR (1952) Evaporation from drops. Chem Eng Prog 48(3):141–146
102. Ranz WE, Marshall WR (1952) Evaporation from drops. Part II. Chem Eng Prog 48 (4):173–180
103. Borgianni C, Capitelli M, Cramarossa F, Triolo L, Molinari L (1969) The behaviour of metal oxides injected into an argon induction plasma. Combust Flame 13:181–194
104. Humbert P (1991) Development of pilot set-up for silicon purification by induction thermal plasma and modelling of mass and heat transfers plasma-particles, Ph.D. Thesis, University of Paris VI, ENSCP, Rue P, Curie M

105. Essoltani A, Proulx P, Boulos MI, Gleizes A (1990) Radiation and self-absorption in argon - iron plasmas at atmospheric pressure, J. Anal Atomic Spectr 5:543–547
106. Essoltani A, Proulx P, Boulos MI, Gleizes A (1994) Effect of the presence of iron vapors on the volumetric emission of Ar/Fe and Ar/Fe/H_2 plasmas. Plasma Chem Plasma Proc 14 (3):301–315
107. Cram L (1985) Statistical evaluation of radiative power losses from thermal plasmas due to spectral lines. J Phys D 18:401–411
108. Essoltani E, Proulx P, Boulos MI, Gleizes A (1994) Volumetric emission of argon plasmas in the presence of vapors of Fe, Si and Al. Plasma Chem Plasma Proc 14:437–450
109. Essoltani A, Proulx P, Boulos MI, Gleizes A (1991) Radiative effects on plasma-particle heat transfer in the presence of metallic vapors, 10th International Symposium on Plasma Chemistry. Ehlemann U & et al (eds). University of BOCHUM, Germany, 1
110. Vardelle M, Vardelle A, Li K-I, Fauchais P, Themelis NJ (1996) Coating generation: vaporization of particles in plasma spraying and splat formation. Pure Appl Chem 68 (5):1093–1099
111. Robertson DGC, Jenkins AE (1970). In: Belton GR, Workel WL (eds) Heterogeneous kinetics at elevated temperatures. Plenum Press, New York, NY pp 369–385
112. Li K-I, Vardelle M, Vardelle A, Fauchais P, Trassy C (1995) Comparisons between single and double flow injectors in the plasma spraying process. In: Berndt CC (ed) Thermal spray: practical solutions for engineering problems. ASM International, Materials Park, OH, pp 45–50
113. Gross KA, Fauchais P, Vardelle M, Tikkanen J, Keskinen J (1997) Vaporization and ultrafine particle generation during the plasma spraying process. In: Berndt CC (ed) Thermal spray: a united forum for scientific and technological advances. ASM International, Materials Park, OH, pp 543–548
114. Vardelle A, Vardelle M, Zhang H, Themelis NJ, Gross K (2002) Controlling particle injection in plasma spraying. J Therm Spray Technol 11(2):244–284
115. Etemadi K (1991) Formation of aluminum nitrides in thermal plasmas. Plasma Chem Plasma Proc 11(1):41–56
116. Volenik K, Leitner J, Hanousek F, Dubsky J, Kolman B (1997) Oxides in plasma-sprayed chromium steel. J Therm Spray Technol 6(3):327–334
117. Asaki Z, Fakunaka Y, Nagasi T, Kondo Y (1974) Thermal decomposition of limestone in a fluidized bed. Metallurg Transact B 5:381–390
118. Arnauld PH, Cavadias S, Amouroux J (1985) The interaction of a fluidized bed with a thermal plasma. Application to limestone decomposition. In: Timmermans X (ed) Proceedings of international symposium on plasma chemistry, vol 1. University of Technology of Eindhoven, Netherlands, pp 195–200
119. Amouroux J, Gicquel A, Cavadias S, Morvan D, Arefi F (1985) Progress in the applications of plasma surface modifications and correlations with the chemical properties of the plasma phase. Pure Appl Chem 57(9):1207–1222
120. Vardelle A, Fauchais P (1997) Vaporization and ultra-fine particle generation during the plasma spraying process. In: Berndt CC (ed) Thermal spray: a united forum for scientific and technological advances. ASM International, Materials Park, OH, pp 543–548
121. Espié G, Fauchais P, Labbe JC, Vardelle A, Hannoyer B (2001) Oxidation of iron particles during APS. In: Berndt CC, Khor KA, Lugscheider E (eds) Thermal spray 2001: New surface for a new millenium. ASM International, Materials Park, OH, pp 821–828
122. Volenik K, Chraska P, Dubsky J, Had J, Leitner J, Schneewein O (2003) Oxidation of Ni-based alloys sprayed by a water-stabilized plasma gun (WSP). In: Moreau C, Marple B (eds) Thermal spray 2003: advancing the science and applying the technology. ASM International, Materials Park, OH, pp 1033–1041
123. Espie G, Denoirjean A, Fauchais P, Labbe JC, Dudsky J, Scheeweiss O, Volenik K (2005) In flight oxidation of iron particles sprayed using gas and water stabilized plasma torches. Surf Coat Technol 195:17–28

124. Syed AA, Denoirjean A, Denoirjean P, Labbe JC, Fauchais P (2005) In-flight oxidation of stainless steel in plasma spraying. J Therm Spray Technol 14(1):177–124
125. Smith RW, Matasin ZZ (1992) Reactive plasma spraying of wear-resistant coatings. J Therm Spray Technol 1(1):57–63
126. Jiang XL, Gitzhoffer F, Boulos MI, Tiwari R (1994) Induction plasma reactive deposition of tungsten and titanium carbides. In: Berndt CC, Sampath S (eds) Thermal spray: industrial applications. ASM International, Materials Park, OH, pp 451–456
127. Eckardt T, Malleaer W, Stove D (1994) Reactive plasma spraying of silicon in controlled nitrogen atmosphere. In: Berndt CC, Sampath S (eds) Thermal spray: industrial applications. ASM International, Materials Park, OH, pp 515–520
128. Lugscheider E, Remer P, Zhao L (1996) Reactive plasma spraying of wear resistant coatings of Ti composites. In: Berndt CC (ed) Thermal spray: practical solutions for engineering problems. ASM International, Materials Park, OH, pp 927–932
129. Fauchais P, Vardelle A, Denoirjean A (1997) Reactive thermal plasmas: ultrafine particle synthesis and coating deposition. Surf Coat Technol 979:66–78
130. Dai S, Delplanque J-P, Rangel RH, Lavernia EJ (1998) Modeling of reactive spray atomization and deposition. In: Coddet C (ed) Thermal spray: meeting the challenges of the 21st century, vol 1. ASM International, Materials Park, OH, pp 341–346
131. Fan X, Ishigaki T (1998) Fabrication of composite SiC-MoSi2 powders through plasma reaction process. In: Coddet C (ed) Thermal spray: meeting the challenges of the 21st century, vol 2. ASM International, Materials Park, OH, pp 1161–1166
132. Denoirjean A, Lefort P, Fauchais P (2003) Nitridition process and mechanism of Ti-6Al-4V particles by plasma spraying. Phys Chem Chem Phys 5:5133–5138
133. Dallaire S (1992) Thermal spraying of reactive materials to form wear-resistant composite coatings. J Therm Spray Technol 1(1):41–47
134. Borisov Y, Borisova A (1993) Application of self-propagating high-temperature synthesis in thermal spraying technology. In: Bernicki TF (ed) Thermal spray: research, design and applications. ASM International, Materials Park, OH, pp 139–144
135. Shaw KG, McCoy KP, Trogolo JA (1994) Fabrication of composite spray powders using reaction systems. In: Berndt CC, Sampath S (eds) Thermal spray: industrial applications. ASM International, Materials Park, OH, pp 509–514
136. Deevi SC, Sikka VK, Swindeman CJ, Seals RD (1997) Reactive spraying of nickel-aluminide coatings. J Therm Spray Technol 6(3):335–344
137. Haller B, Bonnet JP, Fauchais P, Grimaud A, Labbe JC (2004) TiC based coatings prepared by combining SHS and plasma spraying. In: Rom CD (ed) ITSC2004 innovative equipment and process technology V. DVS, Düsseldorf, Germany
138. Bach FW, Babiak Z, Duda T, Rothardt T, Tegeder G (2001) Impact of self propagating high temperature synthesis of spraying materials on coatings based on aluminum and metal-oxides. In: Berndt CC, Khor KA, Lugsheider EF (eds) Thermal spray 2001: new surfaces for a new millenium. ASM International, Materials Park OH, pp 497–502
139. Haller B (2006) Study of a process combining plasma spraying and SHS: application to Ti-graphite mixtures, PhD Thesis (in French), University of Limoges, France
140. Dallaire S (1982) Influence of temperature on the bonding mechanism of plasma-sprayed coatings. Thin Solid Films 95:237–241
141. Borisov YuS, Borisova AL, Shvedova LK (1986) Transition metal-non metallic refractory compound composite powders for thermal spraying. In: Advances in thermal spraying. Pergamon Press, Canada, pp 323–329
142. Legoux JG, Dallaire S (1993) Copper-TiB_2 coatings by plasma spraying reactive micropellets. In: Berndt CC (ed) Proceedings of the 1993 thermal spray conference. ASM International, Materials Park OH, pp 429–432
143. Cliche G, Dallaire S (1991) Synthesis and deposition of TiC-Fe coatings by plasma spraying. Surf Coat Technol 46:199–206

144. Dallaire S, Cliche G (1992) The influence of composition and process parameters on the microstructure of TiC-Fe multiphase and multilayer coatings. Surf Coat Technol 50:233–239
145. Dallaire S, Champagne B (1984) Plasma spray synthesis of TiB_2-Fe coatings. Thin Solid Films 118:477–483
146. Neiser RA, Smith MF, Dykhuisen RC (1998) Oxidation in wire HVOF-sprayed steel. J Therm Spray Technol 7(4):537–545
147. Espié G, Fauchais P, Hannoyer B, Labbe JC, Vardelle A (1999) Effect of metal particles oxidation during the APS on the wettability. In: Fauchais P, Van der Mullen J, Heberlein J (eds) Heat and mass transfer under plasma condition, vol 891. Annals of NY Academy of Sciences, New York, NY, pp 143–151
148. FIDAP code distributed by Fluent Inc., Lebanon, NH, USA
149. Ponticaud C, Grimaud A, Denoirjean A, Lefort P, Fauchais P (2001) Titanium powder nitridation by reactive plasma spraying. In: Fauchais P, Amouroux J, Elchinger MF (eds) Progress in plasma processing of materials. Begell House, New York, NY, pp 527–536
150. Renouard-Vallet G (2003) Plasma spraying of dense YSZ electrolyte for SOFCs, PhD Thesis, University of Limoges, France and University of Sherbrooke, CN, (in French)
151. Padet JP (1991) Flowing fluids, methods and models. Masson, Paris, in French
152. Ben Ettouil F (2008) Fast modelling of powder treatment in d.c. plasma spraying, Ph.D Thesis, University of Limoges, France
153. Cheng D, Xu Q, Trapaga G, Lavernia EJ (2001) A numerical study of high-velocity oxygen fuel thermal spraying process. Part I: gas phase dynamics. Metallurg Mater Transact A 32A:1609–1620
154. Swank WP, Chang CH, Fincke JR, Haggard DC (1996) Measured and simulated particle flow field parameters in a high power plasma spray. In: Berndt CC (ed) Thermal spray: practical solution for engineering problems. ASM International, Materials Park, OH, pp 541–547
155. Crowe CT, Stock DE (1976) A computer solution for two-dimensional, fluid-particle flows. Int J Num Methods Eng 10:185–196
156. Dukowicz JK (1980) A particle-fluid numerical model for liquid sprays. J Comput Phys 35:229–253
157. Belashchenko VE, Chernyak YB (1993) Stochastic approach to the modeling and optimization of thermal spray coating formation. J Therm Spray Technol 2(2):159–164
158. Pfender E, Chang CH (1998) Plasma spray jets and plasma-particulate interaction: modeling and experiments. In: Coddet C (ed) Thermal spray: meeting the challenges of 21st century. ASM International, Materials Park, OH, pp 315–328
159. Mariaux G, Baudry C, Vardelle A (2001) 3-D modelling of gas flow and particles spray jet in plasma spraying. In: Berndt CC, Khor KA, Lugsheider E (eds) Thermal spray: new surfaces for a new millenium. ASM International, Materials Park, OH, pp 933–942
160. Mostaghimi J, Chandra S, Ghafouri-Azar R, Dolatabadi A (2003) Modeling thermal spray coating processes: a powerful tool in design and optimization. Surf Coat Technol 163–164:1–11
161. Gawne DT, Liu B, Bao Y, Zhang T (2005) Modelling of plasma–particle two-phase flow using statistical techniques. Surf Coat Technol 191(2–3):242–254
162. Mingheng L, Christofides PD (2004) Feedback control of HVOF thermal spray process accounting for powder size distribution. J Therm Spray Technol 13(1):108–120
163. Cheng D, Trapaga G, McKelliget JW, Lavernia EJ (2001) Mathematical modeling of high velocity oxygen fuel thermal spraying: an overview. Key Eng Mater 197:1–25
164. Bisson JF, Moreau C (2003) Effect of plasma fluctuations on in-flight particle parameters. J Therm Spray Technol 12(2):38–43
165. Proulx P, Mostaghimi J, Boulos MI (1983) Plasma-particle interaction effects in induction plasma modelling under dense loading conditions, 6th International Symposium on Plasma Chemistry, Montréal. Boulos MI (ed) University of Sherbrooke, CN, 1:59–68
166. Mostaghimi J, Proulx P, Boulos MI, Barnes RM (1985) Computer modeling of the emission patterns for a spectrochemical. ICP Spectro-Chem Acta 40B:153–166

167. Proulx P, Mostaghimi J, Boulos MI (1985) Computer modeling of the emission patterns for a spectrochemical ICP. Int J Heat Mass Transfer 28:1327–1336
168. Mostaghimi J, Pfender E (1984) Effects of metallic vapor on the properties of an argon arc plasma. Plasma Chem Plasma Proc 4(2):129–139
169. Proulx P, Mostaghimi J, Boulos MI (1987) Heating of powders in an r.f. inductively coupled plasma under dense loading conditions. Plasma Chem Plasma Proc 7(1):29–52
170. Vardelle A, Vardelle M, Fauchais P, Proulx P, Boulos MI (1992) Loading effect by oxide powders in DC plasma jets. In: Berndt CC (ed) Thermal spray: Int. advances in coatings technology. ASM International, Materials Park, OH, pp 543–548
171. Yang X, Eidelman S (1996) Numerical analysis of a high-velocity oxygen-fuel thermal spray system. J Therm Spray Technol 5(2):175–184
172. Taylor K, Jodoin B, Karov J (2006) Particle loading effect in cold spray. J Therm Spray Technol 15(2):273–279
173. Karthikeyan J, Berndt CC, Tikkanen J, Wang JY, King AH, Herman H (1997) Preparation of nanophase materials by thermal spray processing of liquid precursors. Nanostruct Mater 9:137–140
174. Bouyer E, Gitzhoffer F, Boulos MI (1997) Experimental study of suspension plasma spraying of hydroxyapatite. In: Fauchais P (ed) Progress in plasma processing of materials. Begell House, New York, NY, pp 735–750
175. Bouyer E, Müller M, Dard N, Gitzhofer F, Boulos MI (1997) Suspension plasma spraying for powder preparation. In: Fauchais P (ed) Progress in plasma processing of materials. Begell House, New York, NY, pp 751–759
176. Bouyer E, Branston DW, Lins G, Müller M, Verleger J, Von Bradke M (2001) Deposition of yttria-stabilized zirconia coatings using liquid precursors. In: Fauchais P (ed) Progress in plasma processing of materials. Begell House, New York, NY, pp 501–506
177. Yang G-J, Li C-J, Han F, Mav S-F (2003) TiO_2 photocatalyst by thermal spraying with liquid feedstock. In: Moreau C, Murple B (eds) Thermal spray 2003: Advancing the science and applying the technology. ASM International, Materials Park, OH, pp 675–680
178. Yang G, Zhang H, Biswas P (1996) Computer modeling of the emission patterns for a spectrochemical ICP. Nanostruct Mater 7(6):675–689
179. Blazdell P, Kuroda S (2000) Plasma spraying of submicron ceramic suspensions using a continuous ink jet printer. Surf Coat Technol 123(2–3):239–246
180. Wittmann K, Blein F, Coudert J-F, Fauchais P (2001) Control of the injection of an alumina suspension containing nanograins in a D.C. plasma. In: Berndt CC, Khor KA, Lugscheider E (eds) Thermal spray 2001: New surface for a new millennium. ASM International, Materials Park, OH, pp 375–382
181. Gitzhofer F, Bonneau M-E, Boulos MI (2001) Double-doped ceria electrolyte synthesized by solution plasma spraying with induction plasma technology. In: Berndt CC, Khor KA, Lugscheider E (eds) Thermal spray 2001: new surface for a new millennium. ASM International, Materials Park, OH, pp 61–68
182. Wittmann K, Fazilleau J, Coudert J-F, Fauchais P, Blein F (2002) A new process to deposit thin coatings by injecting nanoparticles suspensions in a d.c. plasma jet. In: Lugscheider E (ed) Proceedings of ITSC 2002. DVS, Düsseldorf, Germany, pp 519–522
183. Kuroda S, Blazdell P (2002) Suspension plasma spraying of ceramics by using an ink printer. In: Lugscheider E (ed) Proceedings of ITSC 2002. DVS, Düsseldorf, Germany, pp 539–543
184. Fazilleau J, Delbos C, Violier M, Coudert J-F, Fauchais P, Bianchi L, Wittmann-Ténèze K (2003) Influence of substrate temperature on formation of micrometric splats obtained by plasma spraying liquid suspension. In: Moreau C, Murple B (eds) Thermal spray 2003: advancing the science and applying the technology. ASM International, Materials Park, OH, pp 889–895
185. Delbos C, Fazilleau J, Coudert J-F, Fauchais P, Bianchi L, Wittmann-Ténèze K (2003) Plasma spray elaboration of fine nanostructured YSZ coatings by liquid suspension injection.

In: Moreau C, Murple B (eds) Thermal spray 2003: advancing the science and applying the technology. ASM International, Materials Park, OH, pp 661–667
186. Fazilleau J, Delbos C, Coudert J-F, Fauchais P, Denoirjean A, Bianchi L, Wittmann-Ténèze K (2003) Studies of micrometric splats obtained by suspension DC plasma spraying. In: R. d'Agostino (ed) 16th International Symposium on Plasma Chemistry (electronic version). University of Bari, Italy
187. Delbos C, Fazilleau J, Rat V, Coudert J-F, Fauchais P, Bianchi L Finely structured ceramic coatings elaborated by liquid suspension injection in a DC plasma jet. In: Proceedings of ITSC 2004. DVS Düsseldorf, Germany (electronic version).
188. Fauchais P, Rat V, Delbos C, Coudert JF, Chartier T, Bianchi L (2005) Understanding of suspension dc plasma spraying of finely structured coating for SOFC. IEEE Trans Plasma Sci 33:920–930
189. Fauchais P, Vardelle M, Coudert JF, Vardelle A, Delbos C, Fazilleau J (2005) Plasma spraying from thick to thin coatings and micro to nano structured coatings. Pure Appl Chem 77:475–485
190. Fazilleau J, Delbos C, Rat V, Coudert JF, Fauchais P, Pateyron B (2006) Phenomena involved in suspension plasma spraying, part 1: suspension injection and behavior. Plasma Chem Plasma Proc 26(4):371–391
191. Fauchais P, Montavon G (2010) Latest developments in suspension and liquid precursor thermal spraying. J Therm Spray Technol 19:226–239
192. Viswanathan V, Laha T, Balani K, Agarwal A, Seal S (2006) Challenges and advances in nanocomposite processing techniques. Mater Sci Eng R54:121–285
193. Gadow R, Kern F, Killinger A (2008) Manufacturing technologies for nanocomposite ceramic structural materials and coatings. Mater Sci Eng B148
194. Gell M, Jordan EH, Sohn YH, Goberman D, Shaw L, Xiao TD (2001) Development and implementation of plasma sprayed nanostructured ceramic coatings. Surf Coat Technol 146–147:48–54
195. Chen H, Lee SW, Choi CH, Hur BY, Zeng Y, Zheng XB, Ding CX (2004) Plasma sprayed nanostrucutred zirconia coatings deposited from different powders with nano-scale substructure. J Mater Sci 39:4701–4703
196. Gell M, Jordan EH, Teicholz M, Cetegen BM, Padture N, Xie L, Chen D, Ma X, Roth J (2008) Thermal barrier coatings made by the solution precursor plasma spray process. J Therm Spray Technol 17(1):124–135
197. Chen D, Jordan EH, Gell M (2008) Effect of solution concentration on splat formation and coating microstructure using the solution precursor plasma spray process. Surf Coat Technol 202:2132–2138
198. Pawlowski L (2008) Finely grained nanometric and submicrometric coatings by thermal spraying: a review. Surf Coat Technol 202(18):4318–4328
199. Chen D, Jordan E, Gell M (2007) Thermal and crystallization behavior of zirconia precursor used in the solution precursor plasma spray process. J Mater Sci 42:5576–5580
200. Fauchais P, Montavon G, Lima R, Marple B (2011) Engineering a new class of thermal spray nano-based microstructures from agglomerated nanostructured particles, suspensions and solutions: an invited review. J Phys D Appl Phys 44:093001, 53p
201. Kolman D (1997) Modeling of thermal plasma chemical vapor deposition of diamond with liquid feedstock injection. PhD Thesis, University of Minnesota, MN
202. Shan Y, Mosthagimi J (2003) Modeling of transport and evaporation of liquid droplets sprayed into RF-ICPs. In: Moreau C, Marple B (eds) Thermal spray 2003: advancing the science and applying the technology. ASM International, Materials Park, OH, pp 1017–1022
203. Shan Y, Coyle TW, Mostaghimi J (2007) Numerical simulation of droplet break-up and collision in solution precursor plasma spraying. J Therm Spray Technol 16:698–704
204. Marchand C, Vardelle A, Mariaux G, Lefort P (2008) Modelling of the plasma spray process with liquid feedstock injection. Surf Coat Technol 202:4458–4464

205. Basu S, Jordan EH, Cetegen BM (2008) Fluid mechanics and heat transfer of liquid precursor droplets injected into high-temperature plasmas. J Therm Spray Technol 17:60–72
206. Meillot E, Vincent S, Caruyer C, Caltagirone J-P, Damiani D (2009) From DC time-dependent thermal plasma generation to suspension plasma-spraying interactions. J Therm Spray Technol 18:875–886
207. Saha A, Seal S, Cetegen B, Jordan E, Ozturk A, Basu S (2009) Thermo-physical processes in cerium nitrate precursor droplets injected into high temperature plasma. Surf Coat Technol 203:2081–2091
208. Wang AHK, Herman H (1998) Nanomaterial deposits formed by dc plasma spraying of liquid feedstocks. J Am Ceram Soc 81(1):121–128
209. Karthikeyan J, Berndt CC, Tikkanen J, Reddy S, Herman H (1997) Plasma spray synthesis of nanomaterial powders and deposits. Surf Coat Technol 238(2):275–286
210. Kassner H, Siegert R, Hathiramani D, Vassen R, Stöver D (2008) Application of the suspension plasma spraying (SPS) for the manufacture of ceramic coatings. J Therm Spray Technol 17(1):115–123
211. Toma FL, Bertrand G, Rampon R, Klein D, Coddet C (2006) Relationship between the Suspension Properties and Liquid Plasma Sprayed Coating Characteristics. In: ITSC 2006. ASM International, Materials Park, OH, e-proceedings
212. Rampon R, Bertrand G, Toma FL, Coddet C (2006) Liquid plasma sprayed coatings of Yttria stabilized for SOFC electrolyte. In: ITSC 2006. ASM International, Materials Park, OH, e-proceedings
213. Bouyer L, Ma X, Ozturk A, Jordan EH, Padture NP, Cetegen BM, Xiao DT, Gell M (2004) Processing parameter effects on solution precursor plasma spray process spray patterns. Surf Coat Technol 183(1):51–61
214. Bouyer E, Gitzhofer F, Boulos M (1996) Parametric study of suspension plasma sprayed hydroxyapatite. In: Berndt CC (ed) Thermal spray: practical solutions for engineering problems. ASM International, Materials Park, OH, pp 683–691
215. Filkova I, Cedik P (1984) Nozzle atomization in spray drying. In: Mujumdar AS (ed) Advances drying, vol 3. Hemisphere Publication Corporation, New York, NY, pp 181–215
216. Rampon P, Filiatre C, Bertrand G (2008) Suspension plasma spraying of YPSZ coatings for SOFC: suspension atomization and injection. J Therm Spray Technol 17(1):105–114
217. Marchand O, Girardot L, Planche MP, Bertrand P, Bailly Y, Bertrand G (2011) An insight into suspension plasma spray: injection of the suspension and its interaction with the plasma flow. J Therm Spray Technol 20(6):1310–1320
218. Lefebvre AH (1989) Atomizations and sprays. Hemisphere Publication Corporation, New York, NY
219. Jordan EH, Gell M, Bonzani P, Chen D, Basu S, Cetegen B, Wu F, Ma X (2007) Making dense coatings with the solution precursor plasma spray process. In: Marple BR, Hyland MM, Lau Y-C, Li C-J, Lima RS, Montavon G (eds) Thermal spray 2007: global coating solution. ASM International, Materials Park, OH, pp 463–470, e-proceedings
220. Cotler EM, Chen D, Molz RJ (2011) Pressure-based liquid feed system for suspension plasma spray coatings. J Therm Spray Technol 20(4):967–973
221. Fauchais P, Etchart-Salas R, Delbos C, Tognovi M, Rat V, Coudert JF, Chartier T (2007) Suspension and solution plasma spraying of finely structured coatings. J Phys D Appl Phys 40:2394–2406
222. Siegert R, Doring JE, Marque´s JL, Vassen R, Sebold D, Stöver D (2002) Influence of injection parameters on the suspension plasma spraying coating properties. In: Lugscheider E (ed) ITSC 2005. DVS, Düsseldorf, Germany, e-proceedings
223. Oberste-Berghaus J, Legoux J-G, Moreau C (2005) Injection conditions and in-flight particle states in suspension plasma spraying of aluminia and zirconia nano-ceramics. In: ITSC 2005. DVS, Düsseldorf, Germany, e-proceedings

224. Siegert R, Doring J-E, Marque J-L, Vassen R, Sebold D, Stöver D (2004) Denser ceramic coatings obtained by the optimization of the suspension plasma spraying technique. In: ITSC 2004. DVS, Düsseldorf, Germany, e-proceedings
225. Hwang SS, Liu Z, Reitz RD (1996) Breakup mechanisms and drag coefficients of high-speed vaporizing liquid drops. Atomization Sprays 6:353–376
226. Hussary NA, Heberlein JVR (2001) Atomization and particle-jet interactions in the wire-arc spraying process. J Therm Spray Technol 10(4):604–610
227. Gelfand BE (1996) Droplet break-up phenomena in flows with velocity lag. Prog Energ Combust Sci 22:201–265
228. Watanabe T, Ebihara K (2003) Numerical simulation of coalescence and break-up of rising droplets. Comput Fluids 32:823–834
229. Ozturk A, Cetegen M (2004) Modeling of plasma assisted formation of precipitates in zirconia containing liquid precursor droplets. Mater Sci Eng A 384:331–351
230. Ozturk A, Cetegen M (2005) Experiments on ceramic formation from liquid precursor spray axially injected into an oxy-acetylene flame. Acta Mater 53:5203–5211
231. Basu S, Jordan EH, Cetegen BM (2006) Fluid mechanics and heat transfer of liquid precursor droplets injected into high temperature plasmas. J Therm Spray Technol 15(4):576–581
232. Taylor GI (1963) The shape and acceleration of a drop in a high speed air stream, technical report in the Scientific Papers of Taylor GI, (ed)., G.K. Batchelor
233. Lee CS, Reitz RD (2001) Effect of liquid properties on the break-up mechanism of high-speed liquid drops. Atomization Sprays 11:1–18
234. Carruyer C, Vincent S, Meillot E (2011) Caltagirone, modelling of the fragmentation of a water jet in the liquid precursor plasma spraying, 5th International Workshop on Suspension and Solution Plasma Spraying, Tours Sept. 4–6 (2011), CEA Le Ripault
235. Vincent S, Meillot E, Carruyer C, Caltagirone J-P (2011) Analysis by modelling of of the interaction between a thermal flow and a liquid, 5th International Workshop on Suspension and Solution Plasma Spraying, Tours Sept. 4–6 (2011), CEA Le Ripault
236. Jordan EH, Gell M, Benzani P, Chen D, Basa S, Cetegen B, Wa F, Ma XC (2007) Making dense coatings with the solution precursor plasma spray process. In: Marple BR et al (eds) Thermal spray 2007: global coating solutions. ASM International, Materials Park, OH, pp 463–467
237. Marchand C, Chazelas C, Mariaux G, Vardelle A (2007) Liquid precursor plasma spraying: modelling the interaction between the transient plasma jet and the droplets. In: Marple BR et al (eds) Thermal spray 2007: global coating solutions. ASM International, Materials Park, OH, pp 196–201
238. Etchart-Salas R, Rat V, Coudert JF, Fauchais P, Caron N, Wittman K, Alexandre S (2007) Influence of plasma instabilities in ceramic suspension plasma spraying. J Therm Spray Technol 16(5–6):857–865
239. Bouyer E, Gitzhofer F, Boulos MI (1997) Suspension plasma spraying for hydroxyapatite powder preparation by RF plasma. IEEE Trans Plasma Sci 25(5):1066–1072
240. Bouyer E, Gitzhofer F, Boulos MI (1997) The suspension plasma spraying of bioceramics by induction plasma. JOM 49(2):58–68

Chapter 5
Combustion Spraying Systems

Abbreviations

D-gun	Detonation gun
HVAF	High Velocity Air-Fuel
HVOF	High Velocity Oxy-Fuel
SHS	Self-propagating High Temperature Synthesis
slm	standard liters per minute
YSZ	Yttria stabilized zirconia

5.1 Historical Perspective and General Remarks

The growth of combustion processes along the years was driven both by scientific and technical developments providing disruptive innovations and by the market requirements (e.g., the development of HVOF spraying by Browning in 1983 was pushed forward by the need to produce WC–Co cermet coatings with superior properties). Table 5.1 lists major dates related to the development of the most important combustion spray processes.

Combustion spray guns are devices for feeding, accelerating, heating, and directing the flow of a spray material pattern. Historically three types were used:

Flames spraying using mostly oxyacetylene torches achieving premixed combustion temperatures up to about 3,000 K. Sprayed materials are introduced generally axially into the gun. Flame velocities below 100 m/s characterize this process. Historically speaking, this technique has been the first to be developed in 1909 by Maximilian Ulrich Schoop.

High velocity oxy-fuel flame (HVOF) spraying (or supersonic flame spraying) where the *flame or deflagration* of a gaseous or liquid hydrocarbon molecule (C_xH_y) is achieved at an adjustable stoichiometry with an oxidizer, which is either oxygen or air in a chamber at pressures between 0.24 and 0.82 MPa. The chamber is

P.L. Fauchais et al., *Thermal Spray Fundamentals: From Powder to Part*, 227
DOI 10.1007/978-0-387-68991-3_5, © Springer Science+Business Media New York 2014

Table 5.1 Major dates related to the development of the major thermal spray processes

Year	Process	Energy generation	Inventor(s)	References
1909	Flame spraying (FS)	Combustion (diffusive)	Schoop (Switzerland)	[1]
1955	Detonation gun s praying (D-Gun)	Combustion (detonation)	Gfeller and Baiker[a] (USA)	[2]
1983	Supersonic flame spraying (HVOF)	Combustion (deflagration)	Browning (USA)	[3]

[a]Union Carbide, today Praxair Surface Technology (USA)

connected to a convergent–divergent Laval nozzle achieving very high gas velocities (up to 2,200 m/s, which is to say, about Mach 2 when considering the local pressure and temperature). Recently new guns using kerosene instead of fuel gas have been developed with chamber pressures up to 1 MPa. The trend is also to reduce the gases temperature and increase their velocity by injecting noncombustible gas (nitrogen, for example, in the combustion chamber).

Detonation generally in an acetylene or hydrogen–oxygen mixture contained in a tube closed at one of its ends. The shock wave, generated by the enthalpy of reaction in the highly compressed explosive medium (about 2 MPa) accelerates the particles, which are heated by the combustion. Gas velocities higher than 2,000 m/s are commonly achieved. Contrary to the two previous processes where combustible gases and powders are continuously fed within the gun, combustible gas and powder are fed in cycles repeated at a frequency ranging from 3 to 100 Hz. In the following the three techniques and their developments will be described in detail.

5.2 Flame Spraying

5.2.1 Principle

Flame spraying requires the melting of the sprayed material. Flame spray uses the chemical energy of fuel gases to generate the high temperature flow. Oxyacetylene torches are the most common ones. The mixture of acetylene (C_2H_2)–oxygen (O_2) at a stoichiometric ratio yields a temperature of 3,410 K at atmospheric pressure, which is the highest temperature of all combustible gases (C_nH_m) at this pressure (see Table 3.1 in Chap. 3). Stoichiometry corresponds to the full transformation of C into CO_2 and H into H_2O, according to the global reaction:

$$2C_2H_2 + 5O_2 \rightarrow 4CO_2 + 2H_2O \tag{5.1}$$

The mixture is called fuel rich if $R' > 1$ and fuel lean if $R' < 1$. R' is defined as

$$R' = (F/A)/(F/A)_{\text{stoichio}} \tag{5.2}$$

where F is the fuel volume or mass and A the oxidizer volume or mass (see Chap. 3 for more details). Powders, wires, rods, and cords are introduced axially through the rear of the nozzle into the flame burning at the nozzle exit. The feedstock materials are melted and the particles or droplets accelerated toward the substrate surface by the expanding hot gas flow and air jets. The main difference between delivery of the feedstock as powder or as wire, cord, or rod is the melting capability. As the flame length is limited and the particle velocity is a few tens of m/s, the maximum temperature that particles can achieve after their flight is about $T_p = 0.7T_g$ to $0.8T_g$, T_g being the gas temperature, i.e., about 2,300 K for T_p. Thus most ceramic materials are not melted. In contrast, the wire, rod, or cord is advanced in the flame in such a way that its tip is melted and then atomized by the atomizing gas (generally air). Thus the material temperature can reach 0.95 T_g, and even zirconia can be melted [4].

5.2.2 *Powder Flame Spraying*

5.2.2.1 Spray Conditions

Figure 5.1 represents the principle of powder flame spraying. The premixed mixture of acetylene and oxygen is fed to the nozzle extremity through a ring of 16–18 orifices (each below 1 mm in diameter to avoid the flash back: see Chap. 3, Sect. 3.1.4.1). Unburned gas feeding velocity v_u has to be adjusted to the flame velocity S_L (see Chap. 3 Sect. 3.1.4.1). As shown in Fig. 5.2, if v_u is too high the flame is blown-out and if it is too low flash back occurs, except if the feeding orifice diameters are small enough to destroy all radicals, but in this case the flame extinguishes.

The mixture burns outside and around the area where particles are injected (Fig. 5.1) with a carrier gas. It is important to emphasize that the power dissipated in the flame P_F depends on the fuel gas and oxidizer chosen (highest values being obtained with O_2 and C_2H_2 mixture as shown in Table 3.1 in the Chap. 3). Of course the power dissipated in the flame, P_F, depends on the ratio fuel/oxidizer (about 1/1.6 for the O_2–C_2H_2 mixture considered) and on the combustible gas feeding flow rate $\dot{m}_u$. Practically P_F is proportional to $\dot{m}_{O_2}$ because the amount of oxygen is the factor limiting P_F [5]:

$$P_F \sim \dot{m}_{O_2}(\text{kg/s}) \tag{5.3}$$

The power P_F is quite comparable to that of plasma spray torches. For example, in conditions used by Wigren et al. [5] $P_F = 1.354$ A, where A is the oxygen flow rate in slm. With 27 slm, $P_F = 36.6$ kW!

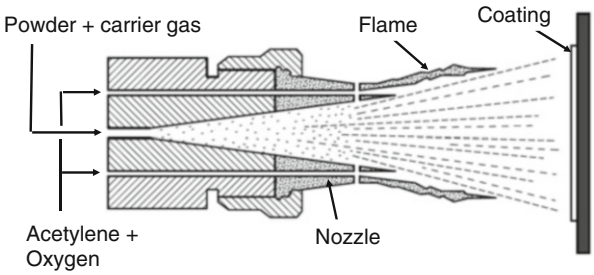


Fig. 5.1 Powder flame spraying principle (courtesy of Sultzer Metco)

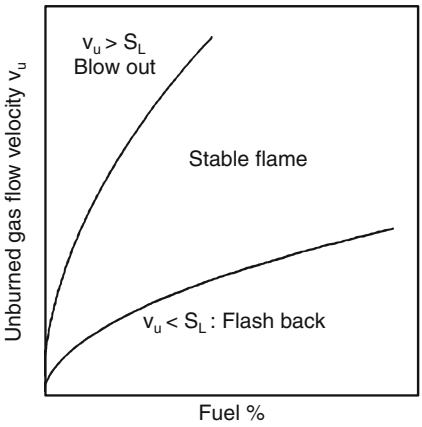


Fig 5.2 Schematic diagram of premixed flame stability. Reprinted with kind permission from ASM International [5]

To our best knowledge, the low velocity oxygen combustion flame process has been modeled only by Bandgopadhyag and Nylen [6, 7], see Sect. 5.2.4, while many papers have been published about HVOF process modeling (see Sect. 5.3.6), at the present time. The premixed acetylene–oxygen mixture (56 slm with 34 slm O_2 and 22 slm C_2H_2) was fed through a ring of 16 orifices (0.8 mm in internal diameter), yielding symmetric process geometry. The mixture of reacting gas flow was modeled using the standard k–ε turbulence gas model. As the process involves chemical reactions, fast moving and turbulent gas flow, a generalized finite rate formulation was applied. This approach is based on the solution of the species transport equations for reactants and product concentrations, based on the chemical reaction mechanisms defined to achieve the global reaction of Eq. (5.1) (see Sect. 5.2.4). Figure 5.3 shows jet gas temperatures and speeds, typically below 100 m/s, generating maximum particle speeds below 60 m/s before impact. Flame temperatures are generally above 2,600 °C and controlled by the parameter R' defined previously and the mixing patterns of the combustion gases with the surrounding air. The latter is adding oxidizer gas.

Bandgopadhyag and Nylen [7] have calculated and measured the temperatures and velocities of nickel-covered bentonite particles (5–120 μm) injected axially into the flame described in Fig. 5.3. Figure 5.4a, b indicate that the simulated particle velocity distribution resembles the measured one with a DPV2000.

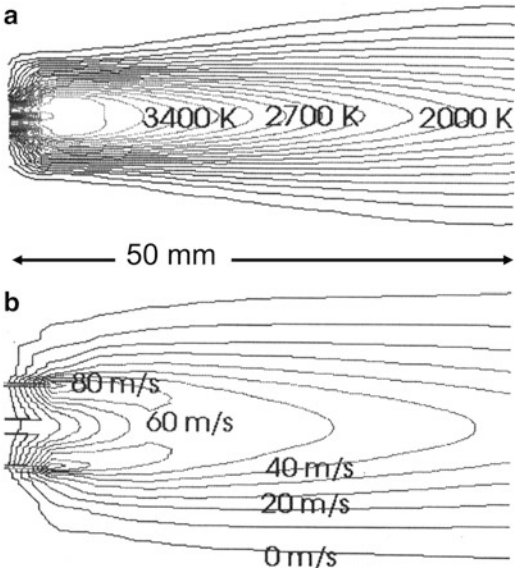


Fig. 5.3 (**a**) Gas temperature and (**b**) velocity fields, for an oxy-acetylene flame: central orifice diameter 3.2 mm, gas mixture inlet diameter 0.8 mm × 16, mixture flow rate 56 slm, O_2/C_2H_2 mixing ratio 34/22. Reprinted with kind permission from Springer Science Business Media [7], copyright © ASM International

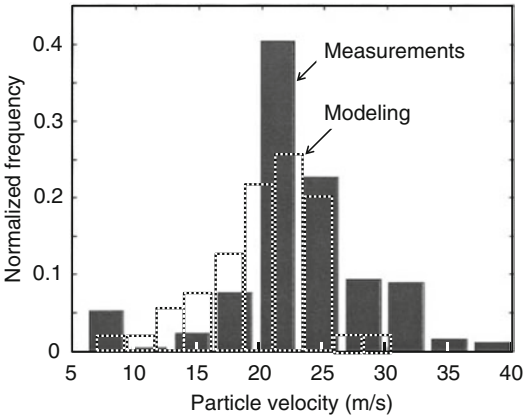


Fig. 5.4 Nickel covered bentonite (5–120 μm) particles injected into the flame presented in Fig. 5.3, (**a**) *Solid lines*, measured velocity distribution, (**b**) *Dotted lines*, calculated velocity distribution. Reprinted with kind permission from ASM International [6]

The experimental distribution [7] has a pronounced peak at around 22 m/s. The simulated distribution has a somewhat less pronounced peak, but this also occurs at 22 m/s. The simulated distribution has a wider range than the measured distribution. Furthermore, a small number of particles at velocities exceeding 30 m/s are present in the measurements. In flame spraying particle velocities are generally below a few tens of m/s.

By varying the flow rates of acetylene and oxygen, the flame can be made either oxidizing (fuel lean) or reducing (fuel rich). A reducing flame limits metal oxidation. The powder is fed either by gravity or preferably with a powder feeder. In spite of the low gas velocities, the carrier gas flow rates, generally argon or nitrogen,

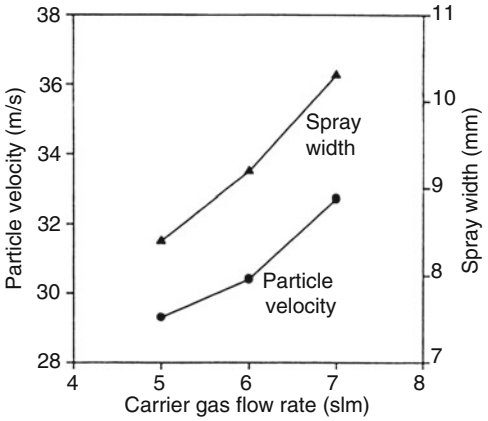


Fig. 5.5 Dependence of particle velocities and spray width on the carrier gas flow rate (N_2) (powder feed rate 17 g/min, 28 slm O_2 and 18 slm C_2H_2, Metco 6PII with 7C-M nozzle). Reprinted with kind permission from ASM International [5]

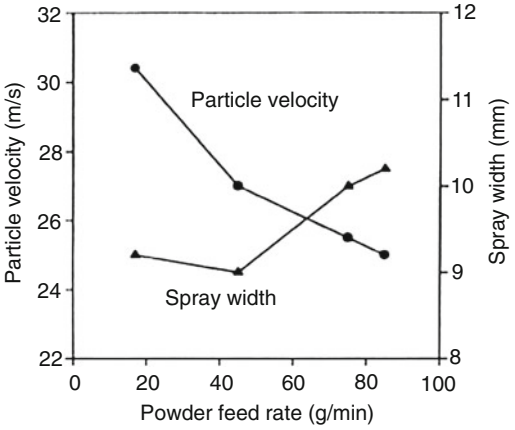


Fig. 5.6 Dependence of particle velocities and spray width on the powder feed rate of NiCrAl/Bentonite (Metco 312 NS) powder feed rate 17 g/min, 28 slm O_2 and 18 slm C_2H_2, Metco 6PII with 7C-M nozzle. Reprinted with kind permission from ASM International [5]

have limited influence (a few m/s) on particle velocities, but they increase the spray spot diameter (see Fig. 5.5). Changing the fuel and oxygen flow rates from 24/18 slm to 34/22 slm increases the power dissipated by 21 % and, accordingly, the gas velocity by 22 %, but correspondingly the particle mean velocity is raised by only 13 % and the mean temperature by 4 % [5]. However, the highest temperature of NiCrAl/bentonite particles is obtained with a ratio of oxygen/acetylene lower than 1.4 (1.6 at stoichiometry) [5]. As in all spray processes, increasing the powder feed rate too much cools and reduces the flame velocity and temperature (loading effect), reducing particle mean velocities and temperatures as well as increasing the spray width as illustrated in Fig. 5.6.

Flame spray processes typically yield coating densities ranging from 85 to 98 % and a rather high degree of oxidation (up to 20 %).

5.2.2.2 Materials Used

(a) Metals
Mainly those that are easy to melt (Pb, Ag, Zn, Al, Al-12 wt.% Si, Al–5 wt. % Mg, Al–Zn, Cu and Cu alloys: Cu–10 wt.% Al, Cu–10 wt.% Zn, Cu–40 wt.% Zn, Cu–30 wt.% Zn, Cu–5 wt.% Sn, Ni, Ni–20 wt.% Cr, steel (0.1 wt.% C or 0.1 wt.% Cr, 0.25 wt.% C, 0.4 wt.% C, 0.8 wt.% C) and Mo (see, for example, [8–13]),

(b) Self Fluxing Alloys
Self fluxing alloys contain Si and B (for example, CrBFeSiCNi) which are used as deoxidizers with a reaction of the type:

$$(\mathrm{FeCr})_x\mathrm{O}_{x+y} + 2\,\mathrm{B} + 2\,\mathrm{Si} \rightarrow x\mathrm{Fe} + x\mathrm{Cr} + \mathrm{B_2O}_x.\mathrm{SiO}_y \tag{5.4}$$

$\mathrm{B_2O}_x.\mathrm{SiO}_y$ is a borosilicate. This process requires a thermal post-treatment of the coating. This "fusing" step is commonly carried out with oxy-acetylene torches very well suited to reheat the coating over the minimum of 1,040 °C. Of course other means can be used such as furnace, induction (if the part diameter is almost constant), laser,... This "fusing" treatment excludes treating coatings on aluminum alloys! During reheating oxide diffuses toward the coating surface where it is mechanically removed (turning, milling,...). The process results in rather dense and hard coatings [14–18]. These self-fluxing alloys can be reinforced with hard ceramic particles such as WC [19].

(c) Few Ceramic (Oxide) Materials
Few ceramic (oxide) materials (mainly introduced as rods or cords, see Sect. 5.2.3) are also flame sprayed [20–22].

(d) Reactive Spraying
TiC cermets have been obtained by using asphalt as a carbonaceous precursor. The powder is made by mixing ferrotitanium powder and asphalt at 300 °C, which is then pyrolized for 2 h at 600 °C under argon atmosphere (asphalt being completely carbonized). Then the resulting porous mass is crushed to be sprayed. In situ reactions form TiC particles, which are fine, spherical, and uniformly dispersed in the coating [23–25].

(e) Polymers
To reduce the risk of over melting or burning of polymer particles, guns are equipped with a ring of holes trough which air or nitrogen is injected. The cold air or nitrogen ring is disposed inside the ring where combustible gases are introduced (see Fig. 5.7a). Thus the cold gas flow between the flame and the particle protects them against overheating. PEEK coatings are very popular in flame spraying.

The polymer coating structure shows a very dense, well-bounded surface layer, a structure which is due to fusing after, or coincidental with deposition (see, for example, [27] where the remelting is achieved by laser). It should be noted that this combustion flame-laser combination has also been used to

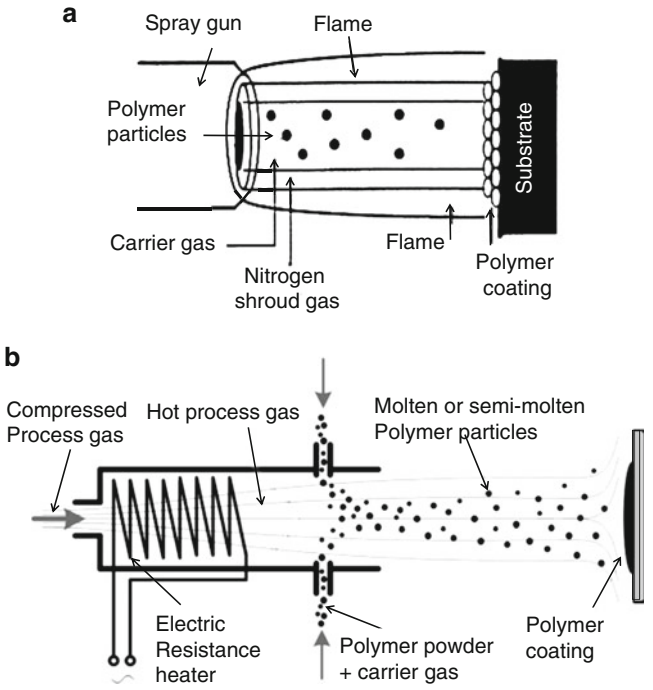


Fig. 5.7 (**a**) Principle of the combustion gun used for polymer spraying. (**b**) Schematic of Resodyn Corporations' Polymer Thermal Spray (PTS) coating process. Reprinted with kind permission from ASM International [30]

prepare multilayer surface coatings of refractory ceramics [28]. However with polymers during deposition and post deposition heating and fusing some overheating can occur very easily. The problem can be reduced when using either the gun presented in Fig. 5.7a or HVOF gun where the high velocities of particles limit the overheating, if the particle sizes distribution is adapted [28]. The heating and fusing operation is more difficult due to the low thermal conductivity of polymers (<0.5 W/m K) resulting in high temperature gradients within coating [29] and the transient heat flux imparted to the coating surface must be carefully controlled. Limitations of the combustion based processes for thermal spray deposition of polymers were the motivation of Isosevic et al. [30] for the development of a low temperature spray process called polymer thermal spray (PTS). A schematic of the PTS coating process is shown in Fig. 5.7b. An electro-resistive heating element heats the main process gas, which can be pure air, nitrogen, an inert gas, or any other pure gas or mixture. The electric heating element can be set to any temperature depending on polymer being processed. The velocity of the main process gas at the nozzle exit can be adjusted in the range of 20–60 m/s. It controls particle in-flight residence time as well as the intensity of forced convection heat over the substrate and/or previously

deposited coating layers. Polymer powder is injected downstream of the main process gas using a carrier gas that can be air, nitrogen, or an inert gas (see Fig. 5.7b). A conventional fluidized bed powder feed system distributes the powder. Two spray guns with power levels, respectively, of 6 kW and 18 kW were available in 2009.

(f) Glass

Refractory glass (Al_2O_3–Y_2O_3–BiO_2) has been flame sprayed onto stainless steel where it formed hard, uniform, and well-adherent coatings [31].

Patents, especially in Japan, have been granted for flame spraying glass or enamel [32–35], bio-glass has been sprayed [36], spraying of enamels on substrates prone to decompose has been achieved [37]. The importance of the heat flux control on the coating formation and the residual stress has been emphasized [37, 38].

5.2.3 *Liquid Flame Spraying*

Liquid flame spraying has been introduced in the mid-1990s: liquid feedstock was atomized and injected in an oxygen–hydrogen flame where the liquid phase was evaporated and thermochemical reactions produced fine or nanometer-sized particles [39]. The process was soon used for glass coloring by flame spraying Co, Cu, and Ag nitrates dissolved in alcohol or water. After evaporation, precursors are transformed into oxides and sprayed onto soda-lime silica glass at 900–1,000 °C. This process has produced blue, blue–green, and yellow colors [40]. The process was also used to deposit finely structured or nanostructured coatings: zirconia, starting from zirconium oxyacetate precursor gas atomized in the flame [41] and nanostructured TiO_2 coatings [42, 43].

5.2.4 *Wire, Rod, or Cord Spraying*

Wire rod- and cord-fed devices, as illustrated in Fig. 5.8, use air turbines or electrical motors, built into the torch, that power drive rolls, which pull feedstock from the source and push it through the nozzle at a controlled velocity. If the velocity is too high the tip cannot melt because its residence time in the flame is too short. The uniform and adapted motion of the wire, adapted to the gas composition, flow rate, and the wire diameter and composition, is the key issue. Typical gas flow rates are as follows: 10–30 slm acetylene, 20–100 slm oxygen, and up to 1 m^3/h (17 slm) air for atomization of the molten tip.

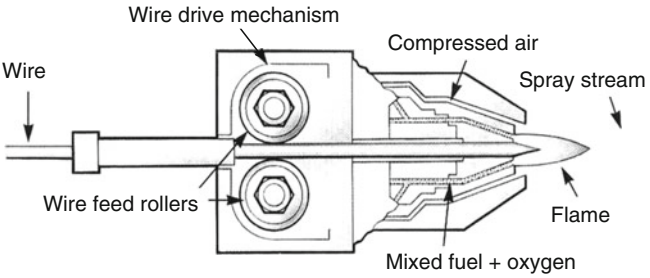


Fig. 5.8 Schematic of a wire or rod or cord flame spray gun (Courtesy of Metallisation Flamespray Dudley, Pear Tree Lane, West Millands, DY2 OXH, England)

5.2.4.1 Wire

Typical wire velocities, depending on the wire material are between 0.6 and 14 m/min. Higher speeds are used to spray lower melting point metals such as Babbitt, tin, and zinc. Figure 5.9 shows the details of the nozzle of the gun. The nozzle produces and shapes the flame and besides guides the wire along its axis. This nozzle can be changed to adapt to wires of different diameters. In Fig. 5.8 the conical shape of the tip can be observed. Assuming that the liquid metal is withdrawn by the atomization gas as soon as it forms, a constant gas temperature and heat transfer coefficient result in a conical wire tip (cone angle of 25–30°), as observed experimentally.

Typical wire diameters used are between 1.2 and 4.76 mm. They must be clean and smooth with a precise dimensional uniformity (between 0.01 and 0.05 mm). They are stored either in coils, spools, or barrels. Wire feed rates depend on sprayed materials and wire diameters, for example, Al: 2–8 kg/h, Zn: 8–30 kg/h, Steel: 2–4.5 kg/h, Mo: 0.7–2.5 kg/h.

Particles are produced by the flow of compressed atomizing gas (generally air), which creates liquid metal sheets that become self-aligned in the flow (see Fig. 2.22 of Chap. 2, illustrated by illustration of Fig. 9.11a, Chap. 9, pictures obtained for wire arc spraying). Waves are created at the sheet surface, due to hydrodynamic instabilities, forming protuberances and inducing the sheet disintegration. The flapping motion of the sheets creates showers of drops, which increases the divergence angle. The large eddy structures formed in the flow also modify particle trajectories [44].

The materials sprayed are:

Pure metals: Al 99 wt.%, Cu (99.5 and 99 wt.%), Mo (99.5, 99 and 98 wt.%), Sn, Zn (99.95 wt.%).

Alloys: Cobalt, Copper, Nickel base, MCrAlY(cored wires), NiAl.

Carbide Cermets (cored wires): Cr_3C_2 with Fe and FeC, WC/W2C + Fe, WC/TiC + Fe, Cr, Ni.

Steels: Low carbon and stainless steel (ductile), Bronze + Al or NiAl.

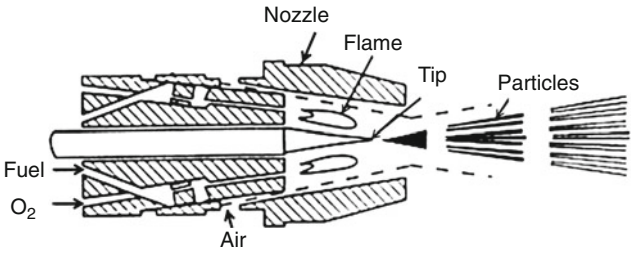


Fig. 5.9 Details of the nozzle for the wire, rod, or cord flame spray gun. Reprinted with kind permission from American Welding Society [4]

Coatings obtained by this process have generally a high porosity (~10 %) and can be highly oxidized, for example, to more than 25 % for air atomized Al. This oxidation can be reduced by a factor 2 when using nitrogen instead of air (see Fig. 5.10). However, considering the flow rates of the atomization gas, this solution is rather expensive.

These coatings are extensively used for corrosion protection, in the automotive industry (Mo on piston rings and for "rain drop erosion" of piston heads), against aqueous corrosion [45] with Al and 80 Ni–20 Cr coatings. However, because of the coating porosity, for corrosion resistance, coatings must be sealed for example with epoxy or silicone if the service temperature is low (<200 °C) [46]. Finally, the process is rather economical and simple; it has high deposition rates (10–40 kg/h), and very good thermal efficiency to melt metals (60–70 %). Moreover the substrate heating by the flame is limited.

5.2.4.2 Rod and Cord

The process has been first developed by Rokide®, now Saint Gobain®. The ceramic particles were sintered to form a rigid rod (diameters between 3.17 and 6.35 mm) but unfortunately the length was limited to 608 mm. Thus, with feeding velocities between 10 and 20 cm/min, the "life time" of a rod is between 3 and 6 min. To improve that "life time," the cord concept was developed.

The cords are made of ceramic particles agglomerated with either an organic binder (the evaporation or decomposition of which starts at 250 °C and is completed at 400 °C) or a mineral binder $Al(OH)_3$ that remains up to 1,500 °C). The diameters are the same as those of rods but the cord length can reach 120 m! The sprayed ceramics are mainly alumina, chromia, titania, zirconia (with calcia, magnesia, yttria as stabilizer) zircon, and alumina–titania. Spray conditions are similar to those of wires.

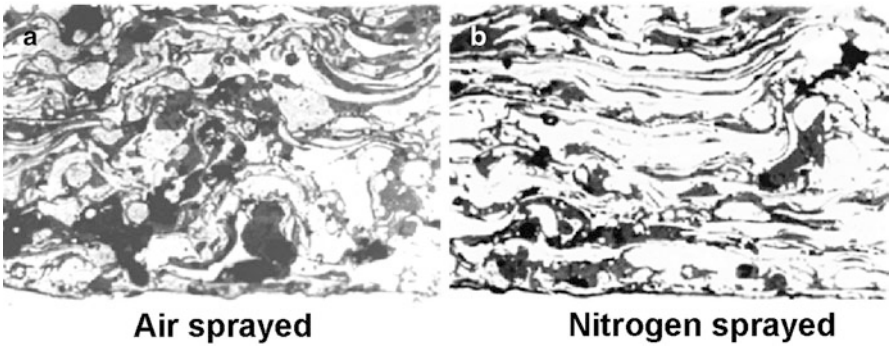


Fig. 5.10 Aluminum coating cross sections wire flame sprayed: (**a**) air atomized, (**b**) nitrogen atomized

5.2.5 Flame Modeling

The most detailed model is that of R. Bandyopadhyay and P. Nylén [7]. The fuel gases, C_2H_2 and O_2, are premixed and injected through a ring of 16 orifices around the nozzle rim, while the powder is transported by argon through the axial orifice. The diffusion combustion of the fuel extends in a free jet transporting the particles to the substrate located about 20 cm from the nozzle exit. The standard k–ε model is used to represent the turbulent gas flow. In the derivation of this model, it is assumed that the flow is fully turbulent, and the effects of molecular viscosity are negligible. To accurately model the combustion process with reasonable computational effort, single or multistep reduced reaction chemistry models might be used. The choice of this turbulence model also enables the use of the eddy-dissipation model as a competing mechanism for species creation/destruction, together with the Arrhenius finite-rate mechanism. As the process involves chemical reactions and fast moving, turbulent gas flows, a generalized finite rate formulation must be applied. The reaction rates influence the rate of creation/destruction of a species, which appears as a source term in the species transport equations. Thus R. Bandyopadhyay and P. Nylén [7] have considered the eddy dissipation concept, as used by Magnussen and Hjertager. In this concept, the rates of species of creation/destruction are calculated using the dominant of the two expressions, in which the turbulent kinetic energy (k) and its dissipation rate (ε) participate. The model is useful for the prediction of premixed and diffusion problems as well as for partially premixed reacting flows. In turbulent reacting flows, each equation is calculated using the Arrhenius reaction rate, the eddy dissipation-model reaction rate, or both, depending on the problem definition [7]. If both are calculated, the limiting (slowest) rate is used as the reaction rate, and the contributions to the source terms in the species conservation and energy equations are calculated from this reaction rate. However such calculations are rather highly time consuming, for example, with the acetylene–oxygen flame, the following 15 species are included:

C_2H_2, O_2, CO_2, H_2O, N_2, Ar, CO, H, H_2, HO_2, OH, O, N, NO, and N_2O. To calculate the concentrations of these substances, 22 reversible reactions are considered. That is why, instead of using complex kinetic reactions, often a global or overall reaction for combustion of the acetylene/oxygen mixture is used [7] such as that of Eq. (5.1). When comparing gas velocity and temperature fields predicted by the single-reaction simulations with those predicted by the multireaction model, the gas temperature and gas velocity fields produced by both models agree quite closely [7]. The convergence time for the simulations without the reversible reactions was significantly shorter, taking only a number of hours instead of a number of days.

5.3 High Velocity Flame Spraying (HVOF–HVAF)

HVOF stands for high velocity oxy-fuel, the gun being fed with combustible gas or fuel and oxygen, while HVAF stands for high velocity air-fuel where oxygen is replaced by air resulting in lower temperatures and higher gas velocities.

5.3.1 HVOF or HVAF Powder Spraying

5.3.1.1 HVOF Processes Description

Union Carbide (now Praxair Surface Technology) has introduced the HVOF process in 1958 by but it was not really commercialized until the early 1980s when the Jet Kote (Deloro Stellite) system was introduced by James Browning [3]. The principle of the Jet Kote, shown schematically in Fig. 5.11a, consists in feeding a high volume of combustible gases into a water-cooled pressurized combustion chamber. The exit of this chamber is at right angles to the exit nozzle. The powder is introduced through a water-cooled injector on the axis of the gas stream in the throat region [47]. The gas velocity is increased through the convergent–divergent nozzle (de Laval type). As in all spray processes when a hot gas exits in the ambient air, the hot jet cools down rather fast due to its expansion and the surrounding air entrainment. To impede this phenomenon it has been proposed to extend the nozzle by a water-cooled barrel (up to 30 cm long), where some energy of the jet is lost but much less than by mixing with the air. Of course, this also requires that particles are not over-melted, or remain below the melting temperature, to avoid deposition on the barrel wall. When comparing a gun with only a simple straight barrel or with a de Laval nozzle, with a divergent section as long as the barrel (see Fig. 5.12), Korpiola et al. [48] have shown, using a 1D compressible flow model (see Chap. 3 Sect. 3.3.5.1), that the gas velocities were about 300 m/s higher with the de Laval nozzle (see Fig. 5.13) having the same divergent section length as that of the barrel (see Fig. 5.12). They have also shown that the gas velocity at the exit plane depends on the fuel/oxygen ratio, but the combustion velocity is almost independent of the

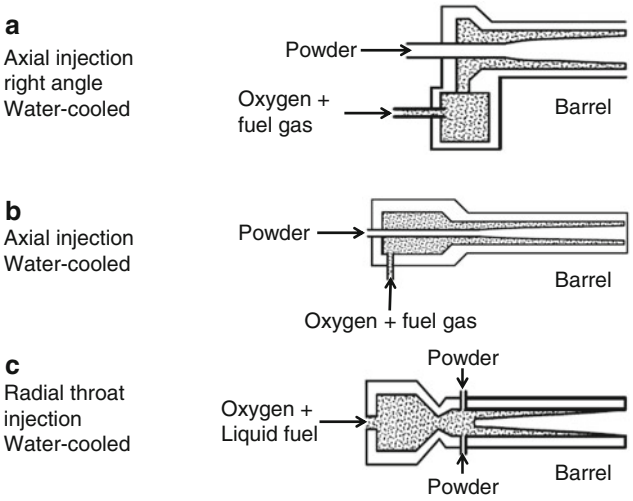


Fig. 5.11 Typical design evolutions of HVOF. (**a**) Principle of the Jet Kote. (**b**) Axial injection and combustion chamber. (**c**) Axial chamber with radial powder injection. Reprinted with kind permission from Springer Science Business Media, copyright © ASM International [47]

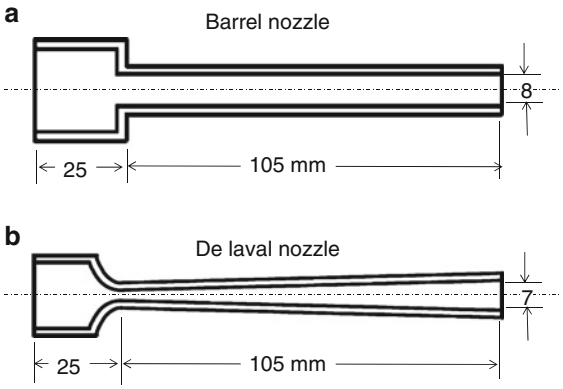


Fig. 5.12 Barrel and de Laval nozzles. Dimensions given in millimeters. Reprinted with kind permission from Springer Science Business Media, copyright © ASM International [48]

total gas flow at constant fuel/oxygen ratio. Typical working pressures are in the range 0.3–0.6 MPa.

The evolution of the water-cooled HVOF design is the axial flow device shown in Fig. 5.11b. The powder is still axially injected (at the bottom of the combustion chamber or close to the nozzle throat with a water cooled injector) into the chamber, positioned coaxially with the nozzle. This design improves the thermal efficiency while providing axial injection [45]. As with the Jet Kote type gun, axial injection of the powder implies using a pressurized powder feeder.

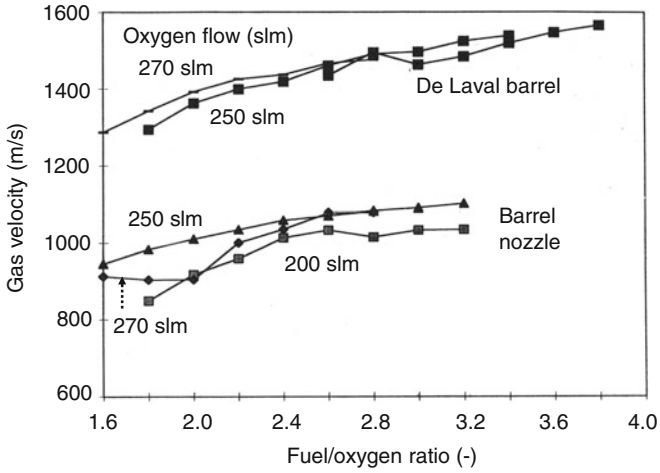


Fig. 5.13 Gas velocity at the exit plane of the HVOF spray gun (H_2/O_2, for different fuel/oxygen ratios) for the two types of gun design [48]: combustion chamber followed by (**a**) a barrel, (**b**) a convergent–divergent (de Laval) nozzle. Reprinted with kind permission from Springer Science Business Media, copyright © ASM International [48]

The last development is that presented in Fig. 5.11c. The chamber is still coaxial with the nozzle but the powder is injected radially beyond the throat at the beginning of the barrel or in the divergent part of the nozzle. Downstream of the throat, the pressure is much lower than in the combustion chamber upstream of the nozzle throat. Thus injecting powders at this point simplifies injection and particle entrainment and permits, if necessary, multiple-port powder injection for a more uniform loading of the exit stream and more efficient use of the available heat. Generally, operating data show that at least twice the spray rate per unit of energy can be achieved with radial injection versus axial injection. Moreover this design has allowed increasing the combustion gas pressure (up to 0.8–0.9 MPa).

Almost simultaneously, guns with the general design of Fig. 5.11b were developed using kerosene instead of combustible gas, and oxygen instead of air allowing very high-dissipated powers (almost 300 kW). With these guns, powders can also be injected radially downstream of the torch throat. Such high powers result in large thermal stresses and oxidation of gun components, particularly the combustion chamber and nozzle, for which the water cooling must be carefully designed. However the use of a liquid fuel simplifies the spraying process, improves the operational safety, and decreases costs without degrading operational parameters.

Over the last two decades, according to Gärtner et al. [49] the development of HVOF systems has been aimed at reducing the temperature of particles and increasing their velocity (Fig. 5.14). Higher particle velocities were obtained by using converging–diverging de Laval-type nozzle designs and higher gas pressures. With a chamber pressure of up to 1 MPa, HVOF spray systems of the third generation (DJ2700, DJ2800, JP5000) accelerate spray particles to velocities of

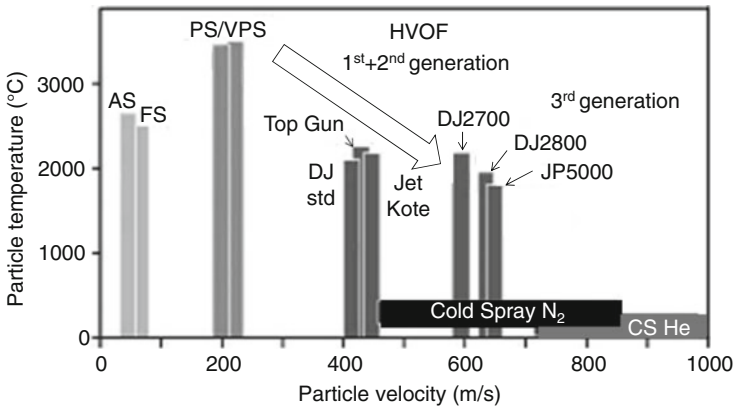


Fig. 5.14 Particle temperatures and velocities obtained in different thermal spray processes, as measured for high-density materials. The *arrow* indicates the observed trend of recent developments (AS: Powder flame spraying, *FS* Wire flame spraying, *PS* Air plasma spraying, *VPS* Vacuum plasma spraying, *CS* Cold Spray). Reprinted with kind permission from Springer Science Business Media, copyright © ASM International [49]

about 650 m/s. For HVAF guns (see Sect. 5.3.1.5) pressures can reach 2 MPa. Coating microstructures demonstrate that only small particles or fractions of larger ones are molten before the impact onto the substrate. A further reduction in particle temperatures below the melting temperatures of metals requires a substantial increase in velocity, which can only be realized by optimizing the expansion ratio in the diverging nozzle section and by using higher chamber pressures through the injection of noncombustible gases. The last developments correspond to power levels up to 300 kW (kerosene 31 slm, O_2 965 slm, air 500 slm) the flame being ignited in the combustion chamber with a hydrogen pilot flame (88 slm).

5.3.1.2 HVOF Gas Flow Description

HVOF systems use liquid kerosene and gaseous hydrogen, propylene, propane (which is also used liquid), methane, acetylene, as well as specialty gases such as, for example, methylacetylene–propadiene-stabilized gas, for fuel (see properties of conventional gases in Chap. 3), and oxygen as oxidizer gas. Velocities at the exit of the nozzle can be as high as 1,900 m/s. Such flows generate oblique shock waves and shock diamonds (see Fig. 5.15). The diamonds are brighter because of local higher pressure and, therefore, temperature in those regions.

5.3.1.3 Results of HVOF Gas Flow Modeling

Much effort has been devoted to the flow modeling. From simple isentropic 1D flows [47, 48] to 3D supersonic flows [50–61], see Sect. 5.3.6. The chemical reaction, which is a very complex problem (see Sect. 5.3.6), is generally treated

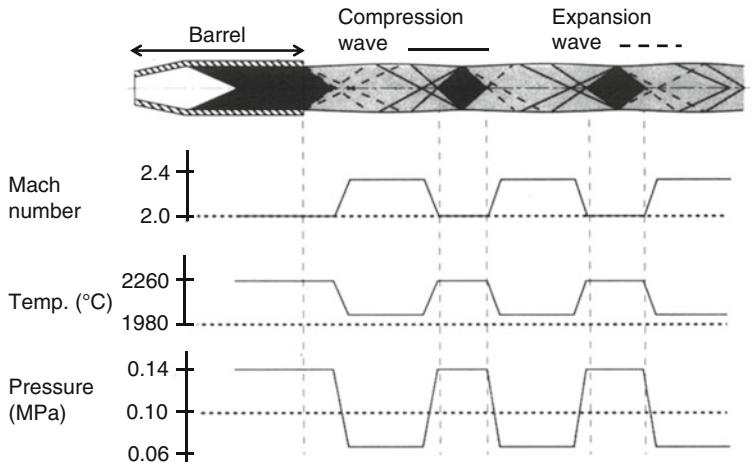


Fig. 5.15 Schematic of oblique shock waves at the barrel exit of a HVOF gun together with axial velocity (Mach number), temperature, and pressure distributions. Reprinted with kind permission from Springer Science Business Media, copyright © ASM International [47]

as an approximate, single-step, equilibrium formulation that takes into account the effects of dissociation:

$$C_xH_y + zO_2 \rightarrow aCO_2 + bCO + cH + dH_2 + eH_2O + fO + gOH \qquad (5.5)$$

Oberkampf and Talpallikar [51, 52] were the firsts who suggested this approach. In general, modeling results match rather well with experimental results, as for example the pressure variation along the centreline of the nozzle. Under- and over-expanded flows (the flow is ideally expanded if the pressure at the nozzle exit, p_e, is equal to the surrounding atmospheric pressure, p_a, it is under-expanded if $p_e > p_a$ and over-expanded if $p_e < p_a$) have been studied for different gas mixtures together with different nozzle designs. As could be expected the latter plays a key role in the flow optimization.

Typical results from Li and Christofides [60] will be presented to illustrate possibilities of 2D sophisticated calculations (see Sect. 5.3.6.2) performed for a Diamond Jet hybrid gun. Figure 5.16 shows a schematic diagram of the torch, which is of the type shown schematically in Fig. 5.11b.

The propylene fuel gas is mixed with oxygen through a siphon system and fed to the air cap, where they react to produce high temperature combustion gases. The exhaust gases, together with the air injected from the annular inlet orifice, expand through the nozzle to reach supersonic velocity. The air cap is cooled by both water and air ("hybrid") to prevent it from being melted. It is assumed that the walls of the torch are maintained at a constant temperature of 400 K. The powder particles are injected at the central inlet nozzle using nitrogen as the carrier gas. The different gas flow rates are the following: propylene 83 slm, oxygen 273 slm, air 404 slm, nitrogen carrier gas 13.45 slm, the total mass flow rate being 18.10 g/s.

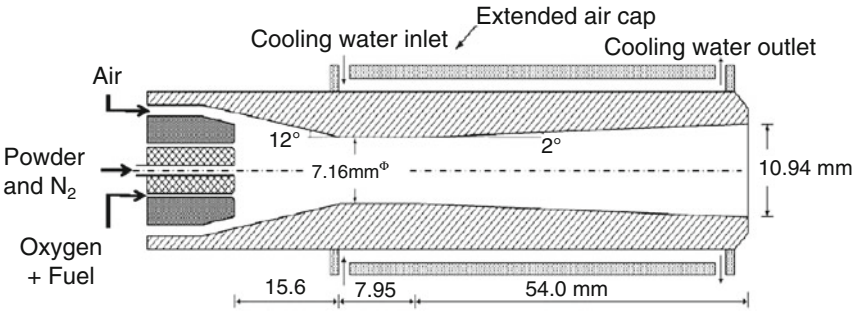


Fig. 5.16 Schematic diagram of the Diamond Jet hybrid thermal spray gun. Reprinted with kind permission from Elsevier [60]

The equivalence ratio, R (fuel/oxygen ratio divided by its stoichiometric value, see Eq. (5.2)) is 1.045, and propylene is in excess. First a 1D process was used by the authors [60] to calculate the chamber pressure and then they used a chemical equilibrium program code developed by Gordon and McBride [61] to get the reaction formula [see Eq. (5.5)] for given partial pressures of oxygen and propylene. Subsequently, the CFD simulation was run and the final pressure compared with the one used for deriving the reaction. Trial and error shows that the chamber pressure is about 0.6 MPa and the partial pressures of oxygen and propylene are about 0.34 MPa. The simulated contours and centreline profiles of static pressure, Mach number, axial velocity, and temperature in the internal and external fields are shown in Fig. 5.17 [60]. In the combustion chamber (convergent section of the air cap), the reaction of the premixed oxygen and propylene results in an increase of gas temperature above 3,000 K, and a pressure of 0.6 MPa is maintained. As the exhaust gases expand through the convergent–divergent nozzle, the pressure (Fig. 5.17a) decreases and the gas velocity (Fig. 5.17b) increases continuously. At the throat of the nozzle, the Mach number is close to 1. The gas is accelerated to supersonic velocity in the divergent section of the nozzle and reaches a Mach number of 2 at the exit of the nozzle (Fig. 5.17c). Simulation shows that the pressure at the exit of the air cap is 0.06 MPa, which implies that the flow is over-expanded. The over-expanded flow condition gives a slightly higher gas velocity, and more kinetic energy can be transferred to the powders. It is important to note that although the gas temperature inside of the torch is very high, its value at the centreline, however, is less than that outside of the torch (Fig. 5.17d). This also implies that the external thermal field plays a very important role in particle heating.

The over-expanded flow pattern involved in the HVOF thermal spray process is illustrated in Fig. 5.18 [60]. At the exit of the nozzle, the shock front begins obliquely as a conical surface and is cut off by a "Mach shock disc" perpendicular to the axis. Behind the incident and Mach shock front, a reflected shock front and a jet boundary develop. As the reflected shock front meets the jet boundary, reflected expansion waves develop. These reflected expansion waves converge before reaching the opposite boundaries and give rise to shock fronts, which meet the jet

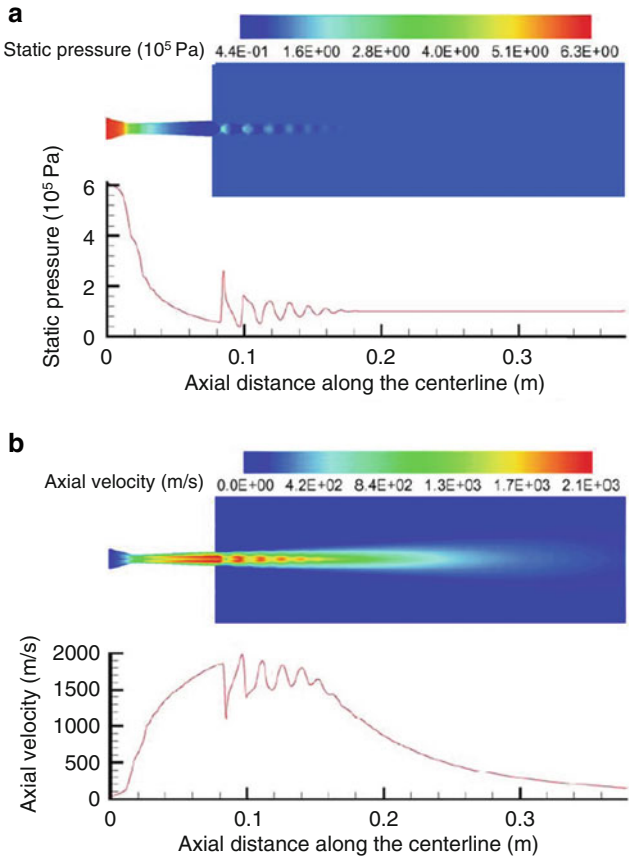


Fig. 5.17 Contours of gas properties (*upper plot*) and centreline profiles of gas properties (*lower plot*): (**a**) static pressure, (**b**) axial velocity, (**c**) Mach number, and (**d**) static temperature. Reprinted with kind permission from Elsevier [60]

boundary again and the whole process repeats. This periodic jet pattern is eventually blurred and dies out due to the action of viscosity at the jet boundary. The contour of gas temperature in the external field is given in Fig. 5.17d. It is shown that the gas temperature is relatively low at the exit of the torch (approximately 1,800 K). However, passing through the first shock leads to a sharp increase in the gas temperature (approximately 2,500 K). The location of the first shock is 7 mm from the nozzle exit.

The main parameters controlling the flow are the nozzle and barrel designs, the choice of gases, the richness of the mixture, and its total flow rate (often linked to the gas pressure in the combustion chamber):

The nozzle design has been extensively studied by modeling [50–60]. Work has been devoted to design a nozzle that provides improved performance in the areas of deposition efficiency, particle in-flight oxidation, and flexibility to allow deposition of ceramic coatings. Based on a numerical analysis, a new attachment to a standard

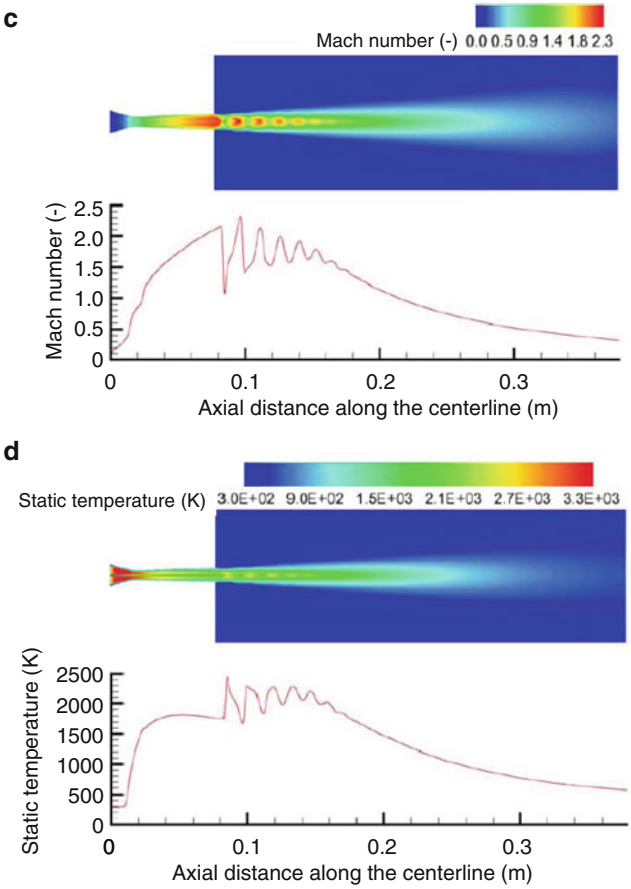


Fig. 5.17 (continued)

HVOF torch was modeled [57], designed (see Fig. 5.19), tested, and used to produce thermal spray coatings. Performance of the attachment was investigated by spraying several coating materials including metal and ceramic powders. Particle characteristics and spatial distribution, as well as gas phase composition were compared for the new attachment and the standard HVOF gun. The attachment provides better particle spatial distribution, combined with higher particle velocity and temperature.

The choice of the ratio fuel/oxygen (F/A) is also very important because it controls the gas temperature and the metal particle oxidation level. For example, calculations by Gu et al. [53], with a gun, similar to that presented in Fig. 5.11b and working with the mixture C_3H_6–O_2, show that the temperatures that are reached within the combustion chamber vary with the F/A ratio. There is also found to be a dependence on total gas flow: the higher flow rate, as expected, giving a marginally higher maximum combustion temperature. Compared to the combustion temperature calculated by another author for the same mixture of propylene–oxygen but at

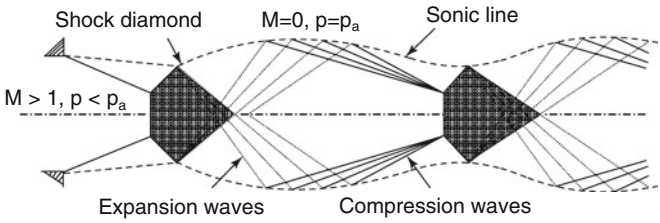


Fig. 5.18 Schematic of wave structure in the over-expanded jet. Reprinted with kind permission from Elsevier [60]

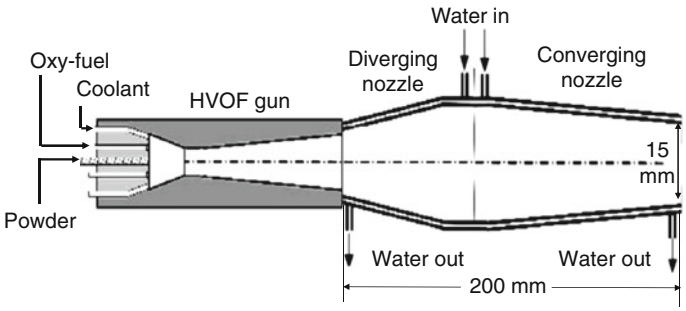


Fig. 5.19 New attachment configurations: Diverging–converging. Reprinted with kind permission from Springer Science Business Media, copyright © ASM International [57]

0.1 MPa, the temperature difference is very small, as it could be expected (see Chap. 3 Sect. 3.1.2). Yang et al. [62] have calculated the adiabatic combustion temperature of natural gas (CH_4) for different conditions. The oxygen flow rate was varied according to stoichiometric conditions (Richness), air was added between 50 and 145 slm in order to allow a larger evolution of the flame temperature, see Fig. 5.20. The oxygen content in the added air was taken into account for the determination of the richness. Figure 5.21 from Gu et al. [53] shows the adiabatic flame temperature evolution as a function of the richness condition for two combustion systems. The adiabatic flame temperature reaches a peak close to the stoichiometric combustion temperature on the slightly fuel-rich side ($R < 1$). It was also observed that an additional gas (i.e., air or nitrogen) is more efficient in decreasing flame temperature on the fuel-rich side.

The effect of the gas flow rate has been studied by Cheng et al. [54]. For many metallic or cermet materials (mostly with carbides), oxidation and partial decarburization must be avoided or at least drastically reduced. This can be achieved by diminishing the gas temperature while increasing its velocity [54]. Using a propylene–oxygen mixture at the nozzle exit of the Sulzer-Metco Diamond Jet gun (type of that presented in Fig. 5.16) with a convergent–divergent nozzle, one obtains a supersonic jet. A fuel gas is premixed with oxygen in a proprietary siphon system in the front portion of the gun. The thoroughly mixed gases are then ejected from the annular gap to the convergent–divergent nozzle and externally ignited.

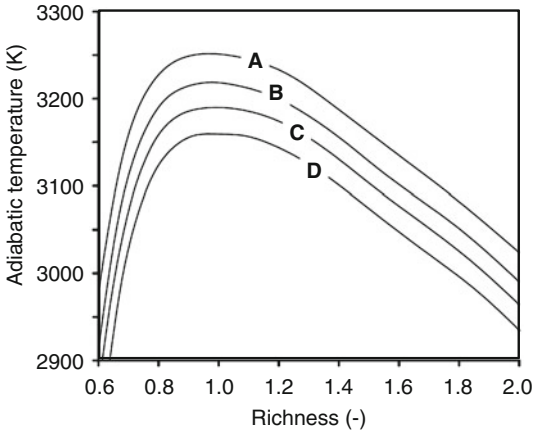


Fig. 5.20 Theoretical adiabatic flame temperatures for different combustion systems at 0.5 MPa (absolute pressure): A: CH_4 (200 slm)-O_2, B: CH_4 (200 slm)–O_2–air (50 slm), C: CH_4 (200 slm)–O_2–air (95 slm), D: CH_4 (200 slm)–O_2–air (145 slm). Reprinted with kind permission from Springer Science Business Media, copyright © ASM International [62]

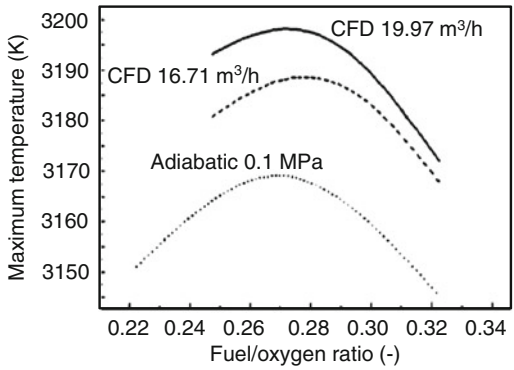


Fig. 5.21 Variation of maximum combustion temperature with fuel–oxygen ratio for CFD simulations at 19.97 and 16.71 m^3/h. Also shown is the variation of the adiabatic flame temperature at 0.1 MPa. Reprinted with kind permission from Springer Science Business Media, copyright © ASM International [53]

Table 5.2 Relative mass flow rates of inlet gases (10^3 kg/s) for different cases compared to those of the standard case after Cheng et al. Reprinted with kind permission from Springer Science Business Media [54]

Cases	Propylene	Oxygen	Nitrogen	Air
REF	1.3	3.05	4.45×10^{-2}	2.55
TF1	0.43	1.0	1.01×10^{-2}	0.84
TF2	0.87	2.04	2.04×10^{-2}	1.71
TF4	1.73	4.05	4.05×10^{-2}	3.39

The exhaust gases, along with the compressed air injected from the annular inlet orifice, form a circular flame configuration that surrounds the powder particle input from the central inlet hole. The relative mass flow rates used in calculations are presented in Table 5.2.

Increasing the total flow rate has little effect on the gas velocity and temperature inside the nozzle in the range investigated in the present study. That is, the gas flow inside the nozzle is choked. However, the increase leads to a significant increase in the pressure inside the nozzle as shown in Fig. 5.22a.

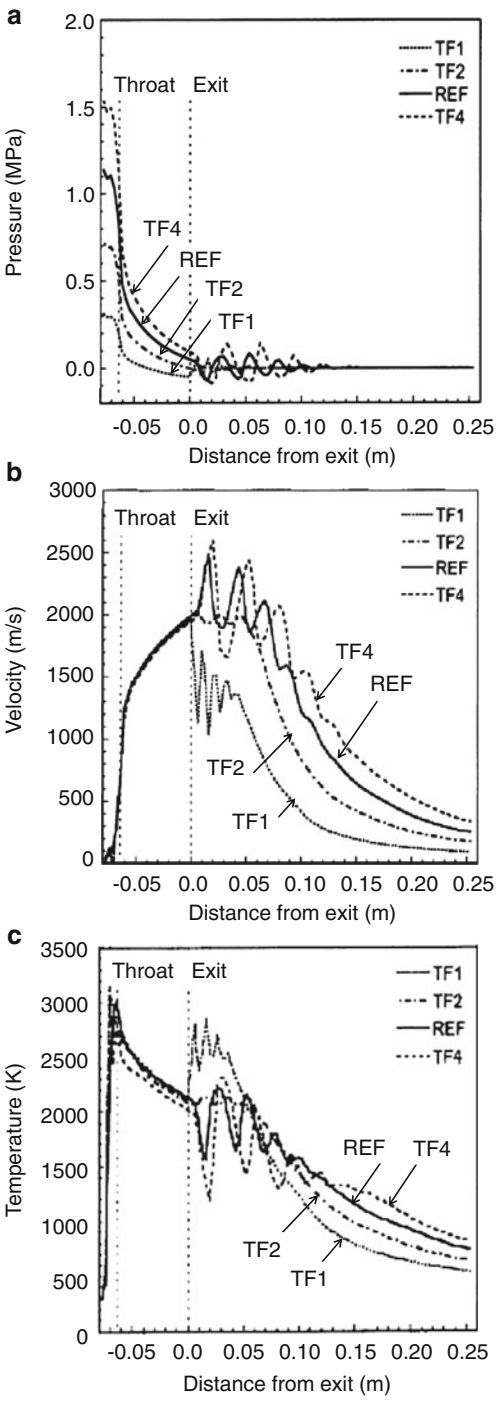


Fig. 5.22 Effect of total gas flow rate on the (**a**), pressure (**b**) velocity, and (**c**) temperature, along the centerline (propylene–oxygen mixture, Sulzer-Metco Diamond Jet gun) REF and TF4 are under-expanded jets, while TF1 and TF2 are over-expanded. Reprinted with kind permission from Springer Science Business Media [54]

At the nozzle exit, the pressures on the centerlines reach either positive or negative values with respect to the surroundings. A positive value indicates that the static pressure is higher than the ambient pressure and that, therefore, the flow is under-expanded. This situation is obtained for high gas flow rates. A negative value indicates that the static pressure is lower than the ambient pressure and that the flow is over-expanded [54]. Whatever the flow at the nozzle exit may be, under- or over-expanded, shock diamonds are observed resulting in more or less important velocity and temperature variations along the jet axis as illustrated in Fig. 5.22b, c.

Such temperature and velocity variations can affect the heat and momentum transfers to small particles (below 30–20 μm depending on their specific mass). The shock diamonds and the bow shock created close to the substrate affect mainly the small particles, for example, those below 25 μm for MCrAlY particles [62].

5.3.1.4 HVOF Particle Temperatures and Velocities

The important point is to calculate particle temperature and velocity distributions within such hot flows. This is achieved by using the conventional equations taking into account the drag force exerted on the particle [50–53, 55, 59, 62–67] (see also for details Chap. 4). The drag coefficient is corrected for the particle morphology [64] or, what is particularly important, for gas compressibility effects at supersonic velocities [65]. Such calculations show, as for other spray processes, the drastic importance of the particle size on their temperatures and velocities at impact.

For example, in the flow conditions similar to those presented in Fig. 5.22 [54] the axial temperature evolution of WC–18Co particles (82 wt.% WC and 18 wt.% Co) with six different diameters is presented in Fig. 5.23 [64].

As can be seen in Fig. 5.23, the 2 and 5 μm particles follow closely the gas temperature. These small particles reach gas temperature before entering the divergent portion inside the gun and continuously cool down with the decreasing gas temperature. As cold ambient air is entrained, it drastically cools the gas jet, and the particle temperature drops rapidly as well. Beyond a distance of 0.24 m from the nozzle exit, the temperature of 2 μm particles equals the gas temperature. The particles with diameters of 10 and 20 μm reach the gas temperature inside the convergent portion of the nozzle, and after exiting the gun nozzle, their temperatures decrease monotonically. The temperatures for particles larger than 20 μm remain relatively unchanged after exiting the nozzle due to their high thermal inertia. The oblique shocks at the nozzle exit perturb strongly the temperature of particles smaller than 20 μm. Similar results were obtained by Srivatsan et al. [63] who have studied the influence of the oblique shock at the nozzle exit and the bow shock in front of the substrate on MCrAlY particles, 15 and 30 μm in diameter. It was found that 15 μm particles, being very light, are largely affected by the shock diamonds at the nozzle exit and bow shock near the substrate, whereas 30 μm particles are least affected by either shock diamonds or bow shocks. This is due to larger Stokes numbers (see Eq. (4.25) Chap. 4) associated with 30 μm particles, which is the ratio of particle response time to a time characteristic of the fluid

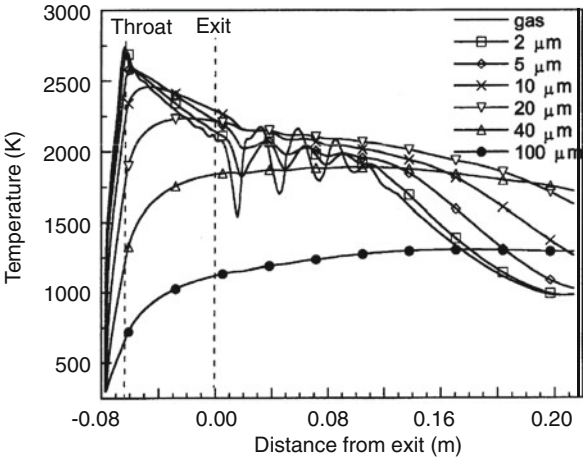


Fig. 5.23 Predicted temperatures of spherical WC (82 wt.%)–Co particles with different diameters as a function of distance from the gun exit for axial flow. Gas flow rates: propylene = $6.2 \times 3 \times 10^{-5}$ mol/s, oxygen = 20.3×10^{-5} mol/s, nitrogen = 0.99×10^{-5} mol/s, and cooling air = 30×10^{-5} mol/s. Reprinted with kind permission from Springer Science Business Media [64]

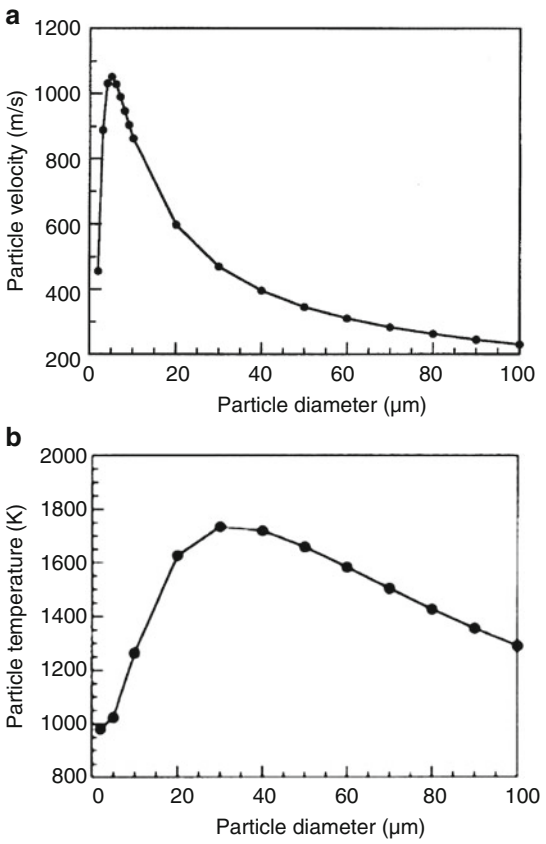


Fig. 5.24 Predicted effect of particle size on its (**a**) velocity and (**b**) temperature, at a spray distance of 0.254 m. Gas flow rates: propylene, 6.2×10^{-5} mol/s; oxygen, 20.3×10^{-5} mol/s; nitrogen, 0.99×10^{-5} mol/s; and cooling air 30×10^{-5} mol/s. Reprinted with kind permission from Springer Science Business Media [64]

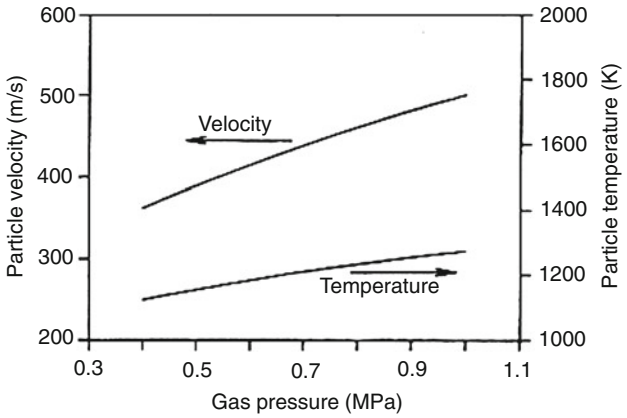


Fig. 5.25 Calculated velocity and temperature of a 38 μm stainless steel sphere at the exit of the conical nozzle for a range of chamber pressures. Modified Tafa JP-5000 system HVOF gun burning kerosene with gaseous oxygen [66]

motion. They have also studied the choice of substrate configuration. A convex substrate is better when compared with flat and concave configurations. Although the shape of the concave substrate is favorable for capturing all the particles, the strength of the bow shock formed on a concave surface is very high and leads to dispersion of most of the lighter particles.

The impact temperatures and velocities of particles thus depend strongly on their sizes as illustrated in Fig. 5.24a, b from Cheng et al. [64] and also on distance between nozzle exit and the substrate.

These figures show that the most critical parameter to be concerned about for HVOF spraying is the particle velocity. As seen in Fig. 5.24a, for size distributions between 10 and 60 μm, typically used in thermal spraying applications, particle velocities are in the range between 310 and 860 m/s at a typical spray distance of 0.254 m. This difference in velocities is equivalent to a kinetic energy per unit mass of the impinging particle, which is different by one order of magnitude. Of course, this will lead to different deformation conditions as splats are being formed, and the higher the velocity, the better is the coating quality. This emphasizes the importance of using powders with relatively narrow size distributions. As shown in Fig. 5.24b the effect of size distribution is less drastic on particle temperatures.

Calculations [66] have also shown that for a given spray gun (type of Fig. 5.11c) and a combustible gas mixture, the stainless steel particle (28 μm in mean diameter) velocity is almost independent of the axial injector position and varies almost linearly with the chamber pressure, as shown in Fig. 5.25.

The temperature variation is significantly less. The temperature is, however, very sensitive to the radial injector position which has been varied from upstream of the nozzle throat to different positions downstream of it. Particle injection location was found to determine the residence time of particles within the nozzle, thus providing a means to control particle temperature. Finally, injection location had

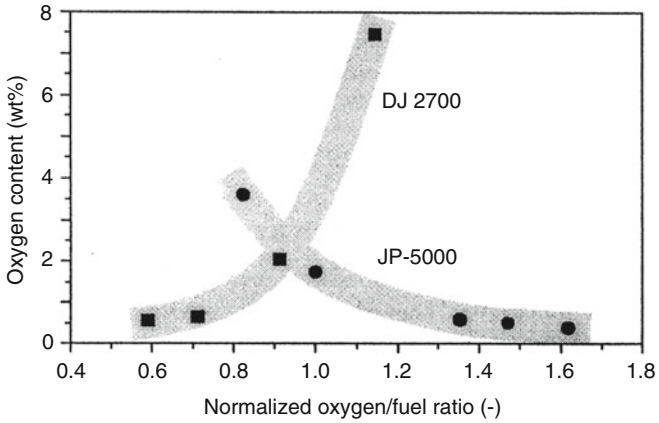


Fig. 5.26 Variation of stainless steel 316L oxidation with the oxygen/fuel ratio of combustible gases. Reprinted with kind permission from Springer Science Business Media, copyright © ASM International [68]

a negligible effect on particle velocity according to the numerical model. Experiments revealed that the impact velocity and temperature of 38 μm stainless steel particles could be controlled within the ranges 340–660 m/s and 1,630 and 2,160 K, respectively.

5.3.1.5 Particle Oxidation

Oxidation is a key parameter for a process that is mainly devoted to spraying metals or composites with metal matrix. Moreover, particles are often combined with carbide particles the decomposition of which is very sensitive to oxidation. Carbides also tend to be dissolved into the metal matrix when its temperature is too high.

Inside the gun (combustion chamber, nozzle, and barrel) and flame core, oxidation is present due to the excess oxygen (lean flame). However the particle temperature plays a key role in the oxidation process, especially if it is above the melting temperature: the oxygen content within a steel coating varies from 0.25 wt.% for particles below 1,700 K to 0.8 wt.% for particles at 1,800 K [68]! The variation of oxidation with the oxygen/fuel ratio of the combustible gases does not necessarily vary as it could be expected [68] (Fig. 5.26). With the DJ-2700 gun with axial injection of particles (particle temperatures higher than when injected radially into a JP-5000 gun), the excess of oxygen increases drastically the oxygen content of the coating (316L). In contrast, with the JP-5000 where the particle temperature is about 800 K lower, the excess of oxygen cools the particles more, and the effect is reverse: the more oxygen in the flame, the less oxide in the coating.

Oxidation, as shown by Dobler et al. [68] occurs only little in the jet core and more in the mixing region with the surrounding air (see Fig. 5.27 [69]), and, at last

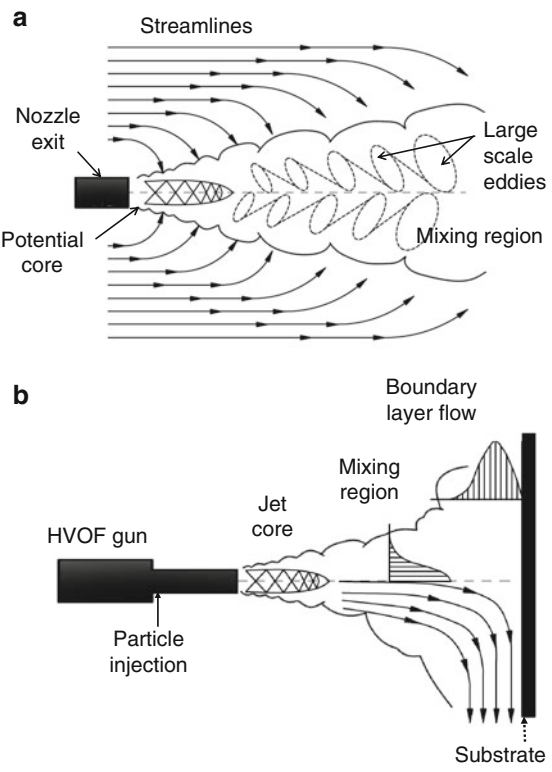


Fig. 5.27 Schematic drawing of HVOF jet mixing with the surrounding gas (**a**) details of the flow (**b**) different regions of the spray process. Reprinted with kind permission from ASM International [69]

within the coating during its formation. To reduce oxidation, a shroud gas can be used [69].

However shroud gas flow rates (nitrogen) must be very high. For an O_2 flow rate of 727 slm and kerosene flow rate of 0.42 slm (gun type of Fig. 5.12c), the nitrogen flow rate reaches 0.45 kg/s (about 21.6 m^3/s!) to reduce the oxygen content of pure iron from 3 wt.% to 1 wt.% as shown in Fig. 5.28 [69]. To reduce oxidation with a shroud gas but with much lower shroud gas flow rate, Ishikawa et al. [70] have developed (see Fig. 5.29) a gas-shroud attachment to use with commercial HVOF guns (see Fig. 5.11c).

The gas shroud set-up has two important effects: particle (WC–Co) mean velocities are increased (with a reducing flame at a pressure of 0.72 MPa) from 760 m/s to 850 m/s with the shroud, while their mean temperatures drop from 1,950 °C to 1,830 °C. Accordingly, the density of the sprayed coating was improved, the degree of decomposition of WC dropped from 6 % to 2.5 %, and coatings were superior both in corrosion and wear resistance compared to those obtained with no shroud.

To check the influence of the gun design, a series of experiments [71] were performed with the same powder, an agglomerated and sintered WC–Co 83–17

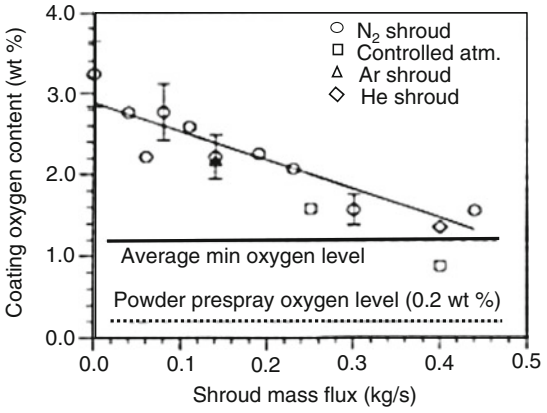


Fig. 5.28 Evolution of the coating oxygen content with the mass flow rate of shroud gas for different shroud gases. Reprinted with kind permission from ASM International [69]

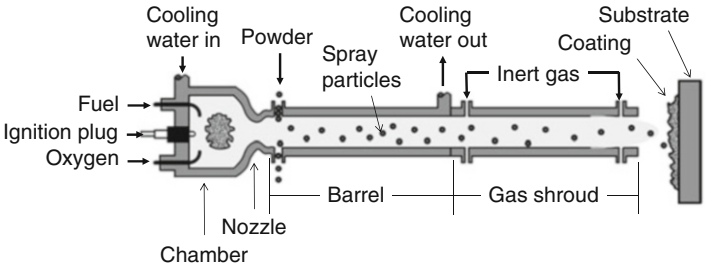


Fig. 5.29 Schematic drawing of commercial high-pressure HVOF (JP5000) with a gas shroud. Reprinted with kind permission from Springer Science Business Media [70], copyright © ASM International

with a particle size range of –45 + 10 µm. The powder was sprayed with the HVOF systems Jet Kote (Stellite Coatings, Goshen, IN), Top Gun (UTP Schweißmaterial, Bad Krozingen, Germany), Diamond Jet (DJ) Standard, DJ 2600, DJ 2700 (Sulzer Metco, Westbury, NY), JP-5000 (Tafa, Concord, NH), and Top Gun-K (GTV, Luckenbach, Germany). The degree of phase transformations depends on the heat transferred to the particles in the respective spray system, on the flame temperature of the fuel used, and on the type of spray powder [71]. Phase transformations increase when the injection of the powder occurs in a region where the flame temperature is highest such as in the Top Gun system, where the powder is injected directly into the combustion chamber. Less phase transformations occur when the powder is injected behind the combustion chamber in a region where the flame temperature is low, as in the JP-5000 and Top Gun-K system, or when the flame temperature is lowered by cooling air as in the DJ 2600 and 2700 systems [69]. Also, the use of dense spray powders, which are heated up less in the spray process, or powders that already contain some amounts of h-phase reduce phase transformations. Decarburization of an agglomerated and sintered WC–Co

(83–17 wt.%) powder ranges from 25 to 70 % for the various spray systems and fuels. But the properties of the coatings such as hardness and wear resistance are not influenced when the carbon loss remains below 60 %. Hardness and bond strength of the coatings are mainly determined by the impact velocity of the particles, and are, therefore, higher when systems with a converging–diverging Laval nozzle are used, which provide superior particle velocities.

5.3.1.6 HVAF and Modified HVOF Processes

For many metallic or cermet materials (mostly with carbides), oxidation and partial decarburization must be avoided or at least drastically reduced. This can be achieved by diminishing the gas temperature while increasing its velocity.

The design of Fig. 5.11c has allowed J. W. Browning to develop the HVAF process: instead of combustible gas, liquid petroleum is used and air replaces oxygen [72], which requires at least 5 times higher flow rates than with pure oxygen. For the same fuel–oxygen richness, nitrogen does not participate in the combustion but must be heated, thus resulting in lower temperatures (see Chap. 3 Sect. 3.1.2). The combustion chamber pressure is over 0.8 MPa and it corresponds to airflows in the 8–10 m^3/min range (for a HVOF gun of the first-generation gas flow rates are below 1m^3/min), inducing very high gas velocities (up to 2,000 m/s) [73]. Lower temperatures and higher velocities are beneficial to limit particle oxidation (see Sect. 5.3.1.4). Moreover the gun can be cooled by the airflow, and its efficiency can reach 90%. Flame ignition is generally made with pure oxygen. For example, Evdokimenko et al. [74] have calculated temperatures in the chamber of a HVAF gun working at 1 MPa with three different gases at stoichiometric composition. With hydrogen $T = 2{,}383$ K, with methane $T = 2{,}267$ K and finally with kerosene $T = 2{,}321$ K.

According to Evdokimenko et al. [74], the American firm "Draco Technologies" (Hanover, N.H., G. Browning, President) has placed on the market a number of specialized spraying equipment—the "Astrojet" seriesdesigned for stationary use in installations. The largest of these, "Astrojet-600", requires 17 m^3/min compressed air and 1.45 kg/min kerosene at a pressure of 2.0 MPa in the combustion chamber. This method of air–fuel high-velocity flame spraying fully satisfies requirements for the deposition of metallic anticorrosive coatings on large-scale structures. Quality aluminum coatings with a wide range of thickness, cohesive strength above 20.0 MPa, and porosity of the order of 1 % can be obtained on steel substrates by spraying powders with different particle sizes [74]. It is worth noting that HVAF systems are designed for spraying not only low-melting metals but also stainless steel, nickel–chrome, and even WC-based composite powders.

To reduce the HVAF process temperature and the particle oxidation, the injection of a liquid upstream of the powder injection but downstream of the nozzle is possible, as shown in Fig. 5.30 [59]. With water flow rates of about 20–30 kg/h, the gas temperature and velocity are about 600–700 K and 700–800 m/s, respectively. These characteristics are close to those of the cold spray process.

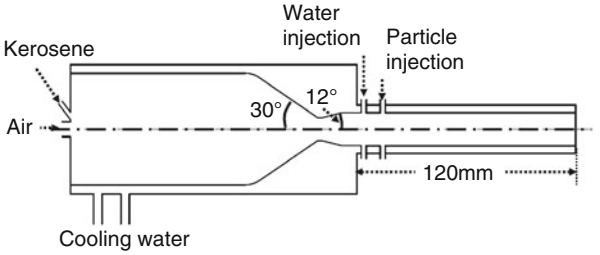


Fig. 5.30 Schematic diagram of low temperature high velocity air fuel spraying gun and nozzle with water injection downstream of the nozzle throat. Reprinted with kind permission from Springer Science Business Media [59], copyright © ASM International

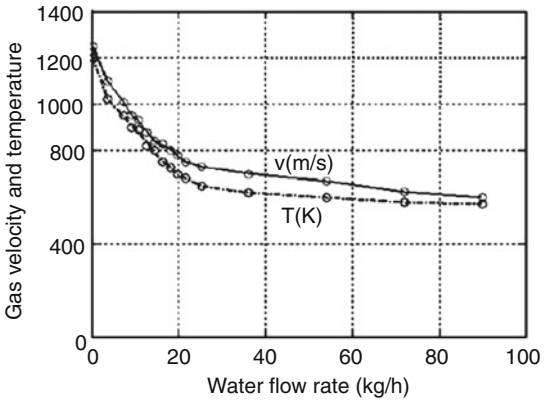


Fig. 5.31 Variation of gas velocity and temperature with water flow rate injected into the gun depicted in Fig. 5.30. Reprinted with kind permission from Springer Science Business Media [59], copyright © ASM International

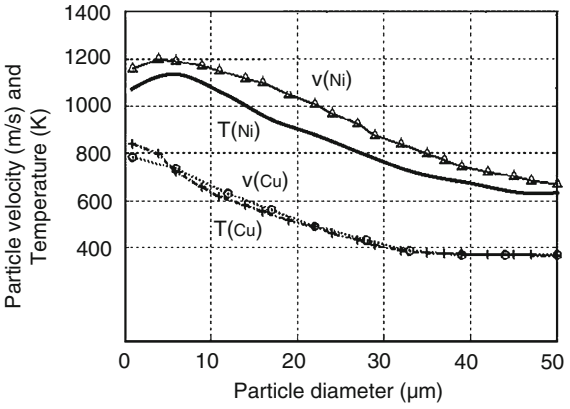


Fig. 5.32 Copper and nickel particle behavior at gun exit with water injection. Reprinted with kind permission from Springer Science Business Media [59], copyright © ASM International

Figure 5.31 shows that, as could be expected, both temperature and velocity are reduced. The optimum water flow rate seems to be 20 slm; above this value the cooling is inefficient.

In the case of water injection (see Fig. 5.30), where during the process the atomized water is vaporized, nickel and copper particles can be easily injected up to the flame core due to their higher density [59]. The particle in-flight behavior in the gun is shown in Fig. 5.32. For example, at the gun exit, the velocities and

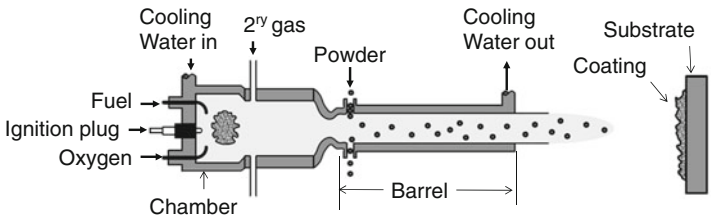


Fig. 5.33 Schematic of modified HVOF gun with an intermediate mixing chamber. Reprinted with kind permission from Springer Science Business Media [75], copyright © ASM International

temperatures of Cu particles with diameters ranging between 1 and 50 μm, vary between 700 and 300 m/s and between 900 and 400 K, respectively.

As previously mentioned, best results for HVOF or HVAF coatings (high density, low oxidation, no decomposition of carbides) are obtained when raising the particle velocities while decreasing their temperatures. That is why Kawakita et al. [75] have modified the gun depicted in Fig. 5.11c by adding a mixing chamber between the combustion chamber and the nozzle, as shown in Fig. 5.33. The combustion gas generated within the combustion chamber is mixed with nitrogen to lower its temperature. Compared to the HVAF process, injection of nitrogen gives more flexibility to tailor temperatures and velocities by adjusting the nitrogen flow rate. Typical working conditions for a modified JP-5000 are the following: kerosene from 0.29 to 0.35 slm, oxygen between 0.55 and 0.73 m^3/min, nitrogen from 0.5 to 2 m^3/min.

For example when spraying titanium on a steel substrate, dense coatings were obtained which provide excellent corrosion protection in artificial seawater in a laboratory test for over one month [75].

Titanium powder was sprayed by the modified HVOF process presented in Fig. 5.33 [75]. The results clearly reveal the effectiveness of controlling the temperature and the composition of the gas environment where the titanium powder is introduced. Especially, cooling of the jet flame prior to supplying the powder allowed reduction of the oxygen content of the resulting coating to the level of the titanium feedstock, suggesting this process might compete with cold spraying. Figure 5.34 shows the dependence of the titanium coating oxygen content and porosity with the nitrogen flow rate injected between the combustion chamber and the nozzle (see Fig. 5.33) [76]. Due to the flow, the gas cooling and the resulting lower particle temperatures led to a decrease of the oxidation level from 5.4 wt.% at 500 slm N_2 to 0.22 at 2,000 slm (spray distance 280 mm). However, over 1,000 slm the porosity increases with large average pore sizes because particle temperatures become too low, and particles lose their plasticity and deformability at impact. Thus, as usual, a compromise must be found.

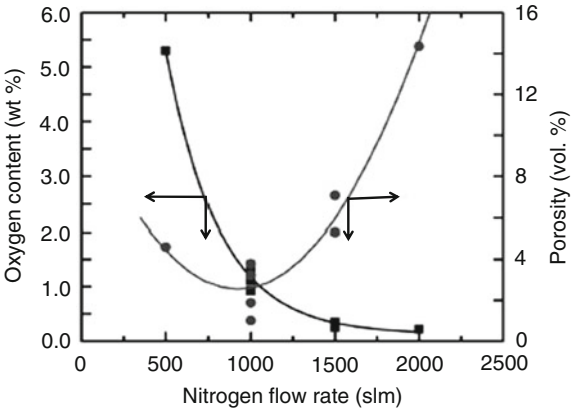


Fig. 5.34 Dependence of titanium (average particles size 28 μm) coating oxygen content and porosity on nitrogen flow rate, sprayed with the gun depicted in Fig. 5.33. Reprinted with kind permission from Springer Science Business Media [76], copyright © ASM International

5.3.1.7 Coating Formation

Trompetter et al. [77] made an interesting study of splat formation. They used an HVAF gun with a gas temperature of about 1,300 °C, below the melting point of NiCr powder (T_m = 1,400 °C). The particle velocity was about 670 m/s. When sprayed on soft substrates (compared to the NiCr hardness) predominantly solid splats were observed, which showed deep penetration, while on hard substrates that resisted to particle penetration, a higher percentage of molten splats was observed. They proposed an explanation of this observation by considering an increased conversion of particle kinetic energy into heat with increased particle plastic deformation with harder substrates.

The second effect of the high velocity impacts is a peening action and results in compressive residual stresses in coatings. The first work on this topic was that of Kuroda et al. [78]. They found that the intensity of the peening action and the resultant compressive stress by HVOF-sprayed particles increase with the kinetic energy of the sprayed particles. Measurements revealed that the residual stress at the surface of the HVOF coatings is low, often in tension, but the stress inside the coatings is at a high level of compression. This low value at the surface reflects the lack of peening effect of the last deposited layer. Normally, the quenching stress due to fast cooling of the splat is always tensile, and only the peening effect can transform this tensile stress into a compressive one. Other researchers [79–82] have confirmed these results. For example, with Ti-6Al-4V values of + 531 MPa were obtained [82], and similar values were observed for superalloy bond coats [81]. Such values, strongly linked to the impact velocity, vary from about 100 MPa at 500 m/s to 400 MPa at 650 m/s for 316L coatings [80]. Of course the substrate is also affected by this peening effect which, for example, for a stainless steel substrate, affects a region of approximately 100 μm depth, producing an increased sub-surface hardening. When these coatings are submitted to high temperature conditions, a recrystallization process takes place and the hardness decreases with the compressive residual stress.

Finally, the HVOF process provides high-density coatings (less than 3 % porosity) due to the high impact energy of particles (between 400 and 650 m/s) [83]. The short residence times of particles with rather low temperatures (by increasing the gas flow rate) allows deposition of particles slightly below the melting temperature, thus reducing oxidation and decomposition of materials such as WC. The particles have better bonding due to the high impact velocity and less degradation of the sprayed materials. Thus, such coatings have better wear resistance and higher hardness than those sprayed by flames or plasmas, and now, with the third generation of spray guns, sufficiently low porosity is obtained that these coatings can be used for corrosion protection. Coatings have mostly compressive residual stress, while those sprayed by flames or plasma is often tensile.

5.3.1.8 Summary of HVOF and HVAF Torch Evolution

Wielage et al. [84] summarize this status: "Presently developed new HVOF spraying guns operating at increased combustion chamber pressures show high potential for spraying of coatings consisting of metals that do not feature the outstanding ductility of pure copper or aluminum. High deposition efficiency, i.e., up to 85 %, at considerable powder feed rate of 4.5 kg/h is already possible for spraying of corrosion protective iron- or nickel-based coatings like AISI 446, AISI 316L, or MCrAlYs. Also spraying of highly reactive materials like titanium under atmospheric conditions becomes feasible. Both dense coatings for corrosion protection purposes and porous coatings for biomedical applications can be produced." [84].

5.3.2 HVOF Wire Spraying

One of the drawbacks of wire flame spraying is the relatively low velocity of particles at impact resulting in very porous coatings (over 10 %). On the other hand, wire flame spraying can be performed at high rates (up to 10 kg/h), which is often a key factor in process economics. Thus HVOF wire spraying has been intensively studied for the automotive industry. A schematic of a typical wire HVOF torch (Metco DJRW Diamond Jet gun) is given in Fig. 5.35.

The nozzle exit diameter is 8.7 mm and a typical wire diameter is 3.2 mm. The gas flow rates are 47 slm propylene, 212 slm oxygen, and 519 slm atomizing air. With a steel wire, these conditions have resulted in a droplet size distribution between 10 and 80 μm with velocities around 250 m/s. With a Flameter gun from Praxair, Neiser et al. measured [85] stainless steel droplet velocities of 540 m/s for 10 μm, 395 m/s for 20 μm, while their temperature was close to 2,200 K. Neiser et al. [85–87] have shown that the high gas velocity induces a convection phenomenon within liquid particles removing continuously fresh metal at their surface and moving the oxygen or the oxides formed at the droplet surfaces to the inside. Thus, within coatings one finds FeO inside the splats resulting from this convection

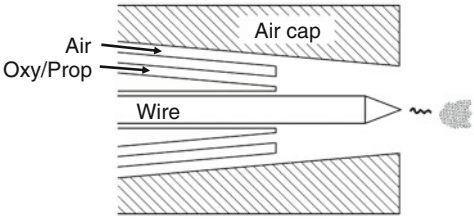


Fig. 5.35 Schematic diagram of the HVOF torch and the wire melting and atomization process. Reprinted with kind permission from ASM International [85]

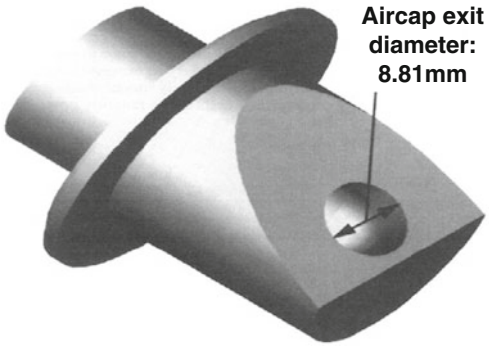


Fig. 5.36 Curved aircap adapted to the HVOF wire gun schemed in Fig. 5.35. Reprinted with kind permission from Springer Science Business Media [88], copyright © ASM International

phenomenon, while the splat surface is oxidized due to oxidation produced by diffusion at the droplet surfaces further from the nozzle exit where conditions for convection movements inside liquid droplets are no more existing. To spray steel inside aluminum–silicon cylinder bores for the automotive industry, a curved air cap has been adapted to the Metco rotating torch (DJRW Diamond jet) (Fig. 5.36).

Hassan et al. [88] and Lopez et al. [86] have calculated the flow (still with the axial position of the wire: see Fig. 5.35). Calculations and measurements give particle velocities at impact between 200 and 250 m/s. Of course, molybdenum has also been sprayed [89]. Coatings obtained with Mo + 25 wt.% NiCrBSi were compared to those sprayed by wire flame and d.c. plasma jets. Those sprayed by HVOF have a lower friction resistance than the plasma sprayed coatings, and they are harder and more wear resistant than those sprayed by wire flame. Low carbon steel was sprayed with methane and oxygen [90]. Such coatings are used for corrosion protection using Ni–Cr wires [91] and NiCrBSi, Cr_3C_2–NiCr and Stellite-6 [92]. With porosities of less than 1 %, the coatings sprayed with a HVOF wire fuel–oxygen gun have shown good resistance to hot corrosion, especially the Ni–20Cr coatings.

At last it must be mentioned that a hybrid spray process has been developed [93] which combines arc spray with a HVOF/plasma jet gun. In this system, shown schematically in Fig. 5.37 the material to be sprayed is introduced in one of the following ways:

- Via arcing of wires only
- Full hybrid mode with both arcing of wires and a powder or wire through the HVOF gun

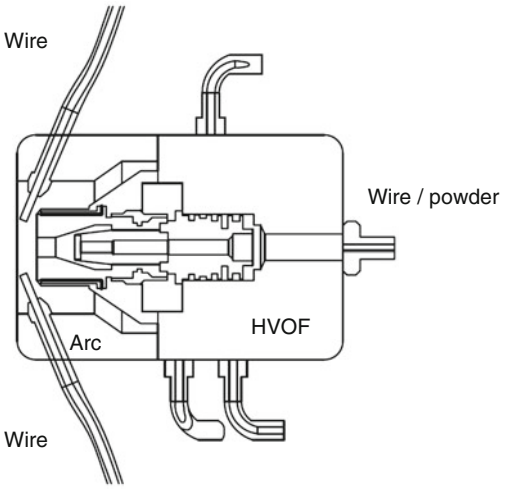


Fig. 5.37 Hybrid spray torch comprising wire arc and HVOF gun. The torch can be operated in the partial-hybrid mode using two-wire arcing, or in the full-hybrid mode using two-wire arcing and powder through the HVOF nozzle, or in the HVOF mode with material fed as powder or as wire. Reprinted with kind permission from Springer Science Business Media [93], copyright © ASM International

- Pure HVOF mode with either wire or powder fed to the HVOF gun
- According to the authors, this system provides very dense coatings compared to arc-sprayed ones [93]

5.3.3 Applications: General Remarks

HVOF produces cermets, metals and a few ceramic protective coatings, which are typically 100–300 μm thick, onto surfaces of engineering components to allow them functioning under extreme conditions. Initially, the focus was on wear-resistant coatings, but now the coatings are extensively studied for their corrosion and oxidation resistance which can be better than those produced by other spraying technologies. These coatings have found wide applications in marine, aircraft, automotive, and other industries. They are used for reclaiming a wide range of petrochemical process components.

5.3.4 Coatings Sprayed with Combustible Gases and Oxygen

5.3.4.1 Metals

Pure aluminum coatings with low porosity were obtained with the lowest oxygen/fuel ratio with HVOF [94], and porosity values down to 1 % were obtained with HVAF [74]. Iron-aluminide was sprayed with HVOF with 7–15 wt.% oxide inclusion [95]. Among alloys the most popular is Ni–Cr for which adherence is very high

on stainless steel substrates (more than 100 MPa) and is not affected by thermal fatigue [96]. When HVAF sprayed onto aluminum substrates, NiCr particles exhibit a strong bond with the substrate with an important penetration into it but with no evidence of chemical bonding [97]. NiCr or NiCrSiB coatings are used against the severe corrosive environment in waste to energy boilers [98, 99]. NiCrMoNb is also used against corrosion [100].

In thermal barrier coatings, upon exposure to high-temperature gases, a thin oxide scale, the thermally grown oxide (TGO), forms at the bond coat/top coat interface and continues to grow in thickness during thermal cycling. The TGO uneven and rapid growth results in localized stress concentrations where cracks can nucleate and initiate the failure dynamics. To achieve a dense and uniform α-Al_2O_3 TGO scale with a slow growth rate HVOF coatings of super alloys have been used [101–113]. Coatings have been studied for the influence of various parameters such as bond coat thickness and roughness, composition, mechanical properties evolution through the top coat, bond coat, substrate, spray process,... HVOF-sprayed bond coat coatings have been compared to those obtained by plasma spraying (APS and VPS), cold spraying, and D-gun. They have higher aluminum content, and the thermally grown oxide (TGO) developed during cyclic oxidation contains less mixed oxide clusters and a stable Al_2O_3 layer. Thus the TGO has a low growth rate and low tendency for crack propagation that leads to an improved TBC durability. Typical HVOF bond coat of NiCrAlY (Cr: 24–26, Al: 4–6, Y: 0.4–0.7, Ni: bal.) with a narrow size distribution (47–57 μm) sprayed with JP-5000 HP/HVOF (kerosene–oxygen) is presented in Fig. 5.38a representing substrate, bond coat, and top coat, the bond coat microstructure being presented in Fig. 5.38b. It has a lamellar structure containing dispersed inclusions of aluminum oxide, as well as pores of varying sizes for a total porosity of 3.2 %. Its average roughness Ra is 5.38 μm. The bond coat presents broader and lower diffraction peaks of the γ-Ni_3Al phase than the starting NiCrAlY powder.

HVOF metal coatings (Stellite®6) have an excellent resistance to cavitation erosion [114]. Bulk amorphous coatings (NiTiZrSiSn) have also been successfully sprayed when reducing the in-flight oxidation by reducing the oxygen to fuel gas ratio [115].

5.3.4.2 Cermets

These coatings have been intensively studied from the beginning, and the success of HVOF or HVAF processes relies on them [116–128]. The cermets, which are mostly sprayed are WC–Co and Cr_3C_2–NiCr. One of the key issues for coating quality is to avoid carbide decomposition or at least reducing it as much as possible. Spraying with fuel rich mixtures [118] and using HVAF preferentially to HVOF [120, 121] allows reducing drastically or even avoiding carbide decomposition. These coatings are used for their wear resistance (friction and erosion) and corrosion resistance, especially for those containing NiCr. Other composites are also sprayed, such as MoB/CoCr [128] against erosion by molten Al–Zn alloys,

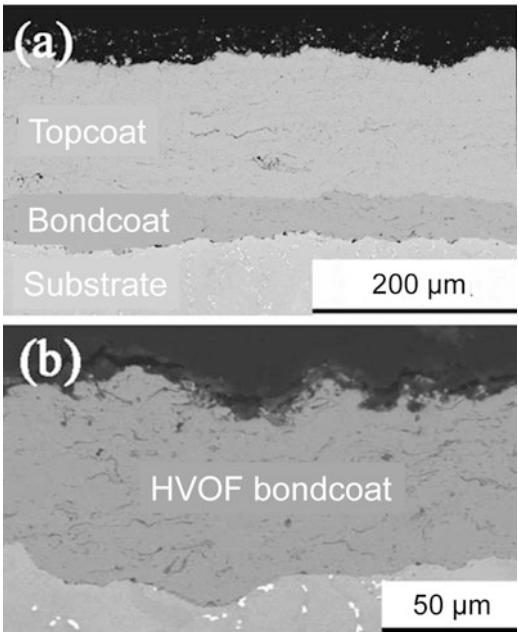


Fig. 5.38 (**a**) Cross section of detonation-sprayed TBC using hollow sphere YSZ powder D-gun sprayed with the HVOF bond coat. (**b**) Microstructure of the HVOF NiCrAlY coating in the as-sprayed state. Reprinted with kind permission from Elsevier [113]

Ni–Ti–C [129], which, by SHS reaction, after spraying, contains TiC in a Ni-rich solution together with NiTi, TiO_2, and $NiTiO_3$, and lastly silicon nitride-based coatings [130], where the silicon nitride is imbedded in a complex oxide binder matrix. Such coatings exhibit satisfactory corrosion and thermal shock resistance.

5.3.4.3 Ceramics

Ceramic coatings are not the strongest point of HVOF or HVAF processes because the process is more prone to achieve high velocities than high temperatures. Titania is rather well melted in processes working with propylene [131, 132]. High Weibull modulus values are obtained compared to other spray techniques and coatings are very dense and uniform, rutile being the major phase. Alumina is mostly sprayed with chromia, which allows stabilizing the α phase [133]. At last zirconia stabilized with yttria with particles below 10 µm can be sprayed, and it is suggested that sintering can play a role with good adhesive and cohesive coatings [134].

5.3.4.4 Polymers

Among the sprayed polymers Nylon 11 is the one most frequently used, with or without ceramic doping [135–137]. The residence time in the HVOF is generally short enough (~1 ms) to limit its degradation and a change of its color. Such

coatings, when used for their dry sliding wear performance, are more wear resistant without doping powders because those additions may lead to abrasive and fatigue wear.

5.3.5 Coatings Sprayed with Liquid Fuel and Oxygen

When comparing Ni–20 wt.% Cr sprayed with gaseous or liquid fuel, the latter results in less oxidation, less porosity, and less evidence of melting. Accordingly, such coatings are able to withstand more than 3,000 h exposure to neutral salt spray tests without substrate corrosion which is two orders of magnitude more than what is obtained with gaseous fuels [138]. Materials sprayed are almost the same as those sprayed with gaseous fuel. The main differences are the higher velocities and the lower temperatures.

With copper particles sprayed at 500 m/s, very dense coatings were obtained when the particle temperatures were such that the particles were highly deformable just below the melting temperature [139]. The same results were obtained with stainless steel, which, with addition of molybdenum, resulted in good corrosion resistance coatings [140] that were also harder than wrought material [141]. Stellite®-6 was also excellent for repair cavitation damage in turbines and pumps [142]. Similar results were obtained with Ni–Cr coatings which had adhesion values of over 70 MPa on 9Cr–1Mo steel, and which presented an excellent steam-oxidation resistance [143, 144]. When spraying MCrAlY coatings with such HVOF guns with an inert gas shroud, the coating oxygen levels were almost as low as those obtained in vacuum plasma spraying (VPS) [145]. It was also possible to achieve amorphous phase formation of Zr-based alloy coatings (up to 62 %) due to low oxide formation. Of course if the coating is overheated by spraying it with too low standoff distance [146] no amorphization is possible. When heat treating Co–Mo–Cr–Si coatings at 600 °C, the hardness increases and the friction between the coating and an alumina pin diminishes [147].

With cermets WC–Co, Cr_3C_2–NiCr [148–155] rather dense coatings are obtained. Cr_3C_2–NiCr coatings are more protective against corrosion than WC–Co ones. This fact is attributed to the formation of Cr_2O_3, NiO, $NiCr_2O_4$ [151]. WC–20 wt.% Cr_3C_2–7 wt.% Ni cermet coatings have good resistance to sliding wear [152]. Adding WC to the powder [153] improved the hardness of WC–Co–Cr. Cr_3C_2–NiCr coatings on Ni base super alloys provided a good resistance to hot corrosion [154]. At last, WC–Co + CoMoCrSi coatings are harder but less tough than electrolytic hard chrome (EHC) coatings, and their two-body sliding resistance definitively overcomes that of EHC coatings, but they experience a comparable or even higher mass loss when subjected to three-body abrasion conditions [152]. WC–NiCrFeSiB coatings on Ni- and Fe-based super alloys show excellent oxidation and hot corrosion resistance at 800 °C [155].

Liquid fuel HVOF is also used to spray materials in which solid lubricants are incorporated such as WC–Co and fluorinated ethylene–propylene (FEP) copolymer-based material [156] or iron sulfide [157].

As with flame or gaseous fuel HVOF, SHS (Self-propagating high temperature synthesis) reactions can be produced upon spraying, for example, with SiO_2/Ni/Al–Si–Mg powder resulting in composite materials of $MgAl_2O_4$, Mg_2Si in an Al–Si matrix [158]. A rapid formation of aluminide ($NiAl_3$) can be produced by an exothermic reaction of plated nickel with Al–Si–Mg core powder [158]. In both cases reactions start in-flight and finish during splat layering. Such composites are rather hard.

5.3.6 HVOF–HVAF Modeling

5.3.6.1 1D Calculations

In simplified 1D models, it is assumed that most of the reactions occur in the combustion chamber (convergent part of the nozzle) and the reactions move forward following an equilibrium chemistry model. This assumption is based on the fact that the residence time of the gas in the combustion chamber is much longer than in the subsequent parts. The heat released from the exothermic reaction increases the gas temperature. During passage through the nozzle, the thermal energy is partially converted into kinetic energy. If the effects of water cooling and friction on the wall are ignored, several relationships can be derived from the governing mass, momentum, and energy conservation equations [47, 159] to relate the gas properties between two positions (1 and 2) in the nozzle (Roberson and Crowe (1997) [159]).

$$\begin{aligned}
\frac{A_2}{A_2} &= \frac{M_1}{M_2}\left\{\frac{1+[(\gamma-1)/2]M_2^2}{1+[(\gamma-1)/2]M_1^2}\right\}^{(\gamma+1)/2(\gamma-1)}, \\
\frac{T_2}{T_1} &= \frac{1+[(\gamma-1)/2]M_1^2}{1+[(\gamma-1)/2]M_2^2}, \\
\frac{P_2}{P_1} &= \left\{\frac{1+[(\gamma-1)/2]M_1^2}{1+[(\gamma-1)/2]M_2^2}\right\}^{\gamma/(\gamma-1)}, \\
\frac{\rho_2}{\rho_1} &= \left\{\frac{1+[(\gamma-1)/2]M_1^2}{1+[(\gamma-1)/2]M_2^2}\right\}^{1/(\gamma-1)}
\end{aligned} \tag{5.6}$$

where A is the cross-sectional area perpendicular to the flow direction, T is the gas temperature, ρ is the gas mass density, p is the pressure, γ is the specific heat ratio,

and M is the Mach number defined as the ratio of gas velocity to the local sound velocity $\left(a = \sqrt{r \cdot p/\rho}\right)$. Since the flow is choked at the throat area, where the Mach number is 1, the mass flow rate m° at the throat of the nozzle is given by

$$m^{\circ} = A_{\mathrm{t}}.a_{\mathrm{t}}.\rho_{\mathrm{t0}} \tag{5.7}$$

where the subscript t denotes throat, A_{t} is the throat area, a_{t} the sound velocity at the throat. m° should match the specified mass flow rate at the entrance of the torch.

Based on this, different calculations can be performed:

1. Thorpe and Richter [47] calculated first the gas temperature T_{g} assuming an equilibrium combustion at the chamber pressure p_0, resulting in the temperature T_0 after corrections accounting for thermal losses at the chamber wall. T_0, p_0, and the corresponding specific mass ρ_0 allow calculation of the temperature, pressure, and specific mass at the throat using equations related to an isentropic flow:

$$\begin{aligned} T_{\mathrm{t}} &= \frac{2.T_0}{\gamma + 1} \\ p_{\mathrm{t}} &= p_0 \left(\frac{2}{\gamma + 1}\right)^{\frac{\gamma}{\gamma + 1}} \\ \rho_{\mathrm{t}} &= \rho_0 \left(\frac{2}{\gamma + 1}\right)^{\frac{1}{\gamma + 1}} \end{aligned} \tag{5.8}$$

   Once T_{t}, p_{t}, and ρ_{t} are determined, Eq. (5.7), where m° is known, allows determining the throat area, A_{t}. Equation (5.6) where $M_1 = 1$ allow calculating the Mach number, M_2, at the nozzle exit if the exit area is known, or the exit area for a given exit Mach number. Such calculations result in gas velocity values, which are in quite acceptable agreement with measurements [47].
2. Based on Eqs. (5.6) and (5.8), an iterative procedure is used to determine the combustion properties. Once the gas properties at a specific point are determined, the entire internal flow/thermal field can be readily solved using Eq. (5.6) [150, 151, 160–162].

   Since the capture of shock diamonds using a one-dimensional model is very difficult, the supersonic free jet in the external flow field is modeled by taking advantage of the experimentally measured data available for supersonic free jets [159]:

$$\overline{gp} = 1 - \exp\left(\frac{\alpha}{1 - \overline{x}/\beta}\right) \tag{5.9}$$

   where gp refers to normalized gas properties $(v/v_{\mathrm{e}}$, $(T - T_{\mathrm{a}})/(T_{\mathrm{e}} - T_{\mathrm{a}}))$ and $(\rho - \rho_{\mathrm{a}})/(\rho_{\mathrm{e}} - \rho_{\mathrm{a}})$, where the subscripts a and e stand for atmospheric condition

and nozzle exit condition, respectively), $\overline{x}$ is the normalized axial distance from the exit of the nozzle ($\overline{x} = x/D$, where D is the diameter of the nozzle exit) α and β, are constants.

5.3.6.2 2D Or 3D Calculations

(i) Combustion Calculation

Liquid fuel and oxygen are generally premixed before being introduced into the combustion chamber. When using a liquid gas such as propane, it is assumed that the liquid evaporates to a gas state and mixes perfectly with oxygen before combustion. This assumption is valid, for example, for liquid propane due to its unique characteristics of extremely low boiling point. When kerosene is used, the numerical model needs to include the effect of droplet evaporation and flow interaction [162].

In most cases the effects of dissociations and intermediate reactions are represented by an equilibrium formulation as follows:

$$n_1 C_x H_y + n_2 O_2 \rightarrow n_3 CO_2 + n_4 H_2O + n_5 CO + n_6 HO + n_7 O_2 + n_8 O + n_9 H_2 + n_{10} H \tag{5.10}$$

An eddy dissipation model [163] is used to solve this global reaction [162]. This approach is based on the solution of transport equations for species mass fractions. The reaction rates are assumed to be controlled by the turbulence instead of the calculation of Arrhenius chemical kinetics.

(ii) Flow Calculation

The governing equations for the HVOF thermal spray process are the conservation of mass, momentum, and energy with the ideal gas law. The direct solution of these conservation equations for high-Reynolds number turbulent compressible flow is far beyond the current computation capacity [60]. However, by applying Reynolds or Favre averaging, these equations can be simplified in such a way that the small-scale turbulent fluctuations do not have to be directly simulated, and consequently, the computational load can be significantly reduced. In Reynolds or Favre averaging, the solution variables are decomposed into the mean (time- or density-averaged) and fluctuating components:

Reynolds (or time) averaging:

$$\phi = \overline{\phi} + \phi', \text{with } \overline{\phi} = \frac{1}{\Delta t}\int_{t_0}^{t_0+\Delta t} \phi \, dt \text{ and } \overline{\phi}' = 0. \tag{5.11}$$

Favre (or density) averaging:

$$\phi = \widetilde{\phi} + \phi'', \text{with } \widetilde{\phi} = \overline{\rho\phi}\,\overline{\rho} \text{ and } \widetilde{\phi}'' = 0. \tag{5.12}$$

The instantaneous continuity and momentum equations, described in Sect. 3.3.2 of Chap. 3, are modified by substituting the above expressions, and taking a time average (Reynolds) of pressure and density, and density average (Favre) of all the other quantities. Due to high Reynolds numbers and large pressure gradients in the nozzle, the renormalization group (RNG) *k–ε turbulence* model is used with the nonequilibrium wall function treatment to enhance the prediction of the wall shear and heat transfer [60]. In most cases the process model of gas dynamics is implemented into Fluent, the commercial CFD software, and is solved by finite volume method. The interested reader can see papers [53, 54, 59, 60, 63, 86].

5.4 Detonation Gun (D-Gun)

In contrast to other combustion processes, where the flame is a subsonic wave sustained by a chemical reaction, detonation is a shock wave sustained by the energy of chemical reactions in the compressed explosive gas mixture. In flames, hot gases have a low density ($\rho_b/\rho_u \sim 0.06–0.25$), where ρ_b is the specific mass of burned gases and ρ_u that of unburned ones, and a pressure slightly below atmospheric pressure ($p_b \sim 0.8–0.9 \times p_u$). In contrast, if in a detonation process the pressure of unburned gases is atmospheric pressure, in the detonation wave $p_b/p_u \sim 13–25$ and $\rho_b/\rho_u \sim$ ‘1.4–2 [164] (see also Chap. 3 Sect. 3.1.4.2).

5.4.1 Process Description

In general, a gaseous detonation consists of a shock wave and a reaction zone, which is tightly coupled. The ideal detonation travels at an almost constant speed close to the Chapman–Jouguet velocity (v_{CJ}), which is between 1,500 and 3,000 m/s in gases, depending on the type and composition of the fuel–oxidizer gases). The pressure just behind the detonation wave can be as high as 20–30 times the ambient pressure.

According to Kadyrov [165] the process comprises four steps: (a) injection of an oxygen and fuel mixture into the combustion chamber, (b) injection of the powder dose and then of nitrogen between ignition point and gas mixture to separate the gas supply from the explosive gas mixture and prevent backfiring (the detonation wave can propagate in all directions, including into the gas supply, creating an explosion hazard), (c) ignition of gas mixture and creation of the detonation, powder acceleration by the detonation wave, impact of particles onto the substrate, and (d) purging of the barrel using nitrogen gas [165]. The scheme of the different stages of the detonation process is shown in Fig. 5.39.

Once the barrel is purged, the process starts over. Steps (a) and (b) are the preparatory ones, while steps (c) and (d) are self-governing ones independent of

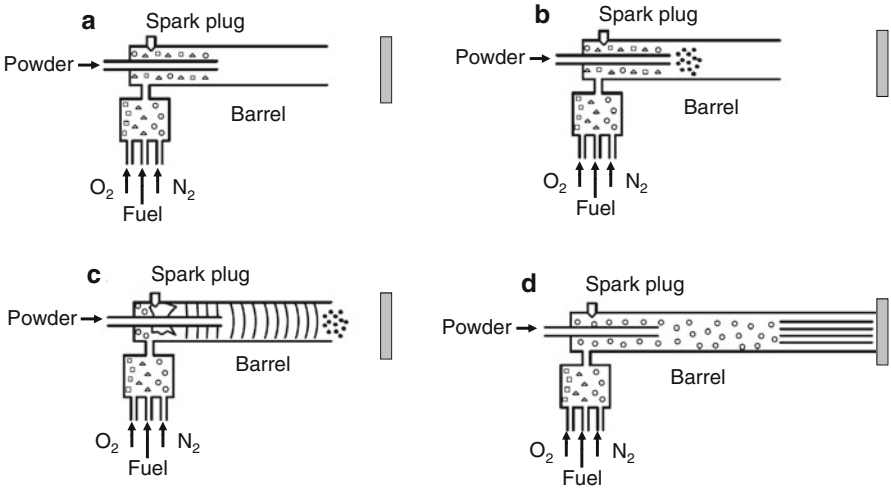


Fig. 5.39 Schematic of the detonation process cycle, using nitrogen as a buffer gas: (**a**) injection of fuel and oxygen into combustion chamber, (**b**) injection of powder and nitrogen gas, (**c**) gas detonation and powder acceleration, (**d**) chamber exhausting. Reprinted with kind permission from Springer Science Business Media [165], copyright © ASM International

the process control system. The injection of fuel into the D gun and the mixing of fuel with incoming oxidizer or injection of fuel–oxidizer mixture start the new operation cycle. A mechanical or electromagnetic valve is used in industrial guns to prevent detonations or shocks into the feeding system and provide a sufficient time for mixing of the fuel with the oxidizer.

In fact it is also possible to describe the process more precisely, as did Kharlamov [166], in nine steps instead of the fourth of Kadyrov [165].

Accordingly Detonation guns can be designed with different versions of combination of working cycle steps [165]. According to Astakhov [165] the detonation coating quality depends on the three important following stages of the process:

5.4.1.1 (a) First Stage Comprising

- The process parameters: the composition of the gas mixture, degree of filling of the barrel, powder charge, particle sizes, particle shapes, position and concentration of the powder cloud in the barrel at the time of detonation initiation (the optimal powder charge is around 0.25 g), and the distance from the nozzle to the substrate.
- Design features of the spraying machine: the size and shape of the barrel, the location where the mixture is ignited, and the location of feeding the powder into the barrel, and firing rate.

5.4.1.2 (b) Second Stage with

– The energy characteristics (gas temperature and velocity) and powder particles, the pressure and density of the gas, and the period during which the powder is in the high temperature flow (two-phase flow exists no longer than about 5×10^{-3} s).

5.4.1.3 (c) Third Stage Including

The temperature and pressure in the zone of physical and chemical processes between the contacting materials and the duration of these processes controlling bonds formed between the interacting materials at the coating–substrate or coating previously deposited layers interface. The process is intermittent in nature (between a few Hz and 100 Hz), which makes it possible to keep the substrate at low temperature (typically $< 100\ ^{\circ}C$). The operating frequency f of a given detonation gun is defined as $1/t_c$, where the cycle duration t_c is, in general, composed of six characteristic time intervals [166]: filling of barrel by fresh gas mixture Δt_{gfl}, filling of barrel with powder Δt_{pfl}, purging Δt_{pr}, detonation initiation, Δt_{in}, detonation traversing the barrel Δt_{tr}, and exhaust of detonation products and powder particles Δt_{ex}, i.e.,

$$t_c = \Delta t_{gfl} + \Delta t_{pfl} + \Delta t_{pr} + \Delta t_{in} + \Delta t_{tr} + \Delta t_{ex} \tag{5.13}$$

The dynamic filling, Δt_{gfl}, and exhaust/purging, Δt_{pr}, processes have the longest duration and can be shortened by operating at higher dynamic pressures, but with some upper limit due to filling losses. The length and the volume of the barrel together with the pre-detonation chamber and the filling velocity determine the filling time, Δt_{gfl}, since the mass flow into the combustor has to traverse the combustor length [166]. Compressibility effects occurring when injected gas velocity is over Mach 0.5 limit the fill rate. A full cycle of the detonation gun, t_c, can then be calculated by summing each characteristic times. An optimum exists because of the coupling of the length, dynamic pressure, and operating frequency of a barrel. Practical values are up to 100 Hz for a 1 m long combustor operating at an initial pressure of 0.1 MPa [166]. When using multiple injection locations this frequency limit could be overcome [168]. The length of the barrel can reach $100 \times d_b$ where d_b is the barrel internal diameter [166]. However, half of the gas thermal energy is lost after $40 \times d_b$!

The minimum barrel diameter depends on heat losses to the tube wall and is typically 15–20 mm for most fuels and particle materials for a realistic 20 μm roughness of the channel walls. A barrel 15 mm in diameter is sufficient for spraying cermets of tungsten carbide–metal when using acetylene, and a barrel 40 mm in diameter is necessary when using propane [169]. According to Kharlamov Y. A. [166], varying the barrel cross-sectional area along its length, as presented in his paper, provides a uniform filling of the barrel. It is possible to use

a nozzle at the barrel end to improve the performance of the D gun [168]. Contrary to nozzles of steady-flow devices, D gun nozzles operate at essentially unsteady conditions and their design and optimization require considering the whole operation process. Attachment of a nozzle to the end of the detonation tube makes it possible to gradually expand gases and decrease the rate of pressure drop in the tube. However, the nozzle increases the length of the barrel and thereby decreases the operation frequency.

Wang et al. [170] have proposed another solution to avoid that the sprayed particles follow the expansion of the high pressure flow exiting the detonation barrel, high-pressure flow exiting the detonation barrel. The dispersion of sprayed particles results in diameters of sprayed spots deposited on the substrate larger than the inner diameter of the barrel. The use of the separation device, shown in Fig. 5.40, in the D-gun spraying system narrows the stream of the detonation products and prevents the dispersed and solidified particles from reaching the substrate or the sprayed splats. The tightening flange and separation liner plate were precisely linked with the barrel sleeve by four long support screws and flange bolts. The inner diameter of the separation liner plate is the same as that of the barrel, so that it can accurately separate the spraying powder from the spraying flow. The outer diameter of the separation liner plate is five times the size of its inner diameter, which can ensure the spraying powder outside the designated area to be intercepted completely. The separation liner plate must often be replaced or cleaned after being used for a period of time due to the partially dispersed spraying powder deposited constantly on it. By comparison of WC–Co coatings achieved without and with the separation plate, the surface roughness Ra, the porosity, and wear rate decrease respectively by 77 %, 41 %, 40 %, and 20 %. The Vickers microhardness HV, the Knoop microhardness in both directions (parallel and orthogonal to the coating) HKcs∞, HKcs$\|$, the elastic modulus Ecs∞, Ecs$\|$, and the adhesive strength increase by 12 %, 13 %, 13 %, 32 %, 36 %, and 16 %, respectively [169].

Intensive turbulence, caused by the roughness of the internal D gun wall modifies the hot gas turbulence, thus promoting the heat losses to the wall but also more uniform mixing of the powder with the combustion products. Roughness can be achieved by threaded grooves of various profiles, made along the entire length of the barrel, or in individual sections [166]. When the grooves are located in the barrel inlet section, the pre-detonation distance is shortened, whereas their location at its outlet improves powder mixing and intensifies heat exchange.

In fact, as pointed out at the beginning of this section, idealized schemes of the process imply perfect premixing of fuel and oxidizer, steady-state initial conditions in the detonation gun, localized instantaneous detonation initiation, thermodynamically equilibrium pressure, temperature and composition of detonation products in a planar, constant speed, classical Chapman–Jouget detonation, and an adapted ideal nozzle. In addition it implies perfect inlets with full pressure recovery and infinitely fast response mechanical valves [168]. This is far from being the case. Because of rigorous safety regulations, it is generally not recommended that perfectly premixed fuel and oxidizers are utilized in practical devices. As the

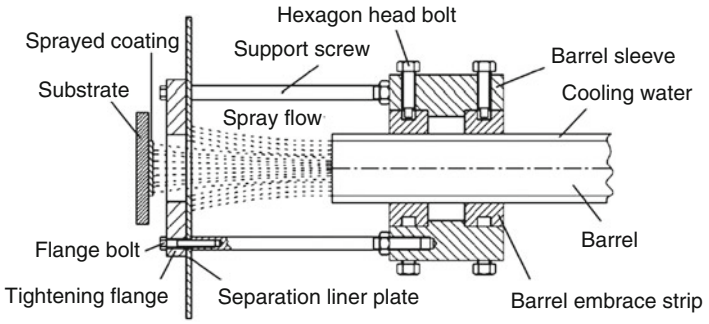


Fig. 5.40 Sketch of a separation device used in the D-gun spraying system. Reprinted with kind permission from Elsevier [170]

operation cycle of detonation guns is transient and the time available for mixing is very short as compared to the steady-state analogs, mixing enhancement can become a crucial issue [167].

Astakhov [167] has proposed and patented (in the USA, Germany, Japan, France, and Switzerland) a new detonation spraying method that provides a more homogeneous detonation mixture. It differs from the traditional method by continuous feed (stationary gas flow) of a mixture of combustible gases (for example, oxygen and acetylene) to the combustion chamber. The process is made periodic and the gas mixture is kept away from the detonation products by feeding periodically a neutral gas (nitrogen, argon) between the supply of powder and the point of ignition of the gas mixture. Since the pressure of nitrogen is 2.5–3.0 times higher than the pressure of the combustible gases, they are prevented from entering. The quality of coatings obtained with that method is described as excellent [167].

The consumption of gas per unit mass of sprayed matter is four to eight times less than that for HVOF spraying [165]. The frequency and noise levels (about 145 dBA) require the detonation to be confined in acoustical enclosures. According to Kadyrov [165] one can image propagation of the detonation wave as a stationary distribution of density, temperature, pressure, and velocity moving with some speed distribution. Figure 5.41 gives a qualitative picture of the detonation parameters [165]. It is assumed that the thickness of the reaction zone is very thin and that the zone of the reaction products is separated from the initial gas mixture by the detonation wave front. At the leading edge of the detonation wave, the temperature increases drastically, and then behind the front rises gradually in the reaction zone before decreasing gradually with increasing distance from the wave front (Fig. 5.41B). There are also step like increases in pressure and specific mass density at the detonation wave front followed by a gradual decrease behind (Fig. 5.41A, C). For other information see Chap. 3 Sect. 3.1.4.

Generally, the addition of light gases (He, H_2) increases the detonation velocity, while the addition of heavier gases decreases the speed. The velocity of the detonation wave varies between 1,000 and 3,000 m/s depending on the composition

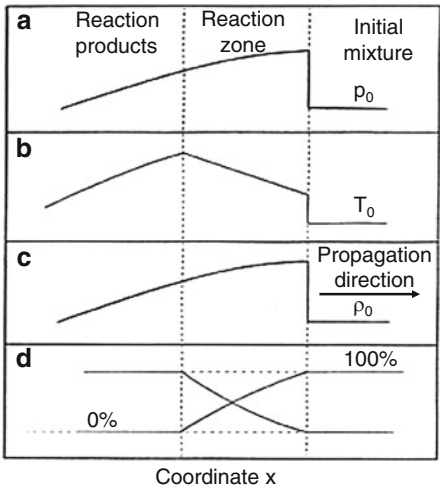


Fig. 5.41 Qualitative picture of detonation parameter variations in the gas (**a**) pressure, (**b**) temperature, (**c**) specific mass, (**d**) distribution of the detonation velocity, D, and un-burned gases. Reprinted with kind permission from Springer Science Business Media [165], copyright © ASM International

of the gas mixture. It is independent of the barrel diameter, provided it exceeds a critical diameter. Once the detonation occurs (ignition at the open end or closed end of the barrel) [165, 171] its theoretical velocity D (m/s) can be calculated through:

$$D = \sqrt{2(\gamma^2 - 1)Q_0} \tag{5.14}$$

where γ is the ratio of specific heats of the burned gases and Q_0 the specific energy of detonation. Temperature, T_1, and pressure, p_1, of the detonation products are given [165] by:

$$T_1 = \frac{2.\gamma}{\gamma + 1}.\frac{Q_0}{c_v} \tag{5.15}$$

$$p_1 = 2(\gamma + 1)\rho_0.Q_0 \tag{5.16}$$

Finally all parameters of the detonation are very sensitive to the composition of the combustible fuel, as well as to the fuel/oxygen ratio. This is illustrated in Fig. 5.42 representing the detonation wave velocity calculated with Eq. (5.14) for different oxygen/acetylene ratios and different nitrogen vol. percentages.

The detonation velocity increases when the amount of oxygen decreases for a stoichiometric acetylene /oxygen mixture. When introducing a small percentage of nitrogen, the velocity is drastically reduced (for example, 3 vol.% of nitrogen reduces the detonation velocity by 600–800 m/s. This addition allows tailoring the particle impact parameters. Similar calculations using Eqs. (5.14)–(5.16) for hydrogen/oxygen mixtures are summarized in Table 5.3.

Of course, more sophisticated calculations of detonations can be performed [172–174]. They account for the strong discontinuity of parameters at the barrel exit, the fuel–oxidizer mixture composition, the design of the gun, and the degree of barrel filling.

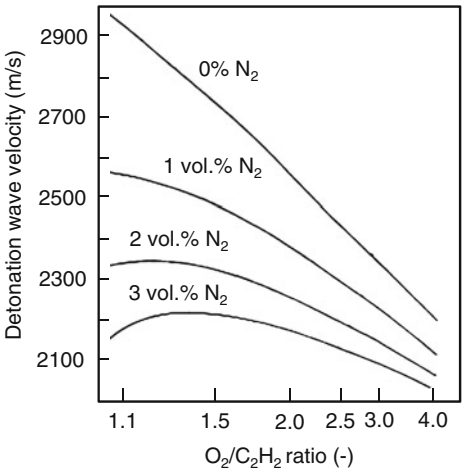


Fig 5.42 Effect of nitrogen gas on the detonation speed for different reverse equivalence ratios (1/*R* see Eq. (3.3)) of oxygen/acetylene mixtures into which a given vol.% of nitrogen is introduced. Reprinted with kind permission from Springer Science Business Media [165], copyright © ASM International

Table 5.3 Parameters of the detonation wave in hydrogen/oxygen mixtures with the addition of different gases. Reprinted with kind permission from Springer Science Business Media [165], copyright © ASM International

Fuel mixture	p_2/p_1	T_2 (K)	D (m/s)
$2H_2 + O_2$	18.0	3,283	2,806
$(2H_2 + O_2) + O_2$	17.4	3,390	2,302
$(2H_2 + O_2) + 4H_2$	16.0	2,976	3,627
$(2H_2 + O_2) + N_2$	17.4	3,367	2,378
$(2H_2 + O_2) + 3N_2$	15.6	3,003	2,033
$(2H_2 + O_2) + 1.5Ar$	17.6	3,412	2,117

5.4.2 In-Flight Particle Properties

Heat and momentum transfer to particles are calculated by using the conventional equations of motion and heat transfer [167, 173] with or without corrections for supersonic velocities. The formation of the gas–mixture–powder system is the key parameter in pulsed detonation thermal spraying. It is linked to the geometry of the system, the detonation mixture, the particle injection mode (axial being much better than radial [172]), the particle size distribution and morphology, and loading location

All calculations point out the importance of the position where particles are injected. This is illustrated in Fig. 5.43, which shows the influence of the distance between the point of detonation wave creation and the point of particle injection (loading distance).

For example, with a loading distance of 20 cm and an O_2/C_2H_2 mixture, the maximum velocity is 837 m/s against 1,152 m/s for a loading distance of 60 cm. Ramadan and Butler [175] have given a more detailed analysis of powder injection. Their model is related to one cycle of pulsed detonation thermal spraying and it

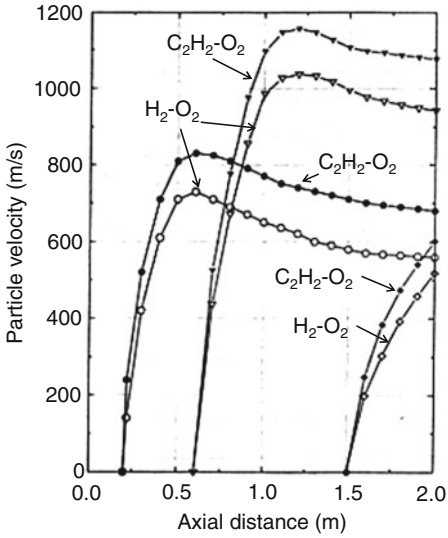


Fig. 5.43 Velocity of 20 μm Al_2O_3 particles versus axial distance for oxygen/acetylene (filled symbols) and oxygen/hydrogen (open symbols) stoichiometric mixtures for different injection locations. Reprinted with kind permission from Springer Science Business Media [165], copyright © ASM International

considers a two-component, compressible, reactive, two-dimensional, axisymmetric flow model, with a one-way coupling between the gas and the particulate phase.

Ramadan and Butler [175] have considered cylindrical detonation guns 25 mm in internal diameter with different lengths, L. The reactive gas mixture used is $C_2H_2/O_2/N_2$, with O/C = 1, $N_2(\%) = 40$, and the resulting detonation wave speed for this mixture is 2,464 m/s. The sprayed particles were alumina with three different diameters: 10, 20 and 30 μm. The standoff distance taken is six tube diameters, i.e., the substrate is far enough from the barrel exit plane so that the gas expands freely with negligible shock reflection effects. Figure 5.44a, b presents the dependencies of solid particle velocities and temperatures on their axial location, x_i, as well as the gas velocities and temperatures at the particle location. In this calculation the initial loading location is $x_i/L = 0.2$ and $L = 1$ m (injection position far from optimal). Hot gases also heat particles to high temperatures that can reach the melting point, depending on their sizes (Fig. 5.44b) and injection location (not represented here).

Finally, the analysis of Ramadan and Butler [175] shows that the geometrical configuration of the Detonation gun, the particle size, the loading locations and the standoff distances are important parameters in determining the properties of the end product. In general, increasing the standoff distance results in an increase in velocity and a decrease in temperature of the particle at impact on the target surface. Increasing the standoff distance also results in less uniform properties of the coating layer where the properties of the coating layer are dependent on the particle characteristics upon impact on the target surface. The particle terminal velocity and temperature are strongly dependent on the particle axial loading location with a weak dependence on its radial loading location. To achieve a coating layer with uniform properties the powder material should be loaded over a narrow range of axial locations.

The mass of powder injected into the barrel is usually smaller than 10–20 % of the gas weight. This is determined not by the deficit of gas energy but by the

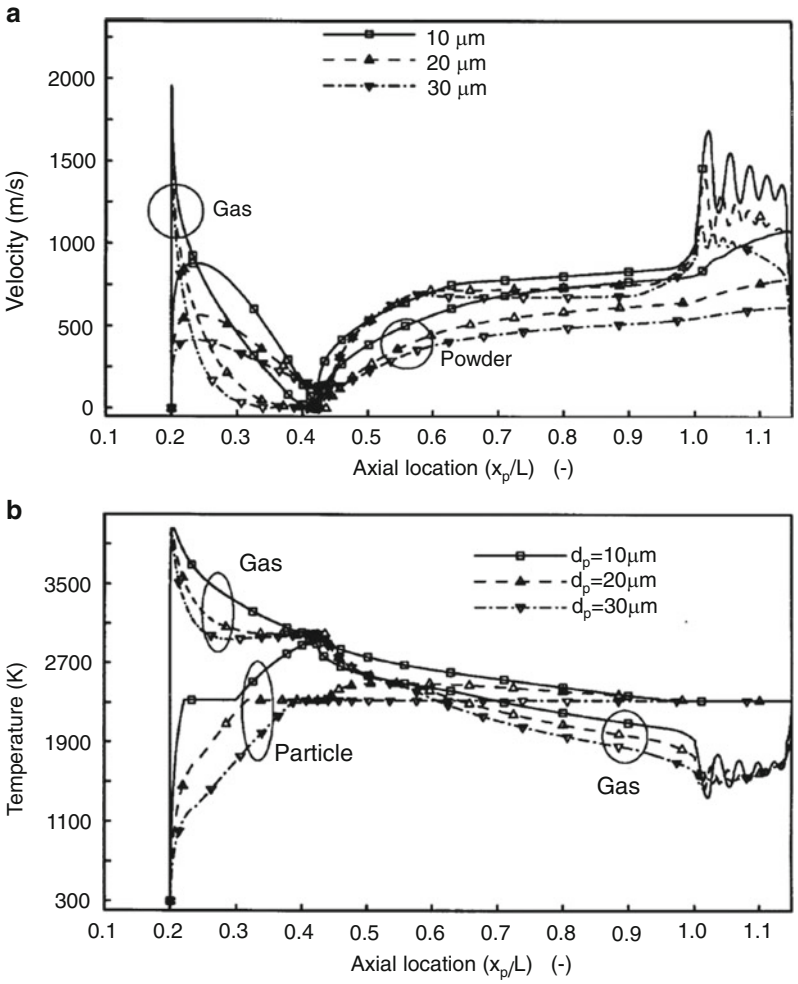


Fig. 5.44 (**a**) Particle velocity versus its axial location, and gas velocity at the particle location, (**b**) particle temperature versus its axial location, and gas temperature at the particle location. Calculations made for axial loading distance $x_i/L = 0.2$ and radial loading distance $y_i/r = 0.05$ ($L = 1.0$ m, $d = 0.025$, stand-off distance = 6d, $C_2H_2/O_2/N_2$, with O/C = 1, $N_2(\%) = 40$). Reprinted with kind permission from Springer Science Business Media [175], copyright © ASM International

influence of this dose on the properties of coatings obtained. In the case of one shot, the coating should mainly consist of individual particles located separately. If the dose is too high, a continuous film is formed in one shot. Because of the rapid cooling, cracks are formed in this film [169].

The sprayed particle size distribution is also very important for coating properties [174]. A decrease in powder size reduces roughness and porosity in the case of NiCr and Al_2O_3 but has a marginal effect for WC–Co due to the flow of the softer

binder (Co) phases, especially when a coarser particle size is utilized. The toughness of the Al_2O_3 and WC–Co coatings are dependent on the presence respectively of W_2C in WC–Co and α –Al_2O_3 in alumina ones. The wear resistance is only marginally affected by the powder size for WC–Co coatings, in contrast to Al_2O_3 coatings where it is very sensitive to the particle size distribution. Finally the authors [174] conclude that commercial powders with size distributions of 10–44 μm can be used.

To conclude, the design of a D gun with all its devices is not simple. Kharlamov [166] has summarized all the issues to ensure rapid development of a detonation wave within a short cycle time. With high impact velocities, and temperatures, which can be controlled in the range 0.9 T_m to T_m, T_m being the melting temperature, very dense coatings can be obtained. D-gun spraying usually produces denser coatings than any other thermal spray technique.

5.4.3 Graded Coatings

Different spray parameters for the detonation gun can be precisely controlled for each shot. Therefore, the "shot control method" has an excellent advantage of spraying both ceramic and metal powders with their optimum spraying parameters since, basically only one type of powder is deposited per individual shot to produce a coating mixture of ceramics and metals [176]. Therefore, graded coatings, having a compositional gradient through thickness can be produced by spraying several coating layers with increasing ratios of ceramic to metal shots in a sequence as shown in Fig. 5.45. Other fabrication methods for such coatings, such as the mixed powder method, are difficult to be optimized, the spraying parameters for ceramics and metals being very different due to the large difference in their material properties, e.g., melting temperature.

5.4.4 Coating Properties

The most important and well-developed applications of the D gun are the deposition of wear-resistant, thermo-barrier, electro-insulating, and high temperature oxidation-resistant coatings.

5.4.4.1 Plain Fatigue and Fretting Fatigue

Cu–Ni–In coatings were used to test the improvement of plain fatigue and fretting fatigue of an Al–Mg–Si alloy substrate [177]. Coatings 40 μm thick were found to give the best result. The same Cu–Ni–In coatings deposited on Ti alloys were beneficial. The detrimental effect of life reduction due to fretting was relatively larger in the Al alloy substrate compared to the Ti alloy one. This result was explained in terms of differences in the values of surface hardness, surface

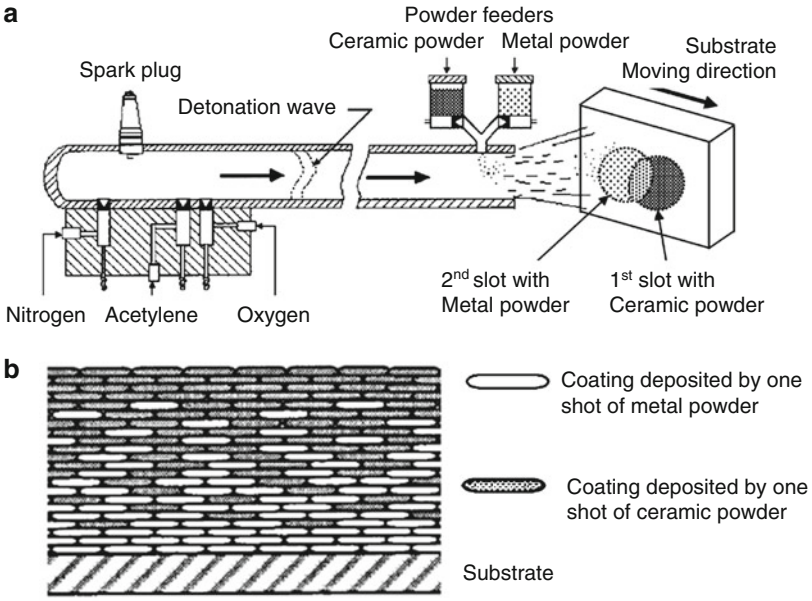


Fig. 5.45 Schematic illustration showing the deposition scheme to produce graded coatings, having a compositional gradient through thickness, by applying the "shot control method" (**a**) D-gun with one radial injection and two powder feeders, (**b**) graded coating: white color coating deposited by one shot of metal, black color coating deposited by one shot of ceramic. Reprinted with kind permission from Elsevier [176]

roughness, surface residual stress, and friction stress [178]. Cu–Ni–In powder was deposited on Ti–6Al–4V fatigue test samples using plasma spray and detonation gun (D-gun) spray processes [179]. The D-gun sprayed coating was dense with lower porosity compared with the plasma-sprayed coating. The hardness value of the D-gun-sprayed coating was higher than that of the plasma-sprayed coating and of the substrate because of its higher density and cohesive strength. Coating surfaces were very rough in both coatings. While the D-gun-sprayed coating had higher compressive residual stresses, the plasma-sprayed coating exhibited lower values of compressive residual stresses and even tensile residual stresses. Higher surface hardness and higher compressive residual stress of the D-gun-sprayed specimens were responsible for their superior fretting fatigue lives compared with the plasma-sprayed specimens [179].

5.4.4.2 Oxidation-Resistant Coatings

In the initial oxidation process of eutectic (β–NiAl + γ-Re) coatings, rhenium partially evaporates in the form of volatile oxides. Instead of rhenium oxides, a protective alumina layer forms on the coating surface. The oxidation process is reduced as Al_2O_3 is formed. It has been established that the air oxidation resistance

of eutectic (β–NiAl + γ-Re) alloy coatings substantially increases at 800–1,100 °C as compared with single-phase NiAl intermetallic coatings. The ratio of alumina and nickel formation rates is the key factor for the oxidation of these coatings. The scale formed on the single-phase NiAl intermetallic coating consists of an Al_2O_3 monolayer with spinel inclusions, while a two-layer protective scale forms on the eutectic (β–NiAl + γ-Re) alloy coating: spinel external layer and alumina internal layer, which has a better resistance to oxidation up to 1,100°C [180].

5.4.4.3 Thermal Barrier Coatings (TBCs)

(a) TBC's Bond Coat

For thermal barrier bond coats Ti–Al–Cr [181] and MCrAlY [113, 181–185] coatings were tested. The behavior of TiAlCr depends on the substrate structure, which determines the nature of diffusion. NiCrAlY coatings displayed a very favorable oxidation resistance; the aluminum layer formed being kept intact for over 300 h at 1,050°C. NiCrAlY coatings sprayed using a D-gun and LPPS showed a splat layer structure in the as-sprayed state [185]. The difference is that an oxidation reaction took place during D-gun spraying and Al_2O_3 distributed on the splat boundaries of as-sprayed D-gun NiCrAlY coatings. Isothermally oxidized at 1,050 °C for 300 h, both coatings showed favorable oxidation resistance and an Al_2O_3 scale was formed on their surface, although oxidation resistance of D-gun NiCrAlY coatings was inferior to that of LPPS NiCrAlY coatings. D-gun NiCrAlY coatings have higher surface hardness. D-gun NiCrAlY coatings should be considered at first when the working conditions are in the high dynamic load or low oxidizing air range [181]. HVOF and D-gun techniques were employed to deposit the Ni–25Cr–5Al–0.5Y bond coat (BC) of a thermal barrier coating with the YSZ top coat detonation sprayed using hollow spherical YSZ powder [183]. The oxidation rate of the TBC system at 1,100 °C is two times lower with the HVOF-sprayed NiCrAlY (see Fig. 5.38b) than with the D-gun-sprayed one (see Fig. 5.46) both processes using the same NiCrAlY powder. A significant number of Cr_2O_3 and $NiCr_2O_4$ oxide nodules can be formed on top of the D-gun NiCrAlY coating after 10 h oxidation at 1,100 °C, while more α-Al_2O_3 is present for the HVOF-sprayed coating. The coarse surface roughness in the case of the D-gun bond coat (Ra = 6.61 μm against 5.38 μm for the HVOF bond coat) and the higher porosity (7.8 % for the D-gun BC against 3.2 % for the HVOF BC) have a detrimental effect on the oxidation behavior of the TBC system. The fine α-Al_2O_3 dispersion formed during HVOF spraying exerts a beneficial effect on the oxidation resistance of the HVOF NiCrAlY coatings by serving as initial alumina nuclei and promoting development of a protective TGO scale [113].

(b) TBC's Ceramic Layer

Yttria partially stabilized zirconia was D-gun sprayed on a Ni-base superalloy, M38G [186]. The D-gun-sprayed TBC had a very low thermal conductivity of 1.0–1.4 W/m K, close to that of the plasma-sprayed YSZ coatings and much

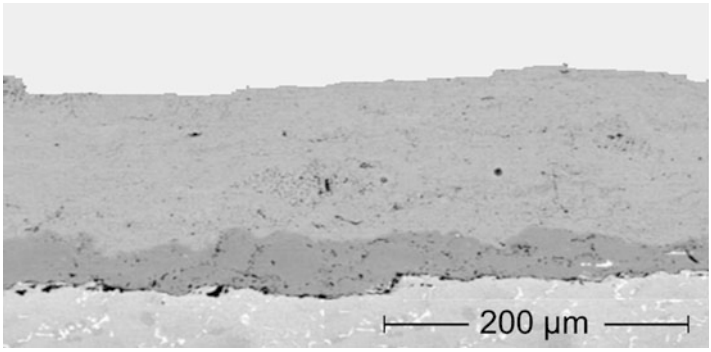


Fig. 5.46 Cross sections of detonation-sprayed TBCs using YSZ fused and crushed powder for the top coat and NiCrAlY for the bond coat (same powder as that used for the HVOF-sprayed bond coat presented in Fig. 5.38. Reprinted with kind permission from Elsevier [113]

lower than their EB-PVD counterparts. The TBCs exhibited excellent resistance to thermal shock up to 400 cycles of 1,050 °C to room temperature (forced air cooling) and 200 cycles of 1,100 °C to room temperature (forced water quenching). As cycles proceeded, the development of Ni/Co-rich TGO and t-to-m transformation within the ceramic coat could account for eventual spallation [183]. Similar results were obtained, through optimizing the spray parameters (especially the ratio of C_2H_2 to O_2) [187]. The oxidation behaviors at 1,000 and 1,100 °C were studied. TBCs detonation sprayed were uniform and dense, with a few micro-cracks in the ceramic coats and a rough surface of bond coats. At the high temperature, the dense detonation sprayed ceramic coats with low porosity could obviously decrease the diffusive channels for oxygen and reduce the oxygen pressure (P_{O2}) at the ceramic–bond coat interface [188]. NiCrAlY/YPSZ and NiCrAlY/NiAl/YPSZ thermal barrier coatings (TBCs) were also successfully deposited by detonation spraying [184]. TBCs included a uniform ceramic coat containing a few micro-cracks and a bond coat with a rough surface. Results were similar to those previously discussed. Figure 5.47 from Yuan et al. [113] presents a fractured YSZ TBC's top coat obtained by D-gun (acetylene–oxygen [189])-sprayed hollow sphere particles 10–75 µm in diameter. The microstructure of the top coat is similar to APS ones with regard to the lamellar microstructure (A in Fig. 5.47). It means that it was built up by layering individual splats resulting from impacting melted or semi-molten particles. The large, equiaxed voids are probably due to particles that did not fully melt (B in Fig. 5.47). Splat are approximately 3–6 µm thick and hundreds of micrometers in diameter. The thermal conductivity is similar to that obtained with APS coatings.

(c) Graded Coatings

At last, functionally graded thermal barrier coatings (FGM TBC) have been fabricated by the D-gun spray process according to the "shot control method" [175]. The gradient ranged from 100 % NiCrAlY metal on the substrate to

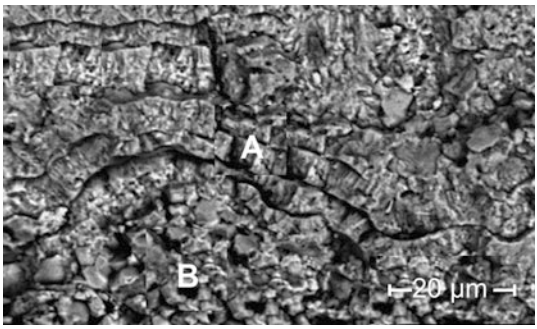


Fig. 5.47 Fractured YSZ top coat obtained by D-gun spraying (acetylene–oxygen mixture) hollow sphere particles 10–75 µm in diameter (as-sprayed state). Reprinted with kind permission from Elsevier [111]

100 % ZrO_2–8 wt.% Y_2O_3 ceramic for the top coat and consisted of a finely mixed microstructure of metals and ceramics with no obvious interfaces between the layers.

5.4.4.4 Wear-Resistant Coatings

The hardness of coatings is conventionally used as the primary correlating parameter for evaluating wear resistance [187, 188] six Authors have studied large varieties of coatings (WC–Co, TiMo(CN), TiN–CoN, Al_2O_3, Al_2O_3–TiO_2 with different size distributions and obtained by different manufacturing processes) deposited with the D-gun process with a range of process parameters for each coating. Coatings were characterized in terms of phase content and distribution, porosity, micro hardness, and evaluated for erosion, abrasion, and sliding wear resistance. Results [188] show that tribiological properties of the coatings are more strongly influenced by the coating process parameters themselves rather than microstructural parameters like phase content and distribution, porosity, etc.

(a) WC–Co

Suresh Babu et al. [189] have shown that the microstructure, in terms of nature/extent of decomposition of WC as well as properties of WC–12 wt.% Co coatings, is critically dependent on the variations of oxygen–fuel ratio. Murthy et al. [191] have studied, WC–10Co–4Cr and Cr_3C_2–20(NiCr) coatings, deposited by HVOF and D-gun processes. The abrasion tests were done using a three-body solid particle rubber wheel test rig using silica grits as the abrasive medium. The D-gun coating performed slightly better than the HVOF one possibly due to the higher residual compressive stresses of the former, and the WC-based coating had higher wear resistance compared to the Cr_3C_2-based coating. Also, the thermally sprayed carbide-based coatings have excellent wear resistance with respect to the hard chrome coatings [191]. Wang et al. [192] have emphasized that the compressive stress of WC–Co coatings (peening effect of high spraying

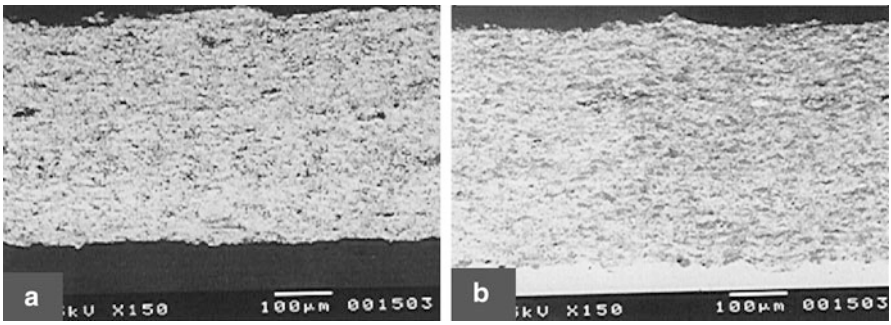


Fig. 5.48 SEM micrographs of transverse section of WC–10Co–4Cr coating in as-sprayed condition: (**a**) HVOF coating, (**b**) DS coating. Reprinted with kind permission from Elsevier [198]

velocity and kinetic energy during the D-Gun process) could significantly improve the coating properties, whereas the tensile stress impaired the coating properties. Park et al. [193] have sprayed WC–12 wt.% Co, commercial feedstock, with carbide grain size of approximately 100–200 nm. Post-heat treatment of WC–Co coatings modified their resistance because microhardness increased, while fracture toughness and wear resistance increased by increasing the temperature to 800 °C, but decreased after heat treatment at 900 °C. The amorphous phase disappeared and other carbide phases such as W_3Co_3C and W_6Co_6C formed during heat treatment above 700 °C. The improved properties were attributed to microstructural changes. Du et al. [194] have studied the influence of process variables on the qualities of D-gun sprayed WC–Co coatings. Suresh Babu et al. [195] have shown that the feedstock size influences the phase composition and porosity of WC–Co coatings, imparting variations in the coating hardness, fracture toughness, and wear properties. The fine and narrow size range of WC–Co coating exhibited superior wear resistance. Oliker et al. [196] have also shown that powder structure is important. The use of powders with highly porous particles results in the formation of porous coatings with low wear resistance. Du et al. [197] have studied the fabrication and evaluation of D-gun sprayed WC–Co coating with self-lubricating property.

Murthy et al. [191] have studied WC–10Co–4Cr and Cr3C2–20(NiCr) coatings, deposited by HVOF and D-gun processes, and low stress abrasion wear resistance of these coatings have been compared. Figure 5.48 from Murthy et al. [198] presents SEM micrographs of transverse section of WC–10Co–4Cr coatings HVOF and D-gun sprayed. The DJ2600 HVOF gun was working with H_2 (3.6 m^3/h), O_2 (1.8 m^3/h), and air (1.2 m^3/h), while the D-gun used O_2/C_2H_2 (1/1.23 volume ratio) and the powder size was between 11 and 53 µm. Figure 5.49 shows that the D-gun coating is slightly denser than the HVOF one, as confirmed by a porosity of 1.3 % against 1.6 %. Correlatively the microhardness ($HV_{0.3}$) is 792 for the HVOL coating against 849 for the D-gun one. Figure 5.49a, b represents HVOF and D-gun coatings, respectively, after grinding surface damage induced in both cases. Coatings were ground with a diamond resin-bonded

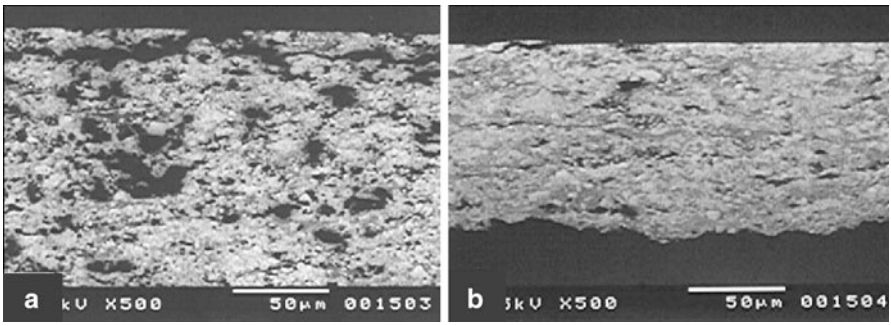


Fig. 5.49 SEM micrographs of transverse section of WC–10Co–4Cr coating in as-ground condition: (**a**) HVOF coating, (**b**) DS coating [198]

wheel to achieve a final surface roughness of Ra < 0.2 µm. The grinding induced surface damage in both the cases as shown in Fig. 5.49a, b. The microstructure of the HVOF coating developed numerous cracks beneath the surface up to a depth of 150–200 µm. However, such cracks were minimum in the case of D-gun sprayed samples (Fig. 5.49b). The erosion resistance of the D-gun coating was found to be higher compared to that of the HVOF coating in the as-coated condition. This is possibly due to the slightly higher microhardness, lower porosity, and possibly higher residual compressive stresses of the DS coating [198].

Usually results show that the D-gun coatings performs slightly better than the HVOF coatings possibly due to the higher residual compressive stresses induced by the former process, and WC-based coatings have higher wear resistance in comparison to Cr_3C_2-based coating. Also, the thermally sprayed carbide-based coatings have excellent wear resistance with respect to the hard chrome coatings.

(b) Alumina

The structure of D-gun-sprayed Al_2O_3 coatings was investigated by Li et al. [199] using a copper electroplating technique with a typical layer structure with poor bonding at interfaces between flattened particles. The mean bonding ratio of bonded interface to total apparent bonding interface area was about 10 %. However, a high particle velocity may result in a rough surface for individual flattened particles, which is effective for better interlocking of flattened particles. The good wear resistance might be mainly due to the mechanical interlocking effect between flattened particles. As for WC–Co, the feedstock size was also found to influence the phase composition of Al_2O_3. The coarse ($d_{50} = 18$ µm) and narrow ($d_{50} = 10$ µm) size distribution Al_2O_3 coating exhibited better performance under abrasion and sliding wear modes, however, under erosion wear mode the as-received Al_2O_3 ($d_{50} = 14$ µm) coating exhibited better performance. Saravanan et al. [200] have conducted a Taguchi-full factorial (L16) design parametric study, to optimize the D-gun spray process parameters. For hardness the significant factors of influence were spray distance, carrier gas flow rate, and fuel to O_2 ratio selected in that order.

They showed that alumina coatings of highest hardness 1363 H and lowest porosity 1.45 % could be obtained for specific spray parameters. Other authors have also sprayed alumina coatings [200–204].

(c) Alumina–Titania

D-gun-sprayed coatings of Al_2O_3–TiO_2 [205] (13 wt.%) , with a particle size of 22–45 μm, have low porosity, high density, hardness above 1,000 $HV_{0.5}$, and, at the same time, a considerably improved frictional wear resistance compared to that of the AISI 1045 steel substrate. A preliminary preparation of the substrate surface by compressed air-enhanced grit blasting is necessary for the coating to adhere well to the substrate. R. Venkataraman et al. [205] have studied phases present in D-gun sprayed Al_2O_3–TiO_2 (13 wt.%) and compared them to those obtained with plasma spraying. Semenov and Cetegen [206] have studied D-gun spraying of nanostructured alumina–titania (12 wt.%) coatings, starting from commercial agglomerated nanostructured particles. XRD spectrum peaks of α-Al_2O_3 (113) and γ-Al_2O_3 (400) for the feedstock powder allowed determining the fraction of melted powder. Detonation coatings contain α-Al_2O_3 phase due to some melting but the relative amount is smaller than that of γ-Al_2O_3 based on the relative values of the X-ray line intensities. These findings combined suggest that the detonation deposition process could be successfully employed in the deposition of nanostructured alumina–titania coatings.

Coatings exhibited lower erosion wear resistance than bulk alumina but better resistance to abrasion wear, especially Al_2O_3 + 3 wt.% TiO_2 and Al_2O_3 + 40 wt.% ZrO_2. Compared to alumina coatings that are plasma sprayed and contain up to 98 % of γ-alumina, D-gun coatings have γ-alumina phase content of less than 60 %, and about 30 % of α-alumina phase content, the balance being β- and δ-alumina phases [206].

(d) Tribological Coatings

Sundararajan et al. [207] have studied the tribological performance of 200 μm thick TiMo(CN)–28Co and TiMo(CN)–36NiCo coatings obtained using a D-gun. Powders were prepared by SHS and had the following characteristics: TiMo(CN)–36NiCo, d_{50} = 36.4 μm irregular and blocky shaped, phases being $TiC_{0.7}N_{0.3}$, Co, Ni, and TiMo(CN)–28Co, d_{50} = 23.3 μm, irregular shaped, phases being $TiC_{0.7}N_{0.3}$, Co. In both coatings the best tribological performance and also the lowest porosity were obtained at intermediate oxygen/acetylene ratios. When comparing the tribological performance of the optimized TiMo (CN) type coatings with that of optimized WC–Co ones, the abrasion resistance is comparable. However, the erosion and sliding wear resistance of TiMo (CN) type coatings were considerably lower than those of the WC–Co coatings. Du et al. [208] have deposited WC–Co/Mo–Ni coatings by D-gun, using a commercial WC–Co powder and a MoS_2–Ni powder, the spray condition being adapted to both powders. The MoS_2 composition was kept and distributed homogeneously. Coatings had self-lubricating properties. MoS_2 lowered the wear rate under dry sliding conditions when its content was lower than 4.9 wt.%.

(f) Corrosion and Wear-Resistant Coatings

Cr_3C_2 (75 wt.%)–NiCr D-gun-sprayed coatings on high temperature structure steel DIN 12CrMo44 [209] were dense with good bonding to substrate as well as

high resistance to high temperature oxidation and wear. Reports from the in-service test at Bao Shan Steel Company indicate that such coatings have at least doubled the roll life. Cr_3C_2–NiCr cermet coatings were deposited on two Ni-based superalloys, namely, Superni 75 and Superni 718 and one Fe-based super alloy, Superfer 800H by the D-gun thermal spray process [210]. The cyclic hot-corrosion studies were conducted on uncoated as well as D-gun-coated super alloys in the presence of a mixture of 75 wt.% Na_2SO_4 + 25 wt.% K_2SO_4 film at 900 °C for 100 cycles. It was observed that Cr_3C_2–NiCr-coated superalloy showed better hot-corrosion resistance than the uncoated super alloys, as a result of the formation of continuous and protective oxides of chromium, nickel, and their spinel. Cr_3C_2–NiCr coatings were D-gun sprayed on Superni 75, Superni 718, and Superfer 800H super alloys [211]. Coatings exhibited nearly uniform, adherent, and dense microstructure with porosity less than 0.8%. These coatings were found to be very effective in decreasing the corrosion rate in a molten salt environment (Na_2SO_4–60% V_2O_5) at high temperature 900 °C for 100 cycles. Particularly, the coating deposited on Superfer 800H showed a better hot-corrosion protection as compared to Superni 75 and Superni 718. The cyclic oxidation behavior of the same coatings on the same superalloy at 900 °C for 100 cycles in air under cyclic heating and cooling conditions has been investigated [212]. In all the coated super alloys, the chromium, iron, silicon, and titanium were oxidized in the inter-splat region, whereas splats, which consisted mainly of Ni remained un-oxidized. The parabolic rate constants of Cr_3C_2–NiCr-coated alloys were lower than that of the bare superalloy. The cyclic oxidation behavior of the same coatings on the same superalloy at 900 °C for 100 cycles in air under cyclic heating and cooling conditions has been investigated [212]. In all the coated superalloy, the chromium, iron, silicon, and titanium were oxidized in the inter-splat region, whereas splats, which consisted mainly of Ni remained un-oxidized. The parabolic oxidation rate of Cr_3C_2–NiCr-coated alloys was lower than that of the bare super alloys. To prolong the life of steel slab continuous casting rolls, Cr_3C_2–NiCr D-gun spray coatings were processed on the roll surface (DIN 12CrMo44) in a steelmaking plant in China [213]. The wear resistance of the coated samples reduced the risk of seizure compared to uncoated samples, at room and elevated temperatures with any load and sliding velocity. It must also be emphasized that Cr_3C_2–20(NiCr) coatings have an excellent wear resistance [191, 213], however lower than that of WC–Co ones. When they are exposed to high temperatures (over 600 °C), their corrosion resistance is improved [214, 215].

(g) Erosion Resistance

It is known that addition of Cr to WC–Co improves binding of the metallic matrix with the WC grains and provides better wear-resistant coatings. Thus, WC–Co–Cr is considered to be a potentially better wear-resistant coating material as compared to WC–Co. The thermally sprayed carbide coatings are in general surface finished by machining or grinding after the coating process. A WC–10Co–4Cr powder has been sprayed [198] on medium carbon steel using D-gun and HVOF processes. Some of the coated specimens were further ground by a diamond wheel with controlled parameters and both “as-coated” and

"as-ground" conditions have been tested for solid particle erosion behavior. It has been found that surface grinding improved the erosion resistance. A detailed analysis indicates that the increase in residual stress in the ground specimen is a possible cause for the improvement in erosion resistance. Sand erosion studies of D-gun sprayed WC–Co–Cr have been undertaken [214] using a sand/water jet impingement rig. The erosion rate of coatings compared well with sintered tungsten carbide–cobalt–chrome for low energy impacts, but the sintered material outperforms the sprayed material for high-energy impacts by a factor of four. This fact is the result from the anisotropic microstructure of coatings with preferred crack propagation parallel to the coating surface, followed by crack interlinking and spalling. The influence of slurry jet angle was found to be more pronounced under low energy conditions where maximum erosion occurred at 90° and the minimum at 30° in contrast to the high-energy erosion rates which were independent of jet angle.

WC–12%Co and WC–17%Co coatings were deposited [217] by detonation spraying on three different substrate materials: mild steel, commercially pure (CP) aluminum, and CP titanium to test their dynamic hardness by a drop weight system. WC–Co coatings exhibit higher hardness under impact at high strain rate. The dynamic hardness of a WC–Co coating is maximum on aluminum substrate and minimum on mild steel substrate. The identical coating exhibits intermediate hardness on titanium substrate.

Other Cermets

Metal–matrix composites (MMCs), containing large ceramic particles as superabrasives, are typically used for grinding stone, minerals, and concrete. Sintering and brazing are the key manufacturing technologies for grinding tool production. However, restricted geometry flexibility and the absence of repair possibilities for damaged tool surfaces, as well as difficulties of controlling material interfaces, are the main weaknesses of these production processes. Thermal spraying offers the possibility to avoid these restrictions [218]. Cu base coatings containing large ceramic particles (Al_2O_3 and SiC particles larger than 150 μm) gave high abrasiveness for grinding stones and concrete [219].

FeTi–SiC coatings gave very high hardness (7,900 MPa) when spraying agglomerated powders with fine SiC [220, 221]. Coatings contained $TiSi_2$, TiSi, Ti_5Si_3, FeTiSi, and the porosity was below 2% [221]. Detonation coatings of mechanically Ti–Al-alloyed powders [221], contained titanium aluminide with inclusion of nitrides, depending on the working gas environment. With the mechanically alloyed powder Ti–50Al, coatings can be consolidated by the formation of the compound Al_2TiO_5 obtained when the working gas is oxidizing [221]. Filimonov et al. [222] have considered the mechanisms of structure formation during gas detonation spraying of coatings of $TiAl_3$ and Ni_3Al intermetallic compounds produced under equilibrium and nonequilibrium synthesis conditions.

Podchernyaeva et al. [223] have investigated the composition, structure, and wear rate of detonation coatings on steel 30KhGSNA deposited from composite

powders based on $TiC_{0.5}N_{0.5}$ with refractory additions of SiC, AlN, and a Ni–Cr metallic binder. It was shown that at a load of 10 MPa these coatings exhibited substantially less wear and a larger range of sliding velocities with a stable value of wear than coatings of the hard alloy WC–15% Co.

A kind of Ti–Fe–Ni–C compound powder was prepared by a novel precursor pyrolysis process using ferro-titanium, carbonyl nickel powder, and sucrose as raw materials [224]. The powder had a very compact structure and was uniform in particle size. The TiC–Fe36Ni composite coatings were simultaneously in situ synthesized by reactive D-gun spraying using this powder. The coatings presented typical morphology of thermally sprayed coatings with two different areas: one was the area of TiC distribution where the round fine TiC particles (from 300 nm to 1 μm) were dispersed in the Fe36Ni alloy matrix; the other was the area of TiC accumulation (from 2 to 4 μm). The surface hardness of the composite coating reached about $94 \pm 2(HV_{15N})$.

The effects of the powder particle size and the acetylene/oxygen gas flow ratio during the D-gun spray process on the amount of molybdenum phase, porosity, and hardness of the coatings using MoB powder were investigated by Yang et al. [225]. The results show that the presence of metallic molybdenum in the coating results from decomposition of MoB powder during thermal spray. The compositions of the coatings are metallic Mo, MoB, and Mo_2B, which are different from the phases of the original powder. Similar results were obtained by Gao et al. [226]

Alloys

Senderowski and Bojar [227, 228] have studied D-gun sprayed NiAl and NiCr intermediate layers underneath the intermetallic Fe–Al type coatings on a plain carbon steel substrate The interface layers are responsible for hardness, bond strength, thermal stability, and adhesive strength of the whole coating structure. The physical–chemical properties of the intermediate layers, combined with a unique, very dense and pore-free intermetallic Fe–Al coating obtained from self-decomposing powders resulted in a more complex structure. It enabled independent control of its functional properties and considerably reduced negative gradients of stress and temperature influencing the substrate and increasing adhesion strength.

Min'kov et al. [229] have studied the possibility of using D-gun spraying of self-fluxing alloys (79 % Ni, 15 % Cr, 3 % Si, 2.4 % B) for restoring the drying cylinders on spinning machines.

5.4.4.5 D-gun Modeling (1D)

Assuming that the detonation wave front has a negligible thickness and propagates with no losses (adiabatic behavior), the integration of conservation equations allows obtaining the conditions relating the gas parameters before and behind the propagation wave front [165]:

$$\rho_b u_b = \rho_u u_u \tag{5.17}$$

$$p_b + \rho_b u_b^2 = p_u + \rho_u u_u^2 \tag{5.18}$$

$$h_b + u_b^2/2 = h_u + u_u^2/2 + q \tag{5.19}$$

u_i is the velocity (m/s), ρ_i the specific mass (kg/m^3), q the chemical energy release at constant pressure (J/kg), and h the enthalpy (J/kg). The subscript u corresponds to the parameters of the unburned gas (before the detonation wave front), while the subscript b denotes parameters of the burned gas in the immediate vicinity behind the front. u is the gas velocity with respect to the detonation wave front. In the laboratory coordinate system, the velocity ahead of the wave front is zero, the wave front velocity is u_u, and $(u_u - u_b)$ is the velocity of the burned gases with respect to the D-gun wall.

Perfect gas law is generally assumed:

$$p_u = \rho_u R T_u \tag{5.20}$$

$$p_b = \rho_b R T_b \tag{5.21}$$

R being the specific perfect gas constant (J/K kg).

Eliminating velocities u_1 and u_2 from Eqs. (5.15)–(5.17) gives the Hugoniot conditions:

$$h_u - h_b + q = (p_u - p_b)(V_u + V_b)/2 \tag{5.22}$$

$$\varepsilon_u - \varepsilon_b + q = (p_u + p_b)(V_b - V_u)/2 \tag{5.23}$$

where V_i is the specific volume (m^3/kg) and ε_i the internal specific energy (J/kg).

These relations describe the Hugoniot adiabatic condition and relate the pressure and specific volume of detonation products to the parameters of the initial mixture p_u and v_u and the reaction energy q [172]. At the Chapman–Jouget point [165] on the Hugoniot curve the following additional condition is introduced:

$$(\partial p_b/\partial V_b)_S = (p_b - p_u)/(V_u - V_b) \tag{5.24}$$

where S is the entropy (J/K).

Using this condition allows calculating all major parameters of the detonation products as a function of q, p_u, u_u, and γ_b (ratio of specific heats). In case of strong detonations, equations are simplified. In a strong detonation the amount of energy q is much higher than the internal gas energy: $q/\varepsilon \gg 1$, which is equivalent to $q/a_u^2 \gg 1$, where c_1 is the sound velocity in unburned gas. The sound velocity is given by

$$a = \sqrt{\gamma R_u T} \tag{5.25}$$

where R_u is the universal perfect gas constant (8.32 J/K mol)

At the Chapman–Jouget surface, the velocity of detonation is equal to the speed of wave propagation in the detonation products (with respect to the laboratory coordinate system) [166]:

$$D = u_b + a_u \tag{5.26}$$

In these conditions, for example, the velocity of the detonation wave front in the laboratory coordinate system, D, is given [167] by Eq. (5.14):

Temperature and pressure of the burned gases are given by

$$T_b = 2\gamma_b q/\left(c_V^2(\gamma_b + 1)\right) \tag{5.27}$$

$$p_2 = 2(\gamma_b - 1)\rho_u q \tag{5.28}$$

As in the case of HVOF or HVAF, calculations are based on the solution of conservation equations and the interested reader can look at the papers [167–170, 175].

5.5 Summary and Conclusions

This chapter was devoted to spray processes where thermal and kinetic energies are generated chemically through the combustion (or detonation) of fuels (gaseous or liquid) with oxygen or air. The oldest process is flame spraying, which appears in 1910 and is still in common use. Oxyacetylene torches are the most common and undoubtedly this process is the cheapest one. The use of rods or cords has allowed spraying ceramics, which otherwise as powders would not have been melted. The main limitation of the flame process is the relatively low velocity of sprayed particles (<60–80 m/s) resulting in porous coatings. Oxide inclusions are also present due to the high degree of interaction between fully molten droplets and the surrounding atmosphere.

The Detonation gun (D-gun) appeared in Western countries in the 1950s. In this process very high thermal and kinetic energies were achieved by producing a detonation in an explosive mixture (mostly acetylene–oxygen) confined in a tube closed at one end into which powder is introduced. Of course the process is cyclic (6–100 Hz) with the introduction of the explosive gases and powder dose, the detonation, ignited by a spark plug followed by the purging of burned gases. The process generates high particle velocities (500–900 m/s) and fully molten particles (even ceramic ones provided their size is small < 30 μm). Thus coatings are dense (less than 2 % porosity), well bonded, with compressive stress, and their oxidation is limited.

In the 1960s, to compete with the D-gun deposition, the HVOF process was introduced where the combustion flame is produced in a pressurized chamber followed by a convergent–divergent nozzle and a barrel to limit the surrounding atmosphere entrainment. First developed with gaseous combustible gases and oxygen, it was extended by replacing oxygen by air (HVAF process) to reduce

the gas temperature and increase its velocity. The next step was the high power HVOF torches working with kerosene followed by HVOF processes where noncombustible gas (nitrogen) was introduced in the combustion chamber or water injected downstream of the nozzle throat. These new torches were aimed at reducing the gas temperature and increasing its velocity. Coatings obtained with HVOF torches are rather dense and their oxidation level is rather low. Of course, the density increases with particle impact velocity that varies with the combustible gas or liquid used with either oxygen or air or nitrogen addition in the combustion chamber. Velocities between 400 and 900 m/s can be achieved for the same particles depending on the spray conditions and gun used. With high velocities (>700 m/s) it becomes possible to spray particles below their melting point and thus with low oxidation level. However it must be emphasized that these processes are not suited to spraying ceramics.

Nomenclature

Latin Alphabet

a	Sound velocity, $a = \sqrt{\frac{\gamma p}{\rho_g}}$ (m/s)
A	Oxidizer volume or mass (m^3 or kg)
A_i	Is the cross-sectional area perpendicular to the flow direction (m^2)
A_t	Throat area (m^2)
D	Detonation wave velocity (m/s)
F	Fuel volume or mass (m^3 or kg)
F/A	Ratio of fuel to oxidizer number of moles
h_i	Enthalpy (J/kg)
$\overset{\circ}{m}_{O_2}$	Oxygen gas feeding flow rate (kg/s)
M	Mach number, ratio of gas velocity to the local sound velocity
p	Pressure (Pa)
p_t	Gas pressure at the throat (Pa)
P_F	Power dissipated in the flame (kW)
q	Chemical energy release at constant pressure (J/kg)
Q_o	Specific energy of detonation (J)
R	Specific perfect gas constant (J/K kg)
R_u	Universal perfect gas constant (8.32 J/K mol)
R'	Equivalence ratio or richness: $R' = (F/A)/(F/A)_{stoichiometry}$
t_c	Detonation cycle duration time (s)
T_g	Gas temperature (K)
T_m	Melting temperature (K)
T_p	Particle temperature (K)
T_t	Temperature at the throat (K)
u_b	Burned gas velocity with respect to the detonation wave front (m/s)
u_u	Unburned gas feeding velocity (m/s)
$u_u - u_b$	Velocity of the burned gases with respect to the D-gun wall (m/s)

Greek Alphabet

Δt_i Characteristic time intervals of a detonation (s)
ϕ Dummy variable
ϕ' Time- (or Reynolds) averaged dumb variable
ϕ'' Density-averaged dumb variable
γ Specific heats ratio
ρ_g Gas mass density (kg/m^3)
ρ_p Particle mass density (kg/m^3)
ρ_t Gas mass density at the throat (kg/m^3)

Subscripts

b Burned gases (in the immediate vicinity behind the front)
g Gas
p Particle
t Throat
u Unburned gas (before the detonation wave front)

References

1. Anon (1913) Metal plating with the air brush, vol 1. Scientific American, New York, NY, pp 346–352
2. Smith RW (1991) Plasma spray processing... The state of the art and future. From a surface to a materials processing technology. In: Proceedings of the 2nd Plasma Technik symposium, Vol. 1. Plasma Technik, Wohlen, Switzerland, pp 13–38
3. Browning JA (1983) Highly concentrated supersonic liquefied material flame spray method and apparatus. US patent # 4,416,421, November (1983)
4. Thermal Spraying, Practice, Theory and Application (1985). American Welding Society, Miami, Fl
5. Wigren J et al (1996) On-line diagnostics of traditional flame spraying as a tool to increase reproducibility. In: Berndt CC (ed) Proceedings of national thermal spray conference. ASM International, Materials Park, OH, pp 675–681
6. Nylén P, Bandyopadhyay R (2000) A computational fluid dynamic analysis of gas and particle flow in flame spraying. In: Berndt CC (ed) Thermal spray: surface engineering via applied research. ASM International, Materials Park, OH, pp 237–244
7. Bandyopadhyay R, Nylén P (2003) A computational fluid dynamic analysis of gas and particle flow in flame spraying. J Therm Spray Technol 12(4):492–503
8. Pombo Rodriguez HRM, Paredes RSC, Calixto A, Wido SH (2007) Comparison of aluminum coatings deposited by flame spray and by electric arc spray. Surf Coat Technol 202:172–179
9. Panossian Z, Mariaca L, Morcillo M, Flores S, Rocha J, Pen JJ, Herrera F, Corvo F, Sanchez M, Rincon OT, Pridybailo G, Simancas J (2005) Steel cathodic protection afforded by zinc, aluminium and zinc/aluminium alloy coatings in the atmosphere. Surf Coat Technol 190:244–248
10. Paredes RSC, Amico SC, d'Oliveira ASCM (2006) The effect of roughness and pre-heating of the substrate on the morphology of aluminium coatings deposited by thermal spraying. Surf Coat Technol 200:3049–3055

11. Vijaya BM, Krishna Kumar R, Prabhakar O, Gowri Shankar N (1996) Simultaneous optimization of flame spraying process parameters for high quality molybdenum coatings using Taguchi methods. Surf Coat Technol 79:276–288
12. Brantner HP, Pippan R, Prantl W (2003) Local and global fracture toughness of a flame sprayed molybdenum coating. J Therm Spray Technol 12(4):560–571
13. Laribi M, Vannes AB, Treheux D (2006) On a determination of wear resistance and adhesion of molybdenum, Cr–Ni and Cr–Mn steel coatings thermally sprayed on a 35CrMo4 steel. Surf Coat Technol 200:2704–2710
14. Lin L, Hanb K (1998) Optimization of surface properties by flame spray coating and boriding. Surf Coat Technol 106:100–105
15. Planche MP, Liao H, Normand B, Coddet C (2005) Relationships between NiCrBSi particle characteristics and corresponding coating properties using different thermal spraying processes. Surf Coat Technol 200:2465–2473
16. Navas C, Colaço R, de Damborenea J, Vilar R (2006) Abrasive wear behaviour of laser clad and flame sprayed-melted NiCrBSi coatings. Surf Coat Technol 200:6854–6862
17. Sakata K, Nakano K, Miyahara H, Matsubara Y, Ogi K (2007) Microstructure control of thermally sprayed co-based self-fluxing alloy coatings by diffusion treatment. J Therm Spray Technol 16(5–6):991–997
18. Harsha S, Dwivedi DK, and Agarwal A Influence of CrC addition in Ni-Cr-Si-B flame sprayed coatings on microstructure, microhardness and wear behaviour. Int J Adv Manuf Technol DOI:10.1007/s00170-007-1072-2
19. Harsha S, Dwivedi DK, Agrawal A (2007) Influence of WC addition in Co–Cr–W–Ni–C flame sprayed coatings on microstructure, microhardness and wear behaviour. Surf Coat Technol 201:5766–5775
20. Mesrati N, Ajhrourh H, Nguyen D, Treheux D (2000) Thermal spraying and adhesion of oxides onto graphite. J Therm Spray Technol 9(1):95–99
21. Barthel K, Rambert S, Siegmann S (2000) Microstructure and polarization resistance of thermally sprayed composite cathodes for solid oxide fuel cell use. J Therm Spray Technol 9 (3):343–347
22. Jorge LF, Duarte TP, Maia R (2003) Development of coated ceramic components for the aluminium industry. J Therm Spray Technol 12(2):250–257
23. Liu CS, Huang JH, Yin S (2002) The influence of composition and process parameters on the microstructure of TiC-Fe coatings obtained by reactive flame spray process. J Mater Sci 37:5241–5245
24. Hui L, Huang J (2005) Reactive thermal spraying of TiC-Fe composite coating by using asphalt as carbonaceous precursor. J Mater Sci 40:4149–4151
25. Liu HY, Huang JH (2006) Reactive flame spraying of TiC–Fe cermet coating using asphalt as a carbonaceous precursor. Surf Coat Technol 200:5328–5333
26. Zhang G, Liao H, Yu H, Costil S, Mhaisalkar SG, Bordes J-M, Coddet C (2006) Deposition of PEEK coatings using a combined flame spraying–laser remelting process. Surf Coat Technol 201:243–249
27. Li JF, Li L, Stott FH (2004) Multi-layered surface coatings of refractory ceramics prepared by combined laser and flame spraying. Surf Coat Technol 180–181:500–505
28. Ivosevic M, Cairncross RA, Knight R (2007) Melting and degradation of nylon-11 particles during HVOF combustion spraying. J Appl Polym Sci 105(2):827–837
29. Gawne DT, Zhang T, Bao Y (2001) Heating effect of flame impingement on polymer coatings. In: Berndt C, Khor K, Lugscheider E (eds) Thermal spray 2001: new surfaces for a New millennium. ASM International, Materials Park, OH, pp 307–313
30. Ivosevic M, Coguill SL, Galbraith SL (2009) Polymer thermal spraying: a novel coating process. In: Marple BR, Hyland MM, Lau Y-C, Li C-J, Lima RS, Montavon G (eds) Thermal spray 2009: proceedings of the international thermal spray conference. ASM International, Materials Park, OH, pp 1078–1083
31. Sainz MA, Osendi MI, Miranzo P (2008) Protective Si–Al–O–Y glass coatings on stainless steel in situ prepared by combustion flame spraying. Surf Coat Technol 202:1712–1717

32. Masataka M, Kazumi K, Substrate for flame-sprayed tile, Japanese patent JP1192777, 02-08-1989
33. Koji N, Kunio H, Eiichi Y, Glass-coated metallic work piece, Japanese patent JP2011749, 16-01-1990
34. Hideki I, Shibakumaran U and Kazumasa G, Method for thermally spraying and grazing cement martial, Japanese patent JP3033084, 13-02-1991
35. Tatsuya N, Izozou K, Haruyuki M, Yasuhi S, Improved glaze application for coating and flame spraying and glaze, Japanese patent JP63277583, 15-11-1988
36. Lugsheider E, Remer P, Nyland A, Siking R (1995) Thermal spraying of Bio-active glass ceramics. In: Berndt CC, Sampath S (eds) Thermal spray: science and technology. ASM International, Materials Park, OH, pp 583–587
37. Arcondéguy A, Grimaud A, Denoirjean A, Gasnier G, Huguet C, Pateyron B, Montavon G (2007) Flame-sprayed glaze coatings: effect of operating parameters and feedstock characteristics onto coating structures. J Therm Spray Technol 16(5–6):978–990
38. Zhang T, Qiu Z, Bao Y, Gawne GT, Zhang K (2000) Temperature profile and thermal stress analysis of plasma sprayed glass-composite coatings. In: Berndt CC (ed) Thermal spray: surface engineering via applied research. ASM International, Materials Park, OH, pp 355–361
39. Tikkanen J, Gross KA, Berndt CC, Pitkatnen V, Keskinen J, Raghu S, Rajala M, Karthikeyan J (1997) Characteristics of the liquid flame spray process. Surf Coat Technol 90:210–216
40. Gross KA, Tikkanen J, Keskinen J, Pitkänen V, Eerola M, Siikamaki R, Rajala M (1999) Liquid flame spraying for glass coloring. J Therm Spray Technol 8(4):583–589
41. Poirier T, Vardelle A, Elchinger MF, Vardelle M, Grimaud A, Vesteghem H (2003) Deposition of nanoparticle suspensions by aerosol flame spraying: model of the spray and impact processes. J Therm Spray Technol 12(3):393–402
42. Guan-Jun Y, Li C-J, Wang YY (2005) Phase formation of nano-TiO_2 particles during flame spraying with liquid feedstock. J Therm Spray Technol 14(4):480–486
43. Guan-Jun Y, Li CJ, Huang XC, Li CX, Wang YY (2007) Influence of silver doping on photocatalytic activity of liquid-flame-sprayed-nanostructured TiO2 coating. J Therm Spray Technol 16(5–6):881–885
44. Hussary NA, Heberlein JVR (2007) Effect of system parameters on metal breakup and particle formation in the wire arc spray process. J Therm Spray Technol 16(1):140–152
45. Ishikawa K, Suzuki T, Tobe S, Kitamura Y (2001) Resistance of thermal-sprayed duplex coating composed of aluminum and 80ni-20cr alloy against aqueous corrosion. J Therm Spray Technol 10(3):520–525
46. Ishikawa K, Suzuki T, Kitamura Y, Tobe S (1999) Corrosion resistance of thermal sprayed titanium coatings in chloride solution. J Therm Spray Technol 8(2):273–278
47. Thorpe ML, Richter HJ (1992) A pragmatic analysis and comparison of HVOF processes. J Therm Spray Technol 1(2):161–170
48. Korpiola K, Hirvonen JP, Laas L, Rossi F (1997) The influence of the nozzle design on HVOF exit gas velocity and coating microstructure. J Therm Spray Technol 6(4):469–474
49. Gärtner F, Stoltenhoff T, Schmidt T, Kreye H (2006) The cold spray process and its potential for industrial applications. J Therm Spray Technol 15(2):223–232
50. Tawfik HH, Zimmerman F (1997) Mathematical modeling of the gas and powder flow in HVOF systems. J Therm Spray Technol 6(3):345–352
51. Oberkampf WL, Talpallikar M (1996) Analysis of a high velocity oxygen-fuel (HVOF) thermal spray torch part1: numerical simulation. J Thermal Spray Technol 5(1):53–61
52. Oberkampf WL, Talpallikar M (1996) Analysis of a high velocity oxygen-fuel (HVOF) thermal spray torch part 2: computational results. J Thermal Spray Technol 5(1):62–68
53. Gu S, Eastwick CN, Simmons KA, McCartney DG (2001) Computational fluid dynamic modeling of gas flow characteristics in a high-velocity oxy-fuel thermal spray system. J Therm Spray Technol 10(3):461–469
54. Cheng D, Xu Q, Trapaga G, Lavernia EJ (2001) A numerical study of high-velocity oxygen fuel thermal spraying process. Part I: gas phase dynamics. Metallurg Mater Transact A 32A:1609–1620

55. Sakaki K, Shimizu Y (2001) Effect of the increase in the entrance convergent section length of the gun nozzle on the high-velocity oxygen fuel and cold spray process. J Therm Spray Technol 10(3):487–496
56. Katanoda H, Matsuoka T, Kuroda S, Kawakita J, Fukanuma H, Matsuo K (2005) Aerodynamic study on supersonic flows in high-velocity oxy-fuel thermal spray process. J Therm Sci 14(2):126–129
57. Dolatabadi A, Pershin V, Mostaghimi J (2005) New attachment for controlling gas flow in the HVOF process. J Therm Spray Technol 14(1):91–99
58. Katanoda H, Yamamoto H, Matsuo K (2006) Numerical simulation on supersonic flow in high velocity oxy fuel termal spray gun. J Therm Sci 15(1):65–70
59. Yuan X, Wang H, Hou G, Zha B (2006) Numerical modelling of a low temperature high velocity air fuel spraying process with injection of liquid and metal particles. J Therm Spray Technol 15(3):413–421
60. Li M, Christofides PD (2005) Multi-scale modeling and analysis of an industrial HVOF thermal spray process. Chem Eng Sci 60:3649–3669
61. Gordon S, McBride BJ (1994) Computer program for calculation of complex chemical equilibrium compositions and applications. NASA Reference Publication 1311, Lewis Research Center, Cleveland, OH, USA
62. Yang Y, Liao H, Coddet C (2002) Simulation and application of a HVOF process for MCrAlY thermal spraying. J Therm Spray Technol 11(1):36–43
63. Srivatsan VR, Dolatabadi A (2006) Simulation of particle-shock interaction in a high velocity oxygen fuel process. J Therm Spray Technol 15(4):481–487
64. Cheng D, Xu Q, Trapaga G, Lavernia EJ (2001) The effect of particle size and morphology on the in-flight behavior of particles during high-velocity oxyfuel thermal spraying. Metallurg Mater Transact B 32B:525–535
65. Gu S, McCartney DG, Eastwick CN, Simmons K (2004) Numerical modeling of in-flight characteristics of Inconel 625 particles during high-velocity oxy-fuel thermal spraying. J Therm Spray Technol 13(2):200–213
66. Hanson TC, Hackett CM, Settles GS (2002) Independent control of HVOF particle velocity and temperature. J Therm Spray Technol 11(1):75–85
67. He J, Ice M, Lavernia E (2001) Particle melting behavior during high-velocity oxygen fuel thermal spraying. J Therm Spray Technol 10(1):83–93
68. Dobler K, Kreye H, Schwetzke R (2000) Oxidation of stainless steel in the high velocity oxy-fuel process. J Therm Spray Technol 9(3):407–413
69. Hackett CM, Settles GS (1995) Research on HVOF gas shrouding for coating oxidation control. In: Berndt CC, Sampath S (eds) Thermal spray: science and technology. ASM International, Materials Park OH, pp 21–29
70. Ishikawa Y, Kawakita J, Osawa S, Itsukaichi T, Sakamoto Y, Takaya M, Kuroda S (2005) Evaluation of corrosion and wear resistance of hard cermet coatings sprayed by using an improved HVOF process. J Therm Spray Technol 14(3):384–390
71. Schwetzke R, Kreye H (1999) Microstructure and properties of tungsten carbide coatings sprayed with various high-velocity oxygen fuel spray systems. J Therm Spray Technol 8 (3):433–439
72. Browning JA (1992) Hypervelocity impact fusion-a technical note. J Therm Spray Technol 1 (4):289–29
73. Browning JA (1999) Viewing the future of HVOF and HVAF thermal spraying. J Therm Spray Technol 8(3):351–356
74. Evdokimenko YI, Kisel VM, Kadyrov VK, Korol' AA, Get'man OI (2001) High-velocity flame spraying of powder aluminium protective coatings. Powder Metallurg Metal Ceramics 40(3-4):121–126
75. Kawakita J, Kuroda S, Fukushima T, Katanoda H, Matsuo K, Fukanuma H (2006) Dense titanium coatings by modified HVOF spraying. Surf Coat Technol 201:1250–1255

76. Wu T, Kuroda S, Kawakita J, Katanoga K, Reed R (2006) Processing and properties of titanium coatings produced by warm spraying. In: Marple B et al (eds) Thermal spray: building on 100 years of success. ASM International, Materials Park, OH, e-proceedings
77. Trompetter W, Hyland M, McGrouther D, Munroe P, Markwitz A (2006) Effect of substrate hardness on splat morphology in high-velocity thermal spray coatings. J Therm Spray Technol 15(4):663–669
78. Kuroda S, Tashiro Y, Yumoto H, Taira S, Fukanuma H, Tobe S (2001) Peening action and residual stresses in high-velocity oxygen fuel thermal spraying of 316L stainless steel. J Therm Spray Technol 10(2):367–374
79. Totemeier TC, Wright RN, Swank WD (2002) Microstructure and stresses in HVOF sprayed iron aluminide coatings. J Therm Spray Technol 11(3):400–408
80. Totemeier TC, Wright RN, Swank WD (2004) Residual stresses in high-velocity oxy-fuel metallic coatings. Metallurg Mater Transact A 35A:1807–1814
81. Lima CRC, Nin J, Guilemany JM (2006) Evaluation of residual stresses of thermal barrier coatings with HVOF thermally sprayed bond coats using the Modified Layer Removal Method (MLRM). Surf Coat Technol 200:5963–5972
82. Yilbas BS, Arif AFM (2007) Residual stress analysis for HVOF diamalloy 1005 coating on Ti–6Al–4V alloy. Surf Coat Technol 202:559–568
83. Sidhu TS, Prakash S, Agrawal RD (2005) Science for production studies on the properties of high-velocity oxy-fuel thermal spray coatings for higher temperature applications. Mater Sci 41(6):805–823
84. Wielage B, Wank A, Pokhmurska H, Grund T, Rupprecht C, Reisel G, Friesen E (2006) Development and trends in HVOF spraying technology. Surf Coat Technol 201:2032–2037
85. Neiser RA, Brockmann JE, O'Hern TJ, Dyhkuizen RC, Smith MF, Roemer TJ, Teets RE (1995) Wire melting and droplet atomization in a HVOF jet. In: Berndt CC, Sampath S (eds) Thermal spray science and technology. ASM International, Materials Park, OH, pp 99–104
86. Lopez AR, Hassan B, Oberkampf WL, Neiser RA, Roemer TJ (1998) Computational fluid dynamics analysis of a wire-feed, high-velocity oxygen fuel (HVOF) thermal spray torch. J Therm Spray Technol 7(3):374–382
87. Neiser RA, Smith MF, Dykhuizen RC (1998) Oxidation in wire HVOF-sprayed steel. J Therm Spray Technol 7(4):537–545
88. Hassan B, Lopez AR, Oberkampf WL (1998) Computational analysis of a three-dimensional high-velocity oxygen fuel (HVOF) thermal spray torch. J Therm Spray Technol 7(1):71–77
89. Modi SC, Calla E (2001) A study of high-velocity combustion wire molybdenum coatings. J Therm Spray Technol 10(3):480–486
90. Edrisy A, Perry T, Alpas AT (2005) Wear mechanism maps for thermal-spray steel coatings. Metallurg Mater Transact 36A:2737–2750
91. Sidhu TS, Prakash S, Agrawal RD (2006) Characterisation of NiCr wire coatings on Ni- and Fe-based superalloys by the HVOF process. Surf Coat Technol 200:5542–5549
92. Sidhu TS, Prakash S, Agrawal RD (2006) Hot corrosion resistance of high-velocity oxyfuel sprayed coatings on a nickel-base superalloy in molten salt environment. J Therm Spray Technol 15(3):387–399
93. Stanisic J, Kosikowski D, Mohanty PS (2006) High-speed visualization and plume characterization of the hybrid spray process. J Therm Spray Technol 15(4):750–758
94. Chow R, Decker TA, Gansert RV, Gansert D, Lee D (2003) Properties of aluminium deposited by a HVOF process. J Therm Spray Technol 12(2):208–213
95. Totemeier TC, Wright RN, Swank WD (2003) Mechanical and physical properties of high-velocity oxy-fuel–sprayed iron aluminide coatings. Metallurg Mater Transact A 34A:2223–2231
96. Higuera V, Belzunce FJ, Carriles A, Poveda S (2002) Influence of the thermal-spray procedure on the properties of a nickel-chromium coating. J Mater Sci 37:649–654
97. Trompetter WJ, Hyland M, Munroe P, Markwitz A (2005) Evidence of mechanical interlocking of NiCr particles thermally sprayed onto Al substrates. J Therm Spray Technol 14(4):524–529

98. Chang-Jiu L, Wang YY (2002) Effect of particle state on the adhesive strength of HVOF sprayed metallic coating. J Therm Spray Technol 11(4):523–529
99. Yuuzou K (2007) Application of high temperature corrosion-resistant materials and coatings under severe corrosive environment in waste-to-energy boilers. J Therm Spray Technol 16 (2):202–213
100. Yilbas BS, Khalid M, Abdul-Aleem BJ (2003) Corrosion behavior of HVOF coated sheets. J Therm Spray Technol 12(4):572–575
101. Young-myung Y, Liao H, Coddet C (2002) Simulation and application of a HVOF process for MCrAlY thermal spraying. J Therm Spray Technol 11(1):36–43
102. Lima CRC, Guilemany JM (2007) Adhesion improvements of thermal barrier coatings with HVOF thermally sprayed bond coats. Surf Coat Technol 201:4694–4701
103. Chen WR, Wua X, Marple BR, Nagy DR, Patnaik PC (2008) TGO growth behaviour in TBCs with APS and HVOF bond coats. Surf Coat Technol 202(12):2677–2683
104. Brandl W, Toma D, Kruger J, Grabke HJ, Matthäus G (1997) The oxidation behaviour of HVOF thermal-sprayed MCrAlY coatings. Surf Coat Technol 93–95:21–26
105. Scrivani A, Bardi U, Carrafiello L, Lavacchi A, Niccolai F et al (2003) A comparative study of high velocity oxygen fuel, vacuum plasma spray, and axial plasma spray for the deposition of CoNiCrAlY bond coat alloy. J Therm Spray Technol 12(4):504–507
106. Rajasekaran B, Mauer G, Vaßen R (2011) Enhanced characteristics of HVOF-sprayed MCrAlY Bond Coats for TBC applications. J Therm Spray Technol 20(6):1209–1216
107. Ni LY, Liu C, Huang H, Zhou CG (2011) Thermal cycling behavior of thermal barrier coatings with HVOF NiCrAlY bond coat. J Therm Spray Technol 20(5):1133–1138
108. Kwon J-Y, Lee J-H, Jung Y-G, Paik U (2006) Effect of bond coat nature and thickness on mechanical characteristic and contact damage of zirconia-based thermal barrier coatings. Surf Coat Technol 201:3483–3490
109. Lima CRC, Guilemany JM (1997) The oxidation behaviour of HVOF thermal-sprayed MCrAlY coatings. Surf Coat Technol 93–95:21–26
110. Richer P, Yandouzi M, Beauvais L, Jodoin B (2010) Oxidation behaviour of CoNiCrAlY bond coats produced by plasma, HVOF and cold gas dynamic spraying. Surf Coat Technol 204:3962–3974
111. Fossati A, Di Ferdinando M, Lavacchi A, Bardi U, Giolli C (2010) Scrivani Improvement of the isothermal oxidation resistance of CoNiCrAlY coating sprayed by High Velocity Oxygen Fuel. Surf Coat Technol 204:3723–3728
112. Jang H-J, Park D-H, Junga Y-G, Jang J-C, Choi S-C, Paik U (2006) Mechanical characterization and thermal behavior of HVOF-sprayed bond coat in thermal barrier coatings (TBCs). Surf Coat Technol 200:4355–4362
113. Yuan FH, Chen ZX, Huang ZW, Wang ZG, Zhu SJ (2008) Oxidation behavior of thermal barrier coatings with HVOF and detonation-sprayed NiCrAlY bondcoats. Corros Sci 50:1608–1617
114. Kumar Ashok J, Boy RZ, Stephenson LD (2005) Thermal spray and weld repair alloys for the repair of cavitation damage in turbines and pumps: a technical note. J Therm Spray Technol 14(2):177–182
115. Hanshin C, Lee S, Kim B, Jo H, Lee C (2005) Effect of in-flight particle oxidation on the phase evolution of HVOF NiTiZrSiSn bulk amorphous coating. J Mater Sci 40:6121–6126
116. Dent AH, DePalo S, Sampath S (2002) Examination of the wear properties of HVOF sprayed nanostructured and conventional WC-Co Cermets with different binder phase contents. J Therm Spray Technol 11(4):551–558
117. Ahmed R, Hadfield M (2002) Mechanisms of fatigue failure in thermal spray coatings. J Therm Spray Technol 11(4):551–558
118. Maria P, Zhao L, Zwick J, Bobzin K, Lugscheider E (2006) Investigation of HVOF spraying on magnesium alloys. Surf Coat Technol 201:3269–3274

119. Perry JM, Neville A, Hodgkiess T (2002) A comparison of the corrosion behavior of WC-Co-Cr and WC-Co HVOF thermally sprayed coatings by in situ atomic force microscopy (AFM). J Therm Spray Technol 11(4):536–541
120. Deng C, Liu M, Wu C, Zhou K, Song J (2007) Impingement resistance of HVAF WC-based coatings. J Therm Spray Technol 16(5–6):604–609
121. Jacobs L, Hyland MM, De Bonte M (1999) Study of the influence of microstructural properties on the sliding-wear behavior of HVOF and HVAF sprayed WC-cermet coatings. J Therm Spray Technol 8(1):125–132
122. Jacobs L, Hyland MM, De Bonte M (1998) Comparative study of WC-cermet coatings sprayed via the HVOF and the HVAF process. J Therm Spray Technol 7(2):213–218
123. Marple BR, Lima RS (2005) Process temperature/velocity-hardness-wear relationships for high-velocity oxyfuel sprayed nanostructured and conventional cermet coatings. Therm Spray Technol 14(1):67–76
124. Moskowitz L, Trelewicz K (1997) HVOF coatings for heavy-wear, high-impact applications. J Therm Spray Technol 6(3):294–299
125. Guilemany JM, Espallargas N, Suegama PH, Benedetti AV, Fernández J (2005) High-velocity oxyfuel Cr_3C_2-NiCr replacing hard chromium coatings. J Therm Spray Technol 14 (3):335–341
126. Gang-Chang J, Li CJ, Wang YY, Li WY (2007) Erosion performance of HVOF-sprayed Cr_3C_2-NiCr coatings. J Therm Spray Technol 16(4):557–565
127. Matthews S, Hyland M, James B (2004) Long-yerm carbide development in high-velocity oxygen fuel/high-velocity air fuel Cr_3C_2-NiCr coatings heat treated at 900°C. J Therm Spray Technol 13(4):526–536
128. Mizuno H, Kitamura J (2007) MoB/CoCr cermet coatings by HVOF spraying against erosion by molten Al-Zn Alloy. J Therm Spray Technol 16(3):404–413
129. Horlock AJ, Sadeghian Z, McCartney DG, Shipway PH (2005) High-velocity oxyfuel reactive spraying of mechanically alloyed Ni-Ti-C powders. J Therm Spray Technol 14(1):77–84
130. Thiele S, Heimann RB, Berger L-M, Herrmann M, Nebelung M, Schnick T, Wielage B, Vuoristo P (2002) Microstructure and properties of thermally sprayed silicon nitride-based coatings. J Therm Spray Technol 11(2):218–225
131. Lima RS, Marple BR (2003) High weibull modulus HVOF Titania coatings. J Therm Spray Technol 12(2):240–249
132. Lima RS, Marple BR (2003) Optimized HVOF Titania coatings. J Therm Spray Technol 12 (3):360–369
133. Stahr CC, Saaro S, Berger L-M, Dubsky´ J, Neufuss K, Hermann M (2006) Dependence of the stabilization of α-alumina on the spray process. J Therm Spray Technol 16(5–6):822–830
134. Dobbins TA, Knight R, Mayo MJ (2003) HVOF thermal spray deposited Y_2O_3-stabilized ZrO_2 coatings for thermal barrier applications. J Therm Spray Technol 12(2):214–225
135. Petrovicova E, Knight R, Schadler LS, Twardowski TE (2000) Nylon 11/Silica nanocomposite coatings applied by the HVOF process. II. Mechanical and barrier properties. J Appl Polym Sci 78:2272–2289
136. Ivosevic M, Knight R, Kalidindi SR, Palmese GR, Sutter JK (2005) Adhesive/cohesive properties of thermally sprayed functionally graded coatings for polymer matrix composites. J Therm Spray Technol 14(1):45–51
137. Jackson L, Ivosevic M, Knight R, Cairncross RA (2007) Sliding wear properties of HVOF thermally sprayed nylon-11 and nylon-11/ceramic composites on steel. J Therm Spray Technol 16(5–6):927–932
138. Aalamialeagha ME, Harris SJ, Emamighomi M (2003) Influence of the HVOF spraying process on the microstructure and corrosion behaviour of Ni-20%Cr coatings. J Mater Sci 38:4587–4596
139. Kawakitaa Jin, Isoyamab K, Kurodaa S, Yumoto H (2006) Effects of deformability of HVOF sprayed copper particles on the density of resultant coatings. Surf Coat Technol 200:4414–4423

140. Kawakitaa Jin, Kuroda S, Fukushima T, Kodama T (2005) Improvement of corrosion resistance of high-velocity oxyfuel-sprayed stainless steel coatings by addition of molybdenum. J Therm Spray Technol 14(2):224–230
141. Totemeier TC (2005) Effect of high-velocity oxygen-fuel thermal spraying on the physical and mechanical properties of type 316 stainless steel. J Therm Spray Technol 14(3):369–372
142. Ashok Kumar J, Boy RZ, Stephenson LD (2005) Thermal spray and weld repair alloys for the repair of cavitation damage in turbines and pumps: a technical note. J Therm Spray Technol 14(2):177–183
143. Sundararajan T, Kuroda S, Abe F (2004) Effect of thermal spray on the microstructure and adhesive strength of high-velocity oxy-fuel–sprayed Ni-Cr coatings on 9Cr-1Mo steel. Metallurg Mater Transact A 35A:3187–3199
144. Sundararajan T, Kuroda S, Abe F (2004) Steam oxidation of 80Ni-20Cr high-velocity oxyfuel coatings on 9Cr-1Mo steel: diffusion-induced phase transformations in the substrate adjacent to the coating. Metallurg Mater Transact A 36A:2165–2174
145. Pant BK, Arya V, Mann BS (2007) Development of low-oxide MCrAlY coatings for gas turbine applications. J Therm Spray Technol 16(2):275–280
146. Kim HJ, Lim KM, Seong BG, Park CG (2001) Amorphous phase formation of Zr-based alloy coating by HVOF spraying process. J Mater Sci 36:49–54
147. Bolelli G, Lusvarghi L (2006) Heat treatment effects on the tribological performance of HVOF sprayed Co-Mo-Cr-Si coatings. J Therm Spray Technol 15(4):802–810
148. de Villiers LHL, Richter PW, Benson JM, Young PM (1998) Parameter Study of HP/HVOF Deposited WC-Co Coatings. Journal of Thermal Spray Technology 7(1):97–107
149. Otsubo F, Era H, Uchida T, Kishitake K (2000) Properties of Cr_3C_2-NiCr cermet coating sprayed by high power plasma and high velocity oxy-fuel processes. J Therm Spray Technol 9(4):499–504
150. Sidhu HS, Sidhu BS, Prakash S (2007) Hot corrosion behavior of hvof sprayed coatings on ASTM SA213-T11 Steel. J Therm Spray Technol 16(3):349–354
151. Bolelli G, Cannillo V, Lusvarghi L, Ricco S (2006) Mechanical and tribological properties of electrolytic hard chrome and HVOF-sprayed coatings. Surf Coat Technol 200:2995–3009
152. Yasunari I, Kuroda S, Kawakita J, Sakamoto Y, Takaya M (2007) Sliding wear properties of HVOF sprayed WC–20%Cr_3C_2–7%Ni cermet coatings. Surf Coat Technol 201:4718–4727
153. Maiti AK, Mukhopadhyay N, Raman R (2007) Effect of adding WC powder to the feedstock of WC–Co–Cr based HVOF coating and its impact on erosion and abrasion resistance. Surf Coat Technol 201:7781–7788
154. Sidhu TS, Prakash S, Agrawal RD (2006) Characterizations and hot corrosion resistance of Cr_3C_2-NiCr coating on Ni-base superalloys in an aggressive environment. J Therm Spray Technol 15(4):811–816
155. Sidhu TS, Malik A, Prakash S, Agrawal RD (2007) Oxidation and hot corrosion resistance of HVOF WC-NiCrFeSiB coating on Ni- and Fe-based superalloys. J Therm Spray Technol 16 (5–6):844–849
156. Marple BR, Voyer J (2001) Improved wear performance by the incorporation of solid lubricants during thermal spraying. J Therm Spray Technol 10(4):626–636
157. Wang Y (2004) Nano- and submicron-structured sulfide self-lubricating coatings produced by thermal spraying. Tribol Lett 17(2):165–168
158. Ozdemir I, Hamanaka I, Tsunekawa Y, Okumiya M (2005) In-process exothermic reaction in high-velocity oxyfuel and plasma spraying with SiO_2/Ni/Al-Si-Mg composite powder. J Therm Spray Technol 14(3):321–329
159. Roberson JA, Crowe CT (1997) Engineering fluid dynamics, 6th edn. Wiley, New York, NY
160. Li M, Shi D, Christofides PD (2004) Diamond jet hybrid HVOF thermal spray: gas-phase and particle behaviour modelling and feed back control design. Ind Eng Chem Res 43:3632–3652
161. Li M, Shi D, Christofides PD (2004) Model-based estimation and control of particle velocity and melting in HVOF thermal spray. Chem Eng Sci 59:5647–5656
162. Kamnis S, Gu S (2006) Numerical modelling of propane combustion in a high velocity oxygen–fuel thermal spray gun. Chem Eng Proc 45:246–253

163. Furuhata T, Tanno S, Miura T, Ikeda Y, Nakajima T (1997) Performance of numerical spray combustion simulation. Energ Convers Manage 38(10–13):1111–1122
164. Glassman I (1977) Combustion. Academic, New York, NY
165. Kadyrov E, Kadyrov V (1995) Gas dynamical parameters of detonation powder spraying. J Therm Spray Technol 4(3):280–286
166. Kharlamov YA (2004) Gaseous pulse detonation spraying: current status, challenges, and future perspective. In: Lugsheider E (ed) ITSC 2008 : Thermal spray crossing borders. DVS, Düsseldorf, Germany, E-proceedings
167. Astakhov EA (2008) Controlling the properties of detonation-sprayed coatings: major aspects. Powder Metallurg Metal Ceramics 47(1–2):70–79
168. Roy GD, Frolov SM, Borisov AA, Netzer DW (2004) Pulse detonation propulsion: challenges, current status, and future perspective. Prog Energ Combust Sci 30:545–672
169. Nikolaev YA, Vasil'ev AA, Ul'yanitskii BY (2003) Gas detonation and its application in engineering and technologies (review). Combust Explos Shock Waves 39(4):382–410
170. Wang T-G, Zhao S-S, Hua W-G, Gong J, Sun C (2009) Design of a separation device used in detonation gun spraying system and its effects on the performance of WC–Co coatings. Surf Coat Technol 203:1637–1644
171. Kadyrov E (1996) Gas-particle interaction in detonation spraying systems. J Therm Spray Technol 5(2):185–195
172. Gavrilenko TP, Nikolaev YA (2006) Limits of gaseous detonation spraying combustion. Explos Shock Waves 42(5):594–597
173. Gavrilenko TP, Nikolaev YA (2007) Calculation of detonation gas spraying combustion. Explos Shock Waves 43(6):724–731
174. Cannon JE, Alkam M, Butler PB (2008) Efficiency of pulsed detonation thermal spraying. J Therm Spray Technol 17(4):456–464
175. Ramadan K, Barry Butler P (2004) Analysis of particle dynamics and heat transfer in detonation thermal spraying systems. J Therm Spray Technol 13(2):248–264
176. Kim JH, Kim MC, Park CG (2003) Evaluation of functionally graded thermal barrier coatings fabricated by detonation gun spray technique. Surf Coat Technol 168:275–280
177. Rajasekaran B, Ganesh Sundara Raman S, Joshi SV, Sundararajan G (2006) Effect of detonation gun sprayed Cu–Ni–In coating on plain fatigue and fretting fatigue behaviour of Al–Mg–Si alloy. Surf Coat Technol 201:1548–1558
178. Ganesh Sundara Raman S, Rajasekaran B, Joshi SV, Sundararajan G (2007) Influence of substrate material on plain fatigue and fretting fatigue behavior of detonation gun sprayed Cu-Ni-In Coating. J Therm Spray Technol 16(4):571–579
179. Rajasekaran B, Ganesh Sundara Raman S, Rajasekaran B, Joshi SV, Sundararajan G (2008) Performance of plasma sprayed and detonation gun sprayed Cu–Ni–In coatings on Ti–6Al–4V under plain fatigue and fretting fatigue loading. Mater Sci Eng A 479:83–92
180. Oliker VE, Barabash MY, Grechishkin EF, Timofeeva II, Gridasova TY (2007) High-temperature air oxidation based on eutectic (β-NiAl + γ- and NiAl intermetallide. Powder Metallurg Metal Ceramics 46(3–4):175–181
181. Oliker VE, Pritulyak AA, Syrovatka VL, Grechishkin EF, Gridasova TY (2007) Formation and high-temperature oxidation of thermal-barrier coatings with Ti–Al–Cr binding layer. Powder Metallurg Metal Ceramics 46(9–10):483–491
182. Belzunce FJ, Higuera V, Poveda S, Carriles A (2002) High temperature of HFPD thermal-sprayed MCrAlY coatings in simulated gas turbine environments. J Therm Spray Technol 11 (4):461–467
183. Yu-Juan Z, Sun XF, Guana HR, Hua ZQ (2002) 1050°C isothermal oxidation behavior of detonation gun sprayed NiCrAlY coating. Surf Coat Technol 161:302–305
184. Taylor TA, Knapp JK (1995) Dispersion-strengthened Modified MCrAlY Coatings Produced by Reactive Deposition. Surf Coat Technol 76–77:34–40
185. Zhang YJ, Sun XF, Zhang YC, Jin T, Deng CG, Guan HR, Hu ZQ (2003) A comparative study of DS NiCrAlY coating and LPPS NiCrAlY coating. Mater Sci Eng A360:65–69

186. Ke PL, Wu YN, Wang QM, Gong J, Sun C, Wen LS (2005) Study on thermal barrier coatings deposited by detonation gun. Surf Coat Technol 200:2271–2276
187. Wu YN, Wang FH, Hua WG, Gong J, Sun C, Wen LS (2003) Oxidation behavior of thermal barrier coatings obtained by detonation spraying. Surf Coat Technol 166:189–194
188. Wu YN, Ke PL, Wang QM, Sun C, Wang FH (2004) High temperature properties of thermal barrier coatings obtained by detonation spraying. Corros Sci 46:2925–2935
189. Suresh BP, Basu B, Sundararajan G (2008) Processing–structure–property correlation and decarburization phenomenon in detonation sprayed WC–12Co coatings. Acta Mater 56:5012–5026
190. Sundararajan G, Sen D, Sivakumar G (2005) The tribological behaviour of detonation sprayed coatings: the importance of coating process parameters. Wear 258:377–391
191. Murthy JKN, Venkataraman B (2006) Abrasive wear behaviour of WC–CoCr and Cr_3C_2–20 (NiCr) deposited by HVOF and detonation spray processes. Surf Coat Technol 200:2642–2652
192. Wang T-G, Zhao S-S, Hua W-G, Li J-B, Gong J, Sun C (2010) Estimation of residual stress and its effects on the mechanical properties of detonation gun sprayed WC–Co coatings. Mater Sci Eng A 527(3):454–461
193. Park SY, Kim MC, Park CG (2007) Mechanical properties and microstructure evolution of the nano WC–Co coatings fabricated by detonation gun spraying with post heat treatment. Mater Sci Eng A 449–451:894–897
194. Du H, Hua W, Liu J, Gong J, Sun C, Wen L (2005) Influence of process variables on the qualities of detonation gun sprayed WC–Co coatings. Mater Sci Eng A 408:202–210
195. Suresh BP, Rao DS, Rao GVN, Sundararajan G (2007) Effect of feedstock size and its distribution on the properties of detonation sprayed coatings. J Therm Spray Technol 16 (2):281–290
196. Oliker VE, Grechishkin EF, Polotai VV, Loskutov MG, Timofeeva II (2004) Influence of the structure and properties of WC-Co alloy powders on the structure and wear resistance of detonation coatings. Powder Metallurg Metal Ceramics 43(5–6):258–264
197. Du H, Sun C, Hua WG, Zhang YS, Han Z, Wang TG, Gong J, Lee SW (2006) Fabrication and evaluation of D-gun sprayed WC–Co coating with self-lubricating property. Tribol Lett 23 (3):261–266
198. Murthy JKN, Rao DS, Venkataraman B (2001) Effect of grinding on the erosion behaviour of a WC–Co–Cr coating deposited by HVOF and detonation gun spray processes. Wear 249:592–600
199. Li C-J, Ohmori A (1996) The lamellar structure of a detonation gun sprayed $A1_2O_3$ coating. Surf Coat Technol 82:254–258
200. Saravanan P, Selvarajan V, Rao DS, Joshi SV, Sundararajan G (2000) Influence of process variables on the quality of detonation gun sprayed alumina coating. Surf Coat Technol 123:44–54
201. Niemi K, Vuoristo P, Mantyla T (1994) Properties of alumina-based coatings deposited by plasma spray and detonation gun spray processes. J Therm Spray Technol 3(2):99–203
202. Saravanan P, Selvarajan V, Srivastava MP, Rao DS, Joshi SV, Sundararajan G (2000) Study of plasma- and detonation gun-sprayed alumina coatings using taguchi experimental design. J Therm Spray Technol 9(4):505–512
203. Pogrebnyak AD, Tyurin YN, Ivanov YF, Kobzev AP, Kul'ment'eva OP, Il'yashenko MI (2000) Preparation and Investigation of the Structure and Properties of Al_2O_3 Plasma-Detonation Coatings. Tech Phys Lett 26(11):960–963
204. Sobiecki JR, Ewertowshi J, Babul T, Wierzchon T (2004) Properties of alumina coatings produced by gas-detonation method. Surf Coat Technol 180–181:556–560
205. Venkataraman R, Ravikumar B, Krishnamurthy R, Das DK (2006) A study on phase stability observed in as sprayed Alumina-13 wt.% Titania coatings grown by detonation gun and plasma spraying on low alloy steel substrates. Surf Coat Technol 201:3087–3095

206. Semenov SY, Cetegen BM (2002) Experiments and modeling of the deposition of nanostructured alumina–titania coatings by detonation waves. Mater Sci Eng A335:67–81
207. Sundararajan G, Sivakumar G, Sen D, Srinivasa Rao D, Ravichandra G (2010) The tribological behaviour of detonation sprayed TiMo(CN) based cermet coatings. Int J Refract Metals Hard Mater 28:71–81
208. Du H, Sun C, Hua W, Wang T, Gong J, Jiang X, Wohn Lee S (2007) Structure, mechanical and sliding wear properties of WC–Co/MoS2–Ni coatings by detonation gun spray. Mater Sci Eng A 445–446:122–134
209. Wang J, Li Zhang B, Sun YZ (2000) Study of the Cr_3C_2-NiCr detonation spray coating. Surf Coat Technol 130:69–73
210. Sundararajan G, Sivakumar G, Sen D, Srinivasa Rao D, Ravichandra G (2010) The tribological behaviour of detonation sprayed TiMo(CN) based cermet coatings, Int. J Refract Metals Hard Mater 28:71–81
211. Kamal S, Jayaganthan R, Prakash S, Kumar S (2008) Hot corrosion behavior of detonation gun sprayed Cr_3C_2–NiCr coatings on Ni and Fe-based superalloys in Na_2SO_4–60% V_2O_5 environment at 900∘C. J Alloys Compd 463:358–372
212. Kamal S, Jayaganthan R, Prakash S (2009) High temperature oxidation studies of detonation-gun-sprayed Cr_3C_2–NiCr coating on Fe- and Ni-based superalloys in air under cyclic condition at 900∘C. J Alloys Compd 472:378–389
213. Wang J, Sun B, Guo Q, Nishio M, Ogawa H (2002) Wear resistance of a detonation spray coating. J Therm Spray Technol 11(2):261–265
214. Jun W, Sun B, Guo Q, Nishio M, Ogawa H (2002) Wear resistance of a Cr_3C_2-NiCr detonation spray coating. J Therm Spray Technol 11(2):261–265
215. Murthy JKN, Bysakh S, Gopinath K, Venkataraman B (2007) Microstructure dependent erosion in Cr_3C_2–20(NiCr) coating deposited by a detonation gun. Surf Coat Technol 202:1–12
216. Wood RJK, Mellor BG, Binfield ML (1997) Binfield, Sand erosion performance of detonation gun applied tungsten carbide/cobalt-chromium coatings. Wear 211:70–83
217. Manish R (2002) Dynamic hardness detonation sprayed WC-Co coatings. J Therm Spray Technol 11(3):393–399
218. Oliker VE, Sirovatka VL, Timofeeva II, Gridasova TY, Hrechyshkin YF (2006) Formation of detonation coatings based on titanium aluminide alloys and aluminium titanate ceramic sprayed from mechanically alloyed powders Ti—Al. Surf Coat Technol 200:3573–3581
219. Tillmann W, Vogli E, Nebel J (2007) Development of detonation flame sprayed cu-base coatings containing large ceramic particles. J Therm Spray Technol 16(5–6):751–758
220. Astakhov EA, Mits IV, Kaplina GS, Kokorina NN, Kil'dii AI (2005) Study of the process of phase formation during detonation spraying of composite powders of the FeTi − SiC system. Powder Metallurg Metal Ceramics 44(1–2):55–59
221. Oliker VE, Sirovatka VL, Timofeeva II, Grechishkin EF, Gridasova TY (2005) Effects of properties of titanium aluminide powders and detonation spraying conditions on phase and structure formation in coatings. Powder Metallurg Metal Ceramics 44(9–10):472–480
222. Filimonov VY, Yakovlev VI, Korchagin MA, Loginova MV, Semenchina AS, Afanas'ev AV (2008) Structure formation during gas-detonation spraying of coatings from composite powders $TiAl_3$ and Ni_3Al. Combust Explos Shock Waves 44(5):591–596
223. Podchernyaeva IA, Shchepetov VV, Panasyuk AD, Gromenko VY, Yurechko DV, Katashinskii VP (2003) Refractory and ceramic materials structure and properties of wear-resistant detonation coatings based on titanium carbonitride. Powder Metallurg Metal Ceramics 42(9–10):497–502
224. Zhu JL, Huang JH, Wang HT, Xu JL, Zhao XK, Zhang H (2008) In-situ synthesis and microstructure of TiC–Fe36Ni composite coatings by reactive detonation-gun spraying. Mater Lett 62:2009–2012
225. Yang G, Zu-kun H, Xiaolei X, Gang X (2001) Formation of molybdenum boride cermet coating by the detonation spray process. J Therm Spray Technol 10(3):456–460

226. Gao Y, Zu-kun H, Xiaolei X, Gang X (2001) Formation of molybdenum boride cermet coating by the detonation spray process. J Therm Spray Technol 10(3):456–460
227. Senderowski C, Bojar Z (2008) Gas detonation spray forming of Fe–Al coatings in the presence of interlayer. Surf Coat Technol 202:3538–3548
228. Senderowski C, Bojar Z (2009) Influence of detonation gun spraying conditions on the quality of Fe-Al intermetallic protective coatings in the presence of NiAl and NiCr interlayers. J Therm Spray Technol 18(3):435–447
229. Min'kov DV, Lakunin VY, Kartashov ST, Bashkirov OM, Ivanov AS, Kasatkin AV, Min'kov MD (2008) Restoration of drying cylinders on spinning machines by gas detonation spraying. Fibre Chem 40(6):545–547

Chapter 6
Cold Spray

Abbreviations

ABS	Adiabatic shear band
LPCS	Low pressure cold spray
HV	Vickers hardness
PGDS	Pulsed gas dynamic spraying
PIC	Particle impact conditions
WS	Window of spray ability

6.1 Introduction to the Different Cold Spray Processes

6.1.1 High-Pressure Cold Spray

6.1.1.1 Conventional Cold Spray

A group of scientists from the Institute of Theoretical and Applied Mechanics of the Siberian Branch of the Russian Academy of Sciences (ITAM of RAS) in Novosibirsk, Russia [1] developed the old Spray (CS) process in the mid-1980s. They successfully deposited a wide range of pure metals, metal alloys, and composites onto a variety of substrate materials and demonstrated the feasibility of cold spray for various applications. According to [2] a US patent on the cold spray technology was issued in 1994 [2] and a European patent was granted in 1995 [3].

Cold spray is probably the spray process to which the largest numbers of publications and patents [1] have been devoted over the past decade. It is a kinetic spray process, utilizing supersonic jets of compressed gas to accelerate, near-room temperature powder particles, to ultrahigh velocities [4, 5]. The solid *ductile* particles, traveling at velocities between 300 and 1,500 m/s, plastically deform on impact with the substrate, and consolidate to create a coating [2, 4, 5]. However it

P.L. Fauchais et al., *Thermal Spray Fundamentals: From Powder to Part*,
DOI 10.1007/978-0-387-68991-3_6, © Springer Science+Business Media New York 2014

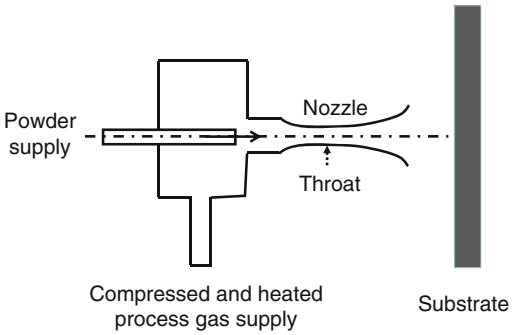


Fig. 6.1 Typical cold spray system geometry. Reprinted with kind permission from Springer Science Business Media, copyright © ASM International [3]

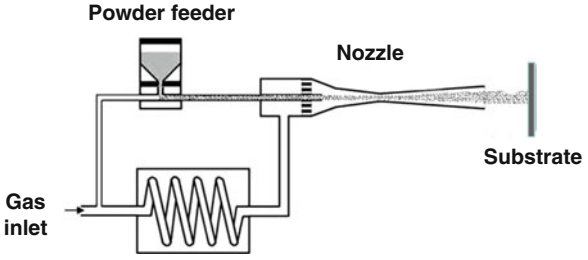


Fig. 6.2 Schematic of the conventional cold spray process principle. Reprinted with kind permission from Springer Science Business Media, copyright © ASM International [6]

implies that particle velocities at impact are higher than a so-called critical velocity, which depends on particle material, size, and morphology. The fundamental phenomenon in the cold spray process is the gas-dynamic acceleration of particles to supersonic velocities and hence to high kinetic energies. This is achieved using convergent–divergent de Laval nozzles as shown in Fig. 6.1 [3].

The upstream gas pressure in a typical cold spray system varies between 2 and 4 MPa (300–600 psig). Gases used are N_2, He, or their mixtures, at relatively high flow rates (up to 4 m^3/min). The gas has to be preheated up to 700–800°C to avoid condensation once it undergoes sonic expansion. Moreover, this heating increases the particle temperature and velocity and thus assists in its deformation upon impact. When spraying with helium, the system should be operated in an enclosure in order to allow for the recycling of the gas and reduce the overall process cost.

Since the particles are injected upstream of the nozzle, (see Fig. 6.2), the powder feeder has to be especially designed to operate at high pressures, slightly above the upstream pressure of the process compressed gas supply. Particles adhere onto the substrate only if their impact velocity is above a critical value, depending on the sprayed material, and is typically in the range of 500–900 m/s. Feedstock powders should be relatively fine with a mean particle diameter in the range of 1 and 50 μm. Deposition efficiencies can be as high as 70–90 wt.% of the injected powder. The spray trace is typically below 25 mm^2 and spray rates of 3–5 kg/h are normally achieved. It is also important to emphasize that, throughout the cold spray process, the substrate is not heated. Since the feed powder remains in the solid state [4, 5], the deleterious effects of oxidation, evaporation, melting, crystallization,

residual stresses (except peening effect), debonding, gas release, and other common problems in traditional thermal spray processes can be avoided. Owing to the impact-fusion coating process, only ductile metals (Zn, Ag, Cu, Al, Ti, Nb, Mo, etc.), alloys (Ni–Cr, Cu–Al, Ni alloys, MCrAlYs, etc.) and polymers can be sprayed.

The overall success of conventional cold spray is probably due to the following process characteristics [2, 4, 5]:

- Oxide level in the coatings of metals or alloys is limited to that of the feedstock.
- Coatings can be deposited on temperature-sensitive materials such as polymers without using sophisticated cooling devices.
- Coatings are very dense and exhibit microstructures identical to those of the feed-stock materials.
- The spray trace is well defined and relatively small (between 1 and 25 mm^2) allowing a precise control of the deposition area.
- Stress generated is compressive allowing spraying thick coatings (up to 50 mm) without adhesion failure.
- Deposition rates are relatively high which makes it attractive for industry.

However *only ductile particles* can be sprayed. The *process uses large flow rates of nitrogen or helium* (1–2 m^3/min), the price of which is not negligible. This is especially the case for helium that requires spraying in closed chambers to recycle it. The spray plume is rather small (below 1 cm in diameter). According to the high impact velocities the sprayed metal is hardened, resulting in a low ductility of coatings.

The first users were the automotive and aerospace industries and a strong interest seems to be developing in the electronic industry [4, 5].

6.1.1.2 Kinetic Spray Process

Van Steenkiste et al. [7–10] have developed a new process called kinetic spray process presented in Fig. 6.3. Instead of using nitrogen or helium as working gas it works with preheated air (2 MPa, 18 g/s), and the powder, carried by nitrogen, from the high-pressure powder feeder is premixed with the working gas in a chamber. The powder carrier gas can be also preheated to increase particles velocity. The ratio cross-sectional area of working gas to powder injector is between 126 and 388, which are 2.5–7.5 less than in conventional cold spray. The mixture of gas and particles, with sizes between 50 and 200 μm, flows through a de Laval-type nozzle, particles being accelerated due to drag effects of the high velocity gas. Mean critical velocities of the larger particles ($d > 50$ μm) are significantly smaller than those of the smaller particles in cold spray process ($d < 50$ μm). The smaller powder injection tube diameters of the kinetic spray process appear to be the most important difference with the cold spray process. According to Van Steenkiste and Smith [10] "Resulting higher gas temperatures and possibly lower turbulence upstream of the throat are kinetic spray properties discussed as potential explanations for observed differences between the kinetic and cold spray process properties."

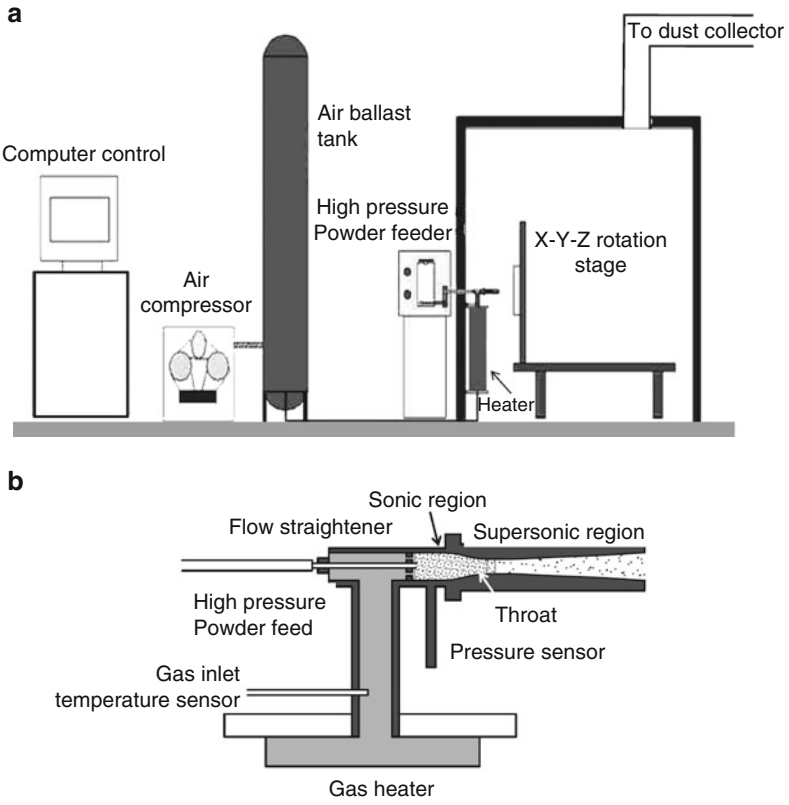


Fig. 6.3 (**a**) Schematic diagram of the kinetic spray equipment. (**b**) Close-up diagram of the nozzle region. Reprinted with kind permission from Elsevier [9]

6.1.1.3 Pulsed Gas Dynamic Spraying Process

The low particle impact temperature in conventional cold spray process is problematic when spraying hard particles for which it is difficult to achieve sufficiently high velocities to reach the critical value. Therefore, a new coating process, the pulsed gas dynamic spraying (PGDS) has been developed [11–13]. This process allows accelerating in an inert gas the feedstock particles to high impact velocities at intermediate temperatures. This higher particle impact temperature, resulting in its enhanced plastic deformation, requires lower critical velocity compared to the conventional cold spray process. The PGDS process is shown schematically in Fig. 6.4. It comprises a long smooth wall pipe, of circular cross section, which is divided into two compartments separated by a valve ($V_{H/L}$). The first compartment, called the shock generator, connected to a high-pressure gas supply, is initially kept at high pressure p_{int} (3.0 MPa), controlled by a pressure regulator. The second compartment, the spraying gun, is opened at the end and kept at atmospheric

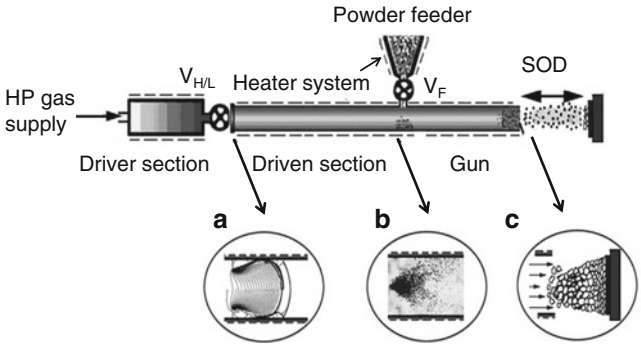


Fig. 6.4 Principle of the Pulsed Gas Dynamic Spraying process (PGDS). Reprinted with kind permission from Elsevier [13]

pressure (p_{atm}). When opening rapidly, for a short period of time, the valve ($V_{H/L}$) separating both sections a shock wave, depending on the initial pressure ratio (p_{int}/p_{atm}), is generated and propagates into the spraying gun, accelerating and heating the powder present in the gun. This operation is repeated at a set frequency. During each cycle, or pulse, a controlled quantity of the feedstock powder is dropped down from the feeder to the tube by opening the feeder valve (V_f), and closing it prior to the passage of the shock wave. Electrical heaters allow preheating both the gas and the powder. For a more detailed description of the process see the paper of Jodoin et al. [11]. The aim of this process is to exploit the benefits of both HVOF and cold spray. It is expected to achieve high impact velocities, similar to those obtained in conventional cold spray and intermediate temperatures (below the melting point) in a nonreacting gas. The detailed description of the process is presented in Fig. 6.5 [11].

The process uses compression waves (CW) produced at constant frequency and injected into a quiescent inert gas in a spray gun containing the powder feedstock material (Fig. 6.5a). The CW coalesces to form shock waves and generates behind their passage in the gun a high-speed intermediate temperature flow (Fig. 6.5b). The induced flow heats and accelerates the powder feedstock material towards the substrate (Fig. 6.5b′ & b″). Modeling of this process has shown that He gives the highest velocities and temperatures [11].

6.1.2 Low Pressure Cold Spray

Blends of ductile materials (> 50 vol.%) with brittle metals or ceramics can also be used in a modified version of cold spray called, "Low Pressure Cold Spray—LPCS" process. In this case, the upstream pressure is below 1 MPa, typically 0.5 MPa with a much lower (about one order of magnitude) gas flow rate of about 0.4 m^3/min. A lower power is accordingly required to preheat the spray gas, which is normally air

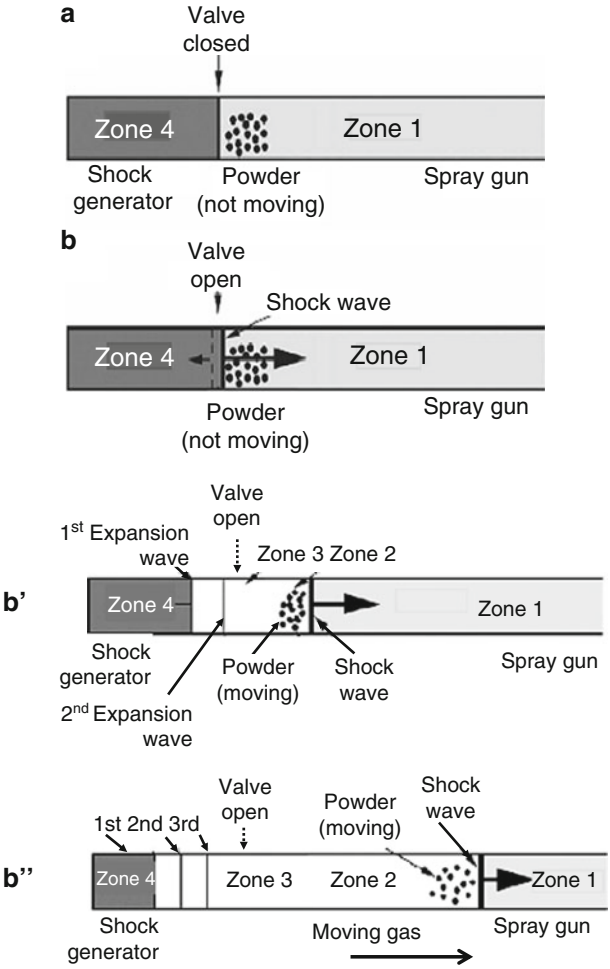


Fig. 6.5 Schematic of one-pulse spray cycle. The opening and closure of the valve located between the shock generator and the spraying gun result in a shock wave moving toward the gun exit entraining the powder in a high-velocity intermediate temperature flow. Reprinted with kind permission from Elsevier [11]

and, therefore, cheaper than N_2 or He [14–18]. Particles are injected downstream of the nozzle throat (see Fig. 6.6, which is an illustration of the SIMAT process). With gas velocities in the 300–400 m/s ranges, the critical velocity of particles is not attained. To achieve coatings, metal particles are mixed with ceramic ones, which mostly rebound upon impact, as shown in Fig. 6.7. Their role is to apply compressive stress to the metal particles on the substrate and the previously deposited layers [19]. Of course, the deposition efficiency is often lower compared to the more standard high-pressure cold spray process. The LPCS process is attractive for short run-production [14–19].

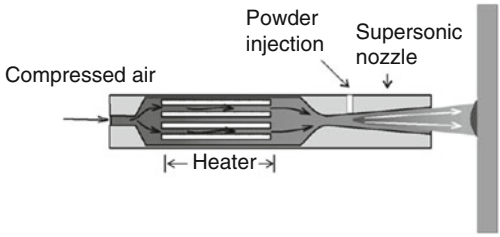


Fig. 6.6 Schematic of the Supersonically Induced Mechanical Alloy Technology (SIMAT®), also known as Gas-dynamic spraying, low pressure cold spray process principle. Reprinted with kind permission of ASM [14]

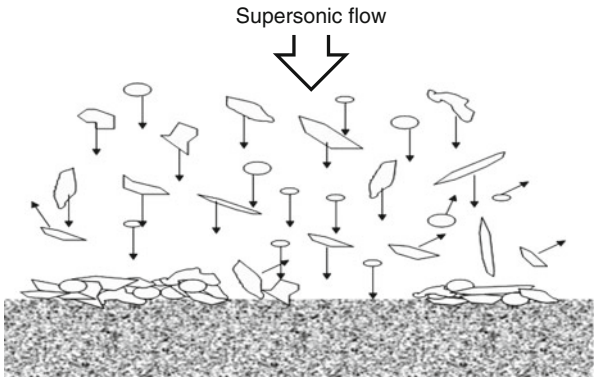


Fig. 6.7 Schematic of the particle deposition SIMAT ® low-pressure cold spray process: the ceramic particles rebound upon impact and apply compressive stress to ductile particles, which form the coating. Reprinted with kind permission of ASM [14]

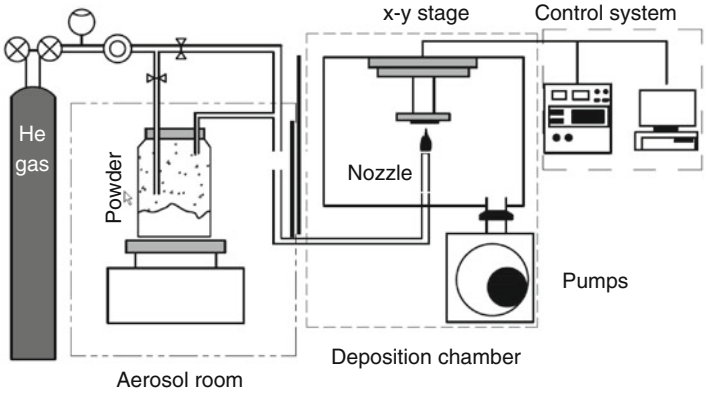


Fig. 6.8 Schematic diagram of vacuum cold spray system. Reprinted with kind permission of ASM [20]

6.1.3 Vacuum Cold Spray

A very simple system, shown schematically in Fig. 6.8 was used to deposit TiO_2 nanometer-sized powders (~200 nm). It consists of a vacuum chamber and vacuum pump, an aerosol chamber, an accelerating gas feeding unit, a particle-accelerating nozzle, a two-dimensional worktable, and a control unit. Helium was used as

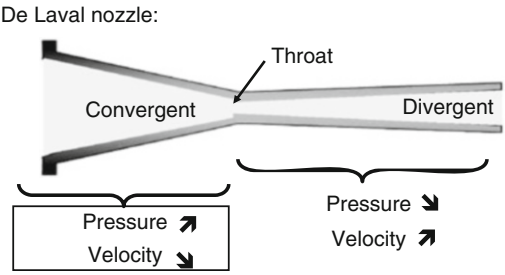


Fig. 6.9 Schematic diagram of de Laval nozzle

accelerating gas (3 slm), the chamber pressure was 2×10^{-3} Pa, and could be varied between 100–5000 Pa, and the orifice of the square nozzle was 2.5×0.2 mm^2. The system deposited TiO_2 coatings on ITO conducting glass [20]. The influence of annealing of the coating between 450 and 500°C yielded both higher photocatalytic activity and better adhesion [20–23]. Other vacuum cold spray systems are described in patents (see Irissou et al [1]).

6.2 High-Pressure Cold Spray Process

6.2.1 Process Gas Dynamics

In the cold spray process, since the process gas accelerates particles, the maximum gas velocity achieved limits the particle velocity. That is why the control of the gas flow pattern is one of the key aspects of the process development [4, 5]. Many studies have been devoted to the optimization of the process gas dynamics through improved nozzle designs [3, 4, 16, 24–28].

6.2.1.1 One-Dimensional Geometry and Isentropic Expansion of the Flow

Historically, one-dimensional isentropic flow analysis has been used to show how to generate a supersonic flow. This analysis assumes that the flow inside a variable area duct is one dimensional, in steady-state, and that there is no chemical reaction, no external work done on the flow, no change in the potential energy, no heat transfer occurring, and the flow is reversible.

(a) Very Simple Models

The simplest models consider a one-dimensional geometry of the de Laval nozzle (see Fig. 6.9) and an isentropic expansion of the flow, from the nozzle throat to its exit [3].

The process gas flow is assumed to originate from a large chamber or duct where the pressure is equal to the stagnation pressure (p_0), the temperature (T_o), and where the gas velocity is zero. For practical purposes, this matches the conditions upstream of the nozzle throat provided that the flow area is three times larger than the throat area [3]. At the throat, the Mach number is unity. The local velocity in the divergent section of the nozzle can be calculated as follows:

$$u_g = M\sqrt{T.\gamma.R/M_g} \tag{6.1}$$

where, u_g is the gas velocity, M the Mach number, R is the universal gas constant, γ the specific heats ratio (c_p/c_v), M_g the molar mass of the gas, and T the temperature at the considered location, which is linked to the initial gas temperature T_0 by

$$T_0/T = 1 + (\gamma - 1)/2 \tag{6.2}$$

For monatomic gases, $\gamma = 1.66$, while for diatomic gases $\gamma = 1.4$. Equation (6.1) demonstrates well the interest of using He instead of N_2: the quantity R/M_g being 296.78 (J/K.kg) for N_2 compared to 2007.15 (J/K.kg) for He. The mass balance yields the gas density at the throat:

$$\rho* = \dot{m}/(v^*.A^*) \tag{6.3}$$

where $\dot{m}$ is the gas mass flow rate, v* and A*, respectively, the throat velocity and throat area. Using the perfect gas law [3], the pressure at the throat is obtained:

$$p* = \rho^*.R_u.T^* \tag{6.4}$$

with $R_u = R/M_g$, From the throat pressure, the stagnation pressure can be calculated. Of course if sonic conditions are to be maintained at the throat, the throat pressure must be above the ambient pressure, or the pressure in the spray chamber. Current cold spray systems operating conditions have an exit pressure well below the ambient pressure to obtain maximum spray particle velocities. Thus, the gas flow is said to be overexpanded. This results in a flow outside of the nozzle that cannot be solved by simple one-dimensional gas dynamic equations. However, the one-dimensional results [3] still apply inside the nozzle as long as the overexpansion is not so important as to cause a normal shock inside the nozzle. The exit Mach number can then be calculated when the exit area is specified. With the exit Mach number known, the other gas conditions can be obtained from conventional isentropic flow relationships [3] (see Sect. 6.6.1)

The acceleration of one particle is a function of the drag force exerted on it (see Chap. 4 Sect. 4.2.2.1), and, assuming that the particle velocity is low compared to that of the gas, the particle velocity becomes [3]

$$u_p = u_g.\sqrt{\frac{C_D.A_p.\rho_p.x}{m_p}} \tag{6.5}$$

where u_p is the particle velocity, u_g that of the gas, C_D the drag coefficient, A_p the particle cross-sectional area, m_p the particle mass, ρ_p the particle specific mass, x the distance traveled by the particle. For a constant drag coefficient, C_D, it can be deduced from Eq. (6.5), that the spray particle velocity is proportional to the square root of the ratio of the distance traveled, x, divided by the particle diameter. It also shows the relatively important influence of the specific mass of the gas (ρ_g). The gas dynamic equations reveal, on the other hand, that the gas mass density decreases as the gas velocity increases through the supersonic nozzle. Thus, there exists an optimal condition that yields a maximum acceleration, which corresponds to conditions where a maximum drag force is exerted on the particle. The latter can be estimated by differentiating the right-hand side of the drag force equation with respect to pressure (or temperature for they are related via the isentropic flow assumption). Then the maximum drag force is estimated by using the perfect gas relations. Note that both the gas mass density and the gas velocity are dependent on the pressure level to which the gas is expanded [3]. Finally, one finds that a gas velocity corresponding to a Mach number of 1.4 yields near optimal conditions that maximize the acceleration of the sprayed particles.

(b) More Complex Models

Under the assumptions recalled at the beginning of Sect. 6.2.1.1 the mass conservation, energy conservation, and second law of thermodynamics show that the general geometry required to accelerate a subsonic flow to the supersonic regime is the convergent–divergent nozzle presented in Fig. 6.9 [25]. With this geometry, the fluid is continuously accelerated from low subsonic to supersonic velocity. Another requirement must also be fulfilled to create a supersonic flow: the pressure ratio between the stagnation pressure p_0 of the flow and the backpressure p_b outside the nozzle must be sufficiently high. The design pressure ratio $(p_b/p_0)_d$ for a shock less supersonic nozzle flow is found with the one-dimensional isentropic relation for an adiabatic perfect gas. Under the stated assumptions the back pressure and the stagnation pressure are the only parameters controlling the exit design Mach number (M_e) [25, 29]:

$$\left(\frac{p_0}{p_b}\right)_d = \left(\frac{\gamma+1}{2+(\gamma-1)M_e^2}\right)^{\frac{\gamma}{\gamma-1}} \tag{6.6}$$

Once the desired exit Mach number and the backpressure are known, the required stagnation pressure is found from Eq. (6.6). However, even if the design pressure ratio is used $(p_b/p_0)_d$, not all convergent–divergent nozzles will produce the desired supersonic flow. The right specific nozzle geometry must be used. The design requirement from the one-dimensional isentropic flow analysis is entirely fulfilled if the design pressure ratio is used with the proper throat to exit area ratio given by [25, 29]

$$\frac{A_e}{A*} = \frac{1}{M_e}\left\{\left(\frac{2}{\gamma+1}\right)\left[1+\left(\frac{\gamma-1}{2}\right)M_e^2\right]\right\}^{\frac{\gamma+1}{2(\gamma-1)}} \tag{6.7}$$

According to Eq. (6.6), the stagnation pressure, but not the stagnation temperature, plays a fundamental role in the process of generating a supersonic flow at a specific exit Mach number. The pressure ratio and the specific geometry (through its exit to throat area ratio, A_e/A_t) determine the exit Mach number. However, the stagnation temperature has a direct influence on the exit velocity of the fluid [25]. For a perfect gas, the speed of sound, c, is given by Eq. (8)

$$c = \sqrt{\frac{\gamma.R.T}{M_g}} \tag{6.8}$$

where R is the perfect gas constant (8.32 J/K/mol) and M_g the molar mass of the gas (kg/mol). Since the velocity of the fluid is given by the relation $v = c.\ M_e$, the temperature plays a direct role in the exit velocity of the fluid. From the energy conservation law, the perfect gas law and the expression of sound velocity we obtain

$$\frac{T_0}{T_e} = \left\{1+\left(\frac{\gamma-1}{2}\right)M_e^2\right\} \tag{6.9}$$

The results of calculations [25] show that the required stagnation gas temperature drops with the increasing gas exit Mach number, resulting in a smaller heater needed. The solid particles injected in the jet will encounter temperatures ranging from the exit jet temperature T_e to the stagnation temperature T_0. The latter is found not only inside the tank at the stagnation section but also at the stagnation point, on the substrate, as the flow is heated during its deceleration. Setting the maximum allowable T_0 to 1,000 K, based on the current practice in cold spray shows that the minimum exit Mach number should generally be kept above 1.5. This limit increases with the required exit velocity [25]. For more details the interested reader can look at the papers [3, 18, 25, 30].

6.2.1.2 Effect of Boundary Layer and the Shock on the Substrate

To accelerate particles in the nozzle up to the gas velocity, it is necessary to increase the nozzle length L. However, as the nozzle length increases, the boundary layer thickness increases. This leads to a decrease of the effective nozzle cross-sectional area downstream in comparison to its geometrical cross-sectional area. As a result, the gas velocity decreases at the nozzle exit in comparison to the ideal gas flow velocity [25] as calculated previously. The boundary and compressed layers, not considered before, have a non-negligible influence on the final particle velocity; the

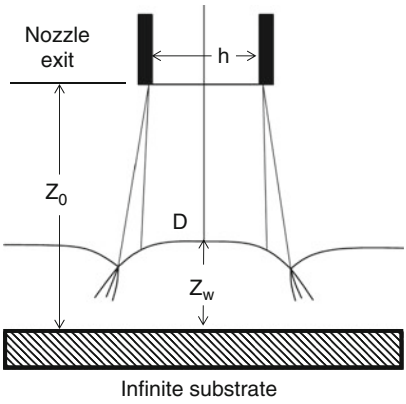


Fig. 6.10 Schematic of the supersonic gas jet impinging on a flat unrestricted obstacle. *D* detached shock, *h* square nozzle thickness, and Z_0 distance from nozzle exit to the obstacle. Reprinted with kind permission from Springer Science Business Media, copyright © ASM International [25]

smaller the size of the particles, the greater is their influence [25]. This effect should be taken into account especially in the case of the cold spray nozzle design, because the particle size of the commonly used powders is small and the impact particle velocity is very important. When the supersonic jet impinges on an obstacle positioned perpendicularly to the flow (Fig. 6.10), a deceleration and deviation of the gas flow occurs in front of the obstacle surface. The transition from a high-velocity supersonic flow to a low velocity subsonic flow occurs in a shock wave that appears at some distance Z_w from the substrate surface.

A high-pressure and high-density gas layer is created between the substrate surface and the shock. Small particles (especially those below 5 μm) of the deposited material coming through this compressed layer will lose some of their velocity while crossing the shock front. This loss becomes greater the greater the compressed layer thickness is [26], which is another good reason to limit the Mach number.

6.2.1.3 2D and 3D Compressible Models

The equations governing the steady state flow are the mass, momentum, and energy conservation equations (Chap. 3 and especially Sect. 3.3.7.2). According to Jodoin [27], due to the transonic nature of the flow under study, this set of equations is classified as elliptic in the subsonic part of the flow, parabolic in the sonic part of the flow, and hyperbolic in the supersonic part of the flow [27]. This difference in the classification of the equations is linked to the way the perturbations are transmitted in the flow. To properly represent the physical system, the numerical discretization scheme must reproduce this physical feature. This feature increases the level of complexity involved in solving the governing equations since the numerical discretization scheme used to solve each set of equations is different. A k–ε model represents the turbulence in the flow. As the flow is compressible, the gas mass density is not constant. Using, in first approximation, the ideal gas law to

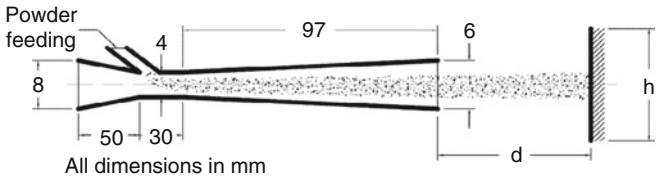


Fig. 6.11 Schematic of the cold spray torch nozzle used by Samareh and Dolatabadi [30] and the substrate. Reprinted with kind permission from Springer Science Business Media, copyright © ASM International

calculate mass density, in order to have the compressibility effects taken into account, closes the system of equations [27].

Models can be 2D [27, 28] or 3D [30] which allows a following of the effects of the nozzle exit–substrate distance as well as the substrate shape (for the 3D model), and characterizing the shock wave, which is present in front of the substrate. For example, Samareh and Dolatabadi [30] have calculated the gas phase pressure and Mach number evolutions along the cold spray torch (see Fig. 6.11) axis, taking into account the position of the flat substrate placed orthogonally to the torch axis.

Calculations [30], show that placing the substrate at a distance of 10 mm from the nozzle exit will result in the lowest peak pressure (see Fig. 6.12a). Indeed, the substrate location is of primary importance as it determines the landing situation for particles. Because of the strong bow shock formed on the substrate, a high-stagnation pressure zone is created near the plate, resulting, as explained before, in a deceleration of the particles as well as off-normal impact on the substrate. The deviation of particle trajectories from the centerline and those particles that hit the substrate with a low-normal impact velocity, reducing their bond to it, are directly responsible of the reduction in the deposition efficiency. The Mach number also varies with the substrate position, as illustrated in Fig. 6.12b.

For the gas–particle interactions the conventional equations are used with the drag coefficient, C_D, for particle acceleration, and with the Nusselt number, Nu, for the heat transfer. Of course these coefficients must be corrected, especially to account for the compressibility effect. For example, for C_D the approximation of Henderson is used (see Samareh and Dolatabadi [30] and also Chap. 4 section "Influence of the injector acceleration and inclination").

Voyer et al. [31] have used FLUENT to calculate the compressible flow of N_2 gas with an initial temperature of 593 K, a pressure of 2.5 MPa in a standard nozzle. Results are presented in Fig. 6.13 for the gas temperature and velocity and for the temperature and the velocity of a Cu particle 15 μm in diameter.

As can be seen, the gas acceleration starts before the throat and is almost finished in the first third of the divergent section. The gas temperature starts to decrease before the throat and, when the jet expands, falls far below room temperature. In the free jet, after the nozzle exit, irregular changes of gas properties (T_g, v_g) are due to compression shocks. Particle velocity, v_p, rises sharply in the first half of the divergent section of the nozzle. As the gas velocity is larger than that of the particle, its acceleration is still important even when the gas velocity has reached a plateau.

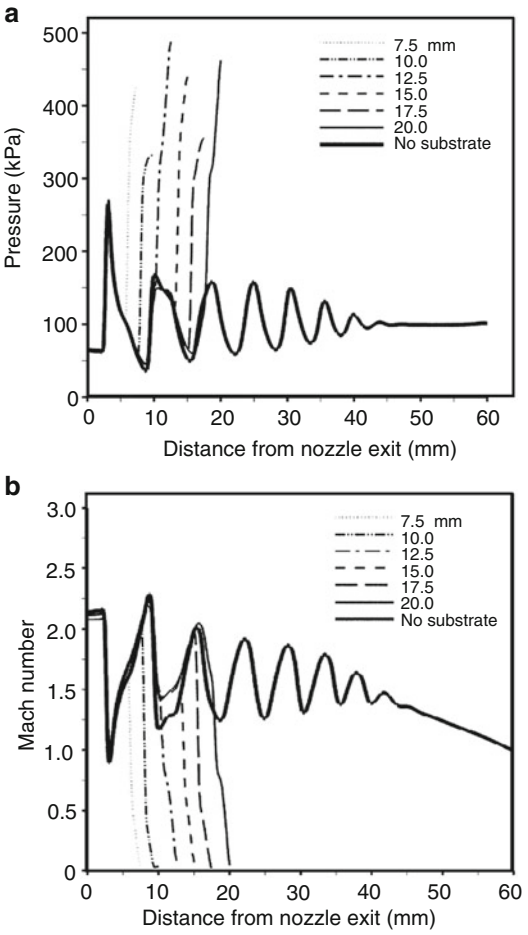


Fig. 6.12 (**a**) Pressure variations along the centerline for various standoff distances for a flat square substrate. (**b**) Mach number variations along the centerline for various standoff distances for the same substrate. Reprinted with kind permission from Springer Science Business Media [6.], copyright © ASM International [30]

Particle heating occurs in the convergent part of the nozzle and then the particle temperature decreases but much less than that of the gas. The shock waves do not affect particle temperature, T_p, and velocity.

Voyer et al. [31] have also calculated the influence of the initial pressure and temperature on the temperature and velocity of 15 μm Cu particles at the nozzle exit, using a 1D model, which is good for showing trends. When increasing, the initial temperature from 373 to 873 K for a fixed inlet gas pressure of 2.5 MPa, the particle temperature increases linearly from 200 K to about 440 K, while the velocity increases almost linearly from about 520 to 660 m/s (see Fig. 6.14), i.e., 25 % against more than 200 % increase for temperature.

Figure 6.15 represents the variation with inlet pressure of the temperature and velocity of the 15 μm Cu particle at the nozzle exit for a standard nozzle and the N_2 gas at an initial temperature of 673 K. As it could be expected the particle

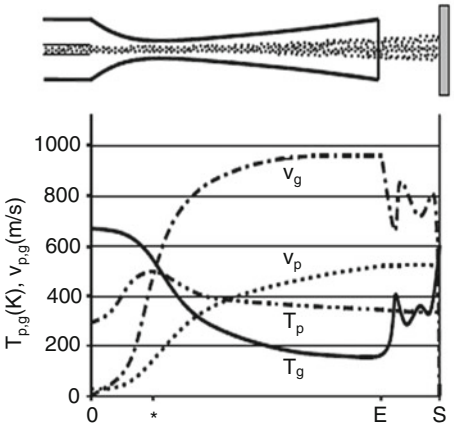


Fig. 6.13 Gas temperature, T_g, and velocity, v_g, evolutions along the nozzle axis for a N_2 flow ($T_0 = 573$ K, $p_0 = 2.5$ MPa, standard nozzle), and Cu particle (15 μm) velocity, v_p and temperature, T_p, evolutions along the axis (* nozzle throat, E nozzle exit, S substrate). Reprinted with kind permission of ASM [31]

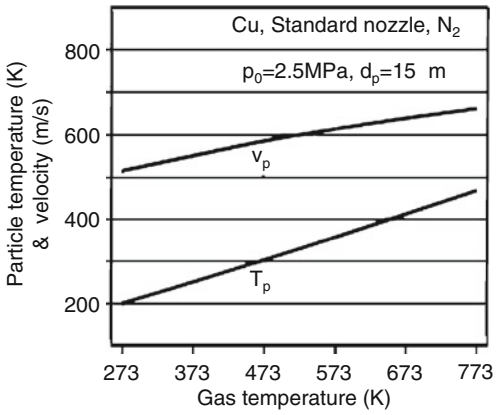


Fig. 6.14 Dependence of the particle temperature and velocity at the nozzle exit on the initial gas temperature for a standard nozzle, an initial pressure of 2.5 MPa and N_2 gas. Reprinted with kind permission of ASM [31]

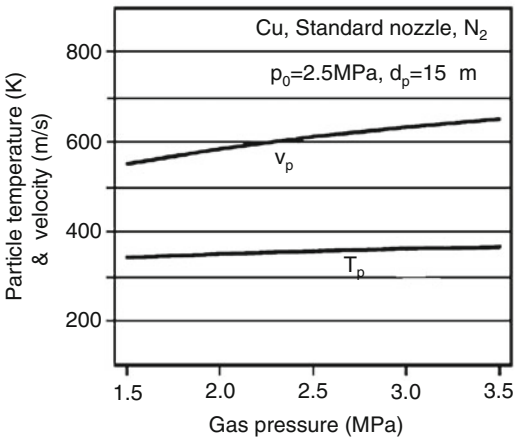


Fig. 6.15 Dependence of the particle temperature and velocity at the nozzle exit with the inlet gas pressure for a standard nozzle, an initial temperature of 673 K and N_2 gas. Reprinted with kind permission of ASM [31]

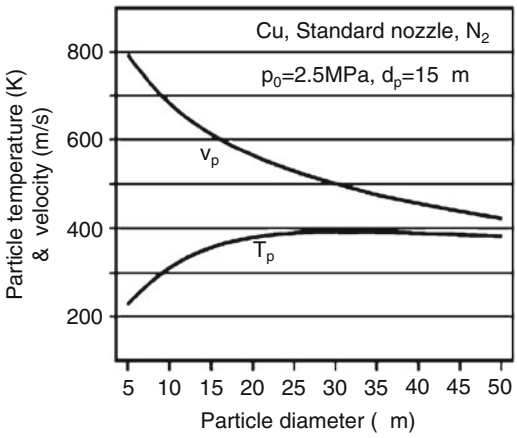


Fig. 6.16 Dependence of the Cu particle temperature and velocity on its size at the nozzle exit: standard nozzle, N_2 as process gas, 2.5 MPa, 673 K. Reprinted with kind permission of ASM [31]

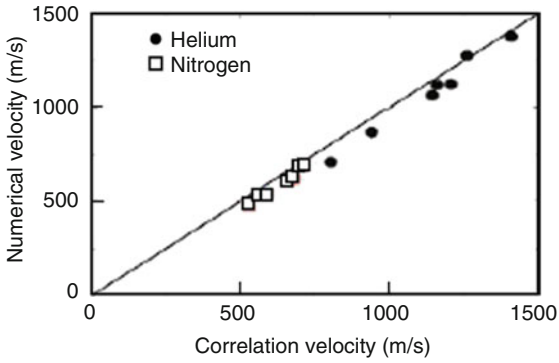


Fig. 6.17 Comparisons of the Alkhimov correlation to numerical results from Sandia's one-dimensional computer code for both aluminum and copper. Reprinted with kind permission of ASM [32]

temperature is insensitive to the inlet pressure, while its velocity varies between about 550 and 650 m/s corresponding to an increase of 15 % when the inlet pressure is more than doubled.

Of course, the particle size also plays an important role. Figure 6.16, from Voyer et al. [31], shows the influence of the Cu particle size on its temperature and velocity at the nozzle exit.

As expected, smaller particles (about <25 μm) possess a much higher velocity and, accordingly, their residence time is smaller as well as their temperature.

Dykhuizen and Neiser [32] have studied the influence of the process gas: nitrogen versus helium with the Sandia nozzle. They have compared copper and aluminum particle (about 15 μm in diameter) velocities measured at the nozzle exit, with the values calculated from the empirical expression proposed by Alkhimov et al [33]. Figure 6.17 presents the results of these measurements and calculations. It is clear that higher velocities are obtained with helium.

Such results are confirmed by the work of Li et al. [34] who have studied the influence of the spray gas (N_2 and He) and copper particle sizes on their velocities at

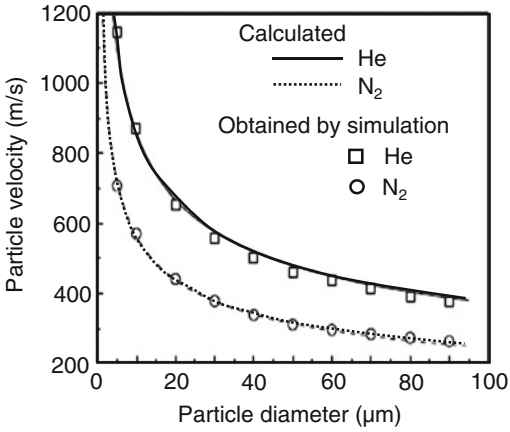


Fig. 6.18 Effect of particle diameter on particle velocity with He and N_2 gases operated at the inlet pressure of 2 MPa and a temperature of 340°C. Reprinted with kind permission from Elsevier [34]

impact. Results, calculated with a conventional model, are presented in Fig. 6.18. It is interesting to note that the velocity evolution with particle diameters, d_p, is well represented by the empirical expression:

$$v_p = k/d_p^n \tag{6.10}$$

One of the main advantages of 2- or 3D compressible models is that they allow representation of shock waves and their interactions with small particles. As emphasized by Jodoin [27], the discontinuity has no effect on the particles by itself, but since the shock wave considerably changes the gas flow properties, and in particular the gas mass density and velocity, this effect is referred to as the shock–particle interaction. The particles injected in the jet will be exposed to temperatures ranging from the nozzle exit temperature (the coldest temperature in the flow) to the stagnation temperature. The latter is experienced by the particles near the stagnation point on the substrate. For example, in the calculation (two-dimensional axisymmetric analysis) of Jodoin [27] for a Ma = 1.7 impinging jet, the stagnation pressure and the stagnation temperature are, respectively, 145 kPa and 22°C. The exhaust backpressure is fixed by the atmospheric pressure at 100 kPa. The non-slip and adiabatic conditions are used at the nozzle walls. With the presence of a shock wave inside the nozzle, the flow decelerates to subsonic speed. The substrate standoff distance is set at 10 mm from the exit of the nozzle. The no-slip velocity condition is used at the substrate surfaces and these surfaces are assumed to be at a uniform and constant temperature of 22°C. The stagnation temperature after the shock wave is not affected significantly and remains nearly constant. In contrast, in Fig. 6.19 showing the gas velocity contours [27], it can be seen that the velocity decreases sharply through the shock wave close to the substrate [27].

To predict the particle position and velocity along the axis, the one-dimensional particle model has been used with the 2D flow calculation results. From a kinematic point of view, the equations allowing calculation of the velocity of a particle show

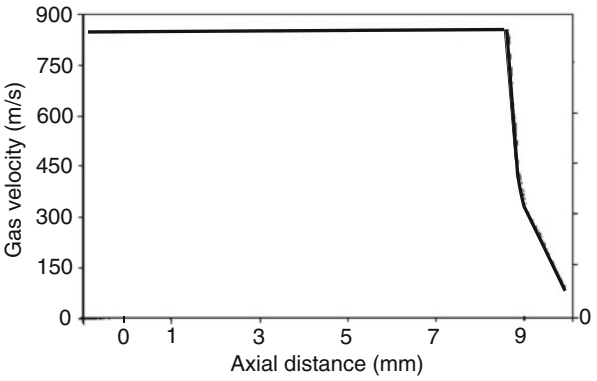


Fig. 6.19 Gas velocity along the axis of the Mach = 1.7 jet. Axial positions = 0 at nozzle exit, 10 mm substrate. The sharp reduction of the velocity caused by the shock wave close to the substrate is shown. Reprinted with kind permission from Springer Science Business Media [6.], copyright © ASM International [27]

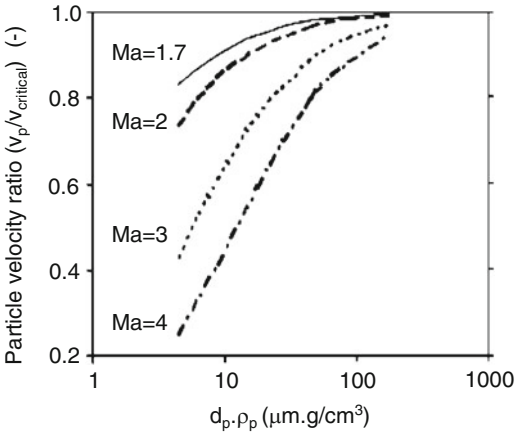


Fig. 6.20 Particle velocity ratio ($v_p/v_{critical}$) after the shock wave for particles with different $r_{part}.\rho_{part}$ based on the two-dimensional flow field. Four pre-shock Mach numbers are shown: 1.7, 2, 3, and 4. Reprinted with kind permission from Springer Science Business Media, copyright © ASM International [27]

that the important physical parameter controlling the response of the particles is the product $r_{part}.\rho_{part}$ [27], where r_{part} is the particle radius and ρ_{part} its specific mass. This factor takes into consideration the type and size of the particle. Particles of two different materials will experience the same trajectory and velocity if they have the same $r_{part}.\ \rho_{part}$. Four different supersonic flows were studied with different pre-shock Mach numbers: respectively 1.7, 2, 3, and 4. The exit gas velocity and pressure were set constant at 850 m/s and 100 kPa [27]. Figure 6.20 shows the effects of the shock wave on the velocity ratio $v_p/v_{critical}$ for particles having different $r_{part}.\rho_{part}$. The effect of the shock wave is rather important on particles having low values of $r_{part}.\rho_{part}$. For example, even for an exit Mach number of 1.7, the velocity ratio of the particles at the substrate surface for $r_{part.}.\rho_{part} = 8\ \mu m \cdot g/cm^3$ is reduced by a factor of 0.90 over the short shock–substrate distance and to as low as 0.40 for the case of an exit Mach number of 4.

The conclusions of Jodoin [27] are that in order to achieve a sufficiently high-exit jet velocity to insure that the particle velocities are over their critical value,

different nozzle designs need to be used. Nozzles with a low design Mach number will require a higher stagnation temperature to produce the required velocity. This may lead to temperatures in the vicinity of the substrate that are high enough to reduce the benefits of the cold spray process since the substrate will be exposed to these temperatures. Calculations showed that for the range of velocity used in cold spray, the design Mach number of an air nozzle should be limited to 1.5 and above to avoid too high temperatures in the vicinity of the substrate. Analyses showed that for large/heavy particles ($r_{\text{part}}.\rho_{\text{part}} > 200$ μm.g/cm^3), the shock wave has a limited but noticeable effect on the impact velocity. This effect increases with the Mach number and becomes important at a Mach number around 3. For small/light particles ($r_{\text{part}}.\rho_{\text{part}} < 50$ μm · g/cm^3), the effect of the shock–particle interactions is very strong, even at short standoff distance and at a Mach number as low as 2 [27]. Of course, other authors, for example, Katanoda et al. [35] have used the two-dimensional axisymmetric, time-dependent Navier–Stokes equations along with the k–ε turbulence model [30]. The governing equations are solved sequentially in an implicit, iterative manner using a finite difference formulation.

The best description of 3D models used is that of Samareh and Dolatabadi [30]. The ideal gas law is used to calculate mass density, in order to have the compressibility effects taken into account. Since the flow is high speed and compressible, viscosity changes with temperature become important. In order to account for this effect, the three coefficients Sutherland viscosity law is used, which is specially suggested for high-speed compressible flows [30]. Due to the presence of diamond shocks at the nozzle exit and a bow shock on the substrate, the flow will experience sharp gradients and steep changes in pressure and velocity. Therefore, the RSM (Reynolds Stress Model) turbulence model is used in the simulation of Samareh and Dolatabadi [30] as it takes into account the compressibility effect as well as streamline curvature, swirl, rotation, and rapid changes in strain rate in a more rigorous manner compared to other models and will result in higher accuracy. However, as this method creates a high degree of coupling between the momentum equation and the turbulence stresses in the flow, calculations can be more susceptible to stability and convergence difficulties compared to the k–ε model. In order to overcome this problem, for each case, the calculation begins with the k–ε model with low under-relaxation factors and is then switched to the RSM scheme.

Samareh et al. [36] have compared calculations with measurements (cutting-edge flow visualization and particle velocimetry) for the torch from CGT company equipped with nozzles: A "v27," called 1 in the following and "v24" called 2. The torch was run with nitrogen with a stagnation pressure of about 3 MPa. The copper particles (1–25 μm) were injected with nitrogen at a rate of 3 g/s. They found that using RSM, a drag law covering all speed flows, and two-way coupled Lagrangian particle tracking result in capturing shocks and expansion waves virtually identical to those observed in the experiments. Injecting the particles to the gas flow is accompanied with a momentum exchange between the gas and solid particle phases. Particles are accelerated and the gas flow decelerates accordingly. The higher the particle loading, the larger the momentum deficit of the gas flows.

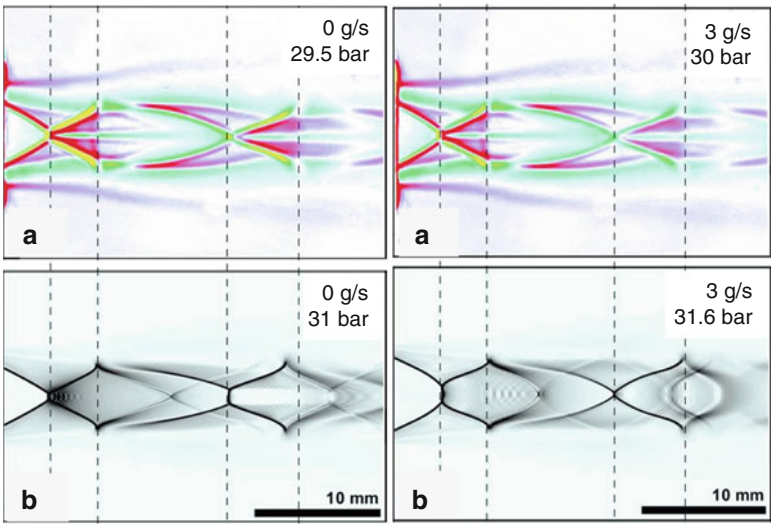


Fig. 6.21 (**a**) Measured and (**b**) calculated pressure gradient contours of the flow behind nozzle 1 at constant gas flow rates of 25.4 and 27.8 g/s, respectively, with and without particle injection. The uncertainties of the measured pressures and mass flow are estimated to be 0.1 MPa and 10 %, respectively. Direction is from left to right, flow separation occurs inside nozzle. No substrate was present. Reprinted with kind permission from Springer Science Business Media [36], copyright © ASM International

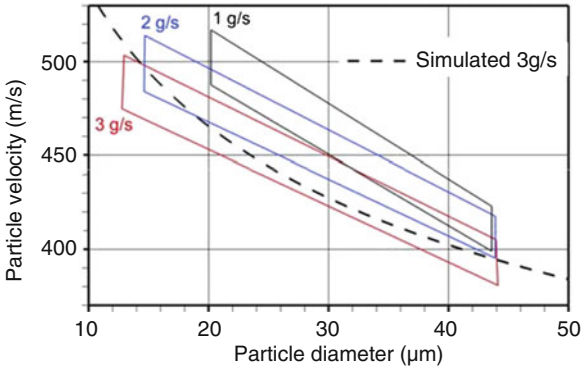


Fig. 6.22 Particle velocities measured in the 2-mm radial distance from the centreline of the flow behind nozzle 1, as function of particle diameter for varying powder injection rates. The trapezoidal regions indicate the 2σ confidence bands for the mean velocity. Reprinted with kind permission from Springer Science Business Media [36], copyright © ASM International

Typical results are illustrated in Figs. 6.21 and 6.22. In Fig. 6.21 are presented the calculated and measured pressure gradient (gas flow was simultaneously mapped using a noncommercial optical flow imaging system developed at Siemens). A visible difference between both flows in Fig. 6.21 is that the separation from the interior

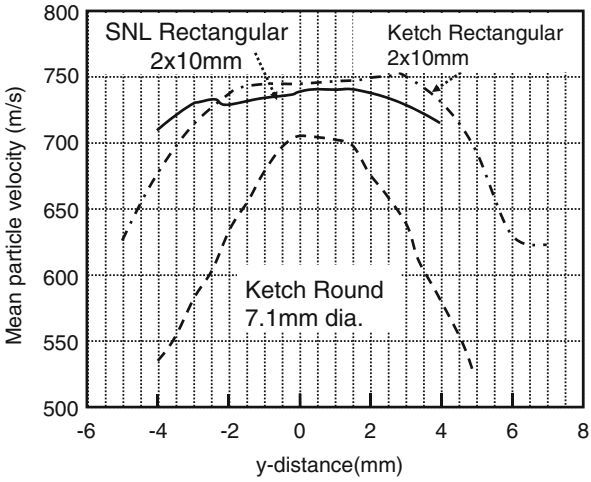


Fig. 6.23 Comparison of mean particle velocity distributions, at 25 mm standoff distance, for round ($d = 7.1$ mm) and rectangular (2×10 mm) spray nozzles: He, 2.1 MPa, 325°C, Cu particles 20–5 μm. Reprinted with kind permission of ASM [39]

nozzle wall occurs a bit earlier without the powder injection. The free jet shock and expansion waves are altered when coating particles are injected (even with 10 % of the gas flow). For instance, the Mach number at the nozzle exit decreases from 2.4 for the free jet case to 2.1 when particles are injected (3 g/s), while the gas velocity at the nozzle exit falls from 820 to 770 m/s and temperature rises by 40 K.

Particle velocities where measured with the Spray-Watch® system. Figure 6.22 shows the decreasing gas velocity at increasing feed rate. Particles 25 μm in diameter lose 6 % of their velocity, when the injection rate is increased from 1 to 3 g/s. At 3 g/s the calculated particle velocity for 3 g/s powder injection is in good agreement with measurements.

6.2.1.4 Nozzle Design

Different nozzle designs have been developed [37]. Of course, as emphasized previously, for a given material, the particle velocity varies significantly with its size. For example, with copper particles and air as driving gas at 25°C with a pressure of 2.1 MPa, the following velocities were achieved: 600 m/s for 5 μm in diameter and 400 m/s for 22 μm in diameter [38]. However, also for particle velocities the nozzle design plays a key role. This is illustrated in Fig. 6.23 from R. E. Blose et al [39] showing the radial distribution of the velocity of Cu particles (20–5 μm) sprayed with helium (2.1 MPa, 325°C). Three nozzles were used, two rectangular and a round one. It is obvious that velocities obtained with the rectangular nozzles at 25 mm standoff distance yield more uniform particle velocity distributions.

Gärtner et al. [40] made calculations for two nozzle configurations, a standard trumpet-shaped nozzle and a bell-shaped (MOC-designed) nozzle, respectively. Results show significant differences in particle acceleration for 20 μm copper particles sprayed with nitrogen (3 MPa and 320°C). With the standard trumpet-shaped nozzle the particle is accelerated to 500 m/s, compared to 580 m/s for the bell-shaped nozzle.

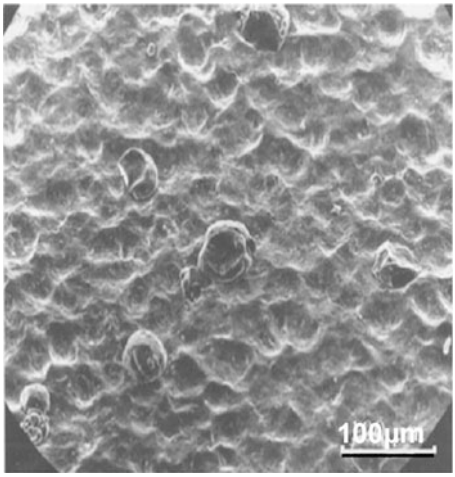


Fig. 6.24 Copper substrate surface after a 25 s delay in a two-phase jet. Impact of aluminum particles (30 µm) onto a copper substrate. Reprinted with kind permission from Springer Science Business Media [41], copyright © ASM International

6.2.2 Coating Adhesion and Cohesion

6.2.2.1 Deposition of the First Layer

(a) Induction Time

When starting with a smooth surface, particles are not attaching at first and they rebound, thus cleaning and deforming the surface. At a time t_i (~ few tens of seconds) called induction time, particles begin to attach, provided their velocity is higher than a critical velocity, v_c. This is illustrated in Fig. 6.24 from Klinkov and Kosarev [41]. Once the cleaning and deformation of the substrate surface are achieved ($t > t_i$) the attachment occurs in an avalanche-like manner, rapidly forming the coating.

The figure shows the copper substrate 25 s after the beginning of the spray process (He, 2.0 MPa, 300 K, aluminum particles), at an instant just before coating starts to grow. The induction time is related to the particle concentration in the flow and the particle velocity [41].

(b) Particle and Substrate Deformation

Upon impact, when the energy is sufficient, the stress applied to the particle is generally higher than its yield stress and thus its deformation is plastic. The pressure at impact, depending on the particle size, specific mass, and impact velocity, can easily reach 40–50 MPa (for about a few tens nanoseconds), and it diminishes afterwards due to the increase of the contact area. The resulting plastic deformation wave corresponds to the propagation of structure defects. Upon impact, high-plastic strain rates occur in the immediate vicinity of the contact zone resulting in adiabatic

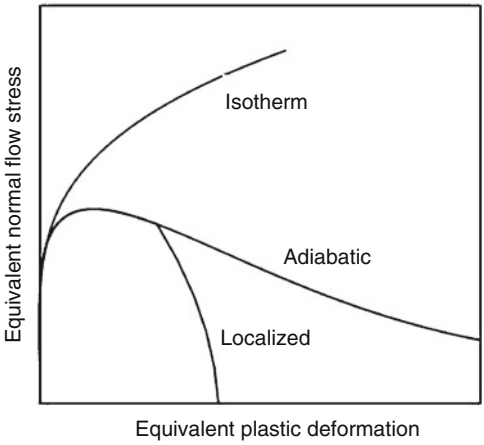


Fig. 6.25 Curves representing the stress–strain in a solid for isothermal, adiabatic, and localized deformation. Reprinted with kind permission from Elsevier [42]

heating (due to the short time during which the high pressure occurs). More than 90 % of the impact energy is converted into heat, softening locally the material [42].

The impacting of the particles onto the substrate can be subdivided into two phases [43]:

- Pressure build-up and elastic deformation of the particles up to the dynamic flow limit.
- Plastic deformation with significant deformation of the material structure and warming due to deformation.

According to the work of Assadi et al. [44] the strong and fast heating of the particle induces locally a transition of the deformation mode from a plastic behavior to a more viscous phenomenon. The mechanical resistance of the material is much lower and a structural instability appears easing the adiabatic shear phenomenon. This is illustrated in Fig. 6.25 [42] showing the relationships existing between stress and strain during the dynamic deformation of a solid.

These curves are explained by the Grujicic et al. [42] as follows: The stress–strain curve called *Isotherm* in Fig. 6.25 shows a monotonic increase of the flow stress with plastic strain. Under adiabatic conditions, the temperature increases with the heat generated by the plastic strain energy dissipated and the material is softened. Thus, as shown with the *Adiabatic* curve in Fig. 6.25, the flow stress reaches a maximum value because the rate of strain hardening decreases. However, as emphasized by Grujicic et al. [42] "fluctuations in stress, strain, temperature or microstructure, and the instability of strain softening can give rise to plastic flow (shear) localization." Correspondingly "shearing and heating (and consequently softening) become highly localized, while the straining and heating in the surrounding material regions practically stops. This, in turn, causes the flow stress to quickly drop to zero" [42], as illustrated with the *Localized* curve in Fig. 6.25 from Schmidt et al [45].

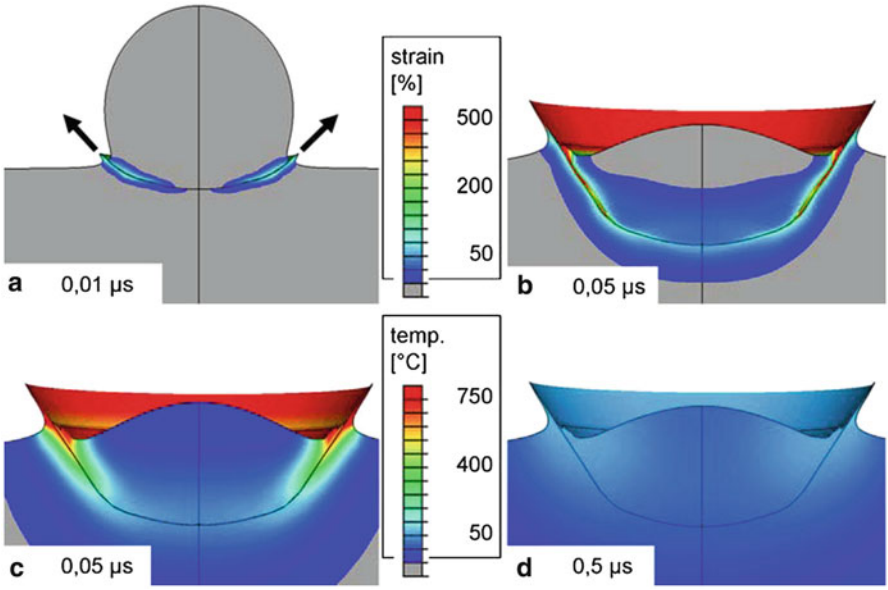


Fig. 6.26 Single sequences of an impact of a 25 µm Cu particle to a Cu substrate with 500 m/s at an initial temperature of 20 °C. (**a**, **b**) Strain field and (**c**, **d**) temperature field. For the analysis a thermally coupled axisymmetric model was used. Reprinted with kind permission from Springer Science Business Media [45], copyright © ASM International

(c) Phenomena at Impact

Numerical simulations of the particle impact were performed [42, 43, 45] to obtain information about the impact loading of the particles: local distribution and temporal evolution of pressure, stress, strain, and temperature. At the beginning of the impact, a strong pressure field propagates spherically (elastic deformation) into the particle and substrate from the point of first contact, A common feature in all simulations is that there is markedly inhomogeneous deformation of particles and localized heating of the interacting surfaces as a result of impact [45]. The pressure gradient at the gap between the colliding interfaces generates a shear load, which accelerates the material laterally and thereby causes localized shear straining. Fig. 6.26a [45] presents the first instant of impact of a Cu particle onto a Cu substrate and Fig. 6.26b the shear straining development. The viscous flow in the impact region generates an outflowing material jet, see Fig. 6.26(a), with material temperatures close to the melting temperature. This phenomenon of jetting is also a known feature in explosive cladding [43]. When the impact pressure and the respective deformation are high enough, this shear straining leads to adiabatic shear instabilities. This means that thermal softening is locally dominant over strain and strain-rate hardening, which leads to a discontinuous jump in strain and temperature and an immediate breakdown of stress. This illustrated in Fig. 6.26c and d corresponding respectively to the beginning of impact (0.05 µs) and late after it (0.5 µs).

The shear instabilities result in solid-state jets of material extruded from the interface between the impinging particle and substrate. The oxide layer is partially removed allowing true metal-to-metal contact [43, 44]. Such contacts have been observed for example by following the formation of non-uniform intermetallic layers at the particle–substrate boundaries on Al–Cu [45–144] or by using high-resolution microstructure investigations at interfaces [46].

According to Grujicic et al. [42] adhesion in cold spray is a nano-length scale phenomenon involving atomic interactions between the contacting surfaces and not atomic diffusion. It requires clean surfaces and relatively high contact pressures to make the surfaces mutually conforming. The adiabatic softening of the material in the particle/substrate interfacial region combined with relatively high contact pressures and the partial removal of oxide layers promote the formation of mutually conforming contacting surfaces via plastic deformation of the contacting surfaces.

To illustrate the importance of the particle size and velocity on the adiabatic softening Schmidt et al. [45] have calculated the temporal evolution of the copper particle temperature. This temperature is the average temperature of the elements in the highly strained contact zone. Figure 6.27 represents this time evolution for 5 and 25 μm Cu particles impacting at 400, 500, and 600 m/s.

The average temperature at the selected part of the interface for 5 μm particles is only slightly increased (Fig. 6.27a), and even higher impact velocities do not lead to shear instabilities [45]. The 25 μm particle shows a sudden temperature rise, indicating shear instabilities, which occur at velocities of 500 m/s or above that. The 25 and 50 μm particles (Fig. 6.27b for 25 μm) show a temperature rise and shear instability at the particle–substrate interface for 500 and 600 m/s, respectively [45].

Li et al. [47] have also studied the possibility for the particle to melt upon impact, adiabatic conditions being dissipated as heat. They show that for most spray materials it is possible to experience a local melting at the contact interfaces between deposited particles. Low melting point and reactions with atmosphere are the two main factors contributing to impact fusion. A poor thermal diffusivity also can play a role. For example, impact fusion has been observed when spraying zinc [48].

(d) Minimum Particle Diameter

As shown in Fig. 6.27a from [45] for copper particles 5 μm in diameter impacting at different velocities the temperature is always rather low, which never leads to shear instabilities and thus no chance for particles to bond. Schmidt et al. [43] have also expressed analytically this effect. These authors have established an equation giving a critical particle diameter above which thermal diffusion is slow enough to allow localized shear instability occurring at the surface of an impacting spherical particle. Smaller particles will not reach conditions for bonding. The equation is as follows:

$$d_{\mathrm{crit}} = 36.\kappa_{\mathrm{p}}.\left(c_{\mathrm{p}}.\rho_{\mathrm{p}}.v_{\mathrm{p}}\right)^{-1}, \tag{6.11}$$

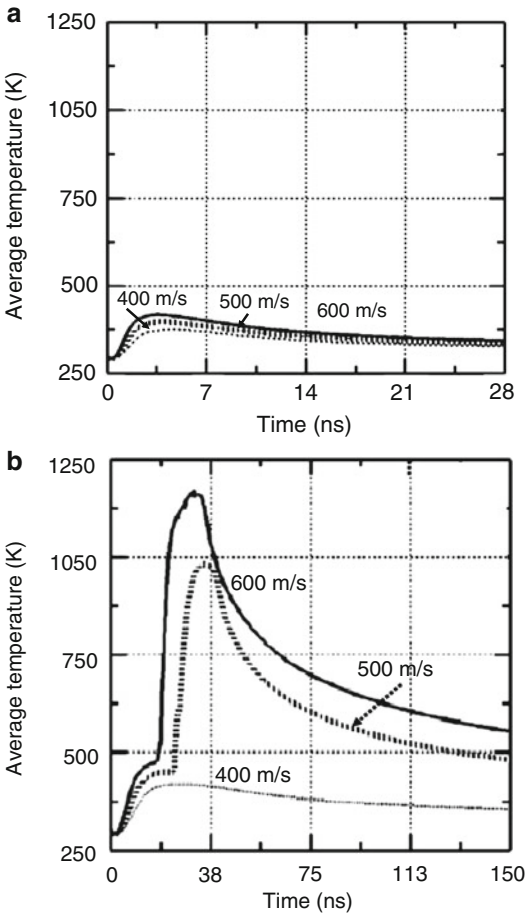


Fig. 6.27 Temporal evolution of the temperature at the monitored volume (sheared interface) of copper particles with different impact velocities and two sizes: (**a**) 5 μm and (**b**) 25 μm. Reprinted with kind permission from Springer Science Business Media [45], copyright © ASM International

where κ_p, ρ_p, c_p are respectively the thermal conductivity, specific mass, and specific heat at constant pressure of the particle, while v_p is its impact velocity. Figure 6.28 represents d_{crit} for different materials.

The values presented in Fig. 6.28 indicate that for tin, copper, silver, and gold, thermal diffusion limits bonding of small particles, whereas spraying of titanium and steel 316 L is less restricted by this effect.

(e) Critical Velocity

As illustrated schematically in Fig. 6.29 from Gârtner et al. [40], particles impacting at low velocities will abrade the substrate material, whereas at higher velocities, deposition and coating formation can occur.

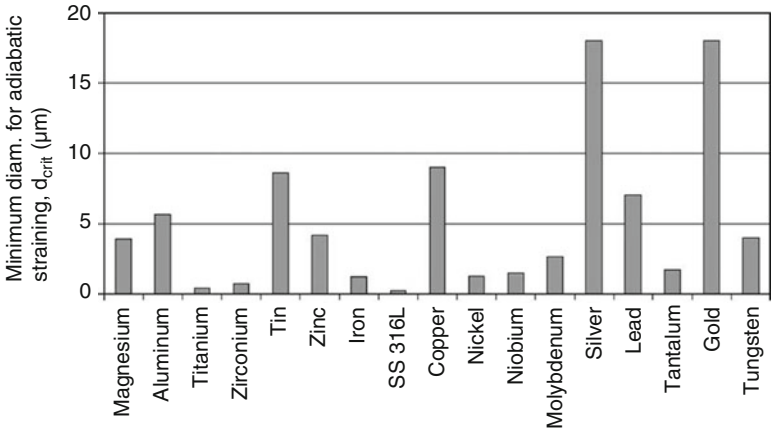


Fig. 6.28 Minimum particle diameter for localized adiabatic straining during impact calculated for different materials with semi-empirical Eq. (6.11). Reprinted with kind permission from Elsevier [43]

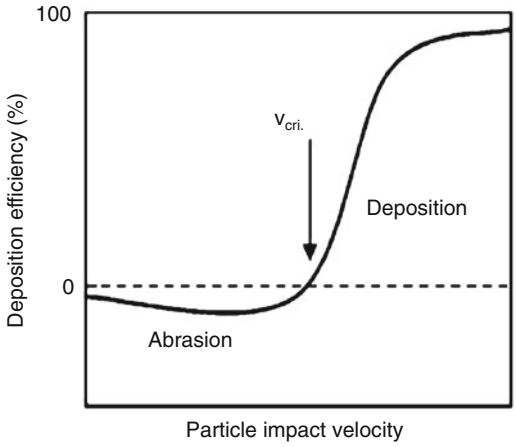


Fig. 6.29 Schematic of the correlation between particle velocity and deposition efficiency. The transition between abrasion in the low velocity range and deposition for high velocities defines the critical velocity, v_c. Reprinted with kind permission from Springer Science Business Media [40], copyright © ASM International

Of course as velocity varies strongly with the particle size (smaller particles are significantly faster) the amount of adhering material is correlated to the respective distribution of a given powder. The critical velocity is thus that of the largest particle that bonds to the substrate. Papyrin et al. [50] have developed a simple model based on the comparison of adhesion energy and energy of elastic deformation generated under particle impact. They have studied the influence of particle size and velocity for which the adhesion energy exceeds that of elastic deformation, thus resulting in the formation of the first coating layer. Based on this concept of bonding by shear instabilities and combining the results from modeling and experimental investigations, analytical expressions have been established to predict the ranges of optimum

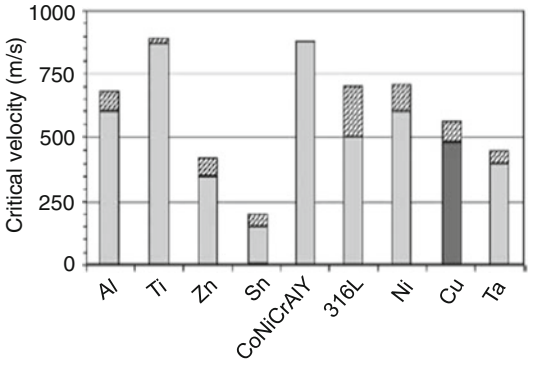


Fig. 6.30 Experimentally determined critical velocities of various spray materials onto a copper substrate. The error bar accounts for differences caused by the range of available powder sizes. Reprinted with kind permission from Springer Science Business Media [40], copyright © ASM International

spray conditions. Those have been determined according to properties of sprayed materials and substrates, spray particle sizes, and temperatures [43].

Critical velocities have been determined for various spray materials and substrates. For example, Gärtner et al. [40] have studied the critical velocities of different sprayed materials *onto a copper substrate*. If the size cut of the powder contains only negligible amounts of fine particles, the cumulative size distribution can be correlated directly to the deposition efficiency in cold spraying. Results are summarized in Fig. 6.30.

In materials of similar crystallographic structures (i.e., face-centered cubic) and stiffness (such as aluminum and copper), the mass density plays a role in bonding. When comparing Ti and Zn (hexagonal close-packed metals), the melting temperature or mechanical strength plays a role. The very high values of v_c for Ti and CoNiCrAlY requires He for spraying them. For more details see [43].

With the kinetic spray process (see Sect. 6.1.1.2) Van Steenkiste et al. [9, 10] have sprayed aluminum and copper particles with sizes between 50 and 200 μm and they found this coating process fundamentally different from that for smaller particles. It seems that mean critical velocities for the larger particles ($d_p > 50$ μm) are substantially less than those reported for particles of average diameter 10 or 20 μm [9, 10]. This is perhaps due to the fact that the particles are not perfectly spherical (the contact point has a smaller radius of curvature than $d_p/2$) and have a larger momentum that can cause an impact stress exceeding the yield stress. Perhaps also the fracture of the particle oxide layer before plastic deformation is more important here. Moreover the smaller injector tube (compared to conventional cold spray) increases deposition efficiencies for larger particles, but there is no definitive answer to the physics behind this observation [10].

(f) Empirical Expressions for the Critical Velocity

Of course this section deals with conventional cold spray. Assadi et al. [44] have modeled the deformation of particles upon impact by using the finite element program ABAQUS/Explicit version 6.2-1. The analysis accounted for strain

hardening, strain-rate hardening, and thermal softening, and heating due to frictional, plastic and viscous dissipation. The heating was assumed to be adiabatic. The model was developed for copper and results were in relatively good agreement with experimental results. To extend the results of the modeling to other materials and spraying conditions, the effect of various process parameters and material properties on the calculated critical velocity was estimated by using a specific method [44]. In this method the effect of small changes in material and process parameters on the critical velocity has been estimated. The overall effect of these parameters can be summarized in the following simple formula:

$$v_{\mathrm{cr}} = 667 - 14\rho_{\mathrm{part}} + 0.08T_{\mathrm{m}} + 0.1\sigma_{\mathrm{u}} - 0.4T_{\mathrm{i}} \tag{6.12}$$

where ρ_{part} is the mass density in g/cm^3, T_{m} is the melting temperature in °C, σ_{u} is the ultimate strength in MPa, and T_{i} is the initial particle temperature in °C.

Schmidt et al. [43] have used another method to calculate the critical velocity:

- First they have considered the impact dynamic effects through the interplay between material strength and dynamic load, resulting in a critical mechanical velocity.
- Second they have considered the energy balance between thermal dissipation and provided kinetic energy, resulting in a critical thermal velocity.
- Third they have combined both velocities by using a weighting factor of 0.5, which matches better with experimental results than both velocities on their own.
- Of course both equations contain calibration factors (respectively $F1$ and $F2$), which were generated by correlating calculated critical velocities on the basis of materials properties with experimentally determined critical velocities resulting in $F1 = 1.2, F2 = 0.3$.

Finally the expression obtained is as follows:

$$v_{\mathrm{crit}}^{\mathrm{th,mech}} = \sqrt{\frac{F_1 \cdot 4 \cdot \sigma_{\mathrm{TS}} \cdot \left(1 - \frac{T_{\mathrm{i}} - T_{\mathrm{R}}}{T_{\mathrm{m}} - T_{\mathrm{R}}}\right)}{\rho} + F_2 \cdot c_{\mathrm{p}} \cdot (T_{\mathrm{m}} - T_{\mathrm{i}})} \tag{6.13}$$

where, c_{p} is the specific heat (J/K.kg), T_{i} the impact temperature (K), T_{m} the melting temperature (K), T_{R} the reference temperature (293 K), σ_{TS} the tensile strength (MPa), and ρ the specific mass (kg/m^3).

Figure 6.31, from Schmidt et al. [43], represents the results for the calculation of critical impact velocities with Eq. (6.13) for 25 µm particles of different metals. The comparison with experiments (see Fig. 6.30) is good.

In Fig. 6.32, calculated and experimentally determined critical impact velocities are compared for cold spraying and for 20 mm ball impacts [43]. The correlation is much better than the results obtained using Eq. (6.7) of Assadi et al. [44]. This is especially the case with tin and tantalum, which have significantly different properties from copper. The difference between v_{crit} of copper calculated with

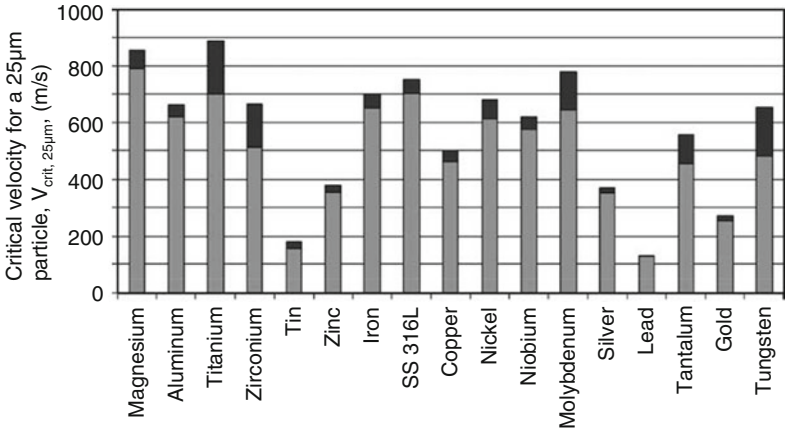


Fig. 6.31 Critical impact velocity for a 25 µm particle calculated for different materials with Eq. (6.13). The *dark gray* levels indicate a range of uncertainty with respect to the range of available materials data. Reprinted with kind permission from Elsevier [43]

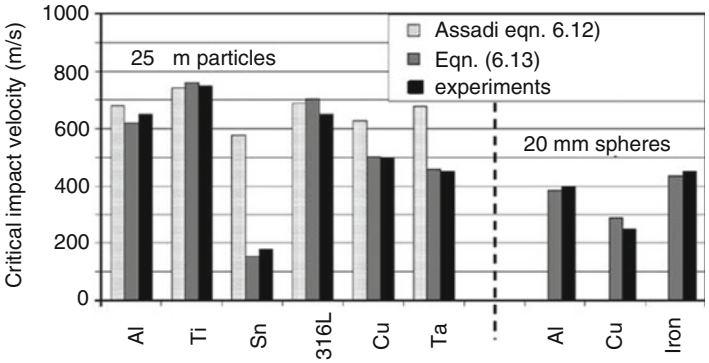


Fig. 6.32 Comparison of calculated v_{crit}, using Eqs. (6.12) and (6.13) with experimental results of spray experiments and impact tests. Reprinted with kind permission from Elsevier [43]

Eqs. (6.12) and (6.13) is based on differences in calibration data, in terms of particle size. With experimentally determined hardness values of spray powders, the tensile strength in Eqn. (6.13) can also be replaced by the Vickers hardness to estimate critical velocity (here with $F1 = 3.8$ and the same thermal correlation factor $F2 = 0.3$).

(g) Material Suitability

A systematic approach of material suitability for the cold spray process can be found in [50] where authors say that the suitability of materials for the cold spray process must be affected on the basis of the deformation properties. The mobility of

dislocations in the crystal lattice drops in a graded classification of the crystal structures [51]:

- Face-centered cubic (fcc) with large number of sliding planes, results in good deformability (Al, Cu, Ag, Au, Pt, Ni, and γ-Fe).
- Close-packed hexagonal (cph), where the number of sliding planes is greatly reduced, corresponds to poorer deformability (Cd, Zn, Co, Mg, and Ti).
- Body-centered cubic (bcc) (also transitional states) represents the lowest deformability of the three structures (W, Ta, Mo, Nb, V, Cr, α-Fe, and β-Ti).

Of course groups of tetragonal or trigonal crystal systems including oxides, exhibit low plasticity, and thus are not suitable for the cold spray process.

(h) Substrate

The substrate also plays a key role in the deposit formation. For example, adhesion has been studied for tin, ABS, copper, Al alloy, brass, different tool steels, carbon steel, glass, and alumina substrates (hardness varying from 0.08 to 10.7 GPa) on which aluminum powder (15–75 μm) was sprayed [52, 53]. It has been shown that initiation onto soft metallic substrates is difficult due to the lack of deformation of the aluminum particles. The initiation of aluminum deposition increases with the substrate hardness. Clear evidence of metal jetting was observed upon deposition onto steel substrates, where the most rapid initiation is observed. Deposition onto aluminum was difficult due to the aluminum oxide layer on the substrate. Deposition onto non-metallic substrates was difficult due to lack of a metallic bond that can be formed [52]. For particles with a low hardness sprayed onto a hard substrate, the adhesion can occur only on rough substrates (mechanical adhesion) [53, 54].

Of course the deformation of the substrate and the impacting particles are strongly linked to the particle velocity above the critical velocity [53, 54] and Fig. 6.33 from Raletz [55] presents the deformation of Ni particles with different impact velocities on a stainless steel (304 L) substrate. With the velocity increase, images show the better penetration of particles into the substrate and a lip angled away from the splat, which is composed mostly of nickel.

6.2.2.2 Coating Formation

(a) Basic Phenomena

Once the first layer has been deposited, the next particles impact on the same material. A decrease or increase of the growth rate should be considered according to the changes in the interaction conditions with the surface [41]. Steenkiste et al. [9] have sprayed aluminum particles (mostly over 50 μm) with the kinetic spray process onto brass substrates with a de Laval rectangular nozzle using air at

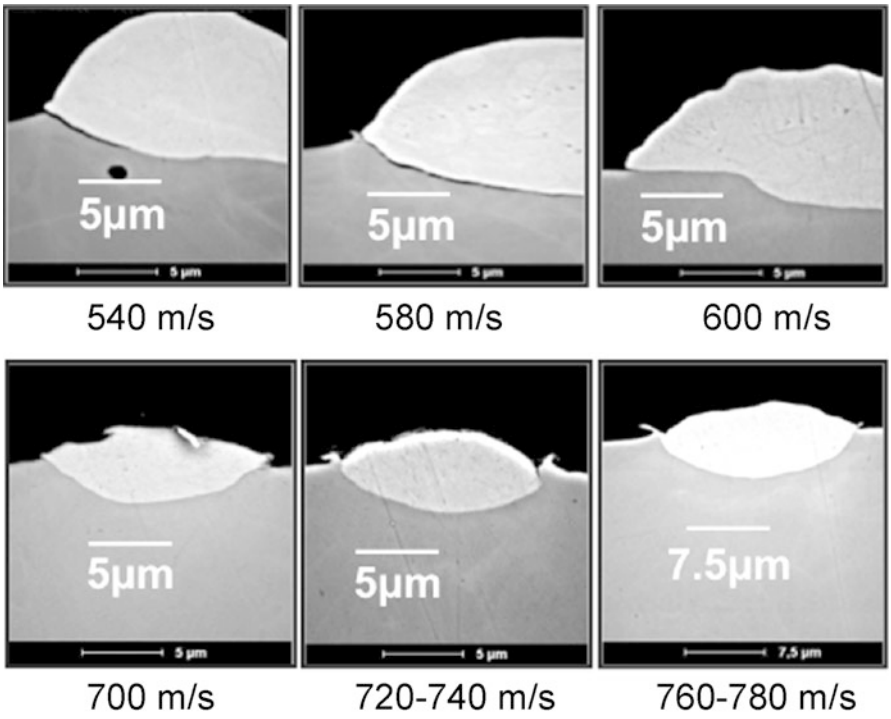


Fig. 6.33 Deformation of Ni particles impacting with different velocities onto a stainless steel substrate (304 L). Reprinted with kind permission of Dr. F. Raletz [55]

315°C and a pressure of 2 MPa. They have deposited, above the critical velocity v_c, with a stationary torch, a 83 mm thick coating, the etched cross section of which is presented in Fig. 6.34. It can be observed that the coating is less and less dense when its thickness increases. This is due to the following reasons:

Close to the substrate is the first layer, built after substrate cratering.

The number of impacts, resulting in deposited particles, is maximum close to the substrate center and diminishes with the distance from it. According to the jet divergence, particles traveling in the jet periphery do not impinge on the substrate perpendicularly (reduced normal impact velocity) and erode the coating during formation.

The new incoming particles deform and realign the just previously deposited ones.

The successive impacts induce metallic bond formation between particles (particle–particle bonding) and void reduction.

At last the successive impacts have a peening effect and create further densification and work hardening of the coating. That is why the top layers that have received much less impacts than the deeper ones and are more porous.

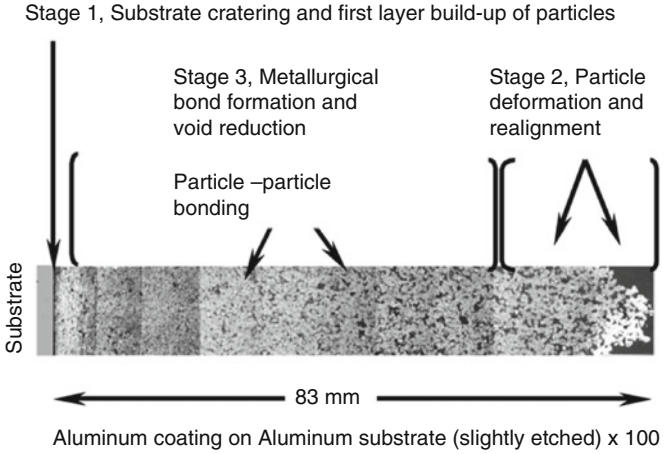


Fig. 6.34 Optical micrograph of an etched cross section of a thick Al sample prepared at 315°C, showing stage 1-type, stage 2-type, and stage 3-type behavior of the bonding process. Reprinted with kind permission from Elsevier [9]

The coating adhesion is due to the importance of plastic deformation (adiabatic shear instabilities), which occurs at the particle-particle interfaces. Gärtner et al. [40] have sprayed copper coatings (−25 + 5 μm powder) onto copper substrate with N_2 (3 MPa and 300°C) with a standard trumpet-shaped nozzle. Figure 6.35a present the resulting coating with porosity below 1 %. The tuned etching of sample cross section (Fig. 6.35b) reveals the internal grain boundaries of former spray particles. Authors point out that such chemical attack would be too strong for more open defects. Figure 6.35b "reveals grain boundaries inside the former spray particles and highly deformed grains close to particle–particle interfaces. In addition, a fairly high amount of 30–40 % of the overall particle–particle interface cuts appear in a similar contrast as normal grain boundaries" [40]. Gärtner et al. [40] with a new nozzle design working with N_2 (3 MPa and 500°C) and using coarser Cu particles (−38 + 10 μm) obtained the etched coating cross section presented in Fig. 6.36. The comparison with Fig. 6.35b shows that higher velocities and higher process gas temperatures result in a higher degree of deformation inside former spray particles of copper coatings.

The analysis of Gärtner et al. [57] suggests that the specific mass and temperature of particles have significant effects on critical velocities. If the particle velocity becomes too high and reaches the velocity range of hydrodynamic penetration, the impacting particle will cause strong erosion. Schmidt et al. have calculated [43, 58] such velocities, called erosion velocity, $v_{erosion}$. It can be observed that they are higher than the critical velocities (see Fig. 6.37).

Such calculations have allowed defining the variation of v_c and $v_{erosion}$ with particle temperature at impact. The area between v_c and $v_{erosion}$ describes the window of spray ability, WS, which can additionally be limited by a region of brittle material or limited ductility at lower temperatures. In the WS region,

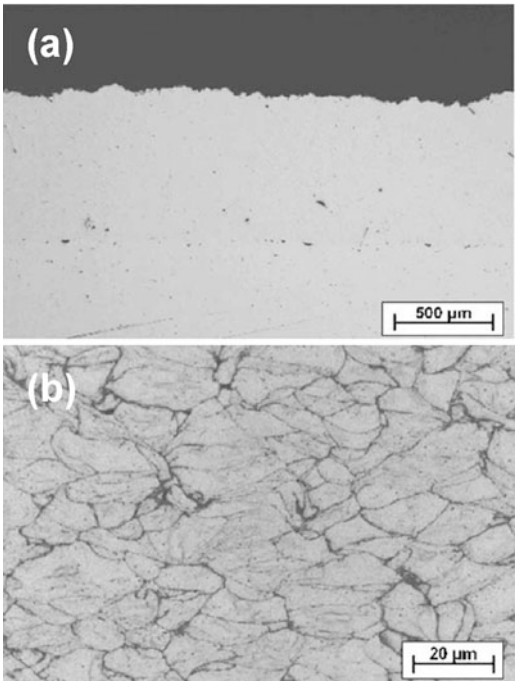


Fig. 6.35 Cu on Cu substrate cold sprayed with a trumpet-shaped standard nozzle (powder −22 + 5 µm; process gas N_2; temperature 320°C; pressure 3 MPa); (**a**) overview; (**b**) close-up. The close-up view of the etched cross section (**b**) reveals grain boundaries and particle–particle interfaces. Reprinted with kind permission from Springer Science Business Media [40], copyright © ASM International

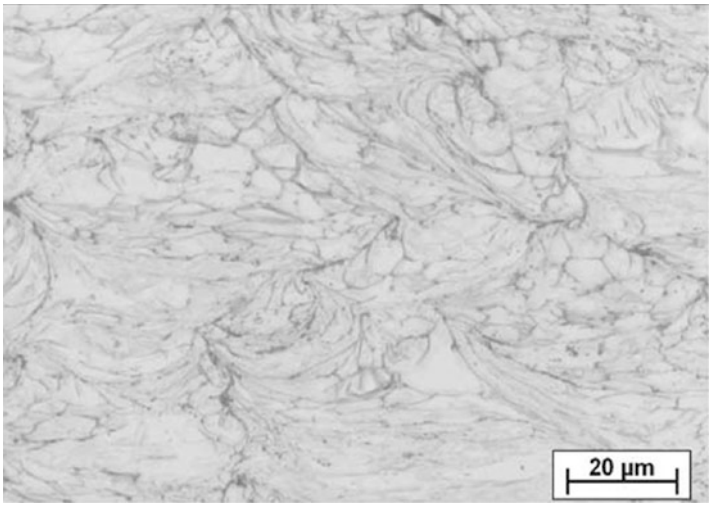


Fig. 6.36 Cu on Cu substrate cold sprayed with a bell-shaped MOC-designed nozzle (powder −38 + 10 µm; process gas N_2; temperature 500°C; pressure 3 MPa); etched cross section. Reprinted with kind permission from Springer Science Business Media [40], copyright © ASM International

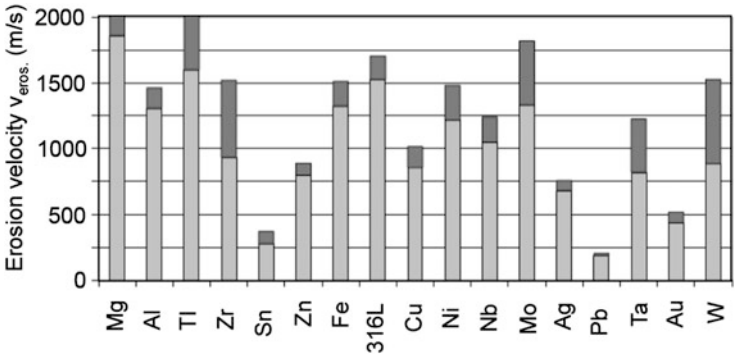


Fig. 6.37 Erosion velocities of different metals calculated by Schmidt et al [43] for 25 µm particles. Reprinted with kind permission of Elsevier

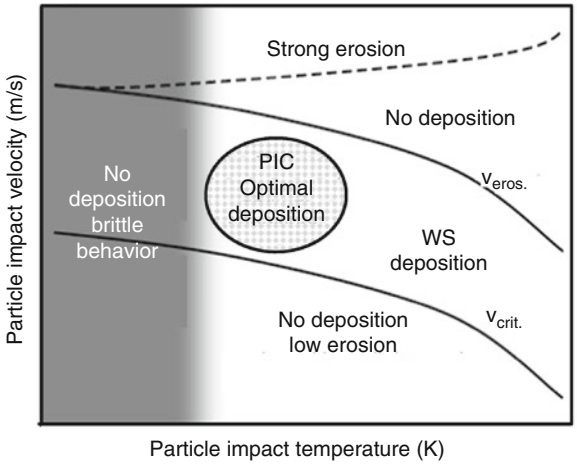


Fig. 6.38 Particle velocity over particle temperature superposed with the window of sprayability (WS) and the optimum particle impact conditions (PIC). Reprinted with kind permission from Elsevier [43]

impacting particles cause deposition. The particle impact conditions PIC represent the optimal conditions (see Fig. 6.38) [43, 57].

The erosion velocity also depends on the particle size as illustrated in Fig. 6.39 from J. W. Wu et al. [59]. v_c is almost independent of the particle size, as already emphasized by numerous authors, while the $v_{erosion}$ diminishes drastically with the particle size. This erosion velocity is obtained by comparing the adhesion energy to the rebound energy.

(b) Deposition Efficiency

Papyrin et al. [see his Chapter in the book edited by Champagne 4, 5, 60] have studied the coating formation on the basis of an analytical approach. These authors took into account the influence of the coating erosion by the reflected particles.

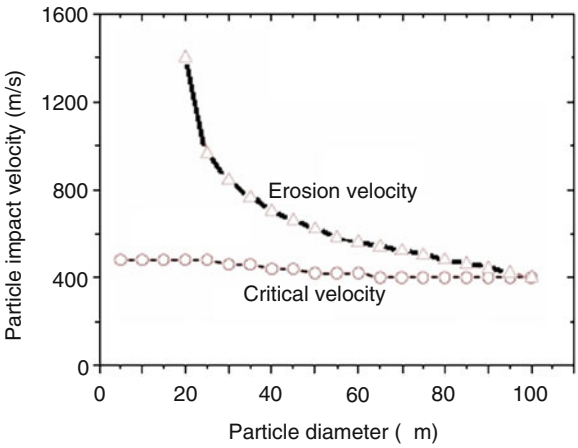


Fig. 6.39 Calculated critical and erosion velocities (sometimes called maximal velocity) for various sized Al–Si feedstock particles deposited onto a mild steel substrate. Reprinted with kind permission of ASM [59]

Qualitative dependences of the coating mass increases have been calculated for different values of probabilities of adhesion and erosion processes. In case of significant erosion ($q > 0.5$) the thickness of the first layer does not increase during the coating process. The parameter q is defined as

$$q = p_{\mathrm{er}}/(p_{\mathrm{c}} + p_{\mathrm{er}}), \tag{6.14}$$

where p_{er} is the probability of erosion while p_{c} is that of deposition. When adhesion prevails over erosion ($q < 0.5$) the coating mass increases linearly with time at long times, and its growth rate equals the difference between adhesion and erosion [60]. Alkhimov et al. [61] have presented experimental results on the dependencies of the coefficient of particle deposition $\Delta m/M_{\mathrm{o}}$, which characterizes the ratio of the substrate mass increase Δm to the total amount of mass of the consumed powder $M_{0,}$ on the particle impact velocity. The coatings were applied to stationary substrates under conditions of strictly dosed portions of various metallic powders with a particle size of 1–50 μm. The experimental values of the deposition coefficient for aluminum, copper, and nickel powders versus the particle velocity, which were obtained by accelerating the particles with a mixture of air and helium, are shown in Fig. 6.40 (curves 1–3). It can be seen that, for the considered metallic particles ($d_{\mathrm{p}} < 50$ μm), there exist critical velocities v_{cr} ~500–600 m/s for their interaction with the substrate. The conventional process of relatively low erosion is observed for $v_{\mathrm{p}} < v_{\mathrm{c}}$; for $v_{\mathrm{p}} > v_{\mathrm{c}}$, a dense metallic layer is formed on the substrate surface, and the character of coating formation changes abruptly as the velocity is further increased. In particular, the value of the deposition coefficient for the examined powders increases from zero to 0.4–0.8 for $v_{\mathrm{p}} \sim 1{,}000$ m/s. For Al, Cu, and Ni, the curves 4–6 in Fig. 6.40 show the same data, but with the particle velocity calculated

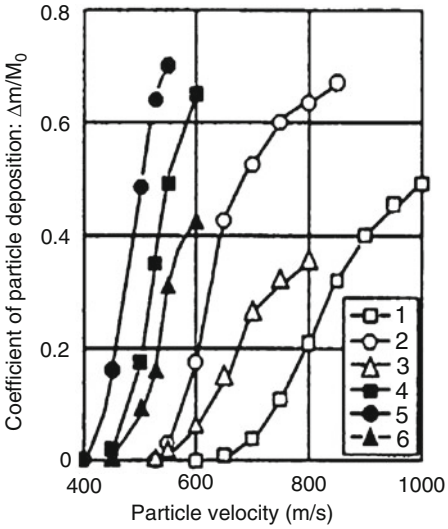


Fig. 6.40 Dependence of the coefficient of particle deposition $\Delta m/M_o$ on the impact velocity for aluminum (1), copper (2), and nickel (3) particles on a copper substrate ([4] Sect. I.2 of the book [4]), spraying being achieved with air-He mixtures. Curves 4–6 show, respectively, the same data, but depending on the particle velocity calculated for the corresponding temperatures obtained with heated air. Reprinted with kind permission from Woodhead Publishing

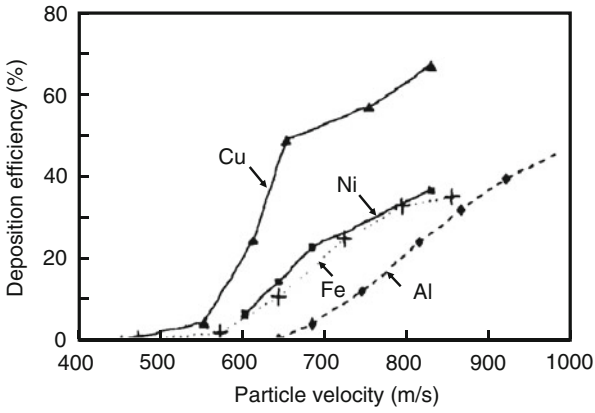


Fig. 6.41 Deposition efficiency versus particle velocity (Sect. I.2 of book [4]). Reprinted with kind permission from Springer Science Business Media [3], copyright © ASM International

for the temperature to which the air is heated. Compared to results obtained with the air and helium mixture at $T_o = 300$ K it can be concluded that the higher particle temperatures significantly affect the spray process (Sect. I.2 of the book [4, 5, 60]).

Similar results for Cu, Fe, Ni, and Al coatings were obtained by the same authors cited by Dykhuizen and Smith [3] (see Fig. 6.41).

For more details about cold-sprayed coating generation see Chap. 13 Sects. 13.4.3 and 13.7.3.

6.2.3 Deposition Parameters

6.2.3.1 Spray Conditions

(a) Spray Gases

First of all, as already indicated previously, helium is the gas resulting in the highest velocities both of the gas and particles [24, 40, 55]. For example, using He instead of N_2 allows increasing aluminum particle velocities by about 60 % (for the same gun nozzle, gas pressure and temperature) [32]. If 5 vol.% air is introduced into the He gas, the velocity, v_g, is reduced by 14 %, with 10 vol.% air v_g is diminished by 22 % and with 15 vol.% air the reduction of v_g reaches 29 %. If air is used instead of He, the gas velocity drops by 66 %. However, He, due to its low specific mass requires more time for particles to reach their maximum velocity relatively to the gas velocity (see the expressions of the drag coefficient in Chap. 4 Sect. 4.2.2.1). For example, the maximum velocity for Cu particles (19 μm in diameter) is 62 % that of the nitrogen gas at the nozzle exit compared to 42 % of the He gas [38].

If the influence of the gas pressure, p_g, is significant for low-pressure cold spray, it is much less so at higher pressures: roughly, the particle velocity varies as the logarithm of the pressure. For example, [38] when increasing the gas pressure from 1.5 to 3 MPa, v_p increases by 15 %, but the increase is only 5 % for a pressure increase from 2.4 to 2.9 MPa. Stoltenhoff et al. [24] obtained similar results. The gas pressure has little influence on the particle temperature (see Fig. 6.15). When increasing the gas temperature, T_g, the particle velocity increases (see Fig. 6.14 from [31]) as does, almost linearly, the particle temperature. If the particle velocity is kept constant while the gas temperature is varying, the deposition efficiency is not modified, the coating density is similar but the adhesion is improving. Han et al. [62] obtained similar results.

(b) Nozzle Design

As already mentioned, the nozzle geometry plays a very important role for particle axial and radial velocities [25, 26, 28, 37, 39, 40, 43, 63, 64]. For example, Stoltenhoff et al. [64] have shown that with four different nozzles characterized by different expansion ratios (6 or 9), shapes (conical and bell), and lengths of the diverging sections, the deposition efficiency varies from 38 % to 72 %! The highest deposition efficiency is obtained with the longest nozzle, an expansion factor of 9 and a bell-shaped nozzle. However there is an optimum in the gas velocity. Dykhuisen and Smith [3] were the firsts who have shown that, when increasing the gas velocity or its Mach number, M, a maximum velocity of the particles was obtained for a value $M = \sqrt{2}$. Jodoin [27] has shown that the design of the Mach number of an air nozzle should be not higher than 1.5 to avoid use of too high temperatures.

The interaction between the substrate and the high-velocity gas jet is not simple at all as shown by Kosarev et al. [16] for supersonic nozzles with rectangular sections and a Mach number at the nozzle exit between 2 and 3.5. This problem has also been emphasized by Samareh and Dolatabadi [30], see for example Fig. 6.12. Studies have shown that various modes of the supersonic gas jet interaction with the flat substrate can take place: the classic mode and the mode with the jet oscillations. The main parameters influencing the transition from one mode to another are jet pressures ratio, distance, and jet thickness. The classic mode occurs at near isobaric exhausting and small distances and in order to find the optimum standoff distance for the substrate, the interactions between the shock diamonds formed in the jet and the bow shock formed at the substrate must be carefully examined [27]. The bow shock, where the axial gas velocity is drastically reduced [27] while the temperature is increased, interacts with particles, especially the smallest (for the conditions of Samareh and Dolatabadi [30] those with sizes below 25 μm).

Reducing the intensity of this bow shock implies also diminishing the Mach number to $M = 1.5$ [27]. The problem is then to accelerate the particles sufficiently to a value above the critical velocity value, which sometimes requires using a higher inlet gas temperature. However, to keep the benefits of the cold spray, depending on the material sprayed, the temperature to which the substrate is subjected must also be limited. The nozzle roughness also plays a role in determining the gas velocity [25]. A roughness, Ra, of 1 μm has a negligible influence but when particles stick on the nozzle wall the roughness can reach 100 μm, and comparing a new nozzle and a nozzle coated with particles, the velocity loss is about 80 m/s. Thus this phenomenon must be considered in the nozzle design and the choice of materials (for example, by use of hard ceramic nozzles).

6.2.3.2 Particles

(a) Spray Angle

The particle velocity must be above the critical velocity, v_c, and the impact angle, θ, must be close to 90°. The particle velocity normal to the substrate varies as v_p. sin θ, thus with decreasing angle, v_p can become lower than the critical velocity, v_c, and particles will not deposit. For example, C.-J. Li et al [34, 65] have calculated the deposition efficiencies for various spray conditions using copper particles with sizes between 22.6 and 142.6 μm. In Fig. 6.42 from Li et al. [34] is presented the comparison of calculated and measured relative deposition efficiencies for He gas (2 MPa, 340°C). The agreement is very good. The drop of the relative deposition efficiency with the impact angle is important below about 70°.

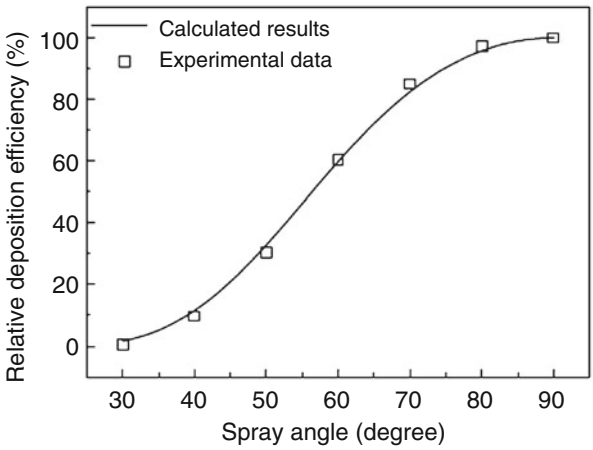


Fig. 6.42 Comparison of relative deposition efficiency calculated theoretically with those measured under helium gas operated at the inlet pressure of 2 MPa and temperature of 340°C versus spray angle (Cu particles 5–25 μm). with kind permission from Elsevier [34]

(b) Influence of Particle Diameter, Specific Mass, and Specific Heat

The parameters that were studied systematically were the influence of various parameters on the critical velocity and deposition efficiency [24, 27, 28, 34, 35, 41, 55, 66–69]. Of course, when increasing the particle size, the particle velocity decreases for the same spray conditions as illustrated in Fig. 6.16 for copper particles with N_2. Of course it must be kept in mind that particles have size distributions: the bigger particles will be slower and the smaller particles will be faster. Thus particles over a certain size may have velocities below the critical one and will not contribute to the deposition. H. Katanoda et al. [35, 67] have searched for a parameter combination that is independent of the material type and that affects the particle velocity and temperature. Using N_2 and He as the process gases with stagnation pressures of 3 MPa and gas temperatures upstream of the nozzle throat of 576 K, and spraying Cu, Ti, and WC–12Co, they have shown that the particle diameter multiplied by the material specific mass is the material-independent parameter, which affects the particle velocity. The maximum velocity is obtained for a parameter combination of 0.020 kg/m^2 for N_2 and 0.0065 for He.

The square of the particle diameter multiplied by the material specific mass and the specific heat is the material-independent parameter combination, which affects the particle temperature.

(c) Particle Temperature

The deposition efficiency increases with the particle temperature at impact for the same velocity (for all sprayed materials temperature increase implies the Young's modulus reduction). For example, Lee et al. [66] cold sprayed Cu–20 wt.% Sn alloy (bronze) particles with a mean size of 20 μm onto aluminum with nitrogen, different

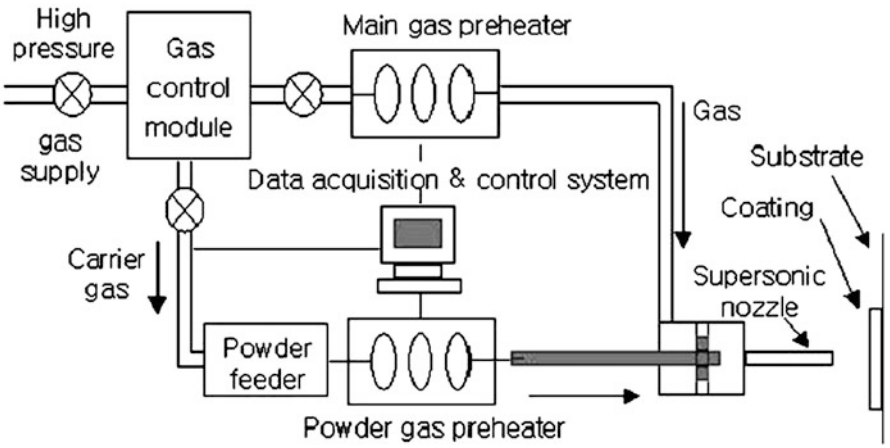


Fig. 6.43 Diagram of the cold spray equipment with a powder heater. Reprinted with kind permission from Elsevier [71]

process gas pressures, and temperatures. For particles with velocities of 550 m/s, the deposition efficiency was respectively about 35 % with the gas at 300°C, 62 % at 400°C and 75 % at 500°C. The critical velocity diminishes with increasing process gas temperature.

One way to achieve higher temperatures of the particles, independently of that of the spray gas, consists in heating the carrier gas separately. New cold spray devices are equipped with a particle heating system before their injection into the nozzle by using a heated carrier gas as proposed by Papyrin et al. [70]. The principle of the device is shown in Fig. 6.43 from Kim et al. [71]. A gas heater is added downstream of the powder feeder and as close as possible to the injector. For example, the heater consists of a stainless steel tube (about 3 mm in internal diameter and 300 mm in length) thermally insulated and heated by induction [55]. However heat losses occur in the soft pipe connecting the heater to the gun, especially when this pipe is long (10 to 15 m are possible). Depending on the carrier gas flow rate, the gas temperature can reach up to 680 °C. To achieve higher temperatures, up to 1000 °C, in the recent guns the heater (up to 22 kW) is integrated in the gun. But heating temperature must be adapted to the sprayed material. If particles are heated too much they become sticky and the control of their mass flow is difficult. Nozzle clogging and sticking to interior walls can also start. Surface oxidation of particles can also be increased especially if air is used as spray gas (kinetic process).

Figure 6.44 shows the dependence of Ni particle deposition efficiency on the mean particle velocity deposited on stainless steel for different preheating temperatures [55]. It can be seen that increasing the particle temperature by 530°C increases the Ni deposition efficiency by about 13 % for the different velocities considered, which is less than that obtained with the lower melting point Cu–Sn alloy.

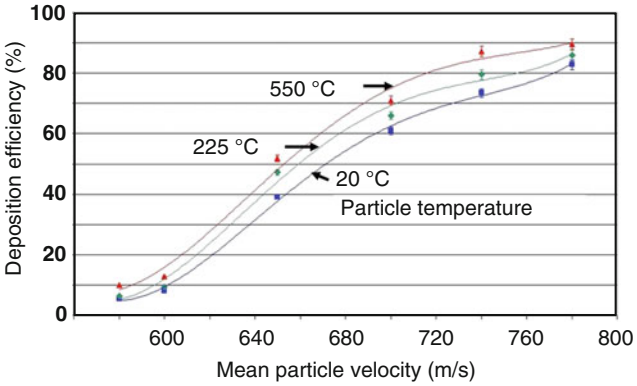


Fig. 6.44 Dependence of Ni particle deposition efficiency on the mean particle velocity for deposition on stainless steel for different preheating temperatures. Reprinted with kind permission from Dr. F. Raletz [55]

(d) Laser-Assisted Cold Spray

When spraying harder materials than Cu, Al, Ag, Zn, such as Ti alloys or Mo, it becomes necessary to heat the spray gas more and to use helium instead of nitrogen with pressures up to 4 MPa, corresponding to He flow rates in the order of 3 m^3/min. However, heating the spray gas too much increases the risk of nozzle fouling with low melting temperature particles. That is why it has been proposed to preheat the substrate with a laser just prior to particle deposition [72–74]. Impact temperatures are then increased, through the local heating of the substrate by the laser (of course below the melting temperatures both of substrate and particles). Thus coatings can be obtained with less spray gas preheating and lower particle velocities (no need to use helium, which costs about 80 times more than nitrogen (Sect. I.5 of book [4] and [74]) with no helium recycling).

Compared to conventional cold spray, the amount of heat and the rate at which it is applied and removed from the impact zone affects both the rate of deposition and the properties of the material [74]. It is also possible to see an annealing effect if the deposited particles are cooled at a suitable rate to allow recovery.

For example, Bray et al. [74] have demonstrated that this method was viable for the deposition of metallic coatings, especially titanium. Oxide-free titanium coatings have been deposited without the use of gas heating at velocities around half of those required in cold spray. For impact velocities of approximately 400 m/s, dense coatings (porosity below 1 %) were produced between 650 and 900°C, well below the melting point of titanium (1,668°C). The oxygen content of cold-sprayed titanium coatings, including those laser treated, was below 0.6 wt.% to be compared with the 5 wt.% obtained with shrouded HVOF sprayed ones.

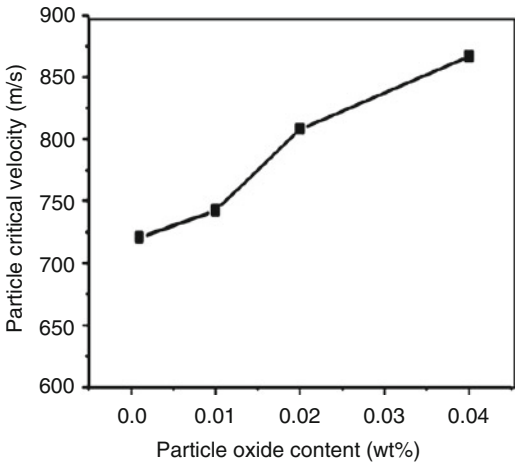


Fig. 6.45 Critical velocity of four kinds of Al feedstock with different oxygen contents. Reprinted with kind permission from Springer Science Business Media [75], copyright © ASM International

(e) Particle Oxidation

Particle oxidation is also very important as shown by Kang et al. [75]. They have sprayed aluminum particles as received, etched, oxidized in a furnace at 150°C for 15 min and at room temperature for 7 days under atmospheric condition, thus varying the oxygen content from close to 0 to 0.04 wt.%. The corresponding critical velocity for deposition on aluminum substrates varied from 750 m/s to more than 850 m/s as shown in Fig. 6.45.

(f) Carrier Gas

A minimum gas flow rate is necessary to avoid injector clogging, but too high flow rates accelerate particles and reduce their residence time, and also modify the gas temperature at the nozzle throat. An optimum must be found between spraying hotter particles (thus more ductile) and faster particles [62]. Both computational simulations and experiments demonstrated that a lower powder feed gas flow rate produced a higher mean gas temperature at the throat. This increased mean gas temperature tends to increase the particle temperature (Fig. 6.46a) but not the particle velocity as shown in Fig. 6.46b.

Moreover in most cases, even when using He as process gas, the carrier gas is nitrogen, which mixes with the helium in the nozzle and reduces the particle velocities. Balani et al. [76] have shown that aluminum coatings were denser with pure He as carrier gas when compared to a mixture He–20 vol.% N_2.

(g) Loading Effect

Varying the mass flow rate at which the feed stock particles are fed can change the thickness of the coating [77]. Is it a loading effect? Once a maximum powder flow

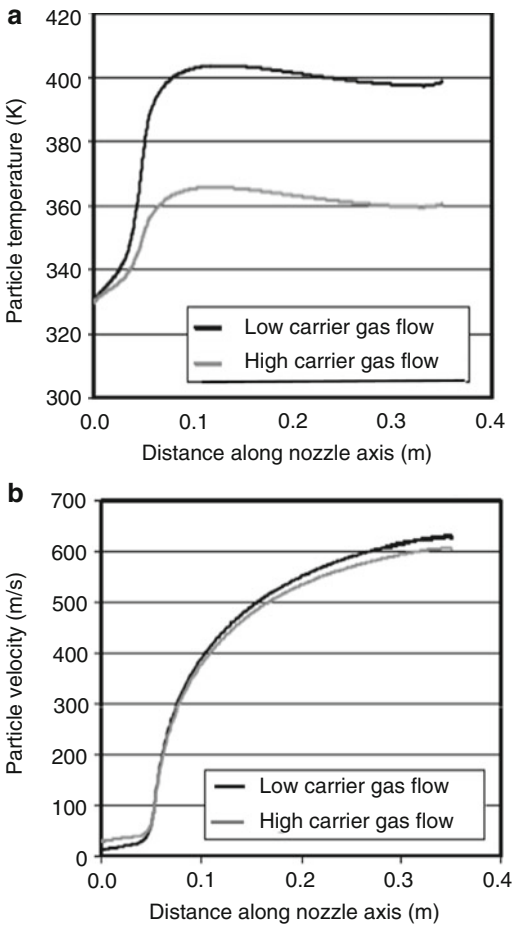


Fig. 6.46 Computational results showing the axial aluminum particle (**a**) temperature and (**b**) velocity distributions for two-carrier gas flow rates. Reprinted with kind permission from Springer Science Business Media [62], copyright © ASM International

rate is reached, too many particles impact the surface, resulting in excessive residual stress causing the coating to peel. This phenomenon is linked to an excessive particle bombardment per unit area of the substrate. This is illustrated in Fig. 6.47 representing the coating thickness evolution, as determined from the SEM images of the various coatings, on aluminum substrates as a function of the copper powder mass flow rate used.

(h) External Parameters

Nozzle clogging is sometimes a concern when spraying metallic powders. A patent [5] has been granted to a method describing a mixture with two particle populations.

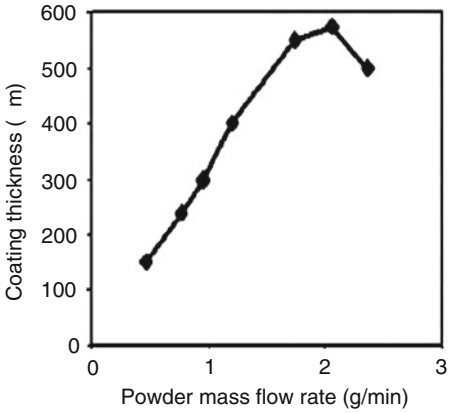


Fig. 6.47 Cold spray copper coating thicknesses on aluminum substrates as a function of the powder mass flow rate and a propellant gas temperature of 5°C. Reprinted with kind permission from Springer Science Business Media [77], copyright © ASM International

One of the populations is selected such that its velocity is below v_c and it differs from the other in terms of size, yield strength, and material nature. It thus maintains the supersonic nozzle in a nonobstructed condition, cleaning it. It also allows raising the main gas operating temperature, thereby increasing the deposition efficiency of the powder the velocity of which is above the critical value.

Besides the size of particles, their morphology also plays a key role [78]. For example, angular particles of both stainless steel and bronze powders were significantly faster (~80 m/s) than spherical particles.

(i) Heat Treatment After Spraying

Powders, substrates, and certainly heat treatment affect the adhesion strengths of the cold-sprayed Cu and Ni–20Cr coatings [68]. Moreover, heat treatment increases adhesion strength with increasing annealing temperatures. The annealed coatings are softer than the as-sprayed coatings due to recovering and recrystallization mechanisms by the heat treatment [68].

6.2.3.3 Substrates

As already emphasized previously, the substrate hardness relative to that of the impacting particles plays a key role [51, 53] (Sect. 6.1.2.a. devoted to deposition of the first layer). For example, [52] for aluminum particles, the initiation of deposition onto soft metallic substrates is difficult due to the lack of deformation of the aluminum particles. In fact, deposition onto a tin substrate resulted in melting of the tin. Ease of initiation of aluminum deposition increases as the hardness of metallic substrates increases. The substrate temperature also is important since the deformation process leading to particle bonding and coating formation takes place

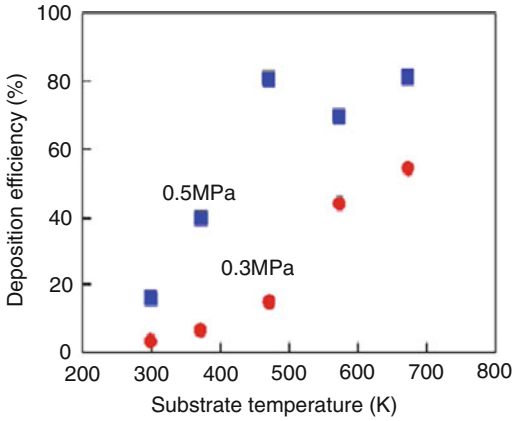


Fig. 6.48 Relation between deposition efficiency and both substrate temperature and gas pressure (He gas temperature: RT, Cu particle size: 5 μm). Reprinted with kind permission from Springer Science Business Media [80], copyright © ASM International

both on the particle and the substrate side [79]. Of course the deposition efficiency changes as a function of the process gas temperature, which influences both the particle velocity and the substrate surface temperature. Legoux et al. [79] have heated the carbon–steel substrate with a resistor at constant gun temperature. For a low pressure gun (N_2 below 0.62 MPa), the substrate temperature increase has raised the deposition efficiency of Al, reduced that of Zn (the surface temperature might have been too high for this low melting temperature material) and has had no effect on Sn. Fukumoto et al. [80], again with a rather low pressure gun (air, 0.4–1 MPa) have shown for Cu particles on stainless steel and Al that the deposition efficiency was increased when the substrate temperature was raised. It can be seen in Fig. 6.48 that the deposition efficiency on AISI 304 substrates can be improved significantly by increasing the substrate temperature, even under conditions without any heating of the working gas, in other words, without any heating of the particles.

Sakaki et al. [81] obtained similar results with a conventional cold spray gun (N_2 at 3 MPa) spraying Cu and Ti onto a mild steel substrate. They also have shown that a gun traverse speed increase (from 20 to 100 mm/s) has a negative effect on the deposition efficiency, as shown in Fig. 6.49.

6.2.3.4 Composite Materials

The easiest way to spray composite coatings made of different metals or alloys is to use preliminarily prepared powder either as mixtures of both powders or as composite particles made by agglomeration or cladding or mechanically alloying... Although this method is straightforward, it has several drawbacks [16]:

- Impossibility to change the components ratio in the powder mixture during the spraying process (no through-thickness compositional gradient).

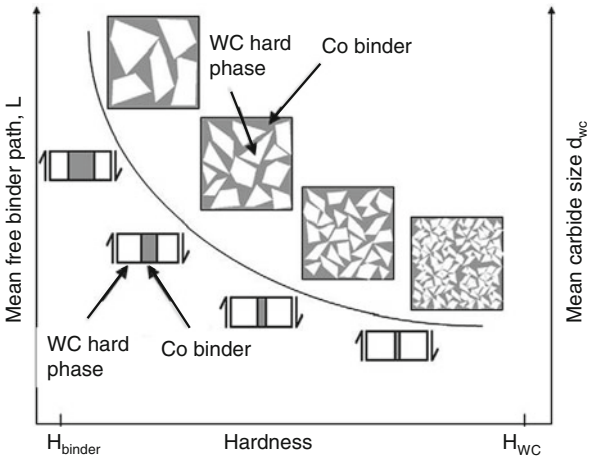


Fig. 6.49 Effect of mean free binder path (L) and mean carbide size D_{WC} on coating hardness. Reprinted with kind permission from Elsevier [82]

- Critical values of the particle in-flight parameters (velocity and temperature) are strongly dependent of the nature of the sprayed materials. Especially for powder mixtures, particles can achieve certain velocity and temperature that may be appropriate for spraying one component but ineffective for the other.

When one material is ductile while the other is brittle, the problem is more complex. Ceramics when cold sprayed produce no coating but erode the substrate surface and also the gun nozzle surface, especially the throat. However, the possibility to deposit preliminary prepared metal–ceramic mixtures or metal and ceramic particles injected in different areas of the spray gun is reported as well as deposition of composite particles made by agglomeration or cladding or mechanically alloying.... However the ratio ceramic/metal, as well as the size of the ceramic particles must be carefully chosen.

(a) Cermets with Tungsten Carbide

A typical example is the cermets containing carbides, which have the tendency to decompose when sprayed by conventional thermal spray processes such as plasma or HVOF. This is especially the case when the carbide particle sizes are small and tend to be nanometer sized. Thus cold spray, where particles are accelerated by a low temperature supersonic gas flow to a high velocity, should be promising if impacting particles and previously deposited underlying particles have sufficient deformation. Siao Ming Ang et al. [82] have cold sprayed, on stainless steel substrates, micro- and nanostructured powders with similar Co content (17 wt.%). The working gas was high-pressure helium at 1.2–1.5 MPa, the gas in the prechamber being preheated to ~873 K. The mean size of the particles was about 31 μm: microstructured ones were sintered and crushed with WC grains of 2–3 μm, while nanostructured ones were wet chemically synthesized and agglomerated with WC

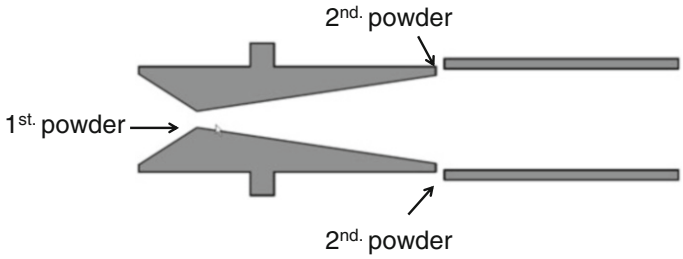


Fig. 6.50 Nozzle design with two points of powder injection into the stream. Reprinted with kind permission from Elsevier [85]

grain sizes of 40–700 nm and 80–800 nm, respectively. Micrometer-structured WC–Co feedstock did not permit coating build up due to simultaneous erosion and deposition effects on the surface. It seems that the substrate deformation allows particle penetration, resulting in the formation of the first layer of the coating via interlocking with the metallic Co, WC particles, and steel substrate. Fine WC particles (< 1 μm) were observed near the substrate interface and larger WC particles (1–2 μm) in the vicinity of the first layer surface. It seems that particles have not enough metallic Co binder and critical velocities and thus erode and reduce WC particle sizes of the first WC–Co layer. With the nanostructured particles the minimum conditions for deformation and deposition seem to be satisfied. Siao Ming Ang et al. [82] have introduced the mean free path of the WC particles, measuring the thickness of the binder layers between the WC particles and related to the plastic deformation. The effect of this mean free path is illustrated in Fig. 6.49 showing how the coating hardness is expected to increase as the particle size of the ceramic decreases and with greater number of fragmented WC particles.

Gao et al. [83] studied deposition behavior of nanostructured WC–Co spray particles with different hardness impacting on the substrate during cold spray process. The porosities of the three powders were respectively, 43.8 ± 1.3 %, 29.8 ± 1.1 %, and 4.9 ± 1.2 %, and the corresponding micro-hardness of the three powders were 0.78 ± 0.02, 5.48 ± 0.46, and 13.17 ± 2.47 GPa. The process used helium for both accelerating and feeding the powder, the He gas being at a pressure of either 2.0 MPa or 2.5 MPa and a temperature 650°C. The standoff distance was 20 mm and different substrates were used with hardness from 2 to 8 GPa. With the two porous powders coatings were formed on all substrates, while with the dense one (porosity around 5 %), sprayed particles can only be embedded into soft stainless steel surfaces. Kim et al. [71] obtained similar results with nanostructured WC–12 %Co particles sprayed with helium at 3.1 MPa and preheated to 600°C. They showed that there was no detrimental phase transformation and/or decarburization of WC by cold spray deposition. Coating showed a very high hardness ($\sim$2050 HV_{5N}). They emphasized that powder preheating (500°C for the powder) was one of the most crucial parameters.

At last Yandouzi et al. [12] have compared nanostructured WC–Co coatings sprayed by conventional cold spray (CGDS process) and pulsed gas dynamic spray process (PGDS), the advantage of the latter being the high impact velocities and intermediate temperatures. They found that there was no degradation of the phase with both processes but dense coatings without major defects were difficult to obtain when using the CGDS process. With the PGDS process it was possible to produce coatings with low porosity if the feedstock powder was preheated above 573 K. The same authors [13] sprayed six commercial types of WC–Co powders with the PGDS process. The PGDS optimum process parameters were material dependent. It was found that sintered and cast and crushed powders with similar chemical composition produced coatings with similar porosity level and hardness but the latter type produced coatings with more cracks, attributed to the bulky dense aspect of the powder. The study also revealed that larger agglomerated and sintered powder particles deformed better on impact with the substrate and formed better coatings (reduced porosity and higher hardness) due to the larger volume of softer material available for deformation.

(b) Other Cermets

Composite metal–ceramic coatings were deposited by CS using injection either of the metal powder in the subsonic zone, and of the ceramic powder in the supersonic zone of the de Laval nozzle (separate injection) or, injected in the subsonic zone either a mixture of both components (blend metal–ceramic) or particles made of both components by cladding or ball-milling.

i. Separate Injection

Kosarev et al. [16], Shkodkin et al. [84], Klinkov et al [85, 86], Sova et al. [87–89], Spencer et al. [90] among others, have used this technique. According to Klinkov et al. [85] the most effective method to spray multicomponent coatings would be heating and accelerating each component under spraying conditions appropriate for this particular component. For that they have designed an axisymmetric nozzle with two points of powder injection schematically presented in Fig. 6.50. The metal powder is injected in the subsonic part for the effective heating of the particles. As for the ceramic particles, their temperature is not important they are injected in the supersonic part avoiding erosion of the nozzle throat. Of course, this process requires two powder feeders.

Sova et al. [87–89] have sprayed soft metal particles (Al with $d_{50} = 25$ μm, Cu $d_{50} = 39$ μm) with fine (around 20 μm) or large (around 130 μm) ceramic powders (Al_2O_3 and SiC) onto grit-blasted aluminum substrates. Ceramic powders were injected either downstream of the nozzle (configuration A) or with metal particles in the subsonic part of it (configuration B). The ceramic particle velocity before impact was measured in both spray configurations. The difference in velocity of the ceramic particles of the same size injected in configurations A

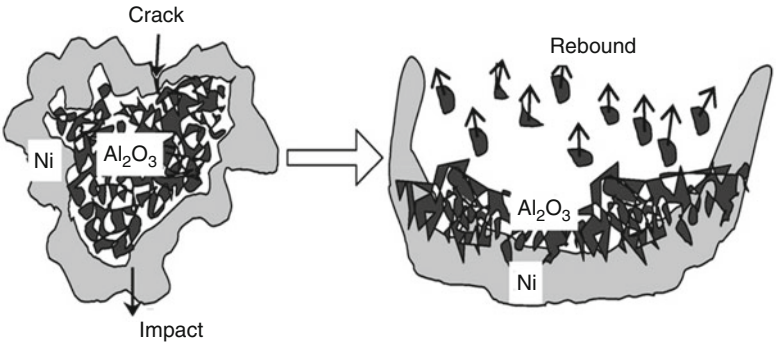


Fig. 6.51 Schematic diagram of the impacting process of a Ni-coated Al_2O_3 composite particle resulting in the rebound and embedding of Al_2O_3 particles. Reprinted with kind permission from Elsevier [96]

and B does not exceed 100 m/s. The velocity of ceramic particles larger than 100 μm is less than 200 m/s. Ceramic powders of fine fractions enhance the coating growth, while ceramic powders of large fractions considerably hinder coating growth. Only a small part of fine ceramic particles is embedded in the coating. Metal particles form a metal matrix with uniformly distributed separate ceramic particles interlocked within it. No large ceramic particles > 100 μm were found in the coating when spraying coarse powders. Sova et al. [87] conclude by underlying the importance of the ceramic particle velocity that must have a minimum velocity to penetrate into the coating. When spraying soft metals (Al, Cu) with fine ceramic powders the "critical" temperature of the metals decreases compared to pure metals.

ii. Metal–Ceramic Blends

In this case the blend is injected in the subsonic zone. Besides those already cited [86, 89] many papers have been devoted to this technique [91–95]. For example SiC-reinforced aluminum alloy [92], Al with Al_2O_3 or SiC [94], Al reinforced with TiN [93], rare earth $Nd_2Fe_{14}B$ permanent magnet with Al [91], Ni–Al_2O_3 coating [95]. Only two typical results will be presented. To produce $Nd_2Fe_{14}B$ permanent magnet/aluminum composite coatings, King et al. [91] blended $Nd_2Fe_{14}B$ powder with aluminum powder (20–80 vol.%). They used nitrogen at 2.6 MPa heated to 200–480°C. The hard $Nd_2Fe_{14}B$ particles tended to fracture and fragment upon impact, while aluminum underwent severe plastic deformation, eliminating pores, and trapping $Nd_2Fe_{14}B$ within the coating. Higher spray temperatures and finer $Nd_2Fe_{14}B$ particle sizes improved their retention rate within the composite structure. Of course the magnetic properties of $Nd_2Fe_{14}B$ remained unaffected by the cold spray process. According to King et al. [91]: with the spray conditions used, only a small proportion of $Nd_2Fe_{14}B$ particles were able to

penetrate deeply into aluminum. But among elastically rebounding particles, those with a small enough rebound momentum to be overcome by new arriving particles were imbedded in the coating. The cold-sprayed [95] Ni–Al_2O_3 coating on Inconel 600 substrate with the ratio of Ni-60 wt.% and α-Al_2O_3-40 wt.% presented a compact microstructure and low porosity. The bonding mechanism was dominated by deformation and interlocking of the interparticles accompanied with local metallurgical bonding.

iii. Particles Made of Metal and Ceramic

According to Li et al. [96] an effective way to increase the volume fraction of hard particles in the composite is to prepare the feedstock powder with a higher volume fraction of hard particles. For that they used the hydrothermal hydrogen reduction method commonly used to prepare the Ni-coated composite materials with graphite, diamond, and alumina. With this technique fine Al_2O_3 particles are clad by a nonuniform Ni layer about 20 μm thick. Figure 6.51 represents what happens to particles at impact. The volume fraction of Al_2O_3 in the composite was about 29 ± 6 vol.% against 40–45 vol.% in the feedstock, probably due to the rebound of some Al_2O_3 particles (see Fig. 6.51). The microhardness of the composite coating was beyond the strain-hardening effect, which was about 173 ± 33$HV_{0.2}$.

Wang et al. [97] have cold-sprayed (N_2 at 2 MPa and 500°C) a ball-milled mixture $Fe_{60}Al_{40}$–10 vol.% Al_2O_3, the starting alumina particles mean size being 5 μm. The metastable microstructure of the milled feedstock was completely retained in the coating. The Fe/Al alloy in the coating was completely transformed to an FeAl intermetallic phase by the annealing treatment of the as-sprayed coatings at a temperature higher than 600°C. Luo et al. [98] have deposited (He at 2.2 MPa and 600°C) the mechanically alloyed composite powder cBNp/NiCrAl. The coating presented a dense microstructure and cBN particles were uniformly dispersed in the NiCrAl matrix although a limited fraction of NiCrAl lamellae were present in the coating.

(c) Composite Metals

Cold spray coatings are essentially achieved by spraying mixtures of the components, as illustrated by the few following examples. Lee et al. [99] have cold sprayed (air at 0.8 MPa and 280°C) pure Al and Ni powders mixture (respectively, 75:25 and 90:10 wt.%). The Ni particles were finely dispersed and embedded in the Al matrix. Above 450°C of post-annealing temperature, the Al_3Ni and Al_3Ni_2 phases were observed in the cold-sprayed Al–Ni coatings, the Ni particles being fully consumed via compounding reaction with Al at 550°C. In another paper Lee et al. [100] investigated the effects of gas pressure on the morphology evolution of cold-sprayed Al–Ni system. Under low pressure (0.7 MPa), large amount of defects were created at the interfaces. These effects gradually decreased as pressure

increased. They supposed that the peening effects, depending on gas pressure, could alter the main route of Al consumption during annealing. Novoselova et al. [101] cold-sprayed titanium and aluminum powder mixtures that were then converted to titanium aluminide with suitable heat treatments. The desirable set of intermetallic phases ($TiAl_3$, r-$TiAl_2$, TiAl, and Ti_3Al) was obtained by varying heat treatment conditions. While the porosity in the as-sprayed precursor deposits was about zero, significant porosity developed during heat treatment.

6.3 Coating Materials and Applications

6.3.1 General Remarks

In his editorial of a special issue of Journal of Thermal Spray Technology E. Lugscheider [102] has emphasized the broad variety of feedstock materials used in cold spray. As other thermal spray coatings cold spray ones have been successfully used:

Against corrosion and wear [103]

For repair, especially magnesium parts [103]

For electromagnetic interference shielding [103]

For demanding electric, electronic, or thermal applications as well as efficient deposition of soldering or brazing alloys [104] (generation of solderable surfaces on materials with poor wettability such as heat sinks with copper on aluminum), conducting structures on nonmetal composite layers (the cold-sprayed metal–matrix composite coating is dense, with a strong bonding between the metal matrix and the dispersant [104].

6.3.2 Metals

A variety of coatings have been applied using the cold spray process. These include pure metals (Ag, Al, Cu, Fe, Mo, Ta, Ti, Zn,. . .), low alloy steels, Ni–Cr alloys, Ni base superalloy, stainless steel, Zn alloys, Al alloys, Cu alloys, MCrAlY, etc. A correlation between deformation properties and bonding type for the three iso-mechanical groups (fcc: face-centered cubic, bcc: body-centered cubic, and hcp: hexagonal close-packed) is supplied by plotting the product of the shear modulus and the modulus of compression as a function of the normalized temperature $T_0/(T_0 + T_m)$ with $T_0 = 273$ K and T_m the melting temperature of the material [51] (Fig. 6.52). The product of the shear modulus and modulus of compression takes into consideration two important material parameters and clarifies the distribution of the data points. The representation permits a rough classification of suitability for the

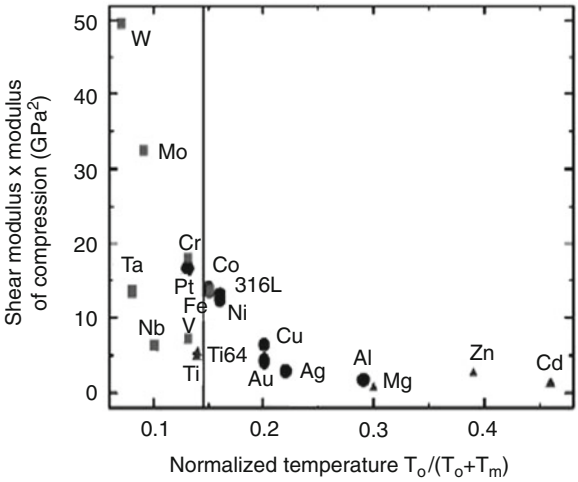


Fig. 6.52 Parameterized representation of the plastic properties of various materials (the product of the shear modulus and the modulus of compression) as a function of the normalized temperature $T_0/(T_0 + T_m)$ with $T_0 = 273$ K and T_m the melting temperature of the material. Characteristics are for $T = 293$ K. Reprinted with kind permission from Springer Science Business Media [51], copyright © ASM International

Table 6.1 Properties, materials, and applications of cold gas-sprayed layers. Reprinted with kind permission from Springer Science Business Media [103], copyright © ASM International

Application/purpose of the cold sprayed layer	Typical materials	Advantages of cold spraying and cold spray
Corrosion protection	Zn, Ni, brass	Little porosity
Conductor, thermal management	Cu, Al, steel, Ni	Little porosity, low oxygen
Repair, structural coatings	Alloys, soldering/brazing	Little porosity, no phase change
Solder/braze deposition	Alloys	Strong bonding, no phase change, low oxygen content
Solderability	Cu	Low oxygen content

cold spray process. Empirically, the plotted line corresponds to a T_m of ~1,600°C, at which temperature difficulties must be expected with regard to compacting.

In addition, the bonding type can be characterized in a simplified manner by the melting temperature, which can be used as an evaluation criterion. At approximately 1,600°C, a significantly more difficult compaction ability is to be defined in the cold spray process on the basis of the experiments and the data published in the literature. Excellent results have been obtained with materials that have low melting point and mechanical strength, Zn, Al, and Cu being ideal. Good results are obtained with Fe and Ni base materials provided higher temperatures and velocities are used to spray. Recent application development efforts are based on several advantages of the cold spray process or cold-sprayed layers. Table 6.1 from S. Marx et al. [103] contains the decisive advantages for some applications.

Cold spray produces ultrapure coatings with unique characteristics that can be used in the following applications:

6.3.2.1 Aluminum

When cold sprayed the oxygen content increases at the maximum by 0.02 wt.% and the porosity is close to zero. Thus the process can be used for the spray forming of aluminum components with elastic modulus, ultimate tensile strength, and elongation similar to those of wrought aluminum. The high bond strength of cold-sprayed aluminum layers on glass or ceramic substrates seems also promising, and such layers can be used as intermediate or bond layers for other coatings. Aluminum alloy coatings can be deposited for brazing. They comprise Al–12 wt.% Si (for the brazing filler metal), Zn (for corrosion protection), and KAlF4 (flux powder), and they are more and more used in brazed aluminum heat exchangers, for example in air conditioning equipment. Al–13Co–26Ce alloys give rise to a substantial reduction in fatigue effects in comparison with uncoated and Al clad-coated substrates. It was proposed that any crack propagation in the coating was arrested by the residual compressive stresses contained in the coating [104–109]. Lee et al. [109] have repaired aluminum molds by cold spraying aluminum. To check the recovered molding capability, polymer (Polystyrol) products were fabricated by injection molding using the repaired mold. Experimental results showed that the mold repair process using cold spray deposition and machining can be applied in the mold repair industry. Bobzin et al. [110] have cold-sprayed AlSi12 and AlSi10Cu4 onto Mg-containing aluminum alloys 6063 and 5754. Some coated samples were brazed under argon atmosphere without any fluxes. The results show that AlSi12 had much better deposition behavior than AlSi10Cu4. Due to the rupture of oxide scales, Cu and Si diffused into the substrate and a metallurgical bond formed between the brazing alloys and the substrates during heat-treatment. The coated samples could be brazed without any fluxes.

As magnesium alloys have poor corrosion resistance, DeForce et al. [111] have applied to a magnesium alloy (ZE41A-T5 Mg) a corrosion-resistant barrier coating made of high-purity Al–5 wt.% Mg that has galvanic compatibility with magnesium and a hardness value as high as that of magnesium. The coating resulted in the best overall performance, including a high hardness, 125 HV_{1N}, and adhesion strength, over 60 MPa, when treated for over 1,000 h in a salt spray chamber and with a low galvanic current.

Nanocrystalline coatings have also been sprayed by cold spray:

Richer et al. [112] have cold sprayed with helium Al–Mg feedstock powder, characterized by a broad particle size distribution. Hardness measurements and TEM inspection demonstrated that the microstructure of the original feedstock powder was conserved throughout the cold spray process and that no increase in hardness due to cold working of particles was observed.

Zhang et al. [113] have cold sprayed with nitrogen aluminum alloy 2009 using a powder mixture of nano crystalline and as-atomized powders, the latter being bigger than the former. The density of the coating was much higher than that of a coating using pure nanocrystalline powder. Ajdelsztajn et al. [114] have successfully cold sprayed conventional and nano crystalline Al–Cu–Mg–Fe–Ni–Sc coatings.

The conventional cold-sprayed coating showed negligible porosity and an excellent interface with the substrate material. This was not the case for the nano crystalline one, in which the porosity level was in the range of 5–10 %. The microstructure of the feedstock powders (atomized and cryomilled) was retained after the cold spray process. The difference in porosity between both coatings was explained by the hardness and microstructure of the corresponding feedstock powder: the softer and coarse-grain conventional powder experienced generalized adiabatic shear instability upon impact, resulting in a dense coating, whereas the harder and fine-grain cryomilled powder did not exhibit the same extent of deformation, resulting in a less dense coating. The conventional powder showed work hardening during impact, thus increasing the hardness of the conventional coating compared with the feedstock powder. On the other hand, the hardness of the nanocrystalline coating was similar to that of the feedstock powder, suggesting that no work hardening took place in this case. The Vickers microhardness of the nanocrystalline coating was, despite the porosity, much higher than that of the conventional coating.

6.3.2.2 Copper

Metallization: the combination of the low porosity and the low O_2 content contributes to excellent electrical properties of coatings (close to those of bulk material). Cu coatings also display excellent tensile properties. They are used extensively in electrical metallization including plastic parts, current carrying thick films in the automotive industry: for example, on a heat sink of aluminum to solder power transistors. The cold-sprayed copper layer removes the natural oxide film and provides a solderable surface for the tin- or copper-plated area of the electronic part. Moreover copper conducts very rapidly the heat dissipated to the heat sink. Papers about cold-sprayed copper can be found for example in references [115–126]. Fukumoto et al. [123] have studied systematically copper splat formation on smooth substrates, with particularly the metal jetting behavior of the particles related to some process factors. Koivuluoto et al. [122] showed that cold-sprayed Cu coatings (coarser particle size) were dense according to SEM analysis and open cell potential measurements. Eason et al. [124] have produced dense bulk material obtained by continuous spray deposits 25 mm thick, the elevated microhardness in the as-sprayed coatings resulting from the cold work hardening. Post-annealed microhardness values indicated the potential for strengthened bulk materials through cold spray processing, exceeding the performance of typical P/M material. Donner et al. [125] have shown that copper coatings with high electrical conductivity (98 % of that of bulk material) were successfully deposited onto insulating alumina thermal spray ceramic coatings by cold gas spraying. The adhesion was good when achieved via an activation of the ceramic surface. Activation consisted of preheating the substrates to remove adsorbed water and of using chemical activation by interlayers to improve coating build-up. Jin et al. [126] attempted to manufacture Cu–In coating layer via the cold spray process and investigated the applicability of the layer as a sputtering target material.

They demonstrated that Cu–In coating layer manufactured via cold spray process with an annealing heat treatment can be applicable as sputtering target in the future. The Cu coatings have also been used as magnetic shielding coatings on electronic components [2, 103].

6.3.2.3 Nickel

In general, nickel coatings are used for corrosion and wear protection layers. Cold-sprayed nickel layers are used as base or intermediate layers and they are less expensive than electroplated coatings. They are also used in coatings for induction heating on cooking appliances or cooking pots. However Koivuluoto and Vuoristo [127] have shown that if cold sprayed Ni and Ni–30 %Cu coatings seemed to be dense according to the SEM studies, corrosion tests showed some through porosity in the cold-sprayed Ni and Ni–30 %Cu coatings. The weak points were on the particle boundaries where the bonding is not strong and uniform enough between the particles. Koivuluoto and Vuoristo [127] also studied denseness improvement of cold-sprayed Ni, Ni–20Cu, Ni–20Cr, Ni–20Cr + Al_2O_3, and Ni–20Cr + WC–10Co–4Cr coatings. Denseness, evaluated by corrosion tests, of the Ni coating was improved with optimized spraying parameters whereas denseness of Ni–20Cr coatings was increased with added hard particles in the powder mixture. In addition, denseness of Ni–20Cu coatings was improved by heat treatments. With cold spray, very dense and well-adhering thick induction heating layers are deposited by a single processing step onto metallic or even nonmetallic cooking utensils [128]. Zhang et al. [129] have synthesized by ball milling of nickel–aluminum powder a mixture with a Ni/Al atomic ratio of 1:1. The powder was deposited by cold spraying using N_2 as accelerating gas. The annealing of the resulting Ni/Al alloy coating at a temperature higher than 850°C leads to complete transformation from Ni/Al alloy to NiAl intermetallic compound. When cold spraying with helium Ni–50Cr on two boiler steels SA-213-T22 and SA 516 (Grade 70), Bala et al. [130] demonstrated that coatings were very useful in developing hot corrosion resistance in the aggressive environment of Na_2SO_4–60 % V_2O_5 at 900°C.

6.3.2.4 Selective Galvanizing

Corrosion protection for automotive body and chassis structures relies primarily on the use of percolated (galvanized) steel and post-manufacturing processes. Cold spraying has been found to be a useful approach for selective protection of a localized area. Zn and Al–Zn coatings are used [2, 39, 107].

6.3.2.5 Superalloys

Typical applications studied are oxidation-resistant MCrAlY bond coats [131], IN718 coatings for localized repair [132]. It is possible to deposit the CoNiCrAlY coating on an Inconel 625 substrate by the cold spray technique. From the results of a laser shock impact test, the adhesion requires higher velocity and specific phase combination. From STEM-EDX results of as-sprayed coatings and SEM, EPMA results, the bonding between CoNiCrAlY coating and an Inconel 625 substrate occurred to only the γ/γ'-(Ni/Ni_3Al) phase of CoNiCrAlY within the substrate [133]. IN718 coatings were produced on IN718 plates with very good bonding and very low oxide content [132]. Such coatings have been studied as bond coats of TBCs [133, 134]. Richer et al. [133] demonstrated the occurrence of microstructural changes during the deposition process of CoNiCrAlY coatings. Evidence of grain refinement of the initially large γ-matrix grains as well as dissolution of the fine β-phase precipitates was observed. Such transformations of the deposited material's microstructure were attributed to the intense plastic deformation. Chen et al. [134] showed that the TBCs with HVOF- and cold spray CoNiCrAlY bond coats had an extended durability, compared to the TBC with APS CoNiCrAlY bond coat. However, the durability of cold spray CoNiCrAlY was not as good as the HVOF CoNiCrAlY.

6.3.2.6 Titanium

Cold-sprayed coatings are very promising against fatigue and for wear resistance, for example, on internal surfaces of cylinder blocks of internal combustion engines, pumps, and hydraulic cylinders for automotive, heavy machinery, forgings, and extrusions. Many studies are devoted to Ti or TiAl coatings to achieve layers as dense as possible with limited residual stress [135–143]. Binder et al. [139] have shown that using nitrogen as process gas at a pressure of 4 MPa and a temperature of 1,000°C resulted in ultimate strengths of about 450 MPa, similar to those of pure bulk material. Bonding is most prominently caused by shear instabilities under plastic deformation and only to a minor extent by the heat of friction. Christoulis et al. [140] studied the deposition of cold-sprayed titanium onto various substrates. The use of helium as the processing gas led to a dramatic improvement in coating properties: deposition efficiency, mean thickness, and porosity. Despite the use of a coarse powder, the formation of titanium cold-sprayed coatings of high density at high deposition efficiency was achieved. Zahiri et al. [142] also showed that coatings densification was improved by using helium. Densification (2 % porosity) was achieved by heating particles up to 700°C, and the metallurgical bond with the substrate was obtained by vacuum heat treatment at 955°C for 8 h. Li et al. [143] showed that when using big particles (45–160 μm) porous coatings were obtained. After annealing at 850°C for 4 h under vacuum condition, the Ti coating also presented a porous

structure with more uniformly distributed small pores. A metallurgical bonding between the deposited particles was formed through the annealing treatment. The adhesive strength of coating was significantly improved after annealing as well as the microhardness. Cinca et al. [144] cold-sprayed Ti onto aluminum alloy 7075-T6, highly used in aeronautic engineering, to protect it from corrosion. They have studied it as an alternative to other deposition techniques such as electrodeposition, chemical vapor deposition, and vacuum plasma spray, which are more expensive. They obtained dense Ti coatings with thicknesses larger than 300 μm and no microstructural changes.

6.3.2.7 Iron and Steel

Cold spraying of high purity iron as an intermediate layer was found to permit the use of more conventional welding processes for the repair and material buildup on dies formed by the thermal spray process [145]. Fe-based amorphous alloy (Fe–Cr–Mo–W–C–Mn–Si–B) coatings on Al-6061 were successfully deposited with negligible porosity and good values of hardness and elastic modulus [146]. Metastable alloys (Al–Fe–V–Si), which have good weld ability and a low thermal expansion coefficient, were successfully cold sprayed and the complex microstructure of the powder was retained after spraying [147]. A nanostructured Fe/Al alloy powder was prepared by a ball-milling process in the study by Wang et al. [148]. The cold-sprayed Fe/Al alloy coating evolved in situ into an intermetallic compound coating through a post-heat treatment. Results showed that the milled Fe–40Al powder exhibits lamellar microstructure. The microstructure of the as-sprayed Fe(Al) coating depended significantly on that of the as-milled powder. The heat treatment temperature significantly influenced the in situ evolution of the intermetallic compound. The heat treatment at a temperature of 500°C resulted in the complete transformation of Fe(Al) solid solution to FeAl intermetallic compound.

Stainless steel was sprayed on aluminum against wear (for example, on a cylinder, with a specially designed gun [149]). Spencer and Zhang [150] studied the porosity of 316 L stainless steel cold spray coatings. They applied the powder metallurgy practice of mixing particle size distributions to improve coating density. Results showed that coatings sprayed using mixed particle size distributions can have similar properties to those sprayed using fine particles alone. Beyond a critical coating thickness the substrate is no longer attacked in polarization tests.

6.3.2.8 Tantalum

Cold spray seems to be an alternative technique to the currently used vacuum plasma spraying. The main advantage of cold spray is the very low level of oxidation during processing of this metal, which is very sensitive to oxidation. It has been demonstrated that Ta coatings can be produced in air with excellent

adhesion, low porosity, and increased hardness. Of course, better coatings were obtained when He was used [151]. Koivuluoto et al. [152] have investigated the microstructural details, denseness, and corrosion resistance (in 3.5 wt.% NaCl and 40 wt.% H_2SO_4 solutions at room temperature and 80°C) of two cold-sprayed tantalum coatings. Standard and improved tantalum powders were tested with different spraying conditions. The cold-sprayed tantalum coating prepared with improved tantalum powder showed excellent corrosion resistance.

6.3.2.9 Pure Silicon

It has been deposited as anode for lithium secondary batteries. The average thickness of the as-deposited silicon anodes is between 0.4 and 0.7 μm. Silicon anodes (20 mm by 20 mm) have a capacity of about 1.5–2.5 mAh [153].

6.3.2.10 Pure Silver

Manhar Chavan et al. [154] have investigated the process parameters and heat treatment on the thermal and electrical properties of silver powders (water atomized) cold sprayed. The optimized Ag coating, in the as-coated condition, exhibits an unusually high electrical conductivity of the order of 70 % of the bulk Ag value. The influence of heat treatment of the "as-coated" cold-sprayed Ag coating on its electrical conductivity is complex and depends also strongly upon the atmosphere where it is performed.

6.3.2.11 Metallic Coatings on Polymers

Zhou et al. [155] have cold-sprayed (with nitrogen as spray and carrier gas) Al and Al/Cu coatings on the surface of carbon fiber-reinforced polymer matrix composite (PMC). Results have shown the deposition of metallic coatings directly onto the PMC surface was possible with reasonable bonding of feedstock and substrate material. Lupoi and O'Neil [156] have studied the potential of cold spray process to produce metallic coatings on nonmetallic surfaces such as polymers and composites for engineering applications. They analyzed copper, aluminum, and tin powder on a range of substrates such as PC/ABS, polyamide-6, polypropylene, polystyrene, and a glass fiber composite material.

6.3.3 Composites

Such coatings are mainly used for wear protection. They have been developed for example to spray the following materials.

6.3.3.1 Pure Iron (99.5 %) Or Stainless Steel (304 L) Reinforced by Diamond

The composites Fe (5–25 μm) and SUS304 stainless steel (5–45 μm) contained, respectively, 46 and 12 % diamond fraction [157]. The coating adhesion on an Al alloy (ASTM 6061) was over 100 MPa. Some of the diamond particles within coatings were fractured. Some of these coatings were coated with Ti.

6.3.3.2 Aluminum and Copper

Aluminum has been reinforced by different ceramic particles. Aluminum (6061-T6) was reinforced by B_4C (up to 20 vol.%) [158]. Postdeposition heat treatments and mechanical property tests were performed and results indicated that adequate strength and ductility were obtained. However elastic modulus was lower than expected, probably due to B_4C particles fracturing upon impact. Aluminum coatings have also been reinforced with SiC [92, 159]. The composite coating microstructure, thickness, porosity, and composition were compared to an Al–12Si coating. The results show that 45 % of the SiC mixed with the aluminum matrix was retained in the composite coatings. These SiC particles exhibit a reasonably uniform distribution within the aluminum matrix. The coating thickness and adhesion strength were not affected by the SiC content. However, the coatings became more porous by increasing the SiC volume fraction of the blended powders [159]. Yong et al. [160] have successfully cold-sprayed SiC and Al_2O_3 with Al. The adhesion and compactness depended on the quantities and sizes of the starting materials.

It was experimentally shown that when spraying soft metals (Al, Cu) with fine ceramic powders the "critical" temperature of the metals decreased compared to pure metals. Ceramic powders of fine fractions produce a strong activation effect on the spraying process and enhance the coating growth, while ceramic powders of large fractions considerably hinder coating growth [86, 87]. The experiments demonstrated the importance of the ceramic particle velocity for the cermet coating formation. Stable cermet coating formation is possible if the ceramic particles are accelerated to an optimal level: ceramic particles accelerated to a high velocity penetrate into the coating, while low-velocity ceramic particles rebound from its surface. Irissou et al. [161] showed that the addition of Al_2O_3 to Al powder increased the adhesion of the coating on the substrate (up to 60 MPa for samples produced with more than 30 wt.% Al_2O_3) due to the creation of micro-asperities by the hard ceramic particles. Moreover the inclusion of alumina particles in the aluminum coatings had no detrimental effect on the corrosion protection of the substrate. Poirier et al. [162] used cold spray to consolidate milled Al and Al_2O_3/Al nanocomposite powders as well as the initial unmilled and un-reinforced Al powder. Results showed that the large increase in hardness of the Al powder after mechanical milling is preserved after cold spraying. Good quality coating with low porosity is obtained from milled Al. However, the addition of Al_2O_3 to the Al powder during milling decreased the powder and coating nano-hardness.

The coating produced from the milled Al_2O_3/Al mixture also showed lower particle cohesion and higher amount of porosity.

Aluminum and Al6061 aluminum alloy-based Al_2O_3 particle-reinforced composite coatings were sprayed by Spencer et al. [90] on AZ91E Mg substrates using cold spray. The strength of the coating/substrate interface in tension was found to be higher than that of the coating itself. The coatings have corrosion resistance similar to that of bulk pure aluminum in both salt spray and electrochemical tests. The wear resistance of the coatings is significantly better than that of the AZ91 Mg substrate, but the significant result is that the wear rate of the coatings is several decades lower than that of various bulks Al alloys tested for comparison. Kong et al. [163] prepared by cold spray a novel $TiAl_3$–Al coating onto Ti–22Al–26Nb (at.%) substrate for high temperature protection. The coating was sprayed with premixed Al and Ti powders. The as-sprayed specimens were subjected to heat treatment (630°C during 5 h) under Argon gas flow of 40 mL/min. The composite coating was mainly composed of $TiAl_3$ embedded in the matrix of residual aluminum. The oxidation test indicated that this composite coating was very effective in improving the high-temperature oxidation resistance of the substrate alloy at 950°C in the tested 150 cycles without any sign of degradation.

Van Steenkiste [164] produced composite coatings with different rare earth iron alloys (REFe2) and several ductile matrices. Composite coatings of Terfenol-D [$(Tb_{0.3}\ Dy_{0.7}\ )Fe_{1.9}$] and $SmFe_2$ were combined with ductile matrices of aluminum, copper, iron, and molybdenum. Evidence of an induced magnetic coercivity was measured for the REFe2-Mo (Hci = 3.7 kOe) and Fe composite coatings. Coatings were produced on flat substrates and shafts. $Nd_2Fe_{14}B$ permanent magnet/aluminum composite coatings were produced by cold spray deposition by King et al. [90]. Isotropic $Nd_2Fe_{14}B$ powder was blended with aluminum powder to make mixtures of 20–80 vol.% $Nd_2Fe_{14}B$, and these mixtures were sprayed at temperatures of 200–480°C. The hard $Nd_2Fe_{14}B$ particles tended to fracture and fragment upon impact, while aluminum underwent strong plastic deformation, eliminating pores, and trapping $Nd_2Fe_{14}B$ within the coating. It was found that higher spray temperatures and finer $Nd_2Fe_{14}B$ particle sizes improved their retention rate. The magnetic properties of $Nd_2Fe_{14}B$ remained unaffected by the cold spray process.

6.3.3.3 Fabrication of Cermet Coatings

WC–Co with nano- and microstructured feedstock powders by cold spray deposition [165]. There was no detrimental transformation and/or decarburization of WC by cold spray deposition. It was observed that nano-sized WC in the feedstock powder is maintained in the cold spray deposits. It seems that nano-sized WC is advantageous over micron-sized WC in cold spray deposition because higher particle velocities can be obtained with the same gas velocity. Kim et al. [71] deposited by cold spray process using helium with reasonable powder preheating WC–12 %Co powders with nano-sized WC. The results showed that there were no detrimental phase transformation and/or decarburization of WC, and the nano-sized nature of the

WC in the feedstock powder was maintained in coatings. The porosity was low and the hardness high (~2050 HV_5). Kim et al. [166] cold sprayed the same particles using nitrogen and helium gases. Best results were obtained with nanometer-sized WC particles. Powder preheating was one of the most crucial parameters for the cold spray deposition in the commercial production point of view.

The cold spray process was successful in applying Cr_3C_2–25 wt.%NiCr and Cr_3C_2–25 wt.%Ni coatings on 4,140 alloys for wear-resistant applications [167]. The average Vickers hardness of the Cr_3C_2-based coatings range from 300 to 900 HV_3. This strongly suggests that the hardness (and thus wear resistance) can be tailored over a wide range of values to meet a variety of hardness specifications.

6.3.3.4 Fe–Al Intermetallic Compounds

At last, Fe–Al intermetallic compounds have been produced using a ball-milled metastable Fe–Al–WC powder, spraying it by cold spray and then annealing the coatings at a temperature above 500°C to form Fe–Al intermetallic compounds. The as-sprayed coating hardness was 648 HV, and it decreased upon annealing only if the corresponding temperature was above 550°C [168].

6.3.4 Ceramics

To the best of our knowledge, TiO_2 is the only ceramic material that has been cold sprayed. In spite of its nonductile behavior, it can be successfully sprayed if a powder is prepared through agglomerating ultrafine (between 10 and 100 mm) primary particles, such agglomerated particles presenting a "ductile" behavior. The interest in TiO_2 lies in its photo-catalytic properties and pure anatase crystalline structure is used as feedstock. The advantage of the cold spray process is the avoidance of transformation of anatase by avoiding the heating present in HVOF-sprayed titanium or plasma spray processes. Yang et al. [169] successfully deposited through cold spray TiO_2 photo-catalytic films up to 15 μm thick with a rough surface and porous structure, as it could be expected. The photo-catalytic performance was examined through acetaldehyde degradation under ultraviolet illumination, for which the film was very active. Yamada et al. [170] also cold-sprayed TiO_2. They showed that the process gas used was not an important factor to fabricate anatase TiO_2 coatings, the use of inexpensive nitrogen instead of helium being an important economy factor. The thickness of coatings increased with increasing process gas temperature and the adhesion strength on Cu substrate reached 25 MPa at nitrogen pressure of 1 MPa. The powder preparation was a key factor to achieve good coatings. They used a simple hydrolysis method of titanyl sulfate ($TiOSO_4$) in distilled water with a small addition of inorganic salt [171]. The solution was stirred on a hot plate to hold the temperature at 120°C for 8 h after which a white precipitate was formed. The precipitate was then dried in an oven for 10 h at 120°C to obtain a powder of pure anatase [171]. The powder was then agglomerated with fine nano primary

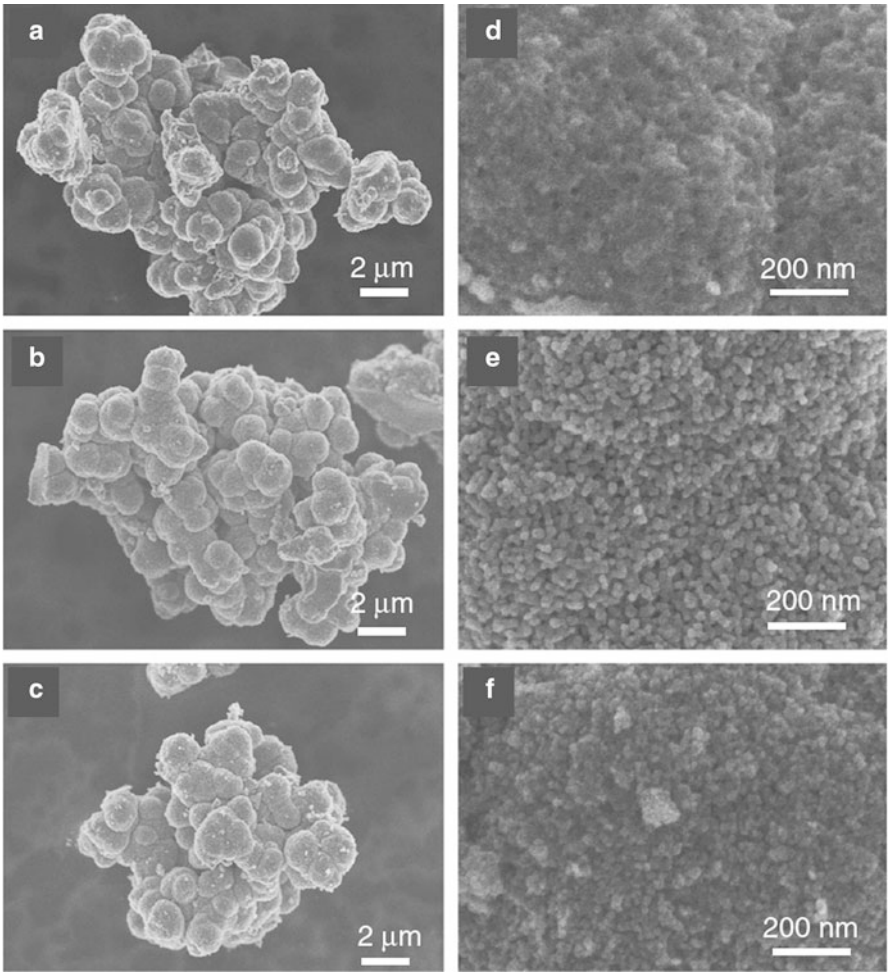


Fig. 6.53 FE-SEM images taken at low magnification of (**a**) as-synthesized, (**b**) annealed, and (**c**) hydrothermal-treated TiO_2 powders; and at high magnification of (**d**) as-synthesized, (**e**) annealed, and (**f**) hydrothermal-treated TiO_2 powders. Reprinted with kind permission from Elsevier [171]

particles, with different post-synthesis treatments leading to different TiO_2 nanostructures but without alteration of the anatase phase. Annealing at 600°C for 1 h caused a significant growth of primary particles with the existence of internal pores within a particle. On the other hand, hydrothermal treatment, performed by soaking the TiO_2 powder with distilled water in an autoclave and heat treating it at 150°C for 5 h produced a unique oriented agglomeration structure where the primary particles were agglomerated in one single crystal axes (see TEM images in Fig. 15.5a, b showing, respectively, the powder as-synthesized and hydrothermally treated). Figure 6.53 shows the powder morphologies obtained by the FE-SEM.

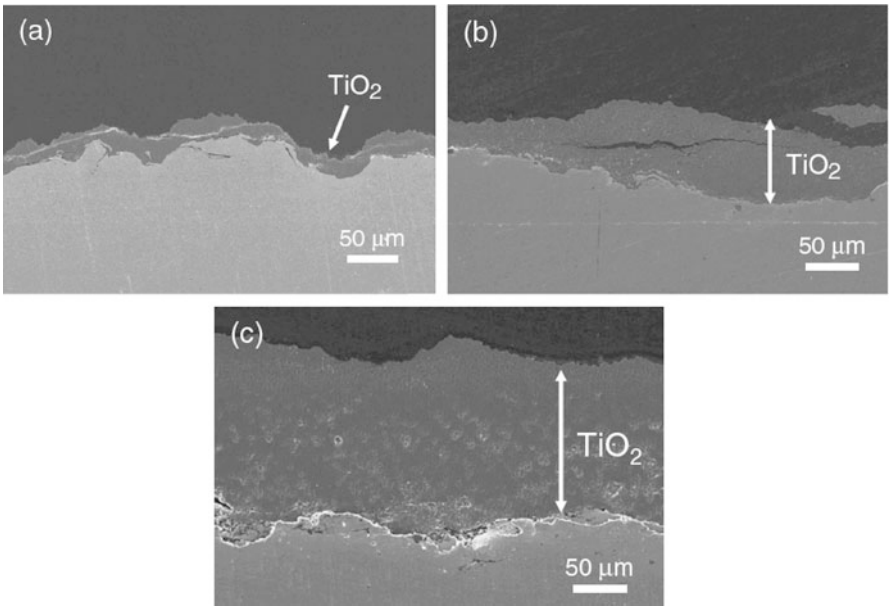


Fig. 6.54 Cold-sprayed coatings (same spray conditions) of (**a**) as-synthesized, (**b**) annealed, and (**c**) hydrothermal-treated TiO_2 powders deposited on copper. Reprinted with kind permission from Elsevier [171]

From the TEM images [171], the particle sizes of as-synthesized, hydrothermal treated, and annealed powders were determined to be about 3, 5, and 25 nm, respectively. Coatings were achieved with the three powders and results are presented in Fig. 6.54. With as-synthesized particles only embedment was observed (Fig. 6.54a), while both other powders formed coatings (Fig. 6.54b, c), the hydrothermal-treated TiO_2 being the thicker with about 150 µm (Fig. 6.54c).

The photo-catalytic activity of the coatings was similar or better than that of the feedstock powder due to the formation of a large reaction area. To conclude this work Yamada et al. [170, 171] concluded that the three major factors to achieve TiO_2 coatings on different substrates (with hardnesses between 45 and 700 HV) are the following:

Porous agglomerates with sizes between 10 and 20 µm
Nano-scaled primary particles agglomerated with a porous structure
Primary particles agglomerated and oriented with single crystal axis

Other works are devoted to ceramic spraying, for example alumina nanoparticles are prepared by a sol-gel technique before being agglomerated and cold sprayed

6.4 Low Pressure Cold Spray (LPCS)

6.4.1 Coating Formation

As already emphasized in Sect. 6.1.3, low pressure ($p_g < 1$ MPa) guns have been developed, for a process being also called Gas Dynamic Spray (GDS), [15–19]. They include a heated compressed air or nitrogen or helium supply, a supersonic nozzle with radial injection of the powder downstream of the throat, and a powder feeder (see Fig. 6.6). With these guns special high pressure pumps are not necessary, the gas flow rates are in the range 0.2–0.5 m^3/min compared to 1.3–5 m^3/min, and thus the heating power is much less, about 10 kW, compared to the 40–70 kW required in conventional cold spray. However, particles generally do not reach the critical velocity and the compaction of the particles must be optimized by the selection of powder types and powder particle size distributions [15–19]. Thus one drawback of the system is that powder recuperation is hardly possible for multicomponent mixtures because of the change in composition after spraying. The addition of very dissimilar powder components, such as ceramic and metal, can enhance processing efficiency by improving the self-cleaning of the substrate or, in the case of ceramic particles, by contributing to the consolidation of the coating via mechanical peening during its formation and consolidation [18]. In these systems (DYMET, SIMAT,...) the dominant mechanism is believed to be analogous to impact compaction, wherein localized pressure waves develop in the solid material upon impact of the incoming particles producing deformation both of the impacting particle and the substrate [19]. Maev and Leshchinsky [172] have studied this particle shock consolidation, their work being based on the "adiabatic shear band" ABS [173] applied to mixtures consisting of particles of various size and specific mass. The principle is illustrated in Fig. 6.55.

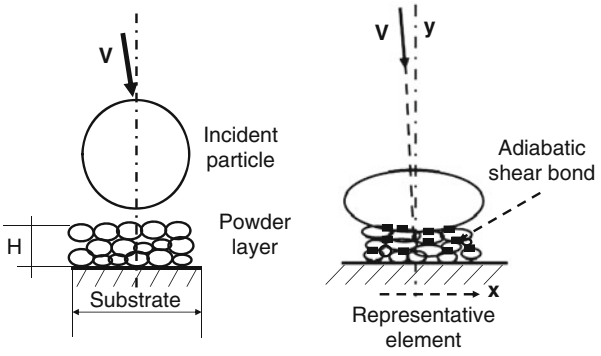


Fig. 6.55 Bimodal powder mixture: large particle impinges upon the layer of smaller particles with the formation of adiabatic shear stress. Reprinted with kind permission from ASM International [172]

6.4.2 Examples of Coatings

A few coatings, such as Cu-based, W-reinforced, and Ni-based TiC reinforced composite coatings have been produced [174] to increase the load bearing capacity, and hence the load and sliding speed range within which the dry sliding wear is low. The dry sliding characteristics depended on the applied load and structure of the composite coatings.

Near net-shaped parts have been produced with Al particles (45–150 μm) and small Al_2O_3 particles (5–10 μm). Coatings presented very low residual porosity (more than 97 % of theoretical density) [175]. However if coating properties were close to those of wrought aluminum, they were less ductile. The hardness was in the range 90–100 $HV_{0.1N}$.

The work of Irissou et al. [161] was related to the influence of the Al particle size and Al_2O_3 mass fraction in Al–Al_2O_3 powder mixtures on the coating deposition and properties. For the two Al powders used, d_{50} was either 91 or 36 μm. Because the mean velocity of the particles was a function of their size, the Al powder having the larger particle size distribution had a significantly smaller volume fraction of particles with velocities higher than the critical one. The deposition efficiency was consequently lower. However, coatings with the starting powder based on the larger Al particles were harder than the coatings made with the smaller size Al powder mixtures. This was likely due to the more important peening effect of the large particles due to their higher kinetic energy. The addition of Al_2O_3 ($d_{50} = 25.5$ μm) to the Al powders helped improving the coating deposition. Optimal deposition efficiency was found for a mass fraction of about 30 % of Al_2O_3 in the starting powder. Abrasion resistance was found to be independent of the alumina mass fraction in the coatings. Al_2O_3 particles played only a role of peening and roughening of the layers during deposition. However, their inclusion in the coatings was limited to about 25 wt.%. The bonding between Al and Al_2O_3 was therefore believed to be weak and resulted in poor cohesion between the two powder types. This limited any possible improvement of the abrasion resistance of the composite coatings. The adhesion was higher than 60 MPa for samples produced with more than 30 wt.% Al_2O_3. The Al–Al_2O_3 coatings proved to be as efficient as pure Al coatings in providing corrosion protection against alternating immersion in saltwater and exposure to salt spray. The inclusion of alumina particles in the aluminum coatings had no detrimental effect on the corrosion protection [161].

Ogawa et al. [176] have studied the possibility of using the low-pressure cold spray technique of aluminum on aluminum alloys instead of welding for repairing cracks. Their work was focused on the active newly formed surface after the aluminum particle deposition. They found that for efficient particle deposition it was necessary to activate the newly formed surface by several impingements because the existence of inactive native oxide films had an adverse effect on the deposition. Furthermore, the strength of a cold-sprayed specimen was found to be higher than that of a cold-rolled specimen under compressive loading.

Koivuluoto et al. [177] have used the low-pressure cold spraying process (0.9 MPa and preheating to 650°C) to spray metallic powders with alumina

particles. Soft metallic coatings (Cu, Ni, and Zn) with a ceramic hard phase can be used for different application areas, e.g., thick coatings and coatings for electrical and thermal conduction and corrosion protection applications. LPCS coatings seemed to be dense according to (SEM), however through porosity was observed in structures through corrosion tests. Bond strengths of LPCS Cu and Zn coatings were found to be 20–30 MPa, and hardness was high indicating reinforcement and work hardening.

Koivuluoto and Vuoristo [178] have shown that the powder type and composition have a very important role in the production of metallic and metallic–ceramic coatings by using the low-pressure cold spray process. They have evaluated the effect of different particle types of Cu powder and different compositions of added Al_2O_3 particles on the microstructure, fracture behavior, denseness, and mechanical properties. Spherical and dendritic Cu particles were tested together with 0, 10, 30, and 50 vol.% Al_2O_3 additions. Coating denseness and particle deformation level increased with the hard particle addition. Furthermore, hardness and bond strength increased with increasing Al_2O_3 fractions. In the comparison between different powder types, spherical Cu particles led to denser and less oxide-containing coating structure due to the highly deformed particles.

Kulmala and Vuoristo [73] have applied the laser-assisted cold spraying (see Sect. 6.2.3.2) to low-pressure cold spraying and called it Laser-Assisted Low Pressure Cold Spray (LALPCS). The purpose of the additional energy from the laser beam is to create denser and more adherent coatings, enhance deposition efficiency, and increase the variety of coating materials. They studied copper and nickel powders with additions of alumina powder on carbon steel. Coatings were sprayed using air as process gas. A 6 kW continuous wave high-power diode laser and a low-pressure cold spraying unit were used in the experiments. The coating density was tested with open cell potential measurements. Results showed that laser irradiation improved the coating density and also enhanced deposition efficiency.

Aluminum components are difficult to repair by welding due to its high-specific thermal conductivity and high coefficient of thermal expansion. The low-pressure cold spray technique can be used instead of welding for repairing cracks, as shown by Ogawa et al. [176]. These authors have focused their study to the effect of surface conditions on aluminum particle deposition and mechanical properties of resulting coatings. They found that for efficient particle deposition it was necessary to obtain an active newly formed surface of the substrate and particle surfaces by several impingements because of the existence of inactive native oxide films. Furthermore, the strength of a cold-sprayed specimen was found to be higher than that of a cold-rolled specimen under compressive loading.

Al–10Sn and Al–20Sn binary alloy coatings have been successfully deposited onto Al6061, copper, and SUS304 substrates with the low-pressure cold spray process with He as propellant gas. However, with particle sizes between 5 and 40 μm the deposition efficiency was 11.2 % at best [179]. Both coatings had similar hardness. There was no significant difference of tin content between the coating and the feedstock powders. A higher critical velocity for Al–Sn binary alloy powder was estimated to exist compared to pure aluminum powders.

SiC (45–50 μm) and Al_2O_3 (>50 μm) with Al (≤45 μm) were successfully sprayed onto a silicon substrate. The adhesion and compactness of coatings depended on the quantities and size of the starting materials [160].

Lee Ha Yong et al. [180] have even prepared WO_3 films by this low-pressure cold spray process working with air, the powder size range being 30–50 μm. During this process, secondary particles of irregular shapes, possibly with highly jagged surfaces are formed due to fracturing of the arriving particles, and mechanical interlocking rather than peening and void reduction can be achieved. However, because particles at the interface seem to be more densely packed and well interlocked, additional energy for enhancing micro interlocking and/or some chemical bonding between the coating and the substrate could be supplied by consecutive bombardment. These studies demonstrate the potential of the technology; however, the process needs further research and development.

6.5 Summary and Conclusions

Cold spray processes, with the operating gases nitrogen or helium at high pressure, are emerging technologies that address shortcomings of the other thermal spray processes. Their main interests lie in their ability to spray: high purity materials, with no modification of the oxide content of sprayed metallic powders, on substrates that are very sensitive to oxidation, coatings with properties close to those of wrought materials, localized deposits for repair purposes. However such processes can only spray ductile materials: metals or alloys but also cermets. However since 2006 works are devoted to ceramic coatings cold sprayed, achieved by spraying agglomerated nanometer sized particles, such as those produced by sol gel process. Best results are obtained with helium as spray gas but with gas flow rates as high as a few m^3/min implying a need for reducing costs by spraying in a closed vessel in order to recycle 90–95 % of the gas used. To avoid liquefaction of the spray gas when accelerated in a Laval-type nozzle and improve the ductility of impacting particles it must be heated to temperatures up to 650°C depending on the sprayed material (for example, 120°C for Al and 650°C for MCrAlY). According to the high-gas flow rates, heating power levels can reach 70 kW. To improve the process and coating qualities, it is possible to preheat sprayed powders, and/or heat the substrate or previously deposited layers with a laser just prior to particle deposition. In parallel to the relatively high-pressure (1–4 MPa) cold spray guns, equipment has been developed to spray with air (or nitrogen) as gas, at a working pressure below 1 MPa and rather low air flow rate (<0.4 m^3/min) requiring less heating energy (<10 kW). These low-pressure guns are well suited for short run production. As most particles do not reach the critical velocity, their compaction must be optimized by the selection of powder types and powder particle size distributions, multicomponent mixtures (metal and ceramic) being generally used. Of course powder recuperation is hardly possible with these mixtures. Coating deposition can also be laser assisted in this case.

Nomenclature

Latin Alphabet

A^*	Throat area (m^2)
A_p	Particle cross section (m^2)
C_D	Drag coefficient (−)
c_p	Specific heat (J/K.kg)
d_p	Particle diameter (m)
m°	Gas mass flow rate (kg/s)
m_p	Particle mass (kg)
M	Mach number
Me	Nozzle exit Mach number
M_0	Mass of the consumed powder during cold spray process (kg)
M_g	Molar mass of the gas (kg/mol)
p^*	Pressure at the throat (Pa)
p_{er}	Probability of erosion
p_c	Probability of deposition
r_{part}	Particle radius (m)
R	Universal gas constant (8.32 J/K.mol)
R_u	Universal gas constant, R, divided by the molar mass of the gas, M_g (J/K.kg)
T_i	Impact temperature (K)
T_m	Melting temperature (K)
T_0	Initial gas temperature (K)
T_R	Reference temperature (293 K)
T^*	Temperature at the nozzle throat (K)
u_g	Gas velocity (m/s)
u_p	Particle velocity (m/s)
v^*	Throat velocity (m/s)
v_c	Impacting particle critical velocity (m/s)
$v_{erosion}$	Impacting particle erosion velocity (m/s)
x	Distance traveled by the particle (m)

Greek Alphabet

Δm	Increment of mass amount deposited on the substrate (kg)
γ	Specific heat ratio ($\gamma = c_p/c_V$)
ρ_{part}	Particle-specific mass (kg/m^3)
σ_{TS}	Tensile strength (MPa)

References

1. Irissou E, Legoux J-G, Ryabinin AN, Jodoin B, Moreau C (2008) Review on cold spray process and technology: part I – intellectual property. J Therm Spray Technol 17(4):495–516
2. Davis JR (ed) (2004) Handbook of thermal spray technology. ASM International, Materials Park, OH
3. Dykhuizen RC, Smith MF (1998) Gas dynamic principles of cold spray. J Therm Spray Technol 7(2):205–212
4. Champagne V (ed) (2007) The cold spray materials deposition process: fundamentals and applications. Woodhead Publications, Cambridge
5. Papyrin A (2001) Cold spray technology. Adv Mater Process 159:49–51
6. Champagne VK Jr, Helfritch D, Leyman P, Grendahl S, Klotz B (2005) Interface material mixing formed by the deposition of copper on aluminum by means of the cold spray process. J Therm Spray Technol 14(3):330–335
7. Van Steenkiste TH, Smith JR, Teets RE, Moleski JJ, Gorkiewicz DW 2000 U.S. Patent 6,139,913, Kinetic spray coating method and apparatus
8. Van Steenkiste TH, Smith JR, Teets RE, Moleski JJ, Gorkiewicz DW (2001) U.S. Patent 6,283,386B1, Kinetic spray coating apparatus
9. Van Steenkiste TH, Smith JR, Teets RE (2002) Aluminum coatings via kinetic spray with relatively large powder particles. Surf Coat Technol 54:237–52
10. Van Steenkiste T, Smith JR (2004) Evaluation of coatings produced via kinetic and cold spray processes. J Therm Spray Technol 13(2):274–282
11. Jodoin B, Richer P, Bérubé G, Ajdelsztajn L, Erdi-Betchi A, Yandouzi M (2007) Pulsed-gas dynamic spraying: process analysis, development and selected coating examples. Surf Coat Technol 201:7544–7551
12. Yandouzi M, Sansoucy E, Ajdelsztajn L, Jodoin B (2007) WC-based cermet coatings produced by cold gas dynamic and pulsed gas dynamic spraying processes. Surf Coat Technol 202:382–39
13. Yandouzi M, Ajdelsztajn L, Jodoin B (2008) WC-based composite coatings prepared by the pulsed gas dynamic spraying process: Effect of the feedstock powders. Surf Coat Technol 202:3866–3877
14. Boro Djordjevic B, Maev RG (2006) SIMAT application for aerospace corrosion protection and structural repair. In: Marple B (ed) ITSC 2006. ASM International, Materials Park, OH, e-proceedings
15. Kashirin A, Klynev O, Buzdygar T, Shkodin A (2007) DYMET technology evolution and application. In: Marple BR et al (eds) Thermal spray 2007: global coating solutions. ASM International, Materials Park, OH, e-proceedings
16. Kosarev VF, Alkhimov AP, Klinkov SV, Papyrin AN (2003) On some aspects of gas dynamics of the cold spray process. J Therm Spray Technol 12(2):265–281
17. Alkimov AP, Kosarev VF, Nesterovich NI, Papyrin AN "Method of Applying Coatings," Russian Patent No. 1,618,778, Sept 8, 1990 (Priority of the Invention: Jun 6, 1986)
18. Alkimov AP, Papyrin AN, Kosarev VF, Nesterovich NI, Shushpanov MM Gas dynamic spraying method for applying a coating. US Patent No. 5,302,414, Apr 12, 1994, Re-examination Certificate, Feb 25, 1997
19. Alkimov AP, Papyrin AN, Kosarev VF, Nesterovich NI, Shushpanov MM "Method and Device for Coating," European Patent No. 0484533, Jan 25, 1995
20. Fan S-Q, Yang G-J, Liu G-J, Li C-X, Li C-J, Zhang LZ (2006) Characterization of microstructure of TiO_2 coating deposited by vacuum cold spraying. In: Marple B et al (eds) Proceedings of the 2006 thermal spray conference. ASM International, Materials Park, OH, e-proceedings
21. Sheng-Qiang F, Guan-Jun Y, Guang-Jian L, Cheng-Xin L, Chang-jiu L, Ling-Zi Z (2006) Characterization of microstructure of TiO2 coating deposited by vacuum cold spraying. J Therm Spray Technol 15(4):513–520

22. Guan-Jun Y, Li C-J, Fan S-Q, Wang Y-Y, Li C-X (2007) Influence of annealing on photocatalytic performance and adhesion of vacuum cold-sprayed nanostructured TiO_2 coating. J Therm Spray Technol 16(5–6):873–880
23. Sheng-Qiang F, Li C-J, Yang G-J, Zhang L-Z, Gao J-C, Xi Y-X (2007) Fabrication of nano-TiO_2 coating for dye-sensitized solar cell by vacuum cold spraying at room temperature. J Therm Spray Technol 16(5–6):893–897
24. Stoltenhoff T, Kreye H, Richter HJ (2002) An analysis of the cold spray process and its coatings. J Therm Spray Technol 11(4):542–550
25. Alkhimov AP, Kosarev VF, Klinkov SV (2001) The features of cold spray nozzle design. J Therm Spray Technol 10(2):375–381
26. Sakaki K, Shimizu Y (2001) Effect of the increase in the entrance convergent section length of the gun nozzle on the high-velocity oxygen fuel and cold spray process. J Therm Spray Technol 10(3):487–496
27. Jodoin B (2002) Cold spray nozzle Mach number limitation. J Therm Spray Technol 11(4):496–507
28. Wen-Ya L, Li C-J (2005) Optimal design of a novel cold spray gun nozzle at a limited space. J Therm Spray Technol 14(3):391–396
29. Shapiro AH (1953) The dynamics and thermodynamics of compressible fluid flow. Ronald Press, New York
30. Samareh B, Dolatabadi A (2007) A three-dimensional analysis of the cold spray process: the effects of substrate location and shape. J Therm Spray Technol 16(5–6):634–642
31. Voyer J, Stoltenhoff T, Kreye H (2003) Development of cold gas sprayed coatings. In: Moreau C, Marple B (eds) ITSC 2003. ASM International, Materials Park, OH, pp 71–78
32. Dykhuizen RC, Neiser RA (2003) Optimizing the cold spray process. In: Moreau C, Marple B (eds) ITSC 2003. ASM International, Materials Park, OH, pp 19–26
33. Alkhimov AP, Klinkov SV, Kosarev VF (2000) Study of heat exchange of supersonic plane jet with obstacle at gas-dynamic spraying. Thermophys Aeromechanics 7(3):375–82
34. Chang-Jiu L, Li W-Y, Wang Y-Y, Yang G-J, Fukanuma H (2005) A theoretical model for prediction of deposition efficiency in cold spraying. Thin Solid Films 489:79–85
35. Katanoda H, Fukuhara M, Iino N (2007) Numerical study of combination parameters for particle impact velocity and temperature in cold spray. J Therm Spray Technol 16(5–6):627–633
36. Samareh B, Stier O, Lüthen V, Dolatabadi A (2009) Assessment of CFD modeling via flow visualization in cold spray process. J Therm Spray Technol 18(5–6):934–943
37. Heinrich P, Kreye H, Stoltenhoff T (2005) Laval nozzle for thermal and kinetic spraying, U.S. Patent 2005/0001075 A1, January 6, 2005
38. Gilmore DL, Dykhuizen RC, Neiser RA, Roemer TJ, Smith MF (1999) Particle velocity and deposition efficiency in the cold spray process. J Therm Spray Technol 8(4):576–582
39. Blose RE, Roemer TJ, Mayer AJ, Beatty DE, Papyrin AN (2003) Automated cold spray system: description of equipment and performance data. In: Moreau C, Marple B (eds) Thermal spray 2003: advancing the science & applying the technology. ASM International, Materials Park, OH, pp 103–111
40. Gärtner F, Stoltenhoff T, Schmidt T, Kreye H (2006) The cold spray process and its potential for industrial applications. J Therm Spray Technol 15(2):223–232
41. Klinkov SV, Kosarev VF (2006) Measurements of cold spray deposition efficiency. J Therm Spray Technol 15(3):364–371
42. Grujicic M, Zhao CL, DeRosset WS, Helfritch D (2004) Adiabatic shear instability based mechanism for particles/substrate bonding in the cold-gas dynamic-spray process. Mater Design 25:681–688
43. Schmidt T, Gärtner F, Assadi H, Kreye H (2006) Development of a generalized parameter window for cold spray deposition. Acta Materialia 54:729–742
44. Assadi H, Gartner F, Stoltenhoff T, Kreye H (2003) Bonding mechanism in cold gas spraying. Acta Mater 51:4379–4394

45. Schmidt T, Assadi H, Gärtner F, Richter H, Kreye H, Klassen T (2009) From particle acceleration to impact and bonding in cold spraying. J Therm Spray Technol 18(5–6):794–808
46. Price TS, Shipway PH, McCartney DG, Calla E, Zhang D (2007) A method for characterizing the degree of inter-particle bond formation in cold sprayed coatings. J Therm Spray Technol 16(4):566–570
47. Wank A, Wielage B, Podlesak H, Grund T (2006) High-resolution microstructural investigations of interfaces between light metal alloy substrates and cold gas-sprayed coatings. J Therm Spray Technol 15(2):280–283
48. Li W-Y, Zhang C, Guo XP, Dembinski L, Liao H, Coddet C (2007) Impact fusion of particle interfaces in cold spraying and its effect on coating microstructure. In: Marple BR, Hyland MM, Lau Y-C, Li C-J, Lima RS, Montavon G (eds) Thermal spray 2007: global coating solutions. ASM International, Materials Park, OH
49. Li C-J, Wen-Ya L, Fukanuma H (2004) Impact fusion phenomenon during cold spraying of zinc, in ITSC 2004. DVS, Dusseldorf, Germany, e-proceedings
50. Papyrin AN, Klinkov SV, Kosarev VF (2003) Modeling of particle-substrate adhesive interaction under the cold spray process. In: Moreau C, Marple B (eds) Thermal spray 2003: advancing the science & applying the technology. ASM International, Materials Park, OH, pp 27–35
51. Vlcek J, Gimeno L, Huber H, Lugscheider E (2005) A systematic approach to material eligibility for the cold-spray process. J Therm Spray Technol 14(1):125–133
52. Zhang D, Shipway PH, McCartney DG (2005) Cold gas dynamic spraying of aluminum: the role of substrate characteristics in deposit formation. J Therm Spray Technol 14(1):109–116
53. Zhang D, Shipway PH, McCartney DG (2003) Particle-substrate interactions in cold gas dynamic spraying. In: Moreau C, Marple B (eds) Thermal spray 2003: advancing the science & applying the technology. ASM International, Materials Park, OH, pp 45–52
54. Dykhuizen RC, Smith MF, Gilmore DL, Neiser RA, Jiang X, Sampath S (1999) Impact of high velocity cold spray particles. J Therm Spray Technol 8(4):559–564
55. Raletz F (2005) Contribution to the development of a Cold Gas Dynamic Spray system (C.G. D.S.) for the realization of nickel coatings. Ph. D, University of Limoges, France, in French
56. Alkhimov AP, Klinkov SV, Shin SM, Lee CH, Kim HJ (2006) Effect of particle temperature on the critical velocity for particle deposition by kinetic spraying. In: Marple B (ed) Thermal spray 2006. ASM International, Materials Park, OH, e-proc
57. Gärtner F, Borchers C, Stoltenhoff T, Kreye H (2003) Numerical and microstructural investigations of the bonding mechanisms in cold spraying. In: Moreau C, Marple B (eds) Thermal spray 2003: advancing the science & applying the technology. ASM International, Materials Park, OH, pp 1–8
58. Schmidt T, Gärtner F, Stoltenhoff T, Kreye H, Assadi H (2005) High velocity impact phenomena and coating quality in cold spraying. In: Lugsheider E (ed) ITSC 2005. DVS, Dusseldorf, Germany, e-proc
59. Wu JW, Fang HY, Lee CH, Yoon SH, Kim HJ (2006) Critical and maximum velocities in kinetic spraying. In: Marple BR et al (eds) Thermal spray. ASM International, Materials Park, OH, e-proc
60. Papyrin AN, Konsarev VF, Kinkov SV (2006) Effect of coating erosion on the cold spray process. In: Marple B (ed) Thermal spray 2006. ASM International, Materials Park, OH, e-proc
61. Alkhimov AP, Kosarev VF, Papyrin AN (1998) Gas dynamic spraying. an experimental study of the spraying process. J Appl Mech Tech Phys 39(2):318–323
62. Han T, Zhao Z, Gillispie BA, Smith JR (2004) A fundamental study of the kinetic spray process, ITSC 2004. DVS, Düsseldorf, Germany, e.proceedings
63. Li W-Y, Liao HL, Zang G, Coddet C, Wang H-T, Li C-J (2006) Optimal design of a convergent-barrel cold spray nozzle by numerical method. In: Marple B (ed) Thermal spray 2006. ASM International, Materials Park, OH, e-proc

64. Stoltenhoff T, Voyer J, Kreye H (2002) Cold spraying: state of the art and applicability. In: Lugsheider E (ed) ITSC 2002. DVS, Dusseldorf, Germany, e-proceedings
65. Chang-Jiu L, Li W-Y, Liao H (2006) Examination of the critical velocity for deposition of particles in cold spraying. J Therm Spray Technol 15(2):212–222
66. Lee JH, Kim JS, Shin SM, Lee CH, Kim HJ (2006) Effect of particle temperature on the critical velocity for particle deposition by kinetic spraying. In: Marple B (ed) Thermal spray 2006. ASM International, Materials Park, OH, e-proc
67. Katanoda H, Fukuhara M, Iino N (2007) Numerical study of combination parameters for particle impact velocity and temperature in cold spray. In: Marple BR et al (eds) Thermal spray 2007: global coating solutions. ASM International, Materials Park, OH, e-proceedings
68. Mäkinen H, Lagerbom J, Vuoristo P (2007) Adhesion of cold sprayed coatings: effect of powder, substrate, and heat treatment. In: Marple BR et al (eds) Thermal spray 2007: global coating solutions. ASM International, Materials Park, OH, e-proceedings
69. Helfritch D, Champagne V (2006) Optimal particle size for the cold spray process. In: Marple B (ed) Thermal spray 2006. ASM International, Materials Park, OH, e-proc
70. Papyrin AN, Alkhimov AP, Kosarev VF (1993) Device for applying coatings by deposition, SU1674585, year of priority (issued): 1989
71. Kim H-J, Lee C-H, Hwang S-Y (2005) Superhard nano WC–12%Co coating by cold spray deposition. Mater Sci Eng A 391:243–248
72. Zieris R, Nowotny S, Berger L-M, Haubold L, Beyer E (2003) Characterization of coatings deposited by laser-assisted atmospheric plasma spraying, CD-ROM. In: Proceeding of the international thermal spray conference.ASM International, Materials Park, OH
73. Kulmala M, Vuoristo P (2008) Influence of process conditions in laser-assisted low-pressure cold spraying. Surf Coat Technol 202:4503–4508
74. Bray M, Cockburn A, O'Neill W (2009) The laser-assisted cold spray process and deposit characterisation. Surf Coat Technol 203:2851–2857
75. Kang KC, Yoon SH, Ji YG, Lee C (2007) Oxidation effects on the critical velocity of pure al feedstock deposition in the kinetic spraying process. In: Marple BR et al (eds) Thermal spray 2007: global coating solutions. ASM International, Materials Park, OH, e-proc
76. Balani K, Laha T, Agarwal A, Karthikeyan J, Munroe N (2005) Effect of carrier gases on microstructural and electrochemical behavior of cold-sprayed 1100 aluminum coating. Surf Coat Technol 195:272–279
77. Taylor K, Jodoin B, Karov J (2006) Particle loading effect in cold spray. J Therm Spray Technol 15(2):273–279
78. Fukanama H, Ohno N, Sun B, Huang R (2006) The influence of particle morphology on in-flight particle velocity in cold spray. In: Marple B (ed) Thermal spray 2006. ASM International, Materials Park, OH, e-proc
79. Legoux JG, Irissou E, Moreau M (2007) Effect of substrate temperature on the formation mechanism of cold-sprayed aluminum, zinc and tin coatings. J Therm Spray Technol 16 (5–6):643–650
80. Fukumoto M, Wada H, Tanabe K, Yamada M, Yamaguchi E, Niwa A, Sugimoto M, Izawa M (2007) Effect of substrate temperature on deposition behavior of copper particles on substrate surfaces in the cold spray process. J Therm Spray Technol 16(5–6):643–650
81. Sakaki K, Tajima T, Li H, Shinkai S, Shimizu Y (2004) Influence of substrate conditions and traverse speed on cold sprayed coatings, ITSC 2004. DVS, Düsseldorf, Germany, e. proceedings
82. Siao Ming Ang A, Berndt CC, Cheang P (2011) Deposition effects of WC particle size on cold-sprayed WC–Co coatings. Surf Coat Technol 205:3260–3267
83. Gao P-H, Li C-J, Yang G-J, Li Y-G, Li C-X (2008) Influence of substrate hardness on deposition behavior of single porous WC-12Co particle in cold spraying. Surf Coat Technol 203:384–390

84. Shkodkin A, Kashirin A, Klyuev O, Buzdygar T (2006) Metal particle deposition stimulation by surface abrasive treatment in gas dynamic spraying. J Therm Spray Technol 15(3):382–386
85. Klinkov SV, Kosarev VF, Sova AA, Smurov I (2008) Deposition of multicomponent coatings by cold spray. Surf Coat Technol 202:5858–5862
86. Klinkov SV, Kosarev VF, Sova AA, Smurov I (2009) Calculation of particle parameters spraying of metal-ceramic mixtures. J Therm Spray Technol 18(5–6):944–956
87. Sova A, Papyrin A, Smurov I (2009) Influence of ceramic powder size on process of cermet coating formation by cold spray. J Therm Spray Technol 18(4):633–641
88. Sova A, Pervushin D, Smurov I (2010) Development of multimaterial coatings by cold spray and gas detonation spraying. Surf Coat Technol 205:1108–1114
89. Sova A, Kosarev VF, Papyrin A, Smurov I (2011) Effect of ceramic particle velocity on cold spray deposition of metal-ceramic coatings. J Therm Spray Technol 20(1–2):285–291
90. Spencer K, Fabijanic DM, Zhang M-X (2009) The use of Al-Al_2O_3 cold spray coatings to improve the surface properties of magnesium alloys. Surf Coat Technol 204:336–344
91. King PC, Zahiri SH, Jahedi MZ (2007) Rare earth/metal composite formation by cold spray. J Therm Spray Technol 17(2):221–227
92. Sansoucy E, Marcoux P, Ajdelsztajn L, Jodoin B (2008) Properties of SiC-reinforced aluminum alloy coatings produced by the cold gas dynamic spraying process. Surf Coat Technol 202:3988–3996
93. Li W-Y, Zhang G, Liao HL, Coddet C (2008) Characterizations of cold sprayed TiN particle reinforced Al2319 composite coating. J Mater Proc Technol 202:508–513
94. Tao Y, Xiong T, Sun C, Jin H, Du H, Li T (2009) Effect of α-Al2O3 on the properties of cold sprayed Al/α-Al2O3 composite coatings on AZ91D magnesium alloy. Appl Surf Sci 256:261–266
95. Hu HX, Jiang SL, Tao YS, Xiong TY, Zheng YG (2011) Cavitation erosion and jet impingement erosion mechanism of cold sprayed Ni–Al_2O_3 coating. Nuc Eng Design 241:4929–4937
96. Li W-Y, Zhang C, Liao H, Li J, Coddet C (2008) Characterizations of cold-sprayed nickel–alumina composite coating with relatively large nickel-coated alumina powder. Surf Coat Technol 202:4855–4860
97. Wang H-T, Li C-J, Yang G-J, Li C-X (2009) Effect of heat treatment on the microstructure and property of cold-sprayed nanostructured FeAl/Al_2O_3 intermetallic composite coating. Vacuum 83:146–152
98. Luo X-T, Yang G-J, Li C-J (2011) Multiple strengthening mechanisms of cold-sprayed cBNp/NiCrAl composite coating. Surf Coat Technol 205:4808–4813
99. Lee HY, Hun Jung S, Yong Lee S, Hyun Ko K (2007) Alloying of cold-sprayed Al–Ni composite coatings by post-annealing. Appl Surf Sci 253:3496–3502
100. Lee H, Shin H, Ko K (2010) Effects of gas pressure of cold spray on the formation of Al-based intermetallic compound. J Therm Spray Technol 19(1–2):102–109
101. Novoselova T, Celotto S, Morgan R, Foxa P, O'Neill W (2007) Formation of TiAl intermetallics by heat treatment of cold-sprayed precursor deposits. J Alloys Comp 436:69–77
102. Lugsheider E (2006) High kinetic process developments in thermal spray technology. J Therm Spray Technol 15(2):155–156
103. Marx S, Paul A, Köhler A, Hüttl G (2006) Cold spraying: innovative layers for new applications. J Therm Spray Techno 15(2):177–183
104. Li W-Y, Zhang C, Guo XP, Liao HL, Coddet C (2007) Deposition characteristics of Al-12Si alloy coating fabricated by cold spraying with relatively large powder particles. In: Marple BR et al (eds) Thermal spray 2007: global coating solutions. ASM International, Materials Park, OH, e-proc
105. Hall AC, Cook DJ, Neiser RA, Roemer TJ, Hirschfeld DA (2006) The effect of a simple annealing heat treatment on the mechanical properties of cold-sprayed aluminium. J Therm Spray Technol 15(2):233–238

106. Yoon SH, Lee C, Kim HJ (2007) Process development of brazed aluminium heat exchanger using a kinetic spraying process. In: Marple BR et al (eds) Thermal spray 2007: global coating solutions. ASM International, Materials Park, OH, e-proc
107. Makinen H, Lagerbom J, Vuoristo P (2006) Mechanical properties and corrosion resistance of cold sprayed coatings. In: Marple B et al (eds) Proceedings of the 2006 thermal spray conference. ASM International, Materials Park, OH, e-proceedings
108. Sansoucy E, Kim GE, Moran AL, Jodoin B (2007) Mechanical characteristics of Al-Co-Ce coatings produced by the cold spray process. J Therm Spray Technol 16(5–6):651–660
109. Lee JC, Kang HJ, Chu WS, Ah SH (2007) Repair of damaged mold surface by cold-spray method. Ann CIRP 56(1):577–580
110. Bobzin K, Zhao L, Ernst F, Richardt K (2008) Flux-free brazing of Mg-containing aluminium alloys by means of cold spraying. Front Mech Eng China 3(4):355–359
111. DeForce BS, Eden TJ, Potter JK (2011) Cold spray Al-5% Mg coatings for the corrosion protection of magnesium alloys. J Therm Spray Technol 20(6):1352–1358
112. Richer P, Jodoin B, Ajdelsztajn L, Lavernia EJ (2006) Substrate roughness and thickness effects on cold spray nanocrystalline Al-Mg coatings. J Therm Spray Technol 15(2):246–254
113. Zhang YY, Wu XK, Cui H, Zhang JS (2011) Cold-spray processing of a high density nano crystalline aluminium alloy 2009 coating using a mixture of as-atomized and as-cryomilled powders. J Therm Spray Technol 20(5):1125–1132
114. Ajdelsztajn L, Zúñiga A, Jodoin B, Lavernia EJ (2006) Cold-Spray Processing of a Nanocrystalline Al-Cu-Mg-Fe-Ni Alloy with Sc. J Therm Spray Technol 15(2):184–190
115. Kairet T, Degrez M, Campana F, Janssen J-P (2007) Influence of the powder size distribution on the microstructure of cold sprayed copper coatings studied by X-ray diffraction. In: Marple BR et al (eds) Thermal spray 2007: global coating solutions. ASM International, Materials Park, OH, e-proc
116. Sudharshan PP, Srinivasa Rao D, Joshi SV, Sundararajan G (2007) Effect of process parameters and heat treatments on properties of cold sprayed copper coatings. J Therm Spray Technol 16(3):424–434
117. Sudharshan Phani P, Srinivasa Rao D, Tanabe K, Yamada M, Yamaguchi E, Niwa A, Sugimoto M, Izawa M (2007) Deposition behavior of sprayed metallic particle on substrate surface in cold spray process. In: Marple BR et al (eds) Thermal spray 2007: global coating solutions. ASM International, Materials Park, OH, e-proc
118. Kairet T, Di Stephano G, Degrez M, Campana F, Janssen J-P (2006) Comparison between coatings from two different copper powders: mechanical properties, hardness and bond strength. In: Marple B et al (eds) Proceedings of the 2006 thermal spray conference. ASM International, Materials Park, OH, e-proceedings
119. Calla E, McCartney DG, Shipway PH (2006) Effect of deposition conditions on the properties and annealing behavior of cold-sprayed copper. J Therm Spray Technol 15(2):255–262
120. Zahiri SH, Fraser D, Gulizia S, Jahedi M (2006) Effect of processing conditions on porosity formation in cold gas dynamic spraying of copper. J Therm Spray Technol 15(3):422–430
121. McCune RC, Donlon WT, Popoola OO, Cartwright EL (2000) Characterization of copper layers produced by cold gas-dynamic spraying. J Therm Spray Technol 9(1):73–82
122. Koivuluoto H, Lagerbom J, Vuoristo P (2007) Microstructural studies of cold sprayed copper, nickel, and nickel-30% copper coatings. J Therm Spray Technol 16(4):488–497
123. Fukumoto M, Mashiko M, Yamada M, Yamaguchi E (2010) Deposition behavior of copper fine particles onto flat substrate surface in cold spraying. J Therm Spray Technol 19 (1–2):89–94
124. Eason PD, Fewkes JA, Kennett SC, Eden TJ, Tello K, Kaufman MJ, Tiryakioglu M (2011) On the characterization of bulk copper produced by cold gas dynamic spray processing in as fabricated and annealed conditions. Mater Sci Eng A 528:8174–8178
125. Donner K-R, Gaertner F, Klassen T (2011) Metallization of thin Al_2O_3 layers in power electronics using cold gas spraying. J Therm Spray Technol 20(1–2):299–306

126. Jin Y-M, Cho J-H, Park D-Y, Kim J-H, Lee K-A (2011) Manufacturing and macroscopic properties of cold sprayed cu-in coating material for sputtering target. J Therm Spray Technol 20(3):497–507
127. Koivuluoto H, Vuoristo P (2010) Structural analysis of cold-sprayed nickel-based metallic and metallic-ceramic coatings. J Therm Spray Technol 19(5):975–989
128. Blose RE, Walker BH, Froes SH (2006) Depositing titanium alloy additive features to forgings and extrusions using the cold spray process. In: Marple B et al (eds) Proceedings of the 2006 thermal spray conference. ASM International, Materials Park, OH, e-proceedings
129. Zhang Q, Li C-J, Wang X-R, Ren Z-L, Li C-X, Yang G-J (2008) Formation of NiAl intermetallic compound by cold spraying of ball-milled Ni/Al alloy powder through post-annealing treatment. J Therm Spray Technol 17(5–6):715–720
130. Bala N, Singh H, Prakash S (2010) Accelerated hot corrosion studies of cold spray Ni–50Cr coating on boiler steels. Mater Design 31:244–253
131. Ichikawa Y, Sakaguchi K, Ogawa K, Shoji T, Barradas S, Jeandin M, Boustie M (2006) Deposition mechanisms of cold gas dynamic sprayed MCrAlY coatings. In: Marple B et al (eds) Proceedings of the 2007 thermal spray conference. ASM International, Materials Park, OH, e-proceedings
132. Marrocco T, McCartney DG, Shipway PH, Sturgeon AJ (2006) Comparison of microstructure of cold sprayed and thermally sprayed IN718 coatings. In: Marple B et al (eds) Proceedings of the 2006 thermal spray conference. ASM International, Materials Park, OH
133. Richer P, Zúñiga A, Yandouzi M, Jodoin B (2008) CoNiCrAlY microstructural changes induced during cold gas dynamic spraying. Surf Coat Technol 203:364–371
134. Chen WR, Irissou E, Wu X, Legoux J-G, Marple BR (2011) The oxidation behaviour of TBC with cold spray CoNiCrAlY bond coat. J Therm Spray Technol 20(1–2):132–138
135. Chang-Jiu L, Li W-Y (2003) Deposition characteristics of titanium coating in cold spraying. Surf Coat Technol 167:278–283
136. Novoselova T, Fox P, Morgan R, O'Neill W (2006) Experimental study of titanium/aluminium deposits produced by cold gas dynamic spray. Surf Coat Technol 200:2775–2783
137. Price TS, Shipway PH, McCartney D-G (2006) The effect of cold spray deposition of a titanium coating on the fatigue behaviour of a titanium alloy. In: Marple B et al (eds) Proceedings of the 2006 thermal spray conference. ASM International, Materials Park, OH, e-proceedings
138. Marrocco T, McCartney DG, Shipway PH, Sturgeon AJ (2006) Production of titanium deposits by cold-gas dynamic spray: numerical modeling and experimental characterization. In: Marple B et al (eds) Proceedings of the 2006 thermal spray conference. ASM International, Materials Park, OH, e-proceedings
139. Binder K, Gottschalk J, Kollenda M, Gärtner F, Klassen T (2011) Influence of impact angle and gas temperature on mechanical properties of titanium cold spray deposits. J Therm Spray Technol 20(1–2):234–242
140. Christoulis DK, Guetta S, Guipont V, Jeandin M (2011) The influence of the substrate on the deposition of cold-sprayed titanium: an experimental and numerical Study. J Therm Spray Technol 20(3):523–533
141. Lima RS, Kucuk A, Berndt CC (2002) Deposition efficiency, mechanical properties and coating roughness in cold-sprayed titanium. J Mater Sci Lett 21:1687–1689
142. Zahiri SH, Antonio CI, Jahedi M (2009) Elimination of porosity in directly fabricated titanium via cold gas dynamic spraying. J Mater Proc Technol 209:922–929
143. Li W-Y, Zhang C, Liao H, Coddet C (2009) Effect of heat treatment on microstructure and mechanical properties of cold sprayed Ti coatings with relatively large powder particles. J Coat Technol Res 6(3):401–406
144. Cinca N, Barbosa M, Dosta S, Guilemany JM (2010) Study of Ti deposition onto Al alloy by cold gas spraying. Surf Coat Technol 205:1096–1102
145. Sun B, Huang R-Z, Ohno N, Fukanuma H (2006) Effect of spraying parameters on stainless steel particle velocity and deposition efficiency in cold spraying. In: Marple B et al (eds)

Proceedings of the 2006 thermal spray conference. ASM International, Materials Park, OH, e-proceedings
146. Ajdelsztajn L, Jodoin B, Richer P, Sansoucy E, Lavernia EJ (2006) Cold gas dynamic spraying of iron-based amorphous alloy. J Therm Spray Technol 15(4):495–500
147. Jodoin B, Ajdelsztajn L, Bérubé G (2006) Cold spray deposition of metastable alloys. In: Marple B et al (eds) Proceedings of the 2006 thermal spray conference. ASM International, Materials Park, OH, e-proceedings
148. Wang H-T, Li C-J, Yang G-J, Li C-X, Zhang Q, Li W-Y (2007) Microstructural characterization of cold-sprayed nanostructured FeAl intermetallic compound coating and its ball-milled feedstock powders. J Therm Spray Technol 16(5–6):669–676
149. Alexandre S, Laguionie T, Baccaud B (2007) Realization of an internal cold spray coating of stainless steel in an aluminum cylinder. In: Marple BR et al (eds) Thermal spray 2007: global coating solutions. ASM International, Materials Park, OH, e-proc
150. Spencer K, Zhang M-X (2011) Optimisation of stainless steel cold spray coatings using mixed particle size distributions. Surf Coat Technol 205:5135–5140
151. Van Steenkiste T, Gorkiewicz DW (2004) Analysis of tantalum coatings produced by the kinetic spray process. J Therm Spray Technol 13(2):265–273
152. Koivuluoto H, Nakki J, Vuoristo P (2009) Corrosion properties of cold-sprayed tantalum coatings. J Therm Spray Technol 18(1):75–82
153. Sakaki K, Shinkai S, Shimizu Y (2007) Investigation of spray conditions and performances of cold-sprayed pure silicon anodes for lithium secondary batteries. In: Marple BR et al (eds) Thermal spray 2007: global coating solutions. ASM International, Materials Park, OH, e-proc
154. Manhar CN, Ramakrishna M, Sudharshan Phani P, Srinivasa Rao D, Sundararajan G (2011) The influence of process parameters and heat treatment on the properties of cold sprayed silver coatings. Surf Coat Technol 205:4798–4807
155. Zhou XL, Chen AF, Liu JC, Wu XK, Zhang JS (2011) Preparation of metallic coatings on polymer matrix composites by cold spray. Surf Coat Technol 206:132–136
156. Lupoi R, O'Neil W (2010) Deposition of metallic coatings on polymer surfaces using cold spray. Surf Coat Technol 205:2167–2173
157. Kim HJ, Jung DH, Jang JH, Lee CH (2006) Assessment of metal/diamond composite coatings by cold spray deposition. In: Marple B et al (eds) Proceedings of the 2006 thermal spray conference. ASM International, Materials Park, OH, e-proceedings
158. Haynes J, Pandey A, Karthikeyan J, Kay A (2006) Cold sprayed discontinuously reinforced aluminium. In: Marple B et al (eds) Proceedings of the 2006 thermal spray conference. ASM International, Materials Park, OH, e-proceedings
159. Sansoucy E, Ajdelsztajn L, Jodoin B, Marcoux P (2007) Properties of SiC-reinforced aluminium alloy coatings produced by the cold spray deposition process. In: Marple BR et al (eds) Thermal spray 2007: global coating solutions. ASM International, Materials Park, OH
160. Yong LH, Young Ho Y, Lee YC, Hong YP, Ko KH (2004) Cold spray of SiC and Al2O3 with soft metal incorporation: a technical contribution. J Therm Spray Technol 13(2):184–189
161. Irissou E, Legoux J-G, Arsenault B, Moreau C (2007) Investigation of Al-Al_2O_3 cold spray coating formation and properties. J Therm Spray Technol 16(5–6):661–668
162. Poirier D, Legoux J-G, Drew RAL, Gauvin R (2011) Consolidation of Al_2O_3/Al nanocomposite powder by cold spray. J Therm Spray Technol 20(1–2):275–284
163. Kong LY, Shen L, Lu B, Yang R, Cui XY, Li TF, Xiong TY (2010) Preparation of $TiAl_3$-Al composite coating by cold spray and its high temperature oxidation behavior. J Therm Spray Technol 19(6):1206–1210
164. Van Steenkiste T (2006) Kinetic sprayed rare earth iron alloy composite coatings. J Therm Spray Technol 15(4):501–506
165. Hyung-Jun K, Lee C-H, Hwang S-Y (2005) Fabrication of WC–Co coatings by cold spray deposition. Surf Coat Technol 191:335–340

166. Kim H-J, Leeb C-H, Hwang S-Y (2005) Fabrication of WC–Co coatings by cold spray deposition. Surf Coat Technol 191:335–340
167. Wolfe DE, Eden TJ, Potter JK, Jaroh AP (2006) Investigation and characterization of Cr_3C_2-based wear-resistant coatings applied by the cold spray process. J Therm Spray Technol 15(3):400–412
168. Wang H-T, Li C-J, Yang G-J, Li C-X (2006) Formation of Fe-Al intermetallic compound coating through cold spraying. In: Marple B et al (eds) Proceedings of the 2006 thermal spray conference. ASM International, Materials Park, OH, e-proceedings
169. Yang G-J, Li C-J, Han F, Li W-Y, Ohmori A (2008) Low temperature deposition and characterization of TiO_2 photo catalytic film through cold spray. Appl Surf Sci 254:3979–3982
170. Yamada M, Isago H, Nakano H, Fukumoto M (2010) Cold spraying of TiO_2 photocatalyst coating with nitrogen process gas. J Therm Spray Technol 19(6):1218–1223
171. Tjitra SN, Yamada M, Nakano H, Shima K, Isago H, Fukumoto M (2011) The effect of post-treatments on the powder morphology of titanium dioxide (TiO_2) powders synthesized for cold spray. Surf Coat Technol 206:366–371
172. Maev RGR, Leshchinsky V (2006) Low pressure gas dynamic spray: shear localization during particle shock consolidation. In: Marple B et al (eds) Proceedings of the 2006 thermal spray conference. ASM International, Materials Park, OH, e-proceedings
173. Wright JT (2002) The physics and mathematics of adiabatic shear bands. Cambridge University Press, Cambridge
174. Beneteau M, Birtch W, Villafuerte J, Paille J, Petrocik M, Maev RGR, Strumban E, Leshchinsky V (2006) Gas dynamic spray composite coatings for iron and steel castings. In: Marple B et al (eds) Proceedings of the 2006 thermal spray conference. ASM International, Materials Park, OH, e-proceedings
175. Weinert H, Maeva E, Leshchinsky V (2006) Low pressure GAS dynamic spray forming near-net shape parts. In: Marple B et al (eds) Proceedings of the 2006 thermal spray conference. ASM International, Materials Park, OH, e-proceedings
176. Ogawa K, Ito K, Ichimura K, Ichikawa Y, Ohno S, Onda N (2008) Characterization of low-pressure cold-sprayed aluminum coatings. J Therm Spray Technol 17(5–6):728–735
177. Koivuluoto H, Lagerbom J, Kylmälahti M, Vuoristo P (2008) Microstructure and mechanical properties of low-pressure cold-sprayed (LPCS) coatings. J Therm Spray Technol 17:721–727
178. Koivuluoto H, Vuoristo P (2010) Effect of powder type and composition on structure and mechanical properties of Cu + Al_2O_3 coatings prepared by using low-pressure cold spray process. J Therm Spray Technol 19(5):1081–1092
179. Xian-Jin N, Jang J-H, Kim H-J, Li C-J, Lee C (2008) Cold spraying of Al–Sn binary alloy: coating characteristics and particle bonding features. Surf Coat Technol 202(9):1681–1687
180. Yong LH, Young Ho Y, Lee YC, Hong YP, Ko KH (2005) Thin film coatings of WO_3 by cold gas dynamic spray: a technical note. J Therm Spray Technol 14(2):183–186

Chapter 7
D.C. Plasma Spraying

Abbreviations

APS	Atmospheric Plasma Spraying
CBL	Cold Boundary Layer
CPS	Controlled Atmosphere Plasma Spraying
EB-PVD	Electron Beam Physical Vapor Deposition
i.d.	internal diameter
LPPS	Low Pressure Plasma Spraying
PS-PVD	Plasma Spraying Physical Vapor Deposition
PYSZ	Partially Yttria-Stabilized Zirconia
SHS	Self-propagating High-temperature Synthesis
SOFC	Solid Oxide Fuel Cells
TGO	Thermal Grown Oxide
VPS	Vacuum Plasma Spraying
WPS	Water Plasma Spraying

7.1 Description of Concept

In plasma spraying, an electric arc generates plasma within a plasma torch. The arc is struck between a cathode (usually a rod or button-type design) and a cylindrical anode nozzle, and the plasma gas is injected at the base of the cathode, heated by the arc, and exits the nozzle as a high temperature, high velocity jet (see Fig. 7.1). Figure 2.1 presents the details of coating generation by plasma spraying.

Peak temperatures at the nozzle exit can be 12,000–15,000 K, and peak velocities range from 500 to 2,500 m/s, (subsonic velocities at these temperatures) depending on torch design, plasma gases, and operating parameters. The powders of the coating material are generally injected radially into the plasma jet downstream of the arc root either inside the nozzle, while the jet is still confined, or right outside the nozzle, and the angle of injection can be either perpendicular to the jet

P.L. Fauchais et al., *Thermal Spray Fundamentals: From Powder to Part*,
DOI 10.1007/978-0-387-68991-3_7, © Springer Science+Business Media New York 2014

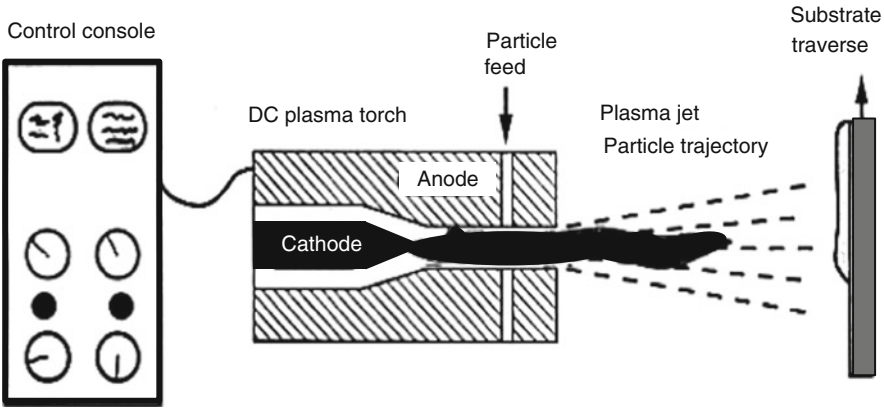


Fig. 7.1 Schematic representation of plasma spray process: the plasma gas entering the torch at the base of the cathode is heated by the arc between the cathode and the cylindrical anode. Spray particles are injected into the plasma jet and transported to the substrate

axis or with a small angle against or in the direction of the plasma flow. However torches exist (for example, the Mettech Axial II torch) where particles are injected axially within three separated plasma jets flowing in a common nozzle and produced by three plasma torches. The spray particles are heated and accelerated by the plasma and transported to the substrate where they form splats and eventually the coating. A movement of the torch relative to the substrate and/or of the substrate relative to the torch permits the deposition of uniform coatings on substrates of different shapes. Usually, as with other thermal spray processes, the coating is built by several passes of the plasma/particle jet over the substrate.

Plasma spraying can be performed as:

1. Atmospheric plasma spraying (APS), where the plasma jet exits the torch into the atmospheric environment.
2. Controlled atmosphere plasma spraying (CPS), where the jet is exiting into a chamber providing the controlled atmosphere (generally argon), e.g., to avoid exposure to oxygen.
3. Low pressure plasma spraying or vacuum plasma spraying (LPPS or VPS) where the jet is exiting the torch into a low pressure chamber at about 10–30 kPa (1.5–4.4 psia).

Recently a hybrid process has been introduced called plasma spraying physical vapor deposition (PS-PVD) with chamber pressure values down to 0.1 kPa. While APS is used in the bulk of the plasma spray applications, CPS or VPS are used for higher value-added applications where the requirement of a higher coating quality justifies the increased expense of using a chamber and pumping systems. PS-PVD has been developed to achieve thermal barrier coatings similar to those obtained by electron beam physical vapor deposition (EB-PVD), which are more expensive than VPS coatings. A further distinction can be made according to the method of

	Torch	Plasma jet	Particles	Substrate
Input parameters	•Current •Plasma gas composition •Flow rate •Nozzle design, erosion •Cooling water flow		•Size distribution •Morphology •Feed rate •Carrier gas flow rate	•Substrate material •Pretreatment •Motion
Operating Characteristics	•Voltage •Voltage fluctuations •Thermal efficiency	•Stability •Geometry •Plasma gas properties •T & V distributions	•Particle trajectory •T_p & V_p distributions •n_p flux distribution	•Coating properties •Porosity •Mechanical properties •Deposition efficiency
	•Torch set up	•Atmosphere •Pressure •Humidity		

Fig. 7.2 Factors influencing the coating properties in plasma spray process

injecting the spray material. In the vast majority of the applications, the spray material is introduced in powder form. However, recent developments have demonstrated the advantages of injecting the material in form of liquid solutions or suspensions. Because of the importance of these new developments, a separate chapter is devoted to them.

The coating properties, as for most thermal spray processes, depend on a large array of process parameters. The primary parameters are the substrate morphology, condition and temperature, the spray particle temperature and velocity, morphology, and size distribution. Spray particle temperature and velocity, in turn, are determined by the plasma jet characteristics, i.e., temperature and velocity distributions and jet stability, thermal conductivity and viscosity of the plasma gas, the powder size distribution and morphology (i.e., shape: spherical or irregular and mass density), and the powder injection dynamics. The plasma jet characteristics are controlled by the torch design, the arc current, the plasma gas, and the plasma jet environment. The influence of the environment in atmospheric plasma spraying includes the atmospheric pressure and the humidity, and changes in these conditions will have to be compensated for by adjusting the operating parameters. Figure 7.2 illustrates how the various parameters influence the plasma spray process.

Plasma spraying is probably the most versatile coating process, and just about any material can be deposited by plasma spraying, even though it may not be the optimal process for some materials. It will be the preferred method for spraying high temperature ceramics, oxides being sprayed by APS and other ones by CPS. The large number of adjustable process parameters allows adaptation of the coating process to a wide range of materials and substrates with different properties. However, the large number of process parameters (up to 60) also poses a disadvantage because the control of all these parameters requires special efforts.

Furthermore, arc instabilities and fluid dynamic jet instabilities exist for the majority of the plasma torches resulting in reduced process reproducibility. Consequently, present research and development efforts are focused on providing torches with more stable operational characteristics and on implementing process control strategies. Control strategies must consider a wide array of time scales associated with the plasma spray process, ranging from splat formation in a few microseconds, plasma and fluid dynamic instabilities on a 100 μs to 1 ms time scale, spray particle heating times of one to a few milliseconds, initial plasma torch "burn-in" time of about 1 h, and changes in torch performance due to erosion in a time frame of several tens of hours. This must be compared to coating process times ranging from less than one minute to many hours, depending on the part to be coated.

In this chapter, the effects of changing operating parameters are described on the plasma characteristics, the particle characteristics in-flight, and the coating characteristics. In addition, a major portion of the chapter is devoted to new developments of equipment and processes, which offer the promise of higher process stability and control. It should be pointed out that several excellent review articles have been published recently providing good overviews of the state of the art and a list of relevant references [1, 2].

7.2 Equipment and Operating Parameters

A typical plasma spray set-up is shown in Fig. 7.3. The central piece of equipment is the plasma torch, and details of torch designs will be discussed in the following section. A process control console allows adjustment of the operating parameters, i.e., the control of arc current, arc initiation, plasma gas flow rates, and powder and carrier gas flow rates. The control console also houses safety interlocks to avoid starting the arc without cooling water flow and without primary plasma gas flow, as well as preventing flow of secondary gas without arc operation. The additional systems necessary for operation are the plasma gas supply system, the power supply system including the high frequency starter unit, the high pressure cooling water system, and the powder feed system.

The plasma gas supply consists of two or more (up to 12–24) high pressure gas cylinders, with the gas flow rates controlled separately in the control console, frequently by means of sonic orifices or, better, by mass flow controllers. The gases are mixed and introduced into the plasma torch. The primary gas should be heavy and must efficiently push the arc root downstream. The most frequently used primary gas is argon because its low energy density results in low torch erosion rates. As secondary gas, to increase the power density, gas velocity, and the heat transfer rates to powders, one uses most frequently hydrogen or helium. However, also nitrogen or carbon dioxide is used as secondary or even primary plasma gases. In particular, for applications requiring high deposition rates and where high power levels are desirable, mixtures of nitrogen and hydrogen are used. It must be emphasized that it is the mass flow rate that is important for controlling the arc

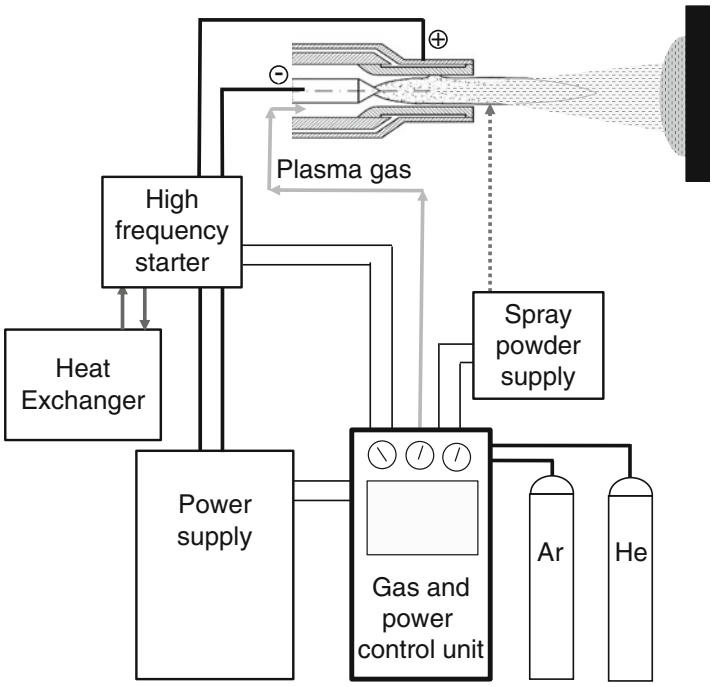


Fig. 7.3 Schematic of a plasma spray system with plasma torch, cooling water supply, gas supply, power supply, high frequency starter, spray powder supply and control unit

inside the torch and not the volumetric flow rate. For example, a flow rate of 30 slm of argon (0.89 g/s) will result in good operating conditions, while a flow rate of 30 slm of hydrogen (0.045 g/s) for the same torch will result in rapid or very rapid erosion of the anode. Increasingly, ternary gas mixtures are being used as plasma gases, such as Ar–H_2–N_2 or Ar–H_2–He, to tailor the plasma properties for optimal heat and momentum transfer to the particles while keeping electrode erosion at acceptable levels [1, 3].

The power supply is usually a current controlled rectifier. While thyristor-controlled rectification is still frequently being found, modern rectifiers use high frequency switching to reduce the size of the inductor necessary for obtaining a smooth d.c. current. The problem with thyristor-controlled rectifiers is that there is an inherent ripple of the d.c. current which is noticeable in the jet as a 300/360 or 600/720 Hz power fluctuation. Inverter-type power supplies rely on high frequency (>15 kHz) switching to deliver smooth current. The open circuit voltages are typically in the 100–200 V range. As a rule of thumb it is necessary to have an open circuit voltage about twice the working voltage, according to the high working voltage at low current used to start the torch with electrode erosion as low as possible. To establish the arc initially, a starting circuit is employed, consisting of a high voltage transformer and capacitor, which allows the breakdown of a spark gap. This breakdown results in a high induced voltage spike in the power supply circuit

leading to a breakdown of the arcing gap and initiation of the current flow. However this type of starter can be very detrimental to electronic devices, which must be disconnected automatically during starting

The cooling water supply consists of a closed loop of deionized or distilled water. The water is pressurized to a pressure in excess of 1 MPa (146 psig), preferably between 1.2 and 1.7 MPa (175–247 psig), and cooled after passage through the torch in a heat exchanger. The high pressure is important because the heat flux to the torch anode is concentrated in a narrow area, and film boiling has to be avoided in the area of maximum heating. The necessary cooling water flow rate can be determined from an estimate of the torch power requirement; typically in the order of 50 % of the power supplied to the torch is carried away by the cooling water. As an example, if the torch is operated at 40 kW, having the cooling water carry 20 kW with a temperature rise of 20 °C requires a flow rate in the order of 14 slm. The cooling water is usually supplied to the torch through the power cables connecting the high frequency starter unit to the torch.

The spray powder supply system consists of a powder hopper, which is heated and vibrating to avoid powder agglomeration and pick-up of moisture. The powder flow can be controlled by various means, e.g., a rotating wheel with a slot, mounted at the bottom of the powder hopper, and the powder transported into the powder supply line is carried to the torch by the carrier gas. It is important to choose a correct combination of mass flow rates of the carrier gas and particle flow because the particle trajectories are determined by the momentum of the individual particles when they are injected into the plasma jet, and the particle velocity is determined by the carrier gas flow rate. Assuring good and steady powder flow by avoiding any accumulation of powder in a section of the supply line where the flow could slow down is of utmost importance because next to the torch operational stability, the powder injection has the strongest influence on coating quality.

Additional ancillary equipment consists of robots moving the torch and the part to be sprayed such that the particle-laden plasma jet impinges as close to perpendicularly to the part surface as possible. A spray booth with ventilation system removes hazardous fumes that are generated when part of the powder evaporates and the nucleation of the vapor generates ultrafine particulates. It also shields the operator from noise and from the ultraviolet radiation from the plasma jet. These ancillary components are described in more detail in Chap. 17.

7.3 Fundamentals of Plasma Torch Design

The electric arc generates the high temperature plasma through resistive energy dissipation by the current flowing through the gas. In order to allow the current to flow through the gas, the gas temperatures must be sufficiently high to have appreciable degrees of ionization resulting in sufficiently high electrical conductivities. For most plasma-forming gases, the required temperatures are 8,000 K and above at atmospheric pressure [4].

The electric arc inside a plasma torch can be divided into the cathode region, the arc column region, and the anode region (see Fig. 7.4a). The schematics of two commercial plasma spray torches are shown in Fig. 7.4b, c. Several different anode nozzle designs exist for both torches, and the anode–cathode combination can be changed to provide optimal particle temperatures and velocities for a specific application.

7.3.1 Torch Cathode

The arc cathode must supply electrons to the arc. In plasma torch designs used for plasma spraying, electrons are supplied through thermionic emission from a hot cathode material. The thermionic emission current can be described by the Richardson–Dushman equation relating the emission to the cathode temperature T_c and work function ϕ_c.

$$j = AT_c^2 \exp(-e\phi_c / kT_c) \tag{7.1}$$

A is an empirical constant, which is about 6×10^5 A/m^2 K^2 for the majority of the cathode materials, e is the electronic charge, and k is the Boltzmann constant. The work function for most materials is around or above 4.0 eV; however, some oxides have work function values of between 2.5 and 3 eV. To obtain a current density of approximately 10^8 A/m^2, as required by the arc, the cathode temperature will have to be about 4,500 K for a cathode material with a work function of 4.5 eV (e.g., for tungsten), but only about 2,700 K for a material with a work function of 2.5 eV. Since tungsten provides a very high melting point and therefore structural stability, but will be molten at 4,500 K, a mixture of tungsten with 1 or 2 % by weight of a material with a low work function value is widely used as torch cathode. The consequence is a significantly reduced cathode operating temperature and longer cathode life. Examples of such materials are ThO_2, La_2O_3, or LaB_6. Cathodes based on tungsten cannot be used with oxidizing gases because the formation of volatile tungsten oxides, at temperatures already below 2,000 K, will result in rapid cathode erosion. For operation with oxidizing gases, button-type electrodes are used where the thermionic emission material is inserted in form of a button into a water-cooled copper holder. The button typically consists of hafnium or zirconium, and the surface of the material is molten. However, the pressure exerted by the arc due to the ion flux to the cathode and due to the magnetic forces resulting from the self magnetic field and the change in current density in front of the cathode will keep the molten material in place [5].

The self magnetic field generates a higher pressure inside the arc than the pressure surrounding the arc, and this pressure differential is proportional to the arc current density. The arc is usually constricted in front of the cathode because of the heat loss from the plasma to the solid material. As a consequence, the pressure close to the cathode is higher than it is farther downstream, resulting in a

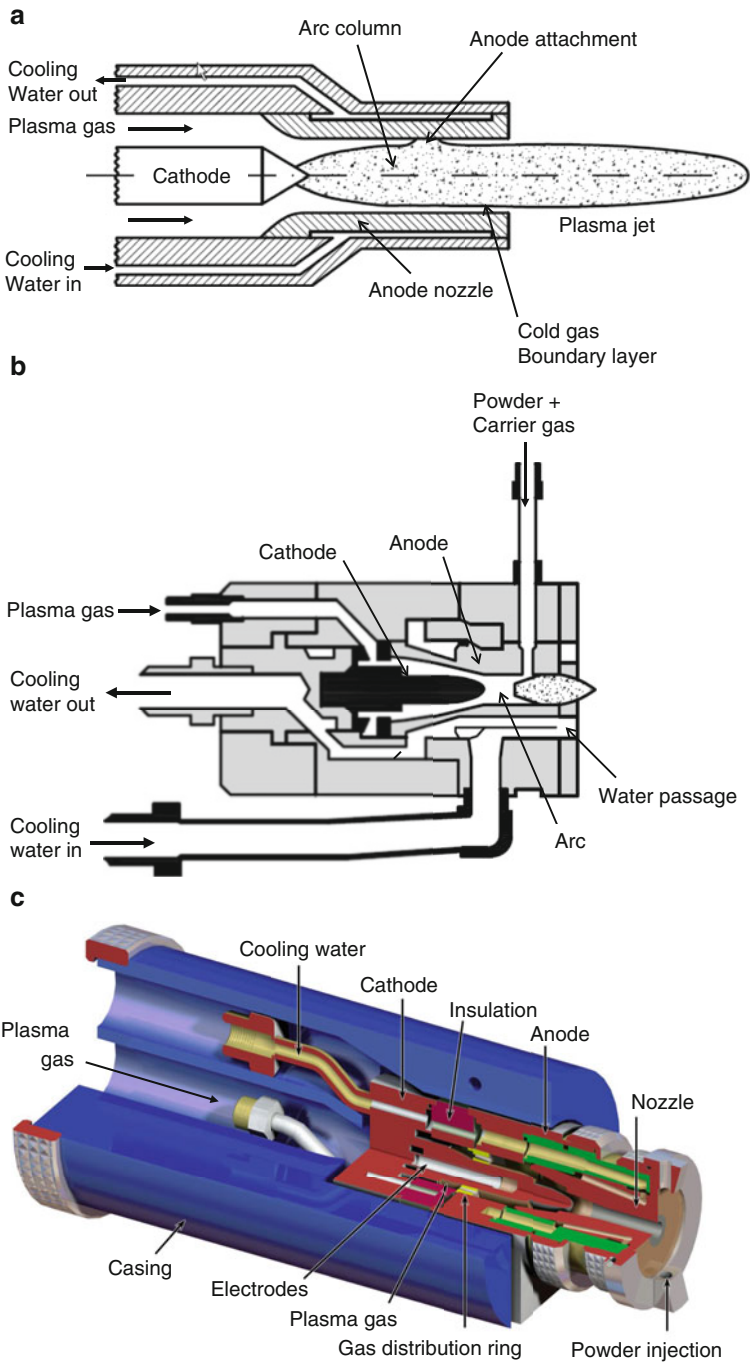


Fig. 7.4 (**a**) Schematic presentation of arc inside a plasma torch. (**b**) Schematic of the commercial plasma torch SG100 from Praxair-TAFA (with kind permission of Praxair-TAFA), and (**c**) of the Sulzer Metco PTF4 torch (with kind permission of Sulzer Metco)

flow away from the cathode, the cathode jet [6]. The flow increases the flow velocity of the superimposed axial gas flow and therefore also the convective cooling of the arc in the vicinity of the cathode, leading to even stronger constriction. The resulting flow velocities can reach several 100 m/s. The highest temperatures in the arc are observed in front of the cathode, reaching values between 20,000 and 30,000 K.

7.3.2 Arc Column

The arc column characteristics are determined by the energy dissipation per unit length, i.e., by the arc current, the plasma gas flow and composition, and the arc channel diameter. The arc column can be described by the conservation equations for mass, momentum, and energy. In principle, Joule heat dissipation, expressed by the product of current density and electrical field strength, is balanced by the heat addition to the plasma gas and the heat losses to the surroundings. If the heat losses to the surroundings increase, the power dissipation has to increase. Since the plasma torches operate with a constant current, higher electric field strengths and arc voltages will compensate for the increased heat loss. Increased heat losses are the result of (a) reduced nozzle diameter, (b) higher total plasma gas flow rates, and (c) increased thermal conductivities and specific heats of the plasma gases. As shown in Chap. 4, the thermal conductivities and specific heats increase from argon to nitrogen and helium (depending on the temperature range) to hydrogen. Accordingly, the column field strengths and arc voltages are increasing from argon arcs to helium and nitrogen arcs to hydrogen arcs, with pure hydrogen arcs typically having four times the arc voltage of an argon arc for similar conditions. However, it must once again be emphasized that to operate the hydrogen arc in a plasma torch, significantly higher volumetric flow rates will be required, with considerably higher voltages as the result. The arc diameter will decrease with increasing energy loss rates.

The species present in the arc column are molecules, atoms, ions, and electrons, and for gas mixtures there will be multiple types of atoms and ions. The strong radial temperature and density gradients result in strong diffusion fluxes, and the diffusion coefficients are quite different for the different species. The consequence is a “demixing” effect where lighter species have higher concentrations in the arc fringes than predicted according to an equilibrium temperature [7, 8]. These effects must be taken into account in particular when heat transfer rates are estimated from plasmas consisting of gas mixtures. The result is that heat transfer rates in the fringes of the arc or arc jet can be higher than expected if diffusion is not taken into account. While electrons would diffuse at very high rates, their diffusion rate is limited by the electric fields generated when electron densities are different from ion densities. Therefore, electrons diffuse only in conjunction with an ion with the ambipolar diffusion rate, which is approximately twice the ion diffusion rate [9]. Furthermore, any mixture containing helium is unlikely to contain any helium

ions because of the high ionization energy of helium compared to all other gases. The consequence is that there is no ambipolar diffusion of He ions, and lower He concentrations are found in the arc fringes [9].

While immense progress has been made with the modeling the arc column in plasma torches [10–14], it still requires significant effort and computational time to use CFD codes as a design tool (see Sect. 7.5). However, an integral energy balance (integrated over the radial coordinate) can provide some information on the arc heating process inside the torch with information, which can be easily obtained:

$$\dot{m}\frac{\Delta\overline{h}}{\Delta z} + Q_{\text{cond}} + Q_{\text{Rad}} = I \times E \tag{7.2}$$

with $\dot{m}$ being the mass flow rate of the plasma gas, $\Delta\overline{h}$ the increase in enthalpy averaged over the cross section per unit length Δz, and Q_{cond} and Q_{rad} the losses to the torch wall by heat conduction and radiation, and $I \times E$ the electric energy dissipated per unit length of the arc. A further integration over the entire arc length will give the energy balance for the torch

$$\dot{m}h_{\text{ave}} = \eta P_{\text{el}} = P_{\text{el}} - Q_{\text{Loss}} \tag{7.3}$$

with h_{ave} the average enthalpy of the gas leaving the torch, η the torch gas heating efficiency, P_{el} the electric power input into the torch (current $\times$ voltage), and Q_{loss} the heat lost to the torch cooling water. The torch average enthalpy is defined as

$$h_{\text{ave}} = 2\pi\frac{\int_0^R \rho v h r \times \mathrm{d}r}{\dot{m}} \tag{7.4}$$

with ρ, v, and h the plasma mass density, velocity, and enthalpy at a given radial location at the torch exit, and R the channel radius. Sometimes the term "average temperature" is used, related to the average enthalpy

$$h_{\text{ave}} = \int_{T_{\text{rel}}}^{T_{\text{ave}}} c_p \times \mathrm{d}T \tag{7.5}$$

with T_{ref} the reference temperature for a zero value of the enthalpy and c_{p} the specific heat at constant pressure of the plasma gas. The average velocity is defined accordingly

$$v_{\text{ave}} = \frac{\dot{m}}{\rho(T_{\text{ave}}) \times A} \tag{7.6}$$

with $\rho(T_{\text{ave}})$ the mass density of the plasma gas at the average temperature, and A the channel cross sectional area. A torch energy balance easily allows determination of the average values of temperature and velocity, but one needs to keep in mind that the peak values for temperature and velocity can easily be twice the average value.

7.3.3 Torch Anode

The torch anode usually consists of a water-cooled copper channel, sometimes lined with a tungsten or tungsten–copper sleeve, and numerous designs exist for tailoring the fluid dynamics within this channel. Nozzle designs can emphasize high gas velocities, high gas temperatures, narrower or wider temperature profiles, and different average arc lengths and consequently arc voltages and torch powers. Typical nozzle diameters are between 6 and 10 mm for arc currents between 300 and 1,000 A. The effect of the diameter on the plasma temperature depends on the operating conditions, but in general a temperature increase is noticed for smaller channel diameters, because the increased electric field strength resulting from the increased heat loss leads to increased local heating of the plasma gas. Because of the nonlinearly varying dependence of the enthalpy on the temperature (e.g., a strong increase with temperature in the ionization region 12,000–15,000 K), a strong increase in power dissipation will increase the enthalpy but only change the temperature by 1,000–2,000 K. The effect of the nozzle diameter on the plasma velocity is stronger, because the flow velocity is inversely proportional to the channel cross-section area, in addition to showing increases due to higher temperatures and lower plasma densities.

What the arc is concerned, the anode is a passive component, just collecting electrons to allow the current to flow from the solid conductors of the electrical circuit to the plasma. The difficulty is that a cold gas boundary layer exists between the plasma and the anode and that nonequilibrium conditions exist in this boundary layer, i.e., higher electron temperatures than heavy particle temperatures, necessary for the current to flow across this boundary layer [15–18]. The current flow is additionally strongly dependent on the electron density gradients and can be expressed by [17]

$$j = \sigma E_x - \frac{\sigma}{e n_\mathrm{e}} \frac{\mathrm{d}p_\mathrm{e}}{\mathrm{d}x} \tag{7.7}$$

where j is the electron current density, σ the electrical conductivity, E_x the electric field normal to the anode surface, e the electronic charge, and n_e and p_e the electron number density and partial pressure, respectively. The strong partial pressure gradient in front of the cooled anode surface results in strong electron diffusion fluxes toward the surface constituting the major component of the current flow.

The heat flux to the anode is strongly tied to the current flow [19, 20]:

$$q = j\phi_w + \left(\frac{5}{2}\frac{k}{e}\right) j T_\mathrm{e} - k_\mathrm{a}\frac{\mathrm{d}T}{\mathrm{d}x} - k_\mathrm{e}\frac{\mathrm{d}T_\mathrm{e}}{\mathrm{d}x} + j_\mathrm{i}(\varepsilon_\mathrm{i} - \phi_w) \tag{7.8}$$

with ϕ_w the work function of the anode material, k the Boltzmann constant, k_a and k_e the heavy particle and electron thermal conductivities, respectively, T_e and T the electron and heavy particle temperatures, respectively, j_i the ion current toward the anode, ε_i the ionization energy of the plasma gas atoms. The first term

on the right-hand side is associated with energy release when the electrons carrying the current to the anode are incorporated into the crystal lattice (condensation energy), the second term is the thermal energy transported by the electrons, the third and fourth terms are the heavy particle and electron conduction terms, respectively, and the fifth term represents the energy released when an ion recombines with an electron at the anode surface. The first three terms are usually the dominant ones [20, 21].

While most commercial plasma torches use anodes with cylindrical nozzle bores, anodes with Laval-type diverging nozzles exits have been used. This type of nozzle provides a somewhat more uniform velocity and temperature distribution at the nozzle exit and somewhat reduced turbulent cold gas entrainment, resulting in a more uniform particle heating and acceleration [22, 23]. More details on the effect of nozzle design are discussed in Sect. 7.6.

7.3.4 Arc Voltage and Power Dissipation

The total power dissipation is determined by the heat loss to the cathode, to the anode, and the enthalpy flow in the plasma jet. Accordingly, the total voltage drop is the sum of the cathode fall voltage, the arc column voltage, and the anode fall voltage. The cathode fall voltage is typically around 10–12 V, which is a significant fraction of the total voltage drop especially for an argon arc. However, the energy loss to the cathode cooling water is only about 5 % of the total energy loss. This apparent discrepancy can be explained by the fact that the thermionic cathode is cooled predominantly by the emission of electrons, i.e., the energy dissipation associated with the cathode fall actually contributes to the gas heating in the column. The magnitude of the anode fall depends strongly on the fluid dynamics in the electrode boundary layer. In general, the direct anode fall is negligible [24], but the voltage drop across the boundary layer between the arc column and the anode surface can amount to several volt. The energy losses from the column have already been discussed. The anode cooling water flow carries the losses from the column as well as the heat transferred to the anode. Typically, the overall losses from the arc to the cooling water amount to 30–60 % of the input power, depending on the operating conditions. The remaining power is carried in the jet and can be used for particle heating.

7.3.5 Arc Stability

Arc stability has to be of central concern in plasma torch design. The arc plasma is easily influenced by asymmetric cooling or by effects of magnetic fields, and these effects can lead to arc extinction. The principal counteracting effect promoting arc stability is an increase in heat loss due to steeper temperature gradients.

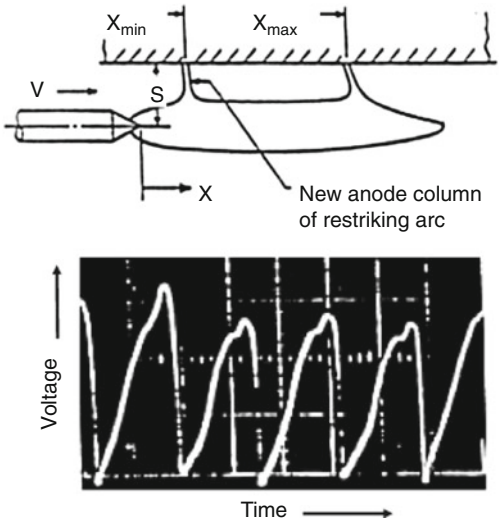


Fig. 7.5 Illustration of the restrike mode of operation of a plasma torch with an upstream connection forming between the arc and the anode nozzle. The oscilloscope image shows the associated voltage trace (Courtesy of Emil Pfender and Steven Wutzke)

However, arc voltage and power dissipation will increase. **Steenbeck's minimum principle** states that the arc will adjust its position such that the overall voltage drop will be a minimum. That means that the preferred arc position is that where the energy loss is minimized [25]. Arcs can be stabilized by a cylindrical wall (e.g., out of water-cooled metal) forcing the arc to remain on the axis of the cylinder (wall stabilization), or it can be stabilized by a superimposed axial cold gas flow, again increasing cooling when the arc moves off the axis (flow stabilization). Flow stabilization is particularly effective when a swirl (or vortex) flow is used because the vortex keeps the light high temperature gases at the flow axis while the heavier cold gases are flowing along the wall. In plasma torches, one usually has a combination of wall and flow stabilization. The preferred position of the arc would be the one where the cathode–anode distance is the smallest. However, at this location the cold gas velocity is usually the highest, resulting in strong cooling of the arc and higher arc voltages. Consequently, the arc attachment is usually found where the fluid dynamic condition brings the plasma close to the anode surface, either through recirculation eddies or through heating of the boundary layer flow [26, 27].

In plasma spraying, the most important instability is the anode attachment instability. The arc root between the column at the axis and the anode surface is exposed to several forces, the dominant one being the drag force exerted by the cold gas in the boundary layer. Because the arc root consists of a very low-density gas, the cold boundary layer flow will go mostly around this bridge between the arc column and the anode, exerting a drag in the downstream direction. This drag is dependent on the momentum of the cold gas flow, i.e., on the boundary layer gas velocity as well as on the mass density of the gas. As a consequence, the arc attachment moves downstream until the voltage between the column and the anode at an upstream location becomes sufficiently high for a breakdown to occur (restrike) [28]. Figure 7.5 shows a schematic of a restriking arc and the associated voltage oscilloscope trace indicating strong

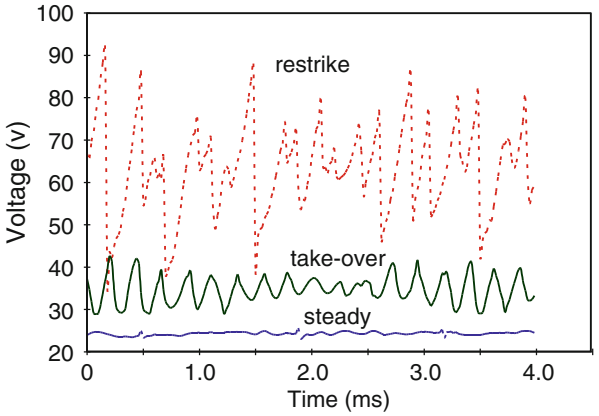


Fig. 7.6 Typical voltage traces for the restrike mode, the take-over mode, and the steady mode of operation of a plasma torch [29]. Reprinted with permission of ASM International. All rights reserved

fluctuations of the arc power. The effect of such fluctuations on particle heating and acceleration will be discussed in Sect. 7.7. Recent flow visualization experiments with a similar set-up of an anode with cold gas flow between the arc and parallel to the anode surface have demonstrated that the location of the restrike is determined by fluid dynamic instabilities like recirculation patterns or Kelvin–Helmholtz instabilities [27].

In general, the arc-anode attachment movement has been divided into three different categories as shown in Fig. 7.6 [29], the *steady mode* of operations with very low fluctuations of the voltage trace, the *take-over mode* of operation with random fluctuations, and the *restrike mode* where the arc attachment moves downstream inside the anode nozzle until an upstream restrike occurs with a new connection between the arc column and the nozzle [30–35].

The total amplitude of fluctuations of the voltage in the restrike mode reaches values of 30–70 % of the average voltage value, having a frequency typically between 2 and 6 kHz. In the take-over mode, the magnitude of the fluctuations is usually in the order of 20–50 % of the mean voltage value, with a much wider Fourier spectrum of the fluctuation frequencies. For the steady mode, only minimal fluctuations are observed at low frequencies, and these fluctuations are not associated with the fluid dynamic behavior of the arc. By assigning a "mode value" of zero to the steady mode, of one to the take-over mode, and of two to the restrike mode, and using an algorithm based on the ratio of the rate of voltage increase vs. the rate of voltage decrease, and of the absolute value of the voltage fluctuation, any arc appearance between the extremes can be quantified by assigning a specific mode value between zero and two to the voltage trace [29]. The mode value for distinguishing the restrike mode from the take-over mode is characterized by the shape factor S, defined as $S =$ (time of voltage increase)/(time of voltage decrease), while the mode value for distinguishing the take-over mode from the steady mode is based on the amplitude factor A of the voltage trace $VA = (\Delta V/V)\ 100\ \%$.

- For $A \geq 10\ \%$ and $S \geq 5$, the arc is in a restrike mode with a mode value of 2
- For $A \geq 10\ \%$ and $S < 1.1$, the arc is in a take-over mode with a mode value of 1

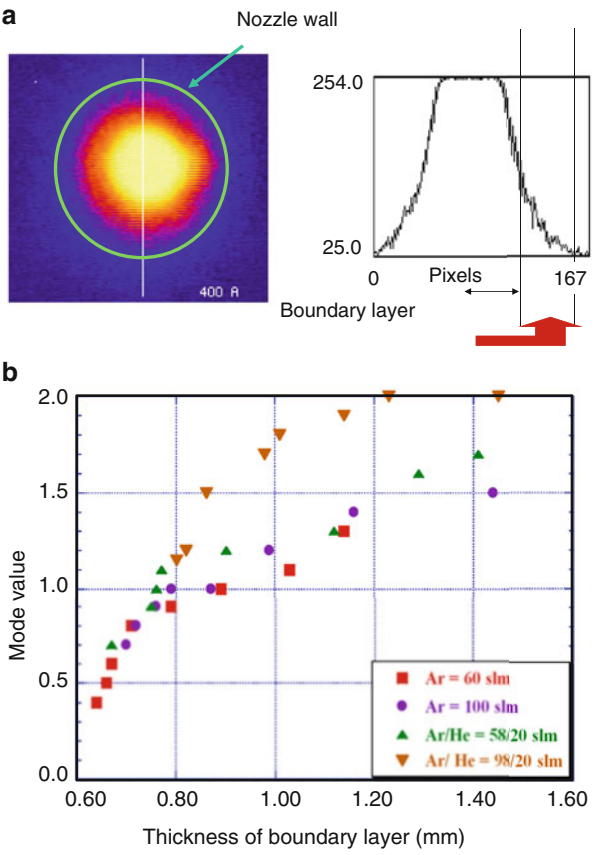


Fig. 7.7 (**a**) End-on image of the arc inside the anode nozzle and the associated intensity scan used for boundary layer thickness measurements. (**b**) The relation between torch operating mode value and boundary layer thickness for a range of operating parameters [32]. Copyright © ASM International. Reprinted with permission

- For $A < 2$ %, the arc is in a steady mode with a mode value of 0
- For $A \geq 10$ % and $S < 5$, the arc is in a restrike–take-over mixed mode, and the mode value is determined as $[1 + (S - 1.1)/3.9]$
- For $2\ \% < A < 10$ %, the arc is in a take-over–steady mixed mode with a mode value of $[(A - 2\ \%)/8\ \%]$

The physical significance of this mode value can be explained on hand of Fig. 7.7 [32], where an end-on picture of the arc inside the nozzle is shown together with an intensity scan giving the arc cross section and the thickness of the boundary layer between the arc and the anode nozzle wall (Fig. 7.7a). It appears that most of the data show a clear correlation between the mode value and the thickness of the boundary layer (Fig. 7.7b). A thicker boundary layer results in a more restrike-like mode, and this thicker boundary layer can be generated by higher gas flow rates, higher hydrogen or helium percentages in the plasma gas, or lower currents. In general, a restrike mode does not occur with a pure argon arc, but addition of hydrogen or nitrogen beyond a certain amount will constrict the arc and increase the boundary layer thickness, favoring a restrike-like behavior. A study of the effect of

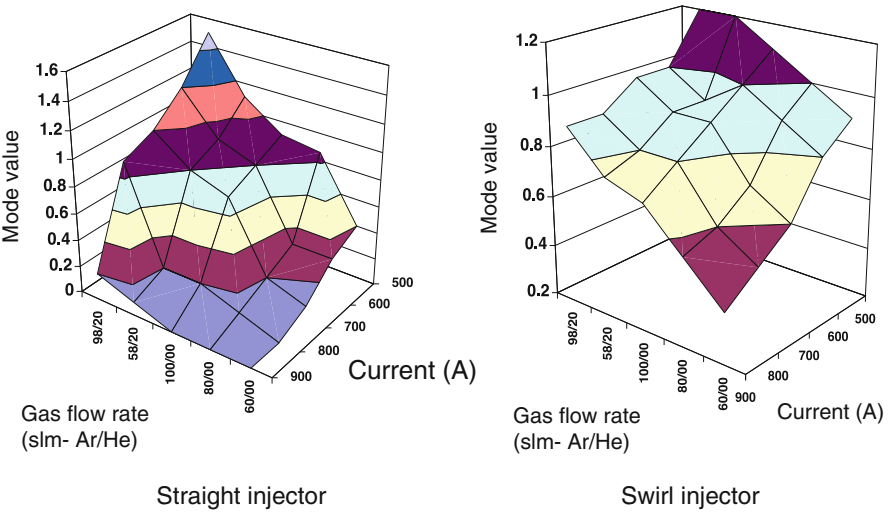


Fig. 7.8 Mode value contours for different arc currents and plasma gas flow rates for a Praxair SG 100 torch with straight injection (*left*) and swirl injection (*right*). The plateau with a mode value between 0.8 and 1 (take-over mode) indicates stable mode of operation [32]. Copyright © ASM International. Reprinted with permission

operating parameters on the boundary layer thickness and the voltage fluctuations for different nozzle designs show that the arc current has the strongest effect on reducing the boundary layer thickness and the arc root fluctuations, but that the effect of increasing the total mass flow rate and the fraction of the secondary gas hydrogen can be different for different nozzle designs, and different if the primary gas is argon or nitrogen [36].

For plasma spraying, usually a mode is preferred where there is some arc motion to distribute the heat input to the anode, but not very strong variations of the voltage and the power as experienced in the restrike mode, i.e., a mode close to the take-over mode value of one. Figure 7.8 [32] shows the mode value distribution for different currents and mass flow rates for a Praxair SG-100 plasma torch for two different plasma gas injection methods, straight injection and swirl injection. It is clear that the distributions for both injection methods have a plateau with a mode value between 0.8 and 1 where small variations of the operating parameters do not change the mode value very much. Lower currents, higher mass flow rates, and higher concentrations of helium in the plasma gas lead to higher mode values, i.e., a more restrike-like behavior.

Coudert and Rat [37–39] have studied the fluctuations of the commercial plasma torch Sulzer Metco F4 working with Ar–H_2 mixtures. For example, with a 6 mm i.d. anode nozzle, an arc current of 600 A and 45 slm Ar, for different H_2 flow rates, the arc voltage power spectra display frequency peaks (a few kHz) with main fluctuation frequencies observed between 4 and 5 kHz, but a secondary peak appears at low hydrogen flow rate at about 7.5 kHz. Attributing the mean arc spot

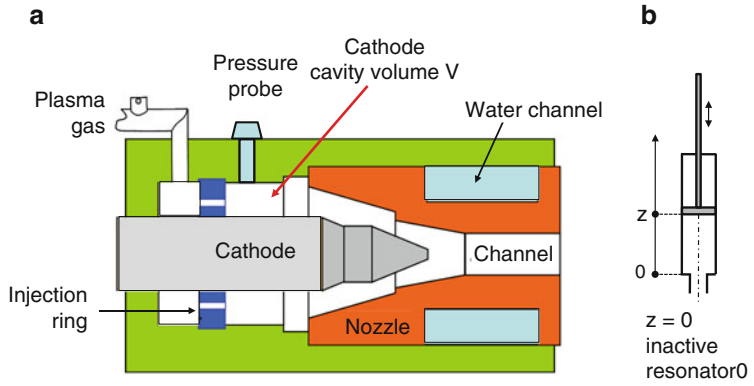


Fig. 7.9 Schematic of (**a**) the PT F4 torch with the cathode cavity volume *V*. (**b**) The acoustic stub fixed on the pressure probe position and acting as resonator on the cathode cavity [39]. Copyright © ASM International. Reprinted with permission

lifetime exclusively to the cold boundary layer (CBL) is not satisfactory because the fluctuation frequency increases as the hydrogen flow rate increases. Moreover, according to the voltage signal, the duration of arc restrikes is about 30–100 µs, that is, frequencies higher than 10 kHz and the evolution of the main fluctuation frequency (4–5 kHz) cannot be described in terms of CBL thickness. Coudert and Rat [39] showed that the restrike mode is superimposed to the main fluctuation of arc voltage, observed around 4–5 kHz. This main oscillation is mainly due to compressibility effects of the plasma-forming gas in the rear part of the plasma torch, that is, in the cathode cavity [37, 38] represented in Fig. 7.9. The plasma torch behaves like a Helmholtz resonator where pressure, inside thecathode cavity, is coupled with the arc voltage. The authors showed that pressure inside this cavity is correlated with the arc voltage. They have correlated the intermittent behavior of the torch and the oscillation modes exchange energy. They also showed that the Helmholtz mode can be damped by the use of an acoustic stub (see Fig. 7.9b) mounted on the plasma torch body at the pressure probe position (see Fig. 7.9a). By adjusting the position, z, of the piston (see Fig. 7.9b) the amplitude of the voltage fluctuations can be reduced. This is illustrated in Fig. 7.10 showing the change of the time dependence of the arc voltage with varying z, generated with an Ar–H_2 (45–10 slm), 500 A arc, and a nozzle with an inner channel diameter of 6 mm. In this figure, arc voltages are raw signals and contain all contributions (modes) described previously. The position $z = 0$ mm corresponds to the situation (Fig. 7.10a), where the acoustic stub is inactive and $z = 1.5 \pm 0.5$ mm to the most effective position to damp the Helmholtz mode. Of course such studies are preliminary ones and additional work is still necessary.

The electrical stability of the arc is determined by its volt–ampere characteristic. The free burning arc has over a range of conditions a falling characteristic, meaning that the voltage decreases with increasing current. Stable operation requires current

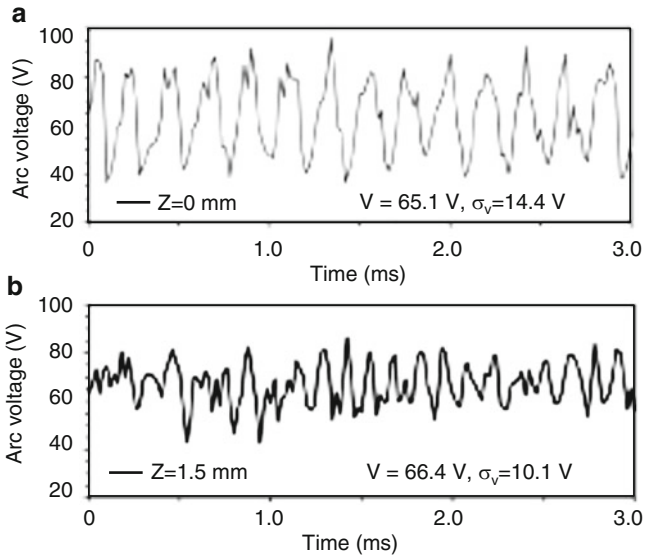


Fig. 7.10 Dependence of arc voltage signal [Ar–H_2 (45–10 slpm), 500 A] on z coordinate giving the piston position of the acoustic stub. (**a**) $z = 0$ mm, (**b**) z = 1.5 mm [39]. Copyright © ASM International. Reprinted with permission

control by the power supply, which is offered by practically all modern dc power supplies. For most plasma torches, the average arc voltage does not change strongly with changing current. However, increasing gas flow rate will increase the arc voltage. The strongest effect has a change in plasma gas composition. A pure argon arc will have the lowest arc voltage, addition of helium or nitrogen will increase the voltage, and hydrogen in the arc will provide the highest voltage, i.e., for a constant current also the highest power dissipation and strongest spray particle heating and acceleration. A variation in pressure will also change the voltage, with lower voltage at lower pressures (reduced heat losses), and higher pressures resulting in increased radiation losses and higher voltages. This holds, of course, only for the same arc current and the same arc length.

7.3.6 Electrode Erosion

Cathode erosion occurs mainly when the current density at the cathode attachment is high enough to result in larger molten volumes. This occurs when (a) the attachment area is constricted, e.g., by having a pointed conical cathode tip, (b) there is a lack of low work function material within the cathode, (c) a strongly constricted arc attachment exists due to the use of a plasma gas like hydrogen resulting in strong arc constriction, and (d) the use of high currents exceeding the cathode design value. The lack of low work function material can occur when

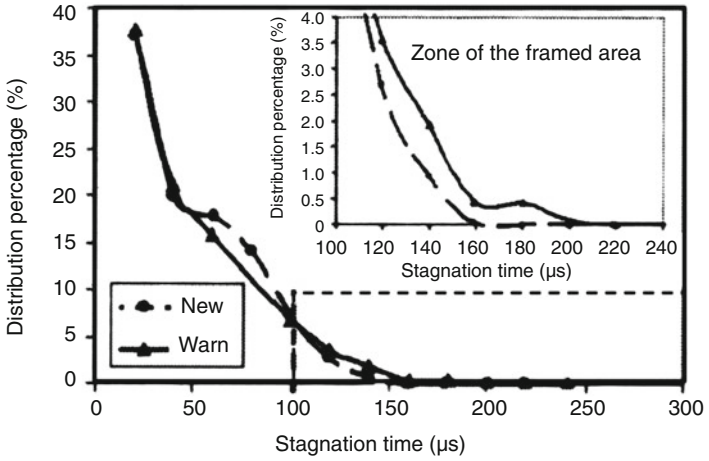


Fig. 7.11 Fraction of occurrences that an arc has a specified residence time at a given location, for a new anode and a used anode. The *inset* shows an increase in residence times above 120 μs for the used anode, indicating accelerating erosion [1] (Copyright IOP Publishing. Reproduced with permission. All rights reserved)

the material addition to the tungsten matrix evaporated faster than it can diffuse to the surface. However, this effect can be mitigated by some redeposition of the material when it is ionized after evaporation and driven back to the cathode surface by the cathode voltage drop [40]. In general, cathode erosion affects torch operation during the first few hours, in particular during the first hour, resulting in a decrease of the arc voltage.

Anode erosion is caused by the strong heat fluxes of the constricted arc attachment between the arc column and the anode surface. For a constricted attachment through a cold gas boundary layer, it has been shown that an instability exists leading to an electron temperature run-away and to localized evaporation of anode material [41]. Slightly used plasma spray torch anodes display this type of erosion. The erosion patterns can result in preferred arc attachment spots leading to increased erosion and establishment of preferred tracks for the arc attachment movements. A study of the erosion patterns and the associated arc voltage traces [42] has shown that the preferred anode attachment slightly moves upstream and becomes slightly more constricted. The amount of erosion has been found to correlate with the residence time of the arc (time of a constant voltage value) at a specific location. Under normal conditions, this residence time varies from 30 to 150 μs, with the lower values occurring much more frequently. The relative distribution of the stationary arc attachment times for a new and worn anode is given in Fig. 7.11 [1]. While for the new anode the attachment times remain smaller than 150 μs, the worn anode shows an increasing fraction of residence times at a specific attachment location exceeding this value. A thermal analysis indicates that with residence times of 150 μs a strong increase in erosion can be expected, i.e., once a slightly eroded spot has formed, the arc prefers to attach at this spot, rapidly increasing the erosion rate [42].

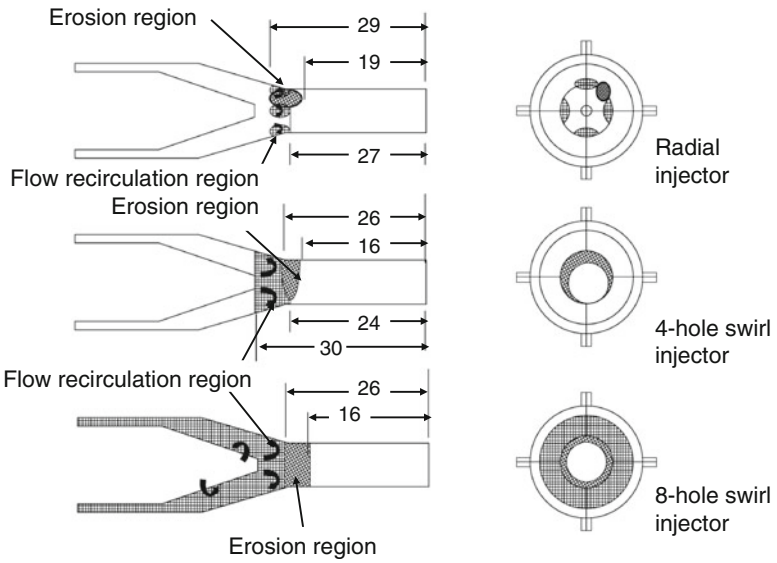


Fig. 7.12 Schematic indication of locations of the flow recirculation region determined by the flow simulation studies (*blue arrows*), the powder deposition as seen in the flow visualization experiments (*light blue areas*), and the erosion pattern observed in the plasma torch (*red area*) for the radial gas injector (*top*), the four-hole swirl gas injector (*center*), and the eight-hole swirl gas injector (*bottom*) [26]. Copyright © ASM International. Reprinted with permission

Clearly, control of the anode heat flux must be achieved to control anode erosion. Increasing the boundary layer thickness, i.e., through increased secondary gas flow, increased total gas flow, increased nozzle diameter or reduced current, will result in reduced conduction heat fluxes but increased current density, and consequently increased heat fluxes associated with electron condensation and electron enthalpy flux. Minimizing anode erosion requires careful optimization of these parameters. For example, increasing the arc current can result in lower anode erosion because the boundary layer thickness is decreased. However, hydrogen in the plasma gas always leads to stronger constriction and increased anode erosion.

Anode erosion can also be strongly influenced by the anode design and the gas injection method. The results of a fluid dynamics study for a commercial plasma torch is given in Fig. 7.12 [26]. To observe the fluid flow in the torch, a glass torch was constructed, the arc heated gases were represented by a flow of heated helium emanating from the cathode tip, and cold argon gas was injected at the base of the cathode as in the regular torch with three different gas injectors, a commercial radial gas injector, a commercial swirl gas injector with four injection holes, and a modified gas injector with eight injection holes. The flow was visualized by introducing fine particles with the gas flow. Flow simulations performed using a commercial CFD code indicated regions of flow recirculation, and the flow visualization experiments indicated powder deposits on the nozzle wall where the recirculation was predicted. Comparison with erosion patterns of an actual plasma

torch with an identical internal geometry indicated that erosion started at the spots where recirculation was predicted and powder deposits were observed. Clearly, radial gas injection results in rapid erosion in a region where recirculation can occur, in a circumferential location between two injection holes. The flow pattern of the four-hole swirl injector indicates that the gas is not swirling uniformly but that stratified flow zones exist with stronger and weaker swirl velocities. Accordingly, there is circumferentially nonuniform erosion of the nozzle wall. The eight-hole swirl gas injector has the least amount of erosion and most uniformly distributed around the circumference, but predominantly in the region of recirculation [26].

Typically, spray torch anodes can be used for 30–60 h before they are eroded to a degree that the coating quality is strongly influenced. However, the number of arc starts has a strong effect on anode erosion because during the initial high frequency breakdown very high currents can flow, resulting in a pitted anode surface. The arc current at the start should be limited to values of 100–150 A and during start usually pure argon flow is used as plasma gas. A study of the long-term stability of the spray torch has shown that over the period between 10 and 40 h of operation the voltage and torch power decrease steadily and the average particle temperatures proportionally [43]. Since coating porosity is a strong function of particle temperature, maintaining a constant coating quality requires adjustment of torch power over this time period.

It is of interest that anode erosion reduces the average value of the arc voltage; however, it leads to increased voltage fluctuations. If the lower voltage effect of erosion is balanced by increasing the fraction of hydrogen in the plasma gas, the average voltage will increase, but so will the fluctuations, resulting in general in poorer coating quality. Both the absolute value of the voltage as well as the amplitude or the frequency of the fluctuations can be used as a measure for erosion and process stability. Additionally, the change in arc fluctuation frequency results in a change of the emitted sound spectrum, and recording this spectrum with a microphone can also be used to detect if erosion has reached unacceptable levels [44].

7.4 Particle Injection

As already mentioned, particle injection affects coating quality immensely. The particle trajectory determines the amount of heating and acceleration a particle experiences, and the time a particle is exposed to the hot plasma is at most a few milliseconds. These residence times, as well as the plasma properties determine the degree of melting of the injected particles. The thermal conductivities of the plasma increase as one proceeds from pure argon to argon–helium mixtures, to argon–hydrogen mixtures and to argon–helium–hydrogen ternary mixtures or N_2–H_2 mixtures, resulting in increased heating rates. However, also the flow velocities increase with the addition of molecular gases, resulting in reduced residence times. Furthermore, too high heating rates will result in evaporation of

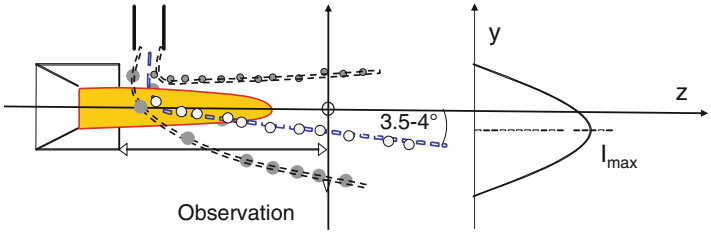


Fig. 7.13 Schematic representation of trajectories of particles with different masses. The heavy particles cross the plasma jet, while the light particles do not penetrate into the plasma. The size distribution of the particles results in a particle flux distribution indicated in the *inset* figure

the particle surface while the particle interior may not be molten yet, in particular with ceramic particles when their thermal conductivity is below 20 W/m K. These issues are discussed in detail in Chap. 4.

The particles are injected into the plasma jet either inside the nozzle or right outside of the nozzle exit, with an injector tube of diameter between 1.2 and 2 mm. The direction of injection can be perpendicular to the jet axis or at a positive or negative angle with respect to the perpendicular direction. Injection with a negative angle with respect to the injector axis (backward injection) can result in higher particle temperatures but somewhat lower particle velocities [45]. Internal injection requires careful adjustment of the carrier gas flow, too high flow rates will result in strong deflection of the plasma jet. As a guideline, carrier gas mass flow rates should be below 10 % of the plasma gas mass flow rates. For external injection, the carrier gas flow rate has less influence [46]. The particles will leave the injector with a relative narrow velocity distribution and with some divergence, and the particle trajectories will be somewhat affected by this fact. However, the strongest effect has the size distribution of the spray powder because the momentum of the particle is proportional to the third power of the particle diameter. For example, if the spray powder has a nominal size distribution of 10–50 μm, the momentum of the particles can vary by a factor of 125 for the same velocity, resulting in vastly different trajectories. In general, small particles remain in the fringes of the jet never reaching the hot core, however, the residence times in the jet are longer in the lower velocity regions and the time needed for melting is shorter for the lower mass particles. The large particles will traverse the jet and remain in the fringes on the opposite side, and it is likely that these particles are not fully molten when they hit the substrate (see Fig. 7.13). The intermediate size particles will have the optimal trajectories for particle heating. However, the particle momentum can be adjusted by the carrier gas flow rate. In general, it is advisable to adjust the flow rate such that the mean particle momentum is equal to the plasma jet momentum flux. But it is possible to reduce the carrier gas flow rate to allow a more favorable trajectory of larger particles [46]. There are several instruments that allow online observation of the particle fluxes/trajectories and that can be used to adjust the carrier gas flow rate to an optimal value for a given particle mass flow rate and torch-operating conditions (see Sect. 16.3.4).

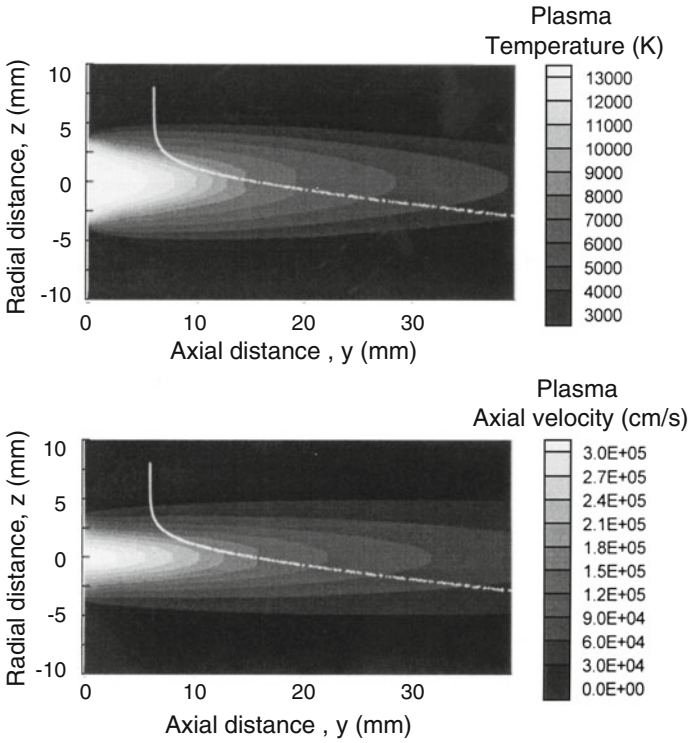


Fig. 7.14 Calculated temperature (*top*) and velocity (*bottom*) profiles assuming cylindrical symmetry and steady state and particle trajectory of YSZ particle with 50 μm diameter, 14.6 m/s injection velocity. The jet was assumed to be generated by a Metco 9MB torch operated at 600 A with a voltage of 70 V, 70 % efficiency, and an argon–hydrogen mixture with flow rates of 40 slm (Ar) + 12 slm (H_2) [47]. Copyright © ASM International. Reprinted with permission

The results of a particle injection model are shown in Fig. 7.14 [47]. A steady-state plasma jet has been simulated with a turbulent two-dimensional CFD code (LAVA), and the particle trajectories have been calculated for specific experimentally determined size distributions, injection velocity distributions, injection velocity direction distributions, and particle density distributions. The particle trajectory shown in Fig. 7.14 is for fixed values of the parameters, namely, 14.6 m/s injection velocity, approximately 50 μm particle diameter, and a mass density of 5,890 kg/m^3 (ZrO_2), and without considering turbulent dispersion. Injection takes place from the positive z-direction outside the torch nozzle. The effect of a measured size distribution is shown in Fig. 7.15 [47], where the spatial distribution of the different sizes at an axial location of 10 cm from the nozzle exit are shown (Fig. 7.15a), as well as the velocity distribution and the temperature distribution for different diameters (Fig. 7.15b, c). The particles with larger diameters are found in the arc fringes with low velocities and low temperatures. Consideration of a

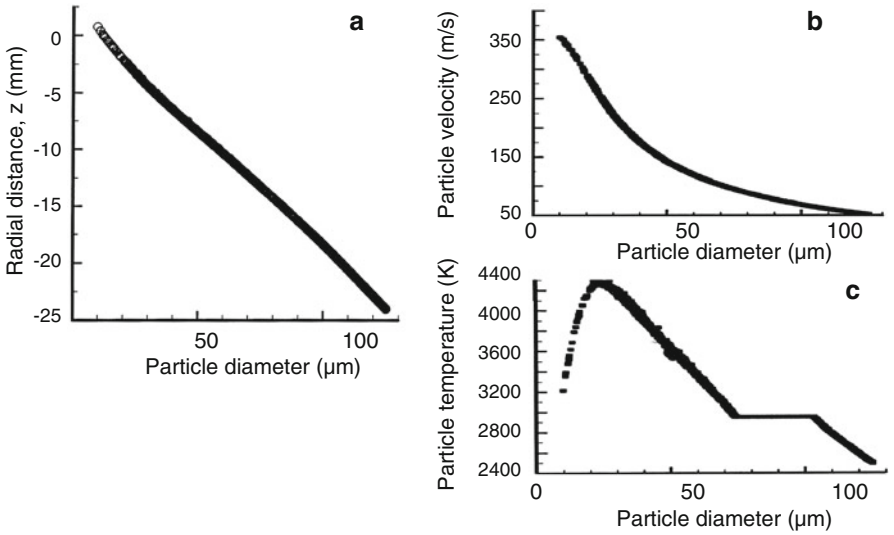


Fig. 7.15 Demonstration of the effect of an experimentally determined particle diameter distributions on (**a**) the simulated distribution of particle location 10 cm from the nozzle exit (injection is from the positive *z*-direction), (**b**) the particle velocity distribution, and (**c**) the particle temperature distribution for YSZ powder; the same operating conditions were assumed as listed in the caption of Fig. 7.14 [47]. Copyright © ASM International. Reprinted with permission

distribution of the magnitude and direction of the injection velocity, the density and including turbulent dispersion essentially results in a broadening of these distributions.

The effect of carrier gas flow rate on the distribution of alumina particles in the plasma jet at an axial distance of 70 mm from the nozzle exit is shown in Fig. 7.16 [46], where the fluxes of the particles have been determined by a spectral intensity measurement integrated over 13 ms. It is clearly seen that for alumina, increasing the carrier gas flow rate to over 5 slm reduces the fluxes of the hot radiating particles, a consequence of fewer particles being in the high temperature region of the jet.

A larger size distribution will result in a larger fraction of particles, which are not fully melted. The unmelted particles may not be incorporated into the coating, or they may be in the coating as unmelted particles rather distinct from the splat structures of the fully molten particles. Unmelted particles in the coating usually increase coating porosity, and if a high coating porosity is desired, a large size distribution will not be of disadvantage. Dense coatings require narrow size distributions and smaller average sizes. The particle morphology also influences the coating microstructure. Irregular-shaped particles such as produced by crushing are more difficult to transport evenly in the powder feed lines, however, the heat and momentum transfer in the plasma is enhanced for such particles, assuring more complete melting of the particles. Particle transport in the supply lines is in general better for spheroidized particles.

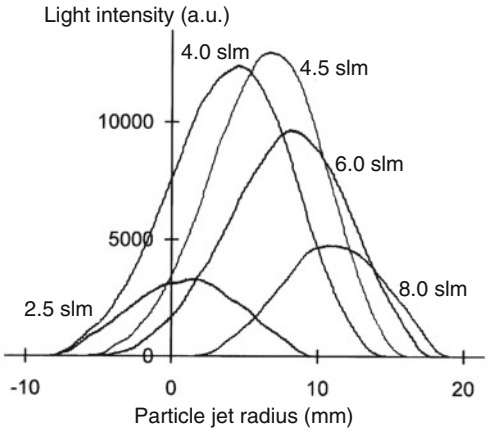


Fig. 7.16 Lateral distribution of light intensity from Al_2O_3 particles with sizes between 22 and 45 μm at a distance 70 mm from the nozzle exit for different carrier gas flow rates. Torch operation at 20 kW, with 45 slm (Ar)+15 slm (H_2); injector diameter 1.75 mm; powder injection *from the left* [46]. Copyright © ASM International. Reprinted with permission

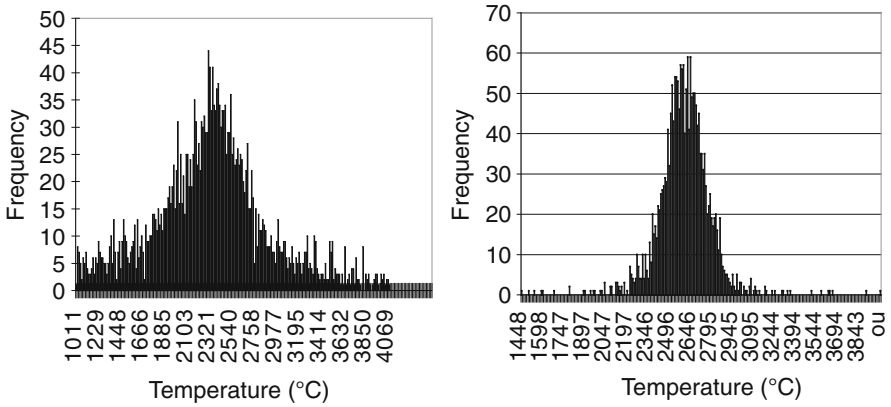


Fig. 7.17 Particle temperature distributions with wind jets (*right*) and without (*left*) showing the removal of slow moving cold particles [49]. Copyright © ASM International. Reprinted with permission

It is of utmost importance that the powder feed lines are kept clean, without strong bends, and without any leaks. Also, any deposit on the particle injection tube will have a disastrous effect.

It is possible to reduce the number of unmelted particles in the coating by utilizing cold gas jets (wind jets) in front of the substrate parallel to the substrate surface. These wind jets influence the trajectories of the slower particles in the fringes (usually including the unmelted particles) such that they will miss the substrate [48]. Figure 7.17 [49] shows the number of particles having a certain

temperature for the cases without wind jets and with wind jets. A narrower size distribution and fewer cold particles are deposited when the wind jets are used.

A special situation arises when graded coatings are desired with a gradual transition from one material to the other, e.g., from a NiCrAlY bond coat to a YSZ thermal barrier coat. In this case, powders of quite different densities and masses have to be injected simultaneously. Investigation of the spray patterns when a mixture of particles is injected has shown that the particle trajectories are not necessarily separating the lighter ceramic from the heavier metallic particles [50]. However, frequently one uses injection of the particles at different axial locations, e.g., the heavier particles internally or closer to the nozzle exit and the ceramic particles slightly farther downstream [51]. Other possibilities for injecting two dissimilar powders is injecting them from opposite directions with different carrier gas flow rates, changing the injection angle such that the heavier particles are injected at an angle against the flow, or using different size distributions [52, 53].

7.5 Plasma Torch and Spray Process Modeling

Numerous models exist for both plasma spray torches and plasma spray processes including the particle trajectories [54–58]. Only a brief overview will be given here, and the reader is encouraged to consult the relevant literature for details. The traditional models assumed axisymmetry and steady state plasmas, allowing a two-dimensional treatment of the torch fluid dynamics. The conservation equations are solved numerically together with the relevant Maxwell equations and thermodynamic equations. Typical boundary conditions are an assumed current density profile at the cathode and an artificially high electrical conductivity in the anode boundary layer to allow current transfer through the low temperature layer while keeping the assumption of LTE. Turbulence is treated using either a K–ε or a Reynolds Stress approach, but usually for low Reynolds numbers. Two-dimensional particle trajectories are calculated in a plane formed by the direction of the particle injection and the torch axis, using the local plasma properties for determining the particle heating and acceleration. Steady state three-dimensional models have demonstrated the effect of the carrier gas on the temperature and velocity distributions of the plasma jet and the particle trajectories [58]. The results show good agreement with time-averaged experimental measurements. However, one has to keep in mind that very strong fluctuations exist of the plasma properties, and averages can reproduce only a part of the process. Nevertheless, such models have been used to evaluate operational characteristics of new torch designs, e.g., for the Sulzer Metco Triplex torch [59, 60], and the potential for expanding their range of operating conditions.

Among the approaches that attempt description of the large-scale turbulence in the jet are the assumption of a time varying radial profile for the plasma temperatures and velocities at the nozzle exit [53, 61, 62], and the use of a two-fluid model [63–65], where one of the fluids is the cold gas moving toward the jet axis while the

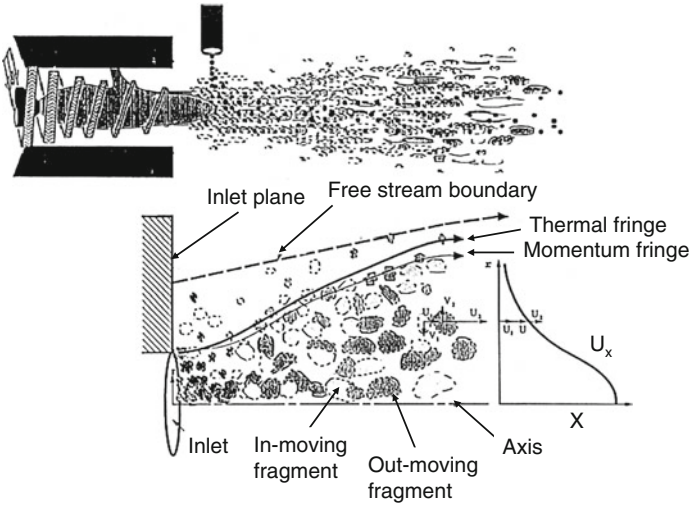


Fig. 7.18 Illustration of two-fluid approach for simulating cold gas entrainment; the plasma jet consists of hot argon plasma with a radial velocity component away from the jet axis, and entrained cold argon gas with a radial velocity component toward the jet axis. Torch operation at 400 A, 23.9 V, with a thermal efficiency of 0.422, and Ar gas flow rate of 35.4 slm, anode nozzle exit 8.5 mm [65] (with kind permission from Springer Science+Business Media B.V.)

other fluid is the hot plasma moving in the outward direction in addition to the movement in the axial direction (see Fig. 7.18) [65]. Calculations have been performed only for argon jets into an argon environment with the assumption of LTE. Both approaches have demonstrated that particles injected with uniform size and velocity experience different heating and acceleration conditions due to the plasma property fluctuations, resulting in different particle trajectories and temperatures at the substrate location. This is shown in Fig. 7.19 [63], in which the results of the two-fluid model show that particles with the same mass and injected with the same velocity can be exposed to plasma temperatures from about 4,000 K to about 11,000 K (Fig. 7.19a) and velocities from 80 to 400 m/s (Fig. 7.19b), depending on if the particle sees the hot plasma or the entrained cold gas bubble. This fact leads to a range of particle temperatures and velocities at the axial position where the substrate would be. Furthermore, because of the different radial velocities in the different gaseous environments, there is a divergence in the particle trajectories (Fig. 7.19c). The two-fluid model has demonstrated further the experimentally confirmed observation that the entrained cold gas bubbles require a significant amount of time to break up and mix with the hot plasma gas, and only at a location typically four to five nozzle diameters from the nozzle exit is the jet composition relatively uniform and less entrainment of larger cold gas bubbles occurs (see Sect. 7.7.1). A simulation of the plasma jet using the LAVA code [66] showed that even with the assumption of a steady arc and turbulence as modeled using a K–ε approach, a significant amount of entrainment can be predicted being responsible for the rapid axial temperature drop

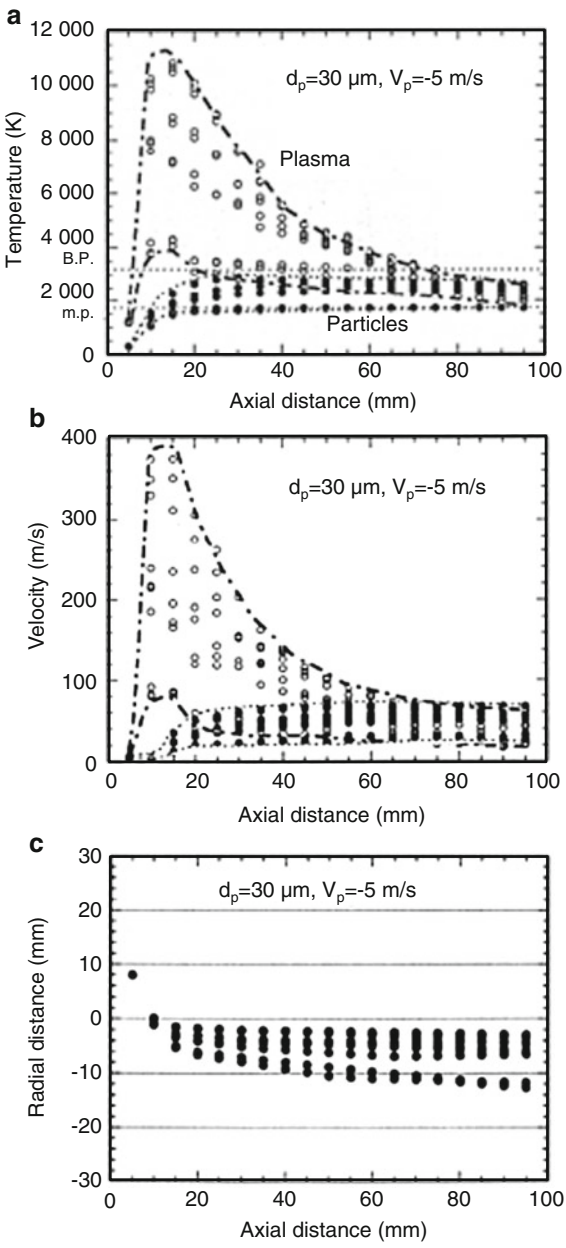


Fig. 7.19 Results of stochastic particle injection model into two-fluid plasma jet; Ni particles are injected 5 mm from the nozzle exit. Particle diameter is 30 μm, particle injection velocity is 5 m/s, torch operation as listed in caption to Fig. 7.18. Ten particles are injected. (**a**) Range of plasma temperatures (*open circles*) resulting in different particle temperatures; (**b**) range of plasma velocities (*open circles*) resulting in different particle velocities; (**c**) dispersion of particle trajectories [63] (reproduced with kind permission of Elsevier)

three to four nozzle diameters downstream of the nozzle exit, results corroborated by experiments (see Sect. 7.7.1) [67].

More recently, fully three-dimensional, time-dependent models have been developed for plasma spray torches [68–70]. Assuming an initial high temperature

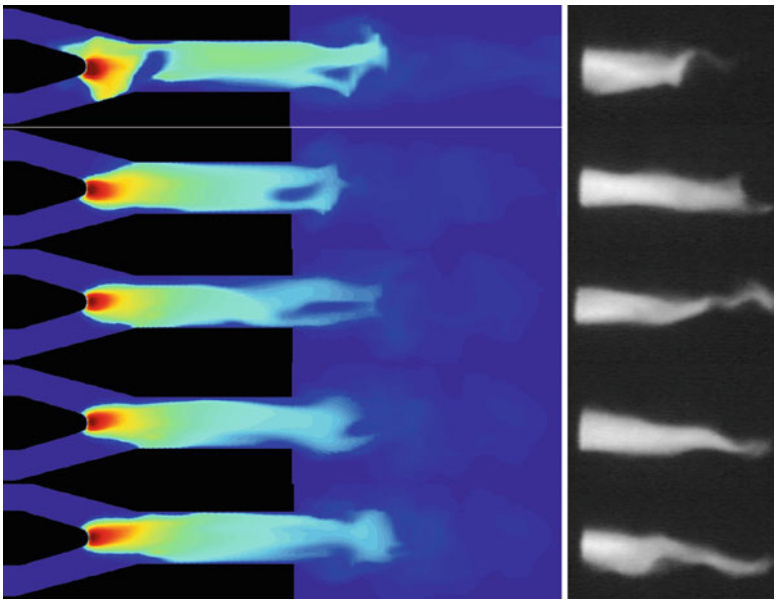


Fig. 7.20 Results of 3D simulation of arc inside plasma torch (J. P. Trelles (2007) personal communication) (reproduced with kind permission of Juan Pablo Trelles)

column between the arc and the anode wall, the arc is established. Upstream restrike is obtained by reestablishing such a column between the main arc and the anode surface at a location where the electric field at the anode surface exceeds a critical value. This way the different voltage fluctuation modes of steady, take-over, and restrike could be reproduced for an argon–hydrogen arc with the assumption of LTE [70]. A similar model has been used to compare the arc movement inside anode nozzles of different designs [13, 14, 71] for torches operating with argon–hydrogen mixtures. This later model has also been used with a modified restrike model for simulating operation of argon–helium-operated torches, simulating the frequencies of the experimental restrike conditions fairly well, however, obtaining too high values for the experimentally observed voltages [72]. Dropping the assumption of LTE and adopting a two-temperature approach for a pure argon arc as well as the assumptions necessary for facilitating the upstream restrike, the experimental values could be simulated well [16]. However, such models are computationally very expensive, and progress in computer and software technology are needed to make such models more widely usable. A review article by Trelles et al. summarizes the different modeling approaches [73].

Figure 7.20 shows the result of a three-dimensional time-dependent simulation of an arc at a specific instant inside a plasma torch, indicating the strong nonuniformity of the arc temperature (J. P. Trelles (2007) personal communication). A comparison of the temperature fields in the plasma jet outside the torch with Schlieren images of the jet shows that the plasma jet fluctuations are quite well represented.

In an effort to provide simplified models for predicting atmospheric pressure plasma spray jet behavior for different nozzle designs and operating parameters, an analytical model has been introduced by Rat et al. [74]. The plasma inside the nozzle is considered as steady and is divided into an arc column and a surrounding cold gas boundary layer, which electrically insulates the arc from the anode nozzle wall. Heat conduction is evaluated by using the Kirchhoff potential as function of the gas-specific enthalpy. The model predicts radial enthalpy and velocity distributions at the nozzle exit, and the predictions agree quite well with experimental data.

7.6 Plasma Torch and Jet Characterization: Time Averaged

Most plasma torches operate in a current control mode, i.e., the current is kept constant through a feedback control loop in the power supply which compensates by changing the voltage in order to maintain the current at the required set value. The current set point, as well as the plasma gas flow rate and composition, are the independent parameters and are chosen by the operator. A specific plasma torch is then characterized by the time-averaged arc voltage, its standard deviation, and the cooling water temperature rise, and these two quantities allow determination of the torch operation, its energy efficiency, and the power carried into the plasma jet, as well as the average specific enthalpy of the plasma gas, its average temperature, and velocity.

The plasma jet can be characterized by several diagnostic methods as described in Chap. 16. Emission spectroscopy, enthalpy probes, and laser scattering can yield the distribution of temperature and electron density in the jet, and laser Doppler anemometry will allow determination of the velocity distributions [75]. Figure 7.21 [76] gives an example of the temperature and velocity distributions in the jet of a plasma spray torch operating with a mixture of nitrogen and hydrogen. A comparison of axial distributions of plasma and particle temperatures and velocities on the jet axis is given in Fig. 7.22 [77] for alumina particles with a Praxair SG 100 torch, operated with 900 A, 47 slm of argon and 22 slm helium. It is clear that particle temperatures and velocities exceed the values of the plasma gas at a typical substrate location (80–100 mm) and that particles cool only slowly after reaching their maximum temperature. Figure 7.23 [77] shows the radial distributions of plasma and particle temperatures and velocities at an axial location 80 mm from the torch. Particles were injected from the negative x-direction. It can be seen that the particle velocities on the side opposite from the injection are higher and exceed the plasma velocities and that the particle temperatures are rather uniform over the cross section and also higher than the plasma temperatures. The authors also observed that the strong deceleration and cooling of the plasma jet is due to cold air entrainment, with the jet at an axial location of 100 mm from the torch consisting to about 80 % of air [77]. The axial decay

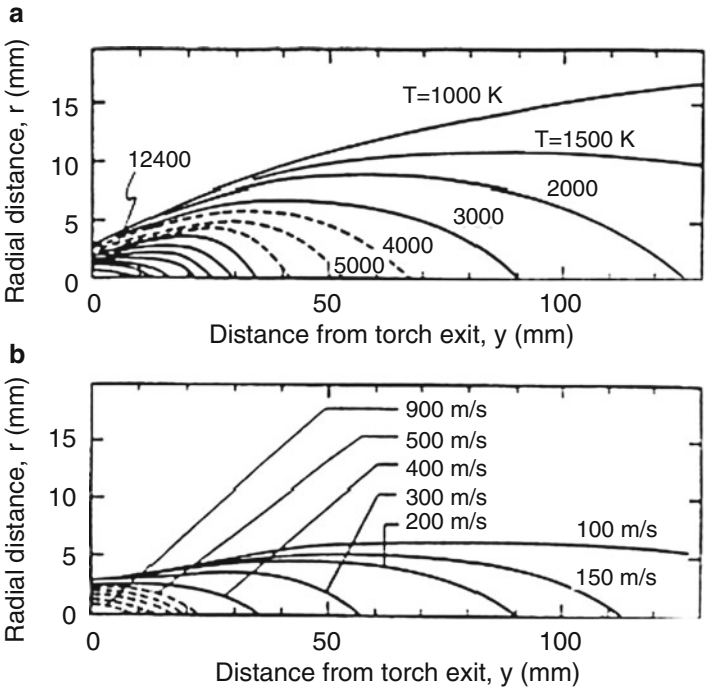


Fig. 7.21 Temperature and velocity contours in d.c. plasma spray jet operated with nitrogen–hydrogen mixture [76] (with kind permission from Springer Science+Business Media B.V.)

of the plasma velocity, as well as the axial velocity distributions of different size particles is shown for an argon–hydrogen plasma jet and compared to theoretical predictions in Fig. 7.24 [76]. The results show that for average quantities the particle velocities reach and surpass the gas velocities at axial distances between 70 and 110 mm from the nozzle exit, depending on their size. In the following, the effect of varying operating conditions on the plasma torch and jet behavior is described as determined by various diagnostics.

7.6.1 Effect of Plasma Gas

As already mentioned, addition of hydrogen or helium to the argon as plasma gas has a strong influence on the arc voltage and torch efficiency (see Fig. 7.25) [78, 79]. As can be seen in this figure, a small addition of hydrogen results in a strong increase in arc voltage and in torch efficiency. This enhanced cooling is due to the fast diffusion of the smaller hydrogen atoms into the arc column fringes, thus increasing drastically the thermal conductivity. It should be mentioned that larger

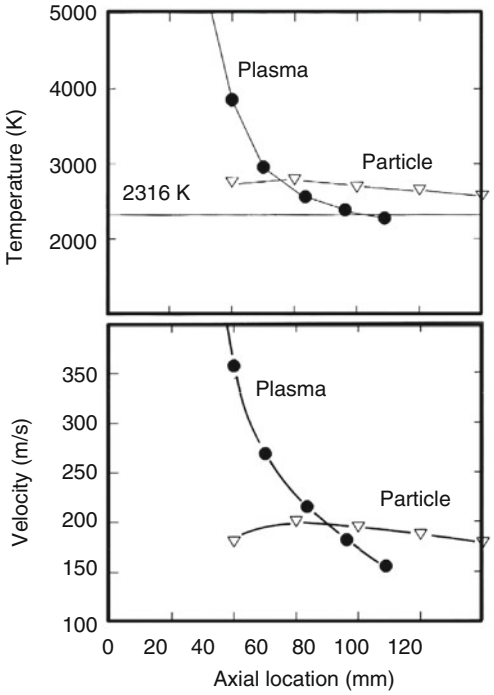


Fig. 7.22 Measured centerline distributions of plasma (*solid symbols*) and particle (*open symbols*) temperatures and velocities, for Al_2O_3 particles sprayed with a Praxair SG 100 torch at 900 A, Ar/He (47/22 slm), 6.1 slm Ar carrier gas, 1.4 kg/h [77] (with kind permission from Springer Science+Business Media B.V.)

amounts of hydrogen will increase electrode erosion significantly and are, therefore, not advisable. The reason for the voltage increase is the much higher specific heat of hydrogen and the higher thermal conductivity, both requiring higher electric fields to sustain an arc in this gas. The higher efficiency can be explained by the fact that the anode heat losses are primarily determined by the current flow, and, for constant current, increased power dissipation due to higher voltages will reduce the fraction of the power transferred to the anode. Also, hydrogen addition will result in smaller arc diameters and less radiation losses.

Figure 7.26 [80] shows the radial velocity distribution of an argon jet 5 mm from the nozzle exit, and that of an argon arc with 20 % hydrogen addition, for approximately the same current. A small addition of hydrogen more than doubles the velocity. It should be noted that the effect on temperature is much less because the high specific heat of hydrogen reduces the temperature.

The effect of hydrogen is less pronounced in nitrogen–hydrogen arcs. However, particle heating will always strongly increase with increasing hydrogen content. Consequently, hydrogen flow rate can be used to adjust particle temperatures for constant power.

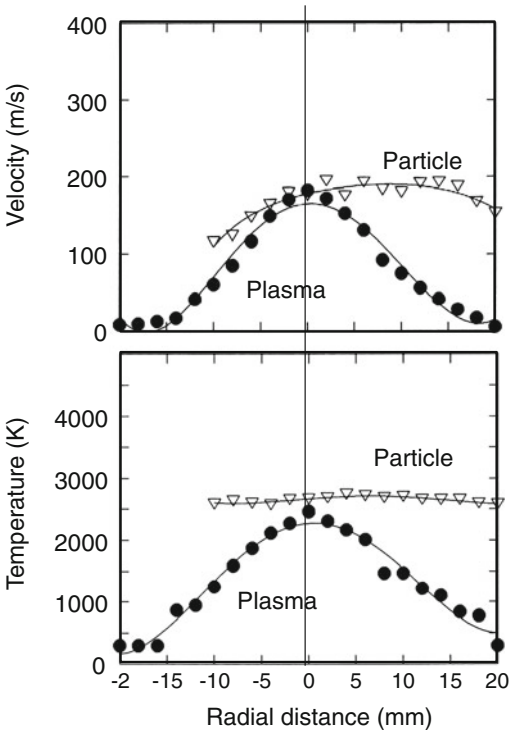


Fig. 7.23 Measured radial distributions of plasma (*solid symbols*) and particle (*open symbols*) temperatures and velocities for Al_2O_3 particles at an axial distance of 80 mm from the torch. Operating conditions as in Fig. 7.22 [77] (with kind permission from Springer Science+ Business Media B.V.)

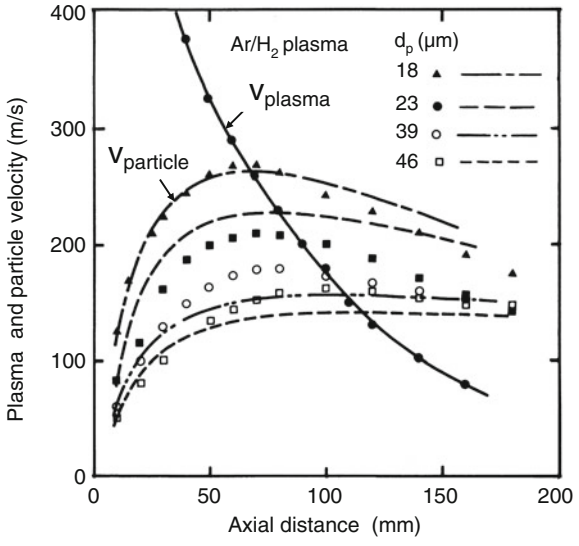


Fig. 7.24 Typical axial plasma and particle velocities for an argon–helium plasma jet [76] (with kind permission from Springer Science+ Business Media B.V.)

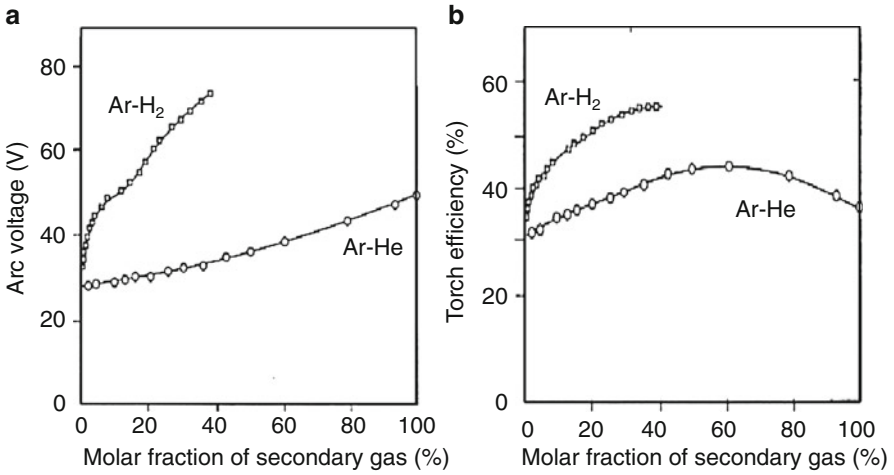


Fig. 7.25 Arc voltage (*left* [78]) and torch efficiency (*right* [79]) as function of the fraction of secondary gas for H_2 and He as secondary gases ([78] *left*). Reprinted with permission of ASM International. All rights reserved. ([79], right), courtesy of P. Roumilhac

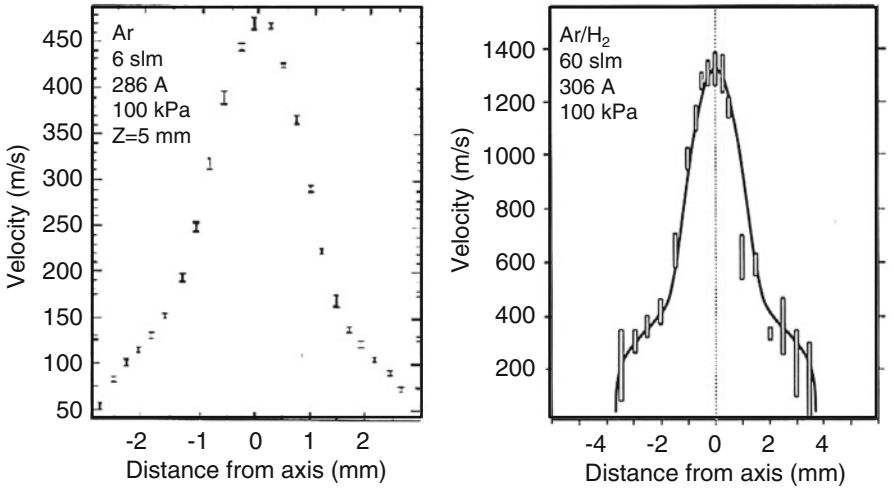


Fig. 7.26 Radial velocity profiles for pure argon jet with 6 slm at 286 A (*left*), and argon–hydrogen jet with 60 slm at 306 A (*right*) [80] (with kind permission from Springer Science+Business Media B.V.)

7.6.2 Effect of Plasma Gas Injector Design

Figure 7.27 [79] shows the arc voltage for different currents and three different plasma gas injector designs, the radial injector, the axial injector, and the vortex or swirl injector. Use of the axial injector results in the highest arc voltages, i.e., the

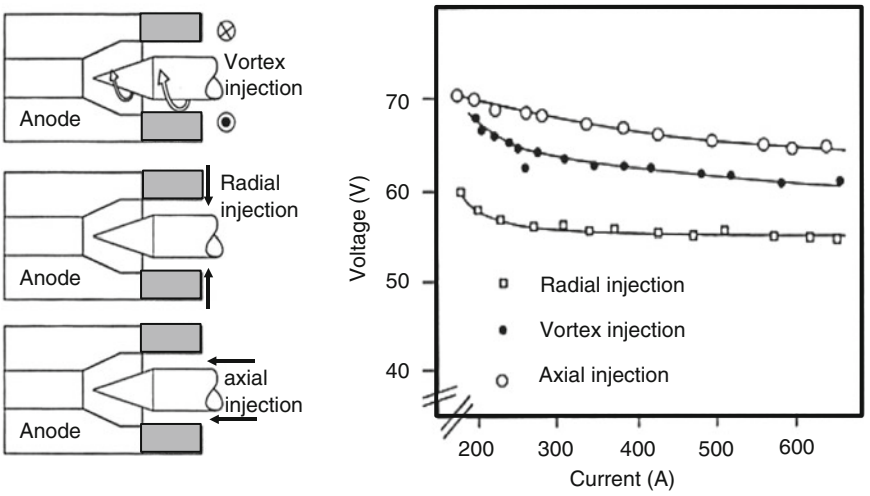


Fig. 7.27 Illustration of different injection modes and arc voltages for the different modes [79] (courtesy of P. Roumilhac)

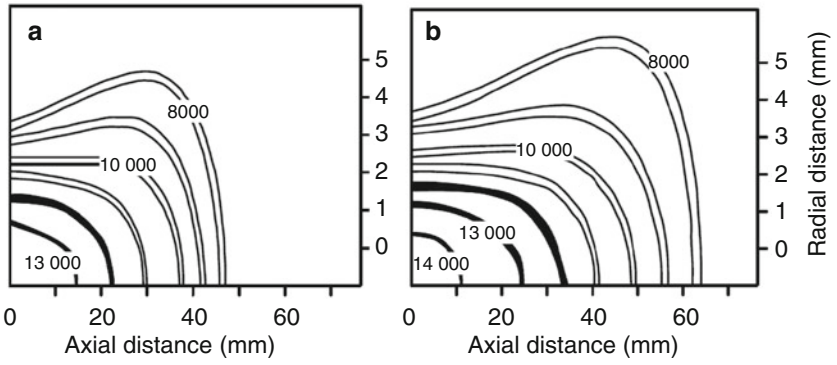


Fig. 7.28 Plasma jet temperature contours for two different injection modes indicating the longer high temperature zone with the axial injection, (**a**) radial injection, (**b**) axial injection (derived from data published in [22])

longest arcs, while radial injection results in the shortest arc. Figure 7.28 [22] illustrates the temperature contours in the plasma jet for the different injector designs, showing significantly lower temperatures for the radial injection, consistent with the observation of higher voltage and power with the axial injection torch. It should be mentioned that the change from swirl injection to radial injection can be gradual by changing the position of the hole through the injection ring from

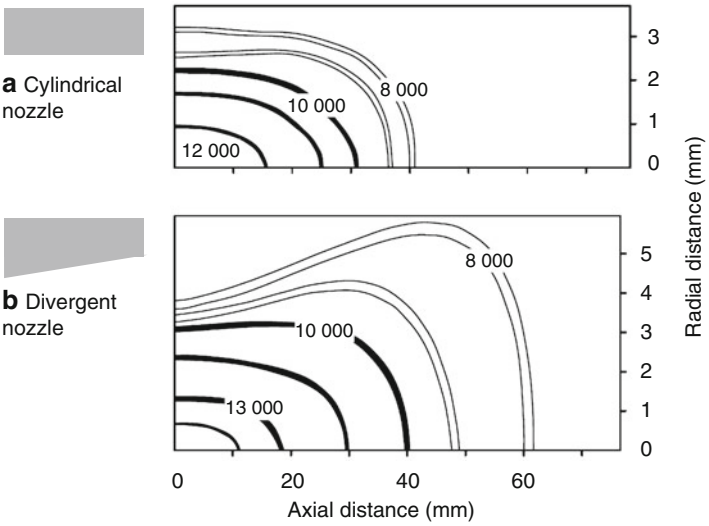


Fig. 7.29 Plasma jet temperature contours for two different nozzle shapes showing the longer and broader jet with a divergent nozzle, (**a**) cylindrical nozzle, (**b**) divergent nozzle [80] (with kind permission from Springer Science+Business Media B.V.)

pointing toward the torch axis (radial injection) to having a purely tangential injection. Intermediate positions have shown to provide more stable plasma jets [81].

7.6.3 Effect of Anode Nozzle Design

The design of the anode nozzle affects the length of the arc, consequently for a given current the power dissipated in the torch, the arc stability, the power loss to the cooling water, and the temperature and velocity distributions in the plasma jet. Numerous nozzle designs exist, giving specific relationships between operating parameters and plasma jet velocity and temperature distributions [23]. Figure 7.29 [80] shows as an example how a small change in the nozzle design by having a slight divergence of the nozzle downstream of the arc attachment changes the jet temperature distributions. There are few general rules on how the nozzle influences the jet because the primary influence is provided by the location of the arc attachment. A smaller nozzle diameter or a constriction of the nozzle downstream of an arcing chamber will result in shorter arcs, lower temperatures at the nozzle exit, but possibly higher velocities for the same current and mass flow rate (see also Sect. 7.3). The effect of a divergent anode nozzle or a Laval-type anode nozzle has been shown to result in less cold gas entrainment [82] and higher deposition efficiencies [83]. Figure 7.30 [84] shows that for Al_2O_3 and YSZ particles the maximum particle velocity (determined from LDA measurements) increases

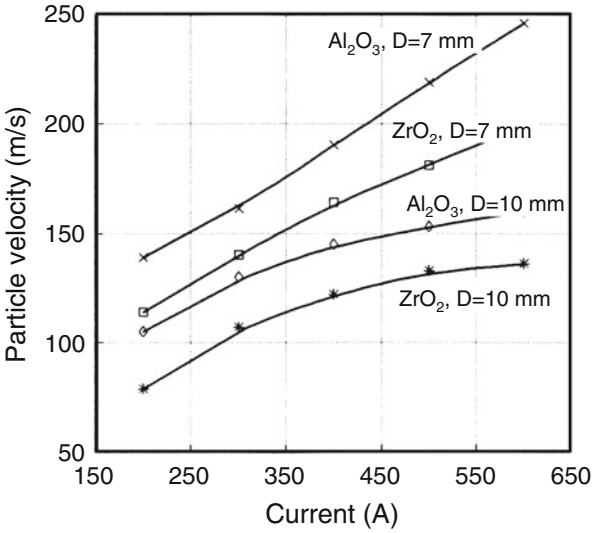


Fig. 7.30 Particle velocity dependencies on arc current for two different nozzle diameters (7 mm and 10 mm) and two different powder materials (Al_2O_3 and YSZ) showing a stronger variation with arc current with the smaller nozzle diameter [84]. Reprinted with permission of ASM International. All rights reserved

linearly with current for a nozzle diameter of 7 mm, while there is a lesser increase with current for a large nozzle diameter of 10 mm, measured at a location 100 mm downstream of the nozzle exit.

A comparison of plasma jet and particle characteristics obtained with a supersonic nozzle (the authors derived from measurements of the pressure drop across the nozzle a Mach number value of $M = 1.6$ at the nozzle exit) and a commercial $M = 1$ nozzle shows that the cold air entrainment is lower by a factor of 2 in the supersonic jet [85]. At a distance of 100 mm from the torch, WC:Co particle velocities at the axis are 380 m/s for the supersonic nozzle vs. 200 m/s for the sonic nozzle. Particle temperatures are given as 3,200 K for the supersonic nozzle vs. 2,300 K for the sonic nozzle. It is interesting to note that the plasma temperatures at the nozzle exit are higher with the sonic nozzle, but the stronger entrainment leads to a faster reduction in temperatures, and at an axial position 100 mm from the nozzle, the gas temperatures are about 1,600 K for the supersonic jet and about 1,100 K for the sonic jet.

In Fig. 7.31 (courtesy of Praxair-TAFA), two different commercial nozzle designs are shown for the SG100 torch (Praxair-TAFA), and the corresponding particle velocity, temperature, size, and flux distributions are shown in Fig. 7.32. The zirconia particles are injected from the positive *y*-direction, and the figure shows the particle characteristics in a plane given by the direction of particle injection (*y*-direction) and perpendicular to the torch axis, as a function of the distance from the torch axis, at an axial location 8 cm from the nozzle exit. Shown are particle velocities, temperatures, diameters, and fluxes, all averaged over 1,000 particles. The normalized flux shown is the ratio of particles detected at a specific *y*-location in particles per second, divided by the particle flux at all y locations. All the data have been obtained with the DPV 2000 instrument (Tecnar Automation, Montreal, Canada), at 800 A arc current, 48 slm Ar and 12 slm He flow, 2.5 slm

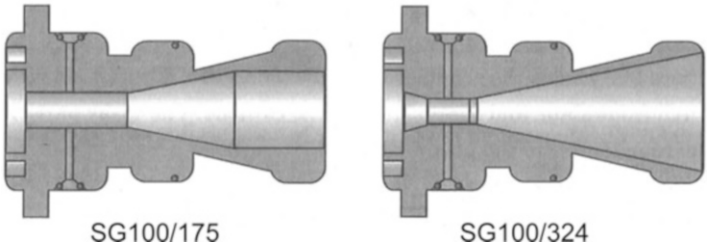


Fig. 7.31 Two different commercial anode nozzles for the Praxair-TAFA SG 100 torch, No. 175 (*left*) and No. 324 (*right*) (reproduced with kind permission of Praxair–TAFA)

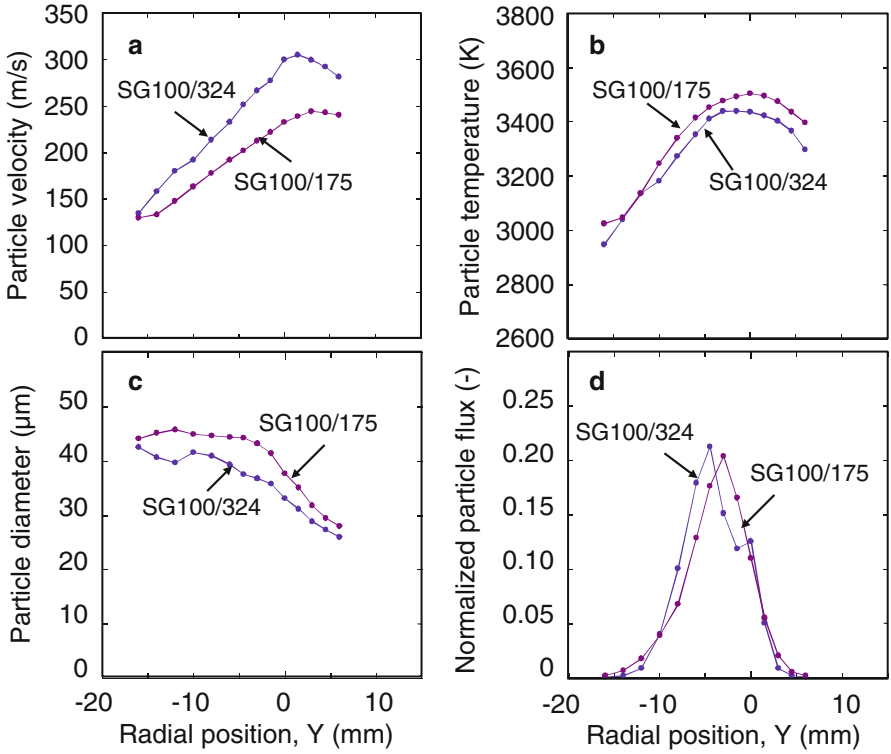


Fig. 7.32 Measurements of the lateral distribution of average values of (**a**) the spray particle velocity, (**b**) the spray particle temperature, (**c**) the spray particle diameter, and (**d**) the relative particle flux for two different anode nozzles shown in Fig. 7.31. Measurements taken with the DPV 2000 at an axial distance of 8 cm from the nozzle. Torch-operating conditions: 800 A, 48 slm Ar + 12 slm He, carrier gas flow 2.5 slm Ar, powder: YSZ (20 %), feed rate 5.8 g/min

argon as carrier gas, and a powder feed rate of 5.8 g/min. The powder has been yttria-stabilized zirconia (YSZ). It is clear that:

1. Highest velocities and temperatures are for the particles on the axis.
2. Highest particle fluxes are below the axis for particle injection above the axis.
3. Largest particles are farthest from the jet axis, have lower temperatures and velocities.
4. Supersonic anode provides higher velocities but lower temperatures.

Comparing these results with those presented by Fincke et al. [86] one must conclude that the specific design of the supersonic nozzle can affect entrainment and the temperature decay and that the observed results may be different for different materials.

7.6.4 Effect of Surrounding Atmosphere

The effect of the surrounding atmosphere is frequently overlooked in plasma spraying. Both the atmospheric pressure and the composition (e.g., humidity) have a strong influence on the jet appearance and the heat and momentum transfer to the spray particles because the surrounding gas is mixed with the plasma gas in the turbulent jet (see Sects. 7.6.3 and 7.7.1). As an example of this influence, Fig. 7.33 [22], shows the lines of constant temperature in an argon–hydrogen plasma jet issuing into an air, nitrogen, or argon atmosphere. It is clear that mixing with air results in the strongest quenching of the jet. The quenching will be even stronger when there is a high humidity in the air. Lower atmospheric pressures not only will result in less quenching and longer jets but will also reduce the heat and momentum transfer to the particles (see Chap. 4).

7.6.5 Effect of Cathode Shape

The tip of the cathode influences the current density in the cathode attachment of the arc, and consequently the acceleration of the plasma gas into the nozzle. Figure 7.34 [87] shows the velocity profiles obtained with a cathode with a sharp conical tip and with one that has a rounded tip. The higher peak velocities and steeper radial profiles with the sharp-tipped cathode are evident. A narrow conical cathode tip will be molten during operation and therefore eroding quickly due to ejection of small molten droplets, resulting in a change of cathode shape within the first hour of operation. This change will be accompanied by a change in the jet characteristics and in the particle heating and acceleration and consequently in the coating characteristics. That means that for a cathode design with a narrow tip, a "burn-in" period will be required before reproducible coatings can be obtained.

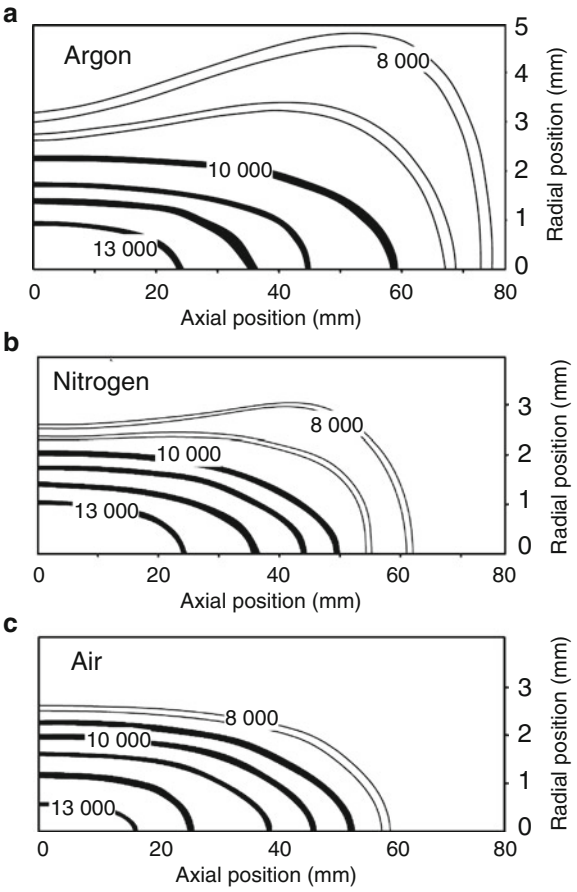


Fig. 7.33 Effect of the environment on plasma jet temperature profiles, with air showing the strongest quench effect. (**a**) Argon ambient gas. (**b**) Nitrogen. (**c**) Air derived from data published in [22]

7.6.6 Effect of Standoff Distance

For every specific plasma spray deposition process there is an optimal standoff distance between the torch and the substrate. This value is typically between 80 and 120 mm, depending on the arc current, plasma gas flow rate, and spray material. At smaller standoff distances, higher particle velocities frequently lead to higher porosities. At larger standoff distances, some re-solidification of only partially molten particles will result in increased porosity and lower deposition efficiency. Fincke et al. [86] find an inverse relationship between the porosity and deposition efficiency, the latter decreasing when the standoff distance is increased. These changes are visualized in Fig. 7.35 [88] which shows the particle temperature and velocity changes with varying current and total plasma gas flow rate for a fixed 33 % of He flow rate as secondary gas. Fincke et al. [89] have shown that by changing the arc current, plasma gas flow rate, and composition, the

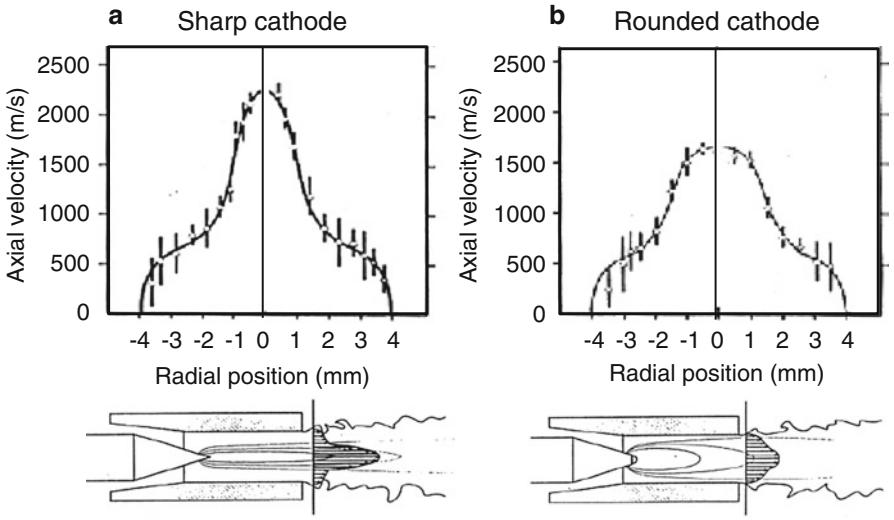


Fig. 7.34 Effect of cathode tip geometry on plasma jet velocity profiles, Ar/Hydrogen plasma (45 slm Ar + 15 slm H_2), 604 A, 7 mm nozzle diameter [87] (reproduced with kind permission of IPCS)

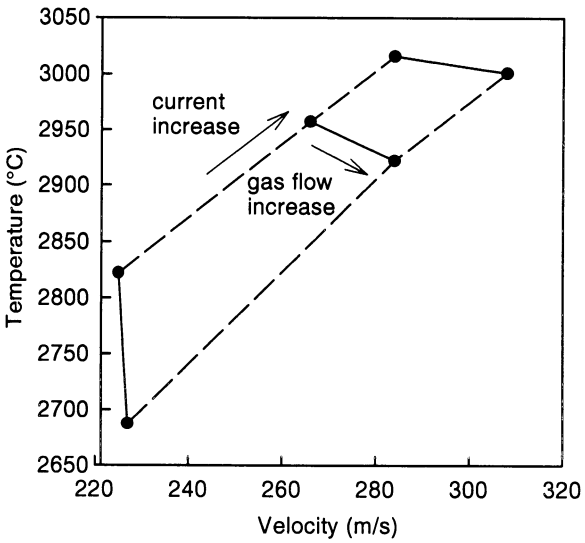


Fig. 7.35 The effect of current and total gas flow rate on average velocity and temperature of YSZ particles (−44 + 11 μm) in an argon–helium (33 vol.%) plasma jet [88]. Reprinted with permission of ASM International. All rights reserved

Table 7.1 Summary of design and operating parameter effects

Increasing ↑	Increases ↑	Decreases ↓
Arc current	T_{gas}, v_{gas}, T_{part}, v_{part}, deposition efficiency	Voltage fluctuations, electrode life
Total gas flow rate	Voltage, v_{gas}, v_{part}, voltage fluctuations	T_{gas}, T_{part}, deposition efficiency
Secondary gas flow	Voltage, voltage-fluctuations, T_{part}, v_{part}	T_{gas} , electrode life
Anode nozzle diameter:	Electrode life, increases voltage fluctuations	Electrode life, T_{gas}, v_{gas}
Anode erosion	Voltage fluctuations	Voltage, T_{part}, v_{part}

average particle temperatures and velocities can be adjusted independently using a feedback control loop with an appropriate diagnostic instrument (see also Chap. 16). Of course, the change in voltage fluctuations needs to be taken into account additionally.

7.6.7 Summary of Design and Operating Parameters

A summary of the effect of the principal design operating parameters for d.c. plasma torches is given in Table 7.1.

7.7 Plasma Jet Characterization: Transient Behavior

7.7.1 Plasma Jet Instability

The unsteady nature of the plasma jet has been the subject of numerous studies [30–39, 90–101]. There are two primary causes for this unsteady behavior (1) the constant movement of the arc root, resulting in voltage and power fluctuations and strong temporal variations of the jet temperature and velocity distributions and (2) the extreme density and viscosity gradients between the low density, high viscosity plasma jet, and the cold gas surroundings [92]. The results are fluctuations as they are shown in a series of high speed images in Fig. 7.36 [1]. In this figure, the spray particles are injected from the top, and the plasma jet exits the nozzle at the right-hand side of the picture. It can be seen that the fluctuations lead to uneven particle heating. Furthermore, the fluctuations lead to the entrainment of cold surrounding gas in the jet, rapidly reducing its average temperature and velocity. Particle velocimetry measurements show that particles injected inside the nozzle have consistently much higher velocities than particles injected outside the nozzle when both types of particles are on the jet axis. The explanation is that the particles

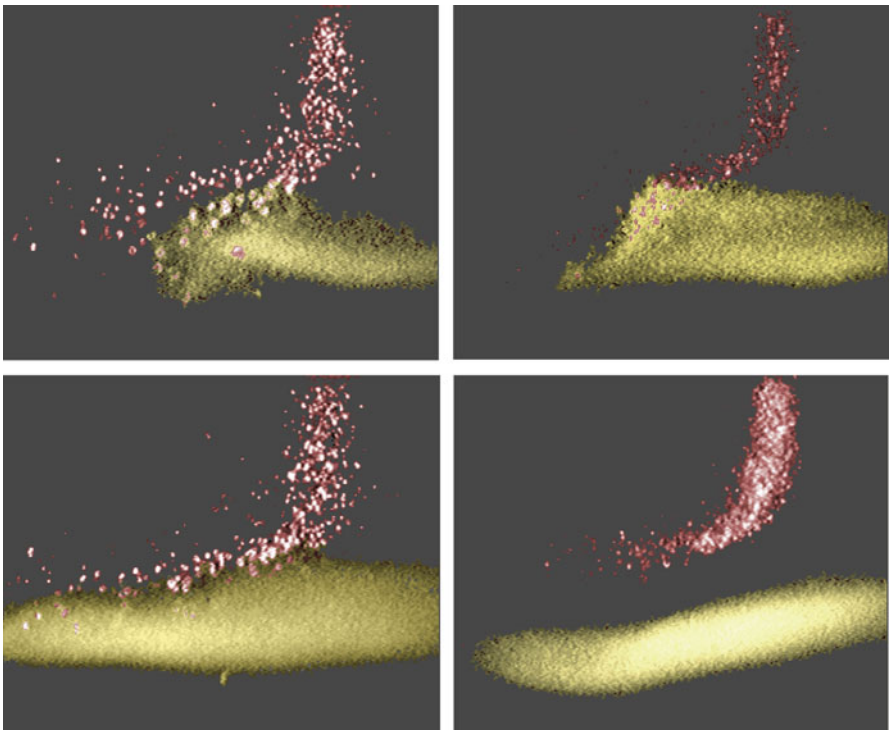


Fig. 7.36 High-speed images showing the fluctuations of the plasma jet and the spray particle fluxes being exposed to varying environments [1] (Copyright IOP Publishing. Reproduced with permission. All rights reserved.)

injected outside the nozzle are entrained in cold gas bubbles which reach the nozzle axis, but do not break up until several nozzle diameters downstream from the nozzle exit [92, 93]. The schematic of such a turbulent low density jet is shown in Fig. 7.37 [92] and compared to a Schlieren image of such a jet. The large-scale eddies in the shear layer are clearly visible. Measurement of the amount of air entrained in an argon plasma jet issuing into an air environment, using gas sampling with enthalpy probes showed that at an axial location 20 mm downstream from the nozzle exit, 50 % of the gas consisted of air [92]. Furthermore, in a set of definitive experiments using enthalpy probe measurements, two-photon Laser-Induced Fluorescence and CARS, the entrainment of air into an argon plasma jet was demonstrated, and the CARS measurements showed that the entrained oxygen remains at a low temperature of about 2,000 K [67]. Figure 7.38 [67] shows the axial temperature decay measured with an enthalpy probe, the fraction of the air in the gas sample obtained with the enthalpy probe, and the temperature of the entrained oxygen derived from CARS measurements of the rotational–vibrational level populations of molecular oxygen. The results clearly

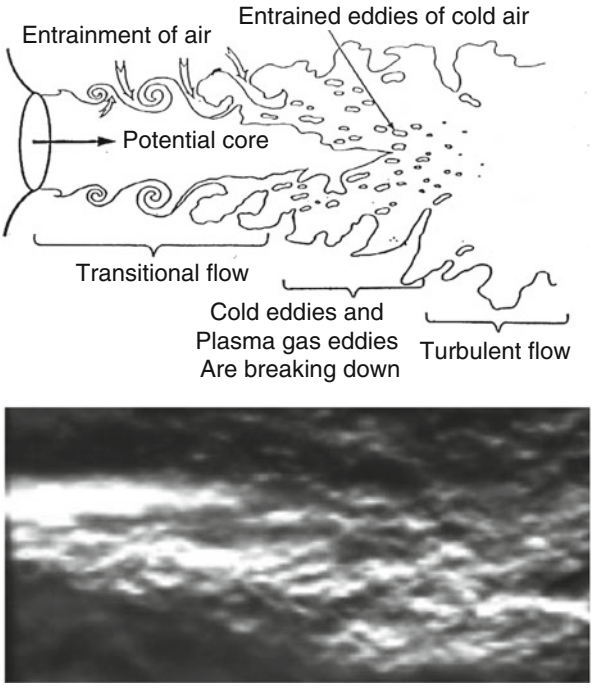


Fig. 7.37 Schematic of the large-scale turbulence and cold gas entrainment in a plasma jet issuing into a cold gas environment and Schlieren images of a turbulent plasma jet [92]. Reprinted with permission of ASM International. All rights reserved

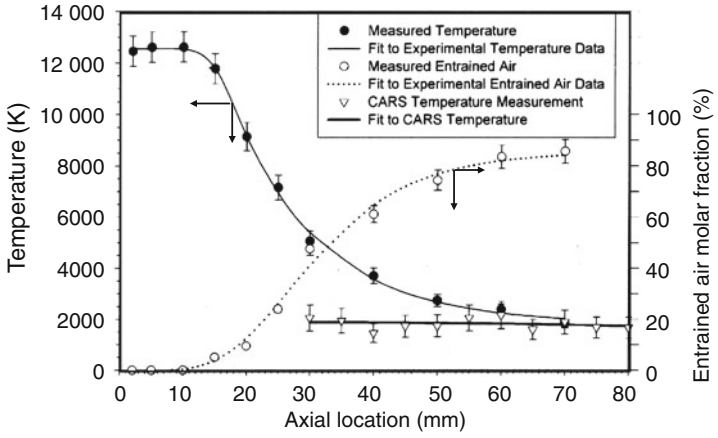


Fig. 7.38 Axial distributions of measured plasma temperatures (enthalpy probe measurements), volume fraction of entrained air in the plasma jet, and temperatures of the entrained oxygen (CARS measurements) showing the low temperatures of the entrained oxygen [67] (reproduced with kind permission of Elsevier)

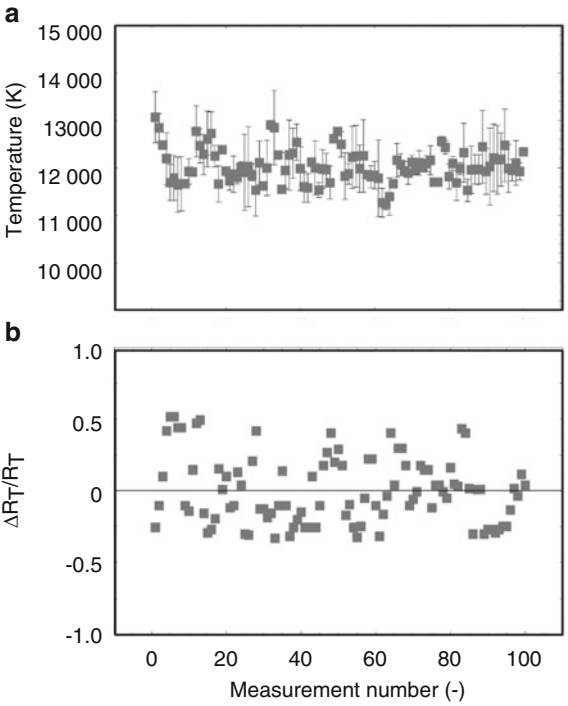


Fig. 7.39 Hundred consecutive measurements of the peak temperature (**a**) and the lateral location relative to the torch nozzle radius of the peak temperature (**b**) at an axial position 11 mm from the nozzle exit, showing peak temperature fluctuations exceeding 2,000 K and peak temperature locations distributed over an area with a radius half of the nozzle radius. Argon plasma jet with 35 slm, 100 kPa, $I = 600$ A. Time resolution of the measurement 50 μs, 5 Hz repetition rate [97] (reproduced with kind permission of IPCS)

indicate the significant difference in temperatures between the plasma jet and the entrained air, as predicted by the simulations (see Sect. 7.5).

Figure 7.39a [97] shows one hundred measured values of peak temperatures in an atmospheric pressure argon plasma jet (35 slm) at an axial location 11 mm from the nozzle exit, derived from spectroscopic measurements of an absolute line intensity with a time resolution of 50 μs. The strong variation of this peak temperature is evident. However, what is even more interesting is the radial position at which this peak temperature has been measured (see Fig. 7.39, right-hand side), ranging from the axis to a position 3 mm from the axis for a nozzle radius of 4 mm [97]. Clearly, the nice axisymmetric distributions obtained with measurements over a time scale of seconds cannot be assumed when processes are considered at or below the millisecond time scale.

7.7.2 Effect of Arc Voltage Fluctuations on Plasma Jet and Particle Characteristics

As mentioned previously, strong arc voltage fluctuations as encountered in a restrike mode of operation are promoted by thick boundary layers between the arc and the anode nozzle wall. These thick boundary layers will exist for conditions

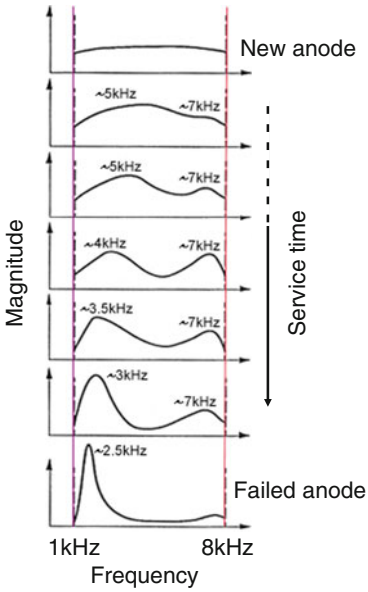


Fig. 7.40 Schematic representation of the Fourier Transform power spectrum of the voltage trace of an arc with a new anode (*top*) to a progressively eroded anode (*bottom*) showing the increase in the power in the 2–4 kHz range and the shift to a somewhat lower frequency [98]. Reprinted with permission of ASM International. All rights reserved

of high plasma gas flow rates and high percentages of hydrogen or helium and for low currents. However, restrike-like behavior can also be found when the anode is eroded and a preferred track exists for the motion of the anode attachment. The restrike motion is usually characterized by a specific frequency in the low kHz range (2–6 kHz), and increased erosion will give rise to a voltage fluctuation with this frequency. Figure 7.40 [98] shows the schematic of a Fourier transform of a voltage fluctuation progressing from a random distribution to a spectrum dominated by a specific frequency as the anode becomes increasingly eroded. Even more sensitive than the Fourier transform of the voltage trace is the spectrum of the sound pressure level as obtained with a microphone [44]. For a good anode, two frequency peaks are observed, one coinciding with the frequency of the voltage peak (in the 2–6 kHz range) and another in the 8–10 kHz range (see Fig. 7.41) [44]. Increasing anode erosion will increase the lower frequency peak with respect to the high frequency peak and shift the low frequency peak to lower frequencies. This diagnostic is a very sensitive indicator for the anode state. It should be mentioned that the peaks and the shifts would be somewhat different for other torch nozzle designs.

The voltage fluctuations caused by an eroded anode have a strong effect on the plasma jet, on the in-flight particle properties, and on the coating. Figure 7.42 [98] shows two high-speed images of a plasma jet obtained with a LaserStrobe camera (Control Vision) at 100 nm exposure time. Figure 7.42a shows a typical image of the jet with a new anode, while Fig. 7.42b shows the image for a strongly eroded anode. The jet length is strongly decreased.

The strong effect of the voltage fluctuations on particle heating and trajectories was reported already by Fincke and Swank in 1991 [96], showing that a fraction of

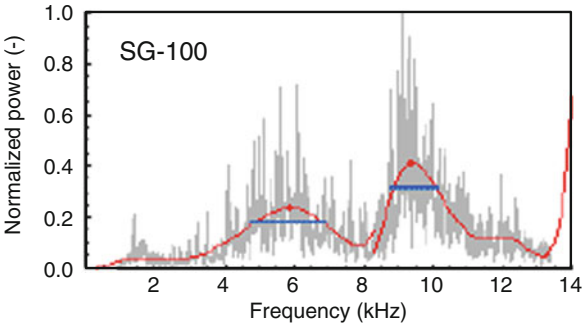


Fig. 7.41 Sound spectrum from Praxair SG 100 torch showing two distinct peaks. The lower frequency peak increases with increasing erosion [44]. Copyright © ASM International. Reprinted with permission

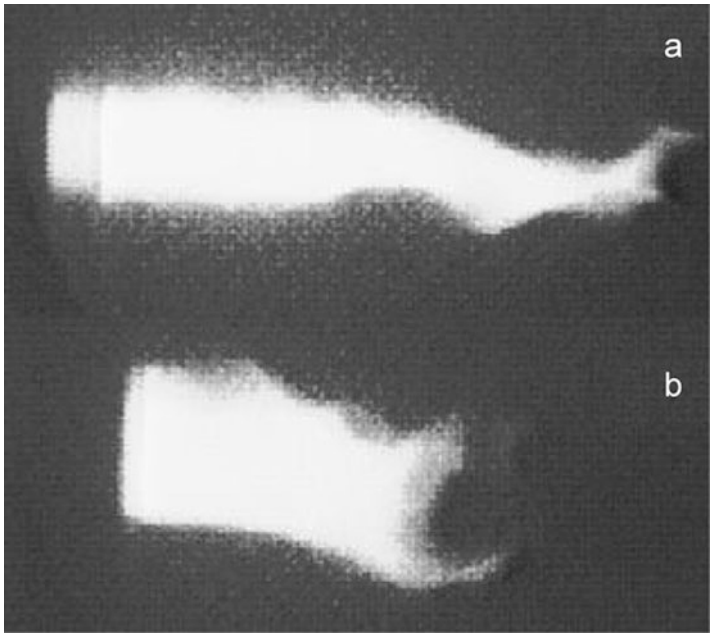


Fig. 7.42 High-speed images (100 ns) of a plasma jet with a new anode (*top*) and an eroded anode (*bottom*) [98]. Reprinted with permission of ASM International. All rights reserved

the particles up to 10 % of the total particle mass remains unheated. In an elegant experiment, Bisson et al. [99] showed the effect of voltage fluctuations on particle temperatures and velocities. A comparator was used to generate a signal when the voltage reached a certain threshold value in a restrike-like mode of operation. After a set delay after this signal, an image of the DPV 2000 gave a velocity and temperature record of a particle associated with a given instantaneous voltage value.

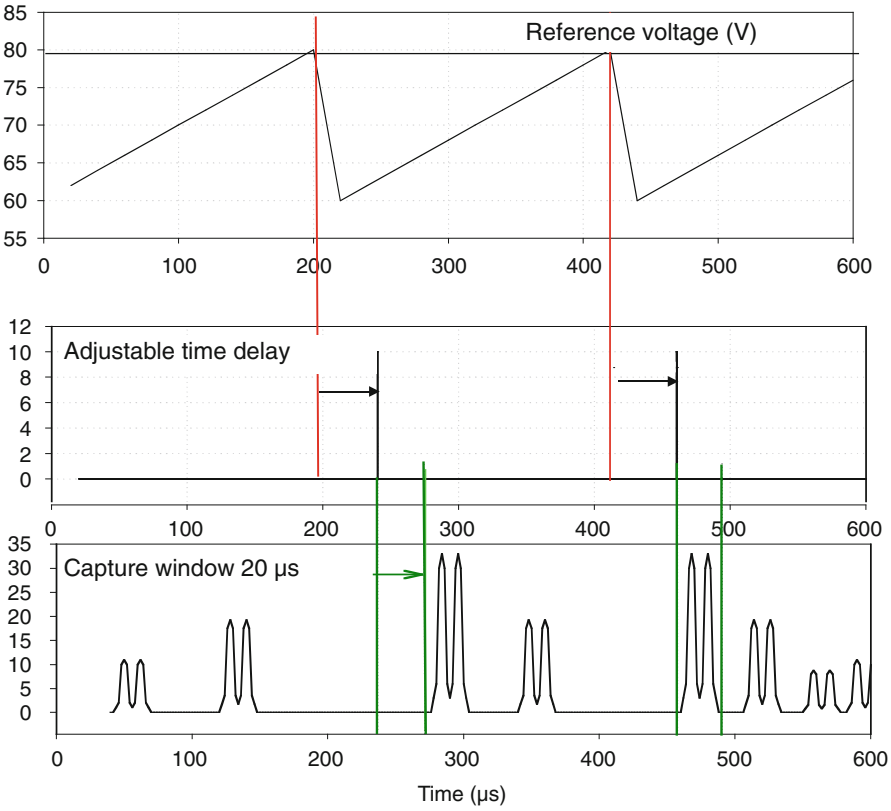


Fig. 7.43 Schematic representation of the triggering sequence of the particle temperature and velocity fluctuation measurements: a comparator triggers an adjustable time delay unit when the arc voltage reaches a certain value, and the time delay unit triggers the DPV 2000 to measure particle temperatures and velocities over a time period of 20 µs [courtesy of Christian Moreau, reproduced with kind permission of the NRC]

Figure 7.43 [courtesy of Christian Moreau] shows the schematic of the timing, and Fig. 7.44 [99] shows the resulting values of alumina particle temperatures and velocities as function of the time delay. The strong fluctuations of 500 °C and 180 m/s with a frequency almost identical to the frequency of the voltage traces are clear.

The amplitude of the fluctuations is damped because the frequency has slight variations. Increasing the arc current reduces the voltage fluctuations and the particle temperature and velocity fluctuations. However, use of the DPV only allows the measurement of the particles hot enough to radiate (above 1,600 °C for a 25 µm size particle with an emissivity of 0.4). By illuminating the plasma jet with a laser and by measuring the radiation backscattered from the particles with one of the channels of the DPV 2000, fluxes of all particles can be measured [100]. Figure 7.45 [100] shows the radial distributions of radiating particles and of low temperature particles, i.e., particles detected with the channel measuring the laser

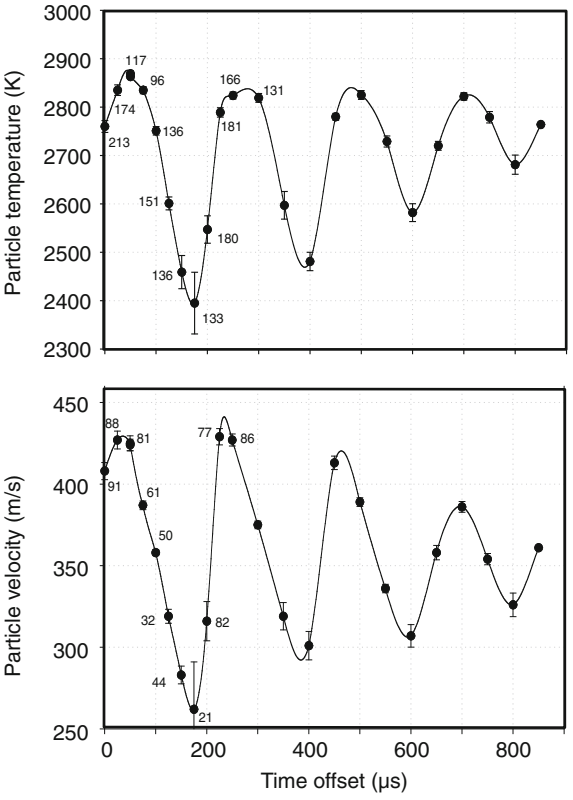


Fig. 7.44 Fluctuations of alumina particle temperatures and velocities with the same frequency as the torch voltage fluctuations 50 mm from the nozzle exit. Sulzer Metco F4 plasma torch operated in restrike mode at 550 A, 35 slm Ar, 10 slm H_2, 3.0 slm carrier gas flow, 1.5 g/min powder flow [99]. Copyright © ASM International. Reprinted with permission

light reflection events where no simultaneous signal is measured of radiation from the particle at a wavelength other than the laser wavelength. Results for two different experimental conditions are shown, one with a current of 300 A and a secondary gas flow rate of 10 slm of hydrogen, and the other with 700 A and 3 slm of hydrogen, all other conditions being the same. These conditions had been chosen to yield about the same average particle temperature of about 2,850 °C, and rather similar particle velocities of 274 and 316 m/s, respectively. The first condition results in a strong restrike mode of torch operation, and strong fluctuations of the particle temperatures and velocities, while the fluctuations for the second set of operating parameters are relatively small. As shown in Fig. 7.45 [100], for the restrike mode of operation a significant fraction of the particles are cold and not detected through emission of thermal radiation, while for the second set of parameters, only few cold particles are detected. It may be concluded that restrike behavior of the arc will result in a larger fraction of unmolten particles and that the use of an instrument like the DPV 2000 alone is insufficient to detect conditions that would result in poor coatings; the transient behavior of the arc needs to be known as well.

The change in the spatial distribution of particle temperatures is shown in Fig. 7.46 [101] for a new anode and an anode that has been used for 37 h.

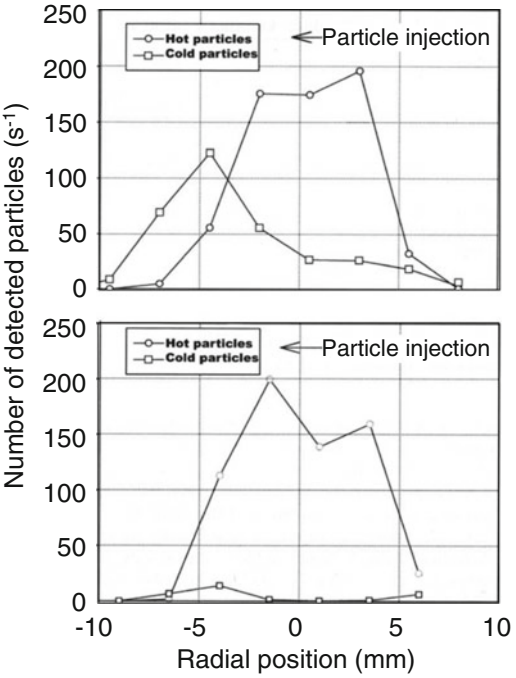


Fig. 7.45 Lateral distribution of hot and cold alumina particles for two different F4-MB torch-operating conditions at a 100 mm standoff distance. *Top*: 300 A, 35 slm Ar, 10 slm H_2, carrier gas 6 slm (restrike mode of operation). *Bottom*: 700 A, 35 slm Ar, 3 slm H_2, carrier gas flow 6 slm (take-over mode of operation). The measured mean particle temperature was the same for both conditions [100]. Copyright © ASM International. Reprinted with permission

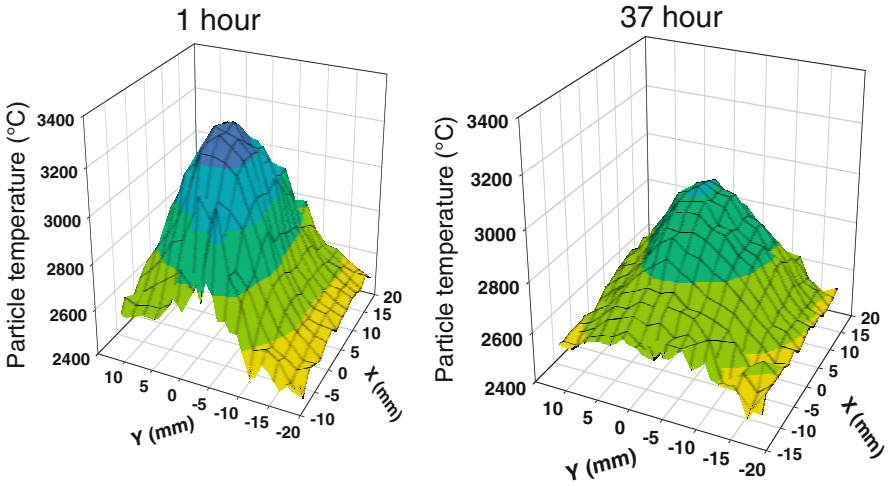


Fig. 7.46 Change of particle temperature distributions during operation from 1 to 37 h [101] (reproduced with kind permission of Trans Tech Publications)

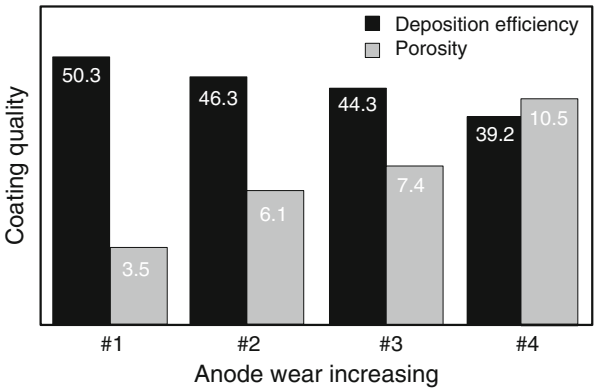


Fig. 7.47 Change of deposition efficiency and coating porosity with increasing anode wear for YSZ particles [98]. Reprinted with permission of ASM International. All rights reserved

A reduction in particle temperature and a widening of the spatial profile is noticeable, attributable to electrode erosion effects. Furthermore, the effect on coatings obtained with anodes of different stages of erosion is shown in Fig. 7.47 [98], which displays an increase in porosity accompanied with a decrease in deposition efficiency with increasing anode erosion.

7.8 Different Plasma Torch Concepts

There are principally four motivations for improving plasma spray torch designs: (a) improving process reliability and reproducibility, (b) increasing deposition rates and improving process economy, (c) improving coating quality/functionality, e.g., for thin coatings or coatings of nano-phase materials, and (d) adapting torches to different applications, such as cylinder bore coatings. The first category contains modifications to the fluid dynamics of the plasma torch, e.g., through gas shrouds or fixed arc attachments. The most notable development in the second category is the water swirl stabilized plasma torch. The third category has its dominant development in the concept of suspension plasma spraying and low-pressure (vacuum) plasma spraying, which will be described in separate sections. Some new developments should also be listed in the third category that combines plasma spraying with vapor deposition techniques. These developments are not presented here. Developments of torches in the last category are presented in a separate section.

7.8.1 Shrouds and Other Fluid Dynamic Jet Stabilization

As described previously, the mixing of the surrounding air with the plasma jet flow cools it down rather fast, mainly due to oxygen dissociation starting at 3,000 K (see Sect. 7.6.4 and Fig. 7.33). To delay this mixing it is possible to use an anode

nozzle extension with the same diameter as that of the nozzle. With an extension 20 mm long of an anode nozzle 6 mm in i.d. and working at 600 A with Ar–H_2 (45–15 slm) as plasma forming gas, Roumilhac [79] has shown that the plasma power was reduced by less than 10 %. The plasma jet core exiting the anode nozzle extension had almost the same length as that of the jet core without the anode nozzle extension. Another important feature of these extensions is that, even with the power lost to cool the extension, the temperatures and velocities of the jet are not drastically reduced at the extension exit. Betoule [102], for a d.c. plasma torch with an anode nozzle i.d. of 7 mm working with an Ar–H_2 mixture (45–15 slm) and an arc current of 600 A corresponding to 40 kW, has measured 2 mm downstream of the nozzle exit on the torch axis a gas temperature of 13,000 K and a velocity of 2,000 m/s. 52 mm downstream on the torch axis, the temperature was 6,200 K and the velocity about 500 m/s. With an extension 50 mm in length with the same i.d., the temperature was 11,000 K and the velocity 1,700 m/s due to 5.7 kW lost in the extension cooling. Unfortunately these nozzle extensions are difficult to use with powder radially injected in the anode nozzle downstream of the arc root, due to their divergent trajectories. However, as shown in Sect. 7.8.3 such extensions can be used with axial injection torches, where the particle jet divergence is much less. In this case, at the extension exit particles reach high velocities; this is especially the case with submicron- or nano-sized particles which, in spite of the Knudsen effect, reach velocities between 500 and 700 m/s (ensemble velocities) at the nozzle extension exit (see Sect. 14.7.1.1). Extensions with a divergent shape and being rather long (about 100 mm), generally called solid shrouds, have been used for spraying and are described in this section. The main problem is again the fully molten particles that can stick on the solid shroud wall. To avoid that, the total angle of the divergent shape must have a value between 40 and 50°. This configuration reduces plasma losses to the shroud wall, but air is entrained within the shroud and to avoid that an inert gas curtain must be provided to the shroud.

Fluid dynamic shrouds, without nozzle extension, provide a curtain of an inert gas between the plasma jet and the surrounding atmosphere. The problem with such shrouds is that the amount of gas in the shroud has to be rather large to match the boundary layer velocity because of the relatively large cross sectional area. With a shroud where argon gas was injected parallel to the flow of the plasma jet through a ring-shaped slit surrounding the jet, it was possible to spray reactive metal particles in an air environment with minimal oxidation. The amount of shroud gas was varied from 100 % to 300 % of the plasma gas mass flow rate, and at 300 % shroud mass gas flow, the oxygen fraction at the center of the jet was less than 0.5 % at a standoff distance of 85 mm. The appropriate selection of the distance between the nozzle wall and the ring-shaped slot was crucial for the success [103]. A similar approach has been taken with an axial injection torch (Axial III from Northwest Mettech, Canada, see Sect. 7.8.3) in a spray process depositing a Hastelloy bond coat [104]. The oxidation of the particles was minimized by using a double shroud with a total gas flow rate of 300 slm for a plasma gas flow rate of 240 slm (75 % Ar, 15 % H_2, 10 % N_2). An inner argon gas shroud surrounded the plasma jet as it exited

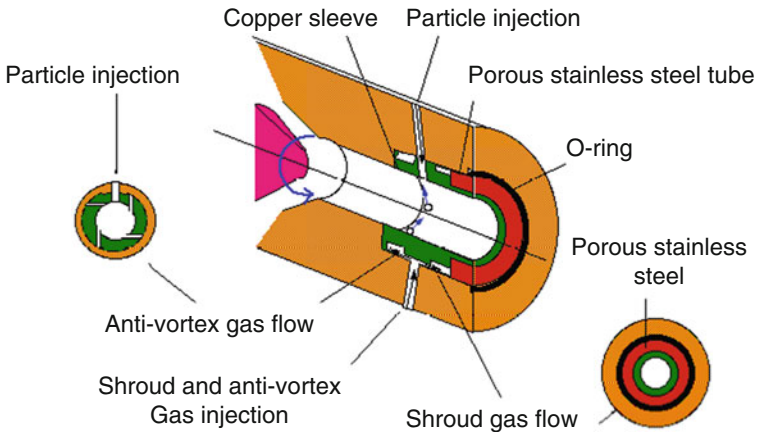


Fig. 7.48 Schematic of modification to SG 100 anode with porous ring shroud and counter swirl [105]. Reprinted with permission of ASM International. All rights reserved

the nozzle, and an outer shroud of nitrogen was introduced further downstream at the end of a cylindrical guide tube for the inner shroud [104].

In a somewhat modified approach, an anode nozzle was modified at its downstream end by fitting a porous ring surrounding the original copper nozzle wall [105, 106]. One of the two powder feed channels of an SG-100 torch was used to provide the shroud gas (see Fig. 7.48) [105]. In some experiments, this shroud was complemented by injecting part of the gas tangentially between the point of the arc attachment and the powder injection point to provide a swirl component opposing the swirl of the plasma gas. The results showed that the particle fluxes were more confined to the central part of the jet and less moved from the vertical injection plane due to the swirl, i.e., more particles remained in the hot core of the plasma jet. These results are shown in Fig. 7.49 [105], obtained with the Laser Strobe system from ControlVision, where the average particle location is shown in a polar plot with the torch axis at the center. Each point presents the average radial location of the particles at a specified distance from the nozzle. The coatings showed lower porosity and higher deposition efficiencies. The amount of shroud gas flow did not exceed the plasma gas flow.

In an approach to control the shear layer turbulence between the plasma jet and the surrounding atmosphere, a ring of micro-jets was used surrounding the plasma jet. The micro-jets do have an effect on the large scale turbulence and increase the length of the plasma jet with flow rates which are only a fraction of the plasma gas flow rate [81]. A similar effect has been observed with an insert at the downstream end of the anode that has a ring of several grooves parallel to the plasma flow requiring no additional gas flow (spline insert). Figure 7.50 [107] shows two Schlieren images illustrating the large-scale turbulence surrounding the plasma jet. The divergence of the jet is reduced and the length of the jet increased with the spline insert. Measurements with the DPV 2000 showed that the particle temperatures and

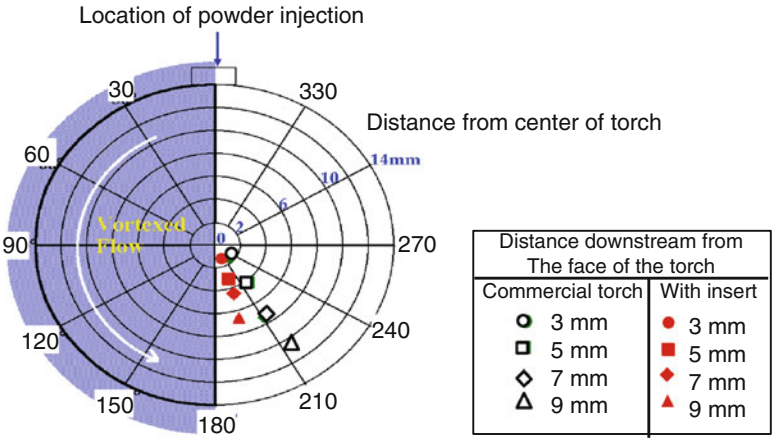


Fig. 7.49 View of mean particle location in a polar plot with the torch axis in the center. The *different symbols* denote different distances from the nozzle exit. The modified nozzle shows a less divergent particle beam and less removed from the central plane [105]. Reprinted with permission of ASM International. All rights reserved

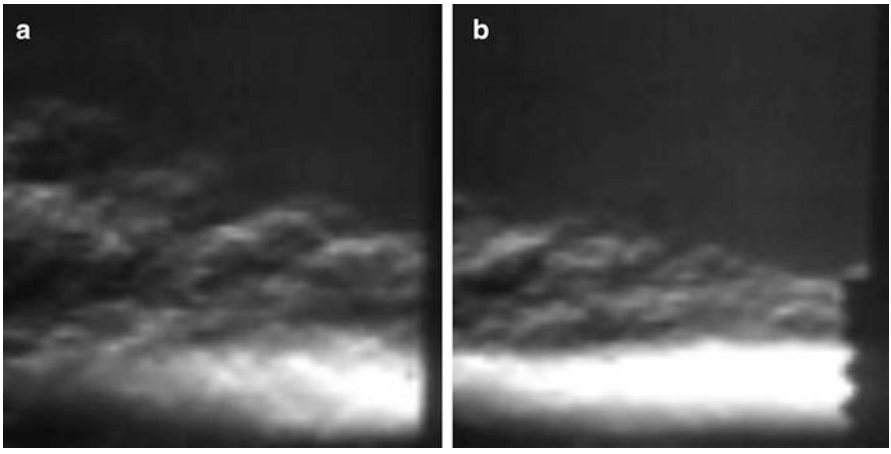


Fig. 7.50 Schlieren images of the plasma jet for (**a**) commercial anode and (**b**) modified anode incorporating axial grooves [107]. Reprinted with permission of ASM International. All rights reserved

velocities were higher with the modified nozzle (see Fig. 7.51) [81]. It is clear that more optimization can be done by tuning the amount of swirl of the plasma gas injection and combining it with a proper shrouding device [108].

As mentioned at the beginning of this section, with a solid shroud air entrainment has to be avoided and this is achieved by injecting argon as a shroud gas [109, 110]. Unfortunately, high mass flow rates are required (200–400 slm of Ar or N_2).

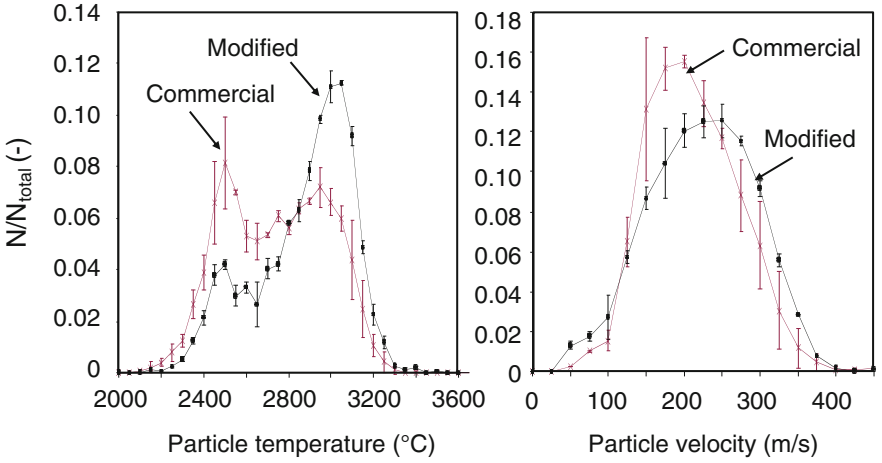


Fig. 7.51 Lateral particle temperature and velocity distributions at an axial location of 80 mm from the nozzle exit for a SG 100 torch operated at 900 A with 49 slm Ar and 21 slm He, carrier gas 2.9 slm, YSZ powder, for a commercial anode and for an anode modified with a micro-jet ring [81] (reproduced with kind permission of IPCS)

A schematic of a nozzle developed by Okada [109], Guest [110] and Houben [111] with a nozzle shield uses radial argon injection at a reduced argon flow rate (~50 slm). The argon injected in the periphery of the shield cover surrounding the shielding nozzle limits the air penetration along the shield cover internal wall where also the plasma gas is ejected. Borisov [112] has designed a nozzle shield where the plasma forming gas is used as shrouding gas (see Fig. 7.52). The plasma gas in the plasma jet fringes is captured at different positions along the nozzle shield, directed to a gas cooling system and then reinjected at the shield bottom along its internal wall, as illustrated in Fig. 7.52. Unfortunately such solid shrouds are mainly designed to spray on flat parts. Industrially, a nozzle shield called Gator Guard is used to spray superalloys [113].

7.8.2 Fixed Anode Attachment Position

Plasma torch designs providing stable arc operation by fixing the anode attachment location have long been used for plasma arc property studies [114–116]. Two ways can be used to elongate the arc: either by using a nozzle with a step diameter change in it or by having the channel consisting of a number of water-cooled segments, electrically insulated from each other and from the anode, called a cascaded arc. One problem with these designs is an enhancement of the anode erosion that occurs with one fixed anode attachment. Limiting it requires reducing the arc current, but the higher arc voltage compensates for the lower power levels (about 3–6 times) that of conventional spray torches.

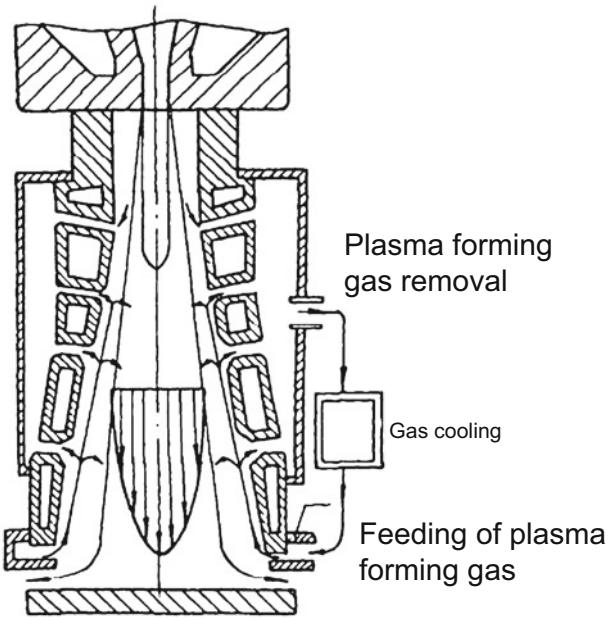


Fig. 7.52 Nozzle shields developed by Borisov [112] reproduced with kind permission of Sulzer Metco AG, Switzerland

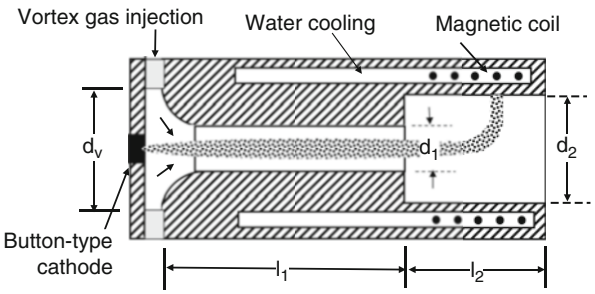


Fig. 7.53 Principle of a plasma torch with a step change in the anode internal diameter (quasi-fixed arc length) [117]. Reproduced with permission of VSP

The anode nozzle with a step change in diameter is represented schematically in Fig. 7.53 [117]. The length ℓ_1 of the smaller diameter (d_1) part has to be shorter than the length ℓ_{ca} that the arc would assume without the step change in the anode diameter d_2. Under such conditions due to the recirculation, which occurs downstream of the step change, the arc strikes close to this step change. To achieve a long free attachment in the nozzle of diameter d_1 a strong vortex must be used with a high swirl that can be achieved when the ratio d_v/d_1 is high, d_v being the diameter of the gas injection tangentially to the arc chamber. This high vortex requires using a

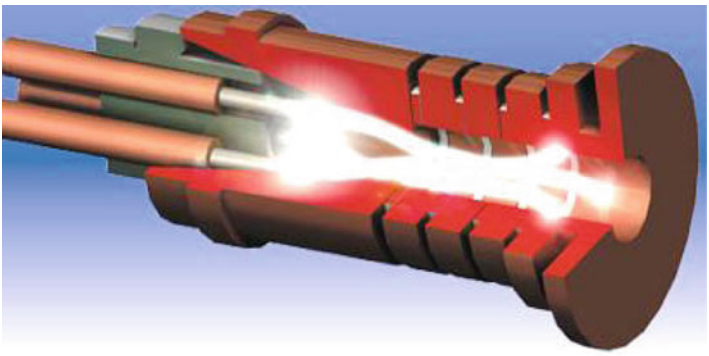


Fig. 7.54 Schematic of Sulzer Metco Triplex Torch (reproduced with kind permission of Sulzer Metco AG, Switzerland)

button type cathode. For low arc currents, the arc characteristic is first slightly decreasing and then slowly increasing [116].

With the cascaded arc, the segment at the downstream end of the channel serves as the anode. The arc can be initiated by having an initial breakdown to the segment closest to the cathode (auxiliary anode), creating a plasma flow inside the channel, and then transferring the arc to the regular downstream anode. A development by the Universität der Bundeswehr, Munich, and Sulzer Metco, has succeeded in solving the problem of increased anode erosion by dividing the arc current into three separate arcs with three cathodes and one anode, but three separate anode attachments ("Triplex" torch, see Fig. 7.54, courtesy of Sulzer Metco) [118, 119]. Several insulated segments form the wall of the arcing channel. This torch offers very stable operation when operated with argon or argon–helium mixtures. The arc root fluctuations at the anode are the same as those obtained at the anode of a conventional torch with a stick type cathode, for example, about 10–15 V for Ar–He plasma. For the latter with a mean voltage V_m of 35 V the ratio $\Delta V/V_m$ at the maximum is 15/35, but with the Triplex torch, where voltage is around 100 V, this ratio becomes 15/100! This torch also offers a significant increase in the powder flow rate. However, powder injection is external to the plasma torch immediately downstream of the anode, and three injectors are adjusted such that they are separated by 120° on the circumference, preferably lining up with the direction between the anode attachments of the three arcs. The improved arc stability, lower turbulence in the jet, and the use of three injection systems allow not only better process control and longer operating times, they also provide higher deposition rates. Anode nozzle i.ds. are between 6 and 9 mm. When observing the plasma jet for small anode nozzle diameters, it can be observed that they are constituted of three lobes as shown Fig. 7.55 (courtesy of Sulzer Metco). Thus particles can be injected either into the lobes or between the lobes, the latter injection being called cage effect. Mauer et al. [120, 121] have studied the resulting plasma jets by emission computer tomography using three CCD cameras rotating around the jet axis and the interaction of the injection conditions on particle properties by DPV-2000 measurements.

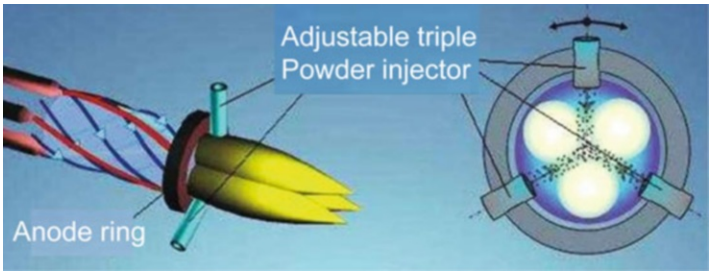


Fig. 7.55 Schematic of the Triplex torch plasma jet with its three lobes (reproduced with kind permission of Sulzer Metco AG, Switzerland)

The tomographic reconstruction of the gas temperature distribution allowed them to relate the injector direction with the regions of high gas temperature and thus of high gas velocity and viscosity. In all investigated cases the most efficient particle heating corresponded to an injection direction between two high temperature lobes, thus confirming the so-called cage effect [121]. The lobe opposite to the injector kept in particular the larger particles properly in the jet center and prevented them from passing through the plume due to their too high momentum. As particle velocities were found to vary only moderately, the particle temperatures were more meaningful when the injection conditions were to be optimized. The results showed that particle injection between the hot lobes, combined with an appropriate carrier gas mass flow rate allowed optimizing the process effectiveness as a function of the size of the injected particles [121].

7.8.3 Central Injection Torches

As discussed previously, injection from one side leads to particle trajectories that result in a classification of particles according to their initial momentum. Particles with higher mass and with a higher injection velocity can penetrate the plasma jet, traverse it, having the majority of their trajectories in the low temperature fringes of the jet on the side opposite of the injection direction. In contrast, particles with too low a momentum (lower mass or lower velocity) will not be able to penetrate the plasma jet, remaining in the fringes on the injection side. Neither one of these particles will have the optimal temperature and velocity for the coating. Several efforts have been undertaken to provide uniform heating of the particles through injection on the axis of the plasma jet. Two such developments shall be described here.

The commercial torch Axial III developed by Northwest Mettech (Canada) [104, 122] consists essentially of three torches arranged such that their axes are parallel and they surround the central powder injector. Each torch has its own cathode and anode, but the jets enter channels directing the flows into a common nozzle (nozzle

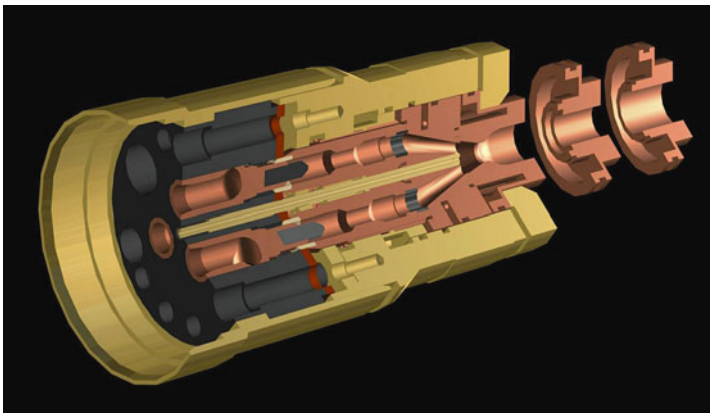


Fig. 7.56 Schematic of Northwest Mettech Axial III central injection torch (courtesy of Northwest Mettech)

extension) with its axis aligned with the central injector. A schematic is shown in Fig. 7.56 (courtesy of Northwest Mettech). The major advantage of such a torch is that the coating quality is less sensitive to the powder material, i.e., size distribution and morphology. However, the problem of plasma property fluctuations due to arc fluctuations remains, but voltage fluctuations of the 3 torches are quite independent. The interest of the nozzle extension is that it delays the mixing with surrounding air with a slow decrease of the temperatures and velocities of the plasma flow within the extension, while without it the drop in plasma temperatures and velocities is by far more important. Thus high particle impact velocities can be almost as high as those obtained with HVOF guns.

Another development based on an early design used for powder synthesis experiments [123, 124] is the triple torch plasma reactor (TTPR) shown schematically in Fig. 7.57 [125]. Three torches are arranged inside a controlled atmosphere chamber with an adjustable angle to the chamber axis and adjustable distances from their suspension on the top flange. The three plasma jets join to form an enlarged plasma region. The powder is injected through an injection tube on the axis of the reactor, right above the location where the three jets join to form the combined jet. Three power supplies are necessary to operate the reactor. Operating currents are between 250 and 320 A with Ar or Ar–H_2 mixtures as the plasma gas. Enthalpy probe characterization of the plasma flow show a rather uniform temperature and velocity over a diameter of several centimeters [126]. The temperature and velocity in the central portion of the plasma jet can be adjusted by changing the carrier gas flow rate, i.e., higher carrier gas flow rates will result in a cooling of the central portion of the jet and reduced particle heating. Clearly, coating of complicated shapes will be difficult because the torches cannot be moved independently, but the substrate can be moved. This torch has been used for specialty coatings, such as the three layers of a solid oxide fuel cell (SOFC), where in a single process the porous Ni–YSZ anode layer, the high density YSZ electrolyte layer (with 99.5 % density), and the porous lanthanum manganite perovskite cathode layer were deposited (see Fig. 7.58) [125]. Another application of

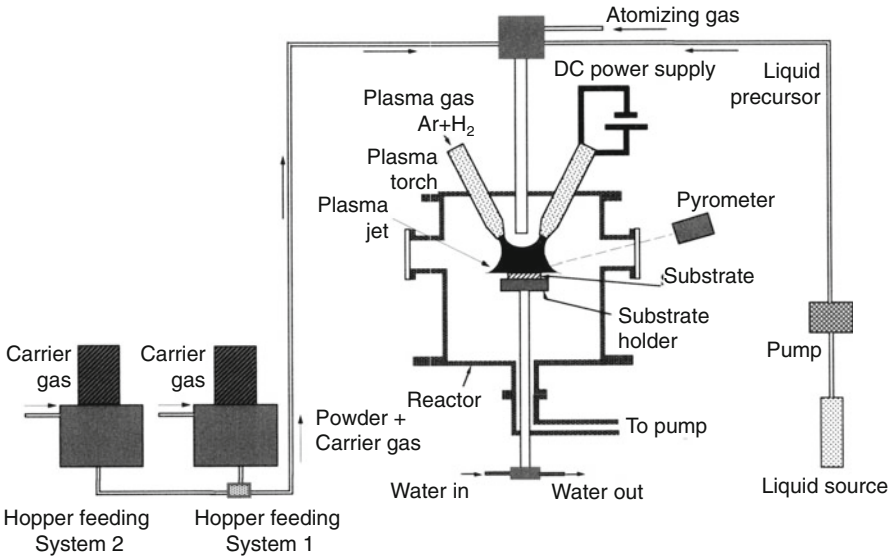


Fig. 7.57 Triple torch plasma reactor with three torches in controlled atmosphere chamber and central injection and multiple powder/liquid feeders [125]. Copyright © ASM International. Reprinted with permission

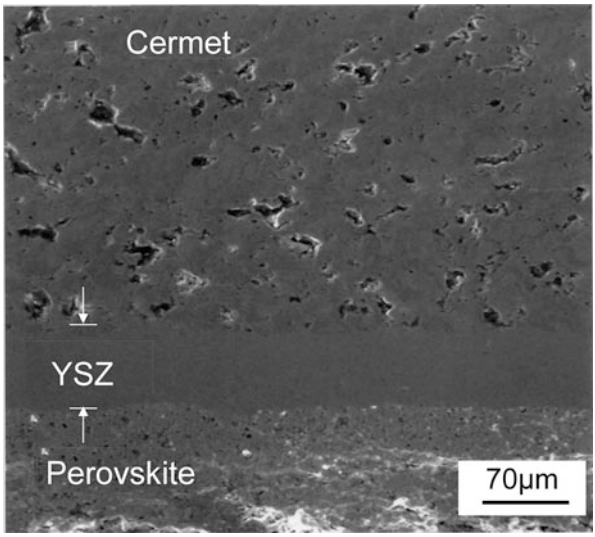


Fig. 7.58 Cross section of three layers of a solid oxide fuel cell deposited sequentially in the triple torch plasma reactor; *top*: YSZ–Ni cermet coating for the anode, *middle*: dense YSZ coating (99.5 % density) for the dielectric layer, *bottom*: lanthanum manganite perovskite layer for the cathode [125]. Copyright © ASM International. Reprinted with permission

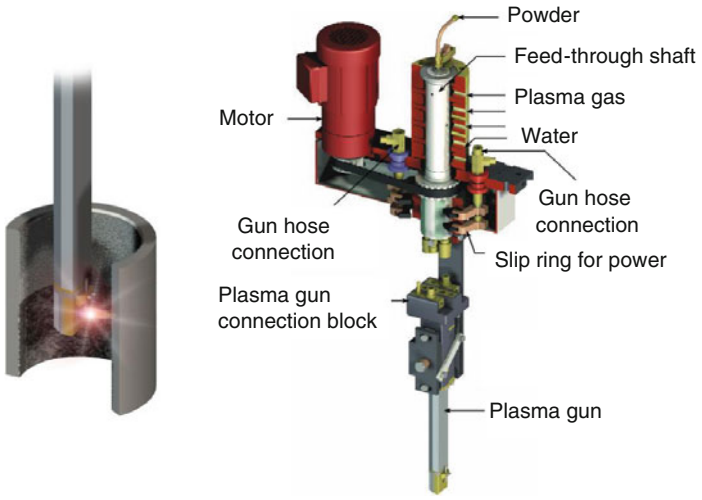


Fig. 7.59 Schematic of Sulzer Metco Rotaplasma torch for coating inside surfaces of cylinders (reproduced with kind permission of Sulzer Metco AG, Switzerland)

this reactor is the deposition of nanophase coatings with the starting powder consisting of agglomerates of nanometer-sized particles. The heating of the particles can be adjusted such that the majority of the particles are deposited in a semi-molten state, preserving the nano-phase microstructure in the coating. Such a layer was deposited as an intermediate strain relief layer between the corrosion resistant mullite coating and the YSZ thermal barrier coating; the thermal expansion mismatch of these two materials could be mitigated to some degree by the nano-phase intermediate layer [127, 128].

7.8.4 Torches for Inside Diameter Coatings

A significant application is the coating of inside diameters of tubes or bore holes. Use of aluminum cylinder blocks in the automobile industry has led to several developments in this area. The most notable of these developments is the RotaPlasma torch by Sulzer Metco [129]. The spray nozzle has its axis perpendicular to the axis of the torch body and the axis of rotation. Figure 7.59 (courtesy of Sulzer Metco) shows a schematic of this torch. The gas and cooling-water connections are made through a rotating feed-through shaft. The torch can be rotated with up to 200 rpm, and inside diameters of as small as 40 mm and as large as 500 mm can be coated, over a length of up to 500 mm. This torch is presently being used commercially for automobile cylinder bore coatings.

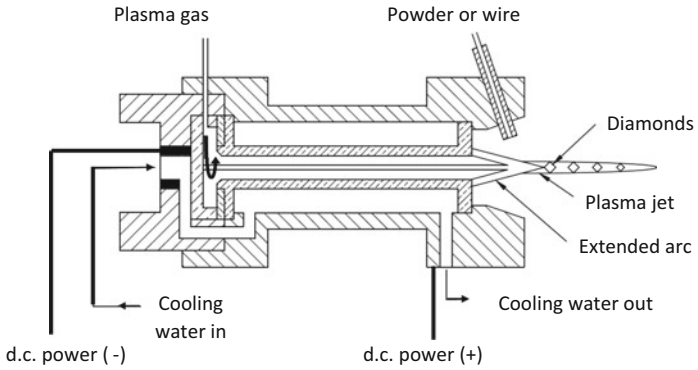


Fig. 7.60 Schematic of the Plazjet d.c. plasma torch [130]. Reproduced with kind permission of Sulzer Metco AG, Switzerland

7.8.5 High-Power Plasma Spray Torch

For increasing the deposition rate, a high-power plasma spray torch has been developed [130]. This torch is based on the concept of Zhukov in the 1960s [116, 117] and described summarily in Sect. 7.8.2. This torch (see Fig. 7.60) has a button-type cathode, plasma gas injection with a strong swirl component, and a very long anode nozzle. The anode nozzle shape may be either a constant diameter cylindrical bore with a length 5–12 times the diameter, a conical bore with a 14 mm diameter inlet and an 8 mm diameter exit, or with a cylindrical bore with a step change in its diameter. This latter design corresponds to a fixed arc length. The choice of different anode designs allows tailoring the particle velocities (highest with the conical design) and temperatures (highest with the step change design). Gas flow rates can be varied over a wide range to up to 250–300 slm of nitrogen and up to 150 slm of hydrogen. This range allows some adjustment of the gas enthalpy vs. gas velocity, i.e., the residence time of the powders in the high temperature zone. The high gas flow rates result in a very long arc (in the order of 125 mm) with a high voltage (in the order of 400 V at 500 A maximum arc current). While the plasma temperatures at these flow rates are not very high (in the order of 10 kK or below), the velocities are very high. This high power allows spray rates of typically 17 kg/h of Cr_2O_3.

7.8.6 Water-Stabilized Plasma Torch

Water as a stabilizing medium for an electric arc has been used already in the 1920s [131] mainly for reaching high plasma temperatures. The high specific heat of water, steam, and the hydrogen/oxygen plasma lead to very constricted arcs, high

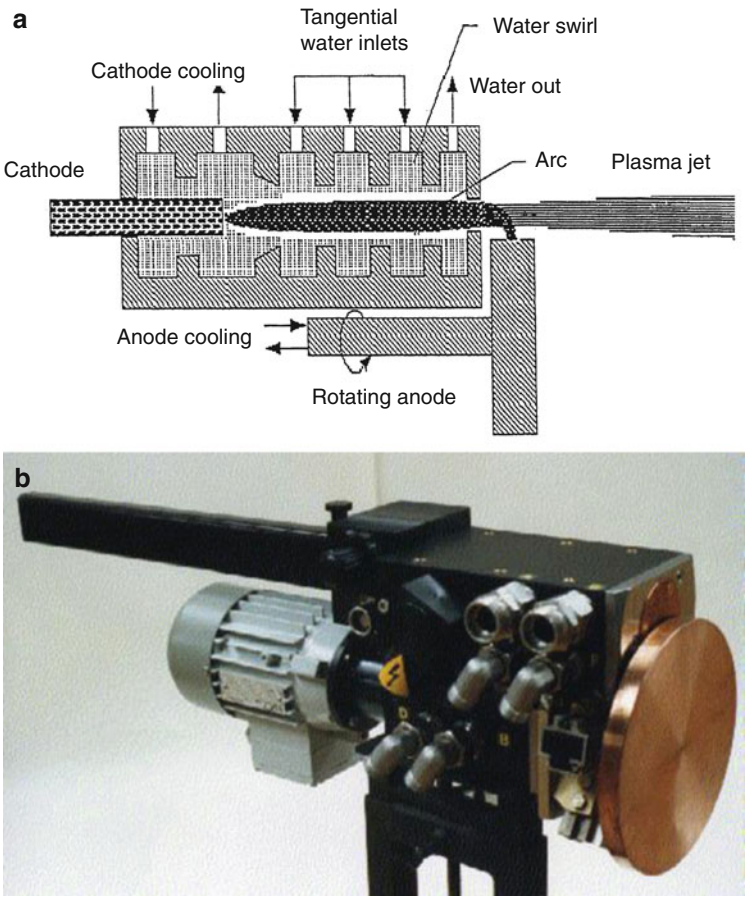


Fig. 7.61 (**a**) Schematic and (**b**) picture of water swirl-stabilized arc torch with external rotating anode (with kind permission of Milan Hrabovsky and the Institute of Plasma Physics of the Czech Academy of Sciences)

arc voltages, and high temperatures. Such a torch was developed for plasma spraying applications by the Institute for Plasma Physics of the Czech Academy of Sciences [132, 133]. Figure 7.61 (courtesy of Milan Hrabovsky) shows a schematic of such a water stabilized plasma torch. The water is introduced into the arcing chamber with a strong swirl component in several sections, and an outlet right before the nozzle allows a return of the unused water. The arc is established through a contact electrode and transferred from the cathode to the external anode. The plasma gas is provided by evaporation of the water, and the plasma exits the torch through a nozzle. The anode is rotating at high speed to distribute the high heat load associated with the hydrogen–oxygen plasma. The graphite cathode is consumable, i.e., it has to be fed continuously during operation. Newer designs use

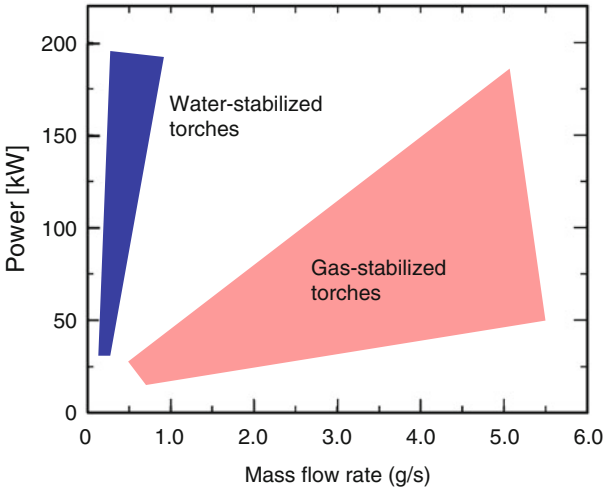


Fig. 7.62 Illustration of torch power variation with plasma mass flow rate for water swirl stabilized and for gas-stabilized torches (with kind permission of Milan Hrabovsky)

a fixed cathode with an argon gas environment in the upstream part of the torch (hybrid torch) providing significantly increased operation times. The strong cooling of the arc results in very high arc voltages (260–300 V) and high torch powers (80–200 kW) for moderate currents (300–600 A). Temperatures at the nozzle exit can reach 28,000 K, and peak plasma velocities of 7,000 m/s have been reported [134]. These values allow spray rates in the range of 25–45 kg/h for ceramics and 80–100 kg/h for metals, an order of magnitude higher than for regular plasma torches operating at 40–50 kW, and still significantly higher than that of a high power gas torch operating at 200 kW with a nitrogen–hydrogen mixture. Figure 7.62 (courtesy of Milan Hrabovsky) compares the range of operating powers for different mass flow rates of the water-stabilized torch and the regular gas plasma torches, showing that only a fraction of the mass is used with the water-stabilized torch achieving the high power and enthalpy levels. The high deposition rates make this torch particularly useful for manufacturing of free-standing shapes or for coating large areas. However, the external rotating anode makes torch movement somewhat more difficult.

7.9 Low Pressure and Controlled Atmosphere Plasma Spraying

The oxidation occurring during atmospheric plasma spraying is detrimental for metals and alloys for both coating properties and adhesion. Controlled atmosphere plasma spraying was developed in 1974 by Mühlberger (Electro Plasma Inc., now

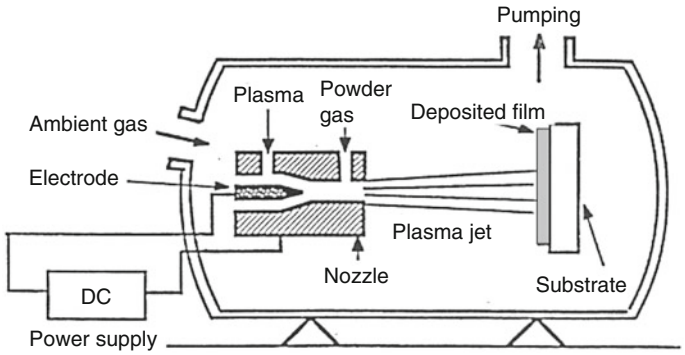


Fig. 7.63 Schematic of low pressure plasma spray installation (Courtesy of Emil Pfender)

Sulzer Metco Inc.) [135, 136]. Most low-pressure plasma spraying is performed in a controlled atmosphere chamber at pressures between 5 and 70 kPa (see schematic in Fig. 7.63). At the lower end of this range and at lower pressures, one frequently talks about "vacuum plasma spraying (VPS)."

This process offers a series of advantages compared to the atmospheric plasma spraying.

1. The controlled atmosphere prevents oxidation of the spray powders in-flight and on the substrate, an important consideration with metal spraying.
2. The higher velocity plasma jet (2,000–3,000 m/s) results in higher particle velocities with the possibility of higher coating densities. Typical particle velocities have been measured of 800–900 m/s for alumina and of 450–650 m/s for YSZ [137].
3. The lower density gradients between the plasma jet and the surroundings result in more stable jets and less cold gas entrainment, with the consequence of more uniform particle heating and acceleration and less divergence of the particle trajectories.
4. The uniformity of the jet temperature and velocity profiles can be further improved by attaching a Laval nozzle to the anode.
5. At the lower pressures, the heat transfer rates to the particles is reduced, however, the longer jets increase the residence time in the plasma; these reduced heating rates result in less superheating of the particle surface and lower temperature differences between particle surface and the particle center.
6. With the plasma torch in operation, striking a low current transferred arc between the torch anode and the substrate (serving as the cathode), cleaning of the substrate surface can be achieved. The formation of cathode spots moving rapidly over the substrate surface results in evaporation of impurities, in particular of oxides, in a timeframe of a few minutes. It is also possible to preheat the substrate by having the substrate positively biased with respect to the torch anode. Passing a current of a few amperes to a few hundred amperes to the substrate, heating to a desired temperature can be achieved without oxidation of

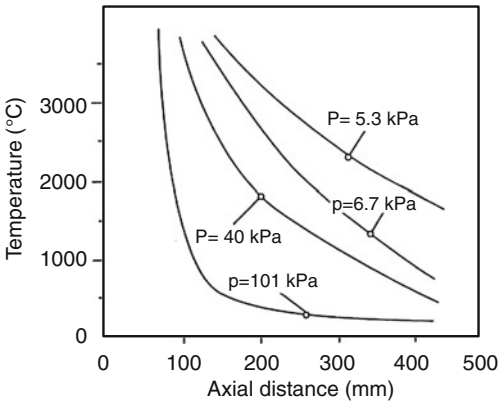


Fig. 7.64 Calculation results of axial temperature profile in a plasma jet at different argon pressures (Courtesy of Emil Pfender)

the substrate surface. This substrate preheating to about 900 °C can promote diffusion bonding of, e.g., an environmental barrier coating with a superalloy substrate.

These advantages come at the price. Besides the large water-cooled chamber with the associated pumping installation, the system requires filters before the pumps, heat exchangers for cooling the exhaust, inert gas manifold for backfilling the chamber, robotic systems adapted to vacuum environment for moving the part and/or the torch, shielding of all cables inside the chamber against exposure to heat and particle fluxes. All of these required features raise the cost of a VPS system significantly, and this increase can be an order of magnitude compared to an APS system with comparable power. One also needs to consider the fluid dynamics inside the chamber to assure that no cold particle deposition occurs due to recirculating flows. Moreover, for industrial use a transfer chamber (load lock) is used that would allow to adjust the pressure, after loading the part to be coated at atmospheric pressure, to the vacuum chamber pressure. This way the pump-down of the main chamber after every spray process can be avoided. Clearly, these additional features and the associated cost increases mean that the applications for VPS coated parts are different from those of APS coated parts and are generally limited to high added value components.

Torch operation is similar to the operation of the APS torches, i.e., with similar arc currents, plasma gas selections and flow rates, power levels, and powder flow rates. However, the torch substrate distance is typically in the range between 250 and 500 mm. Before the start of operation, the chamber is pumped down to a pressure of a few Pascal and then backfilled with high purity argon and pumped down again to the desired operating pressure.

The plasma jet becomes increasingly longer and wider as the pressure decreases because the cooling through the entrained air is avoided [22]. Figure 7.64 shows some modeling results for axial peak temperature distributions of an argon plasma jet issuing into an environment at different pressures showing the much slower temperature decay at lower pressures. Figure 7.65 shows the axial velocity

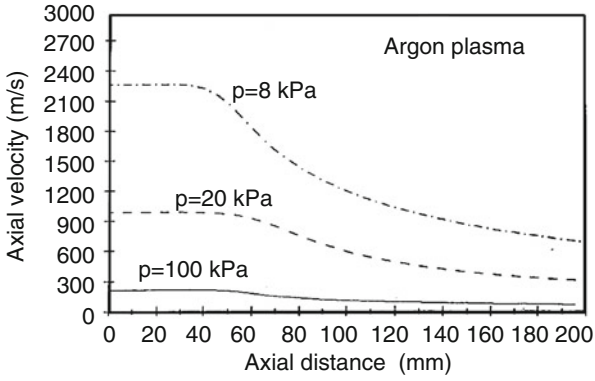


Fig. 7.65 Calculation results of axial velocity profiles in argon at different pressures (Courtesy of Emil Pfender)

distributions for a low power argon plasma jet (8 kW) with 11.6 g/min argon flow for an 8 mm diameter nozzle and three different chamber pressures. The strong increase in velocity even with pure argon is noticeable. The lower axial temperature and velocity gradients are due to the lower large-scale turbulence and less cold gas entrainment, a consequence of the smaller density gradients resulting in less turbulent shear layers. However, the lower densities result in lower electron–ion recombination rates, and deviations from composition equilibrium must be expected.

The effect of going to very low pressures on the plasma jet and particle properties has been nicely shown by Refke et al. [138] using an experimental vacuum chamber and a Sulzer Metco O3CP torch, a set-up that has the capability to be operated down to 0.1 kPa (1.0 mbar) with up to 150 slm of total gas flow rate. Figure 7.66 [138] shows that a reduction of the pressure from 1.0 kPa to 0.2 kPa results in an increase in the plasma jet temperature and velocity as measured with an enthalpy probe for a 1,500 A, Ar–H_2 (100/3 slm) jet. However, since the pressure decrease reduces the heat transfer coefficient, the heat flux to the YSZ particles remains almost constant, and particle temperatures and velocities (as measured with a DPV 2000 system) are slightly higher at 1.0 kPa (see Fig. 7.67) [138]. Reduction of the heat and momentum transfer from the plasma to the particles is enhanced by the Knudsen effect, i.e., the increase in atomic mean free paths compared to the particle dimensions (see Chap. 4). This reduction in heat transfer may pose difficulties for melting refractory particles. The strongest effect of the reduced pressure is seen in the flattening of the radial particle temperature and velocity profiles, as shown in Fig. 7.68 [138] for a Ar/He jet, where the stronger peaks at the higher pressures are evident. The higher absolute values at the higher pressures are in part due to the fact that the axial distance for the higher pressure case was 300 mm while it was 450 mm for the lower pressure case.

A comparison of a NiCoCrAlY coating obtained with a Central Injection APS torch, a HVOF torch and a VPS system showed that the VPS system provided significantly better coatings with regard to lower porosity, lower unmelt density, and practically no oxide formation [139].

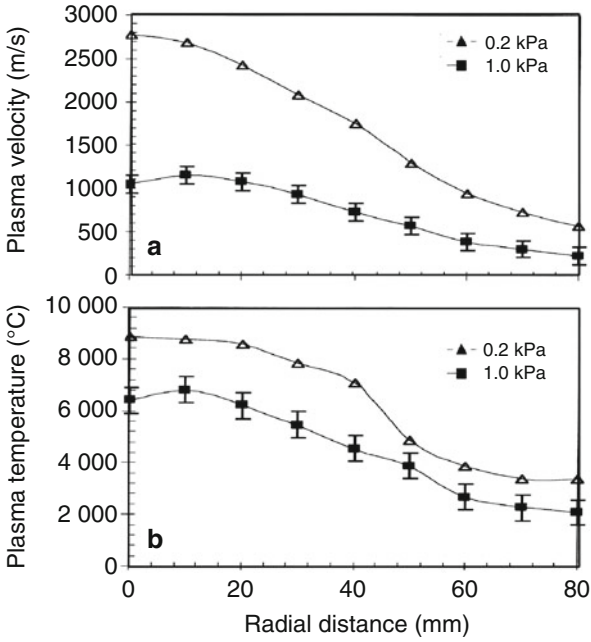


Fig. 7.66 Radial velocity and temperature profiles in an Ar/H_2 (100/3 slm) plasma jet at 1,500 A and an axial position of 775 mm from the nozzle, at pressures of 1.0 kPa and 0.2 kPa showing the increase in temperature and velocity at the lower pressure. Data were obtained with a Sulzer Metco O3CP torch [138]. Reprinted with permission of ASM International. All rights reserved

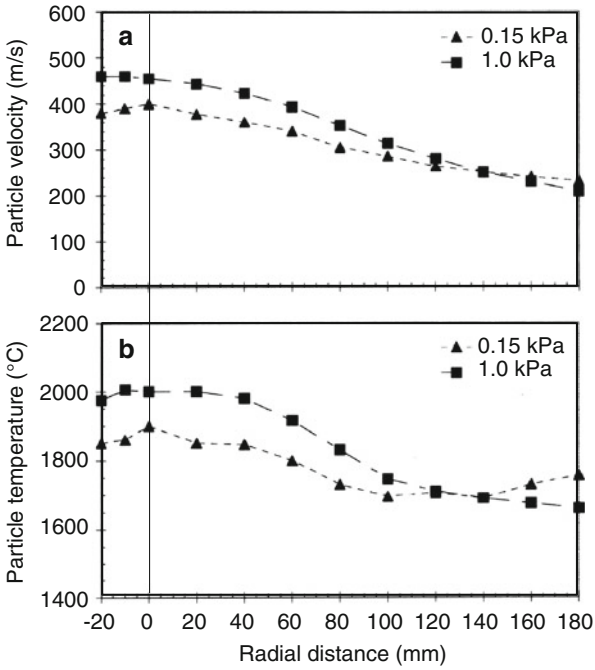


Fig. 7.67 Radial distributions of YSZ particle velocities and temperatures in an Ar/H_2 (100/3 slm) plasma jet at 1,500 A and an axial location 975 mm from the nozzle, at pressures of 1.0 kPa and 0.15 kPa showing slightly higher temperature and velocity values for the higher pressure [138]. Reprinted with permission of ASM International. All rights reserved

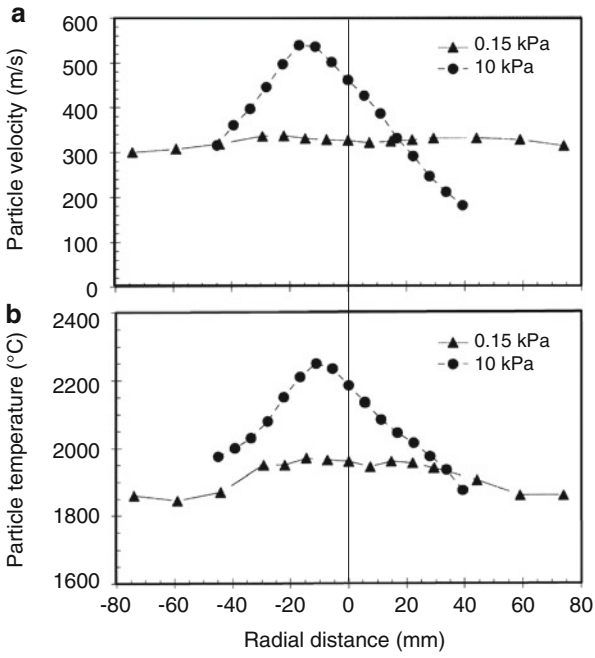


Fig. 7.68 Radial distributions of YSZ particle velocities and temperatures in an Ar/He (50/110 slm) plasma jet at 1,500 A for a pressure of 10 kPa and an axial distance of 300 mm, and of 0.15 kPa and a distance of 450 mm [138]. Reprinted with permission of ASM International. All rights reserved

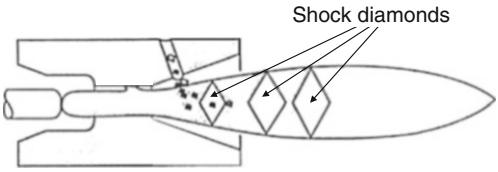


Fig. 7.69 Schematic illustration of shock diamond as consequence of inadequate equilibration between pressures in the jet and in the surroundings

For compressible nozzle flows reaching supersonic speeds inside the nozzle, shock diamonds are usually observed outside the nozzle (see schematic in Fig. 7.69). These shock diamonds occur when the pressure inside the jet is different from the surrounding pressure, and they lead to sudden velocity reductions and can result in a dispersion of the particle trajectories. The jet can be over-expanded, i.e., with a pressure inside the jet lower than the environment pressure or under-expanded with a jet pressure higher than the environment pressure. As a consequence, through the interaction with the environment the jet is compressed or expanded, but an overcompensation may occur resulting in another under-expansion/over-expansion of the flow. A complicated flow structure evolves with shock waves starting at the nozzle exit being reflected at the discontinuity between jet and environment, and these reflected shockwaves create the shock diamonds. The more shock diamonds and the clearer they are visible, the worse the fluid dynamic condition. The use of a properly designed Laval nozzle either as part of the anode

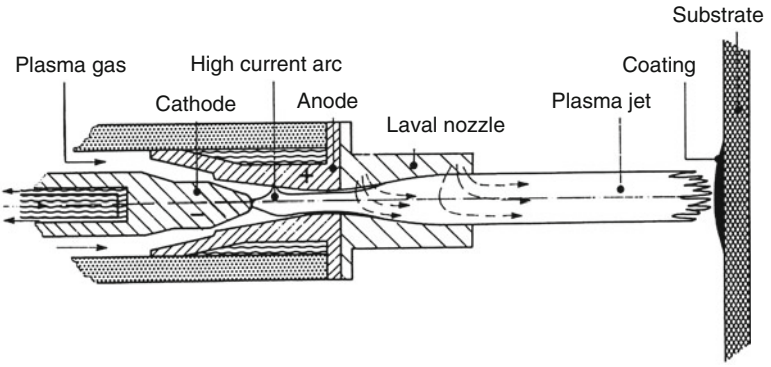


Fig. 7.70 Schematic of torch with Laval nozzle attachment for improved pressure equilibration [140]. Reproduced with kind permission of Sulzer Metco AG, Switzerland

or as an attachment to the anode can significantly improve the results by avoiding the shock structures immediately downstream of the anode nozzle exit [140]. A schematic of a torch with a Laval nozzle attachment is shown in Fig. 7.70 [140]. The Laval nozzle attachment offers an increase of particle velocities by 30–50 % and focuses the particle jet into a direction more parallel to the torch axis [140, 141], resulting in a higher deposition efficiency [23]. As a consequence, the torch current and power level can be reduced.

New developments in vacuum plasma spraying show deposition at lower pressures and a combination of particle spray deposition and vapor deposition processes, resulting in excellent coating quality. However, it must be kept in mind that these coatings are of interest for parts, which have a high value added by the process and will, therefore, be limited to a fraction of the market.

EB-PVD competes with success with conventional plasma spraying for the topcoat of the TBCs used to improve the life and performance of turbine components. It makes it possible to deposit thick (a few hundred micrometers) YSZ coatings with a fine columnar microstructure that results not only in a higher strain tolerance but also higher thermal conductivity than plasma-sprayed coatings [142]. In contrast to plasma spray technology, the EB-PVD process is operated at much lower pressures (0.1–5 Pa) and needs an expensive equipment investment; it exhibits also lower deposition rates. It is a vacuum deposition process where focused high-energy electron beams evaporate the coating material and the vapor phase is transported to the substrate forming a coating.

When used close to atmospheric pressure, thermal plasma jets are rather short, with a potential core of a few centimeters and a plume about twice as long, as illustrated in Fig. 7.71a [143] (courtesy of Sulzer Metco) which shows the picture of a plasma jet issuing in argon. In soft vacuum, the jet will lengthen and enlarge, as shown in Fig. 7.71b: at 30 kPa the plasma plume reaches 0.5 m in length and up to 0.04 m in diameter. The Sulzer Metco company, taking advantage of the characteristics of plasma jets and the possibility to achieve coatings with particular

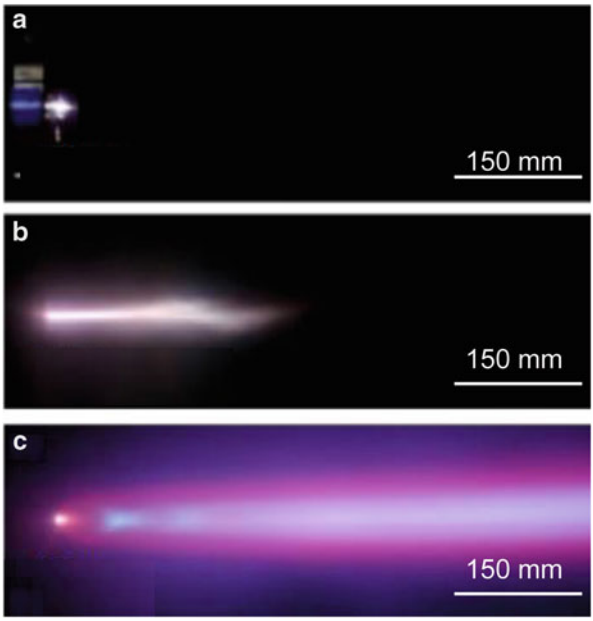


Fig. 7.71 Images of plasma jets in a controlled atmosphere chamber expanding at different pressures: (**a**) 950 kPa (APS), (**b**) 50 kPa (VPS/LPPS), and (**c**) 1 kPa (PS-PVD) and deposition process [143]. Copyright © ASM International. Reprinted with permission

microstructures when the process is operated a low pressure, has developed a new process called PS-PVD. It is based on their expertise in low pressure plasma spraying and involves a high-power plasma spray torch (180 kW–3,000 A, gas flow up to 200 slm) working at a pressure as low as 1 kPa (10 mbar). Under such low pressure conditions, the plasma jet reaches more than 2 m in length and up to 0.4 m in diameter as presented in Fig. 7.71c. With PS-PVD, coatings exhibiting a microstructure similar to that of EB-PVD coatings have been obtained (Fig. 7.72a) using a low powder feed rate, adapted spray conditions, and large spray distance. The YPSZ columns grow perpendicular to the substrate surface, the roughness (Ra) of which was lower than 2 μm, and kept at a temperature in the 1,000 °C range [143]. These columns consist of many fine needles with a high defect density and a high amount of internal porosity. Thanks to the versatility of the PS-PVD process, it also allows deposition of porous coatings with fine particles and splats imbedded in a matrix resulting from vapor deposition as shown in Fig. 7.72b by adapting the spray parameters.

In the range of controlled atmosphere spraying one has the spraying in an inert atmosphere to avoid oxidation and pressures range from 70 to 120 kPa. Oxygen content of less than 7 ppm can be achieved with the use of liquid argon as plasma gas source [144]. The cooling of substrate and coating during spraying is achieved with atomized liquid argon. Avoidance of air entrainment results in plasma jets which are longer by a factor of 1.5–2 [22]. This is an advantage when spraying carbides, borides, or refractory metals, which are very sensitive to oxidation.

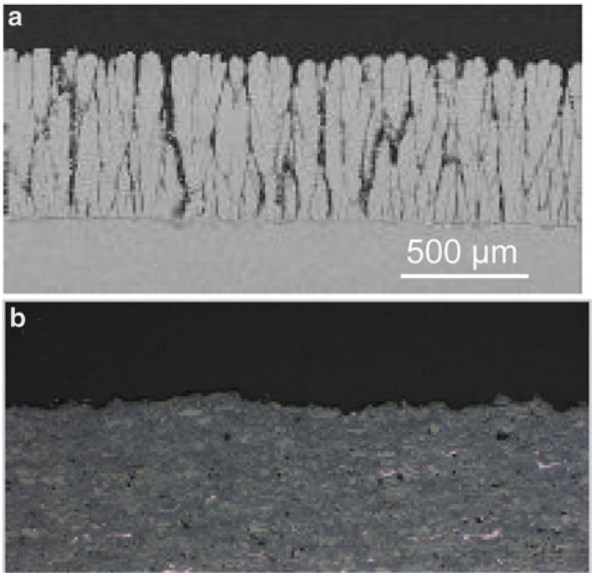


Fig. 7.72 TBC coating of 7YSZ using different PS-PVD plasma parameters showing (**a**) columnar structure and (**b**) splat-like structure [143]. Copyright © ASM International. Reprinted with permission

Spraying at pressures above atmospheric has been demonstrated [145], however, the short plasma jets and the increased electrode erosion have prevented this process for reaching a wide acceptance.

7.10 Plasma-Sprayed Materials and Coatings

As already emphasized, according to temperatures achieved within plasma jets any material can be melted, decomposed, or vaporized, including refractory metals and ceramics, and, according to particle velocities, the kinetic energies at impact result in good flattening. Accordingly coating bond strengths exceed 30 MPa (up to 60–70 MPa). However the weak point of the process is linked to the excellent melting of particles and air entrainment within the plasma jet when spraying in air (APS). Both result in enhanced oxidation, drastically promoted by the convective effect induced by the plasma flow inside the molten drops (see Sect. 4.3.3.7c). Spraying in controlled atmosphere, CPS, reduces drastically this phenomena and allows spraying materials very sensitive to oxidation such as borides, carbides, tungsten, etc. However, this requires using high purity gases, especially argon, and also cooling of the part during spraying with atomized liquid argon. Vacuum plasma spraying, VPS, with broader, longer, and more uniform spray jets than those produced at atmospheric pressure is more tolerant to process parameter changes and, of course, results in very low oxidation levels in the coatings. Moreover, before starting the spray process, but with the plasma jet working, by

running a transferred arc between the torch anode and the part to be sprayed as cathode makes it possible to clean the metallic part surface of its oxide layer. This allows an excellent bonding by diffusion when spraying metals or alloys onto metallic parts. At last, during spraying, it is possible to run another tailored transferred arc between the torch anode nozzle and the part, as secondary anode, in order to increase the part surface temperature to values where metal diffusion is fast and important. Of course, according to the investment, VPS is much more expensive than APS and more expensive than CPS.

It is not surprising that the great success of APS lies in the spraying of oxide materials. For non-oxide ceramics and refractory metals, used mostly in very high temperature and harsh conditions, CPS is the most adopted process, even if VPS is sometimes used. For materials requiring very low oxide levels, VPS is the best suited process, and its great success is the spraying of super alloys for aerospace, aeronautic and land based turbines. Of course APS is also used to spray metals, alloys, and cermets when oxidation is not a problem. In the following the previous remarks will be illustrated by few examples, which represent only a very small part of plasma sprayed coatings.

7.10.1 Oxide Materials

The most frequently sprayed oxides are: Al_2O_2, TiO_2, ZrO_2, $ZrSiO_4$, Cr_2O_3, Y_2O_3, and their mixtures.

7.10.1.1 Alumina

When plasma sprayed, for all fully molten particles the initial α phase is transformed into γ phase upon splat cooling. Unfortunately when the coating is preheated over 950 °C the γ phase is transformed back into the α phase with about 4 vol. % change resulting in coating spallation. Thus plasma-sprayed alumina coatings cannot be used over 800 °C. However spray conditions have been sought, which would keep the α phase. Stahr et al. [146] have studied the stabilization of α alumina by spraying, with APS, WSP, and HVOF, mechanical mixtures of alumina and chromia, as well as pre-alloyed powders consisting of solid solution α-Al_2O_3 with additions of Cr_2O_3. Stabilization of the α phase using the WSP process starting from mechanical mixtures was confirmed. For the WSP process, the positive effect of an increase in the α phase with increasing Cr_2O_3 content in the coating was clearly shown. Contrary to this, in the APS process starting from mechanical mixtures, no stabilization effect was found when mechanically mixed powders were sprayed. However, additional work is necessary to better understand the involved phenomena.

Alumina coatings are mainly used for their good resistance to abrasive wear, sliding wear, and oxidation. Alumina coatings are also used for their dielectric

strength, suitable for insulating coatings extensively used in ozonizers [147]. Kitamura et al. [148] have shown that coating density strongly affects dielectric strength for both Al_2O_3 and Y_2O_3 coatings, while the influence of purity is found to be much less important in their study. Toma et al. [149] have used APS and HVOF processes to prepare alumina (Al_2O_3) and magnesium spinel ($MgAl_2O_4$) coatings designed for insulating applications. Electrical insulating properties (dielectric strength and electrical resistance/resistivity) were very dependent on relative air humidity level and water vapor sorption. Alumina coatings obtained by APS are denser than those flame sprayed [150] and are also used against wear, as well as Cr_2O_3, TiO_2, etc. However wear resistance of sprayed oxide ceramics is not dependent only on the hardness of the coatings but also strongly on their toughness, which is not very high for alumina coatings. Darut et al. [151] have studied the tribological properties of alumina coatings with two different structural scales, a micrometer-sized one manufactured by atmospheric plasma spraying and a sub-micrometer-sized one manufactured by suspension plasma spraying, SPS. Coating architectures were analyzed and their friction coefficients were measured using a dry sliding mode. The friction coefficient was decreased by a factor of two when the characteristic scale was reduced by two orders of magnitude. Accordingly, the wear resistance of SPS coatings was significantly higher than that of APS coatings, thanks to a better toughness of the layer.

Because of their porosity, plasma-sprayed $A1_2O_3$ and Cr_2O_3 coatings must be sealed to improve their corrosion resistance. Leivo et al. [152] used aluminum phosphates to seal them. Phosphates were formed throughout the coating, down to the substrate. The sealing increased the hardness of the coatings by 200–300 Vickers hardness (HV) units. Abrasion and erosion wear resistances were increased by the sealing treatment. Sealing also substantially closed the open porosity, as shown in electrochemical corrosion tests. The sealed structures had good resistance against corrosion during 30 days of immersion in both acidic and alkaline solutions with pH values from 0 to 10. No decrease in abrasion wear resistance was observed after immersion. Berard et al. [153] tested alumina plasma-sprayed coatings, manufactured with feedstock of different particle size distributions, graded alumina–titania coatings, and phosphate-sealed alumina coatings to improve the properties of metallic substrates operating in extreme environments encountered in the processing of nuclear wastes. Such conditions correspond, for example, to aging at moderate temperatures (several months at about 300 °C) coupled to thermal shocks (numerous cycles up to 850 °C for a few seconds, and a few treatments up to 1,500 °C), under a reactive environment made of a complex mixture of acid vapors in the presence of an electric field of a few hundred volts and of radioactivity. Aluminum phosphate impregnation appeared to be an efficient post-treatment to fill connected porosity of these coatings. Mesrati et al. [154] proposed to reduce graphite reactivity and permeability toward oxygen by plasma spraying of Al_2O_3 or ZrO_2. The process required bond coats of Cr_3C_2 or SiC. However, the protection was good only after a post-treatment of the coating based on an impregnation with enamel of the porous oxide.

Keshri and Agarwal [155] have proposed to improve the wear resistance of plasma-sprayed Al_2O_3 using carbon nanotubes (CNT). Composite coatings have been investigated at room temperature (298 K), elevated temperature (873 K), and in sea water. Lowest wear volume loss has been observed in the sea water as compared to dry sliding at 298 and 873 K. Relative improvement in the wear resistance of Al_2O_3–8 wt% CNT coatings compared to Al_2O_3 was 72 % at 298 K, 76 % at 873 K, and 66 % in sea water. This was attributed to (1) larger area coverage by the protective film on the wear surface at room temperature and in sea water, (2) higher fracture toughness of Al_2O_3-CNT coatings due to CNT bridging between splats, and (3) antifriction effect of sea water.

Another important application is the coating of rolls that are used to transport a polymer material past a corona discharge to modify the surface, e.g., to allow printing on it.

7.10.1.2 Titania and Alumina–Titania Coatings

Titania can be used for applications similar to those of alumina but coating hardness is lower as well as the dielectric strength and the resistance to chemical attack.

Titania loses oxygen when plasma sprayed (its color tends to shift from white to gray or even black), the stoichiometry variation of the coatings resulting in a large variation of their electrical properties [156]. Ctibor et al. [157] have sprayed, with the high throughput water-stabilized plasma (WSP), agglomerated nanometer-sized titania powder and a fused and crushed titania. Results indicate that the "nano"-coatings in general exhibit finer pores than coatings of the "conventional" micron-sized powders. The "nano"-coating properties (resistance to slurry abrasion, for example) were better only for carefully selected sets of spraying parameters, which seemed to have a very important impact. Titania coatings could be promising for their photo-catalytic activity if the anatase structure is preserved after spraying, which unfortunately is not the case with plasma spraying. Ye et al. [158] have studied the addition of hydroxyapatite, HAp, $(Ca_{10}(PO_4)6(OH)_2)$ to inhibit the phase transformation of anatase TiO_2 to rutile. The photo-catalytic activity of TiO_2–10 %HAp coating was highest among TiO_2, TiO_2–20 %HAp, and TiO_2–30 %HAp coatings for the optimum adsorption property and anatase content.

Al_2O_3–TiO_2 particles, generally fused and crushed, with different wt% of TiO_2 are extensively used against wear and for their resistance to acids and alkalis. Three different compositions are mainly used:

- Al_2O_3–$3TiO_2$, which is less brittle, but with lower dielectric strength, than pure Al_2O_3 coatings.
- Al_2O_3–$13TiO_2$, which has lower hardness, but higher toughness, and lower dielectric properties than Al_2O_3–$3TiO_2$. This hypoeutectic composition results in coatings where γ-alumina is the main phase [159]. The wear resistance is better than that of alumina coatings, thanks to the increased toughness, in spite of a hardness reduction [160–163].

– Al_2O_3–45TiO_2 coatings (hyper-eutectic composition) present lower hardness and less wear resistance than the preceding ones. This is probably due to the lower hardness and toughness of Al_2TiO_5 (and/or $Al_6Ti_2O_{13}$) aluminum–titanates contained in these coatings.

7.10.1.3 Chromium Oxide

Plasma-sprayed chromium oxide coatings are dense, corrosion, and wear resistant and used on pump seal areas, rolls and wear rings, ceramic anilox rolls used in printing machines working with flexography systems, and they are insoluble in acids, alkalis, and alcohol. In the printing industry the rolls plasma coated with chromium oxide are used to transport the precisely determined quantity of ink in the flexographic printing machines. Of course the powder choice and spray conditions influence coating properties [164]. These coatings are then ground and polished before being laser engraved. Chromium oxide coatings are often used for their tribological properties, as reported, for example, by Ahn and Kwon [165]. Usmani and Tandon [166] have simulated the reciprocating sliding wear under lubrication encountered in internal combustion engines with plasma-sprayed chromium oxide, metal arc-sprayed martensitic stainless steel, and electroplated chromium coatings applied to a steel base material. The chromium oxide coating was found to perform equally well compared to the hard chrome coating that is conventionally used.

7.10.1.4 Zirconia

This is probably one of the most studied plasma-sprayed ceramic for its use in thermal barrier coatings because of its low thermal conductivity (<1.5 W/m K) and excellent thermal shock resistance. It must be stabilized to avoid phase transformation upon heating and cooling. This is achieved with Y_2O_3, CeO_2, or MgO, the higher stabilization temperatures being obtained with Y_2O_3 and CeO_2. When the plasma-sprayed thermal barrier coatings were first used in the late 1980s both for aero-engines [167] and land-based turbines [168], the thermal insulation was achieved with zirconia stabilized by 8 wt% of yttria, PYSZ, which has been established as a standard for the last 20–30 years. Many studies have been devoted to these coatings and their qualities dependent on the powders used and the spray conditions. Ar–H_2 mixtures have been mostly used, although recently the advantages of N_2–H_2 mixtures have been reported [169]. A recent review by Vassen et al. [170] reports that during the last decade a number of ceramic materials, mostly oxides, have been suggested as new thermal barrier coating (TBC) materials. These new compositions (pyrochlores, zirconia doped by different rare-earth cations, hexaaluminates, and perovskites) have been developed to compensate the limited temperature capability of PYSZ, restricted to about 1,200 °C, a value which is insufficient for advanced gas turbines.

It is also important to note that PYSZ are also used in solid oxide fuel cells, SOFC. Fuel cells directly convert chemical energy into electrical energy with the potential of very high-efficiency values, because they are not subject to the Carnot limitation. They typically operate at a high temperature around and above 800 °C and their operation is determined by the electrochemically active ceramic layer [171]. According to the review by Henne [171] different manufacturing methods are in use or under development for the production of the cell components. Among these methods are also plasma spray technologies, as described by Henne [171] and others [125, 172, 173]. In these SOFCs both the cathode [generally strontium-doped lanthanum manganite (LSM)], the electrolyte (PYSZ or YSZ), and the anode (often PYSZ/Ni) are plasma sprayed. The main difficulties are to make the electrolyte as thin as possible (<10 μm, which seems possible with suspension plasma spraying) and impervious to gases, while cathode and anode must be porous. Of course, other ceramics are currently studied as well for these plasma-sprayed SOFC components.

Zirconia has also good wear resistance and it is sprayed together with other oxides. Abdel-Samad et al. [174] showed that by the addition of zirconia to an alumina matrix, the porosity, hardness, and coefficient of friction of the coating were decreased. At the same time the wear resistance was increased due to the higher toughness of this ceramic.

7.10.1.5 Other Oxides

Besides oxides previously cited, which are the most frequently used for plasma spraying, other oxide materials consist of mixtures of different oxides such as Al_2O_3–SiO_2, Al_2O_3–$xTiO_2$–$ySiO_2$, Cr_2O_3–$xTiO_2$, Cr_2O_3–$xTiO_2$–$ySiO_2$, ZrO2–$xTiO_2$–yY_2O_3, ZrO_2–$xCaO$–yAl_2O_3–$zSiO_2$, but also Y_2O_3, HAP, TaO_2, and mullite, and only a few examples will be presented.

Because of the excellent biocompatibility of hydroxyapatite (HAP), plasma-sprayed HAP is widely used to coat orthopedic protheses. During the plasma spraying process, the thermal decomposition of HAP produces [175] tricalcium phosphate (TCP), tetracalcium phosphate (TeCP), calcium oxide (CaO), oxyhydroxyapatite (Oxy-HAP), and a molten phase. Khor et al. [176] have shown that subsequent post-spray heat treatment at 600, 700, and 800 °C for 1 h restored most of the crystalline HA in the coatings. There was also a corresponding increase in the crystalline HAP phase when increasing particle size range. Bond coats based on bioinert ceramic materials such as titania and zirconia were developed to increase the adhesion strength of the coating system hydroxyapatite-bond coat to Ti–6Al–4V alloy surfaces used for hip enoprostheses and dental root implants [177, 178]. To summarize plasma spraying technology is more and more used in fabrication of articles for medical devices.

Plasma treatment is effectively used in the fabrication of microelectronic components especially in dry etching. The halogen-contained plasma at high power levels erodes the film protecting the chamber wall at a high rate, generating a large

amount of particles and requiring frequent maintenance of the production equipment. Plasma-sprayed alumina or yttria coatings [179] have technical and commercial advantages to overcome these problems. Kitamura et al. [180] have shown very recently that yttria coatings obtained by suspension spraying with an axial torch (Mettech Axial III) presented high density, uniform structure, high hardness, high plasma erosion resistance, and retention of a smoother surface after plasma erosion. Although the properties of the best suspension coating are still inferior to bulk Y_2O_3, they are much better than those of the conventional plasma sprayed coatings.

Moldovan et al. [181] have sprayed Ta_2O_5 coatings that can be considered for environmental barrier applications. The as-sprayed coatings were approximately 97–98 % dense and were composed of the low-temperature polymorph, β-Ta_2O_5 and some α-Ta_2O_5. Upon thermal treatment, the α-phase was converted to the low-temperature β-Ta_2O_5 phase.

Among the different ceramic mixtures, plasma sprayed, YSZ-mullite multilayer architectures with compositional grading between the bond coat and YSZ topcoat are potential solutions to ease their coefficient of thermal expansion mismatch induced stress. Cojocaru et al. [182] have identified a better match between the elastic modulus, E, and hardness, H, values of the bond coat, and subsequent layers obtained from powders having similar type and size distribution. Das et al. [183] have plasma sprayed a mixture of zircon and alumina on a mild steel substrate. The coating appeared to be sound and continuous along the interfaces and in the bulk as well. During spraying, zircon sand dissociated into zirconia and silica and a fraction of this silica in turn combined with a fraction of the alumina to form the mullite phase. The presence of the mullite phase enhanced the thermal fatigue characteristics of the coating.

7.10.2 Non-oxide Ceramics

Carbides, borides, and nitrides can be plasma sprayed when they have a melting point that is separated by at least by 300 K from evaporation or decomposition temperatures. These ceramics are also very sensitive to oxidation and must be sprayed in controlled atmosphere or under soft vacuum. They are used for their high temperature resistance in nuclear, military, and aerospace industries, and thus only few papers are published about them. For example Zeng et al. [184] have sprayed in air B_4C particles. Besides B_xC, B_4C, and carbon, other impurity phases exist consisting of B, O, and Fe elements (i.e., Fe_3BO_6). As the carbon phase, the Fe_3BO_6 phase also has a much lower microhardness than the major phase, contributing to the decrease of microhardness of boron carbide coatings. B_4C is an important material for fusion reactors and it has been extensively studied [185]. Its advantages include low atomic number, Z, a relatively high melting point, thermal shock resistance, low vapor pressure, oxygen gettering, chemical

inertness, and easy hydrogen isotope release. Greuner et al. [186] demonstrated that a VPS-based coating technique was suitable for manufacturing the B_4C protection layers on stainless steel wall panels of the W7-X fusion reactor. The other sprayed boride is ZrB_2 for its high hardness, associated with high electrical and thermal conductivities, together with a very high melting point (T_m = 3,313 K). Tului et al. [187] showed that ZrB_2 coatings, deposited by CPS, were good electrical conductors and compared favorably with the reference coatings, in terms of tribological performance, which was not the case of those sprayed by APS. Pulci et al. [188] studied the high temperature mechanical properties of ZrB_2–SiC (30 % vol.)–$MoSi_2$ (10 % vol.) plasma-sprayed coatings at different temperatures (up to 1,500 °C) in air. Results showed an improvement in mechanical properties as the temperature increased up to 1,000 °C. However at 1,500 °C, coatings maintained good mechanical properties but exhibited a plastic behavior.

Carbides are also used for high temperatures applications. Li et al. [189] prepared a dense, thick ZrC coating on the surface of SiC-coated C/C composites by supersonic plasma spraying. The ZrC coating had good adhesion to the SiC inner layer. It greatly improved the ablation resistance of SiC-coated C/C composites.

Another way to prepare non-oxide ceramic coatings is reactive plasma spraying. For example, Hu et al. [190] have prepared SiC coatings for carbon/carbon (C/C) composites by a combination of vacuum plasma spraying technology and heat treatment. The SiC coatings were formed by the reaction of C/C substrates with as-sprayed silicon coatings deposited by vacuum plasma spraying. The preparation temperature and the thickness of the original silicon coatings were shown to have a great influence on the microstructure and the thickness of the synthesized SiC coatings. Siegmann et al. [191] have sprayed by VPS an optimized iron-based alloy consisting of $Fe_{17}Cr_{10}Mn_6VMo$. Particles were nitrogen atomized to create nano-structured hard phases of vanadium nitrides, VN, in each droplet, their size and distribution being adjusted as a function of the N content during the formation process. Using a VPS facility, coatings were sprayed without any oxidation during coating formation and with excellent coating properties. Besides the preceding nitridation of the starting powders, the reactive alloying with N can be achieved during vacuum plasma spraying by the exposure of the particles to a N_2-rich plasma and by creating a N_2-rich environment in the VPS chamber. Borisova and Borisov [192] have presented many carbide coatings that can be prepared by APS by self-propagating high-temperature synthesis, SHS. SHS is accompanied by heat generation in composite powder particles (see Sect. 4.2.4.5). Moreover, this technique allows extending the range of possible compositions of composite powders, compared with the conventional methods. The combination of heating of particles (by hot gas jet) and the additional heat source through the exothermic synthesis of coating material formation from components of composite powder particles increases the thermal energy of sprayed particles, which also can improve the quality of the resultant coatings.

7.10.3 Cermets

A cermet is a composite material composed of ceramic and metallic materials. A cermet is ideally designed to have the optimal properties of both the ceramic and those of the metal especially plastic deformation. The metal is used as a binder for oxides, borides, or carbides. Cermets are used not only for their superior wear and corrosion properties but also in the manufacture of resistors. It must be kept in mind that with the APS process, the metal part of the cermet will be oxidized, but when the ceramic is non-oxide it can be partially or totally decomposed and even dissolved in the molten metal. However partially decomposed carbide can be useful because free carbon is produced resulting in coatings with a low friction coefficient against certain materials. Among the numerous carbide cermets, WC–Co is the most widely applied one, but when plasma sprayed WC is prone to oxidize and/or decompose, while Cr_3C_2–NiCr coatings are more resistant to decomposition at higher temperatures, where corrosion and oxidation can occur simultaneous. Naturally VPS or CPS allows avoiding these problems but their costs cannot compete with those of an HVOF processes producing the same quality of coatings.

For example, Basak et al. [193] have plasma sprayed agglomerated nano-sized powders of alumina (Al_2O_3) and cermet coatings containing alumina dispersed in a FeCu or a FeCuAl matrix. Nanostructured cermet coatings appeared to offer better wear resistance under sliding and abrasion tests than nanostructured Al_2O_3 coatings. The cermet coatings contained up to four different phases after plasma spraying. It was shown that an appropriate balance between hard and soft phases resulted in optimal tribological properties of the nanostructured cermet coatings. Fervel et al. [160] have studied the tribological behavior of plasma-sprayed coatings Al_2O_3, Al_2O_3–TiO_2, Al_2O_3–TiO_2–Cu. in dry conditions. It was found that TiO_2 improved the fracture toughness of coatings and copper reduced friction and wear. Hwang et al. [194] have investigated plasma spray-coated piston rings and cylinder liners for marine diesel engines to find the optimum combination of coating materials. Coating materials studied were Cr_2O_3–NiCr, Cr_2O_3–NiCr–Mo, and Cr_3C_2–NiCr–Mo. They found that a dissimilar coating combination of Cr_2O_3–NiCr–Mo and Cr_3C_2–NiCr–Mo provided the best antiwear performance. The addition of molybdenum was found to be beneficial to improve the wear resistance of the coating.

Instead of using cermet powders, metal and ceramic powders can be sprayed separately as demonstrated by Ageorges et al. [195] with Cr_2O_3 and stainless steel powders. Increasing the stainless steel percentage increased the coating cohesion, while more Cr_2O_3 in coatings resulted in higher hardness and lower weight losses during wear tests in dry abrasion. The study has also shown that the optimum stainless steel percentages in coatings were not identical to reach their maximum resistance to slurry or dry abrasion. Hashemi et al. [196] sprayed Ni–Al–SiC composite powder containing 12 wt% SiC. The powder was prepared by ball milling in a conventional tumbler mill. The results showed that spray parameters have a significant influence on the phase composition and mechanical properties of coatings.

Economou et al. [197] have tested at room temperature and at 550 °C vacuum plasma sprayed NiCrFeAlTi–TiC, NiCr–(Ti, Ta)C, and NiCrMo–(Ti, Ta)C coatings. Air plasma-sprayed NiCr and NiCr–TiC coatings, as well as the high velocity oxy-fuel WC–Co coating, were investigated for comparison. The wear resistance of all coatings decreased at high temperature. The NiCrFeAlTi–TiC coating showed the best wear resistance among the TiC-based coatings. At room temperature and at 550 °C, the WC–Co coating was more wear resistant than the TiC-based coatings, even though the coating cracked in the high temperature tests. The coefficients of friction of the WC–Co coating, tested against sapphire, were lower than those of the TiC-based coatings at room temperature, but not lower than those obtained at 550 °C. These examples illustrate the diversity of plasma-sprayed cermets and of the results obtained. The latter can be very different for the same cermet composition depending not only on the spray parameters, but also on the spray process used and the powder morphologies.

7.10.4 Metals or Alloys

7.10.4.1 Vacuum Plasma-Sprayed Metal Coatings

The VPS development is linked to that of bond coats (MCrAlY coatings) for TBCs in aero-engines. Bond coats [198, 199] are applied to enhance the adherence of the TBC coating to the substrate alloy and to increase the high-temperature oxidation and corrosion resistance of the underlying structural alloy. The protection against oxidizing environments is achieved by forming a thin oxide layer commonly termed as thermally grown oxide, TGO. This layer acts as a barrier between the alloy and the atmosphere and impedes further oxidation. Growth of the TGO occurs either by outward diffusion of metal ions or by inward diffusion of oxygen ions through the oxide layer. The most commonly used TGO is alumina Al_2O_3, which has a slow growth rate and is easily formed on metallic alloys [199]. However to reduce the costs, superalloy coatings are also produced using APS [200], sometimes with shrouded torches [201].

VPS is also used to spray very specific metals such as beryllium [202] for in-situ repair of damaged beryllium surfaces, which are facing the plasma in fusion reactors such as the international thermonuclear experimental reactor (ITER). The effective bond strength and failure characteristics of plasma-sprayed beryllium on beryllium surfaces were determined by mechanical interlocking at low substrate temperatures and increased metallurgical bonding at higher substrate temperatures. VPS can also be used to spray cast iron coatings [203] to hinder graphite formation. Schiller et al. [204] have produced by a VPS process electrode coating for advanced alkaline water electrolysis. Molybdenum-containing Raney nickel coatings were applied for cathodic hydrogen evolution. For the preparation of Raney nickel coatings, a precursor alloy Ni–Al–Mo was sprayed and leached subsequently in a caustic solution to remove the aluminum content, forming a porous, high-surface area nickel–molybdenum layer.

7.10.4.2 Air Plasma-Sprayed Metal Coatings

Most plasma-sprayed alloys are nickel or cobalt or iron based, with, as mentioned previously, superalloys and molybdenum as the metals. Some abradable coatings are also sprayed. Tani and Harada [205] have plasma sprayed, onto the combustion facing surface of steam generating tubes in a heavy oil-fired boiler, Ni–50 mass % Cr alloy coatings for their corrosion resistance. The Ni–50 mass% Cr alloy coating was successful for the suppression of hot corrosion failure of the steam generating tubes of the boiler. Longa-Nava et al. [206] deposited by VPS and APS Cr–Ni–2.5Mo–1Si–0.5B alloys containing 55 or 58 wt% chromium. CO_2-1aser glazing subsequently modified the thermally sprayed coatings. Oxidation and corrosion resistance of the as-sprayed and laser-processed coatings were tested in the presence of $85V_2O_5$–Na_2SO_4 fused salt at 900 °C in air. Hot corrosion resistance of the CrNiMoSiB coatings increased in the following order: VPS, APS, laser-glazed VPS, and laser-glazed APS. Laser glazing enriches the silicon content in the top layers of the coating. Laser-glazed APS CrNiMoSiB coatings exhibited excellent corrosion resistance due to the continuous oxide film of chromia and silica formed on the top surface of the coating. Cyclic oxidation behavior of plasma-sprayed NiCrAlY, Ni–20Cr, Ni_3Al, and Stellite-6 coatings was investigated by Singh et al. [207] in an aggressive environment of Na_2SO_4–60 %V_2O_5. These coatings were deposited on a Ni-base superalloy, namely Superni 600; 10Fe–15.5Cr–0.5Mn–0.2C–Bal Ni (wt%). All of the coatings were found to be useful in reducing the spallation of the substrate superalloy. Moreover, the coatings were successful in maintaining continuous surface contact with the base superalloy during the cyclic oxidation. Miguel et al. [208] sprayed bronze coatings that showed good friction properties (friction coefficient of about 0.3) that remained constant during the entire test. However, bronze–alumina composite coatings obtained by spraying both powders with conditions allowing both powders to be melted produced dense composite coatings with good adhesion and with a general increase in abrasion resistance, even if accompanied by an increase of the friction coefficient.

Coatings of molybdenum, pure or blended with other elements, are often used for their wear resistance, for example, on synchronizer rings or piston rings. Ahn et al. [209] have plasma sprayed four different powders, one of pure molybdenum, the others being blended powders of bronze and aluminum–silicon alloys mixed with molybdenum powders. The wear test results revealed that the wear rate of all coatings increased with increasing wear load and that the blended coatings exhibited better wear resistance than the pure molybdenum coating, although the hardness was lower. The molybdenum coating blended with bronze and aluminum–silicon alloy powders exhibited excellent wear resistance because hard phases such as $CuAl_2$ and Cu_9Al_4 formed inside the coating. Niranatlumpong and Koipraser [210] studied coatings plasma sprayed with various amounts of Mo mixed with NiCrBSi at 0, 25, 50, 75, and 100 wt%. They found that as the Mo/NiCrBSi ratio increases, the wear mechanism changed. Coatings containing 75 %Mo and 25 %NiCrBSi exhibit the highest wear depths corresponding to the cracking of the thin NiCrBSi splats. On the other hand, coatings containing 25 %Mo and 75 %NiCrBSi had the lowest wear depths with no surface cracks.

Plasma-sprayed coatings are also used to produce resistors. For example, Prudenziati and Lassinantti Gualtieri [211] have deposited Ni and Ni20Cr powders to obtain resistors. A clear correlation was found between the oxygen content in the resistors and the temperature dependence of resistance values. The long-term stability of APS Ni-based resistors rendered them excellent candidates for temperature sensors and self-controlled high temperature heaters. Floristán et al. [212] have sprayed by APS electrically conductive coatings on a glass ceramic substrate, using TiO_2 and mixed phases of TiO_2/NiCrAlY. Direct spraying on glass substrates is interesting for industrial applications but the expansion coefficient mismatch is a problem. TiO_2/NiCrAlY mixed phase coatings presented a change in the metal content depending on the spray distance. The most stable system was the TiO_2 coating, with the lowest tensile stresses and the best adhesion. However, the electrical conductivity of the coating restricted its usability to applications, where the resistivity values were not lower than 0.05 Ω cm.

The different coatings presented above illustrate the high versatility of the plasma spray processes. Almost any material with a melting temperature, T_m, that is at least 300 K lower than its decomposition or vaporization temperatures can be sprayed even if T_m is over 4,000 K! However, the oxidation of materials sprayed in air can be significant. The oxidation can be controlled when spraying in soft vacuum or a controlled atmosphere, but at a much higher cost.

7.11 Summary and Conclusions

The typical operating conditions of various spray torches are summarized in Table 7.2. It is clear that the high power torch and the water swirl stabilized torch offer significantly higher deposition rates, whereas the Triplex and the low pressure

Table 7.2 Characteristics of various spray torch-operating conditions

	Plasma gas						
		Flow rate slm		Current	Voltage	Power	Powder flow rate
Type	Type	Primary	Secondary	A	V	kW	kg/h
Conventional	Ar	40–100		500–1,000	30	<30	
	A–He	40–100	5–40	500–900	50	45	6–8
	Ar–H_2	40–100	3–15	700	80	55	
	N_2–H_2	40–100	5–15	500	80	40	
High power	N_2–H_2	300	150	500	400	200	20/45
Triplex	Ar–He	30–60		300	80	20–55	6–10
Water swirl	H_2–O_2			300–600	250–300	80–200	45/100
Low pressure	Ar–H_2	40–60	9	750	70	55	

systems offer improved coating quality and process reliability. In addition, the Triplex torch offers longer electrode life. The water swirl stabilized torch has shorter electrode life times than most other torches, while with the regular conventional torch, electrode life depends on coating requirements, i.e., for high quality coatings the electrodes are replaced more frequently. The choice which equipment or process to use depends on a combination of factors, such as the required coating properties/quality/reproducibility, the value added to the part by the coating, the economics presented by the equipment cost, powder cost, deposition efficiency, and by the process controllability. The discussion in this chapter shows that a wide range exists in each of these factors, and typically a compromise has to be made for getting the optimal result.

Nomenclature

A	The channel cross sectional area (m^2)
A_{RD}	Richardson–Dushman empirical constant (about 6×10^5 A/m^2 K^2 for the majority of the cathode materials)
c_p	The specific heat at constant pressure of the plasma gas (J/kg K)
e	Electronic charge (C)
E	Electric field in the arc column (V/m)
E_x	Electric field normal to the anode surface (V/m)
h	Enthalpy at a given radial location at the torch exit (J/kg)
h_{ave}	Average enthalpy of the gas leaving the torch (J/kg)
I	Arc current (A)
j	Electron current density (A/m^2)
j_i	Ion current towards the anode (A/m^2)
k	Boltzmann constant (1.38×10^{-23} J/K)
k_a	Heavy particle thermal conductivity (W/m K)
k_e	Electron thermal conductivity (W/m K)
$\dot{m}$	Mass flow rate of the plasma gas (kg/s)
n_e	The electron number density (m^{-3})
p_e	Electron partial pressure (Pa)
P_{el}	Electric power input into the torch (W)
Q_{cond}	Loss to the torch wall by heat conduction (J/m)
Q_{loss}	The heat lost to the torch cooling water (W)
Q_{rad}	Loss to the torch wall by radiation (J/m)
R	Arc channel radius (m)
T	Heavy species temperature (K)
T_c	Cathode temperature (K)
T_e	Electrons temperature (K)
T_{ref}	Reference temperature for a zero value of the enthalpy (K)
v	Plasma velocity at given radial location at the torch exit (m/s)

Greek Alphabet

$\Delta\overline{h}$	Increase in enthalpy averaged over the cross section per unit length (J/kg)
Δz	Length variation (m)
ε_i	Ionization energy of the plasma gas (J)
ϕ_c	Work function (V)
ϕ_w	The work function of the anode material (V)
η	The torch gas heating efficiency (%)
ρ	Mass density of the plasma (kg/m^3)
$\rho(T_{ave})$	Mass density of the plasma gas at the average temperature (kg/m^3)
σ	Electrical conductivity (mho/m)

References

1. Fauchais P (2004) Understanding plasma spraying. J Phys D Appl Phys 37:86–108
2. Fauchais P, Vardelle M (2003) How to improve the reliability and reproducibility of plasma sprayed coatings. In: Moreau C, Marple B (eds) Proceedings of thermal spray: Advancing the science and applying the technology, Orlando, FL. ASM International, Materials Park, OH, pp 1165–1173
3. Janisson S, Meillot E, Vardelle A, Coudert J-F, Pateyron B, Fauchais P (1998) Plasma spraying using Ar-He-H2 gas mixtures. In: Coddet C (ed) Proceedings of the 15th international thermal spray conference, Nice, France. ASM International, Materials Park, OH, pp 803–814
4. Boulos M, Fauchais P, Pfender E (1994) Thermal plasma fundamentals and applications, vol 1. Plenum, New York, NY
5. Peters J, Yin F, Borges C, Heberlein J, Hackett C (2005) Erosion mechanisms of hafnium cathodes at high current. J Phys D Appl Phys 38:1781–1794
6. Maecker H (1955) Plasmaströmungen in Lichtbögen infolge eigenmagnetischer Kompression. Z Phys 141:198–216
7. Murphy AB (1996) The influence of demixing on the properties of a free-burning arc. Appl Phys Lett 69:328–330
8. Snyder SC, Murphy AB, Hofeldt DL, Reynolds LD (1995) Diffusion of atomic hydrogen in an atmospheric pressure free-burning arc discharge. Phys Rev E 52:2999–3009
9. Fincke JR, Swank WD, Haggard DC (1993) Entrainment and demixing in subsonic argon: helium plasma jets. J Therm Spray Technol 2(4):345–350
10. Mariaux G, Fauchais P, Vardelle A, Pateyron B (2001) Modeling of the plasma spray process: from powder injection to coating formation. J High Temp Mater Process 5:61–85
11. Baudry C, Vardelle A, Mariaux G, Abbaoui M, Lefort A (2005) Numerical modeling of a dc non-transferred plasma torch: movement of the arc anode attachment and resulting anode erosion. High Temp Mater Processes 9(1):1–18
12. Dussoubs B (1998) 3D modeling of the plasma spray process. Ph.D. Thesis, University of Limoges, Limoges, France
13. Trelles JP, Heberlein J (2006) Simulation results of arc behavior in different plasma spray torches. J Therm Spray Technol 15(4):563–569
14. Trelles JP (2007) Finite element modeling of flow instabilities in arc plasma torches. Ph.D. Thesis, University of Minnesota, Minneapolis

15. Paik S, Huang PC, Heberlein J, Pfender E (1993) Determination of the arc-root position in a DC plasma torch. Plasma Chem Plasma Process 13(3):379–397
16. Trelles JP, Heberlein J, Pfender E (2007) Non-equilibrium modeling of arc plasma torches. J Phys D Appl Phys 40:5937–5952
17. Dinulescu HA, Pfender E (1980) Analysis of the anode boundary layer of high intensity arcs. J Appl Phys 51(6):3149–3157
18. Leveroni E, Rahal AM, Pfender E (1987) Electron temperature measurements in the near-wall region of wall-stabilized arcs. In: Akashi K, Kinbara A (eds) Proceedings of 8th international symposium on plasma chemistry, Tokyo, Japan. University of Tokyo, Tokyo, pp 346–351
19. Pfender E (1994) Thermal plasma-wall boundary layers. In: Fauchais P (ed) Proceedings of international symposium on heat and mass transfer under plasma conditions, Cesme, Turkey. Begell House, New York, NY, pp 223–235
20. Jenista J, Heberlein J, Pfender E (1997) Model for anode heat transfer from an electric arc. In: Fauchais P (ed) Proceedings of fourth international thermal plasma processes conference, Athens, Greece. Begell House, New York, NY, pp 805–815
21. Jenista J, Heberlein J, Pfender E (1997) Numerical model of the anode region of high-current electric arcs. IEEE Trans Plasma Sci 25(5):883–890
22. Roumilhac P, Coudert J-F, Fauchais P (1990) Influence of the arc chamber design and the surrounding atmosphere on the characteristics and temperature distribution of Ar-H2 and Ar-He spraying plasma jets. In: Apelian D, Szekely J (eds) Plasma processing and synthesis of materials, vol 190. MRS, Pittsburgh, PA, pp 227–333
23. Rahmane M, Soucy G, Boulos M, Henne R (1998) Fluid dynamic study of direct current plasma jets for plasma spraying applications. J Therm Spray Technol 7(3):349–356
24. Sanders NA, Pfender E (1984) Measurement of anode falls and anode heat transfer in atmospheric pressure high intensity arcs. J Appl Phys 55(3):714–722
25. Pfender E (1978) Electric arcs and arc gas heaters. In: Hirsh MN, Oskam HJ (eds) Gaseous electronics: electrical discharges, vol 1. Academic, New York, pp 291–398
26. Sun X, Heberlein J (2005) Fluid dynamic effects on plasma torch anode erosion. J Therm Spray Technol 14(1):39–44
27. Yang G, Heberlein J (2007) The anode region of high intensity arcs with cold cross flows. J Phys D Appl Phys 40:5649–5662
28. Wutzke SA, Pfender E, Eckert ERG (1968) Symptomatic behavior of an electric arc with a superimposed flow. AIAA J 6(8):1474–1482
29. Duan Z, Heberlein J (2000) Anode boundary layer effects in plasma spray torches. In: Berndt CC (ed) Proceedings of 1st international thermal spray conference, Montreal, Quebec. ASM International, Materials Park, OH, pp 1–7
30. Coudert J-F, Planche M-P, Fauchais P (1994) Anode-arc attachment instabilities in a spray plasma torch. J High Temp Mater Process 3:639–651
31. Coudert J-F, Planche M-P, Fauchais P (1995) Characterization of d.c. plasma torch voltage fluctuations. Plasma Chem Plasma Process 16(1):211S–227S
32. Duan Z, Heberlein J (2002) Arc instabilities in a plasma spray torch. J Therm Spray Technol 11(1):44–51
33. Duan Z, Janisson S, Wittmann K, Coudert J-F, Heberlein J, Fauchais P (1999) Effects of nozzle fluid dynamics on the dynamic characterisitcs of a plasma spray torch. In: Lugscheider E, Kammer PA (eds) Proceedings of united thermal spray conference, Düsseldorf, Germany. ASM International, Materials Park, OH, pp 247–252
34. Planche M-P, Duan Z, Lagnox O, Heberlein J, Coudert J-F, Pfender E (1997) Study of arc fluctuations with different plasma spray torch configurations. In: Wu CK (ed) Proceedings of 13th international symposium on plasma chemistry, Beijing, P.R. China. International Union of Pure and Applied Chemistry, Zürich, pp 1460–1465
35. Dorier JL, Hollenstein C, Salito A, Loch M, Barbezat G (2000) Influence of external parameters on arc fluctuations in a F4 DC plasma torch used for thermal spraying. In: Berndt

CC (ed) Proceedings of the 1st international thermal spray conference, Montreal, Quebec, Canada. ASM International, Materials Park, OH, pp 37–43
36. Nogues E, Fauchais P, Vardelle M, Granger P (2007) Relation between the arc-root fluctuations, the cold boundary layer thickness and the particle thermal treatment. J Therm Spray Technol 16(5–6):919–926
37. Coudert J-F, Rat V, Rigot D (2007) Influence of Helmholtz oscillations on arc voltage fluctuations in a dc plasma spraying torch. J Phys D Appl Phys 40:7357–7366
38. Coudert J-F, Rat V (2008) Influence of configuration and operating conditions on the electric arc instabilities of a plasma spray torch: role of acoustic resonance. J Phys D Appl Phys 41:205–208
39. Rat V, Coudert J-F (2011) Improvement of plasma spray torch stability by controlling pressure and voltage dynamic coupling. J Therm Spray Technol 20(1–2):28–38
40. Zhou X, Heberlein J (1998) An experimental investigation of factors affecting arc-cathoe erosion. J Phys D Appl Phys 31(19):2577–2590
41. Yang G, Heberlein J (2007) Instabilities in the anode region of atmospheric pressure arc plasmas. Plasma Sources Sci Technol 16:765–772
42. Rigot D, Delluc G, Pateyron B, Coudert J, Fauchais P, Wigren J (2003) Transient evolution and shift of signals emitted by a d.c. plasma gun (type PTF4). J High Temp Mater Process 7:175–186
43. Leblanc L, Moreau C (2002) The long-term stability of plasma spraying. J Therm Spray Technol 11(3):380–386
44. Duan Z, Beall L, Schein J, Heberlein J, Stachowicz M (2000) Diagnostics and modeling of an argon/helium plasma spray process. J Therm Spray Technol 9(2):225–234
45. Bisson JF, Moreau C, Dorfman M, Dambra C, Mailon J (2005) Influence of hydrogen on the microstructure of plasma-sprayed yttria-stabilized zirconia coatings. J Therm Spray Technol 14(1):85–90
46. Vardelle A, Vardelle M, Fauchais P, Li K-I, Dussoubs B, Themelis NJ (2001) Controlling particle injection in plasma spraying. J Thermal Spray Technol 10:267–289
47. Williamson RL, Fincke JR, Chang CH (2002) Numerical study of the relative importance of turbulence, particle size and density, and injection parameters on particle behavior during thermal plasma spraying. J Therm Spray Technol 11(1):107–118
48. Renouard-Vallet G, Bianchi L, Sauvet AL, Fauchais P, Vardelle M, Boulos M, Gitzhofer F (2004) Elaboration of SOFCs electrolyte by air plasma spraying and vacuum plasma spraying: comparison of electrolyte properties. In: Ohmori A (ed) Proceedings of international thermal spray conference, Osaka, Japan. ASM International, Materials Park, OH, pp 132–137
49. Fauchais P, Vardelle M (2010) Sensors in spray processes. J Therm Spray Technol 19(4):668–694
50. Swank WD, Fincke J, Haggard DC, Sampath S, Smith W (1997) The influence of gun parameters on co-injected particles in the spraying of metal-ceramic functionally graded materials. In: Berndt CC (ed) Proceedings of the united thermal spray conference, Indianapolis, IN. ASM International, Materials Park, OH, pp 451–458
51. Wan YP, Gupta V, Deng Q, Sampath S, Prasada V, Williamson RL, Fincke J (2001) Modeling and visualization of plasma spraying of functionally graded materials and its application to the optimization of spray conditions. J Therm Spray Technol 10(2):382–389
52. Dussoubs B, Vardelle A, Mariaux G, Fauchais P, Themelis NJ (1999) Modeling of simultaneous plasma spraying of two powders. In: Lugsheider E, Kammer PA (eds) Proceedings of united thermal spray society, Düsseldorf, Germany. ASM International, Materials Park, OH, pp 793–798
53. Dussoubs B, Vardelle A, Mariaux G, Themelis NJ, Fauchais P (2001) Modeling of plasma spraying of two powders. J Therm Spray Technol 10:105–110
54. Pfender E (1989) Particle behavior in thermal plasmas. Plasma Chem Plamsa Process 9(1):167S–194S

55. Pfender E, Lee YC (1985) Particle dynamics and particle heat and mass transfer in thermal plasmas. Part I. The motion of a single particle without thermal effects. Plasma Chem Plasma Process 5(3):211–237
56. Chyou YP, Pfender E (1989) Modeling of plasma jets with superimposed vortex flow. Plasma Chem Plasma Process 9(2):291–328
57. Chyou YP, Pfender E (1989) Behavior of particulates in thermal plasma flows. Plasma Chem Plamsa Process 9(1):45–71
58. Li HP, Pfender E (2005) Three-dimensional effects inside a dc arc plasma torch. IEEE Trans Plasma Sci 33(2):400–401
59. Muggli F, Molz R, McCullough R, Hawley D (2007) Improvement of plasma gun performance using comprehensive fluid element modeling: Part I. J Therm Spray Technol 16 (5–6):677–683
60. Molz R, McCullough R, Hawley D, Muggli F (2007) Improvement of plasma gun performance using comprehensive fluid element modeling II. J Therm Spray Technol 16 (5–6):684–689
61. Park JH, Duan Z, Heberlein J, Pfender E, Lau YC, Wang HP (1997) Modeling of fluctuations experienced in N_2 and N_2H_2 plasma jets issuing into atmospheric air. In: Wu CK (ed) Proceedings of 13th international symposium on plasma chemistry, Beijing, P.R. China. International Union of Pure and Applied Chemistry, Zurich, pp 326–331
62. Park JH, Heberlein J, Pfender E, Lan YC, Rund J, Wang HP (1999) Particle behavior in a fluctuating plasma jet. In: Fauchais P, Van der Mullen J, Heberlein J (eds) Proceedings of 2nd international symposium on heat and mass transfer under plasma conditions, Antalya, Turkey. New York Academy of Sciences, New York, pp 417–424
63. Huang PC, Heberlein J, Pfender E (1995) Particle behavior in a two-fluid turbulent plasma jet. Surf Coat Technol 73(3):142–151
64. Huang PC, Pfender E, Heberlein J (1995) New modeling approach for calculating particle trajectories in a turbulent plasma spray jet. In: Ohmori A (ed) Proceedings of 14th international thermal spray conference, Kobe, Japan. High Temperature Society of Japan, Osaka, pp 1159–1163
65. Huang PC, Heberlein J, Pfender E (1995) A two-fluid model of turbulence for a thermal plasma jet. Plasma Chem Plasma Process 15(1):25–46
66. Williamson RL, Fincke JR, Crawford DM, Snyder SC, Swank WD, Haggard DC (2003) Entrainment in high-velocity, high-temperature plasma jets. Part II: Computational results and comparison to experiment. Int J Heat Mass Transfer 46:4215–4228
67. Fincke JR, Crawford DM, Snyder SC, Swank WD, Haggard DC, Williamson RL (2003) Entrainment in high-velocity, high temperature plasma jets. Part I: Experimental results. Int J Heat Mass Transfer 46:4201–4213
68. Mariaux G, Baudry C, Vardelle A (2001) 3-D modeling of gas flow and particle spray jet in plasma spraying. In: Berndt CC, Khor KA, Lugsheider E (eds) Proceedings of the international thermal spray conference, Singapore. ASM International, Materials Park, OH, pp 933–942
69. Baudry C, Vardelle A, Mariaux G, Delalondre C, Meillot E (2004) Three-dimensional and time-dependent model of the dynamic behavior of the arc in a plasma spray torch. In: Ohmori A (ed) Proceedings of the international thermal spray conference, Osaka, Japan. ASM International, Materials Park, OH, pp 717–723
70. Moreau E, Chazelas C, Mariaux G, Vardelle A (2006) Modeling of the restrike mode operation of a DC plasma spray torch. J Therm Spray Technol 15(4):524–530
71. Trelles JP, Pfender E, Heberlein J (2006) Multiscale finite element modeling of arc dynamics in a DC plasma torch. Plasma Chem Plasma Process 26:557–575
72. Trelles JP, Pfender E, Heberlein J (2007) Modeling of the arc reattachment process in plasma torches. J Phys D Appl Phys 40:5635–5641
73. Trelles JP, Chazelas C, Vardelle A, Heberlein J (2009) Arc plasma torch modeling. J Therm Spray Technol 18(5–6):728–752

74. Rat V, Coudert J-F (2006) A simplified analytical model for dc plasma spray torch: influence of gas properties and experimental conditions. J Phys D Appl Phys 39:4799–4807
75. Vardelle M, Vardelle A, Fauchais P, Boulos MI (1983) Plasma-particle momentum and heat transfer in modeling and measurements. AIChE 29:236–243
76. Vardelle A, Vardelle M, Fauchais P (1982) Influence of velocity and surface temperature of alumina particles on the properties of plasma sprayed coatings. Plasma Chem Plasma Process 2(3):255–291
77. Fincke J, Swank WD, Haggard DC (1993) Plasma spraying of alumina: plasma and particle flow fields. Plasma Chem Plasma Process 13(4):569–600
78. Roumilhac P, Coudert J-F, Fauchais P (1990) Designing parameters of spraying plasma torches. In: Bernecki T (ed) Proceedings of national thermal spray conference, Long Beach, CA. ASM International, Materials Park, OH, pp 11–19
79. Roumilhac P (1990) Contribution to the metrology and understanding of the DC plasma spray torches and transferred arcs for reclamation at atmospheric pressure. Ph.D. Thesis, Université de Limoges, Limoges, France
80. Coudert J-F, Planche M-P, Fauchais P (1995) Velocity measurement of DC plasma jets based on arc roof fluctuations. Plasma Chem Plasma Process 15(47–70)
81. Outcalt D, Hallberg M, Yang G, Heberlein J, Strykowski P, Pfender E (2007) Diagnostics and control of instabilities in a plasma spray torch. In: Tachibana K (ed) Proceedings of international symposium on plasma chemistry, Kyoto, Japan, 2007. Kyoto University, Kyoto, Unpaginated CD
82. Henne R, Bouyer E, Borck V, Schiller G (2001) Influence of anode nozzle and external torch contour on the quality of the atmospheric dc plasma spray process. In: Berndt CC, Khor KA, Lugsheider E (eds) Proceedings of the international thermal spray conference, Singapore. ASM International, Materials Park, OH, pp 471–478
83. Schwenk A, Gruner H, Zimmermann X, Landes K, Nutsch G (2004) Improved nozzle design of de-laval-type nozzles of the atmospheric plamsa spraying. In: Ohmori A (ed) Proceedings of the international thermal spray conference, Osaka, Japan. ASM International, Materials Park, OH, pp 600–605
84. Coudert J-F, Planche M-P, Betoule O, Vardelle M, Fauchais P (1993) Measurement of flow velocity and correlation to particle velocity under plasma spraying conditions. In: Berndt CC, Bernecki TF (eds) Proceedings of the 5th national thermal spray conference, Anaheim, CA. ASM International, Materials Park, OH, pp 19–24
85. Fincke J, Swank WD, Haggard DC (1993) Atmospheric plasma spraying of WC:Co. In: Harry J (ed) Proceedings of international symposium on plasma chemistry. University of Loughborough, Loughborough, pp 145–149
86. Fincke J, Swank WD (1992) Air plasma spraying of zirconia: spray characteristics, deposition efficiency and porosity control by standoff distance. In: Berndt CC (ed) Proceedings of international thermal spray conference, Orlando, FL. ASM International, Materials Park, OH, pp 513–518
87. Planche M-P, Coudert J-F, Fauchais P (1995) Evolution of the plasma flow characteristics, during the first hours, after replacing the set of electrodes. In: Heberlein JV, Ernie DW, Roberts JT (eds) Proceedings of 12th international symposium on plasma chemistry. University of Minnesota, Minneapolis, MN, pp 1475–1480
88. Prystay M, Gougeon P, Moreau C (1996) Correlation between particle temperatrue and velocity and the structure of plasma sprayed zirconia coatings. In: Berndt CC (ed) Proceedings of the 9th national thermal spray conference, Cincinnati, OH. ASM International, Materials Park, OH, pp 511–516
89. Fincke J, Swank WD, Haggard DC (1995) Feedback control of subsonic plasma spray process: system model. In: Berndt CC, Sampath S (eds) Proceedings of national thermal spray conference, Houston, TX. ASM International, Materials Park, OH, pp 117–122
90. Spores R, Pfender E (1989) Flow structure of a turbulent thermal plasma jet. Surf Coat Technol 37(3):251–270

91. Spores R, Pfender E, Heberlein J (1990) Fluid-dynamic characteristics of a plasma spray jet. In: Solonenko OP, Fedorchenko AI (eds) Proceedings of plasma jets in the development of new material technology, Frunze, USSR. V.S.P, Utrecht, pp 699–716
92. Pfender E, Chen WLT, Spores R (1990) A new look at the thermal and gas dynamic characteristics of a plasma jet. In: Berndt CC (ed) Proceedings of the 3rd national thermal spray conference, Long Beach, CA. ASM International, Materials Park, OH, pp 1–10
93. Pfender E, Fincke J, Spores R (1991) Entrainment of cold gas into thermal plasma jets. Plasma Chem Plasma Process 11(4):529–543
94. Brilhac JF, Pateyron B, Delluc G, Coudert J-F, Fauchais P (1995) Study of the dynamic and static behavior of dc vortex plasma torches. Part I: Button type cathode. Plasma Chem Plasma Process 15(1–2):231–255
95. Duan Z, Wittmann K, Coudert J-F, Heberlein J, Fauchais P (1999) Effects of the cold gas boundary layer on arc fluctuations. In: Hrabovsk'y M, Konrád M, Kopeck'y V (eds) Proceedings of 14th international symposium on plasma chemistry, Prague, Czech Republic. Institute of Plasma Physics, CAS, Prague, pp 233–238
96. Fincke J, Swank WD (1991) The effect of plasma jet fluctuations on particle time-temperature histories. In: Bernecki TF (ed) Proceedings of 4th NTSC, Pittsburgh, PA. ASM International, Materials Park, OH, pp 193–198
97. Gregori G, Kortshagen U, Pfender E, Heberlein J (2003) Time-resolved temperature measurements in a turbulent argon plasma jet. In: d'Agostino R, Favia P, Fracassi F, Palumbo F (eds) Proceedings of 16th international symposium on plasma chemistry, Taormina, Italy, 2003. University of Bari, Italy, Unpaginated CD
98. Duan Z, Beall L, Planche M-P, Heberlein J, Pfender E, Stachowicz M (1997) Arc voltage fluctuations as an indication of spray torch anode condition. In: Berndt CC (ed) Proceedings of 1st united thermal spray conference, Indianapolis, IN. ASM International, Materials Park, OH, pp 407–411
99. Bisson JF, Gauthier B, Moreau C (2003) Effect of plasma fluctuations on in-flight particle parameters. J Therm Spray Technol 12(1):38–43
100. Bisson JF, Moreau C (2003) Effect of direct current plasma fluctuations on in-flight particle parameters: Part II. J Therm Spray Technol 12(2):258–264
101. Moreau C, Leblanc L (2001) Optimization and process control for high performance thermal spray coatings. Key Eng Mater 197:27–58
102. Betoule O (1994) Influence of velocity and temperature distributions of d.c. plasma jets and alumina particles in flight onto coating properties. Universite de Limoges, Limoges
103. Mohanty M, Smith RW, Knight R, Chen WLT, Heberlein J (1996) Shrouded air plasma processing of lightweight coatings. In: Berndt CC (ed) Proceedings of 9th NTSC, Cincinnati, OH. ASM International, Materials Park, OH
104. Burgess A (2002) Hastelloy C-276 parameter study using the axial III plasma spray system. In: Lugsheider E (ed) Proceedings of international thermal spray conference, Essen, Germany. ASM International, Materials Park, OH, pp 516–518
105. Chen HC, Duan Z, Heberlein J, Pfender E (1996) Influence of shroud gas flow and swirl magnitude on arc jet stability and coating quality in plasma spray. In: Berndt CC (ed) Proceedings of thermal spray: Particle solutions for engineering problems, Cincinnati, OH. AMS International, Materials Park, OH, pp 533–561
106. Malmberg S, Leung K, Heberlein J, Pfender E (1995) Particle trajectory control for DC plasma spraying. In: Ohmori A (ed) Proceedings of thermal spraying: Current status and future trends, Kobe, Japan. High Temperature Society of Japan, Kobe, pp 371–375
107. Outcalt D, Hallberg M, Yang G, Strykowski P, Heberlein J, Pfender E (2006) Instabilities in plasma spray jets. In: Marple B (ed) Proceedings of international thermal spray conference, Seattle, WA. ASM International, Materials Park, OH, Unpaginated CD
108. Vincenzi L, Suzuki S, Outcalt D, Heberlein J (2010) Controlling spray torch fluid dynamics – effect on spray particle and coating characteristics. J Therm Spray Technol 19(4):713–722

109. Okada M, Marno H (1968) New plasma spraying and its application. British Welding J.:371–378
110. Guest CJS, Ford KG (1975) US Patent 3892882
111. Houben JM, Zaat JH (1976) Shielded open air plasma spraying of reactive materials. In: Proceedings of 8th international thermal spray conference. American Welding Society, FL, p 78
112. Borisov Y (1993) Structure and parameters of hetergeneous plasma jets shielded by water flow. In: Proceedings of 2nd plasma Technik symposium, Wohlen, Switzerland, pp 1–8
113. Dykhuizen RC, Smith MF (1989) Investigations into the plasma spray process. Surf Coat Technol 37(4):349–358
114. Maecker H (1956) Arc source for spectroscopic measurements of isothermal plasma. Z Naturforsch 11a:457
115. Hermann W, Schade E (1970) Transportfunktionen von Stickstoff bis 26000. KZ Physik 233:333–350
116. Zhukov MF (1994) Linear direct current plasma torches. In: Solonenko OP, Zhukov MF (eds) Proceedings of thermal plasma and new materials technology. Cambridge Interscience, Cambridge, pp 9–21
117. Zhukov MF (1989) Electric arc generators of low temperature plasma. High temperature dust laden jets. VPS, Utrecht
118. Zierhut J, Haslbeck P, Landes KD, Muller M, Schutz M (1998) TRIPLEX – an innovative three-cathode plasma torch. In: Coddet C (ed) Proceedings of international thermal spray conference, Nice, France. ASM International, Materials Park, OH, pp 1374–1380
119. Barbezat G, Landes K (2000) Plasma technology TRIPLEX for the deposition of ceramic coatings in the industry. In: Berndt CC (ed) Proceedings of 1st international thermal spray conference, Montreal, Canada. ASM International, Materials Park, OH, pp 881–885
120. Mauer G, Vaßen R, Stöver D, Kirner S, Marqués JL, Zimmermann S, Forster G, Schein J (2011) Improving power injection in plasma spraying by optical diagnostics of the plasma and particle characterization. J Spray Technol 20(1–2):3–11
121. Mauer G, Vaßen R, Stöver D (2011) Plasma and particle temperature measurements. J Therm Spray Technol 20(3):391–406
122. Moreau C, Gougeon P, Burgess A, Ross D (1995) Characterization of particle flows in an axial injection plasma torch. In: Berndt CC, Sampath S (eds) Proceedings of 8th national thermal spray conference, Houston, TX. ASM International, Materials Park, OH, pp 141–147
123. Lu ZP, Pfender E (1989) Synthesis of AIN powder in a triple torch plasma reactor. In: d'Agostino R (ed) Proceedings of 9th international symposium on plasma chemistry, Pugnochiuso, Italy. University of Bari, Bari, pp 675–680
124. Young RM, Pfender E (1989) A novel approach for introducing particulate matter into thermal plasmas: the triple-cathode arc. Plasma Chem Plasma Process 9(4):465–481
125. Chen HC, Heberlein J, Henne R (2000) Integrated fabrication process for solid oxide fuel cells in a triple torch plasma reactor. J Therm Spray Technol 9(3):348–353
126. Asmann M, Wank A, Kim H, Heberlein J, Pfender E (2001) Characterization of the converging jet region in a triple torch plasma reactor. Plasma Chem Plasma Process 21:37–63
127. Guru DN, Palacio M, Mook W, Chambers M, Racek O, Heberlein J, Gerberich W, Berndt CC (2004) Nanophase partially stabilized zirconia intermediate layer for strain accommodation in a multi-layer thermal barrier coating. In: Ohmori A (ed) Proceedings of international thermal spray conference, Osaka, Japan. ASM International, Materials Park, OH
128. Guru DN, Heberlein J, Mook W, Gerberich W, Berndt CC (2006) Nanostructured partially stabilized zirconia as an interlayer in a multi layered thermal barrier coating. In: Marple B (ed) Proceedings of international thermal spray conference, Seattle, WA. ASM International, Materials Park, OH, Unpaginated CD
129. Barbezat G (2001) The internal plasma spraying on powerful technology for the aerospace and automotive industries. In: Berndt CC, Khor KA, Lugscheider EF (eds) Proceedings of

international thermal spray conference, Singapore. ASM International, Materials Park, OH, pp 135–140
130. Morishita T (1991) Coatings by 250 kW plasma jet spray system. In: Blum-Sandmeier S, Eschnauer H, Huber P, Nicoll A (eds) Proceedings of 2nd plasma technik symposium, Luzern, Switzerland. Plasma Technik, Wohlen, pp 137–145
131. Gerdien H, Lotz A (1922) Wiss. Veröff. Siemens-Konz.489-4
132. Hrabovsky M (1992) Plasma generator with water stabilized DC arc. In: Hooke W, Sindoni E (eds) Proceedings of industrial applications of plasma physics, Varenna, Italy. Italian Physical Society, Varenna, pp 557–562
133. Chraska P, Hrabovsky M (1992) An overview of water stabilized plasma guns and their applications. In: Berndt CC (ed) Proceedings of thermal spray: International advances in coatings technology, Orlando, FL. ASM International, Materials Park, OH, pp 81–85
134. Hrabovsky M, Kopecky V, Sember V (1995) Water stabilized arc as a source of thermal plasma. In: Fauchais P (ed) Proceedings of international symposium on heat and mass transfer under plasma conditions, Cesme, Turkey. Begell House, New York, NY, pp 91–98
135. Muehlberger E (1988) Industrial plasma processing technology. In: Eschnauer H, Huber P, Nicoll AR, Sondermeier S (eds) Proceedings of 1st plasma-technik symposium, Lucerne, Switzerland. Plasma-Technik AG, Wohlen, pp 105–118
136. Meyer PJ, Hawley D (1991) LPPS production systems. In: Bernecki TF (ed) Proceedings of 4th national thermal spray conference, Pittsburgh, PA, 1991. ASM International, Materials Park, OH, pp 29–38
137. Lang M, Henne R, Schaper S, Schiller G (2001) Development and characterization of vacuum plasma sprayed thin film solid oxide fuel cells. J Therm Spray Technol 10(4):618–625
138. Refke A, Barbezat G, Dorier JL, Gindrat M, Hollenstein C (2003) Characterization of LPPS processes under various spray conditions for potential applications. In: Marple B, Moreau C (eds) Proceedings of the international thermal spray conference, Orlando, FL. ASM International, Materials Park, OH, pp 581–588
139. Scrivani A, Bardi U, Carrafiello L, Lavacchi A, Niccolai F, Rizzi G (2003) A comparative study of high velocity oxygen fuel, vacuum plasma spray, and axial plasma spray for the deposition of CoNiCrAlY bond coat alloy. J Therm Spray Technol 12(4):504–507
140. Mayr W, Henne R (1988) Investigation of a VPS burner with laval nozzel using an automated laser doppler measuring system. In: Eschnauer H, Huber P, Nicoll AR, Sandmeier S (eds) Proceedings of 1st plasma-technik symposium, Lucerne, Switzerland. Plasma Technik, Wohlen, pp 87–97
141. Henne R, Mayr W, Reusch A (1993) Influence of nozzle geometry on particle behavior and coating quality in high velocity VPS. In: Proceedings of thermal spray conference TS93, Aachen, Germany. DVS, Aachen, pp 7–11
142. Padture NP, Gell M, Jordan EH (2002) Thermal barrier coatings for gas turbine engine applications. Science 296(5566):280–284
143. von Niessen K, Gindrat M (2011) Plasma sprayed-PVD: a new thermal spray process to deposit out of the vapor phase. J Therm Spray Technol 20(4):736–743
144. Freslon A (1995) Plasma spraying at a controlled temperature and atmosphere. In: Berndt CC, Sampath S (eds) Proceedings of 8th national thermal spray conference, Houston, TX. ASM International, Materials Park, OH, pp 57–63
145. Jäger DA, Stöver D, Schlump W (1992) High pressure plasma spraying in controlled atmosphere up to 2 bars. In: Berndt CC (ed) Proceedings of international thermal spray conference, Orlando, FL. ASM International, Material Park, OH, pp 57–63
146. Stahr C, Saaro S, Berger L-M, Dubsky J, Neufuss K, Hermann M (2007) Dependence of the stabilization of alpha-alumina on the spray process. J Therm Spray Technol 16(5–6):822–830
147. Kogelschatz U (2003) Dielectric-barrier discharges: their history, discharge physics, and industrial applications. Plasma Chem Plasma Process 23(1):1–46

148. Kitamura J, Ibe H, Yuasa F, Mizuno H (2008) Plasma sprayed coatings of high-purity ceramics for semiconductor and flat-panel-display production equipment. J Therm Spray Technol 17(5–6):878–886
149. Toma FL, Scheitz S, Berger L-M, Sauchuk V, Kusnezoff M, Thiele S (2011) Comparative study of the electrical properties and characteristics of thermally sprayed alumina and spinal coatings. J Therm Spray Technol 20(1–2):195–204
150. Costil S, Verdy C, Bolot R, Coddet C (2007) On the role of spraying process on microstructural, mechanical, and thermal response of alumina coatings. J Therm Spray Technol 16 (5–6):839–843
151. Darut G, Ageorges H, Denoirjean A, Montavon G, Fauchais P (2008) Effect of the structural scale of plasma-sprayed alumina coatings on their friction coefficients. J Therm Spray Technol 17(5–6):788–795
152. Leivo EM, Vippola MS, Sorsa PPA, Vuoristo PM, Mantyla TA (1997) Wear and corrosion properties of plasma sprayed AI_2O_3 and Cr_2O_3 coatings sealed by aluminum phosphates. J Therm Spray Technol 6(2):205–210
153. Berard G, Brun P, Lacombe J, Montavon G, Denoirjean A, Antou G (2008) Influence of a sealing treatment on the behavior of plasma-sprayed alumina coatings operating in extreme environments. J Therm Spray Technol 17(3):410–419
154. Mesrati N, Ajhrourh H, Du N, Treheux D (2000) Thermal spraying and adhesion of oxides onto graphite. J Therm Spray Technol 9(1):95–99
155. Keshri AK, Agarwal A (2011) Wear behavior of plasma-sprayed carbon nanotube-reinforced aluminum oxide coating in marine and high-temperature environments. J Therm Spray Technol 20(6):1217–1230
156. Branland N, Meillot E, Fauchais P, Vardelle A, Gitzhofer F, Boulos M (2006) Relationships between microstructure and electrical properties of RF and DC plasma-sprayed titania coatings. J Therm Spray Technol 15(1):53–62
157. Ctibor P, Neufuss K, Chraska P (2006) Microstructure and abrasion resistance of plasma sprayed titania coatings. J Therm Spray Technol 15(4):689–694
158. Ye FX, Ohmori A, Tsumura T, Nakata K, Li CJ (2007) Microstructural analysis and photocatalytic activity of plasma-sprayed titania-hydroxyapatite coatings. J Therm Spray Technol 16(5–6):776–782
159. Ilavsky J, Berndt CC, Herman H, Chraska P, Dubsky J (1997) Alumina-base plasma-sprayed materials – Part II: Phase transformations in aluminas. J Therm Spray Technol 6(4):439–444
160. Fervel V, Normand B, Coddet C (1999) Tribological behavior of plasma sprayed Ai_2O_3-based cermet coatings. Wear 230:70–77
161. Yilmaz R, Kurt AO, Demir A, Tath Z (2007) Effects of TiO_2 on the mechanical properties of the AI_2O_3-TiO_2 plasma sprayed coating. J Eur Ceram Soc 27:1319–1323
162. Fervel V, Normand B, Liao H, Coddet C, Beche E, Berjoan R (1999) Friction and wear mechanisms of thermally sprayed ceramic and cermet coatings. Surf Coat Technol 111 (255–262)
163. Normand B, Fervel V, Coddet C, Nikitine V (2000) Tribological properties of plasma sprayed alumina-titania coatings: role and control of the microstructure. Surf Coat Technol 123:278–287
164. Pawlowski L (1996) Technology of thermally sprayed anilox rolls: state of art, problems, and perspectives. J Therm Spray Technol 5(3):317–334
165. Ahn HS, Kwon OK (1999) Tribological behavior of plasma-sprayed chromium oxide coating. Wear 225–229:814–824
166. Usmani S, Tandon KN (1992) Evaluation of thermally sprayed coatings under reciprocating lubricated wear conditions. J Therm Spray Technol 1(3):249–255
167. Miller RA (1997) Thermal barrier coatings for aircraft engines: history and directions. J Therm Spray Technol 6(1):35–42
168. Parks WP, Hoffman EE, Lee WY, Wright IG (1997) Thermal barrier coatings issues in advanced land-based gas turbines. J Therm Spray Technol 6(2):187–192

169. Marple B, Lima RS, Moreau C, Kruger SE, Xie L, Dorfman M (2007) Yttria-stabilized zirconia thermal barriers sprayed using N_2-H_2 and Ar-H_2 plasmas: influence of processing and heat treatment on coating properties. J Therm Spray Technol 16(5–6):791–797
170. Vaßen R, Jarligo MO, Steinke T, Mack DE, Stöver D (2010) Overview on advanced thermal barrier coatings. Surf Coat Technol 205:938–942
171. Henne R (2007) Solid oxide fuel cells: a challenge for plasma deposition processes. J Therm Spray Technol 16(3):381–403
172. Tsukuda H, Notomi A, Hisatome N (2000) Application of plasma spraying to tubular-type solid oxide fuel cells production. J Therm Spray Technol 9(3):364–368
173. Ma XQ, Zhang H, Dai J, Roth J, Hui R, Xiao TD, Reisner DE (2005) Intermediate temperature solid oxide fuel cell based on fully integrated plasma-sprayed components. J Therm Spray Technol 14(1):61–66
174. Abdel-Samad AA, El-Bahloul AMM, Lugscheider E, Rassoul SA (2000) A comparative study on thermally sprayed alumina based ceramic coatings. J Mater Sci 35:3127–3130
175. Carayon MT, Lacout JL (2003) Study of the Ca/P atomic ratio of the amorphous phase in plasma-sprayed hydroxyapatite coatings. J Solid State Chem 172:339–350
176. Khor KA, Cheang P, Wang Y (1998) Plasma spraying of combustion flame spheroidized hydroxyaptite (HA) powders. J Therm Spray Technol 7(2):254–260
177. Heimann RB (1999) Design of novel plasma sprayed hydroxyapatite-bond coat bioceramic systems. J Therm Spray Technol 8(4):597–603
178. Besov AV, Batrak IK (2005) Application of technology of plasma spraying in the fabrication of articles for medical devices. Powder Metallurgy Metal Ceram 44(9–10):511–516
179. Kitamura J, Mizuno H, Kato N, Aoki I (2006) Ceramic coatings prepared by plasma spraying for semiconductor production equipment. Mater Trans 47(7):1677–1683
180. Kitamura J, Tang Z, Mizuno H, Sato K, Burgess A (2011) Structural, mechanical and erosion properties of yttrium oxide coatings by axial suspension plasma spraying for electronics applications. J Therm Spray Technol 20(1–2):170–185
181. Moldovan M, Weyant CM, Lynn Johnson D, Faber KT (2004) Tantalum oxide coatings as candidate environmental barriers. J Therm Spray Technol 13(1):51–56
182. Cojocaru CV, Wang Y, Moreau C, Lima RS, Mesquita-Guimaraes J, Garcia E, Miranzo P, Osendi MI (2011) Mechanical behavior of air plasma-sprayed YSZ functionally graded mullite coatings investigated via instrumented indentation. J Therm Spray Technol 20(1–2):100–107
183. Das S, Ghosh S, Pandit A, Bandyopadhyay K, Chattopadhyay AB, Das K (2005) Processing and characterisation of plasma sprayed zirconia-alumina-mullite composite coating on a mild-steel substrate. J Mater Sci Lett 0022–2460
184. Zeng Y, Lee SW, Ding C (2002) Study on plasma sprayed boron carbide coating. J Therm Spray Technol 11(1):129–133
185. Matejicek J, Chraska P, Linke J (2007) Thermal spray coatings for fusion applications-review. J Therm Spray Technol 16(1):64–83
186. Greuner H, Balden M et al (2004) Evaluation of vacuum plasma-sprayed boron carbide protection for the stainless steel first wall. J Nucl Mater 329–333:849–854
187. Tului M, Ruffini F, Arezzo F, Lasisz S, Znamirowski Z, Pawlowski L (2002) Some properties of atmospheric air and inert gas high-pressure plasma sprayed ZrB_2 coatings. Surf Coat Technol 151–152:483–489
188. Pulci G, Tului M, Tirillo J, Marra F, Lionetti S, Valente T (2011) High temperature mechanical behavior of UHTC coatings for thermal protection of re-entry vehicles. J Therm Spray Technol 20(1–2):139–144
189. Li HJ, Fu QG, Yao DJ, Wang YJ, Ma C, Wei JF, Han ZH (2011) Microstructures and ablation resistance of ZrC coating for SiC-coated carbon/carbon composites prepared by supersonic plasma spraying. J Therm Spray Technol 20(6):1286–1291
190. Hu C, Niu Y, Li HJ, Ren M, Zheng X, Sun J (2012) SiC coatings for carbon/carbon composites fabricated by vacuum plasma spraying technology. J Therm Spray Technol 21 (1):16–22

191. Siegmann S, Brandt O, Dvorak M (2004) Thermally sprayed wear resistant coatings with nanostructured hard phases. J Therm Spray Technol 31(1):37–43
192. Borisova, Yu S (2008) Self-propagating high-temperature synthesis for the deposition of thermally-sprayed coatings. Powder Metallurgy Metal Ceram 47(1–2):80–94
193. Basak AK, Achanta S, Celis JP, Vardavoulias M, Matteazzi P (2008) Structure and mechanical properties of plasma sprayed nanostructured alumina and FeCuAl-alumina cermet coatings. Surf Coat Technol 202:2368–2373
194. Hwang JH, Han MS, Kim DY, Youn JG (2006) Tribological behavior of plasma spray coatings for marine diesel engine piston ring and cylinder liner. J Mater Eng Perform 15 (3):328–335
195. Ageorges H, Ctibor P, Medarhri Z, Touimi S, Fauchais P (2006) Influence of the metallic matrix ratio on the wear resistance (dry and slurry abrasion) of plasma sprayed cermet (chromia/stainless steel) coatings. Surf Coat Technol 201:2006–2011
196. Hashemi SM, Enayati MH, Fathi MH (2009) Plasma spray coatings of Ni-Al-SiC composite. J Therm Spray Technol 18(2):284–291
197. Economou S, De Bonte M, Celis JP, Smith RW, Lugscheider E (2000) Tribological behaviour at room temperature and at 550°C of TiC-based plasma sprayed coatings in fretting gross slip conditions. Wear 244:165–179
198. Brindley WJ (1997) Properties of plasma-sprayed bond coats. J Therm Spray Technol 6 (1):85–90
199. Feuerstein A, Knapp J, Taylor T, Ashary A, Bolcavage A, Hitchman N (2008) Technical and economical aspects of current thermal barrier coating systems for gas turbine engines by thermal spray and EBPVD: a review. J Therm Spray Technol 17(2):199–213
200. Koomparkping T, Damrongrat S, Niranatlumpong P (2005) Al-rich precipitation in CoNiCrAlY bondcoat at high temperature. J Therm Spray Technol 14(2):264–267
201. Sidhu BS, Prakash S (2007) Analytical studies on the behavior of nickel and cobalt base shrouded plasma spray coatings at elevated temperature in air. Oxid Met 67:279–298
202. Castro RG, Bartlett AH, Hollis KJ, Fields RD (1997) The effect of substrate temperature on the thermally diffusivity and bonding characteristics of plasma sprayed beryllium. Fusion Eng Design 37:243–252
203. Morks MF, Tsunekawa Y, Okumiya M, Shoeib MA (2003) Splat microstructure of plasma sprayed cast iron with different chamber pressures. J Therm Spray Technol 12(2):282
204. Schiller G, Henne R, Borck V (1995) Vacuum plasma spraying of high-performance electrodes for alkaline water electrolysis. J Therm Spray Technol 4(2):185–194
205. Tani K, Harada Y (2007) Enhancement of service life of steam generating tubes in oil-fired boiler for power generation employing plasma spray technology. J Therm Spray Technol 16(1):111–117
206. Longa-Nava E, Takemoto M, Hidaka K (1995) High-temperature corrosion performance of plasma-sprayed CrNiMoSiB coatings. J Therm Spray Technol 4(2):169–174
207. Singh H, Prakash S, Puri D, Phase DM (2006) Cyclic oxidation behavior of some plasma sprayed coatings in Na_2SO_4-60%V_2O_5 environment. J Mater Eng Perform 15(6):729–741
208. Miguel JM, Vizcaino S, Lorenzana C, Cinca N, Guilemany JM (2011) Tribological behavior of bronze composite coatings obtained by plasma thermal spraying. Tribol Lett 42:263–273
209. Ahn J, Hwang B, Lee S (2005) Improvement of wear resistance of plasma-sprayed molybdenum blending coatings. J Therm Spray Technol 14(2):251–257
210. Niranatlumpong P, Koipraser H (2010) The effect of Mo content in plasma-sprayed Mo-NiCrBSi coating on the tribological behavior. Surf Coat Technol 205:483–489
211. Prudenziati M, Lassinantti Gualtieri M (2008) Electrical properties of thermally sprayed Ni and Ni20Cr-based resistors. J Therm Spray Technol 17(3):385–394
212. Floristán M, Fontarnau R, Killinger A, Gadow R (2010) Development of electrically conductive plasma sprayed coatings on glass ceramic substrates. Surf Coat Technol 205:1021–1028

Chapter 8
R.F. Induction Plasma Spraying

Abbreviations

CVD	Chemical vapor deposition
d.c.	Direct current
i.d.	Internal diameter
r.f.	Radio frequency
slm	Standard liters per minute
VIPS	Vacuum induction plasma spraying

8.1 Introduction

Radio frequency (r.f.) induction plasma spraying, or as more commonly known as vacuum induction plasma spraying (VIPS), has attracted increasing attention over the past three decades. While it is not a technology that is posed to replace any of the other plasma spraying technologies such as d.c. plasma spraying, HVOF, or wire arc spraying, it is commercially used in niche applications, such as in perform cladding in the fiber optics industry or X-ray target manufacturing, where the high purity and density of the deposit obtained are of critical importance. VIPS is characterized by the electrodeless nature of the discharge which allows for high purity, and greater flexibility with regard to the chemistry of the plasma gas, and the ease of axial injection of the powder into the center of the plasma jet. Because of the inability to move the plasma torch with respect to the substrate, due to electrical leads constraints, the use of VIPS has been limited to applications where the substrate on which the coating is to be deposited can be easily displaced under the torch. In this context, one of the fastest growing applications of induction plasma spraying is in the area of powder treatment whether for powder densification, purification, and/or spheroidization. The topic will also be further discussed in Chap. 11, on powder preparation.

P.L. Fauchais et al., *Thermal Spray Fundamentals: From Powder to Part*,
DOI 10.1007/978-0-387-68991-3_8, © Springer Science+Business Media New York 2014

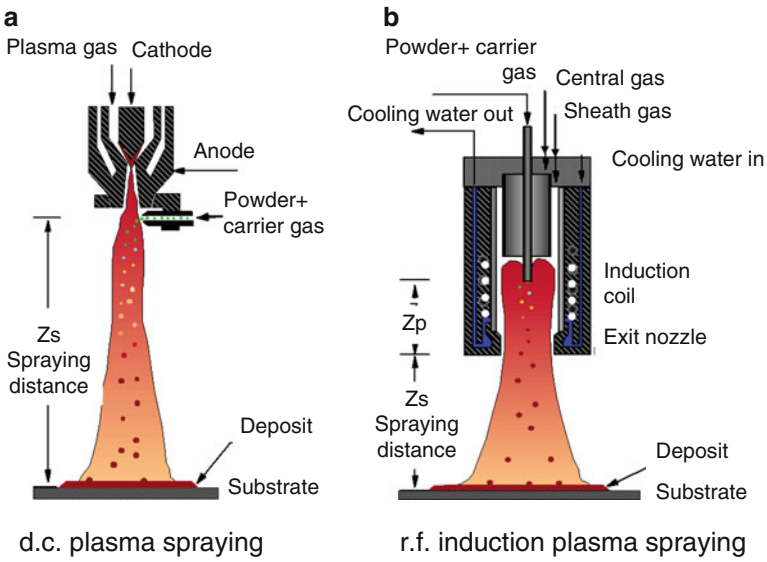


Fig. 8.1 Schematic representations of (**a**) d.c. and (**b**) r.f. induction plasma spraying techniques

Schematic representation of typical plasma spraying setups using d.c. and r.f. induction plasma torches is shown in Fig. 8.1. In the case of d.c. plasma spraying, shown on the left-hand side of Fig. 8.1, the powder to be sprayed is introduced using a carrier gas oriented in the radial direction toward the axis of the flow, either inside the anode nozzle but downstream of the arc root, or external to the nozzle of the plasma torch, downstream of the nozzle exit level. The latter configuration, known as external powder injection, is more commonly used compared to internal powder injection. As the powder penetrates the plasma jet, the individual powder particles are heated in-flight and melted prior to their impact on the substrate where they form the deposit through multiple splat buildups. As mentioned in Chaps. 4 and 7, attention needs to be given to the proper control of the particle injection parameters to insure that the majority of the injected particles acquire an axial trajectory within a narrow cone around the center line of the flow in order to have the best chance of heating, melting, and acquiring the necessary velocity prior to their impact on the surface of the substrate to achieve the best quality deposit.

On the right-hand side of Fig. 8.1, a corresponding setup is shown using an r.f. inductively coupled plasma torch. In this case the discharge is generated through the electromagnetic coupling of the energy from the induction coil to the plasma generated in the discharge cavity. There are no electrodes and the discharge cavity is formed inside a cylindrical tube made of a nonconducting material such as silica or other ceramics. The powder to be treated can be freely injected axially into the center of the discharge using a water-cooled probe oriented along the centerline of

the plasma torch with its tip located at any level within the discharge cavity depending on the time required for the heating and complete melting of the powder. While the particle acceleration and maximum particle velocity achieved is lower in this case compared to the case of d.c. plasma spraying, it does not offer an obstacle to achieving high density deposits. It allows, on the other hand, for the melting of relatively large particles of low thermal conductivity materials. The vast majority of induction plasma systems operate in a confined atmosphere chamber under atmospheric or soft vacuum conditions. Under extreme conditions when the absolute pressure in the chamber is below 1 kPa, the plasma flow at the exit of the torch can reach supersonic flow conditions, which are particularly suited for the deposition of very fine powders.

In this chapter a review is presented of the development of induction plasma technology over the past four decades. The topics covered include the fundamentals of induction plasma torch design, the principal characteristics of the flow, temperature and concentration fields in the discharge, and the basic elements constituting an induction plasma spraying system. This is followed by an analysis of the effect of the operating conditions on the quality of the deposit. Both mathematical modeling results and experimental data are used for this objective. Attention is also given to newly developed variations of the traditional induction plasma spraying technology, such as suspension plasma spraying and supersonic induction plasma spraying. A separate section at the end of this chapter is dedicated to auxiliary equipment needed for induction plasma spraying and safety considerations. Dresvin [1, 2], Eckert [3], and Boulos [4–7] have published several review papers on the broad subject of induction plasma technology. It must be emphasized that induction plasmas have relevancy for thermal spray technology that goes beyond the spraying of coatings or near net shaped parts and includes powder treatment such as spheroidization of the powders used for plasma spraying or the synthesis of nano-sized powders that are used in suspension plasma spraying.

8.2 The r.f. Induction Plasma Torch

8.2.1 Basic Concepts

In contrast to d.c plasma spraying, where the plasma is generated by an arc discharge between two electrodes, the energy transferred into the discharge of r.f induction plasma, is governed by electromagnetic coupling. The basic energy transfer mechanism is identical to that used in the induction heating of metals, with the exception that the load in this case is the plasma gas, rather than a metallic cylinder or crucible. The plasma generation can be described as occurring in the following steps:

1. A high frequency voltage is applied to a water-cooled copper coil surrounding the discharge vessel, resulting in a high frequency current flowing in this coil. This alternating current (coil current) generates a predominantly axial high frequency oscillating magnetic field within the discharge cavity.

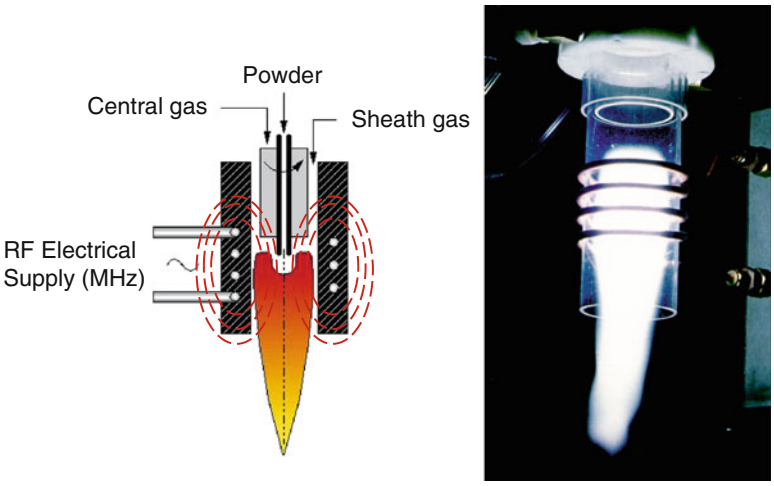


Fig. 8.2 Schematic representation of a typical induction plasma torch and a photograph of an air-cooled, quartz-wall torch, operated at the University of Sherbrooke in 1975

2. This oscillating magnetic field generates a ring-shaped electric field perpendicular to the magnetic field lines, and this electric field results, after the initial breakdown, in a ring-shaped alternating current flow (induction current), which sustains the plasma through Joule heating.
3. The ring-shaped induction current flow in the plasma is in the opposite direction of the current flow in the induction coil, and it generates a corresponding magnetic field in the opposite direction of the field generated by the coil current. As a consequence of these opposing magnetic fields, the net magnetic field intensity in the central part of the discharge tube is suppressed and the induction current flow is confined to an outer annular region close to the inner wall of the plasma confinement tube. The width of this annular, current-carrying region of the discharge is known as the "skin depth" δ_t. The details of the energy coupling are described in the next section.

While the concept behind electrodeless discharges involving the inductive or capacitive coupling of electromagnetic energy into plasma was first identified by Babat [8] in 1947, its demonstration as a research tool for plasma generation was made much later in 1961 by Reed [9–11]. The basic design of the inductively coupled plasma torch as we know it today is shown in Fig. 8.2 together with a photograph of a relatively simple demonstration of the concept for an air-cooled quartz tube, torch operated at the University of Sherbrooke by Boulos and his collaborators in 1975. The plasma torch is composed in this case of a cylindrical quartz tube around which a water-cooled induction coil is wound. The plasma can be sustained, as a stable discharge, as long as the energy coupled into the plasma is sufficient to compensate for conductive, convective, and radiative losses from the plasma to the surrounding. The schematic on the left-hand side of Fig. 8.2 shows a

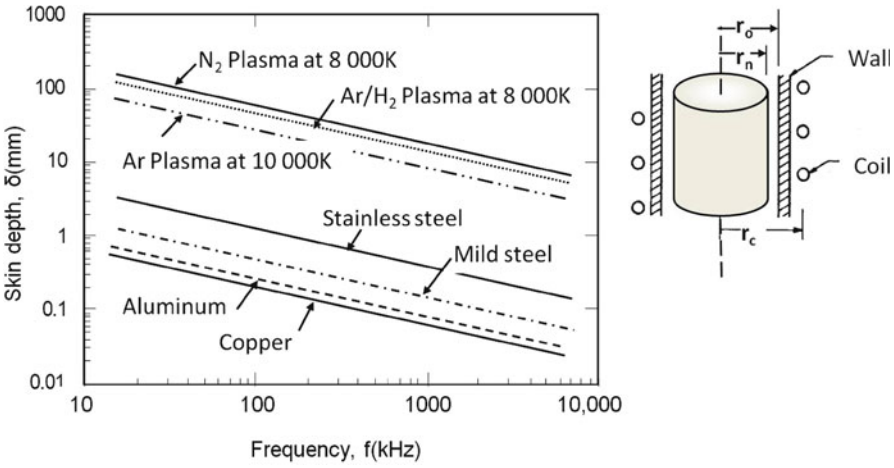


Fig. 8.3 Channel model representation of an induction plasma load and computed skin depth values as function of oscillator frequency for different plasma compositions and metallic load

representation of the magnetic field lines generated by the coil. This schematic also shows the presence of different gas streams introduced into the discharge cavity. These are composed of a sheath gas injected along the inner wall of the plasma confinement tube to protect it from the intense heat to which it is exposed. The central gas stream is injected close to the center of the tube and serves for the stabilization of the discharge. A third gas stream is injected axially along the centerline of the discharge, often referred to as the powder gas, serves for the introduction of the powder or precursor to be treated into the center of the discharge.

8.2.2 Energy Coupling Mechanism

8.2.2.1 Electromagnetic Coupling and Skin Depth

The electromagnetic induction coupling of energy into the plasma is essentially similar to that of the induction heating of metals, which has been known since the beginning of the twentieth century and has found numerous large-scale industrial applications [12, 13]. The fact that, with induction plasmas, the "load" is a conducting gas with a substantially lower electrical conductivity than most metals, has a direct consequence on the range of oscillator frequencies required to sustain such discharges, which are typically in the MHz range, compared to induction heating of metals which is in the kHz range. The relatively simple "channel model" proposed by Freeman and Chase [14, 15] best demonstrate the energy coupling mechanism in the case of inductively coupled plasmas.

According to this model, which is schematically illustrated on the right-hand side of Fig. 8.3, the electrical discharge in the coil region can be represented by a

cylindrical load of radius, r_n with a uniform electrical conductivity, σ_o. Outside this region, ($r_n < r < r_o$), where, r_o is the internal radius of the plasma confining tube, the gas is assumed to be nonconducting and spans the temperature difference between that of the plasma and the wall. The internal radius of the induction coil is designated as r_c, the coil length, L_c, and its number of turns, n_c. The alternating electromagnetic field generated by the applied r.f. current through the induction coil will couple only into the cylindrical load in a similar fashion as in induction heating of metals. Through the solution of the standard electromagnetic induction heating problem, Freeman and Chase [15] demonstrated that the energy will be coupled into the outer shell of the load over a thickness of, δ_t, known as the "*skin depth*," which is function of the electrical conductivity of the load, σ_o , the oscillator frequency, f, and the magnetic permeability of the medium, μ_o. Based on standard electromagnetic formulation, the skin depth can be calculated using the following Eq. (8.1):

$$\delta_t = \frac{1}{\sqrt{\pi \cdot \mu_0 \cdot \sigma_0 \cdot f}} \tag{8.1}$$

It is generally accepted that the magnetic permeability of the medium can be taken as that of free space, $\mu_0 = 4\pi \times 10^{-7}$ (Hy/m), or (V s/A m). For a pure argon plasma at atmospheric pressure with an average temperature of 8,000 K, its corresponding average electrical conductivity, σ_o= 990 A/V m. The skin depth in this case will be equal to approximately 8 mm for an oscillator frequency of 4 MHz. The results of computations of the skin depth as function of oscillator frequency, for the cases of an atmospheric pressure pure Ar plasma at 10,000 K, an Ar/H_2 plasma at 8,000 K, and a pure nitrogen plasma at 8,000 K are given in left-hand side of Fig. 8.3, together with corresponding values for cylindrical metallic loads made of aluminum, copper, mild steel, and stainless steel for comparison. These show skin depth for the case of plasmas, which is almost two orders of magnitude larger than those predicted for metallic loads. As indicated by Eq. (8.1), the only way to reduce the thickness of the skin depth, and accordingly increase the power density into the discharge, is to increase the frequency. As a direct consequence, considerably higher frequency power supplies (typically in the MHz range) are needed for the excitation of inductively coupled discharges, compared to lower frequency (typically in the kHz range) power supplies used for the induction heating of metals.

Measurements of the magnetic field distribution in the discharge cavity in the absence and in the presence of the discharge were reported in the early 1970s by Eckert [16]. The data shown in Fig. 8.4 were obtained using a 3-mm diameter, water-cooled, magnetic induction probe inserted into a relatively large volume, low power density discharge. A water-cooled quartz tube, 155 mm i.d, confined the discharge in this case. The oscillator frequency was 2.6 MHz and the applied r.f. power was estimated at 25 kW. The plasma gas was pure argon at atmospheric pressure with a total gas flow rate into the torch of 120 slm. Curve (a) corresponds to

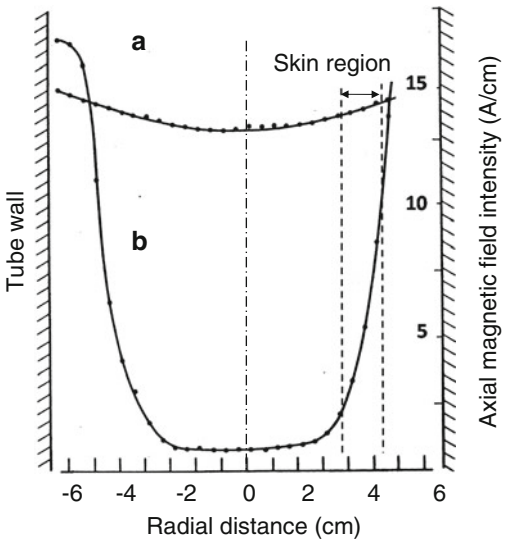


Fig. 8.4 Radial profiles of the magnetic field intensity at the mid-section of the coil of an induction torch in the absence (**a**) and presence (**b**) of the discharge, after Eckert [16]. Copyright [1971], American Institute of Physics, Reproduced with permission. All rights reserved

the axial magnetic field in the coil region in the absence of a discharge, while curve (b) corresponds to the case after ignition of the discharge. In the absence of the plasma, the axial magnetic field is relatively uniform throughout the cross section of the tube with the field intensity decreasing slightly around its axis as one would expect for a "short" inductor coil. In the presence of the plasma, the field drops steeply in the central region of the discharge to around 5 % of its original value due to the interaction between the applied field generated by the current flowing through the inductor coil, and the induced magnetic field, generated by the induced currents in the plasma. Throughout each oscillator half cycle, these two fields, the applied field and the induced field, are opposing each other in the center of the discharge while acting in the same direction in the annular region between the discharge and the induction coil. The skin depth, δ_t, as identified in Fig. 8.4 is estimated to be of the order of 10 mm, which is consistent with its estimate using Eq. (8.1) with $\mu = \mu_o$ the permeability of vacuum $\mu_0 = 4\pi \times 10^{-7}$ Hy/m), and a value of σ_o =1,000 mho/m (10 mho/cm), corresponding to the electrical conductivity of argon at atmospheric pressure at 8,000 K. Outside the discharge region, in the annular space between the plasma column and the wall of the plasma confinement tube, the magnetic field intensity increases by about 10 % over its value in the absence of the discharge (curve a) since both induced and applied magnetic fields are in the same direction.

In a subsequent publication, Eckert [17] extended his magnetic field measurement technique, using a dual magnetic probe system, to determine the difference between the phase angle of the applied and induced magnetic fields. By keeping one of the probes in a fixed position near the plasma boundary and traversing the plasma with the second probe, he could deduce information on the magnetic and electrical fields and the electrical conductivity profiles in the discharge. Results obtained for a

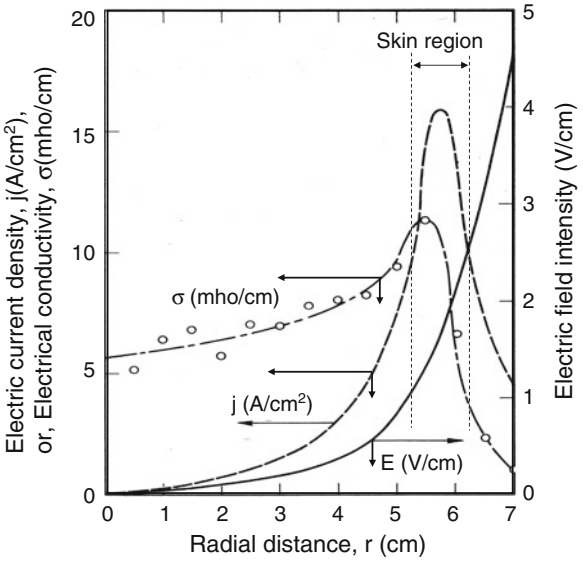


Fig. 8.5 Radial distribution of the magnitude of the induced electric field (E), current density (J) and electrical conductivity (σ) in an Argon induction discharge, $f = 2.6$ MHz, Po = 25 kW, after Eckert [17]. Copyright [1972], American Institute of Physics, Reproduced with permission. All rights reserved

140 mm i.d. induction plasma discharge, operated with pure argon at atmospheric pressure, are presented in Fig. 8.5. The measurements were carried out for an oscillator frequency of 2.6 MHz and an r.f. power of 25 kW. The data are expressed in terms of the electric field $|E|$ (V/cm), and current density $|j|$ (A/cm^2), and electrical conductivity profiles σ (mho/cm) in the middle section of the inductor. In contrast to the monotonic increase of $|E|$ with r, the absolute value of the induced current, $|j|$ passes through a sharp maximum at $r = 58$ mm, which corresponds to about 0.8 of the radius of the plasma confinement tube (r_o=70 mm). The radial profile of the local energy distribution, P, into the discharge can be calculated using these two curves, $|j|$ and $|E|$, as follows:

$$P = |j|.|E| \tag{8.2}$$

Superimposed on this figure are two vertical dotted lines, which identify the region of effective energy dissipation into the discharge corresponding to the "skin region" or "skin depth" estimated to be about 10 mm. From the ratio of the ($|j|/|E|$), Eckert evaluated the radial variation of the electrical conductivity of the plasma,σ, which is also plotted in Fig. 8.5. The results show that σ increases from a value of 600 mho/m (6 mho/cm) at the axis of the discharge to a maximum of 1,150 mho/m (11.5 mho /cm) at $r = 65$ mm and then drops sharply. This kind of variation reflects the annular shape of the energy dissipation zone in the discharge region and is qualitatively consistent with observation revealed by the end view photographs of the discharge shown in Fig. 8.6. It is also responsible for the off-axis maximum observed in temperature profile measurements reported by many authors as discussed in the next section.

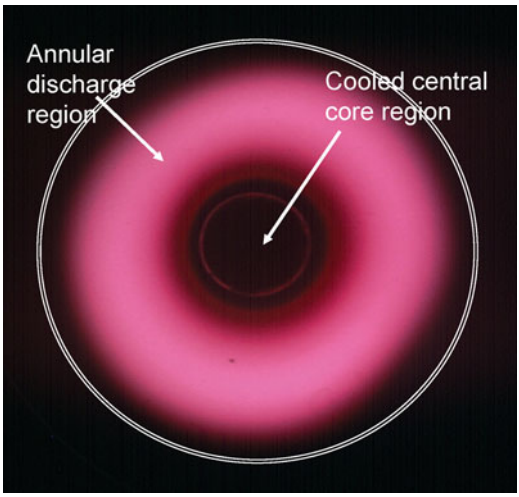


Fig. 8.6 End view of an induction discharge showing the doughnut shape of the energy generation done in the discharge region, Curtsy of M Thorpe

8.2.2.2 Energy Coupling Efficiency

In d.c. plasma sources it is straight forward to determine the plasma power by multiplying the easily measured values of arc current and voltage. In a r.f. power supply, the power delivered by the oscillator circuit is measured as the plate power or the reactive power. The power delivered into the discharge, which is a fraction of the applied power is given by the coupling efficiency, η_c is defined as the ratio of the power coupled into the discharge, P_o, divided by the reactive power, P_{ac}, in the oscillator circuit. This has been shown by Mensingen and Boedecker [18] to be a function of the coupling parameter, κ, defined as $\kappa = \sqrt{2}(r_n/\delta_t)$ and the ratio of the radius of the discharge, r_n to that of the induction coil, r_c. The results given in Fig. 8.7 show a strong dependence of the energy coupling efficiency on both these two parameters with the maximum energy coupling achieved at κ values between 2.5 and 4. The corresponding (r_n/δ_t) values are 1.8–2.8. Because of the strong dependence of the skin depth, δ_t on the oscillator frequency and the electrical conductivity of the plasma, it is important for the design, or selection, of an induction plasma source, to set up in the first place the required discharge diameter, operating pressure, and nature of the plasma gas. These values can then be used to choose the proper operating frequency and necessary discharge power. For example, for an Ar/H_2 discharge operating at atmospheric pressure in a 50 mm i.d. plasma torch, the average discharge temperature will be expected to be around 8,000 K. By using as oscillator frequency in the 1–3 MHz range, the corresponding skin depth will be around 15–20 mm, which is consistent for optimal coupling with a 40 mm discharge diameter.

It may also be noted in Fig. 8.7 that the closer the ratio of (r_n/r_c) is to unity, the higher is the energy coupling efficiency. For most induction plasma torches operating at plate power levels less than 50 kW, geometric considerations limit this parameter, (r_n/r_c), to values in the range of 0.6–0.7. The reason is largely due to the need for adequate cooling of the plasma confinement tube and for avoiding a direct

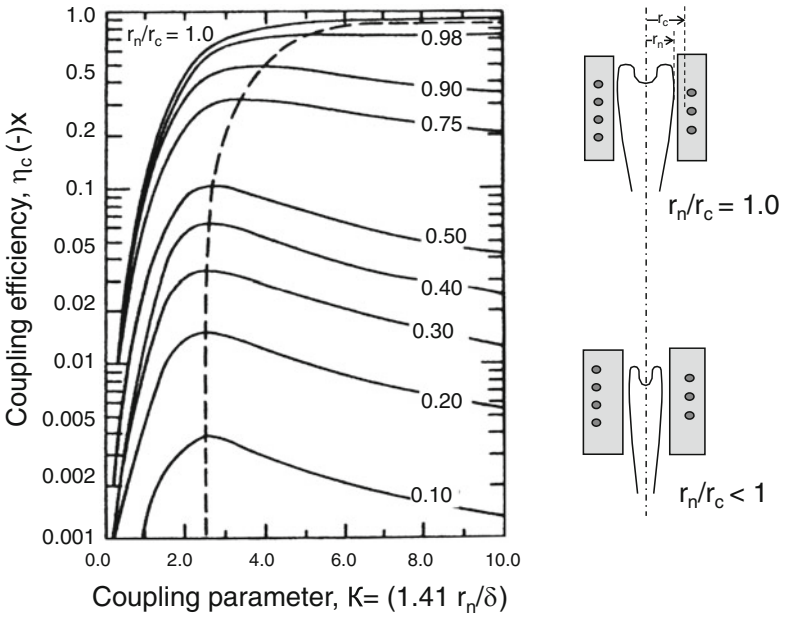


Fig. 8.7 Energy coupling efficiency as function of the coupling parameter and the ratio of the discharge diameter to induction coil diameter, After Mensingen and Boedecker [18]

electrical contact between the induction coil and the plasma. At higher power levels, requiring larger plasma confinement tubes, the ratio of (r_n/r_c) approaches a value of 0.8 or higher depending on the details of the induction plasma torch design, resulting in an improvement of the energy coupling efficiency.

Other than the above-indicated geometric coupling parameters, the efficiency of energy transfer between the electrical circuit and the plasma load also depends on the proper tuning of the oscillating circuit. This is achieved in low power system, up to 10 kW, through the introduction of an appropriate electrical matching circuit, which protects the power supply from impedance fluctuations of the plasma load and allows the power supply to be tuned for a fixed impedance load (generally 50 Ω). In larger power systems, above 10 kW, power losses in the matching network surpass its advantages. It is common in such cases to work with a free oscillating circuit in which the induction plasma load is an integral part of the oscillating circuit. This results in a higher overall energy transfer efficiency, at the expense of tolerating small variations of the oscillating frequency depending on the plasma characteristics.

8.2.2.3 Minimum Sustaining Power

Sustaining a plasma discharge, whether d.c. or r.f. inductively coupled depends on a simple equilibrium between local energy dissipation through ohmic heating and

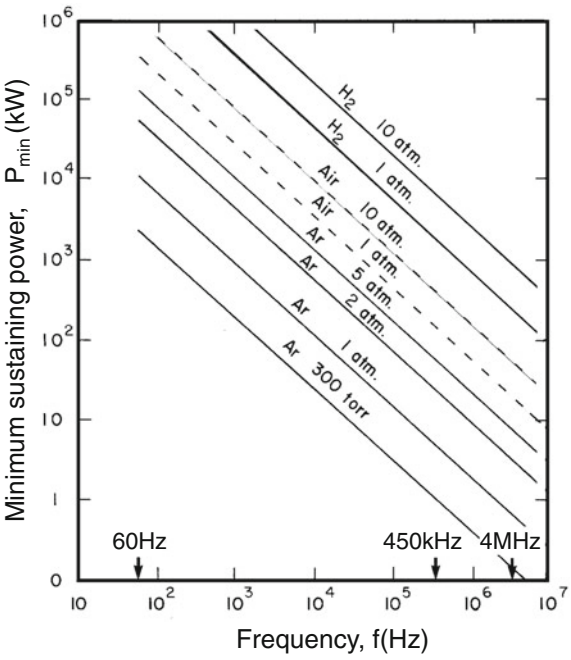


Fig. 8.8 Minimum discharge sustaining power as function of the oscillator frequency for different plasma gases and operating pressures, after Poole et al. [19]

energy losses from the discharge through radiative energy transfer, conduction, and convection to the surroundings of the discharge. r.f. inductively coupled plasmas are no exception in this regard and sustaining such a discharge requires the generation of a sufficiently high energy density to compensate for energy losses and maintain the discharge at the lower limit of its electrical conductivity. It is not surprising to recognize accordingly that molecular gases would require a higher energy density than monatomic gases to be maintained in the plasma state. It is also obvious that maintaining an electrical discharge at high pressure would require higher energy densities than that at a lower pressure.

Based on the analyses presented in Sect. 8.2.3, for a given plasma power, the energy density in the discharge would be inversely proportional to the skin depth. Since the latter is, in turn, inversely proportional to the square root of the oscillator frequency and of the electrical conductivity of the plasma, it is reasonable to expect a direct relationship between the energy density in the discharge and the oscillator frequency. The results presented in Fig. 8.8, by Thorpe and his collaborators [19, 20] based on a simplified mathematical model, clearly indicate that, for a given plasma gas at a given pressure, the minimum power required to sustain a stable discharge, drops exponentially with the increase of the oscillator frequency. While the absolute values given in this example depend on the particular size of the discharge cavity, the trend is clear with a drop of many orders of magnitude of the minimum sustaining power of the discharge, with the increase of the frequency from the kHz to the MHz range. The lowest values of the minimum sustaining

power are obtained for argon plasmas at low pressure and oscillator frequencies in the MHz range. With the increase in pressure, the minimum sustaining power requirement increases. The same effect is noted with the shift of the plasma gas from monatomic to a molecular gas, such as air, with the highest values of the minimum sustaining power required for pure hydrogen above atmospheric pressure.

These results are concurrent with experimental observations made. They also provide a simple explanation for the commonly used practice of igniting an inductively coupled plasma discharge at low pressure with argon as the plasma gas. Once a discharge has been established it is possible to increase the pressure with a corresponding increase in the plasma power. The addition of molecular gases into the discharge can also be made at this stage accompanied by an increase of the discharge power in order to avoid extinction of the discharge.

8.2.3 Induction Plasma Torch Design

8.2.3.1 Flow Stabilization Mechanism

The stability of operation of the induction plasma torch depends to a large extent on the ability to control the aerodynamics of the flow in the discharge. Numerous plasma stabilization flow configurations have been developed over the years. These are summarized in Fig. 8.9, after Dresvin [1]. They can be classified as either "single flux" or "multiple flux" torches.

In the single flux torches, shown in Fig. 8.9a, c, e, g, the plasma gas is introduced into the discharge cavity as a single flow, either axially (Fig. 8.9a), or tangentially (Fig. 8.9c, e, g) oriented at different angles with respect to the axis of the plasma confinement tube. The role of the plasma gas in these cases is to keep the discharge in a central position in the coil region and avoid a too-close contact between the discharge and the inner wall of the plasma confinement tube. Protecting the walls of the plasma confinement tube from thermal damage is a major concern in all of these designs.

In the double flux torches, the plasma gas is introduced into the discharge chamber as two distinct gas streams separated by a concentric quartz tube as shown in Figs. 8.9b, d, f. These configurations are widely used because of their ability to properly protect the plasma confinement tube through the use of a higher sheath gas flow rate. It also offers the added advantage of the possible use of different gas compositions for each of the sheath gas and the central plasma gas stream. In general, when the plasma is formed of a mixture of argon with a molecular gas such as hydrogen, nitrogen, or oxygen, the molecular gas is introduced premixed with the sheath gas. It may be noted from Figs. 8.9b, d, f that the sheath gas is commonly introduced into the plasma torch in an axial flow mode while the central gas is introduced in a tangential flow configuration.

At low pressures and low power levels, a simple air cooling of the external plasma confinement tube is adequate for the protection of the plasma confinement

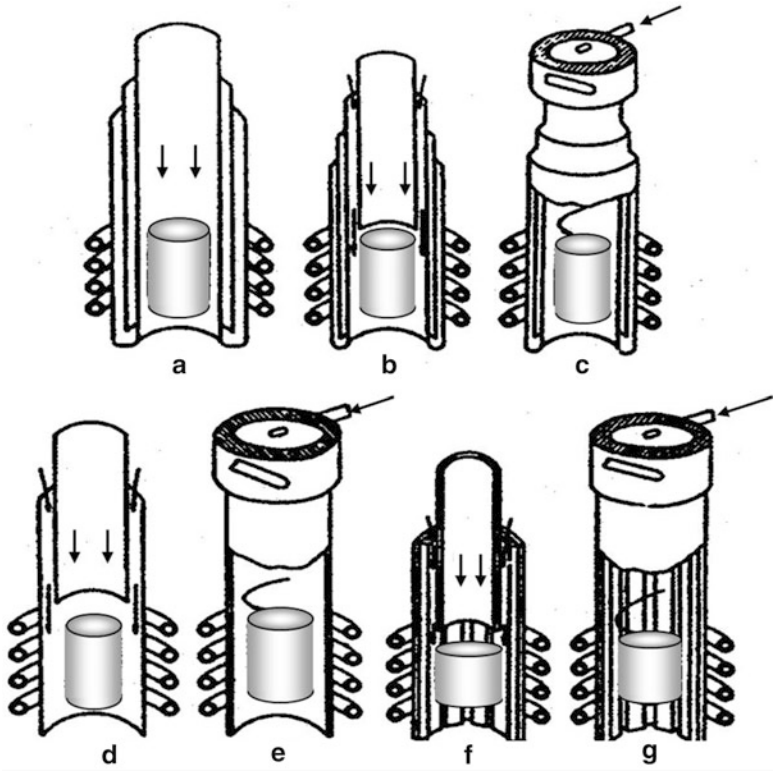


Fig. 8.9 Gas stabilization of induction plasma discharges in the single flux and double flux modes, after Dresvin [2] with kind permission

tube from thermal damage with either modes of plasma stabilization (Fig. 8.9d, e). The photograph given in Fig. 8.2 is a good example of, an air-cooled, double flux stabilized discharge with a 70 mm i.d. plasma confinement tube, operated at atmospheric pressure with pure argon as the plasma gas and a plate power of 12 kW. At higher power levels, external air cooling is not enough to insure a proper protection of the plasma confinement tube. Water cooling is the next step up in these cases as shown in Figs. 8.9a–c. The use of a double or triple wall, water-cooled construction results in a significant increase of the outer diameter of the tube and the corresponding increase of the diameter of the induction coil for the same inner diameter of the plasma confinement tube. This results in a decrease of the ratio of the diameter of the plasma load to that of the induction coil and a corresponding decrease in the energy coupling efficiency. At yet higher power levels, simple water cooling of the walls of the plasma confinement tube is not always enough to insure its adequate protection from the discharge, a water-cooled, segmented metal cage, is inserted in some cases into the discharge cavity of the torch as shown in Fig. 8.9f, g.

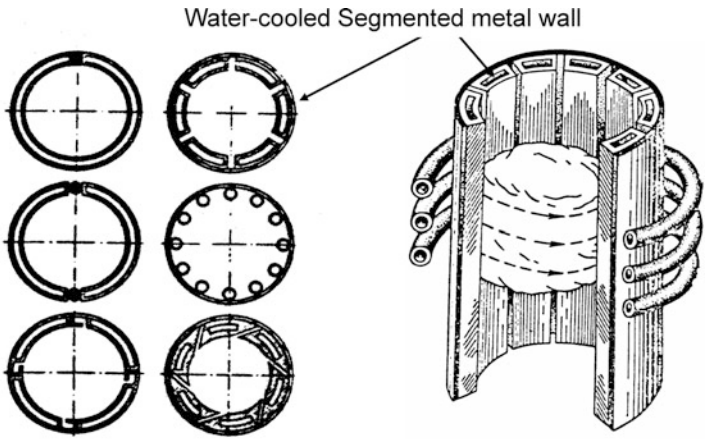


Fig. 8.10 Schematic representation of different metal shield configurations, after Dresvin [1] with kind permission

8.2.3.2 Segmented Metal Wall Torches

Segmented metal wall induction plasma torches were mostly developed in the early 1970s in the former Soviet Union by Dresvin and his collaborators at the St Petersburg Technical University [1, 2]. These torches make use of standard, single or double flux, gas flow configuration in conjunction with a single wall plasma-confinement quartz tube. A segmented, water-cooled, metal shield, often referred to in literature as a "metal cage," is introduced into a standard, quartz wall, plasma confinement tube in order to provide an additional protection to the quartz tube from the plasma discharge. Schematic representations of different segmented metal shield configurations are illustrated in Fig. 8.10. The way the segments work is essentially through the suppression of the induced currents in any given segment through the action of the magnetic fields developed by the currents induced in the neighboring segments. The best results are obtained through the reduction of the gap between successive segments without compromising the electrical insulation between the segments.

The segmented metal wall design, while quite effective in reducing thermal stresses on the quartz plasma confinement tube, suffers from the fact that it is more difficult to ignite and results in a reduction of the overall energy efficiency of the plasma torch. The use of metallic components in contact with the discharge can be a source of contamination of the plasma especially in the presence of corrosive gases.

8.2.3.3 Ceramic Wall Torches

Ceramic wall induction plasma torches make use of the availability of advanced ceramics for the replacement of the quartz plasma confinement tube. The principal properties expected from the ceramic materials to be used are their resistance to chemical attack combined with high thermal conductivity and high thermal shock

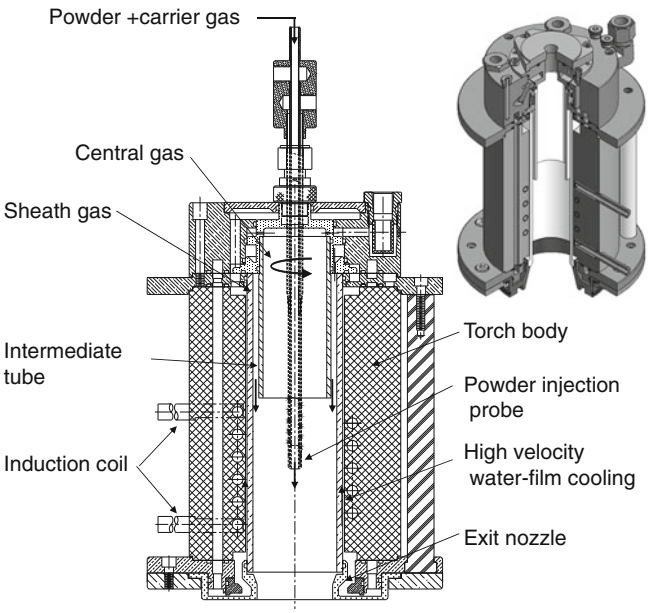


Fig. 8.11 Schematic drawing (*left*) and 3-D representation (*right*) of the ceramic wall induction plasma torch developed by Boulos and Jurewicz, courtesy of Tekna Plasma Systems Inc.

resistance. While a number of materials are available, only one made it to the final design presently manufactured on a commercial scale by Tekna Plasma Systems Inc, in Sherbrooke, Québec, Canada. The basic design of the ceramic wall induction plasma torch was developed in the early 1980s, at the University of Sherbrooke by Boulos and Jurewicz [21, 22]. Further design refinement and scaling-up to the hundreds kW power level, was later completed at Tekna Plasma Systems Inc. [23, 24]. A schematic representation of this induction plasma torch design is given in Fig. 8.11. Its principal characteristics are as follows:

1. The use of a ceramic plasma confinement tube combined with high-velocity, water-film cooling. This is achieved through the incorporation of the induction coil surrounding the ceramic tube into a polymer–matrix composite. Such a torch body is precision machined in order to allow for a very thin gap between the inner surface of the torch body and the outer wall of the ceramic plasma confinement tube. By keeping this gap thickness to less than 1 mm, it is possible to achieve a high velocity of the cooling water flowing in this annular space (above 10 m/s) at a reasonably low overall water flow rate. The results is an efficient cooling of the outer surface of the ceramic tube which allows for its use under the high heat flux conditions associated with the operation of such a torch at high power and high energy density.
2. The incorporation of the water-cooled induction coil in the polymer matrix composite also allows for the precision alignment of the plasma confinement

tube and the coil section. It also facilitates the reproducible assembly of the plasma torch.

3. The aerodynamic design of the upstream torch gas distributor head using a double gas flux design allows for the separate introduction of the sheath and central gas streams. The sheath gas is introduced axially into the annular space between the inner wall of the plasma confinement tube and the outer surface of an intermediate separator tube. The latter which is mostly radiation cooled can be made of quartz or a high temperature ceramic material. The central plasma gas is introduced tangentially into the upper discharge cavity in order to stabilize the discharge and keeps the plasma away from the leading edge of the intermediate separator tube.
4. The axial injection of particles into the center of the discharge cavity through the use of water-cooled metallic injection probes. This allows for the introduction of the material to be treated into the discharge in a non-current-carrying region to avoid the possible extinction of the plasma due to excessive local cooling. It also insures for the proper dispersion and the intimate contact between the injected material streams, whether in the form of powders, liquids, or gaseous streams, and the main plasma flow.
5. The integration into the torch design of a discharge nozzle and a front-mounting flange allows for the control of the plasma flow characteristics at the exit of the torch and the mounting of the torch on the top of a plasma-processing reactor. The use of such nozzles allows for operation under high purity gas tight conditions and for achieving both subsonic and supersonic flow conditions in the discharge plume at the exit of the torch.

Because of the close interdependence between the physical dimension of the induction plasma torch, its nominal design power rating and operating frequency, a single induction plasma torch tends to have a relatively narrow dynamic range of operating conditions. For this reason, Tekna has developed a complete line of induction plasma torches with different internal diameters of the plasma confinement tube for operation at different power levels. Torches optimized for different power levels from 30, up to 200 kW are commercially available. Further development of these torches gave rise to the multi-coil design [23, 24] shown in Fig. 8.12, which can be operated with a dual frequency with the upper coil operated by an r.f. power supply in the MHz range while the lower coils operated with a solid state power supply in the kHz range. The design of these induction plasma torches also allows for the front flange mounting of the torch on the top of a reactor or deposition chamber as well as the insertion of a supersonic Laval nozzle in order to accelerate the plasma flow at the exit of the torch.

8.2.3.4 Hybrid Plasma Torches

The concept of a hybrid induction plasma torch was developed in the late 1970s and early 1980s by Yoshida and Akashi at the University of Tokyo in Japan [25, 26].

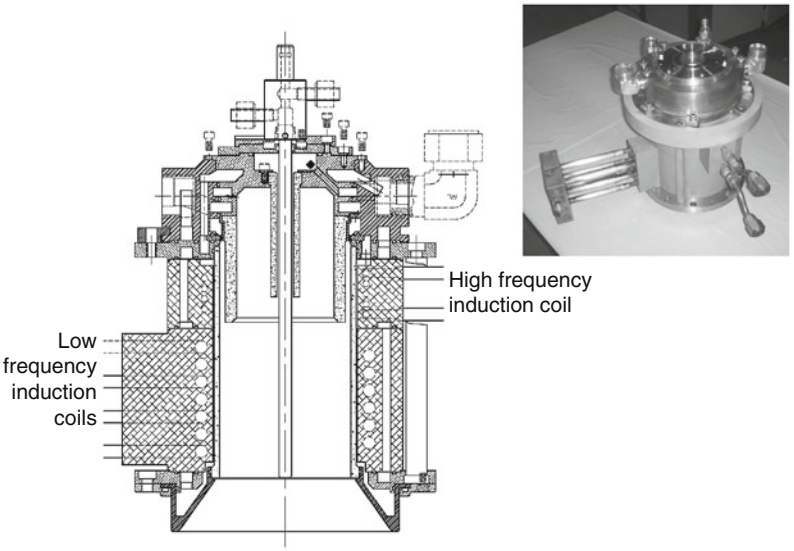


Fig. 8.12 Multi-coil, dual-frequency, induction plasma torch, Model PD-100. Photograph courtesy of Tekna Plasma Systems Inc.

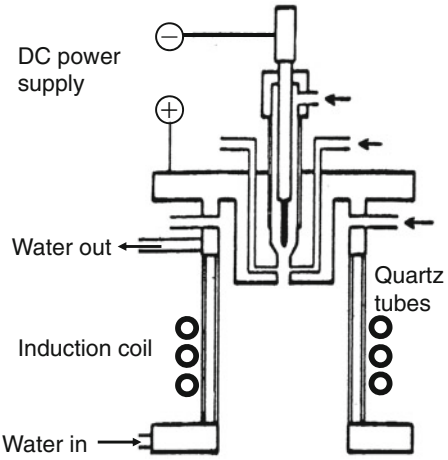


Fig. 8.13 Schematic representation of a D.C./R.F. hybrid plasma torch. After Yoshida et al. [25]. With kind permission from Springer Science + Business Media B.V

The first type of a hybrid plasma torch combines direct current (d.c.) and radio frequency (r.f.) induction plasma technologies. Figure 8.13 shows a typical torch design, which consisted of a d.c. plasma torch coaxially mounted on the top of an r.f. induction plasma torch. The plasma jet from the d.c. torch flows axially into the center of the discharge cavity of the induction plasma torch. The applied r.f. electromagnetic fields generated through the induction coil could then couple into the conducting plasma jet immerging from the d.c. torch and provide

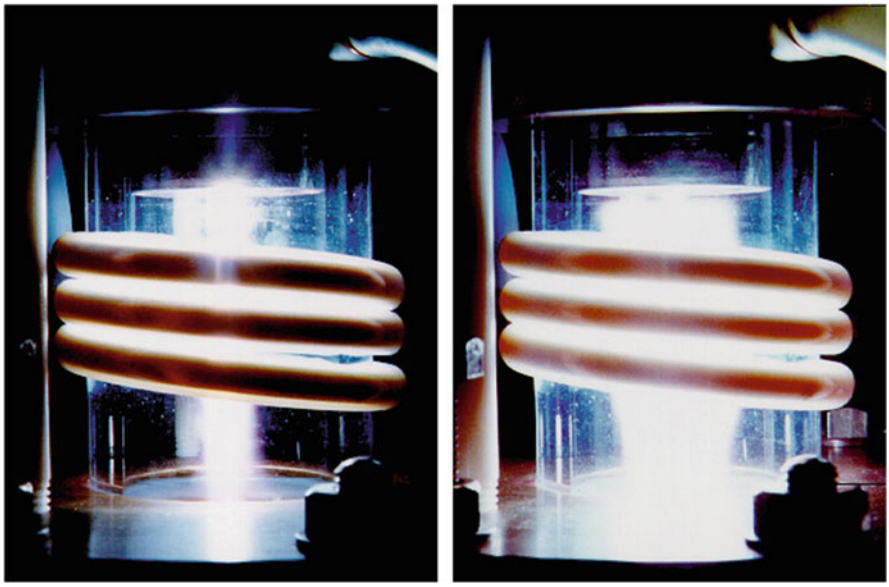


Fig. 8.14 Photograph of a D.C./R.F. hybrid plasma discharge. (*Left*) with the D.C. discharge on (*right*) in the presence of both D.C. and R.F. discharges. Photograph courtesy of Professor T. Yoshida, Tokyo University

the necessary energy for the increase of the volume of the discharge, which filled the discharge cavity defined by the water-cooled, quartz plasma confinement tube. A photograph provided by Professor Yoshida of Tokyo University, Fig. 8.14, shows the discharge in the presence of the d.c. plasma plume only (left) and that in the presence of the combined d.c. and r.f. inductively coupled discharges.

Yoshida and Akashi [25, 26] studied the characteristics of this type of discharge, which was successfully used in a large number of applications in the area of material processing, plasma spraying, and the synthesis of ultrafine powders. A high power installation used, at the University of Tokyo, for the CVD deposition of novel thermal barrier coatings, combines two 150 kW hybrid plasma torches. Systematic efforts were also devoted to the modeling of these hybrid induction plasma discharges in order to identify their principal characteristics and fluid dynamic conditions. These torches were generally operated in the power range of 30–150 kW for the r.f. torches, with the d.c. power typically around 10–15 % of the total applied power to the discharge.

Subsequent studies in Japan were directed to the development of a corresponding r.f./r.f. hybrid plasma torch operating with two independent induction coils powered by separate r.f. power sources oscillating at two different frequencies. These types of torches aimed at achieving a better distribution of the energy in the discharge cavity without the possible introduction of metallic impurities into the plasma caused by the presence of the d.c. plasma torch. A schematic representation of a typical r.f./r.f. hybrid induction plasma torch and a photograph

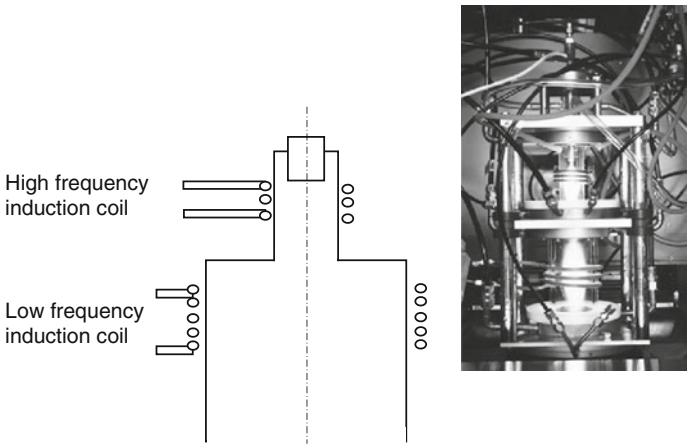


Fig. 8.15 Schematic representation of an r.f./r.f. hybrid induction plasma torch (*left*) and a photograph of such a torch in operation, after Kameyama et al. [27]. Courtesy of Professor T. Yoshida, Tokyo University

of such a discharge system in operation are shown in Fig. 8.15, after Kameyama et al. [27, 28]. The upper coil in this case was powered by a 13.6 MHz r.f. power supply, while the lower coil was powered by a 4 MHz power supply.

8.2.4 Temperature, Fluid Flow, and Concentration Fields

8.2.4.1 Temperature Fields

Numerous studies have been reported dealing with the measurement of the temperature field in an r.f. inductively coupled discharge. In this section a few examples of typical temperature field measurements are presented with the specific objective of revealing the main characteristics of this type of discharge and variation of the temperature field in the discharge with the intensity of the magnetic field (applied power) and the nature of the plasma gas.

Radial temperature profile measurements in the middle section of the induction coil were reported in the early 1970s by Douglas [29]. These were made using emission spectroscopy on a-45 mm i.d. quartz wall inductively coupled discharge, operated at atmospheric pressure with pure argon as the plasma gas. The oscillator frequency was 2 MHz. Typical results obtained for different intensities of applied magnetic fields are given in Fig. 8.16. It may be noted that all distributions show the typical off-axis maximum, which is a direct consequence of the annular mode of energy dissipation into the discharge region. It is important to note that a significant increase of the intensity of the applied magnetic field results in only a slight increase in the maximum temperature of the plasma. The radius of the discharge, as estimated by the outer limit of the temperature profiles, is noted to increases from

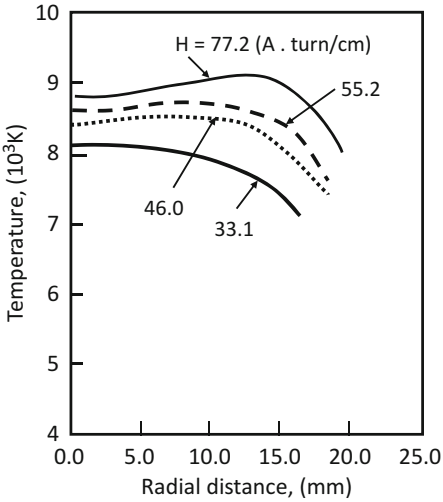


Fig. 8.16 Radial temperature profiles at the middle section of the induction coil for an argon discharge at atmospheric pressure for different axial magnetic field intensities, after Douglas [29]

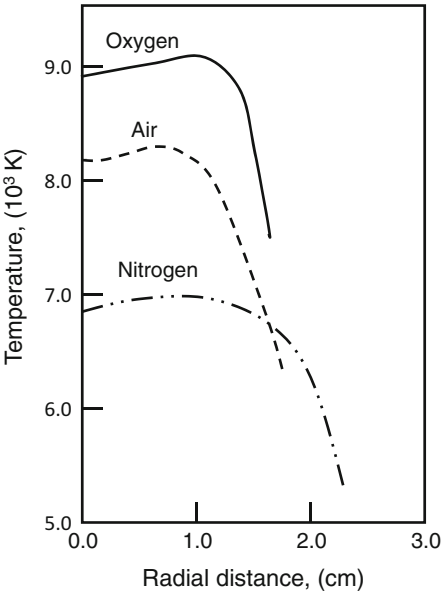


Fig. 8.17 Radial temperature profiles, at the middle section of the induction coil, for atmospheric pressure inductively coupled discharge with different molecular gases. Oscillator frequency = 10–13 MHz and power into the plasma = 8–10 kW. After Dresvin [1] with kind permission

about 16 mm to 20 mm with the doubling of the applied magnetic field (discharge power). The maximum reported temperature in the discharge in this case remains in the range of 8,000–9,000 K.

Dresvin [1] reported a compilation of measurements of the temperature field in r.f. inductively coupled discharges. Typical results are presented in Fig. 8.17 for an atmospheric pressure inductively coupled discharge operated with different plasma gases, oscillator frequencies, in the range of 10–13 MHz, and a total power into

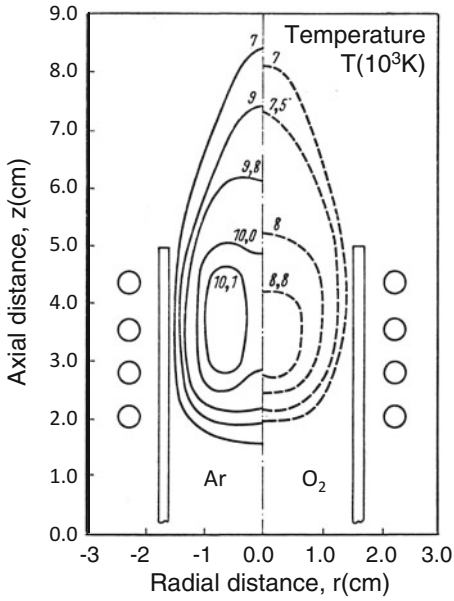


Fig. 8.18 Two-dimensional temperature mapping of inductively coupled atmospheric pressures, discharges of argon (*left*) or oxygen (*right*), under comparable conditions. Total gas flow rate = 30 slm, oscillator frequency = 10 MHz, total plate power = 12 kW for the argon plasma, and 8 kW for the oxygen plasma. Temperature values are given in 1,000 K. After Dresvin [1] with kind permission

the plasma in the range of 8–12 kW. The results reveal a strong dependence of the off-axis maximum temperature, and the size of the discharge region, on the nature of the plasma gas. A relatively high centerline temperature ($T \approx 9,\ 000$ K) is noted for the oxygen plasma compared to that for an air discharge ($T \approx 8,\ 200$ K). The lowest centerline temperature reported is for nitrogen plasma ($T \approx 7,\ 000$ K).

Two-dimensional temperature mappings for atmospheric pressure argon and oxygen plasmas under comparable operating conditions are given in Fig. 8.18. The total gas flow rate was set in each of these two cases at 30 slm. The oscillator frequency was 10 MHz and the r.f. power input was 12 kW for the case of the argon plasma and 8 kW for the oxygen plasma. The results show relatively large volume discharges with a uniform temperature field in both the radial and axial directions.

8.2.4.2 Flow Fields

The flow field in an inductively coupled r.f. discharge is rather complex due to the interaction between the applied magnetic field and the induced electric fields. The resulting ($j \times B$) electromagnetic forces, which act in the radial direction at the middle section of the coil are responsible for the creation of a high-pressure zone in the center of the discharge. This gives rise to the pumping of the plasma flow in both the upstream and the downstream directions, leading to the development of a flow reversal in the upstream direction. A schematic representation by Klubnikin [30] of the flow pattern in the discharge cavity of induction plasma discharge under two different flow conditions is shown in Fig. 8.19a. The corresponding temperature fields in the discharge are shown in Fig. 8.19b. The left-hand side, identified as (1),

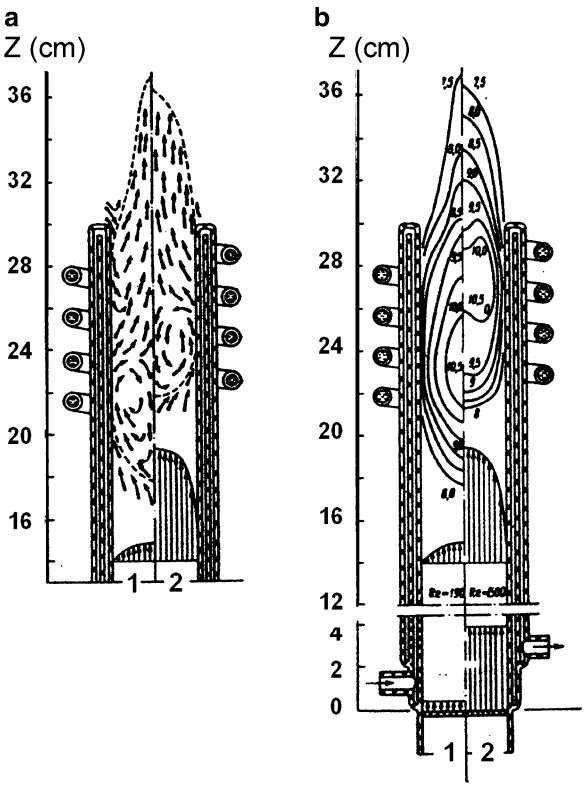


Fig. 8.19 Schematic representation of the flow pattern (a) and temperature distributions (b) for an argon discharge at atmospheric pressure. Torch diameter = 40 mm, $f = 6$ MHz, $P = 7.6$ kW (Case 1). Qo = 5 slm., (Case 2). Qo = 40 slm., after Klubnikin [30]

of each of these two figures corresponds to operation with a low flow rate of the plasma gas into the discharge (5 slm), while the right-hand side of each figure, identified as (2), corresponds to a high flow rate operation (40 slm).

These reveal a flow pattern in the center of the discharge, which is characterized by an electromagnetically induced radial flow towards the center of the discharge at the middle section of the induction coil. This effect is observed in both the low and high flow cases. It can also be observed that in the low flow case (Case 1) the pumping effect is strong enough to entrain gases from the downstream region of the torch, which move upstream along the inner wall of the plasma confinement tube. With the increase of the total gas flow rate into the torch, (Case 2), the center of the discharge is slightly shifted downstream and the radial pumping action in the center of the coil is no longer capable of entraining gas from the downstream end of the torch. The only reverse flow that is maintained in this case is that along the centerline of the discharge on the upstream side of the induction coil. The corresponding temperature contours in Fig. 8.19b reveal a corresponding shift in the position of the discharge with the increase of the total plasma gas flow rate. This schematic is consistent with the observation that the position of the discharge in the induction coil cavity is a result of a delicate balance between the drag forces on the discharge by the plasma and sheath gas flow, and the stabilizing forces

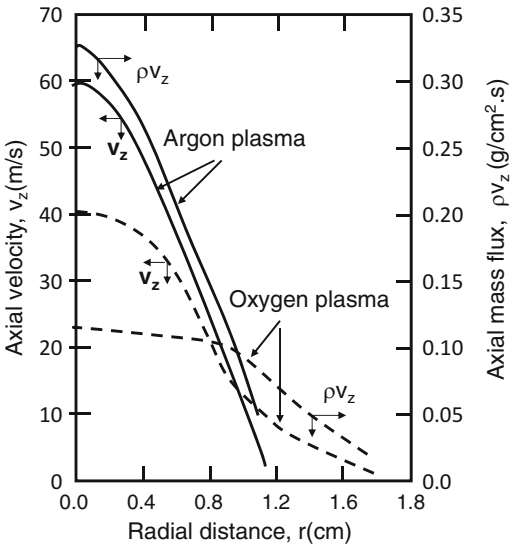


Fig. 8.20 Axial velocity (v_z) and mass flux ($\rho \cdot v_z$) profiles at the exit of a 30 mm i.d. induction plasma torch. $Q_o = 30$ slm., $f =$ 10 MHz, $P = 12$ kW for argon plasma (*solid lines*) and $P = 8$ kW for oxygen plasma (*dotted lines*), after Dresvin [1] with kind permission

created by the electromagnetic pumping and the swirl velocity component which is often introduced into the plasma gas flow for the purpose of enhancing the stability of the discharge. It should be mentioned that increasing the flow rate of the plasma gas into the torch can and will eventually lead to complete extinction of the discharge. The critical total plasma gas flow rate, which can be tolerated by an induction plasma torch, depends on the dimension of the torch, the oscillator frequency, and the applied r.f. power.

It should be pointed out that the observation of the reversed flow on the upstream side of the discharge was reported earlier in the 1960s by Chase [31] using tracer powders, which were shown to bounce-off the upstream side of the discharge repelled by the reverse flow "fountain." The presence of this reversed flow is a distinct characteristic of the induction plasma discharge and requires special attention when using induction plasma torches for the treatment of solid, liquid, or gaseous precursors. Therefore, these materials are usually injected axially into the discharge through a water-cooled feeding tube with its tip reaching in the middle of the induction coil, as shown in Fig. 8.11. While the position of the injection probe can be varied, the location of the probe tip in the center of the induction coil assures that the flow recirculation region is avoided and a full exposure and mixing of the injected material, whether powder, liquid, or gas, with the plasma flow is achieved.

At the exit of the plasma torch, the plasma flow emerges in the form of a low velocity laminar or turbulent jet, depending on the overall flow and operating conditions. Under low-pressure conditions, the length of the core region of the emerging plasma jet can be more than 10 to 15 times the diameter of the exit nozzle of the plasma torch.

Typical axial velocity, v_z, and mass flux, $(\rho \cdot v_z)$, profiles at the exit of a 30 mm i.d. induction plasma torch are given in Fig. 8.20, after Dresvin [1]. These were

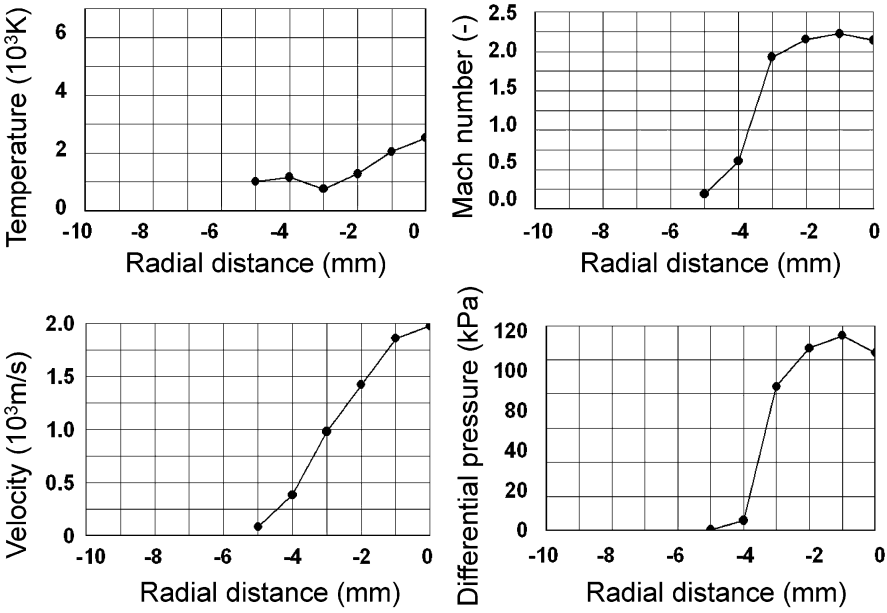


Fig. 8.21 Radial profiles of the local temperature, velocity, Mach number, and differential pressure at a distance of 25 mm from the exit of a M-3 supersonic plasma nozzle attached to a Tekna PL-35 torch operating with Ar/H_2 as the plasma gas (2 % vol. H2), Chamber pressure Pa = 17.1 kPa, Back pressure in the torch, Pb = 212 kPa, after Hollenstein et al. [32] with kind permission

obtained for the same conditions as those for which temperature mappings were given in Fig. 8.18. The measurements were made using water-cooled Pitot tube probes for argon (solid lines) and oxygen (dotted lines) plasmas. The total gas flow rate was 30 slm, oscillator frequency, $f = 10$ MHz, and plate power, $P = 12$ kW for the argon plasma, and 8 kW for the oxygen plasma cases. The results show maximum centerline velocities in the range from 40 to 60 m/s depending on the nature of the plasma gas which is considerably lower than that obtained in standard d.c. plasma jets. It is important to note that the maximum mass flux is also located on the centerline of the discharge, rather than off axis, as observed in d.c. plasma jets. This is a direct consequence of the radial pumping and mixing of the sheath gas toward the center of the discharge at the middle section of the induction coil.

Recent developments of special Laval nozzle adapted to the induction plasma torches allowed for a significant increase of the plasma jet velocity at the exit of the torch to supersonic speed levels. Typical radial profiles of the temperature, axial velocity, local Mach number, and differential pressure are shown in Fig. 8.21 after Hollenstein et al. [32]. These profiles were obtained for an Ar/H_2 (2 % vol. H_2) plasma flow with a water-cooled Laval nozzle designed for operation at Mach number 3.0. The plate power for the discharge was 25 kW. For this nozzle (M-3 nozzle), the results are reported for an axial location $z = 17$ mm. The downstream

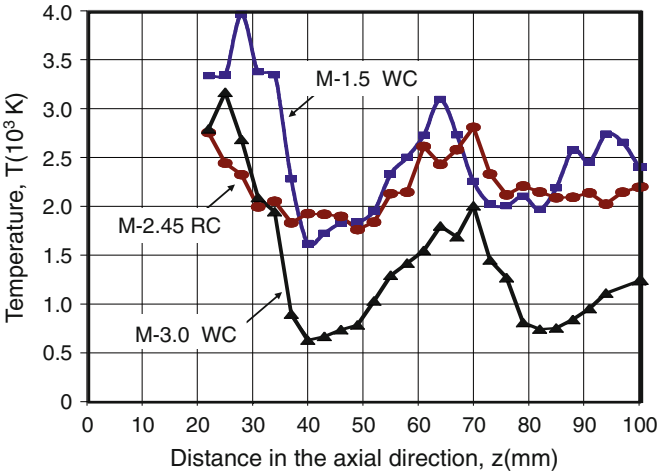


Fig. 8.22 Axial variation of the temperature along the centerline of a supersonic induction plasma jet for different Laval nozzle designs. Plasma gas Ar/H_2 and plasma plate power = 20 kW, after Léveillé et al. [34]. Reprinted with permission of ASM International. All rights reserved

chamber pressure was maintained at 17.1 kPa, while the backpressure in the discharge cavity in the plasma torch was 212 kPa. The results show peak velocities of 2,000 m/s at the centerline of the plasma jet. The local Mach number was close to 2.2, and the local temperature of the plasma flow was below 3,000 K. Similar results were obtained for a nozzle designed for lower velocities (M-1.5).

Further development along these lines aimed at achieving yet higher velocities and improved uniformity of the supersonic plasma flow. Léveillé et al. [33, 34] reported a systematic study of enthalpy probe measurements of the temperature and velocity profiles for an Ar/H_2 plasma jet using both water-cooled (W-C) and radiation-cooled (R-C) Laval nozzles for a wide range of operating conditions. The plasma gas flow rates were maintained at 40 slm Ar + 1.8 slm H_2 for the sheath gas and 20 slm Ar for the central gas. The torch power was set at 20 kW and the absolute pressure in the chamber was 1.5 kPa. Typical results presented in Figs. 8.22 and 8.23 show axial profiles of the temperature and axial velocity of the flow along the centerline of the plasma jet. It can be noted form Fig. 8.23 that the maximum axial velocity achieved in these cases was between 2,000 and 2,300 m/s, which was obtained with the radiation-cooled (R-C), M-2.45 nozzle. The corresponding velocities obtained with the water-cooled (W-C) nozzles were lower by about 500 m/s even for the W-C. M-3 nozzle. As expected the corresponding temperature profiles showed significant axial variations.

8.2.4.3 Concentration Fields

The ability to axially inject reactants into the center of inductively coupled R.F. plasma without disturbing the discharge has long been recognized as being

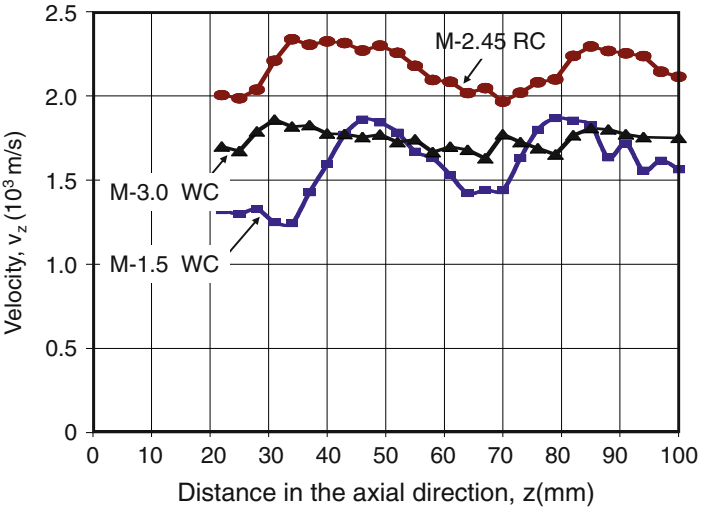


Fig. 8.23 Variation of the axial velocity along the centerline of a supersonic induction plasma jet for different Laval nozzle designs. Plasma gas Ar/H_2 and plasma plate power = 20 kW, after Léveillé et al. [34]. Reprinted with permission of ASM International. All rights reserved

of particular value for the use of this plasma source for chemical synthesis. Special attention has therefore been given to the study of the mass transfer and mixing pattern in the discharge region. Dundas [35] reported in the early 1970s one of the first studies of mass transfer in an inductively coupled discharge. His data presented in terms of two-dimensional concentration mappings in the discharge region for an argon/air system revealed significantly different mixing pattern in the presence and absence of the discharge. The results given in Fig. 8.24 (top) show the molar fraction of air in the mixture in the absence of the discharge, while those given in Fig. 8.24 (bottom) are in the presence of the discharge. The air/argon mass flow ratio is set at 3.33 for both cases. It may be noted from the top figure that in the absence of the discharge, turbulent and intense gas recirculation phenomena are responsible for the instant mixing of the two streams with the molar fraction of air in the mixture reaching 70 % almost instantly at the entrance level of the argon stream in the center of the flow cavity. In the presence of the discharge the corresponding value of the molar fraction of air is less than 0.1 %. The effect is primarily due to the high viscosity of the plasma and complete suppression of turbulence and gas recirculation effects in this case.

Subsequent studies by Boulos [36] have documented these phenomena using photographic and mass spectrometric measurements of the mixing pattern in an inductively coupled R.F. discharge. The photographs given in Fig. 8.25 show a 50 mm i.d. inductively coupled discharge in the presence of a tracer gas axially introduced along the centerline of the discharge. The photograph on the left-hand side of the figure is for a low tracer gas flow rate (less than 1 slm of argon, with a dispersion of ultrafine zirconia powder as tracer), while that on the right-hand side

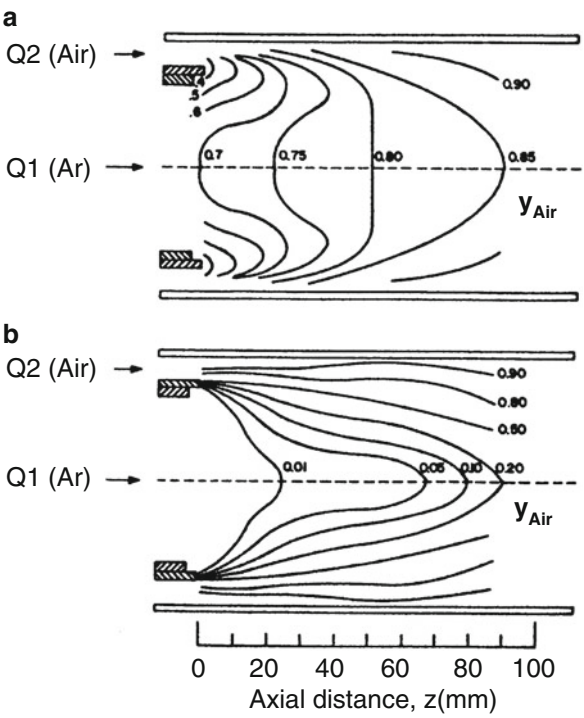


Fig. 8.24 Concentration mapping in induction plasma in the absence (*top*) and presence (*bottom*) of the discharge. Air/Argon mass flow ratio = 3.33, after Dundas [35]

of the figure is for the same discharge in the presence of a stronger tracer gas injection (above 5 slm). The plasma gas was pure argon in this case, operated at atmospheric pressure, with an oscillator frequency of 3 MHz and a plate power of 7 kW.

The significant difference between the mixing patterns in the presence and absence of the discharge was studied by Soucy et al. [37, 38] using mass spectrometric measurements. The set up used for these measurements is shown in Fig. 8.26. The plasma was generated using a Tekna PL-50 torch operated with Ar/H_2 as the sheath gas (89 slm Ar + 9.6 slm H_2), the central gas flow rate was 59 slm, Ar. The chamber pressure was varied between 35 and 93 kPa, and the plate power was set in the range of 13–24 kW. Typical results obtained with axial injection of a nitrogen tracer gas in an Ar/H_2 plasma gas stream are given in Fig. 8.27. In this figure, the concentration profiles of nitrogen along the centerline of the discharge chamber are given when the tracer gas is axially injected into the discharge using a water-cooled probe at a rate of 15 slm (N_2). The probe tip was located at a distance of 78 mm upstream of the exit of the plasma torch. The solid line, which refers to the no plasma case, i.e., cold flow, shows that the nitrogen concentration drops rapidly as the gases emerge from the probe tip reaching almost its asymptotic value of 10 vol.% at the torch exit. In contrast, in the presence of the discharge, dotted lines, whether at a power level of 13 or 24 kW, the nitrogen concentration along the axis remains essentially unchanged for a few centimeters

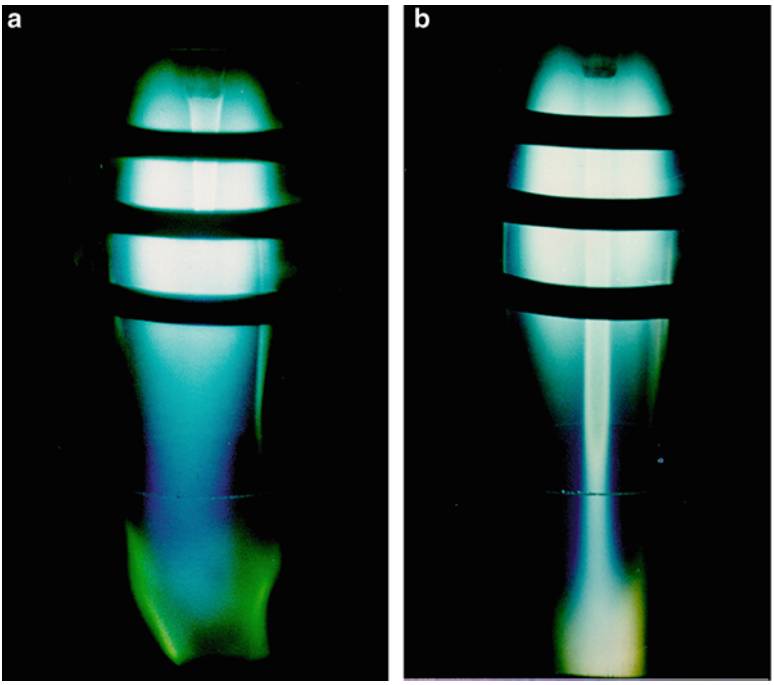


Fig. 8.25 Photographs of an R.F. inductively coupled discharge in the presence of axial injection of a tracer gas along the centerline of the discharge. Pure Argon plasma with an oscillator frequency of 3 MHz and a plate power of 7 kW, after Boulos [36]

within the torch, dropping to N_2 concentration at the exit level of the torch of 30–40 vol.%. The asymptotic value of 10 vol.% N_2 is reached in this case at 150 mm downstream of the torch exit.

The effect of nitrogen gas injection through the central probe, often referred to as powder carrier gas injection, was investigated by Rahmane et al. [39, 40] using an enthalpy probe system. Torch operating parameters were plate power = 20 kW, chamber pressure = 33 kPa, central plasma gas flow of 33 slm of argon, a sheath gas flow of (71 slm Ar + 4 slm H_2), and a probe position 93 mm above the torch exit. Figures 8.28 and 8.29 show the radial distributions of the temperature and the velocity, respectively, at different axial locations, for the case without powder gas injection (left-hand side) and with nitrogen injection at a rate of 8 slm through the central probe (right-hand side). The peak temperature along the centerline of the torch is noted to be reduced, and the corresponding gas velocity increased, as a result of the probe gas injection. Superposed on these figures are the results of flow modeling (solid lines). These show good agreement with the experimental measurements. Figure 8.30 shows the corresponding profiles of the volume fraction of nitrogen in the flow, which are in good agreement with the modeling results. For the position of 22 mm above the torch exit, ($z = -22$ mm) the measured nitrogen volume fraction under "cold flow" conditions are also indicated. These were obtained in the absence of the discharge. They clear show evidence of the rapid

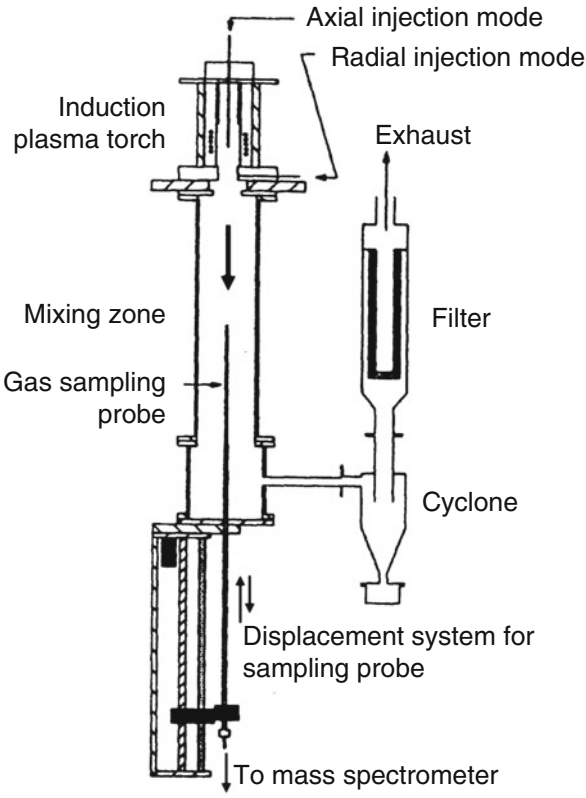


Fig. 8.26 Experimental setup used for the study of mixing phenomena under plasma conditions, after Soucy et al. [37]. With kind permission from Springer Science + Business Media B.V

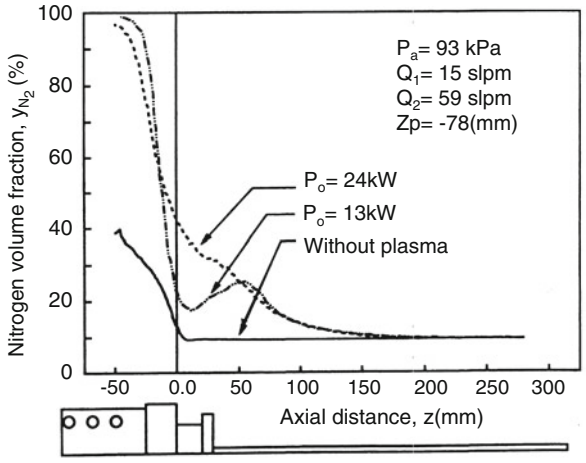


Fig. 8.27 Concentration profiles along the axis of the plasma torch/reactor system for the axial injection of nitrogen in an Ar/H_2 induction plasma, $Q_1 =$ 15 slm. (N_2), Pa = 93 kPa, after Soucy et al. [37]. With kind permission from Springer Science + Business Media B.V

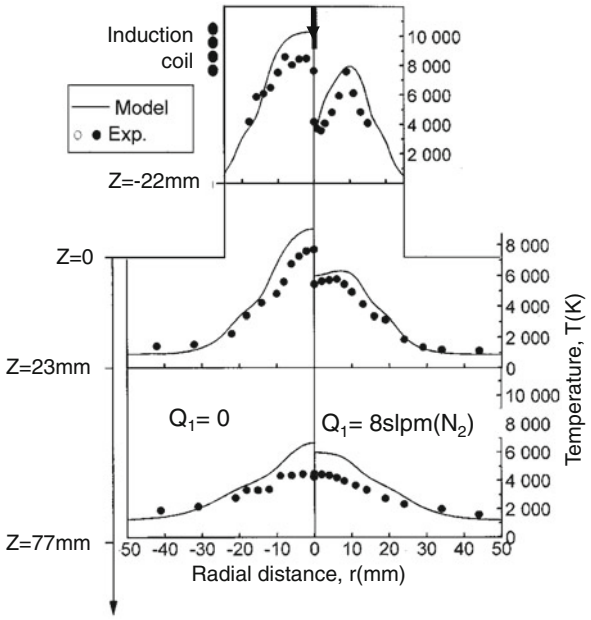


Fig. 8.28 Radial temperature profiles at different levels in an inductively coupled plasma jet in the presence and absence of "powder gas" injection through a central probe in the middle level of the induction coil. Ar/H_2 plasma at 20 kW, 250 Torr, (*left*) powder gas, $Q_1 = 0$, (*right*) powder gas $Q_1 = 8$ slm (N_2), after Rahman et al. [40]. With kind permission from Springer Science + Business Media B.V

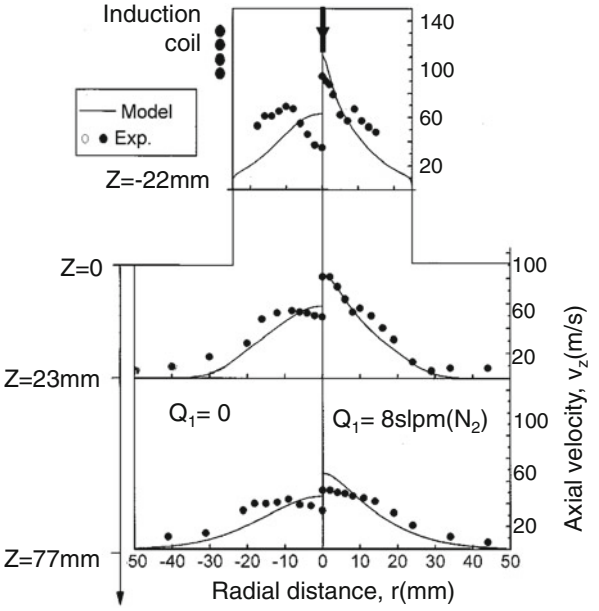


Fig. 8.29 Radial axial velocity profiles at different levels in an inductively coupled plasma in the presence and absence of "powder gas" injection through a central probe in the middle level of the induction coil. Ar/H_2 plasma at 20 kW, 250 Torr, (*left*) powder gas, $Q_1 = 0$, (*right*) powder gas $Q_1 = 8$ slm (N_2), after Rahman et al. [40]. With kind permission from Springer Science + Business Media B.V

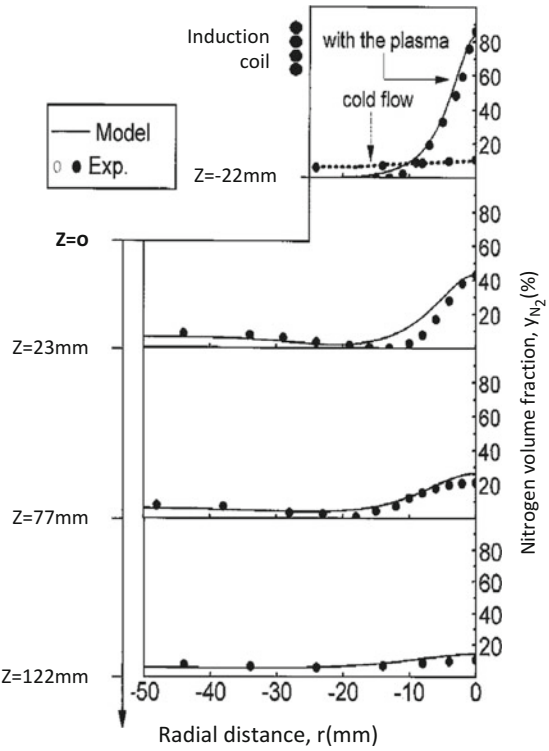


Fig. 8.30 Radial nitrogen concentration profiles at different levels in an inductively coupled plasma in the presence of "powder gas" injection through a central probe in the middle level of the induction coil. Ar/H_2 plasma at 20 kW, 250 Torr, powder gas, $Q_1 = 8$ slm (N_2), after Rahman et al. [40]. With kind permission from Springer Science + Business Media B.V

mixing of the flow under the "cold flow" conditions. In contrast, in the presence of the discharge, the mixing of the different streams is considerably hindered by the high viscosity and low turbulence level in the plasma.

8.3 Modeling of the Inductively Coupled Plasma Discharge

Modeling is an effective tool for the fundamental understanding of the basic phenomena governing materials processing under plasma conditions. Through modeling it is possible to calculate the flow, temperature, and concentration fields in plasma under a wide range of conditions. A considerable research effort was devoted over the past four decades to the modeling of the inductively coupled plasma. In this section no attempt is made to cover this topic in an exhaustive way. Modeling of the r.f. inductively coupled discharge is presented simply as a research tool, similar to previously reviewed diagnostics techniques that contribute to our understanding of the basic phenomena that governs the processing conditions and plasma–particle interactions during typical plasma spraying or powder processing operations. Extensive references are given for a more detailed documentation on the subject. These are grouped by their level of complexity and the principal research groups that have contributed to this field.

One of the first and relatively simple models of the induction plasma was published in 1970 by Eckert [41] who proposed to estimate the average temperature of an inductively coupled discharge through a one-dimensional energy balance between local energy generation and radial heat conduction losses to the plasma confinement tube. The model proposed by Miller and Ayen [42] went one step further by imposing on the discharge a one-dimensional, convective gas flow, and computed the discharge temperature field through an energy balance between local energy generation and conductive and convective energy transfer.

Subsequent studies in this area by Boulos and his collaborators at the University of Sherbrook [43–68] can be traced back to the early 1970s. The model proposed by Boulos [43–50] included a two-dimensional representation of the flow and temperature fields in the discharge through the solution of the Navier–Stokes equations under steady state, laminar flow conditions, with the plasma assumed to be in local thermodynamic equilibrium (LTE). The electromagnetic fields in the discharge were resolved at this stage through a one-dimensional representation of the simplified Maxwell equations. This model was later extended to include nonequilibrium plasmas [49, 53], in-flight particle heating [44], and plasma–particle interactions under dense loading conditions [47]. In the latter case it was possible to predict the local cooling of the plasma resulting from the injection of a particle stream into the discharge. Further development of the model included a two-dimensional representation of the electromagnetic fields [51] using a vector potential representation. Special attention was also given to the inclusion of turbulence in the model [52, 56, 61]. The principal challenge in this case was the simultaneous presence, in the same flow field, of both laminar and turbulent flow regimes, which is a direct consequence of the presence of steep temperature gradients in the discharge. The flow could then be predominantly laminar in the central high temperature region of the discharge, while being fully turbulent in its fringes in the boundary layer region. Further development of induction plasma modeling also included supersonic, compressible flow regions [63, 64]. An integrated representation of the electrical supply source was also included in the model to allow for the calculation of the apparent electrical impedance of the discharge under different conditions [58–60] and [65–68].

Further development of induction plasma modeling was also carried out by Mostaghimi et al. [69] and Develey and his group [70]. The latter was mostly devoted to the representation of the electromagnetic fields in a segmented metal wall plasma torch. More recently Colombo and his collaborators at the University of Bologna in Italy have made major advances in this field by resolving the three-dimensional flow and temperature field, time-dependent problem, which has been the subject of numerous publications [71–82].

In the following section the governing equations and typical results are given for a standard induction plasma torch system used in induction plasma spraying under different operating conditions. The model formulation is based on the earlier discussion of basic concepts of plasma modeling given in Sect. 3.3. For clarity the corresponding equations used for induction plasma modeling are presented in this section for a 2D flow, temperature, concentration, and electromagnetic fields as described by Xue et al. [65].

8.3.1 Basic Assumption

The model is based on the following simplifying assumption:

- Steady state , turbulent flow conditions
- Axisymetric, two-dimensional system of coordinates
- Optically thin plasma
- Plasma in local thermodynamic equilibrium (LTE).
- Negligible displacement current

8.3.2 Governing Equations

The model is based on the solution of the corresponding continuity, momentum, energy and mass conservation equations coupled with the 2D vector potential equations used for the computation of the corresponding electrical and magnetic fields.

8.3.2.1 Continuity Equation

$$\frac{\partial(\rho u)}{\partial z}+\frac{1}{r}\frac{(\rho r v)}{\partial r}=0 \tag{8.3}$$

8.3.2.2 Momentum Equations

$$\rho u\frac{\partial u}{\partial z}+\rho v\frac{\partial u}{\partial r}=-\frac{\partial p}{\partial z}+2\frac{\partial}{\partial z}\left(\mu_{\mathrm{e}}\frac{\partial u}{\partial z}\right)+\frac{1}{r}\frac{\partial}{\partial r}\left[\mu_{\mathrm{e}} r\left(\frac{\partial u}{\partial r}+\frac{\partial v}{\partial z}\right)\right]+F_z \tag{8.4}$$

$$\rho u\frac{\partial v}{\partial z}+\rho v\frac{\partial v}{\partial r}=-\frac{\partial p}{\partial r}+\frac{2}{r}\frac{\partial}{\partial r}\left(\mu_{\mathrm{e}} r\frac{\partial v}{\partial r}\right)+\frac{\partial}{\partial z}\left[\mu_{\mathrm{e}}\left(\frac{\partial u}{\partial r}+\frac{\partial v}{\partial z}\right)\right]+\frac{\rho w^2}{r}+F_r \tag{8.5}$$

$$\rho u\frac{\partial w}{\partial r}+\rho v\frac{\partial w}{\partial z}=\frac{1}{r^2}\frac{\partial}{\partial r}\left[\mu_{\mathrm{e}} r^3\frac{\partial}{\partial r}\left(\frac{w}{r}\right)\right]+\frac{\partial}{\partial r}\left[\mu_{\mathrm{e}}\left(\frac{\partial w}{\partial z}\right)\right]-\frac{\rho w v}{r} \tag{8.6}$$

where, ρ is the mass density, u, ν, and w are the axial, radial, and tangential velocity components, in the z, r, *and* θ directions, respectively. p *is* the pressure and the effective viscosity $\mu_{\mathrm{e}} = \mu + \mu_{\mathrm{t}}$,with μ:molecule viscosity, and μ_{t}: turbulent viscosity. F_r and F_z are the radial and axial components of Lorentz force. These are derived based on the solution of the corresponding vector potential equations for the electromagnetic fields, as described later in Sect. 8.3.2.5, and are given by Eqs. (8.36) and (8.37), respectively. The gravity force is generally neglected in

this case. The molecule viscosity of the gas mixtures μ is computed by the ideal gas mixing law [83]:

$$\mu = \sum_j \frac{X_j \mu_j}{\sum_k X_k \Phi_{jk}} \tag{8.7}$$

where

$$\Phi_{jk} = \left[8\left(1 + \frac{M_j}{M_k}\right)\right]^{-1/2} \left[1 + \left(\frac{\mu_j}{\mu_k}\right)^{1/2} \left(\frac{M_k}{M_j}\right)^{1/4}\right] \tag{8.8}$$

where X_j and μ_j are the mole fraction and the viscosity of species j. For nonideal gas μ may be computed using a simple mass weighted mixing law, as a first approximation:

$$\mu = \sum_j Y_j \mu_j \tag{8.9}$$

where Y_j is the mass fraction.

8.3.2.3 Energy Equation

$$\begin{aligned} &\rho u \frac{\partial}{\partial z}\left(h - \frac{p}{\rho} + \frac{v^2}{2}\right) + \rho v \frac{\partial}{\partial r}\left(h - \frac{p}{\rho} + \frac{v^2}{2}\right) \\ &\quad = \frac{\partial}{\partial z}\left(k_e \frac{\partial}{\partial z} T\right) + \frac{1}{r}\frac{\partial}{\partial r}\left(r k_e \frac{\partial}{\partial r} T\right) - \frac{\partial}{\partial z}\left(\sum_j h_j J_{jz}\right) \\ &\qquad - \frac{1}{r}\frac{\partial}{\partial r}\left(r \sum_j h_j J_{jr}\right) + P_v + (F_r v + F_z u) + P - R \end{aligned} \tag{8.10}$$

where $h = \sum_j Y_j h_j$ is the total enthalpy of mixture and h_j the specific enthalpy of species j. $k_e = k + k_t$ is the effective thermal conductivity, where k and k_t are molecule and the turbulent thermal conductivity, respectively. J_{jz} and J_{jr} are the diffusion flux of species j, which will be discussed in the next section. $P = \sigma|E|^2$ is the local energy generation through ohmic heating which requires the solution of the electromagnetic field vector potential equations as described in Sect. 8.3.2.5, Eq. (8.38). While R is the local volumetric radiation heat losses, is the kinetic energy due to the macroscopic movement of fluids, and $-\frac{p}{\rho}$ is the fluid expansion potential energy. The work done by gravitational force has been neglected. The

pressure work has been joined into the terms on the left side of the Eq. (8.8). $P_v = -\nabla \cdot \left(\overline{\tau} \cdot \vec{V}\right)$ is the viscous power dissipation which causes the energy conversion from the kinetic energy of plasma to the internal thermal energy.

The specific heat C_p and the volumetric radiation power loss of the mixture is computed by the following mixing law [83]:

$$C_\mathrm{p} = \sum_j Y_j c_{p,j}, \tag{8.11}$$

$$R = \sum_j X_j R_i \tag{8.12}$$

where R_j and $c_{p,j}$ are the volumetric radiation power loss and the specific heat of species j. The molecule thermal conductivity of the gas mixture k is computed by the ideal gas mixing law:

$$k = \sum_j \frac{X_j k_i}{\sum_k X_k \Phi_{jk}} \tag{8.13}$$

where k_j is the thermal conductivity of species j. For nonideal gas k may be computed from the simple mass weighted mixing law:

$$k = \sum_j Y_j k_j \tag{8.14}$$

For subsonic flow, and neglecting thermal diffusion, Eq. (8.10) simplifies considerably to the following:

$$\rho u \frac{\partial}{\partial z} h + \rho v \frac{\partial}{\partial r} h = \frac{\partial}{\partial r}\left(k_\mathrm{e} \frac{\partial}{\partial z} T\right) + \frac{1}{r}\frac{\partial}{\partial r}\left(r k_\mathrm{e} \frac{\partial}{\partial r} T\right) + P - R \tag{8.15}$$

8.3.2.4 Species Conservation Equations

$$\frac{1}{r}\frac{\partial}{\partial r}\left(\rho r v_j Y\right) + \frac{\partial}{\partial z}\left(\rho r u_j Y\right) = \frac{1}{r}\frac{\partial}{\partial r}\left[r\left(\rho D_j + \frac{\mu_\mathrm{t}}{Sc_\mathrm{t}}\right)\frac{\partial}{\partial r} Y\right] + \frac{\partial}{\partial z}\left[\left(\rho D_j + \frac{\mu_\mathrm{t}}{Sc_\mathrm{t}}\right)\frac{\partial}{\partial z} Y\right] + S_R \tag{8.16}$$

where μ_t is the turbulent viscosity and Sc_t is the turbulent Schmidt number. And D_j is the mass diffusivity of species j in the mixture. For a binary mixture [83]:

$$D_j = \left(1 - X_j\right) / \sum_{i \neq j} \left(X_i / D_{ij}\right) \tag{8.17}$$

where X_j is the molar fraction of species j. and D_{ij}, the mass diffusivities in the binary mixture of species i and species j

The modified Chapman–Enskog formula [84] can be used to calculate the molecular diffusion coefficient.

$$D_{ij} = 0.0188 \frac{\left[T^3\left(\frac{1}{M_i} + \frac{1}{M_j}\right)\right]^{1/2}}{P\sigma_{ij}^2 \Omega_{\mathrm{D}}} \tag{8.18}$$

where M_i and M_j are the molar weight of species i and j, respectively. P is the absolute pressure, and Ω_{D} is the diffusion collision integral, which is a measure of the interaction of the molecules in the system. Ω_{D} is a function of the quantity T_{D}^*, where

$$T_{\mathrm{D}}^* = k_{\mathrm{B}} T / \varepsilon_{ij} \tag{8.19}$$

k_{B} is the Boltzmann constant, ε_{ij} is the ***geometric*** average:

$$\varepsilon_{ij} = \sqrt{\varepsilon_i \varepsilon_j} \tag{8.20}$$

For a binary mixture, σ_{ij} is calculated as the ***arithmetic*** average of the individual values of σ:

$$\sigma_{ij} = \frac{1}{2}\left(\sigma_i + \sigma_j\right), \tag{8.21}$$

where σ_i and ε_i are the Lennard-Jones energy parameter and characteristic length, respectively. In the present analysis, mass diffusion due to temperature gradients, i. e., the thermal diffusion, is not taken into account. Further information on the corresponding equations can be found in reference [85].

It should be pointed out that the exact treatment of thermal plasma with gas mixture is rather complex. For example in argon–hydrogen plasma, the following six species have to be taken into account, Ar, Ar^+, H_2, H, H^+, and e. The corresponding number of species in air plasma is 11 species. The collision integral between any two species must be known to compute the binary diffusion coefficients. These are not always available for all the gas mixtures. For the exact treatment of argon–hydrogen plasma the reader is referred to [86]. The corresponding collision integral data can be found in [87]. As a first approximation, for the Ar–H_2 plasma, Ar and H_2 are considered as single species, respectively. The binary mass diffusivity is calculated from the kinetic theory using the Lennard-Jones parameters of argon and hydrogen. The dissociation and recombination of H_2 and the ionization and recombination of Ar and H are taken into account through the use of their corresponding transport properties (thermal conductivity, viscosity, electric conductivity) and specific heat. These data are taken from [88].

8.3.2.5 Vector Potential Equations

In the two-dimensional representations of electromagnetic field for plasma heating the inductor (induction coil) is represented as a series of parallel current carrying rings which is assumed infinitely thin. These models generally used a vector potential representation to obtain the electromagnetic field excited by time varying coil current. While earlier models were limited to the computation of the electromagnetic field in the discharge zone, recent developments of these models extended the computational domain for the solution of vector potential equations to outside of the induction coil zone. Such extended field (EF) model [65] greatly simplifies the boundary conditions required for the solution of the vector potential equations and gave rise to more realistic solutions.

The electromagnetic fields generated by the applied time-varying oscillatory coil current are governed by Maxwell equations which can be written in the following general form:

Coulombs law:

$$\nabla \cdot \vec{D} = \varphi, \tag{8.22}$$

Absence of free magnetic poles:

$$\nabla \cdot \vec{B} = 0, \tag{8.23}$$

Faraday's law:

$$\nabla \cdot \vec{E} = -\frac{\partial \vec{B}}{\partial t}, \tag{8.24}$$

Modified Ampere's law:

$$\nabla \times \vec{H} = \vec{J} + \frac{\partial \vec{D}}{\partial t} \tag{8.25}$$

Current continuity:

$$\nabla \cdot \vec{J} + \frac{\partial \varphi}{\partial t} = 0 \tag{8.26}$$

Additional relations: $\vec{D} = \varepsilon \vec{E} = \varepsilon_0 \varepsilon_r \vec{E}$ and $\vec{B} = \mu \vec{H} = \mu_0 \mu_r \vec{H}$

where $\vec{D}, \vec{E}, \vec{H}, \vec{B}, \vec{J}$, and φ are the electric displacement, electric field, magnetic field, and magnetic flux density vectors, current density, and free charge density, respectively.

$\varepsilon = \varepsilon_0 \varepsilon_r$ is the dielectric constant (permittivity) of materials,

$\varepsilon_0 = 8.854 \times 10^{12}$ Farad/m, is the dielectric constant of free space, and ε_r is the relative dielectric constant.

$\mu = \mu_0\mu_r$, the magnetic permeability of materials with $\mu_0 = 4\pi \times 10^7$, the magnetic permeability of vacuum, and μ_r is the relative magnetic permeability. The last term in the right side of Eq. (8.25) is the displacement current.

The simplified physics pictures of the induction plasma heating processes are as follows: A time-varying current passing through the coil excites an alternating magnetic field around the coil. This time-varying magnetic field induces, in turn, an electric field inside and outside of plasma region. Within the plasma region, the induced electric field gives rise to an induced current, which is responsible for the heating and sustaining of the discharge through ohmic heating. The complete picture is, however, slightly more complicated since the induced current in plasma and the coil will, in turn, induce magnetic field according to the modified Ampere's law. The full picture of electromagnetic field can be obtained by solving the Maxwell equations. After complicated mathematical manipulation, Maxwell equations reduce to the following vector potential equations:

$$-\nabla^2\vec{A} = \mu_0\vec{J} - \varepsilon_0\mu_0\frac{\partial^2\vec{A}}{\partial^2 t}, \tag{8.27}$$

Or

$$\begin{aligned} -\nabla^2\vec{A} &= \mu_0\vec{J} - \frac{1}{c^2}\frac{\partial^2\vec{A}}{\partial^2 t}, \\ \vec{E} &= -\frac{\partial\vec{A}}{\partial t}, \end{aligned} \tag{8.28}$$

where $c = 1/\sqrt{\varepsilon_0\mu_0}$ is the speed of light in space. Once $\vec{A}$ is obtained all the other variables can be obtained through Maxwell equations.

Assuming time variation of coil current density $\vec{J}\left(,\vec{r},\mathrm{t}\right) = \vec{J}\left(\vec{r}\right)\cdot\exp(i\omega t)$, where ω is the angle frequency and t is the time, the other field variables $\vec{A}, \vec{E}$, and $\vec{B}$ will also vary in the same way, but will not necessarily all be in phase. The time variation of $\vec{A}$ and $\vec{J}$ in Eq. (8.27) can be eliminated giving rise to

$$-\nabla^2\vec{A} = \mu_0\vec{J} + \frac{\omega^2}{c^2}\vec{A} \tag{8.29}$$

Note that the same symbols are still used to denote these vector quantities even after the elimination of time variations.

In the axisymmetric cylindrical system of coordinates, $\vec{A}$ and $\vec{J}$ possess only tangential components A_θ, and J_θ. J_θ consists of imposed coil current $J_{\theta im}$ by the

applied voltage across the coil and induced current $J_{\theta in}$ in plasma and coil. The θ component equation of Eq. (8.29) is

$$-\nabla^2 A_\theta + \frac{A_\theta}{r^2} = \mu_0 (J_{\theta im} + J_{\theta in}) + \frac{\omega^2}{c^2} A_\theta$$
$$\nabla^2 = \frac{1}{r}\frac{\partial}{\partial z}\left(r\frac{\partial}{\partial r}\right) + \frac{\partial^2}{\partial z^2} \tag{8.30}$$

Rearranging Eq. (8.30) gives

$$-\nabla^2 A_\theta + \left(\frac{1}{r^2} - \frac{\omega^2}{c^2}\right) A_\theta = \mu_0 (J_{\theta im} + J_{\theta in}) \tag{8.31}$$

$$-\nabla^2 A_\theta + \left(\frac{1}{r^2} - \frac{4\pi^2}{\lambda^2}\right) A_\theta = \mu_0 (J_{\theta im} + J_{\theta in}) \tag{8.32}$$

where λ is the wavelength of the imposed electromagnetic field by the oscillatory coil current. For the typical inductive plasma torch, the frequency is generally less than 30 MHz so that λ is larger than 10 m. Since the computational domain for the inductive plasma modeling is generally concerned with a region with a radius considerably smaller than 1 m the displacement current can be safely omitted. The induced current density can be given by

$$J_{\theta in} = \sigma E_\theta = -\sigma \frac{\partial A_\theta}{\partial t} = -i\omega\sigma A_\theta \tag{8.33}$$

where $i = \sqrt{-1}$ and σ is the electrical conductivity of the plasma or the coil material depending on which zone is being considered. Substituting Eq. (8.33) back into Eq. (8.32) yields

$$-\nabla^2 A_\theta + \left(i\mu_0\omega\sigma + \frac{1}{r^2}\right) A_\theta = \mu_0 J_{\theta im} \tag{8.34}$$

This is the final vector potential equation with displacement current being neglected. Once A_θ is obtained, the electromagnetic field can be calculated by the following relations:

$$E_\theta = -i\omega A_\theta, B_r = -\frac{\partial A_\theta}{\partial z} \text{ and } B_z = -\frac{1}{r}\frac{\partial (rA_\theta)}{\partial r} \tag{8.35}$$

The Lorentz force that exerts on the plasma flow is calculated from $\vec{F} = \vec{J} \times \vec{B}$. The components of the time averaged Lorentz force in a time period are

$$F_r = \frac{1}{2}\sigma \cdot \mathrm{Re}\left(E_\theta B_z^*\right) \tag{8.36}$$

and

$$F_z = -\frac{1}{2}\sigma \cdot \mathrm{Re}\left(E_\theta B_r^*\right) \tag{8.37}$$

The superscript * denotes the conjugate and Re denote the real part of the product. The coefficient (½) comes from the time averaging of the Lorentz force in a time period. The time averaged Ohmic heating power density in a period is

$$P_{\mathrm{Oh}} = \frac{1}{2}\sigma \cdot \mathrm{Re}\left(E_\theta E_\theta^*\right) \tag{8.38}$$

In order to obtain the vector potential by solving second differential Eq. (8.36) it is necessary to determine the boundary values for the vector potential.

8.3.2.6 Equations and Boundary Condition for Extended Field Model

According to the extended field model, the computational domain can be classified into three different zones: plasma zone with induced plasma current; coil zone with imposed and induced current, and all other zones which free from any currents. The cross section of current carrying ring of coil is no longer assumed to be infinite thin and the induced current in the coil is not calculated explicitly. It is assumed that the total coil current I_c is the summation of imposed coil current, I_{im} resulting from the applied voltage across the coil, and the current induced in the coil I_{in} by the electromagnetic fields generated by the current induced in the plasma. The general approach used in induction plasma modeling to fix the plasma power, and calculate the corresponding coil current, through an iterative procedure. The corresponding vector potential equations for the different zones in the computational domain can be written as follows.

In plasma flow zone, the only current source is the induced plasma current density and hence the vector potential Eq. (8.35) becomes

$$-\nabla^2 A_\theta + \left(i\mu_0\omega\sigma_{\mathrm{p}} + \frac{1}{r^2}\right)A_\theta = 0 \tag{8.39}$$

or

$$\begin{aligned} -\nabla^2 A_{\theta R} - \mu_0\omega\sigma_{\mathrm{p}} A_{\theta I} + \frac{1}{r^2}A_{\theta R} &= 0 \\ -\nabla^2 A_{\theta I} + \mu_0\omega\sigma_{\mathrm{p}} A_{\theta R} + \frac{1}{r^2}A_{\theta I} &= 0 \end{aligned} \tag{8.40}$$

where σ_{p} is the electrical conductivity of plasma and, $A_{\theta R}$ and $A_{\theta I}$ are the real and imaginary part of vector potential, respectively.

In coil zone, it is assumed that the J_c is the total coil current density, which includes the imposed coil current resulting from the applied voltage across the coil and the induced coil current density. The vector potential equations take the following form

$$-\nabla^2 A_\theta + \frac{1}{r^2} A_\theta = \mu_0 J_c \tag{8.41}$$

or

$$\begin{aligned} -\nabla^2 A_{\theta R} + \frac{1}{r^2} A_{\theta R} &= \mu_0 J_c \\ -\nabla^2 A_{\theta I} + \frac{1}{r^2} A_{\theta I} &= 0 \end{aligned}$$

In all the other zones, which are free from any current sources (imposed or induced), the vector potential equations are simply

$$-\nabla^2 A_\theta + \frac{1}{r^2} A_\theta = 0 \tag{8.42}$$

or

$$\begin{aligned} -\nabla^2 A_{\theta R} + \frac{1}{r^2} A_{\theta R} &= 0 \\ -\nabla^2 A_{\theta I} + \frac{1}{r^2} A_{\theta I} &= 0 \end{aligned}$$

The total coil current takes the following form:

$$J_c(r) = J_0 r_c / r \tag{8.43}$$

where r_c, the coil radius, J_0, the coil current density at the centre of ring of coil, and r the radial distance from to the torch axis to a point on the cross section of the coil ring.

Since the vector potential at outer boundary produced by coil current is inversely proportional to the square of the distance between coil and outer boundary, the vector potential at outer boundary can be set to be zero, provided that such a boundary is far enough from the coil.

$$A_{\theta R} = 0 \text{ and } A_{\theta I} = 0 \tag{8.44}$$

The accuracy of computational results by using the boundary conditions, Eq. (8.44), depends on the outer boundary position. The further the boundary position is placed from the coil the better the computational results, but it requires more computer time to process the increased number of grid nodes in the calculation domain. To check whether the outer boundary is far enough, different positions of the outer boundary are used for the computation. Thus the acceptable distance for

the positioning of the outer boundary is determined empirically through the successive solution of the same equations applied to different positions of the boundary. The outer boundary was finally set at that locus where the computational results of two successive solutions were seen to be essentially identical. The radius of the outer boundary, determined by such method, is generally located at a distance of about five times the plasma radius.

Apart from the outer boundary condition, the interface boundary conditions are also needed to solve the vector potential equations to obtain the vector potential in the whole domain. These can be derived from the interface boundary condition for the electric field. When the electric field crosses the interfaces between the different zones with different permittivity, it has been shown that its tangential component is continuous ($E_{1t} = E_{2t}$) while its normal component jumps ($\varepsilon_1 E_{1n} = \varepsilon_2 E_{2n}$). Therefore the normal component of vector potential jumps, at the interface between different materials, while the tangential component is continuous. It is not easy to set the jumping boundary conditions at the interface. Fortunately, for the axisymmetric coordinate system, the electric field, and accordingly the vector potential, is always parallel to the interfaces so that the continuity interface boundary condition can be applied to the vector potential equations.

Ideal gas mixing law is commonly used to compute the equivalent electrical conductivity, σ, for a plasma with different gas compositions:

$$\sigma_{\mathrm{p}} = \sum_j \frac{X_j \sigma_{pj}}{\sum_k X_k \Phi_{jk}}, \tag{8.45}$$

where σ_{pj} is the electrical conductivity of species j.

8.3.2.7 Turbulence Model

The modeling of induction plasma flows is particularly complicated by the simultaneous presence in the same flow field of both laminar and turbulent flow regimes. These are observed respectively in the high temperature and low temperature regions of the flow. The choice of the turbulence model to be used will accordingly need to adequately represent these two extreme conditions. All the turbulent models described in Sect. 3.3.2.5 with the exception of the DNS (direct numerical simulation), are empirical and therefore approximate. These approximations are introduced in the process to close the Reynolds-averaged Navier–Stokes equation. The model constants employed in the turbulence equations for the turbulent kinetic energy, its dissipation rate, and the Reynolds stresses are all empirically determined. It is therefore not surprising to note that there is no universally correct turbulent model that is suitable for all practical problems. It all depends on how realistic is the closure approximation for that particular problem and how appropriate are the chosen model constants. The ultimate criterion for choosing a turbulent model for a particular problem is eventually to compare the computational

results with the experimental measurements. The turbulence models generally accepted for the modeling of plasma flows are as follows:

- *Standard k–ε model*
- *Reynolds Stress Model (RSM)*
- Direct numerical simulation (DNS)

While the DNS approach is obviously the most exact and adapted for such a problem, the numerical grid used must be fine enough to capture the smallest eddy. Even today's computers are not powerful enough to solve the full Navier–Stokes equation directly for the conditions of high Reynolds number turbulent flows. In this section the Standard k–ε model and Reynolds stress and wall functions are used to simulate the inductive plasma flows. In comparison with the limited experimental measurement, it seems that the Reynolds Stress Model (RSM) [89–91] is the best predictive turbulence model for the inductive plasma flow because it is based on the second moment closure. Details on the governing equations and underlying assumptions for the different turbulence models can be found in the numerous publications on the subject and is beyond the scope of this text. It is important to note, however, that the typical results presented in the next sections were obtained using the RSM turbulence model as described by Xue et al. [65].

8.3.3 Typical Results of Fluid Dynamic Modeling

In this section typical results are given of induction plasma modeling studies under different operating conditions. While these help in establishing a good solid understanding of the characteristics of the flow and temperature and concentration fields in the discharge and the plasma jet, they also provide a good example of the potential of present modeling techniques.

A standard schematic representation of the induction plasma torch as mostly used in all modeling studies is shown in Fig. 8.31. This is based on the double flux torch design with three main gas streams introduced into the torch. The external sheath gas stream, Q_3, is introduced in the annular space between the plasma confinement tube and the intermediate separation tube. The "plasma or central" gas stream, Q_2, is introduced in the central region of the separation tube and usably incorporates a tangential velocity component. The third gas stream, generally referred to as the "powder or carrier" gas stream, Q_1 is usually used for the introduction of the powder or precursor gas stream into the torch. All other dimensions given in Fig. 8.31 are self-explanatory. The most important of which are, r_o inner radius of the plasma confinement tube, r_c the inner radius of the induction coil, and r_1 the inner radius of the powder injection probe. It is important to point out that L_3 represents the position of the tip of the powder injection probe which is an important operational parameter that can be changed from one experiment to the other depending on the properties of the powder being treated/plasma sprayed. The relative position of L_1, the tip of the intermediate separator tube,

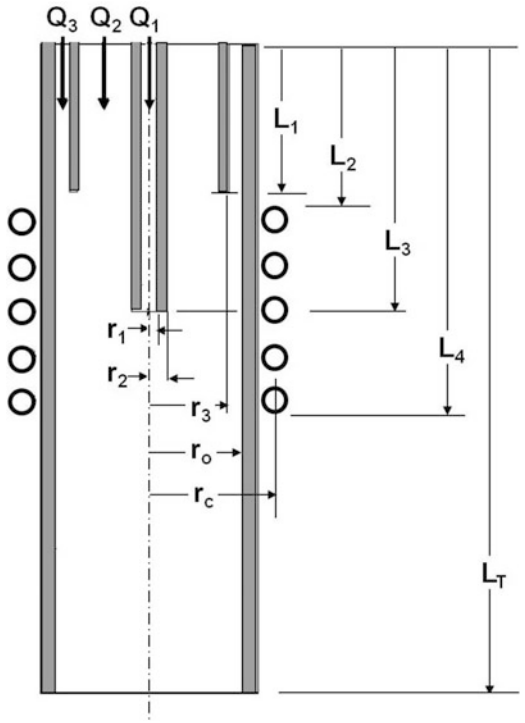


Fig. 8.31 Typical induction plasma geometry and principal dimensional parameters used in induction plasma modeling. After Rahmane et al. [40]. With kind permission from Springer Science + Business Media B.V

compared to L_2, the top level of the induction coil is also an important parameter that can have an important influence on the flow and temperature fields and consequently on the stability of the discharge.

Typical results obtained by Rahmane et al. [39] and [40] on a standard r.f. induction plasma torch model PL-50, with a 50 mm i.d. of the plasma confinement tube were presented in Figs. 8.28, 8.29, and 8.30 together with experimental data which served for the model calibration. These were obtained for plasma operated at 20 kW plate power (about 12 kW coupled into the discharge). The plasma sheath gas was a mixture of Ar and H_2. The plasma was operated at near atmospheric, 82.4 kPa (620 Torr) and low pressure, 33.2 kPa (250 Torr) conditions. The 2D flow streamlines and temperature isocontours are shown on the left-hand side of Fig. 8.32. The corresponding concentration field for H_2 and N_2 are shown on the right-hand side of the same figure. The hydrogen in this case was mixed with the sheath gas, Q_3, while the nitrogen was injected as the powder carrier gas, Q_1. It may be noted that since the hydrogen is injected with the cold and turbulent sheath gas, it mixes at a much faster rate than the nitrogen which is injected in the centre of the high temperature, laminar, discharge zone. Particularly relevant to this study are the results presented in Fig. 8.33. These show the variations along the centerline of the discharge of the (a) effective viscosity, (b) thermal conductivity, and (c) mass diffusivity. In each of these figures, the molecular properties are identified with the subscript "m" while the turbulent properties are identified with the subscript "t."

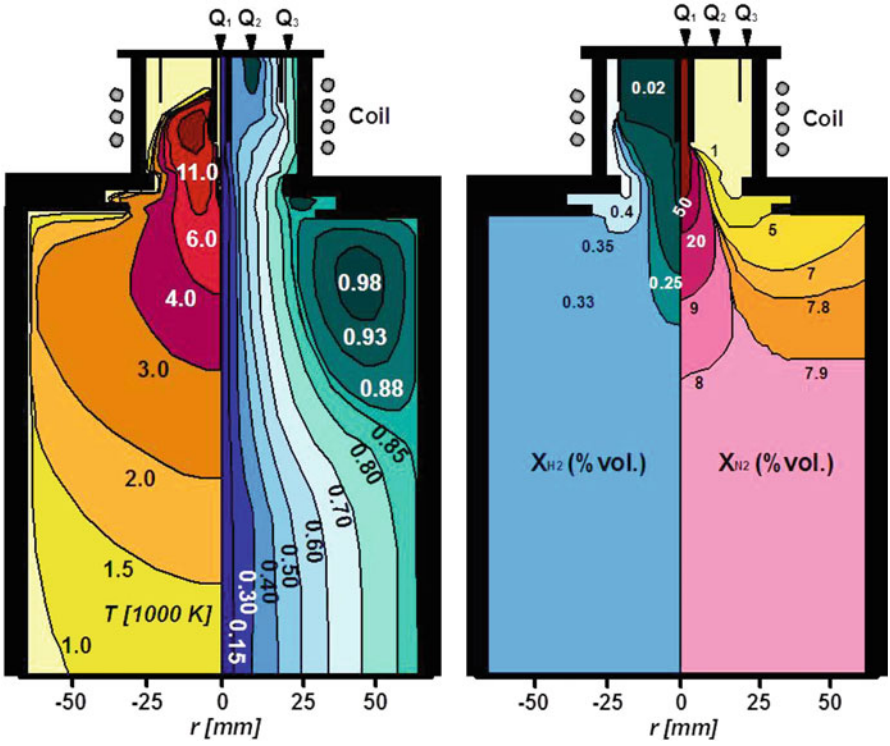


Fig. 8.32 Flow and temperature fields (*left*) and concentration fields (*right*) for an Ar/H_2 plasma (71 slm Ar + 4 slm H_2) at 20 kW with a nitrogen gas injected through the probe with its tip at the center of the induction coil, pressure = 250 Torr. After Rahmane et al. [39] with kind permission

It is significant to note that all of the molecular properties are predominant on the left-hand side of the figure corresponding to the coil, or high temperature, region of the discharge. On the other hand, the turbulent properties are predominant in the right-hand side of the figure, corresponding to the free jet turbulent region of the flow, at the exit of the torch.

Chen and Boulos [56] also reported similar observations by investigating effects of turbulence using the k–ε turbulence model, showing the turbulence viscosity and flow fields for a wide range of Reynolds numbers. The results reviled a high level of turbulence in the entrance region of the plasma gas and near the wall, while the plasma region was always laminar. The high temperature zone is pushed downstream for higher flow rates if turbulence is considered. Ye et al. [61] further improved the turbulence model by including temperature fluctuations and the resulting density fluctuations in the model. However, no major effect of these fluctuations on the turbulence level or the temperature distributions was observed.

In all these models, the characteristics of the power supply have been assumed to be constant with respect to power and frequency. As pointed out earlier, since the plasma is an active part of the power supply circuit, power and frequency changes

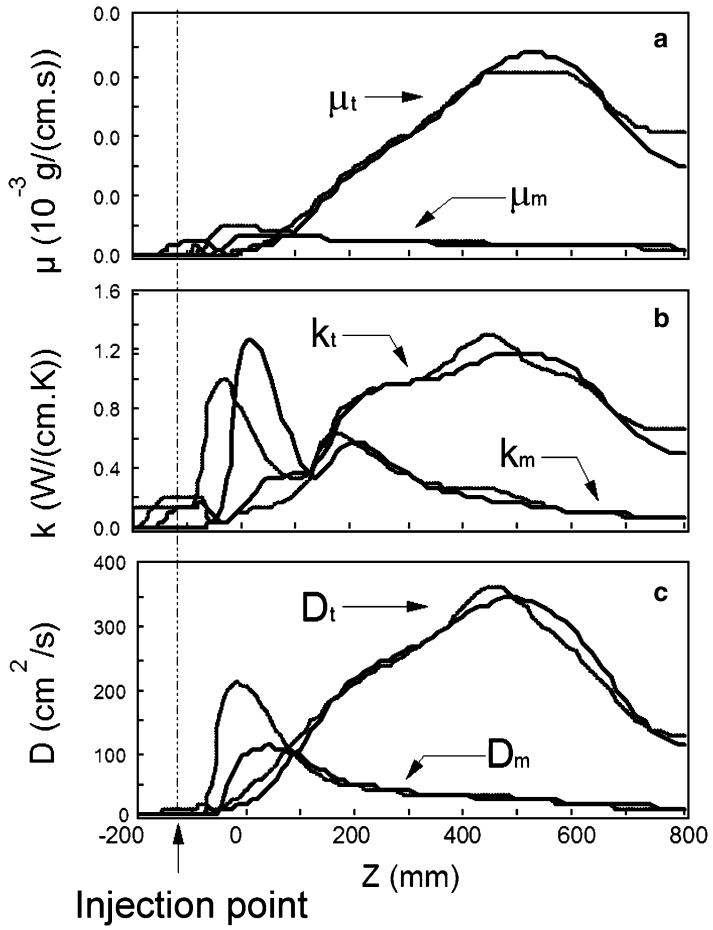


Fig. 8.33 Axial profile of the molecular and turbulent components of the effective (**a**) viscosity, (**b**) thermal conductivity, and (**c**) mass diffusivity along the centerline of the torch and reactor system, Same plasma operating conditions as Fig. 8.37. After Rahmane et al. [40]. With kind permission from Springer

depending on the load presented by the plasma. Merkhouf and Boulos [59] addressed this issue in a model that includes the power supply circuit and with a validation of this model by appropriate measurements. A block diagram of the circuit modeled is shown in Fig. 8.34. Figure 8.35 shows as a result of the calculations a relationship between the plate current and the coil current for different plate voltages for a specific power supply used for the Tekna plasma torch PL-50. The resulting temperature fields in the r.f. discharge are shown in Fig. 8.36 with the corresponding radial temperature profile in the middle section of the coil shown in Fig. 8.37, indicating the strong widening of the plasma region for an increase of the plate voltage from 6 to 9 kV. The total input power and the corresponding coupling efficiency are shown in Fig. 8.38. The plasma and sheath

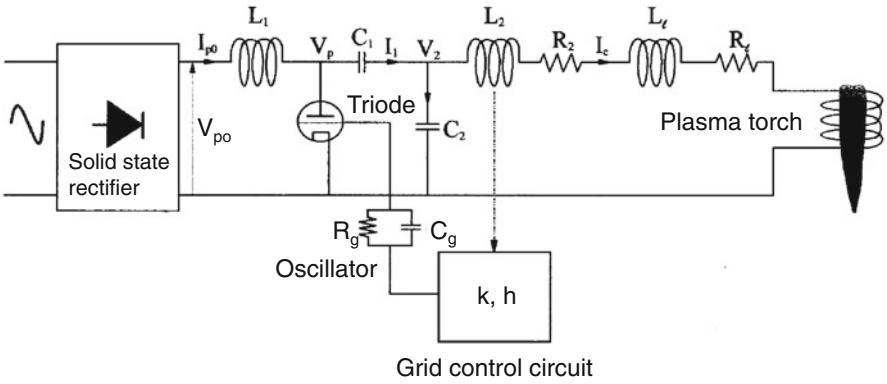


Fig. 8.34 Block diagram for the electrical circuit with the rf plasma torch used in the model. After Merkhouf and Boulos [59]. Copyright IOP Publishing. Reproduced with permission. All rights reserved

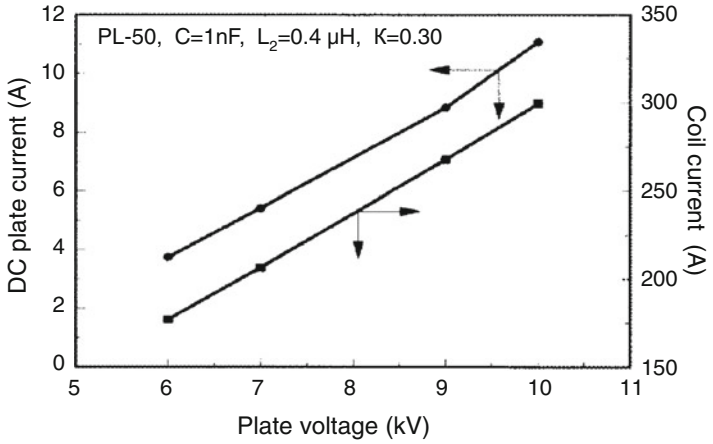


Fig. 8.35 Plate current and coil current as function of plate voltage. After Merkhouf and Boulos [59]. Copyright IOP Publishing. Reproduced with permission. All rights reserved

gas was argon with flow rates of 30 slm and 150 slm, respectively. In a series of electrical and calorimetric measurements, an energy balance was performed for plate voltages of 6.5, 7.0, and 7.5 kV. The power losses can be expressed as the sum of the power loss to the cooling water at the oscillator tube P_{tube}, the rf coil P_{coil}, the central injection tube $P_{\text{injection}}$, and the torch wall P_{torch}.

$$P_{\text{loss}} = P_{\text{tube}} + P_{\text{coil}} + P_{\text{injection}} + P_{\text{torch}} = P_{\text{tube}} + P_{\text{rf}} \tag{8.46}$$

The plasma power is measured by the energy transferred to the cooling water for the chamber into which the plasma jet is exhausted P_{chamber} and for the heat exchanger at the outlet of the chamber P_{exch}.

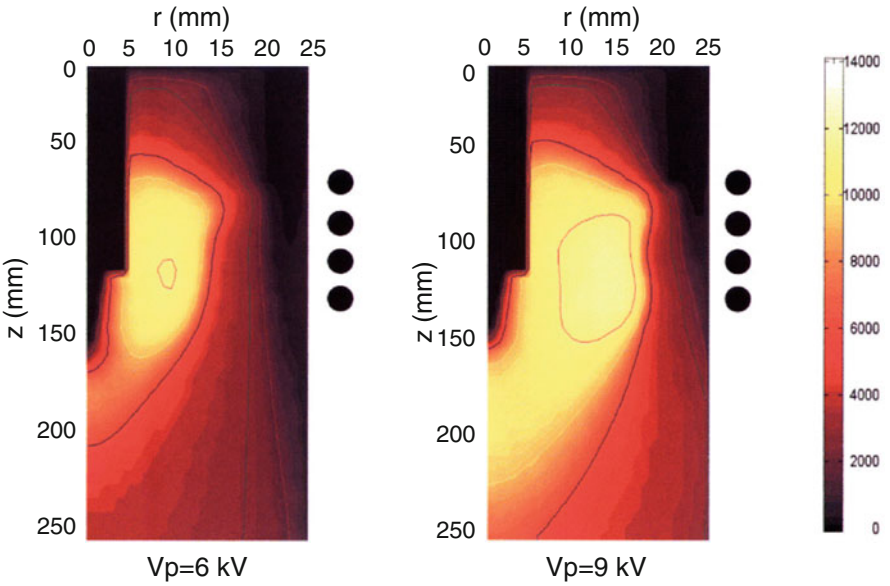


Fig. 8.36 Temperature fields in the r.f. discharge for plate voltages of 6 and 9 kV. After Merkhouf and Boulos [59]. Copyright IOP Publishing. Reproduced with permission. All rights reserved

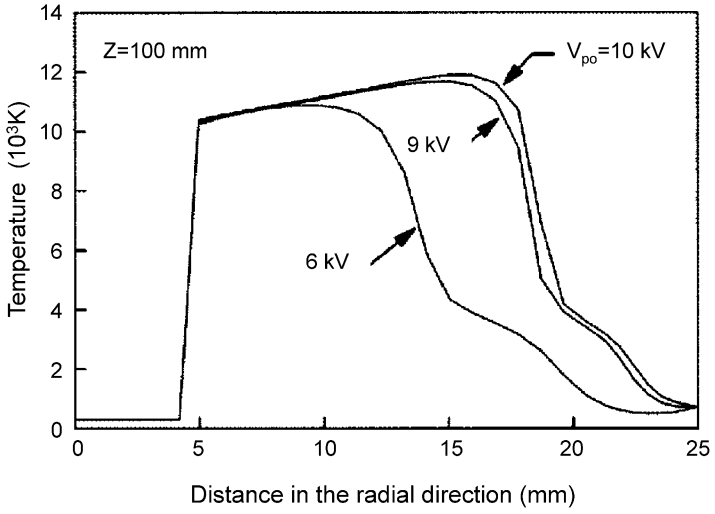


Fig. 8.37 Effect of the plate voltage on the radial temperature profiles at the middle of the induction coil, $z = 100$ mm. After Merkhouf and Boulos [59]. Copyright IOP Publishing. Reproduced with permission. All rights reserved

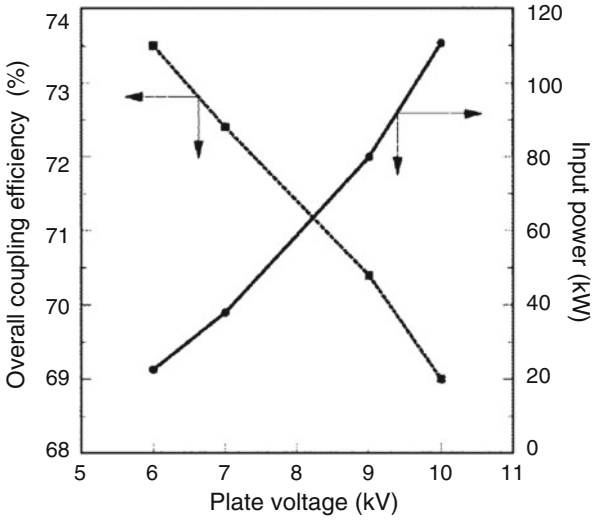


Fig. 8.38 Input power and overall coupling efficiency as a function of plate voltage, After Merkhouf and Boulos [59]. Copyright IOP Publishing. Reproduced with permission. All rights reserved

Table 8.1 Measured power distribution for the Tekna PL-35 plasma torch operated with 30 slm Ar central gas flow and 70 slm Ar sheath gas flow, after Merkhouf and Boulos [60]

Plate voltage, kV	6.5	7.0	7.5
Plate current, A	2.6	3.0	3.5
Plate power, kW	16.9	21.0	26.25
High frequency current, A	152.5	163.5	181.5
High frequency voltage, V	571.2	600	641
Frequency, MHz	4.86	4.87	4.88
P_{tube}, %	32.72	33.33	35.08
P_{rf}, %	64.08	63.14	59.81
P_{plasma}, %	36.5	35.6	33.6

$$P_{plasma} = P_{chamber} + P_{exch} \tag{8.47}$$

The results are given in Table 8.1.

Xue et al. [65] computed with their model the temperature, flow, and concentration fields in an inductively coupled plasma discharge under typical plasma spraying conditions. The results obtained for two chamber pressures of 101 kPa (14.7 psia) and 34.4 kPa (5.0 psia) are given in Figs. 8.39, 8.40, and 8.41. These were obtained for a Tekna PL-50 induction plasma torch (50 mm id), operated using Ar/H_2 as the sheath gas ($Q_3 = 100$ slm Ar + 20 slm H_2), central gas ($Q_2 = 30$ slm Ar), and powder carrier gas ($Q_1 = 5$ slm Ar). The plate power was 70 kW of which 65 % is coupled into the discharge (45 kW). The oscillator frequency was 3 MHz. The temperature field shown in Fig. 8.39 reveals, as expected, a longer plasma jet under low pressure conditions compared to the atmospheric pressure case. The effect is a direct consequence of the proportional increase of the plasma velocity at the exit of the plasma torch. In both cases we note that the powder gas allows for the axial injection of the "powder" into the center of the discharge. The corresponding streamlines in the plasma jet and deposition chamber are shown in Fig. 8.40.

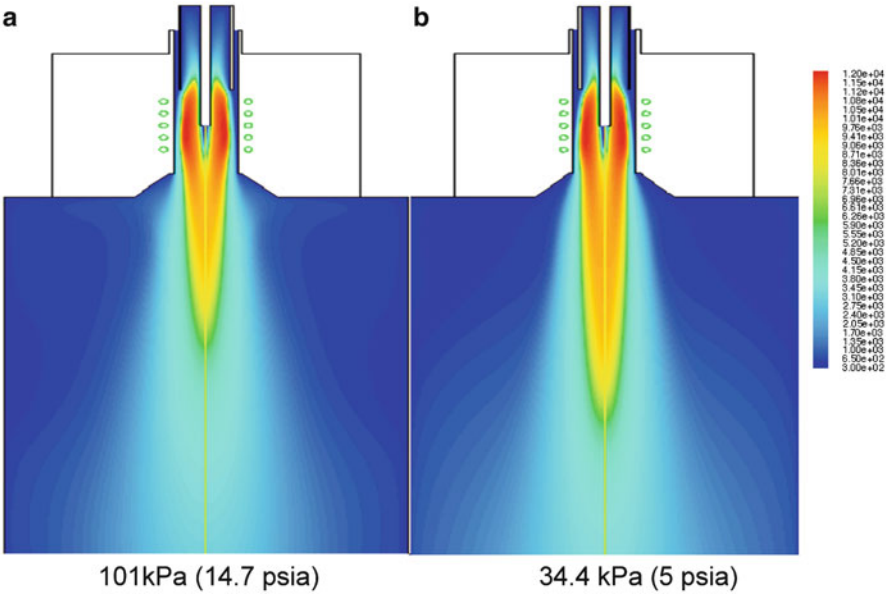


Fig. 8.39 Temperature field for a Tekna PL-50 induction plasma free jet at atmospheric (*left*) and low pressure (*right*) conditions. Ar/H_2 Plasma, plate power = 70 kW. Results supplied by Tekna Plasma Systems Inc. (2012)

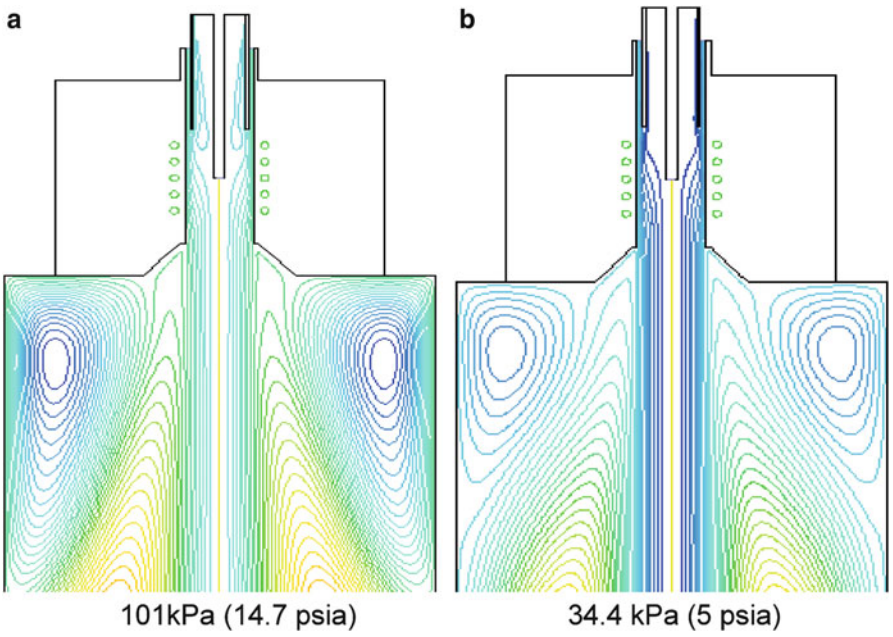


Fig. 8.40 Flow stream lines for a Tekna PL-50 induction plasma free jet at atmospheric (*left*) and low pressure (*right*) conditions. Ar/H_2 Plasma, plate power = 70 kW. Results supplied by Tekna Plasma Systems Inc. (2012)

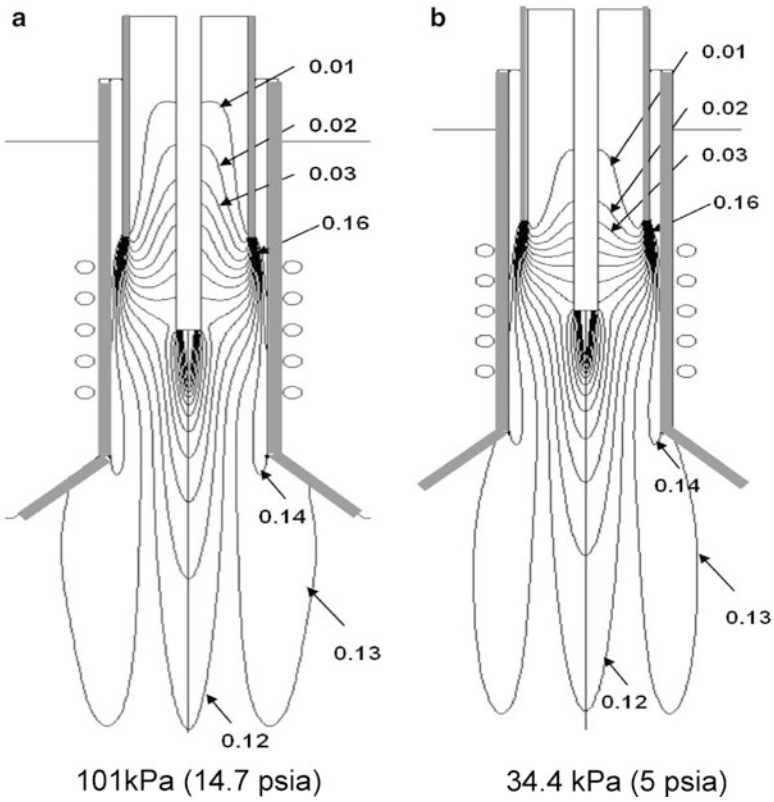


Fig. 8.41 Hydrogen concentration distribution (molar fraction) for a Tekna PL-50 induction plasma free jet, at atmospheric (*left*) and low pressure (*right*) conditions. Ar/H_2 Plasma, plate power = 70 kW. Results supplied by Tekna Plasma Systems Inc. (2012)

The corresponding hydrogen concentration, introduced with Q_3, is given in Fig. 8.41. These show relatively little effect of the pressure on mass transfer phenomena under these conditions. The temperature and axial velocity profiles along the centerline of the plasma torch are given in Figs. 8.42 and 8.43. These show a maximum temperature along the centerline of the discharge of about 10,000 K, with a lower temperature drop with distance in the plume of the jet under low-pressure conditions. The effect is compensated under atmospheric pressure conditions by a slight increase of the discharge power from 70 to 100 kW. The effect of pressure is, however, significantly more important on the axial velocity of the plasma which is noted in Fig. 8.43 to increase from around 70 m/s, under atmospheric pressure conditions, to close to 200 m/s at 34.3 kPa (5 psia). The effect of power on the plasma velocity is considerably less important in this case.

Further computations were carried out with this model for an induction plasma jet in the presence of a substrate under typical plasma spraying conditions. The torch geometry and its principal dimensions are given in Fig. 8.44. The plasma

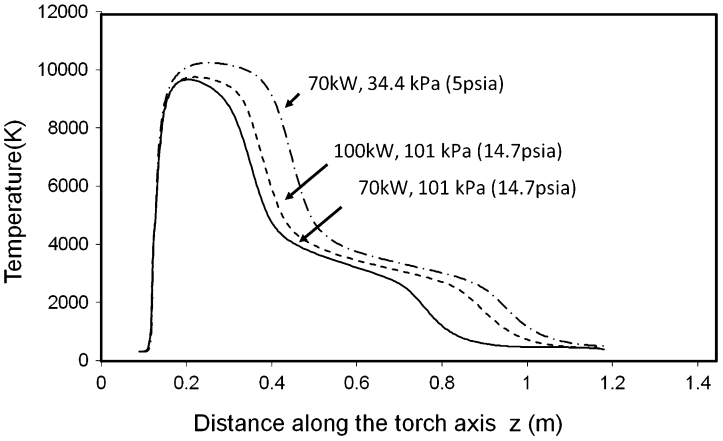


Fig. 8.42 Axial temperature profile along the centerline of a Tekna PL-50 induction plasma free jet at atmospheric and low pressure conditions. Ar/H_2 Plasma, plate power = 70 kW. Results supplied by Tekna Plasma Systems Inc. (2012)

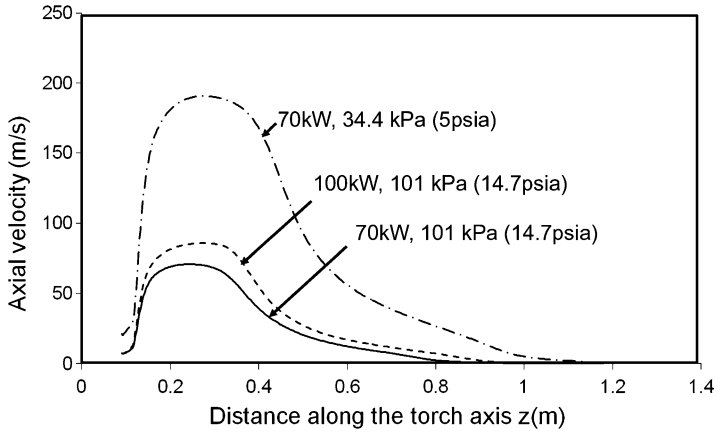


Fig. 8.43 Axial velocity profile along the centerline of a Tekna PL-50 induction plasma free jet at atmospheric and low pressure conditions. Ar/H_2 Plasma, plate power = 70 kW. Results supplied by Tekna Plasma Systems Inc. (2012)

torch used in this case was the same at that used in earlier calculations, a Tekna PL-50 torch. The substrate was in the shape of a disk of 100 mm diameter, placed at a distance of 100 mm downstream of the torch exit. All other operating conditions were identical to those used earlier in the computations given in Figs. 8.39, 8.40, 8.41, 8.42, and 8.43 with the exception of pressure, which was fixed at 34.3 kPa (5 psig). The flow and temperature fields in the discharge are given in Fig. 8.45. These show a strong interaction between the plasma jet immerging from the torch and the substrate on which the flow is directly impinging. Side jets are also being

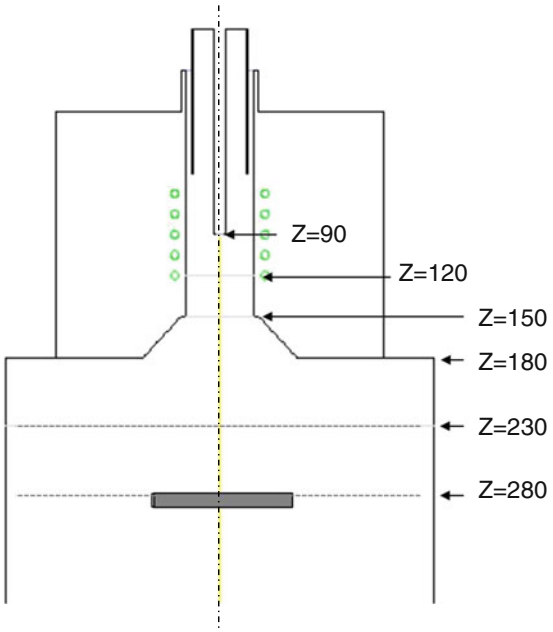


Fig. 8.44 Torch geometry and system of coordinates for an induction plasma vacuum spraying setup. Tekna Plasma Systems Inc. (2012)

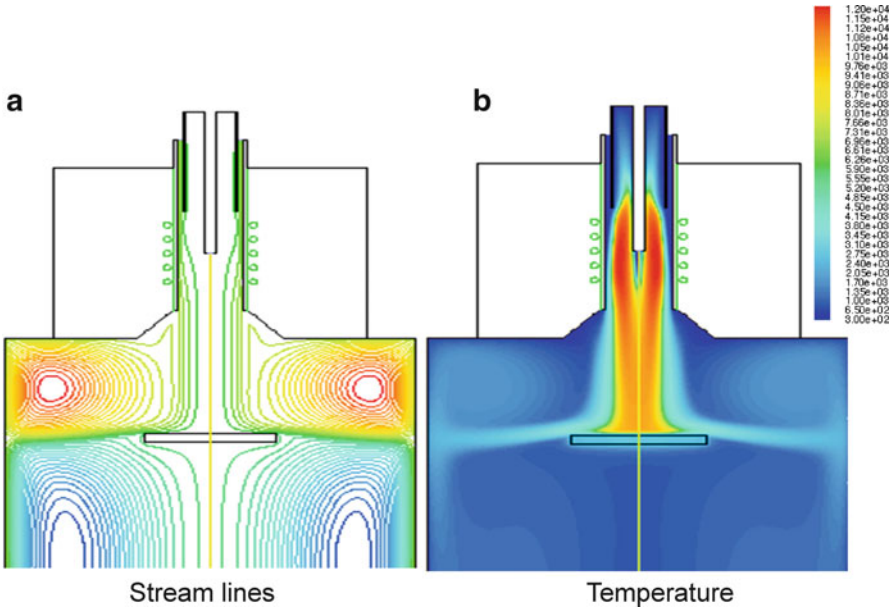


Fig. 8.45 Temperature and flow fields for an impinging induction plasma jet under vacuum plasma spraying conditions. Ar/H_2 Plasma, plate power = 70 kW. Results supplied by Tekna Plasma Systems Inc. (2012)

generated in this case as a result of the impaction on the jet on the substrate, with the corresponding formation of strong recirculation eddies in the deposition chamber. Special attention is to be given in the design of the deposition chamber to avoid such recirculation patterns since they could cause the re-entrainment of powders back into the plasma jet and their entrapment into the coating without proper melting causing defects in the coating.

8.4 Plasma–Particle Interaction Model

The modeling of the plasma flows during thermal spray operations is relatively complex because of the need to take into account plasma–particle interactions effects. This is due to the fact that the presence of the particles in the flow will result in the local cooling of the plasma which will in turn give rise to corresponding changes in the plasma flow and temperature fields. The effect is increasingly more important with the increase of the particle mass feed rate, and is often referred to as the "loading effect," or "plasma–particle interactions under dense loading conditions." It should be emphasized that the basic concepts of plasma–particle interactions, or plasma loading, is equally applicable to all plasma or high temperature flows in which particles are heated in-flight independent of the plasma heating mechanism whether the plasma is a d.c. source or r.f. inductively coupled discharge or any other high temperature source. A detailed analysis of the basic phenomena involved has been reviewed in Chap. 4. In this section a brief outline is given of the modeling approach used and governing equations, followed by typical results published by Boulos and collaborators in the 1980s for the inductively coupled plasma case [44, 47, 50], and [55].

The model used is based on the concept of Particle-Source-In-Cell [PSI-Cell] which is represented schematically in Fig. 8.46. According to this model, the flow field inside the discharge cavity, defined by the cylindrical system of coordinates given on the left-hand side of the figure, can be divided by a fine mesh into small concentric control volumes. As the particle trajectories are calculated, the path of each particle and its corresponding residence time in each of these control volumes can be estimated. Using basic transfer relationships, the net momentum, energy, and mass exchanged between the plasma and the particle during its passage in the control volume can then be calculated. By substituting these values, as source or/sink terms, in the corresponding momentum, energy, and mass conservation equations, it is possible to compute the corresponding plasma flow, temperature, and concentration fields in the presence of the particle flux. While such interactions between the plasma and the particles can involve momentum, energy, and mass transfer, it is generally accepted that the energy transfer is the predominant phenomena compared to momentum and mass transfer. Accordingly only the energy equation is usually modified to take into account the plasma–particle interaction effects. Figure 8.47 shows a block diagram of the computational scheme used according to this model. It is essentially an iterative procedure in which the flow

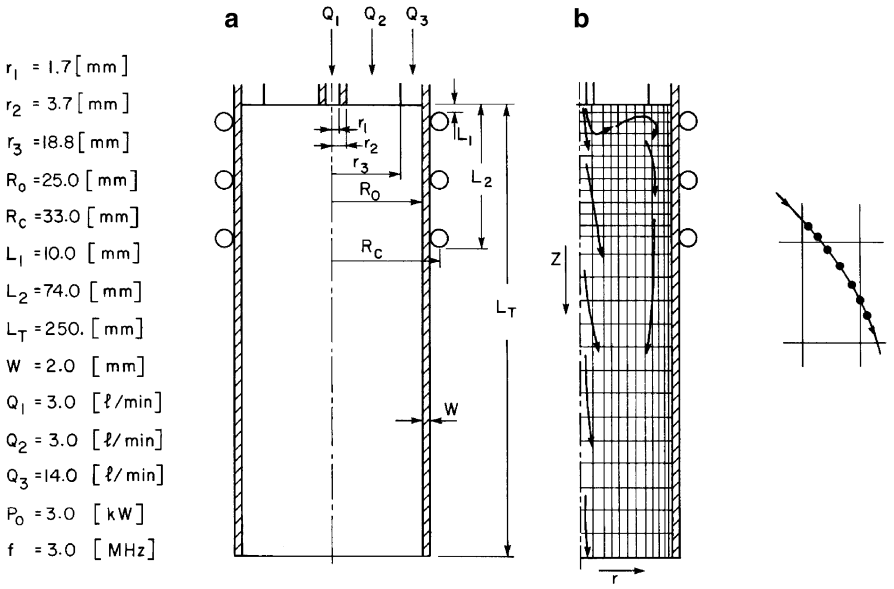


Fig. 8.46 Schematic representation of the induction plasma torch and the computational grid used for the modeling of the plasma–particle interaction effects, after Proulx et al. [47] with kind permission

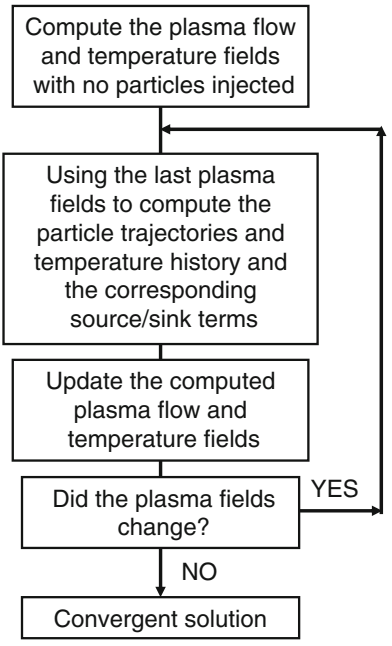


Fig. 8.47 Block diagram for the computation scheme, after Proulx et al. [47] with kind permission

and temperature fields are computed in the first place in the absence of any particles. This is followed by the computation of the individual particle trajectories, temperature history, and the corresponding source/sink terms for each of the individual control volumes. This information is then used to recalculate the flow and temperature fields in the plasma flow taking into account local energy exchange between the plasma and the particles in-flight. Comparing the computed temperature fields with the values used in the previous iterations, it can be determined if the fields changed in any significant way. The iterations are continued until a convergent solution is obtained when the fields do not change between successive iterations.

8.4.1 Governing Equations

8.4.1.1 Continuity, Momentum, Energy, and Mass Conservation Equations

Taking into account plasma–particle interactions, the continuity, momentum, and mass transfer equations can be written in their general form as follows:

Continuity

$$\nabla .\rho u = S_p^c \tag{8.48}$$

Momentum conservation

$$\rho u.\nabla u = -\nabla p + \nabla .\mu \nabla u + J \times B + S_p^M \tag{8.49}$$

Energy conservation

$$\rho u.\nabla h = \nabla \frac{k}{c_p} \nabla h + \sigma E^2 - Q_r + S_p^E \tag{8.50}$$

Mass conservation

$$\rho u.\nabla y = \nabla .D\nabla y + S_p^c \tag{8.51}$$

where, S_p^c , S_p^M and S_p^E are the contributions of the particles to the transport of mass, momentum, and energy, respectively. Neglecting the terms S_p^c and , i.e., the influence of particles on mass and momentum transfer, only Eq. (8.15) will need to be modified as through the addition of as a source or sink term as follows:

$$\rho u \frac{\partial}{\partial z} h + \rho v \frac{\partial}{\partial r} h = \frac{\partial}{\partial z}\left(k_e \frac{\partial}{\partial z} T\right) + \frac{1}{r} \frac{\partial}{\partial r}\left(r k_e \frac{\partial}{\partial r} T\right) + P - R + S_p^E \tag{8.52}$$

For laminar flow, which is the case treated in [47], the values of the effective viscosity, μ_e, and the effective thermal conductivity, k_e, are replaced by the corresponding molecular values. All other electromagnetic fields equations remain unchanged. It is important to note, however, that the results given in [47] were obtained using a simplified one-dimensional representation of the electromagnetic fields and not the full vector potential representation.

8.4.1.2 Particle Trajectory Equations and Plasma–Particle Interactions

Assuming that the only forces affecting an individual particle trajectory are the drag and gravity, the momentum equation for a single particle injected vertically downward into the plasma can be expressed as

$$\frac{\mathrm{d}u_\mathrm{p}}{\mathrm{d}t} = -\frac{3}{4}C_\mathrm{D}\left(u_\mathrm{p} - u\right).U_\mathrm{R}\left(\frac{\rho}{\rho_\mathrm{p}.d_\mathrm{p}}\right) + g \tag{8.53}$$

$$\frac{\mathrm{d}v_\mathrm{p}}{\mathrm{d}t} = -\frac{3}{4}C_\mathrm{D}\left(v_\mathrm{p} - v\right).U_\mathrm{R}\left(\frac{\rho}{\rho_\mathrm{p}.d_\mathrm{p}}\right) \tag{8.54}$$

where C_D is the drag confident, u and v are the axial and radial components of the plasma velocity, u_p and v_p are the axial and radial components of the particle velocity, ρ the plasma density, ρ_p and d_p are the particle density and diameter, respectively, and U_R is the relative velocity between the particle and the plasma.

$$U_\mathrm{R} = \sqrt{\left(u_\mathrm{p} - u\right)^2 + \left(v_\mathrm{p} - v\right)^2} \tag{8.54}$$

The particle temperature is determined by an energy balance

$$Q_{net} = \pi.d_p^2.h_c\left(T - T_p\right) - \pi.d_p^2.\varepsilon.\sigma_s\left(T_p^4 - T_s^4\right) \tag{8.55}$$

where Q_net is the net heat exchange between the particles and its surroundings. An energy balance on the particle using the following equations allows calculating the particle temperature.

$$Q_\mathrm{net} = \left(\frac{\pi}{6}.\rho_\mathrm{p}.d_\mathrm{p}^3.c_\mathrm{p}\right).\frac{\mathrm{d}T_\mathrm{p}}{\mathrm{d}t}\ \text{for}\ T < T_\mathrm{m} \quad \text{and} \quad T_\mathrm{m} < T < T_\mathrm{v} \tag{8.56}$$

$$Q_\mathrm{net} = \left(\frac{\pi}{6}.\rho_\mathrm{p}.d_\mathrm{p}^3.H_\mathrm{m}\right).\frac{\mathrm{d}x}{\mathrm{d}t}\ \text{for}\ T = T_\mathrm{m} \tag{8.57}$$

$$Q_\mathrm{net} = \left(-\frac{\pi}{2}.\rho_\mathrm{p}.d_\mathrm{p}^2.H_\mathrm{v}\right).\frac{\mathrm{d}d_p}{\mathrm{d}t}\ \text{for}\ T = T_\mathrm{v} \tag{8.58}$$

where d_p, T_p, ρ_p, and c_p are the particle diameter, temperature, density, and specific heat, respectively. T_m and T_v are the melting and vaporization temperature of the particle material, while H_m and H_v are the corresponding latent heat of fusion and latent heat of vaporization. x is the molten fraction of the particle mass. The source/sink term in the modified energy equation, Eq. (8.52) is calculated for each control volume i, j based on the net energy exchange between the plasma and all of the particle trajectories crossing the control volume. It is composed of two terms, the first corresponding to the heat exchanged between the particle and the plasma and the second corresponds to the energy needed to superheat any vapors lost from the particles, from the particle vaporization temperature, to the local plasma temperature. It is represented by the following equation:

$$S^E_{p,i,j} = \sum\nolimits_{l,k} C^{l,k}_{i,j} \cdot \left(Q^{l,k}_{p,i,j} + Q^{l,k}_{v,i,j} \right) \tag{8.59}$$

where is the particle concentration in cell (i,j) resulting from the crossing of the particles on the trajectory (l,k).

$$C^{l,k}_{i,j} = \frac{N^{o,l,k} \cdot \tau^{l,k}_{i,j}}{V_{i,j}} \text{ with} N^{o,l,k} = n_{d,l} \cdot n_{r,k} \cdot N^o_t \tag{8.60}$$

$$Q^{l,k}_{p,i,j} = \frac{1}{\tau^{l,k}_{i,j}} \int_0^{\tau^{l,k}_{i,j}} \pi d_p^2 . h_c \left(T_{i,j} - T^{l,k}_{p,i,j} \right) \mathrm{d}t \tag{8.61}$$

$$Q^{l,k}_{v,i,j} = \frac{1}{\tau^{l,k}_{i,j}} \int_0^{\tau^{l,k}_{i,j}} \frac{\pi}{2} d_p^2 . \rho_p \frac{\mathrm{d}d_p}{\mathrm{d}t} . c_{pv} . \left(T_{i,j} - T^{l,k}_{p,i,j} \right) \mathrm{d}t \tag{8.62}$$

8.4.2 Typical Result: Effect of Particle Loading

The first results dealing with particle loading effects in induction plasma modeling were reported in 1985 by Proulx et al. [47]. Computations were carried out in this case for a pure argon, low power, atmospheric pressure, plasma discharge in a 50 mm i.d. quartz plasma confinement tube. The oscillator frequency was 3 MHz, and the net power coupled into the discharge was 3 kW. The total argon gas glow rate was 20 slm.

A fine copper powder, with a mean particle diameter of 70 μm was injected into the center of the discharge at different powder feed rates varying between 1.0 and 20.0 g/min. Typical results obtained for a copper powder feed rate of 5 g/min are given in Fig. 8.48. The plasma temperature and flow field shown on the left-hand side of this figure reveal an off-axis maximum of the plasma temperature of about 9,600 K with the central channel in the flow, where most of the copper particle trajectories are concentrated, considerably cooler. On the right-hand side of this same figure, the corresponding concentration field of the copper vapors in the flow shows a maximum value on the centerline of the discharge. As expected, the cooling effect of the injected copper is increasingly more important with the

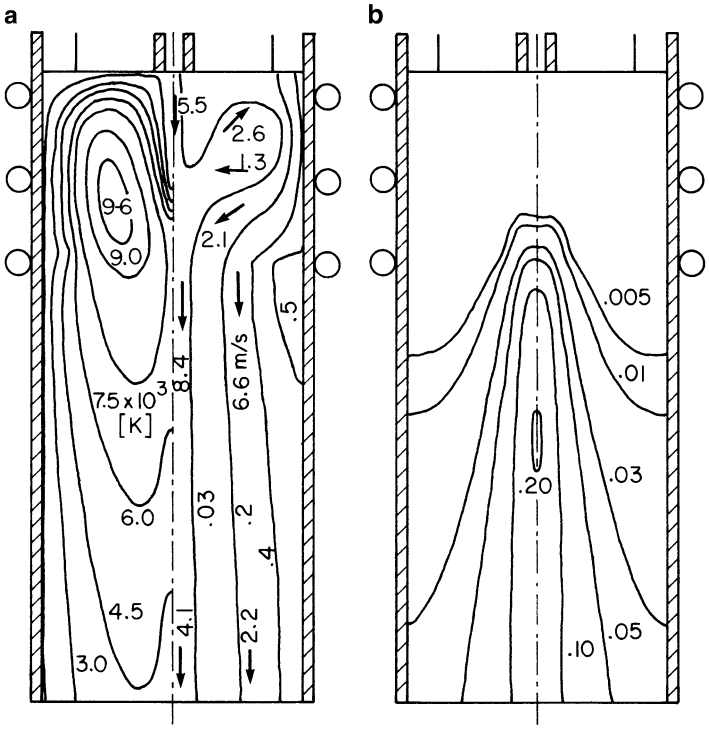


Fig. 8.48 Temperature and flow fields (*left*) and copper vapor concentration iso-contours (*right*), for an argon plasma, 3 kW, in the presence of copper powder axially injected into the center of the discharge at a mass flow rate of 5 g/min. After Proulx et al. [47] with kind permission

increase of the copper powder feed rate. Figures 4.66 and 4.67 show, respectively, the plasma temperature profile along the centerline of the discharge and across the discharge at the middle section of the coil for different copper powder feed rates. It may be noted from Fig. 4.66 that in the absence of powder injection, the maximum plasma temperature reached over the centerline of the discharge is around 9,500 K. With the increase of the copper powder feed rate, the maximum value of the plasma temperature drops systematically down to less than 4,000 K at a copper powder feed rate of 20 g/min. Figure 4.67, reveals, however, that the loading effect caused by the copper powder injection is limited to the central region of the discharge (+/−) 5 mm from the axis where most of the copper powder trajectories are concentrated. A summary of the results obtained in this study is given in Table 8.2 The first column on the left-hand side of the table gives the copper powder feed rate into the plasma, while the second column gives the corresponding copper vaporization rate. The following two columns give the energy transferred from the plasma to the copper particles and to the formed copper vapors respectively. The last column gives the sum of the power that is transferred to the copper particles and vapor as a percentage of the total discharge power. It may be noted that with the increase of the copper powder feed rate, the corresponding rate of copper vaporization increases first. With the further

Table 8.2 Copper powder evaporation rate and energy balance date for copper powder injection into an atmospheric pressure argon induction plasma at 3 kW, after Proulx et al. [47]

m_p (g/min)	m_v (g/min)	Q_p (W)	Q_v (W)	Plasma energy transferred to the particles (%)
1.0	0.50	71	21	3.1
5.0	1.40	255	42	9.9
10.0	1.40	386	35	14.0
15.0	1.16	460	28	16.3
20.0	0.94	511	23	17.8

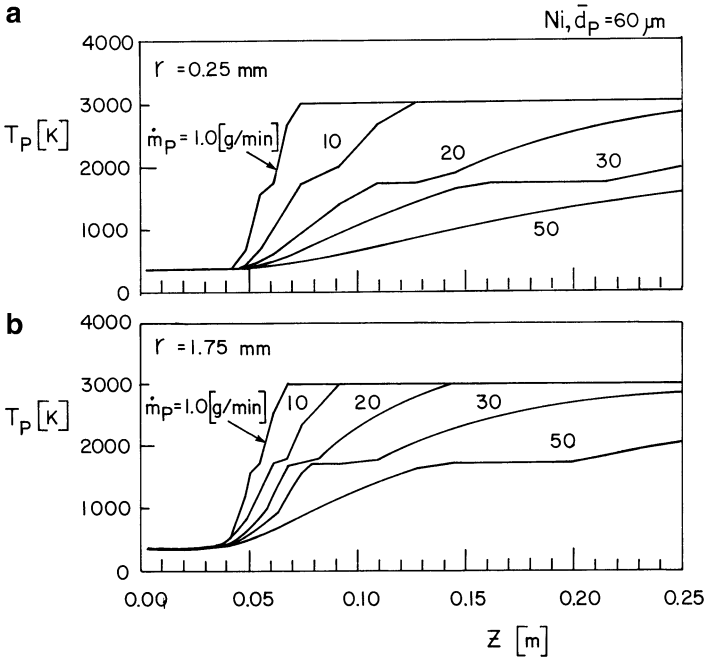


Fig. 8.49 Temperature history for nickel powders traveling along the center of the discharge as function of the powder feed rate. After Proulx et al. [50]. With kind permission from Springer Science + Business Media B.V

increase of the powder feed rate, the powder vaporization rate drops rapidly due to the significant cooling of the plasma. It may also be noted that in all cases the total amount of energy transferred to the powder and vapor increases with the increase of the powder feed rate reaching a plateau around 17–18 % of the total plasma power.

The same phenomenon is also observed with different materials as reported by Proulx et al. [50]. In this study carried out on a 5 kW, atmospheric pressure, pure argon plasma, in which fine powders of Nickel, Alumina, and Tungsten with a mean particle diameter of 60 μm and a standard deviation of 10 μm. The powder feed rate was varied in this case between 1 and 50 g/min. The corresponding temperature history for each of these powders is shown in Fig. 8.49, 8.50, and 8.51. The upper

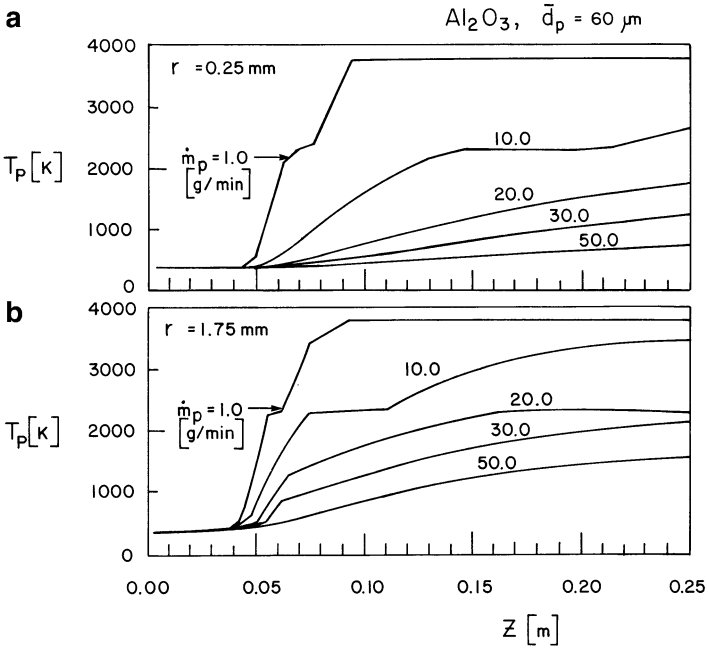


Fig. 8.50 Temperature history for alumina powders traveling along the center of the discharge as function of the powder feed rate. After Proulx et al. [50]. With kind permission from Springer Science + Business Media B.V

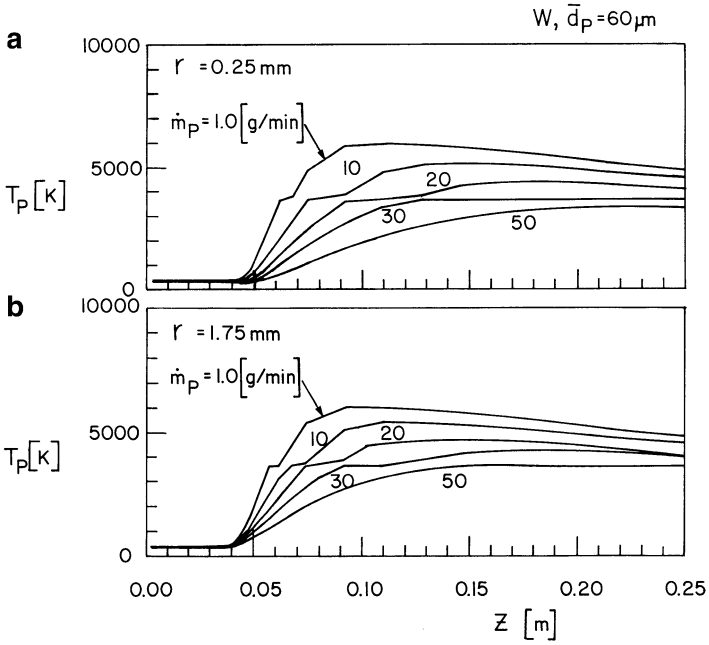


Fig. 8.51 Temperature history for tungsten powders traveling along the center of the discharge as function of the powder feed rate. After Proulx et al. [50]. With kind permission from Springer Science + Business Media B.V

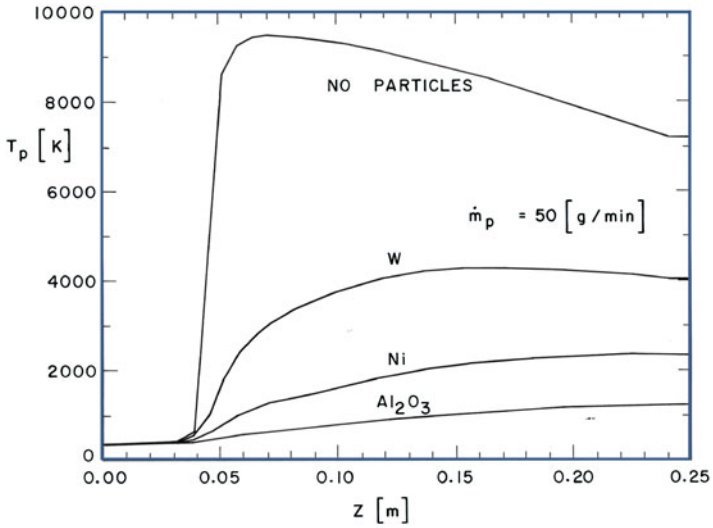


Fig. 8.52 Plasma axial temperature profile along the centerline of the discharge in the presence of powders of different materials injected at a feed rate of 50 g/min. After Proulx et al. [50]. With kind permission from Springer Science + Business Media B.V

part of each of these figures corresponds to the trajectory of a particle initiated at a location of 0.25 mm away from the torch axis, while the lower part of the figure corresponds to a trajectory initiated at 1.75 mm off the torch axis. The individual curves on each of these figures shows the variation of the temperature of particles with a diameter of 60 μm, injected into the plasma at different mass feed rates, as they move toward the downstream end of the flow (left to right). This shows, in most cases, that at low feed rates, the particle temperature rises sharply as it enters the plasma zone reaching rapidly its melting plateau, and in most cases reaching as well the particle evaporation plateau. It is also noted that the individual temperature history of the particles different depending on the initial point of particle injection and the thermophysical properties of the materials treated. The corresponding variation of the plasma temperature along the centerline of the discharge is shown in Fig. 8.52 for a total powder feed rate of 50 g/min. The axial profile of the plasma temperature in the absence of any particle injection is superposed on the figure for comparison. It may be noted that the injection of the particles in the plasma results in a considerable local cooling of the plasma along its axis. The effect, however, varies considerably from one material to the other as function of its thermophysical properties. Consistent with the observation made earlier with the copper powder injection [47], it is also noted in Fig. 8.53 that total amount of energy transferred from the plasma to the particles in-flight increases with the increase of the feed rate, reaching a plateau which is different from one material to the other with a maximum value around 18 % of the total discharge power. The data summarized in Table 8.3 give the mass fraction of the powder injected into the

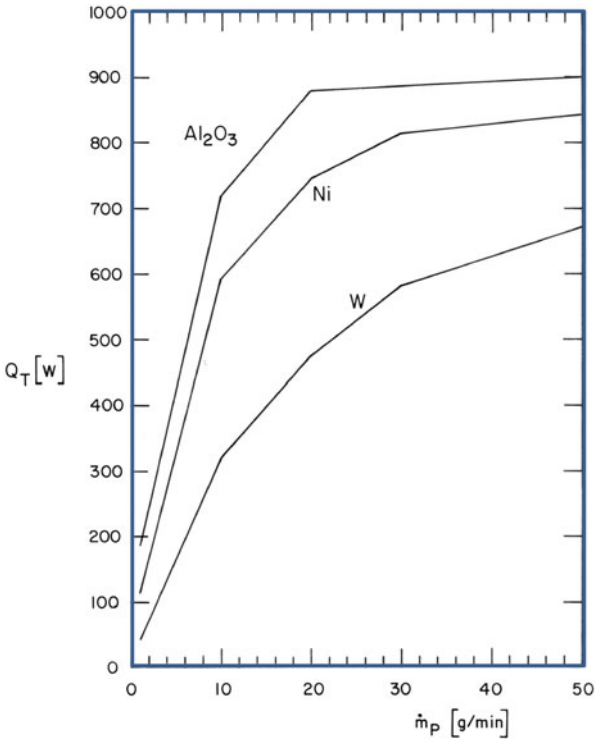


Fig. 8.53 Cumulative energy transferred from the plasma to particles of different materials as function of the powder feed rate. Pure argon plasma with a total power in the discharge of 5 kW. After Proulx et al. [50]. With kind permission from Springer Science + Business Media B.V

Table 8.3 Status of powders of different materials at the downstream end of the plasma torch/reactor system as function of the powder feed rate, after Proulx et al. [50]

		Powder feed rate				
Material	State	1.0 g/min	10 g/min	20 g/min	30 g/min	50 g/min
Alumina	Solid	0	0.02	0.43	0.84	1.00
	Liquid	0.74	0.98	0.57	0.16	0.0
	Vapor	0.26	0.0	0.0	0.0	0.0
Nickel	Solid	0.0	0.0	0.0	0.02	0.19
	Liquid	0.27	0.69	0.88	0.94	0.81
	Vapor	0.73	0.31	0.12	0.04	0.0
Tungsten	Solid	0.0	0.0	0.0	0.05	0.70
	Liquid	0.90	1.0	1.0	0.95	0.30
	Vapor	0.10	0.0	0.0	0.0	0.0

plasma, which is in the vapor, liquid, or solid state at the downstream end of the plasma torch and reactor system as function of the powder feed rate.

For a typical induction plasma spraying setup as described in Fig. 8.44, computations were repeated for the same operating conditions used earlier (Fig. 8.45) except for the introduction into the center of the discharge of a stream of molybdenum powder at different powder feed rates. The powder used in this case had a mean

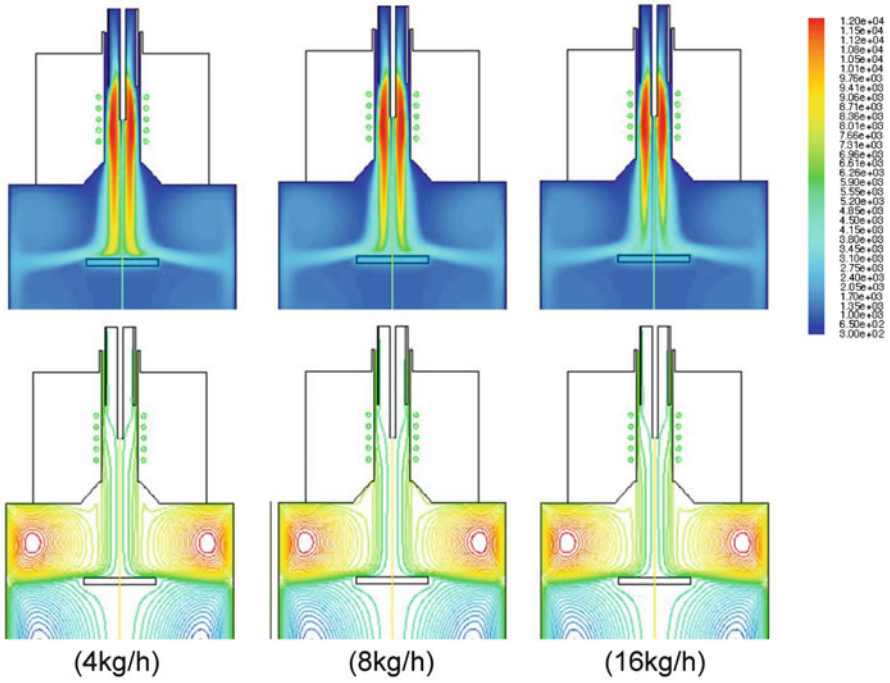


Fig. 8.54 Temperature (*top*) and flow fields (*bottom*) for an impinging induction plasma jet under vacuum plasma spraying conditions, with Molybdenum powder feed rates. Ar/H_2 Plasma, plate power = 70 kW. Results supplied by Tekna Plasma Systems Inc. (2012)

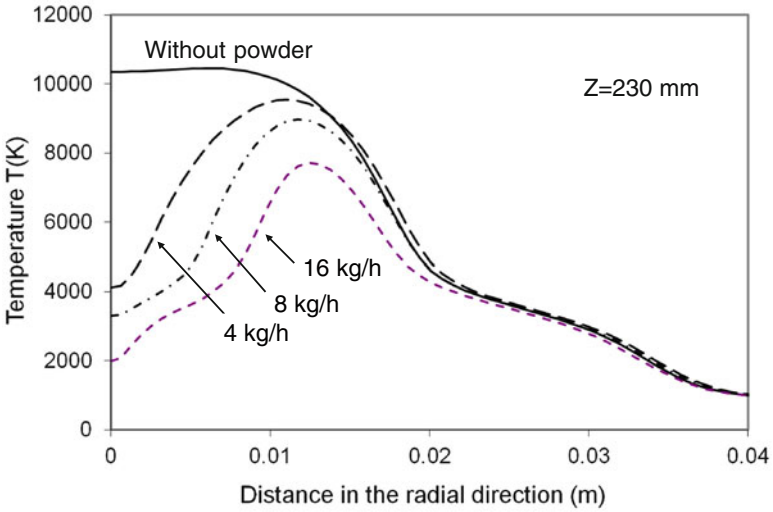


Fig. 8.55 Radial temperature profiles, at $z = 230$ mm, see Fig. 8.50, for an impinging induction plasma jet under vacuum plasma spraying conditions, with Molybdenum powder feed rates varing between 4 kg/h, and 16.0 kg/h. Ar/H_2 Plasma, plate power = 70 kW. Results supplied by Tekna Plasma Systems Inc. (2012)

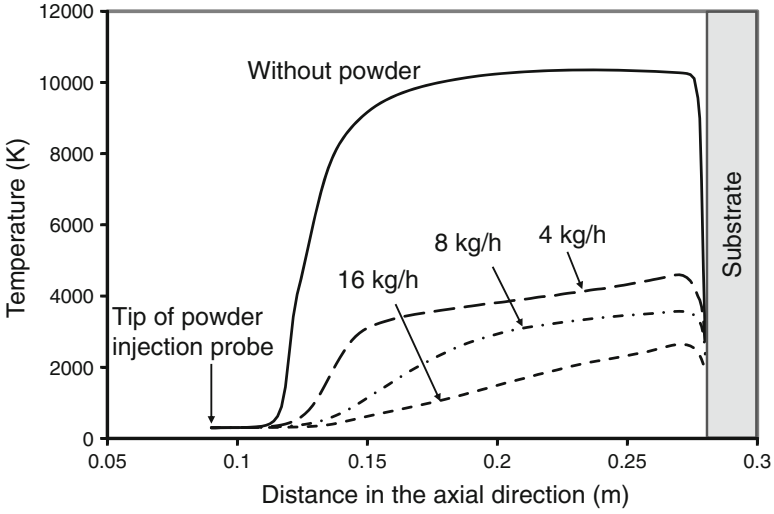


Fig. 8.56 Plasma temperature profiles along the center line of the discharge for an impinging induction plasma jet under vacuum plasma spraying conditions, with Molybdenum powder feed rates of 4 kg/h, 8.0 kg/h, and 16.0 kg/h. Ar/H_2 Plasma, plate power = 70 kW. Results supplied by Tekna Plasma Systems Inc. (2012)

particle diameter, d_{50} of 60 μm, and min and max particle diameters of 40 and 80 μm, respectively. The particles were of pure Molybdenum with the following properties:

Density = 10,200 kg/m^3	Specific heat = 0.25 kJ/kg (°C)
Melting temperature = 2,890 K	Latent heat of fusion = 333.54 kJ/kg
Boiling temperature = 4,912 K	Latent heat of evaporation = 6.23 MJ/kg

The sheath gas (120 slm) was a mixture of Ar/H_2 with a Hydrogen concentration of 16 % vol. while the central gas (30 slm) and the powder carrier gases (5 slm) were pure argon. The powder feed rate was varied between 4, 8, and 16 kg/h for the same plasma power of 70 kW and chamber pressure of 34.4 kPa (5 psia).

The effect of powder injection on the temperature and flow field in the discharge is shown in Fig. 8.54. The upper part of the figure shows effect of increasing the powder feed rate, from 4 kg/h to 8 kg/h and up to 16 kg/h. It is noted that the temperature of the central part of the discharge drops with the increase of the powder feed rate. The effect is less noticeable on the corresponding flow fields on the lower part of the figure. The effect of powder loading on the local radial temperature profiles at the downstream end of the coil (z-230 mm, see Fig. 8.44), is shown in Fig. 8.55. It is noted that the effect is localized around the centerline of the plasma jet with a drop of almost 6,000 K of the axis temperature with a particle feed rate of only 4 kg/h. With the increase of the powder feed rate, the extent of the loading effect is noticeable further away from the flow axis. The effect of powder loading on the plasma temperature along the centerline of the flow is shown in Fig. 8.56 for powder feed rates of 4.0, 8.0, and 16.0 kg/h. The plasma temperature

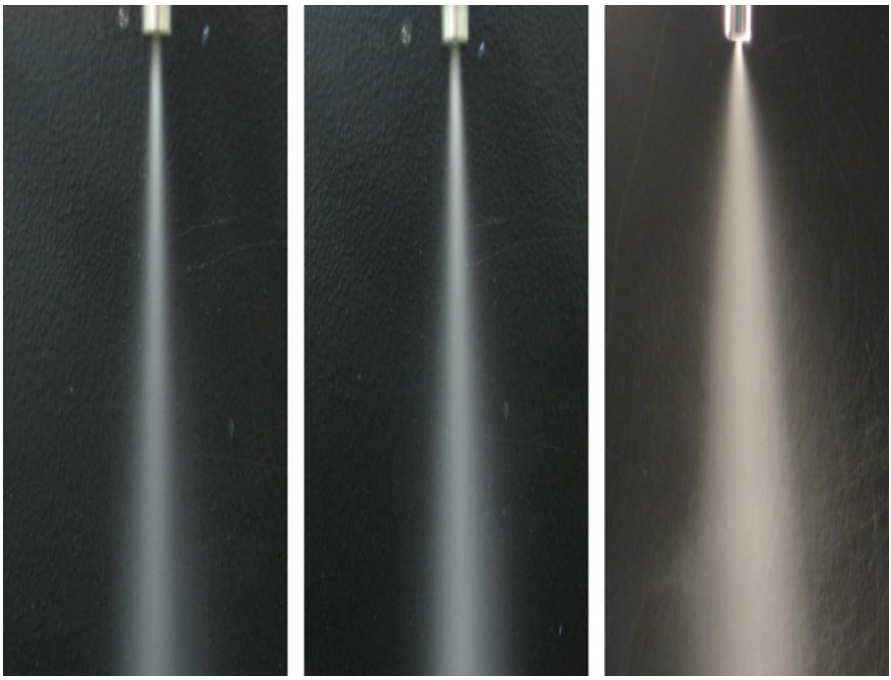


Fig. 8.57 Photographs of a particle jet illustrating the effect of probe design and dispersion gas flow rate on the powder dispersion. Results supplied by Tekna Plasma Systems Inc. (2012)

profile in the absence of any powder feeding is shown for comparison. It is noted that the effect is significant and goes all the way until the plasma jet intercepts with the surface of the substrate on which the molten powder droplets are deposited.

The importance of the plasma–particle interactions phenomena and the resulting loading effects presented in the above discussion, underlined the need for effective means of proper powder dispersion in the plasma flow in order to achieve maximum treatment and/or deposition efficiency. Figure 8.57 shows photographs of a powder dispersion probe developed by Tekna Plasma Systems Inc. for the axial injection of powders in an inductively coupled plasma stream. The photograph on the left-hand side of the Figure shows the powder stream immerging from a standard probe, while the photograph at the center and the right-hand side of the figure shows the corresponding powder stream in the presence of increasing rates of a dispersion gas using the STD series of probes. In order to quantitatively evaluate the impact of proper powder dispersion, computations were carried out for a standard Ar/H_2 plasma flow generated using a PS-70 torch at above atmospheric pressures ($p = 112$ kPa) and 100 kW plate power. A standard Molybdenum powder, similar to that used in earlier modeling work, was injected axially in the center of the discharge at different feed rates and the fraction of the powder molten as it passes through the discharge evaluated.

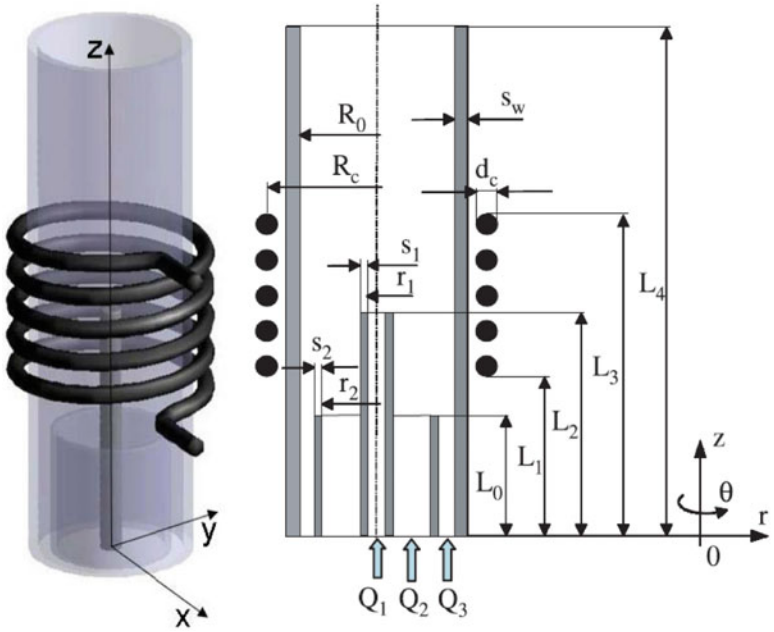


Fig. 8.58 3-D schematic of the induction plasma torch. After Bernardi et al. [73] with kind permission

The results show that with a dispersion angle of 15° the powder is fully molten (100 % melted fraction) at a feed rate of 25.7 kg/h. A similar melting fraction of 100 % is even obtained at a higher powder feed rate of 30 kg/h. It may be noted that the case with straight powder injection results in a pronounced local cooling of the plasma near the axis of the flow. The corresponding effect is distributed over a larger region of the flow, with a lower plasma cooling effect for each of the two cases with a dispersion probe and a dispersion angle $A = 15^{o}$.

Over the past decade, significant improvements in the modeling of plasma–particle interaction effects during induction plasma treatment of powders, whether for simple powder spheroidization or plasma spraying, was developed by Colombo and his collaborators at the University of Bologna [71–82]. Their main contribution is in taking the modeling one step further using 3D modeling codes, which significantly increases model complexity and required computation time. The results, however, reveals for the first time the three-dimensional nature of the flow and the effect of geometrical asymmetries on the 3D plasma temperature field and particle trajectories and dispersion into the discharge. The results reported by Bernardi et al. [73] were essentially for the same torch geometry and operating conditions as those used in an earlier publication by Proulx et al. [50] and presented in Figs. 8.49, 8.50, 8.51, 8.52, and 8.53. The torch geometry used in this case is schematically represented in Fig. 8.58. Special attention was given in this case to the 3D effect of the coil design, as shown on the left-hand side of this figure, and its effect on the temperature fields in the discharge. The corresponding temperature

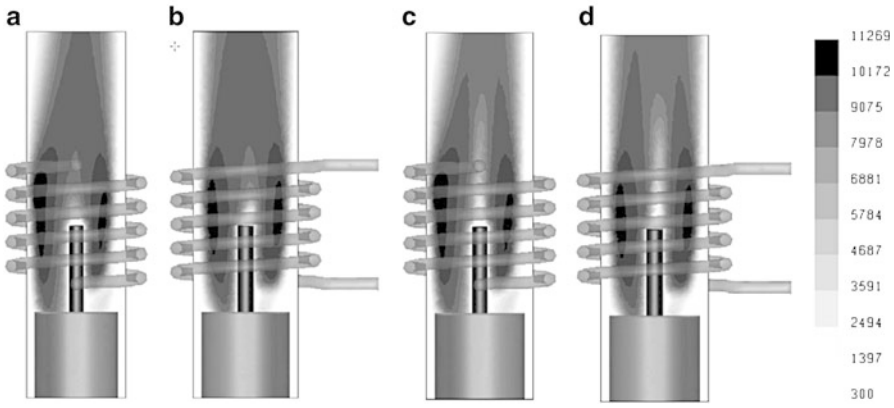


Fig. 8.59 Plasma temperature fields (K) on two orthogonal planes through the axis of the torch. Cases (**a**) and (**b**) without powder injection. Cases (**c**) and (**d**) with 30 μm W powder injection at 20 g/min. After Bernardi et al. [73] with kind permission

fields for a pure argon plasma operated at a frequency of 3 MHz and a net power coupled into the plasma of 25 kW, is shown in Fig. 8.59. The results are presented for two cases in the absence (Fig. 8.59a, b) and the presence (Fig. 8.59c, d) of particles injected into the center of the discharge. For each of these two cases, the corresponding plasma temperature fields are given along two orthogonal planes passing through the axis of the discharge. The results reveal in both cases an important 3D asymmetry of the temperature fields which is due to 3D effect of the coil geometry. As expected, the results also reveal the local cooling of the plasma near the axis of the discharge as a result of Tungsten powder injection, $d_p = 30$ μm, at a feed rate of 20 g/min.

The subsequent study reported by Colombo et al. [81] was focused on the particle loading effects using 3D representation of the flow, temperature, and particle trajectories. A schematic representation of the torch geometry (Tekna Plasma Systems Inc., Model PL-35 torch) and reactor design used for the computations are shown in Fig. 8.60. Computations were carried out for torch operation at atmospheric pressure, with a mixture of Ar/H_2 as sheath gas, and pure Ar as central gas, and a net power dissipated in the discharge of 15 kW. Two oscillator frequencies were used in the computation. These were 3 and 13.56 MHz. The results, given in Fig. 8.61, show the effect of frequency on the temperature fields in the discharge. These are presented as temperature isocontours on two orthogonal planes passing through the axis of the torch, with the results obtained at an oscillator frequency of 3 MHz presented on the left-hand side of the figure (Fig. 8.61a, b), while the results obtained at a frequency of 13.56 MHz are represented on the right-hand side of the figure (Fig. 8.61c, d).

A 3D representation of alumina particle trajectories as they are injected into the center of the discharge is given in Fig. 8.62. The particle size range used in these cases was varied between 25 and 125 μm, and the powder feed rate was 10 g/min.

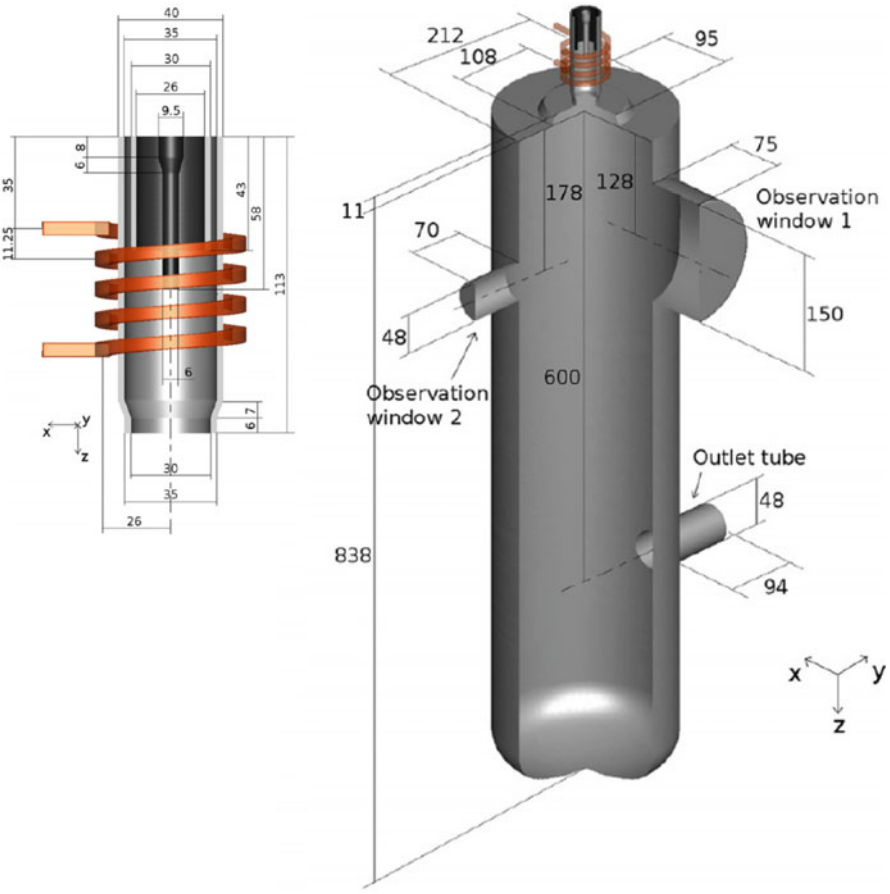


Fig. 8.60 Details of the PL-35 torch geometry and reaction chamber, dimensions in mm. After Colombo et al. [81]. Copyright [2010], American Institute of Physics, Reproduced with permission. All rights reserved

It is noted that the model predicts a widely dispersed and an asymmetric particle distribution, which can have a major impact on particle deposition efficiency during induction plasma spraying operations. The effect of the powder feed rate on the particle temperature history along their trajectories is shown in Fig. 8.63 for alumina powder feed rates of 2, 5, 10, and 20 g/min. These show an increasing loading effect with the increase of the powder feed rate resulting in a significant reduction of the ability to fully melt the powder especially the large article size fractions (75 and 125 μm). A compilation of the results obtained at the two oscillator frequencies considered and for different injection points of the powder along the centerline of the discharge are presented in Figs. 8.64 and 8.65. The location of the probe tip in this case is defined by $h = 45$ or 55 mm, representing the distance between the probe tip and the exit level of the torch nozzle. The results

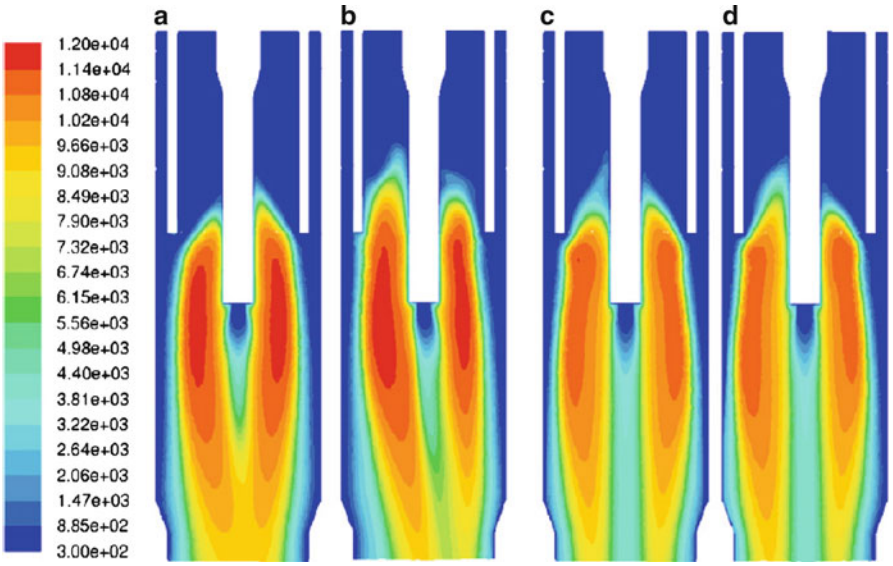


Fig. 8.61 Plasma temperature distribution (K) on two orthogonal planes through the axis of the torch. Cases (**a**) and (**b**) for 3 MHz operation. Cases (**c**) and (**d**) for 13.56 MHz operation, Alumina powder feed rate at 10 g/min, with a probe tip at 55 mm upstream of the torch exit nozzle level. After Colombo et al. [81]. Copyright [2010], American Institute of Physics, Reproduced with permission. All rights reserved

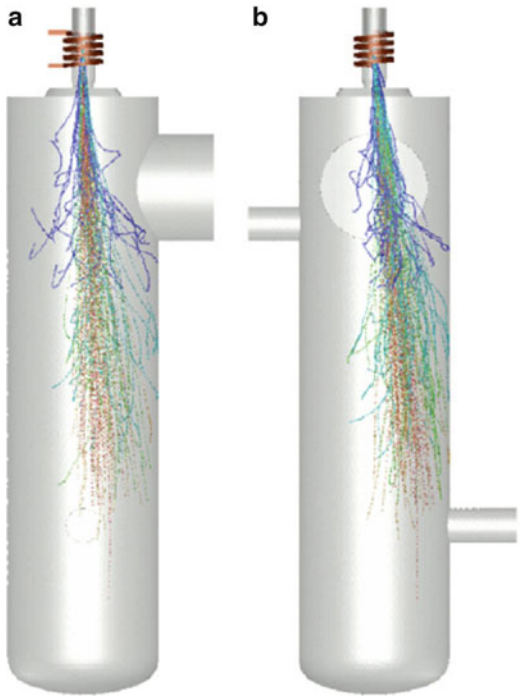


Fig. 8.62 Plasma trajectories on two orthogonal planes passing through the torch and reactor axis, for the case at 3 MHz, powder feed rate of 10 g/min, and probe tip position of 55 mm upstream of the torch exit nozzle. After Colombo et al. [81]. Copyright [2010], American Institute of Physics, Reproduced with permission. All rights reserved

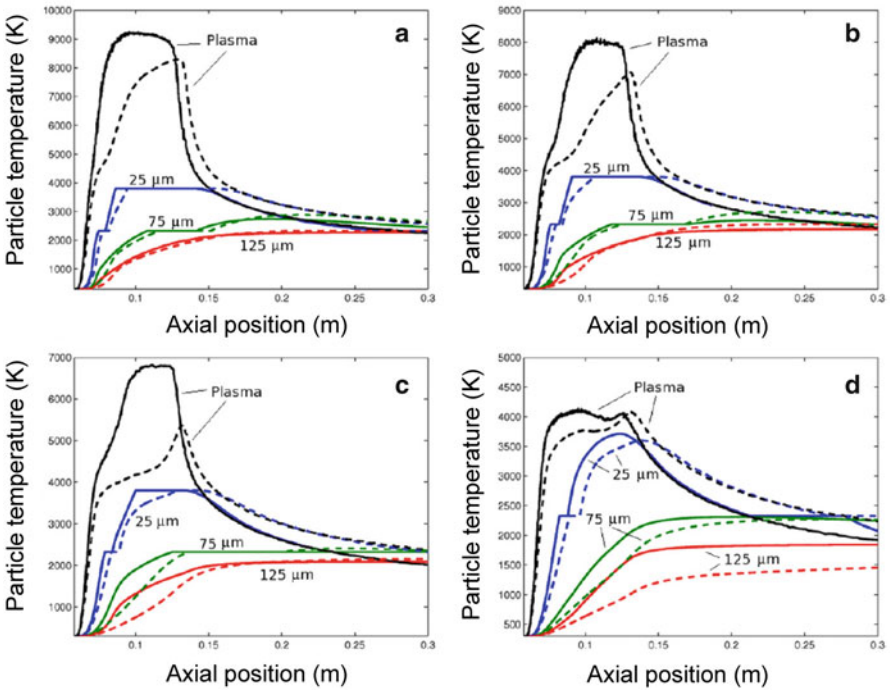


Fig. 8.63 Plasma and mean particle temperature computed along their trajectories for the 3 MHz (*solid line*) and 13.56 MHz (*dashed line*), for different particle diameters and powder feed rates. Probe tip at 55 mm upstream of the torch exit nozzle level. (**a**) mp = 2 g/min, (**b**) mp = 5 g/min, (**c**) mp = 10, and (**d**) mp = 20 g/min. After Colombo et al. [81]. Copyright [2010], American Institute of Physics, Reproduced with permission. All rights reserved

are presented in this case as the mean plasma temperature (K) along the particle trajectory (Fig. 8.63) or the mean plasma temperature as a function of the powder feeding rate (Fig. 8.64), or the integral of the heat transferred to the participle stream (kJ/kg) (Fig. 8.65), as function of the powder feed rate. The results are consistent with earlier observations made by Proulx et al. [50] and given in Fig. 8.54, which shows that the total energy transferred from the plasma to the particles reaching a plateau with the increase of the powder feed rate resulting in a linear drop of the specific energy transferred to the powder expressed in terms of kJ/kg of powder.

8.5 Vacuum Induction Plasma Spraying

8.5.1 Basic Equipment Design

Vacuum induction plasma spraying (VIPS) has been known for the past few decades and used on an industrial scale in a limited number of applications. The deposition of pure silica grain on optical fiber performs, generally known as

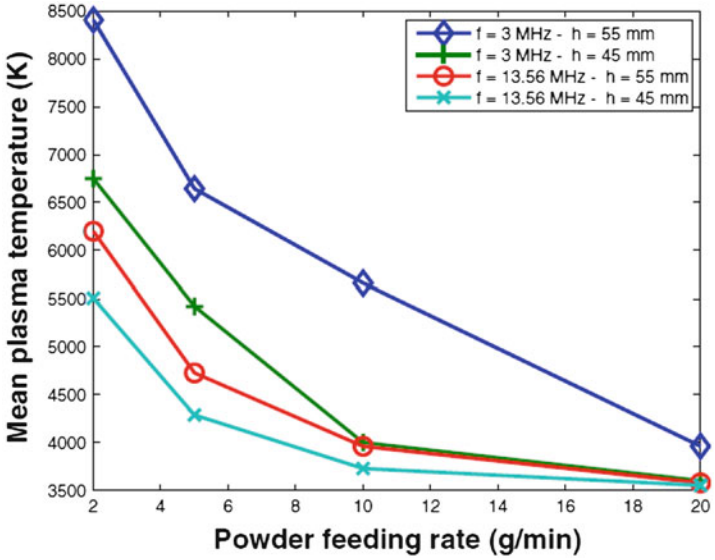


Fig. 8.64 Mean particle temperature computed along their trajectories for the 3 and 13.56 MHz cases. And for two probe tip positions $h = 45$ and 55 mm, as function of the powder feed rate. After Colombo et al. [81]. Copyright [2010], American Institute of Physics, Reproduced with permission. All rights reserved

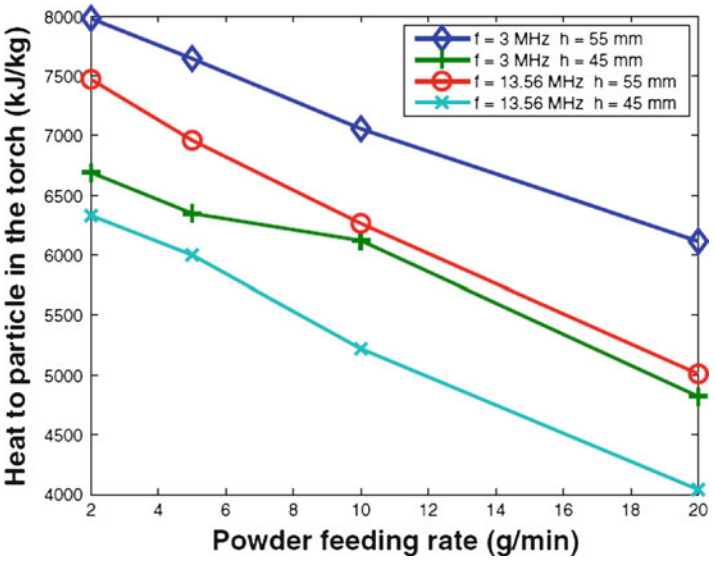


Fig. 8.65 Integral energy transferred from the plasma to the particles along their trajectories for the 3 and 13.56 MHz cases. And for two probe tip positions $h = 45$ and 55 mm, as function of the powder feed rate. After Colombo et al. [81]. Copyright [2010], American Institute of Physics, Reproduced with permission. All rights reserved

preform over-cladding, is a typical example where the technology found a unique application where it was particularly suited because of its ability to maintain the high purity of the deposited material. A typical set up used in such application was reported by Berthou et al. [90]. The silica grain, or deposit precursor, is axially fed through the central injector into the discharge cavity were the grain is heated, melted, and accelerated toward the substrate (perform rod), which is maintained in rotation and linear motion in front of the torch. As the molten silica grains impact on the surface of the perform, they adhere to it forming a clear, bubble free, glass deposit. The technology has been the subject of numerous patents the earliest of which can be traced back to the 1960s and 1970s mostly by Alcatel Corporation.

The wider scale use of r.f. induction plasma technology for plasma spraying applications has been, however, limited due to important differences between a d.c. plasma spraying and r.f. induction plasma spraying in terms of powder injection technique in the torch, torch mobility, and the type of applications that they are best suited for each of these technologies. As schematically presented earlier in Fig. 8.1, induction plasma spraying is characterized by the axial injection of the powder into the center of the discharge in contrast to d.c. plasma spraying in which the powder is typically injected in the radial direction into the plasma jet at the exit of the torch. While axial injection torches have also been developed, using d.c. plasma technology, their design and operation with multiple electrodes is relatively more complex and the in-flight time of the powder in the plasma is almost one order of magnitude shorter in the case of d.c. plasma torches compared to atmospheric pressure r.f. induction plasmas. Because of the relatively long time of flight of the particles in the discharge, which is of the order of 10–20 ms, r.f. induction plasmas allows for the melting and deposition of powders with a considerably larger diameter than possible with d.c. technology. The absence of electrodes and the associated electrode erosion phenomena makes r.f. induction plasmas particularly suited for the spraying of high purity, oxygen-sensitive materials. Moreover, due to the relatively larger plasma jet generated by r.f. induction plasma torches, the injected powder is spread over a larger plasma volume resulting in a generally higher deposition rates over a larger, "sweet-spot," compared to a d.c. torch at a comparable power level.

The principal limitation of r.f. induction plasma spraying is, however, in the large and bulky volume of the r.f. power supplies needed and the inability to independently move the torch with respect to the power supply during the spraying operation. This is a consequence of the fact that the apparent impedance of the r.f. induction plasma torch, which has to be matched with the electrical characteristics of the power supply, is affected by the dimensions and the geometry of the transfer leads. For optimal energy coupling efficiency, the length of these leads should be kept as short as possible. Moreover, considering that most of r.f. induction plasma generators operate at a frequency between 2 and 5 MHz, special precautions need to be given to the proper shielding of the torch in a Faraday cage in order to avoid unacceptable electromagnetic interference (EMI) emitted by the torch which could seriously interfere with the operation of common robotics and computer-controlled accessories of the system.

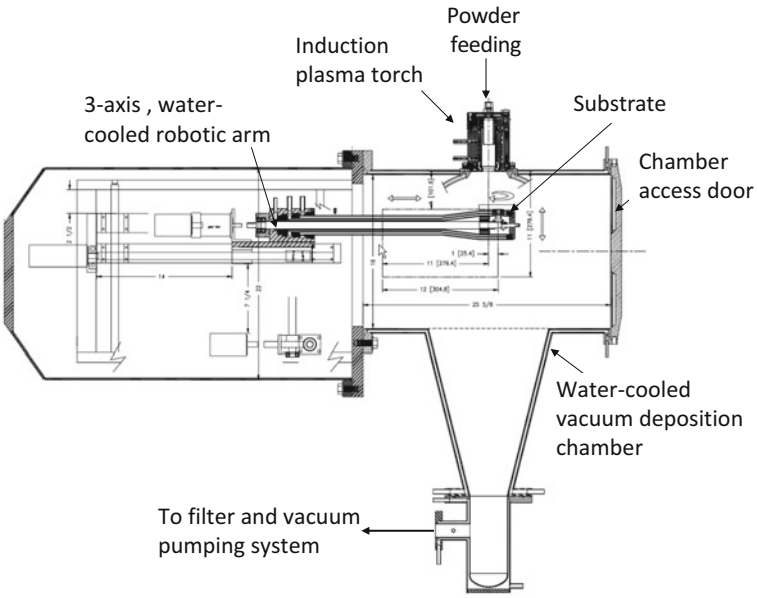


Fig. 8.66 Schematic of a pilot scale vacuum induction plasma spraying (VIPS) chamber. After Tekna Plasma Systems Inc. (2012)

In spite of these important limitations, induction plasma spraying is finding an increasing number of other niche applications involving the deposition of high purity refractory materials in a number of specialized areas such the manufacturing of sputtering targets and near net-shaped parts. In this section a brief description is presented of the main features of a typical induction plasma spraying system. This is followed by a discussion of the relationship between the deposit quality and the principal operating parameters. Examples are given of typical applications of this technology.

A schematic representation of a small-scale pilot vacuum induction plasma spraying chamber is shown in Fig. 8.66. It is composed of a horizontally oriented, water-cooled, stainless steel cylindrical chamber, 0.5 m in internal diameter and 0.64 m long, on which the plasma torch is mounted on the top in a fixed position. A Faraday cage (not shown in the drawing) surrounds the torch to protect the surrounding equipment, instrumentation, and computer-based control modules from EMI originated from the induction coil. Coaxial with the torch is the exit port for the plasma gases and powder overspray. This port is located directly underneath the torch on the opposite side of the chamber. It is of conical shape ending by a water-cooled cylindrical container in which any over-sprayed powder collects by gravity prior to the exit of the plasma gases from a side port. From this port, the gases are directed toward a filter to recover any entrained fumes and fine powders before being sent to the vacuum pumping station. An access door to the deposition chamber is located on the right-hand side of the figure. It is also

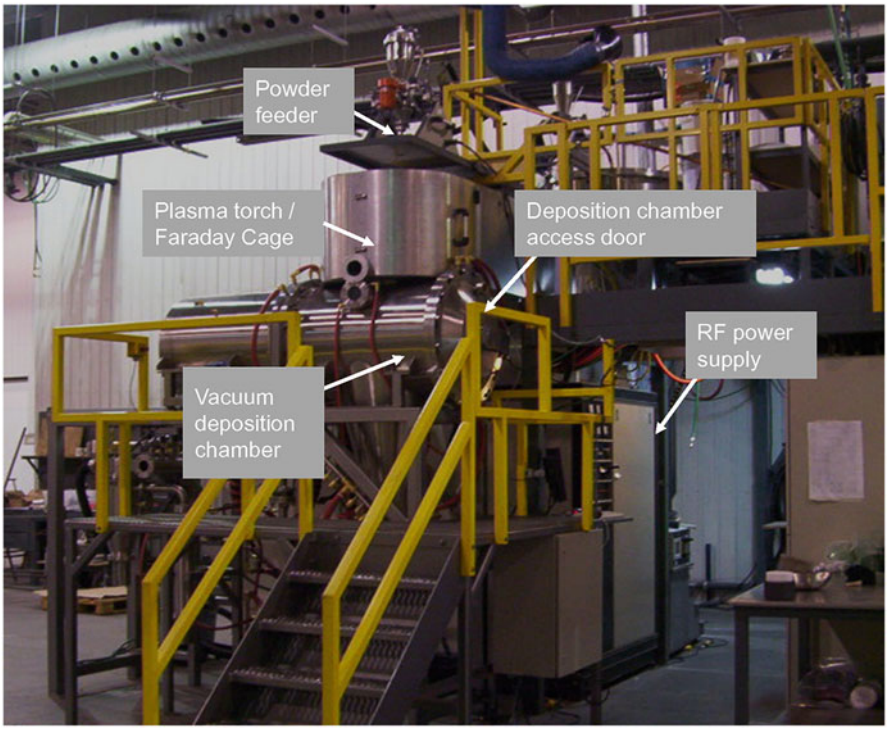


Fig. 8.67 Photograph of a 100 kW vacuum induction plasma spraying (VIPS) chamber. After Tekna Plasma Systems Inc. (2012)

water-cooled and equipped with appropriate seal for maintaining the vacuum tightness of the chamber while allowing for quick opening and closing of the chamber for installation of the substrates to be coated and recovery of the coated components. Opposite to the access door is the mechanical module in which the motors and motion control components are located for a 3-axis robotic arm, which supports the substrate. The water-cooled arm has to allow for the precise control of the exposure of the substrate to the stream of molten particles immerging from exit nozzle of the plasma torch. In standard, pilot installations the robotic arm is designed for the control of the linear motion of the arm in the horizontal direction, the vertical spraying distance between the substrate and the torch exit, and the speed of rotation of the substrate around a vertical or horizontal axis. In more elaborate and larger units a fully equipped five-axis robot can be located in the deposition chamber in order to allow for the articulation of more complex parts underneath the plasma torch. This increases considerably the complexity and the size of the spraying chamber. A photograph of a typical Induction plasma vacuum spraying chamber at Tekna Plasma Systems Inc. is shown in Fig. 8.67. One notices the powder feeder located on the top of the chamber above the induction plasma torch. The latter is not visible since the Faraday cage used for protection from

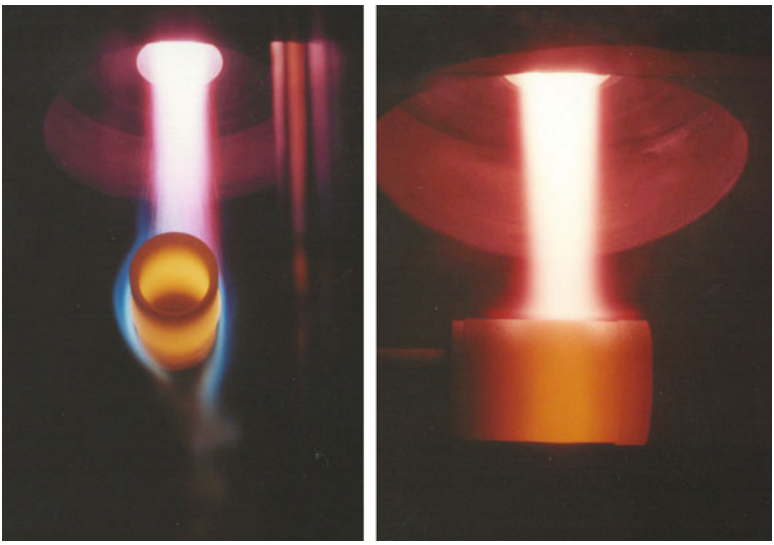


Fig. 8.68 Photograph of VIPS of tungsten on a graphite substrate. Courtsey of the CRTP, University of Sherbrooke (1995)

electromagnetic emission covers the torch. On the bottom, right-hand side of the picture, one notices the r.f. power supply and control panel for the operation of the system.

Photographs of VIPS operations for different applications are given in Figs. 8.68, 8.69, and 8.70. The example given in Fig. 8.68 is for the deposition of a refractory metal such as molybdenum or tungsten on a cylindrical graphite mandrel in order to form a near net-shaped part, which is a standalone component once the graphite substrate is machined out following the deposition step. Examples of such parts of cylindrical, conical, or other more complex shapes are given in Fig. 8.69. Figure 8.70 shows a similar setup in operation for the coating of an X-ray or a sputtering target using VIPS technology. The sheath gas used in this case is composed of 120 slm Ar + 20 slm H_2. The plasma gas is 30 slm Ar, while the powder gas is 8 slm of He. The chamber pressure was 40 kPa (300 Torr), Plate power, 80 kW, and spraying distance 100 mm.

8.5.2 Parametric Analysis and Operating Conditions

In this section an analysis is presented on the influence of principal operating parameters on the quality of the deposit obtained and the deposition efficiency. The basic mechanisms by which most of these parameters can influence the plasma deposition process have already been described in the modeling section. Here only a summary is presented.

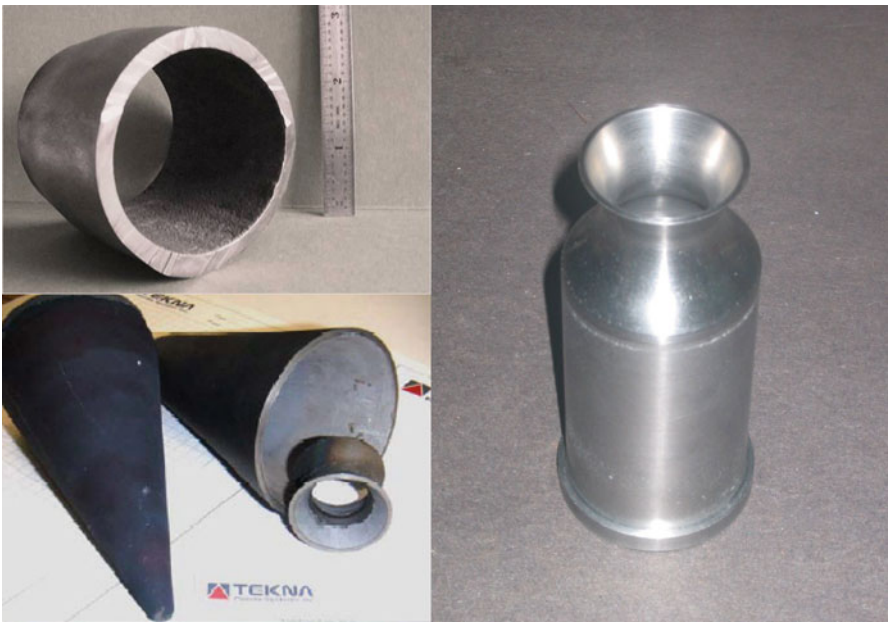


Fig. 8.69 Photograph of VIPS deposited tungsten and molybdenum near net shaped parts. Courtesy of Tekna Plasma Systems Inc. (2005)



Fig. 8.70 Photograph of VIPS of tungsten coating on a graphite substrate. Courtesy of the CRTP, University of Sherbrooke (1995)

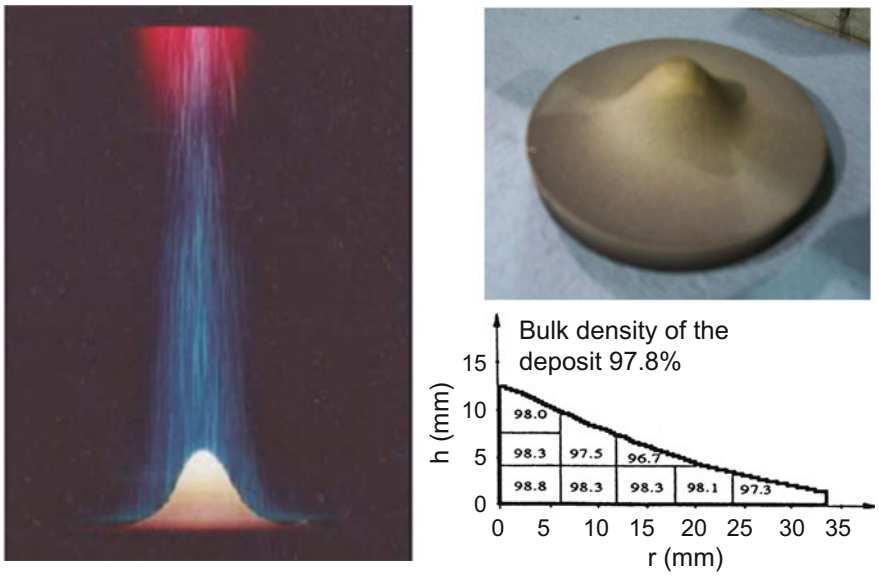


Fig. 8.71 Photograph of VIPS of tungsten on a fixed substrate and a mapping of its apparent density distribution. Plasma plate power 40 kW, chamber pressure 26.6 kPa (200 Torr), spraying distance 200 mm. After Jiang et al. [93]. Reprinted with permission of ASM International. All rights reserved

Boulos and his collaborators [91–99] made a systematic study on the induction plasma deposition of refractory metals. The study reported by Jiang et al. [93] was carried out on the deposition of tungsten on a stationary graphite substrate using a Tekna PL-50 induction plasma torch operated at power levels between 25 and 45 kW using an Ar/H_2 (9 % vol. H_2) mixture as plasma sheath gas and pure Ar as central gas. The chamber pressure was varied between 26.6 and 53.2 kPa (200 to 400 Torr). The spraying distance was varied between 175 and 300 mm, and the powder feed rates was varied between 12 and 40 g/min. A photograph of the deposit during its formation at plate power level of 40 kW, a chamber pressure of 26.6 kPa (200 Torr), and a spraying distance of 200 mm is shown on the left-hand side of Fig. 8.71. A photograph of the deposit obtained and a mapping of its apparent density is given on the right-hand side of the figure. It may be noted that the deposit density varies between 97 and 98 %, the theoretical density of tungsten with the lowest reported densities mostly observed in the fringes of the deposit. The average bulk relative density of the deposit is 97.8 %.

Figures 8.72 and 8.73 shows respectively the variation of the apparent density of the deposit, and the deposition efficiency, with the increase of the spraying distance between 180 and 300 mm, and the chamber pressure from 26.6 kPa (200 Torr) to 53.2 kPa (400 Torr). The deposition efficiency is defined as the ratio of the powder deposited on the substrate to that injected into the plasma torch. It may be noted from Fig. 8.72 that the apparent density of the deposit decreases rapidly with the increase of the spraying distance. The effect reflects the in-flight cooling and

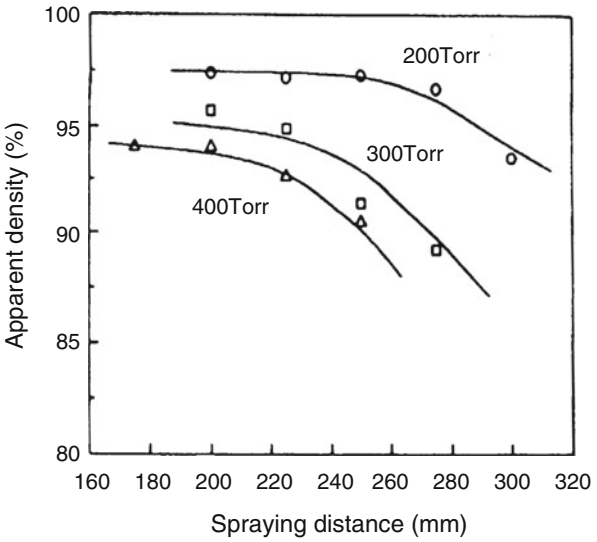


Fig. 8.72 Effect of spraying distance and the chamber pressure on the apparent density of tungsten deposit, Plasma plate power 40 kW. After Jiang et al. [93]. Reprinted with permission of ASM International. All rights reserved

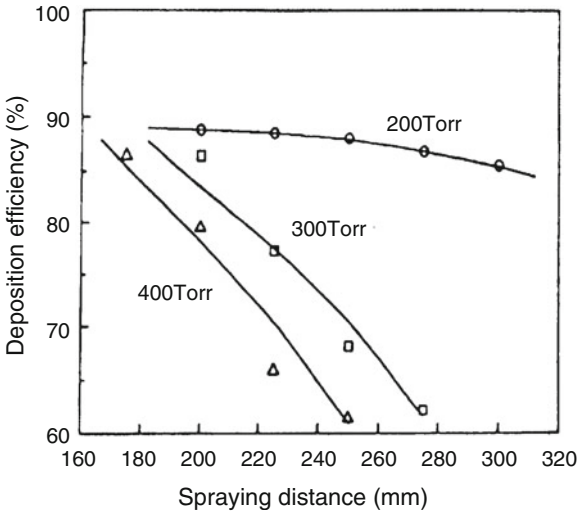


Fig. 8.73 Effect of spraying distance and the chamber pressure on the deposition efficiency of tungsten, Plasma plate power 40 kW. After Jiang et al. [93]. Reprinted with permission of ASM International. All rights reserved

eventual solidification of the powder prior to reaching the substrate. This results in the formation of porosity and defects in the coating and a drop of the deposition efficiency, which is observed in Fig. 8.73. It is important to stress that in the plasma spraying of refractory metals, the in-flight cooling of the particles is largely due to radiation cooling which is very intense at the melting/solidification temperature of such metals and can have a predominant effect on the temperature history of the particles, even during its flight in the plasma with a higher plasma temperature than that of the particle. This can be simply explained by the fact that under such conditions, the radiant heat flux from the particle to the surrounding is higher

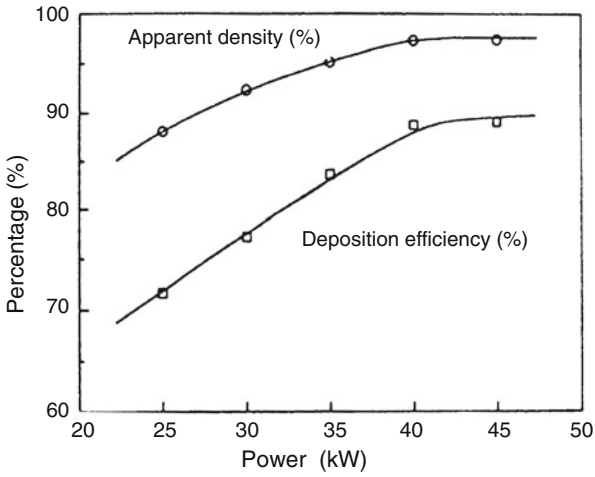


Fig. 8.74 Effect torch plate power on the apparent density and the deposition efficiency of tungsten, Plasma plate power 40 kW. After Jiang et al. [93]. Reprinted with permission of ASM International. All rights reserved

than the heat transferred by conduction and convection from the plasma to the particle. With the drop of the chamber pressure, the flight velocity of the particles increases resulting in a drop of the time of flight of the particles between the exit of the plasma torch and the substrate. The effect results in a reduction of the cooling time of the particle and a corresponding increase of the apparent density of the deposit and of the deposition efficiency even with the substrate locate at 250 or even 300 mm from the exit of the torch. The effect of the plasma power on the apparent density of the deposit obtained and the associated deposition efficiency is shown in Fig. 8.74. It is noted that, as expected, an increase of the plasma power results in a corresponding increase of the deposition efficiency and of the apparent density of the deposit obtained. It is significant to note that at high power levels, deposits of refractory metals could be obtained with apparent densities above 98 % of the theoretical density of the metal and deposition efficiencies as high as 90 %. Such levels of deposition efficiencies are very exceptional compared to those normally achieved using d.c. plasma spraying techniques.

An extended discussion of the mechanism of coating formation and its strong dependence on the individual splat formation and solidification during the induction plasma spraying has been reported by Jiang et al. [95] and Kovarik et al. [97, 98]. These underline the very important role of the substrate temperature on the splat formation mechanism and consequently on the properties of the coating obtained. The underlying mechanisms are very similar to those observed during d.c. plasma spraying and are discussed in significant details in Chap. 7.

The spatial variation of the properties of refractory metals deposits have also been the subject of study at Tekna Plasma Systems Inc by Fan et al. [99]. A typical cross section and apparent density profile for a 200-mm diameter thick tungsten disc made by VIPS on a graphite substrate is shown in Fig. 8.75. The plasma power was in this case 80 kW, the chamber pressure 40 kPa (300 Torr), and the spraying distance 100 mm. During the spraying operation, the substrate was translated

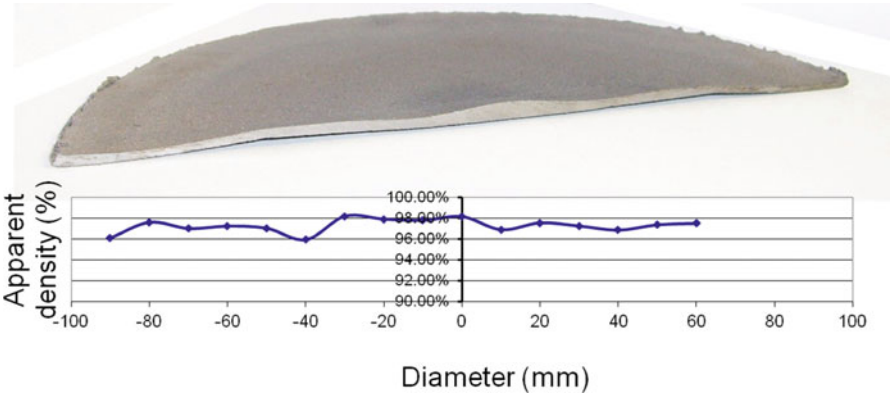


Fig. 8.75 Cross section of a 200-mm diameter tungsten disc made by VIPS on a graphite substrata and the corresponding apparent density profile. Plasma power 80 kW, Chamber pressure, 40 kPa (300 Torr), and spraying distance 100 mm. After Fan et al. Tekna plasma systems (2012)

underneath the plasma jet while being simultaneously rotated around a vertical axis. It is important to stress the need for a detailed simulation of the depositor pattern in such cases order to properly coordinate the speed of rotation and of liner translation depending on the location of the disc in the stream of the molten metal spray. The results show slight variation of the thickness of the coating across the radius of the disc, which can be improved upon by fine tuning the control of the speed of rotation and linear translation. The corresponding density variations across the disc are noted to be in the range of 96–98 % of theoretical density of tungsten. Details of metallographic microstructure of the deposit at different locations on the disc are shown in Figs. 8.76 and 8.77. The micrographs shown in Fig. 8.78 were etched in order to reveal details of the grain structure of the deposit.

The ability to use VIPS technology for the deposition of relatively thick structural discs or cylinders attracted attention for its potential use for the manufacture of near net-shaped parts for a wide range of applications. The first of such applications was in the area of solid oxide fuel cells (SOFC) where VIPS was considered to manufacture the bipolar metallic plates that separated the stacks of the different cell components as shown in Fig. 8.78 after Henne et al. [100, 101]. The results revealed, however, a strong dependence of the porosity of the coating on the spray angle. As shown in Figs. 8.79, 8.80, and 8.81 a very high level of porosity was observed with the decrease of the spray angle below 45°. The effect is not unique to induction plasma spraying since such dependence of the microstructure of coatings has equally been observed in flame and d.c. plasma spraying as well.

Numerous studies dealing with induction plasma spraying of thick coatings or near net-shaped parts have also dealt with the deposition of sputtering targets as reported by Müller et al. [102, 103]. Vacuum induction plasma spraying have also been used for the deposition of a wide range of ceramic materials such as Alumina, YSZ, and Titania as reported by Gitzhofer et al. [104], Fan et al. [105], and Branland [106–108]. These show generally comparable results as with refractory

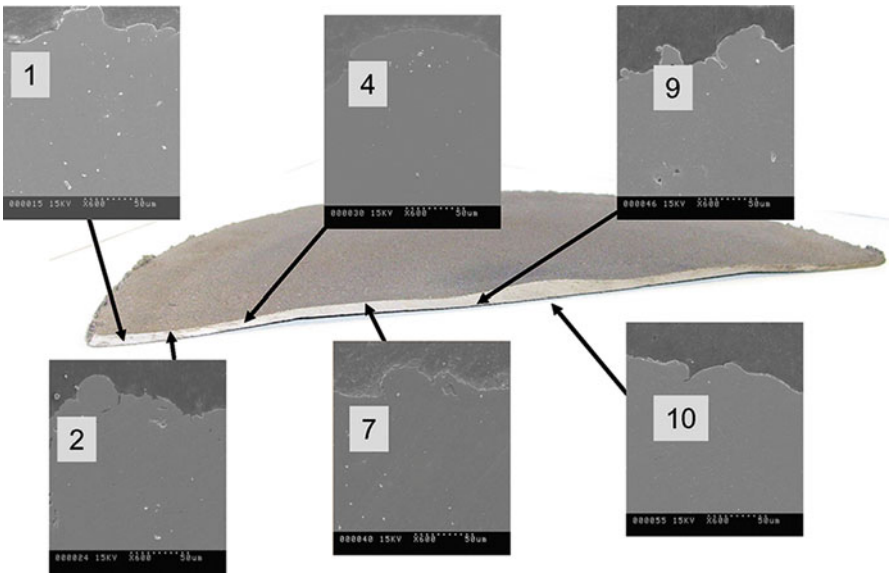


Fig. 8.76 Microstructure of a 200 mm diameter tungsten disc made by VIPS on a graphite substrata. Plasma power 80 kW, Chamber pressure, 40 kPa (300 Torr), and spraying distance 100 mm. After Fan et al. Tekna plasma systems (2012)

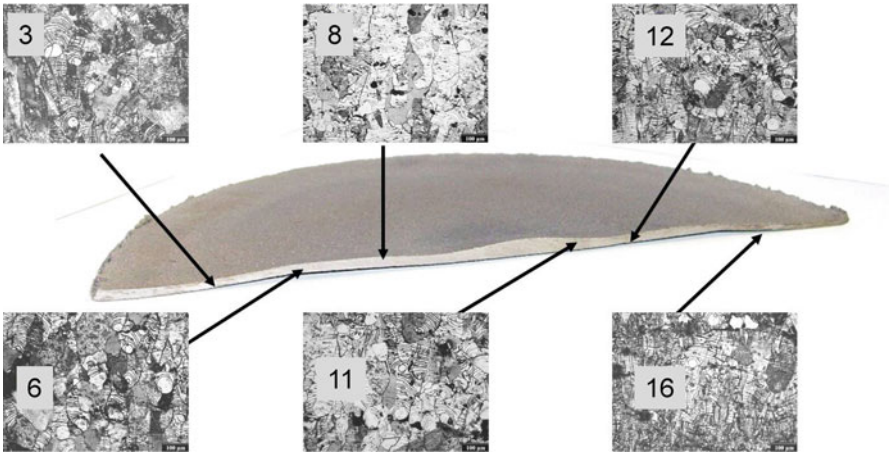


Fig. 8.77 Etched microstructure of a 200-mm diameter tungsten disc made by VIPS on a graphite substrata. Plasma power 80 kW, Chamber pressure, 40 kPa (300 Torr), and spraying distance 100 mm. After Fan et al. Tekna plasma systems (2012)

metals in terms of deposition efficiencies, but not in terms of porosity which is generally higher than the above reported values. Thick ceramic coatings are rather difficult to achieve due to important internal stresses, which develop during the cooling step of the process following the deposition of the coating.

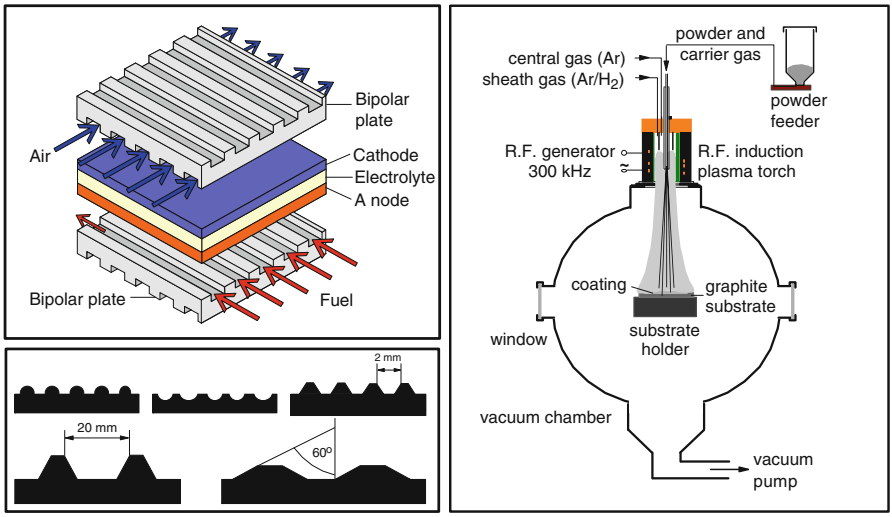


Fig. 8.78 Typical structure of a planar SOFC showing the profile of the bipolar plate (*lower left hand corner*) and induction plasma spraying system. After Henne et al. [100]. Reprinted with permission of ASM International. All rights reserved

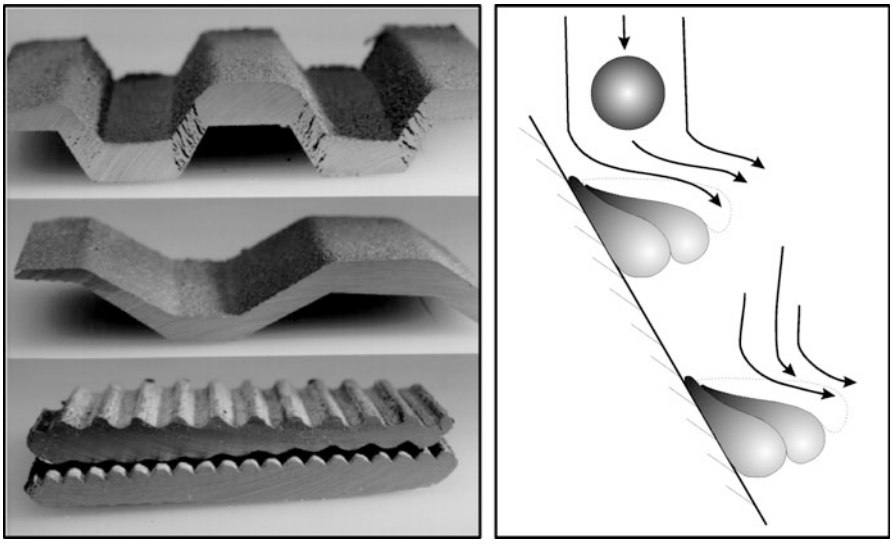


Fig. 8.79 Effect of angle of incidence on deposit formation and its properties. After Henne et al. [100]. Reprinted with permission of ASM International. All rights reserved

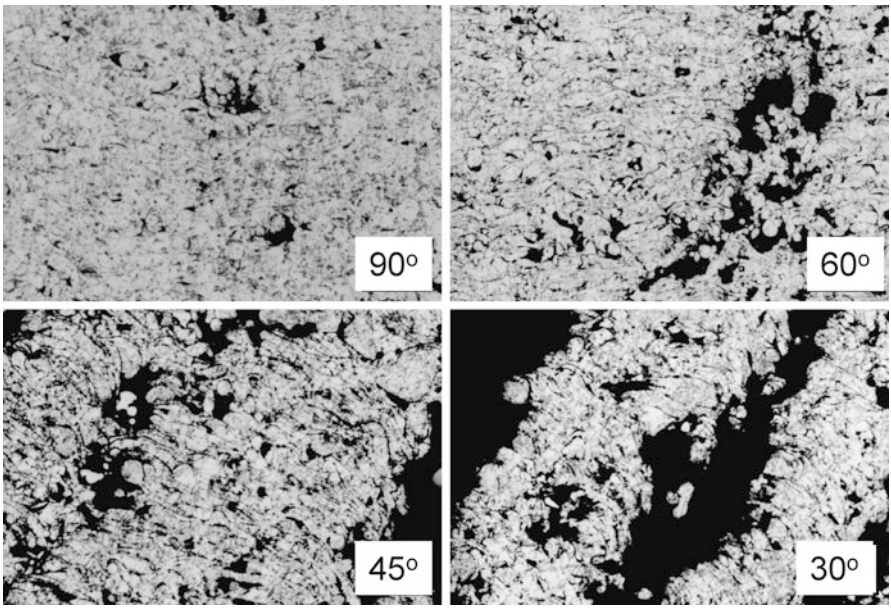


Fig. 8.80 Microstructure of coating made at different angles of incidence of the spray with respect to the substrate. After Henne et al. [100]. Reprinted with permission of ASM International. All rights reserved

8.5.3 Reactive Induction Plasma Spraying

Reactive plasma spraying is a process developed in the 1990s by which the chemical composition of the coating is modified during the coating process. This results in a coating or deposit with a different chemical composition compared to that of the feed material. The chemical transformation is known to take place, either in-flight, through the reaction of the injected particles with the plasma gas, or after the deposition through the reaction of the plasma gas with the formed deposit. In most cases it is believed that both mechanisms contribute to the process.

The studies reported by Jiang et al. [109–113] and by Pu and Boulos [114] give typical examples of the formation of carbides of tungsten, titanium, and of boron through reactive induction plasma spraying. In the study by Jiang et al. [109–113] the carbides coatings were obtained through the reaction of the corresponding metal, pure W or Ti, with a source of carbon such as CH_4 or C_2H_2. In the case of tungsten carbide deposition, the chemical route proposed goes through the formation free carbon as a result of methane thermal decomposition in the plasma, followed by the reaction between the free carbon and the metal in-flight according to the following chemical transformations.

$$CH_4(g) = C(s) + 2H_2(g)$$
$$C(s) + 2W(l) = W_2C(l)$$

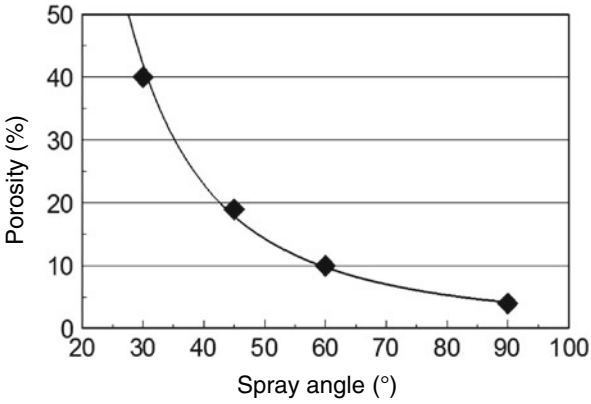


Fig. 8.81 Effect of angle of incidence (spray angle) on the porosity of the coating. After Henne et al. [100]. Reprinted with permission of ASM International. All rights reserved

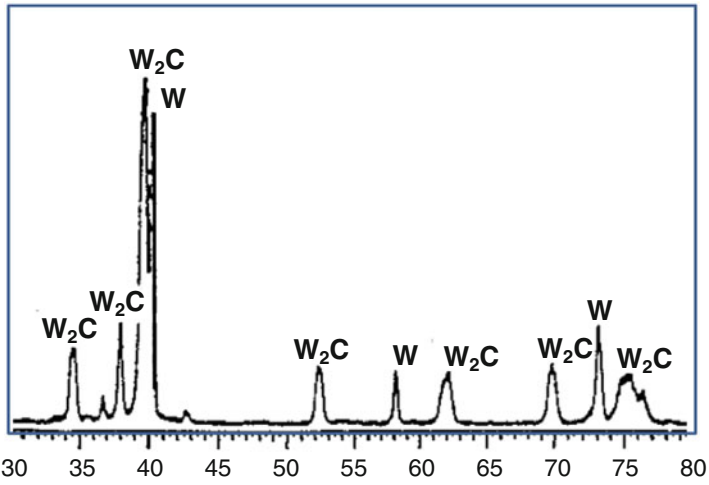


Fig. 8.82 XRD pattern of the in-flight carburized tungsten powder, after Jiang et al. [111] with kind permission

This reaction route is supported by the fact that X-ray diffraction (XRD) pattern of the powder collected, in-flight, Fig. 8.82, shows the powder constituted principally of a mixture of W and W_2C. XRD pattern of the deposit, shown in Fig. 8.83, reveals on the other hand, a continuation of the carburization reaction even after deposit formation giving rise to the transformation of the deposit to a mixture of exclusively WC and W_2C through the following chemical transformations.

$$2W(s) + C(s) = W_2C(s)$$
$$W_2C(s) + C(s) = 2WC(s)$$

A similar reaction route is proposed for the reactive deposition of titanium carbide through the reaction between titanium metal and methane according to the following chemical transformations.

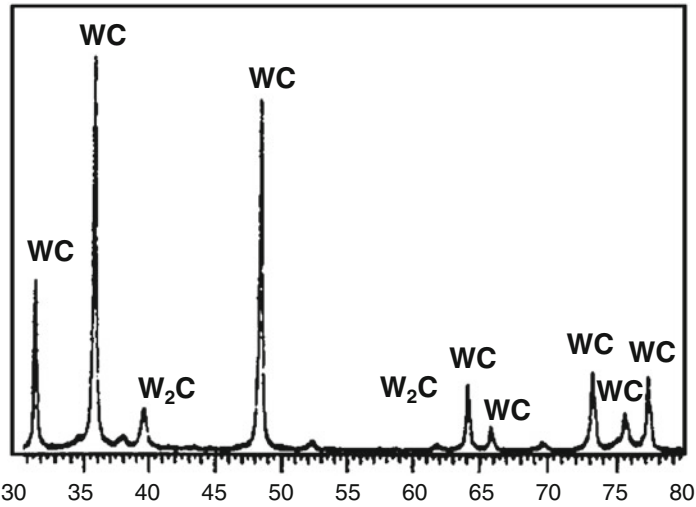


Fig. 8.83 XRD pattern of WC coating formed by in-flight reactive deposition of tungsten powder, after Jiang et al. [111] with kind permission

In-flight carburization

$$\mathrm{CH_4(g) = C(s) + 2H_2(g)}$$
$$\mathrm{Ti(l) + (1 - \mathit{x})C(s) = TiC_{(1-\mathit{x})}(l)}$$

Secondary carburization reactions of the deposit

$$\mathrm{Ti(s) + (1 - \mathit{x})C(s) = TiC_{(1-\mathit{x})}(s)}$$
$$\mathrm{TiC_{(1-\mathit{x})}(l) + \mathit{x}\,C(s) = TiC(s)}$$

These reaction steps are also supported by XRD patterns of the top and bottom of the deposit shown in Figs. 8.84 and 8.85, respectively. The observed difference in composition between the top and bottom layers of the deposit is a clear indication of the continuation of the carburization reaction in the solid state even after the deposit formation.

Pu and Boulos [115] also reported the induction plasma reactive deposition of boron carbide, B_4C. The reaction route used in this case is based on the, in-flight, carburization of boron using methane as the carburizing agent.

8.5.4 Suspension Induction Plasma Spraying

Plasma spraying with injection of a liquid with fine powders suspended in it into the plasma, known as suspension plasma spraying (SPS), was developed in the early 1990s [115]. Over the past two decades it has been increasingly used with both

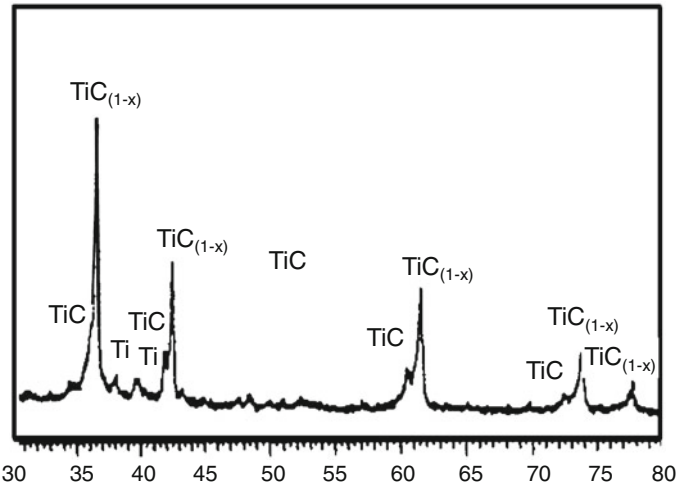


Fig. 8.84 XRD pattern of top layer of Ti/TiC(1−*x*)/TiC coating formed by in-flight reactive deposition of titanium powder, after Jiang et al. [111] with kind permission

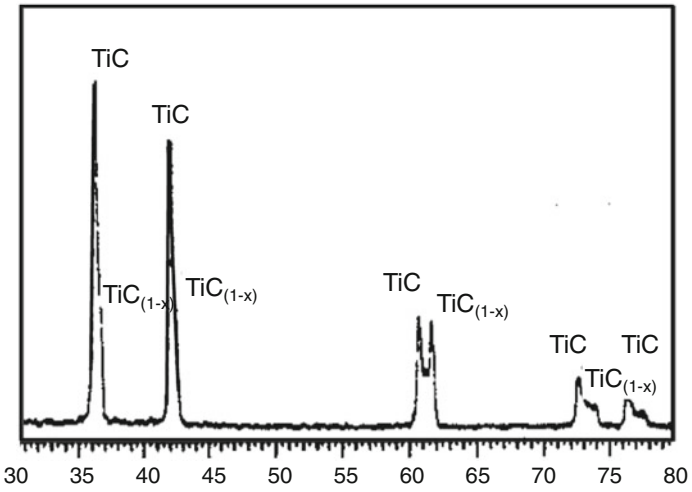


Fig. 8.85 XRD pattern of bottom layer of TiC(1−*x*)/TiC coating formed by in-flight reactive deposition of titanium powder. After Jiang et al. [111] with kind permission

induction and d.c. plasmas spraying operations for the deposition of heat sensitive and nanostructured coatings and materials. The technique will be discussed in detail in Chap. 14. Here, only the concept will be outlined how SPS is working with r.f. induction plasma torches, using the deposition of hydoxyapatite (HA) as an example. Bouyer et al. [116] though [117] have reported numerous publications on

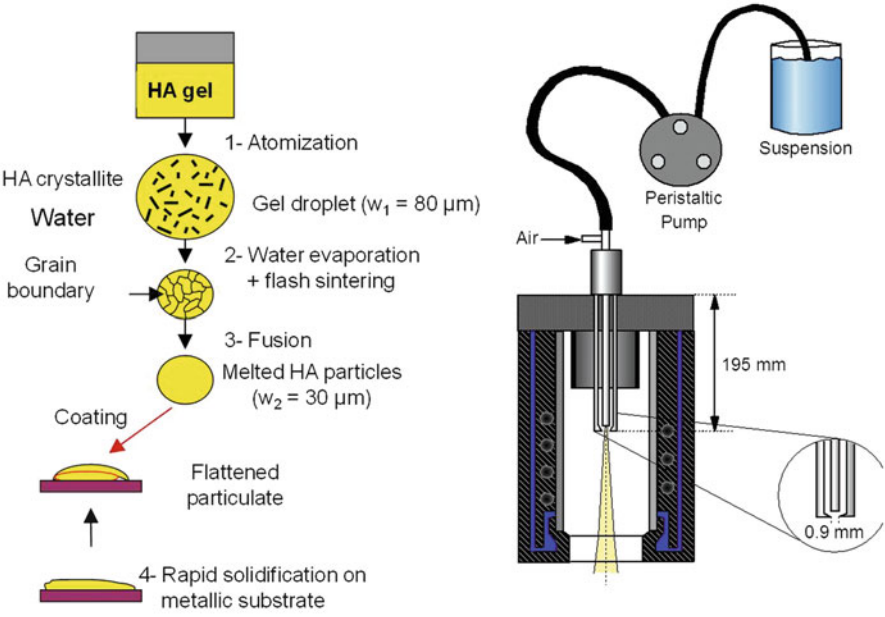


Fig. 8.86 Suspension plasma spraying of hydroxyapatite (HA). *Left*, illustration of the process scheme; *right*, schematic of an experimental setup. After Bouyer et al. [118] with kind permission

the subject. As shown in Fig. 8.86 the aqueous suspension of HA crystals is transported into the atomization probe using a peristaltic pump. An atomizing gas is guided to the probe tip separately from the liquid, and atomization takes place at the probe tip. The atomized droplets have typically diameters in the range of 80 µm. In the plasma, the water evaporates and the agglomerated HA crystals fuse into spherical molten droplets with typical diameters of 30 µm. These molten HA droplets can be allowed to freeze in-flight, forming a dense spherical powder as shown in Fig. 8.87. Alternately they can be directed toward a substrate where they form a coating through the impact, flattening and freezing of the individual droplets on the substrate.

Compared to d.c. suspension plasma spraying, it is easy in induction plasma spraying to bring the suspension into the discharge with the central injection probe, and the atomization is carried out locally through the use of an independently controlled atomizing gas stream. In contrast, the atomization of the suspension in d.c. plasma spraying is carried out by the intense shear of the plasma flow at the point of injection of the suspension into the jet.

Typical results of HA coatings obtained using SPS techniques in an induction plasma torch are given in Fig. 8.88. On the top left-hand side of the figure, micrographs of the HA crystals in the suspension are shown, while micrographs of the coating formed are shown on the bottom left-hand side of the figure. On the right-hand side of the same figure a XRD patter of the, as synthesized, HA crystals is given, while the XTD pattern of the HA coating is shown on the bottom right-hand

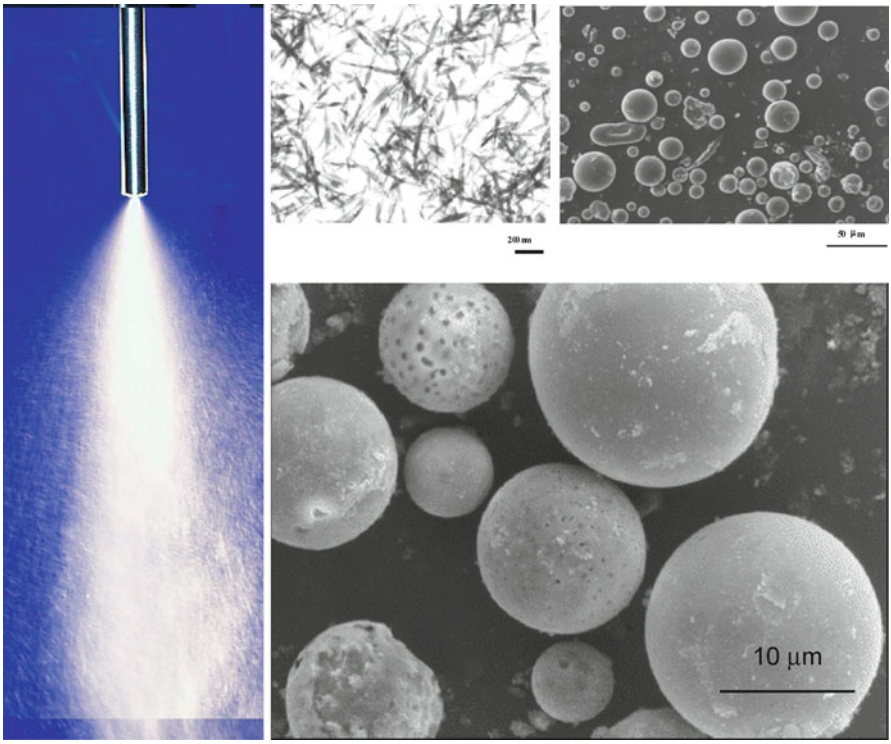


Fig. 8.87 Suspension plasma spraying of hydroxyapatite (HA). *Left*, photograph of atomized jet; *right*, electron micrographs of the HA crystals and SPS formed dense solid HA powders. After Bouyer et al. [118] with kind permission

side of the figure. It may be noted that the HA, which is known to be a rather heat sensitive materials, suffers from minor decomposition as identified by the Tri-Calcium Phosphate (αTCP) and Calcium oxide (CaO) peaks observed in the XRD pattern.

Other examples of applications of SPS using induction plasmas have been reported by Müller et al. [119–121] for the deposition of heat sensitive perovskites for solid oxide fuel cells and spinels for alkaline water electrolysis.

8.5.5 Supersonic Induction Plasma Spraying

Supersonic induction plasma spraying can be achieved though the addition of a converging–diverging Laval nozzle to the plasma torch as previously described in Sect. 8.2.3.3. Typical temperature and velocity profiles in the jet are given in Figs. 8.21, 8.22, and 8.23. A photograph of a supersonic induction plasma spray jet in the presence of fine Yttria-Stabilized Zirconia (YSZ) powder is shown

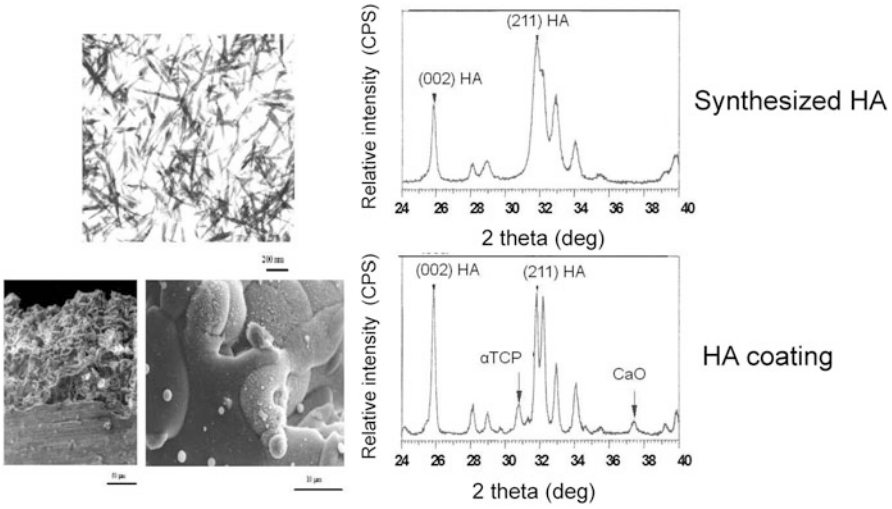


Fig. 8.88 *Left*, electron micrographs of HA crystals and of deposits made using induction plasma SPS. *Right*, XRD of as-synthesized HA crystals and XRD of HA coating. After Bouyer et al. [118] with kind permission

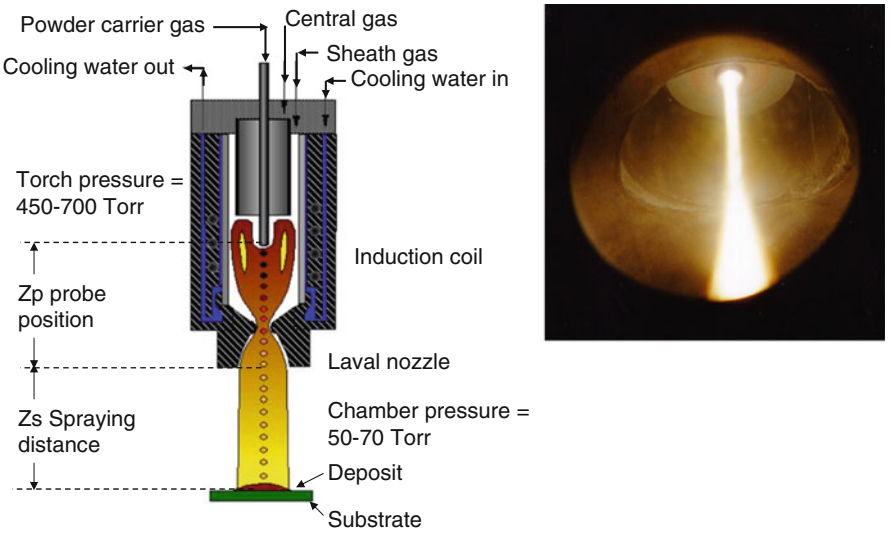


Fig. 8.89 Supersonic induction plasma spraying setup and photograph of the plasma jet in the presence of YSZ powder during a plasma spraying operation. After Mailhot et al. [122]. Reprinted with permission of ASM International. All rights reserved

in Fig. 8.89. Numerous publications on the subject were reported by Mailhot et al. [122–125] and Theophile et al. [126] in connection with a study for the deposition of high density YSZ thin membrane which could be used as an electrolyte for solid oxide fuel cells (SOFC). The plasma gas in this case was a mixture of

Ar/Air (Sheath = 68 slm Air, Central = 21.9 slm Ar, and powder = 0.83 slm Ar), and the YSZ powder feed rate was limited to a few g/min. The chamber pressure was 6.6 kPa and spraying distance of 250 mm. In order to avoid the development of excessive residual stresses in the coating and risk its cracking, the torch power was modulated starting at 30 kW during a 30s preheating step, followed by powder deposition for 10 s at 40 kW, before dropping the torch power to 16 kW for 30 s during the final deposit cooling step. Microscopic observation of the coating sections showed apparent porosity of the coating in the range of 1.15–1.75 % which was consistent with apparent density measurements of the bulk coating using buoyancy measurement techniques. The corresponding apparent porosity of the coating based on bulk density measurement was in the range of 1.31–1.9.

8.6 Summary and Conclusions

Induction plasmas have emerged over the past three or four decades as a potentially powerful tool for materials processing whether for powder spheroidization and densification or nanopowder synthesis. Vacuum induction plasma spraying has also found limited applications for the deposition of protective coating and near net-shaped parts. The main limitation of the technology stems from the fact that the plasma torch cannot be easily translated with respect to the substrate. Rather, the substrate has to be translated with respect to the torch. This resulted in limiting the use of induction plasma technology on an industrial scale to powder processing and the coating of small parts. In this chapter a review is presented of the main design features of induction plasma torches and vacuum induction plasma deposition systems. A description is provided of the main characteristics of the flow and temperature fields in the discharge and of plasma–particle interactions under dense loading conditions. These reviled the predominantly large volume, low velocity nature of the discharge, which allows for a long contact time between the plasma and the particles. These served well for the melting of relatively larger particles compared to d.c. plasma spraying. The absence of electrodes offered the added flexibility of powder treatment of a wide range of chemistries under inert, oxidizing, or reducing atmosphere. Typical examples are given for the use of induction plasma technology for the VIPS, reactive plasma spraying, suspension plasma spraying, and supersonic induction plasma spraying of materials.

Nomenclature

Latin Alphabet

$\vec{A}$ Magnetic vector potential ( )

c Speed of light in space $c = 299{,}792{,}458$ (m/s)

c_p Specific heat (J/K kg)
$\vec{D}$ Electric displacement (C/m^2)
D_j The mass diffusivity of species j in the mixture ( )
E Electric field (V/m
$\vec{E}$ Electric field vector (V/m)
f Oscillator frequency (Hz)
F_r Radial component of Lorentz force (N)
F_z Radial component of Lorentz force (N)
h Total enthalpy of mixture (J/kg)
h_j The specific enthalpy of species j (J/kg)
$\vec{H}$ Magnetic field vector (T)
j Current density (A/m^2)
I_c Coil current (A)
I_{im} Applied coil current (A)
I_{in} Induced current in the coil due to plasma electromagnetic fields (A)
$\vec{J}$ Magnetic flux density vector (W/m^2)
J_{jr} Diffusion flux of species j in radial direction ( )
J_{jz} Diffusion flux of species j in axial direction ( )
k Molecular thermal conductivity (W/m K)
k_e Effective thermal conductivity (W/m K)
k_t Turbulent thermal conductivity (W/m K)
L_c Coil length (m)
M_i Molecular weight of species i (kg/mole)
n_c Coil number of turns
p Pressure (Pa)
P Local energy generation through ohmic heating, $P = \sigma|E|^2$ (W/m^3)
P_v Viscous power dissipation, $P_v = -\nabla \cdot \left(\vec{\tau} \cdot \vec{V}\right)$ (W/m^3)
r_c Internal radius of the induction coil (m)
r_n Radius of equivalent cylindrical load of discharge (m)
r_o Internal radius of the plasma confining tube (m)
R Local volumetric radiation heat losses (W/m^3)
R_j Local volumetric radiation heat losses of species j (W/m^3)
u Axial velocity component (m/s)
v Radial velocity component (m/s)
w Tangential velocity component (m/s)

Greek Alphabet

δ_t Thickness of *skin depth* (m)
ε Dielectric constant (permittivity) of materials $\varepsilon = \varepsilon_0\varepsilon_r$ (Farad/m)
ε_0 Dielectric constant of free space ($\varepsilon_0 = 8.854 \times 10^{12}$) (Farad/m)
ε_r Relative dielectric constant.

φ Free charge density (C/m^3)
Ω_D Diffusion collision integral ( )
η_c Energy coupling efficiency
κ Coupling parameter, $\kappa = \sqrt{2}.r_n/\delta_t$
μ_o Magnetic permeability of the medium (Hy/m)
μ Magnetic permeability of materials $\mu = \mu_0\mu$ (H/m)
μ_o Magnetic permeability of vacuum $\mu_0 = 4\pi \times 10^7$ (H/m)
$_r\mu$ Relative magnetic permeability
μ Molecular viscosity (Pa s)
μ_e Effective viscosity (Pa s)
μ_t Turbulent viscosity (Pa s)
σ_o Electrical conductivity of equivalent load (mho/m) or A/(V m)
ρ Mass density (kg/m^3)

References

1. Dresvin SV (1977) Physics and technology of low temperature plasmas. Iowa State Univ Press, Ames
2. Dresvin SV (1993) The fundamentals of theory and design of HF plasma generators (Translated from Russian)
3. Eckert HU (1974) The induction arc: a state-of-the-art review. High Temp 6:99–134
4. Boulos MI (1985) The inductively coupled r.f. plasma. Pure Appl Chem 57:1321–1352
5. Boulos MI, Induction RF (1992) Plasma spraying, state-of-the-art review. J Therm Spray Technol 1:33–40
6. Boulos MI (1992) Radio-frequency plasma developments, scale-up and industrial applications. J High Temp Chem Proc 1:401–411
7. Boulos MI (1997) The inductively coupled radio frequency plasma. High Temp Mater Process 1:17–39
8. Babat GI (1947) Electrodeless discharges and some allied problems. J Inst Elec Eng 94:27–37
9. Reed TB (1961) Induction coupled plasma torch. J Appl Phys 32:821–824
10. Reed TB (1961) Growth of refractory crystals using the induction plasma torch. J Appl Phys 32:2534–2536
11. Reed TB (1963) Heat transfer intensity from induction plasma flames and oxy-hydrogen flames. J Appl Phys 34:2266–2269
12. Davies J, Simpson P (1979) Induction heating handbook. McGraw Hill, London
13. Zinn S, Semiatin SL (1988) Elements of induction heating. EPRI and ASM International, Palo Alto, CA
14. Freeman MP, Chase JD (1968) Energy-transfer mechanism and typical operating characteristics for the thermal RF plasma generator. J Appl Phys 39:180–190
15. Chase JD (1969) Magnetic pinch effect in the thermal r.f. induction plasma. J Appl Phys 40:318–325
16. Eckert HU (1971) Measurement of the r.f. magnetic field distribution in a thermal induction plasma. J Appl Phys 42:3108–3113

17. Eckert HU (1972) Dual magnetic probe system for phase measurements in thermal induction plasmas. J Appl Phys 43:2707–2713
18. Mensing AE, Boedeker LR (1968) Theoretical investigations on RF induction heated plasmas. NASA CR-1312, 1-75. NASA, Springfield, VA
19. Poole JW, Greeman MP, Doak KW, Thorpe ML (1973), Simulator tests to study hot-flow problems related to a gas core reactor, NASA-CR 2309
20. Thorpe ML, Scammon LW (1968) Induction plasma heating: high power, low frequency operation and pure hydrogen heating, NAS 3-9375. NASA, Cleveland, OH
21. Boulos MI, Jurewicz J (1999) High Performance induction plasma torch with a water-cooled ceramic confinement tube. US Patent, 5,200,595 (April 6, 1993), International Patent Application, PCT/CA92/00156 (April 10, 1992), Japanese Patent, 3,169,962 (March 16, 2001), Canadian Patent, 2,085,133 (April 10, 1992), Chinese Patent, ZL92103380.X (April 11, 1996), European Patent, 533884 (January 22, 1997), Korean Patent, 203,994, 25 Mar 1999
22. Boulos MI, Jurewicz J (1996) Liquid film stabilized induction plasma torch. US Patent, 5,560,844, 1 Oct 1996
23. Boulos M, Jurewicz J (2004) Multi-coil induction plasma torch for solid state power supply. US patent 6,693,253, 17 Feb 2004
24. Boulos M, Jurewicz J (2005) Multi-coil induction plasma torch for solid state power supply. US patent 6,919,527, 19 July 2005
25. Yoshida T, Nakagawa K, Harada T, Akashi K (1981) New design of a radio frequency plasma torch. Plasma Chem Plasma Process 1:113–129
26. Yoshida T, Tawi T, Nishimura H, Akashi K (1983) Characterization of a hybrid plasma and its application to a chemical synthesis. J Appl Phys 54:640–646
27. Kameyama T, Sakanaka K, Motoe A, Tsunoda T, Nakanaga T, Wakayama NI, Takeo H, Fukuda K (1990) Highly efficient and stable radio-frequency thermal plasma system for the production of ultrafine and ultrapure *B*-SiC powder. J Mat Sci 25(2):1058–1065
28. Takeyama T, Fukuda K (1986) Development of an all solid state R.F.-R.F. Thermal plasma reactor. National Chemical Laboratory for Industry, Internal report, vol 21, p 4
29. Douglas TS (1974) Radial temperature profiles in an R.F. plasma over a wide range of applied magnetic flux intensities: theory and experiments. Ph.D. Thesis, Georgia Institute of Technology
30. Klubnikin VS (1975) Thermal and gas dynamic characteristics of an argon induction discharge. High Temp 13:439–446
31. Chase JD (1971) Theoretical and experimental investigation of pressure and flow in induction plasmas. J Appl Phys 42:4870–4879
32. Hollenstein M, Rahman M, Boulos M (1999) Aerodynamic study of the supersonic induction plasma jet, ISPC-14. Czech Republic, 2–6 Aug 1999
33. Léveillé V (2002) Diagnostic du jet de plasma hf supersonique. Université de Sherbrooke, M. Sc.A thesis
34. Léveillé V, Gravelle DV, Boulos MI (2003) Diagnostic study of supersonic plasma flows using enthalpy probe, schlieren and high speed photography. In: International thermal spray conference (ITSC 2003), Orlando, FL
35. Dundas PH (1971) Induction plasma heating, measurement of gas concentrations, temperatures and stagnation head in a binary plasma system. NASA-CR 1527
36. Boulos MI (2001) Visualization and diagnostics of thermal plasma flows. J Vis 4:19–28
37. Soucy G, Jurewicz J, Boulos MI (1994) Mixing study of the induction plasma reactor: part I – axial injection mode. J Plasma Chem Plasma Process 14:43–57
38. Soucy G, Jurewicz J, Boulos MI (1994) Mixing study of the induction plasma reactor: part II – radial injection mode. J Plasma Chem Plasma Process 14:59–71
39. Rahmane M, Soucy G, Boulos MI (1994) Mass transfer in induction plasma reactors. Int J Heat Mass Transfer 37:2035–2046

40. Rahmane M, Soucy G, Boulos MI (1996) Diffusion phenomena of a cold gas in thermal plasma stream. J Plasma Chem Plasma Process 16:169S–189S
41. Eckert HU (1970) Analysis of thermal induction plasma dominated by radial conduction losses. J Appl Phys 41:1520–1527
42. Miller RC, Ayen RJ (1969) Temperature profiles and energy balances for an inductively coupled plasma torch. J Appl Phys 40:5260–5273
43. Boulos MI (1976) Flow temperature field in the fire ball of an inductively coupled plasma. IEEE Trans Plasma Sci PS-4:28–39
44. Boulos MI (1978) Heating of powders in the fire ball of an induction plasma. IEEE Trans Plasma Sci PS-6:93–106
45. Boulos MI, Gagné M, Barnes RM (1980) Computer modelling of an inductively coupled plasma. Can J Chem Eng 58:365–381
46. Mostaghimi J, Proulx P, Boulos MI (1984) Parametric study of the flow and temperature fields in inductively coupled plasma torch. Plasma Chem Plasma Process 4:199–217
47. Proulx P, Mostaghimi J, Boulos MI (1985) Plasma-particle interaction effects in induction plasma modelling under dense loading conditions. Int J Heat Mass Transfer 28:1327–1336
48. Mostaghimi J, Proulx P, Boulos MI (1985) An analysis of the computer modelling of the flow and temperature fields in an inductively coupled R.F. plasma torch. J Numer Heat Transfer 8:187–201
49. Mostaghimi J, Proulx P, Boulos MI (1987) A two-temperature model of the inductively coupled R.F. plasma. J Appl Phys 61:1753–1760
50. Proulx P, Mostaghimi J, Boulos MI (1987) Heating of powders in an R.F. inductively coupled plasma under dense loading conditions. J Plasma Chem Plasma Process 7:29–53
51. Mostaghimi J, Boulos MI (1989) Two-dimensional electromagnetic field effects in inductively coupled plasmas. Plasma Chem Plasma Process 9:25–44
52. El-Hage M, Mostaghimi J, Boulos MI (1989) A turbulent flow model for the R.F. inductively coupled plasma. J Appl Phys 65:4178–4185
53. Mostaghimi J, Boulos MI (1990) Effect of frequency on local thermodynamic equilibrium conditions in an inductively coupled argon plasma at atmospheric pressure. J Phys D Appl Phys 68:2643–2648
54. Proulx P, Mostaghimi J, Boulos MI (1990) Loading and radiation effects in plasma jet modelling. Journal de Physique 51:263–270
55. Proulx P, Mostaghimi J, Boulos MI (1991) Radiative effects in ICP modelling. Int J Heat Mass Transfer 31:2571–2579
56. Chen K, Boulos MI (1994) Turbulence in induction plasma modeling. J Phys D Appl Phys 27:946–952
57. Chen X, Merkhouf A, Boulos MI (1996) Preliminary study of the 3-equation turbulence model of an R.F. plasma torch. In: Proceedings of the 3rd Asia-Pacific conference on plasma science and technology, vol 1, Tokyo, Japan, pp 71–76
58. Merkhouf A, Ye R, Proulx P, Boulos MI (1997) Mathematical modeling of plasma systems. In: Proceedings of the Julian Szekely memorial symposium on materials processing, Boston, MA, pp 509–552
59. Merkhouf A, Boulos MI (1998) Integrated model for the radio-frequency induction plasma torch and power supply. Plasma Sources Sci Technol 7:599–606
60. Merkhouf A, Boulos MI (2000) Distributed energy analysis for an integrated radio frequency induction plasma system. J Phys D Appl Phys 33:1581–1587
61. Ye R, Proulx P, Boulos MI (1999) Turbulence phenomena in the RF induction plasma torch. Int J Heat Mass Transfer 42:1585–1595
62. Ye R, Proulx P, Boulos MI (2000) Particle turbulent dispersion and loading effects in an inductively coupled radio frequency plasma. J Phys D Appl Phys 33:2154–2162
63. Selezneva S, Boulos MI (2001) Supersonic induction plasma jet modelling. Nucl Inst Methods Phys Res B180:306–311

64. Selezneva S, Sember V, Gravelle DV, Boulos MI (2002) Spectroscopic validation oft the supersonic plasma jet model. J Phys D Appl Phys 35:1338–1349
65. Xue S, Proulx P, Boulos MI (2001) Extended – field electromagnetic model for the inductively coupled plasma. J Phys D Appl Phys 34:1897–1906
66. Xue S, Proulx P, Boulos MI (2003) Effect of coil angle in an inductively couple plasma torch: a novel two-dimensional model. Plasma Chem Plasma Process 23:245–263
67. Xue S, Proulx P, Boulos MI (2002) Modelling the effect of ferrite on an inductively coupled plasma torch. Part 1: infinite ferrite permeability. J Phys D Appl Phys 35:1123–1130
68. Xue S, Proulx P, Boulos MI (2002) Modelling the effect of ferrite on an inductively coupled plasma torch. Part 2: finite ferrite permeability. J Phys D Appl Phys 35:1131–1140
69. Kim J, Mostaghimi J, Iravani R (1997) Performance analysis of RF Induction plasma generator using non-linear state approach. IEEE Trans Plasma Sci 25:1023–1028
70. Fouladgar J, Chentouf A, Develey G (1993) The calculation of the impedance of an induction plasma installation by a hybrid finite-element boundary-element method. IEEE Trans Magn 29:2479–2481
71. Bernardi D, Colombo V, Ghedini E, Mentrelli A (2003) Three-dimensional modelling of inductively coupled plasma torches. Eur Phys J D 22:119–125
72. Bernardi D, Colombo V, Ghedini E, Mentrelli A (2003) Comparison of different techniques for the FLUENT-based treatment of the electromagnetic field in inductively-coupled plasma torches. Eur Phys J D 27:55–72
73. Bernardi D, Colombo V, Ghedini E, Mentrelli A, Trombetti T (2004) 3-D numerical simulation of fully-coupled particle heating in ICPTs. Eur Phys J D 28:423–433
74. Bernardi D, Ghedini E, Colombo V (2004) Three dimensional modelling of inductively coupled plasma torches: comparison with experiments and applications. Czech J Phys 54: C489–C515
75. Bernardi D, Colombo V, Ghedini E, Mentrelli A (2004) Numerical simulation for the characterization of operating conditions of RF-RF hybrid plasma torches. Eur Phys J D 28:399–422
76. Bernardi D, Colombo V, Ghedini E, Mentrelli A (2005) 3-D turbulent modeling of an ICPT with detailed gas injection section. IEEE Trans Plasma Sci 33:426–427
77. Bernardi D, Colombo V, Ghedini E, Mentrelli A (2005) Three-dimensional modeling of inductively coupled plasma torches. Pure Appl Chem 77:359–372
78. Colombo V, Ghedini E (2007) 3-D modeling of ICP torches. High Temp Mater Proc 11:283–296
79. Colombo V, Ghedini E, Sanibondi P (2009) Two-temperature thermodynamic and transport properties of argon-hydrogen and nitrogen-hydrogen plasmas. J Phys D Appl Phys 42 (055213):1–12
80. Colombo V, Ghedini E, Sanibondi P (2010) A three-dimensional investigation of the effects of excitation frequency and sheath gas mixing in an atmospheric-pressure inductively coupled plasma system. J Phys D Appl Phys 43(105202):1–14
81. Colombo V, Ghedini E, Sanibondi P (2010) Three-dimensional investigation of particle treatment in a RF thermal plasma with reaction chamber. Plasma Sources Sci Technol 19 (065024):1–13
82. Colombo V, Concetti A, Ghedini E, Gherardi M, Sanibondi P (2011) 3-D time-dependent large eddy simulation of turbulent flows in an inductively coupled thermal plasma torch with reaction chamber. IEEE Trans Plasma Sci 39:2894–2895
83. Birds RB (1960) Transport phenomena. Wiley, New York
84. Hirschfelder JO, Curtiss CF, Byron Bird R (1967) Molecular theory of gases and liquids. Wiley, New York
85. Kuo KKY (1986) Principles of combustion. Wiley, New York
86. Xue S, Murphy AD, Proulx P, Boulos MI (2005) A thermal and chemical non-equilibrium model for multi-component Ar-H_2 plasma. In: International thermal spray conference & exposition (ITSC 2005), Basel, Switzerland, 2–4 May 2005

87. Murphy TB (2000) Transport Coefficients of Hydrogen and Argon–Hydrogen Plasmas, Plasma Chem Plasma Process, **20**, 279–297
88. Boulos MI, Fauchais P, Pfender E (1994) Thermal plasmas, fundamentals and applications, vol 1. Plenum, New York, NY
89. Crowe CT, Sharma MP, Stock DE (1977) The particle-source-in-cell (PSI-Cell) model for gas-droplet flows. J Fluids Eng 99:325–332
90. Berthou H, Neumann V, Hintermann HE (1993) High frequency, inductively coupled plasma torch for pure and doped silica deposition. Surf Coat Technol 61:1164–170
91. Jiang XL, Fan X, Gitzhofer F, Boulos MI (1992) Induction plasma spraying of refractory materials. In: International thermal spraying conference, Orlando, FL, pp 39–44
92. Jiang XL, Tiwari R, Gitzhofer F, Boulos MI (1993) Plasma deposition of refractory metals. In: 5th national thermal spray conference – NTSC'93, Anaheim, CA, pp 309–313
93. Jiang XL, Tiwari R, Gitzhofer F, Boulos MI (1993) On the induction plasma deposition of tungsten metal. J Therm Spray Technol 2:265–270
94. Jiang XL (1994) Induction plasma spraying of refractory metals. Université de Sherbrooke, Ph.D
95. Jiang XL, Boulos MI (2001) Particle melting, flattening and stacking behaviors in induction plasma deposition of tungsten. Trans Nonferrous Metal Soc China 11:811–816
96. Jiang XL, Gitzhofer F, Boulos MI (2004) Plasma spray forming of tungsten coatings on copper electrodes. Trans Nonferrous Met Soc China 14:835–839
97. Kovarik, Xue OS, Fan X, Boulos MI (2006) R.F. plasma deposition of refractory metals: case study for tungsten. ITSS-2006, Seattle, WA
98. Kovarik, Fan OX, Boulos MI (2007) In-flight properties of W particles in an Ar-H_2 plasma. J Therm Spray Technol 16:229–237
99. Fan X, Boulos M (2004) Nesr net shape forming of tungsten material by induction plasm deposition. ITSS 2005, Basel, Switzerland
100. Henne R, Müller M, Pross E, Schiller G, Gitzhofer F, Boulos MI (1999) Near-net-shape forming of metallic bipolar plates for planar solid oxide fuel cells by induction plasma spraying. J Therm Spray Technol 8:110–116
101. Henne R, Müller M, Pross E, Schiller G, Boulos MI, Gitzhofer F (1997) Near-net-shape production of metallic bipolar plates for solid oxide fuel cells (SOFC) by induction plasma spraying. In: 14th international plansee seminar, Austria, vol 1, pp 231–245
102. Müller M., Heinmann RB, Gitzhofer F, Boulos MI (1995) Manufacture of thick chromium coatings by R.F. plasma spraying for PVD sputter targets. In: 8th national thermal spray conference – NTSC'95, Houston, TX, pp 567–572
103. Müller M, Heinmann RB, Gitzhofer F, Boulos MI, Schwarz K (2000) Radio frequency plasma processing to produce chromium sputter targets. J Therm Spray Technol 9:488–493
104. Gitzhofer F, Coulombe S, Fan X, Jiang XL, Boulos MI (1994) Particle splats study and induction plasma spraying of alumina and refractory metals. In: International symposium on heat and mass transfer under plasma conditions, Izmir, Turkey, pp 557–565
105. Fan X, Gitzhofer F, Boulos MI (1998) Investigation of alumina splats formed in the induction plasma process. J Therm Spray Technol 7:197–204
106. Branland N, Meillot E, Fauchais P, Vardelle A, Gitzhofer F, Boulos MI (2003) Study of RF and DC plasma-sprayed TiO_2 coatings: electrical properties and microstructure. In: International thermal spray conference (ITSC 2003), Orlando, FL
107. Branland N, Meillot E, Fauchais P, Vardelle A, Boulos MI, Gitzhofer F, Drouin D, Magny P (2003) Relationships between induction plasma spraying parameters and TiO2 particle characteristics at impact. In: 16th international symposiun on plasma chemistry (ISPC-16), Taormina, Italy
108. Branland N, Meillot E, Fauchais P, Vardelle A, Gitzhofer F, Boulos M (2006) Relationships between microstructure and electrical properties of RF and DC plasma-sprayed titania coatings. J Therm Spray Technol 15:53–62

109. Jiang XL, Gitzhofer F, Boulos MI (1994) Induction plasma reactive deposition of WC and TiC. In: 3rd European congress on thermal plasma processing – TPP-3, Aachen, Germany
110. Jiang XL, Gitzhofer F, Boulos MI, Tiwari R (1994) Induction plasma reactive deposition of tungsten and titanium carbides. In: 7th national thermal spray conference, Boston MA, pp 451–456
111. Jiang XL, Tiwari R, Gitzhofer F, Boulos MI (1995) Reactive deposition of tungsten and titanium carbides by induction plasma. J Mater Sci Lett 30:2325–2328
112. Jiang X-L, Boulos MI (2001) Effect of process parameters on induction plasma reactive deposition of tungsten carbide from tungsten metal powder. Trans Nonferrous Met Soc China 11(5):639–643
113. Jiang XL, Boulos MI (2004) Synthesis of titanium carbide by induction plasma reactive spray. Trans Nonferrous Met Soc China 14(1):15–19
114. Pu W, Boulos MI. Induction plasma spraying of boron carbide coating. In: International thermal symposium conference (ITSC-2004), Osaka, Japan
115. Gitzhofer F, Bouyer E, Boulos MI. Suspension plasma spray deposition. In: International Patent Application, PCT/CA95/00493 (28 Aug 1995), USA Patent, 5,609,921 (11 Mar 1997)
116. Bouyer E, Gitzhofer F, Boulos MI (1995) Suspension plasma spraying of hydroxyapatite. In: 12th international symposium on plasma chemistry – ISPC-12, Minneapolis, MN, vol 2, pp 865–870
117. Bouyer E, Gitzhofer F, Boulos MI (1997) The suspension plasma spraying of bioceramics by induction plasma. J Mater Sci Lett 49:58–62
118. Bouyer E, Gitzhofer F, Boulos MI (1997) Suspension plasma spraying for hydroxyapatite powder preparation by R.F. plasma. IEEE Trans Plasma Sci 25(5):1066–1072
119. Müller M, Schiller G, Gitzhofer F, Boulos MI (1997) Suspension plasma spraying for the preparation of perovskite powders and coatings. In: 1997 national thermal spray conference, Indianapolis, IN
120. Müller M, Schiller G, Gitzhofer F, Boulos MI, Heinmann RB (1997) Suspension plasma spraying of cobalt spinel. In: 1997 national thermal spray conference NTSC'97, Indianapolis, IN
121. Müller M, Henne R, Schiller G, Boulos MI, Gitzhofer F, Heinmann RB (1998) Radio-frequency suspension plasma spraying of cobalt spinel anodes for alkaline water electrolysis. In: International thermal spray conference (ITSC'98), vol 2, Nice, France, pp 1523–1527
122. Mailhot K, Gitzhofer F, Boulos MI (1997) Supersonic induction plasma spraying applied to dense yttria stabilized zirconia electrolyte coatings. In: 13th international symposium on plasma chemistry- ISPC'13, vol 3, Beijing, China, pp 1445–1450
123. Mailhot K, Gitzhofer F, Boulos MI (1997) Supersonic induction plasma spraying of dense YSZ electrolyte membranes. In: 1997 national thermal spray conference NTSC'97, Indianapolis, IN
124. Mailhot K, Gitzhofer F, Boulos MI (1998) Supersonic induction plasma spraying of yttria stabilized zirconia films. In: International thermal spray conference (ITSC'98), vol 2, Nice, France, pp 1419–1424
125. Mailhot K, Gitzhofer F, Boulos MI (1999) Plasma deposition of dense ceramic coatings using supersonic induction plasma. In: UTSC'99 – 2nd united thermal spray conference & exposition – coating in practice, Düsseldorf, Germany
126. Theophile E, Gitzhofer F, Boulos MI (1999) Supersonic induction plasma spraying of yttria stabilized zirconia coatings, ISPC'14, vol IV, Prague, Czech Republic, pp 2145–2148

Chapter 9
Wire Arc Spraying

9.1 Description of Concept

Wire arc spraying is the oldest thermal spray process, having been patented in the USA in 1915 [1]. However, only since the 1960s, there has been progress in expanding the applications based on improvements of the understanding of the essentials of the process using systematic studies with high time resolution [2]. This expansion has accelerated over the past twenty years with several significant improvements in the equipment and processes [3, 4].

In the wire arc spray process the deposition material is introduced in the form of a wire, and it is molten and atomized by an electric arc and a high-velocity gas flow. The wires are electrically connected to a power supply, and the arc is struck between the two wire tips, and the wires are continuously fed such that little variation of the arc gap occurs. A high-velocity gas flow between the wires and across the arc constantly removes the molten material from the wire tips, breaks down the larger droplets into smaller ones in a secondary atomization process, and propels them toward the substrate. Figure 9.1 illustrates this process and Fig. 9.2 shows the shearing of the liquid metal layer from the wire tips by the high-velocity gas flow. There is little heating of the plasma gas; most of the energy is used for melting the metal. Consequently, the droplets experience only cooling during their flight to the substrate. Another consequence is that the sensible heat of the droplet flux essentially determines the heat transfer to the substrate, which is substantially lower than the heat flux experienced in processes in which a high-temperature gas flow is used. Low-melting point substrates can be coated with this process; however, preheating the substrate to improve the coating adhesion would require an additional heat source.

To summarize the advantages of the wire arc spray process:

(a) Use of wire as the starting material is more economical than the use of powder
(b) Small arcing gaps result in lower arc voltages allowing the use of a low-voltage power supply

P.L. Fauchais et al., *Thermal Spray Fundamentals: From Powder to Part*,
DOI 10.1007/978-0-387-68991-3_9, © Springer Science+Business Media New York 2014

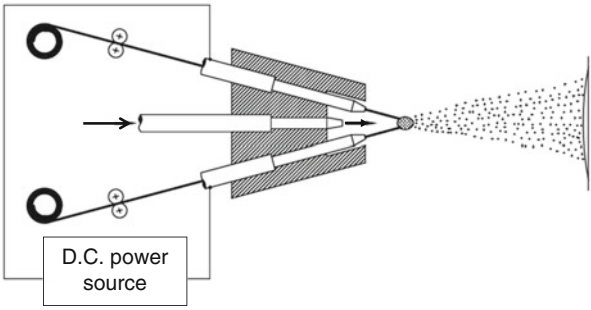


Fig. 9.1 Schematic of wire arc spray setup

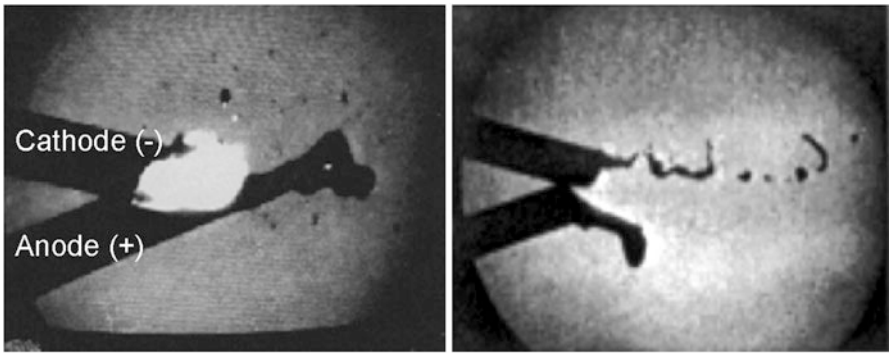


Fig. 9.2 High-speed images of liquid metal droplet formation with 100 ns exposure time

(c) Little heat is transferred to the torch, eliminating the need for water cooling and permitting smaller and simpler torch designs
(d) The high-gas flow rates and the relatively low power result in low gas enthalpies and, consequently, in little substrate heating
(e) The major portion of the electrical energy supplied is used for melting the wire tips, and all material arriving at the substrate was initially molten
(f) The efficient melt rates result in high-deposition rates
(g) Arc initiation through touching of the wires eliminates a high-frequency starting unit

The low level of control that the process offers counters these advantages. The arc experiences a cold gas flow perpendicular to its axis (cross-flow arc), and the melting of the electrodes continuously changes the arc attachments, and both of these effects result in constant arc fluctuations. The instability of the arc results in uneven melt rates, with a wide distribution of metal droplet sizes, and the turbulent flow downstream of the arc leads to secondary atomization of the larger droplets and a dispersion of the droplet trajectories and a wide spray pattern. There is a difference between the melt rates of the wires serving as the arc anode and as the arc cathode. The higher heat fluxes and the more distributed attachment at the anode wire result in the formation of larger droplets and higher melt rates, while the more

constricted attachment at the cathode results in smaller droplets and more evaporation of the metal. This leads, at lower atomizing gas flow rates with limited secondary atomization, to a bimodal distribution of the metal droplet sizes. Furthermore, because of the necessary high-gas flow rates, usually compressed air is used as the atomizing gas, resulting in significant oxidation of the metal droplets. As a consequence, the coatings have usually significantly higher porosity than coatings deposited by most other techniques and higher levels of oxide content. While the wire must be made of ductile material that is an electrical conductor, ceramic materials can be deposited when these ceramics are the filler materials in cored wires.

The process is generally used in the open atmosphere, although controlled atmosphere and low-pressure wire arc spraying processes have been developed. The vast majority of the wire arc installations are using an arc between two wires (twin wire arc deposition), but there are developments of single wire arc processes where the arc is struck between a fixed electrode and the consumable wire. These developments are described in a separate section.

The economics of the process and the limitations on the coating quality have led to establishing this process well in the large-scale manufacturing industry. However, significant research and development efforts over the past two decades have led to improvements in the coating quality and have resulted in a significant growth of arc spray applications.

9.2 Equipment and Operating Parameters

A typical wire arc spray setup is shown in Fig. 9.3. A rectifier supplies d.c. power, usually a thyristor-controlled rectifier. The rectifier must be able to withstand occasional shorting of the output when the wires touch. Since the electrodes are consumable resulting in a varying arc length, the rectifier uses voltage control. The desired voltage is set, and when the melt rate of the wires is higher than the feed rate, the arc voltage will increase surpassing the set point; the power supply control will respond by reducing the arc current, and therefore the melt rate until the set voltage value is again reached. Similarly, when the arcing gap gets too small resulting in too low voltage values, or if the wires even touch resulting in a momentary short, the current will increase to increase the melt rate. However, since the loss of a metal droplet from the wire tips usually leads to a stepwise increase in the arc voltage, one has continuous fluctuations of the arc voltage and arc current (see Fig. 9.4), with the principal frequencies between 500 and 2,000 Hz. These fluctuations can be minimized by judiciously adjusting the arc voltage, the wire feed rate, and the atomizing gas flow. Misalignment of the wire guides such that the two wires do not extend to a single point can also lead to voltage fluctuations, as can a movement of the wire tips due to a remaining cast or cant in the wires. Most wire arc spray operations are performed with voltage settings below 40 V, and the open circuit voltage requirements are between 60 and 80 V, however,

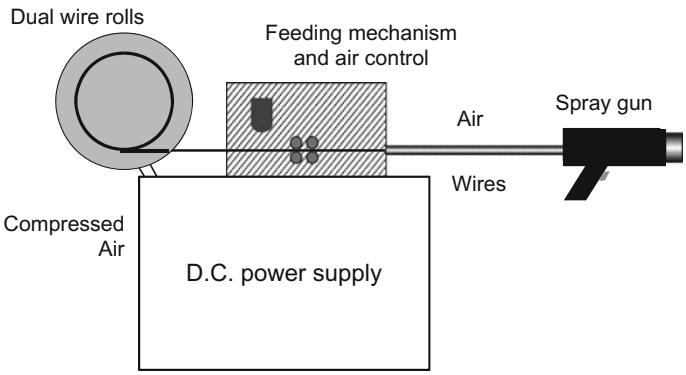
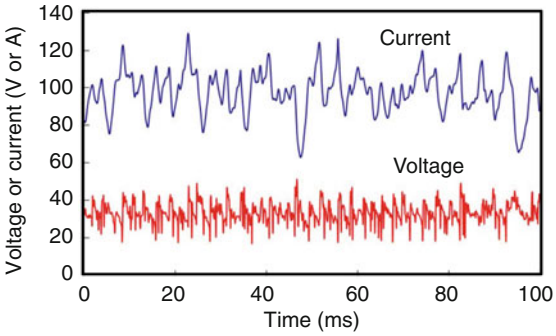


Fig. 9.3 Schematic of wire arc spray system with power supply, control unit, wire supply rolls, compressed gas line, and torch

Fig. 9.4 Illustration of voltage (*bottom*) and current (*top*) fluctuations



the response of the power supply to the constantly varying load can influence the coating quality [4]. The "current control" knob on the power supply controls the wire feed rate, because for a given voltage, higher wire feed rates require higher arc currents.

The wire, necessarily made of ductile and electrically conductive material, is taken from a large spool, and to reduce the wire curvature (cast and cant), it is frequently run through a wire straightener, consisting of an assembly of rolls forcing the wire through a straight path. Without the straightener, the wire tips will have a periodic movement resulting in uneven melt rates. The wire transport rollers are either in the control unit, pushing the two wires to the torch head (push wire feed), or they are mounted on the torch head (pull wire feed). It is also possible to have both a push and pull wire feed for optimal feed speed control and allowing larger distances between the control unit and the torch head (up to 15 m); however, this arrangement requires exact synchronization of the drive motors.

The control unit allows adjustment of the operating voltage, the wire feed rate via the feed motor speed, and the pressure in the line to the torch. The gas is fed from a compressor or from high-pressure gas tanks at pressures of at least 0.6 MPa.

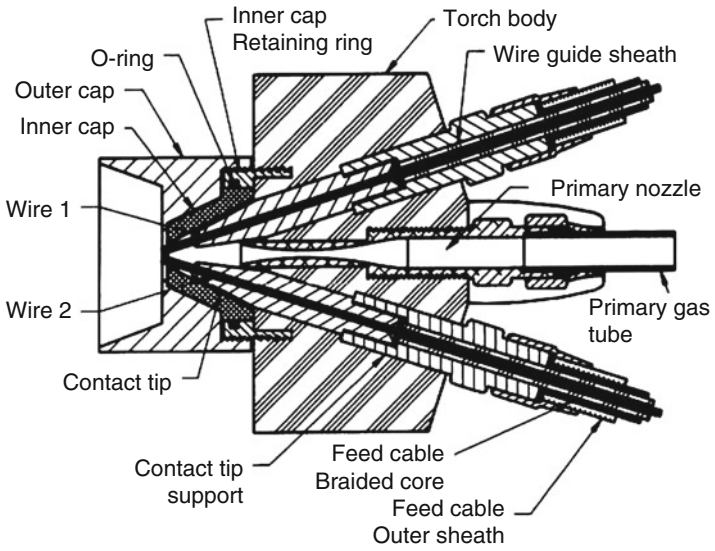


Fig. 9.5 Schematic of wire arc spray torch head (Reproduced with kind permission of R.R. Carlson)

Air is the most commonly used atomizing gas, although nitrogen and CO_2 are being used as well.

The wires are guided inside coaxial hoses to the spray torch, with the metallic layer surrounding the plastic wire tube serving as the power conduit. Also the gas supply tube connects the control unit with the torch. The torch contains wire guides/contact tips, which allow the transfer of current from the power supply to the wire and the nozzle providing the high-velocity gas flow directed toward the wire tips (see Fig. 9.5 [courtesy of R.R. Carlson]). Alignment of the contact tips such that the two wires meet is important for obtaining steady melt rates. The primary atomizing gas nozzle consists usually of a straight bore and is usually operating under choked flow conditions, meaning that sound velocity is reached. Many newer torch designs have a secondary gas flow, i.e., a portion of the gas flow is diverted to flow around the wire guides to the wire tips. A second nozzle (air cap) is mounted surrounding the wire tips or right upstream of the tips (see Fig. 9.6 [courtesy of Praxair TAFA]). This secondary nozzle not only improves the atomization providing higher gas velocities at the wire tips, it can also be used to reduce the jet divergence. The liquid metal atomization process is strongly dependent on the gas velocity, and the fluid dynamic design features of the torch affect the coating quality.

Typical operating parameter ranges are listed in Table 9.1. It should be noted that high-power wire arc coating installations exist operating at up to 1,500 A. These installations are being used mainly for anticorrosion coatings on large surfaces, and they will require water cooling of the contact tips.

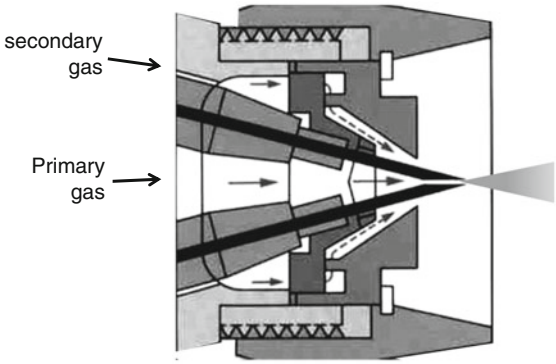


Fig. 9.6 Schematic of wire arc spray head with primary and secondary gas flow (Reproduced with kind permission of Praxair TAFA)

Table 9.1 Typical wire arc operating ranges

Arc voltage:	20–40 V
Arc current:	100–400 A
Wire feed speed:	7–10 m/min
Standoff distance:	10–20 cm
Plasma gases:	Air, nitrogen, CO_2
Plasma gas flow rates:	800–2,400 slm
Gas supply pressure:	0.27–0.6 MPa

9.3 Wire Materials and Specific Applications

Compared to other spray processes, arc spraying presents a higher deposition rate with values ranging, dependent on current (100 to 360 A), from 3 to 15 kg/h for Al, 4.5 to 17 kg/h for stainless, to 10 to 33 kg/h for Zn (200 kg for high-power deposition) [3].

The main requirements for the material to be sprayed by the wire arc spray process are that the material must be electrically conducting and that it can be obtained in the form of a wire without being too brittle or too stiff. Many metals or alloys fulfill this requirement. Therefore, the material to be sprayed is selected according to the application, for which the drawbacks of wire arc spraying—relatively high porosity and oxide contents—are less important than the advantages, in particular the process economy, high-deposition rates, and low substrate heating.

9.3.1 Wires

One of the most important application is corrosion protection using stainless steel, Al or Zn coatings, e.g., in the automobile industry, for marine applications (ship hulls, decks, or platforms) or for infrastructure maintenance (coatings of bridge structures, storage tanks). According to Lester [5] other common anticorrosion application areas are offshore oil platforms, fences, underground pipes, electric

rolled welded (ERW) tube manufacture, multi-void aluminum tube manufacture, LPG cylinders, external and internal steelwork, and playground furniture. The applications of long life corrosion protection of steel structures and maintenance and rehabilitation of machinery parts were mostly developed in China in 2001 [6, 7]. The coating should be as dense as possible (if necessary sealed) if it is an anodic protection (for example, nickel is anodic to steel, and the cathodic area of the steel surface exposed controls the corrosion rate). This is not the case with cathodic protection using zinc or aluminum (see Sect. 15.10.1). Both materials provide an excellent protection in a wide variety of marine and industrial environments. A third material is zinc/aluminum alloy (85 % Zn/15 % Al). According to Lester [5], zinc is used in reasonably low corrosion applications such as water tanks, some bridges, and general structural steelwork. Aluminum is used in harsher corrosion applications such as saltwater and splash-zone areas. In addition, aluminum is used in high-temperature applications, such as flare booms on offshore oilrigs, as the aluminum effectively dissolves into the substrate when exposed to high temperatures (aluminizing). Zinc/aluminum alloy is used in environments where the corrosion resistance of zinc is borderline. A large application for zinc/aluminum coatings is the spraying of ductile iron pipes that are buried in the ground [5].

Zinc–aluminum alloy with a rather low melting point (422.5 °C), and a spray process limiting drastically the substrate heating, can be sprayed onto carbon fiber-reinforced epoxy composites, CFRE. CFRE can degrade or be damaged when the service temperature is over 372 °C, or over 530.8 °C for short time exposure. This Zn–Al coating served as a permeation barrier [6]. In some cases, shot peening densifies soft coatings such as Zn or Al.

When arc-sprayed material is not a cathodic protection, porosity must be minimized, as well as the oxide content, and efforts have been pursued to achieve the required characteristics [7, 8]. Of course an epoxy-sealing coat can eliminate open porosity.

Chang et al. [9] have studied, the corrosion and wear performance of Ni–Ti composite coatings. Coatings were prepared by arc spraying with Ti and Ni wires fed synchronously. Results indicated that some intermetallic compounds such as $TiNi_3$ and Ni–Ti alloy were present within the Ni–Ti coating. The wear resistance of the Ni–Ti composite coating is superior to that of the Ni-sprayed coating but slightly inferior to that of the Ti-sprayed coating. The corrosion resistance of the arc-sprayed Ni–Ti coating is superior to that of Ti but inferior to that of Ni. The formation of $TiN_{0.3}$, TiN, and oxides when spraying titanium wires depends strongly on the atomizing gas used [10]. Nitrogen atomization is efficient in TiN formation by arc spraying. Ar atomization restrains the reaction of titanium with both nitrogen and oxygen and promotes the chemical bonding between the coating and substrate.

Another important application is rebuilding of worn surfaces using NiAl, NiCrAl, AlMg, or Mo, from jet engine parts to rolls, shafts, plungers, crankshafts, etc., of major construction equipment [3, 11, 12]. For these applications, low porosity and low levels of oxidation are desirable, as well as smooth surfaces. Carbon steel coatings are being used in a variety of industries, e.g., as protective

layers on aluminum surfaces. In particular in the automobile industry where effort in weight reduction has led to increased use of aluminum or aluminum alloys, protection of aluminum alloy surfaces resulted in the development of new equipment, processes, and materials. Examples are the coatings of the engine cylinder walls or the valve lifters. Wire arc coatings are functionally better than coatings deposited by electroplating and more economical than plasma-sprayed coatings and can offer acceptable quality [13]. Several developments have been pursued for the coatings of cylinder walls, using single wire arc spray systems as well as twin wire arc spray systems with a 90° nozzle diverting the particle stream. These type of coatings are typically carbon steel based, deposited to thicknesses of 300–400 μm, with porosity required to be less than 5 %, and they must have excellent adhesion [14]. Spraying with air can reduce the carbon content and reduce the wear resistance [13]. Adhesion can be improved by pretreatment of the surface with a fluoride-based flux to reduce the oxide layer and using a NiAl bond coat [15]. Also bronze, brass, or chrome alloys are used. The high-temperature oxidation behavior of arc-sprayed aluminum bronze coatings on steel substrates was studied by Zhang et al. [16] during isothermal exposures in air at 900 °C. The experiments showed that the coatings on steel substrates were not deteriorating and the substrate was well protected. The coatings withstood more than ten thermal shock tests without any coating separation. After exposure at high temperature, the coatings were still adhering well to the steel substrates.

Cooke et al. [17] studied an iron-based material coating (iron–chromium–boron, FeCrB) arc sprayed for improving the wear resistance of sugar mill rollers. According to the results obtained, the coating should be a good candidate for this application. Chen et al. [18] have studied a method to prepare intermetallic Fe–Al composite coatings by spraying twin wires, i.e., a carbon steel wire as the anode and an aluminum wire as the cathode. The inter-deposited Fe–Al coating was transformed in situ to an intermetallic composite coating after a post-annealing treatment. The results showed that the desirable intermetallic phases such as Fe_2Al_5, FeAl, and Fe_3Al were obtained under the annealing condition. The main oxide in the coating was FeO, which can partially transform to Fe_3O_4 at the annealing condition. Wilden et al. [19] have studied the influence of spray parameters, including the plume width, on wire arc coatings of X46Cr13. They showed that for spraying this alloy, it is important to reduce the burn-off of elements. A low-particle temperature process was important to maintain the alloy composition. By using low voltage level at high-atomizing gas pressure and high current, the particle temperature and surface roughness were reduced. Laika et al. [20] wire arc-sprayed Ni on Al_2O_3 substrate. The metal–ceramic interface was well bonded with no pores, flaws, or cracks in the as-sprayed condition. An annealing treatment at 1,273 K for 24 h of the plasma-coated samples did not result in formation of any intermetallic compound or spinel at the Ni/Al_2O_3 interface.

An application of increasing importance is that of spray forming of molds for rapid tooling [21–23]. Typically, thick steel coatings are deposited on substrates like alumina. Requirements are low porosity and high-dimensional stability. For obtaining a 10-mm thick coating of a 300 × 300 mm shell, multiple torches

are used, and the deposition path of the torch movement has been devised such that internal stresses are minimized, i.e., thermally generated stresses are compensated by phase transition stresses [22].

Applications in the electrical and electronic industries include spraying of resistors, capacitors, conducting connections on insulators, and magnetic or radio frequency shielding. Materials used for these applications include NiCr, Al, Cu, and Zn.

9.3.2 Cored Wires

Cored wires with a ductile metal or alloy envelope containing hard particles has extended the use of wire arc spraying to domains, which were previously dominated by plasma and HVOF spraying. Compared to these two processes wire arc spraying is less expensive and permits high-deposition rates coupled with the possibilities of having coating thicknesses over one millimeter. For example, Sampson and Zwetsloot [24] in 1997 have shown that in a coating for a European airline, the wire arc-sprayed NiCrAl structure looked finer with less chipping at the edges than the plasma-sprayed ones. A survey of operators and machinists brought out the benefits of the concentrated spray stream generated by the arc jet system. Reduction of spray times of up to 50 % for the arc jet, combined with a reduction of machining times, and no need to rehabilitate chipped coatings were reported [24]. In 2008, Tillmann et al. [25, 26] performed measurements and modeling of the arc spray process with cored wires.

It is possible to make use of generating alloys in flight or on the surface, such as NiCr with Ni and Cr powders, or compounds like Ni_3Al with a Ni and Al powder mixture [3]. Typical wire diameters are 1.8–2 mm, and the steel wall thickness is about 0.4 mm. Cored wires are predominantly used for obtaining wear-resistant coatings with the hard and brittle compounds used as filler material in low-carbon steel wires. Examples are FeCrB particles with addition of Al powders to provide a metal matrix and reduce porosity [27]. Mixtures of carbides with a metal are frequently used, e.g., WC with Co.

Zhao et al. [28] studied coatings made with a cored wire of 304L stainless steel as sheath material and NiB and WC–12Co as filler materials. The XRD and TEM analyses showed that there was a high-volume fraction of amorphous phase and very fine crystalline grains in the coating, the crystallization of the amorphous phase occurring at 579.2 °C. The abrasive wear test showed that the new Fe-based coating was very wear resistant. Fe–Al intermetallic with excellent erosion, high-temperature oxidation, and sulfidation resistance are potential low-cost high-temperature structural materials. However, their room temperature brittleness limits their industrial application. Meng et al. [29] sprayed on 20G steel by high-velocity arc spraying technology Fe–Al/WC composite coatings and tested their oxidation performance. The composition of the oxidized coating is mainly composed of $A1_2O_3$, Fe_2O_3, Fe_3O_4, and FeO, these phases being distributed

unevenly. The protective $A1_2O_3$ film that forms first preserves the coatings from further oxidation.

Fang et al. [30] produced TiB_2/AI_2O_3 powder by a self-propagating high-temperature synthesis (SHS) reaction and filled an iron envelope with this powder. Ceramic particles were kept solid or semi-molten during spraying. Adding lower melting point, nanostructured ceramic powders to change the atomization characteristics improved the properties of the composite coatings. Fe – TiB_2 – Al_2O_3 seems to have a high potential for abrasive wear applications. Fang et al. [31] also sprayed cored wires to deposit composite coatings consisting of TiB_2 and TiB_2/AI_2O_3 hard particles in a Ni–Cr and stainless steel 304L matrix. Although all the analyzed coatings exhibited similar lamellar structure, remarkable differences not only in the morphology of hard phases and the matrix but also in the size and distribution of hard phases were observed from one coating to another. Tribological behavior of coatings at room temperature and dry sliding wear tests showed by far higher wear resistance than the low-carbon steel substrate under the same conditions. Wear loss of 304L–TiB_2 and Ni – Cr–TiB_2 coatings was nearly 15 times lower than that of the steel substrate. TiB_2 hard phases in coatings bonded well with the metal matrix contributing to the high-wear resistance. Pokhmurska et al. [32] obtained coatings with low porosity and small grains by arc spraying of FeCrB + Al and FeCr + Al + C powder wires in a steel envelope. Wear tests with the block-on-ring configuration at boundary lubrication and friction in an abrasive–oil mixture under 5 MPa pressure have been performed. Results for sprayed coatings of both systems showed their high-wear resistance. Such coatings are widely used in the Ukraine for restoring the worn out components in high-load applications (crankshafts of engines, compressors, pumps, etc.). Skoblo et al. [33] have reconditioned worn crankshafts by depositing a coating from cored wires based on Fe – Cr – Al with Mo, Si, and V as alloying additives. This promoted the formation of a heterogeneous structure and phases providing the requisite hardness in the sprayed layer due to the segregation of dispersed carbides and oxides and the presence of an alloyed matrix α-phase. The coating was wear resistant [34].

Cored wires are also used against erosion. For example, Luo et al. [35] have deposited on 20 steel substrates by the high-velocity arc spraying (HVAS) process three types of FeMnCrAl – Cr_3C_2 coatings with different Al contents. High-temperature erosion (HTE) tests were performed in an erosion tester at different impact angles. Samples with 15 % Al, possessing the lowest porosity and oxide fraction, had the best HTE resistance.

Luo et al. [36] have deposited with cored wires FeMnCr – Cr_3C_2 coatings on low-carbon steel substrates. Thermal shock resistances of the coatings were investigated to assess the influence of Cr_3C_2 content. The experimental results show that the hardness of the coatings increased, bonding strength decreased slightly with the increase of the Cr_3C_2 content of coatings. As a result, the coating with 30 wt% of Cr_3C_2 possessed the best thermal shock resistance. He et al. [34] have prepared, nickel-base cored wires (NiCr envelope containing Ni, Cr, Mo, and CrB). The coatings had a smooth surface and presented a bond strength higher than 40 MPa. Potentiodynamic polarization measurements and salt-spray tests were carried out to

determine the corrosion behavior of the coatings. The results showed that Ni-based coatings containing Mo (5 %) or B (2–4 %) had better antichlorine ion corrosion performance than Ni-based coatings without Mo element or Ni–Cr–Ti coating.

Coatings of reactive materials have been obtained using Ti wires sprayed with Ar/N_2 as atomizing gas and an inert gas shroud in a modified nozzle with a tubular attachment. The resulting coating consisted mostly of a mixture of TiN and Ti. Titanium coatings for corrosion protection have been deposited in a low-pressure wire arc spray process [3]. An interesting application is that of NiTi shape memory alloy films [37]. The films were deposited under low pressure, and the use of a wire arc system is advantageous because the wire has less contamination than the powders resulting in lower impurity in the films.

9.4 Metal Droplet Formation

As already mentioned, the difference in the heat transfer mechanisms between the arc and the anode and the cathode lead to differences in the droplet formation at the anode wire and the cathode wire [2, 3, 38]. This is illustrated in Fig. 9.7 [39], showing a constricted arc attachment at the cathode wire, and a more diffuse attachment at the anode wire, leading to the formation of a large metal sheet from the anode wire with the arc attachment traveling toward the downstream end of this sheet. This effect is shown even more distinctively in Fig. 9.8 [40], where high-speed photographs are correlated with voltage values obtained through synchronization of an oscilloscope with the high-speed CCD camera. Observation of the entire metal droplet jet shows that a periodic variation in particle fluxes can exist (see Fig. 9.9 [39]). Typically a cloud of particles is emitted after a dip in the voltage, indicating a momentary peak in the arc current and melt rate. This cloud is followed by a steady stream of particles for a good part of a millisecond, until the particle stream subsides, the voltage drops to a minimum followed by another burst of particles [41]. The voltage dip can reach a zero value, indicating a touching of the wires. Such a touching of the wires results in an explosive emission of large metal droplets, which are broken up in the secondary atomization zone. Figure 9.10 shows a Schlieren image of such a secondary breakup of a large metal droplet [42]. Clearly, this occurrence results in a widening of the spray pattern and of the particle size distribution.

The primary causes for such voltage fluctuations are:

(a) Improper match of voltage and wire feed rate settings or too low open circuit voltage. Arc extinction may occur indicated by a voltage spike before the dip to zero, caused by the arc blown toward the end of a liquid metal sheet and the disconnecting of the liquid metal
(b) Movement of the wire tips due to the cast and cant in the wires or due to wear of the contact tips
(c) Differences in the melt rates of the anode and cathode wires

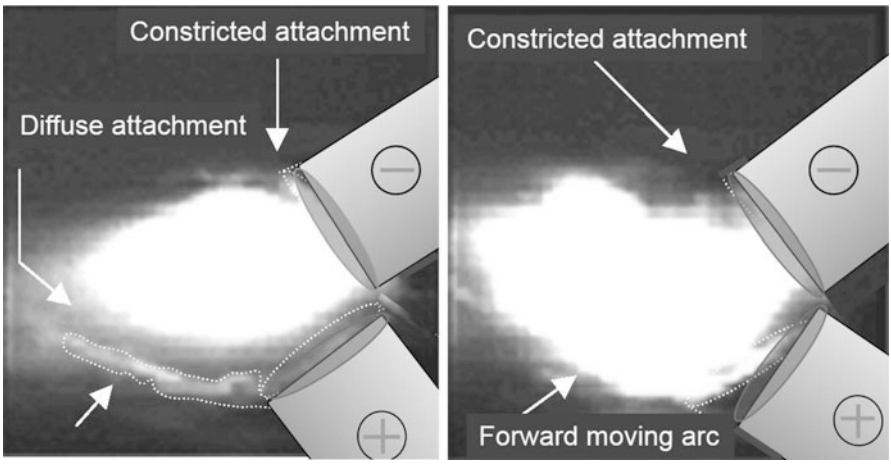


Fig. 9.7 High-speed images of arc attachment on wire tips showing a constricted attachment at the cathode (*top*) wire and a diffuse attachment at the anode wire (*bottom*) [39] (Copyright © ASM International. Reprinted with permission)

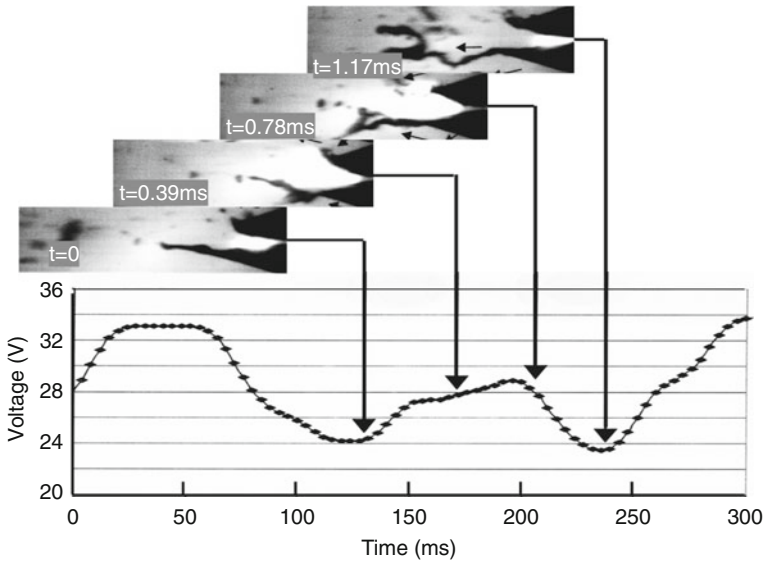


Fig. 9.8 High-speed images of metal droplet formation synchronized with arc voltage trace, showing the forward movement of the anode arc attachment with the associated increase in voltage. Operating parameters: $V = 33$ V, $I = 300$ A, $p = 69$ kPa [40] (Copyright © ASM International. Reprinted with permission)

Metal droplet sizes depend on the atomization mechanisms, i.e., the way the liquid metal layer is sheared initially from the wire tips and on the secondary atomization. Three types of primary atomization mechanisms are most frequently observed, characterized following the categorization introduced in atomization

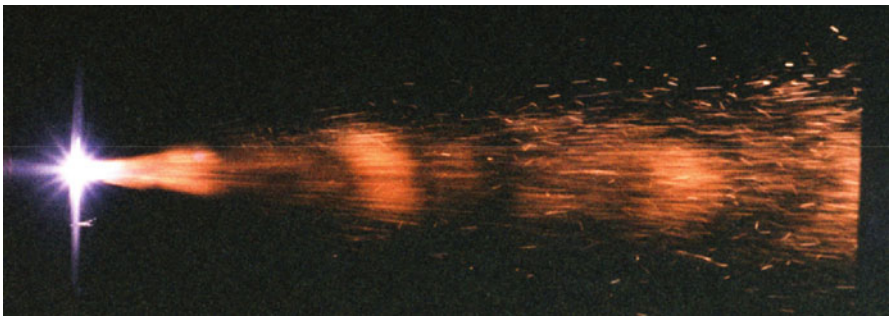


Fig. 9.9 Photograph of a wire arc spray jet showing the periodic variation of droplet fluxes [39] (Copyright © ASM International. Reprinted with permission)

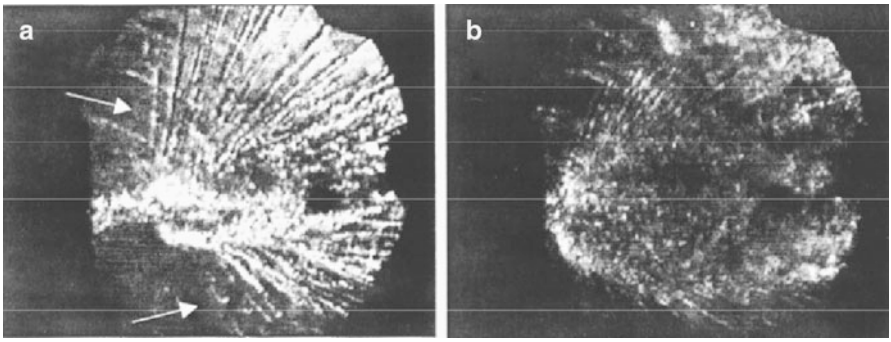


Fig. 9.10 High-speed Schlieren images of the droplet jet from the wire arc spray torch positioned at the *left*, showing the divergence of the droplet beam during a large droplet formation event. The left-hand image shows a secondary atomization event with a larger droplet breaking up into a range of smaller droplets going into a wide range of directions. Such an event occurs typically after a high current surge [42] (Reproduced with kind permission of Nakhleh Hussary)

studies of other liquids [43, 44], the axisymmetric Raleigh breakup, the non-axisymmetric Raleigh breakup, and the membrane breakup. The atomizing gas flow velocity relative to the liquid droplet velocity and the liquid properties such as viscosity, surface tension, and density determines the breakup mechanism. Clearly, the liquid properties in the wire arc spray process are constantly varying, leading to a variation in the breakup behavior. Figure 9.11 [40] schematically illustrates the axisymmetric Raleigh breakup (Fig. 9.11a), the non-axisymmetric Rayleigh breakup (Fig. 9.11b anode) showing the droplet formation from extended liquid metal ligaments, and the membrane-type breakup due to hole formation in a liquid metal sheet (Fig. 9.11b, cathode). Figure 9.12 [40] shows high-speed images of such breakups at the wire tips during spraying using carbon steel wires. The non-axisymmetric breakup is the most frequently observed mechanism at the anode for almost all operating conditions, while the cathode shows a substantial fraction of the time a membrane-type breakup together with the non-axisymmetric breakup,

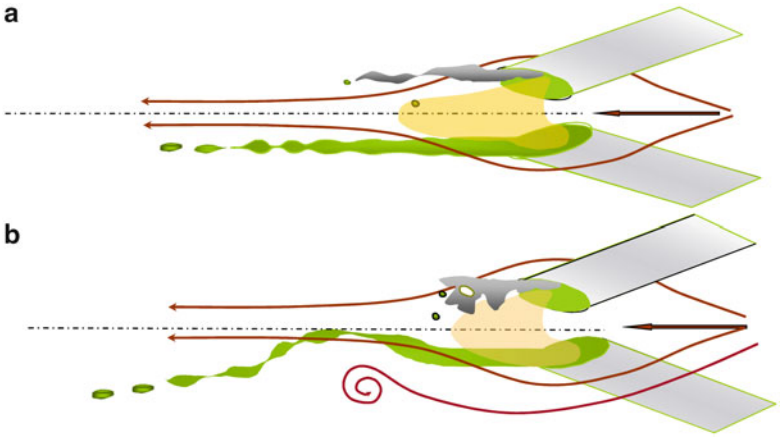


Fig. 9.11 Schematic illustration of (**a**) axisymmetric breakup of anode sheet and (**b**) non-axisymmetric breakup of the anode sheet and membrane-type breakup of the cathode sheet [40] (Copyright © ASM International. Reprinted with permission)

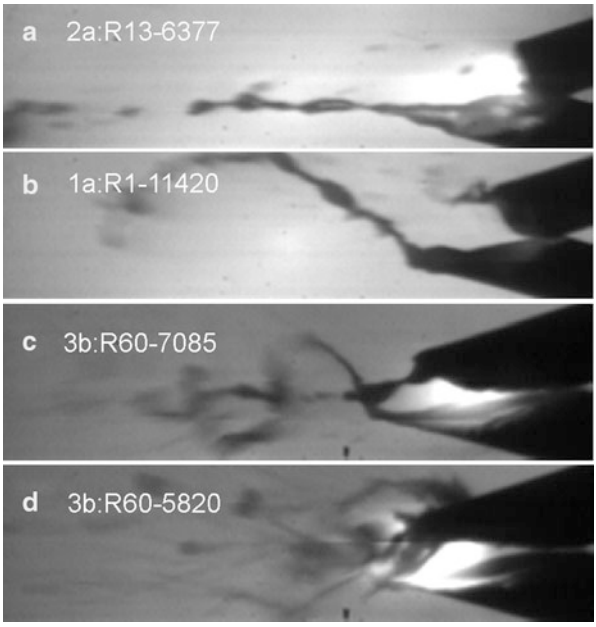


Fig. 9.12 High-speed images of liquid metal atomization of the carbon steel wire tips showing (**a**) disintegration of the anode sheet in an axisymmetric Raleigh breakup, (**b**) a non-axisymmetric Raleigh breakup of a curved anode sheet, (**c**) anode sheet curvature due to large eddies, and (**d**) a membrane-type breakup of the cathode sheet with holes forming in the membrane [40] (Copyright © ASM International. Reprinted with permission)

especially at higher voltages. The high-speed videos (18,000–40,500 frames per second) also showed that increasing the wire feed rate/current setting will increase the amount of molten material, but increasing the voltage will in general not result in larger gaps but rather in arcs that are more strongly bowed in the direction of the flow or are more likely to move toward the end of a liquid metal ligament.

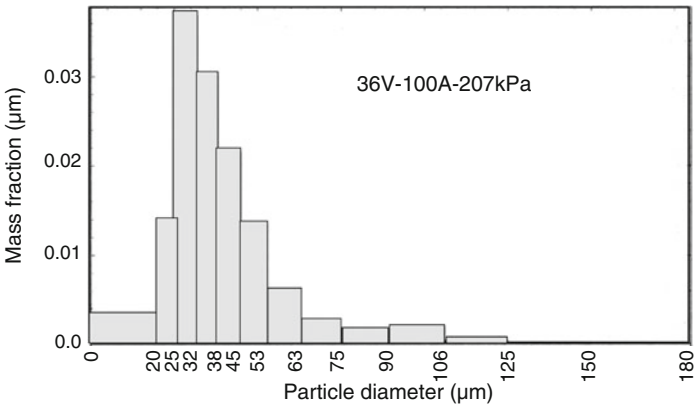


Fig. 9.13 Size distribution of carbon steel droplets collected for the process parameters: $V = 36$ V, $I = 100$ A, $p = 207$ kPa [40] (Copyright © ASM International. Reprinted with permission)

Consequently, one should expect an increase in droplet temperatures with higher voltage settings.

While the atomizing gas velocity influences strongly the primary atomization, in a number of situations, the fluid dynamics of the torch has an even stronger influence on the secondary atomization downstream of the arcing zone. The low-density arc acts as a barrier for the cold gas cross flow, and a substantial portion of the atomizing gas flows around the arc, forming a vortex street behind the obstacle. Metal droplets are further atomized in this vortex street and can change direction, resulting in further dispersion of the spray pattern. A secondary nozzle close to the wire tip location will strongly affect the gas flow, increase the velocity at the wire tips, and reduce the jet divergence.

Figure 9.13 [40] shows a typical size distribution of carbon steel particles obtained by spraying into a layer of ice using a Miller Thermal (now Praxair TAFA) PB400 torch. Shown is the mass fraction within a certain particle diameter range, obtained with a 36 V setting and at a current of 100 A, with an atomizing gas flow rate of approximately 1,100 slm of nitrogen. Figure 9.14 [40] shows the mass mean diameter of the steel particles as a function of the pressure in the torch for different current (wire feed rates) and voltage settings. It must be noted that the pressure at the torch is usually less than half the value of the pressure at the control console, and a pressure of 207 kPa at the torch corresponds to an approximate mass flow rate of 1,100 slm for this torch configuration.

It is clear that (a) the particle diameter decreases strongly with increasing mass flow rate, (b) the particle diameter increases with increasing current, with the increase being stronger at lower currents, and (c) the particle diameter increases with increasing voltage in particular at higher pressures. A correlation has been found with a particle size decreasing with an increase in the aerodynamic Weber number

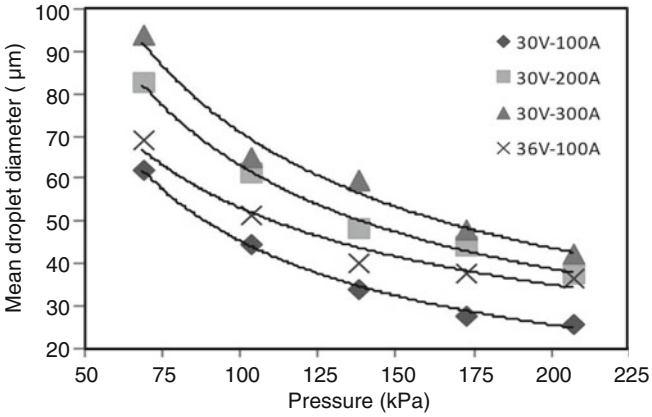


Fig. 9.14 Mass mean droplet diameter dependence on atomizing gas pressure, current, and voltage (carbon steel droplets) [40] (Copyright © ASM International. Reprinted with permission)

$$We = u_{\mathrm{rel}}{}^2 L_{\mathrm{s}} \rho_{\mathrm{g}} / \sigma_{\mathrm{l}} \tag{9.1}$$

where u_{rel} is the relative velocity between the atomizing gas and the metal, L_{s} a characteristic dimension such as the liquid metal sheet thickness, ρ_{g} the mass density of the gas, and σ_{l} the surface tension of the liquid [40, 45]. However, it is difficult to determine the correct values for the parameters determining the Weber number, in particular the relative gas velocity because the gas temperature and velocity at the wire tips are not known. Figure 9.15 [40] shows how the cross-section of a coating is influenced by the change in supply pressure, for a steel wire deposited at 30 V, 300 A. The effect of the smaller particle size due to increased gas velocity is quite obvious.

The effect of the various parameters influencing the gas velocity on droplet size distributions shows clearly that increased velocity will reduce the average droplet size and narrow the distribution. Figure 9.16 [38] shows the size distributions of aluminum droplets obtained by spraying into ice and then determining the size distributions using SEM and image analysis. While there is a bimodal distribution for all supply pressures at the control unit, the increase in the number of particles with smaller diameter with increasing supply pressure is evident. The effect of a Laval nozzle results in a size distribution similar to that in Fig. 9.16c for a supply pressure of 450 kPa. Use of a secondary gas flow and nozzle (high-speed cap) can have an even stronger effect on the particle size distribution [46].

It must be noted that somewhat different results have been observed with different spray installations. In an experiment reported by Liao et al. [47], two different wire materials were used for the anode and cathode wires, e.g., copper and steel, and after spraying into water, the steel particles were separated from the copper ones using a magnetic field. A TAFA 9000 torch was used with three different modifications, (a) a commercial cap with converging nozzle and with secondary gas flow, (b) an upstream convergent–divergent atomization nozzle

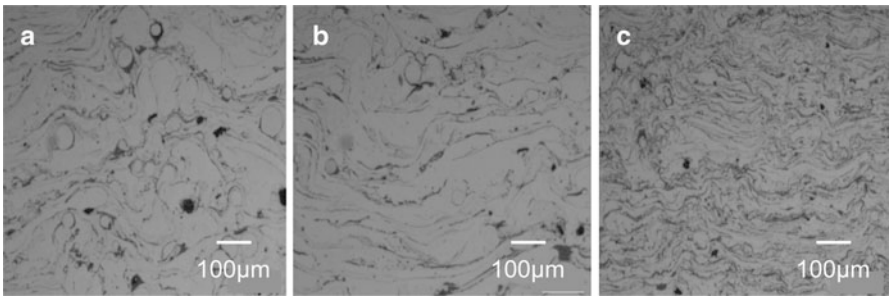


Fig. 9.15 Cross sections of carbon steel coatings deposited at (**a**) 90 kPa, 30 V, 100 A, (**b**) 90 kPa, 30 V, 300 A, and (**c**) 365 kPa, 30 V, 300 A, showing the increase in splat dimensions with increasing current and the reduction with increasing atomizing gas pressure [40] (Copyright © ASM International. Reprinted with permission)

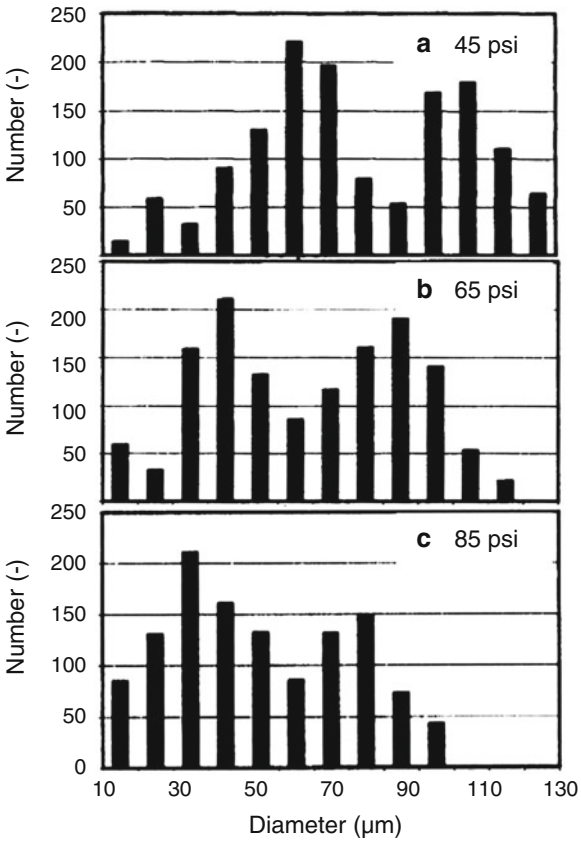


Fig. 9.16 Size distributions of aluminum droplets obtained with atomizing gas pressures of (**a**) 310 kPa (45 psi), (**b**) 450 kPa (65 psi), and (**c**) 590 kPa (85 psi) [38] (Copyright © ASM International. Reprinted with permission)

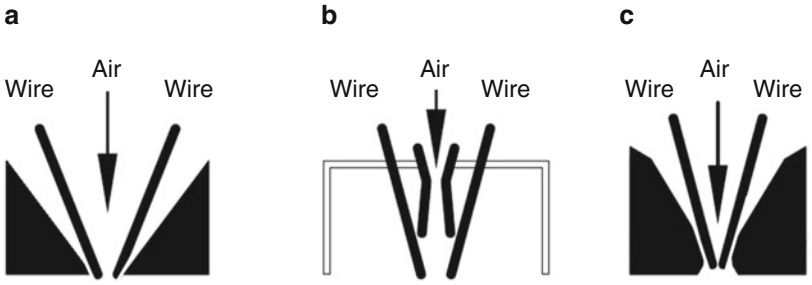


Fig. 9.17 Schematic of different nozzle configurations considered: (**a**) regular atomizing gas nozzle with secondary nozzle (closed configuration), (**b**) Laval-type atomizing gas nozzle without secondary nozzle (open configuration), and (**c**) Laval-type secondary nozzle [47] (Reproduced with kind permission of Elsevier)

without a cap, and (c) a modified cap with a converging–diverging nozzle and secondary gas flow (see section on modeling) (see Fig. 9.17 [47]). Figure 9.18 [47] shows the size distribution of the copper particles sprayed into water with a standoff distance of 30 cm, a torch operating at 30 V and 200 A, for the case of the copper wire being the anode and for the case where it was the cathode, and for two different air supply pressures, 280/280 kPa and 460/490 kPa, respectively, for primary/secondary gas flows.

The following observations are made (see Fig. 9.19 [47]):

(a) Both, the anode and the cathode wire deliver droplets with binary size distributions, i.e., the binary size distributions observed in other experiments are not necessarily due to the different droplet sizes from the anode and the cathode wires.
(b) The size distribution becomes more mono-modal at the higher supply pressure.
(c) The average size of the droplets from the anode wire is approximately the same as that of droplets from the cathode wire for copper, however, for the steel wires, the droplets from the anode are in the average about 20 % larger.
(d) Considering the same polarity, the average size of the steel droplets is larger than that for the copper droplets for the droplets originating from the anode, while the reverse is true for the droplets originating from the cathode. That means that the wire material has a strong influence on the relative importance of the polarity and other operating parameters.
(e) The steel droplets have a size distribution where the two peaks are closer together compared to those for copper shown in Fig. 9.18.
(f) The average particle size is strongly reduced and the distribution is more uniform by going to operating parameters and/or a configuration resulting in higher gas velocities at the wire tips, i.e., using higher gas flow rates or a Laval-type nozzle. The open no-cap configuration yielded the largest average sizes.

An interesting observation is added by Planche et al. [48] who measured droplet size distributions at different distances from the torch axis. A TAFA 9000 torch has

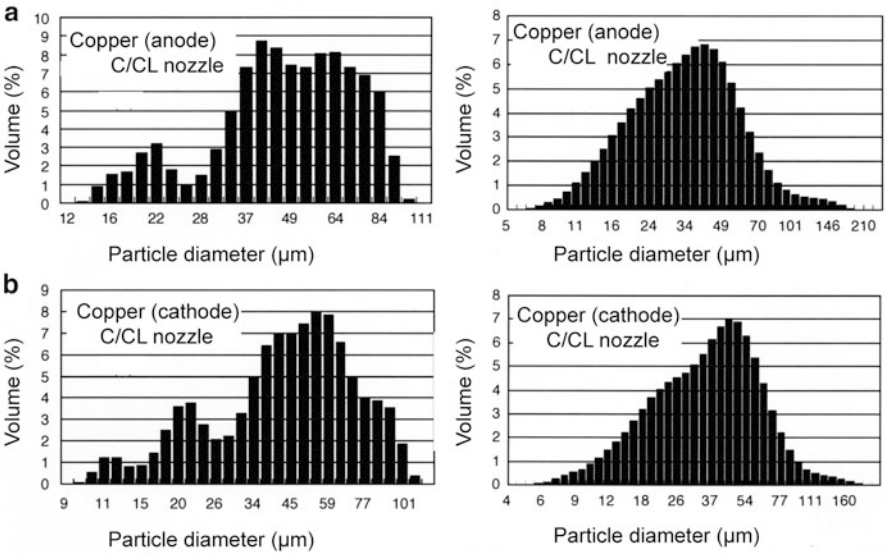


Fig. 9.18 (**a**) Copper droplet size distribution for droplets from the anode wire (*top*) and from the cathode wire (*bottom*) with regular atomization and secondary nozzle and 280 kPa supply pressure for primary and secondary gas flow. (**b**) Copper particle size distribution for droplets from the anode wire (*top*) and from the cathode wire (*bottom*) for regular atomization nozzle and secondary nozzle with 460 kPa primary gas supply pressure and 490 kPa secondary gas supply pressure [47] (Reproduced with kind permission of Elsevier)

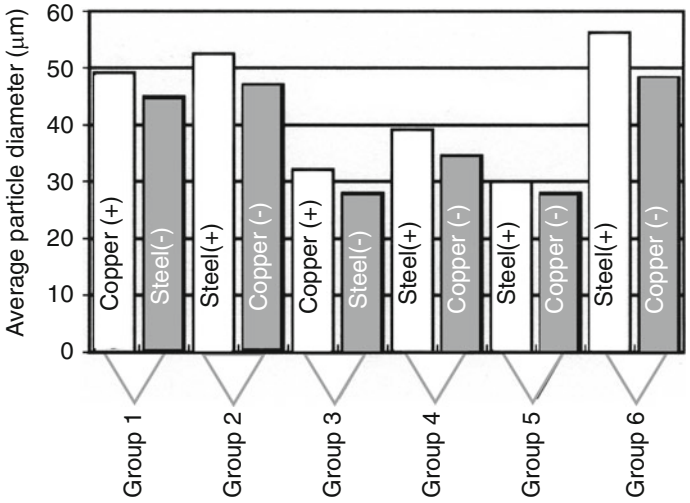


Fig. 9.19 Average droplet sizes for anode wires and cathode wires for the following configurations: Group 1: regular atomizing gas nozzle with secondary nozzle, 280/280 kPa supply pressures. Group 2: regular atomizing gas nozzle with secondary nozzle, 280/280 kPa supply pressures, reversed polarity. Group 3: regular atomizing gas nozzle with secondary nozzle 460/490 kPa supply pressure. Group 4: regular atomizing gas nozzle with secondary nozzle, 460/490 kPa supply pressure, reverse polarity. Group 5: regular atomizing gas nozzle with a Laval-type secondary nozzle, 320/320 kPa supply pressure. Group 6: Laval-type atomizing gas nozzle without secondary nozzle, 320/320 supply pressures [47] (Reproduced with kind permission of Elsevier)

been used with converging cap nozzle, operating at 100, 150, and 200 A and mass flow rates between 1,567 and 2,167 slm. The size distributions were different at different distances from the torch axis, ranging from relatively narrow and monomodal on the axis to multimodal and wider and with larger average diameters at off-axis locations.

Unfortunately, these results cannot completely be generalized and applied to different equipment. In a similar experiment as the one reported by Liao et al. [47], Pourmousa et al. [49] analyzed size distributions of particles from copper and steel wires obtained at different polarities with a Sulzer Metco ValuArc 200 system. The system was operated at 32 V with a wire feed rate of 7 m/min and a supply pressure of 208 kPa resulting in a volumetric flow rate of approximately 1,032 slm. They showed that the resulting size distribution can be fitted by a superposition of two lognormal distributions, and they assumed that one of these belonged to particles from the cathode while the other one to particles from the anode. Applying the assumption of two lognormal distributions to spraying with aluminum wires, and further assuming that the total mass flows from the cathode and the anode would be equal, they investigated the effect of operating parameters on the size distributions. The mass mean diameter decreased with increasing supply pressure, but variation of current (wire feed rate) and voltage had little effect on the mass mean diameter. They further mentioned that since the Weber number would drop rapidly after the wire tips when the velocity difference between the particles and the atomizing gas flow becomes small, there would be little secondary atomization a few millimeters from the tips. However, this last observation does not take into account the large-scale turbulence and the entrainment of slower gas from the surroundings that one frequently sees in the wake of the arc and that may be the cause of the secondary atomization that has been observed in high-speed videography under some conditions.

In an experiment to generate a Ti–Al intermetallic compound in a coating, the droplet formation with a combination of a titanium and an aluminum wire was investigated [50]. It was observed that operation with the Al wire as the anode, the arc was unstable with large voltage fluctuations, attributed to the different melt rates of the wires. With the Ti wire as the anode, a more stable operation was obtained. Instabilities were also observed with two Al wires, while the voltage showed little fluctuation with two Ti wires. The conclusion reached from these experiments was that with low-melting point materials as anode wires it may be difficult to match the wire feed rate with the melt and removal rates, leading to the voltage fluctuations. Larger voltage fluctuations resulted in broader size distributions, and increasing the operating voltage resulted in increased average droplet diameters. Increased atomizing gas flow rates reduced the average droplet size as well as the variation in the sizes. Intermetallic coatings were obtained for higher current operation.

A study in which the anode wire and cathode wire feed rates were varied independently, different regions of arc stability were identified [51, 52]: a stable operating region where the anode wire feed rate is approximately the same as the cathode wire feed rate, a self-regulating operation with the cathode wire feed rate

slightly larger than the anode wire feed rate, and unstable operation when either feed rate (and the current) is too low to melt the wires. Having approximately the same feed rates for the anode and cathode wire results in the highest droplet temperatures and optimal coating adhesion [53, 54], with higher voltages improving the adhesion.

It must be said that droplet atomization in the wire arc spray process is not a closed issue. While it is clear that higher velocity gas flows at the location of the wire tips will result in smaller droplet sizes, it is obvious that the entire fluid dynamics of torch and surroundings affect this process. In particular the role of secondary atomization is presently not fully understood. Furthermore, there appears to be some contradicting evidence reported in the published literature on the effect of the other operating parameters on droplet size distributions and the role of wire polarity. Also, relatively few studies have been performed about the effect of the power supply, e.g., how the rectifier responds to voltage fluctuations.

9.5 Process Characterization

The primary quantity determining the coating properties is the velocity of the atomizing gas and its mass density at the position of the wire tips. This velocity can be changed by several different means:

(a) Upstream pressure change
(b) Change of the primary atomization nozzle shape, i.e., Laval-type nozzle vs. straight bore nozzle
(c) Secondary nozzle around the wire tips (“high-velocity cap”)
(d) Secondary gas flow along wire guides
(e) Shroud gas flow from a secondary nozzle

In the following, the effects of these arrangements will be described on gas velocity, droplet velocity and temperature, droplet trajectories, and coating characteristics such as porosity and oxide content. It is clear that an increase in gas velocity results not only in a stronger accelerating force on the droplet but also, as discussed in Sect. 9.4, in smaller droplets, i.e., in a lower mass to be accelerated. On the other hand, smaller droplet cross sections will result in a smaller drag force.

When considering the effect of changing upstream pressures, one has to consider that the values given in the literature are frequently the pressures at the control console, and that a considerable pressure drop occurs between the control console and the torch head amounting to usually more than 50 %, and possibly more for longer distances. Therefore, the absolute values of the pressure cannot be compared between different experiments, only the relative values showing the trends. Atomizing gas flow rates provide a better indication of the velocity at the wire tips. A nozzle with a converging section followed by a diverging section (Laval-type

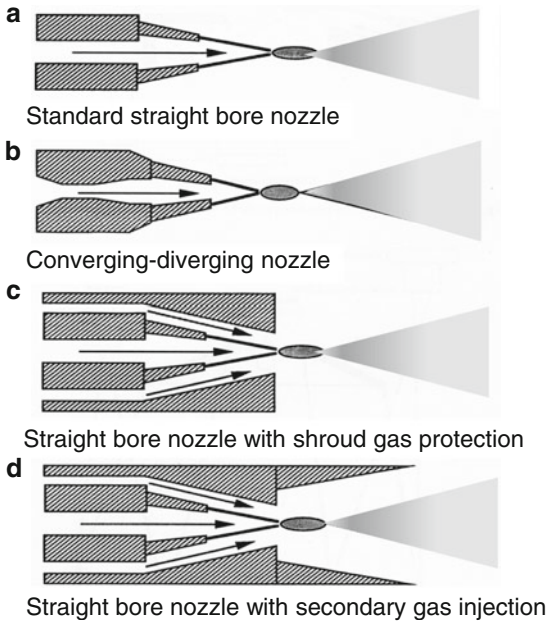


Fig. 9.20 Schematics of different nozzle configurations for changing atomizing gas velocity. (**a**) Standard straight bore nozzle. (**b**) Laval-type nozzle. (**c**) Straight bore nozzle with secondary nozzle and secondary gas flow. (**d**) Straight bore nozzle with secondary gas flow and an additional solid shroud surrounding the droplet jet [38] (Copyright © ASM International. Reprinted with permission)

nozzle) will allow supersonic velocities to be reached at the nozzle exit. Several experimental results are reported for a nozzle with such a shape, however, the shape was not always adjusted exactly for the expected pressure ratio. The secondary nozzle that is now standard on practically all commercial torches provides for the highest velocity values near the wire tips rather than near the exit of the primary nozzle. However, a primary and a secondary nozzle in series result in flow conditions that are difficult to control, and some torch designs have eliminated the primary atomization nozzle. Secondary flow experiments have been conducted with controlled flow added when a secondary nozzle was employed. Frequently the secondary gas flow is provided along the wire guides diverted from the main atomizing gas flow (see Fig. 9.6). Figure 9.20 [38] illustrates schematically the different configurations.

A different nozzle design for obtaining higher droplet velocities similar to the one described in Sect. 5.4 [47] has been presented by Hussary et al. [55]. Here the commercial Miller Thermal (now Praxair TAFA) BP 400 is modified by (a) eliminating the upstream nozzle and introducing a Laval-type nozzle with the wire tips at the nozzle exit plane (CDCP); the nozzle design was based on compressible flow computations for the specific operating conditions; (b) adding a ring of small orifices surrounding the nozzle and providing a shroud gas flow; the orifices are angled toward the jet axis and two different angles were used (SCDCP1 and SCDCP2). Figure 9.21 [42] illustrates this design, and Fig. 9.22 [42] shows the arrangement for providing the gas shroud.

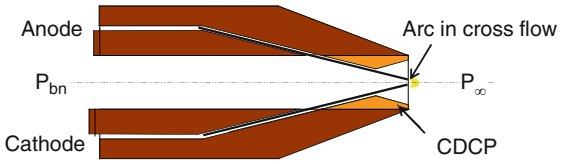


Fig. 9.21 Schematic of Laval-type nozzle surrounding wire tips [42] (Reproduced with kind permission of Nakhleh Hussary)



Fig. 9.22 Schematic of gas shroud arrangement [42] (Reproduced with kind permission of Nakhleh Hussary)

9.5.1 Gas Velocity Measurements

The gas velocity is very difficult to measure during the process because of the associated droplet formation. The heating of a portion of the atomizing gas by the arc increases the gas flow velocity and reduces its density, however, the arc heats only a small fraction of the atomizing gas. Even cold flow measurements using Pitot tubes can produce widely varying results depending on the location of the measurement instrument and the surroundings. It is clear that for almost all operating conditions with a straight bore nozzle for the atomizing gas, the ratio of the pressures on either side of the primary atomizing nozzle is sufficiently high to result in choked flow conditions, i.e., in sonic flow velocity at the nozzle exit. The results of Pitot tube measurements at the location of the wire tips (5 cm from the nozzle exit) are given in Table 9.2 for air as the atomizing gas. Schlieren images of the jet exiting the nozzle show clearly the shock pattern resulting from under-expanded flow exiting the nozzle at sound velocity (see Fig. 9.23) [42]. The mass flow rate of the atomizing gas increases with increasing upstream pressure in spite of the choked nozzle flow conditions because the gas density of the nozzle flow increases, and some of the gas is diverted to flow along the wire guides. Both of these effects will increase the shearing actions on the liquid metal film resulting in

Table 9.2 Gas velocities for two different nozzle geometries without arcing

Nozzle type	Supply pressure (kPa)	Torch inlet pressure (kPa)	Mass flow rate (slm)	Velocity (m/s)	Mach number
Regular	450	202	1,232	334	0.97
Laval	450	220	1,232	352	1.02

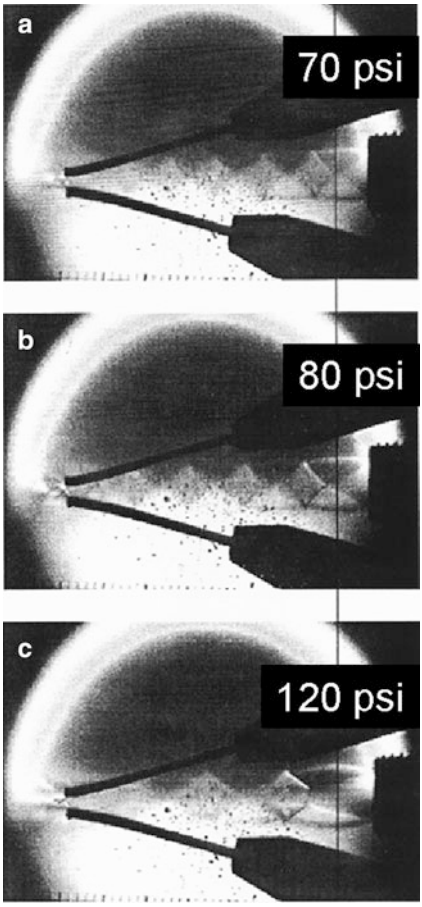


Fig. 9.23 Schlieren images of shock pattern outside atomizing gas nozzle showing under-expanded flow exiting a straight bore nozzle [42] (Reproduced with kind permission of Nakhleh Hussary)

smaller droplet sizes. Also shown in Table 9.2 [42] are the results obtained with a converging–diverging nozzle, labeled Laval-type nozzle. This small change of the nozzle shape resulted in an increase in the velocity to supersonic values.

9.5.2 Metal Droplet Velocity Distributions

The velocity of the droplets increases with atomizing gas flow rate and velocity because of the stronger drag on the droplets and because the particles are smaller.

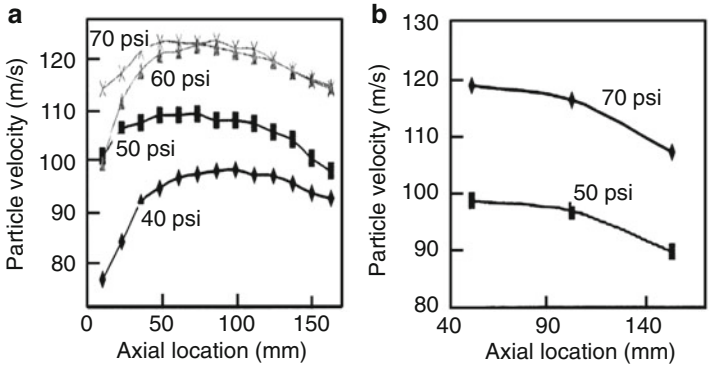


Fig. 9.24 (**a**) Axial distribution of centerline velocity of Al droplets at different atomizing gas supply pressures. (**b**) Axial distribution of Al droplet velocities averaged over the cross section weighted by the local particle fluxes for two different atomizing gas supply pressures [42] (Reproduced with kind permission of Nakhleh Hussary)

Particle velocities have been reported as measured using evaluation of streaks [56] and using the DPV 2000. The effect of secondary gas addition for a torch operating at 30 V, 100 A with a primary gas flow rate of 340 slm (413 kPa), and a secondary flow rate of 85 slm added into the chamber formed by the cap showed a velocity increase from 70 m/s to 105 m/s for stainless steel droplets.

Figure 9.24a [42] shows the axial distributions of the centerline velocity of aluminum droplets for a BP 400 torch operating at 30 V and 100 A for different supply pressures (gas flow rates) of 276 kPa (750 slm), 344.5 kPa (935 slm), 413.5 kPa (1,133 slm), and 482.3 kPa (1,331 slm). These data have been obtained with the DPV 2000. Figure 9.24b shows the axial distributions of the velocities averaged over the cross section and weighted by the droplet number density at every radial location for the same operating conditions. The effect of increasing the supply pressure in commercial equipment is obvious. This effect is also shown in Fig. 9.25a [42] where the spatial distributions of the droplet velocities are displayed in a plane 5 cm from the exit of the secondary nozzle (cap) for two different supply pressures. Figure 9.25b shows the distributions for a different orifice serving as the secondary nozzle, indicating a significantly different distribution of the velocities. Similar results have been obtained by Pourmousa et al. [49, 57] with a commercial spray system (ValuArc from Sulzer Metco) operated at 32 V, a wire feed rate of 7 m/min for the Al wire, and a supply pressure of 208 kPa resulting in a flow rate of 1,032 slm. Figure 9.26 [49] shows the results obtained with a DPV 2000 instrument at a distance of 5 cm from the wire tips, the horizontal (x) and vertical (y) distributions of the droplet velocities, average droplet diameters, and the relative mass flux, i.e., the particle mass flux at a specific location normalized by the total mass flux. The plane of the two wires was the y-plane, and the authors find that the particle flux has less divergence in this plane than in the plane perpendicular to the plane of the two wires thus forming an oval distribution of the mass flux.

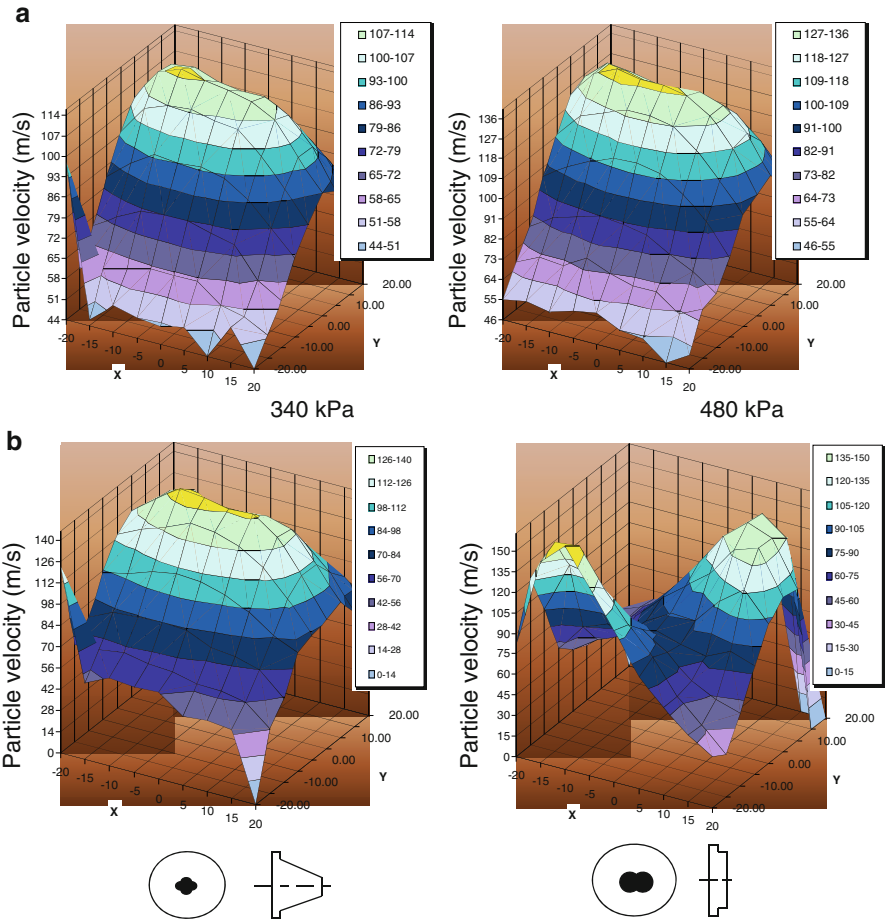


Fig. 9.25 (**a**) Two-dimensional velocity distribution of Al droplets at an axial distance of 5 cm from the secondary nozzle (cap) exit for two different supply pressures. (**b**) Two-dimensional velocity distributions for two different secondary nozzle orifice shapes at axial location 5 cm from the secondary nozzle exit [42] (Reproduced with kind permission of Nakhleh Hussary)

Figure 9.27 [55] shows the axial distributions of the maximum droplet velocities and the particle flux weighted average droplet velocities for aluminum droplets generated with the modified BP 400 torch. For comparison, values obtained with the commercial configuration are included. It is clear that the modification with a Laval-type nozzle at the wire tip location (CDCP) provides a significant increase in droplet velocity, and this increase is further enhanced by the use of the shroud. The use of the modified nozzle and the shroud also significantly reduces the divergence of the droplet jet. This is shown in the Schlieren images of the particle jet in Fig. 9.28 [42], and in the axial distribution of the radial location at which the droplet flux reached a value of 50 % of its

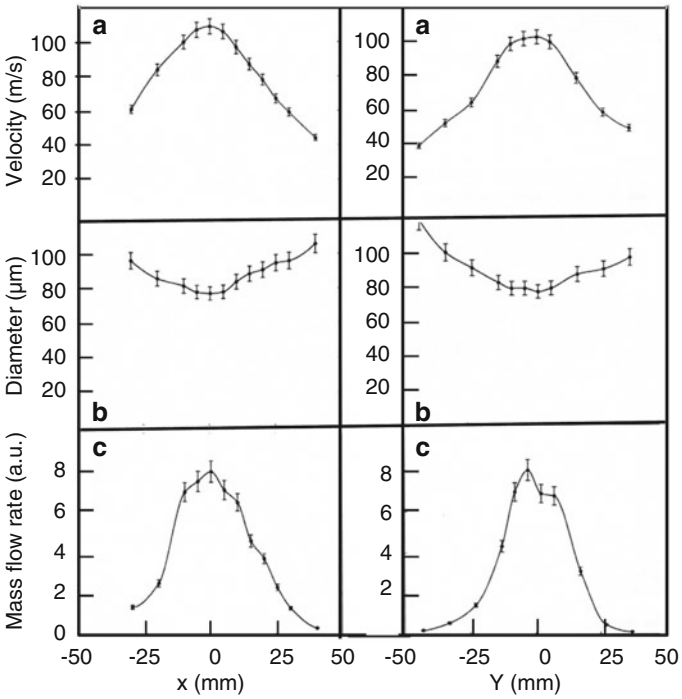


Fig. 9.26 Lateral distribution of (**a**) the droplet velocity, (**b**) droplet size, and (**c**) mass flow rate of aluminum droplets in the horizontal (*left*) and vertical (*right*) directions, at an axial location 5 cm from the nozzle exit. The wires are in the vertical plane [49] (Copyright © ASM International. Reprinted with permission)

maximum (see Fig. 9.29 [55]), as well as the change of the footprint of the deposit on a stationary substrate (see Fig. 9.30 [42]).

Figure 9.31 [58] shows droplet velocities for carbon steel droplets sprayed with the TAFA 9000 system with a converging nozzle and secondary gas flow operated at 30 V, 100 A for a range of atomizing gas flow rates varying from 1,567 to 2,400 slm. These results were obtained with the DPV 2000 with a calibration of the droplet size measurements by spraying into oil and determining the size distributions. This study was extended to yield empirical relationships between the droplet characteristics and various operating parameters and spatial locations for steel wires [48, 59] The range of parameters was 100–200 A current settings, air total atomizing gas flow rates from 1,500 to 2,167 slm, axial spray distances from $z = 200$ to 300 mm, and horizontal (x) and vertical (y) variations of up to 20 and 30 mm from the spray axis, respectively.

The following relationships have been found for I in A and m^{o} in m^3/s [59] relating the droplet properties temperature, velocity, and size with the operating parameters and the position in the jet, given by the coordinates X (perpendicular to the spray direction and perpendicular to the plane of the wires, zero on the torch

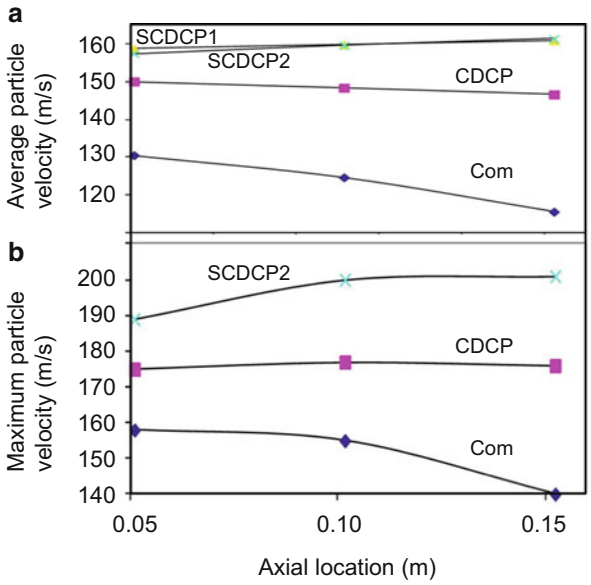


Fig. 9.27 Axial distributions of the peak and weighted average droplet velocities for Al droplets and different nozzle configurations: Commercial nozzle and cap arrangement (Com), Laval-type nozzle in cap (CDCP, see Fig. 9.21), and Laval-type nozzle in cap with additional shroud gas flow with two different angles toward the axis (SCDCP1 and SCDCP2, see Fig. 9.22) showing the significant increase in velocity with the new arrangement [55] (Reproduced with kind permission of the authors)

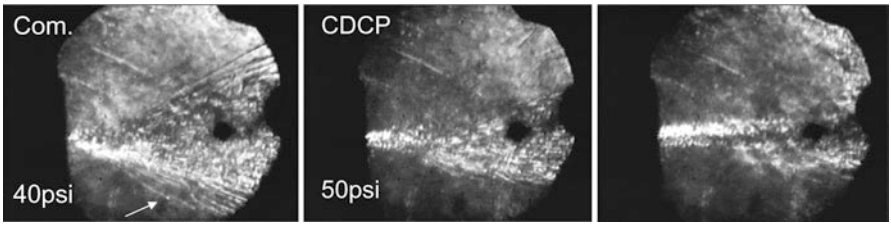


Fig. 9.28 Schlieren images of Al spray droplet jet for different nozzle arrangements: commercial nozzle with cap (*left*), Laval-type nozzle in cap (*center*), and Laval-type nozzle in cap with additional shroud gas flow showing the reduced divergence with the Laval-type nozzle and the shroud gas [42] (Reproduced with kind permission of Nakhleh Hussary)

axis), Y (perpendicular to the spray direction and in the plane formed by the two wires, zero again being the torch axis), and Z the axial coordinate with zero being the torch exit, all coordinates measured in m:

Velocity in m/s:

$$v \propto \frac{\dot{m}^{0.990}}{X^{0.021} Y^{0.025} Z^{0.744} I^{0.070}} \tag{9.2}$$

Temperature in K:

$$T \propto \frac{I^{0.004}}{X^{0.006} Y^{0.002} Z^{0.033} \dot{m}^{0.068}} \tag{9.3}$$

Droplet diameter in μm:

$$D \propto \frac{I^{0.022} X^{0.308}}{Y^{0.006} Z^{0.322} \dot{m}^{2.569}} \tag{9.4}$$

It is interesting to note the strong inverse correlation of droplet diameter with atomizing mass flow rate. The stronger acceleration due to lower mass appears to

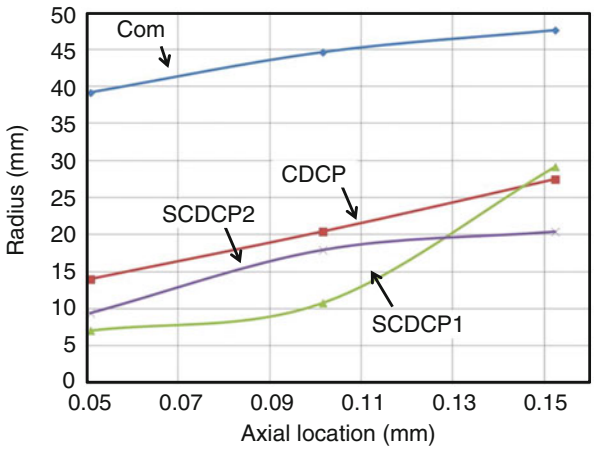


Fig. 9.29 Radial location where the local mass flux is 50 % of the maximum at three different axial locations and for four different nozzle arrangements as described in Fig. 9.27, showing the decrease in jet divergence with shroud gas flow [55] (Reproduced with kind permission of the authors)

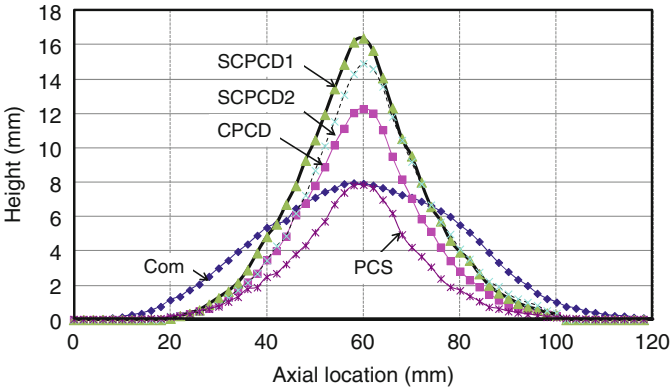


Fig. 9.30 Footprint of Al deposit on stationary substrate with four different nozzle arrangements as described in Fig. 9.27 [42] (Reproduced with kind permission of Nakhleh Hussary)

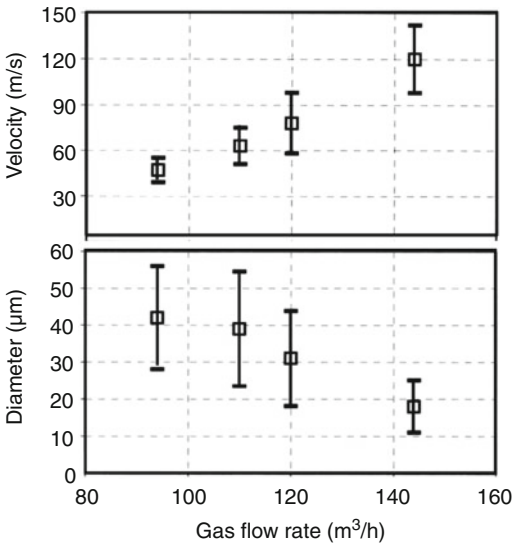


Fig. 9.31 Average carbon steel droplet velocity and droplet size for different atomizing gas flow rates with converging nozzle in cap and secondary gas flow [58] (Reprinted with permission of ASM International. All rights reserved)

off-set the lower drag due to a smaller cross section, resulting in an almost linear increase of the droplet velocity with atomizing gas flow rate.

Another systematic study concentrated on spraying chrome steel wire using air as atomizing gas with a secondary nozzle and secondary gas flow [60]. Operating parameters were varied from 24 to 36 V, 100 to 300 A, and gas supply pressures from 200 to 400 kPa. The droplet velocity was strongly affected by the gas supply pressure increasing from about 75 m/s to about 130 m/s for 32 V 100 A operation [not quite a proportional increase as predicted by Eq. (9.2)]. Increasing the arc current resulted in some drop in droplet velocity (from about 130 m/s at 100 A to about 115 m/s at 300 A and 32 V, 400 kPa). This effect could be explained by a larger droplet diameter at higher currents in qualitative agreement with Eq. (9.2). The effect of voltage was insignificant on droplet velocity, however, stronger on droplet temperatures.

A study of droplet velocities and temperatures for nine different wire materials and different nozzle sizes was reported by Mohanty et al. [61]. A TAFA 8830 torch was used with different caps, operated at 36 V and 200 A and about 1,420 slm of air or nitrogen. At a distance of 16 cm from the nozzle, the average velocities ranged from about 90 m/s for Ni to about 115 m/s for NiAl and about 121 m/s for Mo, with different types of steel and copper in between. No direct relationship with material properties is reported. No significant difference in droplet velocity has been found when nitrogen gas was used instead of air.

It is obvious that droplet velocities are strongly influenced by the torch design, and optimizing droplet velocities will require evaluation of the fluid dynamics inside the torch.

9.5.3 Metal Droplet Temperature

Droplet temperatures are not as strongly affected by the fluid dynamics since all droplets have initially a temperature, which is above the melting temperature of the material. However, oxidation of the droplet surface will result in higher readings of the droplet temperature. For example, in-flight temperature measurements of aluminum droplets will consistently result in temperatures somewhat above the melting point of Al_2O_3, 2,045 °C, because the surface of the droplet is oxidized. It also must be mentioned that wire arc spray droplets are in a condition where convection induced oxidation has been observed, as described in section 4.3.3.7c. This effect of internal convection can explain the very high-oxide content values in excess of 20 % observed with aluminum coatings, and the increase of the oxide content with atomizing gas flow rate is also expected because of the convection of the oxide inside the particle.

As seen from the empirical relation Eq. (9.3), the droplet temperature does not change very much with arc current, atomizing gas flow rate, and horizontal or vertical position, and only a gradual decrease with axial distance is seen. Jandin et al. [58] report a wider spread of droplet temperatures for smaller particles (less than 20 μm diameter), i.e., at higher atomizing gas flow rates. Pourmousa et al. [49, 57] report temperatures of Al droplets decreasing from 2,160 °C to 2,130 °C with an increase of the supply pressure from 236 to 542 kPa with little variation in the horizontal or vertical direction. Wilden et al. [60] report an increase in the temperatures of chrome steel droplets from 2,070 to 2,180 °C when the arc voltage was increased from 24 to 36 V, however, little change of droplet temperatures with current is found, consistent with Eq. (9.3). All temperatures reported indicate a superheating of the droplets significantly above their melting points. For example, Mohanty et al. [61] report temperatures of about 2,275 °C for stainless steel, about 2,370 °C for Ni (melting point 1,455 °C), about 2,610 °C for Cu (melting point 1,085 °C), and about 2,860 °C for Mo (melting point 2,617 °C), all obtained for 32 V, 200 A operation. While no significant dependence on atomizing gas flow rate is seen, a significant effect of the atomizing gas is observed, with steel droplets showing temperatures of about 2,600 °C when atomized with air compared to about 2,430 °C when atomized with nitrogen. This effect is probably due to oxidation providing additional heat. The observation that droplet temperatures increase somewhat for higher gas flow velocities obtained through a different nozzle, i.e., with smaller droplets, supports this conclusion.

The lack of dependence on arc current is clear if one considers that the arc current is actually an indication of wire feed rate, and increased power by increasing the current is used for higher melting rates. The increase in droplet temperature for increasing arc voltage can be explained by the high-speed video observations that increased arc voltage allows the arc to bow more in the downstream direction and to provide more heat to the extended metal ligament. Operation at low arc voltages can result in solidification of particles, particularly when coating at larger standoff distances. There are no droplet temperature measurements that separate the

droplets originating from the cathode and those from the anode. The higher current densities at the cathode would lead one to expect higher droplet temperatures. The higher droplet temperatures observed by Jandin et al. [58] for small droplet sizes may be an indication for a temperature difference between the cathode and the anode droplets.

9.5.4 Coating Characteristics

The principal characteristics of the coating are the porosity and the oxide content or change in elemental composition of the coating. Further characteristics are surface roughness, adhesion, and functional values like hardness. Coating porosity in general decreases with decreasing droplet size, however, oxide content with air-sprayed coatings increases with decreasing particle size because of the larger surface area to mass ratio of smaller particles and because of the increase in internal convection. For example, for the case of spraying aluminum with a 30 V, 150 A setting and a standoff distance of 15 cm, an increase of the supply pressure from 450 kPa to 590 kPa has resulted in a decrease in the porosity from 18 % to 12 %, and in an increase in the oxide content from 19.5 % to 25 % [38].

Significant enhancements can be obtained with the addition of shrouds and the use of nitrogen or CO_2 as atomizing gas. Wang et al. [38] report on spraying stainless steel onto aluminum with a Sulzer Metco 4RG torch with 30 V, 150 A, and a standoff distance of 15 cm, obtaining porosity values of 17 % with air and 12–13 % with CO_2 or N_2. Using a secondary gas flow (see Fig. 9.20) reduced the porosity to 6–8 %. It must be noted that the absolute values of the porosity must be taken with a grain of salt because the variation of the porosity can vary widely across the coating resulting in large standard deviations, and the most widely used method for determining the porosity, image analysis of micrographs, can yield varying results depending on the choices made by the investigator.

The increase in oxide content coupled with a decrease in porosity for increasing gas flow rates is shown in Fig. 9.32 [62], obtained with the Sulzer Metco 4RG torch operated with 34 V and 200 A, and air as the atomizing gas. The results obtained with three configurations are shown, the standard nozzle, the high-velocity cap offering a secondary nozzle around the wire tips, and the standard configuration with a modified primary atomization nozzle to show a Laval-type profile. The lowest porosity and highest oxide content values are obtained with the high-velocity cap. The oxide content can be strongly reduced by using nitrogen or CO_2 as atomizing gas. Wang et al. [38] report oxide content values as determined by Auger spectroscopy of a stainless steel coating as 21 % with air as the atomizing gas, 10–12 % with N_2 or CO_2, and 4–6 % when an inert secondary gas was used (see Fig. 9.33 [63]). All data were obtained with coatings deposited at 30 V, 150 A, 15 cm standoff distance, and 340 slm primary atomization flow rate. Oxidation cannot only result in increased oxide content in the coating; it can also result in a change in the coating composition. For example, in chrome steel

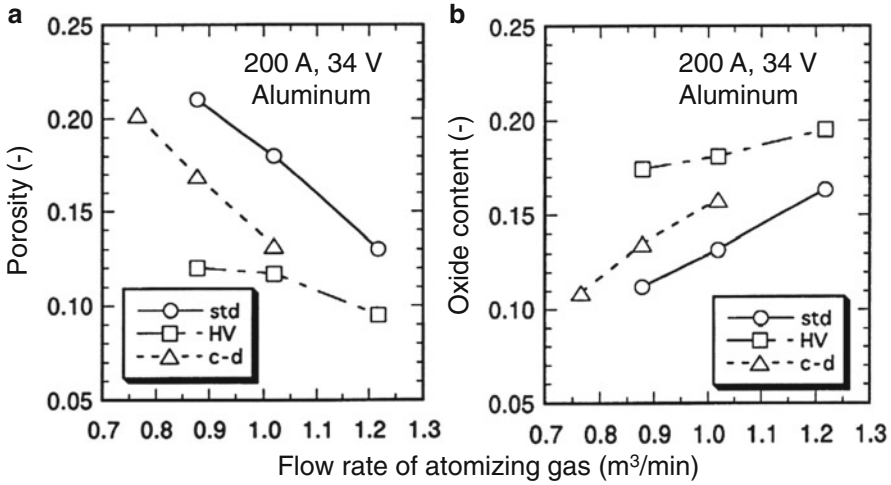


Fig. 9.32 Porosity (**a**) and oxide content (**b**) in Al coating for different atomizing gas flow rates for three different configurations: standard, high-velocity cap, and Laval-type nozzle [62] (Reprinted with permission of ASM International. All rights reserved)

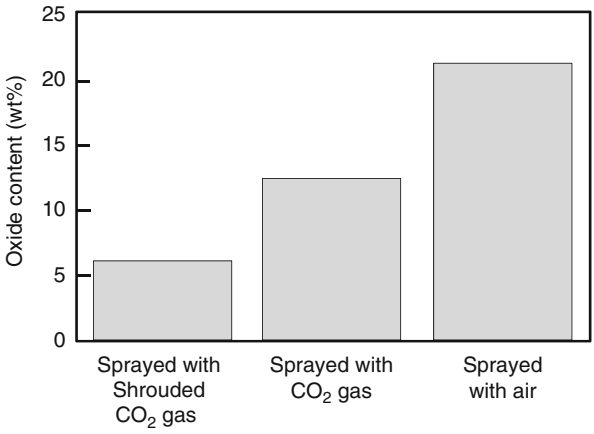


Fig. 9.33 Oxide content in chrome steel coating deposited using air (*right column*), CO_2 (*center*), and CO_2 with additional use of shroud (*left*) [63] (Reprinted with permission of ASM International. All rights reserved)

spraying, the formation of a volatile CrO_3 can reduce the Cr content from 19 % in the wire to 11 % in the coating (see Fig. 9.34 [63]). The use of an inert atomizing gas and an inert secondary gas significantly reduces the Cr loss. Figure 9.35 [58] illustrates how an increase in atomizing gas flow has different results with regard to oxide formation for different atomizing gases: using air, the oxide content in a carbon steel coating increases with increasing gas flow rates (and smaller droplet sizes), whereas for nitrogen as the atomizing gas, a decrease in oxide content is observed when the gas flow rate is increased, possibly due to higher droplet velocities and shorter residence times in the jet. However, the authors also note

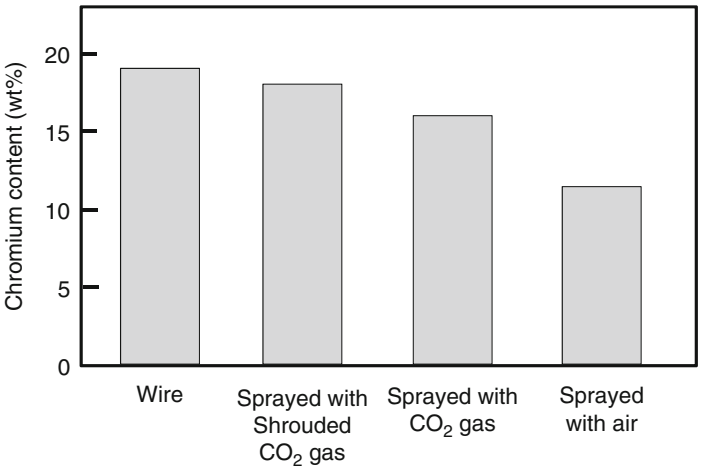


Fig. 9.34 Chromium content in wire and in coatings deposited using CO_2 atomizing gas with shroud, CO_2 atomizing gas without shroud, and air atomization showing the loss of Cr due to volatile oxide formation [63]. Reprinted with permission of ASM International. All rights reserved

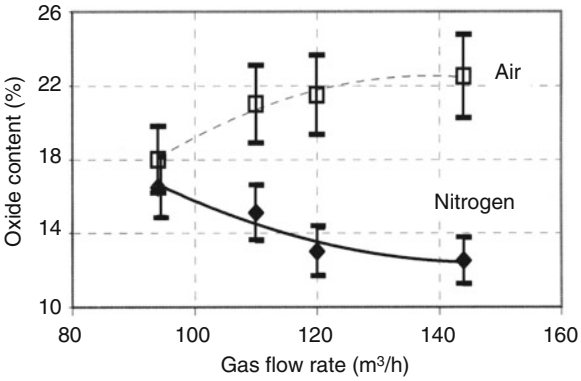


Fig. 9.35 Oxide content in carbon steel coating as function of atomizing gas flow rate for air and for nitrogen as atomizing gas [58] (Reprinted with permission of ASM International. All rights reserved)

that spraying carbon steel with nitrogen can result in a reduction in the amount of carbon in the steel due to reaction with nitrogen and an associated reduction in hardness.

In general, the coating microstructure is more uniform with regular lamellae at the higher gas flow rates, and less surface roughness is observed [46, 48, 58]. A study of the coating formation through investigation of individual splats [48] required preheating of the substrates with an auxiliary heat source, because the splats obtained with cold substrates were extensively fingered and made further analysis difficult.

Increased oxide content usually translates into increased hardness. Smaller particle sizes and associated higher droplet velocities result in lower surface roughness and usually better adhesion. As an example of the improvement of

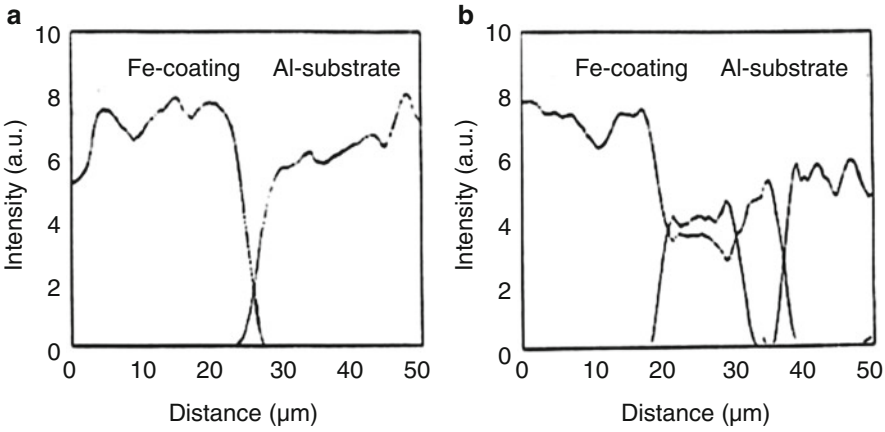


Fig. 9.36 Auger spectrum of interface between steel coating and aluminum substrate for spraying with regular commercial torch and with secondary flow and nozzle showing the formation of an intermetallic bonding layer with higher droplet velocities [38] (Copyright © ASM International. Reprinted with permission)

adhesion with smaller particle sizes and higher particle velocities due to the use of a secondary gas is shown in Fig. 9.36 [38], where the elemental composition across a steel coating on an aluminum substrate is shown. The use of a regular nozzle shows a clear difference in the Auger spectrum between the Fe signal of the coating and the Al signal of the substrate. In contrast, the coating obtained with secondary gas flow shows an intermetallic region between the coating and the substrate with both Al and Fe present. XRD analysis of this region shows indeed the formation of intermetallics at the interface [38]. The formation of the intermetallic is probably due to the higher velocity and higher temperature of the droplet at the moment of impact at the substrate, resulting in local melting of the substrate material.

The effect of the substrate traverse velocity has been investigated by spraying Ni–Cr or chrome steel onto a cylindrical substrate rotating at different speeds giving traverse velocities ranging from 5 to 100 m/min [64]. The lowest porosity has been found at 35 m/min traverse speed, and the effect of lower porosity at increasing traverse velocities below an optimal value has been explained by less densification of the deposited layer by the subsequent droplets (less peening or self densification effect). At low velocities, increased porosity values are explained by more outgassing and increased shrinkage. It also is found that higher currents result in higher porosity values, while higher voltages have little effect on the porosity, but a stronger effect on the loss of alloying elements resulting in reduced hardness values [64], consistent with the observation of higher droplet temperatures at higher voltages.

In summary, it is clear that higher atomizing gas velocities result in smaller particle sizes, higher particle velocities, reduced porosity, and higher oxide

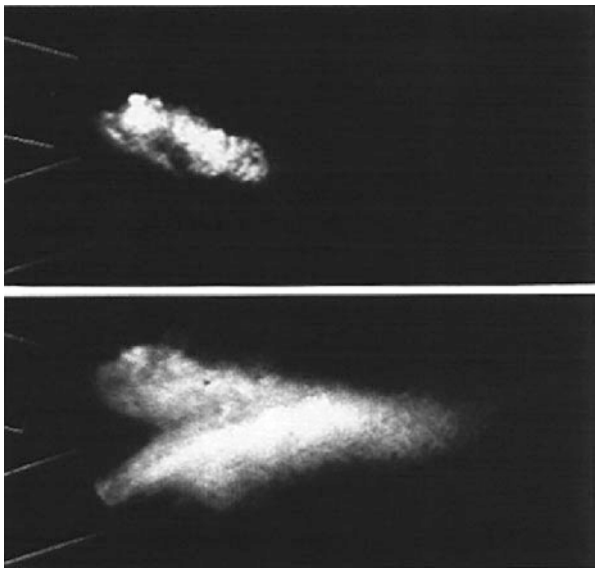


Fig. 9.37 Locations of Al vapor in front of the wire tips (not seen at the left-hand side). The vapor was measured spectroscopically using a line filter for an Al line and a high-speed CCD camera [65] (Reproduced with kind permission of IPCS)

content in the coating. Use of inert atomizing gases like N_2 or CO_2 and inert gas shrouds can reduce the oxidation effect and simultaneously the porosity and improve adhesion.

9.5.5 Fume Formation

The high arc temperatures at the wire tips result in some evaporation of the metal. The evaporated metal oxidizes in the surrounding air, and the oxide is quenched to form ultrafine particles (fumes). The lower the boiling point of the metal, the larger the fume formation. These particles are a health hazard and require either protective equipment (respirators) for the operator or operation in a booth. Figure 9.37 [65] shows the aluminum vapor as measured with a CCD camera and a line filter having transmission at the 313 nm atomic aluminum line, with a 100 ns exposure time. The wire tips are on the left-hand side, the cathode wire in the top position. There is more evaporation observed from the cathode wire, and the evaporation strongly increases with increasing current. Figure 9.38 [65] shows the relative increase in fume formation with increasing arc current and the reduction when using nitrogen as atomizing gas and when using a Laval nozzle. The stronger evaporation from the cathode is due to the higher current and heat flux densities at the cathode resulting in higher droplet temperatures. Use of nitrogen as atomizing gas and a configuration that increases the gas velocity at the wire tips reduces the fume formation, as shown in Fig. 9.38 [65].

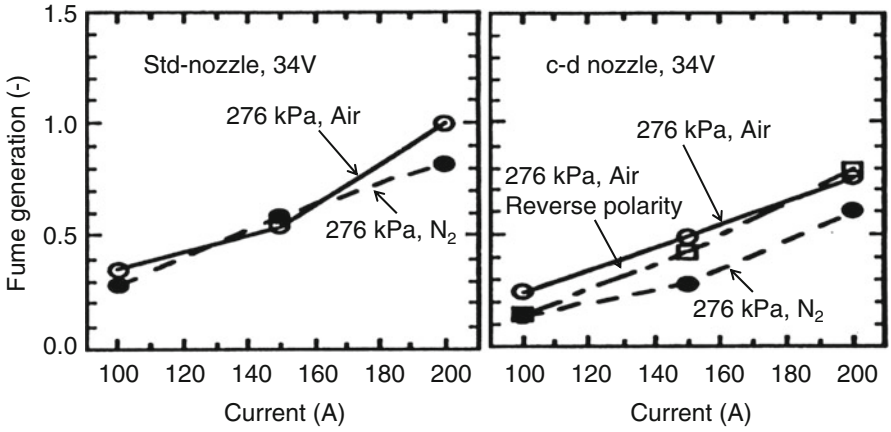


Fig. 9.38 Intensity of Al vapor spectral light emission as function of arc current atomization with air and with N_2 using a Laval-type nozzle, indicating the reduction of vapor with N_2 atomization [65] (Reproduced with kind permission of IPCS)

9.6 Process Modeling

Only a few models have been formulated for the wire arc spray process because of its complexity, requiring by nature three-dimensional, time-dependent treatment, including phase change of the metal electrode and atomization of the liquid metal. One modeling effort has split up the problem into several separate parts: (1) a compressible flow model for the atomizing gas flow upstream of the arc, (2) the 3D model of an arc in cross flow (steady state), with different anode and cathode attachments, yielding temperature and velocity fields, (3) a 2D turbulent plasma jet model, (4) liquid metal atomization models for the cathode and for the anode, and a secondary atomization model [66–68]. The compressible flow model provided input for the arc in cross-flow model, and this model was verified with some previously published experimental data as well as some data obtained for a wire arc configuration but without consumable electrodes and using enthalpy probes to determine plasma temperatures and velocities. Figure 9.39 [66] shows the temperature and velocity distribution in the center plane of the arc. The model captures the differences between the arc anode and cathode attachments, with higher temperatures and velocities at the cathode. But it shows that 5 cm downstream of the electrodes the flow is essentially axisymmetric, justifying a 2D model for the jet region.

The cathode atomization model is essentially a model as developed for metal welding arcs, whereas the anode atomization model uses the boundary layer stripping of the liquid metal sheets and the breakup due to the Kelvin-Helmholtz instability. The secondary breakup model follows an empirical relationship developed by Hsiang and Faeth [69].

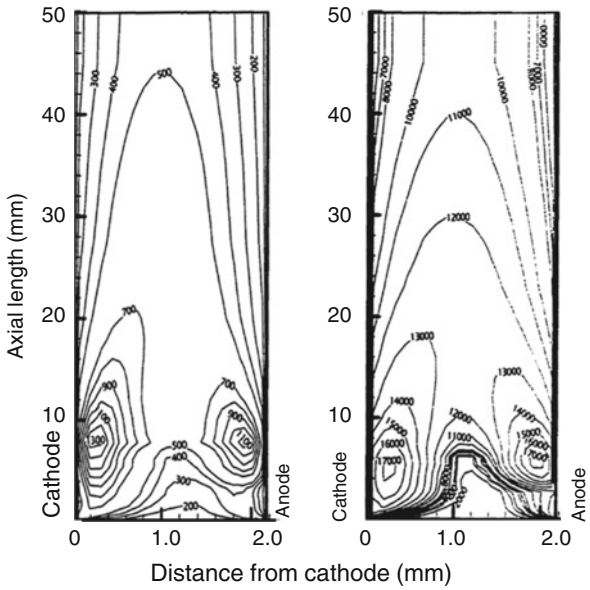


Fig. 9.39 Calculated velocity and temperature distributions in the mid-plane of an arc with cross flow (from the *bottom*). The cathode is on the left-hand side and the anode on the right-hand side [66] (Copyright IOP Publishing. Reproduced with permission. All rights reserved)

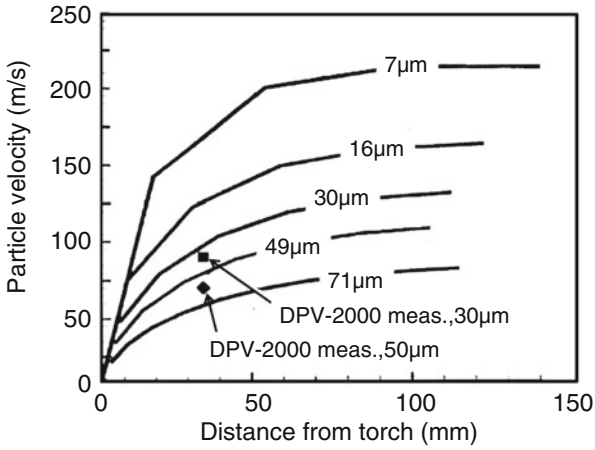


Fig. 9.40 Calculated axial droplet velocity distributions for different droplet sizes. For comparison, two experimentally determined droplet velocities are included, for a 30 μm droplet (*square*) and for a 50 μm droplet (*diamond*) [67] (With kind permission from Springer Science + Business Media B.V)

Figure 9.40 [67] shows calculated particle velocities as function from the distance from the wire tips for different particle sizes. Also shown in the figure are two measured particle velocities using the DPV 2000 and their respective sizes, showing a surprisingly good agreement considering the modeling simplifications. Figures 9.41 and 9.42 [67] show the calculated droplet size distributions (bars) compared to experimentally measured ones (squares) for two different nozzle inlet pressures. It is clear that the shape of the size distribution, going from a bimodal to an almost mono-modal distribution when the nozzle inlet pressure is increased from 300 kPa to 430 kPa is well replicated and shows the increased importance of

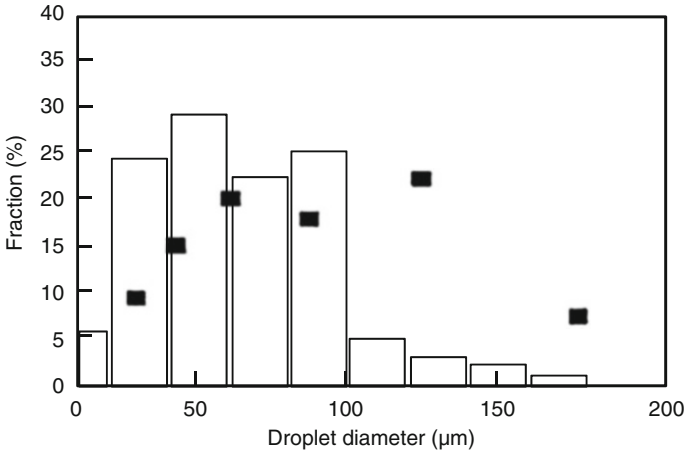


Fig. 9.41 Predicted (*bars*) and measured (*squares*) droplet size distributions for an atomizing gas supply pressure of 300 kPa showing a bimodal distribution [67] (With kind permission from Springer Science + Business Media B.V)

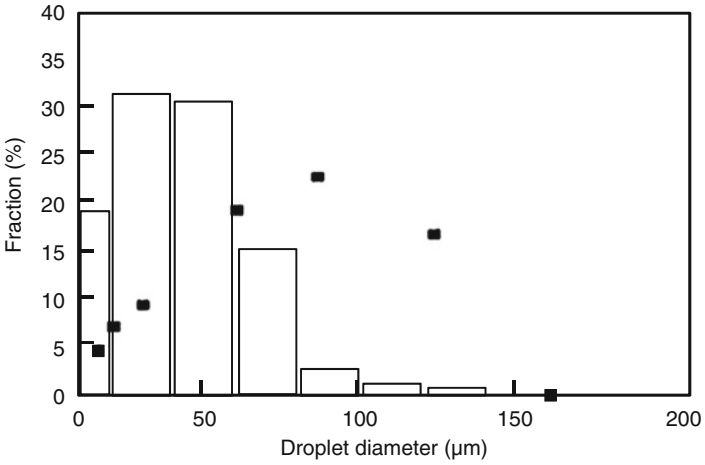


Fig. 9.42 Predicted (*bars*) and measured (*squares*) droplet size distributions for an atomizing gas supply pressure of 430 kPa showing a mono-modal distribution [67] (With kind permission from Springer Science + Business Media B.V)

secondary atomization. However, the calculated sizes are smaller than the measured ones. Clearly, more effort is required for a complete modeling description of the wire arc spray process.

Several CFD calculations were performed for simulating the performance of the TAFA 9000 torch and for optimizing the nozzle designs. Bolot et al. [70] used the commercial PHOENICS code to simulate the exact configuration of the torch.

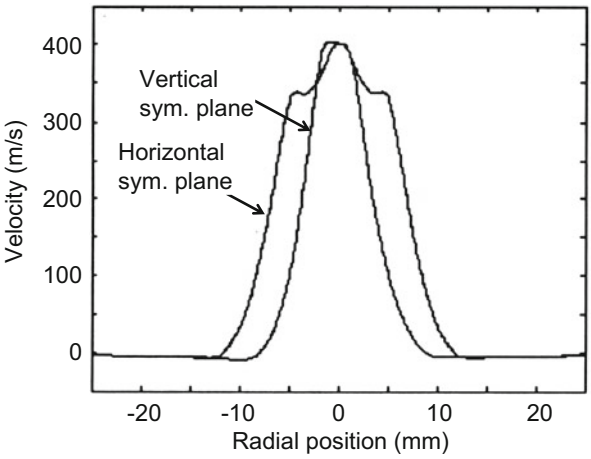


Fig. 9.43 Calculated radial distributions of the axial gas velocity 25 mm from the nozzle exit for two symmetry planes, vertical (plane of the wires) and horizontal, showing the broader profile in the plane perpendicular to the wires. Gas flow rate 1,833 slm (gas supply pressure 285 kPa) [70] (Reprinted with permission of ASM International. All rights reserved)

The effect of the arc on the flow was neglected. Measured relationships between gas flow rate and upstream pressure were used. The results show the gas velocity distributions inside the torch and in the jet. Figure 9.43 [70] shows as an example calculated horizontal and vertical distributions of the axial velocity, indicating the difference. The power required to melt the wires at a given feed rate and to heat the droplets was estimated to be 65 % of the electrical input power. A 2D version of PHOENICS was used to identify nozzle geometries for the same torch that would yield increased droplet velocities [71]. Several designs of the nozzle surrounding the wire tips were simulated, and a design was chosen that had an extension of the nozzle in the downstream direction with a constant cross-sectional area. Experiments performed with such a modified nozzle demonstrated an increase in the droplet velocity by about 20 %. The velocity distributions for the three configurations of the TAFA 9000 torch shown in Fig. 9.17a–c and particle velocities were obtained considering different droplet sizes and acceleration by the gas with the calculated velocity [47], again using the PHOENICS code. The results are shown in Fig. 9.44 [47] where the gas velocities and the velocities of droplets with three different sizes are displayed for two different nozzle arrangements, the Laval-type nozzle without cap (open configuration) and the Laval-type nozzle in the cap. The advantage of having the peak of the gas velocity at the location of the wire tips in the case of the cap is shown clearly, leading to a better acceleration of the droplets.

A similar approach but based on the commercial code FLUENT with a k–ε turbulence model was again applied to the TAFA 9000 torch [71, 72]. The wire material was assumed to be heated to the boiling point, and use of experimentally determined droplet size distributions avoided the requirement of an atomization model. Gas and steel droplet velocity distributions were calculated for the case that there was no effect of the droplets on the gas flow and for the case that the droplets did affect the gas flow. This "loading effect" was found to be significant for higher current (250 A) operation, the axial gas velocity was suppressed by 50 m/s at a

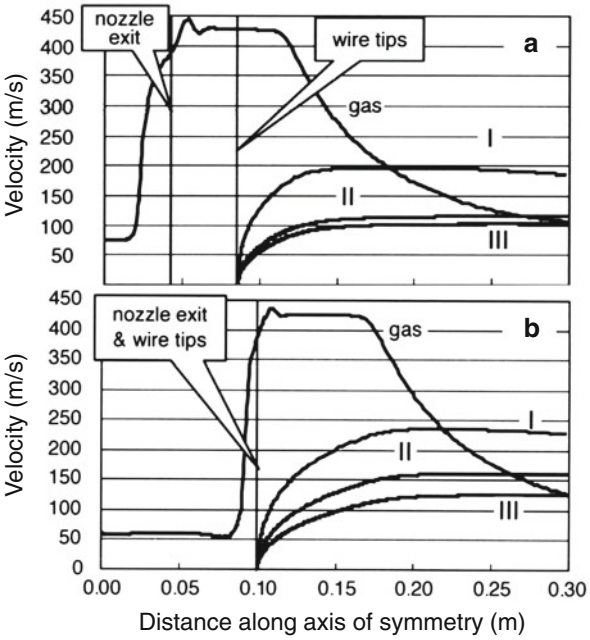


Fig. 9.44 Calculated centerline atomizing gas and droplet velocities for (**a**) the arrangement of a Laval-type atomizing gas nozzle without cap and (**b**) for a secondary nozzle (cap) with Laval-type nozzle. Three different droplet sizes are considered: (I) 10 µm diameter, (II) 51.7 µm diameter, and (III) 70 µm diameter. The higher gas velocities downstream of the wire tips lead to higher droplet velocities. Gas flow rate 2,333 slm [47] (Reproduced with permission of Elsevier)

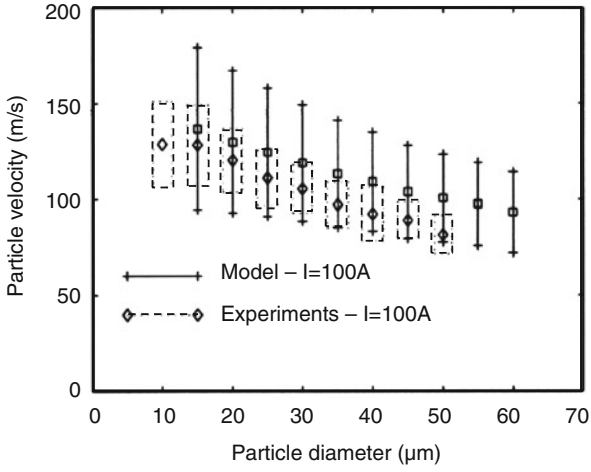


Fig. 9.45 Comparison of calculated and measured particle velocities for different particle sizes [72] (Reproduced with permission of Elsevier)

location 3 cm downstream from the nozzle exit when the interaction with droplets was considered. The effect became less noticeable at farther downstream locations. Again, a different divergence of gas velocities and particle trajectories is observed, with a larger divergence angle in the plane of the wires. This observation is in contrast to that of Pourmousa et al. [49] who observed a larger jet divergence in the plane perpendicular to the plane of the wires, but with a different spray torch. Figure 9.45 [72] shows a comparison of the calculated droplet velocities with

measured ones for an arc current of 100 A. The error bars represent standard deviations. Good agreement is seen for the smaller droplet sizes.

Because of the difficulty of obtaining reliable gas velocity measurements, these simulations are valuable for optimization of nozzle designs and understanding the atomization and droplet acceleration behavior.

9.7 Single Wire Arc Spraying

There have been several efforts pursued for developing a process with one non-consumable electrode and one consumable wire electrode [14, 73–78], a process variously called single wire arc spraying (SWAS), wire arc plasma spraying, or plasma-transferred wire arc spraying. These developments were pursued for different reasons, however, a single wire torch promises a narrower spray pattern and smaller torch design, lighter weight, and significantly reduced gas flow rates. All the materials that are used as wires for the twin wire arc spray process can be used with this process as well.

In several articles [4, 14, 73, 79], a design is described as shown in Fig. 9.46 [14]. The non-consumable thoriated tungsten cathode is placed at the inlet of an air-cooled copper nozzle, and a consumable wire anode is placed downstream of the nozzle exit. The arc is initiated by a breakdown between the cathode and the nozzle and then transferred to the wire anode. The plasma gas is preferably an argon–hydrogen mixture, but other gases have been used including air and nitrogen. A secondary gas enters through a series of openings surrounding the nozzle, and this gas can serve as atomizing gas [15] or as shroud [14, 79] for narrowing the spray pattern. A constant current power supply is used, with currents ranging from 20 to 100 A, with typical operating voltages of around 120 V. Compared to twin wire arc spraying, smaller particle sizes are generated resulting in a finer grain structure of the coating comparable to that of plasma-sprayed coatings. The position of the wire tip can be adjusted by adjusting the operating parameters (current and wire feed rate) as an additional control of coating quality. Typical plasma gas flow

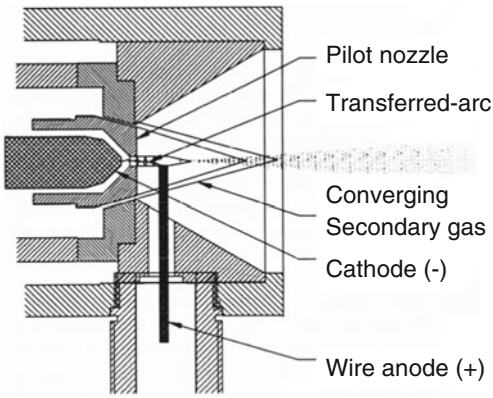


Fig. 9.46 Schematic of single wire plasma-transferred wire arc (PTWA) spray torch [14] (Reprinted with permission of ASM International. All rights reserved)

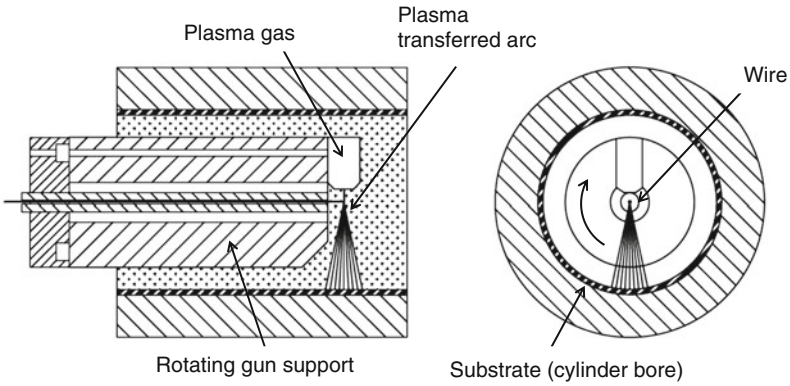


Fig. 9.47 Schematic of use of PTWA spray torch for cylinder bore coating [14] (Reprinted with permission of ASM International. All rights reserved)

rates are 51–71 slm, and shroud gas flow rates range from 621 to 793 slm [79]. Droplet velocities measured using laser Doppler anemometry are 80 m/s for Cu, 98 m/s for stainless steel, and 125 m/s for aluminum when using Ar/H2 and 150 m/s when using air as atomizing gas. The arc current has little effect on the droplet velocity. There can be a powder injected into the liquid droplet stream right downstream of the wire to generate a metal matrix composite coating [14].

The most prominent application of this torch has been the coating of inside cylinder walls of aluminum automobile engine blocks [15, 80], and cylinder walls with i.d.s as small as 75 mm can be coated [14]. Figure 9.47 [14] illustrates the arrangement for an inside cylinder wall coating. For this automotive application, good adhesion is a prime concern, and it has been achieved by using a pretreatment with a fluoride-based flux and a NiAl bond coat before the final low-carbon steel coat is applied [15]. Excellent adhesion has been achieved and porosities of less than 2 %.

A different approach has been pursued by Steffens and Wewel [74] and Steffens and Nassenstein [75]. In this approach an anode nozzle of 2.4 mm diameter surrounds the tip of a cathode wire. The arc is initiated by an rf discharge and operated with a constant current power supply at between 100 A (for stainless steel) and 150 A (for Ti). This process has been developed for the spraying of high purity coatings of Ti or Ta, and a single wire as coating precursor material offers the lowest amount of surface contamination. The spraying has been performed in a controlled atmosphere and under reduced pressure. Typical atomizing gas flow rates of 158 slm are given [74].

Using some features of either of the two mentioned approaches is described by Carlson et al. [76–78]. The wire is surrounded by a nozzle, and a tungsten rod attached to the downstream nozzle face serves as cathode, while the wire serves as the anode (see Fig. 9.48 [77]). A constant current welding power supply has been used, and argon has been used as the atomizing gas with backpressures between 100 and 400 kPa above the atmosphere. Typical arc voltages are between 19 and

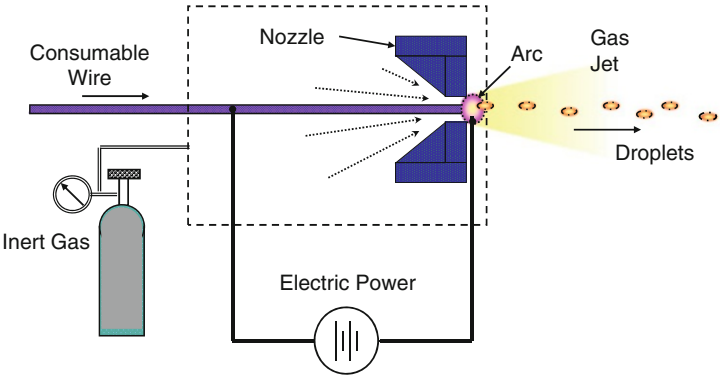


Fig. 9.48 Schematic of High-Definition Single Wire Arc Spray (SWAS) torch [77] (Courtesy of R.R. Carlson. Reprinted with permission of ASM International. All rights reserved)

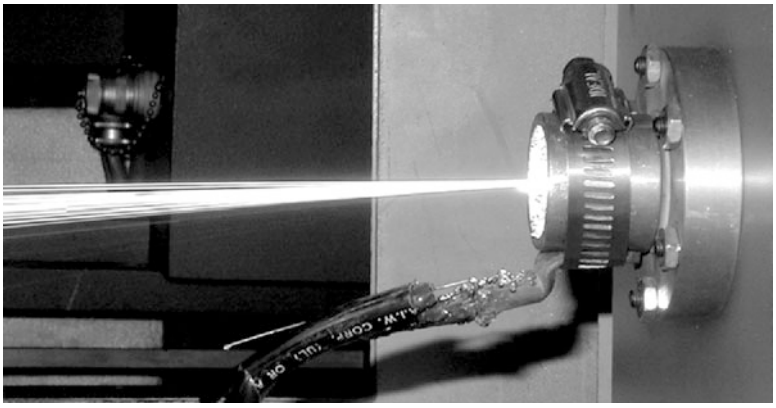


Fig. 9.49 Photograph of particle stream from prototype High-Definition SWAS torch [81] (Reproduced with kind permission of R.R. Carlson)

22 V. This development has been pursued for obtaining narrow particle flux distributions, for coating of small areas such as valve seats. Figure 9.49 [81] shows the particle stream exiting the device. Measured divergence angles are between 2° and 3°, slightly increasing with higher currents and higher back pressures. The wire is fed through a wire straightener before entering the torch to assure minimal lateral movement of the wire tips.

Results have been reported for mild steel wires of 0.584 and 0.762 mm diameter; however, other types of wires have been used. Typical wire feed rates are between 3 and 8.4 m/min, and arc currents are chosen between 35 and 125 A to match the wire feed rates. The gas nozzle diameter is typically 2.5–3 times the wire diameter. Droplet sizes are significantly larger than in any other thermal spray process, with typical mass mean diameters in the order of 300 μm. Figure 9.50 [courtesy of

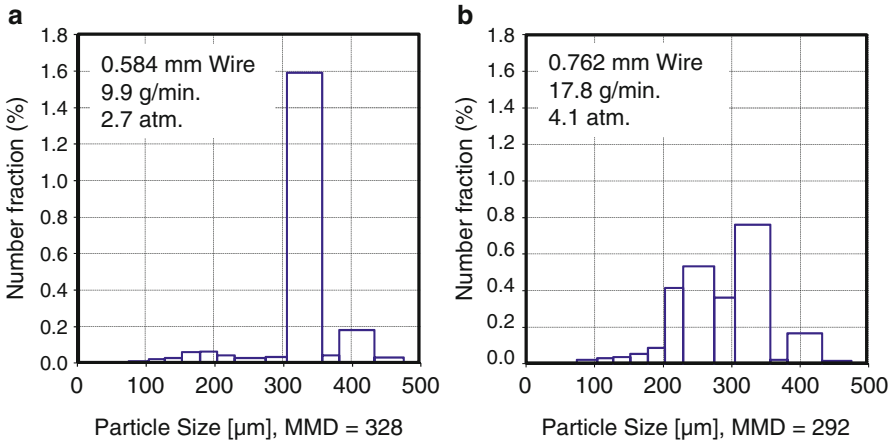


Fig. 9.50 Carbon steel droplet size distributions (shown as number fraction) obtained with the SWAS torch for two different wire diameters, 0.584 and 0.762 mm diameter (Reproduced with kind permission of R.R. Carlson)

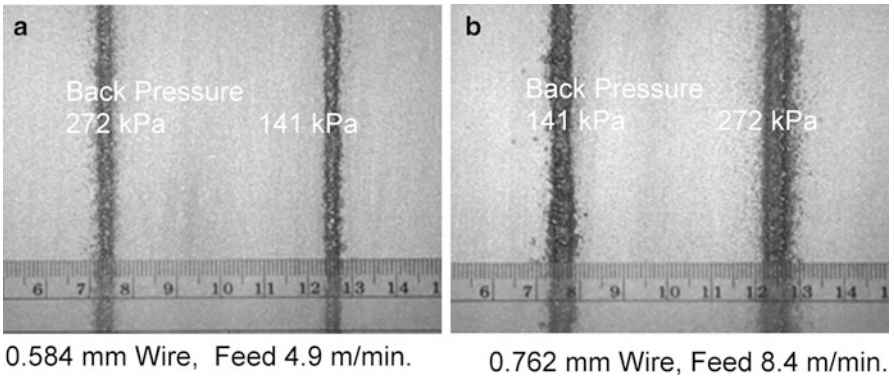


Fig. 9.51 Photograph of mild steel deposit traces on Al substrates for two different wire diameters (**a**) wire diam = 0.584 mm (**b**) wire diam = 0.762 mm, and two different and atomizing gas pressures, 141 and 272 kPa [77] (Courtesy of R.R. Carlson. Reprinted with permission of ASM International. All rights reserved)

R.R. Carlson] shows size distributions of the droplets obtained by spraying into water for two different wire sizes. Droplet size decreases with increasing back pressure and decreases slightly with increasing current. Figure 9.51 [77] shows examples of traces sprayed with this torch, and it is seen that with the smaller wire diameter and the lower back pressure, the deposition foot print is about 3 mm wide. The coating cross sections show dense equiaxed material without the layer structure typical of any other spray coating (see Fig. 9.52 [77]). Deposition efficiencies are between 75 and 86 %, larger for the larger wire size and for higher currents.

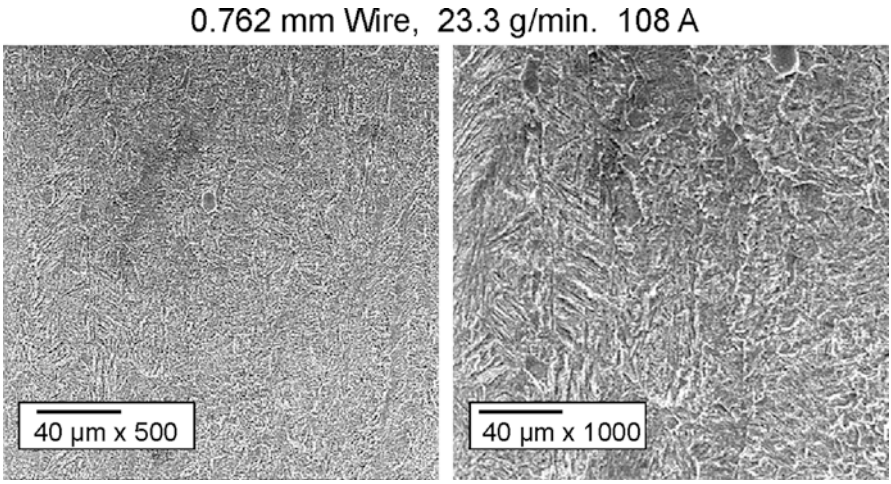


Fig. 9.52 Micrograph of coating cross sections obtained with the High-Definition SWAS torch showing equiaxed large grain deposits [81] (Reproduced with kind permission of R.R. Carlson)

Deposition rates are up to 15.6 g/min for the smaller diameter wire, and up to 25.8 g/min for the larger diameter wire.

The single wire arc technology has demonstrated specific features attractive for some applications. However, at present its potential has not been exploited to a larger degree.

9.8 Special Developments: Low-Pressure Wire Arc and 90° Angle Spraying

Some of the low-pressure wire arc spray developments have been described in the section on single wire arc spraying. Twin wire low-pressure arc spraying has also been reported. The entire wire arc system has been installed in a low-pressure deposition chamber operated at 52.6 kPa (400 Torr) [37]. The purpose for such a process development has been the generation of high purity deposits, for example, of NiTi foils for shape memory applications. Wire arc spraying offers the potential of lower contamination of the feedstock because the wire has less surface area than the powders used for plasma spraying. Using argon as atomizing gas and operating the torch with 9.5 kW, 0.2–0.3 mm thick foils have been generated with about 5 % porosity.

Developments on changing the droplet fluxes by 90° have been pursued for inside cylinder wall coating applications [82, 83]. Figure 9.53 [84] illustrates the approaches that have been pursued for a 90° bending of the droplet jet, as described in [82, 83]. The automobile industry and the introduction of aluminum engine blocks have been the principal driver of such developments. For this application a coating of 300–400 µm is desired with very good adhesion and porosity of less than 5 %. Benary et al. [85] describe an ID extension for a Sulzer Metco Smartarc torch.

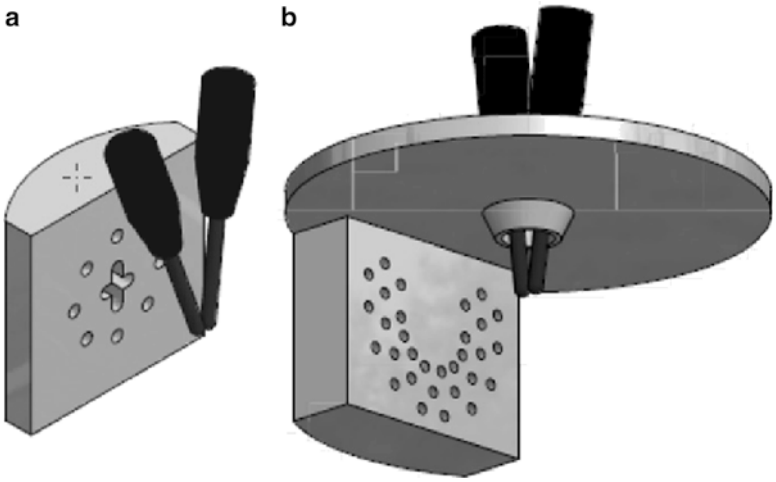


Fig. 9.53 Schematic of nozzle arrangement for 90° angle spraying according to (**a**) Benary [82] and (**b**) Dunkerley et al. [83], as presented in [84] (Reprinted with permission of ASM International. All rights reserved)

Atomization occurs by blowing the gas through a 90° nozzle consisting of several orifices immediately downstream of the initial droplet formation. This perpendicular gas flow is responsible for secondary atomization. The torch is operated with a 28 V, 200 A setting, and 448.2 kPa pressure for the 90° nozzle. Velocities of NiAl droplets as measured with a DPV 2000 instrument are reduced from 88 m/s with straight flow to 66 m/s in the propagation direction with the cross flow. Little effect on the droplet temperature has been noted.

Bolot et al. [84] report on a 90° nozzle optimization effort for the TAFA torch, where a downstream secondary gas flow perpendicular to the original gas flow changes the droplet flow direction. Torch operation is with 30–35 V, 150 A, gas supply pressures of 400–600 kPa, and perpendicular gas flow rates of 1,333–11,667 slm. The wire guides are stationary and only the secondary gas flow nozzle head rotates around the initially formed droplet stream. Consequently, a variation in deposition rate with the circumferential angle is found. Using fluid dynamics calculations with the FLUENT code, the effect of different nozzle designs has been investigated and an optimal nozzle design has been found.

9.9 Summary and Conclusions

The wire arc spray process compared to other thermal spray processes presents the following advantages:

It is one of the simplest and most economical processes.
It has one of the highest deposition rates.
Thick coatings (a few millimeters) can be easily obtained.

The substrate heating is low and usually substrate cooling is not required.
Most of the supplied energy goes into the melting of the coating material, eliminating the need for water cooling.
The system can be moved easily and used on site, for example, to coat a steel bridge.

These advantages are countered by the disadvantages:

The material to be sprayed must be electrically conducting and can only be obtained in form of a wire, which implies that it must be ductile and not too stiff; however, with the cored wires containing brittle material such as refractories or ceramics in a ductile envelope, the problem is solved, at least partially, and, for example, cermet coatings can be obtained.
Coatings are rather porous and their oxide content is higher than with other spray processes.

Wire arc spray coatings have found wide spread use for corrosion protection and wear reduction in large-scale manufacturing or infrastructure maintenance applications where the advantages outweigh the shortcomings. However, continuous improvement in process control and coating quality is leading to a penetration of a market where the coating represents a high-added value to the component. A further diversification of process details and products must be expected.

Nomenclature

D	Droplet diameter, m
I	Arc current, A
L_s	Characteristic length, m
m°	Volumetric gas flow rate, m^3/s
T	Droplet temperature, K
v	Droplet velocity, m/s
X, Y	Coordinates of the droplet in the lateral direction, m
Z	Axial coordinate of the droplet
We	Weber number $We = u_{rel}{}^2 L_s \rho_g / \sigma_l$
u_{rel}	Relative velocity of gas to droplet, m/s
ρ_g	Mass density of gas, kg/m^3
σ_l	Surface tension of liquid (N/m)

References

1. Schoop MU (1915) Apparatus for spraying molten metal and other fusible substances. US Patent No. 1,133,507
2. Steffens HD (1966) Metallurgical changes in the arc spraying of steel. Br Welding J 13(10):597–605

3. Steffens HD, Babiak Z, Wewel M (1990) Recent developments in arc spraying. IEEE Trans Plasma Sci 18(6):974–979
4. Marantz D, Marantz D (1990) State of the art arc spray technology. In: Bernecki TF (ed) Proceedings of the thermal spray research and applications proceedings of the 3rd national thermal spray conference, Long Beach, California. ASM International, Materials Park, OH, pp 113–118
5. Lester T (2005) Metallized coatings application, an overview of the flame-and arc-spraying processes used for surface finishing. Organ Finishing July/August:35–38
6. Liu X (2001) Arc spraying in China. J Therm Spray Technol 10(1):40–43
7. Wang R, Song D, Liu W, He X (2010) Effect of arc spraying power on the microstucture and mechanical properties of Zn-Al coating deposited onto carbon fiber reinforced epoxy composites. Appl Surf Sci 257:203–209
8. Varis T, Rajamake E (2002) Effect of the nozzle design and atomization gas on the properties of the electric arc sprayed Ni18Cr6A12Mn-coatings. In: Lugscheider E (ed) Proceedings of the international thermal spray conference Tagungsband conference proceedings, Essen. ASM Thermal Spray Society, Materials Park, OH, pp 550–552
9. Chang CH, Jeng MC, Su CY, Huang TS (2011) A study of wear and corrosion resistance of arc-sprayed Ni-Ti composite coatings. J Therm Spray Technol 20(6):1278–1285
10. Sakoda N, Hida M, Takemoto Y, Sakakibara A, Tajiri T (2003) Influence of atomoization gas on coating properties under Ti arc spraying. Mater Sci Eng A342:264–269
11. Sampson ER (1993) The economics of arc vs. plasma spray for aircraft components. In: Berndt CC, Bernecki TF (eds) Proceedings of the 5th national thermal spray conference, Anaheim, CA. ASM International, Materials Park, OH, pp 257–262
12. Zajchowski P, Crapo HB (1669) Evaluation of three dual-wire electric arc-sprayed coatings: industrial note. J Therm Spray Technol 5(4):457–462
13. Nakagawa M, Shimoda K, Tomoda T, Koyama M, Ishikawa Y, Nakajima T (1990) Development of mass production technology of arc spraying for automotive engine aluminum alloy valve lifters. In: Proceedings of the 3rd national thermal spray conference, pp 457–464
14. Marantz DR, Kowalsky KA, Marantz D (1991) Wire-arc-plasma spray process—basic principles and its versatility. In: Bernecki TF (ed) Proceedings of the fourth national thermal spray conference, Pittsburgh, PA. ASM International, Materials Park, OH, pp 381–387
15. Cook D, Zaluzec M, Kowalsky KA (2003) Development of thermal spray for automotive cylinder bores. In: Marple B, Moreau C (eds) Proceedings of the 2003 international thermal spray conference, Orlando, FL. ASM International, Materials Park, OH, pp 143–147
16. Zhang ZL, Li DY, Wang SY (2006) High temperature performance of arc-sprayed aluminum bronze coatings for steel. Trans Nonferrous Met Soc 16:868–872
17. Cooke K, Oliver G, Buchanan V, Palmer N (2007) Optimization of the electric wire arc-spraying process for improved wear resistance of sugar mill roller shells. Surf Coat Technol 202:185–188
18. Chen Y, Liang X, Wei S, Liu Y, Xu B (2009) Heat treatment induced intermetallic phase transition of arc-sprayed coating prepared by the wires combination of aluminum-cathode and steel-anode. Appl Surf Sci 255:8299–8304
19. Wilden J, Bergmann JP, Jahn S, Knapp S, van Rodijnen F, Fischer G (2007) Investigation about the chrome steel wire arc spray process and the resulting coating properties. J Therm Spray Technol 16(5–6):759–767
20. Laika A, Chakravarthyb DP, Kale GB (2005) On characterisation of wire-arc-plasma-sprayed Ni on alumina substrate. Mater Charact 55:118–126
21. Fang JC, Xu WJ, Zhao ZY (2005) Arc spray forming. J Mater Process Technol 164–165:1032–1037
22. Grant PS, Duncan SR, Roche A, Johnson CF (2006) Scientific, technological, and economic aspects of rapid tooling by electric arc spray forming. In: Marple B, Hyland MM, Lau Y-C, Lima RS, Voyer J (eds) Proceedings of the 2006 international thermal spray conference, Seattle, Washington, vol 4. ASM International, Materials Park, OH, pp 796–801

23. Newbery AP, Grant PS (2009) Arc sprayed steel: microstructure in severe substrate features. J Therm Spray Technol 18(2):256
24. Sampson ER, Zwetsloot MP (1997) Arc spray process for the aircraft and stationary gas turbine industry. J Therm Spray Technol 6(2):150–152
25. Tillmann W, Vogli E, Abdulgader M (2008) Asymmetric melting behavior in twin wire arc spraying with cored wires. J Therm Spray Technol 17(5–6):974–982
26. Tillmann W, Vogli E, Abdulgader M, Gurris M, Kuzmin D, Turek S (2008) Particle behavior during the arc spraying process with cord wires. J Therm Spray Technol 17(5–6):966–973
27. Pokhmurskii V, Student M, Dovhuny V, Sydorak I, Pokhmurska H (2002) Wear resistance arc-sprayed coating from power wires. In: Lugscheider E (ed) Proceedings of the international thermal spray conference, Essen. ASM Thermal Spray Society, Materials Park, OH, pp 559–562
28. Zhao L, Fu B, He D, Kutschmann P (2009) Development of a new wear resistant coating by arc spraying of a steel-based cored wire. Front Mech Eng 4(1):1–4
29. Meng FJ, Xu BS, Zhu S, Ma SN, Zhang W (2005) Oxidation performance of Fe-AI/WC composite coatings produced by high velocity arc spraying. J Cent South Univ Technol 12(2):222–225
30. Fang JY, Li ZX, Jiang JM, Shi YW (2007) Difference in particle characteristics and coating properties between spraying metallic and ceramic powder cored wires. Trans Nonferrous Met Soc 17:537–542
31. Fang JJ, Li ZX, Shi YW (2008) Microstructure and properties of TiB2 containing coatings prepared by arc spraying. Appl Surf Sci 254:3849–3858
32. Pokhmurska H, Dovhunykb V, Studentb M, Bielanskac E, Beltowska E (2002) Tribological properties of arc sprayed coatings obtained from FeCrB and FeCr-based powder wires. Surf Coat Technol 151–152:490–494
33. Skoblo TS, Vlasovets VM, Moroz VV (2001) Structure and distribution of components in the wroking layers upon reconditioning of parts by electric-arc metallization. Metal Sci Heat Treatment 43(11–12):497–500
34. He D, Dong N, Jiang J (2007) Corrosion behavior of arc sprayed nickel-based b coatings. J Therm Spray Technol 16(5–6):850–586
35. Luo LM, Liu SG, Yu J, Luo J, Li J (2010) Effect of AI content on high temperature erosion properties of arc-sprayed FeMnCrAI/Cr_3C_2 coatings. Trans Nonferrous Met Soc 20:201–206
36. Luo LM, Yu J, Liu SG, Li J (2010) Thermal shock resistance of FeMnCr-Cr3C2 coatings deposited by arc spraying. J Wuhan Univ Technol Mater Sci April:243–247
37. Halter K, Sickinger A, Zysset L, Siegmann S (2003) Low pressure wire arc and vacuum plasma spraying of NiTi shape memory alloys. In: Marple B, Moreau C (eds) Proceedings of the 2003 international thermal spray conference, Orlando, FL. ASM International, Materials Park, OH, pp 289–295
38. Wang X, Heberlein J, Pfender E, Gerberich W (1999) Effect of nozzle configuration, gas pressure and gas type on coating properties in wire arc spray. J Therm Spray Technol 8(4):565–575
39. Hussary NA, Heberlein J (2001) Atomization and particle jet interactions in the wire-arc spaying process. J Therm Spray Technol 10(4):604–610
40. Hussary NA, Heberlein J (2007) Effect of system parameters on metal breakup and particle formation in the wire arc spray process. J Therm Spray Technol 16(1):140–152
41. Sheard J, Heberlein J, Stelson K, Pfender E (1997) Diagnostic development for control of wire-arc spraying. In: Berndt CC (ed) Proceedings of 1st united thermal spray conference, Indianapolis, IN. ASM International, Materials Park, OH, pp 613–618
42. Hussary NA (1999) Fluid dynamic investigations of wire arc spraying process. MS Thesis, University of Minnesota, Minneapolis
43. Chigier N (1981) Energy, combustion and environment. McGraw Hill, New York, NY
44. Mansour A, Chigier N (1990) Disintegration of liquid sheets. Phys Fluids A 2(5):706–719
45. Hussary NA (2003) Investigations into the wire arc spray process. University of Minnesota

46. Wang X, Heberlein J, Pfender E, Gerberich W (1995) Enhancement of coating uniformity with secondary gas atomization in wire arc spray. In: Heberlein J, Ernie DW, Roberts JT (eds) Proceedings of the 12th international symposium on plasma chemistry, Minneapolis, MN. International Union of Pure and Applied Chemistry, pp 907–913
47. Liao H, Zhu YL, Bolot R, Coddet C, Ma SN (2005) Size distribution of particles from individual wires and the effects of nozzle geometry in twin wire arc spraying. Surf Coat Technol 200:2123–2130
48. Planche MP, Lakat A, Liao H, Coddet C (2003) Investigations of in-flight particle characteristics through DPV measurements and correlation with impact analysis and coating properties. In: Marple B, Moreau C (eds) Proceedings of the international thermal spray conference, Orlando, FL. ASM International, Materials Park, OH, pp 1175–1182
49. Pourmousa A, Mostaghimi J, Abedini A, Chandra S (2005) Particle size distribution in a wire-arc spraying system. J Therm Spray Technol 14(4):502–510
50. Watanabe T, Sato T, Nezu A (2002) Electrode phenomena investigation of wire arc spraying for preparation of Ti-Al intermetallic compounds. Thin Solid Films 407:98–103
51. Kawase R, Kureishi M, Minehisa S (1984) Relation between arc spraying condition and adhesive strength of sprayed coating. Trans Jpn Welding Soc 15(2):27–33
52. Kawase R, Kureishi M, Maehara K (1984) Arc phenomena and wire fusion in arc spraying. Trans Jpn Welding Soc 15(2):34–39
53. Kawase R, Kureishi M (1985) Fused metal temperature in arc spraying. Trans Jpn Welding Soc 16(1):82–88
54. Kawase R, Kureishi M (1985) Relation between adhesion strength of arc sprayed coating and fused metal temperature. Trans Jpn Welding Soc 16(2):69–73
55. Hussary NA, Schein J, Heberlein J (1999) Control of jet convergence in wire arc spray systems. In: Lugscheider E, Kammer PA (eds) Proceedings of the united thermal spray conference, Düsseldorf, Germany. ASM International, Materials Park, OH, pp 335–339
56. Wang X, Heberlein J, Pfender E, Gerberich W (1996) Effect of gas velocity and particle velocity on coating adhesion in wire arc spraying. In: Berndt CC (ed) Proceedings of 9th national thermal spray conference, Cincinnati, OH. ASM International, Materials Park, OH, pp 807–811
57. Pourmousa A, Abedini A, Mostaghimi J, Chandra S (2004) Particle diagnostics in wire-arc spraying system. In: Ohmori A (ed) Proceedings of the international thermal spray conference Osaka, Japan. ASM International, Materials Park, OH, pp 962–967
58. Jandin G, Planche M-P, Liao H, Coddet C (2002) Relationships between in-flight particle characteristics and coating microstructure for the twin wire arc spray process. In: Lugscheider E (ed) Proceedings of the international thermal spray conference, Essen. ASM International, Materials Park, OH, pp 954–959
59. Planche M-P, Liao H, Coddet C (2004) Relatioship between in-flight particle characteristics and coating microstructure with a twin wire arc spray process and different working conditions. Surf Coat Technol 182(2–3):215–226
60. Wilden J, Bergmann JP, Jahn S, Knapp S, van Rodijnen F, Fischer G (2007) Investigation about the chrome steel wire arc spray process and the resulting coating properties. In: Marple B, Hyland M, Lau YC, Li CJ, Lima RS, Montavon G (eds) Proceedings of the international thermal spray conference, Beijing, People's Republic of China. ASM International, Materials Park, OH, pp 759–767
61. Mohanty PS, Allor R, Lechowicz P, Parker RA, Craig JE (2003) Particle temperature and velocity characterization in spray tooling process by thermal imaging technique. In: Marple B, Moreau C (eds) Proceedings of the international thermal spray conference, Orlando, FL. ASM International, Materials Park, OH, pp 1183–1190
62. Watanabe T, Wang X, Heberlein J, Pfender E, Herwig W (1996) Voltage and current fluctuations in wire arc spraying as indications for coating properties. In: Berndt CC (ed) Proceedings of 9th national thermal spray conference, Cincinnati, OH. ASM International, Materials Park, OH, pp 577–583

63. Wang X, Heberlein J, Pfender E, Gerberich W (1995) Effect of shrouded CO_2 gas atomization on coating properties in wire arc spray. In: Berndt CC, Sampath S (eds) Proceedings of the 8th national thermal spray conference, Houston, TX. ASM International, Materials Park, OH, pp 31–37
64. Steffens HD, Nasenstein K (1999) Influence of spray velocity on arc-sprayed coating structures. J Therm Spray Technol 8(3):454–460
65. Watanabe T, Wang X, Heberlein J, Pfender E (1995) Fume generation mechanism in wire arc spraying. In: Heberlein J, Ernie DW, Roberts JT (eds) Proceedings of the 12th international symposium on plasma chemistry, Minneapolis, MN. International Union of Pure and Applied Chemistry, pp 889–894
66. Kelkar M, Heberlein J (2000) Physics of an arc in cross flow. J Phys D Appl Phys 33:2172–2182
67. Kelkar M, Heberlein J (2002) Wire-arc spray modeling. Plasma Chem Plasma Process 22(1):1–25
68. Kelkar M, Hussary NA, Schein J, Heberlein J (1998) Optical diagnostics and modeling of gas and droplet flow in wire arc spraying. In: Coddet C (ed) Proceedings of the 15th international thermal spray conference, Nice, France. ASM International, Materials Park, OH, pp 329–324
69. Hsiang LP, Faeth GM (1992) Near-limit drop deformation and secondary breakup. Int J Multiphase Flow 18:635–652
70. Bolot R, Bonnet R, Jandin G, Coddet C (2001) Application of CAD to CFD for the wire arc spray process. In: Berndt CC, Khor KA, Lugscheider E (eds) Proceedings of the international thermal spray conference, Singapore. ASM International, Materials Park, OH, pp 889–894
71. Gedzevicius I, Bolot R, Liao H, Coddet C (2003) Application of CFD for wire-arc nozzle geometry improvement. In: Marple B, Moreau C (eds) Proceedings of the international thermal spray conference, Orlando, FL. ASM International, Materials Park, OH, pp 977–980
72. Bolot R, Planche M-P, Liao H, Coddet C (2008) A three-dimensional model of the wire-arc spray process and its experimental validation. J Mater Process Technol:94–105
73. Kowalsky KA, Marantz DR, Herman H (1991) Characterization of coatings produced by the wire-arc-plasma spray process. In: Bernecki TF (ed) Proceedings of the fourth national thermal spray conference, Pittsburgh, PA. ASM International, Materials Park, OH, pp 389–394
74. Steffens HD, Wewel M (1991) One wire vacuum arc spraying-a new modified process. In: Bernecki TF (ed) Proceedings of the fourth national thermal spray conference, Pittsburgh, PA. ASM International, Materials Park, OH, pp 395–398
75. Steffens HD, Nassenstein K (1994) Recent developments in single-wire vacuum arc spraying. J Therm Spray Technol 3(4):412–417
76. Carlson RR, Heberlein J, Hussary NA, Shi K (2000) High-definition single-wire-arc-spray. In: Berndt CC (ed) Proceedings of the 1st international thermal spray conference, Montreal, QBC. ASM International, Materials Park, OH, pp 709–716
77. Carlson RR, Heberlein J (2001) Effects of operating parameters on high definition single wire arc spraying. In: Berndt CC, Khor KA, Lugscheider E (eds) Proceedings of the international thermal spray conference, Singapore. ASM International, Materials Park, OH, pp 447–453
78. Carlson RR, Heberlein JVR (2002) Single-wire arc spray apparatus and methods for using same. US Patent No. 6,610,959 B2
79. Kowalsky KA, Marantz DR, Neiser R, Smith MF (1992) Diagnostic behavior of the wire-arc-plasma spray process. In: Berndt CC (ed) Proceedings of the thermal spray: international advances in coatings technology, Orlando, FL. ASM International, Materials Park, OH, pp 337–342
80. McCune RC Jr, Reatherford LV, Zaluzec M (1993) Thermally spraying metal/solid lubricant composites using wire feedstock. US Patent No. 5,194,304
81. Carlson RR (2005) Single wire arc spray. University of Minnesota
82. Benary R (2000) Thermal spray gun extension and gas jet member therefore. US Patent No. 6,091,042

83. Dunkerley JP, Friedrich TA, Irons G (1999) Apparatus for rotary spraying a metallic coating. US Patent No. 5,908,670
84. Bolot R, Liao H, Mateus C, Coddet C, Bordes J-M (2007) Optimization of a rotating twin wire-arc spray gun. In: Marple B, Hyland MM, Lau Y-C, Li C-J, Lima RS, Montavon G (eds) Proceedings of the 2007 international thermal spray conference, Beijing, People's Republic of China, vol 5–6. ASM International, Materials Park, OH, pp 783–790
85. Benary R, Margolies J, Gutleber J (1999) A study and comparison of spray stream formation using two wire arc 90-degree, and 0-degree spray processes. In: Lugsheider E, Kammer PA (eds) Proceedings of the united thermal spray conference, Dusseldorf. ASM Thermal Spray Society, Materials Park, OH, pp 242–246

Chapter 10
Plasma-Transferred Arc

Abbreviations

FTC	Fused tungsten carbide
PTA	Plasma-transferred arc
SAW	Submerged arc welding
slm	Standard liters per minute
TIG, MIG	Tungsten inert gas welding or metal inert gas welding, respectively

10.1 Description of Concept

The development of the plasma-transferred arc coating process was directed toward reducing the cost of corrosion and wear-resistant parts. Regular steel parts with an appropriate plasma-transferred arc (PTA) coating can exhibit superior corrosion and wear behavior even compared to specialty alloys. The process is significantly different from the other coating processes as the substrate is part of the electrical circuit that delivers the power for the coating process. The substrate in most of the cases serves as the anode of the arc transferred from the torch and only sometimes as the cathode. Thus it must consist of an electrically conducting material. Figure 10.1 presents a schematic of the system showing a cathode surrounded by a water-cooled copper nozzle constricting the arc between the cathode and the work piece. The plasma gas is introduced at the base of the cathode. The nozzle serves as the "pilot arc" anode, i.e., there is a current supplied by a separate power supply flowing from the nozzle/pilot arc anode to the cathode. This pilot arc pre-ionizes the gap between the cathode and the work piece and allows easy establishment of the transferred arc and a good control of its arc current. The pilot arc further stabilizes the transferred arc when the plasma is cooled by the powder injection and assures the correct positioning of the anode attachment and the powder deposition area. The powder is introduced into the arc plasma though two or more orifices located on a ring surrounding the exit of the nozzle. A further annular

P.L. Fauchais et al., *Thermal Spray Fundamentals: From Powder to Part*, 631
DOI 10.1007/978-0-387-68991-3_10, © Springer Science+Business Media New York 2014

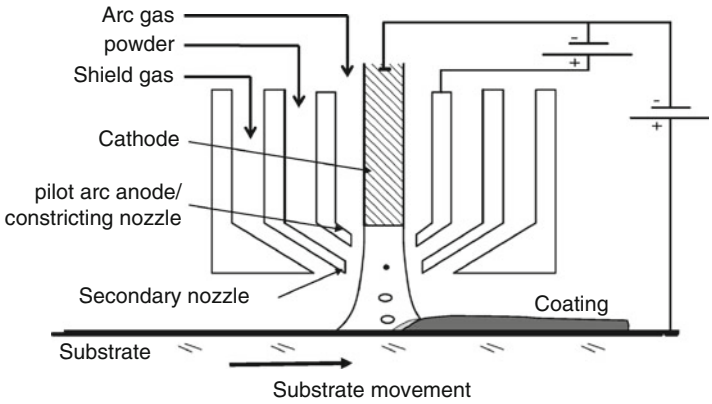


Fig. 10.1 Schematic of PTA torch

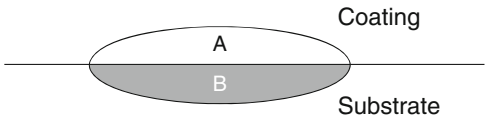


Fig. 10.2 Defining the dilution of a PTA coating

slot surrounding the powder injection ring provides the shield gas flow, necessary to avoid reaction of the molten metal with the environmental air.

The coating is different from those obtained from other thermal spray coating processes because the anode attachment of the arc is heating and to some degree melting the substrate material, and the molten powder of the coating material is mixing with the molten substrate material. The consequence is that a good metallurgical bond or fusion bond is achieved, and that the porosity is very low; however, the heat penetration region and in particular the region where the coating material is mixed with the substrate material can change the properties of both the substrate and the coating. This mixing region is expressed in terms of the "dilution." As illustrated in Fig. 10.2, representing a cross section though a bead, the dilution (D) is defined as the ratio of the area where the substrate and coating materials are mixed (B), to the total area in which the coating material appears ($A + B$). That is,

$$D = B/(A + B)\%$$

The dilution is a major consideration when the functionality of the coating is evaluated, and it depends on the thickness of the coating. For a coating with a thickness larger than 1 mm, dilutions of 5 % or slightly less can be achieved, and thicker coatings can have even lower dilutions.

The transfer of the arc to the work piece makes the PTA process more similar to the weld overlay processes than to the thermal spray processes. The use of powders provides the communality with spray processes. Comparing the PTA process with the other weld overlay processes we can say the following:

10.1.1 Tungsten Inert Gas

Tungsten Inert Gas (TIG) welding uses a free burning, unconstricted arc with the filler material introduced in the form of a wire. The arc has a less stable attachment, produces higher dilution values, and larger heat affected zones compared to the PTA process. Deposition rates are in the order of 3 kg/h or less [1].

10.1.2 Metal Inert Gas

Metal Inert Gas (MIG) welding uses a wire anode and has the work piece as the cathode. This has the advantage that oxide layers on light metals can be cleaned off before deposition. Deposition rates are in the order of 6 to 9 kg/h [1] and the dilution is somewhat less than with the TIG welding process because less energy of the arc is transferred to the cathode, although not as low as with PTA.

In the *Submerged Arc Welding (SAW)* process the coating material is introduced in form of a consumable wire electrode, the other electrode being the work piece. A blanket of flux material, introduced in powder form, surrounds the arc. Currents range from 400 A to 3,000 A. The flux material is typically calcium fluoride with aluminum oxide, with some alloying powders added. Deposition rates are in the order of 15 to 40 kg/h [1], and dilution values are with 15–40 % quite high [2] and require deposition of several layers. This process is advantageous for rapid coating of large areas.

In *laser weld deposition*, the substrate is melted by a laser beam and the deposition material is introduced either in the form of a powder or in the form of a wire. Since the beam can be moved with high precision, this process is used advantageously for coating small areas. The equipment is rather expensive. The same is true for electron beam overlaying, which is used for some special cases.

The *PTA* process combines good control over the process with high-deposition rates (typically 3–10 kg/h, with up to 20 kg/h possible) and good coating quality with practically no porosity and dilution of less than 7 % (better than 5 % have been reported, see next section). Feeding of multiple powders allows a range of coatings to be obtained. Compared to other weld overlay processes, the coating quality is less sensitive to the torch–substrate distance. Compared to other thermal spray processes, PTA has the major advantage that alloy formation can take place in the metal pool during the process, allowing a wider range of metal compound combinations or of metal matrix composite compositions than with any other spray deposition process. Additional advantages [3] are that:

- Less expensive powders can be used
- Very low porosity (almost theoretical density) can be achieved
- Higher deposition rates are possible
- Thicker coatings in one pass can be achieved requiring fewer passes and yielding faster deposition rates
- Better adhesion is obtained though the metallurgical bond

- Higher deposition efficiencies (>95 %) are achieved
- The molten material is protected by a gas shield
- Short stand-off distances (10 to 20 mm) can be used, resulting in more focused deposition
- Smoother surfaces are obtained
- The coatings have fine microstructure and better wear characteristics

The limitations of this process are as follows:

- The requirement of a metallic substrate
- Limitations on the substrate shape complexity
- Dilution changing some of the coating and the substrate properties
- High heat input into the substrate, requiring process modifications or active substrate cooling when smaller size substrates are coated
- In a non-horizontal position the gravitational acceleration has a non-negligible influence on the fluid flow and the coating geometry, an influence that must be counteracted by reducing the energy input per unit length [4]
- Coatings are also dependent on substrate shape such as corners and grooves [5]
- Residual stresses can be rather high
- Metallurgical compatibility between coating and substrate must be considered

While the normal PTA process uses the pilot arc to initiate and stabilize the main arc, a number of processes operate with no current flow to the pilot arc anode once the transferred arc is established, making the process similar to the TIG overlay process. Examples of such processes are included in this chapter as long as they use powder as the coating material.

There are a number of processing parameters that need to be controlled, and the lack of understanding of the process parameter influences and the need for automated controls have slowed the acceptance of this process. However, the excellent coating qualities possible and the significant advances in the process understanding over the last 25 years have resulted in a strong increase in the utilization of PTA. In the following, the equipment and the operating parameters will be discussed. The next section will give an overview of the materials most frequently used and some applications. This section will be followed by a description of the process characteristics that have been determined in specific experiments. A description of the effects of process parameter changes, of equipment and process modifications for specific applications, and finally some specific examples of PTA coating applications conclude this chapter.

10.2 Equipment and Operating Parameters

The equipment consists of the following components (see Fig. 10.3):

(a) The PTA torch, described in more detail below
(b) A two-stage power supply or two independent power supplies, one for the pilot arc and one for the transferred arc; power supply control is for constant current

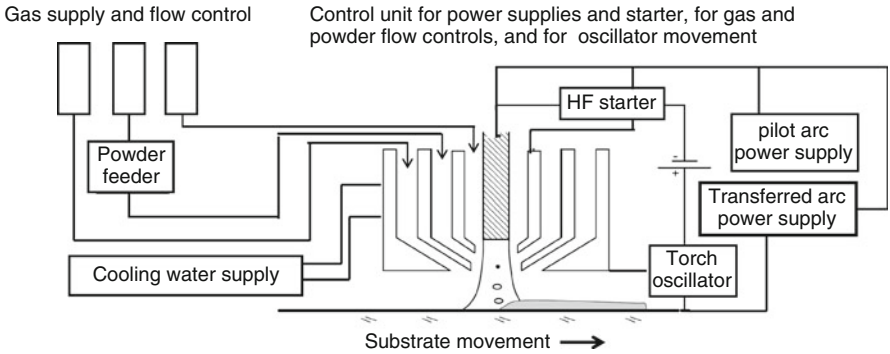


Fig. 10.3 The various components of a PTA system

with relatively low open circuit voltages (<100 V); instead of the two stage power supply, a single d.c. power supply can be used with the pilot arc anode connected to the positive power supply terminal via a resistor [6]

(c) A high-frequency starter unit in the pilot arc circuit to facilitate the initial breakdown and establishment of the pilot arc

(d) A closed loop high-pressure cooling water supply for the torch; typically 6 slm are required at 0.45–0.6 MPa (4.5–6 bar); the heat from the torch is removed by a heat exchanger which is connected to a chilled water circuit or city water circuit

(e) Gas supplies and flow controls for the plasma gas and the shield gas; usually high-purity argon is used as the plasma gas, helium being a possible addition, and argon with addition of 5–7 % hydrogen is used as the shield gas

(f) A powder feeder which is essentially the same as in other thermal spray processes, although the use of larger size powders (typically 50–150 μm) may require some adjustments; multiple powder feeders are used for composite coatings; the powder is transported by a carrier gas (usually argon or argon with a few percent hydrogen) to the torch

(g) A control console which allows selection of the currents, the gas flow rates and the powder feed rates; the control console also houses the interlocks that prevent arc initiation when there is no plasma gas flow and no cooling water flow

(h) Mechanical systems that allow the movement of the substrate and the oscillatory movement of the torch limiting the local heat flux and producing flatter beads; a multi-axis robot could be used; however, the arc transfer to the work piece poses some limitations on the complexity of the shapes that can be coated and therefore the needs for multi-axis robots; the torch oscillatory movement is perpendicular to the substrate movement, has a frequency of about 1 Hz, and increases the bead width to about 10 mm.

The torch consists of a rod cathode, typically 6–8 mm diameter (although smaller diameters have been used), usually made of thoriated tungsten (2 % ThO_2). The plasma gas is introduced into the torch at the base of the cathode, and usually high-purity argon or an argon–helium mixture is used. Downstream of the

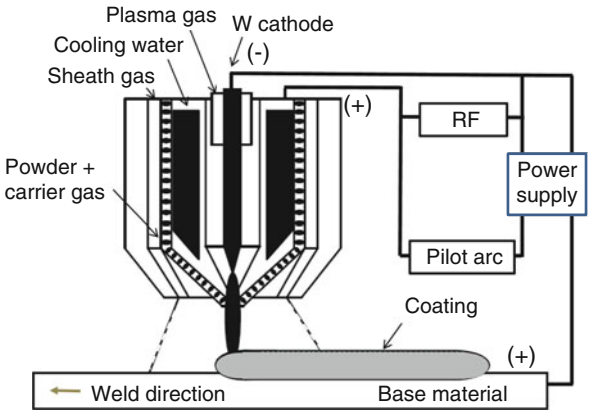


Fig. 10.4 Example of a PTA torch. Reprinted with kind permission from Springer Science Business Media [4], copyright © ASM International

cathode tip is a water-cooled copper nozzle, typically 2–4 mm in diameter, depending on the operating power of the torch. This nozzle serves as the pilot arc anode, and it constricts and stabilizes the arc. Alignment of the cathode with the nozzle axis is crucial for obtaining quality coatings because a slight misalignment can lead to unstable or strongly asymmetric arcs, uneven powder heating, uncontrolled substrate heating, and reduced electrode life. Surrounding this nozzle is a ring with powder injection orifices. The powder is injected, depending on the process and material, either into the arc where it is fully melted or close to be melted, or into the fringes of the arc to keep it only partially melted. In the first case, there is a secondary nozzle (sometimes called focusing nozzle) with a diameter of about double that of the constricting nozzle surrounding the powder injection ring. Torches that do not have this secondary nozzle have the ring surrounding the powder injection orifices at the same level as the constriction nozzle exit, and this arrangement results in powder injection into the fringes of the arc with less heating of the powders. The powder can also be fed into the molten metal pool by an extension of the tube that transports the powder beyond the secondary nozzle to a location close to the substrate surface (see Sect. 10.6). Surrounding this secondary nozzle is the ring introducing the shield gas. The shield gas consists typically of argon with 5–7 % hydrogen added, and it provides a curtain that protects the molten metal from reacting with the surrounding atmosphere. Shield gas flow rates are multiples of the plasma gas flow rates. For deposition of metals that will react with hydrogen, e.g., Ti or Al, pure argon shield gas flows can be used. An example [4] of a PTA torch is shown in Fig. 10.4. Figure 10.5 illustrates the torch movement during the deposition process. The arc attachment on the substrate surface has two movements superposed: (1) the oscillatory movement resulting in speeds of about 40 mm/s (e.g., 10 mm oscillation width with 0.5 Hz oscillation frequency) to 80 mm/s (e.g., 40 mm width with 1 Hz oscillation frequency) and (2) the traverse speed, i.e., the substrate translation with respect to the torch which is in the order of 1.5–2 mm/s.

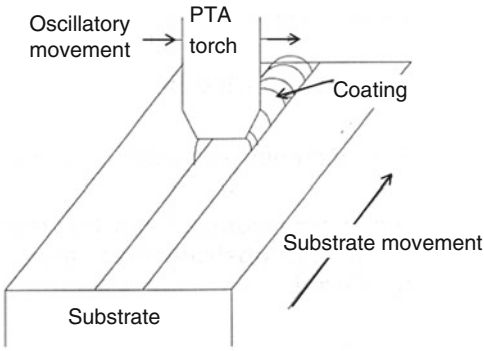


Fig. 10.5 Schematic of PTA deposition process

The PTA process can be divided into three different categories [3, 7] according to the deposition rate and the power used:

(a) Micro PTA for deposition rates of 0.1–2 kg/h, typically used for coating of small components which can absorb little heat, or components with complex shapes [8–11]
(b) Regular PTA for deposition rates of 2–10 kg/h, for the bulk of the PTA coating applications
(c) High-power PTA for deposition rates between 10 and 20 kg/h (or even larger) for rapid coating of large surfaces or large components [2, 12]

Typical operating values are for regular PTA:

Pilot arc current: 0–200 A, with most applications in the 50–100 A range; pilot arc voltage: ~40 V
Transferred arc current: 80–400 A, with most applications between 100 and 300 A transferred arc voltage: ~40 V
Nozzle diameter: 2–4 mm
Plasma gas: Ar or Ar/He, 2–10 slm
Shield gas: Ar with 5–7 % H_2: 10–40 slm, or pure argon
Powder feed rate: 2–10 kg/h
Powder size: 40–250 μm (60–200 μm for most applications)
Carrier gas: Ar or Ar + 5 % H_2: 1–20 slm
Substrate distance: 10–20 mm
Oscillation frequency: ~0.5–1 Hz
Oscillation width: 2–30 mm, mostly between 10 and 20 mm
Traverse speed: 7–10 cm/min for most processes

For Micro PTA, typical operating values are:

Arc current 5–50 A
Arc voltage around 20 V
Nozzle diameter between 1 and 2 mm
Substrate distance 5–10 mm

Plasma gas and flow rate: argon at 0.4–1.4 slm
Shield gas and flow rate: argon + 5–7 % hydrogen, 10–24 slm
Powder feed rate: 0.1–2 kg/h
Carrier gas and flow rate: argon, 1–3.5 slm
Note: for Micro PTA there is frequently no oscillation used, but the traverse speed is increased from 14 to 21 cm/min; this allows deposition with very small bead widths

For high-power PTA, typical operating values are:

Pilot arc current: 0–100 A
Transferred arc current: 200–400 A
Plasma gas flow rate: argon, 3–10 slm
Shield gas: argon with 5–7 % hydrogen, 10–50 slm
Powder feed rate: 10–20 kg/h
Carrier gas: >7 slm are required for powder feed rates above 10 kg/h
Substrate distance: 15–20 mm
Oscillation distance: 20–40 mm
Oscillation frequency: 0.3–1 Hz
Traverse speed: up to 23 cm/min

The coating properties are of course dependent on the operating parameters and the material used, but the range of values is for regular PTA:

Bead thickness: 0.5–6 mm
Bead width: 2–40 mm, mostly around 10 mm
Typical multi-pass coating thickness: 20 mm
Deposition efficiency: 95–98 %
Dilution: 5–7 %, possibly higher for coatings <1 mm thick

For Micro-PTA, bead widths can be as small as 0.5 mm, ranging up to 3 mm, with single pass bead thicknesses 0.5–3 mm, giving bead height to width ratios of 0.5–2 [8].

The dilution increases with the power. The fastest solidification and finest microstructure is obtained with the micro-PTA process.

While the majority of the equipment is automated, handheld torches are also frequently used [13, 14], as any look into an equipment brochure from a torch manufacturer can demonstrate. These torches are primarily used for smaller parts with complex shapes.

There are numerous modifications of the PTA equipment and processes principally to improve control over the powder heating, the substrate heating, and to adjust the process to specific substrate sizes and shapes. These modifications will be discussed in Sect. 10.6.

Loss of deposition material can occur though evaporation of some of the material, and the deposition of low boiling point materials, e.g., zinc, is difficult. Nucleation of the metal vapor leads to the formation of ultrafine particles, and these fumes can be deposited on parts of the torch or on the substrate outside the bead.

Avoiding injection of the powder into the center of the arc, using larger size particles (>60 μm), and increasing the shield gas flow rate and the substrate distance can minimize the problem of the fumes.

10.3 Coating Materials and Applications

As already mentioned, the PTA process gives a choice of a large number of coating materials, various alloys, metal compounds, and metal matrix composites, and there are continuously new coating materials being developed. The largest number of applications is for corrosion and wear-resistant coatings, taking advantage of the superior adhesion and high density of the PTA coatings, and the possibility to select a wide variety of materials systems by mixing the appropriate powders. Coatings have been developed for wear under different corrosive conditions, for abrasive wear, and for wear by erosion due to interaction with particulates. Another important application is the restoration of worn parts to original dimensions. Frequently the restored parts have better corrosion and wear characteristics than the original ones [15]. However, combinations of corrosion and wear resistance usually mean adoption of some compromises. It is beyond the scope of this chapter to list all of the possible material combinations that have been shown to fulfill the needs in a specific application, and specialized review articles can be consulted for these details (e.g., [1]).

The majority of the substrate materials are steels or other ferrous alloys, although with the increase in use of lighter metals for reducing component weight, coatings on aluminum or magnesium are becoming more important. However, light metals such as pure aluminum or magnesium have high thermal diffusivities (9.8×10^{-2} m^2/s for Al and 8.77×10^{-2} m^2/s for Mg) resulting in a broad heating zone which is not easy to control when the melting temperature is approached. In general, the metallurgical compatibility of the substrate material with the coating material has to be considered.

10.3.1 Corrosion and Wear

There are fundamentally two approaches for obtaining a wear- and corrosion-resistant coating. In one approach, a metal alloy is deposited and during the cooling from the molten state hard phases or carbides precipitate. The other approach consists of adding carbides as hard phases into a suitable metal matrix. The addition of carbides will increase the abrasive and erosive wear resistance, but may reduce the corrosion resistance [16]. It also should be noted that hardness and wear resistance give only part of the picture; component life is also determined by the thickness of the wear-resistant coating. Consequently, while it is possible to have very hard and wear-resistant coatings produced by physical vapor deposition (PVD)

or chemical vapor deposition (CVD), these coatings cannot be produced with the thickness that would assure long component life in the construction, mining, or chemical industries. Using PTA, coating thicknesses of several millimeters can be deposited easily.

In general, the metal alloy coatings consist of a Fe–Cr or Fe–Cr–Ni alloy with the addition of a refractory metal, W, Mo, Nb, Ta, or B, and Si and C [3, 12, 14–21]. The most widely used wear resistant coatings are probably Fe–Cr–Mo–C (e.g., for equipment in the construction and mining industries) or Co–Cr–W–C for wear with better corrosion resistance (e.g., food processing knives, drills, valves) [22]. Stellite coatings of valve seats are also widely used. Alloys of Fe–Cr–V–C–B have also excellent wear properties and are more economical than some of the cobalt- or nickel-based alloys [23, 24], with the hardness attributed to the formation of carbo-borides. Other alloys that can form hard phases during spraying and solidification or after treatment are also used. For example, Fe–C–Cr–Cu coatings forming carbides upon spraying and ε-Cu phase upon treatment at 773 K for 35 h, or boride layers on AISI 1018 steel developed using the PTA alloying technique [25–27], or $Fe_2TiSi/-Fe/Ti_5Si_3$ formed when using Fe–Ti–Si–Cr powder blend as the precursor material [28], $(Cr, Fe)_7C_3$ carbide obtained [29] when depositing iron-based coating FeCrSiBC.

The hardness and wear resistance is usually significantly improved by the addition of carbides, however, the carbides may decompose when they are too strongly heated, e.g., in the transferred arc or in a high-temperature molten metal pool. Special injection techniques can remedy this situation (see Sect. 10.6). Some dissolved carbides will form mixed carbide hard phases in the coating. As one of the most popular carbide addition giving the highest hardness is tungsten carbide [17, 30], which can be added (a) in the form of macro-crystalline WC, large enough particles that undergo minimal decomposition (although too large particles tend to settle at the bottom of the weld pool), (b) in the form of fused tungsten carbide (FTC), a eutectic mixture of WC/W_2C, and (c) in form of sintered WC in a cobalt matrix [31, 32]. Other carbides include TiC, VC, NbC, or mixed carbides (W,Ti)C [30, 31]. Different carbides are used with different matrix materials, e.g., (V,W)C, NbC, TiC with a Fe–Cr–C matrix, (W,Ti)C, W_2C with a Co–Cr–W–C matrix. For example, TiC–W–Cr powders formed complex structure comprising primary austenite, martensite, an eutectic of $(Fe,Cr)_7C_3$ carbide and austenite, as well as the uniformly distributed unmelted TiC particles [33]. Undissolved Cr_3C_2 particles and chomium-rich carbides enhanced the hardness and wear resistance of the nickel-based alloy with 30 wt% Cr_3C_2 within a coating deposited by the PTA process [34]. Nanometer-sized Al_2O_3 particles in nickel-based alloy powders promoted the formation of stacking faults and dislocation cell wall. The sliding wear resistance of the coating with Al_2O_3 added was higher than that of the Al_2O_3-free coating [35].

A widely used metal matrix composite is Ni–Cr–B–Si with WC (FTC up to 60 %) [22, 36] or VC (30–50 %) [1] for applications such as extruder screws. Higher corrosion resistance is offered by a Co based alloy (stellite, Co–Cr–W–C with addition of Ni, Mo, or Nb) with 5–25 % WC, TiC, NbC, or VC [17, 30]. A more economical alternative is offered by Fe–Cr–V or Fe–Cr–Nb with 30 % VC

addition [1, 16], Fe–Cr–V–C with VC [37–40], or Fe–V with 50 % VC addition [36], or Fe–Cr–C with 65 wt% WC [41] giving very good combined wear and corrosion resistance.

It should be mentioned that in several cases an intermediate nickel alloy coating is deposited to reduce the formation of unwanted metallic phases [42–44]. In the case of coating aluminum or magnesium substrates, the surface to be coated is covered with an oxide layer. Arcing with reverse polarity, the substrate being the cathode will remove the oxide layer and allow deposition of the coating with a good bonding. More on this topic will be discussed in Sect. 10.6 [3, 45, 46]. Hardening of an Al alloy surface can be accomplished by dispersing a hard material in the molten metal, by adding a metal into the weld pool to generate a hard alloy, or by a combination of these processes [46]. For depositing wear-resistant coatings on aluminum alloys, Al–Cu alloys have been developed (Al–Cu25–Mg25, Al–Si12–Cu25–Ni25, or AlCu4.5–Mg1.8) as matrix materials with up to 70 wt% FTC, and comparison with standard stellite or Ni–Cr–B–Si + 50 % FTC show better wear properties and better corrosion resistance than the nickel-based alloy. Coating of aluminum alloys with Ni has increased surface hardness due to formation of Al–Ni intermetallics [47]. Powder injection can be done in several ways. Injection of a mixture of powders with 10–50 vol.% carbide [47] can result in separation of the components due to different flow properties [17]. Transporting the powders separately to the torch and combining the flows at the torch can improve this situation. The powders can also be injected separately, with the metal matrix material injected into the plasma in front of the molten metal pool and the carbides behind the anode attachment into the molten metal [37]. Powders can also consist of agglomerates of fine particles (~10 μm diameter) of all the materials wanted in the coating, held by an organic binder and generally calcined, prepared in a spray drying process [17, 30].

10.3.2 Self-Lubricating Coatings

Metal matrix composite coatings with potential self-lubricating properties were produced on plain steel substrates using PTA technique [48]. Layers of approximately 1 mm thickness and with various compositions were obtained with additions of MoS_2 and MnS compounds, with different weight percentages, which are known to act as solid lubricants. The addition of MnS was effective in reducing the friction coefficient and the wear rate of the coatings in comparison to the steel substrate, whereas the MoS_2 was ineffective, due to its instability and subsequent redistribution of Mo and S elements during the solidification process [48].

Composite coatings based on co-melting of MoS_2, TiC, and iron ingredients were produced, in an attempt to obtain wear-resistant layers with self-lubricating properties [49]. Experiments have shown that both TiC and MoS_2 dissolve completely in the melt under the plasma arc, whereas their elements, Ti, C, and S, are redistributed in the solidification products forming new compounds. If the original MoS_2 compound is totally absent in the final microstructure, new

complex sulfides have formed. The wear tests performed with a pin-on-disk apparatus have demonstrated improved friction coefficients and lower wear rates in comparison to the steel substrate as well as to the composite containing TiC, but not compared to MoS_2 [49].

10.3.3 Rebuilding of Parts

Various steels or Ni alloys can be used for this purpose, but also, of course any of the previously mentioned materials for addressing specific requirements. Economics will be a major factor deciding what coating material will be used. Frequently the rebuilt parts have better functional properties than the original ones [15].

10.3.4 Free-Standing Shapes

Building free-standing shapes for tool manufacture is a recently developed application [44, 50] making use of tool steel with possible addition of WC or stellite based alloys. Beryllium (Be) is used in many defense and aerospace applications but health hazards associated with this material handling limit the applications. PTA solid free-form fabrication has being evaluated as a Be fabrication technique by Hollis et al. [51].

In addition to the selection for a specific functional performance parameter, one needs to consider the general guidelines that very high hardness will reduce machinability and can lead to crack formation, and a strong difference in the specific density values of the metal matrix material and the carbide addition may result in nonuniform coatings with higher concentrations of the higher density carbides closer to the substrate interface.

The specific applications span a wide range of industries including heavy construction machinery, ship building, farming, tunnel and borehole drilling, chemical processing, automotive, power generation, and food processing. Specific parts that are being coated include rock drills, plow shares, cement crusher rolls, extruder screws, knives, vanes, pump shafts and valves, large Diesel engine valves, valve seats, steam turbine blades, metal forming dies, waste incineration boilers, etc. Some specific cases of coatings for a particular application are described in Sect. 10.7.

10.4 Process Characterization

Considering the importance of this coating process, it is astonishing that relatively few process characterization studies have been performed, compared to other coating processes. The vast majority of the studies have concentrated on evaluating the coating properties, and only few studies exist describing the characteristics of

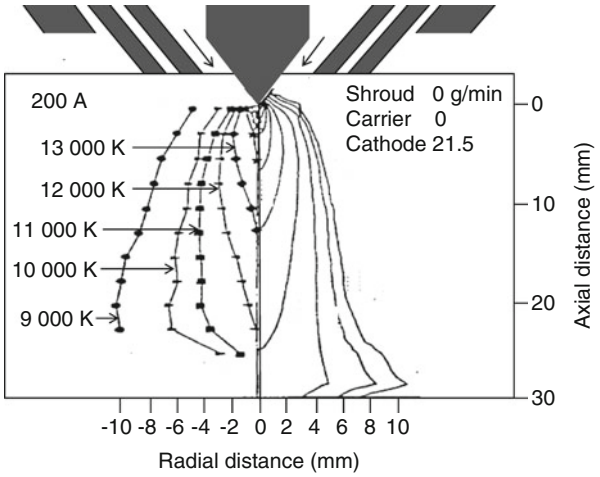


Fig. 10.6 Examples of temperature fields in an argon arc with $I = 200$ A, 1 bar, and substrate distance of 30 mm [57] (Reproduced with kind permission of IPCS)

the arc (e.g., temperature distributions), the powder (e.g., particle temperatures and velocities), and the heat transfer to the substrate. However, the process bears enough similarity to TIG welding and plasma cutting processes that some of the studies involving these processes can be used for understanding the PTA process.

10.4.1 Temperature Distributions in the Arc and Arc Voltages

The temperature distributions and heat fluxes in a TIG welding arc have been well characterized by spectroscopy and by modeling [52–56]. Figure 10.6 [57] shows typical temperature distributions obtained from spectroscopic measurements (left side) and from modeling (right side). The constriction encountered in a PTA arc will increase the peak temperatures on the arc axis and result in higher temperature gradients. The temperature distributions in a plasma cutting arc at different locations between the nozzle and the work piece are described by Peters et al. [58] and an example is shown in Fig. 10.7. The constriction in this configuration is somewhat higher than in a PTA torch, the plasma gas is oxygen also resulting in higher constriction, and there is significantly higher plasma gas flow, and no current transfer to the nozzle. Figures 10.8 and 10.9 show the effects of arc current and plasma gas flow rate, respectively, on the temperature distributions between the nozzle of a plasma welding arc and the substrate [59], as shown by Ducos [15]. It can be seen that for an increase in current from 100 A to 260 A there is little increase in the peak temperature for the nozzle diameter of 3.45 mm, but a widening of the arc and of the anode attachment, resulting in a higher temperature in front of the substrate. Increase of the plasma gas flow rate has a strong effect on the plasma temperature in front the substrate and consequently on the substrate heat transfer.

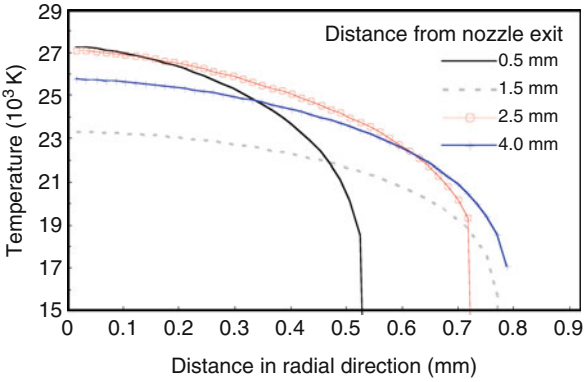


Fig. 10.7 Radial temperature distributions at different axial locations in a cutting arc derived from spectroscopic measurements, $I = 200$ A, nozzle diameter 2 mm, plasma gas flow rate 39 slm oxygen, $d = 13$ mm (Copyright IOP Publishing. Reproduced with permission. All rights reserved)

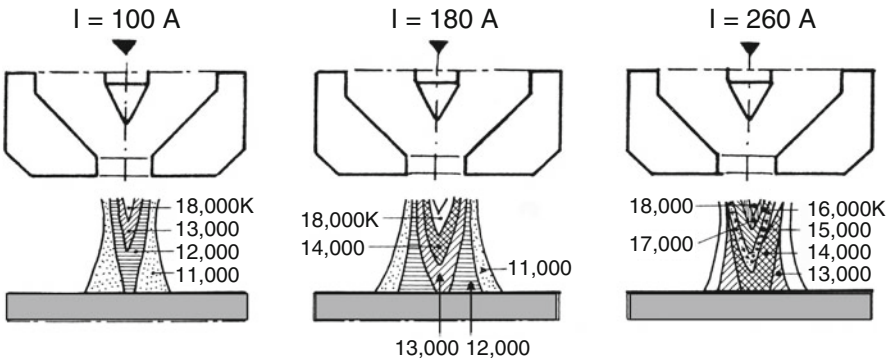


Fig. 10.8 Temperature fields between a plasma-welding torch and a substrate for different arc currents; plasma gas flow 4 slm, argon, pilot arc anode diameter 3.45 mm [59] (Courtesy of M. Ducos with kind permission of Institut de La Soudure)

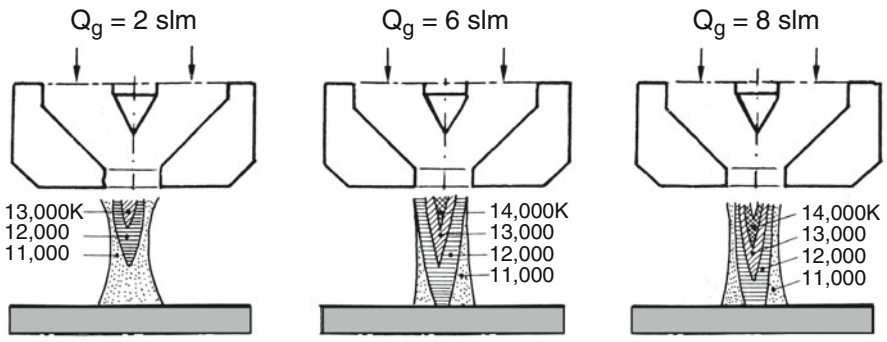


Fig. 10.9 Temperature fields between a plasma-welding torch and a substrate for different plasma gas flow rates; $I = 100$ A, argon, anode nozzle diameter 3.45 mm [59] (Courtesy of M. Ducos with kind permission of Institut de La Soudure)

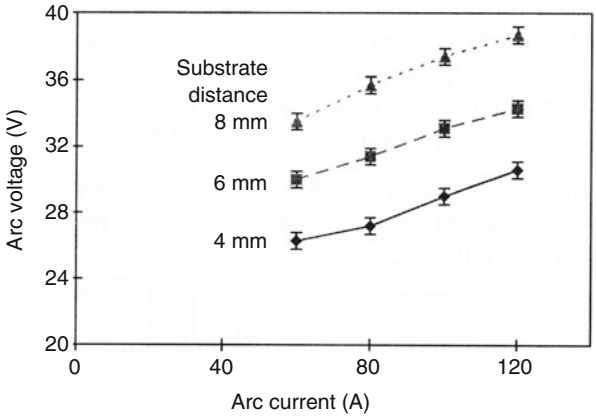


Fig. 10.10 Arc voltage as function of current for different substrate distances for a PTA torch operating with 4 slm of Ar and with a Cu substrate [60]. Reprinted with permission of ASM International. All rights reserved

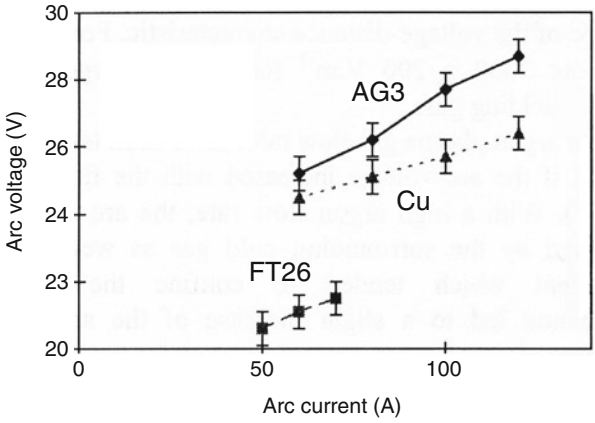


Fig. 10.11 Arc voltage as function of arc current for different anode materials for a PTA torch operating at 4 slm of Ar and with a substrate distance of 6 mm [60]; substrate materials were an Al alloy (AG3), cast iron (FT 26), and copper. Reprinted with permission of ASM International. All rights reserved

Reduction of the nozzle diameter will result in an increase in the heat loss to the nozzle, therefore in the electric field, and consequently in the peak temperature, but also in the plasma gas velocity for the same gas flow rate. This results in increased temperatures in front of the substrate and increased substrate heat fluxes. However a compromise must be found to avoid blowing out the liquid metal, the plasma velocity increase raising the pressure on the liquid ($\rho . v^2$ where ρ is the mass density of the plasma and v its velocity).

The arc in a PTA torch is highly constricted and any increase in current will lead to an increase in arc voltage because of the higher losses to the nozzle as shown in Fig. 10.10 [60]. Of course, there is a linear increase in the arc voltage with standoff distance, as also shown in this figure. Figure 10.11 shows an effect the magnitude of which may be surprising and that is the arc voltage dependence on the substrate material (anode). The highest voltage was observed for Al (25 V at 60 A and 6 mm) and the lowest voltage for cast iron (~21 V at 60 A and 6 mm).

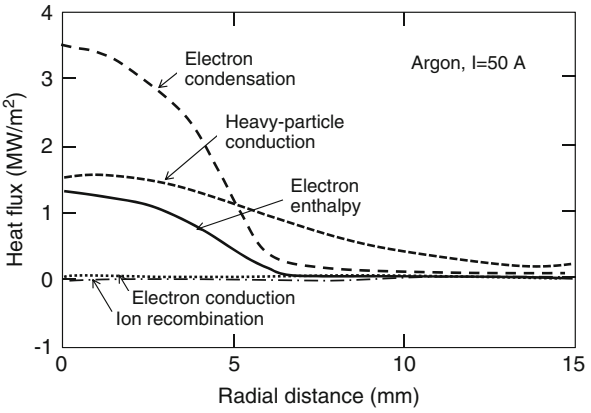


Fig. 10.12 Contributions to the heat flux to the anode surface of a 100 A argon arc at 1 atm with a diffuse anode attachment [64] (Copyright [1997] IEEE. Reprinted, with permission)

10.4.2 Heat Flux to the Substrate

Analytical expressions for anode heat fluxes have been derived [61, 62] and it has been shown that the largest contributions to the heat flux are associated with the electron current transfer from the arc to the anode:

$$q_a = j_e \Phi_a + q_e - k_e \frac{dT_e}{dz} - k_h \frac{dT_h}{dz} + j_i(E_i - \Phi_a) + Q_R \qquad (10.1)$$

with q_a the anode heat flux, j_e the electron current density, Φ_a the workfunction of the anode material, q_e the electron enthalpy flux, k_e, T_e, and k_h, T_h the thermal conductivities and temperatures of the electrons and the heavy particles, respectively, j_i the ion current density, E_i the ionization potential of the plasma gas, and Q_R the heat transfer by radiation [62] The first term on the right-hand side is due to the incorporation of the electrons into the metal lattice, the second term is the enthalpy flux carried by the electrons, the third and fourth terms are the electron and heavy particle conduction, respectively, and the fifth term is the energy release due to recombination of ions diffusing to the anode surface, and the last term expresses the radiation heat flux from the plasma to the anode. The first, second, and fourth terms are usually the most important ones for the heat transfer to the anode [61–64] as shown in Fig. 10.12 [64]. This relation has resulted in good agreements with experimental data for welding arcs. The electron current contribution clearly increases with the electron current density, i.e., the total current and the electron temperature distribution in front of the substrate.

Measured substrate heat fluxes for TIG type welding arcs with different currents in argon are shown in Fig. 10.13 [65]. In these measurements a specially designed heat flux probe has been used [65]. Heat fluxes in a PTA torch are higher because of higher constriction of the arc and because of higher plasma gas flow rates.

Measurements of heat fluxes to the substrate are also reported by Leylavergne et al. [60] for a PTA torch but without powder injection and without pilot arc.

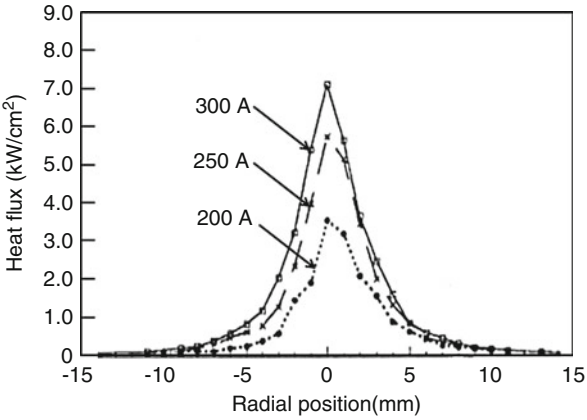


Fig. 10.13 Measured anode heat flux distributions for different currents in argon at 1 atm [65] (Reproduced with kind permission of James Menart)

The measurements were performed, using a calorimetric method, for different arc currents (60 to 120 A), different torch–substrate distances 4, 6, 8 mm), different plasma gas flow rates (3, 4, 5 slm), different He shield gas flow rates (0, 20, 30, 40 slm), and substrates consisting of Cu, an Al alloy, and cast iron. The practically linear increase in voltage with anode distance d for different currents led to the conclusion that the field strength is constant and that mostly the arc radius is increasing with current, according to the approximate relation (Ohm's law)

$$I = \pi r_e^2 \overline{\sigma}_{\mathrm{ar}}\, E \tag{10.2}$$

with I the arc current, r_e the arc radius (radius of current path), $\overline{\sigma}_{\mathrm{ar}}$ the electrical conductivity of argon averaged over the arc cross section, and E the electric field. The heat flux to the anode was calculated according to a slightly modified Eq. (10.1)

$$Q_{\mathrm{an}} = \left[\left(\frac{5}{2}\frac{k_{\mathrm{B}}T_{\mathrm{e}}}{e} + \Phi_{\mathrm{an}} + V_{\mathrm{an}}\right) + (\alpha V A_{\mathrm{con}})\right] \tag{10.3}$$

where T_{e} is the electron temperature, k_{B} the Boltzmann constant, e the electronic charge, Φ_{an} the workfunction of the anode material, V_{an} the anode fall voltage, α the fraction of the electrical power transferred to the anode by convection and radiation, V the arc voltage, and A_{conv} the area over which the convective heat transfer takes place.

Figure 10.14 [60] shows measured heat flux values, increasing with increasing current and increasing anode distance. There is little change of the heat flux with increasing plasma gas flow rate. Assuming that only the heat transfer by convection and radiation is dependent on the anode distance, an extrapolation to a zero distance will give the heat flux due to the current transfer to the anode, which is independent of distance. The different heat fluxes and arc power are shown in Fig. 10.15 and in Table 10.1 [60].

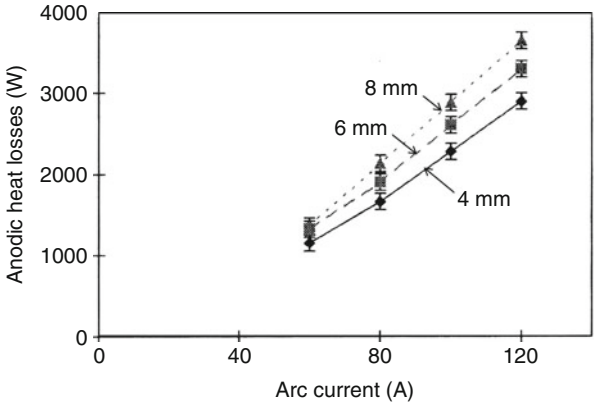


Fig. 10.14 Anode heat transfer as function of arc current and arc length for a Cu anode and 4 slm argon plasma gas flow, without shield gas [60]. Reprinted with permission of ASM International. All rights reserved

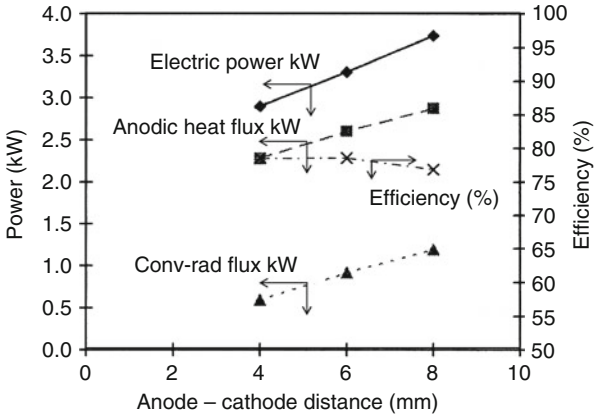


Fig. 10.15 Measured values of electric power input, anode heat flux, and derived values of convective–radiative power loss from the arc and the arc heating efficiency for an Ar mass flow rate of 4 slm, an arc current of 100 A, and a Cu substrate [60]. Reprinted with permission of ASM International. All rights reserved

Table 10.1 Arc power and anode heat transfer for different anode distances for a Cu anode and 100 A arc current (data from [60])

Anode distance, mm	4	6	8
Arc power ($V{\cdot}I$), kW	2.9	3.3	3.7
Q_{an}, kW	2.3	2.55	2.8
Q_{conv}, kW	0.6	0.9	1.2

As noted previously, the majority of the heat transfer is due to the transfer of electron current into the anode. A strong dependence of the heat flux on the anode material is found, with the transfer to the Cu anode being about 50 % higher than that for the cast iron anode. The cast iron substrate showed the largest extent of evaporation and molten droplet ejection, however, these cooling mechanisms could not explain the difference in the measured heat transfer values. Based on a dimensionless analysis for a Cu anode, the following correlation between the operating parameters and the substrate heat transfer has been found

Table 10.2 Substrate heat fluxes for different pilot arc and transferred arc currents, for a nozzle diameter of 4 mm and a plasma gas flow rate of 3.9 slm; adapted from [66]

I_{pilot} (A)	I_{trans} (A)	Q_{sub} (W)	k (cm^{-2})
120	0	275	1.9
200	0	500	
250	0	530	2.9
120	120	2,220	2.6
200	120	2,265	
250	120	2,280	3.9

$$Q_{an} = 62.4 I^{1.36} m_p^{0.046} d^{0.382} \tag{10.4}$$

with Q_{an} the anode heat transfer in W, I the arc current in A, m_p the plasma gas flow rate in kg/s, and d the anode distance in m [60].

Dilthey et al. [66] report on measurements of substrate heat fluxes obtained with a split anode arrangement similar to one described first by Nestor [67]. Two halves of a copper anode, thermally insulated from each other and separately cooled, were used to measure the total heat flux to the substrate and the distribution calorimetrically by moving the substrate across the arc attachment. Assuming a rotational symmetry, the heat flux distribution can be described by a formula as function of a "constriction parameter" k [66]:

$$q(r) = q_m \exp\left(-kr^2\right) \tag{10.5}$$

with $q(r)$ the substrate heat flux, q_m the maximum heat flux for a given condition, and r the radial coordinate. The authors find that for a nozzle diameter of 4 mm, k varies from 1.7 to 3 cm^{-2} depending on current, increasing with the current. A higher k value indicates deeper penetration and higher dilution.

The authors determined the heat fluxes and the k values for different combinations of pilot arc current and transferred arc current. The constriction parameter k varied for a nozzle diameter of 4 mm, a plasma gas flow rate of 3.9 slm, without transferred arc, from 1.9 to 2.9 cm^{-2} when the pilot arc current was increased from 120 to 250 A. For a transferred arc current of 120 A, the values were 2.6–3.9 cm^{-2}. The associated heat fluxes are shown in Table 10.2 [66]. Decreasing the nozzle diameter to 2.5 mm, and the plasma gas flow rate to 1.5 slm, the constriction factor values ranged from 2.45 to 3.45 cm^{-2} without transferred arc for a pilot arc current variation of 100 to 300 A, and from 4.15 to about 4.75 cm^{-2} for pilot arc current variation from 40 to about 250 A, with a transferred arc current of 120 A. The associated heat fluxes were 150–500 W, and 2,130 to about 2,300 W, respectively.

It must be emphasized that Q_{sub} is the total heat transfer to the substrate and that these values include the contribution of the pilot arc power, i.e., are not only due to the anode heat transfer. Substrate melting and coating dilution are determined not only by the substrate heat transfer but also by the distribution of the heat flux, expressed by the constriction parameter k. It can be clearly seen that substrate heating is due to the transferred arc, and the pilot arc contributes only in the order of 10–20 %. About 32–48 % of the electrical energy goes into heating of the substrate [66].

Table 10.3 Mean temperatures for CrNi steel particles, 100–160 µm diameter with plasma gas flow rate of 1.3 slm [66]

I_{pilot} (A)	I_{trans} (A)	Mean particle temperature (K)
150	0	848
0	120	1,641
150	120	1,845

The same authors also measured calorimetrically the heat content of the particles of the material to be deposited and derived mean particle temperatures from these values for CrNi steel particles with a diameter range from 100 to 160 µm. The results are shown in Table 10.3 [66].

It is clear that most particle heating is due to the transferred arc.

One can see from these results that the transferred arc current has the strongest effect on the process, both with respect to substrate heating/dilution and with respect to particle heating/deposition rates. While there have been no measurements of substrate heat fluxes for different plasma gas flow rates, higher gas flow rates increase the plasma temperature in front of the substrate, and consequently also the heat flux, but to a lesser degree than the current because the majority of the heat flux is due to the electron current flow into the substrate material. However, the widening of the temperature profile for higher plasma gas flow rates as well as the higher temperatures would indicate that one should expect that higher deposition rates would be possible with higher plasma gas flow rates.

In the development of a process in which the plasma gas flow was modulated (see Sect. 10.6), Ebert et al. [68] measured the stagnation pressure at the substrate surface with an orifice in the substrate connected to a pressure sensor. Moving the torch over the substrate gave radial pressure profiles, which can be used to represent the velocity profiles. The peak stagnation pressures increase from approximately 330 Pa at a mass flow rate of 1 slm to 430 Pa at a mass flow rate of 2 slm to 525 Pa at a mass flow rate of 3 slm, and to 620 Pa at a mass flow rate of 4 slm at current of 95 A. The full width at half maximum (FWHM) did not change very much when the flow rate was increased and remained between 3 and 4 mm. The pressure is also strongly influenced by the arc current increasing with increasing current and to a lesser extent by the nozzle design (decreasing with increasing diameter) and the substrate distance (decreasing with increasing distance). The higher pressure indicates that a displacement of the molten metal must be expected, and a pressure variation by modulating the plasma gas flow or current will result in molten metal movement that will give a more uniform distribution of high-density carbide particles.

10.4.3 PTA Process Modeling

While numerous models and simulations exist for TIG and MIG welding arcs, very little modeling of the PTA process has been performed. Wilden and coworkers [4, 69] developed a model of the PTA process to identify operating conditions for thin coatings (~500 µm) and for coatings on vertical surfaces, for deposition of Ni on steel. Their model is based on the solution of the conservation equations, but

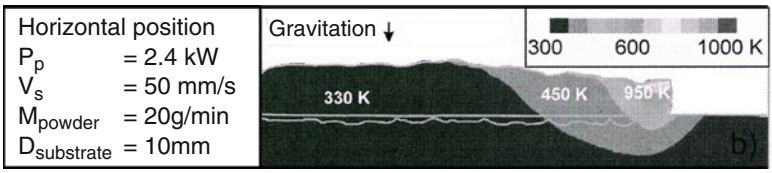


Fig. 10.16 Simulated cross section of a molten metal pool during a PTA coating process of Ni onto a 10 mm thick steel substrate [4]. Copyright © ASM International. Reprinted with permission

assumes instead of a detailed arc model a channel of 2.5 or 2 mm diameter with uniform heat dissipation, and no interaction with the pilot arc anode. The energy is transferred to the substrate and the feed material. A meander like torch movement is assumed. For a 2.5 mm arc diameter, the following operating parameters have been used: I_{pilot} = 10–50 A, I_{trans} = 70–170 A, plasma gas flow rate = 1.5 slm, carrier gas flow rate = 0.4 slm, powder feed rate 0.48–1.2 kg/h, and deposition velocity = 10–90 mm/s (corresponding to an oscillation of 10 mm width at 0.5 Hz to 45 mm width at 1 Hz). The temperature distributions in front of the substrate and the melting of the substrate and the formation of the coating have been modeled for horizontal and vertical substrates. Figure 10.16 [4] shows the distribution of the molten material during the coating formation process. The results indicate:

- A liquid metal pool temperature of about 1,000 K, a pool diameter of 2 mm, and a depth of 1 mm for a 150 A arc current, and a 1.2 kg/h powder feed rate.
- Peak (axial) plasma velocities of 2 m/s for a plasma gas flow rate of 0.5 slm and of 13 m/s for a flow rate of 5 slm are predicted for a plasma power of 4 kW and a nozzle diameter of 2 mm.
- Increasing the arc current from 90 to 150 A results in a strong increase in dilution from 24 to 42 %, but increasing the deposition velocity from 10 to 90 mm/s reduces the dilution from 42 to 30 % at 120 A.
- To deposit coatings of thicknesses of 500 μm or less, the arc current has to be low (90 A or less) and the deposition (oscillatory) speed high (90 mm/s). However, the lower currents may result in uneven thicknesses and the dilution is still rather high requiring further optimization.
- Deposits on vertical surfaces can be obtained with similar parameters as those for thin coatings.

It should be noted that plasma power is given by the product of current and voltage for the pilot arc plus that for the transferred arc, minus the losses to the nozzle.

Experimental validation of this model using a pilot arc current of 10 A, a transferred arc current of 45–90 A, a plasma gas flow rate of 0.5–1.5 slm argon, and a powder feed rate of 0.48–0.72 kg/h, and a deposition speed of 15–30 mm/s qualitatively confirmed the predictions. Thin coatings (<500 μm) have been obtained but with rather high dilutions.

Another modeling effort of the coating formation process is reported by Matthes et al. [70] with the goal to identify the stress distributions in free-standing shapes fabricated by PTA. The heat input into the substrate was given as heat flux across a circular area with a Gaussian distribution. The size of the weld pool and the bead

formation was calculated for a linear motion of the torch and for a superimposed oscillatory movement of 28 mm width and with a velocity of 7 mm/s, while the traverse velocity was 2 mm/s. The oscillation resulted in a lower liquid weld pool temperature, but in a larger area covered by the molten metal. Calculated temperature distribution of the substrate/coating surface was compared with experimentally determined ones and good agreement has been found. The stresses after solidification were tensile close to the bead and compressive farther away from it. The calculated stress values also agreed with the experimentally determined ones.

While many of these characterizations have been performed without powder injection, they allow estimates of how the fundamental properties change when the process parameters are changed. Powder deposition would likely enhance the heat transfer because the deposition of the molten material would transfer some of the arc power that would otherwise be lost to the torch. Summarizing one can say that

- Increasing the transferred arc current has the strongest effect on the substrate heat transfer, increasing the arc radius, the plasma velocity, the melting of the material, the movement of the molten material, and the heating of the powder.
- Increasing the substrate distance also increases the substrate heat transfer because the increased dissipated power will go partially to the substrate; however, an increase in substrate distance results in a decrease in the plasma velocity and therefore a reduction in the molten metal movement.
- Increasing the pilot arc current has a secondary influence on substrate and particle heating and is mainly beneficial for the stability of the transferred arc; of course, the pilot arc current gains in influence at low transferred arc currents.
- The plasma gas flow rate has little influence on the substrate heat transfer, however, the plasma velocity increases and with it the movement of the molten material; also the arc width increases with increasing plasma gas flow rate, and higher deposition rates will be possible.
- Decreasing the nozzle diameter will increase the plasma temperature and velocity and increase the heat flux to the substrate over a smaller area, however, the total heat flux is little affected; higher deposition velocities are possible.
- The substrate heat flux is influenced by the substrate material, increasing with its thermal conductivity when the substrate is cooled, and with its heat capacity for an uncooled substrate.

The effects of the process parameters on the coating properties are discussed in the next section.

10.5 Effect of Process Parameter Changes on Coating Properties

The primary quantities that are of concern are the bead thickness and width, deposition rate and efficiency, dilution, adhesion, and functional performance parameters, e.g., hardness profile, porosity, defect density, resistance to cracking, etc. The functional performance parameters are, of course addressed by the

selection of the powder to be deposited, but they can also be influenced by the process parameters: arc current, pilot arc current, plasma gas flow rate, powder feed rate and carrier gas flow, torch–substrate distance, deposition velocity, and shield gas flow.

Arc current has a strong effect. Increasing current increases substrate heating, melting, dilution, adhesion, bead width and deposition efficiency, and lowers porosity, but decreases bead thickness and may reduce hardness because of increased dilution. Also, high currents may lead to the decomposition or dissolution of the carbide phase, reducing the wear resistance. Too low currents may lead to incomplete melting of the powders.

Pilot arc current has little effect on the coating if all the other parameters are unchanged. However, the pilot arc current can be used to provide increased particle heating when the transferred arc current has to be reduced because the substrate heat transfer has to be reduced. This condition is encountered when (a) low melting point substrates are coated and (b) when dilution needs to be minimized, e.g., in thin coatings. The condition of high-pilot arc current and low-transferred arc current approaches the situation of a plasma spray process.

Torch–substrate distance increases lead to decreased dilution, the effect being stronger for higher currents. At a substrate distance of 20 mm, an increase in current from 150 A to 250 A can be balanced by an increase in powder mass flow rate from 6 kg/h to 10 kg/h, keeping the dilution below 10 %, however, at a substrate distance of 15 mm, the dilution will increase with current in spite of the increase in powder mass flow rate [2].

For increasing the *plasma gas flow rate* mixed results are reported, reduced dilution [15], and increased heat transfer and dilution [2, 47]. The effect is dependent on the arc current and the traverse speed. At high-heat transfer and substrate melting rates, the higher plasma gas flow rate can push the molten material toward the sides and cause turbulence in the molten metal pool and increase dilution.

Increasing the *powder mass flow rate* reduces the dilution, increases bead thickness, but reduces deposition efficiency. Too high powder mass flow rates for a given current will lead to incomplete melting of the powders

An increase in the *traverse velocity* also reduces dilution (although an increase in dilution with traverse velocity is reported in [71]). It also can result in a finer microstructure in high-power PTA deposition due to faster solidification of the molten metal [12]. At the optimal traverse speed the arc attachment is in front of the molten metal pool, however, too fast speeds will result in reduced fusion bonding and too slow speeds will result in increased porosity [12]. Bead width and thickness are reduced (see Fig. 10.17).

The *oscillation width* needs to be adjusted such that the solidification of the molten metal pool during one oscillation is controlled, or that exposure of a part of the molten metal pool to air outside the shield gas envelope is avoided. Typically, oscillation widths remain below 40 mm [12].

What concerns the functional properties, in general they are optimal for the lowest dilution values. However, low dilution values may also be accompanied by low fusion values, i.e., small areas where a metallurgical bond is obtained. DuPont et al. [72]

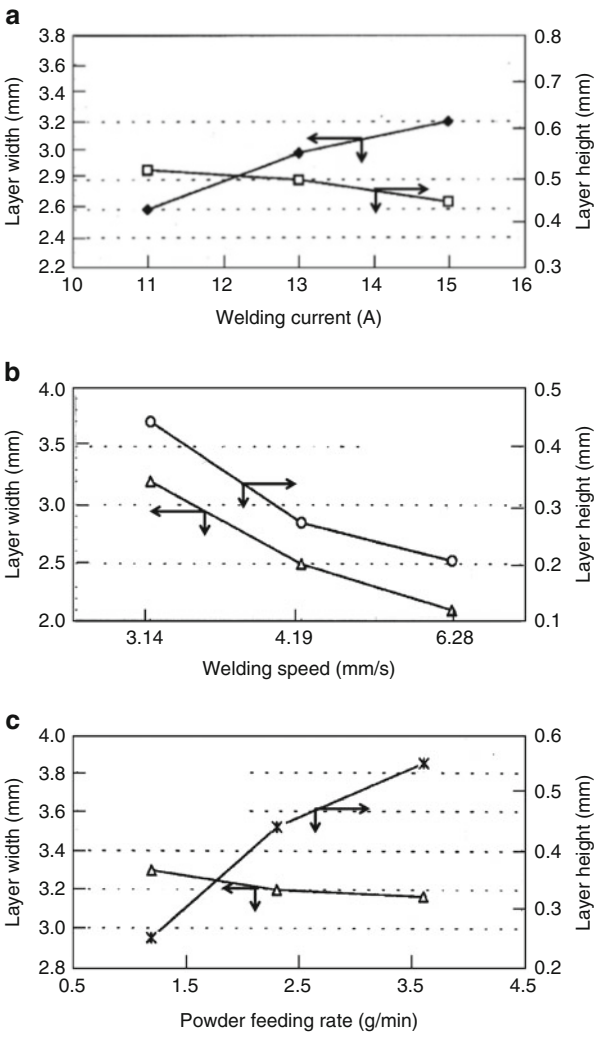


Fig. 10.17 Measured dependencies of bead width and thickness on (**a**) arc current with deposition speed of 3.14 cm/min and powder feed rate of 2.3 g/min, (**b**) deposition speed with arc current 15 A and powder feed rate 2.3 g/min, and (**c**) powder feed rate with arc current 15 A, deposition speed 3.14 cm/min. The other deposition parameters were: substrate distance 3 mm, plasma gas flow rate 0.4 slm, carrier gas flow rate 3.5 slm, and shield gas flow rate 10 slm [50]. With kind permission of Sage Publications

present a correlation of the "fusion factor," i.e., the width of the dilution region over the width of the bead in a coating cross section, with the ratio of powder feed rate over arc power. They report a strong drop off of the fusion factor at a certain value of the metal powder flow rate over the arc power ratio, i.e., if the power is insufficient to melt all of the powder. This drop-off of the fusion factor is accompanied by a drop-off in the deposition efficiency. While these data were obtained for plasma arc weld overlays (no pilot arc), a similar effect must be expected for PTA coatings. A graph showing increases in dilution values with increasing current for different powder flow rates is shown in Fig. 10.18 [2]. A discussion of operating parameter influences on dilution using a response surface analysis is presented in [71].

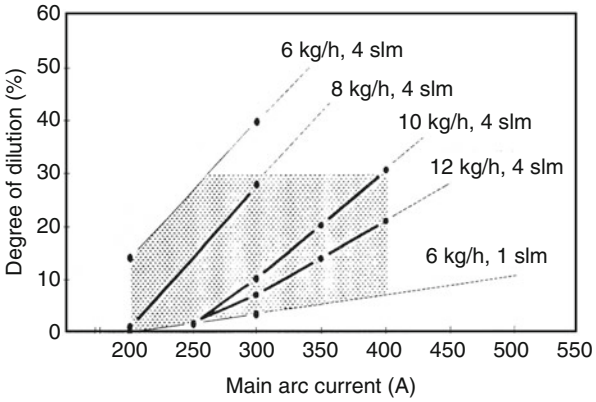


Fig. 10.18 Degree of dilution as function of arc current and powder mass flow rate, work piece St 37, 300 × 100 × 30 mm, shielding gas = 10 slm, transport gas = 3.5 slm, distance of oscillation = 40 mm, oscillation speed = 1.08 m/min, welding speed = 78 mm/min, torch distance = 20 mm [2]. Reprinted with permission of ASM International. All rights reserved

Table 10.4 Effect of increasing process parameter values on coating properties (After M. Ducos [15]). With kind permission of M. Ducos

	I_{pilot}	I_{arc}	m_{powder}	m_{gas}	$v_{travers}$
Bead width	−	++	−		−
Thickness	+	−	++		−−
Deposition efficiency		+	−−		
Surface		+++	−		−
Dilution	−	+++	−−−	++/−−	−−
Hardness	+	−−−	+++	++	++

Just [73] finds higher hardness at lower I, faster cooling, lower dilution, higher impact resistance, but not necessarily better wear because of less bonding between the carbide and the matrix.

A summary of the effect of process parameters has been presented in a table by Ducos [15], and this table is reproduced here as Table 10.4.

10.6 Process Modifications and Adaptations

The principal process modifications other than the adjustments of process parameters for high-deposition rate, high-power PTA or low-deposition rate micro-PTA, or for adjustments for a specific coating/substrate combination are:

- Variations of the ratio of pilot arc current to transferred arc current from zero (plasma weld overlay) to infinite (plasma spray)
- Special powder injection to avoid too strong heating
- Operating with nitrogen for surface nitriding

- Reversing the transferred arc polarity for oxidized surfaces, especially those with thin and impervious oxides, such as Al or Mg
- Modulating the plasma gas flow or the arc current or changing the torch design to affect the heat transfer to the substrate
- Increasing the energy density at low total energies for high velocity, small area depositions (high-energy PTA)
- Combining tape casting with PTA for complex shape coatings
- Combining PTA with MIG or laser welding processes

10.6.1 Variation of Ratio of Pilot Arc Current to Transfer Arc Current

An example of zero pilot arc current deposition (except for arc starting) in a micro-PTA deposition process is described by Wang et al. [50]. A 10–15 A transferred arc was used to deposit a 2–3 mm wide, 0.45–0.55 mm high bead with a 2.3 g/min flow rate of tool steel powders. Deposition parameters were 3 mm standoff distance, 0.4 slm argon plasma gas flow rate, 3.5 slm carrier gas flow rate, 10 slm shield gas flow rate, and 3.14 mm/s deposition speed. Three-dimensional freestanding shapes were fabricated. Tungsten carbide was added with a second powder feeder, and the substrate was preheated to reduce the time for melting. Good control over the arc length was important for getting a uniform product.

10.6.2 Variation of Powder Feed

To avoid overheating of the powders, e.g., carbides leading to their dissolution, injection can be done into the fringes of the arc, or into the molten metal pool through extended tubes [3, 37, 38]. Bouaifi [37] describes the coating of industrial knife edges with a chrome–vanadium steel, and the addition of vanadium carbide though a separate powder feed into the molten metal pool (see Fig. 10.19), reaching this way up to 70 vol.% VC in the coating. Deposition parameters were: arc current 160–230 A, powder mass flow rate 1.5–5.5 kg/h, and a traverse velocity 4–15 cm/min. Some edges had to be ground after the coating deposition.

10.6.3 Nitriding of Coating

Some efforts have been made to increase hardness though nitriding by deposition in a nitrogen atmosphere. Bouaifi et al. [74] describe experiments with nitrogen addition in the plasma gas, with nitrogen as carrier gas, and with nitrogen as the shield gas, depositing Fe–Cr–V–C alloys. Problems were encountered with

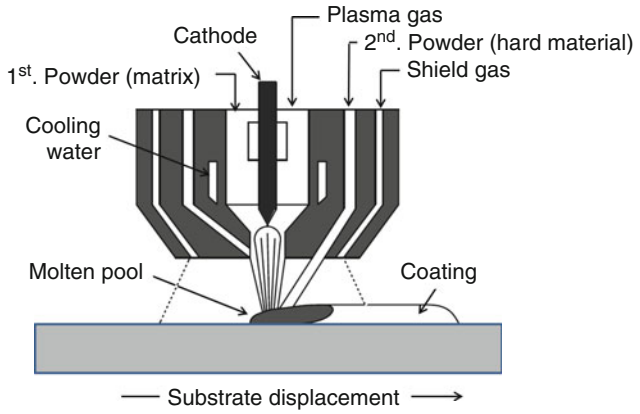


Fig. 10.19 Dual powder feed PTA torch as described by B. Bouaifi [37]. Reproduced with kind permission of the author

nitrogen in the plasma gas: for more than 70 % of N_2 the arc became unstable, and even at lower nitrogen percentages, the stronger constriction of the arc led to more fume formation and shorter electrode lifetimes, as well as to reduced coating adhesion at the bead edges. While the nitrogen content in the shield gas did not influence the coating properties notably, a fraction of 33 % nitrogen in the plasma gas significantly increased the wear resistance of some alloys with incorporation of maximal 0.28 wt% nitrogen. A similar experiment is reported by Bach et al. [75] using plasma weld deposition in a chamber with a nitrogen atmosphere. At 1 atm pressure in the chamber and 10 % N_2 in the plasma gas, nitrogen incorporation into a Cr–Ni steel of up to 0.37 wt% could be achieved. Increasing the chamber pressure reduced the nitrogen content and led to material evaporation.

Wang et al. [76] tried to overcome the problem by depositing the TiN/Ni composite coatings on 7005 aluminum alloy by high-speed jet electroplating, which was then processed with a PTA scanning process. The PTA scanning-treated specimens had a rapidly solidified microstructure consisting of uniformly distributed TiN phase and fine Al_3Ni_2 intermetallic phases. The microhardness was about HV 852 and was seven times higher than that of the aluminum alloy substrate. In comparison with the friction coefficient of 0.35 for TiN/Ni composite coating, the friction coefficient for PTA scanning treated specimen has dropped to 0.25. The corrosion resistance of the composite coating was also greatly improved.

10.6.4 Modulation of Deposition Parameters

The uneven distribution of a high-density carbide (e.g., WC) which, because of gravity, accumulates at the coating-substrate interface, has been addressed by modulation of the plasma gas flow rate [68]. Magnetic valves have been used to

vary the plasma gas flow rate between 1 and 3 slm during deposition of a cobalt alloy with 40 vol.% WC. The arc current has been 95 A, the carrier gas flow rate 2 slm, and the shield gas flow rate 10 slm, and the transverse velocity has been 10 cm/min. A uniform distribution of the carbide in the coating has been obtained for a modulation frequency between 1 and 5 Hz.

To minimize the heat input to small or thin substrates, current modulation has been employed. Shubert [8] describes a micro-PTA process in which a bead is deposited as thin as 0.5 mm, with a bead height to width ratio that could be varied between 0.5 and 2, and with a ratio of bead width to substrate width of 0.5 to 1. An "auxiliary" current of 4–15 A is flowing continuously, and high-current pulses of 0.4 s length with a 25 % duty cycle are superimposed to yield average currents of between 12 and 40 A. the deposition rate has been between 0.3 and 0.5 kg/h, and the deposition speed has been 14–21 cm/min. This process has been applied in particular to the refurbishing of gas turbine parts [8, 9]. Saltzmann [10, 11] describes the refurbishing of superalloy parts in gas turbines with average currents of 3–20 A and with 10–40 ms long high-current pulses. During the high-current pulse the weld pool is created, and it is allowed to solidify during the low current time. The quick solidification times lead to very fine grain structure in the deposits. Very short substrate distances are used (5–10 mm for currents from 10 to 50 A). The powder is delivered into the weld pool though an external feed tube.

A similar approach of pulsing the arc current has been used in a development focused on reducing the distortion of the work piece for a near net-shape application, a stellite 6 coating was deposited on steel with an intermediate Ni alloy coating using a pulsed plasma weld-coating technique [77]. The amount of transferred arc current was periodically varied between a base current value and a pulse current value, and the effect of the current values and the duty cycle of the pulse current have been investigated. Three passes were used to reach the required thickness of 8 mm. The dilution was found to be increasing with the arithmetic mean of the arc current, and with an increase in the ratio of base current to pulse current, as well as with an increase in duty cycle. All these factors influenced the heat input into the substrate, and higher heat inputs increased not only the dilution but also the work piece distortion and reduced the hardness. It was found that good coatings could be deposited with minimal distortion of the substrate material, and the authors comment that this technique is particularly useful for near net-shape manufacture of small parts. D'Oliveira et al. [78] evaluated the effect of pulsed current on a high-carbon cobalt alloy deposited by PTA on carbon steel and stainless steel.

10.6.5 High-Energy PTA

Another development for the purpose to reduce the heat input to smaller parts has been the high-energy PTA by SNMI, Avignon, France [79, 80]. In this development, aimed at wear-resistant coatings of smaller parts like internal combustion engine valves with minimal needs for water cooling, the arc is highly constricted

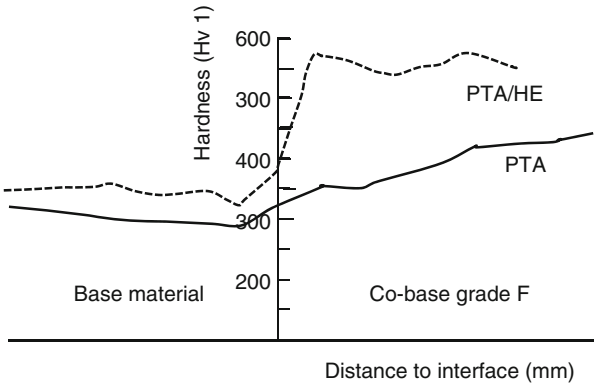


Fig. 10.20 Comparison of hardness profiles across a Co alloy coating on steel for regular PTA and high-energy PTA [79]. Reprinted with permission for Begell House, Inc.

providing a small attachment spot diameter at the work piece, with high current densities and high energy densities. With these high energy densities, the relative torch–substrate movement velocity can be very high, and low penetrations and dilution values are obtained, as well as high cooling rates resulting in a fine microstructure. As relationship between arc attachment spot diameter D, melted layer thickness p, and traverse velocity v the following equation is used:

$$v = \frac{D}{5p^2} \frac{\kappa}{\rho c_\mathrm{p}} \tag{10.6}$$

with κ, ρ, and c_p being the metal properties thermal conductivity, density, and specific heat at constant pressure, respectively, with the condition for the power input at a specific velocity and melt depth given by

$$\frac{VI}{vD} \geq 10^7 \frac{\mathrm{J}}{\mathrm{m}^2} \tag{10.7}$$

As specific examples for such a high-energy value coating process, the following values are given [80]:

1. $I = 120$ A, $D = 3$ mm, $v = 1.06$ m/min, with a deposition rate of approximately 1.8 kg/h (7 g/15 s or 0.47 g/s), nozzle diameter of 3 mm.
2. $I = 60$ A, $D = 2.3$ mm (1.5 mm nozzle diameter), $v = 3.52$ m/min, and a deposition rate of about 0.8 kg/h (0.22 g/s), nozzle diameter of 1.5 mm.

Very low dilution values allow deposition of thin layers. Figure 10.20 [79] shows a comparison of the hardness profiles across a deposited layer of a Co alloy on steel for the regular PTA and the high-energy PTA processes, demonstrating that the final hardness of the coating is reached at lower thicknesses.

10.6.6 PTA Combined with Tape Casting

A combination of tape casting with PTA has been described by Leylavergne et al. [81–84], with the aim of reclamation of worn parts having a complex shape. In this process a slurry has been prepared consisting of a metal powder (NiCu or NiCoCrAlTaY), a solvent (a 73/27 mixture of trichloroethylene/ethanol), a dispersant to assure a uniform distribution of the metal in the solvent (phosphate ether), and a binder (polyvinylbutyral). The substrate was coated with the slurry at a uniform thickness. To obtain a sufficiently high-electrical conductivity for PTA treatment, a heat treatment of the slurry was required. Addition of submicron Ni or C powder also helped increasing the electrical conductivity. The commercial torch (Castolin Eutectic GAP E52) was operated with a transferred arc current of 20–70 A, with 4 slm argon as the plasma gas, 30 slm helium as the shield gas, a torch substrate distance of 5 mm, and an oscillation width and frequency of 3 mm and 3 Hz, respectively. The pilot arc was used for arc initiation to obtain a spot on the surface with sufficient electrical conductivity. During the PTA process, part of the metal particles is blown out, and a deposition efficiency of about 50 % is reported. Uniform films of up to 600 μm thickness have been obtained.

10.6.7 PTA Deposition with a Negative Work Piece Polarity

A number of studies have been directed toward process development for coatings of light metals, i.e., aluminum or magnesium alloys. These metals have low melting points requiring reduced heat input to the substrate, and they have an oxide surface layer that needs to be removed to obtain good adhesion of the coating [1]. As mentioned already in Sect. 10.3, they also have high-thermal diffusivities (9.8×10^{-2} for Al and 8.77×10^{-2} for Mg), resulting in rapid transfer of the heat from the arc attachment to the rest of the substrate. The consequence is that it will take a relatively long time to reach the melting point, but then a major part of the substrate may be molten. Reduction of the overall heat transfer is necessarily accompanied by an increase in the local heat flux, as offered by a reverse arc heating though small cathode spots. Removal of the oxide layer can be achieved by thermal means heating the substrate and melting the oxide with He as addition in the plasma gas. However, this process creates larger melt pools and movement of the molten material [45]. Having the work piece at a negative polarity, i.e., serving as the cathode, will result in lower overall heat transfer, but more concentrated heat fluxes in the continuously moving cathode spots. Cathodic arc de-oxidation has been a standard practice in the metallurgical industry. Dilthey et al. [45] and Lugscheider et al. [46] describe a PTA process with direct current combined polarity heating, in which the pilot arc is established between the tungsten cathode and the pilot arc anode nozzle, but the transferred arc is struck between the pilot arc anode nozzle and the work piece as the cathode. Significant increases in wear

resistance have been achieved by (1) dispersing a hard material such as WC/W_2C into the molten surface of a AlMgSi0.5 alloy, (2) by depositing an aluminum alloy together with a hard material, or (3) by alloying the substrate material with a deposited material to generate hard phases. For this process, the transferred arc current was reduced and the pilot arc current was increased. The pilot arc anode had been designed for improved water cooling to reduce the erosion due to higher thermal loads from two arcs. The same arrangement of a direct current combined polarity has been used for increasing the wear resistance of AlMg4.5Mn [85]. The coating material was a AlCuMg alloy reinforced by up to 70 wt% fused tungsten carbide (WC + W_2C) or up to 50 wt% TiC. With a pilot arc current of 120 A and a transferred arc current of 100 A, a plasma gas flow rate of 0.5–1 slm, a carrier gas flow rate of 4 slm, and a shield gas flow rate of 10 slm, an oscillation width of 10 mm and an oscillation frequency of 1.8 Hz, hard coatings were deposited with significantly improved wear characteristics compared to the base material, by a factor of 40 for the tungsten carbide and a factor 25 for the TiC-containing coatings [85]. The carbide particles were uniformly distributed in the coating. Addition of Ni into the coating material further improved hardness though the formation of hard intermetallic phases, however, the coatings became more brittle.

10.6.8 Hard Coatings on Magnesium

Coating of a magnesium alloy is described by Gebert et al. [86]. Magnesium as a structural material can lead to even more weight reduction than aluminum; however, it has poor corrosion and wear properties. Coatings have been obtained using a matrix material for the composite coating of either Al or AlSi12 with the addition of up to 10 vol.% Mn or Si and reinforcing particles of TiC, SiC or B_4C. The best coatings have been obtained with the work piece at a positive polarity and with about 30 % He added to the plasma gas to increase penetration. A penetration depth of 2–3 mm is obtained. While the TiC and SiC particles have been nonuniformly distributed in the coating, a uniform distribution with the lighter B_4C has been obtained. The hardness increases as well as the wear resistance increases were dependent on the amount of B_4C addition, with 7.5–10 % carbide giving strong improvements particularly in the wear rate.

10.7 Examples of Specific Applications

10.7.1 Increasing Hardness

The largest number of applications is in the area of improving either hardness or wear resistance of components, frequently under corrosive conditions. Lugscheider et al. [30] describe the hardness and wear improvements with a metal matrix

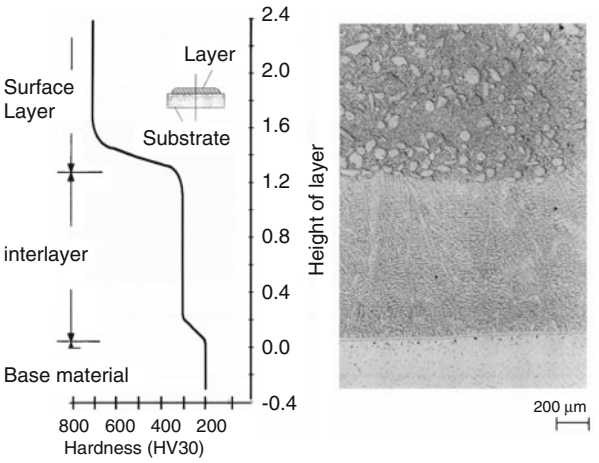


Fig. 10.21 Increase in hardness across a coating on a ball valve consisting of an austenitic steel interlayer and a Ni alloy with FTC reinforcement [17]. Reprinted with permission of ASM International. All rights reserved

composite coating using a cobalt alloy matrix with (WTi)C or TiC, with a deposition rate of 3.3 kg/h and a traverse speed of 9–10 cm/min. The current was 90–100 A, pilot arc current 50 A, and the gas flow rates were 2.5 slm for the Ar plasma gas, 2–3 slm for the carrier gas consisting of Ar + 6.5 % H_2, and 6–7 slm for the shield gas of Ar + 6.5 % H_2. Oscillation width was 10 mm and the oscillation frequency was 0.9 Hz. The highest hardness was achieved with the WC addition, but the lowest wear rate with the TiC. The authors see such coating suitable for applications where corrosion combined with mechanical wear is encountered. A similar process was used to coat ball valves using an Ni–Cr–B–Si alloy reinforced with 50 wt% FTC [17]. To prevent crack formation at the interface, an intermediate austenitic steel layer was deposited, and the parts were preheated to 600 °C. Deposition conditions were for the surface layer: arc current 75 A, pilot arc current 60 A, powder flow 4 kg/h, traverse velocity 8.6 cm/min, substrate distance 15 mm, oscillation width 15 mm, and oscillation frequency 0.7 Hz. A significant increase in hardness and reduction in wear was observed. Figure 10.21 [17] shows the hardness profile next to a micrograph of the coating cross section and the increase in the hardness in the FTC containing surface layer. The steep increases between the layers indicate very low dilution.

10.7.2 Increasing Wear Resistance

Deposition of a wear resistant layer with edge loading for paper or wood cutting knives is described by Bouaifi et al. [37]. A chrome steel matrix is used with up to 70 % VC reinforcement. Deposition current was 200–230 A, deposition rate 3.6–4.8 kg/h, traverse speed 7–10 cm/min. Dual powder injection was used with the carbide injected behind the arc attachment into the weld pool. Significant reduction in wear was observed when the dilution could be kept low.

For the reduction of abrasive wear in elastomer processing machines, different coating techniques were compared by Hartmann et al. [36]. The PTA-deposited FeV18 + 50 % VC showed excellent wear resistance approaching that of specialty metals. This wear resistance value was followed closely by that of PTA deposited Ni–B–Si + 60 % FTC. PTA deposits of Fe–V showed somewhat higher wear, closely followed by HVOF deposited WC–Co–Cr. Wire arc deposits and the presently used weld overlay method have significantly higher wear. It must be pointed out, however, that the PTA and weld-deposited layers are significantly thicker than the spray-deposited layers (3 mm vs. 0.5 mm), thus offering wear resistance for a longer time.

Applications in the steel industry using higher power levels are described by Hallen et al. [12] and Bouaifi et al. [87]. Hallen et al. [12] describe a process of coating parts for cold roll steel mills, using a deposition rate of 12 kg/h, an arc current of 290 A, a traverse velocity of 9.8 cm/min, gas flow rates of 3.2 slm argon for the plasma gas, 9.5 slm for the Ar + 6.5 % H_2 carrier gas, and 13 slm for the Ar + 6.5 % H_2 shield gas. Oscillation width was 40 mm, and the oscillation frequency was 0.38 Hz, and the substrate distance was 15 mm. Ni–Cr–W–C or Co–Cr–W–C coatings were deposited. Bouaifi et al. [87] used a HPTA (high power PTA) process to deposit a wear-resistant coating on continuous casting guide rollers with C4 + FTC. This process was developed to replace a SAW process, which required deposition of thee layers with a total thickness of 15 mm to keep dilution at acceptable levels. At 400 A, a powder feed rate of 8.4 kg/h and a traverse velocity of 14 cm/min were achieved with a dilution of 8 %, and at 500 A, the deposition rate was 10.8 kg/h, the traverse velocity 18 cm/min, but the dilution was 12 %.

Kesavan and Kamaraj [88] report on the sliding wear resistance at elevated temperatures (up to 823 K). A Ni-based alloy (colmonoy 5) was deposited on stainless steel without carbide addition with a current of 150 A, a powder feed rate of 2.1 kg/h, a traverse speed of 7.4 cm/min, with a plasma gas flow of 4.2 slm, a carrier gas flow of 4.1 slm, and a shield gas of 12 slm. The substrate distance was 17 mm, and the oscillation width 15 mm. The substrate was preheated to 573 K. An increase in hardness (about a factor 2.5) was found due to the formation of carbides and borides. The coefficient of friction as well as the wear loss decreases with increasing temperature due to different wear mechanisms.

Bartys and Guerin [89] used the high-energy PTA process to deposit coatings on railway car brakes. The requirement for lightweight and high-energy dissipation led them to compare NiCr–Cr_3C_2 cermet coatings with stellite or Ni alloys on the steel discs, when used with aluminum titanate pads. Stellite proved to give good performance with better adhesion than other coatings.

Deposition of a self lubricating coating is reported by Skarvelis et al. [49] using a slurry-coated steel substrate scanned by a PTA torch. The slurry contained Fe with variable amounts of MoS_2 and TiC. The arc current was 90 A, the traverse speed 12 cm/min, and plasma and shield gas flow rates were 0.7 and 7.1 slm, respectively. It was found that the TiC and the MoS_2 dissolve and that mixed sulfides are generated which do lower the friction and improve wear. A similar approach has been chosen for the deposition of TiB_2 coatings [90]. Water-based slurries of

Fe–B + Ti or of Fe–Ti + FeB were deposited on mild steel substrates, heated at 80 °C for one hour and at 600 °C for a half hour, and then scanned with a PTA torch operated at 120 A with a traverse velocity of 3 cm/min and an oscillation width of 30 mm and a frequency of 0.37 Hz. The results showed a coating composition of Fe–Fe_2B–TiB_2. Similar results could be obtained with a Fe–Ti + B_4C starting powder mixture, however, higher scanning currents were required.

Improvement of toughness and impact resistance of PTA coatings has been investigated by Branagan et al. [91] and by Just et al. [73]. Branagan [91] deposited newly designed chrome steel alloys without a carbide hard phase at 175–200 A, with a deposition rate of 1.74 kg/h and a traverse velocity of 4.5–5 cm/min, with and without substrate preheating. Improved impact resistance was found due to formation of boro-carbide phases (up to 70 vol.%). Just et al. [73] studied the impact resistance of PTA-deposited NiB and Fe–Si–C + 60 wt% FTC, deposited with 70 A and 90 A arc currents at 2.88 kg/h with an oscillation width of 20 mm and an oscillation speed of 20 mm/s. They found that the higher current led to a thicker interface between the matrix material and the carbide and that the lower interface thickness obtained at the lower current reduced the bond strength. The arc current has been found to control the failure mechanism: de-cohesion of the carbide particles at lower current deposits, while carbide cracking is observed at the higher currents and thicker interfaces.

10.7.3 Abrasive Wear in Petrochemical, Mining, and Agricultural Applications

Several studies were performed of the wear by erosion, as encountered in the processing of oil sands, in mining, and in agriculture. Flores et al. [92] exposed coatings of two different Ni–Cr–B–Si alloys with 65 wt% WC addition to erosion by a sand slurry. The WC reinforcement reduced erosion significantly at temperatures of 20 °C, but at a temperature of 65 °C corrosion of matrix material and loss of WC particles were the dominant wear mechanism. At higher sand concentrations in the slurry, erosive wear due to matrix damage and carbide particle fracture was encountered. Controlling precipitation of hard phases during solidification is important for control of erosion, because the mean distance between the hard phase particles should be smaller than the mean diameter of the hard particles. The same authors [41] investigated the erosion mechanisms of a Fe–Cr–C deposit with and without 65 wt% WC addition. Similar effects were found as with the Ni-based alloy matrix. The effect of temperature was again more pronounced than the effect of increased sand content in the slurry. A dry sand–rubber wheel abrasion test was used to evaluate PTA deposited coatings of Ni–B–Si and Ni–B–Cr–Si with 40 or 60 vol.% FTC or micro-crystalline WC, at currents between 120 and 180 A [93]. The Cr containing matrix material and the macro-crystalline WC offer the lowest wear rates, and the wear rate increases with increasing current, except for the case with the Ni–B–Si matrix and 60 vol.% FTC. Specific coatings on specific

components from the oil sand processing industry are described. For a similar range of applications, case studies are reported of a self fluxing alloy Ni–B–Si with Cr and WC additions, at current values between 100 and 300 A [94]. Deposition at higher currents led to some carbide decomposition and increased wear. Comparison of the improvement in wear of the WC coatings deposited with HVOF (WC–Co), with PTA and with a newly developed spray fusion brazing process showed the strongest improvement with the spray fusion deposited layer, closely followed by the PTA deposited layer, and somewhat less improvement with the HVOF-deposited layer.

10.7.4 Combined Corrosion and wear

Improvement of corrosion, erosion, and high temperature wear resistance in machinery for the petrochemical industry has been pursued with PTA coatings of Ni- and Co-based materials [95]. For a coating of pump seal rings, a Ni alloy was chosen with addition of 35 % WC. A handheld torch was used with a current of 63 A, gas flow rates of 0.8 slm for the plasma gas, and 8 slm for the shield gas, and 1 slm for the carrier gas, with a substrate distance of 8–10 mm and an oscillation width of 6 mm. Valve seats and valve cores were coated with a Co-based alloy, at a current of 87 A, flow rates of 1 slm for the plasma gas, 12 slm for the shield gas, and 1.8 slm for the carrier gas, with a substrate distance of 8 mm and an oscillation width of 12 mm. Dilutions of 5–6 % were obtained in a 4-mm thick coating.

A number of coating and process developments have been directed at improving corrosion resistance or wear resistance under corrosive conditions. Gebert et al. [16] have investigated the wear improvement of corrosion resistant coatings and report that addition of 30–50 wt% VC to an Fe-based matrix in a PTA-deposited layer reduced the erosion significantly in food processing applications when no corrosive environment existed, however, Ni alloys had to be used for exposures to inorganic acids to avoid strong corrosion. In many applications, the abrasive wear dominates over the corrosive wear. The coatings of knives in the food industry for abrasive and corrosive wear is described by Heinze et al. [39] and by Gebert and Heinze [40]. A Fe–Cr–V–C–Ni layer with varying amounts of Cr and Ni was deposited at 140–240 A, 2.4–8.4 kg/h, with a traverse speed of 5–15 cm/min [39]. Hardness was increasing with lower Ni content, but corrosion resistance improved with higher Ni content. A content of 2.5 wt% Ni and 15–17 wt% Cr was seen as optimal, improving working life of knives by a factor of three.

Improvement of wear and corrosion resistance using Ni-based matrices reinforced with oxide ceramics has been described by Draugelates et al. [96]. As matrix material served Ni–B–Si or Ni–Mo–Cr–Ti, and the ZrO_2 and Al_2O_3 ceramic powders, fabricated with a Ni–B–Si (50 %) binder via powder metallurgical processing, were added into the weld pool though a second powder feed system. The shield gas was argon with up to 15 % hydrogen. Comparison of the wear rate with plasma-sprayed Cr_2O_3 and Al_2O_3 shows higher wear rates of the

PTA-deposited materials by a factor 2 to 3, however, the larger thicknesses of the deposited layers, 2.5–3 mm for the single pass PTA deposit, 0.5 mm for the plasma-sprayed layer, would offer longer life of the PTA-coated component.

Draugelates et al. [42] describe a deposition process for high-temperature corrosion resistant materials Ti, Zr, and Ta in a protective atmosphere. An intermediate layer of a nickel alloy is used. While coatings of Ti were successfully produced, difficulties were encountered with the Zr and Ta coatings because of the high-melting points of these materials. Using a pulsed PTA deposition process, it was possible to coat steel substrates with a Ti layer using a Cu interlayer [97]. The Cu interlayer reduced the dilution and the formation of intermetallic phases and improved the adhesion of the Ti layer to reach corrosion protection comparable to traditional materials. However, the difference in melting points between Cu and Ti (1,083 °C vs. 1,670 °C) requires good control of the heat fluxes to the substrate, and the high reactivity of Ti with oxygen, nitrogen or hydrogen requires careful shielding of the heated metal which was accomplished by using a controlled atmosphere chamber filled with Ar. The Cu layer was deposited either by explosion cladding or by PTA deposition using 170 A and a traverse velocity of 4 cm/min and a dilution of <5 % was attained. Deposition of the Ti layer was accomplished using a pulsed transferred arc current with a 165 A base value and a 236 A pulse value. Oscillation width was 10 mm, and the traverse velocity was 4 cm/min. During the low current phase of the pulsing cycle, partial solidification occurs, and therefore the bead consists of overlapping sections. Dilution was <10 % for the first layer and <2 % for the second layer, with a total coating thickness of 5–6 mm. The corrosion resistance of the PTA-deposited Ti layer is comparable to that of the reference material consisting of a Ti layer fabricated by explosion cladding.

10.7.5 Refurbishing of Worn Parts

Refurbishing of various gas turbine parts using a micro-PTA process with current pulsing has been described in Sect. 10.6 [8–11]. Another process for coating complex shapes using a handheld PTA torch is described by Schreiber [14] for parts within construction or chemical processing equipment. Deposition of Fe–Cr–Mo–V alloys which reach high hardness due to the formation of fine grain VC during deposition, or with addition of VC, as well as deposition of NiBSi + 60 % FTC is described, with layer thicknesses between 0.3 and 2 mm. Deposition rates are up to 1.5 kg/h, and arc currents can be up to 120 A. Preheating of the substrate with a lower current of 50 A is recommended.

10.7.6 Freestanding Shape Fabrication

A relatively new application of PTA deposition is the fabrication of freestanding shapes or solid free form fabrication. Wang et al. [50] describe the fabrication of three-dimensional shapes using micro-PTA and WC-reinforced tool steel

powders. The arc current was 10–15 A, gas flow rates were 0.4 slm for the plasma gas, 3.5 slm for the carrier gas, and 10 slm for the shield gas, and powder deposition rates were 0.14 kg/h. The substrate was preheated with the 15 A arc for about 180 s, while the traverse speed was set to 6 cm/min. The substrate distance was found to have an effect on the coating because an increase led to an increase in arc voltage and substrate heat transfer. Several different cylindrical shapes were fabricated consisting of 40–80 layers and with average layer thicknesses of 0.35–0.42 mm. One example is a cylinder with 22.4 mm O.D. and 17.2 mm I.D., and in general manufacture of cylindrical tools or tool parts are seen as a suitable application.

Alaluss et al. [44] also describe the fabrication of forming tools with an objective of showing an economical alternative to the machining of a forming tool out of tool steel. They used multiple layers of different materials, starting with layers of a Ni alloy as intermediate and form producing layer. Layers of stellite followed and the surfaces exposed to high wear conditions were treated with deposition of a stellite layer with 10–50 % FTC. The process was demonstrated by the fabrication of a transverse rolling tool, consisting of three layers of the Ni alloy and 4 layers of stellite 12, with an additional layer of stellite with 20 % FTC on the surfaces exposed to wear. The tool was successfully tested in a steel company. The weld direction was changed between successive layers.

Solid free form fabrication of a component made of Be is reported by Hollis et al. [51]. Beryllium offers several advantages for space applications, such as light weight, high stiffness, and a large ratio of the elastic modulus over the cube of the mass density, E/ρ^3; however its danger to human health makes machining cumbersome. Using a controlled atmosphere chamber filled with Ar, the layers were deposited with a 45 A a.c. arc (60 Hz), gas flow rates of 2 slm for the Ar plasma gas, 7 slm for the Ar shield gas, and 2 slm for the Ar carrier gas. The oscillation width was 10 mm. The layers were deposited on a rotating cylinder with a traverse speed of 5 cm/min. The mechanical properties were acceptable for many applications, but somewhat lower than those of hot pressed Be parts; however, it is believed that the mechanical properties could be improved by further developing the process to obtain finer grain sizes.

10.8 Summary and Conclusions

In the PTA-coating process, the substrate serves as one of the arc electrodes, resulting in high-heat transfer rates. The consequences are a good metallurgical bond of the coating to the substrate, very high coating density, and the possibility to generate thick coatings. The major drawback is the limited ability to coat complex shapes, the high level of residual stress, and the requirement of metallurgical compatibility between substrate and coating. There are numerous reports of successful uses of PTA-deposited coatings for reducing wear and corrosion and rebuilding metallic components in almost every industry where thick coatings are

of advantage. This process has led to a number of developments of new materials combinations in metallurgy and in composites, and it is expected that this trend will continue.

Nomenclature

A_{conv}	The area over which the convective heat transfer takes place (m^2)
D	Arc attachment spot diameter (m)
e	Electronic charge (A s)
E	Electric field (V/m)
E_i	Ionization potential of the plasma gas (V)
I	Arc current (A)
j_e	Electron current density (A/m^2)
j_i	The ion current density (A/m^2)
k	Thermal conductivity of electrons (W/m K)
k	"Constriction parameter" (cm^{-2})
k_B	Boltzmann constant (1.38×10^{-23} J/K)
k_h	Thermal conductivity of heavy species (W/m K)
p	Melted layer thickness (m)
q_a	Anode heat flux (W/m^2)
q_e	Electron enthalpy flux (W/m^2)
q_m	Maximum heat flux for a given condition (W/m^2)
$q(r)$	Substrate heat flux (W/m^2)
Q_{sub}	Total heat transfer to the substrate (W)
r	Radial coordinate (m)
r_e	Arc radius (radius of current path) (m)
T_e	Electron temperature (K)
T_h	Heavy species temperature (K)
v	Plasma velocity (m/s)
v	Traverse velocity of the torch (m/s)
V	Arc voltage (V)
V_{an}	The anode fall voltage (V)

Greek Alphabet

α	Fraction of the electrical power transferred to the anode
Φ_a	Work function of the anode material (V)
ρ	Mass density of the plasma (kg/m^3)
$\overline{\sigma}_{ar}$	Electrical conductivity of argon averaged over the arc cross section (mho/m)

References

1. Gebert A, Bouaifi B (2005) Oberflächenschutz durch Auftragschweiβen, Moderne Beschichtungsverfahren. Wiley, New York, NY
2. Hallen H, Lugscheider E, Ait-Mekideche A (1991) Plasma transferred arc surfacing with high deposition rates. In: Bernecki T (ed) Proceedings of the fourth national thermal spray conference, Pittsburgh, PA. ASM International, Materials Park, OH, pp 537–539
3. DuMola RJ, Heath GR (1997) New developments in the plasma transferred arc process. In: Berndt CC (ed) Proceedings of the united thermal spray conference, Indianapolis, IN. ASM International, Materials Park, OH, pp 427–434
4. Wilden J, Bergmann JP, Frank H (2006) Plasma transferred arc welding-modeling and experimental optimization. J Therm Spray Technol 15(4):779–784
5. Gatto A, Bassoli E, Fornari M (2004) Plasma transferred arc deposition of powdered high performance alloys: process parameters optimisation as a function of alloy and geometrical configuration. Surf Coat Technol 187:265–271
6. Wassermann R, Quaas J, Chalard J-C, Noel L, Steine H-T (1978) Installation for surfacing using plasma-arc welding. US Patent 4,125,754
7. Bouaifi B, Schreiber F, Göllner J, Schulze S (1996) Eigenschaften und Beständigkeit von Plasma-Pulver-Auftragschweißungen aus hartstoffverstärkten CrNiMoN-legierten Duplex-Stählen. DVS-Berichte 175:425–428
8. Shubert GC (1987) Welding apparatus method for depositing wear surfacing material and a substrate having a weld bead thereon. US Patent 4,689,463
9. Lindland D, Shubert G (1988) Method for applying a weld bead to a thin section of a substrate. US Patent 4,739,146
10. Saltzmann GA, Wertz TA, Friedman IL (1989) Method for refurbishing cast gas turbine engine components and refurbished component. US Patent 4,878,953
11. Saltzman G, Sahoo P (1991) Applications of plasma arc weld surfacing in turbine engines. In: Berndt CC (ed) Proceedings of the fourth national thermal spray conference, Pittsburgh, PA. ASM International, Materials Park, OH, pp 541–548
12. Hallen H, Mathesius H, Ait-Mekideche A, Hettiger F, Morkramer U, Lugscheider E (1992) New applications for high power PTA surfacing in the steel industry. In: Berndt CC (ed) Proceedings of the international thermal spray conference & exposition, Orlando, FL. ASM International, Materials Park, OH, pp 899–902
13. Kammer PA, Weinstein M, DuMola RJ (1991) Characteristics and applications for composite wear-resistant overlays. In: Bernecki T (ed) Proceedings of the fourth national thermal spray conference, Pittsburgh, PA. ASM International, Materials Park, OH, pp 513–518
14. Schreiber F, Krefeld D (2002) Mobile plasma powder hand deposition welding: practice experience. In: Lugscheider E (ed) Proceedings of the international thermal spray conference 2002, Essen, Germany, 4–6 Mar 2002. DVS, Düsseldorf, Germany, pp 273–277
15. Ducos M (1985) Applications industrielles des plasmas d'arc de faible puissance et des plasmas inductifsinductifs, Les Plasmas dans l'Indudtrie, (ed.) G. Laroche (pub.) Dopée, Electricité de France, France (in French)
16. Gebert A, Wocilka D, Bouaifi B, Alaluss K, Matthes K-J (2008) Neuentwicklungen für den Verschleiβ-und Korrosionsschutz beim Plasma-Pulver-Auftragschweiβen (New developments for wear an corrosion protection by weld surfacing with plasma transmitted arc process). Mat-wiss u Werkstofttech 39(1):99–104
17. Lugscheider E, Ait-Mekideche A (1991) Advances in PTA surfacing. In: Berndt CC (ed) Proceedings of the fourth thermal spray conference, Pittsburgh, PA. ASM International, Materials Park, OH, pp 529–535
18. Yang LJ, Loh NL (1995) The wear properties of plasma transferred arc cladded stellite specimens. Surf Coat Technol 71:196–20
19. Bharath RR, Ramanathan R, Sundararajan B, Srinivasan PB (2008) Optimization of process parameters for deposition of Stellite on S45CrSi93 steel by plasma transferrred arc technique. Mater Des 29:1725–1731

20. Kim HJ, Yoon BH, Lee CH (2002) Wear performance of the Fe-based alloy coatings produced by plasma transferred arc weld-surfacing process. Wear 249:846–852
21. Hou QY, He YZ, Zhang QA, Gao JS (2007) Influence of molybdenum on the microstructure and wear resistance of nickel-based alloy coating obtained by plasma transferred arc process. Mater Des 28:1982–1987
22. Reimann H (1999) Metallic coatings for heavy-wear-protection. In: Lugscheider E, Kammer P (eds) Proceedings of the united thermal spray conference, Düsseldorf, Germany. DVS, Düsseldorf, Germany, pp 86–89
23. Dilthey U, Balashov B, Kondapalli S, Geffers C (2008) Entwicklung einer kostengünstigen und hoch verschleissbeständigen Eisenbasislegierung zum Auftragschweissen. Schweissen und Schneiden 60:200–204
24. Reisgen U, Dilthey U, Balashov B, Kondapalli S, Geffers C (2008) Investigation of wear resistance and microstructure of a newly developed chromium and vanadium containing iron-based hardfacing alloy. Mat-wiss u Werkstofttech 39(6):379–384
25. Hou QY, He Y, Gao J (2006) Microstructure and properties of Fe-C-Cr-Cu coating deposited by plasma transferred arc process. Surf Coat Technol 201:3685–3690
26. Bourithis L, Papaefthymiou S, Papadimitriou GD (2002) Plasma transferred arc boriding of a low carbon steel: microstructure and wear properties. Appl Surf Sci 200:203–218
27. Iakovou R, Bourithis L, Papadimitriou GD (2002) Synthesis of boride coatings on steel using plasma transferred arc (PTA) process and its wear performance. Wear 252:1007–1015
28. Liu YF, Liu XB, Xua XY, Yang SZ (2010) Microstructure and dry sliding wear behavior of Fe_2TiSi/-Fe/Ti_5Si_3. Surf Coat Technol 205:814–819
29. Cheng JB, Xu BS, Liang XB, Wu YX (2008) Microstructure and mechanical characteristics of iron-based coating prepared by plasma transferred arc cladding process. Mater Sci Eng A 492:407–412
30. Lugscheider E, Ait-Mekideche A, Aache AM (1994) Verbesserung der Eigenschaften von Hartlegierungen durch auftraggeschweiβte carbidische Verbundpulver. Schweissen und Schneiden 46(3):109–112
31. Saltzman G (1986) Carbides add muscle to PTA antiwear coatings. Metal Prog 129:25–30
32. Saltzman G, Aufderhaar WB (1984) New antiwear coatings applied by plasma-transferred arc wearsurfacing. Lubr Eng 41:233–241
33. Shi K, Hu S, Zheng H (2011) Microstructure and fatigue properties of plasma transferred arc alloying TiC-W-Cr on gray cast iron. Surf Coat Technol 206:1211–1217
34. Huang Z, Hou Q, Wang P (2008) Microstructure and properties of Cr_3C_2-modified nickel-based alloy coating deposited by plasma transferred arc process. Surf Coat Technol 202:2993–2999
35. Hou Q, Huang Z, Wang JT (2011) Influence of nano-Al_2O_3 particles on the microstructure and wear resistance of nickel-based alloy coating deposited by plasma transferred arc overlay welding. Surf Coat Technol 205:2806–2812
36. Hartmann U, Gebert A, Richter U, Leonhardt G (2007) Erhöhung der Verschleissfestigkeit von Elastomerverarbeitungsmaschinen durch innovative Beschichtungsverfahren. Mat-wiss u Werkstofttech 38(2):155–159
37. Bouaifi B, Gebert A, Heinze H (1993) Plasma-Pulver-Auftragschweiβungen zum Verschleiβschutz abrasiv beanspruchter Bauteile mit Kantenbelastung. Schweissen und Schneiden 45:506–509
38. Bouaifi B, Reichmann B (1997) Neue Anwendungsfelder durch die Entwicklung des Hochleistungs-Plasma-Pulverauftragschweiβens. Schweissen und Schneiden 49:734–736
39. Heinze H, Gebert A, Bouaifi B, Ait-Mekideche A (1999) Korrosionsbeständige Auftragschweisschichten auf Eisenbasis mit hoher Verschleissbeständigkeit. Schweissen und Schneiden 51(9):550–559
40. Gebert A, Heinze H (2002) PTA powder cladding of knives for food processing industry. In: Lugscheider E (ed) Proceedings of ITSC, Essen, Germany. DVS, Düsseldorf, Germany, pp 991–993

41. Flores JF, Neville A, Kapur N, Gnanavelu A (2009) Erosion-corrosion degradation mechanisms of Fe-Cr-C and WC-Fe-Cr-C PTA overlays in concentrated slurries. Wear 267:1811–1820
42. Draugelates U, Bouaifi B, Steinberg H (1993) Korrosionsschutz durch Auftragschweissen mit den reaktiven Metallen Titan, Tantal und Zirkonium. Werkst Korros 44:269–273
43. Tomita T, Takatani Y, Okita K, Harada Y (1998) Improvement of wear property of NbC/high Cr-high Ni overlay alloy coating formed by plasma transferred arc welding process. In: Coddet C (ed) Proceedings of the 15th international thermal spray conference, Nice, France. ASM International, Materials Park, OH, pp 253–258
44. Alaluss K, Matthes K-J (2007) Beanspruchungsgerechte Formgebung von Umformwerkzeugen durch formgebendes Plasma-Pulver-Auftragschweiβen (Load adjusted shaping of forming tools using build-up PTA welding). Mat-wiss u Werkstofttech 38(7):565–571
45. Dilthey U, Kabatnik L, Lugscheider E, Schlimbach K, Langer G (1999) Möglichkeiten zur Steigerung der Oberflächenfestigkeit bei Aluminiumlegierungen mit Plasma-Pulver-Schweiβverfahren (Improving of the wear resistance of aluminum alloys by plasma transferred arc welding). Mat-wiss u Werkstofttech 30(11):697–702
46. Lugscheider E, Langer G, Schlimbach K, Dilthey U, Kabatnik L (1999) Possibilites for improving wear-properties of aluminum-alloys by plasma powder welding process. In: Lugscheider E, Kammer P (eds) Proceedings of the united thermal spray conference, Düsseldorf, Germany. DVS, Düsseldorf, Germany, pp 410–413
47. Deuis RL, Yellup JM, Subramanian C (1998) Metal-matrix composite coatings by PTA surfacing. Compos Sci Technol 58:299–309
48. Skarvelis P, Papadimitriou GD (2009) Microstructural and tribological evaluation of potential self-lubricating coatings with MoS_2\MnS additions produced by the plasma transferred arc technique. Tribol Int 42:1765–1770
49. Skarvelis P, Papadimitriou GD (2009) Plasma transferred arc composite coatings with self lubricating properties, based on Fe and Ti sulfides: microstructure and tribological behavior. Surf Coat Technol 203:1385–1394
50. Wang H, Jiang W, Valant M, Kovacevic R (2003) Microplasma powder deposition as a new solid freeform fabrication process. Proc Inst Mech Eng:1641–1650
51. Hollis K, Bartram B, Withers J, Storm R, Massarello J (2006) Plasma transferred arc deposition of beryllium. J Therm Spray Technol 15(4):785–789
52. Hsu KC, Etemadi K, Pfender E (1983) Studey of the free-burning high-intensity argon arc. J Appl Phys 54(3):1293–1301
53. Lowke JJ, Morrow R, Haidar J (1997) A simplified unified theory of arcs and their electrodes. J Phys D Appl Phys 30:2033–2042
54. Lowke JJ, Tanaka M, Ushio M (2005) Mechanisms giving increased weld depth due to a flux. J Phys D Appl Phys 38(18):3438–3445
55. Bini R, Monno M, Boulos MI (2007) Effect of cathode nozzle geometry and process parameters on the energy distribution for an argon transferred arc. Plasma Chem Plasma Process 27:359–380
56. Etemadi K (1982) Investigation of high-current arcs by computer-controlled plasma spectroscopy. PhD Thesis, University of Minnesota
57. Young RM, Chyou YP, Fleck E, Pfender E (1983) An experimental arc plasma reactor for the synthesis of refractory materials. In: Boulos MI, Munz RJ (eds) Proceedings of the 6th international symposium on plasma chemistry, Montreal, QC. International Union of Pure and Applied Chemistry, pp 211–218
58. Peters J, Heberlein J, Lindsay J (2007) Spectroscopic diagnostics in a highly constricted oxygen arc. J Phys D Appl Phys 40:3960–3971
59. Evrard M, Blanchet B (1970) Etudes des plasmas d'arc du point de vue du soudage. Soudages et Techniques Connexes 7:261–298
60. Leylavergne M, Valetoux H, Coudert JF, Fauchais P, Leroux V (1998) Comparison of the behaviour of copper, cast iron and aluminum alloy substrates heated by a plasma transferred

arc. In: Coddet C (ed) Proceedings of the 15th international thermal spray conference, Nice, France. ASM International, Materials Park, OH, pp 489–495
61. Jenista J, Heberlein J, Pfender E (1997) Model for anode heat transfer from an electric arc. In: Fauchais P (ed) Proceedings of the 4th international thermal plasma processes conference, Athens, Greece. Begell House Inc., New York, NY, pp 805–815
62. Heberlein J, Mentel J, Pfender E (2007) The anode region of electric arcs – a survey. J Phys D Appl Phys 43:023001
63. Yang G, Heberlein J (2008) Anode heat transfer by electron current and electron conduction in an atmospheric pressure argon arc. In: Jemmaa NB (ed) Proceedings of the international conference on electrical contacts, Saint Malo, France. Universite de Rennes, Rennes, France, pp 313–316
64. Jenista J, Heberlein J, Pfender E (1997) Numerical model of the anode region of high-current electric arcs. IEEE Trans Plasma Sci 25(5):883–890
65. Menart JA (1996) Theoretical and experimental investigations of radiative and total heat transfer in thermal plasmas. Ph.D. Thesis, University of Minnesota
66. Dilthey U, Ellermeier J, Gladkij P, Pavlenko AV (1993) Kombiniertes Plasma-Pulver-Auftragschweissen. Schweissen und Schneiden 45(5):241–244
67. Nestor OH (1962) Heat intensity and current density distributions at the anode of high current, inert gas arcs. J Appl Phys 33(5):1638–1648
68. Ebert L, Thurner S, Neyka S (2009) Beeinflussung der Hartstoffverteilung beim Plasma-Pulver-Auftragschweiβen. Influencing the distribution of reinforcing particles in plasma transfer arc welding. Mat.-wiss u. Werkstofttech 40(12):878–881
69. Wilden J, Bergmann JP, Frank H, Pinzl S, Schrieber F (2004) Thin plasma-transferred-arc welded coatings – an alternative to thermally sprayed coatings? In: Ohmori A (ed) Proceedings of the international thermal spray conference, Osaka, Japan. ASM International, Materials Park, OH, pp 556–561
70. Matthes K-J, Alaluss K, Riedel F (2002) Nutzung der Finite-Elemente-Methode zur Optimierung des formgebenden Pulver-Plasmaauftragschweissens für die Herstellung hoch beanspruchbarer Umformwerkzeuge. Schweissen und Schneiden 54(4):178–184
71. Lakshminarayanan AK, Balasubramanian V, Varahamoorthy R, Babu S (2008) Predicting the dilution of plasma transferred arc hardfacing of stellite on carbon steel using response surface methodology. Met Mater Int 14(6):779–789
72. DuPont JN (1998) On optimization of the powder plasma arc surfacing process. Metallugical Mater Trans B 29B:932–934
73. Just C, Badisch E, Wosik J (2010) Influence of welding current on carbide/matrix interface properties in MMCs. J Mater Process Technol 210:408–414
74. Bouaifi B, Ait-Mekideche A, Gebert A, Wocilka D (2001) Nutzung von stickstoffhaltigen Hochtemperaturplasmen zum reaktiven beschichten mittels Plasmaauftragschweiβen. Schweissen und Schneiden 53:478–482
75. Bach F-W, SP, Zühlsdorf J (1999) Plasma powder welding under raised pressure environment. In: Lugscheider E, Kammer P (eds) Proceedings of the united thermal spray conference, Düsseldorf, Germany. DVS, Düsseldorf, Germany, pp 757–760
76. Wang W, Qian SQ, Zhou XY (2009) Microstructure and properties of TiN/Ni composite coating prepared by plasma transferred arc scanning process. Trans Nonferrous Met Soc China 19:1180–1184
77. Matthes K-J, Alaluss K (1996) Formgebendes Plasma-Pulverauftragschweissen mit Impulslichtbogen unter Beachtung minimaler Verformung. Schweissen und Schneiden 48 (9):668–672
78. D'Oliveira CM, Paredes RS, Santos RL (2005) Pulsed current plasma transferred arc hardfacing. Mater Process Technol 171:167–174
79. Proner A, Dacquet JP, Rouanet R (1997) The plasma high energy: a new hardfacing technique. Begell House, Inc., New York, NY
80. Proner A, Ducos M, Dacquet JP (1997) Process for coating of hardfacing a part by means of a plasma tranferred arc. US Patent US 5,624,717

81. Leylavergne M, Chartier T, Grimaud A, Baumard JF, Fauchais P (1998) PTA reclamation of cast iron and aluminum alloys substrate with NiCu film deposited by tape casting. In: Proceedings of the 15th international thermal spray conference, Nice, France, pp 373–377
82. Leylavergne M, Chartier T, Grimaud A, Fauchais P (1999) PTA reclamation of cast iron and nickel-based alloy substrates with films deposited by tape casting. In: Lugscheider PAKE (ed) Proceedings of the united thermal spray conference, Düsseldorf, Germany. DVS, Düsseldorf, Germany, pp 253–258
83. Leylavergne M, Chartier T, Grimaud A, Fauchais P (2000) PTA reclamation of cast iron substrates using tape casting process – the role of the organic binder concentration. In: Berndt CC (ed) Proceedings of the international thermal spray conference, Montreal, Canada. ASM International, Materials Park, OH, pp 1169–1177
84. Leylavergne M, Chartier T, Denoirjean A, Grimaud A, Abelard P, Fauchais P (2001) Cast iron substrates reclamation by tape casting of NiCu treated by plasma transferred arc: optimization of the tape and its plasma treatment. Thin Solid Films 391:1–10
85. Dilthey U, Kondapalli S, Balashow B, Riedel F (2008) Improving wear resistance of aluminium alloys by developing FTC and TiC based composite coatings using plasma powered arc welding process. Surf Eng 24(1):75–80
86. Gebert A, Wocilka D, Bouaifi B, Schütz M (2002) Wear and corrosion prevention at light metals by means of welding methods. In: Lugscheider E (ed) Proceedings of ITSC, Essen, Germany. DVS, Düsseldorf, Germany, pp 268–272
87. Bouaifi B, Plegge T, Sommer D, Hettiger F, Hallen H (1992) High performance plasma-powder weld surfacing – increase in efficiency and in service life of components subject to wear and corrosion. Schweissen und Schneiden 44:675–677
88. Kesavan D, Kamaraj M (2010) The microstructure and high temperature wear performance of a nickel base hardfaced coating. Surf Coat Technol 204:4034–4043
89. Bartys H, Guerin JD, Bricout JP, Oudin J (1998) Thermal spraying applied onto high energy railway braking: characterization of friction performances. In: Coddet C (ed) Proceedings of the 15th international thermal spray conference, Nice, France. ASM International, Materials Park, OH, pp 1127–1132
90. Wang XB, Cai LJ, Yang ZH, Xiao C, Xu LF (2009) Selection of covering materials for synthesising fabrication of TiB2 based coating with PTA process. Surf Eng 25(6):470–475
91. Branagan DJ, Marshall MC, Meacham BE (2006) High toughness high hardness iron based PTAW weld materials. Mater Sci Eng A 428:116–123
92. Flores JF, Neville A, Kapur N, Gnanavelu A (2009) An experimental study of the erosion-corrosion behavior of plasma transferred arc MMCs. Wear 267:213–222
93. Harper DH, Gill MJ, Hart KWD, Anderson M (2002) Plasma transferred arc overlays reduce operating costs in oil sand processing. In: Lugscheider E (ed) Proceedings of the ITSC, Essen, Germany. DVS, Düsseldorf, Germany, pp 278–283
94. Hart KWD, Harper DH, Gill MJ (2000) Case studies in wear resistance using HVOF, PTAW and spray fusion surfacing. In: Berndt CC (ed) Proceedings of the international thermal spray conference, Montreal, Canada. ASM International, Materials Park, OH, pp 1117–1125
95. Huang X, Wang R, Xu LF, Luo H, Yin X (1998) Applications of PTA powder welding in petroleum chemical industry. In: Coddet C (ed) Proceedings of the 15th international thermal spray conference, Nice, France. ASM International, Materials Park, OH, pp 1013–1017
96. Draugelates U, Bouaifi B, Giessler S (1998) Zweipulver-Plasmaauftragschweissen von oxidkeramikhaltigen Nickelbasislegierungen. Schweissen und Schneiden 50:713–716
97. Draugelates U, Bouaifi B, Schreiber F, Göllner J, Schultze S, Boese E (1998) Korrosionsverhalten von Plasma-Auftragschweissungen aus Titan-Legierungen. Mater Corros 49:744–752

Chapter 11
Powders, Wires, Cords, and Rods

Abbreviations

APD	Automatic powder diffraction
AS	Agglomerated and sintered
ASTM	American Society for Testing and Materials
CET	Coefficient of thermal expansion
CNT	Carbon nano tubes
D-gun	Detonation gun
d.c.	Direct current
DNA	Deoxyribo nucleic acid
ECTFE	Ethylene chlorotrifluoroethylene
EDS	Energy dispersion spectroscopy
EDXA	Energy dispersion X-ray absorption
EMAA	Ethylene-methacrylic copolymer
EPMA	Electron micro probe analysis
ETFE	Ethylene tetrafluoroethylene
EVA	Ethylene vinylene acetate
FC	Fused and crushed
FEP	Fluorinated ethylene propylene
GDC	Gadolinia-doped ceria
GFA	Glass forming ability
HA	Hydroxyapatite
HOSP	Hollow spherical particles
HVAF	High-velocity air fuel
HVOF	High-velocity oxy-fuel flame
ICPES	Inductively coupled plasma emission spectroscopy
IMTA	Integrated mechanical and thermal activation
JCPDS	Joint Committee on Powder Diffraction Standards, USA
LCP	Liquid-crystalline polymers
MA	Mechanical alloying

P.L. Fauchais et al., *Thermal Spray Fundamentals: From Powder to Part*,
DOI 10.1007/978-0-387-68991-3_11, © Springer Science+Business Media New York 2014

NIST	National Institute of Standards and Technology
OM	Optical microscopy
PA	Polyamides
PAEK	Polyaryletherketone
PAS	Polyarylene sulfide
PEA	Polyether amide
PES	Polyester
PC	Polycarbonate
PE	Polyethylene
PET	Polyethylene terephthalate
PFA	Perfluoroalkoxy
PMMA	Polymethylmethacrylate
PP	Polypropylene
PPS	Polyphenylene sulfide
PEEK	Poly-ether-ether-ketone
PTFE	Polytetrafluoroethylene
PVDF	Polyvinylidene fluoride
r.f.	Radio frequency
SEM	Scanning electron microscope
SHS	Self-propagating high-temperature synthesis
SOFC	Solid oxide fuel cell
SR	Sedimentation ratio
UHMWPE	Ultra high-molecular weight polyethylene
XRD	X-ray diffraction
XRF	X-ray fluorescence
YAG	Yttrium aluminums garnet

11.1 Powders

11.1.1 Introduction

The structure and properties of coatings obtained by thermal or cold gas spraying depend strongly upon different parameters among which the quality of the powder used plays a key role [1–5]. Powder quality can affect coating performance through one or more of the following effects:

The powder feedstock morphology and particles size distribution; These are closely related to the powder manufacturing route. Over the past decade numerous studies have also been devoted to the formation of nanostructured coatings for which nanostructured particles or particles susceptible to form nanostructured coatings upon cooling are developed.

The transport properties of the powders from the powder feeder to the injector. Transport line clogging can result in low deposition rates and poor deposit quality.

The injection technique used for the introduction of the powder into the energetic gas flow can have a major impact on the resulting particle trajectories and consequently on the particle velocities, temperatures, and indexes of melting (except for cold spray) prior to their impact on the substrate.

Powders are characterized by their:

- Chemical composition with the average and local content of the elements and impurities, especially their homogeneity
- Particle size distribution
- Crystalline structure: phases, alloys
- Moisture content: often an overlooked aspect in powder feeding, but very simple to control with powders placed in a heated oven for some time prior to spraying and then feeding them into the energetic gas stream using a heated powder feeder
- Morphology: fineness, shape, microstructure, porosity. Powders with the same chemical composition and size distribution from different suppliers can have very different morphologies reflecting the various powder manufacturing techniques used

Thermally sprayed coatings can exhibit significant variations in coating quality, even though the starting powders appear to be equivalent with respect to its chemical composition and particle size distribution [6]. This has been demonstrated for plasma spraying [7–12], HVOF [13–16], D-gun [17, 18], and pulsed gas dynamic spraying process [19]. The effect of variation in powder morphology, resulting from variations in the manufacturing process, is observed through variations in their shapes [1]. Irregular-shaped particles range from cubic-like structures to needles, while for blocky shaped particles; the largest and smallest dimensions of each individual particle are rather close. Moreover, while blocky particles are generally dense, spherical and irregular ones can be dense or porous with a rather wide range of porosities [2–5]. Besides the effect of these shapes on particle trajectories, different specific masses, corresponding to particles with different porosities, result in different effective thermal conductivities and diffusivities of the particles, and consequently in different thermal histories of the particles prior to impacting on the substrate.

The flow ability of powders is extremely important in all thermal spray processes. Powders with a poor flow ability (generally measured by Hall Flow, see section 11.1.5.7) gives rise to large variations in powder feed rates and consequently results in poor coatings. The powder mass flow rate also depends directly on its specific mass [20], which is, for a given material, highest with dense spherical particles such as those made using RF induction plasmas [21]. Particle morphology also plays an important role regarding the particle behavior upon penetration within the plasma jet [22]. The fragmentation of agglomerated particles upon penetration into the plasma jet results in the formation of large number of very fine particles which tends to vaporize during their trajectory in the plasma thus significantly reducing the ability of the plasma to melt the larger particles responsible for the coating formation. The homogeneity of particles composition [7, 9] is also a key

parameter for coating behavior, especially at high temperatures. For example, fused and crushed yttria-stabilized zirconia (8 wt%) keep their tetragonal non-transformable structure up to about 1,300 °C, while those prepared by sol–gel process can be heated up to 1,400 °C before transformation occurs [23]. This is due to the more homogeneous distribution of yttria grains (at the nano-scale level) with the sol–gel technique. For complex coatings, such as quasicrystalline [24, 25] or mullite ones [26] there is also a close link between processing, phase structure, crystallinity, and coating properties. The oxidation level of particles during their manufacturing process is also a very important issue because the sprayer, end-user, must never forget that the oxide content in coatings will never be lower than that of powder used in the spraying process. Finally, it must be kept in mind that powder characterization is not necessarily straightforward; for example, the characterization of particle size distribution [27] may vary depending on the particle morphology.

In the following sections devoted to powders, following the presentation of the different powder manufacturing techniques, the methods to classify and characterize them will be discussed. Then a review of powder feeders commonly available and used in thermal spraying operations will be presented. A few examples of the influence of powder manufacturing process on coating properties are discussed at the end of this section.

11.1.2 Powders Manufacturing Techniques

11.1.2.1 Atomization

Atomization is a very common route to manufacture metal and alloy powders [1]. In this process a molten metal is broken into small droplets that are rapidly solidified before their impact onto the walls or bottom of the manufacturing chamber. Atomization is the process used commercially to produce the largest tonnage of metal powders. The starting material, in the form of pure metal or multielement metallic alloy is melted in an induction furnace, arc furnace, or other type of furnace. Following the complete melting and homogenization of the metal charge, the melt is transferred to a melt reservoir from which a constant controlled flow of molten metal is supplied to the atomizing chamber. The molten metal stream, exiting the melt reservoir ladle, is intercepted by the high-velocity stream of the atomizing medium (water, air, or inert gas) disintegrating it into fine droplets that solidify in-flight during their fall through the atomization chamber [28–30]. The two important issues for particles collected at the bottom of the tank (manufacturing chamber) are the size distribution and shape of the formed particles and the degree of oxidation that must be kept as low as possible.

Neutral gases (generally argon or helium) or nitrogen atomization generally gives rise to the formation of particles with good degree of sphericity and low levels of oxidation. Gas atomization processes requires generally large, water-cooled vessels, with controlled atmosphere which makes them a rather expensive

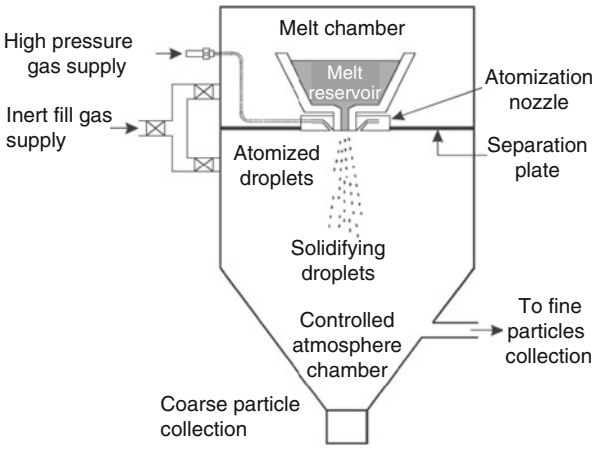


Fig. 11.1 Schematic of the gas atomization process. Reprinted with kind permission from ASM International [2]

powder production process. Gas flow rates, depending on the metal mass treated, are in the range 0.5–2 m^3/kg of atomized powder. Water atomization, on the other hand, is a relatively cheaper process, giving rise to particles with irregular shapes, and a relatively high degree of oxidation. The water/metal ratio is important since there must be enough water to break the metal apart, typical values are 4 to 10 L/kg. In the following a brief description is given of each of these two important powder manufacturing processes.

(a) Gas Atomization

For inert gas-atomized powders, the particle shape depends on the nature of the atomizing gas [29], the way the gas is directed to the molten metal stream [30] and on its pressure [31–33]. The secondary break up in the process of atomization is very important [34]. Sphericity is also correlated to the in-flight particle oxidation [28].

A schematic view of the gas atomization process is given in Fig. 11.1 [30]. It consists of five main parts, namely gas supply system, metal/alloy melting system, atomization nozzle, atomization chamber and powder collection, and gas extraction system. A photograph of a typical university scale experimental gas atomization system is shown in Fig. 11.2 [31]. Such a unit, which can process molten metal batches up to 300 kg, is around 4.5 m in height and 1.25 m in diameter [31]. Figure 11.3 shows the liquid metal jet exiting the atomization nozzle Fig. 11.3a and the same jet atomized, Fig. 11.3b, by the 20 discrete nitrogen jets located concentrically around the metal delivery tube. Lateral spreading occurs at the tip of the melt delivery tube, a conical shape of the atomized spray pattern is formed thanks to nitrogen jets, with supersonic speed, as illustrated in Fig. 11.4. This ensures a strong radial pressure gradient along the melt tip base. In the recirculation zone downstream of the melt tip, the pressure is usually higher at the centerline. This forces the metal outwards into the part of the gas stream where it is most energetic [31]. A discussion and modeling results



Fig. 11.2 Photograph of the Dumlupinar University (Kütahya, Turkey) gas atomization unit. Reprinted with kind permission from Elsevier [31]

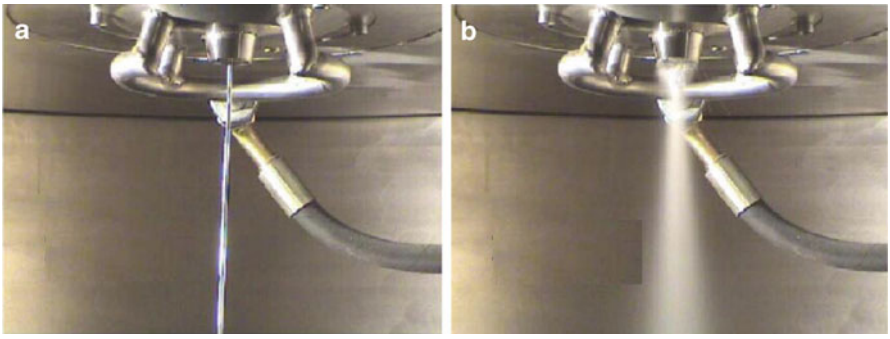


Fig. 11.3 The formation of the atomization process obtained from the recorded video with 40 ms time intervals. (**a**) Melt flow and (**b**) completely formed conical shape of the atomization pattern. Reprinted with kind permission from Elsevier [31]

explain the mechanism of the metal flow breakdown and droplet formation is given by Antipas [32].

The designs of the liquid and gas flows are very important for droplets formation. For example, Allimant et al. [33] have shown that a Laval nozzle is efficient in producing fine and narrow-sized powders. The main parameters of gas atomization are:

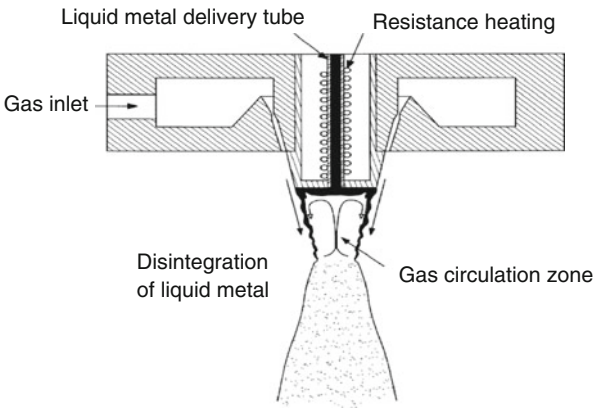


Fig. 11.4 Melt flow and atomization pattern: lateral spreading occurs at the tip of melt delivery tube. Reprinted with kind permission from Elsevier [31]

- The atomizing jet geometry, pressure, velocity. and distance from the liquid jet
- The liquid nozzle geometry and metal flow velocity
- The melt superheat above the metal melting point
- The gas nature, especially its cooling capacity and its purity (to achieve low metal oxidation, purity levels of at least 99.99 % are used)

For example, when comparing the use of helium versus nitrogen as the atomization gas, it is observed that droplets are cooled faster with helium, giving rise to higher content of finer particles in the powder obtained with helium compared to that obtained using nitrogen for the melt atomization. Moreover with helium, formation of nitrides is absolutely impossible and, due to larger extents of undercooling a higher amount of amorphous, or at least metastable, material can be retained [34]. Cooling rates (forced convection) in gas atomization depend on particle sizes and atomizing gas nature, the fastest being obtained with helium. Roughly they range between 10^3 and 10^5 K/s, however, with helium and 10 μm particles they can reach as high as 10^7 K/s. Typical gas flow rates are between 0.5 and 2 m^3/kg, for gas pressures varying from 1.4 to 4.2 MPa [1, 2].

Depending on the atomization parameters, especially the atomization gas pressure, different particle distributions are obtained: mono-modal fine particles distribution to coarse and bimodal one. Typical particle sizes can vary between 10 and 100 μm. The fine size range of the powder particles is generally spherical with smooth surface texture, as illustrated in Fig. 11.5 for Mg particles produced with a low-pressure argon gas [28].

The powders treated by this technique are Co–Cr-base alloys, Ni–Cr-base alloys, Ni-base alloys, Cu-base alloys, Zn, stainless steels, Ni-base superalloys (see, for example, Fig. 11.6) and MCrAlYs [2].

(b) Gas Atomization of Amorphous Alloys

In the past decade, a series of new bulk amorphous alloys with a multicomponent chemistry and high-glass forming ability (GFA) have been developed in zirconium-

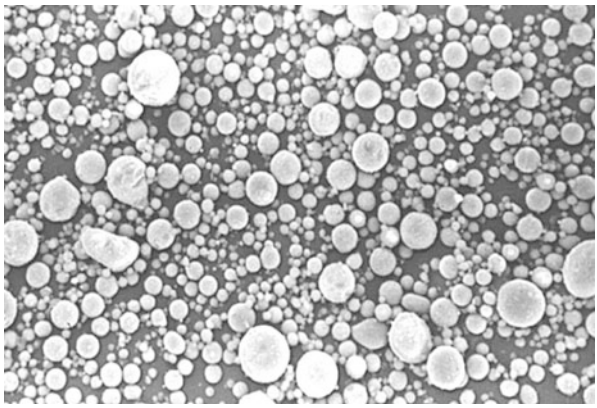


Fig. 11.5 SEM micrographs of Mg powder (particles below 32 μm) produced under low-pressure argon gas. Reprinted with kind permission from Elsevier [28]

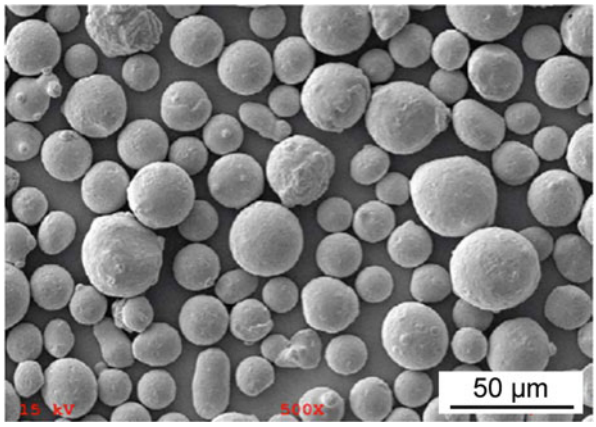


Fig. 11.6 SEM photomicrograph of Diamalloy 1005 (21.5 Cr, 2.5 Fe, 9.0 Mo, 3.7 Nb + Ta, Bal. Ni) showing the gas-atomized morphology typical of these materials. (Courtesy of Sulzer Metco)

, magnesium-, lanthanum-, palladium-, titanium-, and Fe-base systems with various rapid solidification techniques [35–43]. Compared with other amorphous alloy systems, such as zirconium- and lead-base metallic glasses, the advantages of Fe-base amorphous coatings are lower materials cost, higher strength, and higher wear and corrosion resistance. For example, to obtain amorphous and nanocomposite thermally deposited steel coatings, a specialized iron-based composition [42, 43] (Fe63–Cr8–Mo2–B17–C5–Si1–Al4) with a low critical cooling rate (10^4 K/s) for metallic glass formation has been developed. The alloy is processed by inert gas atomization (generally helium) to form micron-sized amorphous spherical particles with a size distribution adapted to thermal spraying and then sprayed to form coatings. The cooling rate of the atomized drops is very important for the amorphous phase formation. For example, Fig. 11.7 represents cross sections of two particles with different sizes: 11 and 59 μm, respectively. The fine powder particles, shown in Fig. 11.7a, subjected to the fastest cooling rate, exhibits an X-ray diffraction pattern typical of an amorphous structure, with a broad

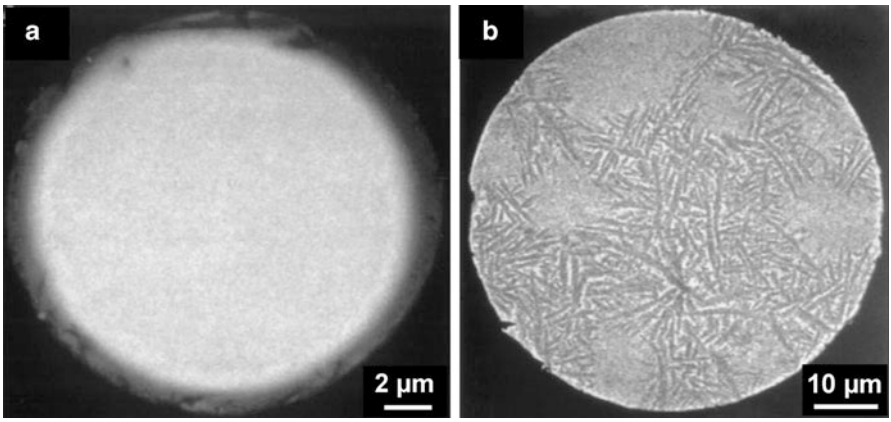


Fig. 11.7 Backscattered electron micrographs of the cross section of two as-atomized powder particles: (**a**) 11 µm particle with an amorphous structure and (**b**) 59 µm particle with a primarily crystalline structure containing pockets of glass. Reprinted with kind permission from Springer Science Business Media [42]

amorphous hump and a lack of Bragg diffraction peaks. The larger particle, shown in Fig. 11.7b, reveals, on the other hand, a higher level of crystallinity, which is consistent with the notion that it would be subjected to a lower cooling rate compared to the finer particle.

Since the mid-1980s a few studies were devoted to the production and properties of air and vacuum plasma-sprayed amorphous/nanocrystalline NiCrB- and FeCrB-based alloys [39]. In-flight particle oxidation must be avoided because it triggers the destabilization of the bulk metallic glass particle, amorphous phase stability, and formability being largely affected by the chemical composition-dependent critical cooling rate. Thus here also inert gas atomization is mandatory to produce amorphous particles.

(c) Water Atomization

Because of its favorable economics, water atomization is widely used for large-scale powder production. The principle of the process is illustrated in Fig. 11.8 [29]. Water jets hit the molten metal stream; droplets are formed by "splash" or "scrape," according to disintegration models, and then freeze, in-flight, before being collected in the water pool at the bottom of the atomizer. To break the molten metal jet apart, the water quantity to molten metal ratios should be in the range of 4–10 L/min per kg of molten metal. Water pressures vary between 30 kPa and 60 MPa. Water atomization results in particle cooling rates in the range of 10^4–10^6 K/s. The high production rates are balanced by [1] the necessity to dewater and dry the particles. The powder produced using water atomization has a typical particle size in the range of 150–400 µm. Finer particles can be

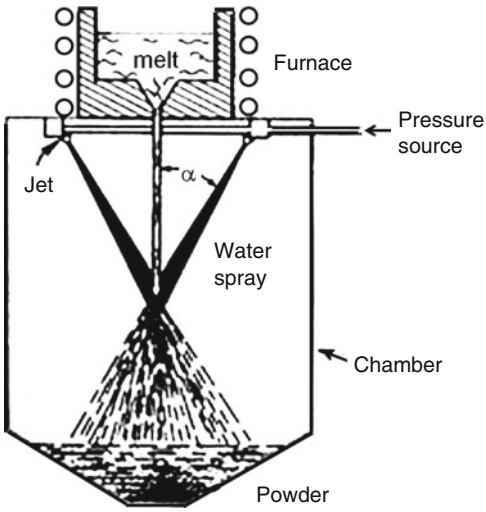


Fig. 11.8 Schematic of a water atomization process. Reprinted with kind permission from ASM International [29]

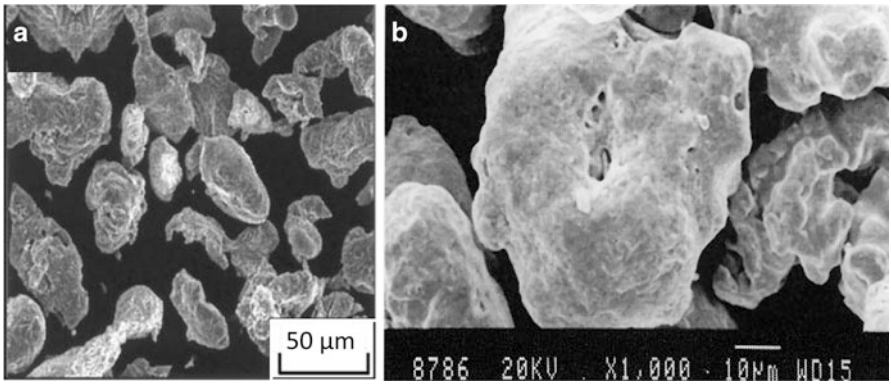


Fig. 11.9 SEM micrographs showing water-atomized cast iron powder: Fe-2.17 at.% C-9.93 at.% Si-3.75 at.% Al. Reprinted with kind permission from Springer Science Business Media [44], copyright © ASM International

obtained using high-water jet velocities. The irregular shape of particles (see, for example, Fig. 11.9) may necessitate better spheroidization which can be achieved through the superheating of the molten metal prior to atomization. Water atomization can result in rather high-oxygen content of the powder obtained, which can require a separate oxygen reduction stage treatment to be performed.

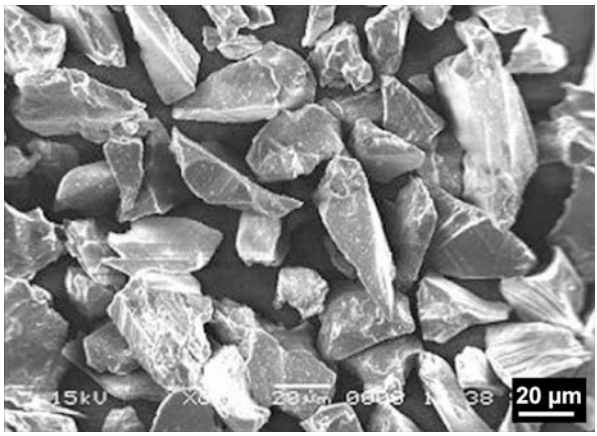


Fig. 11.10 Low-magnification SEM micrograph of as-received irregularly shaped alumina powder [45] obtained by fusing and crushing. Reprinted with kind permission from Springer Science Business Media [45]

11.1.2.2 Fusing and Crushing

This technique is devoted to brittle materials, mainly ceramics. Ceramic materials have, in most cases, melting temperatures over 1,800 °C and require special furnaces. The process is typically carried out in an arc furnace, which can require 10–20 h to melt the core of mixed components in the crucible. After cooling, the outer shell, made of non melted, but partially sintered initial components, is removed and the frozen ceramic block is crushed using conventional attrition mills such as hammer mills, stamping mills, jaw crushers, and gyratory crushers [29]. Particles obtained are angular, dense, and blocky as illustrated in Fig. 11.10 for alumina particles [45].

11.1.2.3 Milling and Sintering

When grinding, many tiny particles (average diameter usually smaller than 5 µm) are produced which are not suitable for spraying. Those small particles can be agglomerated and spray dried (see Sect. 11.1.2.6) or pressed and sintered. In the latter case, they are first compacted (one-direction compaction), with or without a binder, and then sintered. Sintering means heating them in a furnace to a temperature below the melting temperature, but sufficiently high to allow their binding by chemical diffusion between the individual particles [1, 2]. The density of sintered material depends on their compaction and the size distribution of starting particles [46]. When increasing the compaction pressure, the sintering time and temperature, the porosity of the particles obtained is reduced. The sintering and densification step is, however, also accompanying by grain growth which increases with the increase of the sintering temperature. Grain growth is detrimental to the mechanical properties of the particles, especially when dealing with nano-sized grains for the purpose of achieving nanostructure coatings!

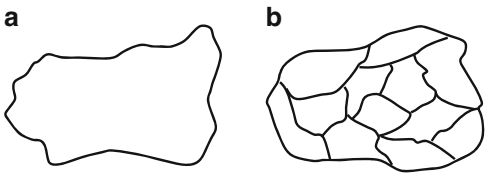


Fig. 11.11 Schematic of (**a**) fused and crushed particles and (**b**) sintered and crushed ones. Reprinted with kind permission from Pergamon press now Elsevier [47]

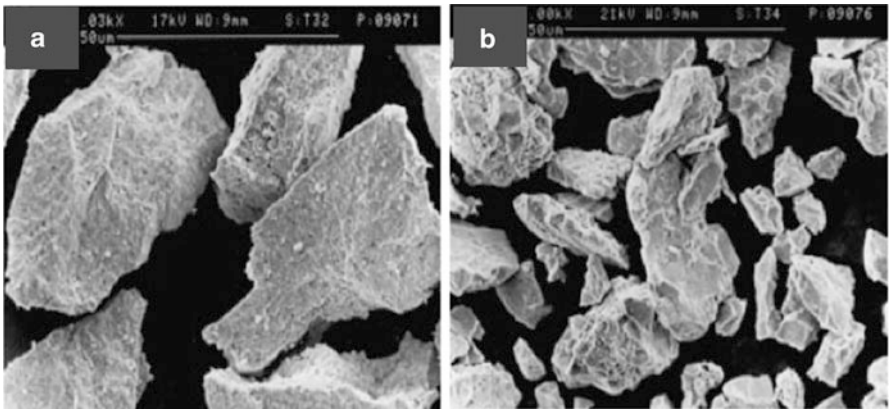


Fig. 11.12 SEM micrographs of sintered and crushed WC–Co–Cr (86–10–4) particles, (**a**) Sulzer Metco Amdry 5843 and (**b**) Starck Amperit 553.065. Reprinted with kind permission from Springer Science Business Media [48], copyright © ASM International

Following the sintering step, the cake obtained is crushed to obtain the size distribution adapted to thermal spraying. Crushing is easier in this case compared to that of fused block as described in the previous section. The particles are blocky and angular and more or less porous. Many carbide-metal or alloy particles are produced by this method. Figure 11.11 illustrates schematically the shapes of fused and crushed particles compared to that of sintered and crushed ones. Figure 11.12 shows fused and crushed WC–Co (83–17) from two different suppliers.

11.1.2.4 Milling

Milling is used when considering brittle particles such as certain metals or metal alloys and ceramics.

(a) Ball Milling

The most common method to reduce the ceramic particle sizes and eliminate aggregates is ball milling [1, 2, 49]. A ball mill is a barrel (usually vulcanized rubber, high-density alumina, stainless steel, but at laboratory scale often made of

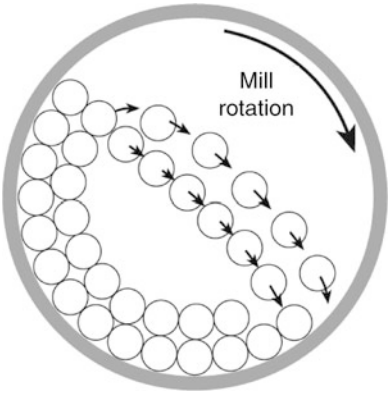


Fig. 11.13 Cross-section of a ball mill showing the movement of the media as the mill rotates about its axis. Reprinted with kind permission from Springer Science Business Media [49]

metal covered with polyurethane or tungsten carbide cermet) that rotates on its axis. The barrel is partially filled with a grinding medium (called media) in the form of spheres, cylinders, or rods. Figure 11.13 shows a cross section of a ball mill. The quantity of the media is such that the rotation of the mill causes it to cascade, creating both shearing and crushing actions on the powder [49].

The media with a high specific mass provides greater impact during tumbling. Alumina, steel, zirconia, and mullite are mostly used media. The choice of media is also based on its cost, wear resistance, and the necessity to limit, as much as possible, contamination of the milled powder. The media size depends on the quantity of powder to be milled, the size of the mill, and the final particle size required: typical diameter values range from a few millimeters to a few centimeters in diameter, the former being used for fine grinding. Very often the powder is milled in a liquid. The main parameters controlling the powder size distribution are:

- The speed of rotation of the mill has to be sufficiently high to insure that the rod or ball mill media drop from the top of the mill onto the grounded material, as shown in Fig. 11.13. At too low velocities the media rolls around the bottom of the mill, while at too high velocities it does not fall due to centrifugal force
- The size of the media
- The milling time

The mean size of milled particles can be as low as 1 μm. This process is very convenient, rather inexpensive, though not yet well understood, and inefficient as less than 2 % of the energy input goes into creating new surfaces. Its main shortcoming is in the relatively long milling time required, and the risk of contamination of the powder produced by impurities originating from the grinding medium.

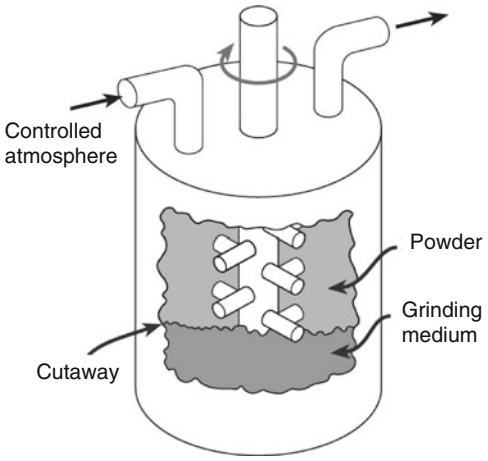


Fig. 11.14 Principle of attrition milling. Reprinted with kind permission from Springer Science Business Media [49]

(b) Attrition Milling

It differs from conventional ball milling in that the slurry containing the particles and media is stirred continuously at frequencies of 1–10 Hz. The stationary grinding chamber, often water cooled, is aligned either vertically, as shown in Fig. 11.14, or horizontally, with the stirrer, having Christmas-tree geometry, located in the center of the chamber [49]. Chamber volume is between 0.004 and 0.4 m^3. The stirrer rotates at about 250 rpm. The media consists of small spheres (0.2–5 mm) that make up between 60 and 90 % of the available mill volume. Most attrition mills work on a continuous basis with the powder to be milled fed in at one end and the milled product collected at the other.

Attrition mills are more energy efficient than the other methods previously described and can handle higher solid contents in the slurry. The rapid milling time, because of the use of small media, helps reduce contamination. Lining the chamber with a polymer or a ceramic and using ceramic stirrers and media can further reduce contamination [49]. To limit agglomeration, organic additives are added in the slurry. Typical particle sizes are between 0.1 and 5 μm. One of the problems with these mills involves separation of fine particles from the slurry. According to Camerucci and Cavalieri [50] high efficiency of the attrition milling obtaining submicron particles sizes is achieved for intermediate rotor speeds, solid contents, and low milling times (longer milling times produce just a slight further size reduction).

(c) Cryomilling

Cooling of the milling media and powders is an effective approach to accelerate the fracture processes and rapidly attain steady-state conditions [51]. Advantages of cryomilling compared to milling at room temperature are the following [51]:

Powder agglomeration and welding to the milling media are suppressed, resulting in a more efficient milling outcome.
Oxidation reactions during milling are reduced under the protection of a nitrogen environment.
The milling time required to attain a nanostructure is significantly reduced, because the low temperature suppresses the annihilation of dislocations and the accumulation of a higher dislocation density is possible.

(d) Other Techniques

Both rotary and vibratory motions were combined in an attritor to produce alumina powders with narrow particle size distributions and finer particle sizes (mean particle diameters in the range 2.05–6.82 μm) for a given milling time [52].

11.1.2.5 Mechanical Alloying and Milling

Mechanical alloying (MA) is a solid-state powder processing technique involving repeated welding, fracturing, and re-welding of powder particles in a high-energy ball mill as detailed in the review paper of Suryanarayana [53]. "Originally developed to produce oxide-dispersion strengthened (ODS) nickel- and iron-base superalloys for applications in the aerospace industry, MA has now been shown to be capable of synthesizing a variety of equilibrium and nonequilibrium alloy phases starting from blended elemental or pre-alloyed powders." Mechanical alloying is a complex process and hence involves optimization of a number of variables to achieve the desired product phase and/or microstructure. Commercially significant quantities of nanostructured materials with grain size in the range of 10–200 nm can be processed using mechanical alloying, which involves the transformation of plasticity-induced dislocation structures into high-angle grain boundaries in metallic powders. Most important parameters that have an effect on the final constitution of the powder are:

- The type of mill
- The milling container
- The milling speed
- The milling time
- The type, size, and size distribution of the grinding medium
- The ball-to-powder weight ratio
- The extent of filling the vial
- The milling atmosphere
- The process control agent
- The milling temperature

Powders used in spray processes are produced with high-energy attritors (see Fig. 11.14), working either with liquid (ethanol, methanol,. . .) or argon atmosphere

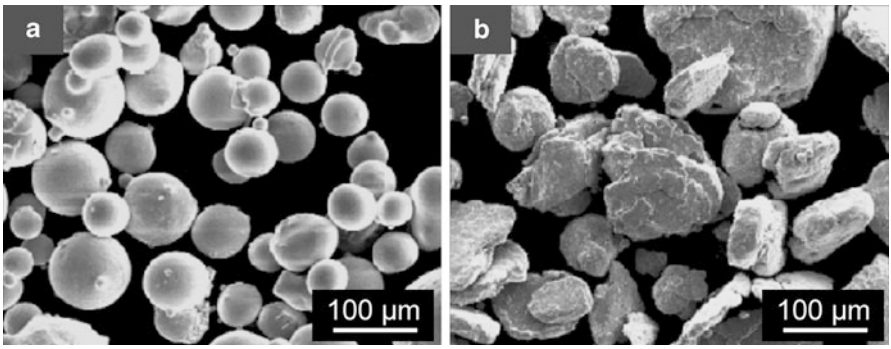


Fig. 11.15 Morphological characteristics of the NiCrAlY powders (**a**) before cryomilling (as received) and (**b**) after cryomilling process. Reprinted with kind permission from Elsevier [54]

or liquid nitrogen: process called cryomilling. The extremely low milling temperature in cryomilling suppresses the recovery and recrystallization and leads to finer grain structures and more rapid grain refinement [51]. Experimental and theoretical studies suggest that for each material, there is a minimum grain size that is obtainable by milling, and that its value is related to the intrinsic properties of the material, such as crystal structure. The results reviewed by Lavernia et al. [51] also demonstrate that cryomilling can be effectively used to manufacture ceramic reinforced metals, in which the size of the reinforcement phase can be modified, depending on the milling parameters. In the following, five typical examples are discussed.

1. Figure 11.15a, b show the morphological differences between the NiCrAlY powders before and after the cryomilling process, respectively [54]. Mechanical cryomilling of the as-received spherical NiCrAlY powders leads to the formation of irregular and flake-shaped agglomerates, as shown in the SEM image (Fig. 11.15b). This morphology is attributed to the continuous welding and fracturing of the powder particles during the mechanical milling process. The average particle size of the powder increases from an as-received value of 28.7 µm, to an average size of the agglomerate and cryomilled powders of 106.0 µm,. The cold welding seems to overcome the fracture process with milling time, resulting in an increase in agglomerate size. The formation of the nanocrystalline structure during cryomilling is considered to be a consequence of plastic deformation at high strain rates [54]. The grain size is in the nanometric range (lower than 50 nm). The increase in oxygen (0.027–0.17 wt %) and nitrogen (0.0048–0.26 wt%) concentration is believed to be a consequence of the incorporation of these elements from the air and liquid nitrogen environment, respectively.
2. A metastable composite Fe60Al40 powder was produced in an attritor filled with argon in which Fe (99.8 wt%) particles below 54 µm and Al (99.5 wt%) with a mean particle size below 74 µm were introduced (with the required FeAl wt%

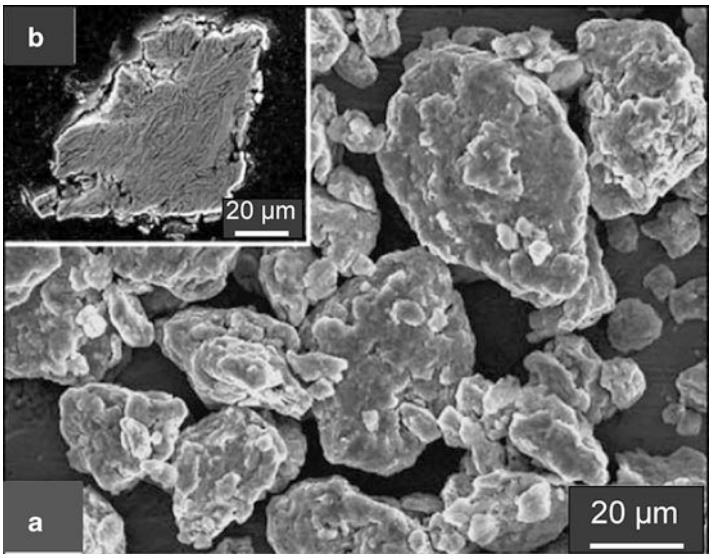


Fig. 11.16 Morphology (**a**) and cross-sectional microstructure and (**b**) of the as-milled Fe60Al40 powder. Reprinted with kind permission from Springer Science Business Media [55], copyright © ASM International

ratio). The milling media being stainless steel balls 5 or 10 mm in diameter and the ball-to-powder weight ratio was 10:1 [55]. Figure 11.16 shows typical SEM images of the morphologies and cross-sectional microstructures of the powder milled for 36 h. The as-milled powder, presented in the aggregated condition, shows an irregular angular morphology (Fig. 11.16a). The cross-sectional microstructure of the as-milled powder, shown in Fig. 11.16b, presents a fine lamellar structure within each particle. Meanwhile, a few relatively thicker layers are still present in the powder. Two distinguishable regions with different microstructural characteristics can be clearly seen. They were typically different in the lamellar thickness. EDXA analysis suggests that the thicker layer is a Fe-rich phase and the fine lamella is a Fe–Al solid solution with high-Al content [55].

3. In the two previous cases particles result from metallurgical agglomeration, which is formed by cold welding. It is no more the case with mixtures of brittle and ductile particles where binder-induced agglomerates are primarily bonded by milling environment and can be decomposed back to their original powder form [56]. By varying the milling conditions, different sizes of the hard phase can be adjusted [56]. Compared to the previous case, the particles obtained are smaller than the starting ones. For example Cr_3C_2-25 (Ni20–Cr) powder was milled in hexane [$H_3C(CH_2)_4CH_3$]. The initial powders are presented in Fig. 11.17a. After 16 h of milling, the pure carbide particles could not be observed anymore. The ductile (soft) Ni-rich phase is no longer seen as spherical particles in the milled powder, but is distributed among the homogeneous finer

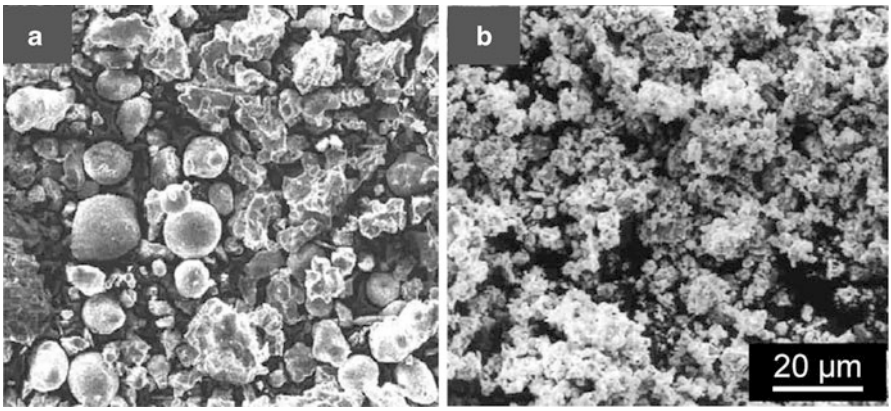


Fig. 11.17 SEM micrographs showing the morphology of the Cr_3C_2–NiCr powder: (**a**) As-received powder and (**b**) 16 h milled powder. Reprinted with kind permission from Elsevier [56]

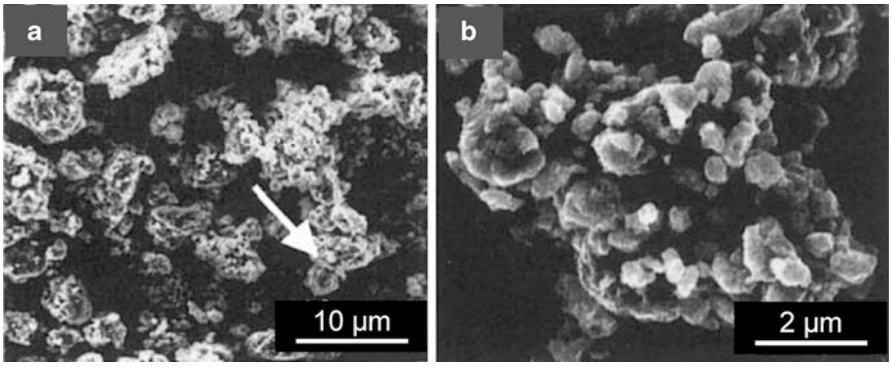


Fig. 11.18 SEM images showing the morphology of the binder-induced, self-agglomerated composite powders. (**a**) 20 h milled powder and (**b**) higher magnification of (**a**). Reprinted with kind permission from Elsevier [56]

particles, see Fig. 11.17b. With an increase in milling time the surface of the powder becomes rough. Figure 11.18a shows almost complete self-agglomeration in the powders that have been milled for 20 h. A higher magnification of the agglomerated powder, indicated by the arrow in Fig. 11.18a, is shown in Fig. 11.18b. X-ray mapping results reveal the particles in Fig. 11.18b to be neither pure carbide nor pure NiCr phase [56].

4. TiC–Ni-based nano-crystalline cermet powders, with fine, homogeneously distributed sub-micrometer-sized hard phases of TiC, have been produced by high-energy ball milling with an industrial-like vibration mill as well as with an attrition mill. It should be noted that at least 95 % of the hard phase particles are

smaller than 300 nm. Milling of the investigated composite material leads to a uniform particle size of 20 μm [57].

5. Thermally sprayed coatings containing solid lubricants such as graphite, Teflon (PTFE), MoS_2, MnS, and CaF_2 reduce the energy loss by friction and weight loss by wear. However these materials are difficult, if not impossible, to thermal spray because both of them decompose easily when overheated and corresponding particle shapes, often close to platelets, have very poor flow ability. Thus in most cases these particles are blended in a certain mass ratio with metal particles and ball milled for a few hours, leading to the powders with either sizes below a few μm [58] or in the few tens of μm, according to the milling conditions [59]. Of course the small particles must then be granulated with some organic binders into a spherical particle of about 45 μm by spray-drying method [58] and eventually sintered before spraying.

11.1.2.6 Spray Drying

In all processes used to manufacture ceramic powders, the size distribution obtained is generally not adapted to that requested for spraying. Especially very often in crushing, grinding, milling, many fine particles (below 5 μm) are produced, which are not usable for conventional spraying without agglomerating them. Moreover to produce cermet particles it is necessary to mix rather fine ceramic and metal or alloy particles and form granules of their mixtures. It is the same problem with nanometer-sized particles that are sprayed either in suspensions injected directly into the hot gases (see Sect. 14.7) or agglomerated as micrometer-sized particles. The spray-drying technique is probably the most versatile one to obtain particles usable in spray processes. In spray-drying agglomerated powders are produced from suspensions (often water based) and called slurry. It must be noted that the formation of a stable suspension containing metal and ceramic particles is not a simple task. If the oxide suspensions are rather easy to stabilize, it is more difficult with a cermet such as WC–Co. This is due to the high specific density of WC–Co powders and the widely different acid/base properties of the two main particle constituents [60]. The formation of a stable suspension for spray drying requires often the addition of a stabilizing surface active agent which helps to avoid the rapid sedimentation of the solids in suspension in order to insure a uniform composition of the powder produced. The addition of a binder may also be necessary in most cases in order to avoid the disintegration of the spray-dried powder prior to its calcination or sintering. The proper choice of the chemical composition of such suspension stabilizer and binder is of critical importance to avoid the addition of impurities and/or residual carbon into the powder.

Drops of suspension are produced with an atomizer and sprayed into a drying chamber where they are heated either into a stream of hot air or by the radiation of the hot chamber wall or both in some cases. The rapid heat and mass transfer that occur during drying, combined with the presence of various slurry compounds, result in dried granules. These granules present large variety of shapes: uniform

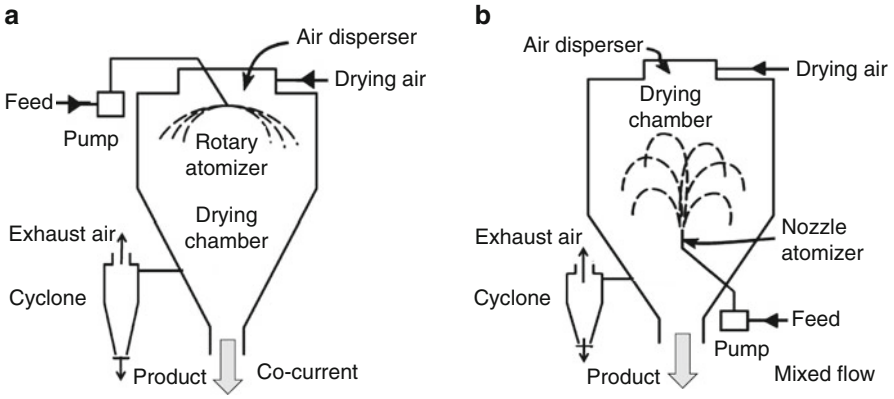


Fig. 11.19 Principle of a spray-drier. (**a**) Centrifugal atomizer with co-current air flow and (**b**) Nozzle atomizer using mixed-flow conditions. Reprinted with kind permission from Springer Science Business Media [49]

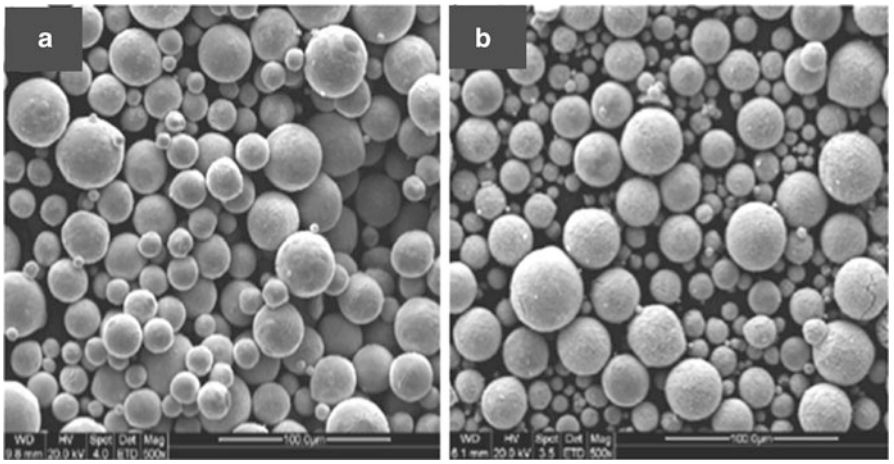


Fig. 11.20 Examples of SEM photos of spray-dried WC–Co (10 wt%) particles (**a**) as spray dried and (**b**) calcined at 700 °C. Reprinted with kind permission from Elsevier [62]

solid spheres or elongated spheres or pancake shaped or donut shaped or needle-like or hollow granules [61]. They are collected downstream of the atomizer, as shown in Fig. 11.19 representing schematically two types of atomizers. Particles are constituted of agglomerated smaller particles in the few micrometers size. For example Fig. 11.20a presents SEM photos of WC–Co (10 wt%) particles as spray dried and Fig. 11.20b the same particles calcinated at 700 °C. The spray-dried powder exhibits smooth surface and spherical shape without agglomeration. After calcination at

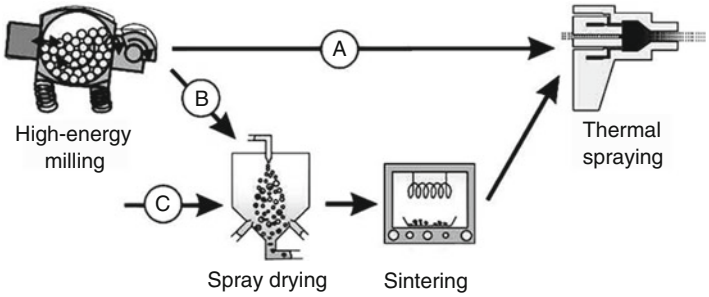


Fig. 11.21 Process routes for the production of thermal spray coatings: (A) milling for direct use as feedstock, (B) milling, spray drying, and sintering, and (C) spray drying, sintering. Reprinted with kind permission from Elsevier [57]

700 °C, surfaces of the particles became rough and porous due to the escape of the gases (NH_3, CO_2, and H_2O) from the decomposition of the spray-dried powder.

Different processing routes, including high-energy milling, spray drying, and sintering, as depicted in Fig. 11.21, allow producing particles with different morphologies [57]. Route A includes milling under agglomerating conditions. By combining the processes of milling, spray drying, and sintering (route B), a refined microstructure can be combined with an open porosity. In order to keep quasi-spherical shapes, particles are sintered in rotating furnaces where diffusion occurs within particles but not between themselves. However, as already mentioned (Sect. 11.1.2.3) the sintering process in route B can cause grain growth and hard phase clusters can be formed [57]. In some cases particles are only calcinated, i.e., fired or heated at a temperature sufficient to eliminate volatile constituents, such as suspension stabilizers and binders, that could result in the explosion of particles upon penetration in the hot gas spray stream. However, calcinated particles generally result in poor coatings.

The spray drying process depends strongly on the way the suspension is prepared. Bertrand et al. [63] have determined the quantitative relation existing between slurry behavior and ceramic granule characteristics. They have shown that the shape of the spray-dried ceramic granules can be predicted by slurry studies, their work being performed with two ceramic oxides: alumina and zirconia. In order to produce spray-dried ceramic powders, the slurry must contain high solid content (from 15 vol.% for zirconia slurry to 30 vol.% for alumina slurry, which means that the solid fraction is 50 wt% for both concentrated ceramic slurries) and be stable during the process. Changing the formulation of the slurry (by varying the pH, the amount of dispersant and the binder) modifies the interparticle interactions and, consequently the state of dispersion of the suspension. The sedimentation test (long time sediment heights as well as sedimentation rates) appears to be appropriate to assess the particles behavior: either particles behave mainly individually, leading to dispersed slurries or particles gather to provide clusters of different shape, size, and strength, leading to flocculated slurries. Generally, it was demonstrated that low sedimentation ratio (SR) values

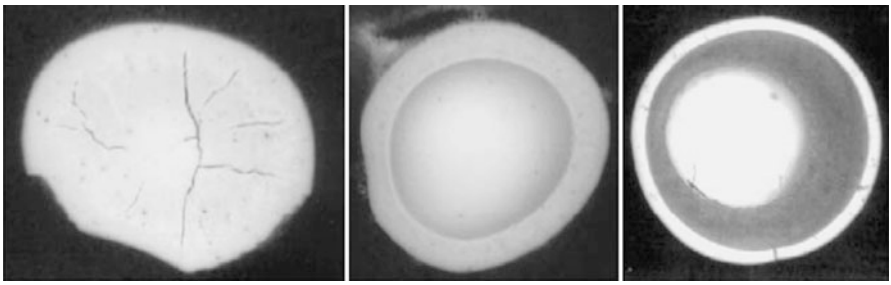


Fig. 11.22 Polished cross sections of dried granules realized from different zirconia-based slurry formulations with various sedimentation ratio RS values (from 0.8 to 0.5 and 0.3). Reprinted with kind permission from Elsevier [63]

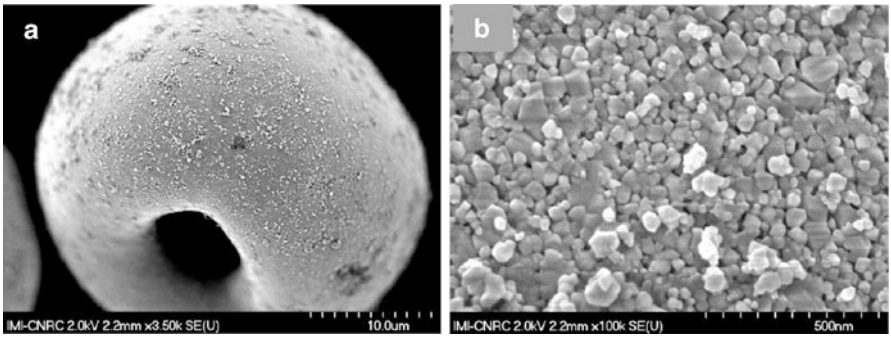


Fig. 11.23 (**a**) Nano spray-dried titania powder. (**b**) Higher magnification view of (**a**) showing the nanostructure of the agglomerate. Reprinted with kind permission from Elsevier [64]

(below, respectively, 0.6 and 0.7 for zirconia and alumina) attributed to disperse slurries provide hollow dried spheres, whereas high SR values, achieved with flocculated slurries, lead to solid dried granules, as illustrated in Fig. 11.22. Besides a linear relation was established for hollow spheres between the sedimentation rate and the shell thickness [63].

This spray drying process can be used with either micrometer- or nanometer-sized particles, as illustrated in Fig. 11.23 for titania nanoparticles [64]. It can be noted in this figure that the spray dried and sintered nano-sized titania particles are hollow and quasispherical. This technique also allows manufacturing powders made of very dissimilar elements. For example agglomerates of particles of aluminum–silicon (Al-Si) eutectic alloy ($d_{50} = 2.4 \pm 1.2$ μm, Al-11.6 wt% Si-0.14 wt% Fe) in which multiwalled carbon nanotubes (CNT) (purity higher than 95 %, diameter = 40–70 nm, length = 1–3 μm) are dispersed by spray drying [65]. 5 wt% CNT were measured within the spray-dried powders. Resulting micrometer-sized particles are displayed in Fig. 11.24.

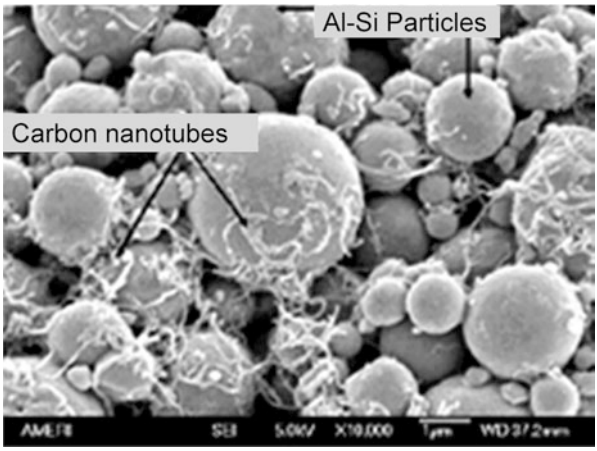


Fig. 11.24 (**a**) Spray-dried Al–Si agglomerate. (**b**) Magnified region within the rectangle in (**a**) showing CNTs within the agglomerate. Reprinted with kind permission from Elsevier [65]

11.1.2.7 Spheroidization

Using dense and spherical particles for spraying results in:

Better flow ability allowing slow or fast particles flow with no pipe clogging and a stable powder feed rate giving rise to denser and uniform

Dense particles resulting in a more uniform heating of the particles which is critically important especially when the particle thermal conductivity is low [66]

Less wear of pipes and feeding systems with smoother particles and thus less coating contamination

Lower porosity of particles due to reactions with warm gases or vaporization, eliminating or at least reducing impurities (by a factor of 10–100 in the ppm range)

(a) Plasma Spheroidization of Powders

The plasma spheroidization of powders is a relatively simple process which is similar to plasma spraying involving the in-flight melting of the particles injected into a plasma jet. The only difference in comparison to plasma spraying is that the formed molten droplets are allow to cool down and resolidify, in-flight, prior to hitting the wall or the bottom of the spheroidization chamber [67]. The process gives rise to the formation of dense, free flowing solid particles, which can be handled easily by most thermal or cold gas spray processes. In a number of cases, the in-flight, plasma melting of the particles also results in the purification of the particle material through distillation of more volatile impurities such as alkali metals and adsorbed gases. While both d.c. and r.f. induction plasma sources

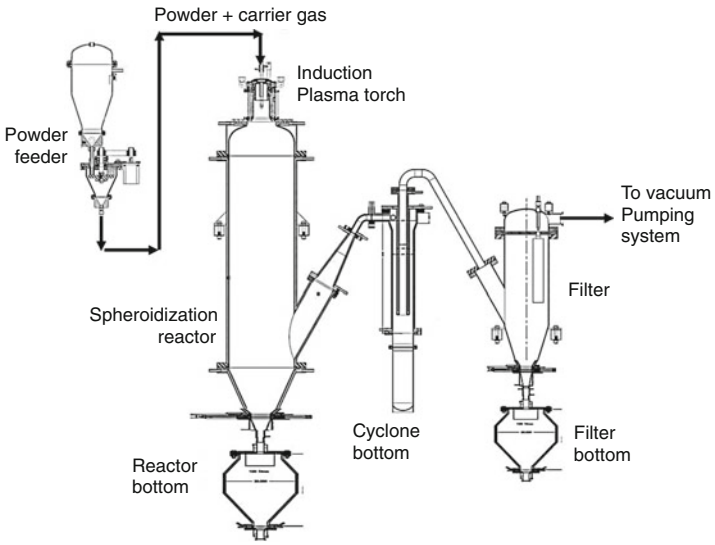


Fig. 11.25 Set-up developed by Tekna for powder spheroidization using r.f. induction plasma technology (http://www.tekna.com) (Courtesy of Tekna)

have been successfully used for powder spheroidization, Induction plasmas offer in most cases a distinct advantage due to the following reasons:

1. Low plasma flow velocity (about 50 m/s) resulting in residence times almost one order of magnitude longer than in d.c. arcs
2. Long residence times allowing for the complete heating and melting of most low thermal conductivity materials for which internal propagation of the thermal front is the limiting step in the particle heating and melting process
3. Possibility to use almost any gas chemistry, whether reducing, inert, or oxidizing, as required by the chemical nature of the processed material. A typical example is the need to use an oxygen rich plasma gas for the spheroidization of oxide ceramics such as silica, SiO_2 to avoid its partial reduction to silicon monoxide, SiO

Different r.f. induction plasma torches have been developed by Tekna Plasma Systems Inc. (http://www.tekna.com) with power levels ranging from 30 to 200 kW working at frequencies between 2 and 4 MHz. A typical, pilot-scale, system developed for induction plasma spheroidization of powders is shown in Fig. 11.25 (http://www.tekna.com) [68]. It comprises essentially of an induction plasma torch located at the top of a large-volume, water-cooled, spheroidization reactor. The powder to be spheroidized is injected axially at the center of the discharge using a water-cooled powder injection probe. The tip of the probe is usually placed at the mid-height of the induction coil. With relatively large and heavier particles, the tip of the probe can be placed slightly above the coil center,

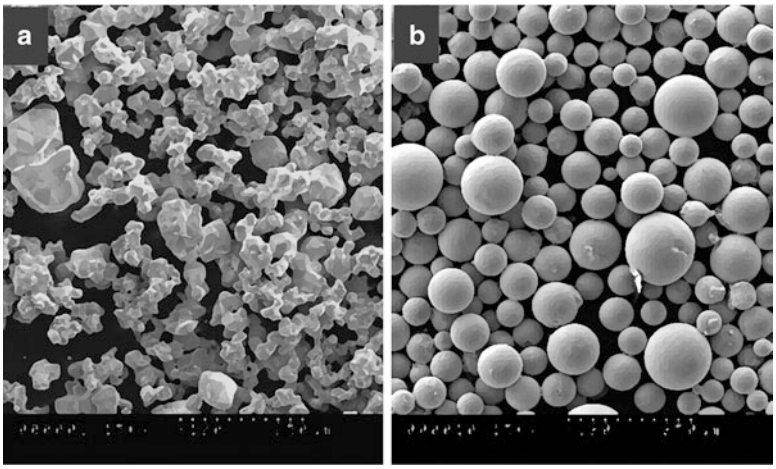


Fig. 11.26 Electron micrographs of tungsten powder before and after r.f. induction plasma spheroidization (http://www.tekna.com) [68] (Courtesy of Tekna)

while with smaller lighter particles, the probe tip is placed below the coil center in order to avoid the deposition of the molten particles on the inner surface of the plasma confinement tube. As the plasma gas entrains the injected particles, the individual particles are heated and melted in-flight. The particle free-fall velocity essentially governs the remaining part of the particle trajectories in the spheroidization reactor. Over this period, the particle cools down and freezes into a solid dense sphere. At the bottom of the spheroidization reactor, the large dense spherical particles are recovered at the reactor bottom, while smaller finer particles are entrained with the plasma gasses exiting from the side of the spheroidization reactor. The plasma gases with any entrained fine powders are directed to a water-cooled cyclone where the fine particles ($d_p \leq$ 1–5 μm) are recovered. Any remaining submicron particles are finally collected in a filter prior to the exhaust of the plasma gases to the gas pumping system.

Most powder spheroidization operations are carried out under near atmospheric pressure, though depending on the nature of the powder being treated, the process can also be carried out under soft vacuum or pressures above atmospheric. Typical results obtained for the spheroidization of tungsten are given in Fig. 11.26. These show electron micrographs of the tungsten powder before and after r.f. induction plasma spheroidization. It should be pointed out that the melting temperature of tungsten is 3,410 °C and its bulk density is 19.3 g/cm^3. Also included on this figure is the tap density of the powder, which is shown to increase from 7,500 to 11,700 kg/m^3 as a result of the plasma spheroidization treatment. The Hall flow index is also show to decrease from no-flow to 7 s/50 g.

Besides the heat and momentum transfers, described in details by Boulos et al. [69], two important points must be underlined:

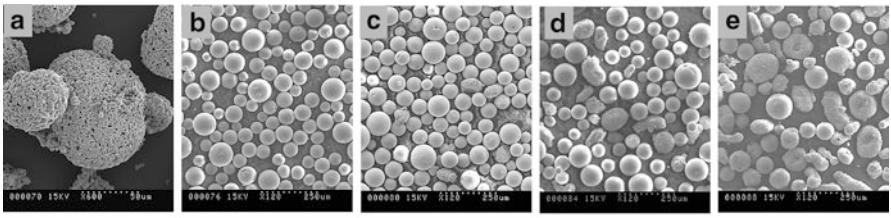


Fig. 11.27 Example of molybdenum powder spheroidization in an r.f. induction plasma system operated using Ar/H_2 as the plasma sheath gas, at a power level of 100 kW, and different powder feed rates varying between 7 and 25 kg/h) (http://www.tekna.com) [68] (Courtesy of Tekna)

Table 11.1 Elemental analysis of molybdenum powder before and after treatment in an Ar/H2 induction plasma at 100 kW at a powder feed rate of 10 kg/h (http://www.tekna.com) (Courtesy of Tekna)

Element	Cr	Fe	Ni	Cu	Mg	Al	O_2
Original powder composition (ppm)	100	70	100	3.5	4.9	2.5	≥1,000
Powder composition after plasma treatment (ppm)	30	25	37	0.39	0.33	0.55	≤100

1. *Losses by radiation* that increase with the particle melting temperature and size, as illustrated in Fig. 4.22
2. *Thermal loading effects* where the increase in the powder feed rate cools down locally the plasma flow through the energy necessary to both melt and vaporize the particles [69] and radiation losses from the particles, the latter being more important for the smallest particles [70].

The maximum quantity of powder particles that can be spheroidized depends on the torch power level and the powder feed rate. Figure 11.27 shows electron micrographs of molybdenum powder, with a particle size in the range of (−60 + 400 Mesh/40–250 μm), spheroidized in a 100 kW, PL-70 r.f. induction plasma torch, using a mixture of Ar/H_2 as the plasma sheath gas, at different powder feeding rates. The micrograph on Fig. 11.27a shows the internal microstructure of the feed material which was prepared by spray-drying and sintering of a fine ($d_p \leq$ 1–5 μm) molybdenum powder. As indicated in the bottom part of that figure, the feed material had a tap density of 3.2 g/cm^3 and a Hall flow index of 36 s/50 g. The micrographs given on Fig. 11.27b–e show the morphology of the powder obtained as a result of spheroidizing the powder in the induction plasma at different feed rates. These were varied respectively from 7, to 14, 20 and 25 kg/h. The corresponding influence on the tap density and the Hall flow index are given in the lower part of the figure. It may be noted that the spheroidization effect is most important at the low powder feed rate of 7 kg/h, where the tap density of the powder increased to 6.35 g/cm^3, and the Hall flow index decreased to 13.0 s/50 g.

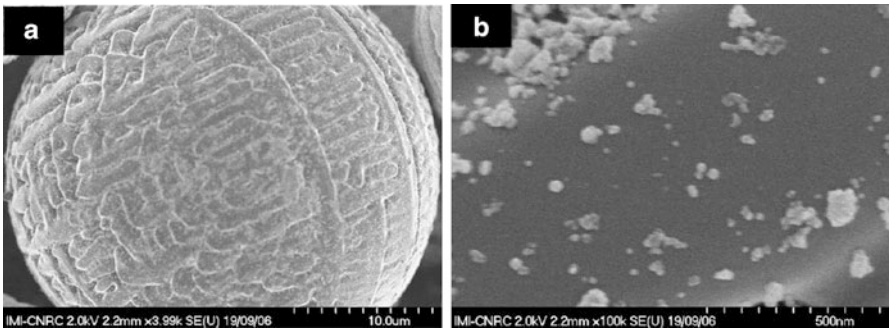


Fig. 11.28 (**a**) Spray-dried titania powder of Fig. 11.22 after being plasma fused (PF). (**b**) Higher magnification view of (**a**) showing the absence of the ultrafine character after the plasma-fusing process. Reprinted with kind permission from Elsevier [64]

With the increase of the powder feed rate to 14 kg/h, the efficiency of the spheroidization process did not seem to drop, with only a very small changes observed in both the tap density and Hall flow index. With the further increase of the powder feed rate to 20 and 15 kg/h, a significant effect of the thermal loading of the plasma is observed, as demonstrated by the lower degree of melting of the powder, especially the larger particles, the drop in the apparent density of the processed powder, and the increase in its Hall flow index. It is important to note that the treatment is accompanied by a drop in the level of impurities in the treated powder as shown in Table 11.1, which was obtained for the same powder when treated at a powder feed rate of 10 kg/h.

The implementation of such a technology on an industrial scale for powder spheroidization has rapidly developed over the past decade. Tekna Advanced Materials Inc. in Sherbrooke, Québec, Canada (http://www.tekna.com) operates an industrial scale installation, with a power level of 200 kW, for particles spheroidization.

d.c. plasma jets have also been used to spheroidize particles; however, it is more complex than r.f. plasmas, especially for ceramics with low thermal conductivities. d.c. plasma jets have higher velocities (more than one order of magnitude) than r.f. ones. It reduces drastically the residence time of particles within them and requires using plasma-forming gases with higher thermal conductivity than pure argon. Unfortunately higher thermal conductivities promote the heat propagation phenomenon and the nonuniform treatment of particles. The melting in a plasma jet (r.f. or d.c.) of nanostructured particles result in the destruction of this nanostructure. This is illustrated in Fig. 11.28 representing the same particle as that shown in Fig. 11.23 after its melting in an argon–hydrogen plasma jet produced with the APS 3 MB torch of Sulzer-Metco [64].

Attempts have been made to produce nanostructure alumina particles by melting them in an Ar–He dc plasma jet, the nozzle of which was adapted to internal injection, and collecting them in water or liquid nitrogen [70]. Particles were spheroidized and those collected in liquid nitrogen (cooling rates calculated in the range of 3.33×10^6 to 2.27×10^8 K/s) were nanostructured, as confirmed by the

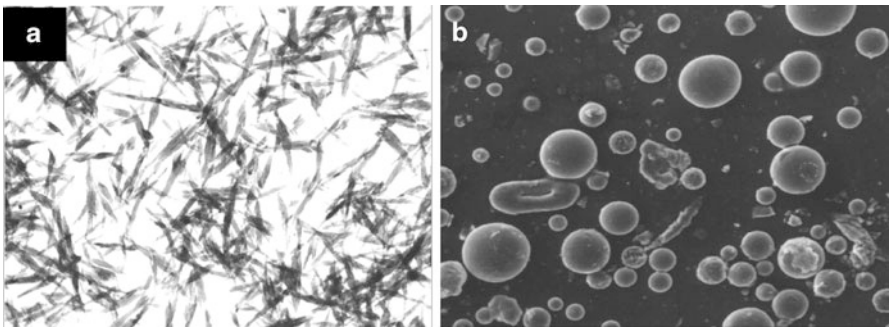


Fig. 11.29 (**a**) TEM picture of the as synthesized HA nanocrystals. (**b**) SEM picture (top view of powders) of particles obtained after heat treatment of the HA suspension drops in an AR r.f. plasma. Reprinted with the kind permission of IEEE Trans Plasma Sci [71]

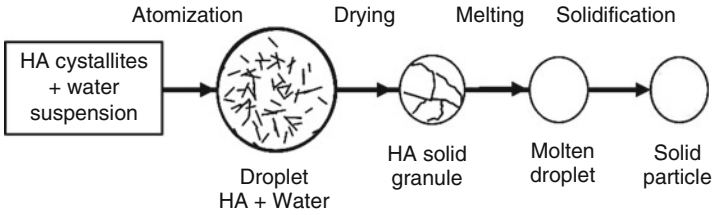


Fig. 11.30 Synthesis process of HA particles. Reprinted with the kind permission of IEEE Trans Plasma Sci [71]

diffraction peaks. The TEM studies corroborated the presence of nanostructure, metastable phase, and amorphous phase formation in the powders. Al_2O_3–TiO_2 (87–13) particles were also spheroidized by flame spraying.

(b) Production of Spherical Particles from Suspension

When chemical routes are used to prepare materials, the formed crystallites are generally at the nano-scale. Therefore it is not simple to achieve dense and spherical powders from them. Bouyer et al. [71] have proposed the densification of hydroxyapatite (HA) by r.f. induction plasma (50 kW from Tekna Plasma Systems Inc in Sherbrooke, Québec, Canada). The HA is synthesized by chemical route and the resulting aqueous precipitate (Fig. 11.29a) is concentrated by centrifugation and heated until reaching a percentage of solid in the suspension of about 40 wt%. The suspension properties are adjusted for decreasing its viscosity down to 0.4 Pa s. The suspension is fed via a peristaltic pump and is gas atomized into the plasma flow to produce droplets with an average diameter in the range of 50–100 μm. The process steps are presented schematically in Fig. 11.30. Because of the low relative

velocity between the droplets and the plasma, the Weber number is below 14 and the droplets are not fragmented during their flight. As the droplets are entrained by the plasma, they are heated and their water content is evaporated giving rise to the formation of solid particles which upon further heating, flash sinter, melt, and finely solidify resulting in the formation of dense spherical particles with an average diameter considerably smaller than the original droplet size in the range of 20–50 μm. As shown in Fig. 11.29b, a small percentage of nonspherical particles can also be formed in the process depending on the quality of the atomization and droplet drying steps.

$LaMnO_3$ particles have also been produced by r.f. suspension plasma spraying [72]. However, they were partially decomposed in spite of the use of an oxygen sheath gas. $La_{0.8}Sr_{0.2}Mo_{3-\delta}$ particles for SOFC's cathode material were also successfully produced [73]. This technology has also an important potential for the preparation of functional materials such as yttrium aluminums garnet (YAG) [74].

11.1.2.8 Cladding

Cladding allows producing composite particles. With this technique particles exhibit a core of one material coated on the outside with a dense and continuous layer, a porous coating, or a heterogeneous one. Lugscheider et al. [75] have presented an excellent overview of the different cladding processes used. They are the following:

(a) Mechanical Alloying with Attritors

The core particles must be mechanically stable during the attrition milling and the ratio of core particles and coating material must be calculated accurately. If the quantity of the coating material is too low, the core material will be crushed, while if it is too high, the coating process will not take place.

(b) Sintering

Coated powders are obtained either using the impact-process sintering or by mixing large particles of one material with submicron-sized particles of the other one before sintering them. The result of the latter process is illustrated in Fig. 11.31 for alumina–titania particles: Al_2O_3 powder (10–45 μm) mixed with submicron-sized TiO_2 before sintering [12].

The different types of coatings that can be obtained by cladding onto the core material are summarized in Fig. 11.32. Electron micrographs of Ni/Al- and Ni/graphite-cladded particles are shown in Fig. 11.33.

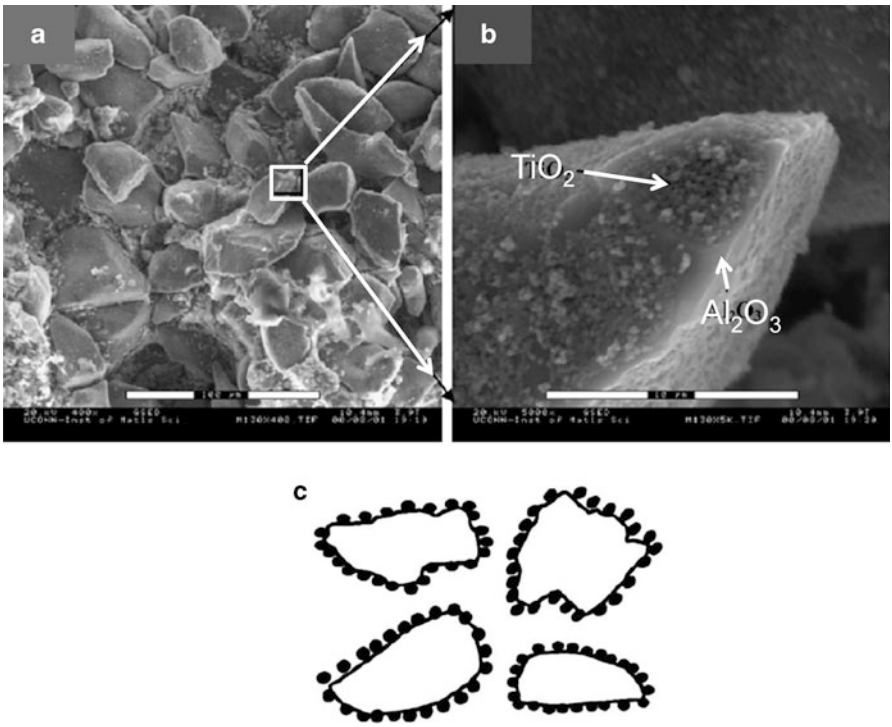


Fig. 11.31 SEM images of (**a**) and (**b**) Metco 130 powder. Two different magnifications are shown to provide an overview of the particle size and the detailed view of the microstructure of the particle. (**c**) Schematic of the powder. Reprinted with kind permission from Elsevier [12]

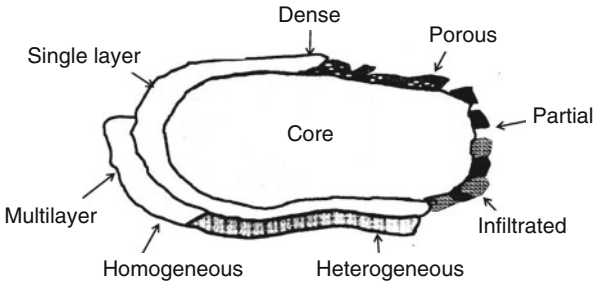


Fig. 11.32 Different types of cladding. (Courtesy of Sulzer Metco for Plasma Technik) [75]

(c) Mechanofusion

This process is used to manufacture composite powders starting from two or more raw powdered materials having different grain sizes [76]. Its principle is shown in Fig. 11.34: a rotating cylinder entrains the powder mixture below two inner

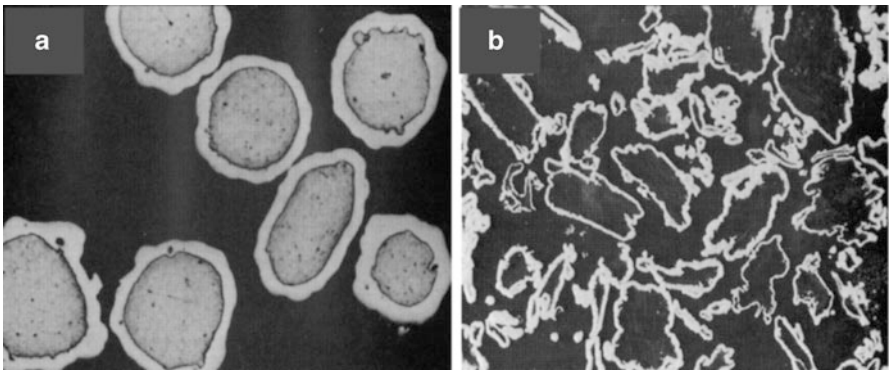


Fig. 11.33 Particles obtained by cladding (**a**) NiAl (80–20) and (**b**) Ni–graphite (85–15) (Courtesy of Sulzer Metco for Plasma Technik) [75]

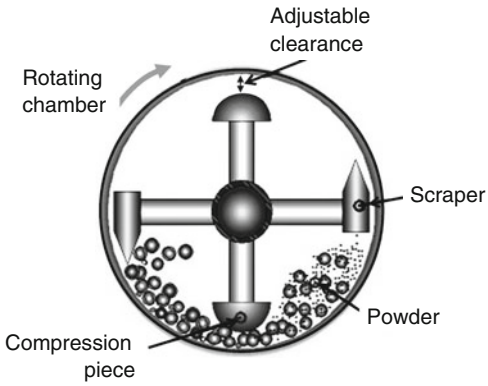


Fig. 11.34 Principle of a mechanofusion process. Reprinted with the kind permission of Dr. R. Cuenca-Alvarez [78]

compression pieces with adjustable clearance between the compression piece and the inner wall of the cylindrical housing. Two scrapers clean the cylinder wall and help the entrainment of the particles mixture below the compression pieces. The raw particles are mixed intensively and subjected to a powerful compression, resulting in strong mechanical forces generating thermal energy. Thereby, the material with the lowest melting temperature is heated to a plastic state or even melts and becomes the core of a composite particle to which the material with the highest melting temperature is welded as a surrounding shell. Figure 11.35 shows 316L stainless-steel particles with a size distribution from 50 to 63 μm coated with pure α-alumina (99.99 %) with a mean particles diameter of 0.6 mm [77]. The composite particles have a spherical shape and their mean diameter, after sieving, is 65 μm, the alumina shell being 2 ± 4 μm thick (Fig. 11.35).

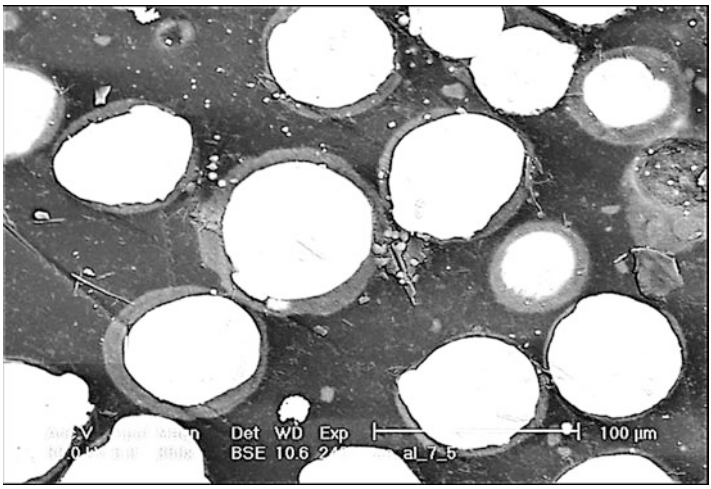


Fig. 11.35 SEM observation of cross section of mechanofused stainless steel/alumina particles. Reprinted with kind permission from Elsevier [77]

(d) Deposition from Gaseous Phase

The most used process is Chemical Vapor Deposition (CVD). It basically consists of coating the particles in a fluidized bed reactor through the thermal decomposition of the vapor precursor. The process, which is mostly a pyrolysis or chemical reduction, requires a close control of the temperature of the fluidized bed and the uniform distribution of the vapor precursor thoughout the bed. The core of the particle to be coated must be stable at the reaction temperature. The maximum thickness of the coating is up to 20 µm. Two problems are encountered: the purity of the coating, which is not the highest, and the stability of the fluidized bed requiring large quantities of fluidizing gas [75]. Metals, alloys, carbides, nitrides, borides, silicides, and oxides are deposited that way. Lugsheider et al. [75] give the list of these materials in their paper. In principle PVD can be used, but compared to CVD the cost is much higher. Particles must withstand temperatures up to 800 °C and pressures between 1 and 10^{-4} Pa. Different techniques are used: evaporation, sputtering, or ion plating [75]. The list of the deposited materials is the same as that of CVD. For more information see [75].

(e) Electrolytic Coatings (Also Called Galvanic Plating)

The particles to be coated (electrically conductive) are at the anode potential, while the material to be deposited is in its metal salt solution. Coating thickness can vary in a very wide range: 0.5–2,000 µm [75]. However coatings are porous and spongy and often irregular.

(f) Chemical Precipitation

It is a very important process based on the electroless reduction of a metal salt solution, also called hyperpoc process (hydrogen-pressure-reducing-powder-coating-process). The core powder to be coated is suspended by mechanical agitation in an aqueous metal salt solution. Introducing hydrogen at elevated temperature and pressure in the autoclave containing the solution and the particle suspension reduces the metal. It requires that the hydrogen potential of the system exceeds the electrode potential of the metal ions. When this condition is fulfilled, the hydrogen reacts with the solution and the metal precipitates. The hydrogen potential increases when the solution pH value and the partial pressure of hydrogen are raised. Typical pressures are in the 2–3 MPa, while the solution is heated at 180–200 °C. The core particles to be coated must be nonreactive to the solution. The metal salts are basically sulfates, nitrates, acetates, carbonates, and also organic metal salts [75]. The deposited layer (Pt, Pd, Au, Ag, CU, Ni, Co, Mo) on the core particles are either homogenous or heterogeneous. Sintering can further consolidate composite particles. For example, this process is used to make NiCrAl/bentonite (silica-based clay) particles. Bentonite core particles are coated with layer (about 2 μm thick) of nickel (starting from a nickel amine sulfate). The nickel is further alloyed with chromium and/or aluminum by pack diffusion [2]. Typically the average core diameter is 85 μm and the deposited layer is about 6 μm, the composition in wt. % being: 20 % bentonite, 5 % chromium, 3 % aluminum, and 72 % nickel. This process can also prepare materials such as graphite or silicate for abradable coatings. MoS_2 powder can be coated with Ni by chemical method. The coated powder has a nominal composition of 22 wt% MoS_2 and 78 wt% Ni, with an average particle size of 50 μm, and an average thickness of Ni layer 5 μm [75].

11.1.2.9 Sol–Gel and Solutions

(a) Sol–Gel

Sol–gel processing can produce ceramic powders, especially oxides (alumina, chromia, partially or totally stabilized zirconia), with a high surface area, which allows sintering to nearly full density at much lower temperatures than are normally required when the particles have been made by other techniques [2, 49]. It also allows, when considering particles with different components, such as yttria partially stabilized zirconia, to have them mixed at nano-metric level.

Sol refers to the initial solution of the chemical components from which the powder is derived. Gel corresponds to the final product of the ceramic material. The process comprises the following steps [49]:

1. *Formation of the solution*. In most sol–gel processes the reactants are solutions of metal alkoxy compounds (resulting from the reaction of metals with

alcohols). Catalysts are often necessary to increase reaction rates. For example, with aluminum the catalyst breaks down the protective oxide layer that forms on the aluminum.
2. *Formation of metal oxide*. Water is added to the alcohol solution. Reactions then occur, such as hydrolysis and condensation. The gel formation depends on the type of alkoxide, the reaction temperature, the amount of water added, and the solution pH. The pH is very important to avoid or promote the formation of agglomerates. Gelation times vary from seconds to several days.
3. *Gel drying and calcination*. When the gel forms it may contain only about 5 vol. % of the oxide. The gel is dried and calcined to completely convert it to oxide. Powders produced by the sol–gel method are amorphous. A crystallization step is required to produce crystalline bodies, which is often performed after sintering. The final density of the product can be varied from low (aggregated sol) to high (well-dispersed sol).

Wang et al. [79], synthetize nanostructured composite powder of $MgO–Y_2O_3$, using magnesium acetate $(CH_3COO)_2$ $Mg{\cdot}4H_2O$, >99 %, and yttrium nitrate $Y(NO_3)_3{\cdot}6H_2O$ >99.9 % as starting chemicals. These products were first dissolved in deionized water, based on the volume fraction ratio of 50:50 of the oxides. After mixing for 10 h, the solution was dried in an oven at 200 °C to form a white gel, then heated in an oven to 600 °C with a heating rate of 20 °C/min. During the heating process, rapid combustion occurred and voluminous fluffy powder was formed. After decarbonization at 600 °C for 2 h, white powder was produced and collected. A ball-milling process with ZrO_2 balls allowed breaking down large agglomerates into micrometer-sized particles. MgO and Y_2O_3 crystals (10–20 nm) were created. The $MgO–Y_2O_3$ nano-powder feedstock was successfully deposited on substrates by APS without the use of spray dry agglomeration [79].

(b) Solutions

Amorphous powders can be used in suspensions and Chen et al. [80] have prepared $Al_2O_3–ZrO_2$ amorphous powders by a chemical solution process. Aluminum nitrate $Al(NO_3)_3{\cdot}9H_2O$, and zirconium acetate $ZrO(OOCCH_3)_3$, were dissolved in deionized water based on molar volumes to produce a ceramic composition of Al_2O_3–40 wt% ZrO_2. The obtained solution was heated at 80 °C and stirred continually to get the sol transformed into a dried gel. The dried gel powders were heated to 750 °C at a heating rate of 10 °C/min and then held for 2 h. The phase composition and microstructure of the as-prepared $Al_2O_3–ZrO_2$ powders heat treated at 750 °C for 2 h was investigated. In the XRD patterns no crystalline peaks appeared (amorphous powders).

Prakash et al. [81] explored the possibility of fabricating thick film of gadolinia-doped ceria (GDC) electrolyte through fabrication methods that lead to the minimization of overall fabrication costs of solid oxide fuel cells (SOFCs). A wide

variety of processes belonging to wet chemical routes are generally used for the synthesis of fine powders of ceria and doped ceria. Thus they tested the solution combustion synthesis to synthesize GDC powders of varying powder characteristics by using different fuels. Nanoparticle-sized GDC powder prepared by using oxalylyl dihydrazide fuel exhibited higher sinter activity and resulted dense pellet with high conductivity (3×10^{-4} S cm^{-1} at 400 °C). These powders exhibited necessary characteristics suitable for wet powder spraying [81]. Due to the high reaction temperature agglomerated particles were formed on using glycine as fuel. Use of ammonium acetate fuel along with reduced amount of glycine yielded micron-sized, plasma spray-able grade GDC powder. These powders resulted in a dense atmosphere plasma-sprayed coating with superior inter-splat adhesion.

11.1.2.10 Self-Propagating High-Temperature Synthesis

Borisova and Borisov [82] have published recently an excellent and complete review of the process. Their definition of the SHS process is as follows: It is a process where the reaction is locally initiated in a thin layer of a reactive mixture of reagents. Once initiated, it is self-propagating, in a wave of gasless combustion, over the entire system through heat transfer from hot interaction products to the next layer of the initial mixture. The thermal activity of the reaction is sufficient to further initiate the process. Reaction products both result from and further promote the process. Therefore, SHS is a highly exothermic interaction of chemical elements (or compounds) in a condensed phase that occurs in combustion conditions. Processes based on SHS are peculiar in that they have high temperatures, ensure rapid synthesis of new materials, are controllable, permit energy saving, ensure purity of the products, etc.

The SHS method was first used to obtain powders of refractory inorganic compounds (carbides, borides, nitrides, silicides, intermetallics, etc.). A cake of the SHS mixture was first prepared, heated in a furnace over the temperature triggering the reaction, and then the cake was crushed to produce the particles. The size of particles was adapted to that requested for spraying. Compared to particles produced with other methods they presented some advantages such as composition, structure, cost, etc.

It is also possible to combine coating deposition with SHS synthesis. In this case the basic reactants are in the solid phase either as agglomerated or cladded particles [82–89]. These particles are sprayed and react during spraying *and particles flattening*, the reaction heat dissipated improving the splats layering. The reaction starts when a critical temperature is reached, which occurs in the periphery of the particle heated by hot gases along its trajectory. Then the reaction propagates toward the particle center at velocities of a few cm/s and, according to the particle size and its residence time in hot gases, the reaction can continue within the deposited particle. Numerous experiments on metal–metal systems in which intermetallics form (Ni–Al, CuAl, Ni–Ti, etc.) and on more complex metal–oxygen-free refractory compound composites (Ti–SiC, Ti–Si_3N_4, Cr–SiC, etc.) have shown that

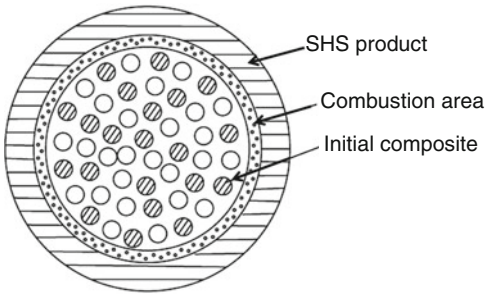


Fig. 11.36 SHS in a spherical powder particle. Reprinted with kind permission from Springer Science Business Media [82]

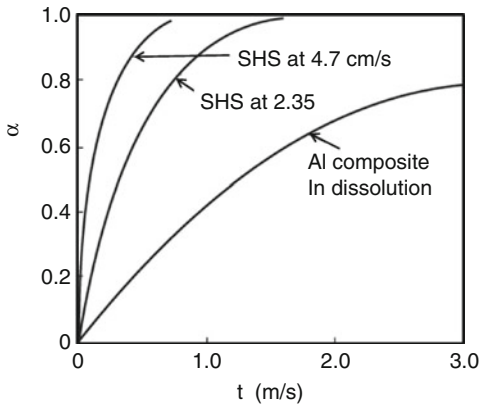


Fig. 11.37 Kinetics of the interaction of components in 80 Ni–20 Al composite in dissolution, and combustion (SHS) at 2.35, and 4.70 cm/s. Reprinted with kind permission from Springer Science Business Media [82]

the abrupt peak of exothermal interaction in differential thermal curves mainly coincides with the moment when the system reaches the melting temperature of the low-melting component or interaction product (for example, low-melting eutectic) [82].

The spraying and synthesis of the material sprayed, which are accompanied by an exothermic effect, were first combined by the Metco Company that used nickel–aluminum composite in the form of aluminum particles coated with nickel [83]. Owing to the clad particle structure, components can interact through dissolution when one of them turns into melt. However, the SHS reaction is more efficient when the particle consists of uniformly mixed exothermically reacting components, as illustrated in Fig. 11.36 [82]. Borisova and Borisov [82] have calculated the evolution with time of the extent of interaction, called α, for the 80Ni–20Al-cladded particles and the composite one (for two reaction velocities: 2.35 and 4.70 cm/s). Results, presented in Fig. 11.37, show that in the composite particles, the SHS interaction substantially intensifies the reaction and heat releases in a shorter period of time, which increases the absolute temperature rise due to the internal heat source. Of course to heat particles without fragmenting them implies that the produced gas expansion during the reaction can escape the particle where SHS reaction occurs.

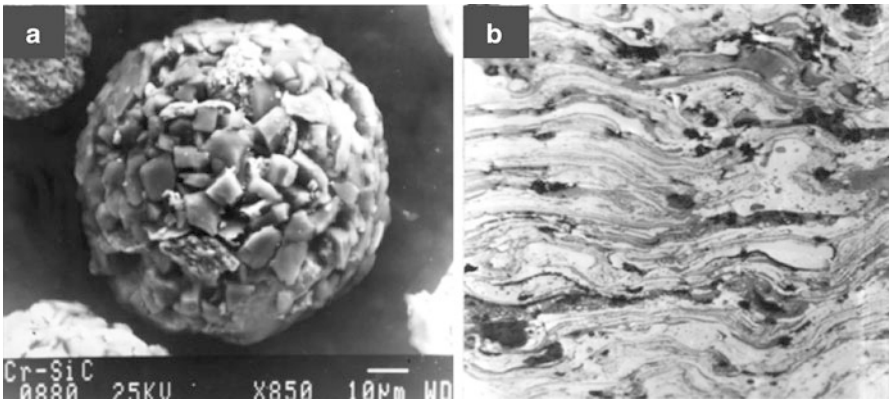


Fig. 11.38 External view of particles in Cr + SiC composite powders conglomerated with organic binder (**a**) and microstructure of a plasma coating of this powder (**b**, ×800). Reprinted with kind permission from Springer Science Business Media [82]

An example of structure of a Cr–SiC composite powder particle and the typical structure of the plasma-sprayed coating are shown in Fig. 11.38. The coating consists of Cr_7C_3, $Cr_{23}C_6$, Cr_5Si_3–xC_x. High hardness and strength of adhesion to steel (σ_{adh} = 26–29 MPa) and wear resistance surpass that of molybdenum coating in oil-abrasive medium and twice that of galvanic chromium coating in dry friction.

Many coatings have been produced by this method; see, for example, the exhaustive list of the review of Borisova and Borisov [82]: transition metal–nonmetal refractory compounds with mixtures of Cr and SiC or B_4C, Ti, and SiC or B_4C or Si_3N_4,... producing coatings with silicides, carbides, borides,... exhibiting excellent resistance to wear [83–88]; copper–TiB_2 coatings starting from agglomerated particles of Ti–bronze and boron, the TiB_2 particles in coatings increasing considerably the hardness of copper matrix [88]; TiB_2 or TiC particles in ferrous matrices to increase their hardness and wear resistance [89],...

11.1.2.11 Other Methods

(a) Use of Adhesives

The core particles, the coating material, and the dissolved organic binder material are mixed intensively and heated. After vaporization of the solvent, the organic binder adheres to the coating material and the core particle.

(b) Blends

Blended powders, generally of two-powder feedstock, are mechanically mixed and then fed to the spray gun through the same port. However if one wants to have similar trajectories for both types of particles, the particle distributions of both powders must be adjusted according to their specific mass. Otherwise spray processes are excellent classifying media, resulting in quite inhomogeneous coatings. The best way is to inject dissimilar particles at two different locations (of course it requires two powder feeders and two injection ports judiciously disposed).

11.1.2.12 Powders with a Metal Matrix in Which Hard Nanometer-Sized Particles Are Uniformly Distributed

One of the main difficulties when spraying particles made of a metal matrix reinforced by carbides is to avoid or at least limit the decarburization. A typical example is that of WC–Co with WC particles in the few micrometer size range, generally produced by spray drying followed by heat treatment. When replacing the micrometer-sized WC particles by nanometer-sized ones, the high surface area of the nanocomposite WC/Co particles facilitates all types of high-temperature reactions, which makes not only the spraying but also the manufacturing of such particles difficult. To overcome the problem, two techniques are used for synthesizing finely divided carbide powders:

- To produce amorphous precursor powder obtained from spray drying an aqueous solution and carburize it in a controlled selective atmosphere to yield the phases pure WC and Co in each composite particle
- To use integrated mechanical and thermal activation (IMTA) process where WC–Co powder is synthesized below 1,000 °C, starting from WO_3, CoO, and graphite powder mixtures

(a) Spray Drying Solutions

According to Seegopaul et al. [90], the combination of solution chemistry with gas–solid reaction processing imparts significant advantages to the spray conversion process (SCP). The process starts from an aqueous solution of soluble salts and any compatible combinations of salts can be spray dried to yield the desired products, such as WC–Co, WCCo–VC, WC–Co–Cr_3C_2, WC–Co–VC–Cr_3C_2 mixtures. Gas phase carburization is then conducted in a fluid bed reactor, with a good control of carbon variation, to yield the nanocomposite hard-metal powder. During the cool down cycle, the high-surface area powder is passivated with oxygen-rich species to avoid spontaneous combustion when exposed to air [91]. The as-produced powder consists of solid agglomerates, which are screened to a relatively narrow size distribution, typically within the range of 15–40 μm

[91]. Seegopaul et al. [90] use milling to break the large particles and ensure uniform mixing of the additives, such as, grain growth inhibitors [90]. Sintering is then performed in hydrogen atmosphere to remove adsorbed oxygen for reduced porosity and optimized carbon balance. Sintering temperature must be well controlled to avoid the destruction of the nanostructured particles [90]. Enhanced WC grain growth occurs early in the sintering cycle, even below the temperature at which the liquid phase is formed. This growth can be largely restricted by the addition of VC [92].

(b) Integrated Mechanical and Thermal Activation

Ban and Shaw [93] have developed a novel approach, termed the integrated mechanical and thermal activation (IMTA) process, which was used to synthesize nanostructured WC–Co powder. The basis of the IMTA process in making nanostructured WC–Co powders is to mechanically activate reactants WO_3, CoO, and graphite at room temperature through high energy milling (the mechanical activation step), followed by completing the synthetic reaction at high temperatures (the thermal activation step) [94]. The amount of free carbon present in the composite powder can be precisely tailored in the IMTA process to prevent decarburization during thermal spraying. IMTA process uses low cost materials while producing nanostructured WC–Co powder that has better powder characteristics (e.g., solid particles rather than hollow ones). Particle sizes ranging from 0.3 to 0.5 μm and an average WC grain size around 30 nm were obtained by IMTA. As these particles were not suitable for thermal spraying (where a range of 5–45 μm, with a mean size around 20 μm is required), they were agglomerated using methylcellulose as the organic binder. These particles HVOF sprayed [94] showed that the ratio of oxygen-to-hydrogen flow rate and the starting powder microstructures had strong effects on decarburization of the nano-coatings. IMTA process has also been used to produce pure nanostructured carbides (SiC and TiC) [95] and nitrides (Si_3N_4, CrN, and TiN) [96].

(c) Other Method

Kurlov et al. [97] have synthesized by the plasma-chemical method with thermochemical treatment WC powder with an average particle size of 35 nm. They produced microcrystalline Co powder with an average particle size of 2.2 μm and nanocrystalline vanadium carbide (VC0.87) powder obtained by high-energy grinding. Then a powder mixture containing 93 wt% WC, 6 wt% Co, and 1 wt% VC0.87 was prepared by multistage mixing in a planetary ball mill with a complex mixing procedure. The nanopowder mixture contained the main components (WC and Co) and inhibiting additives (0.3–0.5 wt% nanocrystalline carbides VC, Cr3C2, and TaC). Then powers must be densified.

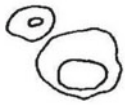
Powder type Manufacturer	Fused and milled	Sintered and milled	Agglomerated and sintered	Spheroidized	Atomized
					
Particle shape	Blocky - angular	Blocky - angular	Spherical	Spherical	Spherical -irregular
Porosity	Dense	Dense - porous	Porous	Dense - hollow	Porous - hollow
Crystalline size	Course-fine	Course - fine	Medium - fine	Medium - fine	Fine
Homogeneity	Alloyed	Alloyed	Alloyed - heterogeneous	Alloyed - heterogeneous	Alloyed

Fig. 11.39 Specific ZrO_2–8 wt% Y_2O_3 powder characteristics depending on their manufacturing route. Reprinted with kind permission from Elsevier [47]

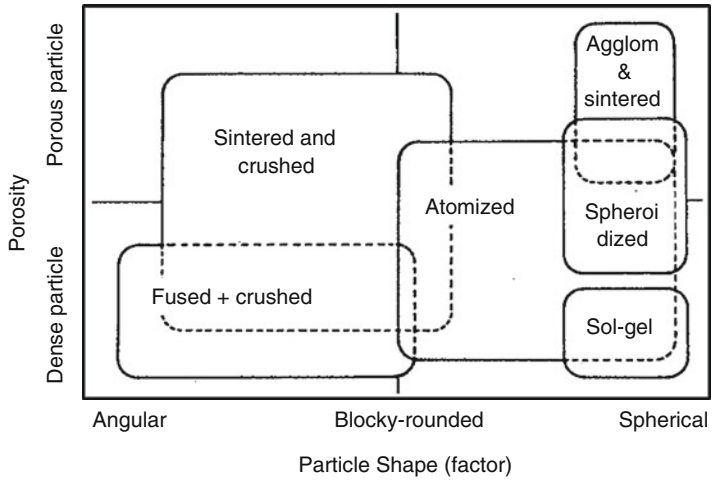


Fig. 11.40 Powder characteristics—porosity and particle shape—as a function of their manufacturing process. Reprinted with kind permission from Elsevier [47]

11.1.2.13 Example: Different Powders of ZrO_2–8 wt% Y_2O_3

The different properties of particles, according to their manufacturing process, were illustrated for ZrO_2–8 wt% Y_2O_3 particles used in thermal barrier coatings

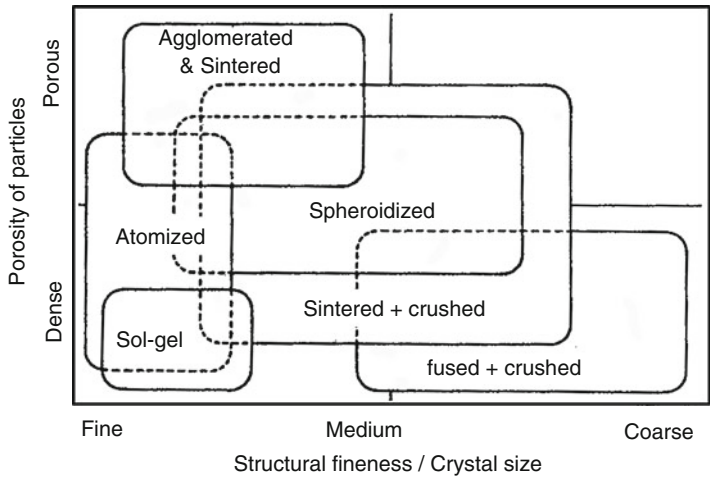


Fig. 11.41 Powder characteristics—porosity and structural fineness—as a function of their manufacturing process. Reprinted with kind permission from Elsevier [47]

Table 11.2 Typical ZrO_2–8 wt% Y_2O_3 powder (90–10 μm) characteristics. Reprinted with kind permission from Elsevier [47]

Powder type	Particle aspect	Bulk density (kg/m^3)	Hall-flow (s/50 g)	Hall-flow (s/cm^3)	ZrO_2 phases (m%)	ZrO_2 phases (c + t%)	Microstructure (μm)
Agglomerated + sintered	Porous spherical	1,800	40	1.4	20	80	1–15
Sintered + crushed	Porous irregular	2,100	40	1.7	15	85	3–15
Spheroidized	Hollow porous spherical	2,300	34	1.6	10	90	<2 (<15)
Atomized	Porous irregular	1,700	50	1.7	0	100	<2
Fused + crushed	Dense irregular	2,700	32	1.7	<5	>95	<90
Sol–gel + calcinated	Dense spherical	2,600	22	1.2	<5	>95	<90

[48]. The shapes and properties of the particles manufactured by different routes are summarized in Fig. 11.39. The trends of the evolution of the porosity with the particles shape factor are presented in Fig. 11.40 and with the structural fineness or crystal size in Fig. 11.41.

A summary of the different properties of ZrO_2–8 wt% Y_2O_3 powders (90–10 μm) is presented in Table 11.2, showing clearly that the injection and spray conditions must be adapted to each powder.

11.1.3 Examples of the Influence of Powder Morphologies on Coating Properties

As Chap. 14 is entirely devoted to nanostructured coatings, in the following only examples of the influence of tens of micrometer-sized particle morphologies will be presented.

11.1.3.1 YSZ Powders

Most ceramic particles are either fused and crushed (FC) or agglomerated by spray drying and then sintered (AS), resulting in spherical and sometimes hollow spheres (HOSP). For example, Streibl et al. [98] have studied with different sensors the temperatures and velocities of YSZ particles sprayed with a 3 MB plasma torch (Sulzer-Metco, Wohlen, Switzerland) working with a plasma gas mixture of nitrogen and hydrogen. The particles used were commercial hollow spherical particles (HOSP), fused and crushed (FC) and agglomerated and sintered (AS), all of them with about the same average diameter (d_{50} of the particle size distribution) and the carrier gas was optimized for each type of them to achieve the same mean trajectory. In-flight measurements have shown that the HOSP particles were indeed the easiest to melt compared to the others. This better heating is due to the lower mass of HOSP particles (the specific mass of such particles can be below 1,000 kg/m^3) compared to that of other types of particles (AS and FC), the lower particle volume, the heat transfer coefficient from the warm gases, as well as the particle surface, being the same. Measurements of thermal conductivities κ_i [99] of corresponding coatings showed that, in the 200–1,200 °C temperature range, $\kappa_{HSOP} < \kappa_{AS} < \kappa_{FC}$ pointing out the important role of inter-lamellar delamination. HOSP particles result in thinner lamellae and consequently a larger fraction of inter-lamellar delamination. Bertrand et al. [100] have compared also YSZ HOSP with an extremely low-specific mass (390 kg/m^3 to be compared to 2,000 kg/m^3 for the commercial HOSP particles and to 2,900 kg/m^3 for FC particles). A decrease in 30 % of as-sprayed apparent κ was obtained, as compared to a standard value, when spraying them (after spray conditions optimization).

11.1.3.2 Al_2O_3–TiO_2 Powders

Wang and Shaw [13] have studied three Al_2O_3–TiO_2 powders with the same chemical composition, but different Al_2O_3–TiO_2 distribution patterns due to different manufacturing methods (spray-drying, FC, and plasma fused) on coating properties. The degree of mixing of the alumina and titania initial particles changes with the powder manufacturing method. It is particularly important for the particles degree of melting, the thermal conductivity of the resulting particles being increased with the better mixing of alumina and titania. It also affects the coating microstructure. TiO_2 lamellae and TiO_2-rich c-Al_2O_3 regions can be

eliminated if the sprayed powder is a mixture of both elements mixed at the sub-micrometer level.

11.1.3.3 WC–Co Powders

The wettability of WC by most binder metals is better than that of the other carbides. This, along with its relative toughness, makes it the most widely used carbide for sintered hard metals. Cobalt is the most commonly used binder because it has excellent carbide wetting and adhesion properties. However WC has no stable molten phase, but it easily transformed to other phases when the carbon content is nonstoichiometric [101]. It is therefore a difficult material to successfully process in the extremely high-temperature oxidizing/decarburizing conditions generated during thermal spraying, particularly plasma spraying [101]. Villiers Lovelock [101] has studied and compared (review of the work performed before 1998) the microstructure and phase composition of WC–Co (12 and 17 wt%) on the phase changes that occur during spraying powders produced from cast/crushed, sintered/crushed, and agglomerated/densified powders. He has discussed in detail the loss of WC during thermal spraying and the resultant coating phase structure. Villiers Lovelock [101] has underlined that published porosity values for the coatings vary between <0.2 % and almost 20 %. Porosity is generally higher for plasma-sprayed coatings than for HVOF and D-gun coatings, as would be expected. The WC grain size in cast/crushed WC–12 % Co powders and the coatings produced from them is larger than that produced from other powder types. Cast/crushed powders exhibit greater loss of visible WC during spraying than the other powder types, and the sintered/crushed powder types appear to be the least susceptible to visible WC loss during spraying. During plasma spraying, the WC–Co powder tends to undergo decarburization, oxidation, reduction by reaction with the H_2 in the plasma gas, and dissolution/reaction between the WC and the cobalt binder metal during spraying, resulting in the formation of hard and brittle phases such as W_2C, Co_3W_3C, Co_6W_6C, Co_2W_4C, $Co_3W_9C_4$, and even WO_3 and tungsten [101]. The binder in thermally sprayed WC–Co coatings is often predominantly amorphous Co/C/W/$Co_xW_yC_z$ due to rapid post-spraying solidification [101]. The extent of the WC transformation during spraying depends on the starting powder type (size, morphology, carbide size), the type of spray process, the amount of oxygen in the environment, including that brought by the cooling air jet and/or that entrained by the hot gases jet increasing with the spray distance, and the spray parameters, the best ones corresponding to the lower temperature (close to Co melting temperature) and the higher velocity. For example, when comparing the same WC–12 wt% Co powder sprayed by high-velocity oxy-fuel (HVOF) and high-velocity air fuel (HVAF), substantial amount of W_2C was identified in the HVOF coatings, as well as a high concentration of tungsten in the binder phase [102]. In contrast with HVAF spraying, where particles temperature is lower and velocity higher, composition and microstructure of coatings were unchanged from that of the powder. Additionally, the wear resistance of the HVAF coatings was superior to

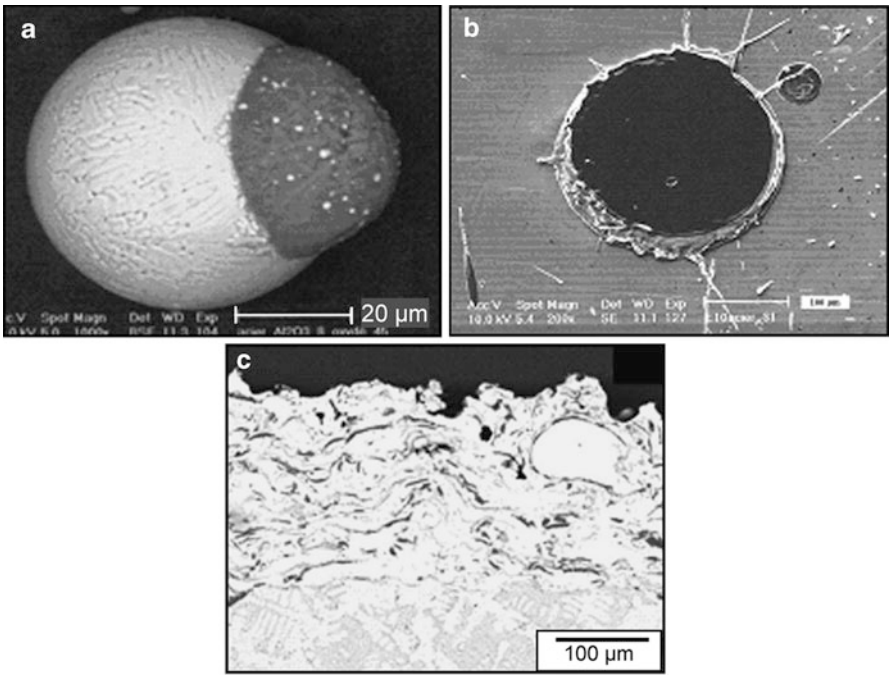


Fig. 11.42 Mechanofused alumina–stainless-steel coatings, (**a**) particle collected after its flight into an Ar–H_2 plasma jet, (**b**) splats collected on a smooth substrate (alumina in black color and stainless-steel in gray color), and (**c**) coating cross section. Reprinted with kind permission from Elsevier [77]

that of the HVOF ones. It has also been shown that WC–17 wt% Co coatings were not primarily influenced by variations in the spray parameters, but were more dependent on the powder composition, particle size range, and manufacturing route [103]. Coatings manufactured with sintered and crushed powder delivered a more consistent and a lower wear rate than the agglomerated and densified powder type, but this effect was possibly related more to the WC grain size (respectively, 1 and 2.6 μm) than to the manufacturing route. The WC particle volume distribution also plays a role in coating properties. For example, Peetsalu et al. [104] have shown that the best dry abrasive wear resistance of WC–Co (15 or 17 wt%) coatings, HVOF sprayed was obtained for a particular WC particle volume distribution: uniform distribution of small-size WC particles (about 1 μm) and a certain amount (5 to 10 vol.%) of larger WC particles (from 2 to 3 μm).

11.1.3.4 Mechanofused Alumina–Stainless Steel Particles

A typical mechanofused alumina–steel particle (see section "(c) Mechanofusion") is presented in Fig. 11.35 [77, 78, 105]. The starting 316L stainless-steel particles with an average diameter of 56 μm are coated with 2 ± 4 μm thick pure α-alumina (99.99 %) particles of 0.6 μm average diameter. Upon spraying both materials are fully melted, and the lighter alumina at the steel core is entrained by the flow either before or behind the steel particle depending on its mass. It results in steel spheres with an alumina cap, as shown in Fig. 11.42a. For particles below about 60 μm, the steel hits the substrate first and two lamellae are formed: a stainless steel one on which lays an alumina one as shown in Fig. 11.42b. Finally, the coating is made of layered steel and alumina lamellae as shown in Fig. 11.42c. Compared to a pure stainless-steel substrate sprayed in the same conditions, the hardness of the alumina–stainless-steel coating is 620 ± 30 HV_{5N} against 460 ± 20 HV_{5N}. To underline the effect of particles in-flight oxidation, the hardness of the bulk-casted identical steel is only 450 ± 15 HV_{5N}.

11.1.3.5 Micrometer-Sized Particles Cold Sprayed

The influence of various parameters (particle diameter, specific mass, material specific heat, etc.) on the critical velocity and deposition efficiency were studied systematically [106–111]. As the deposition efficiency increases with the ductility of the impacting particles, when raising the particle temperature for the same velocity (implying generally Young's modulus reduction) the deposition efficiency is improved. For example, increasing the Ni particle temperature by 530 °C improves the deposition efficiency by about 13 % for the different velocities considered [112]. Particle oxidation, according to the manufacturing technology, also diminishes the particle ductility. For example, Kang et al. [113] have shown that the corresponding critical velocity for deposition of aluminum particles with different oxidation stages (varying the oxygen content from close to 0 to 0.04 wt%) on aluminum substrates varied from 750 m/s to more than 850 m/s.

11.1.4 Conventional Particle Classification Method

The particle size distribution is a key parameter to control particle trajectories on which depend their temperatures and velocities at impact. These trajectories are linked to the particle forces at the injector exit relatively to those imparted to them by the hot flow. As shown in Sect. 4.4.2.3, particle mean velocities at the injector exit are almost the same whatever may be their size. Thus the particle forces are directly proportional to their mass, i.e., to the cube of their diameters. It is thus of primary importance to have particles with a narrow size distribution corresponding

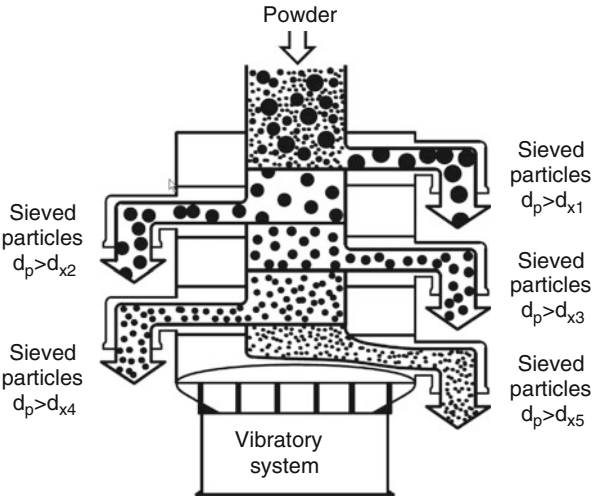


Fig. 11.43 Particle classification by vibratory sieving. Reprinted with kind permission from ASM International [114]

to a ratio of two between the maximum and minimum diameters (already corresponding to a mass ratio of 8!). Of course if rather porous coatings are wanted, broad particle distributions are needed. Moreover in all cases particles with sizes below 5–10 μm, depending on their specific mass, are to be avoided in conventional spraying because they require high carrier gas flow rates perturbing the hot jet and often those traveling in jet fringes create defects in coatings. Thus particle size distribution is very important both for the manufacturer and the sprayer. This aspect of powder technology is referred to as "classification" [114–119]. Whatever the mean used for classification, the powder morphology will also play a role in the classification process: for example, very angular dense particles behave differently than spherical and porous ones.

Among the different methods to classify particles for thermal spraying, the most used ones are sieving either in air or inert gas with or without vibratory system, the lower limit being about 5 μm, or air classification employing cyclones.

11.1.4.1 Sieving

Sieving is the oldest method to sort particles according to size [2, 49, 114–118]. Typically, sieves with decreasing mesh size are stacked with the largest mesh at the top (see Fig. 11.43). A representative weighed sample is poured into the top sieve that has the largest screen openings. Each lower sieve in the column has smaller openings than the one above. The column is typically placed in a mechanical shaker. After the shaking is complete the material on each sieve is weighed. The particle size distribution corresponds to the weighing of amounts of powder in each sieve [118].

The term "mesh size" denotes the number of openings per linear length unit in the sieve screen. The National Institute of Standards and Technology (NIST) developed the sieve numbering system based on the "fourth root of two" ratio;

Table 11.3 Relationship between sieve (or mesh) number and mesh opening size used in thermal spray. Reprinted with kind permission from ASM International [2]

Sieve no.	Mesh opening (μm)	Mesh opening (in.)
100	149	0.0059
120	125	0.0049
140	105	0.0041
170	88	0.0035
200	74	0.0029
230	62	0.0024
270	53	0.0021
325	44	0.0017
400	37	0.0015
500	31	0.0014
600	30	0.00
1200	15	0.00
3000	6	0.00
8000	3	0.00

this series is known as the ASTM E-11 standard (ASTM for American Society for Testing and Materials). This ratio (=1.189) means that the sieve openings are an exact geometric series. It can also be said that the mesh opening of two consecutive sieves has a 1.414 ($\sqrt{2}$) ratio. Table 11.3 [2] gives the relationship between sieve (or mesh) number and mesh opening size, for the meshes used in thermal spray.

The normal wear (deformation, rupture, corrosion of the wires) must be checked regularly to keep the process reliable. However one of the main problem is the embedding of individual particles in the sieve grids, especially for the small mesh opening, thus reducing the sieving efficiency and polluting the next batches. To limit this phenomenon each sieve is vibrated and recently a company [120] has developed a combination of ultrasonic and conventional vibration, which can be retrofitted onto any new or existing vibrating separator or screener. The acoustically developed transducer applies an ultrasonic frequency directly to the screener mesh to break down surface tension, effectively rendering the stainless steel wires friction free. Accurate separation down to 20 μm on even difficult powders can thus be achieved. The limit of such system is about 5 μm. However in production, sieving is not used below 44 μm according to the too long times required and the risk of clogging. Instead of using dry sieving, wet sieving is interesting for materials that are not sensitive to corrosion. Compared to dry sieving, wet sieving allows high throughputs under high-pressure conditions. It implies putting particles in a solution. It also allows separating particles down to a few μm.

11.1.4.2 Air Classification

The other method used employs cyclones and filters to separate particles according to their sizes [2, 49, 114, 120–122]. The principle of a cyclone is given in Fig. 11.44 [2, 114]. The powder is introduced into a spiral-shaped air current flowing toward the center. The air vortex has suitable values of tangential and radial velocities so

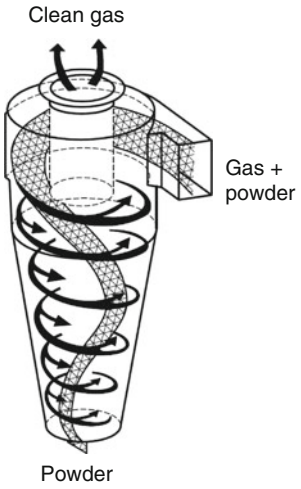


Fig. 11.44 Schematic of a cyclone used for air classification. Reprinted with kind permission from ASM International [2, 114]

that a certain part of the powder is accelerated by the centrifugal force toward the periphery of the whirl, the other part being carried by the air current toward the center of the whirl by aerodynamic means. The shape, size, and specific mass of particles individually determine which direction they will take in the air current. The particle trajectories depend on their momentums when they follow a circular trajectory. The heavier particles will follow the gravity force and thus will be separated from the lighter ones following the swirl flow. The control parameters are the gas pressure drop, the cyclone dimensions, and the inlet particle concentration. It is possible to separate particles down to a few tenths of μm. This method is often used in production to classify particles with sizes below 44 μm, because screens below that value are impractical for production processes [2].

11.1.5 Characterization

As already underlined coating properties depend on the spray process chosen, its optimization but also, to a large extent, on the powder properties. It is thus of primary importance to characterize the sprayed powder parameters such as its chemistry (composition and purity, elements distribution, phase analysis) size distribution, particles morphology and shape, apparent density, and flow ability [115–118].

11.1.5.1 Sampling

To characterize powders, generally a rather low quantity (few grams to few tens of grams) is necessary, compared to a batch of powder representing a few tens of kilograms. It is thus important to pick up a representative sample. The sampling can

be achieved by using an especial "sampler" described by ASTM Standard [123]. It consists of two concentric cylinders that can be twisted relative to each other, capturing powder from specific location within a container. Samples, used in the different characterization technique [2] from different locations, are then combined, blended, and divided.

11.1.5.2 X-ray Diffraction

Phase identification and crystallinity analysis of the powders is carried out with the X-ray diffraction (XRD) technique [124]. The most popular technique is the Debye–Scherer method, employing monochromatic X-radiation. The surface analyzed is typically 15×3–$5\ mm^2$ and the depth analyzed, depending on the material, is between a few μm and 50 μm. The method is based on the relationship existing between the diffraction angle θ and the d-spacing characterizing phase, between the crystallographic planes, according to the Braggs equation. The spectra obtained are compared to databases such as JCPDS (Joint Committee on Powder Diffraction Standards, USA) using devoted computer codes that permit to identify the crystallized phases. The relative phase ratios can be calculated by comparing the areas under peaks in the X-ray diffraction (XRD) pattern. To determine the distribution of phases, the limit of detection corresponds about to 5 wt%. Peak area under corresponding peaks of different phases can be profile fitted using an automatic powder diffraction, APD, profile-fitting program. By measuring the width of X-ray peaks it is possible to obtain the size of the individual crystals or grains.

11.1.5.3 Elements Distribution

Most powders contain different materials and it might be important to determine their distribution in order to see how they are homogenously distributed within each particle. To achieve that particles must be mounted in epoxy resin, using vacuum impregnation, and then the samples polished, using standard metallographic procedures. The samples are then disposed in a SEM (Scanning Electron Microscope) equipped with Electron Micro Probe Analysis (EPMA) or Energy Dispersion Spectroscopy (EDS). These probes allow mapping of the elements (or chemical characterization) within the particles. The principle of the method is based on the interactions between electromagnetic radiation and matter, analyzing X-rays emitted by the matter when hit with charged particles [124]. Each element has a unique atomic structure allowing X-rays characteristics of it. The high-energy beam of charged particles (electrons or protons) is focused into the sample. When the incident beam excites an electron in an inner shell of the atom, ejecting it from the shell it creates an electron hole where the electron was. Then an electron from an outer, higher energy shell fills the hole, and the difference in energy between the higher energy shell and the lower energy shell is released in the form of an X-ray. The number and energy of the X-rays emitted from a specimen are measured by an

energy dispersive spectrometer. The energy of the X-rays is characteristic of the atomic structure of the element. The minimum zone analyzed is about tens μm^2.

11.1.5.4 Composition and Purity

Chemical composition of particles can be obtained by different techniques:

1. *Inductively coupled plasma emission spectroscopy (ICPES)* [125]. A suspension of fine particles is injected in a r.f. plasma where the solvent is first vaporized. The particles contained in the suspension are further heated, melted, and vaporized. The formed vapors mixes with the plasma gases and are heated to sufficiently high temperatures to be identified through their own emission spectrum which serves as the basis for the estimation of their initial concentration in the suspension using emission spectroscopy.
2. *X-ray fluorescence spectroscopy*. The principle is the same as that of EDS, except that the high-energy beam is a primary X-ray excitation source from an X-ray tube [126]. Atoms absorb the X-ray that transfers all of its energy to an innermost electron: "photoelectric effect." If the primary X-ray energy is sufficient, electrons are ejected from the inner shells, creating vacancies. As the atom returns to its stable condition, electrons from the outer shells are transferred to the inner shells giving off a characteristic X-ray whose energy is the difference between the two binding energies of the corresponding shells, allowing one to nondestructively measure the elemental composition of a sample. This process is called "X-ray Fluorescence" or XRF. A typical X-ray spectrum from an irradiated sample will display multiple peaks of different intensities. The spectral lines used for chemical analysis are selected on the basis of intensity, accessibility by the instrument, and lack of line overlaps. The area analyzed has a minimum diameter of 10 mm and a maximum one of 25 mm and its depth, depending on the analyzed material is below 100 μm.
3. *EDS* (see Sect. 11.1.5.3.)

11.1.5.5 Particle Shape

The most direct way to determine the shape and of course the size of a particle is to look at it [118, 119]. To get complete information it is however necessary to observe particles both from the outside and inside. If the size of the particle is >1 μm, then optical microscopy (OM) working with visible light is fine. For more precision SEM is used.

To observe particles from the outside, one of the problems is to obtain a regular distribution of particles on the surface without overlapping. Particle size measurements are made either directly at the microscope or from pictures taken using the microscope. The main challenge is in determining the size and shape of three-dimensional particles on the basis of planar images. Several procedures have been employed for making these measurements but now image analysis methods are

used with computers allowing measuring a large number of particles rather quickly. For submicron particles it is necessary to use scanning electron microscopy (SEM), but the total amount of particles is smaller and it is essential to make sure that the sample examined is representative of the entire powder batch. The morphology observation allows recognizing the different shapes [4]: spheres with dense surface, sphere with rough surface and irregularly rounded, spheres without pores, porous sphere, hollow spheres, dense, angular and blocky porous, coated with dense coating, coated with porous coating.

This observation must be completed by examination of particle cross sections obtained through the encapsulation of the powder in a polymeric cylindrical mounts, which are then polished, and subject to microscopic examination, (see Sect. 15.3) giving information on the particles porosity and internal morphology (assuming that the polishing step has not modified them).

11.1.5.6 Size Distribution

The size distribution is generally calculated by weight in production sieving. The average or mean particle size is not sufficient and it is mandatory to know the upper and lower limits of the powder size distribution. The 90th, d_{p90}, and 10th, d_{p10} percentiles of the distribution define these limits. It means that only 10 % of particles are below d_{p10} and 10 % are over d_{p90}. It is assumed that the size distribution is Gaussian, which is not necessarily true if for example the distribution is bimodal (two-peaks in the size distribution). Moreover the average or mean size of particles and the skew of the distribution are also key parameters [2]. The skew corresponds to the difference between the 50th percentile and the mean size. For example skew can be very important with bimodal distributions. An important problem is the lack of precision for the small values of d_{p10}, especially when particle distribution is obtained by sieving.

(a) Light Scattering

When a beam of light strikes a particle, part of it is transmitted, part is absorbed, and part is scattered. Light scattering is divided into three domains [127] based on a dimensionless size parameter, α, which is defined as

$$\alpha = \pi d_p / \lambda, \tag{11.1}$$

where πd_p is the circumference of the particle and λ the wavelength of incident radiation. If $\alpha << 1$: Rayleigh scattering (Small particle compared to wavelength of light)

$\alpha \approx 1$: Mie scattering (particle about the same size as wavelength of light)
$\alpha >> 1$: Geometric scattering (particle much larger than wavelength of light)

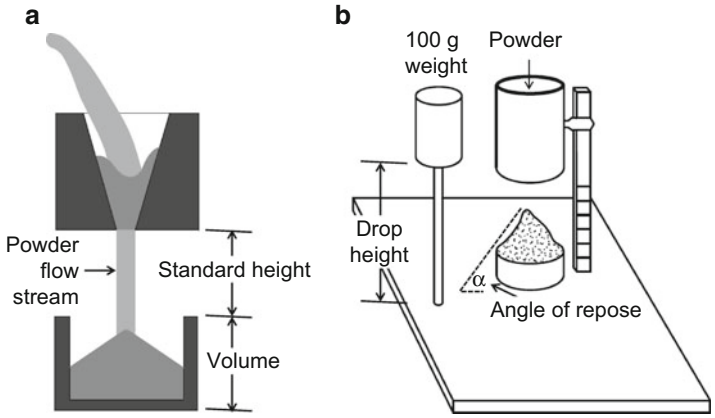


Fig. 11.45 (**a**) Hall flow ability test and (**b**) Angle of repose test. Reprinted with kind permission from ASM International [2]

When $\alpha >> 1$ particles cause Fraunhofer diffraction. The intensity of the forward-scattered light (i.e., light traveling in roughly the same direction as the incident light) is proportional to $d_p{}^2$. The relationship between scattering angle (θ) and d_p is

$$\sin\theta = 1.22\lambda/d_p \tag{11.2}$$

The light source is usually a He–Ne laser with $\lambda = 0.63$ μm. For this wavelength the reliable particle size range is 2–100 μm. Light-scattering methods can be used with particles suspended in either a gas or a liquid, they are rather fast and accurate and only a small sample is needed.

(b) Coulter Counter

Particles suspended in an electrolyte are forced to flow through a narrow orifice on both sides of which an electrode is immersed. As a particle passes through the orifice, it displaces an equivalent volume of electrolyte and causes a change in resistance, R [49]. The magnitude of this change is proportional to the particle size. R changes are converted to voltage pulses that are amplified, sized, and counted to produce data for the size distribution of the suspended particles. The Coulter counter measures particles in a size range 0.5–100 μm.

11.1.5.7 Flow Ability

Flow ability measurements are easy and inexpensive. The most used one, Hall flow ability test presented in Fig. 11.45a, consists in measuring as a function of time the powder flow through a metering orifice at the base of a funnel. The longer is the

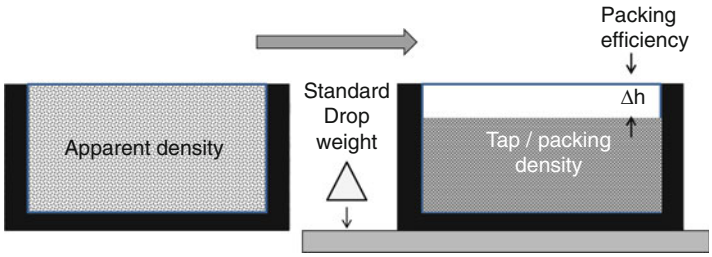


Fig. 11.46 Principle of apparent and tap/packing density measurement. Reprinted with kind permission from ASM International [2]

time for a given powder mass (generally 50 or 100 g) to flow, the poorer is its flow ability [128]. Of course best results are obtained for spherical and dense particles see for example Table 11.2. Another test, also used, is that of angle of repose of the mound of powder formed by dropping it from a specified height through a flow orifice, as shown in Fig. 11.45b. The steepest is the angle of repose; the poorest is the powder flow ability [2].

Another important problem related to powder flow ability is its moisture content. As powders have generally rather high specific surface area they can retain or absorb relatively high quantities of moisture, especially those which material is hygroscopic (water absorbent). This moisture can modify the flow ability of the powder [129] and must be eliminated. This is achieved by placing the powder in the oven prior to spraying, at a temperature slightly over that of water vaporization at atmospheric pressure: 100 °C, and using a heated powder feeder. Of course if the material to be dried is a polymer, the preheating temperature will be less than 100 °C. The preheating time should be at least 8 h. The smaller are particle sizes, the larger is their surface-area-to-volume-ratio, which increases almost exponentially as the particle size decreases, and thus their ability to stock moisture. The preheating time must be increased correspondingly.

11.1.5.8 Apparent Density

Powders packed together will never reach the density of the material with which they are made. Their apparent density or packing density, under gravity conditions, includes all spaces between them and it will depend on particles size distribution, shape, and morphology. As volumetric feeders are based on the apparent density the feed rate changes for the same powder (shape and morphology) if the particles size distribution is modified. The apparent density is very simply measured as shown in Fig. 11.46 [2].

11.1.5.9 Surface Area

The method is based on the adsorption of gases onto a particle surface at low temperature. Brunauer, Emmett, and Teller (BET) method consists in estimating the particle size by determining the surface area of the powder, which is calculated from the N_2-isotherm observed at the boiling point of N_2 [49]. The mass of gas adsorbed is measured as a function of gas pressure at a fixed temperature (typically liquid nitrogen). Since one nitrogen molecule requires a surface area of 0.162 mm^2, the surface area of the particle can be easily estimated in m^2/g. The adsorbates volume, V_m, per unit mass of solid for monolayer coverage is determined by varying the relative pressure, p/p_0, in the range between 0.05 and 0.2, p being the gas pressure and p_0 the saturation vapor pressure for the adsorbates at the adsorption temperature. If V_a is the adsorbates volume at relative pressure p/p_0, V_m is determined by plotting $p/[V_a \cdot (p - p_0)]$ versus p/p_0, that gives a straight line from which V_m can be determined. The specific surface area, S, depends linearly on V_m. Once the particle surface is known the particle radius, r_p, if the particle is a sphere, can be calculated by $r_p = 3\, m_p/(\rho_p\, S_p)$, where ρ is the particle specific mass and m_p its mass.

11.1.6 Powder Feeders

The powder feeder is as important as the spray gun to achieve reliable and reproducible coatings with required properties. It must produce a carrier gas stream in which the powder feedstock is entrained and delivered to the powder injector fixed on the spray gun. The powder issued from the powder feeder must have good flow ability, a regular and reproducible flow rate, whatever may be the particles size distribution, specific mass, and morphology. Of course the carrier gas flow rate must be adjustable, independently of the particle mass flow rate, to transfer to particles the acceleration needed for optimum trajectories when radially injected or that adapted to optimum axial injection. Depending on the spray process used, the powder feeder must be capable of operation at low pressures, atmospheric pressures, or higher as needed for example in HVOF, HVAF, and cold spray processes.

Of course all these requirements are difficult to satisfy, especially if the powder flow ability is poor and/or the particle size is below 10–15 μm. The conventional powder feeders (distributing particles with sizes larger than 10–15 μm) are generally categorized in three basic types: gravity-fed hoppers, volumetric powder feeders, and fluidized-bed powder feeders [2].

11.1.6.1 Gravity Fed Hoppers

This is the oldest type. It comprises a simple cylindrical container, often with a funnel shaped bottom, in which the particles flow freely by gravity. The powder flow rate is controlled by a needle valve located in the funnel exit port. The

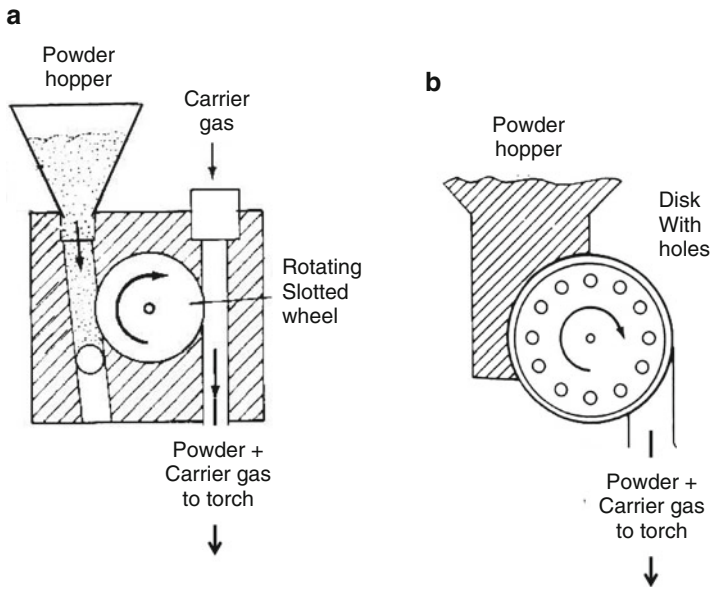


Fig. 11.47 Volumetric powder feeder (**a**) rotating wheel system and (**b**) rotating disk system. Reprinted with kind permission from ASM International [114]

powder falls in a pipe where the carrier gas flows. The feeder can be assisted by a vibration device to improve the powder flow. The system is of course very simple and inexpensive, but it works well only if the power flow ability is good, i.e., with powders, with particles diameters above 10–15 μm, and with adapted morphologies (close to spherical). The powder flow rate is linked to the quantity of powder contained in the container and thus is not very accurate. Of course such feeders cannot be pressurized. It is still used, mainly in powder flame spraying.

11.1.6.2 Volumetric Powder Feeders

They utilize a mechanism to deliver packets of powder in a carburetor, from where the carrier gas entrains them to the particles injector. The different mechanisms involved are screws, slotted wheel, and disk with holes, as shown in Fig. 11.47. In these cases, the transport wheel rotates within the powder bed. Slots or holes are filled with powder from the container, scalpers scraping the excess of powder from the tops of slots or holes in order to feed the carburetor with a predetermined volume of material with each rotation of the wheel or disk. Holes or slots filling can be improved by vibrating the powder feeder, especially for poor flow ability powder. For screw feeders, the end of the screw enters a tube that has the same

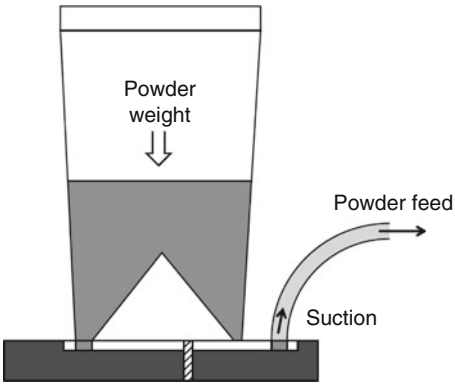


Fig. 11.48 Suction-type volumetric powder feeder. Reprinted with kind permission from ASM International [2]

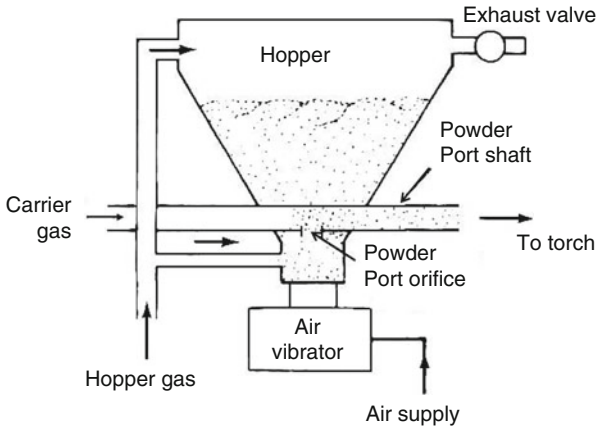


Fig. 11.49 Fluidized-bed powder feeder. Reprinted with kind permission from ASM International [114]

function of the scalper to control the volume distributed by each rotation of the screw into the carburetor.

In most cases particles, fed by gravity into the carburetor, are entrained to the feed hose by a positive gas pressure, with a controlled flow rate. It is also possible to use suction-type volumetric feeder. They comprise a continuous circumferential groove in a powder-transport wheel, filled with powder by gravity [2], as shown in Fig. 11.48. A counter-rotating, inverter conical stirrer helps maintaining a more uniform powder bed density over the feed slots to pack powder into the groove and achieve a uniform stable filling. Powder is picked up by a suction Venturi, through which the carrier gas flows, creating a vacuum that sucks the powder out of the transport wheel [2].

One of the main drawbacks of these powder feeders is the pulsation of the powder feed rate due to the periodic feeding of holes, slots and screw pitches. Different solutions can be used to circumvent the problem: The use of a "cyclone mixer" where powder, exiting the carburetor, is fed tangentially and exit it axially, is an option which can help in damping feed rate pulsations under certain

conditions. Alternately, The use two powder feeders operating out of phase, feeding the same carburetor, to dampen powder feed pulsations.

11.1.6.3 Fluidized-Bed Feeders

In these systems the powder is continuously agitated in a fluidized bed by the fluidizing gas. A pipe with a hole, or port orifice, crosses the bed and the carrier gas entrains the powder at a uniform rate, as depicted schematically in Fig. 11.49 [114]. The bed must be continuously fluidized and the volumes of gas and powder removed continuously replaced [2]. A gravity and/or vibrator feeder is used to maintain the flow of the powder from the hopper into the bed. While such powder feeders are less sensitive to particles morphology, they are more dependent of particle size distribution and mass density. This is due to the way fluidized beds work: particles are fluidized when the pressure drop across the bed is comparable with the weight of the bed. Moreover, for powders with a broad particle size distribution, the smaller and lighter particles will have a tendency to be transported outside the fluidized bed and entrained with the fluidizing gas. The separate control of fluidizing and carrier gases is also trickier.

11.1.6.4 Powder Feeders for Small Particles

To feed powders with particle sizes below 10–15 μm is quite a challenge due to their poor flow ability and their natural tendency to agglomerate and stick together forming bridging and "rate-holes" in the hoppers. Conventional powder feeders cannot be used in these cases and a wide range of novel approaches have be developed for such powders on a case by case basis. In the following, a few examples of such feeders are described.

(a) Powder Pump

A new device for the transport of powders, which sizes are below 10–15 μm, has been developed. The powder pump contains a vacuum source, a pressure source/powder feeding gas, a powder suction line, the powder transport line to the torch, four valves made of special elastic tubes that can be opened and closed mechanically by pistons and a defined volume (dose). If the valves numbers 1 and 2 are closed and the valves 3 and 4 are open, the powder will be sucked through the suction line out of a container into the dose due to the pressure drop produced by the vacuum pump. The dose can have a calibrated volume in the range of 10–1,000 mm^3 as a function of application. After that, the valves 3 and 4 are closed and valves 1 and 2 opened. Now the powder will be pressed out of the dose into the powder feeding line by the pressurized transport gas. The pump design guarantees a 100 % filling and cleaning of the dose. Under atmospheric conditions the working

pressure will be less than 0.2 MPa depending on the powder to be fed and the length of the powder transport line. The powder container can be even an open box, where the powder will be sucked perpendicular out of it. Although, a well-designed powder silo is of advantage regarding feeding regularity and precision.

(b) Vibration Feeder

Vibration feeders have also been used for the feeding of fine powders either through a linear or angular vibration motion, which pushed the powder upstream of a lightly inclined linear or spiral ramp. A thin layer of powder is transported this way at a rate, which depends on the amplitude and frequency of the vibration. At the end of the ramp, the powder falls by gravity into the carburetor where it is mixed with the powder transport gas and conveyed into the powder transport line. For a close control on the transport gas flow rate, the ramp and the vibration mechanism has to be placed inside a gas tight container in which the carrier gas is introduced at a well-controlled gas flow rate. While this type of powder feeders works well with most powder at low feed rates (of the order of grams per minute) very fine submicron powders, will have the tendency to agglomerate, as they are transported over the ramp, forming small "balls" at the carburetor discharge point These will induce important fluctuations of the powder feed rate.

11.1.6.5 Powder Feed Rate Control

Closed-loop feed-rate controllers are necessary on powder feeders to keep the powder mass feed rate as constant as possible [2]. Most of them operate on a loss-in-weight principle. The whole feeder is placed on a sensitive electronic balance that measures the weight loss, as powder is fed to the transport line and injector. The rate of weight change is electronically compared to a preset feed rate. Any variation is compensated by changing the rotation speed of the powder transport wheel, disk, screw, or the gas pressure in order to keep the mass flow as constant as possible.

11.1.7 Hazards Related to Particulate Materials

11.1.7.1 Micrometer-Sized Particles

Particles spread in the atmosphere, when handling powders and/or filling a powder feeder, can be inhaled. After particles are inhaled, depending on their average size, they penetrate to varying depths in the tracheobronchial tree. The tracheobronchial tree is subdivided into three sections: pharynx; trachea, and the bronchi (including the bronchioles) covered by epithelial cilia and mucus cells (the cilia are animated

by Brownian motion); respiratory bronchioles and the pulmonary alveoli covered by an epithelium. The major risks encountered from particles in surrounding atmosphere resulting from the powder feedstock, including dust, created during the spray process have been described in 2003 by Hériaud-Kraemer and his coworkers [130].

Authors [130] have studied:

- The varying penetration depths in the tracheobronchial tree, with the three major factors affecting the particle deposition: morphology, respiratory parameters, and physical characteristics of the particles
- The pulmonary retention level and pulmonary clearance
- The toxicity of some metallic powders

In parallel the authors have also made a survey of French companies that uses thermal spray technology on a large scale. More recently a similar study, related to worker exposure monitoring of suspended particles in thermal spray industry, has also been published in 2007 [131]. Results showed that both particles and heavy metals concentrations were low, even in the production site, which was the most susceptible area. The only exceptions were observed in the case of cleaning and maintenance activities in the thermal spray booth (including powder feeder cleaning) and in the case of spraying outside the booth. Of course low concentrations are observed when most of activities that could produce high-particle concentrations are conducted in closed, well-ventilated systems.

11.1.7.2 Nanomete-Sized Particles

If the manipulation of micro-sized particles seems to be correctly managed, it is another story with nanometer-sized ones. The safety of engineered nanomaterials and the factors those are responsible for their associated hazards are not yet fully understood [132]. The main point for health risk assessment is “genotoxicology” (the study of genetic aberrations following exposure to test agents), as Deoxyribo Nucleic Acid (DNA) damage may initiate and promote carcinogenesis, or impact fertility. If considerable attention has been given to the toxicity of engineered nanomaterials, the importance of their genotoxic potential on human health has been largely overlooked. The review by Singh et al. [132] focuses on the reported abilities of nanoparticles, whether metallic, metal oxides, or others, to damage or interact with DNA, and their “ecogenotoxicity” is also considered. They have highlighted areas that require further attention and recommendations to improve our understanding of the genotoxic potential of engineered nanomaterials are addressed. Their work shows the interest, at least for the feedstock, to have it as suspensions or solutions.

11.2 Wires

Contrarily to powder spraying, the feedstock is introduced as wire (ductile metals or alloys), rod (sintered ceramics), or cord (cellulosic or plastic casing filled with ceramic particles with either an organic or a mineral binder). Wires, rods, and cords are continuously advanced (in most cases axially) at a velocity allowing the spray gun to melt their extremity. The molten material is atomized and accelerated by an auxiliary gas fed in the spray gun and only fully melted particles are accelerated towards the substrate, which is not the case of powders. All these feedstocks are sprayed with flame or HVOF guns, while wire-arc gun is exclusively used for wires or cored wires.

11.2.1 Wire Materials

Wires, see Fig. 2.23a, are necessarily made of ductile materials. For wire arc spraying, they comprise aluminum, copper, iron, molybdenum, nickel, tin, titanium, and zinc base. For flame spraying, the same materials except titanium but with also lead and silver base. Their diameters are between 1.2 and 4.76 mm (1/16 to 3/16 in.). They are supplied in coils, wound on plastic spools, or production packs (drums). Larger, stiffer wires ($d > 2$ mm) are more difficult to feed as uncoiling requires more force and larger wire tension. Moreover the stiffer is the wire the larger is the wire guide erosion. For a regular and reproducible feeding, it is mandatory that wire diameter is well calibrated and its surface as smooth as possible.

Compared to powders their main advantage is the deposition rate. For example, Lester [133] indicates that when spraying Zn/Al (85/15) wires with an oxy-propane flame the throughput is 38 kg/h in continuous mode with a 4.76 mm wire. For wire arc, working with an arc current of 700 A, the throughput reaches 53 kg/h in continuous mode with 3.17 mm wires. The choice between both techniques depends strongly on the engineering situation. The following remarks [133] can be made:

- Typically for Zn and Al, flame spray has higher deposition efficiency than arc spray, which is not necessarily the case for all materials
- Arc-spray parameters are set by simple switches and will not fluctuate
- Flame-spray parameters need to be reset each time the gases are turned off or changed
- Arc spray is very simple to use; once parameters are set, the operator pushes a button, pulls the trigger, and is quickly spraying
- With arc spray, no consideration is required for safe use and storage of flammable gases
- Arc spray only requires the wire to be changed, whereas flame spraying also requires gas bottles to be replaced

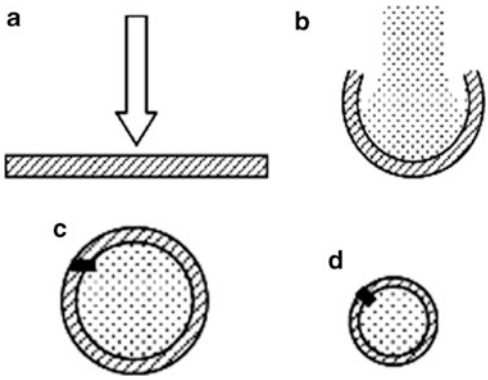


Fig. 11.50 Schematic diagram showing the cross section of the cored wire at various preparation stages. (**a**) Sheet of ductile metal or alloy, (**b**) U-shaped metal or alloy strip filled with powder, (**c**) rolling to 3.8 mm diameter cored wire, and (**d**) rolling to final 2 mm diameter cored wire. Reprinted with kind permission from Elsevier [134]

- Flame spray typically has a finer coating finish, with less porosity and oxide than arc-spray coatings at equivalent spray rates
- Arc-sprayed aluminum has bond strength approximately 2.5 times higher than flame-sprayed aluminum but its oxidation is almost twice higher

11.2.2 Cored Wires

Non-ductile materials can also be used in cored wires, generally wire arc sprayed. They consist of an outer sheath made of ductile material surrounding one or more powdered non-ductile metals or ceramics, as shown in Fig. 2.23b. To prepare cored wires, for example, the ductile metal or alloy belt with a cross section of 12×0.3 mm^2, is rolled [134, 135]. This process gives a U-shaped cross section with the help of three pairs of former rollers Fig. 11.50a. Then different kinds of powders are fed in by powder-feeding equipment, Fig. 11.50b. The U-shaped steel strip containing powders is pressed by four pairs of covering rollers to form cored wires 3.8 mm in diameter, Fig. 11.50c. Then the obtained cored wire is pulled in sequence through 14 dies with gradually reduced diameter to obtain the final cored wire 2 mm in diameter, Fig. 11.50d.

An example of cored wire cross section is presented in Fig. 2.23b and its content in Fig. 2.23c [135]. During the wire arc spraying procedure, the sheath material is fully melted and the powder contained totally or partially melted, the fully melted material being atomized into droplets by compressed air flow. Droplets and partially melted particles are directed towards the substrate, where the form the coating.

11.2.3 Wire Feeders

The driving of the wires is typically achieved either by air motor or electric motor and gearbox arrangement [2, 133]. Three different ways are used to drive wires.

Push only: The wire is pushed from the drive unit to the gun. If the gun is lightweight, the wire position can fluctuate from the drive to the gun reducing the stability and limiting the pushing length to around 5 m. This system is convenient for hand spraying.

Pull only: A drive unit mounted in the gun pulls the wire. The wire position is well defined and in wire arc spraying they are is much more stable, thanks to the feeding rollers that are much closer to the last wire guide. Of course the gun weight is increased and the length of the wire supplied is limited to 5 m. This system is commonly used for automatic spraying.

Push/*pull*: This is obviously a combination of the above two methods, the wire being driven to and pulled from the gun. The wire tip is very stable and its length can reach 20 m. Synchronizing the two-drive units is more complex and the gun weight is higher. Figure 11.51 from [2] schematically represents the principle of wire entrainment device.

The wire entrainment is achieved with electrical or compressed air motors, the first one being the more reliable.

11.3 Rods

Rods are devoted to flame spraying, with an especially designed gun, oxide materials (alumina, alumina-zirconia, chromia, zirconia stabilized with magnesia or calcia, alumina-titania, magnesia-alumina, zirconium silicate,. . .). Rods are manufactured by extrusion followed by sintering and finally machining. Diameters of commercialized rods are: 3.16 mm (1/8″), 4.75 mm (3/16″) and 6.35 mm (1/4″) and their length is 608 mm (24″). This length implies changing the rod very often during the spray process. Figure 11.52 presents different rods from Rockide-Saint Gobain.

11.4 Cords

Cords are the equivalent of wires but they are devoted to feed into flame spray guns ceramic or non-ductile materials. The internal part of the cord is the powdered non-ductile or ceramic material, while the external sheath is made of cellulosic material allowing the flexibility of the cord. They are manufactured by co-extrusion of the sheath and internal material. Ceramic or non-ductile material particles are agglomerated either with an organic binder, decomposing around

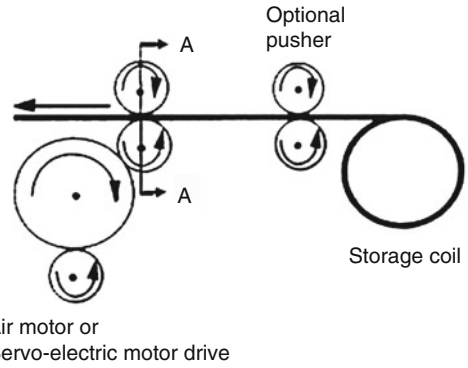


Fig. 11.51 Wire feeding principle. Reprinted with kind permission from ASM International [2]



Fig. 11.52 Rods from Rokide (courtesy of Saint Gobain)

250 °C and that has completely disappeared at 400 °C, or a mineral binder (for example bohemite: $Al(OH)_3$) that keeps the cohesion of ceramic particles up to temperatures close to their melting point. These flexible cords have lengths up to 120 m and must not be regularly and frequently changed as rods. The diameters are the same as those of rods. Figure 11.53 presents a spool of flexicord from Saint Gobain.

11.5 Polymer Particles

11.5.1 General Remarks

11.5.1.1 Definitions

A polymer is a large molecule (macromolecule) composed of repeating structural units. These subunits are typically connected by covalent chemical bonds. The basic

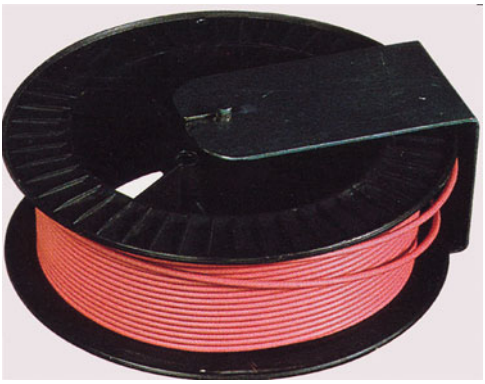


Fig. 11.53 Flexicords of Saint Gobain (courtesy of Saint Gobain)

property of a polymer depends on its constituent monomers, but its microstructure is essentially linked to the arrangement of these monomers within the polymer at the scale of a single chain. These basic structural properties mainly control the bulk physical properties of the polymer. As polymer molecules are so large, they generally pack together in a nonuniform fashion, with ordered or crystalline-like regions mixed together with disordered or amorphous domains. In some cases the entire solid may be amorphous, composed entirely of coiled and tangled macromolecular chains. Crystallinity occurs when linear polymer chains are structurally oriented in a uniform three-dimensional matrix. Increased crystallinity is associated with an increase in rigidity, tensile strength, and opacity (due to light scattering). Amorphous polymers are usually less rigid, weaker, and more easily deformed. The three factors influencing the degree of crystallinity are the chain length, the chain branching, and the interchain bonding. On heating or cooling most polymers undergo thermal transitions changing their morphology: the melt transition, T_m, temperature at which crystalline domains lose their structure, or melt and the glass transition, T_g, temperature below which amorphous domains lose the structural mobility of the polymer chains and become rigid glasses. A more detailed description of polymers is out of the scope of this book and the interested reader can see the books of Mc Crum et al. [136] or the paper of Cowley [137].

Thermosetting plastic (thermoset) is a polymer material that irreversibly cures. The cure can be performed through heat (generally above 200 °C) or a chemical reaction (two-part epoxy, for example) or irradiation such as (electron beam, for example). The curing process transforms the resin into a plastic or rubber by a cross-linking process. The cross-linking process forms a molecule with a larger molecular weight, resulting in a material with a higher melting point. During the reaction, a solid material can be formed. To our best knowledge, only a few attempts have been made to spray thermosets. External substrate preheating to or above the curing temperature might enhance the deposition and curing behavior during the thermal spraying of thermosetting polymers [138].

11.5.1.2 Polymer Coatings

Organic coatings can be sprayed or painted as liquids with the help of organic solvents, but it produces emission of volatile organic compounds (VOCs) increasing the ozone formation, which is less and less recommended. That is why polymers are often deposited directly from dry powders to avoid the use of organic solvents. Electrostatic spraying and fluidized-bed dip coating are considered to be the two primary methods for polymer powder deposition [138, 139]. Both methods are based on capillary fusion of powder particles on either preheated substrate surfaces or during baking.

That is why thermal spraying has been successfully used to deposit polymer coatings [140]. According to Ivosevic [141] the key advantages of using thermal spray are the following:

- Solvent-free deposition
- Possibility to coat large objects in the field under different environmental conditions
- Ability to process polymers with high melt viscosity ($>10^2$ Pa s)
- Ability to produce "ready-to-use" coatings without the need for post-deposition processing
- Possibility to spray polymer/ceramic composites with high reinforcement contents (>5 vol.%)

Unfortunately these advantages are counterbalanced by:

Lower deposition efficiency than conventional means, lower quality surface finish, higher process complexity, and jet/flame temperatures

Potentially degrade polymeric feedstock or previously deposited material with hot gases of the spray process (plasma or flame)

Polymers physical, thermal, and mechanical properties are very different from those of metals, alloys, ceramics, and cermets, thus requiring adapted spray conditions

11.5.2 Sprayed Polymer Powders

Thermally sprayed polymer coatings are increasing in importance as protection against corrosion (gasoline, diesel oil, alcohol, salt spray, more or less acidic liquids, various chemical,. . .) and wear (impact, abrasion, cavitation, sliding, especially due to their low friction coefficient against many materials).

However, according to polymer physical, thermal, and mechanical properties, rather different from those of conventional powders, to their rather easy thermal degradation over low temperatures, the spray parameters (as described in Chap. 13) are rather narrow, especially the particle size distribution, the velocity, and temperature distribution of the hot gases of spray process used, the temperature control

of substrate and coating during spraying, and the substrate preheating prior to spraying.

11.5.2.1 Polymers

Compared to conventional powders (metals, alloys, ceramics, cermets), polymer particles have very different properties:

Polymer thermal conductivity is lower (a few tenths of W/m K) than that of other materials, even lower than that of zirconia (about 1 W/m K). Thus during its flight in the hot gases, steep temperature gradients will develop within the particle with the core unmolten and the surface overheated (see Sect. 4.3.3.3). If the particle is small, overheating resulting in polymer degradation,

According to the rather low mass density of polymers (typically between 1,000 and 2,200 kg/m^3) particle velocities achieved prior to impact will be higher than those of conventional particles for the same particle size and trajectory in the same flame or plasma jet. Polymers typically have three to seven orders of magnitude higher melt viscosity and an order of magnitude lower surface tension than metals [142]. The viscosity is strongly influenced by the polymer molecular weight, M_c, especially over a critical value of M_c. With metals, at the end of particle flattening the inertia force is balanced by the surface tension force (high flattening Weber number), while for polymer particle it is the viscous flow resistance (high flattening Reynolds number). Moreover the viscosity of molten polymer is not Newtonian and presents a shear thinning behavior, implying to consider both the temperature and shear rate when calculating it.

The solidification and spreading kinetics of a polymer particle are also strongly different from those of conventional particles [142]. For example Isocevic et al. [142] explain that under typical flame spray conditions the Peclet number, Pe, for a zinc droplet is in the range 1–10, whereas Pe for a Nylon-11 droplet is almost three orders of magnitude higher ($Pe \approx 3{,}000$). Thus the effect of solidification during Nylon-11 droplet impact can be neglected, the spreading and cooling of Nylon splats occurring over two significantly different time scales. By definition $P_e = t_c/t_s$, where the heat conduction time $t_c \approx {d_p}^2/\alpha$, d_p being the particle diameter (m) and a its thermal diffusivity (m^2/s) and the spreading time $t_s \approx d_p/v_p$, v_p being the particle impact velocity (m/s).

At last larger thermal expansion coefficients of polymers (values up to 150×10^{-6} K^{-1}), compared to those of metal substrates, require spraying rather thin passes.

The other problem is that polymer powders sprayed by electrostatic spraying and fluidized-bed dip have size distributions that are not adapted to thermal spray, requiring sizes approximately between 50 and 200 μm [143]. Thus in the available powders those below 50 μm must be eliminated and the bigger ones cryo-milled in liquid nitrogen.

The different thermal sprayed polymers are the following:

Table 11.4 Properties of Nylon 11, PET, PEEK, PEK, PPS, PES according to powder suppliers

	Nylon 11	PET	PEEK	PEK	PPS	PES
Mass density (kg/m^3)	1,040	1,340–1,400	1,320	1,300	1,400	1,370
Melting point (°C)	175–191	>250	343	–	–	–
Max service T (°C) Vicat[a]	140–160	170	160	–		–
Hardness (MPa)	100 (R) Rockwell	–	28 (HV)	34.4 (HV)	26.5 (HV)	50 (HV)
Tensile strength (MPa)	15–44	55–75	90–100	110	86	90
Flexural strength (MPa)	51.6–89.6	–	185	183	145	120
Glass Trans. T (°C)	42	75	143–148	162	90	225
Water absorption ASTM D-570 %	0.230–1.9	0.16	0.1	–	–	–
Thermal conductivity (W/m K)	0.230–0.346	0.15–0.24	0.25	–	–	–
CTE (μm/K m)	100–150	70	–	–		–

[a]Vicat: determination of the softening point for materials that have no definite melting point, such as plastics. It is taken as the temperature at which the specimen is penetrated to a depth of 1 mm by a flat-ended needle with a 1 square mm circular or square cross section. For the Vicat A test, a load of 10 N is used. For the Vicat B test, the load is 50 N

Table 11.5 Properties of fluoropolymers:polyvinylidene fluoride (PVDF), ethylene chlorotrifluoroethylene (ECTFE), perfluoroalkoxy alkane (PFA), and fluorinated perfluoroethylene-propylene (FEP). Reprinted with kind permission from Elsevier [152]

Property	PVDF	ECTFE	PFA	FEP
Mass density (kg/m^3)	1,780	1,680	2,150	2,150
Melting point (°C)	155–170	240	300–310	250–280
Max service T (°C)	150	166	260	205
Hardness (Shore D)	D70-80	D75	D63-65	D55_66
Tensile strength (MPa)	35–52	31–48	28–30	21–28
Flexural strength (MPa)	59–75	48	–	21
Water absorption ASTM D-570 %	0.04	<0.01	<0.03	<0.01

Nylon 11 has been flame sprayed to study its slurry erosion resistance [142], HVOF sprayed [141] to characterize the resulting splats and coatings, PEEK (Poly-ether-ether-ketone) was flame sprayed and laser remelted [144, 145], flame sprayed to study its crystallinity [146], HVAF sprayed to study its degradation and stability [147], plasma sprayed [148], and HVAF [149] sprayed to study splats formation

PTFE (Polytetrafluoroethylene), polyamides, and UHMWPE (ultra high molecular weight polyethylene) were sprayed with high-energy plasma [150] to study their low friction for high contact pressure rolling/sliding systems.

EMAA (Ethylene-methacrylic copolymer) was flame sprayed to study the splats formation [151].

PVDF (fluoropolymer, polyvinylidene fluoride), ECTFE (ethylene chlorotrifluoroethylene), PFA (perfluoroalkoxy alkane), and FEP (fluorinated perfluoroethylenepropylene) were flame and plasma sprayed against corrosion: salt test and liquid immersion tests (pH values −0.7 and 14) [152].

According to Ivosevic [141] up to 2006 many other polymers have been thermally sprayed: Ethyltetrafluoroethylene (ETFE), Liquid-crystalline polymers (LCP), Polyethylene (PE), Polyaryletherketone (PAEK), Polycarbonate (PC), Polyester (PES), Polypropylene (PP), Polyimide (PMR), Polyethylene terephthalate (PET), Polyphenylene sulfide (PPS), Polymethylmethacrylate (PMMA), Bismaleimide-phenolic resin, Cyanate ester thermosets, Ethylene vinylene acetate (EVA), Ethylene-acrylic acid (EAA) copolymer, Polyamides (PA), Phenolic thermosets, Polyarylene sulfide (PAS) Polyester-epoxy resin, Polyether block amide copolymer, Polyether-amide (PEA) copolymer, Polyethylene-polypropylene copolymer, Polysulphone Polyvinylidene fluoride (PVDF) Post-consumer commingled polymers (PCCP), and since 2006, some others, especially fluoro polymers: A few properties of some polymers are summarized in Tables 11.4 and 11.5.

11.5.2.2 Composites Polymer/Ceramic

An important and growing application area is the deposition of polymer matrix composite coatings [153]. The reinforcing filler (ceramic, metallic or organic) modifies the polymer coating mechanical properties and its chemical resistance and oxidation protection [153]. Reinforcing particles also often improves the powder flow ability and reduces shrinkage due to the significantly lower coefficient of thermal expansion of the filler relative to that of the polymer matrix material. The addition of fillers can also initiate a structural ordering of the macromolecules and change the mechanisms and kinetics of polymer crystallization [141].

As in conventional material spraying, it is not simple to achieve a uniform distribution of the filler within the coating when both powders are in the micrometer size range. When the powders are mixed before being injected they achieve different trajectories according to their sizes and mass densities, which is particularly the case for particles of polymer matrix and ceramic or metallic filler having rather different mass densities. That is why a solution consists in injecting separately both powders, which permits also to tailor their heating within hot gases depending on their injection location [154]. However, according to Sumita et al. [155] the result can strongly depend on the filler particle size. In their study the yield stress of nylon filled with silica decreased by 10 % compared to pure nylon when the silica particle size was 220 μm and increased 20 % when the size was 7 nm. Nylon-11 has been intensively used at the beginning because of the large difference between melting temperature (≈183 °C) and the onset of degradation (≈360 °C). Schadler et al. [153] have used nanometer-sized (in the ten of



Fig. 11.54 Schematic showing the gradient shell distribution of silica particles in nylon [153]

nanometer size range) silica filler particles with nylon-11. The nylon and silica particles were dry ball milled together for 48 h in a ball mill using ER 120A zirconia balls with sphericity of 0.7 and Vickers microhardness of 7 to 9 GPa. This procedure mechanically embedded the smaller silica particles near the surface of the nylon powder particles, but did not completely distribute the silica within the nylon particles. A schematic of the subsequent nylon/silica composite particles is shown in Fig. 11.54. The silica particles were either hydrophobic or hydrophilic. Pin-on-disk sliding wear and scratch tests of the HVOF-sprayed coatings showed marked improvements in wear resistance with the addition of nano-sized silica filler. Hydrophobic silica improved the scratch and wear resistance more than the hydrophilic silica. The greatest improvement in properties was for the 15 vol.% silica–nylon 11 composite which showed a 30 % increase in scratch resistance and a 55 % increase in wear resistance.

Petrovicova [156] reported that HVOF sprayed Nylon-11 coatings with 5–20 vol.% of nano-sized silica (7 nm) had higher crystallinity contents than pure Nylon-11 coatings. It was believed that the nano-sized silica acted as nucleation sites, promoting crystallization and therefore increasing the overall crystallinity level.

Jackson et al. [157] who HVOF sprayed the same particles than Schadler et al. [153] found results contradicting the previous indications. Their same study, however, revealed that the crystallinity of the polymer matrix played a significant role in the wear behavior, as emphasized by Schadler et al. [153], and it is believed that this may have contributed to the behavior observed in this case.

Niezgoda et al. [158] have HVOF-sprayed Nylon-11 reinforced with calcinated alumina (size distribution between 350 nm and 2 μm) and fumed silica (20 and 40 nm). Both ceramic powders were dispersed in a Silquest/toluene solution and stirred for 3 h, then dried at 120 °C to remove the solvent. The Silquest was kept at 5 wt% concentrations to maintain uniform wetting of the reinforcement surface. This treatment created a hydrophobic surface, promoting polymer/ceramic adhesion, and reduced agglomeration of the reinforcement particles. From ball-milled composite feedstock powders, batches of ≈300 g of the D60 nylon-11 were dry ball milled with 10 vol.% of ceramic reinforcement for 48 h at 75 rpm with a 900 g standard charge of alumina milling media. The composite powders were then vacuum dried at 35 °C for 24 h prior to HVOF spraying. The microstructures of the coatings appeared dense, coherent, and well adherent to the substrate. Scratch

testing showed up to 30 % improvements in scratch resistance for the nano-reinforced coatings when compared with pure nylon-11.

Stravato et al. [159] have HVOF-sprayed Nylon-11 + Nano-diamonds. Nylon-11 powder was dry ball-milled together with as-received UD90 nano-diamond powder for 48 h in a Norton Ball Mill using zirconia balls. The milling procedure mechanically embedded the hard reinforcement particles into the surface of the Nylon-11 powder particles. Composite powders with 2.5–10 vol.% (7 to 25 wt%) nano-diamond loadings were produced. Qualitative assessment indicated that coating adhesion was improved through the addition of the nano-diamond to the Nylon-11.

Ivosevic et al. [154] have HVOF-sprayed polyimide (cryomilled to 20–100 μm)/WC–Co (5.6–22.5 μm) functionally graded (FGM) coatings with flame-sprayed WC–Co topcoats. The polymer particles were injected axially against radially for the WC–Co ones. The two- and three-layer composite coatings both exhibited lower pull-off strengths (5–6.2 MPa) than pure polyimide coatings (≈ 8.4 MPa), and in all cases these values were lower than the tensile strength (≈17.6 MPa) of an uncoated PMC substrate used as a reference. The mode of failure in the thermo-setting polyimide was brittle fracture associated with the formation of cracks at inter-pore regions where localized stress concentrations would occur. The two- and three-layer FGM coatings both failed by the same mechanism: a combination of cohesive failure within the composite layer and delamination of the substrate.

Other reinforced polymers with ceramics or metals fillers have been sprayed: metal- and ceramic-polymer composites [160], Polyamide1010 (PA1010) and its composite with nanometer-sized silica (PA1010/n-SiO_2) [161], polyamide1010/n-SiO_2 [161], Al_2O_3–TiO_2/fluoropolymer (PTFE or PFA) composite [162], NiCr or Al_2O_3–ethylene methacrylic acid copolymer [160].

11.6 Summary and Conclusions

Adapted powder to the spray process is one of the keys to good quality coatings. The powder characteristics (size distribution, shape, morphology, apparent density, tap density, chemical homogeneity, and flow ability) must be chosen according to the spray process used and spray parameters. However, as in pastry if a good flour is fundamental, the quality of the cake is strongly linked to the knowledge and experience of the cook and it is the same with spraying. For example when spraying WC–Co cermets, choosing atmospheric plasma spraying is not well adapted, the overmelting promoting WC dissolution in liquid Co and WC decomposition. However if the aim is to produce coatings with a rather low friction coefficient against an adapted material, carbon dissolved within the cobalt matrix is interesting. The best choice to achieve cermets with WC particles homogeneously distributed within cobalt matrix is then using HVAF guns or high power HVOF guns, where the particle temperature is close to, or slightly below, their melting point, but with very high velocities (>500 m/s). The imbedded WC particle size is also an important issue: the smaller they are the

best is their distribution within coatings but the easier they are prone to decompose. Thus, a compromise must be found.

Of course a grain-growth inhibitor can be used, preventing WC dissolution in the binder, but in that case the binder loosely bonds the WC particles.

Among the recent developments in powders production, cryomilling appears to be an important option offering the possibility to obtain nanometer-sized ceramic particles and producing alloyed micrometer-sized particles with nano-sized grains. The manufacturing of complex new bulk amorphous alloys with a multicomponent chemistry and high Glass Forming Ability has also been developed, especially in Fe-base systems with atomization and various rapid solidification techniques. They allow producing amorphous coatings by almost all thermal processes, coatings presenting nanostructures after reheating with very high hardness (not far from those of WC–Co cermets coatings). The recent industrial development of particles spheroidization by RF induction plasmas allows producing dense and spherical particles, mainly of refractory materials, with excellent flow ability for thermal spraying and powder metallurgy. At last the huge quantity of works devoted to the production of manometer-structured coatings must be underlined. All spray techniques are involved. Most developments are devoted to micro-sized agglomerated nano-sized particles or cryomilled particles and also to new suspension spraying process where nanometer-sized particles are injected with a liquid carrier as a suspension. Of course the spray process has to be adapted. For example, the YSZ nanostructure coatings obtained by suspension plasma or HVOF spraying are very promising for SOFCs electrolyte and thermal barrier coatings. Cold-sprayed particles, in which multiwalled carbon nanotubes (CNT) are dispersed, seem to open interesting new avenues for coating reinforcement. For cold spray, developments are in the fields of agglomerated particles, with a good deformation capacity, which are made of mixtures of particles comprising small ones adapted to the process, and large ones having a peening effect.

To summarize new powder manufacturing techniques have shown up recently, especially to spray nanostructure coatings. However, the choice of the spray process and spray parameters, remains as important as the choice of the powder.

For materials sprayed in the shape of wires, cored wires, rods, or cords it is important to underline the need to maintain a close control on their feeding rate into the flame, HVOF, or wire arc. It requires using materials with diameters as constant as possible with very smooth surfaces. The main development seems to be in the field of cored wire that opens interesting possibilities for spraying non-ductile materials.

Polymers spraying seem promising for wear and corrosion resistances. However, according to the very different properties of polymer particles, compared to those of metals, alloys, ceramics, and cermets, spraying is rather complex and the spray conditions are far to be optimized. Powders adapted to thermal spraying do not exist and those commercially available for conventional use of polymers have sizes generally larger than those required for thermal spray. Thus sizes must be adapted by cryomilling, for example. Moreover if polymer coatings reinforced with

ceramics or metals are also promising, the corresponding powders must be prepared by ball milling, the addition of nanometer-sized fillers being probably the most promising.

Nomenclature

Latin Alphabet

d_p Particle diameter (m)
m_p Particle mass (kg)
p Pressure (Pa)
p_0 Saturation vapor pressure (Pa)
r_p Particle radius (m)
S Specific surface area (m^2/g)
V_m Adsorbate volume per unit mass of solid for monolayer coverage (m^3 kg)
V_a Adsorbate volume at relative pressure

Greek Alphabet

α Dimensionless size parameter
λ Wavelength of incident radiation (nm)
θ Scattering angle (°)
ρ_p Particle specific mass (kg/m^3)

References

1. Salman AD, Ghadiri M, Hounslow MJ (eds) (2007) Particle breakage, vol 12, Handbook of powder technology. Elsevier, Amsterdam, pp 1–1227
2. Davis JR (ed) (2004) Handbook of thermal spray technology. ASM International, Materials Park, OH
3. AWS (1985) Thermal spraying, practice, theory and application. American Welding Society, Miami, FL
4. Pawlowski L (1995) The science and engineering of thermal spray coatings. Wiley, New York, NY
5. Fauchais P, Montavon G, Bertrand G (2010) From powders to thermally sprayed coatings. J Therm Spray Technol 19(1–2):56–80
6. Kubel EJ Jr (1990) Powders dictate thermal spray coating properties. Adv Mater Process:24–32
7. Kolman B, Forman J, Dubsky J, Chraska P (1994) Homogeneity studies of powders and plasma sprayed deposits. Mikrochim Acta 114–115:335–42
8. Wigren J, de Vries JF, Greving D (1996) Effects of powder morphology, microstructure and residual stresses on thermal barrier coating thermal shock performance. In: Berndt CC

(ed) Thermal spray: practical solutions for engineering problems. ASM International, Materials Park, OH, pp 855–61
9. Denoirjean A, Vardelle A, Grimaud A, Fauchais P, Lugsheider E, Rass I, Heijen HL, Chandler P, McIntyre R, Cosak T (1992) Comparison of the properties of plasma sprayed stabilized zirconia coatings for different powder morphologies. In: Berndt CC (ed) Thermal spray: international advances in coating technology. ASM International, Materials Park, OH, pp 975–82
10. Vinayo ME, Kassabji F, Guyonnet J, Fauchais P (1985) Plasma sprayed WC-Co coatings influence of the spray conditions. J Vac Sci Technol 3(6):2483–89
11. Diez P, Smith RW (1993) The influence of powder agglomeration methods on plasma sprayed yttria coatings. J Therm Spray Technol 2(2):165–72
12. Wang M, Shaw LL (2007) Effects of the powder manufacturing method on microstructure and wear performance of plasma sprayed alumina–titania coatings. Surf Coat Technol 202:34–44
13. Beczkowiak J, Schwier G (1991) Tailoring carbides and oxides for HVOF. In: Berndt CC, Bernecki TF (eds) Thermal spray: coatings properties, processes and applications. ASM International, Materials Park, OH, pp 121–26
14. Vuoristo P, Mantyla T, Berger LM, Nebelung M (1997) Sprayability and properties of TiC-Ni based powders in the detonation gun and HVOF processes. In: Berndt CC (ed) Thermal spray: a united forum for scientific and technological advances. ASM International, Materials Park, OH, pp 855–61
15. Jarosinski WJ, Gruninger MF, Londry CH (1993) Characterization of tungsten carbide cobalt powders and HVOF coatings. In: Berndt CC, Bernecki TF (eds) Thermal spray coatings: research, design and applications. ASM International, Materials Park, OH, pp 855–61
16. de Villiers Lovelock HL (1998) Powder/processing-structure relationships in WC-Co thermal spray coatings: a review of the published literature. J Therm Spray Technol 7(3):357–373
17. Kim MC, Kim SB, Hong JW (1997) Effect of powder types on mechanical properties of D-Gun coatings. In: Berndt CC (ed) Thermal spray: a united forum for scientific and technological advances. ASM International, Materials Park, OH, pp 791–95
18. Oliker VE, Grechishkin EF, Polotai VV, Loskutov MG, Timofeeva II (2004) Refractory and ceramics materials influence of the structure and properties of WC-Co alloy powders on the structure and wear resistance of detonation coatings. Powder Metall Metal Ceram 43 (5–6):258–264
19. Yandouzi M, Ajdelsztajn L, Jodoin B (2008) WC-based composite coatings prepared by the pulsed gas dynamic spraying process: effect of the feedstock powders. Surf Coat Technol 202:3866–3877
20. Anderson IE, Sordelet DJ, Besser MF, Terpstra RL (1998) Effects of powder morphology on pneumatic feeding and plasma spray deposition. In: Coddet C (ed) Thermal spray: meeting the challenges of the 21st century. ASM International, Materials Park, OH, pp 911–16, Peer reviewed
21. Fan X, Gitzhofer F, Boulos MI (1998) Statistical design of experiments for the spheroidization of powdered alumina by induction plasma processing. J Therm Spray Technol 7(2):247–253
22. Vardelle M, Vardelle A, Fauchais P (1993) Spray parameters and particle behavior relationships during plasma spraying. J Therm Spray Technol 2(1):79–92
23. Boch P, Fauchais P, Lombard D, Rogeaux B, Vardelle M (1985) Plasma sprayed zirconia coatings. Ad Ceram 12:488–503
24. Sordelet DJ, Besser MF, Kramer MJ (1998) Thermal spray quasicrystalline coatings. Part 1: relationships among processing phase structure and splat morphology. In: Coddet C (ed) Thermal spray: meeting the challenges of the 21st century. ASM International, Materials Park, OH, pp 467–72
25. Sordelet D, Besser M (1996) Effect of starting powder particle size and composition on chemistry and structure of Al-Cu-Fe quasicrystalline plasma sprayed coatings. In: Berndt CC (ed) Thermal spray: practical solutions for engineering problems. ASM International, Materials Park, OH, pp 419–28

26. Wang Y, Lima RS, Moreau C, Garcia E, Guimaraes J, Miranzo P, Osendi MI (2009) Mullite coatings produced by APS and SPS: effect of powder morphology and spray processing on the microstructure, crystallinity and mechanical properties. In: Marple BR, Hyland MM, Lau Y-C, Li C-J, Lima RS, Montavon G (eds) Thermal spray 2009: expanding thermal spray performance to new markets and applications. ASM International, Materials Park, OH, pp 97–102
27. Pei P, Kelly J, Malghan S, Dapkunas S (1996) Analysis of zirconia powder for thermal spray: reference material for particle size distribution measurements. In: Berndt CC (ed) Thermal spray: practical solutions for engineering problems. ASM International, Materials Park, OH, pp 263–73
28. Özbilen S (1999) Influence of atomizing gas pressure on particle shape of Al and Mg Powders. Powder Technol 102:109–119
29. Dunkley JJ (1998) Atomization, powder metal technologies and applications, vol 7, ASM handbook. ASM International, Materials Park, OH, pp 35–52
30. Mates SP, Settles GS (2005) A study of liquid metal atomization using close-coupled nozzles. Part1: gas dynamic behavior. Atomization Sprays 15:19–40
31. Ünal R (2006) The influence of the pressure formation at the tip of the melt delivery tube on tin powder size and gas/melt ratio in gas atomization method. J Mater Process Technol 180:291–295
32. Antipas GSE (2006) Modelling of the break up mechanism in gas atomization of liquid metals. Part I: the surface wave formation model. Comput Mater Sci 35:416–422
33. Allimant A, Planche MP, Bailly Y, Dembinski L, Coddet C (2009) Progress in gas atomization of liquid metals by means of a De Laval nozzle. Powder Technol 190:79–83
34. Zambon A (2004) Nitrogen versus helium: effects of the choice of the atomizing gas on the structures of Fe50Ni30Si10B10 and Fe32Ni36Ta7Si8B17 powders. Mater Sci Eng A 375–377:630–637
35. Ajdelsztajn L, Jodoin B, Richer P, Sansoucy E, Lavernia EJ (2006) Cold gas dynamic spraying of iron-base amorphous alloy. J Therm Spray Technol 15(4):495–500 FT60
36. Otsubo F, Era H, Kishitake K (2000) Formation of amorphous Fe-Cr-Mo-8P-2C coatings by the high velocity oxy-fuel process. J Therm Spray Technol 9(4):494–498
37. Das SK, Norin EM, Bye RL (1984) Ni-Mo-Cr-B alloys: corrosion resistant amorphous hardfacing coatings. In: Kear BH, Cohen M (eds) Materials Research Society symposium proceedings, vol 28. Elsevier Science, Amsterdam, pp 233–237
38. Choi H, Kim J, Lee C, Lee KH (2005) Critical factors affecting the amorphous phase formation of NiTiZrSiSn bulk amorphous feedstock in vacuum plasma spray. J Mater Sci 40:3873–3875
39. Dent AH, Horlock AJ, McCartney DG, Harris SJ (1999) The corrosion behavior and microstructure of high-velocity oxy-fuel sprayed nickel-base amorphous/nano-crystalline coatings. J Therm Spray Technol 8(3):399–404
40. Branagan DJ, Swank WD, Meacham BE (2009) Maximizing the glass fraction in iron-based high velocity oxy-fuel coatings. Metall Mater Trans A 40(6):1306–1313
41. Sergueeva AV, Branagan DJ, Mukherjee AK (2008) Microstructure/properties relationship in Fe-based nanomaterials. Mater Sci Eng A 493:237–240
42. Branagan DJ, Swank WD, Haggard DC, Fincke JR (2001) Wear-resistant amorphous and nanocomposite steel coatings. Metall Mater Trans A 32A:2615–2621
43. Branagan DJ, Marshall MC, Meacham BE, Aprigliano LF, Bayles R, Lemieux EJ, Newbauer T, Martin FJ, Farmer JC, Haslam JJ, Day SD (2006) Wear and corrosion resistant amorphous/nanostructured steel coatings for replacement of electrolytic hard chromium. In: Marple BR, Hyland MM, Lau YC, Lima RS, Voyer J (eds) Building on 100 years of success: proceedings of the 2006 international thermal spray conference. ASM International, Materials Park, OH, e-proceedings
44. Tsunekawa Y, Ozdemir I, Okumiya M (2006) Plasma sprayed cast iron coatings containing solid lubricant graphite and h-BN structure. J Therm Spray Technol 15(2):239–245
45. Laha T, Balani K, Agarwal A, Patil S, Seal S (2005) Synthesis of nanostructured spherical aluminum oxide powders by plasma engineering. Metall Mater Trans A 36A:301–309

46. Lee HM, Huang CY, Wang CJ (2009) Forming and sintering behaviors of commercial α-Al_2O_3 powders with different particle size distribution and agglomeration. J Mater Process Technol 209:714–722
47. Schwier C (1986) Plasma spray powders for thermal barrier coating. Adv Thermal Spray. Pergamon Press, pp 277–286
48. Berger L-M, Ettmayer P, Vuoristo P, Mäntylä T, Kunert W (2001) Microstructure and properties of WC-10%Co-4% Cr spray powders and coatings: Part 1. Powder characterization. J Therm Spray Technol 10(2):311–325
49. (2007) Powders, fibers, platelets, and composites, in ceramic materials, chemistry and materials science collection. Springer, New York
50. Camerucci MA, Cavalieri AL (1998) Process parameters in attrition milling of cordierite powders. J Mater Synth Process 6(2):115–121
51. Lavernia EJ, Han BQ, Schoenung JM (2008) Cryomilled nanostructured materials: processing and properties. Mater Sci Eng A 493:207–214
52. Kilinc Y, Öztqrk S, Öztqrk B, Uslan I (2004) Investigation of milling characteristics of alumina powders milled with a newly designed vibratory horizontal attritor. Powder Technol 146:200–205
53. Suryanarayana C (2001) Mechanical alloying and milling. Prog Mater Sci 46:1–184
54. Picas JA, Forn A, Ajdelsztajn L, Schoenung J (2004) Nanocrystalline NiCrAlY powder synthesis by mechanical cryomilling. Powder Technol 148:20–23
55. Wang H-T, Li C-J, Yang G-J, Li C-X, Zhang Q, Li W-Y (2007) Microstructural characterization cold-sprayed nanostructured FeAl intermetallic compound coating and its ball-milled feedstock powders. J Therm Spray Technol 16(5–6):669–676
56. He J, Schoenung JM (2002) Nanostructured coatings, a review. Mater Sci Eng A336:274–319
57. Eigen N, Gärtner F, Klassen T, Aus E, Bormann R, Kreye H (2002) Microstructures and properties of nanostructured thermal sprayed coatings using high-energy milled cermet powders. Surf Coat Technol A336:274–319
58. Zhang X-F, Zhang X-L, Wang A-H, Huang Z-W (2009) Microstructure and properties of HVOF sprayed Ni-based submicron WS2/CaF2 self-lubricating composite coating. Trans Nonferrous Met Soc China 19:85–92
59. Tekmen C, Ozdemir I, Fritsche G, Tsunekawa Y (2009) Structural evolution of mechanically alloyed Al–12Si/TiB2/h–BN composite powder coating by atmospheric plasma spraying. Surf Coat Technol 203(14):2046–2051
60. Oberste-Berghaus J, Marple B, Moreau C (2006) Suspension plasma spraying of nanostructured WC-12Co coatings. J Therm Spray Technol 15(4):676–681
61. Walton DE, Mumford CJ (1999) Spray dried products-characterization of particle morphology. Trans Inst Chem Eng 77:21–38
62. Xiong Z, Shao G, Shi X, Duan X, Yan L (2008) Ultrafine hardmetals prepared by WC–10 wt. % Co composite powder. Int J Refractory Metals Hard Mater 26:242–250
63. Bertrand G, Roya P, Filiatre C, Coddet C (2005) Spray-dried ceramic powders: a quantitative correlation between slurry characteristics and shapes of the granules. Chem Eng Sci 60:95–102
64. Lima RS, Marple BR (2008) Process–property–performance relationships for titanium dioxide coatings engineered from nanostructured and conventional powders. Mater Des 29:1845–1855
65. Baksh SR, Singh V, Balani K, McCartney DG, Seal S, Agarwal A (2008) Carbon nanotube reinforced aluminum composite coating via cold spraying. Surf Coat Technol 202:5162–5169
66. BenEttouil F, Mazhorova O, Pateyron B, Ageorges H, El-Ganaoui M, Fauchais P (2008) Predicting dynamic and thermal histories of agglomerated particles injected within a d.c. plasma jet. Surf Coat Technol 202:4491–4495
67. Dzur B. (2008) Plasma puts heat into spherical powder production. MPR, February, 12–15
68. Boulos M, Ducos M, Fauchais P (2006) (in French) Plasma technology and its potential for powder treatment, Matériaux 2006, Dijon, France, 13–17 Nov 2006. SF2M, Paris, France

69. Boulos M, Fauchais P, Vardelle A, Pfender E (1993) Injection of hot particles in a plasma flame. In: Suryanarayanun R (ed) Plasma spraying theory and applications. World Scientific, Singapore, pp 3–61
70. Dignard NM, Boulos MI (1997) Ceramic and metallic powder spherodization using induction plasma technology. In: Berndt CC (ed) Thermal spray: a united forum for scientific and technological advances. ASM International, Materials Park, OH, pp 1–7
71. Bouyer E, Gitzhofer F, Boulos M (1997) Suspension plasma spraying for hydroxyapatite powder preparation by RF plasma. IEEE Trans Plasma Sci 25(5):1066–1072
72. Schiller G, Müller M, Gitzhofer F (1999) Preparation of perovskite powders and coatings by radio frequency suspension plasma spraying. J Therm Spray Technol 8(3):389–392
73. Bouchard D, Sun L, Gitzhofer F, Brisard GM (2006) Synthesis and characterization of $La_{0.8}Sr_{0.2}MO_{3-\delta}\delta$ (M = Mn, Fe, or Co) cathode materials by induction plasma technology. J Therm Spray Technol 15(1):37–45
74. Ravi BG, Gandhi AS, Guo XZ, Margolies J, Sampath S (2008) Liquid precursor plasma spraying of functional materials: a case study for yttrium aluminium garnet (YAG). J Therm Spray Technol 17(1):82–90
75. Lugscheider E, Loch M, Eschnauer H (1991) Coated powders-the status today. In: Huber P, Echnauer H (eds) 2nd Plasma-Technik symposium, June 1991, vol 2. Plasma Technik, Wholen, CH, pp 339–351
76. Ito H, Umakoshi M, Nakamura R, Yokoyama T, Urayama K, Kato M (1991) Characterization of Ni-Al composite powders formed by mechanofusion. In: Bernecki TF (ed) Thermal spray coatings: properties, processes and applications. ASM International, Materials Park, OH, pp 405–411
77. Ageorges H, Fauchais P (2000) Plasma spraying of stainless-steel particles coated with an alumina shell. Thin Solid Films 370:213–222
78. Cuenca AR (2003) Contribution à l'élaboration de dépôts composites par projection plasma d'arc de poudres élaborées par mechanofusion. Ph.D. thesis, University of Limoges, France, 25 Nov 2003 (in French)
79. Wang J, Jordan EH, Gell M (2010) Plasma sprayed dense MgO-Y2O3 nanocomposite coatings using sol-gel combustion synthesized powder. J Therm Spray Technol 19 (5):873–878
80. Chen D, Jordan EH, Gell M (2009) Microstructure of suspension plasma spray and air plasma spray Al_2O_3-ZrO_2 composite coatings. J Therm Spray Technol 18(3):421–42
81. Prakash S, Grips VKW, Aruna ST (2012) A single step solution combustion approach for preparing gadolinia doped ceria solid oxide fuel cell electrolyte material suitable for wet powder and plasma spraying processes. J Power Source 214:358–364
82. Borisova AL, Borisov Yu S (2008) Self-propagating high-temperature synthesis for the deposition of thermal-sprayed coatings. Powder Metall Metal Ceram 47(1–2):80–94
83. Borisov Y, Borisova A, Shvedova L (1986) Transition metal – nonmetallic refractory compound composite powders for thermal spraying. In: Proceedings of ITSC'86, Montreal, Canada, 8–12 Sept 1986. Pergamon Press, pp 323–330
84. Borisov Y, Borisova A (1992) Application of self-propagating high-temperature synthesis in thermal spraying technology. In: Bernicki TF (ed) Thermal spray: research, design and applications. ASM International, Materials Park, OH, pp 139–144
85. Deevi SC, Sikka VK, Swindeman CJ, Seals RD (1997) Reactive spraying of nickel-aluminide coatings. J Therm Spray Technol 6(3):335–344
86. Haller B, Bonnet J-P, Fauchais P, Grimaud A, Labbe J-C (2005) TiC based coatings prepared by combining SHS and plasma spraying. In: Lugscheider E (ed) Thermal spray connects: explore its surfacing potential! DVS-Verlag GmbH, Düsseldorf, Germany, e-proceedings
87. Dallaire S (1982) Influence of temperature on the bonding mechanism of plasma-sprayed coatings. Thin Solid Films 95:237–241
88. Legoux JG, Dallaire S (1993) Copper-TiB2 coatings by plasma spraying reactive micropellets. In: Berndt CC, Bernecki TF (eds) Thermal spray: research, in design and applications. ASM International, Materials Park, OH, pp 429–432

89. Dallaire S, Cliche G (1992) The influence of composition and process parameters on the microstructure of TiC-Fe multiphase and multilayer coatings. Surf Coat Technol 50:233–239
90. Seegopaul P, McCandlish UE, Shinneman FM (1997) Production capability and powder processing methods for nanostructured WC-Co powder. Int J Refractory Metals Hard Mater 15:133–138
91. Kear BH, Sadangi RK, Jain M, Yao R, Kalman Z, Skandan G, Mayo WE (2000) Thermal sprayed nanostructured WC/Co hardcoatings. J Therm Spray Technol 9(3):399–406
92. Schubert WD, Bock A, Lux B (1995) General aspects and limits of conventional ultrafine WC powder manufacture and hard metal production. Int J Metals Hard Mater 13:281–296
93. Ban Z-G, Shaw L (2002) Synthesis and processing of nanostructured WC-Co materials. J Mater Sci 37:3397–3403
94. Ban Z-G, Shaw LL (2003) Characterization of thermal sprayed nanostructured WC-Co coatings derived from nanocrystalline WC-18wt.% Co powders. J Therm Spray Technol 12(1):112–119
95. Ren R-M, Yang Z-G, Shaw LL (1998) A novel process for synthesizing nanostructured carbides: mechanically activated synthesis. Ceram Eng Sci Proc 19(4):461–68
96. Shaw LL (2000) Processing of nanostructured carbides, nitrides and their composites. Adv Eng Mater 2(11):721–723
97. Kurlov AS, Rempel AA, Blagoveshenskii Yu V, Samokhin AV, Tsvetkov Yu V (2011) Hard alloys WC–Co (6 wt %) and WC–Co (10 wt %) based on nanocrystalline powders. Chem Technol 439(1):213–218
98. Streibl T, Vaidya A, Friis M, Srinivasan V, Sampath S (2006) A critical assessment of particle temperature distributions during plasma spraying: experimental results for YSZ. Plasma Chem Plasma Proc 26(1):73–102
99. Chi W, Sampath S, Wang H (2006) Ambient and high-temperature thermal conductivity of thermal sprayed coatings. J Therm Spray Technol 15(4):773–778
100. Bertrand G, Bertrand P, Roy P, Rio C, Mevrel R (2008) Low conductivity plasma sprayed thermal barrier coating using hollow PSZ spheres: correlation between thermo physical properties and microstructure. Surf Coat Technol 202:1994–2001
101. de Villiers LHL (1998) Powder/processing/structure relationships in WC-Co thermal spray coatings: a review of the published literature. J Therm Spray Technol 7(3):357–373
102. Jacobs L, Hyland MM, De Bonte M (1998) Comparative study of WC-cermet coatings sprayed via the HVOF and the HVAF process. J Therm Spray Technol 7(2):213–218
103. de Villiers Lovelock HL, Richter PW, Benson JM, Young PM (1998) Parameter study of HP/HVOF deposited WC-Co coatings. J Therm Spray Technol 7(1):97–107
104. Peetsalu P, Zimakov S, Pirso J, Mikli V, Tarbe R, Kulu P (2006) Characterization of WC-Co composite thermal spray powders and coatings. Proc Estonian Acad Sci Eng 12(4):435–444
105. Cuenca Alvarez R, Ageorges H, Fauchais P, Fournier P, Smith A (2003) The effect of the mechanofusion process and planetary milling on composite powder preparation: agglomeration and fragmentation. Mater Sci Forum 442:67–72
106. Stoltenhoff T, Kreye H, Richter HJ (2002) An analysis of the cold spray process and its coatings. J Therm Spray Technol 11(4):542–550
107. Klinkov SV, Kosarev VF (2006) Measurements of cold spray deposition efficiency. J Therm Spray Technol 15(3):364–371
108. Li C-J, Li W-Y, Wang Y-Y, Yang G-J, Fukanuma H (2005) A theoretical model for prediction of deposition efficiency in cold spraying. Thin Sol Films 489:79–85
109. Lee JH, Kim JS, Shin SM, Lee CH, Kim HJ (1996) Effect of particle temperature on the critical velocity for particle deposition by kinetic spraying. In: Marple BR, Hyland MM, Lau YC, Lima RS, Voyer J (eds) Building on 100 years of success: proceedings of the 2006 international thermal spray conference. ASM International, Materials Park, OH, e-proceedings
110. Katanoda H, Fukuhara M, Iino N (2007) Numerical study of combination parameters for particle impact velocity and temperature in cold spray. In: Marple BR, Hyland MM, Lau Y-C, Li C-J, Lima RS, Montavon G (eds) Thermal spray 2007: global coating solutions. ASM International, Materials Park, OH, pp 72–77

111. Mäkinen H, Lagerbom J, Vuoristo P (2007) Adhesion of cold sprayed coatings: effect of powder, substrate, and heat treatment. In: Marple BR, Hyland MM, Lau Y-C, Li C-J, Lima RS, Montavon G (eds) Thermal spray 2007: global coating solutions. ASM International, Materials Park, OH, pp 31–36
112. Raletz F (2005) Contribution to the development of a Cold Gas Dynamic Spray system (C.G. D.S.) for the realization of nickel coatings. Ph.D., University of Limoges, France, 17 Oct (in French)
113. Kang KC, Yoon SH, Ji YG, Lee C (2007) Lee, oxidation effects on the critical velocity of pure Al feedstock deposition in the kinetic spraying process. In: Marple BR, Hyland MM, Lau Y-C, Li C-J, Lima RS, Montavon G (eds) Thermal spray 2007: global coating solutions. ASM International, Materials Park, OH, pp 66–71
114. Berndt C (2007) Thermal spray workshop, ITSC courses in conjunction with ITSC 2007 Beijing, May 2007. ASM International, Materials Park, OH
115. Allen T (1997) Particle size measurements (Volume 1: powder sampling and particle size measurements. Volume 2: surface area and pore size determination), 5th edn. Chapman & Hall, London
116. ASTM-B214-07(2011) Standard Test Method for Sieve Analysis of Metal Powders
117. ASTM E2651-10 Standard Guide for Powder Particle Size Analysis
118. Iinoya K, Gotoh K, Higashitani K (1991) Powder technology handbook. Dekker, New York, NY
119. Barth H. (ed.) (1984) Modern methods of particle size analysis, (pub.) John Wiley & Sons
120. Hoffmann AC, Arends H, Sie H (1991) An experimental investigation elucidating the nature of the effect of solids loading on cyclone performance. Filtration and Separation May–June:188–193
121. Hoffmann AC, Van Santen A, Allen WK, Clift R (1992) Effects of geometry and solids loading on the performance of gas cyclones. Powder Technol 70:83–91
122. Ji Z, Xiong Z, Wu X, Chen H, Wu H (2008) Experimental investigations on a cyclone separator performance at an extremely low particle concentration. Powder Technol 191 (3):254–259
123. ASTM WK19862, Standard Practices for Sampling Metal Powders, Revision of B215-04, Active Standard: B215-08.
124. Goldstein JI, Newbury DE, Echlin P, Joy DC, Lyman CE, Lifshin E, Sawyer LC, Michael JR (2003) Scanning electron microscopy and X-ray micro- analysis. Springer, New York, NY
125. Trassy C, Mermet JM (1984) Analytical applications of RF plasmas (in French). Lavoisier, Paris, France
126. Beckhoff B, Kanngießer B, Langhoff N, Wedell R, Wolff H (2006) Handbook of practical X-ray fluorescence analysis. Springer, Berlin
127. van de Hulst HC (1981) Light scattering by small particles. Dover Publications, New York, NY, 470 p
128. ASTM B213 Flow Rate of Metal Powders
129. Stanford MK, Della Corte C (2006) Effect of humidity on the flow characteristics of a composite plasma spray powder. J Therm Spray Technol 15(1):33–36
130. Hériaud-Kraemer H, Montavon G, Hertert S, Robin H, Coddet C (2003) Harmful risks for workers in thermal spraying: a review completed by a survey in a French company. J Therm Spray Technol 12(4):542–554
131. Petsas N, Kouzilos G, Papapanos G, Vardavoulias M, Moutsatsou A (2007) Worker exposure monitoring of suspended particles in a thermal spray industry. J Therm Spray Technol 16(2):214–219
132. Singh N, Manshian B, Jenkins GJS, Griffiths SM, Williams PM, Maffeis TGG, Wright CJ, Doak SH (2009) Nano-genotoxicology: the DNA damaging potential of engineered nano-materials a review. Biomaterials 30:3891–3914
133. Lester T (2005) Metallized coatings application: an overview of the flame- and arc-spraying processes used for surface finishing. Organic finishing July/August:35–39

134. Liu S-G, Wu J-M, Zhang S-C, Rong S-J, Li Z-Z (2007) High temperature erosion properties of arc-sprayed coatings using various cored wires containing Ti–Al intermetallics. Wear 262:555–561
135. Norouzi S (2004) Contribution to the development of hard metal coatings against abrasive wear sprayed by wire arc process. Ph.D. thesis, University of Limoges, France, 30 Nov
136. Mc Crum NG, Buckley CP, Bucknall CB (1997) Principles of polymer engineering. Oxford University Press, Oxford
137. Cowley M (2002) Coating powders and powder coatings—the state of the art. Finishing 26(8):32–36
138. Ivosevic M, Knight R, Kalidindi SR, Palmese GR, Sutter JK, Tsurikov A (2003) Optimal substrate preheating model for thermal spray deposition of thermosets onto polymer matrix composite. In: Moreau C (ed) Proceedings of the ITSC-2003, Orlando, FL. ASM International, Materials Park, OH
139. Åström BT (1997) Manufacturing of polymer composites. Chapman & Hall, London
140. Petrovicova E, Knight R, Schadler LS, Twardowski TE (2002) Thermal spraying of polymers. Int Mater Rev 47(4):169–190
141. Ivosevic M (2006) Splat formation during thermal spraying of polymer particles: mathematical modeling and experimental analysis. Ph.D. thesis, Faculty of Drexel University
142. Ivosevic M, Cairncross RA, Knight R (2006) 3D predictions of thermally sprayed polymer splats: modeling particle acceleration, heating and deformation on impact with a flat substrate. Int J Heat Mass Transf 49:3285–3297
143. Arjula S, Harsha AP, Ghosh MK (2008) Solid-particle erosion behavior of high-performance thermoplastic polymers. J Mater Sci 43:1757–1768
144. Soveja A, Costil S, Liao H, Sallamand P, Coddet C (2010) Remelting of flame spraying PEEK coating using lasers. J Therm Spray Technol 19(1–2):439–447
145. Zhang C, Zhang G, JI V, Liao H, Costil S, Coddet C (2009) Microstructure and mechanical properties of flame-sprayed PEEK coating remelted by laser process. Prog Organic Coat 66:248–253
146. Zhang G, Liao H, Cherigui M, Paulo Davim J, Coddet C (2007) Effect of crystalline structure on the hardness and interfacial adherence of fame sprayed (poly-ether–ether–ketone) coatings. Eur Polym J 43:1077–1082
147. Patel K, Doyle CS, James BJ, Hyland MM (2010) Valence band XPS and FT-IR evaluation of thermal degradation of HVAF thermally sprayed PEEK coatings. Polym Degrad Stab 95:792–797
148. Wu J, Munroe PR, Withy B, Hyland MM (2010) Study of the splat-substrate interface for a PEEK coating plasma-sprayed onto aluminum substrates. J Therm Spray Technol 19(1–2):42–48
149. Withy BP, Hyland MM, James BJ (2008) The effect of surface chemistry and morphology on the properties of HVAF PEEK single splats. J Therm Spray Technol 17(5–6):631–636
150. Niebuhr D, Scholl M (2005) Synthesis and performance of plasma-sprayed polymer/steel coating system. J Therm Spray Technol 14(4):487–494
151. Xie W, Wang J, Berndt CC (2013) Analysis of EMAA deposits on glass and mild steel substrates, Journal of Thermal Spray Technology (published on line)
152. Leivo E, Wilenius T, Kinos T, Vuoristo P, Mäntylä T (2004) Properties of thermally sprayed fluoropolymer PVDF, ECTFE, PFA and FEP coatings. Prog Organic Coat 49(1):69–73
153. Schadler LS, Laul KO, Smith RW, Petrovicova E (1997) Microstructure and mechanical properties of thermally sprayed silica/nylon nanocomposites. J Therm Spray Technol 6(4):475–485
154. Ivosevic M, Knight R, Kalidindi SR, Palmese GR, Sutter JK (2005) Adhesive/cohesive properties of thermally sprayed functionally graded coatings for polymer matrix composites. J Therm Spray Technol 14(1):45–51

155. Sumita M, Tsukumo Y, Miyasaka K, Ishikawa KJ (1983) Effect of re- ducible properties of temperature, rate of strain, and filler content on the tensile yield stress of nylon 6 composites filled with ultra-fine particles. J Macromol Sci Phys B-22(4):601–618
156. Petrovicova E (1999) Structure and properties of polymer nanocomposite coatings applied by the HVOF process. Ph.D. Dissertation, Drexel University, Philadelphia, PA
157. Jackson L, Ivosevic M, Knight R, Cairncross RA (2007) Sliding wear properties of HVOF thermally sprayed nylon-11 and nylon-11/ceramic composites on steel. J Therm Spray Technol 16(5–6):927–932
158. Niezgoda S, Gupta V, Knight R, Cairncross RA, Twardowski TE (2006) Effect of reinforcement size on the scratch resistance and crystallinity of HVOF sprayed nylon-11/ceramic composite coatings. J Therm Spray Technol 15(4):731–738
159. Stravato A, Knight R, Mochalin V, Picardi SC (2008) HVOF-sprayed nylon-11 + nanodiamond composite coatings: production & characterization. J Therm Spray Technol 17(5–6):812–817
160. Berndt CC, Brogan JA, Montavon G, Claudon A, Coddet C (1998) Mechanical properties of metal- and ceramic-polymer composites formed via thermal spray consolidation. J Therm Spray Technol 7(3):337–339
161. Li Y, Ma Y, Xie B, Cao S, Wu Z (2007) Dry friction and wear behavior of flame-sprayed polyamide1010/n-SiO2 composite coatings. Wear 262:1232–1238
162. Mateus C, Costil S, Bolot R, Coddet C (2005) Ceramic/fluoropolymer composite coatings by thermal spraying-a modification of surface properties. Surf Coat Technol 191:108–118

Chapter 12
Surface Preparation

Abbreviation

BS Bond strength

12.1 Introduction

Thermal spraying begins with proper surface preparation, which is absolutely essential. Steps must be undertaken correctly in order for the coating to perform the design expectation [1, 2]. Without surface preparation failure of the coating becomes highly probable because coating adhesion quality is directly related to the cleanliness, the roughness, and sometimes the proper machining for optimal coating performance. The coating material and the nature of the substrate are the major factors in determining what kind of surface preparation is necessary to achieve a resistant bonding. It is also important to keep in mind that the coating must never end abruptly at the part extremity (see Fig. 12.1a, b, where it may act as a stress raiser and where cracks will develop, especially when loads are applied. Coating at the extremity of a part should present a narrow feathered band, rather than a sharp edge (see Fig. 12.1c).

12.2 Machining

Conventional machining: turning or milling allows undercutting the substrate target area to accept the coating. As without undercutting, the coating deposited must never end abruptly. In the undercuts the corners must be chamfered or its cutting edge removed before spraying. The chamfer angle should be about 30° (see Fig. 12.2a). Sharp corners capture loose spray particles, dusts, and debris resulting in porous areas.

P.L. Fauchais et al., *Thermal Spray Fundamentals: From Powder to Part*,
DOI 10.1007/978-0-387-68991-3_12, © Springer Science+Business Media New York 2014

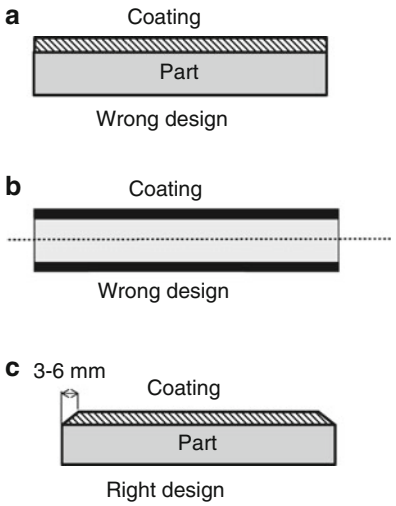


Fig. 12.1 Coating and part: Wrong design with the coating abruptly ending at the extremity of: (**a**) Plane part. (**b**) Cylindrical part. (**c**) Right design with a narrow feathered band rather than a sharp edge. Reprinted with kind permission from ASM International [1] and American Welding Society [3]

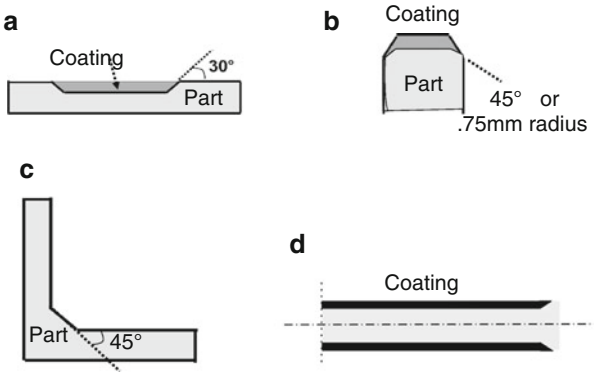


Fig. 12.2 Recommended machining for areas to be sprayed: (**a**) Undercut shape. (**b**) Edge of a sprayed coating. (**c**) Shape for a shoulder to be coated. (**d**) Right design at the coating of a cylindrical part. Reprinted with kind permission from ASM International [1] and American Welding Society [3]

For a part with a sharp corner at 90° the corner must be chamfered at 45° (see Fig. 12.22b) or rounded with radius of 0.75 mm. Otherwise with an abrupt edge, cracks will develop. It is the same if the substrate has a shoulder where it must be chamfered (see Fig. 12.2c). At each extremity of a cylindrical part, a shoulder should be left [3] as illustrated in Fig. 12.2d, an abrupt stop of the coating at the cylinder extremity (see Fig. 12.1c) can lead to crack generation.

Machining is also used for creating grooves or threads into the surface to be sprayed (see Fig. 12.3a) to restrict shrinkage stresses and to disrupt the lamellar pattern of particle deposition in order to break up the shear stresses parallel to the surface (see Fig. 12.3b) [3]. This technique is mainly used for spraying thick coatings or coatings on a substrate with a short radius. The surface is generally

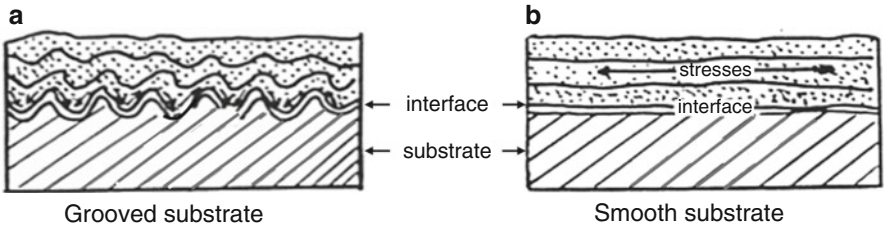


Fig. 12.3 (**a**) Grooved substrate and (**b**) Smooth substrate. Reprinted with kind permission from American Welding Society [3]

roughened after grooving. Two types of grooves are used: V-shaped ones when the V angle relatively to the part surface is 70° with the root rounded or U-shaped grooves, between 1.1 to 1.4 mm in width.

12.3 Cleaning

This is the first step for the substrate preparation. Before spraying, all contaminants, such as scale, oil, grease, and paint must be removed. After removing all contaminants, parts should be protected from airborne debris and fingerprints and should be handled with clean fixtures and materials. In the following a brief description is given of the main cleaning techniques [4] commonly used for substrate preparation.

12.3.1 Vapor Degreasing

It is used to remove organic contaminants [4]. It is fast, efficient, and economical. Hot vapor degreasing is faster and more efficient. Parts should be soaked 15–30 min to remove oil from interstices and surface pores. Porous materials must be soaked for longer times. Most solvents are hazardous and manufacturer's instructions should be followed (usage, location, and disposition). Recycling of solvents is now a requirement for environmental concerns. The most commonly used solvents, in agreement with regulations, are methyl-ethyl-ketone (MEK) and acetone. Aliphatic hydrocarbons are also used but in a blend of other solvents to be less aggressive and drying without forming a film. Isopropyl alcohols are used for precision cleaning but they are not effective on heavy oils and some other contaminants. Large parts can be steamed or submerged into solvents, for example, aqueous washer solutions containing acetic acid. The chlorinated solvents, while very effective, are no more allowed due to environmental restrictions.

12.3.2 Baking in an Oven

Porous parts, such as those resulting from sand castings, which may absorb large quantities of oil, are baked at 315 °C for four hours to dry the oil and prevent bleeding.

12.3.3 Ultrasonic Cleaning

This process is used when contaminants are lodged in a restricted area [4]. The solvent has to be adapted to the problem and the safety requirements. The equipment consists of a holding tank containing the cleaning solution in which the part is soaked and subjected to intense sonication by a series of ultrasonic transducers distributed around the outer walls of the tank.

12.3.4 Wet or Dry Blasting

Wet abrasive blasting uses diluted slurry of abrasive media projected by an air jet onto the surface. Typical slurries are in the ratio 600 kg/m^3 and rust inhibitors must be added. The abrasive size has to be adapted to the work to be done. The treated parts must be carefully rinsed after cleaning.

Dry abrasives are used to remove baked-on-deposits, scale, and oxides. A compressed air stream containing abrasive particles is directed, through a nozzle, toward the part to be treated [5]. The system is similar to grit blasting but it should not be used for roughening because of the contaminants introduced in the grit could end up pollute the treated surface.

12.3.5 Acid Pickling

Dilute acid etching is a very efficient method. The part is immersed totally in an acid solution during a time depending on the material and stock removal desired. After pickling, a hot water rinsing, an alkaline solution, and a careful hot water or steam blast cleaning are necessary.

12.3.6 Brushing

This process is used when only localized cleaning is needed. Small rotary wire brushes driven by a power tool are used in these cases to clean the surface.

12.3.7 Dry Ice Blasting

Dry ice blasting is a blasting method that uses small, compact dry ice pellets, which are not as hard as alternate blasting material. They are made of solid carbon dioxide at a temperature of about −79 °C. Typical pellet sizes are in the few mm range (typically a diameter of 3 mm for a length of 5–15 mm). The dry ice pellets are accelerated in a jet of compressed air similar to that used in traditional blasting methods. It is a mild pretreatment method, since the dry ice pellets are relatively soft (hardness of 2–3 Mohs) thus causing only slight damage (low abrasiveness) to the surface and the fringe area. Moreover it is noncorrosive compared to other blasting agents. The unique feature of dry ice as a blasting material is that it vaporizes on contact with the surface to be cleaned. Upon impact the energy transfer knocks contaminants as in grit blasting. Moreover they also create a micro-thermal shock (the dry ice temperature is of −79 °C) between the surface contaminant and the substrate, inducing cracking, and delamination of the latter. At last the dry ice pellet explodes on impact and warms rapidly, the CO_2 gas expanding partly under the contaminant surface, thus participating in its removal. Dry ice blasting is nonabrasive, and surfaces are therefore treated gently. The system can thus be used on easily damaged surfaces like nickel, chromium, and soft aluminum. Dry ice blasting is ideal for removing contaminants such as adhesives, varnish, oil, grease, and coal dust [6–9]. Dry ice blasting presents the following advantages:

- Cleaning by cryogenic and mechanical effect
- Cooling of substrate and coating during spraying
- Flexibility
- Rather environmental-friendly method

As for other processes, the blasting conditions (shape and dimensions of the blasting nozzle, blasting air pressure, grit flow rate,... must be optimized [10]. For example, Dong et al. [10] have compared plasma sprayed Al_2O_3, CoNiCrAlY, and steel coatings, obtained with either conventional air cooling during spraying or dry ice blasting during spraying. The dry ice blasting nozzle was located just before the plasma torch and substrates were attached to a rotating substrate holder with its axis orthogonal to those of the plasma torch and the blasting nozzle. With dry ice blasting the substrate and coating temperature was reduced by a factor up to 2 compared to air jets cooling. Denser and less oxidized steel and CoNiCrAlY coatings were obtained with dry ice blasting and the adhesive strength of the Al_2O_3 coating obtained was increased by about 30 %. Authors attributed the improvement of the Al_2O_3 coating adhesion to the cleaning effect of the dry ice, the denser non-ceramic coating properties, to the mechanical effect associated with the impact of the dry ice on the surface, and the oxide reduction due to the better cooling efficiency [10].

12.4 Masking

This process is necessary to prevent deposit formation on areas where it is not wanted. It also improves the uniformity of the deposit when coating limited areas. Two types of masks are used depending on the number of parts to be coated [1, 3]. The masks must resists to grit blasting and to spraying because the unwanted spray is collected on the mask.

(a) If a few parts are to be coated tape masking is used. It consists in manually wrapping a tape where the substrate must be protected. This type of mask is called contact mask. The tape is withdrawn after grit blasting and, to get rid of residual glue, the area where it covered the surface must be cleaned with a solvent.
(b) If many parts are to be coated, hard and permanent masking is used. A metal mask is machined and then covered with a protection sheet or tape. The stationary mask, often called shadow mask, is positioned about two to three times the total as-sprayed coating thickness. Of course it must be securely fixed on the part to be sprayed. This protection is renewed after grit blasting a few hundred parts resulting in too much overspray at its surface and heat deformation. With shadow mask grit blasting can be entirely automated.

Coatings resulting from contact mask are somewhat different from shadow ones, as illustrated in Fig. 12.4. As shown in Fig. 12.4, with a contact mask (Fig. 12.4a), the coating edge (Fig. 12.4b) is sharp, is sharp (as without masking presented in Fig. 12.1a, b) and can induce, in that area, debonding of the coating due to stresses when loads are applied. On the contrary with shadow mask (Fig. 12.4c) the coating ends in a narrow feathered band, as recommended for non-protected parts (see Fig. 12.1c).

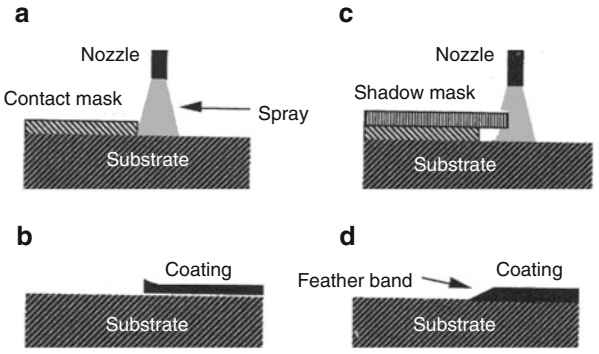


Fig. 12.4 Effect of masking technique on coating profile. (**a**) & (**b**) Contact mask and resulting coating profile. (**c**) & (**d**) Shadow mask and resulting coating profile. Reprinted with kind permission from ASM International [1]

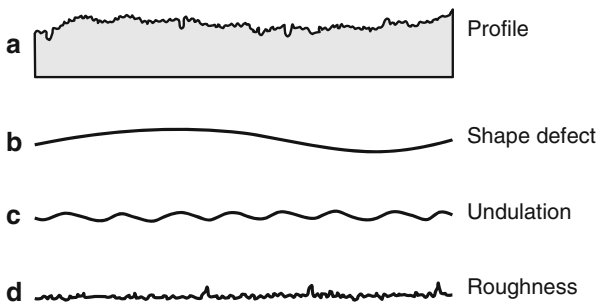


Fig. 12.5 Definitions of surface, (**a**) profile, (**b**) shape defect, (**c**) undulation, and (**d**) roughness. Reprinted with kind permission from Prof. G. Montavon [11]

12.5 Roughening by Grit Blasting

After cleaning, several methods are used to produce a surface to which the sprayed coating will adhere. Dry abrasive grit blasting is probably the most commonly used roughening technique. Dry abrasive particles are propelled toward the substrate at relatively high speeds. On impact, the sharp, angular particles act like chisels, cutting small irregularities into the surface, which have first to be characterized.

12.5.1 Roughness Measurement

First it must be recalled that the surface profile (as shown in Fig. 12.5a) is made up of:

- Shape defects, which are observed at rather large scales of few centimeters (see Fig. 12.5b).
- Undulation (see Fig. 12.5c), which generally corresponds to millimeters scale.
- Roughness (see Fig. 12.5d), which is the parameter to be measured. It has to be separated at least from undulation in the measurement procedure. Roughness is a measure of the texture of a surface. It is quantified by the vertical deviations of a real surface from its ideal form. If these deviations are large, the surface is rough; if they are small the surface is smooth. Roughness is typically considered to be the high frequency, short wavelength component of a measured surface.

  Roughness measurements are performed:

- With a contact skidded instrument, such as the profilometer diamond stylus, the instrument probe scans the surface over a transverse length l_t and records the irregularities over a distance corresponding to the assessment length l_n. A cutoff length (Fig. 12.6) is defined in order to distinguish the possible undulations from the roughness. If the cutoff length is below 1 mm, the undulation is reduced. The assessment length l_n must be at least 5 to 6 times the cutoff

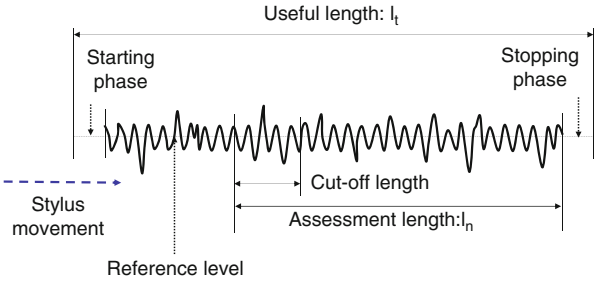


Fig. 12.6 Different length definitions for roughness measurement. Reprinted with kind permission from Prof. G. Montavon [11]

length in order to include both undulation and roughness features. The previous and post-running lengths are discarded from the statistical analysis of the signal [12]. Figure 12.6 illustrates these definitions on a typical roughness profile. The main limitation is the stylus dimensions relative to the size of undercuts. For contact measurements, the most obvious problem is that the stylus may scratch the measured surface. Another problem is that the stylus may be too blunt to reach the bottom of deep valleys and it may round the tips of sharp peaks. In these cases the probe is a physical filter that limits the accuracy of the instrument. Roughness measurements are generally performed in both the longitudinal and transverse directions relative to the substrate. The reported values are the average of 12–18 measurements.

– With noncontact sensors instrument employing optical, ultrasonic, and capacitance methods [13–16], better precision can be obtained though the surface profile can be modified through the sample preparation protocol. In both cases statistics must be performed on data sets (at least 12 collected from randomly chosen orientations) and adjusted by removing the highest and lowest values of the parameters measured. There are also limitations for noncontact instruments. For example, instruments that rely on optical interference cannot resolve features that are less than the wavelength of light used.

In some cases, the physics of the measuring instrument may have a large effect on the data. This is especially true when measuring very smooth surfaces [17]. Of course the interest for smooth surfaces is increasing with the development of new spray technologies such as suspension or solution spraying. In these techniques splat sizes are in the range 0.1–1 μm and thus the roughness is in the same size range. Moreover it has been recently shown that the surface roughness at the nanometer scale can modify the flattening particle wettability, raising the interest for such measurements [18]. An interesting comparison between the different techniques used for measurements at the micrometer scale level is presented in the paper of Conroy et al. [19].

While accurate surface characterization requires three-dimensional (3D) surface measurements that are not provided by 2D measurement systems [20, 21]. 2D surface measurements are more commonly used because of the relative simplicity of the instrumentation involved. It should be noted, however, that traditional

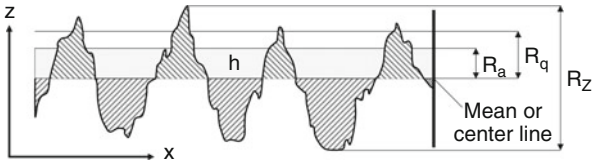


Fig. 12.7 Definitions of the average roughness Ra, root mean square roughness R_q, distance between highest peak and deepest undercut: R_t. Reprinted with kind permission from Prof. G. Montavon [11]

two-dimensional measurements do not reflect the real surface topography of the whole component's geometry [21].

In the following only the 2D measurements will be discussed. Many parameters used to characterize the surface are mainly based on the amplitude or spacing criteria [22, 23]. The most frequently used are:

– The arithmetical average

$$AA = \frac{h_1 + h_2 + \ldots h_N}{N} \tag{12.1}$$

where h_i are the heights of all peaks and undercuts (without regards to the sign) from the centerline and N the number of measurements

– The average roughness

$$\mathrm{Ra} = \frac{1}{\ell} \int_0^{\ell} z(x)\,\mathrm{d}x \tag{12.2}$$

where l is the length analyzed. This measurement represents the mean surface (see Fig. 12.7). As it is a mean integrated value, profiles can exhibit the same Ra but have very different surface morphologies.

– The root mean square roughness (see Fig. 12.7)

$$R_q = \sqrt{\frac{1}{\ell} \int_{\ell} z(x)^2 \mathrm{d}x} = \sigma \tag{12.3}$$

– The Rt or Rz, which is the distance between the highest peak and the deepest undercut and which describes local singularities (see Fig. 12.7). This value is very important for the mechanical adhesion of splats.

– The root mean square value $R_{\Delta q}$ which is obtained from the local profile slope dz (x)/dx of the roughness profile within the single measuring length. $R_{\Delta q}$ is a measure of the standard deviation of the profile angle as given by the formula in Eq. (12.4) and shown in Fig. 12.8

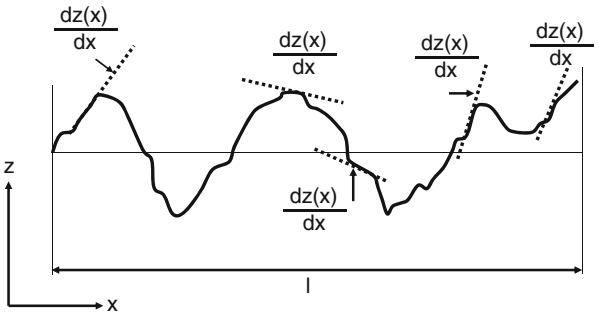


Fig. 12.8 Definition of the slopes used to define $R_{\Delta q}$. Reprinted with kind permission from Prof. P. Nylen [24]

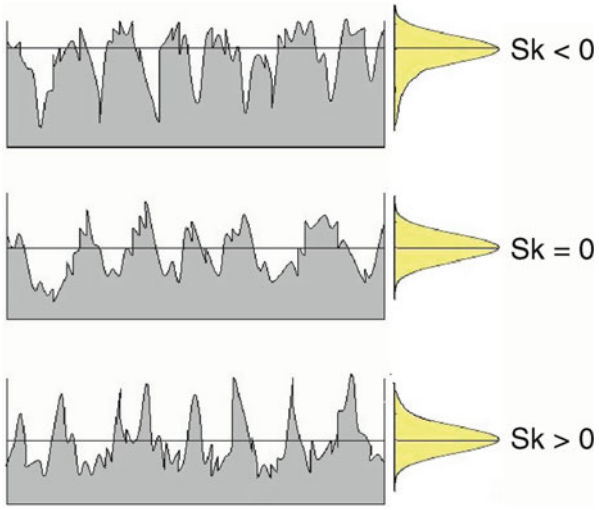


Fig. 12.9 Scheme of surfaces with different skewness. Reprinted with kind permission from Prof. G. Montavon [11]

$$R_{\Delta q} = \sqrt{\frac{1}{\ell}\int_0^{\ell}\left(\frac{\mathrm{d}z(x)}{\mathrm{d}x}\right)^2 \mathrm{d}x} \tag{12.4}$$

– The skewness parameter

$$S_k = \frac{1}{\sigma^3}\int_{-\infty}^{+\infty}(z-m)^3\varphi(x)\,\mathrm{d}x \tag{12.5}$$

where z is the surface height, m its mean value, x the sampling length, σ the root mean square roughness and $\varphi(x)$ the distribution function of the surface heights. The influence of the skewness value on the surface morphology is illustrated in Fig. 12.9. The skewness has been shown to be particularly important at the nanometer scale because it plays a key role on the liquid droplet wetting ability upon flattening and thus on splat formation [18, 25–27].

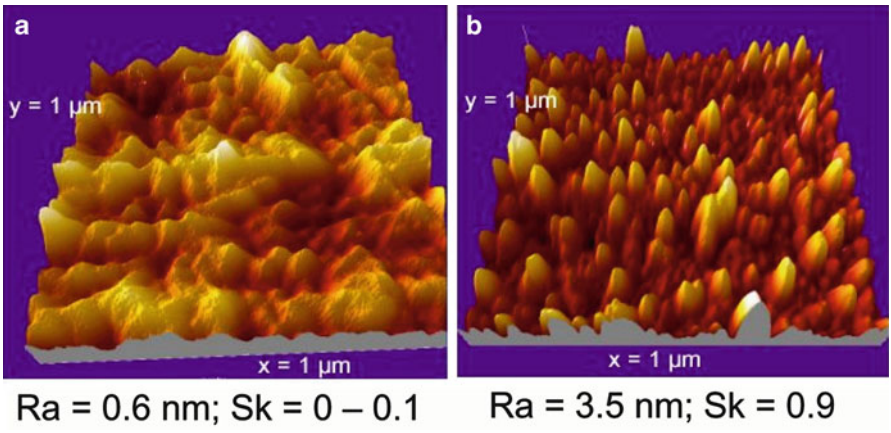


Fig. 12.10 304L stainless steel surface 1 × 1 µm^2, (**a**) kept at room temperature after polishing, (**b**) preheated by a d.c. plasma torch (Ar–H_2) at 250 °C during 120 s. Reprinted with kind permission from Elsevier [18]

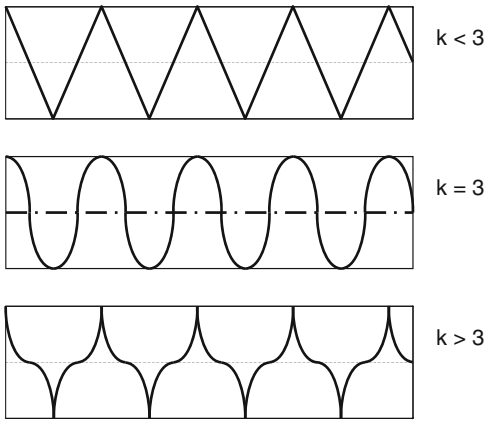


Fig. 12.11 Illustration of surface morphologies and resulting Kurtosis. Reprinted with kind permission from Prof. G. Montavon [11]

Figure 12.10 illustrates practically the skewness effect on a stainless steel 304L kept at room temperature (Fig. 12.10a) with Sk close to 0 and preheated at 250 °C with a d.c. plasma torch (Ar–H_2 plasma) during 120 s resulting in a skewness close to 1 due to surface oxidation (Fig. 12.10b).

– The kurtosis Ku or third moment is used to quantify the anomalies in the heights as illustrated in Fig. 12.11.

Parameters are also used to define the mean spacing R_{sm}. R_{sm} is the arithmetic mean of the widths of the profile within the single measuring length that consecutively cross a lower threshold (C2) and an upper threshold (C1) as given by Eq. (12.6) and shown in Fig. 12.12:

$$R_{sm} = \frac{1}{m}\sum_{i=1}^{m} x_i \tag{12.6}$$

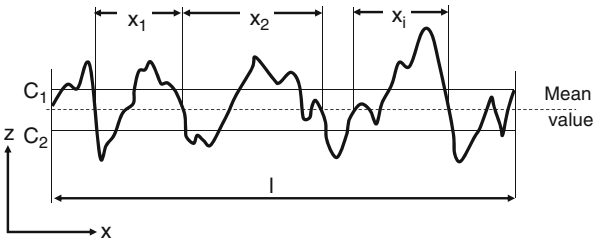


Fig. 12.12 Definition of the arithmetic mean spacing. Reprinted with kind permission from Springer Science Business Media [20]

The question is: which parameter is directly related to the coating adhesion? For example, Bahbou and Nylen [24] have studied the influence of Ra, R_{sm}, and $R_{\Delta q}$ on the adhesion of Ni 5 wt% Al coating plasma sprayed onto Ti6Al4V substrates grit blasted with two brown alumina grit sizes (blasting angle 45°). Results show that the adhesion values measured are poorly correlated with Ra or R_{sm}. However the hybrid parameter containing both amplitude and spacing properties of the surface $R_{\Delta q}$ (i.e., the average slope: see Fig. 12.8) is rather well correlated to the coating adhesion.

Of course many other parameters can be used to characterize surfaces, including fractal dimensions [28–33]. In the latter case however the methodology to accurately describe the surface state is very important and the fractal methodology is sensitive to the measurement scale and to the calculation protocol [32]. To conclude it may be safely stated that the analysis of grit blasted surfaces is far from being a simple problem (see for example [34]).

12.5.2 Grit-Blasting Equipment

The type, size, and degree of automation of any blast system must be tailored to the part. Blasting must always be performed in an enclosure designed for that purpose and equipped with exhaust and dust collection facilities. In order to recycle the grit used, it must be cleaned, rescreened, and sized after each use (generally it falls through a grated floor to a conveyor which transfer it to the cleaning system). Once finer particles and dust have been removed, reusable material is transferred back to the blasting tank. In thermal spraying, mainly two types of machines are used:

- Blast cabinets with suction-type nozzles
- Pressure machines or blast generators

The principle of the suction type gun is presented in Fig. 12.13.

The abrasive medium is dispensed from a hopper and air propelled to the substrate. These machines can be used with almost any type of abrasive with the exception of the larger sizes of crushed iron. This type of machine is less efficient than pressure type machine but the grit flow rate is lower (in a ratio of 3–6) and it is simpler. For more information about grit and air flow rates see the table 1 p. 101 given in [1].

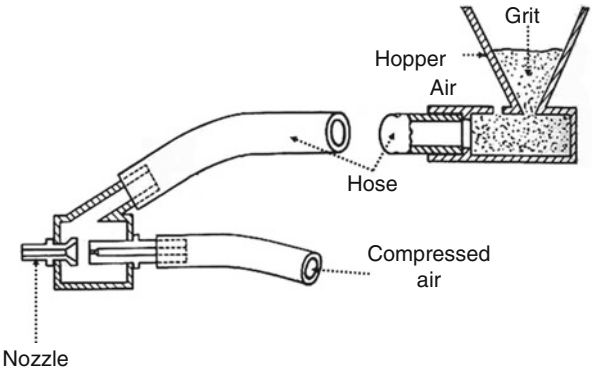


Fig. 12.13 Principle of the suction type gun. Reprinted with kind permission from ASM International [1]

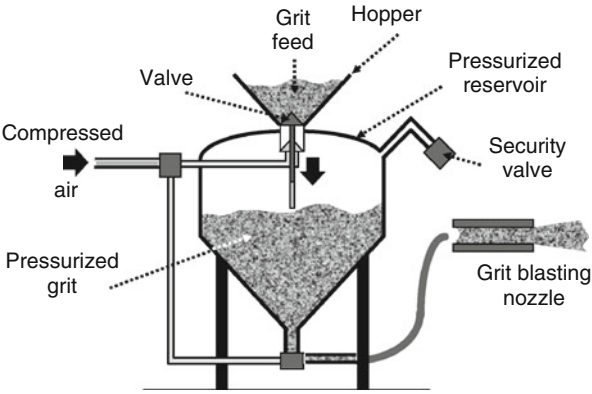


Fig. 12.14 Principle of the pressure type grit-blasting machine. Reprinted with kind permission from American Welding Society [3]

The pressure type machine is shown schematically in Fig. 12.14. It is used for large work pieces requiring high-production rates. They are more effective and efficient than suction type machines, since higher velocities are imparted to the abrasive grains, thus offering greater cutting action. They use a closed reservoir for the abrasive, a carrier gas, and a blasting nozzle. The reservoir is pressurized and the grit carried through the hose and nozzle to the part to be grit blasted. The reservoir must be periodically recharged with the abrasive. It is done automatically when stopping the compressed air releasing the valve at the bottom of the hopper. All types of grit can be used. With this type of machine, the grit velocity is directly linked to the pressure.

12.5.3 Grit-Blasting Nozzles

Straight nozzles are commonly used for industrial scale operation. There are many sizes (diameters), lengths, and configurations as illustrated in Fig. 12.15 for the three most common ones:

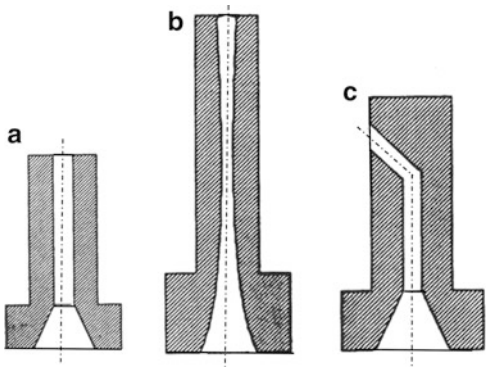


Fig. 12.15 Schematic of three typical grit-blasting nozzles: (**a**) cylindrical or conical, (**b**) Venturi, and (**c**) with deviated jet

Long wear nozzles are generally made of carbide (mainly WC) or a carbide-based [35, 36] composition. They are inserted into a steel or aluminum mounting to protect their hard, brittle, inner core.

The air velocity v_g, which determines the grit particle velocity, depends very strongly on the nozzle internal cross-section area S_n (when compressibility effects are neglected, $m_g^\circ = \rho_g \cdot v_g \cdot S_n$, where m_g° is the air mass flow rate, ρ_g its specific mass). Thus the wear of this nozzle has to be checked very regularly (10 % increase in the diameter results in a 27 % increase of S_n for an 8 mm i.d. nozzle).

12.5.4 Grit Material

Upon impact the abrasive particles induce a plastic deformation of the substrate and the sharp angular particles act like chisels, cutting small irregularities in the surface. In fact, as shown by Griffiths et al. [37]: "two main types of surface damage were observed. The first is produced by an impact from a sharp, angular grit particle, which forms an indentation, often with a lip at its periphery. The crater formed is angular with steep sides and resembles the shape and form of the impinging grit. The crater is formed by plastic indentation of the surface region and elastic compression of the hinterland immediately beneath. It is designated indentation-deformation. The second type of damage is when an impinging particle strikes the surface and micro-machines a crater with a large lip or prow at its exit end. The sharp edge of the particle has cut into the metal, creating a fresh surface, pushing the metal and folding it over onto the undisturbed surface. The crater is more curved than the previous one but still has very angular features particularly in the region of the microchip. This is designated cutting-deformation since it involves fracture as well as elastic-plastic deformation."

The amount of substrate deformation and irregularity created at the surface is a function of the diameter, the specific mass, and the hardness of the impacting particle, and of its speed and angle at which it is directed toward the substrate

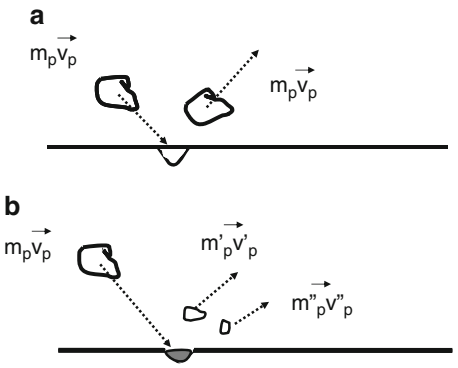


Fig. 12.16 Schematic of the grit particle impact creating an irregularity in the substrate before rebounding (**a**) without breaking and (**b**) with breaking

(see Fig. 12.16a). Of course the substrate deformation and the irregularity formed also depend on the substrate material (hardness, Young's modulus,...). Brittle fracture and/or micro-cutting obtain the surface roughness [38]. After impact the grit particles rebound without or with breaking as illustrated in Figs. 12.16a, b, respectively.

Again it is very important to keep in mind that the particle momentum $m_p.v_p$ depends on its mass which is proportional to the cube of its mean diameter. Thus broken particles, if reused will have a considerably lower momentum, even though, for the same airflow rate, the particle velocity increases when its size decreases.

Since the roughness of the surface depends on the size of the grit, abrasives are supplied in different grades characterized by the screen or sieve used to determine powder size and/or distribution. They are defined by standard mesh sizes (usually between 12 and 320). The smaller is the mesh number, the coarser is the grit. Smaller particles allow for the preparation of a larger area per hour (more particles per unit mass of powder) but the roughness is less. The bigger the particles are, the faster is the material removal from the substrate surface and thus the rougher is the finish. Of course, the larger the particle grit size is, the higher is the compressive peak close to the substrate surface. It is also important to emphasize that the number of particles impacting on a given surface during one second varies with the grit size and decreases when the grit size increases. This is illustrated in Fig. 12.17 after Maruyama et al. [39].

The most commonly used grits are: aluminum oxide, silicon carbide, and steel grit.

12.5.4.1 Aluminum Oxide

It is an angular and durable blasting abrasive that can be recycled (after sieving) many times. It is among harder grits and is used systematically for very hard surfaces (>45 HRC). On soft surfaces (such as aluminum) it may be embedded. When properly crushed, aluminum oxide grits have sharp cutting edges. Its specific

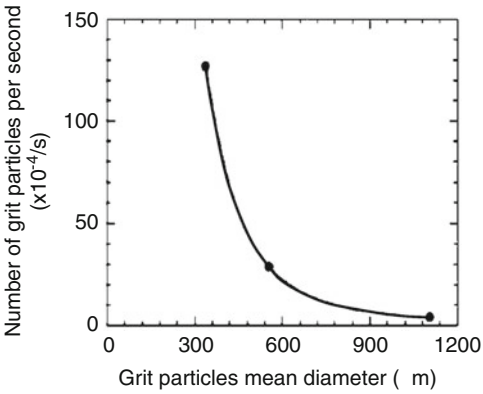


Fig. 12.17 Dependence of the number of grit particles per second on the aluminum grit mean diameter (suction type machine, 6 mm i.d. nozzle, blasting pressure of 0.4 MPa). Reprinted with kind permission from Springer Science Business Media [39], copyright © ASM International

mass about 3,000 kg/m^3 is less than half that of chilled iron grit (about twice as many particles in a kg of grit). There are two types of aluminum oxide:

- Brown aluminum oxide which contains less than 1.5 % free silica, its composition is, for example, 93.3 % Al_2O_3, 3.5 % TiO_2, 1.8 % SiO_2, 0.4 % Fe_2O_3 (CaO and MgO < 1 %), all percentages being in wt%.
- White aluminum, which is 99.5 % pure grade. It is very hard (>9 on the Mohs scale).

12.5.4.2 Silicon Carbide Grits

It is the hardest blasting medium available. High-quality silicon carbide is manufactured to a blocky grain shape that splinters and results in grit particles having rather sharp edges. It may react at high temperatures with various substrates. The concern is that damage to the base material may occur, and coating deterioration may be caused by the combination of silicon and carbon with oxygen as well as the elements present both in the base material and in the coating. On the other hand SiC allows getting "near to zero" contamination at the interface coating/substrate because it dissolves during heat treatment [40]. SiC has a much greater tendency to embed and it breaks down more rapidly than aluminum oxide. However it results in a surface with higher peaks and deeper undercuts when considering the same substrate, the same grit size, and the same blasting conditions. This is illustrated in Fig. 12.18 from Yankee et al. [41].

12.5.4.3 Angular Chilled Iron

The steel used contains more than 0.8 wt% carbon (depending on its hardness) and less than 0.05 wt% of sulfur and phosphorous. Its specific mass is about 7,300 kg/m^3. Different chemistries lead to different hardness:

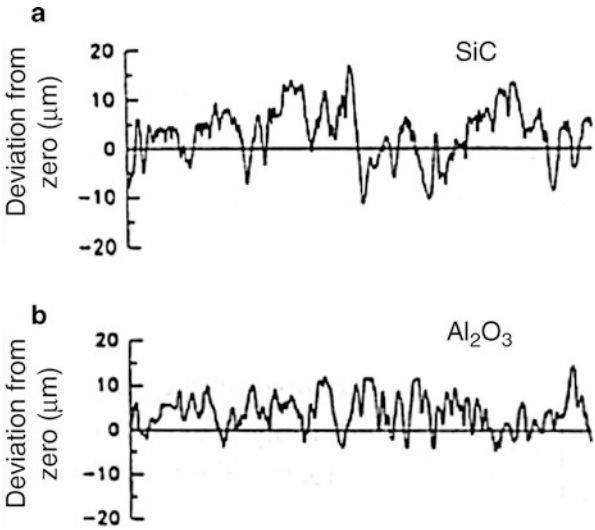


Fig. 12.18 Surface roughness obtained with: (**a**) SiC grit and (**b**) alumina grit. Same substrate, grit size distribution, and blasting conditions. Reprinted with kind permission from ASM International [41]

- The softer one (40–50 HRC) rounds off rapidly and is mainly used for stripping oxides and cleaning
- The harder one (55–65 HRC) maintains its angular shape and provides a good cutting action

12.5.4.4 Other Grits

Silica is inexpensive and widely available. However, it presents an environmental hazard with its possibility of causing silicosis. In some countries, its use is either forbidden or submitted to strict regulations. Crushed garnet: its composition and blasting properties vary widely, depending on the origin of the ore. Crushed slag: it is made from the slag of certain types of furnaces. It is very angular but its silica content must be checked.

12.5.5 Blasting Parameters

As already underlined the blasting parameters are:

– The grit size and composition as well as its impact velocity, the latter being linked to the nozzle internal diameter, the type of blasting machine, the air flow rate (function of its pressure and nozzle i.d.), and the grit size
– The impact angle
– The blasting distance
– The substrate Young's modulus

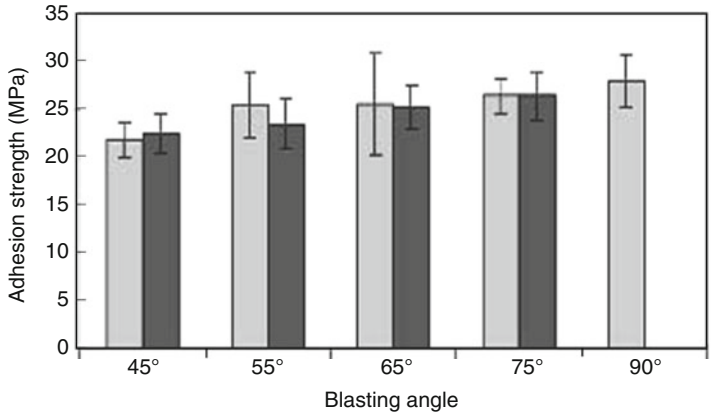


Fig. 12.19 Influence of the grit-blasting/spraying angles on adhesion (Triballoy 800 on Ti6Al4V substrate)—in gray sprayed with the same angle as that of blasting, in black sprayed at 90°. Reprinted with kind permission from Springer Science Business Media [43], copyright © ASM International

12.5.5.1 Impact Angle

The influence of the impact angle is still subject to controversy. However all authors agree on the fact that if a surface is blasted at an angle from one direction and then sprayed at an angle of the opposite direction the coating–substrate bond is very weak. This observation demonstrates that the sprayed particles must penetrate into the surface asperities in order to be mechanically bound to the substrate surface [1]. It could also be said that blasting with an angle results in some sort of "shadowing" effect. The blasting angle is generally varied between 45° and 90° because below 45° the coating adhesion becomes very poor. One observation is that Ra is not affected by the blasting angle variation (between 45° and 90°). However the fractal dimension changes [42]. Similar results were obtained by Mellali et al. [2] who showed that between 60° and 90° the Ra variation was within the error limit. The study of Bahbou et al. [43] spraying Triballoy 800 on Ti6Al4V substrate (grit blasted with alumina: 60 mesh and a suction type machine) has allowed precisely determining the shadowing effect. Results are presented in Fig. 12.19.

The adhesive strength increases with the blasting angle from about 22 MPa at 45° to 28 MPa at 90° (27 % increase) and it increases even more when spraying with the same angle (see Fig. 12.19). This demonstrates the existence of the shadowing effect which is maximal when blasting at 55° and spraying at 90°.

12.5.5.2 Blasting Distance

Figure 12.20 obtained by Mellali et al. [2] with three brown alumina grits shows the Ra dependence on the blasting distance (suction type machine, 8 mm i.d. nozzle). Whatever grit size is used, first Ra increases with the blasting distance, then it reaches a plateau, and then it decreases.

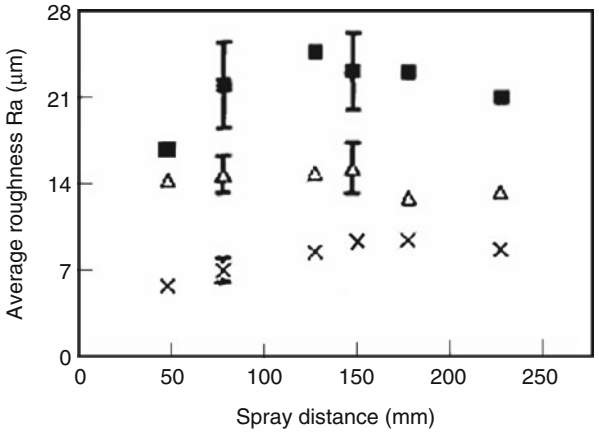


Fig. 12.20 Dependence of the average roughness Ra on the blasting distance for three different brown alumina grits: $d_{50} = 1.4$ mm *square*, $d_{50} = 1$ mm *triangle*, $d_{50} = 0.5$ mm *times*, suction type machine, nozzle i.d. 8 mm, aluminum substrate AU4G. Reprinted with kind permission from Springer Science Business Media [2], copyright © ASM International

Similar results were obtained with cast iron substrates FT25 and hard steel 100C6. The results dispersion increases slightly with distance and the plateau is slightly broader when the Young's modulus of the substrates increases. When the blasting distance, d, is too short, the rebounding particles reduce the number and/or the efficiency of impacting grit particles with which they collide in-flight. When d is too large, the particle velocity decreases, especially that of small particles, which have a lower inertia. It is worth noting that results are more variable when considering R_t instead of Ra. However the general tendency is the same.

12.5.5.3 Blasting Pressure

When increasing the blasting pressure, the particle impact velocity is increased and thus the roughness. However, the effect is rather small with suction type machines [2, 44], but stronger with pressure type machines.

12.5.5.4 Blasting Time

Blasting time is a very important parameter. The blasting time is defined as the time during which each surface unit will be exposed to grit particles. It depends on:

- The radius of the target area a (mm), which increases with the blasting distance (almost linearly) [2], and the nozzle i.d., and is almost insensitive to the grit size
- The displacement velocity of the blasting nozzle v_m (m/s)

For example, Wigren [45] using a diameter ($\varphi = 600$ mm) fixture has established that the blasting time t_b (s) is as follows:

$$t_b = \frac{3.2.a^2.P}{\pi.\varphi.v_m} \tag{12.7}$$

where P is the number of passes. The corresponding values of Ra for different alloys as a function of $(t_b/10^{-3}a^2)$ [according to Eq. (12.7)] are given in Fig. 12.21.

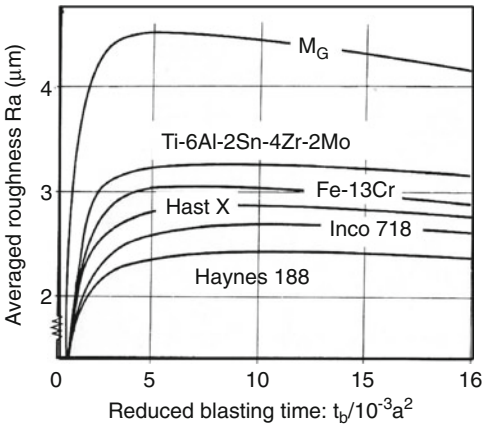


Fig. 12.21 Dependence of the average roughness Ra on the reduced blasting time ($t_b/10^{-3}$ a^2) for various alloys (alumina grit, suction type machine, blasting distance 150 mm, grit flow 2 kg/min). Reprinted with kind permission from ASM International [45]

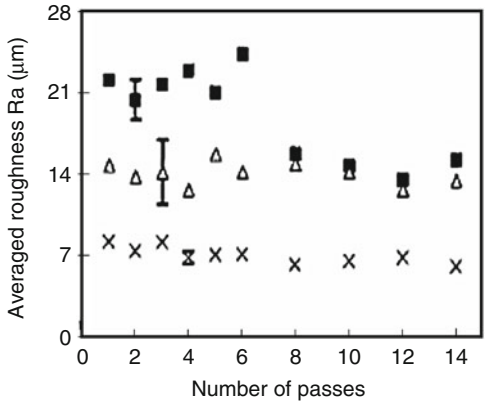


Fig. 12.22 Influence of the number of passes (each pass corresponding to the optimum blasting time) on the average roughness Ra of AU4G substrate for three brown alumina grit sizes ($p = 0.3$ MPa, $d = 130$ mm, suction type machine, nozzle i.d. 8 mm) *square* 1.4 mm, *triangle* 1 mm, *times* 0.5 mm. Reprinted with kind permission from Springer Science Business Media [2], copyright © ASM International

The average roughness increases rapidly with the reduced blasting time, reaching a plateau in a relatively short time (~$0.003 \times a^2 \sim 2.5$–3 s). The time needed to reach this plateau (about 4 reduced times in Fig. 12.21) is the optimum blasting time. Celik et al. [46] obtained a similar result. For longer blasting periods, the roughness decreases slowly but, as it will be shown later, the percentage of residual grit imbedded into the surface increases (see Sect. 12.5.6). Moreover, when increasing the blasting times the substrate hardness increases, with the blasting resulting in some sort of cold work (shot peening effect [47]). Of course the larger the grit size is, the faster is the substrate hardening. This is illustrated in Fig. 12.22 from [2] where an aluminum alloy AU4G substrate has been blasted with three grit sizes of brown alumina for different times. In this figure the time is expressed in terms number of passes, a pass corresponding to the optimum blasting time

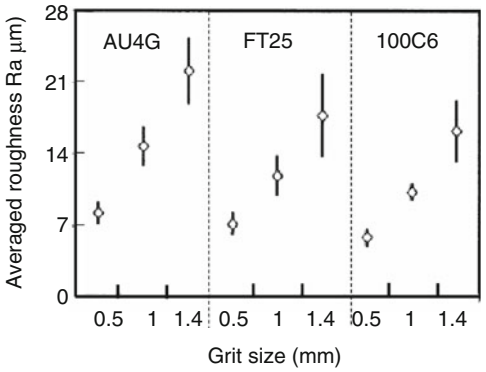


Fig. 12.23 Influence of the brown alumina grit size (0.5, 1 and 1.4 mm) on the average roughness Ra for three substrate materials: AU4G, FT25, and 100C6 ($p = 0.3$ MPa, $d = 130$ mm, optimum time, suction type machine, nozzle i.d. 8 mm). Reprinted with kind permission from Springer Science Business Media [2], copyright © ASM International

(i.e., about 4 reduced time see Fig. 12.21). After 6 passes with the largest grit, suddenly the roughness is reduced by about 39 %. This corresponds to the crushing of the peaks when the hardness underneath increases. For smaller grit sizes, the phenomenon occurs later (for example, 21 passes with the 1 mm grit on AU4G). When considering a harder substrate, for example, 100C6 instead of AU4G, the phenomenon occurs after 11 passes for the 1.4 mm grit.

12.5.5.5 Influence of the Grit

As could be expected, Ra increases when the grit particle size is increased. This is illustrated in Fig. 12.23 from Mellali et al. [2].

A similar result has been obtained by Yang et al. [48] who have shown that for grit sizes over 1.4 mm Ra increases more slowly. The grit nature also plays a role. For example, Mohammadi et al. [49] have blasted a Ti–6Al–4V substrate with alumina grit (300–425 µm) and silica grit (710–1,400 µm) both with suction type machine and silica grit (355–710 µm) with a pressure type machine. The blasting conditions were adapted to obtain for the three grits the same Ra: 3.51 ± 0.15 µm. When spraying hydroxyapatite under the same conditions the following result was obtained for the bond strengths (BS):

- Alumina grit, BS = 24.1 ± 2 MPa
- Silica grit (pressure-type machine), BS = 19.1 ± 3.4 MPa
- Silica grit (suction-type machine), BS = 18.1 ± 3.4 MPa

No clear explanation is given for these results, and the authors do not give grit residue values. The effect of the grit nature (steel grits and conventional grits) on the roughness of A36/1020 steel has also been studied by Varacalle et al. [44].

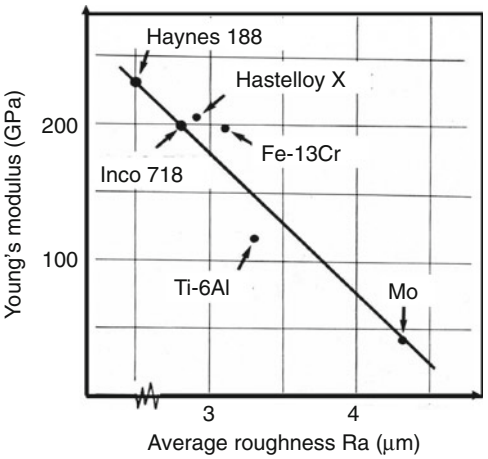


Fig. 12.24 Correlation between average roughness Ra and substrate Young's modulus (same conditions as in caption of Fig. 13.21). Reprinted with kind permission from ASM International [45]

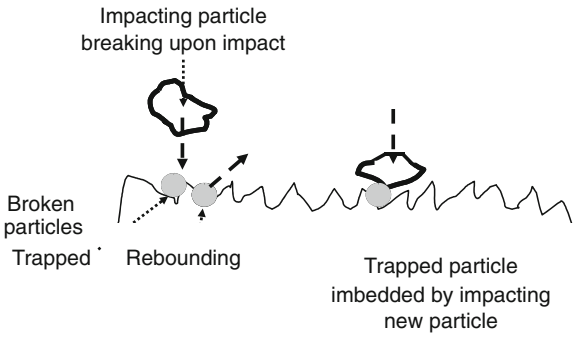


Fig. 12.25 Schematic of the embedding of grit particles at the substrate surface

12.5.5.6 Substrate Young's Modulus

For the same blasting conditions, the Young's modulus of the substrate controls the roughness obtained as shown in Fig. 12.24 from Wigren [45]. For the same blasting conditions the average roughness increases when the Young's modulus decreases.

Similar results can be observed in Fig. 12.23 from Mellali et al. [2], where the Young's modulus are, respectively, 70 GPa for AU4G, 170 GPa for FT25, and 190 GPa for 100C6.

12.5.6 Grit Residues

Unfortunately grit blasting always leaves grit residues embedded into the surface. In most cases the grit embedding happens as shown in Fig. 12.25: an impacting particle is broken at impact and one fragment of it remains at the surface while the

others rebound. Then the next particle impacting on the remaining fragment imbeds it. Of course these phenomena are controlled by on the one hand both grit particle number and momentum, and on the other the Young's modulus of the substrate. The amount of grit residues increases with the substrate ductility which becomes a problem for lightweight alloys.

These residues affect at least the following [44]:

- Surface preparation
- Diffusion between substrate and coating
- Wetting properties of impacting powder droplets on the substrate
- Thermal stress due to thermal expansion coefficient mismatch between grit-matrix and coating first layers

Thus in the following first the influence of the grit blasting parameters on the quantity of grit residues left at the surface and then how to get rid of them will be discussed. All measurements presented were performed at the optimum blasting distance for the different grit sizes and nozzle sizes used. The surface is covered not only by grit residues but also by wear debris produced by the micromachining process. This debris is platelet shape. However these platelets are generally knocked off from the surface by the succeeding impacts of the grit particles.

12.5.6.1 Grit Residues Characterization

The methods used for grit residue evaluation are the following:

- X-ray fluorescence [43, 45]. According to Wigren [45] the analysis of 500 mm^2 area requires about 30 s with a precision better than $\pm$ 10 %.
- Image analysis: when using white alumina grit the imbedded particles are clearly seen with an optical microscope and the ratio of their surface S' to the surface S of the substrate is easy to obtain [2].
- Energy dispersive X ray analysis: for alumina grit containing mainly Al_2O_3 and ZrO_2, Amada et al. [42] have measured Al and Zr at the substrate surface. The image indicating the content of one element was processed by image analysis using back-scattering mode to "see" easily the alumina grit residue and finally, the residual fraction of grits was determined as the ratio of the area covered by the residual grits to the total area of the substrate.
- Dissolution of the blasted surface: Maruyama et al. [39, 50] used this method for carbon steel substrates grit blasted with alumina. After dissolution of the blasted surface in a mixed acid solution, the grit residue removed was weighted and the substrate thickness was measured. The method also allows obtaining the grit particle penetration depth, which can be compared with cross-sectional images of the blasted surface.

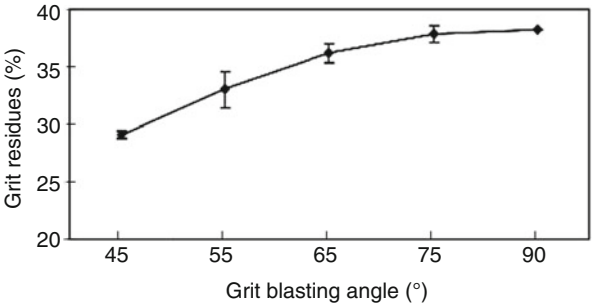


Fig. 12.26 Influence of blasting angle on grit residue amount (percentage by surface area) Ti–6Al–4V substrate, alumina grit. Reprinted with kind permission from Springer Science Business Media [43], copyright © ASM International

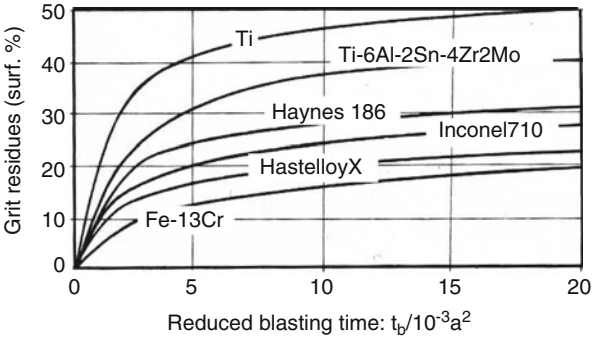


Fig. 12.27 Dependence of the grit residue (surface %) on the reduced blasting time (see Fig. 12.20 caption for different materials). Reprinted with kind permission from ASM International [45]

12.5.6.2 Influence of the Blasting Angle

As it could be expected because grit particles rebounding is easier when the blasting angle is not 90°, the grit residue is lower for a blasting angle of 45° and then increases to reach a maximum at 75° and 90°. This is illustrated in Fig. 12.26 [43].

12.5.6.3 Influence of the Blasting Time

The grit residue increases drastically with the blasting time. As for the substrate average roughness (see Fig. 12.21) the grit residue increases very fast up to a reduced time of about 4 (corresponding to 2.5–3 s) and after this knee increases more slowly but regularly (see Fig. 12.27 from Wigren [45]). Mellali et al. [2] obtained similar results.

12.5.6.4 Influence of the Grit Size

The bigger the grit particles are, the deeper the grit residue is embedded in the substrate (particle mass increases as the cube of its diameter!). This is illustrated in Fig. 12.28 from Maruyama [39].

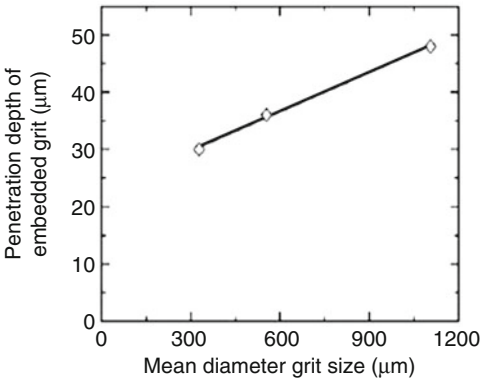


Fig. 12.28 Relationship between the mean diameter of the grit and the penetration depth of the embedded grit (suction type machine, blasting nozzle i.d. 6 mm, blasting pressure 0.4 MPa, white alumina grit, cold rolled carbon steel JIS:S45C). Reprinted with kind permission from Springer Science Business Media [39], copyright © ASM International

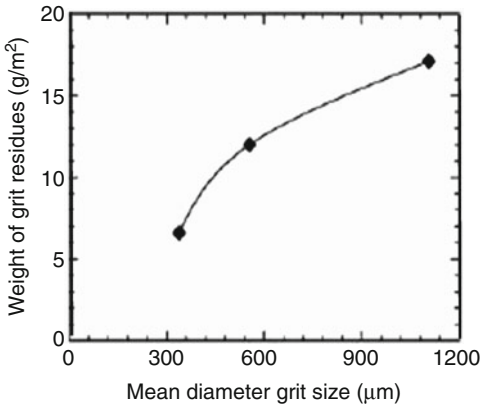


Fig. 12.29 Effect of the mean grit particle diameter on the weight of the residual grit (same conditions as those of Fig. 3.27). Reprinted with kind permission from Springer Science Business Media [39], copyright © ASM International

The weight of the grit residue increases with the grit size as shown in Fig. 12.29 from Maruyama [39]. Mellali et al. [2] obtained a similar result.

Figure 12.30 from Wigren [45] represents the correlation between average roughness and grit residues for different blasting pressures, blasting times, and two blasting angles. It shows that an increased pressure always means increased Ra and increased amount of grit residue, due to the higher energy of the grit particle (the same effect is obtained for a given pressure by increasing the grit particle mean size), and the higher flow of grit particles. The high Ra and low-grit residue percentage are best obtained with high pressure and short time for a given grit size [2]. The blasting angle is not the most important parameter.

12.5.6.5 Grit Residue Removal

The cleaning procedure after grit blasting, to get rid of as much residue as possible, consists in blowing compressed air at a pressure of 0.4–0.5 MPa with a nozzle i.d. of 4 mm for a few tens of seconds and then immersing the substrate in an acetone bath

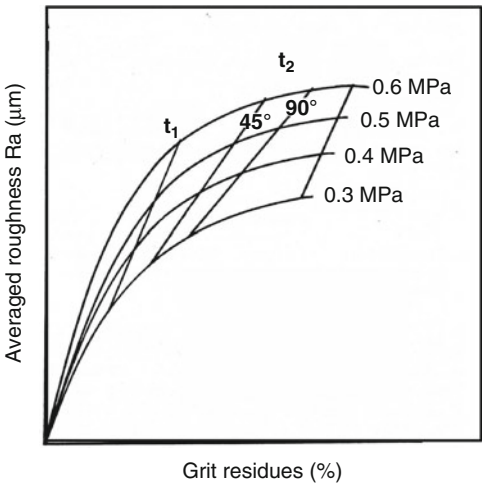


Fig. 12.30 Illustration of the correlation between surface roughness and grit residue, as a function of blasting pressure, angle and blasting time (see blasting conditions in Fig. 3.20 caption: $t_1 = 10^{-3}$ a^{2}s, $t_2 = 3 \times 10^{-3}$ a^{2}s, $t_3 = 12 \times 10^{-3}$ a^{2}s). Reprinted with kind permission from ASM International [45]

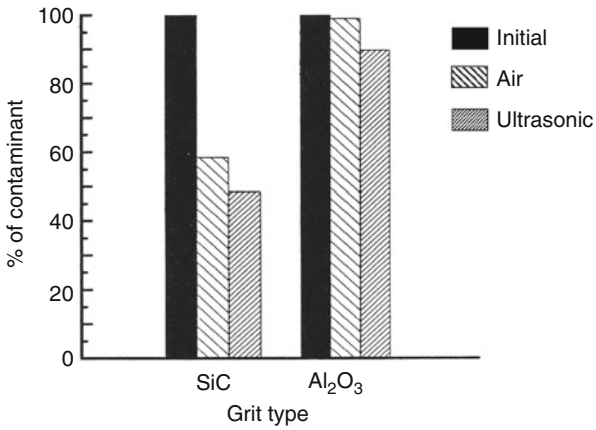


Fig. 12.31 Reduction in contamination, as determined via X-ray fluorescence, for two cleaning procedures (Ti–6Al–4V substrate, 36 mesh grit: SiC or Al_2O, suction type machine, 6.4 mm i.d. nozzle, 0.5 MPa). Reprinted with kind permission from ASM International [41]

solution ultrasonically agitated. As measured by Yankee et al. [41] on Ti–6Al–4V substrates blasted with SiC or Al_2O_3 grit with a size of 36 mesh, the SiC residues are easier to remove than the Al_2O_3 ones. This is illustrated in Fig. 12.31 where the percentage decreases in the original contamination ratio is plotted (the original ratio being normalized at 100 %).

It can be seen that both methods work for SiC but they are much less effective for Al_2O_3, which has the tendency to embed in the Ti–6Al–4V substrate surface. The SiC-roughened substrates were found to contain 7 area % of residue grit, while Al_2O_3-roughened substrate entrained 12 area%. However in spite of that, the adhesion of hydroxyapatite (HA) coatings sprayed under the same conditions presented better adhesion on the alumina grit-blasted substrate and cleaned by air blast (compare Fig. 12.32a to Fig. 12.32b), in spite of the fact that the Ra were similar and the alumina grit residues more important with alumina [41].

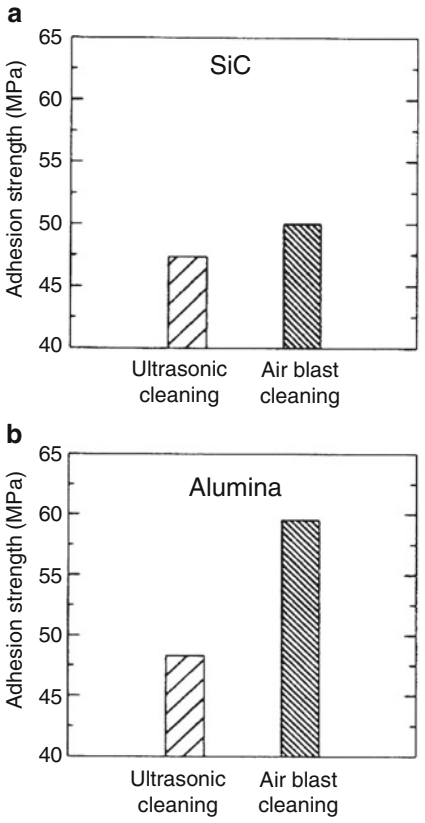


Fig. 12.32 Comparison of adhesion (breaking) strength of HA coatings plasma sprayed on Ti–6Al–4V substrates roughened with (**a**) SiC and (**b**) Al_2O_3. Reprinted with kind permission from ASM International [41]

12.5.7 Grit Wear

The grit wear is strongly linked to the material used, the particle momentum at impact, i.e., the blasting pressure and/or the grit size. For example, SiO_2 is more breakable than SiC, which is more breakable than alumina. For alumina, Mellali et al. [2] have made a systematic study of the grit wear. Figure 12.33 shows three grit size distributions after one cycle (corresponding to the optimum blasting time: the knee in the curves of Fig. 12.21) for three blasting pressures and three grit sizes. The fragmented grit is important especially for the largest particles. A single cycle of the grit significantly increases the quantity of small particles particularly when their velocity (blasting pressure) increases. The grit fragmentation increases with the number of cycles as summarized in Table 12.1 for a suction type machine and a XC38 low-carbon steel substrate.

The authors [2] also show that when using the same grit, without sieving it, to roughen surfaces, the Ra obtained decreased as shown in Fig. 12.34 and the grit residue increases, especially for the larger grit for any substrate [2].

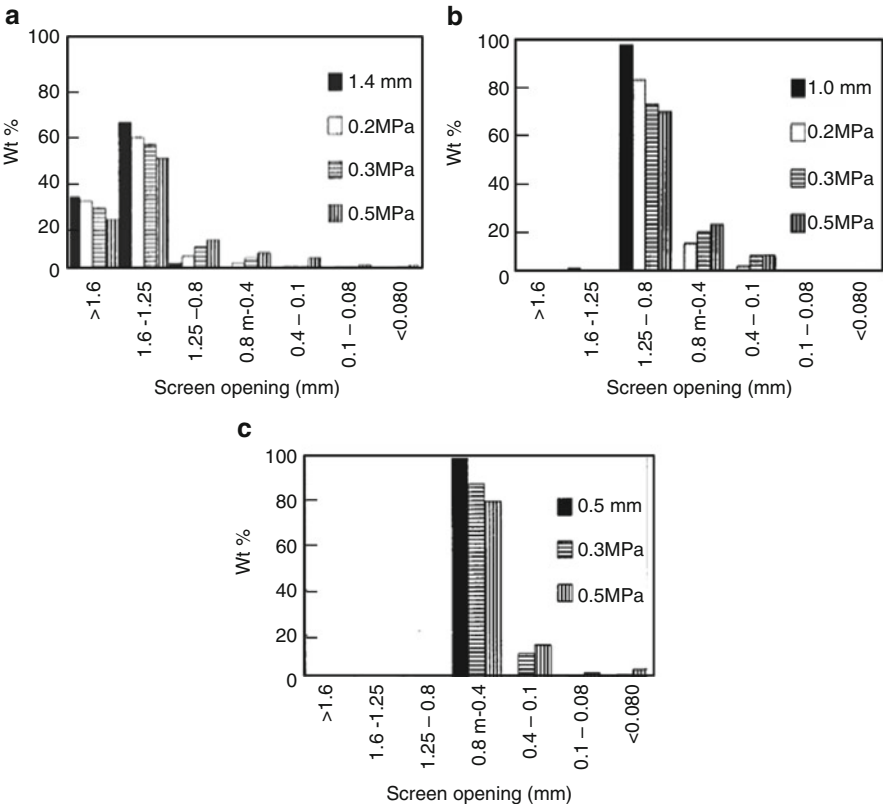


Fig. 12.33 Change of the alumina grit size distribution after one cycle (~3 s) for different blasting pressures and different initial grit sizes. *Black bars* correspond to the initial size distribution (suction type machine, nozzle i.d. 8 mm) (**a**) 1.4 mm, (**b**) 1 mm, and (**c**) 0.5 mm. Reprinted with kind permission from Springer Science Business Media [2], copyright © ASM International

Table 12.1 Weight percentage of grit wear after one and five cycles for three different pressures and grit sizes. Reprinted with kind permission from Springer Science Business Media [2], copyright © ASM International

		Grit wear (wt%)	
Blasting pressure (MPa)	Grit size (mm)	1 cycle	5 cycles
0.2 MPa (30 psig)	0.5	–	–
	1.0	9	27
	1.4	17	39
0.3 MPa (45 psig)	0.5	13	31
	1.0	15	40
	1.4	28	66
0.5 MPa (75 psig)	0.5	20	44
	1.0	26	60
	1.4	31	77

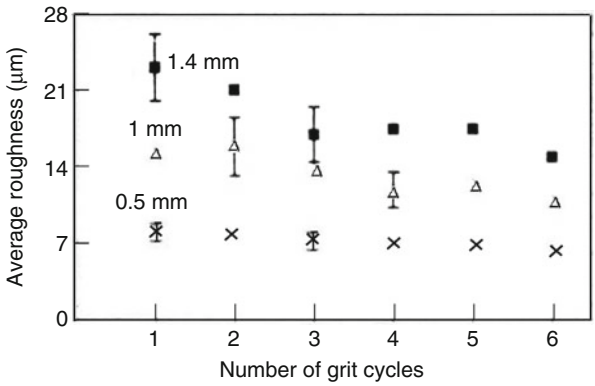


Fig. 12.34 Average roughness of AG4.5 substrates obtained with three different alumina grit sizes (1.4, 1, and 0.5 mm) used for up to six cycles without sieving it. Reprinted with kind permission from Springer Science Business Media [2], copyright © ASM International

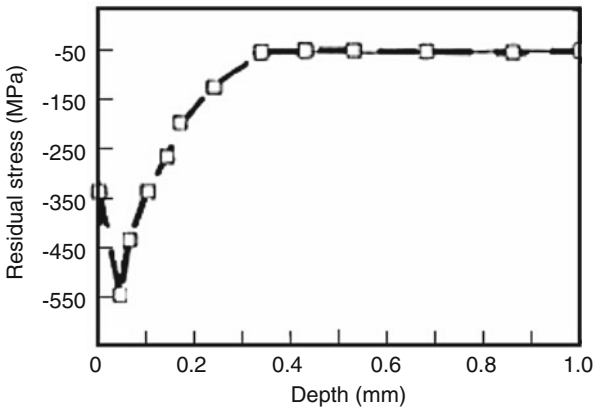


Fig. 12.35 Residual stress distribution, measured by hole drilling method, within a cast iron FT25-blasted substrate (suction type machine, $p = 0.3$ MPa, nozzle i.d. 8 mm, alumina grit 0.5 mm in mean diameter). Reprinted with kind permission from Springer Science Business Media [2], copyright © ASM International

12.5.8 Residual Stress Induced by Grit Blasting

Grit blasting induces compressive stress within metallic substrates [47] by plastic deformation of a layer of about 0.1–0.2 mm in thickness below its surface [2]. This is illustrated in Fig. 12.35 for a cast iron substrate blasted with 0.5 mm alumina grit. With 1.4 mm alumina grit, the maximum compressive residual stress can reach 1,600–2,000 MPa. This stress, of course, modifies the stress distribution between coating and substrate. When spraying materials with high heat content the blasting compressive stress can be partially released when the plastically deformed substrate layer is heated over the recovery temperature [51]. This relaxation is only partial because the spray time is generally shorter than the time necessary for complete relaxation. To relax substrate compressive stress after grit blasting and before spraying, the substrates must be heated in a furnace, where the atmosphere is controlled to avoid oxidation, for example, according to the recommendation of [52].

Table 12.2 Deflection (mm) due to grit blasting of 34CD4 steel flat beams ($2 \times 10 \times 100\ mm^3$) (suction-type machine, nozzle i.d. 8 mm, and one or five cycles) [2]. Reprinted with kind permission from Springer Science Business Media [2], copyright © ASM International

(a) Effect of grit size and pressure

	Pressure (MPa)	Grit size (mm)		
		0.5	1.0	1.4
Deflection (mm)	0.3 (45 psig)	0.32 ± 0.07	0.66 ± 0.05	1.08 ± 0.15
	0.5 (75 psig)	0.43 ± 0.03	0.754 ± 0.04	1.89 ± 0.06

(b) Effect of grit size and blasting time (number of cycles with the grit sieved between each cycle)

	Nb of cycles	Grit size (mm)		
		0.5	1.0	1.4
Deflection (mm)	1	0.32 ± 0.07	0.66 ± 0.05	1.08 ± 0.15
	2	–	0.84 ± 0.06	1.12 ± 0.11
	4	0.37 ± 0.05	1.07 ± 0.05	1.56 ± 0.02

Mellali et al. [2] have studied the influence of the grit-blasting parameters on the residual compressive stress induced by following the deflection of flat beams ($2 \times 10 \times 100\ mm^3$) grit blasted under different conditions. Compared to the hole drilling method, the beam deflection gives only a mean value and no distribution along the substrate thickness but the measurement is straightforward. Table 12.2a summarizes few results obtained with a low-carbon steel substrate (34CD4), grit blasted with three different alumina grits, and two blasting pressures. As could be expected, the deflection increases drastically with the grit size (roughly tripled between a grit of 1.4 mm against one of 0.5 mm) and the blasting pressure, especially for the 1.4 mm grit. The blasting time has also a non-negligible effect, especially for the largest grit (see Table 12.2b).

At last, when martensitic transformation occurs during blasting, for example, when grit blasting an austenitic stainless steel, large distortion can be observed [53].

12.5.9 Conclusion

Grit blasting is a complex process, which has a drastic influence on the adhesion of the sprayed coatings. For the best mechanical adhesion, intuitively the peak heights, characterized by R_t, must be adapted to the mean size of the splats, as illustrated in Fig. 12.36. Of course the spacing between peaks also plays a key role [2, 24, 27].

Indeed to achieve a good mechanical adhesion, it is not sufficient that the size of the peak is adapted to that of the splat size; the flattening liquid drop must also penetrate within the undercuts. For that the impact pressure ($\rho_p \cdot {v_p}^2$) must be larger than the tension force. It results in the following expression:

$$\text{dist} > 4 \cdot \sigma_p / \left(\rho_p \cdot v_p^2 \right) \tag{12.8}$$

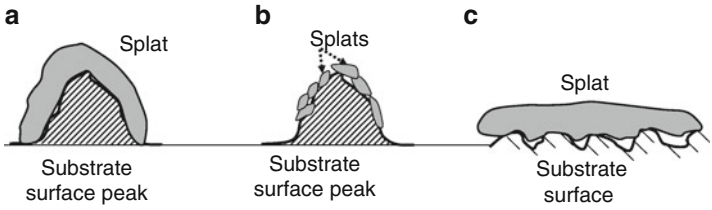


Fig. 12.36 Schematic of splat size relative to grit blasted surface peak sizes. (**a**) Splat size adapted to peak size. (**b**) Too small splat sizes relatively to peak size. (**c**) Too large splat size relatively to peak sizes

Table 12.3 Properties of the main grit materials

Grit material	Properties
Alumina	Hard, angular, durable, easily recycled, embedded in soft surfaces
Silicon carbide	Hardest, very angular, break down easily, produces sharp peaks
Angular chilled iron	Soft (40–50 HRC) rounds off rapidly, hard (40–50 HRC) maintains angular shape
Silica	Inexpensive, angular, breaks down very fast, may cause silicosis

where σ_p is the liquid drop surface tension and dist the characteristic dimension of the under cut. Finally the good criteria must take into account both phenomena. The parameter which seems the most suitable to characterize the surface roughness seems then to be the root mean square value $R_{\Delta q}$ related both to peak sizes and mean distances between peaks. $R_{\Delta q}$ has not yet been systematically studied but the coating adhesion can be rather well related to it [24].

Once the peaks mean size and distance between them have been chosen for a mean splat dimension, the way to achieve the corresponding roughness depends on many parameters:

- Choice of the blasting machine (pressure or suction type)
- Blasting nozzle internal diameter and air pressure controlling the grit particle velocities
- Grit mean size and material controlling, with the particle mean velocity, the mean momentum of grit particles at impact

However it must be kept in mind that the grit residues are also linked to the roughness and thus to particle size, velocity, and material, as well as the residual stress created within the top layer of the substrate. If the latter can be released by heat treatment, the grit residue removal is not easy and the blasting parameters must also be chosen in such a way they are as low as possible (for example, by choosing a smaller grit for obtaining the same roughness [37]).

As will be discussed in Chap. 13, the coating adhesion also depends on the substrate preheating just prior to spraying, for example, to get rid of adsorbates and condensates. Table 12.3 summarizes the effects of the grit choice and Table 12.4

Table 12.4 Influence of the different blasting parameters on the coating roughness, grit residues, and residual stress once blasting distance has been optimized

Grit-blasting parameters	Roughness	Grit residue	Grit wear	Residual stress
Grit size↗	↗	↗	↗	↗
Impact velocity↗ if p ↗ and/or nozzle i.d.↘	↗	↗	↗	↗
Blasting time/ Optimal one t_b	$t < t_b$ ↗ cst. if $t > t_b$	$t > t_b$ ↗	$t > t_b$ ↗	$t > t_b$ ↗
Impact angle: Optimum: 90°	≈cst ."shadowing" effect	45° ↗ 90		
Substrate Young's modulus ↗	↘	↘	↗	

those of the grit-blasting parameters on the substrate modification (roughness, grit residue, residual stress induced) and the grit wear. However it must be kept in mind that all these results depend strongly onto the substrate and especially its Young's modulus. For example, with the same grit b-asting conditions, the substrate roughness decreases if the Young's modulus of the substrate increases.

12.6 High-Pressure Water Jet Roughening

To avoid the embedded contaminants of the grit-blasting process, one of the alternative methods for surface preparation is the use of high-speed fluid jets. The advantage compared to grit blasting is no grit residues, less health hazard, and improved surface cleanness of the substrate. One of the first efforts devoted to this technique using Inconel 718 substrates was that of Taylor [54, 55].

12.6.1 Equipment and Description of the Process

Pumps with pressures up to 360 MPa (54,000 psig) are used. A 0.3 or 0.4 mm diameter sapphire orifice defines the water jet. Either the water jet is translated over the surface of the substrate, or alternately, the substrate is moved transversally underneath the water jet, at velocities between 5 and 200 cm/min. The blasting fluid is often water pretreated by reverse osmosis to fulfill the requirement of the pumping system. The law of Bernoulli gives the velocity of the water jet escaping from the sapphire orifice:

$$v_j = \varphi\sqrt{\frac{p}{\rho_w}} \tag{12.9}$$

where p is the pressure drop (practically the water pressure), ρ_w the specific mass of water, and φ is the nozzle efficiency parameter [56].

The energy of the jet is given by

$$E_{\mathrm{j}} = \frac{m_{\mathrm{w}}}{2} v_{\mathrm{j}}^2 \tag{12.10}$$

where $m_{\mathrm{w}} = m_{\mathrm{w}}^{\circ} \cdot t_{\mathrm{E}}$, with m_{w}° the water jet mass flow rate and t_{E} is the local exposure time ($t_E = L_T/v_{\mathrm{t}}$) with L_T being the length of the profiled section and v_{t} the transverse velocity. The water jet mass flow rate is given by

$$m_{\mathrm{w}}^{\circ} = \alpha \pi d_o^2 v_{\mathrm{j}} \rho_{\mathrm{w}}/4 \tag{12.11}$$

where d_{o} is the sapphire orifice internal diameter and α the outflow parameter.

This results in the expression for jet energy [55]:

$$E_{\mathrm{j}} = \frac{\alpha \pi}{8} d_o^2 v_{\mathrm{j}}^3 \frac{L_T}{v_{\mathrm{t}}} \tag{12.12}$$

For example [55], with $d_{\mathrm{o}} = 0.3$ mm, an exposure time of 600 ms and two water pressures, the following values are obtained:

$$p = 200\,\mathrm{MPa}\,(30,000\,\mathrm{psig}), v_{\mathrm{j}} = 600\,\mathrm{m/s}, E_{\mathrm{j}} = 590\,\mathrm{J}$$
$$p = 275\,\mathrm{MPa}\,(41,000\,\mathrm{psig}), v_{\mathrm{j}} = 704\,\mathrm{m/s}, E_{\mathrm{j}} = 960\,\mathrm{J}.$$

The water jet length consists of a core zone, a transition zone, and a droplet zone [56]. The beginning of the droplet zone is approximately given by the following relationship [57]:

$$L_{\mathrm{c}} \sim 300 \cdot d_{\mathrm{o}} \tag{12.13}$$

where d_{o} is the diameter of the sapphire orifice. For example, with $d_{\mathrm{o}} = 0.3$ mm the droplet zone begins at $L_{\mathrm{c}} \sim 90$ mm from the nozzle exit. Of course the longer the standoff distance is, the larger is the droplet region. The particle velocity decreases with distance. A typical single erosion trace is between 1.5 and 2 mm. The pressure generated by an impacting water drop, p_{I}, is approximated as follows [56]:

$$p_{\mathrm{I}} = \frac{v_{\mathrm{j}} . \rho_w . c_{\mathrm{s}} . \rho_m . c_m}{\rho_w . c_{\mathrm{w}} + \rho_m . c_m} \tag{12.14}$$

where, c_{s} is the shock speed, c_m the sound velocity, and ρ_m the specific mass of the substrate and at last c_{w} the sound velocity in water. The shock speed is given by

$$c_{\mathrm{s}} = c_{\mathrm{w}} + 2 \cdot v_{\mathrm{j}} \tag{12.15}$$

For example [56], for a jet velocity of 600 m/s, with $c_{\mathrm{w}} = 1{,}460$ m/s the impact pressure is $p_{\mathrm{I}} = 1{,}496$ MPa (224,400 psig)! Thus the target, at a given standoff

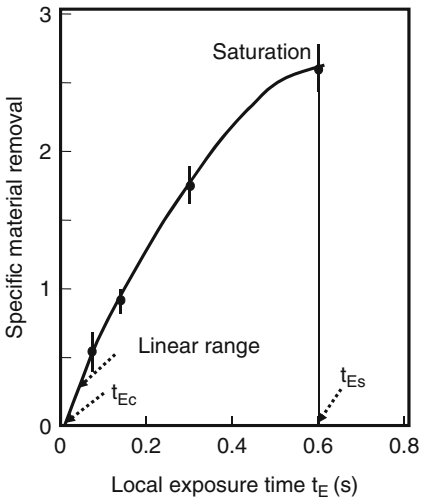


Fig. 12.37 Influence of the water jet time exposure on the specific mass removal. Reprinted with kind permission from Elsevier [56]

distance receives a number of high stress impacts resulting in a non-negligible residual stress below the substrate surface. The additional cyclic component (multiple droplet impact) work hardens and embrittles the surface. For example, after the water jet treatment, the surface hardness of hot-rolled low carbon steel (UH1) is significantly increased: from 24.3 HBR to 41.3 HBR [56].

The substrate material erosion by the water jet requires a minimum local exposure time. This is illustrated in Fig. 12.37 from Momber et al. [56] representing the specific material removal in mg/mm^2 as a function of the local exposure time. Below a critical exposure time t_{EC} no erosion occurs (t_{EC} ~ 0.02 s). When the exposure time increases, the specific material removal increases linearly in the first stage, followed by a gradual drop leading to some sort of saturation where material removal stops at t_{Es}.

The successive phenomena are summarized in Fig. 12.38 from Momber et al. [56]: below t_{EC} probably a certain number of impacting water drops is required to erode material. However the surface below is work harden and embrittle with micro-crack formation. The micro-cracks grow and over the time t_{EC} intersect with each other with material loss occurring. When t_E tends to the saturation time t_{ES}, a fluid film is formed thus damping the impact of the droplets.

12.6.2 Water Jet-Blasting Parameters

The main parameters are the blasting time, stand off distance between the water jet nozzle and the substrate, and pressure as well as the material mechanical properties.

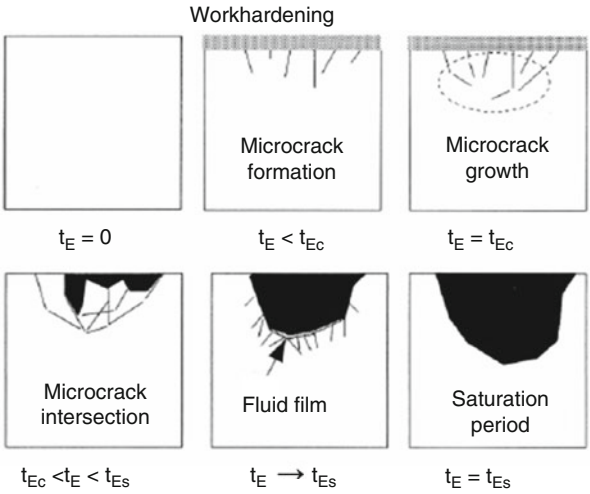


Fig. 12.38 Thresholds and material removal in water jet profiling. Reprinted with kind permission from Elsevier [56]

12.6.2.1 Blasting Distance

As underlined by Taylor [55] and Momber et al. [56], the optimum distance to achieve the best roughening is about 7.6 mm.

12.6.2.2 Blasting Time

The importance of a critical blasting time, t_{Ec} is clearly shown in Fig. 12.38. Taylor [54] has also emphasized that there is "a minimum mass of water required to impinge before there is measurable erosion that is an incubation period." The minimum mass of water per unit surface (kg/m^2) is calculated by dividing the water jet mass flow rate (kg/s) at a given pressure by the product of the water jet width (w) multiplied by its transverse velocity (m/s). In conventional grit blasting roughening occurs after a minimum blasting time, and for a water jet it can be assumed that it corresponds to a minimum mass of water per unit surface (kg/m^2). This is illustrated in Fig. 12.39 from Taylor [54] representing the metal eroded (mg/cm^2) as a function of the mass of water delivered by square centimeters (kg/cm^2) for three blasting pressures.

The effect of the blasting time is also shown in Fig. 12.40 from Taylor [54], where the logarithm of the erosion loss (mg/cm^2) is shown as a function of the logarithm of the traverse rate (cm/min) for two blasting pressures: 207 and 345 MPa (31,050 and 51,750 psig). It can be seen that a small decrease of the blasting time induces a one order of magnitude decrease of the erosion.

The average surface roughness Ra is linked to the erosion loss (mg/cm^2) as shown in Fig. 12.41 from Taylor [55]. Although Ra varies rapidly up to 15 μm with the erosion weight loss, this variation is strongly damped for larger values. The water jet pressure does not seem to have any effect.

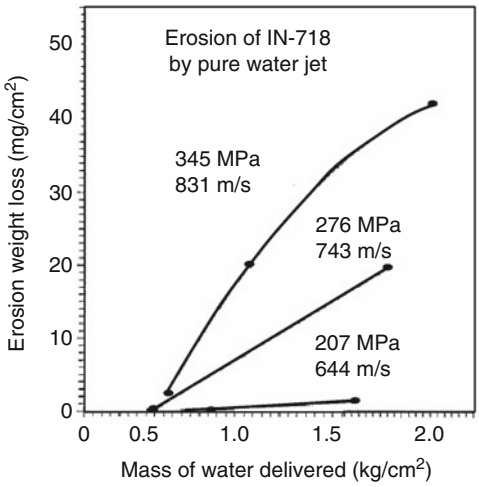


Fig. 12.39 Erosion (mg/cm^2) of IN-718 heat treated for 1 h at 954 °C, as a function of the mass of water delivered (kg/cm^2) for three blasting pressures (nozzle i.d. 0.4 mm). Reprinted with kind permission from Elsevier [54]

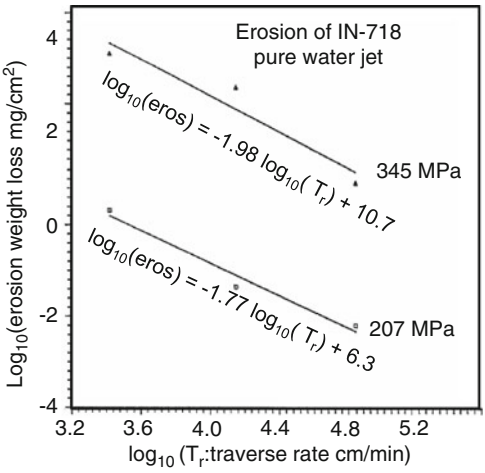


Fig. 12.40 Water jet erosion of IN-718, heat treated for 1 h at 954 °C, $\log_{10} - \log_{10}$ plot of weight loss versus jet traverse rate T_r (cm/min) showing an approximate slope of −2. Reprinted with kind permission from Elsevier [54]

12.6.2.3 Water Jet Pressure

As shown by Eq. (12.9) the water jet velocity depends on the square root of the pressure and according to Eq. (12.14) this has a significant influence on the metal erosion. This is illustrated in Fig. 12.42 from Taylor [54] for IN-718 solution annealed (1 h at 954 °C).

This figure shows a parabolic dependence on pressure, which indicates the existence of a threshold pressure, which is here about 196 MPa (29,400 psig). This threshold pressure can also be observed in Fig. 12.39, where 207 MPa (31,050 psig) is probably very close to it.

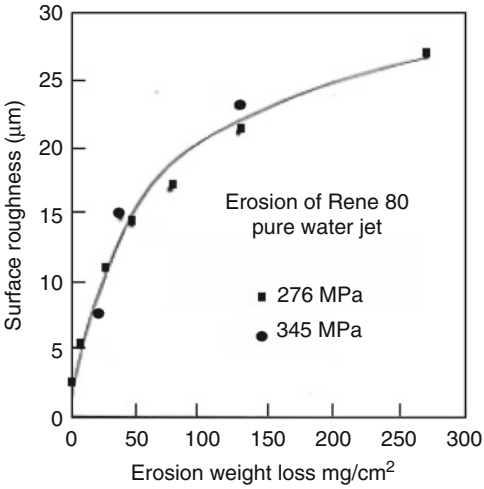


Fig. 12.41 Water jet erosion of Rene 80: dependence of the average roughness Ra on the erosion weight loss: two pressures: 276 and 345 MPa are considered, nozzle i.d. 0.4 mm. Reprinted with kind permission from ASM International [55]

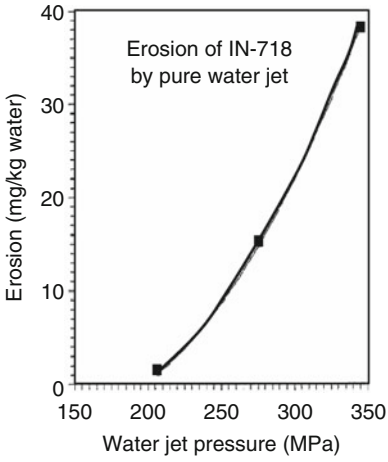


Fig. 12.42 Water jet erosion of IN-718, heat treated 1 h at 954 °C. Weight loss per kilogram of water delivered versus water pressure jet (nozzle i.d. 0.4 mm). Reprinted with kind permission from Elsevier [54]

12.6.2.4 Substrate Material

Figure 12.43 from Taylor [55] correlates the surface roughness of a number of superalloys with their erosion weight losses. There are substantial differences in the roughness achieved with an Inconel sample depending on the heat treatment. The overexposure presents a substantially higher erosion loss and greater roughness. All alloys have a similar behavior for practical applications where Ra is in the range 3–8 µm.

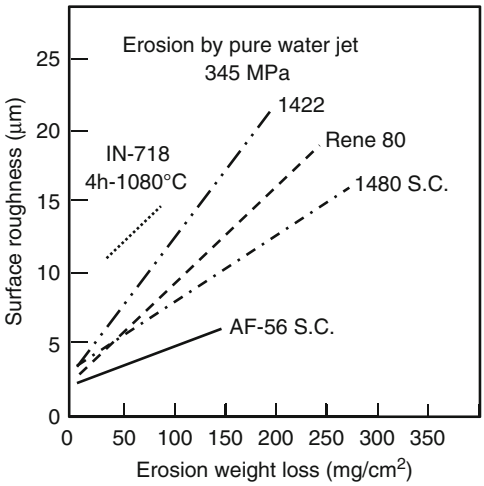


Fig. 12.43 Water jet erosion of various superalloys. Surface roughness versus weight loss. Reprinted with kind permission from Elsevier [55]

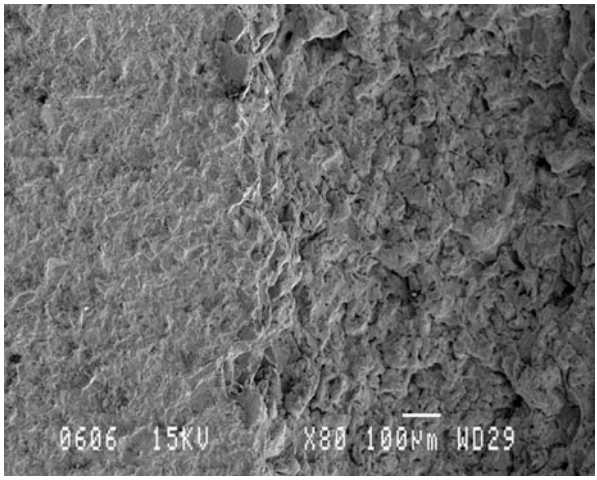


Fig. 12.44 Eroded surface sections (scale 100 µm) of hot-rolled low carbon steel (UH1) *Left*: grit-blasted surface (alumina grit $d_{50} = 165$ µm, nozzle i.d. 8 mm, $p = 0.475$ MPa, suction-type machine) *Right*: water jet blasted (nozzle i.d. 0.3 mm, $p = 248$ MPA). Reprinted with kind permission from Elsevier [56]

12.6.3 Comparison Grit and Water Jet Blasting

Taylor [54] remarks "the detail of eroded surface by water jet increases with increasing magnification, suggesting the water jet erosion produces a fractal surface. The highest magnification micrograph shows a multitude of granular fractures of about 2 µm in size and rather micro-faceted." When compared with conventional grit blasting at the same magnification and for similar average roughness, the feature size is at least an order of magnitude finer in the water jet surface. In contrast the grit-blasted surface appears smoother as the magnification is increased (see, for example, Fig. 12.44 from Momber et al. [56]).

Knapp and Taylor [57] have compared Inconel 718 and Mar-M 509 roughened by water jet and grit blasting and then plasma sprayed with the same superalloy. The have shown superior bounding capabilities of water jet roughened substrates compared to grit blasted substrates. For more details on water jet blasting, the interested reader can consult the reference by Momber and Kovacevic [58].

12.7 Abrasive Water Jetting

It seems that Abrasive Water Jetting (AWJ) can improve pertinent surface characteristics with a higher degree of surface roughness due to the abrasion of the water jet and abrasive particles [59]. In this process the erosion of substrate material is primarily through the action of the abrasive particles, which are accelerated by a thin jet of high velocity water and directed through an AWJ nozzle [5]. Abrasive particles are in the 100–150 mesh range and compared to conventional grit blasting, AWJ reduces grit embedding and grit residues. As for water blasting, the Ra increases with water pressure between (210 and 354 MPa) (31,500 and 53,100 psig), and with blasting time (up to a certain limit). The Ra increases also with the impingement angle, increasing progressively up to 60° and then slightly diminishing [5]. This technique is mainly used for the abrasion and erosion of hard materials [60, 61].

12.8 Laser Treatment: Protal® Process

The idea of laser treatment consists in coupling one or more Q-switched Nd:YAG lasers to the thermal spray torch. The PROTAL process has been developed by Coddet and Marchione [62–65]. It combines in a single step the spraying operation and the surface preparation. The purpose of the laser irradiation is to eliminate the contamination films and oxide layers, to generate a surface state enhancing the deposit adhesion, and to limit the recontamination of the deposited layers by condensed vapors [66].

12.8.1 Laser Ablation

The interaction between a laser beam and a surface is a very complex problem: a part of the laser irradiation is reflected at the surface, a part is transmitted, and the last part is absorbed. The transformation of the irradiated material (heating, melting, and vaporization) is only possible if it is opaque at the considered wavelength. The interaction with the laser irradiation takes place through the free

electrons below the surface. Schematically the laser energy is absorbed following the two main mechanisms, which are the photonic absorption and the inverse bremsstrahlung absorption [67]. Then the process depends on the considered material for:

- Insulating materials the excited electrons are trapped
- Semi-conductor materials, the relaxation is accomplished by heat radiation
- Metallic materials, the relaxation occurs through vibrational excitation (phonons)

Thus the parameters, which are to be considered in laser irradiation–material interaction are the following:

- Substrate nature, its chemical and physical surface properties, its surface micro-geometry (roughness) and for half-transparent materials (such as zirconia, for example, in the 1 μm wavelength range) pores and cracks which reduce the material transmissivity
- Laser beam energy density (J/m^2) and the impact angle. The latter is very important because the absorption of the laser energy by the material diminishes very rapidly when the impact angle (relatively to the normal to the substrate) is increased over 25°
- Nature and pressure of the surrounding atmosphere

In most cases in thermal spraying, substrates are metallic. For a good adhesion of the sprayed particles to the substrate surface, it is necessary first desorbing adsorbates and condensates and then if possible eliminating the oxide layer (when spraying a metal onto a metal). The energy delivered by the laser irradiation must be adapted to what is required and the nature of the contamination [68]. The lowest threshold laser beam energy is required to get rid of the adsorbates and condensates at the surface (the maximum energy of chemisorption is below a few eV).

Higher threshold laser beam energy is required to withdraw the oxide layer at the material surface (*provided it is thin enough: a few tens of nanometers*). Three possibilities must be considered if oxide layer is:

- Transparent to the irradiation wavelength, the energy will be absorbed by the metallic substrate underneath (in general a layer of a few tenths of μm). The resulting thermal effect abruptly expands the surface and induces the breaking and ejection of the oxide layer on top of it
- Semitransparent, intermediate phenomena (absorption by both the oxide layer and substrate) occur
- Opaque, the same phenomena occur as when it was transparent but it is now the oxide layer which is heated

At last the substrate material can be ablated if the laser energy is increased (the highest threshold). Finally to summarize depending on the treated material and its surface properties, different laser thresholds can be chosen to eliminate adsorbates and condensates, adsorbates and condensates together with the oxide layer, to ablate the surface of the metallic substrate.

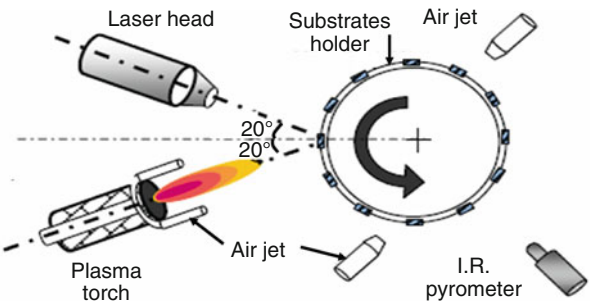


Fig. 12.45 Schematic of the integrated system for the PROTAL® process for air plasma spraying. Reprinted with kind permission from Springer Science Business Media [69], copyright © ASM International

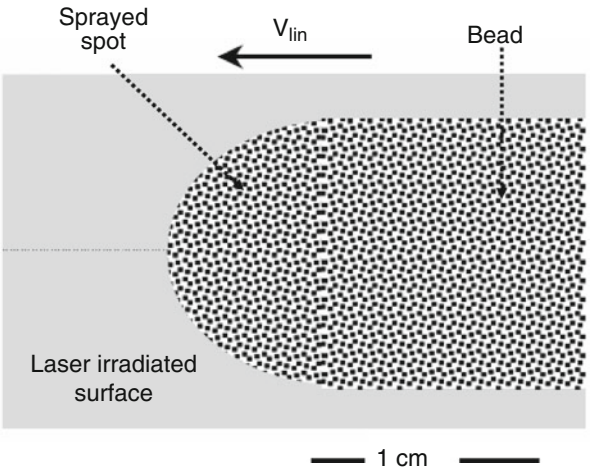


Fig. 12.46 Schematic configuration of the laser-treated zone and of the location of the sprayed particles jet during the PROTAL® process. Reprinted with kind permission from Springer Science Business Media [69], copyright © ASM International

12.8.2 Protal® Experimental Setup

Depending on the thermal and optical characteristics of substrates different phenomena, such as heating, roughening, and ablation can be observed according to the energy density (J/m^2) [66]. It is essential that the laser and spray gun are associated in such geometry that the laser treatment precedes immediately or even overlaps the deposition stage. Figure 12.45 illustrates the integrated systems for the PROTAL® process when plasma spraying in air. The laser head is maintained near the spray torch in front of the sample holder. Both axes of the laser head and plasma torch make an angle of 20° relative to normal axis with respect to the substrate surface.

It is of primary importance that the sprayed spot is in the center of the laser irradiated spot which must be larger than the spraying spot (see Fig. 12.46). Otherwise particles would impact on a nontreated surface.

The laser used in the PROTAL® process is a Q-switched Nd-YAG laser from Quantel (laser blast 1000) which operates at 1,064 μm with an average power output of 40 kW, a maximum pulse frequency of 120 Hz with pulse duration

(FWHM) of 10 ns. The laser beam is transferred through SiO_2 optical fibers. Due to present technical limitations, the power delivery is about 10 W per fiber. A specific optical arrangement allows achieving rectangular-shaped beams with a "top-hat" energy distribution that permitted homogeneous irradiation [69]. The laser head-target distances, defined by the optical system, range from 70 to 120 mm [70]. With this setup energy densities that can be supplied vary from 5 to 25 kJ/m^2.

12.8.3 Example of Results

First of all it must be recalled that all laser parameters will have to be changed according to the material of the treated substrates. To our knowledge only the following substrate materials and coatings have been studied:

- 2017 aluminum-base alloy substrates with pure Cu, Ni–20 wt% Cr, Al_2O_3–13 wt % TiO_2 [66], Ni–5 wt% Al [71] coatings
- Ti–6Al–4V substrate with pure Cu, Ni–20 wt% Cr, Al_2O_3–13 wt% TiO_2 [66], Ni–5 wt% Al [69, 71–74] coatings
- IN718 substrate with Ni–5 wt% Al [73] coating
- Magnesium alloy AZ91 substrate with Ni–20 wt% Cr coating [75]

Moreover the influence of the laser treatment on the surface modification has been studied for the following substrates: pure aluminum (99.99 %) [76], Ti–6Al–4V [77, 78], aluminum alloy A2017, and iron base alloy A430 [78].

The effect of the laser treatment depends on the substrate material, its oxidation (oxide layer thickness, porosity, and crack network), its roughness, and of course on the laser parameters (energy density, number of pulses).

12.8.3.1 Substrate Modifications

For Ti–6Al–4V substrates, the roughness generated by laser treatment varies with the laser energy density and the number of pulses as indicated in Fig. 12.47. A significant increase of Ra begins at 10 kJ/m^2, corresponding to the emergence of craters. Up to 20 kW/m^2 the craters spread all over the surface and correspond to the maximum roughness. Above that value the surface is smoothened and the roughness diminishes. Increasing the number of laser pulses smoothens the surface and protects the early-formed craters, thus the Ra decreases [78]. Figure 12.48a presents the initial state of the Ti–6Al–4V surface and Fig. 12.48b shows the craters after exposure to a single laser pulse of 20 kW/m^2.

Craters are systematically created at surface defect locations, defects such as micro-inclusions or small scratches. The effect of the laser energy density and number of pulses is shown in Fig. 12.49. When comparing Fig. 12.49a, b it can be seen that with the increase of the laser energy density, the induced craters become denser with an enlarged size, linked to more ejected material [77].

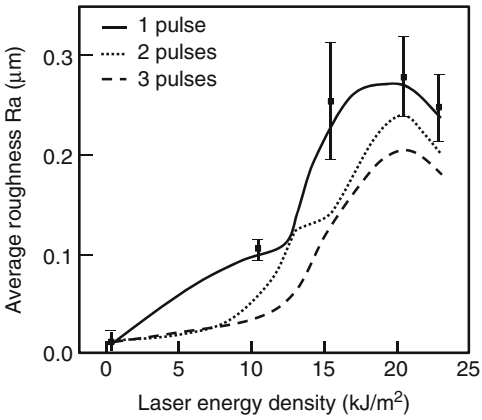


Fig. 12.47 Dependence of a Ti–6Al–4V average surface roughness (Ra) on the laser energy density and number of laser pulses. Reprinted with kind permission from Springer Science Business Media [78], copyright © ASM International

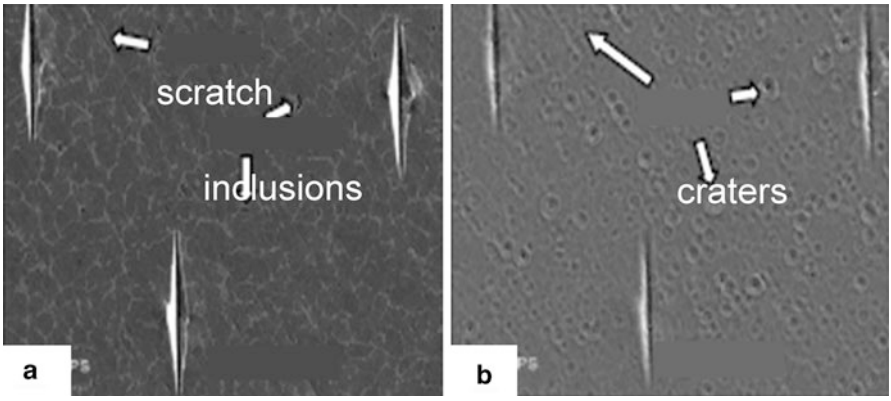


Fig. 12.48 SEM images of the same zone of a Ti–6Al–4V surface: (**a**) initial state, (**b**) surface treated by a single laser pulse at a fluence of 20 kW/m^2. Reprinted with kind permission from Springer Science Business Media [78], copyright © ASM International

With multiple pulses the irradiated surface becomes smooth displaying some periodic variation (Fig. 12.49c) that can be attributed to the laser-induced surface melting at the outermost layer [77]. When the number of laser pulses increases to about 20, a "mud-cracked" morphology is formed on the smooth surface and the surface presents a yellowish color (slight oxidation). If more laser pulses are applied, the "mud-cracked" morphology becomes more distinct with a brighter yellow color which is an indication of the laser induced oxides (Fig. 12.49d) [77]. Correspondingly, the Ra and the skewness S_K vary as indicated in Table 12.5.

Similar results, however with fewer details, have been obtained for other materials [66, 70, 73, 75, 78]: in all cases, craters are formed with laser flux thresholds adapted. Of course when increasing the number of laser pulses, which can also be done by reducing the relative laser-substrate velocity, the substrate temperature increases [72].

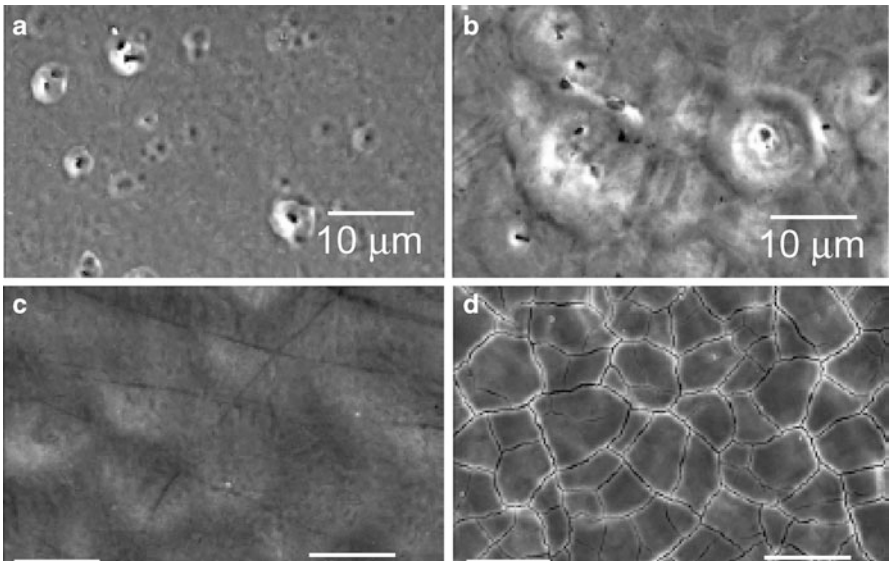


Fig. 12.49 SEM observation of laser irradiated area on Ti–6Al–4V substrate surfaces: (**a**) after a pulse at 10 kJ/m^2, (**b**) 1 pulse of 20 kJ/m^2, (**c**) 10 pulses at 20 kW/m^2, and (**d**) 120 pulses at 20 kJ/m^2. Reprinted with kind permission from ASM International [77].

Table 12.5 Roughness characterization of laser irradiated area on polished Ti–6Al–4V substrate surface (P = pulse). Reprinted with kind permission from ASM International [77]

	Reference	10 kJ/m^2, 1 P	20 kJ/m^2, 1 P	20 kJ/m^2, 20 P	20 kJ/m^2, 100 P
Ra (µm)	0.047	0.13	0.35	0.20	0.25
S_K (-)	−0.09	1.24	0.902	0.096	0.445

12.8.3.2 Splat Formation

For Ni–5 wt% Al sprayed on Ti–6Al–4V splats tend to be disk shaped when the laser heating of substrate reaches about 165 °C. It is worth noting that with the conventional preheating by the plasma jet, the same result is achieved at 250 °C, while the splat is extensively fingered at 165 °C [72].

However if the substrate has been preheated by the plasma torch at about 200 °C, the difference between splats with and without laser treatment is very small [74]. On non-preheated substrates, splats are close to disk shape when laser treatment is used, and are extensively fingered otherwise [74]. Of course the disk-shaped splats are obtained only if the laser energy density is sufficient, i.e., roughly 15 kJ/m^2 [69, 71].

12.8.3.3 Coating Adhesion

Adhesion has been measured either by the interfacial indentation test (see Chap. 15) or the tensile adhesion test (see Chap. 15). However significant differences were observed between the results (tensile adhesion test) of different treatments according to the method used, the interfacial indentation seeming to be more favorable to the PROTAL® process [66]. Compared to the standard preparation (degreasing and grit blasting *but with no preheating*) the PROTAL® process applied to a smooth surface is either equivalent (NiCr coating) or worse (pure Cu or Al_2O_3–TiO_2). However, it must be kept in mind that with the PROTAL® process and the 7.5 kJ/m^2 flux, the Ra is only about 0.09 µm, and the oxide layer has not been completely removed. Moreover, the size of the laser spot is very close to that of the sprayed spot and thus the adhesion is probably poor in the fringes of the sprayed spot.

However the process must be carefully optimized for each substrate and sprayed material. For example, with Ni–20 wt% Cr deposited on magnesium alloy substrates [75] the adhesion reaches 50 MPa for an energy density of 10 kJ/m^2, about 20 MPa with 15 kJ/m^2, and close to 30 MPa for 20 kJ/m^2! When preheating the substrate over the transition temperature (250 °C) for Ni–5 wt% Al sprayed onto Ti–6Al–4V, the adhesion of the coating reaches 30 MPa. On the other hand, when the preheating is followed by one laser pulse at 20 kJ/m^2, it is raised to 40 MPa. To conclude, while this technique seems to be promising because it combines surface preparation with the spray operation, much effort is still necessary to optimize it.

12.9 Summary and Conclusions

The proper preparation of the substrate surface prior to spraying is essential for the coating adhesion. It has to be carried out within the shortest time possible prior to spraying. Surface preparation comprises three steps:

- *Cleaning*, which is the first step to remove contaminants such as oil, greases, paint, rust, scale, and moisture. This operation is quite conventional but it is essential.
- *Roughening* that is crucial for optimal coating adhesion to the substrate. The degree of roughness has to be compatible with the mean size of splats: the R_t (also called R_z) must be about 2.5 times the mean splat diameter, and the spacing between peaks has to be sufficient for the liquid flattening droplet to penetrate between them. The root mean square value $R_{\Delta q}$ seems to be the roughness parameter that correlates the best with the coating adhesion. Roughening can be achieved by grit blasting or water jet. The former is probably the most commonly used. The degree of roughness, grit residues, and blasting induced

stress depends on the blasting system used (suction or pressure type machines), blasting pressure (important for pressure type machine), blasting distance that must be optimized, grit material, and size. Since the grit particles can break down during the blasting operation, the grit used must be continuously sieved, and the fines discarded, in order to maintain a close control on the uniformity and degree of roughness generated. The main disadvantage of grit blasting is the grit residues that must be removed prior to spraying, which is not necessarily easy. The main advantage of water jet, compared to blasting, is that no residue is formed. The degree of roughening depends strongly on the water jet pressure and mass flux of water per unit surface area (kg/m^2). This parameter is calculated by dividing the water jet mass flow rate (kg/s) at a given pressure by the product of the water jet width (w) multiplied by its transverse velocity (m/s). Because of the rapid wear of the equipment and the liquid jet nozzles, which are rather expensive, this technique is mainly used for sophisticated coatings as in aero-engine industry.

– *Adsorbates and condensates elimination* that is performed either by preheating the substrate, generally with the spray torch, to temperatures at which they evaporate, or by blasting the substrate with dry ice just ahead of the spray spot, or by using a laser focused upstream of the spray spot. Substrate preheating is by far the most commonly used on an industrial scale; dry ice blasting has started to be used, while laser pretreatment is a still mainly at the laboratory developed stage.

In all case independent of the technique used, cleaning, roughening, and adsorbates–condensates elimination are all key factors to achieve coatings with good adhesion properties.

Nomenclature

Latin Alphabet

a	Radius of the area hit by blasting particles (m)
AA	Arithmetic average AA $= \frac{h_1+h_2+\ldots h_N}{N}$
c_m	Sound velocity in the substrate (m/s)
c_s	Shock speed in the substrate (m/s)
c_w	Sound velocity in water (m/s)
d	Blasting distance (m)
d_o	Sapphire orifice internal diameter for water jet (m)
E_j	Water jet energy (J)
l_n	Assessment length (m)
l_t	Transverse length (m)
L_T	Length of the profiled section with the water jet (m)
m_g°	Air mass flow rate (kg/s)

m_{w}° Water jet mass flow rate (kg/s)
m_{p}° Grit particle flow rate (kg/s)
p Blasting pressure (MPa)
Ra Average roughness (μm) $\mathrm{Ra} = \frac{1}{\ell}\int_0^{\ell} z(x)\,dx$
R_q Root mean square roughness (μm) $R_q = \sqrt{\frac{1}{\ell}\int_{\ell} z(x)^2 \mathrm{d}x} = \sigma$
R_{t} Distance between the highest peak and the deepest undercut (μm)
R_{sm} Arithmetic mean of the widths of the profile (μm)
$R_{\Delta q}$ Root mean square value $R_{\Delta q} = \sqrt{\frac{1}{\ell}\int_0^{\ell}\left(\frac{\mathrm{d}z(x)}{\mathrm{d}x}\right)^2 \mathrm{d}x}$
S_{n} Blasting nozzle internal surface (m^2)
S_k Skewness parameter $S_k = \frac{1}{\sigma^3}\int_{-\infty}^{+\infty}(z-m)^3\varphi(x)\mathrm{d}x.$
t_{b} Blasting time (s)
t_{E} Local exposure time ($t_{\mathrm{E}} = L_T/v_{\mathrm{t}}$) to the water jet (s)
t_{EC} Critical exposure time to a water jet (s)
v_g Air velocity (m/s)
v_{j} Water jet velocity (m/s)
v_{p} Particle velocity (m/s)
v_{t} Transverse velocity of the water jet/substrate (m/s)

Greek Alphabet

φ Water jet nozzle efficiency parameter (-)
ρ_{g} Air specific mass ($\mathrm{kg/m}^3$)
ρ_{m} Specific mass of the substrate ($\mathrm{kg/m}^3$)
ρ_{w} Specific mass of water ($\mathrm{kg/m}^3$)

References

1. Davis JR (ed) (2004) Handbook of thermal spray technology. ASM International, Materials Park, OH
2. Mellali M, Grimaud A, Léger AC, Fauchais P, Lu J (1997) Alumina grit blasting parameters for surface preparation in the plasma spraying operation. J Therm Spray Technol 6(2):217–227
3. (1985) Thermal spraying, practice, theory and applications. American Welding Society, 550 N. W. LeJeune Road, P. O. 351040, Miami, Florida 33135
4. (1994) ASM handbook volume 05: surface engineering, 1056 pages, ASM Int., Materials Park, OH 44073–0002, USA
5. Wang L (2004) Erosion testing and surface preparation using abrasive water-jetting. J Mater Eng Performance 13(1):103–106

6. Stratford S (2000) Dry ice blasting for paint stripping and surface preparation. Metal Finishing 98(6):493–499
7. Spur G, Uhlmann E, Elbing F (1999) Dry-ice blasting for cleaning: process, optimization and application. Wear 233–235:402–411
8. Elbinga F, Anagrehb N, Dorna L, Uhlmann E (2003) Dry ice blasting as pretreatment of aluminum surfaces to improve the adhesive strength of aluminum bonding joints. Int J Adhes Adhesives 23:69–79
9. Bardi U, Carrafiello L, Groppetti R, Niccolai F, Rizzi G, Scrivani A, Tedeschi F (2004) On the surface preparation of nickel superalloys before CoNiCrAlY deposition by thermal spray. Surf Coat Technol 184:156–162
10. Dong S, Song B, Hansz B, Liao H, Coddet C. Improvement in the microstructure and property of plasma sprayed metallic, alloy and ceramic coatings by using dry ice blasting. In: 5th RIPT conference, CEC Limoges, Dec 2011, e-proceedings
11. Montavon G (2004) Quality control of thermal sprayed coatings, Course Thermal spraying, Aliderte Limoges France
12. (1994) Whitehouse, Handbook of surface metrology. Lavoisier, Paris, 984 pages
13. Vorburger TV, Teague EC (1981) Optical techniques for on-line measurements of surface finish. Precision Eng 3(2):61–83
14. Tonshoff HK, Janocha H, Seidel M (1988) Image processing in a production environment. Ann CIRP 37(2):579–589
15. Shin YC, Oh SJ, Coker SA (1995) Surface roughness measurement by ultrasonic sensing for in-process monitoring. ASME J Eng Ind 117:439–447
16. Bradley C (2000) Automated surface roughness measurement. Int J Adv Manuf Technol 16:668–674
17. Lockwood DJ (2007) Light scattering and nanoscale surface roughness. Springer, New York
18. Cedelle J, Vardelle M, Fauchais P (2006) Influence of stainless steel substrate preheating on surface topography and on millimetre- and micrometer-sized splat formation. Surf Coat Technol 201(3–4):1373–1382
19. Conroy M et al (2005) A comparison of surface metrology techniques. J Phys Conf Ser 13:458–465
20. Hu Zhongxiang, Zhu Lei, Teng Jiaxu, Ma Xuehong, Shi Xiaojun (2008) Evaluation of three-dimensional surface roughness parameters based on digital image processing. Int J Adv Manuf Technol
21. Al-Kindi GA, Shirinzadeh B (2007) An evaluation of surface roughness parameters measurement using vision-based data. Int J Mach Tools Manuf 47:697–708
22. Tomovich SJ, Peng Z (2005) Optimised reflection imaging for surface roughness analysis using confocal laser scanning microscopy and height encoded image processing. J Phys Conf 13:426–429
23. Thomas TR (1999) Rough surfaces. Imperial College press, London
24. Bahbou F, Nylen P (2005) Relationship between surface topography parameters and adhesion strength for plasma spraying. In: Lugscheider E (ed) ITSC 2005. DVS, Düsseldorf, Germany, e-proceedings
25. Fukumoto M, Huang Y (1999) Flattening mechanism in thermal sprayed Ni particles impinging on flat substrate surface. J Therm Spray Technol 8(3):427–432
26. Tanaka Y, Fukumoto M (1999) Investigation of dominating factor on flattening behaviour of plasma sprayed ceramic particles. Surf Coat Technol 12(121):124–130
27. Fukumoto M, Ohgitani I, Yasui T (2004) Effect of substrate surface change on flattening behaviour of thermal sprayed particles. Mater Trans 45(6):1869–1873
28. Amada A, Hirose T (2000) Planar fractal characteristics of blasted surfaces and its relation with adhesion strength of coatings. Surf Coat Technol 130:158–163
29. Amada S, Yamada H (1996) Introduction of fractal dimension to adhesive strength evaluation of plasma-sprayed coatings. Surf Coat Technol 78:50–55

30. Amada S, Hirose T (1998) Influence of the grit blasting pre-treatment on the adhesion strength of plasma sprayed coatings: fractal analysis of roughness. Surf Coat Technol 102:132–137
31. Amada S, Satoh A (2000) Fractal analysis of surface roughened by grit blasting. J Adhes Sci Technol 14(1):27–41
32. Guessasma S, Montavon G, Coddet C (2003) On the implementation of the fractal concept to quantify thermal spray deposit surface characteristics. Surf Coat Technol 173(1):24–38
33. Reisel G, Heimann RB (2004) Correlation between surface roughnesses of plasma sprayed chromium oxide coatings and powder grain size distribution: a fractal approach. Surf Coat Technol 185:215–221
34. Bacova V, Draganovska D (2004) Analysis of the quality of blasted surfaces. Mater Sci 40(1):125–131
35. Deng J, Junlong S (2008) Sand erosion performance of B_4C based ceramic nozzles. Int J Refractory Metals Hard Mater 26:128–134
36. Deng J (2009) Wear behaviors of ceramic nozzles with laminated structure at their entry. Wear 266(1–2):30–36
37. Griffiths BJ, Gawne DT, Dong G (1996) The erosion of steel surfaces by grit-blasting spraying as a preparation for plasma. Wear 194:95–102
38. Bellmann R, Levy A (1981) Erosion mechanism in ductile metals. Wear 70:1–27
39. Maruyama T, Akagi K, Kobayaski T (2006) Effects of blasting parameters on removability of residual grit. J Therm Spray Technol 15(4):817–821
40. Scrivani A, Rizzi G, Giolli C (2006) Improved surface preparation of nickel-superalloys for MCrAlY coatings on gas turbine. In: Larple B et al (eds) Proceedings of the 2006 ITSC conference. ASM International, Materials Park, OH, e-proceedings
41. Yankee SJ, Salsbury RL, Pletka BJ (1991) Quality control of hydroxylapatite coating: properties, processes and applications. In: Bernecki T (ed) Thermal spray 1991. ASM International, Materials Park, OH, pp 505–513
42. Amada S, Hirose T, Senda T (1999) Quantitative evaluation of residual grits under angled blasting. Surf Coat Technol 111:1–9
43. Bahbou MF, Nylen P, Wigren J (2004) Effect of grit blasting and spraying angle on the adhesion strenght of a plasma-sprayed coating. J Therm Spray Technol 13(4):508–514
44. Varacalle DJ Jr, Guillen DP, Deason DM, Rhodaberger W, Sampson E (2006) Effect of grit-blasting on substrate roughness and coating adhesion. J Therm Spray Technol 15(3):348–355
45. Wigren J (1988) Grit blasting as surface preparation before plasma spraying. In: Hauck D (ed) Thermal spray: advances in coatings technology. ASM International, Materials Park, OH, pp 99–104
46. Celik E, Demirkiran AS, Avei E (1999) Effect of grit blasting of substrate on the corrosion behavior of plasma sprayed Al_2O_3 coatings. Surf Coat Technol 116–119:1061–1064
47. He J, Dulin B, Wolfe T (2008) Peening effect of thermal spray coating process. J Therm Spray Technol 17(2):214–220
48. Yang Y, Wang HG, Cao XP, Wang L (2006) Influence of substrate surface roughness on adhesive strength. In: Marple B et al (eds) Proceedings of the 2006 thermal spray conference. ASM International, Materials Park, OH, e-proceedings
49. Mohammadi Z, Ziaei-Moagyed AA, Sheik-Mehdi Mesgar A (2007) Grit blasting of Ti-6Al-4V alloys: optimization and its effect on adhesion strength of plasma sprayed hydroxyapatite coatings. J Mater Proc Technol 194:15–23
50. Maruyama T, Akagi K, Kobayaski T (2007) Effect of the blasting angle on the amount of the residual grit on blasted substrates. In: Marple BP et al (eds) Thermal spray 2007. ASM International, Materials Park, OH, e-proceedings
51. Liao H, Vaslia P, Young Y, Coddet C (1999) Determination of the residual stress distribution from in situ measurements for thermally sprayed WC-Co coatings. J Therm Spray Technol 6(2):235–241
52. (1964) ASM metals handbook, ASM Int., Materials Park, OH 44073–0002, USA

53. Abukawa S, Kobayashi K, Kobayashi Y (2006) The relationship of work distorsion and surface roughness on grit blasting process. In: Marple B et al (eds) Thermal spray 2006. ASM International, Materials Park, OH, e-proceedings
54. Taylor TA (1995) Surface roughening of metallic substrates by high pressure pure waterjet. Surf Coat Technol 76–77:95–100
55. Taylor TA (1995) Surface roughening of superalloys by high pressure water jets. In: Berndt CC, Sampath S (eds) Thermal spray: science and technology. ASM International, Materials Park, OH, pp 351–358
56. Momber AW, Wong YC, Ij R, Budiharma E (2002) Hydrodynamic profiling and grit blasting of low-carbon steel surfaces. Tribology Int 35:271–281
57. Knapp JK, Taylor JA (1996) Waterjet roughened surface analysis and bond strength. Surf Coat Technol 86–87:22–27
58. Momber AW, Kovacevic R (1998) Principles of abrasives water jet machining. Springer, London
59. Kovacevic R, Hashish M, Mohan R, Ramula M, Kim TJ, Geskin ES (1997) State of the art of research and development in abrasive-water-jetting machining. Trans ASME J Manuf Sci Eng 119:776–785
60. Zeng J, Kim TJ (1996) An erosion model for abrasive waterjet milling of polycrystalline ceramics. Wear 199:275–282
61. Ness E, Zibbell R (1996) Abrasion and erosion of hard materials related to wear in the abrasive water jet. Wear 196:120–125
62. Coddet C, Marchione T (1993) Process for the preparation and coating a surface and apparatus for practicing sand process (in French). French patent FR9209277, 21 July 1993
63. Coddet C, Marchione T (1997a) Process for the preparation and coating a surface and apparatus for practicing sand process. European patent extension EP0580534A1, 23 Apr 1997
64. Coddet C, Marchione T (1997b) Process for the preparation and coating a surface and apparatus for practicing sand process. US patent extension, US 5668564, 18 Nov 1997
65. Coddet C, Marchione T (1999) Process for the preparation and coating a surface and apparatus for practicing sand process. Canadian patent extension, CA 2101004, 13 July 1999
66. Coddet C, Montavon G, Ayrault-Costil S, Freneaux O, Rigolet F, Barbezte G, Folio F, Diard A, Wazen P (1999) Surface preparation and thermal spray in a single step: the PROTAL process- example of application for an aluminium-base substrate. J Therm Spray Technol 8 (2):235–242
67. Landau L, Lifshitz E (1984) Statistical physics. MIR, Moscow, Russia
68. Leung NP, Zupka W, Ziemlich W (1992) Cleaning techniques for removal of surface particulates. J Appl Phys 7:3513–3523
69. Li H, Costil S, Liao H-L, Coddet C (2006) Role of the laser surface preparation on the adhesion of Ni-5 wt% Al coatings deposited using the PROTAL® process. J Therm Spray Technol 15(2):191–197
70. Costil S, Li H, Coddet C (2004) New developments in the PROTAL® process. In: ITSC2004. DVS, Düsseldorf, Germany, e-proceedings
71. Li H, Costil S, Liao H-L, Coddet C (2005) Role of laser surface preparation on the adhesion of Ni-5wt% S. CostilAl coatings deposited using the PROTAL® process. In: Lugscheider E (ed) ITSC 2005: explore its potential! ASM International, Materials Park, OH, e-proceedings
72. Liao H, Gammondi A, Costil S, Coddet C (2003) Influence of surface laser cleaning combined with substrate preheating on the splat morphology. In: Moreau C, Marple B (eds) Thermal spray 2003: advancing the science and applying the technology. ASM International, Materials Park, OH, pp 883–888
73. Bahbou F, Nylen P, Barbezat G (2004) A parameter study of the PROTAL® process to optimize the adhesion of Ni5Al coatings. In: ITSC 2004. DVS, Düsseldorf, Germany, e-proceedings

74. Li H, Costil S, Deng S-H, Liao H-L, Coddet C, Ji U, Huang W-J (2006) Benefit of surface oxide removal on thermal spray coating adhesion using the PROTAL® process. In: Marple B (ed) ITSC 2006. ASM International, Materials Park, OH, e-proceedings
75. Li H, Costil S, Deng S-H, Coddet C, Liao H-L, Richardt K, Lugscheider E, Bobzin K (2006) Ni-Cr coatings deposited on a magnesium alloy substrate using the Protal process. In: Marple B (ed) ITSC 2006. ASM International, Materials Park, OH, e-proceedings
76. Barnier V, Costil S, Li H, Coddet C, Oltea R (2007) Study of the aluminium oxidation induced by a Q-switched Nd:YAG laser treatment and its influence on the adhesion properties of a plasma-sprayed alumina coatings. In: Marple B et al (eds) Thermal spray: global coating solutions. ASM International, Materials Park, OH, pp 335–340, e-proceedings
77. Li H, Danlos Y, Costil S, Coddet C (2007) Influence of laser induced surface topography on the surface static wettability in Protal®. In: Marple B et al (eds) Thermal spray (2007), global coating solutions. ASM International, Materials Park, OH, pp 1070–1074, e-proceedings
78. Li H, Costil S, Coddet C (2005) Surface modification induced by the pulse Nd-YAG laser irradiation in the Protal®. In: Lugscheider E (ed) ITSC2005: explore its potential. ASM International, Materials Park, OH, e-proceedings

Chapter 13
Conventional Coating Formation

13.1 Introduction

Thermal spray processes, whether plasma, wire arc, flame, HVOF, HVAF, D-gun, or PTA are relatively mature technologies widely used in industry. They mostly involve the introduction of either particles (in the tens of micrometers size range) into the hot gas stream where they are accelerated and totally or partially melted, or wires, cored wires, rods, and cords and have their tip melted and atomized. The thermal and kinetic energy content of the droplets impinging on the substrate can vary widely with the process used. In spite of the extensive scientific literature published on these processes, they still remain "as much an art as a science" [1]. Moreover, for metals or alloys or composites sprayed in air, high process temperatures tend to increase the in-flight particle oxidation, increasing the oxide content embedded into the coating which can significantly compromise its service performance. It is of course possible to limit the in-flight oxidation of the particles by plasma spraying in a controlled atmosphere (vacuum plasma spraying, VPS). The improvement of the coating quality is, however, associated with a significant increase of the investment needed which can be at least one order of magnitude higher than comparable processes working in an open air envireonment, thus limiting the use of such technologies to high added value products.

Twenty years ago a group of scientists at the Institute of Theoretical and Applied Mechanics of Novosibirsk, Russia [2, 3] developed a new process, called "cold spray," operated at high gas pressures of up to 3 MPa, the high-pressure gas being led into a converging–diverging de Laval-type nozzle. The powder particles are accelerated to velocities of above 600 m/s and kept at temperatures typically around room temperature. The gas can also be preheated to about 600 °C (for details see Chap. 6) in order to increase its nozzle exit velocity. This is generally associated with a corresponding increase of the oxidation level of the coatings compared to that of the sprayed particles. Of course only ductile particles can be sprayed, provided their impact velocity is over a so-called critical velocity. Phenomena at impact are quite different from those obtained with molten particles: they include

P.L. Fauchais et al., *Thermal Spray Fundamentals: From Powder to Part*,
DOI 10.1007/978-0-387-68991-3_13, © Springer Science+Business Media New York 2014

plastic deformation corresponding to the propagation of structure defects and adiabatic heating, due to the short time during which the high pressure occurs, softening locally the material.

The past two decades also saw the development of flame-based spray systems which aimed at reducing the temperature of particles and increasing their velocity [4] (see Fig. 5.14). This was achieved with HVAF and HVOF spraying. In the latter case, particle velocities as high as 650 m/s were obtained using converging–diverging de Laval-type nozzle designs and upstream chamber pressures up to 1 MPa (by injecting nonreactive gases in the combustion chamber). It even became possible to reduce metal or alloy particle temperatures below their melting temperatures with increased velocities (see Chap. 5) resulting in coating densities between those obtained with D-gun and cold spray. In these conditions it is possible to spray ductile particles (in a plastic state below their melting temperature and, of course, less oxidized than those fully melted) and achieve coatings in conditions almost similar to those of cold spray.

Based on the mechanism of coating formation, coatings can be grouped into the following two broad categories:

- Those sprayed with mainly fully melted particles (including metals, alloys, ceramics, and cermets introduced within the spray gun as particles, wires, rods, or cords) flattening upon impact and resulting in splats, with mean diameters between 2 and 6 times that of the impacting particle diameter, the coating being built-up by their layering.
- Those resulting from the deformation of particles (metals, alloys, cermets) either cold and ductile or hot (below their melting temperature) in a plastic state. The deformation of the particle upon impact corresponds to a splat with a diameter rather close to that of the initial particle, with a flattening degree generally below 1.5–2. The coating results from particle plastic deformation and its consolidation is due to the peening effect of the new impacting particles (of course except for the last deposited layers).

The microstructure of sprayed coatings is rather complex, exhibiting anisotropic behavior which is also affected by defects such as pores, cracks, and imbedded unmelted particles. In fact, coating microstructure depends strongly [5–12] on more than 60 independent spray parameters which need to be considered for the optimization of the coating quality. Fortunately the development of sensors [13] (see also Chap. 16), able to work in the harsh environment of spray booths, has allowed achieving a better understanding of coating generation as well as a better control, or at least monitoring, of their formation. These sensors measure particle parameters in-flight: temperature, diameter, velocity, and trajectory distributions for hot ones, and mainly velocity and trajectory distributions for cold ones, particle parameters at impact (images recording of particle flattening and measurement of the splat temperature evolution during its formation and cooling), substrate and coating temperature evolutions, coating thickness. . .(see Chap. 16).

Understanding coating generation starts with particle flattening on the substrate, or the previously deposited layers, and with the cooling of the hot droplets and

flattened particles. In this chapter we will attempt to address the following general questions:

- What are the physical and chemical characteristics of the substrate surface? In all metals, alloys, and cermets (where the matrix is a metal) the substrate surface will be covered with an oxide layer, the thickness and composition of which are dependent on the substrate temperature before spraying.
- Have adsorbates and condensates, present at the substrate surface, been eliminated by preheating just prior to spraying, using dry ice blasting, laser treatment, etc.?
- What are the fundamental phenomena linked to the impact of individual particles?
- How do particles adhere first to the substrate and then to the previously deposited layers? (a coating will never protect a substrate if it does not adhere to it!). Of course melted and unmolten ductile metal, cermet, even ceramic particles, and polymer particles will have to be considered separately.
- How melted or partially melted particles will form splats on smooth substrates or previously deposited layers?
- What happens when melted particles impact on rough substrates or on idealized surfaces with well-defined geometrical patterns?
- How ductile particles impact of on smooth and rough surfaces?
- How are layered splats appearing of melted or ductile particles with:
  - Splat layering with a motionless spray torch
  - Splat layering with the torch moving in one direction relatively to the substrate with the formation of a bead
  - Splat layering with beads overlapping to form a pass, the thickness of which is linked to the spray pattern, as well as successive pass layering
  - Formation of polymer coatings
  - Formation of PTA coatings

Topics covered in this chapter will also include how the use of robots moving the spray torch, and a rotating table on which the substrate is fixed allows controlling the coating thickness on substrates of complex shapes?

- The control of coating temperature during its formation with the impact of hot particles and the jet of hot gases will then be considered.
- The residual stresses, which partly depend on the coating temperature control during spraying and on the impacting particle velocities and temperatures, are then considered with successive discussion of:
  - Temperature control of substrate and coating
  - Development of residual stresses due to quenching, expansion mismatch, temperature gradient, surface preparation, coating geometry, and phase changes

– A short review of the influence of the choice of particle morphologies and wires, cored wires, rods, or cords on coating properties is presented.
– Finally the different means to finish coatings and post-treat them is described.

13.2 Spray Parameters

Spray parameters, as summarized in Fig. 13.1, are the following:

– The spray process used with its working parameters: torch design, nozzle shape and dimensions, mass flow rates, compositions and pressure of spray gases, arc current, etc.
– The powder composition, size distribution, and particle morphologies depending on the manufacturing process, the wire, cored wire, rod, or cord composition and post-treatment
– The powder injection: axial or radial, with the injector position and orientation, internal diameter, carrier gas flow rate, the atomization gas flow rate for the wire, etc.
– The spray distance
– The spray pattern
– The temperature control of substrate and coating during the preheating, spraying, and cooling phases
– The substrate shape, size, thickness, and preparation

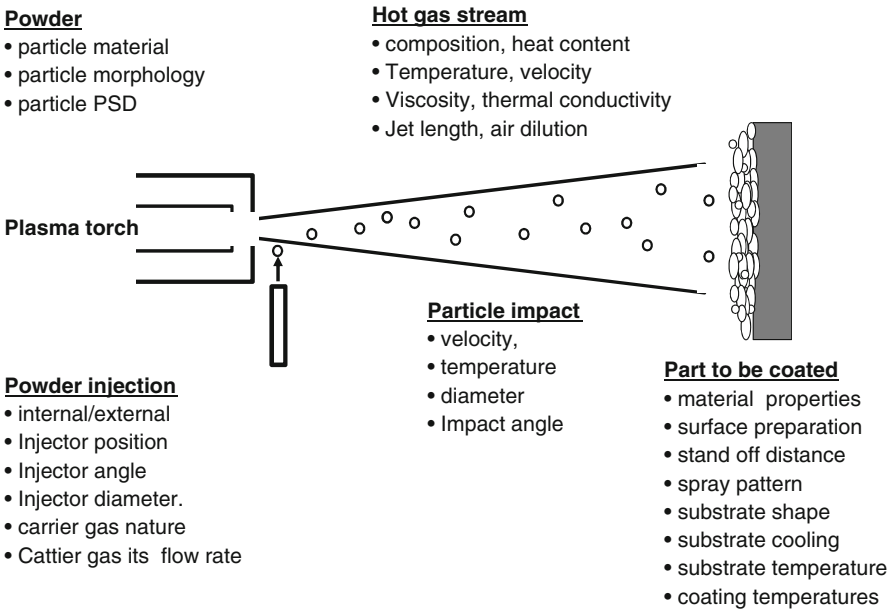


Fig. 13.1 Different spray parameters

Of course the choice of the spray process with the corresponding spray gases defines the gas temperature and velocity ranges, as shown in Fig. 1.5 (see Chap. 1). Of course, these velocities and temperatures are very different according to the spray process used. These different temperatures and especially velocities, as well as the surrounding atmosphere, will result in various coating properties, as illustrated for example in Fig. 2.2a–c (see Chap. 2) presenting the cross sections of the same CoNiCrAlY commercial powder (Sulzer Metco Amdry955) sprayed with three different processes.

As most spray processes are operated in air (atmospheric spraying), the air is entrained within the high-energy jet and thus oxygen (di-atomic or mono-atomic in case of plasmas) reacts with the hot particles in-flight. Besides the entrained air, the oxygen used for the combustion, often performed with an excess of oxygen, can also participate to in-flight particle oxidation. However it must be kept in mind that oxidation also depends strongly on the particle temperature. The in-flight particle oxidation is controlled by diffusion and convection (see Sect. 4.3.3.7). The specific reaction rate constant of diffusion is of an Arrhenius type and roughly increases by one order of magnitude when the temperature increases by 100–200 K. It is thus clear that the oxidation of a fully melted particle will be much more important than that of one in a plastic state, which is in turn higher than that of a cold one, as in cold spray. Moreover oxidation can be promoted, under certain conditions encountered in plasma, HVOF and wire arc spraying, by the convective movement (see Sect. 4.3.3.7) induced by the high-energy jet within the liquid drop (fully melted particle). In this case fresh metal is continuously renewed at the particle surface, while oxide or oxygen is entrained inside the molten particle. Compared to oxidation by diffusion, the oxide content can be multiplied by a factor of 4 to 6! Oxidation can also occur at the surface of successive passes, but the coating temperature control can significantly limit this phenomenon. At last it must be emphasized that oxygen present in the spray jet can also react with the sprayed material to modify its composition. This is, for example, the case of carbides that can be deeply modified or even destroyed by the formation of CO. For example, WC is changed to W_2C and then to W (for more details see Sect. 11.1.3.3). Of course such reactions are also controlled by Arrhenius type laws and drastically reduced when particle temperatures are lowered. To limit oxidation problems spraying in a controlled atmosphere or under soft vacuum is an efficient means, but a rather expensive one. Using shielding devices (elongated spray gun nozzle and/or inert gas flow) also reduces oxidation but generally at the expense of high shield inert gas flow rates (up to more than ten times that of the working gas of the gun).

Once the spray process has been chosen, temperatures and velocities of particles also strongly depend upon particle size distribution and morphology [14] as well as their injection conditions [15] (see Sects. 4.2.2 and 4.4.2). Particles used for spraying have sizes comprised between about 10 μm and 110 μm. However, the choice of the size distribution is a key issue for the coating quality. It must be chosen according to the material sprayed, especially its melting difficulty, and the spray process used. The size distribution must be as narrow as possible to limit the particle trajectory dispersion. Particle trajectories depend on their injection

force, $m_p \cdot \gamma_p$ (Sect. 4.2.2). The particle acceleration γ_p, imparted by the carrier gas flow rate, as shown by the particle mean velocity at the injector exit, is almost independent of the particle size (see Sects. 4.2.1 and 4.2.2). Once the carrier gas flow rate has been chosen, particle forces are linked to their mass, proportional to the cube of their diameter. Trajectory dispersion within energetic gases will be very important, resulting in broad distributions of heat and momentum transfers to particles. Correspondingly, the particle hits the substrate or the previously deposited layers with different velocities and temperatures and of course different melting stages. As pointed out in Sects. 4.2.2.1 and 4.2.2.2, the dispersion effect will be less drastic with axial injection than with radial one. Radial injection in a plasma jet is illustrated in Fig. 2.1. Particles penetrate within the jet, if their mean force is about the same as that imparted to them by the energetic gas. The optimum mean trajectory corresponds roughly to an angle of 3–4° with the torch axis, as illustrated in Fig. 2.19a. Moreover at the injector exit, particle trajectories are not all parallel to the injector axis and the particle flux has a conical shape with a total angle generally below 20°, as illustrated in Fig. 4.58. This is due to the collisions of particles with the injector wall and between themselves. Thus whatever the injection mode will be (axial or radial) it is unavoidable that part of the injected particles travel in the jet fringes, where the heat and momentum transfers are lower, and impact the substrate with an angle and not normally to the substrate. At last the particle morphology, resulting from its manufacturing process (see Chap. 11), plays an important role in their acceleration and heating. For the same material composition, the specific mass can vary in a ratio up to 5 between atomized and agglomerated particles, and the injection acceleration has to be adapted accordingly. The heat transfer is also modified when comparing for example dense and agglomerated particles [16] especially for materials with poor thermal conductivities ($\kappa < 20$ W/m K) where the heat propagation phenomenon becomes important.

To conclude this section, the choice of a spray process defines ranges of temperatures and velocities that can be achieved with particles of specific material having the adapted size distribution. Of course the final impact velocities and temperatures depend on the working parameters chosen for the process and the injection conditions.

13.3 Physical and Chemical Description of Substrates

Most of the following has been published in the review paper of Chandra and Fauchais [17]. The vast majority of substrates used in thermal spray applications are metallic. Metals (except gold and platinum) or alloys have oxidized surfaces even without preheating them (native oxide). Unless oxide layers are removed (with a reversed transferred arc under soft vacuum or using laser pulses) prior to spraying, particles impact on the oxide layer existing on the substrate surface. Then for the following deposited layers, particles also mostly impact on oxides because particles have been oxidized either in-flight or during deposition.

13.3.1 Physical Aspect of Substrate Surfaces

Most studies were performed on smooth surfaces where the observation at the nanometer scale is possible and where the particle flattening can be followed.

13.3.1.1 Substrate Surface Topography

Several authors have pointed out that mean surface roughness R_a of smooth surfaces of metals (except Au and Pt) or alloys increases at the nanometer scale with substrate preheating. Fukumoto et al. [18] have noted that, when a surface was polished to a particular average roughness R_a, coating adhesion was not as high as it was when preheating produced the same roughness. To more accurately characterize the substrate surface they [18] introduced another index of surface topology: skewness (S_K), the definition of which is given in Sect. 12.5.1, Eq. (12.5). The skewness increases from negative values to positive ones upon preheating a polished surface and splat shape changes correspondingly from fingered to disk shaped. Cedelle et al. [19] have shown for a 304L stainless steel substrate that changes in surface topography in the nanometer range have a large effect on the static wetting behavior of molten metal droplets placed on its surface. Hence substrate preheating does not modify just the chemical composition and thickness of the oxide layer on the metallic substrate but also its physical aspect, which plays a key role in the behavior of impacting particles. For $S_K > 0$ (more peaks than undercuts) obtained for 304L stainless steel, preheated at 673 K by a d.c. plasma jet [18–20] or a laser (with a power density over 50 MW/m^2) [21], the resulting zirconia splats were disk shaped and not extensively fingered as when sprayed on the cold substrate ($S_K \sim 0$). For example, Fig. 12.10 (Chap. 12) represents the surface topography of 304L stainless steel after polishing at room temperature (Fig. 12.10a) and preheated at 673 K (Fig. 12.10b). The preheated surface with $S_K \sim 1$ presents more peaks than valleys compared to the non-preheated polished one where $S_K \sim 0$. When the substrate surface is treated with a laser, average roughness R_a and skewness S_K vary with energy density and number of pulses as indicated in Table 12.5.

13.3.1.2 Adsorbates and Condensates

Any surface, especially in the presence of an oxide layer, is polluted by adsorbates and condensates. Upon impact of a molten particle on the substrate, it flattens trapping the adsorbates and any vapors between the flattened droplet surface and the substrate. During a few hundreds of nanoseconds, the local gas pressure can reach a few thousands of MPa. More generally the presence of an evaporable substance on the surface affects significantly the flattening process, through the drop-substrate wettability and the contact resistance created between the flattening particle and substrate [21–24] (see Sect. 13.5.1).

Li et al. [25] have made a careful study of adsorbates and condensates at the substrate surface. Often, water is the main component at the surface. Its adsorption on an oxide surface is usually the result of one of three possible mechanisms, or combinations of them, depending on the temperature, the intrinsic reactivity of the surface, and the number of defect sites at the surface [26]:

- Physisorption of molecular water
- Chemisorption of molecular water
- Chemisorption of molecular water followed by dissociation

Physisorption corresponds to very weak interaction between the substrate and adsorbates, while chemisorption is much stronger and may involve partial charge transfer, which more readily leads to dissociation [26]. Stronger adsorption occurs at steps and defects and new OH_y radicals, resulting from dissociation, bond with a surface metal ion.

When the surface is heated over a critical temperature, adsorbed water species will be desorbed as well as other adsorbed liquids. This desorption process is linked to adsorbed products, surface structural features, and surface materials. Physisorbed molecular water is generally completely removed by preheating above 150 °C. However, with chemisorbed water, the thermal desorption temperature depends on adsorbed features and the subsequent desorbed product. For most oxide-covered metal surfaces it occurs at temperatures ranging from 127 to 320 °C as summarized in the table given in [25] for several oxides and nominal metal surfaces. The authors [25] underline that this desorption temperature range is in good agreement with the substrate preheating temperatures reported as transition temperature over which splats are disk shaped [17–21]. Therefore, they have studied the effect on splat formation of adsorbing and desorbing organic compounds on a stainless steel surface. They brushed xylene, glycol, and glycerol [25] on stainless steel substrates and have shown that when the preheating temperature exceeded the boiling point of these liquids by 50 °C, thermal spray particles impacting on the substrate formed regular disk splats. An interesting question was how long does it takes after preheating and evaporating all adsorbates and condensates for the surface to be covered again by them in the surrounding atmosphere. To answer the question, Fukumoto et al. [27] kept in an air atmosphere at room temperature for a long time the substrate (stainless steel 304L) once it was heated to a temperature where disk-shaped splats were obtained. They investigated the effect of elapsed time after heating on the splat morphology change. Elapsed time was successively 24, 48, 72, 96, and 120 h. The result is shown in Fig. 13.2: 24 h after heating a high fraction of disk-shaped splats was maintained. Afterwards however, the fraction of disk-shaped splats began to decrease. Finally, the fraction of disk splat decreased to less than 50 % over 72 h and more. Of course both Ra and Sk of a once-heated substrate kept in an air atmosphere at room temperature for a long time were unchanged.

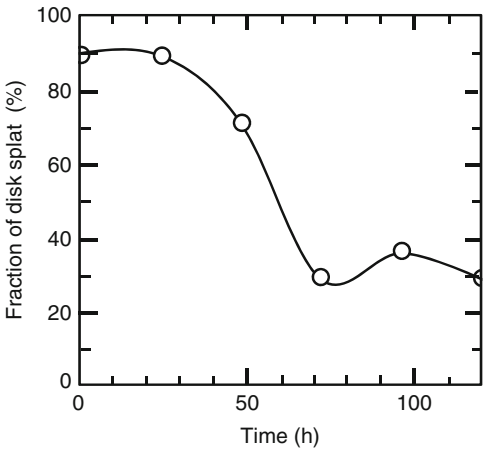


Fig. 13.2 Relationship between elapsed time after heating to 723 K and fraction of disk splats. Reprinted with kind permission from Springer Science Business Media [27], copyright © ASM International

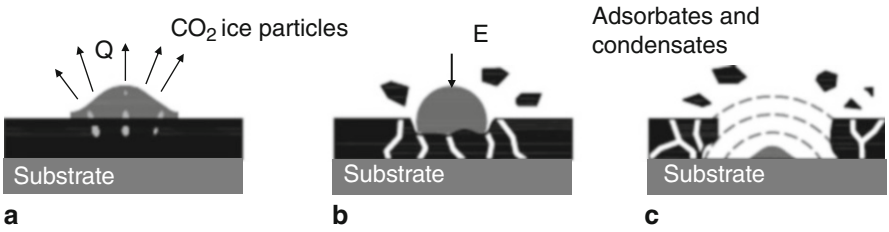


Fig. 13.3 Schematic representation of the elimination of adsorbates and condensates by dry ice pellet blasting: (**a**) The cooling of the impacting ice pellets, 1, solidifies adsorbates and condensates. (**b**) The impact of dry ice pellet on solidified adsorbates and condensates breaks it. (**c**) The following impacting pellets eject broken solid adsorbates and condensates. Reprinted with kind permission from Elsevier [31]

Fukumoto et al. [28] have also investigated the effect of pressure on desorption of adsorbates and condensates. They studied the particle flattening behavior when reducing the chamber pressure (plasma spraying under soft vacuum) on the substrate, which was kept at room temperature. Indirect measurements (determination of the pressure below which splats became disk shaped on different materials) have shown that desorption probably occurs at pressures between 92 and 26 kPa, depending on substrate material.

A laser can also achieve evaporation of adsorbates and condensates provided its energy density is over a certain threshold [29, 30]. This can also be achieved by blasting the substrate surface with dry ice just before the spray spot [31] as explained in Sect. 12.3.7. Dong et al. [31] explain the cleaning by CO2 ice at –79 °C by the process scheme presented in Fig. 13.3.

13.3.2 Oxide Layer Development on Metals or Alloys

The oxide layer formed at the metal or alloy or cermet substrates plays a key role in coating adhesion. The latter, besides the spray conditions, depends on the oxide layer thickness, its structure, and composition, and, sometimes, the corresponding composition gradients between the oxide layer top surface and its interface with the substrate. Many techniques exist to characterize the oxide layer, and the selection of any particular one depends upon the information required (for details see Sect. 15.5).

13.3.2.1 General Remarks

- When preheating a metal or an alloy to get rid of adsorbates and condensates, the oxide layer at its surface will change in thickness, roughness, and composition, since the metal components diffuse differently and their oxidation rates vary. Oxide layers on a substrate surface after preheating can be classified as being either thin (<50 nm) or thick (>100 nm). Thin layers are, for example, observed on titanium and its alloys: for Ti–6Al–4V, the oxide layer thickness is about 25 nm without any heat treatment and reaches 32 nm when preheated at 250 °C [32]. It is the same with stainless steel 316L: about 10 nm before and 25 nm after preheating at 250 °C [32]. Thick layers are observed for low carbon steels and cast irons: on a substrate C 0.49–Si 0.19–S 0.02–Mn 0.59–Fe bal (compositions in wt%) the oxide layer thickness is about 440 nm when preheated at 450 °C [32, 33]!
- Increased oxide layer thickness has two effects: a larger temperature drop across the layer and a reduced resistance to thermal shock. For example, on low carbon steel or cast iron, the impact of alumina or zirconia particles results in the fracture of the oxide layer for about 30 % of impacts [34] (see Fig. 13.4). However, if the impact of stainless steel particles on 1040 steel does not induce any fracture, the coating adhesion strength is reduced by a factor of almost 2 compared to that of coatings deposited on stainless steel substrates preheated under the same conditions. Rupture occurs within the thick hematite layer at the substrate surface for both 1040 steel and low carbon steel.

13.3.2.2 Different Preheating Processes Used

Preheating the substrate over the transition temperature (most probably the temperature above which adsorbates and condensates are removed) modifies the oxide layer thickness, composition, and roughness. However, as previously emphasized, the thermal history of the substrate has a significant effect on oxide layer thickness, composition, and morphology.

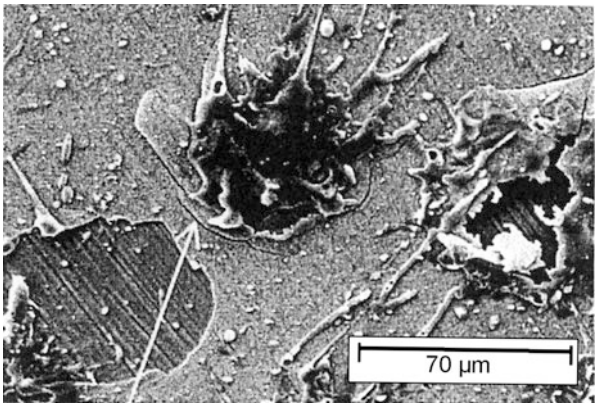


Fig. 13.4 Three alumina splats, plasma sprayed, collected on smooth 1040 steel covered with an oxide layer (173 nm hematite at the top, 305 nm of magnetite beneath): arrow alumina splat, left from it broken oxide layer with no more splat, right from it splat partially broken with broken oxide layer underneath it. Reprinted with kind permission from Springer Science Business Media [34], copyright © ASM International

(a) When the substrate is preheated in a furnace with a controlled atmosphere and well-defined conditions (heating rate, maximum temperature, preheating time, oxygen partial pressure, or controlled atmosphere), oxide layers are reproducible.
(b) When the surface is heated with an electrical resistance while exposed to ambient air, the atmosphere in contact with the surface contains oxygen molecules and different amounts of water vapor. Often, contact between the substrate and the resistance heater used to raise its temperature is not perfect, resulting in uneven heating. For all these reasons, the oxide formation is less well controlled.
(c) When a spray torch is used to preheat the surface, even if the mean heating rate and final temperature can be well defined, the local temperature varies with the movement of the torch relative to the substrate. The surrounding atmosphere is mainly air at atmospheric pressure. With combustion flames (flame spraying, HVOF, HVAF) gas temperatures are below 3,000 K and the entrained air contains mainly molecular oxygen. With plasma jets, gas temperatures of up to 5,000 K can be achieved at spray distances of 80 mm, so the oxygen in contact with substrate surface may be partially or totally atomic oxygen. These devices produce large heating rates (between 1 and 5 K/s). Thus the oxide layers formed generally have compositions and morphologies different from those obtained by more conventional heating [32–35].
(d) Preheating and/or modifying the substrate surface with a laser may also result in oxide layers different from those obtained with a plasma or conventional heating. Very different results can be obtained, depending on the laser used and the substrate treated. Fukumoto et al. [21] have shown that for laser power densities below 50 MW/m^2, the surface roughness does not change and its

Table 13.1 Thickness and composition of the oxide layer formed after Ar–H_2 (25 vol.%) plasma heating at 500 °C on low carbon steel (C 0.49 wt%) [34]. Reprinted with kind permission from ASM International

		wt. fraction of α-Fe_2O_3		
Heating rate (K/s)	Layer thickness (nm)	Grazing XRD	Mössbauer	Identified phases
1.6	600	0.16	0.29	α-Fe, α-Fe_2O_3–Fe_3O_4
2.6	525	0.08	0.27	α-Fe, α-Fe_2O_3–Fe_3O_4
4.5	515	0.04	0.14	α-Fe, α-Fe_2O_3–Fe_3O_4

skewness remains negative or close to zero. It is also possible that the laser irradiation removes part of the oxide layer at the surface [36, 37] if the laser energy density is sufficiently high or if the number of pulses at the same location is increased. It is worth noting that oxide layer elimination requires a much higher energy density than that necessary to remove adsorbates and condensates. Oxide removal is due to mismatch between the coefficients of expansion of the oxide layer and the underlying metal, which is heated by laser irradiation through the transparent or semi-transparent thin oxide layer. For more details see Sect. 12.8.

13.3.2.3 Examples of Oxide Layer Thickness and Composition

While surfaces oxidized by conventional heating have been carefully characterized (composition and thickness of oxide layers), only a few studies have been devoted to surfaces heated by d.c. plasma or HVOF jets and to the best of our knowledge almost none have examined the effect of laser heat treatment (except for color observation and SEM observation of oxide layer surface). For plasma preheating, low carbon steels, stainless steel, cast iron, and titanium alloy (Ti4Al6V) have been studied [32–35, 38]. Four examples will be presented for an Ar–H_2 (25 vol.%) d.c. plasma jet. The oxide layers were characterized as described in Sect. 15.4.

(a) Low carbon steel (C 0.49–Si 0.19–S 0.02–Mn 0.53–Fe bal) preheated for 10 min at 500 °C with 3 heating rates. Results obtained are presented in Table 13.1, which shows that when the heating rate is increased while keeping the preheating temperature the same, both the oxide layer thickness and the weight fraction of hematite (α-Fe_2O_3) decrease. The difference between XRD grazing and Mössbauer results is due to the fact that conversion electron emission comes mainly from the surface and slows down rapidly with the thickness. The oxide layer is heterogeneous, with an upper surface largely constituted of α-Fe_2O_3 and an inner one of Fe_3O_4 [34, 38, 39]. It thus becomes possible to monitor the relative thicknesses of Fe_2O_3 and Fe_3O_4, the former having poor mechanical resistance. For example, when preheating for 10 min the same substrate at 1.4 K/s up to 520 °C, the hematite fraction measured by Mössbauer is 0.85 against 0.62 when preheating to 440 °C at 4 K/s.

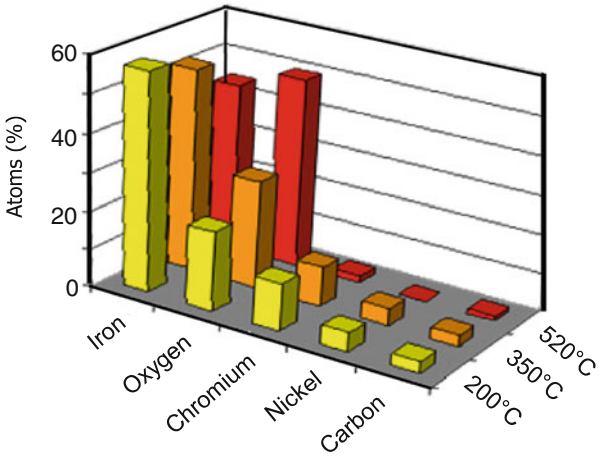


Fig. 13.5 Dependence on the preheating temperature of the oxide layer composition, 40 nm below its surface, of a 316L stainless steel (XPS measurement) [35]. Reprinted with kind permission from ASM International

(b) Ti–6Al–4V preheated during 10 min respectively at 250 °C and 400 °C with a heating rate of 3 K/s. Two phases of Ti are present in the sample, α and β, with the latter diminishing when the temperature increases [32]. For both temperatures the oxide layer thickness is about the same: 32 and 34 nm, respectively. With heating, Al diffuses toward the surface with a ratio Al/Ti > 1. Oxides formed are TiO2 and Al2O3 but the thickness of Al2O3 increases with temperature and, if TiO2 is identified at the surface, TiO is observed at a greater depth [32]. It is also worth noting that impurities at the surface can be detected: Cu coming from the vaporization of the anode material during plasma preheating and Si from the polishing with SiC papers.

(c) Stainless steel 316L [32]. According to Mössbauer spectroscopy the oxide thickness is 25 nm at 250 °C, 40 nm at 400 °C, and 58 nm at 580 °C. At 400 °C a spinel phase can be observed but XPS analysis shows that Cr is present in a very low concentration. At 400 °C and above oxides are hematite and a spinel. The Cr has almost disappeared and the Ni has increased with Fe/Ni $= 3.8$ against 6 in the matrix; thus the spinel should be of the type $NiFe_2O_4$. These evolutions are represented in Fig. 13.5. This result is contrary to that obtained using the same preheating conditions with 304L steel, where the spinel detected, mixed with hematite, was $Fe_{2-x}Cr_xO_3$ [34]. It is interesting to note that with the optical UV/Visible spectroscopy the oxide thickness is not detectable below 350 °C. Over that temperature the oxide thickness increases rather fast, as shown in Fig. 13.6.

(d) Figure 13.7 [33] presents surface topographies along with roughness parameters of 1040 steel substrates preheated to 723 K. Contrary to what can be observed in Fig. 13.7, homogeneously distributed oxide grains were characterized on surfaces of 1040 steel substrates preheated at 573 K. Preheating these substrates at 723 K induced modification in surface topography consisting of plateaus and valleys. The plateaus and valleys observed on substrate surfaces, in Fig. 13.7, can be considered as oxide layers on pearlite and ferrite grains, respectively.

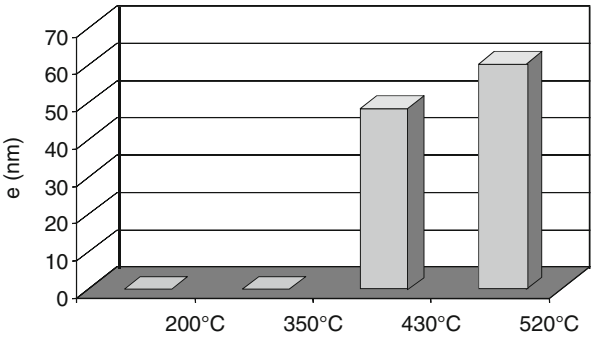


Fig. 13.6 Dependence on the preheating temperature of the oxide layer thickness at the surface of a 316L stainless steel (optical UV/Visible spectroscopy measurement) [35]. Reprinted with kind permission from ASM International

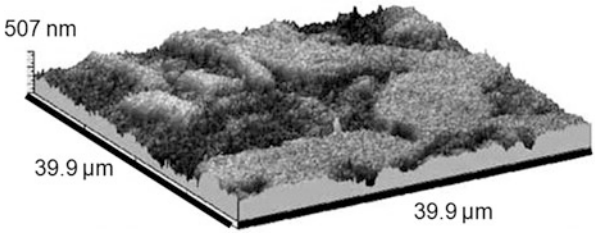


Fig. 13.7 Surface topographies of 1040 steel substrates preheated to 723 K by the plasma jet in air [33]. Reprinted with kind permission from Elsevier

The oxide grains induce an increase in substrate roughness but the major increase in roughness parameters is due to the formation of this plateau–valley surface structure. The average difference of height of oxide layer on pearlite and ferrite grains was measured to be 181 $\pm$ 52 nm and correspondingly the width of valleys was 8.2 $\pm$ 3.7 nm. These results show the difficulties of such analyses, which are very important for understanding variations in coating adhesion.

13.4 Single Particle Impact, Flattening, and Solidification (When Melted)

13.4.1 Introduction

According to the spray process used and, for a given process, the trajectories followed within the high-energy jet, particles impacting the substrate can be:

13.4.1.1 In a Solid State

Particles can be either at temperatures below about 0.4–0.5 times their melting temperature, T_m, which is the case in the cold spray process [12], or below T_m (about 0.7–0.95 times T_m) when sprayed with HVAF [40] or high power HVOF

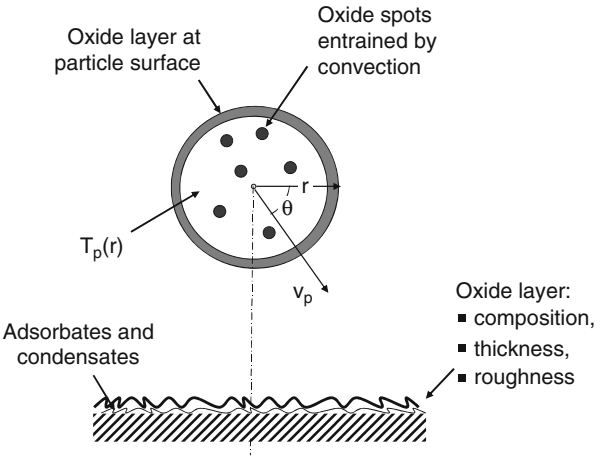


Fig. 13.8 Schematic of the parameters controlling the fully melted particle flattening

with inert gases injected into the combustion chamber [41], or with specially designed HVOF torches [42].

For solid particles, as those sprayed by the cold spray process (see Sect. 6.2.2.1), their impact velocity must be higher than the critical velocity, v_c, (depending on particle ductility) but lower than the erosion velocity, v_r. If possible the impact must be normal to the substrate, otherwise the impact velocity becomes $v_p.(\sin\theta)$, θ being the angle between the axis parallel to the substrate and the direction of impact (see Fig. 13.8). Normal impact corresponds to $\theta = 90°$. With decreasing θ the impact velocity can become lower than the critical one, v_c, and particles will no more deposit and the deposition efficiency diminishes fast (see Fig. 6.42). Moreover the tangential component of momentum of the particle in an angular impact would create a tensile force at the interface, which could be large enough to detach the particle from the substrate, despite the occurrence of shear instability at the interface [43]. The particle deformation is purely plastic because above v_c, the stress applied to the particle is higher than the yield stress. The yield stress diminishes when the temperature increases and, therefore, reaching plastic deformation will be easier with hot particles than with cold ones. In the contact zone adiabatic heating occurs with a transition to an adiabatic shear phenomenon only during the dynamic deformation of the solid [42]. This adiabatic heating results in impacting particle and substrate material softening in the contact zone. However, as described by Grujicic et al. [44] and Grujicic [45] usually in cold spray, the melting of one or both materials is not frequently observed. It is not the same with HVAF or high power HVOF where particles are close to the melting temperature and, due to adiabatic heating, only a rather low amount of additional energy is necessary.

At last it must be emphasized that generally in cold spray the oxide level in the deposited particles is that of the powder used. However with HVOF or HVAF spraying with particles below T_m, the oxide level can be up to ten times higher than that of the initial particles, the oxide being around the impacting particle because it is only diffusion controlled.

13.4.1.2 Molten Particles

With particles in a molten state, either close to T_m as in flame spraying or HVOF or higher than T_m as in plasma spraying, the problem of the impact is quite different from that of solid particles:

- The impacting particle can be modified during its flight in the high-energy jet by its oxidation (see Sects. 2.7.3 and 4.3.3.7) during the heating stage. Oxidation is controlled by diffusion (oxide shell around the particle), increasing with particle temperature and residence time in the hot zone of the jet, and by convection with plasma, HVOF, and wire arc spraying (oxide grains inside the particle), see Fig. 13.8. According to the large difference between oxide and metal melting temperatures, a solid crust can be formed (in the colder zones of the jet) around the particle before its impact on the substrate. This can be observed, for example, in the case of NiAl particles with the formation of an alumina crust.
- Depending on the particle heat conduction or more precisely its Biot number [see Sect. 4.3.1, Eq. (4.28)], the core of the particle can be still solid at impact, modifying deeply its flattening. This is for example the case of polymer particles.
- The substrate roughness, skewness, oxide layer thickness and composition, and the adsorbates and condensates present or not at its surface influence drastically the particle flattening and solidification through its wettability and the thermal contact resistance, see Fig. 13.8.

13.4.2 Different Possibilities of Particle or Splat–Substrate Adhesion

The main adhesion mechanisms for coatings are diffusion, crystallographic structure matching at the interface splat–substrate, adiabatic softening and adiabatic shear localization, chemical, and mechanical.

13.4.2.1 Diffusion

Diffusive adhesion of metals and alloys only occurs when the temperature during coating formation is sufficiently high and no oxide layer exists at the surface. In a simplified approach the thermal diffusion distance, d_d, is given by

$$d_d = \sqrt{D_{th}.t} \tag{13.1}$$

where t is the time during which the contact occurs at temperature T and D_{th} the diffusion coefficient varying as $e^{-E_A/kT}$, where E_A is an activation energy, T the absolute temperature, and k the Boltzmann constant. Thus, good adhesion requires a

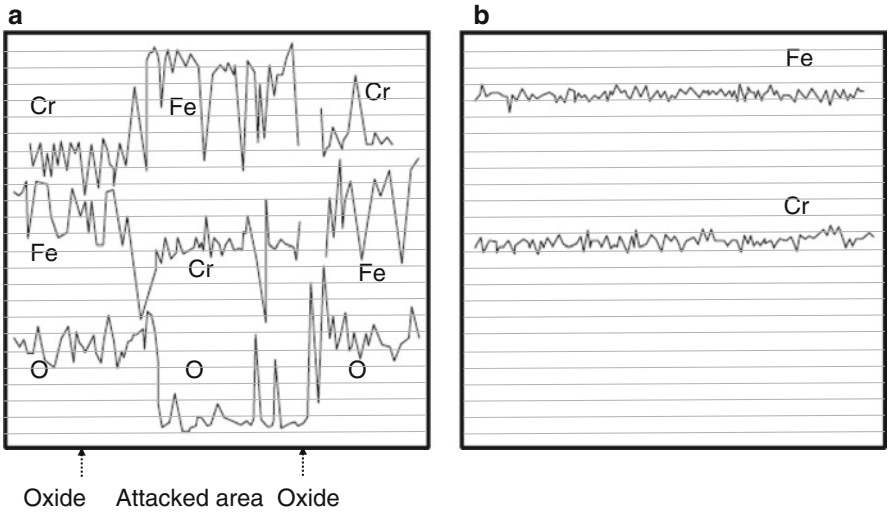


Fig. 13.9 EDS characterization of a SUS304 stainless steel. (**a**) Treated by a reverse transferred arc of 37 A. (**b**) Treated by the same arc for a few minutes and then mirror polished. Reprinted with kind permission from ASM International [46]

high temperature and a sufficient contact time, but diffusion for metals can occur only if the solid oxide layer at the substrate and particle surface is destroyed.

An excellent adhesion between coating and substrate can be achieved, when plasma spraying in soft vacuum. It is the case, for example, when spraying a super alloy on a turbine blade made of another super alloy. The spraying is accomplished with the substrate and coating maintained at about 900 °C, but not above to avoid the formation of undesirable phases. The oxide layer at the substrate surface is removed by establishing a transferred arc between the part to be sprayed, which is then the cathode, and the anode of the torch. Once the plasma jet of the spray torch is established, the medium between the anode nozzle of the torch and the part is electrically conducting. It allows tailoring the arc current of the transferred arc [46]. The arc attachment at the cathode (the part to be sprayed) is erratic and cathode spots are continuously moving. The oxide layer is ejected from the cathode spot and the surface progressively cleaned from its oxides. This is illustrated in Fig. 13.9a showing the cleaning of stainless steel SUS304 after 0.15 s with the transferred arc working at 37 A. At crater positions the oxide has disappeared (at the EDS precision). As shown in Fig. 13.9b, after a treatment of a few minutes, and after surface polishing to a mirror-polish, the oxygen level is very low and the quantities of Fe and Cr are the same as those inside a crater (see Fig. 13.9a). Once the substrate has been cleaned by the reverse transferred arc, it is heated, if necessary with the help of a direct transferred arc (the part is now the anode), to achieve sufficiently high temperatures for the diffusion to occur.

Diffusion can also occur at the splat–substrate interface, but if the temperature of the molten splat is sufficiently high, the time before which solidification starts is a few to ten microseconds. For example [47], at the interface between a YSZ splat

and a 304L stainless steel substrate, a 20–30-nm thick oxide layer is found extending uniformly over the length of the splat cross section. The whole splat is in excellent contact with the substrate, except where cracks in the splat intersect with the substrate. The oxide layer interface includes elements from both the ceramic splat (Zr) and the substrate (Cr, Fe), as determined by EDS using a sufficiently small beam spot size. The relatively thick oxide layer grew during substrate preheating to approximately 450 °C carried out in an ambient atmosphere. The heat transferred from the molten ceramic droplet is sufficient to allow zirconia's cations to diffuse into the oxide layer. However diffusion through a few tens of nanometers is not quite sufficient to achieve a good adhesion.

With a polished Ti–6Al–4V substrate, the presence of alumina diffusing to the substrate surface upon preheating at 400 °C produces excellent adhesion (48 ± 12 MPa) of the sprayed alumina coating. This is probably due to the chemical continuity at the interface substrate coating with the presence of alumina at the surface of the Ti–6Al–4V substrate [32].

As already emphasized previously [48], the substrate heating by the impacting fully melted particle can also promote the diffusion of certain elements of the substrate toward its surface and increase the wettability substrate-flattening particle. With cold-sprayed particles the diffusion is not possible. For example, Grujicic [45] has calculated that with $D_{th} = 10^{-15}$ to 10^{-13} m^2/s and the contact time $t_c = 4 \times 10^{-8}$ s, $\sqrt{D_{th}.t} = 0.004 - 0.1$ nm (fraction of inter-atomic distance), which is by far insufficient for bonding.

13.4.2.2 Crystallographic Structure and Chemical Continuity at the Interface Between Splat and Substrate

Yang et al. [49] have plasma sprayed alumina particles onto single crystalline alumina substrates (α phase) kept at 900 °C. On a cold substrate, due to the fast cooling rate, alumina crystallizes into the metastable γ phase. When the substrate is preheated at 900 °C, the cooling rate of the splat is much slower and the crystallization occurs in α phase, which is also that of the sintered alumina substrate. Moreover, the growth orientation of alumina splat crystal during rapid solidification was exactly the same as the orientation facets of [001] or [110] of the single crystalline alumina substrate, epitaxial solidification taking place during splat cooling.

Alumina particles were plasma sprayed onto alumina polished (Ra ≈ 0.4 μm) plasma-sprayed coatings [50], which were kept at 250 °C before spraying to get rid of adsorbates and condensates. The latter were either as-sprayed (with more than 99 wt% of γ phase) or preheated at 1,373 K at a rate of 5 K/min, annealed for 6 h, and cooled at a rate of 5 K/min resulting in a 100 % α-columnar structure. Some were also preheated to 1,873 K at a temperature ramp of 5 K/min, annealed for 3 h, and cooled at a rate of 5 K/min resulting in a α-granular structure with grains between 3 and 5 μm. As shown in Fig. 13.10a, on the γ-alumina substrate, alumina splats (γ phase) exhibit a columnar and regular structure ~100–150 nm; the adhesion of the alumina coating (300 μm thick) obtained on this smooth substrate is

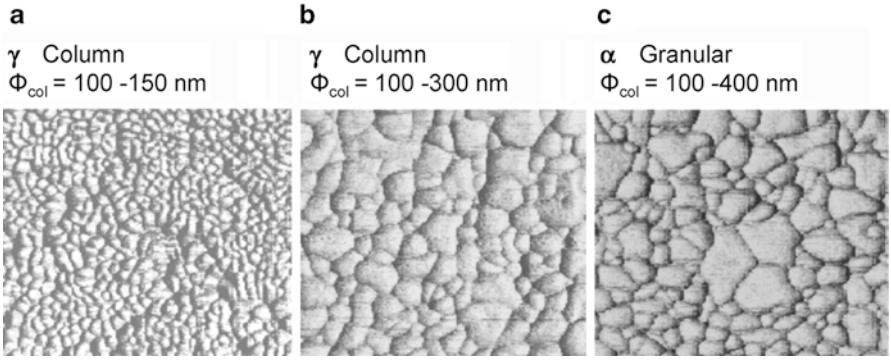


Fig. 13.10 Alumina splats plasma sprayed onto smooth alumina substrates with different microstructures, (**a**) γ columnar, (**b**) α columnar, and (**c**) α granular. Reprinted with kind permission from ASM International [50]

35 ± 3 MPa! On the columnar α-alumina substrate, splats (γ phase) form a columnar and irregular structure ~150–300 nm (see Fig. 13.10b); the adhesion of the coating is only 3 ± 1 MPa. On the α-alumina substrate with a granular structure, splats (γ phase) achieve a very irregular structure ~100–400 nm (see Fig. 13.10c), and splats have the tendency to peel off and it is impossible to achieve any coating.

It has been shown that the pre-oxidation of smooth (Ra $<$ 0.05 μm) low carbon steel substrates in a furnace under a CO2-rich atmosphere at atmospheric pressure allows the formation of a wüstite ($Fe_{1-x}O$) layer. The latter improves significantly the adhesion (>55 MPa) of alumina coatings in spite of the rather low roughness (0.10 μm $<$ Ra $<$ 1.00 μm) of the oxidized surface [51]. It appears that the plasma preheating of steel samples did not modify the morphology of the pre-oxidized wüstite layer formed (Ra ≈ 0.2 μm). In spite of maintaining the surface condition, part of the wüstite scale, very probably the most superficial one, is oxidized into magnetite (Fe_3O_4) [52]. This has already been observed on wüstite and it corresponds to a topotactic phase transformation. This change of composition is liable to occur even inside a grain, so that it may have no harmful consequence on the cohesion of the iron oxide scale. The presence of metastable γ-Al_2O_3 together with α-Al_2O_3 was a little bit surprising because the former phase is generally the only one observed under the spraying conditions used. It is possible that the γ alumina phase was localized in direct contact with magnetite, because they have the same crystallographic structure (spinel) with lattice parameters rather close to 0.793 nm for alumina and of 0.839 nm for magnetite or 0.834 nm for lacunars magnetite. If such an assumption could be verified, it could explain the good adherence of the coating. Indeed, in these conditions, the structure varies from the steel substrate, the α-Fe phase and the wüstite phase at its surface, then the interface comprising magnetite (topotactic transformation), and finally the γ alumina (epitaxial relationship) coating, as shown in Fig. 13.11. This might justify a physical adhesion, and perhaps also a chemical one if a chemical reaction occurs between both spinel phases, which in principle could form mixed oxides.

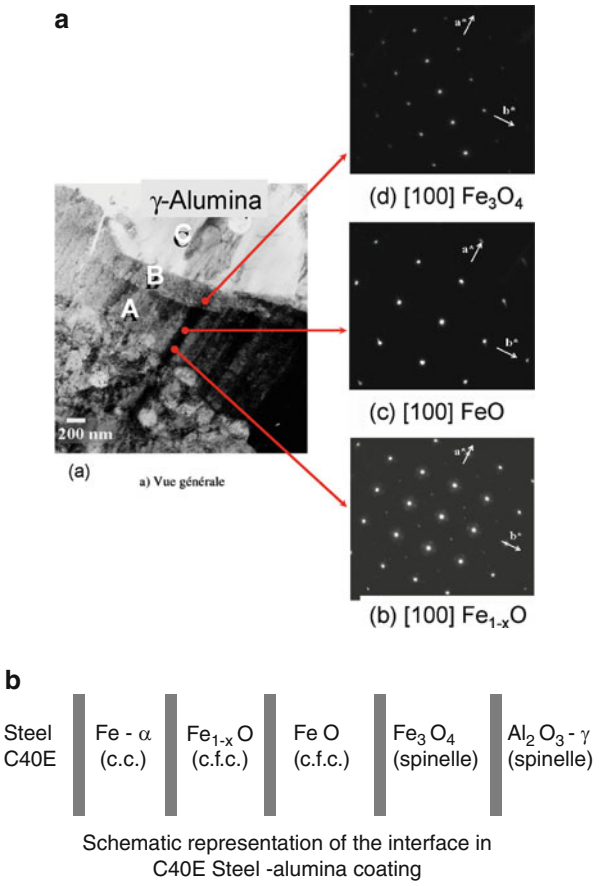


Fig. 13.11 (**a**) TEM image of the interface between low carbon steel C40E and a plasma-sprayed alumina coating: on the left cross section with successively: (**a**) ($Fe_{1-x}O$ and then FeO), (**b**) (Fe_3O_4), C (γ-Al_2O_3), (**b**) schematic of the same interface. Reprinted with kind permission from Dr. S. Valette [38]

13.4.2.3 Adiabatic Softening and Shear Localization

As already mentioned, the average kinetic energy of impacting particles in cold spray is generally insufficient to melt the particle–substrate interface and the contact time at high pressure is very short (a few tens of ns); thus, according to Grujicic [45] the adhesion is an atomic length-scale phenomenon. The occurrence of this adhesion is controlled by the presence of clean surfaces (no oxides) and high contact pressures. The strength of the adhesion depends on [45] the attractive or repulsive character of atomic interactions and the crystallographic and orientation details of the contact surfaces. The adiabatic shear instability and the resultant plastic-flow localization (see Sect. 6.2.2.1) are the key phenomena for the particle-substrate bonding. Grujicic [45] has made a transient non-linear dynamics analysis of the cold-sprayed particle–substrate interactions considering copper and aluminum particles or substrates. Figure 13.12 represents the particle and substrate morphologies at the end of the impact, i.e., 50 ns. Figure 13.12a represents the

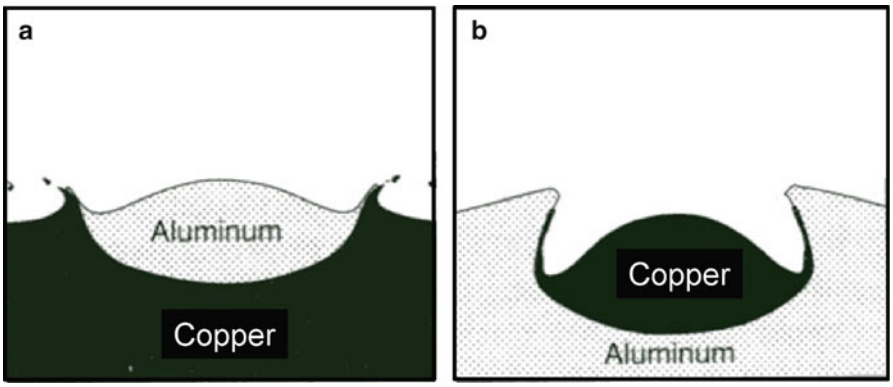


Fig. 13.12 Final calculated shape (impact duration 50 ns) of a 20 μm particle impacting the semi-infinite substrate with a velocity $v = 650$ m/s ($v > v_c$), (**a**) Al particle on a Cu substrate. (**b**) Cu particle on an Al substrate. Reprinted with kind permission from Woodhead publishing [45]

impact of the aluminum particle onto the semi-infinite substrate made of copper, the particle diameter being 20 μm and its impact velocity 650 m/s, slightly over the critical velocity for this combination. Results of Grujicic [45], not presented here, show that the particle aspect ratio decreases, while the substrate crater depth increases with the particle–substrate contact time. During the impact, a jet composed of both the particle and substrate materials is formed at the particle-substrate contact surface, and at the end of the impact pressure it forms a lip pointing away from the flattened particle (see Fig. 13.12a). With the impact of a copper particle (same diameter and impact velocity) onto an aluminum substrate, as the particle–substrate contact time increases, the crater depth and width increase while the flattened particle aspect ratio diminishes. At the end of the process (see Fig. 13.12b), compared to the case of an Al particle on a Cu substrate (Fig. 13.12a), the crater depth is more important and the flattened particle aspect ratio is lower. The length of the interfacial jets is more important. Guetta et al. [53] observed experimentally similar aspects. The difference in the final shapes of both types of calculated impact is linked to the higher kinetic energy of the copper particle due to its higher mass and the larger strength of Cu compared to Al. When the impact velocity is lower than the critical one, the interfacial jet comprises only one material. According to Grujicic [45] the interfacial jets plays a key role in removing oxides and other surface films for both materials. However it must be emphasized that an induction time exists before particles stick to the substrate (see section "(a) Induction Time"), which probably corresponds to the first removal of substrate oxide. Grujicic [45] suggested that once the interfacial jets were formed, cleaning the contact surfaces, "some type of nano/micro length-scale mechanical material mixing contributes to particle-substrate bonding." They suggested that this phenomenon is due to the instabilities created at the interface, creating interfacial roll-ups and vortices. Of course the mutual solubility of the two metals plays a key role. Also the impact velocities during the induction time can begin to form

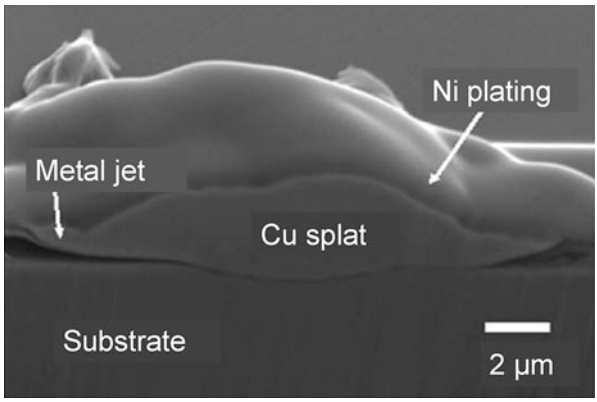


Fig. 13.13 Cross-sectional microstructure of individual deposited Cu particle (mean diameter 5 μm) cold sprayed onto stainless steel SUS304 substrate with N_2 (1–3 MPa and 673 K). Reprinted with kind permission from Springer Science Business Media [54], copyright © ASM International

reentrant cavities, creating a rivet-like particle-cavity assembly. Fukumoto et al. [54] cold-sprayed Cu particles with a mean diameter of 5 μm onto stainless steel SUS304 substrate with a self-designed cold spray gun working with N_2 (1–3 MPa and 673 K) to study the jetting phenomenon. They studied the surface by atomic force microscopy, the cross section microstructure of an individual particle by focused ion beam and transmission electron microscopy for the coating/substrate interface microstructure. The interface microstructure between sprayed particle and substrate revealed an amorphous-like band region at interface during coating fabrication at high power conditions. For the deposition mechanism of the cold-sprayed particles onto the substrate surface, the deformation of the particles initially induces the destruction of its surface oxide and the appearance of the active fresh surface of the material probably enhances the bonding between particles and substrate. On the other hand, in coating fabrication at high power conditions, bonding between particle and substrate may be possibly formed via oxygen-rich amorphous like layer at the interface. With high impact velocities, the substrate at the collision center deformed remarkably and metal jetting along the interface between particle and substrate occurred at the periphery of the flattened particle resulting in a good bonding of the particles. Figure 13.13 of a Cu splat shows well the metal jet, similar to that drawn in Fig. 13.12a. When comparing the fraction of metal jet evolution, increasing with the process gas pressure, with that of the deposition efficiency, it is clear that the latter increases almost as the former. Authors [54] conclude that "the positive control and high efficiency coating formation are possible by setting the spray conditions in which the metal jetting preferentially recognized on the collision of an individual particle onto the substrate surface."

The strength of the substrate material is very important for the deposition of the particle. Zhang et al. [55] have studied the impact of Al particles on substrates with different characteristics. They showed that initiation of deposition onto soft metallic substrates was difficult due to the lack of deformation of the aluminum particles. Deposition onto a tin substrate resulted in its melting, the strength of the interface was therefore very low, and Al particles rebounded from the surface, only the very small ones being trapped in the tin. The ease of initiation of aluminum deposition

increased as the hardness of metallic substrates increased. For example, metal jetting was observed when depositing onto steel substrates, where also the most rapid initiation was observed. Deposition onto aluminum was difficult, due to the tenacious nature of the oxide film on the substrate. Deposition onto nonmetallic substrates (ranging from polymers to ceramics) was difficult because of the lack of metallic bond that can be formed. Hussain et al. [56] have studied the bonding mechanism of copper particles onto aluminum alloy substrates prepared with three different procedures termed as ground with 58.5 μm SiC paper, polished, and grit-blasted with grit size of ~500 μm, respectively. In addition, some substrates were annealed following surface preparation to allow a separation of the effects of work hardening during preparation from those of changes in surface morphology. They concluded that two types of bonding must be considered: metallurgical bonding between the substrate and the coating and interlocked material due to material extruded from the substrate during impact of the particles, which is then interlocked within the coating structure. Of course, as shown by Huang and Fukanuma [57] for Cu particles onto Al alloy substrates, the particle velocity (over v_c) plays an important role in improving adhesive strength based on plastic deformation. It is also beneficial to the mechanical interlocking effect resulting in excellent bonding between the coating and substrate.

The situation is somewhat different with HVOF- or HVAF-sprayed particles below but close to the melting temperature. For example, Trompetter et al. [40] HVAF-sprayed NiCr alloy particles onto a variety of substrate materials. Soft substrates predominantly had deeply penetrating solid splats, whereas harder substrates that resisted particle penetration had a higher percentage of molten splats. A possible explanation was that in the process of plastic deformation, melting occurred. The percentage of melted particles was greater for harder substrates. The percentage of molten splats increased with the particle velocity. Moreover, as in the cold spray process, the impact velocity must be sufficiently high ($v > v_c$) to break surface oxides and to achieve sufficient plastic deformation for successful bonding.

13.4.2.4 Chemical

Chemical adhesion requires that the impacting droplet melts the substrate and a chemical compound of both liquids exists. For example, when Mo particles impact on steel, the melting temperature and effusivity (defined as $(\rho_p.c_p.\kappa_p)^{0.5}$) of the Mo droplet are higher than those of the steel substrate, which melts and reacts to form a chemical compound, $MoFe_2$. Mo particle flattening on a stainless steel substrate results in splats formed of different pieces as shown in Fig. 13.14a from Li et al. [58]. This type of splashing is due to a localized melting of the substrate surface by the impacting droplet. The melted crater on the substrate surface alters the flow direction of the droplet fluid and tends to form a free liquid jet that detaches from the substrate surface Fig. 13.14b. Cracking occurs within the Mo splat due to the restraining of the splat contraction during cooling and due to the low plasticity

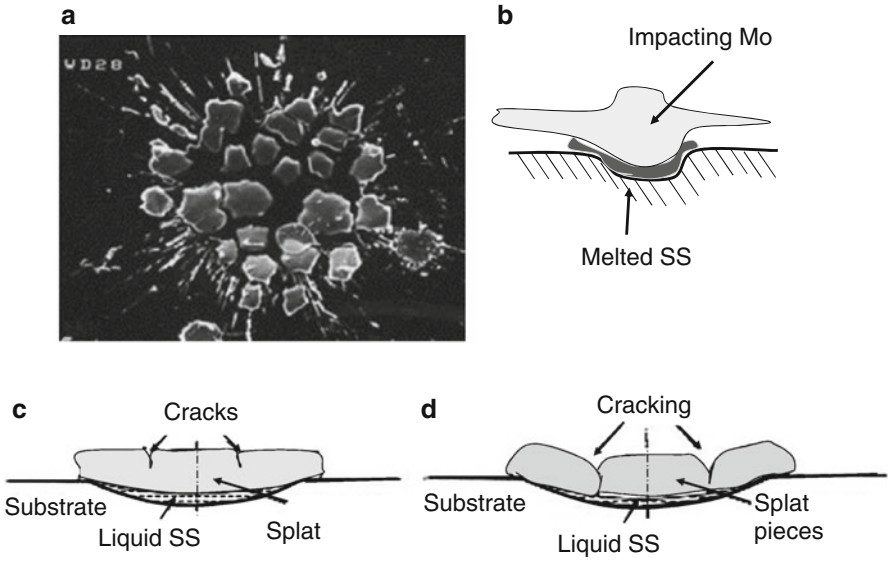


Fig. 13.14 (**a**) Mo splat on stainless steel (SS) substrate. (**b**) Schematic diagram of droplet impact inducing substrate melting. (**c**) Crack initiation in the Mo splat. (**d**) Displacement by floating of the cracked pieces on low melting point liquid. Reprinted with kind permission from Springer Science Business Media, copyright © ASM International [58]

of the solidified splat material [58]. The liquid film, mainly resulting from the steel substrate material, between the Mo flattening particle and the substrate promotes the floating of Mo pieces initiated from cracks.

A chemical reaction also occurs when a cast iron particle impacts on an Al–Si–Cu aluminum alloy substrate preheated to above 400 K where probably the thin alumina layer is melted or eroded. As it has been observed [59], a thin (a few hundreds of nanometers) $FeAl_2O_4$ layer is formed between the splat and substrate. Even if the substrate is not melted upon impact, the high temperature induced in the substrate oxide layer can greatly promote adhesion. Deformed substrate ridges, probably due to the slight melting of the substrate surface, are formed immediately adjacent to the splat periphery sprayed at high substrate temperatures. The flattening ratio decreases with preheating, because the ridges act as an obstacle to the splat expansion.

13.4.2.5 Mechanical

(a) Unmelted Particles

In the cold spray process mechanical bonding can occur for some particles at the substrate surface. It is the case when cold spraying aluminum particles onto glass or alumina substrates with which no metallic bond can be formed [55]. With a polymer

substrate all the damage occurs in the polymer but the aluminum particles are not deformed at all and no bonding occurs. Trompetter et al. [60] have studied the interface between Ni–Cr (20 wt%) particles HVAF sprayed and an aluminum substrate with FIB, cross-sectional SEM, and cross-sectional TEM. The gas temperature was 1,300 °C, while the melting temperature of NiCr particles was 1,400 °C, resulting in particles in a plastic state at impact. The observation of interfacial formations together with no evidence of chemical bonding across the interface suggest that mechanical interlocking was the dominant bonding mechanism for Ni–chrome alloy.

In the cold spray process of Cu particles, when grit blasting of aluminum alloy substrate [55] was performed, bonding was significantly reduced by grit embedment during blasting. It seemed also that the grit-blasted surface restricted the materials jet formation upon impact of the copper particles resulting in less successful removal of oxide from the interface and hence a weaker metallurgical bond.

(b) Molten Particles

Mechanical adhesion takes place when the substrate is roughened, for example, by grit blasting, but, compared to cold spray, with molten particles the phenomena are quite different. Flattening particles and resulting splats impacting on the rough surface shrink while cooling and adhere to the surface because of the frictional force that develops [59, 61–63]. This adhesion depends both on the amplitude of roughness, often characterized by the distance between the highest peak and the deepest undercut (R_t), and on the spacing between peaks and valleys. Bahbou and Nylen [62] have established that a good correlation exists between the adhesion strength of NiAl (5 wt%) coatings on a Ti–6Al–4V substrate, and the root mean square value $R_{\Delta q}$ of the substrate, which takes into account both the amplitude and spacing of peaks (see Sect. 12.5.1). The correlation is rather poor when variables such as R_a, R_t, or the peak spacing are considered individually. As emphasized previously (see Sect. 12.5.9) for the best mechanical adhesion, the peak heights, characterized by R_t, must be adapted to the mean size of the splats, as illustrated in Fig. 12.36.

As for smooth surfaces, the presence of adsorbed contaminants on the substrate may also affect the strength of adhesion. Preheating the grit-blasted surface before spraying removes adsorbates and condensates and improves coating adhesion by a factor of 2 to 4 [63]. Thus the adhesion and cohesion strengths of coatings, as well as other thermomechanical properties, are strongly linked to the quality of contact between splats and the substrate or the previously deposited coating layers. That is why the grit residues must be as low as possible, which depends on the grit-blasting conditions [63, 64] (see also Sect. 12.5.5.5).

13.4.3 Splat Formation from Unmelted Particles Impacting on Smooth Substrates

13.4.3.1 Introduction

The particle after its flattening is called splat and is characterized by its flattening parameter or degree defined as

$$\xi = D/d_p \tag{13.2}$$

where D is the flattening particle diameter and d_p that of the particle before impact. Of course the flattening degree will depend strongly on the particle impact velocity and is state at impact: solid or liquid. The first remark is that the splat diameter is easy to determine if the splat is close to disk shaped (Fig. 13.15a) but more difficult to determine with unmelted particles or exploded molten particles (Fig. 13.15b where a mean diameter, D_m, is defined), but it gives a good trend. Particle velocities vary (see Fig. 1.5) between a few tens of m/s for flame spraying up to almost 800 to 1,000 m/s for cold spray and D-gun deposition.

The corresponding particle flattening varies between about 50 ns (cold spray) and about 10 μs (flame spraying). Experiments to follow particle impact onto the substrate are very complex (see Sect. 16.7.2.1) and require that such investigations are performed only on smooth substrates, because of the necessity of keeping a good depth of field to observe flattening particles with microscopes or special optics,. Besides splat observation with microscopes, other techniques must be used. For a single molten droplet, fast pyrometers (50 ns response time) are used to measure its temperature evolution prior to and during flattening. In parallel with this technique impacting droplets can be photographed with a camera triggered by the pyrometer signal. It is possible to trigger the camera at different flattening times to obtain the corresponding images of flattening particles. Assuming that all impacting particles have the same impact parameters it becomes possible to have the time history of the flattening particle. It is the only way to proceed because one particle takes approximately 0.5–2 μs to flatten. As the fastest cameras can take about one image per microsecond (see Sect. 16.7.2.1), it is impossible to follow directly the flattening phenomenon. In all other cases, what is compared is the

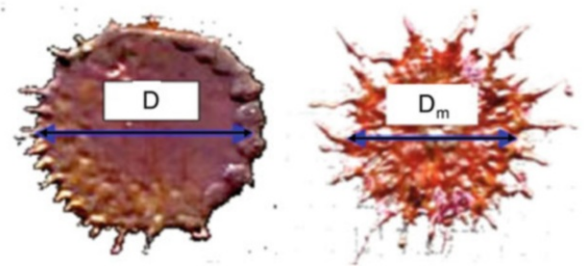


Fig. 13.15 Definition of the splat (YSZ) mean diameter: (**a**) Disk-shaped splat and (**b**) Fingered splat

particle before impact and the resulting splat studied with an optical microscope, a focused ion beam (FIB), cross-sectional scanning electron microscopy (SEM), and cross-sectional transmission electron microscopy (TEM). Moreover it is possible to measure particle velocities, temperatures (above about 1,400 K), and diameters (see Chap. 16, Sects. 16.3.2–16.3.5) and, for certain experimental conditions, to correlate these measurements to splat shape. It is also possible to follow the flattening particle temperature evolution during its flattening and cooling in plasma spraying (see Sect. 16.7.2.1). However, to observe flattening and cooling of micrometer-sized particles, long distance microscope objectives or dedicated optics are necessary [13] for which the field of depth is at most a few tens of micrometers, thus precluding measurements on rough surfaces generally encountered in thermal spray.

13.4.3.2 High-Pressure Cold Spray Conditions

As emphasized in Sect. 6.2.2.1, cold-sprayed particles must have impact velocities higher than a so-called critical velocity (see Fig. 6.29) to adhere to the substrate. As particles are in a solid state the flattening degree is relatively small, at the maximum about 2, depending on particle plasticity and generally below 1.5. As mentioned in Sect. 13.4.2.2, bonding between particle and substrate requires that the oxide layers are removed and that adiabatic shear instability and the resultant plastic-flow localization will occur. The particle and substrate deformations upon impact depend strongly on the particle impact velocity (above the critical velocity) and the relative hardness particle/substrate. Compared to the sprayed particle, the harder the substrate is the less it is deformed. This is illustrated for example in Fig. 13.12a, b.

Klinkov and Konsarev [65], considering aluminum particles impacting on a copper substrate with velocities higher than the critical one, have shown that before a time t_i particles do not attach but rebound, thus cleaning and deforming the surface. At the time t_i, the particles begin to attach because a sufficient level of the surface activation is reached. The oxide layer is partially removed allowing true metal-to-metal contact [12, 45, 54, 66, 67], the oxide layer acting as diffusion barrier. After t_i particles attach in an avalanche-like manner, rapidly forming a coating (see Fig. 6.29). This time t_i is called the induction time (or the time of deposition delay). It is related to the particle concentration in the flow and the impact velocity. Fig. 13.16 shows the evolution of t_i decreasing to zero with the impact velocity increase [65] for aluminum particles impacting on the copper substrate. Attachment with t_i close to zero means that particles attach to a nonactivated surface. The mass flow rate of the powder per unit area in this experiment was 0.06 kg/m^2 s.

Of course the impact velocity must be lower than the erosion velocity (section "(a) Basic Phenomena). The analysis of Assadi et al. [43] suggests that mass density and particle temperature have significant effects on the critical velocity and are thus two of the most influential parameters in cold gas spraying. Fukumoto et al. [66], considering copper particles impacting on stainless steel AISI 304 and aluminum

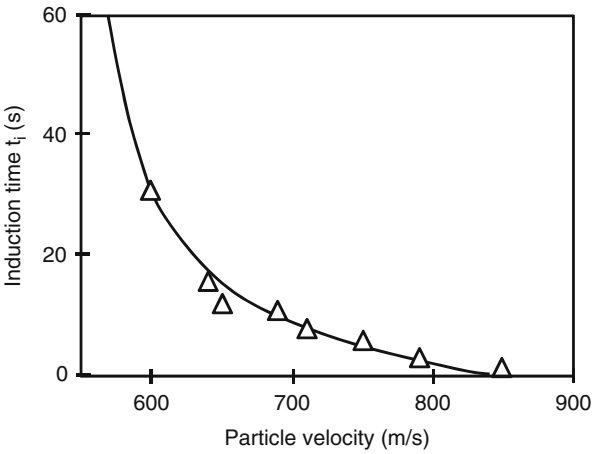


Fig. 13.16 Dependence of t_i (induction time) on the impact velocity for aluminum particles impacting on a copper substrate. Reprinted with kind permission from Springer Science Business Media [65], copyright © ASM International

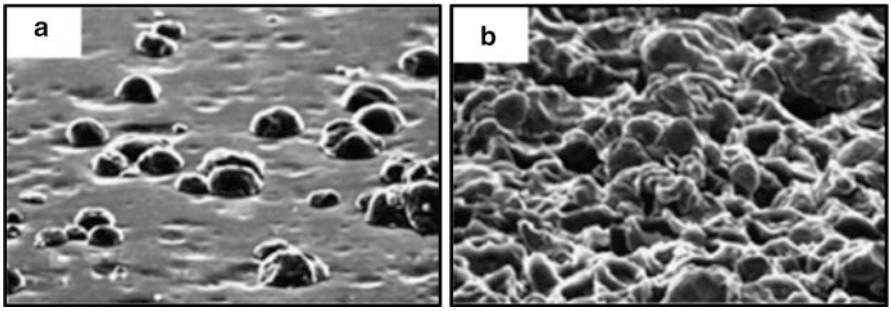


Fig. 13.17 Morphologies of collected copper particles (gas pressure: 0.7 MPa, helium temperature: 723 K, particle size: 5 μm). (**a**) AISI 304 substrate surface. (**b**) A6063 substrate surface. Reprinted with kind permission from Springer Science Business Media [66], copyright © ASM International

alloy A6063 substrates, have shown that extreme roughening is observed on the A6063 substrate, as illustrated in Fig. 13.17.

They have also shown that substrate heating is quite effective for the formation of the first layer resulting in a higher deposition ratio in the cold spray process. This tendency was promoted more effectively using helium instead of air or nitrogen as a working gas. Both higher velocity and temperature of the particles sprayed are the necessary conditions for the higher deposition ratio in the cold spraying. Instead of particle heating, substrate heating may bring about the equivalent effect for particle deposition [66]. The substrate material also plays a key role in the deposit formation. For example, aluminum splat formation has been studied for substrates made of tin, copper, Al alloy, brass, different tool steels, low carbon steel, glass, and alumina (hardness varying from 0.08 GPa to 10.7 GPa) [58, 67]. It has been shown that initiation of deposition onto soft metallic substrates is difficult due to the lack of deformation of the aluminum particles. The initiation of aluminum deposition

increases with the substrate hardness. Deposition of aluminum particles onto aluminum is difficult due to the thin aluminum oxide layer on the substrate, which deforms with the underlying aluminum. Of course deposition onto nonmetallic substrates is difficult due to lack of metallic bond that can be formed [55]. To conclude this part more work on the interface between a cold-sprayed particle and the substrate is necessary to improve our understanding of the involved phenomena.

13.4.3.3 Unmelted Particles (High Power HVOF or HVAF Sprayed)

When spraying with high power HVOF guns, where, for example, nitrogen is introduced in the combustion chamber, or HVAF guns, the gas temperature can be lower than the melting temperature of sprayed metals or alloys that can impact in solid phase a few hundred degrees below their melting temperature. For example, Trompetter et al. [60] have studied Ni–Cr (Ni80/Cr20, 5–45 μm) alloy particles HVAF sprayed onto Al substrates. For a chamber pressure of 414 kPa, the gas temperature falls to ~1,300 °C in the diverging section of the HVAF torch nozzle, which is below the melting point of NiCr powder (T_m = 1,400 °C). Moreover the residence time of the spray particles in the gas jet is quite short (~200 μs for a particle velocity of 700 m/s and a spray distance of 150 mm). The particle substrate interface was investigated with focused ion beam microscopy, cross-sectional scanning electron microscopy, and cross-sectional transmission electron microscopy. No evidence of melting or chemical bonding was found in the samples. Instead, evidence of mechanical bonding was found quite similar to that predicted by Grujicic et al. [44, 45] in high-pressure cold spray. Interlocking features were found at certain locations along the particle–substrate interfaces. Vortices of aluminum were found to extend 100 to 1,000 nm from the substrate into thermally sprayed NiCr particles [60]. As illustrated in Fig. 13.18, the size of the turbulent features was proportional to the particle diameter, which is in agreement with the amount of interfacial instability estimated by Reynolds number calculations.

Trompetter et al. [68] have also studied the influence of the substrate surface oxides on NiCr splat–Al substrate bonding sprayed in the previous conditions. No splats were found on the aluminum oxy-hydroxide oxide layer (845 nm), whereas bonding did occur on an alumina layer (650 nm) grown on an aluminum substrate. Cross sections of solid splats showed that the aluminum substrate and surface oxide had been deformed during the particle impact. This has resulted in some locations where the oxide was as thin as 20 nm but was still present between the splat and the substrate even in these very thin local regions. Cross-sectional measurements of molten particles show that the oxide has been penetrated in several locations allowing close proximity of the splat metal to the substrate metal to occur [68]. At last, Trompetter et al. [40] have studied the same Ni–Cr (Ni80/Cr20, 5–45 μm) alloy particles HVAF sprayed onto a variety of substrate materials (Al, Cu, Fe, Ti, Ta, glassy C, Si), the hardnesses of which varied from 338 MPa to 10,082 MPa. Although the various substrate materials were coated using identical powder material and thermal spray conditions, the type and variation of splat

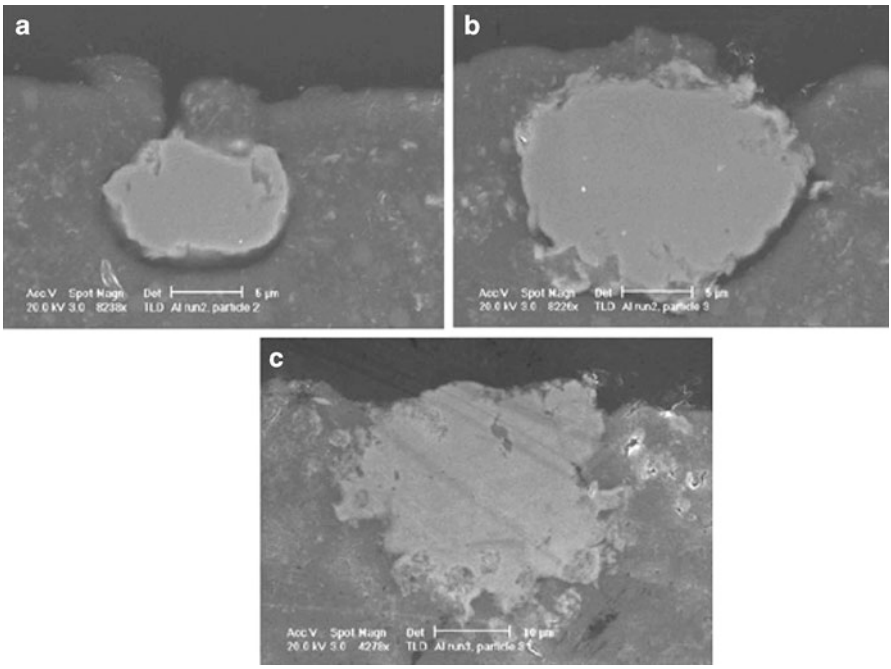


Fig. 13.18 Cross-sectional SEM images of individual NiCr particles embedded in an Al substrate with varying degrees of interfacial contact and interfacial turbulence: (**a**) low level of interfacial turbulence ($d_p = 14$ μm), (**b**) medium level of interfacial turbulence ($d_p = 21$ μm), and (**c**) high level of interfacial turbulence ($d_p = 36$ μm). Reprinted with kind permission from Springer Science Business Media [60], copyright © ASM International

morphologies were strongly dependent on the substrate material. On the Al substrate 52 % of solid splats and 45 % of semi-molten ones were observed. With the very hard substrates (glassy C and Si) 81–70 % of molten splats were obtained, while with Ti, Cu, Fe, Ta substrates semi-molten splat fractions were between 45 and 57 % with fully molten ones between 23 and 31 %. However it must be emphasized that percentages do not vary linearly with the hardness. This is illustrated in Fig. 13.19a showing that the solid splat has penetrated deeply into the Al substrate while on the Si substrate, Fig. 13.19b, the deformation is negligible. Fig. 13.19c, d illustrate are semi-molten splats obtained on Ti and glassy C substrates and Fig. 13.19e, f present molten splats on Ta and glassy C.

Trompetter et al. [40] found that conversion of particle kinetic energy into plastic deformation and heat, dependent on substrate hardness, can make a significant contribution toward explaining the observed behavior. When impacting on soft substrates a low percentage (<10 %) of kinetic energy is converted into plastic deformation and heat. Conversely, when particles suffered heavy deformation impacting onto hard substrates most of the particle kinetic energy (e.g., 95 %) would have been converted into plastic deformation and heat, as illustrated in Fig. 13.20.

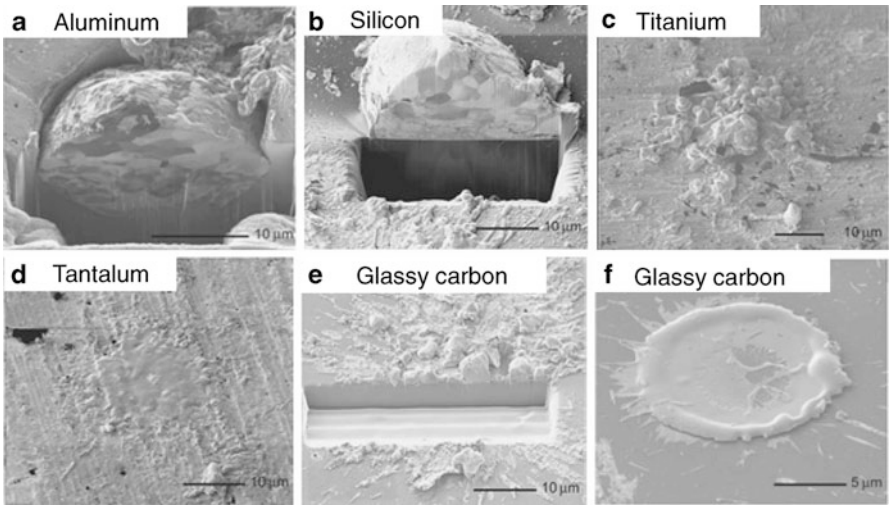


Fig. 13.19 NiCr particles HVAF sprayed and resulting in solid splats on (**a**) Al and (**b**) Si (sectioned); semi-molten splats on (**c**) Ti and (**d**) glassy carbon (sectioned); (**e**) molten-splash splat on Ta and molten-disc splat on glassy carbon. Reprinted with kind permission from Springer Science Business Media [40], copyright © ASM International

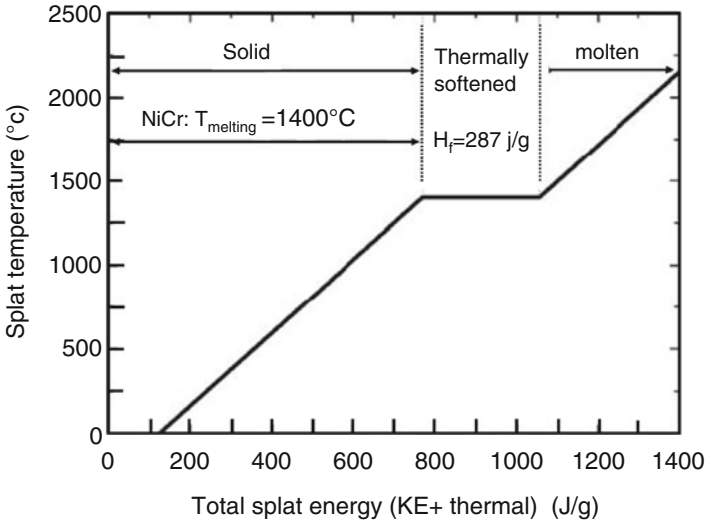


Fig. 13.20 Relationship between splat thermal energy and temperature. Reprinted with kind permission from Springer Science Business Media [40], copyright © ASM International

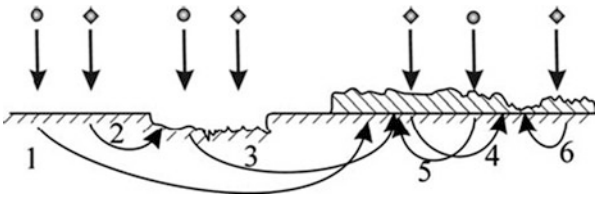


Fig. 13.21 Different phenomena involved in the formation of a coating from a sprayed metal-ceramic mixture. Involved processes: (1) adhesion of a metal particle to initially nonactivated substrate surface (transition s_s to s_c), (2) impact of an abrasive particle onto non-activated substrate surface (transition s_s to s_{sa}), (3) adhesion of a metal particle to activated substrate surface (transition s_{sa} to s_c), (4) impact of an abrasive particle onto the formed coating (transition s_c to s_{ca}), (5) adhesion of a metal particle to activated coating surface (transition s_{ca} to s_c), and (6) impact of an abrasive particle onto the activated portion of the coating (transition s_{ca} to s_{sa}). Reprinted with kind permission from Springer Science Business Media [69], copyright © ASM International

13.4.3.4 Unmelted Particles from Low-Pressure Cold Spray

Klinkov and Kosarev [69] have developed a two-probability model to theoretically analyze the influence of surface erosion and activation due to abrasive particles impacting on the substrate (coating) surface on the total deposition efficiency of a sprayed mixture of abrasive and metal particles. Relations for the total deposition efficiency derived with regard to the activation effect due to abrasive particles were obtained. The spray gun was working with air (pressure 1.6 MPa, temperature 550–750 K) with the two-component system: copper ($d_{50} = 30$ μm)–silicon carbide with different sizes (8, 14, or 40 μm). The presence of abrasive particles in the mixture enhances the adhesion probability of metal particles to the surface, even if, due to dilution, it decreases the concentration of metal particles in the mixture. The impact of ceramic particles also exerts an erosive action on the surface. The involved process is summarized in Fig. 13.21, where the areas of nonactivated s_c and activated s_{ca} coating surfaces are presented, and also the corresponding areas of nonactivated s_s and activated s_{sa} substrate surfaces. The modeling data were found to be in a good qualitative agreement with experimental data. This suggests that the model developed by Klinkov and Kosarev [69] provide an adequate description of the kinetics of coating growth from sprayed metal–ceramics mixtures.

Koivuluoto and Vuoristo [70] have shown that Cu + Al_2O_3 coatings are strongly influenced by the powder characteristics of Cu particles (spherical and dendritic) and volume percentage of Al_2O_3 (0, 10, 30, and 50 vol.%). Coating denseness and particle deformation level increased with the hard particle addition. Furthermore, hardness and bond strength increased with increasing Al_2O_3 fractions. In the comparison between different powder types, spherical Cu particles led to the denser and less oxide-containing coating structure due to the highly deformed particles.

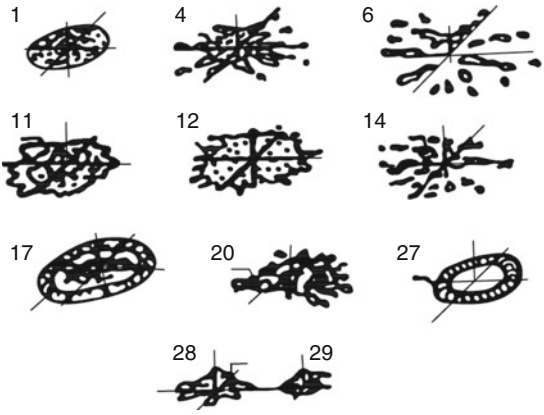


Fig. 13.22 Different morphologies of splats collected on a smooth substrate after Kudinov [72]: 1 and 4 fully melted, 6 and 11 fully melted with gas inclusions, 14 superheating with strong evaporation, 17 melted shell surrounding a solid core, 20 solid shell with a melted core, 27 solidified crown, melted interface and solid core, 28 and 29 ductile particles with high velocities

13.4.4 Splat Formation from Molten Particles Impacting onto Smooth Substrates

13.4.4.1 Introduction

Two types of impacts are generally considered: normal impact, optimum for coating generation, and off-normal one (see Sect. 13.6) where the impact velocity is reduced. However normal impact cannot always be achieved when the part to be sprayed has steep angular area or convex or concave zones with small radii and also because the spray jet is slightly divergent with particles in its fringes impacting the substrate, kept normal to the jet axis, with an angle generally between 70 and 110°.

Kudinov et al. [72] at the beginning of the 1980s were the first to make some sort of zoological classification of splat shapes on a smooth surface shown in Fig. 13.22.

Splat shapes depend on a large number of factors, including the presence of contaminants at the substrate surface, the partial solidification of the particle in-flight resulting in formation of a solid shell around the liquid central part (this occurs especially for low thermal conductivity materials), the degree of in-flight oxidation, the superheating of the particle, etc. According to recent work [73–76] where the flattening of droplets has been followed, the main types of splats are those presented in Fig. 13.23. Of course with sprayed materials, which effusivity is close to that of substrate shapes, as that presented in Fig. 13.13, are also observed.

What makes the study of particle flattening at impact very complex is that it depends on many parameters comprising:

– The particle, or more precisely the droplet, impact parameters: its diameter, velocity, and temperature, which can be nonuniform within the droplet, its

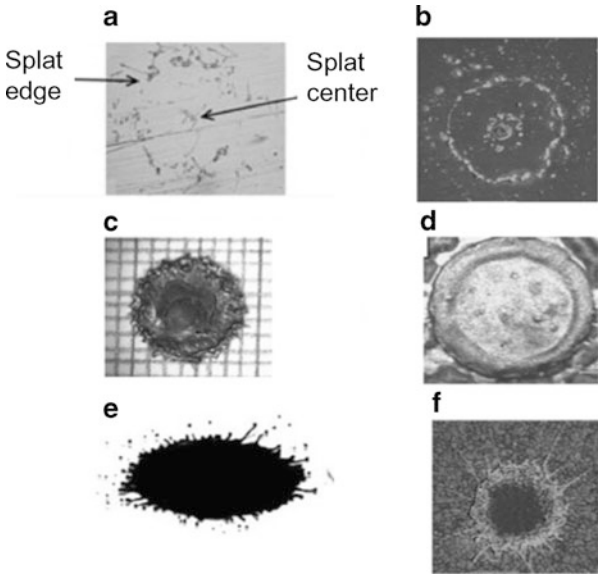


Fig. 13.23 Main types of molten splats: (**a**) and (**b**) extensively fragmented: (**a**) alumina on cold 304 stainless steel (SS) [74]. Reprinted with kind permission from Springer Science Business Media [74], copyright © ASM International, (**b**) Ni on 304 SS pre-oxidized at 150 °C [73]. Reprinted with kind permission from Elsevier. (**c**) and (**d**) close to disk shape: (**c**) Cu on AISI304 SS [75], reprinted with kind permission from Springer Science Business Media. copyright © ASM International, (**d**) alumina on low carbon steel preheated at 200 °C [76], Reprinted with kind permission from Elsevier, and (**e**) and (**f**) Fingered: (**e**) alumina on SS preheated at 400 °C [74]. Reprinted with kind permission from Springer Science Business Media, copyright © ASM International. (**f**) Ni on pre-oxidized SS at 650 °C [73], reprinted with kind permission from Elsevier

oxidation forming a shell at its surface that can be either solid or liquid, and also existing oxide nodules inside the particle (see Fig. 13.8).

– The substrate surface, with, for metals, alloys, and cermets, the oxide layer composition and thickness, the substrate skewness, the adsorbates, and condensates present (see Fig. 13.8).
– All parameters linked to the droplet and substrate combine to control the splat formation. The flattening droplet velocity depends on the transformation of the initial vertical impact velocity into a horizontal one, the liquid-substrate wettability, but also on its solidification. The flattening droplet solidification is closely linked to its thickness and the thermal contact resistance, R_{th}, with the substrate, or previously deposited layers. These two parameters vary along the flattening droplet radius, r, especially R_{th} is closely correlated to the local pressure diminishing with r.

Since the beginning of the 1980s much work was devoted to the study of the impact and deformation of a single thermal spray molten particle to form a solid splat. Fauchais et al. [71] in 2004 and Chandra and Fauchais in 2009 [17] reviewed these studies. Those studies emphasized the difficulty of determining the impact of

particles in a molten state with sizes between 20 and 60 μm and velocities ranging between 50 and 600 m/s. The flattening time of such molten particles is only a few microseconds, and solidification starts before flattening is completed.

(a) Measurements

In Sect. 13.5.1 it has already been emphasized that it is impossible to follow continuously the flattening of molten particle plasma or HVOF sprayed, and the trick used to obtain successive images at different impact times has been to observe different particles assumed to impact with the same parameters (for details see Sect. 16.7.2.1). To follow particle-flattening, millimeter-sized particles have been used. They are easier to observe as they have flattening times of several milliseconds, and thus their impact can be followed with high-speed video cameras. However, applying these observations to thermal-sprayed particles requires matching the values of all the dimensionless numbers (*Reynolds*, *Weber*, *Peclet*, *Stephan*, *Biot*) that control impact dynamics (see below section "(b) Modeling"), which is possible when considering one dimensionless number, such as We, but rarely possible for all of them. Moreover, if for micrometer-sized particles the ratio of the flow boundary layer of the flattening particle to its thickness is close to unity, with millimeter-sized particles it is a few orders of magnitude higher [73].

(b) Modeling

Many analytical models using dimensionless numbers have been developed and the interested reader can see the review paper of Amster et al. [77] or the paper of Fauchais et al. [71]. These models assume a two-dimensional geometry and a perfect contact between flattening particle and substrate ($R_{th} = 10^{-8}$ m^2 K/W). Also very often it is assumed that solidification occurs once flattening is completed. The particle flattening is characterized by Reynolds, *Re*, Weber, *We*, Sommerfeld, *K*, numbers, and its cooling by Stephan, *St*, Peclet, *Pe*, and Biot, *Bi*, numbers. These numbers allow predicting the effect of particle parameters on splat formation. However, they cannot predict the breakup or splashing of the flattening particle on the surface. That is why computational fluid mechanics must be used to simulate thermal spray particle impact and gain insight into mechanisms that determine the shape of a splat. However, such a simulation presents many challenges:

- Simulating thermal spray particle impact requires solving simultaneously momentum and energy conservation equations, while accounting for phase change within the solidifying droplet. A three-dimensional transient model is required to simulate droplet splashing or interactions between multiple droplets, which places significant demands on computing facilities. If gas entrapment under splats is to be modeled a two-fluid model is required, which includes flows in both the droplet and the ambient atmosphere.

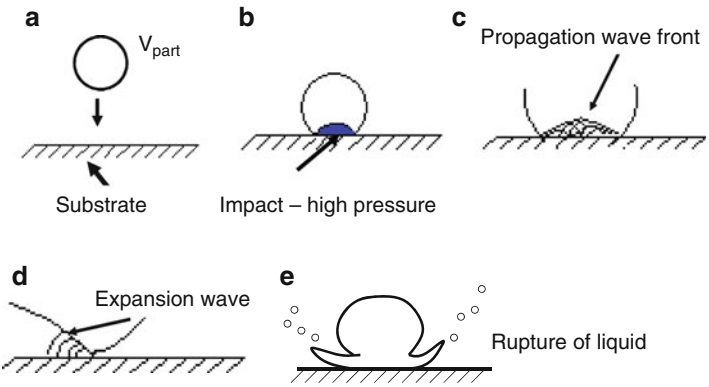


Fig. 13.24 Successive phenomena of impact splashing: (**a**) particle before impact, (**b**) impact generating a very high pressure, (**c**) propagation of a wave front, (**d**) expansion wave at the triple point, and (**e**) rupture of liquid [77]. Reprinted with kind permission from Maney Publishing

- The model must track the free surface of the particle, which undergoes very large and rapid deformation.
- Representing boundary conditions realistically is a challenge. A contact-angle at the liquid–solid contact line must be specified as well as a thermal contact resistance at the interface between the splat and the substrate, if possible varying with time and flattening particle radius. Both are very difficult, if not actually impossible, to determine experimentally.
- Most models that have been developed assume that thermodynamic equilibrium exists and that particles freeze at a well-defined solidification temperature. In reality the rate of cooling is very high when a particle impacts a surface and significant undercooling may exist.
- Results from numerical models are sensitive to fluid properties such as viscosity and surface tension, which vary, sometimes drastically, with droplet temperature and are often not well known for liquid materials such as zirconia.

References [78–81] present a few examples of models developed in the last decade.

13.4.4.2 The First Instants of Impact

The impact pressure $\rho_p \cdot v_p^2$ increases drastically with the particle velocity: if we compare the impact pressure obtained for the same particle at the same temperature, we obtain values for r.f. plasma spraying of an impact velocity v_p (Fig. 13.24a) of 50 m/s a reference pressure p_{ref}, for d.c. plasma spraying with an impact velocity of 200 m/s, $p = 16 \times p_{ref}$ and for spraying with HVOF at 500 m/s, $p = 100 \times p_{ref}$. The impact pressure, linked to compressibility effects, can be very high (over 100 MPa). The impact generates a pressure pulse distributed along a radius r_m smaller than the final splat radius: $r_m = d_p \cdot v_p/(2c_l)$ (Fig. 13.24b), where c_l is the

sound velocity in the liquid drop [77]. As typical sound velocities in liquid metals are a few thousand m/s, r_m is about 10 % of the impacting particle diameter. Within r_m the vaporization of adsorbates and condensates is generally negligible. In general compressibility effects are also neglected. Then the wave front propagates, see Fig. 13.24c, resulting in an expansion wave (Fig. 13.24d) and induces rupture of the liquid and droplet formation at the triple interface, see Fig. 13.24e.

Impact splashing occurs immediately after impact (within the first 100 ns) and is driven by fluid instabilities, before any solidification can take place. It depends, at least for water droplets that have been studied in detail, on the Sommerfeld parameter, K, defined as

$$K = We^{0,5}\,\mathrm{Re}^{0,25} \tag{13.3}$$

where We is the Weber number and Re the Reynolds number of the particle at impact. Thus

$$\mathrm{K} = \left[\frac{\rho v d}{\mu}\right]^{0,5}\left[\frac{\rho \mu^2 d}{\sigma}\right]^{0,25} \tag{13.4}$$

ρ, v, d, μ, and σ being, respectively, the mass density, the velocity, the diameter, the viscosity, and the surface tension of the impacting droplet.

A value of $K < 3$ corresponds to a rebound; $3 < K < 58$ results in deposition, and $K > 58$ induces splashing. These critical values are somewhat different for fully melted materials, as shown by Escure et al. [82]. Figure 13.24e from Armster et al. [77] shows how impact splashing occurs and Fig. 13.25 shows the impact splashing of alumina particles (22–44 μm) plasma sprayed, with different Sommerfeld parameters, onto a stainless steel substrate [82]. The droplets ejected have diameters below one micrometer and they reach distances of a few mm above the substrate, outside the dynamic boundary layer. From a practical point of view these tiny particles reach distances above the substrate that are generally outside the fluid boundary layer. Thus they are entrained by hot gases far from the substrate and the coating being deposited, creating no defect within coating.

13.4.4.3 Molten Particle Flattening and Solidification

This the case of particles sprayed by flame, plasma, HVOF, and D-gun.

(a) General Remarks

Figure 13.26a represents the particle impact at time 0 and the impact pressure time evolution at radius 0 when the particle flattens. The high pressure within the particle forces melted material to flow laterally and eventually can deform the substrate if its material is too ductile. The kinetic energy of the particle is transformed into work of viscous deformation and surface energy. The contact pressure spreads out and

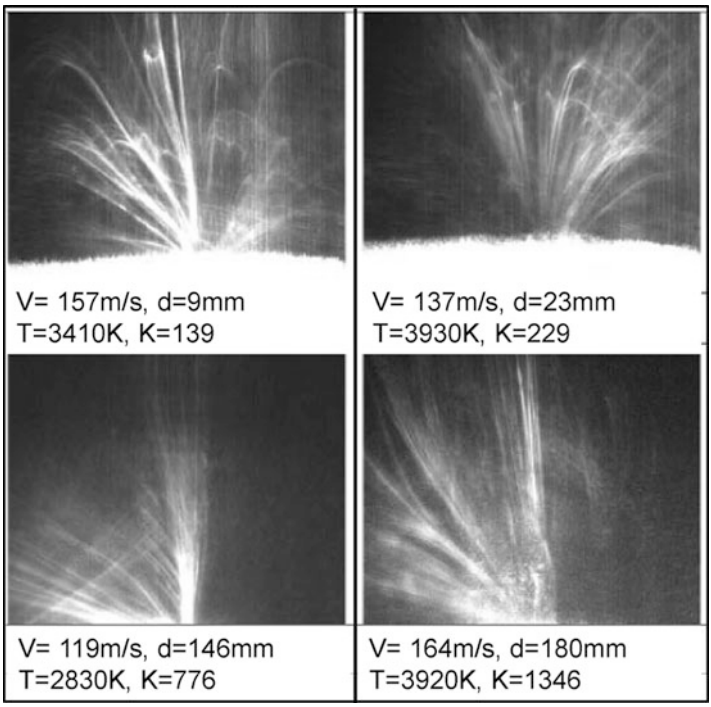


Fig. 13.25 Impact splashing of 3 plasma-sprayed alumina particles with different impact parameters and thus Sommerfeld parameters, pictures taken with a long exposure time of 1 ms [82]. Reprinted with kind permission from Springer Science Business Media

dissipates quickly with droplet flattening, as shown in Fig. 13.26a. Figure 13.26b represents the flattening droplet at time t_k when the flattening particle reaches the radius r_k, in this figure is also shown the pressure time evolution at radius r_k. It is worth noting that a high pressure starts only to exist when the flattening particle reaches r_k. Of course the pressure at position r_k is smaller than at $t = 0$. Such pressure time variations along the flattening particle diameter play a key role in its flattening and solidification behavior. Especially in regions where the flattening degree of the droplet reaches a value of 1.5–2 the pressure is not high enough to overcome other forces such as those due to evaporated adsorbates and condensates at the substrate surface [83]. Upon contact of the molten particle at high temperature, adsorbates and condensates evaporate on the substrate very rapidly (in a few hundreds of nanoseconds) raising the pressure under the flattening particle and decreasing its contact with the substrate. This results in a lifting of the liquid that is flowing on the substrate surface, as illustrated schematically in Fig. 13.27, and the flattening droplet spreads much more than on the same substrate without adsorbates and condensates. In the central zone where the impact pressure is the highest and

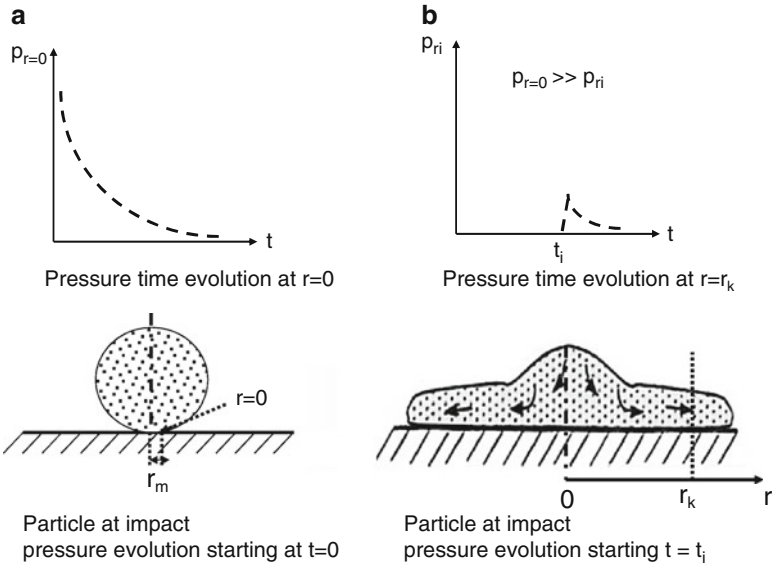


Fig. 13.26 (**a**) Droplet impact at time 0 with the impact pressure time evolution at radius 0. (**b**) Droplet at time t_k with the pressure time evolution at radius r_k

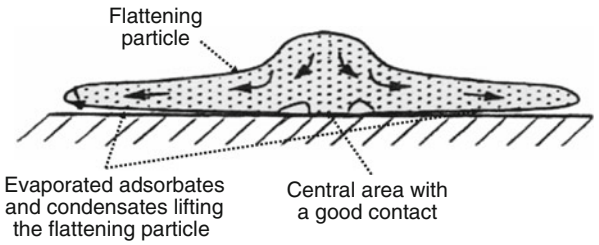


Fig. 13.27 Schematic representation of droplet flattening on a substrate at room temperature where adsorbates and condensates exist: the droplet is lifted over the substrate surface, and in the central zone, where the pressure is the highest, only a few contact points exist

can therefore overcome the vapor pressure, only a few contact points between the splat and the substrate are observed (see Fig. 13.23a, b). Thus, compared to a surface where adsorbates and condensates have been eliminated, the contact surface between splat and substrate is drastically reduced by a ratio of 2–6.

It is also important to recall that the particle morphology (depending on its manufacturing process) plays an important role in its melting and flattening through the temperature and velocity distributions of impacting particles [84, 85].

Table 13.2 Values of transition temperature obtained for different materials plasma or HVOF sprayed onto stainless steel substrates ASI304 [89]. Reprinted with kind permission from ASM International

Powder material	Spraying device	Transition temperature (K)
Ni	APS	610
Mo	APS	474
Cu	APS	394
Cr	APS	387
Cu–30Zn	APS	505
Cu–30Zn	HVOF	455
Ni	HVOF	560
Ni–5Al	HVOF	440
Ni–10Cr	HVOF	400
Ni–20Cr	HVOF	360
Cr	HVOF	345
Al_2O_3	APS	318
TiO_2	APS	350
YSZ	APS	345

Substrate: AISI 304 Stainless steel

(b) Adsorbates and Condensates: Transition Temperature

The quantity of adsorbates and condensates depends strongly on the oxides formed at the metal or alloy substrate. For example, the surface layers on aluminum and stainless steel formed under ambient conditions are mixtures of oxides and oxyhydroxides [25, 86–90]. Heat treatment of the substrate just prior to spraying causes changes in the relative amounts of these species and consequent release of gases from the surface and can also induce segregation of elements on the surface due to differences in free energy of oxide formation [88]. Fukumoto et al. [28] have defined the transition temperature, T_t, as the critical substrate temperature over which more than 50 % of splats are disk shaped. Results are illustrated in Table 13.2 from Fukumoto [89] presenting some values of T_t obtained for different materials sprayed by plasma or HVOF onto a stainless steel substrate ASI304. The transition temperature has been correlated with the vaporization of adsorbates and condensates on the surface and also, under certain circumstances, with the improvement of the droplet wettability on the substrate. The necessity of preheating the substrate to get rid of adsorbates and condensates has also been demonstrated for PEEK splats on aluminum substrates [91].

Figures 13.28 and 13.29 present two examples of splats collected on smooth stainless steel substrates preheated or not. Figure 13.28 shows YPSZ particles [92] and Fig. 13.29 Ni particles [89]. On room temperature (RT) substrates, splats of both materials are extensively fingered, while on substrates preheated over T_t they are disk shaped. For the YPSZ splats on RT substrates the fraction of the surface in good contact with the substrate is about 20 %, while on the preheated substrate it is around 60 %. Figure 13.30 shows the bottom surface of the Nickel splat on the RT

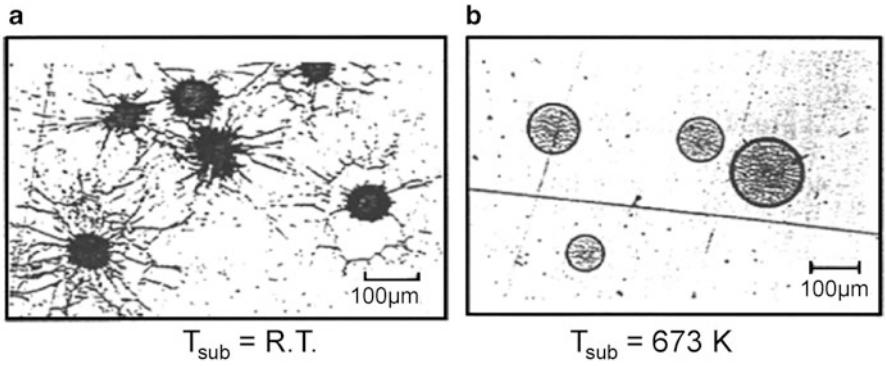


Fig. 13.28 YSZ splats plasma sprayed onto a stainless steel ASI304 substrate. (**a**) At room temperature and (**b**) preheated at 673 K. Reprinted with kind permission from Elsevier [92]

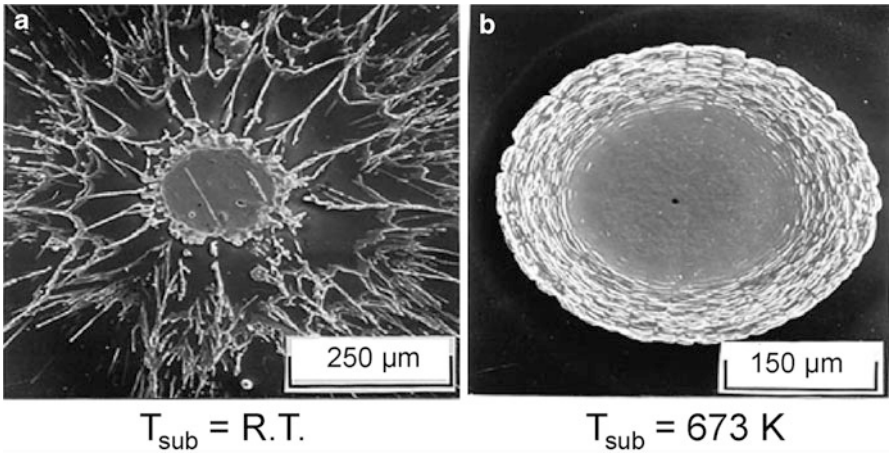


Fig. 13.29 Nickel splats plasma sprayed onto a stainless steel ASI304 substrate. (**a**) At room temperature and (**b**) preheated at 673 K. Reprinted with kind permission from ASM International [89]

substrate. It can be seen that the central part of the splat, which in Fig. 13.30a seems to be in good contact with the substrate, has in fact some sort of lace surface with many holes corresponding to a poor contact area (Fig. 13.30b, c). This is in contrast to the Ni splat on the preheated substrate (Fig. 13.31), where the bottom part shows an excellent contact except in its periphery.

The transition temperature plays a key role in eliminating contaminants at the substrate surface when spraying in an air atmosphere or in a controlled atmosphere at atmospheric pressure. However the preheating temperature must be limited to the transition one because preheating substrates at too high temperatures can modify the oxide layer thickness, its composition and also its Skewness [19].

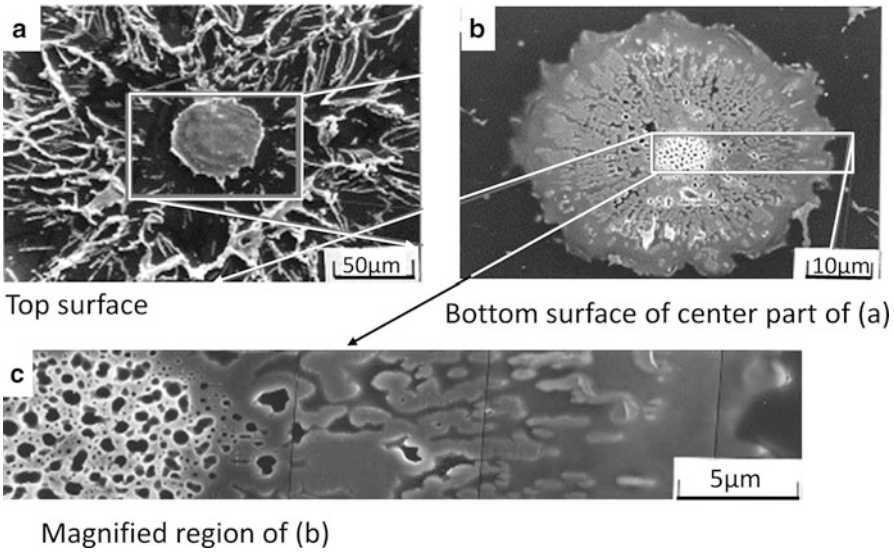


Fig. 13.30 Bottom of nickel splats plasma sprayed onto a stainless steel ASI304 substrate at room temperature. Reprinted with kind permission from ASM International [89]

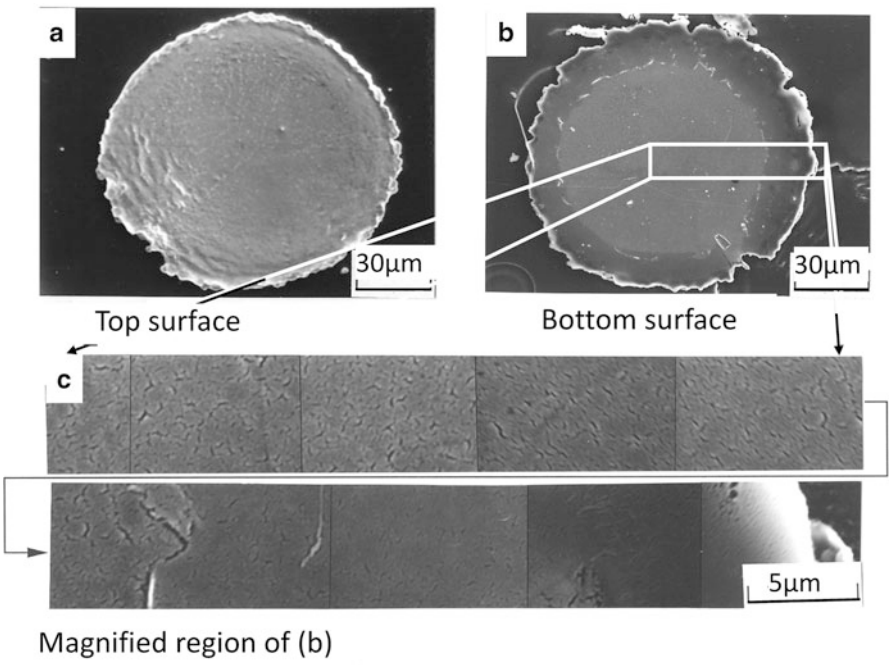


Fig. 13.31 Bottom of nickel splats plasma sprayed onto a stainless steel ASI304 substrate at 673 K. Reprinted with kind permission from ASM International [89]

Table 13.3 Flattening degree and splat thickness of zirconia particles 30 μm in diameter impacting at 3,200 K on a smooth substrate with different velocities

Impact velocity (m/s)	25	135	200	400
Flattening degree	3.6	5	5.5	6.3
Splat thickness (μm)	2.4	1.2	1.04	0.8

When the pressure is reduced as in soft vacuum spraying, a transition pressure also exists, as shown by Fukumoto et al. [28, 75, 93]. Without preheating no chemical modification of the surface occurs when the pressure is lowered, and desorption is the only possible physical change occurring. However transition pressures for different materials do not follow the same classification as that obtained for transition temperatures. The differences are probably linked to the native oxide layers of the different substrates, which also depend on surface preparation.

(c) Droplet Flattening

The first studies on this topic used analytical expressions [77] such as those of Madejski [94], Williams and Jones [95], Yoshida et al. [96], Fantassi et al. [97]. The analytical expression, established by Madejski [94], assuming that the solidification started only when flattening was completed, related the flattening degree ξ, Eq. (13.2), to the particle Reynolds and Weber numbers at impact:

$$\frac{3\xi^2}{We} + \frac{1}{\mathrm{Re}}\left(\frac{\xi}{1.2941}\right)^5 = 1 \tag{13.5}$$

Assuming that the Weber number of the particle is larger than 100, which is the case for most thermal spray processes, at least at the beginning of the flattening process. The splat diameter D, assumed to be a disk, is linked to the impacting particle diameter d_p by expressions of the type:

$$D/d_p = A \cdot \mathrm{Re}^{0.2} \tag{13.6}$$

where A is a constant with a value between 1.2941 for a perfect disk shape according to Madejski [94] and 0.83 for extensively fingered splats [96] where only the central part of the splat is considered being a disk. The flattening degree increases with impact velocity for the same temperature, and the splat thickness, e, diminishes accordingly. The thickness can be calculated by assuming that the liquid spherical particle of diameter d_p is transformed into a perfect disk, with a volume of $e \cdot \Pi \cdot D^2/4$. Table 13.3 gives a few values of flattening degrees and splat thicknesses of zirconia particles impacting with a temperature of 3,200 K with different velocities.

However the impact parameters are not sufficient at all to characterize the particle flattening. Once the droplet has started to flatten, the substrate parameters play a key role. They comprise the substrate material, its mechanical and thermal properties, especially its diffusivity, its oxide layer characteristics (if any), its roughness, and last its surface temperature to get rid of adsorbates and condensates. Depending on the impact velocity, the particle flattening time varies between a few microseconds ($v_p < 50$ m/s) and a few tenths of microseconds ($v_p > 400$ m/s).

Assuming that all adsorbates and condensates have been eliminated before the droplet impact, its flattening depends on the wettability between droplet and substrate:

- Generally the wettability of oxidized particles on the oxide layer on a substrate surface is better than that of nonoxidized particles.
- The wettability of a liquid material on its solid is generally good (case of the droplet impact on previously deposited layers).
- The increase of substrate roughness hinders the liquid spreading and splats are smaller than on the same smooth surface, with irregular morphologies and the formation of many voids, including some rather large ones (few micrometers). However higher surface roughness results in higher wettability of the substrate [17, 18, 21, 27, 28, 71]. As the thickness of the oxide layer increases the roughness [17, 27], it modifies the wettability.
- Of course the composition, thickness, and morphology of the oxide layer on the surface of the substrate, both parameters affected by the preheating temperature, the preheating time and rate, play a key role on the wettability. As shown by Cedelle et al. [19], preheating a 304L stainless steel substrate increases its roughness with its skewness becoming positive at the nanometer scale and its wettability is improved.
- The wettability also depends on the substrate thermal conductivity, as shown by Tanaka and Fukumoto [98] for ceramic particles impacting different substrates. The higher the thermal conductivity of the substrate is, the poorer is its wettability.
- At last the wettability can be improved by the diffusion of substrate elements toward its surface thanks to its heating by the flattening droplet. Brossard et al. [48] have demonstrated this for the impact of NiCr droplets on a stainless steel substrate, with the diffusion of Mg and Cr toward substrate surface.
- The wettability can also be modified by the existence of solid pieces of oxides at the flattening particle surface. That can occur, for example, when particles, such NiAl, contain aluminum and solid alumina is formed at the molten particle surface when the particle temperature is below 2,000 K.

To account for the substrate-flattening droplet wettability variation, Tanaka and Fukumoto [98] have proposed to use a new criterion K_f, based on the flattening information of the droplet. It was obtained by using the maximum flattening velocity v_f and splat thickness b into the Sommerfeld parameter, K (Eq. 13.4), instead of the impact velocity v_p and droplet initial diameter d_p. Of course the main problem with this equation is the evaluation of v_f. According to the last developments in

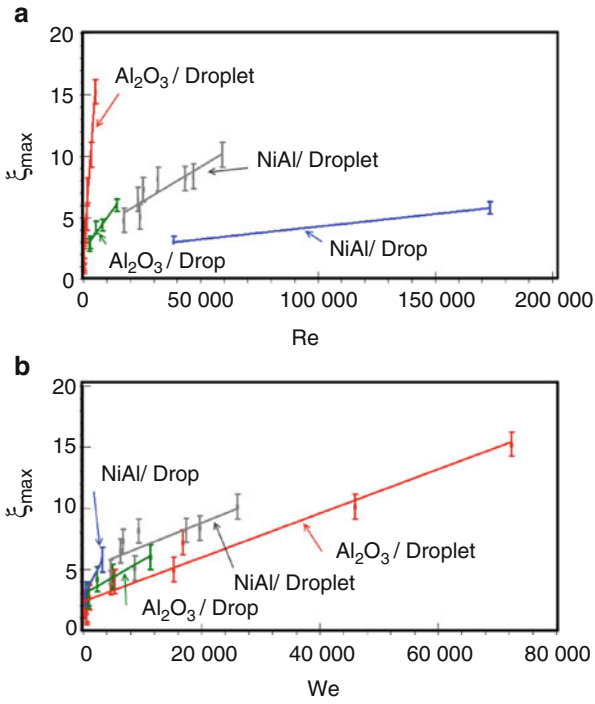


Fig. 13.32 Evolutions of the flattening particles (metal and ceramic) at two scales, with (**a**) the Reynolds ($Re = \rho v_e R_{max}/\mu$), (**b**) the Weber ($We = \rho {v_e}^2 R_{max}/\sigma$), the speed taken into account being that of the liquid on the substrate and characteristic dimension being equal to the radius of maximum flattening. Reprinted with kind permission from Dr. S. Goutier [99]

measuring v_f (Sect. 16.7.2.1) Goutier et al. [74] have calculated the Reynolds and Weber numbers of the flattening droplets. To calculate the Weber and the Reynolds numbers of the flow, the mean flattening velocity, v_e, is considered. If the measurement of the flattening velocity of millimeter-sized drops is simple, that of micrometer-sized droplets is complex because it is not possible to follow the particle flattening in real time. It is thus necessary to make some assumptions to determine the flattening speed. The only solution, to determine the flattening time, is to measure the time necessary to reach the maximum flattening diameter. So it must be to consider that during flattening the cooling is negligible. To confirm this assumption, it can be noticed that the maximum of the pyrometer signal is reached at the maximum flattening. By measuring the maximum flattening diameter (Dmax), thanks to the images [74] and the time corresponding to the maximum of the pyrometer signal at a given wavelength, it is possible to calculate a mean flattening velocity. By using images of the fast camera (10,000 frames/s), it is possible to deduce the time of the maximum flattening diameter of the droplets to calculate this mean velocity. Curves presented in Fig. 13.32 have been obtained by considering the mean flattening speed to calculate the corresponding Reynolds and Weber numbers, together with the dimensionless maximum flattening radius. No relationship exists between Re and the maximum flattening when the material (metal or ceramic) and diameters (40 μm: droplets to 5 mm: drops) of the impacting particle are modified. But, the evolution of the lamella diameter seems

to be strongly related to the evolution of We. Indeed, the flattening curves corresponding to various conditions of the substrate (cold, hot) and of the particles (metal, ceramic) are close to each other. This means that the maximum flattening is controlled by the competition between the surface tension and inertia energies. That also means that the effects of the surface tension are preserved during the modification of the particle scale, due to the weak variation of the surface tension when the liquid is cooling. This is not the case of the viscous effects, which are strongly related to liquid cooling. When calculating the Weber number with the diameter of the impacting particle instead of the splat maximum diameter and of course the mean flattening velocity much better results are obtained, as shown in Fig. 16.51

Clearly, much effort is still necessary to better understand the flattening phenomena especially to link the previous results to the solidification behavior that was neglected in the flattening description.

(d) Droplet Solidification

The material solidification depends on splat thickness, thermal diffusivities of both sprayed material and underlying solid layer, and the quality of contact between the latter and the flattening particle. Unfortunately the quality of contact at the interface is a function of the particle impact pressure that varies drastically and nonuniformly along the contact surface during impact (see Fig. 13.26). Here again the higher the impact velocity will be, the higher will be the impact pressure and the smaller the thickness of the flattening droplet. Thus high impact velocities improve the flattening particle solidification. Compared to flattening times, solidification times are 5 to 10 times longer, but generally solidification starts before flattening is terminated. When solidification starts it can modify the liquid flow at the flattening droplet surface. The contact splat surface will never represent the whole splat surface, a very good contact corresponding to 60–70 %, and a poor one 10–20 % [71]. Even when the contact is good, at the splat rim, where the contact pressure is very low and the surface tension at its maximum, splat curling occurs with the formation of a rounded rim due to the surface tension [100]. The contact of the external radius of the flattening particle with the substrate is very poor, thereby inducing a slower liquid cooling, not directly toward the substrate or the previously deposited layers but through the already solidified part of the splat. Here again, the higher the impact velocity will be, the higher will be the impact pressure and the smaller the flattening droplet thickness.

To illustrate the influence of two critical parameters, real contact between splat and substrate and splat thickness, results of a simple 1D transient calculation will be presented. In this calculation the splat with a disk shape is uniformly in contact with the substrate through a thermal contact resistance R_{th}, either low ($R_{th} = 10{-}7$ or 10^{-8} m^2 K/W corresponding to a perfect contact) or high ($R_{th} = 10^{-6}$ m^2 K/W corresponding to a relatively poor contact) [71]. It must be emphasized that the assumption of a uniform and constant thermal contact resistance to thermally

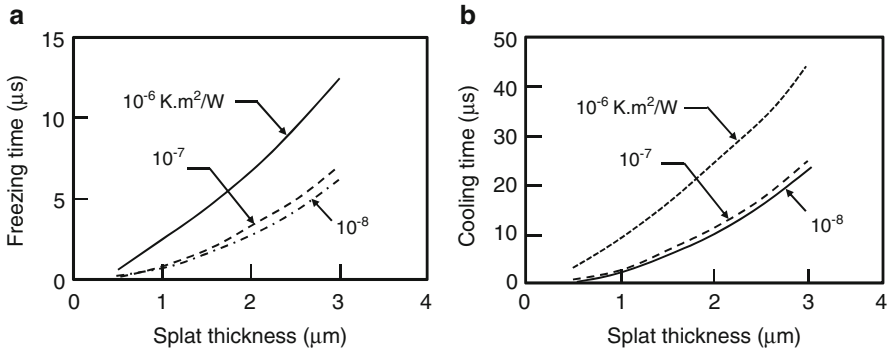


Fig. 13.33 Dependence on the splat thickness of the (**a**) freezing time, (**b**) cooling time, of disk-shaped zirconia splats deposited on a 304L stainless steel substrate, for three different thermal contact resistances. Reprinted with kind permission from Springer Science Business Media [101], copyright © ASM International

characterize the splat–substrate interface is an over-simplification, in reality, as previously mentioned, R_{th} varies with time and particle flattening radius. Figure 13.33a presents results related to freezing time (solidification being supposed to occur at melting temperature) and Fig. 13.33b is related to cooling time (when the splat reaches the substrate temperature). As can be seen results obtained with $R_{th} = 10^{-7}$ or 10^{-8} m^2 K/W are almost the same, the difference being important for $R_{th} = 10^{-6}$ m^2 K/W and the increase of the splat thickness raises both freezing and cooling times. It is important to note that the flattening particle and resulting splat cooling depend essentially on the heat conduction through the substrate or the previously deposited layers. Compared to convective cooling, even when boosted by blowing air jets at the splat top surface, conduction represents between 90 and 95 % of the heat withdrawal.

As illustrated in Fig. 13.34 for a zirconia splat, the thermal diffusivity of which is low, when the thermal contact resistance R_{th} is low the splat bottom temperature is close to that of the substrate (heated by the flattening particle), while with a high R_{th} the substrate is poorly heated and the splat bottom temperature is close to that of its top.

When solidification starts it can, especially for low thermal contact resistances, modify the liquid flow at the flattening droplet surface. It is important to keep in mind that the thermomechanical properties of coatings depend strongly on the real surface contact between splats and substrate and between themselves.

In areas of good contact, depending on the impacting droplet temperature, substrate diffusivity, oxide layer thickness and composition, and dimension of asperities, some melting can occur at the substrate surface, but the thicknesses involved are relatively small (few tens of nanometers) [48]. This phenomenon is generally not sufficient to achieve good adhesion.

In fact heterogeneous nucleation takes place at a temperature lower than the melting one (undercooling) and depends on many parameters, among them the contact angle liquid substrate (wettability) and the thermal contact resistance.

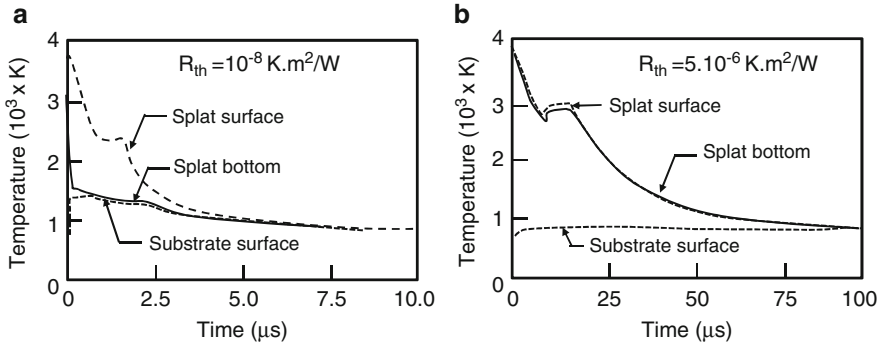


Fig. 13.34 Time dependence of the top and bottom temperatures of disk-shaped zirconia splats as well as of the 304L stainless steel substrate surface temperature for two thermal contact resistances: (**a**) $R_{th} = 10^{-8}$ m^2 K/W, (**b**) $R_{th} = 5 \times 10^{-6}$ m^2 K/W. Reprinted with the kind permission of Prof. A. Vardelle

Table 13.4 Thermal contact resistances measured for different particle materials impacting onto different substrate materials at room temperature or preheated over the transition temperature. Reprinted with kind permission from International Journal of Heat and Mass Transfer [103]

Material/substrate	Substrate temperature °C	R_{th} m^2 K/W ($\times$107)
Mo/glass	27	490 ± 55
	400	6.5 ± 1.0
Mo/inconel	27	190 ± 15
	400	12 ± 2.0
	Preheated–cooled to RT	55 ± 10
Zirconia/glass	27	220 ± 30
	400	10 ± 3.0

Unfortunately for particle flattening these data are impossible to measure and to the best of our knowledge heterogeneous nucleation has been taken into account only in 1D models [102]. Results show that the cooling curves obtained are not very different from those shown in Figs. 13.33 and 13.34 except for temperatures lower than 100 to 200 K.

All experimental studies have shown that the cooling rate of a particle impacting on a surface preheated above T_t is up to two orders of magnitude faster than it is on a cold surface. A high cooling rate corresponds to low thermal contact resistance at the splat–substrate interface. For example McDonald et al. [103] plasma sprayed molybdenum and yttria-stabilized zirconia particles onto glass and Inconel 625 substrates held at either room temperature or 400 °C. Samples of Inconel 625 were also preheated for 3 h and then air cooled to room temperature before spraying. The analysis showed that the thermal contact resistance between the heated or preheated surfaces and splats was more than an order of magnitude smaller than that on nonheated surfaces held at room temperature (see Table 13.4). Particles impacting on the heated or preheated surfaces had cooling rates that were

significantly faster than those on surfaces held at room temperature, which was attributed to smaller thermal contact resistance.

Flattening phenomena are strongly linked to thermal phenomena, including contaminants, controlling the real thermal contact between flattening particle and substrate. Thus Dhiman et al. [73] proposed a single parameter to estimate the importance of freezing during solidification and predict the likelihood of splat break-up. When a molten droplet lands on a solid surface, it spreads into a thin splat of uniform thickness h. If the substrate is at a temperature lower than the melting point of the droplet, a solid layer of thickness s grows in the flattening particle from its bottom during the time it takes to reach its maximum spread. The solidification parameter (Θ) is defined as the ratio of the solid layer thickness to splat thickness:

$$\Theta = s/h \tag{13.7}$$

Dhiman et al. [73] developed an analytical and complex expression to calculate the value of Θ as a function of the dimensionless parameters Re, We, Ste, Pe, and Bi. It is important to note that the splat–substrate thermal contact resistance is included in the Biot number. The magnitude of Θ can be used to predict what the final shape of the splat will be, and what the mechanism of the break-up is, if it occurs. Three outcomes are possible during spreading:

(a) If the solid layer is very thin ($s << h$, or $\Theta << 1$), it will have no effect on spreading. The splat will spread into a thin liquid sheet and ruptures internally. This will lead to extensive fragmentation, producing a small central splat surrounded by a ring of debris Fig. 13.35a. It is the case when adsorbates and condensates are present.
(b) If the solid layer grows by a significant amount during spreading ($s \sim 0.1h$ to $0.3h$ or $\Theta \sim 0.1$ to 0.3), it will restrain the splat from spreading too far and becoming thin enough to rupture. In this case, a disk-type shape splat will be produced see Fig. 14.35b.
(c) If solidification is very rapid ($s \sim h$, or $\Theta \sim 1$), the solid layer will obstruct the outward spreading liquid. A splat with fingers radiating out from its periphery will be produced, see Fig. 14.35c.

Comparison with experimental photographs showed that the value of the solidification parameter gave a reasonably accurate method of predicting the shape of the final splat. Figure 13.35 shows photographs of splats taken both during and after impact, illustrating the three different modes of splat impact. In Fig. 13.35a, for molybdenum and nickel particles landing on substrates at room temperature, thermal contact resistance was high ($\sim 10^{-5}$ m^2 K/W) and $\Theta \sim 0.01$. The splats spread into a thin film that ruptured internally and fragmented. The final splats all showed a central portion at the point of impact that adhered strongly to the substrate, surrounded by a ring.

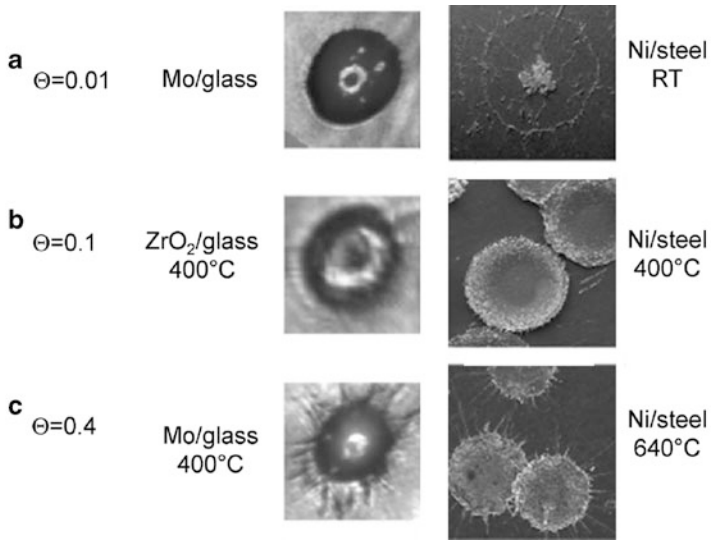


Fig. 13.35 Photographs during and after impact for splats (**a**) Fragmenting during impact, (**b**) forming disk splats, and (**c**) undergoing freezing-induced break-up. Reprinted with kind permission from Elsevier [73]

Increasing the substrate temperature to values above the transition temperature reduces the thermal contact resistance by an order of magnitude, since it evaporated adsorbed contaminants on the surface. Figure 13.35b shows impacts of zirconia and nickel particles on surfaces heated to 400 °C which had R_{th} ~10^{-6} m^2 K/W and correspondingly $\Theta \sim 0.1$. Solidification occurs near the end of droplet flattening, when the spreading liquid has not enough momentum to jet over the solid rim and instead came to rest forming a circular splat with smooth edges.

If Θ is increased further ($\Theta \sim 0.4$, see Fig. 13.35c), the solid layer growth is sufficiently rapid to obstruct the flow of the liquid early during spreading. The liquid has enough momentum that it jetted outward, producing fingers radiating out from the central splat. For nickel particles spreading on a steel substrate oxidized by heating to 640 °C (Fig. 13.35c) the splat is intact and smooth at the center, where solidification is slow. The edges, which solidify very rapidly, have a rough surface since surface tension has not time to level irregularities before solidification occurred. Molybdenum splats on a glass surface heated to 400 °C also have fingers radiating out.

At last it must be mentioned that for splats collected on smooth surfaces kept at room temperature, all the splashed material or droplets or fingers collected around their central part (see, for example, Fig. 13.35a) have very poor adhesion and can be removed easily by the tip of the roughness gauge. This means that any new splat deposited on these dispersed materials will have a lower adhesion than it would have had on a clean surface. In contrast, splats obtained on surfaces preheated over the transition temperature have a much better adherence and cannot be separated by the tip of the roughness gauge.

(e) Splat Fragmentation

Fragmentation occurs late during impact, when the particle is almost completely flattened, and both flow and solidification phenomena are involved. Generally, particles sprayed onto a substrate held at room temperature form splats that are extensively fragmented, while preheating the surface above the transition temperature, T_t, results in disk-shaped splats. T_t is much lower than the melting temperatures of either the substrate or the impacting particle and seems to correspond to the evaporation of contaminants. The splat fragmentation can be linked to

- Instabilities at the edge of the liquid sheet rapidly decelerating and becoming unstable [74].
- The solidification of the flattening particle in its periphery, the outward flowing liquid, jetting over the top of the solid layer, becoming unstable and breaking-up [73].
- The poor contact of the hot flattening particle with the substrate (fast desorption of adsorbates and condensates during the contact). The flattening particle spreads to its maximum extent within a few μs after impact, forming a thin sheet with a diameter up to 10 times that of the initial droplet and a thickness of only about 0.5 μm [103, 104]. The liquid sheet then begins to rupture, initially around the solidified central core and later at other sites. At the end splats disintegrate almost completely and only a central solidified core remains at the substrate surface.

With HVOF spraying, initially the particle is melted and, during its first contact with the substrate, the impact creates a shock wave inside the lamella and in the substrate. After impact the flattening particle forms either a "pancake-" shaped lamella or splat (associated with moderate particle velocities and moderate heat contents) shown in Fig. 13.36a or a flower-type lamella (connected with an elevated velocity of the particle and an elevated heat content) as shown in Fig. 13.36b [105]. Although the authors do not discuss at all the substrate preheating effect, Fig. 13.36 represents well the types of splats and the substrate deformation observed with HVOF when particles are fully melted. Fukumoto et al. [89] have observed the same preheating effect on plasma and HVOF-sprayed splats (see Table 13.4).

Similar results were obtained with D-gun spraying, with which, depending on spray conditions sprayed particles can be fully or partially melted upon impact. Ulianitsky et al. [106] sprayed with Computer Controlled Detonation Spraying (CCDS) device CCDS2000, working with different gas mixtures, Ni and Cu particles, which velocities and temperatures were measured or calculated in-flight prior to impact. Results are presented in Fig. 13.37. Ni splat in Fig. 13.37b was in a semi-melted state at impact, its temperature being close to the melting one ($T_m = 1{,}726$ K). Figure 13.37a corresponds to an initially solid Ni particle, which becomes melted at the interface upon its impact with the substrate due to kinetic energy release. Figure 13.37c corresponds to splashing for the fully melted Ni splat. With overheated Cu splat ($T_m = 1{,}358$ K, the particle impacting at 2,200 K) presented in Fig. 13.37c adsorbates and condensates have resulted in the liquid

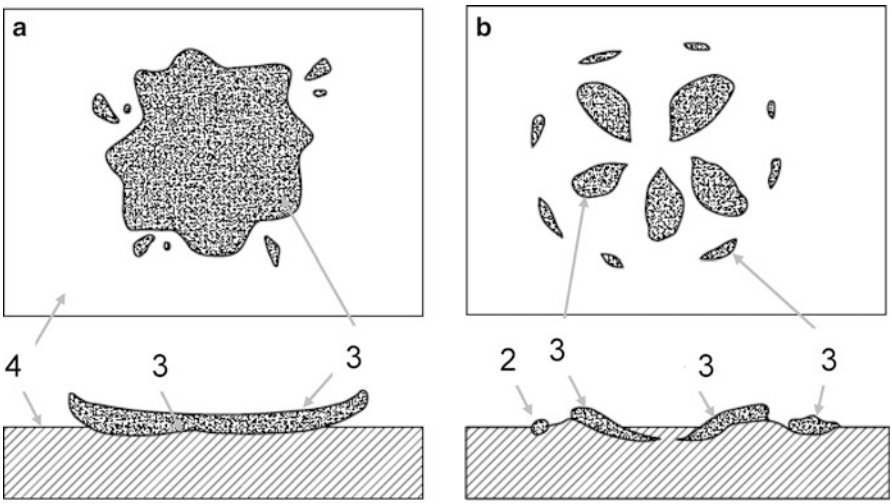


Fig. 13.36 Two morphological forms of lamellae splashed on the substrate: (**a**) pancake, (**b**) flower, (1) crack, (2) deformed substrate, (3) corona, (4) substrate, (5) lamella, (I) top view, (II) X-section view. Reprinted with kind permission from Springer Science Business Media [105]

fast expansion and a result similar to that presented in Fig. 13.23a, b. For YSZ particles, to our best knowledge, no splats were presented, but the fractured YSZ topcoat obtained with D-gun spraying and presented in Fig. 5.47 section "(b) TBC's Ceramic Layer" shows that the coating is made of layered splats.

(f) Modeling

Numerical codes can simulate fluid flow and heat transfer during particle impacts quite accurately, the main difficulty being quantitatively describing the interface between the splat and the substrate. The interface is defined in models only by specifying values of the thermal contact resistance (R_{th}) and liquid–solid contact angle. During droplet flattening, the flow is mostly driven by fluid inertia, but at the end of its flattening, if it is still liquid, fluid motion becomes sensitive to contact angle. Thus the value of thermal contact resistance is very important in the modeling. Pasandideh-Fard et al. [80] modeled the splashing of an impacting nickel particle. Figure 13.38 shows a sequence of computer-generated images showing successive stages of the impact of a 60-μm diameter nickel particle, at a temperature of 1,600 °C (150 °C above the melting point of nickel) on a stainless steel substrate initially at 290 °C, R_{th} being assumed constant and equal to 10^{-7} m^2 K/W. Because of small variations in the liquid velocity around the periphery of the drop a fluid instability was created, leading to the formation of fingers of liquid around the drop that grew larger and detached to form small satellite droplets. Simulations in which

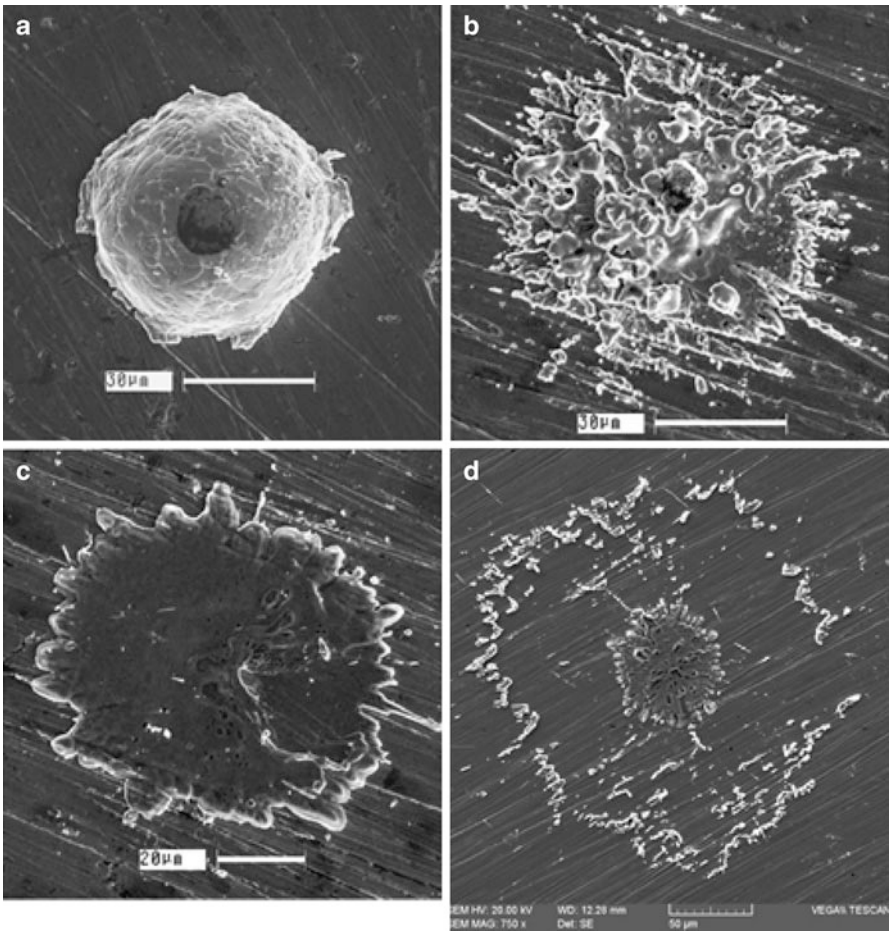


Fig. 13.37 Splat morphology of particles D-gun sprayed at different v_p & T_p collision conditions: Calculated (v_p & T_p) values: (**a**) Ni: $v_p \approx 360$ m/s, $T_p \approx 1{,}450$ K; (**b**) Ni: $v_p \approx 420$ m/s, $T_p \approx 1{,}700$ K; (**c**) Ni: $v_p \approx 460$ m/s, $T_p \approx 2{,}200$ K, (**d**) Cu: $T_p \approx 2{,}200$ K. Reprinted with kind permission from Springer Science Business Media [105], copyright © ASM International

the substrate temperature was increased from 290 to 400 °C produced little change in the impact process, since the droplet temperature was so high that this relatively small change in substrate temperature did not reduce heat transfer significantly. However, increasing R_{th} delayed the onset of solidification until the droplet had finished spreading. Figure 13.39 shows simulations with all parameters the same as those in Fig. 13.38, except that substrate temperature was raised to 400 °C and R_{th} was increased to 10^{-6} m^2 K/W). In this case, the droplet spread completely before a significant amount of solidification occurred, and the flow was not destabilized by the solid layer, leaving a disk-shaped splat, looking much like those observed experimentally on surfaces above the transition temperature. Fauchais et al. [71]

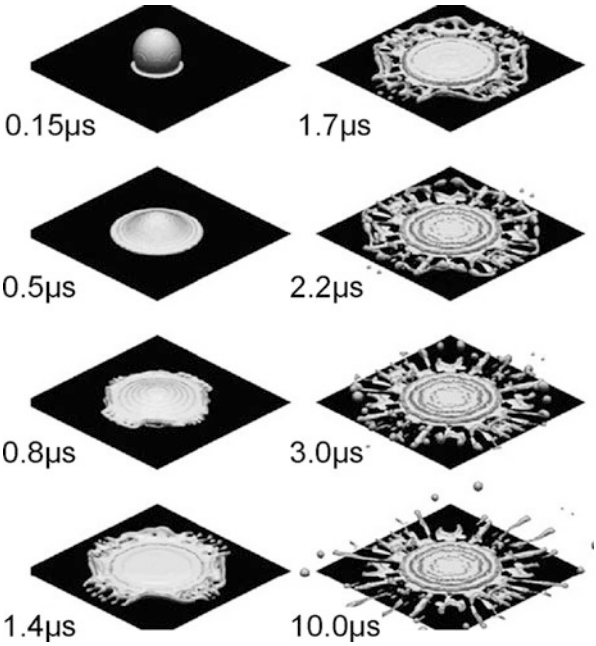


Fig. 13.38 Simulations showing the impact of a 60 μm diameter molten nickel particle at 1,600 °C landing with a velocity of 73 m/s on a stainless steel plate initially at a temperature of 290 °C. The contact resistance at the substrate surface was assumed to be 10^{-7} m^2 K/W. Reprinted with kind permission from Springer Science Business Media [80], copyright © ASM International

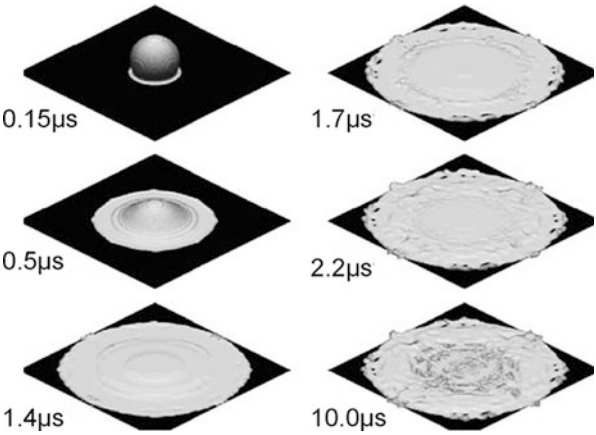


Fig. 13.39 Simulations showing the impact of a 60 μm diameter molten nickel particle at 1,600 °C landing with a velocity of 73 m/s on a stainless steel plate initially at a temperature of 400 °C. The contact resistance at the droplet-substrate interface was assumed to be 10^{-6} m^2 K/W. Reprinted with kind permission from Springer Science Business Media [80], copyright © ASM International

pointed out that these results from models appear to contradict experimental observation, where splashing occurs when the contact resistance was high, not when it was low, as in these simulations. To simulate results obtained with cold surfaces McDonald et al. [107] specified a spatially varying thermal contact resistance between a molybdenum splat and glass substrate held at room temperature in a 3D numerical model. A thermal contact resistance of 10^{-7} m^2 K/W was specified for the splat central core in contact with the glass. The diameter of the

Table 13.5 WC particle size distributions in WC-12 % Co particles (15–45 μm). Reprinted with kind permission from Elsevier [108]

Type	A	B	C	D	E	F
WC size (μm)	0.2	1.0 ~ 1.5	2.0 ~ 2.5	3.0 ~ 4.0	5.0 ~ 7.0	1.0 ~ 5.0

central core was measured from images of the splat after spreading, fragmentation, and solidification. Under the rest of the splat, a thermal contact resistance of 5.0×10^{-5} m^2 K/W was specified. The results from the numerical simulation show that as the splat spreads, it fragments from the solidified central core. Since the thermal contact resistance in the central core is small compared to the rest of the splat, it solidifies faster and remains attached to the substrate. The rest of the splat, in liquid form, continues to spread and disintegrate. Finally, a central solidified core is left on the substrate, surrounded by a ring of debris (see a similar behavior in Fig. 13.23b). The numerical simulations agree qualitatively with experimental observations. These few results show that models can reproduce the experiments provided the parameters controlling the phenomena at the interface (R_{th} and wet ability) are correctly specified.

(g) Impact of Cermet Particles Normal to the Substrate

Fully or partially melted cermet particles have a behavior different from that of metal, alloy, or ceramic particles. Upon impact the metal or alloy matrix is melted or in a plastic state, while the ceramic particles imbedded are not melted at all. HVOF or HVAF or D-gun processes are spraying most of the cermet coatings, and the impact of cermet particles will be illustrated with the work of Watanabe et al. [108]. They have sprayed WC–12 wt% Co on carbon steel (0.45 % C) substrates using the HVOF JP5000 torch from Praxair Technology Inc. (USA),. The substrate surface was mirror-finished by mechanical polishing before spraying. Six commercially available WC–Co powders were sprayed with kerosene (0.38 L/min) and oxygen (944 slm). These powders had similar size distributions of 15–45 μm with the same composition, but differed in the size distributions of the WC particles contained in one composite WC–12 % Co powder particle. Table 13.5 presents their classification.

Splats and coatings of the six types of WC–12 wt% Co were investigated. The interface fracture toughness was evaluated by a pre-notched four-point bending test, and the microstructure of the splat around the interface was examined by SEM and FIB cross-sectioning. Figure 13.40a, b. shows images of the disc-shaped type A and type E splats, and their respective cross sections along the dotted lines in Fig. 13.40c, d. These images were obtained by sectioning splats with FIB equipment and then observing them with SEM. EDX analysis revealed that splats consisted of the W–Co metal binder phases and the carbides. XRD analysis of the coatings showed the crystalline peaks of WC, W_2C, and W. There is a clear

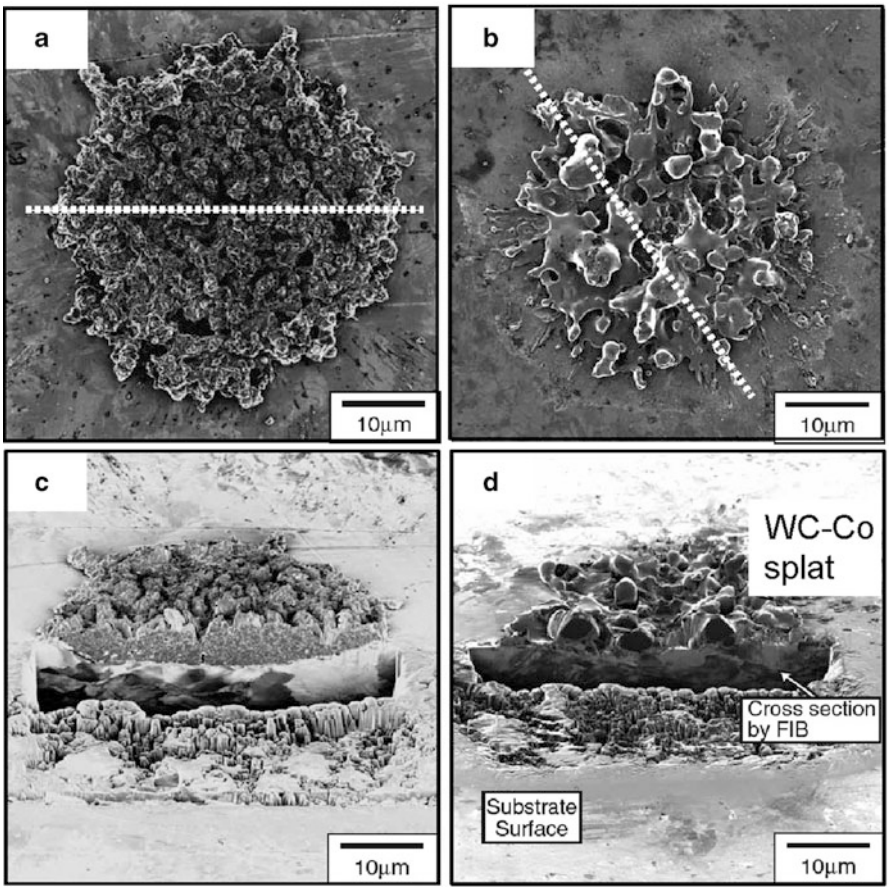


Fig. 13.40 SEM and FIB images of WC–2 wt% Co HVOF sprayed on carbon steel (0.45 % C) substrates: type A and type E splats in top view (**a**, **b**), and in a cross section of the splats (**c**, **d**). Reprinted with kind permission from Elsevier [108]

tendency of the increase of W_2C peak as the carbide size decreases. Interfaces of both splats display concave peripheries, implying substrate deformation by the high kinetic energy of the molten particles upon impact.

The maximum thickness of the splats was about 4 μm for all of them, but the type A splat had more uniform thickness over the splat. In contrast, a cross section of the type E splat indicates a nonuniform feature due to the existence of large particles. The smaller WC particle at the interface in the type E splats was compressed by the larger WC particle just above it and inbedded into the substrate. In contrast, no such carbides intruded into the substrate in type A and thus the interface is much smoother than that of type E coatings. The WC particle size in the original powders was found to significantly affect the interface fracture toughness, which generally increases as the WC particle size in the original powder increases. The key factors in realizing the

excellent adhesion of this coating system is considered to be compression and densification of the surrounding microstructure by the impact of WC particles, intrusion of the particles into the substrate, and plastic deformation of W–Co alloy phases around a crack tip, which functions as the energy dissipation mechanism for crack propagation in the coating [107].

13.4.5 Splat Formation from Partially Molten Particles on Smooth Substrates

In most cases this type of splat is obtained when plasma spraying ceramic particles or polymer particles with any of the spray processes, and sometimes when HVOF or HVAF spraying particles below their melting temperature (see for example Fig. 13.18a, b). In the following two examples are presented of zirconia particles being plasma sprayed and polymer particles.

13.4.5.1 Zirconia Particles Plasma Sprayed

Splats obtained are those of Fig. 13.22 numbered 27–29 [108]. Che-Ming Wu et al. [109] have calculated what happens at impact of partially molten yttria-stabilized zirconia particles. The model employs the immersed boundary (IB) method for imposing the no-slip condition along the solid in order to accurately capture the interaction of the flow with the solid core. The heat transfer effects on the flow field are neglected, considering that solidification time is typically one order of magnitude larger than the spreading time of molten droplets impacting a surface. Two particles sizes (50 and 100 μm) were considered, the size of the solid core of the particles being varied. Che-Ming Wu et al. [109] showed that, when the solid core is small compared to the particle diameter, the impact is similar to the impact of a fully molten droplet. However, as the solid core becomes bigger, splashing occurs.

13.4.5.2 Impact of Polymer Particles

When molten polymer droplets hit the surface, as for droplets of conventional materials, they solidify into distinct “frozen” splats. An example of several Nylon-11 splats deposited on a glass substrate using the HVOF spray process is shown in Fig. 13.41 from Isocevic [111]. The quasi-small spheres observed, probably correspond to small particles traveling in the jet fringes and sufficiently heated to stick on the substrate. The “fried egg”-shaped splats correspond to bigger particles with a molten shell surrounding the unmelted core. This feature results from the large radial temperature profile (poor thermal conductivity of particles ≈0.23–0.34 W/m K), corresponding to the low temperature, high viscosity core and the high temperature, low viscosity shell.

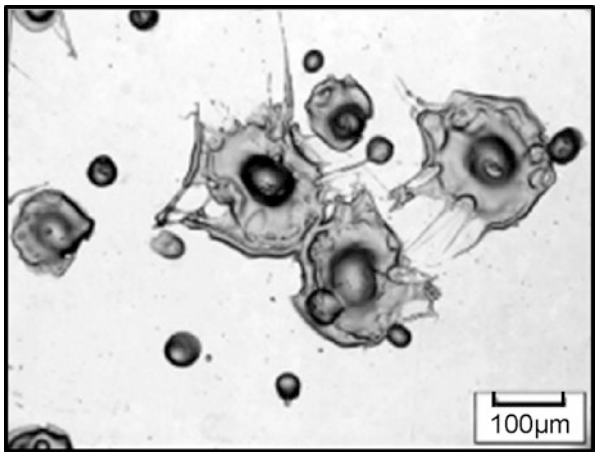


Fig. 13.41 Nylon-11 splats deposited onto a glass slide substrate at room temperature and traversing rapidly the hot gases of the HVOF jet. Reprinted with kind permission from Elsevier [111]

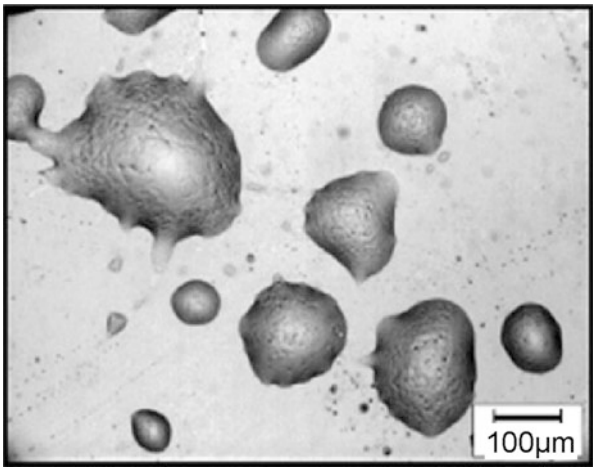


Fig. 13.42 Nylon-11 splats deposited onto a glass slide preheated to ~190 °C, slide traversing rapidly the HVOF jet, and then let cool down to room temperature. Reprinted with kind permission from Elsevier [111]

When the substrate was preheated to a temperature around the melting temperature of Nylon-11 (~190 °C) splats exhibited a flattened hemispherical shape, as shown in Fig. 13.42 [110]. This was attributed to the postdeposition flow activated primarily by surface tension, after the initial "fried-egg" splats were fully melted by the preheated substrate, shown schematically in Fig. 13.43 [110].

Isocevic et al. [111] have modeled HVOF spraying of Nylon-11. Their heat and mass transfer equations were identical to those used with conventional particles taking into account the heat propagation phenomenon (see Sect. 4.3.2) but molten

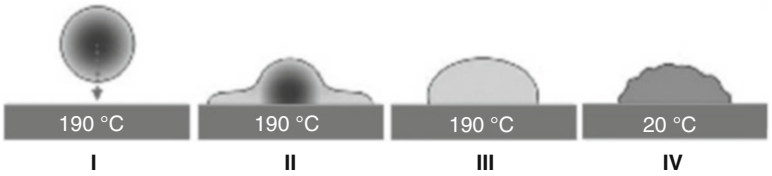


Fig. 13.43 Schematic of the deformation behavior sequence of a polymer particle after impact onto a preheated substrate: (I) partially melted particle before impact; (II) "fried-egg" shaped splat; (III) complete melting and postdeposition flow of a droplet; (IV) droplet shrinkage during cooling. Reprinted with kind permission from International Journal of Heat and Mass Transfer [111]

nylon 11 was modeled as a generalized Newtonian fluid with temperature and shear rate dependent viscosity. Predictions, in good agreement with experiments showed that larger polymer particles (i.e., 90–120 μm) develop steep internal temperature gradients between the core and the surface during HVOF spraying. They conclude by emphasizing that optimal thermal spray process for polymers should utilize a low gas temperature (~ 400–500 °C) to prevent overheating of the polymer particles, a high gas velocity to provide high kinetic energy for spreading of the high melt viscosity particles, and a sufficiently long dwell time for more uniform particle melting.

Other studies were also devoted to splat formation of different polymer materials:

– PEEK was flame sprayed by Alamara et al. [112] with radial injection. Splats, collected on glass slides, kept at room temperature, presented a "fried egg" shape and, according to the spray distance, they presented either disk-shaped or splashed patterns. Decreasing the standoff distance from 35 to 15 cm produced coherent, integral disk-shaped splats that exhibited minimum splashing behavior. Withy et al. [113] HVAF sprayed the particles on aluminum substrates with six different pretreatments. Surface morphology was the main factor found to influence the splat area density, the area of single splats, and the circularity of single splats on substrates maintained at 323 °C. Substrate surface chemistry was however found to have an influence on the area density of deposited single splats, where surface morphology alone cannot explain the significant differences between the six different pretreated substrates. Patel et al. [114] have studied the degradation of PEEK particles HVAF sprayed. Flame impingement onto the just deposited coating degrades the molecular structure of PEEK. Splat circularity was steady around 0.9, indicating that the deposited particles exhibited a circular shape at all stand off distances SODs. When there is significant flame impingement onto the just deposited coating, as with the coatings produced at 200 mm spray distance, hydrocarbons from the flame react with the coating surface.
– PP (polypropylene) splats were sprayed onto a glass substrate at room temperature using the flame spray process, at various SODs [115]. The results of this

study indicated that increasing the SOD from 10 cm to 25 cm reduced the splat thickness and deposition efficiency (as in previous cases splats were "fried egg" shaped), though an increase in splash area was demonstrated. Splat circularity was steady around 0.9, indicating that the deposited particles exhibited a circular shape at all SODs.

To conclude this part the important points of splat formation are:

- The optimization of spray conditions in correlation with particle size distribution. However even when these conditions are optimized, due to the poor thermal conductivity of polymers, particle impact with a rather steep radial temperature gradient within the particle and consequently a steeper viscosity radial distribution (formation of "fried egg"-shaped splats).
- The necessity to keep the substrate temperature slightly lower than that of the polymer melting temperature to achieve the complete melting of splats.
- The careful control of the surface temperature of splats and substrate to avoid splat degradation. This can be achieved by playing with the spray distance in addition to external cooling means.

13.4.6 Splat Formation from Unmelted Particles Off Normal on Smooth Substrates

As already pointed out in section "(a) Spray Angle", the particle velocity, v_p, normal to the substrate varies as $v_p.\sin\theta$, (see Fig. 13.8 for the definition of θ) thus with decreasing angle v_p can become lower than the critical velocity, v_c, and particles will not deposit. Generally the deposition efficiency drops significantly when this angle is below 70 °. Besides the reduction of the impact velocity, a shear stress is imposed on the flattening impacting particle reducing its adhesion.

13.4.7 Flattening and Solidification of Molten Particle on a Smooth Substrate

13.4.7.1 Impact Splashing

With an inclined substrate, the impact velocity is the normal velocity $v_n = v_p \cdot \cos\varphi$, while the tangential velocity $v_t = v_p \cdot \sin\varphi$ (see Fig. 13.44a) controls the movement in the slope direction. Upon impact, as with substrates normal to the particle velocity vector, impact splashing occurs. However the tiny droplets are no more uniformly distributed around the substrate normal but are all centered in the direction symmetrical to the impact velocity relative to the normal, as shown in Fig. 13.44b.

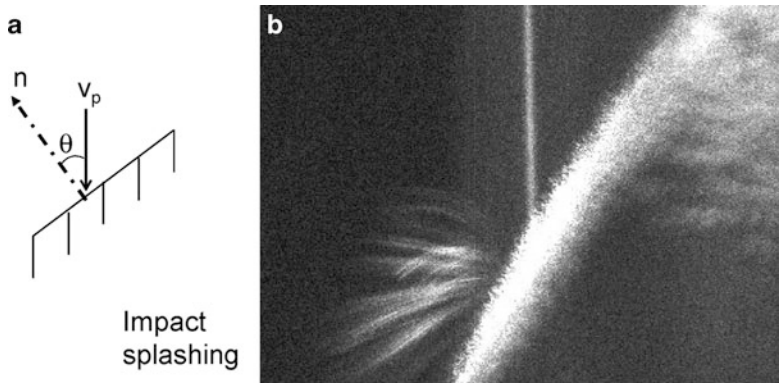


Fig. 13.44 (**a**) Definition of the impact angle in off-normal impacts and (**b**) impact splashing on inclined substrates. Reprinted with kind permission from Springer Science Business Media [82]

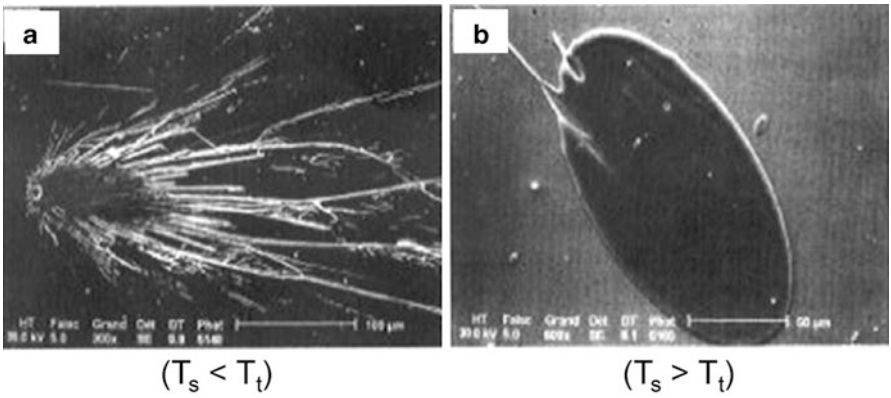


Fig. 13.45 Impact of alumina plasma-sprayed particles ($d_p = 58$ μm, $v_p = 138$ m/s, $T_p = 2{,}400$ K) onto an inclined ASI304 stainless steel (impact angle 30°). (**a**) Room temperature substrate. (**b**) Preheated substrate over transition temperature. Reprinted with kind permission from Elsevier [92]

13.4.7.2 Flattening Splashing

On cold substrates, splats are extensively fingered, especially in the substrate inclination direction as shown in Fig. 13.45a. Authors [92, 116–118] have shown that on stainless steel, copper and a few other polished substrates ($R_a < 0.1$μm) preheated over the transition temperature, when the spray angle, φ, increases from 0° to 75°, splats have an elliptical shape, as shown in Fig. 13.45b, the ratio of the major to the minor axes increasing when the spray angle increases. For different materials (alumina, zirconia, titania, Al, Ni, Astroloy, and Cu), the relationship between the major and minor axes shows a strong linearity over a wide range of

splat sizes. This observation implies that the elongation factor EF (ratio between the major and minor axes) does not depend on particle diameter and impact velocity but only on spray angle. The splat thickness increases slightly along the inclined surface and it becomes progressively thicker in the direction of the inclined surface when the spray angle increases. This probably explains why, when the spray angle exceeds a critical value, which depends on the sprayed material and the substrate material, splashing occurs in the inclination direction even on substrates preheated above the transition temperature.

As already mentioned previously for splats collected on cold substrates orthogonal to the spray torch axis, the tip of the roughness meter can very easily dislodge fingers or splashed material.

13.5 Splat Formation on Rough Surfaces

The experimental study of the flattening of particles on rough surfaces is very difficult because it is impossible to obtain images of the particle flattening due to the too small field of depth of microscopes on rough surfaces. Of course it is possible to follow the temperature evolution of the flattening particle and characterize the splat obtained.

13.5.1 Solid Ductile Particles

13.5.1.1 High Pressure Cold Spray

In most cases spraying is performed on smooth substrates. However for particles with a low hardness sprayed onto a hard substrate, the adhesion can occur only on rough substrates (mechanical adhesion) [55].

Hussain et al. [56] have cold-sprayed copper particles onto aluminum alloy substrates, the surfaces of which had been prepared in a variety of ways including grit blasting with Al_2O_3 with a grit size of ~500 μm (the effects of the corresponding work hardening (see section 13.10.1.2a) being removed by annealing or not). The coating-substrate adhesion onto a grit-blasted surface (whether or not the effects of work hardening had been removed by annealing) was significantly reduced by grit embedment into the aluminum surface during blasting. They have also postulated that the grit-blasted surface has restricted the jet formation upon impact of the copper particles resulting in less successful removal of oxide from the interface and hence a weaker metallurgical bond. On the other hand Koivuluoto et al. [119] have used grit blasting to deposit tantalum on low carbon steel.

13.5.1.2 Low Pressure Cold Spray

Authors use substrates with or without grit blasting. For example, Koivuluoto and Vuoristo [70] have used grit blasting to produce coatings with Cu + Al_2O_3 but no clear details are given.

13.5.2 Molten Metal, Alloy, Ceramic, and Cermet Particles

13.5.2.1 Idealized Surfaces

Shinoda et al. [120] conducted an experimental study in which the surface roughness was artificially created and could be well characterized. Micro-patterns were fabricated on quartz glass substrates by photolithography followed by wet etching. Four micro-patterns were used, their depths/heights were kept at approximately 1 μm (corresponding to $R_a = 0.5$ μm) and their spacing was varied from 4 to 20 μm. The anisotropic deformation of molten alumina droplets (sieved through a 35–65 μm mesh), sprayed with hybrid plasma (d.c.–r.f.), was observed on these substrates preheated to 700 K. Air was entrapped in each splat off-center, regardless of the type, size, and pattern layout. Droplet spread was affected by a roughness as small as $R_a = 0.5$ μm influencing the fingering of splats.

Almost at the same time Parizi et al. [121] presented numerical simulation results for molten nickel and zirconia (YZS) droplets impacting on different micro scale-patterned surfaces of silicon. The numerical simulation clearly showed the effect of surface roughness and solidification on the shape of the final splat, as well as the pore creation beneath the sprayed material. They used 3D transient computational fluid dynamic software, solving the full Navier–Stokes equation, including heat transfer and phase change. A volume of fluid (VOF) tracking algorithm was used to track the droplet-free surface, and the thermal contact resistance at the droplet–substrate interface was also taken into account. Droplet sizes ranged from 15 to 60 μm with impact velocities of 70–250 m/s. The substrate surface pattern was made of regular arrays of cubes 1–3 μm in height, spaced either 1 μm or 5 μm from each other. In the following a few results of this study are presented. Figure 13.46 presents the schematic set up for the patterned surface.

In Fig. 13.47 images are compared of a splat obtained from experiments (a) and a modeled splat (b) and of splat cross sections obtained from an experimental splat (c) and from a modeled one (d). The final splat diameter obtained from the simulation was 180 μm, which is comparable to the average value of 195 μm that can be measured from the experiment (mean value of the splat diameter, excluding all splashes or fingers in splat periphery out of this mean diameter perimeter). When comparing the cross sections (Fig. 13.47c, d) it can be seen that cavities between the textured posts on the substrate are filled with the droplet material in the middle of the splat, whereas close to its boundaries cavities are partially filled or remain

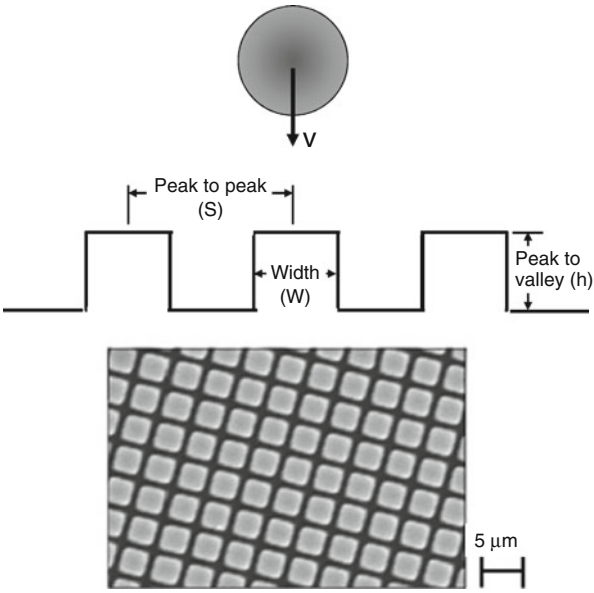


Fig. 13.46 (**a**) Schematic set up for simulation of the droplet impact on a patterned surface: peak to peak distance (*s*), width (*w*), peak to valley distance (*h*), and distance between two peaks (dist) of the cubes and (**b**) SEM image of a typical textured silicon wafer. Reprinted with kind permission from Springer Science Business Media [121], copyright © ASM International

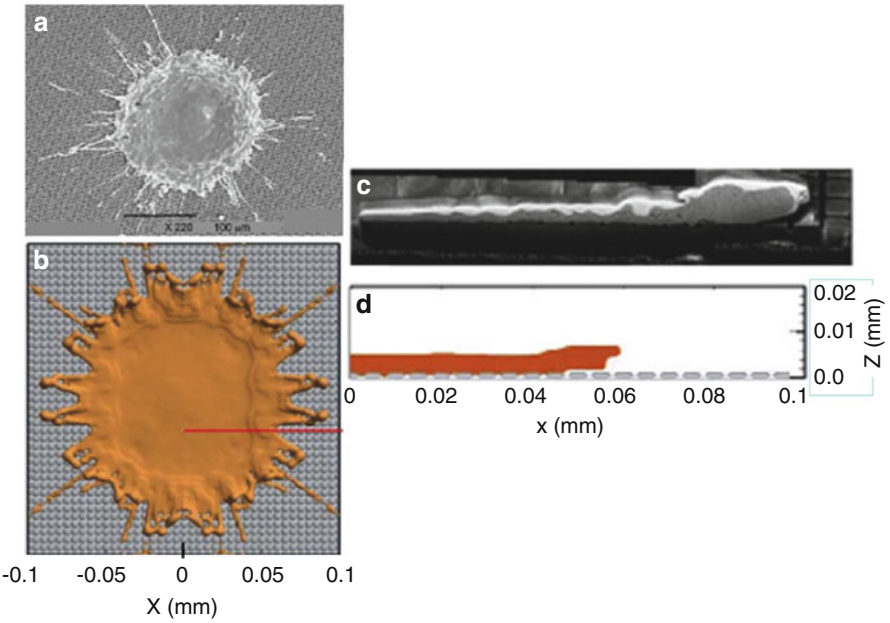


Fig. 13.47 (**a**) SEM image of the splat shape of nickel ($d_p = 50 \pm 3$ µm, $T_p = 2{,}390 \pm 70$ °C, $v_p = 70 \pm 2$ m/s) on a silicon substrate preheated to 350 °C with 1 µm high and 1 µm spacing between the cubes 4 µm in width, taken from experiments [104], (**b**) numerical modeling result for a splat shape of nickel on silicon with the same conditions as in the experiments and assuming a thermal contact resistance: $R_{th} = 5 \times 10^{-6}$ m^2 K/W, (**c**) cross section of the nickel splat, the close-up of the cut showing that the posts close to the center of the splat are filled with material, and (**d**) cross section of the computed splat. Reprinted with kind permission from Springer Science Business Media [121], copyright © ASM International

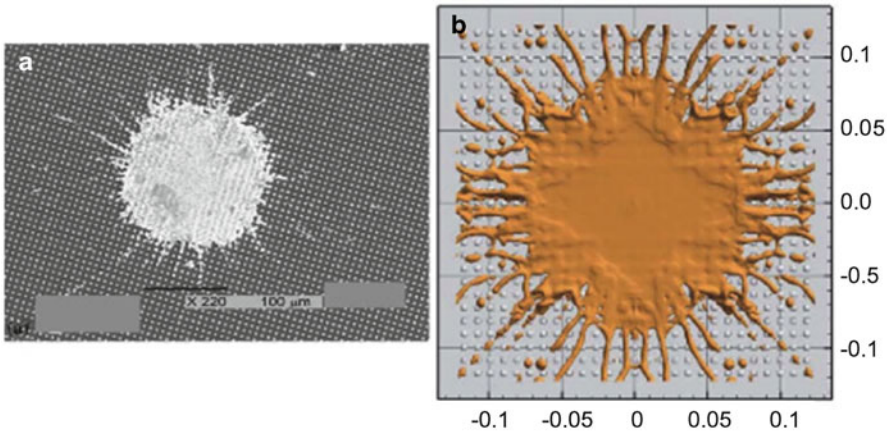


Fig. 13.48 Same SEM image as in Fig. 13.34 except that the impact conditions of the nickel splat are slightly different ($d_p = 60 \pm 3$ µm, $T_p = 2{,}225 \pm 20$ °C, $v_p = 73 \pm 2$ m/s) as well as the silicon pattern (1 µm high and 5 µm spacing between the cubes 4 µm in width); preheated to 350 °C, (**a**) is taken from experiments [104], (**b**) is numerical result for the same conditions with $R_{th} = 2 \times 10^{-6}$ m^2 K/W. Reprinted with kind permission from Springer Science Business Media [121], copyright © ASM International

completely open. Close to the impact point of the droplet, where the kinetic energy of the liquid and its normal velocity are the highest, the cavities on the surface are filled up regardless of the size. As the normal velocity of the liquid is reduced and the liquid spreads in radial direction, the liquid energy is not enough anymore to fill cavities.

Figure 13.48a, b shows the same SEM images (Fig. 13.48a) and numerical results, (Fig. 13.48b) respectively, for a nickel splat on 1 µm height, 5 µm spaced textured silicon.

Splat fingering is more important but the filling of cavities is better.

Parizi et al. [121] have also studied the impact of zirconia particles; Fig. 13.49 shows the calculated top view (a) and cross section (b) of the splat. The initial velocity of the droplet in this case was more than three times that of the nickel splat (250 m/s compared to 70 m/s). Also, relative to the nickel splat, the thermal contact resistance chosen for the calculation is 200 times less and thus the rate of heat transfer between the substrate and the splat is increased causing a more rapid solidification of the splat on the surface. The shape of the splat in this case is closer to a square than a circle and most of the cavities in between the roughness posts are filled with the material.

Such calculations have the potential to be used for characterizing the pore sizes and locations in the coating layers that result from unfilled cavities.

13.5.2.2 Real Surfaces

Most phenomena occurring when particles impact on rough surfaces normal to their trajectory have been described in the review by Fauchais et al. [71]:

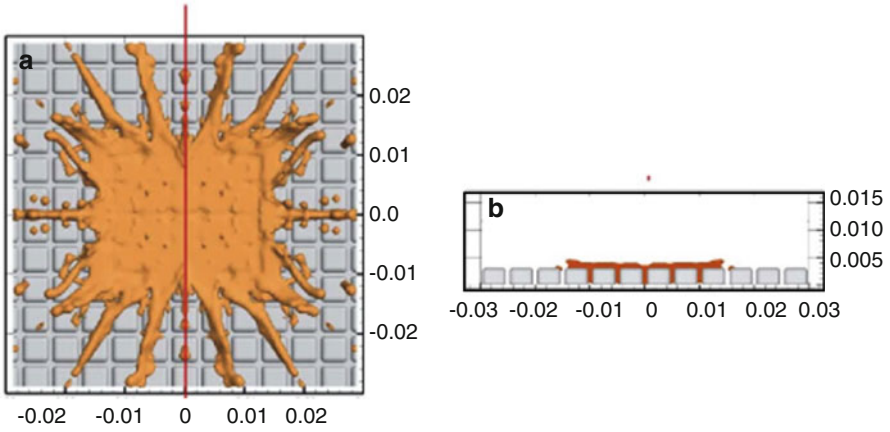


Fig. 13.49 Numerical result for a YSZ splat ($d_p = 15$ µm, $T_p = 2{,}900$ °C, $v_p = 250$ m/s) on patterned silicon substrate, preheated to 350 °C with 3.3 µm high and 1 µm spacing between the cubes 4 µm in width, $R_{th} = 10^{-8}$ m^2 K/W. (**a**) Top view and (**b**) Cross section. Reprinted with kind permission from Springer Science Business Media [121], copyright © ASM International

- Surface roughness promotes adhesion. However the mechanical grip between the substrate asperities depends on the size of the splat compared to that of the surface peaks, which can be characterized by their R_t (distance between their highest peak and deepest under cut). Roughly, the splat dimension must be between 1.5 and 3 times R_t, as shown in Fig. 12.36a. If the splat size is too small, as shown in Fig. 12.36b, the adhesion will be very poor, which is the same is the splat size is big compared to the substrate roughness as illustrated in Fig. 12.36c. However Bahbou and Nylen [61] have studied the influence of R_a, R_t ,R_{sm}, and $R_{\Delta q}$ (see Sect. 12.5.1 for the definitions) on the adhesion of Ni–Al (5 wt%) coating plasma sprayed onto Ti6Al4V substrates, grit blasted with two brown alumina grit sizes (blasting angle 45°). Results show that the adhesion values measured are poorly correlated with R_a or R_{sm}. However the hybrid parameter containing both amplitude and spacing properties of the surface $R_{\Delta q}$ (i.e., the average slope: see Fig. 12.7) is rather well correlated to the coating adhesion.
- Mehdizadeh et al. [122] have shown that for a good contact the liquid must penetrate into the cavities, which requires that the impact pressure is high enough. In the center of the impact the pressure is given by $\rho_p \cdot v_p^2$, where ρ_p and v_p are, respectively, the impacting melted particle specific mass and velocity, if σ_p is the droplet surface tension and w the mean width of the cavity, one must have

$$w > 4\sigma_p \cdot \rho_p^{-1} \cdot v_p^{-2} \tag{13.8}$$

If this condition is not fulfilled, the liquid will not penetrate down to the bottom of the cavity. For example, in the splat fringes, where the pressure is low and with

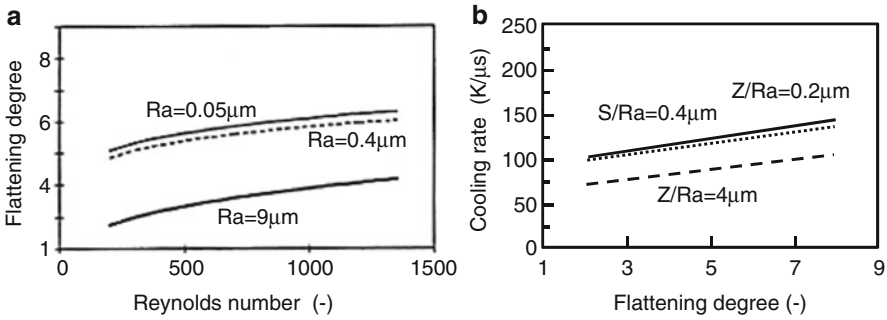


Fig. 13.50 For zirconia particles (22–44 µm) plasma sprayed on substrates with different roughness dependence of the measured: (**a**) flattening degree with the particle Reynolds number, (**b**) cooling rate with the flattening degree

the splat curling, the liquid material does not penetrate into the cavities as shown in Fig. 13.47d. Here again it must be emphasized that when grit residues block cavities, the adhesion of the splat on it becomes very poor. Moreover, often the grit residues have an expansion coefficient different from that of the splat and substrate, inducing stresses upon heating and cooling.

The spreading of the droplet is limited by surface irregularities. It is also much more difficult to analyze the oxide layer thickness and composition formed at the rough substrate surface. Roughness results in smaller and thicker splats with slower cooling, as well as in an important flattening splashing behavior and a poorer contact than that on smooth substrates. This is illustrated in Fig. 13.50 from University of Limoges, for zirconia particles $22 < d_p < 44$ µm, $v_p = 200$ m/s, $T_p = 3{,}200$ K, impacting on smooth ($R_a = 0.05$ µm) or grit-blasted ASI304 stainless steel substrates ($R_a = 0.4$ and 9 µm). In Fig. 13.50a, where the flattening degree, ξ, of the particles is presented, it can be seen that a R_a of only 0.4 µm does not perturb ξ very much, while with $R_a = 9$ µm, ξ is reduced by a factor of about 2. If the splat cooling rate is almost unchanged for $R_a = 0.4$ µm, it is reduced by about 25 % for $R_a = 9$ µm, as shown in Fig. 13.50b. Raessi et al. [123] have also studied the effect of surface roughness on splat shapes.

- At last, as for smooth surfaces, the role of contaminants (adsorbates and condensates) is also important and preheating the substrate over the transition temperature must be performed to eliminate them. This preheating, usually improves the coating adhesion by a factor of 2 to 4.

13.5.3 Polymer Particles

To the best of our knowledge very few studies have been devoted to polymer splat formation on rough surfaces. Ivosevic et al. [124] have studied HVOF-sprayed Nylon-11 particles onto 4140 steel grit blasted with alumina grits of different sizes. The increase of substrate roughness promoted splat instability, resulting in radial

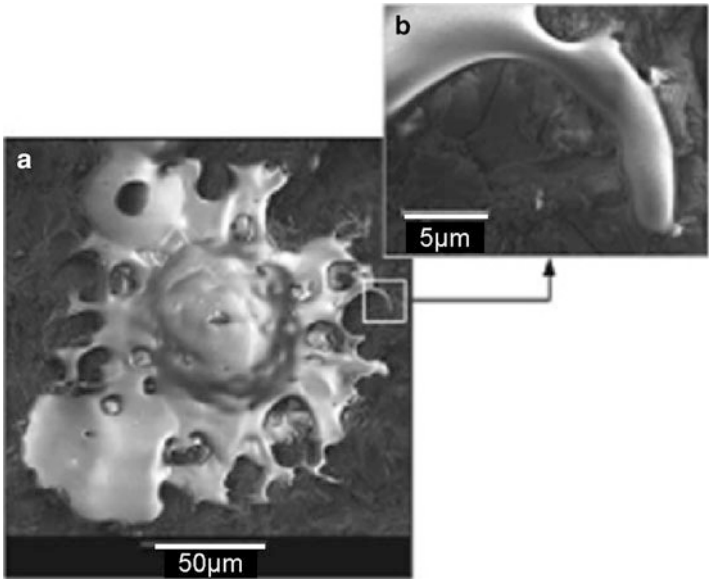


Fig. 13.51 Nylon 11 splat on a grit-blasted steel substrate. Enlarged view of a peripheral splat finger is shown in (**a**). Reprinted with kind permission from Springer Science Business Media [124], copyright © ASM International

jetting and breakup, and producing more irregularly shaped splat shapes on rougher surfaces (Fig. 13.51).

13.6 Coating Formation

Coatings are obtained with a given spray pattern dependent on the relative movement of the torch with respect to the substrate and for a given standoff distance. For a better understanding of the coating generation, the relative movement torch/substrate will be decomposed into three parts: motionless torch and substrate, 1D motion torch/substrate with the bead formation, and pass formation with overlapping beads.

13.6.1 Molten Particles Deposited by Thermal Spraying

13.6.1.1 Principles of Coating Generation

Two types of injection are used: radial, as shown schematically in Fig. 2.17a, and axial, as shown in Fig. 2.17b. In radial injection the particle mean injection force has to be adapted, through the carrier gas flow rate, to that given by the hot gas jet to particles (see Sect. 4.4.2), while in axial injection the carrier gas has less effect on particle trajectories (see Sect. 4.4.2).

Coating properties, whatever the spray process used, depend on splat formation and layering. Typical examples of coatings sprayed with fully melted particles have been presented in Fig. 2.27 for a stainless steel coating (304L) on a low carbon (1040) steel substrate, and in Fig. 2.28 for a zirconia YPSZ (8 wt%) coating on a super-alloy, both coatings being plasma sprayed. Figure 2.2 also presents the same CoNiCrAlY coating sprayed, respectively, by HVOF, Fig. 2.2a, VPS Fig. 2.2b, and APS (Mettech Axial III torch) Fig. 2.2c. When looking at the etched cross sections of those coatings one can observe layered splats with more or fewer contacts between themselves, globular pores of different sizes (from a few tenths of micrometers to a few micrometers), unmelted particles, cracks, especially in the ceramic coating, and oxides (for metals or alloys). Of course when comparing coatings sprayed by APS, VPS, and HVOF, porosities, oxide content, and splat layering are different.

The complexity of the spray process is summarized in Fig. 13.52 [6]. Figure 13.52a represents the way particles, conveyed by a carrier gas and radially injected into the spray jet (for 30 μm particles about 107–109 particles are injected during one second) with the resulting splat formation (Fig. 13.52b) and layering (Fig. 13.52c). According to particle velocities, their residence times in the hot gases and the jet plume are between 0.1 and a few milliseconds. In Fig. 13.52d are indicated the wide range of times involved in conventional coating formation [125], varying from microseconds to hours (the size of the parts to be coated can be between a few centimeters and tens of meters). Such time and size ranges make the comprehensive study of thermal spray processes very complex. Finally, the materials deposited represent a hierarchy of microstructures across various length scales: nano-elements, micro-sized grains contained within meso-scale splat structures and a variety of nano-, micro-, and meso-scale defect structures comprising voids, microcracks, and oriented boundaries.

The coating microstructure depends on:

– The real contact between the splat and the substrate or the previously deposited layers, which is strongly linked to the substrate preheating temperature above the transition temperature to get rid of adsorbates and condensates (see Sect. 13.5.1.1). However this preheating has to be carefully controlled to limit as much as possible the development of the oxide layer at the surface of metal or alloy substrates (see Sect. 13.3.2). As shown very schematically in Fig. 13.53a, the real contact between layered splats determines the coating properties such as thermal conductivity, Young's modulus, etc. Between layered splats, or first splats and the substrate, there exist inter-lamellar pores, the size of which is drastically exaggerated in the figure. The inter-lamellar flat pores are thin voids, orthogonal to the spray direction, filling spaces between splats. These inter-lamellar pores are part of coating porosity and their thickness is a few hundredths to a few tenths of micrometers. The real contact between splats increases with particle impact velocities, provided that they are not either too much superheated or below their melting temperature. To demonstrate that the splat thickness is not the only parameter controlling coating properties, let us consider a 300 μm coating achieved by layering 100 splats, 3 μm thick each, or 300 splats 1 μm thick each, and assume a

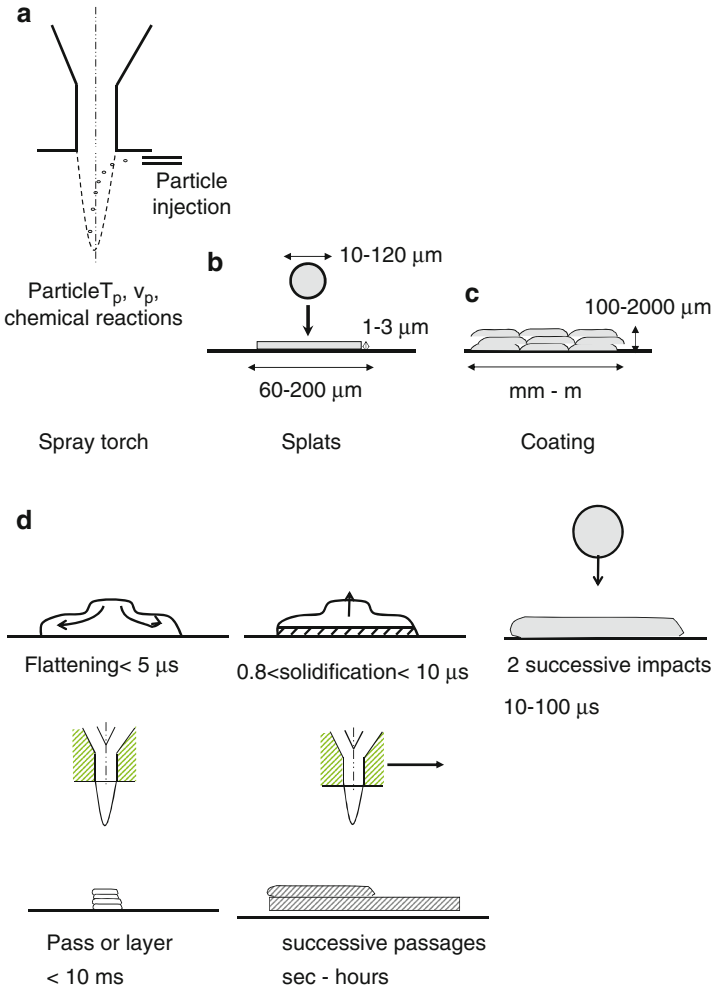


Fig. 13.52 Principle of thermally sprayed coating formation, excluding cold spray. (**a**) Radial injection. (**b**) Typical particle and splat sizes as well as coating thicknesses in conventional coatings. (**c**) Time ranges in coating formation (plasma, HVOF, HVAF, D-gun sprayed). (**d**) Different characteristic times: flattening,solidification, between successive impacts, for pass formation and for coating generation. Reprinted with kind permission from IOP organization [6]

real contact of 30 % between splats whatever maybe their thickness [126]. The mean real contact, MR, between the 300 layered 1 µm thick splats is $MR_1 = 299 \times 30/299 = 30$ %. When considering 3 µm thick splats that can be considered as three layered 1 µm with perfect contact, one 3 µm thick splat corresponds to two-layered splats with a 100 % contact (Fig. 13.53b). The same calculation results in: $MR_2 = (99 \times 30 + 200 \times 100)/299 = 76.6$ %. Of course if it is assumed that the real contact between 1 µm thick splats is 60 % and that between 3 µm thick ones

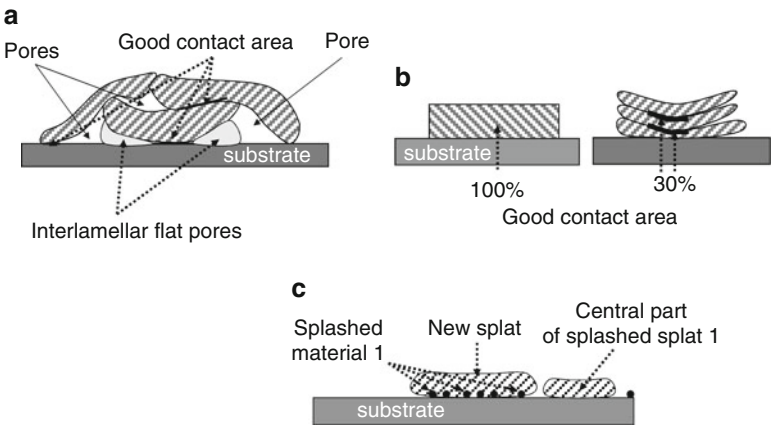


Fig. 13.53 (**a**) Schematically shown contacts between layered splats or first splats and substrate with inter-lamellar contacts, the size of which is drastically exaggerated. (**b**) Same thickness of 3 μm achieved with either a single splat or 3 layered ones. (**c**) New splat deposited in the periphery of a splashed splat with poor contact with substrate due to splashed material

is 15 %, $MR_1 = 60$ % while $MR_2 = 71.8$ %. However the main problem, whatever the mean splat thickness may be, is to know the real surface contact percentage between splats (which is not at all easy to determine).

– Splashing of the melted particles during flattening upon impact can drastically affect the coating properties [127–129]. The lower adhesion of splats deposited on splashed material, as described schematically in Fig. 13.53c, can become more important when spraying metals because splashed material is oxidized rather fast due to the small droplet sizes. Buildup of splashed particles around perturbations on otherwise smooth surfaces was observed under plasma spray conditions [129]. It was also shown that the substrate geometry affects the flow of impacting and splashing particles: flat and cylindrical specimens were used by Racek [130] to investigate the effect of the surface curvature when spraying CrC–NiCr coatings by HVOF. Less splashed particles would be observed on the cylindrical surface, 90 mm in diameter, Fig. 13.54. Due to the surface curvature of the cylindrical surface, the droplets or fragments would travel higher above the surface and fewer protrusions would extend to their path.

Besides these, other important defects, called speckles, can be generated [130] by this splashed material. They will be discussed in section 13.7.1.4.b.

– Pores, often called globular, which are formed during coating generation, are illustrated in Fig. 13.53. Pores are due to the shadowing effect (Fig. 13.55a), narrow holes in valleys between splats are not completely filled as explained by Eq. (13.7) (Fig. 13.55b), due to unmolten or partially melted particles that create the worst defects within coatings (Fig. 13.55c), or due to exploded particles (Fig. 13.55d). These globular pores are distributed more or less homogeneously and their potential to deteriorate coating properties is proportional

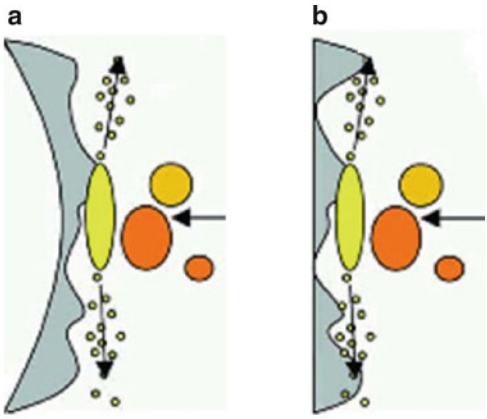


Fig. 13.54 The relation between the substrate curvature and the mechanism of collection of splashed material: (**a**) cylindrical and (**b**) flat surface. Reprinted with kind permission from Springer Science Business Media [130], copyright © ASM International

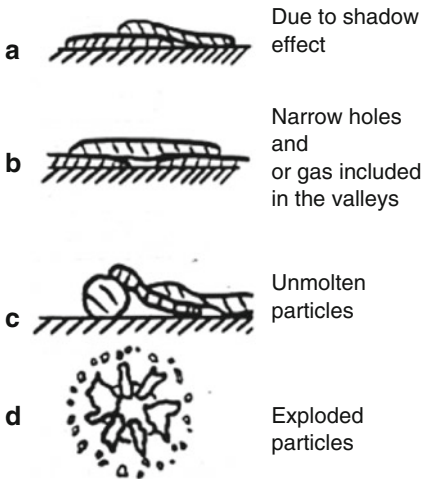


Fig. 13.55 Schematic representation of globular pores within coatings, (**a**) shadow effect, (**b**) narrow holes in valleys between splats, and (**c**) unmelted or partially melted particles, d. exploded particles

to their size [131]. That is why in order to reduce the porosity, the incorporation in the coating of large unmelted particles, which are sufficiently heated to stick, or of partially melted particles, must be avoided. This can be done by choosing carefully the particle size distribution and optimizing the particle injection, especially for radial injection. However, sometimes a compromise has to be found between having most particles fully melted but with a rather high oxide content and more unmelted particles with lower oxide content [132].

– Pores that are not really pores but cracks formed during residual stresses relaxation. They comprise mainly:
– Micro-cracks within splats resulting from quenching stress relaxation, not the worst for coating porosity, observed in ceramic materials, these splats are always parallel to the spray direction.

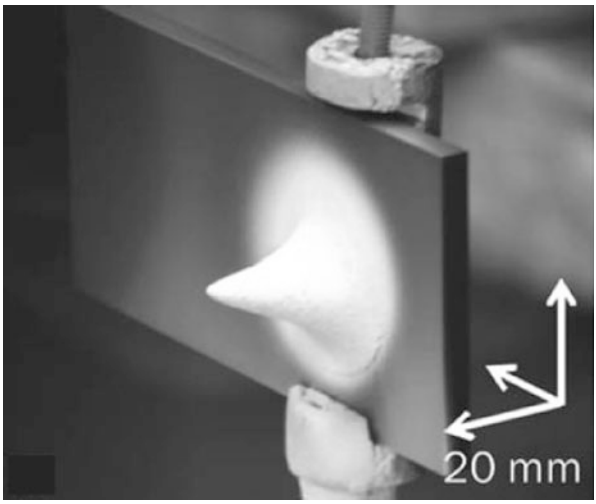


Fig. 13.56 Tower deposited when plasma-spraying yttria partially stabilized zirconia with motionless torch and substrate. Reprinted with kind permission from Springer Science Business Media [134], copyright © ASM International

– Macro-cracks running through layered splats especially at their interfaces; these tend to initiate interconnected porosities. They are often due to the relaxation of an expansion mismatch stress (see Sect. 13.9). They are flat pores and often contribute to the open porosity of coatings. Other stress relaxations can occur but they can be avoided by optimizing spray or service conditions. They will be described in Sect. 13.11.
– At last another important source of defects is the impact angle that reduces the normal impact velocity, resulting in elongated splats (Sect. 13.4.7.2). Spraying with an angle above a certain value, depending on particle and substrate materials, will promote splashing even on substrates preheated above the transition temperature.

To conclude, as in most spray conditions, a careful optimization of the spray parameters, including morphology and size distribution of particles, must be made to achieve coatings with properties expected in service conditions. The importance of the choice of sprayed particles to limit their oxidation is for example illustrated by the work of Zeng et al. [133] who plasma sprayed (APS) Ni–Cr-based alloy powder with Si (4.3 wt%), B (3.0 wt%), and C (0.8 wt%) additions. They showed that the addition of Si and B to iron effectively reduced the oxygen contents in the coatings, especially during the in-flight period at higher particle temperature.

13.6.1.2 Splat Layering: Motionless Torch and Substrate

Figure 13.56 from Shinoda et al. [134] shows the tower appearance of the obtained samples. This yttria partially stabilized zirconia tower was plasma sprayed at the powder feed rate of 7 g/min for 186 s. The deposition region was 36 mm in diameter and the height of the tower was 21 mm. Particles in the hot gas jet have, in first

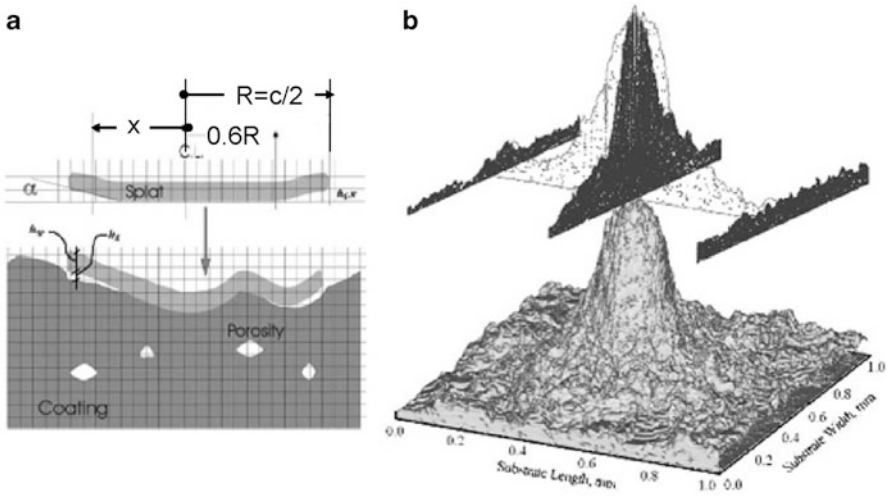


Fig. 13.57 (**a**) Curl-up of splats after impact. Splats were assumed to detach from the substrate, starting at a distance 0.6 R from the center, with an angle α. (**b**) Model of deposition of nickel particles in plasma spray by a spray gun held stationary over the substrate. Reprinted with kind permission from Springer Science Business Media [1], copyright © ASM International

approximation, a Gaussian distribution, not necessarily symmetrical in 3D, either with the same axis as that of the hot gas jet (axial injection) or making an angle of 3–4° with it (radial injection). The conical tower shape results from the layering of the Gaussian shape of the successive layers but also on the impact angle. Most particles, except those traveling in the wings of the Gaussian distribution, impact almost orthogonally to the substrate, while some, which have lower temperatures and velocities, impact with a non-negligible angle (generally between 70 and 110°). Thus these last particles are less likely to attach to the substrate or the previously deposited layers. As time elapses, the central part of the deposited Gaussian distribution grows faster than its wings, creating a cone with an ever-increasing angle. Because of the steeper angle, fewer and fewer particles from the particle jet wings and also from its central part stick to the cone periphery resulting in the conical tower shape presented in Fig. 13.56.

Ghafouri-Azar et al. [1] have modeled the formation of such a conical tower. They use a three-dimensional, stochastic model of thermal spray coating build-up. The model assigns impact properties to molten droplets landing on the substrate by generating random values of process parameters, assuming that these properties follow normal distributions with user-specified mean and standard deviations. Rules are prescribed to calculate splat sizes after droplet impact and their interaction with each other. Porosity is assumed to be solely due to the curl-up of the splats as a result of thermal stresses, as shown in Fig. 13.57a. A Cartesian grid is used to define the computational domain and to track the shape and position of the deposited coating. The surface of the coating and the location of pores within it

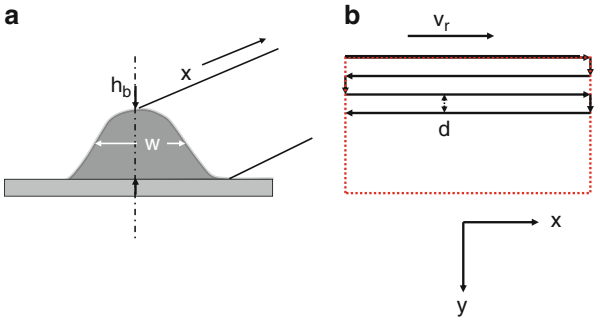


Fig. 13.58 (**a**) Schematic representation of a bead and (**b**) Typical spray pattern on a flat substrate

are specified using a variable known as the "volume fraction," defined as the fraction of the volume of a computational cell occupied by coating material. They modeled plasma spraying of nickel particles, and the resulting conical tower (Fig. 13.57b) is in good agreement with experimental results.

The story is rather different for D-gun-sprayed coatings deposited in a discrete manner, i.e., by each shot (or each explosion), as shown Sect. 5.4.2. In this process molten particles spread out and splatter as they strike the surface to form an approximately 10 μm thick coating deposit with a diameter that can be slightly larger than the i.d. of the D-gun barrel, as shown in Fig. 5.45. The deposited material larger than the inner diameter of the barrel at each shot is due to the particles following the expansion of the high-pressure flow exiting the detonation barrel. As pointed out in Sect. 5.4.1, it can be avoided by using a separation device, shown in Fig. 5.40.

13.6.1.3 Splat Layering: Bead Formation

A bead is obtained (Fig. 13.56a) when translating the torch relatively to the substrate (1D movement) at a given relative velocity torch-substrate, v_r, for example, in the x direction. The bead parameters, its height h_b and its width w_b at mid-height, depend on the spray process, the torch working conditions, the relative velocity torch-substrate v_r, the powder mass flow rate $\dot{m}_p^{\circ}$, the particle size distribution, the deposition efficiency η_d, the torch nozzle internal diameter d_n, the injection conditions, and the spray distance. The bead height h_b is particularly sensitive to v_r, the deposition efficiency, decreasing with increasing distance above a certain value, and the spray distance. The bead width w_b is linked to the nozzle internal diameter, d_n, the injection conditions, especially the injector i.d., and the spray distance. The number of particles N_1 (s^{-1}) sprayed per second is always impressive (Fig. 13.58). It is calculated by using Eq. (13.8):

$$N_1 = \dot{m}_p^{\circ} \cdot \eta_d \cdot m_p^{-1} \tag{13.9}$$

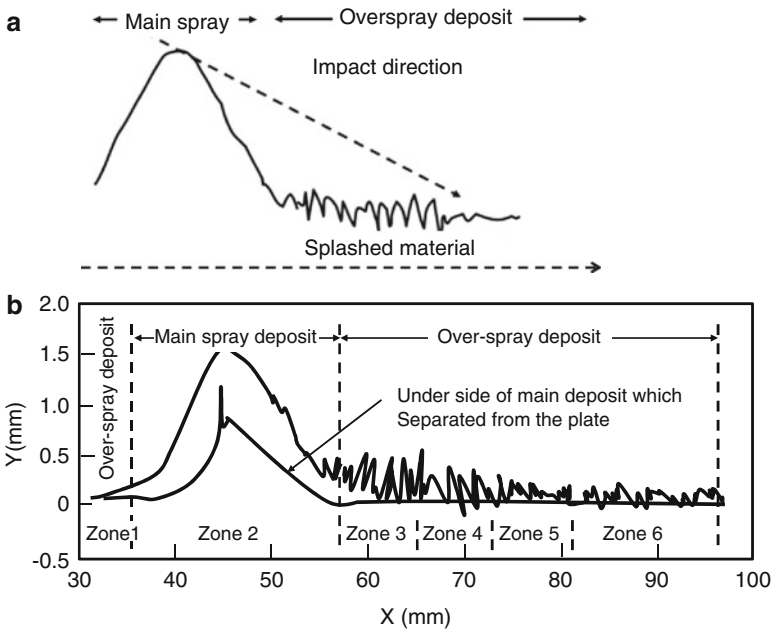


Fig. 13.59 (**a**) Splashed material from inclined spraying where the bead intercepts part of the impacting particles. (**b**) Digitized data for the shape of the deposit cross section obtained from the experiment. Reprinted with kind permission from Springer Science Business Media [135], copyright © ASM International

where $\dot{m}_p$ is the powder mass flow rate (kg/s), η_d the powder mass deposition efficiency, and m_p the particle mass (kg). For example, considering plasma-sprayed alumina particles with a mean diameter $d_p = 30\,\mu m$, a particle feed rate of 6 kg/h, and a deposition efficiency of 0.5, Eq. (13.8) gives $N_1 = 7.1010$ particles per second!

In fact the Gaussian bead shape is (see 4.4.2 and 4.4.3) in good agreement with the distribution of hot particles shown in Fig. 2.32. First, in the bead wings particles impact with an angle and lower velocities and temperatures that result in a more porous area with a poorer contact between splats, see Sect. 13.9.1.1. Also in the wings of the bead, frequently particles appear which are not well exposed to the hot jet, but are sufficiently heated to stick to the bead wing (see Fig. 2.32). Moreover these particles, at least the metallic ones, are easily oxidized in-flight and they may form the major source of oxide inclusions in sprayed coatings, and thus create defects. Another important point is the risk, when spraying off-normal angles, to have particles intercepted by the bead rebounding and splashing on the other side of it, as shown in Fig. 13.59a. The adhesion of the splashed material being very poor, it will be the same with the next bead deposited on top of it [135]. Figure 13.59b presents the digitized photograph of the deposit cross section obtained with 15 successive passes along the same bead sprayed with an HVOF gun and a spray angle of 51°. The portion of the deposit near the impact zone of the main spray jet is relatively thick with small roughness elements on it. This portion of the deposit

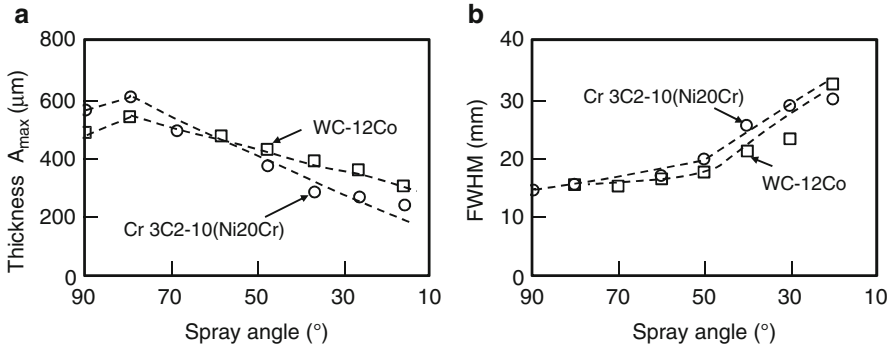


Fig. 13.60 Dependence on the spray angle of plasma-sprayed WC–12Co and Cr3C2–10 (Ni–20Cr) beads. (**a**). Thickness h_b. (**b**) Width at mid height w_b. Reprinted with kind permission from Springer Science Business Media [136], copyright © ASM International

has buckled and separated from the plate due to the thermal stresses created by the transfer of a large amount of heat in the thermal spray material to the plate and deposit. A large amount of splashing occurred when the thermal spray droplets impacted on the target surface (at least 23 %). The splashed material, called overspray, redeposit over large areas on the target surface and is composed of isolated columns with large spaces between them.

Tillmann et al. [136] studied the influence of the spray angle (between 90 and 20°) on plasma-sprayed WC–12Co and Cr3C2–10(Ni–20Cr) coatings. Each sprayed bead was characterized by a Gaussian fit. Furthermore, metallographic studies of the surface roughness, porosity, hardness, and morphology were carried out and the deposition efficiency as well as the tensile strength was measured. The thermally sprayed coatings show a clear dependence on the spray angle. A decrease in spray angle changes the thickness, width, and form of the spray beads. Coatings become rougher and their quality decreases. Fig. 13.60 represents the evolutions of the thickness h_b of the bead (Fig. 13.60a) and its width w_b at mid-height (Fig. 13.60b). The thickness is maximum for 80° and decreases after that, while the width increases slowly down to 50° and much more afterwards. At smaller spray angles the normal component of the particle velocity regarding the substrate surface diminishes and at the same time the tangential component increases and, besides the splat elongation (see Sect. 13.5.3), the probability rises to bounce off a sprayed particle from the specimen [136]. For the considered materials, the porosity is not really affected up to 50°, but it increases drastically afterwards, being multiplied by a factor of up to 3 at 20°.

13.6.1.4 Coating: Pass Formation

To form a pass from beads the torch has to be moved according to a given spray pattern such as, for example, that presented in Fig. 13.58b.

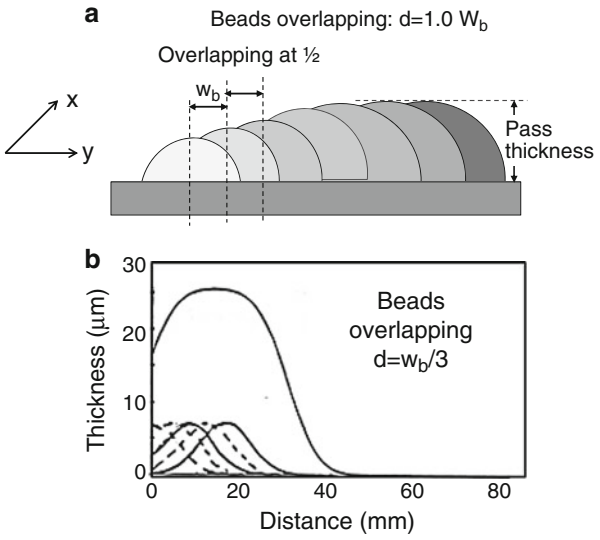


Fig. 13.61 (**a**) Definition of the spray direction (x) and the distance between two successive beads. (**b**) Example of overlapping at a ratio of 0.33

(a) Effect of Spray Pattern

The movement of the torch has a significant influence on the heat and mass transfer during the coating process [137]. The structure and final properties of the coating can be improved by adjusting the movement direction and speed profiles of the torch. Thus, the manufacturing of coatings on complex geometries requires the generation of an optimized movement with a defined torch velocity [132].

Pass results of the overlapping of successive beads, deposited in the x direction (Fig. 13.61a), the next bead being deposited at a distance d in the y direction (Fig. 13.58a), and its thickness depends on the overlapping ratio, as shown in Fig. 13.61b. For a plane substrate, the distance d between successive beads in the y direction is calculated as the bead width at mid-height w_b generally multiplied by a given number, generally called overlapping ratio, f, (typically 0.33, 0.5, 1.0, 2.0, 3.0). The choice of the beads overlapping ratio depends on their thickness and the surface undulation that is acceptable. For a medium thick bead (7–8 µm) an overlapping of 1.0 results in an undulation of about 3 µm while with an overlap ratio of 0.33, the undulation is about 1 µm [138]. This is also illustrated in Fig. 13.62a from Fasching et al. [139] simulating the first layer of the pass in dependence of the track gap ($d = f.w_b$) with f =0.5, 1.0, 2.0, 3.0. The simulation is based on a symmetric Gaussian distribution and shows the cross section normal to the spray line. As it can be seen the undulation diminishes when f increases, but the pass thickness also increases correspondingly, which does not necessarily help to control temperature gradients within passes, especially when spraying low thermal conductivity materials.

The undulation increases when passes sprayed with the same procedure are superimposed. To smoothen the surface of thick passes, the starting point of the next

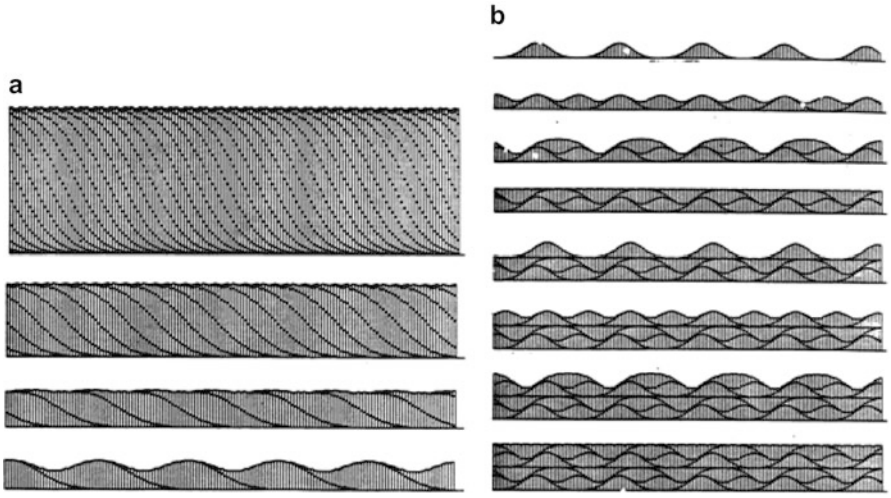


Fig. 13.62 Simulations: (**a**) showing the cross section, normal to the spray line, of the first layer of the pass in dependence of the track gap ($d = f{\cdot}w_b$) with f =0.5, 1.0, 2.0, 3.0, (**b**) smoothing the surface of a thick coating by starting the next passes with different starting points. Reprinted with kind permission from ASM International [139]

pass must be chosen such that the first bead of the next pass is shifted in such a way that it starts in between the beads previously deposited. Figure 13.62b from Fasching et al. [139] illustrates how the evenness diminishes the coating roughness, for an increasing number of layers, by choosing properly the starting point of the next pass.

(b) Other Important Effects

Another important point that must be emphasized is the spray distance which, especially for plasma spraying, plays a key role, not only in the heat transferred to the substrate or coating under construction but also in the bead thickness and width at mid-height. Finally the standoff distance results from a compromise between the locations of particle maximum velocities and temperatures, heat transferred to the substrate, which decreases almost exponentially with the spray distance, and particle inertia. For example, in plasma spraying typical standoff distances are between 100 and 120 mm to achieve heat fluxes below 2 MW/m^2 (see Sect. 13.8). The maximum particle velocities and temperatures are obtained between 60 and 80 mm, where the heat fluxes, reach 5–6 MW/m^2 and are more difficult to control with cooling systems. The final spray distance also depends on particle sizes, i.e., particle inertia: a particle 10 μm in diameter is cooling and slowing down much faster than a 50 μm one. It thus becomes mandatory to spray small particles at shorter distances at the expense of a higher heat flux imposed onto the substrate.

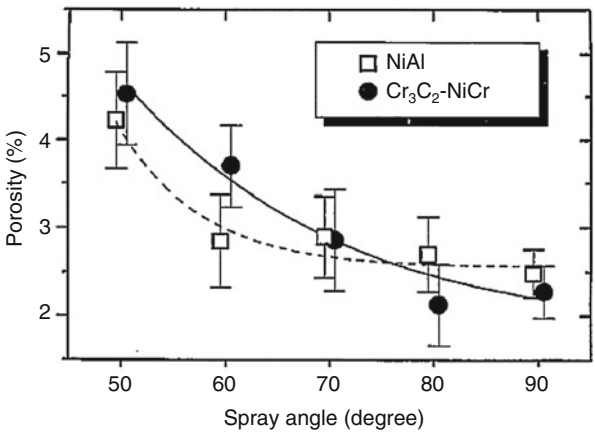


Fig. 13.63 Variation of porosity with spray angle for Cr3C2–NiCr (mean diameter 25 μm) and NiAl (mean diameter 60 μm) coatings plasma sprayed. Reprinted with kind permission from Elsevier [123]

The other key point is the spray angle that must be kept as much as possible close to 90°. For example, Leigh and Berndt [140] have made a systematic study of Cr_3C_2–NiCr (mean diameter 25 μm) and NiAl (mean diameter 60 μm) coatings plasma sprayed. They have varied the spray angle between 90° (normal impact) and 50° and found that the porosity was the lowest for both materials at 90°, as shown in Fig. 13.63, and increased when the angle decreased. The surface roughness of the Cr_3C_2–NiCr deposit was not sensitive to the spray angle, whereas NiAl exhibited an increase as the spray angle decreased. Micro-hardness, tensile adhesion strength, and interfacial fracture toughness decreased with spray angle. The change of these properties with spray angle was attributed to (1) the morphology of the splats (see Sect. 13.4.1), (2) the change of the local spray angle with some shadow effect, and (3) the change of the normal momentum component of particles impacting on the substrate or previously deposited layers.

Racek [130] has shown when HVOF spraying Cr_3C_2–NiCr coatings, localized porosity, and high oxide content can be formed due to re-deposition of splashed metallic particles. Macro-roughness features like speckles were formed when higher particle velocities were used on cold substrates, as illustrated in Fig. 13.64a, showing the coating cross section with a speckle. The speckle grew in size progressively with coating deposition forming an approximately conical volume of high porosity. Its highly porous microstructure consisted of small highly oxidized particles. Racek [130] has hypothesized that droplets or fragments of splashed or fractured particles are responsible for the effect that lead to a speckle formation. Since the trajectories of the splashed particles are more parallel to the substrate, particles re-deposited primarily on surfaces inclined to the substrate plane such as the sides of a substrate protrusion, Fig. 13.64b. As the speckle or protrusion height over the surrounding coating surface increases, the effect is multiplied due to the increased projected area where the splashed particles deposited, Fig. 13.42b. Fortunately [130], adjusting the process parameters such as flow of the process gases and the standoff distance can

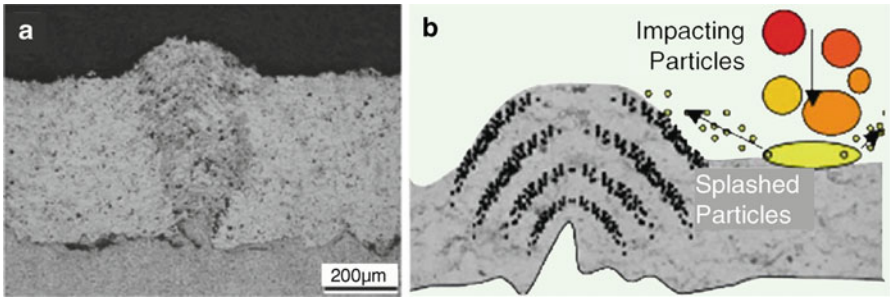


Fig. 13.64 (**a**) Optical micrograph of the cross section of a Cr3C2–Ni HVOF coating: (**a**) porosity speckle emanating from a substrate protrusion, (**b**) suggested mechanism of the speckle formation. Reprinted with kind permission from Springer Science Business Media [130], copyright © ASM International

effectively control the splashing phenomenon. Substrate temperature and chemical composition also strongly affects the particle deposition.

A similar phenomenon was observed with plasma-sprayed suspension coatings, see Sect. 14.7.1.2. According to the very important disparity between the size of peaks of the roughened surface, characterized by its R_a, and the sprayed particle sizes (a ratio of 75 or more), the speckle was more important than that obtained with conventional coatings, as shown in Fig. 14.30.

For D-gun-sprayed coatings, the new deposited shot overlaps with the previous one, as shown in Fig. 5.45, both shots being of either the same or different materials (to achieve graded coatings). Finally the coating is built by the overlapping of the successive shots as illustrated in Fig. 5.45b.

13.6.2 Polymer Coatings

Compared to coatings achieved with conventional particles, bead formation and overlapping are similar. However polymer coating formation depends strongly upon the specific properties of these materials, especially their low thermal conductivities and high viscosities. The crystallinity of coatings, depending on their cooling, plays also a key role in coating properties.

13.6.2.1 Control of Particle in-Flight Melting

The first necessity is to adapt the spray conditions and the polymer particle sizes to melt them partially with no overheating. This requires that overheating of the smallest particles and insufficient melting of the bigger ones be avoided. Then the residence time of particles must be adapted in order to avoid overheating. This is, for example, illustrated in the work of Alamara et al. [112] who sprayed with the

oxyacetylene flame process polypropylene (PP) splats, the powder being externally fed. The collected splats showed that three zones could be recognized on the basis of standoff distance. There is a transition from low to high stand-off distances; i.e., (1) a partially melted splat zone with no or little splashing and less flow deformation due to insufficient heating, (2) a fully melted splat zone with or without splashing and full flow deformation due to sufficient heating, and (3) a splat evaporation zone and highly deformed splats with full flow deformation due to particle overheating.

Bao et al. [141] have succeeded to flame spray ultra-high molecular weight polyethylene UHMWPE coatings with relative molecular weights up to six million. The deposition of pure UHMWPE was sensitive to the processing conditions and powder characteristics. However the use of a low molecular weight ethylene acrylic acid (EAA) as a matrix phase for UHMWPE provided substantial gains in the adhesion and ductility of the coating while maintaining the wear performance.

13.6.2.2 Substrate Preheating

The substrate must be preheated to a temperature close to the polymer melting temperature to achieve the complete melting of the flattened particles and the uniform flow of the melted polymer. Using high velocity particles, such as those obtained with HVOF spraying, helps in reducing the viscosity problem thanks to its shear rate dependence. Poly(tetrafluoroethylenecohexafluoro-propylene) (FEP), with a melting temperature of 261 °C, and the degradation of which starting at 408 °C, was flame sprayed onto grit-blasted steel (AISI-1045) substrates preheated between 270 and 300 °C [142]. No chemical changes were involved in the flame spraying process. PEEK coatings using an HVOF process (Stellite Jet Kote II) were sprayed by Patel et al. [143] onto ANSI stainless steel 304 substrates that have been subjected to three different pretreatments to investigate the effect of varying surface roughness and chemistry on the coatings formation. The three surface treatments were as received degreased, chemically etched and steel grit blasted, including substrates with the same R_a but with different skewness (positive, negative, or zero). The formation of surface roughness on these substrates with a positively skewed distribution can be produced using an etching process. A positively skewed roughness with an adapted magnitude promotes mechanical interlocking. PEEK coatings on surfaces with positive skewness (S_k) show better coating adhesion than similar surfaces with negative skewness.

13.6.2.3 Coating Temperature Control

The surface of the deposited last pass of polymer must be kept at a temperature close to the polymer melting temperature but not too much above it. It is easier to say this than to do it because due to the low thermal conductivity of the polymer only a small quantity of heat is removed through the already deposited layers and

the substrate, opposite to coatings sprayed with conventional powders (even zirconia). To avoid overheating of the last deposited pass and its degradation it is possible to play with the spray distance, the translation velocity of the torch, the cooling systems acting on the coating surface with blown compressed air, etc. Patel et al. [114, 143] have studied the effect of flame impingement on PEEK coating degradation. When there is significant flame impingement onto the just deposited coating, as with coatings produced at 200 mm spray distance, hydrocarbons from the flame react with the coating surface. The extent of thermal degradation decreases with increasing spray distance. The choice of spray gun nozzle did not have as great an effect as spray distance.

13.6.2.4 Coating Cooling Rate: Crystallinity

Once the coating is deposited its cooling rate also plays a key role in controlling its crystallinity. Normanda et al. [144] have flame (acetylene–oxygen)-sprayed PEEK coatings applying two cooling conditions to modify the PEEK crystal structure. A slow cooling, achieved by ambient air, allowed obtaining a partially crystallized structure. The crystallinity was estimated, by DSC measurements, at 36 %. A rapid cooling ensured by water quenching permitted to freeze an amorphous state. The same study indicated the presence of $–CH_2–$ groups in the main chain of PEEK. The explanation given by authors relied on the reactions of acetylene with carbon and hydrogen at high temperature. Li et al. [145] and Zhang et al. [146] have also flame-sprayed (acetylene–oxygen) PEEK coating samples. The substrates were preheated to 400 °C (PEEK melting temperature of 343 °C). Different types of coatings were sprayed with the same spray conditions but different cooling rates [144, 145]: quenched into iced water immediately after spraying and annealed at different temperatures (180 to 300 °C) for different holding times (from 1 to 30 min). The annealed samples have a semicrystalline structure, and the quenched sample crystallinity reached 36 %. The analytical results indicated that two crystal entities emerged from the coating during the isothermal treatment following a stepwise crystallization fashion. The semicrystalline coatings exhibit higher hardness, lower friction coefficients, and wear rates. The increase of the annealing temperature and the holding time in the studied range could lead to a higher coating hardness.

13.6.2.5 Polymer Coatings Post-treatment

Polymer spraying has a certain number of limitations, particularly on the coating quality such as high porosity, low interfacial adherence, etc. For that reason a thermal post-processing step is often necessary. Poly-ethylene-terephthalates (PETs) obtained from used soda bottles were thermally sprayed by HVOF (kerosene–oxygen-ni–rogen) [147]. Heat-treated thermally sprayed coatings delivered a better

tribological performance than virgin PET, as indicated by their lower friction coefficient and lower wear rate against a hardened steel pin. Soveja et al. [148] and Zhang et al. [149] have studied the effects produced during a laser beam heat treatment (Nd:YAG, CO_2, or diode lasers) on the morphological structure (compactness) of PEEK and PTFE coatings, which were flame sprayed, and on the mechanical properties (adherence and tribological properties). Whatever laser wavelengths were used, the results showed a good effect of the laser treatment: improvement of both polymer coating compactness and its adherence to the substrate. The coatings' mechanical properties were correlated with their resulting structures.

13.6.2.6 Polymer Coatings Reinforced with Hard Particles

Using polymer matrix coatings filled with commercial or nanometer-sized ceramic (e.g., silica or alumina) reinforcements or fillers have been reported to improve polymer-coating properties. However the strong velocity and temperature gradients of thermal spray jets, together with variations in particle size, mass density, and morphology can, result in significant segregation when such dissimilar materials are co-sprayed.

Ivosevic et al. [150] have sprayed functionally graded materials (FGMs) comprising layers of pure thermosetting polyimide, polyimide + WC–Co, and pure WC–Co onto polymer matrix composites (PMCs). For that PMR-II (thermoset polyimide) particles (20–100 μm) were injected axially into the Jet Kote II HVOF gun, working with hydrogen and oxygen, while WC–Co particles (5.6–22.5 μm) were fed externally. The WC–Co top coat was flame sprayed. The drastic difference of mass densities of polymer (1,390 kg/m^3) and WC–CO (12,500 kg/m^3) must be pointed out. Substrates were grit blasted and preheated (230–340 °C). The relative proportions (on a pore-free basis) of polyimide matrix and WC–Co filler were 58 and 42 %, respectively. The porosity of the pure polyimide coating was determined to be 26 %. The two- and three-layer FGM coatings both failed by the same mechanism: a combination of cohesive failure within the composite layer and a delamination from the substrate.

Berndt et al. [151] have flame sprayed (propane/air mixture) ethylene methacrylic acid copolymer powder (115 μm) mixed either with nickel–chromium alloy particles (mean size 23 μm) or alumina particles (mean size 16 μm). In both cases tensile strength, elongation to break, and energy to break decrease with the filler content.

Jackson et al. have HVOF (hydrogen–oxygen) sprayed [152] nylon particles (10–180 μm) together with nominal 10 vol.% of nano and multiscale silica reinforcements. Combining Nylon-11 and silica in a 9:1 ratio by volume produced composite feedstock particles. The nanometer-sized particles were made of fumed silica (7 nm mean size), while the multiscale reinforcement comprised equal proportions of each of the five particle sizes ((7, 12, 20, 40 nm, and 10 μm), physically

blended prior to ball milling. Each composition was ball-milled for 48 h, using zirconia balls, to ensure sufficient embedding within coating of the softer Nylon-11 with the silica (see Sect. 11.5.2.2). Nylon-11 coatings reinforced with 7 nm silica exhibited greater sliding wear resistance than pure Nylon-11, but they were better than coatings with the multi-scale silica reinforcement. The same study, however, revealed that the crystallinity of the polymer matrix played a significant role in the wear behavior. The advantage of pure Nylon-11 coating is probably due to the occurrence of two additional wear mechanisms: abrasive and fatigue wear.

Another way to spray composite ceramic-polymer coatings is that proposed by Mateus et al. [153]. They have used plasma spraying (Ar–25 vol.% H_2 mixture) where alumina–titania (3 wt%) particles (30 μm in mean diameter) were injected at the anode nozzle exit, while the PTFE (20 μm in mean diameter) and PFA (30 μm in mean diameter) particles were injected 30 mm downstream with the injector oriented toward downstream of the plasma plume flow. The sprayed polymer particles represented only 8 vol.% of the total sprayed materials. A well-melted ceramic matrix in which rounded polymer particles are randomly distributed characterizes the composite coatings. The as-sprayed polymer particles kept at the coatings surface can however be spread, thanks to a thermal treatment at 350 °C for 15 min. Unlike with spraying of PFA, a large material loss was noticed during the spraying of PTFE. Thus, the highest polymer/ceramic ratio is observed in the coatings made with the separate injection of the Al_2O_3–TiO_2 and PFA powders. The friction tests carried out with thermally treated coatings show that the friction coefficient and the wear of the steel 100C6 balls depend on the amount of polymer (PTFE or PFA) at the coatings surface. To keep it high enough, because surface particles reach quickly the decomposition temperature, cooling and spray conditions must be well controlled. The polymer viscosity at the melting state is also a predominant parameter: a low value promotes a good splashing of the melted particles on the surface substrate and also a good particles adhesion. Thus with PFA a better adhesion is obtained than wit PTFE.

Good results have been obtained with polymer particles doped with nanometer-sized hard particles (silica or diamond). For example, Schadler et al. [154] have HVOF (H_2-O_2)-sprayed nylon-11 particles ball-milled with either 7 nm or 12 nm silica powders treated to be either hydrophobic or hydrophilic, respectively. Compared to pure nylon coatings, scratch resistance improved by 30 % and wear resistance by 50 %. The surface chemistry of the silica filler affected the final coating properties. Silica particles with a hydrophobic (methylated) surface resulted in better mechanical properties than those with a hydrophilic (hydroxylated) surface. Stravato et al. [155] have HVOF-sprayed Nylon-11 particles ball-milled with zirconia balls. Qualitative assessment indicated that coating adhesion was improved through the addition of the nanometer-sized diamond to the Nylon-11. Feedstock preparation is an important aspect and further work is clearly needed to investigate and optimize the process for better dispersion and covalent bonding of the nano-diamond particles to the polymer matrix and for characterizing the improvement in properties as a function of nano-diamond content.

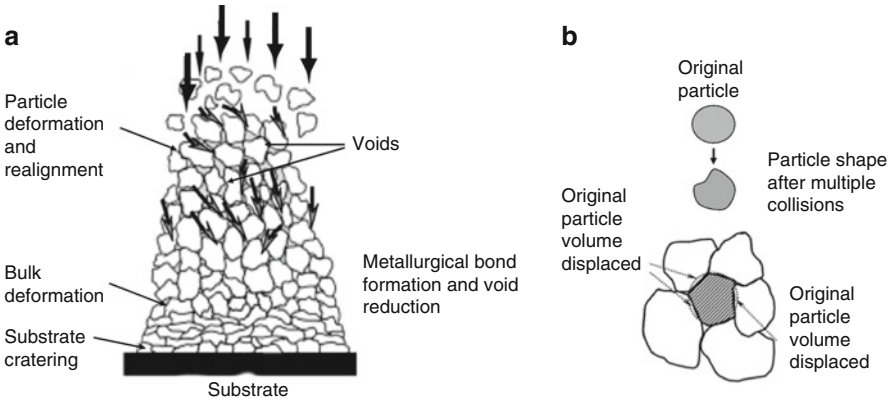


Fig. 13.65 (**a**) Schematic of the progressive plastic deformation of impacting particles when spraying with a fixed nozzle and substrate. (**b**) Schematic diagram of the transformation process from stage 2-type behavior to stage 3-type behavior. The *dashed outline* is the original contour of an ideal spherical particle surface. The *dark line* is the contour of the particle's surface after densification and deformation has occurred. Reprinted with kind permission from Elsevier [156]

13.6.3 Ductile Particles

In cold spray once the first layer has been deposited, the next particles impact on the same material. A decrease or increase of the growth rate should be considered according to the changes in the interaction conditions with the new surface. When spraying (above the critical velocity v_c) with a stationary torch, the coating has a conical shape depending on the nozzle geometry and particle mass flow rate. Depending on the jet divergence, particles traveling in the jet periphery do not impinge on the substrate perpendicularly and erode the coating during its formation. Van Steenkiste et al. [156] sprayed Al particles (the majority having diameters >50 μm) on a brass substrate with a cold spray process where the gas was air pressurized at 2.0 MPa and heated between 208 and 371 °C. The converging–diverging supersonic gun nozzle had a rectangular exit aperture of approximately 2.10 mm with an approximate throat diameter of 3 mm and an 80 mm length (throat to nozzle exit). The coating cross section (schematically presented in Fig. 13.65a) exhibits distinct areas with very different morphologies. Close to the substrate the coating is dense, while farther away the density diminishes [156]. It is clear that the densification is linked to the successive impacts of the incoming particles [156]. For a better description of the involved phenomena, they have considered four stages:

(a) Substrate cratering and first layer build up of particles (see Sect. 6.2.2.1)
(b) Particle deformation and realignment (multilayer coating buildup). For a better understanding Fig. 13.65b, from Van Steenkiste et al. [156], shows particle rotation and deformation inducing void reduction initiated by the collision of

the incident particle with the surface particles, which in turn are forced into their neighbors

(c) Metallic bond formation between particles (particle–particle bonding) and void reduction.

(d) Further densification and work hardening of the coating (excess kinetic energy required for this stage)

The coating adhesion is determined by the plastic deformation (adiabatic shear instabilities), which occurs at the particle–particle interfaces when the impact velocity is above the critical velocity [157].

As is the case for fully melted particles, the impact angle also plays an important role. For example Li et al. [158] have studied the critical velocity for particle deposition in cold spraying through numerical simulation [159] and experiments using Cu powders. The critical velocity was linked to particle size distribution parameters and spray angle through the relative deposition efficiency. For results related to the effect of impact angle, presented in Fig. 13.66, they used nitrogen at 2 MPa preheated, respectively, to 265 °C and 400 °C. As can be seen, in both cases the relative deposition efficiency is zero for angles less than 50°.

Overlapping beads will make coatings, as with spraying of fully melted particles (thermal spraying). Compared to beads obtained with thermal spraying, the wings of cold-sprayed coatings are more abrupt, particles impacting with an angle reaching rapidly a velocity below the critical value. An example of a cold-sprayed copper coating (particle diameter 5–22 μm) is presented in Fig. 13.67 from Stoltenhoff et al. [160]. With a transverse sweep rate speed of the substrate of 125 mm/s and with line spacing of 1.7 mm, a thickness of 200–230 μm per layer was deposited with a deposition efficiency of 72 %. Figure 13.67a shows optical micrographs of the polished coating cross section. In comparison to thermal spray coatings, the coating is very dense and low in oxide content. Microstructure images show no evidence of pores. Differences in the coating density compared with solid Cu can only be determined using leak tests in which a vacuum of $10-12$ kPa is produced on one side of the coating and in which the opposite side is exposed to He. A coating with a thickness of 5.5 mm yielded a leak rate of only $10-10$ kPa l/s, which roughly corresponds to the requirements for high-vacuum components [160]. The etched cross section (Fig. 13.67b) shows the deformation of the sprayed spherical particles with a rather good contact between layered particles and few tiny pores. Of course oxidation (coating oxygen content of less than 0.1 wt%) is that of the original particles [160].

Koivuluoto et al. [161] obtained similar results when cold spraying copper, nickel, and nickel–30 % copper coatings. SEM analysis of etched coating cross sections showed the particle boundaries, deformation, and microstructure inside the sprayed particles. Coatings seemed to be dense according to the SEM studies. However, corrosion tests showed some through porosity in the cold-sprayed Ni and Ni–30 % Cu coatings. The weak-points were on the particle boundaries where the bonding is not strong and uniform enough between the particles. Zahiri et al. [162] have studied the effects of temperature, pressure, and particle size

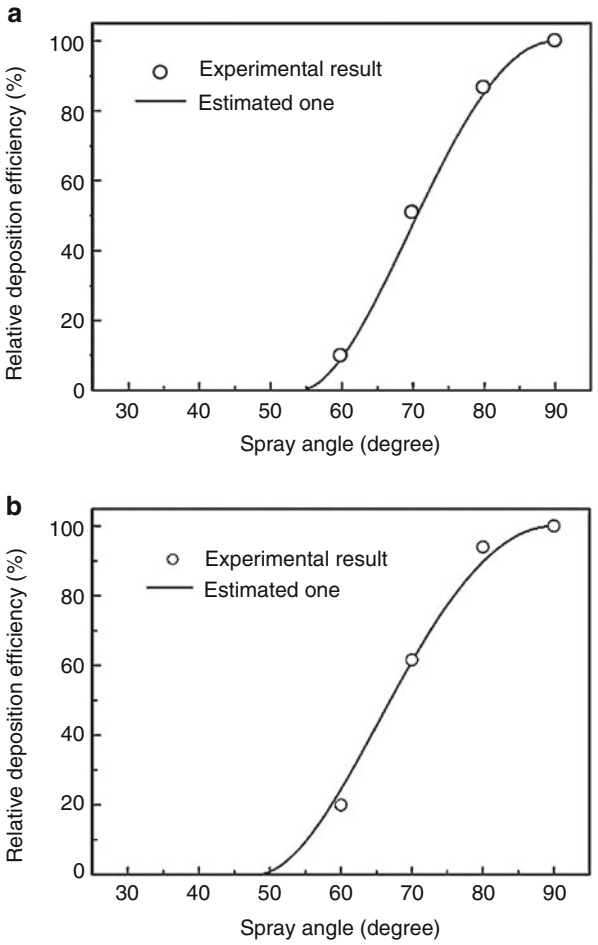


Fig. 13.66 Relative deposition efficiency versus spray angle at different particle velocity distributions obtained under different conditions comparing the measured data with the fitted result, nitrogen preheated at 400 °C pressure, (**a**) 1 MPa; (**b**) 2.6 MPa. Reprinted with kind permission from Springer Science Business Media [158], copyright © ASM International

with respect to porosity formation in cold-sprayed copper particles onto aluminum substrates. It is observed that an increase in spray temperature from 300 to 630 °C results in a decrease in the volume fraction of porosity from 44 to 2.5 μm. Similarly, an increase in temperature leads to a decline in average size of pores. These observations are due to the fact that an increase in spray temperature raises the particle velocity and the particle temperature. Furthermore, Zahiri et al. [162] have presented a schematic representation of the particle size distribution effect on porosity formation in Fig. 13.68. Three powder size distributions are considered:

(a) Powder with a large particle size and a narrow particle size distribution

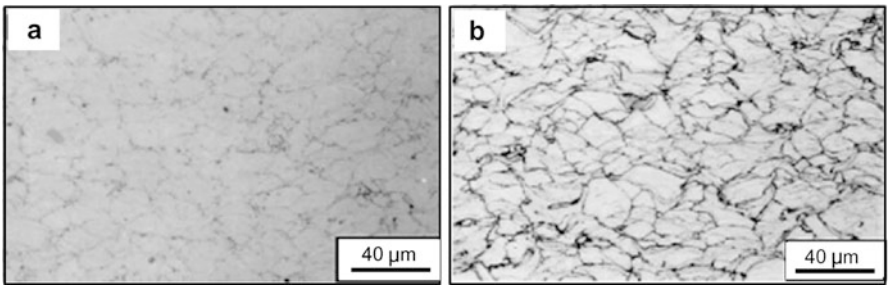


Fig. 13.67 Optical microscopy of the cross section of a cold sprayed Cu coating: (**a**) polished, (**b**) etched. Reprinted with kind permission from Springer Science Business Media [160], copyright © ASM International

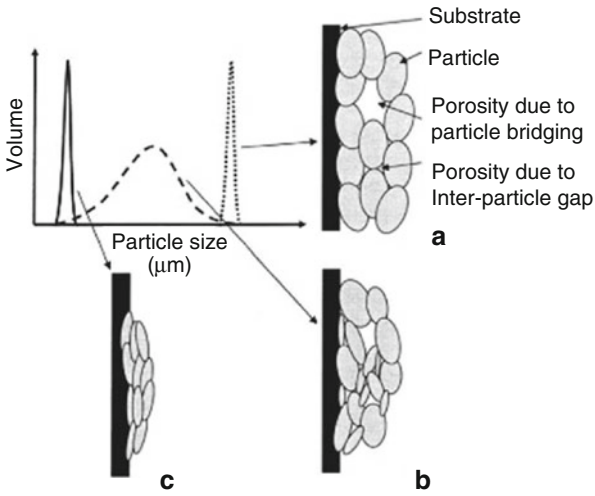


Fig. 13.68 Effect of powder of (**a**) large particle size and a narrow particle size distribution, (**b**) a mixture of small and large particle size with a broad particle size distribution, and (**c**) a small particle size with a narrow particle size distribution on porosity formation in cold spray process. Reprinted with kind permission from Springer Science Business Media [162], copyright © ASM International

(b) Powder with a mixture of small and large particles that represents a broad particle size distribution
(c) Powder with a small particle size and narrow particle size distribution

In the ideal case, (a) large particles achieve lower velocities than the small ones and, if their velocity is above the critical one, a limited plastic deformation (flattening) occurs. Porosities in the microstructure probably develop due to interparticle gaps and bridging of the particles (Fig. 13.68a). At the opposite case (c) small particles achieve the maximum velocity (in the gas stream) required for particles to significantly deform and eliminate voids between particles. This leads to a considerable reduction in porosity and the average pore size (Fig. 13.68c). For a mixture of large and small particles, case (b), small particles acquire enough

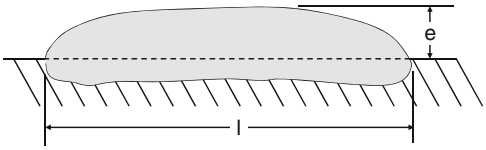


Fig. 13.69 Typical cross section of a PTA bead obtained with the part to be coated as anode. Reprinted with kind permission from Dr. M. Ducos [163]

velocity (kinetic energy) to deform significantly (Fig. 13.68b). However, the large particles (similar to the schematic in Fig. 13.68a) do not considerably deform. This results in a heterogeneous porosity formation with small and large cavities [162].

This short description of coating formation with ductile particles shows that it is quite different from that obtained with thermal spray processes with fully or partially melted particles.

13.6.4 PTA Coatings

As described in Chap. 10, in PTA spraying the substrate is part of the electrical circuit that delivers the power for the coating process, and the molten powder of the coating material is mixed with the molten substrate material. Moreover, compared to other coating processes the torch has also an oscillatory movement limiting the local heat flux and producing flatter beads. Figure 13.69 presents a typical cross section of a PTA bead obtained with the part to be coated as anode [163]. At can be seen the bead is rather flat, which is due both to the flow of molten-sprayed material and the oscillatory movement. The top of the bead presents irregularities [164] linked to the oscillatory movement. According to Ducos [163] the deposition distance and the arc current of the pilot arc have no characteristic influence on the bead shape and deposition efficiency. When the transferred arc current increases, the bead becomes wider, less thick, and the deposition efficiency is raised. The increase of the powder flow rate induces thicker beads and lower deposition efficiencies.

However parameters controlling bead formation also determine the dilution, which increases if the transferred arc current increases, decreases if the powder flow rate is raised or the relative velocity torch–substrate increased.

According to Gatto et al. [165] the quality of the deposition is strongly determined by an optimal reciprocal positioning and movement between the torch and the part to be coated, especially for critical geometries. Thus an accurate design of the process, in particular of the deposit geometry and of the torch tool path is mandatory.

13.6.5 Coatings Obtained by Very Low Pressure Plasma Spray

The very low pressure plasma spray (VLPPS) process has been developed with the aim of depositing uniform and thin coatings with large area coverage by plasma spraying [166]. At typical pressures of 100–200 Pa, the characteristics of the plasma jet change compared to conventional low pressure plasma spraying processes (LPPS or VPS) operating at 5–20 kPa. As described by Gindrat et al. [167] as the ambient pressure is significantly below the exit pressure of the jet (above atmospheric pressure), the plasma jet becomes under-expanded with a hot and dense plume exiting the nozzle. The plasma velocity is almost constant over a large distance from the nozzle exit. Furthermore, at these low pressures the collision frequency is distinctly reduced and the mean free path is strongly increased, the flow being laminar. Enthalpy probe measurements showed that the axial temperature profile of the plasma jet is at higher levels and more uniform compared to conventional spray processes at higher chamber pressures [166]. Depending on the power level of the plasma torch used (between 40 and 160 kW) the injected powder material is either only molten into liquid droplets, or evaporated if the power level is high enough.

13.6.5.1 Dense and Thin Coatings

These coatings are sprayed at pressures in the range of 100–200 Pa with power levels below 60 kW and typical jet dimensions are >1 m in length and >0.2 m in diameter depending on the working parameters. These particular plasma characteristics offer enhanced possibilities to spray thin and dense ceramics. Oxygen ion conducting membrane layers were sprayed using a spray dried $Ba_{0.5}Sr_{0.5}Fe_{0.2}Co_{0.8}O_3$ powder ($d < 45$ µm) with the VLPPS process at 150 Pa working with Ar/N_2/He plasma forming gas mixtures at power levels between 44.7 and 51.2 kW [166]. No hydrogen was used as secondary plasma gas to avoid decomposition due to reduction. The stainless steel substrate was preheated to 500 °C before spraying. The composition of the plasma gas was very important for coating properties, only a small gap existing between sufficient melting of the perovskite particles and the beginning of their decomposition. Moreover sufficient gas-tight coatings have not been successfully obtained for gas separating membrane applications. In contrast, VLPPS-sprayed Mg-spinel ($-25 + 5$ µm) SOFC insulation layers were gas tight and showed adequate electrical resistances at a coating thickness of approximately 40 µm.

Zotov et al. [168] have deposited $La_{0.6}Sr_{0.4}Fe_{0.8}Co_{0.2}O_{3-\delta}$ (LSFC powder spray pyrolyzed) coatings using a pure Ar–He plasma with a power level of 55 kW at a chamber pressure of 200 Pa. Unfortunately, the decomposition of the LSFC powder occurred with loss of oxygen. In addition to the LSFC perovskite, these coatings contained $SrLaFeO_4$, Fe_{3-x} Co_xO_4, CoO, and FeCo phases in different amounts. Coating morphologies were strongly dependent on the Ar–He gas mixture

[168]. With Ar-rich plasma without additional oxygen homogeneous coatings with layered microstructures were formed with porosities decreasing with increasing substrate temperature. In contrast, with He-rich plasma more porous columnar microstructures were obtained. When additional oxygen was pumped into the vacuum chamber and the torch power lowered, coatings contained more than 85 % perovskite phase and only a few percent $Fe_{3-x}Co_xO_4$ and/or CoO. Morphologies of the LSFC coatings obtained with additional oxygen were linked to the substrate temperature, the deposition rate, and the plasma jet velocities. An increase of the plasma jet velocity leads to the formation of homogeneous coatings [168]. These results show that further optimization of the powder injection, the spray parameters, and a better understanding of the growth mechanisms are still necessary to obtain homogeneous gas-tight LSFC coatings, suitable for membrane applications [168].

13.6.5.2 Coatings from Vapor Phase

Hafiz et al. [169] have developed a novel method for generating and depositing nanoparticles to form nanocrystalline films, patterns, and structures. They called it "hypersonic plasma particle deposition." Gas phase products are injected into a reactive thermal plasma that is expanded into a low-pressure chamber via a convergent boron nitride nozzle. The high temperature (~4,000 K) in the injection region of the BN nozzle dissociates the gas-phase reactants (for instance $SiCl_4$ + CH_4 for producing SiC deposits) into their elemental constituents. Then the expansion through the nozzle results in super-saturation of the reactant vapors and consequent nucleation of particles. The substrate is placed 20 mm downstream of the nozzle in the low-pressure chamber (at ~267 Pa versus ~60 kPa in the injection region) [169]. This distance results in hypersonic velocities at impact due to under-expansion of the flow. Short residence times inhibit particle growth, and most particles remain between 10 and 40 nm in diameter. The particles deposited are directly nucleated from gaseous precursors, eliminating the need for powder feeding and producing dense and hard Si–Ti–N films that are inherently nanostructured [169].

The need for better performance from advanced turbine engines requires higher operating efficiencies and longer operating lifetimes. EB-PVD processes operate at low pressures (0.1–5 Pa) [170] and work well but are very expensive. Because of the lower application cost, and a large installed equipment base of the plasma spray process, Sulzer-Metco Co. has developed thermal plasma torches working at pressures as low as 100 Pa to process the coating material [171]. This involves a technique based on a partial or nearly complete evaporation of the feed material. The powder is injected into the plasma torch (two- or fourfold internal powder injection) to produce a coating either from molten particles or from vapor depending on the powder, torch operating conditions and working pressure. This process is called either plasma spraying-physical vapor deposition (PS-PVD) or very low pressure plasma spraying (VLPPS). The PS-PVD technology, with a modified plasma gun, works at reduced ambient pressure (down to 100 Pa) and

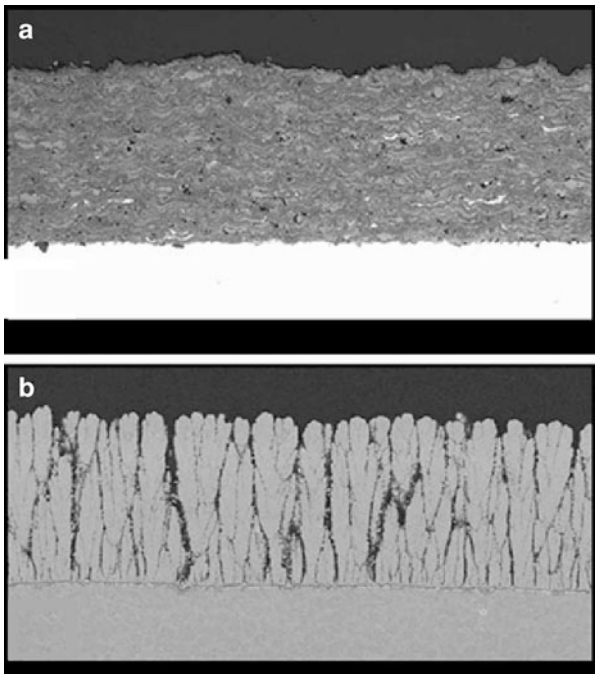


Fig. 13.70 TBC coating of 7 YSZ using different PS-PVD plasma parameters showing (**a**) splat-like structure and (**b**) columnar structure. Reprinted with kind permission from Springer Science Business Media [171], copyright © ASM International

increased power level (total gas flow up to 200 slm and power levels up to 180 kW with 3,000 A). Under such a pressure condition, the plasma jet reaches more than 2 m in length and up to 0.4 m in diameter, as shown in Fig. 7.71c. At this pressure, the plasma jet interaction with the surrounding atmosphere is very weak.

Preheating and cleaning of the substrate can be performed using the plasma or an integrated transferred arc processing to optimize the coating adhesion. Typical substrate temperatures during the spray process can vary between 900 and 1,100 °C depending on the spray conditions and substrate material. In general, a higher substrate temperature is advantageous for the formation of a well-defined columnar microstructure. Depending on the working conditions either splat-like or columnar structures are obtained, as shown in Fig. 13.70. The columnar structure is obtained when using a low powder feed rate, a specific mixture of argon and other plasma gases, a high power level to vaporize the injected particles, and a large spray distance.

Von Niessen and Gindrat [172], using the very low-pressure plasma spraying process (VLPPS), showed that it was possible to produce from the vapor phase coatings with columnar microstructure. The single columns consist of many fine needles with a high defect density and a high amount of internal porosity, as shown in Fig. 13.70. With this morphology, the coatings have proven to be highly strain tolerant during furnace cycling tests and offer a low thermal conductivity. The erosion resistance is lower than that of EB-PVD coatings but at a level of standard APS TBC coatings with 15 % porosity. Moreover this technology offers a high potential to support the development of new non-line-of-sight coating.

Hospach et al. [173] have obtained columnar-structured YSZ layers between 20 and 750 µm. The geometry and arrangement of the sample and the sample holder showed a big influence on the coating quality. The tested columnar-structured TBCs failed after 1,000 cycles, which are fairly close to the already established APS-generated coatings. While this process is promising, a better understanding of phenomena is mandatory to further improve the results. The same authors [174] have shown that this process offers many opportunities to modify the coating microstructure from dense coatings (droplet deposition) to columnar ones. In between exists a quasi-vapor deposition from clusters resulting in columnar coatings with high porosity and growth rate. With the long and wide plasma plume homogeneous coatings are obtained.

Mauer et al. [175] made a careful study of the way coatings were produced with agglomerated 7YSZ ($d_{50} = 8$ µm) and fused and crushed TiO2 ($d_{50} = 13$ µm) particles. To ensure an evaporation of the feedstock, high-power density inside the nozzle in proximity to the location of injection together with well-selected feedstock characteristics are required. Even if the jet excitation temperature can reach values in the range of 8,000–10,000 K, because of its low density no further particle heating is possible. Besides evaporation, the formation of nano-sized clusters is observed. For the coating growth Mauer et al. [175] have used the structure zone model (SZM), initially developed by Thornton [176] for magnetron-sputtered coatings. Different growth mechanisms occurred like shadowing and surface and bulk diffusion. However the vapor deposition of compact columnar structures is only possible if the surface mobility of the "adatoms" is sufficient, an adatom being an atom that lies on a crystal surface, and can be thought of as the opposite of a surface vacancy. High substrate temperatures and low deposition rates are the conditions to obtain vapor deposition. These conditions are defined by the ratio $T_s/T_m > 0.6$ and the area specific impingement rates $\dot{n} = \frac{\dot{N}}{N_A}$, where $\dot{N}$ represents the area specific impingement rate (particles/m^2 s) and N_A the Avogadro number (mol^{-1}). Fig. 13.71 from Mauer et al. [175] present the SZM in the VLPPS process as far as the zones could be identified. The nomenclature of the zones corresponds to the Thornton SZM. By calculating the homologous temperatures and mole rates, experiments with different materials could be considered in the same diagram. The activation energy for surface diffusion was estimated by Mauer et al. [175] to be 141 kJ/mol for YSZ, which is relatively low.

13.6.6 Use of Robot Manipulators

Candel and Gadow [137] have pointed out that microstructural homogeneity, process reproducibility, and precise dimensional tolerances are indispensable requirements in manufacturing of coatings. Net shape and high precision dimensional deposition of coatings are essential for cost efficiency, especially in the case of hard coatings that require machining and finishing. The movement and velocity of the robot-guided torch is of crucial importance for the final properties of the

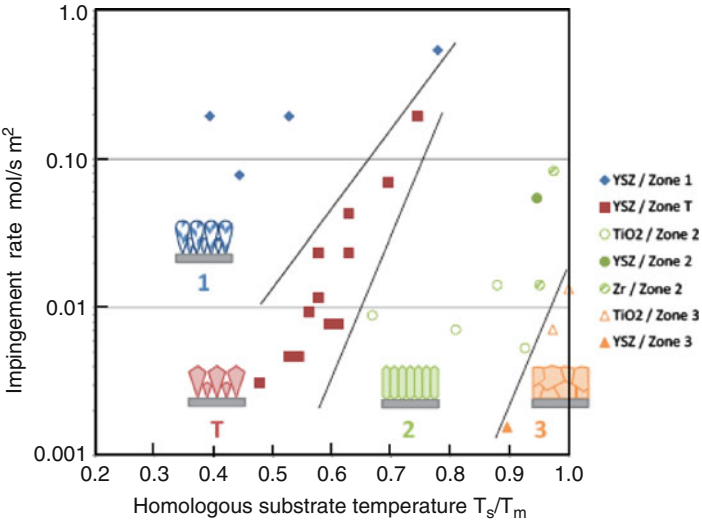


Fig. 13.71 Very low pressure plasma spraying structure zone model: (1) Porous structure consisting of tapered crystallites separated by voids, (T) Transition structure consisting of densely packed fibrous grains. (2) Columnar grains. (3) Recrystallized grain structure. Reprinted with kind permission from ASM International [175]

coating: thickness, roughness, adhesion, porosity, thermal stress distribution, etc. This is especially true for net-shaped coatings on complex 3D geometries. It is thus mandatory to develop software toolkits for the offline generation, simulation, and implementation of movement (position and orientation) of the spray torches [132]. The trajectory generation of the robot, defined through the movement of the tool center point (TCP), is important and time consuming, except maybe on 2D surfaces. As previously mentioned, to achieve a coating thickness as constant as possible and good adhesion of the coating, the relative velocity torch-part must be as constant as possible, velocity defined by the TCP, as well as the overlapping distance of successive beads, and the torch axis must be kept normal to the coating surface. However, such requirements are not necessarily easy to achieve on a curved work piece [177]. The problem may become more complex if, as is often the case in spray processes, the part to be sprayed is disposed on a mechanical unit that provides an external axis of translation or rotation. For example, the rotation of the part can make the robot movement easier to control, if the robot controls it. Two programming methods are possible: online and offline. The first one is easy to operate but difficult for complex parts, while the other can overcome the online programming uncertainties by using the computer-aided design files of the part [178–182]. For example, Hansbo and Nylén [178] using the first method have considered the case when the substrate to be sprayed is rotationally symmetric and rotating during spraying. The angular velocity was then often varied during the process according to the radius of the object, so that the rotational surface velocity

at the object was kept approximately constant, and the robot moved back and forth along a curve in a plane. As shown by the numerical examples given, this method reduced the deviation from the optimum thickness in all cases considered and often gave excellent results with final layer thicknesses close to optimal. However, the method is not fail-safe and they have no mathematical proof of convergence to a local optimum.

The offline programming, used by Fang et al. [177] and Candel and Gadow [180], is focused on the trajectory generation according to the part shape and trajectory optimization depending on the choice of kinematic parameters. This method reduces the difficulty of robot programming and is, therefore, more reliable. For example, the method allows optimizing [180] the robot trajectory when it contains a large change of torch orientation that otherwise would correspond to a reduction of the TCP speed.

With the offline programming technology the local heat load can be considered. Floristán et al. [182], with offline programming, have applied a thermal surface load on the substrate surface to model the heat transfer. The moving hot spot describes the programmed spray path and gives the heat contribution from the plasma and the particles. The velocity torch–substrate is considered in the simulation by the loading times at each node, which are obtained from the robot-programming tool. The heat flux is simulated as a Gaussian distribution on the substrate and it is oriented at each node according to the torch orientation relative to the substrate at that point of the trajectory [182]. Of course this implies measuring first the heat fluxes from hot gases at different positions in the hot jet.

13.6.7 Coating Structure Modeling

Effective physical and mechanical properties of coatings are strongly dependent on the coating microstructure: real contacts between layered splats on the one hand and first splats and substrate on the other, and on pores and also cracks, especially for ceramic coatings. Moreover sprayed coatings present nonperiodic microstructures that make model formulations difficult. Thus a global model taking into account all these phenomena does not exist yet, and according to the complexity of each one of these, it will probably take a rather long time before such a model will be developed. That is why recently a few simplified models have been developed to relate coating microstructure to its effective properties.

Harding et al. [183] were among the firsts to describe the particle flattening based on the available theoretical, numerical, and experimental findings, and they established a set of physically based rules for combining these events to obtain the coating. The model has eliminated unphysical correlations observed in previous models and represents better the YSZ coating microstructure.

Ghafouri-Azar et al. [1] have proposed a sophisticated three-dimensional, stochastic model of a thermal spray coating, predicting coating porosity, thickness, roughness, and the variation of these properties with spray parameters. The model

assigns impact properties to molten droplets landing on the substrate by generating random values of process parameters, assuming that these properties follow normal distributions with user-specified means and standard deviations. Rules are prescribed to calculate splat sizes after droplet impact and their interaction with each other. Porosity is assumed to be solely due to the curl-up of the splats as a result of thermal stresses. They use a Cartesian grid to define the computational domain and to track the shape and position of the deposited coating. The surface of the coating and the location of pores within it are specified using a variable known as the "volume fraction," defined as the fraction of the volume of a computational cell occupied by coating material. Predicted trends agree with experimental observation.

Bobzin et al. [184] have proposed two different numerical approaches to calculate coating porosity:

- A CFD method based on the numerical solution of the governing conservation equations of the particle impact on the solid substrate. With this model, an impact of three particles was analyzed but splashing was neglected.
- The SMP-model calculating the impact and overlaying of discretized splat-discs on the substrate that is a fast tool for predicting the distribution of pore accumulations and the resulting shape of the coating surface.

In another paper Bobzin et al. [185] have applied mathematical homogenization to APS coatings in order to avoid the representation of the whole coating microstructure in FEM simulations and to study the influence of the coating microstructure on its elastic properties.

Sevostianov and Kachanov [186] have focused their paper on micromechanics-based models that explicitly express the elastic and conductive properties of plasma-sprayed ceramic coatings in terms of relevant microstructural parameters. These parameters reflect, in an integral way, the density and the orientation distribution of micro-cracks, and they apply to strongly oblate pores as well. The effect of various "irregularities" of crack shapes is also discussed and finally case studies of YSZ coatings demonstrate how the micromechanics-based modeling can be used and directly interfaced with 2D image data.

These few examples of models illustrate difficulties of the different approaches and how far we are from having a universal and reliable model.

13.7 Temperature Control of Substrate and Coating in Thermal Spraying

13.7.1 Introduction

With thermal spray processes, except of course with cold spray, the substrate and coating under formation receive two different heat fluxes: that from the hot gases and that from hot particles. If the particle injection is radial, both heat fluxes have different axes as illustrated in Fig. 13.72, while they have the same axis with axial powder injection.

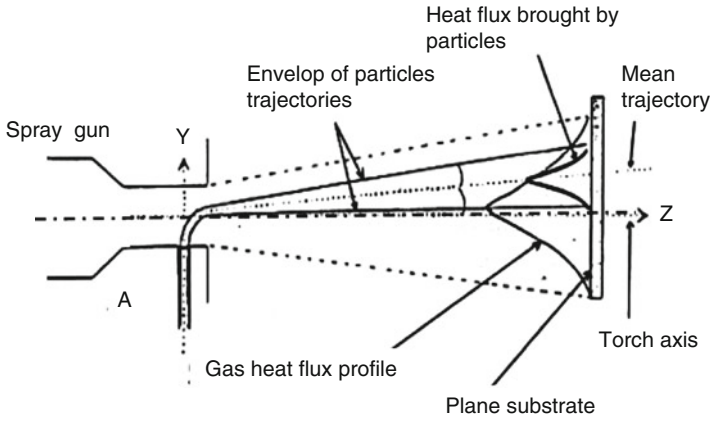


Fig. 13.72 Schematic of heat flux distribution from hot gases and from sprayed particles imposed initially onto the substrate and then onto the coating being deposited, for the case of radial particle injection into the jet

Whatever the spray process may be, the torch is moved, more or less rapidly (up to 1.5–2 m/s), relative to the substrate, and thus heat fluxes are transient, or more precisely cyclic with the beads overlapping, forming passes. The heat flux due to hot gases is almost negligible with wire arc spraying and D-gun spraying (substrate heating, without cooling systems, is in the 100 °C range). However, this it is not the case with flame, HVOF, HVAF, and plasma spraying, systems for which external cooling means are generally mandatory. The PTA process corresponds to another situation where the heat flux must be sufficient to create a molten pool locally (under the plasma transferred arc) where the particles, heated in the arc, are melted.

The temperature of the substrate and the coating being deposited are closely linked to the following parameters: the spray process used, the spray distance (due to the mixing with the surrounding atmosphere the hot gas heat flux decreasing almost exponentially with the increase of the spray distance), thermal properties of the substrate and the sprayed material (heat absorption of the substrate, $m.c_p$ in J/K, is quite different for a 0.5 mm thick substrate than for a 50 mm thick one, with the same other dimensions), relative velocity torch–substrate (the residence time of the torch moved at 1 cm/s is 100 times longer than that of one moved at 1 m/s !), and cooling systems (compressed air blown at the substrate surface is less efficient than a spray of liquid argon, but the cost of the latter is a few orders of magnitude higher).

Temperature monitoring before the spray process during preheating, during the spray process, and afterwards (cooling stage) is a key issue for:

– Coating adhesion: the substrate must be preheated above the transition temperature before performing spraying to get rid of adsorbates and condensates and to improve the coating adhesion and decrease the quantity of splashed material.

As mentioned previously, preheating can be replaced by dry ice blasting in front of the sprayed spot (see Sect. 12.3.7) or by laser treating in front of the sprayed spot (see Sect. 12.8).
- Avoiding temperature gradients within coatings, especially those made of materials of low thermal conductivities, (κ < 30–40 W/m K), particularly to limit or suppress the resulting stress and eventually undesirable phase changes. That implies spraying relatively thin passes (<10 μm) for low κ materials,
- The temperature at which the coating is kept during spraying and then during coating and substrate cooling is very important to tailor the coating residual stress distribution.

If the heat exchanges are considered at the splat level for conventional particles, typical times are in the microsecond time range for the particle flattening and a few microseconds for its cooling, the next splat impacting at the same location about 10 μs later. Of course such measurements, for a better understanding of the thermal spray process, are performed in laboratories but not in spray booths. In industrial spray processes the important temperature which can be measured rather easily with conventional pyrometers, is the time averaged temperature in the tenths of second range, responsible for the residual stress distribution within coating and substrate.

In the following will be presented successively:

- Splat cooling
- Different cooling devices
- Means to control temperature during the spray process

13.7.2 Splat Cooling

Besides the heat flux from the spay torch imposed at the splat location, the thermal history during splat layering is closely linked to the number of splats impacting at the same location during the torch movement (a typical splat diameter is in the range 50–150 μm) [187–191]. This flux depends not only on the powder flow rate, deposition efficiency, and relative torch–substrate velocity but also on the thermal properties of the substrate and the previously deposited layers and the substrate mass and thickness, i.e., the ability to conduct away the heat brought by the solidifying splats and the hot gas heat flux. Under conventional spray conditions, a pass thickness is between 3 and 15 μm, corresponding roughly to about 3–15 layered splats in HVOF or d.c. plasma spraying. Kuroda et al. [187] were the first to propose a method to estimate this time temperature history. The simplified transient 1D model of Leger et al. [191] predicts the cooling of layered splats, assuming that (1) solidification occurs at the melting temperature, (2) the contact splat–substrate and splat-previously deposited layers are characterized by thermal contact resistances, (3) a time t_i exists between successive impacts, and (4) different heat fluxes for the hot gases are imposed. This model shows that splat cooling is mainly due,

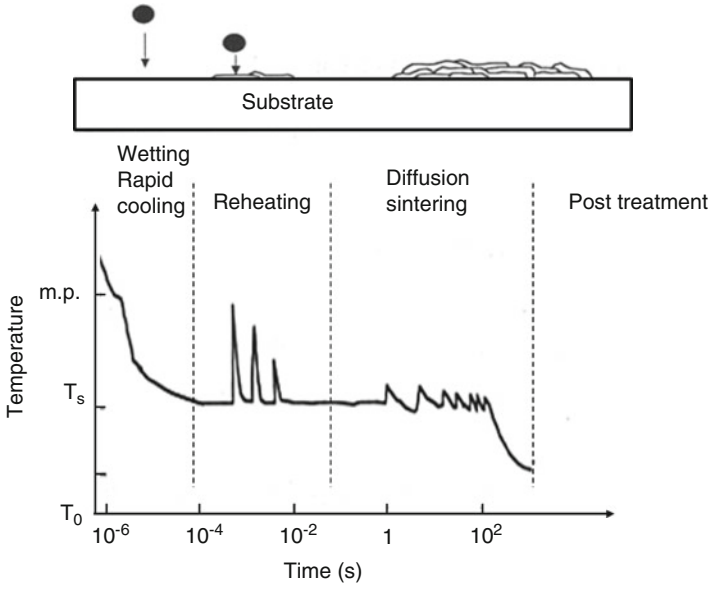


Fig. 13.73 Temperature time history (1D transient model) of the bottom of the first alumina splat deposited on a low carbon steel XC38 substrate, 5 mm thick. The temperature of the impacting particle is 3,000 K, resulting splat thickness 1 μm, time between each splat 15 μs, four splats layered in a sequence and 1.1×10^{-3} s between each torch passage. Reprinted with kind permission from ASM International [191]

about 95 %, to heat conduction toward the substrate or previously layered splats. Convective cooling by the cold gases close to the substrate when the torch is moved to another position and radiation from the cooling splats at the coating surface also contributes, by about 5 %, to the cooling of the layered splats. When the thermal conductivity of the sprayed coating is higher than 50 W/m K, the gas cooling is more efficient (up to 15 %) than for lower thermal conductivity materials. For example, Fig. 13.73 presents the impacts of alumina particles at 3,000 K, forming splats 1 μm thick and 120 μm in diameter on low carbon steel XC38. The thermal contact resistance splat–substrate and splat–splat is assumed to be 5×10^{-7} m^2 K/W, and the time between two successive splats impacting at the same location is 15 μs. During splat layering the heat flux brought by the plasma jet is 2 MW/m^2. Once 4 splats are layered the torch comes back to the same location 1.1×10^{-3} s later. The temperature time history presented in Fig. 13.73 is that of the bottom surface of the first splat. When the first splat is formed it cools down very fast, the melting temperature being reached in about 1.1 μs, then it takes around 10 μs to cool down to the substrate preheating temperature of 700 K. When the next splat arrives 15 μs later it reheats the first splat to almost the alumina melting temperature, the solidified first splat insulating partially its bottom surface. The next impacting splats reheat less and less the bottom surface of the first one. Of course, the successively layered four splats (1.1×10^{-3} s between each passages of the torch) reheat very

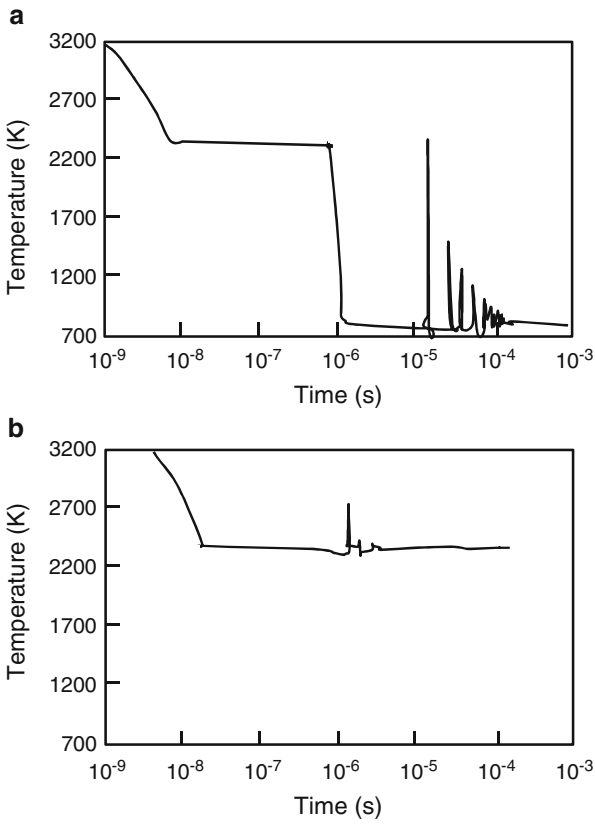


Fig. 13.74 Temperature time history (1D transient model) of the bottom of the first alumina splat 1 μm thick formed by particles impacting at 3,200 K on a low carbon steel XC38 substrate. (**a**) 3 splats layered in one pass. (**b**) 180 splats layered on the previously deposited alumina layer also 180 μm thick. Reprinted with kind permission from ASM International [191]

little the first splat, due to the thicker and thicker layered splats insulating more and more the bottom surface of the first one.

In Fig. 13.74a almost the same result is presented as in the previous figure, except that the initial temperature of the impacting particle is 3,200 K, the torch is moved at 1 m/s , and only 3 splats are layered during one passage on the substrate, preheated to 720 K. The time between two successive passages of the torch is identical to the previous one. As can be seen in Fig. 13.74a each splat has plenty of time to cool down between the reheating by the next impacting particle. However the story is quite different when the velocity torch–substrate is drastically reduced (by a factor of 60) to layer 180 splats per pass. Once the first pass is deposited, the next one, 2 min later, impacts on a thick insulating material, which has still a surface temperature of 2,000 K. Thus, according to the rather low thermal conductivity of the first alumina layer and its high surface temperature, the successive splats of the second pass are kept in a molten state, as shown in Fig. 13.74b.

Of course this case is far from those used in most spray protocols, even if it allows achieving ceramic coatings with vertical cracks from bottom to top, thus presenting an excellent compliance. Such calculations also show the necessity to spray thin

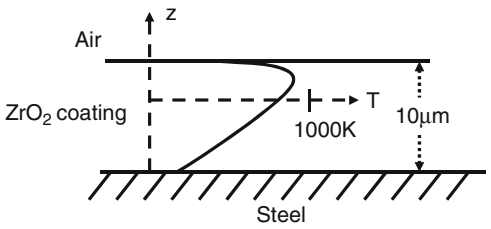


Fig. 13.75 Temperature gradient within a zirconia pass 10 µm thick sprayed on a stainless steel substrate (1D transient model)

passes (<10 µm) of materials with low thermal conductivity (<30–40 W/m K). For a very low thermal conductivity material such as zirconia (about 1 W/m K) a 10 µm thick pass creates already a temperature gradient of about 70 K/µm, as shown in Fig. 13.75. To conclude, the lower the thermal conductivity of the sprayed material is, the thinner the pass must be to limit temperature gradients.

The temperature problem within the successive passes is even worse with thermal conductivities in the range of a few tenths of µm, such as those of polymers.

13.7.3 Cooling Methods

13.7.3.1 Heat Fluxes Contributing to Substrate and Coating Heating

Particle cooling, as described in the previous section, occurs mainly through the substrate and the previously deposited layers. The hot gas heat flux hitting the surface of the substrate during preheating, and then the coating during its formation, contribute to its heating, and cooling gas jets are mainly used to reduce the coating surface temperature. When considering the different spray processes, the following considerations apply to the heat flux imposed onto the substrate and coating:

- The highest heat flux is obtained with suspension and solution plasma spraying where spray distances are in the 30–40 mm for rod type cathode plasma spray torches, and about the same for the tri-cathode Triplex Pro torch (with fluxes slightly higher than for the former), and 60–80 mm for the Axial III torch of Mettech Inc. Heat fluxes under such conditions can be as high as 40–50 MW/m^2.
- When spraying micrometer-sized particles with these torches, spray distances are between 80 and 150 mm and heat fluxes are in the 4–2 MW/m^2 range.
- With HVOF spraying of micrometer-sized particles, heat fluxes at substrate position that have been reported are similar to or smaller than those of plasma torches.
- For flame spraying, heat fluxes are below 1 MW/m^2, lower values being attained when accelerating particles or when atomizing wires with compressed air jets.
- With wire arc spraying the heat flux is below 0.1 MW/m^2.

Of course, to this gas heat flux must be added that of hot-sprayed particles. The maximum heat flux transported by particles depends strongly on the pass thickness

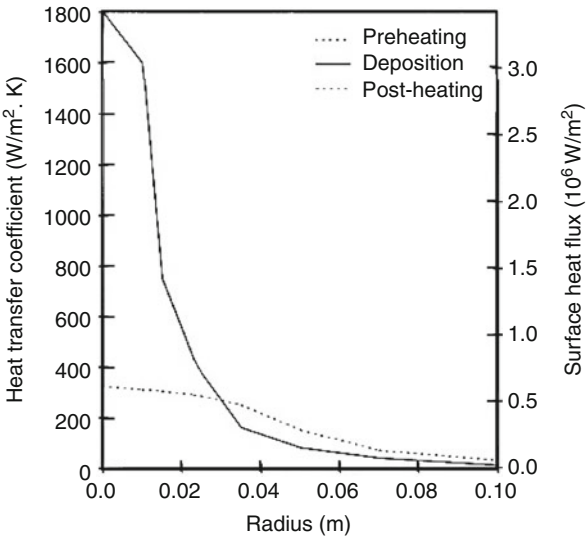


Fig. 13.76 Heat transfer coefficients and heat fluxes over the distance from the axis of the HVOF gun during preheating, deposition and postheating (JP-5,000, Tafa Inc., inside gun diameter 11 mm, kerosene 19.5 l/h, oxygen 893 l/min, spray distance 380 mm, sprayed material: WC–Co 8.5 kg/h). Reprinted with kind permission from Elsevier [193]

and the sprayed material. With d.c. plasma jets and radial injection both heat flux peaks have different locations, as illustrated in Fig. 13.72. Gas heat fluxes have roughly a Gaussian shape, at least for d.c. plasma [188] or HVOF jets [193]. This is illustrated in Fig. 13.76 for a JP5000 HVOF gun working with kerosene and oxygen. The spray distance, as pointed out above, is very important. Hackett and Settles [194] have shown that after a 4 s exposure to the JP5000 flame at a 270 mm spray distance, the temperature increase of the substrate is already 400 °C, against 100 °C at 350 mm. The coating temperature plays a key role in the coating oxidation (at least for metals, alloys, cermets, and non-oxide ceramics). For example, when spraying aluminum particles, the oxygen content of the coating was about 0.23 wt% if the substrate temperature rise was only 100 °C, against 0.4 wt% for a rise to 400 °C [194]. Similar results were obtained by modeling [195].

The heat flux decreases almost exponentially with the spray distance. With the jet expansion in the surrounding atmosphere, both the jet velocity and temperature decrease very rapidly, as shown, for example, for plasma jets [196, 197]. An illustration of the maximum heat flux dependence on the spay distance is presented in Fig. 13.77 for an Ar–H_2 plasma jet working with 4 different power levels. If at 80 mm the heat fluxes can be above 4 MW/m^2, they are around 2 MW/m^2 or less at 100 mm. This explains why, in spite of the fact that the maximum particle velocities and temperatures are obtained around 60–80 mm, spray distances are often preferred between 100 and 120 mm where the heat flux control is easier. It must be noted that the presence of the substrate intercepting the hot gas jet increases the gas temperature close to the surface by a few hundred degree Celsius [198].

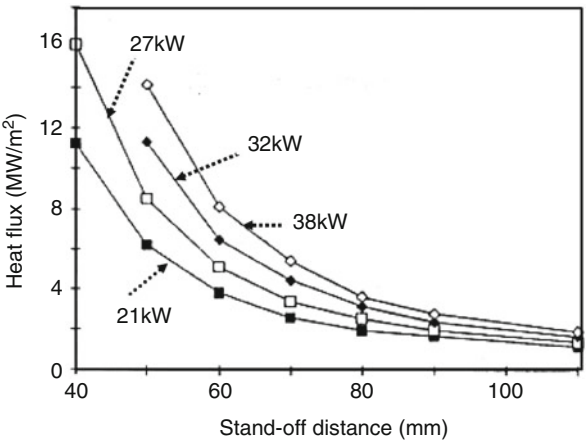


Fig. 13.77 Dependence on the spray distance of the maximum heat flux imposed by a d.c. plasma jet flowing in air at atmospheric pressure (Ar 45 slm–H_2 15 slm, nozzle internal diameter 7 mm) for four power levels. Reprinted with the kind permission from Dr. F. Monerie-Moulin [192]

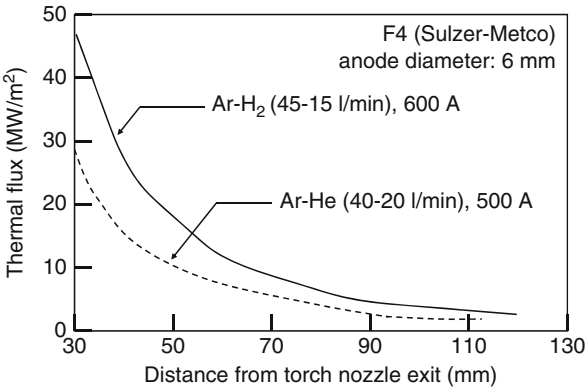


Fig. 13.78 Heat flux evolution along the axis of a rod type cathode torch (PTF4 torch of Sulzer-Metco) when spraying suspensions or solutions: torch anode nozzle internal diameter 6 mm, Ar 45 slm, H_2 15 slm, 600 A, 72 V (*red curve*) and Ar40 slm, He20 slm, 600 A (*green curve*) [199]. Reprinted with kind permission from Dr. E. Brousse

Heat fluxes become higher, as shown in Fig. 13.78 [199], and thus much more difficult to control, with suspension or solution plasma spraying where spray distances are between 30 and 50 mm for a rod type cathode torch. Such heat fluxes also strongly modify the coating microstructures. Of course these fluxes also depend on the plasma forming gases used and, according to the lower voltage and thermal conductivity of Ar–He mixtures, heat fluxes can be half of those obtained with Ar–H_2 with the same plasma torch working with the same arc current [200].

The spray pattern and the torch/substrate velocity play also a key role in the hot gas and particle heat transfer. Thus, according to Floristán et al. [182], robot trajectory planning should integrate not only an accurate definition and control of process kinematics but also an optimal thermal guidance during deposition. The planning of robot trajectories should consequently integrate the analysis of heat and mass transfer during deposition.

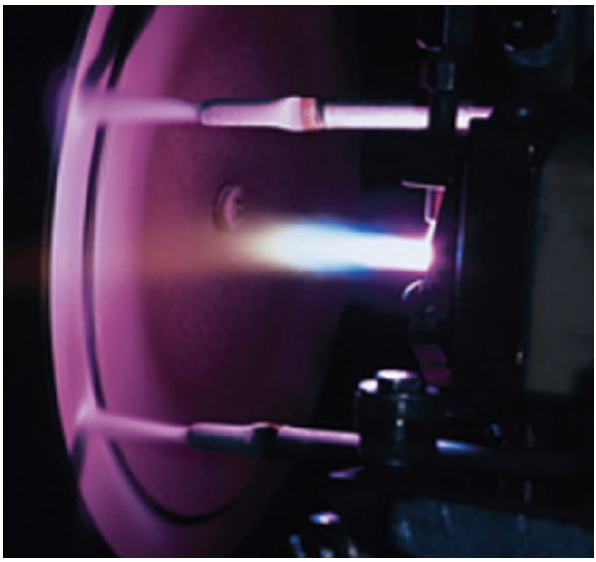


Fig. 13.79 Typical cooling nozzles fixed on the spray torch and moving with it, after LINSPRAY. Courtesy of Linde Company [201]

13.7.3.2 Cooling Methods

To monitor the surface temperature of the substrate and then that of the coating during deposition, different means can be used: compressed air jets, CO_2 ice/snow, liquid nitrogen, and liquid argon. Whatever the cooling device may be, the most common design of the cooling system is that represented in Fig. 13.79 with two nozzles fixed on the spray torch and moved with it.

– With air jets, the cooling is purely convective and depends strongly on the air velocity controlled by the air flow rate, the cooling air nozzle internal diameter, and the distance nozzle part that must be rather short to avoid the air jet expansion. Besides the typical cooling nozzles presented in Fig. 13.79, air-cooling setups as those presented in Fig. 13.80 can be used. They comprise a nozzle, called R in Fig. 13.80 fixed or not to the torch with a slot shape (typically 0.8 mm in width and 30–40 mm in length), and another slot, called wind jet, noted B in Fig. 13.80, intercepting the hot gas and particle jet about 20 mm before the substrate. Wind jets, to the best of our knowledge, have been used essentially with plasma spraying and, as explained in the next section, their main role is not only cooling but also to eliminate particles poorly heated while traveling in the plasma jet periphery.
– With the ice/snow or liquid nitrogen or liquid argon the latent heat of vaporization and lower temperatures contribute much to the cooling. The main properties of these species are summarized in Table 13.6.

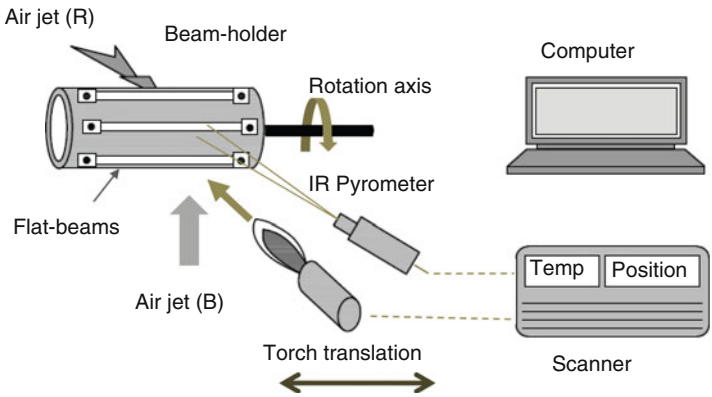


Fig. 13.80 Example of cooling nozzles with a slot shape, R: nozzle attached to the spray torch and cooling the deposited pass, B: nozzle, attached to the spray torch, intercepting jets of hot gases and particles in front of the substrate (about 20 mm), called wind jet

Table 13.6 Thermal properties of gases used to cool coatings with liquid or frozen gases

Gas	Freezing temperature (°C)	Evaporation or sublimation temperature (°C)	Vaporization enthalpy (kJ/kg)	Specific heat (J/kg K)
Argon	−210	−196	198	1,036
Nitrogen	−189	−185	160	520
CO2	−56	−78	307	

- Cooling systems with liquefied gases consist of a high-pressure tank containing the liquid, withdrawal valves, safety valves, a pressure gauge, a high-pressure hose with a good thermal insulation, valves, filters, atomization nozzle, nozzle holders, and a control panel.
- Carbon dioxide has no liquid state at pressures below 0.51 MPa. Depending on its size the tank is kept at a pressure either of 1.8 or 5.6 MPa. At 0.1 MPa, the gas condenses directly as a solid at temperatures below −78 °C and the solid sublimes directly to a gas above −78 °C. In its solid state, carbon dioxide is commonly called dry ice. It is generally made of pellets in the few mm size range (typically a diameter of 3 mm for a length of 5–15 mm), which sublimes at contact with the part. Depending on the atomization nozzle the quantities of CO_2 vary between 0.165 and 1.200 kg/min. It takes about 0.2 kg of dry ice per kg of metal to reduce the temperature by 98 °C [201].
- With atomized liquid nitrogen 0.5–1 L of liquid nitrogen is needed per kg of metal to reduce the temperature from +20 °C to –196 °C ($\Delta T = 216$ °C) [201, 202].
- Liquid argon is used only when spraying in argon-controlled atmosphere to spray refractory materials prone to decompose or react, such as TiB_2, for example.

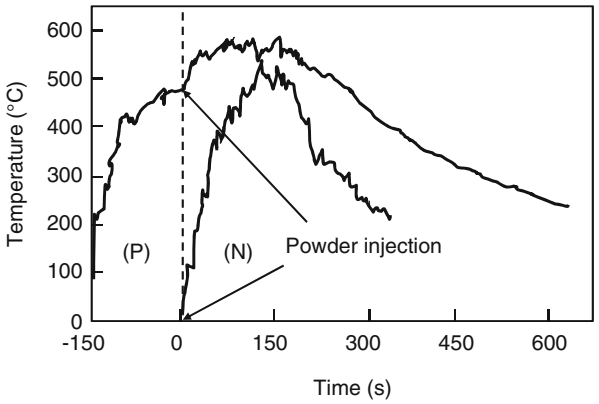


Fig. 13.81 Time evolution of the surface temperature of substrate and alumina coating (fused and crushed particles 22–44 μm) during: preheating, spraying and cooling (curve P), spraying and cooling (curve N). PTF4 type plasma torch, nozzle i.d. 7 mm, Ar 45 slm, H_2 15 slm, 35 kW, coating thickness 300 μm[204]. Reprinted with the kind permission from Dr. A. Haddadi

13.7.4 Coating Mean Temperature Control

The main role of the cooling devices is to keep the coating temperature as constant as possible during spraying, and to avoid temperature gradients, especially when the sprayed material thermal conductivity is low ($\kappa < 30$–40 W/m K) [203, 204]. This is illustrated in Fig. 13.81 showing (a) the surface temperature dependence (curve P) of the substrate during 150 s of preheating with the plasma torch (without powder), and then of the alumina coating during 200 s of spraying with air cooling nozzles, followed by coating and substrate natural cooling for 400 s and (b) the same dependencies but without preheating and no air cooling.

Without preheating and cooling during spraying, the temperature gradient within the alumina coating ($\kappa \approx 18$ W/m K) is about 1,600 °C/mm! After preheating the substrate with the plasma torch and the cooling air jets, the preheating temperature is increased by about 100 °C when the coating process starts, but equilibrium is reached in less than 30 s and then the surface temperature of the coating being deposited remains almost constant. Of course, for controlling such temperature dependencies with alumina, the pass thickness must be below 10 μm.

With a wind jet, facing the plasma jet and fixed on the plasma torch, situated 20 mm in front of the substrate, with spray distances of either 80 or 100 mm, the heat flux on the substrate depends on the air flow rate within the jet as shown in Fig. 13.82. With an airflow rate of 20 m^3/h, the heat flux is reduced by a factor of 5 to 6.

However the main interest in the wind jet is not the cooling effect, but the possibility to get rid of unmelted particles traveling in the plasma jet fringes. Unfortunately, also some fully melted small particles are removed. The wind jet principle is shown in Fig. 2.31. The particles removed from the jet have lower momentums than the other ones because of their lower velocity (those traveling in the jet fringes) or their smaller size. Moreover, the wind jet reduces the velocity of

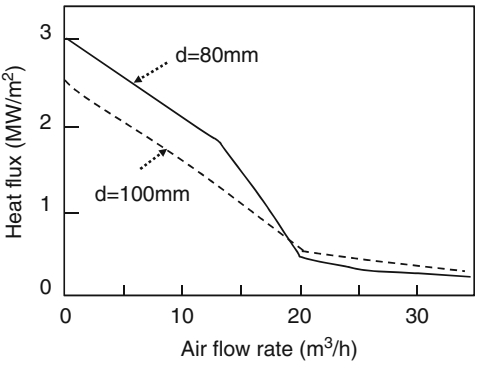


Fig. 13.82 Dependence of the maximum axial heat fluxes of the d.c. plasma jet (characteristics given in Fig. 13.66 caption) on the cooling air flow rate at 80 and 100 mm standoff distances. Wind jet, moved with the torch and fixed to be 20 mm in front of the substrate, is 40 mm in length and 0.8 mm in width [192]. Reprinted with the kind permission from Dr. F. Monerie-Moulin

the particles crossing the jet by about 20–30 m/s and the temperature by about 200–300 °C [97, 205]. In spite of these drawbacks, the use of wind jets presents some advantages as illustrated below. Renouard-Vallet [205] pursued spraying of yttria (13 wt%)-stabilized zirconia (YSZ) particles (fused and crushed with a size distribution between 5 and 22 μm) using a vacuum plasma spray process (VPS) to produce about 50 μm thick and dense electrolyte layers for SOFCs. A PTF4 torch, equipped with a Laval nozzle, was used working with an Ar–H_2 mixture (40 slm–6 slm), an arc current of 750 A in a soft vacuum chamber where the pressure was kept at 8 kPa. The in-flight particle temperature distribution (measured with a DPV 2000, see Chap. 16, focused at the substrate location on the particle jet axis) is presented Fig. 16.22a. Coatings were also kept at 550 °C during spraying (with the help of cryogenic cooling), and cross sections are presented in Fig. 13.83a. The porosity was 10.9 % (measured by image analysis of the cross sections), and the ionic conductivity was 1.9×10^{-2} S/m (that of sintered YSZ being 1 S/m). Such a low ionic conductivity corresponds to rather poor contacts between layered splats. To get rid of unmelted particles, a wind jet has been used, blowing argon orthogonally to the particle jet 3 cm in front of the substrate. The corresponding particle temperature distribution is shown in Fig. 16.22b. Compared to the temperature distributions without wind jet (Fig. 16.22a), the distribution with wind jets is much narrower, with values between about 2,200 and 2,950 °C, and the mean value is slightly higher. According to particle velocities (see Sects. 16.3.3 and 16.3.4) the wind jet has removed both the high velocity tiny hot particles and the low velocity bigger cold particles. The hot particles with an intermediate size were slightly slowed down (less than 20 m/s). Splats collected are now rather close to disk shapes with a mean diameter of 30 μm, a mean thickness of 1.5 μm (against 4 μm without wind jet) corresponding to a flattening degree of 4. The coating obtained with the wind jet (also kept at 550 °C during spraying) is presented in Fig. 13.83b. Compared to that without wind jet (Fig. 13.83a) it is denser with 6.1 % porosity, and its ionic conductivity was 5×10^{-1} S/m corresponding to a much better contact between layered splats.

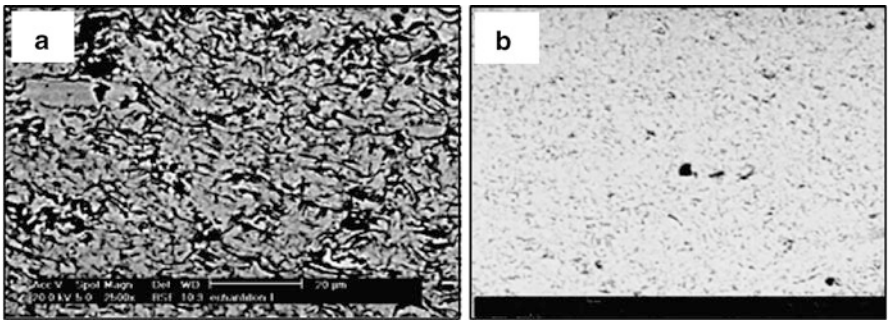


Fig. 13.83 Coatings obtained with the spray conditions of Fig. 16.23. (**a**) Spraying performed without wind jet. (**b**) With wind jet. Reprinted with kind permission from Springer Science Business Media [13], copyright © ASM International

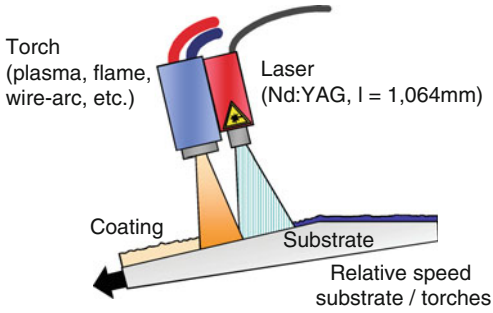


Fig. 13.84 Principle of the substrate preheating with a laser focused just in front of the sprayed spot [207], Reprinted with kind permission from Springer Science Business Media, copyright © ASM International

At last it must be recalled that preheating the substrate to get rid of adsorbates and condensates can be performed with a laser, attached to the torch and irradiating the substrate surface in advance of the sprayed spot [206, 207], as illustrated in Fig. 13.84 [207]. For more details see Sect. 12.8.2.

13.8 Influence of Powder Manufacturing Process on Coating Properties

13.8.1 Chemical Reactions

Except in cold spraying, in which case particle surface temperatures do not exceed a few hundred degrees Celsius, particles react with their surrounding atmosphere, especially air where most spray processes take place. Those reactions are mostly controlled by diffusion [208] or convection [209] (see sect. 4.3.3.7a and c). Convection occurs in plasma, HVOF, and wire arc spraying under certain

conditions. This phenomenon can increase drastically the reaction rate (by up to a factor of 5) compared to pure diffusion. According to the Arrhenius law, the reaction kinetics increases drastically with temperature (about one order of magnitude for a temperature increase of 100–200 °C). Thus, for example, oxidation is rather high in plasma spraying, where particles are often superheated, and decreases in HVOF spraying, especially with high power torches (working with kerosene) or in HVAF where particle temperatures are rather low (close to or below the melting point), and velocities are above 500 m/s.

It is also possible to use basic reactants in the solid phase either as agglomerated or clad particles [210, 211]. Heating of the particle by warm gases triggers (like a match) the self-propagation high-temperature synthesis (SHS). For more details see Sect. 4.3.3.7b.

For cermets containing carbides or nitrides the main phenomena that occur during thermal spray processes and that influence the coating performance are the oxidation and high-temperature decomposition of the non-oxide ceramic. For example with WC–Co, the decomposition of tungsten carbide (WC) gives rise to the formation of di-tungsten carbide (W_2C) as well as a high concentration of metallic tungsten (W) dissolved in the binder phase. These phenomena are promoted when the particle temperature increases above its melting temperature. For example, when comparing the same WC–12 wt% Co powder sprayed by high-velocity oxy-fuel (HVOF) and high-velocity air fuel (HVAF) processes, a substantial amount of W_2C was identified in the HVOF coatings, as well as a high concentration of tungsten in the binder phase [212]. This indicates that oxidation and dissolution processes change the composition and microstructure from powder to coating during spraying. In contrast with HVAF spraying, where particle temperatures are lower and velocities higher, composition and microstructure of coatings were unchanged from that of the powder. Additionally, the wear resistance of the HVAF coatings was superior to that of the HVOF coatings. It has also been shown that WC–17 wt% Co coatings were not primarily influenced by variations in the spray parameters, but were more dependent on the powder composition, WC particle size range, and manufacturing route [213]. Coatings manufactured with sintered and crushed powder delivered a more consistent and a lower wear rate than the agglomerated and densified powder type, but this effect was possibly related more to the WC grain size (respectively, 1 and 2.6 μm) than to the manufacturing route. De Villiers Lovelock [214] has presented a review of the work performed before 1998 on the phase changes that occur during spraying WC–12 wt% Co and WC–17 wt% Co coatings, and differences obtained when using cast and crushed, sintered and crushed, and agglomerated and densified powder types. Similar research was performed on the influence of composition and microstructure of agglomerated and sintered (AS) WC–VC–Co powders, on coatings sprayed by HVOF [215]. When HVOF spraying WC–Co (6 wt%, instead of the conventional 17 wt%) spray dried and cobalt clad particles (11 wt%) [216], the wear resistance (using a Tabor abrasive test to characterize fretting resistance) of the coating was close to that obtained with hard chromium.

Spraying metal particles in controlled atmosphere containing hydrocarbons or nitrogen produce many other species such as carbides or nitrides: TiC + Ti, SiC + Si, W + W_xC_y, Mo + MoC_2, NiCr/Ti + TiC + Cr_xC_y, FeCrAlY + Cr_xFe_y + Fe_xC_y, Mo + $MoSi_2$, Ti + TiB_2, etc. [217–224]. Of course the reaction must occur in solid or liquid phase and not in gas phase such as that producing AlN.

13.8.2 Particle Morphology

As already emphasized in Chap. 11, the powder morphology has a great influence on coating properties, especially for ceramics and cermets [225]. Most ceramic particles are either fused and crushed (FC) or agglomerated by spray drying (AS) and then sintered (resulting in spherical and sometimes hollow spheres [HOSP]). For example, Streibl et al. [85] have studied with different sensors the temperatures and velocities of YSZ particles sprayed with a 3 MB plasma torch (Sulzer-Metco, Wohlen, Switzerland) working with a plasma gas mixture of nitrogen and hydrogen. The particles used were commercial HOSP, FC, and AS, all of them with about the same average diameter (d_{50} of the particle size distribution) and the carrier gas was optimized for each type of them. In-flight measurements have shown that the HOSP particles were indeed the easiest to melt compared to the others. This better heating is due to the lower mass of HOSP particles (the specific mass of such particles can be below 1,000 kg/m3) compared to that of the other types of particles (AS and FC), the particle surface and the heat transfer coefficient from the warm gases being the same. Measurements of thermal conductivities κ_i [226] of corresponding coatings showed that, in the 200–1,200 °C temperature range, $\kappa_{HSOP} < \kappa_{AS} < \kappa_{FC}$ pointing out the important role of inter-lamellar delamination. HOSP particles result in thinner lamellae and consequently a larger fraction of inter-lamellar delamination. Bertrand et al. [227] have compared also YSZ HOSP with an extremely low-specific mass (390 kg/m^3 to be compared to 2,000 kg/m3 for the commercial HOSP particles and to 5,900 kg/m^3 for FC particles). A decrease in 30 % of as-sprayed apparent κ was obtained, as compared to a standard value, when spraying them under optimized spray conditions. Wang and Shaw [228] have studied three Al_2O_3–TiO_2 powders with the same chemical composition, but different Al_2O_3–TiO_2 distribution patterns due to different manufacturing methods (spray drying, FC, and plasma fused) on coating properties. The powder manufacturing method changes the degree of the initial mixing of the alumina and titania particles. This is particularly important for the degree of melting of the particles, the thermal conductivity of the resulting mixture being increased with the better mixing of alumina and titania. It also affects the coating microstructure. TiO_2 lamellae and TiO_2-rich γ-Al_2O_3 regions can be eliminated if the sprayed powder is a mixture of both elements mixed at the sub-micrometer level.

The second case considered deals with thermally sprayed coatings manufactured with micrometer-sized composite particles: as problems linked to carbide-metal composites have been already discussed in Sect. 11.1.3.3, only one example of

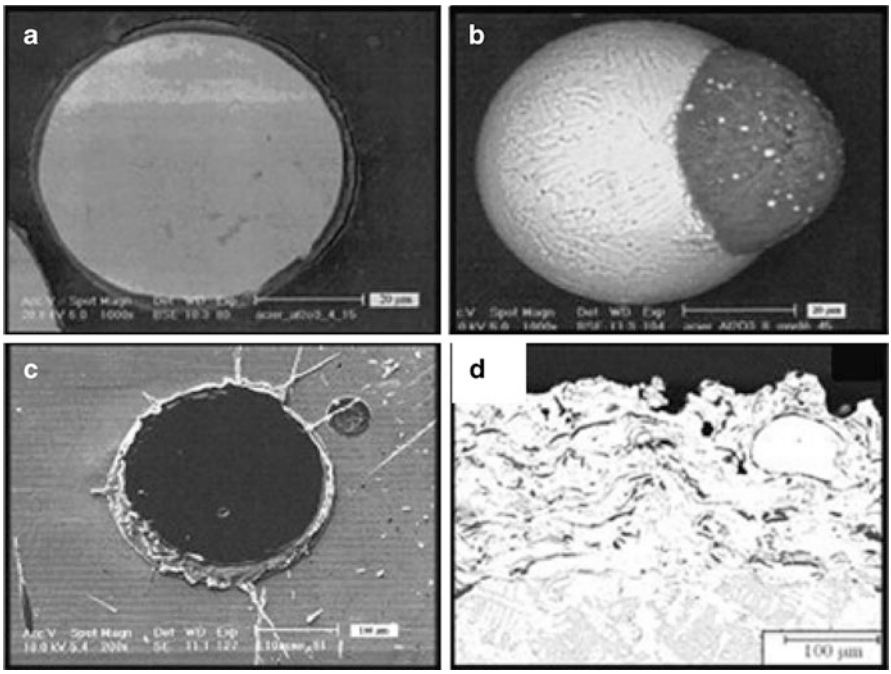


Fig. 13.85 Mechanofused alumina–stainless-steel coatings, (**a**) particle cross section, (**b**) particle collected after its flight in an Ar–H2 plasma jet, (**c**) lamellae collected on a smooth substrate (alumina in black color and stainless-steel in gray color), (**d**) coating cross section with 6 wt% alumina [231]. Reprinted with the kind permission from Dr Cuenca Alvarez

a metal-oxide cermet will be described here. A typical mechanofused alumina–steel particle is presented in Fig. 13.85a [229–231]. The starting 316L stainless-steel particles with an average diameter of 56 µm are coated with a 2–4 µm thick layer of pure α-alumina (99.99 %) particles of 0.6 µm average diameter. Upon spraying, both materials are fully melted, and the lighter alumina at the steel core is entrained by the flow either before or behind the steel particle depending on its mass. The result is a steel sphere with an alumina cap, as shown in Fig. 13.85b. For particles below about 60 µm, the steel hits the substrate first and two lamellae are formed: a stainless steel one on which an alumina one is deposited, as shown in Fig. 13.85c. Finally, the coating is made of layered steel and alumina lamellae as shown in Fig. 13.85d. Compared to a pure stainless-steel substrate sprayed under the same conditions, the hardness of the alumina–stainless-steel coating is 620 ± 30 HV5N against 660 ± 20 HV5N. To underline the effect of in-flight particle oxidation, the hardness of the bulk identical cast steel is only 450 ± 15 HV5N.

The third case considered deals with cold gas-sprayed coatings manufactured with micrometer-sized particles. The influence of various parameters (particle diameter, specific mass, material specific heat, etc.) on the critical velocity and deposition efficiency were studied systematically [65, 160, 232–238].

The deposition efficiency increases with the particle temperature at impact for the same velocity (temperature increase implies Young's modulus reduction over values depending on materials). The critical velocity diminishes with increasing process gas temperature. It can be seen that increasing the particle temperature by 530 °C increases the Ni deposition efficiency by about 13 % for the different velocities considered [239]. Particle oxidation is also very important as shown by Kang et al. [240]. The corresponding critical velocity for deposition of aluminum particles with different oxidation stages (varying the oxygen content from close to 0 to 0.04 wt%) on aluminum substrates varied from 750 m/s to more than 850 m/s. At last, as for hot spray processes, the particle morphology plays a key role in deposition efficiency and coating properties. For example Seo et al. [241] have shown that coatings sprayed with spherical copper particles showed superior thermal conductive characteristics than coatings sprayed with nonspherical particles. They attributed this result to the irregular morphology of powders, resulting in higher coating porosities (7–10 %) in the as-sprayed state compared to coatings deposited with spherical powders. The irregular particles seem to create many interfacial voids between splats inside coatings. Ning et al. [242], spraying Cu particles with spherical and irregular morphologies with a low pressure Dymet 420 process found that the powder morphology could significantly affect the in-flight particle velocity. The powder with irregular morphology had a higher in-flight particle velocity than that with spherical morphology of same size.

13.8.3 Nanostructured Agglomerated Particles

The problem related to thermally sprayed coatings, manufactured from micrometer-sized agglomerates of nanometer-sized ceramic particles, to produce coatings with bimodal structures (nanometer-sized grains imbedded in micrometer-sized ones) is discussed in Sect. 14.3. In the following the fact will be illustrated, through two examples, that the final coating structure depends both on the spray process and the manufacturing method of particles.

The first example is related to WC–Co particles with nanometer-sized WC sprayed by HVOF [243–245] or plasma [246]. The extent of decarburization observed is larger (because of the higher specific surface of the particles) than that in the micro-sized WC coating material. However when using a grain-growth inhibitor the amount of the non-WC/Co phases was greatly reduced within the coatings, influencing strongly the microstructure and other properties of coatings. Preventing WC dissolution in the binder, not only maintains very small grains, but also maintains their original shape. However if the grain growth inhibitor is effective in retarding decarburization, it decreases the cohesion between WC and binder!

The second example is related to thermally sprayed coatings manufactured from alloy micrometer-sized particles made of nanometer-sized grains. Coatings were obtained with a high power HVOF torch to keep as much as possible the nanocrystalline structure. Coatings possess both nanocrystalline regions (grains of a few tens of

nanometers) and submicron grain regions. The oxidation behavior of nanostructure NiCrAlY coatings, obtained from HVOF-sprayed cryomilled particles, was investigated after heat treatments in air, at 1,000 °C, for various times [247]. Oxidation led to the formation of a continuous alumina layer, without the presence of other mixed oxides.

13.9 Influence of Wire, Cored Wires, Rods, and Cords on Coating Properties

As emphasized previously for powders (Sect. 11.1.6), spray conditions modify the composition, structure, morphology of coatings compared to that of wire, cored wire, rod,. . ., feedstock, which is illustrated below through a few examples.

13.9.1 Flame or HVOF or HVAF-Sprayed Wires

13.9.1.1 Flame Spraying

As explained in Sect. 5.2, flame spraying is a process where hot gases are rather slow resulting in particle velocities below 100 m/s and for drops atomized by air jets from wires or rods or cords in particle velocities below 150 m/s. Thus the oxidation phenomenon will be controlled exclusively by diffusion (see Sect. 4.3.3.7).

For example, the flame spray process was used to produce aluminum-coated fabric composites with two different flame spray processes (powder and wire) [248]. Coatings produced using wire as raw material have a much better morphology than those produced using powder as starting material. Successful preliminary tests for Al–polyester composites, used as current collectors, show that application-specific electrically conductive composites with adjustable-specific surface conductivity values and microstructures can be produced on flexible fabric substrates without inducing any thermal or chemical damages to the fabric material.

Rodriguez et al. [249] have compared aluminum coatings sprayed by flame (FS) and electric arc (EA). The XPS analysis of the aluminum coating deposited by EA indicated that the layer of aluminum oxide/hydroxide persisted for a longer sputtering time on the lamella than in that deposited by FS. This difference may also indicate the formation of different aluminum compounds. X-ray diffraction revealed that the principal phase was bayerite in the FS process and boehmite in the coating deposited by EA. It should be noted that the heat source and the deposition material are determining factors in the protection process. In the period during which the coatings of this study were subjected to saline mist, both the FS and EA deposition methods provided satisfactory barrier protection.

Drops resulting from flame-sprayed molybdenum wires are oxidized in-flight and coatings containing oxides, improving their friction against other metals, are

extensively used in industrial applications. They enhance the performance of engineering components such as pistons, piston rings, and shafts. However improved resistance to thermal degradation, corrosion, and wear must be achieved. Moreover in all these applications, the performance of the coating is dependent upon its cohesive and adhesive strengths, which are affected by the spraying process parameters employed during the coating deposition process, particularly the substrate preheating. In the study of Babu et al. [250], the spray process parameters were optimized using Taguchi techniques, especially to achieve high cohesive strengths that were correlated to changes in the microstructure.

13.9.1.2 HVOF Spraying

Coating density is increased if the drop velocities are drastically increased, which can be achieved by HVOF spraying (see Sect. 5.3.2).

Neiser et al. [209], HVOF spraying mild steel wire (AISI 1025), were the firsts to show that convective oxidation occurred, based on in-flight measurements of the droplet velocities and temperatures which were mostly over the melting temperature, (see Sect. 5.3.2). The spherical shape of the Fe and FeO inclusions within coatings confirmed this.

Sidhu et al. [251] successfully obtained NiCr coatings up to a thickness of $<$300 to 330 μm by the HVOF process with liquid petroleum gas (LPG) as fuel gas. The microhardness measurement across the cross section of the coating showed that hardness values were high compared with those of the steel substrates. Micrographs showed that NiCr powder coatings possess some semi-melted particles, inclusions, oxides, and a coarse grain structure, whereas the NiCr wire coatings possess a fine, layered, dense, and uniform structure. The NiCr wire coating also has very low porosity and higher erosion resistance compared to the NiCr powder coating.

13.9.1.3 HVAF Spraying

To achieve high droplet velocities and limit their temperatures, Gorlach [252] has used a high velocity air flame (HVAF) process to spray Zn–Al coatings. HVAF-sprayed coatings showed considerably higher bond strength than coatings obtained by the conventional methods, indicating the advantage of this method in areas where the adhesion strength is critically important. The highly dense structure of the coating obtained with HVAF eliminates a need for a top paint coat, which is typically applied on metal-sprayed coatings to extend service life. The thermal-sprayed coatings exhibited dense structure, low presence of oxides, and high resistance to corrosion. High spray rate and good coating quality make the HVAF thermal spray method a viable alternative to the conventional thermal spraying technologies, such as wire flame and twin-wire arc.

13.9.2 Flame-Sprayed Rods

Among materials, ceramic coatings present several interesting aspects such as wear resistance, corrosion protection, as well as thermal or electrical insulation. This is true particularly for alumina coatings, which appear as the most commonly used. From all spraying processes, atmospheric plasma spraying (APS) is a rather well established for ceramics but it is relatively expensive. Costil et al. [253] have compared plasma-sprayed alumina coatings to those obtained by rod flame spraying with a lower economical impact. They used alumina rods from RokideTM sprayed with the Master Jet® gun. Both types of coating characteristics were different. The alumina coatings obtained with the APS technique were denser with a thinner microstructure compared to those sprayed by flame. This way, their mechanical as well as their thermal properties are quite different, which can be advantageous depending on the applications.

13.9.3 Arc Sprayed

Although arc spraying is not a new technique, recent developments of arc spraying systems, spray wires, a better understanding of the coating mechanisms and the dynamic behavior of the spray process have made it a very active thermal spray process.

13.9.3.1 Wires

According to spray conditions, convective oxidation can take place (see Sect. 4.3.3.7c), this is particularly important for low melting temperature materials such as aluminum, zinc etc. For example, Post Guillen and Williams [254] have examined the in-flight oxidation of aluminum sprayed in air using the twin wire electric arc (TWEA) thermal spray process. Aerodynamic shear at the droplet surface increases the amount of in-flight oxidation by promoting entrainment of the surface oxides within the molten droplet and continually exposing fresh fluid available for oxidation. Mathematical predictions confirm experimental measurements that reveal an elevated, nearly constant surface temperature (<2,273 K) of drops during flight. The calculated oxide volume fraction of a "typical" droplet with internal circulation compares favorably to the experimentally determined oxide content (3.3–12.7 %) for a typical TWEA-sprayed aluminum coating sprayed onto a room temperature substrate. It is concluded that internal circulation due to convective movements within the molten aluminum droplet is a significant source of oxidation. This effect produces an oxide content nearly two orders of magnitude larger than that of a droplet without continual oxidation.

13.9.3.2 Cored Wires

If arc sprayed wires have usually a good resistance to corrosion or oxidation, unfortunately their erosion resistance, especially at high temperature is relatively poor. The advantage of cored wires is that within the ductile sheath it is possible to add powders of very different materials from metals to ceramics, as illustrated in the following few examples.

(a) Metals

For example, He et al. [255], have shown that coatings sprayed with a NiCr sheath cored wire containing 5 wt% Mo or 2–4 wt% B, had better antichlorine ion corrosion performance than that of Ni-base coatings without Mo and PS45 (Ni–Cr–Ti) coatings. The coatings had a compact surface and a bond strength higher than 40 MPa.

Skoblo et al. [256] studied the structure of coatings obtained from powder wires on a substrate of ferro–chrome–aluminum with additional alloying elements added into the charge in different proportions (Mo, Si, V, C). This promotes the formation of a heterogeneous structure and phases providing the requisite hardness in the sprayed layer due to the segregation of dispersed special carbides and oxides and the presence of an alloyed matrix α-phase.

Student et al. [257] studied the kinetics of oxidation at 700 °C of electric-arc dispersion-hardened coatings of the Fe–Cr–B–Al system alloyed with 6 % Ni, 3 % W, 1 % Mo, and 1 % V (powder charge filling of 20–27 %) by spraying from powder-core wires. All coatings sprayed from the powder-core wires are characterized by the presence of both external and internal oxidation. When holding coatings at 700 °C for 100 h, the dispersed phases of Fe_3 Al and Ni_3 Al intermetallic compounds, the borides Fe_2 B and CrB, and $Me_{23}C_6$ special carbides alloyed with the tungsten, molybdenum, and vanadium are separated in the structure of the coating, which significantly increases its microhardness.

(b) Ceramics and Cermets

Xua et al. [258] have studied the sliding wear behavior of Fe–Al and Fe–Al/WC iron aluminide-based coatings prepared by high velocity arc spraying (HVAS) with cored wires. The effect of normal load on friction coefficient and wear rate of the coatings was studied. The main phases in both coatings were iron aluminide (Fe_3Al and FeAl), and α-WC/W_2C particles were embedded in the matrix of the composite coating. With WC hard particles, the Fe–Al/WC composite coating exhibited higher wear resistance than the Fe–Al coating, but both coatings had almost the same friction coefficient. The predominant wear mechanism of the coatings appears to be delamination.

Zhao et al. [259] have designed and deposited a cored wire with 304 L stainless steel as sheath material and NiB and WC–12Co as filler materials to produce a

new wear-resistant coating containing amorphous phases by arc spraying. DTA measurements revealed that the crystallization of the amorphous phase occurred at 579.2 °C. Because metallurgical processes for single droplets were non-homogenous during spraying, the lamellae in the coating have different hardness values, which lie between about 700 and 1,250 HVN. The abrasive wear test showed that the new Fe-based coating was very wear resistant.

Liu et al. [260] prepared cored wires with three Ti–Al series intermetallic compounds, $TiAl_3$, TiAl, and Ti_3Al, which were sprayed on low carbon steel substrates by a supersonic arc spraying process. The high temperature erosion (HTE) resistance of coatings decreased in the order of (from best to worst) $TiAl_3$, TiAl, and Ti_3Al. The arc-sprayed coatings prepared using cored wire containing $TiAl_3$ and TiAl powders exhibited better or comparable HTE resistance than that containing a commercial Cr_3C_2-based composite powder, although the hardness of the former two coatings was somewhat lower. Oxides resulted from oxidation of both the cored alloy powders and the mild steel sheaths were also identified between the laminated layers.

13.10 Stresses Within Coatings

Two types of stresses are considered:

- Residual stress is commonly defined as the stress that remains in a body after its manufacturing and is not being subjected to external forces. It can be detrimental or beneficial to the performance of a material.
- Service stresses due, for example, to thermal effects in thermal barriers (including cyclic heating and cooling associated with engine operation, constrained oxide growth on the bond coat at the ceramic/bond coat interface, in-plane compressive residual stresses), or mechanical effects as in thermal spray coatings submitted to fatigue in rolling/sliding contacts. Also other stresses can occur, mainly during service conditions: chemically induced stresses resulting from volume changes when chemical reactions, precipitations, or phase transformations occur (for example, heating a γ-Al_2O_3 coating over 1,000 °C induces its transformation into α-Al_2O_3).

13.10.1 Residual Stress

The residual stresses in a component arise from mainly three different origins [261]:

- Thermally induced stresses resulting from nonuniform heating and cooling during manufacturing and processing. In a thermally sprayed coating the final residual stress state through the whole coating/substrate system is determined by the superposition of stresses induced during the spray process: quenching,

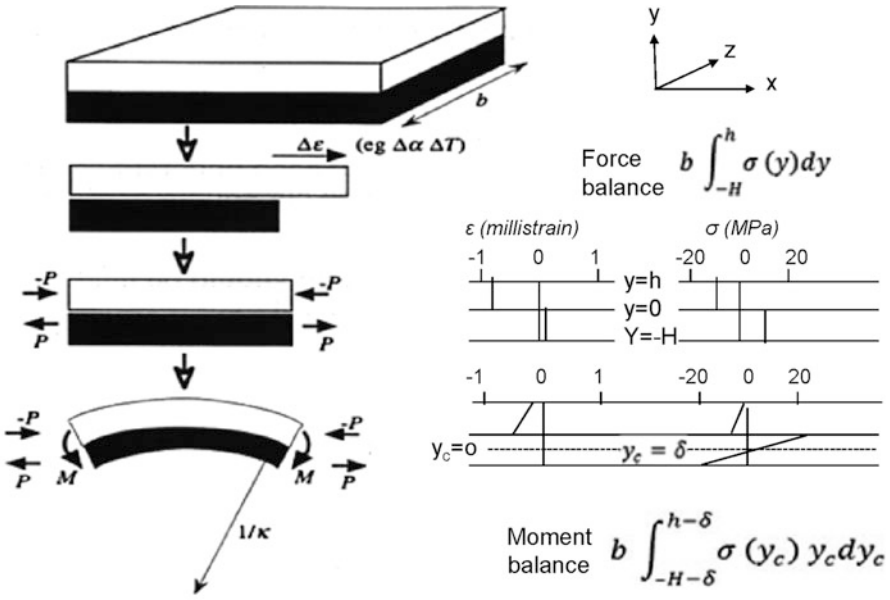


Fig. 13.86 Schematic of the generation of curvature in a flat bimaterial plate as a result of the imposition of a uniform, linear misfit strain, $\Delta\varepsilon$. Reprinted with kind permission from Springer Science Business Media [262], copyright © ASM International

thermal mismatch, and through thickness thermal gradients. The latter stress can be avoided or significantly limited by keeping the time average coating temperature as constant as possible.

– Mechanically induced stresses that are generated during manufacturing processes (such as grinding, blasting, and machining) and that can produce nonuniform plastic deformation. For spray processes where particles achieve velocities over 500–600 m/s (HVOF, HVAF, D-gun, cold spray) their peening effect must be considered because it results in a compressive stress states in the coating, similar to that obtained in the substrate by grit blasting.

13.10.1.1 Thermal Stresses

Clyne and Gill [262] gave an excellent overview of the different thermal stresses contributing to the residual stress after coating generation. A good explanation of stress induced by a thermal effect is given in Fig. 13.86 from Clyne and Gill [262]. They considered a pair of plates bonded together with a misfit strain $\Delta\varepsilon$ in the x-direction (Fig. 13.86) and they assumed that the behavior is purely elastic. The resultant stress distribution, $\sigma_x(y)$, and curvature, K', can be obtained from simple beam bending theory. First, the misfit strain is removed by the application of two equal and opposite forces ($-P'$ and P'). When the two plates are joined, this

results in an unbalanced moment, M, Balancing this moment generates curvature of the composite plate. The moment is given by

$$M = P \cdot \left(H + h^{'}\right)/2 \tag{13.10}$$

where h' and H are the thicknesses of the deposit and substrate, respectively. Then, the curvature of a beam, K' (equal to the through-thickness gradient of strain), can be expressed as the bending moment divided by the beam stiffness, Ξ:

$$K^{'} = M/\Xi \tag{13.11}$$

so that P can be expressed as

$$P = 2 \cdot \Xi \cdot K^{'} \cdot \left(h^{'} + H\right)^{-1} \tag{13.12}$$

Finally, using the expression of the beam stiffness, calculating the misfit strain, $\Delta\varepsilon$ for a change arising from temperature variation) according to forces P, it is possible to obtain a complex expression of K' depending upon the Young's moduli of coating and substrate, their respective thicknesses h' and H (for details see [262]). Of course the curvature depends strongly upon the respective thicknesses of coating and substrate as well as their Young's moduli. For example, it will be negligible when $h'/H \ll 1$. For a given h'/H ratio, the curvature is inversely proportional to the substrate thickness [262]. This means that use of relatively thin substrates is essential to obtain a sufficiently large curvature to achieve a good precision stress measurement through beam curvature [263].

(a) Quenching Stress

Quenching stress occurs due to the rapid quenching of flattened fully molten droplets when they solidify upon impact on the substrate or the previously deposited layer. It arises from the hindered contraction of the individual splats as they cool from the temperature T_p, below the melting temperature where they are no more in a plastic state (however one considers generally that $T_p = T_m$, melting temperature), to the temperature Tsub of the underlying material of the substrate or the previously deposited layers. Of course quenching stress is always tensile and its value depends on the real contact between splat and substrate or the splat and the underlying layer on the one hand and on the relaxation phenomena taking place on the other hand. The theoretical value of the quenching stress is given by

$$\sigma_q^{\circ} = E_c \times \alpha_c \times \left(T_p - T_{sub}\right) \tag{13.13}$$

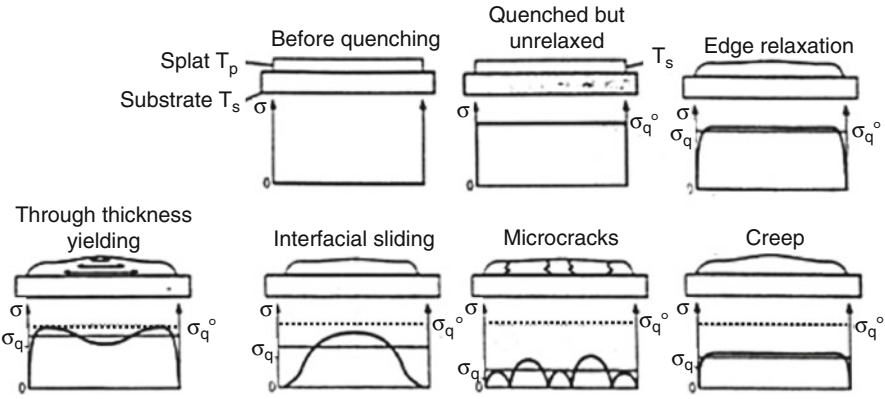


Fig. 13.87 Different mechanisms for quenching stress relaxation. Reprinted with kind permission from Elsevier [267]

where E_c is Young's modulus (GPa) and α_c (K^{-1}) the expansion coefficient of the splat, σ_q° being in MPa. Instead of using Young's modulus of the coating, it is recommended to use the effective Young's modulus $E'_c = E_c \cdot (1 - \nu')^{-1}$, where ν' is Poisson's ratio [263]. More complex expressions are also used [263]. However, even with a perfect contact between splat and the underlying layer the quenching stress is often much less than σ_q° because of the relaxation mechanisms that occur, reducing it to a value σ_q which reflects the degree of relaxation within splats. To illustrate that, when considering the case of alumina, assuming that E_c and α_c values are those of the bulk material, for a 100 °C cooling, σ_q° from Eq. (13.12) is already 100 MPa, while experimental values for splats cooled down to room temperature are about 10 MPa! In general quenching stresses of different materials are lower than 100 MPa. As could be expected, the quenching stress is almost independent of the substrate material [264–267].

The relaxation mechanisms are summarized in Fig. 13.87 from Gill [267]:

- For metals or alloys edge relaxation, through-thickness yielding, interfacial sliding, and creep
- For ceramics mainly cracks with possible interfacial sliding

Quenching stress has been studied mainly for plasma- (air or vacuum) and HVOF-sprayed coatings. Kuroda and Clyne [267] and Clyne T.W. and S.C. Gill [262] are shown in Fig. 13.88. They [262] have emphasized that maximum theoretical values for the quenching stress are typically of the order of 1 GPa. This is due to the various stress-relaxation mechanisms, such as interfacial sliding, which can occur during the quenching process. While many ceramic materials undergo extensive micro cracking, metallic deposits are prone to plastic yielding or creep (see Fig. 13.87). This explains why, depending on the strength of the metal, reductions in quenching stress occur at relatively high temperatures with the misfit strain tending to zero, as the homologous temperature tends to unity.

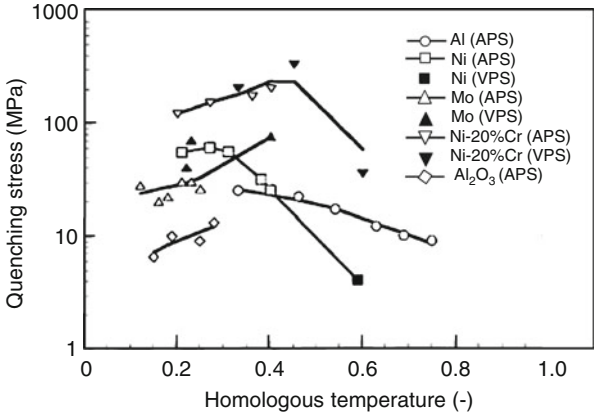


Fig. 13.88 Experimental quenching stresses for plasma spraying in air (APS) or in vacuum (VPS). The values are plotted against the ratio of the specimen temperature to the melting temperature of the deposit (homologous temperature). The data were obtained from specimen curvature measurements during spraying. Reprinted with kind permission from Springer Science Business Media [262], copyright © ASM International

Differences between the data for plasma spraying in air or in vacuum are not significant.

For metals, depending on their strengths, reductions in quenching stress occur when moving to relatively high temperatures for substrate preheating with relaxation phenomena (through-thickness yielding, interfacial sliding, and creep). At lower temperatures, all materials tend to show gradual increases with temperature, which is attributed to improvements in inter-splat bonding.

Of course impact conditions and inter-splat bond strength play a key role. For example, for HVOF or D-gun spraying, according to the high particle impact velocities, but with particle temperatures lower than those obtained with plasma, wire arc, flame spraying, the quenching stress is different, but still tensile. However a high-temperature shot-peening process also occurs (see section 13.11.1.2b below for details), for particle velocities over 500–600 m/s, creating compressive stresses within the coating [261, 263, 268–278].

(b) Expansion Mismatch Stress

Thermal mismatch stress, σ_d, occurs during cooling but after solidification due to difference in thermal expansion coefficients between each deposited layer and the substrate material. Simple elastic analysis of in-plasma stresses of thin coatings attached to a thick substrate results in the simple expression:

$$\sigma_d = E_c \cdot (T_s - T_{RT}) \cdot (\alpha_s - \alpha_c) \cdot \left(1 + 2\left(E_c h' / E_s H\right)\right)^{-1} \tag{13.14}$$

where E_c and E_s are the coating and substrate Young's moduli, α_s and α_c the expansion coefficients of substrate and coating. Of course if one has a thick substrate and a thin coating ($h'/H \ll 1$) σ_d becomes

$$\sigma_d = E_c \cdot (T_s - T_{RT}) \cdot (\alpha_s - \alpha_c) \tag{13.15}$$

This equation shows that if $\alpha_c > \alpha_s$ the expansion mismatch is compressive ($\sigma_d < 0$), while if $\alpha_c > \alpha_s$ the expansion mismatch is tensile ($\sigma_d > 0$).

The expansion mismatch thermal stress must be systematically considered for all coating processes except cold spray. However in most cases the cold spray is performed above room temperature and after deposition the coating and substrate will cool to room temperature generating a thermal misfit [279]. Of course it depends on the cooling range and difference in thermal expansion coefficients between the coating and substrate materials.

(c) Stress Due to Temperature Gradient

The relatively high heat fluxes imposed on coating and substrate during spraying can cause high thermal gradients, especially for sprayed materials with low thermal conductivity ($\kappa_c < 30$ W/m/K), which generate differential thermal expansion at different depths resulting in local misfit strains. Thermal gradients increase also if the coating surface temperature is not kept constant during spraying thanks to adapted cooling devices blowing on the coating surface under construction. Stresses and bending moments will therefore rise. Although they are expected to disappear when the thermal gradient vanishes, they can induce nonelastic effects and thus must be avoided [262]. This can be achieved by adjusting the cooling devices, the spray pattern, and the pass thickness, especially for low thermal conductivity sprayed materials.

13.10.1.2 Mechanically Induced Stresses

(a) Grit Blasting

During grit blasting [262] compressive residual stresses are generated and distributed within a thin layer beneath the grit-blasted substrate surface. Grit blasting modifies the grain shapes, as in cold working. He et al. [273] have shown that initial equiaxed grains of 1010 carbon steel in the deformed regions of a substrate are elongated and spirally oriented surrounding the impact spots. There are no visible changes in this microstructure caused by thermal spraying, and the elongated grain regions are completely unchanged in the coated substrate. Figure 12.35 (Chap. 12) from Mellali et al. [280] shows the residual stress distribution within a cast iron FT25 substrate, grit blasted with 0.5 mm white alumina. The area plastically affected in the substrate is about 0.4 mm thick as shown in Fig. 12.35.

The maximum stress, corresponding to the depth of the plastically deformed zone, was reached at 0.05 mm from the substrate surface. The magnitude and the depth of the zone affected by the grit blasting are strongly dependent on the blasting conditions (particularly the impact velocity and the size of particles, or more precisely momenta of grit particles) and on Young's modulus of the substrate material. Lima et al. [276] obtained similar results for UNS G41350 steel substrates. When grit blasting thin beams (with thickness below about 4–5 mm), the grit-blasting stress induces a curvature of the beam that depends on blasting conditions and the beam Young's module. A possibility to reduce the beam bending is to grit blast it on both sides, with the same blasting conditions.

The grit blasting stress can be relaxed by heating substrates over the material recovery temperature ($\approx 0.4T_m$, T_m being the material melting temperature), in a controlled atmosphere furnace to avoid oxidation.

(b) Peening Effect

For spray processes where particle velocities are above 500–600 m/s a high-temperature shot-peening process occurs [268–278] resulting in a compressive stress. The interaction between impacting particles and substrate depends on the relative hardness value of the impacting particle and the substrate. When a hard particle is sprayed onto a soft substrate, the substrate is deformed (it can even be locally molten), and its surface is penetrated by the impacting particle. In contrast, when a soft particle is sprayed onto a hard substrate, the majority of the impacting particle's kinetic energy is transformed into thermal energy, the particle itself deforms, even melts [273]. It is generally assumed that the substrate, which had been already hardened by grit blasting, is not affected and no further mechanical hardening is created. The superposition of quenching and peening stress induces a nonlinear stress that is first tensile, decreasing with the coating thickness and becoming compressive beyond a given thickness [275]. To illustrate the peening effect, Sampath et al. [270] have compared the stress distribution within Ni–5 wt% Al coatings wire arc sprayed (WA), air plasma sprayed (APS), HVOF sprayed, and cold sprayed (CS). The steel substrate and coating were air cooled during the spray process. The stress distribution was determined by neutron diffraction (see Sect. 15.7.5.2). Near-surface effects, when the gauge volume was partially out of the material, were determined on a stress-free reference and subtracted. In the APS deposit, as shown in Fig. 13.89a, the overall stress within the coating is slightly tensile and it increases toward the deposit surface, due to the buildup of deposit layers with tensile quenching stress. To accommodate this coating stress the stress in the substrate (bending effect) will display a gradient from compression, near the interface with the coating, to tension on the back surface. In the case of wire arc spraying, the stress gradient is somewhat higher, while in the substrate it is negligible. Sampath et al. [270] explain that behavior by the change in quenching stress during the deposit buildup and the low deposit modulus, stemming from higher porosity resulting in insignificant substrate bending. In the HVOF deposit,

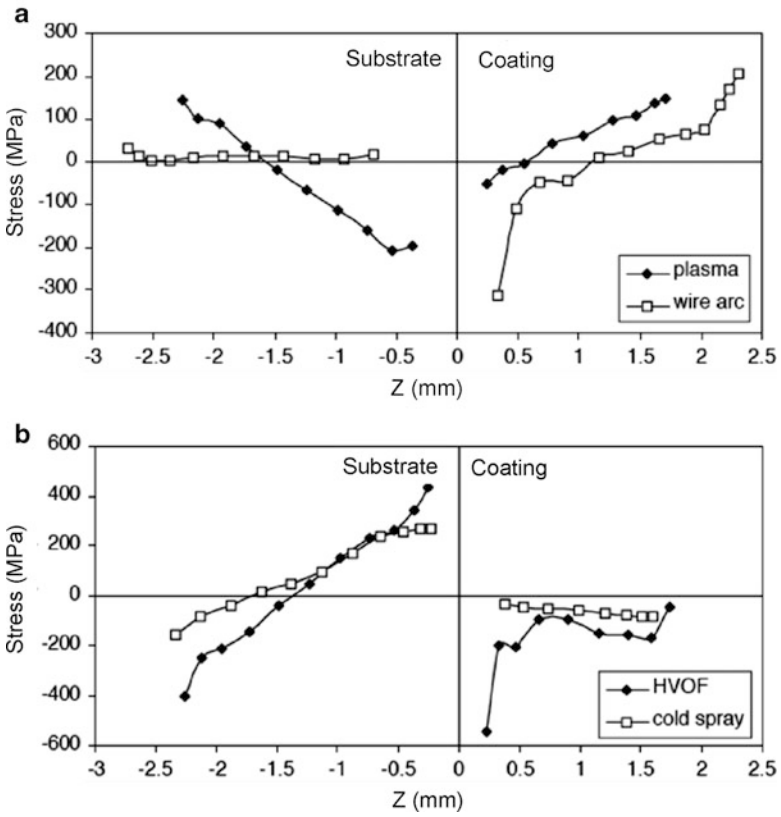


Fig. 13.89 Through-thickness profile of the residual stress in Ni–5 wt% Al deposits on steel substrate sprayed respectively by: (**a**) plasma and wire arc and (**b**) HVOF and cold spray [270]. Reprinted with kind permission from Elsevier

see Fig. 13.89b from [270], the stress is mainly compressive in spite of quenching and thermal stresses, the very high velocity impact of the particles on pre-deposited layers resulting in the peening effect generating compressive residual stress as already emphasized by Kuroda et al. [269]. This results in high tensile stress within substrate close to the interface with coating. Similarly in the cold-sprayed coating, the stress is compressive [270] as well. There is a slight gradient toward compression near the surface. Sampath et al. [270] explain this effect by the fact that the peening action of impinging particles affects only the immediately adjacent material, while the layers further beneath are shifted a little toward tension, to maintain a force balance.

Figure 13.90 from Wang et al. [275] presents the dependence on the coating thickness of the residual stress of D-Gun sprayed WC–Co coatings. In Zone A the residual stress is of tensile nature and decreases dramatically (by ≈1.28 MPa/μm) with a coating thickness increase up to 317.4 μm. When the coating thickness is larger

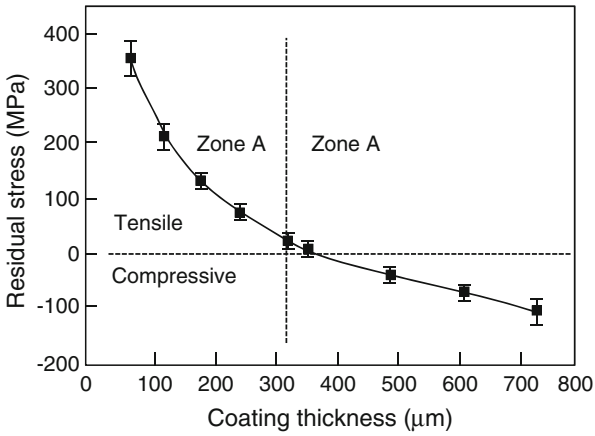


Fig. 13.90 Dependence on the coating thickness of the residual stress of D-Gun sprayed WC–Co coatings [275]. Reprinted with kind permission from Elsevier

than 317.4 μm (Zone B), the residual stress decreases at a lower rate (by ≈0.31 MPa/μm) and varies gradually from a tensile nature to a compressive one.

The stress distribution in cold-sprayed coatings is mainly compressive and it seems [281] that it is determined almost entirely by the plastic deformation process (peening) of the particles of the spray material. Luzin et al. [281] have measured the residual stresses profiles in Cu and Al cold spray coatings by neutron diffraction. The in-plane residual stress profiles are shown in Fig. 13.91a–d. Both Cu coatings on Cu or Al substrates show a significant compressive residual stress at the surface 50–80 MPa, while the surface residual stress of the Al coatings on the same substrates is less than 10 MPa. The overall stress profile of the two Cu coatings is similar, regardless of the substrate material, and the same can be said of the Al coatings. The experimental residual stress distributions were treated [281] empirically using Tsui and Clyne's progressive deposition model to demonstrate that the residual stresses accumulate mainly by kinetic and not thermal effects, and these effects were characterized quantitatively. The measured compressive residual stresses were determined almost entirely by the plastic deformation process (peening) of the particles of the spray material. An attempt has been made [281] to explain the higher residual in-plane stress in the Cu coatings by using a physically based model of residual stress accumulation in a shot-peened surface. Calculations within this model in the case of Al and Cu demonstrated that the balance between the elasto-plastic properties of the material and the spraying conditions defines the resultant residual stress.

(c) Other Stresses

Almost all techniques used to prepare the substrate, machining, grinding, cold work, etc., produce nonuniform plastic deformation and create stresses that may or may not impact the coating [277]. They are discussed in the following section.

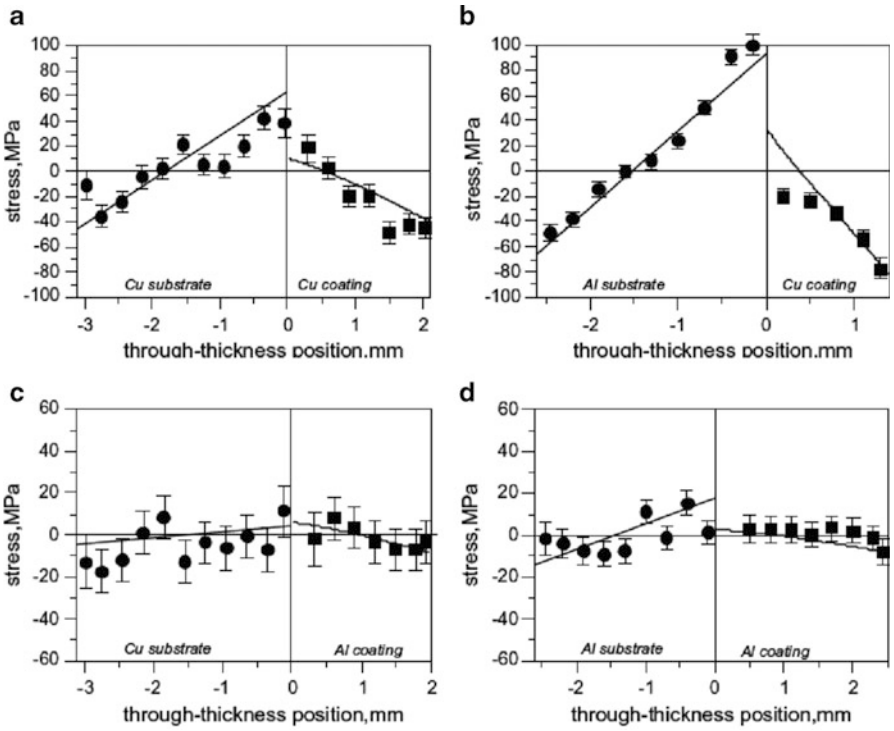


Fig. 13.91 Measurement (*symbols*) and model fit (*solid lines*) of the through thickness in-plane stress distributions for (**a**) Cu/Cu sample, (**b**) Cu/Al sample, (**c**) Al/Cu sample, and (**d**) Al/Al sample [281]. Reprinted with kind permission from Elsevier

13.10.1.3 Resulting Residual Stress

At the end of the coating process the residual stress state through the whole coating/substrate system is determined by the superposition of stresses of different nature induced during the spray process: quenching, thermal mismatch, and peening stresses, together with the compressive stress state of the substrate induced during the grit blasting prior to spraying. This is illustrated in Fig. 13.92 from Lyphout et al. [261], it is worth noting that in this figure the grit blasting stress has been assumed negligible.

The stress distribution, its intensity and sign in the coating, is strongly dependent on the specific spray process [270] and processing conditions [272, 274, 275]. The residual stress distribution can be measured (see Chap. 15) or calculated. Calculations can be performed either by using analytical expressions such as those given by Clyne and Gill [262], Clyne [278], Stokes and Looney [263], Wang et al. [275], and Kroupa [282] who has considered non-homogeneous elastic properties depending on the coordinate z perpendicular to the interface (case of any graded or layered coatings), or by using finite element methods [261, 282–285] with, for example, the ABAQUS

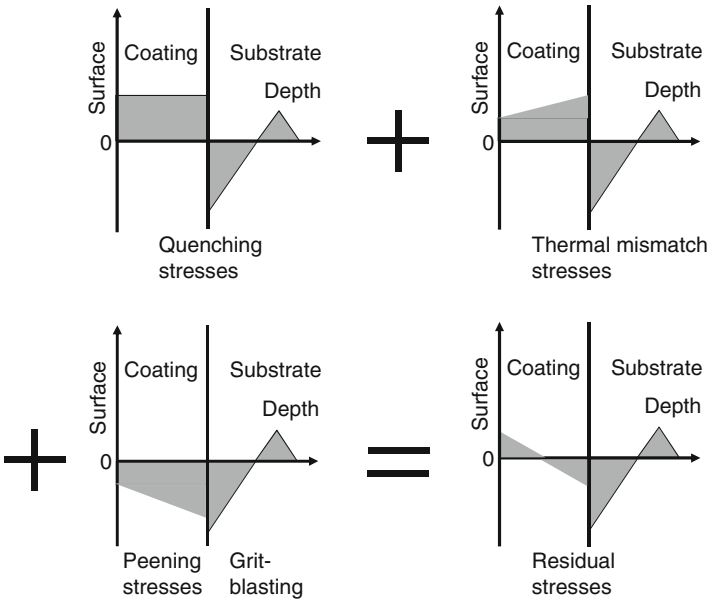


Fig. 13.92 Schematic representation of radial residual stress distribution in HVOF sprayed coating/substrate system. Reprinted with kind permission from Springer Science Business Media [261], copyright © ASM International

code [271, 282]. Ghafouri-Azar et al. [286] using the experimental spray parameters as inputs to a 3D stochastic model have simulated coating formation. They used an object-oriented finite element code (OOF) developed at the National Institute of Standards and Technology to calculate residual stresses in the coating. The model, with an adaptive meshing technique, discretized the coating microstructure into a mesh suitable for finite element analysis. The coating geometry used either micrographs of coating cross sections or computer-generated images of coatings.

Whatever the model or calculation method may be, one of the most important difficulties is that the mechanical properties of coatings, depending strongly on spray conditions, can be quite different from those of bulk materials given in tables. In particular, a very difficult problem is the calculation of the quenching stress taking into account the relaxation phenomena.

13.10.1.4 Effect of Residual Stress on Coating Adhesion

Coating adhesion is a very important property that is linked to the critical strain energy release rate for the interface, G_{ic}, or the closely related critical interfacial stress-intensity factor, K_{ic} at the interface between coating and substrate [262, 287, 288]. In the simplest case of a thin coating with a *uniform* misfit strain, the strain

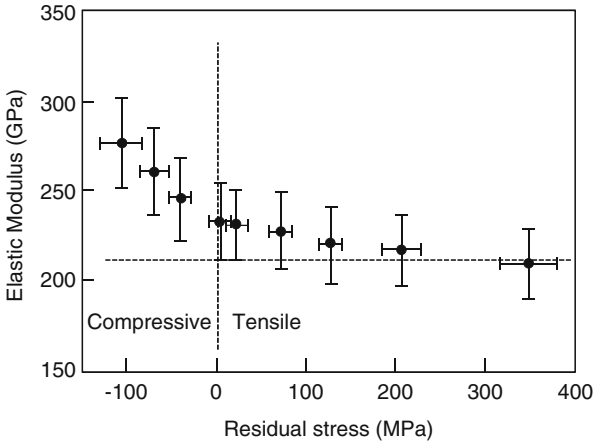


Fig. 13.93 Variations of the elastic modulus with the residual stress evolution through coating thickness see Fig. 13.90 (D-Gun sprayed WC–Co). Reprinted with kind permission from Elsevier [275]

energy release is simply the stored elastic strain energy per unit interfacial area. Assuming that $h' \ll H$ the expression for the strain energy release becomes

$$G = \sigma_c^2 \cdot h' \cdot (2 \cdot E_c)^{-1} \tag{13.16}$$

Once the stress is known at the point where debonding occurs, G_{ic} can be taken as equal to the value of G (J/m^2) at this point.

Unfortunately, the analysis is complicated by the fact that the stress field at the crack tip may not represent conditions of a pure crack opening (mode I) [262]. In contrast to a homogeneous medium, the crack is confined to a particular geometric path and, depending on the toughness of the interface and of the two media on either side, crack propagation may continue within the interface also with a shear stress (mixed modes I and II).

Debonding may also occur under combined residual and applied stresses (for example, generated by the application of an external mechanical load). At last, for an edge crack the driving force near the specimen edge can be reduced during the initial stages of the propagation. That is why at the edge of the coated substrate proper machining must avoid sharp corners, such as an abrupt stop of the coating at the end of a cylinder as explained in Sect. 12.2. Of course the problem is very complex, but it is very important to reduce the initiation of the spallation by tailoring the stress distribution through appropriate spray conditions [262]. Many models have been devoted to the stress distribution calculation [236, 263, 272, 273, 278, 282–288], all emphasize the importance of having low tensile, or better even compressive stress in the coating near the interface. The residual stress also modifies the coating mechanical properties (elastic modulus, hardness) both increasing when the compressive stress is raised [276], as shown in Fig. 13.93. The increase of these mechanical properties results from the elastic closure of small porosities or micro-cracks.

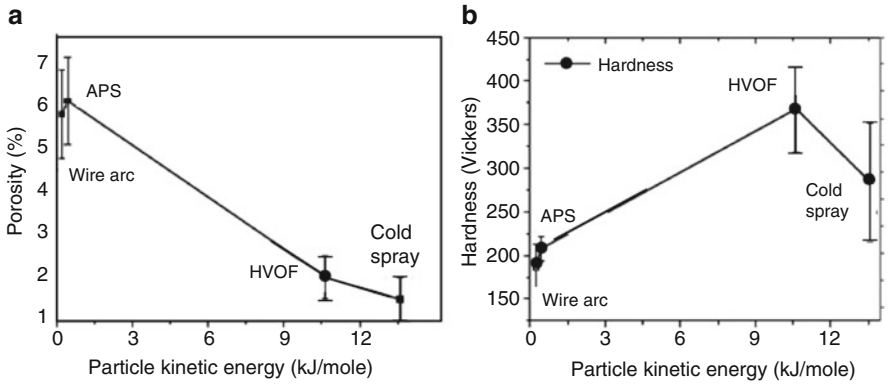


Fig. 13.94 Influence of particle kinetic energy on Ni–5 wt% Al deposits sprayed by wire arc, APS, HVOF, cold spray; (**a**) porosity, (**b**) hardness. Reprinted with kind permission from Elsevier [270]

However, it must be kept in mind that coating properties are strongly linked to the real contacts between splats, which do not necessarily depend on the impact energy of particles. This is illustrated in Fig. 13.94 from Sampath et al. [270] who have compared the porosity and hardness of Ni–5 wt% Al coatings sprayed by wire arc, APS, HVOF, and cold spray.

As shown in Fig. 13.94a, the deposit porosity decreases with increasing particle kinetic energy, but the hardness drops from HVOF deposit to cold-sprayed deposit even though the particle kinetic energy is doubled, see Fig. 13.94b. This implies that deposit properties are strongly linked to the real contacts between splats and not only to the coating porosity or density.

Coating thermal conductivity, closely linked to the real contacts between splats, is the lowest for cold sprayed (11 W/m K) and APS (10.7 W/m K) coatings, slightly higher for the wire arc deposit (17 W/m K), in spite of the lowest impact velocity, and the highest (22.2 W/m K) for HVOF coatings. By analyzing the microstructure of HVOF, APS, and cold spraying parameters, it is clear that a combination of high kinetic energy and a high thermal energy promotes enhanced splat–splat interaction and a consequent improvement in interlayer/inter-splat adhesion, as reflected by the increase in thermal conductivity. The low porosity associated with dynamic compaction in cold spraying does not automatically provide enhanced inter-splat contact. The wire arc-sprayed material has a coarse porosity and large metallurgical bonded regions with no interfaces. The cold-sprayed material consists of a network of fine interconnected interparticle separations with a lack of metallurgical bonding [270].

Tensile stresses within a coating may also induce debonding when the coating thickness increases. For example, Greving et al. [289] have shown that if residual stress measurements indicate that coating thickness for wire arc-sprayed nickel–5 wt% aluminum coatings on AISI 1018 steel minimally influences the residual stress, the degradation of bond strength is raised with increasing coating thickness. They attribute that to the fact that thicker coatings cause higher tensile edge

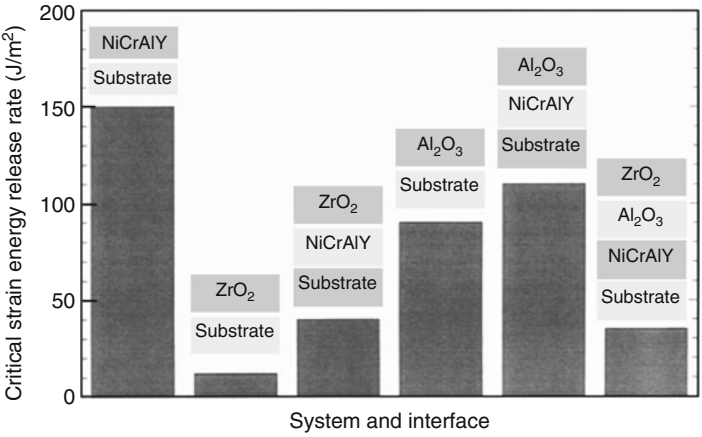


Fig. 13.95 Experimental data for interfacial toughness of various interfaces within multilayer ceramic coating–metal–substrate with or without NiCrAlY bond coat. The schematic above each bar indicates the interface that was measured and the specimen geometry (subs. = substrate). Reprinted with kind permission from Springer Science Business Media [262], copyright © ASM International

stresses, increase the tendency for debonding, and hence reduce the applied stress required to cause debonding.

Such considerations are especially important for coatings used at high temperatures such as thermal barrier coatings. That is why, especially for ceramic materials, which have lower expansion coefficients compared to those of the metal substrate, bond coats (generally about 100 µm thick) are used between the substrate and the ceramic. Their role is to increase the interfacial toughness. For example, Tsui and Clyne [290] studied the evolution of experimentally measured toughness for various interfaces, including some that might form if an alumina oxidation barrier was introduced between the bond coat and the topcoat. The results are presented in Fig. 13.95 from Clyne and Gill [262].

Besides superalloys that can work at temperatures up to about 1,300 °C, other metals are used as bond coats, especially molybdenum, nickel–aluminum composites or alloys and nickel–chromium alloys. NiAl alloys or composites are rather popular because of their good resistance at high temperatures and their ease of application to various substrates. NiCr and, of course, MCrAlY have the best resistance to thermal shocks. Table 13.7 [291] presents the maximum service temperatures of the mostly used bond coats

13.10.2 Service Stresses

In service conditions coatings can be submitted to thermal loads, temperature gradients, fatigue,... resulting in new stresses that have to be calculated according to the residual stress linked to the spray process. Moreover service conditions can

Table 13.7 Approximate maximum service temperatures for common bond coatings. Reprinted with kind permission from American Welding Society [291]

Bond coat	°C
Mo	315
80Ni–20Al	620
95Ni–5Al	1,010
80Ni–20Cr	1,260
94NiCr–6Al	980

also induce phase or chemical changes resulting in what is called intrinsic stresses. In the following only two examples will be considered: thermal barrier coatings and fatigue of tribological coatings.

13.10.2.1 Intrinsic Stresses

The intrinsic growth stresses are due to chemical reactions, phase transformations, and energetic particle bombardment. For thermally sprayed coatings when chemical reactions or phase changes occur, a change in volume occurs generating stresses that can be compressive when the volume increases, or tensile when it is decreased. Such volume transformations occur generally during service conditions. A typical example is the transformation of plasma-sprayed γ-alumina into α-alumina occurring at about 1,000 °C and resulting in an increase of the volume with coating spallation as possible consequence. Thus coatings must be used at temperatures below those at which such transformations occur.

13.10.2.2 Thermal Stresses

(a) Thermal Barrier Coatings

Gas turbine engines use nickel- and cobalt-base superalloys in the turbine components, such as airfoils, combustors, transition ducts, and seals [292]. Increased thermal efficiency demands that the turbine inlet temperature be significantly increased, without structural failure of components from melting, creep, oxidation, thermal fatigue, or other degradation mechanisms. Therefore, the surface temperature of these components must be maintained low enough to retain material properties within acceptable bonds. Due to its low thermal conductivity and good thermocyclic durability when stabilized against phase transformation, zirconia has become the ceramic of choice that is sprayed on a bond coat (see Sect. 13.10.1.4).

Thermal stresses induced by high heat fluxes are not only responsible for the delamination of the topcoat but also the oxidation of the bond coat by the hot oxidizing gases diffusing through the porous top coat is also very important [283, 292, 293]. At the rough bond coat, differential thermal contraction induces

tensile radial stress in the ceramic above asperities and compressive in-plane stress, thus cracks propagate tangentially from the tip of asperities and stop above valleys (location of state of tri-axial compression). When the bond coat is oxidized, the tensile radial component and the compressive component above valleys decrease resulting in easier crack extension and coating failure. Although many factors control TBC failure, the thermally grown oxide (TGO) layer development and subsequent thickening is generally considered as the most important factor. Calculations by Koolloos and Houben [293] show that pre-oxidation of the bond coat has a beneficial effect on lifetime in the case of a thermal load where oxidation is the main cause of failure. The pre-oxidation time and temperature must be chosen such that a dense alumina layer is formed and the forming of spinel-type structures is avoided.

Another problem that must be addressed is that the high thermal gradients commonly present in TBCs under service conditions lead to widely varying conditions within the top coat. Sintering is likely to occur much more rapidly near the free surface, not only because the temperatures are higher there, but because the residual stresses tend to be more compressive [294]. It is known that tensile stresses retard the progression of sintering.

At the end of the nineties, demands on engine performance have required the implementation of even thicker coatings for increased thermal protection. TBCs with a thickness of more than 1 mm are being developed to fulfill the demand, but these present new problems unseen with traditional thinner TBCs. A major problem concerning the thick coating is a low thermal shock resistance when the coating is subjected to thermal shock loads [295]. Segmentation cracks (orthogonal to the substrate and coating) enable TBCs to tolerate greater strains, thereby improving thermal shock behavior of TBCs. By depositing the zirconia (totally or partially stabilized) either by an electron beam evaporation-physical vapor deposition (EB-PVD) process [296] or "hot-spraying" particles without cooling during spraying resulting in an increased surface temperature [295, 297] it was possible to create segmentation crack network. These techniques allowed achieving compliant microstructures of the top coat accommodating the ceramic–super alloy thermal expansion mismatch strains. However the drawback of the compliant coating microstructure is an easier access of oxidizing gases to the bond coat surface, the protection of which against oxidation must be improved [296].

Unconventional plasma-sprayed thermal barrier coating (TBC) systems were also produced [298]. Approximately 250 μm thick 8YPSZ (8 wt%) coatings were directly sprayed onto grit-blasted surfaces of desulfurized PWA 1484, superalloy with excellent oxidation resistance, without a bond coat. To avoid edge-initiated failure, the surfaces of PWA 1484 were machined with a grid of grooves or ribs ($\sim$250 μm wide and high) to break up the shear stresses parallel to the surface (as shown in Fig. 12.3). In this case, failure occurred only as independent, single-segment events. For grooved samples, 1,100 °C segment life was extended to $\sim$ 1,000 h for 5 mm wide segments, with no failure observed out to 2,000 h for segments $\leq$2.5 mm wide. Ribbed samples were even more durable, and segments $\leq$6 mm remained intact for 2,000 h. Larger segments failed by buckling at times inversely related to the segment width.

(b) Functionally Graded Materials

Functionally graded materials (FGMs), whose compositional gradients are designed to have unique properties that are not available from a homogenous material, have great potential for severe thermal loading [299, 300]. FGMs overcome the drawbacks, such as cracking, of the multilayer composite plates that have been commonly used as thermal barriers [299]. For example, Nemat-Alla [300] has determined, based on the minimum value of the maximum normalized equivalent stresses, the optimum composition of the ZrO_2/6061–T6/Ti–6Al–4V 2D-FGM in x- and y directions, respectively. Shabana and Noda [301] have studied the FGM composite of aluminum and partially stabilized zirconia with volume fractions continuously varying through the thickness. Several functional forms of gradation of the constituents in the FGM layer were examined to reach the optimum profile giving the minimum stress level for the FGM structure under thermo-elasto-plastic behavior..

13.10.2.3 Fatigue of Tribological Coatings

Only two examples will be given:

- Thermal spray coatings can provide a cost-effective solution for rolling/sliding contacts and other novel tribological applications, if the durability of these coatings is demonstrated. Ahmed and Hadfield [302] have studied various cermet (WC–Co) and ceramic (Al_2O_3) coatings deposited by detonation gun (D-Gun), high-velocity oxy-fuel (HVOF), and high-velocity plasma spraying (HVPS) techniques, in a range of coating thicknesses (20–250 μm) on various steel substrates to determine the different competing failure modes. Four modes of fatigue-wear failure were identified as abrasive, delamination, bulk deformation, and spalling. These failure modes compete during fatigue failure, and eventual coating failure may be either due to one or a combination of these modes. Coating failures were attributed to micro- and macro-cracking of either the coating material or the coating substrate interface, which also resulted in the attenuation of compressive residual stress.
- Ibrahim and Berndt [303] have compared, with a detailed analysis of fatigue and deformation two groups of AISI 4340 steel specimens, one sprayed with HVOF WC–Co coating and the other plated with hard chrome. Rotating beam wear-fatigue tests were performed on the coated and uncoated specimens. The HVOF system produced a near-theoretical dense WC–Co coating that exhibited a high elastic modulus, which imparted high compressive residual stress to the substrate. The hard chrome plating process induced a tensile residual stress in the substrate that allowed the crack initiation process to start at the periphery of the specimen. Thus, the rate of the wear-fatigue process increased and the wear-fatigue strength decreased [303].

13.10.3 Conclusions Relative to Residual Stresses

Residual stresses within coatings and substrates, with or without bond coat, play an important role in coating behavior in service conditions. They depend strongly not only on the process and spray conditions used but also on the real contacts between splats, contacts linked to particle velocities and temperatures at impact, and not only to one of these parameters. They can be calculated either by analytical expression or sophisticated Finite Element Methods in order to predict the coating spallation depending on the critical strain energy release rate for the interface. However stress calculations depend on coating mechanical properties, again linked to real splat contacts, which are a function of the spray process, and these properties must be measured to obtain calculation results close to reality.

13.11 Finishing Coatings

After spraying coatings are treated to achieve the final dimension and obtain a smooth surface. However, machining of coatings can be troublesome with materials that are abrasion resistant, porous, with sometimes poorly bonded (often mainly mechanical bond) particles or splats that can pull out easily, with low thermal conductivity (at least lower than that of the bulk material) reducing the heat transfer and increasing drastically the coating surface temperature during grinding for example. Thus in general the accepted methods, practices, and techniques used to machine wrought material do not apply to the same material when sprayed [291].

13.11.1 Machining (Turning, Milling)

For metal coatings turning and milling can be easily used to establish the final dimension and remove the as-deposited coating roughness. However cutting lubricants, oils, and coolants will penetrate and remain in coatings with open porosities and remain after machining [10] if the coated part is not treated afterwards. For cermets, especially those with carbide grains, carbide tools are recommended because such coatings are very abrasive. For ceramic coatings only grinding is possible.

13.11.2 Grinding

The required finish and tolerance of ceramic coatings in general needs grinding. As with turning and milling, grinding conditions of ceramic-sprayed coatings are widely different from those of wrought or cast materials. Individual particles or

splats can be pulled out, or even the whole coating can delaminate from the substrate. The ductility of ceramic coatings is very low and, besides the poor thermal conductivity of coatings, the contact between coating and substrate is never perfect, and heat conduction toward the metal substrate is reduced. At last, ceramic coatings are porous and whatever may be the quality of the grinding, the surface will always have holes after grinding.

Machines commonly used are outside diameter grinders (cylindrical and centerless), surface grinders (horizontal and vertical spindle), and internal grinders [304]. However to work on complex shape parts, such as turbine blades, 6 axes machines with pressure control are required. To achieve complex machining at the coating surface, such as airflow channels for air sustained rotating machines, ultrasonic machining can be used. In this machining a constant stream of abrasive slurry (diamond, boron carbide, silicon carbide, alumina, etc.) passes between the tool and the work piece. The vibrating tool, combined with the abrasive slurry, abrades the material uniformly, leaving a precise reverse image of the tool shape. The tool must have lower hardness and toughness than those of the ceramic coating to be machined.

Compared to machining of metal coatings, grinding is rather expensive and thus the quantity of material to be taken off must be as low as possible, implying that the coating thickness is as close as possible to the final dimension (±5 μm at the maximum).

Wet grinding is preferred to dry grinding because of the greater latitude in abrasive and wheel selection; it also allows using harder wheels resulting in better finishes and less dressing [10]. The selection of the grinding wheel depends on the coating hardness and microstructure. The handbook of thermal spray technology [10] proposes a few rules for this selection.

The grinding variables: wheel speed, work speed, area of contact, grinding fluid filtration, and proper fluid concentration are also important parameters. At last, after a period of time when the abrasive grains of the wheel have wear or when the wheel face becomes loaded with the ground material, the wheel must be dressed with a diamond tool.

13.11.3 Abrasive Belt Grinding and Polishing

Metal, cermet, and ceramic-sprayed coatings can be ground and polished with coated abrasive belts. The main advantages of these belts are that they cut without overheating; they need no dressing and can be rapidly changed when worn. The coated part is mounted in a fixture or positioned on a lathe. The part is either transverse or rotated under the belt head. Belt speed is generally 30–40 m/s, while the part speed varies between 0.13 and 1 m/s. The grain size of belts can be adapted to rapid stock removal or to improve finish.

13.11.4 Other Finishing Methods

13.11.4.1 Hand Stoning, Buffing, and Polishing

Hand stoning, buffing, and polishing can be accomplished with abrasive stone, stick, wheel, or paper [291]. Hands stoning and buffing give excellent results on soft metals with a bright finish, provided abrasive sizes are progressively decreased from coarse to fine. However the abrasive device is rapidly loaded and must be frequently dressed. Carbon and stainless steel coatings are difficult to hand stone to a good finish. Ceramics or cermets can be hand stoned to a light finish (well suited for parts with unusual contours). However with these techniques it is difficult to maintain a uniform thickness.

13.11.4.2 Tumbling and Burnishing

For large quantities of small parts or when parts have unusual contours, tumbling, and burnishing are well adapted. Tumbling is performed in a vibrating or rotating tub with an abrasive medium and water, while burnishing is the same but with hard metal balls instead of the abrasive. These hard balls are used to compress the surface, the final smoothness of which depends on pressure and frequency of ball-to-part contacts [291].

13.12 Post Treatment of Coatings

As already mentioned, sprayed coatings are more or less porous with porosities that can be interconnected and extend from the coating surface to the substrate or the bond coat. Post treatments of coatings are performed to enhance the bond strength, relax partially or totally residual stress, create compressive residual stress, close or reduce porosity, especially the interconnected one, create a barrier to corrosive or oxidizing products, improve coating homogeneity, improve splat or particle cohesion, obtain hard phase precipitation, or induce chemical modifications [10]. This is achieved by using different techniques, including fusion of self-fluxing alloys, heat treating or annealing, hot isostatic pressing (HIP), austempering, laser glazing, sealing, spark plasma sintering, peening densification, and diffusion. It is clear that heat treatment processes, where the coating top surface is heated to melt it partially or totally, either by flame, plasma or laser, may induce cracks as soon as temperature gradients are high.

13.12.1 Fusion of Self-Fluxing Alloys

13.12.1.1 Principle

Coatings are submitted to a post thermal treatment at a temperature between the solidus and liquidus states of the alloy, where important diffusion processes take place. This temperature is usually in the range 1,200–1,400 K. As already noted in Chap. 2, self-fluxing alloys contain boron and silicon (for example, CrBFeSiCNi), which are used as deoxidizers. As deposited self-fluxing alloys are rather porous. Upon coating reheating densification occurs (most of the pores are eliminated) and borosilicate ($B_2O_x.SiO_y$) is formed, according to reaction (5.4) in Chap. 5, and diffuses toward the coating surface as slag, which is mechanically removed afterwards by turning, milling, etc. The coating shrinkage can reach 20 vol.%, and the silicon and boron form complex silicides and borides, dispersed within the coating [10, 291]. At last, the high fusion temperature allows diffusion between substrate and coating and between splats, improving the bond strength and the coating cohesion. Of course the fusing temperature depends on the self-fluxing alloy chosen (between 1,020 and 1,121 °C), and it is very important to control it. A too high temperature results in excessive fluxing, depleting the alloy of silicon and/or boron and creating more slag. Too low temperatures induce poor bonding and high porosity.

13.12.1.2 Fusing Processes

The cheapest fusing method uses a flame torch or torches (depending on the part size) working with oxygen and either acetylene or propane. This process can be well adapted to parts with axial symmetry. A low flame velocity must be used to avoid blowing molten metal. The part and coating are gradually and uniformly heated to 760–870 °C before elevating the coating temperature to its fusing range. The torch movement and the surface temperature must be controlled if possible with automatic torch fusing equipment [291]. With furnace fusing, the heating, cooling, and working atmosphere can be easily controlled. Vacuum furnaces are also used. Industrially, furnace fusing is used for components with complex shapes or large parts, which are difficult to heat uniformly with flames.

Induction fusing is rather popular due to the savings in fusion time and energy cost. Laser fusing, if the right parameters are selected, can provide good quality coatings and the heating can be very well controlled. However it is generally preferable to preheat the part in a furnace and then let it cool slowly for example by placing it in vermiculite [291]. Nevertheless there are no significant differences in wear behavior of NiCrBSi coatings treated with flame or laser fusing [305].

13.12.1.3 Fusing Problems

Crack formation occurs when alloys are brittle and when the expansion mismatch between coating and substrate is high. To limit their formation, temperature gradients must be avoided with a uniform heating and a slow cooling. The latter is achieved with a furnace or by immersing the part in an insulating medium such as vermiculite.

Porosity, as noted previously, occurs with under-fusing (incomplete melting, wetting, and fluxing) or overheating. A problem of non-uniform heating can be observed with large parts. Nonuniform heating can also be observed with parts that are hollow or vary in wall thickness. High sulfur, selenium, or lead in the base metal can also cause porosity problems [291].

13.12.1.4 Examples of Results

Only a few examples are given to illustrate the complexity of the fusing process. Akebono et al. [306] have flame sprayed a Ni-based self-fluxing alloy and fused it in a vacuum furnace. They tested three fusing temperatures and three fusing times. Results are largely dependent on (a) size and population of porosities in the coating and (b) the hardness of the matrix (Ni-rich solid solution) of the coating. Gomez-del Rio et al. [307] have compared laser-cladding (LC), flame sprayed (FS) combined with surface flame treatment, and flame sprayed (FS) combined with laser treatment. All coatings show a similar microstructure composed mainly of a Ni solid solution matrix with dendritic structure and common phases precipitated on it with different distribution, size, and shape depending on the type of deposition process and the controlling coating properties.

Miguel et al. [308] have compared tribological properties of NiCrBSi coatings obtained by spray and fuse and as-sprayed coatings obtained by atmospheric plasma spraying (APS) and high velocity oxy fuel (HVOF) spraying. The fuse process produced precipitate growth as well as an improvement of the coating porosity to 0 % (according to the measurement precision). The spray and fused coating had a slightly lower hardness than the HVOF one (667 ± 142 against 819 ± 78 HV10), but its sliding wear resistance was the best. The main wear mechanism was adhesion between coating surface and the sliding surface, but abrasion and delamination also took place.

Shrestha et al. [309] have studied erosion–corrosion characteristics of self-fluxing NiCrMoSiB coatings deposited onto carbon steel (BS970 EN8) and stainless steel (UNS 31603) substrates using a commercial HVOF thermal spray process. The coatings were studied in as-sprayed, vacuum-sealed (by polymer impregnation), and vacuum furnace fused conditions. The study showed that the effect of sealing by polymer impregnation did not significantly alter the erosion–corrosion behavior of the sprayed coating. However, there was an improvement in erosion–corrosion durability afforded by the postfusion process.

Serres et al. [310] have studied NiCrBSi coatings produced by APS and in situ laser irradiated by a diode laser. In situ irradiation (laser remelting after plasma spraying) is very suitable to reduce environmental impacts. The in situ process allows the construction of denser coatings than APS with finer structures, without cracks and porosity. The coating is metallurgical bonded to the substrate. The in situ process allows the construction of denser coatings than APS with finer structures, without cracks and porosity. This treatment is also more environmentally friendly than hard chromium plating, thus it can be another alternative.

13.12.2 Heat Treating or Annealing

13.12.2.1 Definition

By definition annealing corresponds to a heat treatment that alters the microstructure of a material causing change in properties such as strength, hardness, ductility, etc. For thermally sprayed coatings, annealing or heat treating is performed [10] at high temperatures, but well below the coating melting temperature, Tm. It takes place at atmospheric pressure in air or more generally in a controlled atmosphere or under vacuum. The treatment induces changes in microstructure and thermomechanical properties, formation of amorphous phase, relaxation of residual stress (temperature must be over that of recovery $\approx 0.4 \times T_m$), diffusion between substrate and coating improving the bond strength, coating densification by increasing inter-splat cohesion, recrystallization and grain growth occurring through sintering, reduction of coating oxide content when heated in hydrogen atmosphere or complete oxidation when heated in oxygen atmosphere, carbide precipitation from solid solutions with cobalt, thus enhancing the coating toughness, modification of electrical properties.

13.12.2.2 Examples of Results

Gärtner et al. [311] have shown that the mechanical properties of cold-sprayed coatings improve substantially with heat treatment more than any other thermally sprayed coatings, mainly thanks to diffusion effects during their annealing. Stoltenhoff et al. [312] found that annealed cold-sprayed coatings exhibit superior electrical properties compared to HVOF coatings. Copper coatings at different coating parameters were cold sprayed by Sudharshan Phani et al. [313] and subjected to various post-treatments. The electrical conductivity was improved with heat treatment carried out in vacuum at different temperatures and for different durations. Calla et al. [314] have shown that the copper cold spray conditions play a role in the annealing mechanisms.

Koivuluoto et al. [161] have studied cold-sprayed Cu, Ni, and Ni–30 wt% Cu, and the effect of annealing on microstructure and corrosion behavior. Cold-sprayed

Ni coating became denser during heat treatment. Hall et al. [315] showed that annealed cold-sprayed Al samples exhibited mechanical properties that were similar to those of wrought 1100 H14 aluminum. The annealed samples showed a reduction in ultimate strength but a dramatic increase in ductility, with up to 10 % elongation. Zhang et al. [316] have cold-sprayed Ni/Al alloy powders, synthesized by ball milling of a nickel–aluminum powder mixture with a Ni/Al atomic ratio of 1:1. The as-sprayed alloy coating exhibited a laminar microstructure retained from the mechanically alloyed powder. The annealing of the subsequent Ni/Al alloy coating at a temperature higher than 850 °C leads to complete transformation from a Ni/Al alloy to a NiAl intermetallic compound. Wang et al. [317] cold-sprayed an iron/aluminum composite coating using iron and aluminum powder mixtures. The coating was annealed at different temperatures aiming at forming an iron aluminide intermetallic coating. By increasing the annealing temperature to 900 °C, the deposit transformed to a mainly FeAl phase with a trace of remaining Fe phase. Li et al. [318] have deposited by cold spraying a thick and relatively porous Ti coating. After annealing at 850 °C for 4 h under vacuum conditions, the Ti coating still presented a porous structure but with more uniformly distributed small pores and metallurgical bonding between the deposited particles. The optimized cold spray parameters led Zahiri et al. [319] to produce a dense cold spray structure. Annealing improved its ductility by nucleation and growth of equiaxed grains, which include an ultrafine grain structure. Yang et al. [320] have deposited through vacuum cold spray a nano-TiO_2 photo-catalytic coating using both a composite powder (nano TiO_2 powder and polyethylene glycol) and nano TiO_2 powder. They found that the photo-catalytic activity of the coating deposited by the composite powders was significantly influenced by the annealing temperature. Better adhesion was achieved when the coating was annealed at temperatures between 450 and 500 °C. The adhesion of the coatings deposited with the composite powder was better than the primary nano-TiO_2 powder and presented a higher photo-catalytic activity than that deposited with the primary nanoparticles. The high activity was attributed to the existence of large pores that benefits the contaminant transportation in the porous coating.

Prudenziati and Gualtieri [321] have studied electrical properties in the temperature range 20–500 °C, of resistors made of Ni and Ni20Cr-sprayed powders by five laboratories. Annealing at temperatures from 200 to 400 °C resulted in an irreversible decrease of resistance. Karthikeyan et al. [322] have studied the effect of powder, spray, and coating parameters on superconducting properties of plasma-sprayed $Y_1Ba_2Cu_3O_{7-x}$ coatings. Optimizing spray parameters yielded strong, adherent, and dense coatings on many substrates. Oxygen annealing at 950 °C for an hour turned the coating from an insulator to a 90 K superconductor.

The manifold of structural defects governs the effective elastic properties of coatings, and they change as the defect structure changes during annealing. Damani and Wanner [323] have studied the micro-structural development in plasma-sprayed alumina (Al_2O_3), as a function of annealing temperature. Results showed that annealing even at moderate homologous temperatures already had a noticeable effect on the elastic properties. The effective elastic behavior of the material was

described by the generalized Hooke's law and the velocities of elastic waves propagating in the directions of the principal material axes were measured using an ultrasonic spectroscopy technique. Upon annealing at higher temperatures, very strong elastic constant changes were observed: increases of about 300 % as compared with the as-sprayed material. Marrocco et al. [324] investigated HVOF sprayed quaternary Al–Sn-based alloys. The as-sprayed deposits have microstructures that differ significantly from those of the gas-atomized feedstock powders. Annealing at 300 °C causes the dispersed Sn phase to coarsen and increases the fraction of NiAl3 and Si precipitates in the Ni- and Si-containing coatings, respectively, compared with the as-deposited alloy.

The phase transformation of plasma-sprayed yttria partially stabilized zirconia (Y-PSZ) coatings has been extensively studied. For example, coatings were exposed to an alternating heat treatment at different temperatures, after annealing at 773 K and 1,073 K in order to control stress relief [325]. The response of Y-PSZ plasma-sprayed deposits to annealing at 1,000, 1,200, and 1,400 °C with times from 1 to 1,000 h has been evaluated [326]. Results show that the yttria concentration of the as-sprayed tetragonal zirconia component generally decreased with increasing annealing temperature and time. Markocsan et al. [327] have analyzed the influence of a long heat treatment (2,000 h/1,200 °C) on different coating characteristics of two types of TBC systems, partially stabilized with either yttria or dysprosia (i.e., YPSZ and DyPSZ). The microstructure analysis revealed that the coating microstructure was significantly dependent on both spraying parameters and heat treatment conditions. Li et al. [328] have cold sprayed a dense NiCoCrAlTaY bond coat without oxidation during spraying. They have shown that through control of the pretreatment condition, the fast grown spinel can be changed to exclusive α-Al_2O_3 due to limited oxidation of the superalloy bond coat during cold spraying, which led to an increase of thermal cycle life time by as much as a factor of 10.

Laribi et al. [329] have studied the influence of a nickel–aluminum (80:20 %) bond coat post-annealing it at 850 °C in air for 1 h on the residual stress in two sprayed superalloys: blend of Cr–Ni steel and Cr–Mn steel on the one hand, and molybdenum on the other hand. With the post annealing stress was relaxed in both cases.

13.12.3 Hot Isostatic Pressing

Hot isostatic pressing (HIP) is the simultaneous application of heat (temperatures below the melting point, about 1,100 °C for steel and 975 °C for nickel) and pressure between 50 and 300 MPa in an inert atmosphere to an encapsulated coated substrate. The heat promotes diffusion (enhanced bond strength and splat cohesion), and the pressure collapses and shrinks pores. Of course at those temperatures the residual stress is relaxed and the fracture toughness is enhanced [10, 291]. The main industrial application is for near net-shaped components thermally sprayed with high-added values, according to the relatively high cost of the process.

For example, Stewart and Ahmed [330] have investigated the influence of the HIP on the Rolling Contact Fatigue (RCF) performance of thermally sprayed WC–12 wt% Co coatings. By increasing the HIP temperature to 1,200 °C, and maintaining full film lubrication, it is possible to achieve a fatigue life in excess of 70 million stress cycles without failure in relatively thin (50 μm) cermet coatings. Stoica1 et al. [331] have HIP treated (850 °C for one hour) WC–12Co coatings sprayed by a HVOF system onto SUJ-2 bearing steel substrate. The sliding wear performance of test coupons was drastically improved, not only in terms of coating wear but also in terms of the total volume loss.

Khor and Loh [332] studied HIP treatment at increasing temperatures and pressures of plasma sprayed Ni-based alloy coatings. HIP changed the microstructure and increased the microhardness of the coatings. Results showed that, for temperatures below 750 °C, the elastic modulus of HIPed coatings was larger than that of as-sprayed coatings.

Abdel-Samad et al. [333] have studied the influence of hot isostatic pressing on thermal fatigue resistance of plasma-sprayed coatings onto die-casting molds. HIP treatment was performed at 1,100 °C and a pressure of 100 MPa for 6 h using argon gas, heating for 3 h and slow cooling to room temperature. The hardness did not decrease, residual stresses were attenuated, and the fatigue life of steel die specimens was increased. The HIPed coatings showed low residual tensile stress indicating their high relaxation through the HIPing process.

13.12.4 Austempering Heat Treatment

Another means to promote diffusion at the substrate and coating interface and to collapse the internal pores is austempering. The heat treatment is performed in molten salt baths. For example, Lenling et al. [334] have immersed coated samples in an 870 °C neutral salt for 30 min and then quenched them in a neutral salt bath at 315 °C for 30 min. Finally the parts were cooled and rinsed with room temperature water. Coatings, about 250 μm thick, were composites WC–Co and Ni-based alloys plasma sprayed onto AISI 5150 steel substrates. The percentage of WC phase was increased and less desirable carbide phases formed during plasma spraying were eliminated. The bond to substrate was improved, the coating hardness increased, and residual compressive stresses were induced.

13.12.5 Laser Glazing

The advantage of laser heat treating and glazing is that the thermal energy applied is perfectly controlled with respect to the amount and the location on the surface to be treated. Lasers used are mainly CO_2 continuous wave (c.w.) lasers at 10.6

μm with power levels up to 5 kW, diode lasers with power levels in the few kW range, CO_2 pulsed lasers with power levels of a few hundred watts and neodymium-doped-yttrium-aluminum-garnet (Nd/YAG laser) at 1.06 μm. For all treated surfaces, the intensity of the hemispherical reflection coefficient, R, must be considered, the energy or power absorbed by the surface being proportional to $(1–R)$. With a wide range of energy densities, possible accurate temperature profiles can be obtained at precise locations in different depths of the coating. The treatment is limited to heat treating or melting of the surface (laser glazing). In the latter case, the rapid solidification through the coating and substrate allows microstructural refinements and other metallurgical changes modifying coating properties, wear, or corrosion resistance and tribological properties [10]. Of course it must be kept in mind that for sprayed materials with low thermal conductivity (below 30–40 W/m/K) temperature gradients can induce important stresses, which will result in relaxation by macro-cracks orthogonal to the coating. A few examples illustrate advantages of laser glazing.

13.12.5.1 Continuous Wave (c.w.) CO_2 Lasers

Plasma-sprayed zircon ($ZrSiO_4$) coatings are generally made of ZrO_2 and SiO_2 due to the fast quenching of dissociated zircon. Schelz et al. [335] have shown that, by using low-energy (8W) CO_2 laser treatment, the inverse reaction occurs, unfortunately with a low recombination rate. When glassy particles are incorporated in the coating with a large-size distribution from approximately 10 μm to more than 100 μm, the result is a production of a substantial amount of recombined $ZrSiO_4$ when the same laser parameters are used. Thus, the laser treatment with additives may provide technological benefits over other heat treatment techniques where high-temperature annealing (1,600–1,900 K) must be used for the same result.

The microstructure, electrochemical, and wear performances of HVOF WC–24 % Cr_3C_2–6 % Ni coatings on inconel were modified greatly by laser heat treatment [336]. The laser beam spot was elliptical 5 × 4 mm^2 with a power of 400 W. The relative content of Cr_3C_2 and Ni in HVOF sprayed coatings had increased, as well as the coating hardness, after laser heat treatment, and a dense interface between the coating and substrate was obtained. Laser heat treatment was also helpful to form denser oxide tribo-film and improve the cohesion of WC, Cr_3C_2, and Ni phases, together with an improvement of the wear performance of the coating.

Pokhmurska and Ciach [337] have remelted (Fe–Cr–B) + Al-based electric arc sprayed coatings with a CO_2 c.w. laser The surface was covered with a graphite-based antireflection coating. Laser melting markedly improved coating microstructure and density, with much better chemical homogeneity. Results also demonstrated an improvement of mechanical and corrosion properties of the coatings.

Al_2O_3–13 wt.% TiO_2 plasma-sprayed coatings onto a titanium alloy (Ti–6Al–4V) substrate were remelted with a c.w. CO_2 laser [338]. The laser-remelted coatings (LRmC) possessed a much denser and more homogenous structure and excellent metallurgical bonding to the substrate. The average porosity of the LRmC was reduced

to 0.9 %, compared with 6.2 % of the as-sprayed coatings. The metastable γ-Al_2O_3 phase in the as-sprayed coatings transformed to stable α-Al_2O_3 during laser remelting. The microhardness of the coatings was enhanced to 1,000–1,400 HV0.3 after laser remelting, which was much higher than that of the plasma-sprayed coatings.

Aluminum coatings on austenitic stainless steel substrates were laser remelted (c.w. 5 kW CO_2 laser) [339]. The residual porosity was eliminated and phases were mainly AlFeNi, Cr, and CrFeNi. A metallurgical bond between the coatings and the base metal was formed after laser surface remelting.

13.12.5.2 Pulsed CO_2 Lasers

Continuous wave CO_2 laser and a pulsed laser with cylindrical focal lens have been used to glaze the surface layer of plasma-sprayed ZrO_2–20 wt% Y O_3/MCrAlY coatings [340]. Defects, such as bubbles or depressions, were usually generated with a continuous wave laser, but a high-quality glazed layer was produced using a pulsed laser. The surface roughness of the plasma-sprayed ceramic coatings was significantly improved by laser glazing. The surface roughness decreased slightly as the pulse frequency increased for the glazed surface.

Pulsed laser glazing of plasma-sprayed hydroxyapatite coatings modified the morphology of their surface as well as their phase composition [341]. The surface became smoother and the phase content was richer in α-tricalcium phosphate, tetracalcium phosphate (TTCP) than that of as-sprayed deposits, TCP and TTCP are the products of HA decomposition. The fraction of TTCP was larger in all samples treated with a laser.

13.12.5.3 Pulsed Nd/YAG Lasers

Ni–20Cr and Stellite-6 powders have been sprayed on boiler tube steels with a shrouded plasma spray process using NiCrAlY as bond coat [342]. The coatings showed some porosity (2–4 %). Laser remelting of the coating was performed with a pulsed Nd: YAG laser: 300 W with pulse energy of 6 J and pulse width of 20 μs, the repetition rate being 10 Hz. It appeared to be effective in reducing the porosity to less than 0.5 %. However laser remelting further led to a significant dilution of the coating due to surface alloying of the coating with the bond coat and substrate. Laser remelting of the coatings led to a decrease in microhardness.

Laser surface melting was shown to reduce surface roughness of a cordierite glass coating which was air plasma sprayed [343]. Subsequent de-vitrification of the cordierite was found to depend upon the physical and chemical alterations induced by the laser treatment. Crystallization in the as-sprayed coating was controlled by the TiO_2 distribution in the coating microstructure. After laser treatment, the de-vitrification was dominated by nucleation at micro-cracks, since the inter-splat structure was homogenized both physically by the removal of splat boundaries and chemically by the redistribution of TiO_2 in the coating.

Improvement in copper erosion resistance at temperatures between 25 °C and 300 °C can be obtained by forming copper coatings containing 45 vol.% boride particles. To resist erosion due to impact of coarse iron ore particles, these coatings must possess microstructural features, which are larger than the size of impacting particles. Laser melting of plasma-sprayed Cu–boride coatings produces large intricate islands of ductile and hard phases [344]. The peculiar microstructure architecture developed upon laser melting was found suitable to withstand erosion attacks.

13.12.5.4 Power Diode Laser

Ahmed et al. [345] have HVOF sprayed Ni-based superalloy Inconel 625 coatings and laser re-melted them using a high power diode laser. The performance gap between bulk and HVOF sprayed Inconel 625 is largely due to galvanic corrosion between Cr-depleted re-solidified regions and non-melted material in the coatings. Laser surface melting of HVOF coatings of Inconel 625 largely improved the corrosion resistance due to the elimination of both porosity and localized regions of material depleted in Cr.

Several studies have been undertaken recently to adapt yttria partially stabilized zirconia (YPSZ) thermal barrier coating (TBC) characteristics during their manufacturing process. Antou et al. [346] have treated the coating pass by pass as it was manufactured with a 3 kW diode laser at 848 nm. The input energy effect was studied by varying the scanning velocity (between 35 and 60 m/min), and consequently the irradiation time (between 1.8 and 3.1 ms, respectively). Experiments showed that the coating thermal conductivity was lowered by more than 20 % and that coating resistance to isothermal shocks was increased significantly.

13.12.6 Sealing

13.12.6.1 General Remarks

As thermally sprayed coatings (except PTA) are more or less porous with connected porosities they are not very suitable for corrosion protection. This situation can be drastically improved by curing their inter-connected porosities through sealing them. The advantages of sealing are the following [10]:

- Prevention of the corrosive substance (liquids or gases) from penetrating the coating and attacking the coating/substrate interface
- Limitations of the lodging of wear debris in the coating
- Enhancement of inter-splat cohesion
- Production of special surface properties such as nonstick surfaces
- Extension of the life of aluminum or zinc coatings on steel to prevent corrosion

13.12.6.2 Sealing Processes

Knuuttila et al. [347] gave an excellent description of the process presenting various sealant types and impregnation methods, as well as factors influencing impregnation. Impregnation methods can be divided into four categories: atmospheric pressure impregnation, low-pressure impregnation, overpressure impregnation, and a combination of these. The method of choice depends on the size of the coated component, the required penetration depth, and the sealant, the choice of which also depends on the coating material and the application:

- Low-pressure or overpressure impregnation is suitable for small components.
- Atmospheric pressure impregnation is economically viable for larger components but the result depends strongly upon the sealant-coating wettability (in fact it is the dynamic wetting angle that has to be considered) and the sealant viscosity. Sealing requires controlling humidity by keeping the surface temperature above the dew point where water condenses to any surface. The sealant deposition techniques used are brushing, dipping, or spraying.

The advantage of low pressure is the removal of moisture and air from pores and cracks improving the sealant penetration depth. However the pressure must be adjusted to the sealant vapor pressure to avoid excessive evaporation.

Overpressure impregnation is much less sensitive to the sealant coating contact angle that can be over 90°.

Sealants for impregnation are either organic or inorganic or metals. In sealing the aim is to seal the porosity to as great a depth as possible. However, there are applications where only a relatively thin sealant layer is considered optimum [347]. A low interfacial surface tension between the coating and the sealant is the most important factor dictating the penetration depth. The pore size distribution of the coating is equally important; larger pores might not become filled due to lowered capillary pressure.

(a) Organic Sealants

The often-used organic sealants are based on epoxies, phenolics, furans, polymethacrylates, silicones, polyesters, polyurethanes, and polyvinylesters. Waxes can be used as well. The choice depends upon the service temperature. For example, wax can be used only in cold conditions, phenolic resins up to 150–260 °C and methacrylate up to 150 °C [291]. A good sealing depends on how coatings were treated before impregnation and how long the impregnation time was. These sealants are cured by heat, ultraviolet light, or high-energy radiation [347]. However curing the sealants induces some shrinkage, and only low curing shrinkages can prevent the transport of electrolyte through the coating [348].

(b) Inorganic Sealants

These are mostly used for high-temperature applications. Besides aluminum phosphates and sodium and ethyl silicates, various sol–gel type solutions and chromic acid have been used for sealing purposes. For example, phosphate acts as refractory glue that forms solid bridges over pores and cracks; it has also a beneficial effect in transforming the residual stress of the coating into compression. Sol–gel processes refer to the formation of a stable sol, the hydrolyzing of the sol to a gel, and the calcinating of the gel at elevated temperature to oxide. The sol includes a variety of metal alkoxides, nitrates, or hydroxides [347].

(c) Metals

Molten metals are used for sealing and strengthening purposes. The metal-coating wetting is a key issue. For example, zirconia is completely wetted by pure manganese [347].

(d) Other Means

These include electroplating or enamel deposition.

13.12.6.3 Examples of Results

(a) Organic Sealants

Shrestha et al. [349] have studied the erosion–corrosion characteristics of a Ni–Cr–Mo–Si–B coating applied by a high-velocity oxy-fuel (HVOF) process onto an austenitic stainless steel as sprayed, after vacuum sealing with polymer impregnation, and after vacuum furnace fusion. Erosion–corrosion was produced by the impact of a liquid jet of 3.5 % NaCl solution at 18 °C at a velocity of 17 m/s, with or without 800 ppm silica sand. The study showed that sealing with polymer impregnation did not significantly modify the erosion–corrosion behavior of the sprayed coating. However, there was a significant improvement obtained by the postfusion process in coating durability under these erosion-corrosion conditions.

Kim et al. [350] have sealed Al_2O_3–13 wt% TiO_2 using three commercial polymeric sealants. The penetration depth of the sealants into the ceramic coating was from 0.2 to 0.5 mm depending on the sealants used. All of the micro-hardness, two-body abrasive wear resistance, bond strength, and surface roughness of the ceramic coating after the sealing treatment were improved. Three-point bending stress of the ceramic coating after the sealing treatment was decreased. This was attributed to the reduced micro-crack toughening effect since the cracks propagate easily through the lamellas of the coating without crack deflection and/or branching after the sealing treatment.

Ctibor et al. [351] studied unsealed and epoxy resin sealed plasma-sprayed specimens prepared from alumina as well as alumina–13 % titania. It was shown that the abrasion wear resistance of the epoxy resin sealed coatings is significantly better than that of the as-sprayed coatings for both types of applied tests.

(b) Inorganic Sealant

One of the most popular sealants, especially for ceramics, is aluminum phosphate. Leivo et al. [352] have studied plasma-sprayed Al_2O_3 and Cr_2O_3 coatings sealed by aluminum phosphates. Phosphates were formed throughout the coating, down to the substrate. The sealing increased the hardness of the coatings by 200–300 Vickers hardness (HV) units. Abrasion and erosion wear resistances were increased by the sealing treatment. The treatment also significantly reduced open porosity, as shown in electrochemical corrosion tests.

Ahmaniemi et al. [353, 354] have modified thick (1,000 μm) thermal barrier coatings ($25CeO_2$–$2.5Y_2O_3$–ZrO_2, 22MgO–ZrO_2, $8Y_2O_3$–ZrO_2) for diesel engines with laser glazing and phosphate-based sealing treatments. In phosphate-sealed coatings the penetration depth of the sealant was approximately 300–400 μm and micro-hardness at the range of 825–882 HV0.3. The open porosity of the phosphate sealed coatings was reduced by 24–48 % depending on the coating material. The optimal thickness of the melted layer in laser-glazed coatings was 50–150 mm. In all cases the melted zone was significantly densified and a vertical macro-crack network was introduced.

The same authors [355] have studied in three test series several modified thick thermal barrier coatings, in which the maximum coating temperature was fixed to 1,000, 1,150, and 1,300 °C. The modified coating structures were all segmentation-cracked coatings either by using specific spraying parameters or by laser glazing. Some of these coatings were surface-sealed, using aluminum phosphate or a sol–gel-based sealant. Laser glazing significantly decreased the bending modulus of the $8Y_2O_3$–ZrO_2 coating. Correspondingly, aluminum phosphate sealing had an opposite effect. Both sealing treatments reduced the thermal cycling resistance of the segmentation-cracked coatings. The decrease of the thermal cycling resistance of aluminum phosphate sealing was rather high, whereas in sol–gel sealing it was moderate.

Ahmaniemi et al. [355] studied the residual stress induced by an aluminum phosphate sealing of plasma-sprayed alumina and chromia coatings. Sealing treatments were performed at 200, 300, and 400 °C with treatment times for these temperatures of 16, 4, and 2 h, respectively. Strengthening of the alumina coating is mainly based on chemical reactions between the coating and the sealant, leading to bonding phosphate phases and obviously higher stiffness of the coating. The aluminum phosphate sealing treatment changes stress states of the alumina and chromia coatings toward compression. The tensile stress state of the Al_2O_3 coating decreases during the sealing treatment and the stress becomes even compressive when measured with the hole-drilling method. The aluminum phosphate sealing

treatment temperature seems to influence strongly the residual stress state of chromia coatings. Higher sealing treatment temperature leads to higher compressive stress state and better abrasion wear resistance.

Troczynski et al. [357] have sealed zirconia thermal barrier coatings using sol–gel alumina. The overall reduction of porosity was however small (from ~12 to ~11 %), preserving the strain and thermal shock tolerance of the coatings. Burner rig tests showed an increase in sealed coating lifetime under thermomechanical fatigue conditions.

Electrodeposition of Ni has been used in an attempt to seal the open porosity of plasma-sprayed alumina coatings [358]. It is a promising sealing treatment for sprayed alumina coatings intended for tribological applications. The hardness and coating cohesion increased and the wear resistance was found to increase markedly in all wear tests as a result of the sealing. Conventional Ni plating was successfully used [359] to seal the surface pores of an arc-sprayed coating. Electroplating of Ni seals the pores and provides a smooth finish to the sample, enhancing the corrosion resistance of a Hastelloy coating.

The oxidation and hot-corrosion behavior of a Co–Ni–Cr–Al–Y coating produced by high-velocity oxygen fuel (HVOF) with and without an enamel coating were investigated [360] in air at 900 °C and in molten 75 wt% NaCl + 25 wt% Na2SO4 at 850 °C. The results show that the enamel coating possesses excellent hot corrosion resistance in a molten salt, in comparison with the as-sprayed coating. In the hot-corrosion tests, breakaway corrosion did not occur on the samples with the enamel coating and the composition of the enamel did not significantly change?

Caron et al. [361] have developed a stable hermetic seal composed of a ceramic matrix charged with glass particles, atmospheric plasma sprayed to obtain efficient air tightness between two SOFC cells. The developed seal was found to be solid, undistortable, and adhesive to its support at ambient temperature. The sealing properties were acquired when the SOFC was put into service: the glassy phase migrated into the peculiar plasma-sprayed microstructure of the ceramic matrix toward the interface leading to the air tightness of the deposit. With the seal, the leak rate observed at 7 kPa was 0.43 Pa l/s, i.e., below the requirement of the US Department of Energy, which is 0.5 Pa l/s.

13.12.7 Spark Plasma Sintering

Spark plasma sintering (SPS), applied under compressive loading, is a new process for the densification of porous materials. The sparks are generated between the particles and cause the material to be heated rapidly.

Khor et al. [362] have applied SPS for fabricating high performance yttria-stabilized zirconia (YSZ) electrolyte for SOFC starting from detached plasma-sprayed coating. SPS was performed at 1,200, 1,400, and 1,500 °C, each sintering cycle having a holding time of 3 min. A microstructure transition occurred above

1,200 °C, where the typical plasma sprayed lamella structure transformed to a granular-type structure, but the phase composition remained the same. The thermal conductivity of the as-sprayed YSZ was greatly increased (up to two times) by the SPS post-spray heat treatment, and there was an optimum of multiple SPS cycles for the enhancement of the thermal conductivity. The ion conduction resistivity was reduced drastically with an increase of the SPS temperature for multiple SPS cycles.

Prawara et al. [363] also used SPS to densify a ZrO_2–25 wt% MgO flame-sprayed coating on a steel substrate. In the SPS process, the thermal spray-coated steel was exposed to rapid heating under vacuum at temperatures of 900, 950, and 1,000 °C under compressive load for 10 min. The as-sprayed coating had high porosities of up to 22 %, but the porosity fell to below 5 % after SPS treatment. The bond strength and micro-hardness of the coating were also increased. These properties could be controlled by adjustment of the SPS temperature and the compressive load.

13.12.8 Peening or Rolling Densification

To close surface connected pores and improve surface smoothness, shot peening or rolling can mechanically treat metallic-sprayed coatings [291]. This treatment results in pore closure and development of compressive residual stress. A few examples are given below.

Zhou et al. [364] have shot peened, with different lengths of operating time, a CoCrAlY bond coat on a disk-shaped Ni-based superalloy. A moderate shot peening processing modified the surface of the bond coat and improved its oxidation resistance. The surface roughness (Ra) of the specimen without shot peening was around 2.6 μm and 1.09 μm after 3 cycles of shot peening. An EB-PVD YSZ coating was deposited on the compacted bond coat and the coating exhibited a satisfactory thermal cycling lifetime of 1,643 cycles at 1,293 K. The shot peening process increased the axial fatigue strength of AISI 4340 steel WC–10Ni HVOF sprayed by Junior et al. [365]. The fatigue limit increased by 13.3 % from 750 MPa to 850 MPa.

Kubiak et al. [366] investigated a shot peening treatment and a WC–17 % Co coating applied to 30NiCrMo steel against 52100 steel under plain fretting and complex fretting fatigue loading. Only WC–17 % Co decreased the value of the coefficient of friction. Shot peening treatment had very little influence on fretting wear resistance under gross slip conditions and had no influence on the crack nucleation threshold, but performed well against crack propagation under plain fretting and the studied fretting fatigue conditions.

Marin de Camargo et al. [367] evaluated a tungsten carbide cobalt (WC–17 % Co) coating applied on an Al 7050-T7451 alloy by the high velocity oxy fuel (HVOF) process, used to replace anodizing. Anodic films were grown on 7050-T7451 aluminum alloy by sulfuric acid anodizing, chromic acid anodizing, and hard anodizing. Experimental results revealed increase in the fatigue strength of Al 7050-T7451 alloy associated with the WC 17 % Co coating. But a reduction in

fatigue life occurred in the shot peened and coated condition.. The shot peening process may induce surface modification, such as surface roughening that, considering fatigue damage, accelerates nucleation and fatigue crack propagation.

Costa et al. [368] studied the influence of a WC–10 % Co–4 % Cr coating deposited by HVOF on the fatigue strength of a Ti–6Al–4V alloy. Comparison of the fatigue strength of the coated specimens and the base material shows a decrease when the parts are coated. They observed that the effect is more pronounced in high cycle fatigue tests. The shot peening prior to the thermal spray coating is an efficient surface treatment to improve fatigue resistance of coated Ti–6Al–4V.

13.12.9 Diffusion

Aluminum may be diffused into a steel or silicon bronze substrate to protect against the corrosive action of gases at temperatures of up to 870 °C [291]. After being sprayed, the part is coated with a bituminous aluminum sealer or other suitable material. It is then held at 788 °C during the appropriate time for diffusion depending on the thickness.

13.13 Summary and Conclusions

Thermally sprayed coating properties are quite different from those of bulk materials. They result from the interaction of solid particles or wire or rod or cord with high energy gases produced by flame, HVOF, HVAF, D-gun, plasma, transferred arc, wire arc, and cold spray. In all thermal processes high-energy gases are hot except in cold spray, and have temperature (except for cold spray) and velocity distributions, which differ according to the process used and its working parameters. Depending on particle impact velocities and temperatures, strongly linked to the spray process, layered splats have different percentages (about 20–60 %) of real surface contact between themselves or between them and the substrate. These contacts also strongly depend, at least for those between first splats and substrate, on the substrate preheating temperature and the elimination of adsorbates and condensates, among other parameters. When spraying polymers, due to their viscosity, a few orders of magnitude higher than that of conventional melted sprayed materials, the substrate must be preheated close to the polymer melting temperature. It is also preferable to spray with HVOF or HVAF guns to beneficiate of the shear thinning behavior of viscosity. Moreover, these processes limit the residence time of polymer particles within the hot jet, limiting or avoiding their decomposition. According to the very low thermal conductivity of polymers, generally below 0.2 W/m/K, heat propagation within particles is important and their central core is generally unmelted upon impact. This is also a good reason to preheat the substrate close to the polymer melting temperature. Cold-sprayed

particles form coatings by deformation of ductile cold particles when their impact velocity is above the so-called critical velocity. If these coatings are often almost fully dense, the contact between layered deformed particles is generally rather poor (less than that with other thermal spray processes). Coating properties (mechanical, thermal, electrical,. . .) depend strongly upon:

- The real contact between layered splats or plastically deformed particles
- The different defects generated during spraying: unmelted particles, pores either globular or elongated (those between splats), micro-cracks resulting from quenching stress in ceramic splats and macro-cracks propagating generally parallel to layered splats
- For cermet coatings the size of ceramic particles (generally WC or Cr_3C_2) imbedded within the sprayed particles
- The substrate roughness and its adaptation to the mean splat size and melting state
- The residual stress distribution within the coating, depending on the spray process but also on the coating and substrate temperature monitoring before (preheating), during (coating generation), and after spraying (cooling); for example, a tensile stress within the coating close to the substrate interface is generally detrimental to the coating adhesion under service conditions and must be avoided or limited.

Coating properties, besides depending on the spray process used, are also strongly dependent on the spray pattern and the coating time averaged (a few tenths of seconds) temperature distribution during the whole spray process. Sophisticated spray robots are required not only to control the spray pattern, especially for parts with complex shapes, but also to control locally the heat flux imposed by hot gases and hot particles. Well-controlled cooling systems must be used during spraying to monitor the coating temperature distribution. The parameters controlling the heat transfer to the substrate and coating under formation are particularly important when spraying polymers. The substrate must be preheated close to the polymer melting temperature, but their decomposition temperature is close to their melting one. As the thermal conductivity of polymers is very low, the precise control of the surface temperature of the coating under formation is mandatory. This is achieved by adapting the spray distance, the cooling system, the thickness of the pass and the duration of the heating by hot gases and particles, both through control of the spray pattern.

All the spray processes are complementary and not competitive, even if for each process some overlap with others exists. The choice of the spray process depends on the coating service conditions but also on the price the customer is ready to pay to obtain much better service conditions (for example, by spraying the same material with flame or HVOF).

Defects present in thermal sprayed coatings can be totally or partially cured by using post-treatments including: fusion of self-fluxing alloys, heat treatment or annealing, hot isostatic pressing (HIP), austempering, laser glazing, sealing, spark plasma sintering, peening densification, and diffusion. These treatments allow mainly relaxation of residual stresses, densification of the coating with increased inter-splat cohesion, and changing the coating microstructure and service

properties. Those performed at high temperature further promote diffusion between substrate and coating, improving the bond strength, and leading to precipitation of carbides from solid solutions with cobalt, thus enhancing the coating toughness, etc. However, as for the spray pattern and coating temperature monitoring, the post-treatment must be well controlled (temperature, surrounding atmosphere) to achieve reproducible and reliable properties.

At last it must be emphasized that coating properties such as microstructure, adhesion–cohesion, toughness, hardness, etc., must be analyzed regularly during the production to control the reliability and reproducibility of coatings. However the particular structure of coatings with defects is quite different from those of bulk materials when conventional measuring techniques are used.

Nomenclature

Latin Alphabet

a	Ratio of flattening velocity v_f to droplet impact velocity v_p
a_i	Thermal diffusivity (i = s for solid phase, i = l for liquid phase) (m^2/s)
A/C	Adhesion/cohesion of a coating (MPa)
b	Splat thickness (m)
Bi	Biot number ($Bi = d_p/(R_{th} \cdot \kappa_d)$
c	Sound velocity (m/s)
c_l	Sound velocity within the liquid droplet (m/s)
c_{pi}	Specific heat at constant pressure (i = s solid phase, i = l liquid phase) (J/kg.K)
d	Distance in the y direction between successive beads sprayed in x direction (m)
d_d	Thermal diffusion distance (m)
d_p	Impacting droplet diameter (m)
D	Equivalent splat diameter (m)
e_f	Thermal effusivity $e_f = (\rho_p \cdot c_{pp} \cdot \kappa_p)^{1/2}$ ($J/m^2\ K\ s^{0.5}$)
E_c	Young's modulus (GPa)
EF	Shape factor; ratio of the major to the minor axis of an elliptical splat
G	Strain energy release rate (J/m^2)
h	Convective heat transfer coefficient ($W/m^2\ K$)
h'	Coating thickness (m)
h_b	Bead height (μm)
h_c	Convective heat transfer coefficient ($\theta = 0$) ($W/m^2\ K$)
H	Substrate thickness (m)
K	Sommerfeld parameter at impact $K = We^{1/2}Re^{1/4}(-)$
K_f	Flattening splashing parameter
K_{ic}	Critical interfacial stress-intensity factor ($Pa\ m^{1/2}$)
K_{fc}	Critical value of K_f
K'	Beam curvature (m^{-1})

L_p Latent heat of solidification (J/kg)
m_p The particle mass (kg)
$\overset{\circ}{m}_p$ The powder mass flow rate (kg/s)
M Bending moment of a beam (N.m)
Ma Impact Mach number; $Ma = v_p/c_l$
p_h Water hammer pressure; $p_h = \rho_1 \cdot c_l \cdot v_p$(Pa)
p_t Transition pressure (Pa)
P Splat perimeter (m)
P' Force (N)
Pe Peclet number ($Pe = v_p \cdot d_p/a_p$)
r Radius (m)
Ra Average rougness (μm)
Re Particle Reynolds number at impact ($\mathrm{Re} = v_p \cdot d_p \cdot \rho_p/\mu_p$)
$\mathrm{Re_N}$ Reynolds number of the particle at its the normal impact velocity v_N, (-)
R_t Roughness: distance between the highest peak and the deepest undercut (μm)
R_{th} Thermal contact resistance (K m^2/W)
s Thickness of droplet's solidified layer (m)
s^* Dimensionless solid layer thickness ($s^* = s/d_p$)
S Splat surface (m^2)
SF Splat shape factor; $\mathrm{SF} = P/4 \cdot \pi \cdot \mathrm{S}(m^{-1})$
Ste_l Stephan number for the liquid phase ($Ste_l = c_p \cdot (T_p - T_m)/L_p$)
Ste_s Stephan number for the solid phase ($Ste_s = c_{ps}(T_m - T_o)/L_p$)
t Process time (s)
t_c Wave propagation time ($t_c = d_p \cdot v_p/4c_l^2$) (s)
t_i Induction time in cold spray process (or time of deposition delay) (s)
t_{ps} Preheating time (s)
T_m Melting temperature (K)
T_{mean} Coating temperature (K)
T_p Droplet temperature (K)
T_{ps} Preheating temperature (K)
T_s Substrate temperature (K)
T_t Transition temperature (K)
v_f Maximum flattening velocity (m/s)
v_N Normal component of the particle impact velocity ($v_N = v_p \cdot \cos\varphi$) (m/s)
v_p Particle impact velocity (m/s)
v_r The relative velocity spray torch-substrate (m/s)
v_s Solidification velocity (m/s)
v_m Heating rate (K/s)
w_b Bead width at mid-height (μm)
We Weber number at impact ($\mathrm{We} = \rho_p \cdot v_p^2 \cdot d_p/\sigma_p$)
x Characteristic system dimension (m)

Greek Alphabet

$\alpha_c\, t$	Expansion coefficient of the splat (K^{-1})
$\Delta\varepsilon$	Misfit strain
ε	Strain
φ	Angle between particle trajectory and an axis normal to the substrate (°)
η	Dimensionless radius ($\eta = 2 \cdot r/d_p$)
η_d	Deposition efficiency
θ	Contact or wetting angle (°)
K	Thermal conductivity (W/m K)
μ	Viscosity of molten particle (Pa s)
μ_o	Viscosity of molten particle at its melting temperature (Pa.s)
ν	Kinematic viscosity; $\nu = \mu/\rho$ (m^2/s)
ν'	Poisson's ratio
σ	Stress (Pa)
σ_p	Surface tension (J/m^2) or (N/m)
σ_q	Quenching stress after relaxation phenomena (MPa)
σ_q°	Quenching stress (MPa)
Ξ	Flexural beam stiffness (Pa m^4)

References

1. Ghafouri-Azar R, Mostaghimi J, Chandra S, Charmchi M (2003) A stochastic model to simulate the formation of a thermal spray coating. J Therm Spray Technol 12(1):53–69
2. Alkhimov AP, Kosarev VF, Nesterovich NI, Papyrin AN (1986) Method of applying coatings. Russian Patent 1618778, 8 Sept 1990, priority of the invention June 6
3. Alkhimov AP, Papyrin AN, Kosarev VF, Nesterovich NI, Shushpanov MM (1994) Gas-dynamic spray method for applying a coating. U.S. Patent 5,302,414, April 12
4. Gärtner F, Stoltenhoff T, Schmidt T, Kreye H (2006) The cold spray process and its potential for industrial applications. J Therm Spray Technol 15(2):223–232
5. Fauchais P, Vardelle A, Dussoubs B (2001) Quo vadis thermal spraying – invited paper. J Therm Spray Technol 10:44–66
6. Fauchais P (2004) Understanding plasma spraying. J Phys D 37:86–108
7. Hearley JA, Little JA, Sturgeon AJ (2000) The effect of spray parameters on the properties of high velocity oxy-fuel NiAl intermetallic coatings. Surf Coat Technol 123:210–218
8. Sampath S, Herman H (1996) Rapid solidification and microstructure development during plasma spraying deposition. J Therm Spray Deposit 5(4):445–456
9. Sampath S, Jiang X, Kulkarni A, Matejicek J, Gilmore DL, Neiser RA (2003) Development of process maps for plasma spray: case study for molybdenum. Mater Sci Eng A 348:54–66
10. Davis JR (2004) Handbook of thermal spray technology. ASM International, Materials Park, OH
11. Azarmi F, Coyle TW, Mostaghimi J (2008) Optimization of atmospheric plasma spray process parameters using a design of experiment for alloy 625 COATINGS. J Therm Spray Technol 17(1):144–155

12. Schmidt T, Gärtner F, Assadi H, Kreye H (2006) Development of a generalized parameter window for cold spray deposition. Acta Mater 54:729–742
13. Fauchais P, Vardelle M (2010) Sensors in spray processes – an invited review. J Therm Spray Technol 19(4):668–694
14. Fauchais P, Montavon G, Bertrand G (2010) From powders to thermally sprayed coatings. J Therm Spray Technol 19(1–2):56–80
15. Vardelle M, Vardelle A, Fauchais P, Li K-I, Dussoubs B, Themelis NJ (2001) Controlling particle injection in plasma spraying. J Therm Spray Technol 10:267–286
16. Ben Ettouil F, Mazhorova O, Pateyron B, Hélène Ageorges, El Ganaoui M, Fauchais P (2008) Predicting dynamic and thermal histories of agglomerated particles injected within a d.c. plasma jet. Surf Coat Technol 202(18):4491–4495
17. Chandra S, Fauchais P (2009) Formation of solid splats during thermal spray deposition. J Therm Spray Technol 18(2):148–180
18. Fukumoto M, Ohgitani I, Nagai H, Yasni T. Effect of substrate surface change by heating on flattening behavior of thermal sprayed particles. In: Lugscheider E (ed) ITSC 2005. DVS, Düsseldorf, Germany, e-proceedings
19. Cedelle J, Vardelle M, Fauchais P (2006) Influence of stainless steel substrate preheating on surface topography and on millimeter- and micrometer-sized splat formation. Surf Coat Technol 201:1373–1382
20. McDonald A, Moreau C, Chandra S (2007) Effect of substrate oxidation on spreading of plasma-sprayed nickel on stainless steel. Surf Coat Technol 202:23–33
21. Fukumoto M, Nagui H, Yasui T (2006) Influence of surface character change of substrate due to heating on flattening behavior of thermal sprayed particles. In: Marple B et al (eds) ITSC 2006. ASM International, Materials Park, OH
22. Li C-J, Li J-L, Wang WB (1998) The effect of substrate preheating and surface organic covering on splat formation. In: Coddet C (ed) Thermal spray: meeting the challenges of the 21st century. ASM International, Materials Park, OH, pp 473–480
23. Li C-J, Li J-L, Wang WB, Fu A-J, Ohmori A (1999) A mechanism of the splashing during droplet splatting. In: Lugscheider E, Kammer PA (eds) Thermal spraying, in united spray conference proceedings, Düsseldorf. DVS, Düsseldorf, Germany, pp 530–535
24. Li H, Danlos Y, Costil S, Coddet C (2007) Influence of laser induced surface topography on the surface static wettability in Protal®. In: Marple B et al (eds) Thermal spray (2007) global coating solutions. ASM International, Materials Park, OH, pp 1070–1074, e-proceedings
25. Li C-J, Li J-L (2004) Evaporated-gas-induced splashing model for splat formation during plasma spraying. Surf Coat Technol 184:13–23
26. Henrich VE, Cox PA (1994) The surface science of metal oxides. Cambridge University Press, Cambridge
27. Fukumoto M, Nagai H, Yasui T (2006) Influence of surface character change of substrate due to heating on flattening behavior of thermal sprayed particles. J Therm Spray Technol 15 (4):759–764
28. Fukumoto M, Yamaguchi T, Yamada M, Yasui T (2007) Splash splat to disk splat transition behavior in plasma-sprayed metallic materials. J Therm Spray Technol 16(5–6):905–912
29. Coddet C, Montavon G, Ayrault-Costil S, Freneaux O, Rigolet F, Barbezat G, Foliot F, Diard A, Wazen P (1999) Surface preparation and thermal spray in a single step: the PROTAL process – example of application for an aluminium-base substrate. J Therm Spray Technol 8(2):235–242
30. Costil S, Liao H, Gammondi A, Coddet C (2005) Influence of surface laser cleaning combined with substrate preheating on splat morphology. J Therm Spray Technol 14 (1):31–38
31. Dong S, Song B, Hansz B, Liao H, Coddet C. Improvement in the microstructure and property of plasma sprayed metallic, alloy and ceramic coatings by using dry ice blasting. In: 5th RIPT conference, CEC, Limoges, Dec 2011, e-proceedings

32. Haure T. Multifunctional layers obtained by a multi-technique process, Ph.D. University of Limoges, France, Nov 2003
33. Syed AA, Denoirjean A, Hannoyer B, Fauchais P, Denoirjean P, Khan AA, Labbe JC (2005) Influence of substrate surface conditions on the plasma sprayed ceramic and metallic particles flattening. Surf Coat Technol 200:2317–2331
34. Pech J (1999) Preoxidation generated by blown arc d.c. plasma jets. Relationship between surface, oxidation and adhesion of plasma sprayed coatings. Ph.D., University of Rouen, France
35. Pech J, Hannoyer B (2000) Influence of the oxide layer by d.c. plasma preheating on the adhesion coating and role of the initial surface pretreatment. Surf Interface Anal 30:585–588
36. Li H, Costil S, Liao H-L, Li C-J, Planche MP, Coddet C (2006) Effect of surface conditions on the flattening behavior of plasma sprayed Cu splats. Surf Coat Technol 200:5435–5446
37. Li H, Costil S, Deng S-H, Liao H-L, Coddet C, Ji V, Huang W-J (2006) Benefit of surface oxide removal on thermal spray coating adhesion using the PROTAL process. In: Marple B et al (eds) ITSC 2006. ASM International, Materials Park, OH, e-proceedings
38. Valette S (2004) Influence of the preoxidation of a steel substrate on the adhesion of an alumina coating plasma sprayed. Ph.D. Thesis, University of Limoges, France, Nov
39. Pech J, Hannoyer B, Lagnoux O, Denoirjean A, Fauchais P (1999) Influence of the preheating parameters on the plasma jet oxidation of a low carbon steel. In: Fauchais P, Amouroux J (eds) Progress in plasma processing of materials. Begell House, New York, pp 543–551
40. Trompetter W, Hyland M, McGrouther D, Munroe P, Markwitz A (2006) Effect of substrate hardness on splat morphology in high-velocity thermal spray coatings. J Therm Spray Technol 15(4):663–669
41. Kawakita J, Kuroda S, Fukushima T, Katanoda H, Matsuo K, Fukanuma H (2006) Dense titanium coatings by modified HVOF spraying. Surf Coat Technol 201:1250–1255
42. Hanson TC, Hackett CM, Settles GS (2002) Independent control of HVOF particle velocity and temperature. J Therm Spray Technol 11(1):75–85
43. Assadi H, Gartner F, Stoltenhoff T, Kreye H (2003) Bonding mechanism in cold gas spraying. Acta Mater 51:4379–4394
44. Grujicic M, Saylor JR, Beasley DE, DeRosset WS, Helfritch D (2003) Computational analysis of the interfacial bonding between feed-powder particles and the substrate in the cold-gas dynamic-spray process. Appl Surf Sci 219:211–227
45. Grujicic M (2007) Particle/substrate interaction in the cold-spray bonding process. In: Champagne VK (ed) The cold spray materials deposition process. Woodhead Publishing Ltd, Cambridge, pp 148–177
46. Itoh A, Takeda K, Itoh M, Koga M (1990) Pretreatements of substrates by using reversed transferred arc in low pressure plasma spray. In: Bernicki F (ed) Thermal spray: research and applications. ASM International, Materials Park, OH, pp 245–252
47. Chraska T, King AH (2002) Effect of different substrate conditions upon interface with plasma sprayed zirconia—a TEM study. Surf Coat Technol 157:238–246
48. Brossard S, Munroe PR, Tran AT, Hyland MM (2010) Study of the splat microstructure and the effects of substrate heating on the splat formation for Ni-Cr particles plasma sprayed onto stainless steel substrates. J Therm Spray Technol 19(5):1100–1114
49. Yang E-J, Yang G-J, Luo X-T, Li C-J, Takahashi M (2012) Epitaxial grain growth during splat cooling of alumina droplets produced by atmospheric plasma spraying. In: ITSC 2012. ASM International, Materials Park, OH, e-proceedings
50. Denoirjean A, Grimaud A, Fauchais P, Tristant P, Tixier C, Desmaison J (1998) Splat formation, first step for multitechnique deposition of plasma spraying and microwave plasma enhanced CVD. In: Coddet C (ed) Thermal spray: meeting in challenges of the 21st century, vol 2. ASM International, Materials Park, OH, pp 1369–74
51. Maitre A, Denoirjean A, Fauchais P, Lefort P (2002) Plasma-jet coating of pre-oxidized XC38 steel: influence of the nature of the oxide layer. Phys Chem Chem Phys 4 (15):3887–3893

52. Valette S, Denoirjean A, Danoix R, Hannoyer B, Lefez B, Lopitaux J, Lefort P, Fauchais P. Interaction between a thin non continuous d.c. plasma sprayed alumina layer and pre-oxidized low carbon substrate. In: Lugsheider E et al (eds) ITSC 2005. DVS, Düsseldorf, Germany, e-proceedings
53. Guetta S, Berger MH, Borit F, Guipont V, Jeandin M, Boustie M, Ichikawa Y, Sakaguchi K, Ogawa K (2009) Influence of particle velocity on adhesion of cold-sprayed splats. J Therm Spray Technol 18(3):331–342
54. Fukumoto M, Mashiko M, Yamada M, Yamaguchi E (2010) Deposition behavior of copper fine particles onto flat substrate surface in cold spraying. J Therm Spray Technol 19 (1–2):89–94
55. Zhang D, Shipway PH, McCartney DG (2005) Cold gas dynamic spraying of aluminum: the role of substrate characteristics in deposit formation. J Therm Spray Technol 14(1):109–116
56. Hussain T, McCartney DG, Shipway PH, Zhang D (2009) Bonding mechanisms in cold spraying: the contributions of metallurgical and mechanical components. J Therm Spray Technol 18(3):364–379
57. Huang R, Fukanuma H (2012) Study of the influence of particle velocity on adhesive strength of cold spray deposits. J Therm Spray Technol, 21(3–4):541–549
58. Li C-J, Li C-X, Yang G-J, Wang Y-Y (2006) Examination of substrate surface melting-induced splashing during splat formation in plasma spraying. J Therm Spray Technol 15 (4):717–724
59. Morks MF, Tsunekawa Y, Okumiya M, Shoeib MA (2002) Splat morphology and micro-structure of plasma sprayed cast iron with different preheat substrate temperatures. J Therm Spray Technol 11(2):226–232
60. Trompetter WJ, Hyland M, Munroe P, Markwitz A (2005) Evidence of mechanical interlocking of NiCr particles thermally sprayed onto Al substrates. J Therm Spray Technol 14(4):524–529
61. Bahbou F, Nylen P (2005) Relationship between surface topography parameters and adhesion strength for plasma spraying. In: Lugscheider E (ed) ITSC 2005. DVS, Düsseldorf, Germany, e-proceedings
62. Bahbou MF, Nylén P (2007) On-line measurement of plasma-sprayed Ni-particles during impact on a Ti-surface: influence of surface oxidation. J Therm Spray Technol 16(4):506–511
63. Fauchais P, Vardelle M, Vardelle A, Bianchi L, Léger AC (1996) Parameters controlling the generation and properties of plasma sprayed zirconia coatings. Plasma Chem Plasma Proc 16 (1):99S–125S
64. Maruyama T, Akagi K, Kobayashi T (2006) Effects of blasting parameters on removability of residual grit. J Therm Spray Technol 15(4):817–821
65. Klinkov SV, Kosarev VF (2006) Measurements of cold spray deposition efficiency. J Therm Spray Technol 15(3):364–371
66. Fukumoto M, Wada H, Tanabe K, Yamada M, Yamaguchi E, Niwa A, Sugimoto M, Izawa M (2007) Effect of substrate temperature on deposition behavior of copper particles on substrate surfaces in the cold spray process. J Therm Spray Technol 16(5–6):643–650
67. Papyrin AN, Klinkov SV, Kosarev VF (2003) Modeling of particle-substrate adhesive interaction under the cold spray process. In: Moreau C, Marple B (eds) Thermal spray 2003: advancing the science & applying the technology. ASM International, Materials Park, OH, pp 27–35
68. Trompetter W, Hyland M, McGrouther D, Munroe P, Markwitz A (2010) The effect of substrate surface oxides on the bonding of NiCr alloy particles HVAF thermally sprayed onto aluminum substrates. J Therm Spray Technol 19(5):1024–1031
69. Klinkov SV, Kosarev VF. Cold spraying activation using an abrasive admixture. J Therm Spray Technol. Published on line 29 Mar 2012
70. Koivuluoto H, Vuoristo P (2010) Effect of powder type and composition on structure and mechanical properties of Cu + Al2O3 coatings prepared by using low-pressure cold spray process. J Therm Spray Technol 19(5):1081–1092

71. Fauchais P, Fukumoto M, Vardelle A, Vardelle M (2004) Knowledge concerning splat formation: an invited review. J Therm Spray Technol 13(3):337–360
72. Kudinov VV et al. (1981) In high temp. Dust laden jets. VSL, NL, pp 381–392
73. Dhiman R, McDonald AG, Chandra S (2007) Predicting splat morphology in a thermal spray process. Surf Coat Technol 201:7789–7801
74. Goutier S, Vardelle M, Labbe JC, Fauchais P (2011) Flattening and cooling of millimeter- and micrometer-sized alumina drops. J Therm Spray Technol 20(1–2):59–67
75. Fukumoto M, Yang K, Tanaka K, Usami T, Yasui T, Yamada M (2011) Effect of substrate temperature and ambient pressure on heat transfer at interface between molten droplet and substrate surface. J Therm Spray Technol 20(1–2):48–58
76. Sabiruddina K, Bandyopadhyay PP, Bolelli G, Lusvarghi L (2011) Variation of splat shape with processing conditions in plasma sprayed alumina coatings. J Mater Process Technol 211:450–462
77. Armster SQ, Delplanque J-P, Rein M, Lavernia EJ (2002) Thermo-fluid mechanisms controlling droplet based materials processes. Int Mater Rev 7(6):265–301
78. Pasandideh-Fard M, Qiao YM, Chandra S, Mostaghimi J (1996) Capillary effects during droplet impact on a solid surface. Phys Fluids 8:650–659
79. Bussmann M, Chandra S, Mostaghimi J (2000) Modeling the splashing of a droplet impacting a solid surface. Phys Fluids 12:3121–3132
80. Pasandideh-Fard M, Pershin V, Chandra S, Mostaghimi J (2002) Splat shapes in a thermal spray coating process: simulations and experiments. J Therm Spray Technol 11:206–217
81. Xue M, Heichal Y, Chandra S, Mostaghimi J (2007) Modeling the impact of a molten metal droplet on a solid surface using variable interfacial thermal contact resistance. J Mater Sci 42:9–18
82. Escure C, Vardelle M, Fauchais P (2003) Experimental and theoretical study of the impact of alumina droplet on cold and hot substrates. Plasma Chem Plasma Process 3:291–309
83. Chang-Jiu L, Li J-L (2004) Transient contact pressure during flattening of thermal spray droplet and its effect on splat formation. J Therm Spray Technol 13(2):229–238
84. Elsebaei A, Heberlein J, Elshaer M, Farouk A (2010) Comparison of in-flight particle properties, splat formation, and coating microstructure for regular and nano-YSZ powders. J Therm Spray Technol 19(1–2):2–10
85. Streibl T, Vaidya A, Friis M, Srinivasan V, Sampath S (2006) A critical assessment of particle temperature distributions during plasma spraying: experimental results for YSZ. Plasma Chem Plasma Proc 26(1):73–102
86. Withy B, Hyland M, James B (2006) Pretreatment effects on the surface chemistry and morphology of aluminium. Int J Modern Phys B 20(25–27):3611–3616
87. Tran ATT, Hyland MM, Qiu T, Withy B, James BJ (2008) Effects of surface chemistry on splat formation during plasma spraying. J Therm Spray Technol 17(5–6):637–645
88. Birks N, Meier GH, Pettit FS (2006) Introduction to the high-temperature oxidations of metals. Cambridge University Press, Cambridge
89. Fukumoto M (2004) Particle flattening behavior in thermal spray process. In: ITSC course, Osaka, Japan, 7–8 May
90. Yang K, Fukumoto M, Yasui T, Yamada M (2010) Study of substrate preheating on flattening behavior of thermal-sprayed copper particles. J Therm Spray Technol 19(6):1195–1205
91. Wu J, Munroe PR, Withy B, Hyland MM (2010) Study of the splat-substrate interface for a PEEK coating plasma-sprayed onto aluminum substrates. J Therm Spray Technol 19 (1–2):42–48
92. Bianchi L, Denoirjean A, Blein F, Fauchais P (1977) Microstructural investigation of plasma sprayed ceramic splats. Thin Solid Films 299:125–135
93. Yang K, Tomita K, Fukumoto M, Yamada M, Yasui T (2009) Effect of ambient pressure on flattening behavior of thermal sprayed particles. J Therm Spray Technol 18(4):510–518
94. Madejski J (1976) Solidification of droplets on a cold surface. Int J Heat Mass Transfer 19:1009–1013

95. Williams CA, Jones H (1975) The effect of melt superheat and impact velocity on splat thickness. Mater Sci Eng 19:293–297
96. Yoshida T, Okada T, Hamatani H, Kumaoka H (1992) Integrated fabrication process for solid oxide fuel cells using novel plasma spraying. Plasma Sources Sci Technol 1:195–201
97. Fantassi S, Vardelle M, Vardelle A, Fauchais P (1993) Influence of the velocity of plasma-sprayed particles on splat formation. J Therm Spray Technol 2(4):379–384
98. Tanaka Y, Fukumoto M (1999) Investigation of dominating factors on flattening behavior of plasma sprayed ceramic particles. Surf Coat Technol 120–121:124–130
99. Goutier S (2010) Etude expérimentale de l'impact et de la solidification de gouttes céramiques et métalliques de tailles micrométrique et millimétrique sur différents types de substrats: compréhension du mécanisme de formation des dépôts par projection thermique. Ph.D. thesis, University of Limoges, France, 7 Dec
100. Xue M, Chandra S, Mostaghimi J (2006) Investigation of splat curling up in thermal spray coatings. J Therm Spray Technol 15(4):531–536
101. Vardelle M, Vardelle A, Leger AC, Fauchais P, Gobin D (1994) Influence of particle parameters at impact on splat formation and solidification in plasma spraying processes. J Therm Spray Technol 4(1):50–58
102. Lahmar-Mebdoua Y, Vardelle A, Fauchais P, Gobin D (2009) Splat heat transfer and crystal growth under thermal spray conditions. High Temp Mater Process 13(1):77–91
103. McDonald A, Moreau C, Chandra S (2007) Thermal contact resistance between plasma-sprayed particles and flat surfaces. Int J Heat Mass Transfer 50:1737–1749
104. McDonald A, Lamontagne M, Moreau C, Chandra S (2006) Impact of plasma-sprayed metal particles on hot and cold glass surfaces. Thin Solid Films 514:212–222
105. Sidhu TS, Prakash S, Agrawal RD (2005) Studies on the properties of high-velocity oxy-fuel thermal spray coatings for higher temperature applications. Mater Sci 41(6):805–823
106. Ulianitsky V, Shtertser A, Zlobin S, Smurov I (2011) Computer-controlled detonation spraying: from process fundamentals toward advanced applications. J Therm Spray Technol 20(4):791–801
107. McDonald A, Xue M, Chandra S, Mostaghimi J, Moreau C (2007) Modeling fragmentation of plasma-sprayed particles impacting on a solid surface at room temperature. C R Mecanique 335:351–356
108. Watanabe M, Owada A, Kuroda S, Gotoh Y (2006) Effect of WC size on interface fracture toughness of WC–Co HVOF sprayed coatings. Surf Coat Technol 201:619–627
109. Che-Ming Wu T, Bussmann M, Mostaghimi J (2009) The impact of a partially molten YSZ particle. J Therm Spray Technol 18(5–6):957–964
110. Ivosevic M (2006) Splat Formation during thermal spraying of polymer particles: mathematical modeling and experimental analysis. Ph.D. Thesis, Faculty of Drexel University
111. Ivosevic M, Cairncross RA, Knight R (2006) 3D predictions of thermally sprayed polymer splats: modeling particle acceleration, heating and deformation on impact with a flat substrate. Int J Heat Mass Transfer 49:3285–3297
112. Alamara K, Saber-Samandari S, Berndt CC (2010) Splat formation of polypropylene flame sprayed onto a flat surface. Surf Coat Technol 205:2518–2524
113. Withy BP, Hyland MM, James BJ (2008) The effect of surface chemistry and morphology on the properties of HVAF PEEK single splats. J Therm Spray Technol 17(5–6):631–636
114. Patel K, Doyle CS, James BJ, Hyland MM (2010) Valence band XPS and FT-IR evaluation of thermal degradation of HVAF thermally sprayed PEEK coatings. Polym Degrad Stab 95:792–797
115. Alamara K, Saber-Samandari S, Berndt CC (2011) Splat taxonomy of polymeric thermal spray coating. Surf Coat Technol 205:5028–5034
116. Kang CW, Ng HW (2006) Splat morphology and spreading behavior due to oblique impact of droplets onto substrates in plasma spray coating process. Surf Coat Technol 200:5462–5477

117. Salimijazi HR, Pershin L, Coyle TW, Mostaghimi J, Chandra S, Lau YC, Rosenzweig L, Moran E (2007) Effect of droplet characteristics and substrate surface topography on the final morphology of plasma-sprayed zirconia single splats. J Therm Spray Technol 16(2):291–299
118. Kang CW, Ng HW, Yu SCM (2006) Imaging diagnostics study on obliquely impacting plasma-sprayed particles near to the substrate. J Therm Spray Technol 15(1):118–130
119. Koivuluoto H, Näkki J, Vuoristo P (2009) Corrosion properties of cold-sprayed tantalum coatings. J Therm Spray Technol 18(1):75–82
120. Shinoda K, Yamada A, Kambara M, Kojima Y, Yoshida T (2007) Deformation of alumina droplets on micro-patterned substrates under plasma spraying conditions. J Therm Spray Technol 16(2):300–305
121. Parizi HB, Rosenzweig L, Mostaghimi J, Chandra S, Coyle T, Salimi H, Pershin L, McDonald A, Moreau C (2008) Numerical simulation of droplet impact on patterned surfaces. J Therm Spray Technol 16(5–6):713–721
122. Mehdizadeh NZ, Chandra S, Mostaghimi J (2002) Effect of substrate temperature and roughness on coating formation. In: Lugscheider E (ed) Proceedings of the ITSC 2002. DVS, Düsseldorf, Germany, pp 830–37
123. Raessi M, Mostaghimi J, Bussmann M (2006) Effect of surface roughness on splat shapes in the plasma spray coating process. Thin Solid Films 506–507:133–135
124. Ivosevic M, Gupta V, Baldoni JA, Cairncross RA, Twardowski TE, Knight R (2006) Effect of substrate roughness on splatting behavior of HVOF sprayed polymer particles: modeling and experiments. J Therm Spray Technol 15(4):725–730
125. Vardelle A, Moreau C, Fauchais P (2000) The dynamics of deposit formation in thermal spray processes. MRS Bull 25:32–37
126. Renouard-Vallet G, Bianchi L, Fauchais P, Vardelle M, Boulos M, Gitzhofer F (2005) Influence of spray technology on ionic conductivity of yttria stabilized zirconia. J High Temp Mater Process 9(2):195–210
127. Gawne DT, Griffiths BJ, Dong G (1995) Splat morphology and adhesion of thermally sprayed coatings. In: Ohmori A (ed) Thermal spraying: current status and future trends, Kobe, Japan. High Temperature Society of Japan, Osaka, pp 779–784
128. Newbery AP, Grant PS (2000) Droplet splashing during arc spraying of steel and the effect on deposit microstructure. J Therm Spray Technol 9(2):250–258
129. Trice RW, Faber KT (2000) Role of lamellae morphology on the microstructural development and mechanical properties of small-particle plasma-sprayed alumina. J Am Ceram Soc 83(4):889–896
130. Racek O (2010) The effect of HVOF particle-substrate interactions on local variations in the coating microstructure and the corrosion resistance. J Therm Spray Technol 19(5):841–851
131. Ctibor P, Lechnerová R, Beneš V (2006) Quantitative analysis of pores of two types in a plasma-sprayed coating. Mater Charact 56:297–304
132. Saaedi J, Coyle TW, Arabi H, Mirdamadi S, Mostaghimi J (2010) Effects of HVOF process parameters on the properties of Ni-Cr coatings. J Therm Spray Technol 19(3):521–530
133. Zeng Z, Kuroda S, Kawakita J, Komatsu M, Era H (2010) Effects of some light alloying elements on the oxidation behavior of Fe and Ni-Cr based alloys during air plasma spraying. J Therm Spray Technol 19(1–2):128–136
134. Shinoda K, Murakami H, Kuroda S, Takehara K, Oki S (2008) In situ visualization of impacting phenomena of plasma-sprayed zirconia: from single splat to coating formation. J Therm Spray Technol 17(5–6):623–630
135. Kanouff MP, Neiser RA, Roemer TJ (1998) Surface roughness of thermal spray coatings made with off-normal spray angle. J Therm Spray Technol 7(2):219–228
136. Tillmann W, Vogli E, Krebs B (2008) Influence of the spray angle on the characteristics of atmospheric plasma sprayed hard material based coatings. J Therm Spray Technol 17 (5–6):948–955
137. Candel A, Gadow R (2006) Optimized multiaxis robot kinematic for HVOF spray coatings on complex shaped substrates. Surf Coat Technol 201:2065–2071

138. Montillet D, Dombre E, Valentin FD, Goubot JM (1999) Modeling, simulating and optimizing the robotized plasma deposition: an expression approach. In: Lugsheider E, Kammer PA (eds) Thermal spray. DVS, Düsseldorf, Germany, pp 507–512
139. Fasching MM, Weiss LE, Prinz FB (1992) Optimization of robotic trajectories for thermal spray shape deposition. In: Berndt CC (ed) Thermal spray: advances in coatings technology. ASM International, Materials Park, OH, pp 221–226
140. Leigh SH, Berndt CC (1997) Evaluation of off-angle thermal spray. Surf Coat Technol 89:213–224
141. Bao Y, Zhang T, Gawne DT (2005) Influence of composition and process parameters on the thermal spray deposition of UHMWPE coatings. J Mater Sci 40:77–85
142. Feng Z, Xu H, Yan F (2008) Preparation of flame sprayed poly(tetrafluoroethylene-co-hexafluoropropylene) coatings and their tribological properties under water lubrication. Appl Surf Sci 255:2408–2413
143. Patel K, Doyle CS, Yonekura D, James BJ (2010) Effect of surface roughness parameters on thermally sprayed PEEK coatings. Surf Coat Technol 204:3567–3572
144. Normanda B, Takenouti H, Keddama M, Liao H, Monteil G, Coddet C (2004) Electrochemical impedance spectroscopy and dielectric properties of polymer: application to PEEK thermally sprayed coating. Electrochim Acta 49:2981–2986
145. Li J, Liao H, Coddet C (2002) Friction and wear behavior of flame-sprayed PEEK coatings. Wear 252:824–831
146. Zhang G, Liao H, Yu H, Ji V, Huang W, Mhaisalkar SG, Coddet C (2006) Correlation of crystallization behavior and mechanical properties of thermal sprayed PEEK coating. Surf Coat Technol 200:6690–6695
147. Branco JRT, Campos SV (1999) Wear behavior of thermally sprayed PET. Surf Coat Technol 120–121:476–481
148. Soveja A, Costil S, Liao H, Sallamand P, Coddet C (2010) Remelting of flame spraying PEEK coating using lasers. J Therm Spray Technol 19(1–2):439–447
149. Zhanga C, Zhang G, Ji V, Liao H, Costil S, Coddet C (2009) Microstructure and mechanical properties of flame-sprayed PEEK coating remelted by laser process. Prog Organic Coat 66:248–253
150. Ivosevic M, Knight R, Kalidindi SR, Palmese GR, Sutter JK (2005) Adhesive/cohesive properties of thermally sprayed functionally graded coatings for polymer matrix composites. J Therm Spray Technol 14(1):45–51
151. Berndt CC, Brogan JA, Montavon G, Claudon A, Coddet C (1998) Mechanical properties of metal- and ceramic-polymer composites formed via thermal spray consolidation. J Therm Spray Technol 7(3):337–339
152. Jackson L, Ivosevic M, Knight R, Cairncross RA (2007) Sliding wear properties of HV thermally sprayed nylon-11 and nylon-11/ceramic composites on steel. J Therm Spray Technol 16(5–6):927–932
153. Mateus C, Costil S, Bolot R, Coddet C (2005) Ceramic/fluoropolymer composite coatings by thermal spraying-a modification of surface properties. Surf Coat Technol 191:108–118
154. Schadler LS, Laul KO, Smith RW, Petrovicova E (1997) Microstructure and mechanical properties of thermally sprayed silica/nylon nanocomposites. J Therm Spray Technol 6 (4):475–485
155. Stravato A, Knight R, Mochalin V, Picardi SC (2008) HVOF-sprayed nylon-11 + nanodiamond composite coatings: production & characterization. J Therm Spray Technol 17(5–6):812–817
156. Van Steenkiste TH, Smith JR, Teets RE (2002) Aluminum coatings via kinetic spray with relatively large powder particles. Surf Coat Technol 154(2–3):237–252
157. Gärtner F, Borchers C, Stoltenhoff T, Kreye H (2003) Numerical and microstructural investigations of the bonding mechanisms in cold spraying. In: Moreau C, Marple B (eds) Thermal spray 2003: advancing the science & applying the technology. ASM International, Materials Park, OH, pp 1–8

158. Li C-J, Li W-Y, Liao H (2006) Examination of the critical velocity for deposition of particles in cold spraying. J Therm Spray Technol 15(2):212–222
159. Li C-J, Li W-Y, Wang Y-Y, Yang G-J, Fukanuma H (2005) A theoretical model for prediction of deposition efficiency in cold spraying. Thin Solid Films 485:79–85
160. Stoltenhoff T, Kreye H, Richter HJ (2002) An analysis of the cold spray process and its coatings. J Therm Spray Technol 11(4):542–550
161. Koivuluoto H, Lagerbom J, Vuoristo P (2007) Microstructural studies of cold sprayed copper, nickel, and nickel-30% copper coatings. J Therm Spray Technol 16(4):488–497
162. Zahiri SH, Fraser D, Gulizia S, Jahedi M (2006) Effect of processing conditions on porosity formation in cold gas dynamic spraying of copper. J Therm Spray Technol 15(3):422–430
163. Ducos M (1985) Industrial applications of arc and RF inductive plasmas of low power. In: Plasmas in industry. Dopee diffusion, 77210 Avon, France (in French), pp 251–263
164. Wilden J, Bergmann JP, Frank H (2006) Plasma transferred arc welding—modeling and experimental optimization. J Therm Spray Technol 15(4):779–784
165. Gatto A, Bassoli E, Fornari M (2004) Plasma transferred arc deposition of powdered high performances alloys: process parameters optimization as a function of alloy and geometrical configuration. Surf Coat Technol 187:265–271
166. Mauer G, Vaßen R, Stöver D (2010) Thin and dense ceramic coatings by plasma spraying at very low pressure. J Therm Spray Technol 19(1–2):495–501
167. Gindrat M, Dorier J-L, Hollenstein C, Loch M, Refke A, Salito A, Barbezat G (2002) Effect of specific operating conditions on the properties of LPPS plasma jets expanding at low pressure. In: Lugscheider E, Berndt CC (eds) International thermal spray conference. Verlag für Schweißen und verwandte Verfahren DVS-Verlag, Dusseldorf, Germany, pp 459–464
168. Zotov N, Hospach A, Mauer G, Sebold D, Vaßen R (2012) Deposition of La1-xSrxFe1-yCoyO3-δ Coatings with different phase compositions and microstructures by low-pressure plasma spraying-thin film (LPPS-TF) processes. J Therm Spray Technol 21(3–4):441–447
169. Hafiz J, Mukherjee R, Wang X, McMurry PH, Heberlein JVR, Girshick SL (2006) Hypersonic plasma particle deposition-a hybrid between plasma spraying and vapor deposition. J Therm Spray Technol 15(4):822–826
170. Doering T (2007) PVD and PACVD (DLC) coating technologies and applications. In: International SAMPE symposium and exhibition, proceedings, vol 52, 8pp
171. von Niessen K, Gindrat M, Refke A (2010) Vapor phase deposition using plasma spray-PVD. J Therm Spray Technol 19(1–2):502–509
172. von Niessen K, Gindrat M (2011) Plasma spray-PVD: a new thermal spray process to deposit out of the vapor phase. J Therm Spray Technol 20(4):736–743
173. Hospach A, Mauer G, Vaßen R, Stöver D (2011) Columnar-structured thermal barrier coatings (TBCs) by thin film low-pressure plasma spraying (LPPS-TF). J Therm Spray Technol 20(1–2):116–120
174. Hospach A, Mauer G, Vaßen R, Stöver D (2012) Characteristics of ceramic coatings made by thin film low pressure plasma spraying (LPPS-TF). J Therm Spray Technol 21(3–4):435–440
175. Mauer G, Hospach A, Zotov N, Vaßen R (2012) Process conditions and microstructures of ceramic coatings by gas phase deposition based on plasma spraying. In: Lima RS et al (eds) Thermal spray 2012 proceedings. ASM International, Materials Park, OH, e-proceedings
176. Thornton JA (1975) Influence of substrate temperature and deposition rate on structure of thick sputtered Cu coatings. J Vac Sci Technol 12(4):830–835
177. Fang D, Deng S, Liao H, Coddet C (2010) The effect of robot kinematics on the coating thickness uniformity. J Therm Spray Technol 19(4):796–804
178. Hansbo A, Nylén P (1999) Models for the simulation of spray deposition and robot motion optimization in thermal spraying of rotating objects. Surf Coat Technol 122:191–201
179. Fasching M, Prinz F, Weiss L (1993) Planning robotic trajectories for thermal spray shape deposition. J Therm Spray Technol 2:45–50

180. Candel A, Gadow R (2009) Trajectory generation and coupled numerical simulation for thermal spraying applications on complex geometries. J Therm Spray Technol 18 (5–6):981–987
181. Gadow R, Candel A, Floristan M (2010) Optimized robot trajectory generation for thermal spraying operations and high quality coatings on free-form surfaces. Surf Coat Technol 205:1074–1079
182. Floristán M, Montesinos JA, García-Marín JA, Killinger A, Gadow R (2012) Robot trajectory planning for high quality thermal spray coating processes on complex shaped components. In: ITSC 2012. ASM International, Materials Park, OH, e-proceedings
183. Harding JH, Mulheran PA, Cirolini S, Marchese M, Jacucci G (1995) Modeling the deposition of thermal barrier coatings. J Therm Spray Technol 4(1):34–40
184. Bobzin K, Bagcivan N, Parkot D, Scha¨fer M, Petkovic´ I (2009) Modeling and simulation of microstructure formation for porosity prediction in thermal barrier coatings under air plasma spraying condition. J Therm Spray Technol 18(5–6):975–980
185. Bobzin K, Bagcivan N, Parkot D, Kashko T, Laschet G, Scheele J (2009) Influence of the definition of the representative volume element on effective thermoelastic properties of thermal barrier coatings with random microstructure. J Therm Spray Technol 18(5–6):988–995
186. Sevostianov I, Kachanov M (2009) Elastic and conductive properties of plasma-sprayed ceramic coatings in relation to their microstructure: an overview. J Therm Spray Technol 18(5–6):822–834
187. Kuroda S, Dento T, Kitahara S (1995) Quenching stress in plasma sprayed coatings and its correlation with the deposit microstructure. J Therm Spray Technol 4:75–87
188. Monnerie-Moulin F, Gitzhofer F, Fauchais P, Boulos M, Vardelle A (1992) Flux transmitted to a cold substrate by a d.c. Ar-H2 spraying plasma jet. J High Temp Mater Process 1 (3):249–257
189. Haddadi A, Nardou F, Fauchais P, Grimaud A, Leger AC (1997) Influence of substrate and coating temperature on columnar growth within plasma sprayed zirconia and alumina coatings. In: Berndt CC (ed) Thermal spray. A united forum for scientific and technological advances. ASM International, Materials Park, OH, pp 671–680
190. Fauchais P, Vardelle A, Vardelle M, Denoirjean A, Pateyron B, El Ganaoui M (2001) Formation and layering of alumina splats: thermal history of coating formation, resulting residual stresses and coating microstructure. In: Berndt CC, Khor KA, Lugsheider E (eds) Thermal spray 2001: new surfaces for a new millenium. ASM International, Materials Park, OH, pp 865–873
191. Leger AC, Haddadi A, Pateyron B, Delluc G, Grimaud A, Nardou F, Fauchais P (1998) Residual stresses during coating generation: plasma sprayed alumina coating on XC38, measurements and calculations. In: Coddet C (ed) Thermal spray: meeting the challenge of the 21st century. ASM International, Materials Park, OH, pp 895–903
192. Monerie-Moulin F, Gitzhofer F, Fauchais P, Boulos M, Vardelle A (1992) Heat flux transmitted to a cold substrate by a d.c. Ar-H2 plasma jet. J High Temp Chem Process 1:249–258
193. Honner M, Cerveny P, Franta V, Cejka F (1998) Heat transfer during HVOF deposition. Surf Coat Technol 106:94–99
194. Hackett CM, Settles GS (1994) Turbulent mixing of the HVOF thermal spray and coating oxidation. In: Berndt CC, Sampath S (eds) Proceedings of the 7th national spray conference. ASM International, Materials Park, OH, pp 307–312
195. Li M, Shi D, Christofides PD (2005) Modeling and control of HVOF thermal spray processing of WC–Co coatings. Powder Technol 156:177–194
196. Coudert JF, Planche MP, Fauchais P (1995) Velocity measurements of dc plasma jets based on arc root fluctuations. Plasma Chem Plasma Process 15(1):47–69
197. Fauchais P, Coudert JF (1996) Mesures de température dans les plasmas thermiques. Revue Générale de Thermique 35(413):324–337

198. Lapierre D, Kearney RJ, Vardelle M, Vardelle A, Fauchais P (1994) Effects of a substrate on the temperature distribution in argon-hydrogen thermal plasma jet. Plasma Chem Plasma Process 14(4):407–423
199. Brousse E. Elaboration by thermal spraying of finely structured elements of high temperature electrolyser for hydrogen production: processes, structures and characteristics. Ph.D. Thesis, University of Limoges, France, Sept 2010 (in French)
200. Fauchais P, Etchart-Salas R, Rat V, Coudert J-F, Caron N, Wittmann-Ténèze K (2008) Parameters controlling liquid plasma spraying: solutions, sols or suspensions. J Therm Spray Technol 17(1):31–59
201. LINSPRAY CO2 cooling for thermal spraying, pdf document. http://www.linde.com
202. Gosh R (2007) Cryogenic nitrogen gas cooling for thermal spray coatings. Spray Time 14(4):1–4
203. Leger AC, Grimaud A, Fauchais P, Delluc G (1997) Influence of the torch to substrate velocity and resulting temperature on the residual stresses in alumina plasma sprayed coatings. In: Berndt CC (ed) Proceedings of the 1st unified thermal spray conference. ASM International, Materials Park, OH, pp 823–829
204. Haddadi A (1998) Zirconia and alumina coatings plasma sprayed: columnar growth, residual stress and modeling. Ph.D. Thesis, University of Limoges, France, 22 Jul (in French)
205. Renouard-Vallet G (2004) Elaboration by plasma spraying of dense and thin (a few tens of micro meters) yttria stabilized zirconia electrolytes for SOFCs. Ph.D. Thesis, University of Limoges, France, 8 Feb
206. PROTAL process, worldwide patented, original patent: FR9209277
207. Li H, Costil S, Liao H-L, Coddet C (2006) Role of the laser surface preparation on the adhesion of Ni-5wt% Al coatings deposited using the PROTAL® process. J Therm Spray Technol 15(2):191–197
208. Robertson DGC, Jenkins AE (1970) The reaction of liquid iron and its alloys in pure oxygen, heterogeneous kinetics at elevated temperatures. In: Belton GR, Workel WL (ed) Plenum Press, New York, NY, pp 369–385
209. Neiser RA, Smith MF, Dykhuisen RC (1998) Oxidation in wire HVOF-sprayed steel. J Therm Spray Technol 7(4):537–545
210. Dallaire S (1992) Thermal spraying of reactive materials to form wear-resistant composite coatings. J Therm Spray Technol 1(1):41–47
211. Borisova AL, Borisov YS (2008) Self-propagating high-temperature synthesis for the deposition of thermal-sprayed coatings. Powder Metall Metal Ceram 47(1–2):80–94
212. Jacobs L, Hyland MM, De Bonte M (1998) Comparative study of WC-cermet coatings sprayed via the HVOF and the HVAF process. J Therm Spray Technol 7(2):213–218
213. de Villiers Lovelock HL, Richter PW, Benson JM, Young PM (1998) Parameter study of HP/HVOF deposited WC-Co coatings. J Therm Spray Technol 7(1):97–107
214. de Villiers Lovelock HL (1998) Powder/processing-structure relationships in WC-Co thermal spray coatings: a review of the published literature. J Therm Spray Technol 7(3):357–373
215. Luyckx S, Machio CN (2007) Characterization of WC-VC-Co thermal spray powders and coatings. Int J Refract Met Hard Mater 25:11–15
216. Sherman AJ, Engleman PG (2009) Metal clad cermet powders: processing and properties. In: Marple BR, Hyland MM, Lau Y-C, Li C-J, Lima RS, Montavon G (eds) Thermal spray 2009: expanding thermal spray performance to new markets and applications. ASM International, Materials Park, OH, pp 36–840
217. Smith RW, Mutasin ZZ (1992) Reactive plasma spraying of wear-resistant coatings. J Therm Spray Technol 1(1):57–63
218. Eckardt T, Malleaer W, Stove D (1994) Reactive plasma spraying of silicon in controlled nitrogen atmosphere. In: Berndt CC, Sampath S (eds) Thermal spray: industrial applications. ASM International, Materials Park, OH, pp 515–520
219. Fauchais P, Vardelle A, Denoirjean A (1997) Reactive thermal plasmas: ultrafine particle synthesis and coating deposition. Surf Coat Technol 979:66–78

220. Denoirjean A, Lefort P, Fauchais P (2003) Nitridition process and mechanism of Ti-6Al-4V particles by plasma spraying. Phys Chem Phys 5:5133–5138
221. Zou D, Yan D, Xiao L, Dong Y (2008) Characterization of nanostructured TiN coatings fabricated by reactive plasma spraying. Surf Coat Technol 202:1928–1934
222. Kobayashi A (2000) Formation of TiN coatings by gas tunnel type plasma reactive spraying. Surf Coat Technol 132:152–157
223. Inagaki M, Yokogawa Y, Kameyama T (2003) Bond strength improvement of hydroxyapatite titanium composite coating by partial nitriding during R.F.-thermal plasma spraying. Surf Coat Technol 173:1–8
224. Yamada M, Kouzaki Y, Yasui T, Fukumoto M (2006) Fabrication of iron nitride coatings by reactive R.F. plasma spraying. Surf Coat Technol 201:1745–1751
225. Allen AJ, Long GG, Boukari H, Ilavsky J, Kulkarni A, Sampath S, Herman H, Goland AN (2001) Microstructural characterization studies to relate the properties of thermal spray coatings to feedstock and spray conditions. Surf Coat Technol 146–147:544–552
226. Chi W, Sampath S, Wang H (2006) Ambient and high-temperature thermal conductivity of thermal sprayed coatings. J Therm Spray Technol 15(4):773–778
227. Bertrand G, Bertrand P, Roy P, Rio C, Mevrel R (2008) Low conductivity plasma sprayed thermal barrier coating using hollow PSZ spheres: correlation between thermophysical properties and microstructure. Surf Coat Technol 202:1994–2001
228. Wang M, Shaw LL (2007) Effects of the powder manufacturing method on microstructure and wear performance of plasma sprayed alumina-titania coatings. Surf Coat Technol 202:34–44
229. Ageorges H, Fauchais P (2000) Plasma spraying of stainless-steel particles coated with an alumina shell. Thin Solid Films 370:213–222
230. Cuenca Alvarez R, Ageorges H, Fauchais P, Fournier P, Smith A (2003) The effect of the mechanofusion process and planetary milling on composite powder preparation: agglomeration and fragmentation. Mater Sci Forum 442:67–72
231. Cuenca-Alvarez R (2003) Contribution to the elaboration of composites coatings by mechanofused powders direct current plasma sprayed. Ph.D. Thesis, University of Limoges, France (in French)
232. Li C-J, Li W-Y, Wang Y-Y, Yang G-J, Fukanuma H (2005) A theoretical model for prediction of deposition efficiency in cold spraying. Thin Solid Films 489:79–85
233. Alkhimov AP, Klinkov SV, Kosarev VF (2000) Study of heat exchange of supersonic plane jet with obstacle at gas-dynamic spraying. Thermophys Aeromech 7(3):375–382
234. Lee JH, Kim JS, Shin SM, Lee CH, Kim HJ (2006) Effect of particle temperature on the critical velocity for particle deposition by kinetic spraying. In: Marple BR, Hyland MM, Lau Y-C, Lima RS, Voyer J (eds) Building on 100 years of success: proceedings of the international thermal spray conference 2006. ASM International, Materials Park, OH, e-proceedings
235. Katanoda H, Fukuhara M, Iino N (2007) Numerical study of combination parameters for particle impact velocity and temperature in cold spray. J Therm Spray Technol 15(5–6):627–633
236. Katanoda H, Fukuhara M, Iino N (2007) Numerical study of combination parameters for particle impact velocity and temperature in cold spray. In: Marple BR, Hyland MM, Lau Y-C, Li C-J, Lima RS, Montavon G (eds) Thermal spray 2007: global coating solutions. ASM International, Materials Park, OH, pp 72–77
237. Mäkinen H, Lagerbom J, Vuoristo P (2007) Adhesion of cold sprayed coatings: effect of powder, substrate, and heat treatment. In: Marple BR, Hyland MM, Lau Y-C, Li C-J, Lima RS, Montavon G (eds) Thermal spray 2007: global coating solutions. ASM International, Materials Park, OH, pp 31–36
238. Helfritch D, Champagne V (2006) Optimal particle size for the cold spray process. In: Marple BR, Hyland MM, Lau Y-C, Lima RS, Voyer J (eds) Building on 100 years of success: proceedings of the international thermal spray conference 2006. ASM International, Materials Park, OH, e-proceedings

239. Dykhuizen RC, Smith MF, Gilmore DL, Neiser RA, Jiang X, Sampath S (1999) Impact of high velocity cold spray particles. J Therm Spray Technol 8(4):559–564
240. Kang KC, Yoon SH, Ji YG, Lee C (2007) Oxidation effects on the critical velocity of pure Al feedstock deposition in the kinetic spraying process. In: Marple BR, Hyland MM, Lau Y-C, Li C-J, Lima RS, Montavon G (eds) Thermal spray 2007: global coating solutions. ASM International, Materials Park, OH, pp 66–71
241. Seo D, Ogawa K, Sakaguchi K, Miyamoto N, Tsuzuki Y (2012) Parameter study influencing thermal conductivity of annealed pure copper coatings deposited by selective cold spray processes. Surf Coat Technol 206:2316–2324
242. Ning X-J, Jang J-H, Kim H-J (2007) The effects of powder properties on in-flight particle velocity and deposition process during low pressure cold spray process. Appl Surf Sci 253:7449–7455
243. Marple BR, Lima RS (2005) Process temperature/velocity-hardness-wear relationships for high-velocity oxyfuel sprayed nanostructured and conventional cermet coatings. J Therm Spray Technol 14(1):67–76
244. Bartuli C, Valente T, Cipri F, Bemporad E, Tului M (2005) Parametric study of an HVOF process for the deposition of nanostructured WC-Co coatings. J Therm Spray Technol 14(2):187–195
245. Guilemany JM, Dosta S, Miguel JR (2006) The enhancement of the properties of WC-Co HVOF coatings through the use of nanostructured and microstructured feedstock powders. Surf Coat Technol 201:1180–1190
246. Siegmann S, Brandt O, Dvorak M (2004) Thermally sprayed wear resistant coatings with nanostructured hard phases. J Therm Spray Technol 13(1):37–43
247. Ajdelsztajn L, Tang F, Kim GE, Provenzano V, Schoenung JM (2005) Synthesis and oxidation behavior of nano-crystalline MCrAlY bond coatings. J Therm Spray Technol 14(1):23–30
248. Voyer J, Schulz P, Schreiber M (2008) Electrically conductive flame sprayed aluminum coatings on textile substrates. J Therm Spray Technol 17(5–6):818–823
249. Pombo Rodriguez RMH, Paredes RSC, Wido SH, Calixto A (2007) Comparison of aluminum coatings deposited by flame spray and by electric arc spray. Surf Coat Technol 202:172–179
250. Babu VM, Krishna Kumar R, Prabhakar O, Gowri Shankar N (1996) Simultaneous optimization of flame spraying process parameters for high quality molybdenum coatings using Taguchi methods. Surf Coat Technol 79:276–288
251. Singh Sidhu H, Singh Sidhu B, Prakash S (2006) Comparative characteristic and erosion behavior of NiCr coatings deposited by various high-velocity oxyfuel spray processes. J Mater Eng Performance 15(6):699–704
252. Gorlach IA (2009) A new method for thermal spraying of Zn–Al coatings. Thin Solid Films 517:5270–5273
253. Costil S, Verdy C, Bolot R, Coddet C (2007) On the role of spraying process on microstructural, mechanical, and thermal response of alumina coatings. J Therm Spray Technol 16(5–6):839–843
254. Post Guillen D, Williams BG (2006) In-flight oxidation of aluminum in the twin-wire electric arc process. J Therm Spray Technol 15(1):63–71
255. He D, Dong N, Jiang J (2007) Corrosion behavior of arc sprayed nickel-base coatings. J Therm Spray Technol 16(5–6):850–856
256. Skoblo TS, Vlasovets VM, Moroz VV (2001) Structure and distributions of components in the working layer upon reconditioning by electric-arc metallization. Metal Sci Heat Treatment 43(11–12):497–500
257. Student M, Dzioba Yu, Hvozdets'kyi V, Pokhmurs'ka H, Wielage B, Grund T (2008) High-temperature corrosion of electric-arc coatings sprayed from core wires based on the Fe-Cr-B-Al system. Mater Sci 44(5):693–699

258. Xua B, Zhua Z, Maa S, Zhang W, Liu W (2004) Sliding wear behavior of Fe–Al and Fe–Al/WC coatings prepared by high velocity arc spraying. Wear 257:1089–1095
259. Zhao L, Fu B, He D, Kutschmann P (2009) Development of a new wear resistant coating by arc spraying of a steel-based cored wire. Front Mech Eng China 4(1):1–4
260. Liu S-G, Wu J-M, Zhang S-C, Rong S-J, Li Z-Z (2007) High temperature erosion properties of arc-sprayed coatings using various cored wires containing Ti–Al intermetallics. Wear 262:555–561
261. Lyphout C, Nylén P, Manescu A, Pirling T (2008) Residual stresses distribution through thick HVOF sprayed Inconel 718 coatings. J Therm Spray Technol 17(5–6):915–923
262. Clyne TW, Gill SC (1996) Residual stresses in thermal spray coatings and their effect on interfacial adhesion: a review of recent work. J Therm Spray Technol 5(4):401–418
263. Stokes J, Looney L (2008) Predicting quenching and cooling stresses within HVOF deposits. J Therm Spray Technol 17(5–6):908–914
264. Gill C. Residual stresses in plasma sprayed deposits. Ph.D. Thesis, Apr 1991, Gonville and Caius College, Cambridge
265. S. Kuroda, T. Fukushima, S. Kitakara. Generation mechanisms of residual stress in plasma sprayed coatings. In: Proceedings of the 11th international vacuum congress, 17th conference on solid surfaces, Sept 1989, Köln, F.R.G
266. Kuroda S, Clyne TW (1991) The origin and quantification of the quenching stress associated with splat cooling during spray deposition. In: Eschnauer H, Hüber P, Nicoll A, Sandmeier SB (eds) Proceedings of the 2nd Plasma-Technik Syrup, vol 1. Plasma-Technik, Wohlen, Switzerland, pp 273–284
267. Kuroda S, Clyne TW (1991) The quenching stresses in thermally sprayed coatings. Thin Solid Films 200:49–66
268. Kuroda S, Tashiro Y, Yumoto H, Taira S, Fukanuma H (1997) Measurement of stress development during HVOF thermal spray. In: Berndt CC (ed) Thermal spray: a united forum for scientific and technological advances. ASM International, Materials Park, OH, pp 805–811
269. Kuroda S, Tashiro Y, Yumoto H, Taira S, Fukanuma H, Tobe S (2001) Peening action and residual stresses in high-velocity oxygen fuel thermal spraying of 316L stainless steel. J Therm Spray Technol 10(2):367–374
270. Sampath S, Jiang XY, Matejicek J, Prchlik L, Kulkarni A, Vaidya A (2004) Role of thermal spray processing method on the microstructure, residual stress and properties of coatings: an integrated study for Ni–5 wt.%Al bond coats. Mater Sci Eng A364:216–231
271. Bansal P, Shipway PH, Leen SB (2006) Effect of particle impact on residual stress development in HVOF sprayed coatings. J Therm Spray Technol 15(4):570–575
272. Bansal P, Shipway PH, Leen SB (2007) Residual stresses in high-velocity oxy-fuel thermally sprayed coatings – modelling the effect of particle velocity and temperature during the spraying process. Acta Materialia 55:5089–5101
273. He J, Dulin B, Wolfe T (2008) Peening effect of thermal spray coating process. J Therm Spray Technol 17(2):214–220
274. Bolelli G, Lusvarghi L, Varis T, Turunen E, Leoni M, Scardi P, Azanza-Ricardo CL, Barletta M (2008) Residual stresses in HVOF-sprayed ceramic coatings. Surf Coat Technol 202:4810–4819
275. Wang T-G, Zhao S-S, Hua W-G, Li J-B, Gong J, Sun C (2010) Estimation of residual stress and its effects on the mechanical properties of detonation gun sprayed WC–Co coatings. Mater Sci Eng A527:454–461
276. Lima CRC, Nin J, Guilemany JM (2006) Evaluation of residual stresses of thermal barrier coatings with HVOF thermally sprayed bond coats using the modified layer removal method (MLRM). Surf Coat Technol 200:5963–5972
277. Jiang Yi, Bin-Shi Xu, Hai-dou Wang (2005) Residual stresses within sprayed coatings. J Cent South Univ Technol 12 (Suppl 2):53–58

278. Clyne TW (2001) Residual stresses in thick and thin surface coating, encyclopedia of materials: science and technology. Elsevier, Oxford, pp 8126–8134
279. Spencer K, Luzin V, Matthews N, Zhang M-X (2012) Residual stresses in cold spray Al coatings: the effect of alloying and of process parameters. Surf Coat Technol 206(19–20):4249–4255
280. Mellali M, Grimaud A, Léger AC, Fauchais P, Lu J (1997) Alumina grit blasting parameters for surface preparation in the plasma spraying operation. J Therm Spray Technol 6(2):217–227
281. Luzin V, Spencer K, Zhang M-X (2011) Residual stress and thermo-mechanical properties of cold spray metal coatings. Acta Materialia 59:1259–1270
282. Kroupa F (1997) Residual stresses in thick, non-homogeneous coatings. J Therm Spray Technol 6(3):309–319
283. Chang GC, Phucharoen W, Miller RA (1987) Finite element thermal stress solutions for thermal barrier coatings. Surf Coat Technol 32(1–4):307–325
284. Yokoyama K, Watanabe M, Kuroda S, Gotoh Y, Schmidt T, Gärtner F (2006) Simulation of solid particle impact behavior for spray processes. Mater Trans 47(7):1697–1702
285. Samadi H, Coyle TW (2009) Modeling the build-up of internal stresses in multilayer thick thermal barrier coatings. J Therm Spray Technol 18(5–6):996–1003
286. Ghafouri-Azar R, Mostaghimi J, Chandra S (2006) Modeling development of residual stresses in thermal spray coatings. Comput Mater Sci 35:13–26
287. Clyne W (1996) Residual stresses in surface coatings and their effects on interfacial debonding. Key Eng Mater 116(7):307–330
288. Gill SC, Clyne TW (1990) Stress distributions and material response in thermal spraying of metallic and ceramic deposits. Metall Trans B 21:377–385
289. Greving DJ, Shadley JR, Rybicki EF (1994) Effects of coating thickness and residual stresses on the bond strength of ASTM C633-79 thermal spray coating test specimens. J Therm Spray Technol 3(4):371–378
290. Tsui YC, Clyne TW (1996) Adhesion of thermal barrier coating systems and incorporation of an oxidation barrier layer. In: Berndt CC (ed) Thermal spray: practical solutions for engineering problems. ASM International, Materials Park, OH, pp 275–284
291. AWS (1985) Thermal spraying: practice, theory and application. American Welding Society, Miami, FL
292. Bose S, DeMasi-Marcin J (1997) Thermal barrier coating experience in gas turbine engines at Pratt & Whitney. J Therm Spray Technol 6(1):99–104
293. Koolloos MFJ, Houben JM (2000) Behavior of plasma-sprayed thermal barrier coatings during thermal cycling and the effect of a preoxidized NiCrAlY bond coat. J Therm Spray Technol 9(1):49–58
294. Tsipas SA, Golosnoy IO, Damani R, Clyne TW (2004) The effect of a high thermal gradient on sintering and stiffening in the top coat of a thermal barrier coating system. J Therm Spray Technol 13(3):370–376
295. Guo HB, Kuroda S, Murakamia H (2006) Segmented thermal barrier coatings produced by atmospheric plasma spraying hollow powders. Thin Solid Films 506–507:136–139
296. Strangman T, Raybould D, Jameel A, Baker W (2007) Damage mechanisms, life prediction, and development of EB-PVD thermal barrier coatings for turbine airfoils. Surf Coat Technol 202:658–664
297. Tricoire Au, Fauchais P, Braillard P, Malie A, Bengtsson A (2005) New concepts for plasma sprayed zirconia TBCs for aeronautical applications. In: International thermal spray conference 2005 – Basel, CH. DVS, Düsseldorf, Germany (DVD), e-proceedings
298. Smialek JL (2004) Improved oxidation life of segmented plasma sprayed 8YSZ thermal barrier coatings. J Therm Spray Technol 13(1):66–75
299. Choules BD, Kokini K (1996) Architecture of functionally graded ceramic coating against surface thermal fracture. ASME J Eng Mater Technol 118:522–528

300. Nemat-Alla M (2009) Reduction of thermal stresses by composition optimization of two-dimensional functionally graded materials. Acta Mech 208:147–161
301. Shabana YM, Noda N (2002) Geometry effects of substrate and coating layers on the thermal stress response of FGM structure. Acta Mech 159:143–156
302. Ahmed R, Hadfield M (2002) Mechanisms of fatigue failure in thermal spray coatings. J Therm Spray Technol 11(3):333–349
303. Ibrahim A, Berndt CC (2007) Fatigue and deformation of HVOF sprayed WC–Co coatings and hard chrome plating. Mater Sci Eng A 456:114–119
304. Malkin S, Guo C (2008) Grinding technology: theory and applications of machining with abrasives. Industrial Press, New York, NY
305. Gonzalez R, Cadenas M, Fernandez R, Cortizo JL, Rodrıguez E (2007) Wear behaviour of flame sprayed NiCrBSi coating remelted by flame or by laser. Wear 262:301–307
306. Akebono H, Komotori J, Shimizu M (2008) Effect of coating microstructure on the fatigue properties of steel thermally sprayed with Ni-based self-fluxing alloy. Int J Fatigue 30:814–821
307. Gomez-del Rio T, Garrido MA, Fernandez JE, Cadenas M, Rodrıgueza J (2008) Influence of the deposition techniques on the mechanical properties and microstructure of NiCrBSi coatings. J Mater Process Technol 204:304–312
308. Miguel JM, Guilemany JM, Vizcaino S (2003) Tribological study of NiCrBSi coating obtained by different processes. Tribol Int 36:181–187
309. Shrestha S, Hodgkiess T, Neville A (2005) Erosion–corrosion behaviour of high-velocity oxy-fuel Ni–Cr–Mo–Si–B coatings under high-velocity seawater jet impingement. Wear 259:208–218
310. Serres N, Hlawka F, Costil S, Langlade C, Machi F (2010) Microstructures and environmental assessment of metallic NiCrBSi coatings manufactured via hybrid plasma spray process. Surf Coat Technol 205(4):1039–1046
311. Gärtner F, Stoltenhoff T, Voyer J, Kreye H, Riekehr S, Kocak M (2006) Mechanical properties of cold sprayed and thermally sprayed copper coatings. Surf Coat Technol 200:6770–6782
312. Stoltenhoff T, Borchers C, Gartner F, Kreye H (2006) Microstructures and key properties of cold sprayed and thermally sprayed copper coatings. Surf Coat Technol 200:4947–4960
313. Phani SP, Srinivasa Rao D, Joshi SV, Sundararajan G (2007) Effect of process parameters and heat treatments on properties of cold sprayed copper coatings. J Therm Spray Technol 16 (3):425–434
314. Calla E, McCartney DG, Shipway PH (2006) Effect of deposition conditions on the properties and annealing behavior of cold-sprayed copper. J Therm Spray Technol 15(2):255–262
315. Hall AC, Cook DJ, Neiser RA, Roemer TJ, Hirschfeld DA (2006) The effect of a simple annealing heat treatment on the mechanical properties of cold-sprayed aluminum. J Therm Spray Technol 15(2):233–238
316. Zhang Q, Li C-J, Wang X-R, Ren Z-L, Li C-X, Yang G-J (2008) Formation of NiAl intermetallic compound by cold spraying of ball-milled Ni/Al alloy powder through post-annealing treatment. J Therm Spray Technol 17(5–6):715–720
317. Wang H-T, Li C-J, Yang G-J, Li C-X (2008) Cold spraying of Fe/Al powder mixture: coating characteristics and influence of heat treatment on the phase structure. Appl Surf Sci 255:2538–2544
318. Li W-Y, Zhang C, Liao H, Coddet C (2009) Effect of heat treatment on microstructure and mechanical properties of cold sprayed Ti coatings with relatively large powder particles. J Coat Technol Res 6(3):401–406
319. Zahiri SH, Fraser D, Jahedi M (2009) Recrystallization of cold spray-fabricated CP titanium structures. J Therm Spray Technol 18(1):16–22
320. Yang G-J, Li C-J, Fan S-Q, Wang Y-Y, Li C-X (2007) Influence of annealing on photocatalytic performance and adhesion of vacuum cold-sprayed nanostructured TiO2 coating. J Therm Spray Technol 16(5–6):873–880

321. Prudenziati M, Gualtieri ML (2008) Electrical properties of thermally sprayed Ni- and Ni20Cr-based resistors. J Therm Spray Technol 17(3):385–394
322. Karthikeyan J, Sreekumar KP, Venkatramani N, Kurup MB, Patil DS, Rohatgi VK (1989) Effect of process parameters on the properties of plasma-sprayed superconducting Y1Ba2Cu3O7-x coatings. Appl Phys A Mater Sci Process 48(5):489–492
323. Damani RJ, Wanner A (2000) Microstructure and elastic properties of plasma-sprayed alumina. J Mater Sci 35(17):4307–4318
324. Marrocco T, Driver LC, Harris SJ, McCartney DG (2006) Microstructure and properties of thermally sprayed Al-Sn-based alloys for plain bearing applications. J Therm Spray Technol 15(4):634–639
325. Yasuda K, Takeda H (2000) Phase transformation during alternating aging at 473 K and at 773 K in the plasma-sprayed yttria stabilized zirconia coating. J Mater Sci 35(17):4379–4383
326. Ilavsky J, Wallace J, Stalick JK (2001) Thermal spray yttria-stabilized zirconia phase changes during annealing. J Therm Spray Technol 10(3):497–501
327. Markocsan N, Nylén P, Wigren J, Li X-H, Tricoire A (2009) Effect of thermal aging on microstructure and functional properties of zirconia-base thermal barrier coatings. J Therm Spray Technol 18(2):201–208
328. Li Y, Li C-J, Zhang Q, Yang G-J, Li C-X (2010) Influence of TGO composition on the thermal shock lifetime of thermal barrier coatings with cold-sprayed MCrAlY bond coat. J Therm Spray Technol 19(1–2):168–177
329. Laribi M, Vannes AB, Mesrati N, Treheux D (2003) Metallurgical characterization and determination of residual stresses of coatings formed by thermal spraying. J Therm Spray Technol 12(2):234–239
330. Stewart S, Ahmed R (2003) Contact fatigue failure modes in hot isostatically pressed WC-12%Co Coatings. Surf Coat Technol 172:204–216
331. Stoica V, Ahmed R, Golshan M, Tobe S (2004) Sliding wear evaluation of hot isostatically pressed thermal spray ceramet coatings. J Therm Spray Technol 13(1):93–107
332. Khor KA, Loh NL (1994) Hot isostatic pressing of plasma sprayed Ni-base alloys. J Therm Spray Technol 3(1):57–62
333. Abdel-Samad A, Lugscheider E, Bobzin K, Maes M (2006) The influence of hot isostatic pressing on plasma sprayed coatings properties. Surf Coat Technol 201:1224–1227
334. Lenling WJ, Smith MF, Henfling JA (1991) Beneficial effects of austempering post-treatment on tungsten carbide based wear coatings. In: Bernecki TF (ed) Thermal spray research and applications. ASM International, Materials Park, OH, pp 227–232
335. Schelz S, Enguehard F, Caron N, Plessis D, Minot B, Guillet F, Longuet J-L, Teneze N, Bruneton E (2008) Recombination of silica and zirconia into zircon by means of laser treatment of plasma-sprayed coatings. J Mater Sci 43:1948–1957
336. Zhanga Shi Hong, Jae Hong Yoon, Ming Xi Li, Tong Yul Cho, Yun Kon Joo, Jae Young Cho (2010) Influence of CO2 laser heat treatment on surface properties, electrochemical and tribological performance of HVOF sprayed WC–24%Cr3C2–6%Ni coating. Mater Chem Phys 119:458–464
337. Pokhmurska A, Ciach R (2000) Microstructure and properties of laser treated arc sprayed and plasma sprayed coatings. Surf Coat Technol 125:415–418
338. Wang Y, Li CG, Tian W, Yang Y (2009) Laser surface remelting of plasma sprayed nanostructured Al2O3–13wt%TiO2 coatings on titanium alloy. Appl Surf Sci 255:8603–8610
339. Song RG, U, He WZ, Huang WD (2000) Effects of laser surface remelting on hydrogen permeation resistance of thermally-sprayed pure aluminum coatings. Surf Coat Technol 130:20–23
340. Tsai HL, Tsai PC (1998) Laser glazing of plasma-sprayed zirconia coatings. J Mater Eng Performance 7(2):258–264

341. Dyshlovenko S, Pawlowski L, Smurov I, Veiko V (2006) Pulsed laser modification of plasma-sprayed coatings: experimental processing of hydroxyapatite and numerical simulation. Surf Coat Technol 201:2248–2255
342. Sidhu Buta Singh, Puri D, Prakash S (2005) Mechanical and metallurgical properties of plasma sprayed and laser remelted Ni–20Cr and Stellite-6 coatings. J Mater Process Technol 159:347–355
343. Razavy FG, Van Aken DC, Smith JD (2003) Effect of laser surface melting upon the devitrification of plasma sprayed cordierite. Mater Sci Eng A362:213–222
344. Dallaire S, Dubé D, Fiset M (1999) Laser melting of plasma-sprayed copper–ceramic coatings for improved erosion resistance. Wear 231:102–107
345. Ahmed N, Bakare MS, McCartney DG, Voisey KT (2010) The effects of microstructural features on the performance gap in corrosion resistance between bulk and HVOF sprayed Inconel 625. Surf Coat Technol 204:2294–2301
346. Antou G, Hlawka F, Cornet A, Montavon G, Coddet C, Machi F (2004) Processing of yttria partially stabilized zirconia thermal barrier coatings implementing a high-power laser diode. J Therm Spray Technol 13(3):381–389
347. Knuuttila J, Sorsa P, Mäntylä T (1999) Sealing of thermal spray coatings by impregnation. J Therm Spray Technol 8(2):251–257
348. Knuuttila J, Sorsa P, Mäntylä T, Knuuttila J, Sorsa P (1999) Sealing of thermal spray coatings by impregnation. J Therm Spray Technol 8(2):249–25
349. Shrestha S, Hodgkiess T, Neville A (2001) The effect of post-treatment of a high-velocity oxy-fuel Ni-Cr-Mo-Si-B coating part 2: erosion-corrosion behavior. J Therm Spray Technol 10(4):656–665
350. Kim H-J, Lee C-H, Kweon Y-G (2001) The effects of sealing on the mechanical properties of the plasma-sprayed alumina-titania coating. Surf Coat Technol 139:75–80
351. Ctibor P, Neufuss K, Zahalka F, Kolman B (2007) Plasma sprayed ceramic coatings without and with epoxy resin sealing treatment and their wear resistance. Wear 262:1274–1280
352. Leivo EM, Vippola MS, Sorsa PPA, Vuoristo PMJ, Mäntylä TA (1997) Wear and corrosion properties of plasma sprayed AI2O3 and Cr2O3 coatings sealed by aluminum phosphates. J Therm Spray Technol 6(2):205–210
353. Ahmaniemi S, Vippola M, Vuoristo P, Mäntylä T, Cernuschi F, Lutterotti L (2004) Modified thick thermal barrier coatings: microstructural characterization. J Eur Ceram Soc 24:2247–2258
354. Ahmaniemi S, Tuominen J, Vuoristo P, Mäntylä T (2002) Sealing procedures for thick thermal barrier coatings. J Therm Spray Technol 11(3):320–332
355. Ahmaniemi S, Vuoristo P, Mäntylä T, Gualco C, Bonadei A, Di R (2005) Thermal cycling resistance of modified thick thermal barrier coatings. Surf Coat Technol 190:378–387
356. Ahmaniemi S, Vippola M, Vuoristo P, Mäntylä T, Buchmann M, Gadow R (2002) Residual stresses in aluminium phosphate sealed plasma sprayed oxide coatings and their effect on abrasive wear. Wear 252:614–623
357. Troczynski T, Yang Q, John G (1999) Post-deposition treatment of zirconia thermal barrier coatings using Sol-Gel alumina. J Therm Spray Technol 8(2):229–234
358. Westergård R, Hogmark S (2004) Sealing to improve the wear properties of plasma sprayed alumina by electro-deposited Ni. Wear 256:1153–1162
359. Panadda N, Koiprasert H (2006) Improved corrosion resistance of thermally sprayed coating via surface grinding and electroplating techniques. Surf Coat Technol 201:737–743
360. Xie D, Xiong Y, Wang F (2003) Effect of an enamel coating on the oxidation and hot corrosion behavior of an HVOF-sprayed Co–Ni–Cr–Al–Y coating. Oxidation Metals 59 (5/6):503–516
361. Caron N, Bianchi L, Méthout S (2008) Development of a functional sealing layer for SOFC applications. J Therm Spray Technol 17(5–6):598–602
362. Khor KA, Yu L-G, Chan SH, Chen XJ (2003) Densification of plasma sprayed YSZ electrolytes by spark plasma sintering (SPS). J Eur Ceram Soc 23:1855–1863

363. Prawara B, Yara H, Miyagi Y, Fukushima T (2003) Spark plasma sintering as a post-spray treatment for thermally-sprayed coatings. Surf Coat Technol 162:234–241
364. Zhou Zhao-huia, Sheng-kaia Gong, He-feia Li, Hui-bina Xu, Chun-gang Zhang, Lub Wang (2007) Effects of shot peening process on thermal cycling lifetime of TBCs prepared by EB-PVD. Chin J Aeronautics 20:145–147
365. Junior GS, Voorwald HJC, Vieira LFS, Cioffi MOH, Bonora RG (2010) Evaluation of WC-10Ni thermal spray coating with shot peening on the fatigue strength of AISI 4340 steel. Procedia Eng 2:649–656
366. Kubiak K, Fouvry S, Marechal AM, Vernet JM (2006) Behaviour of shot peening combined with WC–Co HVOF coating under complex fretting wear and fretting fatigue loading conditions. Surf Coat Technol 201:4323–4328
367. Marin de Camargo José André, Herman Jacobus Cornelis, Voorwald Maria Odila Hilário Cioffi, Midori Yoshikawa Pitanga Costa (2007) Coating residual stress effects on fatigue performance of 7050-T7451 aluminum alloy. Surf Coat Technol 201:9448–9455
368. Costa MYP, Venditti MLR, Voorwald HJC, Cioffi MOH, Cruz TG. Effect of WC–10% Co–4%Cr coating on the Ti–6Al–4V alloy fatigue strength. Mater Sci

Chapter 14
Nanostructured or Finely Structured Coatings

Abbreviations

APS	Atmospheric plasma spraying
BGCCs	Bioactive glass–ceramic coatings
CGDS	Cold gas dynamic spraying
CVD	Chemical vapor deposition
d.c.	Direct current
EB-PVD	Electron beam-physical vapor deposition
ETAB	Enhanced Taylor's analogy break-up
FESEM	Field emission scanning electron microscopy
FCT	Furnace cycle test
GDC	Gadolinia-doped ceria
GFA	Glass forming ability
HA	Hydroxyapatite ($Ca_{l0}(PO_4)6(OH)$)
HCA	Hydroxide carbonate apatite
HPAL	High-pressure acid-leach
HVAF	High velocity air fuel flame
HVOF	High velocity oxy-fuel flame
HVSFS	High velocity suspension flame spraying
i.d.	Internal diameter
IT-SOFCs	Intermediate temperature solid oxide fuel cells
JETS	Jet engine thermal shocks furnace cycle test (FCT)
LCA	Life Assessment Impact
LSCF	Lanthanum strontium cobalt iron oxide (La_xSr_{1-x} $Co_yFe_{1-y}O_{3-\delta}$)
MWCNT	Multiwalled carbon nanometer-sized tubes
Nd-YAG	Neodinium-doped yttrium aluminum garnet
PAA	Ammonium polyacrylic acid
PBTCA	2-Phosphonobutane-1, 2, 4-tricarboxylic acid
PE-CVD	Plasma-enhanced-chemical vapor deposition
PEI	Polyethyleneimine

P.L. Fauchais et al., *Thermal Spray Fundamentals: From Powder to Part*,
DOI 10.1007/978-0-387-68991-3_14, © Springer Science+Business Media New York 2014

PGDS	Pulsed gas dynamic spraying
PIV	Particle image velocimetry
PTA	Plasma transferred arc
PVD	Physical vapor deposition
r.f.	Radio frequency
RH	Relative air humidity
SBF	Simulated body fluid
SDC	Samaria-doped ceria
SEM	Scanning electron microscopy
slm	Standard liters per minute
SOFCs	Solid oxide fuel cells
SolPS	r.f. Solution plasma spraying
SPS	Suspension plasma spraying
SPPS	Solution precursor plasma spraying
SPS	Suspension plasma spraying
SPTS	Solution precursor thermal spraying
STS	Suspension thermal spraying
TAB	Taylor's analogy break-up
TBCs	Thermal barrier coatings
TIG	Tungsten inert gas
We	Weber number
YAG	Yttrium aluminum garnet
YPSZ	Yttria partially stabilized zirconia
YSZ	Yttria-stabilized zirconia

14.1 Introduction

14.1.1 Why Nanostructured Coatings

According to the definition of the US National Nanotechnology Initiative, USNNI, "nanometer-sized" materials, or more commonly referred to as "nanosized" or "nanostructured" materials, are materials with a particle diameter or an internal structure with at least one dimension smaller than 100 nm. From the pioneering works of McPherson in 1973, who was among the first to identify nano-size features in thermally sprayed alumina coatings, to recent and most advanced work aimed at manufacturing nanostructured coatings from nanosize feedstock particles, the thermal spray community has been actively involved in this area for more than 30 years. Nano-sized materials are at the frontier of materials science due to their remarkable, and in some cases novel, properties [1, 2]. This results in particular from the surface-to-bulk ratio, and interface density between features, that are much higher in nanostructured materials compared to those of coarser particle (e.g., micro-sized) materials. The physical mechanisms involved leading to those remarkable

properties lies, at such dimensions, between atom quantum effects (e.g., phonon scattering, surface plasmon, etc.) and bulk behaviors (e.g., cohesion, etc.).

Due to the large volume fraction of the internal interfaces, nanostructured coatings should exhibit better properties than conventional microstructured coatings. For example, considering ceramics, they should exhibit in a noticeable increase in dimensional stability, lower thermal diffusivity and hysteresis (due to phonon scattering by boundary defects), higher hardness and toughness (due to small grain sizes), better wear resistance (due to higher hardness, grain-sliding plasticity, and the change of fracture and material-removal mechanism due to ultrafine particle size) [3, 4]. Moreover generally nanostructured coatings are not necessarily harder than the conventional ones, but they tend to be much tougher. This is explained by the crack arresting effect. In conventional thermal-sprayed coatings the crack tends to propagate along splat boundaries due to the weak intersplat bonding. For the nanostructured coating the splat-to-splat cohesion is generally better and the coating is rather homogeneous with splat sizes in the 100 nm range, thus crack propagation is limited. It is also important to point out that most of the research performed over the last decade has been devoted to nanostructured ceramics. To illustrate the interest of these coatings a few examples are briefly described.

1. *Spraying of agglomerated nanometer-sized particles* [5]. As described in next subsection, among the different processes developed to produce such coatings, spraying of micro-sized particles made of agglomerated nano-sized ones has been the first to be sufficiently developed, well characterized, with resulting coatings tested in service. For example, for a pure ceramic abradable coating design, the concept of the porous nano-zones, if embedded in the coating microstructure in "sufficient numbers," could be employed to lower the overall stiffness of the coating, allowing the tip of a metallic turbine blade to wear off some of the coating, creating the "seal effect," without damaging the blade. Al_2O_3–13 wt% TiO_2 HVOF-sprayed ultrafine coating exhibited a 4-fold improvement in wear performance. Evolution of the crack propagation resistance for the alumina–titania coatings showed to be the main reason for the superior wear behavior of the ultrafine coating. Improved bond strength values have been reported for these coatings when compared with their conventional counterparts. It seems that dense nano-zones would tend to impede crack propagation at the interface, which would enhance interfacial toughness and the bond strength levels of the coating. Nanostructured alumina–titania coatings deposited by APS are in use to protect the main propulsion shafts of ships of the US Navy. After 4 years of use in naval applications no significant damage was recorded in these types of coatings. It has been shown that HVOF-sprayed nano-TiO_2–hydroxyapatite (HA) composite coatings exhibit bond strength levels of at least 2.5 times that of thermally sprayed conventional HA coatings. Also these coatings exhibit bio-performance levels equivalent or superior to those of an HA coating, which is the current state-of-the-art material.

2. *Iron-based coatings with metallic glass formation forming nanostructures upon reheating* [6, 7]. Specialized iron-based complex composition with a low critical cooling rate (10^4 K/s) for metallic glass formation has been developed. Coatings with thicknesses up to 1.5 mm, obtained by almost all spray processes, except cold spray, presented interesting properties, even when sprayed in air. d.c. plasma or HVOF-sprayed powders such as $Fe_{63}Cr_8Mo_2B_{17}C_5Si_1Al_4$, resulted in coatings with an exceptional resistance to two-body abrasion, and a higher hardness levels compared to that found in conventional steels. The as-sprayed amorphous coatings showed hardness of 10.2–10.7 GPa and after reheating up to 750 °C or 800 °C for one hour (devitrified nano-composite), their hardness was 11.4–12.8 GPa. With twin wire-arc spraying the SHS8000, iron-based glass forming alloy, coatings were formed primarily of an amorphous matrix with very fine dispersed nano-crystals ferrites and $M_2(C,B)_1$ compounds with a hardness in the range 1.05–1.2 GPa. When exposed to 649 °C, the microhardness increased up to ~2 GPa, very significant hardening. The wear resistance to dry sand/rubber wheel abrasion was improved by a factor of 3.5. A similar improvement was also obtained for elevated-temperature erosion resistance. Wire-arc coatings of SHS7170 resist erosion almost independently of contact angle, at temperatures up to 600 °C which is particularly important for real-world boiler applications. The iron alloys developed for PTA spraying had a high hardness, up to Rc 66, due to their fine structure consisting of a high volume fraction of boro-carbides phases. The toughness measured with a Palmqvist method, was up to 74.7 MPa $m^{1/2}$, which could adequately be described through a crack bridging model.
3. *Suspensions or solution-sprayed coatings* [5, 8, 9]. Suspension plasma spraying (SPS), high velocity suspension flame spraying (HVSFS), or solution precursor plasma spraying (SPPS) have been used for the preparation of nanostructured thermal barrier coatings with a very fine porosity, high segmentation crack density, and low Young's modulus. The segmentation cracks survived thermal cycling test. The advantages of SPS were partially lost at very high temperatures (1,400 °C) when YSZ was chosen as coating material. Investigations are ongoing to reduce the amount of overspray embedded in the coatings and to reduce the sintering tendency. SPPS combines the advantages of EB-PVD and plasma or HVOF spraying processes: good strain tolerance and low apparent thermal conductivity with improved bond strength. The spallation life was improved by a factor of 2.5 compared with APS coatings on the same bond coat and substrate and by a factor of 1.5 compared with high-quality EB-PVD coatings. Many studies have also been devoted to solid oxide fuel cells (SOFC) components made by SPS and SPPS and some results are promising. With suspension alumina coatings by HVSFS, low wear rates, nearly one order of magnitude better than for standard micrometer-sized APS and HVOF coatings, were measured using dry sliding tests. The friction coefficient of Al_2O_3 coatings was decreased by a factor of four (0.2 for SPS coatings sprayed with the 0.4 μm mean diameter feedstock, compared to 0.8–0.9 for the APS one). The wear rate was 30 times lower for SPS coatings compared to that of APS coatings. HVSFS

of nano-TiO_2–HA composite coatings exhibit bond strength levels of at least 2.5 times higher than those of thermally sprayed conventional HA coatings with equivalent or superior bio-performance levels compared to a standard HA coating. HVSFS was used to deposit bioactive glass coatings. In vitro bioactivity tests indicated that the coatings interacted remarkably with the simulated body fluid (SBF), developing a thick silica-rich layer containing hydroxyapatite crystals.

14.1.2 How to Spray Nanostructure Coatings?

When spraying conventionally micro-sized particles with nanostructures, their melting automatically destroys the nanostructure. While this is not the case in cold spray, but the sprayed nanostructured particles must be ductile enough. Thus processing of nanoparticles is not simple as pointed out in the review of the different processes by Viswanathan et al. [10]. Among the possible routes thermal spray is very promising [11] to achieve nano– or finely structured materials due to a rapid solidification rate. This opens the way to prepare advanced materials with unique properties.

One of the major drawbacks of processing nano-sized particles by thermal spraying is the problem of injecting them into the core of the high enthalpy flow, since the particle injection force has to be of the same order of that imparted to them by the flow [12]. Decreasing the particle average size down to the nano-size requires, besides other technological issues, increasing the particle injection momentum by significantly of increase of cold carrier gas flow rate, this to a point where it disrupts the high enthalpy flow (disruption occurs usually for a gas mass flow rate equal to or higher than one sixth of the high enthalpy flow rate). To circumvent this phenomenon, two routes can be followed: spraying micrometer-sized particles as in conventional thermal spraying, but made of nano-sized agglomerated particles (see Sect. 11.1.2.6), or spraying sub-micrometer or nano-sized particles using a liquid carrier instead of gas (see Sect. 4.5) [13]. For details see the review of Fauchais et al. [5]. In both cases, when spraying materials that are not oxides, care must be taken to avoid the in-flight oxidation of the particles, since the presence of the oxide between layered splats (or particles) diminishes the contacts between them and consequently degrades the coating properties and especially their resistance to corrosion. Compared to conventional coatings (with micrometric structures), the oxide layers are more detrimental with nanostructured coating.

Since the beginning of the mid-1990s, much work have been devoted to the use of the spray technology for the deposition of finely or nanostructured coatings. To produce finely structured coatings by thermal spray techniques, five routes have been suggested:

1. Conventional spraying by plasma, wire arc, PTA, HVOF (with particle or drop sizes in the tens of μm range) of very complex alloys containing multiple

elements (7–9 different components) having a low critical cooling rate (10^4 K/s) for metallic glass formation, in the case when cooled-down, to a undercooling temperature below the glass transition temperature. After deposition, upon subsequent heating in the 500–750 °C range, the metallic glass precursor transforms, through a solid-solid state deglazing, into multiple crystalline phases where the resulting structures are nano-scaled [7, 14].

2. Spraying of conventional micro-sized particles, by plasma or HVOF (in the 30–90 μm range), made of agglomerated nano-sized particles (mainly ceramics) [15] and operating the spray systems in relatively narrow spray window [5], in order to have the particles only partially melted [16]. The molten part of the larger particles, or the smaller fully melted particles act as "cement" bonding thereby unmelted nano-sized grains. Coatings exhibit a two-scale architecture, often called bimodal (finding application, for example, in thermal barrier abradable coatings made of partially stabilized zirconia).
3. Cold spraying of agglomerated nano or amorphous particles [17].
4. When considering particles in the sub-micro- or nano-scale size range, gas can be no longer applied for carrying (see Sect. 4.4.2) and thus the use of a liquid carrier becomes mandatory. With the liquid, injected as jet or drops, two routes can be implemented, the liquid containing:

   (a) sub-micron- or nano-sized particles via a suspension. Once the liquid has been fragmented and vaporized by the plasma flow or the HVOF flame, particles contained in droplets are heated, accelerated, and sprayed as molten droplets onto the substrate. On a metallic substrate, the first droplets result in the formation of splats, whose equivalent diameters range between 0.1 and 2 μm with an average thicknesses between 20 and 300 nm. However on substrates with poor thermal diffusivity (or on the first deposited layers of poorly conductive materials) and with a high thermal flux from hot gases (up to 20–40 MW/m^2), cooling may be delayed. Thus the surface tension may take over and molten particles recover their spherical shape before solidification and forming coatings with granular structures. The stacking of splats or liquid particles forms finely structured coatings, often with a granular structure [5, 18]. It is also possible to spray a suspension of molecularly mixed amorphous powders as feedstock [19]. According to some authors this is an ideal process for the deposition of homogeneously distributed multicomponent ceramics coatings.
   (b) With solutions of precursors of materials to be deposited, as with suspension, the liquid undergoes rapid fragmentation and evaporation once injected in the plasma jet. This is followed by precipitation or gelation, pyrolysis, and melting to result finally in the impact of molten liquid droplets with average diameters ranging from a few tenths to a few micrometers [5, 20]. A sol–gel colloidal solution can also be used instead of the solution [21].

14.2 Spraying of Complex Alloys Containing Multiple Elements to Form Amorphous Coatings

According to Sergueeva et al. [22]: "Crystallization of metallic glasses has been successfully used as one of the methods for nano-crystalline material production in various alloy systems, e.g., in Fe-, Ni-, and Co-based alloys. This type of transformation involves decomposition of single-phase supersaturated solid solutions into multiphase nano-scale microstructures. To obtain a nano-scale structure, the crystallization process should proceed with the largest nucleation rate possible while suppressing the crystal growth rate as much as possible. Such conditions can be obtained for compositions of some alloys by applying specific methods of heat treatment.... Among metallic glasses those that undergo primary crystallization with a time-dependent, long-range diffusion controlled growth rate are the most suitable candidates for nanometer crystallization".

The methodology involves designing alloys that have low-critical cooling rates for metallic glass formation that result in the formation of amorphous coatings when thermally deposited. The amorphous coatings, when heated (after spraying) above their crystallization temperature are devitrified. Since the diffusion rate in the solid state is very low at the transformation temperature (typically 0.4–0.7 T_m for iron alloys), nano-scale microstructures are formed [6, 23–25].

In the past decade, a series of new bulk amorphous alloys with a multicomponent chemistry and high-glass forming ability (GFA) have been developed in zirconium-, magnesium-, lanthanum-, palladium-, titanium-, and Fe-base systems with various rapid solidification techniques [23–25]. Compared with other amorphous alloy systems, such as zirconium- and lead-base metallic glasses, the advantages of Fe-base amorphous coatings are lower materials cost, higher strength, and higher wear and corrosion resistance. However to be suitable for thermal spray processes such materials should be produced by gas atomization.

14.2.1 Amorphous Alloys Containing Phosphorus

Complex alloys containing phosphorus are known to present amorphous phases and can be produced by gas atomization. Alloy powders of Fe–10 % Cr–8 % P–2 % C (10 Cr), Fe–20 % Cr–8 % P–2 % C(20 Cr), and Fe–10 % Cr–10 % Mo–8 % P–2 % C(10Mo) compositions (in wt%) were sprayed by the high velocity oxy-fuel (HVOF) process under different conditions where the oxygen and fuel pressures of the HVOF process were changed to vary the flame temperature [26]. The melting point of particles was under 1,273 K and their size distribution between 10 and 45 μm. Amorphous coatings with a small amount of crystalline phases were obtained from the 10Cr and 20Cr alloys and a 100 % amorphous coating was formed from the 10Mo alloy. The volume fraction of the crystalline material increased slightly with the rise of the flame temperature. The coatings appeared

very dense, although some pores and oxide films were visible in the coatings. The hardness of the 10Cr and 20Cr coatings was 600–700 HV_{5N}. On the other hand, the 10 Mo coatings composed of a perfect amorphous phase reveal a constant hardness of 560 HV_{5N} independently of the spray condition. The as-sprayed coatings of the 10Cr and 20Cr alloys exhibited the activation–passivation transition. In contrast, the as-sprayed coating of the 10Mo alloy composed of a 100 % amorphous phase structure had excellent corrosion resistance in 1 N H_2SO_4 and 1 N HCl solutions [26].

14.2.2 NiCrB and FeCrB Alloys

Since the mid-1980s studies were devoted to the production and the properties of air and vacuum plasma or HVOF-sprayed amorphous/nanometer crystalline NiCrB- and FeCrB-based alloys [27–31]. For example, NiCrMoB alloys [31] were sprayed with a HVOF Miller spray system (Praxair Surface Technologies, Appleton, WI) with hydrogen as a fuel gas and gas and oxygen (H_2 to O_2 gas ratio 3 to 1). Both powders (two different NiCrMoB alloys: 25–63 μm) and deposits contained substantial quantities of amorphous/nano-crystalline matrices (as shown by the significant broadening of the fcc nickel peak at $2\theta = 44°$). Hardness values were in excess of 610 ± 10 HV_{3N}. Higher molybdenum and boron levels led to higher hardness values of up to 810 ± 15 HV_{3N} · The deposited layers were found to contain fine Cr_5B_3 precipitates within the metallic matrix phase. The predominant oxide phase, Cr_2O_3, occurred principally with a columnar-grained morphology at inter-splat boundaries. Anodic polarization curves showed that in 0.5 M H_2SO_4 a passive region occurred between approximately +100 and +900 mV (SCE). Increased molybdenum and boron levels modified the pre-passivation corrosion current density but had little effect on either passive current density or the onset of trans-passive corrosion. The potentiodynamic corrosion testing also demonstrated that the corrosion behavior of the experimental coatings A and B was similar to that of HVOF-sprayed Inconel 625. However, the presence of oxides at inter-splat boundaries leads to passive current densities higher than those observed in wrought alloys or melt spun ribbons.

In-flight particle oxidation during atmospheric plasma spraying [APS] and high velocity oxy-fuel [HVOF] spraying is however unavoidable. For example, with NiTiZrSiSn there is a preferential oxidation of Zr and Ti in an in-flight particle [32]. As a matter of fact, oxidation triggers the destabilization of the bulk of metallic glass particles because amorphous phase stability and formability are largely affected by the chemical composition depending on the critical cooling rate. With the HVOF process (H_2–O_2 mixture) [7] above the 0.20 O_2/H_2 ratio, severe oxidation was observed, inducing destabilization of the amorphous phase.

14.2.3 Iron-Based Amorphous Alloys

Nano-scale steels have appeared at the end of the past century and the first advances have boosted the field of hard magnets made of neodymium, iron, and boron. Branagan et al. [33] succeeded to synthesize nano-scale metal matrix composite microstructures in a 9-element modified Nd–Fe–B alloy, optimizing the magnetic behavior of permanent magnets

To obtain amorphous and nano-scale composite thermally deposited steel coatings a specialized iron-based composition (Fe63Cr8Mo2B17C5Si1Al4) with a low-critical cooling rate (10^4 K/s) for metallic glass formation has been developed. The alloy is processed by inert gas atomization to avoid oxidation and to form micron-sized amorphous spherical particles with a size distribution adapted to thermal spraying. The particle size distribution is particularly important because the particles have to melt to form the amorphous coatings. Collecting and quenching sprayed particles was performed to verify the particle characteristics. The results show that a significant fraction of the less-than-50 μm particles are amorphous, while particles greater than 75 μm are crystalline. In Fig. 11.7, backscattered electron micrographs indicate that small particles (<20 μm) have an absence of structure, while larger powder particles (50–75 μm) exhibit a primarily crystalline structure with areas of uncrystallized glass.

A primarily amorphous structure is formed in the as-sprayed coatings (using d.c. plasma or HVOF), independent of coating thickness. After a heat treatment above the crystallization temperature (568 °C which is less than half the melting temperature), the coatings are devitrified into a multiphase nano-composite microstructure with 75–125 nm grains containing a distribution of 20 nm second-phase grain-boundary precipitates [6]. A strong effect of annealing conditions on the nature of crystallization products and, as a result, on the mechanical behavior of the alloy has been revealed [6]. Accordingly, depending on the microstructure produced and the deformation conditions chosen, a wide variety of strength/elongation properties can be generated for various potential applications. To illustrate what happens when spraying such materials and reheating the deposit them the results obtained by Branagan [34] by melt spinning are presented below. He has considered a 5-element glass-forming steel alloy with the following stoichiometry, Fe63.2Cr15.8B17W2C2. The as-cast microstructure was found to be formed by a dendritic solidification morphology, resulting in a multiphase structure with an average phase scale from 1 to 5 μm (see Fig. 14.1a). Phases in the ingot were determined from X-ray diffraction and were found to include α-Fe, M23C6 and M3B. The same 5-element steel was processed by melt spinning at 15 m/s to form a homogeneous glass (glass-to-crystalline peak at 536 °C). After heat-treating the glass above 536 °C, complete deglazing occurred through the solid–solid-state transformation. The nanometer scale structures are shown in the TEM micrographs in Fig. 14.1b–d, respectively, obtained after heat treatment at 700 °C, 750 °C, and 850 °C for 1 h.

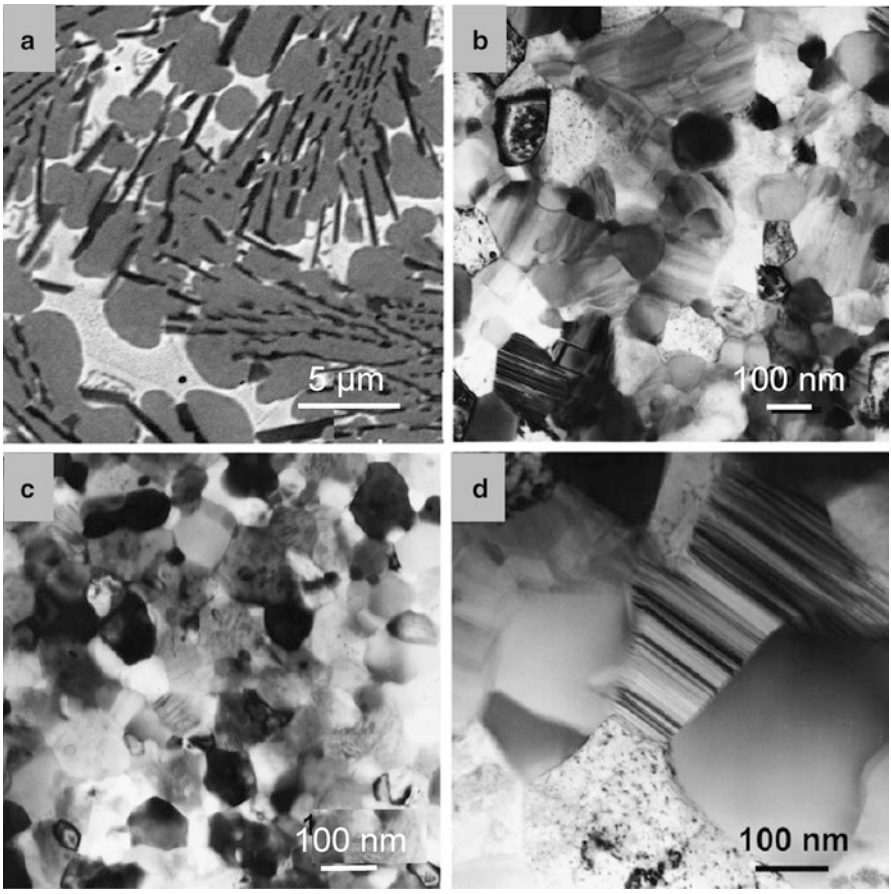


Fig. 14.1 Electron microcopy images of a 5-element steel alloy; (**a**) backscattered electron image of an as-cast ingot, (**b**) transmission electron image of ribbon heat-treated at 700 °C, (**c**) transmission electron image of ribbon heat treated at 750 °C, and (**d**) transmission electron image of ribbon heat treated at 850 °C. Reprinted with kind permission from Elsevier [34]

The phase size is still considered nano-scale up to at least 750 °C, with only a small change from the average size of 25 nm when heat treated from 700 to 750 °C. At the 850 °C heat treatment, extensive grain growth has clearly occurred with phase sizes approximately double those of the lower temperature heat treated samples [34]. When heat-treated at or below 700 °C, the nanometer scale microstructure is found to exhibit a hardness which is approximately 8.83 GPa higher than the micrometer scale microstructure. The nanometer-structured metal hardness exhibits two plateaus with little change in hardness from 600 to 700 °C, followed by a very significant drop in hardness from 700 to 750 °C, and then by a leveling off with finally another significant drop in hardness at 850 °C. Thus in engineering

structures to improve properties, microstructural size alone is not the only important facet of the microstructure and other microstructural aspects must be considered. For more details, see the paper of Branagan [34].

Using HVOF deposition, the adhesion strength of the coatings was found to be excellent for a wide variety of metallic substrates. Good wear resistance was obtained in the three-body slurry abrasion tests [6]. Due to the high hardness, the amorphous and nano-composite coatings experienced good wear characteristics. No wear was found in the two-body abrasion tests in the as-sprayed or heat-treated plasma coatings. This was surprising, since the Si_3N_4 pin was much harder than both the as-sprayed and heat-treated coatings. The NanoSteel Company was recently created to develop and market a range of patented high-performance Super Hard Steel materials. For example, the new Fe-based commercial alloy (Fe52.3Mn2Cr19Mo2.5W1.7B16C4Si2.5) demonstrates strength of more than 6 GPa at room temperature [22], which is much stronger than the commonly used high strength (0.24–0.9 GPa) or even ultrahigh strength steels (0.9–1.5 GPa) of today. Such coatings can be applied with a wide variety of processes: thermal spraying, welding (MIG and PTA), and laser cladding. They are mostly made of Fe–Cr–Mo–W–C–Mn–Si–B or Cr–Mo–B–Si–W–Mn–C–Nb–Fe.

Certain iron-based glass forming materials such as SAM2X5 have an optimized chemistry with a protective adherent oxide layer and in principle a good corrosion resistance. However, Branagan et al. [7] have emphasized that when using optimized HVOF spray parameters to achieve high-density coatings, the development of the glass structure seems to be the dominant factor affecting corrosion performance. All HVOF coatings, regardless of powder lot were found to be primarily amorphous with only subtle differences in crystallinity. However, because the larger particles in the distribution are not completely remelted during spraying, the starting crystallinity in the feedstock powder is found to be an important factor. It is believed that the cores of these larger particles cause the coarsening of the microstructure. These pockets or bands of crystallinity can initiate anodic attack and result in reduced corrosion performance. Thus for a good resistance to corrosion the glass content in the feedstock powder is a paramount factor and must be maximized.

Due to their high abrasion, erosion, and corrosion resistance, hardness and toughness, the main applications of such coatings are boiler tube refurbishment, hard chrome replacement, hard facing, pumps, etc. Generally HVOF spraying is used because of the high particle velocities resulting in dense coatings. The SAM2XS amorphous steel has been used to replace hard chromium [35]. Coatings, sprayed with a JP5000 HVOF gun, were found to be nanometer-structured, hard (about 1,000 HV_{3N} as sprayed and 1,200 HV_{3N} after heat treatment at 700 °C for 10 min, approaching hardness of WC-Co coatings), with an excellent corrosion resistance to sea water and salt fog environment, and a wear resistance far superior to that of stainless steel used for this corrosion resistance. The SHS7574 powder from NanoSteel was successively sprayed with a D-gun and HVOF [36]. In both cases coatings were dense but those sprayed with a D-gun showed better adhesion and presented very good wear resistance.

Branagan et al. [14] have introduced a new iron-base cored wire, SHS7170, which readily forms nanometer composite coatings when sprayed using the wire arc process and exhibits a combination of properties that are superior to the existing available materials for high temperature boiler applications. The oxide content in the coatings is very low and is typically <1 vol.%. The bond strengths are remarkable for wire arc coatings and represent some of the best-published values, along with high toughness and resiliency. The as-sprayed SHS7170 wire arc coatings are found to develop an amorphous matrix structure containing starburst-shaped boride and carbide crystallites with sizes ranging from 60 to 140 nm. After heating to temperatures above the peak crystalline temperature (566 °C), a solid/state transformation occurs that results in the formation of an intimate three-phase matrix structure consisting of the same complex boride and carbide phases, along with α-iron interdispersed on a structural scale from 60 to 110 nm. The nanometer composite microstructure contains clean grain boundaries, which are found to be extremely stable and resist coarsening throughout the range of temperatures found in boilers. The SHS7170 coatings exhibit high bond strength along with high toughness and resiliency. The elevated-temperature erosion resistance of the SHS7170 wire arc coatings was found to be superior based on thickness loss compared with the existing wire arc coatings that have been tested.

Recently a new iron-based alloy SHS7170 has been developed [14]. Upon wire arc spraying, it forms an amorphous matrix with very fine dispersed nanometer-sized crystals that were identified as ferrites and $M_2(C,B)_1$ compounds. When exposed to elevated temperatures, the microhardness slightly increases at relatively low temperatures from 316 °C to 482 °C, and it dramatically increases up to ~1.77 MPa when the temperature is raised to 649 °C. The wear resistance was improved by a factor of 3.5 with the significant hardening. The SHS7170 coatings were found to exhibit high bond strength along with high toughness and resiliency. The elevated-temperature erosion resistance of the SHS7170 wire arc coatings was found to be superior based on thickness loss compared with the existing wire-arc coatings that have been tested. SHS7170 coatings resisted erosion almost independently of contact angle and at temperatures at least up to 600 °C. Zhou et al. [37] have shown that the SHS8000 coatings exhibited high bond strength along with high toughness and resiliency. The development of the time–temperature–transformation diagram for the SHS8000 coating allowed predicting the coating performance as a function of temperature and time during elevated temperature exposure.

Fe-base nano-crystalline SHS7172CP1 (particles with diameters 53–150 μm ranging) wear-resistant materials have been cladded on aluminum alloys using a PTA with a negative work piece polarity (see Sect. 10.6.7) process where the heat input into the base material and the formation of spatter can be limited [38]. The dilution is limited to approximately 5 %, while the high conductivity of the base material is responsible for a high cooling rate, which induces nano-crystalline solidification.

14.3 Agglomerated Ceramic Particles Spraying with Hot Gases

14.3.1 Spray Conditions

In order to spray nano-sized particles using regular powder feeders the nano-sized ceramic particles are agglomerated via spray drying (and then sintered) into micro-sized particles. For details about the powders used see Sect. 11.1.2.6. It is important to point out that for these particles, finding the trade off threshold between providing cohesive strength and maintaining the nanostructural character of the feedstock is paramount, i.e., too high heat-treatment temperatures and/or long heat-treatment times may cause the partial or total loss of the nanostructural character of the powder due to particle coarsening and sintering effects [5].

These agglomerated particles can be either dense, or rather porous. Finally [5] not all so-called nanostructured agglomerated powders commercially available are formed via the agglomeration of individual nanostructured particles. For example, Fig. 14.2a shows a spray-dried "nanostructured" agglomerated Al_2O_3–13 wt% TiO_2 (alumina–titania) powder particle (Nanox S2613S, Inframat Corp., Farmington, CT, USA). By viewing this particle at higher magnification (Fig. 14.2b) it is possible to observe that the agglomerate exhibits individual particles varying from about 15 to 300 nm [9]. Therefore, it is suggested that the term "ultrafine" agglomerate is more scientifically rigorous to describe the morphology of these types of powders, which are formed from a mixture of nanometer and sub-micrometer-sized particles.

Lima and Marple [15] have recently published an excellent overview of the spray process of agglomerated nanometer-structured ceramic particles. The spray processes, except cold spray, are intrinsically associated with the melting of particles, or at least their partial melting. Without some particle melting it is extremely difficult to produce thermal spray coatings, especially ceramic ones. Thermal spraying nanostructured powders is thus a challenge: if all powder

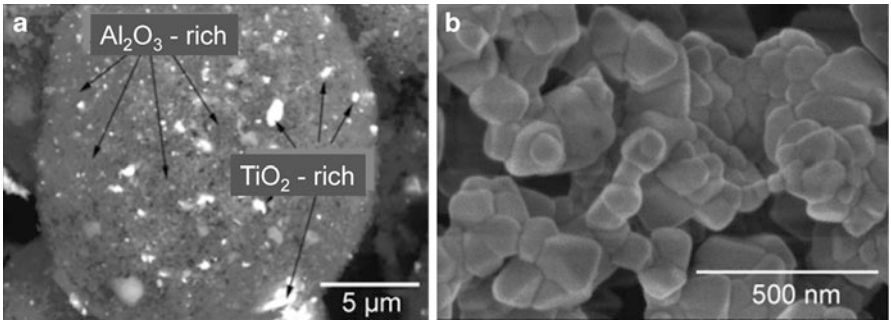


Fig. 14.2 (**a**) Spray-dried agglomerated Al_2O_3–13 wt% TiO_2 particle. (**b**) Higher magnification view showing the "ultrafine" character of the agglomerate. Reprinted with kind permission from IOP organization [5]

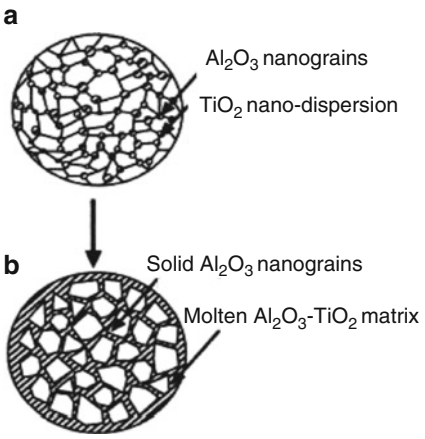


Fig. 14.3 Schematic of (**a**) A reconstituted Al_2O_3–TiO_2 granule and (**b**) the partly melted granule where solid Al_2O_3 nanometer grains exist within a liquid TiO_2. The viscosity of such a "mushy" granule depends on the volume fraction of the liquid TiO_2 and the temperature. Reprinted with kind permission from Elsevier [40]

particles are fully molten in the thermal spray jet, all the initial nano-structures will disappear. In order to overcome this challenge, it is necessary to carefully control the temperature and size distribution of the particles in the thermal spray jet to keep part of the particles in a semi-molten state. Based on this fact, the expression "nanostructured thermal spray coating" is not the most accurate to designate or represent these types of coatings. The expression "bimodal coating," representing the mixture of particles in the coating microstructure that were previously semimolten and fully molten in the spray jet, is more scientifically rigorous. However, as the term "nanostructured thermal spray coatings" is the most widely used by the thermal spray community to designate these types of coatings, it will also be employed in this manuscript [5].

Shaw et al. were among the firsts [39] to plasma spray Al_2O_3–13 wt% TiO_2-agglomerated nano-sized particles. They showed that the phase content and grain size of the coating exhibit a strong dependency on the spray temperature. Figure 14.3a shows schematically a micro-sized granule containing hundreds of nano-sized Al_2O_3 and TiO_2 particles. If, during the short exposure to the plasma jet, the temperature to which particles will be submitted is low enough, the TiO_2 particles (melting temperatures of 1,854 °C) will be melted, while the Al_2O_3 nano-grains (melting temperatures 2,040 °C) will remain unmelted (see Fig. 14.3b) [39]. Of course, besides the temperature and size distribution of the particles, the control of the melting also depends on the way particles have been manufactured [40].

With zirconia particles the problem is even more complex because particles of the average size must be only partially melted: a molten shell surrounding an unmelted core (see Fig. 14.4). For example Fig. 4.42 of Sect. 4.3.3.4 presents the calculated evolution of the melt front within three agglomerated zirconia particles of different sizes as a function of the axial position in a plasma jet [16]. It allows evaluating the size of the nanometer-structured core, preserved at the end of the heat treatment of zirconia particles (the mass density of porous particles used for calculations was 2,840 kg/m^3). The particle, 40 μm in diameter, is totally melted

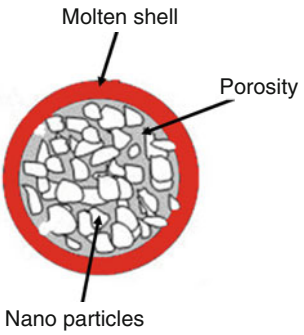


Fig. 14.4 Mechanism of nanostructured coating building. Reprinted with kind permission from Elsevier [16]

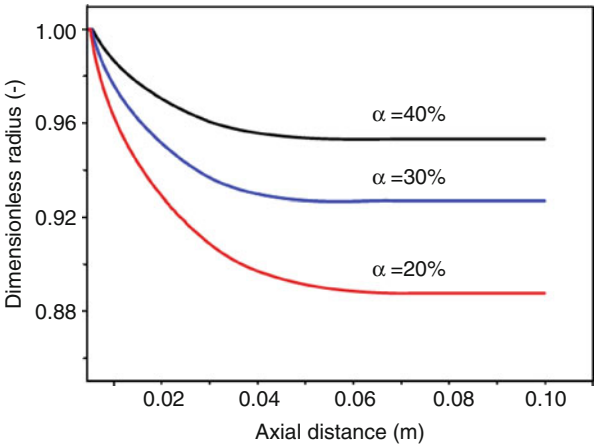


Fig. 14.5 Axial evolution of the radius of agglomerated zirconia particle ($d_p = 60$ µm) with different porosities: 20 %; 30 %; and 40 %. Reprinted with kind permission from Elsevier [16]

after a 40 mm trajectory, whereas within particles of 50 and 60 µm diameter, nanostructured solid cores remain, respectively, of 27 and 56 µm in diameter corresponding to 54 and 71 % of their initial diameter. This result shows that, for these plasma spray conditions (60 slm, Ar + 25 vol.% H_2, nozzle internal diameter 7 mm, effective thermal power 18.24 kW), there is a lower limit to the particle size below which a nanostructured solid core cannot be retained. The dense zirconia particle, 50 µm in diameter, melts much more than the porous particle due to the better heat propagation. Of course, different results are obtained when considering particles with different porosities corresponding to different powder manufacturing processes (see Sect. 11.1.2.6). The particle diameter also varies, controlled by both its surface vaporization and densification due to the porosity loss, as illustrated in Fig. 14.5 for 60 µm zirconia particles with different porosities. As it could be expected, the size of the nanostructured core increases when porosity increases. Figure 14.6 illustrates the evolution of the melting front as a function of the axial position for three zirconia particles 60 µm in diameter but with different porosities.

To spray these nanostructured agglomerates, the spray parameters must be optimized to produce conditions (particle temperatures and velocities) that result in only

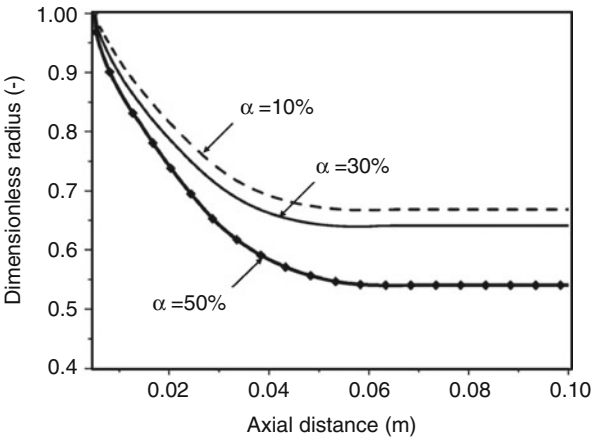


Fig. 14.6 Axial evolution of the melting front in agglomerated zirconia particles ($d_p = 60$ μm) with different porosities: 10 %; 30 %; 50 % corresponding respectively to thermal conductivities $\kappa = 1.49$; 1.16; 0.83 W/m K. Reprinted with kind permission from Elsevier [16]

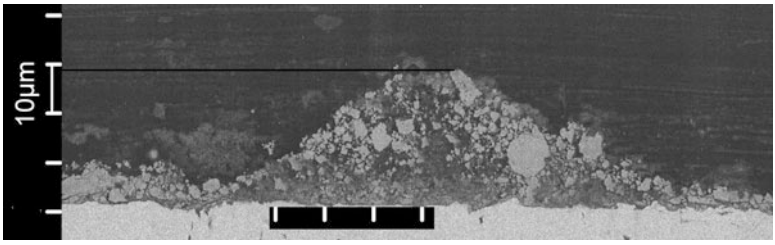


Fig. 14.7 Cross-sectional view of a splat resulting of semimolten structure of agglomerated nanometer-sized particles of YPSZ (8 wt% of Y_2O_3) sprayed by triple torch plasma reactor working with Argon. Reprinted with kind permission from Prof. J. Heberlein [41]

partial melting of agglomerates (to avoid the complete loss of the nanostructure). However a sufficiently high degree of melting must be obtained to ensure effective deposition on the substrate and the formation of the so-called nano-zones [15].

Guru and Heberlein [41] have used the triple torch plasma reactor (TTPR), for details see Fig. 7.57, along with a custom-designed shutter mechanism to deposit splat samples of agglomerated nano-sized particles of YPSZ (8 wt% of Y_2O_3). The TTPR was working with pure argon and the particle size distribution was 15–150 μm. A typical splat, deposited on polished Mo substrate, is presented in Fig. 14.7. The photo shows the features of a semimolten agglomerate particle having the nano-phase structure preserved. A layer of such particles has shown some plastic deformation properties making it suitable as a strain relief intermediate layer between two layers with different thermal expansion characteristics. Many solid particles are present within the melted matrix. The splat shape shown in Fig. 14.7 is conical because only a shell of the particle was fully melted and the impact velocity was relatively low.

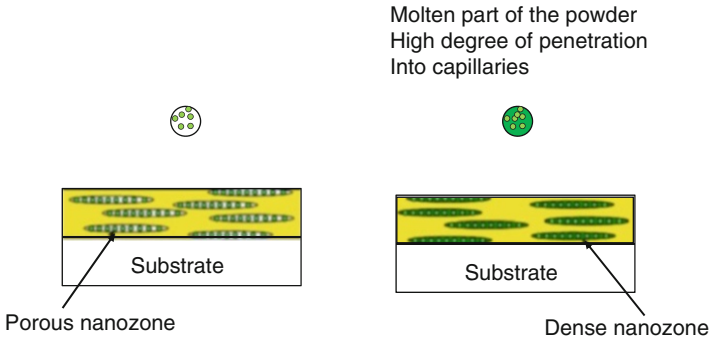


Fig. 14.8 Schematic of the embedding of porous and dense nanozones throughout the coating microstructure during thermal spraying. Reprinted with kind permission from IOP organization [5]

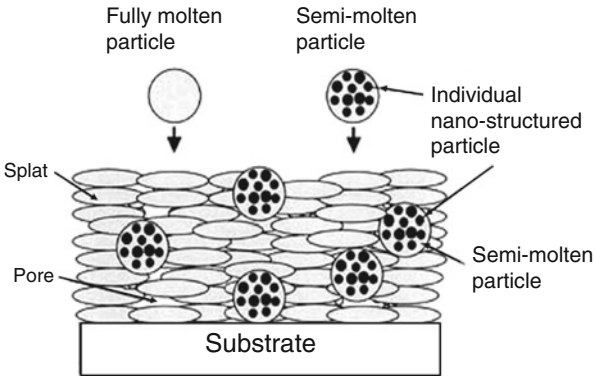


Fig. 14.9 Typical schematic (cross section) of the bimodal microstructure of thermal spray coatings formed by fully molten and semimolten nanostructured agglomerated particles. Reprinted with kind permission from Springer Science Business Media [15], copyright © ASM International

One of the critical goals of parameter optimization is to control the density of the nano-sized zones, i.e., the density of the semimolten nanostructured agglomerates embedded in the coating microstructure [5]. This is achieved by finding the conditions to adjust the amount of the molten part of each semimolten particle that penetrates into the capillaries (i.e., the non-molten particle core) of the agglomerates (Fig. 14.4) during flight within the thermal spray jet and/or at the impact on the substrate surface and subsequent re-solidification. It is important to point out that by introducing porous or dense nano-sized zones throughout the coating microstructure, it is possible to engineer coatings with very different and even opposite properties for a variety of purposes [5]. For example, for thermal barrier and abradable seal application, the presence of porous nanometer-sized zones is paramount. On the other hand, for anti-wear applications, dense nanometer-sized zones are absolutely required to induce high levels of wear resistance [15], as will be discussed later on. A schematic of the embedding of porous and dense nanometer-sized zones throughout the coating microstructure can be found in Fig. 14.8.

As shown in Fig. 14.9 [15] the coating microstructure is formed by semimolten feedstock particles that are spread throughout the coating microstructure and are

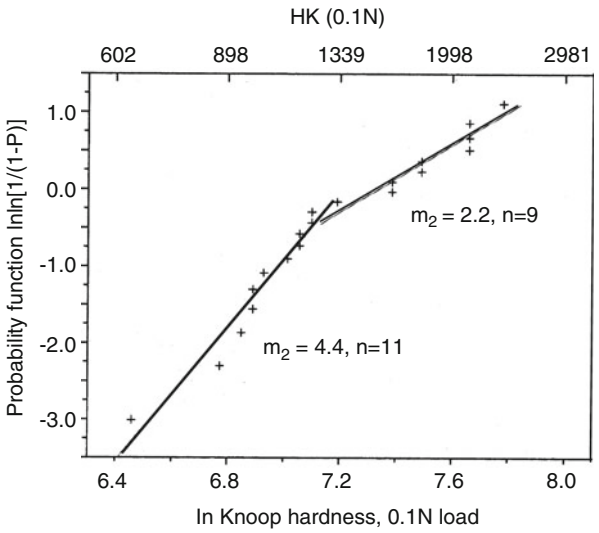


Fig. 14.10 Weibull plot of Knoop microhardness for the nanostructured coating (Nanox S4007) plasma sprayed with the Metco 3MB (40 slm Ar, 12 slm H_2, 600 A, 40 kW). Reprinted with kind permission from Elsevier [42]

surrounded by fully molten particles that act as a cement or binder. Such nanostructured thermal spray coatings exhibit significantly higher crack propagation resistance or relative toughness when compared to conventional coatings.

Some authors [42] have described these coatings as exhibiting a "bimodal microstructure." This is illustrated in Fig. 14.10 for nanostructured YPSZ (ZrO_2–7 wt% Y_2O_3) experimental feedstock Nanox S4007 (Inframat, North Haven, CT) plasma sprayed in air on low-carbon steel substrates. The Metco 3 MB torch (GH nozzle, powder port c2) torch was used with 40 slm Ar, 12 slm H_2, 600 A, at 40 kW. The nanostructured coatings show hardness values similar to those of conventional coatings (with the same size distribution) in the low slope regions of the Weibull plots. Since the conventional coating primarily represents the behavior of fully molten particles, this observation indicates that the low slope regions of the Weibull plots reflect microstructural features of the nanostructured feedstock, which are fully molten. On the other hand, the high slope regions at low hardness values represent the non-molten feedstock particles in the coating microstructure [42].

To achieve this bimodal structure, the temperature of the powder particles should be maintained such that it is not significantly higher than the melting point of the material [5]. The main technique employed for optimizing the spray parameters to engineer coatings produced from nanostructured agglomerated particles is in-flight particle temperature and velocity monitoring. One of the major advantages of in-flight particle monitoring is the fact that it can be employed to optimize spray parameters for plasma spray, flame spray, and high velocity oxy-fuel (HVOF) torches [5]. An essential element of using in-flight particle monitoring to engineer nanostructured coatings is the knowledge of the melting point of the material to be sprayed [15]. Lima et al. [43] have sprayed, using an air plasma spray (APS) torch

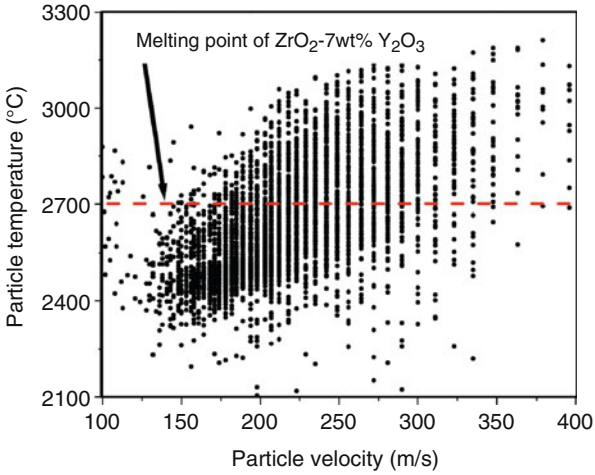


Fig. 14.11 In-flight particle surface temperature and velocity during the plasma spraying of nanostructured agglomerated YSZ particles. Reprinted with kind permission from IOP organization [5]

(F4-MB), the same nano-sized particles (ZrO_2–7 wt% Y_2O_3 Nanox S4007). Figure 14.11 shows the distribution of particle temperatures and velocities of plasma-sprayed YPSZ particles (measured with the DPV2000, Tecnar Automation, Saint-Hubert, QC, Canada). The in-flight particle characteristics were monitored at the same spray distance as used to deposit the coating.

The melting point of YSZ or YPSZ is around 2,700 °C. By controlling and adjusting the main plasma spray parameters (i.e., torch power, gas flow rates, current, and spray distance), it is possible to control the temperature distribution of the particles. If the majority of the particles in Fig. 14.11 are below the melting point of the YSZ, no effective coating deposition will occur. On the other hand, if the majority of the particles are located above the melting point of the material, although a high deposition efficiency could be achieved, most of the nanostructural character of the feedstock would tend to be destroyed during deposition. It can also induce deeper penetration/infiltration of the molten part, formed near the surface of the agglomerates, into their non-molten cores (capillaries) to form dense nanometer-sized zones. At the conditions depicted in Fig. 14.11 the average particle temperature and velocity are 2,633 ± 174 °C and 213 ± 52 m/s, respectively. Therefore, distribution of particles within the plasma spray jet is around the melting point of YPSZ, i.e., approximately 50 % of the particles are above and 50 % below 2,700 °C. Achieving this type of distribution is an important factor in preserving and embedding part of the original porous nanostructure of the powder throughout the coating microstructure. However, the particle temperature and velocity distributions are not the only important factors in the processing [5]. The particle size distribution is also a key factor. For example, the YPSZ agglomerates used are exhibiting a distribution varying from about 40 to 160 μm [5]. Considering the fact that those typical particle size distributions for thermal spraying are generally found within the range of 10–90 μm, these sprayed particles tend to be quite large. Large particles are necessary in agglomerated nano-sized plasma spraying to avoid a high

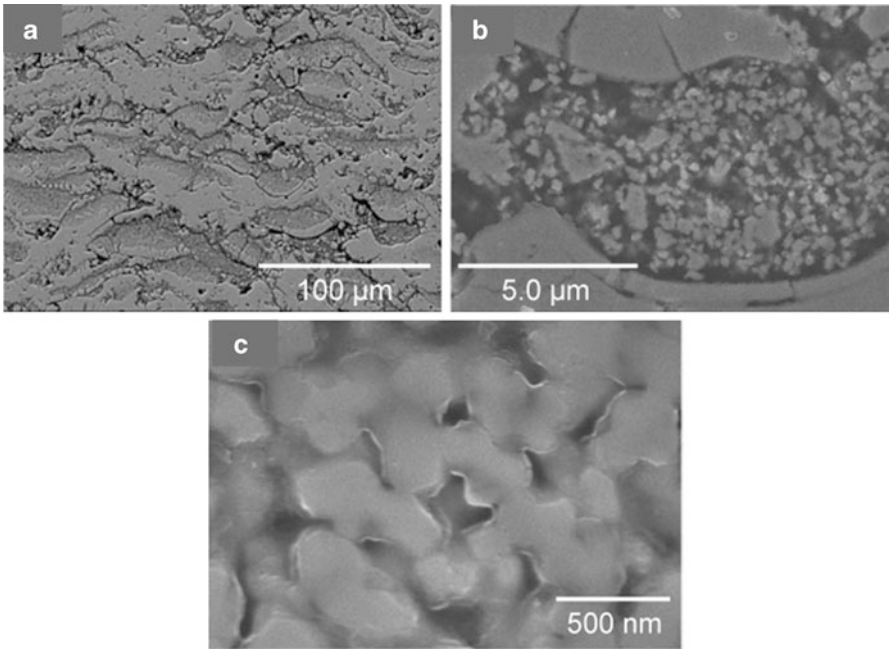


Fig. 14.12 (**a**) Microstructure of the nano-structured zirconia–yttria coating made from a nano-structured feedstock. (**b**) Darker colored region containing the semimolten feedstock particles. (**c**) Detail of semimolten feedstock contained in dark zone of (**b**). Reprinted with kind permission from IOP organization [42]

degree of particle melting caused by the high temperatures of the plasma jet [5]. As described by Fauchais [44], the plasma temperatures a few millimeters downstream of the plasma torch nozzle can be as high as ~15,000 K, i.e., many times higher than the melting point of any material known in nature. In addition, the particle velocities in the plasma jet, in the order of ~150–300 m/s (Fig. 14.11), are considered to be relatively low compared to those possible for some thermal spray processes. Consequently, the dwell time of these particles in the plasma jet is considered to be "sufficient" to induce a high degree of particle melting. The use of large agglomerates is paramount to engineer architectures that exhibit porous nanometer zones embedded in the coating microstructure (Fig. 14.12). This figure shows the microstructure of the coating produced. Lighter colored and darker colored zones can be distinguished in the coating microstructure (Fig. 14.12a), i.e., the bimodal distribution. In the darker colored zones, at higher SEM magnifications (Fig. 14.12b, c), it is possible to recognize the similarities with the morphology of the nano-YPSZ feedstock. The zones like those shown in Fig. 14.12b, c correspond to semimolten nanostructured agglomerated YPSZ particles that became embedded in the coating microstructure. This is achieved when the molten part of each semimolten particle does not exhibit a high level of penetration into the capillaries of the agglomerates during flight and upon impact and resolidification.

Nanostructured YSZ coatings exhibiting these porous nano-zones may be very good candidates for thermal barrier coatings (TBCs) and pure ceramic abradable coatings for the hot sections of gas turbine engines [15, 43, 45]. The percentage of semimolten porous agglomerates embedded in the coating microstructure of Fig. 14.12 was estimated via image analysis to be around 35 %.

As pointed out by Lima and Marple [15], the key parameter to engineer coatings with very pronounced differences in microstructural characteristics and mechanical performance is the density of the nano-sized zones. This density depends on thermal processing, spraying conditions, and feedstock characteristics (e.g., diameter and density). The nanometer-zones that form the coating can be porous, like the original feedstock (see Fig. 14.12b, c), or can be much denser. The porous nanometer-sized zones are expected to appear when the molten part of the agglomerated semimolten particle does not fully infiltrate its non-molten core during thermal spraying. Using very porous nanostructured agglomerated particles can help obtaining porous nano-sized zones. On the other hand, the dense nano-sized zones probably occur when the molten part of an agglomerated semimolten particle fully or almost fully infiltrates into the small capillaries of its non-molten core, either in the spray jet or at impact with the substrate.

Spraying nanostructured powders with less control of temperatures may become possible if compensated by a significant high particle velocity (e.g., HVOF particle velocities) [15]. The control of particles melting is more difficult with plasma spraying [46] than with HVOF process, in spite of the fact that spraying ceramic materials by HVOF is a challenge. This is due to the high melting point of ceramic materials and the low flame temperatures of HVOF torches (<3,000 °C). HVOF spraying seems to be more adapted to ceramic materials which melting temperature is relatively low such as titania or hydroxyapatite. However controlling the density of the nano-sized zones makes it possible to engineer very distinct properties in thermal spray coatings produced from nanostructured agglomerated powders [5]. Dense nano-sized zones are extremely important if the goal is to produce high performing antiwear coatings. Dense nano-sized zones are obtained when the molten part of each semimolten particle exhibits a high level of penetration/infiltration into the capillaries of the agglomerates (non-molten particle core) before and/or at the impact on the substrate surface and subsequent resolidification [5, 15, 47]. To achieve these dense nano-sized zones or dense ultrafine zones to engineer high performing antiwear coatings, the “ultrafine” alumina–titania ceramic powder of Fig. 14.2 was sprayed via HVOF. The HVOF technique was chosen due to the fact that the powder particles can be accelerated to velocities up to 800–1,000 m/s, thereby producing highly dense coatings, which are paramount for antiwear applications [5]. As previously mentioned, the drawback of this technique is found in its low-thermal spray jet temperature levels. In spite of the fact that HVOF temperature levels are higher than the melting point of the majority of the engineering materials, the high particle velocities shorten considerably the dwell time of the particles in the spray jet. From a certain point of view, it can be stated that HVOF processing (i.e., high velocity and low temperature) is the opposite of plasma spray processing (i.e., low velocity and high temperature). This is the main reason why

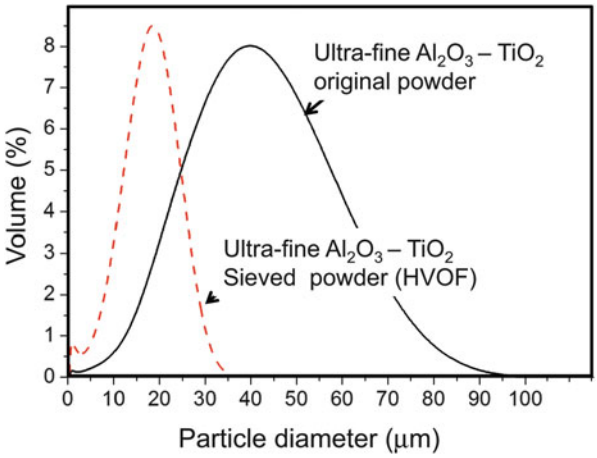


Fig. 14.13 Original and sieved particle size cuts for the ultrafine alumina–titania powder of Fig. 14.2. Reprinted with kind permission from IOP organization [47]

ceramics are typically sprayed via plasma spray process. The HVOF processing is generally employed to spray materials that are sensitive to high temperatures, such as metals or cermets (e.g., WC–Co and Cr_3C_2–NiCr). The first challenge to be overcome when spraying pure ceramics via HVOF is found in the particle size distribution [5]. As previously explained, for plasma spraying, to produce and embed porous nano-sized zones in the coating microstructure it is necessary to employ large particles with a wide particle size distribution (40–160 μm). In HVOF, to produce and embed dense nano-sized zones in the coating microstructure, it is necessary to employ small particles with a narrow particle size distribution. The small particles are absolutely necessary to compensate for (1) the low temperature of the HVOF jet and (2) the short dwell time of these particles in the jet. By doing so, the probability of creating an environment where the molten part of each semimolten particle penetrates/infiltrates deeply into the capillaries of the agglomerates (non-molten particle core) before and/or at the impact on the substrate surface is maximized [5]. Figure 14.13 shows the particle size distribution of the spray-dried ultrafine alumina–titania agglomerates depicted in Fig. 14.3. The particle size distribution of the original (i.e., as-purchased) powder varies from ~5 to 90 μm. To produce a powder with a size distribution more appropriate for use with HVOF, this material was sieved to yield a product having particles within the size range of 5–30 μm (Fig. 14.13).

For comparison, a conventional Al_2O_3–13 wt% TiO_2 powder (Amperit 744.0, H. C. Starck, Goslar, Germany) was also sprayed via HVOF process (DJ2700-hybrid, Sulzer Metco, Westbury, NY, USA). The powder was constituted from a blend of fused and crushed alumina and titania particles [47]. The particle size distribution for this powder was ~5–25 μm, i.e., within the typical particle size range for HVOF torches. The melting point of the Al_2O_3–13 wt% TiO_2 composition is ~1,900 °C. The in-flight particle characteristics were monitored and adjusted (using DPV 2000, Tecnar Automation, Saint-Hubert, QC, Canada), and the results are shown in Fig. 14.14. It is possible to observe that the overall temperature distributions of particles from both powders are well above the melting point of

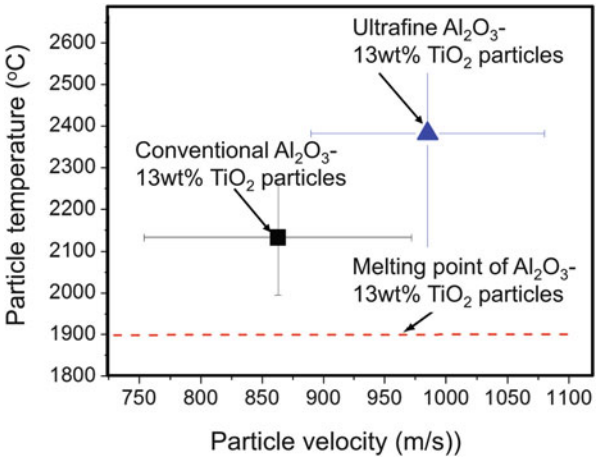


Fig. 14.14 Particle temperature and velocity levels for the ultrafine and conventional alumina–titania powders. Reprinted with kind permission from IOP organization [5]

the alumina–titania composition. As it was the case for the nanostructured YPSZ coatings, the in-flight particle characteristics were being monitored at the same spray distance used to deposit the coatings.

It is important to point out that this type of in-flight particle monitoring is based on pyrometer measurements, i.e., the temperature measurements represent the external temperature of the particle. Therefore, even if the temperatures at the outer surface of the particles are above the melting point of the material, it does not necessarily mean that the inner cores of the particles are also fully molten. It has to be stressed that the velocities in the HVOF jet, are in the range of 900–1,100 m/s for the ultrafine agglomerates (Fig. 14.14), which is considered high for thermal spraying. Consequently, the dwell time of these particles in the HVOF jet is considered to be "short" and higher particle temperatures and smaller particle diameters must compensate for these short-heating times.

Lima and Marple [48] have compared coatings sprayed by HVOF (Diamond Jet 2700-hybrid, Sulzer Metco) using nanostructured titania feedstock (Altair VHP-DCS, 5–20 μm) to plasma-sprayed coatings (APS torch SG100 Praxair) using conventional alumina–titania (Al_2O_3–13 wt% TiO_2) feedstock (Metco 130 nominal particle size range from 15 to 53 μm). The particle temperature and velocity of the feedstock particles in-flight in both spray jets were measured using the DPV 2000 at the spray distance at which the substrates would be positioned when depositing a coating (APS system 6.4 cm; HVOF system 20 cm). As it could be expected the air plasma-sprayed alumina–titania coating was 33 % harder than the HVOF-sprayed nanostructured titania. But the nanostructured titania coating exhibited a superior abrasion wear resistance (27 % lower volume loss) when compared with the air plasma-sprayed conventional alumina–titania. It also exhibited a crack propagation resistance almost twice that of the air plasma-sprayed conventional alumina–titania coating (i.e., the nanostructured coating is tougher than the conventional one).

Table 14.1 Spray parameters to achieve dense nano-sized zones by APS or HVOF or porous nano-sized ones by APS

	Particle size distribution	Particles surface average temperature	Spray distance
APS (porous nanostructured zones)	Large particles exhibiting a wide particle size distribution, e.g., ~10–150 μm	$\overline{T}$ and σ_T must be adjusted (via spray parameters and particle size distribution) to overlap the melting point of the material	Adjusted to be the initial point at which $\overline{T}$ and σ_T overlap the material melting point
APS (dense nanostructured zones)	The typical particle size distribution for APS systems should be used, e.g., within the range ~5–90 μm	$\overline{T}$ and σ_T must be adjusted (via spray parameters and particle size distribution) to overlap the melting point T_M of the material	Compromise between the previous condition and a larger spray distance[a] such as that used for conventional powders
HVOF (dense nanostructured zones)	Small particles exhibiting a narrow particle size distribution should be used, e.g., ~5–30 μm	$\overline{T}$ and σ_T must be adjusted (via spray parameters and particle size distribution) to be over the melting point T_M of the material	Due to the small size of the agglomerates, the spray distance should be around the minimum one required to achieve $\overline{T} > T_M$

[a]Larger spray distances yield longer dwell times and induce a higher degree of particle melting and infiltration into the capillaries of the non-molten cores

To conclude, spraying agglomerated-nanosized particles, to obtain bimodal structures, is not simple and requires staying within a rather narrow spray window. However, as pointed out in the review [5] Lima and Marple have delineated some general and practical engineering guidelines based on previous experimental results and Table 14.1 summarizes the different conditions to achieve dense nano-sized zones by APS or HVOF or porous nano-sized ones by APS. The first point is the necessity to use a sensor measuring the particle temperatures and velocities distributions (particularly the average temperature $\overline{T}$ and its standard deviation σ_T), and not ensemble measurements (see Sect. 16.3.4.2). Such measurements should be performed at the same spray distance used to deposit the coating. The particle size distribution is the other key parameter controlling the coating bimodal structure and the nano-zones density.

14.3.2 Applications

The bimodal nanostructured coatings can be engineered to exhibit different properties and microstructures (sometimes with completely opposite performance characteristics such as antiwear and abradable coatings!) by spraying nanostructured ceramic agglomerated powders via air plasma spray (APS) or high velocity oxy-fuel (HVOF) [15].

14.3.2.1 Wear-Resistant Coatings

Compared to titania or alumina–titania conventional coatings, those made with nanostructured agglomerated particles, either plasma [49–58] or HVOF [47, 48, 59–69] sprayed, have better abrasion or sliding wear performance [15]. Such coatings exhibit significantly higher crack propagation resistance or relative toughness when compared to conventional ones [15]. The hardness of conventional and nanostructured coatings are generally about the same.

The thermal diffusivity of the nanostructured Al_2O_3–3 wt% TiO_2 coating was higher compared with that of the corresponding conventional coating at temperatures ranging from 200 to 1,000 °C [69]. Zirconia nanostructured plasma-sprayed coatings have also been used against wear. The nanostructured coating reduced the wear rate of this coating against stainless steel [70, 71].

Lima and Marple [5] have compared the abrasion wear behavior of coatings sprayed with conventional Al_2O_3–13 wt% TiO_2 powder (Amperit 744.0, H. C. Starck, Goslar, Germany) and the nanostructured agglomerated powder depicted in Fig. 14.2 with the size distribution presented in Fig. 14.13, both sprayed via HVOF (DJ2700-hybrid, Sulzer Metco, Westbury, NY, USA). The comparison was achieved via the measurement of volume loss after abrasive wear testing. The ultrafine coating exhibited a 4-fold improvement in wear performance. The superior abrasion wear performance of the ultrafine coating could not be explained based on Vickers microhardness values. Both coatings exhibited average Vickers microhardness number values of ~800_{3N} [47]. It has to be pointed out that Turunen et al. [72] compared the abrasion wear resistance of nanostructured and conventional alumina (Al_2O_3) coatings deposited via HVOF, and they observed superior wear behavior of the nanostructured coating. The evolution of the crack propagation resistance for the alumina–titania coatings turned out to be the main reason for the superior wear behavior of the ultrafine coating (Fig. 14.15) [47]. The evaluation of the crack propagation resistance, which is a measure of relative toughness, is done by indenting the cross section of the coatings using a Vickers indenter (5 N load) with one of its diagonals parallel to the substrate surface to induce crack propagation in between layers. From tip-to-tip, the crack length of the conventional coating (Fig. 14.15a) was found to be ~40 % longer than that of the ultrafine one (Fig. 14.15b). Therefore, the ultrafine coating is significantly tougher than its conventional counterpart.

The discussion below follows that presented in [5]. The question that arises is related to the role of the ultrafine structure of the agglomerated powder in the enhancement of the coating toughness. Gell et al. [51] and Luo et al. [73] observed that the enhanced toughness of these types of coatings was related to crack arresting and deflection when passing through dense nano-zones embedded in the coating microstructure. McPherson has shown [74] that for conventional thermal spray ceramic coatings, cracks will tend to propagate between adjacent layers of the coatings (i.e., the splat boundaries), which are the weakest link of the microstructure. When the microstructure of the ultrafine coating of Fig. 14.15b is analyzed at

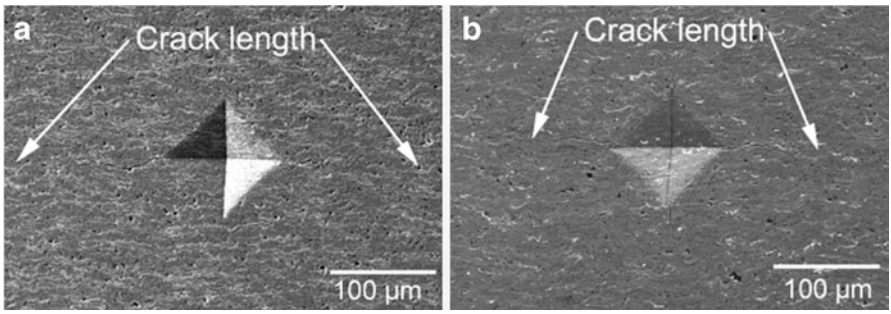


Fig. 14.15 Crack propagation induced by indention on the cross section of the (**a**) conventional and (**b**) ultrafine alumina–titania coatings. Reprinted with kind permission from Elsevier [47]

higher magnifications by using a SEM, it is possible to observe lamellar zones constituted of a finely dispersed material (Fig. 14.16a) distributed evenly within the coating cross-sectional microstructure [47]. By analyzing one of these finely dispersed regions in more detail (Fig. 14.16b) and comparing it with the microstructure of the ultrafine agglomerated powder (Fig. 14.2), one can realize from the similarities that these finely dispersed zones are semimolten ultrafine particles embedded in the coating microstructure. However, due to processing conditions (i.e., particle temperature, velocity, diameter, and dwell time), the molten part from the surface of the agglomerates deeply infiltrated into the capillaries of the non-molten cores, thereby creating dense ultrafine microstructure zones after particle impact and resolidification, as also estimated by Shaw et al. [46]. The percentage of semimolten dense agglomerates embedded in the coating microstructure of Figs. 14.15b and 14.16 was estimated via image analysis to be ~50 % [47]. When the left crack tip of the ultrafine coating of Fig. 14.15b is observed in detail at higher SEM magnifications (Fig. 14.16c), it is noticed that the crack is deflected and arrested when passing thorough a dense ultrafine zone. As in these coatings the microstructure is disrupted periodically by these zones, the crack propagation encounters barriers to propagate through the well-defined layered structure, thereby enhancing coating toughness, as also observed by Gell et al. [51] and Luo et al. [73]. Improved bond strength values have been reported for these coatings when compared to their conventional counterparts [15]. The explanation for this improved bond strength is similar to that used to explain the enhanced toughness. According to Bansal et al. [75], for coatings produced from nanostructured agglomerated powders, the interfaces between the dense nanometer zones and the substrate surface did not exhibit micrometer cracks or gaps, whereas for those of the conventional coatings, micro-sized cracks or gaps were observed. Therefore, the dense nano-zones would tend to impede crack propagation at the interface, which would enhance interfacial toughness and the bond strength levels of the coating. It has to be pointed out that other authors are attributing these higher toughness levels to an enhanced inter-lamellar strength, and not crack path deflection. Ahn et al. [76] observed that in spray-dried nanostructured agglomerated powders,

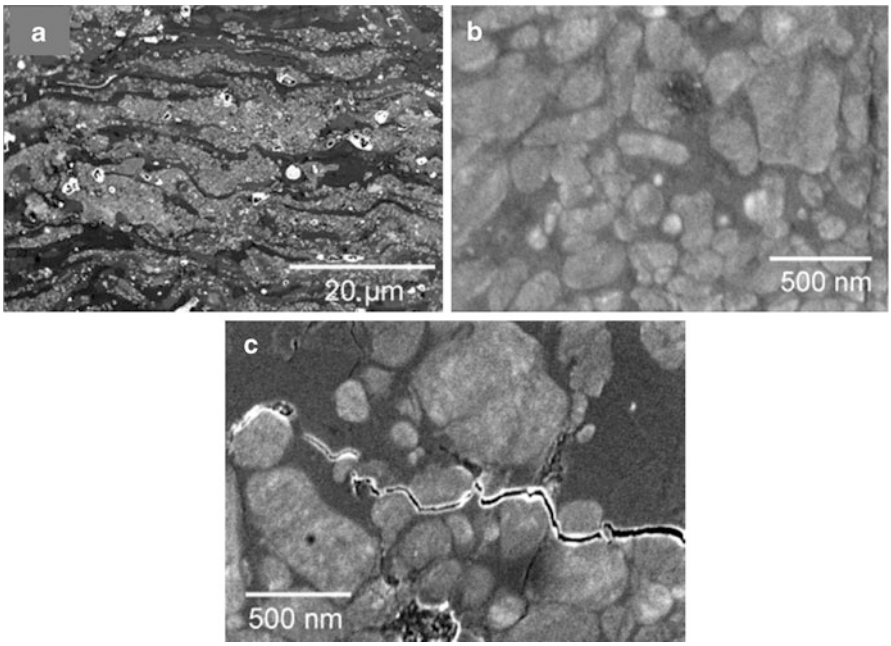


Fig. 14.16 Higher magnification views (cross section) of the ultrafine coating of Fig. 14.15b. (**a**) Overall view of the dense ultrafine zones. (**b**) Localized view of a dense ultrafine zone. (**c**) Crack tip arresting via path deflection by passing thorough a dense ultrafine zone. Reprinted with kind permission from Elsevier [47]

the individual alumina and titania particles are intimately mixed, as readily observed in Fig. 14.2. The same degree of homogeneous mixture is not found in conventional particles. The melting point of pure alumina is 2,050 °C, whereas that of pure titania is 1,855 °C. An addition of 13 wt% of titania into alumina results in a lowering of the melting point of the compound to ~1,900 °C. Therefore, Al_2O_3–13 wt% TiO_2 "well-mixed" agglomerates (Fig. 14.2) would tend to arrive at the substrate exhibiting lower viscosity levels due to the lowering of the melting point, than those of the conventional particles. These lower viscosity levels would translate into an enhanced splat-to-splat cohesion, which would then improve the toughness of the coating. By looking at Fig. 14.15, it is possible to observe a "lower" degree of homogeneity of the coating produced form the conventional powder (Fig. 14.15a) when compared to that produced from the ultrafine powder (Fig. 14.15b). For the conventional coating the alumina-rich (dark) and titania-rich (light) phases are quite well defined, i.e., not well mixed. As titania has lower mechanical strength levels than alumina, it probably creates weak-link zones in between layers of the conventional coating. Therefore, based on these various studies it is believed that for alumina–titania coatings produced from nanostructured or ultrafine powders, two distinct mechanisms are acting together to enhance coating toughness: (1) crack path deflection and (2) enhanced splat-to-splat contact.

Such coatings for antiwear purposes are used in the "real world" applications [5]. Nanostructured alumina–titania coatings deposited by APS are in use to protect the main propulsion shafts of ships of the US Navy. After 4 years of use in naval applications no significant damage was recorded in these types of coatings. This work was based on a research led by the University of Connecticut (USA) [46, 51, 73, 75]. Nanostructured titania thermal spray coatings have been developed and applied with success by Perpetual Technologies (Ile des Soeurs, QC, Canada) in ball valves for autoclaves that operate at high temperature (~260 °C), at high pressure (~5.5 MPa), in corrosive sulphuric acid (>95 %), and at relatively high solids content (>20 wt%) [77]. The in-field performance of this nanostructured coating was compared to that of a conventional one. After 10 months of service the coatings were inspected. The ball valve coated with the conventional coating exhibited delaminating in several areas and had to be replaced, whereas the ball valve coated with the nanostructured coating was nearly intact and put back into service.

14.3.2.2 Abradable Coatings

By embedding a significant amount of semimolten porous particles in the coating microstructure, the ceramic coating becomes friable, producing a nanostructured ceramic abradable coating as shown by Lima et al. [5, 43]. The gap (i.e., clearance) between the tip of the turbine blades and the turbine case should be as tight as possible to improve engine efficiency and performance. It could be stated that abradable coatings are the "opposite" of antiwear coatings, i.e., they must possess a friable structure. It is a challenge to engineer these coatings because they must be at the same time readily abradable and able to withstand the harsh environment of the turbine engine, as described by Ghasripoor et al. [78]. The conventional abradable seal is a composite coating typically made from a metallic-based material, a self-lubricating phase and many pores. Due to environmental and economic issues, there is a significant driving force to increase the combustion temperature of gas turbines. Higher combustion temperatures will generate higher efficiency and less pollution. The abradable coatings have also to follow this trend. To achieve this objective two types of high temperature abradables are currently in use. One is based on a powder composite formed from a metallic superalloy (e.g., CoNiCrAlY), a self-lubricating agent (e.g., BN), and a polymer. The second one is based on a powder composite formed from YSZ, BN, and a polymer. For both cases, the polymer is introduced into the coating microstructure during deposition and burned off in a postdeposition heat treatment to create a large porosity network to make both types of coatings friable. This approach has challenges due to the fact it is difficult to engineer homogeneous microstructures when materials of very distinct physical and chemical properties are sprayed together (e.g., metal + polymer and ceramic + polymer). In addition, the postdeposition heat treatment necessary to burn the polymer off the coating microstructure represents an additional issue of cost and time. Therefore, the use of a pure ceramic abradable material could

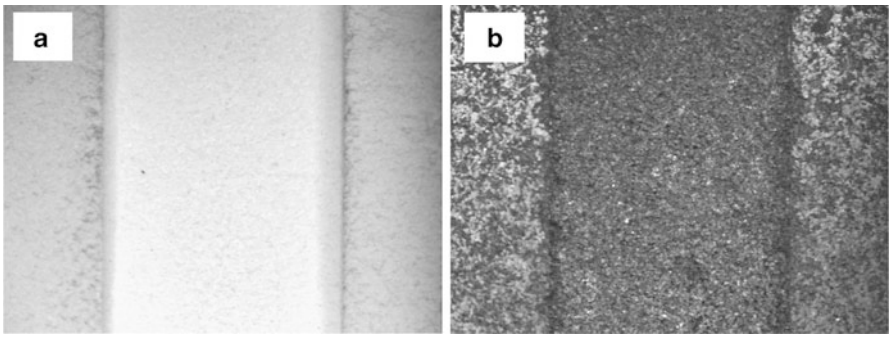


Fig. 14.17 (**a**) Wear scar (*top surface*) of the nanostructured YSZ coating after rub-rig testing. (**b**) Wear scar (*top surface*) of a state-of-the-art high temperature metal-based abradable coating after rub-rig testing. Reprinted with kind permission from Springer Science Business Media [15], copyright © ASM International

be a major advance in producing the next generation of high-temperature abradable coatings. However, the lack of plasticity of ceramic materials is a major barrier impeding progress in achieving this goal. For a pure ceramic abradable coating design, the concept of the porous nanometer-sized zones, if embedded in the coating microstructure in "sufficient numbers," could be employed to lower the overall stiffness of the coating, allowing the tip of a metallic turbine blade to wear off some of the coating, creating the "seal effect," without damaging the blade [5]. Figure 14.17a shows the wear scar after rub-rig testing for abradables on the top surface of the nanostructured YSZ coating of Fig. 14.12. The rub-rig is a standard test to evaluate the abradability of a coating. Essentially, a metallic blade is placed at the edge of a spinning wheel, which exhibits rotating speeds and incremental incursion rates similar to those of a real turbine engine. By rubbing the blade tip against the top surface of the coating and analyzing the blade tip and the coating wear scar after testing, it is possible to infer the degree of abradability of the material.

By looking at Fig. 14.17a it is possible to observe the absence of macro-cracks or any major damage, delaminating, or debonding in the coating structure after being rubbed off by the tip of a metallic blade. The wear scar is "well-shaped" and smooth, and no wear on the blade was recorded. By comparison, a state-of-the-art metallic-based high temperature abradable (CoNiCrAlY + BN + polyester) was tested under the same conditions (Fig. 14.17b). The volume losses of both coatings were measured and they exhibited an almost identical value [15]. Consequently, these results show that the ceramic abradable exhibited a performance level similar to that of the state-of-the-art metallic-based abradable. Therefore, based on the information and promising results available in this section, it can be envisioned that the use of nanostructured YSZ coatings engineered to contain porous nanometer-sized zones for thermal barriers and abradables may become major applications of this technology for the next decade.

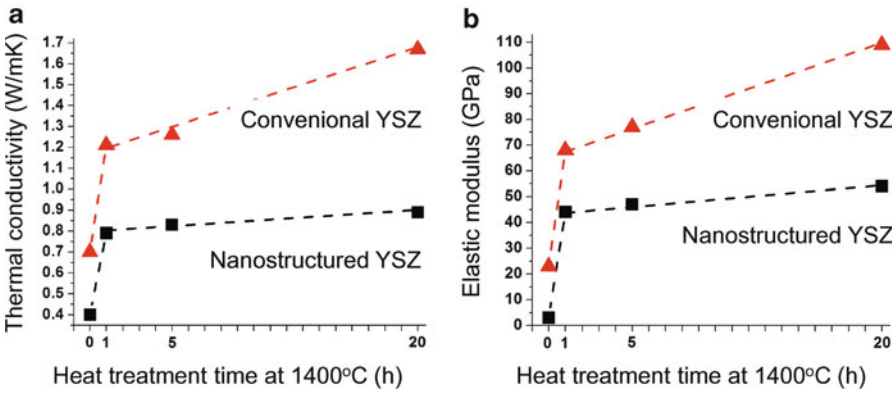


Fig. 14.18 (**a**) Thermal conductivity and (**b**) elastic module values evolution of as-sprayed and heat-treated nanostructured and conventional YSZ coatings at 1,400 °C. Reprinted with kind permission from Springer Science Business Media [91], copyright © ASM International

14.3.2.3 Thermal Barrier Coatings

Much work has been performed on plasma-sprayed nanostructured TBC coatings [79–89]. Lima and Marple [5, 15] have extensively studied these coatings. TBCs are made from low-thermal conductivity (<2 W/m/K) ceramics that also exhibit high mechanical and chemical stability at high temperatures. According to Padture et al. [90], they are employed to protect and insulate the metallic components of the hot sections of gas turbine engines (e.g., blades, vanes, and combustion chambers) from the hot gas stream provided by the fuel combustion, allowing higher combustion temperatures and improving engine efficiency. These turbine engines are employed in aerospace propulsion, power generation, and marine propulsion.

Regarding TBC applications, basically the porous nanometer-sized zones will reduce significantly the increase of the elastic modulus and thermal conductivity values of these coatings when exposed at high temperatures by counteracting densification effects via differential sintering, which are highly desired characteristics for TBC applications. In fact, it has been shown that for specific coatings in some studies the growth rate of the thermal conductivity (Fig. 14.18a) and elastic modulus (Fig. 14.18b) values of conventional YPSZ TBCs at 1,400 °C were approximately 5 times higher than those of the nanostructured YPSZ TBCs [91, 92]. By looking at Fig. 14.19 it is possible to understand how the differential sintering mechanism works. The as-sprayed coating (Fig. 14.19a) exhibits the typical porous nanometer-sized zones of Fig. 14.12. The overall coating porosity increased after an exposure at 1,400 °C for 20 h (Fig. 14.19b), which is a counter-intuitive effect. Essentially, the nanometer-sized zones sinter at much faster rate than the coating matrix, thereby inducing porosity and reducing the growth rate of thermal conductivity and elastic modulus values, which are governed by sintering. When the conventional YSZ is observed, from the as-sprayed (Fig. 14.20a) to the heat-treated (Fig. 14.20b) coating, the "expected" behavior for a ceramic is noticed,

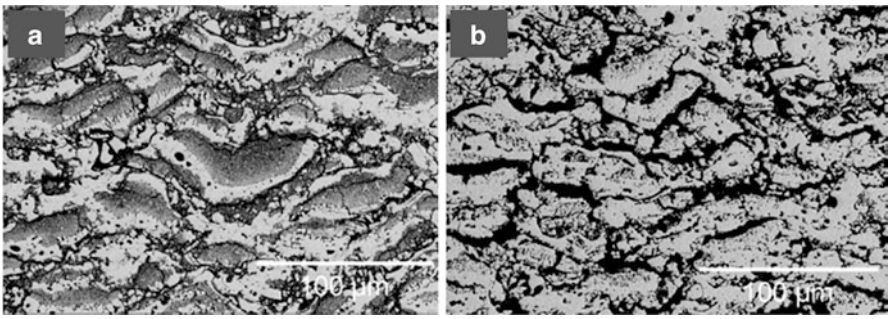


Fig. 14.19 Cross section of an (**a**) as-sprayed and (**b**) heat-treated nanostructured YPSZ coating at 1,400 °C for 20 h. Reprinted with kind permission from Springer Science Business Media [91], copyright © ASM International

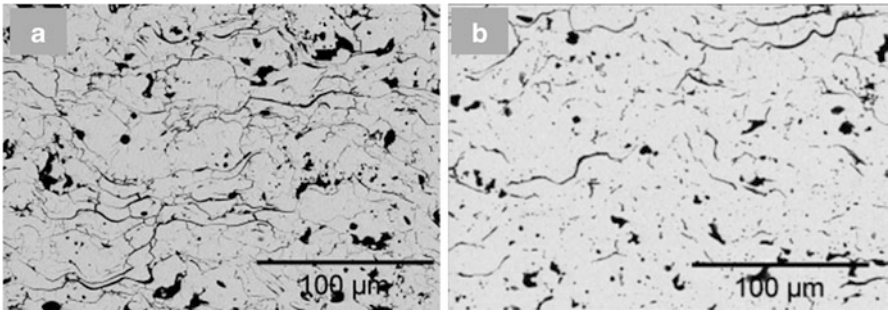


Fig. 14.20 Cross section of an (**a**) as-sprayed and (**b**) heat-treated conventional YPSZ coating at 1,400 °C for 20 h. Reprinted with kind permission from Springer Science Business Media [91], copyright © ASM International

i.e., there is a significant reduction of the overall coating porosity due to sintering effects, which yields higher values of thermal conductivity and elastic modulus.

More information about the mechanism of differential sintering on TBCs can be found elsewhere [45, 91]. In addition to sintering resistance, Liang and Ding [83], Wang et al. [92], and Liu et al. [93] have reported superior thermal shock resistance levels of TBCs produced from nanostructured agglomerated YSZ powders compared to those of TBCs deposited using conventional YSZ powders. Zhou et al. [94] studied the thermal cycling oxidation of nanostructured and conventional YSZ TBCs and reported a superior performance of the nanostructured ones. Therefore, the APS YSZ coatings engineered from nanostructured agglomerated powders have the potential to become the next generation of TBCs. As summarized by Lima and Marple [15] nanostructured TBCs have the following advantages: lower thermal diffusivity, higher (2–4 times) thermal shock resistance, higher creep rate, and healing of the nano-porosity.

As previously discussed, nanostructured YPSZ coatings have demonstrated superior sintering resistance when compared to those of conventional ones [45, 91]. These characteristics are very important because a high increase of elastic modulus and thermal diffusivity/conductivity values caused by sintering hinders the use of these coatings as TBCs. The superior thermal cycle and shock resistances of the nanostructured YSZ coatings [83, 92–94] show that they may become an important alternative as TBCs in gas turbines for the next decade.

14.3.2.4 Biomedical Applications

For biomedical applications, mainly two materials are used: hydroxyapatite and titania [95–100]. The calcium phosphate hydroxyapatite (HA) ($Ca_5(PO_4)_3(OH)$) is the standard thermal spray ceramic coating applied on implants for load bearing applications, such as acetabular cups and hip joints [101]. In spite of this successful application, there are concerns regarding the long-term prognostics of these coatings, which may be hindered by coating dissolution and low mechanical performance [102, 103]. Therefore, it is possible to find nano-sized zones at the coating/substrate interface, in the internal structure of the coating, as well as on its surface. It has to be pointed out that thermal spray coatings produced from conventional powders do not exhibit a significant presence of nano-sized zones on their surfaces. It has been shown that HVOF-sprayed nano-sized TiO_2–HA composite coatings exhibit bond strength levels of at least 2.5 times that of thermally sprayed HA coatings. In addition, these coatings exhibited bio-performance levels equivalent or superior to those of HA coatings, which are the current state-of-the-art material. It was hypothesized that one of the reasons for this enhanced behavior was related to the presence of nano-sized zones on the coating surface [104, 105]. Again the comments in the review of Lima and Marple [5, 15] summarize well the results:

- Osteoblast cell culture (in vitro) shows that the HA coatings with a high content of both crystalline HA and nanostructures are preferred for cell proliferation.
- HVOF-sprayed nanometer-sized TiO_2 coatings have bond strength values at least 2.4 times higher than those of HA coatings on Ti–6Al–4V substrates. In vivo tests (with rabbits) showed that these coatings (deposited on Ti–6Al–4V substrates) have a higher degree of bone apposition when compared to those of uncoated Ti–6Al–4V substrate.

14.3.2.5 Other Applications

The nanostructured titania coatings provided superior resistance against abrasive and erosive wear for ball valves destined for high-pressure acid-leach (HPAL) service [106]. The thermal shock behavior of nanostructured Al_2O_3/13 wt% TiO_2 plasma-sprayed coatings was much higher than that of conventional coatings [107].

14.4 Attrition or Ball Milled Cermets or Alloy Particles Sprayed with Hot Gases

Another possibility to achieve coatings with nano-sized particles is to spray nanocrystalline powders and melt them only partially.

(a) During thermal spraying of ceramics, even with adapted spray conditions (discussed below), small particles exceed the melting temperature of the alloy or the binder phase for cermets. In contrast larger particles have the melting temperature exceeded only near the surface, whereas particle cores can remain solid. In volumes that remain solid, micrometer-structural changes are negligible (slow kinetics of solid state diffusion) due to the very short exposure to high temperatures during the spray process [108]. The final crystallite size of the melted alloy or binder phase is determined by the cooling rate during solidification, high cooling rates resulting in much finer crystallites. With cermets, the behavior of the hard phase will strongly depend on the grain size and spatial distributions. In volumes where the binder phase is melted, obvious changes in the microstructure of both the nanostructured and the micro-structured cermet material due to the spraying process will be observed. In contrast to the crystallite size of the binder phase, the diameters and distribution of the hard phases depend on their initial size and solubility in the solid and liquid state of the binder phase.

(b) To spray nanostructured alloys or cermets, two techniques (HVOF or vacuum plasma spraying) are mainly used to achieve temperatures slightly above the melting temperature of the alloy or cermet binder:

With HVOF (see Sect. 5.3.1.4), depending on the selection of fuel gas and proportion of the fuel gas to oxygen, the sprayed powder particles experience much lower temperatures (gas temperatures below 3,000 °C) compared to plasma spraying. Moreover the spray velocity in HVOF spraying (700–1, 400 m/s) is much higher than in plasma spraying, which causes a higher degree of particle impact in the HVOF process. This heavy impact may lead to fragmentation of resolidifying particles and thus formation of large number of nucleation sites, which may cause a higher extent of grain refinement in the deposit structure.

With vacuum plasma spraying (see Sect. 7.9) the plasma jet temperature, except in the few first millimeters of the jet, is relatively low (below 5,000 K) and the Knudsen effect (see Sect. 4.3.2) reduces the heat transfer. Moreover, particle velocities are higher than those obtained with conventional torches used in atmospheric spraying. Of course to limit the particle heating, atmospheric argon plasma spraying could be used, but oxidation would be unavoidable. Probably the most important advantage of vacuum plasma spraying is the low oxygen pressure reducing drastically the particle and coating oxidation phenomena.

(c) The last important points are the particle oxidation in flight and the coating oxidation during its deposition. Since the agglomerate size of the nano-crystalline particles is higher than that of the conventional powders, it can be expected that the chemical reactivity of nano-crystalline powders will increase due to the increased surface area. It may result in an increased proportion of oxide phases throughout the grains. For cermets containing materials highly reactive to oxygen, such as WC, some decomposition could occur. It is thus important to control the composition of combustion gases used in HVOF. Vacuum plasma spraying will result in less oxidation than HVOF. This is particularly important for the inter-pass oxidation, which is a consequence of the high temperature that the coating experienced during the spray process. During the time between passes, the coating surface is still at a high temperature and, in the presence of air starts to oxidize (as in HVOF or argon plasma spraying in air).

14.4.1 Alloys

Inert gas atomized ASTM F75 Co-based super alloy powders (Cr–28.55 wt%, Mo–5.958, Si–0.53 %, C–0.30 %. Fe–0.27 % Ni–0.13 %, Mn–0.09 %, balance Co, Starmet Corp.) have been mechanically milled in methanol environment for 10 h to produce nano-crystalline powders with an average grain size of 12 nm, determined by TEM dark field imaging [109]. An argon plasma jet (Sulzer Metco 7 M) sprayed these particles onto Ti substrates, and the resultant coating remained nano-crystalline with an average grain size of 21 nm. Furthermore, the micro-hardness and porosity of the nano-crystalline Co–Cr coating are found to be higher than those from the conventional Co–Cr coating, indicating that nano-crystalline coatings may be potential coating candidates for implant applications. It was speculated that the marginal increase in micro-hardness of the nano-crystalline Co–Cr coatings might be due to the presence of an increased proportion of oxide phases throughout the grains.

Cryomilled Ni powders were sprayed with Sulzer Metco Diamond Jet DJ 2600 [110]. The coating was composed of nano-crystalline grains with an average size of 92.5 $\pm$ 41.6 nm (the nanostructure was retained) and with extremely fine NiO particles of 5 nm diameter distributed homogeneously inside the grains. Adjusting the spraying conditions, FeNb microcrystalline powders allowed obtaining amorphous coating, while for the FeSi alloy powder, amorphization was obtained with the addition of boron [111]. Ball milled Fe-based powder with additions of Si, B, Nb, and Cu elements were HVOF sprayed (Sulzer Metco CDS with a mixture CH_4/O_2 (%) = 0.4) [112]. The powders sprayed were Fe93.5–Si6.5, Fe86.5–Si13.5, Fe75–Si6.5–B18.5, Fe75–Si15–B10, and Fe73.5–Si13.5–B9–Nb3–Cu1 (atomic percentages). Amorphous and nanostructured phases were present in the coatings. Coatings produced had a soft ferromagnetic character, the additions of nonmagnetic elements such as boron, niobium, and copper incorporated in the milled powders

having little effect on these properties. However the nanostructure phase had a significant effect on modifying the magnetic properties of deposits.

Super alloys were also sprayed with an HVOF processes:

- Inconel 718 alloy powder, methanol, or cryo-milled producing nano-crystalline coatings exhibiting thermal stability against grain growth up to 1,273 K [113].
- Oxidation of nano-grain CoNiCrAlY coatings made from cryo-milled powder was studied at 1,000 °C [114, 115].
- Nano-crystalline NiCrAlY was produced [116] by cryo-milling and sprayed with the Diamond Jet DJ 2700 (Sulzer Metco). The final microstructure of the nanostructured coating had a fine grain structure characterized by a "multimodal structure," in which both nano-crystalline regions (approximately 75 nm) and submicron grain regions (from 120 to 550 nm) were observed. The oxidation behavior of nanostructured NiCrAlY coatings was investigated after heat treatments in air, at 1,000 °C, for various times. Oxidation led to the formation of a continuous alumina layer, without the presence of other mixed oxides [116].

14.4.2 Cermets

One of the problems when spraying carbide cermets is the decarburization. Moreover, even under HVOF spraying conditions, the extent of decarburization observed in the nano-sized coating material is larger than that in the micro-coating material, because of the high specific surface area of the particles. In particular, heterogeneous melting and localized superheating of the nano-powder, with high surface area is considered to be the controlling factor in decarburization.

14.4.2.1 WC–Co

He and Schoenung [117] have presented an excellent review of the problems involved with spraying WC–Co. They showed that it was possible to produce nanostructured WC–Co powders without non-WC/Co phases although a high percentage of non-WC/Co phases is frequently reported in conventional WC–Co powders. Nanostructured WC–Co powders experienced higher particle temperatures during spraying than those of the corresponding conventional powder. Therefore, if the same spraying parameters were used, WC particles in nanostructured powders suffered from severe decomposition, degrading the performance of corresponding WC–Co coatings. By controlling agglomerate size of the feedstock powder, fuel chemistry, and fuel–oxygen ratio, near nanostructured WC–Co coatings with a low amount of non-WC/Co phases were successfully deposited. These coatings had increased hardness, toughness, and wear resistance. Qiao et al. [118] showed that when HVOF spraying nanostructured powders having the shape of hollow spheres, particles rapidly reached high temperatures in the various

deposition processes and were subject to extensive decarburization. HVOF-sprayed nanostructured WC–12 wt% Co were compared to Cr_3C_2–NiCr coatings [119]. Results showed that the WC–Co coatings had a nanostructure consisting of nano-sized WC carbide particles in an amorphous matrix phase, while in the nanostructured Cr_3C_2–NiCr a few elongated amorphous phases discontinuously distributed in the coating were observed.

Much work has been devoted to nanostructured WC–Co spraying mainly by HVOF [120–129] and much less by d.c. plasma spraying [130]. In nanostructured WC–Co powders manufactured recently, the amount of the non-WC/Co phases was greatly reduced. A grain-growth inhibitor has a strong influence on the microstructure and other properties of the coatings. Preventing WC dissolution in the binder, not only maintains very small grains but also maintains their original shape; it is effective in retarding decarburization but it decreases the cohesion between WC and the binder [125]. Superior sliding wear resistance is obtained from coatings deposited with near nano-powders containing an antigrowth additive [125].

14.4.2.2 Cr_3C_2–NiCr

Compared to WC–Co system coatings the main shortcomings of Cr_3C_2–NiCr coatings are lower hardness and subsequent low wear resistance, but they are frequently used as protective coatings for application in corrosive environments at elevated temperatures.

Nanostructured Cr_3C_2–25(Ni20Cr) coatings are synthesized using mechanical milling and sprayed by HVOF or HVAF. Their decomposition seems to be less than that of WC–Co [131–133]. Better results are obtained with coatings sprayed by HVAF [132]. After 30 days at 900 °C, the carbide morphology of both HVOF and HVAF coatings was comparable, tending toward an expansive structure of coalesced carbide grains [132]. Nano-crystalline coatings exhibit a 20 % increase in hardness, a 40 % decrease in surface roughness, and comparable fracture toughness and elastic modulus compared to conventional coatings [133].

14.4.2.3 Other Cermets

A typical example is the Y_2O_3-reinforced milled FeAl sprayed by a Plasma-Technik CDS 100 HVOF torch. The coating displayed the typical dual aspect consisting of fully melted and well-flattened splats together with retained unmelted powder particles, which both contained nano-sized grains: columnar nano-sized grains formed by rapid solidification in the fully melted splats and equiaxed nano-sized grains retained in a deformed matrix at the core of the unmelted powder particles. Oxidation and Al evaporation during thermal spraying led to a modification of the chemistry of the melted zones. The associated Al depletion resulted in the formation of the Fe_3Al phase and more complex structures [134].

When cryo-milling Ni powders [135], the presence of ultrafine AlN particles drastically decreased the dimension of the formed agglomerates and increased their surface roughness. The AlN phase was broken down into ultrafine particles of approximately 30 nm in size. These particles were dispersed in the Ni matrix and enhanced the development of a nano-crystalline structure in the Ni matrix during cryo-milling. A Sulzer Metco DJ 2600 HVOF gun was used to spray these particles. AlN nanometer-sized grains were present in the coatings, and they also led to an increase in the amount of the NiO phase, distributed in the coating in the form of ultrafine, round particles. Indentation fracture indicated that the fine, dispersed AlN particles raised the apparent toughness of the Ni coating. The increase in microhardness resulted from both grain refinement and the presence of ultrafine particles.

TiC–Ni-based composites [108] and Al_2O_3 and Al_2O_3–Ni [72] resulted in high quality coatings with optimized HVOF spray parameters. Introduction of nickel alloying decreased hardness and wear resistance of the coatings, but increased their toughness.

Using plasma spraying, a coating of Al_2O_3 dispersed in a FeCu or FeCuAl matrix [136] appeared to offer better wear resistance under sliding and abrasion tests than nanostructured Al_2O_3 coatings, and nanostructured YSZ/NiO anodes provided larger triple phase boundaries for hydrogen oxidation reactions in SOFCs [137].

14.5 Spraying Hypereutectic Alloys with Hot Gases

When melting alloys that exceed the solubility limit, upon solidification a single solid solution is produced. However when alloys continue to cool down, a solid-state reaction occurs, permitting a second solid phase to precipitate from the original one and keeping a nanostructure in the coating, if the cooling is fast enough. This effect has been observed both with plasma and HVOF spraying.

Free-standing ring-shaped Al–21Si nanometer composite structures were fabricated by HVOF spraying of gas atomized hypereutectic Al–21 wt% Si alloy powders (15–45 mm) [138]. Figure 14.21 presents a cross-sectional micrograph of the coating structure showing a homogenous and highly dense splat structure, consisting of ultrafine primary (2–4 μm) Si grains and a network of Si in the eutectic Al–Si matrix. Formation of a thin oxide layer of uneven thickness can also be observed on the splat surfaces. The module of elasticity (138 ±17 GPa) shows an intermediate value between those of pure Al (71.9 GPa) and Si (162.9 GPa). The Vickers microhardness value (441 ± 34 N) was also better than that of a conventionally cast eutectic.

A freestanding bulk nano-crystalline structure was vacuum plasma sprayed starting from a hypereutectic Al–21 wt% Si micron size (15–45 μm) gas-atomized powder [139]. The cross sections of the coating exhibited a dense splat structure containing fine eutectic Al–Si grains with homogenously distributed ultrafine primary Si (about 1 μm) particles throughout the eutectic Al–Si matrix

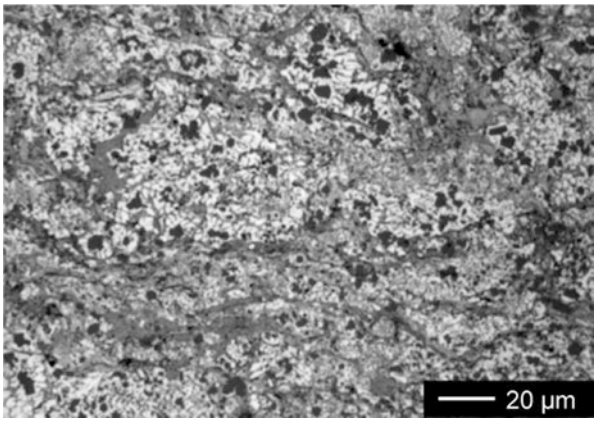


Fig. 14.21 Optical micrograph of the cross section of a HVOF sprayed Al–Si composite structure showing ultrafine primary (2–4 µm) Si and a network of Si in the eutectic Al–Si matrix. Reprinted with kind permission from Springer Science Business Media [138]

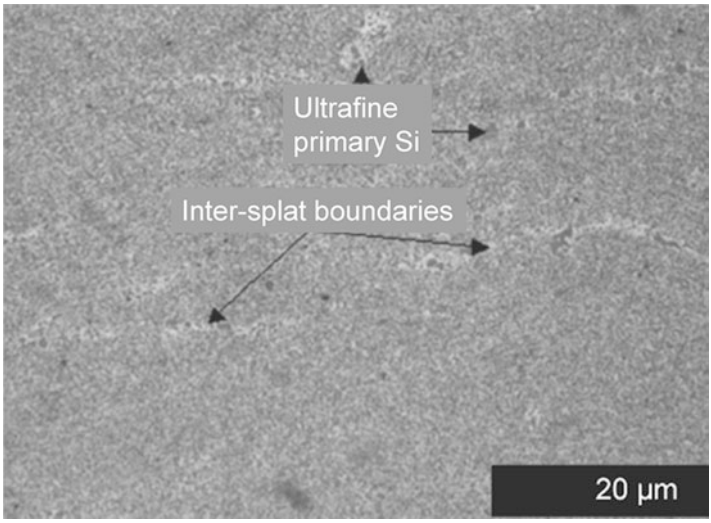


Fig. 14.22 Cross-sectional optical micrograph of the VPS formed Al–Si deposit showing the presence of eutectic Al–Si grains, ultrafine primary silicon particles and a network of silicon particles. Reprinted with kind permission from Elsevier [139]

(Fig. 14.22). The ultrafine primary Si particles precipitated from the Al–Si alloy due to the rapid solidification in VPS process. Further decrease in size of Si particle was due to fragmentation attributed to high velocity impact of the molten powder.

Gas atomized hypereutectic Al–21 wt% Si alloy powder was blended and mixed with multiwalled carbon nano-tubes (10 wt%) before being ball milled. The blended powder was plasma sprayed (SG 100 Praxair gun) [140, 141]. The multiwalled

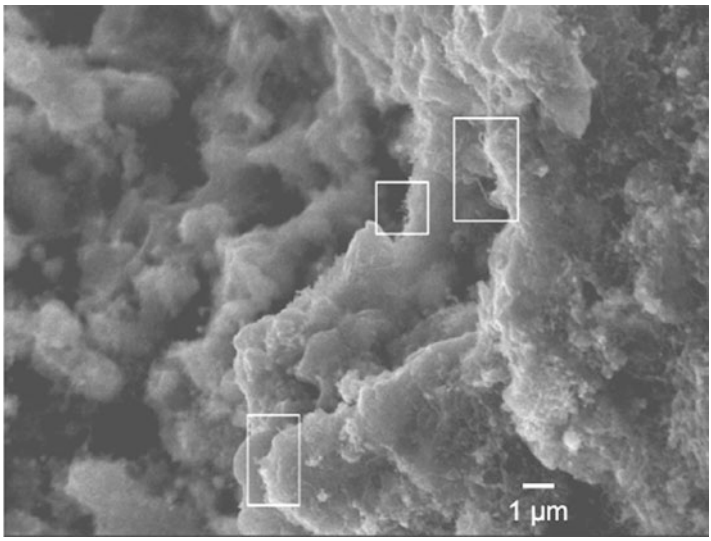


Fig. 14.23 Low magnification SEM image of fractured surface of a composite cone structure, showing the retention of carbon nanotubes. Reprinted with kind permission from Elsevier [140]

carbon nano-tubes (MWCNT) were successfully retained in the spray formed composite structure (Fig. 14.23). The formation of a β-SiC layer, rather than aluminum carbides at the interface of Al–Si matrix and MWCNT reinforcement, has been confirmed. The β-SiC formation occurred in an ultrathin layer (2–5 nm), attributed to the higher rate of reaction at the triple point of MWCNT/Al–Si alloy/vapor [141].

14.6 Production of Nanostructured Coatings by Cold Spray

Compared to the other spray processes with hot gases, the only way to achieve nanostructured material by cold spraying is to spray nano-powders or micro-size powders with nano-sized grains or to spray composite agglomerates made either of micron- and nanoparticles or of only nanoparticles. However it must be kept in mind that the sprayed particles must be sufficiently ductile.

14.6.1 Alloys

Cold spray deposition of conventional and nanocrystalline (atomized and cryomilled) (Al–Cu–Mg–Fe–Ni–Sc) coatings was successfully achieved [142]. The conventional cold-sprayed coating showed negligible porosity and an excellent

interface with the substrate material. This was not the case for the nano-crystalline coating, in which the porosity level was in the range of 5–10 %. The microstructure of the feedstock powder was retained after the cold spray process. The difference in porosity between the conventional and nano-crystalline coatings can be explained by the hardness and microstructure of the corresponding feedstock powder, the extent of deformation of which is much less, resulting in a less dense coating. The hardness of the nano-crystalline coating was similar to that of the feedstock powder, suggesting that no work hardening took place [142].

Nano-crystalline Al 5083 coatings were cold sprayed with helium without preheating of the carrier gas [17] onto a grit-blasted aluminum substrate. The critical velocity (over 700 m/s) was successfully achieved. The cold-sprayed coating showed negligible porosity and the interface with the substrate material was excellent. Wang et al. [143] produced by ball milling a metastable Fe(Al) alloy powder with morphology and size distribution suitable for cold spraying. The prepared powder exhibited a lamellar microstructure. The metastable microstructure of the milled Fe(Al) feedstock was completely retained in the coating using cold spraying. The FeAl intermetallic phase was formed during the heat treatment of the as-sprayed coatings at a temperature of 500 °C [143]. Nickel powder was mechanically milled in liquid nitrogen to achieve small nonspherical powder particles with a mean size of 15 μm with an average nano-crystalline grain size in the range of 20–30 nm [144]. The cryo-milled powder was sprayed with He (also used as carrier gas) onto grit-blasted aluminum substrates using the cold spray process. The Ni coating showed negligible porosity, and the grain structure of the powder was retained. Microhardness values were comparable to the results obtained by electrodeposition. Nanostructured NiCrAlY starting powders were produced using a high-energy milling process and subsequently a coating was deposited on a IN738 substrate by cold spraying maintaining the feedstock nanostructure [145]. The shot-peened coating presented a rather good resistance to oxidation.

14.6.2 Composites

The difficulty wih cold spraying composites lies in the necessity to spray ductile particles, which is not necessarily the case for WC–Co particles. The WC–12Co powder sprayed by Li et al. [146] exhibited a spherical morphology with nano-sized WC particles partially bonded together and voids appearing within particles Fig. 14.24. According to the XRD pattern the powder consisted of two phases of WC and Co. Critical velocities of about 915 m/s were measured. Coating microhardness was about 1,800 $HV_{0.3N}$, a value similar to that of sintered bulk material of a similar composition and microstructure. A certain degree of deformation of both impacting particle and deposited layer is required. This is illustrated by Li et al. [146] who cold sprayed with He a powder made from agglomeration of nano-sized WC with cobalt followed by partial sintering. The powder particles had

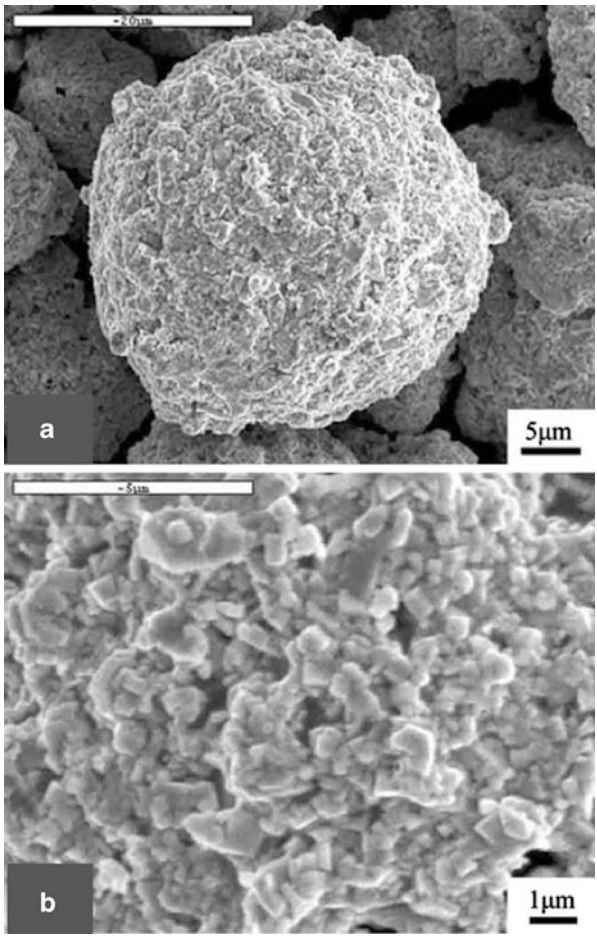


Fig. 14.24 Morphology of nanostructured WC–12Co feedstock (**a**) with detailed surface structure and (**b**) at a high magnification. Reprinted with kind permission from Springer Science Business Media [146], copyright © ASM International

a size range from 5 to 44 μm. The nominal WC grain size was 50–500 nm. As shown in Fig. 14.25 small particles (about 10 μm) are almost completely embedded, into the stainless steel substrate, while large particles penetration is much less. With nanostructured WC–Co, a porous structure, originating from the agglomeration, permits the pseudo-deformation through compaction of particles and the buildup of a thick coating Therefore, it can be considered that a WC–Co powder with WC loosely bonded by the binder is suitable for cold spraying. The annealing treatment at a temperature of 1,000 °C had little influence on the microhardness of the coating. However it seemed that the bonding between deposited WC–Co particles and the toughness of the resulting coatings can be improved by post-annealing treatment [147].

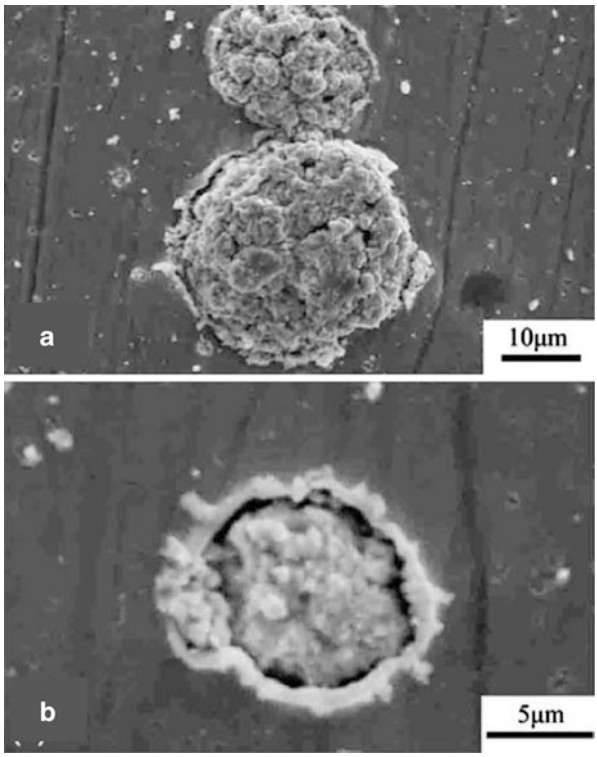


Fig. 14.25 WC–Co particles penetrated into the stainless steel substrate. (**a**) Two particles of different diameters penetrating to different depths; the large particle penetrated less deeply than the small particle and (**b**) a smaller particle of about 10 μm diameter has almost completely embedded into the substrate. Reprinted with kind permission from Springer Science Business Media [146], copyright © ASM International

The production of cermet coatings with conventional and nano-crystalline feedstock powders by cold gas dynamic spraying (CGDS) and pulsed gas dynamic spraying (PGDS) processes was performed by Yandouzi et al. [147]. No degradation of the phase (phase transformation and/or decarburization of WC) was observed. Dense coatings without major defects were difficult to obtain when using the CGDS process. Coatings with low porosity were obtained when the feedstock powder was preheated above 573 K. The nanostructure of the feedstock powder was preserved.

14.6.3 Amorphous Alloys

Cold-sprayed Fe-base amorphous alloy coatings were successfully produced. The coatings showed a negligible porosity and excellent interfaces with the substrate material [148]. The microstructure of the feedstock powder (gas atomized) was retained after the spray process. The use of an amorphous Al–Co–Ce powder to produce nanostructured coatings with high degree of bonding to aluminum substrates alloys was also demonstrated [149].

14.7 Solutions or Suspensions Spraying

To produce finely structured coatings by thermal spray techniques using liquid injection, two routes have been suggested:

- Spraying submicron-sized or nano-sized ceramic or cermet particles via a suspension [150–152]. Once drops have been fragmented and vaporized by the plasma flow or the HVOF flame (see Sect. 4.5), particles contained in the droplets are heated and sprayed onto the substrate. Splats collected on cold substrates have diameters ranging between 0.1 and 2 μm and average thicknesses between 20 and 300 nm. The stacking of splats or grain shaped particles (resulting from flattened liquid droplets recalescence) form finely structured coatings.
- Spray solutions of final material precursors. As with suspension, the liquid undergoes rapid fragmentation and evaporation once injected in the plasma jet. This is followed by precipitation or gelation, pyrolysis, and melting to result finally in the impact of molten liquid droplets with average diameters ranging from 0.1 to a few micrometers [153–156].

These new spray techniques differ from the conventional one (solid particles in the tens of micrometers size range) both in measurements and modeling.

(a) Measurements. In contrast to conventional particles in-flight, liquid drops and droplets emit no radiation and thus the only way to see them is to illuminate them with a laser pulse, as described in Sect. 16.5.3. This system also allows accounting for effects of voltage fluctuations, the image being triggered when the voltage reaches a given threshold value [152]. The liquid penetration can be characterized by taking, under the same conditions, several images (during few seconds or more) that are superposed when the plasma high luminosity, masking the low one of the liquid, has been eliminated. A much more sophisticated technique of shadography with a double-pulsed Nd:YAG laser (532 nm wavelength with 8 ns pulse duration) can be used [157–159] and is described in Sect. 16.5.3.2. It is then possible to discriminate droplets with diameters of about 5 μm at the best and measure their number, velocity and diameter distributions in a relatively small volume ($2.25 \times 1.8 \times 1\ mm^3$). To measure velocities of small droplets (<5 μm) only the particle image velocimetry (PIV) can give accurate results [160], and this method is described in Sect. 16.5.3.1. The plasma jet cooling by the liquid vaporization can be measured by emission spectroscopy [151], but plasma computer tomography (PCT) is mandatory to obtain real temperature distributions [161], as described in section "(b) Emission Spectroscopy of Nonsymmetrical Jets". Of course, (50–60 mm) downstream of the torch nozzle exit, enthalpy probes can be used [162], also described in Sect. 16.3.3.3, which is a much faster technique than PCT. Soysal and Ansar [163] have proposed to use infrared images emitted by hot liquid vapors to characterize the influence of combustible liquid injection into the atmospheric plasma jet, see Sect. 16.5.3.2. Of course, as in conventional spraying, emission spectroscopy can be used to detect evaporation of microparticles [162].

(b) Models. Models used for liquid–plasma jet interaction are very complex because they must take into account a two-phase flow, drop and droplet fragmentation, evaporation as discussed in Sect. 4.5.2. In addition, the thermal history and chemistry and eventually coalescence have to be considered, together with the time variation of the plasma flow fields resulting from the anodic arc root movement on the anode wall, the jet turbulence, and also compressibility effects [164–168]. For fragmentation, two types of models are used. The breakup models, such as TAB or ETAB are used, and Basu and Cetegen [168] were the only ones to integrate the droplet vaporization and the internal precipitation into the calculations. The second route attempts to analyze the injection of a continuous liquid jet into the plasma with regard to its primary and then secondary breakup [165, 166]. This route implies the development of novel numerical multiscale approaches. If the Ohnesorge number [see Eq. (4.69)] Oh < 0.1, breakup modes depend only on the Weber number, *We*, [see Eq. (4.68)]. According to Eq. (4.68), We is proportional to the drop diameter and inversely proportional to the liquid surface tension, σ_l. With drops over 200 μm and ethanol (low σ_l) as solvent in an Ar–H_2 plasma [165, 166], We values over 350 are easily reached within the plasma jet core, except maybe in the jet fringes, and drops can experience different breakup regimes, the catastrophic one inducing a very rapid breakup into tiny droplets, thus limiting their acceleration. In contrast, when injected drop sizes are below 50–60 μm, and the plasma flow mean velocity is lower, when using larger anode nozzle internal diameter, the We reaches a few tens in the central part of the plasma jet. Of course with big drops, increasing the surface tension of the liquid, σ_l, can reduce the Weber number.

14.7.1 Sub-Micrometer and Nanometer-Sized Particles in Plasma or HVOF Jets

14.7.1.1 Particle Inertia

Compared to micro-sized solid particles (generally a few tens of micrometers), sub-micro- and nano-sized ones have a very low mass. Such particles are found either in suspensions or are formed in solutions after pyrolysis, sintering, and melting. Shifting from 10 to 0.1 μm particle corresponds to a mass reduction in a ratio of 10^{-6}! To achieve the same injection force, the acceleration should be increased by a factor of 10^6, which is impossible with a gas carrier without perturbing drastically the plasma jet. That is why a liquid carrier, about 1,000 times heavier than the gas, is used in suspension spraying.

Moreover the drag coefficient, C_D, controlling the particle acceleration by the plasma flow, is drastically reduced by the Knudsen effect (see Sects. 4.2.2.2b and 4.3.3.2, Table 4.3), which is not the case with a HVOF flame. Thus small

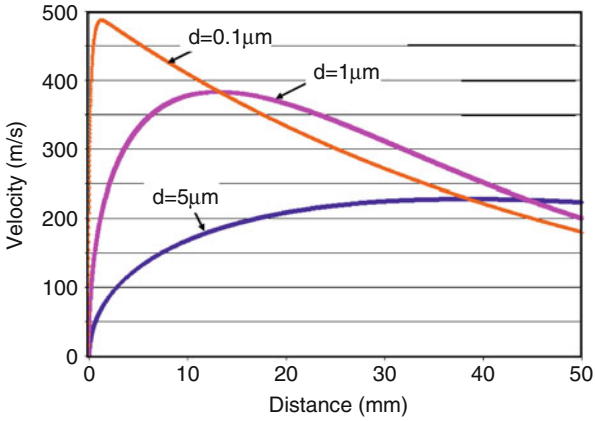


Fig. 14.26 Computed evolutions of particle velocities as a function of the covered distance in a Ar–H_2 plasma jet with a 6mm nozzle diameter and a net power of 32 kW supplied to the gas. Reprinted with kind permission from Springer Science Business Media [169]

particles are poorly accelerated by the plasma flow and the characteristic time for the momentum transfer is multiplied by a factor of more than 200 with a 0.1 µm particle compared to a 10 µm one. Of course the problem is even worse when shifting from 0.1 to 0.01 µm. This is illustrated in Fig. 14.26 from Delbos et al. [169] who have calculated the velocity of zirconia particles "deposited" with a zero velocity at the jet axis at the nozzle exit (no penetration problem) where the velocity of the Ar–H_2 plasma was 2,500 m/s. The nano-particle with a diameter of 0.1 µm, with its very low inertia, is first very rapidly accelerated and reaches a maximum velocity of 480 m/s after 2 mm trajectory, while the gas velocity is still more than 2,300 m/s. The Knudsen effect takes over even more rapidly (the Drag coefficient is multiplied by 0.046) and farther than 2 mm trajectory the particle velocity decreases regularly. On the contrary, with the 5 µm (Drag coefficient multiplied by 0.26) the particle acceleration is regular and its maximum velocity is reached at about 40 mm downstream of the nozzle exit. With the 1 µm particle (C_D multiplied by 0.13) the maximum velocity is reached at 15 mm. This is illustrated in Fig. 14.26. Such values are over estimated because they were calculated for particles "deposited" on the axis at the torch nozze exit, while in spray conditions particles are radially injected and cross-areas where gas velocity is much lower than that along the jet axis. That is why in spray conditions with torches using stick type cathodes the solid particle velocity is that achieved by its carrier droplet just prior to its vaporization. At last, with its low inertia, the nano-particle velocity decreases almost as fast as that of the gas and it is the main reason to use very short spray distances (30–50 mm stand-off distance).

This problem is of course drastically reduced when longer plasmas are used, such as those produced with the Axial III torch. In this torch three plasma jets, produced by separated cathodes and anodes, are gathered together, constricted in an interchangeable extension nozzle, and the resulting plasma jet flows out the extension and expands in the surrounding atmosphere. Suspensions are injected between the three converging plasma jets, axially before the nozzle extension and

accelerated by the long plasma flow within the extension. As pointed out in Sect. 7.8.1, with an extension 50 mm long after the nozzle of a stick type cathode torch the gas velocity is still 1,700 m/s, while at that distance without the extension nozzle the velocity of the expanded plasma jet is only 500 m/s. In these circumstances the gas velocity inside the interchangeable extension is only slightly reduced (about 10–30 % depending on the extension length) compared to that obtained at the nozzle exit of each converging three torches. In such conditions, sub-micro- or nano-sized particles are well accelerated in spite of the Knudsen effect. Of course when the jet expands in air after the interchangeable nozzle, the gas velocity decreases almost as fast as that exiting torches with stick-type cathodes and the spray distance must also be reduced compared to that used for conventional spraying.

With HVOF spraying, gas temperatures are below 2,800–3,200 K and the Knudsen effect is drastically reduced, most authors neglecting it for particles diameters as low as 1 μm and even, which might be more questionable, for particles 0.1 μm in diameter or even less. Anyhow most particles sprayed by HVSFS are bigger than 0.1 μm and the Knudsen effect calculated for a 0.1 μm particle in hydrogen–oxygen flame at 1 MPa corresponds to a CD coefficient multiplied by 0.6 to be compared to the 0.046 in Ar–H_2 plasma. To characterize flame flows, small particles (in the μm size range) are added to the atmospheric flame flow and PIV measurements are performed downstream of the injection where it is assumed that particles have reached the same velocity as that of the flow (see Sect. 16.5.3.1).

14.7.1.2 Particle Trajectory

Thermophoresis force, F_{th}, occurs when small particles are subjected to a temperature gradient (see Sect. 4.2.3.2 and Fig. 4.19). This effect means that small particles with trajectories in the plasma core can escape from it when approaching a high temperature gradient zone, and can be ejected into the jet fringes, as shown schematically in Fig. 4.19. Moreover, small particles can follow the gas flow developing parallel to the substrate surface close to it and thus never impact on it, as shown schematically in Fig. 14.27.

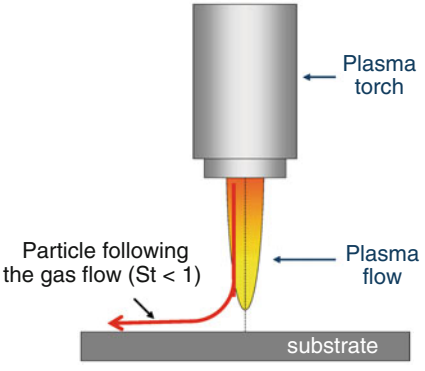


Fig. 14.27 Schematic of a sub-micro- or nanometer particle following the hot gas flow because its Stokes number is <1

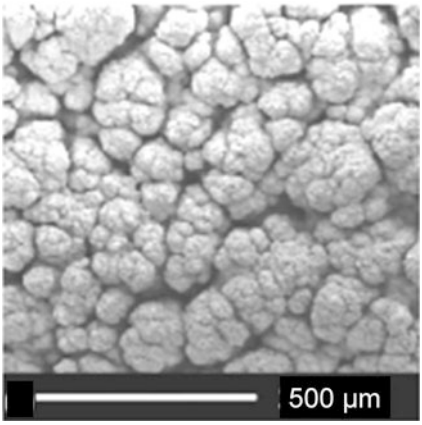


Fig. 14.28 SEM images showing the top surface of a coating sprayed on 24-grit alumina-blasted copper substrate with a standoff distance of 5 cm, mechanical injection with an injection pressure of 45 MPa for an injector nozzle diameter of 230 µm, a suspension flow of 52 ml/min, a coating pass thickness of 1 µm, with a SG-100 plasma torch using 3083-129 cathode, 3083-175 anode, 3083-113 gas injector, and a 6-mm internal diameter nozzle, operated at a current of 1,000 A with 20 slm Ar and 60 slm He, producing a gun voltage of 50 V. Reprinted with kind permission from Elsevier [170]

This situation occurs when their velocity is below that corresponding to a Stokes number, St, below 1 [13]:

$$St = \frac{\rho_p d_p^2 \nu_p}{\mu_g \ell_{BL}} \tag{14.1}$$

Subscripts p and g are related to particles and gas, respectively, ρ being the specific mass (kg/m^3), d the diameter (m), v the velocity (m/s), μ the molecular viscosity (Pa. s), and l_{BL} the thickness of the flow boundary layer, BL, in front of the substrate (m). l_{BL}, varies as the inverse of the square root of the gas velocity close to the substrate and can be lower than 0.1 mm. For example, with an Ar–H_2 plasma, produced with a stick type cathode torch, $St = 1$ for $v_p = 300$ m/s, $l_{BL} = 0.1$ mm, and $d_p = 60$ nm. The higher the spray distance will be, the lower the particle velocity and the thicker the BL close to substrate, reducing correspondingly the probability to reach the substrate. The entrainment of the nano- or sub-micrometer particles by the gas flow can either eliminate these particles from the coating generation or create defects. Defects are due to the substrate asperities: a roughness with a Ra of 1 µm (relatively smooth surface for conventional particles) corresponds to peaks up to 8 µm which are huge compared to the impacting particles sizes.

The first type of defects have been described by VanEvery et al. [170] who have plasma sprayed coatings from suspensions of nanometer-sized (85 ± 13 nm) YSZ powders in ethanol. They varied the liquid injection pressure and the pass thickness, the standoff distance being 5 cm, the spray conditions being given in Fig. 14.28 caption. Coatings were sprayed directly on 24-grit alumina-blasted copper

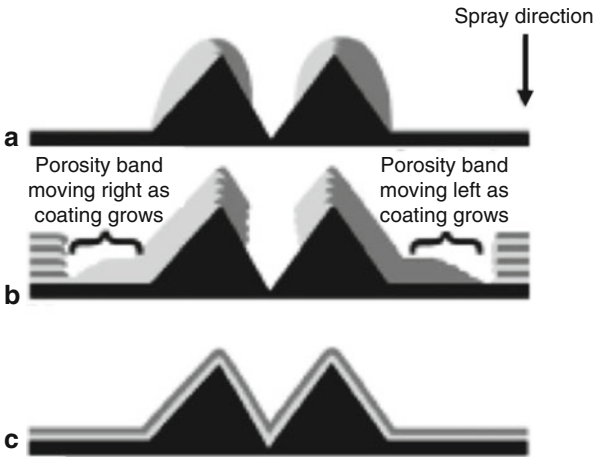


Fig. 14.29 Schematic illustration of the deposition characteristics occurring on and away from substrate surface asperities during (**a**) 1SD, (**b**) 2SD, and (**c**) 3SD. The spray direction is the same in each figure. The black regions denote the substrate. The light gray regions represent material deposited by droplets having a substrate parallel velocity component directed from left to right, and the dark gray regions represent material deposited by droplets having a substrate parallel velocity component directed from right to left. Reprinted with kind permission from Elsevier [170]

substrates. Figure 14.28 presents the top surface of the coatings with a cauliflower aspect resulting from particles defection by asperities close to the substrate.

This type of defect corresponds to the formation of coarse columnar microstructure due to droplet trajectories close to the substrate with shadow effects. From microstructural observations and predictions of droplet flight paths VanEvery et al. [170] suggested that the change in relative influences of drag and inertial forces with YSZ droplet size can result in three types of spray deposition, schematically presented in Fig. 14.29. In the type 1 of spray deposition (1 SD) the plasma drag forces during substrate impingement dominate the droplet inertia and redirect the droplet velocity from normal to along to the substrate surface. Consequently, droplets impact preferentially on asperities, generating deposits that grow to become columnar structures separated by linear porosity bands. With the type 2 deposition (2 SD type), the droplet velocity remains mostly normal to the substrate surface, but the impinging plasma drag influences the droplet trajectories such that surface asperities block deposition in downstream regions and create porosity bands. In the type 3 deposition (3 SD type), the coating microstructure exhibits no signs of droplets being influenced by drag from the plasma impingement. For more details about the different types, see [170]. This has been mainly observed with suspensions, particles formed from solutions being generally bigger in the sub-micrometer size range.

The second type of defects that can be observed corresponds to the formation of stacking defects, called speckles, which are very important if the ratio $Ra/d_{50} > 2$ [171, 172]. Ra is the mean roughness, while d_{50} is the mass median diameter of

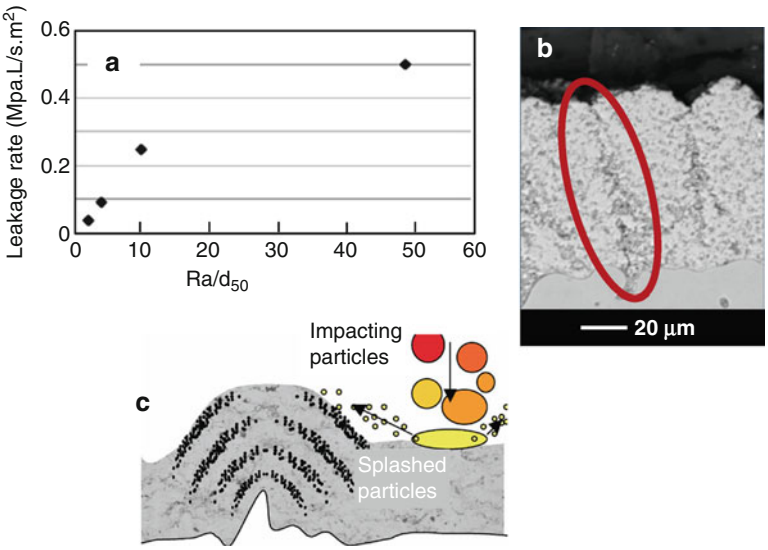


Fig. 14.30 YPSZ coating sprayed onto a substrate exhibiting a ratio average substrate roughness Ra to the feedstock particle average diameter d_{50} of (**a**) 2 times or (**b**) 50 times, where columnar stacking defects develop through the coating thickness [171] (**c**) Suggested mechanism of the speckle formation [173]. Reprinted with kind permission from Dr. E. Brousse [171]

particles contained in the suspension or formed in the solutions. Indeed, large columnar stacking defects develop through the coating when the substrate surface roughness is higher than the feedstock particle average diameter. Brousse et al. [171, 172] have studied the influence of substrate roughness on coating structure and the corresponding leakage rate, results being presented in Fig. 14.30a. Reducing the stacking defects, as presented in Fig. 14.30b, to enhance gas tightness, requires spraying onto smooth polished substrates. For example, with a ratio $Ra/d_{50} = 2$ the leakage rate of the YPSZ suspension coating is only 0.02 MPa L/s m [171]. When $Ra/d_{50} = 50$ the leakage rate becomes 0.5. This columnar stacking defect, presented in Fig. 14.30b, can be explained, as for conventional coatings, by the formation of a speckle (see section 13.6.1.1.b). The formation mechanism of this speckle suggested by Racek [173] is presented in Fig. 14.30c.

14.7.1.3 Particle Flattening

When collecting on a flat substrate splats resulting from the flattening and subsequent solidification of conventional molten particles, the flattening degree, ξ, (ratio of splat mean diameter to that of impacting particle) is typically in the range of 4–7. In contrast, for submicron- or nanometer-sized particles of the same material and

with similar temperature, $\xi < 2$ [5, 151, 169]. That is due to the much lower impact kinetic energy of the small particle but also to its much smaller diameter (Young-Laplace equation stating that the pressure difference across the fluid interface is inversely proportional to the principal radii of curvature).

14.7.1.4 Particle Heat Transfer

Similar to the effect on the drag coefficient, the Knudsen effect reduces drastically the heat transfer coefficient (see Sect. 4.3.3.2); however, the heating is rather fast due to the low mass of nano-particles. Another interesting phenomenon is observed when the spray distance is short (<50 mm with a PTF4 torch) with heat fluxes imposed by plasma >30 MW/m^2 [169, 171] and with a substrate or a previously deposited layer with a low thermal conductivity which is sufficiently insulating. Under these conditions the heat flux delays the solidification of the flattened nano- or sub-micro-sized particle, and the surface tension results in spheroidizing the flattened particles, resulting in a coating with a granular structure [169], as illustrated in the section 14.7.6.3.b "(i) Plasma Spraying" Fig. 14.67.

To conclude this part, the smaller the sprayed particles are, the higher is the probability that they do not reach the substrate with the right impact parameters to form a coating. Sufficiently high impact velocities are only achieved through the velocities of the particle mother droplets.

14.7.2 Liquid Injection

14.7.2.1 Radial Injection into Plasma and HVOF Jets

(i) When spraying solid particles with a size range in the tens of micrometers (conventional spraying), the optimal trajectory is obtained by adjusting the injection force to that imparted to the penetrating particle by the hot gas jet:

$$m_{50} \cdot \gamma_{50} \approx S_{50} \cdot \rho \cdot v^2 \tag{14.2}$$

where m_{50} is the mass median corresponding to the log normal distribution of the mass median diameter d_{50}, γ_{50} the corresponding acceleration, S_{50} the cross section of the d_{50} particle, ρ the mass density of hot gases, and v the hot gas velocity. Of course this expression is oversimplified and in the real world one must take into account the fact that ρ and v vary continuously along the particle trajectory. Moreover, even if vaporization occurs, it happens only when particles have already penetrated into the hot gas jet core, and the trajectory is that determined by the initial particle size. The problem is far more complex with a liquid that is fragmented upon penetration in the high velocity hot gases and then vaporized (the corresponding time t_v being 2 to 3 orders of magnitude

longer than that of the fragmentation time t_f [151]). Thus the mass and correspondingly the cross section of the drops decrease continuously upon their penetration into the hot gases. In order to achieve the drop penetration into the hot gas jet core, the initial velocity must be much higher compared to that which should be given to the initial drop if its diameter was kept constant. Thus the condition for a good radial penetration implies, as explained in Sect. 4.5.2, that

$$\rho_l v_1^2 >> \rho v^2 \tag{14.3}$$

where the index l corresponds to the liquid while no index is related to the hot gas jet.

The fragmentation and vaporization processes of the liquid jets or drops are described in detail in Sects. 4.5.3 and 4.5.4. Drops or jets will be fragmented first in tiny droplets (few micrometers) before being vaporized. Figure 14.31 illustrates the liquid fragmentation upon its penetration within an Ar–He plasma jet (here a suspension in ethanol of YSZ nanometer-sized particles, 20–300 nm, with a load of 10 wt%). As can be seen, fragmentation starts in the plasma jet core fringes: as soon as the Weber number of the suspension [see Eq. (4.68)] is higher than 12–14, droplets can be fragmented in the jet fringes. Then these droplets traveling in the jet fringes are evaporated, but unfortunately in this zone particles contained in suspension droplets are not melted, but heated enough to stick on the previously deposited layers of the coating, thus creating defects. In case of solutions they are poorly pyrolyzed and also imbedded in the coating being formed as a mud-like film. Fragmentation keeps going with further penetration into the hot plasma core, creating first large drops (the image resolution is about 30×30 μm^2) and smaller and smaller ones appearing as clouds, with a color, resulting from laser illumination, which is slightly different from that of the plasma jet image. To Illustrate Eq. (14.3), for the conditions of Fig. 14.31, $\rho_1 v_1^2 = 0.6$ MPa while $\rho v^2 = 0.015$ MPa!

Thus, the liquid should be injected with a device allowing controlled drop dispersion and velocities that are easier to describe than to achieve (see Sect. 4.5.1). According to the complexity of liquid penetration, this process must be controlled on line with appropriate diagnostics (see Sect. 16.7.3).

(ii) For fragmentation of drops and droplets, depending on their Weber number, different breakup mechanisms are considered and classified as: (1) bag breakup ($12 < We < 100$), deformation of the drop as a bag-like structure that is stretched and swept off in the flow direction, (2) stripping breakup ($100 < We < 350$): thin sheets are drawn from the periphery of the deforming droplets, and (3) catastrophic breakup ($We > 350$) which is a multistage breaking process [157]. With catastrophic breakup, liquid fragmentation in tiny droplets is very fast, and the acceleration of their solid sub-micro- or nano-sized particles is very poor due to Knudsen effect. When the liquid precursor is injected as liquid

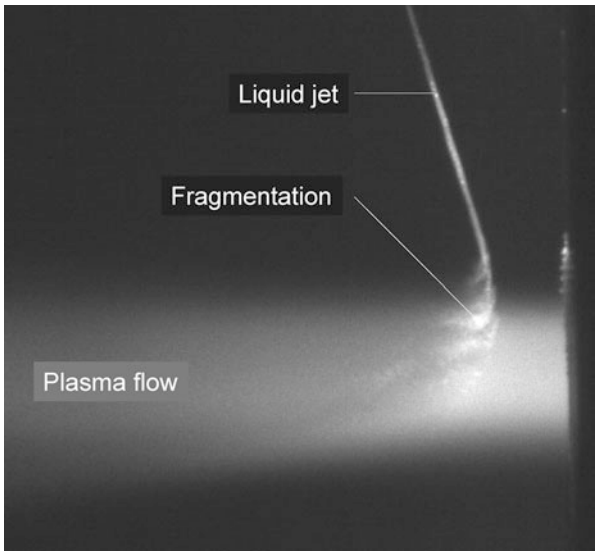


Fig. 14.31 Suspension fragmentation in an Ar–He stable plasma jet (Ar: 30 slm, He: 30 slm, I: 700 A, anode nozzle internal diameter at exit: 6 mm, liquid injection velocity: 26 m/s, average voltage $V_m = 40$ V, relative voltage variation $\Delta V/V_m = 0.3$). Reprinted with kind permission from Springer Science Business Media [151], copyright © ASM International

jet, it undergoes primary breakup by the plasma flow while blobs and droplets generally undergo secondary breakup in the flow [157].

If the drop diameter depends on the injection setup (see Sect. 4.5), the choice of the solvent to prepare the suspension or solution is also very important. The surface tension of the drop determines the final size of droplets that are finally rapidly vaporized once fragmented (see Fig. 4.75). This final size of droplets before their fast evaporation is very important for the type of coating obtained. With the solutions, if the droplet size is too large (>5–10 μm) the precursor solute concentrates as a shell that pyrolyzes and that can reach the coating being formed incompletely treated. When drops are smaller, pyrolysation covers rapidly the whole volume, get sintered, and then melted forming splats upon impact [20, 155, 174]. Generally a droplet corresponds to one particle well melted or a shell just pyrolyzed or parts of this shell. With suspensions, coating formation depends on the solid particle morphologies, the propensity for forming aggregates being very important for particles obtained by a chemical route, while it is much less with attrition-milled particles. Aggregates either form big particles, as shown by the size of collected splats, or explode resulting in dispersed trajectories and unmelted particles. As with conventional spraying, the size distribution width of particles within suspension must also be limited to reduce the trajectory dispersion. With particles in the sub-micron- or nano-size, splats collected sometimes correspond to bigger particles, due to the coalescence of fully melted, initially smaller particles [5, 151]. This phenomenon is also observed when spraying suspensions of different particles such as zirconia and alumina [175–178], Co_2O_3 and Ni_2O_3 (grain sizes of 30 to 60 nm), or TiO_2 and Cr_2O_3 (median crystallite size of 100 nm) [179].

(iii) Another point that must be emphasized is that, to overcome the Stokes effect [see Sect. 14.7.1.2 and Eq. (14.1)], the substrate must be disposed relatively close to the distance where most droplets have been vaporized. It must correspond to a distance sufficient to melt particles but avoiding they slow down too much. This results in rather short spray distances, for example, between 30 and 50 mm downstream of the nozzle exit when plasma spraying with a stick-type cathode torch. At such distances heat fluxes can reach a few tens of MW/m^2 that can modify strongly the heat transferred to the coating under construction and thus its structure.

(iv) The vaporization of the liquid and the heating of the vapor to the temperature of the hot gases, especially the plasma, consumes from 20 to 40 % of the hot gas enthalpy, at least for plasma jets. Section 4.5.5 describes in detail the important cooling of the plasma or HVOF jet by the liquid vaporization. The consequence is that, compared to conventional coatings, torch power levels should be at least 30–40 % higher to compensate for the energy necessary to vaporize the liquid carrier. At last, Sect. 4.5.6 describes the sensitivity of liquid injection to arc root fluctuations for plasma jets (the effect being far more important than that observed when injecting particles in conventional spraying), which requires use of low fluctuating plasma jets when spraying liquids. Unfortunately, the strong fluctuations with H_2 in the plasma forming gas require the use of He as secondary gas, which reduces the voltage and thus also the power level. Such fluctuations are also observed when using nitrogen as primary forming gas. For HVOF guns working with C_2H_2 or liquid fuel the injection of the solution or the suspension should be radially downstream of the nozzle. Using organic solvent does not help, through its combustion, to compensate for the energy lost by its vaporization and transformation into plasma. Indeed combustion can only occur in areas where temperature is below about 3,000 K, and where a sufficient quantity of oxygen has been entrained. See, for example, enthalpy probe measurements presented in Sect. 16.3.1.5. The problem of oxygen entrainement can be partially overcome by using atomization of the suspension by air.

14.7.2.2 Axial Injection

In contrast to radial injection, the injection velocity with axial injection must be sufficient for drop penetration into the high-energy jet, but afterwards the velocity difference between drop and gas flow should assure their fragmentation and subsequent vaporization. However, as in radial injection, the liquid injector must provide a relatively narrow trajectory distribution with controlled drop velocities.

(a) d.c. Plasmas

With a d.c. plasma gun such as the Mettech plasma torch, three plasma jets converge in a nozzle, the liquid drops being injected where the separate jets converge, and they are entrained by the high velocity converging plasma

jets which provide a sucking action [5]. The other advantages of this configuration are that fragmentation and vaporization occur in the high velocity and high-temperature plasma jet inside the convergent torch nozzle that can be longer than that of a fee jet flowing in air. The power level can reach up to 2.5–3 times that of the conventional stick-type cathode plasma guns. The length of the common nozzle is a few tens of millimeters, and fragmentation and vaporization occur inside the convergent torch nozzle. In spite of the Knudsen effect, particles are well accelerated in the extension nozzle where the plasma velocity is not drastically reduced (10–30 % depending on the extension length). For example, Oberste-Berghaus et al. [175] for nano- or sub-micro-sized alumina and zirconia mixed particles have obtained ensemble velocities between 500 and 770 m/s.

For solutions, Basu et al. [20] have shown that the quality and property of the coating microstructure depends upon the injection type and droplet sizes. For axial injection of solutions, smaller initial diameter droplets are favorable for getting pyrolyzed. In the axial mode, the droplets are injected right into the high-temperature plasma core. Hence they readily go through the maximum possible heating rate helping the pyrolization process to develop within the whole droplet.

(b) HVOF

Any liquid, being water or organic, starts to evaporate rapidly when introduced into the flame of the combustion chamber causing two important effects: (1) a significant cooling of the flame and (2) strong disturbance of the free expanding hot gas stream due to the evaporation process caused by the expanding vapor [180]. Vaporization and pressure increase can modify the jet temperature and velocity distribution in the expanding nozzle and hence produce different resulting particle morphologies [181]. An HVOF process using micro-sized particles (a process called high velocity suspension flame spraying: HVSFS [180]), according to Domongo et al. [181], comprises the following series of complex processes: (1) transformation of chemical energy into thermal energy of the gas; (2) conversion of thermal energy into kinetic energy of the gas by expansion through the nozzle, including energy transfer from the gas to particles during this expansion process; (3) free jet flow field with flow patterns strongly depending on the pressure difference between nozzle outlet and the atmospheric pressure; and (4) conversion of the particles' kinetic and thermal energies into viscous deformation work and surface energy during coating deposition. First results were obtained with propane as fuel gas (fuel/oxygen ratio of 0.9) and ethanol as suspension medium. The evolution of the mass fractions of propane, ethanol, oxygen, and the exhaust gases along the torch centerline shows a clear correlation with the temperature of the gases. Ethanol evaporates no earlier than inside the expansion nozzle due to the injection conditions. Also, the increase in pressure in the combustion chamber due to ethanol evaporation leads to delayed evaporation. Ethanol evaporation results in a rapid decrease in flame temperature, which is not

compensated by gaseous ethanol combustion. At the same time, oxygen is not completely consumed by the ethanol combustion. The diffusion process (non-premixed combustion) controls reaction kinetics, under the boundary condition of a high gas velocity. This also means that the gas temperature in the nozzle cannot be influenced by the oxygen content in the premixed oxy/fuel mixture. As a consequence, the spray particles, which are heated only after release from the suspension droplets, are heated at lower gas temperatures and with lower dwell time compared to the conventional HVOF process. The only possibility to change the heating characteristics of the spray particles is to move the position of ethanol evaporation inside the combustion chamber, for example, by modifying the combustion chamber (mainly through the increase of its length) [182, 183]. It is also possible to modify the composition of the liquid phase, in particular the ratio between water and organic liquid phase (isopropanol), which is an important parameter for controlling the flame temperature in the HVSFS process. Indeed, water absorbs energy from the flame as it is vaporized and heated, whereas the organic liquid phase (isopropanol) contributes to the heat generation process by burning after vaporization [183, 184].

(c) r.f. Plasmas

With r.f. plasmas, flow velocities being below 100 m/s, fragmentation does not occur. With no fragmentation three cases can be encountered, of course for all of them the solvent is progressively vaporized, then (1) for suspensions made of particles agglomerating easily, such as those prepared by chemical routes, the solid particles sinter and then melt forming material drops in the tens of micro-size range, the molten drop impacting onto the substrate to form coatings as in conventional spraying, (2) for suspensions made of particles hardly agglomerating, each solid particle is melted separately before impacting the substrate forming splats with diameters in the few micrometer range or below, (3) solutions are completely vaporized in the plasma, and then nanostructured particles are synthesized in flight by homogeneous nucleation from the supersaturated precursor vapor, to subsequently build up a coating with high porosity.

1. A good example is the production of hydroxyapatite (HA: $Ca_{l0}(PO_4)6(OH)$) coatings or micrometer-sized powders described by Bouyer et al. [185]. HA material in the form of an atomized colloidal water suspension was fed into the center of an inductively coupled r.f. argon plasma discharge. The HA suspension was brought into the plasma discharge core via a gas-atomizing probe fed with a peristaltic pump. As mentioned previously the relative gas-drop velocity is too small ($<$50 m/s) to fragment the drops ($<$100 μm) that are only successively flash-dried and melted, then deposited on the substrate to be coated or collected in-flight as spherical particles. The induction plasma allows sufficient time for the droplet drying and melting steps. The first part of the drop trajectories are within a pure Ar plasma with a rather low heat transfer coefficient and it is only downwards that this coefficient increases with the diffusion of the diatomic sheath gas (oxygen) into the torch central part. Figure 11.29a presents the suspension with

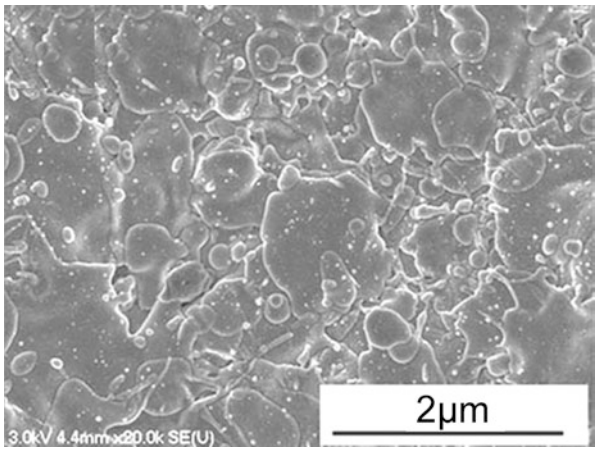


Fig. 14.32 FESEM micrographs of a r.f. suspension plasma-sprayed GDC coating top surface. Reprinted with kind permission from Springer Science Business Media [186], copyright © ASM International

needles of HA. Figure 11.30 shows the three main steps for HA deposit preparation. Finally Fig. 11.29b presents the mostly spherical HA particles obtained. The authors have shown the feasibility of SPS for HA deposition with high deposition rates (>150 μm/min.) and also for spheroidized powder production. Oxygen as sheath gas helps in limiting the decomposition of HA during plasma treatment. As a general rule, this decomposition can be either avoided or at least minimized by using an appropriate choice of plasma gas, namely, a plasma–sheath gas mixture with moderate enthalpy and high oxidizing potential. For example, hydrogen acts as a harmful gas for the HA stabilization, while oxygen is beneficial. In addition, the presence of water in the suspension contributes to the resistance of the apatite structure to decomposition during the high-temperature treatment by maintaining a high partial pressure of water vapor in the deposition reactor. Varying both the atomization parameters and the suspension properties can control HA SPS powder.

2. When r.f. spraying gadolinia-doped ceria (GDC) with particle mean sizes of 0.6 μm (particles with no agglomerating tendency) in suspension in distilled water, the resulting coating, as shown in Fig. 14.32, consists of layered splats with typical diameters from 0.2 to 2 μm corresponding to a flattening ratio below 2.7 [186]. First the solvent is vaporized and then the solid particles melted.
3. In the r.f. Solution Plasma spraying, called SolPS process, described by Jia and Gitzhofer [186], the GDC solutions of nitrate hexahydrate were completely vaporized in the plasma and then nanostructured GDC particles were synthesized in flight by homogeneous nucleation from the supersaturated precursor vapor, to subsequently build up a coating with high porosity, as illustrated in Fig. 14.33. The formation of globular GDC coatings was observed over the entire experimental range of this study. Similarly Shen et al. [187] have r.f. sprayed solutions of Lanthanum strontium cobalt iron oxide ($La_xSr_{1-x}\,Co_yFe_{1-y}O_{3-\delta}$) and GDC to produce a composite nanopowder, which was used in a next step to produce cathode coatings for intermediate temperature solid oxide fuel cells (IT-SOFCs)

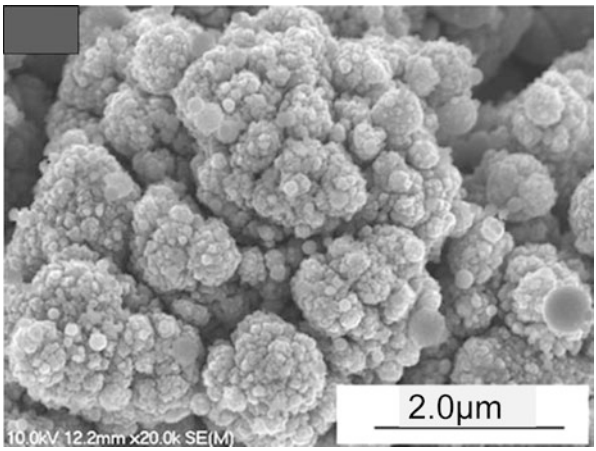


Fig. 14.33 SEM micrograph of the surface of SPS cathode coating. Reprinted with kind permission from Springer Science Business Media [187], copyright © ASM International

by suspension plasma spray (SPS), It has been possible to achieve a homogeneously mixed nanometer-sized composite GDC/LSCF powder without using a prolonged period of mechanical mixing. The nanometer-sized powders exhibited a perovskite structure and a fluorite structure as well as separated GDC and LSCF phases. By applying a low feeding rate, it was easy to synthesize nanometer-sized powders with different compositions by only adjusting the metal nitrate concentrations in the precursor solution. All synthesized powders were spherical with a diameter between 10 and 60 nm regardless of their composition. The deposited coating had a homogeneous nano-cauliflower structure, similar to that presented in Fig. 14.33, with an average porosity of 51 %.

14.7.3 Spray Torches Used

14.7.3.1 General Remarks

Radial liquid injection results in drop fragmentation before the vaporization of the resulting droplets [13]. In plasma flows, this vaporization followed by the transformation of vapor into plasma, drastically cool down the plasma flows even if the liquid is combustible. The combustion can occur only far downstream of the nozzle exit where the air entrainment is sufficiently important, i.e., at distances longer than the standoff distances with which suspensions or solutions are sprayed. However, when using a gas-atomized liquid, with air as atomization gas, combustion of the combustible solvent (ethanol in the experiment performed with a Triplex I torch by Vassen et al. [188]) can occur rapidly in the plasma jet and increase the gas temperature and velocity, as measured with an enthalpy probe 5 cm downstream of the nozzle exit (see Figs. 16.9 and 16.10).

With HVSFS, as previously indicated, almost no fragmentation occurs in the combustion chamber [183]. The liquid drops are vaporized cooling the flame and increasing significantly the combustion chamber pressure. With HVOF guns, designed for spraying conventional particles (in the tens of micrometer range), organic solvent is even not completely evaporated inside the expansion nozzle. Thus the decrease in flame temperature is not compensated by gaseous organic solvent combustion. The spray particles (mainly suspensions are sprayed) are released and heated only downstream of the nozzle throat.

Another very important point is that plasma spray torches must achieve high flow velocities in order to accelerate sufficiently the mother droplets, the particles contained in the droplets or formed being otherwise poorly accelerated due to the Knudsen effect.

14.7.3.2 d.c. Plasma Torches Used

To spray solutions or suspensions different types of torches are used:

- The conventional ones with a stick-type cathode (30–50 kW power levels) are working with Ar–H_2, Ar–He, or Ar–H_2–He plasma-forming gas mixtures. If hydrogen provides excellent heat transfer, it also induces very high arc root fluctuations resulting in important voltage fluctuations having a mean amplitude ΔV relative to the time averaged voltage $\overline{V}$, in the order of $\Delta V/\overline{V} < 1.5$. In contrast, Ar–He mixtures result in $\Delta V/\overline{V} < 0.25$ [18]. The role of these fluctuations can be illustrated with the following example. When using a PTF4 (Plasma Technik) torch with a 6 mm internal diameter nozzle, an arc current of 500 A with 45 slm Ar and 15 slm H_2, the mean voltage is 60 V with a minimum value of 40 V and a maximum one of 80 V. Figure 14.34 presents two pictures of the plasma jet taken, respectively, at the minimum and the maximum voltages. The velocity difference between both jets is about 800 m/s, which corresponds to $\Delta(\rho v^2) \sim 320$ %! For more details about these fluctuations see Sect. 7.3.5. Such voltage variations modify deeply the liquid penetration [151]. This is illustrated in Fig. 4.79 for the Ar/H_2 (45/15 slm) d.c. plasma jet, which plasma jet length fluctuations with voltage are illustrated in Fig. 14.34. On the contrary with the more stable Ar–He plasma presented in Fig. 4.73 the dispersion is drastically reduced. For more details about the drastic dispersion occurring in Ar–H_2 plasma jets, see Sect. 4.5.6. With these plasma torches the plasma jet core, corresponding to the high gas velocity, is short (a few tens of mm) and the gas velocity with the jet expansion in the surrounding atmosphere decreases very fast. Thus, with this gas velocity fast decrease and the Knudsen effect small particle velocities are low.
- The Triplex torch (Sulzer Metco, Wohlen, Switzerland) with three cathodes and three independent electric sources results in three arcs attaching at a single anode, with insulating rings between the cathode and the anode permitting the generation of longer electric arcs compared to conventional rod-type cathode

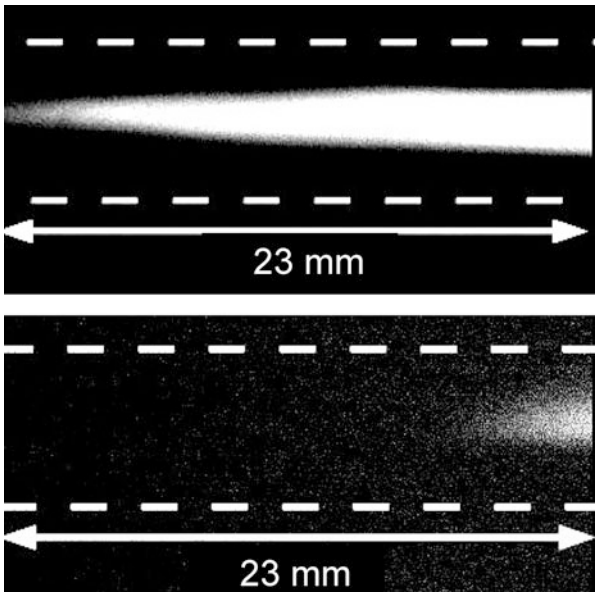


Fig. 14.34 Pictures of an Ar–H_2 plasma jet (PTF4 plasma torch, 6 mm i.d. anode nozzle, 45 slm Ar, 15 slm H_2, 500 A, $\bar{V} = 60$ V) taken at the maximum (80 V) and minimum (40 V) voltages. Reprinted with kind permission from Springer Science Business Media [169]

plasma torches. Mean voltages can reach here 100–120 V with Ar–He plasma gas mixture, instead of less than 40 V with conventional torches. Thus, if ΔV is still about 10 V, the $\Delta V/V$ ratio is below 0.1. This system has been used for example to spray suspensions [190].

The Axial III torch (Mettech, Vancouver, Canada) gun contains three cathodes and three anodes and is operated by three power supplies. The three plasma jets converge within an interchangeable nozzle, and liquid feedstock is injected axially between the three plasma jets [175, 191]. This configuration minimizes drastically the Knudsen effect problem because longer plasmas are obtained. They comprise the interchangeable water-cooled exit nozzle with a length of a few tens of mm where the gas velocity is not very much reduced, followed by the plasma jet, expanding in the surrounding atmosphere where, as with stick type cathodes gun, the gas velocity decreases rapidly. With this torch, where power levels can reach 150 kW, both the evaporation of the solvent does not reduce too much the gas temperature and the nano-sized particle velocities reach 800 m/s resulting in better flattening on the substrate [191]. Also, particle temperatures at impact are higher (e.g., about 2,200 °C for WC–Co particles, which is not necessarily the optimum for such particles since decarburization occurs!). With this technique, the spray distance is also shorter, due to the low inertia of particles, than when spraying micro-sized particles: about 50–60 mm against 150 mm. Wang et al. [192] have shown that when spraying the YSZ electrolyte of half cells of an SOFC, the coating density increased as plasma torch input power increased, in good correlation with the higher particle velocities and their higher degree of melting.

14.7.3.3 r.f. Torches Used

Torches with power levels between 35 and 50 kW, see Boulos [193] and Chapt. 8, are generally used [186, 187], with or without a supersonic nozzle (diameter = 24.2 mm), in order to increase the plasma velocity.

14.7.3.4 HVOF Torches Used

Torches with axial injection such as DJ2700 (Sulzer Metco, Wohlen, Switzerland) [191, 194] or Top-Gun (GTV, Düsseldorf, Germany) [9, 181, 183, 184] are used in the HVSFS process. When the suspension is made of water, poor coatings are obtained due to insufficient flame enthalpy. Much better results are obtained with ethanol, but even a low percentage of water in ethanol drastically cools the flame. Injecting combustible liquids raises the combustion chamber pressure resulting in instabilities in the acetylene flow (acetylene–oxygen giving the highest combustion temperature). Thus propane and ethane are used [181, 182] to achieve stable flames with the Top-Gun system, while with the DJ2700 one, Oberste-Berghauss et al. have chosen propylene [175]. Spray guns have been modified especially for the injection system and also to obtain optimal combustion with longer combustion chambers. As with plasma torches, spray distances are significantly lower (60–110 mm) than when spraying particles in the tens of micrometers range (150–200 mm). These spray distances, significantly higher than those with conventional plasma torches, are possible; thanks to the much higher gas velocities and lower temperatures decreasing the gas mean free path and thus the Knudsen effect.

14.7.4 Solutions or Suspensions Preparation

Either for solutions or suspensions, the main constituent is the solvent which is either water or an organic liquid, the most frequently used one being ethanol. As it can be expected, fragmentation of the liquid depends mainly upon its surface tension, σ_s, and also, but to a lesser extent, on its viscosity, μ_s, while its vaporization is linked to its thermal properties. Table 14.2 presents some values for five liquids often used as solvents.

Water requires more energy than ethanol but less than pentanol and triethanolamine to get vaporized. The lowest surface tension is that of ethanol. Nevertheless, all, except water, contain carbon, which pollute the coatings. Moreover, for an easier liquid injection, the viscosity of the suspension or the solution must remain as close as possible to that of the solvent. At last it must be pointed out that combustion of ethanol, pentanol, and triethanolamine, reheating the hot gases, can occur only if oxygen is present and gas temperatures are below the combustion temperature. It means that combustion is possible with HVOF, once the liquids are

Table 14.2 Main characteristics of solvents used in suspension or solution spraying

Liquid	Boiling temperature (°C)	Viscosity (mPa. s)	Surface tension (mN/m)	Vaporization energy (kJ/mole)	Energy of combustion (MJ/kg)
Water	99.98	1.74	71.97	40.67	
Ethanol	78	1.0	22.27	38.6	29
Triethanolamine	335	–	45.95	67.7	34.2
Pentanole	137–139	4.0	25	44.6	35
Isopropanol	82.5	2.37	23	44.0	30.5

vaporized, and in the plume of plasma jets run in air but at spray distances higher than those used to spray suspensions or solutions, or when the drops are injected with a gas containing oxygen.

14.7.4.1 Solutions

Compared to other spray techniques, solutions with a mixing at the molecular level of the constituent chemicals allow an excellent chemical homogeneity [195]. Several liquid precursors, such as solution/sol/polymeric complexes, have been evaluated for different oxide systems [196]. The success in forming the phase required for a given system depends on the decomposition characteristics of the different precursors. They include (a) mixture of nitrates in water/ethanol solution, (b) mixtures of nitrates and metal-organics in isopropanol (hybrid sol), (c) mixed citrate/nitrate solution (polymeric complex), and (d) co-precipitation followed by peptization (gel dispersion in water/ethanol). It is important to mention that the molecular level mixing of constituents results in chemical homogeneity. It also allows creating metastable coating phases due to rapid cooling of ultrafine splats during deposition [197]. For example, alumina, YSZ, and zirconia were produced by aluminum isopropoxides, zirconium butoxides, zirconium acetate, and yttrium acetate in isopropanol with n-butanol and distilled water as solvents [198, 199, 201]. Other researchers have used aqueous solutions of zirconium, yttrium, and aluminum salts [199, 200]. Aqueous solutions allow higher precursor concentrations than organic ones that are less expensive to produce and are safer to store and handle. According to work related to spray pyrolysis, volumetric precipitation, when heating droplets within the plasma jet, depends on the solute initial concentration and its value relative to the equilibrium saturation. The equilibrium saturation concentration is determined by concentrating the precursor in an evaporator at room temperature until precipitation occurs [200]. This permits then to prepare several solutions with different concentrations. This results in different viscosities, surface tensions, and specific masses: viscosity increases (by a factor of 5) and surface tension decreases (by a factor of 1.23) when increasing the solution concentration in a ratio of 4. It must be moreover emphasized that the solutions behave as the solvent; i.e., as a Newtonian fluid.

The precursor concentration in solutions can be varied up to the equilibrium saturation [202]. In their study of 7YSZ solutions, Chen et al. [200] have considered two different precursor concentrations: one of high molar concentration (2.4 M) that is 4 times higher than that of the low concentration (0.6 M). When the initial 7YSZ precursor is concentrated four times in water, the solution viscosity increases from 1.4×10^{-3} to 7.0×10^{-3} Pa s, and the surface tension decreases from 4.82×10^{-2} to 4.663×10^{-2} N/m. Both precursors pyrolyze below 450 °C and crystallize at ~500 °C [201]. This indicates that the solution precursor concentration has little effect on the precursor pyrolysis and crystallization temperatures. The concentration of precursors produces almost no variation in the solution specific mass and surface tension, but large variations in the solution viscosity. Chen et al. [203] studied also the influence of the properties of the liquid phase. Of course results are quite similar to those observed with suspensions: droplets with a high surface tension and also high boiling point of the liquid phase experience incomplete liquid phase evaporation in the plasma jet, while droplets created from a low surface tension and low-boiling point liquid phase undergo rapid liquid phase evaporation.

As with suspensions, liquid vaporization and then gaseous phase heating in HVSFS or transformation into plasma in plasma spraying, consumes energy. Thus it cools the flame or plasma jet downstream, where higher energy would be necessary to pyrolyze solutions or melt particles contained in suspension droplets. Moreover, with solutions often precursors undergo significant endothermic processes in the early stages of heating [204]. As pointed out by Muoto et al. [204], this endothermic behavior can be significant in solution precursor plasma spraying (SPPS) because the material is traveling in a plasma jet, the temperature of which is dropping rapidly. Endothermic behavior at low temperatures will delay particle heating and pushing the location where the melting point is reached further downstream. It appears, from the work of Muoto et al. [204], that the two characteristics that distinguish the desirable YSZ precursor from others is the propensity for the YSZ precursor to form dense oxide particles and the absence of endothermic events during pyrolysis. Dense particles are better at making dense coatings because they will impinge on the substrate at near normal incidence (Stokes number effect), and therefore do not introduce porosity associated with the arriving particle. These authors have plasma sprayed binary mixtures of yttrium nitrate or yttrium acetate, combined with magnesium nitrate or magnesium acetate (the 4 combinations being tested), with water as the solvent to produce Y_2O_3–MgO nano-composites. Moreover, they have added ammonium acetate (CH_3COONH_4) to their solution of nitrates to increase the exothermicity of the decomposition process. Acetates can oxidize in the air that is present during spraying, and the nitrate can act as an oxidizer for the acetate in the acetate–nitrate combinations. Coatings obtained with the ammonium acetate were denser than the four other ones. This relatively high density was attributed to a combination of two factors: (1) the exothermic decomposition characteristics of the precursor and (2) the formation of oxide particles which are not too flakey or fluffy to remain entrained in the core of the plasma jet. However, if the processes are too highly exothermic then the oxide particles may

shatter in the plasma, causing them to travel along the colder periphery of the jet; also, the increased heat resulting from excessive exothermic reactions may overheat the substrate [204].

14.7.4.2 Suspensions

The easiest way to produce a suspension is to make a simple slurry with particles and a solvent, particle sizes varying from a few tens of nanometers to micrometers. The most frequently used solvents are alcohols (ethanol or isopropanol) or water or a mixture of both [205, 206]. After stirring, the suspension stability can be tested by sedimentation. Typical values of slurry stability are a few tens of minutes, the stability increasing with the powder load [207]. Slurries with TiO_2 and ZrO_2 have been prepared that way [205–208] as well as with Al_2O_3 and ZrO_2–Al_2O_3 mixtures [209]. For example, with zirconia, a phosphate ester has been used [151] that provides a combination of electrostatic and steric repulsions. The pH adjustment is also an important factor to be taken into consideration. However, nano-sized particles of oxides have the tendency to agglomerate or aggregate, even when stirring the suspension. The stability problem can be overcome by using a suitable dispersant, which adsorbs on the particle surface and allows an effective dispersion of particles by electrostatic, steric, or electro-steric repulsions. The percentage of dispersant must be adjusted in such a way that it displays the minimum viscosity of the suspension with a shear-thinning behavior [151]. This behavior means that when the shear stress imposed by the plasma flow is low, the suspension viscosity is high, and it decreases drastically when the shear stress increases as the drop penetrates more deeply into the plasma flow. For example, with zirconia, a phosphate ester that provides a combination of electrostatic and steric repulsion has been used [152]. With a mixture of WC–Co [191], the problem is more complex due to the different acid/base properties of both components: WC or, more precisely, WO_3 at its surface is a Lewis acid, while CoO is basic. Thus, a complex equilibrium between the dispersing agent and the suspension pH must be found; for example, the latter must be adjusted to less basic conditions, but avoiding the cobalt dissolution. Similar problems have been observed with Ni.

At last, it must be pointed out that when the wt% of powder increases the viscosity of the suspension increases too. Different products can be added to the liquid phase to modify its surface tension and/or its viscosity [210, 211]. It is also possible to modify the suspension by adding viscous ethylene glycol (the boiling point of which is 200 °C) at the expense of an additional thermal load on the plasma [175]. The addition of binders also controls the suspension viscosity almost independently of the dispersion. For internal feeding against the pressure in axial injection, especially in combustion chambers (HVSFS), the choice of appropriate rheological properties may be critical in terms of a constant suspension feeding and transport, because any sedimentation of the solid phase will cause clogging in the feeding line [192]. Arevalo-Quintero et al. [212] have investigated the behavior of YSZ, samaria-doped ceria (SDC), and mixtures of YSZ and SDC powders in aqueous suspensions.

They have determined the optimum dispersant concentrations of three potential dispersant materials (ammonium polyacrylic acid, PAA, polyethyleneimine PEI, and 2-phosphonobutane-1, 2, 4-tricarboxylic acid PBTCA) on the suspension stability.

A key point to achieve good spray conditions is to adapt the size distribution of particles within the suspension to the heat transfer from the hot gases and to limit the width of the particle size distribution [8] (as in conventional spraying). This will allow reducing the trajectory dispersion. At last, powders that have the tendency to agglomerate or aggregate, which is often the case with nano-sized particles, especially oxides, when prepared by chemical routes, must be avoided.

14.7.4.3 Sol Preparation: A New Process Called "PROSOL"

A new process called "PROSOL" [213] has recently been developed by the CEA Le Ripault to avoid the drawbacks of suspensions with solid particles. It consists of injecting a stabilized suspension of nanometer-sized particles (1–100 nm). This kind of sol–gel solution, called colloidal, is prepared by the hydrolysis and condensation of metallic precursors: the inorganic polymerization reaction (nucleation and growth) is controlled by varying the chemical conditions (pH, hydrolysis ratio, etc.) and allows preparing colloidal particles (1–100-nm particles) directly dispersed in the liquid medium [21]. The method of stabilization permits avoiding the use of additives such as dispersant or adding ultrasound during the deposition phase. Consequently, the main advantages are the purity of the deposited material, a very low level of agglomeration and aggregation, well-structured nanometer coatings featuring sizes below 100 nm, simplification of the process, and the capability of reaching sub-micrometric thickness with high deposition efficiency.

14.7.4.4 Suspensions of Amorphous Powders

Amorphous powders can be used in suspensions [19]. Chen et al. [19] have prepared Al_2O_3–ZrO_2 amorphous powders by a chemical solution process. Aluminum nitrate $(Al(NO_3)\cdot 9H_2O)_3$, and zirconium acetate $(ZrO(OOCCH_3)_3$, were dissolved in deionized water based on molar volumes to produce a ceramic composition of Al_2O_3–40 wt% ZrO_2. The obtained solution was heated at 80 °C and stirred continually to get the sol transformed into a dried gel. The dried gel powders were heated to 750 °C at a heating rate of 10 °C/min and then held for 2 h. The phase composition and microstructure of the as-prepared Al2O3–ZrO_2 powders heat treated at 750 °C for 2 h was investigated. In the XRD patterns no crystalline peaks appeared (amorphous powders). To prepare the suspension, the powder, with an average particle size of ~5 μm, was mixed and ball-milled in ethanol using ZrO_2 balls with a loading rate of 50 wt% for 24 h [19].

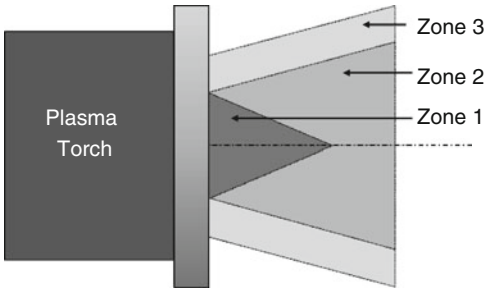


Fig. 14.35 Schematic of the three major zones of a stationary d.c. plasma flow. Reprinted with kind permission from Springer Science Business Media, copyright © ASM International [196]

14.7.5 Liquid Stream: Hot Flow Interactions

14.7.5.1 General Remarks

Liquid stream or drop fragmentation depends strongly upon the dimensionless Weber number, We, and Ohnesorge number, Oh, (see Sects. 4.5.3 and 14.7.2). When considering a plasma jet, three major zones can be identified [189, 192] (Fig. 14.35):

- The plasma jet core (zone 1 in Fig. 14.35)
- The plasma plume (zone 2 in Fig. 14.35) where the heat and momentum capabilities from the plasma are drastically reduced compared to those in zone 1
- The plasma fringes (zone 3 in Fig. 14.35) where fragmentation can occur but where the droplet heat treatment will be insufficient

It will be thus of prime importance to inject the liquid as close as possible to the torch nozzle exit and have it penetrating into zone 1 without being fragmented in zone 3. For HVSFS where injection is mainly axial, it is necessary to treat completely the suspension solvent in the combustion chamber (vaporization followed for combustible solvent by full combustion). It explains the use of combustion chambers longer than those used for conventional HVOF [181–183].

Once the drops or the stream are/is fragmented into droplets of a few micrometers, the vaporization becomes very fast. Indeed the fragmentation time is about two to three orders of magnitude shorter than the vaporization time [151, 152]. The fragmentation depends strongly upon the Weber number (see (2) in Sect. 14.7.2.1) and, for example, if $We > 350$ (catastrophic breakup) in less than 10 mm trajectory in the plasma jet the liquid is fragmented in droplets smaller than a few μm, droplet sizes that are poorly accelerated due to Knudsen effect (see Sect. 14.7.1.1). In most cases of solution or suspension plasma spraying, the whole mechanisms (fragmentation + vaporization) is achieved about 20–40 mm downstream of the injection location [152], depending on the solvent used, plasma torch power level, and plasma flow velocity. Once fragmentation in droplets below a few μm is achieved, the fast vaporization of liquid and the heating of the resulting gases cool down drastically the hot gas flow (20–30 % of the energy available) [152]. That means that because of this hot gas cooling, the low inertia of the sub-micro- or nano-sized

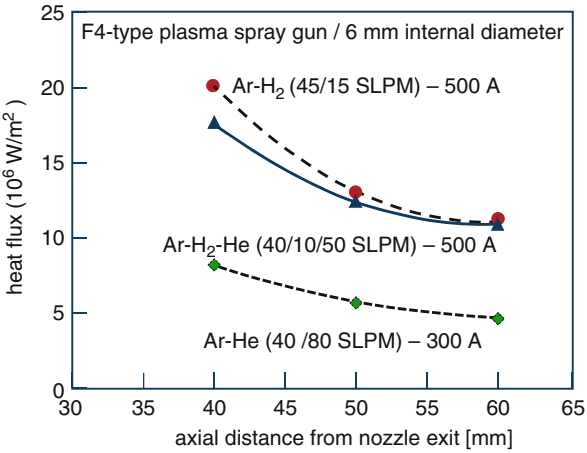


Fig. 14.36 Dependence on the spray distance of the heat flux imparted by a stick-type cathode torch (6 mm i.d. anode nozzle) working with Ar–H_2, Ar–He, and Ar–He–H_2 plasma-forming gas mixtures. Reprinted with kind permission from Dr. E. Brousse [171]

particles [5] the Knudsen effect, not very important in HVSFS, and the Stokes effect [see Eq. (14.1)], the spray distance has to be shorter than that in conventional spraying: 30–50 mm against 100–120 mm for conventional plasma spraying [189] and 60–90 mm with axial injection HVOF against 150–300 mm for conventional HVOF spraying [180]. Correspondingly, the heat flux imposed by the plasma to the coating and the substrate can be up to 40 MW m^{-2}, as illustrated in Fig. 14.36, while in conventional spraying typical heat fluxes are about 2 MW m^{-2} [189].

At last, according to the drastic importance of the liquid momentum density [see Eq. (14.3)] for radial injection, the atomization process when resulting in drops of different sizes and velocities does not appear to be necessarily well adapted to achieve the optimum penetration of the liquid, even with improved atomizers [160, 214] (see also Sect. 4.5.1.1). However it must be pointed out that, if originally only laboratories have designed the liquid injectors, in 2011 an industrial injector, based on atomization studies, has been offered by Sulzer Metco [215].

Undoubtedly, besides the solvent, the precursors in solutions and the particles and their dispersant in suspensions, the liquid injection, penetration, dispersion, and fragmentation in droplets below 10 μm within the hot gases is one of the key issues for nanostructured coatings [158, 159]. To understand better the phenomena involved, models of the liquid–plasma interactions have been developed (see "(b) Models" in Sect. 14.7.a). These models rely on the We and Oh numbers as well as the constants and parameters of previous models that have been established for conditions rather different from those prevailing in liquid plasma spraying, and their extension to these conditions should be validated. The model validation through experiments is also difficult (see Sect. 14.7.a). To illustrate the droplet formation, examples of images obtained by shadowgraphy are presented in Fig. 14.37. Figure 14.37a presents one image taken with laser illumination and pulse duration of 8 ns, while Fig. 14.37b presents 50 images recorded by the shadowgraphy system and averaged. The image acquisition at a frequency of 6 Hz allowed taking into account the plasma jet instabilities. And the superposition

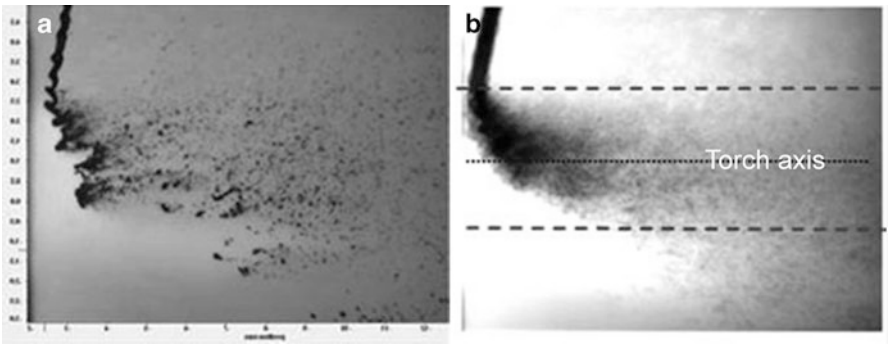


Fig. 14.37 Liquid feedstock interaction with the plasma flow and average trajectories of the drops downstream of the torch outlet (Ar–H_2: 33–10 slm). Reprinted with kind permission from Springer Science Business Media [159], copyright © ASM International

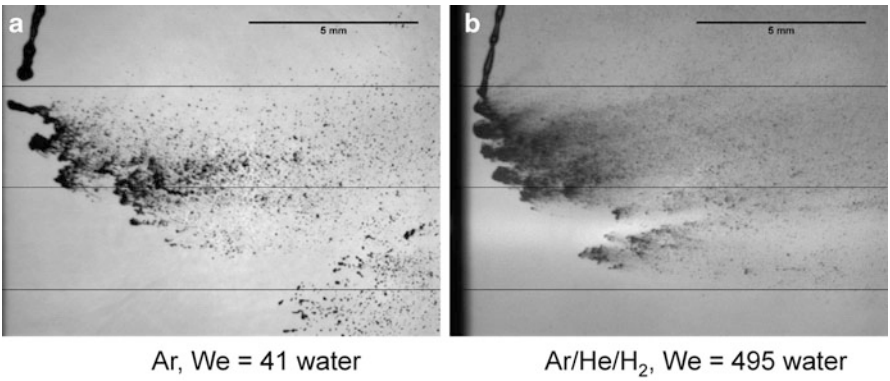


Fig. 14.38 Visualization of a water jet injection within two plasma jets with different Weber numbers: (**a**) Ar We = 41, (**b**) Ar–He–H_2 We = 495. *Horizontal lines* correspond to the nozzle axis and limits (torch i.d. 6 mm). Reprinted with kind permission from Dr. D. Damiani [216]

of images, triggered at the same voltage level, allowed visualizing the average trajectories of the drops.

Of course the primary fragmentation depends strongly on the Weber number resulting from the plasma jet, the velocity and specific mass of which depend on the drop or jet trajectory through the radial and axial positions where these numbers are calculated. However it is possible to calculate rapidly the main value of the Weber number of the plasma jet, assuming that all the energy supplied is distributed uniformly in the plasma jet section at the nozzle exit. Such calculations have been performed by D. Damiani [216] and Meillot et al. [217] and results are shown in Fig. 14.38 for a water jet injected within two different plasmas: Ar We = 41 and Ar–He–H_2 We = 495. It can be readily seen that the primary fragmentation is by far more important with the mixture than with pure Ar.

The drops formed are then fragmented farther downstream, more tiny droplets being formed 15 mm downstream with the mixture compared to the Ar plasma. It can be seen in Fig. 14.38b that fragmentation increases from the jet fringes to the jet axis and farther.

For example, Fig. 16.57 from Bertolissi et al. [159] show the detected number of droplets of a solution in ethanol 15 mm downstream of their injection location (the liquid jet of mechanical injection being focused to the axis of the anode nozzle exit) for 3 spray conditions (Ar, Ar–H_2, Ar–He–H_2). The liquid injector nozzle was 200 μm in i.d. corresponding about to about injected liquid jet diameter of 400 μm. This figure shows clearly that fragmentation increases with plasma jet velocity and power dissipated in the torch, the highest values being obtained with the Ar–H_2–He mixture. When injecting water or ethanol, Fig. 16.58 [158] shows that at 15 mm most of the ethanol droplets are fragmented below 5 μm, while this is far from being the case for water droplets. At 40 mm, ethanol droplets are necessarily below 5 μm because none is seen, which is not the case with water (see Fig. 16.58) and with these spray conditions 20 mm downstream of the nozzle exit no ethanol droplet can be observed. Once droplets cannot be measured with this device, pictures such as that presented in Fig. 16.55b show a "mist" of particles. According to calculations such as those presented in Fig. 4.75, it can be inferred that once droplets have reached a size below a few μm they vaporize and free the solid particles contained for suspensions and pyrolyze, then sinter, and at last melt for solutions. However, according to the drastic Knudsen effect for particles around or below 1 μm, the velocity of the resulting melted or partially melted particles will be mainly that imparted to their mother droplet.

14.7.5.2 Solutions

As described by the model of Ozturk and Cetegen [218] and Basu et al. [174], besides the momentum and heat transfer equations for the interactions between drops or droplets and plasma, the conservation of solute mass and energy equation have to be considered. As for the suspension drops, solution drops are first fragmented, the heating of the droplets precipitating the solute as a shell. Then, compared to the suspension droplets, where the diameter is controlled by the solvent evaporation, the solution droplet size is now fixed by the outer diameter of the precipitate shell formed through the droplet heating. The interior of the droplet is divided into three zones: solid shell, liquid core, and a vapor annulus between them. Depending on the solute and solvent characteristics and thermophysical conditions controlling the precipitation, the shell will be more or less porous. The pressure of the vapor inside it, depending on the rate of vapor leaving it, that is, the shell porosity, can be calculated as well as the critical pressure over which the shell will fracture (if its failure stress is known). The precipitate formation depends on droplet sizes and solute initial mass fraction. In small droplets (5 μm in diameter), precipitation, whatever may be the initial solute level, encompass the whole droplet, thus creating solid particles [174]. For larger

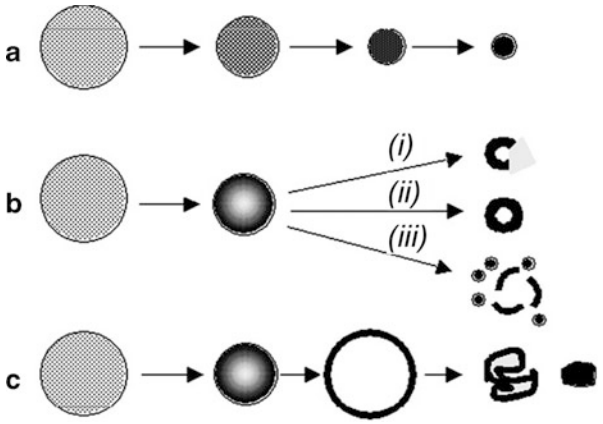


Fig. 14.39 Different routes for droplet vaporization and solid precipitations: (**a**) Uniform concentration leading to solid particles by volume precipitation. (**b**) Super-saturation near the surface: (**i**) low permeable shell leading to fragmented shell formation, (**ii**) high permeable shell leading to unfragmented shell formation, (**iii**) impermeable shell leading to droplet internal heating, pressurization and droplet breakup, secondary atomization. (**c**) Elastic shell formation causing inflation and deflation by solid consolidation. Reprinted with kind permission from Elsevier [219]

particles (only particles up to 40 μm were modeled) a shell precipitate is formed and subsequently fragments, depending on the vapor pressure within particle. To summarize, Saha et al. [219] show that different particle morphologies result from the different processes undergone by drops or droplets, processes linked to their trajectories in hot gases. Finally these morphologies include solid particles, hollow shells, and fragmented shells as shown in Fig. 14.39a–c. Small droplets with high solute diffusivity exhibit a propensity to precipitate volumetrically to form solid particles as shown in Fig. 14.39a. Rapid vaporization combined with low solute diffusivity and large droplet sizes can lead to significant increase in solute concentration near the droplet surface resulting in surface precipitation to form a crust around the liquid core of the droplet. The crust/shell may have varied levels of porosity. Shells having low porosity usually rupture due to internal pressurization to form shell fragments (path I in Fig. 14.39b). Shells that are completely impervious rupture and secondary atomization having a trapped liquid core may be observed (path III in Fig. 14.39b). For shells with a high level of porosity, the internal pressure rise is counterbalanced by the vapor venting through the pores resulting in hollow shells (path II in Fig. 14.39b). For particular precursors, elastic inflation and subsequent collapse and rupture of the shell can also be observed (Fig. 14.39c). The particle morphology resulting from droplet processing is hence sensitive to the solute chemistry, mass diffusivity, solute solubility, droplet size, thermal history, injection type, and velocity [219]. In summary, according to the calculations of Saha et al. [219], the final coating microstructure depends upon the size of the droplet, not on directly whether they follow a trajectory on the torch axis or a deviated path after primary precipitation. Globally, droplets in the size range 5 or

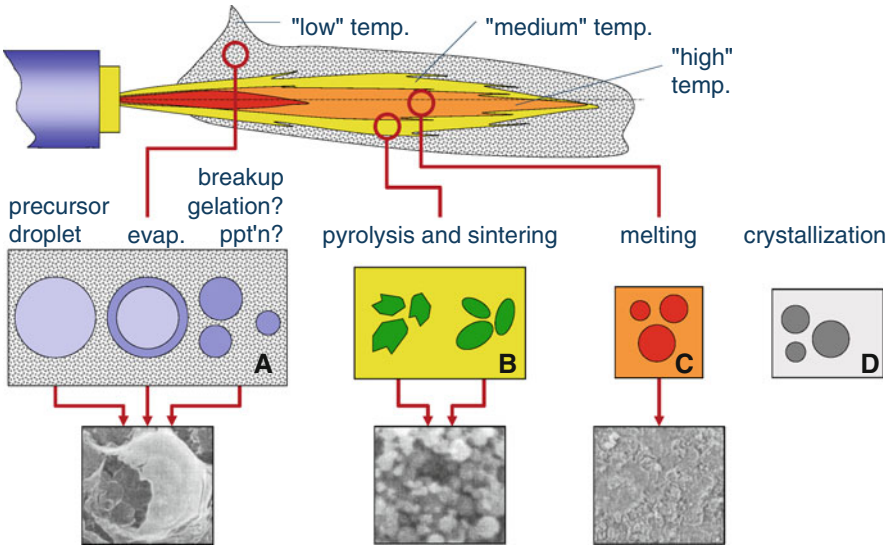


Fig. 14.40 Schematic illustration of the different treatments of solution droplets within a d.c. plasma jet. Reprinted with kind permission from Springer Science Business Media [155], copyright © ASM International

10 μm get pyrolyzed completely before reaching the substrate, while the 20 μm and larger droplets remain partially pyrolyzed. Ozturk and Cetegen [218] presented similar results.

Thus, the drop fragmentation and the resulting droplet penetration into the plasma jet core or its fringes again play a key role as pointed out by Jordan et al. [155] and Gell et al. [196]. Figure 14.40 from [155] illustrates the different mechanisms including precursor solute precipitation, pyrolysis, sintering, melting, and crystallization. According to Gell et al. [167] and Jordan et al. [155], particles traveling in the hot core of the plasma jet exhibit mechanisms A, B, and C of Fig. 14.40. If the standoff distance increases molten particles may resolidify and crystallize before impact (D mechanism). When droplets travel in the jet fringes but still in the hot area ($T < 4{,}000$–$5{,}000$ K), A and B (Fig. 14.40) mechanisms are the most probable. At last, for droplets traveling in the low temperature regions of the jet, some precursor solution can reach the substrate in liquid form.

Works have been devoted to the different parameters controlling the solution spraying [155, 200, 219–221]. To elucidate the difference in deposition mechanisms of precursor droplets, two different substrate arrangements were employed with a stationary plasma torch [155]. In order to investigate the spray patterns produced under various processing conditions, Xie et al. [220], used the spray experiment shown schematically in Fig. 14.41. In this experiment, the plasma torch moves only in one direction and the substrate is held stationary to obtain a bead, which thickness can be amplified by multiple passes. Due to the vast differences in the temperature histories experienced by the precursor droplets

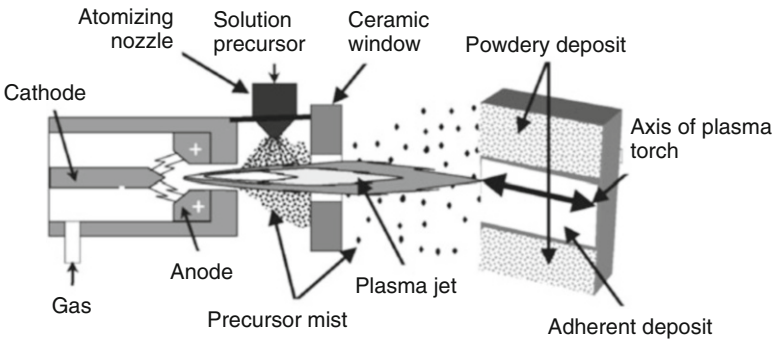


Fig. 14.41 Schematic of the window-shield fixed scan spray set-up. Reprinted with kind permission from Elsevier [220]

traveling in the core of the plasma jet on the one hand and in its fringes on the other, the central part of the bead and its fringes are rather different. To study only the central part of the bead, they placed a ceramic plate with a 20-mm diameter hole in its center, in the front of the plasma torch, and aligned with its centerline. Thus the coating material traveling in the outer region of the plasma jet was shielded from the substrate. Xie et al. [221] sprayed an aqueous chemical precursor feedstock, resulting in a ZrO_2–7 wt% Y_2O_3 ceramic solid solution, with a Metco 9MB plasma torch (35–45 kW) working with a mixture of Ar and H_2. Coatings were collected on the substrate preheated to 500 °C. It was found that the deposits from the precursor injected into the hot region of the plasma jet are crystalline 7-YSZ, while those from the precursor droplets riding along the cold region of the plasma jet are amorphous and contain significant amount of water. The morphology of the deposits that contain significant amount of water is illustrated in Fig. 14.42a. They were collected on the substrate preheated to 500 °C. Figure 14.42b–d, at higher magnification, shows the individual features of the deposit. Figure 14.42b shows a hollow shell, while Fig. 14.41c shows a partially broken shell. Figure 14.42d shows a completely broken shell. During evaporation of the remaining solvent, the deposits appear to inflate (Fig. 14.42b), fracture (Fig. 14.41c), and rupture (Fig. 14.42d). These types of deposits were rarely observed on substrate with no-preheat, reinforcing the notion that evaporation of the wet-precursor occurs after the precursor has landed on the hot substrate.

Coatings (made with the ceramic shield of Fig. 14.41) from the jet hot region are different [221]. The first morphology comprises splat-like features, as shown in Fig. 14.43a. The diameters of the "splats" in the SPPS coating (Fig. 14.43a) range from 0.5 to 5 μm. The second morphology is the fine spherical particles, as indicated in Fig. 14.43a. The third morphology is shown in Fig. 14.43b, which also appears to be "splat" like. A higher magnification image (Fig. 14.43c) shows that this deposit is rough and consists of angular grains of sizes ranging from tens to hundreds of nanometers.

The initial solution concentration also plays a key role in the droplet pyrolysis. Once the solvent is selected (water, ethanol, isopropanol, etc.), the solution

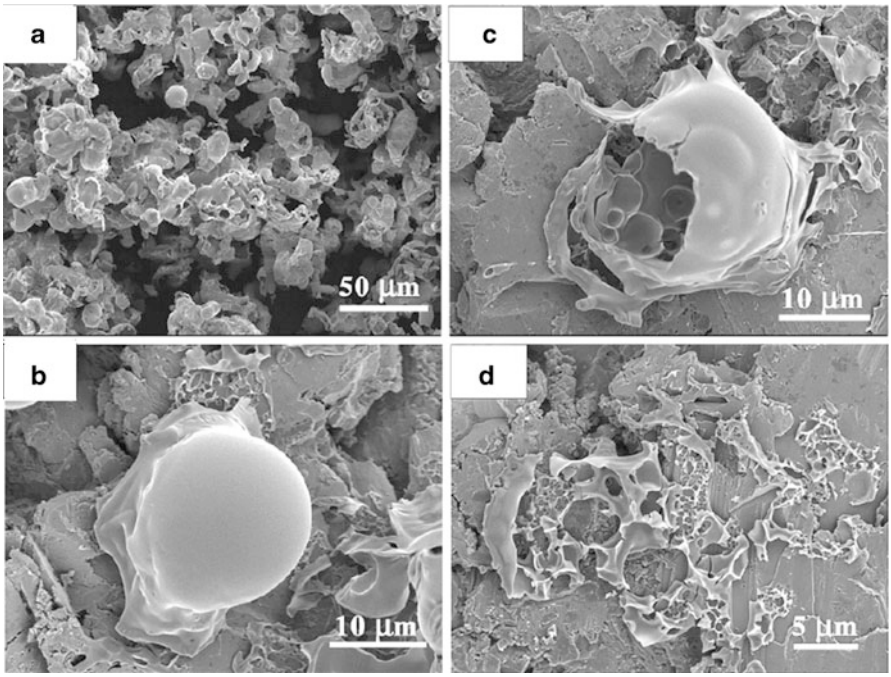


Fig. 14.42 SEM micrographs of deposit from wet-precursor (30 mm offset and 500 °C substrate): (**a**) overview; (**b–d**) detailed views of the individual deposit. Reprinted with kind permission from Elsevier [221]

concentration can be varied up to the equilibrium saturation concentration. A high concentration close to the equilibrium saturation concentration tends to produce volume precipitation [155, 200, 219–221]. Collecting beads, or more precisely overlapped beads obtained by passing the torch a given number of times at the same position, gives relevant information on the heat treatment of the particles [206] by considering the central part and edges of the beads. Figure 14.44 from Chen et al. [211] shows typical SEM microstructures of the collected solution coatings of Y-PSZ on substrates at room temperature from low (A) and high concentration (B) solutions, respectively. No splats are observed in the central zone of the deposited bead with the low concentration solution precursor, mainly composed of ruptured bubbles and a small volume fraction of solid spheres (<0.5 µm) (Fig. 14.44a). The deposited bead central zone made from the high concentration solution is mainly composed of overlapping splats, with an average diameter ranging from 0.5 to 2 µm, and a small amount of unmelted solid spheres (< 0.5 µm) (Fig. 14.43c). The deposited bead edges from both dilute and concentrated solutions (Fig. 14.43b, d) are made of un-pyrolyzed precursor containing significant amounts of water. The mud-like cracks presented at the edges are the result of shrinkage due to liquid phase evaporation.

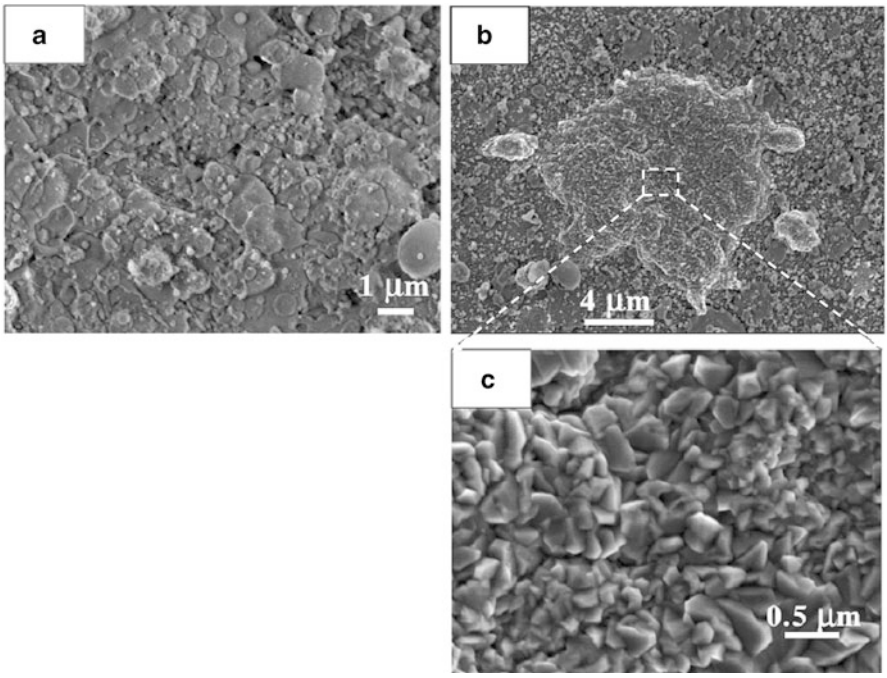


Fig. 14.43 SEM micrograph of the top view of the deposit collected on window-shielded substrate: (**a**) showing "splats," (**b**) showing a "splat"-like large deposit, and (**c**) a higher magnification SEM image showing fine, equiaxed grain structure. Reprinted with kind permission from Elsevier [221]

At last it must be recalled that by adding to the solution a component to increase the exothermal potential of the decomposition process helps to achieve denser coatings (see Sect. 14.7.2.1).

14.7.5.3 Suspensions

The selection of the particles (morphology and size distributions) and their mass load in the suspension are key parameters. Typical mass loads vary between 5 and 20 wt%. However, with a plasma spray torch with a rod-type cathode, coatings manufactured with a suspension containing particle mass load over 10 % are less cohesive [13] (due very likely to the loading effect on the plasma flow), unless the hot gas enthalpy is increased. The size distribution and particle morphologies are also important parameters to consider. Results will be drastically different depending on the ability of solid particles contained in the liquid to agglomerate, or worse, to aggregate. For example, particles (yttria partially stabilized zirconia: YPSZ) made by attrition milling, after the solvent evaporation, are accelerated (their initial velocities being those gained by droplets before their complete vaporization), heated, and melted by the plasma as shown schematically in Fig. 14.45.

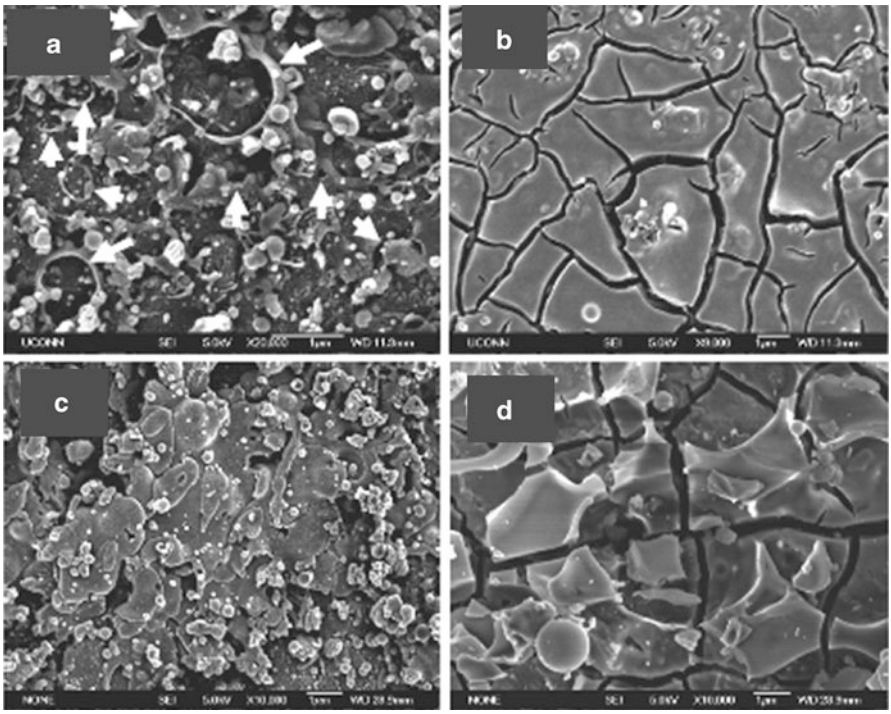


Fig. 14.44 Deposited beads collected on room temperature substrate by single scan experiment. (**A**) From diluted precursor (**a**) deposited bead central zone, (**b**) deposited bead edge. (**B**) From high concentration precursor: (**c**) deposited bead central zone, (**d**) deposited bead edge. Reprinted with kind permission from Elsevier [200]

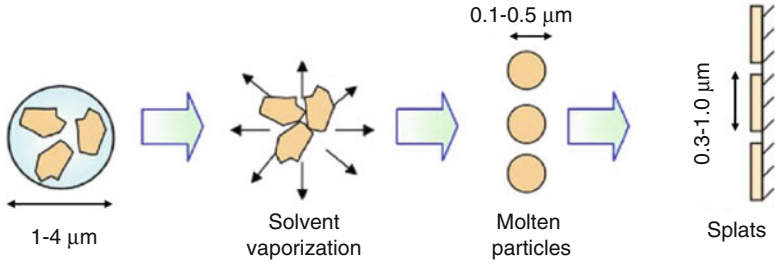


Fig. 14.45 Schematic of suspension droplet treatment when containing attrition-milled particles. Reprinted with kind permission from Springer Science Business Media [169]

When using nano-sized particles obtained by a chemical process (commercial YPSZ Tosoh powder), where the size distribution is between 0.1 and 3 µm, due to the agglomeration and aggregation of the initial grains (mean size of 25 nm), the behavior upon solvent vaporization is different. It seems that the bigger

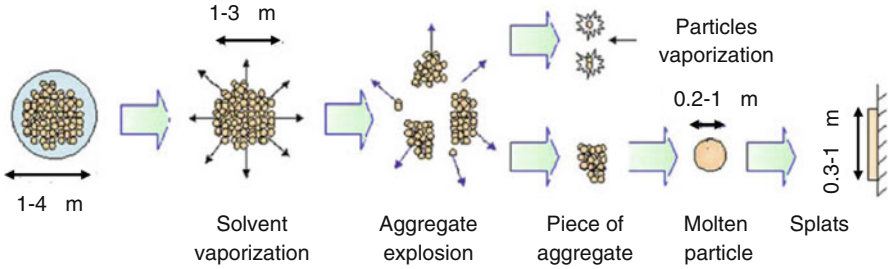


Fig. 14.46 Scheme of the suspension droplet treatment in the plasma jet for the Tosoh nanometric powder containing aggregates and agglomerates resulting in a size distribution between 0.1 and 3 μm. Reprinted with kind permission from Springer Science Business Media [169]

agglomerates or aggregates explode upon solvent evaporation resulting in molten particles and smaller particle evaporation as illustrated in Fig. 14.46.

14.7.5.4 Conclusions

Small particles contained in suspensions or formed in solutions are poorly accelerated by the plasma flow. That is why finally the solid particle velocity contained in suspensions is that achieved by its carrier droplet just prior its vaporization. For solutions, droplets vaporization is stopped by pyrolization followed by sintering and thus the final size of particles formed is bigger than those contained in suspensions (typically a few μm).

When the liquid jet or drops penetrate radially the plasma jet, they are either progressively fragmented in droplets if the Weber number is below 200–300 or very rapidly if $We > 350$. Thus their volumes and apparent surfaces become smaller. The later will be the fragmentation, the higher will be the solid particle velocities. The different values of the Weber numbers along drop and droplet trajectories will condition their fragmentation. To delay fragmentation without modifying the spray and injection conditions, the Weber number can be reduced when shifting from ethanol to water or when reducing the size of initial drops.

With axial injection in HVOF guns, the solvent is mainly evaporated in the combustion chamber, if it is long enough, the solid particles contained in suspensions, being accelerated by the flow downstream of the nozzle throat. Compared to plasma jets, their acceleration is much better than in conventional plasma jets because, trajectories in hot gases are longer, the Knudsen effect is much lower and the gas mass density higher. To our best knowledge no solutions have been sprayed that way. For axial injection with the Mettech Axial torch no clear explanation of the phenomena can be given because no measurements can be performed where drops are injected. However drops are probably fragmented when entrained in the convergin three plasma jets and it can be supposed that drops vaporization plays a key role. As the high temperature plasma core is much longer than with conventional plasma jets, particles reach higher velocities.

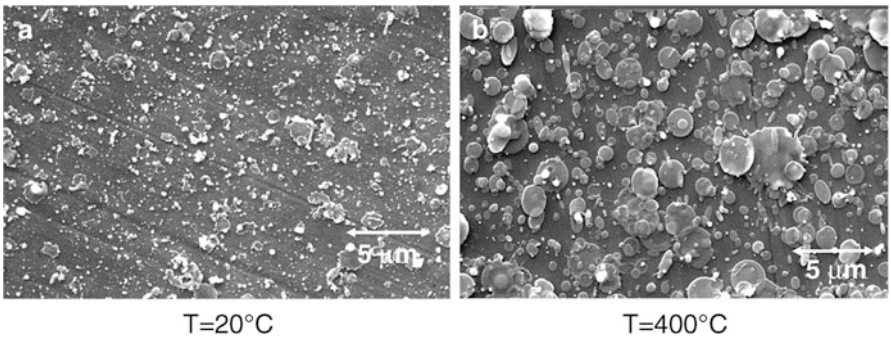


Fig. 14.47 YSZ splats collected on mirror-polished stainless steel substrates (**a**) cold and (**b**) preheated. Spray conditions identical to those of Fig. 13.15 ethanol suspension with 10 wt% Tososh powder. Reprinted with kind permission from Springer Science Business Media [13], copyright © ASM International

14.7.6 Coating Manufacturing Mechanisms

14.7.6.1 Splats

To collect solid sub-micrometric particles, after their plasma treatment, one way is to intercept the particles on a polished stainless steel or glass substrate positioned at the extremity of a pendulum and traversing the jet at about 1 m/s at different distances from the nozzle exit [151, 169, 222, 223]. Of course, the melted particles flatten and form splats, while those completely resolidified or not melted rebound or form some sort of gel phase for poorly treated droplets. Similar results are be obtained by moving rapidly (1 m/s) the torch relatively to the substrate positioned at different distances. Of course, to collect such tiny splats the substrate surface has to be polished. Besides, as in conventional plasma spraying [224], preheating the substrate over the transition temperature (see Sect. 13.4) allows obtaining close to disk-shaped splats while on cold substrates splats with irregular shape are collected, as shown in Fig. 14.47.

(a) Solutions

The surface of spray beads can be divided into adherent deposits (bead central part) and powdery deposits (bead edges) that correspond to the hot and cold regions of the plasma jet, respectively. Four deposition mechanisms, corresponding to splat formation or particle deposition have been identified [196, 221]:

1. Smaller droplets that undergo further heating to a fully molten state and crystallize upon impact to form ultrafine (0.5–2 µm average diameter) splats, as illustrated in Fig. 14.48a.
2. At certain spray distances, droplets undergo resolidification and crystallization before impact upon the substrate to form fine crystallized spheres, as illustrated in Fig. 14.48b.

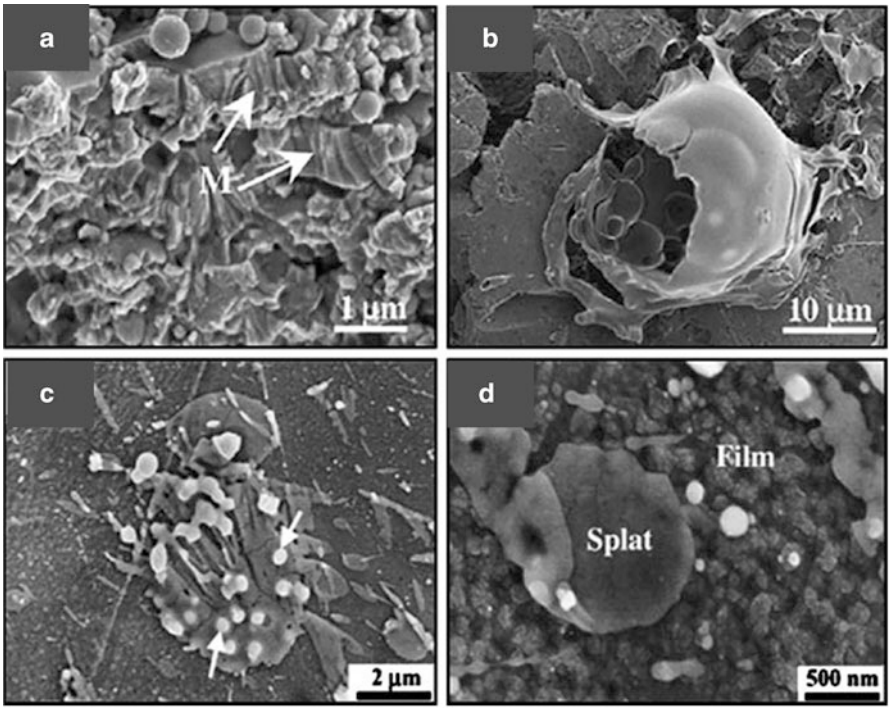


Fig. 14.48 Several deposition modes of SPPS. (**a**) Fine splats, (**b**) crystallized spheres, (**c**) ruptured shell, and (**d**) vapor deposited film. Reprinted with kind permission from Springer Science Business Media [196], copyright © ASM International

3. Droplets entrained in the cold regions of the thermal jet where they experience sufficient heating to cause solute evaporation leading to the formation of a gel phase, deposited on the substrate. Some droplets also form a pyrolyzed shell containing un-pyrolyzed solution that fracture during deposition, as illustrated in Fig. 14.48c.
4. Some precursor solution droplets can reach the substrate in liquid form, having undergone none of the aforementioned processes, as illustrated in Fig. 14.48d.

(b) Suspensions

Splats, obtained when spraying a suspension containing attrition-milled particles, are presented in Fig. 14.49 from Delbos et al. [169]. On the whole the flattening degree is below 2 and the splat distribution follows rather well the particle size distribution. However some splats are bigger than those that should be observed with such flattening degree. They probably correspond to droplets that have contained a few particles that have melted together. This is confirmed when spraying suspensions of two different powders [178]. However when spraying a solution of alumina and YPSZ particles, splats of alumina and YSZ

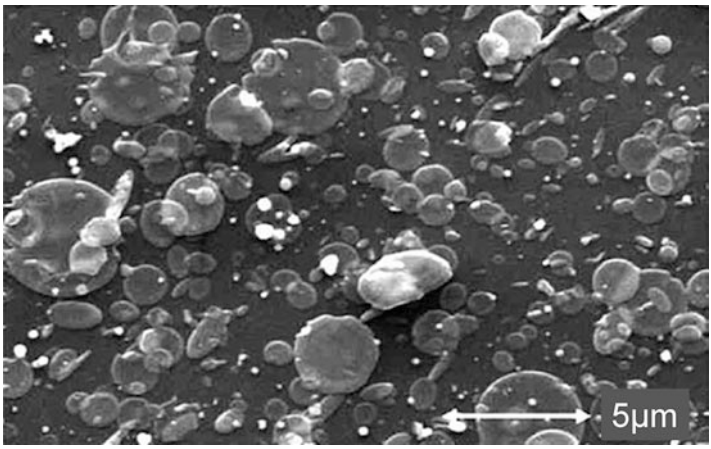


Fig. 14.49 Splats collected on a glass beam when spraying an ethanol suspension of attrition-milled YSZ particles with a distribution of 0.2–3 µm and sprayed with an Ar–H_2 plasma (45–15 slm, $h = 17.9$ MJ/kg). Reprinted with kind permission from Springer Science Business Media [169]

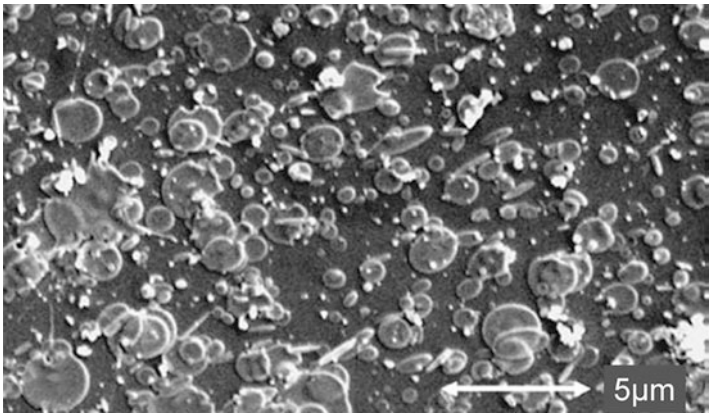


Fig. 14.50 Splats collected on a glass beam when spraying an ethanol suspension of attrition-milled YSZ particles with a distribution of 0.2–3 µm and sprayed with an Ar–H_2–He plasma (40–10–30 slm, $h = 22.3$ MJ/kg). Reprinted with kind permission from Springer Science Business Media [169]

were obtained and the resulting coating was made of layered alumina and YPSZ splats [222]. However, due to the good heat transfer of hydrogen (see spray conditions in Fig. 14.49 caption), particles below 0.4 µm are either vaporized and afterwards recondensed or, for those only melted in-flight, resolidified at the spray distance.

For YPSZ powder made of nanometer-sized particles, which agglomerate easily, even with a dispersant, splats collected have a rather wide distribution, as shown in Fig. 14.50. Most splats collected are below 1µm, but few of them are collected with diameters up to 2 µm.

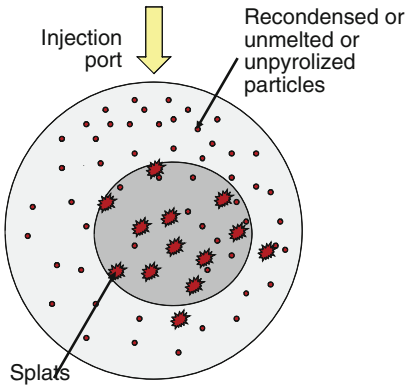


Fig. 14.51 Schematic distribution of splats and particles collected on a disk-shaped substrate: PT-F4 torch nozzle 6 mm i.d., Ar–H_2 (45–15 slm), I = 500 A, zirconia suspension 7 wt%, particle size (0.1–3 μm). Reprinted with kind permission from Dr. Etchart-Salas [189]

Thus, agglomerations of such particles must be avoided or at least limited [151], which can be achieved, for example, by attrition or ball milling the suspension after its preparation.

It is also possible to collect splats and particles on a substrate protected by a water-cooled shield, positioned at the end of an actuator and intercepting particles and plasma fluxes. The substrate is exposed to the particle flux only during a few tenths of seconds. To enlarge the collecting zone of splats and particles in one direction, the line-scan test, as developed by Bianchi et al. [225] for conventional spraying, can also be used. Siegert et al. [226] have also used a similar device. Such systems allow collecting splats and almost spherical particles distributed as shown schematically in Fig. 14.51. Particles that have traveled in the hot zones of the jet (zone 1 of Fig. 14.35) are well melted and form splats, while those that have traveled in the jet fringes (Zone 2 and 3 in Fig. 14.35) form tiny spheres sticking all around the central zone (see Fig. 14.51).

This figure illustrates well that the particles treated in zone 1 of Fig. 14.35 form splats, the layering of which will result in dense coatings, while those traveling in zones 2 and 3 of Fig.14.35 will result in the powdery part of coatings. With solutions similar results are obtained with a mud-like cracked film in the periphery (see Fig. 14.42). Under the repeated scan of the high temperature plasma jet, the mud-like film in situ evaporates, pyrolyzes, and crystallizes on the substrate and results in a porous coating.

14.7.6.2 Spray Beads

The degree of melting of particles can be evaluated with a line-scan-spray experiment considering either a simple bead in one passage or overlapped beads with successive passes [218, 221]. The bead thickness depends upon the relative torch/substrate velocity, the number of passes, the suspension or solution flow rates and the injection parameters, the mass load of powder particles in suspension or the

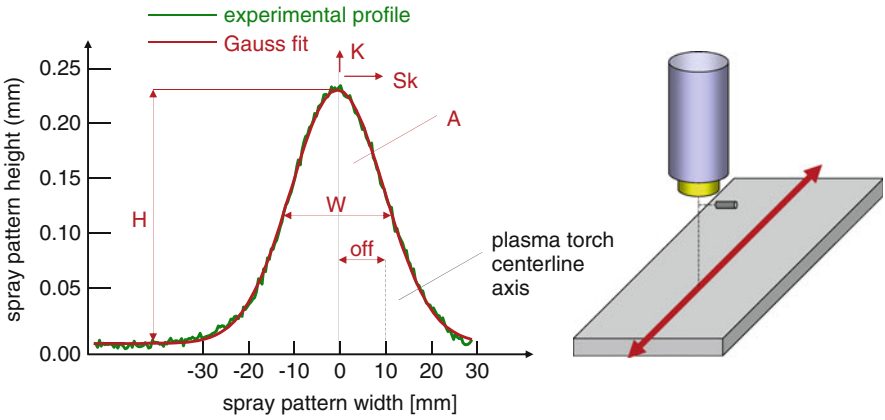


Fig. 14.52 Typical spray bead manufactured by suspension plasma spraying with the schematic of the corresponding torch movement

solution concentration and, of course, the torch-operating conditions. A typical bead, manufactured by suspension plasma spraying, is presented in Fig. 14.52 together with the schematic of the torch movement. It can be seen that the bead can be fit rather well with a Gaussian profile. Xie et al. [220] have obtained similar beads with solutions.

(a) Solutions

Xie et al. [220, 221] and Chen et al. [200] have studied beads obtained with YSZ solutions and a conventional plasma spray torch under various operating conditions. The beads can be divided into adherent deposit and powdery deposit corresponding respectively to particles traveling in warm or cold regions of the plasma jet. Adherent deposits seem to result from precursors traveling in both the warm and cold regions, the poorly treated precursor issued from cold regions being incorporated into the adherent deposit. Powdery deposits in the edges of the spray bead correspond to precursors traveling in the low temperature regions (fringes). Figure 14.53a is a representative macro-photo of samples produced in the fixed scan spray experiments, and Fig. 14.53b–d is the top view of the illustrated regions of the sample. As shown in Fig. 14.53b and d, the powdery deposits consist of loosely connected powders, while the structure of the adherent deposits is dense as shown in Fig. 14.53c.

Chen et al. [203] have studied the influence of the precursor concentrations. The central part of the spray bead deposited on a cold substrate consists of semi-pyrolyzed material that will form soft and porous coatings. Upon impacting the substrate at room temperature, the shells on the droplet surfaces fracture and form bubbles. However, bubbles evolve to spongy deposits when the substrate temperature is raised to 450 °C. In contrast, the high concentration precursor experiences volume precipitation leading to a fully melted lamella

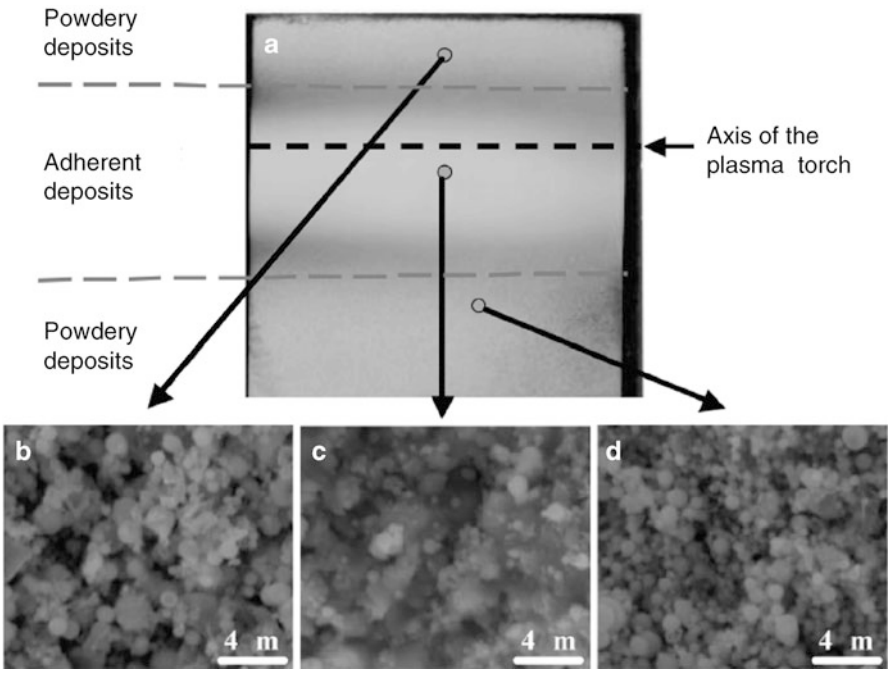


Fig. 14.53 Top view of the samples deposited using SPPS. (**a**) Macrophoto, (**b** and **d**) micrograph of the powdery deposits, and (**c**) micrograph of the adherent deposits. Reprinted with kind permission from Elsevier [220]

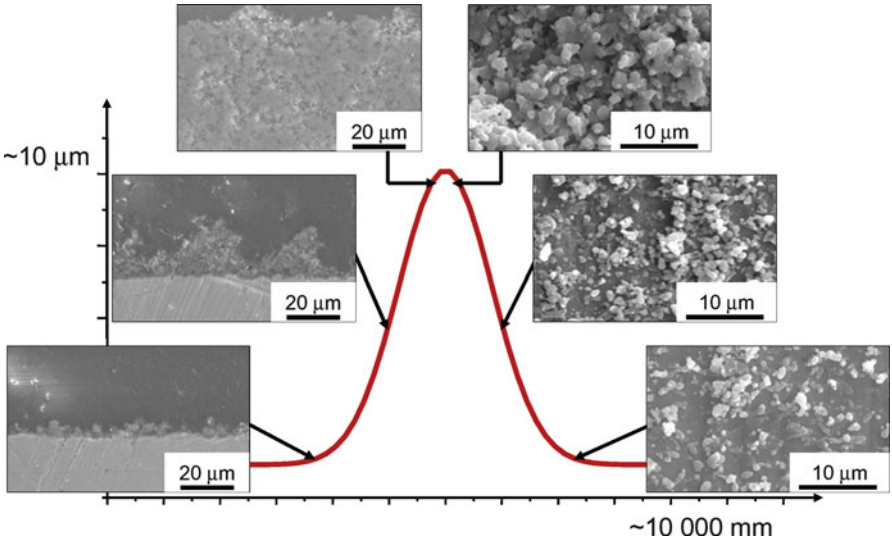


Fig. 14.54 Structure of an alumina suspension sprayed bead (particles size 0.02–1.0 µm, spray conditions see Fig. 14.26 caption). Reprinted with kind permission from Elsevier [228]

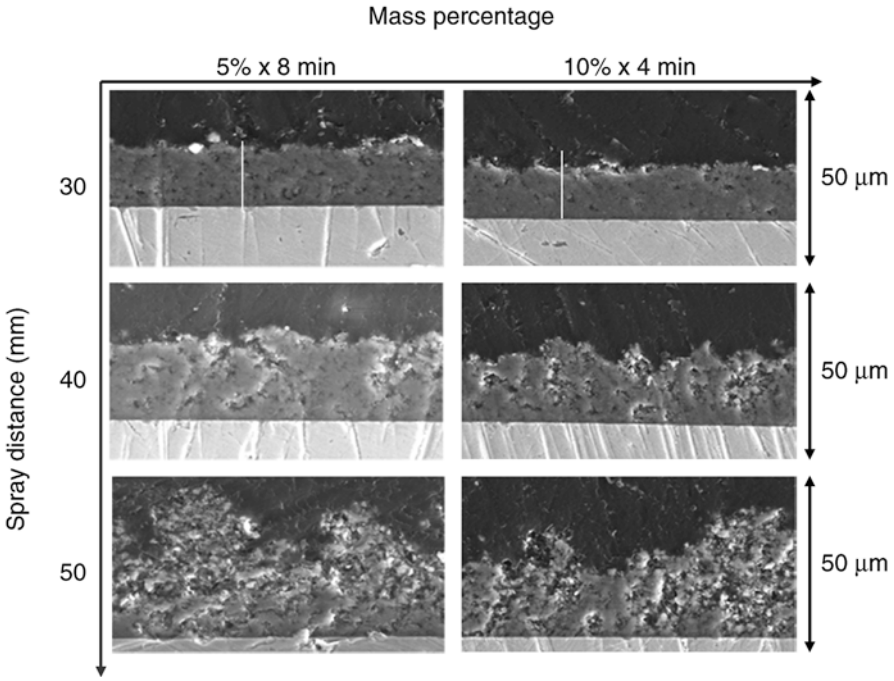


Fig. 14.55 Alumina suspension plasma-sprayed microstructures obtained with the spray conditions depicted in Fig. 14.31 for three different spray distances (30, 40, 50 mm) and two powder mass loads (5 and 10 wt%). Reprinted with kind permission from Springer Science Business Media [227], copyright © ASM International

microstructure and resulting in a dense coating. In both cases, non-pyrolyzed material will in situ pyrolyze and form aggregates when the substrate temperature is above the precursor pyrolysis temperature. This pyrolysis also occurs when reheating the coating by the successive torch passes [196].

(b) Suspensions

A similar observation can be made when considering, the spray beads obtained with suspensions, see Fig. 14.54 [227, 228]. The central part of the bead is relatively dense and mainly consists of mainly a few splats, spherical particles, and unmelted ones.

This central part corresponds to particles that have been well treated in the plasma core plus particles that have traveled in colder zones. In the bead at mid-height, the coating is less dense with many unmelted particles. At last, in the edges of the bead, the coating is fully powdery. To our knowledge, no bead was studied in experiments with axial injection (Mettech plasma torch or HVOF torches). It is also interesting to study the influence of the spray parameters on the bead morphology [227, 228]. Figure 14.55, depicting the influence of the spray distance and the mass percentage

of the particles, illustrates the influence of spray parameters. The densest coating is obtained at a spray distance of 30 mm (when the plasma heat flux reaches 15 MW/m^2). The density seems to be slightly lower with the 10 wt% mass load compared to the 5 wt% one. The coating thickness, when the spray time and the mass load are doubled, is also slightly diminished, which is probably due to the loading effect. When spraying at 40 mm, beads are thicker than at 30 mm but less dense (due to the incorporation of more untreated particles) and it is worst at 50 mm.

14.7.6.3 Coatings

As discussed in the previous section, when superposing beads during spraying, more or less non-pyrolyzed particles (solution spraying) or poorly treated particles (suspension spraying) are embedded in the coating during deposition. The key parameters on which coating properties depend are the following [5]:

1. The momentum of drops/momentum density of the liquid stream that controls the drop penetration into the plasma jet hot core. When considering atomized drops, it is thus of primary importance to generate a pattern of small dimensions and with a narrow range of trajectories, a narrow drop size distribution (see Fig. 4.71) together with a narrow drop velocity distribution [214].
2. For solutions, a high concentration precursor (close to equilibrium saturation) to promote volume precipitation leading to a fully melted splat microstructure and a high-density coating [200].
3. For suspensions, the size distribution and the particle morphology (linked to their manufacturing process) [5].
4. The type of liquid phase [203]: droplets with a liquid phase with high surface tension and high boiling point experience incomplete liquid phase evaporation in the thermal jet. For solutions, the result is a mud-like cracked film on the substrate leading to a porous coating. Droplets created from a low surface tension and low-boiling point liquid phase undergo rapid liquid phase evaporation, solute precipitation, pyrolysis, melting process in the plasma jet and form splats upon impact on the substrate, the stacking of which result in a dense coating. For suspensions the solid particles contained in the liquid droplets that are incompletely evaporated are poorly treated [229].
5. The substrate and coating temperature during spraying. For suspensions and solutions, substrates must be preheated over the transition temperature to get rid of adsorbates and condensates. For solutions, non-pyrolyzed materials are pyrolyzed at the substrate surface and form aggregates when the substrate temperature is above the precursor pyrolysis temperature. This pyrolysis also occurs when reheating the coating by the successive torch passes [196, 203]. Under the repeated processing by the high-temperature thermal jet, the mud-like film (for example, formed when spraying droplets with a high surface tension and high-boiling point liquid phase) in situ evaporates, pyrolyzes, and crystallizes on the substrate and results in porous coatings. For suspensions, the high temperature substrate and coating, as well as the hot gas heat flux can delay the splat cooling, resulting in the recoil of the liquid flattened drop before solidification starts.

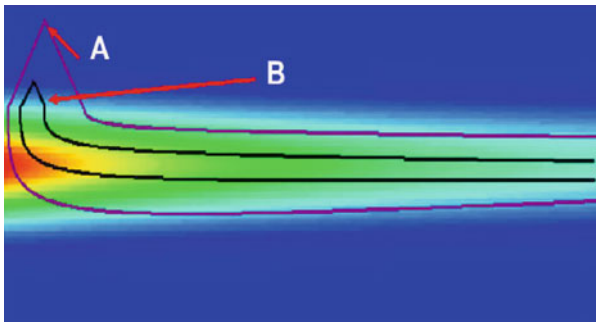


Fig. 14.56 Possible liquid droplet trajectory distributions in a d.c. plasma jet. Reprinted with kind permission from ASM International [214]

6. At last the surface roughness Ra must be adapted to the size of particles d_{50} with a ratio $Ra/d_{50} < 1–2$ (see Sect. 14.7.1.2 and) to avoid speckles [173] and cauliflower [170]-type coatings.

(a) Solutions

In solution spraying the amount of non-decomposed precursor can be controlled by spray parameters, primarily droplet injection momentum density, spray droplet sizes, and trajectories dispersions, as well as precursor concentration [196]. Figure 14.56 illustrates the necessity to adjust the liquid droplet trajectories to achieve a distribution as narrow as possible in the hot core of the plasma jet and obtain uniform dynamic and thermal treatments.

When overlapping beads contain un-pyrolyzed particles (mainly those in the jet fringes) embedded within the layers during manufacturing (see section "(a) Solutions"), upon heat exposure either by subsequent plasma torch passes or postdeposition treatment, their pyrolysis generates tensile stress driving the formation of vertical cracks [214, 229], as illustrated in Fig. 14.57a.

Coatings are made of micron-sized lamellae, which have grain sizes smaller than 30 nm, and they exhibit a porous architecture at two scales (nano- and micro-scales) made of voids and through-thickness stress relieving intra-lamellar cracks. The unique intra-lamellar cracks could result from pyrolyzation shrinkage. Porosities, as those shown in Fig. 14.57b, result also from the entrapment of poorly treated droplets in the coating. The fraction of un-pyrolyzed material has hence to be carefully controlled through the drop atomization (size and trajectory distributions), the spray pattern, and the solution concentration. To manufacture a dense (and hard) coating under the same operating conditions, the fraction of poorly treated material in the jet fringes needs to be significantly reduced, if not suppressed. Besides the optimization of the drop injection, dense coatings are linked to solutions with high concentrations [214]. Figure 14.58 shows that many more splats are observed at the surface of a coating sprayed with a high solution concentration than with a low concentration. With optimized conditions, coating architectures as those presented in Fig. 14.59 are obtained. Those layers are reasonably dense (88 % total pore level), hard (1023 VHN, average value), and exhibit no apparent intra-lamellar cracking.

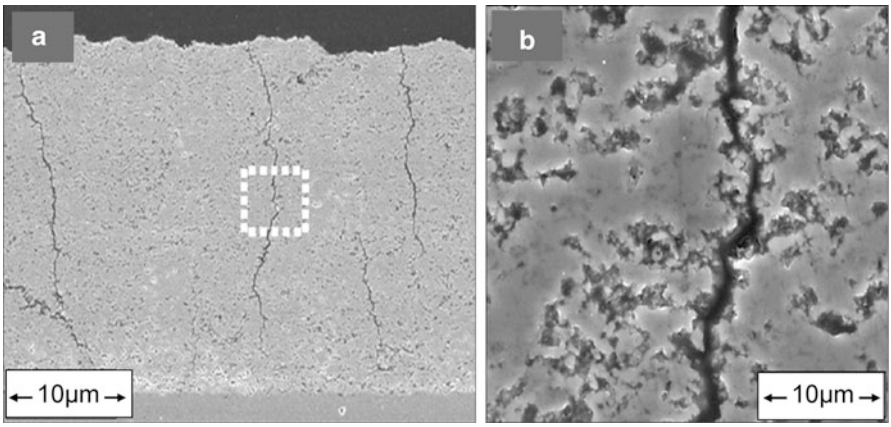


Fig. 14.57 Intra-lamellar cracked zirconia coatings deposited by solution plasma spraying with an Ar–H_2 plasma produced by a 9-MB Sulzer Metco d.c. plasma torch [214] (**a**) general view (**b**) detail. Reprinted with kind permission from ASM International [214]

(b) Suspensions

In HVOF or plasma suspension spraying, it is crucial to achieve particle melting, or particles close to the melting state, at impact. In spite of their much lower temperature, HVOF jets provide good heat transfer, with particles in the sub-micron or few micron size, compared to that of plasma jets where the Knudsen effect is drastic (see Sect. 4.5.4). Moreover, when using water instead of ethanol as suspension solvent, the resulting coatings are generally more porous than those achieved with ethanol [5, 13]. What concern the online monitoring of suspension spraying (as well as that of solution spraying) most studies have been parametric ones, as illustrated in [170, 230, 231] for conventional d.c. plasma torches or for the Mettech Axial III torch [198]. In the following, to illustrate the influence of the different parameters for plasma spraying, only results will be presented of plasma-sprayed suspensions of partially yttria-stabilized zirconia.

(i) Plasma Spraying

Influence of Particle Morphologies and Size Distributions The effects of powders are also linked to the choice of the plasma-forming gas adapted to particles to be treated. In the following it is illustrated with different yttria (8 mol %) partially stabilized zirconia particles, the size distributions of which are summarized in Table 14.3 [171, 189, 232]. All suspensions were sprayed with either Ar–H_2 or Ar–H_2 or Ar–He plasmas produced with a stick cathode torch at the same spray distance of 40 mm [189, 232].

First of all, when using nanometer-sized particles, which have the tendency to agglomerate and aggregate, such as the Tosoh TZ-8Y, resulting in a broad particle size distribution between 0.1 and 3.5 µm, the coating is very porous as illustrated in Fig. 14.59a.

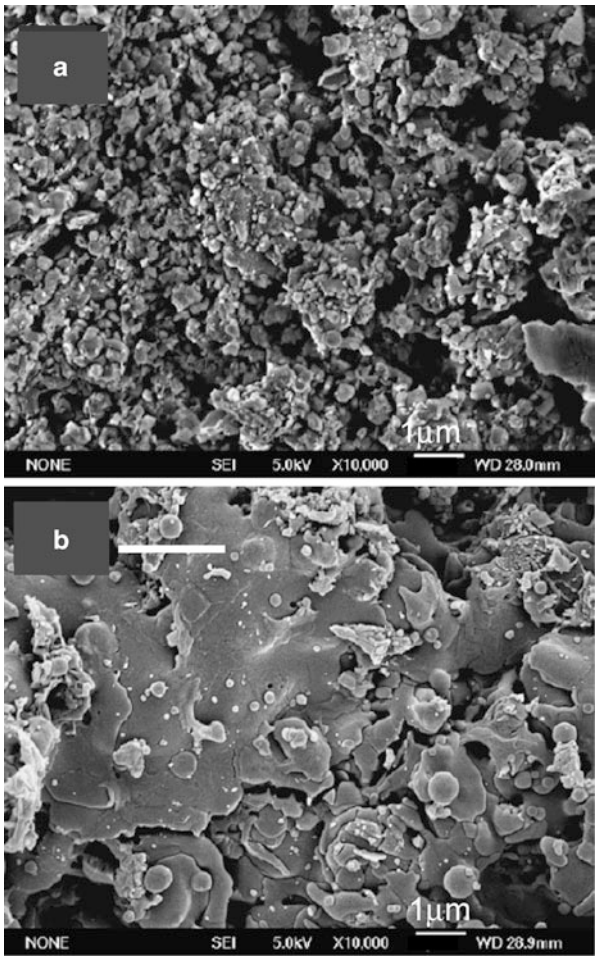


Fig. 14.58 Coating surface morphologies from solution precursors. (**a**) Low concentration. (**b**) High concentration. Reprinted with kind permission from Elsevier [200]

Fig. 14.60a presents the Tosoh powder, the size grading of which is large (see Table 14.3 and Fig. 14.60b) with nanoparticles, and their agglomerates or aggregates, the typical specific surface area being 13 $m^2.g^{-1}$. A typical coating obtained with this powder onto a 316L stainless steel substrate with a Ra of 0,05 µm is presented in Fig. 14.61a. It was sprayed at 40 mm standoff distance with Ar–H_2 plasma (45-15 slm) working at 500 A and an anode nozzle 6 mm in i.d. (enthalpy of 17.9 MJ/kg). The liquid was injected as a jet (aimed at the nozzle exit axis without plasma), which injection pressure corresponded to the optimized penetration of the suspension (see Fig. 4.79). Figure 14.61a shows the very porous coating with a columnar structure. Thin coating cross sections (below a few µm) have been analyzed to compare the initial particle distribution to those of the splats and spheres within the coating and results are presented in Fig. 14.61b. All splats have sizes over 0.2 µm, which means that the smallest fully melted particles

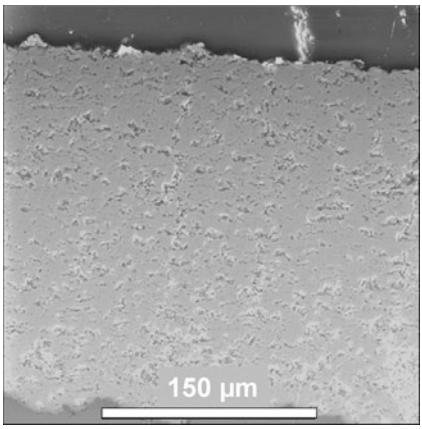


Fig. 14.59 Dense and hard zirconia coatings deposited by solution plasma spraying with an Ar–H_2 plasma using a capillary atomizer. Reprinted with kind permission from ASM International [214]

Table 14.3 Powders used in suspensions by Delbos [232] and by Etchart-Salas [189] Delbos: Tosoh-TZ-8Y and Medipur attrition milled) (Etchart-Salas: Marion powder resulting from soft chemistry, UC-001h and UC-002h both attrition milled)

	$d_{0.1}$ µm	$d_{0.5}$ µm	$d_{0.9}$ µm	Mean grain size, nm	Powder wt%
Tosoh-TZ-8Y	0.1	1.5	3.5	30	7
Medipur attrition milled	0.15	1	3	>150	7
Marion	0.03	0.06	0.76	20–40	20
UC-001h attrition milled	0.03	0.05	0.29	30	20
UC-002h attrition milled	0.26	0.39	0.7	260	20

impacting the substrate are about 0.1 µm in diameter. The spheres correspond probably to small particles, bigger than 0.1 µm, which were melted rapidly but have started to solidify before reaching the substrate. It means that coatings are mostly formed; thanks to particles over 0.1 µm. Due to Knudsen effect, temperatures of the smaller particles are below the melting point and/or their velocities not high enough to achieve Stokes numbers over one. The columnar structure is essentially due to the high voltage fluctuations (between 40 and 80 V for a mean voltage of 60 V), the impact velocity of particles injected at low voltage being too low to achieve Stokes numbers > 1, thus promoting the shadow effect described in Sect. 14.7.1.2. Moreover the agglomerate fragmentation creates a large dispersion of trajectories and nonuniform treatment of particles resulting in coatings with poor cohesion. Tiny particles were also probably evaporated and then recondensed on the coating during its formation creating defects. The agglomerate fragmentation creates a large dispersion of trajectories and nonuniform treatment of particles resulting in coatings with poor cohesion. To clarify the role of the different particle sizes, the small particles were separated from the big ones (aggregates and agglomerates in the few micrometer-sized range). It was achieved by forming an ethanol suspension with no dispersant and by its sedimentation during a sufficient time (42 h 25 min) to achieve particles separation. Figure 14.62 represents the powder distribution of the micron-sized agglomerates and aggregates sprayed with the same

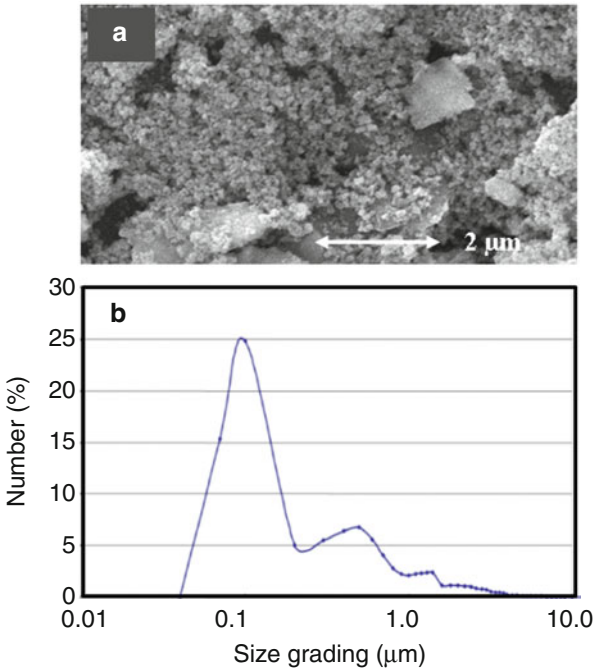


Fig. 14.60 (**a**) SEM view of Tosoh powder. (**b**) Size grading of the powder by number [232]

spray conditions together with resulting splats and spheres. These two distributions are rather similar to those presented in Fig. 14.61 obtained with the initial powder, confirming that coating result mainly of particles with sizes over a few tenths of microns. At last the small particles (< 0.3 µm) have been sprayed in the same conditions, and Fig. 14.63 shows that the splat distributions of both, the sub-micron- and micro-sized particles, are quite similar, coatings formed with splats result mainly of micro-sized particles.

A suspension of Tosoh powder, where most aggregates and agglomerates were taken away, was also sprayed with the same torch but using Ar–He (40-80 slm) plasma with a current of 500 A corresponding to an enthalpy of 13 MJ/kg and a mean gas velocity of 1,425 m/s, against 17.9 MJ/kg and 1,312 m s^{-1} for Ar–H_2 plasma. The coating cross section and its fracture are presented in Fig. 14.64a, b. With this more stable plasma (V_m =62 V and $\Delta V = 15$ V) no more columnar structure, as that shown in Fig.14.61a, is achieved. Figure 14.64a shows that the coating is relatively dense with big pores and the fractured coating, shown in Fig. 14.64b shows that it is mostly granular (the explanation is given farther in this section) with most particles with sizes over 0.05 µm. It must also be noted that the deposition of the same coating thickness is about twice longer than that obtained with initial Tosoh powder sprayed with the Ar–H_2 plasma. It seems that with this faster plasma jet with low voltage fluctuations the small particles reach sufficient velocities and temperatures to be imbedded within the coating under formation.

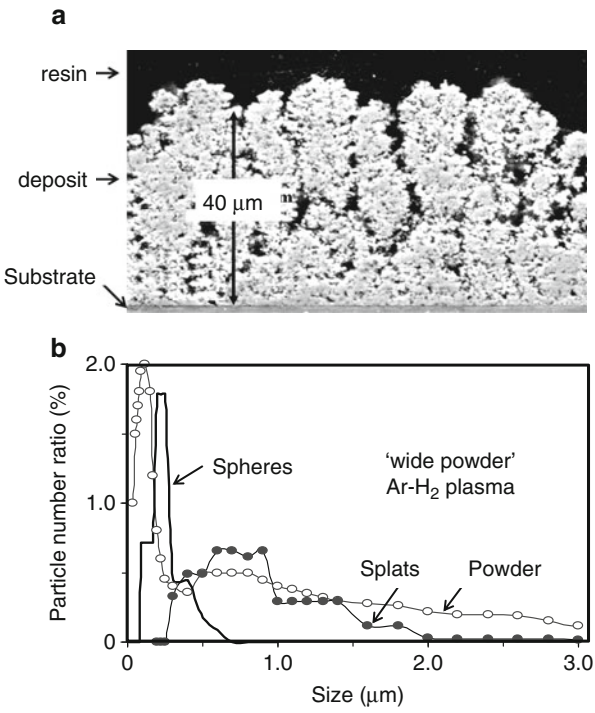


Fig. 14.61 (**a**) Coating cross section obtained with the suspension of Tosoh powder, ethanol 10 wt% YSZ, 2 vol.% dispersing agent, sprayed with Ar–H_2 plasma : 45–15 slm, $h = 17.9$ MJ/kg. (**b**) Size distributions of initial powder, splats, and spheroidized particles. Reprinted with kind permission from Springer Science Business Media [169]

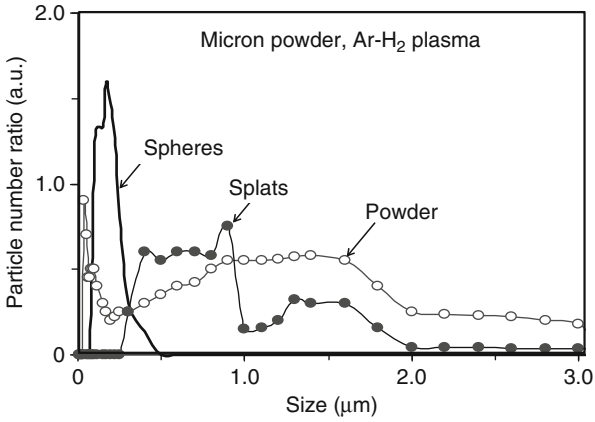


Fig. 14.62 Size distributions of initial powder, splats, and spheroidized particles obtained when spraying suspension of agglomerates and aggregates with the spray conditions depicted in the caption of Fig. 14.61. Reprinted with kind permission from Springer Science Business Media [169]

Then, Delbos [232] has sprayed attrition milled (during 13 h), fused, and crushed particles of Medipur (initial size distribution 5–25 µm). Figure 14.65a presents a SEM view of these particles and Fig. 14.65b their size distribution.

The suspension of attrition-milled Medipur particles was sprayed first with the same conditions as those used for Tosoh powder suspension (Ar–H_2 plasma) and

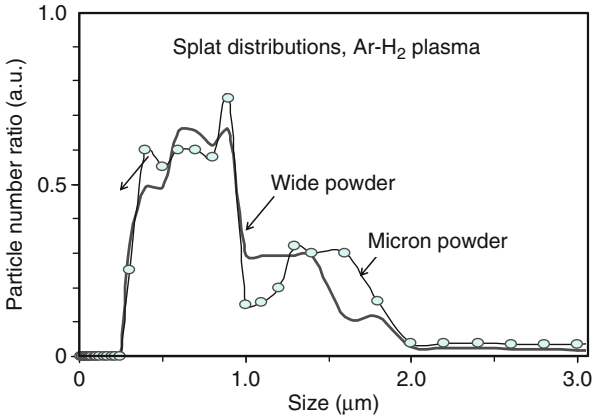


Fig. 14.63 Size distributions of splats obtained when spraying suspensions on the one hand of agglomerates and aggregates (micron particles) and on the other of the Tosoh powder with the spray conditions depicted in the caption of Fig. 14.61. Reprinted with kind permission from Dr. Delbos [232]

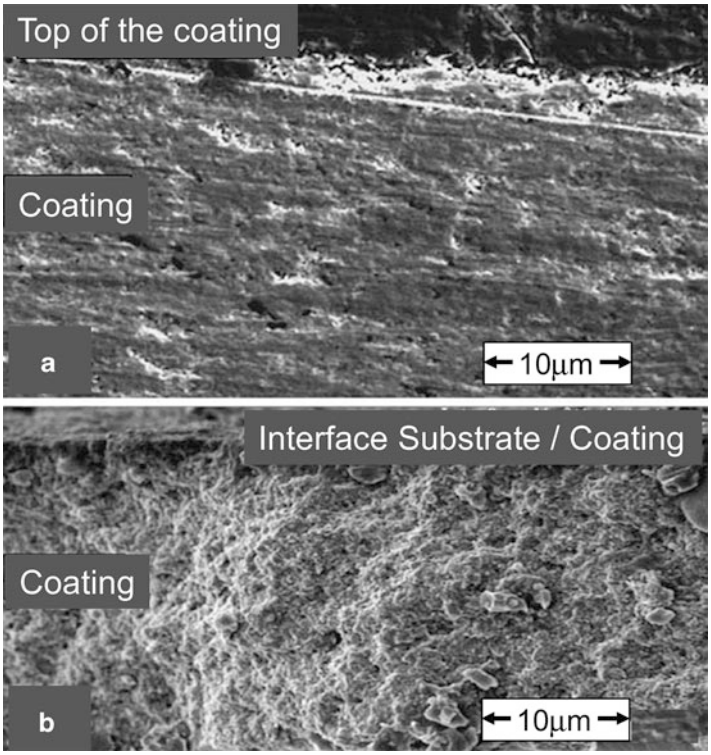


Fig. 14.64 Coating achieved with Ar–He plasma (40–80 slm), anode nozzle i.d. 6 mm, $I = 500$A, 17.9 MJ/kg: (**a**) Cross section. (**b**) Fractured cross-section. Reprinted with kind permission from Springer Science Business Media [169]

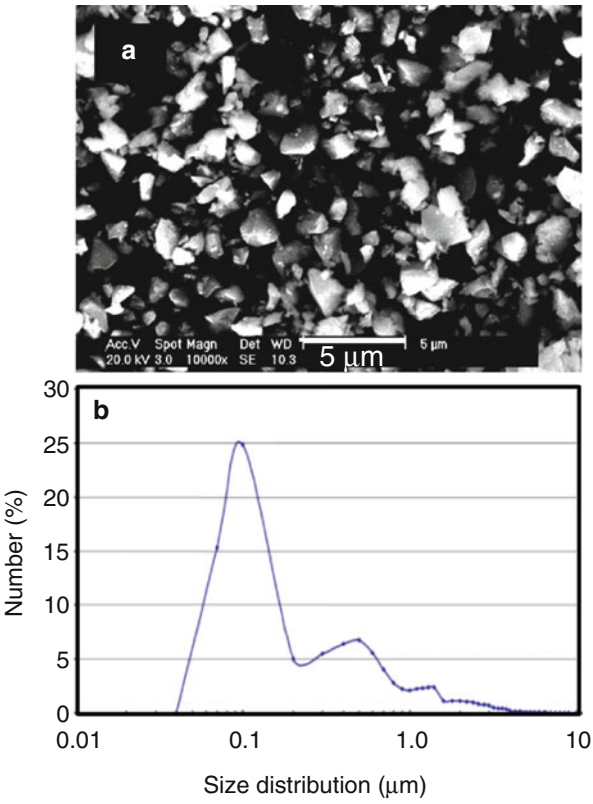


Fig. 14.65 (**a**) SEM view of attrition milled Medipur powder. (**b**) Powder size distribution. Reprinted with kind permission from Dr. Delbos [232]

the corresponding coating cross section is presented Fig. 14.66a. For this coating, many tiny particles, almost spherical, in the range of 0.05–0.3 µm, are contained in the pores. As with Tosoh powder most splats (studied when spraying layers a few µm thick) have sizes over 0.2 µm (see Fig. 14.67). The coating is denser and less porous (6 %) than those obtained with Tosoh powder.

In order to improve the heat transfer, this suspension was also sprayed with Ar–H_2–He plasma, which enthalpy was 22.3 MJ/kg against 17.9 for the Ar–H_2 one, the corresponding coating cross section being presented in Fig. 14.66b. In spite of the fact that, with this plasma forming gases containing 10 vol.% of H_2 the voltage fluctuations are not negligible ($V_m = 75.1$ V and $\Delta V = 30$ V), the coating presented in Fig. 14.66b is rather dense (about 7 % porosity). Compared to the coating presented in Fig. 14.66a, with the same suspension flow rate (which injection was optimized for these spray conditions) and pass number, the coating thickness is increased by almost 50 % due probably to the better melting of particles.

Etchart-Salas [189] has studied 3 powders (see Table 14.3): Marion powder made by a "soft chemistry process" and two Unitec Ceramic powders fused and crushed and then milled: UC-001h and UC-002h. The size distributions are presented in

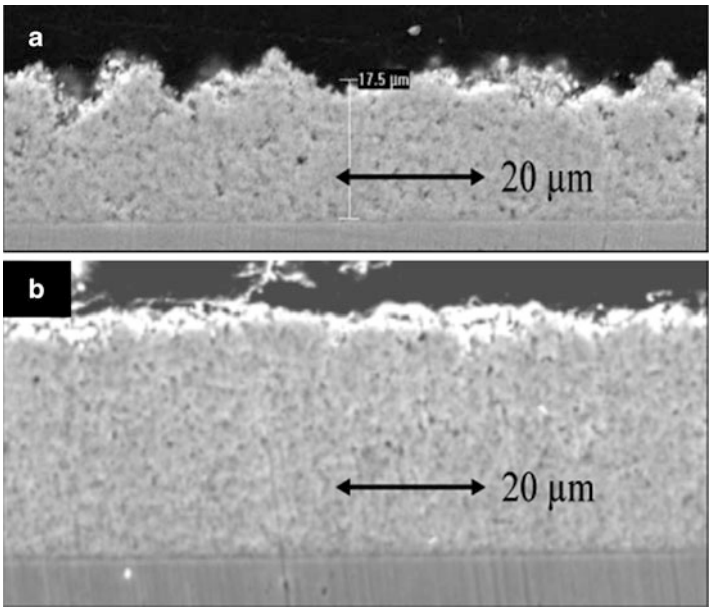


Fig. 14.66 Attrition-milled Medipur powder suspension sprayed: (**a**) with the Ar–H_2 plasma jet used to spray Tosoh powder suspension (see Fig. 14.61 caption), (**b**) with a more powerful jet: Ar–H_2–He (40–10–50 slm), anode nozzle i.d. 6 mm, $h = 22.3$ MJ/kg. Reprinted with kind permission from Dr. Delbos [232]

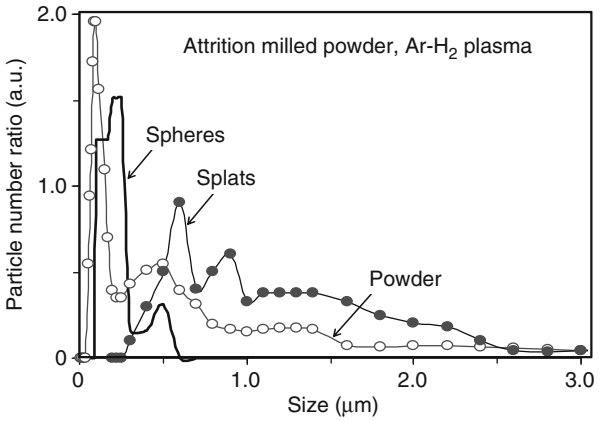


Fig. 14.67 Size distributions of initial powder, splats, and spheroidized particles obtained when spraying suspension of attrition-milled Medipur powder with the spray conditions depicted in the caption of Fig. 14.61. Reprinted with kind permission from Dr. Delbos [232]

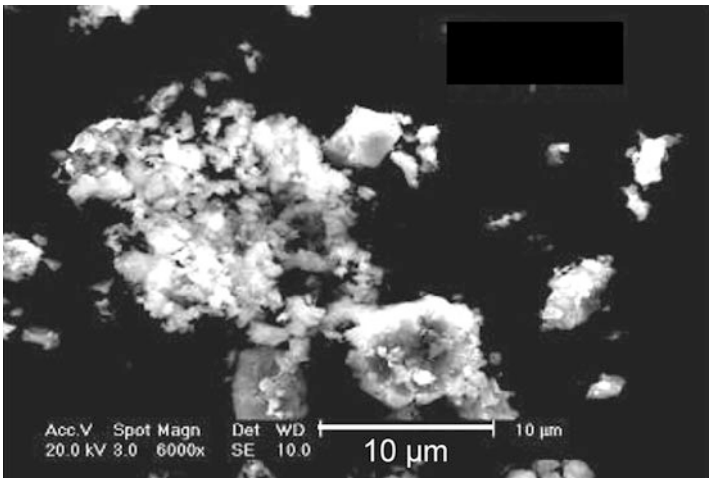


Fig. 14.68 SEM picture of the Marion powder [189]

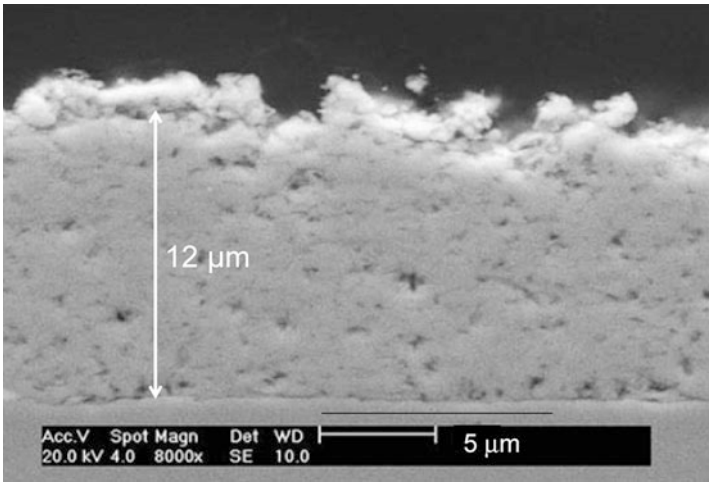


Fig. 14.69 YSZ coating obtained with a suspension with 20 wt% of Marion powder (nanograins) (Table 14.3) in ethanol injected in Ar–He (30–30 slpm) plasma jet (700 A) where the enthalpy is 17.9 MJ/kg and the anode nozzle 6 mm in i.d. Reprinted with kind permission from Springer Science Business Media [13], copyright © ASM International

Table 14.3. In all cases the injection with liquid jets of suspensions, all containing 20 wt% of particles, has been optimized. The Marion powder, presented in Fig. 14.68, is made of nanometer-sized grains (20–40 nm) and presents much less agglomerates and especially aggregates than the Tosoh powder, and its size distribution is between 0.03 and 0.9 Δm. When it is sprayed (see Fig. 14.69) with Ar–He plasma (30–30 slm with low fluctuations: $V_m = 50.9$ V and $\Delta V = 18$ V), the coating

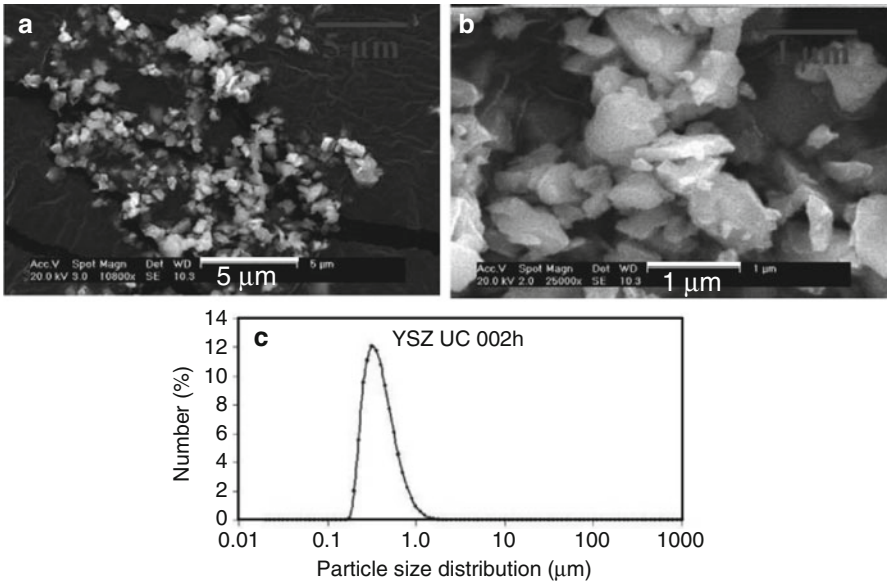


Fig. 14.70 Unitec powder 001h attrition milled: (**a, b**) SEM pictures at two different scales (**c**) size distribution by number. Reprinted with kind permission from Springer Science Business Media [151]

is rather dense (porosity of 4.7 %) and its morphology is close to that of the coating obtained with Medipur attrition-milled powder and the Ar–H_2–He plasma (see Fig. 14.66b).

When spraying suspension of the attrition-milled powder (UC.001h), shown in Fig. 14.70a, b at two different scales, and, the size distribution (see Fig. 14.70c) of which is between 0.03 and 0.29 µm, with few agglomerates between 0.3 and 1 µm, slightly denser coatings (porosity 4 %) than those achieved with Marion powder are obtained, as shown in Fig. 14.71, [189].

Similar results are obtained when bigger particles with sizes between 0.26 and 0.7 µm (Unitec UC-002h), also attrition milled, are used.

Unmolten Tiny Particles These tiny particles have a strong tendency to stick to hot ($T > 1{,}000$ °C) zirconia layers and create defects, especially between successive passes. When injecting the suspension at the end of each pass when starting to spray the next one, particles traveling in jet fringes stick on the previously deposited and still very hot pass. This is illustrated in Fig. 14.72 showing the deposition of successive pass with the defects created between them by this deposition of unmelted tiny particles.

The result is illustrated in Fig. 14.73 with coatings obtained with Unitec UC-002h powder (attrition milled with a rather narrow size distribution, see Fig. 14.70c). In Fig. 14.73a the fluctuating Ar–H_2 plasma jet was used with the injection conditions optimized. The formation of columnar structure can be observed, but smoothed compared to that obtained when spraying with the same conditions Tosoh powder

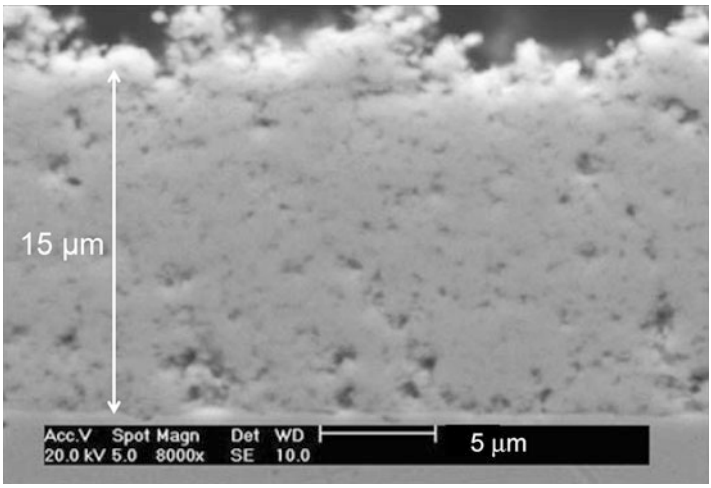


Fig. 14.71 YSZ coating obtained with a suspension with 20 wt% of UC-001 attrition-milled powder (Table 1) in ethanol injected into a Ar–He (30–30 slpm) plasma jet where the enthalpy is 17.9 MJ/kg and the anode nozzle is 6 mm in i.d. Reprinted with kind permission from Springer Science Business Media [13], copyright © ASM International

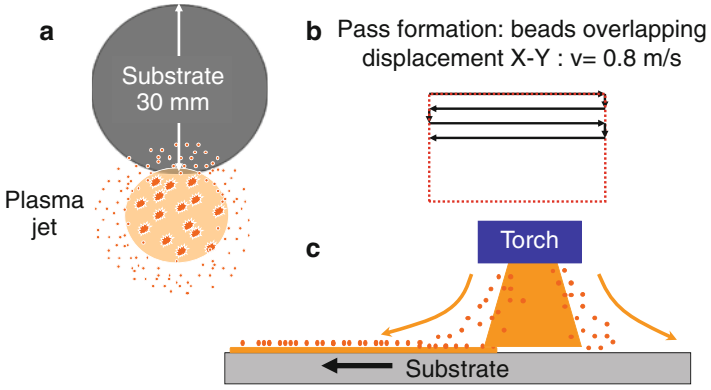


Fig. 14.72 Schematic of successive pass deposition. (**a**) Substrate and particle distribution (well heated in the central part, poorly heated in the periphery). (**b**) Spray pattern. (**c**) Torch movement with the poorly heated particles in the jet fringes. Reprinted with kind permission from Dr. Delbos [232]

(obtained by a chemical route and with a broad size distribution, as shown in Fig. 14.61b). When reducing the suspension penetration in the plasma jet (lower injection pressure) with particles traveling more in the jet fringes, where the plasma jet fluctuations have more influence on particles with lower temperatures and velocities, and the columnar structure is emphasized, as shown in Fig. 14.73b. At last when using Ar–He plasma much more stable than the Ar–H_2 one, the deposition of the unmolten particles between passes is very clearly seen, as shown in

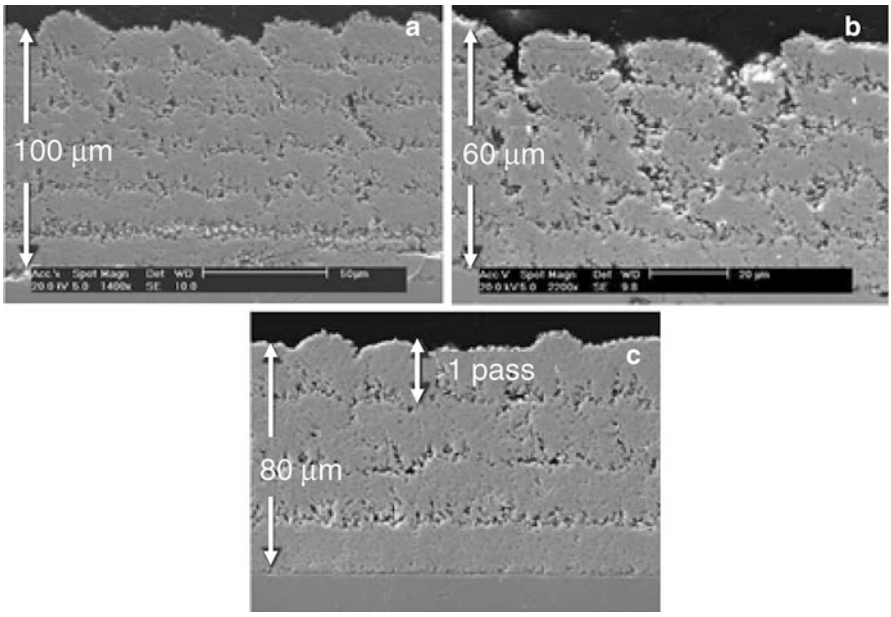


Fig. 14.73 Coatings formed with a PTF4 torch, with a 6mm i.d. anode nozzle, onto a stainless steel smooth substrate (Ra = 0.1 Δm) with a standoff distance of 40 mm, using a suspension (20 wt% of powder) of Unitec UC-002h: (**a**) Ar–H_2 (45–8 slm), I = 500 A, h = 14.5 MJ/kg, with optimized injection, (**b**) same spray condition as with a, but with a reduced injection velocity (less penetration of the suspension within the plasma jet core), (**c**) Ar/He (30/30 slm) plasma, I = 700 A, h = 19.6 MJ/kg, optimized injection. Reprinted with kind permission from IOP organization [5]

Fig. 14.73c. On the cold stainless steel substrate only few unmelted particles have been deposited and the first pass is dense even close to the substrate. It is no more the case for the new successive passes which are more porous close to the previously deposited one. During pass deposition in an x–y pattern with beads overlapping by 1/20, the phenomenon also occurs but the tiny particles are included within beads and less perturb the coating cohesion.

This powdery layer between successive passes can be avoided by changing the spray pattern and the suspension mass load, as is illustrated in Fig. 14.74 representing the same coating as that of Fig. 14.73c. The spray pattern must be such that beads overlapping limit as much as possible the inclusion of particles traveling in jet fringes and also limit the overheating of successive passes also to limit poorly heated particles sticking.

Lamellar or Granular Structures When collecting ceramic sub-micron- or nano-sized molten particles onto a smooth substrate preheated above the transition temperature (∼500 K for YSZ on stainless steel, alumina, superalloys, see Sect. 13.3.1.2), splats are identical to those obtained with micro-sized sprayed particles.

However, for d.c. stick-type cathode spray torches [151], their diameters are generally between 3 and 0.2 µm with thicknesses between 300 and 60 nm,

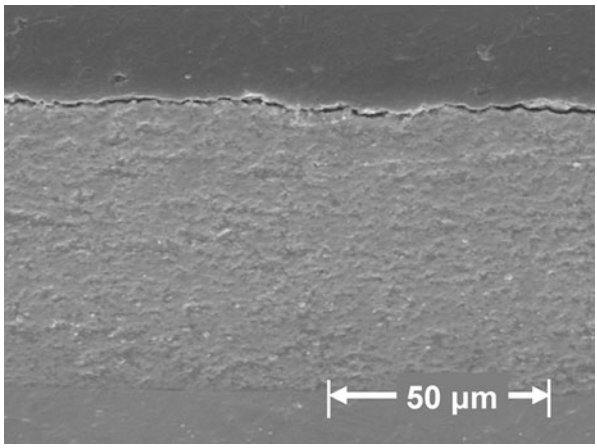


Fig. 14.74 Cross section of the same coating as that presented in Fig. 14.73c but with an optimized spray pattern. Reprinted with kind permission from IOP organization [5]

corresponding to a flattening degree of about 2 at the maximum. This low flattening degree results from lower impact velocities together with larger surface tension due to the small size of the particles. Moreover with these splat sizes, for ceramic materials, no cracks during quenching appear.

When using high enthalpy jets (Ar–H_2–He, 22.3 MJ/kg, with a heat flux of 18 MW/m^2), the structure close to the stainless steel substrate is columnar, resulting from splats layering. The columns develop through a thickness of about 4 µm corresponding to the layering of 5 passes, each of them being 0.8 µm thick. It seems that, after a few layers (a few µm thick), the thermal insulation together with the drastic heat flux from the plasma delays the splat solidification, allowing the surface tension force to take over resulting in quasi-spherical particles in a molten state sticking together before their solidification to achieve the granular structure observed in Fig. 14.75.

Spraying Mixtures of Powders Delbos et al. [222] have used YSZ Tosoh powder, with a specific surface area of 13 m^2/g and alumina powder (Baïkowski CR125) with a specific area of 105 m^2/g to prepare a suspension. They were mixed with the same weight and the suspension solvent was ethanol and the spray parameters were those for the Tosoh powder, except that the nozzle i.d. was 5 mm to increase the plasma jet velocity [222]. Figure 14.76 shows that the structure of the coating is made up of YSZ and alumina splats alternatively layered (there is a difference of contrast between both oxides: gray for alumina and white for YSZ) with thickness lower than 100 nm, as observed with AFM. Moreover, it could be noticed that the contact between splats seems to be excellent. Oberste-Berghaus et al. [208] obtained similar results with an Axial III torch of Mettech. A detailed study of alumina–yttria-stabilized zirconia composite coatings was performed by Tarasi et al. [178] using also Axial III torch of Mettech. They used either agglomerates of nano-particles or suspensions made either with loose nano-powders mixture or loose micro-powders mixture.

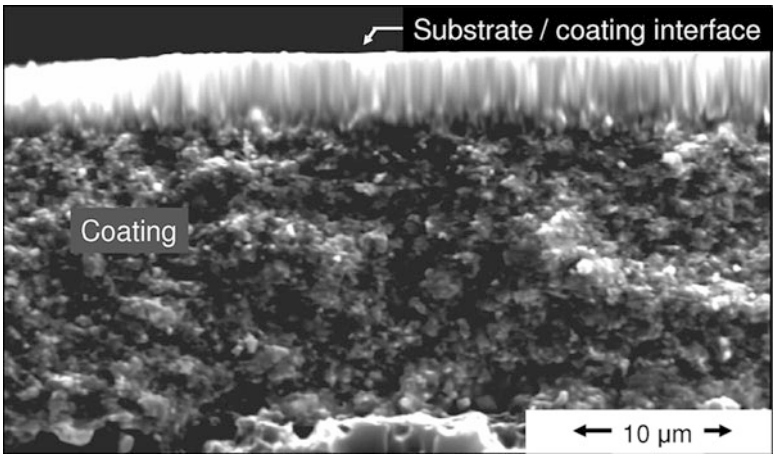


Fig. 14.75 Fractured cross section of a suspension coating sprayed on a 316L stainless steel substrate 40 mm downstream of the nozzle exit with a plasma torch 6 mm in i.d., an attrition milled powder and an Ar–H_2–He: 40–10–30 slm plasma 22.3 MJ/kg, with a heat flux of 18 MW/m^2. Reprinted with kind permission from Springer Science Business Media [169]

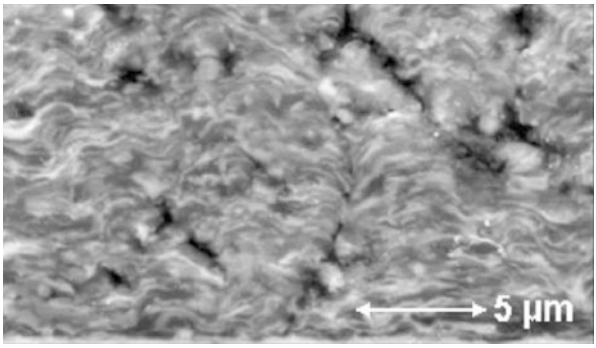


Fig. 14.76 Cross section of an alumina–YSZ coating obtained with suspension spraying with the spray conditions of Fig. 14.75 caption, but with a torch nozzle i.d. of 5 mm instead of 6 mm. Reprinted with kind permission of Dr. Delbos [222]

Through the study of the in-flight collected particles and coatings produced from the two processes, the comparison of fragmentation, melting and mixing phenomena was possible. They showed that both methods can be used in the production of high amorphous coatings provided that the appropriate parameters for each process are utilized. The components in the composite materials sprayed by plasma processes may appear in different forms. They may form crystalline structure of alumina or YSZ with no additional solute atoms. They also can dissolve the solute atoms of the second component and form crystalline solid solutions (even to exceptionally high levels of solubility), and/or form amorphous phase [178].

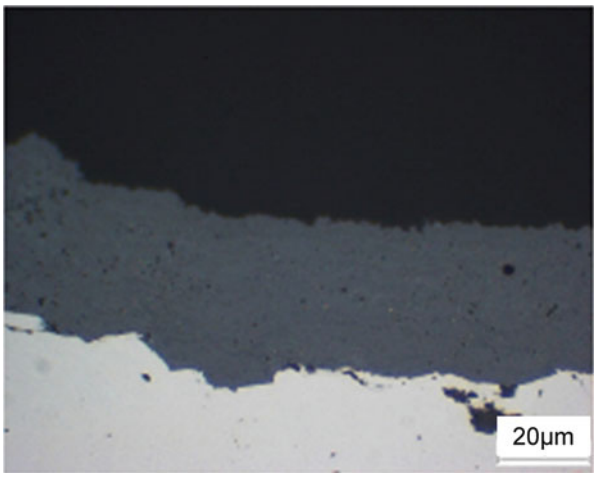


Fig. 14.77 Light microscope image of HVSFS-sprayed TiO_2 coating. Reprinted with kind permission from Elsevier [180]

In-flight melting followed by mixing are crucial processes in amorphous formation. This melting is strongly controlled by the particle velocity, a lower one resulting in higher amorphous content, in spite of the lower cooling rates.

(ii) HVOF Spraying (HVSFS)

An example of HVSFS spraying results is presented with the spraying of TiO_2 nanometer-sized (grain size 12nm) particles onto aluminum substrates [180]. In SEM, the titania nanometer-sized powder appears agglomerated with a primary grain size of approximately 10 nm with agglomerates of about 100 nm. In XRD both the rutile and the anatase phase are detected. The suspension contained 10wt% TiO_2 and the solvent was isopropanol/water with a volume ratio of 90/10, DOLAPIX being the additive. Water (10wt%) was added to facilitate the chemical stabilization of the suspension (but it cools the flame when vaporizing). The HVSFS torch used was based on a Top-Gun-G system (manufactured by GTV) modified to meet suspension spray requirements. Propane and ethene were preferentially chosen as combustion fuels as they allow stable operation of the HVSFS process. The HVSFS torch was operated on a six-axes robot system using a simple meander kinematics with a 2-mm offset. Sample cooling was performed using two air nozzles mounted on the torch. The suspension was fed at a rate of about 8 g/min using a conically shaped 0.3 mm nozzle. The thickness of coating, deposited on aluminum substrate, was around 30 µm, the deposition rate being around 4 µm/cycle. Considering its cross section, the TiO2 coating appears totally dense (Fig. 14.77), homogeneous, no internal structure is visible, and no unmolten particles are detected. The SEM surface image (Fig. 14.78) reveals fully molten splats ranging from a few tenths to about 10 µm. From the XRD data, the main fraction of the coating consists of anatase (approx. 75 %), the rest of the material being rutile. Traces of a sub-stoichiometric species, Ti3O5, could also be identified in the coating.

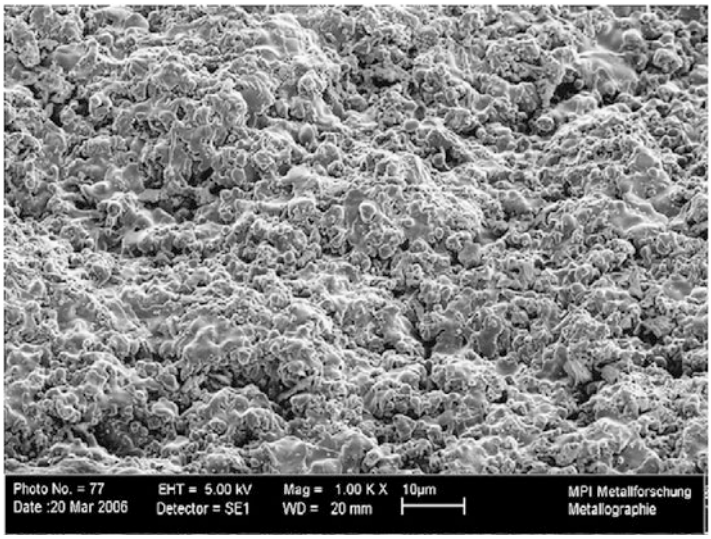


Fig. 14.78 SEM image of HVSFS-sprayed TiO_2 coating surface. Reprinted with kind permission from Elsevier [180]

Toma et al. [233] compared alumina coatings HVSFS sprayed by suspension with particles in the range 0.4–3.5 µm to those obtained with HVOF and particles in the size range 5–25 µm. They used for HVOF spraying a TopGun working with ethylene–oxygen (90–270 slm) with a spray distance of 150 mm and for HVSFS the same gun, which chamber was modified, but working with same gases (75–230 slm) and a standoff distance of 80 mm. The HVSFS coating presents a specific microstructure: partially melted fine particles with elongated shapes (of about 5 µm in length and 150 nm in thickness), nearly spherical µm-sized particles and clusters of agglomerated tiny sub-µm-sized grains embedded in the matrix of well-melted ones (Fig. 14.79). The main crystalline phase is the α-phase representing 60 %. The HVOF coating is more conventional (Fig. 14.80) with layered splats, γ-alumina phase being the main one. The suspension-sprayed Al2O3 coatings present the better electrical resistance stability that can be explained by their specific microstructure and retention of a higher content of α-Al2O3.

Bolelli et al. [184] also HFSFS-sprayed alumina coatings, using seven different Al_2O_3-based suspensions prepared by dispersing two nano-sized Al_2O_3 powders (having analogous size distribution and chemical composition but different surface chemistry), one micron-sized powder and their mixtures in a water + isopropanol solution. HVSFS coatings were deposited using these suspensions as feedstock and adopting two different sets of spray parameters (propane–oxygen either 55–325 slm or 60–350 slm). As with plasma spraying, the characteristics of the suspension, particularly its agglomeration behavior,

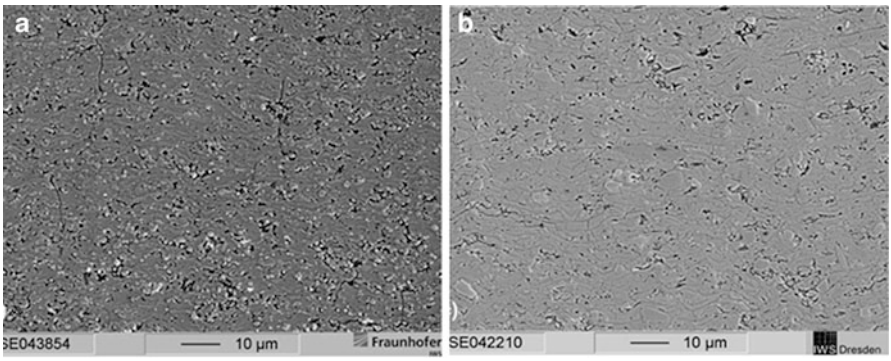


Fig. 14.79 SEM micrographs of cross sections of thermally sprayed alumina coatings. (**a**) Conventional coatings HVOF-sprayed C_2H_4/O_2 (75/230 slm) with particles in the range 5–25 µm. (**b**) Suspension HVOF sprayed C_2H_4/O_2 (90/270 slm) with particles in the range 0.4–3.5 µm. Reprinted with kind permission from Springer Science Business Media [233], copyright © ASM International

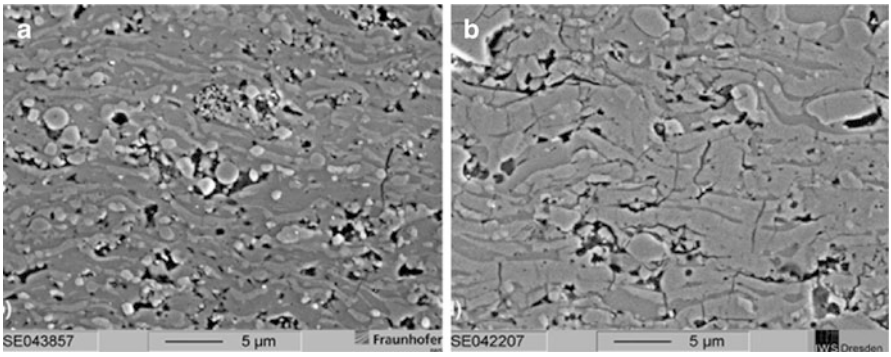


Fig. 14.80 SEM micrographs with higher magnifications of cross sections of HVOF sprayed coatings depicted in Fig. 14.79. (**a**) Conventional and (**b**) Suspension. Reprinted with kind permission from Springer Science Business Media [233], copyright © ASM International

have a significant influence on the coating deposition mechanism and, hence, on its properties [184]. Dense and very smooth (Ra ~ 1.3 µm) coatings, consisting of well-flattened lamellae having a homogeneous size distribution, were obtained with micro-sized (~ 1–2 µm) powders. Spray parameters favoring the breakup of the few agglomerates present in the suspension enhance the deposition efficiency (up to 50 %), as no particle or agglomerate larger than ~2.5 µm can be fully melted. Nano-sized powders, by contrast, generally form stronger agglomerates, which cannot be significantly disrupted by adjusting the spray parameters. When the chosen nanopowder forms small agglomerates (up to a few microns), the deposition efficiency is satisfactory and the coating porosity is limited. If the nanopowder forms large agglomerates (on account of its surface chemistry), poor deposition efficiencies and porous layers are obtained [184].

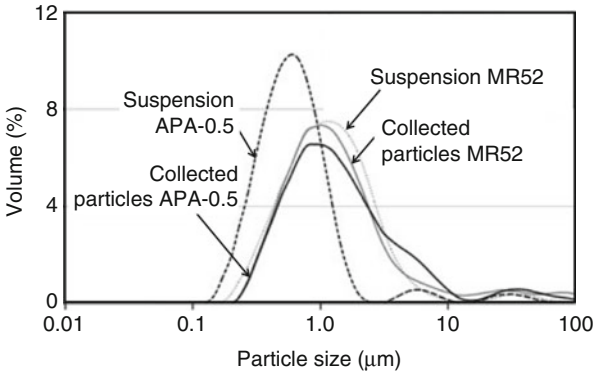


Fig. 14.81 Size distribution of the particles in the used suspensions and of the collected particles from HVSFS spray process for the two used powders. Reprinted with kind permission from Springer Science Business Media [234], copyright © ASM International

Müller et al. [234] have used two different spray processes, suspension plasma spraying (SPS) and HVSFS. They used alumina particles: MR52 (0.33–4.07 μm) and APA-0.5 (0.26–1.19 μm) and suspensions were made either with water or isopropanol. For HVSFS they used a TopGun system equipped with a 22-mm long combustion chamber and working with ethene–oxygen (410 slm) with different oxygen to fuel ratios and a spray distance of 120 mm. For SPS they used a F6-Gun of GTV working with Ar–H_2 (55–12 slm) and standoff distances of 55 mm with water and 75 mm with isopropanol (to benefit from its combustion).

Figure 14.81 represents particle distributions before spraying and collected in water after HVSFS spraying. Collected spray particles produced by HVSFS, exhibited a spherical shape, corresponding to their good melting during their in-flight phase. Those from the coarser MR52 powder exhibit the same size distribution after the spray process as those in the used suspension. The finer APA-0.5 powder has its initial d_{50} value increased from 0.55 μm to a value of 1.23 μm for the collected particles. The size distribution also broadened from a narrow size distribution in the suspension to a broader distribution of the collected particles after spraying. This could be explained by the agglomeration phenomenon. Using water for the suspension results in higher amount of α-alumina phase.

With the SPS process, particle melting was better with isopropanol than with water due to the combustion phenomenon and compared to HVSFS process splat sizes were smaller. When comparing coatings obtained by HVSFS and SPS, α-alumina phase is dominant in the HVSFS coatings, which confirms the better particles melting. Using the SPS process, high coating porosities, up to values of 40 %, were achieved, while with HVSFS low coating porosities (down to 2 %) were obtained.

14.7.6.4 Environmental Impact (Life Assessment Impact: LCA)

The LCA of plasma spray processes using powder, suspension, or solution as feedstock to manufacture zirconia coatings was studied by Moign et al. [235]. The authors pointed out the following points:

– The comparison of the manufacturing of solution for SPPS, suspension for SPS, and powder for APS showed that solution had a lower environmental impact than powder and suspension.
– Different results are obtained when considering the spray process because the amount of electricity used is responsible for about 70–80 % of the environmental impact, and the deposition time linked to deposition efficiency mainly controls the environmental impact. With spraying efficiency of SPS and SPPS of about 30 % at the best against 60 % for the APS process, these processes appear to be much less friendly from an environmental point of view.

14.7.7 Applications

In the following suspension plasma spraying is named: SPS and solution precursor plasma spraying: SPPS. Compared to conventional coatings, those manufactured from solutions or suspensions exhibit quite interesting features such as the absence of lamella boundaries and cracks and porous microstructures with nano-sized grains. Many works have been devoted to many potential applications, as described in the following, but unfortunately, to the best of our knowledge, no industrial developments of these techniques have been mentioned yet.

14.7.7.1 Thermal Barrier Coatings

In the following suspension plasma spraying is named: SPS and solution precursor plasma spraying: SPPS. Compared to conventional coatings, those manufactured from solutions or suspensions exhibit quite interesting features such as the absence of lamella boundaries and cracks and porous microstructures with nano-sized grains. Many works have been devoted to many potential applications, as described in the following, but unfortunately, to the best of our knowledge, no industrial developments of these techniques have been mentioned yet.

(a) Solutions

TBCs were mainly manufactured by solution plasma spraying [155, 156, 196, 221, 229, 236–239]. As explained previously, the coatings contain uniformly distributed cracks, providing a high degree of strain balance to the ceramic topcoat. Compared to APS conventional TBCs, coatings produced by Solution Precursor Plasma Spray (SPPS) demonstrate [154, 196] interesting properties related to their specific features, including ultrafine splats (which form dense coating regions), through thickness vertical cracks, embedded un-pyrolyzed particles, and voids, as shown in Fig. 14.48. The adhesive bond strength, measured according to ASTM C633-79 standard, was 24.2 MPa, while that of conventional APS-deposited coatings was found to be 19.9 MPa [154]. The improved bond strength probably results not only from the finer splat size but

also may be due to an interfacial thin oxide layer that would form on the substrate and would promote adhesion. The vertical crack density increases the in-plane TBC fracture toughness, improving the coatings cyclic durability in the thermal cycling [196]. Gell et al. [196] have shown that, during thermal cycling, the spallation life was improved by a factor of 2.5 compared to APS coatings on the same bond coat and substrate, and by a factor of 1.5 compared to high-properties EB-PVD coatings. The apparent thermal conductivity, as measured by laser-flash technique from 100 to 1,000 °C, has been found to be approximately 1.0–1.2 W m^{-1} K^{-1}, a value lower than that of EB-PVD coatings, but higher than that of conventional APS coatings. Probably this high conductivity (relative to APS coatings) is due to the increased internal contact area of solution-sprayed coatings. The thermal cyclic stability of these coatings was found to show no significant microstructural or phase changes during 1,090 cycles of 1 h each at 1,121 °C. The critical features of solution coatings, vertical cracks, and ultrafine splats, remained stable throughout the test. Vertical cracks were retained or reformed, even after exposure to 1,500 °C. APS and solution-sprayed TBCs exhibited similar grain growths, density and hardness increase between 1,200 and 1,400 °C. Above 1,400 °C, APS TBCs exhibited a faster rate of grain growth and transformation into monoclinic phase. The microstructural features of these coatings are retained in very thick coatings (up to 4 mm), the spallation lives being significantly less thickness sensitive and demonstrating superior lives.

(b) Suspensions

Work has also been performed with suspensions (suspension plasma spraying, SPS, and high velocity suspension flame spraying, HVSFS) [9, 183, 190, 210]. For example, Kassner et al. [190] have obtained segmented coatings (7 cracks. mm^{-1}) for 300-μm thick coatings obtained by plasma spraying. Ben-Ettouil et al. [240] nevertheless showed that resistances to furnace cycle test (FCT) of YPSZ SPS coatings were higher for coatings exhibiting lower crack density. Besides, the thermal diffusivity of such as-sprayed coatings has been measured at atmospheric pressure to change from 0.015 to 0.025 mm^2/s for a temperature rise from room temperature to 250 °C. Such low values, about 10 times lower than values commonly measured on coatings exhibiting dual architectures (nano- and micro-sized) manufactured with micro-sized agglomerates made of nano-sized particles, can be explained in a first approximation by the peculiar void network architecture (80 % of voids smaller than 30 nm) of such coatings. This architecture induces, besides phonon scattering phenomena in the smallest grains of the coating structure, numerous thermal resistances in the structure, each thermal resistance being increased by rarefaction effects due to small grain volume [239]. Besides, such nano-sized coatings exhibit enhanced optical absorption and strong IR scattering compared to conventional micro-sized YPSZ coatings, due to the number and size of the voids, and due to the density of interfaces in between grains and lamellae forming such coatings [239].

14.7.7.2 Solid Oxy-Fuel Cell Components

Numerous works are in progress in the world for the SOFC [172, 180, 188, 192, 241–254] For the cathode and electrolyte, Kassner et al. [190] have plasma sprayed, using two injectors and a Triplex torch, LSM ($(La_{0.65}Sr_{0.3})MnO_3$) and YPSZ to produce a functional layer for SOFC cathodes. Works have also been devoted to deposition of $LaMnO_3$ perovskite thin films by suspension plasma spraying [247].

According to the small particle size, such coatings should provide a higher amount of triple phase boundaries. The cathode manufacturing by thermal spraying is challenging because $LaMnO_3$ doped with SrO, CaO, etc., is prone to decompose easily above the melting temperature. Monterubio et al. [247] have shown that pure $LaMnO_3$ (the easiest to decompose) can be sprayed, with less than 10 % of La_2O_3 formation, if the feedstock particles were doped with 10 mol.% of MnO_2. In this condition, particles with sizes between 1 (d_{10}) and 5 (d_{90}) μm (mean size d_{50} of 3 μm) were sprayed with a pure Ar d.c. plasma jet to limit, as much as possible, the heat transfer, and consequently the particle temperature. A $La_{0.8}Sr_{0.2}MnO_3$ (LSM) [250] cathode was prepared and its properties were strongly influenced by the spray distance.

Thin (~ 10–20 μm) electrolyte coatings of Y-PSZ by SPS are supposed to reduce Ohmic losses, but these layers must be impervious to gases. Efforts were mainly devoted to the study of the influence of various solid loadings in suspensions together with their state of dispersion, the stability of the suspension (by adjusting the amount of dispersant), the suspension tailored viscosity, the atomization effect (gas-to-liquid mass ratio (ALR), influence of Weber number), the effect of mechanical injection, the solid particle size distribution, and the manufacturing process [152, 171, 188, 190, 222, 231, 242–255]. By adapting the spray conditions, it became possible to achieve a leakage rate of 0.5 MPa L/s m^2 for a 15μm thick electrolyte, which is not yet the requirement of 0.08 MPa L/s m^2 [171].

With the Prosol process [21] (sol suspension), the structure and the proportion of the crystalline phases in the coatings are typically the same as those encountered in the injected sol. Coatings are dense when the sol is processed with high enthalpy plasma flows (20 MJ/kg) and consist mainly of very fine particles. Bouaricha et al. [249] sprayed, with the Axial II torch, suspension of nano-sized particles of samarium-doped ceria (SDC) in order to produce thin electrolyte layers for SOFC applications with reduced both Ohmic losses and operating temperature. Original phase composition was retained and, independently of thermal spray conditions, the SDC coatings retained the nanostructure of the sprayed feedstock. Depending upon plasma spray parameters and substrate temperature, the process can produce a wide variety of structures ranging from porous to dense coatings, with very low open void content.

A method for manufacturing metal-supported SOFCs with atmospheric plasma spraying (APS) is presented in [253], making use of aqueous suspension feedstock for the electrolyte layer and dry powder feedstock for the anode and cathode layers. Even with optimized spray parameters, three main defect types were detected in such suspension plasma sprayed electrolyte layers: (1) through-thickness cracks

(perpendicular to the substrate surface) caused by thermal stresses developing during coating deposition, (2) voids or defects caused by unmelted particles embedded within the coating, and (3) small inter-splat voids. Three different types of dispersant were also considered for ensuring feedstock dispersion and the effects of solid particles loading, dispersant type, and dispersant concentration on suspension properties such as viscosity and feed ability, and layer characteristics such as microstructure and deposited thickness, were also examined [253].

Ni–YSZ anode and YSZ electrolyte half cells were successfully deposited by SPS with the Axial III torch from Mettech on porous Hastelloy X substrates by Wang et al. [192]. The thickness of the anode and electrolyte layers was ~40 μm and 10–20 μm, respectively. The NiO–YSZ coating deposition process was optimized by a design of experiment approach. The YSZ electrolyte spray process was examined by changing one parameter at a time. The maximum power density reached 0.610 W/cm^2 at 750 °C.

14.7.7.3 Wear-Resistant Coatings

(a) WC–Co
WC–Co coatings were deposited using an axial injection plasma torch and an Et-OH suspension of sub-micrometer-sized feedstock powders [256]. With a proper selection of spray parameters, porosities below 0.2 % were achieved with hardness over 700 HV_{3N}. The best coatings corresponded to the highest particle velocities (~800 m/s) and the lowest particle temperatures (at the minimum, 2,200 °C). It seems that the measured carbon loss in the carbide is principally associated to deposition of layers of highly oxidized overspray. The properties of the feedstock powder and feed suspension play a critical role in the resulting coatings quality.

(b) Alumina
Toma et al. [257] provided an overview of suspension-sprayed Al_2O_3 coatings. They sprayed alumina coatings by using SPS and HVSFS (axial injection) spraying [258]. The initial mean particle diameter was 0.3 μm and either water or Et-OH was used for the suspension. Et-OH base suspension spraying with Ar–H_2 plasma-forming gas mixture resulted in 18.9 ± 2.5 % porosity against 11.6 % with an Ar–He one. With HVSFS (acetylene–oxygen) and aqueous suspension, the porosity was 7.6 ± 2.8 %. Toma et al. in another work [233] made a comparative study of the characteristics (microstructure, phase composition, and mechanical properties) and electrical properties (insulating resistance, electrical resistivity, and dielectric strength) of Al_2O_3 coatings produced by conventional HVOF (fed with micrometer-sized particles) and HVFSF fed with a suspension of particles, which size distribution was between 0.4 and 3.5 μm. At low levels of relative humidity, RH $<$ 40 %, the electrical resistivity was on the order of 10^{11} Ω.m for both coatings. At a very high humidity (97 % RH) the electrical resistivity values for the HVFSF coatings were in the range 10^7–10^{11} Ω.m, up to five orders of magnitude higher than

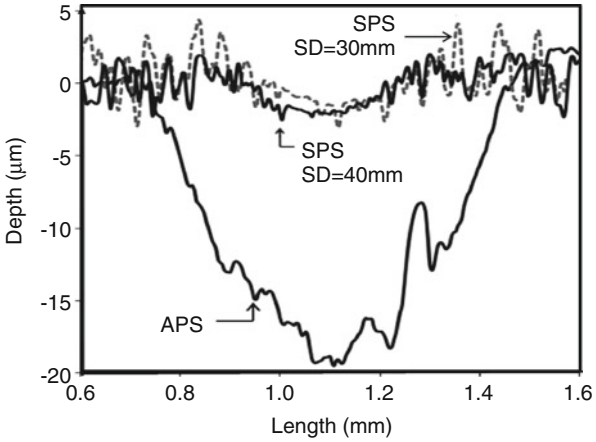


Fig. 14.82 Wear profiles for α-Al_2O_3 micrometer-sized (APS) and sub-micrometer-sized (SPS, spray distance = 30 and 40 mm) structural scales (ball-on-disk friction test, α-Al_2O_3 ball of 6 mm in diameter, 2 N load, relative speed of 0.1 m/s and sliding distance of 1,500 m. The test was operated in the dry mode and the wear scraps were constantly removed by an air jet located behind the contact point). Reprinted with kind permission from Springer Science Business Media [259], copyright © ASM International

those recorded for the HVOF coating (10^6 Ω m). The specific microstructure of the suspension-sprayed coating is probably due to its much lower pore sizes. However, at RH = 97 % the electrical properties were found to degrade significantly (by up to 4–5 orders of magnitude) in these coatings after long-term exposure. The dielectric strength of suspension-sprayed coatings was found to be 19.5–26.8 kV/mm for coating thicknesses ranging from 60 to 200 µm, which is probably due to its microstructure.

Darut et al. [259] compared the tribological properties of alumina coatings structured at two different scales, a micrometer one (d_{50} of particle size distribution of 36 µm) manufactured by APS and a sub-micrometer one (d_{50} of particle size distribution of 0.4 µm) manufactured by SPS. Coating architectures were analyzed and their friction coefficient and wear rate in dry sliding mode measured in ball-on-disk friction conditions (α-Al_2O_3 ball of 6 mm in diameter). The friction coefficient of Al_2O_3 coatings was decreased by two (0.4 for SPS layers to be compared to 0.8–0.9 for APS ones) when the characteristic scale was divided by two orders of magnitude. Moreover, wear rate was 30 times lower for SPS layers compared to the one of APS layers, as shown in Fig. 14.82.

Qiu and Chen [260] manufactured by suspension plasma spraying nanostructured fine alumina coating using nano-scale alumina powders (d ~ 20 nm), ethanol being used as liquid phase. The quality of the coatings strongly depended upon the plasma power, spray distance, liquid phase, solid phase concentration, inner diameter of the suspension injector, and suspension flow rate.

Nanostructured Al2O3–13 wt% TiO_2 coatings were manufactured [261, 262] by plasma spraying with nano-crystalline powders. The TEM analysis revealed

that partially melted Al_2O_3 particles, in the size range of 20–70 nm, were embedded in a TiO_2-rich matrix. The mechanism of the substructure formation was explained in terms of melting and flattening behaviors of the powder particles during plasma spray processing.

Oliker et al. [263] found that SPS alumina coatings exhibited better hardness and mainly toughness than conventionally sprayed coatings.

(c) Zirconia–Alumina

Nanometer-sized composites made of alumina–zirconia can potentially exhibit higher hardness, fracture toughness, slower crack growth, and lower thermal conductivity than alumina or zirconia alone. Both solution [199] and suspension spraying [11, 175, 264–266] were used. Gadow et al. [11] have sprayed by HVSFS a mixture of Al_2O_3 (150 nm) and Y-PSZ (12 nm) dispersed in 30/70wt % isopropanol/water mixtures with a 20wt% solid content. The coatings reveal that nanometer-sized particles of zirconia are embedded in an alumina matrix. The spray conditions were tailored to achieve complete alumina melting with the zirconia particles remaining solid. As the time between melting and reconsolidation is extremely short, the two components are almost immiscible. Oberste-Berghaus et al. [175] have also deposited Al_2O_3–ZrO_2 coatings by SPS and HVSFS, both with axial injection. With optimized spray conditions, the smaller nano-sized particles create fine laminates of alumina and zirconia layers, while slightly larger particles promote pseudo-alloyed alumina–zirconia amorphous phase components. A large variety of microstructures and properties of suspension-sprayed Al_2O_3–ZrO_2 composites was introduced by the different feedstock, spray systems and operating conditions.

Also an alumina/8 wt% YPSZ was deposited by axial injection SPS process by Tarasi et al. [177]. The effects of main deposition operating parameters on the microstructural features were evaluated using the Taguchi design of experiment. The results indicate that thermal diffusivity of the coatings, an important property for potential thermal barrier applications, is barely affected by the changes in porosity content during annealing treatments. At last, Chen et al. [264] have sprayed with a rod-type cathode d.c. plama torch an Al_2O_3–ZrO_2 amorphous powder feedstock [19] the preparation of which was described in Sect. 14.7.4.4.

Solution plasma spraying was used to spray 75 % dense coatings of metastable ceramics in the ZrO_2–10 mol.% Al_2O_3 binary system [199]. The coating microstructure contains a rich variety of features and phases. Coatings were predominantly nanostructured (grain size < 100 nm) and made of tetragonal phase of ZrO_2 with Al^{3+} in solid solution.

Tingaud et al. [265] manufactured by suspension plasma spraying (SPS) several alumina ($d_{50} = 0.6$ μm) and alumina–zirconia (YSZ $d_{50} = 0.4$ μm) composite coatings, varying the operating conditions to achieve dense and cohesive structures. For alumina they measured particle temperatures around 2000 °C and velocities as high as 450 m/s, resulting in coatings with high amount of α-phase. The preliminary results of the SPS wear behavior show rather low friction coefficient and good wear resistance, which is even better with the addition of ZrO_2 in the alumina matrix.

Darut et al. [259] showed that the Al_2O_3-ZrO_2 composite coatings showed higher wear resistance than the Al_2O_3 coatings.

(d) Alumina–Zirconia–Yttria
Solution plasma spraying [201] was used to process the ternary systems (mol%) $10Al_2O_3$–$86.4ZrO_2$–$3.6Y_2O_3$ and $20Al_2O_3$–$76.4ZrO_2$–$3.6Y_2O_3$. The nanostructures (10–40 nm) in both coatings were made predominantly of tetragonal ZrO_2 phase with some cubic phase. The sub-micrometer-sized regions contain, in addition to t-ZrO_2, small amounts of crystalline Al_2O_3 phases. Thus solution plasma spraying allows producing metastable ceramics with unusual structures.

(e) TiO_2–TiC Coatings
Manzat et al. [266, 267] have used HVSFS to spray TiO_2/TiC coatings for automotive engine applications. The suspension was composed of a nano-sized titania and a sub-micron-sized TiC dispersed in isopropanol. They succeeded to achieve spraying onto the inner surfaces of light metal and gray cast cylinder liners. Tests performed under dry sliding and lubricated conditions demonstrated an improved wear resistance compared to gray cast iron.

14.7.7.4 Titania Photo-Catalytic Coatings

Titania photo-catalytic layers were sprayed by suspension plasma spraying [268–282] or HVSFS [183, 283–285]. TiO_2 coatings are mostly designed for photo-catalytic applications. As pointed out by Toma et al. [207, 272, 273, 280], it is generally assumed that the metastable phase, anatase, presents higher photo-catalytic activity than the stable one, rutile. Coatings sprayed with Et-OH base suspensions contained only 23 % of anatase ratio (against 82 vol.% in the feedstock powder) and ensured a very low photo-catalytic decomposition of nitrogen oxides. In contrast, with water base suspensions, the anatase phase and crystallites size were preserved and the conversion rate of pollutant reached 40 % against 32 % for the starting powders [274].

Besides, Tomaszek et al. [275] measured the field emission characteristics of the obtained TiO_2 deposits. The influence of conditioning on emission properties was observed. The lighting segment excited by electrons from the field titania cathode has also been studied by Znamirowski et al. [276]. The titania cathode of the segment was manufactured with suspension plasma spraying. Operating tests reveal effective lighting properties of the segment, with very intense light emitted.

Kozerski et al. [277] studied the influence of the suspension solvent and injection on photo catalytic properties of plasma-sprayed titania suspension. The main conclusion of the study is that the coatings containing mainly rutile are also photo catalytically active for the degradation of aqueous solution of dye methylene blue. The photo-catalytic activity was not found to be correlated with the anatase content; thus further studies should clarify the role of suspension plasma spraying processing parameters, substrate material, suspension formulation, and coating microstructure (porosity, content of hydroxyl groups on the coatings surface, gap energy of the coatings, etc.) on the photo-catalytic activity. Bannier et al. [278]

prepared TiO_2 coatings by suspension plasma spraying from a TiO_2 nanoparticle suspension using two different substrates (a standard stainless steel and a Pyrex glass). They studied the influence of spray parameters and plasma torch design. A large amount of anatase was obtained, ranging from 32 to 72 wt%. Coatings displayed a bimodal microstructure with completely fused areas and non-molten ones with agglomerated anatase nanoparticles. The main parameters controlling this bimodal structure were the spray distance and the cooling. Yuan et al. [279] flame sprayed mixtures of suspensions and powder feedstock. They tailored over a wide range the anatase–rutile ratio and the proportion of nanostructures in the coatings, and up to 30 wt% of anatase in the coatings was obtained. The hybrid micro-/nanostructured TiO_2 coatings exhibited super-hydrophilic performances (0° contact angle). Results were closely linked to the concentration of nano TiO_2 particles (10–30 nm in size) in the starting suspension.

The HVSFS process leaves a fairly large degree of freedom to tailor TiO_2 coating characteristics (thickness, porosity, anatase content, hardness, etc.) according to the required functional properties by adjusting operating spray parameters [283]. For example, coatings with higher anatase content and higher specific surface can be produced to achieve higher photo catalytic efficiency, better than conventional APS and HVOF TiO_2.

Porous titania coatings were plasma sprayed from an aqueous solution containing titanium iso-propoxide [286]. It was shown that when increasing the power level, the anatase phase content decreased and the rutile one increased. In fact, the formation of crystalline anatase and rutile in the as-sprayed coatings was the result of plasma flow heat treatment on the gel like deposit (many non-pyrolized droplets).

14.7.7.5 Coatings for Medical Applications

Bouyer et al. [185] were the firsts to produce by r.f. plasma suspension spraying micrometer-sized Hydroxyapatite (HA) particles that were easy to spray by conventional means. Since then, many efforts were devoted to suspension or solution spraying of HA [287–293]. The development of multilayer coatings of hydroxyapatite (HA) and TiO_2 onto titanium substrates was later studied using suspension plasma spraying [287]. Jaworski et al. [271] have presented the recent developments in suspension d.c. plasma-sprayed HA coatings with rather low thickness (10–50 μm). Two types of coatings were tested: duplex and gradient coatings. The density of coatings was improved as well as their cohesion when increasing the torch power level, but unfortunately the HA was partially decomposed.

Łatka et al. [288] plasma sprayed homemade HA powder. The coatings presented two types of zones: (i) dense ones corresponding to splats, as in conventionally sprayed coatings; (ii) sintered ones containing fine hydroxyapatite grains, corresponding to the fine solids from the initial suspension. The latter disappeared

after soaking the coating in simulated body fluid (SBF), and the pores were filled by the re-precipitated calcium phosphates.

An ethylene glycol-based suspension was HVSFS processed [180] with 13wt% of HA powder, resulting in a dense coating structure with a porosity of about 1 % (coating thickness 50 μm). The coatings consisted of about 90 % of HAP with a small amount of tricalcium phosphate.

Stiegler et al. [293] used the HVSFS technique to deposit HA coatings onto titanium plates. The use of different dispersion media to prepare the HA suspensions affected the microstructure and mechanical properties of the resulting coatings more than the process parameters. However, coatings containing substantial amounts of amorphous phase tended to dissolve very rapidly in the SBF solution and to be replaced by a precipitation layer consisting of crystalline HA.

A phosphorous containing biocompatible glass was also HVSFS processed [294]: coatings displayed a certain porosity that seemed to consist mainly of closed pores with some transverse micro-cracks.

The high-velocity suspension flame spraying technique (HVSFS) was used by Altomare et al. [295] to deposit 45S5 bioactive glass coatings onto titanium substrates, using a suspension of micron-sized glass powders dispersed in a water–isopropanol mixture as feedstock. Depending on the spray parameters, coatings with different porosities and thicknesses were obtained. The sprayed coatings were entirely glassy but exhibited a through-thickness microstructural gradient and the glass network structure was analogous to that of bulk annealed 45S5 bioglass. The interaction mechanisms between coatings and the simulated body fluid (SBF) were also analogous to those of the bulk bioglass. They involved controlled dissolution of the glass, polymerization of an amorphous silica layer on the glass surface itself, and growth of a carbonated hydroxyapatite layer on top of the silica layer. Thus it seems that bioglass poses no trouble related to decomposition and phase alteration and the reactivity of the HVSFS-deposited bioglass coatings seems to be particularly fast, most of the original coating being replaced by the products of the interaction with the simulated body fluid (SBF) in only one week. Xiao et al. [296] have plasma sprayed P_2O_5–Na_2O–CaO–SiO_2 bioactive glass–ceramic coatings (BGCCs), where sol and suspension were used as feedstock. Results indicated that coatings with higher crystallinity were obtained using the sol precursor, while nanostructured coatings predominantly consisting of amorphous phase were synthesized using the suspension precursor. Overall, the liquid precursor plasma spraying process seems to be a promising technique to synthesize nanostructured BGCCs with good in vitro bioactivities. The same authors [297] plasma sprayed a solution to produce the same BGCC on a Ti substrate. The as-deposited coating consisted of two phases, with a predominant amorphous phase and a crystalline phase of $Na_2Ca_2Si_3O_9$. The in vitro bioactivity of the as-deposited coating was studied by SBF soaking. Results suggest that this coating has quick hydroxide carbonate apatite (HCA) formation capability in vitro, likely due to the existence of nanostructure in the as-sprayed coatings.

14.7.7.6 Anti-Corrosion Coatings

A $CaO–ZrO_2–SiO_2$ glass frit was processed by HVSFS [298]. Such glass, if dense, should have excellent anticorrosion properties on metal or ceramic substrates. The coatings obtained were much denser than those formerly investigated and plasma sprayed. Some problems were connected to the formation of molten glass deposits in the combustion chamber and their subsequent embedment in the coating. Work is in progress to overcome this problem and to achieve dense coatings with strong inter-lamellar cohesion.

Waltz et al. [299] have developed a synthesis for the preparation of nano-crystalline magnesium fluoride suspensions, which delivers nearly mono-disperse nanoparticles. These suspensions were deposited with a plasma torch onto TIG welded seams of the magnesium alloy AZ31, thus producing a protective magnesium fluoride layer. The corrosion properties of the magnesium fluoride layer on the welded seams were studied by means of potentiodynamic potential measurements and showed a significant lower corrosion rate.

14.7.7.7 SnO_2 Layers

An aqueous $SnCl_4$ solution feedstock was used to integrate the spray pyrolysis and sintering of nanometer-sized SnO_2 particles in nanometer-sized porous coating production [300]. The coating consisted of interpenetrating pores separating agglomerated particles which themselves and exhibited a layered structure with micropores between the layers. Each layer was comprised of SnO_2 nanometer-sized particles. The structure was apparently formed from overlapping viscous hollow spheres of Sn solution, which were pyrolyzed and annealed in situ. Sensors constructed directly from the porous coatings have good ethanol gas sensitivity at 200 °C.

14.7.7.8 Inconel Coatings

A HVSFS process has been developed to conduct spraying of small Inconel alloy 625 particles in suspension [301]. The coatings exhibited several interesting characteristics for potential applications, including full density, uniform microstructure, and high bond strength. Unfortunately, the preliminary erosion tests, carried out at 90° impact angle, indicated that the conventional HVOF coating was superior to the HVSFS coatings.

14.7.7.9 Antierosion Coatings

Kitamura et al. [302] have sprayed yttrium oxide (Y_2O_3) coatings by axial suspension plasma spraying with fine powders ($d_{50} = 1$ μm). Coatings had high hardness (640 $HV_{1.96N}$), low porosity (0.3-0.4 %), high erosion resistance (about 1.5 times that of bulk yttria) against CF_4-containing plasma and retention of smooth eroded surfaces. This suggested that the axial suspension plasma spraying of Y_2O_3 is applicable to fabricating equipment for electronic devices, such as dry etching.

14.7.7.10 Adhesive Layer on Smooth and Thin Substrate

Vert et al. [303] have studied the use of suspension plasma spraying to manufacture 1-mm thick zirconia coatings on smooth and thin (1 mm) substrates. The spraying conditions were optimized for the deposition of coatings on stainless steel AISI 304L substrates, and the process then adapted for Haynes 230 nickel-based alloy substrates. Special attention was paid to coating adhesion that was investigated by using a Vickers indentation cracking method. The adhesion of various coatings was studied and the effect of the substrate temperature on adhesion confirmed.

14.8 Summary and Conclusions

For about a decade, the interest for manufacturing on large surfaces "thick" finely structured or nanostructured layers have been increasingly growing. If gas condensation routes (CVD, PE-CVD, PVD, EB-PVD, etc.), allow manufacturing of nanostructured architectures, their thicknesses can hardly be higher than a few micrometers, except for EB-PVD. In contrast, conventional plasma spray coating thicknesses between 50 μm to a few millimeters are easily achieved but with no real nanostructured architectures after particle melting.

This explains the interest for the different techniques developed this last decade:

- Spraying with hot gases of amorphous metals, agglomerated ceramic particles, attrition or ball milled cermet or alloy particles, hypereutectic alloys
- Production of nanostructured coatings by cold spray
- Suspension thermal spraying (STS) and solution precursor thermal spraying (SPTS), both allowing achieving finely structured layers of thicknesses varying between a few micrometers up to a few hundreds of micrometers

These techniques seem promising to manufacture dense or porosity controlled coatings and functionally graded layers.

Some industrial applications are already using coatings made from powders with a size range in the tens of micrometers, especially those from amorphous powders. Nevertheless, coatings made from suspensions or solutions injected into hot gases,

are by far more complex because the chemistry (choice of solvent, dispersant, precursors,. . .), the liquid fragmentation and vaporization control the processes. This is probably why publications on first commercial applications are still missing. Moreover, presently diagnostic techniques are not available to measure in-flight droplets below 5 μm, which would permit getting a much better understanding of the phenomena involved. According to all papers published during the last decade, and also the beginning of the new one, the interaction plasma jet and liquid jet or drops is crucial for their fragmentation to sizes below around 10 μm and velocities imparted to particles contained in droplet suspensions or formed from solutions. However to optimize the process first the injection means of the liquid must be improved and new plasma torches developed. Injection setups producing liquid jets or drops with controlled narrow trajectories dispersion, narrow distributions of sizes (if possible around or below 50 μm), and velocities, both varying independently must be developed. To spray them, plasma torches with higher power levels (more than 100 kW), longer plasmas and low voltage fluctuations must be designed. The only one available now in the Axial III of Mettech. At last, the deposition rate, which is about 10–30 % that of conventional coatings, should also be improved. For suspensions HVOF spraying guns, called HVSFS, with longer combustion chambers have been designed to achieve combustion of both combustion gases and organic solvent. Dense and very smooth (Ra ~ 1.3 μm) coatings, consisting of well-flattened lamellae having a homogeneous size distribution, were obtained when micron-sized (~1–2 μm) powders. Both for plasma or HVSFS suspension spraying, the size distribution of particles used in suspension should be as narrow as possible. Mixtures in suspensions with a wide size distribution because of agglomerates and aggregates result in poor coatings. Thus particles having the tendency to agglomerate or aggregate must be avoided.

Thus it could be said that SPS and SPPS are in the same state as conventional spraying was in the 1980s and the beginning of the 1990s. As conventional spraying in the nineties, SPS and SPPS, for the last decade are the subjects of numerous papers in international reviews and conference proceedings. Coatings obtained (mostly ceramics) present very interesting features, especially a much better toughness than conventional coatings.

Numerous studies are still necessary to reach a better understanding of the involved phenomena and for that, the development of diagnostic techniques to either quantify temperature and velocity of the small (between a few tens of nanometers and a few tenths of micrometers) droplets or particles in flight, or to visualize their interactions with hot gases must be improved or newly developed.

No standards have been yet defined both for the spray process and solution or suspension preparation. It is not surprising that, to our best knowledge, no industrial developments of these techniques have been yet mentioned. If many potential applications have been described it is very difficult to predict which one will be the first industrially developed. However, a spray equipment manufacturer has recently proposed an industrial liquid-based feedstock feeder prototype that might be an indication of the potential interest of industry.

As pointed out by Killinger et al. [9]: "to promote industrial implementation, an urgent concern of future research work is to qualify liquid feedstock thermal spray coatings in a more application-oriented way and to communicate the results convincingly. As suspension and solution spray are to be clearly differentiated from classical thermal spray processes, also new industrial standards have to be defined concerning suspension and solution preparation, storage, feeding as well as qualification and handling of raw materials (i.e., ultra-fine powders, solvents, additives, etc.)".

Nomenclature

Latin Alphabet

d_{p}	Particle diameter (m)
d_{l}	Drop or droplet or liquid jet diameter (m)
l_{BL}	Thickness of the flow boundary layer in front of the substrate (m)
St	Stokes number $St = \dfrac{\rho_p d_p^2 \nu_p}{\mu_g \ell_{BL}}$
T_{m}	Material melting temperature (K)
u_{r}	Relative velocity gas-drop or droplet
v	Gas velocity (m/s)
v_{l}	Liquid velocity (m/s)
v_{p}	Particle velocity (m/s)
$\overline{V}$ or V_{m}	Mean voltage (V)
We	Weber number $\mathrm{We} = \dfrac{\rho_{\mathrm{g}} \times \mathrm{u_r^2} \times \mathrm{d}_\ell}{\sigma_\ell}$

Greek Alphabet

ΔV	Voltage fluctuations amplitude (V)
μ_{g}	Molecular viscosity (Pa. s)
ρ or ρ_{g}	Gas specific mass (kg/m^3)
ρ_{l}	Liquid specific mass (kg/m^3)
ρ_{p}	Particle specific mass (kg/m^3)
σ_{l}	Liquid surface tension (N/m)

References

1. McPherson R (1973) Formation of metastable phases in flame and plasma-prepared alumina. J Mater Sci 8:851–858
2. Ashby MF, Ferreira PJ, Schodek DL (2009) Nanomaterials properties. In: Nanomaterials, nanotechnologies and design. Elsevier, Kidlington, pp 199–255
3. Dahotre NB, Nayak S (2005) Nanocoatings for engine application. Surf Coat Technol 194 (1):58–67
4. Lu Y, Liaw PK (2001) The mechanical properties of nanostructured materials. J Metals 53(3):31–35
5. Fauchais P, Montavon G, Lima RS, Marple BR (2011) Engineering a new class of thermal spray nano-based microstructures from agglomerated nanostructured particles, suspensions and solutions: an invited review. J Phys D 44:093001
6. Branagan DJ, Swank WD, Haggard DC, Fincke JR (2001) Wear-resistant amorphous and nanocomposite steel coatings. Metall Mater Trans A 32A:2615–2621
7. Branagan DJ, Swank WD, Meacham BE (2009) Maximizing the glass fraction in iron-based high velocity oxy-fuel coatings. Metall Mater Trans A 40A:1306–1313
8. Guignard A, Mauer G, Vaßen R, Stöver D (2012) Deposition and characteristics of submicrometer-structured thermal barrier coatings by suspension plasma spraying. J Therm Spray Technol 21(3–4):416–424
9. Killinger A, Gadow R, Mauer G, Guignard A, Vaßen R, Stöver D (2011) Review of new developments in suspension and solution precursor thermal spray processes. J Therm Spray Technol 20(4):677–695
10. Viswanathan V, Laha T, Balani K, Agarwal A, Seal S (2006) Challenges and advances in nanocomposite processing techniques. Mat Sci Eng R54:121–285
11. Gadow R, Kern F, Killinger A (2008) Manufacturing technologies for nanocomposite ceramic structural materials and coatings. Mat Sci Eng B148:58–64
12. Fauchais P, Montavon G, Vardelle M, Cedelle J (2006) Developments in direct current plasma spraying. Surf Coat Technol 201(5):1908–1921
13. Fauchais P, Etchart-Salas R, Rat V, Coudert J-F, Car N, Wittmann-Ténèze K (2008) Parameters controlling liquid plasma spraying: solutions, sols or suspensions. J Therm Spray Technol 17(1):31–59
14. Branagan DJ, Breitsameter M, Meacham BE, Belashchenko V (2005) High-performance nanoscale composite coatings for boiler applications. J Therm Spray Technol 14(2):196–204
15. Lima RS, Marple BR (2007) Thermal spray coatings engineered from nanostructured ceramic agglomerated powders for structural, thermal barrier and biomedical applications: a review. J Therm Spray Technol 16(1):40–63
16. Ben-Ettouil F, Mazhorova O, Pateyron B, Ageorges H, El-Ganaoui M, Fauchais P (2008) Predicting dynamic and thermal histories of agglomerated particles injected within a d.c. plasma jet. Surf Coat Technol 202:4491–4495
17. Ajdelsztajn L, Jodoin B, Kim GE, Schoenung JM (2005) Cold spray deposition of nanocrystalline aluminum alloys. Metall Mater Trans A 36A:657–666
18. Fauchais P, Rat V, Coudert J-F, Etchart-Salas R, Montavon G (2008) Operating parameters for suspension and solution plasma-spray coatings. Surf Coat Technol 202:4309–4317
19. Chen D, Jordan EH, Gell M (2009) Microstructure of suspension plasma spray and air plasma spray Al_2O_3-ZrO_2 composite coatings. J Therm Spray Technol 18(3):421–426
20. Basu S, Jordan EH, Cetegen BM (2008) Fluid mechanics and heat transfer of liquid precursor droplets injected into high-temperature plasmas. J Therm Spray Technol 17(1):60–72
21. Wittmann-Ténèze K, Vallé K, Bianchi L, Belleville P, Caron N (2008) Nanostructured zirconia coatings processed by PROSOL deposition. Surf Coat Technol 202:4349–4354
22. Sergueeva AV, Branagan DJ, Mukherjee AK (2008) Microstructure/properties relationship in Fe-based nanomaterials. Mater Sci Eng A 493:237–240

23. Peker A, Johnson WL (1993) A highly processable metallic-glass Zr41.2Ti13.8Cu12.5Ni10.0Be22.5. Appl Phys Lett 63:2342–2344
24. Inoue A (1995) Thermal properties of Zr-TM-B and Zr-TM-Ga (TM = Co, Ni, Cu) amorphous alloys with wide range of supercooling. Mater Trans JIM 36:1411–1419
25. Sergueeva AV, Mara NA, Kuntz JD, Branagan DJ, Mukherjee AK (2004) Shear band formation and ductility of metallic glasses. Mater Sci Eng A 383(2):219–223
26. Otsubo F, Era H, Kishitake K (2000) Formation of amorphous Fe-Cr-Mo-8P-2C coatings by the high velocity oxy-fuel process. J Therm Spray Technol 9(4):494–498
27. Das SK, Norin EM, Bye RL (1984) Ni-Mo-Cr-B alloys: corrosion resistant amorphous hardfacing coatings. In: Kear BH, Cohen M (eds) Materials research society symposium proceedings. Elsevier Science, Amsterdam, pp 233–237
28. Sampath S, Neiser RA, Herman H, Kirkland JP, Elam WT (1993) A structural investigation of a plasma sprayed Ni-Cr based alloy coating. J Mater Res 1:78–86
29. Kishitake K, Era H, Otsubo F (1996) Characterization of plasma sprayed Fe-10Cr-10Mo-(C, B) amorphous coatings. J Therm Spray Technol 5(2):145–153
30. Kishitake K, Era H, Otsubo F (1996) Characterization of plasma sprayed Fe-17Cr-38Mo-4C amorphous coatings crystallizing at extremely high temperature. J Therm Spray Technol 5 (3):283–288
31. Dent AH, Horlock AJ, McCartney DG, Harris SJ (1999) The corrosion behavior and microstructure of high-velocity oxy-fuel sprayed nickel-base amorphous/nanocrystalline coatings. J Therm Spray Technol 8(3):399–404
32. Choi H, Kim J, Lee C, Lee KH (2005) Critical factors affecting the amorphous phase formation of NiTiZrSiSn bulk amorphous feedstock in vacuum plasma spray. J Mater Sci 40:3873–3875
33. Branagan DJ, Kramer MJ, Tang Y, McCallum RW, Crew DC, Lewis LH (2000) Engineering magnetic nanocomposite microstructures. J Mater Sci 35:3459–3466
34. Branagan DJ (2007) Engineering structures to achieve targeted properties in steels on a nanoscale level. Comput Coupling Phase Dia Thermochem 31:343–350
35. Branagan DJ, Marshall MC, Meacham BE, Aprigliano LF, Bayles R, Lemieux EJ, Newbauer T, Martin FJ, Farmer JC, Haslam JJ, Day SD (2006) Wear and corrosion resistant amorphous/nanostructured steel coatings for replacement of electrolytic hard chromium. In: Marple B (ed) Proceedings of the 2006 international thermal spray conference, e-procceedings. ASM International, Materials Park, OH
36. Parco M, Fagoaga I, Bobzin K, Lugsheider E, Zwick J, Hildago G. Developement and characterization of nanostructured iron-based coatings by HFPD and HVOF. In: Marple B (ed) Proceedings of the 2006 international thermal spray conference, e-proceedings. ASM International, Materials Park, OH
37. Zhou J, Walleser JK, Meacham BE, Branagan DJ (2010) Novel in situ transformable coating for elevated-temperature applications. J Therm Spray Technol 19(5):950–957
38. Wilden J, Bergmann JP, Reich S, Schlichting S, Schnick T (2007) Cladding of aluminum substrates with nano crystalline solidifying wear resistant iron-based materials. In: Marple BR, Hyland MM, Lau Y-C, Li C-J, Lima RS, Montavon G (eds) Thermal spray 2007: global coating solutions. ASM International, Materials Park, OH, e-proceedings
39. Shaw LL, Goberman D, Ren R, Gell M, Jiang S, Wang Y, Xiao TD, Strutt PR (2000) The dependency of microstructure and properties of nanostructured coatings on plasma spray conditions. Surf Coat Technol 130:1–8
40. Wang M, Shaw LL (2007) Effects of the powder manufacturing method on microstructure and wear performance of plasma sprayed alumina–titania coatings. Surf Coat Technol 202:34–44
41. Guru D, Heberlein J (2008) Plasma spray processing of nanostructured partially stabilized zirconia for a strain accommodating inter-layer – splat characteristics. In: Lugsheider E (ed) ITSC 2008: thermal spray crossing borders. DVS, Düsseldorf, Germany, e-proceedings

42. Lima RS, Kucuk A, Berndt CC (2002) Bimodal distribution of mechanical properties on plasma sprayed nanostructured partially stabilized zirconia. Mater Sci Eng A A327:224–232
43. Lima RS, Marple BR, Dadouche A, Dmochowski W, Liko B (2006) Nanostructured abradable coatings for high temperature applications. In: Marple BR, Hyland MM, Lau Y-C, Lima RS, Voyer J (eds) Building on 100 years of success: proceedings of the international thermal spray conference 2006. ASM International, Materials Park, OH, e-proceedings
44. Fauchais P (1991) Molten particle deposition. In: Schneider SJ Jr (ed) Engineered materials handbook, vol 4 – ceramics and glasses. ASM International, Materials Park, OH
45. Lima RS, Marple BR (2008) Nanostructured YSZ thermal barrier coatings engineered to counteract sintering effects. Mater Sci Eng A 485:182–193
46. Shaw LL, Goberman D, Ren R, Gell M, Jiang S, Wang Y, Xiao TD, Strutt PR (2003) The dependency of microstructure and properties of nanostructured coatings on plasma spray conditions. Surf Coat Technol 130:1–8
47. Lima RS, Marple BR (2006) From APS to HVOF spraying of conventional and nanostructured titania feedstock powders: a study on the enhancement of the mechanical properties. Surf Coat Technol 200:3428–3437
48. Lima RS, Marple BR (2005) Superior performance of high-velocity oxyfuel-sprayed nanostructured TiO_2 in comparison to air plasma-sprayed conventional Al_2O_3-13TiO_2. J Therm Spray Technol 14(3):397–404
49. Ahmed I, Bergman TL (1999) Thermal modeling of plasma spray deposition of nanostructured ceramics. J Therm Spray Technol 8(2):315–322
50. Zhu Y, Huang M, Huang J, Ding C (1999) Vacuum-plasma sprayed nanostructured titanium oxide films. J Therm Spray Technol 8(2):219–222
51. Gell M, Jordan EH, Sohn YH, Goberman D, Shaw L, Xiao TD (2001) Development and implementation of plasma sprayed nanostructured ceramic coatings. Surf Coat Technol 146–147:48–54
52. Ok Chwa S, Klein D, Toma FL, Bertrand G, Liao H, Coddet C, Ohmori A (2005) Microstructure and mechanical properties of plasma sprayed nanostructured TiO2–Al composite coatings. Surf Coat Technol 194:215–224
53. Wang Y, Jiang S, Wang M, Wang Xiao STD, Strutt PR (2000) Abrasive wear characteristics of plasma sprayed nanostructured alumina/titania coatings. Wear 237:176–185
54. Jiang X-L, Jordan E, Shaw L, Gell M (2003) Mechanism of deformation of nanostructured ceramic coatings. Mater Sci 39(2):305–306
55. Song EP, Ahn J, Lee S, Kim NJ (2006) Microstructure and wear resistance of nanostructured Al2O3–8wt.%TiO2 coatings plasma-sprayed with nanopowders. Surf Coat Technol 201:1309–1315
56. Ctibor P, Neufuss K, Chraska P (2006) Microstructure and abrasion resistance of plasma sprayed titania coatings. J Therm Spray Technol 15(4):689–694
57. Ahn Jeehoon, Byoungchul Hwang, Eun Pil Song, Sunghak Lee, Nack J Kim (2006) Correlation of microstructure and wear resistance of Al_2O_3-TiO_2 coatings plasma sprayed with nanopowders. Metall Mater Trans A 37A:1851–1861
58. Song Eun Pil, Jeehoon Ahn, Sunghak Lee, Nack J Kim (2008) Effects of critical plasma spray parameter and spray distance on wear resistance of Al2O3–8 wt.%TiO2 coatings plasma-sprayed with nanopowders. Surf Coat Technol 202(15): 3625–3632
59. Lima RS, Marple BR (2005) Enhanced ductility in thermally sprayed titania coating synthesized using a nanostructured feedstock. Mater Sci Eng A 395:269–280
60. Lima RS, Marple BR (2000) From APS to HVOF spraying of conventional and nanostructured titania feedstock powders: a study on the enhancement of the mechanical properties. Surf Coat Technol 200:3428–3437
61. Liu Y, Fischer TE, Dent A (2003) Comparison of HVOF and plasma-sprayed alumina/titania coatings—microstructure, mechanical properties and abrasion behavior. Surf Coat Technol 167:68–76

62. Lima RS, Marple BR (2003) High weibull modulus HVOF titania coatings. J Therm Spray Technol 12(2):240–249
63. Lima RS, Marple BR (2003) Optimized HVOF titania coatings. J Therm Spray Technol 12 (3):360–369
64. Turunen E, Varis T, Hannula S-P, Vaidya A, Kulkarni A, Gutleber J, Sampath S, Herman H (2006) On the role of particle state and deposition procedure on mechanical, tribological and dielectric response of high velocity oxy-fuel sprayed alumina coatings. Mater Sci Eng A 415:1–11
65. Lima RS, Moreau C, Marple BR (2007) HVOF-sprayed coatings engineered from mixtures of nanostructured and submicron Al_2O_3-TiO2 powders: an enhanced wear performance. J Therm Spray Technol 16(5–6):866–872
66. Varis T, Knuuttila J, Turunen E, Leivo J, Silvonen J, Oksa M (2007) Improved protection properties by using nanostructured ceramic powders for HVOF coatings. J Therm Spray Technol 16(4):524–532
67. Ibrahim A, Lima RS, Berndt CC, Marple BR (2007) Fatigue and mechanical properties of nanostructured and conventional titania (TiO2) thermal spray coatings. Surf Coat Technol 201:7589–7596
68. Lima RS, Kruger SE, Marple BR (2008) Towards engineering isotropic behaviour of mechanical properties in thermally sprayed ceramic coatings. Surf Coat Technol 202 (15):3643–3652
69. Lin Xinhua, Yi Zeng, Xuebin Zheng, Chuanxian Ding (2005) Thermal diffusivity of plasma sprayed monolithic coating of alumina–3 wt.% titania produced with nanostructured powder. Surf Coat Technol 195:85–90
70. Chen Huang, Chuanxian Ding, Pingyu Zhang, Peiqing La, Soo Wohn Lee (2003) Wear of plasma-sprayed nanostructured zirconia coatings against stainless steel under distilled-water conditions. Surf Coat Technol 173:144–149
71. Shunyan T, Liang B, Ding C, Liao H, Coddet C (2005) Wear characteristics of plasma-sprayed nanostructured yttria partially stabilized zirconia coatings. J Therm Spray Technol 14 (4):518–523
72. Turunen E, Varis T, Gustafsson TE, Keskinen J, Falt T, Hannula S-P (2006) Parameter optimization of HVOF sprayed nanostructured alumina and alumina-nickel composite coatings. Surf Coat Technol 200:4987–4994
73. Luo H, Goberman D, Shaw L, Gell M (2003) Indentation fracture behavior of plasma-sprayed nanostructured Al_2O_3-13wt%TiO_2 coatings. Mater Sci Eng A 346:237–245
74. McPherson R (1989) A review of microstructure and properties of plasma sprayed ceramic coatings. Surf Coat Technol 39–40(1):173–181
75. Bansal P, Padture NP, Vasiliev A (2003) Improved interfacial mechanical properties of Al_2O_3-13wt%TiO_2 plasma-sprayed coatings derived from nanocrystalline powders. Acta Mater 51:2959–2970
76. Ahn J, Hwang B, Song EP, Lee S, Kim NJ (2006) Correlation of microstructure and wear resistance of Al_2O_3-TiO_2 coatings plasma sprayed with nano-powders. Metall Mater Trans A 37A:1851–1861
77. Goberman D, Sohn YH, Shaw L, Jordan EH, Gell M (2002) Microstructured development of Al_2O_3-13wt%TiO_2 plasma sprayed coatings derived from nanocrystalline powders. Acta Mater 50:1141–1152
78. Ghasripoor F, Schmid R, Dorfman MR (1997) Abradable coatings increase gas turbine engine efficiency. Mater World 5(6):328–330
79. Lima RS, Kucuk A, Berndt CC (2001) Evaluation of microhardness and elastic modulus of thermally sprayed nanostructured zirconia coatings. Surf Coat Technol 135:166–172
80. Chen H, Ding CX (2002) Nanostructured zirconia coating prepared by atmospheric plasma spraying. Surf Coat Technol 150:31–36
81. Chen H, Zhou X, Ding C (2003) Investigation of the thermomechanical properties of a plasma-sprayed nanostructured zirconia coating. J Eur Ceram Soc 23:1449–1455

82. Chen H, Lee SW, Choi CH, Hur BY, Zeng Y, Zheng XB, Ding CX (2004) Plasma sprayed nanostrucutred zirconia coatings deposited from different powders with nano-scale substructure. J Mater Res 39:4701–4703
83. Liang B, Ding C (2005) Thermal shock resistances of nanostructured and conventional zirconia coatings deposited by atmospheric plasma spraying. Surf Coat Technol 197:185–192
84. Liang B (2005) Chuanxian ding, phase composition of nanostructured zirconia coatings deposited by air plasma spraying. Surf Coat Technol 191:267–273
85. Liang B, Ding C, Liao H, Coddet C (2006) Phase composition and stability of nanostructured 4.7wt.% yttria-stabilized zirconia coatings deposited by atmospheric plasma spraying. Surf Coat Technol 200:4549–4556
86. Gong WB, Sha CK, Sun DQ, Wang WQ (2006) Microstructures and thermal insulation capability of plasma-sprayed nanostructured ceria stabilized zirconia coatings. Surf Coat Technol 201:3109–3115
87. Racek O, Berndt CC, Guru DN, Heberlein J (2006) Nanostructured and conventional YSZ coatings deposited using APS and TTPR techniques. Surf Coat Technol 201:338–346
88. Soltani R, Garcia E, Coyle TW, Mostaghimi J, Lima RS, Marple BR, Moreau C (2006) Thermomechanical behavior of nanostructured plasma sprayed zirconia coatings. J Therm Spray Technol 15(4):657–662
89. Racek O, Berndt CC (2007) Mechanical property variations within thermal barrier coatings. Surf Coat Technol 202:362–369
90. Padture NP, Gell M, Jordan EH (2002) Thermal barrier coatings for gas turbine engine applications. Science 296:280–284
91. Lima RS, Marple BR (2008) Toward highly sintering-resistant nanostructured ZrO_2-7wt% Y_2O_3 coatings for TBC applications by employing differential sintering. J Therm Spray Technol 17(5–6):846–852
92. Wang WQ, Sha CK, Sun DQ, Gu XY (2006) Microstructural feature, thermal shock resistance and isothermal oxidation resistance of nanostructured zirconia coating. Mater Sci Eng A 424:1–5
93. Liu C-B, Zhang Z-M, Jiang X-L, Liu M, Zhu Z-H (2009) Comparison of thermal shock behaviors between plasma-sprayed nanostructured and conventional zirconia thermal barrier coatings. Trans Nonferrous Metals Soc China 19:99–107
94. Zhou C, Wang N, Xu H (2007) Comparison of thermal cycling behavior of plasma-sprayed nanostructured and traditional thermal barrier coatings. Mater Sci Eng A 452–453:569–574
95. Lima RS, Khor KA, Li H, Cheang P, Marple BR (2005) HVOF spraying of nanostructured hydroxyapatite for biomedical applications. Mater Sci Eng A 396:181–187
96. Li H, Khor KA, Cheang P (2000) Effect of the powders' melting state on the properties of HVOF sprayed hydroxyapatite coatings. Mater Sci Eng A 293:1–80
97. Li H, Khor KA (2006) Characteristics of the nanostructures in thermal sprayed hydroxyapatite coatings and their influence on coating properties. Surf Coat Technol 201:2147–2154
98. Yang YC, Chang C (2003) The bonding of plasma-sprayed hydroxyapatite coatings to titanium: effect of processing, porosity and residual stress. Thin Solid Films 444:260–275
99. Li H, Khor KA, Kumar R, Cheang P (2004) Characterization of hydroxyapatite-nanozirconia composite coatings deposited by high velocity oxy-fuel (HVOF) spray process. Surf Coat Technol 182:227–236
100. Webster TJ, Siegel RW, Bizios R (1999) Osteoblast adhesion on nanophase ceramics. Biomaterials 20:1221–1227
101. Sun L, Berndt CC, Gross KA, Kucuk A (2001) Materials fundamentals and clinical performance of plasma-sprayed hydroxyapatite coatings: a review. J Biomed Mater Res 58:570–592
102. Lai KA (2002) Failure of hydroxyapatite-coated acetabular cups. J Bone Surg (Br) 84-B (5):64646
103. Yang Y-C, Yang C-Y (2013) Mechanical and histological evaluation of a plasma sprayed hydroxyapatite coating on a titanium bond coat. Ceram Int 39: 6509–6516

104. Gutwein LG, Webster TJ (2004) Increased viable osteoblast density in the presence of nanophase compared to conventional alumina and titania particles. Biomaterials 25:4175–4183
105. Lima RS, Li H, Khor KA, Marple BR (2006) Biocompatible nanostructured high-velocity oxyfuel sprayed titania coating: deposition, characterization, and mechanical properties. J Therm Spray Technol 15(4):623–627
106. Kim GE, Walker J (2007) Successful application of nanostructured titanium dioxide coating for high-pressure acid-leach application. J Therm Spray Technol 16(1):34–39
107. Wang Y, Tian W, Yang Y (2007) Thermal shock behaviour of nanostructured and conventional Al_2O_3/13 wt% TiO_2 coatings fabricated by plasma spraying. Surf Coat Technol 201:7746–7754
108. Eigen N, Gartner F, Klassen T, Aust E, Bormann R, Kreye H (2005) Microstructures and properties of nanostructured thermal sprayed coatings using high-energy milled cermet powders. Surf Coat Technol 195:344–357
109. Lau ML, Strock E, Fabel A, Lavernia CJ, Lavernia EJ (1998) Synthesis and characterization of nanocrystalline Co43 coatings by plasma spraying. NanoStructured Mater 10(5):723–730
110. Ajdelsztajn L, Lee J, Chung K, Bastian FL, Lavernia EJ (2002) Synthesis and nanoindentation study of high-velocity oxygen fuel thermal-sprayed nanocrystalline and near-nanocrystalline Ni coatings. Metall Mater Trans A 33A:647–655
111. Cherigui M, Fenineche NE, Coddet C (2005) Structural study of iron-based microstructured and nanostructured powders sprayed by HVOF thermal spraying. Surf Coat Technol 192:19–26
112. Cherigui M, Fenineche NE, Gupta A, Zhang G, Coddet C (2006) Magnetic properties of HVOF thermally sprayed coatings obtained from nanostructured powders. Surf Coat Technol 201:1805–1813
113. Jing HG, Lau ML, Lavernia EJ (1998) Grain growth behavior of nanocrystalline Inonel 718 and Ni powders and coatings. NanoStructured Mater 10(2):169–178
114. Tang F, Ajdelsztajn L, Kim GE, Provenzano V, Schoenung JM (2004) Effects of surface oxidation during HVOF processing on the primary stage oxidation of a CoNiCrAlY coating. Surf Coat Technol 185:228–233
115. Tang F, Ajdelsztajn L, Schoenung JM (2004) Influence of cryomilling on the morphology and composition of the oxide scales formed on HVOF CoNiCrAlY coatings. Oxidation Metals 61 (3/4):219–238
116. Ajdelsztajn L, Tang F, Kim GE, Provenzano V, Schoenung JM (2005) Synthesis and oxidation behavior of nanocrystalline MCrAlY bond coatings. J Therm Spray Technol 14 (1):23–30
117. He J, Schoenung JM (2002) A review on nanostructured WC–Co coatings. Surf Coat Technol 157:72–79
118. Qiao Y, Liu Y, Fischer TE (2000) Sliding and abrasive wear resistance of thermal-sprayed WC-Co coatings. J Therm Spray Technol 10(1):118–125
119. He J, Ice M, Lavernia EJ (2000) Synthesis of nanostructured Cr_3C_2-25(Ni20Cr) coatings. Metall Mater Trans A 31A:555–564
120. Kear BH, Sadangi RK, Jain M, Yao R, Kalman Z, Skandan G, Mayo WE (1999) Thermal sprayed nanostructured WC/Co hardcoatings. J Therm Spray Technol 9(3):399–406
121. He J, Ice M, Dallek S, Lavernia EJ (2000) Synthesis of nanostructured WC-12 wt. % Co coating using mechanical milling and high velocity oxygen fuel thermal spraying. Metall Mater Trans A 31A:541–553
122. Skandan G, Yao R, Sadangi R, Kear BH, Qiao Y, Liu L, Fischer TE (1999) Multimodal coatings: a new concept in thermal spraying. J Therm Spray Technol 9(3):329–331
123. Ban Z-G, Shaw LL (2002) Synthesis and processing of nanostructured WC-Co materials. J Mater Sci 37:3397–3403

124. Dent AH, DePalo S, Samph S (2001) Examination of the wear properties of HVOF sprayed nanostructured and conventional WC-Co cermets with different binder phase contents. J Therm Spray Technol 11(4):551–558
125. Qiao Y, Fischer TE, Andrew Dent (2003) The effects of fuel chemistry and feedstock powder structure on the mechanical and tribological properties of HVOF thermal-sprayed WC–Co coatings with very fine structures. Surf Coat Technol 172:24–41
126. Ban ZG, Shaw LL (2003) Characterization of thermal sprayed nanostructured WC-Co coatings derived from nanocrystalline WC-18wt.%Co powders. J Therm Spray Technol 12 (1):112–119
127. Marple BR, Lima RS (2005) Process temperature/velocity-hardness-wear relationships for high-velocity oxyfuel sprayed nanostructured and conventional cermet coatings. J Therm Spray Technol 14(1):67–76
128. Bartuli C, Valente T, Cipri F, Bemporad E, Tului M (2005) Parametric study of an HVOF process for the deposition of nanostructured WC-Co coatings. J Therm Spray Technol 14 (2):187–195
129. Guilemany JM, Dosta S, Miguel JR (2006) The enhancement of the properties of WC-Co HVOF coatings through the use of nanostructured and microstructured feedstock powders. Surf Coat Technol 201:1180–1190
130. Siegmann S, Brandt O, Dvorak M (2004) Thermally sprayed wear resistant coatings with nanostructured hard phases. J Therm Spray Technol 13(1):37–43
131. He J, Ice M, Schoenung JM, Shin DH, Lavernia EJ (2001) Thermal stability of nanostructured Cr_3C_2-NiCr coatings. J Thermal Spray Technol 10(2):293–300
132. Matthews S, Hyland M, James B (2004) Long-term carbide development in high-velocity oxygen fuel/high-velocity air fuel Cr_3C_2-NiCr coatings heat treated at 900 °C. J Therm Spray Technol 13(4):526–536
133. Roy M, Pauschitz A, Bernardi J, Koch T, Franek F (2006) Microstructure and mechanical properties of HVOF sprayed nanocrystalline Cr_3C_2-25(Ni20Cr) coating. J Therm Spray Technol 15(3):372–381
134. Ji G, Grosdidier T, Morniroli J-P (2007) Microstructure of a high-velocity oxy-fuel thermal-sprayed nanostructured coating obtained from milled powder. Metall Mater Trans A 38A:2455–2463
135. He J, Schoenung JM (2003) Nanocrystalline Ni coatings strengthened with ultrafine particles Ni-AlN HVOF. Metall Mater Trans A 34A:673–683
136. Basak AK, Achanta S, Celis J-P, Vardavoulias M, Matteazzi P (2008) Structure and mechanical properties of plasma sprayed nanostructure ed alumina and FeCuAl–alumina cermet coatings. Surf Coat Technol 202:2368–2373
137. Hwang C, Chia-ho Y (2007) Formation of nanostructured YSZ/Ni anode with pore channels by plasma spraying. Surf Coat Technol 201:5954–5959
138. Laha T, Agarwal A, McKechnie T (2004) Forming nanostructured hypereutectic aluminum via high-velocity oxyfuel spray deposition. JOM J Min Met Mater Soc 56(1):54–56
139. Laha T, Agarwal A, McKechnie T, Rea K, Seal S (2005) Synthesis of bulk nanostructured aluminum alloy component through vacuum plasma spray technique. Acta Mater 53:5429–5438
140. Laha T, Agarwal A, McKechnie T, Seal S (2004) Synthesis and characterization of plasma spray formed carbon nanotube reinforced aluminum composite. Mater Sci Eng A 381:249–258
141. Laha T, Kuchibhatla S, Seal S, Li W, Agarwal A (2007) Interfacial phenomena in thermally sprayed multiwalled carbon nanotube reinforced aluminum nanocomposite. Acta Mater 55:1059–1066
142. Ajdelsztajn L, Zúñiga A, Jodoin B, Lavernia EJ (2006) Cold-spray processing of a nanocrystalline Al-Cu-Mg-Fe-Ni alloy with Sc. J Therm Spray Technol 15(2):184–190

143. Wang H-T, Li C-J, Yang G-J, Li C-X, Zhang Q, Li W-Y (2007) Microstructural characterization of cold-sprayed nanostructured FeAl intermetallic compound coating and its ball-milled feedstock powders. J Therm Spray Technol 16(5–6):669–676
144. Ajdelsztajn L, Jodoin B, Schoenung JM (2006) Synthesis and mechanical properties of nanocrystalline Ni coatings produced by cold gas dynamic spraying. Surf Coat Technol 201:1166–1172
145. Zhang Q, Li C-J, Li C-X, Yang G-J, Lui S-C (2008) Study of oxidation behavior of nanostructured NiCrAlY bond coatings deposited by cold spraying. Surf Coat Technol 202 (14):3378–3384
146. Li C-J, Yang G-J, Gao P-H, Ma J, Wang Y-Y, Li C-X (2007) Characterization of nanostructured WC-Co, deposited by cold spraying. J Therm Spray Technol 16(5–6):1011–1020
147. Yandouzi M, Sansoucy E, Ajdelsztajn L, Jodoin B (2007) WC-based cermet coatings produced by cold gas dynamic and pulsed gas dynamic spraying processes. Surf Coat Technol 202:382–390
148. Ajdelsztajn L, Jodoin B, Richer P, Sansoucy E, Lavernia EJ (2006) Cold gas dynamic spraying of iron-base amorphous alloy. J Therm Spray Technol 15(4):495–500
149. Sansoucy E, Kim GE, Moran AL, Jodoin B (2007) Mechanical characteristics of Al-Co-Ce coatings produced by the cold spray process. J Therm Spray Technol 16(5–6):651–660
150. Fauchais P, Rat V, Delbos C, Coudert J-F, Chartier T, Bianchi L (2005) Understanding of suspension D.C. plasma spraying of finely structured coatings for SOFC. IEEE Trans Plasma Sci 33(2):920–930
151. Fazilleau J, Delbos C, Rat V, Coudert J-F, Fauchais P, Pateyron B (2006) Phenomena involved in suspension plasma spraying part 1: suspension injection and behaviour. Plasma Chem Plasma Process 26(4):371–391
152. Etchart-Salas R, Rat V, Coudert JF, Fauchais P, Caron N, Wittman K, Alexandre S (2007) Influence of plasma instabilities in ceramic suspension plasma spraying. J Therm Spray Technol 16(5–6):857–865
153. Bhatia T, Ozturk A, Xie LD, Jordan EH, Cetegen BM, Gell M, Ma XC, Padture NP (2001) Mechanisms of ceramic coating deposition in solution precursor spray. J Mater Res 17 (9):2363–2372
154. Gell M, Xie LD, Ma XC, Jordan EH, Padture NP (2004) Highly durable thermal barrier coatings made by the solution precursor plasma spray process. Surf Coat Technol 13 (1):97–102
155. Jordan EH, Xie LD, Ma XC, Gell M, Padture NP, Cetegem B, Roth J, Xiao TD, Bryant PEL, Roth J, Xiao TD, Bryant PEC (2004) Superior thermal barrier coatings using solution precursor plasma spray. J Therm Spray Technol 13(1):57–65
156. Padture NP, Schlichting KW, Bhatia T, Ozturk A, Cetegem B, Jordan EH, Gell M, Jiang S, Xiao TD, Strutt PR, Garcia E, Miranzo P, Osendi MI (2001) Towards durable thermal barrier coatings with novel microstructures deposited by solution precursor plasma spray. Acta Mater 49:2251–2257
157. Marchand C, Vardelle A, Mariaux G, Lefort P (2008) Modelling of the plasma spray process with liquid feedstock injection. Surf Coat Technol 202:4458–4464
158. Fauchais P, Vardelle A (2011) Innovative and emerging processes in plasma spraying: from micro- to nanostructured coatings. J Phys D Appl Phys 44:194011 (14pp)
159. Bertolissi G, Chazelas C, Bolelli G, Lusvarghi L, Vardelle M, Vardelle A (2012) Engineering the microstructure of solution precursor plasma-sprayed coatings. J Therm Spray Technol 21(6): 1148–1158
160. Marchand O, Girardot L, Planche MP, Bertrand P, Bailly Y, Bertrand G (2011) An insight into suspension plasma spray: injection of the suspension and its interaction with the plasma flow. J Therm Spray Technol 20(6):1310–1320
161. Landes K (2006) Diagnostics in plasma spraying techniques. Surf Coat Technol 201:1948–1954

162. Mauer G, Guignard A, Vaßen R, Stöver D (2010) Process diagnostics in suspension plasma spraying. Surf Coat Technol 205:961–966
163. Soysal D, Ansar A (2013) A new approach to understand liquid injection into atmospheric plasma jets. Surf Coat Technol 220:187–190
164. Shan Y, Coyle TW, Mostaghimi J (2007) Numerical simulation of droplet break-up and collision in solution precursor plasma spraying. J Therm Spray Technol 16:698–704
165. Vincent S, Balmigere G, Caruyer C, Meillot E, Caltagirone J-P (2009) Contribution to the modeling of the interaction between a plasma flow and a liquid jet. Surf Coat Technol 203:2162–2171
166. Meillot E, Vincent S, Caruyer C, Caltagirone J-P, Damiani D (2009) From DC time-dependent thermal plasma generation to suspension plasma-spraying interactions. J Therm Spray Technol 18:875–86
167. Caruyer C, Vincent S, Meillot E, Caltagirone J-P (2010) Modeling the first instant of the interaction between a liquid and a plasma jet with a compressible approach. Surf Coat Technol 205:974–979
168. Basu S, Cetegen BM (2008) Modeling of liquid ceramic precursor droplets in a high velocity oxy-fuel flame jet. Acta Mater 56:2750–2759
169. Delbos C, Fazilleau J, Rat V, Coudert JF, Fauchais P, Pateyron B (2006) Phenomena involved in suspension plasma spraying part 2: zirconia particle treatment and coating formation. Plasma Chem Plasma Process 26:393–414
170. VanEvery K, Krane MJM, Trice RW (2012) Parametric study of suspension plasma spray processing parameters on coating microstructures manufactured from nanoscale yttria-stabilized zirconia. Surf Coat Technol 206:2464–2473
171. Brousse-Pereira E (2010) Elaboration by thermal spray of finely structured elements of a high temperature electolyser for hydrogen production: processes, structures and characteristics. Ph.D. thesis, University of Limoges, France, 21 Sept 2010
172. Brousse E, Montavon G, Fauchais P, Denoirjean A, Rat V, Coudert J-F, Ageorges H (2008) Thin and dense yttria-partially stabilized zirconia electrolytes for IT-SOFC manufactured by suspension plasma spraying. In: Lugscheider E (ed) Thermal spray crossing borders. DVS, Düsseldorf, Germany, pp 547–552
173. Racek O (2010) The effect of HVOF particle-substrate interactions on local variations in the coating microstructure and the corrosion resistance. J Therm Spray Technol 19(5):841–851
174. Basu S, Jordan EH, Cetegen BM (2006) Fluid mechanics and heat transfer of liquid precursor droplets injected into high temperature plasmas. J Therm Spray Technol 15(4):576–581
175. Oberste-Berghaus J, Legoux J-G, Moreau C, Tarasi F, Chraska T (2008) Mechanical and thermal transport properties of suspension thermal-sprayed alumina-zirconia composite coatings. J Therm Spray Technol 17(1):91–104
176. Oberste Berghaus J, Legoux J-G, Moreau C, Tarasi F, Chráska T (2007) Mechanical and thermal transport properties of suspension thermal sprayed alumina-zirconia composite coatings. In: Marple BR, Hyland MM, Lau Y-C, Li C-J, Lima RS, Montavon G (eds) Thermal spray 2007: global coating solutions. ASM International, Materials Park, OH, e-proceedings
177. Tarasi F, Medraj M, Dolatabadi A, Oberste-Berghaus J, Moreau C (2008) Effective parameters in axial injection suspension plasma spray process of alumina-zirconia ceramics. J Therm Spray Technol 17(5–6):685–691
178. Tarasi F, Medraj M, Dolatabadi A, Oberste-Berghaus J, Moreau C (2011) Amorphous and crystalline phase formation during suspension plasma spraying of the alumina–zirconia composite. J Eur Ceram Soc 31:2903–2913
179. Erne M, Kolar D, Hübsch C, Möhwald M, Bach Fr-W (2012) Synthesis of tribologically favorable coatings for hot extrusion tools by suspension plasma spraying. J Therm Spray Technol 21(3–4):668–675
180. Gadow R, Killinger A, Rauch J (2008) New results in high velocity suspension flame spraying (HVSFS). Surf Coat Technol 202:4329–4336

181. Dongmo E, Gadow R, Killinger A, Wenzelburger M (2009) Modeling of combustion as well as heat, mass, and momentum transfer during thermal spraying by HVOF and HVSFS. J Therm Spray Technol 18(5–6):896–908
182. Dongmo E, Wenzelburger M, Gadow R (2008) Analysis and optimization of the HVOF process by combined experimental and numerical approaches. Surf Coat Technol 202:4470–4478
183. Killinger A, Kuhn M, Gadow R (2006) High-velocity suspension flame spraying (HVSFS), a new approach for spraying nanoparticles with hypersonic speed. Surf Coat Technol 201:1922–1929
184. Bolelli G, Cannillo V, Gadow R, Killinger A, Lusvarghi L, Rauch J, Romagnoli M (2010) Effect of the suspension composition on the microstructural properties of high velocity suspension flame sprayed (HVSFS) Al_2O_3 coatings. Surf Coat Technol 204:1163–1179
185. Bouyer E, Gitzhofer F, Boulos MI (1997) The suspension plasma spraying of bioceramics by induction plasma. JOM February:58–62
186. Jia L, Gitzhofer F (2010) Induction plasma synthesis of nanostructured SOFCs electrolyte using solution and suspension plasma spraying: a comparative study. J Therm Spray Technol 19(3):566–574
187. Shen Y, Almeida VAB, Gitzhofer F (2011) Preparation of nano-composite GDC/LSCF cathode material for IT-SOFC by induction plasma spraying. J Therm Spray Technol 20 (1–2):145–153
188. Vaßen R, Kaßner H, Mauer G, Stöver D (2010) Suspension plasma spraying: process characteristics and applications. J Therm Spray Technol 19(1–2):219–225
189. Etchart-Salas R (2007) D.C. plasma spraying of suspensions of submicronic particles. Experimental and analytic approaches of phenomena implied in the reproducibility and quality of coatings (in French). Ph.D. thesis, University of Limoges, France
190. Kassner H, Siegert R, Hathiramani D, Vassen R, Stoever D (2008) Application of suspension plasma spraying (SPS) for manufacture of ceramic coatings. J Therm Spray Technol 17 (1):115–123
191. Oberste-Berghaus J, Marple B, Moreau C (2006) Suspension plasma spraying of nanostructured WC-12Co coatings. J Therm Spray Technol 15(4):676–681
192. Wang Y, Legoux J-G, Neagu R, Hui S, Marple BR (2012) Suspension plasma spray and performance characterization of half cells with NiO/YSZ anode and YSZ electrolyte. J Therm Spray Technol 21(1):7–16
193. Boulos MI (1992) RF induction plasma spraying: state-of-the-art review. J Therm Spray Technol 1(1):33–40
194. Hui R, Oberste-Berghaus J, Decès-Petit C, Qu W, Yick S, Legoux J-G, Moreau C (2009) High performance metal-supported solid oxide fuel cells fabricated by thermal spray. J Power Source 191:371–376
195. Ravi BG, Sampath S, Gambino R, Devi PS, Parise JB (2006) Plasma spray synthesis from precursors: progress, issues and considerations. J Therm Spray Technol 15(4):701–707
196. Gell M, Jordan EH, Teicholz M, Cetegen BM, Padture N, Xie L, Chen D, Ma X, Roth J (2008) Thermal barrier coatings made by the solution precursor plasma spray process. J Therm Spray Technol 17(1):124–135
197. Karthikeyan J, Berndt CC, Tikkanen J, Reddy S, Herman H (1997) Plasma spray synthesis of nanomaterial powders and deposits. Surf Coat Technol 238(2):275–286
198. Jadhav AD, Padture NP, Jordan EH, Gell M, Miranzo P, Fullu ER (2006) Low thermal conductivity plasma sprayed thermal barrier coatings with engineered microstructure. Acta Mater 54(12):3343–3349
199. Vasiliev AL, Padture NP, Ma X (2006) Coatings of metastable ceramics deposited by solution precursor plasma spray: I-binary ZrO_2-Al_2O_3 system. Acta Mater 54(19):4913–4920
200. Chen D, Jordan EH, Gell M (2008) Effect of solution concentration on splat formation and coating microstructure using the solution precursor plasma spray process. Surf Coat Technol 202:2132–2138

201. Vasiliev AL, Padture NP, Ma XC (2006) Coatings of metastable ceramics deposited by solution-precursor plasma spray: II. Ternary ZrO_2–Y_2O_3–Al_2O_3 system. Acta Mater 54 (19):4921–4936
202. Chen D, Jordan E, Gell M (2007) Thermal and crystallization behavior of zirconia precursor used in the solution precursor plasma spray process. J Mater Sci 42(14):5576–5580
203. Chen D, Jordan EH, Gell M (2010) The solution precursor plasma spray coatings: influence of solvent type. Plasma Chem Plasma Process 30:111–119
204. Muoto CK, Jordan EH, Gell M, Aindow M (2011) Identification of desirable precursor properties for solution precursor plasma spray. J Therm Spray Technol 20(4):802–816
205. Toma FL, Bertrand G, Rampon R, Klein D, Coddet C (2006) Relationship between the suspension properties and liquid plasma sprayed coating characteristics. In: ITSC 2006. ASM International, Materials Park, OH, e-proceedings
206. Rampon R, Bertrand G, Toma FL, Coddet C (2006) Liquid plasma sprayed coatings of yttria stabilized for SOFC electrolyte. In: ITSC 2006. ASM International, Materials Park, OH, e-proceedings
207. Toma FL, Sokolov D, Bertrand G, Klein D, Coddet C, Meunier C (2006) Comparison of the photocatalytic behavior of TiO_2 coatings elaborated by different thermal spray processes. J Therm Spray Technol 15(4):576–581
208. Oberste-Berghaus J, Boccaricha S, Legoux JG, Moreau C, Chraska T (2005) Suspension plasma spraying of nanoceramics using an axial injection torch. In: ITSC 2005, DVS, Dusselörf, Germany, e-proceedings
209. Fazilleau J, Delbos C, Violier M, Coudert JF, Fauchais P, Bianchi L, Wittmann-Teneze K (2003) Influence of substrate temperature on formation of micrometric splats obtained by plasma spraying liquid suspension. In: Marple BR, Moreau C (eds) ITSC 2003. ASM International, Materials Park, OH, pp 889–895
210. Rampon R, Filiatre C, Bertrand G (2008) Suspension plasma spraying of YPSZ coatings: suspension atomization and injection. J Therm Spray Technol 17(1):105–114
211. Rampon R, Toma F-L, Bertrand G, Coddet C (2006) Liquid plasma sprayed coatings of yttria-stabilized zirconia for SOFC electrolytes. J Therm Spray Technol 15(4):682–688
212. Arevalo-Quintero O, Waldbillig D, Kesler O (2011) An investigation of the dispersion of YSZ, SDC, and mixtures of YSZ/SDC powders in aqueous suspensions for application in suspension plasma spraying. Surf Coat Technol 205:5218–5227
213. Patent FR0453390, Revêtement nanostructuré et procédé de revêtement, CEA Le Ripault, Monts, 37, France (in French)
214. Jordan EH, Gell M, Benzani P, Chen D, Basu S, Cetegem B, Wa F, Ma XC (2007) Making dense coatings with the solution precursor plasma spray process. In: Marple BR et al (eds) Thermal spraying 2007:global coating solutions. ASM International, Materials Park, OH, e-proceedings
215. Cotler EM, Chen D, Molz RJ (2011) Pressure-based liquid feed system for suspension plasma spray coatings. J Therm Spray Technol 20(4):967–973
216. Damiani D. Elaboration, fitting in shape and characterization of materials for energy by the interaction radiation-matter. HdR University of Limoges, France, 13 Dec 2012
217. Meillot E, Vert R, Caruyer C, Damiani D, Vardelle M (2011) Manufacturing nanostructured YSZ coatings by suspension plasma spraying (SPS): effect of injection parameters. J Phys D Appl Phys 44:194008 (8pp)
218. Ozturkand A, Cetegen B (2005) Modeling of axially and transversely injected precursor droplets into a plasma environment. Int J Heat Mass Transfer 48(21–22):4367–4383
219. Saha A, Seal S, Cetegen B, Jordan E, Ozturk A, Basu S (2009) Thermo-physical processes in cerium nitrate precursor droplets injected into high temperature plasma. Surf Coat Technol 203:2081–2091
220. Xie L, Ma X, Ozturk A, Jordan EH, Padture NP, Cetegen BM, Xiao DT, Gell M (2004) Processing parameter effects on solution precursor plasma spray process spray patterns. Surf Coat Technol 183(1):51–61

221. Xie L, Ma XC, Jordan EH, Padture NP, Xiao DT, Gell M (2004) Deposition mechanisms of thermal barrier coatings in the solution precursor plasma spray process. Surf Coat Technol 177–178:103–107
222. Delbos C, Fazilleau J, Coudert JF, Fauchais P, Bianchi L (2004) Finely structured ceramic coatings elaborated by liquid suspension injection in a DC plasma jet. In: Thermal spray solutions : advances in technology and application. DVS, Düsseldorf, Germany
223. Wittmann K, Blein F, Fazilleau J, Coudert JF, Fauchais P (2002) A new process to deposit thin coatings by injecting nanoparticles suspensions in a d.c. plasma jet. In: Lugsheider E (ed) ITSC 2002. DVS, Düsseldorf, Germany, e-proceedings
224. Cedelle J, Vardelle M, Fauchais P (2006) Influence of stainless steel substrate preheating on surface topography and on millimeter and micrometer-sized splat formation. Surf Coat Technol 201(3–4):1378–1382
225. Bianchi L, Denoirjean A, Blein F, Fauchais P (1997) Microstructural investigation of plasma sprayed ceramic splats. Thin Solid Films 299:125–135
226. Siegert R, Doring JE, Marque's JL, Vassen R, Sebold D, Stöver D (2005) Influence of injection parameters on the suspension plasma spraying coating properties. In: Lugsheider E (ed) ITSC 2005. DVS, Düsseldorf, Germany, e-proceedings
227. Tingaud O, Grimaud A, Denoirjean A, Montavon G, Rat V, Coudert JF, Fauchais P, Chartier T (2008) Suspension plasma-sprayed alumina coating structures: operating parameters versus coating architecture. J Therm Spray Technol 17(5–6):662–670
228. Tingaud O, Bacciochini A, Montavon G, Denoirjean NA, Fauchais P (2009) Suspension DC plasma spraying of thick finely-structured ceramic coatings: process manufacturing mechanisms. Surf Coat Technol 203:2157–2161
229. Xie L, Chen D, Jordan EH, Padture NP, Ozturk A, Wu F, Ma XC, Cetegem BM, Gell M (2006) Formation of vertical cracks in solution-precursor plasma-sprayed thermal barrier coatings. Surf Coat Technol 201:1058–1064
230. Kozerski S, Łatka L, Pawlowski L, Cernuschi F, Petit F, Pierlot C, Podlesak H, Laval JP (2011) Preliminary study on suspension plasma sprayed ZrO2 + 8 wt.% Y2O3 coatings. J Eur Ceram Soc 31:2089–2098
231. Waldbillig D, Kesler O (2011) Effect of suspension plasma spraying process parameters on YSZ coating microstructure and permeability. Surf Coat Technol 205:5483–5492
232. Delbos C (2004) Contribution to the understanding of liquid injection of ceramics (Y.S.Z., Perovskite. . .) or metals (Ni,. . .) in blown arc plasma jets to achieve finely structured coatings for SOFCs (in French). Ph.D. thesis (in French), University of Limoges, France
233. Toma F-L, Berger L-M, Scheitz S, Langner S, Rödel C, Potthoff A, Sauchuk V, Kusnezoff M (2012) Comparison of the microstructural characteristics and electrical properties of thermally sprayed Al_2O_3 coatings from aqueous suspensions and feedstock powders. J Therm Spray Technol 21(3–4):480–488
234. Müller P, Killinger A, Gadow R (2012) Comparison between high-velocity suspension flame spraying and suspension plasma spraying of alumina. J Therm Spray Technol 21 (6):1120–1128
235. Moign A, Vardelle A, Themelis NJ, Legoux JG (2010) Life cycle assessment of using powder and liquid precursors in plasma spraying: the case of yttria-stabilized zirconia. Surf Coat Technol 205:668–673
236. Xie L, Jordan EH, Padture NP, Gell M (2004) Phase and microstructural stability of solution precursor plasma sprayed thermal barrier coatings. Mater Sci Eng A 381:189–195
237. Madhwal M, Jordan EH, Gell M (2004) Failure mechanisms of dense vertically-cracked thermal barrier coatings. Mater Sci Eng A 384:151–161
238. Low AD, Jadhav NP, Padture EH, Jordan M, Gell P, Miranzo ER (2006) Fuller Jr., Low-thermal-conductivity plasma-sprayed thermal barrier coatings with engineered microstructures. Acta Mater 54:3343–3349
239. Vaßen R, Stuke A, Stöver D (2009) Recent developments in the field of thermal barrier coatings. J Therm Spray Technol 18(2):181–186

240. Ben-Ettouil F, Denoirjean A, Grimaud A, Montavon G, Fauchais P (2009) Sub-micrometer-sized Y-PSZ thermal barrier coatings manufactured by suspension plasma spraying: process, structure and some functional properties. In: ITSC 2009, ASM, Materials Park, OH
241. Bacciochini A, Ben-Ettouil F, Brousse E, Ilavsky J, Montavon G, Denoirjean A, Valette S, Fauchais P (2010) Quantification of void network architectures of as-sprayed and aged nanostructured yttria-stabilized zirconia (YSZ) deposits manufactured by suspension plasma spraying. Surf Coat Technol 205:683–689
242. Fauchais P, Etchart-Salas R, Delbos C, Tognovi M, Rat V, Coudert J-F, Chartier T (2007) Suspension and solution plasma spraying of finely structured layers for SOFCs. J Phys D Appl Phys 40(8):2394–2406
243. Waldbilling D, Kesler O, Tang Z, Burgess A (2007) Suspension plasma spraying of solid oxide fuel cell electrolytes. In: Marple BR et al (eds) Thermal spraying 2007:global coating solutions. ASM International, Materials Park, OH, e-proceedings
244. Stöver D, Hathiramani D, Vaßen R, Damani RJ (2006) Plasma_sprayed components for SOFC applications. Surf Coat Technol 201:2002–2005
245. Brinley E, Babu KS, Seal S (2007) The solution precursor plasma spray processing of nanomaterials. JOM July:54–59
246. Oberste Berghaus J, Legoux J-G, Moreau C, Hui R, Deces-Petit C, Qu W, Yick S, Wang Z, Maric R, Ghosh D (2008) Suspension HVOF spraying of reduced temperature solid oxide fuel cell electrolytes. J Therm Spray Technol 17(5–6):700–707
247. Monterrubio-Badillo C, Ageorges H, Chartier T, Coudert J-F, Fauchais P (2006) Preparation of $LaMnO_3$ perovskite thin films by suspension plasma spraying for SOFC cathodes. Surf Coat Technol 200:3743–3756
248. Wang X-M, Li C-X, Li C-J, Yang G-J (2010) Effect of microstructures on electrochemical behavior of $La_{0.8}Sr_{0.2}MnO_3$ deposited by suspension plasma spraying. Int J Hydrogen Energy. To be published
249. Bouaricha S, Oberste-Berghaus J, Legoux J-G, Moreau C, Ghosh D (2005) Production of doped-ceria plasma sprayed nano-coatings using an internal injection of a suspension containing nanoparticles. In: Lugscheider E (ed) Thermal spray connects: explore its surfacing potential! DVS-Verlag GmbH, Düsseldorf, Germany, e-proceedings
250. Waldbillig D, Kesler O (2009) Characterization of metal-supported axial injection plasma sprayed solid oxide fuel cells with aqueous suspension plasma sprayed electrolyte layers. J Power Sources 191:320–329
251. Marchand O, Bertrand P, Mougin J, Comminges C, Planche M-P, Bertrand G (2010) Characterization of suspension plasma-sprayed solid oxide fuel cell electrodes. Surf Coat Technol 205(4):993–998
252. Michaux P, Montavon G, Grimaud A, Denoirjean A, Fauchais P (2010) Elaboration of porous NiO/8YSZ layers by several SPS and SPPS routes. J Therm Spray Technol 19(1–2):317–327
253. Waldbillig D, Kesler O (2009) The effect of solids and dispersant loadings on the suspension viscosities and deposition rates of suspension plasma sprayed YSZ coatings. Surf Coat Technol 203:2098–2101
254. McCoppin J, Young D, Reitz T, Maleszewski A, Mukhopadhyay S (2011) Solid oxide fuel cell with compositionally graded cathode functional layer deposited by pressure assisted dual-suspension spraying. J Power Sources 196:3761–3765
255. Xiaoming W, Chengxin L, Changjiu L, Lihui T, Guanjun Y (2011) Microstructure and electrochemical behavior of $La_{0.8}Sr_{0.2}MnO_3$ deposited by solution precursor plasma spraying. Rare Metal Mater Eng 40(11):1881–1886
256. Oberste-Berghaus J, Marple B, Moreau C (2006) Suspension plasma spraying of nanostructured WC-12Co coatings. In: Marple BR et al (eds) Thermal spray conference 2006. ASM International, Materials Park, OH, e-proceedings
257. Toma F-L, Berger L-M, Stahr CC, Naumann T, Langner S (2010) Microstructures and functional properties of suspension-sprayed Al_2O_3 and TiO_2 coatings: an overview. J Therm Spray Technol 19(1–2):262–274

258. Toma F-L, Berger L-M, Naumann T, Langner S (2008) Microstructures of nanostructured ceramic coatings obtained by suspension thermal spraying. Surf Coat Technol 202:4343–4348
259. Darut G, Ageorges H, Denoirjean A, Montavon G, Fauchais P (2008) Effect of the structural scale of plasma-sprayed alumina coatings on their friction coefficients. J Therm Spray Technol 17(5–6):788–797
260. Qiu C, Chen Y (2009) Manufacturing process of nanostructured alumina coatings by suspension plasma spraying. J Therm Spray Technol 18(2):272–283
261. Zhang J, He J, Dong Y, Li X, Yan D (2008) Microstructure characteristics of Al_2O_3-13wt.% TiO_2 coating plasma spray deposited with nanocrystalline powders. J Mater Process Technol 197(1–3):31–35
262. Sodeoka S, Suzaki M, Inone T (2006) Mechanical properties of plasma sprayed alumina-zirconia nano-composite film. In: Marple BR et al (eds) Thermal spray conference 2006. ASM International, Materials Park, OH, e-proceedings
263. Oliker VE, Terentev AE, Shvedova LK, Martsenyuk IS (2009) Use of aqueous suspensions in plasma spraying of alumina coatings. Powder Metall Metal Ceram 48(1–2):115–120
264. Chen D, Jordan EH, Gell M (2009) Suspension plasma sprayed composite coating using amorphous powder feedstock. Appl Surf Sci 255:5935–5938
265. Tingaud O, Bertrand P, Bertrand G (2010) Microstructure and tribological behavior of suspension plasma sprayed Al_2O_3 and Al_2O_3–YSZ composite coatings. Surf Coat Technol 205:1004–1008
266. Manzat A, Killinger A, Gadow R (2010) Application of supersonic flame spraying for next generation cylinder liner coatings. In: Wellnitz J (ed) Sustainable automotive technologies. Springer, Berlin, pp 175–181
267. Killinger A, Gadow R, Rempp A, Manzat A (2010) Advanced ceramic tribological layers by thermal spray routes. Adv Sci Technol 66:106–119
268. Tomaszek R, Znamirovski Z, Pawlowski L, Wojnakowski A (2006) Impedance spectroscopy of suspension plasma sprayed titania coatings. Surf Coat Technol 201(5):2099–2102
269. Garcia E, Zhang ZB, Coyle TW, Hao SE, Ma SL (2007) Thermal spraying 2007:global coating solutions. In: Marple BR et al (eds) ASM International, Materials Park, OH
270. Yang G-J, Li C-J, Huang X-C, Wang Y-Y, Li C-X (2007) Influence of silver doping on photocatalytic activity of liquid flame sprayed nanostructured TiO2 coating. In: Marple BR et al (eds) Thermal spray 2007: global coating solutions. ASM International, Materials Park, OH, e-proceedings
271. Jaworski R, Pawlowski L, Roudet F, Kozerski S, Le Maguer A (2008) Recent developments in suspension plasma sprayed titanium oxide and hydroxyapatite coatings influence of suspension plasma spraying process parameters on TiO_2 coatings microstructure. J Therm Spray Technol 17(1):240–247
272. Toma F-L, Bertrand G, Begin S, Meunier C, Barres O, Klein D, Coddet C (2006) Microstructure and environmental functionalities of TiO_2-supported photocatalysts obtained by suspension plasma spraying. Appl Catalysist B 68:74–84
273. Toma F-L, Bertrand G, Chwa SO, Meunier C, Klein D, Coddet C (2006) Comparative study on the photocatalytic decomposition of nitrogen oxides using TiO_2 coatings prepared by conventional plasma spraying and suspension plasma spraying. Surf Coat Technol 200:5855–5862
274. Podlesak H, Pawlowski L, Laureyns J, Jaworski R, Lampke T (2008) Advanced microstructural study of suspension plasma sprayed titanium oxide coatings. Surf Coat Technol 202:3723–3731
275. Tomaszek R, Znamirowski Z, Pawlowski L, Zdanowski J (2007) Effect of conditioning on field electron emission of suspension plasma sprayed TiO_2 coatings. Vacuum 81:1278–1282
276. Znamirowski Z, Ladaczek M (2008) Lighting segment with field electron titania cathode made using suspension plasma spraying. Surf Coat Technol 202:4449–4452

277. Kozerski S, Toma F-L, Pawlowski L, Leupolt B, Latka L, Berger L-M (2010) Suspension plasma sprayed TiO_2 coatings using different injectors and their photocatalytic properties. Surf Coat Technol 205:980–986
278. Bannier E, Darut G, Sánchez E, Denoirjean A, Bordes MC, Salvador MD, Rayón E, Ageorges H (2011) Microstructure and photocatalytic activity of suspension plasma sprayed TiO_2 coatings on steel and glass substrates. Surf Coat Technol 206:378–386
279. Yuan J, Zhan Q, Lei Q, Ding S, Li H (2012) Fabrication and characterization of hybrid micro/nanostructured hydrophilic titania coatings deposited by suspension flame spraying. Appl Surf Sci 258:6672–6678
280. Toma F-L, Berger L-M, Jacquet D, Wicky D, Villaluenga I, de Miguel YR, Lindeløv JS (2009) Comparative study on the photocatalytic behaviour of titanium oxide thermal sprayed coatings from powders and suspensions. Surf Coat Technol 203(15):2150–2156
281. Vaßen R, Yi Z, Kaßner H, Stöver D (2009) Suspension plasma spraying of TiO_2 for the manufacture of photovoltaic cells. Surf Coat Technol 203(15):2146–2149
282. Moroz NA, Umapathy H, Mohanty P (2010) Synthesis and microstructure evolution of nano-titania doped silicon coatings. J Therm Spray Technol 19(1–2):294–302
283. Bolelli G, Cannillo V, Gadow R, Killinger A, Lusvarghi L, Rauch J (2009) Properties of high velocity suspension flame sprayed (HVSFS) TiO_2 coatings. Surf Coat Technol 203:1722–1732
284. Gutzmann H, Kliemann J-O, Albrecht R, Gärtner F, Klassen T, Toma F-L, Berger L-M, Leupolt B (2010) Evaluation of the photocatalytic activity of TiO_2-coatings prepared by different thermal spray techniques. In: Thermal spray: global solutions for future application. DVS-Berichte, Düsseldorf, Germany, pp 182–186
285. Rauch J, Stiegler N, Killinger A, Gadow R (2009) High velocity suspension flame spraying (HVSFS): process development and industrial applications. In: Marple BR et al (eds) Thermal spray 2009: expanding thermal spray performance to new markets and applications. ASM International, Materials Park, OH, pp 150–155
286. Chen D, Jordan EH, Gell M (2008) Porous TiO_2 coating using the solution precursor plasma spray process. Surf Coat Technol 202:6113–6119
287. Tomaszek R, Pawlowski L, Gengembre L, Laureyns J, Le Maguer A (2007) Microstructure of suspension plasma sprayed multilayer coatings of hydroxyapatite and titanium oxide. Surf Coat Technol 201:7432–7440
288. Łatka L, Pawlowski L, Chicot D, Pierlot C, Petit F (2010) Mechanical properties of suspension plasma sprayed hydroxyapatite coatings submitted to simulated body fluid. Surf Coat Technol 205:954–960
289. D'Haese R, Pawlowski L, Bigan M, Jaworski R, Martel M (2010) Phase evolution of hydroxyapatite coatings suspension plasma sprayed using variable parameters in simulated body fluid. Surf Coat Technol 204(8):1236–1246
290. Kozerski S, Pawlowski L, Jaworski R, Roudet F, Petit F (2010) Two zones microstructure of suspension plasma sprayed hydroxyapatite coatings. Surf Coat Technol 204 (9–10):1380–1387
291. Podlesak H, Pawlowski L, dHaese R, Laureyns J, Lampke T, Bellayer S (2010) Advanced microstructural study of suspension plasma sprayed hydroxyapatite coatings. J Therm Spray Technol 19(3):657–664
292. Stiegler N, Killinger A, Gadow R (2010) Hydroxyapatite coatings for biomedical applications deposited by different thermal spray techniques. Surf Coat Technol 205:1157–1164
293. Stiegler N, Bellucci D, Bolelli G, Cannillo V, Gadow R, Killinger A, Lusvarghi L, Sola A (2012) High-velocity suspension flame sprayed (HVSFS) hydroxyapatite coatings for biomedical applications. J Therm Spray Technol 21(2):275–287
294. Bolelli G, Cannillo V, Gadow R, Killinger A, Lusvarghi L, Rauch J (2009) Microstructural and in vitro characterization of high-velocity suspension flame sprayed (HVSFS) bioactive glass coatings. J Eur Ceram Soc 29:2249–2257

295. Altomare L, Bellucci D, Bolelli G, Bonferroni B, Cannillo V, De Nardo L, Gadow R, Killinger A, Lusvarghi L, Sola A, Stiegler N (2011) Microstructure and in vitro behaviour of 45S5 bioglass coatings deposited by high velocity suspension flame spraying (HVSFS). J Mater Sci Mater Med 22:1303–1319
296. Xiao Y, Song L, Liu X, Huang Y, Huang T, Chen J, Wu Y, Wu F (2011) Bioactive glass-ceramic coatings synthesized by the liquid precursor plasma spraying process. J Therm Spray Technol 20(3):560–568
297. Xiao Y, Song L, Liu X, Yi H, Huang T, Wu Y, Chen J, Wu F (2011) Nanostructured bioactive glass–ceramic coatings deposited by the liquid precursor plasma spraying process. Appl Surf Sci 257:1898–1905
298. Bolelli G, Rauch J, Cannillo V, Killinger A, Lusvarghi L, Gadow R (2008) Investigation of high-velocity suspension flame sprayed (HVSFS) glass coatings. Mater Lett 62:2772–2775
299. Waltz F, Swider MA, Hoyer P, Hassel T, Erne M, Möhwald K, Adlung M, Feldhoff A, Wickleder C, Bach F-W, Behrens P (2012) Synthesis of highly stable magnesium fluoride suspensions and their application in the corrosion protection of a magnesium alloy. J Mater Sci 47:176–183
300. Chien K, Coyle TW (2007) Rapid and continuous deposition of porous nanocrystalline sno_2 coating with interpenetrating pores for gas sensor applications. J Therm Spray Technol 16 (5–6):886–892
301. Ma XQ, Roth J, Gandy DW, Frederick GJ (2006) A new high-velocity oxygen fuel process for making finely structured and highly bonded Inconel alloy layers from liquid feedstock. J Therm Spray Technol 15(4):670–675
302. Kitamura J, Tang Z, Mizuno H, Sato K, Burgess A (2011) Structural, mechanical and erosion properties of yttrium oxide coatings by axial suspension plasma spraying for electronics applications. J Therm Spray Technol 20(1–2):170–185
303. Vert R, Chicot D, Dublanche-Tixier C, Meillot E, Vardelle A, Mariaux G (2010) Adhesion of YSZ suspension plasma-sprayed coating on smooth and thin substrates. Surf Coat Technol 205:999–1003

Chapter 15
Coating Characterizations

Abbreviations

a.c.	Alternative current
AE	Acoustic emission
AES	Auger electron spectroscopy
AFM	Atomic force microscopy
AP	Archimedean porosimetry
BSE	Back scattered electrons
CMAS	Calcium–magnesium–aluminosilicate
d.c.	Direct current
DB	Double bar method
DCB	Double cantilever beam test
DOF	Depth of field
DSC	Differential scanning calorimetry
DTA	Differential thermal analysis
EB-PVD	Electron beam physical vapor deposition
EDS	Energy-dispersive X-ray spectroscopy
EIS	Electrochemical impedance spectroscopy
EN	Electrochemical noise
EPMA	Electron probe microanalysis
ESCA	Electron spectroscopy for chemical analysis
EXAFS	Extended X-ray absorption fine structure
FBR	Fluidized bed reactor
FCT	Furnace cycle test
FESEM	Field emission scanning electron microscope
FFT	Fast Fourier transform
FGM	Functional gradient material
FIB	Focused ion beam
FTIR	Fourier transform infrared spectroscopy
FWHM	Full-width at half-maximum

P.L. Fauchais et al., *Thermal Spray Fundamentals: From Powder to Part*, 1113
DOI 10.1007/978-0-387-68991-3_15, © Springer Science+Business Media New York 2014

GP	Gas permeation
HIP	Hot isostatic pressing
HRTEM	High resolution transmission electron microscopy
HU	Universal hardness
HV	Vickers hardness
HVOF	High-velocity oxy-fuel
i.d.	Internal diameter
IA	Image analysis
J.C.P.D.S.	Joint Committee Powder Diffraction Standard
JETS	Jet engine thermal shocks
LASAT	Laser adhesion test
LOM	Light optical microscope
MIP	Mercury intrusion porosimetry
MSANS	Multiple small angle neutron scattering
N	Number of loading cycles
NDT	Nondestructive technique
NEXAFS	Near edge X-ray absorption fine structure
OM	Optical microscopy also called LOM
OOF	Object-oriented finite element analysis of microstructures
P	Pycnometry
PT	Pulsed thermography
R&D	Research and Development
RC	Resistive/capacitive circuit
REV	Representative elementary volume
RFPPS	RF precursor plasma spray synthesis
RPM	Rotation per minute
RVE	Representative volume element
S	Cyclic stress
S.C.E.	Standard calomel electrode
SANS	Small-angle neutron scattering
SAW	Surface acoustic waves
SAXS	Small-angle X-ray scattering
SB	Single bar method
SEM	Scanning electron microscopy
SRV	Sliding, reciprocating, and vibrating friction
ST	Stereological protocols (coupled to image analysis)
STF	Strain to fracture
TAT	Tensile adhesion test
TBC	Thermal barrier coating
TEM	Transmission electron microscopy
TG	Thermo gravimeter
TG-DTA	Thermo gravimeter-differential thermal analysis
TGO	Thermally grown oxide
TSR	Thermal shock resistance
TSS	Thermal spray society

URCAS	Ultrasonic reflection coefficient amplitude spectrum
USAXS	Ultrasmall angle X-ray scattering
XANES	X-ray absorption near edge structure
XAS	X-ray absorption spectroscopy
XPS	X-ray photoelectron spectroscopy
XRD	X-ray diffraction
XRF	X-ray fluorescence
YAG	Yttrium aluminum garnet
YPSZ	Yttria partially stabilized zirconia
YSZ	Yttria-stabilized zirconia

15.1 Introduction to Coating Characterizations and Testing Methods

Coatings as most industrial products must be tested:

- Firstly at the Research and Development stage. They can be then characterized by using techniques more or less sophisticated: metallography and image analysis, materials characterization, void content, and network architecture.
- Secondly in production environment. The tests deal with the control of quality (adhesion–cohesion, mechanical properties, thermal properties, wear resistance, corrosion resistance, ...) and are more targeted toward the service conditions, without neglecting some simple tests from simple visual observation of the coated part to some specific characteristics required by the coating or component specifications.

However, it should be kept in mind that coating properties depend strongly on both the spray conditions and powder used and both must be regularly tested, as described at the end of this section.

At last the aim of this chapter is not to describe in detail all the characterization and testing methods that could be used for thermal spray coatings but to give the reader information about the most used techniques and which information can be drawn from them. The chapter also assembles references where the reader can find detailed description of these techniques. In the following references related to ASTM standards are numbered 15.Letter-number: for example, those related to Thermal properties are 15.Tx_i.

15.1.1 Differences Between Coatings and Bulk Materials

As described in Chap. 13, thermal-sprayed coatings are made of layered splats; the contacts between splats or between splats and substrate surface correspond to few percents of each splat total surface: from 15 to 60 %. The response of these coatings to

any external solicitation will depend strongly on the mean value of these contacts. Moreover, coatings have an anisotropic behavior: for example, hardness measured at coating surface is different from that measured on its cross section. Within splats, according to the fast quenching of the flattening liquid, material grain or column sizes are rather small (below 0.5 μm in diameter). The coating adhesion, as mentioned in Chap. 13, is either mechanical, as in most cases, or chemical for few specific sprayed materials associated with specific substrates, or metallurgical, i.e., controlled by diffusion when metal coatings are plasma sprayed in soft vacuum on hot metal substrates where the oxide layer has been removed. The coating adhesion to substrate is generally below 70 MPa for mechanical adhesion and much higher for diffusion-controlled adhesion. Besides the relatively poor quality of contact between splats, resulting in coating tensile strengths below 60–70 MPa, sprayed coatings properties are also lowered by various defects such as pores, un-melted particles, ...

On the other hand, wrought, forged, cast, or sintered metal materials have quite different properties. For materials prepared by metallurgical processes, grain sizes are larger (a few micrometers, i.e., 10–100 times that of coatings) according to much lower cooling rates and also heat treatments to achieve specific precipitates. Tensile strengths are generally much higher than that of coatings: from a few hundreds to thousands or more MPa.

For sintered engineering ceramic materials, grain sizes are also more important (about 0.6–14 μm) than those of thermal sprayed coatings and if tensile strengths are lower (hundreds MPa) than those of bulk metals, they are still higher than those of coatings.

Thus the preparation of the surfaces or cross sections of coatings used for characterization is relatively different from that of bulk materials.

15.1.2 Characterization and Testing Methods Used for Coatings

The first characteristics that are important and necessary are those related to the coating microstructures at different depths. According to Pawlowski [1] they involve:

- Chemical composition at macro- and micro-scales
- Grain or column morphology and orientation (texture)
- Defects such as voids, unmelted particles, micro- and macro-cracks, and dislocations with their number and distribution

For such characterizations, in most cases, the critical step is the metallographic examination. However the heterogeneous or composite nature of the thermal spray coating can make very difficult the choice of a metallographic preparation protocol (see Sect. 15.3), as underlined by W. Davis in [2] or Wigren and Täng [3]. According to Wigren and Täng [3], the observed coating microstructure depends on a numerous number of possible errors that can often be made in metallographic laboratories. For example, they cited the evaluation of plasma-sprayed WC/Co

coatings sprayed by one supplier and the corresponding metallographic preparation by 27 laboratories that resulted in a wide range of observed properties. Especially the mounting technique (hot and cold under vacuum) may be the single most important step in the whole metallographic procedure. Also improper grinding and polishing can be the source of many problems as well as the measurement system analysis using image analysis [3]. If such methods are mandatory to understand what will be the behavior of coatings: they can be very time consuming and are more used at the R&D level.

Testing methods make it possible to determine properties such as coating adhesion–cohesion, mechanical and thermal properties, or service properties such as wear and corrosion resistance. However, the test results can also depend on the sample preparation techniques. For instance, the adhesion–cohesion test results depend strongly on the penetration of epoxy and pressure used during curing: e.g., [3] the tensile strength of Ni–5Al/Alumina system was found to vary from 60 down to 15 MPa. However, when the coating was dense enough to prevent the penetration of the glue, this variation in tensile results was not observed [3]. Such tests must be as close as possible to real-world coating service conditions to be used at the production stage. In addition they should be rapid to operate and easy to be used by less skilled personnel [1]. These test methods generally consist in observing or measuring the response of coatings to various external solicitations: loads, stress, applied electric signals, or other stimuli [2]. The coating response depends on its physical, chemical, and structural properties that in turn depend to a great extent on the real contacts between splats. To characterize a specific coating property, the coating response to the applied stimulus must be sufficiently important and clear to be measured. For example, when applying a load the response of the coating can be purely elastic or plastic or both and it must be known to interpret correctly the response signal.

The result of every test is practically a number: size of a print for hardness, percent of porosity, thermal signal propagation for thermal diffusivity,.... The numbers obtained from tests are supposed to be representative of the studied property. However numbers are useful only if a certain degree of confidence in them is achieved [2–4]. The measure of confidence is usually expressed statistically as the results of a significant number of tests. The degree of confidence is the highest if a minimal variance or standard deviation from the average value is obtained. For example, a hardness of 400 HV under a load of 5 N is meaningless: the design engineer will be happy if this value is 400 ± 20 HV_5 and very disappointed if it is 400 ± 150 HV_5.

15.1.3 Statistical Methods

Samuel Clemens wrote: “there are three kinds of lies: lies, damned lies, and statistics.” It underlines that statistical methods to characterize sprayed coating properties must be used properly. The complexity of coating structures, their anisotropy implying to consider the measurement directions, their strong dependence on spray conditions and powder characteristics, and the generally wide

scatter in different property values make necessary to perform a statistical analysis when determining a coating property. This will be illustrated for microhardness, which is a basic mechanical property as elastic modulus. They are used to characterize the performance of coatings as they affect the erosion wear-resistance performance, stress strain behavior, contact stress field, coating delaminating, coating fracture, and residual stress state within coatings [5]. However hardness data are often presented in the literature as a single numerical statistic without any details of how the reported value was obtained, which is meaningless.

The measuring equipment, a factor that can affect hardness measurement, must be, as for any type of measuring equipment, tested regularly in order to avoid systematic errors and biases. The coating surface or cross-section preparation is a non-negligible parameter (for more details on preparation see the first four subsections of Sect. 15.3.1). The load also is very important because the indenter penetration increases nonlinearly with it (plastic deformation increases with load). To achieve comparable results the same load must be used with the same time of application. The indentation size effect is of little significance [6] when comparisons are made between samples while keeping the load constant. Indents should only be discounted if there is reason to believe that the measurement is invalid, such as if the testing equipment suffered vibration during the test. Disqualification of outliers to get a "statistically more meaningful result" is not legitimate if, as is usually the case, these represent true variation of the coating structure. Microhardness indentation is also subject to systematic biases between operators that limit the reproducibility of the technique. As it could be expected, these biases increase significantly when the indent size is decreased [7]. Since they may be more important for low loads and high hardness materials, the hardness data reported in the literature for ceramics materials and cemented carbides are not necessarily sound.

Normal, Lognormal, and Weibull distributions are widely used to fit experimental data [8, 15.S1]. Normal and Weibull distributions are currently used to characterize thermal sprayed coatings [8].

15.1.3.1 (a) Normal Distribution

It is very often used. In laboratories when considering N events, x_i, for example, indents, the largest and the smallest values are discarded, before averaging the $N - 2$ remaining values. The standard deviation, σ, is the square root of the average value of $(x - \eta)^2$, where η is the arithmetic mean of the measured values. In the case where x takes random values from a finite data set $x_1, x_2, \ldots, x_N$, with each value having the same probability, the standard deviation is, using summation notation:

$$\sigma = \sqrt{\frac{1}{N}\sum_{i=1}^{N}(x_i - \eta)} \tag{15.1}$$

However the central limit theorem says that the distribution of a sum of many independent, identically distributed random variables tends toward the famous

bell-shaped normal distribution with a probability density function proportional to $\exp(-(x-\eta)^2/2\sigma^2)$, which is a Gaussian distribution. Therefore, the standard deviation is simply a scaling variable that adjusts how broad the curve will be, though also it appears in the normalizing constant to keep the distribution normalized for different widths. When the data distribution is approximately normal then about 68 % of the data values are within one standard deviation of the mean value (mathematically, $\eta \pm \sigma$, where η is the arithmetic mean), about 95 % are within two standard deviations ($\eta \pm 2\sigma$), and about 99.7 % lie within 3 standard deviations ($\eta \pm 3\sigma$).

However the assumption of normal distribution is not always fulfilled for non-homogeneous materials, such as thermal-sprayed coatings, where the dimensions of the microstructural features have a similar order of magnitude than that of the indent depth. In general, flaws such as subsurface porosity, brittleness, and trapped fine particles will result in larger indents, thus producing right- or positively skewed hardness distributions [8]. For an asymmetrical dataset Weibull distribution is more appropriate than Gaussian distribution. Lin and Berndt [9] were among the first to demonstrate that for yttria partially or totally stabilized thermal spray coatings, Weibull statistic is more appropriate.

15.1.3.2 (b) Weibull Statistic

The Weibull distribution function is given by the following equation:

$$F(x,\lambda,m,\delta) = \frac{m}{\lambda}\left(\frac{x-\delta}{\lambda}\right)^{m-1}\exp\left(-\left(\frac{x-\delta}{\lambda}\right)^{m}\right) \tag{15.2}$$

where x is the variable, $m > 0$ is the shape parameter, $\lambda > 0$ the scale parameter, and δ the offset.

In materials science, m, the shape parameter is called Weibull modulus. By plotting $\ln(x-\delta)$ against $\ln\{\ln[1/(1-F(x-\delta))]\}$ and by using a linear regression least-squares fit to calculate the slope and intercept of the best fit straight line, the parameters of the distribution function can be determined [6]. Very often the offset δ is assumed to be zero and the three-factor Weibull distribution is simplified to a two-factor one. "However with modern spreadsheets allowing linear regression and giving the coefficient of determination (r^2 statistic) automatically, finding the offset δ that gives the best fit is trivial, as is the subsequent calculation of the other parameters for this best-fit case" [6]. Thus, when measuring Vickers microhardness HV $= x$, HV-dH is the characteristic hardness with 63.2 % of data points expected to be below this value, and m describes the shape of the distribution. The Weibull distribution is equal to or approximates several other distributions, depending on the value of m: $m = 1$ exponential distribution, $m = 2$ Rayleigh distribution, $m = 2.5$ lognormal distribution, $m = 3.6$ normal distribution, and $m = 5$ peaked normal distribution [6]. At last it must be underlined that Factor and Roman [6] are not favorable to the discounting of lowest and highest values. It affects measures of

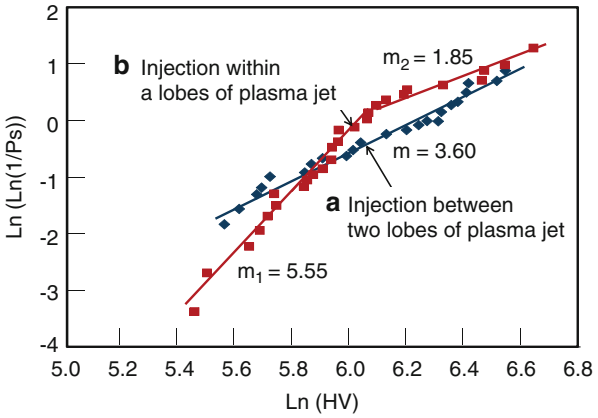


Fig. 15.1 Statistical analysis by microhardness Weibull distribution for coatings achieved by plasma spraying (Triplex II Pro torch anode nozzle i.d. 6.5 mm, $I = 400$ A, 50 % He) of lanthanum manganite doped with strontium ($La_{0.8}Sr_{0.2}MnO_3$: LSM) micrometer-sized particles made of agglomerated nanometer-sized grains: (**a**) injection between two lobes of plasma jet and (**b**) injected within a lobe of plasma jet. Reprinted with kind permission from Dr. E. Brousse [10]

spread such as the range and standard deviation. This also tends to increase the calculated averages, as the data for most coatings are not normally distributed.

An example of Weibull distributions from Brousse [10] is presented in Fig. 15.1. The example is related to the plasma spraying (Triplex II Pro torch) of lanthanum manganite doped with strontium ($La_{0.8}Sr_{0.2}MnO_3$: LSM) under the form of micrometer-sized particles made of agglomerated nanometer-sized grains. With this type of particles when the spray conditions are properly adjusted, coatings are made of nanometer-sized areas imbedded within micrometer-sized ones. Thus, the coating hardness depends strongly on locations where measurements are performed: low values in the nanometer-sized zones and high ones in the others. In Fig. 15.1a the spray conditions were not optimized and only one Weibull modulus was obtained, most sprayed particles being fully melted, while in Fig. 15.1b two Weibull distributions were obtained with the adapted spray conditions resulting in unmelted zones imbedded within fully melted ones. It must be underlined that Weibull distribution is the only way to characterize properly coatings with bimodal distributions.

15.1.3.3 (c) Variance

An important issue when calculating a statistical distribution is the number of data to be considered to have a reliable distribution. It can be determined by calculating the variance according to the number of events, N, taken into consideration. The variance is defined by the mean value of $(x - \eta)^2$, which is very simply calculated, if all events have the same probability, by $(x - \eta)^2/N$.

An example of the variability of Vickers hardness is presented in Fig. 15.2 for plasma-sprayed (Triplex II Pro torch) lanthanum manganite doped with strontium

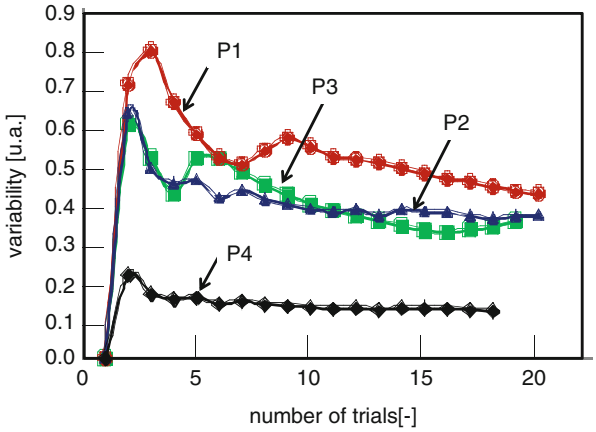


Fig. 15.2 Evolution of the variability of the Vickers hardness with the number of indents considered for different spray conditions (Triplex II Pro, 400A, anode nozzle i.d. 6.5 mm and 9 mm, (P1): $d_a = 6.5$ mm, Ar 60 slm, (P2): $d_a = 6.5$ mm, Ar 58 slm + He 19 slm, (P3): $d_a = 6.5$ mm, Ar 54 slm + He 54 slm, and (P4): $d_a = 9.0$ mm, Ar 60 slm). Reprinted with kind permission from Dr. E. Brousse [10]

($La_{0.8}Sr_{0.2}MnO_3$: LSM) micrometer-sized particles made of agglomerated nanometer-sized grains [10]. Figure 15.2 shows that with the spray conditions 4 (torch with a 9-mm internal diameter anode nozzle) all particles were melted corresponding to the highest hardness 773 ± 55 HV_3, and the variance was stabilized with a low number, 5, of measurements. On the contrary with the other spray conditions the coating hardness was lower (in a ratio of almost twice) with rather large standard deviation and, as shown in Fig. 15.2 the variability was more important (about 0.5 against 0.2 for conditions 4) and a stable value was reached only for 12–14 indents.

Simple, fast, reproducible nondestructive coating test methods are one of the dreams of sprayers. If many works have been achieved in R&D, only a few techniques have diffused in coating industry. This is probably due to the very complex structure of thermally sprayed coatings that is very difficult to interpret through the signals of nondestructive techniques (NDT). The different devices developed in R&D and industry are summarized in the ASM handbook about "Nondestructive evaluation and quality control of materials and manufactured parts" [11] and the ASTM reference [15.ND1]. The few devices that can be used for thermal spray coatings are summarily presented below.

15.2 Nondestructive Methods

15.2.1 Visual Inspection

This NDT allows detecting and examining a variety of surface flaws due to corrosion, contamination, delaminating, quality of surface finish, discontinuities,.... It comprises image sensors for visual records, magnifying systems, dye and

fluorescent penetrants, and magnetic particles for enhancing the observation of cracks or defects. Also, flexible or rigid boroscopes for illuminating and observing internal, closed, or otherwise inaccessible areas [11] can be used, but they are not very useful for coatings. A boroscope is an optical device consisting of a rigid or flexible tube with an eyepiece on one end and an objective lens on the other linked together by a relay optical system in between. The optical system is usually surrounded by optical fibers used for illumination of the remote object. An internal image of the illuminated object is formed by the objective lens and magnified by the eyepiece, which presents it to the viewer's eye.

15.2.2 Laser Inspection

Laser-based measurement systems are used for coating dimensional measurements and surface inspection. For dimension measurements, the following techniques can be used:

- Scanning laser gage. It can exhibit accuracies as high as ± 0.25 μm for parts with diameters of 10–50 mm. This accuracy is less for larger parts.
- Laser triangulation sensors. They measure the standoff distance between a surface and a microprocessor-based sensor and provide quick measurements of deviations due to changes in the surface. With two sensors the part thickness or the inside diameter of bores can be measured.
- Surface inspection to detect surface flaws and roughness.

  For more details, see [11].

15.2.3 Coordinate Measuring Machines

They fulfill demands of manufacturers on manufacturing facilities to provide very accurate and flexible three-dimensional inspection on both in-process, before coating for example, and finished parts; for example, with the coating after machining or rectification, see [11] for details about the method.

15.2.4 Machine Vision and Robotic Evaluation

A machine vision, also computer vision, includes both visual-sensing and interpretive capabilities allowing identifying shapes, measuring distances and ranges, gaging of sizes and dimensions, determining orientation of parts, detecting surface shading, . . . [11].

15.2.5 Acoustic Emission

The principle consists in recording an acoustic emission produced by sudden movement in stressed material. Generally sources of such emission are related to crack growth and/or plastic deformation. In most cases the rapid release of energy from localized source within coating or bulk material [12] produces an elastic stress wave radiating into the structure and exciting a sensitive piezoelectric transducer judiciously positioned. For example, crack formation is analyzed by monitoring acoustic emission (AE) response of deformation activities [13, 14]. AE analysis has been successfully used to monitor cracking in ceramic coatings during mechanical testing (four-point bending [15–17] and thermal cycling [2, 18, 19]). In general, depending on the spray parameters, coatings exhibit different AE responses corresponding to different amounts of AE energy. The number of AE events and AE energy released are measured. It is difficult to separate the AE events related to elastic and plastic deformation and to directly correlate the nature of cracking and the AE energy. However, using multilinear regression analysis, the number of AE events can be correlated to the spray parameters [20]. The Weibull modulus of the energy released during four-point bend test can be calculated [16]. When studying the effect of thermal cycling, the AE behavior monitoring during the heating and cooling periods of a thermal cycle must be separated. These periods show different stress ranges that correspond to different crack lengths and, therefore, correspond to different stress intensity factor ranges [19]. Andrews and Taylor [18] have used acoustic emission (AE) as a quality control test for TBCs, as the test is short and the data can be handled easily by a microprocessor. The test specimens were commercially sprayed straps. The data showed that differences in spraying parameters and microstructure were clearly visible in the emissions during the first thermal cycle.

Recently Zhao et al. [21] have extended the ultrasonic reflection coefficient amplitude spectrum (URCAS) to obtain the coating thickness and its longitudinal velocity at the same time on thick substrates. A model was set up first to represent the ultrasonic waves reflected from a coating system at normal incident. Then, an inverse algorithm based on the Gauss–Newton method was introduced to determine the thickness and velocity by comparing the theoretical and measured URCAS. Experimental validation was performed on the inhomogeneous ZrO_2–7 wt% Y_2O_3 (YSZ) coatings on super alloy substrates. The relative errors of the thickness and velocity measurement were in the ranges of 5.33–5.96 % and 8.95–9.66 % for YSZ coatings. It seems that the URCAS combined with inversion technique can be applied to obtain the thickness and longitudinal velocity of coatings simultaneously.

15.2.6 Laser-Ultrasonic Techniques

Nondestructive ultrasonic techniques have been used to determine the elastic constants, such as Young's modulus and Poisson's ratio, of a variety of bulk materials [22, 23]. However, it is difficult to measure the elastic properties of

thermal spray coatings by conventional ultrasonic techniques due to the porosity and extensive micro cracking. The laser-ultrasonic technique uses surface acoustic waves (SAWs) or Rayleigh waves, propagating along the surface of a material, to obtain information about it. SAWs are generated by the instantaneous local thermal expansion, laser ablation, or high-intensity pulsed ion beam. As the wave motion is concentrated near the surface, it makes SAWs interesting for testing coatings [24] or thin films. The surface waves are generated and detected at lengths much greater than the dimension of the coating thickness and the coating thickness-to-wavelength ratio is the key parameter for the penetration depth of the material [25]. A laser pulse can generate simultaneously many wave modes. The laser and its wave detection are performed on the same surface, but at different places, two types of ultrasonic waves, surface longitudinal and Rayleigh wave velocities, permit measuring Young's modulus, E, and Poisson's ratio, ν. E and ν values measured by Knoop indentation were in good agreement with those obtained with laser-ultrasonic technique for titania coatings plasma and HVOF sprayed [25]. The titania coatings exhibited significantly different Poisson ratio, ν, values, although they had very similar E values. The E values measured on the cross section of WC–Co coatings agreed well with those measured via laser ultrasonic.

Laser (nanosecond pulsed) ultrasonic has also been used for the nondestructive characterization of ceramic coatings (alumina) and the estimation of their adhesion strength on metallic substrates [26].

15.2.7 Thermography

Thermography is a surface thermal radiation measurement technique that is used to detect spatial variations in the measured surface temperature pattern. Thermography reveals flaws by searching anomalous hot spots after thermal excitation. Two types of thermography inspections are used: passive and active. Passive thermography measures the variation of surface radiation to identify anomalous regions. Active thermography uses a controllable thermal source to excite the testing object and reduces the environmental influence such as ambient conditions and emissivity variations [27]. The most efficient thermal tests are the dynamical or active ones, which can detect the presence of subsurface detachments by monitoring the evolution of the coating temperature during a thermal transient pulse. Pulsed thermography (PT) is used today for the inspection of the manufacturing quality of coatings immediately after their deposition. Because of its speed and simplicity, PT allows the design of an automatic inspection procedure for factory quality control [28, 29].

When performing in-field tests on thermal barrier coatings (TBCs) deposited on gas turbine blades, the main problem encountered is the difficulty to correctly interpret the experimental data. Marinetti et al. [30] have defined a procedure to

reliably discriminate thickness changes and real defects and presented and discussed preliminary results. Their approach was based on the analysis of the apparent effusivity profile.

15.2.8 Coating Thickness

Measuring the coating thickness is not necessarily straightforward and the method for thickness evaluation can also be questioned. Wigren and Täng [3] have considered the thickness evaluation of Ni–5Al plasma-sprayed coating. For that they compared two microscope techniques (average and maximum readings) and two types of micrometer (flat and ball end). Thicknesses were given stroke by stroke (2 passes) during the coating buildup. A 50 μm thick metallic coating measured with flat micrometer did not have full metallographic coverage in the above investigation, whereas 50 μm measured with a ball end micrometer did. Important differences in thickness measurements were observed. The measurement tool (flat or ball point micrometer) used for thickness measurements had a significant effect on the reading, as well as the microscope techniques [3].

15.3 Metallography and Image Analysis

Metallography is a critical step to characterize coatings. Sometimes surfaces are rougher than the original grit-blasted surface, which is especially the case for porous and loose structures such as those observed with certain flame-sprayed coatings. Compared to bulk materials coating preparation for metallographic examination is rather difficult. This is due to coating microstructure made of layered splats with porosities and unmelted particles, ceramic coatings that are more brittle than bulk-sintered ceramic materials, mixtures of hard and soft materials in cermets, and mixtures of many phases. All these features are a challenge for conventional metallographers. W. Riggs in the chapter Metallography and Image Analysis in [2] gives an excellent illustration of the effect of the metallographic procedure for a WC–Co coating. One of the main problems related to coatings is linked to particles pullout, especially for cermets. A properly prepared metallographic surface [31–33, 15.Me1–15.Me3] must meet the following criteria:

- Removal of deformation zone produced during rough polishing
- Be flat and free from scratches, stains, and other imperfections
- Contain all nonmetallic inclusions intact
- Show no chipping or galling of hard and brittle inter-metallic compounds
- Be free from all traces of disturbed metal

15.3.1 Coating Preparation

15.3.1.1 Sectioning

The first step of metallographic preparation is sectioning either to reduce the specimen size or examine its cross section or both. Of course the process through heat and deformation must not alter the microstructure. According to the good resistance to compressive loads and the poor ones to tensile ones cutting must be performed from the outermost layer of coating, inward, and then through the coating and not the reverse [2]. To limit the flaws created by cutting, the specimen can be first encapsulated in a cold mount-type epoxy (see Sect. 15.3.1.2) before sectioning, which is an excellent technique but very time consuming.

(a) Abrasive Cutting

This is probably the best solution to eliminate or limit heat and deformation. The cutoff machine and abrasive wheels must be matched. The abrasive is to be chosen according to the material to be cut: diamond, alumina, and silicon carbide are mostly used. Independently of bond hardness, the coarser grit size produces the harder action, while finer grits result in a softer action and a smoother surface. The bonding material, holding abrasive grains in place is either made of resinoid for dry cutting or rubber for wet cutting. Softer bonds are used to cut hard materials, while harder ones are used to cut soft materials. As already emphasized the proper cooling is very important and is achieved by high volume jets or submerged cutting. The cutting speed is also an important parameter and must be adapted to the wheel used.

For thermally sprayed coatings Antou and Montavon recommended [34]:

- Cutting speed should be on the order of a few hundred meters per minute.
- Transverse speed should vary between 0.01 and 0.1 mm/s. It is suggested, when possible, to select the lowest possible transverse speed and use a device in which the cutting speed can be adjusted rather than the cutting load, since in this latter case the cutting speed varies along the sample.
- Water or oil has to be used as lubricant.

Sauer [35] on behalf of the TSS (Thermal Spray Society) Committee on Accepted Practices has also presented the best practices for sectioning sprayed coatings.

(b) Precision Sectioning

Small diameter, 75–125 mm, diamond or CBN (*Cubic Boron Nitride*) rimmed wheels are used. Their speed range extends from a few to 1,000 rpm and the load range, if possible controlled electronically, varies from a few tenths to ten Newtons. The technique gives excellent results for most coatings, but it is rather slow.

To conclude this part applying the following motto is recommended: "Better spend more time for cutting the sample, this will result in reduced polishing time and in less damage to the structure." For more details about cutting, see [2, 32] as well as the recommendations of cutoff machine manufacturers.

15.3.1.2 Mounting

Metallographic samples are mounted to ease their manipulation and protect their edge during preparation. They are encapsulated in cylindrical polymeric mounts. According to Riggs [2] the mount roles are to:

- Ease their gripping by hand or automatic devices but also to firmly hold the specimen
- Have the same response than the specimen during grinding
- Avoid damaging the specimen for example by a too high temperature or pressure
- Penetrate and fill non-occluded (surface-connected pores) but without modifying their original size and shape and also minimizing pullout during grinding and polishing

The main goal of the mounting process is to manufacture a sample that can be easily manipulated and to reinforce the coating prior to polishing or even sectioning

(a) ***Cleaning***: is the first operation to remove oils, dirt, . . ., from the mold. It can be performed with soap and water and afterwards dried after rinsing. The other mean is ultrasonic cleaning.

As previously mentioned by Wigren and Täng [3], "The choice between hot and cold (vacuum) mounting may be the single most important step in the whole metallographic procedure."

(b) ***Hot mounting process***: The compression molding technique consumes the minimum amount of time. It uses thermosetting and thermoplastic materials. The first one requires heat and pressure during the molding cycle and can be ejected at maximum molding temperature. Thermoplastic materials remain fluid at maximum molding temperatures and become dense and transparent with a decrease in temperature and an increase in pressure.

(c) ***Cold-mounting process***: Neither heat nor pressure is applied. The sample is placed in a plastic or rubber cup with epoxies, polyesters, and acrylics all comprising a resin and a hardener. An exothermic reaction occurs during polymerization and thus the mixing by volume or weights of both components is critical. Epoxies and polyesters are transparent, but acrylics are opaque. Epoxy can fill pores if the gas they contain is evacuated. It can be achieved by, if necessary, heating the samples to get rid of water vapor and then by placing the samples in soft vacuum at a pressure such that the boiling of the epoxy is avoided and during 10 min at least. Vacuum impregnation with a suitable liquid epoxy produces nonporous samples well consolidated and rigid. With this technology it becomes possible to distinguish between oxide stringers and delaminations [3].

(d) ***Mounting defects***: They comprise cracking at the corners, bulging in phenolics, soft mounts, and also porous and friable areas (hot mounts), or bubbles (cold mounts).

For more details, see [2, 32–38] as well as the recommendations of cutoff machine manufacturers.

According to Wigren and Täng [3]: "The choice between hot and cold (vacuum) mounting may be the single most important step in the whole metallographic procedure." True microstructure features (cracks, porosities) that never were seen previously are now revealed with cold mount techniques using low viscosity epoxies and thus not allowed in the specifications. The penetration of epoxy during mounting is also crucial for the following steps in the metallographic procedure, especially the grinding step.

15.3.1.3 Grinding

The prepared metallurgical mount is then subjected to a series of grinding and polishing steps in order to achieve a surface suitable for observation at both low and high magnification, see chapter of Riggs in [2]. Of course the grinding procedure depends on the grinded material properties such as hardness and ductility and it must be adapted to each one. The role of grinding, then followed by polishing is to produce samples with:

- True and undisturbed microstructure.
- The larger scratch (polishing artifact) of smaller dimension than that observable at a given magnification.
- Flat specimen with edge rounding: using a polishing surface with high resilience will result in material removal from both the sample surface and the sides. The effect of this is edge rounding and can be seen with mounted specimens if the resin wears at a higher rate than the sample material.

Of course the process parameters, including the coolant lubricant, must be such that overheating does not occur, the high temperatures generated in the grinding zone can cause different types of thermal damages. Wigren and Täng [3] have underlined that many problems can arise from improper grinding/polishing. By far, one of the biggest issues in grinding is the smearing caused by the SiC papers. The most critical are the unfilled pores and cracks in a metallic coating [3]. Long polishing can also bring forward another problem of edge retention, which causes metallic coatings with oxides and pores to be distorted. The width of pores and oxides can also be enlarged. Ceramic coatings can cause other grinding/polishing issues. Many times long polishing times are necessary, because of the damage created by the grinding steps [3].

The first grinding is the coarse one, the purpose of which is to remove the deformation produced during sectioning and achieve a flat surface. It also removes gross amounts of surface material for the micro-sample preparation. The process is performed with abrasive belts or disc-covered rotating wheels and generally water as coolant, which also flush away the surface removal products. In most cases the

abrasive used are alumina or silicon carbide with grit sizes between about 350 and 80 μm. The abrasive action, depending also on the grinding speed, is very aggressive. For more details, see the paper of Puerta [37] on behalf of TSS Committee on Accepted Practices.

The second grinding is fine grinding performed, generally in wet conditions, with bonded grains of alumina, silicon carbide, and emery. Pre-polishing diamond structured discs with diamonds in the size range 3–15 μm can also be used.

A detailed description of grinding materials is given by W. Riggs in the Metallography chapter of [2], where are also specified grinding rates, grinding deformation, and finally material response to various parameters (pressure, abrasive type, abrasion fluid, and time).

15.3.1.4 Polishing

The main objective is to remove the abrasion-damage layer (plastically deformed material, scratches, slip/twin/shear damage layer immediately beneath the surface) produced by the grinding process. The material removal is achieved with either rolling abrasive particles or fixed abrasive particle. To minimize the time and labor interchangeable revolving disks are used, each of which covered with emery paper, cloth, or parchment, according to the stage of polishing for which it is required. The abrasive used should permit accurate sizing, which is the case of diamond abrasives that also have a high hardness, a low coefficient of friction, and excellent inertness. They produce uniform and high rate of material removal with very few induced surface damage. Typically 6-μm mean size is used to achieve the highest removal rates for most materials (rough polishing), the removal rate decreasing very fast for smaller sizes. The type of cloth used is very important for the end result. The final polishing stage removes any deformation zone resulting from the rough polishing. For this polishing, a wide variety of abrasive materials can be used: alumina, chromium oxide, magnesium oxide, colloidal silica, and diamond, with sizes generally around or below 1 μm. The coating materials that are trickier for grinding and polishing are ceramics and cermets. For details about polishing see the Metallography chapter of W. Riggs in [2] or [31–38] or the recommendation of polishing machine manufacturers.

Antou and Montavon [34] recommended to:

- Use semi- or automatic-polishing machine for a higher reproducibility of the operation.
- Adjust independently the load on each sample to polish a given coating nature at the appropriate pressure regardless of the sample size.
- Select identical directions of rotation for the samples and the abrasive support to avoid damage by spallation.

Wigren and Täng [3] underlined that very often long polishing times are necessary, because of the damage created by the grinding steps, especially for ceramic coatings.

15.3.1.5 Etching

Etching is the operation to reveal the microstructural features (grain boundaries, phases, precipitates, and other microstructure constituents) of the *polished* specimen. Etching is achieved through selective chemical attack of the surface. To prevent uneven attack and stains, especially after polishing, the specimen must be washed and degreased in boiling alcohol and then cooled in running water before being etched. Immersing, for a given time, the clean specimen in the etching reagent, performs etching. Then the specimen is quickly removed from the reagent and immediately swilled in running water before being dried in alcohol. The etching reagent is chosen according to the material to be etched, for example, nital reagent (2 volume part of nitric acid, 98 volume part of alcohol) for steels and cast iron. Etching with acid can be enhanced by electric current and becomes electrolytic etching. Many etchants have been developed to reveal the structure of metals and alloys, ceramics, carbides, nitrides, and so forth. While a number of etchants may work for a given metal or alloy, they generally produce different results, in that some etchants may reveal the general structure, while others may be selective to certain phases or constituents. For details, see [32, 33].

15.3.1.6 Focused Ion Beam

Focused ion beam (FIB) has been developed in the semiconductor industry and materials science. It is similar to SEM, but instead of using electrons it works with a focused ion beam. Ions, being far heavier than electrons, have a high momentum but are much slower than electrons [39].

To summarize, ions are positive, large, heavy, and slow; thus ion beams will remove atoms from the coating and/or substrate, and as the beam position, dwell time, and size are very well controlled, it removes material locally in a highly controlled manner, down to the nanometer scale. As with conventional cutting and polishing techniques, ion beams can produce surface damage and implantation that can be minimized by FIB milling with lower voltage. However, for thermally sprayed coatings, it is almost the only mean allowing studying the contact between a splat and the substrate, the conventional means described previously being too aggressive and, in most cases, separating the splat from the substrate. This is, for example, illustrated in Fig. 13.18. FIB can also be used to prepare thin (in the 100-nm range) samples for TEM.

15.3.1.7 Examples of Conventional Coatings Preparation

The Thermal Spray Society (TSS) has tested, through round Robin tests, two different sprayed materials [40] (http://asmcommunity.asminternational.org/portal/site/tss/): Molybdenum coating with some oxide content after spraying in air and Ni–4Cr–4Al/Bentonite coatings containing metallic and nonmetallic phases with a

high porosity level (up to 40 %). Mo coatings are intensively used in aerospace industry and also automotive, marine, and heavy industries. For these coatings, vacuum impregnation with a low-viscosity cold mount epoxy is the recommended mounting method. The amount of material, which must be removed, depends on the sectioning methods employed. All accepted practice preparation procedures utilized combined diamond steps totaling a minimum of five minutes.[1] For abradable coating the possibility to pullout during metallographic preparation is very high as to the elevated porosity with nonmetallic phases generally loosely bonded. Most laboratories identified vacuum impregnation of a castable epoxy as a critical step to ensure such a coating integrity during preparation.[2]

15.3.2 Microscopy

15.3.2.1 Optical Microscopy

Optical microscopy (OM) examination is the first instrument to be used for metallographic observations because it is faster and much less expensive than Scanning Electron Microscopy (SEM). OM covers a large area; the contrast at magnification below 500 is better than that of SEM and at last it can give the natural color of the specimen. In most cases magnifications are between 50 and 1000×. However, with some microscopes, it becomes possible to perform examination at higher magnifications, e.g., 2000×, and even higher, as long as diffraction fringes are not present to distort the image. The resolution limit of the OM is at the best about 0.2–0.3 μm. If necessary, special objectives allow using OM at magnifications below 50×. One of the key parameters is image contrast, which depends on the one hand on the quality of the optics, coatings on lenses, and reduction of flare and glare, and on the other hand on proper specimen preparation and, if necessary, good etching techniques. At last the important characteristic of OM is the depth of field, D, area in front of and behind the specimen that will be in acceptable focus. Figure 15.3 presents a scheme of the depth of field, D, that can be calculated simply by

$$\frac{D}{2}\tan\alpha = \frac{d}{2} \tag{15.3}$$

where α is the beam half angle and d its diameter at the depth of field (DOF) position.

The depth of field is the weak point of OM with D values in the micrometers range or below, for example, $D = 5$ μm for a magnification of 20 corresponding to

[1] ASM Thermal Spray Society (TSS), Accepted Practices Committee on Metallography Accepted Practice–Molybdenum Thermal Spray Coatings, see [40].

[2] ASM Thermal Spray Society (TSS), Accepted Practices Committee on Metallography Accepted Practice–NiCrAl/Bentonite Abradable Coatings, see [40].

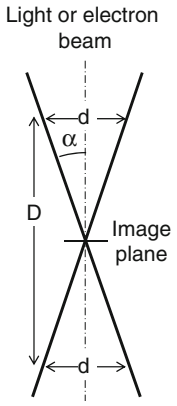


Fig. 15.3 Scheme of the depth of field

a resolution of 5 μm and $D = 0.7$ μm for a magnification of 200 corresponding to a resolution of 0.5 μm.

Most observations are performed with bright field illumination where the image of any flat feature perpendicular to the incident light path is bright or appears to be white. Dark field provides higher contrast images and greater resolution than bright field. The light from features perpendicular to the optical axis is blocked and appears dark, while the light from features inclined to the surface appear bright. Polarized light is also used when studying the structure of metals with non-cubic crystal structures. Tint-etched surfaces, where a thin film (such as a sulfide, molybdate, chromate, or elemental selenium film) is grown epitaxial on the surface to a depth where interference effects are created, when examined with bright field, produce color images. The process can be improved with polarized light. Another imaging mode is differential interference contrast that converts minor height differences on the plane of polish, invisible in bright field, into visible detail.

In many circumstances the ability to capture, display, and preserve specimen images is very important. For that purpose digital microscopes have built-in cameras transmitting the images viewed within the microscope onto a TV or monitor. Adapted softwares allow performing image analysis. For details about optical microscopes, see [32, 33].

15.3.2.2 Scanning Electron Microscopy

In a Scanning Electron Microscope (SEM), an electron beam with an energy ranging from 0.5 to 40 keV is thermionically emitted from an electron gun. The electron beam is focused by one or two condenser lenses to a spot about 0.4–5 nm in diameter. The beam, generally in the final lens, passes through pairs of scanning coils or deflector plates, which deflect it in the x and y axes so that it scans over a rectangular area of the sample surface. The electron beam loses energy by repeated random scattering and absorption within the interaction volume of the specimen,

which extends from less than 100 nm to around 5 μm into the surface. The size of the interaction volume depends on the electron's landing energy, the atomic number of the specimen, and the specimen's mass density. The analysis requires high vacuum conditions and specimens must be vacuum compatible (low vapor pressure) and electrically conductive. The charge-up effects on nonconductive samples can be compensated by reduced probe current, by reduced acceleration voltage or, in most cases, by coating them with a thin metal film (Au, Pt) or carbon layer. Compared to OM, the depth of field of SEM is excellent, for example, at a magnification of 200 the DOF is 100 μm (against 0.7 μm for OM) and at a magnification of 10,000 the DOF is still 2 μm. This allows studying fractured coating surfaces, showing well the splat or grain microstructure. The fractured surface is cut to a suitable size, cleaned of any organic residues, and mounted on a specimen holder for viewing in the SEM. Actually SEM can reach magnifications up to 500,000. As scanning electron microscopes have evolved, the electron beam cross section has become smaller and smaller (they reach now a few nanometers in diameter) increasing magnification several fold. The last generation of SEM, field emission scanning electron microscope (FESEM), has a beam cross section close to one nanometer in diameter. The field emission tip is made up of a sharply etched piece of monocrystalline tungsten. A field applied to the tip causes electrons to tunnel out of the tip and accelerate down the column.

In SEM and FESEM the electrons and photons generated in the excitation volume carry different types of information from the analyzed specimen: secondary electrons, backscattered electrons, absorbed specimen current, and cathodoluminescence.

Secondary electrons are produced when the incident electrons from the beam interact with the atoms in the surface region of specimen. The impact (collision cascade) causes a path change for the incident electron and ionization of several specimen atoms. The ejected electrons leave the atom with a very small kinetic energy (<50 eV) and permit a high resolution (about 3.5 nm) of fine surface morphology. As these electrons are sensitive to the orientation of different surface features they create an image contrast for evaluating the sample's surface topography. SEM is routinely used to observe:

- Single splats
- Surface of as-sprayed coatings
- Metallographic polished surface of coatings or that of their cross section to see layered splats, structure (columnar or granular), pores, voids from pullouts, and cracks
- Fractured surface of as-sprayed coatings
- Backscattered electrons (BSE) are high-energy electrons produced by the elastic collision of the incident electron beam with the electron cone of the sample atoms. Imaging with them provides elemental composition variation and surface topography (resolution about 5.5 nm). The yield is proportional to the atomic number (Z contrast) and depends on the beam energy and incidence angle. They also allow mapping of individual elements

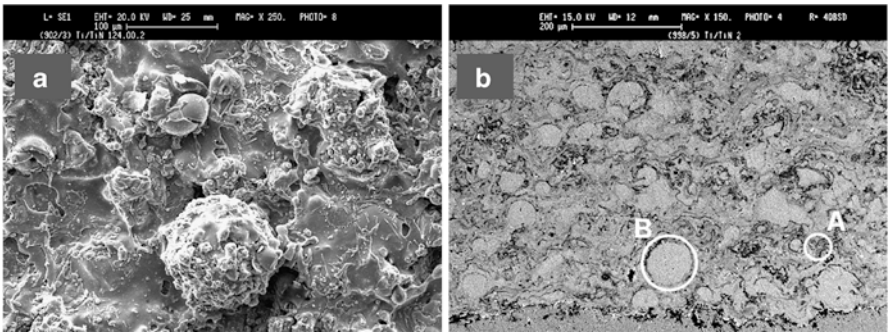


Fig. 15.4 Reactive plasma-sprayed composite Ti–TiN–TixNy: (**a**) SEM image of the surface. (**b**) Cross section of the coating in BSE micrograph (A) nitrided particles and (B) non-nitrided particles. Reprinted with kind permission from Elsevier [41]

An example of SEM images from Ingo et al. [41] is presented in Fig. 15.4 for reactive plasma-sprayed composite Ti–TiN–TixNy coating starting from SP700 powder (Ti–4.5Al–3V–2Mo–2Fe). Figure 15.4a shows the coating surface with high roughness as well as melted and unmolten particles, while Fig. 15.4b presents the coating cross section by Back Scattered Electrons (BSE) allowing distinguishing nitrided and non-nitrided particles.

The electron beam specimen interaction results in the emission of characteristic X-rays, which can be detected and analyzed (Electron Probe Microanalysis, EPMA); see Sect. 15.4.8. For details about scanning electron microscopes, see [32, 33].

15.3.2.3 Image Analysis

Image analysis is extensively used to assess the area percentages of some attributes such as porosity; see the chapter of Riggs in [2] and the book of Russ [42] or to filter images of spray jets, for example, to follow liquid drops injection in a d.c. plasma jet [43]. When a digital image is formed, the digitization process divides it into a horizontal grid of very small regions called “picture elements” or “pixels.” In the computer this digital grid or “bitmap” represents the image. Each pixel is identified by its position in the grid, as referenced by its row (x) and column (y) number. Each pixel has a different color or gray scale value and together they form a representation of the image. Depending on whether pixels are black and white, gray scale, or color, pixels have different bit depths. Bit depth refers to the amount of information allocated to each pixel. For example in digital color, each color occupies 8 bits (1 byte). For example, in a gray scale image each picture element has an assigned intensity ranging from 0 to 255. In image analysis, resolution refers to the number of pixels used to represent the image: more pixels have a higher resolving power. With computers, information from image analysis can be easily modified and/or improved:

- Gray scale adjustment to improve the contrast
- Spatial filtering, which generally results in an image with only edges of high contrast visible, fine detail with low contrast being usually lost to the background
- Noise reduction
- Edge enhancement
- Shape measurement
- Thresholding to select features of interest, ... However it is the step of controversy, the limits to detect the features of interest being strongly operator dependent. For more details, see the paper of Antou and Montavon [34] presenting, from a practical viewpoint, some key points to assess when implementing image analysis coupled to stereological protocols to quantify statistically the architecture of thermal spray coatings and their relevant features (pores, lamellae, and so forth).

Image analysis must be used with care and requires a good knowledge of how information is extracted from the image to achieve reliable data, e.g., porosity. At last one must keep in mind that image analysis cannot give more precision than that given by the microscope observation of the prepared sample.

15.3.2.4 Atomic Force Microscopy

Atomic Force Microscopy (AFM) is based on the specimen surface scan by a cantilever with a sharp tip (probe) at its end. The cantilever is typically made of silicon or silicon nitride with a tip radius of curvature on the order of nanometers. When the tip is brought into proximity of a sample surface, forces between the tip and the sample lead to a deflection of the cantilever according to Hooke's law. Forces implied in AFM include mechanical contact force, van der Waals forces, capillary forces, chemical bonding, electrostatic forces, and magnetic forces. The cantilever deflection is generally measured using a laser spot reflected from its top surface onto an array of photodiodes.

A feedback mechanism makes it possible to adjust the tip-to-sample distance to maintain a constant force between the tip and the sample. For that the sample is moved in the z direction by a piezoelectric tube and in the x and y directions for scanning the sample. See [44] for details about the different AFM modes: topographic, non-topographic, and surface modification.

Compared to SEM, AFM has several advantages: it provides a three-dimensional (3D) surface profile against a 2D one for SEM, it works perfectly well in ambient air or liquid environment, and it can provide higher resolution than SEM. However, it also has some disadvantages: in one pass, SEM can image an area in the order of square millimeters with a depth of field in the order of millimeters, while AFM can only image a maximum height in the order of 10–20 μm and a maximum scanning area of about 150 × 150 μm. The scanning speed of AFM is slower than that of SEM that is capable of scanning at near real time, although at relatively low quality.

In thermal spraying, AFM has been used especially to study splat formation and characterize the variation with oxidation of smooth substrate surface topography at the nanometer scale, see Fig. 12.10 [45] and also Fig. 13.7.

15.3.2.5 Transmission Electron Microscopy

Transmission Electron Microscopy (TEM) works on the same principle as an old-fashioned slide projector, except that an electron beam replaces light. In the projector, the light passing through the film interacts with it. The light going through the film hits the lenses disposed on the other side and the resulting image is projected onto a screen. In a TEM a beam of electrons is focused on a single, pinpoint spot or element on the sample being studied [46]. The electrons interact with the sample and only those that go through unobstructed hit the phosphor screen on the other side. Electrons that hit the screen are converted to light and so an image is formed. The dark areas of the image correspond to areas on the specimen where fewer electrons were able to pass through (either absorbed or scattered upon impact); the lighter areas are where more electrons pass through, although the varying amounts of electrons in these areas enable the user to see structures and gradients. In a TEM, lenses made of electromagnetic devices focus the electron beam to the desired wavelength or size. The amount of power used to generate electrons controls magnification that can be very high, permitting to see objects a few angstroms in size. Of course TEM works under vacuum that can be very low (10^{-7}–10^{-9} Pa) in certain parts.

The drawback of TEM is that specimens studied have to be sliced very thinly (a few micrometers) to ensure that they are electron transparent; they must also be placed in a vacuum. Thus, preparation of specimens is often time consuming. Moreover it requires expert handling to limit the risk of inadvertent damage during the process, especially for ceramic materials. For example, a wedge-polishing technique was used to prepare samples of YSZ single splats [47]. Wedge-polishing device, supplied by different manufacturers, reduces the need for ion milling by mechanically thinning the area of interest to 0.1 μm or less. These polishing kits are recommended for material applications involving microelectronics, metals, ceramics, minerals, and composites. Electron transparency thickness can be reached for TEM analysis.

An important development in the specimen preparation is the use of Focus Ion Beam (FIB) systems operating in a fashion similar to a scanning electron microscope (SEM) (Sect. 15.3.2.2). According to the low pressure (about 10^{-4} Pa), TEM comprises a device to allow the insertion into, motion within, and removal of specimens from the beam path. High-Resolution TEM (HRTEM) is the ultimate tool in imaging defects. In favorable cases it shows directly a two-dimensional projection of the crystal with defects and its magnification can reach 10^6.

TEM allows obtaining information about morphology, crystal size, and chemistry, if equipped as SEM with an EDS (Energy-dispersive X-ray spectroscopy) probe. Two observation modes are used: *Image mode* to observe the specimen morphology with a very high magnification and *Diffraction mode* giving information about the crystalline structure. For example, TEM was used by Tjitra Salim

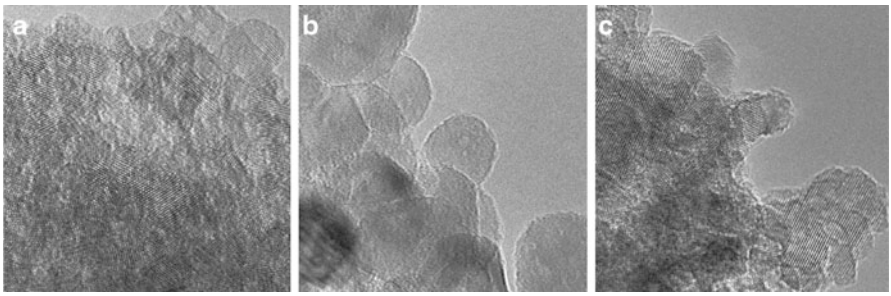


Fig. 15.5 TEM images of (**a**) as-synthesized, (**b**) annealed, and (**c**) hydrothermal treated TiO_2 powders. Reprinted with kind permission from Elsevier [48]

et al. [48] to characterize TiO_2 powders synthesized by hydrolysis of titanyl sulfate ($TiOSO_4$) in distilled water with a small addition of inorganic salt. At a relatively low hydrolysis temperature, pure anatase TiO_2 could be obtained and post-synthesis treatments (annealing or hydrothermal treatment) did not alter this phase structure. The powder was then agglomerated with fine nano-primary particles, with different post-synthesis treatments leading to different TiO_2 nanostructures. Figure 15.5a represents the powder as synthesized, while Fig. 15.5b shows the hydrothermal treated powder with unique oriented agglomeration structures. The hydrothermal treatment consisted in soaking the TiO_2 powder with distilled water in an autoclave and heat treating it at 150 °C for 5 h, and the resulting TEM image is presented in Fig. 15.5c.

Among the numerous papers about thermal sprayed coatings where TEM was used to characterize either powders or coatings or both, Chen et al. [49] characterized nanostructured zirconia particles, Yan et al. [50] studied the structure of coating prepared by reactive plasma spraying Fe_2O_3/Al composite powders, Ma et al. [51] observed grain structures of suspensions of Ni–14.55Cr–3.22B–4.7Si–4.78Fe sprayed by HVOF, Chraska [52] studied microstructures and interfaces of zirconia coatings produced by plasma spraying, …. For more details see [46, 53].

15.4 Materials Characterization

The techniques described below involve nondestructive analytical techniques, which reveal information about the crystallographic structure, chemical composition, and physical properties of coatings. These techniques are based on the observation of the scattered intensity of X-rays, infrared, neutron, and nuclear gamma ray beams hitting a specimen as to incident and scattered angles, polarization, and wavelength or energy.

15.4.1 X-Ray Spectroscopy or X-Ray Fluorescence

When a primary X-ray excitation source strikes a sample, the X-rays can either be absorbed by the atom or scattered through the material. The photoelectric effect occurs when the atom absorbs X-ray, the energy of which is all transferred to an innermost electron. If the primary X-rays have sufficient energy, electrons are ejected from the inner shells, creating vacancies. As the atoms return to stable condition, electrons from the outer shells are transferred to the inner shells. This process creates characteristic X-rays whose energy is the difference between the two binding energies of the corresponding shells. Each element having a unique set of energy levels produces X-rays at a unique set of energies. The theoretical relationship between the measured X-ray intensities and concentrations of elements in the sample allows the nondestructive measure of the elemental composition of a sample. This process is called "X-ray Fluorescence" or XRF. A typical X-ray spectrum from an irradiated sample displays multiple peaks of different intensities. The penetration depth of X-ray depends on the coating material and the wavelength of the beam, but it is generally a few micrometers at the maximum 10–15 μm. For details see [53].

15.4.2 Infrared Spectroscopy

In infrared spectroscopy molecules absorb specific frequencies that are characteristic of their chemical bonds and organization. The frequency of the absorbed radiation matches the frequency of the bond or group that vibrates. The shape of the molecular potential energy surfaces, masses of atoms, and the associated vibration coupling determine the energies. The frequency of the vibrations can be associated with a particular bond type. For example, the characteristic wave numbers of oxides are between 250 and 1,000 cm^{-1}.

Fourier Transform Infrared Spectroscopy (FTIR) refers to a recent development in which infrared light is guided through an interferometer and then through the sample (or vice versa). The data are collected and converted from an interference pattern to a spectrum. The sample's spectrum is then compared to standards as described in [53, 15.Ma1].

In thermal spraying, FTIR has been used to characterize the oxide layer formed at the smooth surface of a metal or alloy substrate according to the preheating conditions prior to spraying [54]. In this case the analysis was performed with a quasi-ranking incidence of the IR light and its depth was between a few nanometers and few micrometers.

15.4.3 Mössbauer Spectroscopy

Mössbauer spectroscopy is a spectroscopic technique based on the recoil-free, resonant absorption, and emission of gamma rays in solids. Typically, three types of nuclear interaction may be observed: an isomer shift, also known as a chemical shift; quadrupole splitting; and magnetic or hyperfine splitting, also known as the Zeeman effect (splitting of a spectral line into several components in the presence of a static magnetic field) [55].

Mössbauer spectroscopy gives local information on the nucleus affected, its vibration state, electron density, and magnetic momentum. These data inform about the valence state of the corresponding atoms, bonds with their neighbors, and positions within the crystalline network.

Mössbauer spectroscopy is well adapted to the study of iron and its oxides as it allows characterizing phases and their relative percentages. It has been used to characterize the oxidation of steel substrates according to the preheating conditions [54]. It has also been used to characterize the in-flight oxidation of plasma-sprayed alloy steel particles [55].

15.4.4 X-Ray Diffraction

X-ray diffraction (XRD) is a versatile, nondestructive technique that reveals detailed information about the chemical composition and crystallographic structure of natural and manufactured materials, including coatings [53, 15.Ma2–15.Ma5]. When a monochromatic X-ray beam with wavelength lambda, λ, is projected onto a crystalline material at an angle theta, θ, diffraction occurs only when the distance traveled by the rays reflected from successive crystal planes differs by an integer number n of wavelengths. Bragg developed a relationship in 1913 to explain why the crystallographic planes of crystals appear to reflect X-ray beams at certain angles of incidence (theta, θ). The variable, d, is the distance between atomic layers with the same Miller indices (h, k, l), in a crystal, and the variable lambda, λ, is the wavelength of the incident X-ray beam and n is an integer, the order of the reflection.

$$n\lambda = 2d_{hkl} \sin\theta \tag{15.4}$$

By varying the angle theta, the Bragg's Law conditions are satisfied by different d-spacings (characterized by Miller indexes) in polycrystalline materials. Plotting the angular positions and intensities of the resultant diffracted peaks of radiation produces a pattern, which is characteristic of the sample. When the sample is a mixture of different phases, the resultant diffractogram is formed by addition of the individual patterns. The identification of crystalline materials is based on the comparison of experimental values of the reticular distances with data of literature. The reference data are that of the Joint Committee Powder Diffraction Standard

(J.C.P.D.S.). XRD is extensively used in thermal spraying, for example, to characterize structural changes between the sprayed powder and coating. It must be underlined that the penetration distance of the X-ray beam into the sample can vary from few to several micrometers depending on the sample characteristics and wavelength of the beam.

XRD is also used to estimate the average grain size of the feedstock and coating. The applicability of this method was confirmed by comparing results from TEM and XRD techniques [52, 56]. The XRD method assumes that the overall broadening of XRD peaks comprises two effects: one arising from the small coherent grain size and one arising from the atomic level micro-strain. i.e., $\Delta d/d$, where d is the atomic spacing. The peak width resulting from a small grain size effect alone can be described by the Scherrer equation [53]:

$$B(2\theta) = \frac{K\lambda}{D\cos\theta} \tag{15.5}$$

where $B(2\theta)$ is the true broadening of the diffraction line measured at full-width at half-maximum (FWHM), λ the wavelength of the X-ray radiation, D the mean dimension of the grains, θ the Bragg angle, and K the Scherrer constant. It depends on how the width is determined, the shape of the crystal, and the size distribution; its common value is 0.9. For more information about the K constant, see JI Langford and AJC Wilson, "Scherrer after sixty years: A survey and some new results in the determination of crystallite size," *J. Appl. Cryst.* **11** (1978) p102–113.

Hugo Rietveld, for the characterization of crystalline materials, showed that the neutron and X-ray diffractions of powder samples result in a pattern characterized by reflections (peaks in intensity) at certain positions. The height, width, and position of these reflections can be used to determine many aspects of the materials structure (see [53]).

X-ray diffraction also makes it possible to measure the angular lattice strain distributions resulting from residual stress. A reflection at high 2-Theta is chosen and the change in the d-spacing with different orientations of the sample is measured. Using Hooke's law, relating stress and strain, the stress can be calculated from the strain distribution.

In amorphous material, the atoms are not arranged in a periodic fashion such that observed with crystals and the scattering intensity is then the summation of each individual atom. Thus, weak X-ray scattering, scattering spreading throughout reciprocal space, and a detailed analysis are required to obtain real-space information characterizing amorphous coatings. Spectra with amorphous elements are characterized by a broad halo as illustrated in Fig. 15.6 from Liu et al. [57]. They have sprayed onto mild steel, by using high-velocity plasma with an axial injection of powder, a FeCrMoMnWBCSi amorphous metallic coating with thickness of about 1 mm and porosity less than 0.1 %. The coating has been compared to as-spun ribbon obtained by melt spinning. XRD pattern of Fig. 15.6 exhibits only a broad halo of fully amorphous phase in the ribbon samples. For the powder, it shows a broad halo and some crystalline peaks due to Fe_2C, Cr_2B, and $M_{23}C_6$, reflecting that

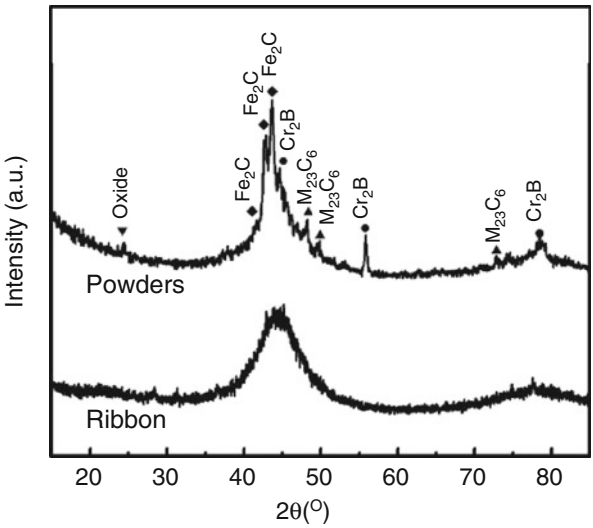


Fig. 15.6 XRD patterns of the as-spun ribbon and the atomized powders of Fe-based alloy. Reprinted with kind permission from Elsevier [57]

the cooling rate of gas atomization is apparently lower than that of melt spinning. These XRD patterns were also compared to those of coatings obtained with different spray conditions. Similar XRD patterns can be found in many references such as, for example, [58, 59].

15.4.5 Small- and Ultrasmall-Angle X-Ray Diffraction (USAXF)

Small-angle X-ray scattering (SAXS) probes structure in the nanometer to micrometer range by measuring scattering intensity at scattering angles 2θ close to 0°. SAXS is used for the structural characterization of solid and liquid materials in the nanometer (nm) range. It probes inhomogeneities of the electron density on a length scale of typically 1–100 nm, thus yielding complementary structural information to XRD data. SAXS is applicable to crystalline and amorphous materials alike. Measurements are commonly performed in transmission geometry, using a narrow, well-collimated, and intense X-ray beam. Scattering angles typically range between 0.1 and 5°. The smallest accessible angle determines the largest resolvable feature size. Some typical applications comprise the determination of nanometer-sized particle and pore size distributions of specific surface areas. For more details, see the book of Guinier and Fournier [60].

However, for coatings, to our best knowledge, Ultrasmall-angle X-ray scattering (USAXS) is used. It is also a nondestructive characterization technique recording elastic scattering of X-rays induced by compositional and structural inhomogeneities [61]. USAXS has been successfully implemented in quantifying void size distribution in YPSZ EB-PVD deposited coatings [62] and also in YPSZ

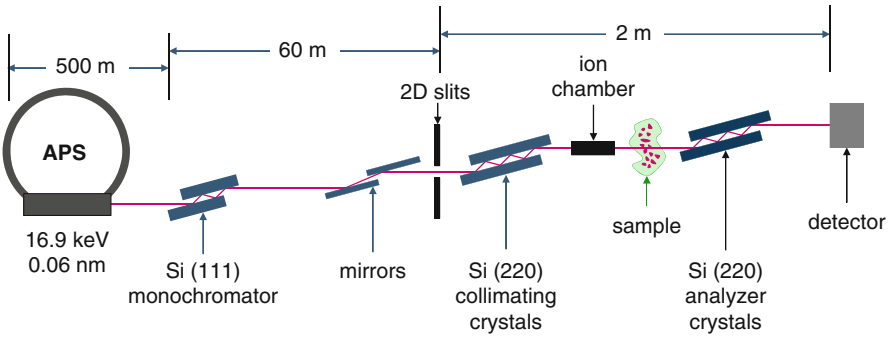


Fig. 15.7 Scheme of the Advanced Photon Source (Argonne National Laboratory, Argonne, IL, USA) (http://usaxs.xor.aps.anl.gov/, see also [64])

($d_{50} = 50$ nm) suspension plasma-sprayed coatings [63]. For the EB-PVD coatings, computer modeling was used to obtain values of stereometric (geometrical and spatial) characteristics of the pore populations in terms of their volume fraction, shape (aspect ratio), size, and orientation, each representing statistical average values based on Gaussian distributions. For the nanometer-sized structured coating about 80 % of voids, in number, exhibited characteristic dimensions smaller than 30 nm, the largest voids in the coatings having characteristic dimensions of a few hundreds of nanometers. Such results are difficult, if not impossible, to obtain from other characterization techniques, since it addresses with a very high resolution to the whole set of scatters (voids in this case) regardless of their characteristics (open, connected, or closed).

For both examples cited above, USAXS experiments were conducted on beam line 32-IDat Advanced Photon Source (Argonne National Laboratory, Argonne, IL, USA). Measurements were performed in transmission geometry. Figure 15.7 gives the characteristic dimensions of this source. The interested reader can find further details on the Web site of Argonne National Laboratory (http://usaxs.xor.aps.anl.gov/, see also [64]).

The USAXS instrument uses Bonse–Hart crystal diffraction optics, which allows recording of small-angle scattering curves using a photodiode detector. q the scattering vector ranges from 10^{-4} to 1 $Å^{-1}$ with an angular resolution of 10^{-4} $Å^{-1}$. The scattering vector $|q|$ [58] is a typically used quantity in small-angle scattering and relates to the diffraction angle (2θ), as known from X-ray diffraction, via the relationship:

$$|q| = \frac{4\Pi \sin\theta}{\lambda} \tag{15.6}$$

where λ is the X-ray wavelength. Combining this equation with Bragg's law, the length scale, L, probed at a given q range follows the general inverse relationship:

$$L \approx \frac{2\pi}{|q|} \tag{15.7}$$

This setup delivers approximately 10^{13} photons per second in about 1 mm^2 area at the sample position, for incident photons with energy around 16.9 keV and corresponding to a wavelength of 0.775 Å. The uncertainty estimation for USAXS results is challenging, and absolute intensity of USAXS calibration was estimated, from repeated measurements, to present an uncertainty of about ±5 % for the total volume content [63].

15.4.6 Neutron Scattering

Small-angle neutron scattering (SANS) is a laboratory technique, similar to the complementary techniques of small-angle X-ray scattering (SAXS) and light scattering. The technique provides valuable information over a wide variety of scientific and technological applications, especially for coatings defects in materials, the data analysis giving information on size, shape, etc. [65–70].

With SANS experiment a beam of neutrons is directed at a sample, which can be for coatings, a solid or a powder. The neutrons are elastically scattered by changes of refractive index on a nanometer scale inside the sample, which is the interaction with the nuclei of the atoms present in the sample. In this experiment, a monochromatic beam of thermalized neutrons passes through the specimen in transmission geometry and the scattered neutrons are recorded on a two-dimensional detector. Figure 15.8a shows the principle of the SANS instrument [69]. Neutrons are capable of interacting strongly with all atoms, in contrast to X-ray techniques where the X-rays interact weakly with hydrogen, the most abundant element. Small-angle neutron scattering is caused by fluctuations of scattering length density $\rho(r)$ on a size scale 1 nm to 5 μm in the studied material. These fluctuations are connected with compositional and/or structural inhomogeneity such as pores. The fluctuations of scattering length density result in the scattering contrast $\Delta\rho(r) = \rho(r) - \overline{\rho}$, where r is the coordinate in the real space and $\overline{\rho}$ the average scattering length density of the sample. The scattering contrast gives rise to the coherent elastic scattering of neutrons to small magnitudes of the scattering vector $|Q|$; see Eq. (15.6), ($Q = k - k_0$, where k is the wave vectors of the incident and scattered neutron, respectively, $|k| = |k_0| = 2\pi/\lambda$, λ being the incident neutron wavelength).

In this experiment [69], a monochromatic beam of thermalized neutrons passes through the specimen in transmission geometry and the scattered neutrons are recorded on a two-dimensional detector, as shown in Fig. 15.8a. Scattering occurs at the void–grain interface due to differences in scattering length density between the material and the pores. The first measurement is the anisotropic Porod scattering (see Fig. 15.8b), where the orientation averaging of the Porod scattering from the sample gives the total void surface area per unit sample volume, independent of the precise void morphology [69]. The second type of measurement is anisotropic multiple SANS (MSANS), involving the measurement of the beam broadening due to anisotropic multiple scattering by long wavelength neutrons [69]. In Porod

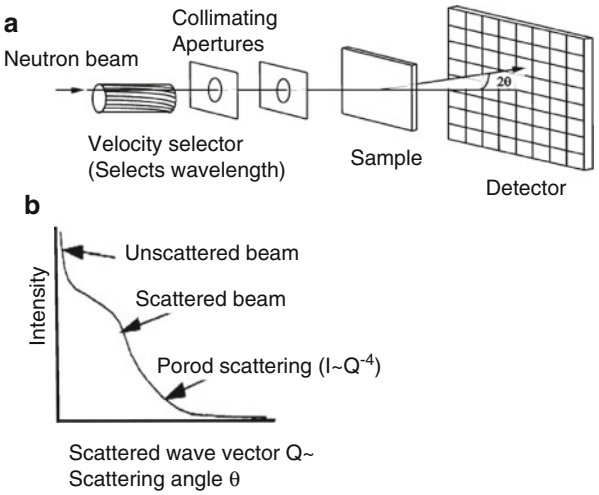


Fig. 15.8 (**a**) Scheme of the SANS instrument. (**b**) Evolution of signal intensity with scattered wave vector Q. Reprinted with kind permission from Elsevier [69]

scattering, the scattering intensity, $I(Q)$, is a function of the magnitude and direction of the scattering vector, Q, and its orientation average, as shown in Fig. 15.8b. More complete microstructural information is obtained by combining MSANS measurements for different sample orientations, anisotropic Porod surface area distributions, and the total porosity determined from precision density measurements [69]. The MSANS beam broadening shows much greater sensitivity to the coarse globular and irregular porosity than does the Porod scattering analysis. For interpretation of the anisotropic MSANS beam-broadening data, the interlamellar pores and intra-splat cracks are considered to comprise two space-filling networks of oblate spheroids, each with a fixed aspect ratio, and the globular pores are considered spheres, as shown in Fig. 15.8c.

Allen et al. [65–70] were among the first to use SANS to determine the porosity of ceramic plasma-sprayed coatings. The voids and the grains within the samples have different scattering length density, ρ, causing some of the neutrons to be scattered at the void/grain interfaces. In the SANS experiment, a beam of "cold" neutrons with wavelength λ, ranging from 5 to 18 Å and controlled by a neutron velocity selector, is passed through parallel-sided sample. Scattered neutrons are recorded in directions orthogonal and parallel to the coating with a two-dimensional area detector. The intensity of the scattering vector varies with the volume fraction of porosities, the scattering contrast $(\Delta\rho)^2$ (square of the difference in scattering length densities between the grains and the void), and on the distribution of void sizes [68]. The scattering curve of intensity vs. scattering angle can be divided into two regions as shown in Fig. 15.8b. The multiple small-angle neutron scattering (MSANS) region is dominated by neutrons scattered many times by large pores inside the sample. The theory of MSANS is useful for pores with sizes in the 0.08–10 μm range. Larger scattering angles are dominated by scattering from the surfaces of pores in a region, which is termed the Porod region [68]. The anisotropy in the Porod scattering is strongly amplified by the shape of the scatterers.

The anisotropy depends not only on the individual pore shapes and preferred orientation but also on the polydispersity of pore shapes and sizes and to some extent on the surface roughness [69].

The major advantages of SANS are (1) it does not require sample preparation and (2) quantitative information can be obtained concerning the separate crack and pore systems, including their distinctive anisotropies [68]. However, the relationship between the SANS results and the underlying structure is more complex and less intuitive than for image analysis. Also the availability of the SANS technique is limited by the need to have access to a powerful neutron source, such as a reactor. Kulkarni et al. [70] described the quantitative characterization of the microstructure of plasma-sprayed partially stabilized zirconia (PSZ) coatings by means of X-ray and neutron-scattering imaging techniques. Petorak et al. [71] have used SEM and Porod's specific surface area analysis of SANS results to determine which void systems, either interlamellar pores or intralamellar cracks, contributed to the observed relaxation of stress in plasma-sprayed coatings when simulating TBC service conditions. Allen et al. [65] explored the relationships between the feedstock or spray process conditions, anisotropic void and crack microstructures of the deposits, and technologically important deposit properties such as thermal conductivity. Kulkarni et al. [69] described the quantitative characterization of the microstructure of plasma-sprayed partially stabilized zirconia (PSZ) coatings by means of X-ray and neutron-scattering imaging techniques.

15.4.7 X-Ray Absorption Spectroscopy

X-ray absorption spectroscopy (XAS) is widely used for determining the local geometric and/or electronic structure of matter. Usually it is performed using synchrotron radiation sources providing intense and tunable X-ray beams. The photon energy is tuned using a crystalline monochromator to a range where core atom electrons can be excited (0.1–100 keV photon energy). According to the core electron which is excited: the principal quantum numbers $n = 1$, 2, and 3 correspond to the K-, L-, and M-shells, respectively. For instance, excitation of a 1s electron occurs at the K-edge, while excitation of a 2p electron occurs at an L-edge. When a monochromatic X-ray beam is directed through a sample and the energy of the X-rays is gradually increased such that the X-ray beam crosses an absorption edge of one of the elements of interest in the sample, the transmitted X-ray light will contain small variations in absorbance, on the high energy side of the absorption edge. These absorbance variations provide information about the structural environment of the atoms surrounding the element whose absorption edge is being examined. An X-ray absorption spectrum is generally divided into four sections (1) pre-edge ($E < E_0$); (2) X-ray absorption near edge structure (XANES), where the energy of the incident X-ray beam is $E = E_0 \pm 10$ eV; (3) near edge X-ray absorption fine structure (NEXAFS), in the region between 10 eV and 50 eV above the edge; and (4) extended X-ray absorption fine structure (EXAFS), which starts

approximately from 50 eV and continues up to 1,000 eV above the edge. One of the main interest of XAS is its tunability allowing probing the environments (molecular structure) of different elements in the sample by selecting the incident X-ray energy. For details, see the book of Bunker [72].

15.4.8 Electron Probe X-Ray Microanalysis

Electron probe microanalysis (EPMA) associated with scanning electron microscopy (SEM) is generally considered as microanalytical technique able to image or analyze materials. Elemental analysis is accomplished at a microscale (about a few μm^2). It makes it possible to identify the elements present and quantify them, down to about 100 ppm with a rather good accuracy. Elements lighter than atomic number 8 cannot be measured without reservations.

EPMA implies that the element densities in the probed volume are uniformly distributed. Thus, to obtain information on a large area, the over-scanning must be avoided and the large area sampled at many discrete points. For details, see [32, 15.Ma6].

15.4.9 Auger Electron Spectroscopy

Auger electron spectroscopy (AES) is used specifically in the study of surfaces. The Auger effect is based on the analysis of energetic electrons emitted from an excited atom after a series of internal relaxation events. Auger effect is produced whenever incident radiation—photons, electrons, and ions—interacts with an atom with an energy exceeding that to remove an inner-shell electron (L, M, . . .) from the atom. This interaction leaves the atom in excited state with a core hole, that is, a missing inner-shell electron. These excited atoms have a limited life and de-excitation occurs very rapidly with the emission of an X-ray or an electron termed Auger electron. SEMs are equipped to detect such electrons and AES is now a practical and straightforward characterization technique for probing chemical and compositional surface environments [32, 15.Ma7].

15.4.10 X-Ray Photoelectron Spectroscopy

X-ray photoelectron spectroscopy (XPS), also known as Electron Spectroscopy for Chemical Analysis (ESCA), is a quantitative spectroscopic technique that measures the elemental composition, chemical state, and electronic state of the elements that exist within a material. The material is irradiated with a beam of X-rays and the kinetic energy and numbers of electrons that escape from the top (1–10 nm) are

measured. XPS works exclusively in ultrahigh vacuum; it allows analyzing the surface chemistry of a material in its "as-received" state or after some treatment. XPS detects all elements with atomic number (Z) of 3 (lithium) and above. Detection limits for most of the elements are in the parts per thousand ranges. For details, see [32, 15.Ma8–15.Ma10].

15.4.11 Other Techniques

The characterization means described above are those mostly used for thermal sprayed coatings, but they are not the only ones. For example, inductively coupled plasma atomic emission spectroscopy can be used for elemental determinations in the concentration range of major to trace. Atomic absorption spectrometry can be used for measuring relatively low concentrations of metallic or semi-metallic elements in a solution of the sample containing the metals . . .. For details, see [53].

15.5 Void Content and Network Architecture

The thermomechanical behavior of coatings and their thermal insulation performances (e.g., thermal barrier coatings) are mostly related to the void architecture typified usually as void network (for example, see [73]). Its quantification is hence fundamental and usually includes several characteristics. Among the principal characteristics one can identify [74]:

1. The void global content (called in some cases as porosity or porosity content or apparent density). It is the most commonly used descriptor of the pore microstructure.
2. The void size distribution. Most manufacturing processes result in a wide range of void sizes rather than a single size. Establishing the extent of sizes and distribution of pores can be of major importance in understanding and controlling material properties as depending on the application and material, large pores or small pores can be wished.
3. The discrimination of voids by shape: globular voids corresponding to features exhibiting low elongation ratio, cracks corresponding to features exhibiting high elongation ratio and preferentially oriented perpendicularly to the substrate surface (from 45° to 135° from substrate surface), and delaminations corresponding to features exhibiting high elongation ratio and preferentially oriented, as for them, parallel to the substrate surface (from 0° to 45° from substrate surface).
4. The void network connectivity, to the coating surface on the one hand (open void content) and to the substrate and coating surface on the other hand (connected void content). Voids being not connected are identified as closed voids. The question arises as to the fraction of pores that can be accessed from the surface.

Table 15.1 Conventional techniques implemented to quantify voids in a porous medium such as a thermal spray coating [76]

technique	methode	void global content	void size distribution	void morphology			void network connectivity		
				globular voids	cracks	delamina-tions	connec-ted void content	open void content	closed void content
P	physical								
IS	electro-chemical								
P	physical								
IP	physical								
	physical								
SANS	physical			*via* void network anisotropy					
T	stereolo-gical								
USAXS	physical								

AP Archimedean porosimetry, *EIS* electrochemical impedance spectroscopy, *GP* gas permeation, *MIP* mercury intrusion porosimetry, *P* pycnometry, *SANS* small-angle neutrons scattering, *ST* stereological protocols (coupled to image analysis), *USAXS* ultrasmall-angle X-ray scattering

5. Pore surface area: surface area of pores, expressed as specific surface area per weight or volume of sample.
6. Pore anisotropy. The anisotropy of the void system can be of major importance especially for highly anisotropic microstructures such as the TBCs microstructures obtained by EB-PVD.

Often the pores in the material are modeled as spherical voids, nicely separated from each other. However this simple model is wrong for the majority of engineered materials. For more complicated pore microstructures, one can imagine pores that are better approximated by other geometrical shapes, such as ellipsoids or platelets [74].

Several methods are commonly implemented to quantify voids network in a porous medium such as thermal spray coating structured at the micrometer scale (see, for example, the reviews of Ilavsky [74] and Andreola et al. [75]):

Physical methods:

Stereological protocols (combined with image analysis)

Electrochemical methods

None of those techniques can address all void network characteristics, as depicted in Table 15.1 from Fauchais et al. [76], which displays the void

characteristics addressed by each technique. The following sections describe some of the major characteristics and main drawbacks when they are applied to nanometer-sized thermal spray coatings.

15.5.1 Archimedean Porosimetry

Archimedean porosimetry (AP) makes it possible to quantify the non-connected porosity [75, 77, 78]. The substrate is generally removed by chemical etching in acid medium in order to weight freestanding coatings before and during immersion into de-mineralized water. Knowing the specific mass of water ρ_{water} (i.e., depending upon temperature), the coating volume is calculated, according to Archimedean, by measuring:

- The dried coating weight, w_{dry}, obtained after careful drying in a furnace
- The wet coating weight, w_{sat} (after complete impregnation of open porosities)
- The weight of water saturated sample immersed in water, w_{wet}

It allows calculating the weight of water displaced, w_{wd},

$$w_{wd} = w_{sat} - w_{wet} \tag{15.8}$$

and then, the bulk volume, V_b:

$$V_b = w_{wd}/\rho_w \tag{15.9}$$

where ρ_w is the water mass density.

The open pores volume, V_p is obtained by calculating the weight of water they contain, w_{wp}:

$$w_{wp} = w_{sat} - w_{dry} \tag{15.10}$$

and then by dividing it by the specific mass of water ρ_w

$$V_p = w_{wp}/\rho_w \tag{15.11}$$

Finally the apparent porosity, ϕ_a is given by

$$\phi_a = V_p/V_g \tag{15.12}$$

A value for porosity can alternatively be calculated from the bulk mass density ρ_{bulk} and particle mass density ρ_{part}:

$$\phi_a = 1 - \rho_{bulk}/\rho_{part} \tag{15.13}$$

Closed or sealed pores are not included in the apparent porosity value. The latter is usually close to the total porosity as long as the closed porosity in the sample is low. The first drawback with Eq. (15.13) is that the coating bulk-specific mass must be known. It depends on the coating phase content that can be analyzed by X-ray diffraction analysis. The second drawback with Eq. (15.12) is related to the sizes of pores. The percolation test of deionized water drops through the coating makes it possible to determine the smallest open pore diameter into which the water percolates. The contact angle, θ, between zirconia and deionized water is about 59° and the surface energy, γ, of deionized water is 72.8 mN/m at room temperature. At atmospheric pressure (about 10^5 Pa), pure water percolates, according to Lucas–Washburn's equation [79], into open voids of equivalent diameter equal or larger than 1.5 μm, while most of open voids in nanometer-sized coatings exhibit characteristic dimensions smaller than micrometer.

15.5.2 Mercury Intrusion Porosimetry (MIP)

The non-wetting mercury percolates through the open voids according to the applied impregnation pressure. This results in the intrusion versus pressure curve, which can be normalized with respect to sample weight or volume [80–83]. The experimental data are analyzed on the basis of the Washburn equation:

$$d = \frac{-4\gamma \cos\theta}{p} \tag{15.14}$$

where d represents the equivalent diameter of intruded pores (m), γ is the surface tension of mercury (N/m), θ is the contact angle between the pore walls and mercury, and p is the applied pressure (Pa). The latter is converted into equivalent pore sizes on the assumption of tubular pores. Often the mercury porosimetry consists of two parts: the low pressure part (0.1–400 kPa) for the measurement of large pores up to a maximum dimension of 60–100 μm, depending on how much mercury is used and the high pressure part (0.1 ± 400 MPa) detecting pores and micro-cracks down to the size of 1.8 nm.

The main drawbacks are that (1) only the open void network is accessible and (2) the necessity to apply high pressure of mercury, which can lead to sample deformation and even structural failures [84] and thus distortion of curves depicting the volume distribution vs. pore characteristic dimension. However, the technique covers a large void size range.

15.5.3 Gas Permeation and Pycnometry

Gas permeation (GP) is measured by applying forced gas (generally air) flow rates on one face of the sample and the other face being kept at a reference pressure

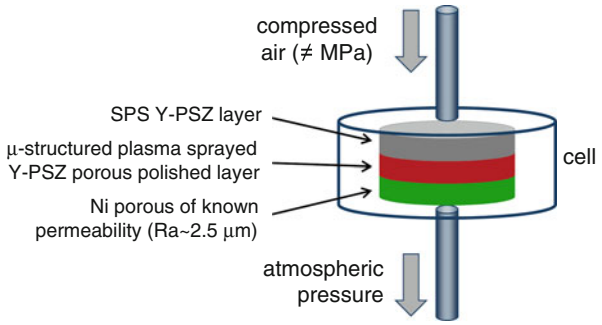


Fig. 15.9 Principle of the permeation measurement of an YSZ coating suspension plasma sprayed. Reprinted with kind permission from Dr. E. Brousse [10]

(usually atmospheric pressure). The resulting pressure drop is measured for each gas flow rate. After checking the linear evolution of the pressure drop with the gas flow rate, the permeability can be determined from the Darcy's law [85]:

$$Q = k\frac{A\,\Delta p}{\mu\, e} \tag{15.15}$$

The leakage rate is then calculated from the linear regression of the curve $\frac{Q}{A}\eta = f\left(\frac{\Delta p}{e}\right)$, where Q is the imposed gas flow (m^3/s), A the sample measured area (m^2), μ the gas viscosity (Pa s), e the sample thickness (m), and Δp the pressure drop (Pa). Measuring the coating gas permeation at elevated temperatures (corresponding usually to coating operating temperature) and selecting several gas natures are the two major advantages of this technique [86–92]. Golosnoy et al. proposed a model of gas permeation in thermally sprayed ceramic coatings [88]. For nanometer-sized coatings resulting from suspension or liquid precursor thermal sprayed coatings, due to their thin thickness, specific dual-layer samples with the under-layer made of a material of known permeation rate have to be manufactured. The specificity of the under-layer can influence the coating void architecture, which would have not been the case if the under-layer had been dense as a conventional substrate [10]. The principle of gas permeation measurement for YSZ suspension plasma-sprayed coating is shown in Fig. 15.9.

Helium pycnometry is used to determine the skeletal density of (non) porous solid and gives indirect information about pore volume and closed porosity. The simplest type of gas pycnometer (no moving parts) consists of two chambers, one (with a removable gas-tight lid) to hold the sample and a second chamber of fixed, known (via calibration) internal volume, referred to as the reference volume or added volume. A valve allows admitting a gas under pressure to one of the chambers. The pressure in the first chamber is measured with a transducer, the two chambers can be connected, and the second chamber can be vented. The working equation of a gas pycnometer wherein the sample chamber is pressurized first is as follows:

$$V_S = V_C + \frac{V_r}{1 - \frac{p_1}{p_2}} \tag{15.16}$$

where V_S is the sample volume, V_C is the volume of the empty sample chamber (known from a prior calibration step), V_r is the volume of the reference volume (again known from a prior calibration step), p_1 is the first pressure (i.e., in the sample chamber only), and p_2 is the second (lower) pressure after expansion of the gas into the combined volumes of sample chamber and reference chamber. While pycnometers of any type are recognized as density measuring devices they are in fact devices for measuring volume only. The volume measured in a gas pycnometer is the amount of three-dimensional space, which is inaccessible to the gas used, i.e., the volume within the sample chamber from which the gas is excluded. Therefore the volume measured depends on the atomic or molecular size of the gas. Helium is most often the prescribed gas, because of the atom small size and also because it is inert. Indeed, gas atoms form a single layer on the total surface of material and penetrate into open and connected porosity. This technique has already been successfully employed to determine plasma coating mass density [88]. However, pycnometry measuring only volumes, the sample weight must also be measured. By comparing with the theoretical mass density this measurement gives the percentage of closed porosity of the sample. It has been used for nanometer-sized suspension plasma sprayed coatings [89].

15.5.4 Small-Angle Neutrons Scattering

A quantitative characterization of the microstructural features has been demonstrated successfully in the case of plasma-sprayed YPSZ coatings, using a combination of anisotropic Porod scattering and MSANS scattering techniques. The experiment is the same as that described in Sect. 15.4.6. The scattering occurs at the void–grain interface due to differences in scattering length density between the material and pores. Two types of measurements are performed: anisotropic Porod scattering and anisotropic multiple SANS (MSANS) [92]. The anisotropic Porod scattering can be divided into two anisotropic contributions: one from interlamellar pores that are predominantly parallel to the substrate and the other from intra-splat cracks that are predominantly perpendicular to the substrate. Orientation averaging of the Porod scattering from the sample makes it possible to obtain the total void surface area per unit sample volume.

Two examples of results are presented in Fig. 15.10 from Ilavsky et al. [68, 92]. Water-stabilized plasma alumina SANS results, presented in Fig. 15.10a, show high anisotropy of the apparent Porod surface area distribution dominated by intralamellar cracks. Apparent Porod surface area can be defined as the Porod surface area, which would be viewed in any particular direction by an observer standing in the center of the sample. Knowledge of this apparent surface area in all directions (over 4π) allows calculation of the quantitative specific surface area in the sample and, if more surface systems can be distinguished, in the surface systems separately.

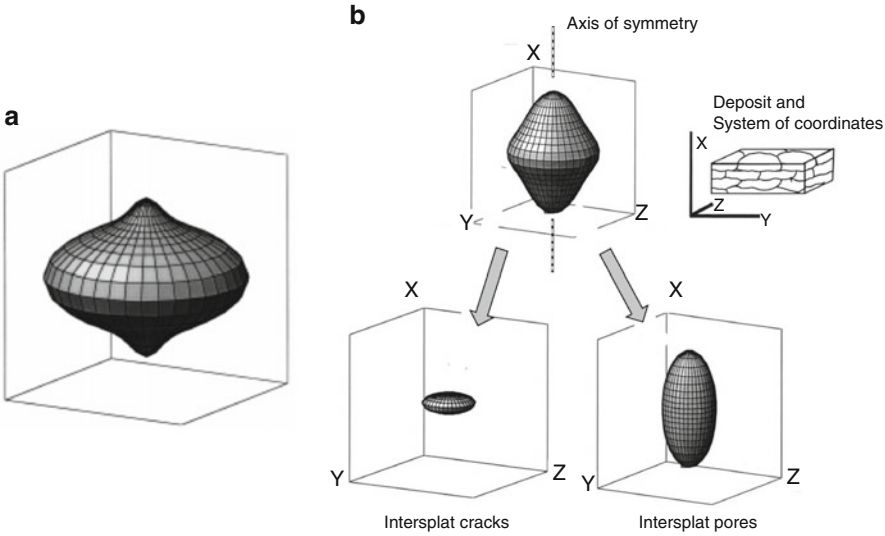


Fig. 15.10 Apparent Porod surface area distribution of (**a**). water-stabilized plasma-deposited alumina and (**b**) gas-stabilized plasma-deposited alumina separated into two separate void surface areas: *Left* (*prolate ellipsoid*) representing intralamellar cracks and *right* (*elongated ellipsoid*) representing interlamellar pores. Reprinted with kind permission from Elsevier [92]

Kulkarni et al. [69] used this method to study the effect of partially stabilized zirconia feedstock characteristics (particle density, size, and shape) on the anisotropic void structure of plasma-sprayed coatings. They correlated the results with the thermal conductivity and elastic modulus of coatings; properties are most sensitive to these microstructural features. Allen et al. [67] have previously done a similar work. Ilavsky et al. [92] have used SANS to study the effect of heating on the pores and cracks in YSZ coatings. Strunz et al. [93] have also studied by SANS the effect of heating on plasma-sprayed TBCs and compared the results with those obtained by mercury porosimetry. Kulkarni et al. [94] have also used SANS to study EB-PVD thermal barrier coatings and quantified the voids in terms of component porosities, anisotropy, size, and gradient through the coating thickness.

15.5.5 Ultrasmall-Angle X-Ray Scattering

Ultrasmall-angle X-ray scattering (USAXS; see Sect. 15.4.5) has been used to characterize EB-PVD thermal barrier coatings [95]. Two data collection methods were combined. In the first, the scattered intensity was measured as a function of $|q|$ (see Eq. 15.6) for each orientation of the sample azimuthal angle α. In the second, the scattered intensity at a fixed $|q|$ was measured as a function of α by rotating the sample in the beam. Variations in the scattering anisotropies

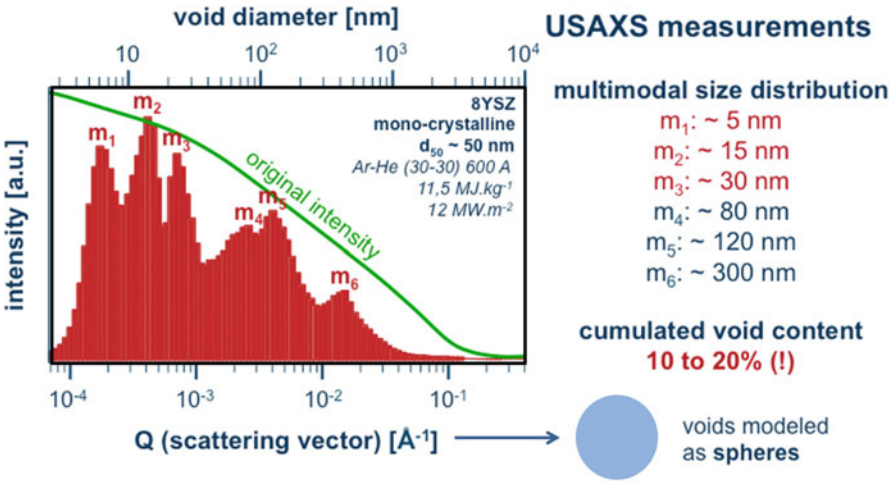


Fig. 15.11 Evolution of the USAXS signal intensity with the q scattering vector (in Ängstrom^{-1}) and the calculated corresponding pore size distributions (YSZ suspension plasma-sprayed coating, suspension particle mean size: 50 nm, Ar–He plasma, 30-mm standoff distance). Reprinted with kind permission from Elsevier [63]

observed at different $|q|$ were associated with the variation in the microstructure anisotropy at different length scales and gave, thus, a quantitative map as a function of the sizes of the scattering populations. The anisotropies in the scattered intensity at different $|q|$ values were presented as a function of azimuthal angle with respect to the substrate-normal direction [94]. Flores Renteria et al. [95] have studied, via USAXS-measurement, the stereometric characteristics of the pores within EB-PVD TBCs. A subsequent use of the appropriate statistically representative values made it possible to predict the thermal conductivity by a noninteracting scheme. The projected values agreed well with the measured values.

USAXS measurement was used by Bacciochini et al. [63] to characterize plasma-sprayed suspensions of YSZ (50-nm average particle diameter, Ar–He plasma gas mixture, 30-mm spray distance). Figure 15.11 shows the evolution of the signal intensity with the $|q|$ scattering vector (in Angström) and the calculated corresponding pore size distribution, assuming that the pores have spherical shapes. Rotating the analyzer and recording the scattered photons received by the detector enabled the measurement of the X-ray scattering from the sample. USAXS data were fully corrected for instrument effects and analyzed using Igor Pro1software from Wave Metrics Inc. (Oswego, OR, USA) coupled to Irena1 package for analyzing small-angle scattering data. The total void content was about 14.3 %. The void distribution was multimodal and characterized by several modes diameters (i.e., average diameter of an equivalent monomodal distribution) contrary to micrometer-sized YSZ coatings, which usually exhibited a bimodal distribution of voids [63]. In SPS coatings, the typical void mode diameters that were identified

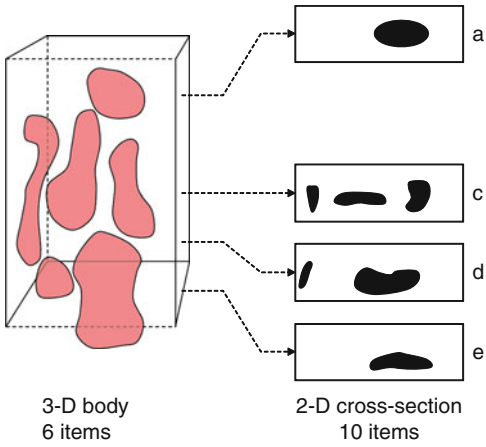


Fig. 15.12 3D or 2D analyses: the Wicksell corpuscule problem. Reprinted with kind permission from Springer Science Business Media [97, 98], copyright © ASM International

are $m_1 < 5$ nm, $m_2 < 15$ nm, $m_3 < 30$ nm, $m_4 < 80$ nm, $m_5 < 120$ nm, and $m_6 < 300$ nm. The most numerous population of voids corresponded to voids exhibiting mode diameter $m_5 < 120$ nm. It is important to underline that commonly applied porosity characterization methods, based on analysis of cross-sectioned coatings or on liquid impregnation, are not suitable to address the void content of SPS nanometer-sized coatings. On the other hand, combination of Helium pycnometry and ultrasmall-angle X-ray scattering proved to be suitable for quantifying SPS deposits void contents with sufficient details. Large populations of nanometer and larger voids have been detected. Their characteristic dimensions cover four orders of magnitude (i.e., from 1 to 10,000 nm). About 90 % of voids (by number) in the coatings exhibit characteristic dimensions smaller than 50 nm. The photon scattering phenomena and thermal resistance effects are most likely responsible for the significantly lower thermal diffusivity values (about 0.025 mm^2/s) measured in the temperature range of 20–300°C for these SPS coatings compared to typical values for micrometer-sized conventional APS coatings.

15.5.6 Stereological Protocols (Coupled to Image Analysis) (ST)

Assuming that resolution limits are considered, porosity within a microstructure can be easily detected by image analysis due to the high degree of contrast between the dark pores (voids) and the more highly reflective coating material [96]. However image analysis gives only 2D pore distributions of the coating cross section (the intersection of the structure with this specific plane). If the cross-section images can show the effect of the coating densification for example after laser remelting [97], it does not mean that such images are representative of the real 3D structure. It is illustrated in Fig. 15.12 from Montavon and Antou [98]

and representing the Wicksell's corpuscule problem demonstrating that "an accurate estimation of the number of objects of interest cannot be obtained from profile counts on individual cross sections." This figure illustrates that the three bodies of the 3D structure cannot be represented by the ten objects resulting from 2D cross sections (a, b, c, d, e).

According to Antou and Montavon [98] the procedure to analyze different 2D cross sections of the 3D coating comprises successively (1) sample preparation, (2) image acquisition, (3) image pretreatment, (4) image treatment, and finally (5) stereology implementation to achieve the quantitative interpretation of the coating architecture. The image acquisition is made either with optical microscopy (OM) equipped with cameras for image analysis, but the resolution is low or by SEM. For SEM, BSE imaging, which is sensitive to the average atomic number of the sample, gives sufficient contrast between dissimilar phases for automatic threshold determination due to the electron–matter interaction. With OM magnification is generally 500 or below, while with SEMs magnification values can be up to 1,000 or more. If high magnification allows seeing many details (pores and cracks), the small surface (between about one-tenth and one square millimeter) analyzed does not necessarily represent the whole coating. Experience indicates that image characteristic dimension should be between 10 and 15 times larger than the objects of interest (voids) to be analyzed to account for the representative elementary volume (REV) of the structure. Thus statistical measurements (in general 10–15 locations within the coating) are necessary to ensure a representative sample for qualitative analysis. Moreover low-magnification images (100×) can also be taken to reveal larger cross sections of the coating for porosity analysis as did, for example, Hanson and Settlese [99] to analyze 316L stainless steel HVOF sprayed coatings.

Several mathematical filters can be implemented to reveal specific structural data from the initial image [100]. The objective of this pretreatment is to remove singularities and to reveal feature outlines prior to morphological analysis. It consists of altering the pixel values (i.e., pixel intensities) using mathematical treatments. Four main types of filters are usually implemented at this stage of the treatment [34]:

- Filters that make it possible to modify the image contrast (linear or nonlinear filters)
- Arithmetic and logic filters
- Spatial filters (linear or nonlinear filters)
- Frequency filters (Fast Fourier Transform, FFT, applicable only on square images)

An example of such a processing is presented in Fig. 15.13 from Antou and Montavon [34], showing the different treatments to discriminate globular pores from cracks of the SEM image of Al_2O_3–13TiO_2 coating plasma sprayed in air.

As coating architectures are heterogeneous they must be characterized at several scales and the size of the representative elementary volume (REV) must be defined to describe the overall structure of the material [34]. The REV must be small

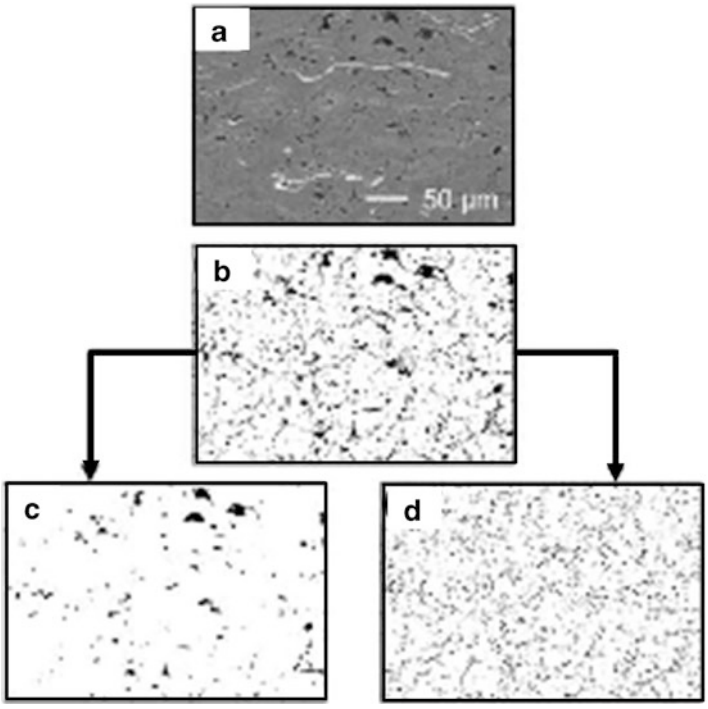


Fig. 15.13 Image analysis for discriminating the globular pores from the crack network: SEM image of an Al_2O_3–$13TiO_2$ coating plasma sprayed in air [34]. (**a**) SEM image, (**b**) image treated by an image analyze software, (**c**) globular pores, and (**d**) cracks isolated implementing several filtering and morphological protocols. Reprinted with kind permission from Springer Science Business Media [34], copyright © ASM International

enough to resolve the thinner details of the structure: high magnification and image resolution. But the REV must be large enough to describe the whole material structure: low magnification. To find the compromise, the evolution of the result variability (standard deviation over average value) must be followed as a function of the considered number of images (Fig. 15.14). The appropriate number of images corresponds to the value where this function tends toward an asymptote.

For example, Zhang et al. [101, 102] have proposed the following procedure divided into four steps, i.e., gray level transformation, fuzzy enhancement of image, binary segment of image, and removing the impurities and identification of pores and micro-cracks. Venkataraman et al. [103] have processed and analyzed the digitally stored images with image analysis software such as Image J and Adobe Photoshop to identify the pores and their distribution. Elsebaei et al. [104] have used the Matlab code to identify the pores and their distribution. The measured data of porosity can be highly scattered. The adjustment of the porosity dataset almost does not lead to the variation of the mean value of porosity calculated from the Gaussian distribution, as shown by Zhang et al. [101]. However, the adjustment of

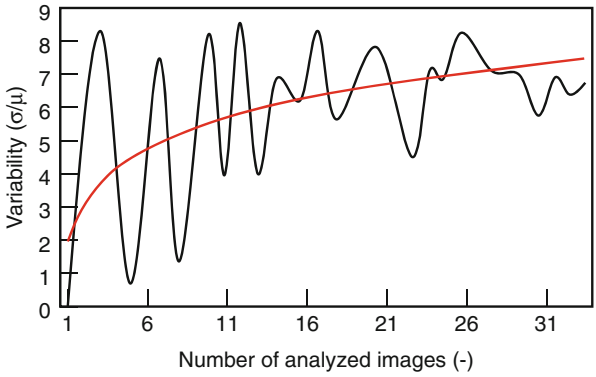


Fig. 15.14 Determination of the number of images to be analyzed. Reprinted with kind permission from Springer Science Business Media [34], copyright © ASM International

the porosity dataset by subtracting the two largest and two smallest data greatly decreases the variance. It was also observed that the measured data of coating porosity might follow the Weibull distribution [103]. The first limitation of this method is the limited resolution, which makes difficult to take into consideration features smaller than 0.1 μm in average value. So, the technique cannot be used to characterize nanometer-structured coatings. The second limitation is the artifacts (i.e., pullouts, scratches, etc.) that result from the cutting and polishing steps [35–37, 100, 105]. This can be particularly the case for cermet coatings where the hard ceramic particles imbedded within the soft metal matrix can be pulled out easily if the polishing step is not made carefully. For example, Nolan and Samandi [105] have shown that the potential for smearing over (or filling in of) pores is important and insufficient polishing can result in considerable underestimation of porosity, thus providing incorrect representation of coating structure.

This method of image analysis is extensively used to characterize the coatings void structure, for example, according to the spray process [106–108], the spray conditions [109], the spray angle [110], and the heat treatment [82].

The coating porosity is often measured using the Delesse principle [111, 112]: if the porosity is randomly distributed throughout the coating, then the percentage of porous area in a coating cross section is identical to the percentage of porous volume in the entire coating. Fowler et al. [113] have shown that image analysis can reproducibly detect and measure microstructural features (pores, cracks, etc.) within thermal spray coatings. They have statistically tested the reliability of these methods for specific experiments and they assume 95 % confidence level. However, coatings are nonuniform in all spatial directions and the 2D approach is not necessarily representing well the structure. Several quantitative tools allowing the quantification of complex structures exist. They are known as stereological protocols [98] and have been used to quantify some specific features of thermal spray coatings [114–116]. Stereological protocols of the first order aim at statistically quantifying 3D structures from 2D randomly oriented plane sections.

The NIST was the first to develop OOF (Object-Oriented Finite Element Analysis of Microstructures) (http://www.ctcms.nist.gov/oof/), a program designed to help materials scientists to calculate macroscopic properties from images of real or

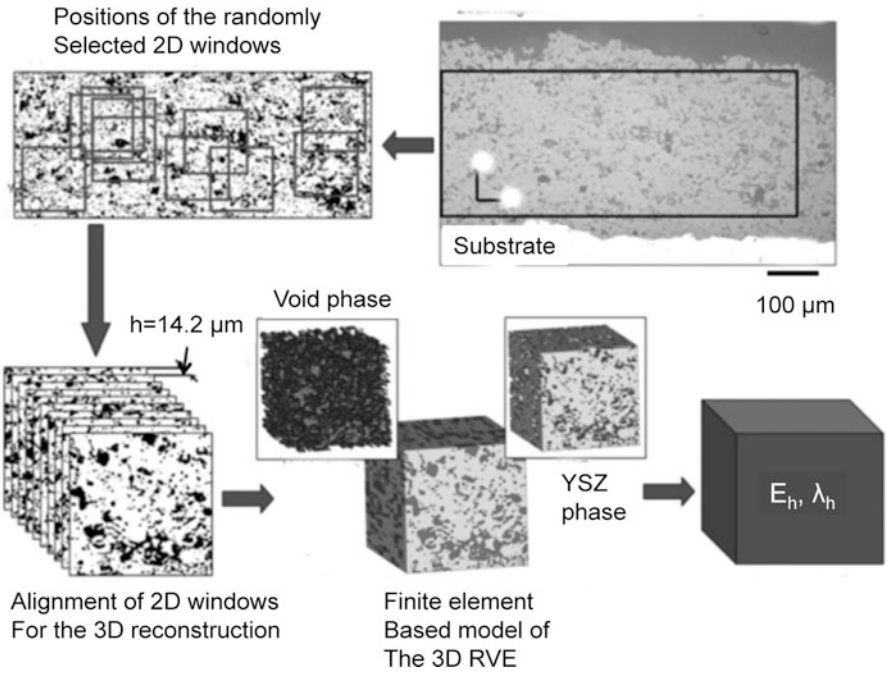


Fig. 15.15 Homogenization of thermally sprayed YSZ coatings obtained by statistical 3D reconstruction approach. Reprinted with kind permission from Springer Science Business Media [124], copyright © ASM International

simulated microstructures. OOF reads an image, assigns material properties to features in the image, and conducts virtual experiments to determine the macroscopic properties of the microstructure. At the beginning two separate versions existed, one only solving elasticity problems and the other solving coupled elasticity and thermal diffusion problems. Now the current version of OOF is OOF2, which improves on OOF1 in a number of ways. OOF2 can solve a much larger variety of physics problems and can be easily extended to cover even more. This program was, for example, used to characterize and predict properties of plasma-sprayed YSZ coatings [69, 117–119] and arc-sprayed WC–FeCSiMn coating [120]. University of Technology of Belfort-Montbéliar (France) also developed a software package TS2C focused on estimation of the thermal conductivity of thermally sprayed coatings [121–123]. Bobzin et al. [124] showed that when using 3D models, the results of the virtual testing and asymptotic homogenization methods match each other more closely compared with the conventional 2D models. Homogenization methods are based on the assumption that a specific small part of the microstructure can be considered to be representative for the entire material. The dimensions of the representative volume element (RVE) are much smaller than those of the entire microstructure. It requires that the RVE contain a sufficient number of microstructural inhomogeneities, so its morphology is

equivalent to that of the entire microstructure [124]. Figure 15.15 presents the way the 3D representation of the RVE has been derived.

The statistical 3D reconstruction approach has been used by Bobzin et al. [124] to calculate the effective properties of a typical YSZ coating in 3D domain. The calculated (with this method) effective values of Young's module and the thermal conductivity of the coating agree with the results of micro-indentation and laser flash measurements. The definition of the distance between 2D images (h), used to reconstruct the 3D representation, is critical for the correctness of the calculated effective properties [124].

15.5.7 Electrochemical Impedance Spectroscopy

The percolation of an electrolyte inside the interconnected void network allows quantifying the void fraction connected to the substrate by analyzing the chemical reaction (passivation most of the time) at the substrate/electrolyte interface. The electrochemical impedance spectroscopy (EIS) technique consists hence in measuring the impedance of the electrochemical cell. In order to access the charge transfer resistance or polarization resistance, EIS results have to be interpreted with the help of a model of the interface. To make an EIS measurement, a small amplitude signal, usually a voltage between 5 and 50 mV, is applied to a specimen over a range of frequencies of 0.001–100,000 Hz. The EIS instrument records the real (resistance) and imaginary (capacitance) components of the impedance response of the system. Depending upon the shape of the EIS spectrum, a circuit model or circuit description code and initial circuit parameters are assumed and input by the operator. The program then fits the best frequency response of the given EIS spectrum to obtain the fitting parameters. The quality of the fitting is judged by how well the fitting curve overlaps the original spectrum. By fitting the EIS data it is possible to obtain a set of parameters, which can be correlated with the coating condition.

A typical EIS for measuring connected porosity in plasma-sprayed TBCs is presented in Fig. 15.16 from Antou and Montavon [116]. They have used a flat cell with a volume of 300 mL at room temperature. The gray alumina sample was used as the working electrode (exposed area of 1 cm^2). A platinum mesh was used as a counter electrode, and an Ag/AgCl electrode was used as a reference. A 0.01 mol/L $K_3Fe(CN)_6/K_4Fe(CN)_6$ aqueous solution was selected as electrolyte due to its highly reversible electrochemical exchange current density and its minimal interference with the system. The three-electrode system was connected to EG&G Parc Model K0235 EIS measurement system. A sinusoidal voltage perturbation of 10 mV amplitude and a frequency range of 1 mHz–100 kHz was input to the system, and the system response was recorded as a Bode plot.

The immersed coating surface behaves as the working electrode [125, 126]. The connectivity of a pore network is related to the quantity of voids, which connects the substrate to the surrounding atmosphere.

A similar system was used by Zhang and Desai [125], Jayaraj et al. [126], Antou et al. [127], and Anderson et al. [128] to study plasma-sprayed TBCs. Bolelli

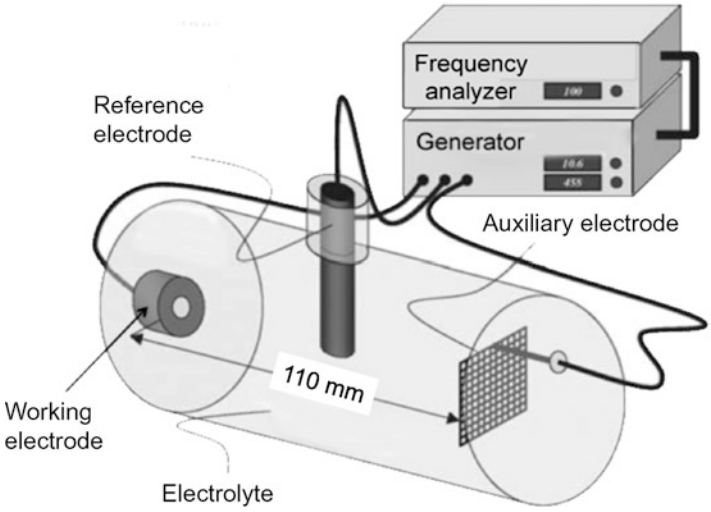


Fig. 15.16 Scheme of electrochemical impedance measurement system. Reprinted with kind permission from Springer Science Business Media [116], copyright © ASM International

et al. [129] have also characterized the connected porosity of high-velocity suspension flame sprayed (HVSFS) Al_2O_3 coatings. Kawakita et al. [130] have studied by EIS the through-porosity of Hastelloy C high-velocity oxy-fuel (HVOF) sprayed coatings by quantitatively analyzing dissolved substances derived from coated steel during immersion in HCl solution. Furthermore, Koivuluoto et al. [131] investigated the denseness of cold-sprayed Cu, Ni, and Zn coatings with corrosion tests to get more information about existing through-porosity (open-porosity). The corrosion tests used were open-cell potential measurement and salt spray fog test.

As previously mentioned, the test of deionized water droplet percolation through the coating indicated that the smallest void diameter into which a liquid such as water percolates through the coating void network was in the order of the micrometer. So the EIS technique is not adapted to most of the nanometer-sized thermal spray coatings.

15.6 Adhesion–Cohesion

15.6.1 Introduction

The quality and performance of thermal spray coatings are strongly dependent on the adhesion between the coating and substrate because the debonding of coating will result in the collapse of the sprayed system. However, the prediction and control of coating adhesion are complex as it depends on:

- The spray process and operating conditions
- The feedstock particle size distribution and morphology

- The substrate material: oxidation stage (oxide composition and thickness); roughness (peaks height in comparison with the splat mean size, and peak separation distance, characterized by the root mean square roughness $R_{\Delta q}$, i.e., the root mean square average of the roughness profile ordinates); cleanliness (removal of surface pollution and grit residue); and preheating prior to spraying at a temperature sufficient to get rid of adsorbates and condensates
- The residual stresses: they depend on the substrate-sprayed material couple, spray conditions, and substrate mean temperature
- The environmental conditions such as the surrounding atmosphere temperature and humidity, externally generated vibration transmitted into the specimen at the time of testing, . . .

Also, the structure of thermal-sprayed coatings is different from that of bulk materials; it generally involves layered splats, the real contact surface of which is between about 15 and 60 % of their surface, unmolten particles, globular pores, cracks, ... Thus, the basic bonding mechanisms between thermal spray coatings and substrate are, as already discussed about splats in Sect. 13.4, strongly dependent on real contacts between splats and between splats and substrate. They are categorized into three major groups (1) mechanical interlocking or anchoring, (2) metal-to-metal bonding (diffusion phenomenon), and (3) chemical bonding (formation of an intermetallic compound with a substrate).

The service failure mode can be described as interfacial (adhesive), cohesive, or mixed interfacial/cohesive [132]. Adhesion can be defined through fracture mechanics [133] that consider the energy required to initiate or propagate cracks and evaluate the adhesion of the coating system in terms of fracture toughness [134]. The experiment must establish the equilibrium condition where the elastic energy provided by an external force (as defined by the geometry of the specimen and applied load) is balanced by the propagation of a *stable* crack [133]. Over a critical value of the strain energy release rate, G_c (stated in J/m^2) crack propagation occurs and thus failure.

15.6.2 Simple Adhesion Tensile Test

The Tensile Adhesion Test (TAT) is used as a routine quality control tool for thermal spray coatings. The TAT arrangement is illustrated in Fig. 15.17a from Lin and Berndt [132]. In this test, the coated sample (a cylinder ∅ 25.4 mm × 25.4 mm long) is glued to an uncoated similar counterpart that is just grit blasted and then tested in tension in a universal testing machine. The value of the tensile load, in which the separation of the coated–uncoated parts occurs, is registered and transformed in an adhesion value, the bond strength, by calculating the load/area relation [135]. Four main standards are used in industry or research laboratories [132]: DIN 50160-A (Germany), AFNOR NF A91-202-79 (France), JIS H8666-80 (Japan), and ASTM C633-01 (2008) (USA) [15.A1]. These standards differ in their specimen geometry (for example, cylinder diameter: 25.2 mm for ASTM against

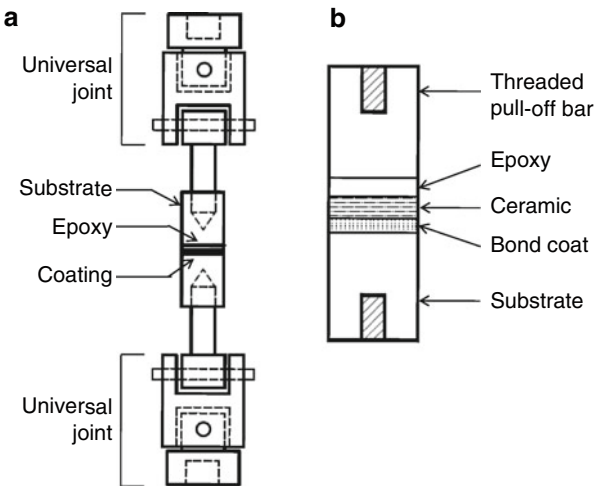


Fig. 15.17 (**a**) Tensile adhesion test configuration specified by ASTM C633-79 and (**b**) tensile adhesion test with cohesive and interfacial ruptures. Reprinted with kind permission from Springer Science Business Media [132], copyright © ASM International

40 mm for DIN and cylinder length 25.4 mm for ASTM and 50 mm for DIN), test methodology, and failure analysis [132].

The failure region indicates the type and characteristic of the failure, according to Fig. 15.17b, that shows a simple coating system. The failure modes of a coating under TAT conditions are (1) interfacial failure, which occurs along the coating/substrate interface, (2) cohesive failure within the coating, and (3) mixed-mode failure, which is a combination of the first two modes. If the coating is a duplex system, as in a TBC, the coating cohesive failure could be located within the bond coat, within the ceramic topcoating or at the bond coat/ceramic interface. Some failures may occur in a combined way, starting in a region and then expanding to other ones [135].

However TAT measurement, whatever maybe the standard used, presents some shortcomings:

- When the glue diffuses within the coating, its tensile resistance can be drastically improved, modifying the results [3]. It appears that the tensile strength achieved on a thermal sprayed coating is very dependent on the penetration of the epoxy and pressure being used during curing. They showed that the tensile strength of a Ni–5Al/Alumina system can vary from 60 down to 15 MPa. In cases, where the coating is dense enough to prevent epoxy penetration (such as WC/Co) of the glue, this tensile variation is not seen.
- The alignment of test fixtures is also very important because it can create nonuniformly distributed stress or stress singularities within the coated sample, such that the failure is not only controlled by the magnitude of the applied tensile force. That is why, as shown in Fig. 15.17a, universal joints are used to center the TAT arrangement.

Han et al. [136] used finite-element analysis to study the stress distribution along the coating/substrate interface; they found that the stress distribution was

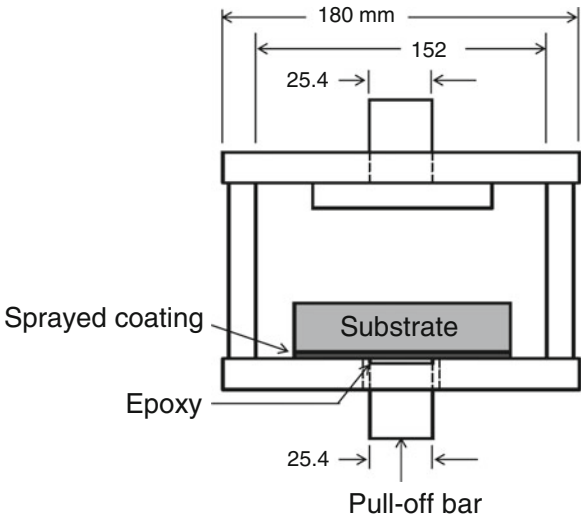


Fig. 15.18 Schematic of TAT assembly for single-bar (SB) method. Reprinted with kind permission from Springer Science Business Media [144], copyright © ASM International

nonuniform and the average adhesion strength underestimated. A modified specimen, 50 % longer than the standard size, was proposed so that a uniform stress can be obtained along the interface. In their tests they found that the determined mean tensile strength with the elongated specimen was 21 % higher than that determined with the ASTM C633-79 standard specimen. So, they concluded [136] that elongated specimens provide more accurate estimates of bond strength than ASTM C633-79 standard specimens.

TAT has been used intensively for many applications, for example, to investigate the effect of grit blasting [137–139], substrate preheating prior to spraying [140], coating thickness [141], spray angle [142], sprayed particle size distribution, and morphologies [143].

15.6.3 Other Types of Tensile Tests

Different tests have been defined [144–146] and few examples are given below.

The modified configuration of the TAT, called single bar (SB) method, according to Leigh and Berndt [144] has been designed for self-alignment and to accommodate flat and wide thermal sprayed-coated specimens, see Fig. 15.18, with sizes up to 152 × 152 × 152 mm^3. The specimen is positioned between two plates that are 178 × 178 mm^2 wide. The bottom plate has a 25.4-mm-diameter hole at the center, through which the glued pull-off bar passes and provides tensile stress to the specimen [144]. This bottom plate and the universal joints at the top and bottom of the fixture result in a self-aligning TAT system. Several tests can be performed on each flat substrate, since the pull-off bar can be repositioned for each TAT.

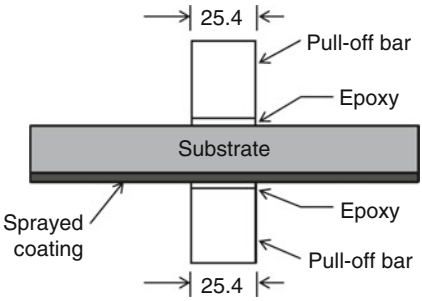


Fig. 15.19 Schematic of TAT assembly for double-bar (DB) method. Reprinted with kind permission from Springer Science Business Media [144], copyright © ASM International

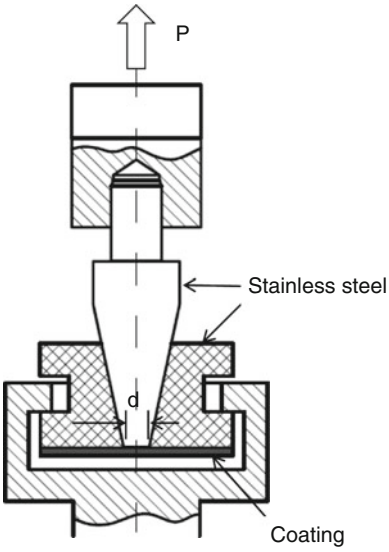


Fig. 15.20 Schematic diagram of the direct pull-off test. Reprinted with kind permission from Elsevier [146]

Another modified TAT, called double bar (DB) method, is shown in Fig. 15.19 from Leigh and Berndt [144]. This method does not require a special testing fixture except two pull-off bars and two universal joints, which are attached to both sides of the flat specimen. As for SB, several tests can be performed on each flat substrate, since the pull-off bar can be repositioned for each TAT, the problem being to maintain the alignment between the two bars.

For coatings with a strong adhesion (>60 MPa), such as those obtained with D-gun or high-power HVOF, the adhesions are measured according to the pull-off method [145] with the application of a force normal to the coating–substrate interface. The schematic diagram of one of these tests is presented in Fig. 15.20 from Du et al. [146]. The substrate comprises two parts with conical shapes: one female and one male made of the same material as that of the used substrate. The surface of joined both parts is continuous and grit blasted to anchor the sprayed coating. Du et al. [146] have sprayed WC–Co powder using a D-gun

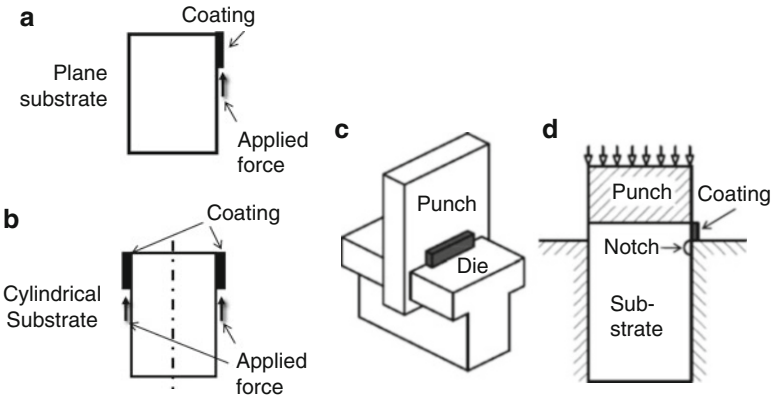


Fig. 15.21 Schematic illustration of shear test: (**a**) Plane substrate, (**b**) cylindrical substrate (**c**) shear test jig, and (**d**) schematic illustration of shear test. Reprinted with kind permission from Elsevier [147]

spray system, onto stainless steel substrate; the tester was also made of stainless steel. They found adhesions values ranging between 120 and 150 MPa, depending on the spray conditions.

15.6.4 Shear Stress

In many cases shearing plays a key role in coating peeling off. The principle of a shear stress test is very simple, as shown in Fig. 15.21a. The coating is deposited onto either plane (Fig. 15.21a) or cylindrical (Fig. 15.21b) substrate and a force parallel to the coating is applied at is extremity as shown schematically in Fig. 15.21a, b. If the shear test piece is rather complex to prepare, it needs no adhesive agent. Moreover, the adhesion strength can be measured using specimens, which are cut out from the products [147].

However, the main disadvantage of this shear test is a possible stress concentration [147] at the corner of the protruded step of a test piece, indicated by a dotted arrow in Fig. 15.21a. It results in a lower value than the true shear strength. That is why Era et al. [147], proposed a shear test piece with a semicircular notch at the corner of a protruded step. Calculations and measurements have demonstrated that the reduction of the stress concentration in a notched test piece (radius over 0.3 mm) is effective for a coating which Young's modulus is equal or larger than that of substrate. The sprayed specimen (Cr_3C_2 cermet coating on mild steel) was cut using a precision machining tool into conventional shear test pieces assuming that no damage occurs to the coating by this machining. Figure 15.21c shows the shear test jig they used and Fig. 15.21d the appearance of the shear test. The shear test jig was precisely made of sintered WC–Co cermet. The clearance between the punch and die was measured to be about 20 μm, corresponding to the interface zone between coating and roughened substrate. The critical shear stress τ_c is calculated by

$$\tau_c = \frac{F}{w\,l} \tag{15.17}$$

where F is the force applied, l is the length of the coating, and w is the coating thickness minus 20 μm.

15.6.5 Fracture Mechanics Approach

The fracture mechanics approach consists in establishing the equilibrium condition where the elastic energy provided by an external force (as defined by the geometry of the specimen and the applied load) is balanced by the propagation of a "stable" crack [132]. One form of this energy-balance criterion derives the strain energy release rate, G (in J/m^2) and is defined as $G = \frac{\partial(W_e - U)}{\partial A}$, where W_e is the work done by external forces (J), U is the elastic energy stored in the system (J), and A is the crack area (m^2). It is convenient to write G as

$$G = \frac{P^2\,\mathrm{d}C}{2w\,\mathrm{d}a_k} \tag{15.18}$$

where P is the force required to extend a crack (N), a_k is the crack length (m), w is the coating thickness (m), and C is the compliance, which is the reverse of the slope of the curve load displacement (m/N). The critical value G_{ic} corresponds to the coating adhesion limit. The strain energy release rate can be related to the fracture toughness, characterizing the interface, K (stated in N/m$^{3/2}$), by

$$K = \frac{\sqrt{E \times G}}{1 - \nu^2} \tag{15.19}$$

where E' is the elastic modulus (MPa) and v is the Poisson's ratio. The toughness represents the ability of a material to deform plastically and absorb energy in the process before fracture occurs.

The TAT can be analyzed according to the fracture mechanics concepts, where the specimen configuration for the TAT geometry is considered as a circumferentially cracked bar (Fig. 15.22). The average fracture strength can be converted into fracture toughness [132] by using Eq. (15.20).

$$K_{1C} = P\left[-1.27 + 1.72\left(\frac{D}{d}\right)\right]D^{-1.5} \quad 0.4 \le \frac{d}{D} \le 0.9 \tag{15.20}$$

where K_{1C} is the critical fracture toughness (N/m$^{3/2}$), P the fracture force (N), D the outside diameter of the bar (m), and d the inside diameter in the circumferentially notched bar (m) (see Fig. 15.22). The average reduced-area ratios range between

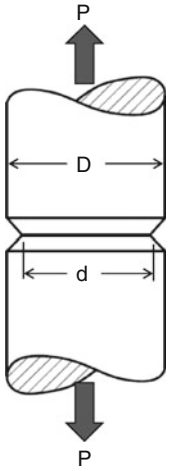


Fig. 15.22 Tensile adhesion test specimen of a circumferentially cracked bar for K_{1c} testing. Reprinted with kind permission from Springer Science Business Media [132], copyright © ASM International

0.74 and 0.86. This reduction in area corresponds to a reduced failure stress of about 80 %, which correlates reasonably well with the underestimation factor of approximately 83 % found by Han et al. [148].

For HVOF-sprayed coatings, the tensile adhesion test is widely used. However, the edge of the substrate is heavily deformed and rounded due to the high impact energy of the sprayed particles. This deformation causes a large scatter of the adhesion test results [149]. To avoid that a pre-crack was formed at the interface of a conventional tensile adhesion test specimen, the coating was sprayed onto the cylindrical substrate used in the ASTM C633-79 test. Before spraying, a carbon layer was placed along the substrate edge with 3 mm width from the edge in order to introduce "a weak bonded region" at the interface as indicated with the black rings in Fig. 15.23. A pencil of 2B grade was used to place the carbon layer. The substrate was set in a lathe-turning machine and rotated. The sharpened pencil was touched on the surface by the precise position controller in order to achieve a uniform carbon layer. This system was used to determine the interfacial toughness, according to the fracture mechanics concepts.

According to Eq. (15.18), the strain energy release rate corresponds to crack opening. Unfortunately, Clyne and Gill [150] have shown that the analysis of interfacial debonding is complicated by the fact that the stress field at the crack tip may not represent conditions of pure crack opening (mode I). "Depending on the toughness of the interface and of the two media on either side, crack propagation may continue within the interface, rather than seeking a mode I path in some other direction, even though the interfacial path is heavily 'mixed mode' (i.e., has a substantial shear component at the crack tip)" [150]. The so-called phase angle, ϕ, is related to the crack-tip stress-intensity factors, K_i (see Eq. 15.21), for mode I and mode II loading by

$$\phi = \tan^{-1}\left(\frac{K_{II}}{K_I}\right) \tag{15.21}$$

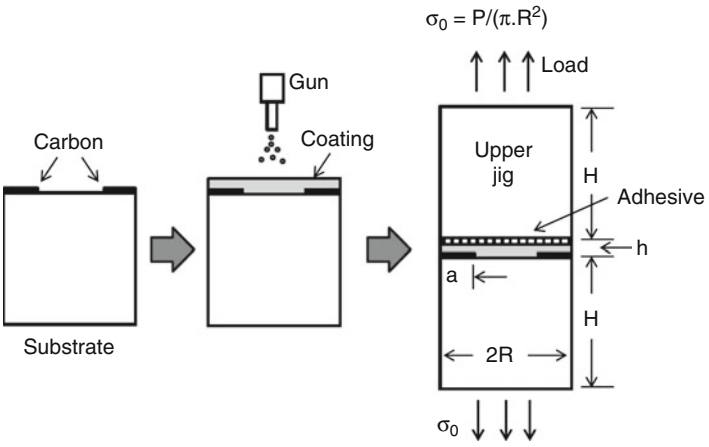


Fig. 15.23 Procedure of sample preparation for the modified adhesion test and schematic of a sample configuration. Reprinted with kind permission from Elsevier [149]

so that $\phi \sim 0$ represents pure opening conditions (mode I) and $\phi \sim 90$ represents pure shear (mode II). The critical value of critical strain energy release rate G_{ic} rises as a shear component is introduced, since this will encourage dissipation of energy at and immediately behind the crack tip as a result of frictional rubbing between asperities. It is expected that roughening of the substrate surface will give rise to a more substantial increase in interfacial toughness if there is a large shear component to the crack-tip driving force. As the dependence of G_{ic} on ϕ is significant, especially over 45°, the interfacial fracture energy values should always be quoted together with ϕ, which values vary widely between different test procedures and are also affected by the presence of residual stresses. Thus, all the adhesion and toughness experiments presented afterwards should be considered with many cares in their interpretation. The same experiment should be used to compare the effect of the different spray parameters on coating adhesion and toughness. Also the results obtained under the same spray conditions with two different measurements devices are not comparable.

15.6.6 Bending Test: Adhesion and Interface Toughness Measurements

They are either three-point measurements where a rectangular coupon is placed on two rolls and a third roll applies a load at the mid-span location as in Fig. 15.24a from Rammo et al. [151] or four-point measurements where four rolls are used to more homogeneously distribute stresses over the test volume, as in Fig. 15.24b from Lin and Berndt [132]. During the three-point test, the upper half of the specimen is

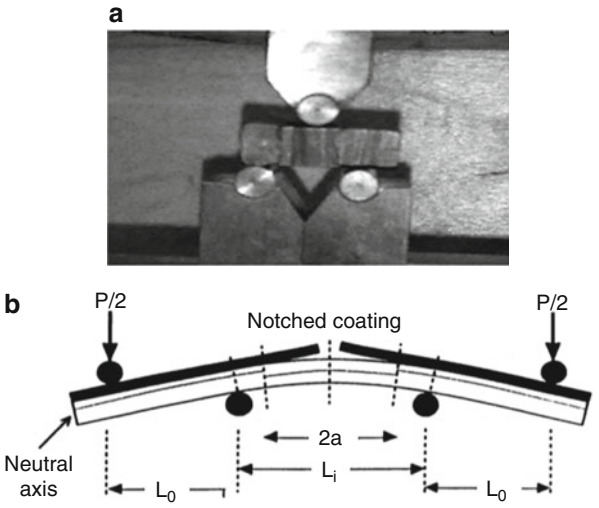


Fig. 15.24 (**a**) Joined sample assembly under three-point adhesion test [151] and (**b**) loading arrangement and specimen geometry to measure coating adhesion in four-point adhesion test. Reprinted with kind permission from Springer Science Business Media [132], copyright © ASM International

under compression, while the complementary half is under tension. With the four-point bend test it is the reverse. This test is more currently used because it is less sensitive to the defects within coatings. However it is a mixed mode system with ϕ comprised between 35 and 60°. The test must enable a symmetric crack to propagate from a perpendicular notch, see Fig. 15.24b, along the weakest interface of a multilayer specimen.

In principle between the two inner loading points, stable crack propagation should occur at a constant load. Théry et al. [152] performed adhesion tests on specimens, either pre-cracked, as shown in Fig. 15.25a or not. Without preset pre-crack a large load is needed to initiate the crack and the specimen could consequently be overloaded. A pre-crack has been successfully realized by introducing a 1-mm large band at the center of the specimens that were not grit blasted prior to spraying [152]. After initiation, catastrophic crack propagation occurred and the force-displacement diagram exhibited no plateau (see Fig. 15.25b), providing no reliable information on the adhesion energy. With a pre-crack a plateau was observed after the peak (see Fig. 15.25c) and reliable adhesion measurements could be performed. The length of the pre-crack might be sufficient to make the critical strain energy release rate, G_{ic}, be independent of it [150].

Acoustic emission (AE) is often used to follow crack propagation [153]. The distribution of AE responses combined with the analysis of crack source parameters is useful for determining the failure modes and the damage progression [153].

This method can also be used to determine the coating toughness. For that the critical strain energy release rate G_{ic} (see Eq. 15.18) must be calculated either from simple equilibrium equation, assuming an elastic behavior, or using more complex expressions such as those deduced from Euler–Bernoulli beam theory [154, 155]. In order to determine G_{ic}, both the applied load and the displacement of the loading points are continuously monitored and recorded. The specimen is loaded until both

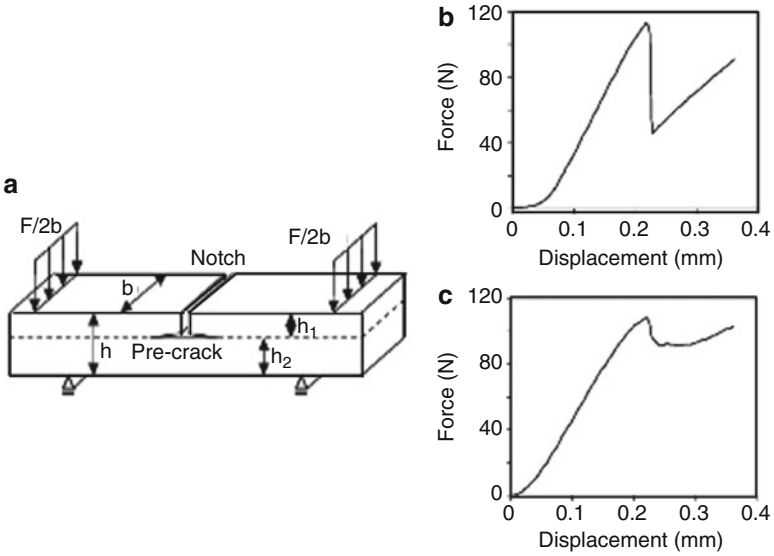


Fig. 15.25 (**a**) Four-point bending specimen with symmetrical interfacial cracks; force-displacement diagrams recorded during the adhesion test. (**b**) Without any pre-crack, the specimen is overloaded so that catastrophic crack propagation occurs and the diagram exhibits no plateau. (**c**) With an efficient pre-crack, stable crack propagation occurs so that the diagram exhibited a plateau. Reprinted with kind permission from Elsevier [152]

cracks have propagated out to the supporting points. The strain is monitored and any cracking detected by AE so that the strain to fracture (STF) is determined. Unfortunately the STF parameter is dependent on the residual stress. For example, Howard and Clyne, as cited by Lin and Berndt [132], used the bi-material notched four-point bending specimen to study the interfacial fracture toughness of vacuum plasma-sprayed titanium coatings. G_{ic} was 6.79 $\pm$ 0.35 J/m^2 for coatings exhibiting residual stress and 2.98 $\pm$ 0.19 J/m^2 for coatings without residual stress.

The four-point test has been used to characterize, for example, plasma-sprayed TBCs [156], 100Cr6 steel coatings thermally sprayed on a 35CrMo4 steel substrate [154], plasma-sprayed ceramics [157], high velocity oxy-fuel-sprayed bioceramic coatings [155], detonation-sprayed MoB–CoCr alloy coatings on 2Cr13 stainless steel substrate [158], ….

15.6.7 Indentation: Interface Toughness Measurement

Compared to the sophisticated adhesion and/or toughness measurements described above, the indentation test is simple as it consists in (1) obtaining polished cross sections of coating and substrate and (2) performing Vickers indentation tests on the interface using different applied loads. Upon indenting

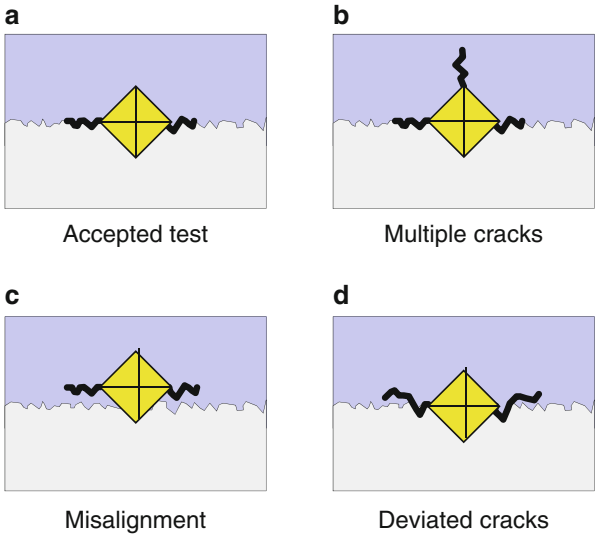


Fig. 15.26 Schematic aspect of the crack generated by interfacial indentation: (**a**) Accepted test, (**b**) multiple cracks, (**c**) misalignment, and (**d**) deviated cracks. Reprinted with kind permission of Prof. G. Montavon [159]

the interface, a plastic deformation zone is created by sharing the combined local properties of the coating and the substrate. When the fracture toughness of this composite interface material coating is reached, a local crack occurs [157, 158] (see Fig. 15.26a [159]). The purpose of the interface indentation test is to give a quantitative measure of the apparent fracture toughness of the above mentioned "interface material." Compared to most of the above tests it does not require the use of a bonder and it may be used for a large range of coating thicknesses, provided they are over 100 μm. However the test needs to be carefully performed and avoid multiple cracks (Fig. 15.26b), misalignment (Fig. 15.26c), and cracks deviation (Fig. 15.26d).

Lesage et al. [160] have developed a procedure for coated materials; it consists of the following:

(a) Applying the Vickers indent with its diagonal coincident with the coating substrate interface
(b) For each indentation test, measuring the value of the half diagonal of the indent, a_c, and the length of the crack l, both at the interface
(c) Plotting these data as a function of the applied load in bi-logarithmic scale, as represented schematically in Fig. 15.27
(d) Determining the coordinates of the critical point indicated in Fig. 15.27 (load P_c, half diagonal of crack length a_c), underneath which no crack is formed

To achieve a quantitative measure of the apparent fracture toughness, the mechanical properties, strength, and elasticity of the interface materials must be known. Neglecting the effect of residual stresses, according to Lesage et al. [160] the apparent interface fracture toughness K_{ca} may be defined as

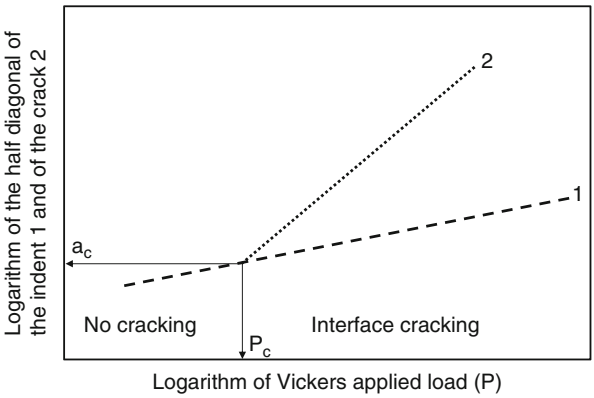


Fig. 15.27 Schematic representation of the results obtained by performing the interface indentation test: *curve 1*: Logarithm of Vickers Hardness indent half diagonal and *curve 2*: logarithm of the interface crack length. Below P_c and a_c no interface cracking is observed. Reprinted with kind permission from Elsevier [160]

$$K_{ca} = 0.015 \frac{P_c}{a_c^{3/2}} \left(\frac{E'}{H}\right)_i^{1/2} \tag{15.22}$$

The quantity $(E/H)_i$ may be expressed as follows:

$$\left(\frac{E'}{H}\right)_i^{1/2} = \frac{\left(\frac{E'}{H}\right)_S^{1/2}}{1 + \left(\frac{H_S}{H_C}\right)^{1/2}} + \frac{\left(\frac{E'}{H}\right)_C^{1/2}}{1 + \left(\frac{H_C}{H_S}\right)^{1/2}} \tag{15.23}$$

where H is the Vickers hardness and E' the Young's modulus. The subscripts i, S, and C stand for interface, substrate, and coating, respectively.

This method was used, for example, to characterize the effect of thermal treatment on the adhesion of thermal-sprayed NiCr coatings [160], the adhesion of plasma-sprayed cermet Cr_3C_2/Ni–Cr coatings [161, 162], and that of NiCr–Cr_3C_2 VPS-sprayed coatings [163].

15.6.8 Other Methods

Only a few of them will be described.

15.6.8.1 Double Cantilever Beam Test

In the simple double cantilever beam (DCB) test on coatings (Fig. 15.28), a tension force is applied to the specimen assembly and displacement is measured by an extensometer placed on the arms [132]. When cracking initiates (decreasing load with increasing extension) the DCB is unloaded. Several loading/unloading

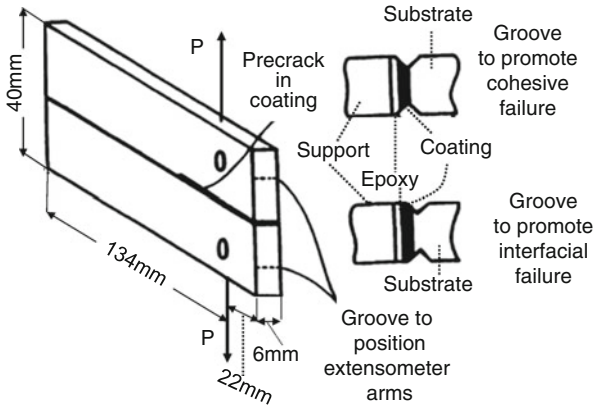


Fig. 15.28 Double cantilever beam specimens used for adhesion measurement. Detail shows the grooving procedure to promote either interfacial or cohesive failure. Reprinted with kind permission from Springer Science Business Media [132], copyright © ASM International

sequences are performed until the specimen completely fails, at which point the morphology can be examined by optical microscopy and scanning electron microscopy (SEM). Of course the fracture toughness of the adhesive must be greater than that of the coating. As illustrated in Fig. 15.28 it is possible to promote either cohesive or interfacial failure. In this test both fracture modes occur and the ϕ angle is between 0 and 50°.

Expression of the fracture toughness can be found in the paper of Lin and Berndt [132].

15.6.8.2 Double Torsion Test

The double torsion test [132] has been applied to thermally sprayed coatings. The prime advantage of this test is that the crack length need not be measured, because cracking occurs at a constant strain energy release rate or stress-intensity factor.

15.6.8.3 Scratch Test

The scratch test is mostly used to characterize thin, hard coatings (TiN and TiC for example). In this test, a loaded Rockwell C diamond stylus (see Sect. 15.7.1.1) is drawn across the coating surface under either constant or gradually increasing load. Often the Acoustic Emission (AE) is also monitored during the scratching procedure to determine precisely the critical load, P_c, at which failure takes place [132]. Erickson et al. [164] have compared scratch test with other tests and Xie and Hawthorne [165] have modeled it. For example, Ma et al. [166] have used this technique to characterize ultrafine-structured alloy HVOF sprayed using a liquid suspension/slurry containing small alloy powders. In their test, 0.2 mm tip radius Rockwell diamond indenter tip was drawn across the coating with a loading rate of 300 N/min, start load of 0.9 N, and end load of 150 N. Using optical microscopy

examinations the critical loads were measured. Sundararajan et al. [167] used this test to get an estimate of the critical load (P_c) at which cracks started appearing at the base of the scratch formed on the cold-sprayed coating surface. Scratch tests were performed on polished and un-etched top surfaces of Cu, Ag, Zn, and SS 316L coatings with different heat treatments.

15.6.8.4 Laser Shock

(a) Coating Adhesion

Based on the work of Bolis et al. [168] laser shock method (LASAT: Laser Adhesion Test) has been used to characterize the interfacial resistance of thermal-sprayed coatings. The pulsed laser was focused on the substrate side on a few mm^2 surfaces, permitting to run different tests on the same sample. Irradiating the surface of a substrate with a high power laser generated a very intense pressure pulse propagating as a shock wave [169]. This shock wave propagated and reflected in the material, creating release waves, the crossing of which led to tensile stresses. Depending on the laser source, the shock pressure can reach few tens GPa during a few ns. To determine the adhesion threshold, shocks were applied to samples with different levels of the incident laser power flux. The de-bonding limit, i.e., when exceeding the interface resistance, was determined from systematic metallographic observations of cross sections of all the laser-shocked specimens. Below and above the laser shock adhesion threshold, two types of velocity profiles of the coating surface were respectively obtained [170]. The first type of velocity signal was for a laser power flux of 18 GW/cm^2, i.e., below the adhesion threshold. The corresponding curve showed two peaks in the velocity amplitude, which corresponded to the interaction of the shock wave with the coating surface. The time between two peaks was that for the shock wave to propagate through the whole coated substrate material and go back. Therefore, the wave could go through the interface, which was the sign there was no interface damage. When increasing the power flux, beyond a certain value the distance between two velocity peaks was shorter and the time between the two peaks corresponded to the time necessary for the wave to cross two times the coating only. This signal was typical of de-bonding at the interface as the shock wave reflects on the void, which was created at the first interaction with the interface. Barradas et al. [169] used a Nd: YAG laser delivering 10-ns Gaussian pulses focused on a 2-mm-diameter spot at the surface of the substrate with a wide range of laser power densities (5–100 GW/cm^2). Laser interferometry allowed measuring the substrate top surface velocity to calibrate LASAT testing numerical simulations in order to calculate the corresponding traction at interface. For the first tests, the tensile stresses in the tested sample were determined using “SHYLAC” finite element code, which allowed one-dimensional simulation only. It corresponded to assuming that the laser beam had a top-hat shape and not a Gaussian one. The first experiments [169] on cold-sprayed Cu onto Al showed that Cu–Cu interlamellar strength was about of

the same order as that of Cu–Al coating–substrate adhesion and demonstrated the feasibility of the LASAT testing as a powerful tool for the measuring of adhesion, including in local zones. Rolland et al. [171] showed that the laser test was reproducible provided that a black overlay was deposited onto the surface prior to testing to achieve a good and constant absorption of the laser pulse. The optimization of the laser test consisted in determining the maximum laser energy without any surface melting. This requirement came from the fact that the laser absorption was not stable as a function of surface temperature and dramatically increased with melting [171]. Rolland et al. [171] carried out finite element calculations using Zebulon® in two steps: i.e., thermal calculations then mechanical calculations. The thermal step consisted in applying a thermal flow on the laser-irradiated zone. The laser power profile was modeled with a spherical approximation [172] with which the minimum laser energy needed to melt the surface was calculated. This power profile was used to involve the defocusing effect of the laser, which evolved from a top hat profile to a Gaussian profile.

LASAT has been used to evaluate the feasibility of metallization of thermoplastic polyamide 66 (PA66) using cold spray of aluminum powder [173]. The need of careful interpretation of LASAT when applied to this kind of deposits was highlighted. However, the potential of the test was demonstrated and criteria for future use established.

Guipont has studied the characterization with LASAT of porous ceramic coatings (YSZ and HAp) plasma sprayed or deposited by a physical process on metal substrates [174]. He showed that, when the laser power corresponding to the adhesion level was reached, a white spot appeared in the ceramic coating at the opposite of the laser impact. This signature of the cracked surface that can be detected with eyes is very convenient.

(b) Splat Adhesion

In cold spray, particle adhesion onto the substrate is influenced by particle impact velocity. Guetta et al. [175] developed an original experimental setup (Fig. 15.29) to discriminate the particles as a function of the levels of impact velocity to investigate the influence of this parameter on the resulting splat adhesion. The sample, the top of which surface showed splats, is placed in front of a polymer plane. The upstream laser shock results in the debonding of splats, which are collected at the polymer surface [175]. For splats, laser interferometry (VISAR in Fig. 15.29) resulted in measuring the substrate top surface velocity. This was used to calibrate LASAT testing numerical simulations before the corresponding traction at interface was calculated. Because splat debonding highly depended on traction at the interface, modifying the laser beam intensity decreased the latter. When the traction was low enough, splats no longer debonded. The level of adhesion was therefore reached. Mechanical adhesion resulted from both solid material jetting, which kept the particle in the substrate and molten material jetting, which overlaid the particle and improved adhesion (for details, see section

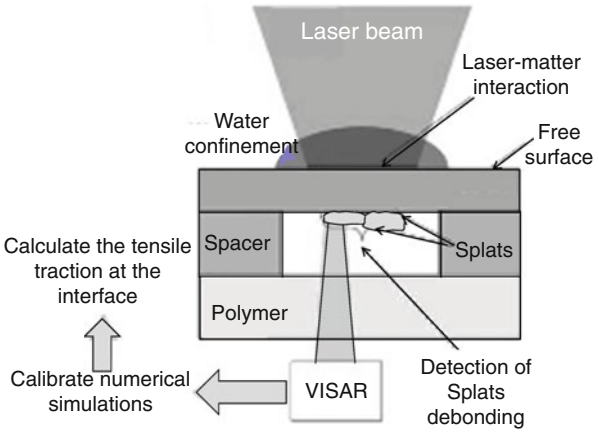


Fig. 15.29 Schematic illustration of LASAT testing setup for splats. Reprinted with kind permission from Springer Science Business Media [175], copyright © ASM International

"Phenomena at Impact" in Chap. 6). TEM observation, simulation, and LASAT experiments allowed correlating nano-scale phenomena to macroscopic parameters such as impact velocity [176].

15.7 Mechanical Properties

Mechanical properties of materials including hardness, adhesion, Young's modulus, toughness, and residual stress are very important for materials and coatings in service conditions. Some tests of these properties are summarized in [15.M1–15.M4].

15.7.1 Hardness and Indentation Test

15.7.1.1 Hardness

Hardness is generally not considered as an intrinsic property of a material or a coating and its value depends on the testing method used [177] as well as for coatings on the direction where the test is performed: at coating surface, orthogonal to splats, or at a cross section parallel to splats. In the latter case the coating must be imbedded in resin, which is not necessarily the case for surface measurements. Cross sections are generally polished, whereas it is not necessarily the case for surfaces. However on nonpolished rough surfaces, the dispersion of results is more important and thus polishing is recommended. For thin coatings the substrate may influence the results and it is generally admitted that for coatings thicker than 250 μm the substrate is no more a problem. As previously underlined, hardness

measurements must be statistical and thus can be performed only with multiple readings, at least 10–15.

The principle of the method is to measure the depth of penetration (in general for nano-hardness) or the width of a print (microhardness or hardness) left by an indenter applied during a given time (usually a few tens of seconds both for loading and unloading) with a given load, P. The latter varies from 0.1 mN to tens of N. The denominations are the following: nano-hardness $P < 0.05$ N, microhardness $0.05 < P <$ 5–10 N, hardness >10 N.

Wigren and Täng [3] have pointed out that microhardness is generally performed as per ASTM E384 [15.M7]. A first general misconception is the number of indentations. It is easily shown that 10 indentations are by far too few. A second issue is the metallographic preparation of the specimen before measurement. A preparation routine that tends to smear the coating (i.e., the use of SiC paper) can lead to an underestimation of the microhardness by about 100 Vickers.

When measuring the depth of penetration a motorized vertical carriage supplies a loading force (from 0.1 mN to kN). The depth of indentation is measured for nano-hardness with a 3-plate capacitance sensor (from 0.1 nm to few μm) and for microhardness with a traditional capacitance sensor (from 0.05 to 250 μm).

For microhardness and hardness measurements, the diameter or diagonals (from about 5 μm to 0.5 mm) of the indents are measured with a digital optical microscope. However, here again to read prints that can be only a few micrometers long the surface preparation also plays a non-negligible role [2]. It is also important to keep a certain distance, depending on the used indenter, between the measurement location and the interface coating–substrate or bond coat.

Hardness testers are compared in [15.M5]. For coating nano-, microhardness, and hardness measurements, four types of indenters are used:

- Berkovitch indenter for nano-hardness measurements. It is a three-sided pyramid, which is geometrically self-similar and has an excellent penetration. It has a very flat profile and a tip radius of about 150 nm, with a total included angle of 142.3° and a semi-apex angle of 65.03°. The Berkovich tip has the same projected area to depth ratio as Vickers indenter. For example, Dey et al. [178] used this method to characterize hydroxyapatite coatings. It is also possible to use a cone of semi apical angle 30°, which penetration depth is higher than that of the Berkovich indenter.
- Vickers indenter. This standard indenter uses a square-based diamond pyramid with an angle between opposite faces of 136° (see Fig. 15.30). Sometimes this test is called diamond pyramid hardness (DPH). The hardness is calculated by

$$\mathrm{HV} = \frac{2P \sin \alpha}{L^2} (\mathrm{MPa}) \tag{15.24}$$

where P is the applied load (N), L the average length of diagonals (m), and α the angle between opposite faces of diamond (136°). The measurement is acceptable only if the length difference between both diagonals (see Fig. 15.30 representing

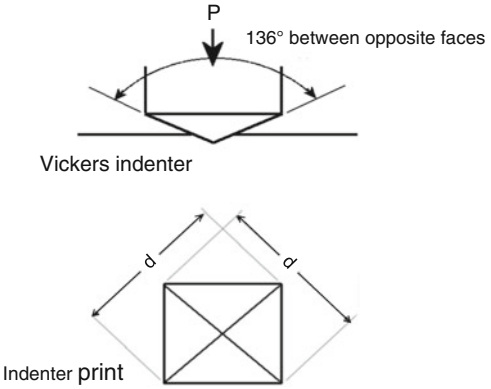


Fig. 15.30 Schematic of a Vickers indenter tip and of its print on the tested coating

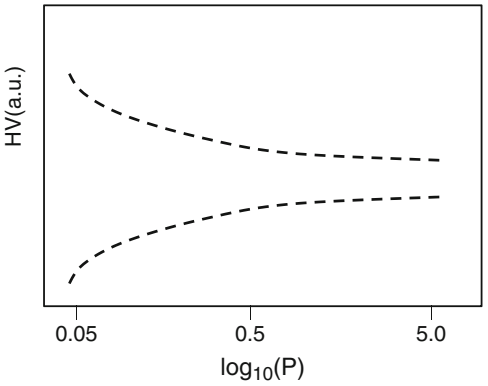


Fig. 15.31 Schematic variation of distributions of maximum and minimum of the Vickers hardnesses of a thermal sprayed coating for different loads

the indenter print) is less than 5 % and if the print is at least half a diagonal length apart from any side of the coating and for measurements on cross sections if the distance from interface or top is larger than 1.5 times the diagonal length.

In principle, because the impressions made by the pyramid indentor are geometrically similar whatever their size, HV should be independent of the load. However localized microstructural variations decrease when the applied load increases. This is due to the particular structure of the sprayed coatings that involve splats more or less in good contacts, voids, unmolten particles, . . ., the indenter with a higher load being in contact with more splats, voids, . . ., and giving a response less and less localized. Thus when the load increases the dispersion of results diminishes. If curves representing the minimum and maximum values measured for different loads are plotted they look as those schematically presented in Fig. 15.31.

Thus it is clear that when hardness measurement is presented it is meaningless if the load at which measurement has been made is not given as well as the measurement dispersion: e.g., 600 ± 60 MPa HV_5. To illustrate that with experimental results let us consider titania (TiO_2) coatings HVOF sprayed by Lima and Marple

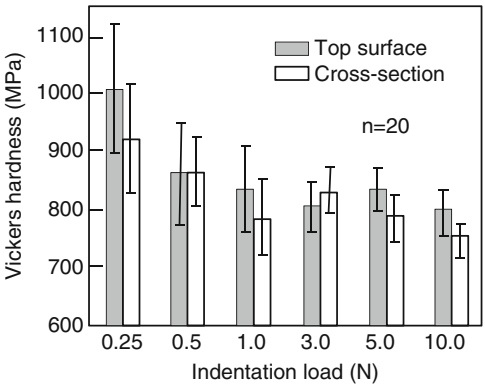


Fig. 15.32 Vickers hardness on the top surface and cross section of HVOF titania coatings for different indentation loads. Reprinted with kind permission from Springer Science Business Media [179], copyright © ASM International

[179]. Figure 15.32 presents hardness measurements on the surface and cross section of the titania coating sprayed on low-carbon steel substrates using a DJ 2700 HVOF torch. The hardness decreased from <900 to 1000 Vickers at an indentation load of 0.25 N to <750–800 Vickers at an indentation load of 10 N, for both the top surface and cross section. At lower loads, the indentation diagonal sizes were quite small indicating that only a small region of the coating was being sampled. For example, at an indentation load of 0.25 N, the indentation diagonal length was approximately 7 μm. This minimized the extent of defects, such as coarse pores, splat boundaries, and micro-cracking, enclosed within the indentation zone. As the indentation load increased, so did the volume of coating being analyzed: at an indentation load of 10 N, the indentation diagonal length was approximately 50 μm. As a consequence, porosity, splat boundaries, and micro-cracking played a significant role on hardness, lowering its value. As previously emphasized the dispersion of the hardness values increased when the load diminished. Globally hardness was smaller on cross sections [179]. Lima et al. [180] also measured the Vickers hardness of nanostructured zirconia coatings.

Knoop indenter is used particularly for very brittle materials, where only a small indentation may be made for testing purposes. The geometry of this indenter is an extended pyramid with a length to width ratio of 7:1 and with face angles of 72°30′ for the long edge and 130° for the short edge, respectively (see Fig. 15.33). The depth of the indentation can be approximated as 1/30 of the long dimension. The Knoop hardness HK or KHN is then given by the formula:

$$\mathrm{HK} = \frac{P}{c_\mathrm{f} L^2}\,(\mathrm{MPa}) \tag{15.25}$$

where L is the length of indentation along its long axis and c_f a correction factor related to the shape of the indenter, ideally 0.070279. For measurements close to the interface or the top for coatings cross sections, the distance must be higher than 0.35 times the length of the longer diagonal. Often Knoop is preferred to measure hardness of ceramic materials because of the longer print of the long diagonal

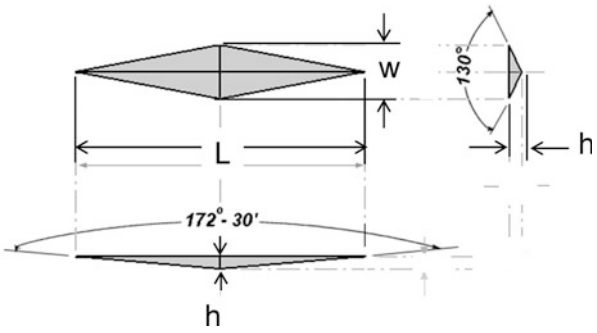


Fig. 15.33 Knoop hardness prints

compared to that of the Vickers indenter under the same load. For example, Lima et al. [181] have measured the Knoop hardness of plasma-sprayed nanostructured partially stabilized zirconia coatings. ASTM tests for Knoop and Vickers hardnesses are given in [15.M6–15.M9].

Rockwell C indenter is a diamond cone with an angle of 120°. The test consists in measuring the additional depth to which an indenter is forced by a heavy load beyond the depth of a previously applied light load. The light load eliminates backlash in the load train: the indenter breaks through slight surface roughness and crush particles of foreign matter [177]. Compared to the two previous techniques, Rockwell C technique is faster due to its minimal surface preparation and its ease of use.

15.7.1.2 Indentation

Upon penetration, under a load, P, within the material of the indenter elastic and plastic deformation phenomena occur resulting in a print. Elastic and/or plastic deformation is linked to the indenter geometry (for example, a spherical indenter result generally in elastic deformation) and to the applied load, low loads corresponding to elastic deformation. However with sharp indenters, plastic deformation occurs with very low loads. The penetration depth, h, depends on the geometry of the indenter and the load. The curve $P(h)$ shown in Fig. 15.34a is obtained by first increasing progressively the load (loading step) and then by reducing it to zero (unloading step). When the maximum load, P_{max}, is reached the maximum depth, h_{max}, is obtained. The unloading curve is different from the loading one (see Fig. 15.34a) because of the plastic deformation induced by the load. Figure 15.34b illustrates the different states induced by the loading and unloading steps. The depth h_{max} results from the sum of the contact depth h_p and displacement of the material surface along the contact perimeter (see Fig. 15.34c). Once the indenter is removed, only the elastic component is recovered, leaving a residual deformation h_r (see Fig. 15.34c). It is worth noting that the length of the Vickers indenter diagonal, observed after unloading, is that corresponding to the

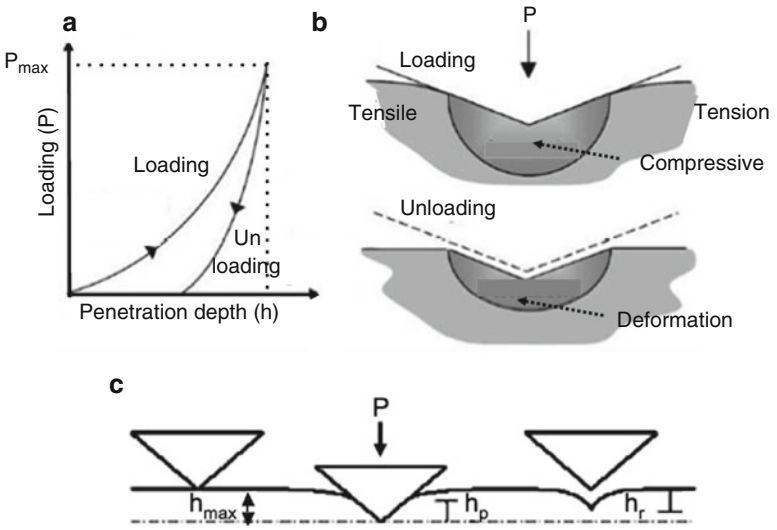


Fig. 15.34 (**a**) Characteristic curves $P(h)$ during loading and unloading, P being the load, and h the indenter penetration depth, (**b**) different states induced by loading and unloading steps, and (**c**) definitions of h_{max}, h_p and h_r

residual deformation. This is different for the Knoop print: upon unloading elastic deformation reduces the length of the shorter diagonal as well as its depth, while the elastic recovery of the longer diagonal is much less. It gives the possibility to determine the Young's modulus [182].

Instrumented indentation method reveals much more information about a thermal spray coating than conventional Vickers or Knoop microhardness methods. It gives information about mechanical properties of the coating such as elastic modulus, elastic/plastic work of indentation, and creep or cyclic behavior [183]. Thanks to its force-displacement recording capability, the instrumented indentation method is able to sense when an indentation is performed on a void: the depth suddenly increases without the corresponding increase in force (Fig. 15.35). The most significant advantage is probably the automation of measurements. For example, this efficient cyclic indentation method allows automatic increase of maximum load on each subsequent cycle. Dataset of indentation depth and hardness or elastic modulus is obtained within ten or twenty minutes depending on the number of cycles [183]. When the coating hardness increases, the loading and unloading curves are shifted to the left as the indenter penetrates less for the same load.

The area between the loading and unloading curve represents the energy dissipated in the coating due to plastic deformation, and the area under the unloading curve represents the elastic energy for deformation. The normal load, P, and the depth of indentation, h, are measured during the indenter penetration [184]. The zero-point, defined as $P = 0$ and $h = 0$, is determined by a change in the

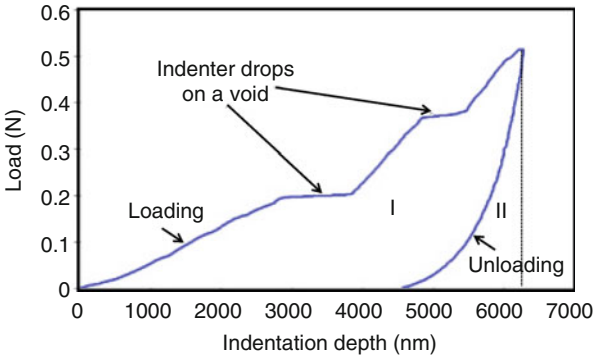


Fig. 15.35 Loading–unloading indentation curve presenting two "indenter drops" due to indentation on voids or other defects, Areas I and II represent plastic deformation and elastic recovery, respectively. Reprinted with kind permission of CSM Instruments application bulletin [183]

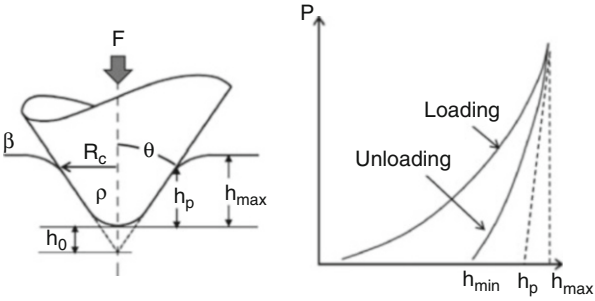


Fig. 15.36 Geometrical parameters under load and typical force-penetration curve, with a rounded cone. Reprinted with kind permission from Springer Science Business Media [184]

force signal as the indenter approaches the test surface. When the indenter is withdrawn the hardness can be calculated for the conical indenter by

$$H = \frac{P}{\pi R_c^2}\,(\text{MPa}) \tag{15.26}$$

The hardness, H, can also be calculated from the depth of the indenter, h_p in Fig. 15.36 (plastic component of the coating deformation only) or from h_{max} (corresponding to both plastic and elastic components) defining the universal hardness, HU [185], which is lower than H. For example with a Vickers indenter one has [115]:

$$H = \frac{L_{max}}{(26.43\,h_p)^2} \quad \text{HU} = \frac{L_{max}}{(26.43\,h_{max})^2} \tag{15.27}$$

Moreover one also must account for the indenter tip that is not sharp but rounded as shown in Fig. 15.36 [184]. Musil et al. [185] have shown that (1) the area between the loading/unloading curve and the value of h decrease with increasing (a) hardness H, (b) effective Young's modulus $E^* = E/(1-\nu^2)$, and (c) universal hardness HU, where E and ν are the Young's modulus and the Poisson ratio,

respectively; and (2) there is no simple relation between the mechanical response of the coating and H or E alone. However, this response is strongly dependent on the ratio H/E. More details will be given about indentation in sections related to Young's modulus and toughness measurements.

15.7.2 Young's Modulus

The elastic constants of thermal spray deposits are strongly dependent on microstructures (depending upon the real contacts between layered splats, cracks, and porosities), which are sensitive to the material processing condition. For example, Leigh and Berndt [115] assumed that the voids within the deposit were ellipsoidal in shape. The structure of the deposit was considered to be transversely isotropic with respect to the spray direction, which required five independent elastic constants of a stiffness tensor. Solid mechanics models containing ellipsoid-shaped voids were applied to obtain the five independent elastic constants of the deposits. The calculated elastic constants were compared to the experimentally determined values. The predicted Young's modulus values from the theoretical calculations were comparable to the obtained experimental values. However, the thin voids and micro-cracks contributed only to a small part of the total porosity; but they had the major influence on the decrease of Young's moduli by small elastic openings and partial closings of their faces. The inter-splat thin voids led to the decrease of Young's module E_3 in the spraying direction, while the intra-splat micro cracks led to the decrease of Young's module E in the directions orthogonal to the spray direction [186]. A few ASTM tests for Young's modulus are given in [15.M10–15.M13]. Experimental values of the Young's modulus can be obtained from the following measurements:

15.7.2.1 Indentation

As already emphasized in Sect. 15.7.1.2, the loading/unloading curves of Berkovitch or conical indenters are related to the ratio H/E and different ways are used to determine the Young's modulus. Roy et al. [187], working with a Berkovitch indenter have used the following expression

$$\frac{1}{E_r} = \frac{(1-\nu^2)}{E'} + \frac{\left(1-\nu_i^2\right)}{E'_i} E_r = \frac{0.89 \times S}{\sqrt{A}} \text{ with} \tag{15.28}$$

where S is the slope of the initial part of the unloading curve (see Fig. 15.36), A is the contact area between the indenter and the substrate, E' and E'_i are the Young's modulus, and ν and ν_I are the Poisson ratio of the coating and the indenter, respectively.

- Ma et al. [188] have used the same approach to investigate a set of approximate relationships between H/E' and We/W for different types of Berkovich tip geometries with different degree of bluntness. We and W are the elastic work and total work corresponding to the areas under the unloading and loading curves recorded in an indentation test.
- Feng and Kang [189, 190] have used a spherical transparent indenter that can directly measure the indentation-induced out-of-plane deformation as well as the indented surface. Coupling with a multiple partial unloading testing procedure, material's Young's modulus was determined.
- Wallace and Ilavsky [191] have used a spherical indenter to measure the elastic constant: Hertzian indentation. They found that planar defects, which contributed only insignificantly to the porosity of the material, had a very strong effect on the elastic modulus. It has been further shown that there are periodic variations in the elastic modulus throughout the thickness that are correlated with the spray parameters of the initial deposit.

15.7.2.2 Four-Points Bending

The setup used for the four-point bending test is that presented in Fig. 15.24b with the coating placed in tension. All the expressions (see, for example, [191–195]) relate the coating Young's modulus, E'_c, to that of the substrate, E'_s, the respective thicknesses of substrate and coating, the relative beam deformation.

Musalek et al. [196] have used different types of loadings: loading up to stepwise increasing loads, with full unloading, loading up to the maximum load, with full unloading, and loading up to stepwise increasing loads, with partial unloading. This allowed observing the coating behavior at different load levels and hysteresis of the stress–strain curves. Coating secant modulus was separated from the total stiffness [197]. Bare substrates were tested to assess their elastic limits. The maximum load applied was then selected accordingly.

15.7.2.3 Knoop Hardness

The elastic modulus of coatings can be determined via Knoop microhardness tests. As already emphasized, the elastic modulus is determined by measuring the major and minor diagonals of a Knoop indenter, respectively [180].

15.7.2.4 Ultrasound Propagation

Landa et al. [186] have studied the dependence of the velocity of the longitudinal ultrasound waves on uniaxial pressure for three types of plasma-sprayed ceramics in two directions. The measurement consisted in recording the acoustic emission (AE) activity (count rate dN/dt) as AE is an important tool for detecting the

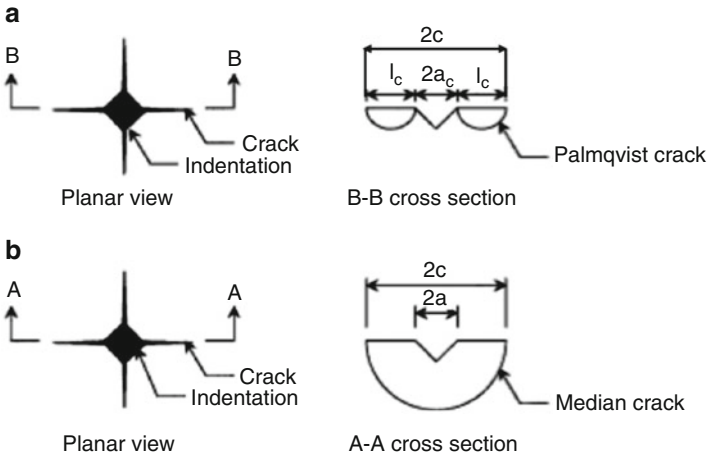


Fig. 15.37 Planar and cross-sectional views of (**a**) the Palmqvist model and (**b**) Median crack model. Reprinted with kind permission from Elsevier [198]

irreversible changes in brittle materials. The Young's modulus determination requires the knowledge of the coating thickness, including during the pressure application. Acoustic emission was monitored to find the maximum pressure, which did not cause any detectable damage. The instantaneous elastic stiffness c33 and c11, calculated from the measured ultrasound velocities, grew with increasing pressure between 0 and 300 MPa in different materials and in different directions 1.4 up to 4.7 times [186]. These results were explained by elastic closing of the inter-splat thin voids and intra-splat micro cracks under pressure. The loading and unloading curves slightly differed, which was explained by relative displacements of the faces of thin voids and micro-cracks oblique to the compression axes, leading to the appearance of friction forces.

15.7.3 Toughness

Among the different mechanical methods that can be used to measure coating toughness, the Palmqvist fracture toughness is popular because no specialized test specimens are necessary and small laboratory samples can be easily tested. Depending on the load applied on a Vickers indenter [198], either Palmqvist cracks appear for a low load regime, while median cracks show up for high load regime. When increasing loads, Palmqvist cracks form first followed by median cracks. Both types of cracks are represented in Fig. 15.37 from Meacham et al. [198]. Unlike the median crack model, also called halfpenny model, Palmqvist cracks tend to be only as deep as the indenter penetration and are independent of each other.

The critical indentation and crack-related dimensions are the indentation half-diagonal length, a_c, the radial surface crack length, c, and the Palmqvist surface crack length, l_c (Fig. 15.37) [199]. Equations to determine fracture toughness take the following general form for halfpenny (Eq. 15.29) and Palmqvist (Eq. 15.30) shaped cracks [199].

$$K_c = k\frac{P}{a_c c^{1/2}} \tag{15.29}$$

$$K_c = k(E/\mathrm{HV})^{2/5}\frac{P}{a_c l_c^{1/2}} \tag{15.30}$$

where according to Emiliani [199], k is a constant determined typically between 0.001 and 0.5, P is the applied indentor load (N), HV is the Vickers microhardness (GPa), E is the elastic modulus (GPa), and a_c, c, l_c are the indentation and crack-related dimensions (m) respectively that of indentor a and that of Palmqvist, as shown in Fig. 15.37. However it must be kept in mind that cracks must have a minimum length, depending on the test used. The AE recorded during macro-indentation shows three distinct stages [199]. The onset of the second stage marked the critical indentation size, for the specific-analyzed coating where radial cracks begin to form. The last stage was associated with the continuation of all mechanisms of accommodation as the indenter descends further into the coating, and therefore changes significantly with load [200].

Vickers indentation with Palmqvist cracks is extensively used for ceramic coatings, see, for example, [201–203]; cermet coatings, see, for example, [200, 204–207]. It is also used for certain metal coatings as, for example, those manufactured by PTA with gas-atomized powder and Wire arc with cored wire, both with a nominal composition of <25 % Cr, <5 % Mn, <10 % Mo, <10 % W, <5 % B, <5 % C, and <5 % Si, the balance being Fe [198]. A few ASTM standards for toughness measurements are presented in [15.M14–15.M19].

15.7.4 Residual Stress

The paper of Clyne and Gill [150] presents an overview of residual stresses associated with thermally sprayed coatings together with the corresponding measurements.

15.7.4.1 X-Ray Diffraction

A very popular method for direct measurement of residual stresses is the monitoring of the shift of selected X-ray diffraction (XRD) peaks [72, 15.M20]. The method is applicable only to materials with well-defined crystal structures. It becomes difficult, as a result of peak broadening, when the grain size is very fine or if

unpredictable variations in composition are likely to occur. The lattice strain is obtained from the shift of hkl peak (where h, k, and l stand for Millers indices of the investigated lattice plane), when compared with that for a corresponding unstrained specimen. The drawbacks of the method are the following:

- The limited penetration depth (10–50 μm) of X-rays through most coating materials depending on the source wavelength and coating material
- The penetration depth is usually about that of the surface roughness of as-sprayed coatings

To overcome the penetration problem, successive layer-removal can be performed but it changes the stress distribution, if not inducing deformation or damage in the underlying material [150].

Although the lattice strain, and hence stress, in a selected in-plane (x) direction can in principle be estimated via the Bragg equation from a single measurement, it is more accurate to examine the variation in peak shift as a function of φ, the angle between the normal to the coating surface (y direction) and the normal to the diffracting planes (which lies in the x–y plane) [150]. The stress can then be obtained from

$$\sigma_x = \left(\frac{E}{1+\nu}\right)_{hkl} \frac{1}{d_0} \left(\frac{\partial d}{\partial \sin^2 \varphi}\right) \tag{15.31}$$

where d is the measured inter-planar spacing and d_0 is the value for an unstrained sample. The Young's modulus, E, and Poisson's ratio, ν, for the hkl planes must be accurately known. In general, they are obtained by experimental measurements, using a sample with a known stress state [153]. As shown in Fig. 15.38, the lattice strain is obtained from the shift of one hkl peak, when compared with that for a corresponding unstrained specimen.

For coatings with different components such as, for example, WC–Co coating, the diffraction peaks of the dominant phase are used [208, 209].

15.7.4.2 Neutron Diffraction

Compared to low-energy X-rays, the main advantage of working with neutrons is the possibility to analyze greater depths, i.e., higher coating thicknesses. Neutrons have the following advantage over X-ray photons: for wavelengths comparable to the atomic spacing, their penetration into engineering materials is in the range of several millimeters, due to their interaction only with nuclei instead of electrons [15.M21].

For example, Lyphout et al. [210] used a monochromatic neutron beam of a cross section of 0.6×0.6 mm^2, in a spatially resolved mode, to determine the residual stress distribution within HVOF-sprayed Inconel 718 Coatings. The Bragg peaks (220) and (111) for Ni-alloy were measured to $2\theta = 86^\circ$ and 47°, using a wavelength, λ, of 0.147 and 0.165 nm, respectively. From the obtained

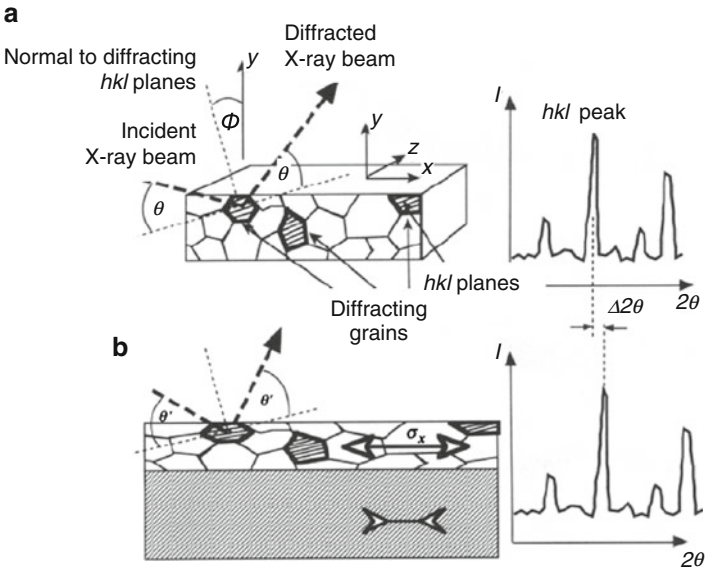


Fig. 15.38 Scheme of the XRD technique for the measurement of residual stresses stresses (**a**) Coating detached from its substrate (un-strained specimen) and (**b**) coating with its substrate (strained specimen). Reprinted with kind permission from Springer Science Business Media [150], copyright © ASM International

diffracted peaks, they used Bragg's law (Eq. 15.4) with the corresponding lattice strain (Eq. 15.30) defined as a function of the "stress-free" lattice parameter d_0.

$$\varepsilon_{hkl} = \frac{(d_{hkl} - d_0)}{d_0} \tag{15.32}$$

where d_{hkl} is the lattice spacing and ε_{hkl} is the lattice strain. Measurements were performed only in radial and axial directions, by scanning the sample from the top to the bottom, using, respectively, the reflection and transmission modes. Sampath et al. [211] have also used neutrons to measure the residual stress distribution within Ni–5 wt%Al bond coats sprayed by different spray techniques.

15.7.4.3 Material Removal

There are two basic methods involving material removal: either a hole is drilled in the specimen or layers are removed by polishing.

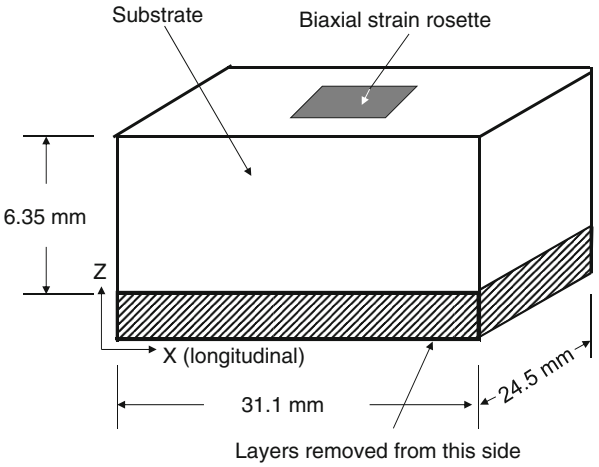


Fig. 15.39 Residual stress specimen ready for layer removal. Reprinted with kind permission from Springer Science Business Media [212], copyright © ASM International

(a) Layer Removal Method

This method was adapted to coatings by Greving et al. [212]; it is based on the concept that removing a layer from the surface of a plate or beam with residual stresses releases a force and moment acting on the remaining piece. It is presumed that the remaining piece is large enough and the layer removed small enough so that the change in strain through the thickness of the remaining piece is linear. A strain rosette (gage) on the remaining piece records the change in strain on the surface opposite the face where the layer was removed. The stresses in the layer removed and the change in stresses of the remaining piece can be calculated from force and moment equilibrium, the linear strain change assumption, the strain rosette readings, and the stress–strain properties of the material [212]. To calculate the residual stress after removal of one layer, one must know the substrate dimensions, the coating thickness before starting removal, its new thickness after removal, the substrate and coating, Young's modulus, and Poisson ratios. A typical specimen for layer removal is presented in Fig. 15.39.

The method was tested for different metal, cermet, or ceramic coatings plasma or HVOF sprayed, with and without bond-coats and with substrate grit blasting [212–215].

(b) Hole Drilling Method

The hole drilling strain gage technique [216–218] is a semidestructive method for the determination of residual stresses in the superficial layers of a solid body. The technique simply consists of two stages (1) removal of stressed material by drilling a small hole (about 2–4 mm diameter) on the surface of the body and (2) measurement of the relaxation strains occurring around the hole by means of an extensimetric rosette [219]. Residual stresses are then calculated from the measured

deformations by means of an analytical model based on the solution of the problem of the loaded wide plate with hole [216–219].

In the case of nonuniform through-thickness stresses, the test must be divided into several small depth increments, and the produced relaxation must be determined for every single incremental step [219]. Results may be affected by various errors [220] such as alignment [221]. The drilling in brittle ceramics with diamond drills requires an adapted cooling [222].

15.7.4.4 Bending

A rather powerful and nondestructive residual stress measurement technique is the in situ curvature method, where the curvature of a thin plate sample is continuously monitored during the deposition process [150, 223–225]. Kuroda et al. [223] were the first to describe such a continuous measurement procedure during thermal spraying. They used lightly contacting knife-edges and recorded the changing curvature during spraying. Later Bolelli et al. [226] used this method to determine the peening action and residual stresses in HVOF spraying of 316L. Gill and Clyne [225] then further developed this technique and made two advances. First, a noncontacting method of curvature measurement was employed with simple video recording, eliminating interference with free bending of the specimen, and allowing the study of a wide range of substrate temperatures. Second, a numerical model was developed that allowed the curvature history to be predicted from thermomechanical boundary conditions and material property including the quenching stress [150]. The main advantage of this technique is that various stress contributions can be separately evaluated, especially the quenching stress, which, up to now, cannot be modeled without many assumptions. However, the use of a thin plate with macroscopic curvature generates very different experimental conditions compared to most industrially relevant applications. The latter involves rather thick, medium- or large-sized components like paper or steelmaking rolls, petrochemical industry ball valves, turbine shafts, train axles, etc. [226]. The main problems of this technique are (1) the different substrate stiffness that can alter the stress distribution, compared to a real application and (2) the average deposition temperature and thermal history of the system that can vary significantly with the substrate heat capacity and torch spray pattern. For example, in the experiment of Hugot et al. [227], a metallic beam ($110 \times 15 \times 2$ mm^3) was fixed on a water-cooled rotating cylinder (Fig. 15.40a). The tangential velocity could be varied between 0.2 and 1.8 m/s, the torch being moved up and down at velocities ranging between 2 and 30 cm/s. The metallic plate was supported onto thin edge knifes and held in position by two springs (Fig. 15.40c). The central deflection was measured with a LD500-5 gauge transducer, the precision of which was 1 μm (Fig. 15.40c). The macroscopic preheating temperature was measured on sample back side by K-type thermocouple (chromel–alumel). This measurement was performed 1 cm ahead of the displacement measurement (Fig. 15.40c). In order to protect the sensors from too high temperatures, a mask was fixed around the substrate (Fig. 15.40b). Two liquid CO_2 atomizing nozzles were positioned around the

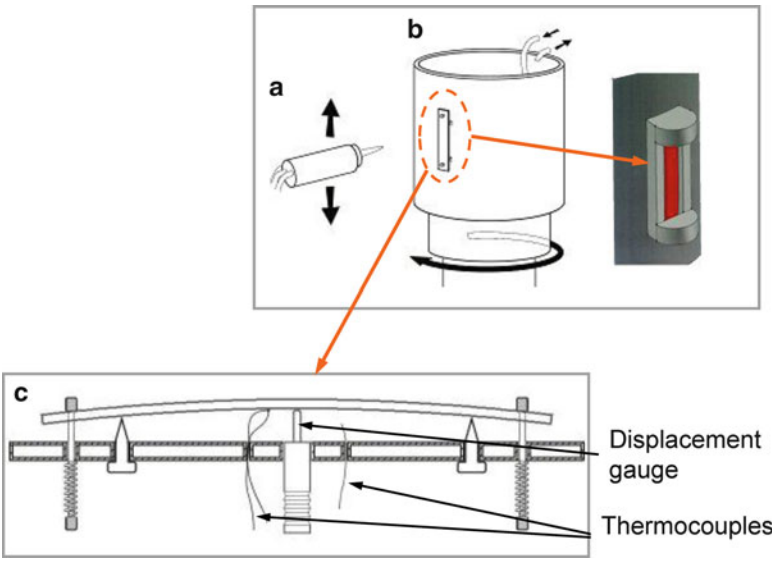


Fig. 15.40 (**a**) Scheme of the experimental stress evaluation device based on beam deflection measurement, (**b**) mask protecting the beam from excessive heating, and (**c**) cross section of the metallic sample and its measurement device. Reprinted with kind permission from Elsevier [227]

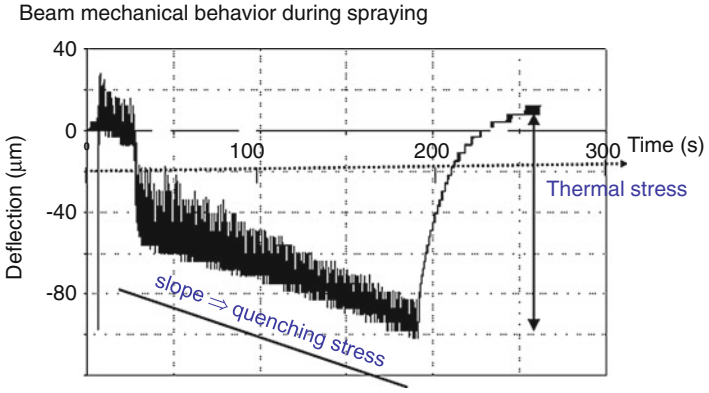


Fig. 15.41 Example of the evolution of the signal measured by the beam displacement gauge (see Fig. 15.40c) during plasma spraying of YSZ on grit-blasted substrate preheated at 200 °C during the first 250 s

rotating cylinder, at 90° and 135° from the plasma torch respectively in order to control the substrate mean temperature. A typical signal obtained is presented in Fig. 15.41 for YSZ coating deposited on a grit-blasted stainless steel substrate. The first 250 s corresponds to the preheating of the substrate up to 200 °C and a beginning of relaxation of the compressive stress induced by grit blasting can be observed. Then during spraying (about 155 s) the slope of the beam deflection

increases linearly (the slope corresponds to the quenching stress). At last, when the plasma jet and particle feeding are stopped, as well as the liquid CO_2 atomization, the coated beam cools down to room temperature in about 700 s. The corresponding gauge signal represents the stress due to the mismatch between substrate and coating expansion coefficients.

Stokes and Looney [228] have listed all the analytical expressions related to quenching and expansion mismatch stress, often used when measuring them, and compared them with the predictions of finite elements model.

15.8 Thermal Properties

The thermal properties of coatings are of primary importance for engineering. The coating linear expansion coefficient, $\alpha_L(K^{-1})$, plays a key role in the coating residual stress due to the difference in expansion coefficients of coating and substrate. In coating service conditions, the service temperature must be such that the stress generated by the expansion mismatch is below that generating the failure of the coating-substrate adhesion. The removal of the heat flux imparted to coating during service conditions depends strongly upon its thermal conductivity, κ (W/m K), which value also controls the temperature gradient generated within coating. Coatings are extensively used as thermal barriers in turbines, automotive engines, ..., and their thermal conductivity, or thermal diffusivity in transient conditions, control their performances. Thermal diffusivity, a (m^2/s), is linked to the thermal conductivity κ, specific heat at constant pressure, c_p (J/K kg), and mass density, ρ (kg/m^3), by the expression:

$$a = \kappa/\rho c_p \tag{15.33}$$

In the following will be presented briefly the measurements of the mass density, expansion coefficient, thermal diffusivity (most measurements of the thermal conductivity are performed through that of the thermal diffusivity), and specific heat capacity at constant pressure. The section will end up with the measurement of thermal shock resistance of coatings.

15.8.1 Mass Density

The mass density of the coating, ρ_{300}, at room temperature (300 K) is mostly determined by Archimedean porosimetry [75] (see Sect. 15.5.1. and Eq. 15.8). To obtain its value at temperature T, the expansion coefficient, α_L must be known. If it is linear and the same in the three directions, $\rho(T)$, T being expressed in Kelvin, is given by the following expression:

$$\rho(T) = \frac{\rho_{300}}{1 + 3\alpha_L(T - 300)} \tag{15.34}$$

Actually, the linear expansion coefficients of coatings with lamellar structure are not the same in the three directions: α_L in the spray direction is different from the linear expansion coefficient in the directions parallel to the substrate. However, in most measurement systems of expansion coefficients, the sample length required is a few millimeters. Such a length is easy to cut within the coating, but unfortunately, in most cases the coating thickness is a few hundreds of micrometers and samples in that direction are not suitable for the measurement.

15.8.2 Expansion Coefficient

This technique implies the precise determination of very small changes in the sample length, which temperature can be as high as 2,000 °C. Different techniques include mechanical dilatometers, optical imaging and interference systems, X-ray diffraction methods, and electrical pulse heating techniques. For details, see the paper of James et al. [229]; see also the ASTM standards [15.T1, 15.T2]. For thermal-sprayed coatings, the mechanical dilatometry is mostly used. The quantity that must be determined is

$$\alpha_L = \frac{1}{L}\frac{dL}{dT} \text{ or sometimes } \alpha_{L_0} = \frac{1}{L_0}\frac{dL}{dT} \tag{15.35}$$

In the first expression L is the sample length at temperature T and in the second at room temperature. An alternative means of quantifying the sample expansion is in terms of the fractional increase in volume per unit rise in temperature:

$$\alpha_V = \frac{1}{V}\left(\frac{dV}{dT}\right)_p \tag{15.36}$$

If the three linear expansion coefficients α_L are the same: $\alpha_V = 3\alpha_L$.

Thermal expansion measurements can also give information when they deviate from linearity, which happens when phase transformation or oxidation occurs and when stresses relax [230]. To avoid the oxidation phenomena the dilatometer furnace must be maintained under controlled atmosphere when studying metals, alloys or cermets.

15.8.3 Thermal Conductivity and Thermal Diffusivity

Thermal conductivity depends on three mechanisms [1, 231]:

Electronic conduction, κ_e, which is the main mechanisms for materials having free electrons (metals and alloys). In general κ_e varies linearly with temperature at low temperatures and is not temperature dependent at higher temperatures.

Lattice conduction (phonon conduction), κ_{Ph}, which is the main mechanism for materials without free electrons, such as ceramics. At low temperatures it depends exponentially upon temperature and the scattering of phonons by geometrical defects. At higher temperatures the Umklapp process occurs and κ_{Ph} varies as the reverse of temperature.

Photon conduction κ_{Ph} is important in optically absorbing dielectric materials (emission, absorption, and re-emission phenomena). κ_{Ph} is proportional to T^3. At high temperatures photons contribute to the conduction through pores, the thermal conductivity of the air or gas contained in the pores being low (~0.026 W/m K).

Thus the thermal conductivity of thermal-sprayed coatings depends strongly on the coating structure, defects, porosity, real contacts between layered splats, and oxide impurity for metals or alloys, which are linked to the fabrication process. For example, the low thermal conductivity of YPSZ plasma-sprayed coatings (about 1–2 W/m K) is due to the material but also to the poor contacts between layered splats that reduce phonons propagation. The sintering of coatings at high-temperature service conditions increases the thermal conductivity or diffusivity of the coating by improving the contacts between layered splats [232, 233]. The results of Chi et al. [234] also pointed out the important role of interlamellar porosity in both room temperature and temperature-dependent thermal conductivity. The modeling of thermal conductivity can be achieved by using a finite element-based approach coupled with SEM image analysis of the coating microstructure for both through-thickness and in-plane directions for a single image [69, 235].

Most measurements of thermal conductivity are performed through thermal diffusivity measurement, which implies measuring the mass density (see Sect. 15.8.1) and the specific heat at constant pressure (see Sect. 15.8.4) to calculate thermal conductivity according to Eq. (15.33). Some of the corresponding ASTM references are [15.T3, 15.T8]. Using a flash laser or Xenon flash lamp can carry out thermal diffusivity measurement. Baba and Ono [236] have developed an advanced laser flash system for thermal diffusivity measurements. The initial and boundary conditions for measurements are well defined and the transient temperature of the specimen is measured with a calibrated radiation thermometer, the entire curve of the measured temperature history being analyzed. Figure 15.42a shows the schematic of IR detector with sample of xenon flash diffusivity system [234]. The front face of a sample (typically a small disk-shaped specimen) is heated by a short xenon lamp pulse (pulse energy 12 J and duration 6–8 ms). The xenon lamp illuminates a 0.8 cm diameter area on the sample surface the temperature rise on its rear surface being detected by an infrared detector and a TV camera monitoring beam profiles. The infrared detector and the sample holder are completely shielded from the flash source by multiple shielding layers and addition of reflecting surfaces. The detector output signal is monitored from the beginning of the test and in between each shot, which assures that the following flash pulse starts only if the temperature of the sample is steady. When the material studied is translucent in the near infrared, as most oxide ceramics (for example, YPSZ), a thin layer of colloidal graphite is painted to make the surfaces opaque prior performing the thermal diffusivity measurement, on both the front and the rear faces of the sample (see Fig. 15.42b).

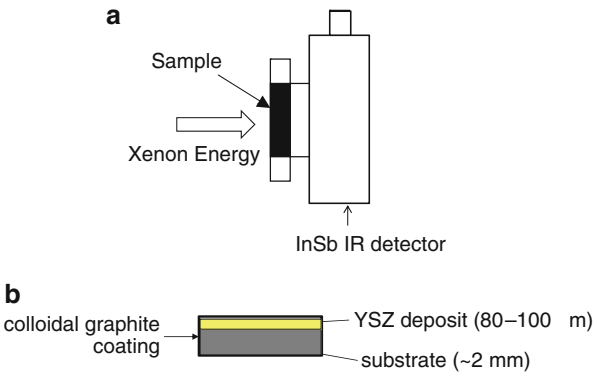


Fig. 15.42 (**a**) Scheme of the laser flash thermal diffusivity measurement system and (**b**) colloidal graphite painted on sample surfaces to make surfaces opaque. Reprinted with kind permission from Springer Science Business Media [234], copyright © ASM International

For evaluating the thermal diffusivity, a, the simple solution proposed by Parker et al. can be used:

$$a = 0.1388 \frac{L^2}{t^{1/2}} \tag{15.37}$$

where $t^{1/2}$ and L are the time corresponding to the half-maximum increase of the temperature and the sample thickness, respectively. The main advantages of this method are the simplicity and rapidity of measurement and the possibility to measure the thermal diffusivity on a wide range of materials within a wide range of temperature [232]. For more details about the method, see the paper of Baba and Ono [236], and, for the reliability of the method, see the paper of Wang and Dinwiddie [237]. The coating diffusivity can be measured with the coating detached from the substrate or with the substrate, provided the thermal properties of the latter are known [238, 239]. This technique can be used for multilayer coatings [240]. It has also been used to characterize nanometer-structured solution plasma-sprayed coatings. The lower thermal conductivity obtained compared to conventional coatings sprayed with micrometer-sized particles has been explained by the distribution and size of pores [119].

Instead of measuring the diffusivity, it is also possible to measure directly the thermal conductivity [241] using axial flow with one-sided guarded hot plate according to ASTM C 177-85, or comparative cut bar, or guarded or unguarded heat flow meter method, etc.

15.8.4 Specific Heat at Constant Pressure

Many different calorimeters make it possible to measure the heat capacity (c_p) of coatings. Most of them give results with a precision of about 1 % [15.T9]. They comprise either one cell, the adiabatic one being the simplest, or two cells where the studied sample is compared to a reference material [15.T10].

15.8.5 Thermal Shock Resistance

Thermal shock is a failure mechanism that occurs in materials, especially ceramics that exhibit a significant temperature gradient when they are subjected to a sudden and dramatic change in temperature. The thermal shock resistance (TSR) describes the ability of the material (for example, a thermal barrier coating) to resist rapid temperature variations without failure. Most methods used to characterize it involve heating the material to high temperature and then quench it by using water, oil, or air as cooling medium. The result depends both on the heating conditions: steady state flow, transient heating by convection, radiation, and the temperature drop. Quench tests generally must be repeated and in that case the number of cycles necessary to cause a defined damage or weight loss can be used as a measure of the thermal shock resistance [242]. According to Hasselman [243], for steady heat flow and an infinite slab symmetrically heated or cooled, the thermal shock resistance (TSR) parameter is defined as

$$\mathrm{TSR} = \frac{\sigma_\mathrm{f}(1-\nu)}{\alpha_\mathrm{L} E} \tag{15.38}$$

where σ_f is the fracture stress, ν the Poisson ratio, E the Young's modulus, and α_L the mean expansion coefficient. Four more shock resistance parameters can be defined [244]. TSR of coatings is measured with the whole system: coating, bond coat, and substrate. It is thus important to keep in mind that the thermal shock must be adapted to the resistance of all components. For example, if the YPSZ topcoat can sustain temperatures up to 1,200 °C and in some cases for relatively short periods 1,300–1,400 °C (military engines), it is not the case of the bond-coat and substrate superalloys. If possible, characterization means must reproduce service conditions, which is not always the case. Again for a thermal barrier coating three tests are commonly used: the jet engine thermal shock (JETS), the furnace cycle test (FCT), and the fluidized bed reactor (FBR) [244]:

- With the JETS the flame of a burner rig heats the coating surface, while the substrate opposite side is air cooled. It creates a thermal gradient of several hundred degrees Celsius across the TBC. The front surface temperature can reach 1,400 °C and can initiate sintering. This test mainly stresses the ceramic layer and bond coat interface thermomechanically, but the bond coat oxidation is rather low. This test is reasonably quick and typically results are available within 2 days for a 2,000-cycle test [244]. Figure 15.43a represents schematically the JETS process.
- In the FCT test the TBC system is oxidized and cycled in a furnace between room temperature and temperatures ranging from 1,100 to 1,200 °C. Thermal gradients across the TBC are moderate during the heat-up phase and significant during the cool-down phase. The sample is exposed for a long time to elevated temperatures, which leads to significant bond coat oxidation. The TBC

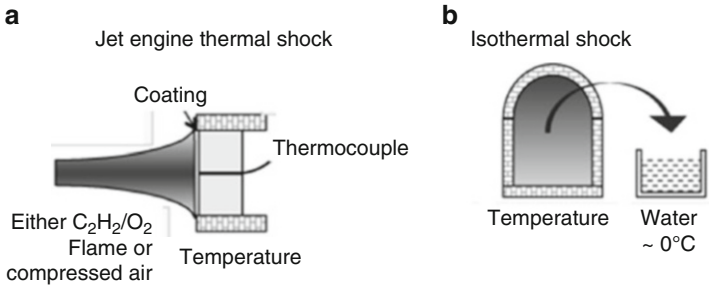


Fig. 15.43 Scheme of two thermal shock setups: (**a**) engine thermal shocks (JETS) heating with a burner rig and cooling with air jet and (**b**) furnace cycle test (FCT) using furnace heating and water soaking cooling. Reprinted with kind permission from Prof. G. Montavon [159]

temperature during soaking is too low to cause pronounced sintering in the ceramic. Figure 15.43b represents schematically the FTC process.

– The third system, FBR, consists of a standard fluidized bed furnace using alumina. It is typically operated at 1,000 °C. Test samples are transported via a pneumatic system into a cooling zone in which compressed air is directed onto the TBC surface.

According to Bolcavage et al. [244]:

– The FCT reflects the actual engine condition because it also degrades the bond coat through severe oxidation but it does not really address TBC degradation in the ceramic layer, which typically initiate above 1,300 °C.
– The JETS test provides performance-ranking data on the ceramic itself thanks to the high thermal gradients within the ceramic layer.
– The fluidized bed used as a quality control tool as the standard 1,000-cycle TCF test, does not discriminate differences well enough to provide quantitative data for a performance ranking.

ASTM references for thermal shock testing are the following [15.T11–15.T15].

Other means are used to produce the thermal shock, such as laser irradiation [245] and infrared irradiation [202]. To increase the thermal gradient after heating, samples can be quenched in iced water instead of air jets [246]. Nusair Khan and Lu [247] have compared TBCs delamination when water quenched or forced air quenched:

– In both cases samples delamination starts from their extreme edges.
– In the case of the water-quenched samples the thickness of the topcoat was only half of its original value, after 220 cycles, whereas in the case of the forced air-quenched samples, the spallation was only confined to the edges and the thickness of the topcoat remained the same even after 1,000 cycles.
– In both cases more TGO growth was observed at the edges compared with the central portion of the samples.

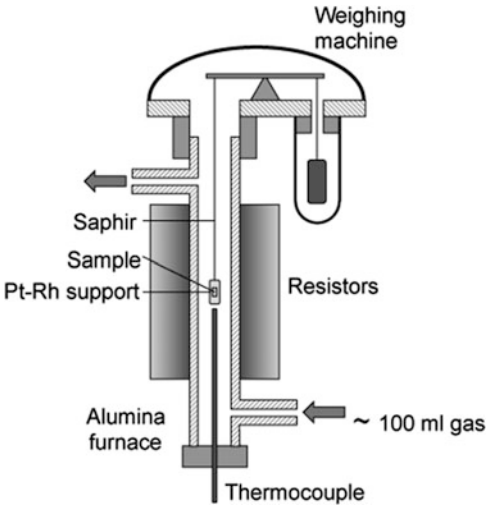


Fig. 15.44 Principle of a thermogravimeter. Reprinted with kind permission from Prof. G. Montavon [159]

To obtain more information than those resulting from visual inspection after a given number of cycles, acoustic emission can be used [19, 244]. As a crack is initiated and propagates through a material, measurable characteristics of the AEs from this event reveal details about the microstructure [18]. AE continuous emission corresponds to plastic deformation mechanisms, while burst-type emission results from micro-cracking in brittle materials, fracture of hard inclusions in alloys, phase transformations, …. Such measurements allow determining when first cracks propagation occurs and the different fracture modes implied [248].

15.8.6 Differential Thermal Analysis, Thermogravimetry, and Differential Scanning Calorimetry

In thermal analysis a physical property of a substance is measured as a function of temperature, which is continuously controlled [249, 250]. Techniques mainly used for characterizations of sprayed coatings or sprayed powders are:

- In Thermogravimeters (TG) the mass of a sample of a substance is recorded, in a controlled atmosphere or air (see Fig. 15.44), as a function of temperature. On the one hand, mass is lost if the substance contains a volatile fraction and TG measurement can be coupled with a device permitting the analysis of volatile products, and on the other, mass is gained with oxidation.
- In Differential Scanning Calorimetry (DSC), the difference in the heat flow absorbed by the test sample is compared with the heat flow absorbed by a reference material, as a function of the temperature. Experiments are performed in a controlled atmosphere. DSC provides information about thermal changes

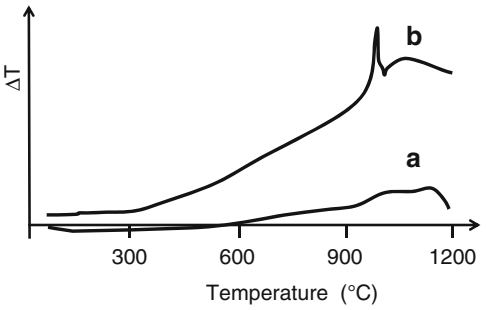


Fig. 15.45 DTA obtained from (a) mullite initial powder and (b) as-sprayed mullite coating at substrate temperature of 300 °C. Reprinted with kind permission from Springer Science Business Media [251], copyright © ASM International

that do not involve a change in sample mass such as phase changes or changes in chemical composition. It also allows checking the material purity through changes in heat of fusion and melting point and studying oxidation in oxidizing atmospheres.

– In Differential Thermal Analysis (DTA), the temperature difference between a substance and a reference material is measured as a function of temperature, both materials being subjected to the same controlled temperature programmed. Experiments are performed in a controlled atmosphere. The reference material is a known substance, generally inactive thermally within the temperature range of interest.

One of the main advantages of thermal analysis systems is that they require rather small samples. For more details about these techniques, the reader can see the books of Sorai and Gakkai [249] or Speyer [250]. In the following are presented a few examples of these techniques used in the thermal spraying area to characterize phase changes in powders or coatings, reactions at high temperatures and oxidation.

15.8.6.1 (a) Phase Changes

Salimijazi et al. [251] have compared plasma-sprayed coatings made with commercially available mullite powder particles and a mixture of mechanically alloyed alumina and silica powder particles. DTA was used to study the phase transformations in the coatings. Figure 15.45 represents the DTA curves obtained from mullite initial powder and as-sprayed mullite coating on stainless steel substrate at temperature of 300 °C. Neither exothermic nor endothermic peaks were observed for the mullite powder. A peak around 980 °C could be observed in the as-sprayed structure that was attributed to the crystallization of amorphous aluminum silicate.

Garcia et al. [252] have air plasma sprayed with an Axial III plasma torch plain mullite, 75 vol.% mullite–25 vol.% Y-ZrO_2, and 50 vol.% mullite–50 vol.% Y-ZrO_2 powders. DTA of as-sprayed plain mullite coatings showed no endothermic or exothermic event, supporting the fact that as-sprayed coating was fully crystallized, which was not the case with the two other powders. The authors stated that mullite crystallization was hindered in the composites during the spray process.

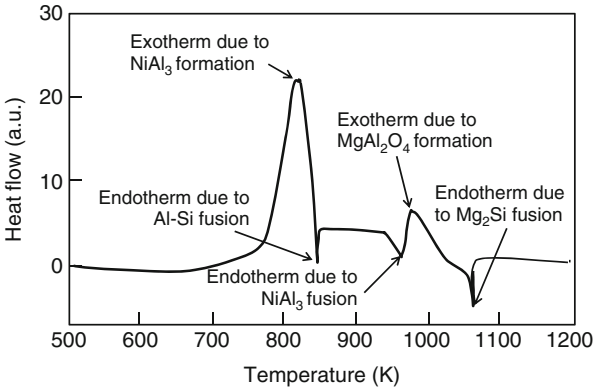


Fig. 15.46 DTA scan of granulated SiO_2/Ni/Al–Si–Mg particles heated to 1,273 K with heating rate of 0.17 K/s in argon atmosphere. Reprinted with kind permission from Springer Science Business Media [254], copyright © ASM International

Liu et al. [253] studied phase changes of plasma-sprayed wollastonite ($CaSiO_3$) coatings. The DTA curves showed that the wollastonite powder had no chemical reactivity from room temperature to 1,000 °C, whereas an obvious exothermic reaction occurred in the wollastonite coatings at about 882 °C. Crystalline wollastonite, glassy phase, and tridymite (SiO_2) were observed in the coating. Tridymite (SiO_2) likely reacted with other compounds such as CaO and glassy phase to form crystalline wollastonite when the coating was heated at about 882 °C.

15.8.6.2 (b) Reactive Plasma Spraying

Reactive thermal spraying, in which thermodynamically stable compounds are formed by expected in-process reactions, has attracted considerable attention as a result of the wide availability of in situ synthesized composite coatings. Ozdemir et al. [254] have HVOF sprayed a composite powder of SiO_2/Ni/Al–Si–Mg onto an aluminum substrate. To identify the reactions which were taking place in flight, they heated the same materials in a DTA over the temperature range of 298 to 1,273 K under argon atmosphere with a heating rate of 0.17 K/s. Figure 15.46 presents the DTA curve.

Deevi et al. [255] have studied the reactive spraying of nickel aluminide when nickel and aluminum powders were plasma sprayed onto carbon steel substrates. To illustrate the exothermic reaction between nickel and aluminum, a mixture of nickel and aluminum in a 1:1 atomic ratio was heated in a (DTA) unit under argon atmosphere. Wang et al. [256] have synthesized by a sol–gel combustion process MgO–Y_2O_3-nanostructured composite powder (volume ratio of 50:50) with crystal sizes in the 10–20 nm ranges. The powder was used for plasma spraying. The formation process was studied by TG-DTA of the 200 °C dried $MgOY_2O_3$ powder precursor as a function of temperature at a heating rate of 10 °C/min. As illustrated in Fig. 15.47, the sample weight decreased continuously with the increasing of temperature up to 1,000 °C, with a total weight loss of about 67 %.

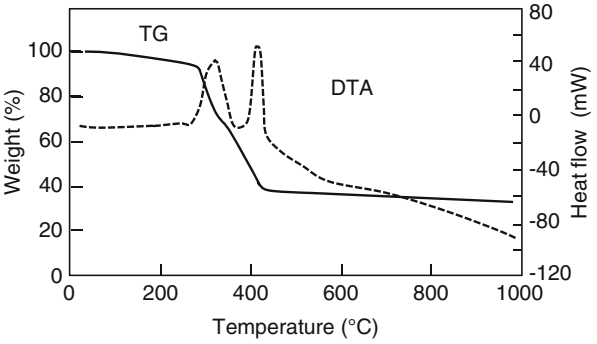


Fig. 15.47 Thermal gravimetric-differential thermal analysis curves of dried MgO–Y_2O_3 precursor at a heating rate of 10 °C/min. Reprinted with kind permission from Springer Science Business Media [256], copyright © ASM International

Two exothermic peaks at 326 and 419 °C were ascribed to the pyrolysis of the precursor (see the DTA curve). The TG curve showed that after 600 °C, the pyrolysis process was completed.

Ravi et al. [257] studied the RF precursor plasma spray synthesis process (RFPPS). It starts with liquid inorganic precursors and directly produces ceramic coatings as yttrium aluminum garnet (YAG). The sols used were either regular or reverse ones [257]. To gain a better insight in the process, thermal analysis (DTA-TG curves) was performed on the coatings. The TG plots showed that the as-sprayed coatings had substantial amount of volatile matter, presumably OH^- ions. However, subsonic-sprayed coatings lost less weight than the supersonic-sprayed coatings, probably due to the relatively longer residence times of particles in subsonic spraying improving pyrolysis of the sols.

15.8.6.3 (c) Oxidation Resistance

Guilemany et al. [258] have explored transition metal aluminide in HVOF-sprayed coatings of two different aluminide (FeAl and $NbAl_3$) feedstock powders in terms of resistance to oxidation and mechanical behavior. They have studied the heat flow and mass gain-temperature dependence for the as-sprayed coatings during the oxidation test in DTA–TGA equipment. The oxidation analysis revealed that despite the high melting point of $NbAl_3$, it suffers from intergranular disintegration at moderate temperatures. The high level of oxidation and coating defects that facilitated oxygen diffusion inwards and Al depletion in the as-sprayed coating itself favored this phenomenon. Fan and Ishigaki [259] used induction plasma spray processing to produce freestanding parts of Mo_5Si_3-B composite and $MoSi_2$ materials. Oxidation resistance of the specimens was evaluated through the TG tests. The specimen temperature was increased at 20 °C/min to the preset temperature, 1,210 °C, and held for 24 h, during which time the mass changes and temperature of the specimens were continuously recorded. The performance of Mo_5Si_3-B composites at high temperature was found to depend strongly on the composite boron content, e.g., at boron contents greater than 1 wt%; composites demonstrated encouraging oxidation resistance in the high-temperature environment.

15.9 Wear Resistance

Wear is generally classified into six distinguishable types [1] as described below according to Craig [260] and Chattopadhyay [261]. Information about standard terminology relating to wear and erosion can be found in [15.W1].

The wear volume, V_w, defined by the following equation, characterizes wear [261]:

$$V_w = K_w \frac{F_N}{H} \times d_w \tag{15.39}$$

where d_w is the sliding distance, F_N the applied normal force, H the hardness or yield stress of the softer surface, and K_w the wear coefficient. The depth of wear δ_w is expressed as

$$\delta_w = K_w \frac{F_N}{H} \cdot \frac{d_w}{A_w} \tag{15.40}$$

where A_w is the area of contact, $V = \delta_w A_w$.

The wear coefficient K_w depends on the wear mode, materials and lubrication system used, type of motion, stress distribution, ... Chattopadhyay [261] has summarized typical values of K_w.

For adhesion wear the following equation is used:

$$\frac{V_w}{d_w} = K_{adh} \cdot \frac{F_N}{H} \tag{15.41}$$

where $K_{adh} = K_w/3$.

In erosive wear, the volume loss is given by

$$V_w = \frac{1/2 mv^2}{H} f(\alpha) \tag{15.42}$$

where H is the hardness or yield strength of the surface material, $mv^2/2$ the kinetic energy of the impacting particles, and $f(\alpha)$ a function of the impingement angle α, which plays a key role in the erosion. For brittle materials V_w increases with higher angles, while it is the reverse for ductile materials.

At last it must be underlined that any kind of wear produced with the adapted testing machine is often measured with the use of optical methods giving the wear track profile as well as the debris distribution.

15.9.1 Abrasive Wears

Abrasive wear occurs when a solid surface experiences the displacement or removal of material as a result of a forceful interaction with another hard surface. Both free-flowing particles and abrasive attached to the counter body cause wear.

Two types of abrasive wear are defined based on the degree of stress in the component surface or the number of components involved. In the two-body abrasion, under low stress conditions, abrasive particles (asperities or hard particles) sliding against the component surface cause scratches, but the stress induced does not cause fragmentation of abrasives. Three-body or high stress abrasion occurs when the abrasive particles are forced between two mating surfaces leading to loss of materials from both component surfaces [261]. A few abrasive tests proposed by ASTM are given in [15.W2–15.W5].

For the abrasive wear tests, in laboratories two main tests are performed [262–266]:

- The pin-shaped material rotates on an abrasive disk, or an abrasive cloth, or paper mounted on a flat disk. The debris can be blown out with a gas jet to determine if their presence improves or not the wear resistance.
- Free or loose abrasive is interposed in between the two surfaces pressed against each other. One is in sliding or rotating motion while the other is stationary.

Many results are described in the literature and a few of them illustrated in the following references [267–273], tests being performed at room or high temperature, depending on the coating application.

15.9.2 Adhesive Wears

Adhesive wear occurs between two surfaces in relative motion because of the inherent roughness of material surfaces. It is also called sliding wear [15.W6]. In adhesive wear, the peaks on the adjacent surfaces that do come into contact plastically deform under pressure and form atomic bonds at the interface and in some cases this is considered solid-phase welding. As the relative motion between the surfaces continues, the shear stress at the bonded contact point increases until the shear strength limit of one of the materials is reached and the contact point is broken, bringing with it a piece of the opposing surface. The broken material can then either be released as debris or remain bonded to the other material's surface [260, 261]. The most used tests are [261–266]:

- The pin-on-disk [15.W7, 15.W8] where a pin specimen, with an extremity either flat or spherical, is tightly pressed against a flat circular-coated disk with a specified load. During the test either the pin or the disk rotates, see Fig. 15.48, and the sliding path forms a circle on the rotating disk surface. The debris can be blown out with a gas jet to determine if their presence improves or not the wear resistance. It is also possible to have the disk vertical and the pin horizontal to entrain the debris by gravity or achieve tests with lubrication.
- The pin-on-plate where the coated plate reciprocates at 50–300 cycles per minute.

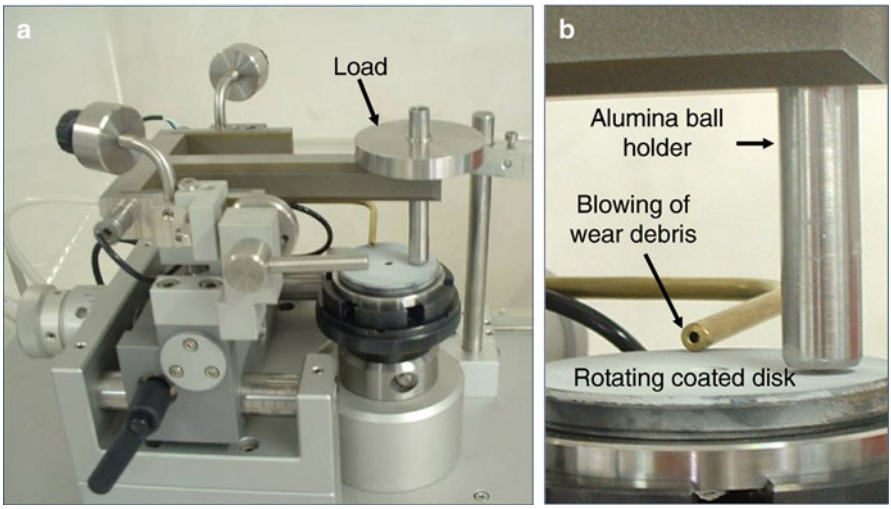


Fig. 15.48 Pin-(here the ball 6 mm in diameter is made of sintered alumina)-on disk test with a rotating coated disk (**a**) General view and (**b**) detailed view

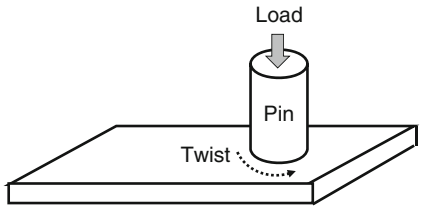


Fig. 15.49 Principle of galling test setup. Reprinted with kind permission from ASM International [261]

– The pin or block-on-ring where the coated sample slides on the edge of a disk or a ring mounted vertically. This test reproduces the type of motion found in engine cam or internal combustion systems.

A few equipments can work at high temperatures to test the evolution of the wear. This is for example the case of the experiment of Yin et al. [274] who studied the sliding wear behavior of HVOF-sprayed Cr_3C_2–NiCr/CeO_2 composite coatings at temperatures up to 800 °C. Friction and wear tests were carried out in a ball-on-disk contact configuration using an SRV (sliding, reciprocating, and vibrating) friction and wear tester.

Many results are described in the literature and a few of them illustrated in the following references [275–280].

The extreme form of adhesive wear is galling that involves excessive friction between the two surfaces, resulting in localized solid-phase welding, and subsequent spalling of the mated parts [261]. This process causes significant damage to the surface of one or both materials. The typical test is shown in Fig. 15.49: the pin

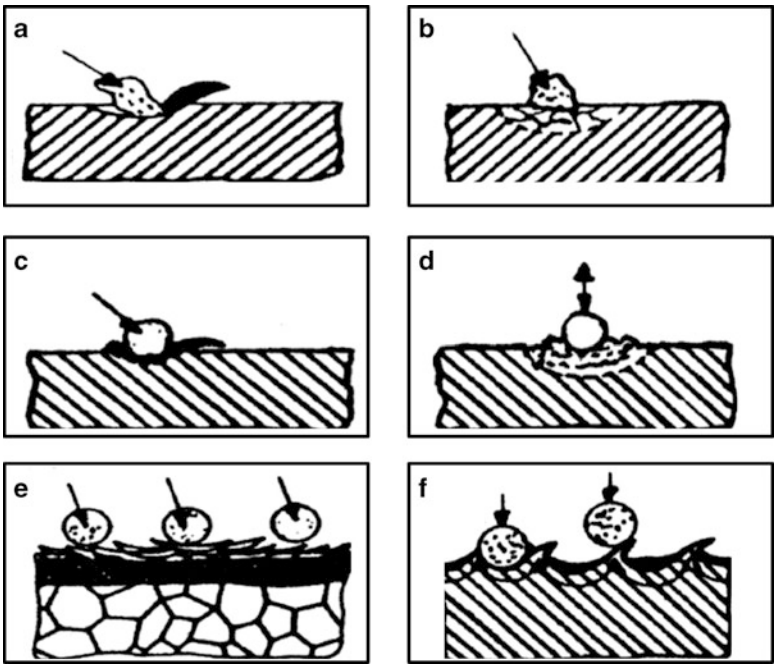


Fig. 15.50 Erosive wear due to particle impact: (**a**) microcutting and microploughing; (**b**) surface cracking; (**c**) extrusion of material at the exit end of the impact craters; (**d**) surface and subsurface fatigue cracks due to repeated impacts; (**e**) formation of thin platelets due to extrusion and forging by repeated impact; and (**f**) formation of platelets by a backward extrusion process. Reprinted with kind permission from Elsevier [262]

specimen, gradually load, against a rotating counter plate material. The load at which the pin tends to gall onto the plate is the galling load [265]. The ASTM test is referenced [15.W8].

15.9.3 Erosive Wear

– Erosive wear is the continuous deterioration of a material by fluid carrying solid particles [15.W6]. When the fluid is traveling in a direction that is normal to the surface of the material, it can be considered as impact wear. The repeated impact by particles that are very small relative to the size of the material being impacted, results in erosive wear. Whatever may be the size of impacting particles, they can cause deformation to the material being impacted that can result in the ejection of particles from the material's surface or the formation of near-surface cracks that under repeated impact can cause pieces of the surface to fracture. Figure 15.50 from Kennedy and Hashmi [262] summarizes the different phenomena implied in erosive wear. One conventional test is described in [15.W10].

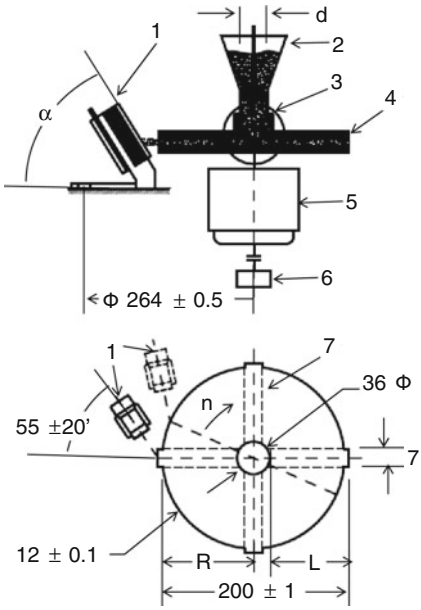


Fig. 15.51 Impact erosive wear tester for testing materials in abradant particles jet: (1) specimens, (2) abradant, (3) shield, (4) rotor, (5) drive motor, (6) rotation frequency gauge, and (7) radial channels. Reprinted with kind permission from Springer Science Business Media [281], copyright © ASM International

– Cavitation wear, occurring during liquid impingement by the collapse of bubbles on the coating solid surface, is also considered as erosive wear. The deformation of solids by the impact of liquid occurs because of the interaction of stress waves generated by the collapsing bubbles with the surface.

For dry erosion wear, the test mostly used consists of repeated impact erosion by a flow of 50 μm mean diameter angular alumina particles exiting a tungsten–carbide nozzle (50 mm in length and 1.5 mm in internal diameter) with a mean velocity of 30 m/s. Crushed silica with grain size below 0.1 mm is also used for erosion tests. As for grit blasting the nozzle wears and must be replaced as soon as its internal diameter has increased by 10 %. Blasting time is generally 10 min and the nozzle axis must be kept orthogonally to coating. When dividing erosion rate (mg/min) by the abrasive flow rate (g/min) one obtains the average erosion rate after dividing the result by the specimen mass density. The averaged erosion rate is thus expressed in mm^3/g.

To characterize the impact erosion in severe but cold conditions, Kulu and Pihl [281] have developed an impact erosion wear tester (Fig. 15.51), based on centrifugal force. It produces a stream of abrading-quartz sand with abrasive particle size of 0.1–0.3 mm and abrasive hardness 1,100–1,200 HV. The velocity of abrasive particles is 80 m/s. It can also use abrasives of different hardness (from 120 to 2,000 HV) such as limestone, glass, iron oxide, quartz, and corundum. The measurements of weight loss permits calculations for weight and volume losses as a measure for wear rate; that is, the loss of mass or volume per one kilo of abrading material in mg/kg and mm^3/kg, respectively. The impact angle, α, can be varied easily, see Fig. 15.51.

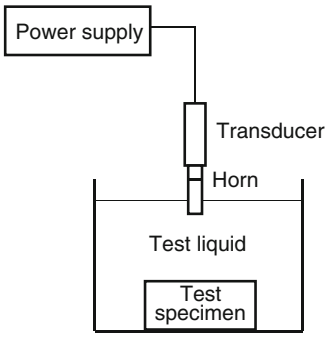


Fig. 15.52 Cavitation erosion test. Reprinted with kind permission from ASM International [261]

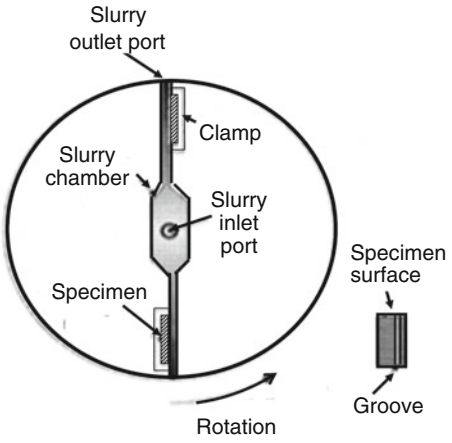


Fig. 15.53 Schematic of the Coriolis erosion tester. Reprinted with kind permission from Elsevier [282]

In liquid cavitation erosion, tensile stresses are generated during liquid impingement by the collapse of bubbles on a solid surface. It results in solid deformation because of the interaction of stress waves generated by the collapsing bubbles. Two ASTM tests are referenced in [15.W11, 15.W12]. According to Chattopadhyay [261] a simple testing method of cavitation is that developed by Shal'nev and represented in Fig. 15.52. The material to be tested is exposed to sound waves, produced by a magneto-striction vibrator with a nickel pipe 20 mm in internal diameter, oscillation frequency of 8,000 Hz, and amplitude of 0.066 mm.

Liquid erosion with slurry, generally an alumina slurry, combines high abrasive conditions with cavitation. For example, the test rig [282] showed in Fig. 15.53 uses a steel wheel, which rotates against a flat-coated specimen in slurry containing sharp alumina particles, subjecting the samples to combined impact erosion. The extent of erosion depends on the composition, size, and shape of the eroding particles, their velocity and angle of impact, and the composition and microstructure of the surface being eroded. The method utilizes the combination of centrifugal and Coriolis accelerations in a revolving rotor to pass slurry rapidly across a test surface

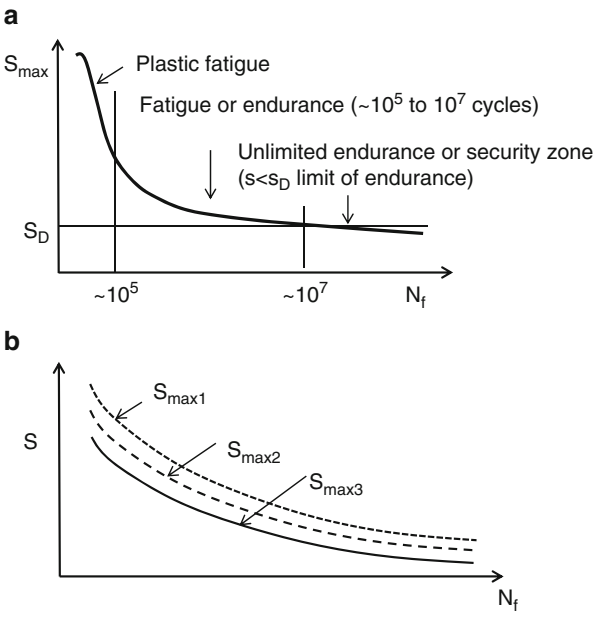


Fig. 15.54 *S–N* diagram plots: nominal stress amplitude *S* versus cycles to failure *N*: (**a**) *S*−*N* curve for fatigue and (**b**) evolution of the *S–N* curve for different S_{max}. Reprinted with kind permission from ASM International [261]

such that the solid particles are forced against the surface, producing wear during their passage. The device allows using flat plate specimens and rotation speeds up to 7,000 rpm, resulting in very short wear test times of 1 or 2 min. For example, a wear scar formed in a ductile material during a Coriolis erosion test shows a progressive increase in depth with distance from the rotation centre of the device.

Different examples of erosive wear for coatings sprayed with various processes are given in the following references [283–289].

15.9.4 Surface Fatigue

Surface fatigue wear not only results in material loss from the surface, but it can also reduce the working life of the engineering component. It is the process leading to progressive localized permanent structural change in a material subjected to fluctuating stresses and strains. The cumulative effects of progressive changes in service conditions may result in cracks and/or complete fracture after a certain number of cycles. For coatings, for example, it happens in contact with a rolling motion. Fatigue is discussed according to two categories based on the number of cycles to failure. In high-cycle fatigue situations, materials performance is commonly characterized by an *S–N* curve, also known as a Wöhler curve. In this test *constant* cyclic stress amplitude *S* is applied to a specimen and the number of loading cycles *N* until the specimen fails is determined. It results in a graph of the magnitude of a cyclic stress (*S*) against the logarithmic scale of cycles to failure (*N*), see Fig. 15.54. The coupon with its coating manifests variation in its number of

cycles to failure, and the *S–N* curve should more properly be an *S–N–P* curve capturing the probability of failure after a given number of cycles of a certain stress. Probability distributions that are common in data analysis and in design against fatigue include lognormal distribution, Weibull distribution and others. High-cycle fatigue occurs under low stress S_{max} and fracture occurs at $N = 10{,}000$ cycles or greater ($N \geq 10^4$).

Low-cycle fatigue is represented by the *E–N* curves (E = strain = $E_p + E_e$, E_p being the plastic strain and E_e the elastic one) and failure occurs below 10,000 cycles ($N < 10^4$). To improve the fatigue resistance, compressive residual stresses can be introduced in the surface by, e.g., shot peening to increase fatigue life. On the contrary, tensile stress decreases the fatigue resistance. Of course fatigue life, as well as the behavior during cyclic loading, varies widely with the material or coating considered. Extreme high or low temperatures can decrease fatigue strength as well as environmental conditions resulting in erosion, corrosion, or gas-phase embrittlement.

Various means are used to characterize coating's fatigue:

- Cyclic fatigue and fracture mechanisms [15.W13], thermomechanical fatigue testing [15.W14], cyclic fatigue, and fracture mechanisms [15.W15–15.W17].
- For highly loaded machine elements such as roller bearings and gears, subjected to a combined rolling/sliding motion, extensive tests have to be performed [290]. Stewart et al. [290] have proposed a modified version of the standard four-ball machine, where steel discs 31 mm in diameter were fabricated, coated, and then HIPed. A number of modifications to the four-ball machine were thus necessary in order to maintain the correct rolling/sliding kinematics. Figure 15.55a, b present the details of the setup. Test results revealed that performance of the coating was dependent on the microstructural changes due to post-treatment. Ahmed and Hadfield [291] have used a similar setup to study different coatings, but in this case the substrate material was either 440-C, M-50 bearing steel, or mild steel in the shape of rolling element ball or cone.
- Zhang et al. [292] have used the rolling contact testing machine developed by Yanshan University in China to the rolling contact fatigue (RCF) resistance and failure mechanisms of plasma-sprayed CrC–NiCr cermet coatings.
- Much less sophisticated tests are those based on Young's modulus measurement at increasing deformation of up 0.3 % [293, 294]. For example, Kovarik et al. [293] have loaded the fatigue samples in reversible bend (as a cantilever beam) at room temperature in a special computer-controlled electromagnetic testing device. An alternating electromagnetic field induced by a pair of coils was used to deflect the free end of the specimen, which was equipped by a yoke. Other authors [295, 296] used specimens supported in the same manner as a cantilevered beam at one end and that were subjected to an alternating force at the other. The fatigue test specimen shown in Fig. 15.56 includes a triangular shape intended to produce a constant stress along the length of the test section.
- Other authors [297, 298] have used rotating-beam fatigue testing machines, where test specimens are coated bars (12.7 mm in diameter). The fatigue

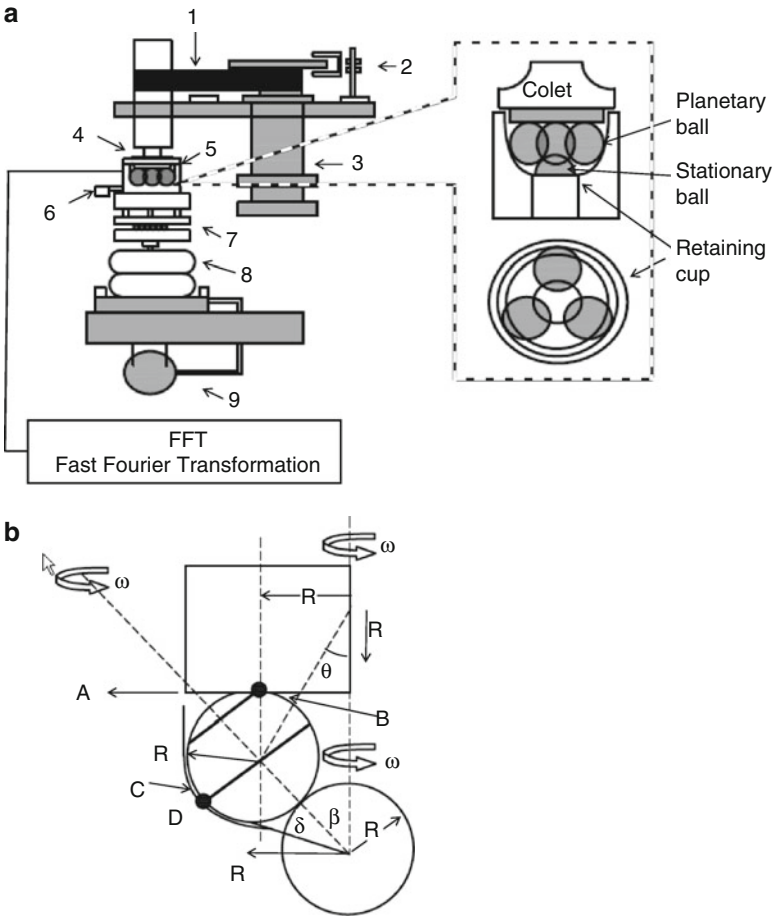


Fig. 15.55 (**a**) Schematic of the modified four-ball machine: 1. Belt drive, 2. speed sensor, 3. spindle-driving motor, 4. coated disc and collet, 5. cup assembly, 6. thermocouple, 7. thrust bearing, 8. bellows, 9. pressure gauge. (**b**) Schematics of ball and disk kinematics in cup assembly: $R_i = 7.75$ mm, $R_p = 6.35$ mm, $\theta = 36.83°$, $\beta = 37.61°$, $\delta = 31.16°$, $\omega = 4000 \pm 10$ rpm). Reprinted with kind permission from Elsevier [290]

experiments were conducted at room temperature under a rotating beam and stress ratio of $R = -1$ configuration at a load frequency of 50 Hz. The maximum load P_{max} generating a tensile stress, considered positive, is equal to the minimum load P_{min} generating a compressive stress, considered negative. The stress ratio corresponds to the ratio of the minimum stress to the maximum one during one cycle of loading in a fatigue test.

- Fatigue resistance has also been tested with a torsional setup [299].
- For the axial fatigue strength test, a sinusoidal load of 20 Hz with load ratio of $R = -1$, at room temperature (23 ± 2 °C), and 35 ± 3 % humidity was applied

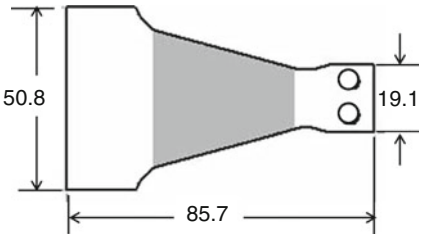


Fig. 15.56 Bending fatigue strength specimen. The *gray region* corresponds to the coated area. Dimensions are in mm. Reprinted with kind permission from Springer Science Business Media [295], copyright © ASM International

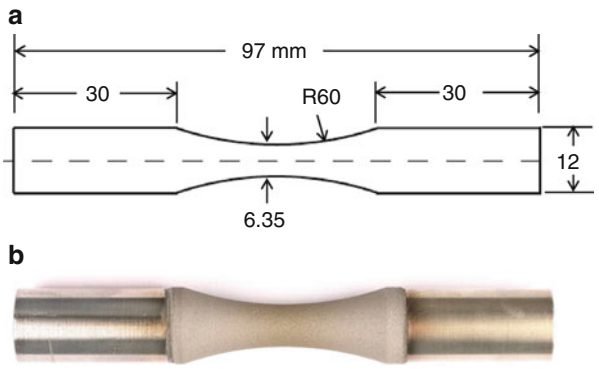


Fig. 15.57 Axial fatigue specimens. All the dimensions are in mm. (**a**) Drawing and (**b**) as WC–CoCr sprayed. Reprinted with kind permission from Springer Science Business Media [300], copyright © ASM International

by Agüero et al. [300]. Experimental tests considered as fatigue strength the specimen fracture or 5×10^6 load cycles. The test was performed on two MTS computer-controlled servo-hydraulic axial fatigue-testing machines, according to the ASTM E466 standard. Figure 15.57 presents the test sample dimensions and a picture of the coated fatigue specimen.

– At last thermal fatigue resistance, generally of TBCs, is tested with furnaces and/or laser [301–304]. For example, Scrivani et al. [301] have tested thick (1.8 mm) plasma-sprayed TBCs by introducing them in a furnace, heating them up to 1,150 °C in 5 min, letting them stabilize at 1,150 °C during 45 min, followed by a 10-min forced air cooling. Failures occurred after 305–455 cycles, depending on the spray conditions. When looking at the limits of the TBC the thermal fatigue resistance increases with amount of porosity in the topcoat. After the thermal cycling tests the compressive in-plane stress increases in the TBC systems and it is less a function of the porosity level of topcoat. Robin et al. [19] also observed the modification of the stress distribution. In their setup coatings were heated by radiating lamps and acoustic emission allowed following cracks formation during the heating and cooling stages. The bond coat or the functional gradient material (FGM) play an important role in the coating resistance to thermal fatigue [304] as illustrated in Fig. 15.58 showing SEM micrographs with interface delamination cracking for non-FGM coating subjected to six thermal fatigue cycles and FGM coating subjected to 10 thermal fatigue cycles. FGM coating has much higher thermal fatigue resistance compared to non-FGM coating system through thermal cycling tests conducted under the simulated advanced gas turbine blade conditions.

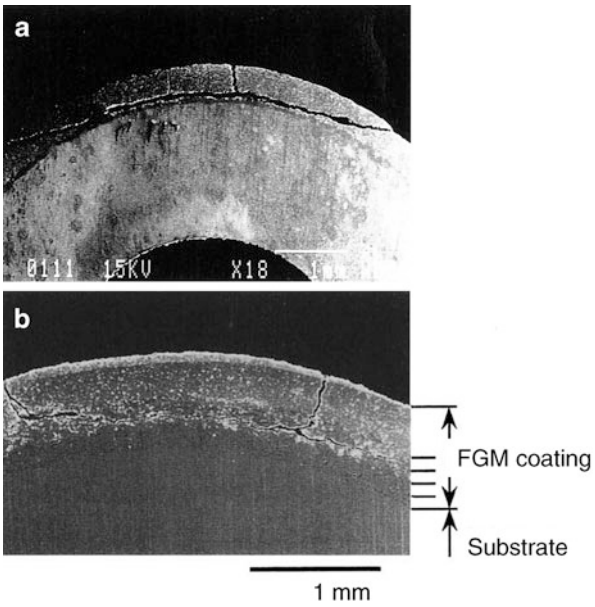


Fig. 15.58 (**a**) SEM micrographs showing interface delamination cracking for non-FGM coating subjected to six thermal fatigue cycles, where the exposed time for every cycle was 70 s and the highest temperature on coating and substrate was 1,200 and 600 °C, respectively. (**b**) SEM micrographs showing interface delamination cracking for FGM coating subjected to 10 thermal fatigue cycles, where laser power was 34 W. Delamination occurred along the boundary between 75 %PSZ/25 %NiCrAlY and 50 %PSZ/50 %NiCrAlY. Reprinted with kind permission from Elsevier [304]

15.9.5 Corrosive Wears

Corrosive wears occurs when the effects of corrosion and wear are combined, resulting in a more rapid degradation of the material's surface [15.W18, 15.W19]. A surface that is corroded or oxidized may be mechanically weakened and more likely to wear at an increased rate. Furthermore, corrosion products including oxide particles that are dislodged from the material's surface can subsequently act as abrasive particles. Stress corrosion failure results from the combined effects of stress and corrosion. At high temperatures reactions with oxygen, carbon, nitrogen, sulfur, or flux (chemical cleaning agent) result in the formation of oxidized, carburized, nitrided, sulfidized, or slag layer on the surface. Temperature and time are the key factors controlling the rate and severity of high temperature corrosive attack [261].

Three types of tests are mainly used:

– Sliding and corrosive test is quite similar to the pin on disk test presented in Fig. 15.48, but a container allows performing the test with lubricant or corrosive

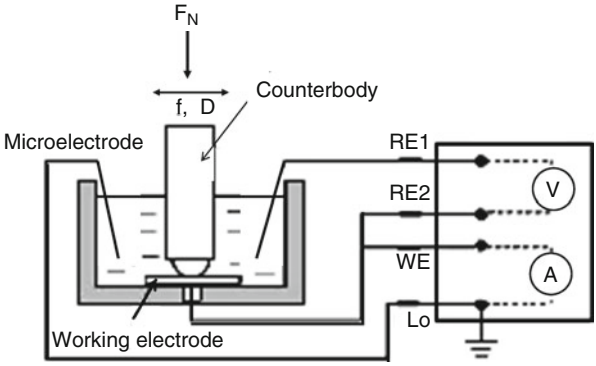


Fig. 15.59 Experimental setup combining a bidirectional sliding test immersed in an electrolyte and electrochemical noise measurements (*WE* working electrode (sample), *RE* reference electrode, *V* voltmeter, and *A* zero resistance ammeter). Reprinted with kind permission from Elsevier [307]

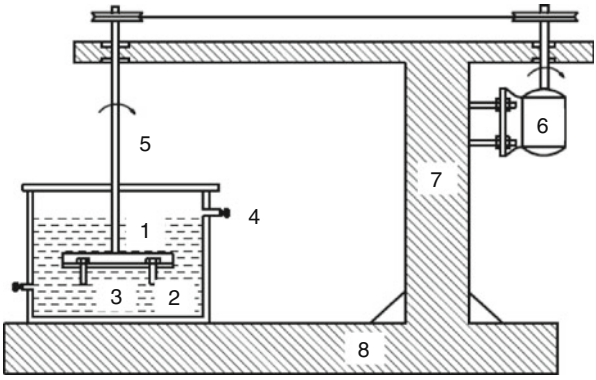


Fig. 15.60 A schematic representation of the slurry wear tester: 1. Disc, 2. sample, 3. slurry media, 4. double wall container, 5. spindle, 6. driving motor, 7. column, 8. machine base. Reprinted with kind permission from Elsevier [308]

solution [305] or both [306]. For example, 10 % H_2SO_4 added to the lubricant with the volume ratio of H_2SO_4 to oil approximately equal to 1:4. It is also possible to perform simultaneously fretting wear test with an electrochemical noise (EN) measurement system, the whole system being in an electrochemical cell, as schematically shown in Fig. 15.59 [307]. Two personal computers control the systems and acquire potential, current, and friction force data. The flat samples are covered with an electrical insulating cover prior to fretting tests leaving an area of 1 cm^2 exposed to the electrolyte. Corundum balls (Ceratec, The Netherlands) with a diameter of 10 mm, a hardness of 2,000 HVN, and a surface roughness $Ra < 0.02$ μm, are used as counter body. Corundum was selected for its high wear resistance, high chemical inertness, and high electrical resistance. Fretting–corrosion experiments are performed at room temperature with a reciprocating ball-on-flat contact configuration. The flat sample is immersed in the Hank's solution for 90 min before starting up experiments in order to reach a stable potential and a low background current.

– Preweighed samples 15 mm in diameter are fixed on a disc attached with an electric motor. The disc is isolated from the samples by painting appropriately and putting a nonconducting adhesive in between. A schematic representation of the slurry-wear test apparatus is shown in Fig. 15.60 from Prasad [308]. Samples

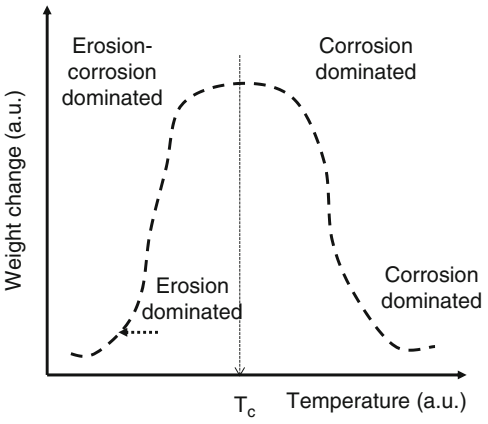


Fig. 15.61 Scheme of corrosion–erosion wear at high temperature. Reprinted with kind permission from ASM International [261]

are rotated at ambient temperature at a given velocity and the travel distance varies in the range of 15–500 km. Changing the content of the solid sand particles (size 212–300 μm) from 0 to 60 wt% in the liquid electrolyte modifies the slurry composition. The electrolyte comprises 4 g sodium chloride plus 5 cc concentrated sulphuric acid dissolved in 10 L of water and has a pH of 1.98 highly acidic in nature. Addition of 20, 40, and 60 wt% sand to the electrolyte changed the pH of the slurry mixture of liquid plus sand to 3.64, 6.85, and 7.12, respectively. Wear rate are computed by weight loss technique. Zhang and Lei [309] conducted a similar experiment.

In high-temperature erosion–corrosion heated fluids containing solid particles lead to material removal from the surface by a specific wear process [310]. The evolution of the weight change of the sample is represented in Fig. 15.61 [261].

Four different behaviors can be observed [261, 311]:

- At low temperature, the material loss is essentially due to erosion.
- Beyond a certain temperature the rate of oxidation increases drastically with temperature. For a temperature in the mid-range, both erosion and oxide scale formation rates remain similar and the wear is erosion–corrosion dominated.
- With the further temperature increase the loss of oxide dominates and over a certain critical temperature, chipping of brittle scale is the main mechanism.
- Above the critical temperature, T_c, the overall weight change from corrosion process tends to zero.

For high temperature tests, for example to reproduce the erosion of fly ash in coal-fired boiler, fly ashes are introduced in a 210 kW laboratory combustion unit using methane as fuel (this type of combustion reproduces well that of coal). Ashes are continuously injected into the combustion chamber by means of a helicoidally feeder [311]. Garcıa et al. [312] have conducted a similar experiment to study the erosive–corrosive wear of Ni–Cr coatings in boilers atmosphere the high temperatures being provided by a burner using methane as fuel. During erosion wear tests,

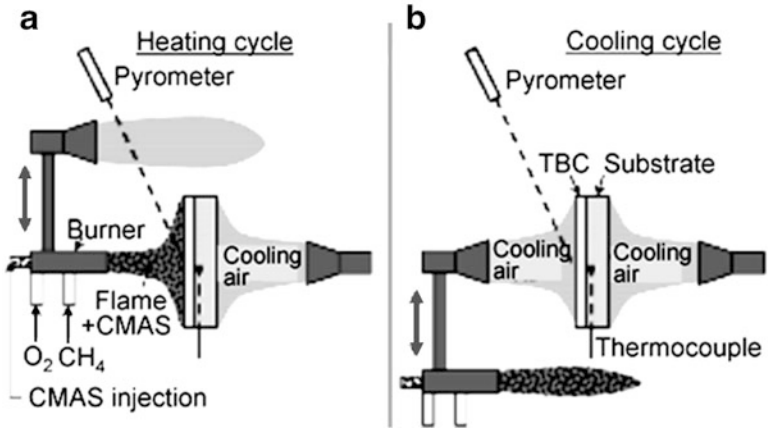


Fig. 15.62 Schematic diagram of thermal-gradient cyclic testing of TBCs with CMAS injection during (**a**) heating and (**b**) cooling cycles. Reprinted with kind permission from Elsevier [313]

ashes retrieved from a 900 MW power plant were injected continuously into the combustion chamber by means of a helicoidally feeder, which pumped the ash into a mixing chamber where the ash was fluidized with air before being incorporated into the chamber. This device allows reproducing, at the laboratory scale, the same operating conditions, which exist in the areas of postcombustion gases in industrial coal-fired power plants.

Degradation of thermal barrier coatings (TBCs) in gas-turbine engines by molten calcium–magnesium–aluminosilicate (CMAS) glassy deposits is becoming a pressing issue, as engines are required to operate under increasingly harsh conditions. Drexler et al. [313] developed a new thermal-cycling test for the evaluation of TBC performance, where a thermal gradient was applied across the TBC, with simultaneous injection of CMAS. The conditions simulated in this new test are closer to actual conditions in engine, as compared to the conventional furnace test without thermal gradient. In a typical test, an equilibrated natural gas/oxygen flame heats the front of the TBC, while compressed air cools the backside (Fig. 15.62a). The front temperature (T_{sur}) is monitored using a long-wavelength (9.6–11.5 μm) pyrometer, and the substrate temperature (TTC) is monitored by a thermocouple (1 mm diameter) placed inside a hole (1.1 mm diameter, 15 mm long) drilled radially into the substrate. The bond coat temperature (T_{sub}) at the ceramic/metal interface is estimated from T_{sur} and TTC. The CMAS suspension is sprayed axially through the gas burner. The heating cycle lasts 5 min. During the cooling cycle (2 min) the cooling air nozzle is brought in front of the TBC (Fig. 15.62b), and the process is repeated.

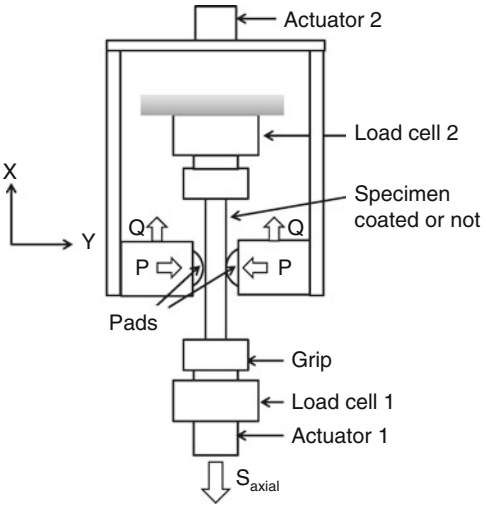


Fig. 15.63 Fretting test apparatus with a servo-hydraulic uniaxial test frame and an additional servo-hydraulic actuator. Reprinted with kind permission from Springer Science Business Media [314]

15.9.6 Fretting

– Fretting wear occurs when surfaces, in intimate contact with each other, are subject to a small amplitude relative motion that is cyclic in nature, such as vibration. Fretting wear is normally accompanied by the corrosion or oxidization of the debris and worn surface. If the debris become embedded in the surface of the softer metal, the wear rate may be reduced, but if the debris remain free at the interface between the two materials, the wear rate may be increased. Fatigue cracks also have a tendency to form in the region of wear. ASTM standards are presented in [15.W20–15.W22].

Figure 15.63 shows schematic of a dual actuator fretting test apparatus used by Lee et al. [314, 315]. It allows conducting fretting tests with any prescribed value of relative displacement at an applied cyclic stress to the specimen. The setup comprises a servo-hydraulic uniaxial test frame and an additional servo-hydraulic actuator (actuator 2 in Fig. 15.63), which is directly connected to the fretting fixture so that independent cyclic movement of the fretting fixture is possible under a given contact load. During fretting the specimen is fatigued at a given stress level thanks to actuator 1. The tangential force, Q, depends on the difference between two load cells located at the bottom and top of the specimen. Fretting fixture can be independently controlled in either load or displacement controlled mode through the actuator 2. The contact load, P, is applied through lateral springs and measured by a pressure gauge.

Another device used by Fridrici et al. [316] is presented in Fig. 15.64. A tension-compression hydraulic machine is used to impose the displacement between the plane and the cylinder. For preselected cycle numbers during a fretting test, the displacement δ, the normal force P, and the tangential force Q are recorded. This enables to plot the fretting loop Q–δ for the preselected cycles.

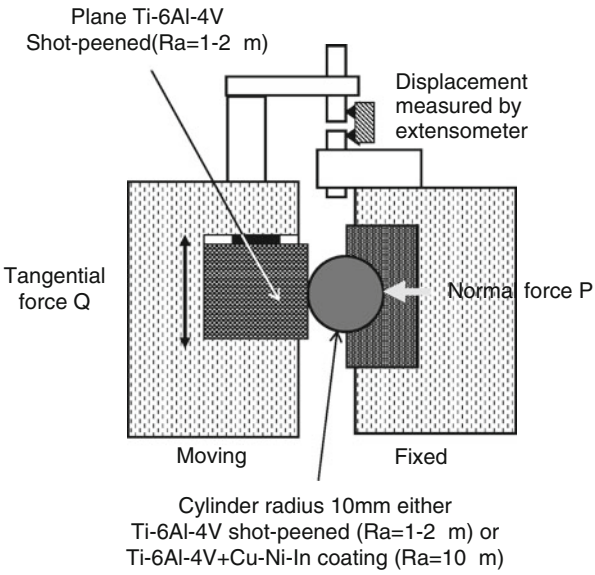


Fig. 15.64 Schematic drawing of fretting-wear rig with a tension-compression hydraulic machine. Reprinted with kind permission from Elsevier [316]

Other fretting tests have been developed. They involve dovetail geometry [317], the temperature of which can be monitored; a tension-compression hydraulic machine [318] where the coated flat specimen is stationary and the 52100 steel ball is vibrated with small reciprocating amplitude; flat-on-flat wear tester designed to simulate the vibrating condition and positioned inside a furnace to obtain an operating condition of 500 °C [319]; and a device in which the fluctuating loading is supplied by a variable crank system [320].

15.10 Corrosion Resistance

15.10.1 General Remarks

In corrosion process materials loss occurs through electrochemical or chemical reaction with the surrounding medium. At high temperatures corrosion reactions are oxidation, carburization, nitriding, halogen erosion, sulfidation, and molten-salt corrosion [261], coatings being mainly concerned by the former and the latter.

The dissolution of metallic elements by the formation of ions by electron loss corresponds to anodic reactions such as

$$\mathrm{M(metal)} \rightarrow \mathrm{M}^{n+} + n\mathrm{e}^{-} \tag{15.43}$$

where M is a metal, M^{n+} a positively charged n times ion, and e^{-} an electron. This electron loss allows the metal ion to bond to other groups of atoms that are

negatively charged, for example, the reaction of water or oxygen with electrons from the metal surface, known as cathodic reaction. Let us consider steel rusting where water (H_2O) and oxygen (O_2) are involved:

$$Fe \rightarrow Fe^{2+} + 2e^{-} \tag{15.44}$$

The free electrons produced react with water and oxygen:

$$O_2 + 2H_2O + 4e^{-} \rightarrow 4OH^{-} \tag{15.45}$$

Both reactions (15.44 and 15.45) can then be written as the global reaction:

$$2Fe + O_2 + 2H_2O \rightarrow 2Fe(OH)_2 \tag{15.46}$$

As O_2 dissolves rapidly in water and because there is generally an excess of it, O_2 reacts with the iron hydroxide to form the hydrated iron oxide, $2Fe_2O_3{\cdot}H_2O$, often called brown rust:

$$4Fe(OH)_2 + O_2 \rightarrow 2H_2O + 2Fe_2O_3 \cdot H_2O \tag{15.47}$$

It is clear from these equations that the corrosion rate is linked to electrons production, corresponding to a corrosion current flow. However, the presence of an impervious oxide layer can inhibit the corrosion and the metal is said passivated.

Corrosion rate equation [261] is expressed by

$$C_T = C_0(\Delta G * /RT) \tag{15.48}$$

where C_T is the corrosion rate at temperature T(K), generally expressed in mm/year or mpy, C_0 is the rate at 0 K, R is the ideal or universal gas constant, and ΔG^* is the activation energy of the corrosion reaction. This equation is transformed in logarithmic form, the energy terms are considered as potentials and rates as currents, resulting in a relationship between corrosion current, I_c, and measured potential, E, of the specimen:

$$E - E_c = \beta \frac{\log I}{\log I_c} \tag{15.49}$$

where E is the measured potential of the specimen when current flows, E_c is the corrosion potential (no current flowing), I is the impressed current, I_c is the corrosion current (no external current), and β is a constant. This equation is used to characterize corrosion by electrochemical measurements, as described later.

The different types of corrosive attack, especially for coatings, are the following:

General corrosion, corresponding to about 30 % of failure, where the average rate of corrosion on the surface is uniform as illustrated in Fig. 15.65a.

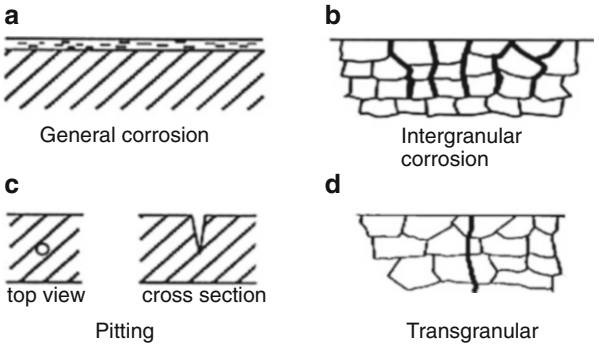


Fig 15.65 Different types of corrosion: (**a**) General corrosion, (**b**) intergranular corrosion, (**c**) pitting, and (**d**) transgranular corrosion

Localized corrosion, about 70 % of failures, comprise of the following:

1. Galvanic corrosion occurring when two dissimilar metals are in contact with each other in a conductive solution (electrolyte), the more anodic metal being corroded, while the more cathodic one is unaffected. The anodic metal corrodes faster because ions from the metal migrate from anode to cathode. There are three conditions that must exist for galvanic corrosion to occur. First there must be two electrochemically dissimilar metals present. Second, there must be an electrically conductive path between the two metals. And third, there must be a conductive path for the metal ions to move from the more anodic metal to the more cathodic metal. If any one of these three conditions does not exist, galvanic corrosion will not occur. The galvanic or electrochemical series ranks metals according to their potential, generally measured with respect to the Standard Calomel Electrode (S.C.E.). Metals can be arranged in a galvanic series representing the potential they develop in a given electrolyte against a standard reference electrode. The relative position of two metals on such a series gives a good indication of which metal is more likely to corrode more quickly. However, other factors such as water aeration and flow rate can influence the process markedly. The results are often viewed as a galvanic corrosion chart or galvanic corrosion (Fig. 15.66).

   This chart says that the "anodic" or "less noble" metals at the negative end of the series, such as magnesium, zinc, and aluminum, are more likely to be attacked than those at the "cathodic" or "noble" end of the series such as gold and graphite. For example, zinc has a negative potential higher than that of iron and it will behave as a cathode relatively to it, while nickel which negative potential is lower than that of iron will behave as an anode relatively to it. The electrolyte, ionic-conducting fluid bridging both metals, plays a key role, as well as the relative surface contact area, the smaller the anodic to cathodic area ratio is the more severe is the anodic metal corrosion. This is very important, for example, to protect low carbon iron from atmospheric corrosion by a coating either anodic (nickel coating) or cathodic (aluminum or zinc). In the first case no discontinuity in the coating can be tolerated, while it has relatively a low importance with cathodic coating, as illustrated in Fig. 15.67. Of course by imposing a voltage between both metals, the current direction can be changed.

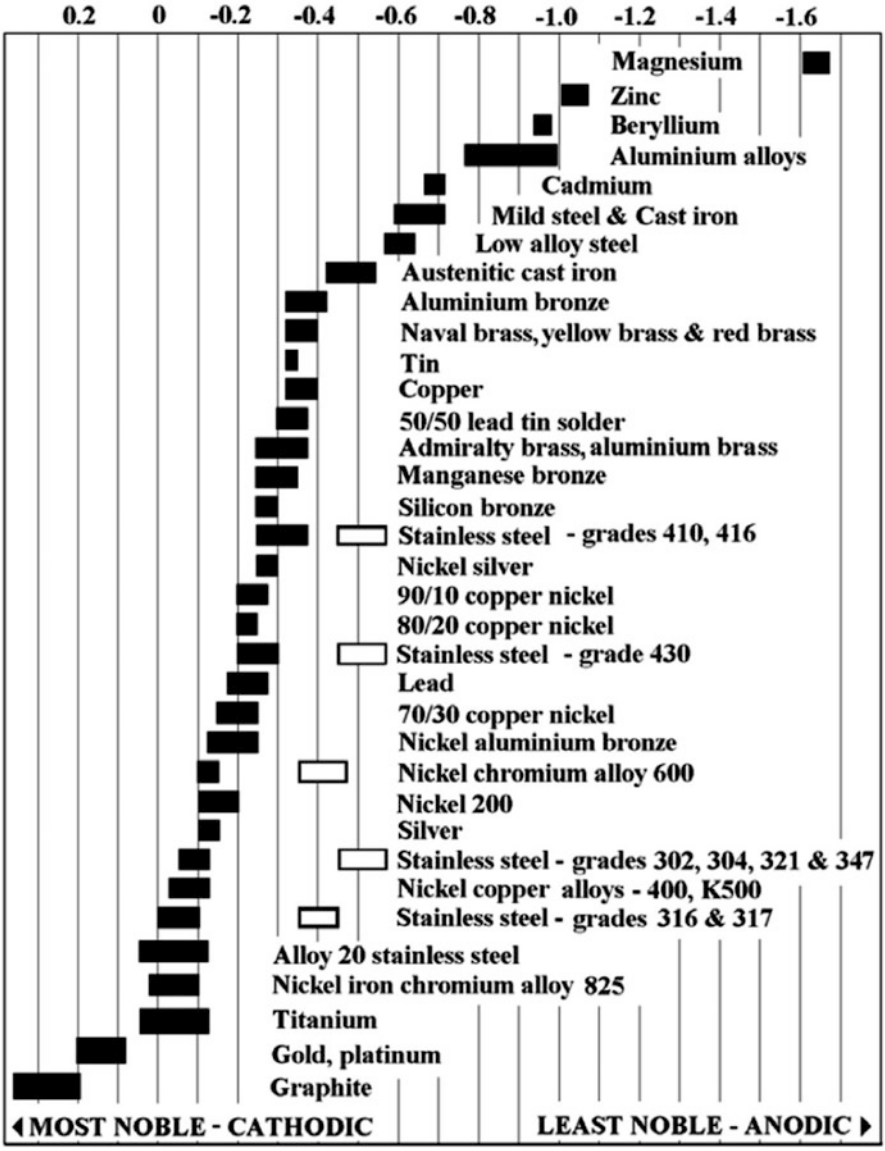


Fig. 15.66 Galvanic corrosion chart: Corrosion potentials in flowing sea water at ambient temperature. The *unshaded symbols* show ranges exhibited by stainless steels in acidic water such as may exist in crevices or in stagnant or low velocity or poorly aerated water. The more Noble materials at the left side tend to be cathodic and hence protected; those at the right are less noble and tend to be anodic and hence corroded in a galvanic couple. Reprinted with kind permission from Elsevier [321]

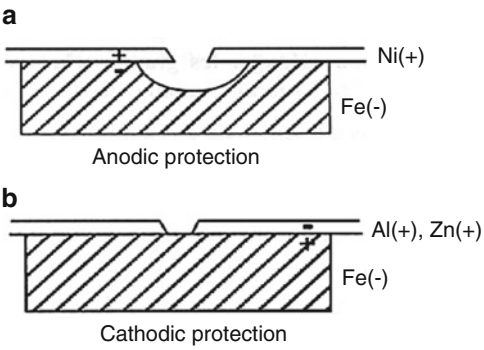


Fig. 15.67 Examples of protective coatings: (**a**) Anodic (no discontinuity allowed in the coating) and (**b**) cathodic (discontinuity allowed in the coating, resulting in almost no corrosion of iron)

2. Intergranular corrosion, illustrated in Fig. 15.65b, occurring when a chemical element is depleted during the coating or bulk material manufacturing, for example during heat treatment.
3. Pitting is a localized corrosion characterized by depression or pit formation on the surface as illustrated in Fig. 15.65c. It occurs, for example, when stainless steel is corroded by chloride-containing solutions. The pit cavities act as stress raisers.
4. Transgranular corrosion is mainly due to high static tensile stress in the presence of a corrosive environment. It can be intergranular but also transgranular when cracking occurs, as illustrated in Fig. 15.65d. Of course the coating material and its microstructure play an important role.

15.10.2 Corrosion Characterization

For terminology and acronyms related to corrosions, see [15.C1].

15.10.2.1 (a) Electrochemical Measurements

ASM 13A book [322] and the following ASTM references [15.C2–15.C13] give a detailed description of the electrochemical techniques.

In direct current (d.c.) method potentiodynamic polarization is used. The coating is insulated by epoxy cold resin mounting, except a surface of about 1 cm^2, which is exposed to a liquid electrolyte and the system is allowed to reach a near-electrochemical equilibrium. The equilibrium corroding potential, E_c, is measured relatively to a reference electrode because the absolute potential of the coating sample relatively to the electrolyte is not accessible. The value of

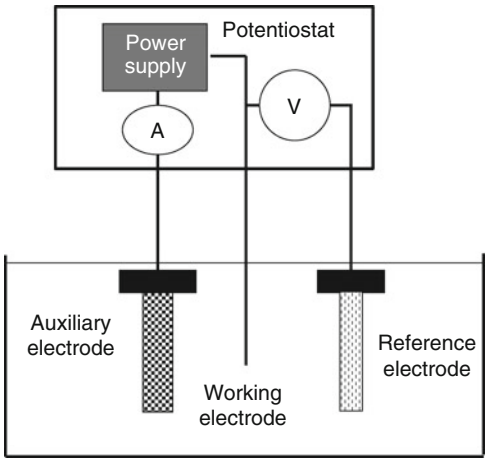


Fig. 15.68 Three-electrode cell used in the electrochemical experiments. Reprinted with kind permission from Springer Science Business Media [323], copyright © ASM International

either the anodic or cathodic current at E_c, called the corrosion current, I_c, would allow calculating the corrosion rate of the metal, but unfortunately it cannot be measured directly. Thus additional electrodes are immersed in the solution, and all of them are connected to a device called a potentiostat that allows changing the potential of the metal sample in a controlled manner and measure the current as a function of the potential. Figure 15.68 from Souza and Neville [323] presents an oversimplified scheme of the three electrodes electrochemical experiment. When the potential of a metal sample in solution is forced away from E_c, it is referred to as polarizing the sample. The response (current) of the sample is measured as it is polarized. The computer controlled potentiostat shift the potential of the working electrode (the specimen) relative to the reference electrode (often saturated calomel electrode) at a predetermined rate (a few mV/min) to potentials more positive than the free corrosion potential (E_c). The current density in the external circuit between the Pt auxiliary electrode and the coating (working electrode) is measured as a function of applied potential until a given current density is reached and then the potential drops at the same rate as on the forward curve. The response is used to develop a model of the sample's corrosion behavior. Various authors achieved similar measurements for cermets or metals either thermal sprayed [324–330] or cold sprayed [331].

Alternating current (a.c.) methods are based on the fact that in presence of an electrolyte, the corroding system is equivalent to an electrical circuit comprising a resistive/capacitive (RC) parallel circuit. It is called Electrochemical Impedance Spectroscopy (EIS). The response of the circuit (computer-driven ac impedance device) to frequencies varying from very low frequencies (10^{-2} Hz) to very high ones (10^5 Hz) allows determining the different elements of the coating equivalent electrical circuit [331].

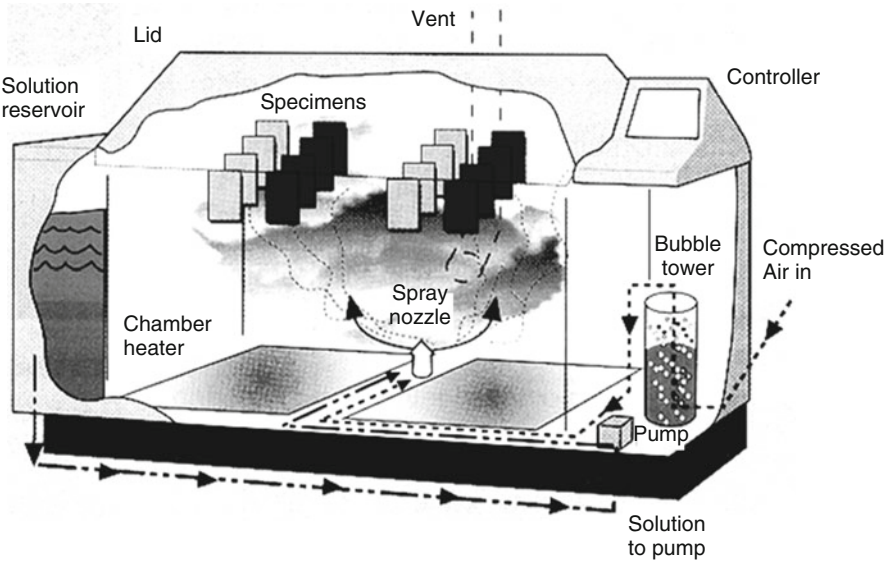


Fig. 15.69 Typical climatic enclosure. Reprinted with kind permission from Prof. G. Montavon [159]

15.10.2.2 (b) Fog and Salt-Spray Test

The corrosion tester is a box; for details, see [15.C14], where a corrosive solution is atomized by humidified compressed air. Air humidification is achieved by passing it through a bubble tower. The box temperature can be adjusted thanks to heaters. In the box, also called climatic enclosure, temperature, airspeed, and relative humidity are controlled. The linear shrinkage, product mass loss or gain of treated samples, is then measured. The tests are performed either continuously or in a cyclic mode: for example, x hours with the solution followed by x hours without solution. Figure 15.69 represents a typical box.

For example, the corrosion resistance of nickel-base cored wires arc-sprayed coatings was tested by this method and by electrochemical corrosion test [332].

15.10.2.3 (c) Molten Salt

According to Sidhu et al. [333–335] vanadium (V), sulfur (S), and sodium (Na) are common impurities in the low-grade petroleum fuels. Molten sulfate vanadate deposits resulting from the condensation of combustion products of such fuels are extremely corrosive to high-temperature materials in the combustion systems. Further, mixture of Na_2SO_4 and V_2O_5 in the ratio of 40:60 constitutes eutectics with a low melting point of 550 °C and provides a very aggressive environment for

hot corrosion to occur. They have applied uniformly a layer of Na_2SO_4–60 %V_2O_5 mixture on the warm specimens. Cyclic studies were performed in molten salt for 50 cycles. Each cycle consisted of 1-h heating at 900 °C in a silicon carbide tube furnace in open air atmosphere followed by 20-min cooling at room temperature. Singh et al. [336] have also studied the corrosion of Ni-base superalloy by Na_2SO_4–60 %V_2O_5 mixture in a furnace at 900 °C.

Guilemany et al. [337] have tested the corrosion resistance of Ni-based coatings applied on municipal solid-waste incinerators by using a blowpipe of hot air that expels air at 650 °C, and propels onto the coating drops of aqueous solution 0.05 M of a eutectic mixture KCl:ZnCl (52:48 wt%).

Li et al. [338] have studied the corrosion of TBCs by CMAS (the acronym of each oxide: CaO, MgO, Al_2O_3, and SiO_2). The CMAS powder was synthesized as tapes of 25.4 mm diameter and glued onto the top of the coating surfaces using cement 520. The infiltration process was accomplished either in a tube furnace or through a flame burner. The coating degradation simulated in this method is similar to reports from field studies of aircraft engines.

15.10.2.4 (d) Oxidation

Matthews et al. [339] have followed the oxidation of Cr_3C_2–NiCr coatings heat treated at 900 °C in still air during different numbers of days. Ye et al. [340] performed a similar work on Cr39Ni7C cermet coatings deposited by Diamond jet spray process. For details about oxidation test, see [15.C15].

15.11 Summary and Conclusions

Sprayed coating characterization is very important. However the needs of research laboratories, often working on relatively small samples, are not at all the same as those of industry working with real part geometry. In laboratories the interest is mostly in the characterization of coating phases, microstructure, and now nanostructure, unmolten particles, voids, and cracks distributions, coating–substrate interface or splat interfaces, …, quantities which are not directly linked to the properties desired in industry. In production, the main interest is in the measurement of the part geometry after spraying and machining, coating thickness, adhesion/cohesion, hardness, stiffness, Young's modulus, thermal conductivity, and diffusivity. Anyhow whatever maybe the measurement it requires using statistical methods (see Sect. 15.1.3) that must be carefully achieved to limit the errors to human ones.

The dream in production would be that all measurements could be achieved by nondestructive methods (Sect. 15.2). However if the coordinate measurements with machine vision and robotic are now well developed, the other methods are still

essentially used in laboratories. Most materials characterizations (see Sect. 15.4), void content, and network architecture (see Sect. 15.5) imply metallographic preparation of samples, techniques rapidly presented in Sect. 15.3. Then the important measurements of adhesion/cohesion, mechanical, and thermal properties are described in Sects. 15.6–15.8. And finally the two last sections deal with wear and corrosion.

All these measurements impact the reproducibility and reliability of thermal-sprayed coating production. Thus the measurement uncertainty must be controlled carefully and statistics used properly. However the human factor still remains very important in coating quality [4].

Nomenclature

Latin Alphabet

a	Thermal diffusivity (m^2/s)
A	Sample measured area or contact area between the indenter and the substrate (μm^2), also crack area (m^2)
a_c	Half-diagonal crack length (μm)
a_k	Crack length (m)
A_w	Area of contact (m^2)
B	Thickness (m)
C	Compliance: ratio of the displacement to the load (m/N)
c_f	Correction factor related to the shape of the indenter
c_p	Specific heat at constant pressure (J/K kg)
C_T	Corrosion rate at temperature T (mm/year or mpy)
d	Equivalent diameter of intruded pores (μm) or inside diameter in the circumferentially notched bar (m)
D	Outside diameter of the bar (m)
d_0	"Stress-free" lattice parameter (nm)
d_{hkl} d	Distance between atomic layers with the same Miller indices (h, k, l)
d_w	Sliding distance (m)
e	Sample thickness (m)
E	Energy (J) or (eV for X-ray, neutron, ...)
E'	Young's modulus (GPa)
E'_c	Young's modulus of the coating (GPa)
E'_s	Young's modulus of the substrate (GPa)
E_c	Corrosion potential (no current flowing) (mV)
F	Force applied (N)
$f(\alpha)$	A function of the impingement angle α (−)
F_N	Applied normal force (N)
G_c	Critical value of the strain energy release rate (J/m^2)

h	Penetration depth of an indenter (μm)
H	Hardness or yield stress (MPa)
HK or KHN	Knoop hardness (MPa)
h_{max}	Penetration depth of an indenter corresponding to both plastic and elastic components (μm)
h_p	Plastic component of penetration depth of an indenter (μm)
h_r	Residual depth of the residual deformation once the indenter is removed (μm)
HV	Vickers hardness (MPa)
HV_x	*hardness* measured with a load of x Newton
I	Impressed current (mA)
I_c	Corrosion current (no external current) (mA)
$\mathbf{k}$	Wave vector of the incident neutron beam
K	Strain energy release rate (related to the fracture toughness) ($N/m^{3/2}$)
$\mathbf{k}_0$	Wave vector of the scattered neutron beam
K_{adh}	Adhesion wear coefficient ($K_{adh} = K_w/3$) (−)
K_c	Fracture toughness ($N/m^{3/2}$)
K_{ca}	Apparent interface fracture toughness ($N/m^{3/2}$)
K_w	Wear coefficient (−)
l	Length of the coating (m)
L	Length scale probed at a given value of the scattering vector or the average length of diagonals of Vickers indenter (m)
l_c	Palmqvist surface crack length (μm)
m	Shape parameter in Weibull distribution
p	Pressure (Pa)
P	Force required extending a crack (N)
P_c	Applied load (N) on an indenter
P_{max}	Maximum load on an indenter (N)
$\mathbf{q}$	Scattering vector
q	Modulus of scattering vector
Q	Imposed gas flow (m^3/s)
S	Slope of the initial part of the unloading curve (−)
TSR	Thermal shock resistance (K)
U	Elastic energy stored in the system (J)
V	Volume (m^3)
V_b	Coating bulk volume (m^3)
V_p	Open pores volume (m^3)
V_w	Wear volume (m^3)
w	Coating thickness (μm)
W	Total work (J)
w_{dry}	The dried coating weight (kg)

W_e Work done by external forces (J) or elastic work (J)
w_{sat} The wet coating weight (kg)
w_{wd} Weight of water displaced (kg)
x_i Measured value of indent, hardness, Young's module ...

Greek Alphabet

α Impingement angle (°), angle between opposite faces of diamond (136°)
φ Angle between the normal to the coating surface (y-direction) (°)
ϕ Phase angle
γ Surface tension (J/m^2 or N/m)
η Arithmetic mean of the sample of N events
κ Thermal conductivity (W/m K)
μ Viscosity (Pa s)
λ Wavelength (nm) or scale parameter in Weibull distribution
ν Poisson's ratio
θ Angle of incidence of analyzing beam or contact angle between a liquid and a solid
ρ Mass density (kg/m^3)
σ Standard deviation
$\rho(r)$ Scattering length density
ϕ_a Apparent porosity (%)
τ_c Critical shear stress (MPa)
κ_e Electronic conduction (W/m K)
σ_f Fracture stress (MPa)
ΔG^* Activation energy of the corrosion reaction (J)
ε_{hkl} Lattice strain (−)
α_L Linear expansion coefficient (K^{-1})
κ_{Ph} Lattice conduction or phonon conduction (W/m K)
α_V Volumetric expansion coefficients, if α_L are the same in the three coordinates direction ($\alpha_V = 3\alpha_L$) (K^{-1})
δ_w Depth of wear (μm)
ρ_X Specific mass or mass density of X (kg/m^3)
Δp Pressure drop (Pa)

ASTM Standards

A: Adhesion–Cohesion

[15.A1] **ASTM C633** Revision/Edition: 01 Chg: W/REAP Date: 00/00/08 Standard test method for adhesion or cohesion strength of thermal spray coatings

C: Corrosion

[15.C1] **ASTM G193** Revision/Edition: 10B Chg: Date: 06/01/10 Standard terminology and acronyms relating to corrosion

[15.C2] **ASTM 03.02** Revision/Edition: 10 Chg: Date: 08/00/10 Corrosion of metals; Wear and corrosion

[15.C3] **ASTM G102** Revision/Edition: 89 Standard practice for calculation of corrosion rates and related information from electrochemical measurements

[15.C4] **ASTM G3** Revision/Edition: 89 Standard practice for conventions applicable to electrochemical measurements in corrosion testing

[15.C5] **BS EN ISO 17475** Revision/Edition: 06 Corrosion of metals and alloys—Electrochemical test methods—Guidelines for conducting potentiostatic and potentiodynamic polarization measurements

[15.C6] **ASTM G5** Revision/Edition: 94 Chg: W/REAP Date: 00/00/04 Standard reference test method for making potentiostatic and potentiodynamic anodic polarization measurements

[15.C7] **ASTM G59** Revision/Edition: 97 Chg: W/REAP Date: 00/00/09 Standard test method for conducting polarization resistance measurements

[15.C8] **ASTM G61** Revision/Edition: 86 Chg: W/REAP Date: 00/00/09 Standard test method for conducting cyclic potentiodynamic polarization measurements for localized corrosion susceptibility of iron-, nickel-, or cobalt-based alloys

[15.C9] **ASTM G102** Revision/Edition: 89 Chg: W/REAP Date: 00/00/10 Standard practice for calculation of corrosion rates and related information from electrochemical measurements

[15.C10] **ASTM G106** Revision/Edition: 89 Chg: W/REAP Date: 00/00/10 Standard practice for verification of algorithm and equipment for electrochemical impedance measurements

[15.C11] **SEMI F77** Revision/Edition: 03 Chg: W/REAP Date: 03/00/10 Test method for electrochemical critical pitting temperature testing of alloy surfaces used in corrosive gas systems

[15.C12] **ASTM G150** Revision/Edition: 99 Chg: W/REAP Date: 00/00/10 Standard test method for electrochemical critical pitting temperature testing of stainless steels

[15.C13] **ASTM G78** Revision/Edition: 01 Chg: W/REAP Date: 00/00/07 Standard guide for crevice corrosion testing of iron-base stainless alloys in seawater and other chloride-containing aqueous environments

[15.C14] **ASTM B117** Revision/Edition: 09 Chg: Date: 07/01/09 Standard practice for operating salt spray (fog) apparatus

[15.C15] **ISO DIS 21608** Revision/Edition: 10 Chg: Date: 10/29/10 Corrosion of metals and alloys—Test method for isothermal-exposure oxidation testing under high-temperature corrosion conditions for metallic materials

M: Mechanical Properties

[15.M1] **ASTM 03.01** Revision/Edition: 10 Chg: Date: 07/00/10 Metals-mechanical testing; elevated and low-temperature tests; Metallography
[15.M2] **ASM METALS HDBK V8** Revision/Edition: 00 Chg: Date: 00/00/00 Mechanical testing and evaluation
[15.M3] **ASTM E6** Revision/Edition: 09B Chg: Date: 05/15/09 Standard terminology relating to methods of mechanical testing
[15.M4] **BS 7134 P4 S4.2** Revision/Edition: 90 Chg: REAF Date: 00/00/96 Testing of engineering ceramics—thermo-mechanical properties—method for determination of thermal diffusivity by the laser flash (or heat pulse) method
[15.M5] **ASTM A833** Revision/Edition: 08A Chg: Date: 11/01/08 Standard practice for indentation hardness of metallic materials by comparison hardness testers
[15.M6] **ASTM C1327** Revision/Edition: 08 Chg: Date: 08/01/08 Standard test method for Vickers indentation hardness of advanced ceramics
[15.M7] **ASTM E384** Revision/Edition: 10 Chg: W/E2 Date: 04/00/10 Standard test method for Knoop and Vickers hardness of materials
[15.M8] **ASTM C1326** Revision/Edition: 08 Chg: W/E1 Date: 09/00/08 Standard test method for Knoop indentation hardness of advanced ceramics
[15.M9] **ASTM C1327-08** Standard test method for Vickers indentation hardness of advanced ceramics
[15.M10] **BS 5600 P4 S4.7** Revision/Edition: 79 Chg: Date: 00/00/79 Determination of the Young's modulus
[15.M11] **JIS Z 2280** Revision/Edition: 93 Chg: W/REAF Date: 10/01/08 Test method for Young's modulus of metallic materials at elevated temperature
[15.M12] **BS DD CEN/TS 1071-7** Revision/Edition: 03 Chg: Date: 10/16/03 Advanced technical ceramics—Methods of test for ceramic coatings—Part 7: Determination of hardness and Young's modulus by instrumented indentation testing
[15.M12] **ASTM C1198** Revision/Edition: 09 Chg: Date: 11/04/09 Standard test method for dynamic Young's modulus, shear modulus and Poisson's ratio for advanced ceramics by sonic resonance
[15.M13] **ASTM C1259** Revision/Edition: 08 Chg: W/E1 Date: 04/00/09 Standard test method for dynamic Young's modulus, shear modulus and Poisson's ratio for advanced ceramics by impulse excitation of vibration
[15.M14] **API TR 6AM** Revision/Edition: 2 Chg: W/REAF Date: 01/00/03 Material toughness
[15.M15] **ASTM C1421** Revision/Edition: 09 Chg: Date: 05/01/09 Standard test methods for determination of fracture toughness of advanced ceramics at ambient temperature
[15.M16] **BS 7448-1** Revision/Edition: 91 Chg: W/REAF Date: 03/00/07 Fracture mechanics toughness tests—Part 1: Method for determination of K1c, critical CTOD and critical J values of metallic materials

[15.M17] **BS EN ISO 12737** Revision/Edition: 06 Chg: Date: 01/12/06 Metallic materials—Determination of plane-strain fracture toughness
[15.M18] **BS ISO 28079** Revision/Edition: 09 Chg: Date: 08/31/09 Hardmetals—Palmquist toughness test
[15.M19] **ASTM STP381** Revision/Edition: 65 Chg: Date: 00/00/65 Fracture toughness testing and its applications
[15.M20] **BS EN 15305** Revision/Edition: 08 Chg: W/CRGD Date: 06/30/09 Non-destructive testing—Standard test method for determining residual stress analysis by X-ray diffraction
[15.M21] **BS DD CEN ISO/TS 21432** Revision/Edition: 06 Chg: W/REAF Date: 12/01/08 Non-destructive testing—Standard test method for determining residual stresses by neutron diffraction

Ma: Materials Characterization

[15.Ma1] **ASTM E204** Revision/Edition: 98 Chg: W/REAP Date: 00/00/07 Standard practices for identification of materials by infrared absorption spectroscopy, using the ASTM coded band and chemical classification index
[15.Ma2] **BS EN 13925-1** Revision/Edition: 03 Chg: W/REAF Date: 12/01/08 Non-destructive testing—X-ray diffraction from polycrystalline and amorphous materials—Part 1: General principles
[15.Ma3] **BS EN 13925-2** Revision/Edition: 03 Chg: W/REAF Date: 12/01/08 Non-destructive testing—X-ray diffraction from polycrystalline and amorphous materials—Part 2: Procedures
[15.Ma4] **NBS MONO 25 SEC 16** Revision/Edition: 79 Chg: Date: 10/00/79 Standard X-ray diffraction powder patterns
[15.Ma5] **ASTM F2024** Revision/Edition: 10 Chg: REIN Date: 06/00/10 Standard practice for X-ray diffraction determination of phase content of plasma-sprayed hydroxyapatite coatings
[15.Ma6] **BS ISO 17470** Revision/Edition: 04 Chg: W/REAF Date: 12/01/08 Microbeam analysis—electron probe microanalysis—Guidelines for qualitative point analysis by wavelength dispersive X-ray spectrometry
[15.Ma7] **BS ISO 18516** Revision/Edition: 06 Chg: W/REAF Date: 06/01/10 Surface chemical analysis—Auger electron spectroscopy and X-ray photoelectron spectroscopy—Determination of lateral resolution
[15.Ma8] **AS ISO 15470** Revision/Edition: 06 Chg: Date: 10/20/06 Surface chemical analysis—X-ray photoelectron spectroscopy—description of selected instrumental performance parameters
[15.Ma9] **BS ISO 10810** Revision/Edition: 10 Chg: Date: 12/31/10 Surface chemical analysis—X-ray photoelectron spectroscopy—guidelines for analysis
[15.Ma10] **BS ISO 15470** Revision/Edition: 05 Chg: W/REAF Date: 10/01/10 Surface chemical analysis—X-ray photoelectron spectroscopy—description of selected performance parameters

Me: Metallography and Image Analysis

[15.Me1] **ASTM E1920** Revision/Edition: 03 Chg: W/REAP Date: 00/00/08 Standard guide for metallographic preparation of thermal sprayed coatings
[15.Me2] **ASTM E3** Revision/Edition: 01 Chg: W/E1 Date: 03/00/09 Guide for metallographic preparation of metallographic specimens
[15.Me3] **ASTM MNL46** Revision/Edition: 07 Chg: Date: 00/00/07 Metallographic and materialographic specimen preparation light microscopy, image analysis and hardness testing

ND: Non-destructive Methods

[15.ND1] **ESDU 91027** Revision/Edition: 91 Chg: W/AA Date: 11/01/93 Non-destructive examination—Choice of methods

S: Statistical Methods

[15.S1] **ASTM C1239-07** Revises ASTM C1239-06a Standard practice for reporting uniaxial strength data and estimating Weibull distribution parameters for advanced ceramics

T: Thermal Properties

[15.T1] **ASTM E228** Revision/Edition: 06 Chg: W/REIN Date: 09/01/06 Standard test method for linear thermal expansion of solid materials with a push-rod dilatometer
[15.T2] **ASTM E289** Revision/Edition: 04 Chg: W/REAP Date: 00/00/10 Standard test method for linear thermal expansion of rigid solids with interferometry
[15.T3] **ASTM C177** Revision/Edition: 10 Chg: Date: 06/01/10 Standard test method for steady-state heat flux measurements and thermal transmission properties by means of the guarded-hot-plate apparatus
[15.T4] **ASTM C201-93** (2009) Standard test method for thermal conductivity of refractories
[15.T5] **ASTM E 1461** Revision/Edition: 07 Chg: Date: 11/01/07 Standard test method for thermal diffusivity of solids by the flash method Disk 6–12 mm diameter; 1.5–4 mm thick diffusivity 0.1–1,000 m^2/s

[15.T6] **ASTM C 714** Revision/Edition: 05 Chg: W/REAP Date: 00/00/10 Standard test method for thermal diffusivity of carbon and graphite by a thermal pulse method; 6–12mm, 2–4 mm thick; 0.04–2.0 cm^2/s

[15.T7] **ASTM C 1470-06** Standard guide for testing the thermal properties of advanced ceramics

[15.T8] **BS 7134 P4 S4.2** Revision/Edition: 90 Chg: REAF Date: 00/00/96 Testing of engineering ceramics—thermo-mechanical properties—method for determination of thermal diffusivity by the laser flash (or heat pulse) method

[15.T9] **ASTM D2766-95(2009)** Standard test method for specific heat of liquids and solids

[15.T10] **ASTM E1269-11** Standard test method for determining specific heat capacity by differential scanning calorimetry

[15.T11] **ASTM C1525** Revision/Edition: 04 Chg: W/REAP Date: 00/00/09 Standard test method for determination of thermal shock resistance for advanced ceramics by water quenching

[15.T12] **FORD FLTM BI 107-05** Revision/Edition: 09 Chg: Date: 02/03/09 Thermal shock for coating adhesion

[15.T13] **JDQ149** Revision/Edition: 02 Chg: Date: 06/27/02 Tests for thermal shock resistance of high temperature coatings

[15.T14] **ASTM C 1171-05** Standard test method for quantitatively measuring the effect of thermal shock and thermal cycling on refractories

[15.T15] **ISO DIS 13123** Revision/Edition: 10 Chg: Date: 07/22/10 Metallic and other inorganic coatings—Test method of cyclic heating for thermal barrier coatings under temperature gradient

V: Void Content and Network Architecture

[15.V1] **E2109-01(2007)** Standard test methods for determining area percentage porosity in thermal sprayed coatings

W: Wear

[15.W1] **ASTM G40** Revision/Edition: 10A Chg: Date: 07/01/10 Standard terminology relating to wear and erosion

[15.W2] **ASTM C704/C704M** Revision/Edition: 09 Chg: W/E1 Date: 08/00/09 Standard test method for abrasion, resistance of refractory materials at room temperature

[15.W3] **ASTM G105** Revision/Edition: 02 Chg: W/REAP Date: 00/00/07 Standard test method for conducting wet sand/rubber wheel abrasion test

[15.W4] **ASTM G132** Revision/Edition: 96 Chg: W/REAP Date: 00/00/07 Standard test method for pin abrasion testing
[15.W5] **ASTM G65** Revision/Edition: 04 Chg: Date: 11/01/04 10 Standard test method for measuring abrasion using the dry sand/rubber wheel apparatus
[15.W6] **ASTM MNL56** Revision/Edition: 07 Chg: Date: 00/00/07 Guide to friction, wear, and erosion testing
[15.W7] **ASTM G99** Revision/Edition: 05 Chg: W/REAP Date: 00/00/10 Standard test method for wear testing with a pin-on-disk apparatus
[15.W8] **ASTM G133** Revision/Edition: 05 Chg: W/REAP Date: 00/00/10 Standard test method for linearly reciprocating ball-on-disk sliding wear
[15.W9] **ASTM G98** Revision/Edition: 09 Chg: Date: 10/01/09 Standard test method for galling resistance of materials
[15.W10] **ASTM G73** Revision/Edition: 10 Chg: Date: 04/01/10 Standard test method for liquid impingement erosion using rotating apparatus
[15.W11] **ASTM G134** Revision/Edition: 95 Chg: W/REAP Date: 00/00/06 Standard test method for erosion of solid materials by a cavitating liquid jet
[15.W12] **ASTM G32** Revision/Edition: 09 Chg: Date: 05/01/09 Standard test method for cavitation erosion using vibratory apparatus
[15.W13] **ASTM E1942** Revision/Edition: 98 Chg: W/REAP Date: 00/00/04 Standard guide for evaluating data acquisition systems used in cyclic fatigue and fracture mechanisms
[15.W14] **ASTM E2368** Revision/Edition: 10 Chg: Date: 05/01/10 Standard practice for strain controlled thermomechanical fatigue testing
[15.W15] **BS 3518-1** Revision/Edition: 93 Chg: W/REAF Date: 01/01/09 Methods of fatigue testing—Part 1: Guide to general principles
[15.W16] **BS 3518-2** Revision/Edition: 62 Chg: W/REAF Date: 01/01/09 Methods of fatigue testing—Part 2: Rotating bending fatigue tests
[15.W17] **BS 3518-3** Revision/Edition: 63 Chg: W/REAF Date: 01/01/09 Methods of fatigue testing—Part 3: Direct stress fatigue tests
[15.W18] **ASTM G119** Revision/Edition: 09 Chg: Date: 07/15/09 Standard guide for determining synergism between wear and corrosion
[15.W19] **ASTM 03.02** Revision/Edition: 10 Chg: Date: 08/00/10 Corrosion of metals; Wear and corrosion
[15.W20] **ASTM G204** Revision/Edition: 10 Chg: Date: 04/01/10 Standard test method for damage to contacting solid surfaces under fretting conditions
[15.W21] **ASTM STP1159** Revision/Edition: 92 Chg: Date: 00/00/92 Standardization of fretting fatigue test methods and equipment
[15.W22] **ASTM STP1367** Revision/Edition: 00 Chg: Date: 02/00/00 Fretting fatigue: current technology and practices

References

1. Pawlowski L (1995) The science and engineering of thermal spray coatings. Wiley, NY (revised version Wiley, Apr 30, 2008, 656 p)
2. Riggs W (2004) Metallography and image analysis. In: Davis JR (ed) Handbook of thermal spray technology. ASM International, Metals Park, OH, pp 224–259, Reprinted with kind permission from ASM International and the Thermal Spray Society 2004
3. Wigren J, Täng K (2007) Quality considerations for the evaluation of thermal spray coatings. J Therm Spray Technol 16(4):533–540
4. Wigren J, Johansson J (2011) Improving reliability of thermal spray coatings in production environment. In: Presented at 3rd plasma round table, 31 Oct–4 Nov 2011, South Africa
5. Li J, Ding C (2001) Determining microhardness and elastic modulus of plasma-sprayed Cr_2C_3-NiCr coatings using Knoop indentation testing. Surf Coat Technol 135:229–237
6. Factor M, Roman I (2000) Vickers micro-indentation of WC-12%Co thermal spray coating. Part 1: Statistical analysis of microhardness data. Surf Coat Technol 132:181–193
7. Factor M, Roman I (2000) Vickers micro-indentation of WC-12%Co thermal spray coating. Part 2: The between-operator reproducibility limits of microhardness measurement and alternative approaches to quantifying hardness of cemented-carbide thermal spray coatings. Surf Coat Technol 132:65–75
8. Walpole RE, Myers RH (1978) Probability and statistics for engineers and scientists, 2nd edn. Macmillan, New York
9. Lin CK, Berndt CC (1993) Microhardness variations in thermally sprayed coatings. In: Berndt CC, Bernicki TF (eds) Proceedings of the national thermal spray conference. ASM International, Materials Park, OH, pp 561–564
10. Brousse E (2010) Elaboration by thermal spraying of finely structured elements of a high temperature electrolyser for hydrogen production: processes, structures and characteristics. Ph.D. thesis, University of Limoges, France (in French)
11. ASM International (2007) ASM handbook: nondestructive evaluation and quality control, vol 17, 9th edn. ASM International, Materials Park, OH
12. Noone MJ, Mehan RL (1974) In: Bradt RC, Hasselman DPH, Lange FF (eds) Fracture mechanics of ceramics. Plenum, New York, pp 201–229
13. Berndt CC (1985) Acoustic emission evaluation of plasma·sprayed thermal barrier coatings. J Eng Gas Turbines Power Trans ASME 107:142–146
14. Voyer J, Gitzhofer F, Boulos MI (1998) Study of the performance of TBC under thermal cycling conditions using an acoustic emission rig. J Therm Spray Technol 7:181–190
15. Kucuk A, Berndt CC, Senturk U, Lima RS, Lima CRC (2000) Influence of plasma spray parameters on mechanical properties of yttria stabilized zirconia coatings. I: Four point bend test. Mater Sci Eng A 284:29–40
16. Lin CK, Berndt CC (1998) Acoustic emission studies on thermal spray materials. Surf Coat Technol 102:1–7
17. Lin CK, Berndt CC, Leigh SH, Murakami K (1997) Acoustic emission studies of alumina-13% titania free-standing forms during four-point bend tests. J Am Ceram Soc 80:2382–2394
18. Andrews DJ, Taylor JAT (2000) Quality control of thermal barrier coatings using acoustic emission. J Therm Spray Technol 9(2):181–190
19. Robin P, Gitzhofer F, Fauchais P, Boulos M (2010) Remaining fatigue life assessment of plasma sprayed thermal barrier coatings. J Therm Spray Technol 19(5):911–920
20. Kucuk A, Berndt CC, Senturk U, Lima RS, Lima CRC (2000) Influence of plasma spray parameters on mechanical properties of yttria stabilized zirconia coatings. II: Acoustic emission response. Mater Sci Eng A284:41–50

21. Zhao Y, Lin L, Li XM, Lei MK (2010) Simultaneous determination of the coating thickness and its longitudinal velocity by ultrasonic nondestructive method. NDT&E Int 43:579–585
22. Boccaccini DN, Boccaccini AR (1997) Dependence of ultrasonic velocity on porosity and pore shape in sintered materials. J Nondestruct Eval 16(4):187–192
23. Asmani M, Kermel C, Leriche A, Ourak M (2001) Influence of porosity on Young's modulus and Poisson's ratio in alumina ceramics. J Eur Ceram Soc 21:1081–1086
24. Ma XQ, Mizutani Y, Takemoto M (2001) Laser-induced surface acoustic waves for evaluation of elastic stiffness of plasma sprayed materials. J Mater Sci 36:5633–5641
25. Lima RS, Kruger SE, Lamouche G, Marple BR (2003) Elastic modulus measurements via laser-ultrasonic and Knoop indentation techniques. In: Moreau C, Marple B (eds) Thermal spray 2003: Advancing the science and applying the technique. ASM International, Materials Park, OH, pp 1369–1378
26. Rosa G, Psyllaki P, Oltra R, Costil S, Coddet C (2001) Simultaneous laser generation and laser ultrasonic detection of the mechanical breakdown of a coating-substrate interface. Ultrasonics 39:355–365
27. Hung YY, Chen YS, Ng SP, Liu L, Huang YH, Luk BL, Ip RWL, Wu CML, Chung PS (2009) Review and comparison of shearography and active thermography for non-destructive evaluation. Mater Sci Eng R 64:73–112
28. Maldague X, Marinetti S (1996) Pulse phase infrared thermography. J Appl Phys 79 (5):2694–2698
29. Shepard SM (2001) Advances in pulsed thermography. In: Proceedings of SPIE, Thermo sense XXIII, Orlando, FL, USA, 16–19 Apr 2001, pp 511–515
30. Marinetti S, Robba D, Cernuschi F, Bison PG, Grinzato E (2007) Thermographic inspection of TBC coated gas turbine blades: discrimination between coating over-thicknesses and adhesion defects. Infrared Phys Technol 49:281–285
31. Van der Voort GF (1999) Metallography principles and practice, Material science and engineering series. ASM International, Materials Park, OH
32. George Vander Voort (ed) (2004) ASM handbook, vol 09, Metallography and microstructures. ASM International, Materials Park, OH, 1184 p
33. Geels K (2007) ASTM MNL46, Metallographic and materialographic specimen preparation, light microscopy, image analysis and hardness testing. ASTM International, West Conshohocken, PA
34. Antou G, Montavon G (2007) Quantifying thermal spray coating architecture by stereological protocols: Part II. Key points to be addressed. J Therm Spray Technol 16(2):168–176
35. Sauer JP (2005) Metallographic preparation and testing of thermal spray coatings: sectioning, TSS committee on accepted practices. J Therm Spray Technol 14(3):313–314
36. Puerta DG (2005) Metallographic preparation and evaluation of thermal spray coatings: mounting, TSS committee on accepted practices. J Therm Spray Technol 14(4):450–452
37. Puerta DG (2006) Metallographic preparation and testing of thermal spray coatings: grinding, TSS committee on accepted practices. J Therm Spray Technol 15(1):31–32
38. Sauer JP, Blann G (2006) Metallographic preparation and testing of thermal spray coatings: fine grinding and polishing, TSS committee on accepted practices. J Therm Spray Technol 15 (2):174–176
39. Giannuzzi LA, Stevens FA (2004) Introduction to focused ion beams: instrumentation, theory, techniques and practice. Springer, Berlin
40. Puerta DG (2008) TSS accepted practices committees—metallography and mechanical testing. J Therm Spray Technol 17(4):435–436
41. Ingo GM, Kaciulis S, Mezzi A, Valente T, Casadei F, Gusmano G (2005) Characterization of composite titanium nitride coatings prepared by reactive plasma spraying. Electrochim Acta 50:4531–4537
42. Russ JC (2011) The image processing handbook, 6th edn. CRC, Taylor & Francis Group, Boca Raton, FL

43. Etchart-Salas R, Rat V, Coudert JF, Fauchais P, Caron N, Wittman K, Alexandre S (2007) Influence of plasma instabilities in ceramic suspension plasma spraying. J Therm Spray Technol 16(5–6):857–865
44. Eaton P, West P (2010) Atomic force microscopy. Oxford University Press, Oxford
45. Cedelle J, Vardelle M, Fauchais P (2006) Influence of stainless steel substrate preheating on surface topography and on millimeter- and micrometer-sized splat formation. Surf Coat Technol 201:1373–1382
46. Williams DB, Carter CB (2009) Transmission electron microscopy, 2nd edn. Springer, New York
47. Chraska T, King AH (2001) Transmission electron microscopy study of rapid solidification of plasma sprayed zirconia — Part I. First splat solidification. Thin Solid Films 397:30–39
48. Tjitra Salim N, Yamada M, Nakano H, Shima K, Isago H, Fukumoto M (2011) The effect of post-treatments on the powder morphology of titanium dioxide (TiO_2) powders synthesized for cold spray. Surf Coat Technol 206:366–371
49. Chen H, Hao Y, Wang H, Tang W (2010) Analysis of the microstructure and thermal shock resistance of laser glazed nanostructured zirconia TBCs. J Therm Spray Technol 19 (3):558–565
50. Yan D, Dong Y, Yang Y, Wang L, Chen X, He J, Zhang J (2011) Microstructure characterization of the $FeAl_2O_4$-based nanostructured composite coating synthesized by plasma spraying Fe_2O_3/Al powders. J Therm Spray Technol 20(6):1269–1277
51. Ma XQ, Gandy DW, Frederick GJ (2008) Innovation of ultrafine structured alloy coatings having superior mechanical properties and high temperature corrosion resistance. J Therm Spray Technol 17(5–6):933–941
52. Chraska T (1999) TEM studies of microstructures and interfaces of zirconia produced by plasma spraying. Ph.D. thesis, State University of New York at Stony Brook, New York
53. ASM International (2008) ASM handbook, vol 10, 8th edn, Materials characterization. ASM International, Materials Park, OH
54. Chandra S, Fauchais P (2009) Formation of solid splats during thermal spray deposition. J Therm Spray Technol 18(2):148–180
55. Volenžk K, Hanousek F, Chraska P, Ilavsky J, Neufuss K (1999) In-flight oxidation of high-alloy steels during plasma spraying. Mater Sci Eng A272:199–206
56. Lima RS, Kucuk A, Berndt CC (2001) Integrity of nanostructured partially stabilized zirconia after plasma spray processing. Mater Sci Eng A313:75–82
57. Liu XQ, Zheng YG, Chang XC, Hou WL, Wang JQ, Tang Z, Burgess A (2009) Microstructure and properties of Fe-based amorphous metallic coating produced by high velocity axial plasma spraying. J Alloys Compd 484:300–307
58. Kishitake K, Era H, Otsubo F (1996) Characterization of plasma sprayed Fe-17Cr-38Mo-4C amorphous coatings crystallizing at extremely high temperature. J Therm Spray Technol 5 (3):283–288
59. Zhao XB, Ye ZH (2012) Microstructure and wear resistance of molybdenum based amorphous nanocrystalline alloy coating fabricated by atmospheric plasma spraying. Surf Coat Technol 228:S226–S270
60. Guinier A, Fournet G (1955) Small-angle scattering of X-rays. Wiley, New York, NY
61. Ilavsky J, Jemian PR, Allen AJ, Zhang F, Levine LE, Long GG (2009) Ultra-small-angle X-ray scattering at the advanced photon source. J Appl Crystallogr 42:1–11
62. Flores A, Renteria, Saruhan B, Ilavsky J, Allenc AJ (2007) Application of USAXS analysis and non-interacting approximation to determine the influence of process parameters and ageing on the thermal conductivity of electron-beam physical vapor deposited thermal barrier coatings. Surf Coat Technol 201:4781–4788
63. Bacciochini A, Ilavsky J, Montavon G, Denoirjean A, Ben-ettouil F, Valette S, Fauchais P, Wittmann-Teneze K (2010) Quantification of void network architectures of suspension plasma-sprayed (SPS) yttria-stabilized zirconia (YSZ) coatings using Ultra-small-angle X-ray scattering (USAXS). Mater Sci Eng A528:91–102

64. Ilavsky J, Jemian PR, Allen AJ, Zhang F, Levine LE, Long GG (2009) Ultra-small-angle X-ray scattering at the advanced photon source. J Appl Crystallogr 42(3):469–479
65. Allen AJ, Long GG, Boukari H, Ilavsky J, Kulkarni A, Sampath S, Herman H, Goland AN (2001) Microstructural characterization studies to relate the properties of thermal spray coatings to feedstock and spray conditions. Surf Coat Technol 146–147:544–552
66. Ilavsky J, Herman H, Berndt CC, Goland AN, Long GG, Krueger S, Allen AJ (1994) In: Berndt CC, Sampath S (eds) Thermal spray industrial applications. ASM International, Materials Park, OH, pp 709–715
67. Allen AJ, Ilavsky J, Long GG, Wallace JS, Berndt CC, Herman H (2001) Micro structural characterization of yttria-stabilized zirconia plasma-sprayed deposits using multiple small-angle neutron scattering. Acta Mater 49:1661–1675
68. Ilavsky J, Long GG, Allen AJ, Leblanc L, Prystay M, Moreau C (1999) Anisotropic microstructure of plasma-sprayed deposits. J Therm Spray Technol 8(3):414–420
69. Kulkarni A, Wang Z, Nakamura T, Sampath S, Goland A, Herman H, Allen J, Ilavsky J, Long GG, Frahm J, Steinbrech RW (2003) Comprehensive microstructural characterization and predictive property modeling of plasma-sprayed zirconia coatings. Acta Mater 51:2457–2475
70. Kulkarni AA, Goland A, Herman H, Allen AJ, Ilavsky J, Long GG, De Carlo F (2005) Advanced microstructural characterization of plasma-sprayed zirconia coatings over extended length scales. J Therm Spray Technol 14(2):239–250
71. Petorak C, Ilavsky J, Wang H, Porter W, Trice R (2010) Microstructural evolution of 7 wt.% Y_2O_3–ZrO_2 thermal barrier coatings due to stress relaxation at elevated temperatures and the concomitant changes in thermal conductivity. Surf Coat Technol 205:57–65
72. Bunker G (2010) Introduction to XAFS: a practical guide to X-ray absorption fine structure spectroscopy. Cambridge University Press, Cambridge
73. Rice RW (1996) Porosity dependence of physical properties of materials: a summary review. Key Eng Mater 115:1–19
74. Ilavsky J (2010) Characterization of complex thermal barrier deposits pore microstructures by a combination of imaging, scattering and intrusion techniques. J Therm Spray Technol 19 (1–2):178–189
75. Andreola F, Leonelli C, Romagnoli M, Miselli P (2000) Techniques used to determine porosity. Am Ceram Soc Bull 79(7):49–52
76. Fauchais P, Montavon G, Lima RS, Marple BR (2011) Engineering a new class of thermal spray nano-based microstructures from agglomerated nanostructured particles. Suspensions and solutions: an invited review. J Phys D 44:093001
77. Mancini CE, Berndt CC, Sun L, Kucuk A (2001) Porosity determinations in thermally sprayed hydroxyapatite coatings. J Mater Sci 36:3891–3896
78. Matějíček J, Kolman B, Dubský J, Neufuss K, Hopkins N, Zwick J (2006) Alternative methods for determination of composition and porosity in abradable materials. Mater Charact 57:17–29
79. Washburn EW (1921) The dynamics of capillary flows. Phys Rev 17:273–283
80. Ilavsky J, Berndt CC, Karthikeyan J (1997) Mercury intrusion porosimetry of plasma-sprayed ceramic. J Mater Sci 32:3925–3932
81. Van Brakel J, Modrý S, Svatá M (1981) Mercury porosimetry: state of the art. Powder Technol 29(1):1–12
82. Siebert B, Funke C, Vaßen R, Stöver D (1999) Changes in porosity and Young's modulus due to sintering of plasma sprayed thermal barrier coatings. J Mater Process Technol 92–93:217–223
83. Mauer G, Vaßen R, Stöver D (2009) Atmospheric plasma spraying of yttria-stabilized zirconia coatings with specific porosity. Surf Coat Technol 204:172–179

84. Zhu S, Pelton RH, Collver K (1995) Mechanistic modelling of fluid permeation through compressible fiber beds. Chem Eng Sci 50(22):3557–3572
85. Wittmann-Ténèze K, Caron N, Alexandre S (2008) Gas permeability of porous plasma-sprayed coatings. J Therm Spray Technol 17(5–6):902–907
86. Li C-J, Ning X-J, Li C-X (2005) Effect of densification processes on the properties of plasma-sprayed YSZ electrolyte coatings for solid oxide fuel cells. Surf Coat Technol 190:60–64
87. Fox AC, Clyne TW (2004) Oxygen transport by gas permeation through the zirconia layer in plasma sprayed thermal barrier coatings. Surf Coat Technol 184:311–321
88. Golosnoy IO, Paul S, Clyne TW (2008) Modelling of gas permeation through ceramic coatings produced by thermal spraying. Acta Mater 56:874–883
89. Reed JS (1995) Principles of ceramics processing. Wiley, New York
90. Curran JA, Clyne TW (2006) Porosity in plasma electrolytic oxide coatings. Acta Mater 54 (7):1985–1993
91. Bacciochini A, Montavon G, Ilavsky J, Denoirjean A, Fauchais P (2010) Porous architecture of SPS thick YSZ coatings structured at the nanometer scale (50 nm). J Therm Spray Technol 19(1–2):198–206
92. Ilavsky J, Long GG, Allen AJ, Berndt CC (1999) Evolution of the void structure in plasma-sprayed YSZ deposits during heating. Mater Sci Eng A272:215–221
93. Strunz P, Schumacher G, Vaßen R, Wiedenmann A (2004) In situ SANS study of pore microstructure in YSZ thermal barrier coatings. Acta Mater 52:3305–3312
94. Kulkarni A, Goland A, Herman H, Allen AJ, Dobbins T, DeCarlo F, Ilavsky J, Long GG, Fang S, Lawton P (2006) Advanced neutron and X-ray techniques for insights into the microstructure of EB-PVD thermal barrier coatings. Mater Sci Eng A 426:43–52
95. Flores Renteria A, Saruhan B, Ilavsky J, Allen AJ (2007) Application of USAXS analysis and non-interacting approximation to determine the influence of process parameters and ageing on the thermal conductivity of electron-beam physical vapor-deposited thermal barrier coatings. Surf Coat Technol 201:4781–4788
96. Deshpande S, Kulkarni A, Sampath S, Herman H (2004) Application of image analysis for characterization of porosity in thermal spray coatings and correlation with small angle neutron scattering. Surf Coat Technol 187:6–16
97. Antou G, Montavon G, Hlawka F, Cornet A, Coddet C, Machi F (2004) Evaluation of modifications induced on pore network and structure of partially stabilized zirconia manufactured by hybrid plasma spray process. Surf Coat Technol 180–181:627–632
98. Montavon G, Antou G (2007) Quantifying thermal spray coating architecture by stereological protocols: Part I. A historical perspective. J Therm Spray Technol 16(1):6–14
99. Hanson TC, Settlese GS (2003) Particle temperature and velocity effects on the porosity and oxidation of an HVOF corrosion-control coating. J Therm Spray Technol 12 (3):403–415
100. Russ JC (1995) The image processing handbook, 2nd edn. CRC, Boca Raton, FL
101. Zhang XC, Xu BS, Xuan FZ, Wang HD, Wu YX, Tu ST (2009) Statistical analyses of porosity variations in plasma-sprayed Ni-based coatings. J Alloys Compd 467:501–508
102. Zhang XC, Xu BS, Xuan FZ, Wang HD, Wu YX (2009) Microstructural and porosity variations in the plasma-sprayed Ni-alloy coatings prepared at different spraying powers. J Alloys Compd 473:145–151
103. Venkataraman R, Das G, Singh SR, Pathak LC, Ghosh RN, Venkataraman B, Krishnamurthy R (2007) Study on influence of porosity, pore size, spatial and topological distribution of pores on microhardness of as plasma sprayed ceramic coatings. Mater Sci Eng A 445–446:269–274
104. Elsebaei A, Heberlein J, Elshaer M, Farouk A (2010) Comparison of in-flight particle properties, splat formation, and coating microstructure for regular and nano-YSZ powders. J Therm Spray Technol 19(1–2):2–10

105. Nolan DJ, Samandi M (1997) Revealing true porosity in WC-Co thermal spray coatings. J Therm Spray Technol 6(4):422–424
106. Kang H-K, Bong Kange S (2004) Behavior of porosity and copper oxidation in W/Cu composite produced by plasma spray. J Therm Spray Technol 13(2):223–228
107. Saravanan P, Selvarajan V, Srivastava MP, Rao DS, Joshi SV, Sundararajan G (2000) Study of plasma- and detonation gun-sprayed alumina coatings using Taguchi experimental design. J Therm Spray Technol 9(4):505–512
108. Yang G, Zu-kun H, Xiaolei X, Gang X (2001) Formation of molybdenum boride cermet coating by the detonation spray process. J Therm Spray Technol 10(3):456–460
109. Scrivani A, Rizzi G, Berndt CC (2008) Enhanced thick thermal barrier coatings that exhibit varying porosity. Mater Sci Eng A 476:1–7
110. Tillmann W, Vogli E, Krebs B (2008) Influence of the spray angle on the characteristics of atmospheric plasma sprayed hard material based coatings. J Therm Spray Technol 17 (5–6):948–955
111. Underwood EE (1970) Quantitative stereology. Addison-Wesley, Reading, MA
112. Russ JC, DeHoff RT (1999) Practical stereology, 2nd edn. Plenum, New York, NY
113. Fowler DB, Riggs W, Russ JC (1990) Inspecting thermal sprayed coatings. Adv Mater Process 11:41–52
114. Montavon G, Coddet C, Berndt CC, Leigh S-H (1998) Microstructural index to quantify thermal spray deposit microstructures using image analysis. J Therm Spray Technol 7 (2):229–241
115. Leigh S-H, Berndt CC (1999) Modelling of elastic constants of plasma spray deposits with ellipsoid-shaped voids. Acta Mater 47(5):1575–1586
116. Antou G, Montavon G, Hlawka F, Cornet A, Coddet C (2006) Exploring thermal spray gray alumina coating pore network architecture by combining stereological protocols and impedance electrochemical spectroscopy. J Therm Spray Technol 15(4):765–772
117. Wang Z, Kulkarni A, Deshpande S, Nakamura T, Herman H (2003) Effects of pores and interfaces on effective properties of plasma sprayed zirconia coatings. Acta Mater 51:5319–5334
118. Michlik P, Berndt CC (2006) Image-based extended finite element modeling of thermal barrier coatings. Surf Coat Technol 201:2369–2380
119. Jadhav AD, Padture NP, Jordan EH, Gell M, Miranzo P, Fuller ER Jr (2006) Low-thermal-conductivity plasma-sprayed thermal barrier coatings with engineered microstructures. Acta Mater 54:3343–3349
120. Tillmann W, Klusemann B, Nebel J, Svendsen B (2011) Analysis of the mechanical properties of an arc-sprayed WC-FeCSiMn coating: nanoindentation and simulation. J Therm Spray Technol 20(1–2):328–335
121. Bolot R, Antou G, Montavon G, Coddet C (2005) A two-dimensional heat transfer model for thermal barrier coating average thermal conductivity computation. Numer Heat Transf A 47 (9):875–898
122. Costil S, Verdy C, Bolot R, Coddet C (2007) On the role of spraying process on microstructural, mechanical, and thermal response of alumina coatings. J Therm Spray Technol 16 (5–6):839–843
123. Bolot R, Seichepine J-L, Hao Qiao J, Coddet C (2011) Predicting the thermal conductivity of AlSi/Polyester abradable coatings: effects of the numerical method. J Therm Spray Technol 20(1–2):39–47
124. Bobzin K, Kopp N, Warda T, Öte M (2012) Determination of the effective properties of thermal spray coatings using 2D and 3D models. J Therm Spray Technol. doi:10.1007/s11666-012-9809-3
125. Zhang J, Desai V (2005) Evaluation of thickness, porosity and pore shape of plasma sprayed TBC by electrochemical impedance spectroscopy. Surf Coat Technol 190:98–109

126. Jayaraj B, Desai VH, Lee CK, Sohn YH (2004) Electrochemical impedance spectroscopy of porous ZrO_2–8 wt.% Y_2O_3 and thermally grown oxide on nickel aluminide. Mater Sci Eng A 372(1–2):278–286
127. Antou G, Montavon G, Hlawka F, Cornet A, Coddet C (2004) Characterizations of the pore-crack network architecture of thermal-sprayed coatings. Mater Charact 53:361–372
128. Anderson PS, Wang X, Xiao P (2004) Impedance spectroscopy study of plasma sprayed and EB-PVD thermal barrier coatings. Surf Coat Technol 185:106–119
129. Bolelli G, Rauch J, Cannillo V, Killinger A, Lusvarghi L, Gadow R (2009) Microstructural and tribological investigation of high-velocity suspension flame sprayed (HVSFS) Al_2O_3 coatings. J Therm Spray Technol 18(1):35–49
130. Kawakita J, Kuroda S, Kodama T (2003) Evaluation of through-porosity of HVOF sprayed coating. Surf Coat Technol 166:17–23
131. Koivuluoto H, Lagerbom J, Kylmälahti M, Vuoristo P (2008) Microstructure and mechanical properties of low-pressure cold-sprayed (LPCS) coatings. J Therm Spray Technol 17 (5–6):721–727
132. Lin CK, Berndt CC (1994) Measurement and analysis of adhesion strength for thermally sprayed coatings. J Therm Spray Technol 3(1):75–104
133. Berndt CC, McPherson R (1981) A fracture mechanics approach to the adhesion of flame and plasma sprayed coatings. Trans Int Eng 6(4):53–58
134. Heintze GN, McPherson R (1988) Fracture toughness of plasma sprayed zirconia coatings. Surf Coat Technol 134:15–23
135. Lima CRC, Guilemany JM (2007) Adhesion improvements of thermal barrier coatings with HVOF thermally sprayed bond coats. Surf Coat Technol 201:4694–4701
136. Han W, Rybicki EE, Shadley JR (1993) An improved specimen geometry for ASTM C633-79 to estimate bond strengths of thermal spray coatings. J Therm Spray Technol 2 (2):145–150
137. Białucki P, Kozerski S (2006) Study of adhesion of different plasma-sprayed coatings to aluminium. Surf Coat Technol 201:2061–2064
138. Amada S, Hirose T (1998) Influence of grit blasting pre-treatment on the adhesion strength of plasma sprayed coatings: fractal analysis of roughness. Surf Coat Technol 102:132–137
139. Staia MH, Ramos E, Carrasquero A, Roman A, Lesage J, Chicot D, Mesmacque G (2000) Effect of substrate roughness induced by grit blasting upon adhesion of WC-17% Co thermal sprayed coatings. Thin Solid Films 377–378:657–664
140. Pershin V, Lufitha M, Chandra S, Mostaghimi J (2003) Effect of substrate temperature on adhesion strength of plasma-sprayed nickel coatings. J Therm Spray Technol 12 (3):370–376
141. Krishnamurthy N, Sharma SC, Murali MS, Mukunda PG (2009) Adhesion behavior of plasma sprayed thermal barrier coatings on Al-6061 and cast iron substrates. Front Mater Sci China 3(3):333–338
142. Bahbou MF, Nylén P, Wigren J (2004) Effect of grit blasting and spraying angle on the adhesion strength of a plasma-sprayed coating. J Therm Spray Technol 13(4):508–514
143. Li C-J, Wang Y-Y (2002) Effect of particle state on the adhesive strength of HVOF sprayed metallic coating. J Therm Spray Technol 11(4):523–529
144. Leigh SH, Berndt CC (1994) A test for coating adhesion on flat substrates–a technical note. J Therm Spray Technol 3(2):184–190
145. Rickerby DS (1988) A review of the methods for the measurement of coating-substrate adhesion. Surf Coat Technol 36(1–2):541–557
146. Du H, Hua W, Liu J, Gong J, Sun C, Wen L (2005) Influence of process variables on the qualities of detonation gun sprayed WC–Co coatings. Mater Sci Eng A 408:202–210
147. Era H, Otsubo F, Uchida T, Fukuda S, Kishitake K (1998) A modified shear test for adhesion evaluation of thermal sprayed coating. Mater Sci Eng A251:166–172

148. Han W, Rybicki EF, Shadley JR (1993) Application of fracture mechanics to the interpretation of bond strength data from ASTM Standard C633-79. J Therm Spray Technol 2 (3):235–241
149. Watanabe M, Kuroda S, Yokoyama K, Inoue T, Gotoh Y (2008) Modified tensile adhesion test for evaluation of interfacial toughness of HVOF sprayed coatings. Surf Coat Technol 202:1746–1752
150. Clyne TW, Gill SC (1996) Residual stresses in thermal spray coatings and their effect on interfacial adhesion: a review of recent work. J Therm Spray Technol 5(4):401–418
151. Rammo NN, Al-Amery HR, Abdul-Jabbar T, Jaffer HI (2009) Adhesion, hardness and structure of thermal sprayed Al/SiC composite, coat on graphite. Surf Coat Technol 203:2891–2895
152. Théry P-Y, Poulain M, Dupeux M, Braccini M (2007) Adhesion energy of a YPSZ EB-PVD layer in two thermal barrier coating systems. Surf Coat Technol 202:648–652
153. Ma XQ, Cho S, Takemoto M (2001) Acoustic emission source analysis of plasma sprayed thermal barrier coatings during four-point bend tests. Surf Coat Technol 139:55–62
154. Bradai MA, Braccini M, Ati A, Bounar N, Benabbas A (2008) Microstructure and adhesion of 100Cr6 steel coatings thermally sprayed on a 35CrMo4 steel substrate. Surf Coat Technol 202:4538–4543
155. Li H, Khor KA, Cheanga P (2002) Young's modulus and fracture toughness determination of high velocity oxy-fuel-sprayed bioceramic coatings. Surf Coat Technol 155:21–32
156. Choi SR, Zhu D, Miller RA (2005) Fracture behavior under mixed-mode loading of ceramic plasma-sprayed thermal barrier coatings at ambient and elevated temperatures. Eng Fract Mech 72:2144–2158
157. Westergård R, Axén N, Wiklund U, Hogmark S (2000) An evaluation of plasma sprayed ceramic coatings by erosion, abrasion and bend testing. Wear 246:12–19
158. Heping L, Nie P, Yan Y, Wang J, Sun B (2010) Characterization and adhesion strength study of detonation-sprayed MoB–CoCr alloy coatings on 2Cr13 stainless steel substrate. J Coat Technol Res 7(6):801–807
159. Montavon G (2004) Quality control of thermal sprayed coatings, course thermal spraying. Aliderte, Limoges
160. Lesage J, Staiab MH, Chicot D, Godoy C, De Mirandad PEV (2000) Effect of thermal treatments on adhesive properties of a NiCr thermal sprayed coating. Thin Solid Films 377–378:681–686
161. Hivart P, Crampon J (2007) Interfacial indentation test and adhesive fracture characteristics of plasma sprayed cermet Cr_3C_2/Ni–Cr coatings. Mech Mater 39:998–1005
162. Marcano Z, Lesage J, Chicot D, Mesmacque G, Puchi-Cabrera ES, Staiaa MH (2008) Microstructure and adhesion of Cr_3C_2–NiCr vacuum plasma sprayed coatings. Surf Coat Technol 202:4406–4410
163. Marot G, Démarécaux P, Lesage J, Hadad M, St. Siegmann, Staia MH (2008) The interfacial indentation test to determine adhesion and residual stresses in NiCr VPS coatings. Surf Coat Technol 202:4411–4416
164. Erickson LC, Westergard R, Wiklund U, Axén N, Hawthorne HM, Hogmark LS (1998) Cohesion in plasma-sprayed coatings–a comparison between evaluation methods. Wear 214:30–37
165. Xie Y, Hawthorne HM (2001) A model for compressive coating stresses in the scratch adhesion test. Surf Coat Technol 141:15–25
166. Ma XQ, Gandy DW, Frederick GJ (2008) Innovation of ultrafine structured alloy coatings having superior mechanical properties and high temperature corrosion resistance. J Therm Spray Technol 17(5–6):933–941
167. Sundararajan G, Chavan NM, Sivakumar G, Sudharshan Phani P (2010) Evaluation of parameters for assessment of inter-splat bond strength in cold-sprayed coatings. J Therm Spray Technol 19(6):1255–1266

168. Bolis C et al (2002) Developments in laser shock adhesion test (LASAT). In: Lugscheider E et al (eds) International thermal spray conference (ITSC 2002). ASM International, Materials Park, OH, pp 587–593
169. Barradas S, Molins R, Jeandin M, Arrigoni M, Boustie M, Bolis C, Berthe L, Ducos M (2005) Application of laser shock adhesion testing to the study of the interlamellar strength and coating–substrate adhesion in cold-sprayed copper coating of aluminum. Surf Coat Technol 197:18–27
170. Barradas S, Borit F, Guipont V, Jeandin M, Bolis C, Boustie M, Berthe L (2002) Laser shock flier impact simulation of particle-substrate interactions in cold spray. In: Lugscheider E, Berndt CC (eds) International thermal spray conference. DVS Deutscher Verband fûr Schweißen, Düsseldorf, pp 592–597
171. Rolland G, Sallamand P, Guipont V, Jeandin M, Boller E, Bourda C (2011) Laser-induced damage in cold-sprayed composite coatings. Surf Coat Technol 205:4915–4927
172. Jeandin M, Christoulis DK, Borit F, Berger MH, Guetta S, Rolland G, Guipont V, Irissou E, Legoux JG, Moreau C, Nivard M, Berthe L, Boustie M, Sakaguchi K, Ichikawa Y, Ogawa K, Costil S (2010) Lasers and thermal spray. Mater Sci Forum 174:638–642
173. Giraud D, Borit F, Guipont V, Jeandin M (2012) Metallization of a polymer using cold spray: application to aluminum coating of polyamide 66. In: Lima RS et al (eds) Thermal spray 2012: proceedings from the international thermal spray conference and exposition. ASM International, Materials Park, OH (e-proc)
174. Guipont V (2013) Microstructures and interfaces ceramic/metal obtained by physical processes. State Thesis, University of Limoges, Limoges
175. Guetta S, Berger MH, Borit F, Guipont V, Jeandin M, Boustie M, Ichikawa Y, Sakaguchi K, Ogawa K (2009) Influence of particle velocity on adhesion of cold-sprayed splats. J Therm Spray Technol 18(3):331–342
176. Christoulis DK, Guetta S, Irissou E, Guipont V, Berger MH, Jeandin M, Legoux J-G, Moreau C, Costil S, Boustie M, Ichikawa Y, Ogawa K (2010) Cold-spraying coupled to nano-pulsed Nd-YaG laser surface pre-treatment. J Therm Spray Technol 19(5):1062–1073
177. Chandler H (ed) (2004) Hardness testing, 2nd edn. ASM, Materials Park, OH
178. Dey A, Mukhopadhyay AK, Gangadharan S, Sinha MK, Basu D (2009) Weibull modulus of nano-hardness and elastic modulus of hydroxyapatite coating. J Mater Sci 44:4911–4918
179. Lima RS, Marple BR (2003) High Weibull modulus HVOF titania coatings. J Therm Spray Technol 12(2):240–249
180. Lima RS, Kucuk A, Berndt CC (2001) Evaluation of microhardness and elastic modulus of thermally sprayed nanostructured zirconia coatings. Surf Coat Technol 135:166–172
181. Lima RS, Kucuk A, Berndt CC (2002) Bimodal distribution of mechanical properties on plasma sprayed nanostructured partially stabilized zirconia. Mater Sci Eng A327:224–232
182. Marshall DB, Noma T, Evans AG (1982) A simple method for determining elastic-modulus-to-hardness ratios using Knoop indentation measurements. Commun Am Ceram Soc 65: C175–C176
183. CSM Instruments (2010) Advanced mechanical surface testing: characterization of thermal spray coatings by instrumented indentation and scratch testing. Part II: Indentation of plasma sprayed coatings. CSM instruments application bulletin, vol 32. CSM Instruments, Peseux
184. Bucaille JL, Felder E, Hochstetter G (2002) Identification of the viscoplastic behavior of a polycarbonate based on experiments and numerical modeling of the nano-indentation test. J Mater Sci 37:3999–4011
185. Musil J, Kunc F, Zeman H, Polakova H (2002) Relationships between hardness, Young's modulus and elastic recovery in hard nanocomposite coatings. Surf Coat Technol 154:304–313
186. Landa M, Kroupa F, Neufuss K, Urbanek P (2003) Effect of uniaxial pressure on ultrasound velocities and elastic moduli in plasma-sprayed ceramics. J Therm Spray Technol 12 (2):226–233

187. Roy M, Pauschitz A, Bernardi J, Koch T, Franek F (2006) Microstructure and mechanical properties of HVOF sprayed nanocrystalline Cr_3C_2-25(Ni20Cr) coating. J Therm Spray Technol 15(3):372–381
188. Ma D, Ong CW, Zhang T (2009) An instrumented indentation method for Young's modulus measurement with accuracy estimation. Exp Mech 49:719–729
189. Feng C, Kang BS (2006) A transparent indenter measurement method for mechanical property evaluation. Exp Mech 46(1):91–103
190. Feng C, Kang BS (2008) Young's modulus measurement using a simplified transparent indenter measurement technique. Exp Mech 48:9–15
191. Wallace JS, Ilavsky J (1998) Elastic modulus measurements in plasma sprayed deposits. J Therm Spray Technol 7(4):521–526
192. Kucuk A, Berndt CC, Senturk U, Lima RS (2000) Influence of plasma spray parameters on mechanical properties of yttria stabilized zirconia coatings. I: Four point bend test. Mater Sci Eng A284:29–40
193. Beghini M, Bertini L, Frendo E (2001) Measurement of coatings' elastic properties by mechanical methods: Part 1. Consideration on experimental errors. Exp Mech 41(4):293–304
194. Beghini M, Benamati G, Bertini L, Frendo F (2001) Measurement of coatings' elastic properties by mechanical methods: Part 2. Application to thermal barrier coatings. Exp Mech 41(4):305–311
195. Podrezov YN, Mil'man YV, Lotsko DV, Lugovoi NL, Verbilo DG, Efimov NA (1999) A method of determining the mechanical properties of a two-layer composite consisting of a steel matrix and a plasma spray coating based on amorphizing powders. Powder Metallurgy Metal Ceram 38(5–6):224–227
196. Musalek R, Matejicek J, Vilemova M, Kovarik O (2010) Non-linear mechanical behavior of plasma sprayed alumina under mechanical and thermal spray loading. J Therm Spray Technol 19(1–2):422–428
197. Harok V, Neufuss K (2001) Elastic and inelastic effects in compression in plasma-sprayed ceramic coatings. J Therm Spray Technol 10(1):126–132
198. Meacham BE, Marshall MC, Branagan DJ (2006) Palmqvist fracture toughness of a new wear-resistant weld alloy. Metall Mater Trans A 37A:3617–3627
199. Emiliani ML (1993) Debond coating requirements for brittle matrix composites. J Mater Sci 28:5280–5296
200. Faisal NH, Steel JA, Ahmed R, Reuben RL (2009) The use of acoustic emission to characterize fracture behavior during Vickers indentation of HVOF thermally sprayed WC-Co coatings. J Therm Spray Technol 18(4):525–535
201. Xie XY, Guo HB, Gong SK (2010) Mechanical properties of $LaTi_2Al_9O_{19}$ and thermal cycling behaviors of plasma-sprayed $LaTi_2Al_9O_{19}$/YSZ thermal barrier coatings. J Therm Spray Technol 19(6):1179–1185
202. Richard CS, Lu J, Béranger G, Decomps F (1995) Study of Cr_2O_3 coatings. Part II: Adhesion to a cast-iron substrate. J Therm Spray Technol 4(4):347–352
203. Berka L, Murafa N (2004) On the estimation of the toughness of surface microcracks. Int J Fracture 128:115–120
204. Lima MM, Godoy C, Avelar-Batista JC, Modenesi PJ (2003) Toughness evaluation of HVOF WC-Co coatings using non-linear regression analysis. Mater Sci Eng A357:337–345
205. Lima MM, Godoy C, Modenesi PJ, Avelar-Batista JC, Davison A, Matthews A (2004) Coating fracture toughness determined by Vickers indentation: an important parameter in cavitation erosion resistance of WC-Co thermally sprayed coatings. Surf Coat Technol 177–178:489–496
206. Chivavibul P, Watanabe M, Kuroda S, Kawakita J, Komatsu M, Sato K, Kitamura J (2010) Effect of powder characteristics on properties of warm-sprayed WC-Co coatings. J Therm Spray Technol 19(1–2):81–88

207. Prudenziati M, Gazzadi GC, Medici M, Dalbagni G, Caliari M (2010) Cr_3C_2-NiCr HVOF-sprayed coatings: microstructure and properties versus powder characteristics and process parameters. J Therm Spray Technol 19(3):541–550
208. Santana YY, Renault PO, Sebastiani M, La Barbera JG, Lesage J, Bemporad E, Le Bourhis E, Puchi-Cabrera ES, Staia MH (2008) Characterization and residual stresses of WC–Co thermally sprayed coatings. Surf Coat Technol 202:4560–4565
209. Taha-al ZY, Hashmi MS, Yilbas BS (2009) Effect of WC on the residual stress in the laser treated HVOF coating. J Mater Process Technol 209:3172–3181
210. Lyphout C, Nylén P, Manescu A, Pirling T (2008) Residual stresses distribution through thick HVOF sprayed Inconel 718 coatings. J Therm Spray Technol 17(5–6):915–923
211. Sampath S, Jiang XY, Matejicek J, Prchlik L, Kulkarni A, Vaidya A (2004) Role of thermal spray processing method on the microstructure, residual stress and properties of coatings: an integrated study for Ni–5 wt.%Al bond coats. Mater Sci Eng A364:216–231
212. Greving DJ, Rybicki EF, Shadley JR (1994) Through-thickness residual stress evaluations for several industrial thermal spray coatings using a modified layer-removal method. J Therm Spray Technol 3(4):379–388
213. Pejryd L, Wigren J, Greving DJ, Shadley JR, Rybicki EE (1995) Residual stresses as a factor in the selection of tungsten carbide coatings for a jet engine application. J Therm Spray Technol 4(3):268–274
214. Greving DJ, Shadley JR, Rybicki EF (1994) Effects of coating thickness and residual stresses on the bond strength of ASTM C633-79 thermal spray coating test specimens. J Therm Spray Technol 3(4):371–378
215. Lima CRC, Nin J, Guilemany JM (2006) Evaluation of residual stresses of thermal barrier coatings with HVOF thermally sprayed bond coats using the modified layer removal method (MLRM). Surf Coat Technol 200:5963–5972
216. Rendler NJ, Vigness I (1966) Hole drilling method of measuring residual stresses. Exp Mech 6(12):577–586
217. Richard CS, Béranger G, Lu J, Flavenot JF, Grégoire T (1996) Four-point bending tests of thermally produced WC-Co coatings. Surf Coat Technol 78(284):294
218. Schajer GS (1988) Measurement of non uniform residual stress using the hole drilling method. Part 1. J Eng Mater Technol 110(4):338–343, Part 2. 110(4):345–349
219. Valente T, Bartuli C, Sebastiani M, Loreto A (2005) Implementation and development of the incremental hole drilling method for the measurement of residual stress in thermal spray coatings. J Therm Spray Technol 14(4):462–470
220. Schajer GS, Altus E (1996) Stress calculation error analysis for incremental hole drilling residual stress measurement. J Eng Mater Technol 118(1):120–126
221. Wang H-P (1979) The alignment error of the hole-drilling method. Exp Mech 19:23–27
222. Balykov AV (2006) Main conditions for efficient drilling of holes in brittle nonmetallic materials using diamonds drills. Mater Process 63(5–6):161–165
223. Kuroda S, Kukushima T, Kitahara S (1988) Simultaneous measurement of coating thickness and deposition stress during thermal spraying. Thin Solid Films 164:157–163
224. Kuroda S, Tashiro Y, Yumoto H, Taira S, Fukanuma H, Tobe S (2001) Peening action and residual stresses in high-velocity oxygen fuel thermal spraying of 316L stainless steel. J Therm Spray Technol 10(2):367–374
225. Gill SC, Clyne TW (1994) Investigation of residual stress generation during thermal spraying by continuous curvature measurement. Thin Solid Films 250:172–180
226. Bolelli G, Lusvarghi L, Varis T, Turunen E, Leoni M, Scardi P, Azanza-Ricardo CL, Barletta M (2008) Residual stresses in HVOF-sprayed ceramic coatings. Surf Coat Technol 202:4810–4819
227. Hugot F, Patru J, Fauchais P, Bianchi L (2007) Modelling of a substrate thermomechanical behavior during plasma spraying. J Mater Process Technol 190(1–3):317–323
228. Stokes J, Looney L (2008) Predicting quenching and cooling stresses within HVOF deposits. J Therm Spray Technol 17(5–6):908–914

229. James JD, Spittle JA, Brown SGR, Evans RW (2001) A review of measurement techniques for the thermal expansion coefficient of metals and alloys at elevated temperatures. Meas Sci Technol 12:R1–R15
230. Ilavsky J, Berndt CC (1998) Thermal expansion properties of metallic and cermet coatings. Surf Coat Technol 102:19–24
231. Wang H, Dinwiddie RB (2004) Development of a lab view based portable thermal diffusivity system. In: Wang H (ed) Thermal conductivity 27, Thermal expansion 15. DESTech, Lancaster, PA, pp 484–492
232. Cernuschi F, Lorenzoni L, Ahmaniemi S, Vuoristo P, Mäntylä T (2005) Studies of the sintering kinetics of thick thermal barrier coatings by thermal diffusivity measurements. J Eur Ceram Soc 25:393–400
233. Gitzhofer F, Lombard D, Vardelle A, Vardelle M, Martin C, Fauchais P (1986) Thermophysical properties of zirconia coatings stabilized with calcia or yttria: influence of spraying parameters and heat treatment. In: Advances in thermal spraying. Pergamon, Oxford, pp 269–275
234. Chi W, Sampath S, Wange H (2006) Ambient and high-temperature thermal conductivity of thermal sprayed coatings. J Therm Spray Technol 15(4):773–778
235. Tan Y, Longtin JP, Sampath S (2006) Modeling thermal conductivity of thermal spray coatings: comparing predictions to experiments. J Therm Spray Technol 15(4):545–552
236. Baba T, Ono A (2001) Improvement of the laser flash method to reduce uncertainty in thermal diffusivity measurements. Meas Sci Technol 12:2046–2057
237. Wang H, Dinwiddie RB (2000) Reliability of laser flash thermal diffusivity measurements of the thermal barrier coatings. J Therm Spray Technol 9(2):210–214
238. He GH, Guo JD, Zhang YY, Wang BQ, Zhou BL (2000) Measurement of thermal diffusivity of thermal control coatings by the flash method using two-layer composite sample. Int J Thermophys 21(2):535–542
239. Rätzer-Scheibe H-J, Schulz U, Krell T (2006) The effect of coating thickness on the thermal conductivity of EB-PVD PYSZ thermal barrier coatings. Surf Coat Technol 200:5636–5644
240. Jennifer SY, Wang H, Porter WD, de Arellano Lopez AR, Faber KT (2001) Thermal conductivity and phase evolution of plasma-sprayed multilayer coatings. J Mater Sci 36:3511–3518
241. Slifka AJ, Filla BJ, Phelps JM, Bancke G, Berndt CC (1998) Thermal conductivity of a zirconia thermal barrier coating. J Therm Spray Technol 7(1):43–46
242. Aksel C, Warren PD (2003) Thermal shock parameters [R, R''' and R''''] of magnesia–spinel composites. J Eur Ceram Soc 23:301–308
243. Hasselman DPH (1970) Thermal stress resistance parameters for brittle refractory ceramics: a compendium. Am Ceram Soc Bull 49(12):1033–1037
244. Bolcavage A, Feuerstein A, Foster J, Moore P (2004) Thermal shock testing of thermal barrier coating/bondcoat systems. J Mater Eng Perform 13(4):389–397
245. Qi ZM, Amada S, Akiyama S, Takahashi C (1988) Evaluation of thermal shock strength of thermal-sprayed coatings by the laser irradiation technique. Surf Coat Technol 110:73–80
246. Irisawa T, Matsumoto H (2006) Thermal shock resistance and adhesion strength of plasma-sprayed alumina coating on cast iron. Thin Solid Films 509:141–144
247. Nusair Khan A, Lu J (2003) Behavior of air plasma sprayed thermal barrier coatings, subject to intense thermal cycling. Surf Coat Technol 166:37–43
248. Ma XQ, Takemoto M (2001) Quantitative acoustic emission analysis of plasma, sprayed thermal barrier coatings subjected to thermal shock tests. Mater Sci Eng A308:101–110
249. Sorai M, Gakkai NN (2004) Comprehensive handbook of calorimetry and thermal analysis. Wiley, New York, 534 p
250. Speyer R (1993) Thermal analysis of materials (Materials engineering). Amazon, Seattle, WA

251. Salimijazi H, Hosseini M, Mostaghimi J, Pershin L, Coyle TW, Samadi H, Shafyei A (2012) Plasma sprayed coating using mullite and mixed alumina/silica powders. J Therm Spray Technol 21(5):825–830
252. Garcia E, Mesquita-Guimaraes J, Miranzo P, Osendi MI, Cojocaru CV, Wang Y, Moreau C, Lima RS (2011) Phase composition and microstructural responses of graded mullite/YSZ coatings under water vapor environments. J Therm Spray Technol 20(1–2):83–91
253. Liu X, Ding C (2002) Thermal properties and microstructure of a plasma sprayed wollastonite coating. J Therm Spray Technol 11(3):375–379
254. Ozdemir I, Hamanaka I, Tsunekawa Y, Okumiya M (2005) In-process exothermic reaction in high-velocity oxyfuel and plasma spraying with SiO_2/Ni/Al-Si-Mg composite powder. J Therm Spray Technol 14(3):321–329
255. Deevi SC, Sikka VK, Swindeman CJ, Seals RD (1997) Reactive spraying of nickel-aluminide coatings. J Therm Spray Technol 6(3):335–344
256. Wang J, Jordan EH, Gell M (2010) Plasma sprayed dense MgO-Y_2O_3 nanocomposite coatings using sol-gel combustion synthesized powder. J Therm Spray Technol 19 (5):873–878
257. Ravi BG, Gandhi AS, Guo XZ, Margolies J, Sampath S (2008) Liquid precursor plasma spraying of functional materials: a case study for yttrium aluminum garnet (YAG). J Therm Spray Technol 17(1):82–90
258. Guilemany JM, Cinca N, Dosta S, Cano IG (2009) FeAl and NbAl3 intermetallic-HVOF coatings: structure and properties. J Therm Spray Technol 18(4):536–545
259. Fan X, Ishigaki T (2001) Mo_5Si_3-B and $MoSi_2$ deposits fabricated by radio frequency induction plasma spraying. J Therm Spray Technol 10(4):611–617
260. Craig BD (2005) Material failure modes, Part II: A brief tutorial on impact, spalling, wear, brinelling, thermal shock, and radiation damage. J Fail Anal Prev 5(6):7–12
261. Chattopadhyay R (2001) Surface wear: analysis, treatment, and prevention. ASM International, Materials Park, OH, 307 p
262. Kennedy DM, Hashmi MSJ (1998) Methods of wear testing for advanced surface coatings and bulk materials. J Mater Process Technol 77:246–253
263. Bolelli G, Cannillo V, Lusvarghi L, Manfredini T (2006) Wear behaviour of thermally sprayed ceramic oxide coatings. Wear 261:1298–1315
264. Cockeram BV, Wilson WL (2001) The hardness, adhesion and wear resistance of coatings developed for cobalt-base alloys. Surf Coat Technol 139:161–182
265. Wielage B, Steinhäuser S, Schnick T, Nickelmann D (1999) Characterization of the wear behavior of thermal sprayed coatings. J Therm Spray Technol 8(4):553–558
266. Schmidt G, Steinhäuser S (1996) Characterization of wear protective coatings. Tribol Int 29 (3):207–214
267. Gawne DT, Qiu Z, Bao Y, Zhang T, Zhang K (2001) Abrasive wear resistance of plasma-sprayed glass-composite coatings. J Therm Spray Technol 10(4):599–603
268. Li C-J, Wang H-T, Yang G-J, Bao C-G (2011) Characterization of high-temperature abrasive wear of cold-sprayed FeAl intermetallic compound coating. J Therm Spray Technol 20:227–233
269. Rainforth WM (2004) The wear behaviour of oxide ceramics—a review. J Mater Sci 39:6705–6721
270. Kim HJ, Kweon YG, Chang RW (1994) Wear and erosion behavior of plasma-sprayed WC-Co coatings. J Therm Spray Technol 3(2):169–178
271. Tillmann W, Vogli E, Baumann I, Matthaeus G, Ostrowski T (2008) Influence of the HVOF gas composition on the thermal spraying of WC-Co submicron powders (28 + 1 μm) to produce superfine structured cermet coatings. J Therm Spray Technol 17(5–6):924–932
272. He D-Y, Fu B-Y, Jiang J-M, Li X-Y (2008) Microstructure and wear performance of arc sprayed Fe-FeB-WC coatings. J Therm Spray Technol 17(5–6):757–761
273. Magnani M, Suegama PH, Espallargas N, Fugivara CS, Dosta S, Guilemany JM, Benedettir AV (2009) Corrosion and wear studies of Cr_3C_2-NiCr-HVOF coatings sprayed on AA7050 T7 under cooling. J Therm Spray Technol 18(3):354–363

274. Yin B, Liu G, Zhou H, Chen J, Yan F (2010) Sliding wear behavior of HVOF-sprayed Cr_3C_2–NiCr/CeO_2 composite coatings at elevated temperature up to 800 °C. Tribol Lett 37:463–475
275. Fernandez JE, Rodriguez R, Wang Y, Vijande R, Rincon A (1995) Sliding wear of a plasma-sprayed A_2O_3 coating. Wear 181–183:417–425
276. Liu Y, Wang HM (2010) Microstructure and wear property of laser-clad Co_3Mo_2Si/Co_{ss} wear resistant coatings. Surf Coat Technol 205:377–382
277. Tiana W, Wang Y, Zhang T, Yang Y (2009) Sliding wear and electrochemical corrosion behavior of plasma sprayed nanocomposite Al_2O_3–13%TiO_2 coatings. Mater Chem Phys 118:37–45
278. Lin JF, Liu MH, Wu JD (1996) Analysis of the friction and wear mechanisms of structural ceramic coatings. Part 1: The effect of processing conditions. Wear 194:1–11
279. Yanga Q, Senda T, Hirose A (2006) Sliding wear behavior of WC–12% Co coatings at elevated temperatures. Surf Coat Technol 200:4208–4212
280. Guilemany JM, Miguel JM, Armada S, Vizcaino S, Climent F (2001) Use of scanning white light interferometry in the characterization of wear mechanisms in thermal-sprayed coatings. Mater Charact 47:307–314
281. Kulu P, Pihl T (2002) Selection criteria for wear resistant powder coatings under extreme erosive wear conditions. J Therm Spray Technol 11(4):517–522
282. Clark HMI, Hawthorne HM, Xie Y (1999) Wear rates and specific energies of some ceramic, cermet and metallic coatings determined in the Coriolis erosion tester. Wear 233–235:319–327
283. Ji G-C, Li C-J, Wang Y-Y, Li W-Y (2007) Erosion performance of HVOF-sprayed Cr_3C_2-NiCr coatings. J Therm Spray Technol 16(4):557–565
284. Dallaire S (2001) Hard arc-sprayed coating with enhanced erosion and abrasion wear resistance. J Therm Spray Technol 10(3):511–519
285. Shivamurthy RC, Kamaraj M, Nagarajan R, Shariff SM, Padmanabham G (2010) Slurry erosion characteristics and erosive wear mechanisms of Co-based and Ni-based coatings formed by laser surface alloying. Metall Mater Trans A 41A:470–486
286. Hejwowski T, Szewczyk S, Weronski A (2000) An investigation of the abrasive and erosive wear of flame-sprayed coatings. J Mater Process Technol 106:54–57
287. Hejwowski T (2009) Erosive and abrasive wear resistance of overlay coatings. Vacuum 83:166–170
288. Mann BS, Arya V (2001) Abrasive and erosive wear characteristics of plasma nitriding and HVOF coatings: their application in hydro turbines. Wear 249:354–360
289. Prasad Sahu S, Satapathy A, Patnaik A, Sreekumar KP, Ananthapadmanabhan PV (2010) Development, characterization and erosion wear response of plasma sprayed fly ash–aluminum coatings. Mater Des 31:1165–1173
290. Stewart S, Ahmed R, Itsukaichi T (2005) Rolling contact fatigue of post-treated WC – NiCrBSi thermal spray coatings. Surf Coat Technol 190(1–2):171–189
291. Ahmed R, Hadfield M (2002) Mechanisms of fatigue failure in thermal spray coatings. J Therm Spray Technol 11(3):334–349
292. Zhang XC, Xu BS, Tu ST, Xuan FZ, Wang HD, Wu YX (2009) Fatigue resistance and failure mechanisms of plasma-sprayed CrC–NiCr cermet coatings in rolling contact. Int J Fatigue 31:906–915
293. Kovarik O, Siegl J, Nohava J, Chraska P (2005) Young's modulus and fatigue behavior of plasma-sprayed alumina coatings. J Therm Spray Technol 14(2):231–238
294. Kovarik O, Siegl J, Prochazka Z (2008) Fatigue behavior of bodies with thermally sprayed metallic and ceramic deposits. J Therm Spray Technol 17(4):525–532
295. McGrann RTR, Greving DJ, Shadley JR, Rybicki EF, Bodger BE, Somerville DA (1998) The effect of residual stress in HVOF tungsten carbide coatings on the fatigue life in bending of thermal spray coated aluminum. J Therm Spray Technol 7(4):546–552
296. Sansoucy E, Kim GE, Moran AL, Jodoin B (2007) Mechanical characteristics of Al-Co-Ce coatings produced by the cold spray process. J Therm Spray Technol 16(5–6):651–660

297. Ibrahim A, Lima RS, Berndt CC, Marple BR (2007) Fatigue and mechanical properties of nanostructured and conventional titania (TiO_2) thermal spray coatings. Surf Coat Technol 201:7589–7596
298. Ibrahim A, Berndt CC (2007) Fatigue and deformation of HVOF sprayed WC–Co coatings and hard chrome plating. Mater Sci Eng A 456:114–119
299. Yan L, Leng Y, Chen J (2003) Torsional fatigue resistance of plasma sprayed HA coating on Ti-6Al-4V. J Mater Sci Mater Med 14:291–295
300. Agüero A, Camón F, García de Blas J, del Hoyo JC, Muelas R, Santaballa A, Ulargui S, Vallés P (2011) HVOF-deposited WCCoCr as replacement for hard Cr in landing gear actuators. J Therm Spray Technol 20(6):1292–1309
301. Scrivani A, Rizzi G, Bardi U, Giolli C, Muniz Miranda M, Ciattini S, Fossati A, Borgioli F (2007) Thermal fatigue behavior of thick and porous thermal barrier coatings systems. J Therm Spray Technol 16(5–6):816–821
302. Giolli C, Scrivani A, Rizzi G, Borgioli F, Bolelli G, Lusvarghi L (2009) Failure mechanism for thermal fatigue of thermal barrier coating systems. J Therm Spray Technol 18(2):223–230
303. Zhu D, Choi SR, Miller RA (2004) Development and thermal fatigue testing of ceramic thermal barrier coatings. Surf Coat Technol 188–189:146–152
304. Zhou YC, Hashida T (2002) Thermal fatigue failure induced by delamination in thermal barrier coating. Int J Fatigue 24:407–417
305. Zhang T, Li DY (2001) Improvement in the resistance of aluminum with yttria particles to sliding wear in air and in a corrosive medium. Wear 251:1250–1256
306. Liu R, Li DY (1999) Protective effect of yttrium additive in lubricants on corrosive wear. Wear 225–229:968–974
307. Basak AK, Matteazzi P, Vardavoulias M, Celis J-P (2006) Corrosion–wear behaviour of thermal sprayed nanostructured FeCu/WC–Co coatings. Wear 261:1042–1050
308. Prasad BK (2000) Effects of alumina particle dispersion on the erosive–corrosive wear response of a zinc-based alloy under changing slurry conditions and distance. Wear 238:151–159
309. Zhang D-W, Lei TC (2003) The microstructure and erosive–corrosive wear performance of laser-clad Ni–Cr3C2 composite coating. Wear 255:129–133
310. Stack MM, Stott FH, Wood GC (1993) Review of mechanisms of erosion-corrosion of alloys at elevated temperatures. Part 2. Wear 162–164:706–712
311. Higuera Hidalgo V, Belzunce Varela J, Carriles Menéndez A, Poveda Martɪnez S (2001) High temperature erosion wear of flame and plasma-sprayed nickel–chromium coatings under simulated coal-fired boiler atmospheres. Wear 247:214–222
312. Garcɪa JR, Cuetos JM, Fernandez E, Higuera V (2007) Laser surface melting Cr–Ni coatings, in the erosive-corrosive atmosphere of boilers. Tribol Lett 28:99–108
313. Drexler JM, Aygun A, Li D, Vaßen R, Steinke T, Padture NP (2010) Thermal-gradient testing of thermal barrier coatings under simultaneous attack by molten glassy deposits and its mitigation. Surf Coat Technol 204:2683–2688
314. Lee H, Mall S, Sanders JH, Sharma SK (2005) Wear analysis of Cu–Al coating on Ti–6Al–4V substrate under fretting condition. Tribol Lett 19(3):239–248
315. Lee H, Mall S, Murray KN (2007) Fretting wear behavior of Cu–Al coating on Ti-6Al-4V substrate under dry and wet (lubricated) contact condition. Tribol Lett 28:19–25
316. Fridrici V, Fouvry S, Kapsa P (2003) Fretting wear behavior of a Cu–Ni–In plasma coating. Surf Coat Technol 163–164:429–434
317. Gean MC, Farris TN (2009) Elevated temperature fretting fatigue of Ti-17 with surface treatments. Tribol Int 42:1340–1345
318. Xu G-Z, Liu J-J, Zhou Z-R (2002) The effect of the third body on the fretting wear behavior of coatings. J Mater Eng Perform 11(3):288–293
319. Koiprasert H, Dumrongrattana S, Niranatlumpong P (2004) Thermally sprayed coatings for protection of fretting wear in land-based gas-turbine engine. Wear 257:1–7

320. Majzoobi GH, Hojjati R, Nematian M, Zalnejad E, Ahmadkhani AR, Hanifepoor E (2010) A new device for fretting fatigue testing. Trans Indian Inst Met 63(2–3):493–497
321. Atlas Steel Technical Note No. 7 "Galvanic corrosion," revised Aug 2010
322. ASM International (2003) Corrosion: fundamentals, testing, and protection. In: ASM handbook, vol 13A. ASM International, Materials Park, OH, pp 509–513
323. Souza VAD, Neville A (2006) Mechanisms and kinetics of WC-Co-Cr high velocity oxy-fuel thermal spray coating degradation in corrosive environments. J Therm Spray Technol 15 (1):106–117
324. Guilemany JM, Espallargas N, Suegama PH, Benedetti AV, Fernández J (2005) High-velocity oxyfuel Cr_3C_2-NiCr replacing hard chromium coatings. J Therm Spray Technol 14 (3):336–341
325. Shrestha S, Neville A, Hodgkiess T (2001) The effect of post-treatment of a high-velocity oxy-fuel Ni-Cr-Mo-Si-B coating. Part I: Microstructure/corrosion behavior relationships. J Therm Spray Technol 10(3):470–479
326. Ishikawa Y, Kawakita J, Osawa S, Itsukaichi T, Sakamoto Y, Takaya M, Kuroda S (2005) Evaluation of corrosion and wear resistance of hard cermet coatings sprayed by using an improved HVOF process. J Therm Spray Technol 14(3):384–390
327. Gobinda CS, Khan TI (2010) The corrosion and wear performance of microcrystalline WC-10Co-4Cr and near-nanocrystalline WC-17Co high velocity oxy-fuel sprayed coatings on steel substrate. Metall Mater Trans A 41A:3000–3009
328. Paul S, Yadav K (2010) Corrosion behavior of surface-treated implant Ti-6Al-4V by electrochemical polarization and impedance studies. J Mater Eng Perform 20(3):422–435
329. Barletta M, Bolelli G, Bonferroni B, Lusvarghi L (2010) Wear and corrosion behavior of HVOF-sprayed WC-CoCr coatings on Al alloys. J Therm Spray Technol 19(1–2):358–367
330. Luiz de Assis S, Wolynec S, Costa I (2006) Corrosion characterization of titanium alloys by electrochemical techniques. Electrochim Acta 51:1815–1819
331. Wang H-R, Hou B-R, Wang J, Wang Q, Li W-Y (2008) Effect of process conditions on microstructure and corrosion resistance of cold-sprayed Ti coatings. J Therm Spray Technol 17(5–6):736–741
332. He D, Dong N, Jiang J (2007) Corrosion behavior of arc sprayed nickel-base coatings. J Therm Spray Technol 16(5–6):850–856
333. Sidhu TS, Prakash S, Agrawal RD (2006) Hot corrosion resistance of high-velocity oxyfuel sprayed coatings on a nickel-base superalloy in molten salt environment. J Therm Spray Technol 15(3):387–399
334. Sidhu TS, Prakash S, Agrawal RD (2007) Study of molten salt corrosion of high velocity oxy-fuel sprayed cermet and nickel-based coatings at 900 °C. Metall Mater Trans A 38A:77–85
335. Sidhu TS, Prakash S, Agrawal RD (2006) Characterizations and hot corrosion resistance of Cr_3C_2-NiCr coating on Ni-base superalloys in an aggressive environment. J Therm Spray Technol 15(4):811–816
336. Singh H, Puri D, Prakash S (2005) Corrosion behavior of plasma-sprayed coatings on a Ni-base superalloy in Na_2SO_4-60 Pct V_2O_3 environment at 900 °C. Metall Mater Trans A 36A:1008–1015
337. Guilemany JM, Torrell M, Miguel JR (2008) Study of the HVOF Ni-based coatings corrosion resistance applied on municipal solid-waste incinerators. J Therm Spray Technol 17 (2):254–262
338. Li L, Hitchman N, Knapp J (2010) Failure of thermal barrier coatings subjected to CMAS attack. J Therm Spray Technol 19(1–2):148–155
339. Matthews S, James B, Hyland M (2010) The effect of heat treatment on the oxidation mechanism of blended powder Cr_3C_2-NiCr coatings. J Therm Spray Technol 19 (1–2):119–127
340. Ye F-X, Wu S-H, Ohmori A (2008) Microstructure and oxidation behavior of Cr39Ni7C cermet coatings deposited by diamond jet spray process. J Therm Spray Technol 17 (5–6):942–947

Chapter 16
Process Diagnostics and Online Monitoring and Control

Abbreviations

ANN	Artificial neural network
APS	Atmospheric plasma spraying
CARS	Coherent anti-stokes Raman spectroscopy
CCD	Coupled charged device
CFD	Computational fluid dynamic
CS-PIV	Cinema-stereoscopic particle image spectroscopy
cw	Continuous wave
d.c.	Direct current
D-gun	Detonation gun
FFT	Fast fourier transformation
FL	Fuzzy logic
HVAF	High-velocity air fuel flame
HVOF	High-velocity oxy-fuel flame
ICCD	Camera intensified coupled charged device camera
i.d.	Internal diameter (mm)
I.R.	Infra red
LASAT	Laser Adhesion Test
LDA	Laser Doppler anemometry
LIF	Laser-induced fluorescence
LTE	Local thermodynamic equilibrium
MI	Melting index
MVE	Total molten volume ensemble
MVF	Molten volume flux
Nd:YAG	Neodymium-doped yttrium aluminum garnet: Nd:$Y_3Al_5O_{12}$
NIR	Near infrared sensor
OPCS-PIV	Orthogonal-plane cinema-stereoscopic particle image spectroscopy
PC	Personal computer
PCT	Plasma computer tomography

P.L. Fauchais et al., *Thermal Spray Fundamentals: From Powder to Part*,
DOI 10.1007/978-0-387-68991-3_16, © Springer Science+Business Media New York 2014

PIV	Particle image velocimetry
PLIF	Planar laser-induced fluorescence
PSI	Particle shape imaging
r.f.	Radio frequency
SDC®	Spray and deposit control
SEM	Scanning electron microscopy
SSMI	Spray stream melting index
TBC	Thermal barrier coating
TTL	Transistor–transistor logic
VPS	Vacuum plasma spraying
YSZ	Yttria-stabilized zirconia

16.1 Introduction

16.1.1 What Is Expected from Thermal-Sprayed Coatings?

Whatever maybe the spray process, the user expects that coating thickness and weight tolerances are respected, the reproducibility of coating microstructure and reliability of service properties are at least good and, if possible, excellent. Good quality control of coatings presents many benefits: reduced rework, predictable performance and life linked to coatings, and high reproducibility with narrow variability. It results in good confidence in engineering and design properties and thus in wider use of coatings because of the reduced warrantee costs and liability risk, in a word, in customer satisfaction. On the contrary a poor control of coating properties with poor reproducibility and wide variability with unpredictable performance and life induce: high rework cost, unpredictable performance and life, high warrantee cost and liability risk, high cost of components with lost production due to failed coating, and poor product resulting from coating. At last failed application results in poisoned market.

16.1.2 Coatings Repeatability, Reliability, and Reproducibility

First it is appropriate to clarify the nuances and terminologies associated with these different terms, especially with respect to industrial plasma spray operations. The definitions of Dwivedi et al. [1], related to the variability in industrial TBC production, can be used whatever the coating sprayed:

1. Repeatability consists in repeating a process to achieve the same coating. For that measurements of specific parameters, based on the real need of coating properties (mechanical, thermal, physical, chemical,. . .) and the actual geometry

of the part to be covered, must be performed. It must be underlined that in production such measurements are not necessarily those achieved in research laboratories. Checking the repeatability [1] implies that variations in the measurements obtained by one person measuring the same attribute with the same measuring equipment are the same, or the variation in measurements obtained when one person takes multiple measurements using the same instrument and techniques on the same parts or items are the same.

2. Reproducibility is generally defined [1] by the variation in average measurements obtained when two or more people inspect the same parts or items using the same measuring technique. Often this term is used to define spatial variations, for instance, when two or more booths/sites seek to reproduce the same coating either through the same or similar processes.
3. Reliability of a coating is the probability that it will adequately perform its specified purpose for a specified period of time under specified environmental conditions [1]. As such, the term reliability captures all the aspects of repeatability and reproducibility and sets fundamental benchmarks at each step of the process.

As for every coating technology, the reliability and reproducibility of thermal-sprayed coatings, including cold spray, were essential in getting these technologies adopted as soon as they were introduced in industrial manufacturing. If one considers only the spray processes, coatings can differ due to [1]:

– Temporal or time-dependent variation within a single spray booth (including those specific to spray process, hardware degradation such as electrodes or nozzle wear, environment with, for example, temperature and humidity variations, and feedstock including the way the powder is stored, its drying or not before spraying, its morphology even if its composition and size distribution are the same,. . .),
– Spatial variation arising from multiple spray booth variability due to different booth configurations, spray torches, and even subtle details. For example the location of the powder feeder relatively to the spray torch, the way it is connected to the torch, including the length and path of the connecting pipe.

However, according to Wigren and Johansson [2], nice words among which are repeatability, reliability, and reproducibility are “mostly about average and standard deviation, σ, versus drawing requirements” [2] and the question is what is really needed. The answer to this question is not simple at all because many parameters are involved in the variability of coatings:

– Monitoring or control of the spray process at different levels (macroscopic working parameters (gases flow rates, arc current, voltage,. . .), microscopic ones (particles injection, particle temperature, velocity distributions in-flight,. . .), substrate preheating, coating, and substrate properties during spraying (residual stresses, Young’s module,. . .),
– Substrate cleaning, preparation including masking,. . .

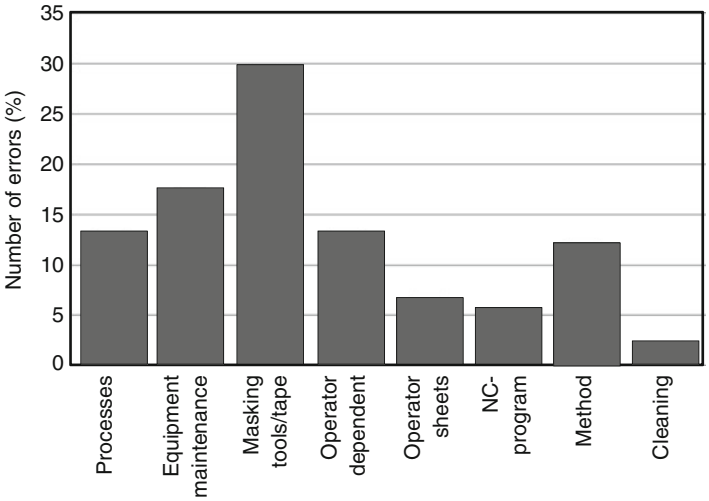


Fig. 16.1 Percentages in the number of errors observed in a production unit according to the different parameters: process, equipment maintenance, masking tools/tape, operator dependent, operation sheets, NC program, method, cleaning. Reprinted with kind permission from Dr. J. Wigren [2]

- Booth conditions (temperature, humidity, evacuation of dust,. . .) and disposition of the different spray equipment: robot and spray torch, mechanical unit where the part to be sprayed is fixed (often a rotating table), powder feeder,. . .
- Measurements of the coating properties: geometry, adhesion and cohesion, mechanical, thermal,. . . properties
- Equipment maintenance
- Operator training and certification, attention (that can depend on the day of the week),. . .
- Operation sheets validation and follow-up

At last, the procedures and systems used to characterize and test coating properties have also to be standardized and carefully run. Indeed, many measurements depend on the quality of coating surface or the preparation of sample cross section.

Wigren and Johansson [2] have presented (see Fig. 16.1) the percentages in the number of errors observed in a production unit and resulting in parts rejected. As it can be seen, that due to the process itself is only a small part (about 13 %) of all of them. Process gives rise to the largest number of works published in the literature, including sensors presented in this chapter, which are essentially devoted to this topic. The use of sensors in real spray conditions is however crucial for improving the reliability of coatings through the better process understanding and its link to coating characteristics. In each case, the different stages of the spray process, i.e., from the preparation of the surface of the part to be covered to the characterization and control of coating properties, and also the equipment maintenance, operator training and certification, and follow-up of spray operation sheets are of key importance. Independently of the process itself, procedures and systems used to

characterize and test coating properties (see Chap. 15) have also to be standardized and carefully run. Indeed, many measurements depend on the quality of coating surface or the preparation of sample cross section.

16.1.3 How Sprayed Coatings Quality Was Improved Through the Spray Process Monitoring

16.1.3.1 At the Beginning

Since the 1960s and almost up to the 1980s, the development of this technology was carried out in an empirical manner. The way to proceed consisted in (1) varying the operating spray parameters such as arc current, anode nozzle internal diameter (i.d.), gas flow rates for plasma spraying, combustible and oxygen gas flow rates, nozzle i.d., gas injection for flame spraying, etc., for a powder with particles of given morphologies and size distribution and (2) characterizing the properties of the resulting coating and evaluating its performance in specific use conditions. The procedure was repeated until certain standards were obtained and the parameter setting was padlocked [3]. Control of these parameters based on experience and trial and error allowed achieving, by this approach, the development of efficient coatings for a broad spectrum of applications. This approach made it possible to develop efficient coatings for a broad spectrum of applications and achieve repeatable and rather reliable products. It allowed developing the monitoring of macroscopic spray parameters (not those of in-flight particles), control of feedstock (particle morphology and size distribution), and the booth-to-booth consistency (equivalency, calibration, qualification, position of powder feeder relatively to spray torch,. . .).

16.1.3.2 Eighties–Nineties

At the end of the 1980s and in the 1990s two new approaches were considered:

– The development of commercially available computerized systems to follow continuously in real-time macroscopic parameters of the process in the spray booth. The parameters were for plasma spraying: arc current, and mass flow rates of plasma forming gases; for flame: combustible gases mass flow rates; for wire arc: arc current and wire advance velocity together with atomizing gas flow rate, etc., and of course for all processes the powder carrier gas mass flow rate for a given injector at a given position, the cooling water temperature and flow rate, the water leakage detection, etc. Unfortunately, spray guns are sensitive to aging: nozzle wear in HVOF, or HVAF spraying, or cold spray, electrodes wear in plasma spraying, small displacement of the injector and its partial clogging. As such variations practically induce almost no apparent change of

the macroscopic spray parameters, procedures had to be defined to take into account these phenomena. For example, in combustion spray guns, combustible gas flow rates, carrier gas flow rate,. . ., do not vary with a slight injector clogging. Such computerized systems, for example, with plasma torches, were taking into account the electrode erosion resulting in voltage decrease for a given arc current. The computer program was increasing the hydrogen flow rate to rise the voltage back to that obtained with a non-eroded anode nozzle. However, the development of sensors measuring particle temperatures and velocities in-flight showed later that such a procedure was generally not the best appropriate for keeping identical the heating and acceleration of particles.

– At the same time, laboratories developed various experiments and techniques to measure:
  - The hot gas flow temperatures and some attempts were also made to measure the gas velocity field
  - The particle trajectories distributions within the hot jets and the effect of the carrier gas flow rate on these trajectories (for a given injector i.d. and position as well as particle characteristics)
  - The particle velocity and temperature distributions at impact
  - The substrate and coating temperature evolution during the spray process, etc.
– At the same time, various experiments and techniques were developed to link the plasma or flame generation first to the heat and momentum transfers to particles and then attempts were made to link these results to the coating buildup and its properties characterization [4]. The importance of controlling in flight hot particle parameters, instead of macroscopic spray ones, was demonstrated in laboratories during the 1980s and 1990s. Rather sophisticated measuring devices were, then, used such as Laser Doppler Anemometry (LDA) for particle velocities and Phase Doppler Shift to also measure their diameters, fast pyrometers (with response time as short as 100 ns) [5–9], and also CCD (charge-coupled device) cameras for the detection of the hot particle trajectories distribution within the plasma jet [10]. Most of these techniques were too sophisticated to be used in the harsh environment of a spray booth, but they have permitted a much better understanding of coating generation. Thus, they helped to shift from a trial-and-error approach to a more scientific one progressively transforming the plasma spray process from an art to a science [11].
– During this period many efforts have also been made to standardize the techniques for coating characterization (metallography and image analysis, materials characterization, void content and network architecture,. . .) and also the control of coating quality (adhesion–cohesion, mechanical properties, thermal properties, wear resistance, corrosion resistance,. . .), the latter being more targeted toward the service conditions.

16.1.3.3 Mid-1990s to Now: Development of Sensors

The techniques developed and/or used in laboratories have been the basis for the development of sensors, less sophisticated but more simple and robust, able to work in the harsh environment of spray booths [12, 13]. At the end of the 1990s, a commercially available in-flight particle condition (temperature, velocity and diameter) monitoring system, the DPV 2000® System (Tecnar Automation, Quebec, CN) was developed, based on the work of Moreau et al. [13]. Almost in parallel, an imaging system for in-flight particle temperature, T_p, and velocity, v_p, measurements the Spray Watch® was developed by Oseir, based on the work of J. Vattulainen et al. [14]. These devices were the firsts that could work in the harsh environment of spray booths. They both allowed monitoring the effect of the conventional spray parameters (gas flow rates, nozzle internal diameter, power level for plasma spray torches, injection conditions, particles size distribution and morphology,. . ..) on the in-flight particle parameters. Extensive research on relationships between in-flight particle parameters and coating properties, see, for example, [14–23] led to a drastic enhancement in the process understanding and to the improvement of coating reproducibility and reliability [14, 17]. However the linkage to coating properties is still some sort of enigma. In fact the following points, which are actually missing, should be developed:

- Real-time process control to improve performance and meet quality requirements.
- Close-loop control for direct, real-time monitoring of process performance via real-time sensing of particle spray parameters.
- Corrective actions setting process variables and post-process examination.

However this implies:

- The necessity to establish for *each coating* with given service properties, relationships between macroscopic spray parameters—sensor parameters—coating thermomechanical properties—service properties.
- The development of new robust and easy-to-use sensors that incorporate these relationships.
- To develop controllers that must be able to modify input spray variable accordingly.

16.1.4 Spray Process Parameters That Should Be Controlled

Roughly parameters that should be controlled can be categorized in three areas:

- The high temperatures (plasma, flame, HVOF, HVAF, D-gun) or high-energy (cold spray) jets or the arc (wire arc) generation, linked to the gun-operating parameters.

- The heating and acceleration of the injected particles. They are linked on the one hand to the high-energy jet temperature and velocity distributions and on the other to particle size distribution, morphology, specific mass, injection velocity, and direction distributions and of course their injection type (radial or axial). All these parameters control the particle diameter, velocity, and temperature distributions at impact onto the substrate or the previously deposited layers.
- The phenomena linked to particles impacting onto the substrate or the previously deposited layers and depending on the one hand on temperatures, velocities, diameters, and oxidation levels of in-flight particles and on the other on the relative movements torch to substrate (robot programming of the spray pattern) and cooling systems. The relative movements torch/substrate also control the orientation of the torch, which axis must be as close as possible to the normal to the substrate at the deposited spot location, the successive passes thickness and finally that of the coating, the temperature of the substrate and coating through monitoring of cooling systems and pass thickness. It must be underlined that the monitoring of coating temperature and its through thickness gradient, during the spray process, are key parameters to control especially the residual stress distribution. At last the substrate preheating permits the elimination of adsorbates and condensates of its surface and controls, to a great extent, the coating adhesion.

This chapter comprises six sections:

- The first short one is related to the high-energy jet measurements
- The second is devoted to sensors characterizing gas flow and particle measurements in-flight
- The third one presents a few examples of sensor applications
- The fourth part is related to coating properties monitoring
- The fifth part explains how coating properties are now monitored and what should be done for a real online control
- The last section presents other possible measurements that could become sensors in the future

16.2 High-Energy Jets Characterization

These measurements, which started in the 1960s, were the firsts developed on plasma or flame torches used for spraying.

16.2.1 Plasma Jets

They have been the first ones to be characterized, with many works devoted to temperature measurements while only a few attempts were made to determine jet velocities.

16.2.1.1 Temperature Measurements

(a) Emission Spectroscopy of Symmetrical Jets

Most measurements, except those made with enthalpy probe, which, in the following, is categorized as a sensor, are based on emission spectroscopy of molecules, atoms, and ions. Such measurements give the population of the emitting excited level [5–7] and assumptions must be made to deduce a temperature from this population. Depending on the assumptions made, different temperatures can be measured. In most cases when measuring plasma jet temperatures in spray conditions it is simply assumed that the plasma is at equilibrium (LTE: Local Thermodynamic Equilibrium) and the different temperatures: electrons, population, Boltzmann, rotational, vibrational,... [5] are the same. At equilibrium, the evolution of the volumetric emission coefficient, ε_λ, can be calculated as a function of temperature for a given pressure [24] and thus temperature can be deduced from ε_λ measurement. However the evolution of ε_λ with temperature is drastic and for atoms it varies in ratios of about 10^{16} to 10^{18} when temperature increases from 3,000 to 14,000 K! At the best, detectors can cover 4 to 5 orders of magnitude and thus the temperature range that can be covered is limited and varies roughly from 8,000 to 13,000 K for argon or nitrogen atoms. This range covers well conventional plasma jet cores (produced by stick type cathode guns). For higher temperatures, such as those obtained in PTA, argon ions, Ar^+, are used and cover values from about 15,000 K to 22,000 K. For lower temperatures (below 8,000 K) such as those obtained in the plasma jet plumes or in high power torches with vortex gas injection and button-type cathodes, where an important mixing with the cold surrounding atmosphere occurs, molecular spectra must be used. The easiest molecular spectra to be used are those of N_2^+ or OH, but they are by far more complex and time consuming than atomic spectra [5, 24]. To record the plasma radiation, a small measurement volume is focused, through a lens, onto the entrance slit of the monochromator. To collect such spectra, spectrometers or monochromators must cover a wavelength range from about 3,000 to 12,000 Ä, depending on the lines or molecular spectra considered, with reasonable accuracy and resolution. The spectral resolution depends on the width of the entrance slit, the resolution of the detector itself, as well as on the accuracy of the diffraction, linked to grooves density in the dispersive element. Spectral resolutions better than a few Ä are easily achieved. The photodetector is now generally made of a diode array, which, when coupled with a computer, permits fast treatment of data, including Abel's inversion.

Unfortunately such diode arrays response time are longer than those of photomultipliers.

Another problem is that the detector collects radiation that is the integrated intensity of the light originating along the line of sight (optical path). Moreover along this line of sight very high temperature and volumetric emission coefficient gradients exist. For example, at anode nozzle exit, with the line of sight aiming the torch axis, temperature varies from 8,000 K in the jet core fringes to about 13,000–14,000 K on the axis. First of all it must be assumed that the plasma jet is optically thin and then that the jet has a perfect axial symmetry. The first point depends on the choice of lines used. The symmetry is almost the case of plasma torches with one stick-type cathode, except when electrode wears irregularly or a too high radial carrier gas injection destroys the symmetry. When these conditions are fulfilled, methods such as Abel's inversion can be used to determine the temperature distributions along the line of sight [5].

The last problem is the anodic arc root fluctuations, the arc attachment being continuously fluctuating resulting in surging and whipping motion of the plasma jet. This is illustrated in Fig. 14.34 showing pictures of the same plasma jet taken at the lowest (about 40 V) and highest voltages (about 80 V) of the fluctuating Ar–H_2 plasma jet (fluctuation frequency of about 5,000 Hz) [25]. In general the frequencies of these fluctuations range from 2 kHz to about 10 kHz and with diatomic gases (Ar–H_2, N_2, N_2–H_2) the ratio of the highest voltage fluctuation ΔV to the mean voltage V_m can reach 2 and sometimes be over, but it is generally below 0.5 for Ar–He mixtures. According to Fig. 14.34, which is among the worst cases, the jet lengths (corresponding to gases with temperatures over 8,000 K), in accordance to these fluctuations, can vary in a ratio that can reach 3.

Monochromators are now equipped with CCD detectors, cooled with liquid nitrogen and computer controlled. They allow a very fast treatment (a few ms) of the recorded data especially for Abel's inversion. As their response times are around milliseconds, fluctuations are integrated and the temperature distribution recorded seems perfectly symmetrical. Such measurements allow visualizing what is the effect of the torch working parameters on the plasma jet core temperature distribution. This is illustrated in Fig. 7.29 showing the effect of the design of the anode nozzle exit onto the plasma jet temperature distribution [25–27]. With a slight divergent nozzle (Fig. 7.29b), the mixing with the surrounding air, as pointed out by Pfender et al. [28], is delayed [27] and the plasma jet lengthen compared to that obtained with a straight nozzle Fig. 7.29a. These two figures represent the plasma jet with a time-averaged (100 ms) temperature distribution, assuming a cylindrical symmetry of the jet, as observed with the eye through a black window.

Unfortunately when taking pictures of a d.c. plasma jet, with a camera at a frequency of 24 Hz and shutter time of 10^{-4} s, one obtains images such as those presented in Fig. 16.2a [29] that are not at all symmetrical. Arc root fluctuations can be taken into account by adding and subtracting the standard deviation to the mean value of the line signal. When doing so, one obtains the temperatures distribution presented in Fig. 16.2b.

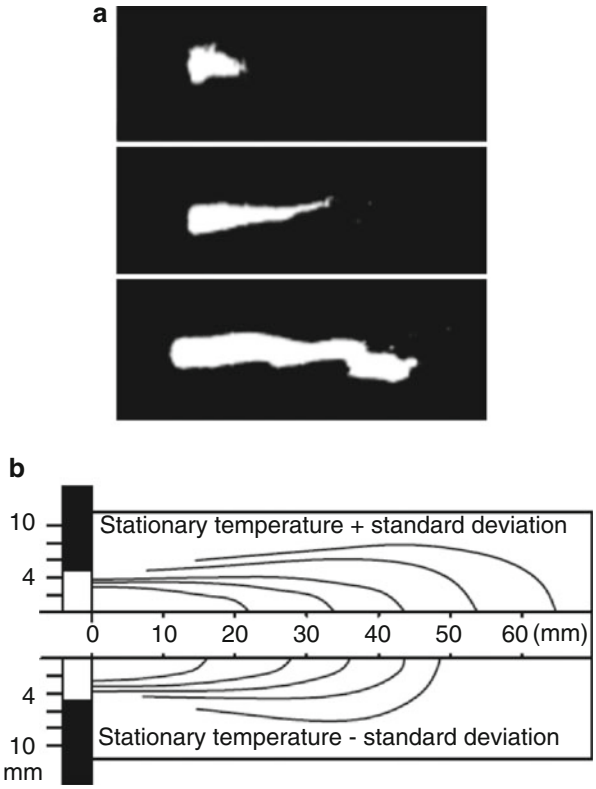


Fig. 16.2 (**a**) Pictures of a d.c. plasma jet taken with a shutter time of 10^{-4} s, (**b**) temperature measured with ArI 738.3 nm line ± standard deviation (measuring time 100 ms). Ar–H_2 (45–15 slm) plasma jet; nozzle i.d. 10 mm, $I = 632$ A, $V = 61$ V, thermal efficiency of the gun 56 %. Reprinted with kind permission from Elsevier for Int. J. Therm. Science [29]

It is difficult to pretend that the temperature distributions presented in Fig. 16.2b are a good representation of images shown in Fig. 16.2a. Thus such measurements for highly fluctuating plasma jets obtained with diatomic plasma-forming gases can only give trends about the plasma jet evolution when modifying plasma torches working parameters. Results obtained with pure argon or argon–helium mixtures are more reliable. To achieve less fluctuating plasma jets, torches with the anode separated from the cathode by insulating rings have been developed (same voltage fluctuation ΔV at the anode but much higher mean voltage V_m due to the arc column lengthening, resulting in $\Delta V/V_m < 0.2$). Among these torches Triplex Pro® from Sulzer Metco comprises three insulated cathode and one anode (see Fig. 7.54) resulting in plasma jets comprising three lobes (see Fig. 7.55) and thus no more symmetric. To measure the temperature of such jets one must use plasma computer tomography (PCT).

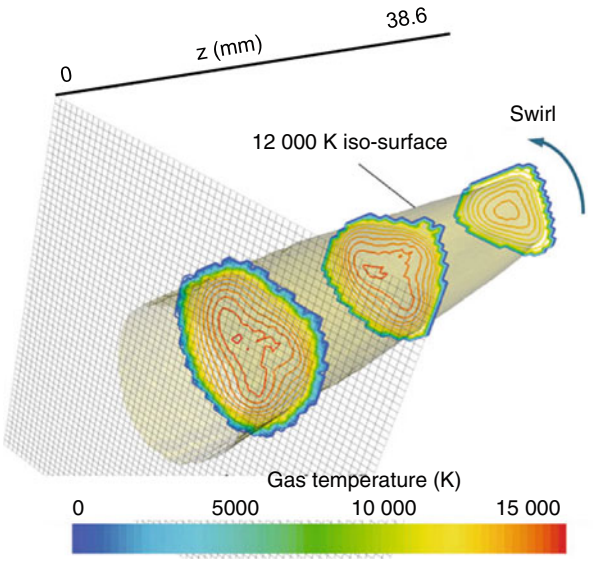


Fig. 16.3 Tomographic reconstruction of gas temperature distribution showing the counterclockwise jet rotation; injector plane cross section, three additional downstream sections and surface of 12,000 K. Reprinted with kind permission from Springer Science Business Media [32], copyright © ASM International

(b) Emission Spectroscopy of Nonsymmetrical Jets

In the plasma computer tomography (PCT) developed by Landes [30], the emitted radiation of the plasma jet is detected under several directions, one after the other and distributed over a sector of 180° in a plane perpendicular to the torch axis. As in conventional emission spectroscopy, a cross section of the plasma jet is imaged, through a lens system, on the entrance slit of the spectrometer and signals in its outlet plane are recorded through a CCD camera. With nonsymmetrical jet it is mandatory to detect, by a tomographic procedure, the emitted radiation under several angles of observation. The necessary conditions to apply this method are highly stationary plasma jets with a definite axis around which the total detecting optical system is rotated. The calculation and storage capacity, necessary for the reconstruction of cross-section images from tomographic data are very high and increase with the third power of cross-section resolution. However customary PCs can reconstruct cross-section images within an acceptable time [31]. For more details on the process see the papers of Landes [30], and Mauer et al. [32].

Mauer et al. [32, 33] have presented results obtained with a three-cathode TriplexPro™ torch [33]. The nozzle diameter was 9 mm, the current 540 A, and the plasma gas flow rates 50 slm Ar and 4 slm He, conditions corresponding to an effective net power of 30.9 kW. Figure 16.3 shows the tomographic reconstruction of gas temperature distribution with the powder injector plane cross-section, three additional downstream sections and the iso-surface of 12,000 K. The gas distribution ring inside the torch induces the counterclockwise jet rotation. The temperature distribution, over the jet cross section in the plane of particle injection, shows characteristic nonrotationally symmetric profiles with a typical triangular shape.

Such tomographic technique could measure the symmetrical plasma jet perturbation by the carrier gas flow rate for which only calculations have been performed [10].

(c) Laser Spectroscopy for Jets at Temperatures Below 8,000 K

More sophisticated techniques such as Coherent Anti-Stokes Raman Spectroscopy (CARS) or Rayleigh scattering are also used, essentially for temperatures below 8,000 K. Coherent Anti-Stokes Raman spectroscopy (CARS) has the advantage of high conversion efficiency, a laser-like coherent signal beam for high collection efficiency, excellent fluorescence and luminosity discrimination, as well as high spatial and temporal resolution [34–38], but it only works with molecular spectra. The CARS signal is generated by crossing three high-powered, pulsed laser beams, called pump beam at frequency ω_1, pump beam at ω_2, and the Stokes beam at ω_S, in a suitable phase-matched geometry. The beam-crossing region is at the common focus of the three laser beams and defines the CARS probe volume, a 50 μm diameter cylinder that is 1 ± 2 mm in length [38].

A broadband approach is generally used to generate the entire CARS spectrum on the time scale of the laser pulse. For example, it has been used in plasma jet fringes to follow the entrainment of the surrounding air into the plasma jet [28]. Molecular nitrogen was the probe and the temperature determination was calibrated against a Pt, Pt–Rd thermocouple.

Integrated Rayleigh scattering, as CARS, presents an excellent spatial resolution: the measuring volume is the intersection of the laser beam and the optical path of the detector and the measurement is local. The temporal resolution is obtained by using pulsed lasers. The Rayleigh signal is proportional to the densities of the atomic and molecular species present at the measuring volume and of course to their Rayleigh cross sections. Assuming equilibrium and using Dalton's law it is possible to determine the temperature [39]. Such measurements have been used to study the influence of the presence or not of a substrate on the temperature distribution in the plume of an Ar–H_2 d.c. plasma jet [40].

16.2.1.2 Velocity Measurements

Very few devices can be used to measure the plasma velocity. To our best knowledge they consist of enthalpy probes for regions where temperatures are roughly below 6,000 K (see Sect. 16.3.1) and a setup based on plasma jet fluctuations. Velocity measurements of flame or cold flows are performed by injecting small particles (in the few μm size range) and measuring their velocity, assumed to be that of the flow, by particle image velocimetry PIV (see Sect. 16.5.3.1).

The enthalpy probe measurements being described in Sect. 16.3.1, only the setup based on plasma fluctuations will be summarily described. The principle of the method developed by Coudert et al. [41, 42] is to measure the time of flight of the

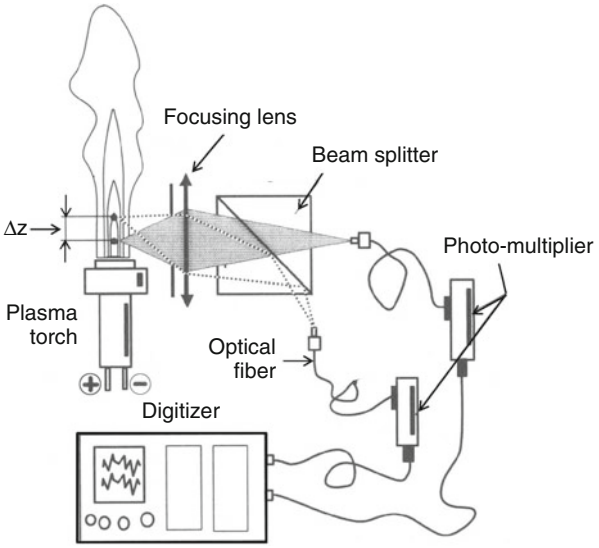


Fig. 16.4 Optical arrangement for the velocity measurements. Reprinted with kind permission from Springer Science Business Media [42]

luminous fluctuations of the plasma ($Ar–H_2$), which are supposed to propagate at the flow velocity. In Fig. 16.4 is shown, the image of the plasma jet split and focused, with a known magnification, in two planes were the wavelength-integrated light is sampled by means of two optical fibers 100 μm in diameter. The distance, Δz, between the two sampling points is adjusted with a precision of 0.02 mm. Because Δz is finite (4 mm in the experiments) the measured velocity corresponded to a space-averaged value. This value is attributed to the velocity in the middle of Δz, which is equivalent to assuming a linear change of the velocity between the two sampling points. The detection is ensured by two photomultipliers. This setup has allowed determining velocity radial and axial distributions in the plasma jet core (where temperatures are over 8,000 K) [42], according to the working conditions of the plasma torch.

Very recently a dedicated PIV system (see Sect. 16.2.2.2 for definition) was implemented to record information on the injection of liquid feedstock and characterize the liquid stream penetration and behavior in the plasma jet. Results will be presented in Sect. 16.5.3.1.

16.2.1.3 Turbulences Characterization

Shadowgraphs of plasma jets [28] reveal the abrupt development of turbulence from the well-behaved laminar flow near the nozzle exit. They reveal typical shear layer instabilities close to the nozzle exit, characterized by the formation of vortex rings around the plasma jet. Farther downstream, the vortex structure breaks down over a relatively short distance, resulting in large-scale turbulence eddies that rapidly penetrate into the core of the plasma jet.

Laser Doppler anemometry of small alumina particles ($d < 3$ μm) was used to measure the turbulence intensity [43]. In the plasma jet fringes where temperatures are below 3,000 K, the Knudsen effect can be neglected and small particles follow the flow velocity. Particles were injected, from an especially designed fluidized bed, inside the nozzle and downstream of the arc root. The turbulence was defined as the ratio of the standard deviation of the individual velocity measurements for a given data point divided by the maximum centerline mean velocity for a given axial distance downstream. As for the shadowgraphs, the results show the rapid increase of the axial velocity fluctuations at the jet edge due to the mixing and entrainment of external air. By injecting small alumina particles around the plasma jet, the velocity of the entrained air was measured along the centerline of the plasma. Such measurements show that the fluid from the plasma jet has a much higher mean velocity than the entrained gas.

16.2.1.4 Electrode Erosion

Plasma torch electrodes wear:

- The cathode tip, conical for a new one, is rounded in about half an hour and then its erosion almost does not participate to the torch mean voltage variation. Of course this is true if the working conditions recommended by the manufacturer, minimum and maximum arc currents values, are respected. This cathode tip rounding modifies the flow velocity as illustrated in Fig. 7.34.
- For the anode the problem is more complex [44] and, depending on operating hours and number of restarts, the arc digs its attachment area as illustrated in Fig. 16.5a [45]. When working time and/or restart number increase, the arc root melts locally the anode wall, digging a deeper and deeper hole. The arc root displacement is thus more and more limited and the mean voltage diminishes. This is illustrated in Fig. 16.5b [45] showing the correlation, for three different working times (10 min, 10 h, 30–40 h), of the voltage and lifetime of the anodic arc root. As it can be seen in Fig. 16.5b, the amplitude of the voltage fluctuations decreases with time with a corresponding increase of the dispersion of the arc root residence time, τ, *especially* for longer periods of operation. Over a certain value of τ, corresponding to the critical time to melt the anode material, the erosion rate increases and so is the depth of the erosion craters as shown in 16.5a and b. This anode erosion has a negative effect on coating deposition efficiency (study performed for YSZ coatings), which value can be reduced from 50 % to 38 % after 20 h working with 40 periods of half an hour each, with the same arc current and plasma-forming gases, the carrier gas being reset to the optimum value after each restart. Correspondingly, the coating porosity increased from 4 to 11 %.

Of course increasing the arc current [46] can compensate the anode erosion and the voltage decrease. However it works when the voltage decrease is not too important. Moreover adding hydrogen to the plasma-forming gas to raise the

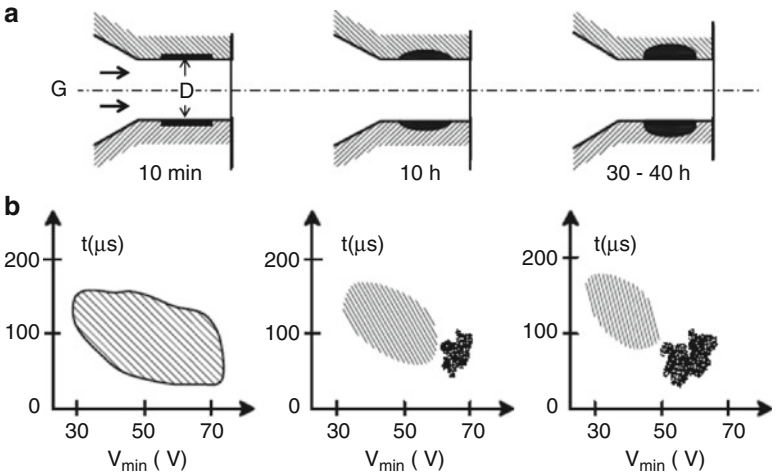


Fig. 16.5 (**a**) Evolution of the anode cross-section arc attachment area after respectively 10 min, 10 h and 30–40 h; (**b**) corresponding evolution of the voltage-arc root residence time distributions. Reprinted with kind permission from Dr. M. P. Planche [45]

voltage at constant arc current modifies not only the voltage but also the heat transfer. As the voltage decrease is not at all linear with the time elapsed, torch electrodes are changed after a given working time to avoid spoiling the production with the occurrence of an unpredicted catastrophic voltage decrease. Rigot et al. [47] have developed an electronic erosion controller with its own program and inerasable memory. The principle is presented in Fig. 16.6 representing the mean voltage time evolution. According to the frequency signal and mean voltage analyses a warning (yellow lamp) is lighted as soon as the mean voltage times evolution reaches the critical zone, the red lamp being lighted as soon as the hazardous zone, where the mean voltage time evolution becomes unpredictable, is reached.

Mauer et al. [48] have studied the influence of the electrodes wear on voltage measurement, power spectra analysis, and particle temperature distributions (using DPV 2000). With the first two measurements it is necessary to have a sequence of measurements under similar spray parameters. On the contrary particle temperature measurements yield an absolute criterion to assess the state of the gun.

16.2.2 Flames and Cold Spray

Compared to plasma jets, flame temperatures are by far lower with maximum in the range of 3,500 K. The high temperature jets can be subsonic with conventional burners or supersonic with HVOF and HVAF. In the following are presented summarily the different means that can be used, except of course the enthalpy

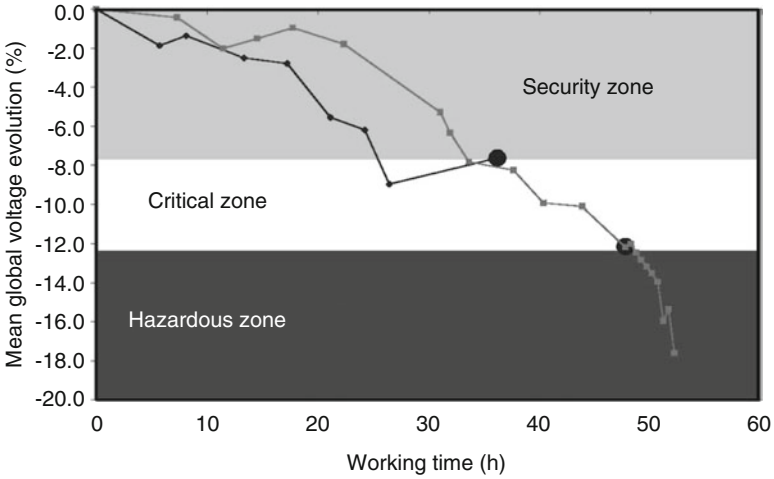


Fig. 16.6 Evolution with working time of the mean torch voltage, for two different sets of electrodes, with the three zones: security (*grey*), critical (*white*), and hazardous (*black*) [47]

probe described later in sensors Sect. 16.3.1. To our best knowledge nothing has been published about detonation characterization as well as on cold flow temperatures.

16.2.2.1 Flame Temperatures

(a) Laser

As for plasma plumes laser techniques are used, a few of them being cited below:

- CARS: for example single-shot temperature and CO_2 concentration measurements were performed in the exhaust stream of a swirl-stabilized, liquid-fueled combustor using dual-pump N_2–CO_2 CARS spectroscopy [49].
- Rayleigh scattering: High-repetition rate laser Rayleigh scattering was used to study the temperature fluctuations, power spectra, gradients, and thermal dissipation rate characteristics of a non-premixed turbulent jet flame at a Reynolds number of 15,200 [50].
- Laser-induced fluorescence (LIF) was used to characterize concentrations of OH, CH, NH, CN, C, and pollutants, NO, CO, to diagnose combustion processes [51]. The technique is based upon UV vibrational Raman scattering technique. The photon-counting system is used for detection of the Stokes and anti-Stokes Raman signals and their amplitude measurements. Rather small laser energy (about 20–25 mJ per pulse) are sufficient to characterize flames at atmospheric pressure. Assuming equilibrium, the Raman scattering signal can be calculated as a function of temperature.

(b) Thermocouple

For thermocouple measurements, radiative heat loss from the junction must be corrected and its effect on the temperature evaluated [52]. Moreover maximum temperatures are below 1,900 °C.

16.2.2.2 Flame and Cold Flow Velocity Measurements: PIV

Flow velocity is also measured by particle imaging velocimetry (PIV), which is a method for visualizing and analyzing field of flows [53, 54]. Small particles (in the μm size range) are added to the flow and measurements are performed downstream of the injection where it is assumed that particles have reached the same velocity as that of the flow (Knudsen effect is generally considered to be negligible below 3,000–3,500 K). The particles motion is dominated by Stokes drag with Stokes number below 1. Assuming that particles are spherical with low Reynolds number (micrometer sized particles and low specific mass), their ability to follow the fluid's flow is directly proportional to the difference in mass density between particles and the fluid and directly proportional to the square of the particles' diameters. Thus the smaller they are the faster they will reach the flow velocity. The scattered light from the particles is dominated by Mie scattering and so is also proportional to the square of the particles' diameters. Finally the particle size needs to be balanced to scatter enough light to accurately visualize all particles within the laser sheet plane but small enough to accurately follow the flow. Moreover for hot gases one must consider the Knudsen effect and the increase of the gas mean free path with temperature. That is why the problem is more complex with plasma than with flames and cold flows. In the PIV method, two images of the field, respectively at times t and $t + \Delta t$, are compared. Particles in the flow are illuminated by short laser pulses and captured with CCD digital cameras with a few hundred nanoseconds of difference between frames. The frames are split into a large number of interrogation areas or windows. In order to compare both images one must find out pairs of small areas (windows), which are the most similar to each other in both images. It is then possible to calculate a displacement vector for each window thanks to signal processing and autocorrelation or cross-correlation techniques. This is converted to a velocity using the time between laser shots and the physical size of each pixel on the camera. The size of the interrogation window should be chosen to have at least six particles per window on average. For example, this technique has been used by Alekseenko et al. [55] to measure the flow structure and velocities of swirling turbulent propane flames and by Yilmaz et al. [56] to characterize diffusion flame oscillations. PIV has also been used by Zahiri et al. [57] to characterize supersonic flow field for a commercially pure titanium powder cold sprayed. Results show that PIV, a whole-flow-field process, is a practical characterization technique for optimization of parameters and validation of the future models for the cold spray process. Newbery and Grant [58] have used PIV and high-speed video

imaging to observe droplet deposition during electric arc spraying, particularly with regard to the behavior of droplets originating from splashing.

16.2.2.3 Measurements Based on Laser Scattering

Lange et al. [59] have studied the location where particles are injected into a gas jet. To avoid contamination of the gas flow by tracer particles, they used non-resonant laser scattering to measure the spatially resolved distribution of drift velocity of fast gas flows, as well as their relative density distribution. Presently flows with temperatures below 4,000 K (high-velocity oxy-fuel spray or cold spray gas) can be measured. Measurements in a supersonic nozzle, obtained by means of laser scattering correlate well with theoretical calculations and particle image velocimetry (PIV) experiments.

16.2.2.4 Turbulences

As for plasma, turbulences play a key role in combustion phenomena. Techniques used are based on pulsed lasers with planar laser-induced fluorescence (PLIF) [52] or cinema-stereoscopic particle image spectroscopy PIV (CS-PIV) and orthogonal-plane cinema-stereoscopic PIV (OPCS-PIV) [60].

16.3 Sensors

By definition a sensor is a device that measures a physical quantity and converts it into a signal, which can be read by an observer or an instrument. In fact those used in spray processes, and described below, are all derived from sophisticated devices used in laboratories to characterize for example particles in-flight. Sensors are robust devices that can survive in the harsh atmosphere of spray booths and are relatively simple to avoid the numerous adjustments necessary for laboratory setups. Two types of sensors exist: those fixed on the spray torch and those fixed aside of it. As the first ones are moved with the torch, they record continuously the measured parameters and any variation is instantly detected. Thus the operator or the closed-loop feedback controller can react at once to correct the problem. Of course these sensors must be rather light (less than one kilogram) and small (less than 400 cm^3). On the other hand, when the sensor is fixed aside, the torch is driven in front of it after a given spray period, usually a few tens of minutes. Thus problems cannot be detected on line and corrected correlatively.

Sensors are used to characterize either hot gases jet or particles in-flight or coating under formation. For particles in-flight, the flux emitted or scattered by hot particles must be higher than that of the radiation from the hot gases. For example, with plasma jets, measurements of the radiation emitted by hot particles

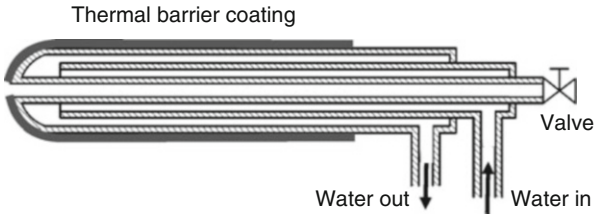


Fig. 16.7 Schematic of one of the smallest enthalpy probes with an external diameter = 3.17 mm (prior to its coating), and an internal diameter of 0.66 mm (Courtesy of Tekna Plasma Systems Inc.) reproduced with permission

are only possible in the plasma plume where the plasma temperature is below 6,000 K.

In the following are presented successively sensors for characterization of:

- Hot gases flow
- Particles in-flight
- Coatings under formation

16.3.1 Hot Gases Flow: Enthalpy Probe

Blais et al. [61] have presented an excellent historical review of the enthalpy probe starting from the work of Grey [62] through the first applications to plasma jets [63–65] to the extensive use of them [66–68] with their coupling with a mass spectrometer to measure local gas composition and at last their use in compressible jets [61, 69]. In 1993 Tekna Co. (CN) has developed a robust, low cost, and unique industrial enthalpy probe to determine enthalpy, temperature, velocity, and composition of d.c. or radio-frequency plasma jets. Tekna's integrated system is user friendly and the computer software controls the whole operation. Moreover a mass spectrometer can be easily integrated to measure local gas compositions.

The probe, as represented schematically in Fig. 16.7, consists of double walled tubing (made of stainless steel) that is cooled by a high-pressure (up to 6 MPa) water circuit, the water flow rate and inlet and outlet temperatures of which are measured. The water cooling is a closed-loop water recirculation system. The system also comprises a gas sampling line and a data acquisition and control unit. The technique is based on a two-step energy balance on the cooling-water circuit of the enthalpy probe. The first step is a "tare" measurement of the heat load to the probe in the absence of gas sampling conditions. The second is a measurement of the heat load under gas sampling conditions. The difference in heat load between the second and first steps represents the energy associated with the extracted gas sample. For a known amount of gas extracted from the plasma, the specific enthalpy associated with the sampled gas can be calculated.

Based on the enthalpy and the composition of the gas mixture, the temperature and the specific density can be determined. Nowadays, enthalpy probes are often covered with a thermal barrier coating (TBC), which provides a larger heat load

difference between the tare and sampling modes, improving the quality of enthalpy measurements [61]. Furthermore, the hot gases can be sampled in order to analyze the composition by integrating a mass spectrometer. In contrast to the previously discussed spectrometric methods (Sect. 16.2), which are nonintrusive, probes are intrusive, i.e., they may disturb the plasma or the flame at the same location at which measurements are being taken. By reducing the probe size (but water cooling must be achieved!), disturbances may be minimized, but not entirely eliminated. This implies that the application of probes for hot gases diagnostics, especially plasmas, requires a careful assessment of possible disturbances caused by the presence of the probe. In order to meet the basic requirements of a viable diagnostic tool, the probe should (1) cause little disturbance of the hot gases, (2) provide sufficient spatial resolution, (3) have a high sensitivity, and (4) be rigid and thermally well protected. The application of enthalpy probes is restricted to dense plasmas in which the mean free path lengths of the various species are very small compared to the probe radius. For flames the mean free path requirement is generally satisfied. In addition, the flow must be steady. In nonsteady flows, the enthalpy probe will measure some average, which is no more a time average but a Favre mass average.

Enthalpy probes are useful for measurements in the temperature range from 2,000 to 9,000–10,000 K. The upper temperature limit is due to the high heat fluxes at the probe tip, which may be as high as 10^9 W/m^2. For reactive gas mixtures (for example, a hydrogen/argon mixture), the upper temperature limit has to be reduced (6,000–7,000 K), because of the high enthalpy, high heat transfer coefficient and the correspondingly high heat fluxes in this situation. The lower temperature limit is mainly due to the decreasing sensitivity as the temperature or enthalpy in the gas is reduced. The plasma enthalpy h_p is given by [61]:

$$h_\mathrm{p} = h_0 + \frac{c_\mathrm{pw}\left(\dot{m}_{wf}\Delta T_\mathrm{f} - \dot{m}_{wnf}\Delta T_{nf}\right)}{\dot{m}_g} \tag{16.1}$$

where c_pw is the specific heat of the water, m_wf is the mass flow rate of the cooling water during sampling gas flow, and ΔT_f is the cooling water temperature difference during sample flow. The nf subscript stands for the non-flow conditions, when no sample is being drawn. The h_o represents the enthalpy of the gas sample at the probe outlet, determined by the specific heat, c_g, of the gas sample. To determine the flow velocity, v_f, assumptions must be made about the flow Mach number, M, ($M = v_\mathrm{f}/a$, where a is the sound velocity).

16.3.1.1 Incompressible Jets

It is generally the case when $M < 0.3$, where the velocity can be determined from Bernoullis's equation:

$$v_f = \sqrt{\frac{2(p_0 - p)}{\rho_f}} \tag{16.2}$$

where p is the pressure of the flow, p_0 the pressure at the stagnation point of the flow (i.e. with a zero velocity), and ρ_f the specific mass of the flow. ρ_f is calculated once temperature and pressure of the flow are known. The measured enthalpy Eq. (16.1) allows determining temperature when assuming equilibrium.

16.3.1.2 Subsonic Jets

In the Mach number range $0.3 \leq M \leq 1$, compressibility must be considered and the velocity expression becomes

$$v_f = \sqrt{\frac{2\gamma RT}{\gamma - 1}\left[\left(\frac{p_0}{p}\right)^{\frac{\gamma}{\gamma-1}} - 1\right]} \tag{16.3}$$

where γ is the ratio of the gas specific heats at constant pressure and volume ($\gamma = c_p/c_v$) and R the ideal gas constant. As for incompressible gas, temperature must be determined from the enthalpy measurement.

16.3.1.3 Supersonic Jets

In the supersonic regime $M > 1$, the problem becomes more complex because of the existence of shock wave and nonequilibrium phenomenon. Thus rather complex equations must be used for which the interested reader can see the paper of Blais et al. [61].

16.3.1.4 Precision of Measurements

First of all, results from the enthalpy probe rely on the energy balance and pressure measurement. Lowering cooling water flow increases the temperature difference between inlet and outlet but raises the risk of the probe destruction, while a too high water flow will decrease the accuracy of temperature difference measurement. Pressure measurements must be performed under iso-kinetic conditions, meaning that the gas velocity at the probe inlet is equal to the free gas stream velocity, condition achieved by adjusting the gas velocity at the probe inlet. Thus, the measurement calibration is a key issue to achieve reliable measurements and calibration factors must be computed and saved. According to Mauer et al. [32] once a full calibration of the system has been completed, a new calibration run should be performed applying the calibration factors obtained previously to confirm

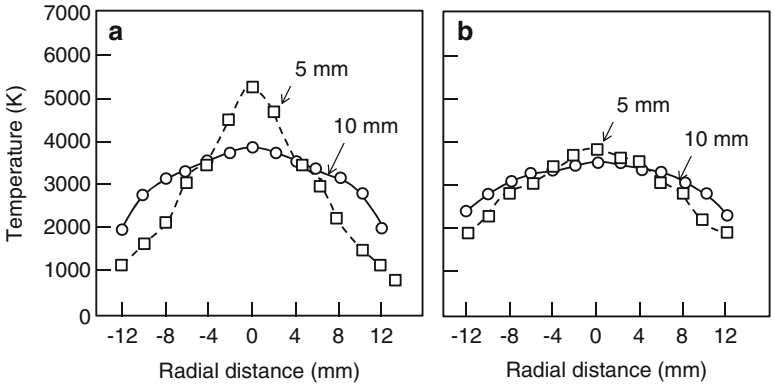


Fig. 16.8 Ar–H_2 plasma radial temperature distributions measured downstream of the nozzle exit at (**a**) 40 mm and (**b**) 60 mm. Reprinted with kind permission from Springer Science Business Media [73], copyright © ASM International

and fine-tune the accuracy. Normally, an accuracy of within 1 % can be obtained in 2–3 calibrations. Jankovic and Mostaghimi [70] have reviewed the errors induced by this measuring setup. It must also be kept in mind that temperature measurements through emission spectroscopy and enthalpy probe do not necessarily give the same results. It has been shown by Pfender et al. [64] who have compared temperatures measured in a d.c. Ar plasma jet at the limit of the jet core, where the fast diffusion of the electrons enhances the inelastic collisions with atomic species and thus give overestimated spectroscopic temperatures. Rajabian et al. [71] published later a more detailed analysis of differences between spectroscopic and enthalpy probe measurements. In their study of a plasma jet produced by a triple torch plasma reactor, Asmann et al. [72] have shown the excellent reproducibility of enthalpy probe measurements.

16.3.1.5 Example of Results

– Steffens and Duda [73] have studied a 9MB plasma torch of Sulzer Metco working with an argon/hydrogen mixture and two different anode designs: 5 and 10 mm i.d. anode nozzles. The closest measurements were achieved 40 mm downstream of the nozzle exit to ensure a safe operation. At that distance, as shown in Fig. 16.8a, the maximum temperature was roughly 1,500 °C lower with the 10 mm nozzle, but the temperature distribution was more uniform, thus improving the heating of the particles traveling in the jet periphery. These different jet characteristics were emphasized by the temperature distribution 60 mm downstream of the nozzle exit, presented in Fig. 16.8b. The maximum temperature at this measurement location was approximately the same, but the gradient to the fringes of the 5 mm anode was larger compared to that of the 10 mm anode.

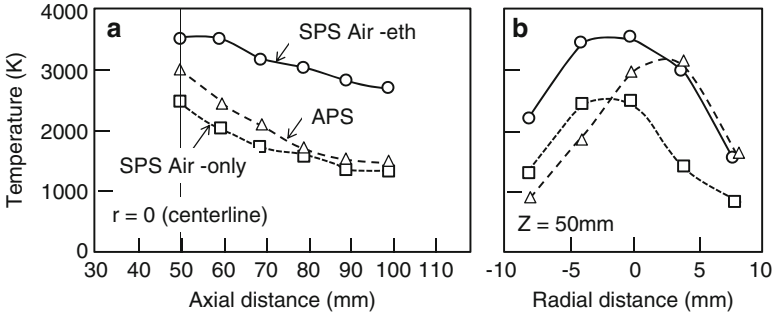


Fig. 16.9 For Triplex Pro plasma torch axial and radial distributions (at an axial distance of 50 mm) of the measured plasma gas temperatures for three cases (APS: without any injection, SPS air + ethanol: two-phase injection of ethanol and air, SPS air only: injection of air without ethanol). Reprinted with kind permission from Springer Science Business Media [74], copyright © ASM International

To better understand the suspension plasma spraying (SPS) process, Vaßen et al. [74] have studied with an enthalpy probe the effect of injection of ethanol in a Triplex Pro torch working with Ar–He (40-10 slm) and an arc current of 250 A (corresponding to 17.3 kW). Figure 16.9 shows the measured plasma gas temperatures axially (Fig. 16.9a) and radially (Fig. 16.9b measured 50 mm downstream of the torch nozzle exit) for three cases: (1) APS: without any injection; (2) SPS air + ethanol: two-phase injection of ethanol and air; (3) SPS air only: injection of air without ethanol. Air injection cools down the plasma plume and shifts the radial temperature distribution downwards (Fig. 16.9b). 50 mm downstream of the nozzle exit, the maximum is moved radially by about 5 mm. If ethanol is added, the maximum temperature rises from 2,458 K (air injection only) to 3,487 K with ethanol due to its combustion enthalpy. With ethanol injection, in axial direction, the maximum CO_2 content of 2.65 vol.% is reached at a distance of 70 mm, indicating that the combustion of the ethanol is completed here. At the same point, the oxygen content is lowered by the combustion from 19.5 vol.% (air injection only) to 13.8 vol.% with ethanol. Figure 16.10 presents the corresponding measured velocity distributions. The same characteristics as those obtained for temperatures are observed. Due to the air injection, the velocities measured at a nozzle distance of 50 mm are lowered from 379 m/s (no injection) to 336 m s^{-1} (air injection only). The combustion of ethanol leads again to an increase to 402 m/s.

16.3.2 Particles In-Flight Distribution

Two types of injection, linked to the spray gun, are used: radial at the nozzle exit (internal or external) or axial [10]. Many works have been devoted to radial injection in d.c. plasma jets [16, 67–88] or HVOF jets [89–92] or D-gun [93]. With radial injection [10], an optimum trajectory is obtained if the force

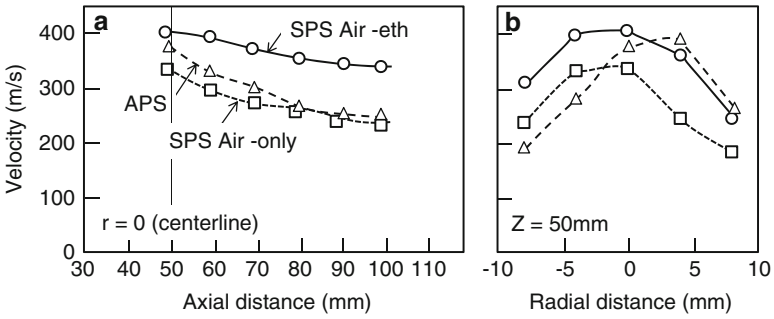


Fig. 16.10 For Triplex Pro plasma torch axial and radial distributions (at an axial distance of 50 mm) of the measured plasma gas velocities for three cases (APS: without any injection, SPS air + ethanol: two-phase injection of ethanol and air, SPS air only: injection of air without ethanol). Reprinted with kind permission from Springer Science Business Media [74], copyright © ASM International

imparted to particles by the hot gases jet is close to that they have at the injector exit. The hot gases force is linked to their momentum density, ρv^2, where ρ is their specific mass and v their velocity and the particle cross-section surface, S_p. This quantity ($S_p \cdot \rho \cdot v^2$) varies along the particle penetration trajectory: velocities and temperatures are increasing from the jet fringes to its center, but ρ is decreasing correspondingly (by less than a few tens of %). The force of injected particles varies with their injection velocity and mass on the one hand and on the carrier gas velocity on the other [see Eq. (4.2)]. According to collisions between particles and the injector wall or between themselves, as well as the high Reynolds number of the carrier gas (very turbulent flow), particles, whatever may be their size, have about the same velocity and thus acceleration [see Eqs. (4.5) and (4.6)] at the injector exit [10]. It means that their size distribution must be as narrow as possible to limit trajectories dispersion. For example, a diameter ratio of 2 between the smallest and the biggest particles (narrow distribution) corresponds already to a ratio of 8 of their mass and thus their forces! Of course the morphology of particles, modifying their mass density must also be considered [94]. The injection velocity of particles must be adapted to their mass and mean size defining their cross-section surface, S_p, and to the mean hot jet momentum density. The latter varies very fast, through the jet velocity, with the jet enthalpy. *It means that for any slight change in the torch-working conditions, the injection velocity, through the carrier gas flow rate, must be adjusted*. Indeed, the carrier gas flow rate must not perturb the hot gas flow [84, 95]. As its flow rate must be increased to increase particles mean velocity, it becomes difficult to inject particles with sizes below 5–10 μm, especially those with a specific mass lower than 3,000 kg/m^3.

Axial injection is used with different spray guns such as flame, some HVOF, or HVAF, detonation, a few d.c. plasmas, all R.F. plasmas, and cold spray [10]. Axial injectors play also a key role [93, 96–106] according both to their position and the particle injection velocity, especially when the gas flow velocity is low as in flame

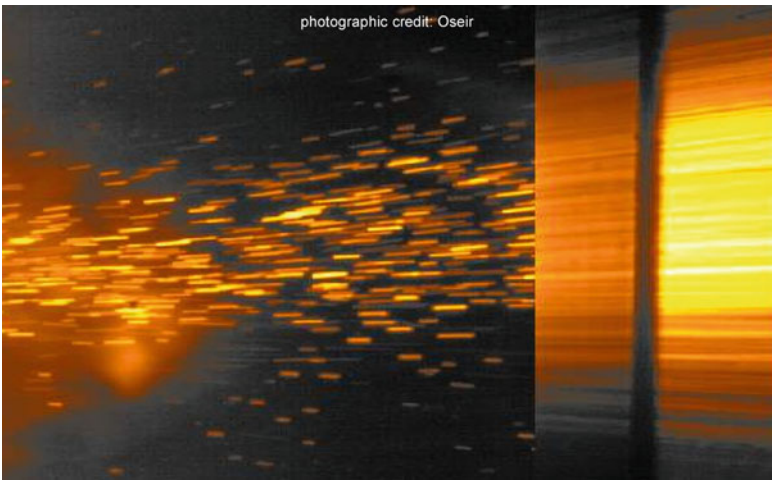


Fig. 16.11 Particles in-flight in the plume of a d.c. plasma jet imaged with a CCD camera and a given shutter time on which depend the line lengths representing them [courtesy of Oseir®]

[96] or RF torches [101]. Many results are presented in references cited above and show the drastic importance of injection optimization. However to achieve reproducible coatings it is of primary importance to follow online with sensors if particles mean trajectory remains optimal in spite of any modification of spray parameters by the operator or after long spray periods resulting in the nozzle wear, for example. Thus the continuous control of hot and cold particle trajectories is as important as their temperatures and velocities that are strongly linked to their trajectories.

16.3.2.1 Hot Particles

The control of hot particle trajectories can be performed in area where the hot gases jet radiation is low enough (for example, in the plume of a plasma jet) and does not overcome rradiation from hot particles [9]. This is illustrated in Fig. 16.11 after from Oseir® showing the image of hot particles in-flight in the plume of a plasma jet. The CCD camera is focused to image the jet plume from a few centimeters to the substrate. It can be seen that, according to the shutter time, lines represent particles and their lengths can be linked to their velocities.

The spray and deposit control (SDC®) [10, 107], based on hot particles radiation, uses either a CCD camera or a photodiode array where the image of a section of the plasma jet plume or the flame is focused. A filter with a 3-nm band pass allows eliminating the most important part of the plasma plume light or that of combustion gases in HVOF. It is possible to record four images and, as the SDC is fixed on the plasma torch or the HVOF gun, the particle trajectories can be continuously monitored. The arrangement is shown in Fig. 16.12, where the SDC, fixed orthogonally to the plane defined by the torch and injector axes, measures the flux of hot

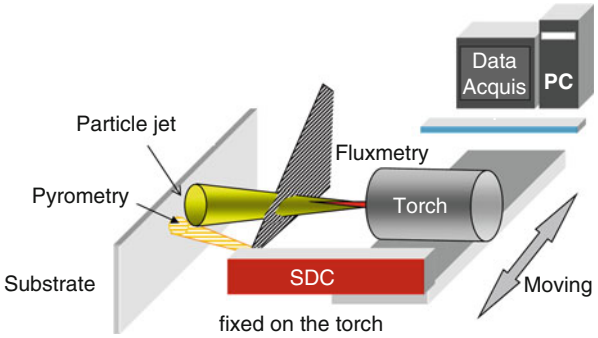


Fig. 16.12 Spray and deposit control setup fixed on the spray torch and following the hot particles radiation in the hot gases jet plume (60 mm downstream of the nozzle exit) and the temperature of the coating behind the sprayed spot. Reprinted with kind permission from Springer Science Business Media [9], copyright © ASM International

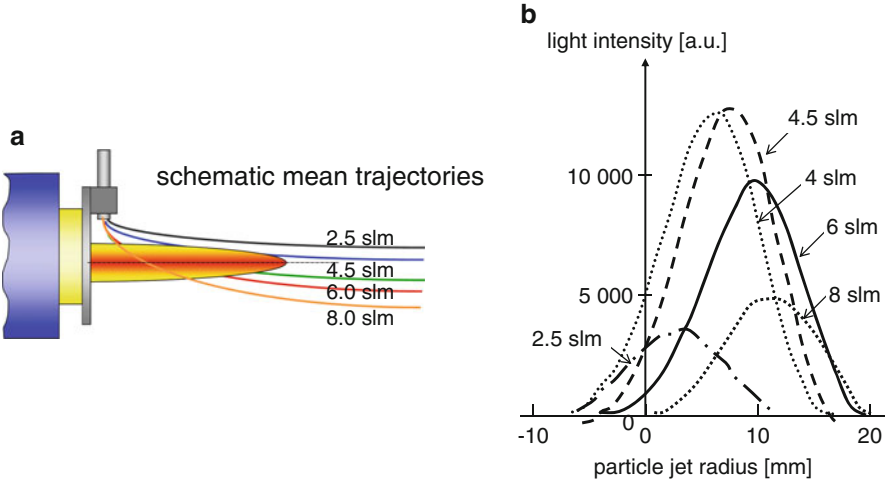


Fig. 16.13 SDC measurement of alumina particles heat flux 60 mm downstream of the nozzle exit of an Ar–H_2 plasma (45 slm Ar, 15 slm H_2, 6 mm i.d., Peff = 20 kW, injector i.d. = 1.75 mm, disposed 3 mm downstream of the nozzle exit and at 8 mm from the torch axis) with different argon carrier gas flow rates. Effects on particles: (**a**) mean trajectories and (**b**) radial distribution of emitted light intensity. Reprinted with kind permission from Springer Science Business Media [9], copyright © ASM International

particles 60 mm downstream of the nozzle exit and, at the same time, the temperature of the coating just behind the sprayed spot.

Figure 16.13 illustrates how SDC works: in Fig. 16.13a are presented schematically the different mean trajectories of particles depending on the carrier gas flow rates and in Fig. 16.13b are shown signals obtained with the SDC for different carrier gas flow rates, all other spray conditions being identical. The maxima observed for

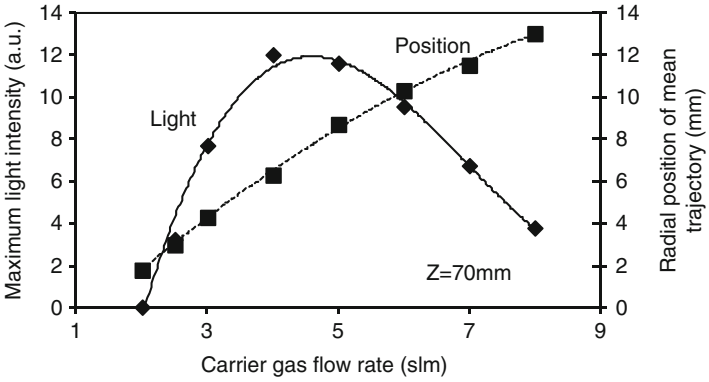


Fig. 16.14 Evolution with the carrier gas flow rate (argon) of the maximum intensity of the light emitted by the hot particles and of its position relatively to the torch axis. Spray conditions given in the caption of Fig. 16.13. Reprinted with kind permission from Springer Science Business Media [9], copyright © ASM International

the different carrier gas flow rates are shifted to the right or the left of the optimal one (corresponding for these spray conditions to an argon carrier gas of 4.5 slm). The optimum trajectory corresponds to a mean trajectory of particles making an angle of 3.5–4° with the torch axis and also induces the best temperature and velocity distributions. When the mean trajectory is not optimal, because the carrier gas flow rate is either too low or too high, particles are less heated and the SDC signal is lower. The type of measurement achieved by the SDC is an ensemble one: along the lines of sight across the hot gases cross section, defined on the one hand by the camera or photodiode optics and on the other by the pixels, and corresponding to a large measurement volume. All particles contained in this large volume are taken into account during the exposure time. This type of measurement is called ensemble measurement and is defined precisely in Sect. 16.3.4. Systematic measurements achieved with different spray conditions [10] have shown that the carrier gas flow rate must be adapted to any slight change of them to keep an optimal trajectory.

The SDC also allows following the evolution, with the carrier gas flow rate, of the maximum of the signal emitted by hot particles as well as the position of this maximum relatively to the torch axis, see Fig. 16.14.

The particle flux imaging® (PFI) from Linspray [30, 108], tested in plasma spraying, records the plasma jet close to the torch and the particle flux (ensemble measurement) in the plasma jet plume and also the sprayed spot in the last version. Using a CCD camera the very luminous plasma jet close to the torch, the less luminous particle flux in the downstream zone, and the spray spot are imaged simultaneously, see Fig. 16.15a.

A PC reduces the information by finding lines of constant radiation intensity in images of the hot plasma jet and the particles flux. These lines can be approximated by ellipses. Their characteristics are typical of the state of the coating process and any variation of macroscopic parameters results in the particles ellipse displacement. This system allows also detecting the possible perturbation of hot gases jet by

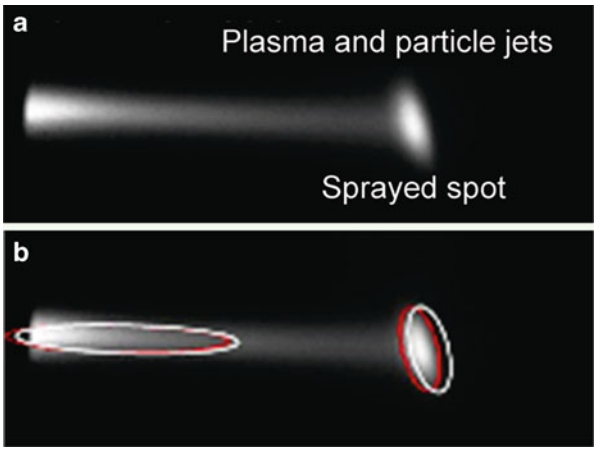


Fig. 16.15 (**a**) Particle flux imaging® (PFI-S) image of a running process (*left*), (**b**) PFI-S image with two calculated ellipses (*right*). Reprinted with kind permission from Elsevier [30]

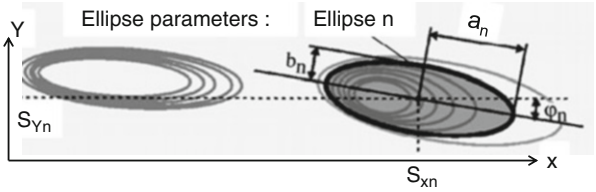


Fig. 16.16 Ellipses characteristics. Reprinted with kind permission from Elsevier [30]

the carrier gas when radially injected. In this way variations in the hot plasma jet as well as in the particle flux can be detected without a precise knowledge of exact physical plasma jet or particle parameters. An example of these two ellipses (plasma jet and spray spot) is presented in Fig. 16.15b. Of course for plasma jets, due to their very high level of radiation, filters with different transmittivity must be used both for plasma and particles. The combined resulting image of the plasma jet and the particle flux represents the actual state of the coating process. The ellipses generated in Fig. 16.16 are characterized by the major axis, a_n, the minor axis, b_n, the x-coordinate, S_{xn}, of the center point, the y-coordinate, S_{yn}, of the center point, the angle, φ_n, between x-axis and major axis, as well as the additional information: number of pixels E_N in the contour and the average gray scale value, E_{avg} of pixels. The PFI® system, as the SDC®, is moved attached to the gun and images continuously the whole area between the gun and the substrate surface, thus allowing an instant response to any change in spray conditions. The PFI technique provides not detailed quantitative physical parameters but by monitoring the process it is a very useful tool for quality control.

The Sprayview® of Tecnar (CN) uses also a CCD camera with adapted filters. It allows, when injection is not optimal, observing phenomena such as fine particles bouncing on the plasma, coarse particles flying all the way through the plasma, etc. The good contrast in between the injected particles and the plasma flame itself permits the visualization of the injection cone and the quantitative characterization

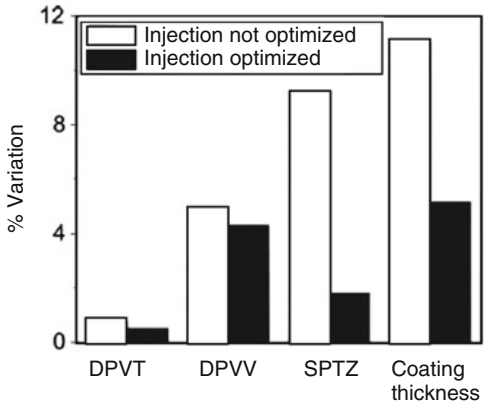


Fig. 16.17 Influence of injection optimization on the variability of particle mean temperature (DPV T) and velocity (DPV V), position of the hot particles jet (SPT Z) and coating thickness (YSZ particles, 10–75 μm, APS 7MB torch from Sulzer Metco with a 8 mm "G" nozzle working with a mixture N_2–H_2). Reprinted with kind permission from Springer Science Business Media [15], copyright © ASM International

of the injection zone, such as cone width and angle, particle mean velocity, acceleration, and trajectory angle. However it is not fixed on the spray gun and the latter must be moved in front of it from times to times.

The hot particle trajectories control can also be achieved with the DPV 2000®, the Plume Spector®, and the Accuraspray® of Tecnar that have been designed to also measure particle temperatures and velocities and are described in Sect. 16.3.3. All these techniques, except the DPV 2000® are ensemble measurements.

Srinivasan et al. [15] have also emphasized the importance of particle trajectories. Figure 16.17 represents the influence of the injection optimization on the variability in particle parameters: temperature, velocity, and position of the hot particles jet and the coating thickness. If, apparently, for the mean values of temperatures and velocities, the trajectory influence is not very important, it is quite different for the coating thickness with an important reduction in its variability. This is due to the fact that, for the optimum trajectory, more particles reach the optimum temperature and velocity, thus improving the deposition efficiency and correlatively increasing the coating thickness.

Zhang et al. [87] have investigated the influence of particles injection angle on particle in-flight behaviors and characteristics at different primary and carrier gas flow rates through an integrated modeling and experimental approach. They showed the importance of injection conditions on particle in-flight status such as temperature (particle's melting status before impact) and velocity.

Srinivasan et al. [88] have shown the existence of a "sweet-spot" in the plasma jet where the particle temperatures and velocities achieved a maximum. This sweet-spot can be characterized by the plume position (location of centroid of the spray stream) rather than carrier gas flow rate and is independent of primary gas flows and other process/material conditions. This result suggests a possible approach to optimize particle injection independent of plasma-forming torch parameters.

16.3.2.2 Cold Particles

Following cold particle trajectories and velocities is also of primary importance for all spray processes [9]. This can be achieved by illuminating all particles (cold and hot ones) with a laser to determine trajectories and velocities of all particles (hot and cold). Then results are compared with those obtained with hot particles (without laser illumination) to determine where cold particles travel. For conventional thermal spray processes it allows optimizing the injector design and follow particles that have not penetrated in the hot gases jet core and travel in its fringes.

One of the problems, especially with plasma jets where heat fluxes can be very high close to the plasma jet core, is to find the right distance between the injector extremity, from which cold particles are injected, and the jet core. If the distance is short, all particles exiting the injector (with cone shaped trajectories, generally with an angle between 10 and 30°) will penetrate within the plasma jet. However, clogging may occur due to the heat flux from the plasma. The solution is then to position the injector farther from the jet as illustrated in Fig. 16.18a from Fauchais and Vardelle [9]. In this case part of the injected particles bypass the jet, as schematically drawn in Fig. 16.18a. Those, which have reached the other side of the jet with a low velocity, are sucked down by the fast flowing hot gases and entrained in the jet fringes. They will certainly not be melted but they can be sufficiently heated to stick to the hot successive passes deposited, especially if the coating surface is hot, creating defects between them. Two solutions are possible: use a water-cooled wall injector that can be disposed closer to the plasma jet, or constricting the particle jet with a double flow injector, as represented in Fig. 16.18b. The gas flow rate around the injector has to be adapted to the carrier gas flow rate [110]. This is illustrated in Fig. 4.58a, where the cold particle flow exiting the injector, 1.8 mm in internal diameter with no gas injected around, is illuminated by the laser. The same injector, but with 3 slm injected around, results in a good constriction of the powder jet, as shown in Fig. 4.58b.

The effect of this constriction is presented in Fig. 4.59, with the hot and cold particles radial distributions, 20 mm downstream of the injector. In the right part of Fig. 4.59, aside of the particle central distribution, for the conventional single injector, a flat distribution is observed, corresponding to particles bypassing the jet, as schematized in Fig. 16.18a. The maximum signal of hot particles (similar to

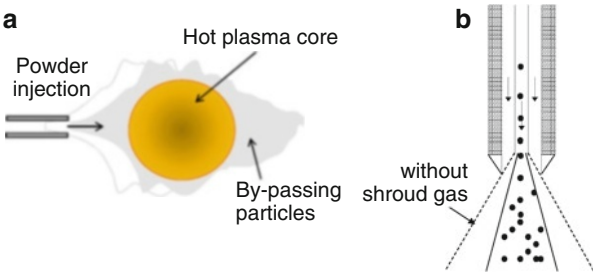


Fig. 16.18 (**a**) Scheme of the powder injection with the injector sufficiently far from the hot plasma core for part of the powder bypassing the jet and (**b**) Double flow injector. Reprinted with kind permission from Springer Science Business Media [10], copyright © ASM International

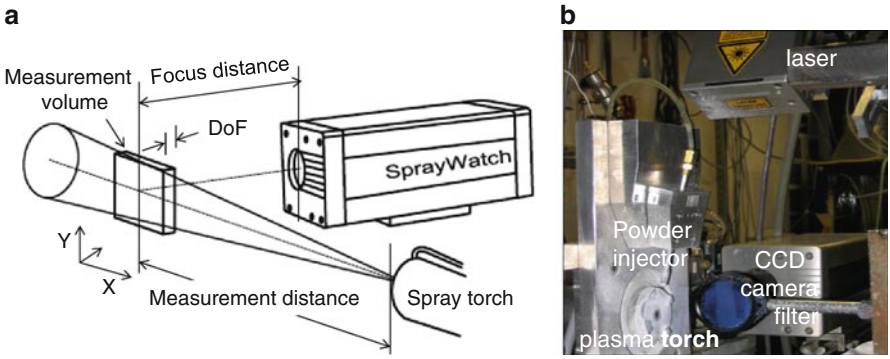


Fig. 16.19 (**a**) Schematic design of the measurement setup where the liquid injection is illuminated by a laser sheet and the corresponding image collected by a CCD camera (that of the SprayWatch of Oseir (FN)). (**b**) Picture of the device with the plasma torch, the laser, and the camera [113]

that presented in Fig. 16.13b), obtained with the single injector flow resulted from a carrier gas flow rate of 6 slm, and its position is of course identical to that obtained with the laser (cold and hot particles). With the double flow injector, most of particles bypassing the jet with a single flow injector, are now penetrating it. It is also interesting to note that the maximum intensity of hot and cold particles is positioned at almost the same radial position as that obtained with the single flow injector. The double flow injector almost does not modify the particles mean trajectory. However it must be noted that with the double flow injector, the carrier gas flow rate is only 3 slm, while that corresponding to the surrounding gas flow is 3 slm (with the single injector this trajectory was obtained with 6 slm). In both cases (single and double flow injector), the mean trajectory is almost the same.

16.3.2.3 Liquid Injection

There is a large development since the beginning of the millennium in suspensions and solutions plasma or HVOF sprayed [111]. One of the main problems is to follow how the liquid jet (mechanical injection) or the liquid drops (atomization) penetrate within the plasma or the HVOF jet [9]. In radial injection, when the hot gases flow hits the liquid jet or drops, first fragmentation takes place and then the resulting tiny droplets (a few μm in diameter) vaporize [111]. Fragmentation times are about 2–3 orders of magnitude smaller than vaporization ones [111]. The setup developed to observe the suspension penetration within the plasma jet [112], consists of a fast shutter camera (that of the Spray Watch) coupled with the laser sheet flash at 808 nm. Figure 16.19a presents the principle of the experiment and Fig. 16.19b the picture of the setup. The image is triggered when the voltage reaches a given threshold. Figure 16.20 [9] represents the corresponding image

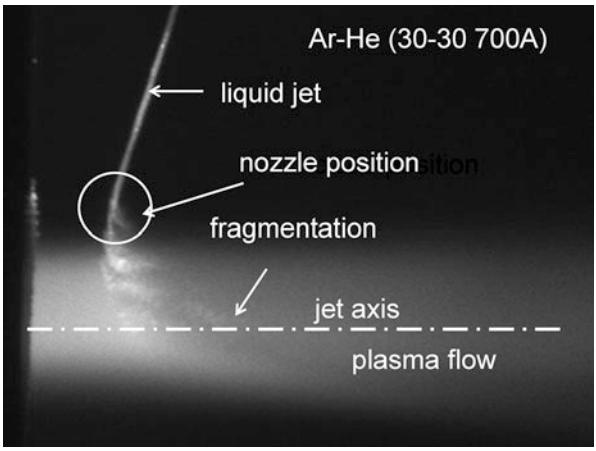


Fig. 16.20 Interaction plasma jet–ethanol suspension, image taken when the fluctuating voltage of the Ar–H_2 plasma was 65 V (Ar 45 slm, H_2 15 slm, nozzle i.d. 6 mm, 500 A). Liquid mechanically injected with a nozzle internal diameter of 150 μm. Reprinted with kind permission from Springer Science Business Media [9], copyright © ASM International

obtained with the mechanical injection of an ethanol suspension injected into an Ar–H_2 plasma jet, image triggered for a 65 V voltage. The dashed line in the figure top corresponds to the anode nozzle top position. The distance between the torch axis and the injector is 23 mm and, just before entering the plasma jet, weak instabilities of the liquid jet can be observed with a wavelength of about 900 nm. Upon its penetration into the jet, and unfortunately also in its fringes, the liquid jet is broken at the neck of its own instabilities by the shear stress produced. Several clouds of material (liquid and/or solid) within the plasma jet are visible in Fig. 16.20. However, it must be kept in mind that, according to the image size and the number of pixels (600 × 600), one pixel represents about 30 μm^2. It is thus impossible to see fragmented droplets sizes of which are below 5 μm in diameter. Clouds are composed of a compact head of suspension and, behind it, some sort of tail with tiny droplets and/or solid particles resulting from the fragmentation that keeps going. The distance between clouds corresponds to 900 μm, which means that the liquid initial velocity (here 26.6 ± 2 m s^{-1}) is kept.

To obtain more information on the plasma and liquid jet interaction, several images taken in the same conditions (in about 1 s) were superposed in order to eliminate the plasma high luminosity masking the low one of the liquid [112]. Before being superposed, each image Fig. 16.21a was filtered to eliminate the plasma luminosity Fig. 16.21b. Then ten images, as that presented in Fig. 16.21b, were superposed to obtain the image of Fig. 16.21c. This final image (Fig. 16.21c) allows determining two characteristic angles of the liquid penetration: the dispersion angle of the liquid in the plasma flow (θ) and the deviation angle of the suspension jet (α). Thus such images permit to optimize the liquid penetration by adjusting its velocity. An example is presented in Fig. 4.74 showing the

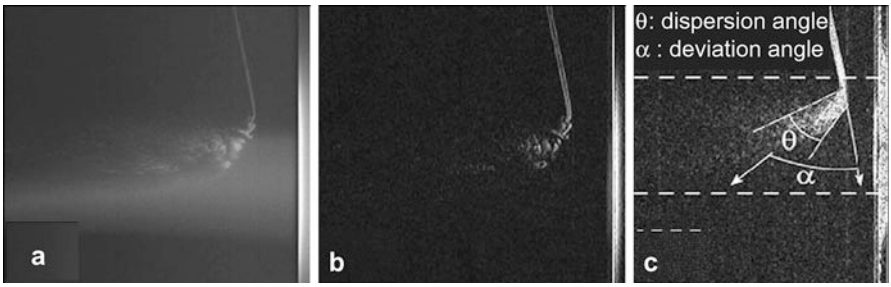


Fig. 16.21 Protocol of image processing: (**a**) original picture, (**b**) image obtained after filtering, and (**c**) result of the sum of several images treated. Reprinted with kind permission from Springer Science Business Media [112], copyright © ASM International

penetration of a zirconia suspension in ethanol injected with two different injection velocities (27 and 33.5 m s^{-1}) into an Ar–He d.c. plasma jet (30–30 slm, 700 A, anode-nozzle i.d. 6.0 mm).

16.3.3 In-Flight Hot Particle Temperature and Velocity Measurement

16.3.3.1 Ensemble or Local Measurements

In fact two types of measurements are considered [9]:

- ***Local measurements with a small measurement*** volume, which can be below 1 mm^3, coupled with relatively high-speed detectors and electronics with band widths on the order of 0.1–1 MHz or greater. In this case the observation of a single particle is possible [5–8]. A sufficient number (several thousands) of individual particles must be observed to achieve an adequate statistical representation of the means and standard deviations of temperatures, velocities, and diameters recorded. Such measurements usually require lightly loaded thermal spray processes and are often performed with particles mass flow rates lower than 0.5–1 kg/h. Of course it is assumed that same results are obtained in real spray conditions, which is true as soon as no loading effect occurs (see Sect. 4.4.4). Moreover recording times are generally at least of a few minutes. DPV 2000, presented in next session, is the typical setup for such measurements.
- ***Large measurement volumes*** containing an important number of particles at a given time. They are called ensemble measurements and they do not attempt to distinguish between individual particles. For example, the measurement volume consists of an approximately cylindrical chord, of few tens of mm^3, through the spray pattern. This chord is preferably oriented in the plane of the injector so that the measurement is insensitive to the movement of the spray pattern relative to the measurement volume [8]. Of course such measurements only give mean values.

Ensemble techniques work equally well for heavily loaded processes such as HVOF spraying and measurement times are a few seconds. For example, such measurements are performed with the Accuraspray or Spray Watch presented in next section.

To illustrate the difference between both techniques [9], and also the fact that ensemble in-flight measurements are not sufficient by themselves to explain coating properties, an example is presented below. Renouard-Vallet [109] aimed at spraying yttria (13 wt%)-stabilized zirconia (YSZ) particles (fused and crushed with a size distribution between 5 and 22 μm) by vacuum plasma spraying (VPS) to produce dense electrolytes about 50 μm thick. A PTF4 torch, equipped with a Laval nozzle, was used working with an Ar–H_2 mixture (40–6 slm), an arc current of 750 A in a soft vacuum chamber where the pressure was kept at 8 kPa. The in-flight particle temperatures distribution (measured with a DPV 2000 focused at the substrate location on the particle jet axis) is presented Fig. 16.22a. The melting temperature, T_m, of YSZ has been indicated in this figure. As it can be seen the temperatures distribution is rather broad: from about 1,000 °C (lower limit of such measurements) to 4,000°C and, if the absolute calibration of the pyrometer is correct, many particles are unmelted, the mean value, T_e in Fig. 16.22a, being below T_m. The mean ensemble temperature measurement (with a Spray Watch focused at the same location as DPV 2000, but measuring the whole jet cross-section), is in good agreement with the mean temperature resulting from the distribution shown in Fig. 16.22a. However, for more precise comparison, distributions obtained from DPV 2000 all over the measurement volume of the Spray Watch and weighted by the particle frequency should have been determined [114]. Particle velocities (DPV 2000) were 150 ± 70 m s^{-1} [109]. Correspondingly splats collected at the standoff distance of 175 mm on a substrate maintained at 550 °C presented different shapes, including partially melted particles, the shape of which was still rather blocky. According to statistical measurements, performed on about 1,200 of them, their mean diameter was 25 μm, with a mean thickness of 4 μm, values corresponding to a flattening degree of 1.8. Coatings were also kept at 550 °C during spraying (with the help of cryogenic cooling) and are presented in Fig. 13.83a. Their porosity was 10.9 % (measured by image analysis of their cross sections) and their ionic conductivity was 1.9×10^{-2} S/m (that of sintered YSZ being 1 S m^{-1}). Such a low ionic conductivity corresponds to rather poor contacts between layered splats. To get rid of unmelted particles and also tiny ones, a "windjet" (see its principle in Fig. 2.33) has been used, blowing argon orthogonally to the particle jet 3 cm ahead of the substrate. The corresponding particle temperatures distribution, presented in Fig. 16.22b, with values between about 2,200 and 2,950 °C, is narrower than that without "windjet" and presented in Fig. 16.22a. Moreover the mean value, T_E, obtained with the Spray Watch, is slightly higher than T_e. Here again ensemble temperature is in good agreement with the mean value of the DPV 2000. The particle velocities (DPV 2000) are now 80 ± 25 m s^{-1}: the high velocity tiny hot particles have been ejected by the "windjet," as well as the low velocity bigger cold particles. The hot particles with an intermediate size were

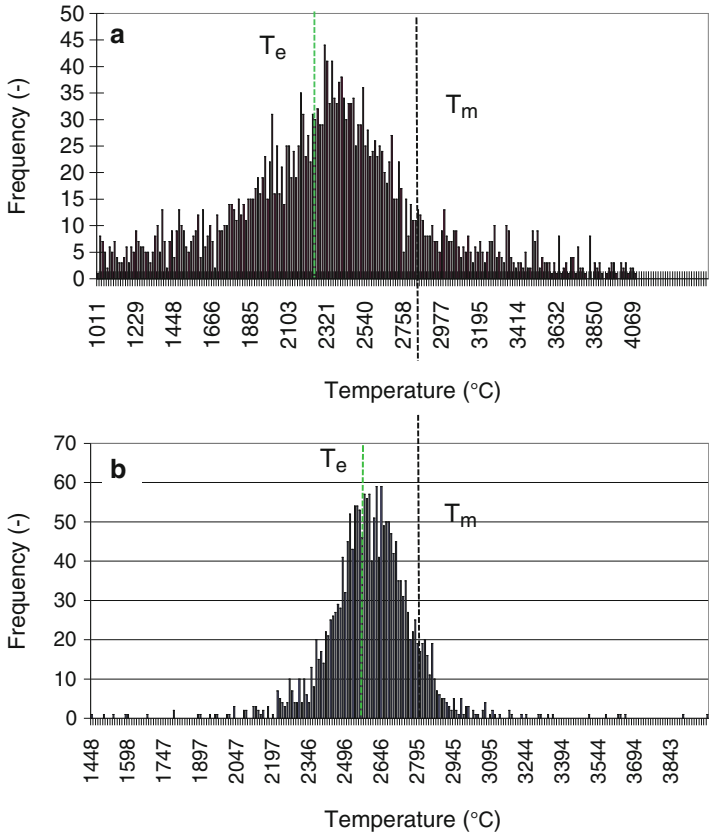


Fig. 16.22 In-flight temperatures distribution of yttria-stabilized zirconia (YSZ) particles (fused and crushed, 5 and 22 μm) sprayed in soft vacuum with a PTF4 torch, Laval nozzle, Ar–H_2 mixture (40 slm–6 slm), 750 A, and measurements performed with a DPV 2000 (statistical distribution) and a Spray Watch (ensemble value T_E). The melting temperature, T_m, is indicated. (**a**) Spraying performed without "windjet", (**b**) with "windjet". Reprinted with kind permission from Springer Science Business Media [9], copyright © ASM International

slightly slowed down. Splats collected are rather close to disk shapes with a mean diameter of 30 μm, a mean thickness of 1.5 μm corresponding to a flattening degree of 4. The coating obtained with the "windjet" (substrate and coating being also kept at 550 °C during spraying) is presented in Fig. 13.83b. Compared to that without "windjet" it is denser (porosity of 6.1 % against 13 wt% without windjet) and its ionic conductivity is now 5×10^{-1} S m^{-1} (against 1.9×10^{-2} S m^{-1} without windjet) corresponding to a much better contact between layered splats.

When looking at the ensemble temperatures the values obtained with and without the "windjet" are close to the mean values deduced from DPV 2000. Spray Watch results correspond to average values representing a wide particle fraction in a comparatively large measurement volume. However the differences

between ensemble results with and without the "windjet" are much less informative than statistical measurements at a given location. Anyhow the drastic difference between coatings presented in Fig. 13.83a, b can only be explained by the important change in statistical temperature distributions together with splat distributions. These results allow understanding that the "windjet" eliminates most unmelted particles, as well as overheated small particles.

Of course ensemble measurement is faster (a few seconds against a few minutes). Mauer et al. [114] have compared different measurements performed with DPV 2000® and Accuraspray-g3®. This comparison was made after measuring and then weighting by the local particle flow rates, the different local mean values of the particle data (temperatures and velocities) at each DPV 2000 grid point that is contained by the Accuraspray-g3 measurement volume. They found that results obtained with both systems were in good agreement, thus confirming the measurement accuracy of both. They have also identified some application limits for the DPV-2000 and the Accuraspray-g3 diagnostic systems when using a few powder species. It is also reported that measurement of particle temperature close to plasma torch exit is generally more difficult to carry out by the Accuraspray-g3 than by the DPV 2000 system [115]. That is probably due to the fact that the plasma radiation is dominant relatively to the particle radiation because of the much larger measurement volume of the Accuraspray-g3. At last, strong evaporation of particles might affect the identification of the particle radiation, especially when large volumes are analyzed.

Srinivasan et al. [15] conducted a systematic study of the variability in particle state and deposit properties from run to run for plasma spraying of YSZ. They showed that using sensors measuring particle temperatures and velocities along with injection optimization certainly offers ease of implementation and benefits with reduction in variability and is worth further consideration.

Sampath et al. [17], comparing local and ensemble measurement systems, found that particle velocities measured from single and ensemble sensors can be correlated but careful consideration is required for understanding temperature results. Particle temperature may not be a sufficient descriptor of the melting state for refractory ceramics and authors suggested that normalized/group parameters are perhaps more appropriate. Parameters such as melting index, kinetic energy, and particle Reynolds number may offer more insights into the description of process states.

Streibl et al. [116] confirmed that many data are lost when using ensemble measurements instead of statistical ones. When considering the temperatures distribution of YSZ particles (fused and crushed with a mean diameter of 38 μm) plasma sprayed (measured with DPV 2000) significantly different particle temperature distributions can be obtained for a given average value, as illustrated in Fig. 16.23.

A trimodal structure can be observed in the temperature distribution, from which a significant melting peak can be extracted. This melting peak is at a constant temperature (for a given calibration setting of the pyrometer detector) and is independent of particle size, powder morphology, and process parameters.

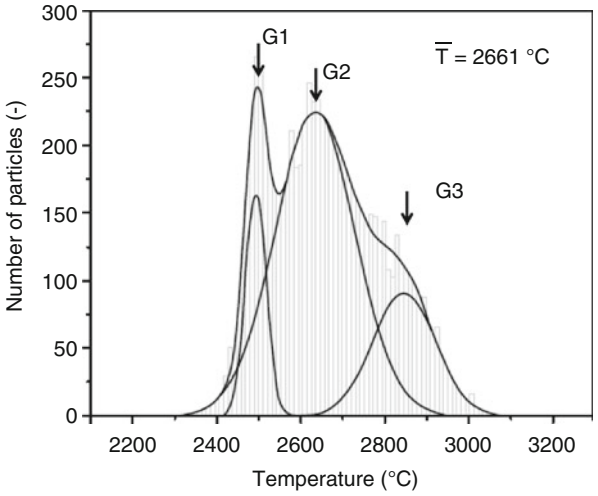


Fig. 16.23 Temperatures distribution of particles (angular dense, 10–90 μm, 8 wt% Y_2O_3 partially stabilized ZrO_2,) plasma sprayed with Sulzer Metco 7MB torch equipped with a "G" nozzle 8 mm in internal diameter. Spray parameters: 47.6 slm of N_2, 5.6 slm of H_2, 550 A current and 3.7 slm of carrier gas. The overall temperature distribution curve has been represented as a sum of three Gaussian curves and the individual peaks of these underlying curves have been label as "G1," "G2," and "G3". Reprinted with kind permission from Springer Science Business Media [116]

The second and third peaks correspond to the particle temperature distributions that relate to process conditions and can therefore be ruled out as a melting state indicator. It is thus of primary importance to look at the distributions themselves, and not an ensemble measurement, to draw conclusions on the melting state of particles.

Recently Colmenares-Angulo et al. [117] performed deliberate particle state variations using atmospheric plasma spray (APS) and high-velocity oxy-fuel flame spraying (HVOF) to create a set of first-order process maps. Particle states were measured simultaneously using five in-flight particle sensors: DPV-2000, Accuraspray, SprayWatch, TDS, and SprayCam. While sensors used similar methods for calculating particle characteristics, absolute values of temperature and velocity were considerably different. Process map trends among sensors are in agreement for the HVOF process, but differ when using plasma spray at high total gas flow conditions. After understanding the stochastic nature of particle detection, they have implemented an open-loop feedback control algorithm to achieve similar particle states with different hydrogen gas flow rates. The resulting particle state window measured by three different sensors under select fixed hydrogen flow rates was significantly narrowed.

16.3.3.2 Particle Temperature and Velocity Measurements

The importance of controlling microscopic parameters such as in-flight hot particle parameters, instead of macroscopic ones (gas flow rates, arc current,...), was demonstrated in laboratories during the 1980s and 1990s [9]. Rather sophisticated measuring devices were used such as Laser Doppler Anemometry (LDA) for particle velocities and Phase Doppler Shift to also measure their diameters, fast pyrometers (with response time as short as 100 ns) [5–7], and also CCD cameras for the detection of the hot particle trajectories distribution within the plasma jet. However such measurements were far to be usable in the harsh environment of spray booths. Moreau et al. [13] were the firsts to develop, a set-up measuring the particle velocity based on the time-of-flight measurement through signals recorded when hot particles passed in front of two slots separated by a known distance. The development of DPV 2000 was based on their work.

As for velocity, up to the mid-nineties, fast pyrometers were developed [5–7] (response time of 100 ns). However contrary to velocity measurements, they are susceptible of errors in the absolute temperature that can reach 20 % in some cases. This is particularly due to the effect of particle emissivity, often unknown or poorly known, and, for ceramic materials, absorption occurring in wavelengths around 1 μm or over. The plasma light scattered by particles must also be taken into account [117]. Of course, relative values of temperature can be measured with a precision of 5 %. Generally temperatures below 1,200 °C are very difficult to measure with a reasonable precision. All sensors described below perform temperature measurements through two-color pyrometer.

(a) Principle of the Different Sensors

Sensors mainly used to measure in-flight particle temperatures and velocities are [9]:

1. DPV 2000® from Tecnar (CN), which is a local measurement, Accuraspray® also from Tecnar that is an ensemble measurement, SprayWatch® from Oseir (FN) also an ensemble measurement setup and finally Flux Sentinel sensor (Cyber Materials Boston, MA, USA). All of them cannot be fixed on the spray torch, which time to time must be positioned in front of them to measure particle temperatures and velocities. Recently Mauer et al. [114] have presented an excellent description of both setups of Tecnar and the description presented below is mainly based on their work.

   Figure 16.24 presents the principle of the DPV 2000. The velocity is obtained by measuring the time between the two signals, which are triggered by a radiating particle passing the two-slit mask of the optoelectronic sensor head (see Fig. 16.24). Knowing the distance between slits and the magnification of the lens, the velocity can be calculated from the two signals. The precision is generally better than 5 %. The temperature is measured by calculating the

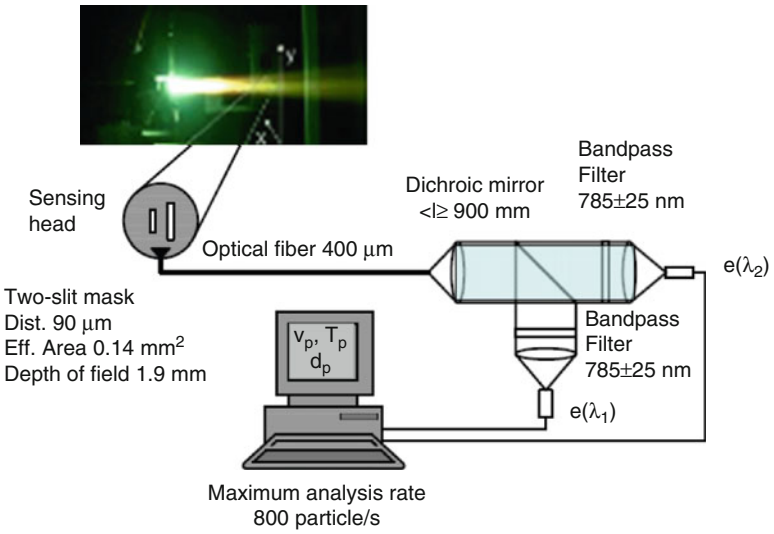


Fig. 16.24 Operation principle of the DPV-2000 diagnostic system. Reprinted with kind permission from Springer Science Business Media [114], copyright © ASM International

ratio of the energy radiated at two different wavelengths, assuming that particles behave as gray body emitters with the same emissivity at both color bands. The particle diameter, assumed to be spherical, can be calculated from the emitted signal of the particle once its temperature and emissivity are known, but the precision is rather poor (at the best 30 %). As the measurement volume is relatively small (<1 mm^3), the data are collected for individual particles. Analyzing at least a few thousands particles at the same location, statistics permit to determine temperatures and velocities distributions, but it requires a few minutes. Moreover, as already mentioned, low particle flow rates (0.5–1.0 kg/h) are needed.

2. Contrary to the DPV-2000 the Accuraspray-g3, from Tecnar (CN), provides ensemble average data of particle characteristics in a measurement volume 25 mm in length and 3 mm in diameter (see Fig. 16.25). Particle velocities are obtained from cross-correlation of signals, which are recorded at two closely spaced locations. The temperatures are determined by two-color pyrometry. Of course mean particle diameter cannot be determined with ensemble measurements in general. The system involves a CCD camera enabling the analysis of the plume appearance (position, width, distribution, intensity) along a line in spray distance perpendicular to the particle jet.

   Experimental correlations with deposited mass have been promising. The pyrometer is based [115] on multiple-color (125-nm-wide color bands) assuming gray body emission and it permits determining the temperature of one particle provided its intensity is significant (gray body above 2,000 K). Frames are sampled at 500 Hz and since the exposure time is longer than the particle's

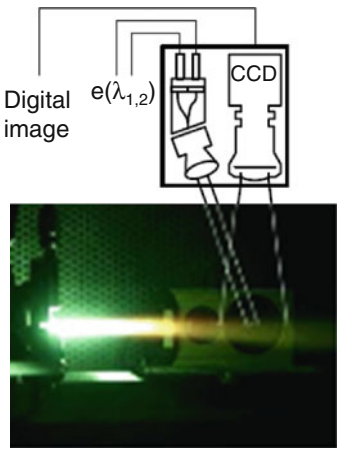


Fig. 16.25 Operation principle of the diagnostic system Accuraspray-g3. Reprinted with kind permission from Springer Science Business Media [114], copyright © ASM International

transit time across the measurement volume, multiple particles are captured in each frame. This approach, as for the other sensors, needs a prior calibration.

3. The Spray Watch from Oseir (Fn), schematically positioned relatively to the spray jet, is presented in Fig. 16.19, and Fig. 16.11 represents particles visualized on the screen of the fast shutter CCD camera. The measurement volume is adjustable from $18 \times 14 \times 5$ mm^3 to $36 \times 28 \times 30$ mm^3. According to Vattulainen et al. [14], hot particles are imaged onto a CCD camera sensor with the aid of a custom designed dichroic double mirror. The front and back surfaces of the mirror are designed to reflect different spectral bands and the corresponding first and second reflections produce spectral two-color double images of single particles onto the CCD sensor. The orientation of the double mirror with respect to the CCD sensor produces an axial shift in the direction of the particle movement between images from the first and second reflections. Parameters are selected to make the different wavelength band images of individual particles partially overlap each other in the middle in order to help particle identification and signal determination during image processing.
4. The ThermaViz™ of Stratonics Inc., CA, USA is based on a CCD camera with 640×480 pixels, working at a rate of 30 Hz [119, 120]. It is a two-color imaging pyrometer at wavelengths of 625 nm and 800 nm. Typical exposure times range from 5 to 20 μs and moreover particle velocities and sizes are determined. As Shape Imaging Watch and Accuraspray it is an ensemble measurement.
5. The Flux Sentinel sensor (Cyber Materials LLC, Boston, MA, USA) [121, 122] is a CCD-based sensor to measure particle temperatures, diameters, and velocities. It has, according to authors [121, 122] the ability to accurately measure diameter in order to ensure the proper volume-weighted contributions of individual particles to the molten volume flux
   - Sense the entire plume and capture a large enough ensemble of particles at a rate commensurate with the demands of real-time control (at a rate of about 500–1,000 particles per second)
   - Quickly determine the plume centroid

Experimental correlations with deposited mass have been promising. "Experiments with different plasma torches showed that molten volume flux measured across the entire plume correlated better with deposited mass than other quantities: number-average particle temperature at the centroid, plume bulk temperature, and overall plume light intensity" [122].

6. With the particle shape imaging setup [30], different particle shapes and orientations can be resolved and the mean diameter of each particle determined with precision. The assumption of spherical particles is no more necessary.
7. Recently the PIV (particle image velocimetry) method, used for many years in fluid mechanics to measure the flow velocity by using tracer particles in the micrometer size range, has been used in thermal spraying to detect either conventional particles in the tens of micrometer-sized [123] or in the sub-micrometer size range [124]. PIV offers the advantage, that the measurement range is not focused in one spot but covers an area. For thermal spraying processes, the size of the measuring area is typically selected in the square centimeter range [123].

(b) Calibration Problems

Whatever may be the sensor used, a prior calibration is mandatory as well as regular ones after a certain time of use. Sprayed particle velocity measurements have a precision better than 5 % [9]. A simple system to calibrate them is to put the detector in front of a rotating cylinder with a narrow slot and containing a light source. The cylinder rotation velocity being well known, the velocity deduced from the signals given by the detector can be calibrated. The calibration is trickier for the pyrometer [32]. The most conventional approach is using a tungsten ribbon lamp calibrated before with a high precision pyrometer or sometimes a blackbody instead of the tungsten ribbon lamp. The main problem is that emissivity of other substances may be significantly different from those of tungsten and black body. Moreover, the calibration is valid only in the temperature range in which the tungsten lamp is operated and for which calibration data are provided [32]. Thus particle temperatures of high-melting point materials such as YSZ may exceed this validity range. Moreover for plasmas, the plasma light scattered by particles is not negligible [118]. Wroblewski et al. [122] and Mates et al. [125], who proposed other means of calibration, have discussed this calibration problem.

(c) Example of Results

(i) Plasma Spraying

One of the first results obtained with the DPV 2000 was the demonstration of the particle temperatures and velocity shifts with the plasma torch electrodes wear during a long-term experiment. The investigation by Leblanc and Moreau [46] was carried out using a model F4-MB plasma gun starting with new electrodes with a

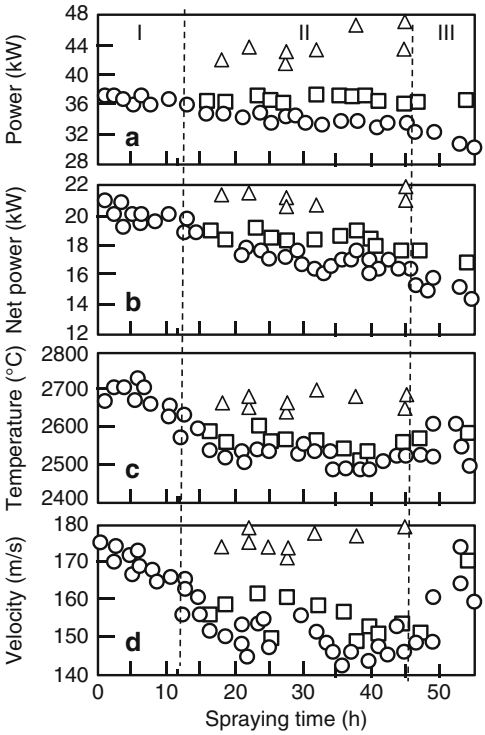


Fig. 16.26 Evolution of the plasma (**a**) gun power and (**b**) net energy, (**c**) in-flight particle temperature, and (**d**) velocity during 55 h of spraying. Nominal operating conditions (*circles*); constant power (*squares*); and constant in-flight particle state (*triangles*). Reprinted with kind permission from Springer Science Business Media [46], copyright © ASM International

1.8 mm diameter external powder injector, the tip of which was located 10 mm away from the gun axis. The sprayed powder, injected from the top into the plasma plume, was a fused and crushed 7 wt% yttria partially stabilized zirconia powder, −45 + 22.5 μm. Those operating conditions were used for more than 50 h of spraying, with an average of 2.5 stops/starts per hour. The DPV 2000 was used to monitor the temperature, velocity, size, and trajectory of the sprayed particles at the nominal stand-off distance. Results were obtained both under the nominal operating conditions, i.e., at constant arc current (circles) and after adjustment of the arc current (squares and triangles). Figure 16.26 presents the time evolution of the power dissipated, the net energy, the particle temperature, and velocity. They show significant variations in the particle state and gun characteristics with spraying time and demonstrate the necessity to modify the spray parameters to keep the particle temperature and velocity at impact as constants as possible. Deposition efficiencies and coating porosities were compared for different spray gun conditions yielding a similar input power. It has been shown that the same input power obtained by increasing the arc current or by increasing the hydrogen flow rate resulted in different coating properties.

The DPV 2000 has, for example, been used to study the influence of the radial injector angle, the secondary hydrogen, and arc current on the deposition efficiency (DE) and microstructure of yttria-stabilized zirconia (YSZ) coatings plasma sprayed [126, 127].

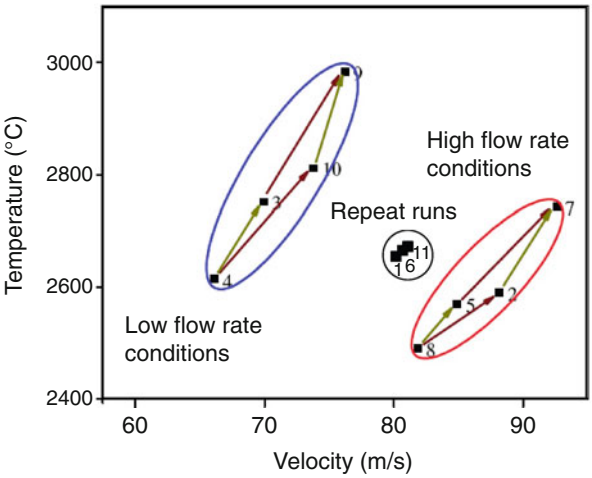


Fig. 16.27 First-order process map for APS of CoNiCrAlY material. Results identify the particle state response for various torch-operating conditions as well as the control vectors identifying the influence of arc current and secondary gas flow rate. Reprinted with kind permission from Springer Science Business Media [17], copyright © ASM International

Marple et al. [128], using Accuraspray, have compared YSZ coatings sprayed with Ar–H_2 and N_2/H_2 plasmas. With N2–H2 plasma gas mixture, higher in-flight particle temperatures and lower particle velocities were produced as compared with Ar–H_2 plasmas. Coatings had similar hardness values; however, the Young's modulus and thermal diffusivity following heat treatment were lower. Planche et al. [16] have studied, with a DPV 2000, alumina particles in-flight and compared measurements with calculations. The calculated particle velocities and temperatures were in good agreement with the experimental results: discrepancies being less than 10 %. Tekmen et al. [129], using Accurasprayg3, have optimized the spraying of cast iron to control the graphite content. A wide range of in-flight particle temperature and velocity values with constant graphite carbon content was determined. Zhang et al. [130] have studied the influence of particle parameters onto the ionic conduction of YSZ. Teckmen et al. [131, 132] have linked the spray conditions to particle parameters and alumina formation when spraying Al–12Si particles. Yin et al. [133] have studied the influence of alumina particle sizes on their in-flight parameters and bonding. Wang et al. [134] have shown the possibility to tailor alumina–zirconia coatings with two powder injection ports. Fang et al. [135] have studied the influence of spray conditions on YSZ particle parameters. Shinoda et al. [136] have studied the powder loading effects for various yttria-stabilized zirconia powders under atmospheric d.c. plasma spraying. Statistical temperature distributions of in-flight particles suggested a rapid increase in the number of semimolten particles above a certain powder-loading rate. Despite drops in the particle temperature and velocity due to the powder loading effect, the deposition efficiency tends to have increased in some cases.

Such measurements allow drawing what Sampath et al. [17] call first order process maps as illustrated in Fig. 16.27. In this figure, are identified the particles (CoNiCrAlY, 38–57 μm) state response for various torch operating conditions as well as the control vectors identifying the influence of the secondary gas flow and

torch current in terms of particle temperatures and velocities. These quantitative vectors can be used as feedback control.

From such measurements Srinivasan et al. [15] estimate that there exist at least a few control protocols to monitor the particle state (predominantly temperature and velocity) with judicious choice of critical parameters. They have controlled the particle state by varying the critical torch parameters (primary gas flow and arc current) in a narrow range using yttria (8 wt%)–zirconia particles with angular shape. The particle state resulting from averaged individual particle measurements (DPV 2000) is surprisingly stable with variability in temperature <1 % and variability in velocity of <4 %. Ensemble approaches yield a somewhat higher variability (5 % in temperature). Despite this, the variability in basic coating attributes, such as thickness and weight, is surprisingly large.

Zhang and Sampath [137] have defined a group of dimensionless parameters, MI and *Re*, to represent particle in-flight status. The melting index (MI) describes the molten state of a given particle by normalizing the measured surface temperature with the dwell time and size. It is assessed as

$$\mathrm{MI} = \frac{\Delta t_{\mathrm{fly}}}{\Delta t_{\mathrm{m}}} = \frac{24\kappa_{\mathrm{p}}}{\rho_{\mathrm{p}} h_{\mathrm{fg}}} \cdot \frac{1}{1 + 4/Bi} \cdot \frac{(T_{\mathrm{f}} - T_{\mathrm{m}}).\Delta t_{\mathrm{fly}}}{d_{\mathrm{p}}^2} \tag{16.4}$$

where κ_{p} is the particle thermal conductivity (W/m.K), ρ_{p} the specific mass of the melted particle (kg m^{-3}), h_{fg} is the enthalpy of fusion (J/kg), Bi, the Biot number, T_{f} is the gas temperature near the in-flight particle (K), T_{p} is the measured particle surface temperature (K), d_{p} is the particle size (m), Δt_{m} is the particle melting time (s), and Δt_{fly} is the particle in-flight time (s), which has the following expression

$$\Delta t_{\mathrm{fly}} = \frac{2L}{v_{\mathrm{p}}} \tag{16.5}$$

where L is the spray distance (m) and v_{p} is the particle velocity (m/s).

Similar to MI they also used particle Reynolds number (*Re*) as another dimensionless method for describing the kinetic state of a particle.

$$\mathrm{Re} = \frac{d_{\mathrm{p}} v_{\mathrm{p}} \rho_{\mathrm{p}}}{\mu_{\mathrm{p}}} \tag{16.6}$$

where μ_{p} is the liquid particle molecular viscosity (Pa/s).

Experimentally and theoretically *Re* has significant effect on particle impact spreading. However this is true as long as the flattening liquid particle surface tension is not considered, i.e., at the right beginning of the impact. Afterwards flattening is controlled by, on the one hand, the wettability flattening particle–substrate depending on substrate layer surface composition and roughness, as well as adsorbates and condensates existing at its surface, and, on the other hand, on the droplet surface tension. For more details see Sect. 13.4.4 and 16.5.2.1.

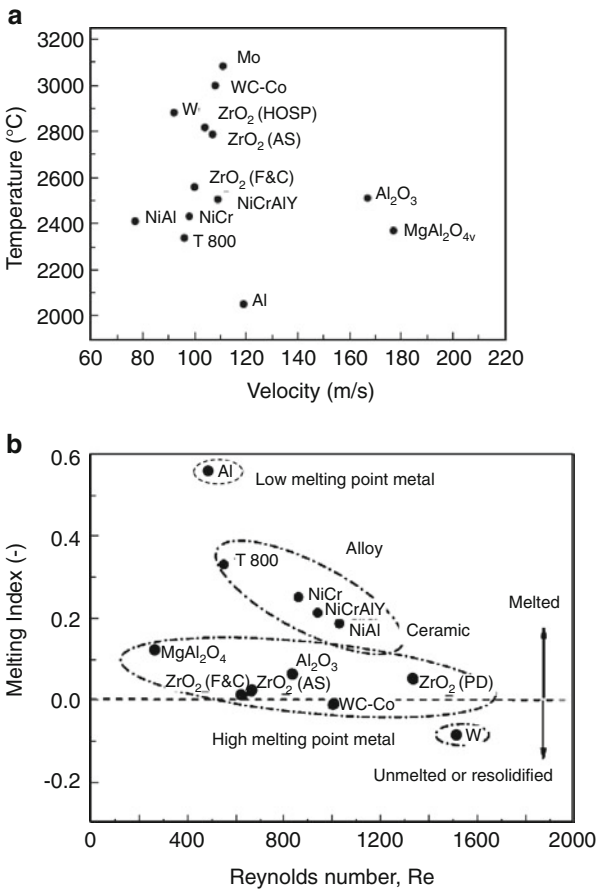


Fig. 16.28 (**a**) T_p-v_p global process map and (**b**) MI–Re global process map. Reprinted with kind permission from Springer Science Business Media [137], copyright © ASM International

Of course to calculate MI and *Re*, statistical measurements are mandatory and DPV 2000 must be used. Figure 16.28 presents a generalized first-order map based on large number of process diagnostic results obtained from multiple materials and processed through a typical air plasma spray torch at one or more process conditions (injection was optimized for each material so as to have maximum heat and momentum transfer for that particular condition). Figure 16.28a is a traditional first-order temperature–velocity representation based on the DPV-generated single particle data. According to their melting temperatures, aluminum is on the bottom of the plot while molybdenum and tungsten are on top. Moreover surface temperature is not necessarily linked to particle melting: low-thermal conductivity material can present an important temperature gradient and metal oxidation also plays a role. The melting percentage of each particle depends on its size, thermal conductivity, latent heat, and residence time in the plasma jet. At last, particle impact velocity is not sufficient to characterize its flattening. According to Zhang and Sampath [137], MI and Re are more appropriate for a more comprehensive

description of particle states. The DPV 2000 single particle data allow calculating the individual particle MI and Re numbers and average values based on these measurements for each of the materials. This is represented in Fig. 16.28b from the T_p, v_p and diameter data obtained for materials in Fig. 16.28a. In the MI–Re-based first-order process map, it is clearly seen that low-melting point Al shows the highest melting state (value of MI), while W shows the lowest value of MI despite representing a much higher temperature in the T_p–v_p-based first-order process map.

Considering particle temperature distributions such as that represented in Fig. 16.23, Srinivasan and Sampath [138] have defined the ratio of sum of area under the completely molten peaks and a factor of the area of the partially molten peak to the total area under the whole distribution, ratio that they called spray stream melting index (SSMI). The SSMI represents the molten content in the spray stream. This approach provides a reliable quantitative representation of the molten content in the spray stream as a whole.

The mass flux of molten particles correlates better with coating thickness than bulk-average temperature or light intensity. However, measurement of molten mass flux for control requires sensors that are capable of sensing particle states at high rates from across a large portion of the full plume. This aim is that of the Flux Sentinel [121, 122]. Only a subset of particles in the jet plume is incorporated in the coating: primarily those that are molten. The characteristics of this molten volume ensemble, MVE, differ from those of the entire ensemble, with the MVE characterized by smaller, hotter, and faster particles. For Wroblewski et al. [122], the total molten volume flux, MVF, is a properly weighted metric that correlates well with deposited mass and is defined by

$$\mathrm{MVF} = \frac{1}{t_M} \sum_{i=1}^{N_{MVE}} \frac{4}{3} \pi (D_i/2)^3 \tag{16.7}$$

where N_{MVE} is the number of particles in the MVF, and t_M is the time over which the particles are captured by the sensor. Volume weighting eliminates the bias toward smaller particles inherent with straight number averages, as illustrated in the number and volume-weighted temperature (Fig. 16.29a) and diameter (Fig. 16.29b). Experiments with different torches showed that molten volume flux measured across the entire plume correlated better with deposited mass than other quantities.

Measuring T_p and v_p has also permitted to better understand the working conditions of the Triplex Pro torch. With the three cathodes and the same anode the plasma jet can be considered as three plasma jets flowing aside. Thus particles treatment will be different when injecting them in one jet or between two of them. Between two jets, the viscosity is lower and the particle penetration easier, while injection in one jet of higher viscosity requires a higher injection force of particles. To study that, Mauer et al. [86] used a nozzle internal diameter of 9 mm and an injector diameter of 1.8 mm, with an angle of 90° relative to the torch axis. The azimuthal injector positions were step-adjustable by 20° between 0° and 80°.

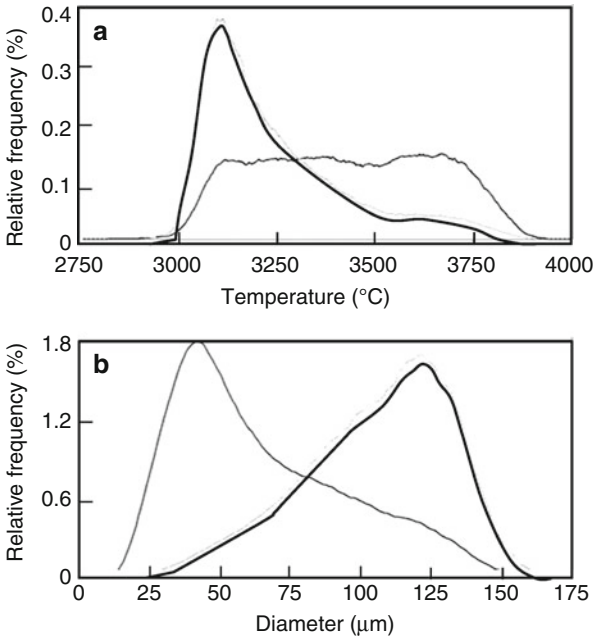


Fig. 16.29 Volume (*gray*) and number (*black*) weighted distributions of (**a**) temperature and (**b**) diameter of only molten particles (Sulzer Metco 7MB torch, nitrogen 40 slm, hydrogen 6 slm, $I = 600$ A, YSZ particles 45–75 μm). Reprinted with kind permission from Springer Science Business Media [122], copyright © ASM International

In Fig. 16.30 injection between two jets is indicated as "between arcs," while that in the jet is called " close to arc." Three spray conditions were used: 40 slm Ar–4 slm He with either $I = 540$ A (case 1) or $I = 470$ A (case 2) and for the third (case 3) 75 slm Ar, 6 slm He, and $I = 540$ A. Results presented in Fig. 16.30 show that the highest temperatures are obtained with case 1 corresponding to a net power of 30.9 kW with gas velocity, v_g, of 1,250 m/s, while similar values are obtained for case 2 and 3 corresponding to, respectively, 25.3 kW with $v_g = 1{,}140$ m/s and 37.6 kW with $v_g = 1{,}940$ m/s. In the three cases the injection between jets results in higher particle temperatures, phenomena called by authors "cage effect."

To spray nanometer-sized agglomerated particles, as emphasized in Sect. 4.3.1, the determination of the spray conditions (particle temperature and velocity distributions) is the key issue [139–142] as illustrated in Fig. 14.11. Indeed the formation of nano-zones depends on the control of the heat propagation within oxide particles through the control of their temperature to achieve coatings with bimodal structure.

(ii) HVOF Spraying

Three oxygen-fuel guns (JP5000, JP5000-ST, Diamond jet DJ2700) and Axial III plasma gun were compared to spray WC–10Co–4Cr powder [23]. The plasma Axial III provided the highest particle temperatures (between 2,000 and 2,600 °C) depending on the spray conditions, while the JP5000 imparted the highest velocities (550–700 m/s). The ST version of JP5000 has provided the same velocity but with

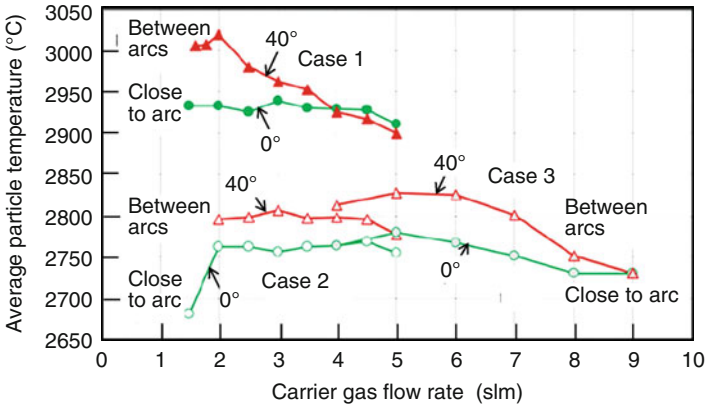


Fig. 16.30 Volume flow-averaged particle temperatures as a function of carrier gas flow and azimuthal injector position (TriplexPro™ torch, case 1 to 3, short injector mount). Reprinted with kind permission from Springer Science Business Media [86], copyright © ASM International

lower temperature (around 1,500 °C). The DJ2700 sprayed particles with temperatures and velocities between those of Axial III and JP5000. Best results were achieved with the lowest particles mean temperature and the highest velocity.

Works were devoted to spraying conventional particles of TiO_2 [143, 144], Al_2O_3 [145], and Inconel [146]. These studies emphasized the importance of impacting particle temperatures on the deposition efficiency and some coating properties.

Valarezo et al. [147] have used the concept of "process maps" to study the fundamentals of process–structure–property relationships in high velocity oxygen fuel (HVOF)-sprayed coatings Ni–20 % Cr.

HVOF has been used to spray agglomerated nanostructured particles: TiO_2 ones [148, 149] and WC–Co ones [150]. In the latter case one powder, called multimodal, has been engineered to have a bimodal WC grain size distribution. It consisted of a 50-to-50 mixture of two size fractions: coarse grains of 1–3 μm and fine grains of 30–50 nm. For all WC–Co powders a process window was defined with respect to particle temperature to achieve the highest resistance to dry abrasion. The multimodal coatings tend to have a higher hardness than conventional ones; however, in terms of abrasion resistance, there is little difference between the best-performing multimodal and conventional coatings. For the nanostructured TiO_2 coatings [148], HVOF sprayed, different spray conditions were studied. It was shown that a linear dependence between particle temperatures and particle velocities existed when spraying this type of powder using HVOF spraying. The higher the average particle temperature and velocity, the higher was the Vickers micro hardness number. Higher particle temperatures and velocities enhanced the inter-splat contact, thereby increasing the cohesive strength of the coating.

To conclude, adjusting through the in-flight mean temperature measurements and the use of either plasmas or HVOF guns with different working conditions and

the choice of the size distribution of nanosized agglomerated particles, allows achieving dense or porous nano-zones [144]. It results in coatings with different properties, from good wear resistance to abradable.

(iii) Wire Arc

DPV 2000 was used to differentiate particles produced by atomization of the molten metal either at the cathode or anode [151]. The spray conditions influence on particle characteristics was studied [152] and experimental results compared with those of CFD study [153]. The model was validated on the basis of comparisons between in-flight droplet velocity measurements performed using the DPV 2000 diagnostic tool.

A hybrid system consisting of a twin-wire arc where the high velocity atomization gas produced by HVOF gun has also been studied [154]. In this system the particle velocities are significantly higher than those in a conventional wire arc, resulting in high-density coatings.

16.3.3.3 Transient Measurements of Particle Temperatures and Velocities

As underlined in the previous section, the particles mean trajectory must be adapted to any change in the spray torch parameters [9]. When d.c. plasma spraying with diatomic gases, voltage fluctuations ΔV can be very high with the ratio $\Delta V/V_m > 1$, where V_m is the mean voltage. As the plasma jet enthalpy, h, can vary with voltage fluctuations, in a ratio of 2 or more, its velocity, v, varies at least in the same ratio and then the momentum density ρv^2 varies in a ratio between 2 and 4. As the response time of the carrier gas is about ten Hertz, while arc root fluctuations are in the 5,000 Hz range, particle trajectories cannot anymore follow the optimum trajectory relatively to the plasma jet different enthalpies, as illustrated in Fig. 7.36, Sect. 7.7.1, for more details see also Fauchais et al. [155]. It can be seen that the particle jet is slightly affected, while the plasma jet fluctuates drastically. It is thus not surprising that particle temperatures and velocities vary with the voltage fluctuation. To follow that Bisson et al. [156, 157] have synchronized the DPV 2000® device with the torch voltage fluctuations. Results are illustrated in Fig. 16.31 from Bisson et al. [156]. They used the DPV 2000 and a comparator generating a pulse when the instant voltage exceeded a threshold. This pulse was used to trigger the DPV 2000 a specific time after the threshold is crossed and particle parameters were measured as functions of the time delay. For alumina particles periodic variations of temperature (about 500°C) and velocity (around 200 m/s) were observed, as illustrated in Fig. 16.31 for particle velocities. The period of the cycles coincides with that of voltage fluctuations (period 220 μs or $f = 4{,}500$ Hz).

Recently Nogues et al. [158] and Goutier et al. [159] have developed a fast bichromatic pyrometer system (100 ns response time), triggered by the arc voltage

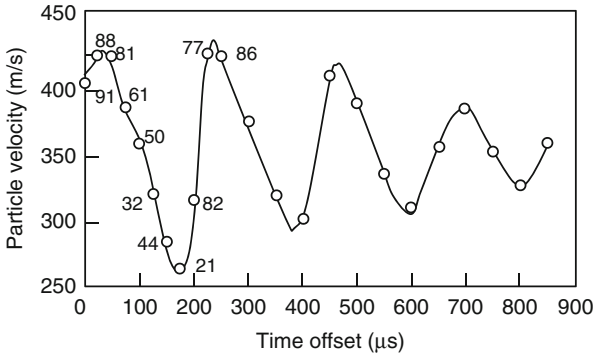


Fig. 16.31 Fluctuations of the velocity of alumina particles (22–45 μm) sprayed with an Ar–H_2 plasma jet (Ar 35 slm, H_2 10 slm, $I = 550$ A, and i.d. 7 mm) as a function of time delay. Reprinted with kind permission from Springer Science Business Media [156], copyright © ASM International

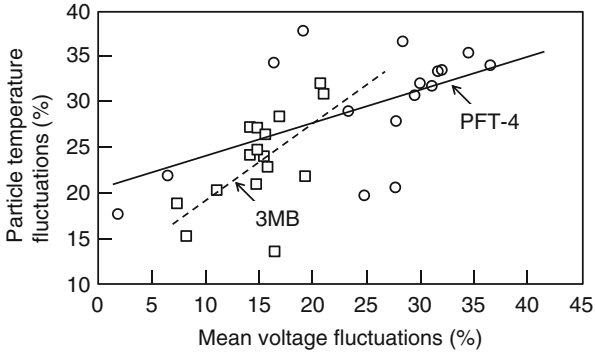


Fig. 16.32 Evolution with mean voltage fluctuations ($\Delta V/V_m$) of the mean particle temperature fluctuations for two different torches (PTF4 and 3MB of Sulzer Metco) working with Ar–H_2 (PTF4) and N_2–H_2 (3MB). Reprinted with kind permission from Elsevier [158]

fluctuations, and allowing a detection time of 2 μs for a single particle. They have compared three plasma torches, one working with Ar–H_2 (PTF4 from Sulzer Metco) and two with N_2–H_2 (3MB torches of Sulzer Metco with different plasma forming gases injectors and anode nozzles). The voltage fluctuation frequency of the PTF4 torch is around 4,000 Hz, while that of the 3MB ones is about 6,000 Hz. Figure 16.32 shows the evolution with the mean voltage fluctuations of the particle temperature fluctuations. Whatever the torch configuration, the temperature fluctuation increases. It means that particles "follow" voltage fluctuations: the more important are the torch fluctuations, the more heterogenic is the particle treatment. The rapid pyrometer allows also obtaining the temperature fast fourier transformation (FFT) curves. The particle temperature fluctuation frequency follows that of arc voltage only in the case of the PTF4 torch working with argon–hydrogen mixtures. It means that voltage fluctuations have no direct influence on the particle treatment when using the 3MB plasma torch working with nitrogen–hydrogen mixtures. The particle velocity fluctuations increase with the mean voltage fluctuations for the Ar–H_2 plasma, while they decrease for the N_2–H_2 plasma in spite of larger mean voltage fluctuations. More works are necessary to achieve a better understanding of these phenomena.

16.3.3.4 Particle Temperature Measurements

The in-flight particle pyrometer (IPP) of Inflight Ltd. Co., ID, USA is a two-color radiation pyrometer, with a long measurement volume (5 mm in diameter and 50 mm in length) providing an average particle temperature (ensemble) measurement at a rate of 10 Hz [160].

16.3.3.5 Particle Size or Diameter

If size measurements with Phase Doppler Shift method (assuming that particles are spherical) [5, 6, 9] were rather precise, it is not really the case with setups based on the radiation energy emitted at one wavelength by the hot particles as in DPV 2000®. The difficulty is that it is necessary to assume spherical particles (not really the worst point of the method) and know precisely the emissivity of hot particles (that is the most critical point) at the temperature measured with the two-color pyrometer. Moreover all particles are not necessarily detected by the system, especially the smallest one. Thus the precision of this measurement is relatively poor (at the best 30 %). That is why such measurements must be calibrated, for example, by collecting particles in water or in oil. Such calibration is especially important with wire arc spray, where the size distribution of droplets, resulting from wire fragmentation, is unknown compared to other spray processes [151]. In the experiment of Planche et al. [152], the static wire arc spray gun was directed toward the ground surface. A screen with a 2.5 mm diameter hole was placed at a distance of 160 mm from the gun. Underneath (40 mm) a tub of oil collected, during about 10 s, particles passing through it. After oil filtering, captured particles were observed and analyzed using optical means. Optical analysis and statistical measurements of particle diameters were then performed. Afterwards the DPV 2000 measurements were achieved at the same locations into the jet as those previously chosen for the capture of the particles. In this way, the calibration of the diameter parameter by the DPV could be made. Of course, diameter measurements are not possible with ensemble measurements.

Particle shape imaging [30] is a laser-based shadow technique with the beam of a linear-polarized Nd–YAG Laser (100 mW continuous wave) split into two parts of equal intensity, which are crossed by mirrors in the focal plane of a long-distance-microscope (Optics). In the image plane an ICCD camera monitors a rectangular region. Particles being outside the depth of focus (940 μm) are projected blurred or with interference effects. A particle crossing the measuring volume creates in principle two shades in the image plane because the particle is located in the two laser beams. The trigger system starts an image acquisition when a particle enters the measurement volume. The image acquisition is started after an adjustable delay time so that in the resulting picture the particle distance from the trigger line corresponds to its velocity. By image processing, particle size can be measured through the number of pixels, which represent the particle in the image. Laser

Doppler Anemometry (LDA) is integrated into the diagnostic system to calibrate the PSI method and to compare the velocity results. With this setup, different particle shapes and orientations can be resolved and the mean diameter of each particle determined with precision. The assumption of spherical particles is no more necessary. In the Flux Sentinel sensor (Cyber Materials LLC, Boston, MA, USA) particle diameter is estimated photometrically and here also calibration is mandatory.

16.3.4 In-Flight Velocity Measurements of Cold Particles

Following cold particle trajectories and velocities is also of primary importance for all spray processes [9]. This can be achieved by illuminating all particles (cold and hot ones) with a laser to determine all particle trajectories and velocities. Then results are compared with those obtained with hot particles (without laser illumination) to determine where cold particles travel and with what velocities, generally smaller than that of hot ones. For conventional thermal spray processes, it allows optimizing the injector design and following particles that have not penetrated in the hot gases jet core and travel in its fringes. For cold spray, particle velocities can be measured and their critical velocity determined if their diameter is also determined, which is not yet possible with the existing sensors if velocities are over 500 m/s. Velocity measurement is achieved by illuminating particles with a laser, which is scanned through the jet cross section, and measuring the bursts of scattered light as the particle flow pass the laser beam [10]. The particle velocity in cold spray process was measured by using laser two-focus anemometer [161]. Jodoin et al. [162] have developed measurements of particles in cold spray process, using the Oseir Spray Watch® combining a fast shutter CCD camera with a high-power pulsed laser diode (Hiwatch) to illuminate particles. The camera exposure time is between 100 ns and 10 ms with a maximum of 7 frames/s. The diode laser produces a laser sheet (at $\lambda = 808$ nm) with a width of 15 mm and a thickness of 1.5 mm, the pulse length being in the 50–2,000 ns ranges. The accuracy in velocity measurement is 1–10 m/s. It is also possible to use the DPV 2000 with particles illuminated by a laser diode (7 W, $\lambda = 830$ nm) [163, 164].

The principle of the near infrared sensor (NIR Sensor, GTV Verschleißschutz GmbH, Luckenbach, Germany) [165] is based on the illumination of single particles in the focus distance by a 10 MHz pulsed infrared laser (1,000 nm), the reflected pulsed laser radiation indicating the passage of single particles through the measurement focus spot, which is small enough to detect one particle (local measurement). The in-flight time is inversely proportional to the particle velocity. Thus the velocity of cold particles can be detected. Furthermore [32] two fast detectors with different spectral ranges between 900 nm and 1,500 nm as well as between 1,500 nm and 2,600 nm, capture, during the time of passage the emitted thermal radiation of the single particles. The ratio of the two emission signals is used for temperature determination according to the two-color pyrometer principle.

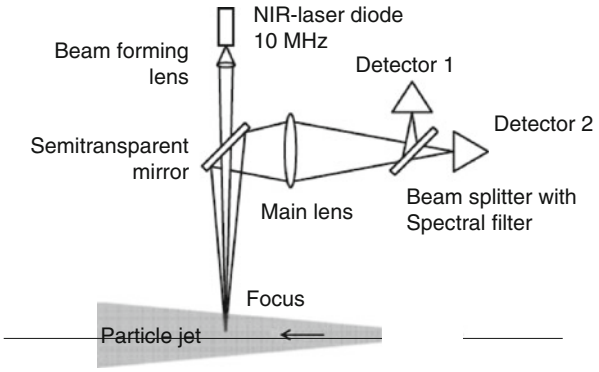


Fig. 16.33 Optical design scheme of the NIR sensor [165] (Courtesy of GTV-MBH D-57629 Luckenbach)

Figure 16.33 presents the scheme of the setup. The detection limits are between 700 and 3,000 °C for temperature, 30–1,200 m/s for velocity and particle diameters over 5 μm. As up to 300,000 single particles per second are detected, statistical distributions and average values can be calculated. Due to operation in the infrared range and the pulsed laser illumination, comparatively cold and slow particles are still detectable.

Examples are presented below to illustrate the interest of such measurements in cold spray. Particle velocities, when cold sprayed, have been measured and compared to models [162, 166], to find the effect of substrate temperature on the formation mechanism of aluminum, zinc, and tin coatings [164], to study the coating buildup mechanisms and properties when cold-spraying aluminum and alumina particles to form cermets [163], and to determine the influence of the powder properties [167].

A complex problem is however to determine the critical velocity of a powder. This critical velocity corresponds to the beginning of the adherence of the impacting particles. However, a powder corresponds to a particle size distribution. When the smallest particles start to adhere, because they have reached their critical velocity, it is not necessarily the case of the bigger ones. The question is then what is the maximum diameter, which can be deposited for the gun working conditions, and how to determine it. What is currently admitted is that the critical velocity corresponds to that of the mean sized particles (mass distribution), which implies that the deposition efficiency is 50 % when measuring the mean velocity (ensemble measurements). However this method is time consuming because not only the mean particles velocity has to be measured but also the deposition efficiency. Moreover it is sometimes difficult to reach a deposition efficiency of 50 %!

For example, Legoux et al. [164] have performed such measurements for aluminum and zinc (Fig. 16.34). It can be seen that the deposition starts to be measurable for average velocities of about 400 and 500 m/s for Zn and Al, respectively. This study also shows that surface temperature at the impact point of a low-pressure cold spray system can be significantly influenced by the process gas temperature. The deposition efficiency changes as a function of the process

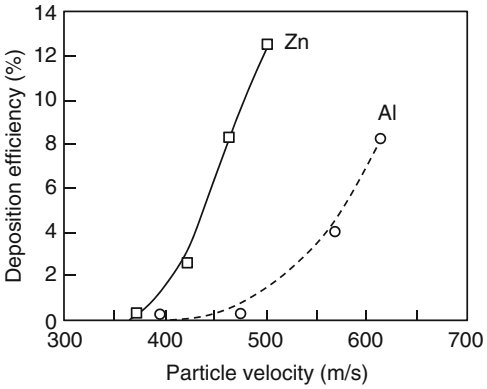


Fig. 16.34 Deposition efficiency as a function of the average particle velocity: Al and Zn particles with an average size of 36.2 and 10.6 μm, respectively. Powders, injected radially, were sprayed with low-pressure cold spray system (SST, Centerline, Ontario, Canada) working with nitrogen at 0.62 MPa and that can be heated in the gun region up to 500 °C. Reprinted with kind permission from Springer Science Business Media [164], copyright © ASM International

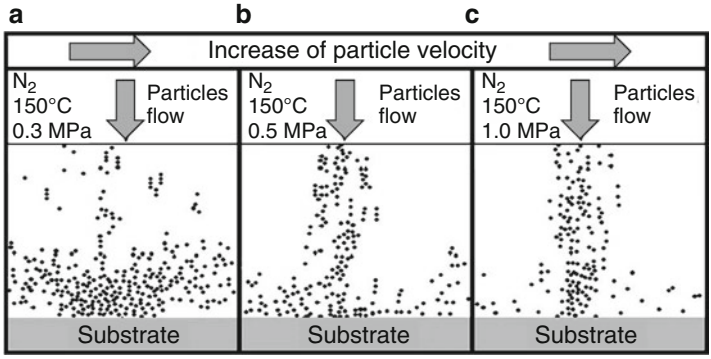


Fig. 16.35 Evolution with the mean impact velocity of the flux distribution of Cu particles impacting on a Cu substrate: images obtained with Spray Watch and laser sheet illumination. Reprinted with kind permission from Elsevier [168]

gas temperature because of the influence of this processing parameter both on the gas velocity and on the substrate surface temperature.

To avoid the deposition efficiency measurement, Raletz et al. [168] have developed a method consisting in determining with the Spray Watch and the particles illuminated by the laser sheet, correlations existing between the impacting particles flux and those rebounding onto the substrate. As the velocity of the rebounding particle is rather low, compared to its impacting velocity (it can be ten times lower), the flux measurement is performed by taking into account all the bright spots on the screen. Contrary to what is done in conventional velocity measurement, with the Spray Watch, it is not necessary that each bright point is aligned with two other ones

to be accounted for the flux, while for the impact velocity only three aligned points are considered. A typical result is shown in Fig. 16.35.

As expected, the particle flux distribution clearly depends on their impact velocity controlled by the spray conditions (nitrogen temperature and pressure):

- In Fig. 16.35a, the gas velocity is relatively low and the particle jet is not sufficiently focused. The concentration of rebounding particles close to the substrate is important and nonuniform.
- In Fig. 16.35b, for these spray conditions, the jet is much better focused but the velocity is still below the critical one and the number of rebounding particles is almost that of the sprayed particles.
- In Fig.16.35c, for these spray conditions, the critical velocity is reached for most particles. The width of the jet is about that of case b but the number of rebounds is drastically reduced.

It is then possible, for the different velocities measured, to experimentally draw radial flux distribution curves representing the number of sticking particles. They are obtained by subtracting from the impacting particles number at each radial position, the maximum value of the rebounding ones calculated in the jet fringes. For each curve, corresponding to each mean impact velocity, the deposition efficiency can be determined.

16.3.5 Are Such Measurements Sufficient to Monitor Coating Properties?

Considering such measurements two questions arise: are they sufficient to determine what will be coating properties [9, 169, 170], and, if not, what is their usefulness?

16.3.5.1 Conventional Hot Processes

- As in these processes, particles at impact must be fully melted or close to their melting point. Are the in-flight particle temperatures measurement sufficiently precise? First the absolute temperature measurement is not very precise; errors in absolute temperature can approach 20 % in some cases (see [5–7, 9] and Sect. 16.3.3.2). Moreover the mean temperature value is not very informative; a value over the melting temperature T_m, does not necessarily means that all particles are fully melted upon impact. Reciprocally a mean temperature below T_m does not mean that all particles are unmelted. The interpretation of coating properties is by far easier with particle temperatures distribution than only mean values or ensemble measurement. That is why authors have proposed instead of temperature nondimensional and/or normalized parameters such as melting

index and particle Reynolds' number [116, 137, 170], molten volume flux [121, 122] as more appropriate descriptions of the particle state at impact.

– Coating properties are strongly linked to each particle flattening, solidification, and resulting splat formation, followed by splats layering, controlling the real contact splat-substrate or splat-previously deposited layers. That is why during the last decade, many works have been devoted to splat formation. These works were performed on smooth surfaces because of the low field depth of the microscope objectives that must be used to visualize them, see [171–174] and the reviews [175, 176]. Results of these studies underline the drastic importance of the substrate preheating over a so-called transition temperature T_t. Over T_t on the one hand adsorbates and condensates at the substrate surface are desorbed and on the other the oxide layer roughness at the surface of metallic substrates might be modified. Besides the modifications of thickness and composition, that of roughness, characterized by its skewness SK at the nanometer scale, may result, in certain cases, in a better wettability of the flattening droplet, also improving its contact with the substrate. To summarize, the quality of the contact splat–substrate is drastically improved when preheating the substrate over, T_t, parameter that is not controlled by particle parameters in flight. Correspondingly the coating adhesion on roughened substrates, with Ra in the few micrometers range, can be increased by a factor of 3 to 4 when they are sprayed after being preheated over T_t [176]. Of course, preheating is generally performed with the spray torch. As most coatings are sprayed on metallic surfaces, it becomes very important to control the preheating time, rate, and temperature in order to monitor the formation of the oxide layer at the substrate surface (its composition and thickness). This is particularly true for certain metals very sensitive to oxidation such as for example low carbon steel [176].
– Besides the oxide formation, the control of the substrate and coating surface temperature before during and after spraying is very important to avoid temperature gradients within coating during its formation, especially when spraying materials with low thermal conductivities (below about 20 W/m K). The temperature distribution within the coating during the spray process influences strongly the residual stress distribution after coating and substrate cooling [177].
– The particle oxidation in flight is also very important for coating properties. When spraying with d.c. plasma or HVOF or HVAF or wire arc guns, besides the oxidation by diffusion, a convective movement within molten particles can be induced by the hot gases flow. It produces a very strong oxidation [178] (up to five times that resulting from diffusion), because convection renews continuously the fresh metal at the particle surface while the oxide formed and/or the oxygen is entrained inside the particle [174, 178–180]. This oxidation phenomenon cannot be detected by particles in-flight measurements.
– The spray pattern is also crucial through the number of passes, the scanning step, the relative speed spray gun-substrate, the spray distance, and the spray angle [181]. These parameters are very important for the control of the coating mean temperature during spraying and the sticking or not at the surface of each pass of the poorly treated particles traveling in the jet fringes (especially the hot smaller ones).

16.3.5.2 Cold Spray

The development of the cold spray technique being more recent, only a few papers were presented about the use of sensors to measure in-flight particle parameters [9]. In this process, as particles are cold (or at least not hot enough to emit sufficient light to be detected by conventional sensors used in thermal spray processes), only velocity measurements are performed [163, 164, 166, 167, 182]. These velocity measurements have been mainly used to characterize the particle critical velocity, which also requires measuring the deposition efficiency. According to the few results published, there is no clear link established between particle velocities (over the critical velocity) and coating properties, provided the impact velocities of particles are over the critical velocity. For example, Raletz et al. [168] have sprayed with helium nickel particles (32–10 μm), for which the deposition efficiency was over 4 % for a mean velocity of 504 m/s. He has shown that, for the same coating thickness, the coatings porosity was, in the measurement precision range, about 2 %, whatever may be the particles mean impact velocity for values varying between 540 and 780 m/s.

16.3.6 Coating Under Formation

16.3.6.1 Hot Gases Heat Flux

Hot gases and the impacting molten or semimolten particles heat the substrate and coating, during spraying [9]. The heat flux, due to the hot gas expansion downstream of the nozzle exit, decreases rather rapidly with the spray distance (almost exponentially). However when spraying solutions or suspensions at very short distances (30–40 mm with plasma jets and 60–90 mm with HVOF jets), heat fluxes can reach a few tens of MW/m^2, especially with plasmas, requiring short residence time of the torch at the same location and efficient cooling systems, generally with gas jets. The heat flux measurement requires, for axis-symmetric jets, calorimetric measurements [183–186]. Commercial calorimeters exist, but generally for heat fluxes below 5 MW/m. For higher fluxes the central part of the calorimeter with a surface between a few tens and a few hundreds of mm^2 is high-pressure (up to 3 MPa) water cooled, and it is surrounded by a ring calorimeter also water cooled, the water connections being such that no heat flux is exchanged between both calorimeters. One of the difficulties is the interpretation of results, the central calorimeter, and especially the ring one modifying the free hot gases flow. At short distances (<50 mm), where most calorimeters give up, a copper target crossing rapidly the jet (30 m/s) allows measuring the total heat flux received from the plasma jet, giving a good approximation of the heat flux [187].

16.3.6.2 Substrate Temperature Control

It has been emphasized that the monitoring of coating temperature before, during, and after spraying is as important for the coating quality, reliability, and reproducibility, as monitoring particle velocities, temperatures, and trajectories [3, 188, 189]. Thus many efforts have been devoted to coating temperature monitoring during the spray process by different means [9]:

- Infra red (IR) pyrometers [190–192], wavelengths over 6 μm being less sensitive to radiation of the plasma or hot gases as well as hot particles [190].
- IR thermography [193–195].
- Embedded and fast response micro-thermocouples in metallic substrate [196, 197] with the still unresolved problem of the lack of good contact between substrate and coating, especially for low-conductivity sprayed materials. Such thermocouples are also used to calibrate the surface temperature measurement with IR pyrometers [198].

Zhang et al. [199] have shown that by simply reducing the spray distance, it is possible to achieve substrate melting and control splat solidification. Of course it requires that a temperature-control device is attached at the backside of the substrate

At last it must be recalled that the coating temperature depends on the pass thickness, especially for low-thermal conductivity (below about 20 W/m.K) sprayed materials, the spray pattern, the spray distance, and the cooling systems used, as well as their positioning.

16.3.6.3 Stress Development During Spraying

To determine the stress formation in situ during spraying, the curvature of a beam, made of the substrate metal, is continuously recorded during the spray process (preheating, coating, and cooling) in parallel with the substrate and coating temperature [9].

The first works on this technique were initiated by Kuroda and Clyne [200–203] at the end of the 1980s and the beginning of the 1980s and then developed by other authors [183, 204–210]. One of the setup used [204] is represented in Fig. 16.36. The beam shaped substrate is fixed at one of its extremity on a water-cooled shield and its curvature is continuously recorded with a sensor (LVDT). Meanwhile the pyrometer of the spray and deposit control (SDC) setup measures continuously first the substrate and then the coating surface temperatures. Of course in parallel the particle trajectories are monitored with the SDC.

Typical signals observed during plasma spraying are presented in Fig.16.37. The fluctuating curve represents the surface temperature evolution. The strong variations are due to the torch pattern during spraying. As the detector is fixed on the torch sometimes it “sees” the substrate or coating hot surfaces and sometimes the

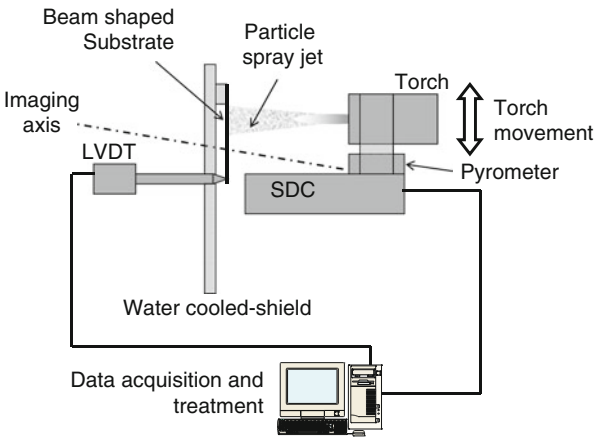


Fig. 16.36 Setup developed with the spray and deposit control to follow continuously the beam-shaped substrate bending before, during, and after spraying while controlling the substrate and coating temperature. Reprinted with kind permission from ASM International [204]

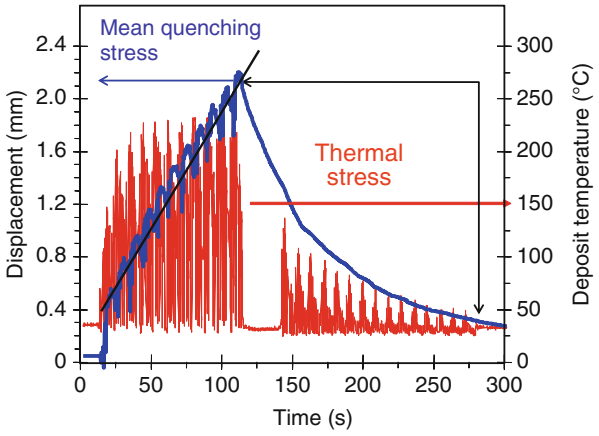


Fig. 16.37 Surface temperatures of substrate and coating evolution during the spray process as well as that of the beam bending. Reprinted with kind permission from ASM International [204]

surrounding of the setup (the water cooled shield). The bending curve with a positive steep slope corresponds to the quenching stress generated during the spray process while that with a decreasing shape corresponds to the expansion mismatch stress developing after spraying when substrate and coating cool down.

16.3.6.4 Coating Thickness Measurement

Coating thickness is one of the most important parameters to monitor and control. Unfortunately most measurements are generally destructive (after spraying) and time consuming. A novel approach has been recently developed [211] enabling on line, real time and noncontact measurement of individual spray pass thickness during deposition.

It is based on simple optical triangulation to detect the smooth step profile of a pass over the immediately adjacent uncoated (or previously coated) surface. The strategy consists in recording the profile of the coating at the frontier between the new layer and the previous one using a laser line projected across the pass edge and captured with CCD camera. Measurements are independent of coating/substrate nature, the surface roughness or the thermal expansion of the coated part. For online tests on cylinders, the precision is about 5 μm.

16.4 Online Control or Monitoring?

16.4.1 Coating Properties Monitoring

As presented in the previous section, sensors have been mainly used to find either relationships existing between in-flight parameters and spray conditions, or compare calculations with measurements, or determine the effect of particle temperatures and/or velocities on a specific property of the coating. Their main goals were to optimize spray parameters, improve the reliability and the reproducibility of coatings, compensate the drift of these in-flight parameters with the erosion of nozzle, electrodes,... and validate models.

However establishing a relationship between in-flight measurements and coating properties is another story, which beginning is just starting [173]. For example, despite the small variability observed in particle state, substantial variability is observed in coating attributes [15]. For that, besides the in-flight measurements, especially particle trajectories distribution, other parameters must be recorded during the spray process, such as the coating mean temperature evolution, the stress distribution evolution, the spray pattern,... and also some coating characteristics such as porosity, phase content, oxide content, thermomechanical properties,... The spray pattern is an important parameter for coatings quality. "Robot trajectory planning for high quality thermal spray coating processes should integrate an accurate definition and control of process kinematics, but it should also give rise to an optimal thermal guidance during deposition" [212].

16.4.1.1 Spray Pattern Through Robot Trajectory Planning

The generation of the trajectory plays an important role in thermal spraying to achieve a uniform thickness with as less as possible of undulations (see Sect. 13.6.1.4), a perfect control of temperature gradients within coatings, depending on the heat flux and pass thickness. When using a robot to control the spray pattern, the reliability and functional properties of the coating can be improved [213]. They can be programmed in two ways: online and offline programming. The online programming method is easy to operate but difficult to use for complex work pieces and the heat transfer is not considered.

The offline programming technology gives much better results and the local heat load considered. The interested reader can find three methods of robot programming in the paper of Deng et al. [213]. Floristán et al. [212], with offline programming, have applied a thermal surface load on the substrate surface to model the heat transfer. The moving hot spot describes the programmed spray path and gives the heat contribution from the plasma and the particles. The velocity torch–substrate is considered in the simulation by the loading times at each node, which are obtained from the robot-programming tool. The heat flux is simulated as a Gaussian distribution on the substrate and it is oriented at each node according to the torch orientation relative to the substrate at that point of the trajectory [212]. Of course this implies measuring first the heat fluxes from hot gases at different positions in the hot jet (see Sect. 16.3.6.1)

16.4.1.2 Coating Monitoring Through In-Flight Particle Parameters

As previously underlined, in spite of many works performed, during the last two decades, there are still no clear relationship between on the one hand in-flight particle parameters, substrate, and coating temperature evolution before, during, and after spraying and coating thermomechanical properties. A factorial design experiment can be performed to link different coating properties such as hardness, oxide content, thickness, porosity, wear resistance,. . . to in-flight particle parameters, coating surface temperature,. . .or spray parameters. For example, it was done by Fris and Persson [214] who found that models based on particle in-flight properties explain the variations in the microstructures of plasma sprayed YSZ as well as or better than the spray gun parameters do. Particle temperatures, T_p, and velocities, v_p, control the porosity, while the substrate temperature and the spray angle control the cracks formation. However the strong correlation between T_p and v_p makes it hard to discern which one of these two parameters affects the microstructure features. Basu et al. [215] and Gevelber et al. [216] have tried developing real-time control for plasma jets. The aim of their work was to measure in-flight particle parameters, spray pattern, including the spray jet position and adjust the torch inputs in order to maintain those states at their set point. It is also possible to define a good working area [169], as did Renault et al. [204, 217] for plasma sprayed CuNiIn (Ni 35 wt%, In 5 wt%) particles (10–45 μm). They used the spray and deposit control (SDC) system fixed on a commercial d.c. plasma torch. The parameters given by the SDC were the maximum intensity emitted by hot particles, the position of this maximum relatively to the torch axis, the distribution width, as well as the substrate and coating temperature. The powder mass flow rate, the spray pattern, and the relative velocity torch/substrate were kept constant, the only variables being the torch input parameters varied around the standard conditions used by SNECMA Co. A factorial design was constructed. Regression equation were established to relate SDC parameters to coating hardness, oxide content wt%, and thickness. Figure 16.38 represents the sensitivity of coating properties to the maximum intensity of hot particles and coating temperature.

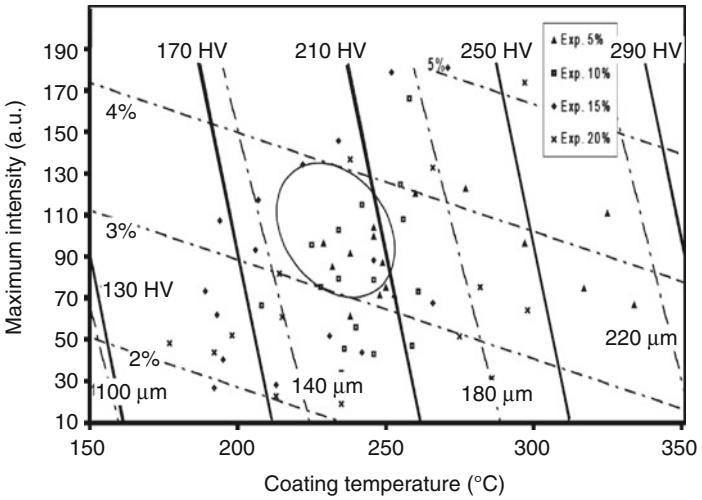


Fig. 16.38 Sensitivity of coating hardness (HV_{3N}), oxide wt% content, and thickness (µm) to the maximum intensity of the SDC and coating temperature during d.c. plasma spraying of NiCuIn particles. Reprinted with kind permission from ASM International [204]. See also [217]

This figure shows that, as soon as the slope of the iso-values is close to be parallel to one of the axes, the coating property studied is very sensitive to the variation of the SDC parameter of the perpendicular axis.

The central zone, surrounded by an ellipse-shaped line, corresponds to the coating properties expected by the manufacturer. As soon as the SDC parameters deviate slightly from this zone, the operator modifies parameters such as the hydrogen flow rate, the carrier gas flow rate, or the cooling airflow rate to keep the SDC parameters in the optimum working zone. This technique has reduced by more than 90 % the number of parts rejected. For other coating properties such as residual stress, measured with the setup presented in Fig. 16.36, the main parameter is the coating temperature during spraying. This is illustrated in Fig. 16.39 showing that by tailoring the temperature variation around that determined by the optimum torch working point, it becomes possible to achieve coatings, which, at room temperature, exhibit either compressive or tensile stress.

S. Sampath et al. [17] have shown that "the representation of the particle state within the temperature-velocity space allows a systematic recognition of the contribution of the process variables and sensitivities." They also showed that if the elastic modulus is a reasonable quantitative descriptor of a coating property, nonlinear response must also be considered for porous coatings, especially when subjected to thermomechanical loading. "Integrated process maps provide a framework comprehending sensors, enable feedback control and, when combined with coating properties, offer a strategy for coating design" [17].

Vaidya et al. [218] and Dwivedi et al. [1] have presented results on process–structure–property relations for plasma spraying of different feedstock

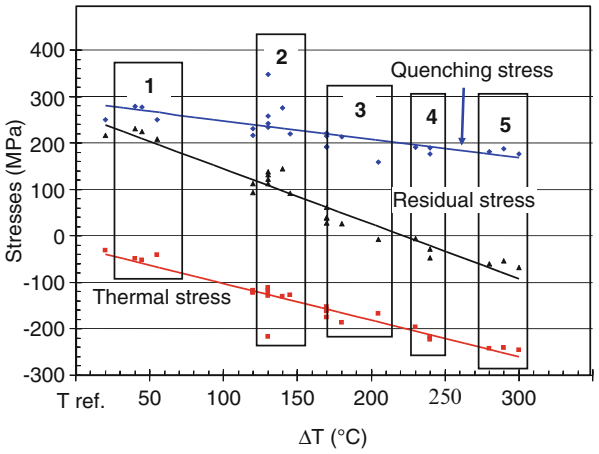


Fig. 16.39 Effect of the evolution of the coating temperature relatively to the spray temperature on the residual stresses: quenching stress, expansion mismatch or thermal stress and resulting residual stress of NiCuIn coatings d.c. plasma sprayed. Reprinted with kind permission from Springer Science Business Media [9], copyright © ASM International [204]

morphologies of YSZ (polyhedral, hollow spherical, and solid spherical). This was achieved by critical examination of the different stages of the spray process, namely, the in-flight particle state and design relevant deposit properties and the interrelations among them. The first-order process map was the relation between the in-flight particle state and the plasma-forming torch parameters and feedstock characteristics. Independent control of particle injection and construction of first-order process maps through the use of dimensionless group parameters enabled a unified assessment of various powder morphologies through the single first-order process map. From these results a critical comparison of only the material response was achieved with second-order maps connecting coating properties (such as the through thickness thermal conductivity, elastic modulus, and nonlinear elasticity relations), to the particle states. However they underlined that postspray characterization using metallography, indentation, and thermal conductivity are prone to higher intrinsic variability associated both with spray conditions and coatings preparation, especially for destructive techniques, which have potential to introduce artifacts. Ex situ curvature sensor technique [219] where coatings sprayed on a beam shaped substrate were thermally cycled, minimize the source of errors associated with the multistep/destructive characterization techniques and provides a novel means to assess their variability. Vaidya et al. [218] and Dwivedi et al. [1] further enable strategies to identify process windows in the particle state space to achieve a specific coating property and to do so reliably.

Valarezo et al. [147] have also used this process-map concept to study NiCr HVOF-sprayed coatings. With the measurements of coating thermal conductivities, electrical conductivities, hardness and elastic modules, and the mean particle temperatures and velocities, they obtained what they called second-order process maps, the first-order ones being those relating spray parameters to particle temperatures and velocities. An example of this second-order map is presented in Fig. 16.40.

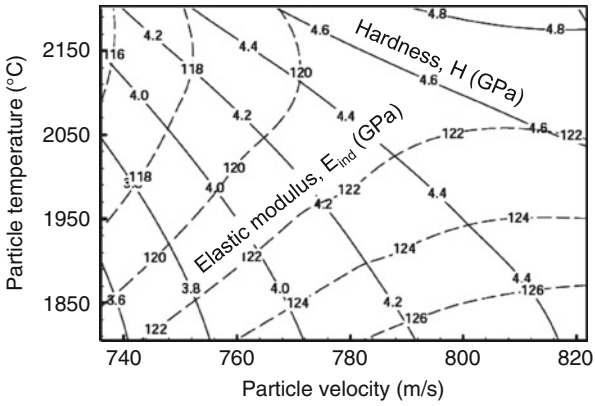


Fig. 16.40 Second-order process maps: elastic modulus and hardness of Ni–20Cr coatings by HVOF-DJ-2700 system: Hardness H (GPa), Elastic Modulus E_{ind} (GPa). Reprinted with kind permission from Springer Science Business Media [147], copyright © ASM International

This methodology addresses the effects of spraying parameters in production of coatings.

16.4.1.3 Artificial Neural Networks and Fuzzy Logic

One of the main problems with diagnostic tools such as those related to in-flight particle temperatures, velocities, and diameters is that they do not offer opportunities to tune the operation conditions. To do so, the sprayer needs [220] a feedback system requiring at least correlations between each processing parameter and each measured characteristic. Artificial intelligence, based on Artificial neural networks (ANN), proved to be a pertinent tool to predict particle in-flight characteristics and coating structural attributes from the knowledge of processing parameters [220]. In the ANN model, the discrimination of complex correlations between the process input (I) and the process output (O) is a simple mathematical operation processed through units called neurons. As shown in Fig. 16.41a from Kanta et al. [221], ANN architecture comprises input layer (receiving input data), one or more hidden layer (s) (connecting input and output layers representing correlations encoded by the system), and output layer (i.e., ANN result). The neuron (elementary processor of the ANN) is represented in Fig. 16.41b, with the input being the sum of flow coming from neurons connected upstream, the activation or transfer function making the input nonlinear and the output, resulting from the transformation, supplying the neurons connected downstream [221]. The strength of a given connection is quantified by a number, which is termed as a weight. For more details about the way the weights are tuned, see Guessasma et al. [220].

For example, Liu et al. [222], in their study of plasma-sprayed Al_2O_3–TiO_2, 13 wt% defined the ANN as follows: 4 neurons in the input layer (current intensity, total mass flow rate, H_2/Ar ratio, and the air cooling flow), 50 and 30 neurons in the 1st layer and the 2nd layer, respectively, forming the so-called hidden layers and 3 neurons in the output layer (particle velocity and temperature and substrate temperature). ANN, experimental database was divided in training, test, and

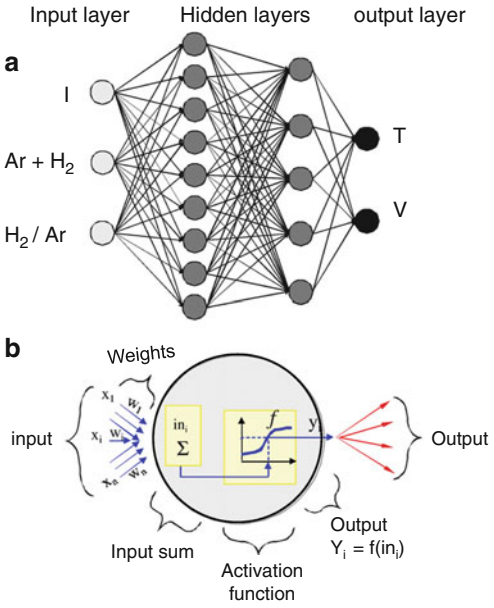


Fig. 16.41 ANN principle: (**a**) typical ANN feed forward architecture, (**b**) neuron model. Reprinted with kind permission from Elsevier [221]

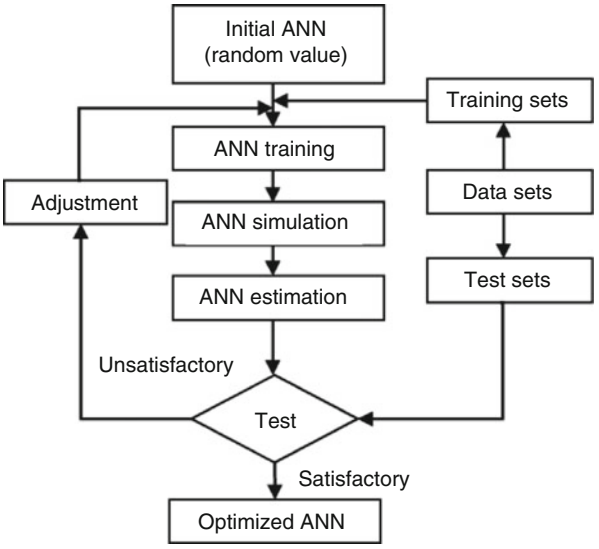


Fig. 16.42 ANN optimization process. Reproduced with the kind permission of ASM [222]

validation samples as shown in Fig. 16.42. After 5,000 iterations, ANN was stopped. Once trained with the results of experiments, ANN can predict the in-flight characteristics of particles and the temperature of the substrate with an error lower than 5 %.

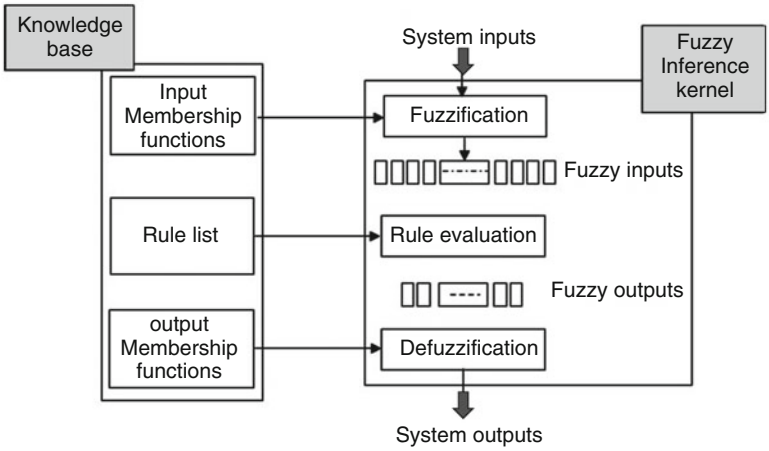


Fig. 16.43 Fuzzy logic basis system. Reproduced with the kind permission of Elsevier [223]

For coatings, the difficulty relies in the fact that any modification of macroscopic parameter spray parameters (arc current, plasma forming gas flow rates) implies modifications of powder carrier gas... All parameters (the previous ones) and the spray pattern as well as the coating surface mean temperature must be optimized and then maintained constant during spraying. Kanta et al. [221, 223] suggested that artificial intelligence (AI) is a suitable approach to predict operating parameters to attain required coating characteristics and correspondingly they implemented ANN and Fuzzy Logic (FL) to predict in-flight particles characteristics as a function of power process parameters. Figure 16.43 from Kanta et al. [223] represents the fuzzy logic basis system. The model, see Fig. 16.43, is generally implemented following three successive steps, namely fuzzification, rule evaluation (or inference), and defuzzification [224].

The fuzzy logic controller was implemented to control and regulate the processing parameters (arc current intensity, total gas flow rate, hydrogen percentage) of plasma-sprayed (APS) alumina–titania (Al_2O_3–TiO_2, 13 % by weight) to the in-flight particle parameters [223]. For example, Fig. 16.44 represents the effect of the hydrogen percentage in the plasma-forming gas on the in-flight particle average velocity and temperature. The predicted results both with ANN and FL indicate the same tendency. When the hydrogen mass percentage varied from 0.25 to 1.50 wt%, the in-flight particle average velocity and temperature increase by 12 % and 6 %, respectively. Authors [223] concluded that these models are powerful techniques that deliver a response within a very short time, once properly prepared. The ANN model seems well adapted for process prediction; whereas the FL model appears more adapted for process control.

ANN was also implemented to predict APS process parameters to manufacture by plasma spraying $Al_2O_3 - TiO_2$ 13 wt% coatings with the desired structural characteristics [221, 223]. Typical results of ANN predicted evolutions are

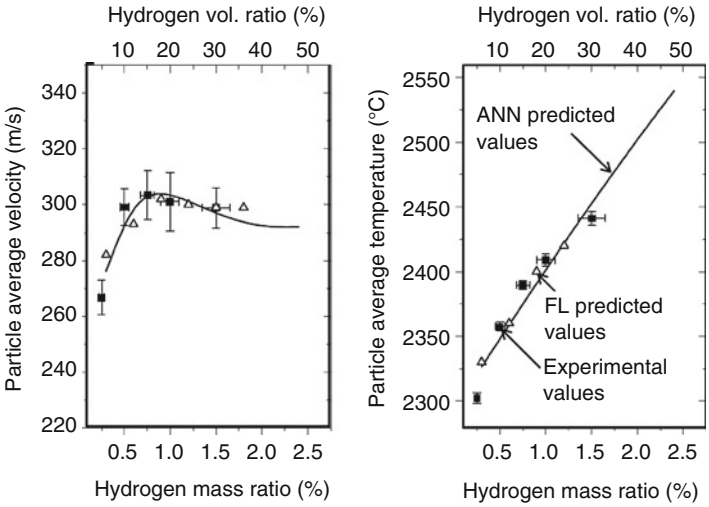


Fig. 16.44 Hydrogen percentage effect on in-flight Al_2O_3–TiO_2 (13 % by weight) particles characteristics. Spraying performed with a Sulzer F4-type plasma torch working with a current of 530 A and a total plasma gas mass flow rate to 72.3 g min^{-1}. Error bars represent standard deviation associated with experimentally determined average values. Reproduced with the kind permission of Elsevier [223]

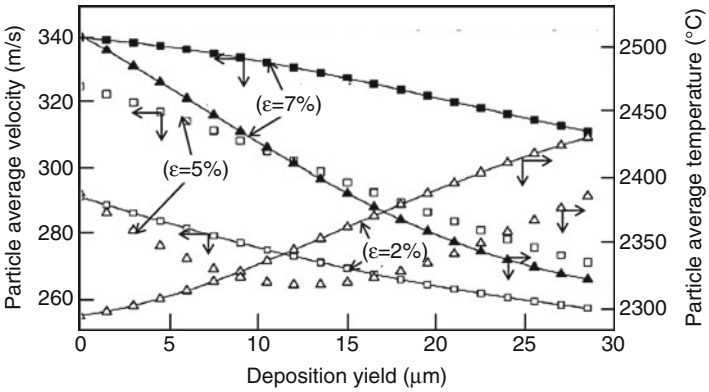


Fig. 16.45 ANN predicted evolution of in-flight particle average characteristics as a function of the porosity for several fixed deposition yields. Reproduced with the kind permission of Elsevier [223]

presented in Fig. 16.45 with in-flight particle average characteristics as a function of deposition yields for several fixed porosities.

The great advantage of ANN over other conventional methods is that it offers a global optimization and does not consider prior assumptions on parameter correlations. However the constraint to obtain a large representation sample is lowered by considering the noise on the measurements.

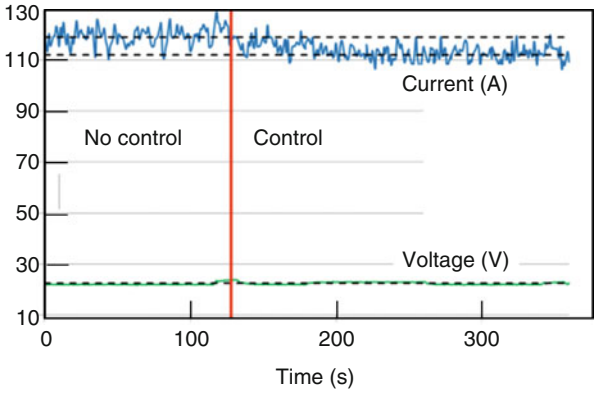


Fig. 16.46 ANN response to a disturbance ($I = 119$ A and $V = 22$ V) when the working parameters are set to $I = 110$ A and $V = 24$ V. Reproduced with the kind permission of Prof. J. Schein [225]

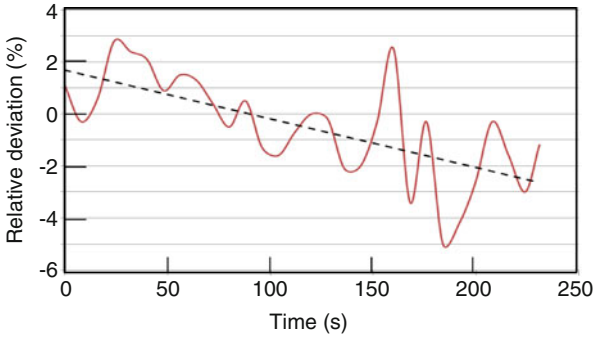


Fig. 16.47 Relative deviation of the vertical axis, b_n, of the particle flux imaging system when new contact sleeves are installed. Reproduced with the kind permission of Prof. J. Schein [233]

Kirner et al. [225], for a wire arc, underlined that, besides the working parameters including measurements of particles in-flight, the process is also influenced by different external effects, e.g., eroded contact sleeves, varying gas supply, fluctuations of wire feed speed,. . .,sleeping operators. To control the wire arc, they have developed ANN-based closed-loop system in connection with the particle flux imaging (PFI) to follow the particles beam in flight. PFI image processing creates an ellipse (see Sect. 16.3.2.1) characterized by its key numbers [30] as illustrated in Fig. 16.16. These parameters are the input data of an ANN, while the output data are the wire arc working parameters: arc current, I, voltage, V, and atomizing gas pressure. Kirner et al. [225] have evaluated the performance of statistical investigations by the method of design of experiments and calculated regression polynomials for the particles ellipse parameters in order to simulate the wire arc spray process by an artificial neural network. For example, Fig. 16.46 presents the system reaction, when a disturbance is created: $I = 119$ A and $V = 22$ V, while the wire arc is set to optimum parameters $I = 110$ A and $V = 24$ V. Of course the response time is more than one minute but the set parameters are re-established.

New contact sleeves also lead to PFI signal changes, especially that of the vertical axis of the ellipse, b_n (see Fig. 16.16) when other parameters are kept constant. This is illustrated in Fig. 16.47 from Kirner et al. [225]. As wire feed

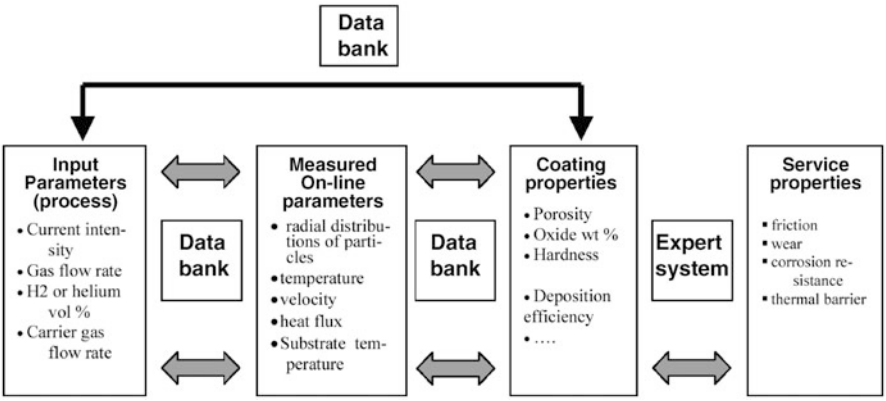


Fig. 16.48 Strategy of a possible on-line control. Reprinted with kind permission from Springer Science Business Media [9], copyright © ASM International [169]

velocity and voltage have a statistically significant effect on b_n, it becomes possible to control this deviation. If these results are promising, work is still needed to improve the system and fast-reacting power supplies should be developed.

16.4.2 Online Control?

A real online control is still a challenge, because nobody, according to the present knowledge, has a clear idea of the effect of the particle velocities and temperatures at impact on the coating thermomechanical properties and especially their service properties. The corresponding strategy for an online control [9] could be that presented in Fig. 16.48 [9] and it should be established for each coating.

16.5 Other Possible Measurements

16.5.1 Particle Vaporization

Two possibilities exist but, to our knowledge, only in laboratory conditions:

- Emission spectroscopy (analysis similar to chemical analysis in ICP plasma). As the sprayed particles are not completely vaporized, a few assumptions are mandatory (gas velocity constant within the analyzed volume, flow laminar in the analyzed volume, LTE prevailing, heat conduction in axial direction negligible) [226].
- Absorption spectroscopy to determine the ground state populations of atoms and ions as spectral lines are absorbed proportionally to the number of absorbing atoms [226–228].

16.5.2 Splat Formation

During the last decade, splat formation measurements have allowed drastic strides in our understanding of coatings formation. Splats layering form the coating that finally presents a hierarchy of microstructures across various length scales: manometer-sized elements, micrometer-sized grains contained within meso-scale splat structures, and a variety of manometer, micrometer, and meso-scale defect structures comprising voids, micro-cracks, and oriented boundaries. The coating microstructure depends on:

- - The splat real contact with substrate or previously deposited layers. Typical contacts vary between about 10–20 % of splat surfaces for poor ones and 60–70 % for good ones [228].
- The splashing of flattening fully melted particles upon impact that can affect drastically coating properties [229, 230].
- Pores, often called globular, formed during coating generation [231].
- Cracks formed during residual stresses relaxation. They comprise [203] micro-cracks within splats resulting from quenching stress relaxation and macro-cracks running through layered splats, often due to the relaxation of expansion mismatch stress.

Of course in this list are not included defects resulting from off-normal angle impacting particles (see Sect. 13.6.1.3), assuming that spraying is achieved keeping the torch orthogonal to substrate.

According to the importance of splat real contacts on coating thermomechanical properties, since the two last decades many works have been devoted to splat studies; see the review papers [175, 176].

16.5.2.1 Case of Molten or Semimolten Particles

According to the importance of splat real contacts on coating thermo-mechanical properties, since the two last decades many works have been devoted to splat studies.

They can be categorized in three types:

- Study of splat–substrate or splat-previously deposited layer interface.
- Modeling of particle flattening of a single particle, mostly onto smooth surfaces.
- Experimental study of the flattening of a single particle on a smooth surface.

(a) Interface Splat–Substrate

The preparation and observation of cross sections at a high spatial resolution is relatively difficult and requires specific instrumentation. Thus only few studies of the direct interaction between splat and substrate and their interface have been

performed at the microscopic level. For example, Otsubo et al. [232] have studied the interface resulting from the reaction between nickel base self-fluxing alloy coating and steel substrate by preparing the TEM specimens with ion milling method [235]. The problem is even more complex with ceramic splats where a modified wedge technique to bring the sample near electron transparency is necessary before ion milling [233]. With the development of the focused ion beam (FIB) technique during the past decade more studies were published these last years [234–241]. These studies were mainly performed for the impact of NiCr, NiAl, Al_2O_3, Al_2O_3–13 wt% TiO_2 plasma-sprayed particles onto aluminum or stainless steel, with or without NiCr bond coats. They showed that the shape and the real contact between splat and polished substrate and the occurrence of interdiffusion depend very strongly on:

– The substrate surface chemistry, i.e., the oxide or oxyhydroxyl layer formed during substrate preheating or boiling treatment as well as the desorption of adsorbates and condensates during preheating
– The wet ability flattening droplet–substrate that can be improved by the diffusion of elements such as Mg and Cr toward substrate surface for NiCr on stainless steel
– The localized interdiffusion between splat and substrate with possible localized melting of the substrate

Also very recently a method based on indentation experiments performed inside a scanning electron microscope (SEM) has been developed to measure the adhesion strength of alumina splats [242].

At last, as described in, Sect. 15.6.8.4 (b), Splat adhesion, Guetta et al. [175, Chap. 15] developed an original experimental setup, called LASAT, (see Fig. 15.29) to discriminate particles as a function of the levels of impact velocity to investigate the influence of this parameter on the resulting splat adhesion. TEM observation, simulation, and LASAT experiments allowed correlating nano-scale phenomena to macroscopic parameters such as impact velocity [176, Chap. 15].

(b) Modeling

Even for the impact of a single fully melted particle the modeling is very complex because results depend on the following:

– The impacting particle parameters (temperature, velocity, impact angle, oxidation stage that can be controlled by diffusion and/or convection phenomena as well as by the quantity of oxygen entrained in the plasma jet along the particle trajectory).
– The substrate parameters (material, initial surface roughness, oxide composition, thickness and roughness depending on substrate preheating conditions, presence of adsorbates and condensates, possible preferential diffusion of substrate elements toward its surface, especially during the impact of the molten droplet,. . .).

As summarized in the three reviews published about the splat formation [175, 176, 243], two types of models have been considered: analytical and numerical.

– Analytical methods [243], characterizing rebounding, deposition, or splashing, are based on dimensionless numbers related to droplet parameters at impact such as Reynolds, Re, Weber, We, Sommerfeld, K. . . numbers. These methods mostly assume incompressible conditions within droplets. But for these flattening parameters the question raised is that the flow of the liquid after a certain degree of flattening does not necessarily depend on the particle impact velocity but on the liquid flow velocity. As soon as the cooling of the flattening droplet is considered, Peclet, Pe, Stephan, Ste, and Biot, Bi numbers must be used. However the weak point of these solidification models is that the thermal contact resistance, R_{th}, between the flattening droplet and substrate must be considered. This key parameter controls the heat transfer and thus the cooling and solidification of the splat under formation as shown, for example, by the 1D model of Dhiman et al. [244].
– Numerical simulations of the fluid flow and heat transfer during the droplet impact result in very sophisticated models as presented in the reviews [175, 176]. However again, the thermal contact resistance between flattening particle and substrate is the key parameter. In fact R_{th} varies with time along the radius of the flattening droplet. This is due to the drastic variation of the impact pressure during flattening [245]. Especially in regions where the flattening degree of droplet reaches values over 1.5 to 2, the pressure is no more high enough to overcome other forces such as that due to vaporized gas from substrate surface, gas resulting from adsorbates and condensates vaporization. Thus instead of a constant value of R_{th}, as assumed by most models, a variable R_{th} should be considered. However the best models assume a given R_{th} value for the central core of the flattening particle and another one, with a higher value, for the rest of it [246]. At last all models developed assume that nucleation occurs at the melting temperature (T_m) that is not the case, nucleation-taking place at a temperature below T_m. However if nucleation can be easily considered in 1D transient models [247], it is unfortunately not the case in 3D transient ones.

(c) Flattening and Cooling Measurements

The coating adhesion–cohesion, as well as its thermomechanical properties depends strongly upon the particle flattening and the corresponding splat formation. In the 1980s and at the beginning of the 1990s splats study was limited to some sort of zoological classification with no systematic study of the effects of the spray conditions and substrate state [248].

The first measurements were those devoted to the flattening particle temperature time evolution; thanks to sophisticated two-color pyrometers with response times in the 50 ns range [175, 176]. However the interpretation of the cooling curves is very difficult and risky without images showing the evolution of the flattening droplet. Unfortunately flattening of plasma-sprayed particles occurs in times of the order of

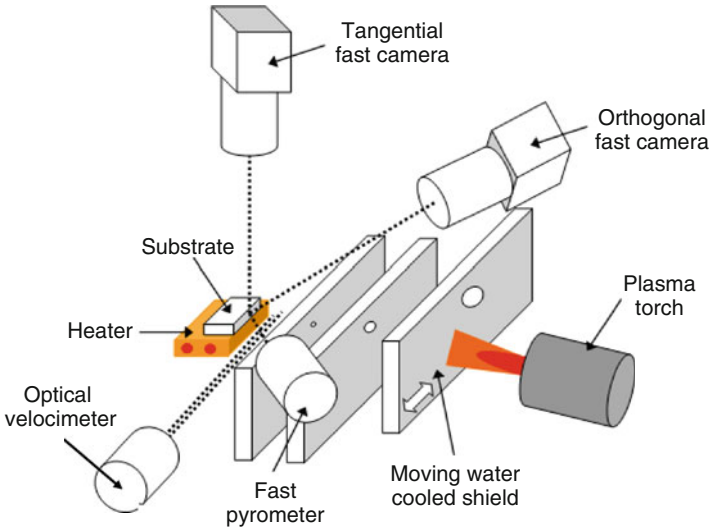


Fig. 16.49 Experimental setup and diagnostics to follow the impact of single tens of micrometer-sized ceramic or metallic particle plasma sprayed. Reprinted with kind permission from Springer Science Business Media [252], copyright © ASM International

one microsecond, while the fastest camera available allows interval between each frame of 1 μs and exposure time of each frame of 500 ns [249]. Solutions have been found by photographing one particle during its flattening in a given time range [250–252]. Thus varying the time range for different particles, assumed to be identical at impact (same diameter, temperature and velocity), it becomes possible to obtain few photographs (less than ten) of the flattening at different times. Such images, with the flattening droplet temperature time evolution and the observation of the resulting splat, allow a much better understanding of the phenomena taking place. Such measurements have confirmed phenomena followed with millimeter-sized drops, the flattening time of which is in the millisecond range and for which fast cameras (~5,000 images s^{-1}) can be used [175, 176]. Also they have demonstrated the importance of substrate preheating over the transition temperature to achieve disk-shaped splats. Dhiman et al. [253] gave an excellent review of how the splat shape depends on the substrate conditions and particle impact parameters. These experiments are rather sophisticated, as illustrated below, and made in laboratories but they are fundamental to understand phenomena controlling coating formation. Examples of diagnostic systems developed are presented in Fig. 16.49 which represents the experimental setup of Goutier et al. [252], where particles were plasma sprayed using a d.c. plasma torch (PTF4 type). Three shielding were used to select particle trajectories close to the plasma jet axis. The first one was a mobile water-cooled shield (hole of 5 mm), which was positioned 70 mm downstream of the torch nozzle exit. The second one (hole of 1.5 mm) was disposed at 80 mm, the last one, with a hole of 600 μm, was positioned at 90 mm. The measuring system comprised the measurements of in-flight droplet velocity by a

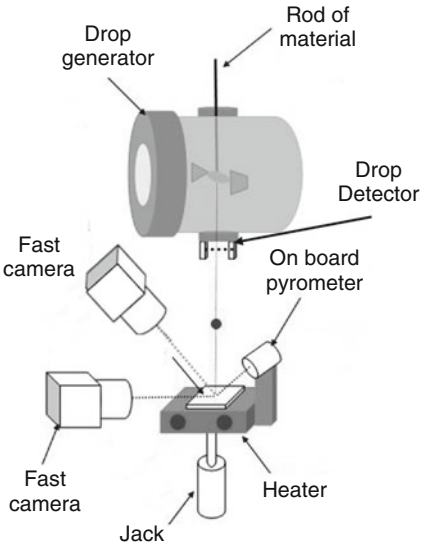


Fig. 16.50 Drop generator and diagnostics for millimeter-sized drops. Reprinted with kind permission from Springer Science Business Media [252], copyright © ASM International

2-point measuring optical detector and temperature by a fast (response time = 50 ns) dichromatic pyrometer following the particle temperature during its flattening and then cooling. The two wavelengths of the dichromatic pyrometer were 0.690 and 0.710 μm, respectively. At last two fast cameras were imaging the flattening droplet orthogonally and parallel to the substrate. However such experiments are extremely difficult and time consuming and that is why, since the beginning of flattening studies, many experiments have been performed on millimeter-sized particles [175, 176]. In this case flattening time is in the millisecond range and fast cameras (5,000 images/s) allow following the whole flattening of a single particle.

Unfortunately almost all experiments with millimeter-sized particles, except those with tiny droplets (not really a sprayed material), have been performed with free falling drops, the velocities of which are below 3 m/s and thus Weber numbers much lower than those of sprayed particles. That is why Goutier et al. [252] have developed a new setup where millimeter-sized drops (metals or ceramics) are sprayed onto a substrate fixed on a pneumatic jack that is moved up during particle fall, thus rising the relative impact velocity up to 10 m/s. Figure 16.50 presents the setup comprising a controlled atmosphere chamber where the rod of material to be melted is heated by an arc, the substrate, electrically preheated, being moved up when the falling drop is detected at the chamber exit. Otherwise, as in the experiment presented in Fig. 16.49, two fast cameras follow the drop flattening and a fast pyrometer its temperature evolution.

The question that is raised is the following: are measurements made at millimeter and micrometer scales comparable? Many results are based on measurements performed with millimeter-sized particles for which it has not been clearly established that flattening behaviors at the micrometer and millimeter scales are

Table 16.1 Reynolds and Weber numbers related to millimeter- and micrometer-sized particles. Reprinted with kind permission from Springer Science Business Media [252], copyright © ASM International

Alumina particles	v_p (m s^{-1})	d_p	Re	We
Micrometer	150	40 μm	430	4,000
Millimeter	1.2	5 mm	430	30
Millimeter	10	5 mm	3,583	2,084

similar, see, for example, the recent papers of Yang et al. [254]. The first question is about the Reynolds and Weber dimensionless numbers, as illustrated in Table 16.1. If with free falling velocities (<3 m/s) it is very easy to achieve same Reynolds numbers, higher velocities are mandatory to increase the millimeter-sized Weber number, which, even with 10 m/s, is only 2,084. While, with a rather low impact velocity (150 m/s) for plasma-sprayed particles, We is already 4,000!

The other important difference is the relative size of the boundary layer at the flattening particle bottom. For the micrometer-sized particles its thickness is close to that of the final splat and thus the flow at the flattening particle bottom is controlled by the boundary layer, while for the millimeter-sized particle the boundary layer thickness is quite negligible relatively to the final splat thickness. All experiments with micrometer-sized particles have shown the existence of a so-called transition temperature, T_t. When the substrate is preheated over T_t splats are mostly disk shaped [175, 176], while they are extensively fingered or fragmented below it. This has been attributed to desorption of adsorbates and condensates or a better wettability flattening droplet–substrate when preheating the substrate or reducing the pressure of its surrounding atmosphere. Correspondingly all models and comparisons with flattening droplet temperature evolution show that over T_t thermal contact resistances are in the 10^{-7}–10^{-8} m^2 K/W ranges, while below T_t they are superior to 10^{-6} m^{2}K/W. At last, a few experiments have been devoted to the measurement of the thermal contact resistance during millimeter-sized drops impact; thanks to a thermocouple measuring at the center of the substrate surface, supposed to be that of the flattening particle, the temperature evolution during flattening was recorded [255–257]. Recently, Goutier [258] has calculated the evolution of the flattening factor ($\xi = \frac{D_p}{d_p}$), where D_p is the diameter of the resulting splat, as a function either of the Reynolds or the Weber numbers for alumina and NiCr micrometer- and millimeter-sized particles. Results are presented in Fig. 13.32. These figures demonstrate that no link exists between the flattening factor and the Reynolds number Re_L of the flattening particle, while the evolution of ξ is not too badly correlated with the flattening Weber number (calculated with the mean flattening velocity of the droplet and the radius of the flattened splat) for different spray conditions, substrate preheating temperature, and different particle materials. No correlation works between ξ and either Re or We calculated with impact parameters. Thus works relating the melting index to the Reynolds number are maybe not the most appropriate. When developing the same

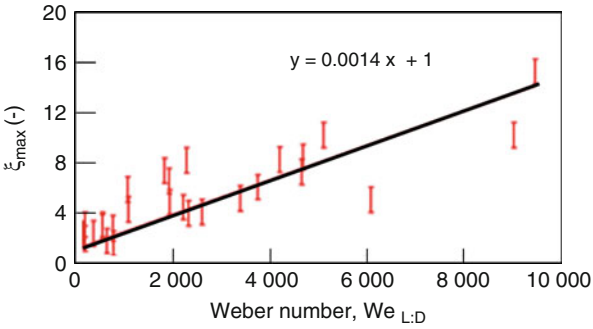


Fig. 16.51 Evolution of the flattening factor ξ of millimeter- and micrometer-sized particles of alumina and NiCr calculated with the flattening Weber number where the impacting particle diameter is used. Reprinted with the kind permission of Dr. S. Goutier [258]

calculation but using the impacting particle diameter instead of the splat diameter, the correlation is much better as illustrated in Fig. 16.51.

To conclude in spite, during the last decade, of all efforts devoted to splat formation on smooth substrates, many works are still necessary for a better understanding of the different phenomena involved.

16.5.2.2 Case of Unmelted Particles

As for conventional thermal spray, the understanding of splat formation is a key issue to improve coating properties. Unfortunately it is more difficult than with molten or semimolten particles. That is due to the fact that cold particles do not emit enough light to be observed directly and the impacting velocities, generally over 500 m s^{-1}, even less allow following the impact with fast cameras. For cold spray process only solid particles impact (resulting in "solid" splats), while with HVAF or high power HVOF processes also molten particles (resulting in "splash" and "disk" splats) and semimolten ones (resulting in "slushy/broken/semimolten" splats are observed [259]. Thus, actually, the only way to study solid splat formation is to observe them, once deposited, with an optical microscope, cross-sectional scanning electron microscopy (SEM) using a focused ion beam (FIB) and cross-sectional transmission electron microscopy (TEM). It means that for solid splats the situation is the same as that occurring at the end of the 1980s for splats resulting from molten or semimolten particles, except that now the impact velocity can be measured and tried to be linked to the splat shape. Such studies have allowed determining cratering of the substrate, splats formed, and material ejection according to the influence of particle sizes, spray conditions (particle velocity and temperature at impact), and substrate hardness and temperature [164, 260–267].

For example, Fukumoto et al. [266] have studied the effect of AISI304 stainless steel substrate temperature on the deposition behavior of Cu particles cold sprayed with helium. The gas temperature was kept as low as possible to eliminate the effect of particle heating. It is clear from Fig. 16.52 that the deposition ability increases, and the number of craters decreases remarkably with the increase in substrate temperature.

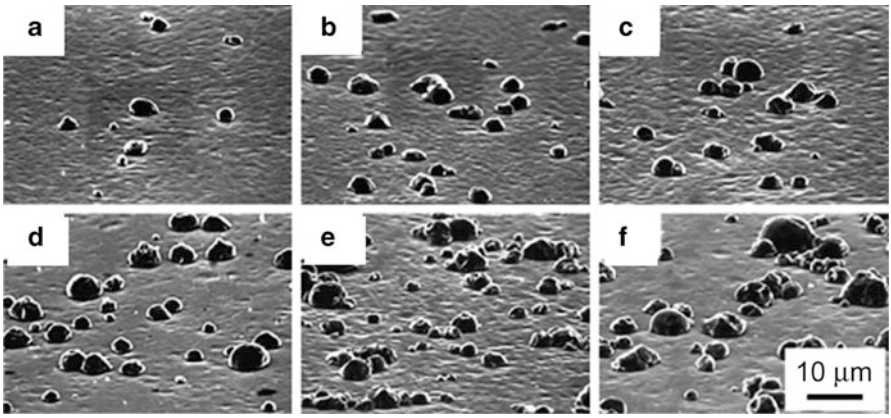


Fig. 16.52 Morphologies of collected particles (particle size: 5 µm, AISI 304 substrate). (**a**) Gas pressure: 0.4 MPa, gas temperature: 523 K. (**b**) 0.5 MPa, 523 K. (**c**) 0.6 MPa, 523 K. (**d**) 0.4 MPa, 923 K. (**e**) 0.5 MPa, 923 K. (**f**) 0.6 MPa, 923 K. Reprinted with kind permission from Springer Science Business Media [266], copyright © ASM International

Such measurements have allowed determining the induction time in cold spray. When starting with a smooth surface, particles are not attaching at first and they rebound, thus cleaning and deforming the surface. At a time t_i (~ few tens of seconds) called induction time, particles begin to attach, provided their velocity is higher than a critical velocity, v_c. This attachment occurs in an avalanche-like manner, rapidly forming the coating. This is illustrated in Fig. 6.24 of Chap. 6 from Klinkov and Kosarev [268].

16.5.3 Plasma-Liquid Injection

As already emphasized in Sect. 16.4.2, the key issue to better understand and control suspension or solution spraying lies in the possibility to follow drops and droplets fragmentation as well as their velocities. Up to now the main measurements were "global," velocity being measured with the Accuraspray system, measurement based on assumptions that were not really checked, and for drops and droplets the visualization of their dispersion within the jet. However two new techniques have recently shown up that are presented below.

16.5.3.1 Particle Imaging Velocity

In conventional PIV measurements (see Sect. 16.2.2.2), flow velocity is determined from the measurement of displacement versus time of imaged particles in a thin light sheet. For suspension spraying, Marchand et al. [124] have used the suspension droplets in the spray and the particles in the plasma flow, as the fed small

particles of conventional PIV, for imaging and velocity calculation. Droplets and particles, located in a plane of the flow, are both illuminated by two laser flashes following each other in short separation time. A camera detects the backscattered light, and two subsequent particle images are recorded. From these images, PIV analysis algorithms calculate droplets displacements and velocities of the entire flow region imaged. For this experiment Marchand et al. [124] used a Nd:YAG dual-pulsed laser (Quantel, Les Ulis, France) to create two collimated, collinear beams each with a pulse duration of 8 ns at wavelength of 532 nm. The laser beams were expanded into 2D light sheet by an arrangement of cylindrical and spherical lenses. The diverging light sheet had a thickness of about 1 mm and was passing through both the suspension atomizing nozzle axis and the torch axis. A PCO SensiCam 12-bit digital CCD camera (1280 $\times$ 1024 pixels) was used for imaging, laser pulses and the CCD camera shutter being synchronized using a TTL computer-controlled synchronizer. As with the bright plasma, a zone expanding 40 mm downstream from the plasma torch nozzle exit is dazzled, two specific filters were employed to prevent both exposures from being dazzled by the plasma. In order to get satisfactory statistical reliability, 50 and 100 pairs of images for the spray of drops originating from the atomizing nozzle and for the particles injected into the plasma flow, respectively, were recorded. For the evaluation of an average displacement of particles on pairs of images, the images were divided into small squares called "interrogation windows" of 32 $\times$ 32 pixels, in the present study. The local displacement vector was then determined for each interrogation box by implementing algorithm analyses based on cross-correlation.

To check the validity of the PIV measurements, Accuraspray was implemented to perform the same measurements in the same suspension spray conditions. Unfortunately results obtained with the PT-F4 torch were around 260–450 m/s, which were twice the values obtained in the PIV. Thus O. Marchand et al. [124] performed the same experiment changing the suspension injection conditions only. At the spray distance of 40 mm, velocities measured by Accuraspray were almost constant at 430 m/s, whereas velocities evaluated from the PIV increases from 110 to 210 m/s. The coating produced at a spray distance of 50 mm was very porous, with a low cohesion compared to the coating sprayed at a distance of 40 mm, which is in good agreement with the particle velocity decrease evidenced by PIV, whereas the Accuraspray results are independent from the spray distance. At last the coating porosity was related to the particle velocity as shown in Fig. 16.53. From Fig. 16.53a it is clear that a linear relation can be established between porosity and PIV measurements, which is not the case with the Accuraspray measurements shown in Fig. 16.53b.

16.5.3.2 Shadography

Marchand et al. [269] used a shadowgraphy technique with a double-pulsed Nd : YAG laser (532 nm wavelength with 8 ns pulse duration) with a beam diffuser for the backlight illumination of the liquid material (see Fig. 16.54). The detection

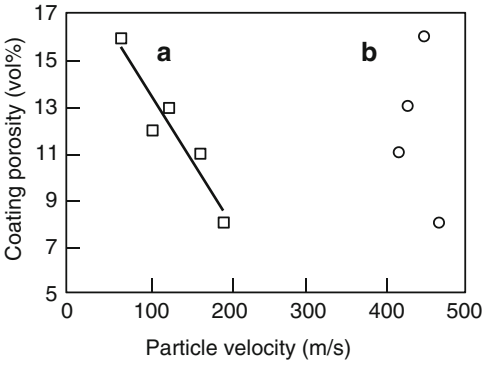


Fig. 16.53 Coating porosity (vol.%) related to particle velocity as determined either by (**a**) PIV technique or (**b**) using Accuraspray measurements (spray conditions defined in [124]). Reprinted with kind permission from Springer Science Business Media [124], copyright © ASM International

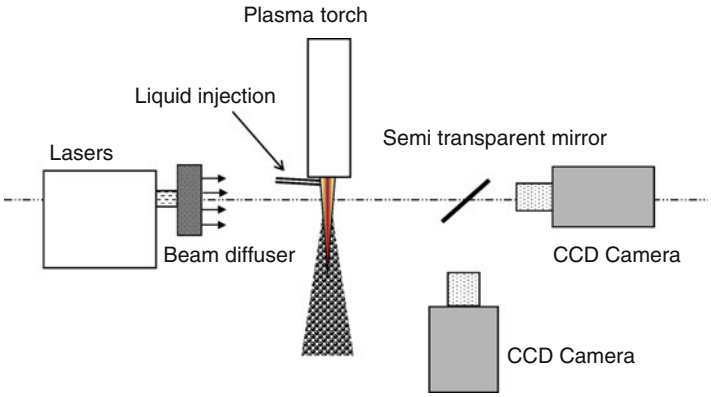


Fig. 16.54 Principle of the shadowgraphy setup. Reprinted with kind permission from IOP organization [270]

system consisted of two charge-coupled device (CCD) cameras with 1,376 × 1,040 pixels and 12 bits resolution and a programmable hardware timing unit controlled the synchronization of the laser with the cameras [270]. This system made it possible to discriminate droplets with diameters of about 2–3 μm at the best, and measure their number, velocity, and diameter distributions in a relatively small volume (2.25 × 1.8 × 1 mm^3).

Some results obtained with this device are shown in Figs. 16.55 and 16.56. Figure 16.55a from Fauchais and Vardelle [270] illustrates the penetration, fragmentation and dispersion into an Ar–H_2 plasma jet of a liquid jet made up of sub-micrometer-sized YSZ suspension in water. Figure 16.55b shows the dispersion of the droplets within two small areas as that indicated by a red square in Fig. 16.55a. However, it is worth to note that the in-flight observation of the material after solvent evaporation would require observing droplets or particles whose diameters are at least an order of magnitude lower, which is actually impossible with this technique.

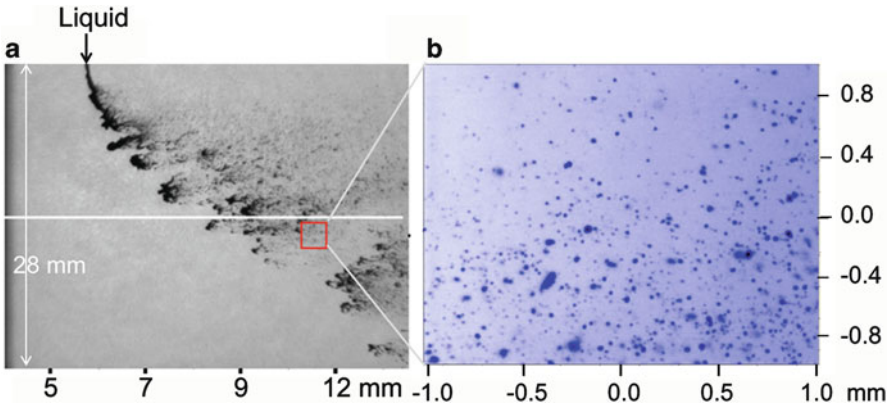


Fig. 16.55 (**a**) Mechanical injection of water suspension of YPSZ (10 wt%, 0.5–1.5 μm) into an Ar–H_2 plasma jet (Ar 33 slm, H_2 10 slm, anode nozzle i.d. 6 mm, arc current 600 A), visualized by shadowgraphy technique. (**b**) Zoom on areas as that is indicated by a violet square in Fig. 16.50a (investigated area: 2.25 × 1.18 mm^2). Reprinted with kind permission from IOP organization [270]

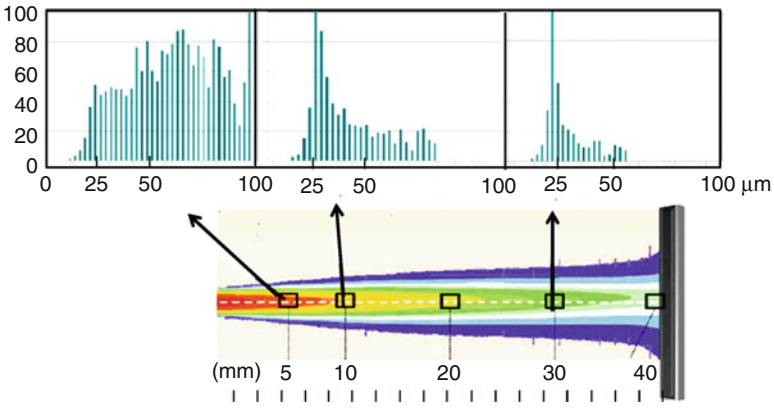


Fig. 16.56 Schematic of the plasma jet with the locations of measurements by shadowgraphy and the corresponding size distributions obtained (spray conditions as in Fig. 16.57a). Reprinted with kind permission from IOP organization [270]

Figure 16.56 presents the droplet size distribution evolution along the plasma jet axis, showing their fragmentation. However, as previously underlined, the real understanding of different phenomena controlling suspensions or solutions spraying requires that droplets or particles could be followed at least down to a few tenths of micrometers.

It is also possible with this setup to visualize the influence of the plasma enthalpy (Fig. 16.57) and that of solvent (Fig. 16.58) on the drops and droplets fragmentation [271]. Figure 16.57 shows that with the high enthalpy plasma, the number of droplets (>5 μm) with ethanol as solvent diminishes rather fast 15 mm downstream

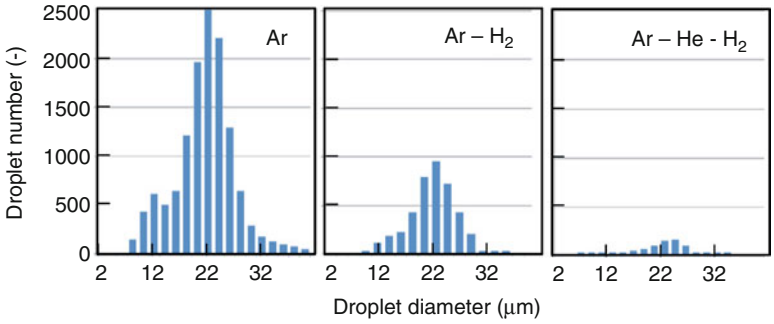


Fig. 16.57 Distribution by number of ethanol-based droplet diameters (>5 µm) 15 mm downstream of their injection in 3 different plasma jets (anode nozzle i.d. 6 mm; Ar 35 slm, $h = 9.1$ MJ/kg; Ar–H_2 33–10 slm, $h = 21$ MJ/kg; Ar–H_2–He 45, 3, 45 slm, $h = 19$ MJ/kg). Reprinted with kind permission from IOP organization [271]

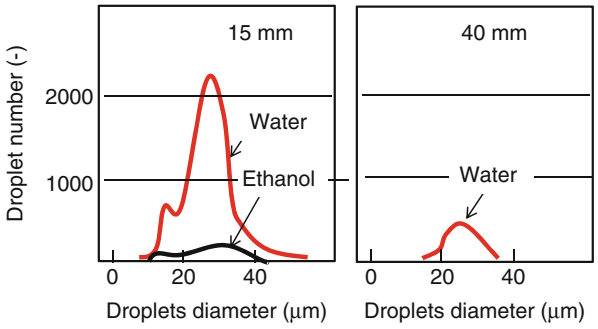


Fig. 16.58 Distribution by number of ethanol and water solvent droplets (>5 µm) at 15 mm and 40 mm downstream of their point of injection in an Ar–H_2–He (45, 3, 45 slm) plasma, $h = 19$ MJ kg^{-1} plasma jet (anode nozzle i.d. 6 mm). Reprinted with kind permission from IOP organization [271]

of the injection. When using water instead of ethanol as solvent, droplets formed from water still exist 40 mm downstream of the injection (see Fig. 16.58), while with ethanol nothing is observed at that distance, all visible droplets (>5 µm) vanishing at 20 mm.

16.5.3.3 Infrared Detection of Liquid Injection

Soysal and Ansar [272] have proposed to use infrared images emitted by liquids and vapors to characterize the influence of liquid injection into the atmospheric plasma jet. They used a camera with an exposure time of 35 µs only detecting a small band of infrared radiation from 1.5 to 5 µm and in the two-dimensional images intensities also depend on concentration densities of emitting species. The chaotic nature of turbulence makes it necessary to examine averaged pictures made of 100 single snapshots. With this setup it is also possible to obtain line profiles along the plasma

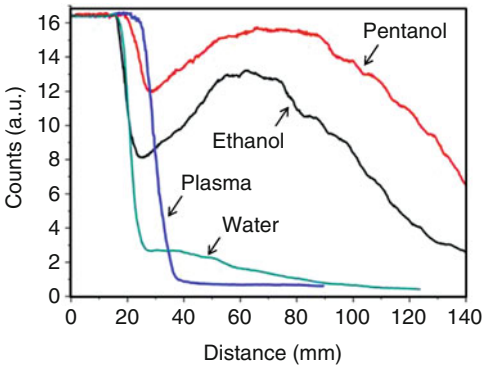


Fig. 16.59 Line profile along the plasma axis of averaged infrared images (500 A, 50 slm Ar, 20 ml/min). Reprinted with kind permission of Elsevier [272]

axis of averaged images of water, ethanol, and pentanol injection as well as the line profile of the plasma plume without any injection, as shown in Fig. 16.59. Compared to the original Ar plasma jet, water cools it rather fast, while in its plume the maxima observed probably come from post-atomization combustion. This combustion can take place only outside the hot plasma plume when temperatures are below 3,000 K. The peak width for ethanol is narrower than that of pentanol, corresponding probably to a faster combustion process. The broad combustion peak of pentanol higher than that of ethanol is due to the higher energy of combustion of pentanol.

16.6 Summary and Conclusions

Since the end of the nineties, sensors, able to work in the harsh environment of spray booths, have been developed and commercialized. They allow following in-flight particle trajectories, temperatures, velocities, sizes, and shapes. Also infrared pyrometers or cameras are used to follow substrate and coating surface temperature evolutions during their preheating, the spray process, and their cooling down. Other sensors allow following the development of stresses during substrate preheating, spraying, and cooling, the Young's module within coating and thickness evolutions during its formation. However coating properties also depend on numerous parameters, which are not necessarily controlled by sensors. For example, other important parameters are the substrate preparation, the way its preheating modifies the oxide layer (composition, thickness, and roughness) at metallic substrate surface, the spray pattern, and its control by robot offline or online programming with a good limitation of temperature gradients within coating during spraying, the particles oxidation in flight depending also on the hot gases velocity and composition, particle morphologies, which depend on their manufacturing process, operator carelessness, equipment maintenance,... Unfortunately, as underlined by Wigren and Johansson [2] coating reliability indeed depends on the process itself that can be controlled by sensors, spray pattern, cooling system,... but

unfortunately not only on them. As shown by Fig. 16.1 the process itself represents about 13 % of the number of errors occurring during coatings manufacturing! However since the use of sensors in spray booths the process reliability has been seriously improved.

Sensors for in-flight particle parameters can either follow single particles or ensemble of particles. In the first case more information is obtained with in-flight particle parameters distribution and not only a mean value as with ensemble measurements. Ensemble measurements require only a few seconds and can be used with the same powder flow rate as that of sprayed coatings. On the contrary statistical measurements performed with the DPV 2000 need at least a few minutes and require much lower flow rates than those used for coatings. All measurements show that the mean values of ensemble measurements are close to those deduced from statistical distributions. Among the in-flight parameters measured, good precisions (5 %) are achieved with velocities and trajectories, which is not the case with temperature. If the relative precision is good (about 5 %), the absolute value can be obtained with an error of 20 % due to the uncertainties about the emission coefficient and the possible radiation absorption by the particle, especially of ceramic materials. Moreover pyrometers must be calibrated regularly and more frequently than other sensors. The precision of particle diameter measurements, based on the light intensity emitted by particles, is also rather poor (up to 30 %) and they must be calibrated by collecting particles after their flight in the hot gases. New measurements based on shadowgraphs and using pulsed lasers, allow a good precision on particle diameters and also permit to access to their shape. Such measurements are however limited to particle velocities below 500 m/s and droplet or particles sizes over 5 μm. Authors found that temperatures and velocities are not the best parameters linked to the coating properties and proposed to consider: the melting index or the molten flux measured across the entire plume or the particles flux and new sensors have been developed for that.

Measurements have also been developed to follow fluxes and velocities of cold particles in-flight by illuminating them with a pulsed laser sheet. For the cold spray process, they allow determining particle velocities. Unfortunately no device permits measuring the particle diameters in cold spray conditions, which requires either deposition efficiency measurement or counting impacting and rebounding particles to determine the critical velocity. The use of laser illumination has also improved drastically the control of the radial injection of cold particles or liquid (suspension or solution spraying) in hot gases.

Most sensors are disposed aside the spray torch that implies measuring the in-flight parameters from times to times. On the contrary sensors, light enough to be fixed on the spray torch, provide information continuously allowing monitoring the torch parameters. These sensors have resulted in a much better understanding of the influence of the spray gun working conditions on the particles in-flight parameters, especially their trajectories, temperatures, and velocities. For example, the measurement of particle temperatures is one of the key parameters to achieve bimodal structure when spraying agglomerated particles made of agglomerated nanometre-sized ones.

The coating formation and properties not only depend on in-flight particles properties but also on the particles flattening, solidification, and layering, which are linked to substrate properties: roughness, oxide layer thickness and composition (most substrates are metallic), temperature evolution,... That is why sensors have been developed to measure substrate and coating mean temperature evolution (with the tenth of second response time), residual stress development during spraying and cooling. Of course the spray pattern is also very important as well as the heat fluxes from the hot gases and particles, as well as the cooling system used during preheating, spraying, and cooling. That is why fluxmeters have been developed for hot gases flux distribution.

Many works are devoted to define "a good working area" through factorial design, using in-flight parameters measurements together with those related to coating generation and coating properties. Other approaches, starting from the same parameters, use artificial intelligence based on ANN that proved to be a pertinent tool to predict particle in-flight characteristics and coating structural attributes from the knowledge of processing parameters.

However, in spite of the great strides made, thanks to sensors used in spray booths, sensors connected to process control unit, a lot of work is still necessary to achieve a real online control of the spray processes.

Everybody agrees on the fact that, since the development of sensors working in spray booths, the coatings reproducibility and reliability have been drastically improved. Moreover sensors have improved our knowledge of the spray process by validating models. Unfortunately for industrial use sensors are expensive. But considering the theme of payback, changes and improvements through in-flight particle control in industries have provided significant savings in material, energy, labor and hardware while adding to the quality of the product [273]. The author [273] however regrets that at the time, little effort was placed on optimizing the process or developing a quantitative return on investment. To conclude with sensors used in industry, the still pending questions are how to optimize the process, achieve a quantitative return on investment, and similarly how to relate such in-flight measurements to coating properties.

Also it must not be forgotten that sensors exist because many works have been developed in laboratories to measure different parameters such as those characterizing the high-energy gas flow (temperature and velocity distributions). These works with those about in-flight particle parameters have permitted to understand better the heat and momentum transfers and optimize them especially through particles injection. That is why the last section of this chapter is devoted to more fundamental works that have focused the attention of searchers these last years: the characterization of new processes such as suspension and solution spraying on the one hand and splats formation in conventional spraying on the other. For suspensions or solutions, many works have been devoted to follow liquid fragmentation and vaporization with sophisticated shadowgraphs and the use of particle image velocimetry. Unfortunately the detection is limited to droplets with sizes over 5 μm and thus the development of new measuring techniques is necessary to understand the process and achieve more reliable coatings. What has been achieved during the

last decade for the impact of fully or partially molten particles on smooth substrates has drastically improved our knowledge about coating formation on the substrate surface. But it is only a part of the story and a lot of work is still necessary to understand and control the flattening particles layering, especially on rough substrates. Moreover for the impact of solid ductile particles (cold spray, HVAF, high power HVOF, D-gun) no such sensor is yet available.

At last the link between on the one hand in-flight measurements (particle temperatures, velocities, diameters,...), coating temperature, and stress evolutions,..., during spray process and on the other coating thermomechanical properties is far to be clear and many works are still necessary before a real online control can be developed.

Nomenclature

Latin Alphabet

a	Sound velocity (m/s)
Bi	Biot number ($Bi = h\,L_c/\kappa_p$)
c_{pw}	The specific heat of the water at constant pressure (J/K kg)
d_p	Particle size (m)
h	Heat transfer coefficient (W/m^2 K)
h_o	Enthalpy of the gas sample at the probe outlet (J/kg)
h_{fg}	Enthalpy of fusion (J/kg)
h_p	Plasma enthalpy (J/kg)
L	Spray distance (m)
L_c	Characteristic length (m)
M	Mach number ($M = v_f/a$, where a is the sound velocity)
m^0_{wf}	Mass flow rate of the cooling water during sampling flow (kg/s)
nf	Subscript stands for the non-flow conditions, when no sample is being drawn
p	Pressure of the flow (Pa)
p_0	Pressure at the stagnation point of the flow (i.e. with a zero velocity) (Pa)
R	Ideal gas constant (8.32 J/K.mole)
Re	Reynolds number $\mathrm{Re} = \dfrac{d_p v_p \rho_p}{\mu_p}$
T_f	Gas temperature near the in-flight particle (K)
T_p	Measured particle surface temperature (K)
T_t	Transition temperature (K)
v_f	Flow velocity (m/s)
v_p	Particle velocity (m/s)
We	Weber number ($We = \frac{\rho_p v_p^2 d_p}{\sigma_p}$)

Greek Alphabet

Δt_m	Particle melting time (s)
Δt_{fly}	Particle in-flight time (s)
ΔT_f	Cooling water temperature difference during sample flow (K)
γ	Ratio of the gas specific heats at constant pressure and volume ($\gamma = c_p/c_v$)
ε_λ	Volumetric emission coefficient of the line at the wavelength λ (W/m^3.ster)
κ_p	Particle thermal conductivity (W/m K)
μ_p	Liquid particle molecular viscosity (Pa/s)
ρ_f	Specific mass of the flow (kg/m^3)
ρ_p	Specific mass of the melted particle (kg/m^3)
σ_p	Surface tension (J/m^2)

References

1. Dwivedi G, Wentz T, Sampath S, Nakamura T (2010) Assessing process and coating reliability through monitoring of process and design relevant coating properties. J Therm Spray Technol 19(4):695–712
2. Wigren J, Johansson J. Improving reliability of thermal spray coatings in production environment. In: Presented at 3rd plasma round table, 31 Oct–4 Nov 2011, South Africa
3. Friis M, Persson C (2003) Control of thermal spray processes by means of process maps and process windows. J Therm Spray Technol 12(1):44–52
4. Fauchais P, Vardelle A, Dussoubs B (2001) Quo vadis thermal spraying? J Therm Spray Technol 10:44–66
5. Fauchais P, Coudert JF, Vardelle M (1989) Diagnostics in thermal plasma processing. In: Auciello O, Flamm DL (eds) Plasma diagnostics, vol 1. Academic, New York, pp 349–446
6. Fauchais P et al (1992) Diagnostics of thermal spraying plasma jets. J Therm Spray Technol 1(2):117–128
7. Coudert JF, Fauchais P, Vardelle M (2002) Diagnostics of plasma spray process and derived on-line control. High Temp Mater Process 6(2):247–265
8. Fincke JR, Haggard DC, Swank WD (2001) Particle temperature measurement in the thermal spray process. J Therm Spray Technol 10(2):255–266
9. Fauchais P, Vardelle M (2010) Sensors in spray processes. J Therm Spray Technol 19(4):668–694
10. Vardelle M, Vardelle A, Fauchais P, Li K-I, Dussoubs B, Themlis NJ (2001) Controlling particle injection in plasma spraying. J Therm Spray Technol 10:267–286
11. Moreau C, Bisson J-F, Lima RS, Marple BR (2005) Diagnostics for advanced materials processing by plasma spraying. Pure Appl Chem 77(2):443–462
12. Li C-J, Wu T, Li C-X, Sun B (2003) Effect of spray particle trajectory on the measurement signal of particle parameters based on thermal radiation. J Therm Spray Technol 12(1):80–94
13. Moreau C, Gougeon P, Lamontagne M, Lacasse V, Vaudreuil G, Cielo P (1994) On-line control of the plasma spraying process by monitoring the temperature, velocity and trajectory of in-flight particles. In: Berndt CC, Sampath S (eds) Thermal spray industrial applications. ASM International, Materials Park, OH, pp 431–37
14. Vattulainen J, Hämäläinen E, Hernberg R, Vuoristo P, Mäntylä T (2001) Novel method for in-flight particle temperature and velocity measurements in plasma spraying using a single CCD camera. J Therm Spray Technol 10(1):94–104

15. Srinivasan V, Vaidya A, Streibl T, Friis M, Sampath S (2006) On the reproducibility of air plasma spray process and control of particle state. J Therm Spray Technol 15(4):739–743
16. Planche MP, Bolot R, Coddet C (2003) In-flight characteristics of plasma sprayed alumina particles: measurements, modeling, and comparison. J Therm Spray Technol 12(1):101–111
17. Sampath S, Srinivasan V, Valarezo A, Vaidya A, Streibl T (2009) Sensing, control, and in situ measurement of coating properties: an integrated approach toward establishing process-property correlations. J Therm Spray Technol 18(2):243–255
18. Prystay M, Gougeon P, Moreau C (1996) Correlation between particle temperature and velocity and the structure of plasma sprayed zirconia coatings. In: Berndt CC (ed) Thermal spray: practical solutions for engineering problems. ASM International, Materials Park, OH, pp 517–523
19. Vardelle M, Vardelle A, Leger AC, Fauchais P, Gobin D (1995) Influence of the particle parameters at impact on splat formation and solidification in plasma spraying processes. J Therm Spray Technol 4(1):50–58
20. Fauchais P, Vardelle M, Vardelle A, Bianchi L (1996) Plasma spray: study of the coating generation. Ceram Int 22:295–303
21. Fauchais P, Vardelle M, Vardelle A, Bianchi L, Leger AC (1996) Parameters controlling the generation and properties of plasma sprayed zirconia coatings. Plasma Chem Plasma Process 16:S99–S126
22. Wang P, Yu SCM, Ng HW (2007) Correlation of plasma sprayed coating deposition efficiency with volume flux measurements by phase doppler anemometry (PDA). Plasma Chem Plasma Process 27:311–336
23. Legoux J-G, Arsenault B, Leblanc L, Bouyer V, Moreau C (2002) Evaluation of four high velocity thermal spray guns using WC-10% Co-4% Cr cermets. J Therm Spray Technol 11(1):86–94
24. Boulos MP, Fauchais P, Pfender E (1994) Thermal plasmas fundamentals and applications, vol 1. Plenum, New York, NY
25. Fauchais P, Rat V, Coudert J-F, Etchart-Salas R, Montavon G (2008) Operating parameters for suspension and solution plasma-spray coatings. Surf Coat Technol 202:4309–4317
26. Roumilhac Ph, Coudert J-F, Fauchais P (1990) Influence of the arc chamber design and of the surrounding atmosphere on the characteristics and temperature distributions of Ar-H_2 and Ar-He spraying plasma jets. In: Apelian D, Szekely J (eds) Plasma processing and synthesis of materials III, vol 190. MRS, Pittsburgh, PA, pp 227–240
27. Roumilhac Ph. Contribution to the measurements and understanding of the spray and reclamation plasma torches at atmospheric pressure. Ph.D. thesis, University of Limoges, France, 12 Mar 1990 (in French)
28. Pfender E, Fincke J, Spores R (1991) Entrainment of cold gas into thermal plasma jets. Plasma Chem Plasma Process 11(4):529–543
29. Fauchais P, Vardelle A (2000) Heat, mass and momentum transfer in coating formation by plasma spraying. Int J Therm Sci 39:852–870
30. Landes K (2006) Diagnostics in plasma spraying techniques. Surf Coat Technol 201:1948–1954
31. Schein J, Richter M, Landes KD, Forster G, Zierhut J, Dzulkor M (2008) Tomographic investigation of plasma jets produced by multielectrode plasma torches. J Therm Spray Technol 17(3):338–343
32. Mauer G, Vaßen R, Stöver D (2011) Plasma and particle temperature measurements in thermal spray: approaches and applications. J Therm Spray Technol 20(3):391–406
33. Mauer G, Vaßen R, Stöver D, Kirner S, Marqués J-L, Zimmermann S, Forster G, Schein J (2010) Improving powder injection in plasma spraying by optical diagnostics of the plasma and particle characterization. In: Thermal spray: global solutions for future applications, 3–5 May 2010, Singapore, DVS-Berichte, vol 264. DVS Media, Düsseldorf, Germany, pp 525–530
34. Eckbreth AC, Anderson TJ (1985) Dual broadband CARS for simultaneous multiple species measurements. Appl Opt 24:2731–2736

35. Eckbreth AC, Anderson TJ (1986) Simultaneous rotational coherent anti-Stokes Raman spectroscopy with arbitrary pump-Stokes spectral separation. Opt Lett 11:496–498
36. Hall RJ, Eckbreth AC (1984) CARS: application to combustion diagnostics. In: Ready JF, Eaf RK (eds) Laser applications, vol 5. Academic, New York
37. Aldén M, Bengtsson PE, Edner H, Kroll S, Nilsson D (1989) Rotational CARS: a comparison of different techniques with emphasis on accuracy in temperature determination. Appl Opt 28:3206–3219
38. Kearney SP, Lucht RP, Jacobi AM (1999) Temperature measurements in convective heat transfer flows using dual-broadband, pure-rotational coherent anti-Stokes Raman spectroscopy (CARS). Exp Therm Fluid Sci 19:13–26
39. Fauchais P, Coudert J-F (1996) Mesures de température dans les plasmas thermiques. Revue Générale de Thermique 35:324–337
40. Lapierre D, Kearney RJ, Vardelle M, Vardelle A, Fauchais P (1994) Effect of a substrate on the temperature distribution in an argon-hydrogen thermal plasma jet. Plasma Chem Plasma Process 14(4):407–423
41. Coudert JF, Planche MP, Fauchais P (1995) Velocity measurement of D.C. plasma based on arc root fluctuations. Plasma Chem Plasma Process 15(1):47–70
42. Planche MP, Coudert JF, Fauchais P (1998) Velocity measurements for arc jets produced by a DC plasma spray torch. Plasma Chem Plasma Process 18(2):263–283
43. Pfender E, Chen WLT, Spores R (1990) A new look at the thermal and gas dynamic characteristics of a plasma jet. In: Bernecki TF (ed) Thermal spray research and applications. ASM International, Materials Park, OH, pp 1–10
44. Duan Z, Beall L, Planche MP, Heberlein J, Pfender E, Stachowicz M (1997) Arc voltage fluctuations as an indication of spray torch anode conditions. In: Berndt CC (ed) Thermal spray: a united forum for scientific and technological advances. ASM International, Materials Park, OH, pp 407–411
45. Planche MP (1995) Contribution to the study of fluctuations in a d.c. plasma torch. Application to the dynamic of the arc understanding and measurement of the flow velocity. PhD Thesis University of Limoges, France, 6 Nov 1995 (in French)
46. Leblanc L, Moreau C (2002) The long-term stability of plasma spraying. J Therm Spray Technol 11(3):380–386
47. Rigot D, Delluc G, Pateyron B, Coudert JF, Fauchais P, Wigren J (2003) Transient evolution and shifts of signals emitted by a d.c. plasma gun (type PTF4). J High Temp Mater Process 2:175–186
48. Mauer G, Marques-Lopez J-L, Vaßen R, Stöver D (2007) Detection of wear in one-cathode plasma torch electrodes and its impact on velocity and temperature of injected particles. J Therm Spray Technol 16(5–6):933–939
49. Roy S, Meyer TR, Lucht RP, Belovich VM, Corporan E, Gord JR (2004) Temperature and CO_2 concentration measurements in the exhaust stream of a liquid-fueled combustor using dual-pump coherent anti-Stokes Raman scattering (CARS) spectroscopy. Combust Flame 138:273–284
50. Wang GH, Clemens NT, Varghese PL (2005) High-repetition rate measurements of temperature and thermal dissipation in a non-premixed turbulent jet flame. Proc Combust Inst 30:691–699
51. Levy Y, Kartvelishvili L (2006) Flame diagnostics based on UV vibrational Raman spectroscopy. Optics Lasers Eng 44:1009–1026
52. Blunck D, Basu S, Zheng Y, Katta V, Gore J (2009) Simultaneous water vapor concentration and temperature measurements in unsteady hydrogen flames. Proc Combust Inst 32:2527–2534
53. Westerweel J (1993) Digital particle image velocimetry – theory and application. Delft University Press
54. Adrian RJ (1988) Double exposure, multiple-field particle image velocimetry for turbulent probability density. Optics Lasers Eng 9:211–228

55. Alekseenko SV, Dulin VM, Kozorezov YS, Markovich DM, Shtork SI, Tokarev MP (2011) Flow structure of swirling turbulent propane flames. Flow Turbulence Combust 87:569–595
56. Yilmaz N, Lucero RE, Burl Donaldson A, Gill W (2009) Flow characterization of diffusion flame oscillations using particle image velocimetry. Exp Fluids 46:737–746
57. Zahiri SH, Yang W, Jahedi M (2009) Characterization of cold spray titanium supersonic jet. J Therm Spray Technol 18(1):110–117
58. Newbery AP, Grant PS (2000) Droplet splashing during arc spraying of steel and the effect on deposit microstructure. J Therm Spray Technol 9(2):250–258
59. Lange S, Sieber M, Forster G, Luis Marqués-Lopez J, Schein J, Kähler CJ (2011) Velocity diagnostics for gas velocity distributions in cold gas and plasma spraying using non-resonant laser scattering. J Therm Spray Technol 20(1–2):12–20
60. Li ZS, Li B, Sun ZW, Bai XS, Aldén M (2010) Turbulence and combustion interaction: high resolution local flame front structure visualization using simultaneous single-shot PLIF imaging of CH, OH, and CH2O in a piloted premixed jet flame. Combust Flame 157:1087–1096
61. Blais A, Jodoin B, Dorier J-L, Gindrat C, Hollenstein C (2005) Inclusion of aerodynamic non-equilibrium effects in supersonic plasma jet enthalpy probe measurements. J Therm Spray Technol 14(3):342–353
62. Grey J, Jacobs PF, Sherman MP (1962) Calorimetric probe for the measurement of extremely high temperatures. Rev Sci Instrum 33(7):738–741
63. Brossa M, Pfender E (1988) Probe measurements in thermal plasma jets. Plasma Chem Plasma Process 8(1):75–90
64. Pfender E, Fincke JR, Spores R (1991) Entrainment of cold gas into thermal plasma jets. Plasma Chem Plasma Process 11(4):529–543
65. Katta S, Lewis JA, Gauvin WH (1973) A plasma calorimetric probe. Rev Sci Instrum 44 (10):1519–1523
66. Capetti A, Pfender E (1989) Probe measurements in argon plasma jets operated in ambient argon. Plasma Chem Plasma Process 9(2):329–341
67. Swank WD, Fincke JR, Haggard DC (1993) Modular enthalpy probe and gas analyzer for thermal plasma measurements. Rev Sci Instrum 64(1):56–62
68. Fincke JR, Chang CH, Swank WD, Haggard DC (1994) Entrainment and demixing in subsonic thermal plasma jets: comparison of measurements and predictions. Int J Heat Mass Transfer 37:1673–1682
69. Fincke JR, Swank WD, Snyder SC, Haggard DC (1993) Enthalpy probe performance in compressible thermal plasma jets. Rev Sci Instrum 64(12):3585–3593
70. Jankovic M, Mostaghimi J (1998) Thermally induced measurement error by a water-cooled enthalpy probe. Plasma Chem Plasma Process 18(1):53–71
71. Rajabian M, Gravelle DV, Vacquié S (2004) Measurements of temperatures and electron number density in an argon–nitrogen plasma jet generated by a dc torch-operation close to supersonic threshold. Plasma Chem Plasma Process 24(2):261–284
72. Asmann M, Wank A, Kim H, Heberlein J, Pfender E (2001) Characterization of the converging jet region in a triple torch plasma reactor. Plasma Chem Plasma Process 21(1):37–63
73. Steffens H-D, Duda T (2000) Enthalpy measurements of direct current plasma jets used for ZrO_2-Y_2O_3 thermal barrier coatings. J Therm Spray Technol 9(2):235–240
74. Vaßen R, Kaßner H, Mauer G, Stöver D (2010) Suspension plasma spraying: process characteristics and applications. J Therm Spray Technol 19(1–2):219–225
75. Janisson S, Meillot E, Vardelle A, Coudert JF, Pateyron B, Fauchais P (1999) Plasma spraying using Ar-He-H_2 gas mixtures. J Therm Spray Technol 8(4):545–552
76. Planche MP, Bolot R, Landemarre O, Coddet C (1998) Comparison between experimental and numerical results obtained on in-flight particles characteristics. In: Coddet C (ed) Thermal spray: meeting the challenges of the 21st century, vol 2. ASM International, Materials Park, OH, pp 355–360

77. Bolot R, Morin V, Coddet C (2001) Correlation between simulations and plasma spray coatings properties. In: Berndt CC, Khor KA, Lugscheider E (eds) Thermal spray 2001: new surface for a new millenium. ASM International, Materials Park, OH, pp 883–888
78. Dussoubs B, Vardelle A, Mariaux G, Themelis NJ, Fauchais P (2001) Modeling of plasma spraying of two powders. J Therm Spray Technol 10(1):105–110
79. Delluc G, Perrin L, Ageorges H, Fauchais P, Pateyron B (2004) Modelling of plasma jet and particle behavior in spraying conditions. In: ITSC 2004, in modeling and simulation V. DVS, Düsseldorf, Germany, C.D. Rom. 35
80. Zhang T, Gawne DT, Liu B (2000) Computer modelling of the influence of process parameters on the heating and acceleration of particles during plasma spraying. Surf Coat Technol 132:233–243
81. Devasenapathi A, Ang CB, Yu SCM, Ng HW (2001) Role of particle injection velocity on coating microstructure of plasma sprayed alumina – validation of process chart. Surf Coat Technol 139:44–54
82. Wilden J, Frank H, Bergmann J-P (2006) Process and microstructure simulation in thermal spraying. Surf Coat Technol 201:1962–1968
83. Kamnis S, Gu S, Zeoli N (2008) Mathematical modelling of Inconel 718 particles in HVOF thermal spraying. Surf Coat Technol 202:2715–2724
84. Liantong A, Gao Y, Zhang T (2007) Effect of powder injection location on ceramic coatings properties when using plasma spray. J Therm Spray Technol 16(5–6):967–973
85. Xiong H-B, Zheng L-L, Sampath S, Williamson RL, Fincke JR (2004) Three-dimensional simulation of plasma spray: effects of carrier gas flow and particle injection on plasma jet and entrained particle behavior. Int J Heat Mass Transfer 47:5189–5200
86. Mauer G, Vaßen R, Stöver D, Kirner S, Marqués J-L, Zimmermann S, Forster G, Schein J (2011) Improving powder injection in plasma spraying by optical diagnostics of the plasma and particle characterization. J Therm Spray Technol 20(1–2):3–11
87. Zhang W, Zheng LL, Zhang H, Sampath S (2007) Study of injection angle and carrier gas flow rate effects on particles in-flight characteristics in plasma spray process: modeling and experiments. Plasma Chem Plasma Process 27:701–716
88. Srinivasan V, Friis M, Vaidya A, Streibl T, Sampath S (2007) Particle injection in direct current air plasma spray: salient observations and optimization strategies. Plasma Chem Plasma Process 27:609–623
89. Li M, Christofides PD (2004) Feedback control of HVOF thermal spray process accounting for powder size distribution. J Therm Spray Technol 13(1):108–120
90. Yuan X, Wang H, Hou G, Zha B (2006) Numerical modeling of a low temperature high velocity air fuel spraying process with injection of liquid and metal particles. J Therm Spray Technol 15(3):413–421
91. Katanoda H, Matsuo K (2003) Analysis of particle behavior in high-velocity oxy-fuel thermal spraying process. J Therm Sci 12(3):279–282
92. Kamnis S, Gu S (2006) 3-D modelling of kerosene-fuelled HVOF thermal spray gun. Chem Eng Sci 61:5427–5439
93. Tillmann W, Vogli E, Nebel J (2007) Development of detonation flame sprayed Cu-base coatings containing large ceramic particles. J Therm Spray Technol 16(5–6):751–758
94. Fauchais P, Montavon G, Bertrand G (2010) From powders to thermally sprayed coatings. Schein 19(1–2):56–80
95. Vardelle A, Fauchais P, Dussoubs B, Themlis JN (1998) Heat generation and particle injection in a thermal plasma torch. Plasma Chem Plasma Process 18:551–574
96. Bandyopadhyay R, Nylén P (2003) A computational fluid dynamic analysis of gas and particle flow in flame spraying. J Therm Spray Technol 12(4):492–503
97. Kadyrov E (1996) Gas-particle interaction in detonation spraying process. J Therm Spray Technol 5(2):185–195
98. Boulos MI (1978) Heating the powders in the fire ball of an induction plasma. IEEE Trans Plasma Sci 6:93–106

99. Gu S, McCartney DG, Eastwick CN, Simmons K (2004) Numerical modeling of in-flight characteristics of Inconel 625 particles during high-velocity oxy-fuel thermal spraying. J Therm Spray Technol 13(2):200–211
100. Boulos MI (1985) The inductively coupled R.F. (radio frequency) plasma. Pure Appl Chem 57(9):1321–1352
101. Boulos MI (1992) RF induction plasma spraying: state-of-the-art review. J Therm Spray Technol 1(1):33–40
102. Abukawa S, Takabate T, Tani K (2006) Effect of powder injection of deposit efficiency in plasma spraying. In: Marple B et al (eds) Proceedings of the 2006 international thermal spray conference. ASM International, Materials Park, OH, e-proceedings
103. Han T, Zhao Z, Gillispie BA, Smith JR (2005) Effects of spray conditions on coating formation by the kinetic spray process. J Therm Spray Technol 14(3):373–383
104. Balani K, Laha T, Agarwal A, Karthikeyan J, Munroe N (2005) Effect of carrier gases on microstructural and electrochemical behavior of cold-sprayed 1100 aluminum coating. Surf Coat Technol 195:272–279
105. Katanoda H, Hagi J, Fukuhara M (2009) One-dimensional analysis of supersonic two-stage HVOF process. J Therm Sci 18(4):332–337
106. Li M, Christofides PD (2006) Computational study of particle in-flight behavior in the HVOF thermal spray process. Chem Eng Sci 61:6540–6552
107. Vardelle M, Bossoutrot C, Renault Th, Braillard F, Hoffmann H. Dispositif et procédé de contrôle d'une projection thermique. SNECMA Services – SPCTS laboratory, published 03/03/2004, Patent n°EP:1 340 578
108. Zierhut J, Landes K, Waas C, Kutscher D, Heinrich P, Krömmer W (1999) Particle flux imaging. In: Lugscheider E (ed) ITSC99 proceedings. DVS, Düsseldorf, Germany, pp 340–344
109. Renouard-Vallet G (2004) Elaboration by plasma spraying of dense and thin (a few tens of micro meters) yttria stabilized zirconia electrolytes for SOFCs. Ph.D. thesis, University of Limoges France, 8 Feb 2004 (in French)
110. Fauchais P, Montavon G, Lima R, Marple B (2011) Engineering a new class of thermal spray nano-based microstructures from agglomerated nanostructured particles, suspensions and solutions: an invited review. J Phys D Appl Phys 44:093001 (53pp)
111. Fauchais P, Etchart-Salas R, Rat V, Coudert JF, Caron N, Wittmann-Ténèze K (2008) Parameters controlling liquid plasma spraying: solutions, sols, or suspensions. J Therm Spray Technol 17(1):31–59
112. Etchart-Salas R, Rat V, Coudert JF, Fauchais P, Caron N, Wittman K, Alexandre S (2007) Influence of plasma instabilities in ceramic suspension plasma spraying. J Therm Spray Technol 16(5–6):857–865
113. Etchart-Salas RDC (2007) Plasma spraying of suspensions of submicronic particles. Experimental and analytic approaches of phenomena implied in the reproducibility and quality of coatings (in French). Ph.D. thesis, University of Limoges, France
114. Mauer G, Vaßen R, Stöver D (2007) Comparison and applications of DPV-2000 and Accuraspray-g3 diagnostic systems. J Therm Spray Technol 16(3):414–424
115. Bissons JF, Lamontagne M, Moreau C, Pouliot L, Blain J, Nadeau F (2001) Ensemble in-flight particle diagnostics under thermal spray conditions. In: Berndt CC, Khor KA, Lugscheider EF (eds) Thermal spray 2001: new surfaces for a new millennium. ASM International, Materials Park, OH, pp 705–714
116. Streibl T, Vaidya A, Friis M, Srinivasan V, Sampath S (2006) A critical assessment of particle temperature distributions during plasma spraying: experimental results for YSZ. Plasma Chem Plasma Process 26(1):73–102
117. Colmenares-Angulo J, Shinoda K, Wentz T, Zhang W, Tan Y, Sampath S (2011) On the response of different particle state sensors to deliberate process variations. J Therm Spray Technol 20(5):1035–1048

118. Gougeon P, Moreau C (1993) In-flight particle surface temperature measurement: influence of the plasma light scattered by the particles. J Therm Spray Technol 2(3):229–233
119. Craig JE, Parker RA, Biancaniello FS, Ridder SD, Mates SP (2000) Particle temperature measurements by spectroscopic and two-wavelength streak imaging. In: Berndt CC (ed) Thermal spray: surface engineering via applied research, Montréal, QC, Canada, 8–11 May 2000. ASM International, Materials Park, OH, pp 51–56
120. Craig JE, Parker RA, Lee DY, Wakeman T, Heberlein J, Guru D (2003) Particle temperature and velocity measurements by two-wavelength streak imaging. In: Marple BR, Moreau C (eds) Thermal spray 2003: advancing the science and applying the technology, 5–8 May 2003, Orlando, FL, vol 2. ASM International, Materials Park, OH, pp 1107–1112
121. Gevelber M, Wroblewski D, Vattiat B, Ghosh O, VanHout M, Basu SN (2008) Issues and requirements for developing a plasma spray deposition rate sensor for real-time control. In: Lugscheider E (ed) Thermal spray 2008: thermal spray crossing borders. DVS, Düsseldorf, Germany, pp 912–916
122. Wroblewski D, Reimann G, Tuttle M, Radgowski D, Cannamela M, Basu SN, Gevelber M (2010) Sensor issues and requirements for developing real-time control for plasma spray deposition. J Therm Spray Technol 19(4):723–735
123. Bach Fr-W, Möhwald K, Rothardt T, Prehm J, Engl L, Hartz K, Drössler B (2004) Particle image velocimetry in thermal spraying. Mater Sci Eng A 383:146–152
124. Marchand O, Girardot L, Planche MP, Bertrand P, Bailly Y, Bertrand G (2011) An Insight into suspension plasma spray: injection of the suspension and its interaction with the plasma flow. J Therm Spray Technol 20(6):1310–1320
125. Mates SP, Basak D, Biancaniello FS, Ridder SD, Geist J (2002) Calibration of a two-color imaging pyrometer and its use for particle measurements in controlled air plasma spray experiments. J Therm Spray Technol 11(2):195–205
126. Bisson JF, Moreau C, Dorfman M, Dambra C, Mallon J (2005) Influence of hydrogen on the microstructure of plasma-sprayed yttria-stabilized zirconia coatings. J Therm Spray Technol 14(1):85–90
127. Prystay M, Gougeon P, Moreau C (2001) Structure of plasma-sprayed zirconia coatings tailored by controlling the temperature and velocity of the sprayed particles. J Therm Spray Technol 10(1):67–75
128. Marple BR, Lima RS, Moreau C, Kruger SE, Xie L, Dorfman MR (2007) Yttria-stabilized zirconia thermal barriers sprayed using N_2-H_2 and Ar-H_2 plasmas: influence of processing and heat treatment on coating properties. J Therm Spray Technol 16(5–6):791–797
129. Tekmen C, Iwata K, Tsunekawa Y, Okumiya M (2009) Controlling graphite content in plasma sprayed cast iron coatings *via* in-flight particle diagnostic. J Mater Process Technol 209:5417–5422
130. Zhang C, Li C-J, Liao H, Planche M-P, Li C-X, Coddet C (2008) Effect of in-flight particle velocity on the performance of plasma-sprayed YSZ electrolyte coating for solid oxide fuel cells. Surf Coat Technol 202:2654–2660
131. Tekmen C, Tsunekawa Y, Okumiya M (2008) Effect of plasma spray parameters on in-flight particle characteristics and in-situ alumina formation. Surf Coat Technol 203:223–228
132. Tekmen C, Yamazaki M, Tsunekawa Y, Okumiya M (2008) In-situ plasma spraying: alumina formation and in-flight particle diagnostic. Surf Coat Technol 202:4163–4169
133. Yin Z, Tao S, Zhoua X, Ding C (2008) Particle in-flight behavior and its influence on the microstructure and mechanical properties of plasma-sprayed Al2O3 coatings. J Eur Ceram Soc 28:1143–1148
134. Wang P, Yu SCM, Ng HW (2004) Particle velocities, sizes and flux distribution in plasma spray with two powder injection ports. Mat Sci Eng A 383:122–136
135. Fang JC, Xu WJ, Zhao ZY, Zeng HP (2007) In-flight behaviors of ZrO_2 particle in plasma spraying. Surf Coat Technol 201:5671–5675
136. Shinoda K, Tan Y, Sampath S (2010) Powder loading effects of yttria-stabilized zirconia in atmospheric dc plasma spraying. Plasma Chem Plasma Process 30:761–778

137. Zhang W, Sampath S (2009) A universal method for representation of in-flight particle characteristics in thermal spray processes. J Therm Spray Technol 18(1):23–34
138. Srinivasan V, Sampath S (2010) Estimation of molten content of the spray stream from analysis of experimental particle diagnostics. J Therm Spray Technol 19(1–2):476–483
139. Lima RS, Moreau C, Marple BR (2007) HVOF-sprayed coatings engineered from mixtures of nanostructured and submicron Al_2O_3-TiO_2 powders: an enhanced wear performance. J Therm Spray Technol 16(5–6):866–872
140. Lima RS, Marple BR (2007) Thermal spray coatings engineered from nanostructured ceramic agglomerated powders for structural, thermal barrier and biomedical applications: a review. J Therm Spray Technol 16(1):40–63
141. Lima RS, Marple BR (2005) Superior performance of high-velocity oxyfuel-sprayed nanostructured TiO_2 in comparison to air plasma-sprayed conventional Al_2O_3-13TiO_2. J Therm Spray Technol 14(3):397–404
142. Lima RS, Marple BR (2008) Nanostructured YSZ thermal barrier coatings engineered to counteract sintering effects. Mater Sci Eng A 485:182–193
143. Lima RS, Marple BR (2003) High weibull modulus HVOF titania coatings. J Therm Spray Technol 12(2):240–249
144. Lima RS, Marple BR (2003) Optimized HVOF titania coatings. J Therm Spray Technol 12 (3):360–369
145. Turunen E, Varis T, Hannula S-P, Vaidya A, Kulkarni A, Gutleber J, Sampath S, Herman H (2006) On the role of particle state and deposition procedure on mechanical, tribological and dielectric response of high velocity oxy-fuel sprayed alumina coatings. Mater Sci Eng A 415:1–11
146. Planche MP, Normand B, Liao H, Rannou G, Coddet C (2002) Influence of HVOF spraying parameters on in-flight characteristics of Inconel 718 particles and correlation with the electrochemical behaviour of the coating. Surf Coat Technol 157:247–256
147. Valarezo WB, Choi W, Chi AG, Sampath S (2010) Process control and characterization of NiCr coatings by HVOF-DJ2700 system: a process map approach. J Therm Spray Technol 19 (5):852–865
148. Gaona M, Lima RS, Marple BR (2008) Influence of particle temperature and velocity on the microstructure and mechanical behaviour of high velocity oxy-fuel (HVOF)-sprayed nanostructured titania coatings. J Mater Process Technol 198:426–435
149. Lima RS, Li H, Khor KA, Marple BR (2006) Biocompatible nanostructured high-velocity oxyfuel sprayed titania coating: deposition, characterization, and mechanical properties. J Therm Spray Technol 15(4):623–627
150. Marple BR, Lima RS (2005) Process temperature/velocity-hardness-wear relationships for high-velocity oxyfuel sprayed nanostructured and conventional cermet coatings. J Therm Spray Technol 14(1):67–76
151. Pourmousa A, Mostaghimi J, Abedini A, Chandra S (2005) Particle size distribution in a wire-arc spraying system. J Therm Spray Technol 14(4):502–510
152. Planche MP, Liao H, Coddet C (2004) Relationships between in-flight particle characteristics and coating microstructure with a twin wire arc spray process and different working conditions. Surf Coat Technol 182:215–226
153. Bolot R, Planche M-P, Liao H, Coddet C (2008) A three-dimensional model of the wire-arc spray process and its experimental validation. J Mater Process Technol 200:94–105
154. Stanisic J, Kosikowski D, Mohanty PS (2006) High-speed visualization and plume characterization of the hybrid spray process. J Therm Spray Technol 15(4):750–758
155. Fauchais P, Coudert JF, Vardelle A (1997) Transient phenomena in plasma torches and in plasma sprayed coating generation. J Phys IV 7:C4184–C4198
156. Bisson JF, Gauthier B, Moreau C (2003) Effect of plasma fluctuations on in-flight particle parameters part I. J Therm Spray Technol 12(1):38–43
157. Bisson JF, Moreau C (2003) Effect of direct-current plasma fluctuations on in-flight particle parameters: part II. J Therm Spray Technol 12(2):258–264

158. Nogues E, Vardelle M, Fauchais P, Granger P (2008) Arc voltage fluctuations: comparison between two plasma torch types. Surf Coat Technol 202:4387–4393
159. Goutier S, Nogue‘s-Delbos E, Vardelle M, Fauchais P (2008) Particle temperature fluctuations in plasma spraying. J Therm Spray Technol 17(5–6):895–901
160. Swank WD, Fincke JR, Haggard DC (1995) Particle temperature sensor for monitoring and control of the thermal spray process. In: Berndt CC, Sampath S (eds) Advances in thermal spray science & technology, 11–15 Sept 1995, Houston, TX. ASM International, Materials Park, OH, pp 111–116
161. Gilmore DL, Dykhuizen RC, Neiser RA, Roemer TJ, Smith MF (1999) Particle velocity and deposition efficiency in the cold spray process. J Therm Spray Technol 8(4):576–582
162. Jodoin B, Raletz F, Vardelle M (2006) Cold spray modeling and validation using an optical diagnostic method. Surf Coat Technol 200(14–15):4424–4432
163. Irissou E, Legoux J-G, Arsenault B, Moreau C (2007) Investigation of Al-Al_2O_3 cold spray coating formation and properties. J Therm Spray Technol 16(5–6):661–668
164. Legoux JG, Irissou E, Moreau C (2007) Effect of substrate temperature on the formation mechanism of cold-sprayed aluminum, zinc and tin coatings. J Therm Spray Technol 16 (5–6):619–626
165. Schwenk A, Wank A, Wallendorf T, Marke S (2010) NIR (Near-Infra-Red) sensor – an alternative diagnostic tool for the online process control of thermal spray processes. In: Thermal spray: global solutions for future applications. DVS-Berichte, Düsseldorf, Germany, vol 264, e-proceedings
166. Li W-Y, Li C-J, Wang H-T, Li C-X, Bang H-S (2006) Measurement and numerical simulation of particle velocity in cold spraying. J Therm Spray Technol 15(4):559–562
167. Xian-Jin N, Jang J-H, Kim H-J (2007) The effects of powder properties on in-flight particle velocity and deposition process during low pressure cold spray process. Appl Surf Sci 253:7449–7455
168. Raletz F, Vardelle M, Ezo’o G (2006) Critical particle velocity under cold spray conditions. Surf Coat Technol 201:1942–1947
169. Fauchais P, Vardelle M (2003) How to improve the reliability and reproducibility of plasma sprayed coatings. In: Marple BR, Moreau C (eds) Thermal spray 2003: advancing the science and applying the technology. ASM International, Materials Park, OH, pp 1165–1173
170. Vaidya A, Streibl T, Li L, Sampath S, Kovarik O, Greenlaw R (2005) An integrated study of thermal spray process–structure–property correlations: a case study for plasma sprayed molybdenum coatings. Mater Sci Eng A 403:191–204
171. Li L, Vaidya A, Sampath S, Xiong H, Zheng L (2006) Particle characterization and splat formation of plasma sprayed zirconia. J Therm Spray Technol 15(1):97–105
172. Montavon G, Berndt CC, Coddet C, Sampath S, Herman H (1997) Quality control of the intrinsic deposition efficiency from the controls of the splat morphologies and the deposit microstructure. J Therm Spray Technol 6(2):153–165
173. Sampath S, Jiang X (2001) Splat formation and microstructure development during plasma spraying: deposition temperature effects. Mater Sci Eng A304–306:144–150
174. Syed AA, Denoirjean A, Hannoyer B, Fauchais P, Denoirjean P, Khan AA, Labbe JC (2005) Influence of substrate surface conditions on the plasma sprayed ceramic and metallic particles flattening. Surf Coat Technol 200(7):2317–2331
175. Fauchais P, Fukumoto M, Vardelle A, Vardelle M (2004) Knowledge concerning splat formation : an invited review. J Therm Spray Technol 13(3):337–360
176. Chandra S, Fauchais P (2009) Formation of solid splats during thermal spray deposition. J Therm Spray Technol 18(2):148–180
177. Gill SC, Clyne TW (1990) Stress distribution and material response in thermal spraying of metallic and ceramic deposits. Met Trans 21B:377–385
178. Neiser RA, Smith MF, Dykhuisen RC (1998) Oxidation in wire HVOF-sprayed steel. J Therm Spray Technol 7(4):537–545

179. Espie G, Denoirjean A, Fauchais P, Labbe JC, Dubsky J, Schneeweiss O, Volenik K (2005) In-flight oxidation of iron particles sprayed using gas and water stabilized plasma torch. Surf Coat Technol 195:17–28
180. Syed AA, Denoirjean A, Fauchais P, Labbe JC (2006) On the oxidation of stainless steel particles in the plasma jet. Surf Coat Technol 200:4368–4382
181. Trifa F-I, Montavon G, Coddet C (2007) Model-based expert system for design and simulation of APS coatings. J Therm Spray Technol 16(1):128–139
182. Schmidt T, Gärtner F, Kreye H (2006) New developments in cold spray based on higher gas and particle temperatures. J Therm Spray Technol 15(4):488–494
183. Hugot F, Patru J, Fauchais P, Bianchi L (2007) Modelling of a substrate thermomechanical behavior during plasma spraying. J Mater Process Technol 190(1–3):317–323
184. Monerie-Moulins F (1993) Contribution to the study of heat fluxes imposed by plasma spraying on substrates and coatings. Ph.D. thesis, University of Limoges
185. Lugscheider E, Ladru F, Fischer A, Herbst C (1998) Plasma sprayed ceramic coatings for electrical purposes—necessity of process control. In: Proceedings of the 24th annual conference of the IEEE industrial electronics society, Aachen, Germany, pp 2284–2289
186. Honner M, Cerveny P, Franta V, Cejka F (1998) Heat transfer during HVOF deposition. Surf Coat Technol 106:94–99
187. Fauchais P, Rat V, Delbos C, Fazilleau J, Coudert JF, Chartier T, Bianchi L (2005) Understanding of suspension dc plasma spraying of finely structured coating for SOFC. IEEE Trans Plasma Sci 33(2):920–930
188. Pawlowski L. The science and engineering of thermal spray coatings. Wiley, New York, NY (1995) and also the revised version. Wiley, Apr 30, 2008, 656 pages
189. Oberste-Berghaus J, Legoux J-G, Moreau C (2005) Injection conditions and in-flight particle states in suspension plasma spraying of alumina and zirconia nano-ceramics. In: ITSC 2005, Düsseldorf, Germany. DVS, 2005, e-proceedings
190. Vardelle M, Renault T, Fauchais P (2002) Choice of an IR pyrometer to measure the surface temperature of a coating during its formation in air plasma spraying. High Temp Mater Process 6(4):469–490
191. Moulla L, Salhi Z, Planche MP, Cherigui M, Coddet C (2005) On the measurement of substrate temperature during thermal spraying. In: Lugscheider E (ed) Thermal spray connects: explore its surfacing potential. DVS, Düsseldorf, Germany, pp 679–683
192. Doubenskaia M, Bertrand P, Smurov I (2006) Pyrometry in laser surface treatment. Surf Coat Technol 201:1955–1961
193. Weisheng X, Zhang H, Wang G, Yang Y (2009) A novel integrated temperature investigation approach of sprayed coatings during APS process. J Mater Process Technol 209:2897–2906
194. Lugscheider E, Ladru F, Gourlaouen V, Gualco C (1998) Enhanced atmospheric plasma spraying of thick TBCs by improved process control and deposition efficiency. In: Coddet C (ed) Thermal spray: meeting the challenges of the 21st century. ASM International, Materials Park, OH, pp 1583–1588
195. Friedrich CJ, Gadow R, Killinger A, Li C (2001) IR thermographic imaging-a powerful tool for on-line process control of thermal spraying. In: Berndt CC, Khor KA, Lugscheider EF (eds) Thermal spray 2001: new surfaces for a new millennium. ASM International, Materials Park, OH, pp 779–786
196. Verdy C, Serio B, Coddet C (1998) In situ temperature measurement using embedded microthermocouples in vacuum plasma sprayed multi-layered structures. In: Coddet C (ed) Thermal spray: meeting the challenges of the 21st century. ASM International, Materials Park, OH, pp 821–824
197. Salimijazi HR, Pershin L, Coyle TW, Mostaghimi J, Chandra S, Lau YC, Rosenzweig L, Moran E (2007) Measuring substrate temperature variation during application of plasma-sprayed zirconia coatings. J Therm Spray Technol 16(4):580–587

198. Jiang X, Matejicek J, Sampath S (1999) Substrate temperature effects on the splat formation, microstructure development and properties of plasma sprayed coatings. Part II: case study for molybdenum. Mater Sci Eng A272:189–198
199. Zhang W, Wei GH, Zhang H, Zheng LL, Welch DO, Sampath S (2007) Toward the achievement of substrate melting and controlled solidification in thermal spraying. Plasma Chem Plasma Process 27:717–736
200. Kuroda S, Fukushima T, Kitahara S (1988) Simultaneous measurement of coating thickness and deposition stress during thermal spraying. Thin Solid Films 164:157–163
201. Kuroda S, Clyne TW (1991) The quenching stress in thermally sprayed coatings. Thin Solid Films 200:49–66
202. Kuroda S, Dento T, Kitahara S (1995) Quenching stress in plasma sprayed coatings and its correlation with the deposit microstructure. J Therm Spray Technol 4(1):75–84
203. Clyne TW, Gill SC (1996) Residual stresses in thermal spray coatings and their effect on interfacial adhesion. J Therm Spray 5(4):401–418
204. Renault T, Vardelle M, Fauchais P, Hoffman H, Braillard F (2001) On-line monitoring (SDC) through coating surface temperature of residual stresses in APS WC-Co 17 wt % coatings on Hastelloy X. In: Berndt CC (ed) Thermal spray: new surfaces for a new millenium. ASM International, Materials Park, OH, pp 743–750
205. Sampath S, Matejicek J (2002) Method and apparatus for determining process-induced stresses and elastic modulus of coatings by in situ measurement. U.S. Patent 6,478,875
206. Matejicek J, Sampath S (2003) In situ measurement of residual stresses and elastic moduli in thermal sprayed coatings – part 1: apparatus and analysis. Acta Materiala 51(3):863–872
207. Matejicek J, Sampath S, Gilmore D, Neiser R (2003) In Situ measurement of residual stresses and elastic moduli in thermal sprayed coatings – part 2: processing effects on properties of Mo coatings. Acta Mater 51(3):873–885
208. Kesler O, Matejicek J, Sampath S, Suresh S, Gnaeupel-Herold T, Brand PC, Prask HJ (1998) Measurement of residual stress in plasma-sprayed metallic, ceramic and composite coatings. Mater Sci Eng A257:215–224
209. Liu Y, Nakamura T, Srinivasan V, Vaidya A, Gouldstone A, Sampath S (2007) Non-linear elastic properties of plasma-sprayed zirconia coatings and associated relationships with processing conditions. Acta Materialia 55:4667–4678
210. Li J, Bolot R, Liao H, Coddet C (2004) Numerical study of residual stresses formation during the APS process. In: Thermal spray solutions, advances in technology and application, Osaka, Japan. ISBN 3-87155-792-7
211. Nadeau A, Pouliot L, Nadeau F, Blain J, Berube SA, Moreau C, Lamontagne M (2006) A new approach to online thickness measurement of thermal spray coatings. J Therm Spray Technol 15(4):744–749
212. Floristán M, Montesinos JA, García-Marín JA, Killinger A, Gadow R (2012) Robot trajectory planning for high quality thermal spray coating processes on complex shaped components. In: ITSC 2012. ASM International, Materials Park, OH, e-proceedings
213. Deng SH, Cai ZH, Fang DD, Liao HL, Montavon G (2012) Application of robot offline programming in thermal spraying. J Therm Spray Technol 206(19–20):3875–3882
214. Friis M, Persson C, Wigren J (2001) Influence of particle in-flight characteristics on the microstructure of atmospheric plasma sprayed yttria stabilized ZrO_2. Surf Coat Technol 141:115–127
215. Basu SN, Ye G, Cui C, Gevelber M et al (2003) Plasma sprayed coatings with engineered microstructures. In: Marple BR, Moreau C (eds) Advancing the science and applying the technology. ASM International, Materials Park, OH
216. Gevelber M, Cui C, Vattiat B, Fieldman Z, Wroblewski D, Basu S (2005) Real time control for plasma spray: sensor issues, torch nonlinearites, and control of coating thickness. In: Lugsheider E (ed) ITSC 2005 proceedings. DVS, Düsseldorf, Germany, e-proceedings

217. Renault T (2001) Control of properties of thermal sprayed coatings: development of a diagnostic sensor of the process working in spray booths on industrial site, 17 Oct 2001. University of Limoges, France (in French)
218. Vaidya A, Srinivasan V, Streibl T, Friis M, Chi W, Sampath S (2008) Process maps for plasma spraying of yttria-stabilized zirconia: an integrated approach to design, optimization and reliability. Mater Sci Eng A 497:239–253
219. Liu YJ, Nakamura T, Dwivedi G, Valarezo A, Sampath S (2008) Anelastic behavior of plasma-sprayed zirconia coatings. J Am Ceram Soc 91(12):4036–4043
220. Guessasma S, Montavon G, Coddet C (2004) Neural computation to predict in-flight particle characteristic dependences from processing parameters in the APS process. J Therm Spray Technol 13(4):570–585
221. Kanta A-F, Montavon G, Planche M-P, Coddet C (2009) In-flight and upon impact particle characteristics modelling in plasma spray process. Surf Coat Technol 203:3361–3369
222. Liu T, Planche M-P, Deng S, Montavon G, Kanta A-F (2012) Spray operating parameters optimization based on artificial intelligence during plasma process. In: Lima RS et al (eds) Thermal spray 2012: proceedings. ASM International, Materials Park, OH, pp 562–567
223. Kanta A-F, Montavon G, Vardelle M, Planche M-P, Berndt CC, Coddet C (2008) Artificial Neural networks vs. fuzzy logic: simple tools to predict and control complex processes—application to plasma spray processes. J Therm Spray Technol 17(3):365–376
224. Ogaji SOT, Marinai L, Sampath S, Singh R, Prober SD (2005) Gas-turbine fault diagnostics: a fuzzy-logic approach. Appl Energy 82(1):81–89
225. Kirner S, Hartz-Behrend K, Zierhut J, Schein J (2012) Control of wire arc spray process using artificial neural networks in connection with a particle flux imaging system. In: 12th high technologies plasma processes, Bologna, Italy, 24–29 June 2012
226. Vardelle A, Vardelle M, Zhang H, Themelis NJ, Gross K (2002) Volatilization of metal powders in plasma sprays. J Therm Spray Technol 11(2):244–252
227. Gross KA, Fauchais P, Vardelle M, Tikkanen J, Keskinen J (1997) Vaporization and ultra-fine particle generation during the plasma spraying process. In: Berndt CC (ed) Thermal spray: a united forum for scientific and technological advances. ASM International, Materials Park, OH, pp 543–549
228. Fauchais P (2004) Understanding plasma spraying. J Phys D 37:86–108
229. Gawne DT, Griffiths BJ, Dong G (1995) Splat morphology and adhesion of thermally sprayed coatings. In: Ohmori A (ed) Thermal spraying: current status and future trends, Kobe, Japan, 1995. High Temperature Society of Japan, pp 779–784
230. Trice RW, Faber KT (2000) Role of lamellae morphology on the microstructural development and mechanical properties of small-particle plasma-sprayed alumina. J Am Ceram Soc 83(4):889–896
231. Ctibor P, Lechnerová R, Beneš V (2006) Quantitative analysis of pores of two types in a plasma-sprayed coating. Mater Charact 56:297–304
232. Otsubo F, Era H, Kishitake K (2000) Interface reaction between nickel-base self-fluxing alloy coating and steel substrate. J Therm Spray Technol 9(2):259–263
233. Chraska T, Kinh AH (2002) Effect of different substrate conditions upon interface with plasma sprayed zirconia. a tem study. Surf Coat Technol 157(2–3):238–46
234. Tran ATT, Hyland MM, Qiu T, Withy B, James BJ (2008) Effects of surface chemistry on splat formation during plasma spraying. J Therm Spray Technol 17(5–6):637–645
235. Brossard S, Munroe PR, Tran ATT, Hyland MM (2010) Study of the splat formation for plasma sprayed NiCr on aluminum substrate as a function of substrate condition. Surf Coat Technol 204:2647–2656
236. Brossard S, Munroe PR, Tran ATT, Hyland MM (2010) Study of the effects of surface chemistry on splat formation for plasma sprayed NiCr onto stainless steel substrates. Surf Coat Technol 204:1599–1607

237. Bolelli G, Kazi Sabiruddin L, Lusvarghi E, Gualtieri E, Valeri S, Bandyopadhyay PP (2010) FIB assisted study of plasma sprayed splat–substrate interfaces: NiAl–stainless steel and alumina–NiAl combinations. Surf Coat Technol 205:363–371
238. Brossard S, Munroe PR, Tran ATT, Hyland MM (2010) Study of the splat microstructure, splat-substrate interface, and the effects of substrate heating on the splat formation for Ni-Cr particles plasma sprayed on to aluminum substrates. J Therm Spray Technol 19 (5):1115–1130
239. Brossard S, Munroe PR, Tran AT, Hyland MM (2010) Study of the splat microstructure and the effects of substrate heating on the splat formation for Ni-Cr particles plasma sprayed onto stainless steel substrates. J Therm Spray Technol 19(5):1100–1114
240. Tran ATT, Hyland MM (2010) The role of substrate surface chemistry on splat formation during plasma spray deposition by experiments and simulations. J Therm Spray Technol 19 (1–2):11–23
241. Tran ATT, Hyland MM, Kentaro Shinoda, Sampath S (2011) Influence of substrate surface conditions on the deposition and spreading of molten droplets. Thin Solid Films 519:2445–2456
242. Balic EE, Hadad M, Bandyopadhyay PP, Michler J (2009) Fundamentals of adhesion of thermal spray coatings: adhesion of single splats. Acta Materialia 57:5921–5926
243. Armster SQ, Delplanque J-P, Rein M, Lavernia EJ (2002) Thermo-fluid mechanisms controlling droplet based materials processes. Int Mater Rev 7(6):265–301
244. Dhiman R, McDonald A, Chandra S (2007) Predicting splat morphology in a thermal spray process. Surf Coat Technol 201:7789–8801
245. Chang-Jiu L, Li J-L (2004) Transient contact pressure during flattening of thermal spray droplet and its effect on splat formation. J Therm Spray Technol 13(2):229–238
246. McDonald A, Xue M, Chandra S, Mostaghimi J, Moreau C (2007) Modeling fragmentation of plasma-sprayed particles impacting on a solid surface at room temperature. C R Mecanique 335:351–356
247. Lahmar-Mebdoua Y, Vardelle A, Fauchais P, Gobin D (2010) Modelling the nucleation process in alumina lamellae deposited on a steel substrate. Int J Therm Sci 49:522–528
248. Kudinov VV et al (1981) High Temperature Dust Laden Jets. VSL, NL: 381–392
249. Shinoda K, Murakami H, Kuroda S, Takehara K, Oki S (2008) In situ visualization of impacting phenomena of plasma-sprayed zirconia: from single splat to coating formation. J Therm Spray Technol 17(5–6):623–630
250. Mehdizadeh NZ, Lamontagne M, Moreau C, Chandra S, Mostaghimi J (2005) Photographing impact of molten molybdenum particles in a plasma spray. J Therm Spray Technol 14 (2):354–361
251. McDonald A, Lamontagne M, Chandra S, Moreau C (2006) Photographing impact of plasma sprayed particles on metal substrates. J Therm Spray Technol 15(4):708–716
252. Goutier S, Vardelle M, Labbe JC, Fauchais P (2011) Flattening and cooling of millimeter- and micrometer-sized alumina drops. J Therm Spray Technol 20(1–2):59–67
253. Dhiman R, McDonald A, Chandra S (2007) Predicting splat morphology in a thermal spray process. Surf Coat Technol 201:7789–7801
254. Yang K, Ebisuno Y, Tanaka K, Fukumoto M, Yasui T, Yamada M (2011) Verification the flattening behavior of thermal-sprayed particles and free-falling droplets through controlling ambient pressure. Surf Coat Technol 205(13–14):3816–3823
255. Heichal Y, Chandra S (2005) Predicting thermal contact resistance between molten metal droplets and a solid surface. J Heat Transfer 127:1269–1275
256. Cedelle J, Vardelle M, Fauchais P (2006) Influence of stainless steel substrate preheating on surface topography and on millimeter- and micrometer-sized splat formation. Surf Coat Technol 201:1373–1382
257. Fukumoto M, Yang K, Tanaka K, Usami T, Yasui T, Yamada M (2011) Effect of substrate temperature and ambient pressure on heat transfer at interface between molten droplet and substrate surface. J Therm Spray Technol 20(1–2):48–58

258. Goutier S. Experimental study of impact and solidification of metal and ceramic liquid particles micrometer and millimeter sized on different types of substrates: understanding of the thermal sprayed coatings formation. Ph.D. thesis, University of Limoges, France, 1 Dec 2010 (in French)
259. Trompetter W, Hyland M, McGrouther D, Munroe P, Markwitz A (2006) Effect of substrate hardness on splat morphology in high-velocity thermal spray coatings. J Therm Spray Technol 15(4):663–669
260. Dykhuizen RC, Smith MF, Gilmore DL, Neiser RA, Jiang X, Sampath S (1999) Impact of high velocity cold spray particles. J Therm Spray Technol 8(4):559–564
261. Sakaki K, Shimizu Y (2001) Effect of the increase in the entrance convergent section length of the gun nozzle on the high-velocity oxygen fuel and cold spray process. J Therm Spray Technol 10(3):487–496
262. Li C-J, Yang G-J, Gao P-H, Ma J, Wang Y-Y, Li C-X (2007) Characterization of nanostructured WC-Co deposited by cold spraying. J Therm Spray Technol 16(5–6):1011–1020
263. Zhang D, Shipway PH, McCartney DG (2007) Cold gas dynamic spraying of aluminum: the role of substrate characteristics in deposit formation. J Therm Spray Technol 14(1):109–116
264. Richer P, Jodoin B, Ajdelsztajn L, Lavernia EJ (2006) Substrate roughness and thickness effects on cold spray nanocrystalline Al-Mg coatings. J Therm Spray Technol 15(2):246–254
265. Champagne VK Jr, Helfritch D, Leyman P, Grendahl S, Klotz B (2005) Interface material mixing formed by the deposition of copper on aluminum by means of the cold spray process. J Therm Spray Technol 14(3):330–254
266. Fukumoto M, Wada H, Tanabe K, Yamada M, Yamaguchi E, Niwa A, Sugimoto M, Izawa M (2007) Effect of substrate temperature on deposition behavior of copper particles on substrate surfaces in the cold spray process. J Therm Spray Technol 16(5–6):643–650
267. Trompetter WJ, Hyland M, Munroe P, Markwitz A (2005) Evidence of mechanical interlocking of NiCr particles thermally sprayed onto Al substrates. J Therm Spray Technol 14(4):524–529
268. Klinkov SV, Kosarev VF (2006) Measurements of cold spray deposition efficiency. J Therm Spray Technol 15(3):364–371
269. Marchand C, Vardelle A, Mariaux G, Lefort P (2008) Modelling of the plasma spray process with liquid feedstock injection. Surf Coat Technol 202:4458–64
270. Fauchais P, Vardelle A (2011) Innovative and emerging processes in plasma spraying : from micro- to nano-structured coatings. J Phys D Appl Phys 44:1–14
271. Fauchais P, Joulia A, Goutier S, Chazelas C, Vardelle M, Vardelle A, Rossignol S (2013) Suspension and solution plasma spraying. J Phys D Appl Phys 46:2240 (14pp)
272. Soysal D, Ansar A (2013) A new approach to understand liquid injection into atmospheric plasma jets. Surf Coat Technol 220:187–190
273. VandenBergh Mo (2009) Sprayed particle diagnostics. Spraytime 16(1):9–12

Chapter 17
Process Integration

Abbreviations

APS	Atmospheric plasma spraying
c.w.	Continuous wave
dBA	Decibel A: weighting in noise measurements
d.c.	Direct current
DLR	German aerospace research center
EB-PVD	Electron beam-physical vapor deposition
FS	Flame sprayed
HEPA	High-efficiency particulate air class filters
HIP	Hot isostatic pressing
HVOF	High-velocity oxy-fuel flame
IR	Infra red
LC	Laser-cladding
LEV	Local exhaust ventilation
LPPS	Low-pressure plasma spraying
LRmC	Laser-remelted coatings
MS-SOFC	Metal supported solid oxide fuel cells
NIOSH	National Institute of Occupational Safety and Health
NRR	Noise reduction rating
OV/P-100	Filters for organic vapor, P oil-proof, 100 corresponds to 99.97 % efficiency
PLCs	Programmable logic controllers
PRPE	Personal respiratory protective equipment
RCF	Rolling contact fatigue
SPS	Spark plasma sintering
UV	Ultra violet

P.L. Fauchais et al., *Thermal Spray Fundamentals: From Powder to Part*,
DOI 10.1007/978-0-387-68991-3_17, © Springer Science+Business Media New York 2014

TBC	Thermal barrier coating
VPS	Vacuum plasma spraying
YPSZ	Yttria partially stabilized zirconia
YSZ	Yttria-stabilized zirconia

17.1 Introduction

This section is devoted to important items that are not directly linked to the different spray processes, the coating formation and applications, but without which coatings production could not exist. As all industrial processes, thermal spray induces potential risks due to gases and powders used, vapors and dusts produced, noise, radiation, high temperatures of the different processes, electrical equipment, use of robots,... Such risks must be prevented not only by individual protections but also mainly by using especially designed enclosures (spray booth), with adapted exhaust and ventilation systems.

Moreover in most cases, coatings are not usable as-sprayed because the dimensions cannot be as precise as requested by specifications, they might be too porous, not enough impervious to gases, liquids,... Thus they have to be machined to achieve the right dimensions, densified for a better wear resistance, sealed to improve their corrosion resistance.

In the following after the description of the different risks induced by thermal spraying, what is called the ancillary equipments (spray booth, ventilation, filters, robots,...) will be described. A special session will then be devoted to the specific equipments for vacuum and inert plasma spraying. The chapter will end with the different machining techniques and processes used for the post-treatment of coatings.

17.2 Potential and Real Risks

As underlined by Montavon and Gross [1]: "Safety of both research and production thermal spray facilities is a major interest of managers, workers, and also environmental, health, and safety regulating bodies around the world." Any activity, and of course thermal spraying, presents a certain level of risks that are either acceptable or unacceptable and must be assessed. For a safer work environment, a plan of action must be put in place to control unacceptable risks [2]. The most important risks are those linked to respiratory problems compared to those due to noise, radiation, explosion, electrocution, and burn. They will be presented successively before the description of the prevention and safety measures.

17.2.1 Powders: Respiratory Problems and Explosions

Thermal spray processes involve powders with sizes in:

– The micro-size range (from a few μm to about 200 μm) corresponding to those sprayed.
– The sub-micro-size range resulting mainly from dusts formed by particle evaporation during spraying, thus consisting of oxide particles, or from particles splashing upon flattening or from particles that after traveling in the jet fringes (poor penetration of the smallest injected ones) rebound on the coating.
– Nano-size range produced when nanometer-sized particles formed from suspensions or solutions travel in the jet fringes and, due to their too low velocity, follow the flow and do not impact on the substrate (Stokes effect).

However powders used to spray are not the only ones to be considered; other activities linked to thermal spraying can also generate particles and/or fumes:

– Grit blasting generates fine particles of the grit medium and of the substrate, the worst case being a cloud of silicon dioxide particles.
– Loading and emptying grit blast cabinets, loading, unloading, and cleaning hoppers, cleaning operations within the thermal spray enclosure.
– Vapors from solvents can also be produced when used during the part-cleaning process.

17.2.1.1 Particles and Pulmonary System

The main risk with particles is their inhalation [3, 4] from which workers must be protected [5]. Depending on their size, particles penetrate in different regions of the tracheobronchial tree [3]:

- The large particles (average diameters ranging from 5 to 30 μm) are stopped in the pharynx.
- The medium particles (average diameters ranging from 1 to 5 μm) are deposited mostly in the trachea and the bronchi.
- The small particles (average diameters smaller than 1 μm) diffuse into the pulmonary alveoli, from which their harmful effect arises.
- Problems could be even worst with nanometer-sized particles even if the properties driving such toxic responses are yet not well understood [6, 7].

All particles penetrating at different levels are partially eliminated by phenomena called pulmonary clearance mechanisms and finally the pulmonary retention level is the deposition level minus the clearance level. Thus pulmonary retention varies as a function of the particle size and the respiratory frequency. Whatever the mode of clearance, the harmful products operate chemically on the organism, which suffers from clamping; the products also operate physically by destroying specific molecular sequences [3].

17.2.1.2 Toxicity of Powders

It is essentially chemical. However it must be underlined that if many studies have been made about the toxicity of metals in various industries, according to Hériaud-Kraemer et al. [3] no study has been conducted at the date of publication and to the knowledge of authors up to now, to specifically assess the toxicity of powders commonly used in thermal spraying. The powders the most susceptible to be dangerous are those containing nickel, cobalt, copper, aluminum, and chromium. Moreover, except aluminum, they are potential occupational carcinogens for humans. The study of Chadwick et al. [8] has shown that levels of exposure to cobalt, chromium, and nickel were highest in plasma sprayers and on occasions exceeded UK Occupational Exposure Limits. Exposure to metals during detonation gun and electric arc spraying was better controlled and levels remained below the relevant [8]. This was especially the case when spraying was performed manually or semi-automatically and where control relies on local exhaust ventilation (LEV) and personal respiratory protective equipment PRPE) [5, 8]. Legislations about the rules related to the exposure of workers to harmful products vary with countries and rely on indexes determining several admitted concentrations of a given product in the atmosphere for a given duration of exposure, permanent or not [3].

17.2.1.3 Explosiveness of Powders

Numerous feedstock powders are in an unsteady thermodynamic state [3]. An ignition source can induce the release of an enthalpy of reaction. Some powders can react explosively with water vapor or oxygen of the surrounding atmosphere; magnesium and zirconium are reactive with carbon dioxide, while aluminum and titanium are reactive with chlorine. The most critical factors [3] are the concentration of particles in the atmosphere (the critical concentration depends on the powder type), their shapes and sizes (small irregular particles are more prone to explosion than large and spherical particles), temperature, pressure, hygrometry, and nature of the ignition source. That is why the local accumulation of powder particles in hazardous areas (spray booth, spray vacuum chamber, etc.) has to be limited by frequent cleanings and appropriate ventilation [3].

The spontaneous inflammation of a powder in air at ambient temperature is defined as pyrophoricity, which differs from the autogenous ignition by the absence of temperature increase [3]. All the metallic powders, whatever their nature, except precious metals, are subjected to pyrophoricity when their sizes are sufficiently small (a few micrometers). Pyrophoricity depends on the size and shape of the particles, their specific surface (below 1 $m^2\ g^{-1}$ the potential risk increases drastically), and oxidation enthalpy.

17.2.2 Gases

However if powders are probably the main risk, spray gases (Ar, N_2, H_2, methane, acetylene,...) and those resulting from the process (CO_2, CO, NO,...) also contribute to hazardous risks.

17.2.2.1 Gases Used for the Spray Process

Problems with gases used for spray processes are the following [9–12]:

- When nonreactive gases at room temperature (nitrogen, argon, and helium), which are inert, colorless, and tasteless, are trapped in a confined area, thus reducing the oxygen normal content (21 vol.%) below 19.5 vol.%, it may result successively in dizziness, unconsciousness, and finally death. When breathing air where oxygen is below 16 vol.%, a person is mentally incapable of diagnosing the situation. The stagnation of argon is the more important because it is heavier than air, but that of nitrogen is almost the same, because its weight is close (only slightly lighter) to that of air. Helium, according to its weight, accumulates in the upper parts of the confined area.
- Pure oxygen gas, used for combustion, is inert, colorless, and tasteless. It is a local irritant to mucous membranes and can result in destruction of lung tissue. It lowers drastically the ignition point of flammable materials (an enrichment of a few % considerably increases the risk of fire) and supports and accelerates the combustion. Oxygen reacts with most organic materials, especially hydrocarbons. Compounds like grease and oil may ignite spontaneously when subjected to oxygen-enriched atmosphere. Cloths saturated with oxygen are highly flammable and may be very easily ignited.
- Combustible gases are flammable and susceptible of explosions (see Sect. 3.1.3.3). The main hazards with these gases are due to their flammability. Table 17.1 from [11] summarizes properties of fuel gases.

However, the ignition energy is also an important parameter to consider, that of hydrogen and acetylene being very low, as shown in Table 17.2.

At last it must be kept in mind that when combustion occurs in a confined area it can displace oxygen needed for breathing.

Table 17.1 Properties of fuel gases mostly used in spray processes [10] (Courtesy of Linde)

		Flammability vol. %		Auto-ignition T (°C)	
	Specific gravity (air =1)	Air	O_2	Air	O_2
Hydrogen	0.0696	4–75	4–94	572	560
Acetylene	0.908	2–82	2–93	305	296
Methane	0.555	5–15	5–60	580	555
Propane	1.550	2.2–9.5	2.3–45	480	470
Propylene	1.476	2–10.5	2.1–53	460	

Table 17.2 Minimum ignition energies of combustible gases mainly used in spray processes (mJ). Reprinted with kind permission of Elsevier [11]

Fuel gas	Ignition energy (mJ)
Hydrogen	0.02
Acetylene	0.02
Methane	0.29
Propane	0.25
Propylene	0.27

- Hydrogen, which is the lightest gas (twice less weight than helium), is colorless, tasteless, and odorless. It burns with an almost invisible flame, making it difficult to see.
- Acetylene (C_2H_2), lighter than air (see Table 17.1), with an odor close to that of garlic, is a very unstable gas that can easily decompose to the point of a deflagration being started (without the presence of air) that will rapidly progress into an explosive detonation. It is also highly explosive with copper, silver, and mercury as well as their salts and compounds.
- Natural gas (CH_4), lighter than air (see Table 17.1), has a faintly disagreeable odor and breathing moderate concentrations can cause drowsiness and dizziness. Typically an identifying odor is added to help in identifying any leakage
- Propane (C_3H_8) heavier than air (see Table 17.1) is a colorless gas, easily liquefied, with a faintly disagreeable odor but, as for methane, identifying odor is added to help in identifying any leakage. It is mostly transported as liquid.
- Propylene (C_3H_6) heavier than air (see Table 17.1) is a colorless gas, easily liquefied, with a faintly sweet odor. At atmospheric pressure and room temperature, propylene is nontoxic. Short-term overexposure to fumes may have anesthetic effects, cause dizziness, nausea, and dryness or irritation of nose; longer-term exposure may cause liver damage.
- Kerosene is a clear, water-white liquid combustible with a mild characteristic odor. A low energy spark (static electricity, for example) can ignite very easily its vapor and thus it must be kept away from sources of ignition.

17.2.2.2 Gases Resulting from the Spray Process

Gases such as nitrogen oxides (NO, NO_2) and phosgene ($COCl_2$) can be produced during the spray process. The nature of the respiratory attack is a function of the spot of action of these harmful substances. Nitrogen oxides and phosgene are insoluble substances penetrating very deeply into the tracheobronchial tree, deep enough to reach the alveoli. The symptoms observed in acute harmful effects range from irritation syndrome to pulmonary edema [3].

Carbon oxide gases (CO and CO_2) are combustion products (as water vapor, which is harmless). CO_2, nonreactive gas heavier than air and corresponding to complete combustion of carbon, can cause asphyxiation and death in confined and poorly ventilated local. CO_2 ice is currently used to cool substrate and coating during the spray process and the resulting CO_2 gas has the same effects as those

resulting from combustion products. The story is worst with carbon monoxide CO (resulting from incomplete carbon combustion), which is colorless, odorless, and tasteless, but highly toxic. It combines with hemoglobin to produce carboxyl-hemoglobin, which is ineffective for delivering oxygen to bodily tissues. Concentrations, as low as 667 ppm, may cause up to 50 % of the body's hemoglobin to convert to carboxyl-hemoglobin. A level of 50 % carboxyl-hemoglobin may result in seizure, coma, and fatality. For example in the USA, the OSHA limits long-term workplace exposure levels above 50 ppm.

17.2.2.3 Gases Storage

Five types of spray gas installations are used:

- Cryogenic liquid tanks (mainly argon, nitrogen, oxygen, and hydrogen)
- Pressurized liquid tanks (propane and propylene)
- Cylinders containing gas dissolved in solvent (acetylene)
- High-pressure cylinders (typically argon, nitrogen, oxygen, helium, and hydrogen) that can be interconnected (often twelve bottles)
- Refrigerated liquid tanks for carbon dioxide used to cool down substrate and coating during the spray process

The main risks are the following:

- Fire and asphyxiation that are by far the main ones
- Liquid or cold gas, especially oxygen, can cause severe frostbite to eyes or skin; of course it is the same with CO_2 ice. Although some local pain may be experienced initially, frozen tissues are painless and a casualty might be unaware. Breathing very cold vapor can cause damage to lungs. At last, unprotected skin coming in contact with un-insulated items of cold equipment (pipe for example) may stick fast and flesh may be torn on removal
- Short-term exposure to propylene fumes may have anesthetic effect

17.2.3 Prevention and Safety Measures

It must be kept in mind that adequate ventilation can eliminate many health and safety concerns. One of the most important protections for workers is performing the spray process in spray booths, provided that, before entering the spray booth after coating a part, a sufficient time elapsed until several air exchanges have been completed. In all other cases either for spraying or cleaning or loading and emptying powders, workers must wear an adequate protection [5].

17.2.3.1 Powders

Two cases must be considered: spraying in spray booth and manual spraying.

Automated spray booths (see Sect. 17.4.1) are well-ventilated areas where no worker is present during spraying. They are connected to dry filtering systems and the spray booth as well as the dry filtering system (typically every 3 months) is cleaned regularly. The efficiency of the filtering systems is also annually checked. Depressions are generated in the spray booths to keep the possible leaks at the lowest possible level. Nonautomated spray booths are connected to a wet filtering system.

In case of manual spraying, on site or nonautomated spray booth, manual sprayers must use protective equipment. While working in the open or in well-ventilated spaces, a simple dust mask may be sufficient. Otherwise semi-disposal masks, full face, are needed, when the contaminant in the air can harm eyes or the face.

Air-purifying respirators are typically negative pressure units in which the user's inhalation draws contaminated air in through a filtration medium and exhalation pushes air out through one-way valves back into the atmosphere [5]. Filtering cartridges can protect either from dust or solvent or chemical products. However, the replaceable filter cartridges must be regularly changed. They can be combined for removing suspended particles and organic vapors. Of course the mask must properly fit and maintained. As a minimum [13] negative pressure half-mask respirator equipped with OV/P-100 filters should be used. OV stands for organic vapor, the P stands for oil-proof, and the 100 stands for 99.97 % efficient against solid or liquid particles, including oil-based particles. These are HEPA-class filters (High-Efficiency Particulate Air) approved for protection against dust, fumes, and mists that have a time-weighted average of less than 0.05 mg per cubic meter or two million particles per cubic foot. These filters generally are color-coded magenta and gray with a black National Institute of Occupational Safety and Health (NIOSH) label. Filters whose elements are encased in a plastic or metal container offer more protection against the open flames and sparks generated by thermal spray processes than low-profile filters with cloth or paper exteriors. If low-profile filters are used, a spark shield should be installed over the element [13]. At last when spraying nanometer-sized particles, filters must be adapted.

If necessary, an air-supplied respirator can be used where the worker wears a half- or full-face mask with breathable air supplied via a pressurized airline. The air must be supplied by a devoted compressor with its own piping system and never for example by the air to run the grit blaster [5].

To find the related standards and documents see the guidelines of Wuest et al. [5].

17.2.3.2 Gases

For process gas supply, from gas storage to spay torches, through piping, pressure relief valves, vents, valves, regulators, flow meters, connections, and hoses, many rules have been defined for safety and are summarized in [9].

For gases generated during the spray process, again good ventilation is the key issue.

Gas analyzers and combustible gas detectors are often incorporated in the design of the thermal equipment to provide information to unsafe conditions [9] when preset levels are attained. They can also be installed in gas storage local to detect leakage. In spray booth they mostly detect un-proper concentration of oxygen and the presence of unacceptable percentages of combustible or other dangerous gas. They can be connected to computerized systems to shutoff valves, ventilation, and/or alarms. They must be disposed according to the weight of the gas relatively to that of air: close to the ground for heavy gases and close to the roof for light ones. Oxygen monitors are usually placed at face level just inside the entrance to spray booths in order to give readings at the operator-breathing zone.

The interested reader will find in the guidelines of Dobler and Gifford [14] the standards, the gas characteristics and application-specific safety hazards/precautions, and a detailed description and all the recommendations to install safely:

- The bulk gas supplies installation, operation, and maintenance
- The connecting pipes (with especially the specific requirements for oxygen)
- The supply piping to the thermal spray cell
- The bulk supply operation and maintenance considerations
- Regulators, flow meters, and hoses
- Check valves, flashback arrestors, and excess flow valves
- Pressure relief valves and vents

17.2.4 Other Risks

17.2.4.1 Noise

The abrupt expansion of the high-temperature jets exiting the spray gun at atmospheric pressure (for example, velocities ranging from 400 to 2,800 m s^{-1} for plasma torches, velocities up to 1,800 m s^{-1} for HVOF spraying) generates an acoustic level far higher than the maximal permitted level of 85 dBA [11] as presented in Table 17.3.

In order to place such values relatively in relation to tolerable noise limit levels, the normal voice level is about 70 dBA, and automobiles on a highway have levels of about 100 dBA. Any exposure over 109 dBA for more than 2 min requires, according to US regulations, hearing protection and 110 dBA or higher is the case encountered with most spray processes. Over 110 dBA serious risk of permanent occupational deafness exists if no action is taken to protect the sprayers.

When spraying outside the booth, hearing protection is mandatory for workers to wear either earplugs or earmuffs with the highest Noise Reduction Rating (NRR) available. In the area of very high noise, both earplug and earmuff must be used. For more details see [5, 15]. At last increasing the distance between the noise source and the workers reduce the sound level: theoretically by 10 dBA at 3 m and 28 at 27 m.

Table 17.3 Sound levels with different spray processes. Reprinted with kind permission from Springer Science Business Media [3, 15], copyright © ASM International, Reprinted with kind permission from ASM [16]

Thermal spray device	Decibel (dBA)
Detonation gun	145
HVOF (liquid fuel)	133
HVOF (gaseous fuel)	125–135
HVAF	133
Wire flame spray	118–122
Powder flame spray	90–125
Rod flame spray gun	125
Wire arc	105–119
Air plasma spraying (APS)	110–125
Vacuum plasma spraying (VPS)	Ambient[a]
Cold spray	110 Ambient[b]
Water-stabilized plasma	125
RF plasma	Ambient[a]

[a]These processes are carried out in vacuum chambers and noise from the gun is considerably attenuated. However, the continuous noise from pumps, fans, power supply, etc., is not negligible and the personnel must be protected
[b]When the cold spray is performed in a closed enclosure in order to recycle gases, especially helium. The same remark can be made for the auxiliary equipment, as for VPS or RF spraying

17.2.4.2 Radiation

For plasma spraying in particular, but less so for flame spraying, high-temperature jets generate radiation in a broad range of wavelengths from ultraviolet (UV) to visible and infrared (IR) [3]. Plasma systems emitting radiation in the range between 280 and 220 nm are dangerous for cornea of the eye that absorbs the UV from these regions easily, leading to a condition called flash burn after prolonged exposure. The severity of flash burn depends on the duration of exposure, UV wavelengths, and the energy level at which the luminance and radiance are produced during the process. Eyes can be damaged without discomfort during exposure [3]. These UV can affect exposed skin, causing sunburn, sun tanning, and changes in skin cell growth. Repeated exposure to UV may decrease skin elasticity. This can give the appearance of premature aging and can lead to a higher risk of skin cancer. Visible and near-IR radiation can also generate an energy density that reaches the retina. When exposed to a luminous source of excessive energy density without any protection, a subject can suffer from a retinal photo-traumatic lesion known as "arc stroke." It is thus important to install UV dark glass or shades over the windows of spray booths and enclosures. Operator must never view the plume of a spray gun without adequate eye protection.

For eye protection [5], safety glass with safety frames, vinyl-framed goggles of soft pliable body design, and welders' goggles are used; such equipment being available with incremental shades of filtration. Of course lenses of eye protectors

must be kept clean. Face shields should be worn to protect eyes and face against flying particles, metal sparks, and chemical/biological splash [5]. Wuest et al. [5] present a chart for eye and face protection.

17.2.4.3 Thermal Risks

Plasma plumes or flames are directional jets; their thermal effect, caused by extreme energy density and very high temperatures, can be detected as far as 1 m past the exit of the guns [3]. The components sprayed reach temperatures from 200 °C to 500 °C in some cases. Severe burns by contact with warm parts represent the major risks encountered by the sprayers. Suitable gloves need be worn when hazards of burns and harmful temperature extremes are present [5]. Gloves must also be used for hazards from chemicals, cuts, lacerations, abrasions, punctures, and biological agents. Glove selection shall be based on performance characteristics of the gloves, conditions, duration of use, and hazards present. For more details see [5].

17.2.4.4 Electric Risks

All thermal spray equipment need electric source with proper voltage and current requirements. Electric risks are especially important with d.c. plasma guns for which a high intensity current and direct current source (i.e., a few hundreds of amperes, up to 1,000 A) are used to generate the plasma jet. Grounding of electrical cabinets, booth walls, and other metallic structures must be provided. Electrical cabinets containing electrical equipment for the control of thermal spray installations must follow regulations. The electrical installation must have overload protection and ground fault interrupters, because most spray devices use water-cooling and leaks of coolant are common, especially during maintenance [3, 4]. In general the use of electrical gloves is recommended [5].

17.2.4.5 Risks Associated with the Use of Robots

A robot arm can move very fast, up to 2 m s^{-1} or even more, and it has no detection capability, rending unavoidable the collision when someone or something is along its trajectory. That is why numerous national and international standards [3, 16] apply when a robotic system is used. Numerous emergency stops must be located on the robot control system, on its power delivery system, and near the spray booth. When an anomaly is detected, the system abruptly stops. Anti-intrusion security systems on doors are frequently implemented in thermal spray booths. When the

operator is in the booth for maintenance, the robot must be set to manual control (velocity lower than 0.25 m s^{-1}) and its control system handled by the operator. Main risks occur during maintenance or when the sprayer intervenes in the booth during production to solve a problem.

17.3 Ancillary Equipment

The necessary additional equipment to spray processes includes the spray booth, the exhaust systems, the power, gas, cooling water, and compressed air supplies, the powder feeder, and the control panel.

17.3.1 The Spray Booth

17.3.1.1 What for?

The structures of spray booths are designed to protect operators from the following major hazards [16]:

- Excessive sound levels (see Sect. 17.2.4.1).
- Powder and dust from the process (see Sect. 17.2.1): part of the particles is not treated in the spray gun and corresponds to overspray which can represent 50 % of the powder fed to the gun. Moreover particles may be partially vaporized, resulting in fumes (mostly oxides) with sizes below 1 μm. Thus high volumes of air are required to capture overspray powder and fumes to protect the operator.
- Heat and volume of hot gases produced by the spray gun (see Sects. 17.2.2.2 and 17.2.3.2) must also be handled by the exhaust system. These gases must be properly ventilated to avoid asphyxiation of operators. Some of them may also induce combustion or explosion. The heat load is moderated by diluting the heat of the jet in the high-volume exhaust airflows, which also avoids the stagnation accumulation of explosive gases in the booth.
- Visible light and ultra violet radiation (see Sect. 17.2.4.2).

The interested reader can find references of standards and documents about spray booths in the document of Gifford et al. [16].

17.3.1.2 Typical Design

The typical configuration is that schemed in Fig. 17.1 from Gifford et al. [16].

The spray booth by itself is an enclosure that works with the ventilation systems to provide an effective control of the major hazards described previously. Its size must be sufficient to allow the operator to prepare the torch and parts to be sprayed

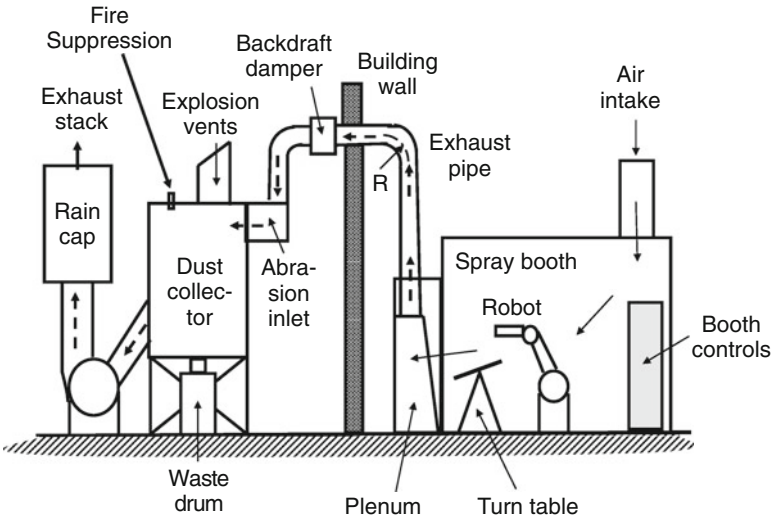


Fig. 17.1 Schematic of the spray booth and the ventilation system. Reprinted with kind permission from ASM International [16]

and to maintain the robotic equipment. It must be designed in such a way that during spraying the operator cannot be inside but control the spray operation from an adjacent room such as illustrated in Fig. 17.2 for a booth with plasma spraying. The visual control of the spray process is achieved through a window with proper radiation filters (which can include pull down shades) and sound proofing or with a CCD camera and a TV screen.

The booth comprises [16] sheet steel panels filled with nonflammable insulation (fiberglass for example) thick enough (in the range of 15 cm) to damp the sound emitted by the process down to tolerable noise limit levels. On the outer side the sheet steel panels are solid, while they are perforated toward the sound source. Detonation devices typically will require double-walled booths with a heavier mass of sound absorbent material. One of the important issues is the door design: it must be sound proof, give good access, and with interlocks to prevent the gun from starting when personnel is inside the booth. The door seals must remain tight and receive regular maintenance. This is also valid for all penetrations or openings of the booth (air inlet, etc.) and ports for continuously feeding and removing parts to increase the productivity.

The booth layout is very important to achieve the total airflow capability and the local velocities, which are critical to capture dust particles and carry them out to the filters. The respiratory ailments caused by feedstock materials appear as the major risk for operators: see, for example, the review of H. Heriaud-Kraemer et al. [3]. To get rid of dusts, the use of laminar flows is mandatory; turbulent flows often create areas where the dust is trapped. In most cases the pressure within the booth is slightly negative by adjusting the exhaust and inlet fans and dampers. This lower pressure results in an inward flow through small leaks, carrying the dust to the

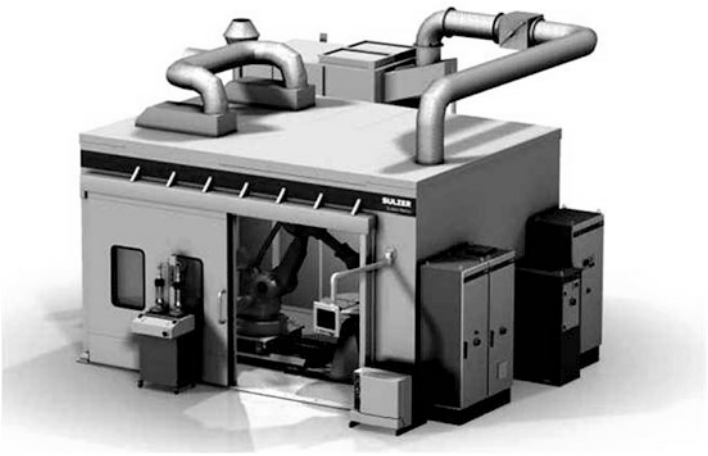


Fig. 17.2 Typical spray booth with an adjacent room for the operator (Courtesy of Sulzer Metco)

filters. At last the booth must have an entry timer to allow the ventilation system to clean the air of hazardous dust after stopping the spray gun. It is also recommended to use a dual-speed exhaust system maintaining a low level ventilation mode at all times when the booth door is open and when operators are inside the booth for maintenance and setup [16].

The air inlet can come from the inside of the building or from the outside but in the latter case consideration must be given to the heating or cooling of this air. The position of the air intake and exhaust plenums is crucial to achieve the laminar flow. It requires using an inlet plenum with many small unevenly distributed inlet air openings and fewer larger openings create turbulence. As much as possible, obstacles (cooling, parts, fixtures,...) must be out of the airflow. The exhaust plenum should be at the opposite end of the spray booth from the air intake to smoothen the flow. The plenum is generally on the wall just beyond the spray area (see, for example, Fig. 17.1). In this figure, the airflow is from the back of the gun to the front, the robot is placed near the center of the booth facing the exhaust plenum/spray hood with the part to be sprayed on the turntable between the exhaust plenum and the robot [16]. Industry standards for the face velocity through the spray booth opening recommend 61 m/min for every 929 cm^2 (1 ft^2). Suppliers and manufactures recommend increasing this airflow by 50 %. Thus a booth opening of 1.2 × 1.2 m^2 would require 91 m^3/min [16] of airflow. However, an air velocity of 91 m/min may adversely affect the spray process. Moreover the total airflow for the spray booth should provide a minimum of five exchanges of the entire booth air volume per minute, which might be difficult to achieve for large booths. The negative pressure in the booth should range from 25 to 124 Pa. The booth must also be regularly cleaned; the frequency depending on the process type, the coating material type, the part configuration, and the system.

17.3.2 Exhaust Systems

The recommended velocity inside the ductwork between the spray booth and the dust collector should be between 17.8 m/s and 20.3 m/s [16]. The lower velocity value is chosen to prevent dust deposition on the walls and the higher value to limit the air and dust momentum. The least number of bends must be used between the collector and the booth. The air velocity when entering the dust collector must be reduced to prevent the erosion of the filters and disperse the air across them. Common cartridge or bag-type filters are used to capture overspray particles and fumes. Filters must be adapted to dusts according to regulations. It is important also to remember that the position in which a filter cartridge is mounted in the dust collector has a major impact on the effectiveness of the pleated media within the filter. Secondary filters (High-Efficiency Particle Air: HEPA) are often used to enhance the cleaning efficiency (they capture 99.7 % of fine particles down to 0.3 μm). Sometimes also cyclones enable to capture large amounts of dust (especially the bigger particles) before they reach the primary dust collector. Ductwork must prevent hot particles from reaching the dust collector. A back-draft damper is recommended at the point where the ductwork leaves the building. It prevents the reverse flow of air from outside into the spray booth when the exhaust system is off and also the back flow of smoke in case of a fire in the dust collector [16]. At last the ventilation should be automatically adjusted to compensate for the loss of airflow because of the dust loading of filters increasing with the working time.

Of course filters must be cleaned or replaced regularly.

17.3.3 Power Supply

The electrical power supply for plasma torches, wire arc torches, etc., must be disposed outside the booth. Electrical cables between gun and power source must be as short as possible, and the high-frequency starter for d.c. arcs must be located as close as possible to the spray gun. This limits the antenna effect of the cables transmitting radiofrequency. For the same reason a certain distance between these cables and the metal conductors (pipes, structural support,...) must exist (depending on the frequencies involved). It is also preferable to separate electrical cabinets, consoles, or electrical boxes from an area where combustible gases are present. If a cabinet contains both combustible gas carrying components and electrical components, it must be designed with strong ventilation [16].

17.3.4 Gas Supply

A bulk supply system is a gas supply source that is permanently plumbed and has a permanent location. Sect. 17.2.2.3 summarizes the different types of gas containers and Sect. 17.2.3.2 the corresponding prevention and safety measures and at last, the reader can find detailed information in references [9, 11, 12, 17]. In spray booths one can find sophisticated gas control consoles. The safety precautions are outlined in [9]. The interested reader can also find information on the industrial gases used and quality issues in [18].

17.3.5 Compressed Air Supply

Compressed air is used in grit blasting and cooling in conjunction with the spray process. It must be free from oil, water, and other contaminates. The air is dried by cooling it down to a few °C in order to condense the water vapor. Then it passes through the oil filter, which can correctly treat only dry air. Of course the oil concentration must be low at the compressor exit. The airflow must be sufficient at the required pressure (generally below 0.1 MPa) and have a constant flow rate. Thus an air-pressurized reservoir is needed.

17.3.6 Cooling Water

Cooling water is needed for plasma, D-gun, and most HVOF spray systems. For example, if the spray gun has a power of 250 kW with a thermal efficiency of 60 % 100 kW go into the cooling water. The pressure is a key issue to increase the boiling temperature of water. Local boiling reduces the heat transfer coefficient by almost two orders of magnitude resulting in a catastrophic overheating. However if the pressure is too high it may deform parts of the gun where they are heated and special hoses are required. Thus, the pressure is generally limited to 1.7 MPa. The water temperature has to be controlled: it must be over the dew point of the environment to prevent condensation, which can be very detrimental in the anode nozzle of a plasma torch or in the chamber of HVOF, and it must be kept at a constant temperature generally 20 °C above the dew point.

Thus closed loop cooling water systems must be used with a capacity adapted to the maximum power to be removed and, if necessary, a cooling system used. At last, mineralized water is not recommended because of calcia deposits forming in the hottest area, reducing the heat transfer where it should be the highest. Deionized water is somewhat corrosive, therefore, the best is to use distilled water and monitor its electrical conductivity regularly to change it when it becomes too conductive.

17.3.7 Micrometer-Sized Powder Feeders and Solutions or Suspensions Feeders

The quality of the powder feeder is as important as that of the spray gun. It must provide a carrier gas stream with a flow rate that must be controlled independently of the powder feed rate. The powder feed stock must have a mass flow rate as constant and controlled as possible [19–21]. Three types of powder feeders are used [19]:

- Gravity-feed hoppers (the oldest one): it consists of a simple container, usually with funnel-shaped bottoms, that allows powder to flow freely, assisted by gravity from the bottom of the funnel. They are inexpensive and trouble-free, provided the feed stock powder is free flowing, but they are not accurate and it is difficult to control the gas flow independently of the powder rate.
- Volumetric powder feeders: packets of powder are delivered by a positive-displacement mechanism into a carburetor where they are picked up by the carrier gas stream. The mechanism involves a screw or a wheel rotating within a bed of powder (see Fig. 11.47). Vibrators can be used for powders with poor flow ability. Scrapers can be used to deliver a constant quantity of powder with the wheel system. Using a "cylinder mixer," which consists of a conical chamber with tangential injection and an axial exit, the powder pulsation due to the principle of the system can be damped.
- Fluidized beds: the powder is fluidized and the design is such that a controlled volume of gas powder is sampled with a tube passing through the bed at a uniform rate (see Fig. 11.49). Their operation is very much affected by the powder characteristics and particle size distribution.

The most sophisticated powder feeders have a feed rate control, achieved with a weight-loss device that uses a load cell to continuously weigh the contents of the hopper. The feed rate is determined by the rate of hopper weight-loss averaged over time. The system is capable to adjust five variations, thus keeping the feed rate constant. At last it is also possible to preheat particles before their injection [22] and according to the authors the preheated powder coatings appear to exhibit enhanced contact between grains.

For liquid injection, as explained in Sect. 4.5.1, two main techniques are used: atomization or mechanical injection. Two phenomena can occur: drops or liquid jet fragmentation into droplets on the one hand and vaporization of droplets on the other hand. Two main injection techniques are used:

- Spray atomization where a low velocity liquid is injected inside a nozzle where it is fragmented by a gas expanding within the body of the nozzle (see Sect. 4.5.1.1 and for example [23–25]). The main problems are the droplets trajectory, velocity, and diameter dispersions.
- Mechanical injection (see Sect. 4.5.1.2 and for example [26, 27]) with the use of either a magnetostrictive rod at the back side of the nozzle which superimposes pressure pulses at variable frequencies (up to a few tens of kHz) [26] or a liquid in a pressurized reservoir from where it is forced through a nozzle of given i.d.

17.3.8 Gun Movements

In spray booths many different spray guns can be used and a wide variety of torches and parts positioning equipment is used to achieve movements in X, Y, or rotary axes. The manipulation equipment is often computer controlled by specific software or hardware, and frequently an operator in close proximity defines the movement. There is a three-dimensional envelope through which the arm can move and a larger area where a safety hazard may result from unexpected arm movement with the possibility for pinch hazard reaction between the arm and other physical elements of both the interiors. Much work has been devoted to planning robotic trajectories for thermal spray deposition on different shapes [28–38].

17.3.9 Control Panel

These panels range from simple to complex [19]. The tendency is now to have closed looped, output based, or adaptive controls especially for complex processes such as plasma spraying or HVOF. These systems control gas mass flow controllers, heat exchangers, cooling water flow rate and inlet and outlet temperatures, powder feed rate controllers, motion controls, and constant current supplies. In each subsystem a set point is specified and the specific quantity is automatically maintained based on the deviation of the output value from the set point. In the advanced control panels the set points of the sub processes are established to a recapture in the computer or programmable logic controllers (PLCs). In the latest control units, the thermal spray plume can be diagnosed through the use of real-time sensor technology. By integrating spray plume monitoring and control earlier in production, greater process reliability, reduced processing time, and processing costs are realized (see Sect. 16.4). During processing, data are recorded for online control and off-line analysis of results and statistical process control.

At last, these control panels have multiple high- and low-limit alarms to warn the operator of potential problems or for shutting down the process.

To summarize the latest control panels contain all electrical, gas, powder controls, and system safety interlocks. They control the whole process in real time and collect process data as well as fault messages.

17.4 Controlled Atmosphere

17.4.1 Soft Vacuum Plasma Spraying

In air spraying and plasma spraying of metals and alloys, in-flight powder oxidation is detrimental for both the coating properties and adhesion. Plasma

spraying under controlled atmosphere was developed on an Industrial scale in 1974 by Mulberger (Electro Plasma Inc. now Sulzer Metco Inc.), see [39, 40]. Historically, after the first presentation about Low Pressure Plasma Spraying 1974 of Erich Mühlberger in London, Herbert Nussbaum, owner of the Company "Plasma Technik" in Wohlen, Switzerland, wanted to increase the plasma activity with development and selling of equipment, particularly for aircraft companies for coating of turbine blades. He contacted Dr. Henne at DLR (German Aerospace Research Center) in Stuttgart for developing, on the base of APS, the VPS technology (The acronym LPPS was protected by Electro Plasma Inc.). Dr. Henne and his coworkers designed and constructed a VPS torch (perhaps for the first time for plasma spraying) with "de Laval nozzle," adapted for a low pressure surrounding. In cooperation with "Plasma Technik" a lot of pioneering work was done, in Stuttgart, and also a first study about the integration of a robot into a vacuum surrounding. In 1980 for the first time the common activity of "Plasma Technik" and DLR on VPS was announced at the Surfair-Congress in Cannes, F. (27–29 May, 1980): R. Henne, and H. Nussbaum: New Developments in the Low Pressure Plasma Spray Coating and in the Automation of this Techniques. This was followed by several papers [41–43]. As an important part of the VPS process, the following papers were devoted to the Laval nozzle [44] and surface cleaning by means of Transferred Arc [45]. By the middle of the 80s Sulzer took control on Plasma Technik AG; several automated VPS systems were already installed at different countries mostly for the aerospace industry. By acquiring several companies, such as Electro Plasma Inc. in (1991), and in Metco (1994), Sulzer, now Sulzer Metco, continued its consolidation in the thermal spray field, including plasma, flame, and wire arc spray sources, spray systems for APS and VPS [46], equipment, material (powders, wires, targets, etc.) rounded with its own development of coating activity on a commercial scale.

The principle of the industrial installation of Electro Plasma Inc. is shown in Fig. 17.3. The equipment is contained in a water-cooled, vacuum-tight chamber, maintained at an absolute pressure between 10 and 70 kPa. Such systems, known as vacuum plasma spraying (VPS) or low-pressure plasma spraying (LPPS) include vacuum pumping, exhaust cooling, filtration, an inert gas backfill manifold, and robots to move the spray gun and the part, as shown in Fig.17.4. More simple devices were developed for batch process, comprising only one transfer chamber as illustrated in Fig. 17.5. As the temperature inside the chamber can reach values between 150 and 200 °C, and moreover since the interior is rather dusty, the arms of the robots have to be protected against heat and dust. Filters must also be disposed between chamber and pumps to trap the dust. Thorough cleaning of the inside of the deposition chamber is necessary on a regular basis for the proper operation of the mechanical components. It is also essential to avoid memory effects when switching from one material system to another.

When the plasma jet flows into an argon atmosphere, it becomes longer and fatter than in air (see Fig. 7.33a compared to Fig. 7.33c and Sect. 7.6.4) because there is no dissociation and ionization of the entrained air, both of which are consuming a lot of energy [48]. Moreover when the surrounding atmosphere

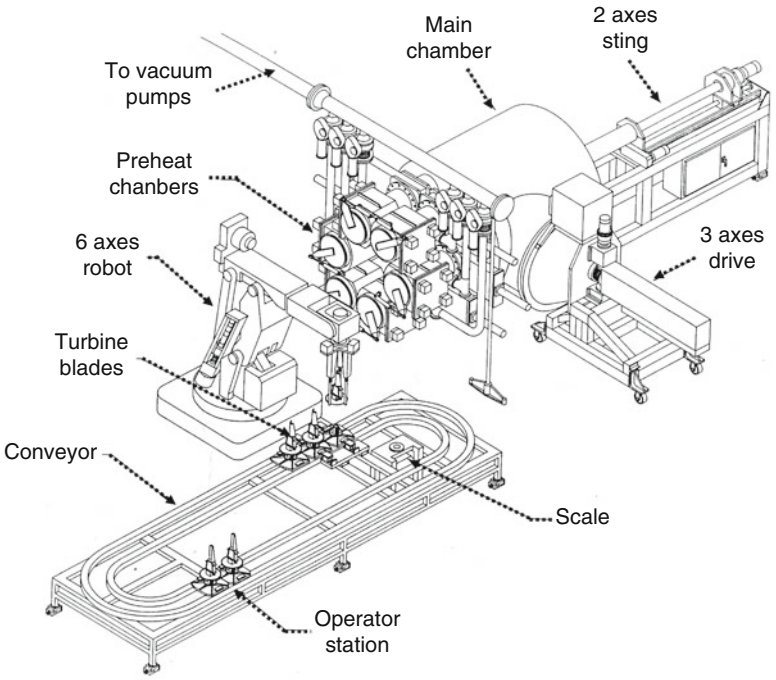


Fig. 17.3 Industrial soft vacuum plasma spray setup to coat turbine blades. Reprinted with kind permission from ASM International [40]

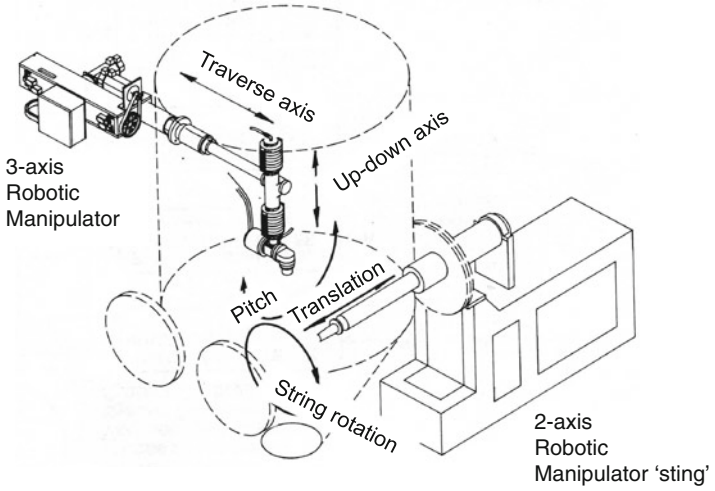


Fig. 17.4 Schematic of the robot manipulating the spray torch and that moving the part to be sprayed. Reprinted with kind permission from ASM International [40]

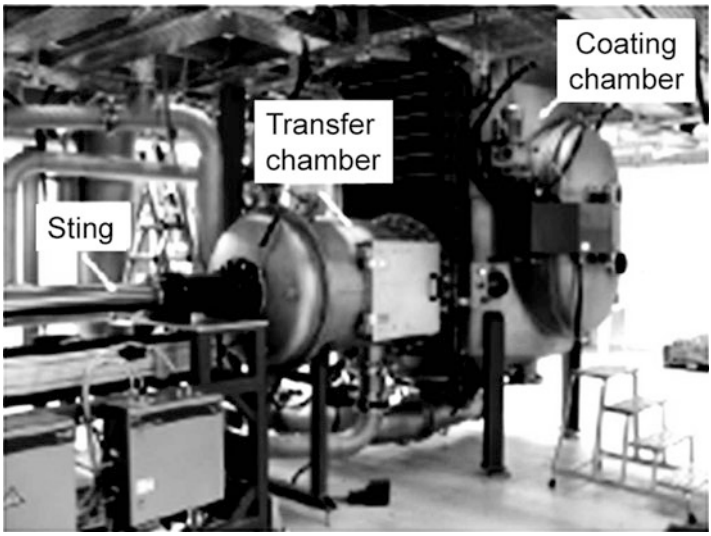


Fig. 17.5 Batch soft vacuum system with vertical process chamber and horizontal part manipulator including a transfer chamber. Reprinted with kind permission from ASM International [47]

pressure diminishes, the gas mean free path increases reducing collisions between gas species and recombination between ions and electrons and atoms (for diatomic species). Thus the plasma jet is elongated with decreasing chamber pressure, as shown in Fig. 17.6.

The chamber is pumped down to a low pressure (a few Pa) and then backfilled with high purity, dry argon to maintain oxygen levels below 30 ppm. These jets have higher velocities and lower plasma densities. Therefore, the jet cooling by the surrounding atmosphere is lower and the chemistry is somewhat frozen resulting in slow recombination. Lower density gradients at the jet boundaries result also in less turbulence and less cold gas mixing. Thus for all these reasons, reducing the chamber pressure results in longer and broader jets. However the plasma jet temperature within the jet downstream of the nozzle exit is lower, ranging for example between 4,000 K and 2,000 K between 100 and 400 mm at 5 kPa. Moreover the Knudsen effect reduces the heat and momentum transfers (see Sect. 4.2.2.2b and 4.3.3.2).

The main advantages are that:

- Coatings are almost oxide free (a quantity slightly higher than the oxide content of sprayed powder).
- The substrate oxide layer can be eliminated by a reverse transferred arc.
- The substrate can be preheated up to 1,000 °C before and during spraying.

The cleaning and heating processes are illustrated in Fig. 17.7. In both cases the plasma jet is ignited, of course with no particles injection, the plasma jet creating an

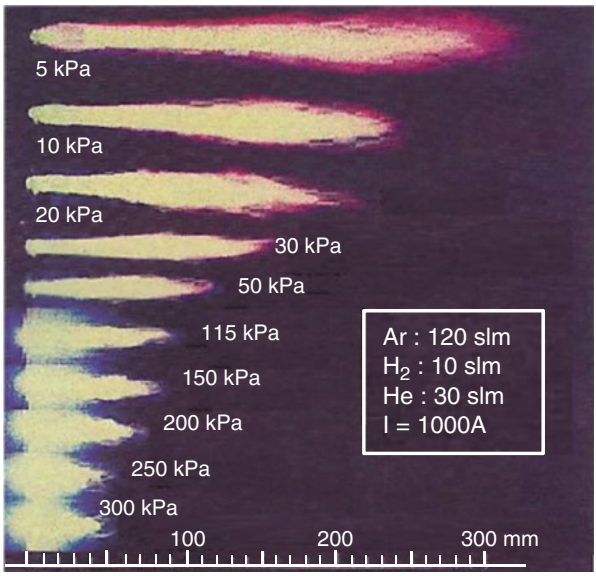


Fig. 17.6 Pressure dependence of plasma jet dimensions. Reprinted with kind permission from Springer Science Business Media [49], copyright © ASM International

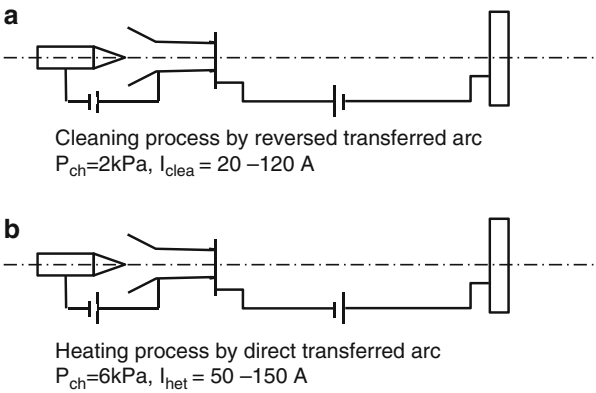


Fig. 17.7 Schematic of the transferred arc cleaning (**a**) and heating (**b**) when vacuum plasma spraying. Reprinted with kind permission from ASM International [50]

ionized volume between the torch nozzle and substrate. Thus it becomes possible to run a transferred arc between these two parts with a tailored arc current (from about 20 to 150 A). For cleaning, the substrate is the cathode (Fig. 17.7a) and for heating the anode Fig. 17.7b. An electrical shield must be used in certain cases to avoid the transferred arc striking on substrate grips, for example. Itoh et al. [50] have cleaned stainless steel (SUS304) coupons 25 mm in diameter placed 400 mm downstream of the nozzle exit in the chamber kept at 3,300 Pa. Some stainless steel coupons were heated in air to 1,000 °C and then mirror polished, the oxide layer being 0.45 μm thick. The reversed transferred arc current was 37 A. The arc cathodic spots moved continuously at the substrate surface. Coupons treated by the reversed arc are presented in Fig. 13.9.

Thus VPS results for metal sprayed on metal substrate in very good coating adhesion by diffusion, once the oxide layer at substrate surface has been removed with the reverse transferred arc (Fig. 17.7a). Of course diffusion requires that during spraying the temperature be kept sufficiently high with the help of the direct transferred arc (Fig. 17.7b) and high coating density.

The industrial use of soft vacuum spraying requires using antechambers to introduce and remove parts without modifying the main chamber pressure. When introducing the part the antechamber is at atmospheric pressure, then it is pumped down to the main chamber pressure once it is closed and the part can be preheated with resistors before being translated to the main chamber. To remove the sprayed part the reverse operation is performed, the preheating stage becoming a cooling stage. Of course a robot inside the chamber is handling the parts to be sprayed and withdrawn. A robot outside the chamber loads and unloads the pre-chambers as illustrated in Fig. 17.3 [40].

The main disadvantages are:

- The considerable capital cost with prices 5 to 20 times higher than those of APS systems depending on the quality requirements of the desired product
- The difficulty to melt in soft vacuum refractory materials, due to the Knudsen effect

17.4.2 Vapor Phase Deposition

As emphasized by Fauchais and Vardelle [51] Electron Beam Physical Vapor Deposition (EB-PVD) is a serious competitor to conventional plasma spraying process for Thermal Barrier Coatings (TBCs). As emphasized by Fauchais and Vardelle [51], they are used to improve the life and performance of turbine components by making it possible to deposit thick coatings, of a few hundred micrometres, with a fine columnar microstructure. While this results in a higher strain tolerance, their effective thermal conductivity are unfortunately higher than that of conventional plasma–sprayed coatings [52]. It makes it possible to deposit thick (a few hundreds of micrometers) yttria-stabilized zirconia (YSZ) coatings with a fine columnar microstructure that results not only in a higher strain tolerance but also unfortunately higher thermal conductivity than plasma-sprayed coatings [52]. In contrast to plasma spray technology, the EB-PVD process is operated at much lower pressures (0.1–5 Pa) [53] and needs an expensive equipment investment; it exhibits also lower deposition rate. It is a vacuum deposition process where focused high-energy electron beams evaporate the coating material and the vapor phase is transported to the substrate, forming a coating. Because of the lower application cost, and the large installed equipment base of plasma spray processes, some of them under development, are based on the use of thermal plasmas to process the coating material. They involve not only the solution precursor plasma spray technique (see Chap. 14) but also techniques based on a partial or nearly

complete evaporation of the powder injected in the plasma flow. The latter techniques make it possible to produce a coating either from molten particles or vapor depending on the powder, torch-operating conditions, and working pressure in the VPS equipment.

In soft vacuum, the plasma jet lengthen and enlarge and, as shown in Fig. 7.71b at 30 kPa, typical pressure in VPS, the plasma plume reaches 0.5 m in length and up to 0.04 m in diameter. The Sulzer Metco Company has developed a new process called plasma spray-physical vapor deposition (PS-PVD). It is based on their expertise in low pressure plasma spraying and involves a high-power plasma spray torch (180 kW–3,000 A, gas flow up to 200 slm) working at a pressure as low as 0.1 kPa (1 mbar). Under such a pressure condition, the plasma jet reaches more than 2 m in length and up to 0.4 m in diameter as presented in Fig. 7.71c. With PS-PVD, coatings exhibiting a columnar microstructure similar to that of EB-PVD coatings have been obtained by using a low powder feed rate, adapted spray conditions, and large spray distance. The YPSZ columns grow perpendicular to the substrate surface whose roughness (Ra) was lower than 2 μm and temperature in the 1,000 °C range [47]. They consist of many fine needles with a high defect density and a high amount of internal porosity (see Fig. 7.72a). Thanks to the versatility of the PS-PVD process, it also makes it possible to achieve porous coatings with fine particles and splats imbedded in a matrix resulting from vapor deposition as shown in Fig. 7.72b by adapting the spray parameters, especially when increasing the powder flow rate to limit its evaporation.

17.4.3 Inert Plasma Spraying

Because of the disadvantages of vacuum plasma spraying, especially the low heat transfer to ceramic particles, inert chamber plasma arc spray has been developed since the 1960s. Commonly, air is removed from the vacuum-tight chamber with a vacuum pump, and the chamber is then backfilled with an inert gas, usually argon, to atmospheric pressure. The oxygen content can be lower than 7 ppm if a liquid argon source is used [54]. Plasma jets in argon atmosphere are broader and longer (about a factor 1.5 to 2) than in air [48]. Such chambers are used to spray carbides, borides, and refractory metals. Liquid argon sprays allow controlling the coating temperature during the spray process [54]. If the chamber volume is above 10 m^3, no cooling is necessary for the chamber walls.

A few tests have been performed using chambers at higher pressure than one atmosphere (up to 0.3 MPa or 3 atm) [55]. However, plasma jets are shorter (see Fig. 17.6) and electrode erosion increases with the increase of the operation pressure above one atmosphere. This is mainly due to the increased radiation form the arc column, and the shrinkage of the cathode attachment with the increase of the operating pressure. The latter gives rise to the increase of the local current density and the thermal load on the electrode, and consequently to higher erosion and lower lifetime of the electrodes.

17.4.4 Cold Spray with Helium

As emphasized in Chap. 6, particle velocities are the highest when using helium in cold spray process, thus improving the quality of coatings and enabling more critical materials, such as titanium, requiring a higher particle speed, to be processed. However, due to the high cost per unit volume and higher flow rate, the cost of spraying with helium is significantly larger than that when using nitrogen [56–58]. To economize on helium resources and keep the coating price to a minimum, helium-recycling plants, already in use in other applications, have been adapted to the needs of cold spraying, for example, by Linde Co. or Praxair Co. In order to avoid unnecessary contamination, the process should be carried out under sealed-off conditions. The uncooled chamber size, working at or close to atmospheric pressure, depends strongly on that of the parts to be treated. The exhaust gas is then conducted through a particle filter and cooled if necessary. The process comprises a compressor and a complex membrane enabling to store recycled helium with a purity of 99 %. Of course new helium is required to replace losses.

17.5 Finishing and Post-Treatment of Coatings

After spraying, coatings are treated to achieve the final dimension and obtain a smooth surface. However, machining of coatings can be troublesome with materials that are abrasion resistant and porous, with sometimes poorly bonded (often mainly mechanical bond) particles or splats that can pull out easily and with low thermal conductivity (at least lower than that of the bulk material) reducing the heat transfer and increasing drastically the coating surface temperature during grinding, for example. Thus in general the accepted methods, practices, and techniques used to machine wrought material do not apply to the same material when sprayed [19].

As already mentioned, sprayed coatings are more or less porous with porosities that can be interconnected and extend from the coating surface to the substrate or the bond coat. Post-treatments of coatings are performed to enhance the bond strength, relax partially or totally residual stress, create compressive residual stress, close or reduce porosity, especially the interconnected one, create a barrier to corrosive or oxidizing products, improve coating homogeneity, improve splat or particle cohesion, obtain hard phase precipitation, or induce chemical modifications [19]. This is achieved by using different techniques, including fusion of self-fluxing alloys, heat treating or annealing, hot isostatic pressing (HIP), austempering, laser glazing, sealing, spark plasma sintering, peening densification, and diffusion. It is clear that heat treatment processes where the coating top surface is heated to melt it partially or totally either by flame, plasma, or laser, may induce cracks, especially with ceramic coatings, as soon as temperature gradients are high.

17.5.1 Finishing

After spraying, coatings are treated to achieve the final dimension and obtain a smooth surface. However, machining of coatings can be troublesome with materials that are abrasion resistant, porous, with sometimes poorly bonded (often mainly mechanical bond) particles or splats that can pull out easily, with low thermal conductivity (at least lower than that of the bulk material) reducing the heat transfer, and increasing drastically the coating surface temperature during grinding, for example. Thus in general the accepted methods, practices, and techniques used to machine wrought material do not apply to the same material when sprayed [59].

17.5.1.1 Machining (Turning, Milling)

For metal coatings turning and milling can be easily used to establish the final dimension and remove the as-deposited coating roughness. However cutting lubricants, oils, and coolants will penetrate and remain in coatings with open porosities and remain after machining [59] if the coated part is not treated afterwards.

For cermets, especially those with carbide grains, carbide tools are recommended because such coatings are very abrasive.

For ceramic coatings only grinding is possible.

17.5.1.2 Grinding

The required finish and tolerance of ceramic coatings in general require grinding. As with turning and milling, grinding conditions of ceramic-sprayed coatings are widely different from those of wrought or cast materials. Individual particles or splats can be pulled out, or even the whole coating can delaminate from the substrate. The ductility of ceramic coatings is very low and, besides the poor thermal conductivity of coatings, the contact between coating and substrate is never perfect, and heat conduction toward the metal substrate is reduced. At last, ceramic coatings are porous and whatever may be the quality of the grinding, the surface will always have holes after grinding.

Machines commonly used are outside diameter grinders (cylindrical and centerless), surface grinders (horizontal and vertical spindle), and internal grinders [60]. However to work on complex shape parts, such as turbine blades, six-axes machines with pressure control are required. To achieve complex machining at the coating surface, such as airflow channels for air sustained rotating machines, ultrasonic machining can be used. In this machining, a constant stream of abrasive (diamond, boron carbide, silicon carbide, alumina,...) slurry passes between the tool and the work piece. The vibrating tool, combined with the abrasive slurry,

abrades the material uniformly, leaving a precise reverse image of the tool shape. The tool must have lower hardness and toughness than the ceramic coating to be machined.

Compared to machining of metal coatings, grinding is rather expensive and thus the quantity of material to be taken off must be as low as possible, implying that the coating thickness is as close as possible to the final dimension (±5 μm at the maximum).

Wet grinding is preferred to dry grinding because of the greater latitude in abrasive and wheel selection; it also allows using harder wheels resulting in better finishes and less dressing [19, 59]. The selection of the grinding wheel depends on the coating hardness and microstructure. The handbook of thermal spray technology [19] proposes a few rules for this selection.

The grinding variables: wheel speed, work speed, area of contact, grinding fluid filtration, and proper fluid concentration are also important parameters. For example, for the grinding wheel selection [59] always use the sharpest wheel possible to cut rapidly without overheating and choose wheels with structures and grades to achieve free cutting action. For the wheel structure the spacing between individual abrasive is one of the key issues as well as the wheel grade, harder wheels lasting longer but cutting slowly and generating more heat. Moreover they require frequent dressing, harder grades used on small areas of contact or narrow wheels. Of course one has to choose the bond-type best suited to the operation and equipment: vitrified bonds, which have a high-stock removal and a good precision tolerance, the operating speed being limited to 33 m s^{-1} or resinoid bonds allowing high speeds, rapid stock removal, and fine finishes. At last the equipment and especially the wheel mounting (balance) must be systematically checked [59, 60]. At last the grinding variables are as follows:

- Proper choice of the wheel speed from which depend the performance, finishing, and stock removal
- High work speed corresponding to aggressive wheels
- Low area of contact, a higher pressure corresponding to larger depth of abrasive penetration
- Use wet grinding, allowing using harder wheels, giving better finishes, and less dressing

At last, after a period of time when the abrasive grains of the wheel have wear, or when the wheel face becomes loaded with the ground material, the wheel must be dressed with a diamond tool [59, 60].

17.5.1.3 Abrasive Belt Grinding and Polishing

Metal, cermets, and ceramic-sprayed coatings can be ground and polished with coated abrasive belts. The main advantages of these belts are that they cut without overheating; they need no dressing and can be rapidly changed when worn. The coated part is fixture or positioned on a lathe. The part is either transverse or rotated

under the belt head. Belt speed is generally between 30 and 40 m/s, while the part speed varies between 0.13 and 1 m/s. The grain size of belts can be adapted to rapid stock removal or to improve finish [59].

17.5.1.4 Super Finishing

It is achieved with abrasive stones or laps oscillating in front of the moving part. The choice of lubricant is critical, high viscosity, reducing cutting action, but giving finer finishes.

17.5.1.5 Other Finishing Methods

(a) Hand Stoning, Buffing, and Polishing

Hand stoning, buffing, and polishing can be accomplished with abrasive stone, stick, wheel, or paper [59]. Hands stoning and buffing give excellent results on soft metals with a bright finish, provided abrasive sizes are progressively decreased from coarse to fine. However the abrasive device is rapidly loaded and must be frequently dressed. Carbon and stainless steel coatings are difficult to hand stone to a good finish. Ceramics or cermets can be hand stoned to a light finish (well suited for parts with unusual contours). However with these techniques it is difficult to maintain a uniform thickness.

(b) Tumbling and Burnishing

For large quantities of small parts or when parts have unusual contours, tumbling and burnishing are well adapted. Tumbling is performed in a vibrating or rotating tub with an abrasive medium and water, while burnishing is the same but with hard metal balls instead of the abrasive. These hard balls are used to compress the surface, the final smoothness of which depends on pressure and frequency of ball-to-part contacts [59].

17.5.2 Fusion of Self-Fluxing Alloys

17.5.2.1 Principle

Coatings are submitted to a post-thermal treatment at a temperature between the solidus and liquidus states of the alloy, where important diffusion processes take place. This temperature is usually in the range 1,200–1,400 K, meaning that low melting temperature metals, such as aluminum are excluded of this process. As

already noted in Chap. 2, self-fluxing alloys contain boron and silicon (for example, CrBFeSiCNi), which are used as deoxidizers. As-deposited self-fluxing alloys are rather porous. Upon coating and reheating, densification occurs (most of the pores are eliminated) and borosilicate (B_2O_x·SiO_y) is formed, according to reaction (see Eq. (5.4) in Sect. 5.2.2.2), and diffuses toward the coating surface as slag, which is mechanically removed afterwards by turning, milling, etc. The coating shrinkage can reach 20 vol.%, and the silicon and boron form complex silicides and borides, dispersed within the coating [19, 59]. At last, the high fusion temperature allows diffusion between substrate and coating and between the splats, improving the bond strength and the coating cohesion. Of course the fusing temperature depends on the self-fluxing alloy chosen (between 1,020 and 1,121 °C) and it is very important to control it. A too high temperature results in excessive fluxing, depleting the alloy of silicon and/or boron and creating more slag. Too low temperatures induce poor bonding and high porosity.

17.5.2.2 Fusing Processes

The cheapest fusing method uses a flame torch or torches (depending on the part size) working with oxygen and either acetylene or propane. This process can be well adapted to parts with axial symmetry. A low flame velocity must be used to avoid blowing molten metal. The part and coating are gradually and uniformly heated to 760–870 °C before elevating the coating temperature to its fusing range. The torch movement and the surface temperature must be controlled if possible with automatic torch fusing equipment [59].

With furnace fusing, the heating, cooling, and working atmosphere can be easily controlled. Vacuum furnaces are also used. Industrially, furnace fusing is used for components with complex shapes or large parts, which are difficult to heat uniformly with flames.

Induction fusing is rather popular due to savings in fusion time and energy cost, but limited to parts with cylindrical symmetry. Laser fusing, if the right parameters are selected, can provide good quality coatings and the heating can be very well controlled. However it is generally preferable to preheat the part in a furnace and then let it cool slowly, for example, by placing it in vermiculite [59]. Nevertheless there are no significant differences in wear behavior of NiCrBSi coatings treated with flame or laser fusing [61].

Crack formation occurs when alloys are brittle and when the expansion mismatch between coating and substrate is high. To limit their formation, temperature gradients must be avoided with a uniform heating and a slow cooling. The latter is achieved with a furnace or by immersing the part in an insulating medium such as vermiculite.

Porosity, as noted previously, occurs with under-fusing (incomplete melting, wetting, and fluxing) or overheating. A problem of nonuniform heating can be

observed with large parts. Nonuniform heating can also be observed with parts that are hollow or vary in wall thickness. High sulfur, selenium, or lead in the base metal can also cause porosity problems [59].

17.5.2.3 Examples of Results

Only a few examples are given to illustrate the complexity of the fusing process.

Akebono et al. [62] have flame sprayed a Ni-based self-fluxing alloy and fused it in a vacuum furnace. They tested three fusing temperatures and three fusing times. Results are largely dependent on (a) size and population of porosities in the coating and (b) the hardness of the matrix (Ni-rich solid solution) of the coating.

Gomez-del Rio et al. [63] have compared laser-cladding (LC), flame sprayed (FS) combined with surface flame treatment, and flame sprayed (FS) combined with laser treatment. All coatings show a similar microstructure composed mainly of a Ni solid solution matrix with dendritic structure and common phases precipitated on it with different distribution, size, and shape depending on the type of deposition process and controlling coating properties.

Miguel et al. [64] have compared tribological properties of NiCrBSi coatings obtained by spray and fuse and as-sprayed coatings obtained by Atmospheric Plasma Spraying (APS) and High-Velocity Oxy Fuel (HVOF) spraying. The fuse process produces precipitate growth as well as an improvement of the coating porosity almost down to 0 % (according to the measurement precision). The spray and fused coating has a slightly lower hardness than the HVOF one (667 ± 142 HV_{10}), but its sliding wear resistance is the best. The main wear mechanism was adhesion between coating surface and the sliding surface, but abrasion and delamination also took place.

Shrestha et al. [65] have studied erosion–corrosion characteristics of self-fluxing NiCrMoSiB coatings deposited onto carbon steel (BS970 EN8) and stainless steel (UNS S31603) substrates using a commercial high-velocity oxy-fuel (HVOF) thermal spray process. The coatings were studied in as-sprayed, vacuum-sealed (by polymer impregnation), and vacuum furnace fused conditions. The study showed that the effect of sealing by polymer impregnation did not significantly alter the erosion–corrosion behavior of the sprayed coating. However, there was an improvement in erosion–corrosion durability afforded by the post-fusion process.

Serres et al. [66] have studied NiCrBSi coatings produced by APS and in situ laser irradiated by a diode laser. In situ irradiation (laser remelting after plasma spraying) is very suitable to reduce environmental impacts. The in situ process allows the construction of denser coatings than APS with finer structures, without cracks and porosity. The coating is metallurgical bonded to the substrate.

17.5.3 Heat Treating or Annealing

17.5.3.1 Definition

By definition annealing corresponds to a heat treatment that alters the microstructure of a material causing change in properties such as strength, hardness, ductility, etc. For thermally sprayed coatings, annealing or heat treating is performed [19] at high temperatures, but well below the coating melting temperature, T_m. It takes place at atmospheric pressure in air or more generally in a controlled atmosphere or under vacuum. It induces changes in microstructure and thermomechanical properties, formation of amorphous phase, relaxation of residual stress (temperature must be over that of recovery $\approx 0.4 \times T_m$), diffusion between substrate and coating improving the bond strength, coating densification by increasing inter-splat cohesion, recrystallization and grain growth occurring through sintering, reduction of coating oxide content when heated in hydrogen atmosphere or complete oxidation when heated in oxygen atmosphere, carbide precipitation from solid solutions with cobalt, thus enhancing the coating toughness and modification of electrical properties.

17.5.3.2 Examples of Results

Gartner et al. [67] have shown that the mechanical properties of cold-sprayed coatings improved substantially with heat treatment unlike other thermal-sprayed coatings, mainly thanks to diffusion effects during their annealing. Stoltenhoff et al. [68] found that annealed cold-sprayed coatings exhibited superior electrical properties compared to HVOF coatings. Copper coatings at different coating parameters were cold sprayed by Sudharshan Phani et al. [69] and subjected to various post-treatments. The electrical conductivity was improved with heat treatment carried out in vacuum at different temperatures and for different durations. Calla et al. [70] have shown that the copper cold spray conditions played a role in the annealing mechanisms.

Koivuluoto et al. [71] have studied cold-sprayed Cu, Ni, and Ni-30 wt% Cu and the effect of annealing on microstructure and corrosion behavior. Cold-sprayed Ni coating became denser during heat treatment. Hall et al. [72] showed that annealed cold-sprayed Al samples exhibited mechanical properties that were similar to those of wrought 1,100 H14 aluminum. The annealed samples showed a reduction in ultimate strength but a dramatic increase in ductility, with up to 10 % elongation. Zhang et al. [73] have cold-sprayed Ni/Al alloy powders, synthesized by ball milling of nickel–aluminum powder mixture with a Ni/Al atomic ratio of 1:1. The as-sprayed alloy coating exhibited a laminar microstructure retained from the mechanically alloyed powder. The annealing of the subsequent Ni/Al alloy coating at a temperature higher than 850 °C led to complete transformation from a Ni/Al alloy to a NiAl intermetallic compound. Wang et al. [74] cold-sprayed

an iron/aluminum composite coating using iron and aluminum powder mixtures. The coating was annealed at different temperatures aiming at forming an iron aluminide intermetallic coating. By increasing the annealing temperature to 900 °C, the deposit transformed to mainly FeAl phase with a trace of remaining Fe phase.

Li et al. [75] have deposited by cold spraying a thick and relatively porous Ti coating. After annealing at 850 °C for 4 h under vacuum conditions, the Ti coating still presented a porous structure but with more uniformly distributed small pores and metallurgical bonding between the deposited particles. The optimized cold spray parameters led Zahiri et al. [76] to produce a dense cold spray structure. Annealing improved its ductility by nucleation and growth of equiaxed grains, which included an ultrafine grain structure. Yang et al. [77] have deposited, through vacuum cold spray, a nanometer-sized TiO_2 photo-catalytic coating using both a composite powder (nanoTiO_2 powder and polyethylene glycol) and nanoTiO_2 powder. They found that the photo-catalytic activity of the coating deposited by the composite powders was significantly influenced by the annealing temperature. Better adhesion was achieved when the coating was annealed at temperatures between 450 and 500 °C. The adhesion of the coatings deposited with the composite powder was better than the primary nanoTiO_2 powder and presented a higher photo-catalytic activity than that deposited with the primary nanoparticles. The high activity was attributed to the existence of large pores that benefits the contaminant transportation in the porous coating.

Prudenziati and Gualtieri [78] have studied electrical properties, in the temperature range 20–500 °C, of resistors made of Ni and Ni20Cr-sprayed powders by five laboratories. Annealing at temperatures from 200 to 400 °C resulted in an irreversible decrease of resistance. Karthikeyan et al. [79] have studied the effect of powder, spray, and coating parameters on superconducting properties of plasma-sprayed $Y_1Ba_2Cu_3O_{7-x}$ coatings. Optimizing spray parameters yielded strong, adherent, and dense coatings on many substrates. Coatings, after oxygen annealing at 950 °C for an hour, turned from insulator to superconductor at 90 K.

The manifold of structural defects governs the effective elastic properties of coatings, and they change as the defect structure changes during annealing. Damani and Wanner [80] have studied the microstructural development in plasma-sprayed alumina (Al_2O_3), as a function of annealing temperature. Results showed that annealing even at moderate homologous temperatures already had a noticeable effect on the elastic properties. Upon annealing at higher temperatures, very strong elastic constant changes were observed: increases of about 300 % as compared with the as-sprayed material. Marrocco et al. [81] investigated HVOF-sprayed quaternary Al–Sn-based alloys. The as-sprayed deposits had microstructures that differed significantly from those of the gas-atomized feedstock powders. Annealing at 300 °C caused the dispersed Sn phase to coarsen and increased the fraction of $NiAl_3$ and Si precipitates in the Ni- and Si-containing coatings, respectively, compared with the as-deposited alloy.

The phase transformation of plasma-sprayed yttria partially stabilized zirconia (YPSZ) coatings has been extensively studied. For example, coatings were exposed to an alternating heat treatment at different temperatures, after annealing at 773 K and 1,073 K in order to control stress relief [82]. The response of YPSZ plasma-sprayed deposits to annealing at 1,000, 1,200, and 1,400 °C with times from 1 to 1,000 h has been evaluated [83]. Results showed that the yttria concentration of the as-sprayed tetragonal zirconia component generally decreased with increasing annealing temperature and time. Markocsan et al. [84] have analyzed the influence of a long heat treatment (2,000 h/1,200 °C) on different coating characteristics of two types of TBC systems, partially stabilized with either yttria or dysprosia (i.e., YPSZ and DyPSZ). The microstructure analysis revealed that the coating microstructure was significantly dependent on both spraying parameters and heat treatment conditions. Li et al. [85] have cold sprayed a dense NiCoCrAlTaY bond coat without oxidation during spraying. They have shown that through control of the pretreatment conditions, the fast grown spinel can be changed to exclusive α-Al_2O_3 due to limited oxidation of the superalloy bond coat during cold spraying, which led to the increase of thermal cyclic life time even by a factor of 10.

Laribi et al. [86] have studied the influence of a nickel–aluminum (80:20 %) bond coat post-annealing at 850 °C in air for 1 h on the residual stress in two sprayed coatings: blend of Cr–Ni steel and Cr–Mn steel on the one hand and molybdenum on the other hand. With the post-annealing, stress was relaxed.

17.5.4 Hot Isostatic Pressing

HIP is the simultaneous application of heat (temperatures below the melting point, about 1,100 °C for steel and 975 °C for nickel) and pressure between 50 and 300 MPa in an inert atmosphere to an encapsulated coated substrate. The heat promotes diffusion (enhanced bond strength and splat cohesion), and the pressure collapses and shrinks pores. Of course at those temperatures the residual stress is relaxed and the fracture toughness is enhanced [19, 59]. The main industrial application is for near net-shaped components thermally sprayed with high-added values, according to the relatively high cost of the process.

For example, Stewart and Ahmed [87] have investigated the influenced of the HIP on the Rolling Contact Fatigue (RCF) performance of thermal spray (WC–12Co) coatings. By increasing the HIP temperature to 1,200 °C and maintaining full film lubrication, it was possible to achieve a fatigue life in excess of 70 million stress cycles without failure in relatively thin (50 μm) cermet coatings. Stoica et al. [88] have HIP treated (850 °C for one hour) WC–12Co coatings sprayed by a HVOF system onto SUJ-2 bearing steel substrate. The sliding wear performance of test coupons was drastically improved not only in terms of coating wear but also in terms of the total volume loss.

Khor and Loh [89] studied HIP treatment at increasing temperatures and pressures of plasma-sprayed Ni-based alloy coatings. HIP changed the microstructure and increased the microhardness of the coatings. Results showed that, for temperatures below 750 °C, the elastic modulus of HIPed coatings was larger than that of as-sprayed coatings. These changes could be related to plastic flow, interlamellar diffusion, and creep that occur at increased temperatures and pressures.

Abdel-Samad et al. [90] have studied the influence of hot isostatic pressing on thermal fatigue resistance of plasma-sprayed coatings onto die-casting molds. HIP treatment was performed at 1,100 °C at a pressure of 100 MPa for 6 h using argon gas, heating for 3 h, and slow cooling to room temperature. The hardness did not decrease, residual stresses were attenuated, and the fatigue life of steel die specimens was increased. The HIPed coatings showed low residual tensile stress indicating their high relaxation through the HIPing process.

17.5.5 Austempering Heat Treatment

Another means to promote diffusion at the substrate and coating interface and to collapse the internal pores is austempering. The heat treatment is performed in molten salt baths. For example, Lenling et al. [91] have immersed coated samples in an 870 °C neutral salt for 30 min and then quenched them in a neutral salt bath at 315 °C for 30 min. Finally the parts were cooled and rinsed with room temperature water. Coatings, about 250 μm thick, were composites of WC–Co and Ni-base, plasma sprayed onto AISI 5150 steel substrates. The percentage of WC phase was increased and less desirable carbide phases formed during plasma spraying were eliminated. The bond to substrate was improved, the coating hardness increased, and residual compressive stress was induced.

17.5.6 Laser Glazing

Laser treatments (auxiliary processes) can be applied before, during, or after thermal spraying (main process), leading to a wide range of coating improvements (microstructure, adhesion, etc.). Garcia-Alonso et al. [92] made an excellent review of laser pretreatments (ablation and texturing) to promote coating/substrate adhesion, hybrid laser treatments applied simultaneously during the spraying process and deeply modifying the coatings microstructure and finally, laser post-treatments to improve coatings density and adhesion, and also induce phase transformations and structure refinement. In this section only laser post-treatments are considered.

The advantage of laser heat treating and glazing is that the thermal energy applied is perfectly controlled with respect to the amount and the location on the surface to be treated. Lasers used are mainly CO_2 continuous wave (c.w.) lasers at 10.6 μm with power levels up to 5 kW, diode lasers with power levels in the

few kW range, CO_2-pulsed lasers with power levels of a few hundred watts and neodymium-doped-yttrium-aluminum-garnet (Nd/YAG laser) at 1.06 μm. For all treated surfaces, the intensity of the hemispherical reflection coefficient, R, must be considered, the energy or power absorbed by the surface being proportional to $(1–R)$. With a wide range of energy densities possible, accurate temperature profiles can be obtained at precise locations in different depths of the coating. The treatment is limited to heat treating or melting of the surface (laser glazing). In the latter case, the rapid solidification through the coating and substrate allows microstructural refinements and other metallurgical changes modifying coating properties, wear or corrosion resistance, and tribological properties [20]. Of course it must be kept in mind that for sprayed materials with low thermal conductivities (below 30–40 W m^{-1} K^{-1}) temperature gradients can induce important stress, which will result in relaxation by macro-cracks orthogonal to the coating.

A few examples illustrate advantages of laser glazing.

Plasma-sprayed zircon ($ZrSiO_4$) coatings are generally made of ZrO_2 and SiO_2 due to the fast quenching of dissociated zircon. Schelz et al. [93] have shown that, by using low-energy (8 W) CO_2 laser treatment, the inverse reaction occurred, unfortunately with a low recombination rate. When glassy particles were incorporated in the coating with a large-size distribution from approximately 10 μm to more than 100 μm, the result was the production of a substantial amount of recombined $ZrSiO_4$ when the same laser parameters were used. Thus, the laser treatment with additives may provide technological benefits over other heat treatment techniques where high-temperature annealing (1,600–1,900 K) must be used for the same result.

The microstructure, electrochemical, and wear performances of HVOF WC–24 % Cr3C2–6 % Ni coatings on Inconel were modified greatly by laser heat treatment [94]. The laser beam spot was elliptical 5 × 4 mm^2 with a power of 400 W. The relative content of Cr_3C_2 and Ni in HVOF-sprayed coatings was increased, as well as the coating hardness, after laser heat treatment, and a dense interface between the coating and substrate was achieved. Laser heat treatment was also helpful to form denser oxide tribo-film and improve the cohesion of WC, Cr_3C_2, and Ni phases, together with better wear performance of the coating.

Pokhmurska and Ciach [95] have remelted (Fe–Cr–B) + Al-based electric arc-sprayed coatings with a CO_2 c.w. laser The surface was covered with a graphite-based antireflection coating. Laser melting markedly improved coating microstructure and density, with much better chemical homogeneity. Results also demonstrated an improvement of mechanical and corrosion properties of coatings.

Al_2O_3–13wt%TiO_2 plasma-sprayed coatings onto a titanium alloy (Ti–6Al–4V) substrate were remelted with a c.w. CO_2 laser [96]. The laser-remelted coatings (LRmC) possessed a much denser and more homogenous structure and excellent metallurgical bonding to the substrate. The average porosity of the LRmC was reduced to 0.9 %, compared with 6.2 % of the as-sprayed coatings. The metastable γ-Al_2O_3 phase in the as-sprayed coatings transformed to stable α-Al_2O_3 during laser remelting, due to the slow cooling. The micro-hardness of the coatings was

enhanced to 1,000–1,400 $HV_{0.3}$ after laser remelting, which was much higher than that of the plasma-sprayed coatings.

Aluminum coatings on austenitic stainless steel substrates were laser remelted (c.w. 5 kW CO_2 laser) [97]. The residual porosity was eliminated and phases were mainly AlFe Ni, Cr, and CrFeNi. A metallurgical bond between the coatings and the base metal was formed after laser surface remelting.

Continuous wave CO_2 laser and a pulsed laser with cylindrical focal lens have been used to glaze the surface layer of plasma-sprayed ZrO_2–20 wt% Y_2O_3/MCrAlY coatings [98]. Defects, such as bubbles or depressions, occurred usually with a continuous wave laser, but a high-quality glazed layer was produced using a pulsed laser. The surface roughness of the plasma-sprayed ceramic coatings was significantly improved by laser glazing. Surface roughness decreased slightly as the pulse frequency increased for the glazed surface.

Pulsed laser glazing of plasma-sprayed hydroxyapatite coatings modified the morphology of their surface as well as their phase composition [99]. The surface became smoother. The phase content was richer in α-tricalcium phosphate, tetracalcium phosphate (TTCP) than that of as-sprayed deposits; TCP and TTCP were the products of HA decomposition. The fraction of TTCP was larger in all samples treated with a laser.

Ni–20Cr and Stellite-6 powders have been sprayed on boiler tube steels with a shrouded plasma spray process using NiCrAlY as bond coat [100]. The coatings showed some porosity (2–4 %). Laser remelting of the coating was performed with a pulsed Nd:YAG laser: 300 W with pulse energy of 6 J and pulse width of 20 μs, the repetition rate being 10 Hz. It appeared to be effective in reducing the porosity to less than 0.5 %. However laser remelting further led to a significant dilution of the coating due to surface alloying of the coating with the bond coat and substrate. Laser remelting of the coatings led to a decrease in micro-hardness.

Laser surface melting was shown to reduce surface roughness of a cordierite glass coating, which was air plasma sprayed [101]. Subsequent devitrification of the cordierite was found to depend upon the physical and chemical alterations induced by the laser treatment. Crystallization in the as-sprayed coating was controlled by the TiO_2 distribution in the coating microstructure. After laser treatment, the devitrification was dominated by nucleation at micro-cracks, since the inter-splat structure was homogenized both physically by the removal of splat boundaries and chemically by the redistribution of TiO_2 in the coating.

Improvement in copper erosion resistance at temperatures comprised between 25 °C and 300 °C can be obtained by forming copper coatings containing 45 vol.% boride particles. To resist erosion due to impact of coarse iron ore particles, these coatings must possess microstructural features, which are larger than the size of impacting particles. Laser melting of plasma-sprayed Cu–boride coatings produced large intricate islands of ductile and hard phases [102]. The peculiar microstructure architecture developed upon laser melting was found suitable to withstand erosion attacks.

Ahmed et al. [103] have HVOF-sprayed Ni-based superalloy Inconel 625 coatings and laser remelted them using a high power diode laser. The performance gap

between bulk and HVOF-sprayed Inconel 625 was largely due to galvanic corrosion between Cr-depleted re-solidified regions and nonmelted material in the coatings. Laser surface melting of HVOF coatings of Inconel 625 largely improved the corrosion resistance due to the elimination of both porosity and localized regions of material depleted in Cr. Several studies have been undertaken recently to adapt yttria partially stabilized zirconia (YPSZ) thermal barrier coating (TBC) characteristics during their manufacturing process. Antou et al. [104] have treated the coating pass by pass, as it was manufactured, with a 3 kW diode laser at 848 nm. The input energy effect was studied by varying the scanning velocity (i.e., between 35 and 60 m min^{-1}), and consequently the irradiation time (i.e., between 1.8 and 3.1 ms, respectively). Experiments showed that coating thermal conductivity was lowered by more than 20 % and coating resistance to isothermal shocks was increased significantly.

17.5.7 Sealing

17.5.7.1 General Remarks

As thermally sprayed coatings are more or less porous with connected porosities, they are not very suitable for corrosion protection. This situation can be drastically improved by curing their interconnected porosities through sealing them.

The advantages of sealing are the following [19]:

- It prevents the corrosive substance (liquids or gases) from penetrating the coating and attacking the coating/substrate interface
- It limits the lodging of wear debris in the coating
- It enhances inter-splat cohesion
- It can provide special surface properties such as nonstick surfaces
- It can extend the life of aluminum or zinc coatings on steel to prevent corrosion

17.5.7.2 Sealing Processes

Knuuttila et al. [105] gave an excellent description of the process presenting various sealant types and impregnation methods, as well as factors influencing impregnation. Impregnation methods can be divided into four categories: atmospheric pressure impregnation, low-pressure impregnation, overpressure impregnation, and a combination of those. The method of choice depends on the size of the coated component, the required penetration depth, and the sealant, the choice of which also depends on the coating material and the application:

- Low-pressure or overpressure impregnation is suitable for small components.
- Atmospheric pressure impregnation is economically viable for larger components but the result depends strongly upon the sealant-coating wet ability (in fact

it is the dynamic wetting angle that has to be considered) and the sealant viscosity. Sealing requires controlling humidity by keeping the surface temperature above the dew point where water condenses to any surface. The techniques used are brushing, dipping, or spraying.

The advantage of low pressure is the removal of moisture and air from pores and cracks improving the sealant penetration depth. However the pressure must be adjusted to the sealant vapor pressure to avoid excessive evaporation.

Overpressure impregnation is much less sensitive to the sealant-coating contact angle that can be over 90°.

Sealants for impregnation are either organic or inorganic materials or metals. In sealing the aim is to seal the porosity to as great a depth as possible. However, there are applications where only a relatively thin sealant layer is considered optimum [99]. A low interfacial surface tension between the coating and the sealant is the most important factor dictating the penetration depth. The pore size distribution of the coating is equally important; larger pores might not become filled due to lowered capillary pressure.

(a) Organic Sealants

The often-used organic sealants are based on epoxies, phenolics, furans, polymethacrylates, silicones, polyesters, polyurethanes, and polyvinylesters. Waxes can be used as well. The choice depends upon the service temperature. For example, wax can be used only in cold conditions, phenolic resins up to 150–260 °C, and methacrylate up to 150 °C [60]. A good sealing depends on how coatings were treated before impregnation and how long the impregnation time was. These sealants are cured by heat, ultraviolet light, or high-energy radiation [106]. However curing the sealants induces some shrinkage, and only low curing shrinkages can prevent the transport of electrolyte through the coating [106].

(b) Inorganic Sealants

They are mostly used for high-temperature applications. Besides aluminum phosphates, sodium and ethyl silicates, various sol–gel type solutions and chromic acid have been used for sealing purposes. For example, phosphate acts as refractory glue that forms solid bridges over pores and cracks; it has also a beneficial effect in transforming the residual stress of the coating into compression. Sol–gel processes refer to the formation of a stable sol, the hydrolyzing of the sol to a gel, and the calcinating of the gel at elevated temperature to oxide. The sol includes a variety of metal alkoxides, nitrates, or hydroxides [105].

(c) Metals

Molten metals are used for sealing and strengthening purposes. The metal-coating wetting is a key issue. For example, zirconia is completely wetted by pure manganese [105].

(d) Other Means

They include electroplating or enamel deposition.

17.5.7.3 Examples of Results

(a) Organic Sealants

Shrestha et al. [107] have studied the erosion–corrosion characteristics of a Ni–Cr–Mo–Si–B coating applied by a high-velocity oxy-fuel (HVOF) process onto an austenitic stainless steel as sprayed, either after vacuum sealing with polymer impregnation or after vacuum furnace fusion. Erosion–corrosion was produced by the impact of a liquid jet of 3.5 % NaCl solution at 18 °C at a velocity of 17 m s^{-1}, with or without 800 ppm silica sand. The study showed that sealing with polymer impregnation did not significantly modify the erosion–corrosion behavior of the sprayed coating. However, there was a significant improvement afforded by the post-fusion process in coating durability.

Kim et al. [108] have sealed Al_2O_3–13 wt% TiO_2 using three commercial polymeric sealants. The penetration depth of sealants into the ceramic coating was from 0.2 to 0.5 mm depending on the sealants used. All of the micro-hardness, two-body abrasive wear resistance, bond strength, and surface roughness of the ceramic coating after the sealing treatment were improved. Three-point bending stress of the ceramic coating after the sealing treatment was decreased. This was attributed to the reduced micro-crack toughening effect since the cracks propagate easily through the splats of the coating without crack deflection and/or branching after the sealing treatment.

Ctibor et al. [109] studied unsealed and epoxy resin-sealed plasma-sprayed specimens prepared from alumina as well as alumina-13 % titania. It was shown that the abrasion wear resistance of the epoxy resin-sealed coatings is significantly better than that of the as-sprayed coatings for both types of applied tests.

(b) Inorganic Sealant

One of the most popular sealants, especially for ceramics, is aluminum phosphate. Leivo et al. [110] have studied plasma-sprayed Al_2O_3 and Cr_2O_3 coatings sealed by aluminum phosphates. Phosphates were formed throughout the coating, down to the

substrate. The sealing increased the hardness of the coatings by 200 to 300 Vickers hardness (HV) units. Abrasion and erosion wear resistances were increased by the sealing treatment. Sealing also substantially closed the open porosity, as shown in electrochemical corrosion tests.

Ahmaniemi et al. [111, 112] have modified thick (1,000 μm) thermal barrier coatings ($25CeO_2$–$2.5Y_2O_3$–ZrO_2, $22MgO$–ZrO_2, $8Y_2O_3$–ZrO_2) for diesel engines with laser glazing and phosphate-based sealing treatments. In phosphate-sealed coatings, the penetration depth of the sealant was approximately 300–400 μm and micro-hardness was at the range of 825–882 $HV_{0.3}$. The open porosity of the phosphate-sealed coatings was reduced by 24–48 % depending on the coating material. The optimal thickness of the melted layer in laser-glazed coatings was 50–150 μm. In all cases the melted zone was significantly densified and a vertical macro-crack network was introduced.

The same authors [113] have studied several modified thick thermal barrier coatings in three test series, in which the maximum coating temperature was fixed to 1,000, 1,150, and 1,300 °C. The modified coating structures were all segmentation-cracked coatings and some of these coatings were surface-sealed, using aluminum phosphate or a sol–gel-based sealant. Both sealing treatments reduced the thermal cycling resistance of the segmentation-cracked coatings. The decrease of the thermal cycling resistance of aluminum phosphate sealing was rather high, whereas in sol–gel sealing it was moderate.

Ahmaniemi et al. [114] studied the residual stress induced by an aluminum phosphate sealing of plasma-sprayed alumina and chromia coatings. Sealing treatments were performed at 200, 300, and 400 °C with treatment times for these temperatures of 16, 4, and 2 h, respectively. Strengthening of alumina coating is mainly based on chemical reactions between the coating and the sealant, leading to bonding phosphate phases and obviously higher stiffness of the coating. The tensile stress state of the Al_2O_3 coating decreased during the sealing treatment and the stress became even compressive as measured with the hole-drilling method. The aluminum phosphate sealing treatment temperature seemed to influence strongly the residual stress state of chromia coatings.

Troczynski et al. [115] have sealed zirconia thermal barrier coatings using sol–gel alumina. The overall reduction of porosity was however small (from ∼12 to ∼11 %), preserving the strain and thermal shock tolerance of the coatings. Burner rig tests showed an increase in sealed coating lifetime under thermomechanical fatigue conditions.

Electrodeposition of Ni has been used in an attempt to seal the open porosity of plasma-sprayed alumina coatings [116]. It is a promising sealing treatment for sprayed alumina coatings intended for tribological applications. The hardness and coating cohesion increased and the wear resistance was found to increase markedly in all wear tests as a result of the sealing.

Conventional Ni plating was successfully used [117] to seal the surface pores of an arc-sprayed coating. Electroplating of Ni sealed the pores and provided a smooth finish to the sample, enhancing the corrosion resistance of a Hastelloy coating.

The oxidation and hot-corrosion behavior of a Co–Ni–Cr–Al–Y coating produced by HVOF with and without an enamel coating were investigated [118] in air at 900 °C and in molten salt 75 wt% NaCl+25 wt% Na_2SO_4 at 850 °C. The results showed that the enamel coating possessed excellent hot corrosion resistance in a molten salt, in comparison with the as-sprayed coating. In the hot-corrosion tests, breakaway corrosion did not occur on the samples with the enamel coating and the composition of the enamel did not significantly change.

For automotive application lightweight so-called metal-supported solid oxide fuel cells (MS-SOFC) have been developed. As usual these cells are serially stacked to achieve technically suitable voltage and power. Each cell is contained between two metal sheets, where these sheets of ferrite steel have to form a gas-tight cassette. But, to prevent electrical short-circuiting of the electrodes, both sheets have to be insulated from each other at the cassette rim. Gas tightness and electrical insulation at once represent a demanding task to solve, considering the strong operating conditions of about 800 °C and the desired lifetime. DLR-Stuttgart (Germany) has successfully developed a reliable sealing system [119–122]. The main problem was here to have a ceramic which was at the same time insulating and could be soldered by means of a metal braze, without losing the insulating property. A patent was filed about the procedure consisting in spraying at vacuum conditions to one sheet a powder mixture of $MgAl_2O_4$ (spinel) and fine titanium hydride or another reactive metal hydride. The metal hydride decomposed within the hot plasma jet into the metal and together with the spinel a cermet arised. At high temperature brazing in atmosphere the metallic component turned into insulating oxide. Because of the high pyrophoric property of these reactive metals the required fine fraction cannot be handled, directly, whereas the hydrides were less problematic. This procedure led to the following positive results applying titanium hydride:

- The titanium bonded the braze for a stable connection.
- The braze was stopped by the titanium and could not reach the other metal side avoiding an electrical short circuit.
- The remaining metallic titanium gathered oxygen and turned into insulating oxide, and closed at the same time open porosity, sealing the cell.

Caron et al. [123] have developed a stable hermetic seal composed of a ceramic matrix charged with glass particles, atmospheric plasma sprayed to obtain efficient air tightness between two SOFC cells. The developed seal was found to be solid, un-distortable, and adhesive to its support at ambient temperature. The sealing properties were acquired when the SOFC was put into service: the glassy phase migrated into the peculiar plasma-sprayed microstructure of the ceramic matrix toward the interface leading to the air tightness of the deposit. With the seal, the leak rate observed at 7 Pa was 0.43 P.L/s, i.e., below the requirement of the US Department of Energy, which is 0.5 P.L/s.

17.5.8 Spark Plasma Sintering

Spark plasma sintering (SPS), applied under compressive loading, is a new process for the densification of porous materials. Sparks are generated between the particles and cause the material to be heated rapidly.

Khor et al. [124] have applied SPS for fabricating high-performance yttria-stabilized zirconia (YSZ) electrolyte for SOFC starting from detached plasma-sprayed coating. SPS was performed at 1,200, 1,400, and 1,500 °C, each sintering cycle having a holding time of 3 min. A microstructure transition occurred above 1,200 °C, where the typical plasma-sprayed lamellar structure transformed to a granular-type structure, but the phase composition remained the same. The thermal conductivity of the as-sprayed YSZ was greatly increased (up to two times) by the SPS post-spray heat treatment, and there was an optimum of multiple SPS cycles for the enhancement of the thermal conductivity. The oxygen ion conduction resistivity was reduced drastically with an increase of the SPS temperature for multiple SPS cycles.

Prawara et al. [125] also used SPS to densify a ZrO_2–25 wt% MgO flame-sprayed coating on a steel substrate. In the SPS process, the thermal spray-coated steel was exposed to rapid heating under vacuum at temperatures of 900, 950, and 1,000 °C under compressive load for 10 min. If the as-sprayed coating had high porosities of up to 22 % the porosity fell to below 5 % after SPS treatment. The bond strength and micro-hardness of the coating were also increased. These properties could be controlled by adjustment of the SPS temperature and the compressive load.

17.5.9 Peening or Rolling Densification

To close surface-connected pores and improve surface smoothness, shot peening or rolling can mechanically treat metallic-sprayed coatings [60]. This treatment resulted in pore closure and development of compressive residual stress. A few examples are given below.

Zhou et al. [126] have shot peened, with different lengths of operating time, a CoCrAlY bond coat on a disk-shaped Ni-based super-alloy. A moderate shot peening processing modified the surface of the bond coat. An EB-PVD (Electron Beam-Physical Vapor Deposition) YSZ coating was deposited, onto the compacted bond coat, and after 3 cycles of shot peening, with a smooth surface, the coating exhibited a satisfactory thermal cycling lifetime of 1,643 cycles at 1,293 K.

The shot peening process increased the axial fatigue strength of AISI 4340 steel WC-10Ni HVOF sprayed by Junior et al. [127]. The fatigue limit increased by 13.3 % from 750 MPa to 850 MPa.

Kubiak et al. [128] investigated a shot peening treatment and a WC–17 % Co coating applied to 30NiCrMo steel against 52100 steel under plain fretting and

complex fretting fatigue loading. Only WC–17 % Co decreased the value of the coefficient of friction. Shot peening treatment had very little influence on fretting wear resistance under gross slip conditions and had no influence on the crack nucleation threshold, but performed well against crack propagation under plain fretting and the studied fretting fatigue conditions.

Marin de Camargo et al. [129] studied WC–17 % Co HVOF-sprayed coatings on an Al 7050-T7451 alloy. The axial fatigue strength of the shot peened coating was improved in comparison to the Al 7050-T7451 substrate HVOF sprayed with WC–17 % Co coating. The shot peening process could induce surface modification, such as surface roughening that, considering fatigue damage, accelerated nucleation and fatigue crack propagation.

Costa et al. [130] studied the influence of a WC–10 % Co–4 % Cr coating deposited by HVOF on the fatigue strength of a Ti–6Al–4 V alloy. Comparison of the fatigue strength of the coated specimens and the base material showed a decrease when the parts were coated. They observed that the effect was more pronounced in high-cycle fatigue tests. The shot peening prior to the thermal spray coating was an efficient surface treatment to improve fatigue resistance of coated Ti–6Al–4 V.

Shot peening of Al wire arc-sprayed coatings was studied by I'Anson et al. [131]; the process being optimized thanks to Taguchi fractional-factorial L4 design parametric study.

Results also depended on the peened layer thickness, which were varied from 83 to 207 μm. The porosity of the un-peened Al layer ranged from 4.33 to 13.63 %, while that of the peened coating layers varied from 0.16 to 0.83 %. The average hardness of the coatings ranged from 61.8 to 74.6 $HV_{0.25N}$ for the peened coatings and was 41.6 for the un-peened coating.

17.5.10 Diffusion

Aluminum may be diffused into a steel or silicon bronze substrate to protect it against the corrosive action of gases at temperatures of up to 870 °C [60]. After being sprayed, the part is coated with a bituminous aluminum sealer or other suitable material. It is then held at 788 °C during the appropriate time for diffusion depending on the thickness.

17.6 Summary and Conclusions

Thermal spray processes as all industrial ones present hazards including radiation, noise, production of toxic gases, use of explosive gases, dusts,... All these problems have been presented in this chapter with the solutions to minimize the risks and the description of adapted booths, control panel, gas handling,... The problems

linked to plasma spraying in soft vacuum or inert atmosphere have also been described.

Defects present in thermal-sprayed coatings can be totally or partially cured by using post-treatments including fusion of self-fluxing alloys, heat treatment or annealing, hot isostatic pressing (HIP), austempering, laser glazing, sealing, spark plasma sintering, peening densification, and diffusion. Treatments at medium temperatures allow mainly relaxation of residual stresses, densification of the coating with increased inter-splat cohesion, and changing the coating microstructure and service properties. Those performed at high temperature further promote diffusion between substrate and coating, improving the bond strength, and leading to precipitation of carbides from solid solutions with cobalt, thus enhancing the coating toughness, etc. Treatments at room temperature such as peening or rolling allow reducing the porosity and increasing the compressive residual stress. However, as for the spray pattern and coating temperature monitoring, the post-treatment must be well controlled (temperature, surrounding atmosphere for those at intermediate or high temperature, peening size, material, impact velocity for peening. . .) to achieve reproducible and reliable properties.

Nomenclature

Latin Alphabet

T_m Melting temperature (K)

References

1. Montavon G, Gross K (2004) Safety issue in thermal spraying: the need for a collaborative effort within the community? J Therm Spray Technol 13(2):155–157
2. Russo L. Safety guidelines for performing risk assessments. ASM Thermal Spray Society, Safety Guidelines, 07/06/2010
3. Hériaud-Kraemer H, Montavon G, Hertert S, Robin H, Coddet C (2003) Harmful risks for workers in thermal spraying: a review completed by a survey in a French Company. J Therm Spray Technol 12(4):542–554
4. Petsas N, Kouzilos G, Papapanos G, Vardavoulias M, Moutsatsou A (2007) Worker exposure monitoring of suspended particles in a thermal spray industry. J Therm Spray Technol 16 (2):214–219
5. Wuest G, Hall A, Crawmer D. Guidelines for the use of personal protective equipment (PPE) in thermal spraying. ASM Thermal Spray Society, 27 pages in Safety Guidelines
6. Fadeel B, Garcia-Bennett AE (2010) Better safe than sorry: understanding the toxicological properties of inorganic nanoparticles manufactured for biomedical applications. Adv Drug Deliv Rev 62:362–374
7. Schulte PA, Murashov V, Zumwalde R, Kuempel ED, Geraci CL (2010) Occupational exposure limits for nanomaterials: state of the art. J Nanoparticle Res 12(6):1971–1987

8. Chadwick JK, Wilson HK, White MA (1997) An investigation of occupational metal exposure in thermal spraying processes. Sci Total Environ 199:115–124
9. Dobler K, Gifford D (2003) Safety guidelines for the handling and use of gases in thermal spraying. Prepared by the ASM-TSS Safety Committee. TSS, ASM International, Materials Park, OH, 27 pages
10. Linde catalogue, Acetylene... there is no better fuel gas for Oxy-fuel gas processes, www.linde-gas.com/
11. Creffield G, Cole M (1999) Safe working practices with thermal spray gases. In: Lugscheider E, Kammer PA (eds) United thermal spray conference, Düsseldorf. DVS, Düsseldorf, Germany, pp 397–401
12. Heinrich P, Penszior C, Meinass H (1999) Industrial gases for thermal spraying-from production to application, with the required purity. In: Lugscheider E, Kammer PA (eds) United thermal spray conference, Düsseldorf. DVS, Düsseldorf, Germany, pp 95–105
13. Howes CP (2001) Thermal spray safety and OSHA compliance, protecting operators from ultraviolet light, fumes, dust, compressed air, gases, Fabricator Magazine July 12
14. Dobler K, Gifford D. Safety guidelines for the handling and use of gases in thermal spraying. ASM Thermal Spray Society, 27 pages in Safety Guidelines
15. Gross KA (2002) Noise emission in thermal spray operations. J Therm Spray Technol 11 (3):350–358
16. Gifford DJ, Pollard L, Wuest G, Fletcher RC (2003) Thermal spray booth design guidelines. Prepared by the ASM-TSS safety committee. ASM International, Materials Park, OH, 47 pages
17. Hale DH, Dobler K, Gifford D (2002) Safety hazards associated with the usage of compressed gases in thermal spraying. In: ITSC 2002. DVS, Düsseldorf, Germany, pp 242–246
18. Kroemmer W, Heinrich P (2006) Influence of industrial gases on the thermal spray process. In: Marple B et al (eds) ITSC 2006. ASM International, Materials Park, OH, e-proceedings
19. Davis JR (2004) Handbook of thermal spray technology. ASM International, Materials Park, OH
20. Crawmer DE, Bartoe RL, Kramer J (1987) Technical note: improved universal powder mass flow control for thermal spray applications. Surf Coat Technol 33:353–365
21. Saenz JA (1988) Technical note: automated powder mass flow monitoring and control system. Surf Coat Technol 34(1):89–99
22. Czernichowski A, Pawlowski L, Nitoumbi B (2000) Injection of hot particles in the plasma flame. J Therm Spray Technol 9(4):458–462
23. Filkova I, Cedik P (1984) Nozzle atomization in spray drying. In: Mujumdar AS (ed) Advances drying, vol 3. Hemisphere Publishing Corporation, New York, NY, pp 181–215
24. Marchand O, Girardot L, Planche MP, Bertrand P, Bailly Y, Bertrand G (2011) An insight into suspension plasma spray: injection of the suspension and its interaction with the plasma flow. J Therm Spray Technol 20(6):1310–1320
25. Cotler EM, Chen D, Molz RJ (2011) Pressure-based liquid feed system for suspension plasma spray coatings. J Therm Spray Technol 20(4):967–973
26. Oberste-Berghaus J, Marple B, Moreau C (2006) Suspension plasma spraying of nanostructured WC-12Co coatings. J Therm Spray Technol 15(4):676–681
27. Etchart-Salas R, Rat V, Coudert JF, Fauchais P, Caron N, Wittman K, Alexandre S (2007) Influence of plasma instabilities in ceramic suspension plasma spraying. J Therm Spray Technol 16(5–6):857–865
28. Kutay A, Weiss LE (1992) Economic analysis of robotic operations: a case study of a thermal spraying robot. Robot Comput Integr Manuf 9(3):279–287
29. Fasching MM, Prinz FB, Weiss LE (1993) Planning robotic trajectories for thermal spray shape deposition. J Therm Spray Technol 2(1):45–57
30. Nylen P, Franssen J, Wretland A, Martensson N (1996) Coating thickness prediction and robot trajectory generation of thermal sprayed coatings. In: Berndt CC (ed) Thermal spray:

prediction and robot trajectory generation of thermal sprayed coatings. Thermal spray: practical solutions for engineering problems. ASM International, Materials Park, OH, pp 693–698
31. Eidelman S, Yang X (1997) Three dimensional simulation of HVOF spray deposition of nanoscale materials. Nanostruct Mater 9(1–8):79–84
32. Bonnet R, Bolot R, Coddet C (1999) Simulation of the thermal spray process and off-line programming. In: Lugscheider E, Kammer PA (eds) United thermal spray conference. DVS, Düsseldorf, Germany, pp 519–526
33. Nylen P, Wigren J, Pejryd L, Hansson M-O (1999) The modelling of coating thickness, heat transfer and fluid flow for a plasma sprayed gas turbine application. J Therm Spray Technol 8 (3):393–398
34. Guessasma S, Trifa F-I, Montavon G, Coddet C (2004) Al_2O_3–13% weight TiO_2 deposit profiles as a function of the atmospheric plasma spraying processing parameters. Mater Des 25(4):307–315
35. Trifa F-I, Montavon G, Coddet C, Nardin P, Abrudeanu M (2005) Geometrical features of plasma-sprayed deposits and their characterization methods. Mater Charact 54(2):157–175
36. Candel A, Gadow R (2009) Trajectory generation and coupled numerical simulation for thermal spraying applications on complex geometries. J Therm Spray Technol 18 (5–6):981–987
37. Floristán M, Montesinos JA, García-Marín JA, Killinger A, Gadow R (2012) Robot trajectory planning for high quality thermal spray coating processes on complex shaped components. In: ITSC 2012. ASM International, Materials Park, OH, e-proceedings
38. Deng SiHao, ZhenHua Cai, DanDan Fang, HanLin Liao, Ghislain Montavon (2012) Application of robot offline programming in thermal spraying. Surf Coat Technol 206 (19–20):3875–3882
39. Muehlberger E (1988) Industrial plasma processing technology. In: Proceedings of the 1st Plasma Technik symposium, vol 3. Plasma Technik, Wohlen, pp 105–118
40. Meyer PJ, Hawley D (1991) Electro Plasma Inc., LPPS production systems. In: Bernecki TF (ed) Thermal spray coatings: properties, processes and applications. ASM International, Materials Park, OH, pp 29–38
41. Henne R, Weber W (1982) Plasmaspritzen im Unterdruck. Ein Verfahren zur Herstellung von dichten Schutzschichten für hochschmelzende Metalle; Proc. 10. Plansee-Seminar, Reutte, A, June 1–5, (1981), which appeared also in High temperature – high pressure, vol 14, pp 237–244
42. Henne R, Schnurnberger W, Weber W (1983) Low pressure plasma spraying – an interesting method to produce electrodes for water electrolysis. In: ITSC 83, 10th international thermal spraying conference, Essen, 2–6 May
43. Henne R, Bradke VM, Schnurnberger W, Weber W (1986) Development and manufacture of electrolyzer components – applying plasma spraying under reduced pressure. In: Proceedings of the 11th international thermal spraying conference, Montreal, Canada, 8–12 Sept 1986. Pergamon Press
44. Mayr W, Henne R (1988) Investigation of a VPS burner with laval nozzle using an automated laser doppler measuring system. In: 1st Plasma Technik symposium, Luzern, vol 1, pp 87–97
45. Henne R, Weber W (1990) Reinigung und Aktivierung von Oberflächen beim Vakuumplasmaspritzen durch "übertragenen Lichtbogen". (Cleaning and activation of surfaces with VPS by means of transferred arc), Thermische Spritzkonferenz TS 90, 29–31 Aug 1990, Essen, Germany. DSV-Report, vol 130, pp 34–37
46. Ambühl P, Meyer P (1999) Thermal coating technology in controlled atmospheres (ChamProTM). In: Lugscheider E, Kammer PA (eds) Proceedings of the ITSC. DVS, Düsseldorf, Germany, pp 291–92
47. von Niessen K, Gindrat M (2010) Vapor phase deposition using a plasma spray process. In: Thermal spray: global solutions, ITSC 2010. DVS, Düsseldorf, Germany, e-proceedings

48. Roumilhac Ph, Coudert JF, Fauchais P (1991) Influence of the arc chamber design and of the surrounding atmosphere on temperature distributions of Ar-H_2 and Ar-He spraying plasma jets. In: Plasma processing and synthesis of materials III, MRS proceedings, vol 190, pp 227–238
49. Sodeoka S, Suzuki M, Ueno K (1996) Effects of high-pressure plasma spraying for yttria-stabilized zirconia coating. J Therm Spray Technol 5(3):277–282
50. Itoh A, Takeda K, Itoh M, Koga M (1991) Pretreatment of substrates by using reversed transferred arc in low pressure plasma spray. In: Berneki F (ed) Thermal spray research and application. ASM International, Materials Park, OH, pp 245–251
51. Fauchais P, Vardelle A (2011) Innovative and emerging processes in plasma spraying: from micro- to nano-structured coatings. J Phys D Appl Phys 44:194011
52. Padture NP, Gell M, Jordan EH (2002) Thermal barrier coatings for gas turbine engine applications. Science 296:280–284
53. Doering T (2007) PVD and PACVD (DLC) coating technologies and applications. In: International SAMPE symposium and exhibition (Proceedings), vol 52, 8p
54. Freslon A (1995) Plasma spraying at controlled temperature and atmosphere. In: Berndt CC, Sampath S (eds) Thermal spray: science and technology. ASM International, Materials Park, OH, pp 57–63
55. Jäger DA, Stöver D, Schlump W (1992) High pressure plasma spraying in controlled atmosphere up to 2 bars. In: Berndt CC (ed) Thermal spray: international advances in coatings technology. ASM International, Materials Park, OH, pp 69–75
56. Pattison SC, Ho JS, Johnson AN, O'Neill W (2007) The economics of the cold spray process. In: Champagne VK (ed) The cold spray materials deposition process, fundamental and applications. Woodhead, Cambridge, pp 72–98
57. Jaynes S, Lauricella F (2003) Helium recovery: design considerations for cold spray systems. In: Moreau C, Marple B (eds) Thermal spray 2003: advancing the science and applying the technology. ASM International, Materials Park, OH, pp 113–116
58. Champagne V (2007) The cold spray materials deposition process. Woodhead, Cambridge
59. AWS (1985) Thermal spraying: practice, theory and application. American Welding Society, Miami, FL
60. Malkin S, Guo C (2008) Grinding technology: theory and applications of machining with abrasives. Industrial Press, New York, NY
61. Gonzalez R, Cadenas M, Fernandez R, Cortizo JL, Rodrıguez E (2007) Wear behaviour of flame sprayed NiCrBSi coating remelted by flame or by laser. Wear 262:301–307
62. Akebono H, Komotori J, Shimizu M (2008) Effect of coating microstructure on the fatigue properties of steel thermally sprayed with Ni-based self-fluxing alloy. Int J Fatigue 30:814–821
63. Gomez-del Rio T, Garrido MA, Fernandez JE, Cadenas M, Rodrıgueza J (2008) Influence of the deposition techniques on the mechanical properties and microstructure of NiCrBSi coatings. J Mater Process Technol 204:304–312
64. Miguel JM, Guilemany JM, Vizcaino S (2003) Tribological study of NiCrBSi coating obtained by different processes. Tribology Int 36:181–187
65. Shrestha S, Hodgkiess T, Neville A (2005) Erosion–corrosion behaviour of high-velocity oxy-fuel Ni–Cr–Mo–Si–B coatings under high-velocity seawater jet impingement. Wear 259:208–218
66. Serres N, Hlawka F, Costil S, Langlade C, Machi F (2010) Microstructures and environmental assessment of metallic NiCrBSi coatings manufactured via hybrid plasma spray process. Surf Coat Technol 205(4):1039–1046
67. Gärtner F, Stoltenhoff T, Voyer J, Kreye H, Riekehr S, Kocak M (2006) Mechanical properties of cold sprayed and thermally sprayed copper coatings. Surf Coat Technol 200:6770–6782
68. Stoltenhoff T, Borchers C, Gärtner F, Kreye H (2006) Microstructures and key properties of cold sprayed and thermally sprayed copper coatings. Surf Coat Technol 200:4947–4960

69. Sudharshan Phani P, Srinivasa Rao D, Joshi SV, Sundararajan G (2007) Effect of process parameters and heat treatments on properties of cold sprayed copper coatings. J Therm Spray Technol 16(3):425–434
70. Calla E, McCartney DG, Shipway PH (2006) Effect of deposition conditions on the properties and annealing behavior of cold-sprayed copper. J Therm Spray Technol 15(2):255–262
71. Koivuluoto H, Lagerbom J, Vuoristo P (2007) Microstructural studies of cold sprayed copper, nickel, and nickel-30% copper coatings. J Therm Spray Technol 16(4):488–497
72. Hall AC, Cook DJ, Neiser RA, Roemer TJ, Hirschfeld DA (2006) The effect of a simple annealing heat treatment on the mechanical properties of cold-sprayed aluminum. J Therm Spray Technol 15(2):233–238
73. Zhang Q, Li C-J, Wang X-R, Ren Z-L, Li C-X, Yang G-J (2008) Formation of NiAl intermetallic compound by cold spraying of ball-milled Ni/Al alloy powder through postannealing treatment. J Therm Spray Technol 17(5–6):715–720
74. Wang H-T, Li C-J, Yang G-J, Li C-X (2008) Cold spraying of Fe/Al powder mixture: coating characteristics and influence of heat treatment on the phase structure. Appl Surf Sci 255:2538–2544
75. Li W-Y, Zhang C, Liao H, Coddet C (2009) Effect of heat treatment on microstructure and mechanical properties of cold sprayed Ti coatings with relatively large powder particles. J Coat Technol Res 6(3):401–406
76. Zahiri SH, Fraser D, Jahedi M (2009) Recrystallization of cold spray-fabricated CP titanium structures. J Therm Spray Technol 18(1):16–22
77. Yang G-J, Li C-J, Fan S-Q, Wang Y-Y, Li C-X (2007) Influence of annealing on photocatalytic performance and adhesion of vacuum cold-sprayed nanostructured TiO2 coating. J Therm Spray Technol 16(5–6):873–880
78. Prudenziati M, Gualtieri ML (2008) Electrical properties of thermally sprayed Ni- and Ni20Cr-based resistors. J Therm Spray Technol 17(3):385–394
79. Karthikeyan J, Sreekumar KP, Venkatramani N, Kurup MB, Patil DS, Rohatgi VK (1989) Effect of process parameters on the properties of plasma-sprayed superconducting Y1Ba2Cu3O7−x coatings. Appl Phys A Mater Sci Process 48(5):489–492
80. Damani RJ, Wanner A (2000) Microstructure and elastic properties of plasma-sprayed alumina. J Mater Sci 35(17):4307–431
81. Marrocco T, Driver LC, Harris SJ, McCartney DG (2006) Microstructure and properties of thermally sprayed Al-Sn-based alloys for plain bearing applications. J Therm Spray Technol 15(4):634–639
82. Yasuda K, Takeda H (2000) Phase transformation during alternating aging at 473 K and at 773 K in the plasma-sprayed yttria stabilized zirconia coating. J Mater Sci 35(17):4379–4383
83. Ilavsky J, Wallace J, Stalick JK (2001) Thermal spray yttria-stabilized zirconia phase changes during annealing. J Therm Spray Technol 10(3):497–501
84. Markocsan N, Nyle´n P, Wigren J, Li X-H, Tricoire A (2009) Effect of thermal aging on microstructure and functional properties of zirconia-base thermal barrier coatings. J Therm Spray Technol 18(2):201–208
85. Li Y, Li C-J, Zhang Q, Yang G-J, Li C-X (2010) Influence of TGO composition on the thermal shock lifetime of thermal barrier coatings with cold-sprayed MCrAlY bond coat. J Therm Spray Technol 19(1–2):168–177
86. Laribi M, Vannes AB, Mesrati N, Treheux D (2003) Metallurgical characterization and determination of residual stresses of coatings formed by thermal spraying. J Therm Spray Technol 12(2):234–239
87. Stewart S, Ahmed R (2003) Contact fatigue failure modes in hot isostatically pressed WC-12%Co coatings. Surf Coat Technol 172:204–216
88. Stoica V, Ahmed R, Golshan M, Tobe S (2004) Sliding wear evaluation of hot isostatically pressed thermal spray ceramet coatings. J Therm Spray Technol 13(1):93–107
89. Khor KA, Loh NL (1994) Hot isostatic pressing of plasma sprayed Ni-base alloys. J Therm Spray Technol 3(1):57–62

90. Abdel-Samad A, Lugscheider E, Bobzin K, Maes M (2006) The influence of hot isostatic pressing on plasma sprayed coatings properties. Surf Coat Technol 201:1224–1227
91. Lenling WJ, Smith MF, Henfling JA (1991) Beneficial effects of austempering post-treatment on tungsten carbide based wear coatings. In: Bernecki TF (ed) Thermal spray research and applications. ASM International, Materials Park, OH, pp 227–232
92. Garcia-Alonso D, Serres N, Demian C, Costil S, Langlade C, Coddet C (2011) Pre-/during-/post-laser processes to enhance the adhesion and mechanical properties of thermal-sprayed coatings with a reduced environmental impact. J Therm Spray Technol 20(4):719–735
93. Schelz S, Enguehard F, Caron N, Plessis D, Minot B, Guillet F, Longuet J-L, Teneze N, Bruneton E (2008) Recombination of silica and zirconia into zircon by means of laser treatment of plasma-sprayed coatings. J Mater Sci 43:1948–1957
94. Zhanga SH, Yoon JH, Li MX, Cho TY, Joo YK, Cho JY (2010) Influence of CO2 laser heat treatment on surface properties, electrochemical and tribological performance of HVOF sprayed WC–24%Cr3C2–6%Ni coating. Mater Chem Phys 119:458–464
95. Pokhmurska A, Ciach R (2000) Microstructure and properties of laser treated arc sprayed and plasma sprayed coatings. Surf Coat Technol 125:415–418
96. Wang Y, Li CG, Tian W, Yang Y (2009) Laser surface remelting of plasma sprayed nanostructured Al_2O_3–13wt%TiO_2 coatings on titanium alloy. Appl Surf Sci 255:8603–8610
97. Song RG, He WZ, Huang WD (2000) Effects of laser surface remelting on hydrogen permeation resistance of thermally-sprayed pure aluminum coatings. Surf Coat Technol 130:20–23
98. Tsai HL, Tsai PC (1998) Laser glazing of plasma-sprayed zirconia coatings. J Mater Eng Performance 7(2):258–264
99. Dyshlovenko S, Pawlowski L, Smurov I, Veiko V (2006) Pulsed laser modification of plasma-sprayed coatings: experimental processing of hydroxyapatite and numerical simulation. Surf Coat Technol 201:2248–2255
100. Sidhu BS, Puri D, Prakash S (2005) Mechanical and metallurgical properties of plasma sprayed and laser remelted Ni–20Cr and Stellite-6 coatings. J Mater Process Technol 159:347–355
101. Razavy FG, Van Aken DC, Smith JD (2003) Effect of laser surface melting upon the devitrification of plasma sprayed cordierite. Mater Sci Eng A362:213–222
102. Dallaire S, Dubé D, Fiset M (1999) Laser melting of plasma-sprayed copper–ceramic coatings for improved erosion resistance. Wear 231:102–107
103. Ahmed N, Bakare MS, McCartney DG, Voisey KT (2010) The effects of microstructural features on the performance gap in corrosion resistance between bulk and HVOF sprayed Inconel 625. Surf Coat Technol 204:2294–2301
104. Antou G, Hlawka F, Cornet A, Montavon G, Coddet C, Machi F (2004) Processing of yttria partially stabilized zirconia thermal barrier coatings implementing a high-power laser diode. J Therm Spray Technol 13(3):381–389
105. Knuuttila J, Sorsa P, Mäntylä T (1999) Sealing of thermal spray coatings by impregnation. J Therm Spray Technol 8(2):251–257
106. Knuuttila J, Sorsa P, Mäntylä T, Knuuttila J, Sorsa P (1999) Sealing of thermal spray coatings by impregnation. J Therm Spray Technol 8(2):249–25
107. Shrestha S, Hodgkiess T, Neville A (2001) The effect of post-treatment of a high-velocity oxy-fuel Ni-Cr-Mo-Si-B coating part 2: erosion-corrosion behavior. J Therm Spray Technol 10(4):656–665
108. Kim H-J, Lee C-H, Kweon Y-G (2001) The effects of sealing on the mechanical properties of the plasma-sprayed alumina-titania coating. Surf Coat Technol 139:75–80
109. Ctibor P, Neufuss K, Zahalka F, Kolman B (2007) Plasma sprayed ceramic coatings without and with epoxy resin sealing treatment and their wear resistance. Wear 262:1274–1280
110. Leivo EM, Vippola MS, Sorsa PPA, Vuoristo PMJ, Mäntylä TA (1997) Wear and corrosion properties of plasma sprayed AI_2O_3 and Cr_2O_3 coatings sealed by aluminum phosphates. J Therm Spray Technol 6(2):205–210

111. Ahmaniemi S, Vippola M, Vuoristo P, Mäntylä T, Cernuschi F, Lutterotti L (2004) Modified thick thermal barrier coatings: microstructural characterization. J Eur Ceramic Soc 24:2247–2258
112. Ahmaniemi S, Tuominen J, Vuoristo P, Mäntylä T (2002) Sealing procedures for thick thermal barrier coatings. J Therm Spray Technol 11(3):320–332
113. Ahmaniemi S, Vuoristo P, Mäntylä T, Gualco C, Bonadei A, Di R (2005) Thermal cycling resistance of modified thick thermal barrier coatings. Surf Coat Technol 190:378–387
114. Ahmaniemi S, Vippola M, Vuoristo P, Mäntylä T, Buchmann M, Gadow R (2002) Residual stresses in aluminium phosphate sealed plasma sprayed oxide coatings and their effect on abrasive wear. Wear 252:614–623
115. Troczynski T, Yang Q, John G (1999) Post-deposition treatment of zirconia thermal barrier coatings using Sol-Gel alumina. J Therm Spray Technol 8(2):229–234
116. Westergård R, Hogmark S (2004) Sealing to improve the wear properties of plasma sprayed alumina by electro-deposited Ni. Wear 256:1153–1162
117. Niranatlumpong P, Koiprasert H (2006) Improved corrosion resistance of thermally sprayed coating via surface grinding and electroplating techniques. Surf Coat Technol 201:737–743
118. Xie D, Xiong Y, Wang F (2003) Effect of an enamel coating on the oxidation and hot corrosion behavior of an HVOF-sprayed Co–Ni–Cr–Al–Y coating. Oxidation Metals 59 (5/6):503–516
119. Henne R, Zerfass HR, Arnold J. Sealing arrangement for a fuel cell stack and process for the production of such a sealing arrangement. Patent Application DEA 102005045053, 21.09.05
120. Henne R (2007) Solid oxide fuel cells: a challenge for plasma deposition processes. J Therm Spray Technol 16(3):381–403
121. Arnold J, Ansar SA, Maier U, Henne R. Insulating and sealing of SOFC devices by plasma spraying ceramic layers. In: International thermal spray conference & exposition, thermal spray 2008: crossing borders (DVS-ASM), Maastricht, The Netherlands, 2–4 June 2008, pp 83–87
122. Arnold J, Ansar SA, Ruckdäschel R, Henne R, Maier U, Grünling HW. Vacuum plasma sprayed insulating layers suitable for brazing in high temperature fuel cells. In: Abstract and manuscript of the ITSC-conference 2011 in Hamburg, no. 276, 27–29 Sept 2011, pp 143–148
123. Caron N, Bianchi L, Méthout S (2008) Development of a functional sealing layer for SOFC applications. J Therm Spray Technol 17(5–6):598–602
124. Khor KA, Yu L-G, Chan SH, Chen XJ (2003) Densification of plasma sprayed YSZ electrolytes by spark plasma sintering (SPS). J Eur Ceram Soc 23:1855–1863
125. Prawara B, Yara H, Miyagi Y, Fukushima T (2003) Spark plasma sintering as a post-spray treatment for thermally-sprayed coatings. Surf Coat Technol 162:234–241
126. Zhou Z-h, Gong S-k, Li H-f, Xu H-b, Zhang C-g, Wang L (2007) Effects of shot peening process on thermal cycling lifetime of TBCs prepared by EB-PVD. Chin J Aeronautics 20:145–147
127. Junior GS, Voorwald HJC, Vieira LFS, Cioffi MOH, Bonora RG (2010) Evaluation of WC-10Ni thermal spray coating with shot peening on the fatigue strength of AISI 4340 steel. Procedia Eng 2:649–656
128. Kubiak K, Fouvry S, Marechal AM, Vernet JM (2006) Behaviour of shot peening combined with WC–Co HVOF coating under complex fretting wear and fretting fatigue loading conditions. Surf Coat Technol 201:4323–4328
129. de Camargo JAM, Cornelis HJ, Cioffi VMOH, Costa MYP (2007) Coating residual stress effects on fatigue performance of 7050-T7451 aluminum alloy. Surf Coat Technol 201:9448–9455
130. Costa MYP, Venditti MLR, Voorwald HJC, Cioffi MOH, Cruz TG (2009) Effect of WC–10% Co–4%Cr coating on the Ti–6Al–4V alloy fatigue strength. Mater Sci Eng A 507:29–36
131. I'Anson K, Riggs WL, Irons G, Steeper TJ, Varacalle DJ Jr (1991) Use of shot peening process for surface modification of thermal spray coatings. In: Bernecki TF (ed) 4th NTSC proceedings. ASM International, Materials Park, OH, pp 139–145

Chapter 18
Industrial Applications of Thermal Spraying Technology

Abbreviations

ACP	Amorphous Calcium Phosphate
APS	Atmospheric Plasma Spraying
BAG	Bioactive Glass
BOF	Basic Oxygen Furnace
BRT	Burner Rig Test
CMAS	Acronym of each oxide deposits CaO, MgO, Al_2O_3, and SiO_2
CNT	Carbon Nano-tubes
CFRP	Carbon Fiber-Reinforced Plastics rolls
C-SS-CS	Composite surface of Stainless Steel and Carbon Steel welded together
CTE	Coefficient of Thermal Expansion
C-W	Corrosion and Wear
dBA	decibel Authorized
d.c.	direct current
D-gun	Detonation-gun
DRC	Diamond-Reinforced Composite
EAF	Electric Arc Furnace
EBC	Environmental Barrier Coating
EB-PVD	Electron Beam-Physical Vapor Deposition
E–C	Erosion–Corrosion
EHC	Electrolytic Hard Chrome
EIS	Electrochemical Impedance Spectroscopy
FAC	Fe-based Alloy Coatings
FBC	Fluidized-Bed Combustor
fcc	Face Center Cubic
FG	Functionally Graded
FGC	Functionally Graded Coating
GDC	$Ce_{0.8}\ Gd_{0.2}\ O_{1.9}$
GS	Gas Shroud

P.L. Fauchais et al., *Thermal Spray Fundamentals: From Powder to Part*,
DOI 10.1007/978-0-387-68991-3_18, © Springer Science+Business Media New York 2014

HA	Hydroxyapatite $Ca_{10}(PO_4)_6(OH)_2$
HAT	HA Top coating
HB	Hardness Brinell
HCC	Hard Chromium Coating
HEPS	High-Energy Plasma Spray
HIP	Hot Isostatically Pressed
HPAL	High-Pressure Acid-Leach
HTBC	50 vol. % HA and 50 vol. % TiO_2 (HT)
HTH	(HA)/HA + TiO_2 bond coat composite
HVAF	High-Velocity Air Flame
HVLF	High-Velocity Liquid Fuel
HVOF	High-Velocity Oxy-fuel Flame
HVPS	High-Velocity Plasma Spray
HVSFS	High-Velocity Suspension Flame Spraying
IACS	International Annealed Copper Standard
IPS	Induction plasma spraying
LaMA	La $MgAl_{11}O_{19}$
LTA	$LaTi_2Al_9O_{19}$
LSCF	$La_{0.6}\ Sr_{0.4}\ Co_{0.2}\ Fe_{0.8}\ O_{32-\delta}$
M	Mole unit
MMCs	Metal Matrix Composites
MSWI	Municipal Solid Waste Incinerators
NTSRS	Net Thermal Spraying Residual Stress
ODS	Oxide-Dispersion Strengthened
OEM	Original Equipment Manufacturer
PA-12	Polyamide 12
PAH	Progressive Abradability Hardness
PECVD	Plasma Enhanced Chemical Vapor Deposition
PEEK	Poly-Ether-Ether-Ketone
PEI	Poly Ether Imide
PGDS	Pulsed Gas Dynamic Spraying
PS	Plasma Sprayed
PS-PVD	Plasma-Sprayed-Plasma Vapor Deposition
PTA	Plasma-Transferred Arc
PVD	Physical Vapor Deposition
QC	Quality Control
r.f.	Radio Frequency
RFC	Rolling Contact Fatigue
RH	Relative air Humidity
SBF	Simulated Body Fluid
SER	Specific Energy Requirement
SLPS	Super solidus Liquid Phase Sintering
SPS	Spark Plasma Sintering
SPS	Suspension Plasma Spraying

SPPS	Solution Precursor Plasma Spraying
SS	Stainless Steel
SSC	Sm0.5 Sr0.5 Co O3
STS	Special Treatment Steel
SW-SS	Spot-Welded Stainless Steel
TBC	Thermal Barrier Coating
TCF	Thermal Cycling Fatigue
TCHT	Thermo Chemical Heat Treatment
TCP	Tricalcium Phosphate
TCR	Temperature Coefficient of Resistance
TF-LPPS	Thin Film-Low Pressure Plasma Spraying
TGO	Thermally Grown Oxide
TSR	Thermal Shock Rig
TTCP	Tetra-Calcium Phosphate
UHTC	Ultrahigh Temperature Ceramics
VIPS	Vacuum Induction Plasma Spraying
VPS	Vacuum Plasma Spraying
WA	Wire Arc
YPSZ	Yttria Partially Stabilized Zirconia
YSZ	Yttria-Stabilized Zirconia
ZFA	ZrO_2–CaF_2–Ag_2O composite coating

18.1 Introduction

At its early stages of development, thermal spray technology was mostly used for the repair, rebuilding, retrofitting, and for surface protection against corrosion, erosion, and wear [1]. Up to the early 1980s, the basic phenomena involved in most of thermal spray processes were poorly understood, with the process parameters based more on the operator experience and skill, rather than on a solid scientific understanding of the phenomena involved. This often resulted in unsatisfactory process reproducibility and reliability. The wider acceptance of the technology for industrial-scale production has started in the late 1980s and early 1990s, with applications limited to high-added value components in the aeronautic and nuclear industry. These were mostly driven by the fact that no alternate viable solutions were available, and design engineers and scientists were used to work with rather complex processes.

Over the past decade, a wide range of industrial-scale surface modification processes became available. These are presently accepted for applications ranging from tribological and wear-resistant applications including lubricity and low-friction surfaces, to resistance to corrosion and/or oxidation, thermal protection, freestanding components, electrical and optical components, electromagnetic shielding, electrical insulation, abradable seals, biomedical applications, superconducting oxides, components with coefficient of thermal expansion tailored

to service conditions, magnetic coatings, solid oxide fuel cells, replacement of hard chromium, as well as ornamental applications. The choice of a specific coating and/or thermal spray process, for a given service condition, depends, however, on the expectation of the user and the cost that could be tolerated for the application. This affected, in turn, the selection of the material to be applied for the coating and the spray process to be used. The coating design process is often complicated by the fact that, in practice, components are not always devoted to a single requirement such as wear or corrosion or electrical insulation or thermal insulation. In most cases, coatings must resist to different combined needs: for example, wear is often linked to corrosion.

The different available spray processes are generally complementary and not competitive and any overlap between them in terms of application is not very broad. To choose one of them, it is important to know the advantages and limitation of each of these processes and to make the proper decision of the best process for each application. A review is given in Sect. 18.2 of the principal characteristics and limitations of different thermal spray processes and the criteria for their selection. The different applications will be briefly described in Sect. 18.3 together with the expected material properties adapted to each one. In Sect. 18.4 current applications of thermal-sprayed coatings by industry are described. As pointed out previously, the cost of the coating plays an important role in the final choice of the spray process. An economic analysis of the different thermal spray processes is presented in Sect. 18.5. A listing of the range of materials that can be used for different applications is provided in the appendix of this chapter.

18.2 Advantages and Limitations of the Different Spray Processes

In the following advantages and limitations of the different processes are presented. A comparative economic analysis of each of these processes is given in Sect. 18.5.

18.2.1 Flame Spraying

Two techniques are used: powder on the one hand and wire, cord, or rod on the other. With powders, the melting temperature of the material can be at best about 70 % of the flame temperature, while with rods or cords, it corresponds to 90–95 % of the flame temperature. The combustion process uses gaseous fuels, and the mean power of a torch is around 40 kW.

18.2.1.1 Powders

(a) As-Sprayed Coating

Sprayed materials are mainly metals or polymers, which are rather easy to melt and spray. Particles are axially injected into the flame. Coatings present a high porosity (>10 vol. %) and a low adhesion (<30 MPa). Powder feed rates is typically between 2 and 10 kg/h, depending on sprayed material and torch used. The deposition efficiency is around 50 %. In-flight oxidation of the powder occurs during processing (oxide content between 6 and 12 wt%). They are used for wear abrasion under low load and wear adhesion under low load. For details see Sect. 5.2.1. Substrate and coating must be cooled during spraying. Flame spraying is generally rather noisy (90–125 dBA).

(b) Remelted Coating (Flame, Furnace, Induction)

Self-fluxing alloys (see Sect. 5.2.2.2) contain Si and B (for example, CrBFeSiCNi) which are used as deoxidizers. When the coating is heat treated at about 1,030 °C they diffuse toward the coating surface trapping the oxygen. It results in coatings with almost no porosity, an excellent adhesion by diffusion at the substrate–coating interface. It is also very easy to deposit materials of brazing type, and composite coatings are possible. Of course these coatings are limited to substrates that can tolerate the fusing temperature (steel and not aluminum for example) and possibly any induced distortion. Such coatings are used against abrasion (friction, erosion) and corrosion (cold or hot).

18.2.1.2 Wire, Rod, or Cord

A compressed air jet atomizes the melted tip of the wire (metallic and ductile) or cored wires (containing ceramics or non-ductile materials), rod, or cord (for ceramics). Due to the compressed gas atomization, the noise level is not negligible. For details see Sect. 5.2.3. Compared to powders, the variety of materials that can be sprayed as wires, rods, or cords are larger. Wires of self-fluxing alloys can also be sprayed. Oxides are of course generated during the process, but less than with powders (about 4–8 wt%), and the deposition efficiency is better (around 70 %). Compared to powders the material flow rate varies from 5 to 25 kg/h. With wires the coating adhesion is slightly better than that obtained with powders. The porosity is similar to that obtained with powders except for ceramic materials that are more porous but present an excellent wear resistance. Generally the metal or alloy coatings are used against wear, especially abrasion or adhesion under low load,

for example, in rotating heavy equipments, piston rings and synchronizing rings, and atmospheric corrosion: bridges, large steel structures, galvanized tubing, ships, . . . The wire flame spray noise level is between 118 and 122 dBA, while with rods it is about 125 dBA. For details see Sect. 5.2.3.

18.2.2 D-Gun Spraying

This process is pulsed at a frequency between 6 and 100 Hz. Particle velocities are due to the energy of a detonation (explosion) (for details see Sect. 5.4.1). The resulting deposit is extremely hard, dense, and tightly bonded to the substrate. The process is the noisiest of all the thermal spray processes (more than 145 dBA). Coatings porosity is low (below 1 vol. %) and its oxygen content is between 0.1 and 0.5 wt%. The deposition efficiency is around 90 %, but powder flow rates are limited to the 1–2 kg/h range. Sprayed materials are mainly powders of metals, alloys, and cermets. Some oxides can also be sprayed by this technique as long as particle sizes are below 20 μm. The main applications are abrasion and adhesion (friction) under low load as well as corrosion. Substrate and coating must be cooled during spraying. For more details see Sect. 5.4.1.

18.2.3 HVOF–HVAF Spraying

HVOF and HVAF are also combustion-driven processes with internal combustion at pressure below 1 MPa for those with gaseous fuel and slightly higher for those with liquid fuels. They produce very high-velocity gas streams, thanks to a convergent–divergent nozzle following the combustion chamber (see Sect. 5.3.1.1). In most cases, particles are axially injected but radial injection is possible with some guns. Power levels for HVOF guns working with gaseous fuels are in the range of 100–120 kW, with a noise level of 125–135 dBA. For those working with liquid fuels, the power can reach 300 kW with a noise level of 133 dBA or more. The actual trend is to increase particle velocities and reduce their temperatures in order to limit their oxidation (see Sect. 5.3.1.5), the high-kinetic energy of particles compensating for the lower temperature. This was first realized with HVAF guns working with air and where the noise level was 133 dBA or more. In the high-power guns, especially designed for that, high quantities (up to 2,000 slm) of nitrogen are injected in the combustion chamber to reduce gas temperature and increase its velocity. Globally this process, working mainly with metals, alloys, and cermets (one of their most successful application) has deposition efficiencies of about 70 % for powder flow rates up to 7.2 kg/h for gaseous-fuel guns, and up to 12 kg/h for liquid-fuel guns with deposition efficiencies roughly of 60–80 %. Resulting coating porosities are a few vol. %, with a good adhesion (>50–60 MPa) and low oxygen content (between 0.5 and a few wt%). Due to shot-peening effect, stresses are compressive and rather

thick coatings can be achieved (up to 6.4 mm). Of course the process is noisy, dusty, and requires special safety precautions for the handling of large flow rates of explosive gases. As with D-guns, the main applications of HVOF and HVAF spraying guns are against wear and corrosion. The wear resistance: sliding/adhesive wear, fretting, erosion or cavitation, of course depending on the material and process parameters chosen, is generally excellent. The corrosion resistance is also very good with the high density of coatings and, according to the sprayed material, they are used for hot corrosion, oxidation, against acidic or alkaline atmospheres and liquids. Substrate and coating must be cooled during spraying. A few processes have been developed to spray wires but in most cases powders are used. For details see Sects. 5.3.1 and 5.3.2

18.2.4 Wire Arc Spraying

Two wires or cored wires are continuously fed to a point where the arc striking at their tips melts them and an atomizing gas form the superheated spray droplets accelerating them toward the substrate. The high-droplet temperatures produce metallurgical interactions or diffusion zones or both after impact with the substrate or previously deposited layers. The maximum arc current, can vary from 200 to 1,500 A. This process spray rates between 5 and 30 kg/h, with deposition efficiency of about 80 %, are higher than most other spray processes. Consequently, it is one of the most economical processes, as long as the materials to be sprayed can be obtained in the form of wires or cored wires. The noise level is similar to that of wire flame process: 118–122 dBA. The oxide content depends strongly on the sprayed materials but is rather high, over 25 wt% for Al, for example. Using nitrogen instead of air as atomizing gas can reduce the oxidation level in the deposit, but depending on the required gas flow rates (around 1.0 m^3/min or more) the process becomes expensive. Porosity is usually over 10 vol. % and the coatings adhesion is medium in the 40 MPa range. An advantage is the minimal heating of the substrate, while the divergence of the spray pattern is a disadvantage. As other spray processes it is noisy and dusty. Coatings can be used for abrasion and adhesion (friction) under low load but their main use is for atmospheric or marine corrosion protection and a broad range of electrical applications. For more details see Sects. 9.2, 9.7, and 9.8.

18.2.5 Plasma Spraying

With temperatures over 8,000 K any material whether metallic or ceramic can be melted. At conventional spray distances, 10–12 cm, the heat flux to the substrate is among the highest ($\approx$2 MW/m^2) and the substrate as well as the coating must be cooled. To avoid oxidation, spraying must be performed under controlled atmosphere or soft vacuum conditions.

18.2.5.1 Air Plasma Spraying

The heat source is a direct current (d.c.) arc through which flows a nonoxidizing and/or non-carburizing gas. In most cases powder injection is radial. For plasma spray torches with one-stick type cathode, power levels range from 30 to 90 kW. For power levels in the range 40–50 kW, the powder flow rate is between 3 and 6 kg/h, the deposition efficiency around 50 %, and the torch noise level between 110 and 125 dBA. With high-power torches (250 kW), powder flow rates as high as 15–20 kg/h can be reached. With tri-cathode torches, torch power varies from 40 to 80 kW. Plasma torches developed by Mettech comprise three-plasma jets converging in a nozzle which length and diameter can be varied; particles are axially injected between the three converging plasma jets and power levels reach 150 kW.

Plasma-sprayed coating porosities are between 2 and 8 vol. %, the oxygen content of metal or alloy coatings being between 1 and 5 wt% and their adhesion is good (>40–50 MPa). They are mainly used to spray oxides. However they present good resistance to abrasive, adhesive, fretting, or sliding wear. They also produce thermally conductive or resistant surfaces. They are used for salvage and restoration of worn surfaces. For details see Sects. 7.3 and 7.8.

18.2.5.2 Inert Atmosphere Plasma Spraying

When oxidation is a problem, metals with high-melting temperature and non-oxide ceramics can be sprayed only in inert atmosphere (chamber filled with argon), at atmospheric pressure or slightly over. The technique is mostly used to melt materials with high-melting temperature, such as TaC, which has a melting temperature close to 4,000 °C. The controlled atmosphere chamber must be water cooled if its volume is below 10 m^3, and industrial scale production of such coatings requires using antechambers (connecting zones) to introduce and remove parts from the chamber, without allowing for air penetrating the main chamber. The noise level is that of the surrounding pumps, fans, and power supply. With all the equipment required, including that of argon gas recycling (see Sect. 17.4.3), the equipment cost is rather high compared to that of air plasma spraying.

18.2.5.3 Vacuum d.c. Plasma Spraying (VPS)

In this case the controlled atmosphere is at a pressure below atmospheric (in the tens of kPa range, see Sects. 17.4.1 and 7.9) and can even be below the 0.1 kPa range, for vapor deposition (see Sect. 17.4.2). According to the plasma jet expansion, the mean ambient temperature in the chamber is over 200 °C. The noise level is similar to that of inert atmosphere spraying. The equipment is more complex than that of inert atmospheric pressure spraying and consequently is the most expensive of all spray processes. One of the advantages of the process, besides the significant

reduction of oxidation, is the possibility to remove the oxide layer from the substrate. This is achieved with a transferred arc etching the surface of the substrate prior to deposition, the part to be coated being in a reversed polarity (cathode of transferred arc). During the deposition step, the part is heated to a sufficiently high temperature to achieve diffusion bonding between the sprayed metal or alloy and substrate, the part being then the anode of the transferred arc. This process is used for high-added value parts, such as turbine blades.

18.2.5.4 Induction Plasma Spraying (VIPS)

Induction plasma spraying is usually carried out under controlled atmosphere at atmospheric pressure (IPS), or soft vacuum conditions, down to 10 kPa (VIPS) (for more details see Sects. 8.2 and 8.5). The process is essentially similar to d.c. vacuum plasma spraying (VPS), with the exception that the torch is fixed with respect to the chamber walls, while the substrate has to be translated in a linear or rotating movement across the stream of molten droplets immerging from the torch at the required spraying distance. With torches i.d. of a few tens of mm, against below 10 mm for d.c. ones, the plasma jet velocity is considerably lower (<100 m/s) than that of a corresponding d.c. plasma jet, at a comparable power rating. It allows spraying bigger particles (up to 200–250 μm) than those sprayed with d.c. torches. Typical plasma power ratings for VIPS installations are in the 50–400 kW range, with corresponding powder feed rates of 2–10 kg/h, depending on the sprayed material. Induction plasma spraying is mostly used for the spraying of metals and ceramics on small parts with a high-added value and coating densities close to 98 % of the theoretical value. VIPS is used on an industrial production scale for the deposition of high purity silica on fiber optics performs and refractory metals on X-Ray targets. However one of their main applications is powder spheroidization to produce powders with an excellent flow ability that are used for many applications not necessarily linked to spray processes. For more details on VIPS equipment, design, and operating conditions see Sect. 8.5.

18.2.6 Plasma-Transferred Arcs (PTA)

The process is a combination of welding and thermal spraying process that requires electrically conductive substrates acting mostly as the anode. The feedstock is wires or powders with particle sizes in 100 μm range. Metals, alloys, and cermets are sprayed using PTA techniques. The different guns are characterized by the maximum current varying from 200 to 600 A. The coatings are thicker than those of other spray processes; they can be 10 mm thick or more, and a metallurgical bond with the substrate is achieved. The substrate must be kept as horizontal as possible during spraying. No porosity is observed and the deposition efficiency is over 90 %.

Powder flow rate can be as high as 18 kg/h or even more with high power devices. The resistance to wear is excellent as well as that to high temperature corrosion. These coatings are used to achieve high-quality rebuild surface, to coat large and heavy parts without cracks or deformation, to produce smooth and highly wear-resistant surfaces. PTA coatings are used against wear in different industries: mining, pulp and paper, oil and gas, power, . . .

18.2.7 Plasma Transferred Arc

The process is significantly different from the other coating processes as the substrate is part of the electrical circuit that delivers the power for the coating process. As the substrate in most of the cases serves as the anode of the arc transferred from the torch it must consist of an electrically conducting material. The stability of the arc is improved when using a "pilot arc" between the cathode and the nozzle of the transferred arc, which becomes the anode of the transferred arc. It requires a two-stage power supply or two independent power supplies. The powder, bigger than with most other spray processes (typically 50 to 150 μm), is introduced into the arc plasma though two or more orifices located on a ring surrounding the exit of the nozzle. A further annular slot surrounding the powder injection ring provides the shield gas flow, necessary to avoid reaction of the molten metal pool with the environmental air. The coating is different from those obtained from other thermal spray coating processes because the arc melts to some degree the substrate material, and the molten powder of the coating material is mixing with the molten substrate material. The consequence is that a good metallurgical bond or fusion bond is achieved, and that the porosity is very low, however, the heat penetration region and in particular the region where the coating material is mixed with the substrate material can change the properties of both the substrate and the coating. This mixing region is expressed in terms of the "dilution". Torches used are divided into three different categories according to the deposition rate and the power used: Micro PTA with deposition rates of 0.1–2 kg/h, used for small components, or components with complex shapes, regular PTA for deposition rates of 2–10 kg/h, and high power PTA for deposition rates between 10 and 20 kg/h.

Compared to other coating processes, the substrate must be metals or alloys, coatings are also metals or alloys with the possibility to achieve cermet coatings, the deposited metal must be compatible with that of substrate. Coatings are also different because they are generally fully dense and considerably thicker than other coatings (up to a few cm). Their main use is for wear and corrosion resistance applications. For more details see Chap. 10.

18.2.8 Cold Spray

Cold spray is mostly used for the spraying of metals on virtually any substrate, with the main advantage of avoiding the in-flight oxidation of the powder and achieving high coating densities. With this spray process, the oxide content of the coating is limited to that of the sprayed powder (for example, less than 100 ppm for copper). After optimization of the spray parameters and proper choice of powder characteristics, the mechanical and electrical properties of as-sprayed coatings are remarkably close to those of bulk materials, especially with very good tensile properties. However the ductility of cold-sprayed coatings can be rather low due to the important work hardening inherent to the process. Coatings are made of pure metals, ferrous, and nonferrous metal alloys, composites, and cermets; provided, they are ductile (at least the matrix for cermets). The noise level is about 110 dBA. For more details see Sect. 6.2. The drawback of the process is the high nitrogen or helium (or both) flow rates needed. With flows in the few m^3/min range within the de Laval-type nozzle, particles achieve very high impact velocities (up to 1,200–1,500 m/s). Recycling helium requires to spray in a controlled atmosphere with the chamber adapted to the part size, and if necessary antechambers to introduce it, and use pumps, filters, and tanks to recycle the gas, thus increasing the investment. In this case, the noise level is that of the surrounding equipment. The deposition rates are in the 2–10 kg/h with deposition efficiency in the 40–90 % range depending strongly of sprayed materials. The first and very successful application was copper metallization, then the selective protection of localized areas against corrosion, rapid tooling repair, electromagnetic shielding, and repair of magnesium components. It is also used for metal restoration and sealing, engine blocks, castings, molds and dies, refrigeration equipment, heat exchangers, for aluminum piston heads, manifolds, disc brakes, for heat sinks for microelectronics (Al and Cu), for solid lubricant matrix with base metals, for electronically conductive coatings (Cu or Al on ceramic or polymeric components), for localized corrosion protection (Zn or Al coatings), . . .

18.3 Thermal-Sprayed Coating Applications

Of course the list presented below is far to be exhaustive and its goal is to emphasize the wide variety of thermal-sprayed coatings. However the reader must keep in mind that the sprayed materials (see Appendix) have mechanical, thermal, service properties different from those of bulk ones. They depend on the real contacts between layered splats, porosities, crack types and distributions, oxide inclusions, materials partial decomposition (WC for example). Coating morphologies and microstructure are linked to the spray process used, the morphology of the sprayed particles, depending on their manufacturing process, the spray parameters, the substrate used, the coating thickness and the possible post-treatments of coatings (annealing, laser, hot isostatic pressing, . . .). For each topic a few examples are given.

18.3.1 Wear Resistant Coatings

"Wear is the problem" and it occurs in almost all industries where thermal-sprayed coatings are used. In all cases, it is a progressive loss of material at the active surface due to the relative movement of another part or particles on this surface. The lifetime of the coating depends on its resistance to wear and its thickness, which can reach up to 10 mm with PTA coatings. The different types of wear are described below, according to [2–8]. For each type of wear, a few examples of coatings are presented.

18.3.1.1 Abrasive Wears

It corresponds to weight loss with grooves, pits, and scores at the surface due to cutting or deformation. It results from either two-body abrasion where the asperities or defects of one of the surface plough or abrade the counter face, or three-body abrasion where hard particles move freely between both surfaces or are imbedded in one of them (for more details see Sect. 15.9.1). The phenomena are promoted when temperature, humidity, aggressiveness of the environment (corrosion) increase. The three-body abrasion depends also on the shape, grain size, and hardness of the abrasive particles and the relative speed of the two bodies. As a general rule abrasion increases drastically as soon as the hardness of one metal or alloy becomes equal to that of the abrasive particles. If the abrasive belongs to the surrounding medium the contact must be protected from it and wear debris must be removed or trapped. At last the roughness of the harder surface must be reduced to the minimum. It must be emphasized that abrasion wear represents more than 50 % of wear. In most cases wear-resistant coatings are hard with a good resistance to heat and chemical attack; coating materials with such properties are [2]:

(a) Self-Fluxing Alloys

If their corrosion resistance is generally excellent, their hardness is not particularly high and they cannot compete with cermets for sliding wear resistance. Thus one can either spray them with hard particles or heat-treat them. This for example the solution proposed by Bolelli and Lusvarghi [9]. After HVOF spraying Co-28 %Mo-17 %Cr-3 %Si coatings, they studied them as-sprayed and after heat treatments at 200, 400, and 600 °C for 1 h. A significant degree of splat boundary oxidation existed in the as-sprayed coating, because of exothermic oxidative reaction occurring at $T > 810$ °C; thus, it had low hardness and toughness, resulting in poor tribological performance. The 600 °C treatment caused the appearance of submicrometric crystalline regions improving hardness and elastic modulus and the sliding wear performance at room temperature was improved. Kulu and Hailing [10] have flame-sprayed NiCrSiB self-fluxing alloy-base composite powders,

containing WC–Co hard metal powders (from 15 to 50 wt%) from used (recycled) hard metals. They compared them with D-gun-sprayed WC–Co particles. The wear resistance of coatings at small impact angles of abrasive particles increased with an increase in matrix phase hardness as well as with an increase in hard phase content in the composite. However the wear resistance of the self-fluxing alloy coatings, reinforced with hard metal particles, was low at straight impact. Sakata et al. [11] have flame-sprayed Co-based (Co–Cr–W–B–Si) self-fluxing alloy coating. The diffusion treatments of thermally sprayed Co-based self-fluxing alloy coating on steel substrate were carried out at 1,370–1,450 K for 600–6,000 s under an Ar gas atmosphere. The proper diffusion treatment precipitated two kinds of fine compounds in Co-based matrix: a chromium boride dissolving cobalt and a tungsten boride containing cobalt and chromium. The size of each precipitate became larger with increasing treatment temperature and time. A coating with the proper size borides showed a superior wear resistance. The diffusion treatment temperature of 1,397–1,406 K substantially improved the abrasion resistance. Otsubo et al. [12] fused flame-sprayed coatings of nickel-base self-fluxing alloy, containing chromium and boron, and also showed that they resulted in complex structures. Kulu and Pihl [13] have sprayed WC–Co systems and self-fluxing alloys, containing tungsten carbide-based hard metal particles [NiCrSiB-(WC-Co)], by the detonation gun, HVOF JP 5000 that they called "continuous detonation spraying," and spray fusion processes. They found that coatings must have the following properties: minimum porosity (less than 3 vol. %), hardness higher than that of the abrasive, and a metal matrix structure containing particles of WC–Co granules, or WC–Co particles to have a good resistance to oblique impact and normal impact. Miranda and Ramalho [14] studied coatings sprayed, with different proportion mixtures, two commercial alloys, a nickel self-fluxing alloy and a tungsten carbide–cobalt. Coatings were sprayed by HVOF and powder oxyacetylene flame processes. The effect of both hard-phase content and coating-spraying technique on abrasion resistance was studied in terms of the coatings' mechanical properties and microstructures. For coatings produced by powder flame spraying, the remelting after spraying led to increased adhesion to the substrate and also higher hardness, especially in the coatings with a larger WC + Co percentage. PTA is used against abrasive wear in petrochemical, mining and agricultural applications see Sect. 10.7.3 of Chap. 10.

(b) Cermet Coatings, Especially Those HVOF or HVAF Sprayed

Coating quality is strongly linked to the spray process and parameters, especially with WC particles. If corrosion problems are also to be considered, Cr is important in the metal matrix. For example, Schwetzke and Kreye [15] have sprayed different WC–Co and WC–Co–Cr powders with various high-velocity oxygen fuel spray systems (Jet Kote, Top Gun, Diamond Jet (DJ) Standard, DJ 2600 and 2700, JP-5000, Top Gun-K). Powders exhibited various degrees of phase transformation during the spray process depending on type of powder, spray system, and spray

parameters. Phase transformations increased when the injection of the powder occurred in a region where the flame temperature was highest, for example, into the combustion chamber of the Top Gun system. Decarburization of agglomerated and sintered WC–Co 83-17 powder ranged from 25 to 70 % for the various spray systems and fuels. When the carbon loss remained below 60 %, the properties of the coatings such as hardness and wear resistance were not influenced. The decarburization seemed to be compensated by the hardening with the formation of a solid solution of cobalt (tungsten, carbon) and hard W_2C and h-phases. If the wear resistance of WC–Co–Cr coatings were comparable to those of WC–Co, the corrosion resistance of WC–Co–Cr was considerably higher.

Kasparova et al. [16] have evaluated the abrasive wear resistance and adhesive strength of HVOF-sprayed WC–Co and the Cr_3C_2–NiCr coatings. They found that high-stress abrasive conditions change the coatings behavior very significantly, particularly that of the Cr_3C_2–NiCr coating. The high-plastic deformation and pulling out of entire splats or splat blocks, especially during abrading by the alumina sand, were detected under the high-stress abrasive conditions for both coatings, but much more with Cr_3C_2–NiCr. As shown by Houdkova et al. [17], the spraying angle is one of the deposition parameters that influence the quality of thermally sprayed coatings. They HVOF (TAFA JP-5000) sprayed WC–Co and Cr_3C_2–NiCr coatings with different spray angles. Their results showed that with a maximum 30° angle diversion from the normal spray direction for WC–Co and 15° angle diversion for Cr_3C_2–NiCr coatings wear resistance was not reduced. Tillmann et al. [18] used statistical design of experiments to identify the most relevant factors influencing the HVOF spraying of fine $75Cr_3C_2$–25(Ni20Cr) powders and find an optimum setting of these factors to produce coatings with improved morphological and mechanical properties. Fine structured coatings obtained showed an extremely dense and finely dispersed structure (porosity <2 vol. %), a high surface quality (Ra < 2 μm) and a high adhesive strength. These coatings showed a high potential to be used as wear-resistant coatings for large tools without any post treatment or surface finish.

Recently, considerable emphasis has been placed on HVOF thermal spraying of nanostructured WC/Co to achieve high hardness combined with excellent wear resistance. However, it appeared difficult to achieve dense coatings and avoid decarburization. Skandan et al. [19] have HVOF-sprayed homogeneously mixed powders. They consisted of WC/12 Co agglomerates in the range 15–40 μm with a carbide grain size of 2–5 μm (70 vol. % of the mixture) and WC/5 Co, forming particles in the range 0.1–0.5 μm with each particle composed of many WC nanometer-sized crystals (~30 nm in diameter). The coating was dense and had no decarburized phases. The abrasion wear resistance was at least 50 % better than that of a pure coarse-grained WC/Co coating. In their review Lima and Marple [20] have presented superior abrasion and sliding wear performance of nanostructured ceramic coatings (Al_2O_3, Al_2O_3–13 wt% TiO_2, Al_2O_3–3 wt% TiO_2, TiO_2, and YSZ) when compared to those of conventional coatings. By employing HVOF and nanosized ceramics, the abrasion wear levels could be reduced by up to 90 % in comparison with the wear performance of optimized APS conventional ceramic

coatings. It was generally observed that the nanostructured coatings were not harder than the conventional ones; however, they tended to be much tougher. Kim and Walker [21] have developed nanostructured titania coating specifically for ball valves destined for high-pressure acid-leach (HPAL) service. These coatings were compared to conventional ones. The nanostructured titania coating provided dramatically superior resistance against abrasive and erosive wear, better wear performance attributed to improved toughness.

Gawne et al. [22] have plasma-sprayed ball-milled mixture of glass and alumina powders to produce alumina–glass composite coatings. The alumina raised the mean hardness from 300 HV for pure glass coatings to 900 HV for a 60 wt% alumina–glass composite coating. The scratch resistance increased by a factor of 3 and the wear resistance by a factor of 5, maximum value obtained with 40–50 vol. % alumina. This alumina content corresponded to the change over from a glass matrix to an alumina matrix. Cipri et al. [23] produced thick alumino-silicate coatings by plasma-spray technique. Coatings, efficiently coupling to metallic substrates even after plastic deformation, exhibited very interesting performance in terms of mechanical properties and fracture toughness (elastic modulus of 43 GPa and K_{1c} of about 2 MPa $m^{1/2}$ for 850 μm thick coatings) and compliance. Thus they showed an excellent refractory behavior allowing a wide use as wear-resistant thermal barrier coatings in metallurgical and glass plants and in high-temperature heat exchangers. At last to illustrate the interest of such coatings, Kang et al. [24] used detonation gun to spray three different WC–Co–Cr, Cr_3C_2–NiCr, and Stellite-21 coatings on high-tensile steel rotavator blades. The wear rates of Cr_3C_2–NiCr and Stellite-21 coated blades showed significant superiority over the uncoated blade, but not as much as shown by WC–Co–Cr coated blade.

18.3.1.2 Erosive Wear

It occurs when hard particles carried by a fluid hit the surface (for details see Sect. 15.9.3). The impact angle plays an important role on the wear rate depending on the surface material: ductile, hard metal, ceramic, . . . [4, 5]. To reduce the wear, one must choose a coating material harder than the abrasive particles, with toughness high enough, especially for inclined impact angle between 30 and 45°, which must be avoided if possible, and the coating roughness must be reduced to the minimum. It is also important to avoid turbulences in service conditions because they increase erosion. The erosion is much more complex than abrasive wear in which the wear resistance is predominantly influenced by the hardness of the coatings. The erosion depends on the response behavior of coatings to the impact of erosive particles at high velocity. It is usually considered that the wear and erosion resistance of cermet coatings are predominating influenced by their microstructures including the splat size, carbide particle size, carbide content, and carbide distribution within a splat, and the cohesion between the splats [25, 26]. For example, Kim et al. [25] showed that inter-splat cohesive strength of coatings, measured by a simple bonding test, was the most significant factor relating to the wear rate of plasma-sprayed

WC-12 wt% Co coatings. As previously emphasized, the microstructure strongly depended on starting powder, spray system, and spray conditions. Other parameters, such as the influence of time, solid loading, impingement angle, temperature, particle velocity, as well as the erosion–corrosion mechanism must also be considered [27]. When comparing the influence of dry and slurry erosion on HVOF coatings, it was shown that erosion rates in dry particle impact were about three orders of magnitude higher than those in slurry systems. This difference probably reflects the real erodent target impact velocities, which are mitigated in the slurry test by the water medium [28]. A few examples are presented below. Ji et al. [29] have HVOF-sprayed Cr_3C_2–NiCr coatings and erosion tests were performed at different jet angles of abrasive particles. The erosion occurred dominantly by spalling of splats from the lamellar interfaces, spalling resulting from the propagation of cracks parallel to the interfaces between the lamellae exposed at the surface and underlying coating. The carbide particle size and content in the coating influenced significantly the erosion performance of Cr_3C_2–NiCr coatings. Yang et al. [30] have compared the high-temperature erosion behavior of HVOF-sprayed Cr_3C_2–NiCr coating with mild steel for circulating fluidized bed boiler tubes. The erosion rate of the HVOF-sprayed Cr_3C_2–NiCr coating was not influenced by the temperature in the range of 300–800 °C, while that of the mild steel at 800 °C was four times that at 300 °C at an erosion angle of 30°. Osawa et al. [31], for WC–Co HVOF-sprayed coatings, have shown that the substrate also played a role in coating erosion resistance. For the studied variety of steel substrates, the near-surface hardness of the substrate resulting from the work hardening caused by peening during the grit blasting and HVOF spraying played a dominant role. It improved the ability of the substrate to support the coating and thus the integrated coating-substrate performance during impact loading. Kulu et al. [32] sprayed, by detonation gun, HVOF JP 5000 spraying, and spray fusion process, tungsten carbide-based hard metal, nickel-based self-fluxing alloy, and composites NiCrSiB. For all of them the erosion was strongly affected by particle impact angle. For all materials tested, the erosion rate was 5–6 times higher at elevated temperature, but in that case, the influence of impact angle had no great effect. Ramesha et al. [33] have plasma-sprayed Inconel-718 (thicknesses of 200 μm and 250 μm) on mild steel. Increased coating thickness decreased the porosity and increased the hardness significantly. Inconel-718 coatings exhibited improved slurry (containing 3.5 vol. % NaCl) erosive wear resistance when compared to uncoated mild steel. The wear resistance increased with coating thickness. Higuera Hidalgo et al. [34] have compared the behavior of plasma- and flame-sprayed modified nickel–chromium alloy (with small aluminum and titanium additions) subjected to the action of simulated post-combustion gases from a coal-fired boiler combustor. With flame, the adherence was much lower even with a bond coat. High-temperature oxidation rate of nickel–chromium coatings in post-combustion gases from coal-fired boilers, (atmospheres with 3–3.5 vol. % of free oxygen) was low. The embedment of fly ash particles on the surface of coatings was especially important at higher temperatures (800 °C). The erosion behavior of nickel–chromium flame and plasma-sprayed coatings at medium temperatures (500 °C) was characterized by low erosion rates

and a ductile erosion mechanism. At 800 °C the wear was essentially corrosive. Krishnamurthy et al. [35] studied the erosion resistance of plasma-sprayed alumina and calcia-stabilized zirconia coatings on Al-6061 substrate. It was found that erosion of coating systems occurred through spalling of lamella exposed on coating surface resulting from cracking along the lamellar interface. Erosion wear was more at 45° angle of impact. Pores seemed to act as stress concentrators and decreased the load-bearing surface. At last, the promising behavior of unconventional nanoscale composite coatings must be underlined. Branagan et al. [36] have wire arc-sprayed amorphous SHS7170. Coatings were found to develop an amorphous matrix structure containing starburst-shaped boride and carbide crystallites with sizes ranging from 60 to 140 nm. The performance of the SHS7170 coatings in boiler environments was measured via elevated temperature erosion experiments conducted at 300, 450, and 600 °C using bed ash from an operating circulating fluidized-bed combustor boiler, and the results were compared with those for existing boiler coatings. The elevated temperature erosion resistance of the SHS7170 wire arc coatings was found to be superior, based on thickness loss, compared with the existing wire arc coatings that have been tested. SHS7170 coatings have resisted to erosion almost independently of contact angle.

18.3.1.3 Friction and Adhesive Wears

It occurs when particles are transferred from one interacting surface to the other. When different materials are in contact, particles are mainly transferred from the softer or weaker material onto the harder one. This wear is promoted when increasing the load and/or the temperature, and under dry friction, or poor lubrication (see Sect. 15.9.2). It depends on the structure, composition, hardness, and melting temperature of the material.

To reduce it, dry friction must be avoided and, if it is not possible, coatings containing solid lubricants or retaining lubricants must be used. The compatibility of materials is also important: the friction coefficient, f ($f = T/N$, $T =$ tangential force, $N =$ Normal force), depends on the couple of materials rubbing against each other. It is also linked to the load, P, (or more precisely the pressure, p), and the relative velocity, v, between both parts (in principle the product, $p \cdot v$, must be below 1 MPa m/s [3]) The roughness of surfaces into contact must be as low as possible and from a rough surface (Ra of a few μm) to a smooth one (Ra < 0.1 μm), f, can be reduced by 60 %. Dry friction, usually results in high local heating and, even with a very low relative velocity, the friction coefficient, f, increases with temperature. Low friction coefficients can be achieved with solid lubricants ($f = 0.001$–0.05), but the relative velocity must be low. Using materials with a high thermal conductivity (both coating and substrate) reduces the heating due to friction. As wear increases with the energy of adhesion, it is also important to avoid micro welding, i.e., to use materials with a low solubility and a narrow range of solid solution (ex: Fe/Al, Fe/Cu). The work of adhesion decreases with the

following couples: metal–metal, metal–ceramic, ceramic–ceramic, metal–polymer, ceramic–polymer, and polymer–polymer. A few examples are presented below.

High stress, due to too high average pressure or very high local pressure that exceed the elastic limit, might be favorable when it strengthens the material by work hardening, but it might result in surface embrittlement of surface layers reducing their fatigue strength. It is promoted by an increase of the friction coefficient or temperature. Here again the worst occurs when cracks propagate.

(a) Ceramic Materials

Pantelis et al. [37] have plasma sprayed a 450 μm thick Al_2O_3 coating deposited on cast iron substrate. Wear tests were carried out with normal force varying from 50 to 160 N, sliding speed of 1.40 m/s, and average relative humidity of 60 %, using as a counter-body a quenched D2 tool steel (D-type tool steels contain between 10 % and 18 % chromium and D2 is very wear resistant but not as tough as lower alloyed steels). The coating wear rate presented three stages. During the first one, the wear rate was decreasing rapidly and the wear of the coating proceeded via adhesion mechanism. During the second stage, wear rate remained almost constant and the wear of the coating was taking place via a combined "polishing/abrasion/fatigue" wear mechanism. During the last stage, wear rate increased rapidly until the total worn of the ceramic layer due to the "easy" removal of the completely cracked remained coating. The D2 tool steel counter-body was also worn out by a combination of wear mechanisms. Sanchez et al. [38] have plasma-sprayed Al_2O_3–13 %TiO_2 coatings on stainless steel substrates from conventional and agglomerated nanostructured powders. The wear resistance of conventional coatings was shown to be lower than that of nanostructured coatings. As already emphasized in Chap. 14, Darut et al. [39] found that the friction coefficient of Al_2O_3 coatings, suspension plasma sprayed (SPS), was decreased by a factor of 2 compared to that obtained with micrometer-sized particles; meanwhile, alumina was not a material suitable for friction layers. Moreover, wear rate was 30 times lower for SPS layers compared to the conventional ones. Bolelli et al. [40] have HVOF-sprayed alumina suspensions and compared them to coatings obtained with conventional powders sprayed with APS and HVOF. With the suspension, porosity is much lower and pores are smaller than in conventional coatings. Moreover, few inter-lamellar or intra-lamellar cracks exist, resulting in reduced pore interconnectivity (evaluated by electrochemical impedance spectroscopy). Such strong inter-lamellar cohesion favors much better dry sliding wear resistance at room temperature and at 400 °C. Ahn and Kwon [41] studied the tribological behavior of plasma-sprayed chromium oxide coatings against cast iron both in dry at 450 °C and lubricated wear tests at room temperature and 200 °C. Under dry sliding conditions, dispersed smooth surface films were formed by plastic deformation of compacted debris particles that adhered to the surface and these films strongly influenced the friction coefficient and wear rate of the coating. Considerable quantity of CrO_3 was detected at room temperature, whereas CrO_2 (more favorable

than CrO_3 in reducing friction) was detected at 450 °C. Under lubricated sliding conditions, tribochemical reaction films of different species of carbon–oxygen bond units were formed depending on the test temperature and they appeared to be effective in reducing friction and preventing wear. Pratap Singh et al. [42] studied the tribological behaviors of plasma-sprayed conventional and nanostructured (agglomerated nanoparticles) Cr_2O_3–3 %TiO_2 ceramic coatings. Samples coated with nanostructured powder exhibited better properties such as higher hardness and less porosity as compared to conventional powder coated samples. Dry sliding wear resistance of nanostructured powder under 60 N load was better than the wear resistance offered by conventional powder under 50 and 60 N load for similar testing conditions. In general, nanostructured powder exhibits a better wear resistance than conventional powder. Tao et al. [43] deposited Al_2O_3 and Cr_2O_3 coatings on stainless steel by atmospheric plasma spraying and tested their dry sliding tribological properties against copper alloy using a block-on-ring configuration at room temperature. The wear resistance of Al_2O_3 coating was superior to that of the Cr_2O_3 coating under these conditions. This was mainly attributed to the better thermal conductivity of Al_2O_3 coating (about 2.8 W/m K for alumina against 2.4 for chromia at 400 °C), which was considered to effectively facilitate the dissipation of tribological heat and alleviate the reduction of hardness due to the accumulated tribological heat. Bolelli et al. [44] plasma-sprayed ceramic coatings (Al_2O_3, Al_2O_3–13 wt% TiO_2, Cr_2O_3) and tested them through pin-on-disk and dry sand–steel wheel tests. The toughest coating (Al_2O_3) displayed the highest wear resistance, which in fact overcame HVOF-sprayed cermets and Cr electroplating, when a low number of wheel revolutions were considered. Against the alumina ball, Al_2O_3 and Al_2O_3–TiO_2 coatings showed high wear rates and friction coefficients (due to chemical affinity), while Cr_2O_3 had better wear resistance, lower friction coefficient, and inflicted less wear on the counterpart. Cr_2O_3 wear scar consisted in plastically deformed splats and debris forming a quite adherent protective tribofilm. In pin-on-disk tests, no coating underwent wear loss against the 100Cr6 ball that possessed lower hardness. Ramachandran et al. [45] studied the friction and wear behaviors of Yttria Stabilized Zirconia (YSZ) coatings, Lanthanum Zirconate (LZ) coatings, and Inconel 738 base material (BM) sliding under unlubricated conditions, against a sintered tungsten carbide surface in a pin-on-disc configuration. They found that the wear resistance of the ceramic coatings got deteriorated with the increase in the percentage volume of porosity.

(b) Cermets

Dallaire [46] studied a cored wire, referred to as Alpha 1800, developed to produce tailored arc-sprayed coatings that were tough enough to resist particle impacts at 90° and sufficiently hard to deflect eroding particles at low impact angles. Results showed that coatings produced with the new cored wire are at least 5 times more erosion resistant and 10 times more abrasion resistant than coatings produced by arc spraying commercial cored wires.

Yang et al. [47] sprayed by a HVOF system three-agglomerated WC–12 wt% Co powders with different carbide grain size distributions. Dry sliding friction and wear behavior of the WC–12 wt% Co coatings was investigated by using sintered alumina (Al_2O_3) as the mating material at 200 °C, 300 °C, and 400 °C. The specific wear rate of the coatings increased when increasing the carbide grain size at a given testing temperature. It decreased when increasing the temperature for a given carbide grain size. The specific wear rate was reduced by more than one order of magnitude when the test temperature was increased from room temperature to 400 °C. The tribofilm formed at higher temperature was denser and more adhesive to the underlying surface, thus providing more surface protection against wear. The results showed that the formation of dense and well-adhered tribofilms played an important role on the low sliding wear rate of the coatings at elevated temperatures.

Yandouzi et al. [48] sprayed by pulsed gas dynamic spraying (PGDS) process both cryo-milled particles made of an Al matrix reinforced with B_4C powders (Al5356 + 20 % B_4C) and conventional composite. The presence of homogeneously distributed fine B_4C reinforcement particles embedded within the nanostructured Al5356 matrix significantly improved the dry sliding wear resistance of the coating. Li et al. [49] cold-sprayed dense Al5356/TiN composites with TiN particles uniformly dispersed in the matrix (50 wt% TiN). The coating porosity was less than 1 vol. %. The deposited composite coating presented an excellent performance compared to that of the composite sprayed without using the ball-milled powder.

Qiao et al. [50] studied the resistance of the coatings to abrasive and un-lubricated sliding wear of 40 WC/Co coatings applied by HVOF, high-energy plasma spray (HEPS), and high-velocity plasma spray (HVPS), using commercial and nanostructured experimental powders. Phase analysis by X-ray diffraction revealed various amounts of decarburization in the coatings, some of which contained WC, W_2C, W, and h phase. The wear resistance was lowered by decarburization, which produced a hard but brittle phase. Jacobs et al. [51] investigated the microstructural properties of WC–Co–Cr and WC–Co coatings deposited by HVOF and HVAF processes. The HVAF-sprayed coatings showed better sliding wear resistance compared to the HVOF coatings. The prime wear mechanism in the WC–Co HVAF coatings was adhesive wear; the lubricious cobalt matrix resulted in very low wear rates and low debris generation. The WC–Co–Cr HVOF coatings wear was linked to "pullouts" that became trapped in the contact zone and acted as a third-body abrasive. The HVAF/WC–Co–Cr coatings exhibited better resistance. Bolelli et al. [52] studied the tribological performance of two Colferoloy Fe–Cr–Ni–Si–B–C coatings HVOF sprayed and they compared them to other coatings. Under sliding wear conditions, these coatings were a good alternative to Ni-based alloy coatings but they could not replace Cr_3C_2–NiCr cermets (best sliding wear). These coatings were unsuitable for dry particle abrasion conditions. At 400 °C, all coatings were softened and their sliding wear behavior was dominated by more severe abrasive grooving and all differences were reduced.

Alam et al. [53] studied the tribological characteristics of low-pressure plasma-sprayed aluminum bronze coatings against steel ball. Under optimum operating conditions, the test samples exhibited a dense microstructure with high hardness, low coefficient of friction, and high wear resistance. Ouyang et al. [54] studied the tribological properties of VPS ZrO_2–CaF_2–Ag_2O composite coating (ZFA). At 300–700 °C, the ZFA coating exhibited lower friction and wear than at room temperature, 200 °C or 800 °C. Ag_2O and CaF_2 acted as solid lubricants effectively at 300–400 and 600–700 °C, respectively. But with the increase of temperature up to 800 °C, the severe adhesive sliding caused more material transfer and tearing out of coating, and finally leads to a high friction and wear.

(c) Metals

Ahn et al. [55] studied the wear resistance of plasma sprayed, on a low-carbon steel substrate, molybdenum blend coatings consisting of powders of bronze and aluminum–silicon alloy powders mixed with molybdenum. The wear test results revealed that the wear rate of all coatings increased with rising wear load and that the blended coatings had better wear resistance than the pure molybdenum coatings, although the hardness was lower. The molybdenum coating blended with bronze and aluminum–silicon alloy powders exhibited excellent wear resistance because hard phases such as $CuAl_2$ and Cu_9Al_4 formed inside the coating. Bolelli et al. [52] studied the tribological performance of two Fe–Cr–Ni–Si–B–C (Colferoloy) alloy coatings manufactured by HVOF thermal spraying, through rubber-wheel dry particle abrasion test and ball-on-disk sliding wear tests. Colferoloy coatings were validated as alternatives to Ni-based alloys and electroplated chromium under sliding wear conditions, but appeared unsuitable for particle abrasion resistance. The different sliding wear behaviors of HVOF-sprayed coatings were explained by coupling micro and nano-hardness to scratch testing, which reflected cracking resistance and plastic deformability. Rodriguez et al. [56] compared NiCrBSi alloys sprayed by either plasma or flame but then fused for the latter. Four sets of specimens were tested varying the composition (with the presence or not of WC in the powders). Coatings were tested in a reciprocating pin on plate wear machine able to select loads ranging from 50 to 200 N and temperatures up to 500 °C. NiCrBSi alloys, deposited by thermally spray techniques, maintained their wear resistant performances up to bulk temperatures of 500 °C. The alloys deposited by flame spraying with fusion had better wear resistance than those deposited by plasma spraying. The presence of tungsten carbide in the powders was not a beneficial factor on the wear performance of thermally sprayed NiCrBSi coatings. PTA is used to increase wear resistance mainly in steel industry, see Sect. 10.7.2 of Chap. 10.

(d) Polymers

At last at low temperatures polymers can be used against friction. Niebuhr and Scholl [57] sprayed with high-energy plasma polymer–steel coatings for high-contact pressure rolling/sliding systems. Polymers were applied as a thin film (75–100 μm) over a thicker (250–750 μm) steel coating. Twin roller rolling/sliding tests were performed at 5 and 35 % creep and contact loads of 1,700 N on a 5 mm contact face. A lower coefficient of friction (0.10–0.15) with increased durability compared with that of AISI 1080 steel thermally sprayed coating (coefficient of friction of 0.46) was observed under these rolling–sliding contact conditions. Li et al. [58] deposited, using the flame spray process, PEEK coatings with three kinds of crystallinities. Investigations were performed under dry sliding conditions against a 100C6 counter-body. The average friction coefficients appeared to decrease while increasing the sliding velocity, but were insensitive to the applied load in the range of investigation. The higher was the crystallinity of the coating, the lower was its average friction coefficient. The wear mechanisms of the different coatings were explained in terms of plastic deformation, plough marks, and fatigue tearing. Li et al. [59] flame sprayed polyamide1010 (PA1010) and its composite with nanometer-sized silica (PA1010/n-SiO_2). The dry friction and wear behaviors of both coatings were investigated under dry sliding conditions. The results showed that the addition of nanometer-sized silica increased the crystallinity of the coatings and reduced friction and wear compared to pure PA1010. The nano-composite coatings, containing 1.5 wt% nanosized silica, displayed better properties.

18.3.1.4 Scuffing

It is a localized damage caused by the occurrence of solid-phase welding between sliding surfaces, without local melting [1]. Scuffing may result from missing of lubricating film and formation of adhesive contact between surfaces and finish with the macro-damage [60]. Żórawski and Kozerski [60] characterized the tribological properties of plasma- and HVOF-sprayed WC–12 Co and Cr_3C_2–25(Ni20Cr) coatings. The WC–12Co coating sprayed using HVOF method showed the best scuffing resistance and the most homogeneous structure. The resistance was better for coatings presenting lower friction coefficient, higher hardness, and being more homogeneous. Edrisy et al. [61] HVOF coated the inner surfaces of the engine blocks working in racetrack conditions. During the deposition of the HVOF 2.5 % Al coating, the gun traveled along the length of the bore as it rotated inside the cylinder and sufficient excess coating was applied so that about 30 % of the coating layer was removed subsequently. Then they studied scuffing damage mechanisms of the engine. The delamination of the tribolayers was the primary source of material removal during scuffing. This process was facilitated by crack formation at the $FeAlO_3$ inclusions as well as fracture along the FeO veins between the iron splats.

18.3.1.5 Cavitation Wear

Cavitation, where pits and pores are formed, results from sudden variations of pressure in the fluid resulting in the creation of shocks waves due to implosion (for more details see Sect. 15.9.3) inducing fatigue phenomenon. Cavitation occurs when the velocity difference between the liquid and solid becomes important. Cavitation can be reduced by a proper design to diminish the low-pressure area. Against it, high toughness alloys with a good resistance to micro-crack formation are mandatory. The surface polishing is also very important; a low Ra can reduce the wear by a factor 5. Of course the proper design of the different parts can reduce drastically cavitation.

Arc spraying has been extensively used against cavitation, but liquid corrosion phenomena must also be considered and thus results depend on hardness and internal coherency of coatings. For example, Kim and Lee [62] have arc sprayed ten different coatings. Stainless steel coatings with the highest hardness showed the best performance against the cavitation erosion. In Al-based coatings, Si addition improved both the hardness and bond strength, resulting in drastic increment of cavitation erosion resistance by about 40 times when adding 12 wt% Si. In terms of marine corrosion resistance, aluminum coating showed the best performance with the aid of the sacrificial anode effect; unfortunately, the addition of Si to Al-based coatings caused surface pitting similar to those of Zn-based coatings. In both the Cu- and Fe-based coatings, interfacial oxidation occurred in between the coating and steel substrate. Hahn and Fischer [63] have tested the cavitation resistance of FeC0.8 coating arc sprayed, FeC0.8 coating HVOF sprayed, and FeCr19C0.1B1.6 coating deposited by plasma-transferred arc fed with wire. They showed that for all coatings the weight loss immediately starts with the beginning of the test. The major acting wear mechanism within cavitation was surface fatigue with splat delamination and cracks propagation along splat interfaces, the worst being when coating had a very low ductility. Kumar et al. [64] have tested 21 different coatings thermal sprayed. The HVOF-sprayed coatings exhibited lower cavitation wear rates than the thermal spray coatings deposited by the plasma spray process. The lowest cavitation rate was for Stellite 6; however, its cavitation rate was 11.7 mg/h, while the corresponding cavitation rate for 308 stainless steel weld metal was 3.2 mg/h. But in slurry erosion wear testing, the volume loss for Stellite 6 coatings was 5.33 mm^3/h, less than half the volume loss of 11.17 mm^3/h for 304 stainless steel. Factor and Roman [65] have subjected a selection of WC–Co and Cr_3C_2–25 %NiCr coatings produced by plasma spray and HVOF deposition techniques to various wear tests designed to simulate abrasion, cavitation, sliding, and particle erosion type wear mechanisms. Cr_3C_2–25 wt% NiCr outperforms the WC–Co samples, and it appeared that the WC–12 wt% Co sample performed better than the WC–17 wt% Co samples. For all samples the wear loss mechanism was clearly that of the delamination of flakes of material. With WC–Co samples, corrosion mechanisms played an important role, possibly through enhanced corrosion resulting from the cavitation mechanisms causing pit corrosion or similar

behavior. Wu et al. [66] studied a WC–Co–Cr coating deposited by HVOF onto a 1Cr18Ni9Ti stainless steel substrate to increase its cavitation erosion resistance. The microstructural analysis of the coating after the cavitation erosion tests indicated that most of the corruptions took place at the interface between the unmolten or half-melted particles and the matrix (Co–Cr), the edge of the pores in the coating, and the boundary of the twin and the grain in the stainless steel 1Cr18Ni9Ti.

Santa et al. [67] studied the slurry and cavitation erosion resistance of six thermal spray coatings and compared to that of an uncoated martensitic stainless steel. The results showed that the slurry erosion resistance of the steel could be improved by up to 16 times through the application of the thermally sprayed coatings. On the other hand, none of the coated specimens showed better cavitation resistance than the uncoated steel in the experiments. Lima et al. [68] deposited four different coatings onto an AISI 1020 steel substrate:

- WC–12 %Co
- As-sprayed (AS) 50 %(WC–12 %Co) + 50 %(NiCr)
- Post-melted (PM) 50 %(WC–12 %Co) + 50 %(NiCr)
- A duplex system comprising a WC–12 % Co top layer and a NiCrAl interlayer

The worst performance in cavitation erosion tests was observed for the WC–12 %Co coating, which showed the highest mass loss throughout the test. Conversely, the "PM" 50 % (WC–12 %Co) + 50 %(NiCr) coating exhibited the best cavitation resistance and a correlation between coating toughness and cavitation resistance could be established. Ding et al. [69] HVOF deposited conventional, submicron, and multimodal WC–12Co cermet coatings. They found that the multimodal WC–12Co coating exhibited the best cavitation erosion resistance among the three coatings tested, the erosion rate was approximately 40 % that of the conventional coating, and the cavitation erosion resistance of multimodal WC–12Co coating was enhanced by above 150 % in comparison with the conventional coating. Dense nanostructure, high microhardness, and strong cohesive strength of WC–12Co coating contributed to the increase in the cavitation erosion performance of multimodal WC–12Co coating.

18.3.1.6 Surface Fatigue Wear

It results in pits and pores that can extend to depths of several tenths of millimeters and are due to cyclic loading contacts, with stresses induced by rolling, shocks, or sliding in a lubricated regime. They depend on material properties: structure, cohesion, elastic limit, toughness, and residual stresses (see Sect. 15.9.4). If tangential stress is predominant, fatigue will start in the "skin" and if shear stress is more important, fatigue will occur essentially in the subsurface. The worst occurs when cracks propagate (see Sect. 15.9.4). The best materials to be used are hard ones with a high toughness. The surface must be smooth with no irregularities where cracks are initiated.

Stewart and Ahmed [70] made in 2002, a review of the thermal-sprayed coatings used in rolling contact fatigue (RFC). Coatings of WC–12 %Co, WC–17 %Co, and WC–10 %Co–4 %Cr, were sprayed on steel substrates using APS or HVOF; those of NiBSiCrFeC, Al_2O_3–TiO_2, Cr_2O_3–SiO_2–TiO_2, Mo were sprayed by APS; those of WC–Co and WC–Cr–Ni were sprayed by HVOF; and those of WC–12 %Co, WC–15 %Co, and Al_2O_3 were sprayed by D-gun. The HVOF-deposited coatings presented superior RCF performance, probably because of their dense microstructure and high cohesive strength combined with a minimum number of detrimental brittle phases. Cermet coatings displayed superior RCF performance followed by ceramic and metallic coating, respectively. Thermal and mechanical mismatch between the coating and the substrate influenced the RCF performance of the coating through the control the degree of compressive residual stress. Coatings thicker than 200 μm displayed superior RCF performance over thinner ones.

Ahmed and Hadfield [71] studied cermet (WC–Co) and ceramic (Al_2O_3) coatings deposited by D-Gun, HVOF, and high-velocity plasma spraying (HVPS) techniques, in a range of coating thicknesses (20–250 μm) on various steel substrates to deliver an overview of the various competing failure modes in rolling/sliding contact. Four modes of fatigue failure, competing during fatigue failure and that can be combined, were identified: abrasive, delamination, bulk deformation, and spalling. The conclusions of authors were the following:

Abrasion can be controlled by appropriate selection of contacting pair and lubrication conditions. Delamination and catastrophic failure mode, can be avoided by appropriate selection of coating thickness and fracture toughness.

Controlling the hardness of substrate and also increasing the coating thickness can avoid bulk failure. Coating failures were attributed to micro- and macrocracking of either the coating material or the coating substrate interface, which also resulted in the attenuation of compressive residual stress. Savarimuthu et al. [72] have studied the possible replacement of chromium electroplated by WC–Co-sprayed coatings for commercial aircraft applications. Decarburization, volume percent and distribution of hard particles, and porosity might more strongly influence wear behavior than residual stresses. Zhang et al. [73] addressed the fatigue behavior and failure mechanisms of plasma-sprayed CrC–NiCr cermet coatings in rolling contact. As emphasized previously, failure modes of coatings could be classified into four main categories, i.e., surface abrasion, spalling, and delamination within the coating and at the coating/substrate interface. The interfacial delamination was the main failure mode of the coatings at high contact stress. The failure mechanisms of coatings were associated with the microstructures and the bonding strengths of coatings, the depths of the orthogonal shear stress, and the maximum shear stress. Berger et al. [74] studied the dependence on substrate hardness of the rolling contact fatigue of HVOF-sprayed WC–17 %Co coatings. Such coatings are for gears and other components with high-load-bearing capacity. The durability of HVOF-sprayed WC–17 wt% Co coatings under rolling contact fatigue loading was significantly improved through the use of substrates of different hardnesses. The highest endurable Hertz pressure for a probability of survival of 50 % at 5×10^7 cycles was obtained for quenched and tempered substrates of

intermediate hardness of 400 HB. Crack formation and subsequent delamination appeared to be the main causes of failure. Bolelli et al. [52] studied the tribological performance of two coatings of Fe–Cr–Ni–Si–B–C (Colferoloy) alloy HVOF sprayed. They compared results to those obtained on Ni–Cr–Fe–Si–B–C and Cr_3C_2–NiCr layers (also HVOF sprayed), hard chromium electroplating, and bulk tool steel. Colferoloy coatings were validated as alternatives to Ni-based alloys and electroplated chromium under sliding wear conditions, but appeared unsuitable for particle abrasion resistance. The different sliding wear behaviors of HVOF-sprayed coatings could be explained by coupling micro- and nano-hardness to scratch testing, which reflected cracking resistance and plastic deformability. Ganesh Sundara Raman et al. [75] D-gun-sprayed Cu–Ni–In coatings on two substrate materials: Ti–6Al–4V and Al-alloy AA-6063. The Cu–Ni–In coating was found to be beneficial on the Ti alloy, but was deleterious on the Al-alloy substrate under both plain fatigue and fretting fatigue loading. The results were explained in terms of differences in the values of surface hardness, surface roughness, surface residual stress, and friction stress. Akebono et al. [76] investigated the factors that most strongly influenced fatigue properties of steel flame sprayed with Ni-based self-fluxing alloy and prepared three types of thermally sprayed specimens, which differed in heating time in the fusing process. The sprayed specimens fused for longer time exhibited lower fatigue strength, because segregation of the chromium compound in the coated microstructures was induced. Therefore, performing the fusion for a shorter time was effective for producing sprayed materials of enhanced fatigue properties.

18.3.1.7 Wear by Fretting and Fretting-Corrosion

Fretting occurs when the two interacting mating surfaces are subjected to an oscillatory motion of small amplitude. It can be more important when corrosion or oxidation occurs, producing for example oxides with ferrous materials (fretting corrosion). In the latter case, the extent and kinetics of phenomena are linked to the balance between the formation of products and their removal through wear. Besides the material properties, the design of the machine must eliminate the micro-movement, trap or remove debris, limit the contact with the environment. Jin et al. [77] have underlined that surface coating may protect the contact area from the fretting damage; however, specific contact condition would govern the effectiveness of the coating. They [77] proposed to classify coatings into two major types: hard and soft. Hard coatings are used in the contact conditions where fretting wear is present or dominant, while soft coatings are used to reduce the fretting fatigue induced failure since they could act as a self-lubricant and reduce the coefficient of friction resulting in improvement in fretting fatigue life. Of course fretting resistance depends on coating and substrate on the one hand and contact conditions (lubricant, pressure, and amplitude of the movement on the other). For example, Kim and Korsunsky [78] studied a pad and a substrate made of Ti–6Al–4V alloy on which was plasma sprayed a metallic interlayer of

Cu59–Ni36–In5. A dry film lubricant layer was then applied on the metallic interlayer and on the pad in the form of epoxy matrix loaded with MoS_2 particles. The coated specimen was clamped between two pads that were pressed against the specimen surface with a contact pressure of ~125 MPa, conditions simulating the geometric and loading conditions experienced in aerospace components. Each fretting test was performed at a frequency of 2.5 Hz. The durability of the coating was increased when increasing its thickness. Jin et al. [77] studied Cu–Al coating on Ti–6Al–4V substrate under fretting fatigue condition. At the low-applied stress amplitudes, the coating survived up to one million cycles. At the high-applied stress amplitudes, either the coating was separated from the substrate due to insufficient interfacial strength or the specimen fractured at locations away from the contact area. Mary et al. [79] performed fretting wear tests up to 500 °C. A representative punch (Ti17)/plane (CuNiIn plasma coating) interface was investigated under air conditions. Wear was studied by varying pressure, sliding amplitude, and temperature. A threshold mean pressure $p_{th} \approx 85$ MPa was identified for the transition from a low to a high wear regime. Temperatures in the range of 20–450 °C did not modify the respective wear processes and consequently did not affect the related wear rates. Hager et al. [80] conducted, for titanium compressor bladed disk assemblies, an in-depth wear analysis on the gross slip fretting wear of Ti6Al4V-mated surfaces as well as Ti6Al4V worn against plasma-sprayed CuNiIn, Al–bronze, Mo, and Ni. Tests were performed at room temperature and 450 °C. To eliminate the stress concentrations, the test geometry was an ellipsoid on a flat plate. They determined that all coatings caused significant damage to the mating Ti6Al4V surfaces and that the wear mechanisms were all similar to those of the uncoated baseline case. In gross slip fretting, these soft thermal spray coatings did not effectively protect the mating Ti6Al4V surfaces without solid lubrication. Koiprasert et al. [81] HVOF sprayed four types of coating (≈300–400 μm), namely, WC–17 % Co ($T < 500$ °C), Cr_3C_2–25 %NiCr ($T < 800$ °C), AlSi graphite, and CoMoCrSi ($T < 800$ °C) on stainless steel substrates. They used an in-house flat-on-flat, fretting wear tester at 500 °C. At that temperature, WC–Co did not perform well, Cr_3C_2–25 %NiCr outperformed WC–Co; but the formation of Cr_2O_3 by oxidation caused rapid wear, AlSi graphite coating did not provide additional wear resistance to the stainless steel. Only the CoMoCrSi coating, with its low porosity, moderate-to-high hardness, and good high temperature corrosion resistance, exhibited the best wear property. Hager et al. [82] plasma-sprayed nickel graphite composite coatings with 5–20 % graphite and studied mitigate fretting wear within Ti6Al4V contacts at room temperature and 450 °C. The embedded graphite particles reduced the friction of the nickel thermal-sprayed coatings during both low and high temperature fretting wear experiments. The wear reduction on the mated Ti6Al4V surfaces was due to the formation of uniform transfer films graphitic based at room temperature and NiO based at 450 °C. Carrasquero et al. [83] investigated the fretting wear performance of a Ni–Cr-based alloy, containing B and C, HVOF sprayed onto a SAE 1045 steel substrate. Tests were conducted on both the uncoated and coated substrate, under un-lubricated dry conditions, at different applied normal loads, cycles, and amplitudes. They showed

that at constant wear amplitude, the wear volume increased with the applied normal load and that at under constant load conditions, the wear volume decreased as the wear test amplitude also decreased, becoming insignificant when it was less than ~100 μm. Tian et al. [84] studied the fretting wear behavior, against a steel ball, of conventional and nanostructured Al_2O_3–13 wt% TiO_2 plasma sprayed. The improved fretting wear resistance of nanostructured coatings was attributed to the nanometer-sized grains, reduced lamellar structures, and amorphous phases. Fretting wear often occurs in hip joints that must be replaced after about 10 years use. Sathish et al. [85] reported on the sliding wear performance of the nanostructured Al_2O_3–$13TiO_2$, ZrO_2, and the bilayered (ZrO_2/Al_2O_3–$13TiO_2$) coated biomedical Ti–13Nb–13Zr alloy in simulated body fluid condition. The bilayered coating exhibited 200- and 500-fold increase in the wear resistances when compared with that of the nanostructured Al_2O_3–$13TiO_2$ and ZrO_2 coatings. This substantial improvement was attributed to the lower porosity and higher adhesion strength of the bilayered coating.

18.3.1.8 Thermal Fatigue and Thermal Shock

Thermal fatigue occurs in components subjected to high temperature gradients resulting from friction or operating environment (for example, external surface subjected to hot gases). It results in high stresses, surface fatigue, and mechanical transfer (transfer of the softer body to the harder one). Of course when thermal fatigue tests are performed in air, very often oxidation problems take an important part in coating resistance. Thermal fatigue characterization is presented in Sect. 15.9.4. Thermal shock occurs when the thermal gradient causes different parts of an object to expand by different amounts, generating stress or strain. At some point, this stress can exceed the strength of the material, causing a crack to form. If nothing stops this crack from propagating through the material, it will cause the object's structure to fail. As described in Sect. 15.8.4, the thermal shock resistance is tested by alternate high-temperature exposure and cooling cycles until failure. For thermal fatigue testing, the heat flux to the sample is applied using a flame, followed by air cooling, with or without convection. On the other hand, in thermal shock tests, the heating is achieved by a furnace (moderate thermal gradients), followed by cooling using cold water (high thermal gradients). Alternately, the heating is made with a flame on one side of the sample, while the opposite side of the sample is air cooled (high thermal gradients). The cooling step can also be achieved through the replacing the flame by an air jet (moderate thermal gradients). The heating step can also be achieved with a fluidized bed or a laser.

(a) Thermal Fatigue

As it could be expected, most studies were devoted to thermal barrier coatings (TBCs). However, the first two following examples are not related to TBCs, which

are depicted in Sect. 18.3.3. Aoh and Chen [86] investigated high temperature (700 °C) wear characteristics of Stellite 6 alloy containing Cr_3C_2 after thermal fatigue and oxidation treatment at 700 °C. The coating was deposited by plasma transferred arc (PTA) process. Thermal fatigue cracks initiated from the surface of Stellite 6 with Cr_3C_2 and propagated into the coating along carbide boundaries. No thermal fatigue crack was observed on sprayed Stellite 6 layer. The Cr_3C_2 content in the alloy enhanced the formation of the oxide layer. Surface oxidation was beneficial to the improvement of wear resistance and the coating exhibited the lowest wear loss if an oxidation treatment at 700 °C/100 h was achieved prior to the wear testing.

According to D'Ans et al. [87] the major wear mode of steel in the aluminum foundry industry is thermal fatigue especially affecting die-casting dies. Steel is also intensively corroded by molten aluminum and, sometimes, sliding wear occurs when extracting the molded parts from the die. D'Ans et al. [87] conducted thermal fatigue tests with samples of hot work tool steel, respectively, untreated, simply borided, and at last protected by a multilayer of YSZ, followed by a nickel superalloy and then a borided layer. Unfortunately the multi-layer coating resistance to thermal fatigue (heating between 500 and 800 °C), turned out to be lower than for a single-treatment solution (boriding) and for plain steel.

Eriksson et al. [88] subjected air plasma-sprayed thermal barrier coatings to isothermal and cyclic heat treatments (Thermal Cycling Fatigue TCF). Specimen subjected to TCF and isothermal oxidation gave very similar interface (Thermally Grown Oxide) TGO thickness and TGO composition. The heat treatment influences the adhesion of TBCs: isothermal oxidation up to 290 h has been shown to have a beneficial effect on adhesion compared to the as-sprayed condition, while cyclic heat treatment has been shown to decrease adhesion. Kwon et al. [89] studied a TBC with topcoat deposited by APS and bond coat by HVOF. Thermal fatigue did not affect the stress–strain curves, except for thermal fatigue for 500 h. However, the thermally grown oxide (TGO) layer thickness was dependent on the exposure time under thermal fatigue, showing a nominal thickness of approximately 4 μm after thermal fatigue for 500 h, independent of the number of thermal fatigue cycles. As the exposure time was increased in the thermal fatigue experiments, the damage to the topcoat was inhibited with less crack coalescence. The higher stiffness in the bond coat induced cracking or delamination at the interface between the bond coat and the substrate, whereas thermal fatigue increased the mechanical properties, especially the elastic modulus, of the bond coat and enhanced the damage tolerance of the TBC system.

(b) Thermal Shock

Luo et al. [90] deposited by high-velocity arc spraying cored wires FeMnCrAl/Cr_3C_2 and FeMnCrAl/Cr_3C_2–Ni9Al coatings onto low-carbon steel substrates. The specimens were placed inside a furnace at 800 °C, held for 15 min and then quenched into a water bath (25 °C). The first type of coating consisted of layered

splat of mainly Fe solid solution phases mixed with oxide phases, unmelted particles, and pores. The second type of coating exhibited higher bonding strength; Ni and Fe formed the diffusion layer that improved the thermal shock resistance. The cracks in the coatings were mainly initiated and propagated along the oxide phases during the thermal shock test. The uniformly shaped pores in the coatings helped preventing crack initiation and propagation. Pan et al. [91] studied the effect of SiC particles on thermal shock resistance of Al_2O_3–20 wt% 8YSZ coatings air plasma sprayed. The thermal shock resistance of Al_2O_3/8YSZ coatings was increased greatly from 5 to 83 cycles with addition of SiC particles at 1,000 °C. Some silicate fibers were formed on the coating surface and through thickness after thermal shock. The $Al_2O_3{\cdot}xSiO_2$ silicate fibers increased greatly the thermal shock resistance of ceramic coatings. Gu et al. [92] plasma sprayed NiCoCrAlY/8YPSZ coating on aluminum alloy (5A06). The failure after thermal shock tests (furnace heating at 400 °C for 0.5 h, then quenched with cold water, and dried by warm air) was mainly due to the stress caused by thermal expansion mismatch between the bond coat and the substrate as well as the galvanic corrosion of the aluminum alloy. Ni–P, Ni–W–P, and Ni–Cu–P as interlayers were electrolessly deposited on the substrate in order to mitigate the thermal stress. Diffusion layers mainly composed of AlNi, Al_3Ni_2, and Al_3Ni were observed between the interlayers and the substrate after thermal shock test. The oxidation of the substrate was effectively inhibited. Ni–P interlayer was superior to the other two interlayers and enhanced the thermal shock life from 38 to more than 200 cycles. Kokini et al. [93] studied plasma-sprayed yttria-stabilized zirconia–NiCoCrAlY bond coat alloy compositionally graded thermal barrier coatings onto Inconel steel subjected to a thermal shock loading. The thermal loading was applied using a continuous CO_2 laser. The results showed that for a given thermal resistance, as the compositional gradation was increased, the maximum surface temperature at which horizontal cracks initiated in the TBC increased. Liang et al. [94] deposited by APS nanostructured and conventional zirconia coatings and studied, by the water quenching method, the thermal shock resistances of as-sprayed coatings. The results showed that the nanostructured as-sprayed coating possessed better thermal shock resistance than the conventional one. The difference in microstructure and microstructural changes occurring during thermal shock cycling explained those results. Gilbert et al. [95] investigated the reduction of time-dependent deformation through the addition of mullite to YSZ based TBCs. Fracture mechanics analyses were performed for three coating architectures: monolithic YSZ, monolithic mullite, and a mullite-YSZ composite. The effect of coating architecture and surface crack morphology on interface fracture was investigated. They found that mullite and YSZ combined to influence the thermal shock behavior of the composite coatings. Composite coatings experienced a reduced driving force for interface fracture compared to monolithic YSZ coatings while having a higher thermal resistance compared to monolithic mullite coatings.

18.3.1.9 Wear by Very High Stresses

It is mostly characterized by dry sliding with a pin-on-disk test and depends on the high load applied and sliding distance, the wear response being dominated by subsurface cracking and removal of materials when sliding. Plasma with ceramics, HVOF, and D-gun with cermets are mainly used. Bolleli et al. [44] have investigated through pin-on-disk and dry sand–steel wheel tests the wear resistance of plasma-sprayed ceramic coatings (Al_2O_3, Al_2O_3–13 %TiO_2, Cr_2O_3). These ceramic coatings were the better performing ones in dry particles abrasion conditions, because they never undergone abrasive grooving but only splats detachment. In the pin-on-disk test, the ability to form a smooth and compact surface film by local plastic deformation was the key property determining coatings performance. Al_2O_3 and Al_2O_3–13 %TiO_2 did not form an adequately compact tribofilm and therefore showed unfavorable properties in terms of sample wear rate, pin wear rate, and friction coefficient. Cr_2O_3, instead, had the ability to form a compact tribofilm by splats plastic deformation; thus, its performances were comparable to HVOF-sprayed ceramics. However, its rather low deposition efficiency (below 45 %) and its propensity to possibly form Cr_6^+ by in-flight thermal alteration were disadvantages that must be considered. Bolelli et al. [44] found that Al_2O_3 coatings, manufactured by the high-velocity suspension flame spraying (HVSFS) technique using a nano-sized powder suspension resulted in few interlamellar or intralamellar cracks, inducing reduced pore interconnectivity. Such strong interlamellar cohesion favored much better dry sliding wear resistance at room temperature and at 400 °C. Ahmaniemi et al. [96] showed that the aluminum phosphate sealing treatment changed stress states of the alumina and chromia coatings toward compression. Tensile stress state of the Al_2O_3 coating decreased during the sealing treatment and was even compressive when measured with hole-drilling method. Dry abrasion resistance increased correlatively. Stress state of sealed Cr_2O_3 coating was more sensitive to sealing treatment temperature. Higher sealing treatment temperature led to higher compressive stress state and better abrasion wear resistance. Chen and Hutchings [97] plasma-sprayed coatings of tungsten carbide with 9, 12, and 17 wt% Co by both air (APS) and low-pressure (VPS) methods. VPS coatings had a lower porosity, better inter-pass bonding, and higher WC contents; these correlated with greater abrasion resistance. All coatings showed poor resistances to high-stress abrasive wear, which was associated with widespread fracture of the carbide constituents of coatings under these conditions. Under low-stress abrasion, however, all coatings showed a substantially greater wear resistance than the steel control. The presence of hard carbides was beneficial, and the VPS coatings all showed a greater wear resistance than the APS ones. Venkateswarlu et al. [98] sprayed diamond reinforced composite coatings deposited with both oxyacetylene flame and HVOF techniques. The feedstock material used for the coating consisted of tungsten carbide (WC) (average particle size: ~2 μm), bronze (average particle size: ~30 μm), and diamond (average particle size: ~25 μm)

powders. In addition to the high hardness of HVOF-sprayed coating, the uniform distribution of diamond particles in the matrix was considered important in the view of reduced matrix deformation. HVOF-sprayed specimen, owing to its lower porosity and higher bond strength between reinforced particulates and the matrix, led to substantial reduction in the deformation of matrix, which in turn facilitated higher wear resistance. To improve the resistance of HVOF sprayed cermets different means were used. For example, Stoica et al. [99] have HVOF (JP5000) sprayed functionally graded WC–NiCrBSi coatings and heat-treated them at 1,200 °C in argon environment. It was possible to achieve higher wear resistance, both in terms of coating wear, as well as the total wear of the test couples. This was attributed to the improvements in the coating microstructure during the heat treatment, which resulted in an improvement in coating's mechanical properties through the formation of hard phases, elimination of brittle W_2C and W, and the establishment of metallurgical bonding within the coating microstructure and at the interface coating–substrate. Valarezo et al. [100] tested the effective damage tolerance of a functionally graded coating (FGC) deposited by HVOF. The thick FGC (≈1.2 mm) consisted of 6 layers with a stepwise change in composition from 100 vol. % ductile AISI316 stainless steel (bottom layer) to 100 vol. % hard WC–12Co (top layer) deposited onto an AISI316 stainless steel substrate. The FGC structure showed the ability to reduce cracking with increased compliance in the top layer during static and dynamic normal contact loading, while retaining excellent sliding wear resistance (ball-on-disk tests). One of the main problems seemed to be the poor characteristics of HVOF-sprayed stainless steel. It suffered from extensive oxidation and phase alteration during spraying, which compromised its mechanical strength and probably impaired its adhesion to the substrate. Bolelli et al. [101] manufactured HVOF-sprayed functionally graded coating, consisting of two NiAl/WC–Co composite layers with increasing cermet content and a pure WC–Co topmost layer. Results showed that the WC–Co/NiAl FGC could provide good wear and corrosion protection to the substrate under very severe conditions, when very thick layers were demanded. This architecture also solved many of the problems highlighted by the previously considered WC–Co/stainless steel FGC. Stoica et al. [102] compared the sliding wear performance of as-sprayed and Hot Isostatically Pressed (HIPed) thermal spray cermet (WC–12Co) coatings. Results indicate that HIPing technique can be successfully applied to post-treat thermal spray cermet coatings for improved sliding wear performance, not only in terms of coating wear but also in terms of the total volume loss for test couples. The process induced phase transformations: elimination of secondary phase W_2C and metallic tungsten W, alteration of amorphous binder phase through recrystallization of Co leading to precipitation of the η carbides. It also developed the metallurgical bonding at the interface between the constituent lamellae of the coating, thereby increasing the coatings Young's modules after HIPing post treatment.

18.3.2 Corrosion and Oxidation Resistant Coating

Corrosion and oxidation correspond to a chemical or electrochemical reaction with the surrounding atmosphere. For details about corrosion either at room or high temperatures, see Sect. 15.10.1. As a general rule, except for sacrificial coatings, those used against corrosion must be as dense as possible and in many cases a post-treatment must be achieved (fusion of self-fluxing alloys, heat-treatment, sealing, austempering, laser glazing, . . . see Sect. 13.12).

18.3.2.1 Room Temperature Corrosion

The different corrosions at room temperature can roughly been categorized in atmospheric or marine corrosion, chemical, or parachemical corrosion.

(a) Atmospheric and Marine Corrosion

Large steel structures such as bridges, pipelines, oil tanks, towers, radio and television masts, overhead walkways, and large manufacturing facilities in the metallurgical, chemical, energy, and other industries must be protected from corrosion. It is the same, but with more difficulties, with structures exposed to moist atmospheres and seawater such as ships, offshore platforms, and seaports [103]. Sørensen et al. [104] have presented a review of anticorrosive coatings for containers, offshore constructions, wind turbines, storage tanks, bridges, rail cars, and petrochemical plants and "marine corrosion" corresponding to coatings for ballast tanks, cargo holds and cargo tanks, decks, and engine rooms on ships.

Flame and wire arc spraying meet such requirements. However, coatings obtained by these methods are relatively porous (up to 20 %). Sacrificial coatings (for example, Zn or Al on steel) are mainly used. Referring to Sect. 15.10.1 such coatings must have a cathodic behavior relatively to the ions of the metal to be protected, steels in almost all cases. As illustrated in Fig. 15.67b, the cathodic protection can be porous without any corrosion of the underneath metal. Zinc performs better than aluminum in alkaline conditions, while aluminum is better in acidic conditions. Zinc–aluminum (Zn–15 wt% Al) seems to combine advantages of both materials. Against marine biofouling, undesirable accumulation of marine organisms on artificial surfaces that are immersed in the sea, Murakami and Shimada [105] have studied flame sprayed aluminum–copper alloy powders, aluminum–copper blend powders, aluminum–zinc blend powders, and a zinc powder. Coatings were immersed in the sea and their corrosion and marine fouling behaviors were examined. The aluminum–copper coatings had poor anticorrosion and antifouling properties. The aluminum–zinc coating with high zinc content and the zinc coating possessed the anticorrosion and antifouling properties [105].

Of course other treatments are possible such as plastic deformation. For example, the initial porosities of 4–14 % (depending on spray conditions) of aluminum coatings, wire arc sprayed, was reduced to 0.16–0.83 % after being shot peened with SiC glass beads of 0.21–0.3 mm [106]. Sealers can also present antifouling properties. Chun-long et al. [107] have arc sprayed aluminum on steel panels and then sealed coatings with nano-composite epoxies especially developed for sealing them. In order to test their performance, some panels were tested in the East China Sea. Test panels were mounted respectively during 3 years, in the marine atmosphere zone, seawater splash zone, tidal zone, and full-immersion zone. Tests included marine atmospheric outdoor exposure test, seawater corrosion test, and coating adhesion test. It was found that the appearance of coating panels was as fine as original but with a little sea species adhering to panels on tidal zone and full-immersion zone. Basically no change in the morphology, bond strength, and any visible coating crack, blister, rust, and break off was observed. Schmidt et al. [108] investigated the corrosion protection performance of 17 different Zn and Al sacrificial coating system configurations during marine atmospheric exposure (20-month exposure time) at Kure Beach, NC, USA. The coating systems incorporated several conversion coating layers, primers, and organic topcoats. The sacrificial Zn coatings provided sacrificial protection at the defects. Of the two thermal spray Zn coatings, flame spray coatings were more protective than arc spray. Han et al. [109] wire arc-sprayed aluminum wire on Special Treatment Steel (STS) 304 base metal. The electrochemical experiment was performed in natural seawater. The coating with the higher thickness represented good corrosion resistance in seawater. Esfahani et al. [110] deposited aluminum coating on mild steel by arc spraying. The corrosion behavior was evaluated by electrochemical impedance spectroscopy (EIS) and polarization tests in 3.5 vol. % NaCl solution. The as-coated samples were also subjected to a 1,500-h salt spray assay. EIS measurements showed that the corrosion performance of the coating was improved during a long-time immersion and exposure to saline mist. This could be due to plugging of pores by corrosion products, which hinder further penetration of the electrolyte through the coating. The twin wire arc-sprayed aluminum coatings could reliably protect steel structures against corrosion in chloride-containing aqueous solutions. Gorlach [111] has developed wire (Zn–Al) spraying by HVAF process. Coatings showed considerably higher bond strength than those obtained by the conventional methods, an advantage in areas where the adhesion strength was critically important. The highly dense coating structure also eliminated the need for a top paint coat, usually applied on metal-sprayed coatings to extend service life. Concrete bridge structural deterioration in coastal marine environments or in areas where deicing salts are used for snow and ice removal is a problem.

To limit atmospheric or marine corrosion, if one uses an anodic protection (for example, nickel is anodic to steel and the cathodic area of steel exposed controls the rate), the coating should be as dense as possible (if necessary sealed). Cramer et al. [112], as well as Holcomb et al. [113], have proposed a cobalt-catalyzed, nonconsumable, thermal-sprayed titanium anode as an alternative to thermal-sprayed zinc anodes for impressed current cathodic protection. Ti was wire arc

sprayed [112], the atomization being performed with nitrogen to limit as much as possible the formation of γ TiO_2. The titanium anode had a porous heterogeneous structure composed of α-titanium containing interstitial oxygen and nitrogen, and a fcc (face cubic centered) phase thought to be Ti(O,N). The final titanium anode thickness was 50–150 μm. Electrochemical aging was studied using catalyzed titanium anodes thermal sprayed on concrete slabs containing a steel mesh cathode. Cobalt catalyst, applied to the anode as an aqueous cobalt nitrate–amine complex, penetrated the anode and accumulated at the anode–concrete interface and in cracks within the concrete adjacent to the interface. Anodic polarization during and after application converted the cobalt to the active catalyst, Co_3O_4. With aging, cobalt catalyst dissolved in the increasingly acid environment of the interface and dispersed into the Ca-deficient, silica-rich reaction zone to reprecipitate and form a more diffuse site for the anode reactions. Stable operation of catalyzed anodes was maintained for a period equivalent to 23 years service at Oregon DOT bridge ICCP conditions with no evidence that operation would degrade with further aging. Early results from the field experiment at the Depoe Bay Bridge suggested anodes may age more slowly at low current densities with lesser impact from acidification [112].

To improve the marine corrosion resistance of stainless steel coatings fabricated by high-velocity oxyfuel (HVOF) spraying with a gas shroud attachment, Kawakita et al. [114] increased the molybdenum (Mo) content of stainless steel with a chemical composition of Fe balance-18 wt% Cr-22 wt% Ni-2–8 wt% Mo. The corrosion rate in sulfuric acid was improved when increasing the molybdenum content. The pitting corrosion resistance in artificial seawater was shifted toward the noble direction with increases in the molybdenum content. The number of rust spots formed by crevice corrosion in artificial seawater decreased after the addition of molybdenum to the coatings.

(b) Chemical or Parachemical Corrosion

Non-sacrificial coatings will never protect the substrate if connected porosities and oxide networks exist, which is the case of most thermal-sprayed coatings. The substrate protection requires using a protective bond coat or producing dense coatings, or sealing them that is generally possible if the service temperature is below few hundreds of Celsius degrees. Austenitic stainless steels, aluminum bronze, nickel-base alloys, MCrAlY, cermets with WC, Cr_2C_3, and matrices containing chromium or nickel or both are used against corrosion, often associated with wear. A few examples will be presented below.

Moskowitz [115] pointed out that the use of vacuum chambers or post-treatments can eliminate most defects, but these methods are costly and impractical on a large scale. Thus he proposed using modified HVOF process using unique inert gas shrouding to achieve highly dense, low-oxide coatings of metallic alloys. Coatings of corrosion-resistant alloys for severe corrosion applications in petroleum industry, such as type 316L stainless steel and Hastelloy C-276, were shown to act as true

corrosion barriers. The oxide content also played a role. For example, 316L stainless steel coatings formed by HVAF and HVOF were applied on carbon steel panels and their resistance to salt spray was tested as sprayed or sealed [116]. When coatings were sealed, corrosion was less on the HVAF coatings than that on the sealed HVOF coating, and almost no corrosion was observed on the sealed coating sprayed with powder of the largest particles (highest porosity) after even 500 h of salt spray testing. While the amount of through pores dominated the corrosion resistance of as-sprayed coatings, the degree of oxidation of the coatings (much less with HVAF) determined the corrosion resistance when sealing was applied.

For applications with a severe wear in oil and gas industry, cermets are used, with however some problems for offshore installations. According to Meng [117] the choice between the wide varieties of tungsten carbides with different alloying binders is not simple. The corrosion resistance must be improved by the proper choice of binder. For example, Souza and Neville [118] have shown that WC–CrNi exhibited passive behavior, as stainless steel, and would be compatible for use as a coating/substrate system when exposed to seawater, which was not the case for WC–CrC–CoCr. As previously mentioned the coating porosity and its oxide content must be as low as possible, which implied using HVOF guns resulting in higher impact velocities (low coating porosity) and lower particle temperatures (less oxidation), for more details see Sect. 5.3.1.5. This was illustrated by the work of Ishikawa et al. [119] who used a commercial HVOF with a gas shroud attachment (GS-HVOF) to prepare WC–CrC–Ni coatings. The density of coatings improved as the velocity of sprayed particles increased. Results of corrosion test indicated that through porosity was eliminated at velocities above 770 m/s with a lower degree of WC degradation. Wear resistance and hardness of coatings prepared by GS-HVOF were superior to those prepared by the conventional HVOF. Fedrizzi et al. [120] showed that Cr_3C_2–NiCr coatings, in sodium chloride solution under sliding wear, presented good barrier properties, and substrate corrosion was never observed. Moreover, when chromium was added to the metal matrix of WC–Co-based systems, tribo-corrosion behavior was enhanced and lower tribo-corrosion rates were measured. Plasma sprayed Cr_2O_3–8 wt% TiO_2 coating was used on hydraulic cylinder piston rods and rolls, but the substrate was rapidly corroded by the diffusion of the corrosive solution through pores: the bond coating was destroyed by the aggressive solution and ceramic coating flakes dropped off. Zhang et al. [121] have sealed coatings with epoxy and silicone resins. The sealing treatment improved the corrosion resistance of coatings significantly by blocking the open pores and cracks of the coating. Sealed by silicone resin, the coating gained remarkable anticorrosion properties, as after 1,200-h salt spray test, there was still no rust on the silicone resin-sealed coating.

For chemical corrosion, the coating material must be adapted to the corrosive medium. Coatings are often used to reduce costs, especially when solutions have been found in the use of sophisticated materials, oxidation-, and corrosion-resistant at high and low temperatures with high strength such as nickel-base superalloy Inconel 625. However, coatings of these materials on cheaper metals would be cheaper than bulk super alloy. Tuominen et al. [122] have shown that Inconel

625 HVOF sprayed presented mechanical and corrosion properties typically inferior to wrought materials due to the chemical and structural inhomogeneity of the thermal-sprayed coating material. Laser remelting, with high-power continuous wave Nd:YAG laser equipped with large beam optics, resulted in homogenization of the sprayed structure. This strongly improved the performance of the laser-remelted coatings in adhesion, wet corrosion, and high-temperature oxidation testing.

A rudder is one of the essential ship components for navigation and safety and services in the complex conditions of cavitation erosion and marine corrosion [122]. Kim and Lee [123] have investigated ten different coatings arc sprayed with Al-, Zn-, Cu-, and Fe-based wire feedstock for a rudder application. In terms of marine corrosion resistance, aluminum coating was the best, while stainless steel coating presented the highest resistance against cavitation erosion. Si addition improved both the hardness and bond strength of Al-based coatings, resulting in drastic increment of cavitation erosion resistance by about 40 times when adding 12 wt% Si. With Cu- and Fe-based coatings, interfacial oxidation occurred in between the coating and steel substrate, leading to interfacial cracks and coating delamination. The same authors, also for rudders, wire arc-sprayed Al–Zn and then sealed them with F–Si sealer, spread with the brush at room temperature for several times. The corrosion rate of the sealed specimen after coating was lower and the hardness higher and they presented good cavitation resistance characteristics [123]. Dent et al. [124] studied the corrosion characteristics in 0.5 M H_2SO_4 of two Ni–Cr–Mo–B alloy powders HVOF sprayed. Both coatings exhibited comparable resistance to corrosion. Microstructural examination of samples revealed the prevalence of degradation at splat boundaries, especially those where significant oxidation of the deposit occurred. Ishikawa et al. [125] wire arc sprayed a duplex coating composed of aluminum on 80Ni–20Cr alloy undercoat. The duplex coating presented an excellent performance in a hot, near neutral aqueous environment. The role of the undercoat layer of the sprayed 80Ni–20Cr alloy was to decrease the surface area of the steel substrate to be protected and reduce the sacrificing load for the aluminum and also to increase the adhesion of the aluminum topcoat by its roughness.

Magnesium alloys present low density and excellent physical and mechanical properties. They are particularly suitable for their use in automotive and aerospace applications, where replacement of steel and aluminum components by magnesium components would contribute to energy savings and reduced environmental impact. However, their drawback is their relatively high corrosion susceptibility and low wear resistance. That is why many studies of thermal spray coatings have been performed to improve their corrosion resistance. Pardo et al. [126] wire arc sprayed aluminum/silicon carbide composite coatings on AZ31, AZ80, and AZ91D magnesium–aluminum alloys. Presences of SiC particles provide higher hardness and wear resistance but not necessarily a better corrosion resistance. Corrosion was investigated in 3.5 wt% NaCl solution at 22 °C. Al/SiC composite coatings in the as-sprayed state revealed high level of porosity with poor bonding at the Al/SiC and coating/substrate interfaces, facilitating the degradation of the magnesium

substrates by galvanic corrosion. Cold-pressing post-treatment produced more compact coatings with improved corrosion performance. Arrabal et al. [127] evaluated also the corrosion behavior of wire arc-sprayed Al/SiC coatings on AZ31, AZ80, and AZ91D Mg–Al–Zn alloys in neutral salt fog (ASTM B 117) and high relative humidity (98 % RH, 50 °C) environments. As Pardo et al. [126], they found that the application of a cold-pressing post-treatment improved the corrosion performance of the coatings. In high humidity atmosphere, corrosion signs were only visible at the Al/SiC interfaces in the outermost surface of the coatings and in salt fog environment the galvanic corrosion of the substrates was delayed. Pokhmurska et al. [128] deposited on magnesium substrates (AM20, AZ31, AZ91) by wire arc spraying Zn, ZnAl4, and ZnAl15 solid wires and cored wires in aluminum core with powder filling containing different hard particles, such as boron, silicon, and tungsten carbide or titanium oxide. Remelting of thermal spray coatings was carried out by means of continuous irradiation of CO_2 laser in nitrogen or argon atmosphere, electron beam in vacuum, and focused tungsten halogen lamp line heater in atmosphere. Electrochemical behavior of modified surface layers was mostly improved due to alloying, homogenization of element distribution, and strong decrease of as-sprayed coating porosity.

18.3.2.2 High Temperature Corrosion

Against carburization, high nickel- and chromium-containing alloys are often used.

Against nitriding, many austenitic stainless steel and nickel base alloys present a good resistance to nitriding in ammonia.

Against sulfidation, certain Hastelloy and CoCrAlY are used.

Against molten salt corrosion resulting from sodium sulfates (such as Na_2SO_4), sodium chlorides (such as NaCl), and vanadium oxides (such as V_2O_5) no protection exists. However, corrosion consists of two stages: initiation and propagation. Thus CoCrAlY is recommended, provided, it contains 10–12 wt% of Al, because it has a very long initiation period.

For oxidation–corrosion resistance, nickel- and/or cobalt-based alloyed coatings are used: high chromium-containing alloys (NiCrMo: Hastelloy or Nistelle, CoCrSiMo: Tribaloy and MCrAlYs) Against molten glass, which is among the most corrosive media, plasma-sprayed coatings of platinum or their alloys are performed, spraying being performed in inert atmosphere where the over spray can be collected. Thermal sprayed ceramics can retard the corrosion. At last Mo–Ni–Cr coatings with addition of MoS_2 are used to reduce the wear and the friction of glass when transferred to mold.

Hot corrosion occurs mainly in thermal barrier coatings (TBCs), boilers, and molds:

– As summarized by Mohan et al. [129] and Jones [130] for TBCs when cost-effective alternative fuels, containing appreciable levels of elemental impurities such as V, Na, S, P, and Ca are used, corrosive compounds such as vanadates and

sulfates might arise as combustion by-products. In addition, TBCs are also increasingly susceptible to degradation by air-ingested CMAS [131] (acronym of each oxide deposits CaO, MgO, Al_2O_3, and SiO_2), especially in aircraft engines that operate in a dust-laden environment. Mohan et al. [129] have studied, at temperatures up to 1,400 °C, the degradation by V_2O_5 and a laboratory-synthesized CMAS of freestanding (on grit-blasted graphite substrates) yttria partially stabilized zirconia and CoNiCrAlY coatings (300 μm). The molten deposits destabilized the YPSZ with the formation of YVO_4 and reacted with the thermally grown oxide with various phase transformations and reaction product formation. CMAS melt readily dissolved the YSZ and then re-precipitated ZrO_2 with a composition based on local melt chemistry that deviates in the content of the Y_2O_3 stabilizer. Extensive dissolution of the TGO α-Al_2O_3 from freestanding APS CoNiCrAlY coatings by CMAS melt was observed. Enriching CMAS composition with Al promoted the crystallization of anorthite platelets and $MgAl_2O_4$ spinel and mitigated CMAS ingression [131]. Li et al. [132] investigated, in laboratory scale, the effect of CMAS. They found that the porous nature of the thermal-sprayed TBCs made them vulnerable to CMAS attack even before discernible chemical reaction started. A denser coating had the potential to resist the CMAS attack for a longer time than a more porous coating. Habibi et al. [133] compared the hot corrosion performance of YSZ, $Gd_2Zr_2O_7$, and YSZ + $Gd_2Zr_2O_7$ composite coatings in the presence of molten mixture of Na_2SO_4 + V_2O_5 at 1,050 °C. For YPSZ results were similar to those of Mohan et al. [129]. For the second composite coating, by the formation of $GdVO_4$, the amount of YVO_4 formed was significantly reduced. Molten salt also reacted with $Gd_2Zr_2O_7$ to form $GdVO_4$, but under 1,050 °C, these coatings were more stable, both thermally and chemically, than YPSZ and exhibited a better hot corrosion resistance. $LaTi_2Al_9O_{19}$ (LTA) exhibited [134] promising potential as a new kind of TBC material, with its excellent high-temperature capability and low thermal conductivity. Xie et al. [134] demonstrated its good chemical stability in molten salt of Na_2SO_4 and NaCl at 1,000 °C. However, the molten salt infiltrated to the bond coat, dissolving the TGO and resulting in hot corrosion of the bond coat. Mei et al. [135] studied the corrosion kinetics and mechanisms of NiCoCrAlTaY cold-sprayed coating and uncoated Mar-M247 superalloy in molten Na_2SO_4 salt vapor. Mass gain and microstructures after 200 h indicated that the NiCoCrAlTaY coating provided good oxidation and corrosion resistance in this vapor at 900 °C. Sidhu et al. [136] HVOF sprayed NiCrBSi, Cr_3C_2–NiCr, Ni–20Cr, and Stellite-6 coatings on a nickel-base superalloy and tested them at 900 °C in the molten salt (Na_2SO_4–60 %V_2O_5) environment under cyclic oxidation conditions. Among them, Ni–20Cr-coated superalloy imparted maximum hot corrosion resistance, whereas Stellite-6 coated indicated minimum resistance. The hot corrosion resistance of all the coatings was attributed to the formation of oxides and spinels of nickel, chromium, or cobalt.

– Hot corrosion degradation of metals and alloys is also a serious problem for many high temperature aggressive environment applications, such as boilers, fluidized bed combustion, and industrial waste incinerators. Chatha et al. [137]

deposited by HVOF process 80Ni–20Cr and 75Cr_3C_2–25(Ni–20Cr) coatings on T91 boiler tube steel. Hot corrosion was studied on bare and HVOF-coated steel specimens after exposure to a molten salt (Na_2SO_4–60 %V_2O_5) environment at 750 °C under cyclic conditions. The 80Ni–20Cr coating was found to be more protective than the cermet coating. Tani and Harada [138] examined the corrosion resistance of Ni–50Cr alloy coating, plasma-sprayed onto the fireside of steam generating tubes in a heavy oil-fired boiler. This coating, applied on steam generating tubes at Tocalo Co. Ltd., had remained for more than 20 years (about 140,000 h) demonstrating the corrosion resistant effect. Bala et al. [139] studied the corrosion resistance of Ni–50Cr coatings cold sprayed on two boiler steels SA-213-T22 and SA 516 (Grade 70). The aggressive environment consisted of Na_2SO_4–60 %V_2O_5 under cyclic conditions at 900 °C. The Ni–50Cr coated steels showed lesser weight gains than the bare metals and the oxide scales remained intact till the end of the experiment. According to Matsubara et al. [140], nickel-based self-fluxing alloy coating extended the service life of furnace wall tubes at waste incineration plants due to its excellent corrosion resistance and heat resistance. Fusing of such coatings by induction heating offered improved efficiency and reliability of products. A successful experimental application of 11 units in a waste incinerator revealed virtually no corrosion on the exposed surfaces and showed an improved water heating efficiency over that of the original tubes. Chatha et al. [141] investigated the corrosion resistance of HVOF sprayed Cr_3C_2–NiCr coating on ASME-SA213-T91 boiler steel without and with post-treatment of the coating by sealing and heat treatment. Corrosion tests consisted of exposure to a molten salt (Na_2SO_4–60 % V_2O_5) environment at 900 °C under cyclic conditions. Post-treated coating resulted to be more effective than as-deposited coating in enhancing the corrosion resistance of T91 steel. Tao et al. [142] HVAF-sprayed conventional and nanostructured NiCrC coatings. Hot corrosion was conducted in the Na_2SO_4–30 %K_2SO_4 environment, in the temperature range of 550–750 °C for periods up to 160 h. Both types of dense coatings possessed high corrosion resistance, especially the nanostructured NiCrC coating. The enhanced grain boundary diffusion in the nanostructured coating not only promoted the formation of a denser Cr_2O_3 scale with a higher rate but also helped to mitigate the Cr depletion at the metal/scale interface. Ceramic coatings are also used against corrosion.

Jansen et al. [143] compared the performance of dicalcium silicate-based coatings plasma sprayed to that of YPSZ coatings. Coatings were exposed to a V_2O_5–15 wt% Na_2SO_4 slag at 700 and 900 °C. At 700 °C, gaseous sulfidation was stimulated by an addition of 0.5 vol. % sulfur dioxide in air. The dicalcium silicate withstood combined attack without debonding, while the YPSZ coating deteriorated and spalled. Hirata et al. [144] investigated the influence of impurities of Al_2O_3 on the hot corrosion resistance against V_2O_5–Na_2SO_4 molten salt. Thickness of damage zone in Al_2O_3 ceramics, whose purity was high, depended linearly on the holding time. On the other hand, thickness of damage zone in Al_2O_3 whose purity was relatively low depended on square root of

holding time. In the impurities, SiO_2 especially affected the corrosion rate influencing the diffusion rate of corrosive elements through grain boundaries and thus the corrosion rate.

– Two examples of mold protection are presented. For the protection of aluminum for injection mold tools, Gibbons and Hansell [145] HVOF or plasma sprayed 100 ± 20 μm thick coatings of WC–10Co–4Cr, Cr_2C_3–20(Ni20Cr), 316 Stainless Steel, or Al_2O_3–40TiO_2. Substrates were made of three grades of aluminum: 2014 (90.4–95.0Al 3.9–5.0Cu 0.5–1.2Si 0.4–1.2Mn), 5083 (92.4–95.6Al 4.0–4.9Mg 0.4–1.0Mn), and 6082 (94.7–98.8Al 0.7–1.3Si 0.4–1.0Mn 0.06–1.2Mg). HVOF, except for the alumina–titania coating only plasma sprayed, was the most suitable of the two types of thermal spray systems evaluated, since APS was unable to provide high bond strengths. Furthermore, the processing by HVOF was not found to be detrimental to the fatigue life of the aluminum substrate. Mizuno and Kitamura [146] HVOF sprayed on AISI 316L substrate MoB/CoCr, a novel cermet material, with high durability in molten alloys for aluminum die-casting parts, and for hot continuous dipping rolls in Zn and Al–Zn plating lines. This coating presented a much higher durability without dissolution in the molten Al–45 wt% Zn alloy. Using undercoat was effective to reduce the influence of large difference in thermal expansion between the MoB/CoCr topcoat and stainless steel substrate. Combinations of topcoat and undercoat thickness were optimized to obtain intrinsic performance.

18.3.2.3 Oxidation

A variety of oxides can form on the surface and the further oxidation depends on the oxide layer forming a stable and continuous film. Of course the oxidation depends on the oxygen affinity of the elements forming the alloy. In most cases Cr and Al additions to the coating's matrix are used to form the oxidation barrier. Their quantity must be important enough to provide the renewal of the oxide layer that must be tough, well adhered and self-healing. Up to 430 °C, chromium–molybdenum steel presents a good resistance to oxidation. Up to 980 °C the high chromium (16–28 wt%)-containing alloys: NiCr, Inconel (Ni–Cr alloys), stellites (Co–Cr alloys), stainless steel present a good resistance. Over that temperature superalloys with aluminum (up to 5 wt%) are used, because aluminum forms an alumina film, which is more adherent than Cr_2O_3, thin enough to be ductile, and nonvolatile at 1,000 °C and over.

Many studies were devoted to the bond coat and the Thermally Grown Oxide (TGO) layer formation. The problem is that MCrAlY coatings contain only limited aluminum content because high values can lead to brittleness and potential crack. For example, Koolloos and Houben [147] have shown that pre-oxidation of the bond coat had a beneficial effect on lifetime when the oxidation was the main cause of failure. The pre-oxidation time and temperature were chosen such that a dense alumina layer was formed and the forming of spinel-type structures avoided. Fossati et al. [148] sprayed by VPS CoNiCrAlY coatings onto CMSX-4 single

crystal nickel superalloy disk substrates. As-sprayed samples were annealed at high temperatures in low vacuum. Three kinds of finishing processes were carried out producing three types of samples: as sprayed, mechanically smoothed by grinding, ground and PVD coated by using aluminum targets in an oxygen atmosphere. Samples were tested under isothermal conditions, in air, at 1,000 °C, and up to 5,000 h. Several differences were observed: grinding operations decreased the oxidation resistance, whereas the PVD process can increase the performances over longer time with respect of the as-sprayed samples. Jiang et al. [149] designed gradient coating that could provide a balance between high Al content and high-stress bearing ability. The gradient coating showed better performance of re-healing alumina β scale due to its possession of more β phase as Al reservoir. The improved high-temperature performance of the gradient coating was due to the Al enrichment of Al in the outer layer. Yuan et al. [150] sprayed the MCrAlY bond coat by HVOF and D-gun processes. The isothermal oxidation rate at 1,100 °C of the TBC system with the HVOF bondcoat was two times lower than that of the TBC system with the detonation-sprayed bondcoat. The rough surface of the detonation-sprayed bondcoat created a large specific surface area and unfavorable oxides on the bondcoat. Pint et al. [151] investigated by furnace cycling several different oxidation-resistant substrates with dry, flowing oxygen at temperatures from 1,000 to 1,200 °C. They determined the cyclic lifetimes of YSZ topcoat plasma sprayed or EB-PVD deposited. For NiAl + Zr (0.05–0.08 at.% Zr) substrate, the testing revealed that a more adherent alumina scale may extend the lifetime of commercial EB-PVD and PS coatings. Oxide-dispersion strengthened (ODS) FeCrAl substrates with YSZ topcoat seemed promising for the metallic skin of the next generation space shuttle. Limarga et al. [152] produced Al_2O_3/ZrO_2 functionally graded (FG) thermal barrier coatings, system incorporating an oxygen barrier layer between bondcoat and topcoat. Alumina has been highlighted as a potential material as oxygen barrier to improve the oxidation resistance of the bond coat since it has very low oxygen diffusivity. The results showed that FG systems exhibited superior mechanical properties and oxidation resistance at the expense of a slightly lower thermal insulating effect. Thin interlayer was preferred in order to minimize the detrimental effect of phase transformation of γ-Al_2O_3 to α-Al_2O_3 that resulted in tensile residual stresses at the interface.

High-temperature oxidation and corrosion phenomena in boilers are the source of many problems. Both the HVAF-sprayed conventional and nanostructured NiCrC coatings possess good properties against the oxidation and hot corrosion attacks [141]. Compared with its conventional counterpart, nanostructured NiCrC coating [141] exhibited better performance, which was believed to result from the faster formation of Cr_2O_3 scale with a denser structure. Even after thermal exposure at 650 °C for over 100 h, the nanostructured coating still kept its mean grain size less than 100 nm and seemed to be stable. Consequently, a large number of grain boundaries in the nanostructured coating served as "short circuit" channels for Cr diffusion [141]. Ramesh et al. [153] HVOF sprayed Ni-based hard facing NiCrFeSiB alloy powder on three kinds of boiler tube steels. Thermo cyclic oxidation studies were performed in static air at 900 °C. NiCrFeSiB-coated steels

showed slow oxidation kinetics and considerably lower weight gains than that of uncoated steels. The superior performance was attributed to continuous and protective thin oxide scale of amorphous SiO_2 and Cr_2O_3 formed on the surface of the oxidized coatings. Kaur et al. [154] deposited with D-gun Cr_3C_2–NiCr coating on T22 boiler steel. High-temperature oxidation in air and oxidation–erosion in actual boiler environment at 700 °C under cyclic conditions were carried out. While the uncoated boiler steel suffered from a catastrophic degradation in the form of intense spalling of the scale, the Cr_3C_2–NiCr coating showed good adherence to the boiler steel during the exposures with no tendency for spallation of its oxide scale. Sidhu et al. [155] HVOF sprayed WC-NiCrFeSiB coating on Ni-based superalloy (Superni 75) and Fe-based superalloy (Superfer 800H). The coated as well as uncoated specimens were exposed to air and molten salt (Na_2SO_4–25 % NaCl) environment at 800 °C under cyclic conditions. The oxides of active elements of the coatings, formed in the surface scale as well as at the boundaries of nickel and tungsten rich splats, have contributed for the oxidation and hot corrosion resistance. These oxides acted as barriers for the diffusion/penetration of the corrosive species through the coatings.

Singh et al. [156] deposited by a shrouded plasma spray process Stellite-6 on two Ni-base superalloys, Superni 601 and Superni 718, and one Fe-base superalloy, Superfer 800H. Oxidation studies were conducted on the coated superalloys in air at 900 °C under cyclic conditions for 50 cycles. The rate of oxidation was observed to be high in the early cycles of the study for the coated superalloys, which may be attributed to the interconnected network of pores and splat boundaries present in the coating structure. The Stellite-6 coating after exposure to air oxidation showed the presence of mainly oxides in its surface scale. The phases revealed where oxides of Cr and Co and spinels containing CoCr mixed oxides were present, oxides reported to be protective in nature against the high-temperature oxidation. Bala et al. [157] have deposited by cold spray Ni–20Cr and Ni–50Cr coatings on two boiler steels. The coatings, in general, were found to follow the parabolic rate of oxidation and were successful in maintaining their surface contact with their respective substrate steels.

18.3.2.4 Corrosive Wear

Corrosive wear occurs when the effects of corrosion and wear are combined, resulting in a more rapid degradation of the material's surface. A surface that is corroded or oxidized may be mechanically weakened and more likely to wear at an increased rate. Furthermore, corrosion products including oxide particles that are dislodged from the material's surface can subsequently act as abrasive particles. Stress corrosion failure results from the combined effects of stress and corrosion. At high temperatures, reactions with oxygen, carbon, nitrogen, sulfur, or flux result in the formation of oxidized, carburized, nitrided, sulfidized, or slag layer on the surface. Temperature and time are the key factors controlling the rate and severity of high-temperature corrosive attack [5].

The effect of fluids containing solid particles is complex and depends on the surface temperature. At low temperature the main phenomenon is erosion, with

increasing temperature both erosion and oxide scale formation are similar. The loss of oxide prevails with further increase of temperature (chipping of the brittle scale). It is thus necessary to use a compatible matrix with hard reinforcing phases such as carbides and oxides. It is also necessary to limit residual stresses within coating for example by using graded layers.

The problem of erosion–corrosion of materials at elevated temperatures is that the extent of wastage in such environments is dependent on a wide variety of parameters, which include properties of the impacting particles (angularity, for example), impact angle, target material, and nature of the corrosive environment, as well as the composition of the oxide scale formed during the erosion–oxidation process.

(a) Low Temperature

Hill et al. [158] investigated HVOF-sprayed coatings of Fe–Cr–C and Fe–Cr–V–C on high-chromium high-carbon tool steels in the as-processed state and after a quenching and tempering treatment. Coatings were also achieved by super solidus liquid phase sintering (SLPS). In comparison, sintered steels were analyzed in the quenched and tempered conditions only. The performed heat treatment was able to improve the properties of both steels leading to an increase of hardness due to martensite formation (SLPS and HVOF) and also carbide precipitation (HVOF) and an assumed increase of wear. The lower corrosion resistance of the high-vanadium tool steel X420CrVMo18-16 in comparison to X190CrVMo20-4 was due to a lower concentration of dissolved chromium in the metal matrix. The HVOF coatings showed a decrease in corrosion resistance in relation to the sintered material because of smaller precipitates and formation of chromium oxides. Kembaiyan and Keshavan [159] deposited, on drill bits in mining, oil and gas drilling, 82W–15Co–3C by Super-D-gun, 8ONi–1OCr–4Fe–4Si–1.8B–.4C by spray fused and laser cladded, Fe–Cr–Ni by wire feeded and fuse welded, WC based by plasma, 36Ni–44W–6Cr–6Co–1.8Si–1.9Fe–1.35B by flame and laser cladded, all heat treated afterwards. The D-gun coating offered beneficial compressive residual stresses on the inserts and cone shell, thereby being the best coating protecting three cone drill bits from corrosion and fluid erosion. Uozato et al. [160] plasma sprayed Fe–C powders, with or without nickel added (up to 14 wt%), on a cast AA383 aluminum alloy plate. Corrosion and wear tests in engine oil with or without sulfuric acid water solutions added were performed as well. The corrosion performance was dependent upon the nickel content. Souza and Neville [118] studied the influence of microstructure on the overall material loss in erosion–corrosion environments for WC–Co–Cr coatings applied by HVOF and D-Gun processes. The work was devoted to the enhancement of erosion due to corrosion effects. HVOF coatings had a slightly lower corrosion resistance than the D-Gun coatings but higher overall erosion–corrosion resistance. The formation of different tungsten species, η phases and a higher Cr amount reduced the toughness of WC–Co–Cr coatings and the corrosion rates under erosion–corrosion. Stainless steel components coated with Inconel-625 are very common in the oil/gas industry. That is why Al-Fadhli

et al. [161] HVOF sprayed Inconel-625 on three different metallic surfaces: (a) plain stainless steel (SS), (b) spot-welded stainless steel (SW-SS), and (c) a composite surface of stainless steel and carbon steel welded together (C-SS-CS). The erosion experiment was carried out using a jet impingement rig through which natural seawater (pH 8.3) or sand slurry was circulated. The coating exhibited excellent erosion–corrosion resistance, as it was not highly affected by the type of substrate material. The coating was found to be highly sensitive to the presence of sand particles in the impinging fluid. As the period of coating exposure to the flow of slurry fluid increased, weight loss increased significantly, the increment being dependent on the type of substrate material.

Polymer coatings have received increased attention as protection against corrosion and wear for several environmental conditions mainly in the automotive, petrochemical, oil, and gas industries. Lima et al. [162] flame-sprayed (Terodyn-System2000 gun of Eutectic) Polyetherimide (PEI), poly-ether-ether-ketone (PEEK), and Polyamide 12 (PA 12) polymers onto carbon steel substrates. The obtained coatings had formed a dense and smooth deposit with good adhesion and no significant defects. The abrasive wear test showed a better performance for polyamide 12 samples, almost twice better than PEEK and 20 % better than PEI. Polyamide 12 and PEEK coatings showed no corrosive attack in a very aggressive H_2SO_4 40 vol. % solution after 2,000 h of testing. Under the experimental conditions used in their work [162], PEEK and PA 12 coatings had a better corrosion performance but PA 12 had much better abrasive wear performance. As the presence of sand and mineral particles flowing in a corrosive fluid produced a high degradation rate of the hydro-transport equipment, Flores et al. [163] studied the erosion–corrosion behavior of two tungsten carbide cermets coatings obtained by PTA process. Two variations of the CNiCrFeBSi matrix, called soft and hard, with different concentration of chromium (Cr), carbon (C), and boron (B) were evaluated with and without reinforcing hard phase. Important microstructural differences were identified between the two Metal Matrix Composites (MMCs). Elongated precipitates rich in W and Cr were identified near the WC grains and in the matrix phase of the WC-hard overlay. Needle-like precipitates with a lower concentration of W were identified in the WC-soft overlay. For both MMCs the γ-Ni phase and silicides were present in the matrix phase. The MMC with the harder matrix showed the lower mass loss and the erosive degradation was predominant in the overall erosion–corrosion process at the lower temperature. A different behavior was observed when the temperature of the testing solution was increased and a low sand concentration was used. PTA coatings are excellent, when wear and corrosion are present at low temperature, see Sect. 10.7.4 of Chap. 10.

(b) High Temperature

Sidhu and Prakash [164] evaluated the erosion–corrosion (E-C) behavior of as-sprayed plasma and laser remelted Stellite-6 coatings on boiler tube steels (3 different ones) in the actual coal fired boiler environment at 755 °C. Coating

has been found to be effective in increasing the E–C resistance of boiler steels in the coal-fired boiler environment. Among the as-coated steels the highest E–C resistance has been observed for T11 steel, probably due to the presence of a continuous chromium-rich band lying at bond coat–substrate interface. A less porous structure obtained after laser remelting was found to be effective for increasing E–C resistance to the given environment for this coated T11 steel. Wang [165] HVOF sprayed Cr_3C_2–NiCr coating and tested them in conditions simulating erosive conditions in tubular heat exchangers of fluidized bed combustor boilers. These coatings showed excellent E–C behavior as compared with 1018 steel, A213 T22 steel. Coating high E–C resistance was attributed to its high compactness, fine grain size structure, and the homogeneous distribution of the skeletal network of hard carbides within a ductile, corrosive-resistant metal binder. Uusitalo et al. [166] sprayed various coatings by HVOF, wire arc, and plasma and simulated the E–C conditions in the superheater section of a circulating fluidized bed combustor by a burner-rig type working at elevated temperature. The gas temperature was 850 °C and the specimen temperature was adjusted to 550 °C by cooling the specimen internally with pressurized air. In E–C tests in presence of chlorine, nickel-based HVOF coatings performed the best, whereas carbide containing HVOF coatings and diffusion coatings wore away. Kaur et al. [154] D-gun sprayed Cr_3C_2–NiCr coating on T22 boiler steel. Coated and not coated boiler steel were subjected to high-temperature oxidation in air and oxidation–erosion in actual boiler environment at 700 °C. The uncoated boiler steel suffered from a catastrophic degradation in the form of intense spalling of the scale in both environments. The Cr_3C_2–NiCr coating showed good adherence to the boiler steel during the exposures with no tendency for spallation of its oxide scale.

Kim and Walker [21] developed a nanostructured titania coating for ball valves destined for high-pressure acid-leach (HPAL) service. The nanostructured titania coating provided dramatically superior resistances against abrasive and erosive wear compared to titania conventional coatings. The enhanced wear performance seemed to be due to improved toughness. The nanostructured titania coating has been applied onto ball valve components in ten locations around the world and has performed very well. PTA coatings are also successful against corrosion and wear at high temperatures, see Sect. 10.7.4 of Chap. 10.

18.3.3 Thermal Protection Coatings

Thermal protection helps reducing exposure temperature of the metal, increases thermal efficiency, often limits oxidation or corrosion, and finally extends the lifetime of the component. The main problem is that good heat flux protection requires low thermal conductivity materials that are generally refractory metals (W, Mo, Ta, Nb) or oxides, the expansion coefficients of which are relatively low compared to those of protected metals or alloys. Thus a bond coat is often

mandatory both to adapt the expansion mismatch and also to protect the metal or alloy from oxidation, the low thermal conductivity oxide coatings being often rather porous.

- Refractory metals give a good protection to high heat fluxes but their resistance to oxidation is relatively poor. Thus they are used against high heat fluxes for short times (rockets for example) or in nonoxidizing environment,
- Alumina can be used up to 900 °C because over that temperature the γ phase of plasma sprayed coatings transform into α phase with an important volume change resulting in coating peeling off.
- Zirconia is the most used material, but it must be stabilized to avoid phase transformations with temperature. The problem is then the price of the stabilizer. The cheapest ones are CaO or MgO but unfortunately over about 600 °C the stabilization becomes inefficient [167] and these powders, especially CaO, are essentially used for diesel engines. For higher temperatures yttria is used either with 7–8 wt% (partially stabilized zirconia: tetragonal phase) or 12 wt% (stabilized zirconia: cubic phase). The maximum service temperature is around 1,200 °C and the thermal conductivity of plasma sprayed coatings is around 1 W/m K. One of the problems of these coatings is their sintering increasing their thermal conductivity. When using powder manufactured from chemical route (sol–gel technique with an intimate mixing of zirconia and yttria at the nanometer level) the maximum temperature reaches 1,350 °C, but the powder price is higher. Other stabilizers are used such as CeO_2, GeO_2, Nb_2O_5, To_2O_5, Sc_2O_3, however, they are more expensive than Y_2O_3 and 24 wt% of them are required for zirconia stabilization. Even if their thermal conductivities are slightly lower than that of ZrO_2–7 wt% Y_2O_3 the maximum service temperature is about the same. Researches are now about pyrochlore structures such as La_2ZrO_7, Nd_2ZrO_7 et $Gd_2Zr_2O_7$ that melt at temperatures over 2,000 K but have no phase change. Another important problem with high-temperature thermal barriers is the compatibility of their coefficient of thermal expansion with that of the substrate especially under conditions of temperature changes (stopping and starting the reactor). Unfortunately, the drawback of the high compliance obtained with the columnar structure of EB-PVD coatings is that it eases the access of high temperature air or CMAS (acronym of each oxide: CaO, MgO, Al_2O_3, and SiO_2) to the bond coat, which resistance must be improved.

18.3.3.1 Thermal Barrier Coatings for Aero Engines

As illustrated in Fig. 1.8, many parts (hundreds of components) are sprayed in an aircraft engine. If at the beginning coatings were APS and VPS sprayed, HVOF spraying has been rapidly adapted to needs and twin-arc spray process is now explored. Coatings are used against fretting wear, to reduce friction, for clearance control, for high temperature protection, as thermal barrier, as seals, to replace hard chromium in landing gear [1].

TBCs were first successfully tested in the turbine section of a research gas turbine engine in the mid-1970s. By the early 1980s they had entered revenue service on the vane platforms of aircraft gas turbine engines [167, 168], and today they are flying in revenue service on vane and blade surfaces [168]. Thermal insulation benefits provided by TBCs and the resulting impact on component creep and thermomechanical fatigue life have made them enablers of high-thrust gas turbine engines. As underlined by Pratt and Whitney, of particular importance is the EB-PVD-based TBC, presenting an excellent compliance upon thermal cycles were then anticipated to improve blade life by a factor of 3 [169]. The aging of TBC's topcoat strongly depends upon the spray conditions and powder morphologies used to spray or deposit it, conditions acting on its sintering [170, 171]. The second problem is the oxidation of bond coat with the formation of Thermally Grown Oxide (TGO) [172–177] as well as the bond coat corrosion with oxides such as CMAS [129, 130, 132, 174] or vanadium oxide [178]. Feuerstein et al. [179] have shown that the most advanced thermal barrier coating (TBC) systems for aircraft engine and power generation hot section components (combustors, blades and vanes) consist of electron beam physical vapor deposition (EBPVD) applied yttria-stabilized zirconia and platinum-modified diffusion aluminide bond coating. Thermally sprayed ceramic and MCrAlY bond coatings, however, are still used extensively for combustors and power generation blades and vanes. Feuerstein et al. [179] have reviewed and compared the state-of-the-art processes for the deposition of TBC systems: shrouded plasma and HVOF for MCrAlY bond coat, plasma for low-density YSZ, and dense vertically cracked Zircoat, platinum aluminide diffusion coatings, EBPVD TBC. They outlined and compared key features of coatings and their cost elements actually used in industry. Vaßen et al. [180, 181] have presented last developments using advanced processing: methods allowing obtaining highly segmented TBCs [182] and the important recent directions of development for TBC systems, including improved processing routes and advanced TBC materials are discussed. Numerous studies were devoted to the resistance of the bond coat [176] and the way to improve it [167, 174] by bond coat treatment, or the choice of the spray process [182, 183]. For the TBC topcoat, promising new technologies such as TF-LPPS (Thin Film-Low Pressure Plasma Spraying) [184, 185] or solution or suspension or nanometer-sized agglomerated particles plasma sprayed will probably play an increasing role in future applications [186].

(a) Conventional Plasma Spraying

The evolution of TBCs for aero engines is well summarized when comparing review papers published at the end of 1990s [187–189] with more recent ones [180, 190, 191] and also those related to coating materials [192–199]. In 1999, Miller [168] said that TBCs have evolved from the laboratory to low risk turbine section applications and then on to an integral part of engine design. Beele et al. [189] underlined that if partially stabilized zirconia became the standard

material very early on, thermal spraying and electron beam physical vapor deposition in the early 1990s were even considered as competing technologies. In 2008 Feuerstein et al. [179] emphasized that "the most advanced thermal barrier coating (TBC) systems for aircraft engine and power generation hot section components consisted of electron beam physical vapor deposition (EBPVD)-applied yttria-stabilized zirconia and platinum-modified diffusion aluminide bond coating. Thermally sprayed ceramic and MCrAlY bond coatings, however, are still used extensively for combustors and power generation blades and vanes." However, as for any industrial production, the coating cost is a key parameter. For thermal spray processes, the labor and material costs are the major ones, while for EBPVD, the equipment cost is substantial (up to 50 % of the cost is for depreciation interest [179]) and its utilization must be effective. During the last decade many works were devoted to bond coats, see [176] and Sect. 18.3.5. Zirconia partially stabilized with yttria (YPSZ) was identified as the best ceramic topcoat material and has been established as standard for the last 30 years. However, correlatively, especially the last decade, other ceramic materials have been studied:

- Zirconia stabilized with CeO_2 [193, 194]: low thermal conductivity, less phase transformation than YSZ, but increased sintering rate compared to YSZ.
- Zirconia partially stabilized with dysprosia [195, 196]: more resistant to sintering than standard YSZ coatings up to 200 h at 1,150 °C, but the thermal properties of which were significantly influenced by the operating conditions. The lowest thermal conductivity at high temperatures was reached with the HOSP 4DyPSZ coatings (0.70 W/m K at 700 °C and 0.76 W/m K at 1,000 °C).
- Pyrochlore structure ($A_2B_2O_7$) materials offer properties comparable to YSZ with a lower thermal conductivity for several zirconate pyrochlores, especially $La_2Zr_2O_7$, that have also an excellent thermal stability [191].
- Zirconia doped by different rare-earth cations with the formation of dopant clusters as in the ZrO_2–Y_2O_3–Nd_2O_3(Gd_2O_3, Sm_2O_3)–Yb_2O_3(Sc_2O_3) [190].
- Hexaaluminates such as (La,Nd)$MAl_{11}O_{19}$, where M could be Mg and Mn to Zn, Cr, and Sm, present excellent longtime sintering resistance and structural stability up to 1,800 °C. For example, Chen et al. [197] have sprayed YSZ-based composite coatings with the addition of $LaMgAl_{11}O_{19}$ (LaMA) as the secondary phase. Unfortunately composite coatings showed much shorter thermal cycling lifetime than the monolithic YSZ coating due to the presence of as-sprayed LaMA (La $MgAl_{11}O_{19}$) coating with a large amount of amorphous phase reducing the thermal insulating efficiency and accelerating the oxidation and degradation of bond coat. Chen et al. [198] also sprayed five layer functionally graded TBC based on LaMA/YSZ system. The amorphous LaMA phase underwent recrystallization processes during high temperature aging, resulting in the formations of LaMA platelet-like grains and imparting the TBC with improved thermal and mechanical properties and a higher strain tolerance. Such coatings presented a good thermal cycling lifetime at the surface testing temperature above 1,350 °C.

- Perovskites (ABO_3 crystal structure such as $BaZrO_3$ or $SrZrO_3$ or $CaZrO_3$) have also been extensively studied [191]. Jarligo et al. [199] synthesized Ba $(Mg_{1/3}Ta_{2/3})O_3$ and La$(Al_{1/4}$ $Mg_{1/2}$ $Ta_{1/4})O_3$ compositions and plasma sprayed them as ceramic topcoats of TBC either in single layer or in double-layer combination with conventional YSZ. The low value of fracture toughness for the complex perovskites and the thermally grown oxide at the topcoat–bondcoat interface of the TBCs were, however, the major factors which led to the coating failure on thermal cycling at about 1,250 °C. Similar results were obtained by Ma et al. [200]. Yu et al. [201] tested $Sm_2Zr_2O_7$ coatings that exhibited low microhardness and elastic modulus, which increased with rise in aging temperature because of the microstructure reconfiguration.
- Other ceramics were also tested. $LaTi_2Al_9O_{19}$ (LTA) was synthesized by solid-state reaction at 1,773 K by Xie et al. [202], and the mechanical properties of the LTA bulk were evaluated. A double-ceramic layer LTA/YSZ TBC structure was proposed and the TBC sprayed by plasma spraying. The LTA/YSZ TBC remained intact even after 3,000 cycles, exhibiting a promising potential as new TBC materials. Guo et al. [203] produced $BaLa_2Ti_3O_{10}$ (BLT) by solid-state reaction and plasma sprayed it. The coating contained segmentation cracks and had a porosity of around 13 %. Thermal cycling result showed that the BLT TBC had a lifetime of more than 1,100 cycles of about 200 h at 1,100 °C and the failure occurred by cracking at TGO.
- Ceramic mixtures were also proposed: Liu et al. [204] showed that the La_2O_3 addition can effectively alleviate the grain growth of YSZ coatings under high temperatures.

Of course, besides the choice of the TBC's materials, works on the process optimization were also developed. Paul et al. [205] studied the influence of the YSZ purity on the YSZ TBS. They showed that reducing the contents of alumina and silica, from 0.1–0.2 wt% down to 0.01–0.05 wt%, induced a significant reduction in the sintering rates. Mihm et al. [206] studied the spray process optimization. Tan et al. [207] showed, with process mapping strategies and spraying hollow powders, that it was feasible to produce tailored microstructures with substantially lower thermal conductivity than generally reported for YSZ TBCs. It also allowed enhancing thermostructural compliance and reducing propensity to sintering during elevated temperature exposure. Guo et al. [208] studied the segmentation cracks density of thick TBCs (1.5 mm) for thermal protection of combustor. A segmentation crack density of 3.65/mm exhibited a thermal cycling lifetime of more than 1,500 cycles at 1,250 °C for the surface/950 °C for the bond coat, indicating an excellent thermal shock resistance. Zhu et al. [209] tested conventional TBCs (APS sprayed ZrO_2–8 wt% Y_2O_3 with a NiCrAlY VPS bond coat) sprayed onto 25.4-mm diameter and 3.2-mm thick nickel base superalloy specimens. A high-power CO_2 laser was used to test the TBC specimens under high temperature (1,287 °C) and high-thermal gradient cyclic conditions. If the initial average cracks propagation rates were in the range of 3–8 μm/cycle, the crack propagation rates increased to 30–40 μm/cycle at later stages of testing and the critical spalling crack size ranged

from 3 to 5 mm. According to Shin et al. [210] the failure of TBC is directly connected to the failure of the blades because the spallation of the ceramic layer accelerates the local corrosion and oxidation. They performed thermal fatigue tests at 1,100 °C and 1,151 °C for coin-type specimens. Delamination cracks occurred at the edge of a specimen first and then the area of the edge delamination gradually increased toward the center. A thermally grown oxide (TGO) was formed and grew at the interface between the topcoat and the bond coat. The crack propagated with increase of cycle number, growth resulting from the TGO formation, and the high normal stress at the edge. Kim et al. [211] also investigated the failure mechanisms of coin-shaped plasma-sprayed TBCs for gas turbine blades due to cyclic thermal fatigue. Hernandez et al. [174] quantified, through finite element analyses, the thermomechanical response of the bond coat (NiCoCrAlY) and the thermally grown oxide (TGO) for a YPSZ. The models they developed include nonlinear and time-dependent behavior such as creep, TGO growth stress, and thermomechanical cyclic loading. Eriksson et al. [87] for the same type of TBCs studied the effect of three different heat treatments: isothermal oxidation, thermal cycling fatigue (TCF), and burner rig test (BRT) using a thermal shock rig (TSR). The specimens subjected to BRT gave much thinner interface TGO due to their shorter exposure time to high temperature, and the TGO consisted almost exclusively of Al_2O_3. TCF-subjected specimens had areas of cracked interface TGO, while the thin interface TGO in the BRT-subjected specimens did not contain any cracks. Jang et al. [212] studied TBCs bond coats (0.08, 0.14, and 0.28 mm) HVOF sprayed. The TGO layer with the thickness of 2.8–3 μm was formed after thermal fatigue tests, showing the same effects in both the temperature and the dwell time. The bond coat thickness did not affect the formation of the TGO layer. As the thickness of the bond coat increased, the damage zone in the substrate decreased, the bond coat acting as a buffer layer under applied loads. Re-sintering of the top coating during the thermal fatigue tests was evident from the fatigue damage and the observed increase in the hardness values. Li et al. [213] examined through thermal cyclic test TBCs behavior with the NiCoCrAlTaY bond coats deposited by cold spraying and low-pressure plasma spraying. The surface of the cold-sprayed bond coat presented a smoother configuration than that of the LPPS-sprayed bond coat. Ni/Cr oxides easily formed on the LPPS bond coat during oxidation. In contrast, TGO on the cold-sprayed bond coat was uniform in both thickness and composition. The uniform protective TGO enhanced the thermal cyclic behavior of the TBCs. These results suggested that cold spraying is a promising process to deposit MCrAlY bond coat for high performance of TBCs.

(b) New Spray Processes

Plasma spray-physical vapor deposition (PS-PVD), recently developed by Sulzer Metco [214], is a low-pressure plasma spray technology to deposit coatings out of the vapor phase. PS-PVD is a part of the family of new hybrid processes. It is then possible to deposit a coating by vaporizing the injected material. Coatings show a

unique columnar microstructure, so far only known from other vapor phase deposition processes like EB-PVD.

But economical evaluations for columnar coatings on turbine components under production conditions show a clear saving potential when using the PS-PVD process. Hospach et al. [184] showed that quasi vapor deposition from clusters resulted in columnar coatings with high porosity and growth rate. The low working pressure (about 100 Pa) increased the size of the plasma plume and enabled homogeneous coatings, which made this process interesting in particular for large-scale applications.

New developments in suspension or solution plasma spraying seem also very promising (see Chap. 14). Vaßen et al. [180] pointed out that suspension spraying offers the manufacture of strain-tolerant, segmented TBCs with low thermal conductivity. In addition, highly reflective coatings, which reduce the thermal load of the parts from radiation, can be produced. Gell et al. [215] showed that solution sprayed TBCs have a microstructure characterized by: strain relieving through thickness vertical cracks, fine, dispersed porosity ultra-fine splats with enhanced splat-to-splat bonding. First tests showed that such coatings have equal or greater durability, lower thermal conductivity, higher in-plane toughness and bond strength, and costs comparable to APS. However, to our best knowledge such coatings have not yet been tested in industry

(c) Coatings Against Fretting

In the lower and higher temperature sections of engines, carbide cermets are the common materials used against fretting. Below 540 °C WC in cobalt matrices (6–12 wt%) with chromium addition (4–12 wt%) are used and at higher temperatures CrC carbides in NiCr matrices are used [1]. HVOF spraying is often used to limit carbides decomposition. CuNiIn is one of the oldest coatings used against fretting [1, 78].

18.3.3.2 Thermal Barrier Coatings for Land-Based Turbines

Coating life for land-based turbines (time to refurbish aircraft turbines), should be approximately 24,000 h, with a majority of all service time at maximum conditions, against 8,000 h for aircraft turbines with only 5–15 % is at maximum conditions. Thus problems of bond coat oxidation, interdiffusion of bond coat and substrate, coating densification, and changes in thermal or mechanical properties of the coating are more important. Accessibility for inspection, repair, and refurbishment is also more difficult for power generation machines than for aircraft engines. Components size is also more important (a factor of 10 for turbine blades), thus requiring adapted spray processes. At last the quality of the combustible is far from that used in aircraft engines [216–220].

Compared to aero engines land-based turbines work in different conditions: the external environment might range from cold (−40 °C) to high temperature (55–60 °C) and corrosive and erosive contaminants due to the environment and fuel are present. Coatings are applied onto bearing journals, bearing seals, sub-shaft journal, labyrinth seals, blades, tip seals, inlet and exhausts, and housing [1]. A detailed description of the different land-based turbines can be found in the paper of Lebedev and Kostennikov [221]. Pomeroy [222] gives a good description of coatings for gas turbine materials and long-term stability issues. Due to the demand to increase turbine inlet temperatures and thus cycle efficiencies, ceramic insulating coatings can be applied to decrease the temperature of the hottest parts of the turbine components by up to 170 °C. A review of the next generation of TBCs for gas turbines is presented by Curry et al. [223].

Turbines are also exposed to excessive amounts of moisture and chlorides and also two types of hot corrosion and oxidation occur:

– Type II hot corrosion occurring at temperatures in the range 500–800 °C and involving the formation of base metal (nickel or cobalt) sulfates which require a certain partial pressure of sulfur trioxide for their stabilization,
– Type I hot corrosion, observed in the range 750–950 °C, involving the transport of sulfur from a sulfatic deposit (generally Na_2SO_4) across a preformed oxide into the metallic material with the formation of the most stable sulfides. Once stable sulfide formers (e.g., Cr) are fully reacted with the sulfur moving across the scale, then base metal sulfides can form with catastrophic consequences as they are molten at the temperatures at which Type I hot corrosion occurs.

At last oxidation starts at temperatures over 1,000 °C.

Sprayed materials with a good corrosion and oxidation resistance are nickel- and/or cobalt-based alloyed coatings [1], such as NiCrMo (Hastelloy or Nistelle), CoCrSiMo (Triballoy), and MCrAlYs plasma or HVOF sprayed. Oxidation- and corrosion-resistant coatings are applied on air inlets, combustor liners, injectors, turbine tip shoes, nozzles, and exhausts [1]. On blades and vanes MCrAlY coatings are used as bond coats and for corrosion–oxidation protection.

For thermal barrier coatings mainly ZrO_2–Y_2O_3 (6–8 wt%), ceria or dysprosia-stabilized zirconia are used [220] and also ceria and yttria-stabilized zirconia or for certain applications calcium titanate [1]. It is worth underlying that for abradable and seals in the low-temperature areas, where moisture is important, porous aluminum-base coatings containing polyester, polyimide or BN, as well as nickel–graphite coatings are used. For higher temperatures (over 450 °C), abradables are made of MCrAlY with BN or polyester [1, 222]. Ceramic abradables have also been introduced but the expansion mismatch with the metal substrate must be accounted for with the cooling of the superalloy.

18.3.3.3 Thermal Barrier Coatings for Diesels

TBC for diesel engines either thick [224], or eventually phosphate sealed [225], or thin [226] are used to:

- Increase the piston head temperature and improve the fuel combustion [227]
- Reduce NO_x emissions [227]
- Reduce the heat rejection [228]
- Improve the usability of vegetable oils as a fuel [229]

18.3.3.4 Other Applications

- Ultrahigh temperature ceramics (UHTC) coatings deposited by plasma spraying are studied, such as ZrB_2–SiC(30 vol. %)–$MoSi_2$ (10 vol. %) [230]. Advanced coating systems based on monazite (two-phase mixture of $LaPO_4$ and Al_2O_3), a weak interphase for oxide composites, have been investigated as a means to increase the service temperatures of thermal protection blankets for re-entry space craft [231].
- Thermal barriers of zirconia stabilized by 8 wt% yttria (8YPSZ) for rare earth magnesium alloy were fabricated by atmospheric plasma spraying [232]. The thermal resistance of coating is obvious. The thermal insulation tests indicated that the coating with a topcoat thickness of 108 μm reduces the substrate temperature for about 80 °C and the coating surface could sustain a temperature of 534 °C. The coating also largely improves hardness, wear, and corrosion resistances of Mg alloy.
- Thermal barrier coatings were fabricated on polyimide matrix composites via air plasma spray process [233]. They consisted of Al (30 μm) as the bond coating and YSZ (130 μm) as the top ceramic. When thermal ablation test was at about 815 °C, the weight loss of the sample decreased from 7.05 % to 1.90 %, while the corresponding mass ablation rate reduced from 0.48 to 0.21 mg/s.
- Other ceramics were studied for TBCs. For example, Limarga et al. [152] studied Al_2O_3/ZrO_2 functionally graded (FG) thermal barrier coatings. The proposed FG system exhibited superior mechanical properties and oxidation resistance at the expense of a slightly lower thermal insulating effect. Thin interlayer was preferred in order to minimize the detrimental effect of phase transformation of γ-Al_2O_3 to α-Al_2O_3 that resulted in tensile residual stresses at the interface. Cojocaru et al. [234] plasma sprayed two different types of mullite powders (spray dried and freeze granulated) and a mullite-YSZ 75/25 vol.% mixture spray-dried powders. They showed that mechanical properties of coatings produced from particles with different morphologies (e.g., spray dried and fused and crushed) could be matched and tailored if the deposition conditions were carefully controlled to produce coatings with similar microstructural features. Suzuki et al. [235] studied plasma-sprayed zircon ($ZrSiO_4$) for an environmental barrier coating (EBC) application and reported that substrate temperature was one of the most important factors to obtain crack-free and

highly adhesive coating. Four different amount of yttria addition: 3, 5, 10, and 20 mol. % of $YO_{1.5}$ into $ZrSiO_4$ were tested. YSZ, zircon, and yttrium silicate were formed in the yttria-added coatings. More amount of yttria addition decreased the zircon formation. This resulted in less porosity in the coating even after the heat treatment at 1,400 °C, thereby improving the coating stability and adhesion.

18.3.4 Clearance Control Coatings

In compressors, gas turbines, and turbochargers, dimensional changes take place between the rotor and stator components because of thermal and mechanical effects during operation. These dimensional changes affect sealing and clearance control systems, consisting of a sacrificial element and a cutting component, are used. Thermal spray coatings, called abradables, and honeycomb seals form effective sacrificial systems. Abradable coatings are machined in situ and consist of a soft metal with polymer particles in cold sections and Ni–graphite or MCrAlY with polyester or BN particles in hot areas [1, 236, 237]. Additives provide the necessary friability, as well as aid in dry lubrication. Other thermal sprayed coatings can also be used on the "cutting" side of the clearance control system, and when the dynamic member of the system is too soft to cut without a coating.

Abradable materials have a strong impact on the turbine efficiency and fuel consumption [238]. At rotating speeds of the order of 10,000 rpm, rotating blade tip may rub against the stationary casing, due to either thermal expansion or misalignment or rotation, inducing strains [239]. Abradable seals act as sacrificial layers between the blades and the casing and are soft enough to avoid significant wear to blade tips, thus allowing much smaller clearances. They also offer a wear protection to the shroud material and rubbing blades. High-temperature abradable seals are used in high-pressure gas turbine of jet engines [238].

Abradable materials are rather complex because they must be abradable with a good resistance and strength as well with a good resistance to oxidation and corrosion. Their porosity also plays a key role and is often achieved by spraying also polymers, which size and volume percentage are critical for optimizing both the "abradability" and erosion-resistance performance. The polymer is then removed by heating the sprayed coating. At last the coating composition must be such that particle debris, released from the coating into the engine, are kept to a minimum. Their composition must also be adapted to the blade materials: titanium or nickel or steel. They are classified in low- and mid- (<540 °C) and high-temperature (540–980 °C) abradables. Low-temperature abradables are aluminum based with graphite or polyester or polyimide or boron nitride, or nickel based with graphite or calcinated bentonite clay [238, 239]. In the cold compressor section aluminum base is preferred due to the high risk of moisture. At high temperature one uses super alloys (MCrAlY with M=Ni or Co or both) with polyester and/or boron nitride or bentonite or graphite. Recently, ceramic mixed

with softer material (BN and polyester) abradable coatings have been developed to reduce slightly the alloy surface temperature. Other seals, which do not interact with the blades, are coatings composed of Babbit (tin–copper–lead), bronze, and AlSi-polyimide. They are used against labyrinth seals along the engine shafts in the compressor and turbine, sealing either gas or oil paths [1].

A few examples are presented below. For high temperature Bardi et al. [240] have tested, for the first stage of industrial gas turbines, the behavior of composite coatings: plasma-sprayed CoNiCrAlY/Al_2O_3 and laser-cladded CoNiCrAlY/graphite coatings. After 1,000 h at 1,100 °C both coatings did not show relevant microstructural modifications. Steinke et al. [241] showed that the hardness could be used as an indication for the abradability. It should be in the range of 500 $HV_{0.5N}$. A hardness of approximately 600 $HV_{0.5N}$ seemed to be the upper end at which a good cut-in was no longer reliably reproducible. Sporer et al. [242] performed abradability tests of YSZ abradables with the Sulzer Innotec test rig that can operate up to 1,200 °C with blade tip speeds up to 410 m/s. At intermediate temperatures (<450–480 °C), AlSi-hexagonal BN or NiCrAl–bentonite are popular [237, 243–246]. For example, the AlSi–hBN coating was characterized by a proportion of about 40 % of hBN "lubricant" particles trapped in the metallic matrix [244]. The amount of porosity was about 5 %. The NiCrAl–bentonite coating contained about 25 % of relatively spherical bentonite particles together with about 30 % porosity constituted mainly of large pores [244]. Comparatively to the hBN particles, the majority of the large bentonite particles and pores in this coating are distributed without significant preferred orientation [244]. Johnston [237] studied the net thermal spraying residual stress (NTSRS) and showed that it was most sensitive to changes in substrate thickness, abradable deposit thickness, and deposit modulus. Such results could be used for the creation of new abradable materials with optimum stress profiles and greater mechanical integrity. Stringer and Marshall [243] studied the wear at high speed: impact velocities between 100 and 200 m/s and incursion rates between 3.4 and 2,000 μm/s. They suggested that the adhesion of abradable material was due to plucking out of complete phases from the abradable coating, rather than a conventional cutting mechanism. Ma and Matthews [239] suggested using "Progressive abradability hardness" (also called "specific grooving energy"), abbreviated as "PAH," to measure abradability in the scratch test. At low temperature Dowson et al. [247] studied, for abradable seals to centrifugal compressors and steam turbines, the development of a new abradable silicon rubber adhesively bonded to a metal substrate. Lima and Marple [20] showed that a material that was generally considered as being hard and stiff, as YSZ, could be engineered to produce a nanostructured 100 % ceramic coating with a friable structure possessing attributes required for an abradable coating. In order to engineer a friable ceramic coating, the molten part of a semi-molten agglomerate particle must not fully infiltrate into the capillaries of its non-molten core during thermal spraying. The porous nano-zones spread throughout the coating microstructure acted as weak links, thereby making the coating friable. Abrasive wear resistant coatings are applied to blade tips and labyrinth seal teeth. They are often made of alumina, alumina–titania, nickel–aluminum cermet, Ni–Cr–Cr_3C_2 cermet.

18.3.5 Bonding Coatings

Bond coats are very important to:

- Improve the coating adhesion by forming an anchoring subcoat or adhering to clean and smooth surfaces that cannot be grit blasted properly (too thin or too hard or with a configuration making roughening difficult)
- Form a layer with an expansion coefficient between that of substrate and topcoat
- Provide an oxidation or corrosion resistant barrier to the substrate

According to the oxidation or corrosion barrier, and the working temperature of the coated part, the bond coat must be properly chosen.

For example, Mo can be used up to 315 °C [2]. NiAl bond coats are oxidation resistant up to 650 °C with Ni–Al (20 wt%) and 800 °C with Ni–Al (5 wt%), but they can also be used against corrosion. For example, Lekatou et al. [248] have investigated the corrosion behavior of an HVOF Ni–5Al/WC–17Co coating on Al-7075 in 0.5 M H_2SO_4. In the temperature range of 25–45 °C, the coating exhibited pseudo-passivity that effectively protected from localized corrosion. In case of surface film disruption, the bond coat successfully hindered corrosion propagation into the Al alloy. Yılmaz [249] has shown that the application of NiAl (5 wt%) bond coat layer in the plasma spraying of Al_2O_3 and Al_2O_3–13 wt% TiO_2 on pure titanium substrate has increased the hardness and bonding strength of coatings. Ni–Cr (20 wt%) bond coats can be used up to 980 °C and are designed to resist oxidation and corrosive gases. Cho et al. [250] coated micron-sized WC-Co powder onto a 420J2 steel substrate and bond coats of Ni, NiCr, and Ni/NiCr using HVOF spraying. The fracture locations were at interfaces with top coatings of WC–Co and NiCr indicating that adhesion between metal/similar metal is much stronger than between metal/cermet (WC–Co) because of the easy diffusion between similar metal atoms. Bond coats for TBCs have been extensively studied. They are of the MCrAlY type with M = Ni, Co, ... that can be doped with Pt, Hf, ... and can support temperatures of 1,100–1,200 °C. A few examples are presented below. Schulz et al. have studied [251] NiPtAl bond coats as well as NiCoCrAlY (X) deposited by LPPS and EB-PVD underneath conventional EB-PVD yttria-stabilized zirconia top coats on three different substrate alloys. The longest lifetimes were achieved on a novel Hf-doped EB-PVD NiCoCrAlY bond coat owing to a differing TGO formation and failure mechanism. Zhao et al. [252] investigated the effect of the Pt content on the durability of thermal barrier coatings (TBCs) with a Pt-enriched $\gamma + \gamma'$ bond coat. During oxidation, impurities such as S, C, and refractory elements segregating to the interface would degrade the TGO adherence to the bond coat. However, a higher content of Pt can inhibit this segregation and thus improve the TBCs life. Tang and Schoenung [253] observed multilayered accumulation of thermally grown oxide (TGO) locally on the tops of the roughness protrusions of the bond coat in thermal barrier coatings. Chen et al. [254] have compared TGO growth and cracking behaviors in TBC systems with APS-, HVOF-, and CGDS-CoNiCrAlY bond coats during thermal exposure.

Results pointed the potential advantage of using CGDS technique to produce TBC bond coats, for its significantly improved durability over the commercial air plasma spray bond coat, as well as its fast deposition rate and low deposition temperature. The TBCs with HVOF bond coats had an extended durability, compared to that obtained by APS but lower than that by CGDS. Other materials than superalloy were tested for TBC bond coat, such as glass–ceramics [255]. The TBC with YSZ top coat, glass–ceramic bond coat, and nickel base superalloy substrate was subjected to static oxidation test at 1,200 °C for 500 h in air. No TGO layer was found between the bond coat and the top coat in the case of glass–ceramic bonded TBC system, while the conventional TBC system exhibited a TGO layer of about 16 μm thickness at the bond coat–top coat interface region.

Bond coats are also used for other applications, as presented below:

- Lu et al. [256] plasma-sprayed two-layer hydroxyapatite (HA)/HA + TiO_2 bond coat composite coating (HTH coating) on titanium. The HA + TiO_2 bond coat (HTBC) consisted of 50 vol. % HA and 50 vol. % TiO_2 (HT). The positive effect of the HTBC on the decrease of residual stress in HA top coating (HAT coating) was evidenced through the observation on the surface cracking. The toughening and strengthening of HTBC was thought to be mainly due to TiO_2. Goller [257] plasma sprayed bioglass, known as 45S5 (45 % SiO_2, 6 % P_2O_5, 24.5 % CaO, and 24.5 % Na_2O all in weight percent) onto a titanium substrate with and without Amdry 6250 (60 % Al_2O_3–40 % TiO_2) as bond coating layer. The adhesive bonding observed at the bioglass metal interface turned into cohesive bonding by application of the bond coating layer.
- Guanhong et al. [258] have deposited on PMCs (carbon fiber reinforced unsaturated polyester) the Al bond coat and Al_2O_3 top coating by APS. The highest shear adhesion strength of the bond coating was 5.21 MPa and the hardness of the surface was much improved by the alumina coating. Liu et al. [259] arc-sprayed Al, Zn, and plasma-sprayed Al, Zn, Ni_3Al, and Cu on carbon-fiber reinforced polyimide substrate as bond coats for erosion and thermal-resistant coating. Ni_3Al or Cu damaged the substrate. Arc-sprayed and plasma-sprayed Al and Zn could be used as bond coat materials. For Zn as bond coat material, depositing method had little influence on shear adhesion strength. For Al as bond coat material, plasma spray was superior to arc spray, preheating improving shear adhesion strength.

18.3.6 Electrical and Electronic Coatings

One of the main problems of electrically conductive thermal sprayed materials, except those cold sprayed or plasma sprayed in soft vacuum VPS (generally VPS is too expensive), is that oxidation during the process increases the electrical resistance of the coating. The anisotropic structure of sprayed coatings also results in strong anisotropy between in-plane and through thickness electrical properties.

Some thermal-sprayed coatings are used to produce heater panel resistance. However, the choice of the resistance material must be such that the variation of its electrical resistance with temperature is as low as possible because otherwise electronic devices must be used to adapt the voltage to the resistance variation.

18.3.6.1 Dielectrics

Alumina is probably the most used material. The α and γ phases present different dielectric constants and loss tangent at high frequency. The γ phase resulting from the spray process can be avoided either by keeping the substrate at 1,000 °C, which is not easy to do with most substrates and requires a careful temperature control during cooling to avoid cracks, or by stabilizing it with elements such as MgO or Cr_2O_3. If the γ phase is not the phase suitable for high-frequency applications, as the α phase, the voltage breakdown is close for both phases. The dielectric properties of alumina coatings depend strongly upon their microstructure and spray conditions [6, 260]. One of the drawbacks is that the alumina coating electrical resistivity is strongly dependent on the air humidity due to the increase in water adsorption in the porous coating, generating ionic conductivity. Toma et al. [261] made the comparative study of the electrical properties and characteristics of thermally sprayed alumina and magnesium spinel coatings sprayed by HVOF and plasma. At low humidity levels, the electrical resistivity of alumina and spinel coatings was comparable (on order of magnitude of 10^{11} Ω m). At a very high humidity level (95 % RH: Relative air Humidity), a dramatic decrease in resistivity of about five orders of magnitude for alumina coatings, and about four orders of magnitude for spinel coatings was observed, water adsorption generating ionic conductivity. HVOF spinel coatings presented the best dielectric strength values ($E_d > 30$ kV/mm against 20 kV/mm for sprayed alumina) and were less sensitive to moisture. Thus, these coatings can be considered as potential candidates for use in insulating applications. Toma et al. [262] studied microstructural characteristics and electrical insulating properties of thermally sprayed alumina coatings produced by suspension HVOF (S-HVOF) and conventional HVOF spray processes. The better electrical resistance stability of the suspension-sprayed Al_2O_3 coatings could be explained by their specific microstructure and retention of a higher content of α-Al_2O_3. Kim et al. [263] studied, for plasma-sprayed Al_2O_3–13 % TiO_2 coatings, the effect of two commercial sealants based on polymers on the electrical insulation properties before and after the impregnation treatment. Cipri et al. [23] studied the interesting electromagnetic properties (complex permittivity) of Al_2O_3–SiO_2 compounds plasma sprayed. For microwave and nuclear fusion applications, BeO is sprayed by inert plasma spraying process but its toxicity requires very stringent spray conditions.

18.3.6.2 Resistors and Conductors

Prudenziati et al. [264–266] have studied Ni, Ni20Cr, or Ni5Al coatings plasma sprayed onto alumina films deposited onto steel plates. They compared electrical properties of resistors prepared with Ni and Ni–20Cr powders by thermal spray processes (APS and HVOF). The resistivity of Ni resistors decreased after annealing at temperatures in the range 200–400 °C may be due to healing of structural defects. On the contrary, the observed increase of resistivity of Ni–20Cr-based resistors was possibly due to ordering of the atoms. The temperature dependence of resistance for Ni-based resistors was invariably the same as for Ni bulk, regardless of sample origin. On the other hand, a large spread in temperature coefficient of resistance (TCR) values of Ni–20Cr-based resistors was observed. Ni-based resistors had an excellent reproducibility of the resistance versus the temperature curves, making them excellent candidates for temperature sensors and self-controlled high temperature heaters.

To limit oxidation in flight, cold spray can be used. In spite of the low flattening degree of cold-sprayed (CS) coatings, the anisotropy does not disappear even after annealing [7]. However, when compared to thermal-sprayed coatings, the electrical resistivity of cold-sprayed ones is lower (3–5 times) [267–269].

18.3.6.3 Electronic Devices

For electronics, the following applications and development areas of cold spray process can be indicated [267]: (1) deposition of electric screening coatings on plastics, (2) generation of conducting structures on nonmetals, and (3) deposition of brazing and soldering alloys.

For example, Gui et al. [270] plasma sprayed, onto a graphite substrate, Al matrix composites with high-SiC volume fraction. Al-55SiC and Al-75SiC powders were milled by stainless steel and ZrO_2 balls in a conventional rotating ball mill for 1–10 h. The SiC particles exhibited a reasonably uniform distribution in the composites sprayed from the milled powders. The Fe contamination occurred to the milled powders when stainless steel balls were used. Waveguide devices for microwave applications were achieved by spraying ferrites and dielectrics.

Yamakawa et al. [271] have studied ceramic trays (a type of kiln furniture) used for firing multilayer ceramic chip capacitors (MLCC) that are used in a large number of electronic appliances. They are being required in more compact sizes, larger capacities, and reduced costs year by year. High-thermal shock resistance and reaction resistance are desired properties for these ceramic trays. They showed that the application of plasma-sprayed ZrO_2 topcoat and an Al_2O_3-sintered basecoat made it possible to enhance longevity and reduce cost.

18.3.6.4 Electromagnetic Shielding

Thermal spray coatings cannot compete with PVD techniques to manufacture electronic devices, but wire arc sprayed coatings are used as shielding material to eliminate electromagnetic and radio frequency interference and dissipate static discharge sparks. Zn and Al are currently used to protect computers, electronic office equipment, medical monitoring devices, housing constructed of temperature-sensitive plastic, rooms containing military computers. Donner et al. [272] have cold-sprayed copper coatings onto previously thermally sprayed Al_2O_3 coatings. They either applied a bondcoat on the ceramic layer or used heated substrates during the cold spray process. By both alternatives, dense copper layers were produced. The electrical conductivity reached 98% of international annealed copper standard (IACS) in the as-sprayed condition on heated substrates, or 90 % of the IACS value after spraying on cold substrates with aluminum bondcoat and additional heat treatment, thus meeting the requirements for electronic applications. Lin et al. [273] plasma sprayed surfaces of copper plates with a thick alumina layer to fabricate a composite with a dielectric performance suitable as substrate in electronic devices with high thermal dissipation. They concluded that an alumina layer thickness of 20 μm provided low surface roughness, low thermal resistance, and highly reliable breakdown voltage (38 V/μm). Most telecommunication systems and wireless networks operate at radio and microwave frequencies. However, due to the ever-increasing exploitation of these frequencies, both electromagnetic (EM) pollution and interference occur [274]. Various plastic- and foam-layered instruments and computer equipment cases require shielding. That can be achieved by wire arc spraying zinc coating on the case. Zinc because of its low melting temperature and wire arc because of the low heat flux of the process. Of course it is better using nitrogen atomization to keep the electrical conductivity of the coating as low as possible with as less as possible oxide within coating. For military applications, the whole room can be shielded with a zinc or aluminum film wire arc sprayed outside of it.

Broadband electromagnetic wave absorbers usually correspond to spinel ferrites and hexa-ferrites operating at 45–75 GHz. Unfortunately these materials are usually decomposed when sprayed. Lisjak et al. [275] found a solution by plasma spraying atomized particles of hexa-ferrite and polymer. The hexa-ferrite crystalline structure was preserved during the spraying, while the polyester partly melted and resolidified during cooling. The coupling of the hexa-ferrite magnetic and dielectric losses with the polyester dielectric losses resulted in the superior properties of the composite coating with respect to the pure single-phase coating of the constituent phases.

18.3.6.5 Magnetic Materials

Nd–Fe–B permanent magnets have been sprayed by vacuum plasma spraying [276]. The review of Sampath [277] presents a few ferrites and soft magnetic materials plasma and HVOF sprayed that could be interesting for industrial applications.

18.3.6.6 Sensor Applications

According to the review paper of Sampath [277], interesting prospective seems to be the innovative Direct Write Thermal Spray (DWTS), which is a new and exciting manufacturing technology capable of depositing a large number of electronic materials on a wide range of substrates, enabling direct write fabrication of multilayer thick film electronic devices. One of the exciting prospects of this technology is the fabrication of integrated, embedded sensors directly onto thermal spray-coated components. Sampath [277] also presents the past, present, and future of thermal spray applications in electronics and sensors. The different dielectrics that are used or that have been used are presented: alumina, beryllia, $MgO–3Al_2O_3$ spinel, alumina–titania, cordierite ($2MgO–2Al_2O_3–5SiO_2$), and forsterite ($MgO–SiO_2$), perovskite-based dielectric systems including lead zirconate titanate (PZT), $BaTiO_3$, and strontium-doped $BaTiO_3$, ... deposited by plasma or HVOF.

18.3.6.7 Other Applications

Cold-sprayed nickel or further ferromagnetic metals and alloys are used as induction heating coats on cooking appliances or cooking pots [268]. Superficial metallization on polymer improves the corrosion-resistant and antiaging property but also achieves some special features such as electrical conductivity, thermal conductivity, electromagnetic shielding, and radial protection [269].

Electrically conductive and flexible aluminum coatings (flame sprayed with powder or wire) were deposited onto diverse polyester textiles for wearable electronics, lighting, or communication in medical techniques [278]. Coatings produced using wire as raw material had much better morphologies than those produced using powder as starting material. Successful preliminary test results for Al–polyester composites used as current collectors showed that application-specific electrically conductive composites with adjustable specific surface conductivity values and microstructures can be produced without inducing any thermal or chemical damages to the fabric material [278].

18.3.7 Freestanding Spray-Formed Parts

The freestanding bodies are produced by plasma spraying for refractory or ceramic materials [279–285] and by HVOF spraying for thin alloys or cermets [286] and also by cold spray [287]. Of course rotationally symmetrical shapes are preferred: the core is easy to produce, the stress in the sprayed material is low and evenly distributed, and at last separating the core from the coating is easier. In most cases the core is made of smooth graphite or other material coated by atomization of a

product preventing the substrate–coating adhesion. It is also possible to achieve very complex shapes, such as manifolds of racecar engines, by spraying on special materials that can be afterwards dissolved. It becomes then possible to coat externally the sprayed ceramic thermal barrier by an alloy to achieve the hot gases tightness. This technique, having a high cost, is hardly suitable for large-scale production, but it offers advantages as far as cost and fast delivery are concerned. For example, sprayed ceramic bodies offer good mechanical strength at high temperatures, excellent electrical insulation at temperatures where glass insulators give-up and chemical resistance against corrosive gases or liquids. For example, in rocketry nozzle inserts are achieved that way. Ceramic tubing is used in furnace construction as well as in chemistry. The production of crucibles for the melting of materials is also an important application. Such crucibles are made of partially (YPSZ) or totally (YSZ) stabilized zirconia, strontium zirconate, alumina, tungsten, and molybdenum. A relatively new application of PTA deposition is the fabrication of freestanding shapes, or solid free form fabrication, see Sect. 10.7.6 of Chap. 10.

A few examples of freestanding coatings are presented below:

- Chen et al. [288] vacuum plasma-sprayed dense, oxide-free and pore-free freestanding forms of NiAl and NiAl-B. The deposits retained the same phase structure as the starting powders. The as-sprayed freestanding deposits exhibited a large grain size due to self-annealing during vacuum plasma spray processing. The hardness of NiA1-B was about 10 % higher than that of NiAI.
- Saeidi et al. [289] produced freestanding VPS and HVOF-sprayed CoNiCrAlY coatings. The as-sprayed HVOF coating retained the γ/β microstructure of the feedstock powder, and the VPS coating consisted of a single γ phase. A 3 h, 1,100 °C heat treatment in vacuum converted the single-phase VPS coating to a two-phase γ/β microstructure and coarsened the γ/β microstructure of the HVOF coating. Oxidation of the freestanding as-sprayed coatings produced a dual-layer oxide consisting of an inner layer of α-Al_2O_3 and an outer spinel layer.
- Fan and Ishigaki [290] used induction plasma spraying to produce free-standing parts of Mo_5Si_3-B composite and $MoSi_2$ materials. The oxidation resistance, up to 1,210 °C, of the former composite was compared with that of the latter, known to be resistant to high-temperature oxidation. At boron contents greater than 1 wt %, composites demonstrated encouraging oxidation resistance and with 2 wt% boron it was comparable to $MoSi_2$ [290].
- Waki et al. [291] sprayed freestanding circular tube specimen of CoNiCrAlY by VPS, HVOF, and APS. They studied the effect of post-spray thermal treatments, in vacuum and in air, on the mechanical properties in the 400–1,100 °C temperature range. High-temperature thermal treatment in air was effective in increasing the bending strength and Young's module. It was especially effective on the APS coatings, which were produced using powders with average size of 60 μm, and on HVOF coatings, those bending strengths increased by approximately three times [291].
- Plasma-sprayed freestanding zircon pipes (inside diameter 83 mm, wall thickness 1.5–2 mm, lengths up to 2,000 mm) are used in furnaces as shields

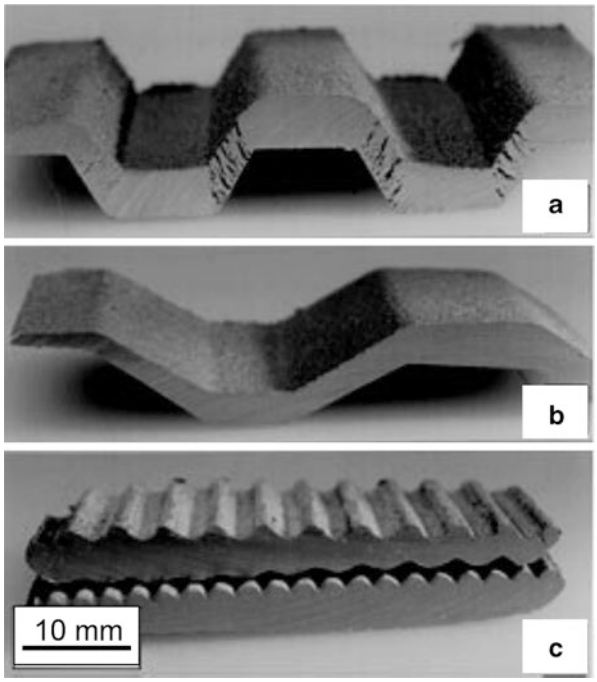


Fig. 18.1 Radio frequency plasma-deposited freestanding parts of bipolar plate material. (**a**) Made with a geometrically extended contour of the substrate (removed), incidence angle at the flanks of 30° (with respect to the direction of the jet). (**b**) Like (**a**), but with an incidence angle of 60°. (**c**) Made with a finer substrate contour. Reprinted with kind permission from Springer Science Business Media [294], copyright © ASM International

for heating elements [292]. The plasma deposits contained glassy silica and various modifications of zirconia in addition to a small amount of the amorphous phase. This combination of zirconia and silica exhibited properties such as a high -thermal shock resistance, good corrosion resistance, and low wettability [292].

– Chen et al. [293] obtained by plasma spraying freestanding $La_2Zr_2O_7$ coatings, using an amorphous La–O–Zr precursor as the feedstock. During thermal spraying, the amorphous powder crystallized, and fine grains were formed, while with crystallized feedstock powder the average grain size was 750 nm. The thermal conductivity of the as-sprayed coating with the amorphous feedstock powder was approximately 0.42 W/m K and its average coefficient of thermal expansion was 11.1×10^{-6}/K, value similar to that of metallic bond coatings [293].
– Henne et al. [294] processed by induction plasma spraying the material of metallic bipolar plates for solid oxide fuel cells, a chromium alloy with the composition 94 % Cr, 5 % Fe, and 1 % Y_2O_3. Freestanding parts had a density above 95 % of the theoretical density of the material. From the deposits obtained, it was positively concluded that, as long as the deposit thickness did not exceed about half the characteristic substrate dimension, the contour of the free side of the deposit sufficiently followed the contour of the substrate [294]. Figure 18.1 presents radio frequency plasma-deposited freestanding parts of bipolar plate material.

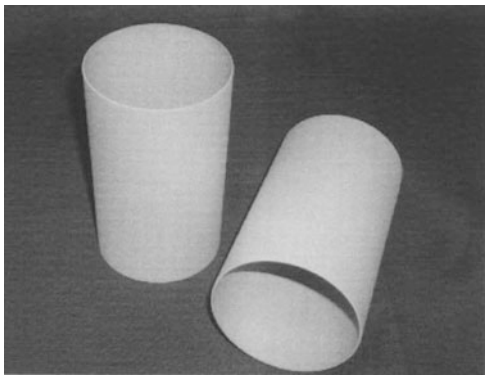


Fig. 18.2 Plasma spray-formed nanostructured aluminum oxide shells with a wall thickness of 0.4–0.6 mm. Reprinted with kind permission from Springer Science Business Media [295], copyright © ASM International

- Agarwal et al. [295] plasma sprayed a mixture of commercially available aluminum oxide powder (99.8 % pure), in the 15–45 μm particle size range, with nanosized aluminum oxide powder (99.9 % pure) thoroughly mixed in a rotating ball (alumina ones) mill for 24 h. Coatings were sprayed on conical mandrels. Spray parameters were controlled with an innovative proprietary cooling technique to retain a large fraction of nanosize Al_2O_3 powder particles in the spray deposit. Nanosize particles were partially melted and trapped between the fully melted coarser (micrometer size) Al_2O_3 grains [295]. Figure 18.2 presents the spray-formed nanostructured alumina-tapered cylindrical cones.
- Laha et al. [296] plasma sprayed freestanding structures hollow conoid (100 mm taper-length, 62 mm diameter, 2 mm thickness) of Al-based nanostructured composite with carbon nanotubes as second phase. Carbon nanotubes (CNT) were successfully retained in the spray-formed composite structure. The CNTs were observed largely between the consecutive Al–Si splats with dangling structure.
- Hussain et al. [297] cold sprayed titanium freestanding coatings, some of them being vacuum heat treated to further decrease porosity levels. Cold spraying using N_2 as a process gas heated to 800 °C deposited titanium with less interconnected porosity than N_2 gas at 600 °C due to a higher degree of particle deformation on impact. Pores above 1 μm were reduced to 0.2 vol. % and the total interconnected porosity to 1.8 vol. % after heat treatment of deposits produced at a process gas temperature of 800 °C.
- Herman et al. [298] sprayed by the VPS process dense deposits of unreinforced and composite matrices of Ni_3A1 alloy and $MoSi_2$. Geibel et al. [279] showed that plasma spray deposition was a suitable technique to produce freestanding, near-net-shaped components of the difficult-to-shape NiAl intermetallic compound.
- Weiss et al. [299] described a new spray-forming process based on thermal spray shape deposition. Shape deposition processes build three-dimensional shapes by incremental material buildup of thin, planar cross-sectional layers.

These processes did not require preformed mandrels and can be used to directly build three-dimensional structures of arbitrary geometrical complexity. The basis for the thermal spray approach was to spray each layer using a disposable mask that had the shape of the current cross section. Masks could be produced from paper rolls, for example, with a CO_2 laser.

18.3.8 Medical Applications

Orthopedic and dental market is developing very fast with either bioinert coatings (Ti–6Al–4V, Ti–6Al–7Nb, Ti–13Nb–13Zr, . . .) or bioactive ones (hydroxyapatite (HA), tricalcium phosphate) [300, 301]. Two types of coatings are used [1]:

Bioinert ones with no activity between them and the bone or soft tissues, the most used materials being Ti and Ti–6Al–4V. These coatings must be porous (at least 30 %).

Bioactive coatings, interacting with bone to promote bonding interfaces, are ceramic coatings with material compositions similar to that of bone tissue (calcium phosphate). The most used ceramic is hydroxyapatite (HA) Ca_{10} $(PO_4)_6$ $(OH)_2$ exhibiting a strong activity to join the bone. Examination of four retrieved HA coated orthopedic prostheses by Gross et al. [302] has indicated bone attachment, along with coating removal, from a range of areas on the prosthesis surface. Coating removal occurred by dissolution provided the higher bone-remodeling rate accompanied by the release of calcium and phosphate. Coatings dissolved faster on elevated areas or those subjected to a higher level of loading. Coatings located in less loaded areas provided a higher longevity. In fact very different methods have been tested to spray HA [303].

RF induction plasma sprayed [304] where the HA coatings, prepared with supersonic plasma nozzle, was highly crystalline in nature with insignificant phase decomposition. Both the crystallinity and purity of HA decreased when sprayed with normal plasma nozzle.

Air plasma-sprayed coatings and HA and HVOF-sprayed nano-titania coatings on Ti–6Al–4V and fiber-reinforced polymer composite substrates [305] were compared. The surface cell coverage after 7 days of incubation was more complete on nano-TiO_2 than HA. Preliminary results indicated that osteoblast activity after 15 days of incubation on nano-TiO_2 was equivalent to or greater than that observed on HA. Chang et al. [306] studied hydroxyapatite coatings sprayed with a vacuum plasma spray system at different power levels. They showed that the spray power greatly affected the crystallinity, chemical composition, and microstructure of as-sprayed hydroxyapatite coatings, which were linked to the melting state of hydroxyapatite powder. Prevéy [307], to overcome the complexities of characterizing plasma-sprayed HA coatings, has developed an external standard method of XRD quantitative analysis that can be applied nondestructively. Khor et al. [308] have studied the formation of a composite made of HA and Ti–6Al–4V, APS or HVOF sprayed, to enhance the poor mechanical properties of hydroxyapatite (HA).

The composite presented excellent bond strength due to the superior interfacial bond between the Ti–6Al–4V rich splats and the substrate. Wang et al. [309] have studied the preparation of a functionally graded bio-ceramic coating composed of essentially calcium phosphate compounds.

HVOF-sprayed HA: compared to plasma-sprayed one, the HVOF system has proven to be a novel method for HA deposition with maximum crystallinity and purity values of 93.81 and 99.84 %, respectively. With FDA-approved plasma spray technique, values of only 87.6 and 99.4 % crystallinity and purity, respectively, were found [310].

HVOF-sprayed nanostructured titania (n-TiO_2) and 10 wt% hydroxyapatite (HA) (n-TiO_2–10 wt% HA) powders have been engineered by Lima et al. [311] as possible future alternatives to HA coatings deposited via air plasma spray (APS).

The n-TiO_2–10 wt% HA coatings exhibited bond strength levels higher than 77 MPa, i.e., at least twice those of APS HA coatings deposited on Ti–6Al–4V substrates. In addition, due to the high stability of TiO_2 in the human body, longevity related concerns of HA coatings, such as dissolution and osteolysis, were unlikely to occur. HA coatings with a high content of both crystalline HA and nanostructures were preferred for cell proliferation [20].

Coatings resulting from agglomerated nanostructure coatings: It was demonstrated by using an osteoblast cell culture (in vitro) that the type of HA coating phase is more important than the nanostructure character of the coating, however, HA coatings with a high content of both crystalline HA and nanostructures were preferred for cell proliferation [20, 311, 312]. Based on cell culture (in vitro) results observed for bulk nanostructured ceramics, the nanostructure zones being found on the TiO_2 coating surface may have played an important role in producing good biocompatibility results. However, up to this point there is no experimental evidence to prove this [20].

ZrO_2/SiO_2 composite coatings have high-abrasive wear resistance compared with pure HA and HA/ZrO_2 coatings because they exhibit high hardness and dense structure. The in vitro test of the composite coatings in simulated body fluid showed a growth of nanometer-sized particles apatite after the immersion of the coatings for 20 days [313].

Well-adherent, flawless, glass–ceramic (SiO_2–CaO–K_2O) coatings on alumina and Ti6Al4V substrates were realized [314, 315]. The obtained results were reproducible and the applied techniques were low cost and not complex. When tested in vitro, the coatings showed an extensive precipitation of a thick HA layer, well adherent to the coatings.

SiO_2–CaO–P_2O_5-based bioactive glasses and glass–ceramics are attractive materials for biomedical applications, because of the excellent levels of bioactivity, which can be achieved by formulating and selecting appropriate compositions [316]. Preliminary results with high-velocity suspension flame spraying bioactive glasses seemed to be promising.

The sprayed coatings can be heat treated:

HA coatings deposited by HVOF spraying showed similar advantages as coatings obtained by APS, but with higher crystallinity. Heat treatment of the coating allowed crystallization of the amorphous calcium phosphate (ACP) present in the coatings [317]. XRD analysis confirmed that the ACP transforms directly to HA and not to other calcium phosphate phases. Similarly functionally graded calcium phosphate coatings were produced on Ti–6Al–4V substrates by plasma spraying [317]. The microstructure of the coating was dense with the typical lamellar structure. The top layer of the coating was mainly composed of a-(Tricalcium Phosphate) TCP, which suggested high bio-resorbability. After post-spray heat treatment, the TCP phase, from either the decomposition of HA or the TCP feedstock, and the tetracalcium phosphate (TTCP) phase were no longer detected by XRD, but the CaO phase remained.

Yu et al. [318] plasma-sprayed HA coatings and post-spray treated them by the spark plasma-sintering (SPS) technique at 500 °C, 600 °C, and 700 °C for duration of 5 and 30 min. The HA coatings treated in SPS for 5 min revealed rapid surface morphological changes during in vitro incubation (up to 12 days), indicating that the surface activity is enhanced by the SPS treatment.

Bellucci et al. [319] coated titanium plates by high-velocity suspension flame spraying (HVSFS) technique using a novel bioactive glass composition based on the K_2O–CaO–P_2O_5–SiO_2 composition ("Bio-K"). On half of the samples, an atmospheric plasma-sprayed (APS) TiO_2 bond coat was preliminarily deposited; suspensions of attrition milled micron-sized glass powders, dispersed in a water and isopropanol mixture, were then sprayed onto both bare and bond-coated plates using five different process parameter sets. All coatings exhibited analogous behavior when soaked in a simulated body fluid (SBF) solution. Their interaction with the SBF involved ion release from the glass, conversion of its surface into an amorphous and hydrated silica layer followed by nucleation, and growth of a carbonated hydroxyapatite film on top of the latter. This interaction seemed particularly fast, as the hydroxyapatite film started to appear after 3 days of soaking.

Other materials were tested for their potential application in biomedicine: Liang et al. [320] plasma sprayed three kinds of powders composed of Ca_2SiO_4, ZrO_2, and $CaZrO_3$ with different Ca_2SiO_4. Results showed that the chemical stability of the coatings was significantly improved compared with pure calcium silicate coatings and increased with the increase of Zr contents. Results indicated that plasma-sprayed coating with 40 wt% of Ca_2SiO_4 had medium dissolution rate and good biological properties, suggesting its potential use as bone implants.

At last bactericidal effects of coatings were also studied.

Preliminary results showed that thermal-sprayed nanostructure TiO_2 coatings exhibited photocatalytic bactericidal activity with *Pseudomonas aeruginosa* [321].

The antibacterial behavior of HA–Ag (silver-doped hydroxyapatite) nanometer-sized powder and their composite coatings were investigated against *Escherichia coli* (DH5a). HA–Ag nanometer-sized powder and PEEK (poly-ether-ether-ketone)-based HA–Ag composite powders were synthesized using in-house powder processing techniques. These nanometer-sized composite powders were

cold sprayed. The results indicated that the antibacterial activity increased with increasing HA–Ag nanometer-sized powder concentration in the composite powder feedstock and cold-sprayed coating [322].

The antibacterial behavior of CS–Cu (chitosan–copper complex) powder and their composite coatings were investigated against *E. coli* (DH5a). The cold-sprayed coatings retained the antibacterial properties of the original feedstock powders [323].

18.3.9 Replacement of Hard Chromium

Electrolytic hard chromium plating is extensively used against wear and sometimes corrosion. However, the chromium plating baths contain chromic acid, in which the chromium is in hexavalent state, known carcinogen. Thus this technology presents harmful effects on the environment and the public health and it has also some intrinsic technical limitations. That is why research efforts on its replacement by sprayed coatings, especially cermet coatings HVOF sprayed, are numerous since the beginning of the 1990s.

Few other examples are presented below:

Sahraoui et al. [324] investigated and compared microstructural properties, wear resistance, and potentials of HVOF-sprayed Tribaloy©-400 (T-400), Cr_3C_2–25 wt% NiCr, and WC–12 wt% Co coatings for a possible replacement of hard chromium plating in gas turbine shafts repair. HVOF carbide-based coatings exhibited higher hardnesses and superior performances in wear resistance than hard chromium coatings. In the case of shafts repair, hard chromium plating process proved to be time consuming and to involve high costs.

Heydarzadeh and Ghadami [325] plasma deposited APS onto steel substrates WC–12 wt% Co powders. Heat treatment of the coatings in an inert atmosphere above 900 °C promoted the formation of Z-carbides from the amorphous phase. Microhardness of coatings for different heat-treating conditions was relatively higher than that of the conventional hard chromium electro deposit.

Ishikawa et al. [119] used a commercial HVOF and a gas shroud attachment HVOF to prepare WC/CrC/Ni cermet coatings under various combustion conditions. The density of coatings improved as the velocity of sprayed particles increased. With the gas-shrouded HVOF, high density was achieved with a lower degree of WC degradation. Such coatings could be alternative candidates of hard chrome plating.

Bolelli et al. [326] studied mechanical properties and tribological behavior (abrasion and un-lubricated sliding wear resistance) of various kinds of electrolytic hard chrome (EHC) coatings and of metallic and cermet HVOF-sprayed coatings (WC–17Co, WC–10Co–4Cr, Co–28Mo–17Cr–3Si). HVOF-sprayed cermet coatings were harder but less tough than EHC ones. Therefore, they undergone a comparable or even higher mass loss when subjected to three-body abrasion conditions. However, their two-body sliding resistance definitely overcame that

of EHC coatings, because they form a tough and uniform surface film protecting them from further damage [326].

Savarimuthu et al. [72] studied sliding wear characteristics of WC thermal spray coatings HVOF sprayed and electroplated chrome tested against Al–Ni–Bz blocks, Cu–Be blocks, and against themselves. The fatigue resistance of WC coatings increased when compressive residual stresses existed.

Deng et al. [327] used high-velocity oxygen/air fuel (HVO/AF) to spray WC-17Co and WC-10Co4Cr on 300M ultrahigh-strength steel. WC-17Co coating exhibited higher fracture toughness than that of WC-10Co4Cr coating. WC-17Co coating demonstrated better impingement resistance than WC-10Co4Cr, and the impingement resistance of chrome electroplating felled between that of WC-17Co and WC-10Co4Cr coatings.

Guilemany et al. [328] compared wear and corrosion properties of Cr_3C_2–NiCr (CC-TS) HVOF sprayed and hard chromium (HC) coatings obtained on a steel substrate. Three orders of magnitude lower volume loss were found for CC-TS (HVOF) after friction tests compared with HC. The best corrosion resistance was also obtained for the CC-TS by HVOF.

Picas et al. [329] compared the mechanical and tribological properties of HVOF CrC75–(NiCr20)25 coatings sprayed from three different agglomerated feedstock powders with various powder size distributions and compared results with conventional hard chromium plating. The CrC–NiCr coating, obtained with the lowest feedstock powder size, presented the best wear resistance under all studied conditions and demonstrated superior performance to hard chrome with regard to mechanical and tribological properties [329].

Staia et al. [330] investigated the tribological behavior of a VPS sprayed Cr_2C_3–25 wt% NiCr chromium carbide coating both in the as-deposited and heat-treated conditions. The samples were subsequently annealed for 2 h at 600 °C, 800 °C, and 900 °C in Ar. The wear values indicated a satisfactory behavior from the tribological point of view. However, the heat treatment had no important consequences on the tribological performance of these coatings. The only problem is that VPS coating is about 4 times more expensive than HVOF ones [330].

Lu et al. [331] compared the microstructure and corrosion behavior of hard chromium coating HCC and plasma-sprayed Fe-based alloy coatings (FAC) on low carbon steel, using the salt-spray test and electrochemical corrosion test. After 60 days of salt-spray test, the weight loss of the FAC was only about 10 % of HCC. After sealing treatment, the defects of pores and micro-cracks existing in FAC disappeared. The sealing treatment further decreased the weight loss of FAC to be about 4 % of HCC [331].

Abdi and Lebaili [332] flame sprayed NiCrBSiCFe coatings for a possible replacement of hard chromium plating in mechanical parts repair. Coatings presented a high hardness after cyclic heat treatment, an excellent resistance to wear and friction, a good corrosion resistance, and an excellent adhesion to steel. Tests have been also positive for the replacement of hard chromium in landing gear by HVOF sprayed WC–CoCr coatings [1, 333, 334].

18.3.10 Applications Under Developments

18.3.10.1 Solid Oxide Fuel Cells

A solid oxide fuel cell (SOFC) is an electrochemical conversion device that produces electricity directly from oxidizing fuel. They are made of four layers comprising three ceramic layers, which are not electrically and ionically active below about 600 °C. Such high operating temperatures result in mechanical and chemical compatibility issues. To achieve an affordable manufacturing cost, the whole SOFCs have been manufactured by plasma spraying: cathode, electrolyte, and anode. One of the disadvantages of the process is the thickness of the electrolyte that must be below a few tens of micrometers and impervious. However, it seems that thin and impervious electrolyte (around 10 μm) can be achieved by suspension plasma spraying. Henne [335] presented in 2007 an excellent overview of thermal-sprayed coatings to make SOFC components and also entire cells. Among the numerous studies, essentially with plasma spraying, published before that year, "only few have proven their potential for a reliable and efficient production of relevant layers and components and promised the status for a technical breakthrough for mass production where a continuous operation with high throughput and yield producing the desired quality is required" [335]. Henne recommends for further developments to improve plasma sources, increase deposition efficiency, work on less costly materials, and combine synthesis and deposition of cell materials based on low-cost precursors. He also evokes the possibility of the recycling of "plasma gas" and overspray [335]. A few examples are given below.

- Takenoiri et al. [336] developed a seal-less planar SOFC consisting of a cell supported with a porous metallic substrate and a metallic separator. The anode and electrolyte were fabricated using flame spraying and APS, respectively, and APS was also used to form a protective coating of the separator. It was shown that the electrical resistance of the separator could be kept lower than $25 \times 10^{-3}\ \Omega\ cm^2$ for at least 3,000 h by the application of $(LaSr)MnO_3$ protective coatings.
- Barthel et al. [337] deposited by thermal spray processes (VPS and flame spraying) porous composite cathodes of $(La_{0.8}\ Sr_{0.2})_{0.98}MnO_3$ (LSM) and ZrO_2–12 % Y_2O_3 (YSZ). The electrochemical performance of the cathodes, evaluated by impedance spectroscopy, indicated significant improvements, especially for the bilayer technique, whereas the concentration profiles of the multilayer gradients still must be optimized. Flame spraying seemed promising.
- $La_{10}\ Mg_{0.2}\ Si_{5.8}\ O_{26.8}$ was prepared by solid-phase sintering and also plasma sprayed by Sun et al. [338]. The amorphous transformation of lanthanum silicates happened during APS process. The heat treatment effectively ameliorated phase composition of as-sprayed coatings, complete recrystallization being achieved after 1,000 °C for 4 h. However, it decreased the permeability of coatings.

- Puranen et al. [339] plasma sprayed Mn–Co–Fe spinel coating on the thin metallic interconnectors in SOFCs. They optimized spray conditions to produce coatings with low thickness and low amount of porosity. The original spinel structure decomposed because of the fast transformation of solid–liquid–solid states but was partially restored by using post-annealing treatment.
- Harris et al. [340] manufactured by axial-injection APS (Mettech Axial torch) single phase and composite cathodes based on LSCF ($La_{0.6}$ $Sr_{0.4}$ $Co_{0.2}$ $Fe_{0.8}$ $O_{32-\delta}$) and SSC ($Sm_{0.5}$ $Sr_{0.5}$ Co O_3). An average surface temperature of approximately 2,200 °C was needed for adequate melting of LSCF particles and approximately 2,100 °C to melt SSC. But too much particle heating resulted in coarser and denser microstructures.
- Suspension plasma spraying [186] seems to be promising for the SOFC cathode deposition, as coatings with high porosity levels in combination with fine pore size can be produced. Shen et al. [341], using induction plasma technology and solution plasma spraying, achieved a homogeneously mixed nano-sized composite GDC/LSCF powder without using a prolonged period of mechanical mixing. The nano-powders exhibited a perovskite structure and a fluorite structure as well as separated GDC ($Ce_{0.8}$ $Gd_{0.2}$ $O_{1.9}$) and LSCF phases. The coatings were homogeneous and porous (51 % porosity) with cauliflower structures. Wang et al. [342] successfully deposited with Axial III Mettech torch Ni–YSZ anode and YSZ electrolyte half-cells on porous Hastelloy X substrates by SPS. The thickness of the anode and electrolyte layers was ~40 μm and 10–20 μm, respectively. The density of YSZ electrolyte coatings increased as plasma torch input power increased. The anodes of the deposited half-cells were porous and electrolytes dense, with no interconnected pores. Michaux et al. [343] prepared and characterized porous anode layers with homogeneous nickel distribution and nanometer sized microstructure for SOFC application. They investigated the effects of some spray parameters on the layer architecture and composition.

18.3.10.2 Other Sensors

For oxygen permeation membranes Zotov et al. [344] prepared $La_{1-x}Sr_xFe_{1-y}$ $Co_yO_{3-\delta}$ (LSFC) coatings by low-pressure plasma spraying thin film processes using different plasma spray parameters. The microstructures of the investigated LSFC coatings depended sensitively on the oxygen partial pressure, the substrate temperature, the plasma jet velocities, and the deposition rate. Coatings deposited with Ar-rich plasma and higher plasma jet velocities were most promising.

Oxygen sensors based on ionic conduction of plasma-sprayed ZrO_2 (measurement of the small electrical current caused by oxygen ions diffusing through the layer) are now extensively used in catalytic car exhaust pipes [345].

18.3.10.3 Decorative Coatings

Thermal spraying is not widely adapted to decorative coatings, and the main efforts were achieved on relatively large structures such as bridges, water tower, chimneys, . . . that were sprayed with zinc or aluminum for corrosion protection. They can be left as-sprayed or sealed with plain or colored sealers. The liquid flame spraying process has been developed to uniformly color hot glass objects [346]. Thermal spraying of concrete or bricks have been performed with glazing materials. Arcondéguy et al. [347, 348] manufactured glaze layers by flame spraying onto substrates that decomposed when heated and for which the traditional glazing process was not appropriate. Adjusting the chemical composition permitted to adjust the transition temperature of the materials. Adjusting their morphology by post-treatment permitted to increase the deposition efficiency and reduce the pore content of the coatings. Of course the decorative value of such coatings is important for the aesthetic but it has a cost.

18.3.10.4 Spent Nuclear Fuel

Many works are now devoted to the containment of spent nuclear fuel that poses a challenge from the perspective of materials science. These applications require to safely provide neutron absorption and corrosion resistance at reasonable costs for very long periods. Identifying a single material that can meet all these requirements has been quasi-impossible and the introduction of coatings seems promising. Alternate coating materials such as amorphous metals and ceramics have been developed and studied to better resist corrosion. Amorphous coatings with boron or other neutron-absorbing element have demonstrated promising results against corrosion [349–353]. The absence of long-range structure (grain boundaries, dislocations, and segregations), in corrosion-resistant materials, further enhances the corrosion resistance of amorphous alloys. One of the most promising formulations was found to be $Fe_{49.7}Cr_{17.7}Mn_{1.9}Mo_{7.4}W_{1.6}B_{15.2}C_{3.8}Si_{2.4}$ (SAM2X5), which included chromium (Cr), molybdenum (Mo), and tungsten (W) for enhanced corrosion resistance, and boron (B) to enable glass formation and neutron absorption [353]. The parent alloy for this series of amorphous alloys, which is known as SAM40 and represented by the formula $Fe_{52.3}Cr_{19}Mn_2Mo_{2.5}W_{1.7}B_{16}C_4Si_{2.5}$, has less molybdenum than SAM2X5 and was originally developed by Branagan [353]. Coatings, HVOF sprayed, have demonstrated phase stability well above 500–600 °C and at high neutron dose (equivalent to 4,000 years inside the container) [351].

Alumina plasma-sprayed coatings manufactured with graded alumina–titania coatings, and phosphate-sealed alumina coatings were investigated to improve the properties of metallic substrates operating in extreme environments of spent nuclear fuel. The effects of particle sizes distribution, phosphate sealant, and graded titania additions on the dielectric strength of the as-sprayed, thermally cycled, and

thermally aged coatings were investigated [354]. Spinel ($MgAl_2O_4$) coatings were also investigated [355]. All studies demonstrated the necessity to have impervious coatings.

18.3.10.5 Combined Cycle Power Plant Combinations

Hardwicke and Lau [356] emphasized that recent power generation company announcements centered on integrating renewable resources onto the power grid for cleaner, more efficient energy generation. They think that these technical breakthroughs can certainly utilize the new developments in the thermal spray industry.

18.3.10.6 Future Nuclear Fusion Reactor

At last thermonuclear fusion is a potential source of cleaner and safer energy for the future. Its technological realization depends on the development of materials able to survive and function in extreme conditions. According to the review of Matejicek et al. [357], materials to be applied in a fusion reactor will be subjected to extreme and complex loading conditions and have to fulfill very complex and sometimes contradicting requirements. A number of the demands on fusion materials can be fulfilled by the application of coatings. Thermal spraying is just one of the available coating technologies. Thermal spray (especially plasma spray) coatings were developed and tested for a variety of applications in fusion environments, including plasma facing components, tritium permeation barriers, and electrical insulation.

18.4 Thermal-Sprayed Coatings by Industry

In his paper [358], published in 1992, Longo had already identified 34 industrial sectors where thermal spray and other coatings were used. The broad base of end-user activity with thermal spray coatings for 12 industrial sectors was profiled in three tables. The main activities he has considered were gas turbine and aircraft, gas turbine and industry, turbine and steam, engines and automotive, engines and diesel, transportation, oil and gas exploration, chemical processing, paper and pulp, defense and aerospace, medical and dental, electric and electronic.

Longo [358] estimated that "the total market was projected to reach 1.8 to 2.0 billion dollars (1990 dollars) by the end of the decade (2000) on the strength of a growing and expanding powder business, a strong demand for standard equipment systems and vacuum plasma systems, and a growing demand for contract coating services."

Twenty-one years later Dorfman and Sharma [359] estimated that the thermal spray industry is worth approximately a $6.5 billion with the majority of revenue generation in coating services, thus underlying the growth of thermal processes.

The last ASM Handbook, Volume 5A: Thermal Spray Technology [360] is a replacement for the Handbook of Thermal Spray Technology [1]. In this book are developed more recent selection of applications, including electronics and semiconductors, automotive, energy, and biomedical. Emergent thermal spray market sectors such as aerospace and industrial gas turbines and important areas of growth such as advanced thermal barrier materials, wear coatings, clearance control coatings, and oxidation/hot corrosion resistant alloys also are reviewed.

18.4.1 Aerospace

Aero engines are probably those where thermal sprayed coatings, especially APS or HVOF sprayed, were extensively developed since the 1970s–1980s. The fan, compressor, combustion chamber, and turbine must be protected with coatings against oxidation, hot gas corrosion, erosion, and wear. Hundreds of components are now sprayed (see Fig. 1.8) in an aero engines used both for military and industrial turbine engine units worldwide. Their main role is to reduce wear, corrosion, and thermal flux, improve the engine efficiency, and promote life extension... In aero engines almost all types of sprayed materials are used (carbides, iron and steel, nickel alloys, cobalt alloys superalloys, nonferrous metals) except the self-fluxing alloys. The following list, far to be exhaustive, presents the different parts where coatings are used [1, 361]:

Against fretting wear, occurring in both lower- and higher temperature sections of engines, carbides, and refractory metals are used, and for clearance control CuNiIn, Nickel–Aluminum-base coatings, for more details (see Sect. 18.3.1.7).

Where rotating parts need some sealing to reduce by-pass of hot combustion or cold compressor gases (through spaces between blade tips and stationary housing) abradable seals are used. For example, in cold sections they are made of polymers and soft metals, while in the hot ones nickel–graphite, superalloy–polyester or boron carbide, YPSZ with polyester or boron carbide, NiCrAl, and bentonite (for more details see Sect. 18.3.4). Seal coatings are also used in the labyrinth seal knife-edges.

For the high-temperature sections, coatings are used on the one hand for protection against corrosion and high-temperature metal fatigue and on the other to reduce the temperature of the metallic substrate to improve components durability and increase fuel efficiency by higher turbine inlet temperatures: thermal barrier coatings. Besides the fuel consumption reduction, emissions of nitrogen oxide, hydrocarbon gases, and smoke are reduced, which is important to have environmental-friendly engines. For example, Airbus A380 and Boeing 787 cope with the limits set by International Civil Aviation Organization (ICAO).

Against corrosion, materials of the family MCrAlYs are used with M being nickel, cobalt, molybdenum, iron, or alloys of these elements (NiCo, CoNi, ...).



Fig. 18.3 Coated gas turbine vanes (courtesy of Sulzer-Metco)



Fig. 18.4 Coated combustion chamber (courtesy of Sulzer-Metco)

These alloys are VPS, HVOF and for some of them cold sprayed. It is important for these materials to reduce or suppress oxidation during spraying and achieve excellent adhesion. The latter is obtained by spraying on substrates cleaned from oxide layer and kept at high temperature to achieve diffusion between coating and substrate, which requires VPS spraying.

Thermal barrier coating systems (TBCs) are widely used in modern gas turbine engines to lower the metal surface temperature in combustor and turbine section hardware. The engine components exposed to the most extreme temperatures are the combustor and the initial rotor blades and nozzle guide vanes of the high-pressure turbine. Metal temperature reductions of up to 165 °C are possible when TBCs are used in conjunction with external film cooling and internal component air cooling [179]; for more details see Sect. 18.3.3.1. TBCs are applied on vane bases, burner cans, after burners, and also other small engine components. An example of coated gas turbine vane is presented in Fig. 18.3 and that of a combustion chamber in Fig. 18.4.

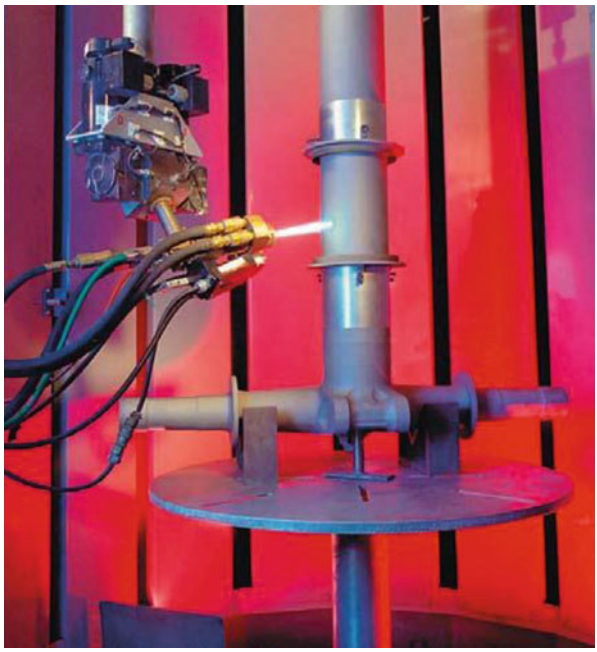


Fig. 18.5 Robot coating a landing gear (courtesy of Sulzer-Metco)

As developed in Sect. 18.3.4, rotating vane assemblies in aircraft engines require limiting the bypass flow of either hot combustion gases or cold compressor gases through the spaces between the blade tips and the stationary housing. These seals can improve drastically the engine efficiency. As developed in Sect. 18.3.4, two types of seals are used: abradable ones that are machined in situ by the rotating components (blades, for example) and labyrinth ones to match stator and rotor components with an intermeshing saw tooth geometry

Against wear, chrome plating has been intensively used because of its durability, ease of application, and low cost. Of course it suffers from pitting, spalling, and other failures under stress. For airlines the replacement of traditional industrial chromium plating process, used in landing gear, is time intensive and the aircraft is out of service for long periods, which is expensive.

Moreover chrome plating has some environmental and health problem with hexavalent chromium emissions. That is why alternatives have been searched to replace it: hard trivalent chrome coating and HVOF or plasma-sprayed coatings. Both present difficulties such as limited coating thickness for trivalent chrome and only line-of-sight geometries for thermal-sprayed coatings [361]. Coatings of tungsten carbides especially developed for landing gears and HVOF sprayed have considerably increased the service life of exposed cylinders and seals used in landing gears. Figure 18.5 presents a robot coating a landing gear.

Tests were also made to prevent corrosion of exhaust silencer segments with aluminum coatings arc sprayed.

18.4.2 Land-Based Turbines

Compared to aero engines the working conditions are tougher according to the longer life time expected (about 3 times longer), the larger size (for example, a ratio of 10 for turbine blades), the poor quality of the fuels used, and the working conditions with external temperatures varying from −40 to 60 °C. For more details see Sects. 18.3.3.2 and 18.3.4. Coatings are applied on bearing journals, bearing seals, stub shaft journals, labyrinth seals, blades nozzles, tip seals, inlets and exhausts, and housings [1, 360]. The overview of Rajendran [238] presents the different coatings used, methods of application and characterization, degradation mechanisms and indicates future directions, which are of use to a practicing industrial engineer. Coatings are applied to the compressor blades and vanes for enhanced erosion resistance. Anti-fretting coating protects the contact area of the dovetail part of the compressor blade root from fretting fatigue failure. Abradable coatings offer close clearance control thereby increasing the engine efficiency. Wear-resistant coatings give extended life of the parts that undergo rotary and reciprocating rubbing motion. Oxidation and corrosion resistant coatings are applied through either diffusion or overlay process. YPSZ (7 wt%) thermal barrier coatings offer increased component life with a decrease in operating temperature of the metal. Hardwicke and Lau [356] in their review paper about advances in thermal spray coatings for gas turbines and energy generation describe functional coatings widely used in energy generation equipment in industries such as renewables, oil and gas propulsion engines, and gas turbines. They present the current status of materials, equipment, processing, and properties' aspects for key coatings in the energy industry, especially the developments in large-scale gas turbines. In addition to the most recent industrial advances in thermal spray technologies, future technical needs are also highlighted. For more details see Sect. 18.3.3.2.

18.4.3 Automotive

Figure 18.6 from Vetter et al. [362] show a variety of car parts treated by different surface technologies (from sprayed coatings to PVD or PECVD). The different coating applications are related to [1, 362–365] the power train components, thermal barriers protecting certain components from overheating, brake discs, cylinder bore in diesel engines, aluminum alloy cylinder bore, exhaust valves, crankshaft, transmission and rear end gear clusters, body and chassis, synchronizer rings, shifter forks, valve seats, and connecting rods.

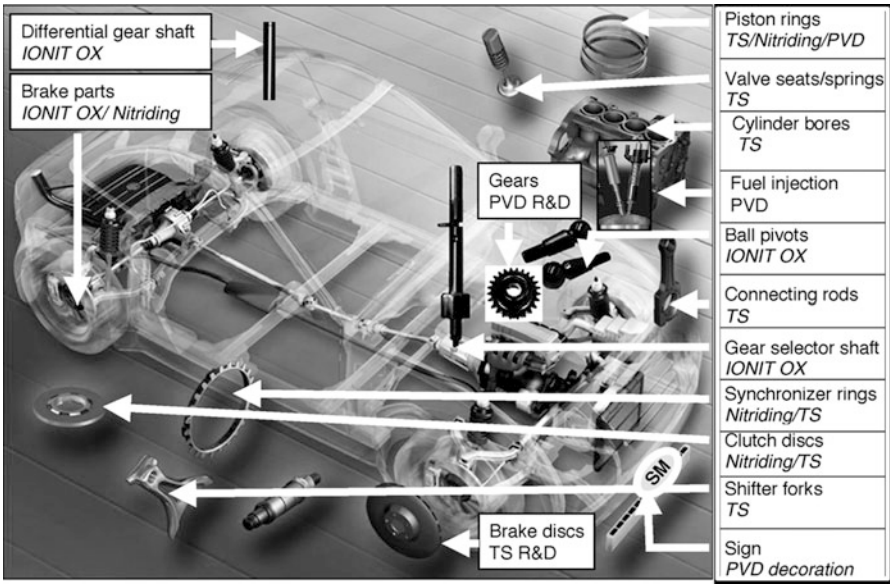


Fig. 18.6 Selected parts to be treated by surface technologies in cars. Reprinted with the kind permission of Elsevier [362]

18.4.3.1 Power Train Components

1. Against hot corrosion: Exhaust systems components (exhaust headers, exhaust pipes) are protected from hot corrosion by aluminum coatings wire arc sprayed.
2. Against wear: piston rings are commonly coated with molybdenum and molybdenum-bearing compounds using the plasma spray process in general. The HVOF spray process is used in the case of high performance piston rings for diesel engines. Molybdenum coatings are also used on aluminum piston skirts to prevent galling. Some aluminum piston tops are coated with molybdenum to limit erosion due to the impingement of fuel from injectors. Cylinder bore in diesel engines are coated with molybdenum plasma sprayed or WC–Co and WC–Co–Cr HVOF sprayed. Such coatings, slightly porous, retain oil and improve friction. Coated transmission parts such as synchronizing rings and shift forks are widely coated using wire flame spraying with molybdenum to provide a constant coefficient of friction and prevent scuffing.

In order to reduce the weight and size of the engine, iron cylinder blocks are replaced by aluminum ones, usually equipped with cast-iron cylinder linings. Instead of them, Sulzer-Metco has been the first to propose aluminum cylinder bores coated with a special iron alloy, to replace the cast-iron cylinder lining. This plasma coating acts as a direct running surface for the similarly coated piston rings, which reduces diesel or gasoline consumption and the amount of oil needed.



Fig. 18.7 Photo of the Rotaplasma process of Sulzer Metco (courtesy of Sultzer Metco)

The process called Rota-plasma developed by Sulzer-Metco was introduced in 2000 for automobile production. It allows coating aluminum alloy (cast aluminum–silicon) cylinder bores to provide a good wear resistance. Coating materials can be: carbon steel with its own oxides wustite and magnetite as solid lubricant, composite of carbon tool steel and molybdenum, corrosion-resistant steel (Cr and Mo alloyed), and metal matrix composite with ceramic particles. The process is entirely automated and lasts about one minute for a bore of conventional car engine (see Fig. 18.7).

The process advantages are the following:

- The pitch distance between the cylinders can be reduced allowing a further reduction of the engine block weight
- The friction between the piston rings and the liner surface can be significantly reduced (more than 30 % in gasoline engines)
- Considering that the majority of the energy losses in the engine is due to thermodynamic cycle efficiency, the potential fuel savings is limited to 4 to 5 %
- Very low surface wear rate (about 5 nm/h of service)

Transmission and rear end gear clusters receive often Mo thin coatings plasma sprayed to lessen the friction and produce smoother movement.

18.4.3.2 Rebuilding and Dimensional Restoration

It concerns crankshafts, clutches, and transmission shafts.

18.4.3.3 Thermal Barrier Coatings (See Sect. 18.3.3.3)

TBCs have been used on piston heads and valves and exhaust ports of high-performance engines. Thick TBCs (0.5–1 mm) on piston heads are attractive for the gains in engine performance and lifetime and the pollution reduction (hydrocarbons and NO_x). TBCs on brake pads insulate the hydraulics and avoid the risk of its boiling, especially on race cars.

They can also be applied externally on manifolds and other exhaust systems when the air cooling becomes insufficient. They increase the efficiency of turbochargers.

18.4.3.4 Other Applications

Metal matrix composites are used in brake discs to tailor the mechanical resistance and the thermal conductivity. The wire arc spray provides low-cost filler for weld seam and is also used for dimensional restoration. Ceramic overlay are sprayed for oxygen sensor protection, the sensor itself using zirconia-sprayed coating.

18.4.4 Electrical and Electronic Industries

First of all thermal spray coatings that allow achieving thick coatings cannot compete with the thin film technology (CVD, PECVD, sputtering, ion plating, . . .) used in electronic devices. However, they can be very useful in capacitors, insulators, resistors, and inductors. Coatings of oxide ceramics (alumina, titanate, beryllia) are used as dielectrics, while metals, and alloys are used for current carrying and bonding to ceramic substrates, metals for electromagnetic shielding, . . . [1, 360]. A few examples are presented below.

Alumina plasma-sprayed coatings are currently used in ozonizers. Standard ozonizer tubes consist of a borosilicate glass tube serving as dielectric with a metal coating applied to the inner surface of the tube serving as the HV-electrode. In order to increase the ozone production efficiency, a material with a higher permittivity is needed. Alumina coatings with a thickness up to 1,000 μm and serving as dielectric is deposited together with the metal electrode on top of the glass tube in ozonizers. Alumina is also used for high-temperature strain gages and insulation of induction heating coils.

Multilayer ceramic chip capacitors (MLCC) are used in a large number of electronic appliances. According to Yamakawa et al. [271] they are being required in more compact sizes, larger capacities, and reduced costs year-by-year and ceramic trays (a type of kiln furniture) are used for firing them. Normally, this ceramic tray consists of an Al_2O_3–SiO_2 body, an Y_2O_3-stabilized ZrO_2 topcoat and Al_2O_3 basecoat. The application of plasma-sprayed ZrO_2 topcoat and an Al_2O_3-sintered basecoat makes it possible to enhance longevity and reduce cost.

Pure beryllia (BeO) present excellent thermal and dielectric properties and is used in many high-performance semiconductor parts for applications such as radio equipment. Some power semiconductor devices use beryllia between the silicon chip and the metal mounting base of the package in order to achieve a lower value of thermal resistance than the alumina currently used. It is also used as a structural ceramic for high-performance microwave devices, vacuum tubes, magnetrons, and gas lasers. Vacuum plasma-sprayed beryllia coatings present excellent properties. Unfortunately their handling, especially that of fine powders, is highly toxic resulting in very stringent safety conditions such as keeping the rooms where spraying is achieved at pressure lower than atmospheric one. These conditions are often economically prohibitive and such coatings are essentially used for army and nuclear applications [1, 360].

According to Smyth and Anderson [366], for electrical heaters, arc-sprayed coatings are used, masking permitting to define the geometry. The choice of the material (NiCr, NiAl, . . .) depends on its resistance variation with temperature that must be as low as possible because the electricity source is a constant voltage one. The resistance depends on the coating oxide content that can also modify the alloy composition, chromium being preferentially oxidized compared to nickel, for example. Most sprayed resistors are used at relatively low temperatures (<250 °C). The resistance value can also be increased when adding alumina particles. Coatings can be sprayed on ceramic material, even polished ones, with a very good adhesion, when eutectics are formed or diffusion occurs. It requires heating the substrate to temperatures close to the sprayed alloy or metal temperature.

Cold-sprayed copper coatings are used to improve the heat conductivity between electronic devices, an underlying copper plate, and a soldered copper-coated heat sink, which is fabricated out of aluminum [267]. Cold spray also permits the generation of solderable surfaces on materials with poor wettability (for example, heat sinks, such as copper on aluminum) [268]. Similarly PTA allows spraying very thick (up to 1 cm or more) copper coatings that are used in powerful computer systems to improve their cooling. These copper layers, Fig. 2.8, achieve a good heat distribution and remove the heat more easily.

Alumina films plasma sprayed are more and more used as insulators in electronic devices. Plasma-sprayed alumina is used for electronic package mount in automotive industry.

Wire arc-sprayed coatings are used as shielding material to eliminate electromagnetic and radio frequency interference and dissipate static discharge sparks. Zn and Al are currently used to protect computers, electronic office equipment,

medical monitoring devices, housing constructed of temperature-sensitive plastic, and rooms containing military computers.

The review paper of Sampath [277] points out the industrial success of the lambda sensor for exhaust gas oxygen measurement for engine fuel control. This sensor uses a porous plasma-sprayed zirconia membrane coating between electrodes. When subjected to a differential partial pressure of oxygen, a rapid variation in electric resistance related to the oxygen partial pressure can be monitored through an electrical circuit [277].

Aluminum coatings, wire arc sprayed, are used in the production of electrolytic condensers. A thin film of copper is sprayed on carbon and ceramic resistors and carbon brushes to provide the electrical connection of high electrical conductivity. Thermal sprayed coatings are also used to produce thick films electrical circuits that can carry higher current than printed ones. The most used materials for these applications are Cu, Al, Zn, and Ag.

18.4.5 Corrosion Applications for Land-Based and Marine Applications

When metal coatings are needed to enhance the properties of a given surface wire combustion spray systems or wire arc spray systems are very good solutions to spray protective coatings, especially sacrificial ones. The investment is rather low and coating adherence is generally good (over 20 MPa), with almost no heating of the substrate. However coatings obtained by these methods are relatively porous (up to 20 %), which is not a problem for sacrificial ones. These coatings are extensively used throughout the maritime, paper/pulp/printing, manufacturing, steel, aerospace, automotive, and railroad industries.

18.4.5.1 Sacrificial Coatings

The corrosion protection of large steel structures such as bridges, pipelines, oil tanks, towers, radio and television masts, overhead walkways, and large manufacturing facilities in the metallurgical, chemical, energy, and other industries is a key issue. The protection of structures exposed to moist atmospheres and seawater such as ships, offshore platforms, seaports, is even more difficult [103, 104], see also Sect. 18.3.2.1. In most cases the surface to be protected is thousands and even tens of thousands of square meters, requiring that coating costs is competitive with those of traditional painting methods. The coating rate must be equal or higher than 10 m^2/h and if possible deposited in one unique pass. The equipment must be mobile and autonomous for operation in field conditions and must work under manual control, automation being generally difficult for large-scale operations, and at last, the spray gun can be up to 30 m from its power supply and control center [103, 104]. Flame wire arc spraying meet such requirements.



Fig. 18.8 Iron bridge arc sprayed with zinc and then painted. Reproduced with kind permission of Dr. M. Ducos [367]

Sacrificial coatings (cathodic behavior relatively to ions, for example, Zn or Al on steel) are mainly used: the thicker they will be the longer will be the protection. Typical thicknesses vary from 50 to 500 μm; the most frequent ones being around 230 μm. Referring to Sect. 15.10.1, such coatings must have a cathodic behavior relatively to the ions of the metal to be protected, in almost all cases steels. Metals used are then zinc, aluminum, and zinc–aluminum. Zinc performs better than aluminum in alkaline conditions, while aluminum is in acidic conditions. Zinc and aluminum replace more and more painting and galvanizing because their lifetime is predictable, they have good erosion resistance and require one application with no drying problems. Sluice gates and canal lock gates of the St. Denis Canal in France, that have been zinc coated in the early 1930s, have remained in perfect condition with virtually no maintenance for decades. According to [1] the lifetime of a 255 μm thick zinc or zinc aluminum coating is about 25 years and it can be extended 15 years by sealing it with vinyl paint. Painting is not the only sealer used; impregnation with special compositions (epoxy resin, silicon resin, . . .) being also intensively used. As soon as sealing is considered, the porosity of these coatings becomes an advantage for the adhesion of the sealer. Figure 18.8 represents an iron bridge arc sprayed with zinc and then painted.

Zinc–aluminum (Zn–15 wt%Al) seems to combine advantages of both materials. If resistance to wear must be improved, aluminum coatings can be sprayed with alumina particles, for example, using cored wires.

In case of the protection of steel reinforcement in concrete, zinc is generally used, but titanium has also been used in spite of the fact it is an anodic protection. In that case the coating is applied directly on the concrete substrate [1, 360]. Aluminum must be avoided where thermite sparkling may occur. That is due to the reaction of rusted steel and aluminum smears when this combustible mix is

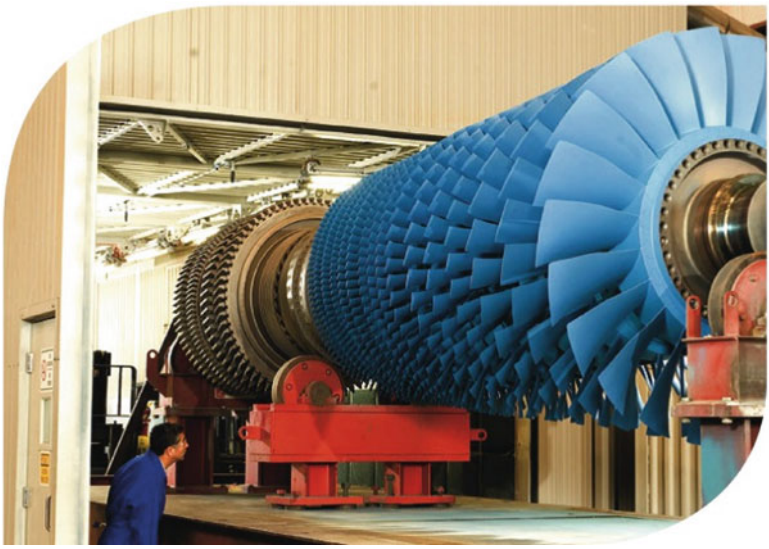


Fig. 18.9 Coated blades of the compressor airfoil of an industrial gas turbine compressor (courtesy of Sulzer-Metco Turbo)

ignited by an impact [1, 360]. Another interest of such coatings is their antifouling properties. Marine biofouling is the undesirable accumulation of marine organisms on artificial surfaces that are immersed in the sea. For example, when marine biofouling occurs on ship hulls, it leads to an increase in weight of the ship and friction to sail.

In the protection from corrosion and/or erosion of industrial gas turbine compressor airfoils, a sacrificial aluminum-filled metallic coating has been recently developed by Sulzer-Metco. The aluminum-filled metallic coating is made conductive via mechanical abrasive finishing. The thickness of these coatings is typically between 25 and 75 μm and the maximum operating temperature 870 °C. Figure 18.9 presents the coated blades of the compressor airfoil.

18.4.5.2 No-Sacrificial Coatings

Austenitic stainless steels, aluminum bronze, nickel-base alloys, MCrAlY, cermets with WC, Cr_2C_3, and matrices containing chromium or nickel or both are used against corrosion, often associated with wear. However such coatings, presenting no galvanic protection, will never protect the substrate if connected porosities and oxide networks exist, which is the case of most thermal sprayed coatings. The substrate protection requires using a protective bond coat or producing dense coatings, or sealing them that is not always possible if the service temperature is over a few hundreds of Celsius degrees.

Coatings of corrosion-resistant alloys for severe petroleum industry corrosion applications, such as type 316L stainless steel and Hastelloy C-276, were shown to act as true corrosion barriers. The oxide content also plays a role (see section "(b) Chemical or Parachemical Corrosion").

For applications with a severe wear in oil and gas industry, cermets are used, with however some problems for offshore installations. According to Meng [117] the corrosion resistance is improved by the proper choice of binder between the wide varieties of tungsten carbides.

18.4.6 Medical Applications

Orthopedic and dental market is developing very fast with either bioinert coatings (Ti–6Al–4V, Ti–6Al–7Nb, Ti–13Nb–13Zr, . . .) or bioactive ones (hydroxyapatite (HA), tricalcium phosphate). Both orthopedic and dental implants receive coatings designed to aid fixation in bone tissues, see Sect. 18.3.8. For example according to [300, 301], the report published in *Implant Dentistry*, estimated that 910,000 dental implant procedures were performed in 2000, and the numbers grew at an annual rate of 18.6 % through 2005. By 2005, annual sales exceeded half a billion dollars. The implant success is dependent on quality bone formation, optimization of the local surface structure, chemistry, morphology, and use of bioactive factors that are equally important [301]. Coated implants are now currently used for tooth, hip, knee, elbow, and shoulder. Two types of coatings are used [1, 360]:

- Bioinert ones with no activity between them and the bone or soft tissues, the most used materials being Ti and Ti–6Al–4V. These coatings must be porous (at least 30 %). Plasma spraying allows preparing porous-graded coatings with dense coating close to substrate to achieve a strong adhesion with substrate and very porous outermost layer (with pore sizes over 100 up to 400 μm). To achieve that, the plasma power was gradually reduced and the particle sizes increased while regulating the degree of powder melting layers to achieve porous graded coatings [300, 301, 360].
- Bioactive coatings, interacting with bone to promote bonding interfaces, are ceramic coatings with material compositions similar to that of bone tissue (calcium phosphate). The most used ceramic is hydroxyapatite (HA) $Ca_{10}(PO_4)_6(OH)_2$ exhibiting a strong activity to join the bone. The provision of a high-calcium and phosphorus-rich environment promotes rapid bone formation within the vicinity of the implant. Unfortunately when HA is plasma sprayed in air, calcium oxide (CaO) is usually formed, thereby affecting the integrity of plasma-sprayed HA coatings. Plasma-sprayed HA coatings also contain other bioresorbable phases, such as tricalcium phosphate (TCP) α or β forms, tetra-calcium phosphate (TTCP), and amorphous calcium phosphate (ACP) [307]. Gross et al. [302] investigated four HA-coated hip components recovered from patients during revision surgery. Analysis of the coating surface indicated

dissolution, osteoclastic resorption, and carbonate apatite precipitation identical to observations from previous in vitro studies. The coating microstructure differed between three coatings that remained on the prosthesis surface, ranging from completely crystalline coatings made by vacuum plasma spraying to less crystalline coatings manufactured by air plasma spraying. Increasing the amorphous and TCP concentration predisposes the coatings to higher dissolution rates [302]. Nelson et al. [368] have deposited by flame spraying powders of titanium alloy (Ti–6Al–4V) and bioactive glass (45S5) to fabricate composite porous coatings for potential use in bone fixation implants. Bioactive glass and titanium alloy powder were blended and deposited in various weight fractions and with two sets of spray conditions, which produced different levels of porosity. The HA formation on the alloy–bioactive glass composite coating suggested that the addition of bioactive glass to the blend may greatly increase the bioactivity of the coating through enhanced surface mineralization. Drnovšek et al. [369] studied the ability of nanoparticle bioactive glass (BAG) to infiltrate into the porous titanium (Ti) layer on Ti-based implants to promote osseointegration. Juhasz and Best [370] reviewed bioactive implants, coatings, and scaffolds made of ceramics, glasses, glass–ceramics, and composites that were able to form a chemical interfacial bond with tissue and can be resorbable or non-resorbable.

The ratio of HA to TCP has been reported to be crucial for bone regeneration. The dissolution rate of HA coating is dependent on the biochemical calcium phosphate phase of the coating as well as coating crystallinity. With adapted spray conditions it is possible to achieve up to 75 % crystallinity for APS, 80 % for HVOF spraying, and 95 % for VPS [302, 303, 306, 311, 312]. The result also depends on powder preparation, best results being obtained with dense HA particles. In Fig. 2.13 is presented the vacuum plasma spraying of (VPS) of HA coating on a knee prosthesis and in Fig. 18.10 a biocompatible coating on the lower part of hip joints.

18.4.7 Ceramic and Glass Manufacturing

For the production of a variety of glasses, platinum is currently used thanks to its high melting point, strength, and resistance to corrosion that allows withstanding the abrasive action of molten glass. Rhodium is often alloyed with platinum to increase the strength of the alloy and extend the life of the equipment. According to the prices of these metals, instead of using them as plates or sheets, they are often plasma sprayed in inert atmosphere chambers where over-sprayed powder can be collected. A ceramic coating, that is reapplied regularly according to its wear [1, 360], can protect these precious metal coatings. The electric glass melting for homogenizing, feeding, and shaping was developed with molybdenum electrode materials, since stirrers, mixing paddles, and some mold surfaces are plasma coated with molybdenum and its alloys [1, 360].

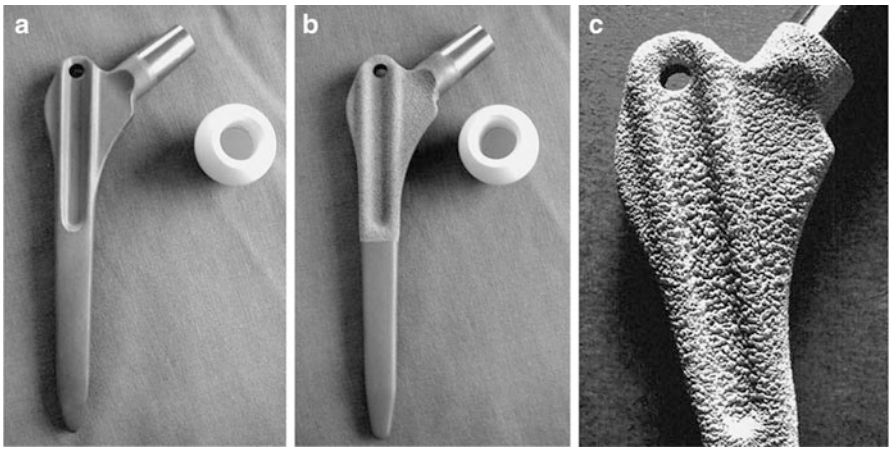


Fig. 18.10 (**a**) Femoral stem Walter, without coating, (**b**) Femoral stem with titanium alloy/hydroxyapatite coating, (**c**) Magnified view of the coating at the proximal end of the porous coated femoral stem [371]

Mold glass material must have sufficient strength, hardness, and accuracy (no deforming process) at high temperature and pressure. Of course, its oxidation resistance must be good, its thermal expansion low, and its thermal conductivity high. Therefore, the mold material choice depends critically on the transition temperature of the glass material. For low temperature-transition-glasses, steel molds with a nickel alloy coating can be used. For example, self-fluxing alloy NiCrBSi flame sprayed and refused. For higher transition temperatures NiCr–Cr_2C_3 or TiC cermets are used.

Hamashima [372] has developed a new boride cermet coating consisting of Mo-system ternary boride and iron-group metal alloys. MoCoB–Co/Cr cermets have a very low friction coefficient with glass at high temperature. The cermet coating has been applied to the lower mold on an industrial scale and the results were very satisfactory. In particular, the production efficiency of the forming process was improved substantially.

18.4.8 Printing Industry

According to Döering et al. [373] "the printing processes need all an ink transferring unit, a print form, and an impression cylinder. They differ in the process of transferring the print image to the substrate, leading to additional cylinders for generating the inverted image—in case of offset printing the so called offset cylinder—or even a shortcut from the ink transferring roller to the print form and directly to the substrate if gravure printing is regarded. Additionally, dampening



Fig. 18.11 SUME™CAL coating after super-finishing on calendar roll (Courtesy of Sulzer-Metco)

units require other surface energy than ink leading rollers. Moreover, the precision of shape and surface roughness of these core components is rather high. Therefore not only the requirements for an appropriate coating in terms of the function but also the requirements for the grinding and finishing step after the coating process are rather high." This will be illustrated with few examples:

- The ink transporting systems in offset printing machines consists of several different rollers, providing a homogenous film of ink for the print form. For example, the duct-roller elevates the ink from the ink box to the ink conditioning system. Its surface roughness R_z must be better than 2 µm and tolerances must be better than 2/1,000 mm in concentricity. Such conditions are achieved with chromia-rich coating consisting of a bond coat (Ni, NiCr, NiAl) and the ceramic topcoat [374].
- Rollers in the paper industry are subject various operating environments resulting in wear, chemical attack from dyes, thermal stress on heated rollers, and mechanical stress from doctor blades. They also must exhibit a high surface finish lasting as long as possible. Figure 18.11 presents a calendar roll coated with the so-called Sulzer-Metco SUME^{TM}CAL developed to meet these requirements.
- In contrast to common offset inking units, the anilox unit consists of a laser-engraved roller, taking the ink from a chamber doctor blade system [373]. The gravure procedure is performed after finishing the roller surface. Producing pure chromia coatings implies using carefully adapted plasma spray conditions and adapted powders, for more details see the works of Pawlowski [6, 374].

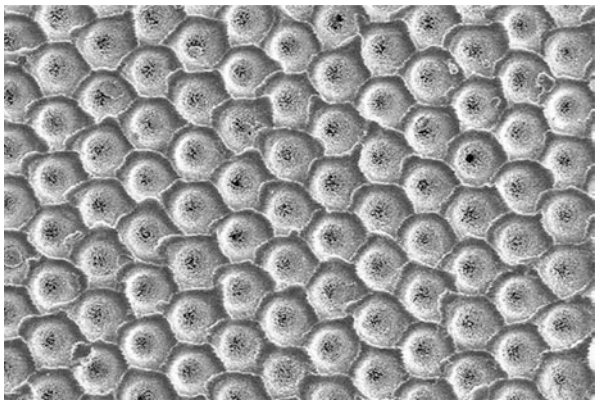


Fig. 18.12 Anilox printing roll with a laser engraved chromium oxide coating (Courtesy of Sulzer-Metco)

– Many other rolls are used in printing machines [374], where different oxides [chromia, alumina–titania (3 or 13 wt%)] are plasma sprayed. Lima and Marple [375] have proposed to replace the alumina–titania conventionally plasma sprayed by HVOF-sprayed nanostructured titania coating exhibiting a very dense (nearly pore free) and uniform isotropic microstructure with an excellent wear and corrosion resistance. Plasma-sprayed chrome oxide coatings for inking rollers exhibit very fine microstructures, which can then be laser engraved with a very small and tight pattern (Fig. 18.12).
– Other rolls such as blanket cylinders are coated with Hastelloy C by either APS or HVOF and at last draw rolls are coated with nickel–chromium [1, 362].

18.4.9 Pulp and Paper

Machines producing paper and cardboard comprise many parts that can be rather important (for example, rolls over one meter in diameter and ten meters in length) with high wear and corrosion problems. Coatings are used in several types of rolls and cylinders, including for instance, center press rolls, dryer cylinders, calender rolls, traction rolls, and Yankee cylinders [376]. Coating materials used are iron- and nickel-base alloys, nickel–chromium self-fluxing alloy, carbides, oxide ceramics, and various multilayers, again depending on the application. For example, rolls are coated by NiCrBSi coatings flame sprayed and others by WC–Co coatings HVOF sprayed. Figure 1.11 presents calendar roll of a paper machine protected by thermal spraying.

Functionally graded (FG) coatings are considered as an option to increase compatibility between ceramic coatings and metallic substrates. In this concept material properties such as CTE (Coefficient of Thermal Expansion) and elastic modulus are designed to gradually change in order to reduce the thermal stresses within the coating. Post-treatments, such as coating with fluoropolymers or sealing



Fig. 18.13 Paper machine center press-roll with a thermally sprayed ceramic coating (Metso Paper Inc.). Reproduced with kind permission of ASM [376]

coatings against corrosive process environments, are also used. A few examples are presented below:

- Press rolls are used to remove as much water from the sheet using mechanical forces. First they were made of granite rock and were very expensive with limited rotation velocity. Now one uses cast iron or steel roll bodies with coatings that are application specific and tailored to perform optimally in various different types of paper production conditions. Factors such as wear and corrosion resistances, and the functionality of the roll surface in the paper manufacturing process, are key properties in these applications [376]. In most cases alumina–titania and chromia coatings are used with HVOF-deposited bond coat [1, 360]. According to the size of the coated cylinders, high-power plasma torches, such as Plazjet, are used for deposition.
- Dryer cylinders of paper machines and large Yankee drying cylinders of tissue paper machines are HVOF thermal spray coated with cermets containing various carbides. According to their weight and size, these components are commonly coated on-site (surface preparation, coating, surface finish) in the paper factory. Ceramic-coated center press rolls are, nowadays, used to replace conventional granite rolls [376]. Ceramic coatings are based on aluminum and chromium oxides with an underlying bond coat and corrosion barrier. They are application specific and tailored to perform optimally in various different types of paper production conditions. According to the size of the components, Metso Paper is the world's leading manufacturer, both in Finland and elsewhere Fig. 18.13 represents a ceramic center press roll of a paper machine after finishing.

Sprayed coatings can also be top-coated with a fluoropolymer layer to improve the release properties of the roll surfaces [376]. Steels with high molybdenum contents (better corrosion resistance and thermal conductivity) HVOF sprayed are also used [1, 360].

- Machine knives (slitters, guillotine, blades) are coated with HVOF sprayed WC–Co coatings and then sharpened [1, 360].
- Carbon Fiber-Reinforced Plastics rolls (CFRP roll), exhibiting excellent characteristics including lightweight, high stiffness, and low flexure, have been increasingly employed in manufacturing industrial fields. Compared to conventional metal rolls, CFRP roll is lighter and stiffer and exhibits lower inertia moment [377]. Unfortunately carbide-cermet coatings failed because of their poor thermal shock resistance on CFPR rolls. Ni-base composite porous coating including ceramics particles developed by Nagai et al. [378] showed high-thermal shock resistance. Five coated rolls were installed in the actual papermaking line. They achieved successful results with 10 % improvement of the line speed, whereby outstanding performance and maintenance-free has been confirmed even after 4 years of use. Yoshiya et al. [377] have developed a 5.4-m long thermal sprayed carbon roller, installed in a paper slitter/winder, that is moving stably at ultrahigh speed, 2,300 m/min, with no abrasive wear. The roller is a formed three-layer structure: a tungsten carbide cermet layer on grooved metal sleeve, which covers the CFRP substrate roller shell. The thermal spray process is the finishing process because no after grinding is performed.
- Blow tanks, that are storage bins, are also on-site HVOF sprayed with WC–Co coatings to improve their wear resistance.

18.4.10 Metal Processing Industries

Many parts in metal working industries are submitted to severe wear and corrosion, which consequences can be reduced by thermal-sprayed coatings. The main parts that can be sprayed are [1, 362, 379] components of electric arc furnace (EAF) and basic oxygen furnace (BOF), molds, casting dies, casting salvage, molten metal containment and delivery, steel mill rolls working in both wet and dry mill environment: entrance and exit rolls of steel processing line, rolls for galvanized and aluminized steel sheets, …. PTA coatings are also used in processing industries, see Sect. 10.7.4 of Chap. 10.

18.4.10.1 Components of Furnaces or Boilers

Boilers are large and expensive installations which suffer enormously from wear caused by corrosion and erosion, aggravated by very high temperatures. The exact type of wear experienced varies from one part of a boiler to another and is

Table 18.1 Different parts of the boiler that can be affected with the corresponding wear phenomena [380]. Reproduced with the kind permission of Castolin, copyright © Castolin Eutectic

	Part of boiler affected	Principal wear phenomena
1	Combustion chamber waterwalls	Corrosion/abrasion/erosion
2	Secondary superheater	Corrosion/oxidation/erosion (ash)
3	Economiser	Erosion (ash)/corrosion
4	Primary superheater	Erosion (ash)/corrosion
5	Reheater	Corrosion/oxidation/erosion (ash)
6	Superheater soot blowers	Erosion (steam)
7	Combustion chamber soot blowers	Erosion (steam)



Fig. 18.14 Flame fusing of flame sprayed self-fluxing alloy on boiler tubes (Courtesy of Castolin)

influenced by the overall design of the boiler and the type of combustible fuel. For example, Table 18.1 from Castolin [380] presents the different parts of the boiler that can be affected with the corresponding wear phenomena.

A wide variety of components associated with electric arc furnace (EAF) and basic oxygen furnace (BOF) are under severe attack from heat, particulate, and acidic gases. Water-cooled components, in the off-gas duct systems such as pans, roofs, boxes, and panels, are subjected to high-velocity combustion gases that contain a number of corrosives chemicals that condense and attack the heat transfer surfaces [381]. Coatings used are those developed for high-temperature wear and corrosion resistance see for example [379, 381–388]. For example, Fig. 18.14 presents the deposition of spray and fuse coating on boiler tubes.

18.4.10.2 Molds

In continuous casting the cast shell in the lower half of the mold abrades and wears the bottom of the mold. Diffusion of the copper substrate from the mold into the surface of the cast product leads to a quality defect called "star cracking" [379]. Chrome- and nickel-based coatings protect copper molds from wear and also enhances caster product quality by greatly reducing cast product contamination and star cracking problems [379]. Thermal barrier coatings are also used to control the heat flow and retard rapid chilling [1, 360, 387]. For very corrosive melts, pure yttria is used instead of zirconia partially stabilized with yttria. Of course bond coats are necessary, and sometimes multilayer coatings, to achieve a good compliance between the expansion coefficients of mold and topcoat. Sanz [387] has studied different coatings to protect the mold wall. Casting salvage is also achieved by filling the voids, after grinding of porosity or wear zones, with plasma or wire arc coatings that are then remachined [1, 360]. Gross and Kovalevskis [388] have shown that metallic molds from iron, nickel, Ni–Al, and Ni–Cr–B–Si can be produced by air plasma spraying onto steel and chrome-plated steel models. The main processing criterion was the mold temperature that must be heated above 400 °C to avoid coating warpage and fragmentation. Heating to 600–700 °C is required to remove coating porosity and reduce coating pullout. Weiss et al. [389] have demonstrated the feasibility of making sprayed steel-faced tooling. Kim and Kweon [390] investigated various flame- and plasma-sprayed coatings to extend the life of these molds. Coating materials studied include plasma-sprayed ceramic coatings with bond coats as well as flame for casting pig iron ingots. Cyclic furnace tests from room temperature to 1,100 °C in air, simulating the thermal cycle in casting, indicated that failure occurred along the interface between the bond coat and the gray iron substrate because of iron oxidation, and not at the interface between the ceramic top coating and the bond coating. The field test results indicated that plasma-sprayed alumina coatings with 200 μm top coating thickness are the most promising materials for pig iron casting.

18.4.10.3 Die Casting

Gibbons and Hansell [391] have shown that two thermal spray materials, one Cr_2C_3–25(Ni–20Cr) and one WC–10Co–4Cr, deposited using JP5000 HVOF hardware, offered properties that could enable low-cost, low-volume production aluminum injection mold tooling to be upgraded to higher volume production tooling. Hot dipping rolls: MoB/CoCr, a novel cermet material for thermal spraying, with high durability in molten alloys has been developed to utilize for aluminum die-casting parts, and for hot continuous dipping rolls in Zn and Al–Zn plating lines [146]. The tests revealed that the MoB/CoCr coating had much higher durability without dissolution in the molten Al–45 wt%Zn alloy. Using undercoat was effective to reduce the influence of large difference in thermal expansion

between the MoB/CoCr topcoat and substrate of stainless steel of AISI 316L, widely used for the hot continuous dipping [146]. MoB-based cermet feedstock powders (MoB/NiCr and MoB/CoCr) were deposited on SKD61 (AISI H-13) substrates used as a preferred die (mold) material [392]. The durability of these coatings on cylindrical specimens against soldering also has been investigated by immersing in molten aluminum alloy (ADC-12) for 25 h at 670 °C and subsequently, compared with that of NiCr and CoMoCr coatings. Both types of MoB-based cermet coatings have shown high soldering resistance as negligible intermetallic formation occurred during the immersion test [392]. Weiss et al. [389] have used arc-sprayed steel-faced tooling to create matched die sets for injection molding applications.

18.4.10.4 Entrance and Exit Rolls of Steel Processing Line

When coating bridle and accumulator rolls in entrance and exit ends of a steel processing line with tungsten carbide coating surface damage on the roll is eliminated and proper grip provided and slippage prevented. The surface coating is properly textured to provide the required characteristics or profile on the strip surface [379]. Multi-component white cast iron is a new alloy that belongs to system Fe–C–Cr–W–Mo–V, HVOF sprayed seems to be promising for rolls [392].

18.4.10.5 Galvanized and Aluminized Steel Sheets

They require very high surface quality, particularly in exposed panels. In continuous galvanizing and aluminizing, the steel strip is dipped in the molten bath through a series of rolls, which control the speed and tension of the strip and guide the steel strip through the molten metal bath. The rolls operating in the molten Zn–Al alloy are subjected to severe corrosive environment and require frequent change and repair [1]. Seonga et al. [394] have shown that WC–Co coatings were not very good with molten Zn–Al. By coating the sink and stabilizer rolls with molybdenum boride, tungsten carbide, and other materials, the rolls remained smoother and produced an improved strip surface.

18.4.11 Petroleum and Chemical Industries

The main problem is to prevent corrosion and wear, all forms of wear, especially those linked to corrosion arising at low, intermediate, and high temperatures. As previously pointed out, against corrosion dense (no-sacrificial) coatings (no pores or cracks and very low oxide level) of the appropriate material are mandatory. For porous coatings, especially ceramic ones, a dense bond coat with a good resistance to the corrosive media is mandatory. Porous coatings can be sealed but



Fig. 18.15 Typical coating against corrosion sprayed on-site onto refinery pipe (Courtesy of Sulzer-Metco)

the seal must be adapted to the service temperature. Moreover many components have sizes that require on-site spraying. Usually dense coatings are obtained with vacuum plasma spraying or D-gun or HVOF, but soft vacuum plasma and D-gun spraying are not adapted to big parts. Thus HVOF spraying, that can be used on-site, is extensively used against corrosion and abrasive and erosive wear mainly with carbide-based cermets [1, 116, 118, 119, 166, 294, 379, 381–384, 397–399]. Of course for the protection of external steel structures, pipes, tanks, ... Al, Zn, or Zn–Al wire arc or flame sprayed are used [1, 103–109], as well as polymers sprayed by flame, HVOF, plasma according to the polymer melting temperature [402]. For example, Fig. 18.15 present an aluminum protection flame sprayed on a refinery pipe.

Coatings in chemical industry are used for pressure and storage vessels with Hastelloy B or C, Inconel 600, for heat-affected zones where solutions found in gas turbines are often used. In some chemical reactors, submitted to strong acids in combination with organic solvents, glass lining are used that are repaired by APS-spraying tantalum, bonding well to the glass, and followed by an overlay of chromium oxide [1, 360]. For example, Moskowitz [115] have tested HVOF process using unique inert gas shrouding to produce highly dense, low-oxide coatings of metallic alloys, which were tested in laboratory and plant, with exposures as long as 5 years. Coatings of corrosion-resistant alloys, such as type 316L stainless steel and Hastelloy C-276, were shown to act as true corrosion barriers.

For the oil, gas, and petrochemical industries, the following components are coated using thermal spray technologies: mud drill rotors, pump impellers, plunger, turbine, rotor shaft of centrifugal compressor/pump, pump shafts, boiler tube, thermo-well, mixing screw, mandrels, actuator shafts and housings, housings and valves, valve gates and seats, ball valve with large diameter, progressive cavity mud motor rotors, rock drill bits, riser tensioner rods, impeller/blade drilling and production risers, sub-sea piping, wellhead connectors, fasteners, compressor rods, mechanical seals, pump impellers, tank linings, external pipe coatings, structural



Fig. 18.16 General view of practical spraying of ball valve by the MET-JET III system. Reprinted with kind permission of ASM [395]



Fig. 18.17 Wear band on drilling pipe PTA coated (courtesy of Castolin)

steel coating, . . . [1, 360]. It also seems that wear-coating applications have started to replace hard chrome [361].

Two examples of coatings used in oil, gas, and petrochemical industries are presented below. Stainless steel ball valves must be wear resistant, have a low friction coefficient, a good erosion and heat resistance, good fatigue strength and seal performances, etc., are significantly improved by applying HVOF coatings [395]. loping trend of these ball valves for highly harsh working conditions. Figure 18.16 shows the practical spraying of a ball valve having a diameter of over 500 mm. Wear bands on drilling pipes, as shown in Fig. 18.17, are PTA coated, for more details see Sects. 10.7.3 and 10.7.4 of Chap. 10.

18.4.12 Electrical Utilities

Coatings against corrosion and wear (C–W) are used in fluidized-bed combustor (FBC) and conventional coal-fired boilers.

18.4.12.1 For Fluidized Bed Combustor Boilers

The problem is linked to the finely divided mixtures of coal and limestone particles eroding and corroding steam pipes and boiler walls, as well as the high sulfur content of coals or low grade combustibles resulting in corrosion at high temperature. Different coatings are used:

- Cr_2O_3 (20 wt%)–Al_2O_3 on NiCrAlY bond coat (against corrosion through the porous ceramic coating) [1, 360], the addition of approximately 20 wt% chromia resulting in the formation of one solid solution of $(Al–Cr)_2O_3$ in the α-modification (working temperatures can reach 1,000 °C and the transformation of γ phase starts around 900 °C).
- HVOF sprayed Cr_3C_2–NiCr coatings with high compactness and fine grain size [165], the wear resistance being due to hard carbides particles homogeneously distributed within coating, the ductile matrix being corrosive-resistant.

18.4.12.2 For Coal-Fired Boilers

Plasma sprayed stellite-6 coating has been found to be effective in increasing the erosion–corrosion resistance of boiler steels in the coal-fired boiler environment. A less porous structure obtained after laser remelting was found to be effective for increasing erosion–corrosion resistance [164]. Inconel systems or high-chromium alloys or chromium–nickel alloys coatings, presenting a good resistance to sulfur, have also been used, sprayed with plasma, wire arc, or HVOF [1, 360]. Notomi and Sakakibara [403] have proposed low cost and high hardness plasma-sprayed coatings, developed by addition of carbon and hardening elements to high chromium cast iron (C–Si–Mn–Cr–Mo–V–other–Fe) used for wear-resistant material. Nitrogen gas atomization was applied to manufacture the powder in order to prevent oxidation of particles. These coatings showed the same or more erosion resistance than Cr_3C_2–NiCr cermet coating and had higher reliability for long period operation and higher practicality.

18.4.13 Textile and Plastic Industries

The abrasive qualities of man-made fibers, particularly nylon and polyester, and the corrosive characteristics of additives, such as fiber finishes and lubricants, combine to deteriorate yarn contact surfaces. High rotation speed of grooved rollers results in considerable abrasion wear. Due to the very high rotational speed, the roller has to be made from aluminum, and therefore, the reduction in wear can only be achieved by the deposition of a coating that also must be as light as possible. For years, thermal spray coatings have been used against wear and corrosion on textile machinery: steel thread guiders, thread breaks, stretch roll, grooved roll, separator roll, oiling roll, draw roll, feed roll, conditioning rollers, snick pins, collets, disk grip, cutter base, feed drum, rotor for open-end, extruder dies, knives, heating bars, heater/hot plate, . . . [1, 360]. The high-velocity rotating parts are often coated with alumina or alumina–titania coatings. TiO_2 addition lowers significantly the microhardness of the alumina coating but increases its toughness [404]. Parts such as knives and extruder dies are coated by HVOF-sprayed tungsten carbides, while textile rolls are plasma sprayed with alumina–titania (13 wt%) as illustrated in Fig. 1.12. A printing roll with laser engraved chromium oxide coating is shown in Fig. 18.12.

Lima and Marple [375] showed that nanostructured titania feedstock HVOF-sprayed exhibited a superior abrasion wear resistance (27 % lower volume loss) when compared with an air plasma-sprayed conventional alumina–titania coating, in spite of the fact that the latter is 33 % harder than the HVOF sprayed titania. The higher wear resistance of the HVOF-sprayed nanostructured titania was provided by the nanostructured zones embedded in the dense and uniform coating microstructure acting as crack arrester. They are probably worth to be tested in textile industry.

18.4.14 Polymers

Thermal spraying polymers [1, 360, 402, 405–417] is one-coat process that acts as both the primer and the sealer, with no additional cure times processes. Polymer thermal spraying is ideally suited for large structures that otherwise could not be dipped in a polymer suspension. Moreover it seems that functionalized polyethylene polymers such as ethylene methacrylic acid copolymer (EMAA) and ethylene acrylic acid (EAA) can be applied in high humidity. Of course the use of polymer coatings depends strongly on its service conditions. Especially it must be kept in mind that melting temperatures vary from 40 to 60 °C for ethylene methacrylic acid copolymer (EMAA) to 300 °C for polyimide. They are deposited onto metals, ceramics, cermets, and composites. . . As they present a high chemical resistance, a high impact, and abrasion resistance at low temperature, they are used in many industries, especially in food industry.

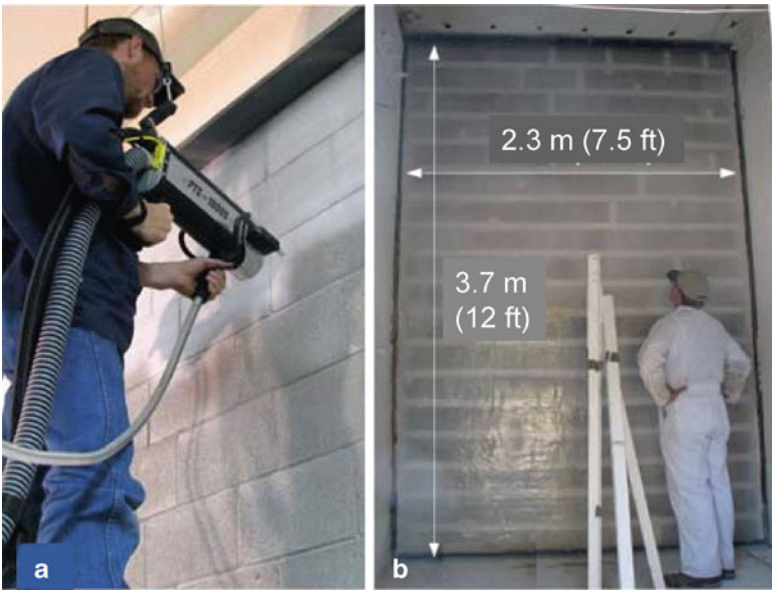


Fig. 18.18 (**a**) thermal spraying of blast mitigation polymer membrane to the internal side of test walls; (**b**) wall dimensions and appearance of a completed membrane. Reprinted with kind permission of ASM [417]

In food industry polymer coatings replace paints on the wall because they have a much better resistance to the chemical products used for cleaning (about 1 week for paint against about a quarter for the polymer coating). They are even used on the floors where polymer coatings doped with alumina particles provide an excellent anti-slip lining, the alumina particles rippling out when people walk on it.

A novel coating process (Polymer Thermal Spray PTS), has been developed by Isocevic et al. [417]. It utilizes an electro-resistive heating element for rigorous temperature control and for heating the main process gas that could be air, nitrogen, inert, or other gases. They have deposited advanced polymer coatings and structures such as (1) blast mitigation coatings for protecting civil structures against external explosions and (2) thermal spray forming of syntactic foams based on polyimide micro-balloons. For blast mitigation, Fig. 18.18 shows thermally sprayed polymer (thermoplastic elastomer) membranes applied to the internal side of the test walls 3.7 × 2.3 m. Figure 18.19 presents the test setup for evaluation of thermally sprayed blast mitigation treatments. The explosion impulse reached 215 kPa and lasted about 50 ms. Both walls successfully passed the test and remained standing. The total wall deflection toward the inside of the test room was 8 in. with no visible damage to the membrane and no flying debris or wall segments penetrated the room.

Spraying syntactic foams based on polyimide micro-balloons was developed [417] in the frame of a research project funded by NASA Langley Research Center.

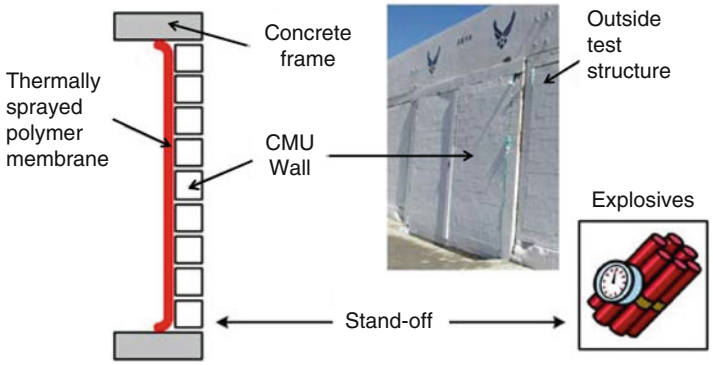


Fig. 18.19 Test setup for evaluation of thermally sprayed blast mitigation treatments. Reprinted with kind permission of ASM [417]

The coating was supposed to be used as high temperature insulation (up to 325 °C) and also satisfy strict flammability regulations relating to the aerospace industry. The polyimide syntactic foam, see Fig. 18.20a, consisted of two NASA Langley-licensed materials, polyimide microspheres (PerFoma-H® from GFT Corporation), and a binder. Polyimide microspheres had a bulk density of 0.043 g/cm^{-3}, a size range 400–800 µm and service temperature between −253 °C and 315 °C. The binding powder and microspheres were thermally co-sprayed using the PTS coating system. The thermally sprayed foam did not support a flame and formed a stable isolative char without smoke at higher temperatures. The foam deposited over various complex shapes is shown in Fig. 18.20b–d and seemed to be interesting for thermal insulation in airspace applications [417].

18.4.15 Reclamation

The effects of wear and corrosion can only be retarded, but not be stopped forever and wear parts must be replaced or resurfaced. It is the same for undersize parts due to manufacturing error. The ability to apply coatings by thermal spraying with a broad spectrum of thickness, finish and composition requirements makes the different thermal spray processes ideal solutions to re-surface components, avoiding their costly replacement. Restoration is performed either with the same material as the base metal or with a more corrosion- and/or wear-resistant material. However, it is better to choose coatings that can be machined. In a wide range of industrial applications, thermal coatings are used to renew components by restoring their specified dimensions and matching and sometimes improving their original performance. Very often it is possible to design a coating that meets the functional requirements of the component, and moreover offers better resistance to corrosion, oxidation, and mechanical wear than the original product. Of course the cost of the

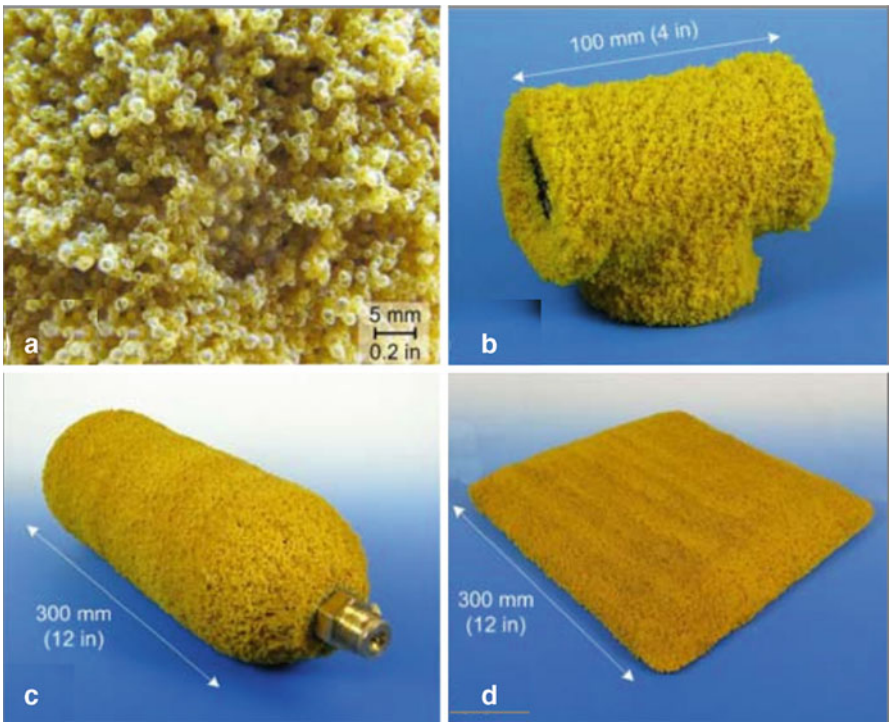


Fig. 18.20 Thermally sprayed syntactic foam based on polyimide micro-balloons; (**a**) foam microstructure; (**b**) thermally sprayed on pipe T joint; (**c**) on a gas cylinder; (**d**) on a flat aluminum plate. Reprinted with kind permission of ASM [417]

resurfacing must be lower than that of a new part (a fraction of it). For example, this technique is particularly used for roller faces and journals, dryer drums for paper-making, pump seals (shafts and sleeves), pump housings, compressor rods, rotary airlocks and feeders, conveyer screws, ... [1, 360]. PTA also are used for refurbishing components, even with a complex shape as turbine, see Sect. 10.7.6 of Chap. 10.

A few examples are given below to illustrate the use of sprayed coatings in re-surfacing components:

- The use of aluminum alloy for injection mold tools, especially for the automotive industry, is not new and has been utilized as bridge tooling to support the manufacture of typically up to 10,000 components. Two thermal spray materials, one Cr_2C_3–25(Ni–20Cr) and one WC–10Co–4Cr, deposited using JP5000 HVOF hardware, have been shown to offer properties that could enable low-cost, low-volume production aluminum injection mold tooling to be upgraded to higher volume production tooling [389].
- The thermal-sprayed Tribaloy T-800 coatings deposited by the HVOF process exhibited lower cavitation wear rates than the stainless steel bulk material [63].

- Massive turbines and the valves used to regulate water flow at hydroelectric dams are often exposed to the wearing effects of high-velocity water containing abrasive particulate. As mentioned by Sulzer-Metco, coatings can replace lost material and, at the same time, provide a more wear-resistant surface, increasing useful life by up to 20 times over the original.
- Hard chromium plating is usually used to restore to original dimensions the worn surfaces of gas turbine shafts. In the case of shafts repair, hard chromium plating process proved to be time consuming and to involve high costs. High hardness and good wear resistance performances of WC–12 %Co HVOF sprayed coatings support their candidature for the replacement of hard chromium plating in this field [326].
- Song et al. [418] have studied the effect of repair of NiCrAlYSi coating after longtime use on the coherence of coating to substrate and mechanical properties of Ni_3Al base alloy IC6. For secondary coating repair, the room temperature tensile properties of base alloy had no obvious change, while stress rupture lives decreased, but still were rather long, compared to the alloy with first repair coating. Therefore, they deduced that NiCrAlYSi coating repair is feasible to prolong the service lives of IC6 turbine vanes.
- Ducos [419] has presented a few industries where PTA is used for resurfacing: extruder screw, vanes, turbine blades, engine valves (especially big diesel engines), and rail train car wheels.
- Isakaev et al. [420] have shown that plasma-sprayed coating of railway frogs, working under contact fatigue and wear-out provides a good solution for repairing them.
- The surfaces of printing press cylinders wear quickly. Coatings of nickel/chrome alloy, Cr_2O_3, and others, have supplanted chrome plating as the preferred method of reclaiming worn cylinders because thermal spray processing is far faster.
- It has been shown that cold spray is a promising cost-effective and environmentally acceptable technology to impart surface protection and restore dimensional tolerances to aluminum alloy [421] or magnesium alloy components on helicopters and fixed-wing aircraft [425]. Kashirin et al. [426] have shown that using a portable cold spray system working with air at pressures below 0.8 MPa, made possible to restore on site aluminum alloy molds for plastics, corrosion defects on car aluminum engines, casting defects for various aluminum alloys, antique art objects such as copper sculptures of Isaac Cathedral in Saint-Petersburg, . . .

18.4.16 Other Applications

As previously described, thermal spray coatings provide superior wear (abrasive, erosive, fretting, . . .) resistance and corrosion protection with coatings having low porosity, high hardness, good toughness for cermets, and great flexibility of composition [1, 360]. Thus they are also used in the following:

- *Mining industry* where good abrasive and/or adhesive resistance is very important. For example, HVOF, PTA (alloys doped with ceramic particles), and wire arc-sprayed cored wire coatings are used on conveyor belt idlers, steel oscillating tub, fan components such as removable leading edges, bolt-covers, blades, deflectors and large inlet entrance cone ducts, scraper or excavator teeth as illustrated in Fig. 2.18.
- *Nuclear industry* where the use of cobalt-based alloys (stellites or cermets matrix) is limited, thus coatings against wear and corrosion rely on nickel alloy-based coatings (NiCr–WC or Cr_3C_2). Cermets with hafnium carbide have been developed that present a large neutron cross section. However sprayed coatings are essentially used in pumps, turbines, heat exchangers, vanes, etc.

  In numerous applications developed at CEA-DEN, French Atomic Agency, Atomic Energy Department, particularly those encountered in the processing of nuclear wastes, metallic components are subjected to extreme environments in service, in terms, for example, of aging at moderated temperature (several months at about 300 °C) coupled to thermal shocks (numerous cycles up to 850 °C for a few seconds and a few ones up to 1,500 °C) under a reactive environment made of a complex mixture of acid vapors in the presence of an electric field of a few hundred volts and a radioactive activity. Berard et al. [354] have tested alumina plasma-sprayed coatings manufactured with feedstock of different particle size distributions, graded alumina–titania coatings, and phosphate-sealed alumina coatings to improve the properties of metallic substrates operating in such extreme environments. The effects of particle size distribution, phosphate sealant, and graded titania additions on the dielectric strength of the as-sprayed, thermally cycled, and thermally aged coatings were investigated. Thermal aging test was realized in furnace at 350 °C for 400 h and thermal shocks tests resulted from cycling the coating between 850 and 150 °C using oxyacetylene flame and compressed air cooling. Aluminum phosphate impregnation appeared to be an efficient post-treatment to fill connected porosity of these coatings. Alumina as-sprayed coatings manufactured with +22–45 μm and +5–20 μm particle size distributions exhibited good dielectric strengths after thermal solicitations compared to those manufactured with larger size distributions or to graded titania coatings.
- *Cement industry*: Again the main role of sprayed coatings is against wear and corrosion in mechanical seal, sleeve, burner tip, boiler tube, thermo-well, kiln support roll, pinion shaft, coating for cement preheat tower, impeller blade, calender roll, cone crusher, and hydraulic rams with acid-resistant coatings.
- *Drawing Machine*: Guide roller and ceramic disc, rod breakdown drawing machine, fine drawing machine, and other accessories.
- *Waste treatment*: Steel tubes oxidation causes an important problem in Municipal Solid Waste Incinerator (MSWI) plants due to burned wastes containing high concentrations of chemically active compounds of alkali, sulfur, phosphorus, and chlorine. Ni-based HVOF coatings are a promising alternative to the MSWI conventional protection against chlorine environments [424].

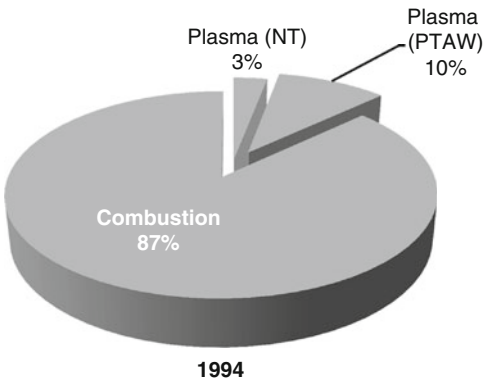


Fig. 18.21 Percentages of the different spray processes in industry in 1994, after M. L. Thorpe, Oral presentation ITSC

– *Sheet metal forming dies*: Conventionally mold and dies are manufactured by machining from bulk metallic materials. Tooling by using arc spray process to spray metal directly onto a 3D master pattern is an alternative method to manufacture mold and dies for plastic injection molding and other applications [1, 360].

18.4.17 Thermal-Sprayed Coatings in the Different Countries

Up to the 1980s thermal spraying was more an art than a science with a reputation of high complexity (up to 60 parameters to be adjusted to achieve coatings with specific service properties) and rather low reproducibility and reliability. Thus it is not surprising that the firsts industries where coatings (except metallization) were successful were those used to rather sophisticate production techniques such as aeronautics and nuclear ones. This is illustrated in Fig. 18.21 from TAFA Co. representing the percentages of the different spray techniques in industry in 1994. It shows that the majority of processes are flame spraying (87 %) with 10 % PTA and 3 % of plasma spraying. Of course such figures give only trends because some spray activities performed in companies, and which activity is not directly linked to spray process, are often ignored.

In the 1980s, thermal spraying has dramatically evolved from an art to a science [428] with many research developments in laboratories and also new spray techniques such as HVOF, HVAF, and arc spraying. This is illustrated in Fig. 18.22, again from TAFA, and representing percentages of the different spray techniques in 2000. Of course flame spraying is now reduced to 50 % and the rest of the market comprises all other techniques except of course cold spray that had not yet diffused in industry at that period. This trend is confirmed by the repartition of the different spray processes in industry in Europe in 1998 [426] presented in Fig. 18.23, where the developments of HVOF and D-gun as well as wire arc are no more negligible.

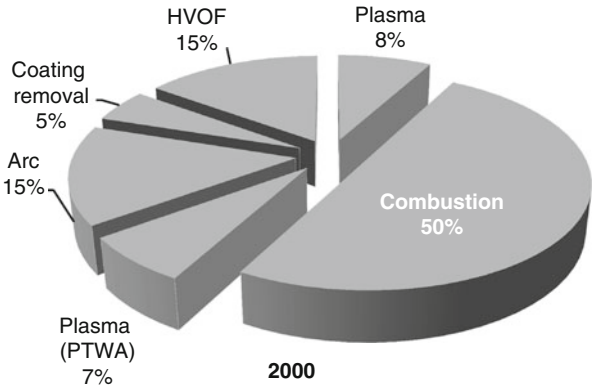


Fig. 18.22 Percentages of the different spray processes in industry in 2000, after M. L. Thorpe, Oral presentation ITSC

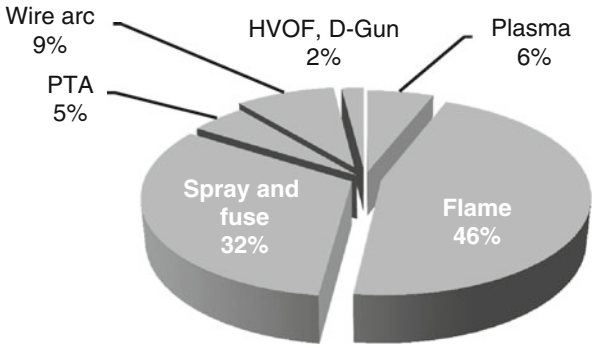


Fig. 18.23 Percentages of the different spray processes in European industry in 1998 after Ducos and Durand. Reprinted with the kind permission of ASM [426]

The distribution of the 615 M€ coating activities in Europe across end-use sectors is presented in Fig. 18.23 from Ducos and Durand [426] (source: MAGETEX study [427]). It can be seen that at the "low end" are mechanical repair and metallic coatings for heavy wear or corrosion protection (including pipes and gas bottles). At the "high end," high value coatings used in aircraft, industrial gas turbines, printing rolls, or medical and dental. In between can be found process industries (primary metals, polymer processing and food, glass, pulp and paper, chemical, oil and gas, textile, . . .), the automotive industry or other OEMs [427] (Fig. 18.24).

Besides new marketing issues of the thermal spray market, the development is linked to a better reproducibility and reliability of substrate surface preparation, spraying, and post-treatment of coatings. Particularly consistent effort has been made in the following areas:

- Better control of surface preparation with a grit residue level as low as possible and a roughness adapted to sprayed particles and a desired grit blasting residual stress level (see Chap. 12).
- Better control of the spray process parameters thanks to computerized control panels (see Chap. 16).

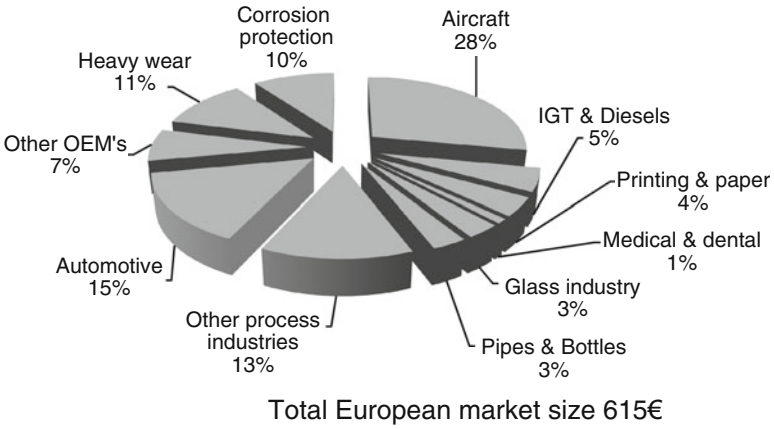


Fig. 18.24 Repartition of the 615 M€ coating activities across end-use sectors in Europe in 1998. Reprinted with the kind permission of ASM [426]

- Development of robust sensors to follow the key parameters of coating manufacturing, i.e., trajectories distribution of hot particles linked to their injection conditions, particle impact velocities and temperatures, coating and substrate temperature, and coating thickness during spraying. For coating and substrate temperature, rather cheap IR and small pyrometers are now available (see Chap. 16).
- More researches about reliable correlations between coating properties and particle impact parameters as well as coating and substrate temperature during spraying, pass thickness, etc., in order to establish feedback control. It is now possible to establish empirical correlations for given spraying conditions and particle parameters at impact, which could be used to keep, with the help of sensors previously described (see Chap. 16), the measured parameters in a "window," resulting in an acceptable coating property.
- Better control of the dust, especially that resulting from the condensation of vaporized material, in the booth and close to the sprayed part.
- Standardization of coating characterization methods that has been started [428].
- Finally, education at all levels that are slowly developed and expert systems need to be created that can help operators and designers.

According to Dorfman and Sharma [359] it is estimated that the TS industry is worth approximately a $6.5 billion with the majority of revenue generation in coating services, see Fig. 18.25a. In terms of market segmentation, approximately 60 % of the total TS market belongs to the turbine industry, 15 % to automotive, and the remaining 25 % is distributed over a large number of other industries, as shown in Fig. 18.25b [359].

Approximately two-thirds of this market is split evenly between North America, Europe, and the Middle East. The balance is from the rest of the world [359]. It is unfortunately difficult to follow the evolution of the industrial spray equipment in

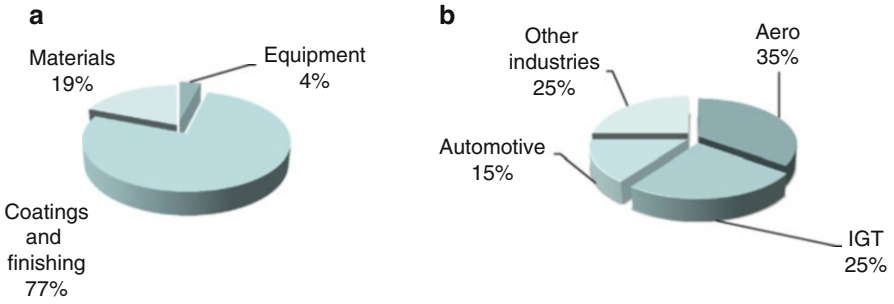


Fig. 18.25 (**a**) Distribution of revenue generation in coating services, (**b**) market segmentation in thermal spray industry. Reprinted with kind permission from Springer Science Business Media [359], copyright © ASM International

the world because few data are published in this field. In connection with the thermal spray conference in 2009 data have been published about thermal spraying in Korea [429], Nordic region of Europe [375], India [430], Japan [431, 432], and also in Asia [433], all these data giving trends about last developments.

Thermal spraying is used widely in many industrial sectors in the Nordic Countries [375]. Important areas where thermal spraying is used are in the manufacture of products for the petroleum, paper, metals, transport, defense, and high-tech machinery industries. In Finland thermal spray technology has wide areas of application in the pulp and paper industries. In Sweden, thermal spray technology is of great importance in the manufacture of aero engines and in industrial gas turbine applications. In Norway thermal spraying is widely used in various offshore applications, including sub-sea oil drilling enterprises. Unfortunately, if the paper indicates that all of the major spray processes are currently used (from flame and arc spraying, to plasma, HVOF and HVAF), depending on the application and type of coating applied, no precision is given about their distribution.

In Japan [431, 432], the growth rate from 2004 to 2006 for the thermal spray industry is estimated to be more than 5 %. Thermal spraying output for fiscal 2004 for the three sectors of the Japanese market were contract job shop productions just under 40 billion Yen, in-house production by large enterprises about 45 billion Yen, and consumables and spray equipment manufacturing 10–15 billion Yen. Figure 18.26 represents the repartition of coating services by job shops in 2004 (total amount of 45 billion Yen) [432]. It is worth noting that the growth rate in the semiconductor/LCD field is very high. Figure 18.27 shows the corresponding distribution among spray processes with the important contribution of APS, HVOF, and the reduction, compared to 2000, of flame-sprayed coatings.

The previous examples were related to countries (Europe, Japan), where research centers and industries have worked on sprayed coatings since the 1970s and 1980s. For countries, which came more recently in the field, the development is also spectacular.

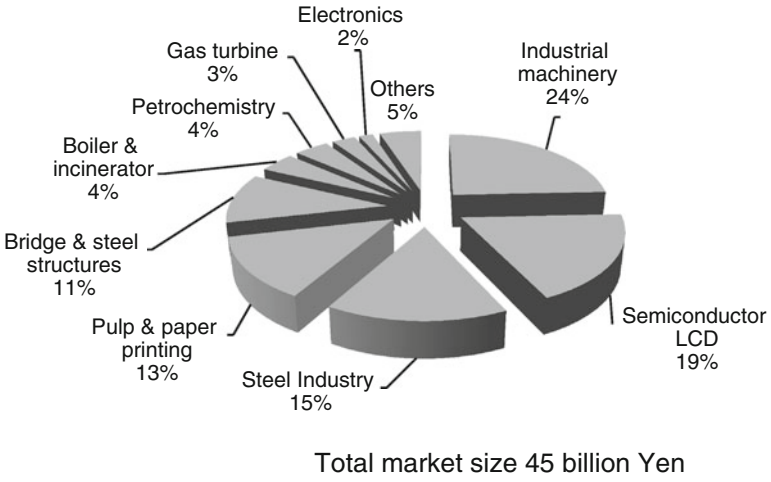


Fig. 18.26 Coating services by job shops in Japan in 2004. Reprinted with kind permission from Springer Science Business Media [432], copyright © ASM International

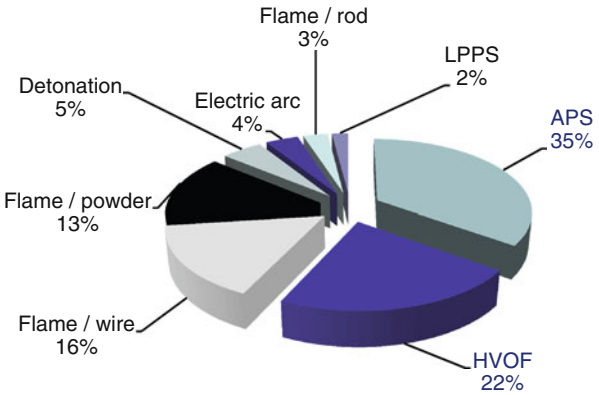


Fig. 18.27 Segmentation of spray process/turnover of contract job shops in fiscal 2004 in Japan. Reprinted with kind permission from Springer Science Business Media [432]. copyright © ASM International

Statistical data [433] show that Chinese applications of plasma spraying are only about 10 % of the total thermal spray market compared with about 50 % in developed countries. According to Li in the paper of Fukumoto [430], the total output of the thermal spray industry in China increased from about US$0.14 billion in 2002 to US$0.24 billion in 2005, representing an annual growth rate of about 20 %. Spray technology has been applied to different industrial fields including steelmaking, textiles, paper and pulp, energy, petroleum and chemicals, aeronautics, and others (Fig. 18.28). The application of thermal spray coatings in the steel industry has been the fastest growing field in the last several years. The energy industry mainly includes coatings for coal-fired power plants and hydro-electric power plants. Applications of thermal spray technology to the aeronautics

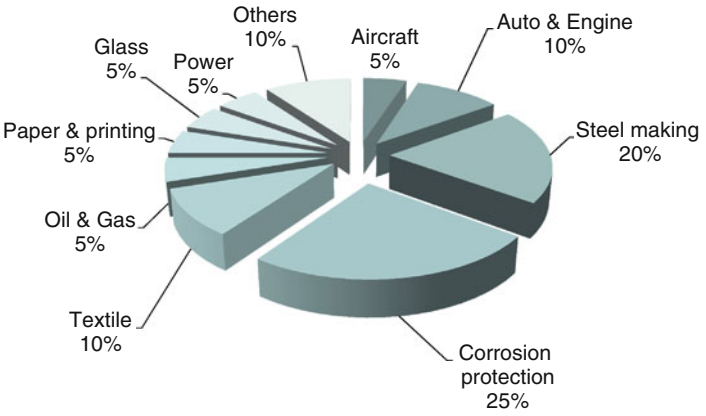


Fig. 18.28 Estimated share of different thermal spray application fields in China. Reprinted with kind permission from Springer Science Business Media [433], copyright © ASM International

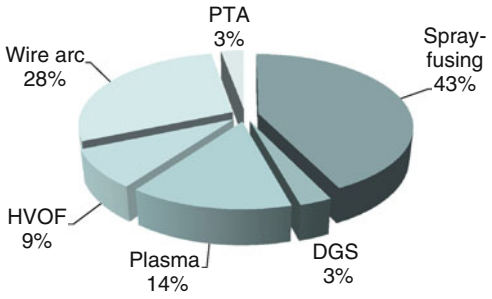


Fig. 18.29 Estimated share of different spray processes in Korea. Reprinted with kind permission of ASM International [429]

industry in China are mainly performed in five large job shops that share 5 % of the total thermal spray output in China. The national program to develop different types of aircraft will promote further fast expansion of R&D and thermal spraying applications in this field. Figure 18.29 shows the distribution among the different spray processes. The plasma spray is about 5 times less than that in other industrial countries. The HVOF market share is probably over the 6 % of Fig. 18.29. Li in the paper of Fukumoto [433] underlines that this figure, compared with those of developed countries, implies the potential for growth in the thermal spray industry in China in the coming decade.

Another country where sprayed coatings are developing is Korea. For example, Fig. 18.30 from Lee [429] gives an idea of estimated share of different spray processes in Korea for the year 2008. As presented in Fig. 18.31 [429], chemical and power plants clearly dominate the market share. Semiconductor and shipbuilding industries also have significant share of the pie. In terms of revenue, semiconductor/LCD, steel making, and power plant industries are the dominant sectors, based on the current fiscal reports, seen in Fig. 18.32.

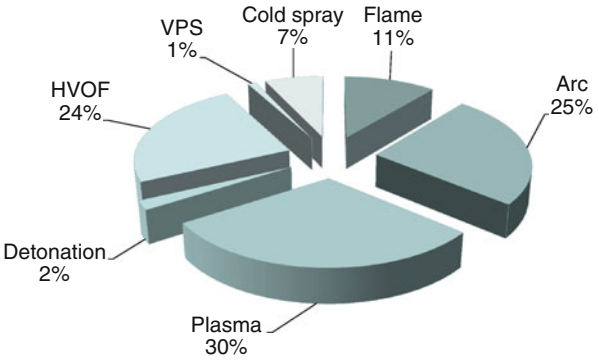


Fig. 18.30 Estimated share of different spray application fields in Korea. Reprinted with kind permission of ASM International [429]

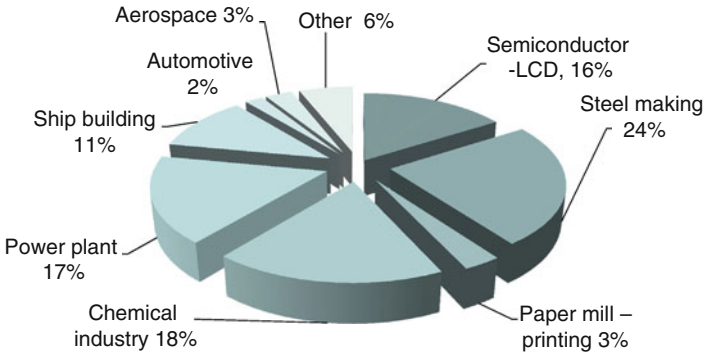


Fig. 18.31 Estimated annual sales of different spray application fields in Korea. Reprinted with kind permission of ASM International [429]

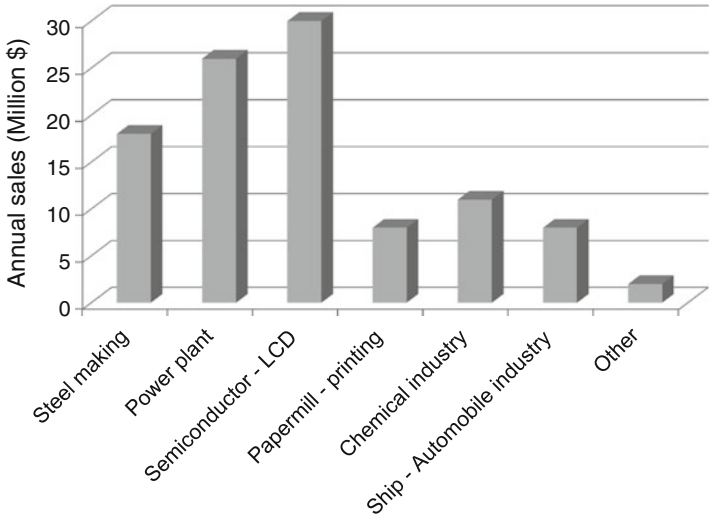


Fig. 18.32 Estimated annual sales of different spray application fields in Korea. Reprinted with kind permission of ASM International [429]

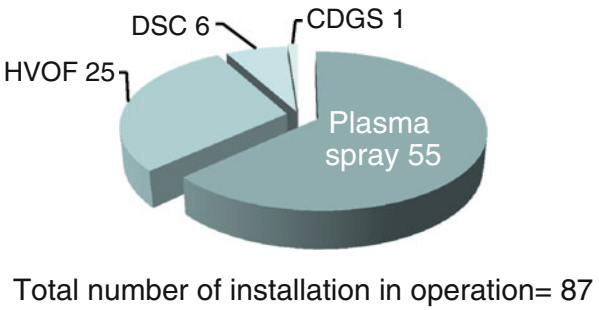


Fig. 18.33 Total number of installations in India by thermal spray variant (excludes flame, arc, and wire spray systems). Reprinted with kind permission of ASM International [430]

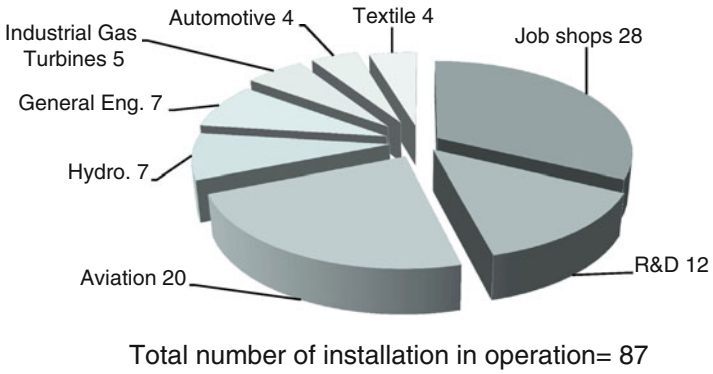


Fig. 18.34 Total number of installations in India by user segment (excludes flame, arc, and wire spray systems). Reprinted with kind permission of ASM International [430]

In India the perceptible change occurred in the 1990s and a good indicator of the success in industry is the growth in sale of spray-grade powder [430] that has been multiplied by a factor 3 between 2000 and 2008. The number of systems, as shown in Fig. 18.33 is still low for country of India's size but it is an important change compared to that prevailed not so long ago. The distribution of the country's thermal spray systems installations among the various segments is presented in Fig. 18.34. The data clearly reveal that the highest number of thermal spray units operate as "job-shops." They play a crucial role both in addressing the needs of a vast majority of industrial users as well as running a crusade to demonstrate "new" applications to the industry and facilitating further growth [430].

To conclude, the coating market is still wide open to (1) protect parts from wear, corrosion, and high heat fluxes; (2) produce parts and manufacture forms and volumes that are difficult or even impossible to obtain using conventional processes; and (3) manufacture parts with complex shapes and material gradients, with associated protection against wear, heat, and other advances challenging operating conditions; and (4) replace hard chrome plating. For example, the automotive industry reveals a wide market with more automated, more reproducible, and less expensive coatings.

18.5 Economic Analysis of the Different Spray Processes

18.5.1 Different Cost Contribution Factors

In spite of its fundamental importance toward the acceptance of a new technology, few papers have been devoted to the economic analysis of thermal spray processes [2, 179, 367, 425–427, 429–436]. This is due to the generally confidential nature of the relevant information in an industrially competitive environment. Moreover, in our rapidly evolving global economy, process economics changes rapidly with time and location. In the context of this book, it is more important to focus on the methodology of carrying out a detailed economic analysis, rather than on the absolute values. These can and will change with time. Emphasis is placed on understanding of the relative importance of the different cost factors in the overall process economics and means of controlling them. Typical examples are provided at the end of this section for the illustration of the methodology and a comparative analysis of the different thermal spray technologies. For a more precise economic analysis, it is best to work with your local provider of thermal spray equipment and materials supplier.

The first step in an overall cost analysis is to identify the different steps of the operation, which can involve a single or multiple process technologies. A typical coating process often involves all or most of the following process steps:

1. Substrate preparation
   - Machining
   - Masking
   - Degreasing
   - Grit blasting
   - Ultrasonic cleaning
2. Coating
   - Part setting up
   - Preheating
   - Coating
   - Online post-treatment (Whenever necessary)
   - Part removal
3. Post-coating operations
   - Off-line post-treatment, annealing, austempering, laser glazing, hot isostatic pressing (whenever necessary)
   - Surface machining, grinding, and polishing
   - De-masking
   - Cleaning
   - Quality control
   - Packing and labeling

The overall cost for the coating for a given part, constitutes essentially of two broad categories of cost contributing factors:

Direct costs (S_{di}); which includes all cost items directly related to each of the different process steps. These depend directly on the complexity of the technology used, the number, size, shape, and complexity of the parts to be coated, and the nature of the coating material. Direct costs are usually calculated on a per hour basis of the operation. Their conversion to cost per part depends on the number of parts that could be produced in 1 h. The principal factors that contribute to the direct cost of a coating operation are

- The cost of material to be sprayed (powder, wires, rods, etc.)
- The cost of gases, electricity, and consumables supplies for the operation
- Direct labor cost for each of the different stages of the operation
- Quality control, packing, and labeling

Indirect costs (S_{in}); often referred to as *fixed cost* or *overhead costs*, include all other expenses, which are related to the investment needed and general running cost of the coating site. The indirect costs factors are usually calculated on a yearly basis of the operation. Their conversion to a per hour basis depends on the number of hours of operation of the coating center per year (N_{hy}). They include, though not limited to, the following:

- Equipment acquisition and amortization of the capital investment
- Building, ancillary equipment, and necessary infrastructure
- Maintenance workshop
- Quality control laboratory
- General administrative and services
- Marketing and financial expenses

The total cost of the coating of a single part is the sum of all direct S_{di}, and indirect S_{in} cost factors, on a per hour basis, multiplied by the number of hours needed per part (N_{hp}).

$$\text{Total cost per part}\,(/\text{part}) = \left[S_{di}(/\text{h}) + S_{in}(/\text{y})/N_{hy}(\text{h/y})\right] \times N_{hp}(\text{h/part}) \tag{18.1}$$

18.5.2 Direct Cost Factors

18.5.2.1 The Cost of Materials

This is often the most important single cost item of the coating operation. It varies widely depending on the nature of the coating material, its purity, and its form. As presented in Chap. 11, coating material are available as powders, wires, cords, or rods depending on the coating technology used. By far the most common form of materials used in coating operations is powders with particle size ranging from 5 to 10 μm up to a few hundred microns in diameter or more. Generally the cost of a powder increases rapidly with the following parameters:

- *The purity level of the material*. For example, a 5N Si powder would cost almost one order of magnitude higher than a 3N Si.
- *Oxygen level*. For example, a grade 1 Titanium powder with an oxygen level lower than 1,200 ppm will cost considerably more than a grade 2 powder of the same particle size but with an oxygen level in the 2,500 ppm or grade 4 with an oxygen level of 4,000 ppm.
- *Particle size distribution*. The narrower the particle size distribution of the powder, the higher will be the cost of the powder on a $/kg basis.
- *Powder morphology*. Generally, spherical, free-flowing dense powders will have a higher cost than a standard spray dried or fused and crushed powder.
- *Specialty alloys* When custom made, with tightly controlled specification of its elemental analysis, the powder will cost considerably more that standard materials.

It is important to underline that these parameters are also interactive between them. For example, a Titanium powder with a particle size $\leq$45 μm and an oxygen content of less than 1,300 ppm (grade 1), will be more difficult to obtain, and would be significantly more expensive, than a Titanium powder with the same oxygen level (grade 1), but a coarser particle size range (45–106 μm). Delivery time and volume of annual consumption can also have a significant influence on the cost of powders. The same reasoning equally applies for other materials in the form of cords, wires, or rods.

The key parameters that influences the quantity of material needed to spray a part are:

- The surface to be coated, A_c, taking into account its shape complexity, its holes distribution that must be protected, and the sprayed material lost at edges.
- The average thickness of the coating, δ_c, (including the mean thickness that has to be removed from the as-sprayed part to achieve the final specified dimensions, sprayed coatings dimensional precision being in the range of tenths of millimeters).

These two quantities, together with the feed stock specific mass, ρ_p, (kg/m^3),

and the deposition efficiency, η_c (%), (which depends strongly on the spray process and the geometry of the part to be coated), allow calculating the powder quantity necessary for each part, m_p (kg),

$$m_p = \frac{\delta_c \cdot A_c \cdot \rho_p}{\eta_c} \tag{18.2}$$

It is important to underline the very important impact of the deposition efficiency on the overall cost of materials in the coating process. This is because overspray powders, which do not end up in the coating, are collected from the exhaust gases or ambient air strictly for environmental reasons, and are never recycled in the coating operation because of the risk of introducing major defects in the coating.

Table 18.2 Investment costs of equipment for spray processes in 2006. Reprinted with the kind permission of Dr. M. Ducos [367]

	Value in Euro (€)	Value in US$
Manual powder or wire flame	About 5,000	About 6,500
Automated powder or wire flame	5,000–10,000	6,500–13,000
HVOF–HVAF	50,000–100,000	65,000–130,000
Arc–spray	9,000–22,500	11,700–29,250
APS	75,000–185,000	97,500–240,500
VPS–CAPS	600,000 to >2 M	780,000 to >2.6M
PTA	50,000–75,000	65,000–97,500

One way of reducing powder waist, and accordingly reduce powder consumption in the spray process, is through automation. For example, if a multi-axis robot handles the arc spray gun, the operation of powder feeder can be synchronized with the robot to stop spraying during substrate transfer or repositioning, thus reducing feed stock losses and coating costs.

18.5.2.2 The Cost of Gases, Electricity, and Consumables

The cost of gases can represent an important component of the cost of the coating operation. This depends significantly on the nature of the gases used, their purity level, and overall volume flow rates required for the coating operation. The unit cost of gases ($/m^3) also depends on the overall size of the operation and the associated gas consumption. For example, the cost for industrial purity argon gas in North America can be more than 5 times higher when in the form of compressed gas cylinders compared to cryogenic form in industrial scale Dewar's. A compilation of typical cost of gases used in thermal spray and cold spray coating operations in North America and Europe is given in Table 18.2. These values are based on 2013 prices and should be adjusted for inflation and price changes in subsequent years. It is important to note that the decision on which size of gas packaging to use is essentially based on the volume of the operation. For example, the use of cryogenic gases, while generally less expensive per m^3 of gas used, can be completely offset by the constant loss factor which has to be bleed to the atmosphere from cryogenic containers for any prolonged period of time in which the gas is not in use. Compressed gas cylinders, or bulk packs, required manual handling and rental fee for the cylinders, which in large volume operation can be important especially if the operation requires a wide range of different specialty gases. Generally, the cost of the gas varies drastically with its consumption and on-site storage linked to the corresponding delivery mode [435] (from cylinder, vehicles delivering liquid gases with different storage volumes and pressures, trailer for He, bulk vehicle).

With cold spray process the gas consumption rate, as illustrated in Fig. 18.35, depends on the process variables, the type of gas, operating pressure and temperature and finally of nozzle internal diameter [435]. The use of Helium in cold spray

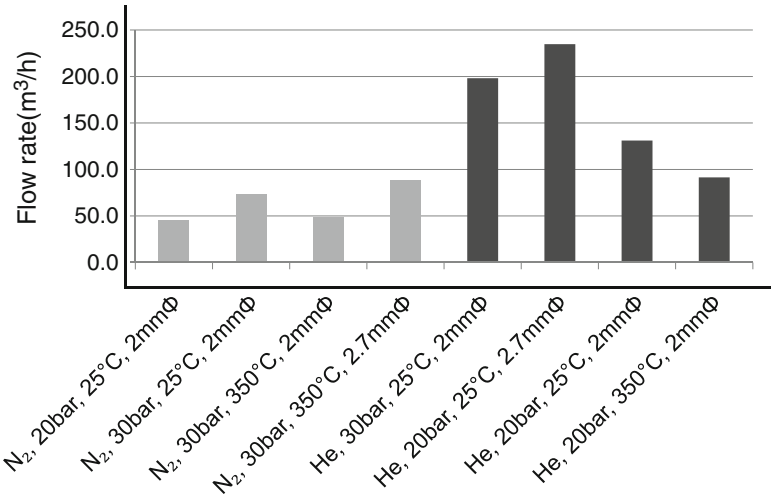


Fig. 18.35 Gas consumption rates for different cold spray systems configurations [435]

requires flow rates that are 4.2 times higher than those for N_2, due to the large difference in sonic velocity. Increasing the gas temperature, on the other hand, allows for the decrease of the gas consumption.

Gas recycling and on-site gas generation are two of the common means of reducing the cost of gases in the coating operation. Gas recycling is generally limited to operation in a closed environment such as in vacuum plasma spraying, whether d.c. or r.f. induction plasma. More recently, gas recycling has been increasingly introduced in cold spray operations, which requires often the use of Helium at relatively large volume flow rates with a significant financial burden on the operation. Gas recycling in this case has to be associated with a gas cleaning and recompression operation. On-site gas generation on the other hand is only used in large volume operation, which justifies the capital investment whether for the generation of oxygen or nitrogen on side through cryogenic distillation or hydrogen through water electrolysis.

The cost of energy, whether in the form of fuels in combustion spraying, or electrical, in plasma spray operations, varies considerably with type of technology used and the scale of operation. A comparison of the power requirement by different spray technologies is given in Fig. 18.36. This shows that HVOF and high-velocity liquid fuel (HVLF) technologies are among the largest energy consumers. This is supplied in this case in the form of liquid or gaseous fuels. Comparative data on the efficiency of different spray processes and the associated specific energy requirement (SER) of different spray processes is given in Figs. 18.37 and 18.38, respectively.

Molz and Hawley [436] have pointed out that the comparison of the effective performance of each process, in relation to each other, is hampered and difficult to compare on an equal basis. Thus they proposed a more generic and global method,

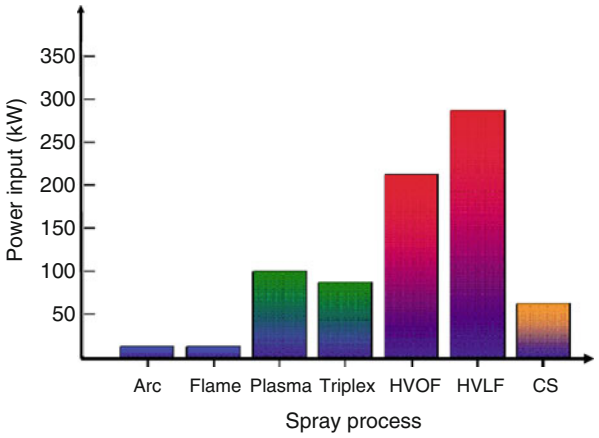


Fig. 18.36 Total power consumption by spray process. Reprinted with kind permission of ASM International [436]

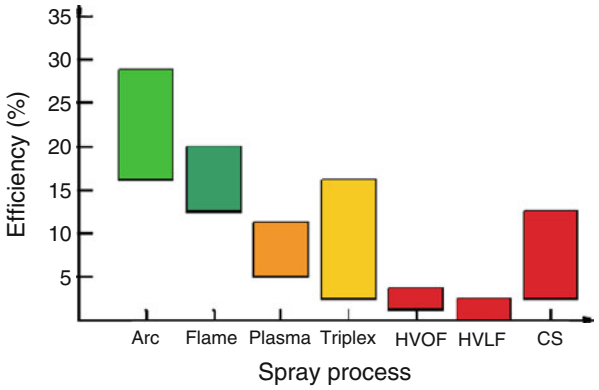


Fig. 18.37 Spray process efficiencies. Reprinted with kind permission of ASM International [436]

based on deriving a unified process efficiency formula that takes into account all energy inputs and energy outputs of a process in the same energy units. They made a direct comparison of process efficiency for each process and specific coating conditions. For example, the energy input to the "system" could either be already included in the supply to the thermal spray gun or created (as in combustion guns) within the gun itself. Two sources exist, one for the gas itself being used (in raw form prior to any reaction) and one for the material input into the system. This illustrated in Fig. 18.36 from Molz and Hawley [436] representing the total energy required (input) for a process. As for each process the total range of input energy is large, they have plotted the range of energies instead of the maximum amount of energy consumed. As it could have been expected, flame and wire arc spraying exhibit the lowest energy consumptions. Figure 18.37 from Molz and Hawley [436] represents the process efficiency for each thermal spray process based on the measured power output in terms of particle temperatures and velocities. The drawback of these calculations is that they are based on the particle temperature measured assuming that it is representative of the total thermal energy

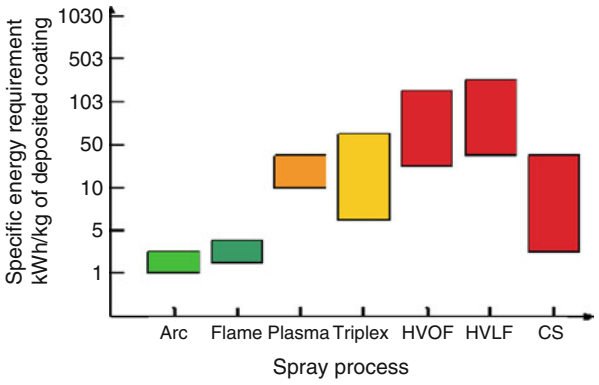


Fig. 18.38 Energy ranges to deposit 1 kg of coating for different spray processes. Reprinted with kind permission of ASM International [436]

state of the particle. However, Fig. 18.37 shows that arc has the highest efficiency, but still barely manages to achieve 30 % efficiency at the best operating parameters. The difference between arc and combustion is the lower efficiency derived from using a combustion process. HVOF processes have the lowest efficiency (in the 2 % range). The third figure (Fig. 18.38) of Molz and Hawley [436] represents the energy consumed per kg of coating deposited. The scaling in Fig. 18.38 is now logarithmic in order to fit the entire range of values in. The typical high velocity coatings such as carbides, with lower deposit efficiency and higher energy input, require considerably more energy to deposit per unit mass, almost one order of magnitude higher than that to spray pure ceramics or metals.

Electric energy-based technologies such as plasma and arcs, uses typically industrial electricity rates which are composed of two components:

- *Power* (*kW*), which is set by an annual agreement with the electric energy utilities reflecting the overall size of the operation and its peak energy demand.
- *Energy* (*kWh*) is the electrical energy consumption by the operation for running the plasma system as well as all of the ancillary equipment.

Electricity cost for building illumination, heating, and other operations is not included under direct cost of the operation. These constitute part of the indirect costs. Electricity rates vary widely between locations and period of operation over the range $0.09–0.15/kWh.

The cost of consumables and spare parts also varies widely with the nature of the spray process and the complexity of the part. For example, in d.c. plasma spraying operation whether atmospheric or under vacuum, a close monitoring of the state of the electrodes is essential for insuring a consistent quality of the coating. Generally, the allowed life of the electrodes is based on the recommendations of the equipment manufacturer and/or the operator experience. It is generally accepted practice to replace consumable parts in a setup after a well-defined lifetime, rather than wait for a disruption of the operation and a failure of the quality of the coating. It has to be recognized that the cost of a failed coating is not limited to the loss of the coating martial and associated labor and expenses, but also the damage caused to the part

being coated, which can be order of magnitude higher than that of the coating operation itself. The cost of consumables is not limited to torch components; it can also include certain important components of the plasma generating equipment. In induction plasma spraying, for example, the r.f. power supply has a triode tube which need to be replaced depending on its projected lifetime, which can be in the 10,000–20,000 h. The triode life also depends on the mode of operation and the number of starts and stops per hour of unit. In a 100 kW installation, the cost of such a components can be in the US$15,000–20,000 range.

The cost of consumables also includes the cost of masking tapes used to protect the surface which should not be exposed to sand blasting or coating, the cost of the grit, used in the sand blasting operation prior to coating, and cost of grinding and polishing materials and supplies used for surface finishing of the part.

18.5.2.3 Direct Labor Cost

In thermal spray operations, direct labor cost is inversely proportional to the degree of automation of the operation. The higher is the level of automation and the larger is the scale of the operation; the lower will be the direct cost of labor per part. In a typical coating operation direct labor is needed for:

- Preparation of the part to be coated, including its, masking, sandblasting, and cleaning
- Setting up of the part in the coating booth. Starting of the operation, preheating, and coating, followed by removal of the part from the rig
- Cleaning of the part, surface machining, grinding, and polishing
- De-masking and cleaning
- Quality control
- Packing and labeling

The total cost of labor for the coating operation is also relatively sensitive to the overall management of the facility and the efficient definition of the operation steps and the definition of responsibilities.

18.5.2.4 Direct Cost for Quality Control, Packing, and Labeling

This depends on the maturity of the technology used for the coating operation and on the nature of the parts to be coated. The most stringent quality control rules are generally applied for medical and aerospace applications, where very rigorous quality control (QC) procedures are needed and have to be strictly in forced. Other applications, with generally lower value items, such as in automobile industry, quality control on individual parts would be too expensive. The industry has to rely in this case on well-developed, mature, and reliable technologies.

The overall cost of quality control includes direct and indirect cost factors. Basic investment in QC in instrumentation and laboratory equipment will go under

indirect cost, while the labor cost associated with the QC procedures will go under *direct cost* and will depend on whether it is applied on all of the coated parts or on randomly selected parts. For obvious reasons, QC procedures tend to use nondestructive testing as much as possible in order to avoid sacrificing the part being tested. In the development stage of a new part, both nondestructive and destructive testing procedures are generally needed.

18.5.3 Indirect or Fixed Cost Factors

18.5.3.1 Capital Investments

This covers the total investment needed for the setting up of the operation. It includes

- Cost of land, building, and building permits including environmental studies necessary for the setting up of the operation
- Ancillary equipments and infrastructure including spray booth, dust collection and disposal, air cleaners, sound control, operator safety equipment
- Production equipment including spray system and associated operations, instrumentation, and data acquisition
- Equipments for post-treatment and finishing including heat treatment furnaces, laser glazing, hot isostatic pressing, machining, grinding and polishing equipments
- Maintenance workshop
- Quality control laboratory
- Storage space for materials, supplies, spare parts, and finished part
- Office space

Direct investment for the acquisition of the coating production equipments rarely exceeds 15–20 % of the total investment needed for the setting up of a new production facility. The investment structure needed for the expansion of an existing facility can be different with a considerably higher percentage needed for the acquisition of the production equipment.

Capital investment contributes to indirect production cost through the amortization of the investment made. It is important to note that the amortization rules vary from country to country as well as between the different types of investments. For example, investments for the building and infrastructure is generally depreciated over a 25-year period, production equipment, over a 5–7-year period, while computer and automation equipments may need to be amortized over a 3–5-year period due to the rapid evolution of the technology. The simplest method of calculating amortization cost per hour of operation, S_{ih}, is based on a linear amortization over the number of year over which the equipment is depreciated, N_y, divided by the number of operating hours per year, N_{hy}, as follows:

Table 18.3 Investment costs of ancillary equipments in 2006. Reprinted with the kind permission of Dr. M. Ducos [367]

	Value in Euro (€)	Value in US$
Grit blasting	10,000–40,000	13,000–52,000
Linear movements	35,000–75,000	45,500–97,5000
Robot	75,000–150,000	97,500–195,000
Spray booth	12,000–25,000	15,600–32,500
Ventilation and filtering	30,000–45,000	39,000–58,500
Machining and grinding	200,000–1M	260,000–1.3M
Quality control	75,000–200,000	97,500–260,000

$$S_{\mathrm{ih}} = \frac{P_{\mathrm{e}}}{N_{\mathrm{y}} \times N_{\mathrm{hy}}}, \tag{18.3}$$

where P_{e} is the cost of the equipment. For more information on investment cost calculation, the interested reader can see the paper of de Munter et al. [431]. Typical investment costs estimates for coating equipments and ancillary equipments are given in Tables 18.3 and 18.4, respectively, based on a study by Magetex [427] and presented by Ducos [367]. These were compiled in 2006.

18.5.3.2 Other Indirect or Fixed Costs

These include essentially the cost of general administration and services, insurances, marketing, and financial services. These are strongly dependent on the scale of the operation and its location.

18.5.4 Few Examples

18.5.4.1 Cost of d.c. Plasma Spraying of Partially Yttria-Stabilized Zirconia

To illustrate the relative importance of each of these cost factors, de Botton [425] in his master of science, calculated the costs for d.c. plasma spraying of partially yttria-stabilized zirconia (PYSZ) coatings on a flat 1 m^2 surface. The coating thickness was 300 μm. The spray rate was 3 kg/h, with a deposition efficiency of 60 % and a coating density of 0.9. Losses at holes and edges were assumed to be of 10 %.

For the costs calculation he assumed 5 years to recover investment, a capital cost of 10 %, a maintenance cost of 4 %, 250 production days, and a total productive time per year of 4,000 h. Results are summarized in Figs. 18.39 and 18.40 which represent the different factor of prices per sprayed part. It is obvious from this figure

Table 18.4 Evaluation of the NiCrAlY coating cost for Plazjet and arc spray processes. Reprinted with kind permission from Springer Science Business Media, copyright © ASM International [437]

	Plazjet	Arc Jet 9000 (N2)	Arc Jet 9000 (Air)
System cost (US$)	198,000	3,800	23,800
Amortization time (years)	5	5	5
Material feed rate (kg/h)	12	12	12
Spraying time per year (h)	278	278	278
Amortization (US$/kg of coating)	19.83	2.38	2.38
NiCrAlY powder and wire (US$/kg)	90	63	63
Powder cost (US$/kg of coating)	1.26	0.11	0.11
Electric power (kW)	115	10	10
Electric energy cost per (US$/100 kWh)	7.90	7.90	7.90
Energy cost US$/kg of coating	1.26	0.11	0.11
Plasma and atomization gas flow rates (m^3/h)	9.6	105	65
Gas cost (US$/100 m^3)	3.40	3.40	0.50
Gas consumption (m^3/year)	2,670	29,200	18,000
Electrodes and tips costs (US$)	635	6	6
Electrodes and tips lifetime (h)	12	6	6
Consumable cost US$/kg of coating	7.39	0.63	0.18
Production cost US$/kg of coating	162.10	154.80	107.30
Labor cost US$/kg of coating	8.45	8.45	8.45
Production cost without amortization US$/kg	158.65	105.74	105.29
Total production cost US$/kg of coating	178.48	108.12	107.67

[a]The production cost was calculated per kilogram of coating at a deposition rate of 12 kg/h and a deposition efficiency of 60 %. The total production was set to 2 tons per year. Coatings were sprayed without substrate cooling

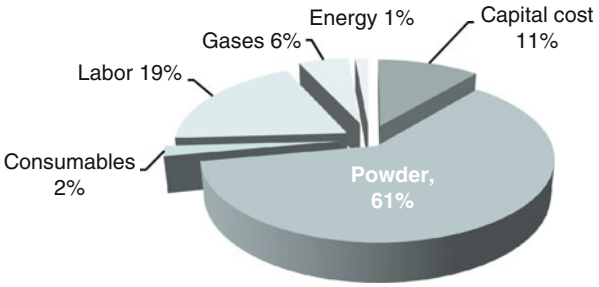


Fig. 18.39 Spray costs distribution of YPSZ coatings. Reprinted with the kind permission of MIT [425]

that the most important one is the powder, followed by labor (automation can reduce it notably) and capital cost. Figure 18.40 shows that after the coating cost (81.9 %), the grinding process is the most important (11.5 %) followed by the surface preparation (4.4 %). The quality control and storage represent only 2.1 %.

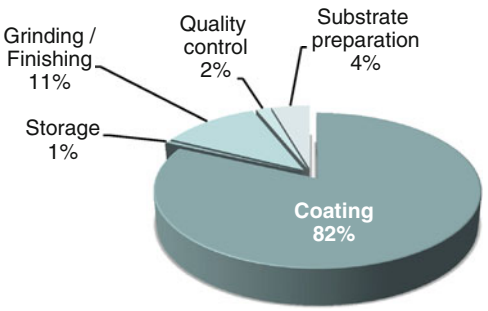


Fig. 18.40 Total costs distribution of YPSZ coatings. Reprinted with the kind permission of MIT [425]

Table 18.5 Different costs for manually wire arc-spraying zinc on 1 m^2 of steel. Reprinted with kind permission of Dr. M. Ducos [367]

Thickness	120 µm
Labor	40 €/h
Zn wire	2 €/h
Amortizing	3 y and 1.200 h/y
Surface preparation	7.3 €
Spraying (air atomization)	6.9 €
Amortizing	1.0 €
Total	15.2 €/m^2

18.5.4.2 MCrAlY Coatings Sprayed by Arc Spray and High-Power Plasma Spraying

In the work of Sacriste et al. [437] the bond coat of TBCs was deposited on large-sized substrates and used under given working conditions: vacuum and corrosion by hot liquids but with no thermal cycling. As the thickness of the topcoat was limited to 200 µm for this application, the roughness of the bond coat must also be low (*Ra* must be less than 10 µm). The substrate was a nickel-based super alloy, with a surface area of 100 × 50 mm^2 and a thickness of 2 mm. For deposition, the following setups were used to deposit the bond coat:

- The TAFA PlazJet gun model 7070 equipped with a 120-mm long anode and working with a mixture of nitrogen and hydrogen, the powder being injected at feed rates up to 12 kg/h.
- The twin-wire arc spray system used in this study was a TAFA model Arc Jet 9000. Wires were fed with the push–pull system capable to work with wires and cored wires 7.50 m in length. The NiCrAlY material was available as cored wire with a NiCr envelope containing particles of Al, Cr, and Y. Air and nitrogen were used as atomization gases with different air caps. After optimization of the spray conditions, Table 18.5 summarizes the different costs of the three coatings.

According to Sacriste et al. [437], coatings obtained by arc spraying exhibited a higher surface roughness due to a relatively low particle velocity compared to that obtained with the Plazjet process. The deposition efficiency was the same as that obtained with the Plazjet gun, for both air and nitrogen atomizing gas. The

Table 18.6 Spray conditions and costs of APS- and WA-Sprayed NiAl (5 wt%) 1.8 mm thick coatings for aeronautic application. Reprinted with kind permission of Dr. M. Ducos [367]

	Air plasma sprayed	Wire arc sprayed
Deposition rate (kg/h)	2.5	11.2
Deposition efficiency (%)	60	70
Material costs (€/kg)	35 (powder)	45 (wire)
Spray time (h)	2.93	0.56
Material used (kg)	7.33	6.29
Replacement parts (€)	13.49	0.45
Gases and electricity (€)	30.26	1.4

use of nitrogen atomization resulted in a 10 wt% reduction of the oxygen content, but no changes were observed in the bond strength (higher than 40 MPa). The composition of the arc-sprayed NiCrAlY coatings was very heterogeneous, which was attributed to the wire manufacturing method.

Considering only the costs of these coatings [437], Table 18.5 shows that the arc spray process, using air or nitrogen atomization, is about 40 % less expensive than the Plazjet process. As with the majority of spraying systems, the material feed stock is the most expensive parameter for both systems. In this study, it represents about 84 % of the total coating price for Plazjet and 97 % for arc spraying, while, since the deposition rate is high, the labor cost represents less than 5 % for Plazjet and of the order of 7 % for arc spraying. The major cost point of the Plazjet system is its purchasing cost. It represents 11 % of total production cost, whereas it is about 2 % for the arc spray system. The difference in the electric power shows that arc spraying is more thermally efficient than plasma spraying, as it requires a power of 10 kW to spray 12 kg of NiCrAlY material per hour, whereas Plazjet needs, at least, 110 kW.

18.5.4.3 Manual Wire Flame Zn Coating per Square Meter

According to Ducos [367] and calculations of MAGETEX [427] the different costs for manually wire arc-spraying zinc on 1 m^2 of steel are summarized in Table 18.6.

With this spray process, which is the cheapest, the surface preparation becomes slightly more important than the spray cost. According also to the low investment cost, amortizing is rather low as already emphasized in Table 18.6 for wire arc spraying.

18.5.4.4 Cost Comparison Between APS and Wire Arc for NiAl (Aeronautic)

Ducos [367] has evaluated the cost of a NiAl coating 1.8 mm thick for aeronautic application plasma (APS) and wire arc (WA) sprayed. Coatings are performed with robotized setups according to conditions and costs summarized in Table 18.7.

Table 18.7 Thermal processes used by various industrial segments. Reprinted with the kind permission of SPRAYTIME a publication of the International Thermal Spray Association, a standing committee of the American Welding Society [439]

Industry	Oxy-fuel	Spray/fuse	HVOF	D-gun	Air Plasma	Vac-plasma	Shroud Plasma
Aero gas turbine	✓		✓	✓	✓	✓	✓
Stationary gas turbine	✓		✓	✓	✓	✓	
Hydro-steam turbine	✓		✓	✓	✓	✓	✓
Automotive engines	✓		✓		✓		
Diesel engines	✓		✓		✓		
Transportation non-engine	✓			✓	✓		
Agriculture implementations	✓	✓			✓		
Railroad	✓		✓		✓		
Iron and steel manufacture	✓	✓			✓		
Steel rolling mills	✓	✓	✓		✓		
Iron and steel casting			✓		✓		
Forging	✓		✓				
Copper and brass mills	✓						
Ship and boat manufacture and repair	✓						
Oil and gas exploration	✓	✓	✓	✓	✓		
Mining, construction, and dredging	✓	✓	✓		✓		
Rock products	✓	✓	✓		✓		
Screening							
Cement and structural clay	✓	✓	✓				
Chemical processing	✓	✓	✓	✓	✓		
Rubber and plastic manufacture	✓	✓	✓		✓		
Textile	✓		✓	✓	✓		
Food processing	✓	✓	✓	✓	✓		
Electrical utilities			✓		✓		
Pulp and paper	✓		✓		✓		
Printing equipment			✓	✓	✓		
Defense and aerospace	✓		✓	✓	✓	✓	
Nuclear			✓	✓	✓		
Medical			✓	✓	✓	✓	✓
Business equipment			✓	✓	✓		
Electrical and electronic			✓	✓	✓	✓	
Architectural	✓	✓			✓		
Glass manufacture		✓		✓	✓		

Figure 18.41 presents the costs distribution of the different items of the spray process for APS. It can be seen, as for YPSZ coatings (see Sect. 18.5.4.1), the most important cost factor is the powder (51 %) followed by the investment amortization (22 %) and labor (18 %). Gases electricity and replacement parts represent only 9 %. The distribution of other costs (surface preparation, grit blasting and cleaning,

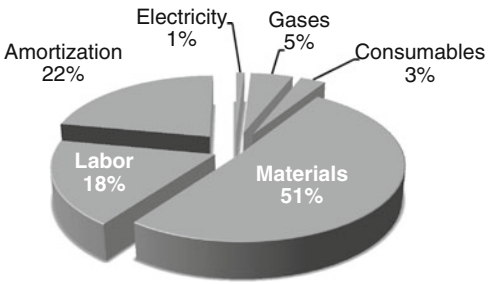


Fig. 18.41 Distribution of spray costs for a 1.8 mm thick NiAl (5 wt%) coating plasma sprayed in air. Reprinted with kind permission of Dr. M. Ducos [367]

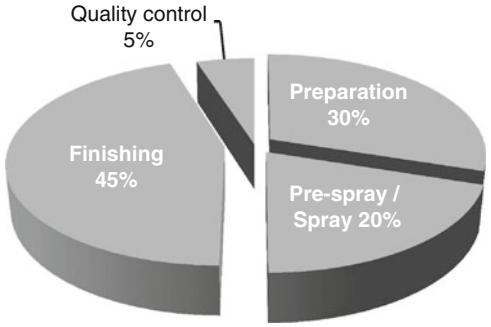


Fig. 18.42 Distribution of pre- and post-spray costs for a 1.8 mm thick NiAl (5 wt%) coating plasma sprayed in air. Reprinted with kind permission of Dr. M. Ducos [367]

finishing, and quality control) is presented in Fig. 18.42. It can represent 50–80 % of the spray costs.

Finally Fig. 18.43 represents the cost distribution per sprayed hour for the APS and WA coatings. The WA coating cost per hour is about 60 % of that of the APS coating that is mainly due to the investment and labor costs.

18.5.4.5 Cost Comparison for Hard Chromium Replacement on a Jack

Based on same principles, Ducos [426] calculated the costs per m^2 of Al_2O_3–TiO_2 (13 wt%) APS sprayed, WC–Co HVOF sprayed, and NiCrBSi HVOF sprayed to replace electrolytic hard chromium. Results are presented in Fig. 18.44. They show that the cheapest coating is that of NiCrBSi HVOF sprayed, but its cost (21.6 €) is higher than that of hard chromium (18 €), followed by the ceramic coating plasma sprayed in air, but to which the cost of the bond coat must be added (46.6 + 20 = 66.6 €) and then by the WC–Co HVOF-sprayed coating (122.5 €), which is essentially due to the powder cost.

Coating price is linked to many parameters and in any application it must be compared to the money saved by reducing wear, corrosion, . . . and improving the lifetime of the part. Its competitiveness is generally very good when used to repair. Anyhow, as shown in the examples presented, besides the main cost that is that of

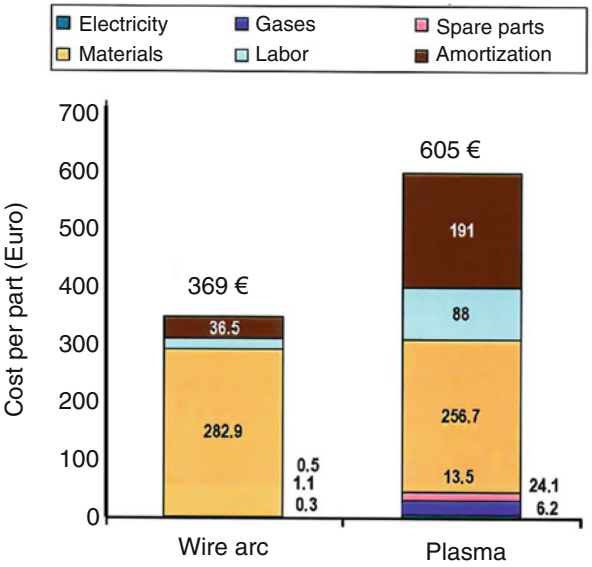


Fig. 18.43 Comparison of the cost per part of 1.8 mm thick NiAl (5 wt%) coatings plasma sprayed in air or wire arc sprayed. Reprinted with kind permission of Dr. M. Ducos [367]

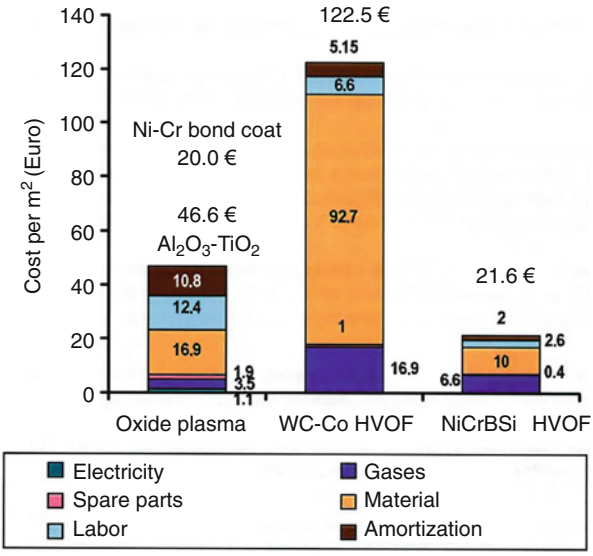


Fig. 18.44 Comparison of the costs per m^2 of Al_2O_3–TiO_2 (13 wt%) APS sprayed, WC–Co HVOF sprayed, NiCrBSi HVOF sprayed to replace hard chromium. Reprinted with kind permission of ASM International [426]

powder or wire or rod or cord, the amortization of the spray process can become very important when comparing flame or wire arc spraying to other processes (plasma, HVOF, ...) and, of course, when considering VPS this item becomes drastically important (see Table 18.3).

18.6 Summary and Conclusions

Moign et al. [438] have tried evaluating the comparison of life cycle assessment (LCA) of electroplating and various thermal spray processes (plasma, twin-wire arc, HVOF, and cold spraying) for the formation of nickel coatings. According to the number of parameters that can affect the final result, it is not an easy task. Comparing damages to human health and resources is that thermal spraying processes have a similar impact, while electroplating exhibits a lower impact when alumina for grit blasting is recycled two times. These results show that the nickel production process and also the alumina production for grit blasting have the largest impact, in comparison to energy production and other processes used during the coating step itself. The electroplating process can also be highly pollutant in countries that do not apply stringent environmental regulations on air and water emissions. Moreover, to be more realistic, the environmental impact of nickel electroplating processes should incorporate the environmental impacts of the production of the chemicals used in this process.

Thermal-sprayed coatings, including cold spray are more and more used in industry because of the following advantages:

- They provide specific properties onto substrates which properties are very different from those of the sprayed coating.
- They can be applied with rather low or no heat input to substrates (allowing for example spraying ceramics onto polymer substrates).
- Virtually any material that melts without decomposing or vaporizing can be sprayed. Moreover when preparing powders or wires for spraying it is possible to achieve cermets, very complex metal or ceramic mixtures, opening new possibilities to obtain very sophisticated coatings that can be tailored to the wished service property.
- Sprayed coatings can be stripped off and the worn or damaged coatings can be recoated without changing part properties and dimensions.
- Some spray processes can be moved on site, allowing spraying rapidly big parts, which displacement would otherwise be rather long and expensive.

Of course these coatings have also drawbacks such as:

- They are a line of sight technology, for example, making impossible coating small and deep cavities.
- Most of them have lamellar structures with contacts between layered splats that, depending on spray conditions, represent between 15 and 60 % of the splat surfaces.
- They have pores, cracks, ... that can be connected, depending on the spray process chosen and spray conditions, and that must be sealed for certain applications.

Of course the choice of a spray process, in connection with the sprayed material, depends on the specific properties expected from the coating on the one hand and on the cost of the coating also linked to the process and to the sprayed material. For example, spraying platinum or nickel alloy with the same process makes a huge difference in the coating cost for the same surface and thickness.

Finally the following tables prepared by the International Thermal Spray Association [436] summarize the different processes used in industry (Table 18.8), the coating application according to industry served (Table 18.9), and materials sprayed in industry. Unfortunately, these tables give no information about the industrial use of cold spray coatings, which is probably due to the fact that this process has been introduced at the end of the 1980s. Even in the recent book about cold spray [7] published in 2007 very few information is given about the industrial use.

Appendix: Use of the Different Spray Materials

In this appendix only basic information about the main sprayed materials and the most frequently sprayed materials are presented. For more detailed information the reader must consult the different powder and wire suppliers. It must also be kept in mind that the coating resulting from the spray process has properties (thermal and electrical conductivities for example) different from those of powder or wire properties. Such differences result from the increase of the oxide content, the pores generated during spraying, the real contacts between layered splats, ... Properties also depend on the way the sprayed material has been manufactured. In the following X-20Y-10Z means 20 wt% of Y, 10 wt% of Z, the balance being X.

A.1 Metals

Aluminum Al (99 wt%) $T_m = 660$ °C:

- Good corrosion resistance in industrial atmospheric conditions
- Good electrical and thermal conductivity
- Soft and ductile → repair Al alloys
- Non-magnetic (electromagnetic shielding)
- Sprayed by flame (powder or wire), wire arc, plasma, and cold spray

Aluminum base Al–Si (95/5 or 12 wt%)

- Salvage of parts made of Al, Mg, and their alloys: excellent finish
- Sprayed by flame (powder or wire), wire arc, plasma, and cold spray

Table 18.8 Thermal spray processes used by various industrial segments. Reprinted with the kind permission of SPRAYTIME a publication of the International Thermal Spray Association, a standing committee of the American Welding Society [439]

Industry	Wear							Clearance Control			Corross/	Electrical	
	Abrasive	Adhesive	Fretting	Erosion	Cavitation	Impact	TBC	Abradable	Abrasive	Restoration	Oxidat	Resistance	Conduct
Aero gas turbine	✓	✓	✓	✓			✓	✓	✓	✓	✓		
Stationary gas turbine	✓	✓	✓	✓			✓	✓	✓	✓	✓		
Hydro-steam turbine	✓	✓	✓	✓	✓					✓	✓		
Automotive engines	✓	✓		✓		✓	✓	✓	✓	✓	✓	✓	
Diesel engines	✓	✓		✓		✓	✓			✓	✓		
Transportation non-engine	✓	✓					✓			✓	✓	✓	
Agriculture implementations	✓			✓		✓				✓			
Railroad	✓	✓				✓				✓	✓		✓
Iron and steel manufacture	✓			✓		✓				✓	✓		
Steel rolling mills	✓	✓				✓				✓	✓		
Iron and steel casting	✓			✓		✓				✓	✓		
Forging	✓	✓				✓				✓	✓		
Copper and brass mills	✓									✓	✓		
Ship and boat manufacture/repair	✓			✓						✓	✓		
Oil and gas exploration	✓	✓		✓		✓				✓	✓		

(continued)

Table 18.8 (continued)

Industry	Wear							Clearance Control			Corross/	Electrical	
	Abrasive	Adhesive	Fretting	Erosion	Cavitation	Impact	TBC	Abradable	Abrasive	Restoration	Oxidat	Resistance	Conduct
Mining, construction, and dredging	✓			✓	✓	✓				✓	✓		
Rock products	✓					✓				✓	✓		
Screening	✓					✓				✓	✓		
Cement and structural clay	✓					✓				✓	✓		
Chemical processing	✓			✓						✓	✓		
Rubber and plastic manufacture	✓			✓		✓				✓	✓		
Textile	✓									✓			
Food processing	✓									✓			
Electrical utilities	✓	✓		✓	✓	✓				✓	✓		
Pulp and paper	✓				✓	✓				✓	✓		
Printing equipment	✓	✓								✓			
Defense and aerospace	✓	✓	✓	✓	✓	✓	✓			✓			
Nuclear											✓		
Medical	✓		✓								✓		
Business equipment	✓	✓	✓										
Electrical and electronic										✓	✓		
Architectural	✓					✓							
Glass manufacture	✓	✓								✓	✓		

Table 18.9 Thermal spray-coating applications according to industry served. Reprinted with the kind permission of SPRAYTIME a publication of the International Thermal Spray Association, a standing committee of the American Welding Society [439]

Industry	Chrome carbide	Self-fluxing	Iron and Steel	Nickel alloys	Superalloys	MCrAlY	Cobalt alloys	Non-ferrous
Aero gas turbine	✓		✓	✓	✓	✓	✓	✓
Stationary gas turbine	✓		✓	✓	✓	✓	✓	✓
Hydro-steam turbine	✓	✓	✓	✓	✓		✓	✓
Automotive engines	✓			✓	✓	✓	✓	
Diesel engines	✓		✓	✓	✓	✓	✓	
Transportation non-Engine			✓	✓				✓
Agriculture implementations		✓	✓	✓				✓
Railroad		✓	✓	✓				✓
Iron and steel manufacture		✓	✓	✓	✓		✓	✓
Steel rolling mills		✓	✓	✓	✓		✓	✓
Iron and steel casting		✓	✓					✓
Forging		✓	✓	✓	✓		✓	
Copper and brass mills							✓	
Ship and boat manufacture/repair			✓	✓				✓
Oil and gas exploration		✓	✓	✓			✓	✓
Mining, construction, and dredging		✓	✓					✓
Rock products		✓	✓					✓
Screaming			✓					
Cement and structural clay		✓	✓					✓
Chemical processing			✓	✓	✓		✓	
Rubber and plastic manufacture		✓	✓	✓			✓	
Textile			✓					
Food processing		✓	✓					
Electrical utilities		✓	✓	✓			✓	✓
Pulp and paper		✓	✓	✓				✓

(continued)

Table 18.9 (continued)

Industry	Chrome carbide	Self-fluxing	Iron and Steel	Nickel alloys	Superalloys	MCrAlY	Cobalt alloys	Non-ferrous
Printing equipment								✓
Defense and aerospace	✓	✓	✓	✓	✓	✓	✓	✓
Nuclear								
Medical								✓
Business equipment								✓
Electrical and electronic								✓
Architectural	✓							✓
Glass manufacture	✓	✓	✓					

Cobalt based powders (Pure cobalt $T_m = 1{,}495$ °C):

- Stellite® (Co–xCr–yW–zC)
- Against galling, cavitation
- For metal friction, high angle erosion, high temperature hardness, good resistance to abrasion, rather good wettability
- Very good oxidation resistance
- Replace WC in high temperature applications
- Repair of Cobalt-based parts
- Sprayed by HVOF, flame, PTA, Plasma

Triballoy® (Co–xCr–yMo–zSi) or (Co–xCr–yMo–zSi–tNi)

- Against galling for metal to metal friction
- High temperature hardness
- Good resistance to corrosion and oxidation
- Very good wear properties from room temperature to 860 °C
- Sprayed by HVOF, flame, PTA, Plasma

Co–25.5Cr–10.5Ni–7.5W–0.5C

- High abrasive, sliding fretting and cavitation wear resistance up to 800–850 °C
- Good oxidation resistance
- Behave well between 540 and 840 °C
- Sprayed by HVOF, flame, PTA, plasma

Co–28Mo–8Cr–2Si

- Up to 760 °C low coefficient of friction
- Good corrosion resistance
- Sprayed by HVOF, flame, PTA, plasma

Co–28Mo–17Cr–3Si

- Excellent sliding wears resistance
- Good hot corrosion resistance and moderate oxidation resistance up to 800 °C
- Sprayed by HVOF, flame, PTA, plasma

Copper Cu (99 wt%) ($T_m = 1{,}084$ °C)

- Very good electrical and thermal conductivities
- Good resistance to inks (paper and printing)
- Used to repair Cu base alloys
- Non-magnetic (electromagnetic shielding)
- Sprayed by flame (powder or wire), wire arc, plasma, HVOF, and cold spray

Copper-based powder: Cu–36Ni–5In ($T_m = 1{,}150\ ^\circ C$):

- Very dense coatings with good resistance to galling and fretting
- Sprayed by flame (powder or wire), wire arc, plasma, HVOF, and cold spray

Aluminum Bronze Cu–9.5Al–1Fe:

- For pumps (against cavitation)
- Piston guides (soft bearing surfaces)
- Shifter forks and compressor air seals (friction)
- Strength and hardness twice that of other bronzes
- Sprayed by flame (powder or wire), wire arc, plasma, HVOF, and cold spray

Supra bronze: Cu–40Zn–0.8Sn–0.75Fe–0.24Mn

- For metallizing work
- Sprayed by flame (powder or wire), wire arc, plasma, HVOF, and cold spray

Iron-based powders (Pure iron $T_m = 1{,}538\ ^\circ C$)

Low carbon steels (C $<$ 0.25 wt%):

- An inexpensive low carbon steel powder
- Corrosion resistant $\rightarrow$ repair + good wear resistance in lubricated service
- May contain martensitic phases
- Produces machinable coatings
- Sprayed by flame, wire arc, plasma, HVOF, and cold spray

High carbon steels (C $>$ 0.8 wt%)

- Reclamation
- Wear and erosion resistance
- Sprayed by flame, wire arc, plasma, HVOF

Stainless steels (SS) Fe-13 or 14Cr–1Ni:

- Good resistance to wear and corrosion
- Best all purpose (SS)
- Sprayed by flame, wire arc, plasma, HVOF

Stainless steels (SS) Fe–18Cr–8Mg–5Ni:

- Reclamation
- Corrosion protection
- Low shrinkage and good machinability
- Sprayed by flame, wire arc, plasma, HVOF

Stainless steels (SS) Fe–17Cr–12NI–2.5Mo–1Si–0.1C (ASI 316):

- Corrosion protection
- Dimensional restoration

– Cavitation and low temperature erosion resistance
– Sprayed by wire or powder flame, wire arc, HVOF

Cored Wires (wire arc sprayed):

– Some of them (Fe–Cr–P–C–. . .) form amorphous phases upon spraying
– Rather good resistance to corrosion (for example, with H_2SO_4)
– Good resistance to abrasion

Molybdenum Mo (Pure molybdenum $T_m = 2{,}623\ ^\circ C$)

– Self bonding to most metallic surfaces, especially steels
– Natural lubricity and high hardness: good wear properties
– Maximum service temperature 316 °C
– Salvage and build-up of Ni base alloy components
– High density coatings
– Fretting resistant
– Used for pump parts, diesel engine fuel, injectors, piston rings, synchronized ring, press fits, valves, gears, cam followers, . . .
– Sprayed by HVOF, flame (powder or wire), wire arc, plasma

Self-fluxing alloys: Mo+25 (Ni–Cr–B–Si–Fe)

– High wear resistance, low friction coefficient
– Against steel, good scuff resistance
– Can be used for hard facing, hard bearing surfaces
– Against abrasion

Nickel Ni (99.5 wt%) (Pure nickel $T_m = 1{,}455\ ^\circ C$)

– Good bonding to steel
– Good corrosion and oxidation resistance up to 980 °C
– Resist heat and prevent scaling of carbon and low alloy steels in hot atmospheres
– Salvage and build-up of Ni base alloys
– Easily machined
– Sprayed by HVOF, flame (powder or wire), wire arc, plasma

Ni–20Cr:

– Good surface appearance
– Good machinability
– Protective coatings against oxidizing gases at high temperature (up to 980 °C)
– Electrical conductors
– Surfacing

– Other different types of NiCr (Cr 10–17 wt%) but also addition of Fe, Mo with specific applications (see suppliers guides); for example:

Ni–16Cr–8Fe

– Machinable "stainless" coatings for salvage and build-up applications on corrosion resistant steels
– Sprayed by HVOF, flame (powder or wire), wire arc, plasma

Ni–18Cr–6Al (composite or clad):

– Good oxidation resistance
– Good machinability
– Bonding and surfacing layers
– Self-bonds to most metallic surfaces
– Sprayed by HVOF, flame (powder or wire), wire arc, plasma

Ni–20Cr–10W–9Mo–4Cu–1C–1B–1Fe:

– Wear and corrosion protection
– Coatings contain some amounts of glassy phases (due to addition of refractory metals and metalloids)
– Sprayed by HVOF, flame (powder or wire), wire arc, plasma

Ni–5Al (clad):

– Good hardness and refractoriness (formation of nickel aluminide)
– Oxidation and abrasion resistant
– Adhere very well to smooth substrates
– Bond coat
– Resizing of over machined parts or of worn-out parts
– Possible: Al 20 wt% (clad) → self-bonds to most metal surfaces
– Sprayed by HVOF, flame (powder or wire), wire arc, plasma

Nickel-based self-fluxing alloys

– Ni–10Cr–2.5B–2.5Fe–2.5Si–0.15C
– The only one producing machinable-fused coating
– Resistance to abrasive wear, fretting, cavitation, and erosion up to 840 °C
– Ni–17Cr–4Fe–4Si–3.5B–1C
– Dense coating good corrosion resistance
– Ni–17Cr–4Fe–4Si–3.5B–1C
– Dense, hard, oxide free coating
– Piston rings, cylinder liners, utility exhaust fan

Superalloys: M.Cr.Al.Y with M = Ni, Co, Fe, Ni–Co

- Composition optimized: for substrate compatibility and environmental resistance
- Protection against corrosion and oxidation in high temperature applications:
- Aero gas turbines
- Marine turbines
- Stationary gas turbines
- Design criteria—Avoid phase transformation during engine start up and shut down, Avoid brittle phases (ex μ, σ, αCr)
- Limit brittleness increasing with oxide content
- Form a stable and adherent oxide scale of Al_2O_3 (addition of active elements: 0.5 % wt Y)
- Increase corrosion resistance (by increasing Cr content)
- Control thermal expansion coefficient: increasing with Cr and decreasing with Al
- Keep ductile coatings (ductile to brittle temperature influenced by Cr and Al contents)
- Many compositions exist
- Sprayed by HVOF, plasma (if possible under soft-vacuum to limit oxidation)

A.2 Ceramics (Oxides)

For most oxides the thermal expansion coefficient is low compared to that of most metals and it has to be taken into account because they are often used at high temperature.

Alumina Al_2O_3 (T_m = 2,050 °C)

- Main problem: Starting from α phase, melting and fast cooling (spraying) result in γ phase. Unfortunately around 1,000 °C γ phase transforms into α phase with a volume increase of about 4 % resulting in coating peeling off. Thus coatings should be used below 900 °C
- They are not too sensitive to oxygen losses
- They have a good resistance to abrasive, sliding and friction wear up to approximately 800 °C
- Poor resistance to shock or impact loading
- High dielectric strength, good electrical insulating coatings
- Reactive with molten salts
- Porous coatings
- Sprayed mainly by plasma, sometimes by HVOF (particles below 22 μm in diameter) and also by flame (rods or cords)

Titanium dioxide TiO_2 (T_m = 1,843 °C)

- Very sensitive to oxygen losses resulting in strong modifications of coating properties: color from white to black and especially electrical properties
- Loss and gain of oxygen reversible
- Very good wettability
- Excellent surface finish
- Excellent adhesion
- Rather low porosity
- Sprayed by plasma, HVOF, and also by flame (rods or cords)

Alumina–Titanium dioxide Al_2O_3–xTiO_2

- TiO_2 in the range 2–50 wt% (most common: 3–13–40 wt%):

  Lowers Al_2O_3 coatings porosity.

Al_2O_3–3TiO_2

- Can be used with most acids and alkalis
- Good for abrasion, erosion, and sliding wear
- Maximum service temperature 840 °C
- Less brittle but lower dielectric strength than pure Al_2O_3 coatings
- Sprayed by plasma

Al_2O_3–13TiO_2

- Applications similar to those of Al_2O_3–3TiO_2 but lower hardness and dielectric strength and less resistance to chemical attack
- Maximum service temperature 540 °C
- Sprayed by plasma

Al_2O_3–40TiO_2

- Formation of Al_2TiO_5
- Softer and less resistant to chemicals
- Excellent finishing properties
- Sprayed by plasma
- Other compositions are used, for example, with SiO_2 below 2 wt%

Chromium Oxide Cr_2O_3 (T_m = 2,435 °C)

- Its stoichiometry depends strongly upon spray conditions (high oxygen pressure needed), and sub-stoichiometric coatings have a metallic behavior with a poor corrosion resistance
- Coatings have high hardness (1900–2000 HV_{5N})
- Excellent wear resistance
- Low porosity

- Excellent finish
- Used on sliding surfaces
- Good wear resistance
- Insoluble in acids, alkalis, and alcohol
- Maximum service temperature 540 °C
- Excellent engraving properties
- Sprayed by plasma, HVOF, and also by flame (rods or cords)

Cr_2O_3–$3TiO_2$–$5SiO_2$

- TiO_2 limits oxygen losses
- Resist better than Cr_2O_3 to impacts
- High wear and corrosion resistance

Hydroxyapatite $Ca_5\ (PO_4)_3\ OH$

- For coating medical and dental implants
- Biocompatible and bioactive (main constituent of bones)
- Sprayed by plasma

Zirconia, ZrO_2

- Interesting mechanical properties
- Good wear resistance
- Low thermal conductivity (1–5 W/m K)
- Three phases: monoclinic (m), tetragonal (t), and cubic (c). Upon cooling around 1,000 °C, cubic or tetragonal phases transform into monoclinic with volume increase of about 10 % and coating peeling off. Thus only totally (c phase) or partially (t′ non-transformable t phase) stabilized zirconia can be sprayed.

  Most used stabilizers are CaO, MgO, Y_2O_3, CeO_2. CaO and MgO are rather cheap but the maximum service temperature is about 500 °C. Very good results are obtained with Y_2O_3; with about 8 wt% t′ phase is obtained, while with13 wt% c phase is obtained, as with 24–25 wt% CeO_2. The maximum service temperature (about 1,350 °C at the best) depends not only on the phase (best results with c phase) but also on the way the powder is manufactured (see Sect. 11.1.2.9) best results being obtained when zirconia and stabilizer particles are very small and uniformly distributed.
- Coatings have excellent thermal shock resistance and good oxidation and corrosion resistance.
- They are mainly used as thermal barriers.
- Sprayed by plasma and also by flame (rods or cords)

Zircon $ZrSiO_4$ (infusible)

- Dissociated during spraying (65 % ZrO_2, 35 % SiO_2)
- Not wetted by liquid metals: used for casting
- Good resistance to liquid glass.
- Good resistance to combustion gases

A.3 Cermets

They are made of a metal matrix, to achieve a good toughness, where are imbedded ceramic particles either of oxides or carbides for the hardness and wear resistance. Here again the manufacturing process plays a key role, for example, sintered particles behaving very differently than blended ones.

With oxides. In most cases they are blends. For example

$$Al_2O_3–30(Ni–20Al)$$

- Denser coatings than pure ceramic, more abrasion, and shock resistant, hard, and smooth
- Addition of alumina particles modifies the electrical resistance of the metal matrix

MCrAlY + Al_2O_3 (<3 μm)

- Hardness increases with Al_2O_3 content
- Electrical resistance decreases with Al_2O_3 %

With carbides (the most used)
Most used ones are:
WC, Cr_3C_2, and also sometimes TiC

- If all of them have melting temperatures over 1,900 °C (for example, T_m = 2,870 °C for WC) they are relatively sensitive to oxidation
- WC oxidation starts at 500–600 °C and oxidation produces W_2C decomposing into W over 1300 °C

Cr_3C_2

- Is not the only chromium carbide: Cr_7C_3 (T_m = 1,782 °C), $Cr_{23}C_6$ (T_m = 1,518 °C). Cr_3C_2 is mostly used in spraying and its oxidation starts at 800–900 °C, however, $Cr_{23}C_6$ has an excellent wear resistance.

TiC

- Has a unique cubic phase (T_m = 3,170 °C), which oxidation starts at 800–900 °C.
- At last carbides dissolve more or less in the liquid metal or alloy matrix, the dissolution increasing with temperature over the matrix melting temperature. The metal matrix lowers the wear resistance of carbides but increases resistance to mechanical or thermal shock. Phase changes of metal matrix must be avoided during the service (for example, that of Co occurs at about 480 °C). To conclude chemical changes occur during spraying especially in air atmosphere: oxidation, decomposition, and dilution. Thus microstructural properties of sprayed cermets

depend strongly on spray conditions (VPS, IPS, APS, HVOF, HVAF, ...), particle morphology and manufacturing process, and ceramic mean grain size. Only a few examples are given below:

WC–8Co

- Dense, hard wear-resistant coating
- Sprayed by plasma, HVOF, HVAF

WC–12Co

- Excellent low-temperature wear resistance
- Sprayed by plasma, HVOF, HVAF

WC–17Co

- Higher Co level improves toughness and fretting resistance
- Cannot be used in corrosive media

Cr_3C_2–25(Ni–20Cr)

- Oxidation resistant up to 900 °C
- Good corrosion resistance
- Excellent for high-temperature cavitation, abrasion, and sliding wear

Cr_3C_2–7(Ni–20Cr)

- Very good resistance to high temperature fretting and wear (higher carbide content increases hardness)

A.4 Abradables

They are designed to wear preferentially upon contact with mating part in order to automatically establish clearance. They comprise a metal matrix and non-metallic filler such as graphite, polyester, polymide, boron nitride, and friable material, the role of filler being to weaken the matrix integrity. The metal matrix is made of Ni, Al, Cu, Co bases, and superalloys.

The main difference of the base material is related to service temperature.

- Al–Si with C: up to 315–425 °C
- Al–Si with polyester: up to 350 °C
- The filler content can be varied
- Both are used for the compressor section of jet engines
- Co–polyester–BN
- They are used up to 700 °C
- Cu: Aluminum bronze alloy–polyester or Cu–14polyester–8Al–1Fe–5Binder

- Maximum service temperature: 650 °C
- Ni–graphite
- They are used up to 480 °C
- Also self-lubricating
- MCrAlY–polyester and/or BN
- Temperatures up to 1,200–1,300 °C

Nomenclature

Latin Alphabet

Ah	Amount to be amortized per hour of equipment work (€/h or USD/h)
Ap	Amortization cost per kilogram of powder used (€/kg or USD/kg)
Fr	Process gas flow rate per hour (m^3/h)
Nh	The number of hours devoted per year to spray the specific coating
Ny	Number of years of the amortization period
p	Pressure (Pa)
Pc	Deposited powder cost per kilogram (€/kg or USD/kg)
Pcc	Cost of each component (electrodes, nozzle, O-ring, . . .) (€ or USD)
Pcp	Deposited powder cost per hour (€/h or USD/h)
Pe	Cost of the equipment (€ or USD)
Pee	Cost of 100 kW (€ or USD)
Pen	Energy cost per deposited powder kilogram (€/kg or USD/kg)
Pep	Cost of components related to the deposition of powder kilogram (€/kg or USD/kg)
Pg	Gas price per 100 m^3 (€ or USD)
Pgp	Gas price per kilogram deposited (€/kg or USD/kg)
Pp	Energy cost per deposited powder kilogram (€/kg or USD/kg)
Pt	Plasma torch power (kW)
qp	Powder quantity necessary for each part (kg)
Qp	Quantity of powder sprayed per hour (kg/h)
Sc	Surface to be coated (m^2)
tc	Mean life time of each component (electrodes, nozzle, O-ring, . . .) (h)
tp	Time necessary to spray the part (h)
v	Velocity (m/s)
wc	Thickness of the coating including the overspray before machining (mm)

Greek Alphabet

η_e	Percentage corresponding to effective spray due to loss at holes and edges (%)
η_p	Powder or wire deposition efficiency
ρ_p	Feed stock specific mass (kg/m^3)

References

1. Davis JR (ed) (2004) Handbook of thermal spray technology. Sections introduction to applications for thermal spray processing and selected applications. ASM International, Materials Park, OH
2. American Welding Society (1985) Thermal spraying, practice, theory and application. American Welding Society, Miami, FL
3. Cartier M (2003) Handbook of surface treatments and coatings. ASME Press, New York, 412 p
4. Zhum Gahr KH (1987) Microstructure and wear of materials. Elsevier, Amsterdam
5. Chattopadhyay R (2001) Surface wear: analysis, treatment, and prevention. ASM International, Materials Park, OH, 307 p
6. Pawlowski L (1995) The science and engineering of thermal spray coatings. Wiley, New York
7. Champagne VK (2007) The cold spray materials deposition process; fundamental and applications. Woodhead, Cambridge, 362 p
8. Sobolev VV, Guilemany JM, Nutting J (2004) High velocity oxy-fuel spraying. Maney for the Institute of Materials, Minerals and Mining, London
9. Bolelli G, Lusvarghi L (2006) Heat treatment effects on the tribological performance of HVOF sprayed Co-Mo-Cr-Si coatings. J Therm Spray Technol 15(4):802–810
10. Kulu P, Hailing J (1998) Recycled hard metal-base wear-resistant composite coatings. J Therm Spray Technol 7(2):173–178
11. Sakata K, Nakano K, Miyahara H, Matsubara Y, Ogi K (2007) Microstructure control of thermally sprayed Co-based self-fluxing alloy coatings by diffusion treatment. J Therm Spray Technol 16(5–6):991–997
12. Otsubo F, Era H, Kishitake K (2000) Structure and phases in nickel-base self-fluxing alloy coating containing high chromium and boron. J Therm Spray Technol 9(1):107–113
13. Kulu P, Pihl T (2002) Selection criteria for wear resistant powder coatings under extreme erosive wear conditions. J Therm Spray Technol 11(4):517–522
14. Miranda JC, Ramalho A (2001) Abrasion resistance of thermal sprayed composite coatings with a nickel alloy matrix and a WC hard phase. Effect of deposition technique and re-melting. Tribol Lett 11(1):37–48
15. Schwetzke R, Kreye H (1999) Microstructure and properties of tungsten carbide coatings sprayed with various high-velocity oxygen fuel spray systems. J Therm Spray Technol 8 (3):433–439
16. Kasparova M, Zahalka F, Houdkova S (2011) WC-Co and Cr_3C_2-NiCr coatings in low- and high-stress abrasive conditions. J Therm Spray Technol 20(3):412–424
17. Houdkova S, Kasparova M, Zahalka F (2010) The influence of spraying angle on properties of HVOF sprayed hardmetal coatings. J Therm Spray Technol 19(5):893–901
18. Tillmann W, Vogli E, Baumann I, Kopp G, Weihs C (2010) Desirability-based multi-criteria optimization of HVOF spray experiments to manufacture fine structured wear-resistant $75Cr_3C_2$-25(NiCr20) coatings. J Therm Spray Technol 19(1–2):393–408
19. Skandan G, Yao R, Sadangi R, Kear BH, Qiao Y, Liu L, Fischer TE (2000) Multimodal coatings: a new concept in thermal spraying. J Therm Spray Technol 9(3):329–331
20. Lima RS, Marple BR (2007) Thermal spray coatings engineered from nanostructured ceramic agglomerated powders for structural, thermal barrier and biomedical applications: a review. J Therm Spray Technol 16(1):40–63
21. Kim GE, Walker J (2007) Successful application of nanostructured titanium dioxide coating for high-pressure acid-leach application. J Therm Spray Technol 16(1):34–39
22. Gawne DT, Qiu Z, Bao Y, Zhang T, Zhang K (2001) Abrasive wear resistance of plasma-sprayed glass-composite coatings. J Therm Spray Technol 10(4):599–603

23. Cipri F, Bartuli C, Valente T, Casadei F (2007) Electromagnetic and mechanical properties of silica-aluminosilicates plasma sprayed composite coatings. J Therm Spray Technol 16(5–6):831–838
24. Kang AS, Grewal JS, Jain D, Kang S (2012) Wear behavior of thermal spray coatings on rotavator blades. J Therm Spray Technol 21(2):355–359
25. Kim HJ, Kweon YG, Chang RW (1994) Wear and erosion behavior of plasma-sprayed WC-Co coatings. J Therm Spray Technol 3(2):169–178
26. Wang BQ, Luer K (1994) The erosion-oxidation behavior of HVOF Cr_3C_2-NiCr cermet coating. Wear 174:177–185
27. Kenichi S, Nakahama S, Hattori S, Nakano K (2005) Slurry wear and cavitation erosion of thermal-sprayed cermets. Wear 258:768–775
28. Hawthorne HM, Arsenault B, Immarigeon JP, Legoux JG, Parameswaran VR (1999) Comparison of slurry and dry erosion behavior of some HVOF thermal sprayed coatings. Wear 225–229:825–834
29. Ji G-C, Li C-J, Wang Y-Y, Li W-Y (2007) Erosion performance of HVOF-sprayed Cr3C2-NiCr coatings. J Therm Spray Technol 16(4):557–565
30. Yang G-J, Li C-J, Zhang S-J, Li C-X (2008) High-temperature erosion of HVOF sprayed Cr_3C_2-NiCr coating and mild steel for boiler tubes. J Therm Spray Technol 17(5–6):782–787
31. Osawa S, Itsukaichi T, Ahmed R (2005) Influence of substrate properties on the impact resistance of WC cermet coatings. J Therm Spray Technol 14(4):495–501
32. Kulu P, Hussainova L, Veinthal R (2005) Solid particle erosion of thermal sprayed coatings. Wear 258:488–496
33. Ramesha CS, Devaraja DS, Keshavamurthya R, Sridharb BR (2011) Slurry erosive wear behavior of thermally sprayed Inconel-718 coatings by APS process. Wear 271:1365–1371
34. Higuera HV, Belzunce Varela J, Carriles Menéndez A, Poveda Martiınez S (2001) High temperature erosion wear of flame and plasma-sprayed nickel–chromium coatings under simulated coal-fired boiler atmospheres. Wear 247:214–222
35. Krishnamurthy N, Murali MS, Venkataraman B, Mukunda PG (2012) Characterization and solid particle erosion behavior of plasma sprayed alumina and calcia-stabilized zirconia coatings on Al-6061 substrate. Wear 274–275:15–27
36. Branagan DJ, Breitsameter M, Meacham BE, Belashchenko V (2005) High-performance nanoscale composite coatings for boiler applications. J Therm Spray Technol 14(2):196–204
37. Pantelis DI, Psyllaki P, Alexopoulos N (2000) Tribological behavior of plasma-sprayed Al_2O_3 coatings under severe wear conditions. Wear 237:197–204
38. Sanchez E, Bannier E, Cantavella V, Salvador MD, Klyatskina E, Morgiel J, Grzonka J, Boccaccini AR (2008) Deposition of Al_2O_3-TiO_2 nanostructured powders by atmospheric plasma spraying. J Therm Spray Technol 17(3):329–337
39. Darut G, Ageorges H, Denoirjean A, Montavon G, Fauchias P (2008) Effect of the structural scale of plasma-sprayed alumina coatings on their friction coefficients. J Therm Spray Technol 17(5–6):788–797
40. Bolelli G, Rauch J, Cannillo V, Killinger A, Lusvarghi L, Gadow R (2009) Microstructural and tribological investigation of high-velocity suspension flame sprayed (HVSFS) Al_2O_3 coatings. J Therm Spray Technol 18(1):35–48
41. Ahn H-S, Kwon O-K (1999) Tribological behaviour of plasma-sprayed chromium oxide coating. Wear 225–229:814–824
42. Pratap Singh V, Sil A, Jayaganthan R (2011) Tribological behavior of plasma sprayed Cr_2O_3–3%TiO_2 coatings. Wear 272:149–158
43. Tao S, Yin Z, Zhou X, Ding C (2010) Sliding wear characteristics of plasma-sprayed Al_2O_3 and Cr_2O_3 coatings against copper alloy under severe conditions. Tribol Int 43:69–75
44. Bolelli G, Cannillo V, Lusvarghi L, Manfredini T (2006) Wear behaviour of thermally sprayed ceramic oxide coatings. Wear 261:1298–1315

45. Ramachandran CS, Balasubramanian V, Ananthapadmanabhan PV, Viswabaskaran V (2012) Understanding the dry sliding wear behaviour of atmospheric plasma-sprayed rare earth oxide coatings. Mater Design 39:234–252
46. Dallaire S (2001) Hard arc-sprayed coating with enhanced erosion and abrasion wear resistance. J Therm Spray Technol 10(3):511–519
47. Yang Q, Senda T, Hirose A (2006) Sliding wear behavior of WC–12% Co coatings at elevated temperatures. Surf Coat Technol 200:4208–4212
48. Yandouzi M, Bu H, Brochu M, Jodoin B (2012) Nanostructured Al-based metal matrix composite coating production by pulsed gas dynamic spraying process. J Therm Spray Technol 21(3–4):609–619
49. Li W-Y, Zhang G, Zhang C, Elkedim O, Liao H, Coddet C (2008) Effect of ball milling of feedstock powder on microstructure and properties of TiN particle-reinforced Al alloy-based composites fabricated by cold spraying. J Therm Spray Technol 17(3):316–322
50. Qiao Y, Liu Y-R, Fischer TE (2001) Sliding and abrasive wear resistance of thermal-sprayed WC-CO coatings. J Therm Spray Technol 10(1):118–125
51. Jacobs L, Hyland MM, De Bonte M (1999) Study of the influence of microstructural properties on the sliding-wear behavior of HVOF and HVAF sprayed WC-cermet coatings. J Therm Spray Technol 8(1):125–132
52. Bolelli G, Bonferroni B, Laurila J, Lusvarghi L, Milantia A, Niemi K, Vuoristo P (2012) Micromechanical properties and sliding wear behaviour of HVOF-sprayed Fe-based alloy coatings. Wear 276–277:29–47
53. Alam S, Sasaki S, Shimura H (2001) Friction and wear characteristics of aluminum bronze coatings on steel substrates sprayed by a low pressure plasma technique. Wear 248:75–81
54. Ouyang JH, Sasaki S, Umeda K (2001) Microstructure and tribological properties of low-pressure plasma-sprayed ZrO_2–CaF_2–Ag_2O composite coating at elevated temperature. Wear 249:440–451
55. Ahn J, Hwang B, Lee S (2005) Improvement of wear resistance of plasma-sprayed molybdenum blend coatings. J Therm Spray Technol 14(2):251–257
56. Rodriguez J, Martin A, Fernández R, Fernández JE (2003) An experimental study of the wear performance of NiCrBSi thermal spray coatings. Wear 255:950–955
57. Niebuhr D, Scholl M (2005) Synthesis and performance of plasma-sprayed polymer/steel coating system. J Therm Spray Technol 14(4):487–494
58. Li J, Liao H, Coddet C (2002) Friction and wear behavior of flame-sprayed PEEK coatings. Wear 252:824–831
59. Li Y, Ma Y, Xie B, Cao S, Wu Z (2007) Dry friction and wear behavior of flame-sprayed polyamide1010/n-SiO_2 composite coatings. Wear 262:1232–1238
60. Żórawski W, Kozerski S (2008) Scuffing resistance of plasma and HVOF sprayed WC-12Co and Cr_3C_2-25(Ni20Cr) coatings. Surf Coat Technol 202:4453–4457
61. Edrisy A, Perry T, Alpas AT (2005) Investigation of scuffing damage in aluminum engines with thermal spray coatings. Wear 259:1056–1062
62. Kim J-H, Lee M-H (2010) A study on cavitation erosion and corrosion behavior of Al-, Zn-, Cu-, and Fe-based coatings prepared by arc spraying. J Therm Spray Technol 19 (6):1224–1230
63. Hahn M, Fischer A (2010) Characterization of thermal spray coatings for cylinder running surfaces of diesel engines. J Therm Spray Technol 19(5):866–872
64. Kumar A, Boy J, Zatorski R, Stephenson LD (2005) Thermal spray and weld repair alloys for the repair of cavitation damage in turbines and pumps: a technical note. J Therm Spray Technol 14(2):177–182
65. Factor M, Roman I (2002) Use of microhardness as a simple means of estimating relative wear resistance of carbide thermal spray coatings: Part 2. Wear resistance of cemented carbide coatings. J Therm Spray Technol 11(4):482–495

66. Wu Y, Hong S, Zhang J, He Z, Guo W, Wang Q, Li G (2012) Microstructure and cavitation erosion behavior of WC–Co–Cr coating on 1Cr18Ni9Ti stainless steel by HVOF thermal spraying. Int J Refract Metals Hard Mater 32:21–26
67. Santa JF, Espitia LA, Blanco JA, Romo SA, Toro A (2009) Slurry and cavitation erosion resistance of thermal spray coatings. Wear 267:160–167
68. Lima MM, Godoy C, Modenesi PJ, Avelar-Batista JC, Davison A, Matthews A (2004) Coating fracture toughness determined by Vickers indentation: an important parameter in cavitation erosion resistance of WC–Co thermally sprayed coatings. Surf Coat Technol 177–178:489–496
69. Ding Z-X, Chen W, Wang Q (2011) Resistance of cavitation erosion of multimodal WC-12Co coatings sprayed by HVOF. Trans Nonferrous Met Soc China 21:2231–2236
70. Stewart S, Ahmed R (2002) Rolling contact fatigue of surface coatings—a review. Wear 253:1132–1144
71. Ahmed R, Hadfield M (2002) Mechanisms of fatigue failure in thermal spray coatings. J Therm Spray Technol 11(3):333–349
72. Savarimuthu AC, Taber HF, Megat I, Shadley JR, Rybicki EF, Cornell WC, Emery WA, Somerville DA, Nuse JD (2001) Sliding wear behavior of tungsten carbide thermal spray coatings for replacement of chromium electroplate in aircraft applications. J Therm Spray Technol 10(3):502–510
73. Zhang XC, Xu BS, Xuan FZ, Tu ST, Wang HD, Wu YX (2008) Rolling contact fatigue behavior of plasma-sprayed CrC–NiCr cermet coatings. Wear 265:1875–1883
74. Berger L-M, Lipp K, Spatzier J, Bretschneider J (2011) Dependence of the rolling contact fatigue of HVOF-sprayed WC–17%Co hardmetal coatings on substrate hardness. Wear 271:2080–2088
75. Ganesh Sundara Raman S, Rajasekaran B, Joshi SV, Sundararajan G (2007) Influence of substrate material on plain fatigue and fretting fatigue behavior of detonation gun sprayed Cu-Ni-In coating. J Therm Spray Technol 16(4):571–579
76. Akebono H, Komotori J, Shimizu M (2008) Effect of coating microstructure on the fatigue properties of steel thermally sprayed with Ni-based self-fluxing alloy. Int J Fatigue 30:814–821
77. Jin O, Mall S, Sanders JH, Sharma SK (2006) Durability of Cu–Al coating on Ti–6Al–4V substrate under fretting fatigue. Surf Coat Technol 201:1704–1710
78. Kim K, Korsunsky AM (2011) Effects of imposed displacement and initial coating thickness on fretting behaviour of a thermally sprayed coating. Wear 271(7–8):1080–1085
79. Mary C, Fouvry S, Martin JM, Bonnet B (2011) Pressure and temperature effects on Fretting Wear damage of a Cu–Ni–In plasma coating versus Ti17 titanium alloy contact. Wear 272:18–37
80. Hager CH Jr, Sanders JH, Sharma S (2008) Un-lubricated gross slip fretting wear of metallic plasma-sprayed coatings for Ti6Al4V surfaces. Wear 265:439–451
81. Koiprasert H, Dumrongrattana S, Niranatlumpong P (2004) Thermally sprayed coatings for protection of fretting wear in land-based gas-turbine engine. Wear 257:1–7
82. Hager CH Jr, Sanders J, Sharma S, Voevodin AA (2009) The use of nickel graphite composite coatings for the mitigation of gross slip fretting wear on Ti6Al4V interfaces. Wear 267:1470–1481
83. Carrasquero EJ, Lesage J, Puchi-Cabrera ES, Staia MH (2008) Fretting wear of HVOF Ni–Cr based alloy deposited on SAE 1045 steel. Surf Coat Technol 202:4544–4551
84. Tian W, Wang Y, Yang Y (2008) Fretting wear behavior of conventional and nanostructured Al2O3–13 wt%TiO2 coatings fabricated by plasma spray. Wear 265:1700–1707
85. Sathish S, Geetha M, Aruna ST, Balaji N, Rajam KS, Asokamani R (2011) Sliding wear behavior of plasma sprayed nanoceramic coatings for biomedical applications. Wear 271:934–941
86. Aoh J-N, Chen J-C (2001) On the wear characteristics of cobalt-based hardfacing layer after thermal fatigue and oxidation. Wear 250:611–620

87. D'Ans P, Dille J, Degrez M (2011) Thermal fatigue resistance of plasma sprayed yttria-stabilised zirconia onto borided hot work tool steel, bonded with a NiCrAlY coating: experiments and modeling. Surf Coat Technol 205:3378–3386
88. Eriksson R, Brodin H, Johansson S, Östergren L, Li X-H (2011) Influence of isothermal and cyclic heat treatments on the adhesion of plasma sprayed thermal barrier coatings. Surf Coat Technol 205:5422–5429
89. Kwon J-Y, Lee J-H, Kim H-C, Jung Y-G, Paik U, Lee K-S (2006) Effect of thermal fatigue on mechanical characteristics and contact damage of zirconia-based thermal barrier coatings with HVOF-sprayed bond coat. Mater Sci Eng A 429:173–180
90. Luo L, Liu S, Li J, Wu Y (2011) Thermal shock resistance of FeMnCrAl/Cr3C2–Ni9Al coatings deposited by high velocity arc spraying. Surf Coat Technol 205:3467–3471
91. Pan ZY, Wang Y, Wang CH, Sun XG, Wang L (2012) The effect of SiC particles on thermal shock behavior of Al2O3/8YSZ coatings fabricated by atmospheric plasma spraying. Surf Coat Technol 206:2484–2498
92. Gu L, Chen X, Fan X, Liu Y, Zou B, Wang Y, Cao X (2011) Improvement of thermal shock resistance for thermal barrier coating on aluminum alloy with various electroless interlayers. Surf Coat Technol 206:29–36
93. Kokini K, DeJonge J, Rangaraj S, Beardsley B (2002) Thermal shock of functionally graded thermal barrier coatings with similar thermal resistance. Surf Coat Technol 154:223–231
94. Liang B, Ding C (2005) Thermal shock resistances of nanostructured and conventional zirconia coatings deposited by atmospheric plasma spraying. Surf Coat Technol 197:185–192
95. Gilbert A, Kokini K, Sankarasubramanian S (2008) Thermal fracture of zirconia–mullite composite thermal barrier coatings under thermal shock: a numerical study. Surf Coat Technol 203:91–98
96. Ahmaniemi S, Vippola M, Vuoristo P, Mäntylä T, Buchmann M, Gadow R (2002) Residual stresses in aluminum phosphate sealed plasma sprayed oxide coatings and their effect on abrasive wear. Wear 252:614–623
97. Chen H, Hutchings IM (1998) Abrasive wear resistance of plasma-sprayed tungsten carbide–cobalt coatings. Surf Coat Technol 107:106–114
98. Venkateswarlu K, Rajinikanth V, Naveen T, Dhiraj Prasad Sinha (2009) Abrasive wear behavior of thermally sprayed diamond reinforced composite coating deposited with both oxy-acetylene and HVOF techniques. Wear 266:995–1002
99. Stoica V, Ahmed R, Itsukaichi T (2005) Influence of heat-treatment on the sliding wear of thermal spray cermet coatings. Surf Coat Technol 199:7–21
100. Valarezo A, Bolelli G, Choi WB, Sampath S, Cannillo V, Lusvarghi L, Rosa R (2010) Damage tolerant functionally graded WC–Co/stainless steel HVOF coatings. Surf Coat Technol 205:2197–2208
101. Bolelli, Cannillo V, Lusvarghi L, Rosa R, Valarezo A, Choi WB, Dey R, Weyant C, Sampath S (2012) Functionally graded WC–Co/NiAl HVOF coatings for damage tolerance, wear and corrosion protection. Surf Coat Technol 206:2585–2601
102. Stoica V, Ahmed R, Golshan M, Tobe S (2004) Sliding wear evaluation of hot isostatically pressed thermal spray cermet coatings. J Therm Spray Technol 13(1):93–107
103. Evdokimenko Yu I, Kisel' VM, Kadyrov VK, Korol' AA, Get'man OI (2001) High-velocity flame spraying of powder aluminum protective coatings. Powder Metallurgy Metal Ceram 40 (3–4):121–126
104. Sørensen PA, Kiil S, Dam-Johansen K, Weinell CE (2009) Anticorrosive coatings: a review. J Coat Technol Res 6(2):135–176
105. Murakami K, Shimada M (2009) Development of thermal spray coatings with corrosion protection and antifouling properties. In: Marple BR, Hyland MM, Lau Y-C, Li C-J, Lima RS, Montavon G (eds) Thermal spray 2009: Proceedings of the international thermal spray conference. ASM International, Materials Park, OH, pp 1041–1044
106. Pacheo da Silva C et al (1991) 2nd Plasma Technik Symposium 1. Plasma Technik, Wohlen, pp 363–373

107. Chun-long Y, Yun-qi A, Ya-tan S (2009) Three years corrosion tests of nanocomposite epoxy sealer for metalized coatings on the East China Sea. In: Marple BR, Hyland MM, Lau Y-C, Li C-J, Lima RS, Montavon G (eds) Thermal spray 2009: Proceedings of the international thermal spray conference. ASM International, Materials Park, OH, pp 1090–1093
108. Schmidt DP, Shaw BA, Sikora E, Shaw WW, Laliberte LH (2006) Corrosion protection assessment of sacrificial coating systems as a function of exposure time in a marine environment. Prog Org Coat 57:352–364
109. Han M-S, Woo Y-B, Ko S-C, Jeong Y-J, Jang S-K, Kim S-J (2009) Effects of thickness of Al thermal spray coating for STS 304. Trans Nonferrous Met Soc China 19:925–929
110. Esfahani EA, Salimijazi H, Golozar MA, Mostaghimi J, Pershin L (2012) Study of corrosion behavior of arc sprayed aluminum coating on mild steel. J Therm Spray Technol. doi:10.1007/s11666-012-9810-x
111. Gorlach IA (2009) A new method for thermal spraying of Zn–Al coatings. Thin Solid Films 517:5270–5273
112. Cramer SD, Covino BS Jr, Holcomb GR, Bullard SJ, Collins WK, Govier RD, Wilson RD, Laylor HM (1999) Thermal sprayed titanium anode for cathodic protection of reinforced concrete bridges. J Therm Spray Technol 8(1):133–145
113. Holcomb GR, Cramer SD, Bullard SJ, Covino Jr BS, Collins WK, Govier RD, McGill GE (1997) Characterization of thermal-sprayed titanium anodes for cathodic protection. In: Berndt CC (ed) Thermal spray: a united forum for scientific and technological advances. ASM International, Materials Park, OH, pp 141–150
114. Kawakita J, Kuroda S, Fukushima T, Kodama T (2005) Improvement of corrosion resistance of high-velocity oxyfuel-sprayed stainless steel coatings by addition of molybdenum. J Therm Spray Technol 14(2):225–230
115. Moskowitz LN (1993) Application of HVOF thermal spraying to solve corrosion problems in the petroleum industry—an industrial note. J Therm Spray Technol 2(1):21–29
116. Zeng Z, Sakoda N, Tajiri T, Kuroda S (2008) Structure and corrosion behavior of 316L stainless steel coatings formed by HVAF spraying with and without sealing. Surf Coat Technol 203:284–290
117. Meng H (2010) The performance of different WC-based cermet coatings in oil and gas applications–a comparison. In: ITSC 2010 Thermal spray: global solutions, future applications. DVS, Düsseldorf, e-Proc
118. Souza VAD, Neville A (2007) Aspects of microstructure on the synergy and overall material loss of thermal spray coatings in erosion–corrosion environments. Wear 263:339–346
119. Ishikawa Y, Kawakita J, Osawa S, Itsukaichi T, Sakamoto Y, Takaya M, Kuroda S (2005) Evaluation of corrosion and wear resistance of hard cermet coatings sprayed by using an improved HVOF process. J Therm Spray Technol 14(3):384–390
120. Fedrizzi L, Valentinelli L, Rossi S, Segna S (2007) Tribocorrosion behaviour of HVOF cermet coatings. Corros Sci 49:2781–2799
121. Zhang J, Wang Z, Lin P, Lu W, Zhou Z, Jiang S (2011) Effect of sealing treatment on corrosion resistance of plasma-sprayed NiCrAl/Cr_2O_3-8 wt.%TiO_2 coating. J Therm Spray Technol 20(3):508–513
122. Tuominen J, Vuoristo P, Mäntylä T, Kylmälahti M, Vihinen J et al (2000) Improving corrosion properties of high-velocity oxy-fuel sprayed inconel 625 by using a high-power continuous wave neodymium-doped yttrium aluminum garnet laser. J Therm Spray Technol 9(4):513–519
123. Kim S-J, Lee S-J (2011) Effects of F−Si sealer on electrochemical characteristics of 15% Al−85%Zn alloy thermal spray coating. Trans Nonferrous Met Soc China 21:2798–2804
124. Dent AH, Horlock AJ, McCartney DG, Harris SJ (1999) The corrosion behavior and microstructure of high-velocity oxy-fuel sprayed nickel-base amorphous/nanocrystalline coatings. J Therm Spray Technol 8(3):399–404

125. Ishikawa K, Suzuki T, Tobe S, Kitamura Y (2001) Resistance of thermal-sprayed duplex coating composed of aluminum and 80Ni-20Cr alloy against aqueous corrosion. J Therm Spray Technol 10(3):520–525
126. Pardo A, Merino MC, Mohedano M, Casajús P, Coy AE, Arrabal R (2009) Corrosion behaviour of Mg/Al alloys with composite coatings. Surf Coat Technol 203:1252–1263
127. Arrabal R, Pardo A, Merino MC, Mohedano M, Casajús P, Merino S (2010) Al/SiC thermal spray coatings for corrosion protection of Mg–Al alloys in humid and saline environments. Surf Coat Technol 204:2767–2774
128. Pokhmurska H, Wielage B, Lampke T, Grund T, Student M, Chervinska N (2008) Post-treatment of thermal spray coatings on magnesium. Surf Coat Technol 202:4515–4524
129. Mohan P, Patterson T, Yao B, Sohn Y (2010) Degradation of thermal barrier coatings by fuel impurities and CMAS: thermochemical interactions and mitigation approaches. J Therm Spray Technol 19(1–2):156–167
130. Jones RL (1997) Some aspects of the hot corrosion of thermal barrier coatings. J Therm Spray Technol 6(1):77–84
131. Hitchman LN, Knapp J (2010) Failure of thermal barrier coatings subjected to CMAS attack. J Therm Spray Technol 19(1–2):148–155
132. Li L, Hitchman N, Knapp J (2010) Failure of thermal barrier coatings subjected to CMAS attack. J Therm Spray Technol 19(1–2):148–155
133. Habibi MH, Li Wang, Guo SM (2012) Evolution of hot corrosion resistance of YSZ, $Gd_2Zr_2O_7$, and $Gd_2Zr_2O_7$ + YSZ composite thermal barrier coatings in Na_2SO_4 + V_2O_5 at 1050 °C. J Eur Ceram Soc 32:1635–1642
134. Xie X, Guo H, Gong S, Xu H (2012) Hot corrosion behavior of double-ceramic-layer $LaTi_2Al_9O_{19}$/YSZ thermal barrier coatings. Chin J Aeronautics 25:137–142
135. Mei H, Liu Y, Cheng L, Zhang L (2012) Corrosion mechanism of a NiCoCrAlTaY coated Mar-M247 superalloy in molten salt vapor. Corros Sci 55:201–204
136. Sidhu TS, Prakash S, Agrawal RD (2006) Hot corrosion resistance of high-velocity oxyfuel sprayed coatings on a nickel-base superalloy in molten salt environment. J Therm Spray Technol 15(3):387–399
137. Chatha SS, Sidhu HS, Sidhu BS (2012) High temperature hot corrosion behaviour of NiCr and Cr_3C_2–NiCr coatings on T91 boiler steel in an aggressive environment at 750 °C. Surf Coat Technol 206:3839–3850
138. Tani K, Harada Y (2007) Enhancement of service life of steam generating tubes in oil-fired boiler for power generation employing plasma spray technology. J Therm Spray Technol 16 (1):111–117
139. Bala N, Singh H, Prakash S (2010) Accelerated hot corrosion studies of cold spray Ni–50Cr coating on boiler steels. Mater Design 31:244–253
140. Matsubara Y, Sochi Y, Tanabe M, Takeya A (2007) Advanced coatings on furnace wall tubes. J Therm Spray Technol 16(2):195–201
141. Chatha SS, Sidhu HS, Sidhu BS (2012) The effects of post-treatment on the hot corrosion behavior of the HVOF-sprayed Cr_3C_2–NiCr coating. Surf Coat Technol 206:4212–4224
142. Tao K, Zhou X-L, Cui H, Zhang J-S (2009) Oxidation and hot corrosion behaviors of HVAF-sprayed conventional and nanostructured NiCrC coatings. Trans Nonferrous Met Soc China 19:1151–1160
143. Jansen F, Xi W, Dorfman MR, Peters JA, Nagy DR (2002) Performance of di-calcium silicate coatings in hot-corrosive environment. Surf Coat Technol 149:57–61
144. Hirata T, Ota S, Morimoto T (2003) Influence of impurities in Al_2O_3 ceramics on hot corrosion resistance against molten salt. J Eur Ceram Soc 23:91–97
145. Gibbons GJ, Hansell RG (2008) Thermal-sprayed coatings on aluminium for mould tool protection and upgrade. J Mater Process Technol 204:184–191
146. Mizuno H, Kitamura J (2007) MoB/CoCr cermet coatings by HVOF spraying against erosion by molten Al-Zn alloy. J Therm Spray Technol 16(3):404–413

147. Koolloos MFJ, Houben JM (2000) Behavior of plasma-sprayed thermal barrier coatings during thermal cycling and the effect of a preoxidized NiCrAlY bond coat. J Therm Spray Technol 9(1):49–58
148. Fossati A, DiFerdinando M, Bardi U, Scrivani A, Giolli C (2012) Influence of surface finishing on the oxidation behaviour of VPS MCrAlY coatings. J Therm Spray Technol 21(2):314–324
149. Jiang SM, Li HQ, Ma J, Xu CZ, Gong J, Sun C (2010) High temperature corrosion behavior of a gradient NiCoCrAlYSi coating II: oxidation and hot corrosion. Corros Sci 52:2316–2322
150. Yuan FH, Chen ZX, Huang ZW, Wang ZG, Zhu SJ (2008) Oxidation behavior of thermal barrier coatings with HVOF and detonation-sprayed NiCrAlY bond coats. Corros Sci 50:1608–1617
151. Pint BA, Wright IG, Brindley WJ (2000) Evaluation of thermal barrier coating systems on novel substrates. J Therm Spray Technol 9(2):198–203
152. Limarga AM, Widjaja S, Yip TH (2005) Mechanical properties and oxidation resistance of plasma-sprayed multilayered Al_2O_3/ZrO_2 thermal barrier coatings. Surf Coat Technol 197:93–102
153. Ramesh MR, Prakash S, Nath SK, Pawan Kumar Sapra, Krishnamurthy N (2011) Evaluation of thermocyclic oxidation behavior of HVOF-sprayed NiCrFeSiB coatings on boiler tube steels. J Therm Spray Technol 20(5):992–1000
154. Kaur M, Singh H, Prakash S (2011) Surface engineering analysis of detonation-gun sprayed Cr3C2–NiCr coating under high-temperature oxidation and oxidation–erosion environments. Surf Coat Technol 206:530–541
155. Sidhu TS, Malik A, Prakash S, Agrawal RD (2007) Oxidation and hot corrosion resistance of HVOF WC-NiCrFeSiB coating on Ni- and Fe-based superalloys at 800 °C. J Therm Spray Technol 16(5–6):844–849
156. Singh H, Puri D, Prakash S, Rama Rao VV (2006) On the high-temperature oxidation protection behavior of plasma-sprayed stellite-6 coatings. Metallurgical Mater Trans A 37A:3048–3056
157. Bala N, Singh H, Prakash S (2011) Characterization and high-temperature oxidation behavior of cold-sprayed Ni-20Cr and Ni-50Cr coatings on boiler steels. Metallurgical Mater Trans A 42A:3399–3416
158. Hill H, Weber S, Raab U, Theisen W, Wagner L (2012) Influence of processing and heat treatment on corrosion resistance and properties of high alloyed steel coatings. J Therm Spray Technol 21(5):987–994
159. Kembaiyan KT, Keshavan K (1995) Combating severe fluid erosion and corrosion of drill bits using thermal spray coatings. Wear 186–187:487–492
160. Uozato S, Nakata K, Ushio M (2003) Corrosion and wear behaviors of ferrous powder thermal spray coatings on aluminum alloy. Surf Coat Technol 169–170:691–694
161. Al-Fadhli HY, Stokes J, Hashmi MSJ, Yilbas BS (2006) The erosion–corrosion behaviour of high velocity oxy-fuel (HVOF) thermally sprayed inconel-625 coatings on different metallic surfaces. Surf Coat Technol 200:5782–5788
162. Lima CRC, de Souza NFC, Camargo F (2012) Study of wear and corrosion performance of thermal sprayed engineering polymers. Surf Coat Technol 220:140–143
163. Flores JF, Neville A, Kapur N, Gnanavelu A (2009) An experimental study of the erosion–corrosion behavior of plasma transferred arc MMCs. Wear 267:213–222
164. Sidhu BS, Prakash S (2006) Erosion-corrosion of plasma as sprayed and laser remelted Stellite-6 coatings in a coal fired boiler. Wear 260:1035–1044
165. Wang B (1996) Erosion-corrosion of thermal sprayed coatings in FBC boilers. Wear 199:24–32
166. Uusitalo MA, Vuoristo PMJ, Mäntylä TA (2002) Elevated temperature erosion–corrosion coatings in chlorine containing environments of thermal sprayed. Wear 252:586–594

167. Billah BM, Ahmad Khalid F, Nusair Khan A (2012) Behavior of calcia-stabilized zirconia coating at high temperature, deposited by air plasma spraying system. J Therm Spray Technol 21(1):121–131
168. Miller RA (1997) Thermal barrier coatings for aircraft engines: history and directions. J Therm Spray Technol 6(1):35–42
169. Schulz U, Bernardi O, Ebach-Stahl A, Vaßen R, Sebold D (2008) Improvement of EB-PVD thermal barrier coatings by treatments of a vacuum plasma-sprayed bond coat. Surf Coat Technol 203:160–170
170. Bose S, de Masi-Marcin J (1997) Thermal barrier coating experience in gas turbine engines at Pratt & Whitney. J Therm Spray Technol 6(1):99–104
171. Cipitria A, Golosnoy IO, Clyne TW (2009) A sintering model for plasma-sprayed zirconia TBCs. Part I: Free-standing coatings. Acta Mater 57:980–992
172. Markocsan N, Nylén P, Wigren J, Li X-H, Tricoire A (2009) Effect of thermal aging on microstructure and functional properties of zirconia-base thermal barrier coatings. J Therm Spray Technol 18(2):201–208
173. Golosnoy IO, Cipitria A, Clyne TW (2009) Heat transfer through plasma-sprayed thermal barrier coatings in gas turbines: a review of recent work. J Therm Spray Technol 18 (5–6):809–821
174. Hernandez MT, Karlsson AM, Bartsch M (2009) On TGO creep and the initiation of a class of fatigue cracks in thermal barrier coatings. Surf Coat Technol 203:3549–3558
175. Vaßen R, Giesen S, Stöver D (2009) Lifetime of plasma-sprayed thermal barrier coatings: comparison of numerical and experimental results. J Therm Spray Technol 18(5–6):835–845
176. Toscano J, Vaβen R, Gil A, Subanovic M, Naumenko D, Singheiser L, Quadakkers WJ (2006) Parameters affecting TGO growth and adherence on MCrAlY-bond coats for TBC's. Surf Coat Technol 201:3906–3910
177. Pint BA, Haynes JA, Zhang Y (2010) Effect of superalloy substrate and bond coating on TBC lifetime. Surf Coat Technol 205:1236–1240
178. Chen Z, Mabon J, Wen J-G, Trice R (2009) Degradation of plasma-sprayed yttria-stabilized zirconia coatings via ingress of vanadium oxide. J Eur Ceram Soc 29:1647–1656
179. Feuerstein A, Knapp J, Taylor T, Ashary A, Bolcavage A, Hitchman N (2008) Technical and economical aspects of current thermal barrier coating systems for gas turbine engines by thermal spray and EBPVD: a review. J Therm Spray Technol 17(2):199–213
180. Vaßen R, Jarligo MO, Steinke T, Mack DE, Stöver D (2010) Overview on advanced thermal barrier coatings. Surf Coat Technol 205:938–942
181. Vaßen R, Stuke A, Stöver D (2009) Recent developments in the field of thermal barrier coatings. J Therm Spray Technol 18(2):181–186
182. Richer P, Yandouzi M, Beauvais L, Jodoin B (2010) Oxidation behaviour of CoNiCrAlY bond coats produced by plasma, HVOF and cold gas dynamic spraying. Surf Coat Technol 204:3962–3974
183. Karger M, Vaßen R, Stöver D (2011) Atmospheric plasma sprayed thermal barrier coatings with high segmentation crack densities: spraying process, microstructure and thermal cycling behaviour. Surf Coat Technol 206:16–23
184. Hospach A, Mauer G, Vaßen R, Stöver D (2012) Characteristics of ceramic coatings made by thin film low pressure plasma spraying (LPPS-TF). J Therm Spray Technol 21(3–4):435–440
185. Muehlberger E, Meyer P (2009) LPPS – thin film processes: overview of origin and future possibilities. In: Marple BR, Hyland MM, Lau Y-C, Li C-J, Lima RS, Montavon G (eds) Thermal spray 2009: Proceedings of the international thermal spray conference. ASM International, Materials Park, OH, pp 737–740
186. Fauchais P, Montavon G, Lima RS, Marple BR (2011) Engineering a new class of thermal spray nano-based microstructures from agglomerated nanostructured particles, suspensions and solutions: an invited review. J Phys D Appl Phys 44:093001

187. Musil J, Alaya M, Oberacker R (1997) Plasma-sprayed duplex and graded partially stabilized zirconia thermal barrier coatings: deposition process and properties. J Therm Spray Technol 6 (4):449–455
188. Soechting FO (1999) A design perspective on thermal barrier coatings. J Therm Spray Technol 8(4):505–511
189. Beele W, Marijnissen G, van Lieshout A (1999) The evolution of thermal barrier coatings—status and upcoming solutions for today's key issues. Surf Coat Technol 120–121:61–67
190. Gupta M, Curry N, Nylén P, Markocsan N, Vaßen R (2012) Design of next generation thermal barrier coatings — experiments and modeling. Surf Coat Technol 220:20–26
191. Cao XQ, Vaßen R, Stöver D (2004) Ceramic materials for thermal barrier coatings. J Eur Ceram Soc 24:1–10
192. Haynes JA, Ferber MK, Porter WD (2000) Thermal cycling behavior of plasma-sprayed thermal barrier coatings with various MCrAIX bond coats. J Therm Spray Technol 9 (1):38–48
193. Hamacha R, Fauchais P, Nardou E (1996) Influence of dopant on the behaviour under thermal cycling of two plasma sprayed zirconia coatings, Part 1: Relationship between powder characteristics and coating properties. J Therm Spray Technol 5(4):431–438
194. Ma B, Li Y, Su K (2009) Characterization of ceria–yttria stabilized zirconia plasma-sprayed coatings. Appl Surf Sci 255:7234–7237
195. Markocsan N, Nylén P, Wigren J, Li X-H (2007) Low thermal conductivity coatings for gas turbine applications. J Therm Spray Technol 16(4):498–505
196. Curry N, Donoghue J (2012) Evolution of thermal conductivity of dysprosia stabilised thermal barrier coating systems during heat treatment. Surf Coat Technol 209:38–43
197. Chen X, Zou B, Wang Y, Ma H, Cao X (2011) Microstructure and thermal cycling behavior of air plasma-sprayed YSZ/LaMgAl11O19 composite coatings. J Therm Spray Technol 20 (6):1328–1338
198. Chen X, Gu L, Zou B, Wang Y, Cao X (2012) New functionally graded thermal barrier coating system based on LaMgAl11O19/YSZ prepared by air plasma spraying. Surf Coat Technol 206:2265–2274
199. Jarligo MO, Mack DE, Vaßen R, Stöver D (2009) Application of plasma-sprayed complex perovskites as thermal barrier coatings. J Therm Spray Technol 18(2):187–193
200. Ma W, Jarligo MO, Mack DE, Pitzer D, Malzbender J, Vaßen R, Stöver D (2008) New generation perovskite thermal barrier coating materials. J Therm Spray Technol 17 (5–6):831–837
201. Yu J, Zhao H, Zhou X, Tao S, Ding C (2011) Effect of thermal aging on microstructure and mechanical properties of plasma-sprayed samarium zirconate coatings. J Therm Spray Technol 20(5):1056–1062
202. Xie XY, Guo HB, Gong SK (2010) Mechanical properties of $LaTi_2Al_9O_{19}$ and thermal cycling behaviors of plasma-sprayed $LaTi_2Al_9O_{19}$/YSZ thermal barrier coatings. J Therm Spray Technol 19(6):1179–1185
203. Guo H, Zhang H, Ma G, Gong S (2009) Thermo-physical and thermal cycling properties of plasma-sprayed $BaLa_2Ti_3O_{10}$ coating as potential thermal barrier materials. Surf Coat Technol 204:691–696
204. Liu Y, Gao YF, Tao SY, Zhou XM, Li WD, Luo HJ, Ding CX (2008) Microstructure of plasma sprayed La_2O_3-modified YSZ coatings. J Therm Spray Technol 17(5–6):603–607
205. Paul S, Cipitria A, Golosnoy IO, Xie L, Dorfman MR, Clyne TW (2007) Effects of impurity content on the sintering characteristics of plasma-sprayed zirconia. J Therm Spray Technol 16(5–6):798–803
206. Mihm S, Duda T, Gruner H, Thomas G, Dzur B (2012) Method and process development of advanced atmospheric plasma spraying for thermal barrier coatings. J Therm Spray Technol 21(3–4):400–408

207. Tan Y, Srinivasan V, Nakamura T, Sampath S, Bertrand P, Bertrand G (2012) TBC optimizing compliance and thermal conductivity of plasma sprayed thermal barrier coatings via controlled powders and processing strategies. J Therm Spray Technol 21(5):950–962
208. Guo HB, Vaßen R, Stöver D (2004) Atmospheric plasma sprayed thick thermal barrier coatings with high segmentation crack density. Surf Coat Technol 186:353–363
209. Zhu D, Choi SR, Miller RA (2004) Development and thermal fatigue testing of ceramic thermal barrier coatings. Surf Coat Technol 188–189:146–152
210. Shin I-H, Koo J-M, Seok C-S, Yang S-H, Lee T-W, Kim B-S (2011) Estimation of spallation life of thermal barrier coating of gas turbine blade by thermal fatigue test. Surf Coat Technol 205:S157–S160
211. Kim D-J, Shin I-H, Koo J-M, Seok C-S, Lee T-W (2010) Failure mechanisms of coin-type plasma-sprayed thermal barrier coatings with thermal fatigue. Surf Coat Technol 205: S451–S458
212. Jang H-J, Park D-H, Junga Y-G, Jang J-C, Choi S-C, Pai U (2006) Mechanical characterization and thermal behavior of HVOF-sprayed bond coat in thermal barrier coatings (TBCs). Surf Coat Technol 200:4355–4362
213. Li Y, Li C-J, Yang G-J, Xing L-K (2010) Thermal fatigue behavior of thermal barrier coatings with the MCrAlY bond coats by cold spraying and low-pressure plasma spraying. Surf Coat Technol 205:2225–2233
214. von Niessen K, Gindrat M, Refke A (2010) Vapor phase deposition using plasma spray-PVD™. J Therm Spray Technol 19(1–2):502–509
215. Gell M, Jordan EH, Teicholz M, Cetegen BM, Padture N, Xie L, Chen D, Ma X, Roth J (2008) Thermal barrier coatings made by the solution precursor plasma spray process. J Therm Spray Technol 17(1):124–135
216. Mutasim Z, Brentnall W (1997) Thermal barrier coatings for industrial gas turbine applications: an industrial note. J Therm Spray Technol 6(1):105–108
217. Nelson WA, Orenstein RM (1997) Land based gas turbines TBC experience in land-based gas turbines. J Therm Spray Technol 6(2):176–180
218. Parks WP, Hoffman EE, Lee WY, Wright IG (1997) Thermal barrier coatings issues in advanced land-based gas turbines. J Therm Spray Technol 6(2):187–192
219. Tamura M, Takahashi M, Ishii J, Suzuki K, Sato M, Shimomur K (1999) Multilayered thermal barrier coating for land-based gas turbines. J Therm Spray Technol 8(1):68–72
220. Wright IG, Gibbons TB (2007) Recent developments in gas turbine materials and technology and their implications for syngas firing. Int J Hydrogen Energy 32:3610–3621
221. Lebedev AS, Kostennikov SV (2008) Trends in increasing gas-turbine units efficiency. Therm Eng 55(6):461–468
222. Pomeroy MJ (2005) Coatings for gas turbine materials and long-term stability issues. Mater Design 26:223–231
223. Curry N, Markocsan N, Li X-H, Tricoire A, Dorfman M (2011) Next generation thermal barrier coatings for the gas turbine industry. J Therm Spray Technol 20(1–2):108–115
224. Beardsley MB (1997) Thick thermal barrier coatings for diesel engines. J Therm Spray Technol 6(2):181–186
225. Ahmaniemi S, Tuominen J, Vuoristo P, Mäntylä T (2002) Sealing procedures for thick thermal barrier coatings. J Therm Spray Technol 11(3):320–332
226. Hejwowski T, Weronski A (2002) The effect of thermal barrier coatings on diesel engine performance. Vacuum 65:427–432
227. Buyukkaya E, Cerit M (2007) Thermal analysis of a ceramic coating diesel engine piston using 3-D finite element method. Surf Coat Technol 202:398–402
228. Parlak A, Yasar H, Eldogan O (2005) The effect of thermal barrier coating on a turbo-charged diesel engine performance and exergy potential of the exhaust gas. Energy Convers Manag 46:489–499
229. İşcan B, Aydın H (2012) Improving the usability of vegetable oils as a fuel in a low heat rejection diesel engine. Fuel Process Technol 98:59–64

230. Pulci G, Tului M, Tirillo J, Marra F, Lionetti S, Valente T (2011) High temperature mechanical behavior of UHTC coatings for thermal protection of re-entry vehicles. J Therm Spray Technol 20(1–2):139–144
231. Davis JB, Marshall DB, Oka KS, Housley RM, Morgan PED (1999) Ceramic composites for thermal protection systems. Composites A 30:483–488
232. Fan X, Liu Y, Xu Z, Wang Y, Zou B, Gu L, Wang C, Chen X, Khan ZS, Yang D, Cao X (2011) Preparation and characterization of 8YSZ thermal barrier coatings on rare earth-magnesium alloy. J Therm Spray Technol 20(4):948–957
233. Huang W, Fan X, Zhao Y, Zhou X, Meng X, Wang Y, Zou B, Cao X, Wang Z (2012) Fabrication of thermal barrier coatings onto polyimide matrix composites via air plasma spray process. Surf Coat Technol 207:421–429
234. Cojocaru CV, Wang Y, Moreau C, Lima RS, Mesquita-Guimarães J, Garcia E, Miranzo P, Osendi MI (2011) Mechanical behavior of air plasma-sprayed YSZ functionally graded mullite coatings investigated via instrumented indentation. J Therm Spray Technol 20 (1–2):101–107
235. Suzuki M, Sodeoka S, Inoue T (2008) Zircon-based ceramics composite coating for zircon-based ceramics composite. J Therm Spray Technol 17(3):404–409
236. Ma X, Matthews A (2009) Evaluation of abradable seal coating mechanical properties. Wear 267:1501–1510
237. Johnston RE (2011) Mechanical characterization of AlSi-hBN, NiCrAl-Bentonite, and NiCrAl-Bentonite-hBN freestanding abradable coatings. Surf Coat Technol 205:3268–3273
238. Rajendran R (2012) Gas turbine coatings – an overview. Eng Fail Anal 26:355–369
239. Ma X, Matthews A (2007) Investigation of abradable seal coating performance using scratch testing. Surf Coat Technol 202:1214–1220
240. Bardi U, Giolli C, Scrivani A, Rizzi G, Borgioli F, Fossati A, Partes K, Seefeld T, Sporer D, Refke A (2008) Development and investigation on new composite and ceramic coatings as possible abradable seals. J Therm Spray Technol 17(5–6):805–811
241. Steinke T, Mauer G, Vaßen R, Stöver D, Roth-Fagaraseanu D, Hancock M (2010) Process design and monitoring for plasma sprayed abradable coatings. J Therm Spray Technol 19 (4):756–764
242. Sporer D, Dorfman M, Xie L, Refke A, Giovannetti I, Giannozzi M (2007) Processing and properties of advanced ceramic abradable coatings. In: Marple MR, Hyland MM, Lau Y-C, Li C-J, Lima RS, Montavon G (eds) Thermal spray 2007: global coating solutions. ASM International, Materials Park, OH, pp 495–500
243. Stringer J, Marshall MB (2012) High speed wear testing of an abradable coating. Wear 294–295:257–263
244. Faraoun HI, Grosdidier T, Seichepine J-L, Goran D, Aourag H, Coddet C, Zwick J, Hopkins N (2006) Improvement of thermally sprayed abradable coating by microstructure control. Surf Coat Technol 201:2303–2312
245. Johnston RE (2009) The sensitivity of abradable coating residual stresses to varying material properties. J Therm Spray Technol 101318(5–6):1004–1013
246. Bounazef M, Guessasmaa S, Ait Saadi B (2004) The wear, deterioration and transformation phenomena of abradable coating BN–SiAl–bounding organic element, caused by the friction between the blades and the turbine casing. Mater Lett 58:3375–3380
247. Dowson P, Walker MS, Watson AP (2004) Development of abradable and rub-tolerant seal materials for application in centrifugal compressors and steam turbines. Seal Technol Dec:5–10
248. Lekatou A, Regoutas E, Karantzalis AE (2008) Corrosion behaviour of cermet-based coatings with a bond coat in 0.5 M H_2SO_4. Corros Sci 50:3389–3400
249. Yılmaz S (2009) An evaluation of plasma-sprayed coatings based on Al_2O_3 and Al_2O_3–13 wt. % TiO_2 with bond coat on pure titanium substrate. Ceram Int 35:2017–2022
250. Cho TY, Hong Yoon J, Young Cho J, Kon Joo Y, Ho Kang J, Zhang S, Gon Chun H, Young Hwang S, Chol Kwon S (2009) Surface properties and tensile bond strength of HVOF thermal

spray coatings of WC-Co powder onto the surface of 420J2 steel and the bond coats of Ni, NiCr, and Ni/NiCr. Surf Coat Technol 203:3250–3253
251. Schulz U, Fritscher K, Ebach-Stahl A (2008) Cyclic behavior of EB-PVD thermal barrier coating systems with modified bond coats. Surf Coat Technol 203:449–455
252. Zhao X, Xiao P (2008) Effect of platinum on the durability of thermal barrier systems with a $\gamma+\gamma'$ bond coat. Thin Solid Films 517:828–834
253. Tang F, Schoenung JM (2005) Local accumulation of thermally grown oxide in plasma-sprayed thermal barrier coatings with rough top-coat/bond-coat interfaces. Scr Mater 52:905–909
254. Chen WR, Irissou E, Wu X, Legoux J-G, Marple BR (2011) The oxidation behavior of TBC with cold spray CoNiCrAlY bond coat. J Therm Spray Technol 20(1–2):132–138
255. Das S, Datta S, Basu D, Das GC (2009) Glass–ceramics as oxidation resistant bond coat in thermal barrier coating system. Ceram Int 35:1403–1406
256. Lu Y-P, Li M-S, Li S-T, Wang Z-G, Zhu R-F (2004) Plasma-sprayed hydroxyapatite-titania composite bond coat for hydroxyapatite coating on titanium substrate. Biomaterials 25:4393–4403
257. Goller G (2004) The effect of bond coat on mechanical properties of plasma sprayed bioglass-titanium coatings. Ceram Int 30:351–355
258. Guanhong S, Xiaodong H, Jiuxing J, Yue S (2011) Parametric study of Al and Al_2O_3 ceramic coatings deposited by air plasma spray onto polymer substrate. Appl Surf Sci 257:7864–7870
259. Liu A, Guo M, Gao J, Zhao M (2006) Influence of bond coat on shear adhesion strength of erosion and thermal resistant coating for carbon fiber reinforced thermosetting polyimide. Surf Coat Technol 201:2696–2700
260. Beauvais S, Guipont V, Jeandin M, Juve D, Treheux D, Robisson A, Saenger R (2005) Influence of defect orientation on electrical insulating properties of plasma-sprayed alumina coatings. J Electroceram 15:65–74
261. Toma F-L, Scheitz S, Berger L-M, Sauchuk V, Kusnezoff M, Thiele S (2011) Comparative study of the electrical properties and characteristics of thermally sprayed alumina and spinel coatings. J Therm Spray Technol 20(1–2):195–204
262. Toma F-L, Berger L-M, Scheitz S, Langner S, Rödel C, Potthoff A, Sauchuk V, Kusnezoff M (2012) Comparison of the microstructural characteristics and electrical properties of thermally sprayed Al_2O_3 coatings from aqueous suspensions and feedstock powders. J Therm Spray Technol 21(3–4):480–488
263. Kim H-J, Odoul S, Lee C-H, Kweon Y-G (2001) The electrical insulation behavior and sealing effects of plasma-sprayed alumina-titania coatings. Surf Coat Technol 140:293–301
264. Prudenziati M, Gualtieri ML (2008) Electrical properties of thermally sprayed Ni- and Ni20Cr-based resistors. J Therm Spray Technol 17(3):385–394
265. Prudenziati M, Cirri G, Dal Bo P (2006) Novel high-temperature reliable heaters in plasma spray technology. J Therm Spray Technol 15(3):329–331
266. Prudenziati M (2008) Development and the implementation of high-temperature reliable heaters in plasma spray technology. J Therm Spray Technol 17(2):234–243
267. Gärtner F, Stoltenhoff T, Schmidt T, Kreye H (2006) The cold spray process and its potential for industrial applications. J Therm Spray Technol 15(2):223–232
268. Marx S, Paul A, Köhler A, Hüttl G (2006) Cold spraying: innovative layers for new applications. J Therm Spray Technol 15(2):177–183
269. Wu X-K, Zhang J-S, Zhou X-L, Cui H, Liu J-C (2012) Advanced cold spray technology: deposition characteristics and potential applications. Sci China Technol Sci 55(2):357–368
270. Gui M, Kang SB, Euh K (2004) Al-SiC powder preparation for electronic packaging aluminum composites by plasma spray processing. J Therm Spray Technol 13(2):214–222
271. Yamakawa O, Nihonmatsu H, Morisasa M, Hotta H (2009) Plasma sprayed ceramic tray members for firing ceramic capacitor. In: Marple BR, Hyland MM, Lau Y-C, Li C-J, Lima RS, Montavon G (eds) Thermal spray 2009: Proceedings of the international thermal spray conference. ASM International, Materials Park, OH, pp 624–627

272. Donner K-R, Gärtner F, Klassen T (2011) Metallization of thin Al_2O_3 layers in power electronics using cold gas spraying. J Therm Spray Technol 20(1–2):299–306
273. Lin KH, Xu ZH, Lin ST (2011) A study on microstructure and dielectric performances of alumina/copper composites by plasma spray coating. J Mater Eng Perform 20(2):231–237
274. Osbond P (1992) Plasma sprayed anti-reflection coatings for micro-wave optical components. Adv Mater 4:807–809
275. Lisjak D, Bégard M, Bruehl M, Bobzin K, Hujanen A, Lintunen P, Bolelli G, Lusvarghi L, Ovtar S, Drofenik M (2011) Hexaferrite/polyester composite coatings for electromagnetic-wave absorbers. J Therm Spray Technol 20(3):638–644
276. Rieger G, Wecker J, Rodewald W, Sattler W, Bach FW, Duda T, Unterberg W (2000) Nd-Fe-B permanent magnets (thick films) produced by a vacuum-plasma-spraying process. J Appl Phys 87(9):5329–5331
277. Sampath S (2010) Thermal spray applications in electronics and sensors: past, present, and future. J Therm Spray Technol 19(5):921–949
278. Voyer J, Schulz P, Schreiber M (2008) Electrically conductive flame sprayed aluminum coatings on textile substrates. J Therm Spray Technol 17(5–6):818–823
279. Geibel A, Froyen L, Delaey L, Leuven KU (1996) Plasma spray forming: an alternate route for manufacturing free-standing components. J Therm Spray Technol 5(4):419–430
280. Devasenapathi A, Ng HW, Yu SCM, Indra AB (2002) Forming near net shape free-standing components by plasma spraying. Mater Lett 57:882–886
281. Chráska P, Neufuss K, Herman H (1997) Plasma spraying of zircon. J Therm Spray Technol 6 (4):445–448
282. Neufuss K, Chráska P, Kolman B, Sampath S, Trávnícek Z (1997) Properties of plasma-sprayed freestanding ceramic parts. J Therm Spray Technol 6(4):434–438
283. Shi S, Hwang J-Y (2003) Plasma spray fabrication of near-net-shape ceramic objects. J Miner Mater Charact Eng 2(2):145–150
284. Patel RR, Keshri AK, Dulikravich GS, Agarwal A (2010) An experimental and computational methodology for near net shape fabrication of thin walled ceramic structures by plasma spray forming. J Mater Process Technol 210:1260–1269
285. Brožek V, Ctibor P, Cheong DI, Yang S-H (2009) Plasma spraying of zirconium carbide-hafnium carbide-tungsten cermets. Powder Metallurgy Prog 9:1–49
286. Helali M, Hashmi MSJ (1996) Production of free-standing objects by high velocity oxy-fuel (HVOF) thermal spraying process. J Mater Process Technol 56:431–438
287. Pattison J, Celotto S, Morgan R, Bray M, O'Neill W (2007) Cold gas dynamic manufacturing: a non-thermal approach to freeform fabrication. Int J Machine Tools Manuf 47:627–634
288. Chen JZ, Herman H, Safai S (1993) Evaluation of NiAI and NiAI-B deposited by vacuum plasma spray. J Therm Spray Technol 2(4):357–361
289. Saeidi S, Voisey KT, McCartney DG (2009) The effect of heat treatment on the oxidation behavior of HVOF and VPS CoNiCrAlY coatings. J Therm Spray Technol 18(2):209–216
290. Fan X, Ishigaki T (2001) Mo_5Si_3-B and $MoSi_2$ deposits fabricated by radio frequency induction plasma spraying. J Therm Spray Technol 10(4):611–617
291. Waki H, Kitamura T, Kobayashi A (2009) Effect of thermal treatment on high-temperature mechanical properties enhancement in LPPS, HVOF, and APS CoNiCrAlY coatings. J Therm Spray Technol 18(4):500–509
292. Chraska P, Neufuss K, Herman H (1997) Plasma spraying of zircon. J Therm Spray Technol 6 (4):445–448
293. Chen H, Gao Y, Luo H, Tao S (2011) Preparation and thermophysical properties of $La_2Zr_2O_7$ coatings by thermal spraying of an amorphous precursor. J Therm Spray Technol 20 (6):1201–1208
294. Henne R, Müller M, Proß E, Schiller G, Gitzhofer F, Boulos M (1999) Near-net-shape forming of metallic bipolar plates for planar solid oxide fuel cells by induction plasma spraying. J Therm Spray Technol 8(1):110–116

295. Agarwal A, McKechnie T, Seal S (2003) Net shape nanostructured aluminum oxide structures fabricated by plasma spray forming. J Therm Spray Technol 12(3):350–359
296. Laha T, Agarwal A, McKechnie T, Seal S (2004) Synthesis and characterization of plasma spray formed carbon nanotube reinforced aluminum composite. Mater Sci Eng A 381:249–258
297. Hussain T, McCartney DG, Shipway PH, Marrocco T (2011) Corrosion behavior of cold sprayed titanium coatings and free standing deposits. J Therm Spray Technol 20 (1–2):260–274
298. Herman H, Sampath S, Tiwari R, Neiser R (1994) Plasma spray forming of intermetallics and their composites. J Therm Spray Technol 3(3):295–296
299. Weiss LE, Prinz FB, Adams DA, Siewiorek DP (1992) Thermal spray shape deposition. J Therm Spray Technol 1(3):231–237
300. Yang Y, Oh N, Liu Y, Chen W, Oh S, Appleford M, Kim S, Kim K, Park S, Bumgardner J, Haggard W, Ong J (2006) Enhancing osseo-integration using surface-modified titanium implants. JOM 58:71–76
301. Ong JL, Appleford M, Oh S, Yang Y, Chen W-H et al (2006) The characterization and development of bioactive hydroxyapatite coatings. JOM 58(7):67–69
302. Gross KA, Walsh W, Swarts E (2004) Analysis of retrieved hydroxyapatite-coated hip prostheses. J Therm Spray Technol 13(2):190–199
303. Khor KA, Cheang P, Wang Y (1997) The thermal spray processing of HA powders and coatings. JOM Feb:51–57
304. Roy M, Bandyopadhyay A, Bose S (2011) Induction plasma sprayed nano hydroxyapatite coatings on titanium for orthopaedic and dental implants. Surf Coat Technol 205:2785–2792
305. Legoux J-G, Chellat F, Lima RS, Marple BR, Bureau MN, Shen H, Candeliere GA (2006) Development of osteoblast colonies on new bioactive coatings. J Therm Spray Technol 15 (4):628–633
306. Chang C, Shi J, Huang J, Hu Z, Ding C (1998) Effects of power level on characteristics of vacuum plasma sprayed hydroxyapatite coating. J Therm Spray Technol 7(4):484–488
307. Prevéy PS (2000) X-ray diffraction characterization of crystallinity and phase composition in plasma-sprayed hydroxyapatite coatings. J Therm Spray Technol 9(3):369–376
308. Khor KA, Yip CS, Cheang P (1997) Ti-6AI-4 hydroxyapatite composite coatings prepared by thermal spray techniques. J Therm Spray Technol 6(1):109–115
309. Wang Y, Khor KA, Cheang P (1998) Thermal spraying of functionally graded calcium phosphate coatings for biomedical implants. J Therm Spray Technol 7(1):50–57
310. Hasan S, Stokes J (2011) Design of experiment analysis of the Sulzer Metco DJ high velocity oxy-fuel coating of hydroxyapatite for orthopedic applications. J Therm Spray Technol 20 (1–2):186–194
311. Lima RS, Dimitrievska S, Bureau MN, Marple BR, Petit A, Mwale F, Antoniou J (2010) HVOF-sprayed Nano TiO_2-HA coatings exhibiting enhanced biocompatibility. J Therm Spray Technol 19(1–2):336–343
312. Lima RS, Li H, Khor KA, Marple BR (2006) Biocompatible nanostructured high-velocity oxyfuel sprayed titania coating: deposition, characterization, and mechanical properties. J Therm Spray Technol 15(4):623–627
313. Morks MF, Kobayashi A (2008) Development of ZrO_2/SiO_2 bioinert ceramic coatings for biomedical application. J Mech Behav Biomed Mater 1:165–171
314. Vitale-Brovarone C, Verné E (2005) SiO_2-CaO-K_2O coatings on alumina and Ti6Al4V substrates for biomedical applications. J Mater Sci Mater Med 16:863–871
315. Xie Y, Zheng X, Ding C, Zhai W, Chang J, Ji H (2009) Preparation and characterization of CaO-ZrO_2-SiO_2 coating for potential application in biomedicine. J Therm Spray Technol 18(4):678–685
316. Bolelli G, Cannillo V, Gadow R, Killinger A, Lusvarghi L, Rauch J (2009) Microstructural and in vitro characterisation of high-velocity suspension flame sprayed (HVSFS) bioactive glass coatings. J Eur Ceram Soc 29:2249–2257

317. Fernandez J, Gaona M, Guilemany JM (2007) Effect of heat treatments on HVOF hydroxyapatite coatings. J Therm Spray Technol 16(2):220–228
318. Yu L-G, Khor KA, Li H, Cheang P (2003) Effect of spark plasma sintering on the microstructure and in vitro behavior of plasma sprayed HA coatings. Biomaterials 24:2695–2705
319. Bellucci D, Bolelli G, Cannillo V, Gadow R, Killinger A, Lusvarghi L, Sola A, Stiegler N (2012) High velocity suspension flame sprayed (HVSFS) potassium-based bioactive glass coatings with and without TiO_2 bond coat. Surf Coat Technol 206:3857–3868
320. Liang Y, Xie Y, Ji H, Huang L, Zheng X (2010) Chemical stability and biological properties of plasma-sprayed CaO-SiO_2-ZrO_2 coatings. J Therm Spray Technol 19(6):1171–1178
321. Jeffery B, Peppler M, Lima RS, McDonald A (2010) Bactericidal effects of HVOF-sprayed nanostructured TiO_2 on Pseudomonas aeruginosa. J Therm Spray Technol 19(1–2):344–349
322. Sanpo N, Lu Tan M, Cheang P, Khor KA (2009) Antibacterial property of cold-sprayed HA-Ag/PEEK coating. J Therm Spray Technol 18(1):10–15
323. Sanpo N, Ming Ang S, Cheang P, Khor KA (2009) Antibacterial property of cold sprayed chitosan-Cu/Al coating. J Therm Spray Technol 18(4):600–608
324. Sahraoui T, Fenineche N-E, Montavon G, Coddet C (2004) Alternative to chromium: characteristics and wear behavior of HVOF coatings for gas turbine shafts repair (heavy-duty). J Mater Process Technol 152:43–55
325. Heydarzadeh SM, Ghadami F (2010) Comparative tribological study of air plasma sprayed WC–12% coating versus conventional hard chromium electro deposit. Tribol Int 43:882–886
326. Bolelli G, Cannillo V, Lusvarghi L, Ricco S (2006) Mechanical and tribological properties of electrolytic hard chrome and HVOF-sprayed coatings. Surf Coat Technol 200:2995–3009
327. Deng C, Liu M, Wu C, Zhou K, Song J (2007) Impingement resistance of HVAF WC-based coatings. J Therm Spray Technol 16(5–6):604–609
328. Guilemany JM, Espallargas N, Suegama PH, Benedetti AV, Fernández J (2005) High-velocity oxyfuel Cr_3C_2-NiCr replacing hard chromium coatings. J Therm Spray Technol 14 (3):335–341
329. Picas JA, Forna A, Matthäus G (2006) HVOF coatings as an alternative to hard chrome for pistons and valves. Wear 261:477–484
330. Staia MH, Suárez M, Chicot D, Lesage J, Iost A, Puchi-Cabrera ES (2012) Cr_2C_3–NiCr VPS thermal spray coatings as candidate for chromium replacement. Surf Coat Technol 220:225–231
331. Lu W, Wu Y, Zhang J, Hong S, Zhang J, Li G (2011) Microstructure and corrosion resistance of plasma sprayed Fe-based alloy coating as an alternative to hard chromium. J Therm Spray Technol 20(5):1063–1070
332. Abdi S, Lebaili S (2008) Alternative to chromium, a hard alloy powder NiCrBCSi (Fe) coatings thermally sprayed on 60CrMn4 steel. Phase and comportements. Phys Proc 2:1005–1014
333. Matthäus G, Henry J, Ackermann D (2009) Further developments in internal diameter HVOF application of WC-CoCr for hard chrome replacement in critical applications such as landing gear. In: Marple BR, Hyland MM, Lau Y-C, Li C-J, Lima RS, Montavon G (eds) Thermal spray 2009: Proceedings of the international thermal spray conference. ASM International, Materials Park, OH, pp 722–724
334. Krishnan N, Vardelle A, Legoux JG (2008) A life cycle comparison of hard chrome and thermal sprayed coatings: a case example of aircraft landing gears. In: Lugscheider E (ed) Thermal spray conference: Crossing the border. DVS, Dûsseldorf, e-Proc
335. Henne R (2007) Solid oxide fuel cells: a challenge for plasma deposition processes. J Therm Spray Technol 16(3):381–403
336. Takenoiri S, Kadokawa N, Koseki K (2000) Development of metallic substrate supported planar solid oxide fuel cells fabricated by atmospheric plasma spraying. J Therm Spray Technol 3639(3):360–363

337. Barthel K, Rambert S, Barthel S, Rambert S, Siegmann S (2000) Microstructure and polarization resistance of thermally sprayed composite cathodes for solid oxide fuel cell use. J Therm Spray Technol 9(3):343–347
338. Sun F, Zhang N, Liao H, Li J (2012) Effect of heat treatment temperature on performance of plasma-sprayed apatite-lanthanum silicate coatings as electrolytes for IT-SOFC. J Therm Spray Technol 21(6):1257–1267
339. Puranen J, Lagerbom J, Hyvärinen L, Kylmälahti M, Himanen O, Pihlatie M, Kiviaho J, Vuoristo P (2011) The structure and properties of plasma sprayed iron oxide doped manganese cobalt oxide spinel coatings for SOFC metallic interconnectors. J Therm Spray Technol 20(1–2):154–159
340. Harris J, Qureshi M, Kesler O (2012) Deposition of composite LSCF-SDC and SSC-SDC cathodes by axial-injection plasma spraying. J Therm Spray Technol 21(3–4):461–468
341. Shen Y, Alexandra V, Almeida B, François Gitzhofer (2011) Preparation of nanocomposite GDC/LSCF cathode material for IT-SOFC by induction plasma spraying. J Therm Spray Technol 20(1–2):145–153
342. Wang Y, Legoux J-G, Neagu R, Hui S, Marple BR (2012) Suspension plasma spray and performance characterization of half cells with NiO/YSZ anode and YSZ electrolyte. J Therm Spray Technol 21(1):7–15
343. Michaux P, Montavon G, Grimaud A, Denoirjean A, Fauchais P (2010) Elaboration of porous NiO/8YSZ layers by several SPS and SPPS routes. J Therm Spray Technol 19(1–2):317–327
344. Zotov N, Hospach A, Mauer G, Sebold D, Vaßen R (2012) Deposition of La12xSrxFe12yCoyO32d coatings with different phase compositions and microstructures by low-pressure plasma spraying-thin film (LPPS-TF) processes. J Therm Spray Technol 21 (3–4):441–447
345. Fedtke P, Wienecke M, Bunescu M-C, Barfels T, Deistung K, Pietrzak M (2004) Yttria-stabilized zirconia films deposited by plasma spraying and sputtering. J Solid State Electrochem 8:626–632
346. Gross KA, Tikkanen J, Keskinen J, Pitkänen V, Eerola M, Siikamaki R, Rajala M (1999) Liquid flame spraying for glass coloring. J Therm Spray Technol 8(4):583–589
347. Arcondéguy A, Grimaud A, Denoirjean A, Gasgnier G, Huguet C, Pateyron B, Montavon G (2007) Flame-sprayed glaze coatings: effects of operating parameters and feedstock characteristics onto coating structures. J Therm Spray Technol 16(5–6):978–990
348. Arcondéguy A, Gasgnier G, Montavon G, Pateyron B, Denoirjean A, Grimaud A, Huguet C (2008) Effects of spraying parameters onto flame-sprayed glaze coating structures. Surf Coat Technol 202:4444–4448
349. Blink J, Farmer J, Choi J, Saw C (2009) Applications in the nuclear industry for thermal spray amorphous metal and ceramic coatings. Metallurgical Mater Trans A 40A:1344–1354
350. Farmer JC, Choi J-S (2007) Criticality-control applications in the nuclear industry for thermal spray amorphous metal and ceramic coatings, UCRL-TR-234171. Lawrence Livermore National Laboratory, Aug 31, pp 1–7
351. Blink J, Choi J, Farmer J (2007) Applications in the nuclear industry for thermal spray amorphous metal and ceramic coatings, UCRL-CONF-232603. Lawrence Livermore National Laboratory, July 9, pp 1–14
352. Farmer J, Choi J, Saw C, Haslam J, Day D, Hailey P, Lian T, Rebak R, Perepezko J, Payer J, Branagan D, Beardsley B, D'Amato A, Aprigliano L (2009) Iron-based amorphous metals: high-performance corrosion-resistant material development. Metallurgical Mater Trans A 40A:1289–1305
353. Branagan D (2004) Properties of amorphous/partially crystalline coatings. US Patent 20040253381
354. Berard G, Brun P, Lacombe J, Montavon G, Denoirjean A, Antou G (2008) Influence of a sealing treatment on the behavior of plasma-sprayed alumina coatings operating in extreme environments. J Therm Spray Technol 17(3):410–419

355. Haslam JJ, Farmer JC, Hopper RW, Wilfinger KR (2005) Ceramic coatings for a corrosion-resistant nuclear waste container evaluated in simulated ground water at 90 °C. Metallurgical Mater Trans A 36A:1085–1095
356. Hardwicke CU, Lau Y-C (2013) Advances in thermal spray coatings for gas turbines and energy generation: a review. J Therm Spray Technol 22(5):564–576
357. Matejıcek J, Chraska P, Linke J (2007) Thermal spray coatings for fusion applications—review. J Therm Spray Technol 16(1):64–83
358. Longo FN (1992) Industrial guide–markets, materials, and applications for thermal-sprayed coatings. J Therm Spray Technol 1(2):143–145
359. Dorfman M, Sharma A (2013) Commentary challenges and strategies for growth of thermal spray markets: the six-pillar plan. J Therm Spray Technol Comment 22(5):559–563
360. Tucker RC (ed) (2013) ASM handbook, vol 5A: Thermal spray technology. ASM International, Materials Park, OH
361. Thintri Inc. (2013) Thermal spray wear coatings find growing markets and greater competition. Spraytime 20(1):1–36
362. Vetter J, Barbezat G, Crummenauer J, Avissar J (2005) Surface treatment selections for automotive applications. Surf Coat Technol 200:1962–1968
363. Barbezat G (2006) Application of thermal spraying in the automobile industry. Surf Coat Technol 201:2028–2031
364. Barbezat G (2005) Advanced thermal spray technology and coating for lightweight engine blocks for the automotive industry. Surf Coat Technol 200:1990–1993
365. Barbezat G (2003) Low-cost high-performance coatings produced by internal plasma spraying for the production of high efficiency engines. In: Moreau C, Marple B (eds) International thermal spray conference 2003. ASM International, Materials Park, OH, pp 139–142
366. Smyth RT, Anderson JC (1975) Production of resistors by arc plasma spraying. Electrocompon Sci Technol 2:135–145
367. Ducos M (2006) Evaluating the costs of thermal spraying, ALIDERTE course. ALIDERTE, Limoges (in French)
368. Nelson GM, Nychka JA, McDonald AG (2011) Flame spray deposition of titanium alloy-bioactive glass composite coatings. J Therm Spray Technol 20(6):1339–1351
369. Drnovšek N, Novak S, Dragin U, Čeh M, Gorenšek M, Gradišar M (2012) Bioactive glass enhances bone ingrowth into the porous titanium coating on orthopaedic implants. Int Orthop 36:1739–1745
370. Juhasz JA, Best SM (2012) Bioactive ceramics: processing, structures and properties. J Mater Sci 47:610–624
371. Landor I, Vavrik P, Sosna A, Jahoda D, Hahn H, Daniel M (2007) Hydroxyapatite porous coating and the osteointegration of the total hip replacement. Arch Orthop Trauma Surg 127 (2):81–89
372. Hamashima K (2007) Application of new boride cermet coating to forming of glass sheets. J Therm Spray Technol 16(1):32–33
373. Döring J-E, Hoebener F, Langer G (2008) Review of applications of thermal spraying in the printing industry in respect to OEMs. In: Lugscheider E (ed) Thermal spray conference: Crossing the border. DVS, Düsseldorf, e-Proc
374. Pawlowski L (1996) Technology of thermally sprayed anilox rolls: state of art, problems, and perspectives. J Therm Spray Technol 5(3):317–334
375. Lima RS, Marple BR (2005) Superior performance of high-velocity oxyfuel-sprayed nanostructured TiO_2 in comparison to air plasma-sprayed conventional Al_2O_3-13TiO_2. J Therm Spray Technol 14(3):397–404
376. Vuoristo P, Nylén P (2009) Industrial and research activities in thermal spray technology in the Nordic region of Europe. In: Marple BR, Hyland MM, Lau Y-C, Li C-J, Lima RS, Montavon G (eds) Thermal spray 2009: Proceedings of the international thermal spray conference. ASM International, Materials Park, OH, pp 517–522, e-Proc

377. Yoshiya A, Shigemura S, Nagai M, Yamanaka M (2009) Advances of thermal sprayed carbon roller in paper industry. In: Marple BR, Hyland MM, Lau Y-C, Li C-J, Lima RS, Montavon G (eds) Thermal spray 2009: Proceedings of the international thermal spray conference. ASM International, Materials Park, OH, pp 601–606
378. Nagai M, Shigemura S, Yoshiya A (2009) Thermal-sprayed CFRP roll with resistant to thermal shock and wear - for papermaking machine. In: Marple BR, Hyland MM, Lau Y-C, Li C-J, Lima RS, Montavon G (eds) Thermal spray 2009: Proceedings of the international thermal spray conference. ASM International, Materials Park, OH, pp 607–611
379. Iyengar RK (2009) Thermal spray coating for steel processing. Technovations International, Littleton, MA
380. Process Industries: Power, http://www.castolin.com
381. Kaushal G, Singh H, Prakash S (2011) High-temperature erosion-corrosion performance of high-velocity oxy-fuel sprayed Ni-20Cr coating in actual boiler environment. Metallurgical Mater Trans A 42(7):1836–1846
382. Espallargas N, Berget J, Guilemany JM, Benedetti AV, Suegama PH (2008) Cr_3C_2–NiCr and WC–Ni thermal spray coatings as alternatives to hard chromium for erosion–corrosion resistance. Surf Coat Technol 202:1405–1417
383. Wang B-Q, Verstak A (1999) Elevated temperature erosion of HVOF Cr_3C_2/TiC– NiCrMo cermet coating. Wear 233–235:342–351
384. Higuera HV, Belzunce Varela FJ, Carriles Menéndez A, Poveda Martinez S (2001) A comparative study of high-temperature erosion wear of plasma-sprayed NiCrBSiFe and WC–NiCrBSiFe coatings under simulated coal-fired boiler conditions. Tribol Int 34:161–169
385. Sidhu TS, Prakash S, Agrawal RD (2005) Studies on the properties of high-velocity oxy-fuel thermal spray coatings for higher temperature applications. Mater Sci 41(6):805–823
386. Sidhu HS, Sidhu BS, Prakash S (2006) Comparative characteristic and erosion behavior of NiCr coatings deposited by various high-velocity oxyfuel spray processes. J Mater Eng Perform 5(6):699–704
387. Sanz A (2001) Tribological behavior of coatings for continuous casting of steel. Surf Coat Technol 146–147:55–64
388. Gross KA, Kovalevskis A (1996) Mold manufacture with plasma spraying. J Therm Spray Technol 5(4):469–475
389. Weiss LE, Thuel DG, Schultz L, Prinz FB (1994) Arc-sprayed steel-faced tooling. J Therm Spray Technol 3(3):275–281
390. Kim H-J, Kweon Y-G (1996) The application of thermal sprayed coatings for pig iron ingot molds. J Therm Spray Technol 5(4):463–468
391. Gibbons GJ, Hansell RG (2006) Down-selection and optimization of thermal-sprayed coatings for aluminum mould tool protection and upgrade. J Therm Spray Technol 15(3):340–347
392. Khan FF, Bae G, Kang K, Na H, Kim J, Jeong T, Lee C (2011) Evaluation of die-soldering and erosion resistance of high velocity oxy-fuel sprayed MoB-based cermet coatings. J Therm Spray Technol 20(5):1022–1034
393. Maranho O, Rodrigues D, Boccalini M, Sinatora A (2009) Bond strength of multicomponent white cast iron coatings applied by HVOF thermal spray process. J Therm Spray Technol 18 (4):708–713
394. Seonga BG, Hwanga SY, Kima MC, Kimb KY (2001) Reaction of WC-Co coating with molten zinc in a zinc pot of a continuous galvanizing line. Surf Coat Technol 138:101–110
395. Huang XO, Wang RJ, Zhang TJ, Luo HJ, Lü YF (2007) Several application cases of thermal spraying technology on industrial components and its considerations. In: Marple BR, Hyland MM, Lau Y-C, Li C-J, Lima RS, Montavon G (eds) Thermal spray 2007: Global coating solutions. ASM International, Materials Park, OH, e-Proc
396. Vicenzi J, Marques CM, Bergmann CP (2008) Hot and cold erosive wear of thermal sprayed NiCr-based coatings: influence of porosity and oxidation. Surf Coat Technol 202:3688–3697
397. Bolelli G, Lusvarghi L, Giovanardi R (2008) A comparison between the corrosion resistances of some HVOF-sprayed metal alloy coatings. Surf Coat Technol 202:4793–4809

398. Godoya C, Lima MM, Castro MMR, Avelar-Batista JC (2004) Structural changes in high-velocity oxy-fuel thermally sprayed WC–Co coatings for improved corrosion resistance. Surf Coat Technol 188–189:1–6
399. Choa JE, Hwang SY, Kim KY (2006) Corrosion behavior of thermal sprayed WC cermet coatings having various metallic binders in strong acidic environment. Surf Coat Technol 200:2653–2662
400. Bolelli G, Giovnardi R, Lusvarghi L, Manfredini T (2006) Corrosion resistance of HVOF-sprayed coatings for hard chrome replacement. Corros Sci 48:3375–3397
401. Perry JM, Neville A, Wilson VA, Hodgkiess T (2001) Assessment of the corrosion rates and mechanisms of a WC-Co-Cr HVOF coating in static and liquid-solid impingement saline environments. Surf Coat Technol 137:43–51
402. Petrovicova E, Schadler LS (2002) Thermal spraying of polymers. Int Mater Rev 47 (4):169–190
403. Notomi A, Sakakibara N (2009) Recent application of thermal spray to thermal power plants. In: Marple BR, Hyland MM, Lau Y-C, Li C-J, Lima RS, Montavon G (eds) Thermal spray 2009: Proceedings of the international thermal spray conference. ASM International, Materials Park, OH, pp 1106–1111
404. Yilmaz R, Kurt AO, Demir A, Tatli Z (2007) Effects of TiO_2 on the mechanical properties of the Al_2O_3–TiO_2 plasma sprayed coating. J Eur Ceram Soc 27:1319–1323
405. Lathabai S, Ottmuller M, Fernandez I (1998) Solid particle erosion behaviour of thermal sprayed ceramic, metallic and polymer coatings. Wear 221:93–108
406. Lins VFC, Branco JRT, Diniz FRC, Brogan JC, Berndt CC (2007) Erosion behavior of thermal sprayed, recycled polymer and ethylene–methacrylic acid composite coatings. Wear 262:274–281
407. Berndt CC, Brogan JA, Montavon G, Claudon A, Coddet C (1998) Mechanical properties of metal- and ceramic-polymer composites formed via thermal spray consolidation. J Therm Spray Technol 7(3):337–339
408. Leivo E, Wilenius T, Kinos T, Vuoristo P, Mäntylä T (2004) Properties of thermally sprayed fluoropolymer PVDF, ECTFE, PFA and FEP coatings. Prog Org Coat 49:69–73
409. Zhang T, Gawne DT, Bao Y (1997) The influence of process parameters on the degradation of thermally sprayed polymer coatings. Surf Coat Technol 96:337–344
410. Chen H, Zhao H, Qu J, Shao H (1999) Erosion-corrosion of thermal-sprayed nylon coatings. Wear 233–235:431–435
411. Zhang G, Liao H, Cherigui M, Paulo Davim J, Coddet C (2007) Effect of crystalline structure on the hardness and interfacial adherence of flame sprayed (poly-ether–ether–ketone) coatings. Eur Polym J 43:1077–1082
412. Zhang G, Liao H, Yu H, Ji V, Huang W, Mhaisalkar SG, Coddet C (2006) Correlation of crystallization behavior and mechanical properties of thermal sprayed PEEK coating. Surf Coat Technol 200:6690–6695
413. Zhang C, Zhang G, Ji V, Liao H, Costil S, Coddet C (2009) Microstructure and mechanical properties of flame-sprayed PEEK coating remelted by laser process. Prog Org Coat 66:248–253
414. Sweet GK (1993) Applying thermoplastic/thermoset powder with a modified plasma system. In: Berndt CC, Bernicki F (eds) Proceedings of the 1993 national thermal spray conference. ASM International, Materials Park, OH, pp 381–384
415. Brogan JA, Margolies S, Sampath H, Herman CC, Berndt SD (1995) Adhesion of combustion-sprayed polymer coatings. In: Berndt CC, Sampath S (eds) Thermal spray science and technology. ASM International, Materials Park, OH, pp 521–526
416. Henne RH, Schitter C (1995) Plasma spraying of high performance thermoplastics. In: Berndt CC, Sampath S (eds) Thermal spray science and technology. ASM International, Materials Park, OH, pp 527–532
417. Ivosevic M, Coguill SL, Galbraith SL (2009) Polymer thermal spraying: a novel coating process. In: Marple BR, Hyland MM, Lau Y-C, Li C-J, Lima RS, Montavon G (eds) Thermal

spray 2009: Proceedings of the international thermal spray conference. ASM International, Materials Park, OH, pp 1078–1083
418. Song JX, Han YF, Li SS, Xiao CB (2005) Repair of NiCrAlYSi overlay coating on Ni3Al base alloy IC6. Intermetallics 13:351–355
419. Ducos M (1988) Plasma transferred arc reclamation. In: Laroche G, Orfeuil M (eds) Plasmas in industry. Dopee Diffusion, France, pp 251–262 (in French)
420. Isakaev E, Yablonsky A, Kogan A, Katarzhis V, Kutnov V, Ivanov P (1999) The repair of railway frogs using plasma sprayed coatings, heat and mass transfer under plasma conditions. Ann NY Acad Sci 891:231–235
421. Tapphorn R, Henness J, Gabel H (2009) Kinetic metallization-a repair process for damaged IVD-Al coatings, Mg, and Al alloy components. In: Marple BR, Hyland MM, Lau Y-C, Li C-J, Lima RS, Montavon G (eds) Thermal spray 2009: Proceedings of the international thermal spray conference. ASM International, Materials Park, OH, pp 261–266
422. Champagne VK (2008) The repair of magnesium rotorcraft components by cold spray. J Fail Anal Prevent 8:164–175
423. Kashirin A, Klyuev O, Buzdygar T, Shkodkin A (2007) DYMET technology evolution and application. In: Marple BR, Hyland MM, Lau Y-C, Li C-J, Lima RS, Montavon G (eds) Thermal spray 2007: Global coating solutions. ASM International, Materials Park, OH, pp 141–145
424. Guilemany JM, Torrell M, Miguel JR (2007) Properties of HVOF coating of Ni based alloy for MSWI boilers protection. In: Marple BR, Hyland MM, Lau Y-C, Li C-J, Lima RS, Montavon G (eds) Thermal spray 2007: Global coating solutions. ASM International, Materials Park, OH, pp 1115–1119, e-Proc
425. de Botton O (1988) Master of Science in Technology and Policy. MIT, Cambridge, MA
426. Ducos M, Durand JP (2001) Thermal coatings in Europe, a business perspective. In: Berndt CC, Khor KH, Lugscheider E (eds) Thermal spray 2001. ASM International, Materials Park, OH, pp 1267–1276
427. MAGETEX (n.d.) Thermal coatings in Europe: a business prospective. MAGETEX, Les bureaux de Sèvres, 2 rue Troyon, 92316 Sèvres
428. Wigren J, Kristina Täng (2007) Quality considerations for the evaluation of thermal spray coatings. J Therm Spray Technol 16(4):533–540
429. Lee C (2009) Market direction and application opportunities for T/S growth in Korea. In: Marple BR, Hyland MM, Lau Y-C, Li C-J, Lima RS, Montavon G (eds) Thermal spray 2009: Proceedings of the international thermal spray conference. ASM International, Materials Park, OH, pp 505–510, e-Proc
430. Sundararajan G, Mahajan YR, Joshi SV (2009) Thermal spraying in India: status and prospects. In: Marple BR, Hyland MM, Lau Y-C, Li C-J, Lima RS, Montavon G (eds) Thermal spray 2009: Proceedings of the international thermal spray conference. ASM International, Materials Park, OH, pp 511–516
431. Tani K, Nakahira H (1992) Status of thermal spray technology in Japan. J Therm Spray Technol 1(4):333–339
432. Nakahira A (2009) Current status and future prospect of thermal spray coating applications and coating service market of job shops in Japan. In: Marple BR, Hyland MM, Lau Y-C, Li C-J, Lima RS, Montavon G (eds) Thermal spray 2009: Proceedings of the international thermal spray conference. ASM International, Materials Park, OH, pp 499–504, e-Proc
433. Fukumoto M (2008) The current status of thermal spraying in Asia; Hwang SY Status of thermal spraying in Korea; Li C-J The current state of thermal spray activities in China; Tani K, Nakahira A The current status of thermal spray in Japan; Khor MKA Thermal spray activities in Singapore. J Therm Spray Technol 17(1): 5–13
434. de Munter AJ, Bult A, de Jong JA (2002) On the economical and environmental aspects of TSA coatings. In: Lugscheider E (ed) International thermal spray conference 2002. DVS, Düsseldorf, e-Proc

435. Celotto S, Pattison J, Ho JS, Johnson AN, O'Neill W (2007) The economics of the cold spray process. In: Champagne V (ed) Cold spray materials deposition process - fundamentals and applications. Woodhead, Sawston
436. Molz R, Hawley D (2007) A method of evaluating thermal spray process performance. In: Marple BR, Hyland MM, Lau Y-C, Li C-J, Lima RS, Montavon G (eds) Thermal spray 2007: Global coating solutions. ASM International, Materials Park, OH, e-Proc
437. Sacriste D, Goubot N, Dhers J, Ducos M, Vardelle A (2001) An evaluation of the electric arc spray and (HPPS) processes for the manufacturing of high power plasma spraying MCrAlY coatings. J Therm Spray Technol 10(2):352–358
438. Moign A, Vardelle A, Legoux JG, Themelis NJ (2009) LCA Comparison of electroplating and other thermal spray processes. In: Marple BR, Hyland MM, Lau Y-C, Li C-J, Lima RS, Montavon G (eds) Thermal spray 2009: Proceedings of the international thermal spray conference. ASM International, Materials Park, OH, pp 1207–1212, e-Proc
439. International Thermal Spray Association, What is thermal spray. http://www.thermalspray.org